ADVANCED IMAGING AND MAPPING IN BRAIN TUMORS

EDITED BY: Nico Sollmann, Alexandra Golby and Sandro M. Krieg
PUBLISHED IN: Frontiers in Neuroscience, Frontiers in Oncology, Frontiers in Neurology, Frontiers in Neuroimaging and Frontiers in Human Neuroscience



frontiers Research Topics



frontiers

Frontiers eBook Copyright Statement

The copyright in the text of individual articles in this eBook is the property of their respective authors or their respective institutions or funders. The copyright in graphics and images within each article may be subject to copyright of other parties. In both cases this is subject to a license granted to Frontiers.

The compilation of articles constituting this eBook is the property of Frontiers.

Each article within this eBook, and the eBook itself, are published under the most recent version of the Creative Commons CC-BY licence. The version current at the date of publication of this eBook is CC-BY 4.0. If the CC-BY licence is updated, the licence granted by Frontiers is automatically updated to the new version.

When exercising any right under the CC-BY licence, Frontiers must be attributed as the original publisher of the article or eBook, as applicable.

Authors have the responsibility of ensuring that any graphics or other materials which are the property of others may be included in the CC-BY licence, but this should be checked before relying on the CC-BY licence to reproduce those materials. Any copyright notices relating to those materials must be complied with.

Copyright and source acknowledgement notices may not be removed and must be displayed in any copy, derivative work or partial copy which includes the elements in question.

All copyright, and all rights therein, are protected by national and international copyright laws. The above represents a summary only. For further information please read Frontiers' Conditions for Website Use and Copyright Statement, and the applicable CC-BY licence.

ISSN 1664-8714
ISBN 978-2-83250-835-0
DOI 10.3389/978-2-83250-835-0

About Frontiers

Frontiers is more than just an open-access publisher of scholarly articles: it is a pioneering approach to the world of academia, radically improving the way scholarly research is managed. The grand vision of Frontiers is a world where all people have an equal opportunity to seek, share and generate knowledge. Frontiers provides immediate and permanent online open access to all its publications, but this alone is not enough to realize our grand goals.

Frontiers Journal Series

The Frontiers Journal Series is a multi-tier and interdisciplinary set of open-access, online journals, promising a paradigm shift from the current review, selection and dissemination processes in academic publishing. All Frontiers journals are driven by researchers for researchers; therefore, they constitute a service to the scholarly community. At the same time, the Frontiers Journal Series operates on a revolutionary invention, the tiered publishing system, initially addressing specific communities of scholars, and gradually climbing up to broader public understanding, thus serving the interests of the lay society, too.

Dedication to Quality

Each Frontiers article is a landmark of the highest quality, thanks to genuinely collaborative interactions between authors and review editors, who include some of the world's best academicians. Research must be certified by peers before entering a stream of knowledge that may eventually reach the public - and shape society; therefore, Frontiers only applies the most rigorous and unbiased reviews.
Frontiers revolutionizes research publishing by freely delivering the most outstanding research, evaluated with no bias from both the academic and social point of view. By applying the most advanced information technologies, Frontiers is catapulting scholarly publishing into a new generation.

What are Frontiers Research Topics?

Frontiers Research Topics are very popular trademarks of the Frontiers Journals Series: they are collections of at least ten articles, all centered on a particular subject. With their unique mix of varied contributions from Original Research to Review Articles, Frontiers Research Topics unify the most influential researchers, the latest key findings and historical advances in a hot research area! Find out more on how to host your own Frontiers Research Topic or contribute to one as an author by contacting the Frontiers Editorial Office: frontiersin.org/about/contact

ADVANCED IMAGING AND MAPPING IN BRAIN TUMORS

Topic Editors:
Nico Sollmann, University of California, San Francisco, United States
Alexandra Golby, Harvard Medical School, United States
Sandro M. Krieg, Technical University of Munich, Germany

Citation: Sollmann, N., Golby, A., Krieg, S. M., eds. (2022). Advanced Imaging and Mapping in Brain Tumors. Lausanne: Frontiers Media SA.
doi: 10.3389/978-2-83250-835-0

Table of Contents

09 ***Peritumoral Brain Edema in Meningiomas May Be Related to Glymphatic Dysfunction***
Cheng Hong Toh, Tiing Yee Siow and Mauricio Castillo

17 ***Combining Electrostimulation With Fiber Tracking to Stratify the Inferior Fronto-Occipital Fasciculus***
Alexandre Roux, Anne-Laure Lemaitre, Jeremy Deverdun, Sam Ng, Hugues Duffau and Guillaume Herbet

29 ***Diagnostic Accuracy of PET for Differentiating True Glioma Progression From Post Treatment-Related Changes: A Systematic Review and Meta-Analysis***
Meng Cui, Rocío Isabel Zorrilla-Veloz, Jian Hu, Bing Guan and Xiaodong Ma

42 ***Multimodal Simulation of a Novel Device for a Safe and Effective External Ventricular Drain Placement***
Giuseppe Emmanuele Umana, Gianluca Scalia, Kaan Yagmurlu, Rosalia Mineo, Simone Di Bella, Matteo Giunta, Angelo Spitaleri, Rosario Maugeri, Francesca Graziano, Marco Fricia, Giovanni Federico Nicoletti, Santino Ottavio Tomasi, Giuseppe Raudino, Bipin Chaurasia, Gianluca Bellocchi, Maurizio Salvati, Domenico Gerardo Iacopino, Salvatore Cicero, Massimiliano Visocchi and Lidia Strigari

55 ***Imaging-Genomics in Glioblastoma: Combining Molecular and Imaging Signatures***
Dongming Liu, Jiu Chen, Xinhua Hu, Kun Yang, Yong Liu, Guanjie Hu, Honglin Ge, Wenbin Zhang and Hongyi Liu

68 ***Fluorescence Lifetime Imaging and Spectroscopic Co-Validation for Protoporphyrin IX-Guided Tumor Visualization in Neurosurgery***
David Reichert, Mikael T. Erkkilae, Johanna Gesperger, Lisa I. Wadiura, Alexandra Lang, Thomas Roetzer, Adelheid Woehrer, Marco Andreana, Angelika Unterhuber, Marco Wilzbach, Christoph Hauger, Wolfgang Drexler, Barbara Kiesel, Georg Widhalm and Rainer A. Leitgeb

81 ***Factors Associated With Dysfunction of Glymphatic System in Patients With Glioma***
Cheng Hong Toh and Tiing Yee Siow

89 ***Exploring Peritumoral Neural Tracts by Using Neurite Orientation Dispersion and Density Imaging***
Shin Tai Chong, Xinrui Liu, Hung-Wen Kao, Chien-Yuan Eddy Lin, Chih-Chin Heather Hsu, Yi-Chia Kung, Kuan-Tsen Kuo, Chu-Chung Huang, Chun-Yi Zac Lo, Yunqian Li, Gang Zhao and Ching-Po Lin

104 ***Diagnostic and Prognostic Potential of ^{18}F-FET PET in the Differential Diagnosis of Glioma Recurrence and Treatment-Induced Changes After Chemoradiation Therapy***
Monica Celli, Paola Caroli, Elena Amadori, Donatella Arpa, Lorena Gurrieri, Giulia Ghigi, Patrizia Cenni, Giovanni Paganelli and Federica Matteucci

114 ***Dynamic ^{18}F-FDopa PET Imaging for Newly Diagnosed Gliomas: Is a Semiquantitative Model Sufficient?***
Timothée Zaragori, Matthieu Doyen, Fabien Rech, Marie Blonski, Luc Taillandier, Laëtitia Imbert and Antoine Verger

125 ***Case Report: Disruption of Resting-State Networks and Cognitive Deficits After Whole Brain Irradiation for Singular Brain Metastasis***
Martin Kocher, Christiane Jockwitz, Christoph Lerche, Michael Sabel, Philipp Lohmann, Gabriele Stoffels, Christian Filss, Felix M. Mottaghy, Maximilian I. Ruge, Gereon R. Fink, Nadim J. Shah, Norbert Galldiks, Svenja Caspers and Karl-Josef Langen

134 ***Resting-State Functional Magnetic Resonance Imaging Networks as a Quantitative Metric for Impact of Neurosurgical Interventions***
Peter H. Yang, Carl D. Hacker, Bhuvic Patel, Andy G. S. Daniel and Eric C. Leuthardt

144 ***Assessment of Isocitrate Dehydrogenase 1 Genotype and Cell Proliferation in Gliomas Using Multiple Diffusion Magnetic Resonance Imaging***
Yan Xie, Shihui Li, Nanxi Shen, Tongjia Gan, Shun Zhang, Weiyin Vivian Liu and Wenzhen Zhu

154 ***A Data-Based Approach for Selecting Pre- and Intra-Operative Language Mapping Tasks***
Justyna O. Ekert, Matthew A. Kirkman, Mohamed L. Seghier, David W. Green and Cathy J. Price

168 ***Turbo Gradient and Spin Echo PROPELLER-Diffusion Weighted Imaging for Orbital Tumors: A Comparative Study With Readout-Segmented Echo-Planar Imaging***
Qing Fu, Xiang-chuang Kong, Ding-Xi Liu, Kun Zhou, Yi-hao Guo, Zi-Qiao Lei, Chuan-sheng Zheng and Fan Yang

179 ***Assessment of Sodium MRI at 7 Tesla as Predictor of Therapy Response and Survival in Glioblastoma Patients***
Daniel Paech, Sebastian Regnery, Tanja Platt, Nicolas G. R. Behl, Nina Weckesser, Paul Windisch, Katerina Deike-Hofmann, Wolfgang Wick, Martin Bendszus, Stefan Rieken, Laila König, Mark E. Ladd, Heinz-Peter Schlemmer, Jürgen Debus and Sebastian Adeberg

188 ***Combined Application of Sodium Fluorescein and Neuronavigation Techniques in the Resection of Brain Gliomas***
Zhan Xue, Lu Kong, Shuyu Hao, Yu Wang, Guijun Jia, Zhen Wu, Wang Jia, Junting Zhang and Liwei Zhang

194 ***Resting-State Electroencephalography Functional Connectivity Networks Relate to Pre- and Postoperative Language Functioning in Low-Grade Glioma and Meningioma Patients***
Nienke Wolthuis, Djaina Satoer, Wencke Veenstra, Marion Smits, Michiel Wagemakers, Arnaud Vincent, Roelien Bastiaanse, Perumpillichira J. Cherian and Ingeborg Bosma

208 ***Tracking the Corticospinal Tract in Patients With High-Grade Glioma: Clinical Evaluation of Multi-Level Fiber Tracking and Comparison to Conventional Deterministic Approaches***
Andrey Zhylka, Nico Sollmann, Florian Kofler, Ahmed Radwan, Alberto De Luca, Jens Gempt, Benedikt Wiestler, Bjoern Menze, Sandro M. Krieg, Claus Zimmer, Jan S. Kirschke, Stefan Sunaert, Alexander Leemans and Josien P. W. Pluim

223 ***Automatic Radiotherapy Planning for Glioblastoma Radiotherapy With Sparing of the Hippocampus and nTMS-Defined Motor Cortex***
Michaela Schuermann, Yvonne Dzierma, Frank Nuesken, Joachim Oertel, Christian Rübe and Patrick Melchior

238 ***Dual-Task nTMS Mapping to Visualize the Cortico-Subcortical Language Network and Capture Postoperative Outcome—A Patient Series in Neurosurgery***
Ann-Katrin Ohlerth, Roelien Bastiaanse, Lyndsey Nickels, Beate Neu, Wei Zhang, Sebastian Ille, Nico Sollmann and Sandro M. Krieg

252 ***Radiomics Analysis Based on Magnetic Resonance Imaging for Preoperative Overall Survival Prediction in Isocitrate Dehydrogenase Wild-Type Glioblastoma***
Shouchao Wang, Feng Xiao, Wenbo Sun, Chao Yang, Chao Ma, Yong Huang, Dan Xu, Lanqing Li, Jun Chen, Huan Li and Haibo Xu

263 ***Decreasing Shortest Path Length of the Sensorimotor Network Induces Frontal Glioma-Related Epilepsy***
Shengyu Fang, Lianwang Li, Shimeng Weng, Yuhao Guo, Zhong Zhang, Lei Wang, Xing Fan, Yinyan Wang and Tao Jiang

275 ***Advanced Imaging Techniques for Newly Diagnosed and Recurrent Gliomas***
Luis R. Carrete, Jacob S. Young and Soonmee Cha

297 ***High-Grade Glioma Treatment Response Monitoring Biomarkers: A Position Statement on the Evidence Supporting the Use of Advanced MRI Techniques in the Clinic, and the Latest Bench-to-Bedside Developments. Part 2: Spectroscopy, Chemical Exchange Saturation, Multiparametric Imaging, and Radiomics***
Thomas C. Booth, Evita C. Wiegers, Esther A. H. Warnert, Kathleen M. Schmainda, Frank Riemer, Ruben E. Nechifor, Vera C. Keil, Gilbert Hangel, Patrícia Figueiredo, Maria Del Mar Álvarez-Torres and Otto M. Henriksen on behalf of the European Cooperation in Science Technology (COST) Glioma MR Imaging 2.0 (GliMR) initiative

319 ***Validation of Non-invasive Language Mapping Modalities for Eloquent Tumor Resection: A Pilot Study***
Matthew Muir, Rajan Patel, Jeffrey Traylor, Dhiego Chaves de Almeida Bastos, Sarah Prinsloo, Ho-Ling Liu, Kyle Noll, Jeffrey Wefel, Sudhakar Tummala, Vinodh Kumar and Sujit Prabhu

332 ***High-Grade Glioma Treatment Response Monitoring Biomarkers: A Position Statement on the Evidence Supporting the Use of Advanced MRI Techniques in the Clinic, and the Latest Bench-to-Bedside Developments. Part 1: Perfusion and Diffusion Techniques***
Otto M. Henriksen, María del Mar Álvarez-Torres, Patricia Figueiredo, Gilbert Hangel, Vera C. Keil, Ruben E. Nechifor, Frank Riemer, Kathleen M. Schmainda, Esther A. H. Warnert, Evita C. Wiegers and Thomas C. Booth on behalf of the European Cooperation in Science and Technology (COST) Glioma MR Imaging 2.0 (GliMR) Initiative

359 ***Case Report: ALK-Positive Histiocytosis With* KIF5B-ALK *Fusion in Cerebrum-Disseminated Lesions in a Child***
Yi Guo, Hai-bo Qu, Gang Ning, Feng-lin Jia, Hong Liu, Xin-mao Ma and Yi Liao

367 ***Automation of Cranial Nerve Tractography by Filtering Tractograms for Skull Base Surgery***
Méghane Decroocq, Morgane Des Ligneris, Titouan Poquillon, Maxime Vincent, Manon Aubert, Timothée Jacquesson and Carole Frindel

384 ***Ultra-High-Field MRI in the Diagnosis and Management of Gliomas: A Systematic Review***
Annabelle Shaffer, Susanna S. Kwok, Anant Naik, Aaron T. Anderson, Fan Lam, Tracey Wszalek, Paul M. Arnold and Wael Hassaneen

395 ***Multiparametric Intraoperative Ultrasound in Oncological Neurosurgery: A Pictorial Essay***
Francesco Prada, Riccardo Ciocca, Nicoletta Corradino, Matteo Gionso, Luca Raspagliesi, Ignazio Gaspare Vetrano, Fabio Doniselli, Massimiliano Del Bene and Francesco DiMeco

406 ***Contralesional Sensorimotor Network Participates in Motor Functional Compensation in Glioma Patients***
Shengyu Fang, Lianwang Li, Shimeng Weng, Yuhao Guo, Zhang Zhong, Xing Fan, Tao Jiang and Yinyan Wang

418 ***Non-Invasive Prediction of Survival Time of Midline Glioma Patients Using Machine Learning on Multiparametric MRI Radiomics Features***
Da-Biao Deng, Yu-Ting Liao, Jiang-Fen Zhou, Li-Na Cheng, Peng He, Sheng-Nan Wu, Wen-Sheng Wang and Quan Zhou

429 ***Intraoperative Real-Time Near-Infrared Image-Guided Surgery to Identify Intracranial Meningiomas* via *Microscope***
Jun Muto, Yutaka Mine, Yuya Nishiyama, Kazuhiro Murayama, Seiji Yamada, Daijiro Kojima, Motoharu Hayakawa, Kazuhide Adachi, Mitsuhiro Hasegawa, John Y. K. Lee and Yuichi Hirose

440 ***Navigated Intraoperative 3D Ultrasound in Glioblastoma Surgery: Analysis of Imaging Features and Impact on Extent of Resection***
Benjamin Saß, Darko Zivkovic, Mirza Pojskic, Christopher Nimsky and Miriam H. A. Bopp

451 ***Differentiation of Meningiomas and Gliomas by Amide Proton Transfer Imaging: A Preliminary Study of Brain Tumour Infiltration***
Han-Wen Zhang, Xiao-Lei Liu, Hong-Bo Zhang, Ying-Qi Li, Yu-li Wang, Yu-Ning Feng, Kan Deng, Yi Lei, Biao Huang and Fan Lin

460 ***Surgical Effects of Resecting Skull Base Tumors Using Pre-operative Multimodal Image Fusion Technology: A Retrospective Study***
Zhi-heng Jian, Jia-yan Li, Kai-hua Wu, Yu Li, Shi-xue Li, Hai-dong Chen and Gang Chen

469 ***The Effect of Right Temporal Lobe Gliomas on Left and Right Hemisphere Neural Processing During Speech Perception and Production Tasks***
Adam Kenji Yamamoto, Ana Sanjuán, Rebecca Pope, Oiwi Parker Jones, Thomas M. H. Hope, Susan Prejawa, Marion Oberhuber, Laura Mancini, Justyna O. Ekert, Andrea Garjardo-Vidal, Megan Creasey, Tarek A. Yousry, David W. Green and Cathy J. Price

488 ***3D Amide Proton Transfer Weighted Brain Tumor Imaging With Compressed SENSE: Effects of Different Acceleration Factors***
Nan Zhang, Haonan Zhang, Bingbing Gao, Yanwei Miao, Ailian Liu, Qingwei Song, Liangjie Lin and Jiazheng Wang

499 ***Surgery of Motor Eloquent Glioblastoma Guided by TMS-Informed Tractography: Driving Resection Completeness Towards Prolonged Survival***
Carolin Weiss Lucas, Andrea Maria Faymonville, Ricardo Loução, Catharina Schroeter, Charlotte Nettekoven, Ana-Maria Oros-Peusquens, Karl Josef Langen, N. Jon Shah, Gabriele Stoffels, Volker Neuschmelting, Tobias Blau, Hannah Neuschmelting, Martin Hellmich, Martin Kocher, Christian Grefkes and Roland Goldbrunner

517 ***Laterality and Sex Differences of Human Lateral Habenula Afferent and Efferent Fiber Tracts***
Frederick L. Hitti, Drew Parker, Andrew I. Yang, Steven Brem and Ragini Verma

525 ***Evaluation of HIF-1α Expression in a Rat Glioma Model Using Intravoxel Incoherent Motion and R2* Mapping***
Dongdong Wang, Yiping Lu, Xuanxuan Li, Nan Mei, Pu-Yeh Wu, Daoying Geng, Hao Wu and Bo Yin

532 ***Diagnostic Accuracy of the Diffusion-Weighted Imaging Method Used in Association With the Apparent Diffusion Coefficient for Differentiating Between Primary Central Nervous System Lymphoma and High-Grade Glioma: Systematic Review and Meta-Analysis***
Xiaoli Du, Yue He and Wei Lin

545 ***Decoding the Heterogeneity of Malignant Gliomas by PET and MRI for Spatial Habitat Analysis of Hypoxia, Perfusion, and Diffusion Imaging: A Preliminary Study***
Michele Bailo, Nicolò Pecco, Marcella Callea, Paola Scifo, Filippo Gagliardi, Luca Presotto, Valentino Bettinardi, Federico Fallanca, Paola Mapelli, Luigi Gianolli, Claudio Doglioni, Nicoletta Anzalone, Maria Picchio, Pietro Mortini, Andrea Falini and Antonella Castellano

566 ***Case Report: Atypical Solitary Brain Metastasis: The Role of MR Spectroscopy In Differential Diagnosis***
Dusko Kozic, Nebojsa Lasica, Danica Grujicic, Savo Raicevic, Natasa Prvulovic Bunovic, Igor Nosek and Jasmina Boban

571 ***Differentiation Between Glioma Recurrence and Treatment Effects Using Amide Proton Transfer Imaging: A Mini-Bayesian Bivariate Meta-Analysis***
Kai Chen, Xi-Wen Jiang, Li-jing Deng and Hua-Long She

582 ***Diffusion Tensor Imaging, Intra-Operative Neurophysiological Monitoring and Small Craniotomy: Results in a Consecutive Series of 103 Gliomas***
Giorgio Carrabba, Giorgio Fiore, Andrea Di Cristofori, Cristina Bana, Linda Borellini, Barbara Zarino, Giorgio Conte, Fabio Triulzi, Alessandra Rocca, Carlo Giussani, Manuela Caroli, Marco Locatelli and Giulio Bertani

602 ***Predicting the True Extent of Glioblastoma Based on Probabilistic Tractography***
David Kis, Laszlo Szivos, Mark Rekecki, Bayan Salam Shukir, Adrienn Mate, Katalin Hideghety and Pal Barzo

616 ***Clinical Implementation of Artificial Intelligence in Neuroradiology With Development of a Novel Workflow-Efficient Picture Archiving and Communication System-Based Automated Brain Tumor Segmentation and Radiomic Feature Extraction***
Mariam Aboian, Khaled Bousabarah, Eve Kazarian, Tal Zeevi, Wolfgang Holler, Sara Merkaj, Gabriel Cassinelli Petersen, Ryan Bahar, Harry Subramanian, Pranay Sunku, Elizabeth Schrickel, Jitendra Bhawnani, Mathew Zawalich, Amit Mahajan, Ajay Malhotra, Sam Payabvash, Irena Tocino, MingDe Lin and Malte Westerhoff

frontiers in Neuroscience

ORIGINAL RESEARCH
published: 22 April 2021
doi: 10.3389/fnins.2021.674898

Peritumoral Brain Edema in Meningiomas May Be Related to Glymphatic Dysfunction

Cheng Hong Toh[1,2], Tiing Yee Siow[1] and Mauricio Castillo[3]*

[1] Department of Medical Imaging and Intervention, Chang Gung Memorial Hospital at Linkou, Taoyuan, Taiwan, [2] College of Medicine, Chang Gung University, Taoyuan, Taiwan, [3] Department of Radiology, University of North Carolina School of Medicine, Chapel Hill, NC, United States

The pathogenesis of peritumoral brain edema (PTBE) in meningiomas remains unclear. The glymphatic system is recently recognized as a pathway for waste clearance and maintaining fluid balance in the brain parenchymal interstitium. We aimed to investigate if the PTBE volume of meningiomas correlates with their glymphatic function. A total of 80 meningioma patients (mean age, 58.8 years; 37 men) and 44 normal subjects (mean age 53.3 years; 23 men) who had preoperative diffusion-tensor imaging for calculation of the analysis along the perivascular space (ALPS) index were retrospectively included. Information collected from each patient included sex, age, tumor grade, Ki-67 index, tumor location, tumor volume, PTBE volume and ALPS index. Comparisons of ALPS index among meningiomas without PTBE, meningiomas with PTBE, and normal subjects were performed using analysis of covariance with Bonferroni correction and adjustments for age and sex. Pearson correlation coefficient and multivariable linear regression analyses were performed to identify factors associated with PTBE volume. Group comparisons revealed that the ALPS index was significantly higher ($P < 0.05$) in meningiomas without PTBE vs. meningiomas with PTBE and normal subjects. On the other hand, ALPS index was not different between meningiomas with PTBE and normal subjects. On Pearson correlation and multivariable linear regression analyses, the ALPS index was the only factor significantly ($P < 0.05$) associated with PTBE volume. In conclusion, PTBE volume inversely correlated with ALPS index in meningiomas. PTBE formation in meningiomas may be related to glymphatic dysfunction.

Keywords: meningioma, peritumoral brain edema, glymphatic system, diffusion-tensor imaging, brain interstitial fluid

OPEN ACCESS

Edited by:
Nico Sollmann, Technical University of Munich, Germany

Reviewed by:
Michael Sughrue, University of New South Wales, Australia
Alexey Surov, Leipzig University, Germany

****Correspondence:***
Cheng Hong Toh
eldomtoh@hotmail.com

Specialty section:
This article was submitted to Brain Imaging Methods, a section of the journal Frontiers in Neuroscience

Received: *02 March 2021*
Accepted: *06 April 2021*
Published: *22 April 2021*

Citation:
Toh CH, Siow TY and Castillo M (2021) Peritumoral Brain Edema in Meningiomas May Be Related to Glymphatic Dysfunction. Front. Neurosci. 15:674898. doi: 10.3389/fnins.2021.674898

INTRODUCTION

Meningiomas account for 37.6% of primary brain tumors in population-based studies (Ostrom et al., 2019). Up to 67% of meningiomas have peritumoral brain edema (PTBE) (Hou et al., 2013). PTBE increases intracranial pressure, complicates surgical resection, and is associated with higher risk of seizures (Simis et al., 2008), postoperative intracranial hemorrhages (Sindou and Alaywan, 1998) and recurrences (Mantle et al., 1999; Simis et al., 2008). Pathogenesis of PTBE remains unclear and there are conflicting reports on correlations between PTBE extension and imaging features such as tumor size or volume (Bitzer et al., 1997; Tamiya et al., 2001; Paek et al., 2002;

Lee et al., 2008; Simis et al., 2008; Kim et al., 2011), tumor-brain interface (Tamiya et al., 2001; Nakano et al., 2002; Simis et al., 2008; Kim et al., 2011; Sapkota et al., 2020), tumor location (Osawa et al., 2013; Sapkota et al., 2020), venous outflow obstruction (Kim et al., 2019), tumor blood supply pattern (Tamiya et al., 2001; Osawa et al., 2013), and tumor T2-weighted signal (Tamiya et al., 2001; Nakano et al., 2002; Kim et al., 2011; Sapkota et al., 2020).

The glymphatic system is recently recognized as a pathway for waste clearance and maintaining fluid balance in the brain parenchymal interstitium (Rasmussen et al., 2018). CSF from the subarachnoid space flows into brain parenchyma through periarterial spaces of the penetrating arteries under the influence of Aquaporin-4 water channels and mixes with parenchymal interstitial fluid. The interstitial fluid moves with its solutes toward the perivenous and perineuronal spaces, where it leaves brain parenchyma. From there, CSF exits the intracranial compartment via the perineural sheaths of some cranial and spinal nerves, dural lymphatics, and arachnoid granulations. Glymphatic failure has been proposed as a final pathway to dementia (Nedergaard and Goldman, 2020) and is responsible for early tissue swelling and edema after ischemic infarct (Mestre et al., 2020). In glioma-bearing mice, CSF flow to extracranial spaces is reduced (Ma et al., 2019b) but in extra-axial tumors such as meningiomas, alterations of glymphatic function related to PTBE remain unclear.

In the diffusion tensor image analysis along the perivascular space (DTI-ALPS) method (Taoka et al., 2017), ALPS index, a diffusion metric that estimates the diffusivity along the perivascular spaces of medullary veins, has been used to assess glymphatic function. Alterations of the ALPS index correlate with the Mini-Mental State Examination score of dementia patients and is thought to reflect glymphatic dysfunction (Taoka et al., 2017). ALPS index is also significantly lower in normal pressure hydrocephalus patients and suggests glymphatic dysfunction as evidenced by delayed clearance of intrathecally injected gadobutrol (Ringstad et al., 2017; Eide and Ringstad, 2019). Therefore, the ALPS index may serve as a surrogate marker for identifying altered glymphatic function and quantifying glymphatic activity.

To the best of our knowledge, the relationship between the function of the glymphatic system and PTBE of meningiomas has not been investigated. The DTI-ALPS method may help understand the role of the glymphatic system in PTBE formation and may aid in the development of treatments for reducing PTBE preoperatively. We hypothesized that PTBE of meningiomas is associated with dysfunction of glymphatic system as evidenced by an altered ALPS index.

MATERIALS AND METHODS

Study Subjects

Approval for reviewing the patients' clinical data and preoperative MRI findings was obtained from our Institutional Review Board. Between 2006 and 2017, a total of 90 consecutive patients with a histopathological diagnosis of meningioma underwent preoperative DTI at our institution. A total of 10 patients were excluded due to motion artifacts (n = 2), bihemispheric tumors (n = 4), infratentorial tumors (n = 2) and *trans*-arterial tumor embolization before MRI examinations (n = 4). Thus, a total of 80 patients (43 women, 37 men; mean age, 58.8 ± 13.5 years; age range, 24–90 years) were analyzed. No patients had begun corticosteroid treatment, radiation therapy, chemotherapy or had previous brain surgery at the time of their MRI studies. An overview of patient characteristics is found in **Table 1**. As healthy controls, 44 subjects (21 women, 23 men; mean age 53.3 ± 10.0 years; age range, 27–83 years) with normal brain MRI examinations were also included.

Clinical and Imaging Information

Patient medical records and MRI studies were retrospectively reviewed to collect clinical and imaging information including sex, age, tumor grade (grade I or grade II/III), tumor proliferation index Ki-67, tumor location, and the side of the cerebral hemisphere or posterior fossa in which the tumor was located (right or left). Histopathologic diagnosis was made by a board-certified neuropathologist with 20 years of experience. Tumors

TABLE 1 | Patient characteristics.

Characteristics	All meningioma
No. of patients	80
Mean age ± SD (y)	58.8 ± 13.5
Sex	
Man	37
Woman	43
Tumor location	
Sphenoid ridge	12
Parasellar	1
Frontal base	2
Convexity	39
Parasagittal	23
Intraventricular	2
Tentorium	1
Tumor grade	
Grade I	61
Grade II	15
Grade III	4
Tumor volume (cm^3)	
1–8	7
8–27	15
27–64	28
64–125	22
>125	8
Edema volume (cm^3)	
0	24
1–27	15
27–64	15
64–125	17
>125	9

Except where indicated, data are numbers of patients. SD = standard deviation.

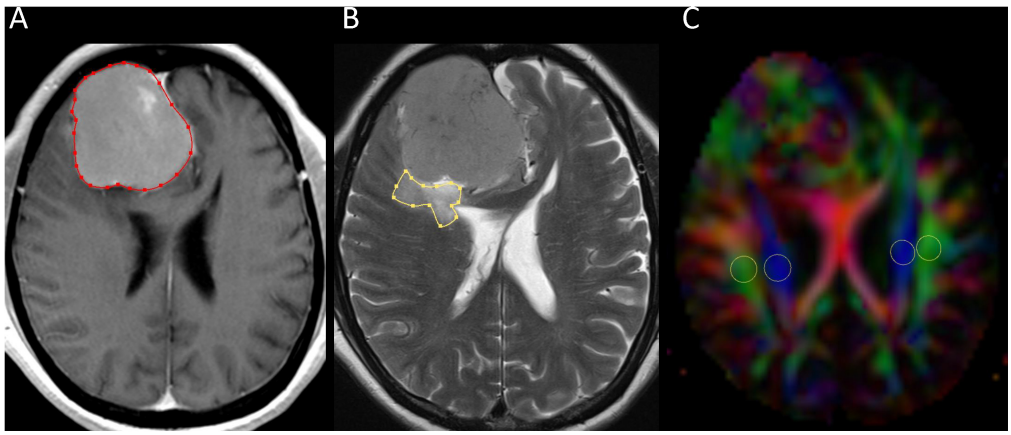

FIGURE 1 | Example of how regions of interest (ROIs) were segmented. Transverse contrast-enhanced T1-weighted **(A)** and T2-weighted **(B)** images show manually drawn ROIs for measurement of meningioma and peritumoral brain edema volumes. Directionally encoded color map **(C)** illustrates ROIs of projection (blue area) and association (green area) fibers in bilateral periventricular regions.

were graded according to the 2016 World Health Organization classification. Tumor locations were skull base (frontal base, tuberculum sellae, parasellar, sphenoid ridge) and non-skull base (other locations).

MRI

All MRI studies were performed using a 3T unit (Magnetom Tim Trio, Siemens, Erlangen, Germany) with a 12-channel phased-array head coil. All examinations included a T2-weighted, DTI, and T1-weighted sequences acquired in transverse plane before and after administration of 0.1 mmol/kg body weight gadopentetate dimeglumine (Magnevist; Schering, Berlin, Germany).

Diffusion tensor image was performed using a single-shot EPI with the following parameters: TR msec/TE msec, 5800/83; diffusion gradient encoding in 20 directions; b = 0, 1000 s/mm^2; FOV, 256 × 256 mm; matrix size, 128 × 128; section thickness, 2 mm; and number of signals acquired, 4. A total of 50–60 sections without intersection gap were used to cover the cerebral hemispheres, brainstem and cerebellum. Generalized autocalibrating partially parallel acquisitions (GRAPPA) with reduction factor set at two were used during DTI acquisitions. Contrast-enhanced T1-weighted images (TR/TE, 2000/2.63 ms; section thickness, 1 mm; TI, 900 ms; acquisition matrix, 224 × 256 and FOV, 224 × 256 mm) were acquired after completion of the DTI sequence.

Measurements of Tumor and PTBE Volume

Two neuroradiologists (with 16 and 6 years of experience) independently measured tumor and PTBE volumes of meningiomas using the software nordicICE (nordic Image Control and Evaluation Version 2, Nordic Imaging Lab, Bergen, Norway). A polygonal region-of-interest (ROI) was manually drawn to include the entire tumor on each transverse contrast-enhanced T1-weighted image. The ROIs on all images were then combined to form a whole tumor volume-of-interest for calculations of tumor volume. If multiple tumors were present, all of them were measured and their volumes summed up. The same method was used for the calculation of PTBE volume on transverse T2-weighted images. All ROIs did not include dural tails, areas of necrosis, or presumed calcification. An example of ROI segmentation is shown in **Figure 1**.

Diffusion Tensor Image Analysis Along the Periventricular Space (DTI-ALPS)

Diffusion tensor image analysis along the perivascular space method (Taoka et al., 2017) was used to evaluate the glymphatic functions. This method evaluates the diffusivity along the perivascular space on a transverse slice at the level of lateral ventricle body. The medullary veins, accompanied by the perivascular spaces run perpendicular to the ventricular walls at the level of the lateral ventricular body in a right-left or left-right direction (i.e., x-axis in image coordinate). In this level, the corticofugal corona radiata projection fibers run in the craniocaudal direction (i.e., z-axis in image coordinate) adjacent to the lateral ventricles. The superior longitudinal fascicle, which represents the association fibers runs in the anterior-posterior direction (i.e., y-axis in image coordinate) and is located lateral to the corona radiata. As the perivascular space is nearly perpendicular to both the projection fibers and association fibers, the major differences between x-axis diffusivity in both fibers (D_{xproj} and D_{xassoc} for x-axis diffusivity in projection fiber and association fiber, respectively) and the diffusivity that is perpendicular to the x-axis and to the direction of fiber tracts (y-axis for projection fiber, where the diffusivity denoted as D_{yproj}; z-axis for association fiber, where the diffusivity denoted as D_{zassoc}) is the existence of perivascular space. To quantify glymphatic activity, ALPS index is defined as follows:

$$\text{ALPS index} = \frac{\text{mean}\left(D_{xproj}, D_{xassoc}\right)}{\text{mean}\left(D_{yproj}, D_{zassoc}\right)} \quad (1)$$

Diffusion metric images were generated by using 3D Slicer version 4.10.2[1]. Two neuroradiologists independently drew the ROIs of bilateral projection (mean size, 29 ± 17 mm^2) and association fibers (mean size, 26 ± 17 mm^2) on a slice at the level of the lateral ventricular body based on directionality encoded map. ALPS index was computed according to the equation above (1). An example of ROI placement for ALPS index measurement is shown in **Figure 1**.

Statistical Analysis

A commercially available statistical software package (SPSS 22; IBM, Armonk, NY, United States) was used for analysis, and *P* values < 0.05 were considered to indicate a statistical significance. Continuous variables are denoted as mean ± standard deviation, unless otherwise noted. The Kolmogorov-Smirnov test was used to assess the normality of continuous variables and guide the selection of a parametric or nonparametric test for comparison of variables.

The interobserver variability in the measurements of PTBE volume, tumor volume and ALPS index was assessed by intraclass correlation coefficients (ICCs) with 95% confidence intervals (CIs) based on an absolute-agreement, two-way random-effects model. The final values of PTBE volume, tumor volume, and ALPS index were obtained by taking the mean of two observers' independent measurements.

Because there are no reference ranges for human ALPS index, potential interhemispheric, sex, and age differences in ALPS index were taken into account when comparing between normal subjects and meningioma patients. As such, comparisons of normal subjects with patients having right-side and left-side meningiomas were performed separately. Differences in bilateral ALPS indices among meningiomas without PTBE, meningiomas with PTBE, and normal subjects were assessed using analysis of covariance with Bonferroni correction and adjustments for age and sex.

In the group of meningiomas with PTBE, correlations of PTBE volume with age, sex, tumor grade, Ki-67, tumor location, tumor volume, and ALPS index were analyzed with the Pearson correlation coefficient. Variance inflation factors were used to detect multicollinearity. All variables were entered as potential covariates in the stepwise multivariable linear regression analysis to assess their associations with PTBE volume.

RESULTS

Among 80 patients, 44 had right-side meningiomas and 36 had left-side meningiomas. A total of 15 meningiomas were in deep locations (12 sphenoid ridge, 1 parasellar, and 2 frontal base). Other tumor locations included the convexities (n = 39), parasagittal (n = 23), tentorial (n = 1), and intraventricular (n = 2). Tumor grades were grade I in 61 patients, grade II in 15, and grade III in 4. Mean Ki-67 (%) was 4.8 ± 3.1 (range, 1 to 12).

There were excellent interobserver agreements in the measurements of meningioma volumes (ICC = 0.997, 95% CI = 0.995–0.998, $P < 0.001$), PTBE volumes (ICC = 0.996, 95% CI = 0.994–0.997, $P < 0.001$), right ALPS index (ICC = 0.960, 95% CI = 0.884–0.950, $P < 0.001$) and left ALPS index (ICC = 0.934, 95% CI = 0.900–0.57, $P < 0.001$). Mean meningioma volume (cm^3) of 80 patients of was 58.6 ± 45.3 (range, 3.1–202.9). PTBE was present in 56 patients, with a mean volume (cm^3) of 67.1 ± 46.8 (range, 4.1 to 171.3). PTBE was absent in 24 (30%) patients.

Results of comparing the ALPS index among meningiomas without PTBE, meningiomas with PTBE and normal subjects are summarized in **Table 2**. The right ALPS index of right-side meningiomas without PTBE, right-side meningiomas with PTBE, and normal subjects was 1.502 ± 0.089, 1.260 ± 0.112, and 1.215 ± 0.093, respectively. The right ALPS index of meningiomas without PTBE was significantly higher than that of meningiomas with PTBE ($P < 0.001$) and normal subjects ($P < 0.001$). The right ALPS index was not significantly different between meningiomas with PTBE and normal subjects ($P = 0.060$). The contralateral (left) ALPS index of the three groups was not statistically significant ($P = 0.148$). **Figure 2** shows the differences in right ALPS index among the three groups.

The left ALPS index of left-side meningiomas without PTBE, left-side meningiomas with PTBE, and normal subjects was 1.513 ± 0.198, 1.304 ± 0.178, and 1.273 ± 0.105, respectively. The left ALPS index of meningiomas without PTBE was significantly higher than that of meningiomas with PTBE ($P = 0.002$) and normal subjects ($P < 0.001$). The left ALPS index was not significantly different between meningiomas with PTBE and normal subjects ($P = 0.840$). The contralateral (right) ALPS index of the three groups was not statistically significant ($P = 0.625$). **Figure 3** shows the differences in left ALPS index among the three groups.

In the group of meningiomas with PTBE, volume of PTBE correlated inversely with ALPS index ipsilateral to tumor ($r = -0.680$, $P < 0.001$). No correlations were found between PTBE volume and age ($r = -0.007$, $P = 0.956$), sex ($r = 0.165$, $P = 0.224$), tumor volume ($r = -0.167$, $P = 0.220$), tumor location ($r = 0.004$, $P = 0.976$), tumor grade ($r = 0.053$, $P = 0.696$), or Ki-67 ($r = 0.185$, $P = 0.337$). **Figure 4** shows the correlation between PTBE volume and ALPS index ipsilateral to meningiomas. On stepwise multiple linear regression analysis, ALPS index ipsilateral to tumor ($\beta = -0.632$; $P < 0.001$) was the only factor associated with PTBE volume. No correlations were found between PTBE volume and age ($P = 0.226$), sex ($P = 0.856$), tumor volume ($P = 0.141$), tumor location ($P = 0.759$), tumor grade ($P = 0.713$), or Ki-67 ($P = 0.393$).

DISCUSSION

In the present study, the ALPS index of meningiomas without PTBE was significantly higher than those of meningiomas with PTBE and normal subjects. Among meningiomas with PTBE, ALPS index is inversely correlated with PTBE volume. The relationship between PTBE volume and ALPS index of meningiomas suggested that PTBE formation may be related to glymphatic dysfunction.

[1] http://www.slicer.org

TABLE 2 | Comparisons of ALPS index among meningiomas without PTBE, meningiomas with PTBE and normal subjects.

Index	Right-side meningioma		Normal subject (n = 44)	PTBE− vs. PTBE+		PTBE− vs. normal subject		PTBE+ vs. normal subject	
	PTBE− (n = 13)	PTBE+ (n = 31)		P-value	95% CI	P-value	95% CI	P-value	95% CI
Right ALPS	1.502 ± 0.089	1.260 ± 0.112	1.215 ± 0.093	<0.001	0.140, 0.304	<0.001	0.204, 0.357	0.060	−0.002, 0.118
Left ALPS	1.353 ± 0.213	1.263 ± 0.173	1.273 ± 0.105	0.615	−0.057, 0.183	0.158	−0.022, 0.203	1.000	−0.060, 0.115
	Left-side meningioma		Normal subject (n = 44)						
	PTBE- (n = 11)	PTBE+ (n = 25)							
Right ALPS	1.272 ± 0.167	1.198 ± 0.204	1.215 ± 0.093	1.000	−0.079, 0.175	1.000	−0.075, 0.158	1.000	−0.095, 0.082
Left ALPS	1.513 ± 0.198	1.304 ± 0.178	1.273 ± 0.105	0.002	0.060, 0.317	<.001	0.110, 0.347	0.840	−0.050, 0.130

Data are mean ± SD; CI, confidence interval; PTBE−, meningiomas without peritumoral brain edema; PTBE+, meningiomas with peritumoral brain edema.

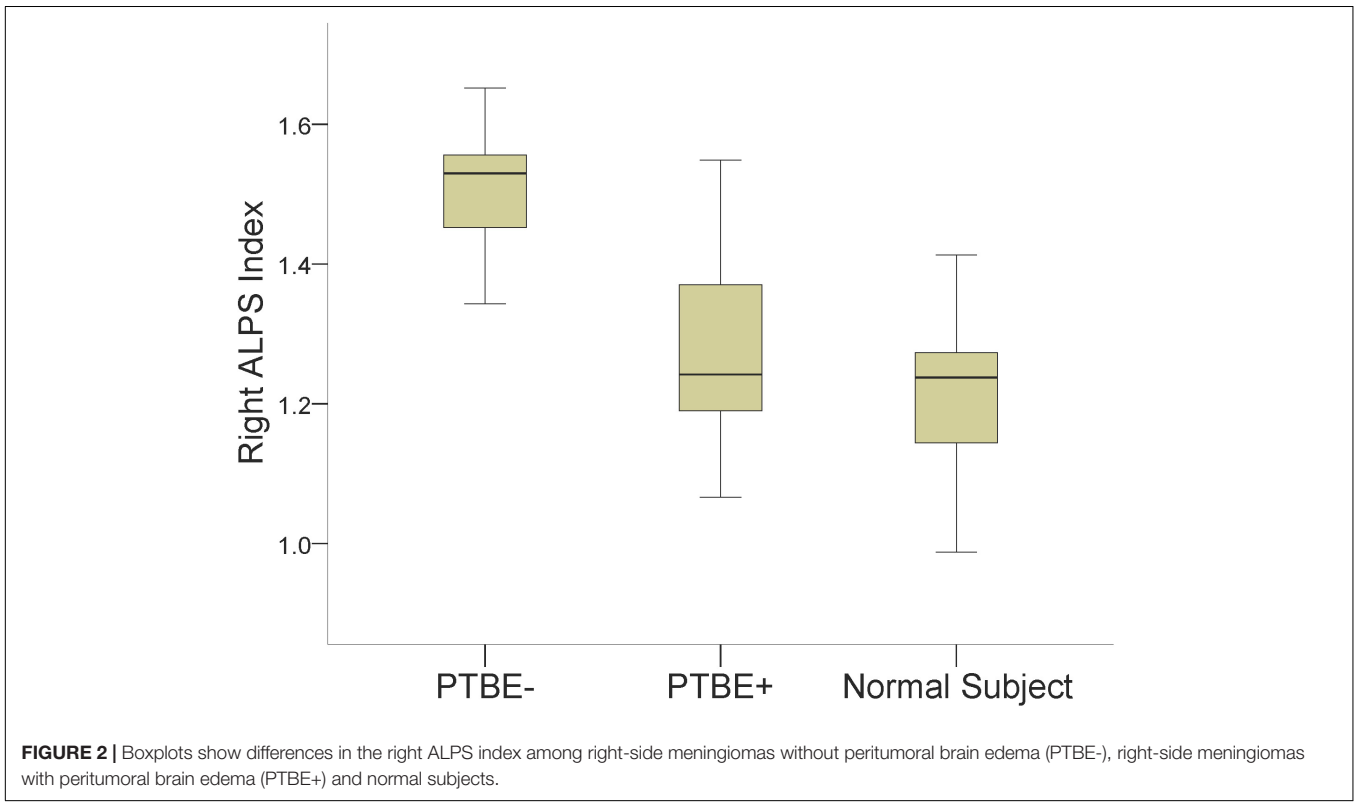

FIGURE 2 | Boxplots show differences in the right ALPS index among right-side meningiomas without peritumoral brain edema (PTBE-), right-side meningiomas with peritumoral brain edema (PTBE+) and normal subjects.

The associations of PTBE extensions with many imaging, histologic and molecular features of meningioma have been reported. The brain parenchyma compression theory states that large meningiomas lead to compression, ischemia, and edema (Lobato et al., 1996). However, the associations between PTBE extension and tumor volume have been inconsistent. While some studies (Bitzer et al., 1997; Simis et al., 2008) reported positive correlations between PTBE extension and tumor volume, others found no correlations (Paek et al., 2002; Lee et al., 2008; Sapkota et al., 2020; Toh and Castillo, 2021). Some studies attributed frequently found and prominent PTBE in meningiomas with T2 hyperintensity to higher water content (Nakano et al., 2002; Lee et al., 2008; Kim et al., 2011; Sapkota et al., 2020). However, this explanation is not supported by a recent study (Toh and Castillo, 2021) which found no differences in tumor T2-weighted signal intensity and apparent diffusion coefficient between meningiomas without and with PTBE. In their study, the only factor associated with PTBE was tumor FA which reflects interstitial fluid flow directionality. Similar to a previous study (Gawlitza et al., 2017), our study shows no correlations between PTBE and histologic grade or Ki-67 index. Other studies reported correlations between PTBE and molecular features of meningioma including the expressions of vascular endothelial growth factor, aquaporin 4, and matrix metalloproteinase 9 (Gawlitza et al., 2017; Berhouma et al., 2019). Although some of these imaging, histologic and molecular findings of meningioma may be associated with PTBE, the underlying mechanisms for extra-axial tumor characteristics to cause intra-axial PTBE remain unclear. In our study, glymphatic function was the only significant factor associated with PTBE

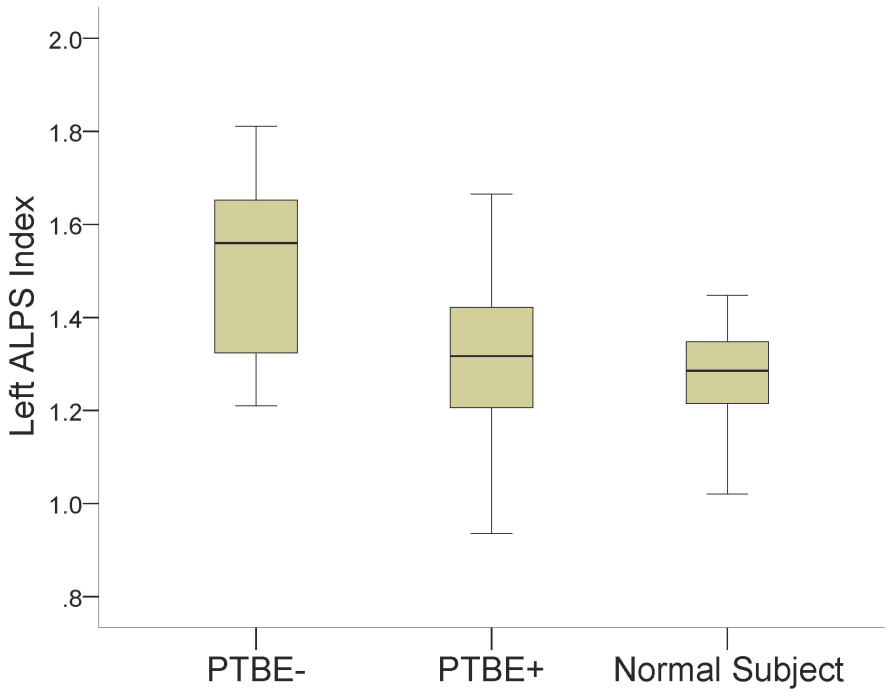

FIGURE 3 | Boxplots show differences in the left ALPS index among left-side meningiomas without peritumoral brain edema (PTBE-), left-side meningiomas with peritumoral brain edema (PTBE+) and normal subjects.

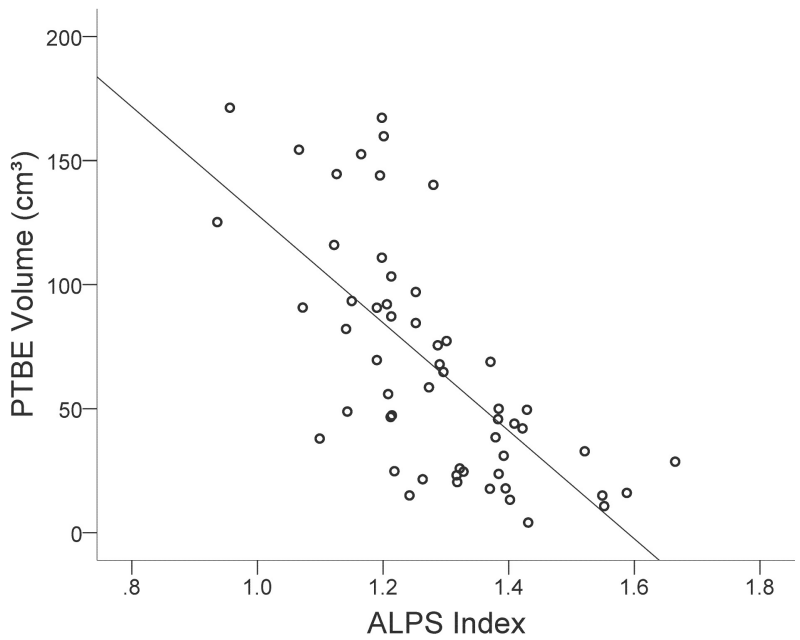

FIGURE 4 | Scatterplot with regression line shows the negative correlation ($r = -0.680$, $P < 0.001$) between peritumoral brain edema (PTBE) volume (cm^3) and ALPS index of meningiomas.

volume. To the best of our knowledge, this correlation has not been reported previously.

In the glymphatic pathway, a convective influx of CSF is balanced by the perivenous efflux of interstitial fluid (Iliff et al., 2012). The growth of meningiomas may disrupt this balance and result in the accumulation of interstitial fluid, i.e., PTBE. Compared to ALPS index of meningiomas with PTBE and normal subjects, the significantly higher ALPS index in meningiomas without PTBE may suggest increased glymphatic function that facilitates interstitial fluid clearance that reduces

or prevents the formation of PTBE. In contrast, ALPS index was not significantly different between meningiomas with PTBE and normal subjects, indicating that no significant changes in glymphatic function for meningiomas with PTBE versus normal subjects. We herein speculate that changes in glymphatic function in response to meningioma growth may have an important role in PTBE formation. Insufficient glymphatic function for interstitial fluid clearance may result in PTBE formation.

As shown in previous studies, alterations in glymphatic function vary with diseases. Decreased glymphatic function and subsequently impaired waste clearance have been reported in Alzheimer's disease, normal pressure hydrocephalus, small vessel disease, and traumatic brain injury (Nedergaard and Goldman, 2020). On the other hand, some clinical conditions are associated with increased glymphatic function. In acute ischemic infarction, edema appears to be caused by a rapid influx of CSF into the brain parenchyma (Mestre et al., 2020). In mice harboring gliomas and melanomas, glymphatic function is increased to reduce PTBE by remodeling of meningeal lymphatic vessels (MLVs) which is downstream of the glymphatic system (Hu et al., 2020). In mice with defective MLVs, impaired drainage of brain parenchymal interstitial fluid aggravates PTBE. Therefore, the increased glymphatic function observed in meningiomas without PTBE may be explained by tumor-induced remodeling of MLVs which facilitate efflux of interstitial fluid from the brain parenchyma. Alternatively, the higher ALPS index in meningiomas without PTBE suggests that this group of patients may have more glymphatic reserve capacity, which serves to relieve the PTBE.

In intra-axial tumors, tumor interstitium directly contacts the surrounding brain parenchyma. Their PTBE may be caused by disruption of the blood-brain barrier (Stummer, 2007) and vasogenic edema associated with tumor cell infiltration. In this setting, it would be difficult to determine the contribution of glymphatic dysfunction to PTBE formation. In contrast, meningioma is a good disease model to study the role of glymphatic system in PTBE formation since it is an extra-axial tumor, and in most cases, is separated from brain parenchyma by pia-arachnoid membrane. The relationship between PTBE volume and ALPS index of meningiomas observed in our study suggests that PTBE formation may be related to glymphatic dysfunction. To date, most studies of the human glymphatic system have focused on mapping its pathways (Ma et al., 2017, 2019a). To the best of our knowledge, no human studies have investigated tumor-related glymphatic dysfunction and thus, further studies are needed to confirm our observations.

MRI studies have confirmed the presence of glymphatic system in the human brain (Ma et al., 2017, 2019a). Intrathecal injection of gadolinium-based contrast agents allows simultaneous visualization of glymphatic system clearance, deep cervical lymph nodes, and putative meningeal lymphatic vessels (Zhou et al., 2020). However, this method is invasive and the off-label use of gadolinium-based contrast agents has potential neurotoxicity. Alternatively, several diffusion imaging-based techniques including DTI-ALPS (Taoka et al., 2017; Harrison et al., 2018; Debacker et al., 2020), have been used to investigate water movement along the perivascular spaces as a reflection of glymphatic system function. Besides being non-invasive, this approach measures glymphatic function quantitatively and reproducibly and allows investigating longitudinal changes of glymphatic function in the same subjects as well as comparison of glymphatic function across different patient groups.

There are limitations to our study. First, the glymphatic system has only recently been recognized and there are no well-established non-invasive methods to measure its function in humans. As fluid dynamics within each anatomical region are not yet fully understood, it is not known in which segments of glymphatic pathway should fluid flow be measured for an estimation of overall glymphatic function. Second, ALPS index evaluates water flow along deep medullary veins and it remains unclear if this measurement reflects the overall function of glymphatic system or just the efflux of interstitial fluid at the perivenous spaces. The correlation between water diffusivity in right-to-left direction along deep medullary veins and the glymphatic activity needs further validation. Third, our findings may not fully explain the pathogenesis of PTBE in meningiomas, but they may suggest a new approach to reduce PTBE, i.e., improving glymphatic function.

In conclusion, we found an inverse relationship between PTBE volume and ALPS index in meningiomas. PTBE formation in meningiomas may be related to dysfunction of the glymphatic system. Insufficient glymphatic function for interstitial fluid clearance during meningioma growth may explain PTBE formation.

DATA AVAILABILITY STATEMENT

Raw data supporting conclusions of this article are available from the corresponding author after signing an agreement.

ETHICS STATEMENT

The studies involving human participants were reviewed and approved by the Chang Gung Medical Foundation Institutional Review Board. Written informed consent for participation was not required for this study in accordance with the national legislation and the institutional requirements.

AUTHOR CONTRIBUTIONS

CT, TS, and MC contributed to conception and design of the study. CT and TS contributed to acquisition and analysis of data. CT and MC contributed to drafting the text and preparation of figures. CT wrote the first draft of the manuscript. All authors read and approved the final manuscript.

FUNDING

This study was funded by the National Science Council Taiwan (NSC-102-2314-B-182-055 to CT).

REFERENCES

Berhouma, M., Jacquesson, T., Jouanneau, E., and Cotton, F. (2019). Pathogenesis of peri-tumoral edema in intracranial meningiomas. *Neurosurg. Rev.* 42, 59–71. doi: 10.1007/s10143-017-0897-x

Bitzer, M., Wockel, L., Morgalla, M., Keller, C., Friese, S., Heiss, E., et al. (1997). Peritumoural brain oedema in intracranial meningiomas: influence of tumour size, location and histology. *Acta Neurochir. (Wien)* 139, 1136–1142. doi: 10.1007/bf01410973

Debacker, C., Djemai, B., Ciobanu, L., Tsurugizawa, T., and Le Bihan, D. (2020). Diffusion MRI reveals in vivo and non-invasively changes in astrocyte function induced by an aquaporin-4 inhibitor. *PLoS One* 15:e0229702. doi: 10.1371/journal.pone.0229702

Eide, P. K., and Ringstad, G. (2019). Delayed clearance of cerebrospinal fluid tracer from entorhinal cortex in idiopathic normal pressure hydrocephalus: a glymphatic magnetic resonance imaging study. *J. Cereb. Blood Flow Metab.* 39, 1355–1368. doi: 10.1177/0271678x18760974

Gawlitza, M., Fiedler, E., Schob, S., Hoffmann, K. T., and Surov, A. (2017). Peritumoral brain edema in meningiomas depends on aquaporin-4 expression and not on tumor grade, tumor volume, cell count, or Ki-67 labeling index. *Mol. Imaging Biol.* 19, 298–304. doi: 10.1007/s11307-016-1000-7

Harrison, I. F., Siow, B., Akilo, A. B., Evans, P. G., Ismail, O., Ohene, Y., et al. (2018). Non-invasive imaging of CSF-mediated brain clearance pathways via assessment of perivascular fluid movement with diffusion tensor MRI. *Elife* 7:e34028.

Hou, J., Kshettry, V. R., Selman, W. R., and Bambakidis, N. C. (2013). Peritumoral brain edema in intracranial meningiomas: the emergence of vascular endothelial growth factor-directed therapy. *Neurosurg. Focus* 35:E2.

Hu, X., Deng, Q., Ma, L., Li, Q., Chen, Y., Liao, Y., et al. (2020). Meningeal lymphatic vessels regulate brain tumor drainage and immunity. *Cell Res.* 30, 229–243. doi: 10.1038/s41422-020-0287-8

Iliff, J. J., Wang, M., Liao, Y., Plogg, B. A., Peng, W., Gundersen, G. A., et al. (2012). A paravascular pathway facilitates CSF flow through the brain parenchyma and the clearance of interstitial solutes, including amyloid β. *Sci. Transl. Med.* 4:147ra111. doi: 10.1126/scitranslmed.3003748

Kim, B. W., Kim, M. S., Kim, S. W., Chang, C. H., and Kim, O. L. (2011). Peritumoral brain edema in meningiomas : correlation of radiologic and pathologic features. *J. Korean. Neurosurg. Soc.* 49, 26–30. doi: 10.3340/jkns.2011.49.1.26

Kim, J. H., Moon, K. S., Jung, J. H., Jang, W. Y., Jung, T. Y., Kim, I. Y., et al. (2019). Importance of collateral venous circulation on indocyanine green videoangiography in intracranial meningioma resection: direct evidence for venous compression theory in peritumoral edema formation. *J. Neurosurg.* 132, 1715–1723. doi: 10.3171/2019.3.jns182308

Lee, K. J., Joo, W. I., Rha, H. K., Park, H. K., Chough, J. K., Hong, Y. K., et al. (2008). Peritumoral brain edema in meningiomas: correlations between magnetic resonance imaging, angiography, and pathology. *Surg. Neurol.* 69, 350–355; discussion355.

Lobato, R. D., Alday, R., Gomez, P. A., Rivas, J. J., Dominguez, J., Cabrera, A., et al. (1996). Brain oedema in patients with intracranial meningioma. Correlation between clinical, radiological, and histological factors and the presence and intensity of oedema. *Acta Neurochir. (Wien)* 138, 485–493; discussion493–484.

Ma, Q., Ineichen, B. V., Detmar, M., and Proulx, S. T. (2017). Outflow of cerebrospinal fluid is predominantly through lymphatic vessels and is reduced in aged mice. *Nat. Commun.* 8:1434.

Ma, Q., Ries, M., Decker, Y., Müller, A., Riner, C., Bücker, A., et al. (2019a). Rapid lymphatic efflux limits cerebrospinal fluid flow to the brain. *Acta Neuropathol.* 137, 151–165. doi: 10.1007/s00401-018-1916-x

Ma, Q., Schlegel, F., Bachmann, S. B., Schneider, H., Decker, Y., Rudin, M., et al. (2019b). Lymphatic outflow of cerebrospinal fluid is reduced in glioma. *Sci. Rep.* 9:14815.

Mantle, R. E., Lach, B., Delgado, M. R., Baeesa, S., and Belanger, G. (1999). Predicting the probability of meningioma recurrence based on the quantity of peritumoral brain edema on computerized tomography scanning. *J. Neurosurg.* 91, 375–383. doi: 10.3171/jns.1999.91.3.0375

Mestre, H., Du, T., Sweeney, A. M., Liu, G., Samson, A. J., Peng, W., et al. (2020). Cerebrospinal fluid influx drives acute ischemic tissue swelling. *Science* 367:eaax7171. doi: 10.1126/science.aax7171

Nakano, T., Asano, K., Miura, H., Itoh, S., and Suzuki, S. (2002). Meningiomas with brain edema: radiological characteristics on MRI and review of the literature. *Clin. Imaging* 26, 243–249.

Nedergaard, M., and Goldman, S. A. (2020). Glymphatic failure as a final common pathway to dementia. *Science* 370, 50–56. doi: 10.1126/science.abb8739

Osawa, T., Tosaka, M., Nagaishi, M., and Yoshimoto, Y. (2013). Factors affecting peritumoral brain edema in meningioma: special histological subtypes with prominently extensive edema. *J. Neurooncol.* 111, 49–57. doi: 10.1007/s11060-012-0989-y

Ostrom, Q. T., Cioffi, G., Gittleman, H., Patil, N., Waite, K., Kruchko, C., et al. (2019). CBTRUS statistical report: primary brain and other central nervous system tumors diagnosed in the United States in 2012-2016. *Neuro Oncol.* 21, v1–v100.

Paek, S. H., Kim, C. Y., Kim, Y. Y., Park, I. A., Kim, M. S., Kim, D. G., et al. (2002). Correlation of clinical and biological parameters with peritumoral edema in meningioma. *J. Neurooncol.* 60, 235–245.

Rasmussen, M. K., Mestre, H., and Nedergaard, M. (2018). The glymphatic pathway in neurological disorders. *Lancet Neurol.* 17, 1016–1024. doi: 10.1016/s1474-4422(18)30318-1

Ringstad, G., Vatnehol, S.a.S, and Eide, P. K. (2017). Glymphatic MRI in idiopathic normal pressure hydrocephalus. *Brain* 140, 2691–2705. doi: 10.1093/brain/awx191

Sapkota, M. R., Yang, Z., Zhu, D., Zhang, Y., Yuan, T., Gao, J., et al. (2020). Evaluation of epidemiologic factors, radiographic features, and pathologic findings for predicting peritumoral brain edema in meningiomas. *J. Magn. Reson. Imaging* 52, 174–182. doi: 10.1002/jmri.27046

Simis, A., Pires De Aguiar, P. H., Leite, C. C., Santana, P. A. Jr., Rosemberg, S., and Teixeira, M. J. (2008). Peritumoral brain edema in benign meningiomas: correlation with clinical, radiologic, and surgical factors and possible role on recurrence. *Surg. Neurol.* 70, 471–477; discussion477.

Sindou, M. P., and Alaywan, M. (1998). Most intracranial meningiomas are not cleavable tumors: anatomic-surgical evidence and angiographic predictibility. *Neurosurgery* 42, 476–480. doi: 10.1097/00006123-199803000-00007

Stummer, W. (2007). Mechanisms of tumor-related brain edema. *Neurosurg. Focus* 22:E8.

Tamiya, T., Ono, Y., Matsumoto, K., and Ohmoto, T. (2001). Peritumoral brain edema in intracranial meningiomas: effects of radiological and histological factors. *Neurosurgery* 49, 1046–1051; discussion1051–1042.

Taoka, T., Masutani, Y., Kawai, H., Nakane, T., Matsuoka, K., Yasuno, F., et al. (2017). Evaluation of glymphatic system activity with the diffusion MR technique: diffusion tensor image analysis along the perivascular space (DTI-ALPS) in Alzheimer's disease cases. *Jpn. J. Radiol.* 35, 172–178. doi: 10.1007/s11604-017-0617-z

Toh, C. H., and Castillo, M. (2021). Peritumoral brain edema volume in meningioma correlates with tumor fractional anisotropy but not apparent diffusion coefficient or cerebral blood volume. *Neuroradiology*. doi: 10.1007/s00234-021-02646-6

Zhou, Y., Cai, J., Zhang, W., Gong, X., Yan, S., Zhang, K., et al. (2020). Impairment of the glymphatic pathway and putative meningeal lymphatic vessels in the aging human. *Ann. Neurol.* 87, 357–369. doi: 10.1002/ana.25670

Conflict of Interest: The authors declare that the research was conducted in the absence of any commercial or financial relationships that could be construed as a potential conflict of interest.

Copyright © 2021 Toh, Siow and Castillo. This is an open-access article distributed under the terms of the Creative Commons Attribution License (CC BY). The use, distribution or reproduction in other forums is permitted, provided the original author(s) and the copyright owner(s) are credited and that the original publication in this journal is cited, in accordance with accepted academic practice. No use, distribution or reproduction is permitted which does not comply with these terms.

frontiers in Neuroscience

ORIGINAL RESEARCH
published: 20 May 2021
doi: 10.3389/fnins.2021.683348

Combining Electrostimulation With Fiber Tracking to Stratify the Inferior Fronto-Occipital Fasciculus

Alexandre Roux[1,2,3], Anne-Laure Lemaitre[4], Jeremy Deverdun[5,6], Sam Ng[4,7], Hugues Duffau[4,7] and Guillaume Herbet[4,7]*

[1] Department of Neurosurgery, GHU Paris, Sainte-Anne Hospital, Paris, France, [2] Université de Paris, Sorbonne Paris Cité, Paris, France, [3] Inserm UMR 1266, IMA-Brain, Institute of Psychiatry and Neurosciences of Paris, Paris, France, [4] Department of Neurosurgery, Gui de Chauliac Hospital, Montpellier University Medical Center, Montpellier, France, [5] Department of Neuroradiology, Gui de Chauliac Hospital, Montpellier University Medical Center, Montpellier, France, [6] I2FH, Institut d'Imagerie Fonctionnelle Humaine, Gui de Chauliac Hospital, Montpellier University Medical Center, Montpellier, France, [7] Institute of Functional Genomics, University of Montpellier, INSERM, CNRS, Montpellier, France

The inferior fronto-occipital fasciculus (IFOF) is one of the longest association fiber tracts of the brain. According to the most recent anatomical studies, it may be formed by several layers, suggesting a role in multiple cognitive functions. However, to date, no attempt has been made to dissociate the functional contribution of the IFOF subpathways. In this study, real-time, cortico-subcortical mapping with direct electrostimulation was performed in 111 patients operated on in wide-awake surgery for a right low-grade glioma. Patients performed two behavioral tasks during stimulation, tapping, respectively, mentalizing and visual semantic cognition—two functions supposed to be partly mediated by the IFOF. Responsive white matter sites were first subjected to a clustering analysis to assess potential topological differences in network organization. Then they were used as seeds to generate streamline tractograms based on the HC1021 diffusion dataset (template-based approach). The tractograms obtained for each function were overlapped and contrasted to determine whether some fiber pathways were more frequently involved in one or the other function. The obtained results not only provided strong evidence for a role of the right IFOF in both functions, but also revealed that the tract is dissociable into two functional strata according to a ventral (semantic) and dorsal (mentalizing) compartmentalization. Besides, they showed a high degree of anatomo-functionnal variability across patients in the functional implication of the IFOF, possibly related to symmetrical/hemispheric differences in network organization. Collectively, these findings support the view that the right IFOF is a functionally multi-layered structure, with nevertheless interindividual variations.

Keywords: diffuse glioma, non-verbal semantic cognition, mentalizing, inferior fronto-occipital fasciculus, electrostimulation

OPEN ACCESS

Edited by:
Nico Sollmann, Technical University of Munich, Germany

Reviewed by:
Sandro M. Krieg, Technical University of Munich, Germany
Michael Sughrue, University of New South Wales, Australia

****Correspondence:***
Hugues Duffau
hugues.duffau@chu.montpellier.fr

Specialty section:
This article was submitted to Brain Imaging Methods, a section of the journal Frontiers in Neuroscience

Received: *20 March 2021*
Accepted: *23 April 2021*
Published: *20 May 2021*

Citation:
Roux A, Lemaitre A-L, Deverdun J, Ng S, Duffau H and Herbet G (2021) Combining Electrostimulation With Fiber Tracking to Stratify the Inferior Fronto-Occipital Fasciculus. Front. Neurosci. 15:683348. doi: 10.3389/fnins.2021.683348

INTRODUCTION

The inferior fronto-occipital fasciculus (IFOF) is one of the longest association fiber tract of the brain; it interconnects the frontal lobe to different territories of the posterior cortex (Schmahmann and Pandya, 2007). Although the earliest descriptions of the IFOF are long-lasting (Burdach, 1822; Dejerine and Dejerine-Klumpke, 1895; Trolard, 1906; Curran, 1909),

the interest for this ventral fasciculus has renewed only recently—especially because of the revival of post-mortem anatomical dissection techniques (Martino et al., 2010; Sarubbo et al., 2013) and the development of tractographic imaging that allows indirect visualization of fiber pathways (Catani et al., 2002; Mori et al., 2002, 2005; Schmahmann and Pandya, 2007; Thiebaut de Schotten et al., 2012; Caverzasi et al., 2014). The IFOF has been thought to be specific to humans, but recent evidence indicates that it may be in fact present in the monkey brain (Sarubbo et al., 2019).

Anatomical studies suggest that the IFOF is not a monolithic white matter (WM) tract, but rather organized into distinct anatomical strata. The first modern dissection work has shown that the IFOF may be split into two layers, a superficial one and a deeper one (Martino et al., 2010). The former connects the frontal lobe to both the superior parietal lobule and the postero-superior part of the occipital lobe, whereas the latter interconnects the frontal lobe with the postero-inferior part of the occipital lobe and the postero-basal temporal areas. More recently, a study combining anatomical dissection and diffusion imaging has allowed disentangling the frontal projections of the two layers (Sarubbo et al., 2013). The superficial layer terminates in the inferior frontal gyrus, while the deep one ends in different prefrontal areas thus forming different subpathways: the anterior sublayer has cortical terminations in both the orbito-frontal cortex and the frontal pole, the middle sublayer in the lateral orbito-frontal cortex and the middle frontal gyrus, and the posterior sublayer mainly in the dorsolateral prefrontal cortex. According to another work using diffusion spectrum imaging, the connective architecture of the IFOF may be even more complex than previously thought, with possibly five layers that would be "trackable" from their prefrontal terminations (Wu et al., 2016). Other studies confirmed that the IFOF projects into many areas of the brain; among them, some were not previously identified as receiving connective inputs from the tract such as the angular gyrus or the posterior temporal cortex (Caverzasi et al., 2014; Hau et al., 2016; Wu et al., 2016). These studies also showed that the IFOF cortical terminations are highly variable across individuals, with the exception of projections targeting the inferior frontal, lateral orbito-frontal, and lateral occipital gyri (Hau et al., 2016).

This multi-layered organization agrees with the array of functions that have been assigned to the IFOF. Neuromodulation studies using direct electrostimulation mapping, the only technique allowing direct access to tract functions (Duffau, 2015), have demonstrated a role of this connection in verbal and visual semantic cognition (Duffau et al., 2005; Moritz-Gasser et al., 2013; Herbet et al., 2017a), and mentalizing (Yordanova et al., 2017), a finding that have been now replicated in lesion mapping works (Almairac et al., 2015; Mirman et al., 2015; Marino Dávolos et al., 2020). Other studies suggested a role in emotion recognition (Philippi et al., 2009; Crespi et al., 2014), spatial cognition and neglect (Urbanski et al., 2008; Herbet et al., 2017b), face recognition (Thomas et al., 2009) and orthographic processes (Vandermosten et al., 2012; Wang et al., 2020). However, neither of these studies has attempted and succeeded to relate the putative functions of the IFOF to specific sublayers.

With the purpose of investigating whether distinct right IFOF sublayers might be specifically devoted to either mentalizing or visual semantic cognition, we analyzed a unique dataset gained from direct brain stimulation mapping achieved in awake patients, combined with q-space diffusion-based fiber-track imaging. The secondary objective was to explore the existence of potential interindividual variations in the functional compartmentalization of the IFOF.

MATERIALS AND METHODS

Patients

All patients recruited in this study were consecutively operated on for a histopathologically proven supratentorial diffuse low-grade glioma at Montpellier University Hospital's Department of Neurosurgery over a period of 5 years. They were included if they met the following criteria: (i) a surgical resection performed in "awake" condition with a cortico-sub-cortical mapping by means of direct electrostimulation; (ii) a glioma close to or infiltrating at least in part the IFOF in the right hemisphere; (iii) an intraoperative mapping of mentalizing and/or visual semantic cognition (see below for a comprehensive description of the behavioral tasks); and (iv) available 3-month postoperative anatomical MRI. Patients showing a preoperative impairment of mentalizing or visual semantic cognition not allowing to objectively probe these functions during the mapping were excluded (no patients were excluded by this criterion).

A total of 189 patients with a right supratentorial low-grade diffuse glioma were initially screened. Among those, we excluded 71 patients for whom the IFOF was not stimulated during the surgical procedure because the tumors were distant from the tract and its interconnected areas. The final sample thus consisted of 111 patients (46 females and 65 males), with a mean $\pm$ SD age of 39.8 $\pm$ 10.4 years (range: 23–70 years). All patients except 18 were right-handed (5 ambidextrous and 13 left-handed).

"Awake" Surgery Procedure

All patients included in this study benefited from a "wide-awake" surgical procedure performed by the same well-experienced neurosurgeon (HD). An intraoperative multifunctional mapping was systematically achieved at both the cortical and axonal levels by means of direct electrostimulation. The general principles of such a surgical approach has been comprehensively described by our research group in another works (Duffau et al., 2005; Tate et al., 2014). Briefly, after craniotomy and dural opening under general anaesthesia, the patient was awoken and the cortical surface was exposed. Next, the tumor gross limits were identified by intraoperative ultrasound and visually indicated with sterile letter tags, placed directly on the cortex. Direct electrical stimulations were then performed using a biphasic electric current (60 Hz frequency, 1 ms pulse-width, amplitude 2–5 mA) delivered by a bipolar probe with 5 mm inter-tip space (NIMBUS Stimulator, Newmedic, France). A sensorimotor and speech mapping was first performed. A small current was initially used and incrementally increased up by step of 0.5 mA until a reliable speech arrest, or motor or sensory response

was triggered. This stimulation threshold was maintained during the remaining of the cortical and subcortical mapping. The cerebral cortex was then mapped with different behavioral tasks, including tasks tapping into aspects of mentalizing and visual semantic cognition. To both limit the spread of current through the brain tissue and preserve response specificity, the length of stimulation never exceeded 4 s. All the exposed cortical surface was mapped, and cortical areas whose stimulations induced three non-consecutive, identical perturbations was accepted as responsive for the function under scrutiny (Ojemann and Mateer, 1979); they were subsequently marked with sterile tags. Patients' functions were monitored by a senior clinical neuropsychologist, blinded to when stimulations were applied. After the completion of cortical mapping, several photographs were taken for off-line treatment of data. Then, glioma removal was started. With the progress of resection, the WM tracts were gradually accessible for stimulation. WM sites associated with recurrent functional responses were marked with sterile tags. New photographs from different angles of view were taken.

Intraoperative Behavioral Paradigms

The behavioral paradigm to assess mentalizing "on-line" has been previously described in another study (Herbet et al., 2015) and is schematically illustrated in **Figure 1A**. It is an adapted version of the well-used "Read the Mind in the Eyes" task (hereafter, RME), initially developed by Baron-Cohen et al. (2001) to gauge social intelligence in autistic patients. In the standard version of the task, the participant is asked to choose among four complex mental states the one that best matches with what the person seen on a photograph is feeling or thinking. Only the eye region of the face is shown. This version, composed of 36 items, was systematically achieved the day before surgery. Due to the inherent complexity of the RME task, only two mental states were used during the intraoperative mapping in order to decrease the number of false positive manifestations and thus the number of required stimulations. For the same reason, only succeeded items during the preoperative assessment were included in the intraoperative protocol.

To assess visual semantic cognition, the Pyramids and Palm Trees test (hereafter, PPTT) was used (Howard et al., 1992). This force-choice task, in which the participant is required to form a semantic association, comprises 52 black and white items in its standard version. For each target item, two further pictures are proposed. The patient is asked to select the one that best matches with the target picture according to the most straightforward semantic link. As for the RME task, the PPTT was achieved the day before surgery, and impaired patients were dismissed from the mapping. Items associated with incorrect responses were excluded from the intraoperative materials. The intraoperative protocol is described in **Figure 1B**.

To demonstrate specificity, and depending on which networks were damaged by the tumor, anatomical sites associated with mentalizing and/or visual semantic impairments were also stimulated while the patients were performing other behavior tasks. This included a naming task (Duffau et al., 2005), a line bisection task (Herbet et al., 2017b), a motor task (Rech et al., 2019), and a passive somatosensory task (Tate et al., 2014). In this study, only semantic and mentalizing sites are reported.

It is worth mentioning that, on the total of patients included (n = 111), 104 (93.7%) patients were intraoperatively assessed for visual semantic cognition, 90 (81.1%) for mentalizing and 83 (74.8%) for both functions.

Imaging Acquisition and Spatial Normalization

Structural MRI datasets were collected 3 months after surgery on either a 1.5T (Avanto, Siemens Medical Systems, Erlangen, Germany) or a 3T MR imaging scanner (Skyra, Siemens Medical Systems, Erlangen, Germany), as part of the routine management protocol. For the purpose of the current work, standard 3D gadolinium-enhanced axial T1-weighted images were used. The 1.5T/3T MRI parameters were as follows: repetition time 1,880/1,700 ms; echo time 3.4/2.5 ms; inversion time 1,100/922 ms; field of view 256 × 256/250 × 250 mm; flip angle 15/9°; voxel size 1 × 1 × 1 mm^3 and; 176 axial slices.

All individual MRI datasets were registered to the Montreal Neurological Institute (MNI) 152 template with an isotropic resolution of 1-mm. This work was achieved using SPM12 software[1] implemented in MATLAB environment (Matrix Laboratory, MathWorks, Inc.—R2018a), with standard parameters. At this stage, all MRIs were visually inspected to ensure sufficient quality. All registrations were satisfactory.

Distribution of Stimulation-Related Anatomical Sites

The coordinates of each anatomical site was manually plotted onto the patients' respective normalized MRI. They were established by using a combination of intraoperative photos taken from different points of view (allowing to precisely identify the location of functional sites indicated by sterile numbered tags), written surgical reports, cortical (e.g., gyri, sulci and vessels) and subcortical (e.g., edges of the resection cavity) landmarks identifiable on both the normalized MRI and the intraoperative photos. This method has been successfully applied in recent studies (e.g., Sarubbo et al., 2020). The accuracy of coordinate positioning was systematically checked by the senior author. When a disagreement occurred, the location of problematic sites was remapped in a consensual manner. The MNI coordinates (x, y, z) were recorded in separate databases as a function of the behavior tasks (i.e., PPTT or RME or both) and the stimulation location (i.e., cortical vs. subcortical). Then, for each stimulation site, a spherical volume of interest (VOI) was generated using the MarsBaR toolbox[2] with a radius of 2.5 mm corresponding to the spatial resolution of the bipolar stimulator.

To demonstrate reliability in the way stimulation sites were positioned, we asked an independent operator with certified expertise in neurosurgery and neuroanatomy, and fully blind to both the general purpose and the results of the study, to position again 40 subcortical sites randomly selected among the

[1] http://www.fil.ion.ucl.ac.uk/spm/

[2] http://marsbar.sourceforge.net

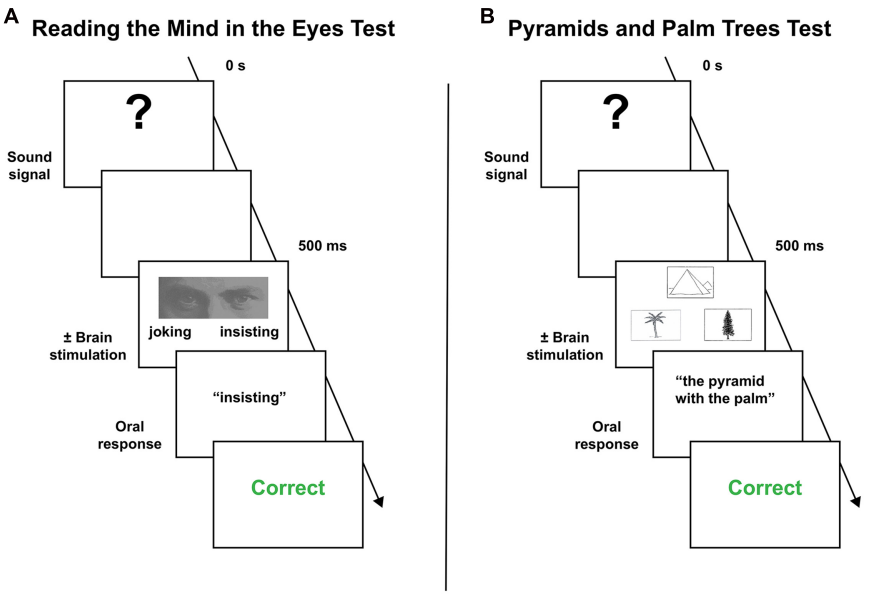

FIGURE 1 | Behavior paradigms employed during the intraoperative mapping. **(A)** Mentalizing task. **(B)** Visual semantic cognition task (see the main text to a complete description of the behavioral procedure).

105 subcortical sites already positioned by the first operator (i.e., subcortical sites either associated with mentalizing or visual semantic cognition during electrostimulation). To obtain a quantitative index of inter-operator reliability, three parametric correlations were performed, one for each axis. We further statistically compared the coordinates between both operators. We also calculated both the mean and the standard deviation of the absolute difference in site estimates (one for each axis) in order to provide a measure of error (see Herbet et al., 2019 for a comparable method).

Clustering Analysis of Subcortical Data

In view of the apparent topological heterogeneity between the distribution of the mentalizing and the semantic subcortical sites, at least in the WM deep in the prefrontal and the posterior parietal cortices (see below), a clustering analysis was conducted with each stimulation dataset. As a first step, we used the Duda-Hart procedure (Duda and Hart, 1973) to decide whether the data should be split into two or more clusters. Then, when the null hypothesis of homogeneity was rejected at $p < 0.05$, we performed a formal clustering analysis with the *k*-means algorithm, by varying *k* from 2 to 10 with 100 iterations. Clusters were formed by observations that maximize between-cluster distances using a squared Euclidean distance-based measure. The optimal number of clusters was estimated with a leave-one-out cross-validation procedure. To assess the statistical differences between the clusters in each stimulation dataset, an ANOVA was performed for each coordinate. The analyses were mainly achieved with SPSS[3] and the "Flexible Procedures for Clustering" (FPC) package (Hennig, 2020) implemented in *R* environment[4].

Disconnection Analysis: A Population-Based Approach With the HCP-1021 Diffusion Data

Our aim here was to dissociate the WM fiber connections specific either to mentalizing or visual semantic cognition. As a first step, a population-based template was constructed based on the diffusion data of 1,021 participants from the Human Connectome Project (2017 Q4, 1,200-subject release). A multishell diffusion scheme was used; the *b*-values were 1,000, 2,000, and 3,000 s/mm^2. The number of diffusion-sampling directions was 90 for each *b*-value. The in-plane resolution, as well as the slice thickness, was 1.25 mm. The diffusion data were reconstructed in the MNI space using *q*-space diffeomorphic reconstruction (Yeh and Tseng, 2011) to obtain the spin distribution function (Yeh et al., 2010). A diffusion sampling length ratio of 2.5 was used, and the output resolution was 2 mm. The restricted diffusion was quantified using restricted diffusion imaging (Yeh et al., 2017). The analysis was conducted using DSI Studio[5].

Each 5-mm (in diameter) subcortical spherical VOI was used as seeds for fiber tracking allowing us to generate a map of the fiber connections passing through or originating from this VOI. The same tracking parameters were maintained across all tractographies performed; this included a tracking threshold automatically determined using the Otsu's method, an angular threshold of 55°, a step size of 1 mm, a minimal and maximal length of 10 and 300 mm, respectively. To estimate

[3]https://www.ibm.com

[4]https://R-project.org/

[5]http://dsi-studio.labsolver.org

fiber direction, the standard trilinear interpolation method was selected. Streamlines were tracked using the Euler Algorithm.

Once all tractographies were performed, they were transformed into binarized maps. These maps were overlaid according to the associated impairment (i.e., mentalizing *or* visual semantic cognition) using MRIcron software. Then MRIcron's subtraction plot function was employed to identify the WM voxels the most frequently and specifically "disconnected" during mentalizing vs. semantic electrostimulation, and *vice versa*.

Standard Protocol Approvals, Registrations and Patient Consents

Data were acquired as part of the current clinical practice and were retrospectively studied. Patients consented to the extraction of data from their medical records. We conducted this study in compliance with the ethical standards of our institution for a retrospective study.

RESULTS

Patients' Clinical Characteristics and Tumor Topography

A total of 111 patients (46 females) presenting with a right supratentorial diffuse low-grade glioma fulfilled all inclusion criteria and thus constituted the final sample. An overview of the patients' sociodemographic and clinical data is provided in **Table 1**. Consistent with the preferential distribution of low-grade glioma (Herbet et al., 2016), the most common location was in the frontal and the insular cortex. The mean pre-operative tumor volume was 51.0 ± 41.7 cm^3.

TABLE 1 | Main characteristics of the study sample.

Parameters	*n*	%
Clinical characteristics at diagnosis		
Sex		
Female	46	41.4
Male	65	58.6
Age, years (mean, SD) 39.8 ± 10.4		
≤40	64	57.7
>40	47	42.3
Handedness		
Right-handed	93	83.8
Left-handed	13	11.7
Ambidextrous	5	4.5
Presenting symptom		
Incidental	29	26.1
Epileptic seizure	80	72.1
Neurological focal deficit	2	1.8
Imaging characteristics at diagnosis		
Topography of tumor		
Frontal	45	40.6
Fronto-temporo-insular	25	22.5
Temporal	12	10.8
Parietal	7	6.3
Fronto-insular	6	5.4
Temporo-insular	4	3.6
Temporo-occipital	3	2.7
Insular	3	2.7
Fronto-cingular	3	2.7
Fronto-temporo-parieto-insular	2	1.8
Fronto-parieto-insular	1	0.9
Tumor volume, cm^3 (mean, SD) 51.0 ± 41.7		
<50	67	60.4
≥50	44	39.6
Treatment-related characteristics		
Extent of resection, percent (mean, SD) 92.8 ± 8.8		
<90%	29	26.1
≥90%	82	73.9

Inter-Operator Reliability in Site Estimates

The results from correlation analyses performed between the MNI coordinates of each operator indicated $r_{40} = 0.93$, $r_{40} = 0.99$ and $r_{40} = 0.97$ for, respectively, the *x*-, *y*-, and *z*-axis. No significant difference was found in estimates between both operators for the *x*- ($t_{39} = 0.14$, $p = 0.89$), *y*- ($t_{39} = 1.57$, $p = 0.12$) and *z*-axis ($t_{39} = 0.90$, $p = 0.37$). The mean ± SD of the absolute difference between both operators was 0.08 mm ± 3.36 for the *x*-axis, 1.27 mm ± 5.12 for the *y*-axis, and 0.87 mm ± 6.1 for the *z*-axis. These analyses clearly indicate that the positioning work was reliable and accurate.

Topological Organization of Cortical Sites

In total, 101 cortical sites were identified across patients; among these, 57 were specifically associated with mentalizing (**Figure 2**, orange circles), 41 with visual semantic cognition (**Figure 2**, blue circles) and 3 with both functions (called "aspecific sites") (**Figure 2**, red circles). Mentalizing sites were distributed in IFG (pars opercularis, $n = 24$; pars triangularis, $n = 10$; pars orbitalis, $n = 1$), in dlPFC ($n = 20$) and in the superior temporal gyrus (STG, $n = 2$). Semantic sites were mainly located in dlPFC ($n = 30$), and to a lesser extent in the mid-to-posterior STG ($n = 7$) and in IFG (pars opercularis, $n = 1$; pars triangularis, $n = 3$). Among the three "aspecific" sites, two were located in STG and one in dlPFC. To summarize, the spatial distribution of mentalizing and semantic sites were relatively similar across patients, except for IFG that was clearly under-represented for visual semantic cognition.

Topological Organization of Subcortical Sites

Overall, 105 sites were detected during subcortical stimulation: 46 were specific to mentalizing, 49 to semantic cognition, and 10 were associated with both functions. The distribution of these anatomical sites is provided in **Figure 3A**, the vast majority of which were located along the topological positioning of the IFOF according to the most recent anatomical studies using either DTI (**Figure 3B**) or post-mortem dissection (**Figure 3C**). Visually, although the two distributions were quite similar, though, two differences were noticeable: indeed, mentalizing sites

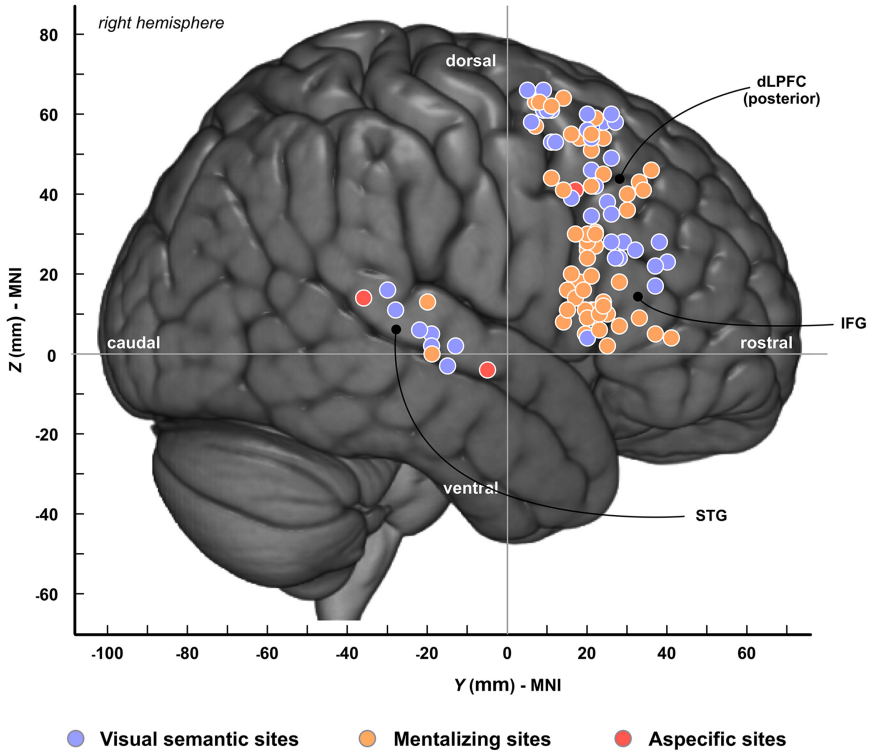

FIGURE 2 | Spatial topography of cortical sites. Cortical sites are plotted onto the MNI-152 template. Colors refer to the type of neuropsychological impairments induced by electrostimulation. Blue, visual semantic cognition; Orange, mentalizing; Red, sites associated with both visual semantic cognition and mentalizing. dlPFC, dorsolateral prefrontal cortex; IFG, inferior frontal gyrus; STG, superior temporal gyrus.

were over-represented in the WM fibers underlying the anterior part of both dlPFC and pars triangularis whereas visual semantic cognition were rather over-represented in the WM fibers of the posterior parietal cortex (**Figure 3A**).

Relationships Between Cortical and Subcortical Sites, and Between Functions

In total, 83 patients benefited from a mapping concerning both mentalizing and visual semantic cognition. At the cortical level, at least one anatomical site for each function was identified in 16 patients (19.3%). Conversely, 14 (16.9%) patients uniquely showed one (or more) site(s) for visual semantic cognition, and 35 (42.2%) for mentalizing. Note that no cortical responses were found in 18 patients (21.6%) for these functions.

As regards with subcortical mapping, 16 patients (19.3%) showed at least one anatomical site for each function. 16 (19.3%) patients uniquely showed one (or more) site(s) for visual semantic cognition, and 33 (39.8%) for mentalizing. No subcortical responses were found in 18 patients (21.6%).

Collectively, these results show a high inter-individual variability in the functional involvement of the IFOF with, nevertheless, a more frequent implication for mentalizing vs. visual semantics (2-tailed t-test for proportion comparison, $p = 0.004$). Interestingly, this variability echoed those identified at the cortical level with, again, an over-involvement of mentalizing vs. visual semantic cognition ($p = 0.002$).

As a significant proportion of patients was left-handed, we checked whether the distribution of functional sites could be considered as equivalent between left-handed and right-handed patients. The proportion of unmasked cortical sites were not different for mentalizing ($p = 0.46$) and visual semantic cognition ($p = 0.78$). However, although no difference was revealed for semantic cognition at the subcortical level ($p = 0.21$), this was not the case for mentalizing ($p = 0.017$) (left-handed patients showed a lower rate of subcortical sites). This suggests that the right white matter network is less engaged in left-handed patients for mentalizing.

Clustering Analysis Results

Both mentalizing and non-verbal semantic cognition stimulation datasets were allowed to be clustered according the Duda-Hart statistics ($p < 0.05$). For mentalizing, a 5-cluster solution model was found to best fit the data (training error = 0.037). The MNI coordinates between the five clusters were significantly different (x: $F = 559.01$, $p < 0.001$; y: $F = 77.48$, $p < 0.001$; z: $F = 104.16$, $p < 0.001$). For visual semantic cognition, a 6-cluster solution model was estimated as the most appropriate for the data (training error = 0.033) and, again, the between-coordinates differences were significant (x: $F = 326.28$, $p < 0.001$; y: $F = 47.18$, $p < 0.001$; z: $F = 99.68$, $p < 0.001$). The

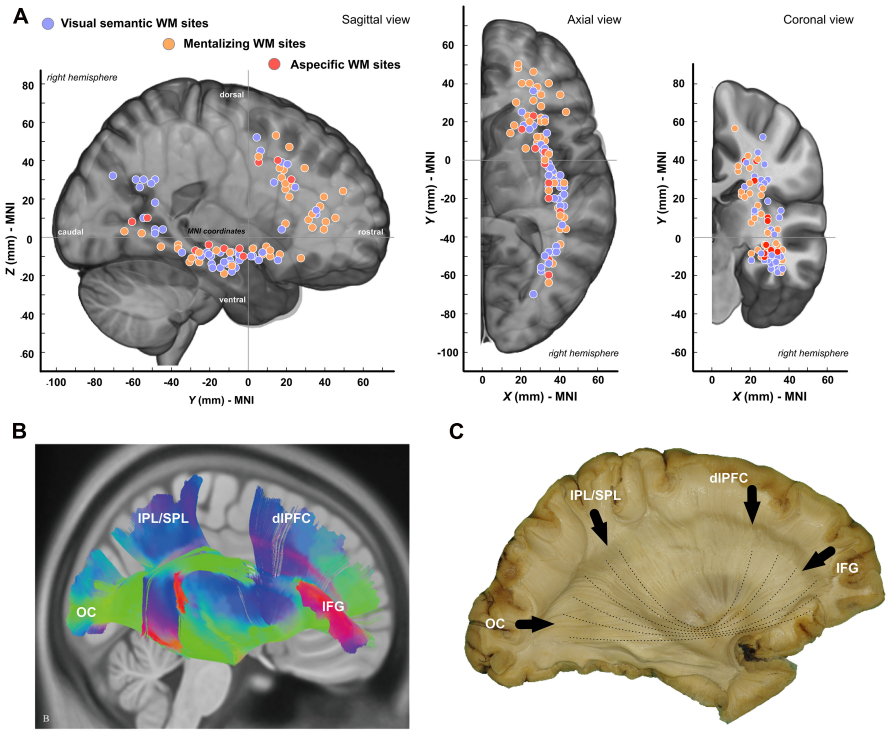

FIGURE 3 | Spatial distribution of white matter sites. **(A)** Tridimensional distribution of WM sites. **(B)** Template-based fiber tracking of the right IFOF with q-diffusion imaging (from Wu et al., 2016). **(C)** Anatomical dissection of the right IFOF (personal materials). OC, occipital pole; IPL, inferior parietal lobule; SPL, superior parietal lobule; dlPFC, dorsolateral prefrontal Cortex; IFG, inferior frontal gyrus.

centroids ± SD of the clusters are reported in **Table 2** and plotted in **Figure 4**. To summarize, a high topological similarity was found for both functions in the prefrontal dorsolateral, subinsular/anterior extreme capsule and temporal WM. Dissimilarities were, however, observed in the WM of the antero-dorsal pars triangularis (cluster specific to mentalizing) and in WM of the angular gyrus (cluster specific to visual semantic cognition).

Disconnection Analysis

The disconnection analysis, summarized in **Figure 5**, first confirmed that the most "disconnected" voxels during stimulations associated with either mentalizing or visual semantic cognition mainly belonged to the right IFOF. However, the subtraction between mentalizing and visual semantic cognition binarized streamline tractograms (and vice versa) revealed some noticeable differences: WM semantic sites were more frequently crossed by orbitofrontal and mid-to-post temporal IFOF streamlines whereas WM mentalizing sites were more frequently crossed by fronto-parietal and dorsal temporal stem/extreme/external capsule streamlines. These differences were moderate because not exceeding 25%.

DISCUSSION

By virtue of their brain-wide cortical projections, association fiber pathways are vital building blocks in integrating information within and across neurocognitive networks (Herbet and Duffau, 2020). Until recently, association tracts were frequently viewed as monolithic structures, the primary consequence of which was a tendency to conceptualize them as monofunctional pieces. However, recent works using tractography imaging or anatomical dissection has provided evidence that association tracts are in fact formed by multiple anatomical layers and thus are possibly involved in different functions (Martino et al., 2010; Wu et al., 2016; Latini et al., 2017; Herbet et al., 2018). The IFOF is no exception to the rule, as its connective architecture is complex. This tract may indeed be segregated into two (Martino et al., 2010; Sarubbo et al., 2013) or more (Wu et al., 2016) sublayers with distinct frontal or posterior terminations. In this context, the present study was an attempt to dissociate two functional pathways into the right IFOF with the major advantage of using stimulation mapping—the sole available method allowing direct functional interrogation of WM tracts (Duffau, 2015).

First of all, the results confirmed that the right IFOF is a critical WM connection in the networks supporting, respectively, visual semantic cognition and mentalizing, as suggested in other neuromodulation (Moritz-Gasser et al., 2013; Herbet et al., 2017a; Yordanova et al., 2017) or neuroimaging studies (Mirman et al., 2015; Grosse Wiesmann et al., 2017). Cortical sites were indeed observed in structures known to receive connective inputs from the IFOF, including posterior dlPFC, IFG and STG (Sarubbo et al., 2013; Caverzasi et al., 2014; Hau et al., 2016; Wu et al., 2016). Most importantly, the subcortical sites were mainly situated

TABLE 2 | Cluster coordinates.

Parameters	Clusters	Clusters location	Number of cases for clustering	MNI coordinates ± SD		
				X	*Y*	*Z*
Mentalizing	Cluster 1	Temporal	8	35 ± 3	−9 ± 7	−11 ± 4
	Cluster 2	Antero-dorsal pars triangularis	9	24 ± 5	37 ± 11	16 ± 6
	Cluster 3	Posterior dlPFC	11	23 ± 6	18 ± 7	36 ± 9
	Cluster 4	Subinsular/anterior extreme capsule	8	31 ± 5	20 ± 12	−5 ± 6
	Cluster 5	Sagittal stratum	10	40 ± 3	−37 ± 13	−6 ± 5
Visual semantic cognition	Cluster 1	Posterior dlPFC	6	28 ± 6	15 ± 8	38 ± 10
	Cluster 2	Subinsular/anterior extreme capsule	4	26 ± 1	27 ± 11	5 ± 12
	Cluster 3	Temporal	13	41 ± 2	−19 ± 7	−12 ± 4
	Cluster 4	Sagittal stratum	5	36 ± 2	−49 ± 4	8 ± 7
	Cluster 5	Temporal	15	34 ± 2	−3 ± 6	−11 ± 2
	Cluster 6	Angular gyrus	6	31 ± 3	−56 ± 8	29 ± 2

SD, standard deviation; dlPFC, Dorsolateral Prefrontal Cortex; MNI, Montréal Neurological Institute.

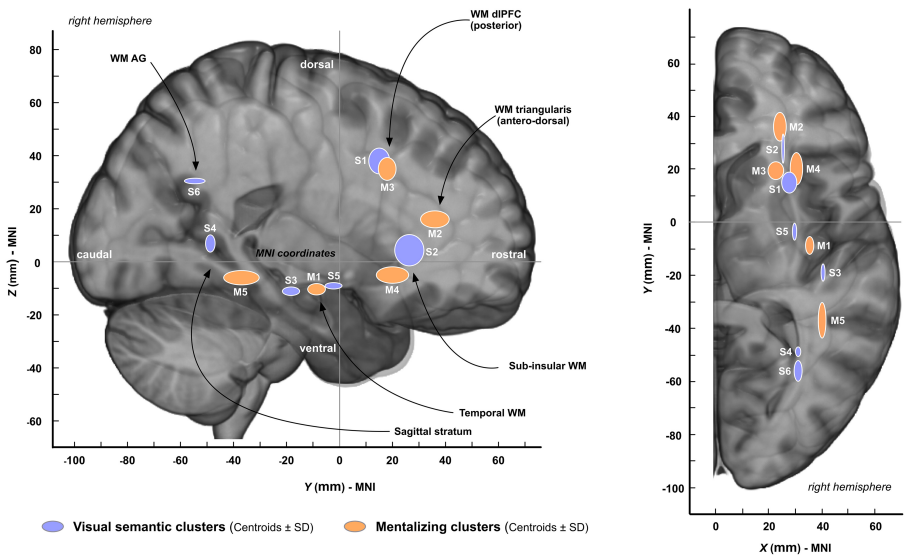

FIGURE 4 | Results from the clustering analysis. The coordinates of each cluster are represented by centroids ± SD (see **Table 2** for the precise MNI coordinates). "S" means "semantic cluster" and "M" means "mentalizing cluster." AG, angular gyrus; dlPFC, dorsolateral prefrontal cortex.

along the typical course of the IFOF (**Figure 3**). Furthermore, the overlap maps of individual tractograms showed that streamlines generated from subcortical sites belonged in average to the right IFOF, again, for both functions. As matter of fact, the maximum overlaps occurred at the level of the temporal stem, a classical anatomical reference not only to identify the tract during neurosurgery (Duffau et al., 2005) but also to track it with diffusion imaging (steam-based approach)—as the entire range of IFOF fibers pass through this region (Hau et al., 2016; Wu et al., 2016).

The main goal of this study was to determine whether the IFOF might be dissociated into (at least) two anatomical strata, each of them specifically devoted either to semantic cognition or to mentalizing. The results obtained support at least partially this hypothesis. First, consistent with the general distribution of subcortical sites (**Figure 3**), subcortical clustering analyses revealed that mentalizing sites were over-represented deep in the white matter underlying pars triangularis whereas semantic sites were rather over-represented in the depth of the angular gyrus, suggesting that the IFOF fibers involved in each function are dissociable, but only at the level of the terminal parts of the tract (**Figure 4**). Second, the subtraction analyses indicated (i) that semantic sites were more frequently crossed by ventral streamlines compared to mentalizing sites, including IFOF orbito-frontal and mid-to-posterior temporal fibers; (ii) conversely that mentalizing sites were more frequently crossed by more dorsal streamlines compared to semantic sites, including fibers passing through the dorsal part of the temporal stem, fibers in the depth of pars triangularis, and fibers belonging to the superior longitudinal fasciculus (SLF) (**Figure 5**). This pattern of result suggests a functional compartmentalization of the IFOF, with distinct sublayers at the subcortical level (stem

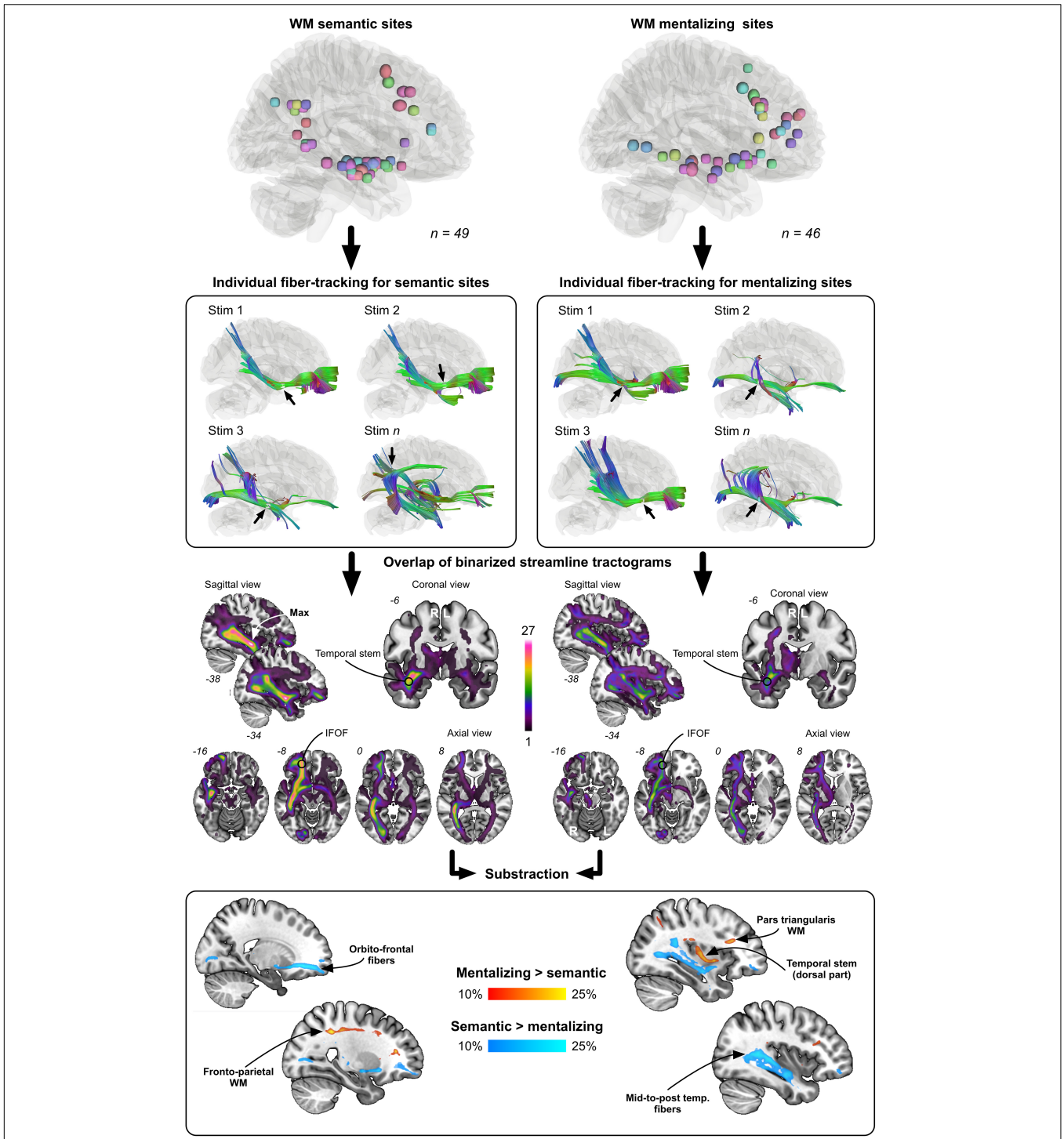

FIGURE 5 | Results from the disconnection analysis. Each WM site was used to generate individual streamline tractograms. These tractograms were next binarized and overlapped according to each function (semantics vs. mentalizing). Last, the overlap maps were contrasted to visualize the fiber pathways the most frequently and specifically tracked from mentalizing sites (red to yellow color) and semantic sites (dark blue to light blue color).

of the bundle) as well as regarding their terminal parts. More specifically, a "ventral" IFOF sublayer may be implicated in visual semantic processing whereas a "dorsal" IFOF layer may be rather implicated in mentalizing with an additional contribution of the SLF, as previously suggested in lesion mapping studies (Herbet et al., 2014; Grosse Wiesmann et al., 2017).

This interpretation may be criticized on the ground that the subtraction analyses revealed only low to moderate differences

between streamline distributions associated with semantic cognition vs. mentalizing and vice versa (max 25%). This was, however, expected for anatomical reasons. Indeed, a large proportion of stimulation sites was unmasked within the temporal stem. Given the width of this bottleneck structure [around 11 mm at the level of the limen insulae (Martino et al., 2010)] and the spatial resolution of the bipolar stimulator (5 mm), dissociating IFOF WM subpathways in this area is actually challenging. Besides, as reported by Wu et al. (2016), the fibers forming the different IFOF layers are relatively intermingled in the temporal stem, not organized into well-structured bundles. Consequently, the difference we found in the subtraction analyses were not so large because related to subcortical sites (and their associated streamlines) located outside the temporal stem, which were clearly less numerous. Note that in a recent study aimed at disentangling the motor-speech from the lexical semantic fiber pathways, comparable differences in streamline distribution was observed (a quite similar approach was used) (Corrivetti et al., 2019).

Remarkably, a high degree of anatomo-functional variations was identified across patients at both the cortical and subcortical level. More specifically, four patterns were observed: (i) a contribution to both categories of functions; (ii) a unique contribution to semantic cognition; (iii) a unique contribution to mentalizing; (iv) no contribution at all—knowing that mentalizing was over-represented compared with visual semantic cognition. Before elaborating further on this finding, two notes of caution are necessary. First, the fact that no response was identified for either mentalizing or semantics (or both), and most notably at the subcortical level, does not necessary mean that the IFOF was not implicated. Indeed, as patients were operated on according to the individual functional margins (i.e., the surgery procedure stopped when a functional response was repeatedly evoked during stimulation), some IFOF fibers were not stimulated, typically those running in the deeper component of the tract. Second, the pattern "no contribution at all" is quite artificial because uniquely appropriate when considering the cortical and subcortical levels, independently. Indeed, according to the inclusion criteria, patients took place in this study if at least one positive response was observed during the mapping. In other words, a few patients could show a functional response at the cortical level but not at the subcortical level and *vice versa*; this is not surprising because again all IFOF fibers were not stimulated and only the exposed cortical surface during surgery was stimulated. This implies, in the latter case, that some important cortical sites could have been missed because not accessible to the surgery procedure. With these limits in mind, our results nevertheless suggest an across-subject anatomo-functional variation that may be related to hemispheric dominance. This is especially reminiscent of a study by Catani et al. (2007) in which interhemispheric differences were found in the WM connections of the language network, from strongly left lateralized to bilateral symmetrical distribution. Consequently, a valuable extension of our study would be to assess to what extent semantic and mentalizing performances are related to left-right differences in network topology by combining fMRI and diffusion imaging in healthy participants. Besides, it is worth recalling that handedness may influence the interindividual variations we discussed above, as subcortical sites for mentalizing were less frequent in left-handed vs. right-handed patients.

Last, a few cortical and subcortical sites were associated with both types of functional responses. This result can be interpreted in two ways: either both functional networks were impaired by stimulation, meaning that the spatial resolution of stimulation was not enough to mark topological differences, or a more domain-general control or attention network was temporary disrupted. The latter explanation has to be prioritized, as the aspecific sites were observed uniquely at the cortical level in dlPFC, a region which is known to be involved in such networks (Chein and Schneider, 2005; Duncan, 2010). Besides, at the subcortical level where amodal sites were also observed, the IFOF is believed to support some kinds of amodal processing, especially in the context of semantic cognition (Moritz-Gasser et al., 2013).

The current study had some limitations. First, the positioning of anatomical sites relied on the use of anatomical landmarks identifiable on structural MRI and intraoperative photos. This procedure could lead to potential inaccuracies, but we showed an excellent inter-rater reliability in this mapping work – as in another recent work (Herbet et al., 2019). Second, a template-based approach was adopted to generate streamline tractograms from stimulation sites. Admittedly, the use of patient diffusion data would have been better. However, there are important difficulties to perform streamline tractography in subcortical structures impaired by lesional infiltrations. Third, low-grade gliomas are disproportionally located in paralimbic areas, implying that posterior structures were less stimulated. A larger set of posterior sites would have certainly help better dissociating the IFOF sublayers. Last, even if the IFOF is considered as a poorly compensable tract (Herbet et al., 2016), we cannot rule out that the possibility that neuroplastic compensations occurred.

In brief, the current study not only confirms that the network mediated by the IFOF is implied in both visual semantic cognition and mentalizing, but also suggests that the tract is dissociable into two functional strata according to a ventral (semantic) and dorsal (mentalizing) compartmentalization. Although this general finding needs to be replicated in healthy participants with other imaging modalities (e.g., coupling navigated transcranial magnetic stimulation with diffusion MRI to track white matter pathways from cortical sites), from a clinical standpoint, they are of central interest for the surgical planning of patients presenting with a tumor in the vicinity of this anatomical connectivity.

DATA AVAILABILITY STATEMENT

The original contributions presented in the study are included in the article/supplementary material, further inquiries can be directed to the corresponding author/s.

ETHICS STATEMENT

Ethical review and approval was not required for the study on human participants in accordance with the local legislation and

institutional requirements. The patients/participants provided their written informed consent to participate in this study.

AUTHOR CONTRIBUTIONS

AR, HD, and GH: conception and design of the study. AR, A-LL, HD, and GH: acquisition and analysis of data and drafting a significant portion of the manuscript and figures. JD and SN: analysis of data. SN, HD, and GH: critical review of the manuscript. All authors contributed to the article and approved the submitted version.

ACKNOWLEDGMENTS

AR would like to thank Johan Pallud for his valuable advice and the *Nuovo-Soldati Foundation* for Cancer Research for their support.

REFERENCES

Almairac, F., Herbet, G., Moritz-Gasser, S., de Champfleur, N. M., and Duffau, H. (2015). The left inferior fronto-occipital fasciculus subserves language semantics: a multilevel lesion study. *Brain Struct. Funct.* 220, 1983–1995. doi: 10.1007/s00429-014-0773-1

Baron-Cohen, S., Wheelwright, S., Hill, J., Raste, Y., and Plumb, I. (2001). The "Reading the Mind in the Eyes" test revised version: a study with normal adults, and adults with Asperger syndrome or high-functioning autism. *J. Child Psychol. Psychiatry* 42, 241–251. doi: 10.1111/1469-7610.00715

Burdach, K. F. (1822). *Vom Baue Und Leben Des Gehirns,* Dyk. 2.

Catani, M., Allin, M. P. G., Husain, M., Pugliese, L., Mesulam, M. M., Murray, R. M., et al. (2007). Symmetries in human brain language pathways correlate with verbal recall. *Proc. Natl. Acad. Sci. U.S.A.* 104, 17163–17168. doi: 10.1073/pnas.0702116104

Catani, M., Howard, R. J., Pajevic, S., and Jones, D. K. (2002). Virtual in vivo interactive dissection of white matter fasciculi in the human brain. *NeuroImage* 17, 77–94. doi: 10.1006/nimg.2002.1136

Caverzasi, E., Papinutto, N., Amirbekian, B., Berger, M. S., and Henry, R. G. (2014). Q-ball of inferior fronto-occipital fasciculus and beyond. *PloS One* 9:e100274. doi: 10.1371/journal.pone.0100274

Chein, J. M., and Schneider, W. (2005). Neuroimaging studies of practice-related change: fMRI and meta-analytic evidence of a domain-general control network for learning. *Brain Res. Cogn. Brain Res.* 25, 607–623. doi: 10.1016/j.cogbrainres.2005.08.013

Corrivetti, F., Thiebaut de Schotten, M., Poisson, I., Froelich, S., Descoteaux, M., Rheault, F., et al. (2019). Dissociating motor-speech from lexico-semantic systems in the left frontal lobe: insights from a series of 17 awake intraoperative mappings in glioma patients. *Brain Stuct. Funct.* 224, 1151–1165. doi: 10.1007/s00429-019-01827-7

Crespi, C., Cerami, C., Dodich, A., Canessa, N., Arpone, M., Iannaccone, S., et al. (2014). Microstructural white matter correlates of emotion recognition impairment in Amyotrophic Lateral Sclerosis. *Cortex J. Devoted Study Nerv. Syst. Behav.* 53, 1–8. doi: 10.1016/j.cortex.2014.01.002

Curran, E. J. (1909). A new association fiber tract in the cerebrum with remarks on the fiber tract dissection method of studying the brain. *J. Comp. Neurol. Psychol.* 19, 645–656. doi: 10.1002/cne.920190603

Dejerine, J., and Dejerine-Klumpke, A. (1895). *Anatomie des Centres Nerveux*. Paris: Rueff.

Duda, R. O., and Hart, P. E. (1973). *Pattern Classification and Scene Analysis*. New York, NY: John Wiley & Sons Inc.

Duffau, H. (2015). Stimulation mapping of white matter tracts to study brain functional connectivity. *Nat. Rev. Neurol.* 11, 255–265. doi: 10.1038/nrneurol.2015.51

Duffau, H., Gatignol, P., Mandonnet, E., Peruzzi, P., Tzourio-Mazoyer, N., and Capelle, L. (2005). New insights into the anatomo-functional connectivity of the semantic system: a study using cortico-subcortical electrostimulations. *Brain J. Neurol.* 128, 797–810. doi: 10.1093/brain/awh423

Duncan, J. (2010). The multiple-demand (MD) system of the primate brain: mental programs for intelligent behaviour. *Trends Cogn. Sci.* 14, 172–179. doi: 10.1016/j.tics.2010.01.004

Grosse Wiesmann, C., Schreiber, J., Singer, T., Steinbeis, N., and Friederici, A. D. (2017). White matter maturation is associated with the emergence of Theory of Mind in early childhood. *Nat. Commun.* 8:14692. doi: 10.1038/ncomms14692

Hau, J., Sarubbo, S., Perchey, G., Crivello, F., Zago, L., Mellet, E., et al. (2016). Cortical terminations of the inferior Fronto-Occipital and uncinate fasciculi: anatomical stem-based virtual dissection. *Front. Neuroanat.* 10:58. doi: 10.3389/fnana.2016.00058

Hennig, C. (2020). *fpc: Flexible Procedures for Clustering*. Available online at: https://CRAN.R-project.org/package=fpc (accessed December 6, 2020).

Herbet, G., and Duffau, H. (2020). Revisiting the functional anatomy of the human brain: toward a meta-networking theory of cerebral functions. *Physiol. Rev.* 100, 1181–1228. doi: 10.1152/physrev.00033.2019

Herbet, G., Lafargue, G., Bonnetblanc, F., Moritz-Gasser, S., Menjot de Champfleur, N., and Duffau, H. (2014). Inferring a dual-stream model of mentalizing from associative white matter fibres disconnection. *Brain J. Neurol.* 137, 944–959. doi: 10.1093/brain/awt370

Herbet, G., Lafargue, G., Moritz-Gasser, S., Bonnetblanc, F., and Duffau, H. (2015). Interfering with the neural activity of mirror-related frontal areas impairs mentalistic inferences. *Brain Struct. Funct.* 220, 2159–2169. doi: 10.1007/s00429-014-0777-x

Herbet, G., Maheu, M., Costi, E., Lafargue, G., and Duffau, H. (2016). Mapping neuroplastic potential in brain-damaged patients. *Brain J. Neurol.* 139, 829–844. doi: 10.1093/brain/awv394

Herbet, G., Moritz-Gasser, S., and Duffau, H. (2017a). Direct evidence for the contributive role of the right inferior fronto-occipital fasciculus in non-verbal semantic cognition. *Brain Struct. Funct.* 222, 1597–1610. doi: 10.1007/s00429-016-1294-x

Herbet, G., Moritz-Gasser, S., Lemaitre, A.-L., Almairac, F., and Duffau, H. (2019). Functional compensation of the left inferior longitudinal fasciculus for picture naming. *Cogn. Neuropsychol.* 36, 140–157. doi: 10.1080/02643294.2018.1477749

Herbet, G., Yordanova, Y. N., and Duffau, H. (2017b). Left spatial neglect evoked by electrostimulation of the right inferior fronto-occipital fasciculus. *Brain Topogr.* 30, 747–756. doi: 10.1007/s10548-017-0574-y

Herbet, G., Zemmoura, I., and Duffau, H. (2018). Functional anatomy of the inferior longitudinal fasciculus: from historical reports to current hypotheses. *Front. Neuroanat.* 12:77. doi: 10.3389/fnana.2018.00077

Howard, D., Patterson, K. E., and Company, T. V. T. (1992). *The Pyramids and Palm Trees Test: a Test of Semantic Access From Words and Pictures*. Bury St Edmunds: Thames Valley Test Company.

Latini, F., Mårtensson, J., Larsson, E.-M., Fredrikson, M., Åhs, F., Hjortberg, M., et al. (2017). Segmentation of the inferior longitudinal fasciculus in the human brain: a white matter dissection and diffusion tensor tractography study. *Brain Res.* 1675, 102–115. doi: 10.1016/j.brainres.2017.09.005

Marino Dávolos, J., Arias, J. C., and Jefferies, E. (2020). Linking individual differences in semantic cognition to white matter microstructure. *Neuropsychologia* 141:107438. doi: 10.1016/j.neuropsychologia.2020.107438

Martino, J., Brogna, C., Robles, S. G., Vergani, F., and Duffau, H. (2010). Anatomic dissection of the inferior fronto-occipital fasciculus revisited in the lights of brain stimulation data. *Cortex J. Devoted Study Nerv. Syst. Behav.* 46, 691–699. doi: 10.1016/j.cortex.2009.07.015

Mirman, D., Chen, Q., Zhang, Y., Wang, Z., Faseyitan, O. K., Coslett, H. B., et al. (2015). Neural organization of spoken language revealed by lesion–symptom mapping. *Nat. Commun.* 6:6762. doi: 10.1038/ncomms7762

Mori, S., Frederiksen, K., van Zijl, P. C. M., Stieltjes, B., Kraut, M. A., Solaiyappan, M., et al. (2002). Brain white matter anatomy of tumor patients evaluated

with diffusion tensor imaging. *Ann. Neurol.* 51, 377–380. doi: 10.1002/ana.10137

Mori, S., Wakana, S., van Zijl, P. C. M., and Nagae-Poetscher, L. M. (2005). *Mri Atlas Of Human White Matter*, 1st Edn. Amsterdam: Elsevier Science Ltd.

Moritz-Gasser, S., Herbet, G., and Duffau, H. (2013). Mapping the connectivity underlying multimodal (verbal and non-verbal) semantic processing: a brain electrostimulation study. *Neuropsychologia* 51, 1814–1822. doi: 10.1016/j.neuropsychologia.2013.06.007

Ojemann, G., and Mateer, C. (1979). Human language cortex: localization of memory, syntax, and sequential motor-phoneme identification systems. *Science* 205, 1401–1403. doi: 10.1126/science.472757

Philippi, C. L., Mehta, S., Grabowski, T., Adolphs, R., and Rudrauf, D. (2009). Damage to association fiber tracts impairs recognition of the facial expression of emotion. *J. Neurosci.* 29, 15089–15099. doi: 10.1523/JNEUROSCI.0796-09.2009

Rech, F., Herbet, G., Gaudeau, Y., Mézières, S., Moureau, J.-M., Moritz-Gasser, S., et al. (2019). A probabilistic map of negative motor areas of the upper limb and face: a brain stimulation study. *Brain J. Neurol.* 142, 952–965. doi: 10.1093/brain/awz021

Sarubbo, S., De Benedictis, A., Maldonado, I. L., Basso, G., and Duffau, H. (2013). Frontal terminations for the inferior fronto-occipital fascicle: anatomical dissection, DTI study and functional considerations on a multi-component bundle. *Brain Struct. Funct.* 218, 21–37. doi: 10.1007/s00429-011-0372-3

Sarubbo, S., Petit, L., De Benedictis, A., Chioffi, F., Ptito, M., and Dyrby, T. B. (2019). Uncovering the inferior fronto-occipital fascicle and its topological organization in non-human primates: the missing connection for language evolution. *Brain Struct. Funct.* 224, 1553–1567. doi: 10.1007/s00429-019-01856-2

Sarubbo, S., Tate, M., De Benedictis, A., Meler, S., Moritz-Gasser, S., Herbet, G., et al. (2020). Mapping critical cortical hubs and white matter pathways by direct electrostimulation: an original functional atlas of the human brain. *Neuroimage* 205:166237. doi: 10.1016/j.neuroimage.2019.116237

Schmahmann, J. D., and Pandya, D. N. (2007). The complex history of the fronto-occipital fasciculus. *J. Hist. Neurosci.* 16, 362–377. doi: 10.1080/09647040600620468

Tate, M. C., Herbet, G., Moritz-Gasser, S., Tate, J. E., and Duffau, H. (2014). Probabilistic map of critical functional regions of the human cerebral cortex: Broca's area revisited. *Brain J. Neurol.* 137, 2773–2782. doi: 10.1093/brain/awu168

Thiebaut de Schotten, M., Dell'Acqua, F., Valabregue, R., and Catani, M. (2012). Monkey to human comparative anatomy of the frontal lobe association tracts. *Cortex J. Devoted Study Nerv. Syst. Behav.* 48, 82–96. doi: 10.1016/j.cortex.2011.10.001

Thomas, C., Avidan, G., Humphreys, K., Jung, K., Gao, F., and Behrmann, M. (2009). Reduced structural connectivity in ventral visual cortex in congenital prosopagnosia. *Nat. Neurosci.* 12, 29–31. doi: 10.1038/nn.2224

Trolard, P. (1906). Le faisceau longitudinal inférieur du cerveau. *Rev. Neurol. (Paris)* 14, 440–446.

Urbanski, M., Thiebaut de Schotten, M., Rodrigo, S., Catani, M., Oppenheim, C., Touzé, E., et al. (2008). Brain networks of spatial awareness: evidence from diffusion tensor imaging tractography. *J. Neurol. Neurosurg. Psychiatry* 79, 598–601. doi: 10.1136/jnnp.2007.126276

Vandermosten, M., Boets, B., Poelmans, H., Sunaert, S., Wouters, J., and Ghesquière, P. (2012). A tractography study in dyslexia: neuroanatomic correlates of orthographic, phonological and speech processing. *Brain J. Neurol.* 135, 935–948. doi: 10.1093/brain/awr363

Wang, K., Li, X., Huang, R., Ding, J., Song, L., and Han, Z. (2020). The left inferior longitudinal fasciculus supports orthographic processing: evidence from a lesion-behavior mapping analysis. *Brain Lang.* 201, 104721. doi: 10.1016/j.bandl.2019.104721

Wu, Y., Sun, D., Wang, Y., and Wang, Y. (2016). Subcomponents and connectivity of the inferior fronto-occipital fasciculus revealed by diffusion spectrum imaging fiber tracking. *Front. Neuroanat.* 10:88. doi: 10.3389/fnana.2016.00088

Yeh, F.-C., Liu, L., Hitchens, T. K., and Wu, Y. L. (2017). Mapping immune cell infiltration using restricted diffusion MRI. *Magn. Reson. Med.* 77, 603–612. doi: 10.1002/mrm.26143

Yeh, F.-C., and Tseng, W.-Y. I. (2011). NTU-90: a high angular resolution brain atlas constructed by q-space diffeomorphic reconstruction. *NeuroImage* 58, 91–99. doi: 10.1016/j.neuroimage.2011.06.021

Yeh, F.-C., Wedeen, V. J., and Tseng, W.-Y. I. (2010). Generalized q-sampling imaging. *IEEE Trans. Med. Imaging* 29, 1626–1635. doi: 10.1109/TMI.2010.2045126

Yordanova, Y. N., Duffau, H., and Herbet, G. (2017). Neural pathways subserving face-based mentalizing. *Brain Struct. Funct.* 222, 3087–3105. doi: 10.1007/s00429-017-1388-0

Conflict of Interest: The authors declare that the research was conducted in the absence of any commercial or financial relationships that could be construed as a potential conflict of interest.

Copyright © 2021 Roux, Lemaitre, Deverdun, Ng, Duffau and Herbet. This is an open-access article distributed under the terms of the Creative Commons Attribution License (CC BY). The use, distribution or reproduction in other forums is permitted, provided the original author(s) and the copyright owner(s) are credited and that the original publication in this journal is cited, in accordance with accepted academic practice. No use, distribution or reproduction is permitted which does not comply with these terms.

frontiers in Neurology

SYSTEMATIC REVIEW
published: 20 May 2021
doi: 10.3389/fneur.2021.671867

Diagnostic Accuracy of PET for Differentiating True Glioma Progression From Post Treatment-Related Changes: A Systematic Review and Meta-Analysis

Meng Cui[1,2†], *Rocío Isabel Zorrilla-Veloz*[3,4†], *Jian Hu*[3,4], *Bing Guan*[5*] and *Xiaodong Ma*[1,2*]

[1] Medical School of Chinese People's Liberation Army, Beijing, China, [2] Department of Neurosurgery, The First Medical Centre of Chinese People's Liberation Army General Hospital, Beijing, China, [3] Department of Cancer Biology, The University of Texas MD Anderson Cancer Center, Houston, TX, United States, [4] The University of Texas MD Anderson Cancer Centre UT Health Graduate School of Biomedical Sciences, Houston, TX, United States, [5] Department of Health Economics, The First Medical Centre of Chinese People's Liberation Army General Hospital, Beijing, China

OPEN ACCESS

Edited by:
Sandro M. Krieg,
Technical University of Munich, Germany

Reviewed by:
Marcus Unterrainer,
Ludwig Maximilian University of Munich, Germany
Nico Sollmann,
Technical University of Munich, Germany

***Correspondence:**
Xiaodong Ma
xiaodongm@hotmail.com
Bing Guan
bgbj@sina.com

[†]These authors have contributed equally to this work

Specialty section:
This article was submitted to Neuro-Oncology and Neurosurgical Oncology, a section of the journal Frontiers in Neurology

Received: 24 February 2021
Accepted: 24 March 2021
Published: 20 May 2021

Citation:
Cui M, Zorrilla-Veloz RI, Hu J, Guan B and Ma X (2021) Diagnostic Accuracy of PET for Differentiating True Glioma Progression From Post Treatment-Related Changes: A Systematic Review and Meta-Analysis. Front. Neurol. 12:671867. doi: 10.3389/fneur.2021.671867

Purpose: To evaluate the diagnostic accuracy of PET with different radiotracers and parameters in differentiating between true glioma progression (TPR) and post treatment-related change (PTRC).

Methods: Studies on using PET to differentiate between TPR and PTRC were screened from the PubMed and Embase databases. By following the PRISMA checklist, the quality assessment of included studies was performed, the true positive and negative values (TP and TN), false positive and negative values (FP and FN), and general characteristics of all the included studies were extracted. Results of PET consistent with reference standard were defined as TP or TN. The pooled sensitivity (Sen), specificity (Spe), and hierarchical summary receiver operating characteristic curves (HSROC) were generated to evaluate the diagnostic accuracy.

Results: The 33 included studies had 1,734 patients with 1,811 lesions suspected of glioma recurrence. Fifteen studies tested the accuracy of ^{18}F-FET PET, 12 tested ^{18}F-FDG PET, seven tested ^{11}C-MET PET, and three tested ^{18}F-DOPA PET. ^{18}F-FET PET showed a pooled Sen and Spe of 0.88 (95% CI: 0.80, 0.93) and 0.78 (0.69, 0.85), respectively. In the subgroup analysis of FET-PET, diagnostic accuracy of high-grade gliomas (HGGs) was higher than that of mixed-grade gliomas ($P_{\text{interaction}} = 0.04$). ^{18}F-FDG PET showed a pooled Sen and Spe of 0.78 (95% CI: 0.71, 0.83) and 0.87 (0.80, 0.92), the Spe of the HGGs group was lower than that of the low-grade gliomas group (0.82 vs. 0.90, $P = 0.02$). ^{11}C-MET PET had a pooled Sen and Spe of 0.92 (95% CI: 0.83, 0.96) and 0.78 (0.69, 0.86). ^{18}F-DOPA PET had a pooled Sen and Spe of 0.85 (95% CI: 0.80, 0.89) and 0.70 (0.60, 0.79). FET-PET combined with MRI had a pooled Sen and Spe of 0.88 (95% CI: 0.78, 0.94) and 0.76 (0.57, 0.88). Multi-parameters analysis of FET-PET had pooled Sen and Spe values of 0.88 (95% CI: 0.81, 0.92) and 0.79 (0.63, 0.89).

Conclusion: PET has a moderate diagnostic accuracy in differentiating between TPR and PTRC. The high Sen of amino acid PET and high Spe of FDG-PET suggest that the combination of commonly used FET-PET and FDG-PET may be more accurate and promising, especially for low-grade glioma.

Keywords: glioma, positron emission tomography, glioma progression, treatment outcome, meta-analysis

INTRODUCTION

Glioma is the most common primary brain tumor. It includes low-grade gliomas (LGGs) and high-grade gliomas (HGGs). The annual incidence of gliomas is approximately six cases per 100,000 individuals worldwide (1). Maximizing extent of resection (EOR) was demonstrated to be associated with improved outcomes, including progression-free survival and overall survival, by multiple retrospective analyses (2, 3). According to the NCCN guidelines, the standard treatment method for LGGs is surgical gross total resection combined with radiotherapy (RT) and adjuvant chemotherapy (CT) of temozolomide (TMZ) or PCV (procarbazine, lomustine, vincristine); for HGGs it is total resection followed by concurrent and adjuvant chemotherapy of TMZ or PCV (more than six cycles) (4–6).

Tumor progression monitoring is very important for patients with glioma after treatment. A confirmed diagnosis of tumor recurrence or progression guides surgeon and patients for the next treatment strategy. Progression and recurrence can be described as true glioma progression (TPR), while all treatment effects can (e.g., radiation necrosis and pseudoprogression) be described as post treatment-related change (PTRC). The wrong differentiation between TPR and PTRC will cause the wrong decision to be made by surgeon and patients, for example an unnecessary secondary surgery or the best surgery opportunity missed. Assessment of the glioma treatment response to differentiate between PTRC and TPR remains as much of a challenge as the treatment (7, 8).

At present, imaging follow-up was still the most common method to monitor TPR. Gadolinium-enhanced T1-weighted magnetic resonance imaging (G-T1-MRI) is often the choice for monitoring glioma patients' response to PTRC and TPR. However, this test often gets a false positive result because it only detects the disruption of the blood-brain barrier and not the tumor activity specifically. To overcome the limitations of G-T1-MRI, multimodal MRI has been proposed, including magnetic resonance spectroscopy (MRS), diffusion-weighted imaging (DWI), and perfusion-weighted imaging (PWI), among others (9, 10). Some previous meta-analyses had demonstrated the relative high diagnostic accuracy of MRS and PWI but low accuracy of DWI (11–13). However, these methods also sometimes caused false positive or false negative results because of their inability to provide metabolic information of lesions directly.

Due to the challenge to accurately determine brain tumor response by MRI both in daily practice and clinical trials, radiolabeled amino acid-positron emission tomography (PET) was proposed in the management of brain tumors by the RANO (Response Assessment in Neuro-Oncology) group (14). The radiotracers include O-(2-[^{18}F] fluoroethyl)-L-tyrosine (^{18}F-FET), ^{18}F-fluorodeoxyglucose (^{18}F-FDG), ^{11}C-methionine (^{11}C-MET), 3,4-dihydroxy-6-[18F]-fluoro-l-phenylalanine (^{18}F-DOPA), and ^{11}C-choline (^{11}C-CHO), among others. PET of various tracers can visualize biological processes such as cell proliferation, membrane biosynthesis, glucose consumption, and uptake of amino acid analogs. Hence PET provides additional insight beyond MRI into the biology and treatment response of gliomas which may be used for non-invasive grading, differential diagnosis, delineation of tumor extent, surgical and radiotherapy treatment planning, post treatment surveillance, and prognostication (15). Many previous studies have demonstrated the usefulness of PET for the assessment of the treatment response of glioma (16, 17), yet a systematic review and meta-analysis of the diagnostic accuracy of PET using different radiotracers and parameters is lacking. Here, we conducted a systematic review and meta-analysis to assess the diagnostic accuracy of PET at differentiating TPR and PTRC.

Abbreviations: ^{11}C-CHO, ^{11}C-choline; DCE, dynamic contrast-enhanced; DOR, diagnostic odds ratio; DSC, dynamic susceptibility contrast; DWI, diffusion-weighted imaging; FDG, ^{18}F-fluorodeoxyglucose; ^{18}F-FET, O-(2-[^{18}F]fluoroethyl)-L-tyrosine; ^{18}F-FLT, ^{18}F-fluorothymidine; ^{18}F-DOPA, 3,4-dihydroxy-6-[18F]-fluoro-l-phenylalanine; HGGs, high-grade gliomas; LGGs, low-grade gliomas; LR+, positive likelihood ratio; LR–, negative likelihood ratio; ^{11}C-MET, ^{11}C-methionine; MRS, magnetic resonance spectroscopy; PTRC, post treatment-related change; PWI, perfusion-weighted imaging; ROIs, regions of interest; SUV, standardized uptake value; TBR, tumor-to-brain ratio; TBRmax/mean, tumor-to-brain maximum/mean ratio (calculated by dividing the max or mean SUV of the tumor ROIs by the max or mean SUV of healthy brain tissue); TMZ, temozolomide; TPR, true progression; TTP, time-to-peak (the time in minutes from the beginning of the dynamic acquisition to the time at which the maximum SUV of the lesion occurred).

METHODS

Search Strategy

This systematic review and meta-analysis was performed according to the Preferred Reporting Items for Systematic Reviews and Meta-Analysis (PRISMA) criteria (**Supplementary Material 1**). It was registered on PROSPERO with registration number CRD42020197852. PubMed and Embase were searched using the key words as follows: "glioma" or "glioblastoma" or "astrocytoma" or "oligodendroglioma" or "oligoastrocytoma"; and "Positron Emission Tomography" or "PET;" and "progression" or "recurrence" or "recurrent" or "relapse" or "pseudoprogression" or "necrosis" or

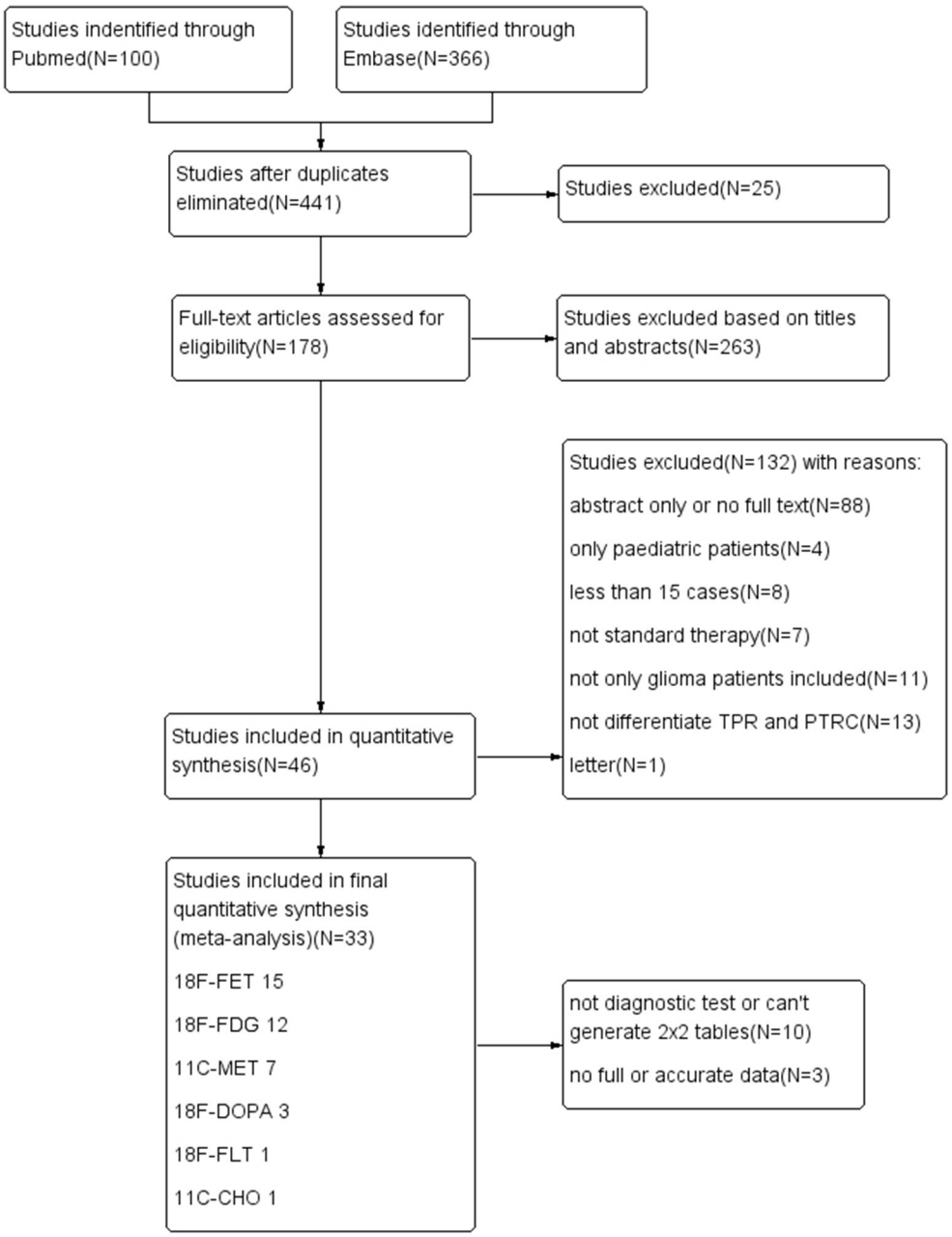

FIGURE 1 | Flow diagram of the study-screening process.

"posttreatment." The detailed search strategy is shown in **Supplementary Material 2**.

Selection Criteria

The inclusion criteria were as follows: English language, publication from January 1999 to December 2019, clinical diagnostic test for glioma with adequate PET data (radiotracers, imaging technique, parameters, etc.), more than 15 patients, adult patients with glioma treated with standard therapy (surgery+RT/CT), diagnostic test involving PET to differentiate between TPR and PTRC compared to a definite reference standard diagnosis (histology or clinical/imaging follow-up), and 2×2 tables from which true positives (TP), false positives (FP), false negatives (FN), and true negatives (TN) could be extracted. The reference standard of clinical/imaging follow-up was reasonable according to RANO criteria. For WHO grade II gliomas, the PTRC required that both the clinical and the radiological situation had to be stable/improved for at least 12 months without administration of another therapy. For WHO grade III-IV gliomas, the classification of PTRC required at

least 6 months of stable or improved clinical and radiological condition, as well as no change in tumor treatment. TPR was considered present when lesions continued to increase in size on at least two subsequent MRI scans, paralleled by a deterioration in performance status, or when a patient died of glioma, which ever occurred first (18).

Exclusion criteria were the inclusion of other tumor entities besides glioma (such as brain metastases, lymphomas, or meningiomas); pediatric glioma patients; *in vitro* or animal studies; publication as a review, letter, comment, case report, or abstract; and treatment methods other than standard therapy recommended by NCCN guidelines (6), such as antiangiogenic bevacizumab therapy, intracavitary radiation, and tumor-treating field therapy.

Data Extraction and Quality Assessment

After duplicates were eliminated, studies were screened for eligibility based first on their title and abstract and subsequently on their full text independently by a board-certified neurosurgeon with 6 years of experience and a neuro-oncologist with 5 years of experience. Study quality was assessed independently according to the quality assessment of diagnostic accuracy studies (QUADAS-2) (19). Then these two authors reviewed in detail the abstracts, methods, results, figures, and tables. Extracted data consisted of true positives (TP), false positives (FP), true negatives (TN), and false negatives (FN); if raw numbers were not reported in the papers, we calculated them from the sensitivity (Sen) and specificity (Spe). The general characteristics extracted from each study were the total number of patients, study design, patient selection criteria, therapy method, mean or median age, sex, reference standard of diagnosis (histopathology or clinical/MRI follow-up), time point at which tumor progression was suspected, PET characteristics and time at which PET was performed, and parameters of PET with or without cut-off value. Disagreements were reassessed by the two authors together to reach a consensus.

Statistical Analysis

By using Meta-Disc statistical software version 1.4, we first evaluated the heterogeneity between each study caused by the threshold effect. The Spearman correlation coefficient between the logit of Sen and the logit of (1–Spe) was computed to assess the threshold effect (20). A strong positive correlation would suggest a threshold effect with $P < 0.05$.

Then, we used Stata 14.0 to perform the statistical analysis: (1) To evaluate the extent of heterogeneity in each study, we used the Q test and the inconsistency index (I^2) of the diagnostic odds ratio (DOR: the ratio of LR+ and LR-). Heterogeneity was considered to be significant if $P < 0.1$ or $I^2 > 50\%$. In this case, the Sen and Spe of the studies were pooled using a random-effects model. Otherwise, a fixed-effects model was used (21). (2) The pooled Sen, Spe, and DOR with their 95% confidence intervals (CIs) were calculated for all studies and are presented as forest plots. If any cells of studies contained a count of zero, a value of one was added to replace zero in order to avoid

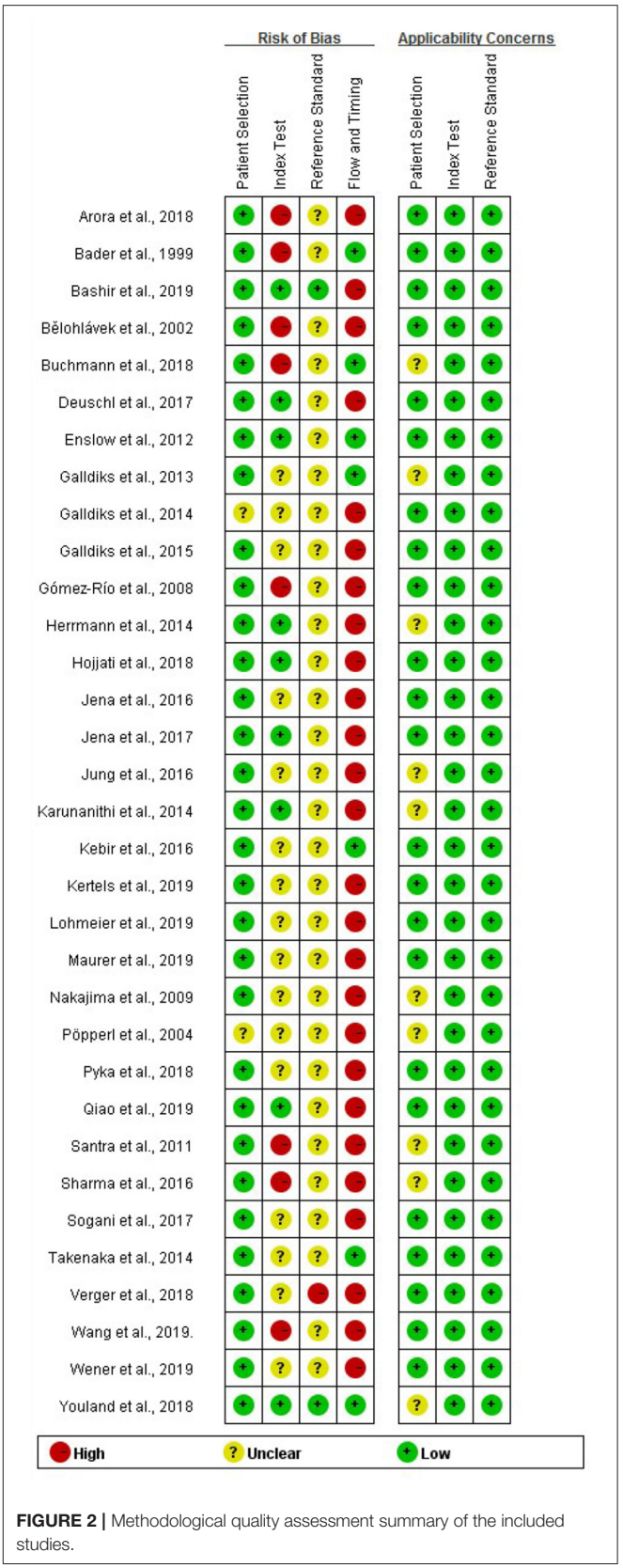

FIGURE 2 | Methodological quality assessment summary of the included studies.

any impossibilities in odds calculations for studies with a Sen or Spe of 100%. (3) The hierarchical logistic regression model was used to generate hierarchical summary receiver operating characteristic (HSROC) curves and area under the curve (AUC) to evaluate the diagnostic accuracy (22–24). (4) We assessed publication bias visually by using a scatter plot (X axis was log DOR, Y axis was $ESS^{1/2}$, which is the inverse of the square root of effective sample size). A symmetric funnel shape and $P > 0.01$ in Deeks' asymmetry test indicated the absence of publication bias; otherwise, there was significant bias.

Subgroup analysis was performed using meta-regression if ≥3 studies could be included, and meta-regression tests were used to analyze differences between subgroups.

RESULTS

Characteristics of Included Studies

A flow diagram describing our study search process is provided in **Figure 1**. The results of the quality assessment are presented in **Supplementary Material 3** and **Figure 2**. In brief, the quality of the included studies was satisfactory.

In total, the 33 included studies (retrospective = 21, prospective = 12) consisted of 1,734 patients and 1,811 lesions suspected of glioma recurrence. The mean ages ranged from 33.9 to 59.5 years. There were 1,110 males and 624 females. The lesions comprised 388 (21.4%) LGGs (WHO grades I and II) and 1,300 (71.8%) HGGs (WHO grades III and IV). In addition, 16 (0.9%) were other kinds of brain tumors, and 107 (5.9%) pathology results of lesions were not mentioned or determined.

Among the included studies, 15 tested the accuracy of ^{18}F-FET PET (25–39), 12 tested ^{18}F-FDG PET (40–51), seven tested ^{11}C-MET PET (46, 47, 51–55), three tested ^{18}F-DOPA PET (45, 56, 57), one tested ^{18}F-FLT PET (44), and 1 tested ^{11}C-CHO PET (46). Of all the included lesions, 836 (46.0%) had histopathology as the reference standard, 549 (30.2%) had clinical combined with imaging follow-up, and 81 (4.5%) only had imaging or clinical follow-up. Though the remaining 353 (19.4%) cases had either a combination or individual use of histopathology and clinical and imaging follow-up as the reference standard, the detailed data were not reported in these four studies (43, 47, 49, 51). The total incidence of TPR was 77.4% (1,394/1,801) in all patients. The incidence of TPR in HGG and LGG patients was 80.5% (577/717) and 63.1% (106/168), respectively. The incidence of PTRC was 22.6% (407/1,801) among all patients, 19.5% (140/717) in patients with HGG, and 36.9% (62/168) in patients with LGG (**Supplementary Material 4**).

Quantitative Synthesis

The pooled results and subgroup analysis are shown in **Tables 1**, **2**, respectively. The HSROC curves are shown in **Figure 3**. The forest plots are shown in **Figure 4**.

^{18}F-FET PET (TBRmax, TBRmean, TTP)

The pooled weighted values of tumor-to-brain maximum ratio (TBRmax) tests were Sen = 0.88 (95% CI: 0.80, 0.93), Spe = 0.78 (0.69, 0.85), DOR = 26 (12, 57), and AUC of HSROC curve = 0.86 (0.83, 0.89). The Sen of these studies had high heterogeneity ($P < 0.1$, $I^2 = 85.3\%$). Subgroup analysis of glioma histopathology showed that the HGG subgroup of the FET-PET test group benefitted from higher accuracy than the mixed-grade group ($P_{interaction} = 0.04$). Subgroup analysis of PET scans (static and dynamic scan groups) showed no significant difference in diagnostic accuracy ($P_{interaction} = 0.54$). Different time points of PET scans may influence the diagnostic accuracy, but subgroup analysis indicated no difference between the ≤7-day and >7-day groups after suspicious recurrence.

Thresholds of the tumor-to-brain mean ratio (TBRmean) ranged from 1.52 to 2.98. The Spearman's correlation coefficient (ρ) was −0.677 ($P = 0.022$), which indicated that a threshold effect was detected only in this group when quantitative synthesis was performed. Therefore, the Sen and Spe of studies could not be pooled directly. The AUC of the HSROC curve was 0.90 (0.87, 0.92), which was used to evaluate the diagnostic accuracy of the TBRmean tests of FET-PET.

The pooled weighted values of time-to-peak (TTP) tests were Sen = 0.80 (95% CI: 0.68, 0.88), Spe = 0.67 (0.48, 0.81), DOR = 8 (4, 16), and AUC = 0.81 (0.77, 0.84).

^{18}F-FDG PET

The pooled weighted values were Sen = 0.78 (95% CI: 0.71, 0.83), Spe = 0.87 (0.80, 0.92), and DOR = 23 (14, 39). The AUC of the HSROC curve was 0.90 (0.87, 0.92). Subgroup analysis of PET visual assessment and semiquantitative analysis of one parameter (such as TBR and SUV) were performed. The difference in Spe between these two groups was statistically significant ($P < 0.05$). Subgroup analysis of glioma histopathology showed that the mixed-grade group and LGG group had higher pooled Spe than the HGG group according to the FDG-PET test (0.87 vs. 0.82 [$P < 0.05$], 0.90 vs. 0.82 [$P = 0.02$]). However, the pooled Sen of the HGG group was not significantly different from those of the other two groups (both $P > 0.05$).

^{11}C-MET PET (TBR)

Heterogeneity was detected in pooled Sen ($P < 0.1$, $I^2 = 86.3\%$). The pooled Sen, Spe, and DOR were 0.92 (95% CI: 0.83, 0.96), 0.78 (0.69, 0.86), and 39 (15, 105), respectively. The AUC of the HSROC curve was 0.82 (0.78, 0.85). The subgroup of HGGs and the subgroup of mixed grades were analyzed, but no significant differences in diagnostic accuracy were detected (all $P > 0.05$). Subgroup analysis of time points showed a higher pooled Spe of the >20 months after radiotherapy group than the <20 months group ($P = 0.04$), but the diagnostic accuracy in these two groups was not different ($P_{interaction} = 0.11$).

^{18}F-DOPA PET (TBRmax, Visual)

The pooled values of Sen, Spe, and DOR were 0.85 (95% CI: 0.80, 0.89), 0.70 (0.60, 0.79), and 13 (7, 24), respectively. The AUC of the HSROC curve was 0.85 (0.82, 0.88). Subgroup analysis showed that there were significant differences between the visual and semiquantitative groups regarding sensitivity ($P < 0.05$).

Publication Bias Assessment

Publication bias did not exist in the FET-PET (TBRmax), FDG-PET, or ^{18}F-DOPA-PET studies ($P = 0.85$, $P = 0.99$, $P = 0.40$),

TABLE 1 | Pooled Sen, Spe, DOR, and heterogeneity analysis results of PET tests of different radiotracers and techniques.

Radiotracer and test technique	Quantitative parameter	Threshold range	ρ and P value	Heterogeneity of pooled Sen (upper) and Spe (lower) (*P*-value of Q test and I^2)	Pooled Sen and its 95%CI	Pooled Spe and its 95%CI	Pooled DOR and its 95%CI	AUC of HSROC
^{18}F-FET	TBR_{max} (810 tests)	1.95,3.52	0.068 ($P = 0.816$)	**§$P < 0.1$, $I^2 = 85.3\%$** ‖$P = 0.09$, $I^2 = 36.1\%$	0.88 (0.80,0.93)	0.78 (0.69,0.85)	26 (12,57)	0.86 (0.83, 0.89)
	TBR_{mean} (713 tests)	1.52,2.98	**−0.677 ($P = 0.022$)**	NA*	NA*	NA*	NA*	0.90 (0.87, 0.92)
	TTP (317 tests)	20,45	0.714 ($P = 0.111$)	**§$P = 0.03$, $I^2 = 59.1\%$** ¶$P = 0.1$, $I^2 = 45.2\%$	0.80 (0.68,0.88)	0.67 (0.48,0.81)	8 (4,16)	0.81 (0.77, 0.84)
^{18}F-FDG (631 tests)	NA†	NA†	0.432 ($P = 0.161$)	−‖$P = 0.04$, $I^2 = 46.4\%$ ¶$P = 0.5$, $I^2 = 0.0\%$	0.78 (0.71,0.83)	0.87 (0.80,0.92)	23 (14,39)	0.90 (0.87, 0.92)
^{11}C-MET	TBR (409 tests)	1.43,2.51	0.559 ($P = 0.192$)	**§$P < 0.1$, $I^2 = 86.3\%$** ¶$P = 0.35$, $I^2 = 10.8\%$	0.92 (0.83,0.96)	0.78 (0.69,0.86)	39 (15,105)	0.82 (0.78, 0.85)
^{18}F-DOPA	TBR_{max} (175 tests), visual (175 tests)	NA†	−0.638 ($P = 0.173$)	¶$P = 0.30$, $I^2 = 18.2\%$ ¶$P = 0.61$, $I^2 = 0.0\%$	0.85 (0.80,0.89)	0.70 (0.60,0.79)	13 (7,24)	0.85 (0.82, 0.88)
FET-PET and MRI (190 tests)	NA‡	NA‡	0.316 ($P = 0.648$)	**§$P = 0.06$, $I^2 = 60.2\%$** ¶$P = 0.16$, $I^2 = 42.5\%$	0.88 (0.78,0.94)	0.76 (0.57,0.88)	23 (9,59)	0.90 (0.87, 0.92)
FET-PET static/dynamic multi-parameters analysis (354 tests)	NA‡	NA‡	−0.100 ($P = 0.873$)	‖$P = 0.09$, $I^2 = 49.5\%$ ¶$P = 0.30$, $I^2 = 18.4\%$	0.88 (0.81,0.92)	0.79 (0.63,0.89)	26 (9,78)	0.91 (0.88, 0.93)

AUC, area under receiver operating curve; CI, confidence interval; DOR, diagnostic odds ratio; HSROC, hierarchical summary receiver operating characteristic; NA, not available because of the threshold effect existed; NA†, not available because not all the studies used quantitative parameter analysis of PET; NA‡, not available because different parameters were used among studies; ρ, Spearman correlation coefficient; TBR, tumor-to-brain ratio; TTP, time-to-peak; §, significant heterogeneity; ‖, slight heterogeneity; ¶, no heterogeneity; #, some studies only reported the value of TBR, so it was used instead of TBRmax or TBRmean to analyze the pooled effect. Bold face type indicates statistical significance.*

TABLE 2 | Subgroup analysis between LGGs, mixed-grade gliomas, and HGGs; between static PET scan and dynamic PET scan; and between visual assessment of the PET scan and semi-quantitative parametric analysis.

Radiotracer and parameter	Subgroup	Number of studies/PET scan tests	Pooled Sen and its 95%CI	*P*-value	Pooled Spe and its 95%CI	*P*-value	Pooled DOR and its 95%CI	AUC	$P^{*}_{interaction}$
^{18}F-FET, TBR_{max}	HGGs	6/333	0.92 (0.85,0.98)	0.51	0.88 (0.79,0.96)	0.90	75 (18,304)	0.92	**0.04**
	Gliomas of mixed grades	8/477	0.84 (0.75,0.93)		0.71 (0.61,0.81)		12 (6,23)	0.80	
	Static scan	5/311	0.94 (0.88,0.99)	0.80	0.76 (0.62,0.90)	0.09	47 (7,299)	0.92	0.10
	Dynamic scan	9/810	0.82 (0.73,0.91)		0.79 (0.71,0.88)		15 (7,32)	0.86	
	PET performed ≤7d after SRR	3/108	0.84 (0.76,0.92)	0.19	0.79 (0.56,1.00)	0.64	NA	NA	0.34
	PET performed >7d after SRR	4/233	0.76 (0.68,0.84)		0.82 (0.68,0.95)		NA	NA	
^{18}F-FDG	Visual assessment	8/355	0.76 (0.63,0.85)	0.30	0.90 (0.81,0.95)	**<0.05**	29 (14,60)	0.92	0.17
	Semi-quantitative parametric analysis	7/349	0.83 (0.73,0.90)		0.82 (0.72,0.89)		23 (10,51)	0.85	
	HGGs	11/214	0.76 (0.68,0.83)		0.82 (0.70,0.90)		15 (7,33)	0.84	
	Gliomas of mixed grades	7/417	0.76 (0.58,0.88)	0.31†	0.87 (0.80,0.92)	**<0.05**†	21 (8,52)	0.88	0.64†
	LGGs	5/141	0.61 (0.34,0.83)	0.83†	0.90 (0.77,0.96)	**0.02**†	15 (3,88)	0.90	0.10†
^{11}C-MET, TBR	HGGs	3/248	0.94 (0.87,1.00)	0.95	0.82 (0.69,0.95)	0.47	71 (20,251)	0.95	0.58
	Gliomas of mixed grades	4/384	0.89 (0.78,0.99)		0.77 (0.67,0.86)		29 (7, 117)	0.79	
	PET performed <20 m after RT	2/92	0.96 (0.91,1.00)	0.89	0.71 (0.53,0.89)	**0.04**	NA	NA	0.11
	PET performed >20 m after RT	4/110	091 (0.84,0.97)		0.89 (0.79,0.99)		NA	NA	
^{18}F-DOPA	Visual assessment	3/175	0.86 (0.80,0.92)	**<0.05**	0.72 (0.59,0.86)	0.22	16 (4,62)	0.93	0.8
	Semi-quantitative analysis of TBR_{max}	3/175	0.84 (0.77,0.90)		0.68 (0.54,0.83)		14 (4,50)	0.85	

*AUC, area under receiver operating curve; CI, confidence interval; DOR, diagnostic odds ratio; HGGs, high-grade gliomas; LGGs, low-grade gliomas; SRR, suspicious recurrence of glioma; TBR, tumor-to-brain ratio. Bold face type indicates statistical significance. *Based on meta regression. †Compared with group of HGGs.*

while bias may have existed in the MET-PET (TBR) studies ($P = 0.01$) (**Figure 5**).

MRI Combined With FET-PET and Multi-Parameter FET-PET

The pooled Sen, Spe, and DOR of the FET-PET/MRI group were 0.88 (95% CI: 0.78, 0.94), 0.76 (0.57, 0.88), and 23 (9, 59), respectively. The AUC of the HSROC curve was 0.90 (0.87, 0.92). The multi-parameter FET-PET test had pooled Sen, Spe, DOR, and AUC values of 0.88 (95% CI: 0.81, 0.92), 0.79 (0.63, 0.89), 26 (9, 78), and 0.91 (0.88, 0.93), respectively. Publication bias did not exist between these studies ($P = 0.66$, $P = 0.65$).

DISCUSSION

To overcome the limitations of MRI, PET-CT has been suggested by RANO for the management of glioma in addition to conventional MRI at every disease stage (58). Many studies have explored the diagnostic accuracy of PET labeled by different radiotracers, which indicates its potential value. Static and dynamic PET scans can acquire different parameters to assess diagnosis. Static scans can calculate SUVmax, SUVmean, TBRmax, and TBRmean to analyze the characteristics of radiotracer uptake in lesions and unaffected brain tissue to differentiate between tumor and normal brain tissue. Dynamic scanning brings in the variable of time and can depict the time-activity curves (TACs) of radiotracer uptake by lesions, and can then identify tumors by calculating TTP or slope (the change in SUV per hour) or by visually assessing the shape of TACs (28, 30, 39). All these parameters are believed to improve the diagnostic accuracy of PET tests compared to visual assessments alone.

According to the pooled AUC of HSROC curves in this meta-analysis, the diagnostic accuracy of ^{18}FET-PET was similar to that of ^{18}F-FDG PET, which was higher than that of ^{18}F-DOPA PET and ^{11}C-MET PET.

^{18}F-FET PET had a high diagnostic accuracy for TBR. Subgroup analysis demonstrated a higher test accuracy for HGGs than gliomas of mixed grades ($P_{interaction} = 0.04$). Because of the higher recurrence rate of HGGs than LGGs, FET-PET will benefit HGG patients more during monitoring recurrence after surgery (**Table 2**). Compared with dynamic scanning, static FET-PET scanning may have

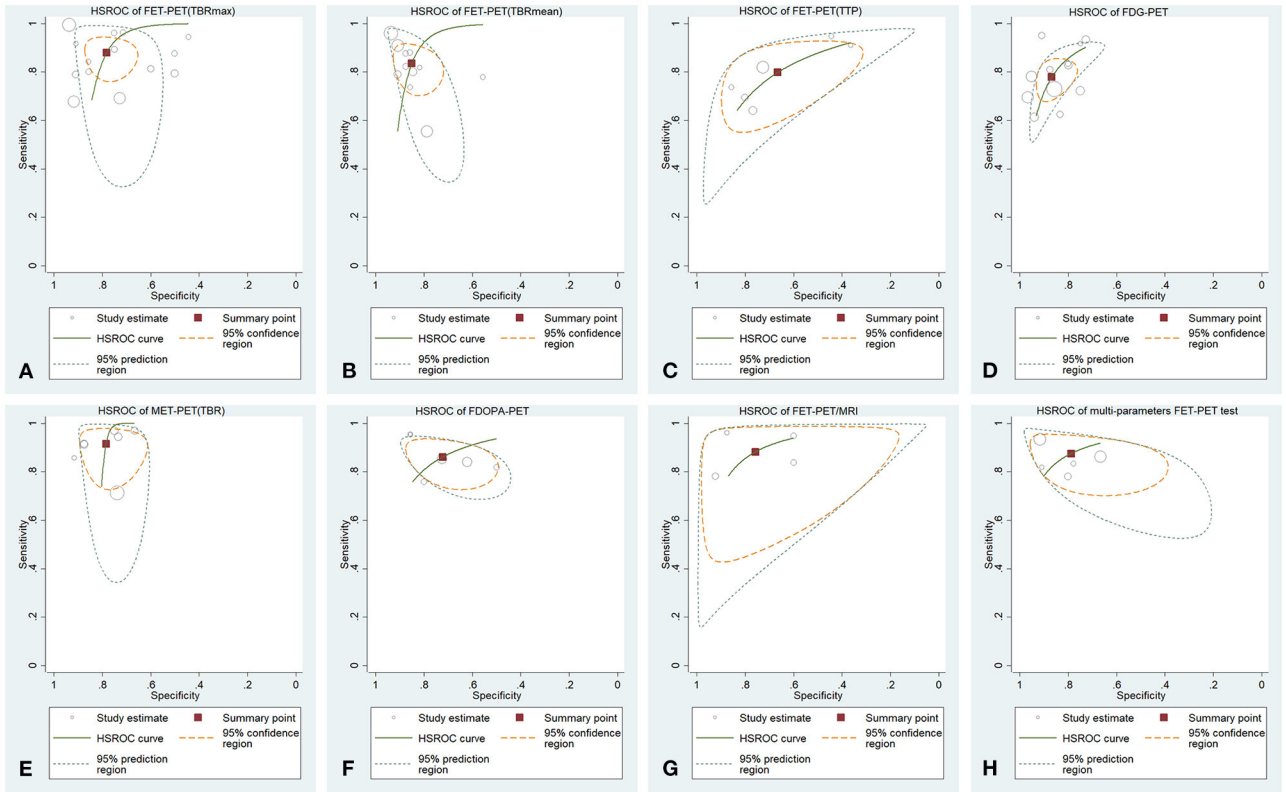

FIGURE 3 | HSROC curves for **(A)** ^{18}F-FET PET (TBRmax), **(B)** ^{18}F-FET PET (TBRmean), **(C)** ^{18}F-FET PET (TTP), **(D)** ^{18}F-FDG PET, **(E)** ^{11}C-MET PET (TBR), **(F)** ^{18}F-DOPA PET, **(G)** FET-PET/MRI, and **(H)** multi-parameters FET-PET.

similar accuracy for the differential diagnosis between TPR and PTRC ($P_{\text{interaction}} = 0.10$).

A common PET modality for the central nervous system (53, 59), ^{11}C-MET PET had good test accuracy when calculating TBR (pooled set: 0.92, Spe: 0.78). Although the accuracy of ^{11}C-MET PET was not different between the HGG group and the mixed-grade group ($P_{\text{interaction}} = 0.58$), a trend of higher diagnostic accuracy in the HGG group was detected. As seen for FET-PET, this result also indicated a better performance of MET-PET for HGG patients. ^{18}F-DOPA is a kind of amino acid radiotracer that can be transported across the intact blood-brain barrier, but it is scarcely used or researched (60). The accuracy of 18F-DOPA PET was not superior to that of FET- or MET-PET in our analysis, which will limit the use of FDOPA-PET.

Because of the limited number of studies that reported the time when PET was performed, only the FET-PET TBRmax and MET-PET TBR could be evaluated for the influence of time point by subgroup analysis in this review. Because of the pseudoprogression caused by radiotherapy, the symptoms of patients and MRI always showed false positive results, which can be falsely considered as tumor recurrence. In our analysis, a longer time after radiotherapy showed a higher Spe of MET-PET, which indicated that the PET scan may need to be performed in the appropriate time window (perhaps a longer time after radiotherapy). Further research is needed to identify the best time point for performing PET after there is suspicious recurrence on MRI.

^{18}F-FDG is a common radiotracer used in PET scans, but it always fails to differentiate between tumors and the brain due to the similarly high uptake rates of glucose in normal brain tissue (61). In this review, the accuracy of FDG-PET showed a similar accuracy to amino acid PET (**Table 1**). Compared to amino acid PET, FDG-PET had a higher Spe but a lower Sen, so we can predict that the combination of these two radiotracers would acquire better diagnostic performance. In the subgroup analysis (**Table 2**), the pooled Spe of visual assessment was higher than that of semiquantitative parametric analysis ($P < 0.05$). Compared to the mixed-grade glioma group and LGG group, the HGG group had a lower Spe ($P < 0.05$, $P = 0.02$). These results demonstrate that the high Spe of FDG-PET may be derived from the visual assessment of PET and the testing of LGG patients. Thus, visual assessment should also be an important part of PET tests in addition to parametric analysis. For HGG patients, the accuracy of amino acid PET was satisfactory, while for postoperative recurrence tests of LGG patients, amino acid PET was not good enough and should be combined with FDG-PET to acquire a higher Spe.

A confirmed diagnosis of recurrence during the follow-up of glioma patients is most important for choosing the next treatment method (secondary surgery or others). MRI is the

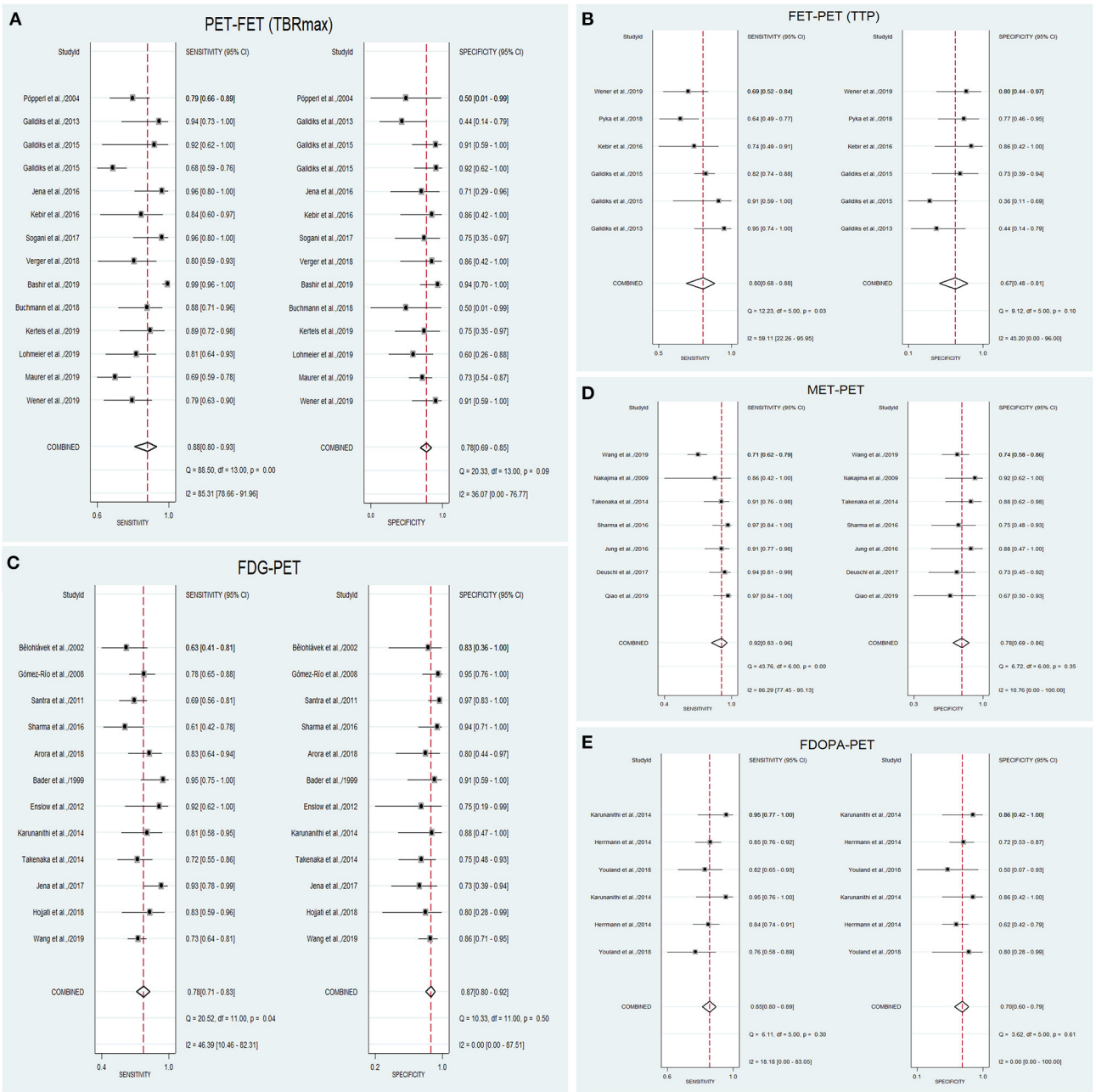

FIGURE 4 | Forest plots for **(A)** ^{18}F-FET PET (TBRmax), **(B)** ^{18}F-FET PET (TTP), **(C)** ^{18}F-FDG PET, **(D)** ^{11}C-MET PET (TBR), and **(E)** ^{18}F-DOPA PET.

most common and valuable method to monitor recurrence at present. From a review of some previous meta-analyses, the diagnostic accuracy of anatomical G-T1-MRI and advanced MRI is summarized in **Table 3**. The accuracy of G-T1-MRI and DWI was obviously not adequate for the diagnosis of glioma recurrence (10, 13). Advanced MRI showed a higher accuracy (11, 12, 62–64). Compared to advanced MRI, PET with different radiotracers did not present an obvious superiority in the differential diagnosis of glioma recurrence (**Table 1**). However, the high Sen of amino acid PET and high Spe of FDG-PET may suggest their combination in future applications of diagnosis.

Some previous meta-analyses evaluated the accuracy of PET, which did not show an obviously better performance than advanced MRI. Moreover, none of them took the different parameters (TBR, TTP, etc.) of PET into consideration (63–67). Along with the evaluation of PET with different tracers, this meta-analysis concentrated on the different accuracy of parameters of PET scans and showed more accuracy in the static parameter TBRmax of FET-PET than the dynamic parameter

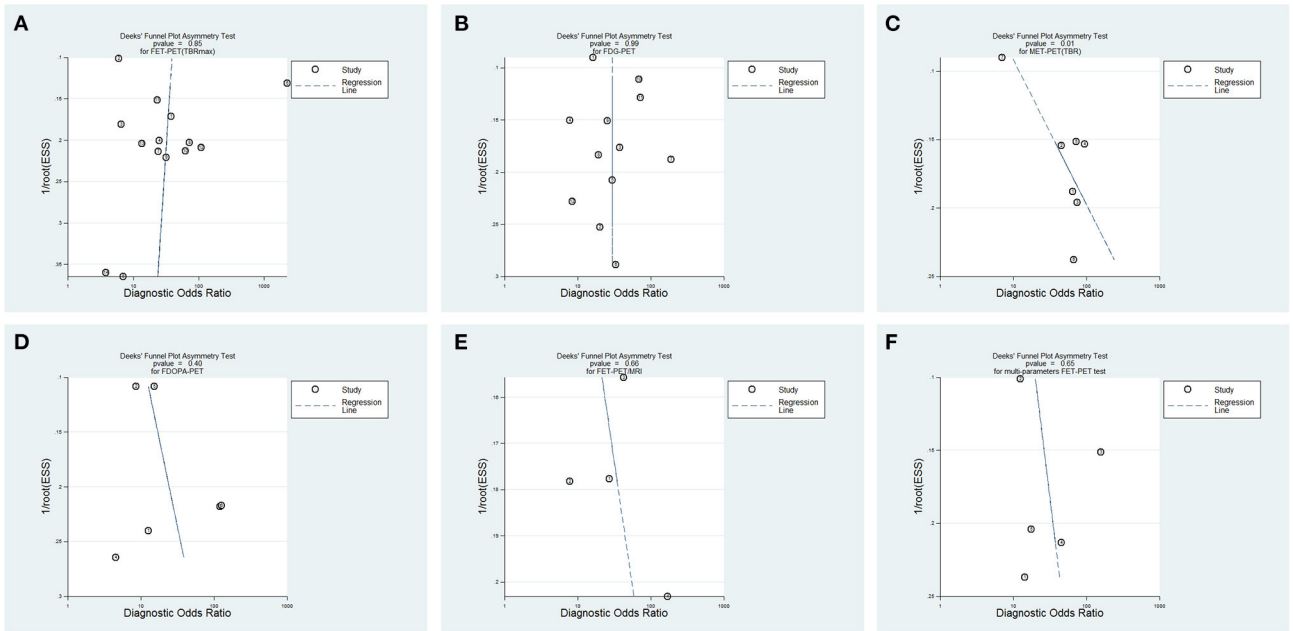

FIGURE 5 | Funnel plots of publication bias for different PET tests. **(A)** ^{18}F-FET PET (TBRmax), **(B)** ^{18}F-FDG PET, **(C)** ^{11}C-MET PET (TBR), **(D)** ^{18}F-DOPA PET, **(E)** FET-PET/MRI, and **(F)** multi-parameters FET-PET.

TABLE 3 | Previous meta-analysis of MRI accuracy for diagnosis of glioma recurrence.

MRI	Study	Pooled Sen and its 95%CI	Pooled Spe and its 95%CI	DOR and its 95%CI	AUC
Anatomical G-T1-MRI	(13)	0.68 (0.51,0.81)	0.77 (0.45,0.93)	NR	NR
	(64)	0.48 (0.08,0.90)	0.85 (0.39,0.98)	NR	NR
ADC of DWI	(13)	0.71 (0.60,0.80)	0.87 (0.77,0.93)	NR	NR
MRS	(63)	0.87 (0.80,0.92)	0.86 (0.77,0.93)	NR	0.93
	(13)	0.91 (0.79,0.97)	0.95 (0.65,0.99)	NR	NR
	(64)	0.82 (0.68,0.90)	0.79 (0.69,0.87)	NR	NR
Cho/NAA of MRS	(11)	0.88 (0.81,0.93)	0.86 (0.76,0.93)	37 (12,84)	0.92
Cho/Cr of MRS	(11)	0.83 (0.77,0.89)	0.83 (0.74,0.90)	24 (12,49)	0.90
DSC of PWI	(62)	0.88 (0.82,0.93)	0.85 (0.75,0.92)	42 (19,94)	0.93
	(12)	0.90 (0.85,0.94)	0.88 (0.83,0.92)	NR	NR
	(13)	0.87 (0.82,0.91)	0.86 (0.77,0.91)	NR	NR
DCE of PWI	(12)	0.89 (0.78,0.96)	0.85 (0.77,0.91)	NR	NR
	(13)	0.92 (0.73,0.98)	0.85 (0.76,0.92)	NR	NR

ADC, apparent diffusion coefficient; Cho/Cr, choline/creatine; Cho/NAA, choline/N-acetyl-aspartate; DCE, dynamic contrast-enhanced; DSC, dynamic susceptibility contrast; DWI, diffusion-weighted imaging; G-T1-MRI, gadolinium-enhanced T1-weighted magnetic resonance; MRS, magnetic resonance spectroscopy; PWI, perfusion-weighted imaging; NR, not reported.

TTP. However, most studies in this review only performed static parameter analysis, and the accuracy of dynamic parameter analysis needs more research for evaluation. Regardless of these results, as a supplement to MRI, PET with different tracers and parameters can provide additional useful information by evaluating different metabolic pathways.

Furthermore, the accuracy of FET-PET multi-parameter analysis or FET-PET/MRI in this meta-analysis was similar to that of FET-PET TBR alone (**Table 1**). FET-PET multi-parameter analysis and hybrid PET/MRI also were not more accurate than advanced MRI. Although hybrid PET/MRI seemed to be a promising technique for recurrent glioma diagnosis, quantitative meta-analyses are scarce, and its accuracy in our analysis was not satisfactory (7, 68). PET-CT was also commonly used to differentiate TPR and PTRC in patients with brain metastases. A meta-analysis showed that pooled Sen and Spe of FDG-PET were 0.83 (95% CI: 0.74, 0.92) and 0.88 (0.81, 0.95), respectively. The pooled Sen and Spe of amino acid PET were 0.84 (0.79, 0.90) and 0.85 (0.80, 0.91) (69). These results were similar to the results in this review, thus it demonstrated similar diagnostic

accuracy of PET differentiating TPR and PTRC both in glioma and brain metastases.

To acquire high diagnostic accuracy in the management of glioma as well as high feasibility and low cost to patients, the method of radiomics analysis is applied broadly now. PET radiomics combines datasets of static and dynamic PET parameters to make full use of imaging information. Precise image segmentation and feature extraction using different classification methods make it more accuracy in diagnosis. However, many studies demonstrated that a PET radiomics model had higher accuracy than the PET single parameter analysis in differentiating TPR from PTRC (70, 71). Feature-based PET/MRI radiomics also showed higher accuracy (72). One study used FDG PET, MET PET, and structural MRI images to develop an integrated radiomics-based model which showed a very high diagnostic accuracy with an AUC of 0.99 (51). In this review we did not cover radiomics. Multi-parameter PET radiomics combined with other imaging modalities has indeed great potential in differentiating TRP and PTRC, and its diagnostic performance should be summarized and evaluated in future.

Some limitations exist in this meta-analysis. First, while 33 studies were included, only three tested ^{18}F-DOPA PET, one tested ^{18}F-FLT PET, and one tested ^{11}C-CHO PET. So their credible diagnostic accuracy cannot be found in this review. The accuracy of ^{18}F-FET, ^{11}C-MET, and ^{18}F-FDG PET which was synthesized in this review was credible due to the support of enough studies. Second, some studies included a small number of patients, so the correction of zero replaced by 1 in 2 × 2 tables caused a large effect on these studies.

CONCLUSION

This meta-analysis demonstrates that PET with different radiotracers has a moderate diagnostic accuracy in differentiating between glioma progression or recurrence and post treatment-related changes. However, their performance does not show an obvious advantage over advanced MRI. The high Sen of amino acid PET and high Spe of FDG-PET suggest that the combination of these two methods will yield a higher accuracy. The PET multi-parameter analysis and PET/MRI have a great clinical application prospect, their diagnostic performances require further research in large sample sizes in multicenter studies.

DATA AVAILABILITY STATEMENT

The original contributions generated for this study are included in the article/**Supplementary Material**, further inquiries can be directed to the corresponding author/s.

AUTHOR CONTRIBUTIONS

MC: conceptualization, methodology, software, formal analysis, resources, data curation, writing-original draft, and writing reviewing and editing. RZ-V: methodology, software, formal analysis, resources, data curation, and writing-reviewing and editing. JH: supervision and writing-reviewing and editing. BG: supervision and writing-reviewing and editing. XM: supervision and project administration. All authors contributed to the article and approved the submitted version.

ACKNOWLEDGMENTS

Thanks to Yihong Chi from the Department of Information Technology in Xian Janssen Pharmaceutical Ltd for her work and contribution to this research (including data analysis and visualization).

SUPPLEMENTARY MATERIAL

The Supplementary Material for this article can be found online at: https://www.frontiersin.org/articles/10.3389/fneur.2021.671867/full#supplementary-material

REFERENCES

1. Fisher JL, Schwartzbaum JA, Wrensch M, Wiemels JL. Epidemiology of brain tumors. *Neurol Clin.* (2007) 25:867–90. doi: 10.1016/j.ncl.2007.07.002
2. Chaichana KL, Jusue-Torres I, Navarro-Ramirez R, Raza SM, Pascual-Gallego M, Ibrahim A, et al. Establishing percent resection and residual volume thresholds affecting survival and recurrence for patients with newly diagnosed intracranial glioblastoma. *Neuro Oncol.* (2014) 16:113–22. doi: 10.1093/neuonc/not137
3. D'Amico RS, Englander ZK, Canoll P, Bruce JN. Extent of resection in Glioma-A review of the cutting edge. *World Neurosurg.* (2017) 103:538–49. doi: 10.1016/j.wneu.2017.04.041
4. Stupp R, Mason WP, van den Bent MJ, Weller M, Fisher B, Taphoorn MJ, et al. Radiotherapy plus concomitant and adjuvant temozolomide for glioblastoma. *N Engl J Med.* (2005) 352:987–96. doi: 10.1056/NEJMoa043330
5. Nabors LB, Portnow J, Ammirati M, Brem H, Brown P, Butowski N, et al. Central nervous system cancers, version 2.2014. Featured updates to the NCCN guidelines. *J Natl Compr Canc Netw.* (2014) 12:1517–23. doi: 10.6004/jnccn.2014.0151
6. Nabors LB, Portnow J, Ammirati M, Baehring J, Brem H, Butowski N, et al. NCCN guidelines insights: central nervous system cancers, version 1.2017. *J Natl Compr Canc Netw.* (2017) 15:1331–45. doi: 10.6004/jnccn.2017.0166
7. Dhermain FG, Hau P, Lanfermann H, Jacobs AH, van den Bent MJ. Advanced MRI and PET imaging for assessment of treatment response in patients with gliomas. *Lancet Neurol.* (2010) 9:906–20. doi: 10.1016/S1474-4422(10)70181-2
8. Ahluwalia MS, Wen PY. Antiangiogenic therapy for patients with glioblastoma: current challenges in imaging and future directions. *Expert Rev Anticancer Ther.* (2011) 11:653–6. doi: 10.1586/era.11.35
9. Bobek-Billewicz B, Stasik-Pres G, Majchrzak H, Zarudzki L. Differentiation between brain tumor recurrence and radiation injury using perfusion, diffusion-weighted imaging and MR spectroscopy. *Folia Neuropathol.* (2010) 48:81–92. doi: 10.3109/15513815.2010.505628
10. Verma N, Cowperthwaite MC, Burnett MG, Markey MK. Differentiating tumor recurrence from treatment necrosis: a review of neuro-oncologic imaging strategies. *Neuro Oncol.* (2013) 15:515–34. doi: 10.1093/neuonc/nos307
11. Zhang H, Ma L, Wang Q, Zheng X, Wu C, Xu BN. Role of magnetic resonance spectroscopy for the differentiation of recurrent glioma from

radiation necrosis: a systematic review and meta-analysis. *Eur J Radiol.* (2014) 83:2181–9. doi: 10.1016/j.ejrad.2014.09.018
12. Patel P, Baradaran H, Delgado D, Askin G, Christos P, John Tsiouris A, et al. MR perfusion-weighted imaging in the evaluation of high-grade gliomas after treatment: a systematic review and meta-analysis. *Neuro Oncol.* (2017) 19:118–27. doi: 10.1093/neuonc/now148
13. van Dijken BRJ, van Laar PJ, Holtman GA, van der Hoorn A. Diagnostic accuracy of magnetic resonance imaging techniques for treatment response evaluation in patients with high-grade glioma, a systematic review and meta-analysis. *Eur Radiol.* (2017) 27:4129–44. doi: 10.1007/s00330-017-4789-9
14. Albert NL, Weller M, Suchorska B, Galldiks N, Soffietti R, Kim MM, et al. Response assessment in neuro-oncology working group and European Association for Neuro-Oncology recommendations for the clinical use of PET imaging in gliomas. *Neuro Oncol.* (2016) 18:1199–208. doi: 10.1093/neuonc/now058
15. la Fougere C, Suchorska B, Bartenstein P, Kreth FW, Tonn JC. Molecular imaging of gliomas with PET: opportunities and limitations. *Neuro Oncol.* (2011) 13:806–19. doi: 10.1093/neuonc/nor054
16. Cannon DM, Kruser TJ, Khuntia D. Principles and application of PET in brain tumors. *PET Clin.* (2011) 6:131–48. doi: 10.1016/j.cpet.2011.02.004
17. Tsiouris S, Bougias C, Fotopoulos A. Principles and current trends in the correlative evaluation of glioma by advanced MRI techniques and PET. *Hell J Nucl Med.* (2019) 22:206–19.
18. Chukwueke UN, Wen PY. Use of the Response Assessment in Neuro-Oncology (RANO) criteria in clinical trials and clinical practice. *CNS Oncol.* (2019) 8:CNS28. doi: 10.2217/cns-2018-0007
19. Whiting P, Rutjes AW, Reitsma JB, Bossuyt PM, Kleijnen J. The development of QUADAS: a tool for the quality assessment of studies of diagnostic accuracy included in systematic reviews. *BMC Med Res Methodol.* (2003) 3:25. doi: 10.1186/1471-2288-3-25
20. Zamora J, Abraira V, Muriel A, Khan K, Coomarasamy A. Meta-DiSc: a software for meta-analysis of test accuracy data. *BMC Med Res Methodol.* (2006) 6:31. doi: 10.1186/1471-2288-6-31
21. Leeflang MM. Systematic reviews and meta-analyses of diagnostic test accuracy. *Clin Microbiol Infect.* (2014) 20:105–13. doi: 10.1111/1469-0691.12474
22. Kim KW, Lee J, Choi SH, Huh J, Park SH. Systematic review and meta-analysis of studies evaluating diagnostic test accuracy: a practical review for clinical researchers-part I. General guidance and tips. *Korean J Radiol.* (2015) 16:1175–87. doi: 10.3348/kjr.2015.16.6.1175
23. Lee J, Kim KW, Choi SH, Huh J, Park SH. Systematic review and meta-analysis of studies evaluating diagnostic test accuracy: a practical review for clinical researchers-part II. Statistical methods of meta-analysis. *Korean J Radiol.* (2015) 16:1188–96. doi: 10.3348/kjr.2015.16.6.1188
24. Suh CH, Park SH. Successful publication of systematic review and meta-analysis of studies evaluating diagnostic test accuracy. *Korean J Radiol.* (2016) 17:5–6. doi: 10.3348/kjr.2016.17.1.5
25. Pöpperl G, Götz C, Rachinger W, Gildehaus FJ, Tonn JC, Tatsch K. Value of O-(2-[18F]fluoroethyl)-L-tyrosine PET for the diagnosis of recurrent glioma. *Eur J Nucl Med Mol Imaging.* (2004) 31:1464–70. doi: 10.1007/s00259-004-1590-1
26. Galldiks N, Stoffels G, Ruge MI, Rapp M, Sabel M, Reifenberger G, et al. Role of O-(2-18F-fluoroethyl)-L-tyrosine PET as a diagnostic tool for detection of malignant progression in patients with low-grade glioma. *J Nucl Med.* (2013) 54:2046–54. doi: 10.2967/jnumed.113.123836
27. Galldiks N, Dunkl V, Stoffels G, Hutterer M, Rapp M, Sabel M, et al. Diagnosis of pseudoprogression in patients with glioblastoma using O-(2-[18F]fluoroethyl)-L-tyrosine PET. *Eur J Nucl Med Mol Imaging.* (2015) 42:685–95. doi: 10.1007/s00259-014-2959-4
28. Galldiks N, Stoffels G, Filss C, Rapp M, Blau T, Tscherpel C, et al. The use of dynamic O-(2-18F-fluoroethyl)-l-tyrosine PET in the diagnosis of patients with progressive and recurrent glioma. *Neuro Oncol.* (2015) 17:1293–300. doi: 10.1093/neuonc/nov088
29. Jena A, Taneja S, Gambhir A, Mishra AK, D'Souza MM, Verma SM, et al. Glioma recurrence versus radiation necrosis: single-session multiparametric approach using simultaneous O-(2-18F-Fluoroethyl)-L-tyrosine PET/MRI. *Clin Nucl Med.* (2016) 41:e228–36. doi: 10.1097/RLU.0000000000001152
30. Kebir S, Fimmers R, Galldiks N, Schafer N, Mack F, Schaub C, et al. Late pseudoprogression in glioblastoma: diagnostic value of dynamic O-(2-[18F]fluoroethyl)-L-tyrosine PET. *Clin Cancer Res.* (2016) 22:2190–6. doi: 10.1158/1078-0432.CCR-15-1334
31. Sogani SK, Jena A, Taneja S, Gambhir A, Mishra AK, D'Souza MM, et al. Potential for differentiation of glioma recurrence from radionecrosis using integrated 18F-fluoroethyl-L-tyrosine (FET) positron emission tomography/magnetic resonance imaging: a prospective evaluation. *Neurol India.* (2017) 65:293–301. doi: 10.4103/neuroindia.NI_101_16
32. Pyka T, Hiob D, Preibisch C, Gempt J, Wiestler B, Schlegel J, et al. Diagnosis of glioma recurrence using multiparametric dynamic 18F-fluoroethyl-tyrosine PET-MRI. *Eur J Radiol.* (2018) 103:32–7. doi: 10.1016/j.ejrad.2018.04.003
33. Verger A, Filss CP, Lohmann P, Stoffels G, Sabel M, Wittsack HJ, et al. Comparison of O-(2-18F-Fluoroethyl)-L-tyrosine positron emission tomography and perfusion-weighted magnetic resonance imaging in the diagnosis of patients with progressive and recurrent glioma: a hybrid positron emission tomography/magnetic resonance study. *World Neurosurg.* (2018) 113:e727–37. doi: 10.1016/j.wneu.2018.02.139
34. Bashir A, Mathilde Jacobsen S, Molby Henriksen O, Broholm H, Urup T, Grunnet K, et al. Recurrent glioblastoma versus late posttreatment changes: diagnostic accuracy of O-(2-[18F]fluoroethyl)-L-tyrosine positron emission tomography (18F-FET PET). *Neuro Oncol.* (2019) 21:1595–606. doi: 10.1093/neuonc/noz166
35. Buchmann N, Gempt J, Ryang YM, Pyka T, Kirschke JS, Meyer B, et al. Can early postoperative O-(2-(18F)Fluoroethyl)-l-tyrosine positron emission tomography after resection of glioblastoma predict the location of later tumor recurrence? *World Neurosurg.* (2019) 121:e467–74. doi: 10.1016/j.wneu.2018.09.139
36. Kertels O, Mihovilovic MI, Linsenmann T, Kessler AF, Tran-Gia J, Kircher M, et al. Clinical utility of different approaches for detection of late pseudoprogression in glioblastoma with O-(2-[18F]fluoroethyl)-l-tyrosine PET. *Clin Nucl Med.* (2019) 44:695–701. doi: 10.1097/RLU.0000000000002652
37. Lohmeier J, Bohner G, Siebert E, Brenner W, Hamm B, Makowski MR. Quantitative biparametric analysis of hybrid (18)F-FET PET/MR-neuroimaging for differentiation between treatment response and recurrent glioma. *Sci Rep.* (2019) 9:14603. doi: 10.1038/s41598-019-50182-4
38. Maurer GD, Brucker DP, Stoffels G, Filipski K, Filss CP, Mottaghy FM, et al. (18)F-FET PET imaging in differentiating glioma progression from treatment-related changes - a single-center experience. *J Nucl Med.* (2020) 61:505–11. doi: 10.2967/jnumed.119.234757
39. Werner JM, Stoffels G, Lichtenstein T, Borggrefe J, Lohmann P, Ceccon G, et al. Differentiation of treatment-related changes from tumour progression: a direct comparison between dynamic FET PET and ADC values obtained from DWI MRI. *Eur J Nucl Med Mol Imaging.* (2019) 46:1889–901. doi: 10.1007/s00259-019-04384-7
40. Bader JB, Samnick S, Moringlane JR, Feiden W, Schaefer A, Kremp S, et al. Evaluation of L-3-[123I]iodo-α-methyltyrosine SPET and [18F]fluorodeoxyglucose PET in the detection and grading of recurrences in patients pretreated for gliomas at follow-up: a comparative study with stereotactic biopsy. *Eur J Nucl Med.* (1999) 26:144–51. doi: 10.1007/s002590050370
41. Bělohlávek O, Klener J, Vymazal J, Dbalý V, Tovaryš F. The diagnostics of recurrent gliomas using FDG-PET: Still questionable? *Nucl Med Rev.* (2002) 5:127–30.
42. Gómez-Río M, Rodríguez-Fernández A, Ramos-Font C, López-Ramírez E, Llamas-Elvira JM. Diagnostic accuracy of 201Thallium-SPECT and 18F-FDG-PET in the clinical assessment of glioma recurrence. *Eur J Nucl Med Mol Imaging.* (2008) 35:966–75. doi: 10.1007/s00259-007-0661-5
43. Santra A, Kumar R, Sharma P, Bal C, Julka PK, Malhotra A. Detection of recurrence in glioma: a comparative prospective study between Tc-99m GHA SPECT and F-18 FDG PET/CT. *Clin Nucl Med.* (2011) 36:650–5. doi: 10.1097/RLU.0b013e318217aee0
44. Enslow MS, Zollinger LV, Morton KA, Butterfield RI, Kadrmas DJ, Christian PE, et al. Comparison of 18F-fluorodeoxyglucose and 18F- fluorothymidine PET in differentiating radiation necrosis from recurrent glioma. *Clin Nucl Med.* (2012) 37:854–61. doi: 10.1097/RLU.0b013e318262c76a
45. Karunanithi S, Sharma P, Kumar A, Khangembam BC, Bandopadhyaya GP, Kumar R, et al. 18F-FDOPA PET/CT for detection of recurrence in patients

with glioma: prospective comparison with 18F-FDG PET/CT. *Eur J Nucl Med Mol Imaging.* (2013) 40:1025–35. doi: 10.1007/s00259-013-2384-0
46. Takenaka S, Asano Y, Shinoda J, Nomura Y, Yonezawa S, Miwa K, et al. Comparison of 11c-methionine, 11c-choline, and 18f-fluorodeoxyglucose-positron emission tomography for distinguishing glioma recurrence from radiation necrosis. *Neurol Med Chir.* (2014) 54:280–9. doi: 10.2176/nmc.oa2013-0117
47. Sharma R, D'Souza M, Jaimini A, Hazari PP, Saw S, Pandey S, et al. A comparison study of 11 C-methionine and 18 F-fluorodeoxyglucose positron emission tomography-computed tomography scans in evaluation of patients with recurrent brain tumors. *Indian J Nucl Med.* (2016) 31:93–102. doi: 10.4103/0972-3919.178254
48. Jena A, Taneja S, Jha A, Damesha NK, Negi P, Jadhav GK, et al. Multiparametric Evaluation in differentiating glioma recurrence from treatment-induced necrosis using simultaneous (18)F-FDG-PET/MRI: a single-institution retrospective study. *AJNR Am J Neuroradiol.* (2017) 38:899–907. doi: 10.3174/ajnr.A5124
49. Arora G, Sharma P, Sharma A, Mishra AK, Hazari PP, Biswas A, et al. 99mTc-methionine hybrid SPECT/CT for detection of recurrent glioma: comparison with 18F-FDG PET/CT and contrast-enhanced MRI. *Clin Nucl Med.* (2018) 43:e132–8. doi: 10.1097/RLU.0000000000002036
50. Hojjati M, Badve C, Garg V, Tatsuoka C, Rogers L, Sloan A, et al. Role of FDG-PET/MRI, FDG-PET/CT, and dynamic susceptibility contrast perfusion mri in differentiating radiation necrosis from tumor recurrence in glioblastomas. *J Neuroimaging.* (2018) 28:118–25. doi: 10.1111/jon.12460
51. Wang K, Qiao Z, Zhao X, Li X, Wang X, Wu T, et al. Individualized discrimination of tumor recurrence from radiation necrosis in glioma patients using an integrated radiomics-based model. *Eur J Nucl Med Mol Imaging.* (2019) 47:1400–11. doi: 10.1007/s00259-019-04604-0
52. Nakajima T, Kumabe T, Kanamori M, Saito R, Tashiro M, Watanabe M, et al. Differential diagnosis between radiation necrosis and glioma progression using sequential proton magnetic resonance spectroscopy and methionine positron emission tomography. *Neurol Med Chir.* (2009) 49:394–401. doi: 10.2176/nmc.49.394
53. Jung TY, Min JJ, Bom HS, Jung S, Kim IY, Lim SH, et al. Prognostic value of post-treatment metabolic tumor volume from 11C-methionine PET/CT in recurrent malignant glioma. *Neurosurg Rev.* (2017) 40:223–9. doi: 10.1007/s10143-016-0748-1
54. Deuschl C, Kirchner J, Poeppel TD, Schaarschmidt B, Kebir S, El Hindy N, et al. 11C–MET PET/MRI for detection of recurrent glioma. *Eur J Nucl Med Mol Imaging.* (2018) 45:593–601. doi: 10.1007/s00259-017-3916-9
55. Qiao Z, Zhao X, Wang K, Zhang Y, Fan D, Yu T, et al. Utility of dynamic susceptibility contrast perfusion-weighted MR imaging and11C-methionine PET/CT for differentiation of tumor recurrence from radiation injury in patients with high-grade gliomas. *Am J Neuroradiol.* (2019) 40:253–9. doi: 10.3174/ajnr.A5952
56. Herrmann K, Czernin J, Cloughesy T, Lai A, Pomykala KL, Benz MR, et al. Comparison of visual and semiquantitative analysis of 18F-FDOPA- PET/CT for recurrence detection in glioblastoma patients. *Neuro Oncol.* (2014) 16:603–9. doi: 10.1093/neuonc/not166
57. Youland RS, Pafundi DH, Brinkmann DH, Lowe VJ, Morris JM, Kemp BJ, et al. Prospective trial evaluating the sensitivity and specificity of 3,4-dihydroxy-6-[18F]-fluoro-L-phenylalanine (18F-DOPA) PET and MRI in patients with recurrent gliomas. *J Neurooncol.* (2018) 137:583–91. doi: 10.1007/s11060-018-2750-7
58. Law I, Albert NL, Arbizu J, Boellaard R, Drzezga A, Galldiks N, et al. Joint EANM/EANO/RANO practice guidelines/SNMMI procedure standards for imaging of gliomas using PET with radiolabelled amino acids and [(18)F]FDG: version 1.0. *Eur J Nucl Med Mol Imaging.* (2019) 46:540–57. doi: 10.1007/s00259-018-4207-9
59. Yano H, Shinoda J, Iwama T. Clinical utility of positron emission tomography in patients with malignant glioma. *Neurol Med Chir.* (2017) 57:312–20. doi: 10.2176/nmc.ra.2016-0312
60. Youland RS, Kitange GJ, Peterson TE, Pafundi DH, Ramiscal JA, Pokorny JL, et al. The role of LAT1 in (18)F-DOPA uptake in malignant gliomas. *J Neurooncol.* (2013) 111:11–8. doi: 10.1007/s11060-012-0986-1
61. Herholz K, Langen KJ, Schiepers C, Mountz JM. Brain tumors. *Semin Nucl Med.* (2012) 42:356–70. doi: 10.1053/j.semnuclmed.2012.06.001
62. Deng SM, Zhang B, Wu YW, Zhang W, Chen YY. Detection of glioma recurrence by (1)(1)C-methionine positron emission tomography and dynamic susceptibility contrast-enhanced magnetic resonance imaging: a meta-analysis. *Nucl Med Commun.* (2013) 34:758–66. doi: 10.1097/MNM.0b013e328361f598
63. Wang X, Hu X, Xie P, Li W, Li X, Ma L. Comparison of magnetic resonance spectroscopy and positron emission tomography in detection of tumor recurrence in posttreatment of glioma: a diagnostic meta-analysis. *Asia Pac J Clin Oncol.* (2015) 11:97–105. doi: 10.1111/ajco.12202
64. Furuse M, Nonoguchi N, Yamada K, Shiga T, Combes JD, Ikeda N, et al. Radiological diagnosis of brain radiation necrosis after cranial irradiation for brain tumor: a systematic review. *Radiat Oncol.* (2019) 14:28. doi: 10.1186/s13014-019-1228-x
65. Nihashi T, Dahabreh IJ, Terasawa T. Diagnostic accuracy of PET for recurrent glioma diagnosis: a meta-analysis. *AJNR Am J Neuroradiol.* (2013) 34:944–50. doi: 10.3174/ajnr.A3324
66. Yu J, Zheng J, Xu W, Weng J, Gao L, Tao L, et al. Accuracy of (18)F-FDOPA positron emission tomography and (18)F-FET positron emission tomography for differentiating radiation necrosis from brain tumor recurrence. *World Neurosurg.* (2018) 114:e1211–24. doi: 10.1016/j.wneu.2018.03.179
67. Treglia G, Muoio B, Trevisi G, Mattoli MV, Albano D, Bertagna F, et al. Diagnostic performance and prognostic value of PET/CT with different tracers for brain tumors: a systematic review of published meta-analyses. *Int J Mol Sci.* (2019) 20:4669. doi: 10.3390/ijms20194669
68. Yang Y, He MZ, Li T, Yang X. MRI combined with PET-CT of different tracers to improve the accuracy of glioma diagnosis: a systematic review and meta-analysis. *Neurosurg Rev.* (2019) 42:185–95. doi: 10.1007/s10143-017-0906-0
69. Suh CH, Kim HS, Jung SC, Choi CG, Kim SJ. Comparison of MRI and PET as potential surrogate endpoints for treatment response after stereotactic radiosurgery in patients with brain metastasis. *AJR Am J Roentgenol.* (2018) 211:1332–41. doi: 10.2214/AJR.18.19674
70. Hotta M, Minamimoto R, Miwa K. 11C-methionine-PET for differentiating recurrent brain tumor from radiation necrosis: radiomics approach with random forest classifier. *Sci Rep.* (2019) 9:15666. doi: 10.1038/s41598-019-52279-2
71. Lohmann P, Elahmadawy MA, Gutsche R, Werner JM, Bauer EK, Ceccon G, et al. FET PET radiomics for differentiating pseudoprogression from early tumor progression in glioma patients post-chemoradiation. *Cancers.* (2020) 12:3835. doi: 10.3390/cancers12123835
72. Lohmann P, Meissner AK, Kocher M, Bauer EK, Werner JM, Fink GR, et al. Feature-based PET/MRI radiomics in patients with brain tumors. *Neurooncol Adv.* (2020) 2(Suppl. 4):iv15–21. doi: 10.1093/noajnl/vdaa118

Conflict of Interest: The authors declare that the research was conducted in the absence of any commercial or financial relationships that could be construed as a potential conflict of interest.

Copyright © 2021 Cui, Zorrilla-Veloz, Hu, Guan and Ma. This is an open-access article distributed under the terms of the Creative Commons Attribution License (CC BY). The use, distribution or reproduction in other forums is permitted, provided the original author(s) and the copyright owner(s) are credited and that the original publication in this journal is cited, in accordance with accepted academic practice. No use, distribution or reproduction is permitted which does not comply with these terms.

frontiers in Neuroscience

ORIGINAL RESEARCH
published: 14 June 2021
doi: 10.3389/fnins.2021.690705

Multimodal Simulation of a Novel Device for a Safe and Effective External Ventricular Drain Placement

Giuseppe Emmanuele Umana[1], Gianluca Scalia[2], Kaan Yagmurlu[3], Rosalia Mineo[4,5], Simone Di Bella[4,5], Matteo Giunta[4], Angelo Spitaleri[1], Rosario Maugeri[6], Francesca Graziano[2,6], Marco Fricia[1], Giovanni Federico Nicoletti[2], Santino Ottavio Tomasi[7], Giuseppe Raudino[8], Bipin Chaurasia[9], Gianluca Bellocchi[10], Maurizio Salvati[11], Domenico Gerardo Iacopino[6], Salvatore Cicero[1], Massimiliano Visocchi[12] and Lidia Strigari[13]*

[1] Department of Neurosurgery, Trauma Center, Gamma Knife Center, Cannizzaro Hospital, Catania, Italy, [2] Department of Neurosurgery, Highly Specialized Hospital and of National Importance "Garibaldi," Catania, Italy, [3] Department of Neurological Surgery, University of Virginia, Charlottesville, VA, United States, [4] MT Ortho Srl, Aci Sant'Antonio, Catania, Italy, [5] DICAR, University of Catania, Catania, Italy, [6] Department of Experimental Biomedicine and Clinical Neurosciences, School of Medicine, Postgraduate Residency Program in Neurological Surgery, Neurosurgical Clinic, AOUP "Paolo Giaccone," Palermo, Italy, [7] Department of Neurosurgery, Christian-Doppler-Klinik, Paracelsus Private Medical University, Salzburg, Austria, [8] Department of Neurosurgery, Humanitas University, Catania, Italy, [9] Department of Neurosurgery, Neurosurgery Clinic, Birgunj, Nepal, [10] Department of Otorhinolaryngology, San Camillo Forlanini Hospital, Rome, Italy, [11] Department of Neurosurgery, Policlinico Tor Vergata, Rome, Italy, [12] Craniovertebral Junction Operative Unit, Master CVJ Surgical Approach Research Center, Institute of Neurosurgery, Policlinic "A. Gemelli", Catholic University, Rome, Italy, [13] Department of Medical Physics, IRCCS University Hospital of Bologna, Bologna, Italy

OPEN ACCESS

Edited by:
Sandro M. Krieg,
Technical University of Munich, Germany

Reviewed by:
Camilo Molina,
Washington University School of Medicine, United States
Asem Salma,
Mercy Health – St. Rita's Neuroscience Institute, United States

***Correspondence:**
Giuseppe Emmanuele Umana
umana.nch@gmail.com

Specialty section:
This article was submitted to Brain Imaging Methods, a section of the journal Frontiers in Neuroscience

Received: 03 April 2021
Accepted: 04 May 2021
Published: 14 June 2021

Citation:
Umana GE, Scalia G, Yagmurlu K, Mineo R, Di Bella S, Giunta M, Spitaleri A, Maugeri R, Graziano F, Fricia M, Nicoletti GF, Tomasi SO, Raudino G, Chaurasia B, Bellocchi G, Salvati M, Iacopino DG, Cicero S, Visocchi M and Strigari L (2021) Multimodal Simulation of a Novel Device for a Safe and Effective External Ventricular Drain Placement. Front. Neurosci. 15:690705. doi: 10.3389/fnins.2021.690705

Background: External ventricular drain (EVD) placement is mandatory for several pathologies. The misplacement rate of the EVD varies widely in literature, ranging from 12.3 to 60%. The purpose of this simulation study is to provide preliminary data about the possibility of increasing the safety of one of the most common life-saving procedures in neurosurgery by testing a new device for EVD placement.

Methods: We used a novel guide for positioning the ventricular catheter (patent RM2014A000376). The trajectory was assessed using 25 anonymized head CT scans. The data sets were used to conduct three-dimensional computer-based and combined navigation and augmented reality-based simulations using plaster models. The data set inclusion criteria were volumetric head CT scan, without midline shift, of patients older than 18. Evans' index was used to quantify the ventricle's size. We excluded patients with slit ventricles, midline shift, skull fractures, or complex skull malformations. The proximal end of the device was tested on the cadaver.

Results: The cadaveric tests proved that a surgeon could use the device without any external help. The multimodal simulation showed Kakarla grade 1 in all cases but one (grade 2) on both sides, after right and left EVD placement. The mean Evans' index was 0.28. The geometric principles that explain the device's efficacy can be summarized

by studying the properties of circumference and chord. The contact occurs, for each section considered, at the extreme points of the chord. Its axis, perpendicular to the plane tangent to the spherical surface at the entry point, corresponds to the direction of entry of the catheter guided by the instrument.

Conclusion: According to our multimodal simulation on cadavers, 3D computer-based simulation, 3D plaster modeling, 3D neuronavigation, and augmented reality, the device promises to offer safer and effective EVD placement. Further validation in future clinical studies is recommended.

Keywords: hydrocephalus, shunt, ventricle, cerebral hypertension, ventricular catheter

INTRODUCTION

External ventricular drain (EVD) placement is mandatory for several pathologies, both in emergency and elective surgery. It allows reducing life-threatening intracranial hypertension, thus rapidly improving the patient's clinical conditions and sometimes saving the patient's life. The misplacement rate of the ventricular catheters reported in the literature varies widely, ranging from 12.3 to 60% (Saladino et al., 2009; Toma et al., 2009; Park et al., 2011; Bergdal et al., 2013; Chai et al., 2013; Rehman et al., 2013; Phillips et al., 2014), with possible serious complications (e.g., cerebral hematomas, neurological deficits, and seizures) (Woernle et al., 2011; Rosenbaum et al., 2013). This misplacement rate has been considered as the baseline for our results, and we aimed to obtain a lower misplacement rate in a simulation setting. The misplacement rates reported in literature are high, probably due to the use of EVD also in patients affected by midline shift or slit ventricles and in procedures performed by non-neurosurgeons in remote areas with logistic difficulties. Numerous studies have already been published about the reduction of complication after EVD, which is currently a freehand procedure, performed only according to anatomical landmarks that help to introduce the catheter perpendicularly to the burr hole; the perpendicularity is a critical element for the correct positioning of the catheter (Gil et al., 2002; Shimizu et al., 2004; Lee et al., 2008, 2020; Mahan et al., 2013; Patil et al., 2013; Jakola et al., 2014; Siesjö, 2014; Shtaya et al., 2018; Thomale et al., 2018; Wilson et al., 2018; Fuller et al., 2020; Park et al., 2020; Sun et al., 2020; Amoo et al., 2021; Cabrilo et al., 2021; Pishjoo et al., 2021).

One study reported the results in 17 patients, using a guide that allows obtaining perpendicularity (Ghajar, 1985): this study reported obtaining cerebrospinal fluid (CSF) on the first attempt, providing initial evidence of the strong correlation between the perpendicular trajectory offered by their device and the correct positioning of the catheter. In 11 out of 17 patients (64%), the correct positioning at the level of the ipsilateral anterior frontal horn of the ventricle was confirmed by intraoperative fluoroscopy and postoperative CT scan. However, this guide was not suitable for neuronavigation, a useful tool when midline shift is present.

The development of new devices is one of the purest forms of surgical research, but it is rare and challenging, since most of the technical discoveries have already been reported. We highlight the experimental nature of this study, in which we used merged technologies to assess the accuracy and validate the trajectory offered by the device, which allows to immediately obtain the perpendicularity required and, indicated in literature, for correct EVD placement.

The purpose of this study is to provide preliminary data about the possibility of increasing the safety of one of the most common life-saving procedures in neurosurgery by testing a new device for EVD placement.

MATERIALS AND METHODS

We used a novel guide for positioning the ventricular catheter (patent RM2014A000376), which is neither invasive nor implanted on the patient, and it does not modify the standard surgical protocol for EVD placement. We used a cadaveric specimen, already used for a cadaver lab during the "First European advanced course on surgical techniques for the obstructive sleep apnea-hypopnea syndrome" in Rome, to develop the device's proximal end, which is the key: it is fixed to the skull, it does not go beyond the dura mater, and, above all, it has a perpendicular trajectory. Several bilateral, precoronal, and prefrontal tests were performed to improve the device's insertion into the burr hole. The cadaveric specimen was not used to assess catheter trajectory. The entry points were precoronal: 7–11 cm from the nasion and 3 cm from the midline.

The trajectory was assessed using 25 anonymized head CT scans of patients with a mean Evans's index of 0.28. The data sets were used to conduct three-dimensional computer-based and augmented reality-based simulations. Data set inclusion criteria were volumetric head CT scan without midline shift of patients older than 18. Evans' index was used to quantify the ventricle's size. We excluded patients with slit ventricles, midline shift, skull fractures, or complex skull malformations.

Methodologic Highlights

I. Precoronaric burr hole, 11 cm from the nasion and 5–3 cm from midline and dura mater incision.
II. Internal bone spur removal if the bone is very thin, <8 mm.

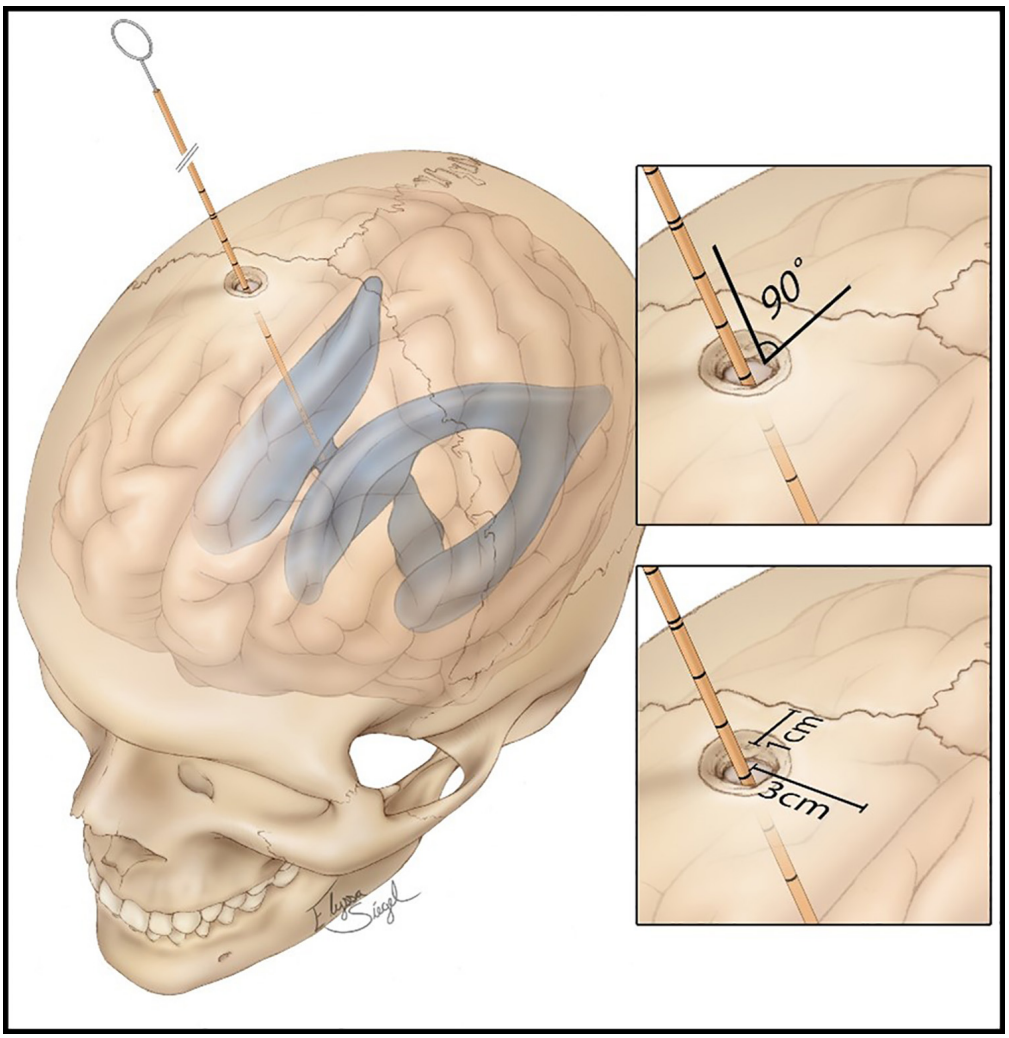

FIGURE 1 | Standard procedure of external ventricular drain (EVD) placement, showing the distances from the coronal suture, midline, and the angle of 90° of the catheter, aiming to perpendicularity. Source: https://assets.neurosurgicalatlas.com/volumes/ATLAS/1-PRINCIPLES_OF_CRANIAL_SURGERY/16-External_Ventricular_Drain/PCS_ExtIntraventDrain_03.jpg (last accessed: March 30, 2021).

III. Insert the device inside the burr hole; associate the navigation reference if midline shift is present.
IV. Insert the catheter inside the device, remove the mandrel, and remove the device.
V. Catheter tunneling.

Standard Procedure

- Step 1: In the standard freehand procedure, the skin incision can be either linear or curvilinear.
- Step 2: A burr hole is placed 10–11 cm from the nasion and 2.5–3 cm on the right of the midline. The burr hole is performed with a 14-mm perforator (**Figure 1**).
- Step 3: The dura mater is coagulated and cut with a no. 11 blade, and a small corticectomy is performed.
- Step 4: The catheter is introduced for 6 cm from the external cortical bone of the skull, looking for the perpendicularity (90°) compared with the outer skull, having as reference the mid-pupillary line, the external acoustic meatus, and the medial canthus; these are the landmarks for directing the tip of the catheter toward the ipsilateral Monro foramen.
- Step 5: Once the catheter is inserted and CSF is obtained, the catheter is tunneled and connected to the external drainage system.

Device Description

The device's peculiarity (**Figure 2**) is identifiable in the bone support base, which allows the fast and non-invasive achievement of the correct trajectory (perpendicular to the curvature of the skull). The distal cylindrical component maintains the trajectory during the insertion and allows interfacing with the neuronavigation, using the navigated stylet or universal reference systems of the common brands. The device can be sterilized multiple times, saving costs. It is semitransparent, allowing

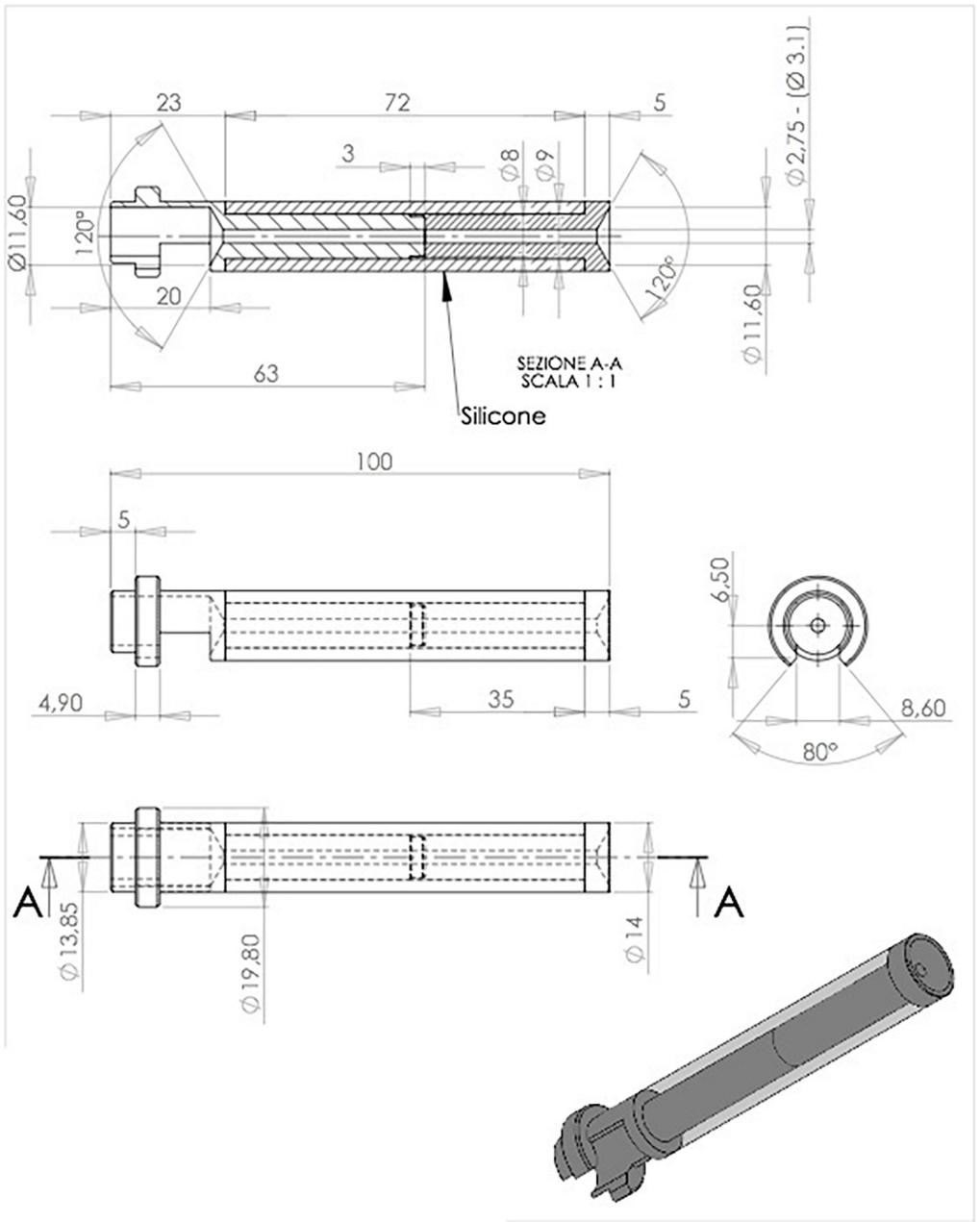

FIGURE 2 | External ventricular drain (EVD) device, detailed illustration.

to visualize the number indicating the catheter's length, thus controlling the depth of insertion (**Figure 3**).

Simulation

3D Computer-Based Simulation

Twenty-five anonymized head CT scan data sets were uploaded, and 3D head models were obtained. The skull and ventricles were reconstructed. The 3D rendering of the ventricles was highlighted and visualized together with the skull, removing the brain. A 3D representation of the device was created and positioned in Kocher's point, along its offset and directed proximally, toward the lateral ventricles. The device was positioned perpendicular to the skull by imposing the flat part of the device's proximal end on the skull's curvature.

3D Computer-Based Simulation Protocol

This protocol was designed to virtually simulate the EVD procedure performed with the aid of the novel device in the most realistic way. This device allows the catheter's insertion in a guided way; mainly, it ensures the catheter to be inserted

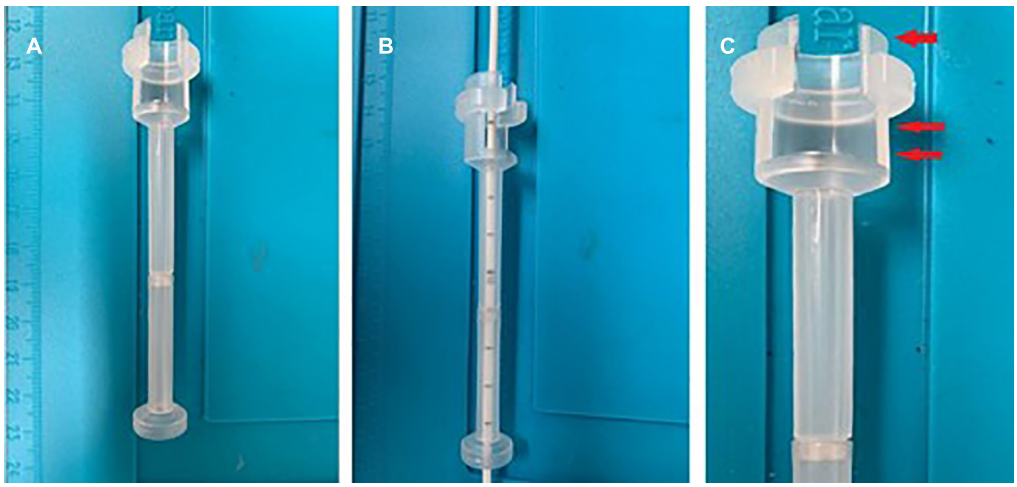

FIGURE 3 | The device is semitransparent, allowing catheter control during insertion **(A,B)**. The catheter's proximal end (arrow), which helps to fix the device to the skull with the correct trajectory. The proximal end also presents a window to clamp the catheter before removing the mandrel (double arrows) **(C)**.

perpendicular to the skull's surface, providing a higher success rate. This simulation can be summarized in seven phases:

- Phase 1: Reconstruction of the 3D model. The 3D model of the patient's bone is created using the Mimics software (Materialize, Leuven Belgium) from the CT images data set (**Figure 4A**).
- Phase 2: Identification of the catheter entry point. The 3D model just obtained is imported into the Materialize® 3-Matic software. In this virtual-like environment, using a measuring instrument along curved surfaces, we move 100/110 mm, starting from the glabella, along the sagittal plane, and then 30 mm along the coronal plane, thus identifying the entry point of the catheter (**Figure 4B**).
- Phase 3: Simulation of the burr hole. Performing a Boolean operation of subtraction between solids, the first surgical phase of the external ventricular drain (EDV) placement, represented by the burr hole, is simulated by subtracting a cylinder with a diameter of 14 mm from the 3D model of the skull (**Figure 4C**).
- Phase 4: Identification of the contact surface. At this point, the surgical procedure involves the positioning of the device inside the hole, orthogonally to the contact surface. To virtually simulate this surgical phase, the instrument/skull contact surface ensemble was isolated, consisting of a crown with an external diameter of 20 mm (coinciding with the outer diameter of the instrument in contact with the skull) and an internal diameter of 14 mm (inner diameter of the burr hole) (**Figure 4D**).
- Phase 5: Identification of the normal to the contact surface. The plane that best fits the newly isolated surface is then identified. The normal to this plane will specify the device's direction of insertion (**Figure 4E**).
- Phase 6: Catheter entry simulation. This phase allows the virtual simulation of the catheter's insertion. A cylindrical solid with a diameter of 2.7 mm is created, and it is translated along the direction normal to the plane for a length of 60 mm (**Figure 4F**).
- Phase 7: Verification of correct catheter placement. The cylinder thus positioned is then imported into the Mimics software, where it can be viewed on the patient's CT images. In this way, it is possible to verify that the cylinder, simulating the catheter, reaches the ipsilateral lateral ventricle (**Figure 4G**).

Modeling

Twenty-five plaster models of the patients' anatomy were created (Fin-Ceramica, Faenza, Italy) and used for combined 3D neuronavigation and augmented reality-based navigation (**Figure 5**). These plaster models are usually used for cranioplasty planning; thus, their accuracy to the patient's anatomy is the highest available.

Augmented Reality-Based Simulation

We used Microsoft's HoloLens mixed reality glasses and Virtual Surgery Intelligence (VSI) (ApoQlar, Hamburg, Germany). The model can be moved and "edited" in space via gesture control, and speech control can be used to record videos or take pictures. We uploaded the head CT scan data set and STL file of the device to reconstruct the patient's anatomy and the holographic rendering of the device, respectively, to improve the immersive experience of the simulation (**Figure 6**).

3D Neuronavigation-Based Simulation

We conducted a 3D neuronavigation-based simulation by performing a CT scan of the 3D plaster model. The data set obtained was merged with the patient's head CT scan to allow visualization of the ventricles. The 3D model was then uploaded in BrainLab (Munich, Germany) planning station and used to simulate the introduction of the ventricular catheter in the plaster

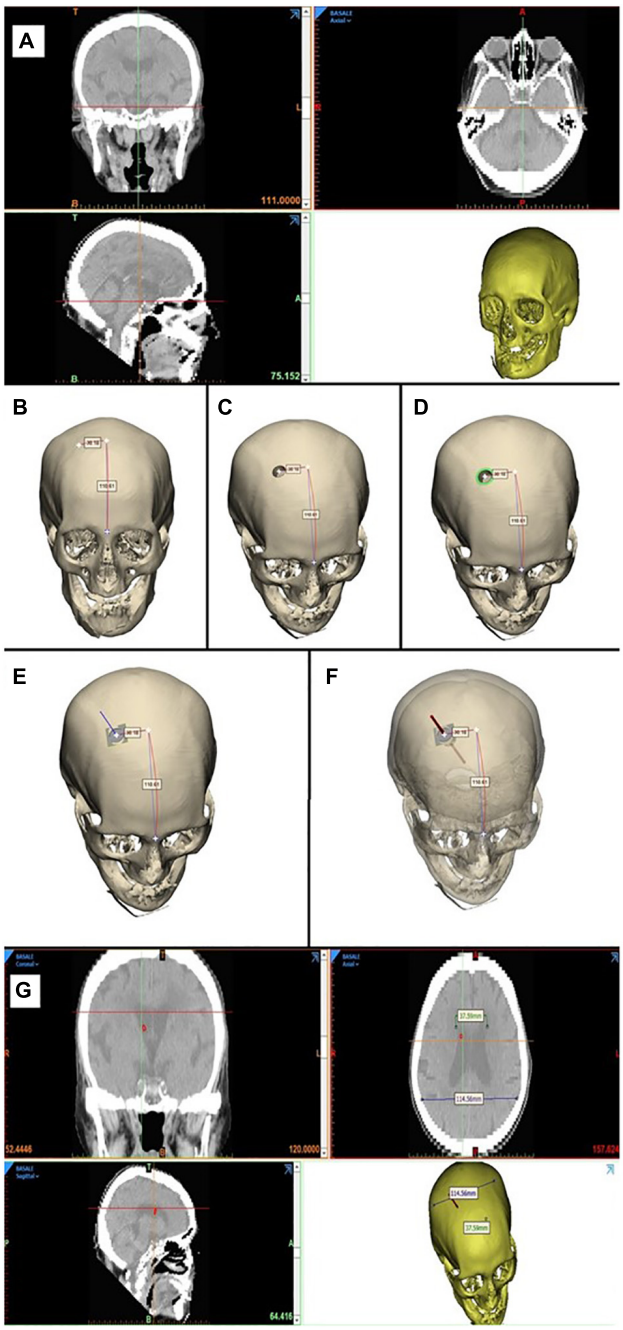

FIGURE 4 | 3D computer-based simulation **(A)**, showing the entry point definition based on anatomical landmarks, to both the right and left, Evans' evaluation, simulation of the catheter placement **(B–F)**, bilaterally obtaining grade A positioning **(G)**.

model, with the device overlapped on its holographic representation, verifying the correct trajectory navigating the catheter. The navigation could be associated with neuronavigation by using a navigated stylet or other navigation tools.

Accuracy

The accuracy was assessed according to the Kakarla classification (**Figure 7**; Kakarla et al., 2008), which includes three grades (**Table 1**). The device's accuracy has been proven to be equal to that of the neuronavigation because we applied the device according to craniometric parameters and using plaster models; furthermore, we applied the navigated stylet to confirm the accuracy of the trajectory provided by the guide. The 3D computer-based navigation should be considered a fine simulation step that geometrically demonstrates the mathematical reasons on which the device's efficacy is based. The computer did not adjust the trajectory to bias the results and obtain the desired results; instead, it allowed to get the correct measures. The software allows to apply the device perpendicularly to the skull surface and, only after this step, to evaluate its trajectory.

We suggest considering this computer-based simulation step as the finest and most objective way to test the device in a simulation setting. In daily life, the head's position can affect the accuracy of the EVD placement; thus, a guide that is of aid to get perpendicularity independently from the head position would be of great benefit.

RESULTS

The trajectory was assessed using an anonymized head CT scan of 25 patients (14 males and 11 females) with a median age of 71 (range 36–90) years. The mean of the Evans' index was 0.28 (±0.03 standard deviation); see **Table 2**. The catheter tip distribution was calculated in 23/25 and 24/25 cases in the right and left hemispheres, respectively. The calculation was not performed in patients with a tumoral mass in the right hemisphere, and, in one case, the CT images did not include the entire skull.

The catheter tip distribution in the craniocaudal (CC) and in the latero-lateral (LL) position, calculated in our cohort using the computer-based simulation in the left and right brain hemispheres, is shown in **Figure 8**.

Figure 9 shows catheter tip distribution against patients' sex/gender, highlighting, as expected, that CC position is lower for female than male patients due to skull shape and anatomical characteristics (t-test, $p = 0.0003$).

The cadaveric tests proved that any surgeon could use the device without any external help because it shows a good fixation inside the burr hole. The internal bone border created by the burr hole perforator, close to the dura, should be removed with a Kerrison rongeur to obtain the complete insertion of the proximal end of the device. The burr hole should have a minimum thickness of 5 mm for optimal insertion of the device. Thus, only in the case of a thick skull is it possible not to remove the inner skull layer and directly use the device.

The multimodal simulation performed with 3D neuronavigation and computer-based simulation showed Kakarla grade 1 in both sides after right and left EVD

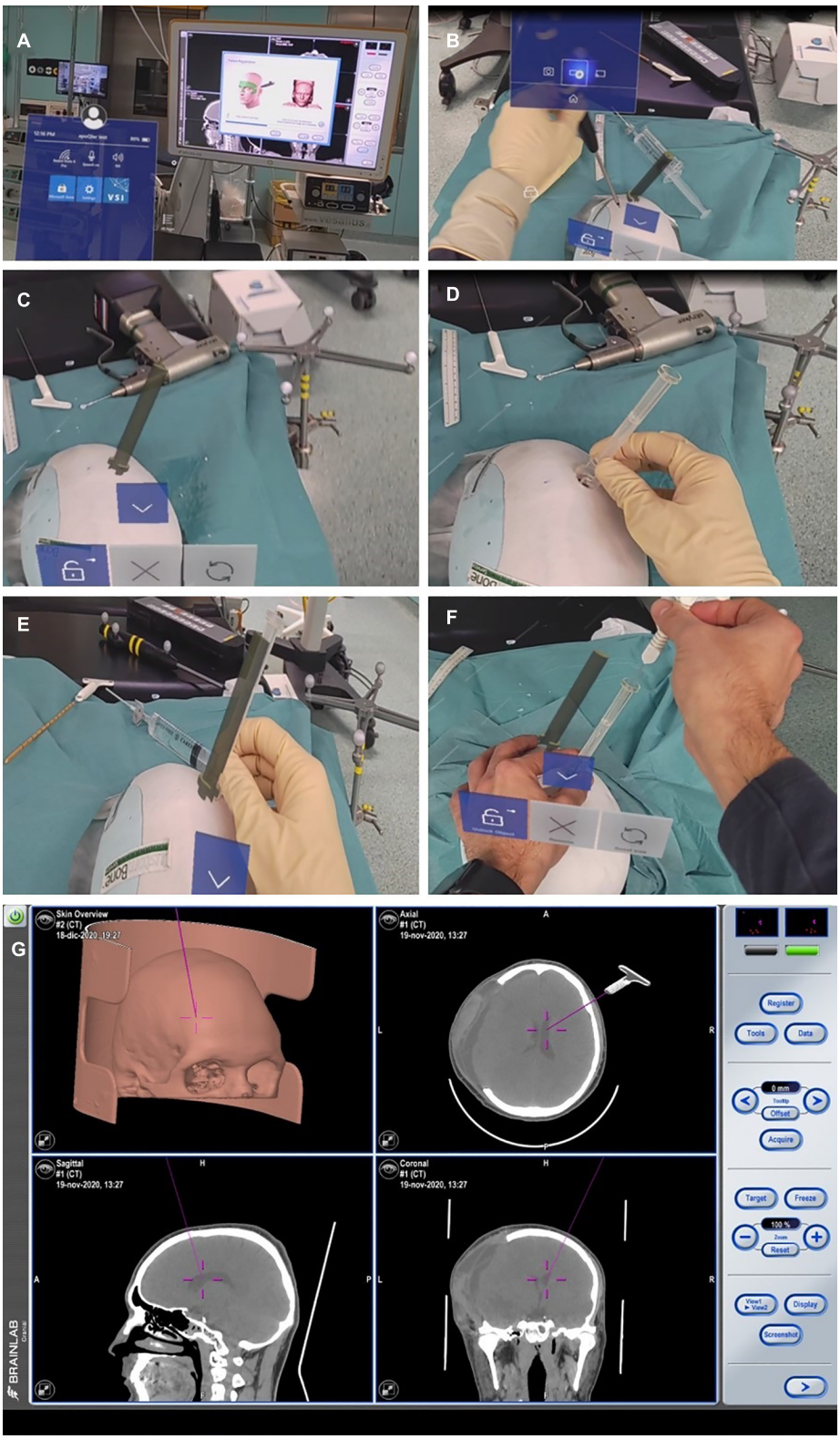

FIGURE 5 | Finceramica plaster model navigation after merging the patient's CT scan (already treated for post-traumatic craniotomy, but with no midline shift). **(A,B)** Superficial tracing for navigation registration (BrainLab) of the plaster model. **(C)** Entry point definition with a holographic representation of the device. **(D)** Positioning of the real device on the defined entry point. **(E)** Overlap of the holographic device with the real one, to match the entry point. **(F)** Introduction of the navigated stylet inside the device. **(G)** Its representation with the standard navigation.

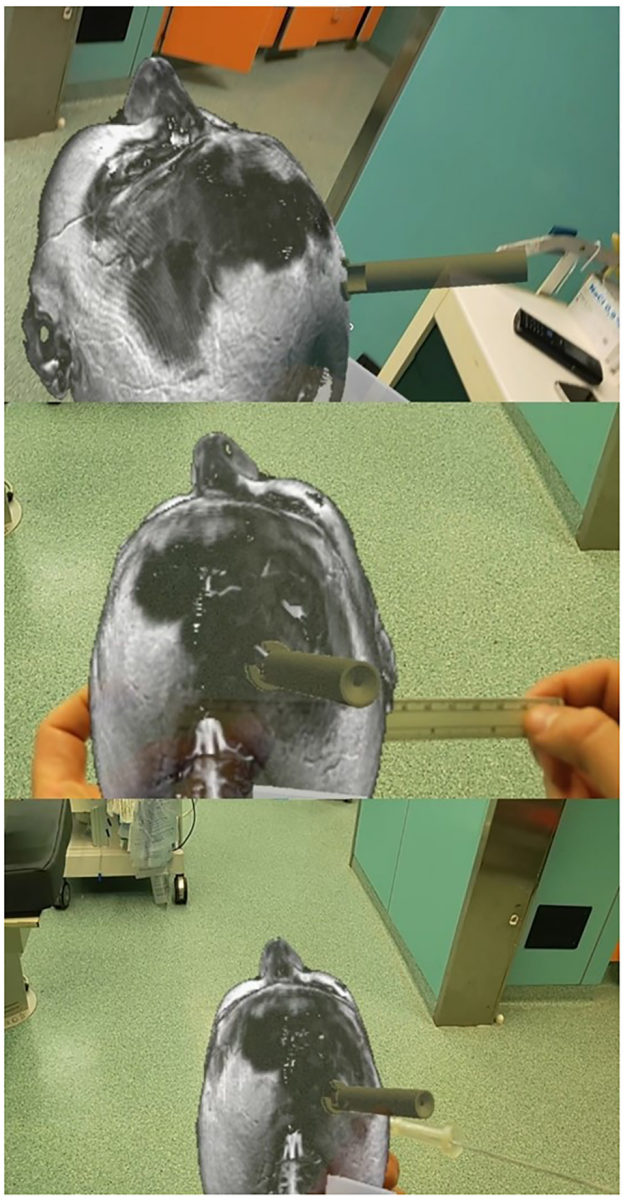

FIGURE 6 | Augmented reality-based simulation (ApoQlar) to locate the entry point. A real ruler was overlapped on the hologram based on both MRI and CT scans; the actual device was overlapped over its holographic reconstruction, and the navigated stylet was introduced to improve familiarity with the procedure and technology.

placements, in all cases but one, classified as grade 2. We considered only Kocher's point, 11 cm from the nasion and 3 cm from the midline. The simulation with augmented reality, associated with 3D navigation using plaster skulls, demonstrated that the device positioned with the aid of mixed reality allowed an excellent entry point definition, as confirmed by the 3D navigation. The mean Evans' index was 0.28 (**Table 2**).

Geometric Considerations

The contact between the trocar and the skull occurs on a crown of points small enough to be assimilated to a circumference. Therefore, in order to study the geometric characteristics at the interface, we can analyze what happens in a generic section, as shown in **Figure 10**.

The problem thus leads back to studying the geometric properties of circumference and chord (**Figure 11**).

Contact occurs, for each section considered, at the extreme points of the chord (A and B in **Figure 11**). Its axis, perpendicular to the plane tangent to the spherical surface at the entry point, corresponds to the direction of entry of the catheter guided by the instrument (**Figure 12**).

DISCUSSION

General Considerations

International recommendations for EVD placement suggest performing another burr hole if no CSF is obtained after more than three attempts (Greenberg, 2019), indirectly confirming that EVD misplacement is a risk that everybody will experience during their professional lives. The incidence of misplacement of the ventricular catheters reported in the literature is high, ranging from 12.3 to 60% according to the statistics (Saladino et al., 2009; Toma et al., 2009; Park et al., 2011; Bergdal et al., 2013; Chai et al., 2013; Rehman et al., 2013; Phillips et al., 2014), with possible associated complications (cerebral hematomas, neurological deficits, and seizures), which can dramatically worsen a patient's clinical conditions (Woernle et al., 2011; Rosenbaum et al., 2013). Of notice, using the freehand technique, the only indirect sign of ventricular reach is the CSF drained from the distal catheter end, which does not give any information on the catheter's trajectory.

Traversing brain parenchyma means creating damage from the cortex to the ventricle, with the risk of injury to cranial nerves, vessels, basal nuclei, or even the brainstem in case of mispositioning (Chai et al., 2013; Rosenbaum et al., 2013). Repeated attempts or even performing a second, contralateral, burr hole exponentially increases the risk of damage to eloquent structures.

We highlight the experimental nature of this study, in which we used merged technologies to assess the accuracy of the device. The use of the guide, together with the navigation, offered the possibility to assess the accuracy of the trajectory offered by the device, since CSF drain was not possible in a simulation setting.

Device Technique

The present novel device aims to obtain the perpendicularity relative to the bone surface, thus reducing EVD misplacement rate without modifying the standard EVD placement method.

Once the device is introduced into the skull, the catheter will follow a perpendicular route to the ventricle without further trajectory adjustments, thus allowing EVD placement independently from the head's position. The device's utility

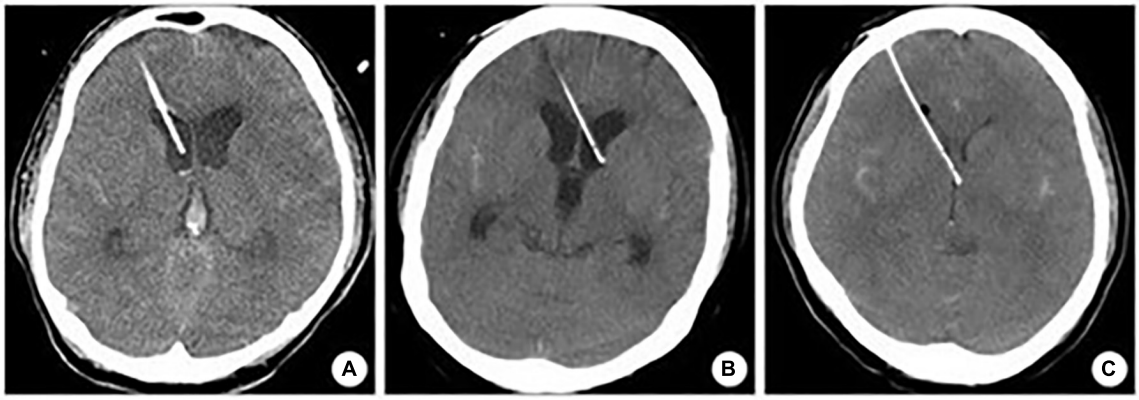

FIGURE 7 | Kakarla grading system. **(A)** Homolateral lateral ventricle positioning. **(B)** Contralateral lateral ventricle positioning. **(C)** Misplacement.

includes the possibility to perform ventricular catheter placement with the same head rotation as used for ventriculoperitoneal shunt placement.

The device's proximal end shows a notch that prevents excessive insertion, thus avoiding parenchymal lesion. Still, the essential function is represented by its geometric characteristic of a plane superimposed on the skull, which can be assimilated to a sphere, thus reproducing the tangent of a sphere, which in turn helps to achieve the needed perpendicularity. The critical point of the procedure is the correct selection of the burr hole, which must be performed at the desired location, 11 cm from the nasion and 3 cm from midline; of course, a wrong burr hole placement will alter the entire procedure, as what happens in the standard freehand technique. The novel guide is entirely non-invasive, so it does not add any injury to the patient. The burr hole angle does not affect the trajectory because the device works on the skull's surface, and the internal bone border can be removed.

This preliminary, non-invasive investigation is expected to improve the learning curves of these procedures and decrease the rates of misplacement of the ventricular catheters by adopting a patient-specific approach. The process can be performed with no additional dose of ionizing radiation, just by using the conventional imaging acquired before the surgical procedure. The device can be used on its own but is neuronavigation-ready. Navigation is handy in the case of midline shifts, in which the normal anatomy is altered and it is not possible to use the typical anatomical landmarks and in the case of "slit ventricles," in which the target is challenging to reach (Gil et al., 2002; Mahan et al., 2013; Jakola et al., 2014; Thomale et al., 2018). If used on a patient with no midline shift, the device is as accurate as navigation, which is then unnecessary, thus saving costs (Chai et al., 2013).

Utility in Low- and Middle-Income Countries

The low economic impact is of great importance since this device could be particularly useful in low- and middle-income countries (LMICs), in which EVD placement is performed by non-neurosurgeons, mostly general surgeons, in remote areas where referral to neurosurgeons is time-consuming or impossible or the patients' clinical conditions are worsening rapidly (Robertson et al., 2019a,b,c; Fuller et al., 2020). The aid of a simple guide for EVD placement could be of great benefit in those contexts, helping surgeons and improving outcomes. Given the high incidence of mispositioning among the neurosurgical statistics reported in the literature (Saladino et al., 2009; Toma et al., 2009; Park et al., 2011; Bergdal et al., 2013; Chai et al., 2013; Rehman et al., 2013; Phillips et al., 2014), the incidence of mispositioning in LMICs could be expected to be higher. The possibility of using a device that offers similar accuracy to neuronavigation could be of great benefit for LMICs, where expensive tools for neuronavigation are not available and non-neurosurgeons often perform EVD procedures in remote areas.

Multimodal Simulation Tests

We did not consider midline shift because it includes an extensive range of conditions, causing the data to be non-homogeneous, and it is out of the interest of the study, which is focused on the assessment of the possibility to get the perpendicularity in the majority of cases in which EVD is required, i.e., patients affected by hydrocephalus, with no midline shift. Patients who require EVD placement should be

TABLE 1 | Kakarla grading system for ventricular catheter tip mispositioning.

Grade	Placement accuracy	Catheter's tip location
A	Optimal/ adequate	Ipsilateral frontal horn, including the tip of the third ventricle
B	Suboptimal (shallow)	Contralateral frontal horn
C	Suboptimal	Corpus callosum/interhemispheric fissure in eloquent tissue brainstem/cerebellum/internal capsule/basal ganglia/thalamus/occipital cortex/basal cisterns

TABLE 2 | Computer-based simulation with report of Evans' index, depth in both sides, and data analysis.

Evans' index	Positive R	Positive L	Depth R	Depth L	Age	Sex	Right X	Right Y	Left X	Left Y
0.286	Yes	Yes	60	60	71	M	4.29	28.58	3.53	32.12
0.275	No	Yes	60	60	53	F	4.77	16.52	0	17.83
0.298	Yes	Yes	60	60	69	M	8.48	25.68	7.25	26.45
0.297	Yes	Yes	60	60	80	F	4.19	27.91	4.2	26.71
0.252	Yes	Yes	60	60	73	F	−1.64	14.95	0	14.91
0.334	Yes	Yes	60	60	73	M	7.66	16.61	1.74	17.9
0.237	Yes	Yes	60	60	85	F	5.9	18.68	3.83	20.23
0.328	Yes	Yes	60	60	82	F	7.97	26.65	7.95	20.4
0.314	Yes	Yes	60	60	68	M	8.56	22.6	3.64	25.79
0.289	Yes	Yes	50	60	71	M	11.46	26.19	2.52	32.37
0.26	Yes	Yes	60	60	59	F	3.54	20.98	2.83	22.48
0.321	Yes	Yes	60	60	76	M	7.32	24.8	9.38	28.67
0.277	Yes	Yes	60	60	83	F	11.67	24.36	5.25	26.5
0.306	Yes	Yes	60	60	78	M	11.45	31.62	8.78	36.24
0.309	Yes	Yes	60	60	64	M	6.47	25.67	1.38	27.39
0.267	Yes	Yes	60	60	63	F	3.65	29.26	4.51	28.06
0.293	Yes	Yes	60	60	78	M	9.86	28.35	9.64	27.78
0.259	Yes	Yes	60	60	36	F	6.91	22.7	1.55	25.91
0.319	Yes	Yes	60	60	50	M	3.66	29.97	−1.7	29.81
0.273	Yes	Yes	60	60	52	F	4.64	22.85	9.38	23.83
0.267	Yes	Yes	60	60	75	M	6.83	23.03	4.7	25.01
0.231	Yes	Yes	60	60	50	F	2.03	23.43	3.16	23.44
0.272	Yes	Yes	60	60	86	M	7.62	30.68	7.08	28.88

distinguished from those requiring other surgeries, like patients affected by midline shift, in whom a craniotomy is usually needed. All this would have included biases and methodological inaccuracies that are not desirable and are not the core of this simulation study.

To obtain reliable results, we performed multimodal simulation by using the most advanced tools available. Plaster models of the skull were created to verify the accuracy of entry point definition by merging craniometric measures, augmented holographic reality reconstruction of the device, and 3D navigation. The latter was also used to assess the target by using a navigated stylet through the device, positioned inside the burr hole created in the plaster model. Augmented reality was also used to simulate the procedure using a holographic representation of both the skull and the device, thus improving familiarity with the simulation process and optimizing the device use. Of the

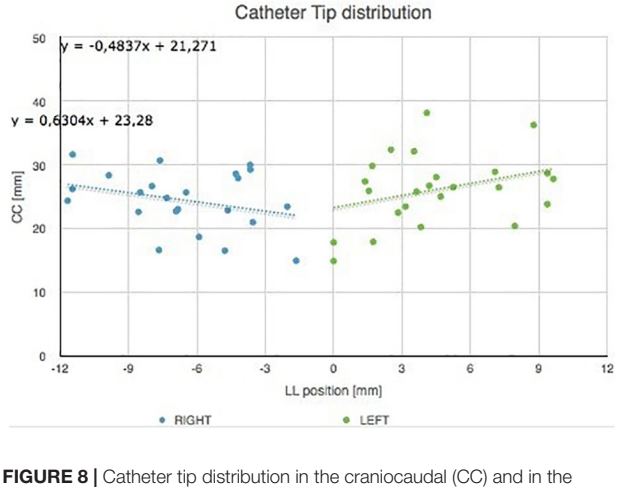

FIGURE 8 | Catheter tip distribution in the craniocaudal (CC) and in the latero-lateral (LL) position in the left and right brain hemispheres, calculated in our cohort using the augmented reality tool. The trend lines of catheter tip position in the right and left lobes are indicated.

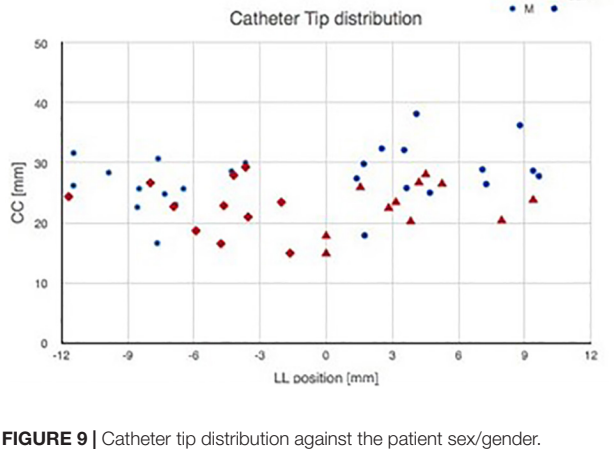

FIGURE 9 | Catheter tip distribution against the patient sex/gender.

utmost importance, the computer-based simulation using engineering software allows us to demonstrate the device's accuracy mathematically.

According to our preliminary simulation study, the guide is a reliable device that deserves further investigation in larger cohorts and clinical settings. Considering a misplacement rate, reported in literature, of 12–60%, our results suggest that the device could improve safety and reduce the misplacement rate. Of course, clinical tests will provide more realistic data about its strength and limitations.

This study has been endorsed by the International Society of Reconstructive Neurosurgery (ISRN), and it has been proposed and accepted by five centers in Europe (Cannizzaro Hospital, Catania, Italy; Christian Doppler-Klinik – Universitätsklinikum der PMU, Salzburg, Austria; Fondazione Policlinico Universitario A. Gemelli IRCCS, Catholic University, Rome, Italy; Tor Vergata University Medical School, Rome, Italy; and Highly Specialized Hospital of National Importance Garibaldi, Catania, Italy), which could be further extended if needed.

Multimodal simulation offers unheard-of opportunities, allowing professionals to experience surgical procedures in a virtual setting that replicates, with high efficacy, the actual clinical practice, but with the further advantage of quantitatively analyzing all the steps, with the final aim to favor a safer and effective quality of care. Even in future clinical studies that we will promote, the association with neuronavigation will offer greater safety in EVD placement with this novel device.

Only after getting enough volume of data confirming the safety of EVD placement with this device would the procedure be performed only device-based with reasonable safety and efficacy. Again, this is a simulation, an experimental study to validate the trajectory offered by the device and its property to get the perpendicularity required immediately, indicated in literature to achieve the correct EVD placement.

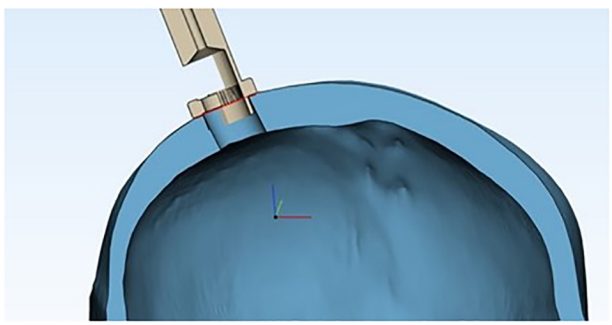

FIGURE 10 | Cross section of the device's proximal end inside the burr hole, showing the skull's geometric properties, assuming the skull as a sphere and the burr hole as a chord.

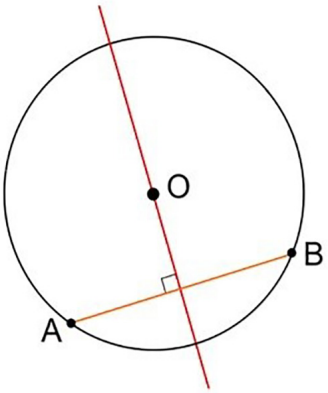

FIGURE 11 | Geometric representation of the perpendicularity obtained, considering the plane as tangent to the spherical surface at the entry point.

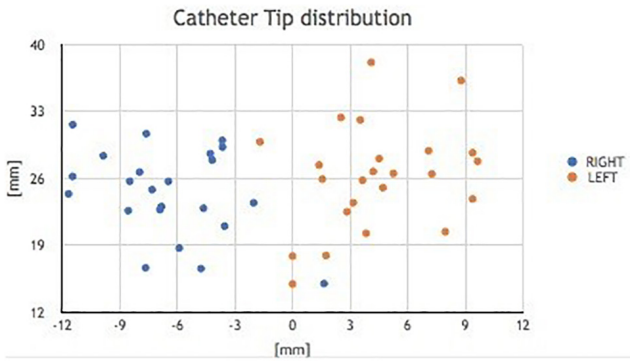

FIGURE 12 | Catheter tip distribution to the right and left.

CONCLUSION

This study provides encouraging results on a simple, cheap device for EVD placement. Our multimodal simulation, through cadaveric, 3D computer-based simulation, 3D plaster modeling, 3D neuronavigation, and augmented reality, shows that the device could offer a safer and more effective EVD placement. Our results should be validated in a multicenter clinical study, based on the encouraging data obtained in the present simulation study.

PATENTS

Number RM2014A000376: Guide for the positioning of cerebral catheters in neuronavigation, for the monitoring of intracranial pressure, CSF drainage in the case of sub-arachnoid hemorrhage or hydrocephalus; possible extension of drainage of abscesses and cerebral hematoma evacuation.

DATA AVAILABILITY STATEMENT

The original contributions presented in the study are included in the article/supplementary material, further inquiries can be directed to the corresponding author/s.

AUTHOR CONTRIBUTIONS

GU: conceptualization, writing—original draft preparation, supervision, and project administration. GU and LS: methodology. GS: methodology, form analysis, and writing—review and editing. RMi, SD, MG, and AS: software. SC, MV, DI, and GB: validation. GU, GS, LS, and KY: formal analysis and writing—review and editing. GU, MF, ST, GN, GR, and FG: investigation. GU, RMi, SD, and MG: resources. RMi, SD, and MG: data curation. GU, MS, and RMa: visualization. LS: funding acquisition. All authors have read and agreed to the published version of the manuscript.

ACKNOWLEDGMENTS

We wish to thank Profs. M. F. Fraioli and F. G. Garaci for their support in the preliminary steps. A special thanks to ApoQlar (Sirko Pelzl and Liliana Duarte) and MtOrtho (Gianluca Tropea) for their technical support for augmented reality and 3D computer reconstruction simulations, respectively. Thanks to Lorenzo Falcolini and Federico Righetti, who provided the prototypes of the device for testing.

REFERENCES

Amoo, M., Henry, J., and Javadpour, M. (2021). Common trajectories for freehand frontal ventriculostomy: a systematic review. *World Neurosurg.* 146, 292–297. doi: 10.1016/j.wneu.2020.11.065

Bergdal, O., Springborg, J. B., Holst, A. V., Hauerberg, J., Way, S., Breum, P., et al. (2013). Accuracy of tunnelated vs. bolt-connected external ventricular drains. *Clin. Neurol. Neurosurg.* 115, 1972–1975. doi: 10.1016/j.clineuro.2013.05.026

Cabrilo, I., Craven, C. L., Dasgupta, D., Reddy, U., and Toma, A. K. (2021). Accuracy of bolt external ventricular drain insertion by neurosurgeons of different experience. *Acta Neurochir. (Wien)* 163, 1121–1126. doi: 10.1007/s00701-021-04712-7

Chai, F. Y., Farizal, F., and Jegan, T. (2013). Coma due to malplaced external ventricular drain. *Turk Neurosurg.* 23, 561–563. doi: 10.5137/1019-5149.JTN.5724-12.1

Fuller, A. T., Barkley, A., Du, R., Elahi, C., MScGH, Tafreshi, A. R., et al. (2020). Global neurosurgery: a scoping review detailing the current state of international neurosurgical outreach. *J. Neurosurg. [Online ahead of pring]* 1–9. doi: 10.3171/2020.2.JNS192517

Ghajar, J. B. (1985). A guide for ventricular catheter placement. Technical note. *J. Neurosurg.* 63, 985–986. doi: 10.3171/jns.1985.63.6.0985

Gil, Z., Siomin, V., Beni-Adani, L., Sira, B., and Constantini, S. (2002). Ventricular catheter placement in children with hydrocephalus and small ventricles: the use of a frameless neuronavigation system. *Childs Nerv. Syst.* 18, 26–29. doi: 10.1007/s00381-001-0550-3

Greenberg, M. S. (2019). *Handbook of Neurosurgery*, 9th Edn. New York, NY: Thieme Medical Publishers Inc.

Jakola, A. S., Reinertsen, I., Selbekk, T., Solheim, O., Lindseth, F., Gulati, S., et al. (2014). Three-dimensional ultrasound-guided placement of ventricular catheters. *World Neurosurg.* 82, 536.e5–539.e5. doi: 10.1016/j.wneu.2013.08.021

Kakarla, U. K., Kim, L. J., Chang, S. W., Theodore, N., and Spetzler, R. F. (2008). Safety and accuracy of bedside external ventricular drain placement. *Neurosurgery* 63(Suppl. 1), ONS162–ONS166, discussion ONS166-ONS167. doi: 10.1227/01.neu.0000335031.23521.d0<pmid<

Lee, C. K., Tay, L. L., Ng, W. H., Ng, I., and Ang, B. T. (2008). Optimization of ventricular catheter placement via posterior approaches: a virtual reality simulation study. *Surg. Neurol.* 70, 274–277. doi: 10.1016/j.surneu.2007.07.020 discussion 277-8,

Lee, K. S., Zhang, J. J. Y., Bolem, N., Leong, M. L., Goh, C. P., Hassan, R., et al. (2020). Freehand insertion of external ventricular drainage catheter: evaluation of accuracy in a single center. *Asian J. Neurosurg.* 15, 45–50. doi: 10.4103/ajns.AJNS_292_19

Mahan, M., Spetzler, R. F., and Nakaji, P. (2013). Electromagnetic stereotactic navigation for external ventricular drain placement in the intensive care unit. *J. Clin. Neurosci.* 20, 1718–1722. doi: 10.1016/j.jocn.2013.03.005

Park, B., Han, S., Byoun, H. S., Han, S., Choi, S. W., and Lim, J. (2020). The assessment of geometric reliability of conventional trajectory of ventriculostomy in a three dimensional virtual model and proposal of a new trajectory. *Neurol. Med. Chir. (Tokyo)* 60, 264–270. doi: 10.2176/nmc.oa.2019-0304

Park, Y. G., Woo, H. J., Kim, E., and Park, J. (2011). Accuracy and safety of bedside external ventricular drain placement at two different cranial sites : kocher's point versus forehead. *J. Korean Neurosurg. Soc.* 50, 317–321. doi: 10.3340/jkns.2011.50.4.317

Patil, V., Lacson, R., Vosburgh, K. G., Wong, J. M., Prevedello, L., Andriole, K., et al. (2013). Factors associated with external ventricular drain placement accuracy: data from an electronic health record repository. *Acta Neurochir. (Wien)* 155, 1773–1779. doi: 10.1007/s00701-013-1769-y

Phillips, S. B., Delly, F., Nelson, C., and Krishnamurthy, S. (2014). Bedside external ventricular drain placement: can multiple passes be predicted on the computed tomography scan before the procedure? *World Neurosurg.* 82, 739–744. doi: 10.1016/j.wneu.2013.08.030

Pishjoo, M., Khatibi, K., Etemadrezaie, H., Zabihyan, S., Ganjeifar, B., Safdari, M., et al. (2021). Determinants of accuracy of freehand external ventricular drain placement by neurosurgical trainees. *Acta Neurochir. (Wien)* 163, 1113–1119. doi: 10.1007/s00701-020-04671-5

Rehman, T., Rehman, A., Ali, R., Rehman, A., Bashir, H., Ahmed Bhimani, S., et al. (2013). A radiographic analysis of ventricular trajectories. *World Neurosurg.* 80, 173–178. doi: 10.1016/j.wneu.2012.12.012

Robertson, F. C., Briones, R., Mekary, R. A., Baticulon, R. E., Jimenez, M. A., Leather, A. J. M., et al. (2019a). Task-sharing for emergency neurosurgery: a retrospective cohort study in the Philippines. *World Neurosurg. X* 6:100058. doi: 10.1016/j.wnsx.2019.100058

Robertson, F. C., Esene, I. N., Kolias, A. G., Kamalo, P., Fieggen, G., Gormley, W. B., et al. (2019b). Task-shifting and task-sharing in neurosurgery: an international survey of current practices in low- and middle-income countries. *World Neurosurg. X* 6:100059. doi: 10.1016/j.wnsx.2019.100059

Robertson, F. C., Esene, I. N., Kolias, A. G., Khan, T., Rosseau, G., Gormley, W. B., et al. (2019c). Global perspectives on task shifting and task sharing in neurosurgery. *World Neurosurg. X* 6:100060. doi: 10.1016/j.wnsx.2019.100060

Rosenbaum, B. P., Wheeler, A. M., and Krishnaney, A. A. (2013). External ventricular drain placement causing upgaze palsy: case report. *Clin. Neurol. Neurosurg.* 115, 1514–1516. doi: 10.1016/j.clineuro.2012.12.008

Saladino, A., White, J. B., Wijdicks, E. F., and Lanzino, G. (2009). Malplacement of ventricular catheters by neurosurgeons: a single institution experience. *Neurocrit. Care* 10, 248–252. doi: 10.1007/s12028-008-9154-z

Shimizu, S., Tanaka, R., Iida, H., and Fujii, K. (2004). Manual occipital ventricular puncture for cerebrospinal fluid shunt surgery: can aiming be standardized? *Neurol. Med. Chir. (Tokyo)* 44, 353–357. discussion 358, doi: 10.2176/nmc.44.353

Shtaya, A., Roach, J., Sadek, A. R., Gaastra, B., Hempenstall, J., and Bulters, D. (2018). Image guidance and improved accuracy of external ventricular drain tip position particularly in patients with small ventricles. *J. Neurosurg. [Online ahead of print]* 1–6. doi: 10.3171/2017.11.JNS171892

Siesjö, P. (2014). The enigma of external ventricular drain placement. *World Neurosurg.* 82, 597–598. doi: 10.1016/j.wneu.2013.10.056

Sun, Z., Wu, L., Liu, Z., Zhong, W., Kou, Z., and Liu, J. (2020). Optimizing accuracy of freehand cannulation of the ipsilateral ventricle for intracranial pressure monitoring in patients with brain trauma. *Quant. Imaging Med. Surg.* 10, 2144–2156. doi: 10.21037/qims-20-128

Thomale, U. W., Schaumann, A., Stockhammer, F., Giese, H., Schuster, D., Kästner, S., et al. (2018). GAVCA Study: randomized, multicenter trial to evaluate the quality of ventricular catheter placement with a mobile health assisted guidance technique. *Neurosurgery* 83, 252–262. doi: 10.1093/neuros/nyx420

Toma, A. K., Camp, S., Watkins, L. D., Grieve, J., and Kitchen, N. D. (2009). External ventricular drain insertion accuracy: is there a need for change in practice? *Neurosurgery* 65, 1197–1200, discussion 1200-1201 doi: 10.1227/01.NEU.0000356973.39913.0B

Wilson, M. P., O'Kelly, C., Jack, A. S., and Rempel, J. (2018). Utilizing preprocedural CT scans to identify patients at risk for suboptimal external ventricular drain placement with the freehand insertion technique. *J. Neurosurg. [Online ahead of print]* 1–7. doi: 10.3171/2018.1.JNS172839

Woernle, C. M., Burkhardt, J. K., Bellut, D., Krayenbuehl, N., and Bertalanffy, H. (2011). Do iatrogenic factors bias the placement of external ventricular catheters?–a single institute experience and review of the literature. *Neurol. Med. Chir. (Tokyo)* 51, 180–186. doi: 10.2176/nmc.51.180

Conflict of Interest: Authors RMi, SD, and MG are employed by the company MtOrtho which does not produce the device. They simply used the software to obtain calculations.

The remaining authors declare that the research was conducted in the absence of any commercial or financial relationships that could be construed as a potential conflict of interest.

Copyright © 2021 Umana, Scalia, Yagmurlu, Mineo, Di Bella, Giunta, Spitaleri, Maugeri, Graziano, Fricia, Nicoletti, Tomasi, Raudino, Chaurasia, Bellocchi, Salvati, Iacopino, Cicero, Visocchi and Strigari. This is an open-access article distributed under the terms of the Creative Commons Attribution License (CC BY). The use, distribution or reproduction in other forums is permitted, provided the original author(s) and the copyright owner(s) are credited and that the original publication in this journal is cited, in accordance with accepted academic practice. No use, distribution or reproduction is permitted which does not comply with these terms.

frontiers in Oncology

REVIEW
published: 06 July 2021
doi: 10.3389/fonc.2021.699265

Imaging-Genomics in Glioblastoma: Combining Molecular and Imaging Signatures

Dongming Liu[1†], Jiu Chen[2,3†], Xinhua Hu[1,3], Kun Yang[1], Yong Liu[1], Guanjie Hu[1], Honglin Ge[1], Wenbin Zhang[1,3] and Hongyi Liu[1,3*]*

[1] Department of Neurosurgery, The Affiliated Brain Hospital of Nanjing Medical University, Nanjing, China, [2] Institute of Neuropsychiatry, The Affiliated Brain Hospital of Nanjing Medical University, Fourth Clinical College of Nanjing Medical University, Nanjing, China, [3] Department of Neurosurgery, Institute of Brain Sciences, The Affilated Nanjing Brain Hosptial of Nanjing Medical University, Nanjing, China

Based on artificial intelligence (AI), computer-assisted medical diagnosis can scientifically and efficiently deal with a large quantity of medical imaging data. AI technologies including deep learning have shown remarkable progress across medical image recognition and genome analysis. Imaging-genomics attempts to explore the associations between potential gene expression patterns and specific imaging phenotypes. These associations provide potential cellular pathophysiology information, allowing sampling of the lesion habitat with high spatial resolution. Glioblastoma (GB) poses spatial and temporal heterogeneous characteristics, challenging to current precise diagnosis and treatments for the disease. Imaging-genomics provides a powerful tool for non-invasive global assessment of GB and its response to treatment. Imaging-genomics also has the potential to advance our understanding of underlying cancer biology, gene alterations, and corresponding biological processes. This article reviews the recent progress in the utilization of the imaging-genomics analysis in GB patients, focusing on its implications and prospects in individualized diagnosis and management.

Keywords: glioblastoma, radiomics, imaging genomics, artificial intelligence, machine learning, deep learning

OPEN ACCESS

Edited by:
Nico Sollmann, University of California, San Francisco, United States

Reviewed by:
Milan Girish Chheda, Washington University School of Medicine in St. Louis, United States
Manjari Pandey, West Cancer Center, United States
Vasileios Stathias, University of Miami, United States

***Correspondence:**
Hongyi Liu
njnkyylhy@163.com
Wenbin Zhang
wenbinzhang@njmu.edu.cn

[†]These authors have contributed equally to this work and share first authorship

Specialty section:
This article was submitted to Neuro-Oncology and Neurosurgical Oncology, a section of the journal Frontiers in Oncology

Received: *23 April 2021*
Accepted: *23 June 2021*
Published: *06 July 2021*

Citation:
Liu D, Chen J, Hu X, Yang K, Liu Y, Hu G, Ge H, Zhang W and Liu H (2021) Imaging-Genomics in Glioblastoma: Combining Molecular and Imaging Signatures. Front. Oncol. 11:699265. doi: 10.3389/fonc.2021.699265

Abbreviation: AI, Artificial intelligence; AUC, Area under receiver operating characteristic curve; CNNs, Convolutional neural networks; CNS, Central nervous system; CpG, Cytosine-phosphate-guanine; EGFR, Epidermal growth factor receptor; FLAIR, Fluid-attenuated inversion recovery; GB, Glioblastomas; GO, Gene Ontology; GSEA, Gene set enrichment analysis; 2HG, R(-)-2-hydroxyglutarate; IBSI, Image biomarker standardization initiative; IDH, Isocitrate dehydrogenase; LASSO, Least absolute shrinkage and selection operator; MRI, Magnetic resonance imaging; MGMT, O(6)-methylguanine-DNA methyltransferase; NF1, Neurofibromatosis 1; OS, Overall survival; PET, Positron emission tomography; PFS, Progression-free survival; PTEN, Gene of phosphate and tension homology deleted on chromosome ten; PIK3, Phosphatidylinositol-3-OH kinase; RB1, Retinoblastoma 1; RF, Random forest; RNN, Recurrent neural network; ROI, Region of interest; RRS, Radiomic risk score; RTK, Receptor tyrosine kinase; SMOTE, Synthetic minority oversampling technique, SVM, Support vector machines; TCGA, The Cancer Genome Atlas; TCIA, The Cancer Imaging Archive; TMZ, Temozolomide; TPOT, Tree-based Pipeline Optimization Tool; WHO, World Health Organization.

INTRODUCTION

Glioblastoma (GB) is the most common malignant primary brain tumor in adults, accounts for 48.3% of malignant brain tumors (1). Much work has focused on GB, given that it has the characteristics of infiltrating the surrounding brain tissue (2), and has an aggressive course and extremely grim prognosis (3). Gene expression profiling has provided new perspectives for the identification of tumor-associated genetic mutation, biomarkers, and therapeutic targets of glioblastoma (4, 5). The 2016 central nervous system (CNS) tumor classification of the World Health Organization (WHO) incorporated molecular markers into traditionally histopathological classification, providing an integrated phenotypic and genetic classification (6). Recently, based on transcriptomic profiling, GBs have been divided into proneural, classical, and mesenchymal subtypes (7).

The characteristic neuroradiological findings raise the initial suspicion for GB and determine the initial surgical approach and plan. Diagnosis is confirmed through histo-molecular evaluation of the tissue post-biopsy/resection. Traditional magnetic resonance imaging (MRI) has greatly improved the diagnostic efficiency of intracranial lesions, but there are still limitations in the definitive diagnosis of brain tumors. Over the past few decades, there has been a rapid development towards the application of quantitative parametric MRI techniques for GB evaluation (8). More recently, advanced computer technology has permeated the field of modern medicine, making precision medicine an inevitable trend in the development of clinical medicine. Artificial intelligence (AI) is a broad term that covers a wide range of disciplines including computer vision, machine learning, and more. Deep learning is a branch of machine learning that uses artificial neural networks as a framework to learn and characterize databases. There has been growing interest in the application of AI techniques to neuroimaging research, making machine learning and deep learning algorithms critical to the radiomics procedures.

Radiomics utilizes high-throughput radiomics features and mathematical models to quantify tumor characteristics, allowing the non-invasive capture of microscale information hidden within medical imaging (9, 10). As an important branch of radiomics, imaging-genomics (also known as radiogenomics) further links imaging characteristics (phenotypes) with genetic, mutational, and expression patterns (11, 12). The basic hypothesis of imaging-genomics is that the expression of a specific set of genes or molecular alterations affects the extractable imaging phenotypes (13). A particular focus of imaging-genomics analysis has been on the association between imaging characteristics and gene expression patterns, including the expression of individual genes and the expression of specific gene subgroups (14). Just like the resolution and complexity that genomics has brought to tumor biology, imaging-genomics also brings similar effects to traditional medical images. The ultimate goal of radiomics is to maximize the utilization of medical imaging information to help clinicians make clinical decisions, so as to minimize the possibility of potential invasive maneuvers. The increasing importance of genetic markers has also led to the rapid growth of GB imaging-genomics research, with progressively greater complexity, including the combination of artificial intelligence (AI) technology. More recently, deep learning using convolutional neural networks has further improved radiogenomics prediction (15, 16), providing unique opportunities and challenges for the diagnosis and treatment evaluation of GB.

Herein, we will review the latest researches on radiomics and imaging-genomics of GB. First, we briefly introduced the genomic characteristics of GB and the principle of imaging-genomics, and then summarized the findings of the latest research. Finally, we will present our opinions on its current challenges, and potential future directions.

GENOMICS IN GLIOBLASTOMA

Traditionally, GBs can be divided into "primary" and "secondary" GBs. The vast majority of GB (about 90%) develop rapidly *de novo* in elderly patients and are mostly isocitrate dehydrogenase (IDH) wild-type. While secondary GBs develops from a preexisting lower-grade glioma in younger patients and usually carry mutations in IDH (17). Radiologically, primary GBs are widely distributed in the brain, while secondary GBs are preferentially located in the area of the frontal lobe surrounding the rostral extension of the lateral ventricle in younger patients (17, 18). Primary and secondary GBs are largely histologically indistinguishable, but they are different in genetic and epigenetic profiles (17). The genomic and transcriptome characteristics of these tumors have revealed the key alterations that may contribute to the classification and evaluation of the disease (4, 19, 20) (17) (21).Different bioinformatics algorithms have identified several genes as significantly mutated in GB, including but not limited to epidermal growth factor receptor (EGFR), TP53, PTEN, Neurofibromatosis 1 (NF1), and RB1 (20, 21). Additionally, genomic analysis based on multiple sampling from the same neoplasm suggests that transcriptome subtypes are heterogeneous in GB (22) (23). Patient-specific intratumor heterogeneity of GB underlies variation in response to treatment, which contributes to the eventual failure of treatment (22, 24, 25), including drug resistance, radiotherapy resistance, and fast and incurable tumor recurrence. Thus, relying only on single tissue samples from individual patients to understand the cancer dynamics of GB is challenging.

The whole-genome sequence analysis has revealed the genetic and epigenetic landscapes of human brain GB (4, 20). Complex gene interaction events and molecular modulation networks are involved in the occurrence and development of GBs (4, 5, 26). It is expected that one or several biomarkers will provide information to help clinicians make the diagnosis, and enable clinical experts to make the best choice among various treatment options, such as surgery and/or chemotherapy, and/or radiotherapy, and/or targeted therapy. Numerous studies have identified alterations of several core signaling pathways in GB, including the RB1 pathway, the TP53 pathway, and the PI3K/PTEN pathway (4, 21). The heterogeneity of GB cells (26)

suggests that targeting strategies based on multiple elements of different signaling pathways might constitute a more efficient therapy for GB (5).

Given its invasive and infiltrating nature, GB is essentially considered to be a disease of the entire brain (27). Surgical biopsy is currently the standard procedure for providing the genomics information of GB. However, a biopsy is not only highly invasive, but its accuracy is also limited by the biopsy site, resection type, and disease variability. Compared with traditional genomic analysis, imaging-genomics has the advantage of assessing the entire tumor volume, and non-invasively provides a "virtual biopsy" by predicting specific gene status, biological processes, and even core signaling pathways of GB (28–30) (28, 29, 31). High-resolution imaging technologies can present the tumor completely and three-dimensionally. Based on this property, imaging-genomics can associate the radiological phenotypes (such as shape or texture) of a specific spatial location (such as necrosis, high perfusion, or even more subtle subregions) with the tumoral molecular characteristics of the same location. Also, by associating the genetic status of the biopsy location with the quantitative imaging features, imaging-genomics has the potential to help characterize tumoral genetic heterogeneity (30), which shows diagnostic value under the context of individualized oncology.

RADIOMICS AND IMAGING-GENOMICS OF GLIOBLASTOMA

Traditional pathology and radiology have been primarily focused on the associations between histopathologic and visual imaging findings, while radiomics and imaging-genomics focus on exploring the relationships between imaging phenotypes and biological characteristics (11, 12). Generally, radiomics is dedicated to discovering the biological significance (such as predicting survival and treatment prognosis) of specific imaging phenotype, which when correlated with genomics is termed imaging-genomics. Imaging-genomics analysis helps to understand the biological associations behind image phenotypes, explain how biological processes are reflected in imaging, and define imaging markers associated with molecular biological characteristics. When constructing an imaging genomic map of GB, several dimensions need to be considered, including the disease course, imaging category, lesion delineation, features extraction and selection, and biological data type, as well as model building or integration (11). Typically, the imaging features used in a radiomics or imaging-genomics study are mainly divided into two categories, namely manually defined features and deep learning features.

Feature Extraction, Selection, and Corresponding Modeling

Manually Defined Features

Manually defined feature-based imaging-genomics utilizes specific mathematical algorithms to extract features from pre-depicted regions of interest (ROI) (**Figure 1**). After feature extraction and feature selection, machine learning models are used to solve classification and/or regression problems. Usually, the steps of the process mentioned above includes a few phases as following: 1) Data acquisition; 2) Image pre-processing, including multiparametric imaging registration, noise reduction, intensity and/or orientation normalization, spatial resampling, and corrections of MRI field inhomogeneities; 3) Segmentation of ROI, segment the tumors into necrosis, enhancement, edema, and peritumoral parts, etc. by manual

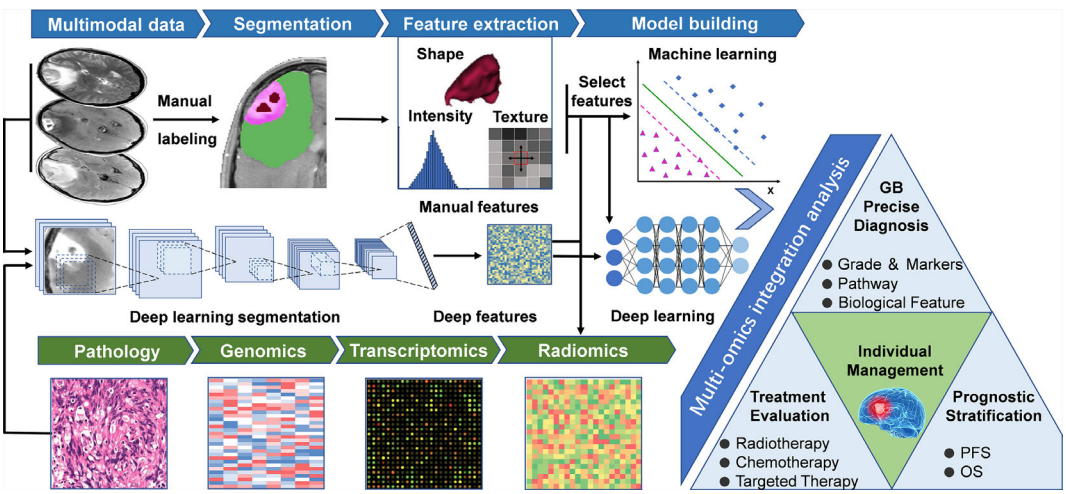

FIGURE 1 | General workflow of radiomics studies in neuro-oncology. The workflow of a radiomics study, including the following steps: (1) Multimodal imaging and biological data acquisition; (2) Data preprocessing and standardization; (3) Delineation of regions of interest, including manual segmentation and deep learning-based segmentation; (4) Radiomics feature extraction using predefined algorithms or deep learning techniques; (5) Data analysis, feature reduction, and/or selection for further analysis of machine learning and/or deep neural networks; (6) Multi-omics and clinical information integrated model training and testing, guiding individualized disease diagnosis, treatment evaluation, and prognosis prediction. GB, Glioblastoma; OS, Overall Survival; PFS, Progression free survival.

delineation or (semi-) automated algorithms; 4) Feature extraction, extract different kinds of quantitative features that reflect the heterogeneity of tumors, including shape features, histogram-based features, textural features, and higher-order statistics features; 5) Feature selection, including supervised and unsupervised methods to overcome the issue of redundancy and overfitting that may be seen with multitudinous features; 6) Model building and evaluation, build a mathematical model (such as regression models, random forest (RF), and/or support vector machines (SVM) based on the selected features to predict a known, underlying ground truth, including specific genetic mutation or pathway alterations. In general, training set data is used for learning to fit the parameters of a classifier, while the validation set is used to tune the parameters of the model. Ideally, after model training and validation, the final models should be applied to the test set (unexposed independent data) to evaluate the performance of the final model. A robust radiomic model must be validated by independent, external data to show its value for clinical promotion and application.

Deep Learning-Based Features

Deep learning, a subcategory of machine learning based on neural networks (32), represents a class of algorithms that use stacked neural network structures (33). In deep learning-based imaging-genomics, different network structures such as auto-encoders or convolutional neural networks (CNNs) are utilized to mine the hidden features from the initial data (15, 34). The typical way to extract deep learning features is to train a deep learning model using observed indicators, and then extract the outputs of specific layers as deep learning features (35). For example, the results of the final fully connected layer of CNNs or the final convolutional layer of auto-encoder can be extracted as deep learning features (36). The extracted deep features can either be trained by an artificial neural network for classification and prediction (15) or leave the network and fit into different classifiers (35) (such as SVM, RF) to generate a model (**Figure 1**), the latter process is similar to the approach of manually defined feature-based imaging-genomics. Recently, deep learning has been successfully applied in digital pathology to segment nuclei and for the classification of molecular markers (37, 38). Deep learning-based imaging-genomics usually requires relatively large datasets. Auto-encoders provide an alternative method to extract deep features when there is not enough data to train a deep learning model (34, 36). Another technique to overcome this limitation is transfer learning (39, 40), which essentially uses a pre-trained network (usually on natural images) to solve the data set needs of deep network training (34). **Figure 1** describes the main workflow of the above two methods, and **Table 1** summarizes several radiomics studies designed according to this workflow.

Imaging-Genomics of Glioblastoma

As a subclass of radiomics, imaging-genomics focuses more on the relationships between imaging characteristics of a disease, and its gene expression patterns, gene mutations, and other genomic-related characteristics (11). The gene expression patterns for constructing these relationships include not only the expression of a single gene (45, 50), but also the measures that summarize expressions of specific gene subsets (14, 29, 51, 52), the corresponding signal pathways (29, 53), and consequent biological effects (28, 54). 'Imaging-genomics' research also refers to a study aimed at discovering those relationships.

In addition to predicting the expression status of specific molecular markers, the current imaging genomics researches can

TABLE 1 | Applications of radiomics for predicting specific molecular markers in GB.

Study	Imaging Modality	Molecular signature(s)	No. of Patients Training + Testing	No. of features Initial	No. of features Final	Performance AUC/Accuracy	Features selection and Model building
Li et al. (41)	MRI, T1+T1CE+T2+Flair	IDH1 status	225 (118 + 107)	1614	8	0.96[a]	RF-Boruta, RF
Chang et al. (42)	MRI, T1+T1CE+T2+Flair	IDH1,MGMT,and 1p/19q	259 (80%+20%)	NA	NA	(IDH1) 94%[b]	CNNs
Zhang et al. (43)	MRI,T1+T1CE+T2+ Flair +DWI	IDH1/2	120 (90 + 30)	2970	387	0.92[a]	Correlation coefficient, RF
Li et al. (44)	PET	IDH1/2	127 (84 + 43)	1561	11	0.90[a]	Lasso, Multivariate logistic regression
Wei et al. (45)	MRI, T1CE+Flair+DWI	MGMT	105 (74 + 31)	3051	13	0.90[a]	Correlation coefficient, MRMR, Logistic regression
Li et al. (46)	MRI, T1+T1CE+T2+Flair	MGMT	193 (133 + 60)	1705	6	0.88[a]	Correlation coefficient, RF-Boruta, RF
Qian et al. (47)	PET	MGMT	86 (59 + 27)	1450	3	80%[b]	Correlation coefficient, RF Extra trees, SVM, Neural network
Su et al. (48)	MRI, T1+T1CE+T2+Flair	H3 K27M	100 (75 + 25)	85	10	0.85[a]	TPOT
Choi et al. (15)	MRI, T1CE+T2+Flair	IDH1/2 status	1166 (727 + 439)	NA	NA	0.96[a]	CNNs, RF
Jin et al. (38)	H&E Pathological slides	IDH1/2 and 1p/19q	323 (267 + 56)	NA	NA	87.6%[b]	CNNs
Liu et al. (49)	H&E Pathological slides	IDH1/2 status	200 (6:1:1)	NA	NA	0.931[a]	CNNs

CNNs, Convolutional neural networks; DWI, Diffusion Weighted Imaging; Flair, Fluid-attenuated inversion recovery; H&E, haematoxylin and eosin; IDH, Isocitrate dehydrogenase; Lasso, Least absolute shrinkage and selection operator; MGMT, O (6)-methylguanine-DNA methyltransferase; MRI, Magnetic resonance imaging; MRMR, Minimum redundancy and maximum relevance algorithm; NA, Not available; PET, Positron emission tomography; 1p19q, the co-deletion status of the 1p/19q chromosome arms; RF, Random forest; SVM, Support vector machines; T1, T1-weighted MRI; T2, T2-weighted MRI; T1CE, contrast-enhanced T1-weighted MRI; TPOT, the Tree-based Pipeline Optimization Tool.

The values in the performance column were achieved using the best model in the test set. [a] and [b] are used to mark the AUC and accuracy values, respectively.

be divided into several directions. On the one hand, researchers can first identify the prognostic imaging features (like OS or progression-free survival, PFS) to calculate individualized indicators (such as radiomic risk score, RRS), based on which patients will be further classified into different subgroups (low- or high-risk groups). Some bioinformatics analysis methods such as Gene Ontology (GO), Gene Set Enrichment Analysis (GSEA) analysis can be further used to detect differences in molecular biology of different subgroups, corresponding signal pathways, and downstream biological processes (28, 54, 55). Another research paradigm is the reverse process of the above method (13, 56). Bioinformatics analysis can reveal the pathways, biological processes, and expression of protein corresponding to specific molecular markers detected by sequencing technique. These biological processes can finally be mapped in the form of different imaging phenotypes (like necrosis or edema) on multi-modal images, and then captured by the quantitative radiomic features (such as shape, texture, or wavelet). A pioneering radiogenomics study by Zinn et al. (13) showed that radiomic-features could significantly predict periostin expression status in GB patients (Area under the receiver operating characteristic curve, AUC=76.56%) and orthotopic xenografts (AUC=92.26%). The authors tried to establish causality between radiomic texture features and expression levels in a pre-clinical model. This was one of the first radiogenomics studies highlighting a causal linkage between specific gene expression status and radiomic-features of GB. This kind of research paradigm is more suitable for the verification of the radiogenomics model and its corresponding conclusions. However, to date, it has not been elucidated how specific biological processes reflect phenotypes through imaging. Additional multidisciplinary studies in the future are needed to shed more light on this subject. **Figure 2** describes the common steps of an imaging-genomic study and **Table 2** summarizes several imaging-genomic studies in patients with GB.

Although imaging-genomics has broad application prospects, current researches mainly focus on one or several aspects of the procedures and purpose discussed above. Here, we will review the recent progress in the utilization of the imaging-genomics analysis in GB patients.

PROGRESS OF IMAGING-GENOMICS IN GB

Candidate Molecular Alterations

Isocitrate Dehydrogenase 1 and 1p/19q Codeletion

Genetic analysis revealed that the IDH1 gene mutations exist in approximately 12% of GB (21). Tumor-related IDH1 mutations result in the enhancement of enzyme function, which causes the accumulation of R(-)-2-hydroxyglutarate (2HG), and the accumulation of 2HG might drive oncogenesis (60). IDH1 mutation is also an independent factor for predicting the prognosis of patients with glioma (61), and the IDH and 1p/19q codeletion status has been introduced into the revised WHO classification of CNS tumors (6).

There have been numerous studies attempted to reveal the links between the IDH1 and 1p/19q codeletion status with the imaging-phenotypic appearance of GB (15, 38, 41–43). A model for predicting the state of molecular markers (such as IDH1) needs to take into account the distribution of data, considering that the vast majority of GB are IDH1 wild types (17). In this context, some techniques (like the synthetic minority oversampling technique (SMOTE) and adaptive synthetic) have been proven to have better performance in some cases (62). In a study of 225 GB patients by Li et al. (41), after balancing the data with the SMOTE algorithm, the model combining all-region (necrosis, enhancement, non-enhancement, and edema areas) radiomics features with clinical information achieved the best performance of a 97% accuracy. The radiomics model with multi-regional features has the potential to predict the IDH1 mutation status of GB patients, and the data balance is beneficial to improve the classification performance. Li and colleagues (44) used 18F-fluorodeoxyglucos PET scans from 127 patients, after feature selection through least absolute shrinkage and selection operator (LASSO), the final SVM model used 11 features and yielded an area under curve (AUC) of 90% in the validation set. In general, radiomics utilizing multimodal images seems to achieve better performance than a single modality. Nevertheless, there are also exceptions. Using a 3D-Dense-UNets approach, Yogananda et al. (63) reported a mean accuracy of 97.14% in predicting IDH status. Interestingly, the authors demonstrated similar performance when comparing the T2-based network with the multi-contrast network. One possible reason is that the deep-learning networks using conventional single-modality MR images avoid the effect of head motion due to long scan times, which helps promote clinical translation.

Choi et al. combined perfusion and conventional MRI for the prediction of IDH genotype in a group of 463 patients. The authors reported that the long short-term memory model, a type of recurrent neural network (RNN), showed performance with an accuracy of 92.8% in the validation set and 91.7% in the test set (50). Also, the RNN model can provide certain interpretability by demonstrating which temporal features are crucial for the prediction of IDH genotypes. By performing principal component analysis on their final CNN layer, Chang and co-workers (42) selected the imaging features and obtained a prediction accuracy of 94% for IDH status and 92% for 1p19q codeletion. Recently, Choi and colleagues (15) used MRI data from multiple centers to predict IDH genotypes in a cohort of 1,166 patients with glioma (WHO grade II-IV). Researchers developed an automated approach containing two CNN models, one for tumor segmentation and the other for IDH status prediction. Finally, the automated model achieved the highest diagnostic accuracy of 93.8% and 87.9% in the internal and external test set, respectively. A fully automated process is conducive to the repeatability and generalization of results, which reduces the interference of human factors and is beneficial to future application and promotion of the models.

O (6)-Methylguanine-DNA Methyltransferase

The MGMT gene encodes a DNA repair enzyme named O6-alkylguanine DNA alkyltransferase (64). In this process, the methylmoiety is transferred onto the MGMT protein and thus

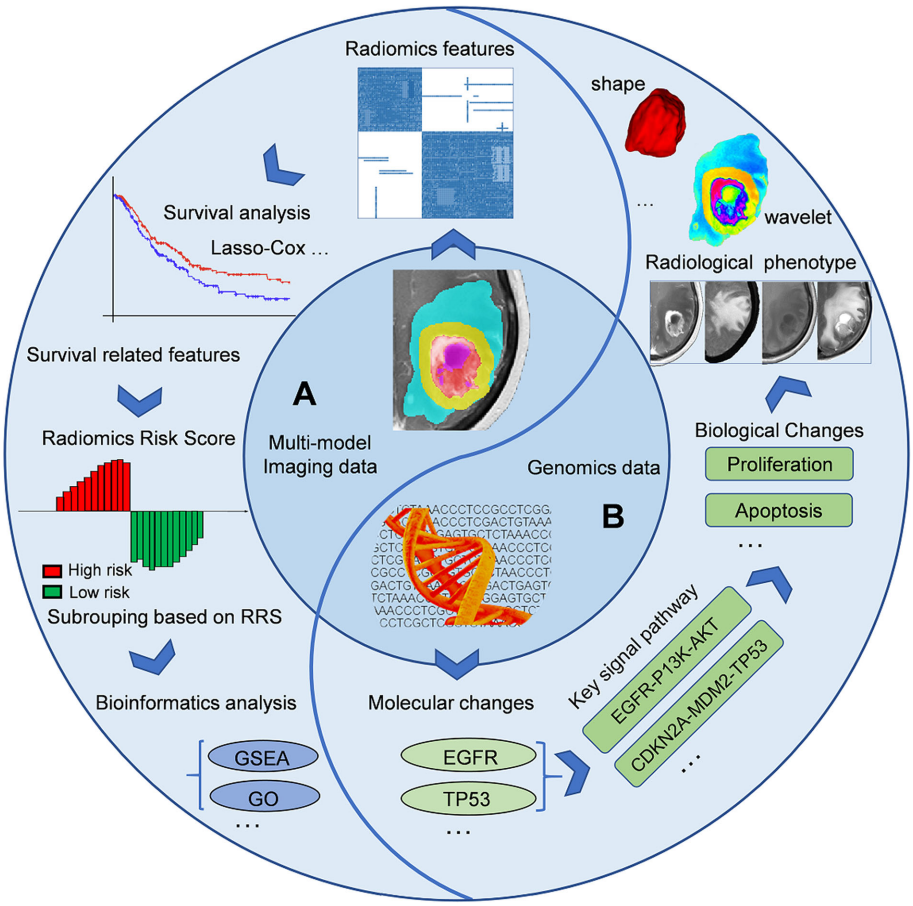

FIGURE 2 | General workflow of imaging-genomics studies. A imaging-genomics research can generally build the relationship between imaging phenotypes and genetic characteristics from two perspectives. **(A)**, Left semicircle, from imaging phenotypes to genomic characteristics: using features extracted from the sub-areas of tumors in multi-modal images to construct individualized RRS or divide patients into different subgroups, and utilize the corresponding sequencing data for further bioinformatics analysis (such as GO or GSEA). **(B)**, Right semicircle, from genomic characteristics to imaging phenotypes: bioinformatics analysis can reveal the pathways, biological processes, and expression of protein corresponding to specific molecular markers detected by sequencing technique. These biological processes can finally be mapped in the form of different imaging phenotypes (like necrosis or edema) on multi-modal images, and then captured by the quantitative radiomic features (such as shape, texture, or wavelet features). EGFR, Epidermal growth factor receptor; GO, Gene Ontology; GSEA, Gene set enrichment analysis; RRS, Radiomic risk score.

is consumed (64, 65). The epigenetic modification of the cytosine-phosphate-guanine (CpG) island at specific CpG sites of the MGMT promoter silences the gene, resulting in low DNA alkylation repair efficiency and enhanced response to temozolomide (TMZ) (66, 67).

The methylation status of the MGMT gene promoter has been considered as a crucial biomarker of tumor response to TMZ chemotherapy. Consequently, it has become an important molecular marker in imaging-genomics research (68–71). Sasaki and colleagues (72) extracted features from MRI data of 201 newly diagnosed GB patients. The diagnostic model of MGMT promoter using two significant Gray-level Co-occurrence Matrix texture features selected by LASSO only yielded a low accuracy of 67%, which remains insufficient for practical use. Wei and colleagues (45) found that the fusion radiomics signature (clinical factors and texture features) showed great performance for predicting MGMT promoter status of glioma, with an AUC value of 0.902 in the validation cohort. Moreover, the model could classify patients into low-risk and high-risk groups for overall survival (OS) after TMZ chemotherapy, which may serve as a basis for individualized treatment recommendations. Li et al. (46) predicted the MGMT promoter methylation used 1,705 radiomics features from multiregional and multiparametric MRI in multicenter cohorts. The final model achieved an accuracy of 80% in the test dataset. Distinguished from the studies in the past (43), however, this study suggested that combing clinical factors with radiomics features did not improve the prediction performance.

PET-based radiomics is also a promising method to noninvasively evaluate the MGMT status of gliomas. Qian et al. (47) extracted features from PET images of 86 patients with GB. Features were selected by comparing the weighted feature coefficient and filtering with bivariate analysis. The Random Forest model using the appropriate parameters from

TABLE 2 | Applications of imaging-genomics for exploring potential signaling pathway or biological processes or in GB.

Study	Imaging Modality	General Purpose	Total Patients Training + Testing	No. of features Initial + Final		Performance AUC/ Accuracy	Statistical Analysis
Choi et al. (51)	MRI, T1+T1CE+T2 +Flair	Exploring biological characteristics behind imaging phenotypes in GB.	200 (144 + 56)	478	7	NA	Lasso-Cox, RRS, GSEA
Itakura et al (57).	MRI, T1CE	Verifying distinct pathway changes behind different imaging subtypes of GB.	265 (121 + 144)	388	388	NA	k-means consensus clustering, IGP
Beig et al. (28)	MRI, T1CE+T2 +Flair	Exploring prognostic stratification-based biological processes in GB.	203 (130 + 73)	2850	25	0.84[c]	Lasso-Cox, RRS, GO, GSEA
Park et al. (29)	MRI,T1+T1CE +T2DWI +Flair +DSC	Identifying Core signaling pathway in GB. (RTK, p53, and RB1 pathways).	120 (85 + 35)	6472	123	(RTK) 0.88[a]	Lasso, RF, logistic regression,
Akbari et al. (58)	MRI, T1+T1CE+T2 +Flair	Predicting status of EGFRvIII and exploring associated biological processes.	129 (75 + 54)	NA	NA	0.86[a]	Multivariate model, SVM
Zinn et al. (52)	MRI, T1+T1CE +Flair	TP53-PTEN-EGFR mutational landscape in GB.	29	2480	457	NA	Spearman rank correlation Hierarchical clustering
Beig et al. (53)	MRI, T1CE+ T2 +Flair	Predicting hypoxia pathway and overall survival in GB.	115 (85 + 30)	270	8	0.83[c]	GSEA, Cox model, Unsupervised clustering
Hsu et al. (59)	MRI, T1CE+ DWI	Classifying immunophenotypes of GB by radiomic features.	116 (32 + 84)	9809	76	79%[b]	RF, Information gain, GSEA Logistic regression
Beig et al. (54)	MRI, T1CE+ T2 +Flair	Identifying sex-specific biological processes and prognostic of GB.	313 (130 + 183)	2850	8	0.88[c]	Lasso-Cox, RRS, GO, GSEA
Zinn et al. (13)	MRI, T1CE+ T2 +Flair	Validating causality between Periostin expression status and MRI-features in GB.	93 (xenografts=40)	4880	31	0.93[a] (xenografts)	Lasso, GSEA, XGboost

DSC, Dynamic susceptibility contrast; DWI, Diffusion weighted imaging; EGFR, Epidermal growth factor receptor; Flair, Fluid-attenuated inversion recovery; GO, Gene ontology; GSEA, Gene set enrichment analysis; IGP, in-group proportion statistic; Lasso, Least absolute shrinkage and selection operator; MRI, Magnetic resonance imaging; NA, Not available; PET, Positron emission tomography; RB1, Retinoblastoma 1; RF, Random forest; RRS, Radiomic risk score; RTK, Receptor tyrosine kinase; SVM, Support vector machines; T1, T1-weighted MRI; T2, T2-weighted MRI; T1CE, contrast-enhanced T1-weighted MRI; XGboost, Extreme Gradient Boosting.

The values in the performance column were achieved using the best model in the test set. [a], [b], and [c] are used to mark the AUC, accuracy, and concordance index values, respectively.

the grid search achieved 80% ± 10% accuracy for the prediction of MGMT promoter status. Kong et al. (73) used PET images from 107 patients with WHO grade II-IV primary diffuse gliomas for prediction. Using Wilcoxon ranksum test for features selection, a radiomics signature comprising five final features for the prediction of MGMT promoter status could be identified, yielding an AUC of 0.86 in the validation sets. However, this model lacks further validation on an external dataset.

The CNN-based classifiers achieved the accuracy from 82.7% to 94.9% in predicting the methylation status of MGMT promoter in GB (74, 75). Chen et al. (74) utilized a deep learning pipeline for automatic tumor segmentation and MGMT promoter status prediction in an end-to-end manner for GB patients. The better tumor segmentation and MGMT prediction performance both came from Fluid-attenuated inversion recovery (FLAIR) images. The CNN-based prediction model in this study had only 4 layers and achieved an accuracy of 82.7%, which might be further improved by a deeper network architecture with multi-layers. Korfiatis et al. (75) compared three different residual deep neural network (ResNet) architectures to evaluate their performance in predicting MGMT promoter status in patients with GB. The researchers found that the ResNet50 architecture (the deepest model with 50 layers) outperformed the two shallower architectures (ResNet18 with 18 layers, ResNet34 with 34 layers), and achieved an accuracy of 94.9% in the test set. Networks with deeper architectures could potentially improve the performance of the model, which also increases the risk of overfitting. Transfer learning and fine-tuning of the existing pre-trained network are alternative methods to improve the utilization of the limited data (34).

Other Potential Genetic/Molecular Markers

EGFR is a transmembrane tyrosine kinase that regulates normal cellular growth in epithelial cell lines. The most common EGFR mutant in GB is EGFRvIII, which is found in 31% of patients (76). Using support vector machine–based approaches, Akbari et al. (58) construct an imaging signature of EGFRvIII and achieved an accuracy of 87% in 129 patients with primary GB. The authors also reported that EGFRvIII mutant GB exhibit increased neovascularization and cell density, which is consistent with a more infiltrative phenotype. Zinn and colleagues (52) demonstrated a relationship between MRI radiomics signatures and the TP53-PTEN-EGFR mutational landscape in 29 GB patients from The Cancer Genome Atlas (TCGA). The radiomics features generated by texture analysis revealed different cellular biofunctions, such as angiogenesis, invasion, and immune response. Despite some gaps exist, glioma radiomics landscape is approaching its genomic counterpart in heterogeneity and complexity.

Diffuse midline glioma with histone H3-K27M mutation is a newly defined entity in the WHO group of grade IV diffuse gliomas (77). Those tumors carry a poor prognosis and frequently occur in brainstem, thalamus in the pediatric population. The underlying histological and radiographic variations (78) make it possible to predict the H3-K27M status of a tumor using radiomics analysis. Su and colleagues (48)

performed an automated machine learning analysis on MRI data from 100 patients with midline gliomas. After feature selection and model optimization using The Tree-based Pipeline Optimization Tool (TPOT), they finally obtained an AUC of 0.903 and an average precision of 0.911 for the prediction of H3 K27M mutant status in midline glioma. Automated machine learning methods (such as TPOT) are relatively researcher-independent, which increases the robustness of the results.

Signaling Pathways and Biological Processes

Genomic analysis has identified a highly interconnected network of aberrations in GB, including three major pathways: receptor tyrosine kinase (RTK), the retinoblastoma 1 (RB), and tumor protein p53 tumor suppressor pathways (4). Radiogenomics studies have revealed the relationship between different imaging features and certain signaling pathways or biological processes.

In a study of 120 patients with GB, using diffusion, perfusion MRI, and next-generation sequencing technology, Park and colleague (29) combined radiomic and genomic features to predict core signaling pathways in IDH wild-type GB. Different types of radiomic features were identified by the combined radiogenomics model, corresponding to RTK, P53, and RB pathways respectively. This study demonstrates that MRI features can help noninvasively identify the core signaling pathway alterations in GB, which may further support the use of targeted therapy for glioblastoma rather than a one-size-fits-all approach. Another study based on perfusion MRI showed that the elevated perfusion features were significantly associated with poor patient survival in a subgroup of GB patients. Angiogenesis and hypoxia pathways were enriched in this subgroup, suggesting the possible efficacy of anti-angiogenic therapy (79). Similarly, imaging features from enhancing tumor and edematous regions were identified to be associated with the hypoxia pathway (53), imaging markers of hypoxia can discriminate GB patients as short, mid, and long-term survivors.

Radiogenomics studies also highlight sex-related biological variations in GB patients. Colen et al. (80) revealed sex-specific molecular mechanisms for cell death (MYC oncogenic in female GB patients, TP53 apoptotic in male GB patients). Similarly, a recent study by Beig et al. (54) suggested that higher expression of texture features from enhancing tumor regions seemed to be more enriched in 'high-risk' group in the male population. This result appeared to be opposite in the female population, in which the same features were enriched in the 'low-risk' group. These findings suggesting the importance of treating sex as a covariate in the design of a radiogenomics study.

Heterogeneity and Molecular Subtype

Intra-tumoral Heterogeneity in GB has been a topic of long-standing interest (23, 81). Spatio-temporally comprehensive assessment of the tumor heterogeneity requires multiple spatially sampling at different time points. In daily clinical practice, effective tissue sampling remains a significant challenge in accurately evaluating the intratumoral heterogeneity of a GB. Radiogenomics has shown the initial prospects for spatially evaluating the regional and genetically distinct subtypes that coexist within a single GB tumor (30, 82). By collected 48 image-guided biopsies from 13 GBs, Hu et al. (30) co-registered each biopsy location with MRI texture map to correlate spatially matched imaging measurements with regional genetic status. They identified significant imaging correlations for several driver genes, including EGFR, PTEN, RB1, TP53, and more. The author also emphasized that even within one tumor segment (such as the enhancement part in T1 contrast-enhanced MRI), regional genetic diversity can also exist. This suggests the need to improve the image-based assessment of genetic heterogeneity beyond the use of the subregion presented in a single imaging mode.

Images contain information about tumor phenotypes that are regulated not only by cell-intrinsic biological processes but also by the tumor microenvironment (59, 83–85). Recently, machine learning-based radiomics models demonstrated the capacity to evaluate enrichment levels of different immune cells in GB patients. Using radiomics features of MR images, the radiomics models could classify the immunophenotypes of GB and can predict patient prognosis (59). Lin et al. (84) used a consistent clustering method to classify radiological features into two subgroups. The two subtypes have significantly different histological stages and molecular factors (such as IDH and MGMT). Furthermore, biological information analysis hinted that the inferior prognosis subtype may be more responsive to immunotherapy. At the same time, if GB patients receive immunotherapy (such as immune checkpoint blockade therapy), the responses of therapy might also be distinguished by radiomics signatures noninvasively (86). Cho et al. (83) revealed that immune cell markers have significant correlations with perfusion and diffusion MRI features in a study of 60 GB patients. The apparent diffusion coefficient values were correlated with the expression level of immune cell markers, which can be used as an immune biomarker to predict the progression and prognosis of GB patients. It should be noted that many classification methods based on radiomics characteristics are still in an early developmental stage. Although these potential associations are encouraging, some conclusions still need further verification.

Prognostic Stratification-Based Tumor Biological Characteristics

A large number of retrospective studies have revealed the link between the radiomics characteristics and survival time of GB patients (70, 87). According to radiomics risk stratification, some studies (28, 54, 84, 88) also tried to explore the corresponding tumor biological information. Based on survival-related imaging features, some studies (28, 54) construct individualized RRS, by which the patients will be divided into subgroups with different risk stratifications. Further, bioinformatics analysis such as GO and/or GSEA will be used to identify the signaling pathway networks or specific biological characteristics that were associated with RRS features. For example, using data from public platforms, Beig and colleagues (28) extracted 936

3D-radiomics features from T1, T2, and Flair MR images of 203 patients with GB. Finally, the GO and GSEA revealed associations of RRS signatures with signaling pathways for cell adhesion, cell differentiation, and angiogenesis. A somewhat similar approach was followed by Choi et al. (51) who used RRS weighted by Lasso-Cox model to classify patients with GB. Finally, GSEA suggested that the transcriptomic characteristics enriched in personalized subtypes were consistent with radiomics phenotypes. For example, the rim-enhancing necrotic subtype could be described by T2-derived radiomic features and further highlighted by the inflammatory genomic signatures.

Radiogenomics has the potential to unravel the molecular underpinning behind the imaging-derived phenotypes. However, these associations seem to be indirect, since they were constructed through survival variables, such as OS and PFS. Indirect associations may obscure or expand the relationships between radiomics characteristics and molecular phenotypes. In addition to using optimized AI models to integrate all such information, radiogenomics biological validation in animal models (13) would be a promising direction in the future.

Personalized Treatment and Assessment

At present, several studies are exploring combination imaging-genomics with the assessment of early treatment response. Imaging biomarkers have shown great potential to stratify the therapeutic response of patients with recurrent glioblastoma treated with bevacizumab (89). EGFR extracellular domain mutations in GB also present opportunities for imaging and therapeutic development (56). Wei and colleagues (45) used logistic regression to generate a fusion radiomics signature based on conventional MRI of 105 patients with WHO grade II-IV astrocytomas. The fusion signature exhibited great power for predicting the methylation status of MGMT promoter and evaluating temozolomide (TMZ) chemotherapy effect. Petrova et al. (90) collected perfusion and diffusion images from 54 subjects with recurrent GB and subsequently treated with bevacizumab. Among the six different classifiers, the authors found that SVM was able to identify 97% of subjects that would respond to bevacizumab with accuracy for PFS and OS of 82% and 78%. This can help assess whether a GB patient can benefit from anti-angiogenic therapy. However, the model still needs to prove its repeatability and generalizability in an extensive cohort study.

GB is a heterogeneous disease composed of multiple molecular subtypes with different clinical courses, leading to different treatment strategies and prognoses. Radiomics and genomics attempt to explain the diversity of tumors from different perspectives. A more fused model might be used to integrate clinical information and all experimental data of an individual, and propose corresponding molecular networks specific to a personalized GB for efficient early-stage diagnosis, precise treatment recommendations, and prognostic assessment. At present, the underlying transformation of imaging-genomics remains only at an early stage of the investigation. Imaging signatures identified by animal models may be useful for future clinical trials enriched for patients with specific subtypes of GB (13, 86).

FUTURE CHALLENGES

Big Data and Data Sharing

One of the fundamental challenges in imaging-genomics research is the availability of large, standardized, well-annotated data sets. Many studies lacked external testing for evaluating the performance of the models due to the limit of data. While external testing is crucial to confirm model generalizability across different institutions. Data sharing between institutes would bring new opportunities for researchers. The Cancer Imaging Archive (TCIA, https://www.cancerimagingarchive.net/) (91), a part of the Cancer Genome Atlas (TCGA), can provide open-access cancer medical imaging and corresponding genome resources to support imaging-genomics researches (59, 63). Some information about the tumors and corresponding supporting data has been summarized on the TCIA website (https://www.cancerimagingarchive.net/collections/).

Radiological images and biological data from CPTAC (Clinical Proteomic Tumor Analysis Consortium, https://proteomics.cancer.gov/programs/cptac) (92, 93) have also been made publicly available to enable researchers to investigate the imaging phenotypes which may correlate to corresponding genomic, proteomic, and clinical data (28, 54). Additionally, the Ivy Glioblastoma Atlas Project (IvyGAP, http://glioblastoma.alleninstitute.org/) (94) provides resources for exploring the anatomic and genetic basis of GB at the radiological and molecular levels. The dataset contains RNA sequencing data, tissue sections, as well as partial MR data in TCIA. Data from these public databases has motivated and continues to motivate the technological exploration and development in imaging-genomics field. However, such data are far from sufficient. Further researches focused on developing improved algorithms (such as transfer learning or data augmentation technologies) optimized for smaller datasets are also needed.

Quality Control, Interpretability, and Application Challenge

Even for the same data, two different calculation software might generate different feature values (95). The lack of standardized definitions will hamper the clinical use of the models. Undoubtedly, quality control and repeatability should run through the entire imaging genomic study, including data collection, preprocessing, delineation of ROIs, features extraction and selection, model building, and verification. Lambin et al. (10) have proposed the radiomics quality score (RQS) to assess the quality of radiomics studies, which plays a guiding role in improving the initial design of an imaging-genomics research. The Image Biomarker Standardization Initiative (IBSI) also produced and validated a series of consensus-based reference values for radiomics features (95). These reference values can be used to check whether a radiomics

software complies with IBSI standards. Improved research quality and reproducibility can promote the clinical translation of radiomics.

In the clinical setting, there are still many obstacles to the standardized processing of data and the effective deployment of the pre-trained models. The lack of sufficient verification of a model will inevitably limit its further application. Additionally, it is also important to note that features and models generated by AI (especially deep learning) often lack clear interpretable parameters. Even if AI algorithms provide good predictive results, the models and deep features are difficult for clinicians to interpret, which limits the integration of radiomics into routine clinical practice. In the context of a regulated healthcare environment, this "black box" problem of AI algorithms is particularly outstanding. Visualization of models and features is an alternative way to alleviate this problem. Interpretability in AI is an emerging field of increased research efforts in the data science community.

Multi-Omics Integration

Multi-omics is undergoing the big data revolution. Genomic analysis such as gene mutation or altered gene expression alone does not always reflect the real change of the corresponding protein and downstream metabolite. The intricate connections between tumor biology and holistic phenotype could have been better captured by multidimensional data and multi-omics models. In recent years, leveraging AI and digital pathology has shown significant promise in cancer diagnosis (38, 49). Remarkably, there have been attempts to integrate pathological section data and radiological data (96), which is called a new term as radopathomics. The fusion signature combining information from distinct dimensions could better predict discrepancies of treatment response. These results have exhibited the great potential of radiomics in the integration of modern precision medicine.

Predictably, the evolution of the radiomics field will gradually differentiate into "radio-…omics", such as radio-proteomics, radiopatho-genomic, or even radio-metabonomics in the coming future, dependent on the source used. As such, current imaging-genomic association maps entail integrations of large, "multi-omic" data sets with imaging to bridge the missing links. Certainly, such a large number of omics features can easily lead to overfitting. Optimal feature reduction and selection methods and appropriate model validation are also needed to deal with the problem of "Curse of Dimensionality".

CONCLUSION

The evolution of the field of radiomics and radiogenomics is similar to the emergence of the microscope in pathology. It is foreseeable that based on multi-parameter imaging features, more biological information can be mined to evaluate the biological characteristics of GB for supporting individualized patients management. However, many challenges still exist and much work needs to be done. Better interpretability and validation of these tools will make imaging genomics more acceptable in this field. Even though the translation of these models from research to clinical practice is still in progress, they provide promise for guiding precision medicine and subsequent individualized therapeutic intervention.

AUTHOR CONTRIBUTIONS

HL and WZ conceived this review, organized, and critically revised the manuscript. DL and JC did major work of the manuscript. XH, KY, YL, GH, and HG made contributions to the writing and revising of the manuscript. All authors contributed to the article and approved the submitted version.

FUNDING

This study was supported by grants from the National Natural Science Foundation of China (No. 81972350, 81701671), the project of Jiangsu Provincial Medical Youth Talent (No. QNRC2016047), the Medical Scientific and Technologic Development Project of Nanjing (No. ZKX15035), the Jiangsu Provincial Medical Innovation Team (No. CXTDA2017050), the Medical Science and Technology Development Foundation of Nanjing (No. ZDX16011), and the Nanjing Medical Science and technique Development Foundation (No. QRX17087).

REFERENCES

1. Ostrom QT, Cioffi G, Gittleman H, Patil N, Waite K, Kruchko C, et al. Cbtrus Statistical Report: Primary Brain and Other Central Nervous System Tumors Diagnosed in the United States in 2012-2016. *Neuro-oncology* (2019) 21:v1–v100. doi: 10.1093/neuonc/noz150
2. Glas M, Rath BH, Simon M, Reinartz R, Schramme A, Trageser D, et al. Residual Tumor Cells are Unique Cellular Targets in Glioblastoma. *Ann Neurol* (2010) 68(2):264–9. doi: 10.1002/ana.22036
3. Stupp R, Taillibert S, Kanner A, Read W, Steinberg D, Lhermitte B, et al. Effect of Tumor-Treating Fields Plus Maintenance Temozolomide vs Maintenance Temozolomide Alone on Survival in Patients With Glioblastoma: A Randomized Clinical Trial. *JAMA* (2017) 318(23):2306–16. doi: 10.1001/jama.2017.18718
4. Chin L, Meyerson M, Aldape K, Bigner D, Mikkelsen T, Vandenberg S, et al. Comprehensive Genomic Characterization Defines Human Glioblastoma Genes and Core Pathways. *Nature* (2008) 455(7216):1061–8. doi: 10.1038/nature07385
5. Pearson JRD, Regad T. Targeting Cellular Pathways in Glioblastoma Multiforme. *Signal Transduct Target Ther* (2017) 2:17040. doi: 10.1038/sigtrans.2017.40
6. Louis DN, Perry A, Reifenberger G, Von Deimling A, Figarella-Branger D, Cavenee WK, et al. The 2016 World Health Organization Classification of Tumors of the Central Nervous System: a Summary. *Acta Neuropathol* (2016) 131(6):803–20. doi: 10.1007/s00401-016-1545-1
7. Wang Q, Hu B, Hu X, Kim H, Squatrito M, Scarpace L, et al. Tumor Evolution of Glioma-Intrinsic Gene Expression Subtypes Associates With Immunological Changes in the Microenvironment. *Cancer Cell* (2017) 32(1):42–56.e6. doi: 10.1016/j.ccell.2017.06.003

8. Villanueva-Meyer JE, Mabray MC, Cha S. Current Clinical Brain Tumor Imaging. *Neurosurgery* (2017) 81(3):397–415. doi: 10.1093/neuros/nyx103
9. Lambin P, Rios-Velazquez E, Leijenaar R, Carvalho S, Van Stiphout Rg, Granton P, et al. Radiomics: Extracting More Information From Medical Images Using Advanced Feature Analysis. *Eur J Cancer (Oxford Engl 1990)* (2012) 48(4):441–6. doi: 10.1016/j.ejca.2011.11.036
10. Lambin P, Leijenaar R, Deist TM, Peerlings J, De Jong E, Van Timmeren J, et al. Radiomics: The Bridge Between Medical Imaging and Personalized Medicine. *Nat Rev Clin Oncol* (2017) 14(12):749–62. doi: 10.1038/nrclinonc.2017.141
11. Kuo MD, Jamshidi N. Behind the Numbers: Decoding Molecular Phenotypes With Radiogenomics–Guiding Principles and Technical Considerations. *Radiology* (2014) 270(2):320–5. doi: 10.1148/radiol.13132195
12. Ellingson BM. Radiogenomics and Imaging Phenotypes in Glioblastoma: Novel Observations and Correlation With Molecular Characteristics. *Curr Neurol Neurosci Rep* (2015) 15(1):506. doi: 10.1007/s11910-014-0506-0
13. Zinn PO, Singh SK, Kotrotsou A, Hassan I, Thomas G, Luedi MM, et al. A Coclinical Radiogenomic Validation Study: Conserved Magnetic Resonance Radiomic Appearance of Periostin-Expressing Glioblastoma in Patients and Xenograft Models. *Clin Cancer Res* (2018) 24(24):6288–99. doi: 10.1158/1078-0432.CCR-17-3420
14. Mazurowski MA. Radiogenomics: What it is and Why it is Important. *J Am Coll Radiol JACR* (2015) 12(8):862–6. doi: 10.1016/j.jacr.2015.04.019
15. Choi YS, Bae S, Chang JH, Kang SG, Kim SH, Kim J, et al. Fully Automated Hybrid Approach to Predict the IDH Mutation Status of Gliomas Via Deep Learning and Radiomics. *Neuro Oncol* (2020) 23(2):304–13. doi: 10.1093/neuonc/noaa177 noaa177.
16. Fukuma R, Yanagisawa T, Kinoshita M, Shinozaki T, Arita H, Kawaguchi A, et al. Prediction of IDH and TERT Promoter Mutations in Low-Grade Glioma From Magnetic Resonance Images Using a Convolutional Neural Network. *Sci Rep* (2019) 9(1):20311. doi: 10.1038/s41598-019-56767-3
17. Ohgaki H, Kleihues P. The Definition of Primary and Secondary Glioblastoma. *Clin Cancer Res* (2013) 19(4):764–72. doi: 10.1158/1078-0432.CCR-12-3002
18. Lai A, Kharbanda S, Pope WB, Tran A, Solis OE, Peale F, et al. Evidence for Sequenced Molecular Evolution of IDH1 Mutant Glioblastoma From a Distinct Cell of Origin. *J Clin Oncol* (2011) 29(34):4482–90. doi: 10.1200/jco.2010.33.8715
19. Aldape K, Zadeh G, Mansouri S, Reifenberger G, Von Deimling A. Glioblastoma: Pathology, Molecular Mechanisms and Markers. *Acta Neuropathol* (2015) 129(6):829–48. doi: 10.1007/s00401-015-1432-1
20. Brennan CW, Verhaak RG, Mckenna A, Campos B, Noushmehr H, Salama SR, et al. The Somatic Genomic Landscape of Glioblastoma. *Cell* (2013) 155(2):462–77. doi: 10.1016/j.cell.2013.09.034
21. Parsons DW, Jones S, Zhang X, Lin JC, Leary RJ, Angenendt P, et al. An Integrated Genomic Analysis of Human Glioblastoma Multiforme. *Science* (2008) 321(5897):1807–12. doi: 10.1126/science.1164382
22. Turner NC, Reis-Filho JS. Genetic Heterogeneity and Cancer Drug Resistance. *Lancet Oncol* (2012) 13(4):e178–85. doi: 10.1016/s1470-2045(11)70335-7
23. Sottoriva A, Spiteri I, Piccirillo SG, Touloumis A, Collins VP, Marioni JC, et al. Intratumor Heterogeneity in Human Glioblastoma Reflects Cancer Evolutionary Dynamics. *Proc Natl Acad Sci USA* (2013) 110(10):4009–14. doi: 10.1073/pnas.1219747110
24. Wang J, Cazzato E, Ladewig E, Frattini V, Rosenbloom DI, Zairis S, et al. Clonal Evolution of Glioblastoma Under Therapy. *Nat Genet* (2016) 48(7):768–76. doi: 10.1038/ng.3590
25. Francis JM, Zhang CZ, Maire CL, Jung J, Manzo VE, Adalsteinsson VA, et al. EGFR Variant Heterogeneity in Glioblastoma Resolved Through Single-Nucleus Sequencing. *Cancer Discovery* (2014) 4(8):956–71. doi: 10.1158/2159-8290.CD-13-0879
26. Köber V, Yang J, Barah P, Wu Y, Stichel D, Gu Z, et al. Evolutionary Trajectories of IDH(WT) Glioblastomas Reveal a Common Path of Early Tumorigenesis Instigated Years Ahead of Initial Diagnosis. *Cancer Cell* (2019) 35(4):692–704.e12. doi: 10.1016/j.ccell.2019.02.007
27. Agarwal S, Sane R, Oberoi R, Ohlfest JR, Elmquist WF. Delivery of Molecularly Targeted Therapy to Malignant Glioma, a Disease of the Whole Brain. *Expert Rev Mol Med* (2011) 13:e17. doi: 10.1017/s1462399411001888
28. Beig N, Bera K, Prasanna P, Antunes J, Correa R, Singh S, et al. Radiogenomic-Based Survival Risk Stratification of Tumor Habitat on Gd-T1w MRI is Associated With Biological Processes in Glioblastoma. *Clin Cancer Res* (2020) 26(8):1866–76. doi: 10.1158/1078-0432.ccr-19-2556
29. Park JE, Kim HS, Park SY, Nam SJ, Chun SM, Jo Y, et al. Prediction of Core Signaling Pathway by Using Diffusion- and Perfusion-based Mri Radiomics and Next-generation Sequencing in Isocitrate Dehydrogenase Wild-type Glioblastoma. *Radiology* (2020) 294(2):388–97. doi: 10.1148/radiol.2019190913
30. Hu LS, Ning S, Eschbacher JM, Baxter LC, Gaw N, Ranjbar S, et al. Radiogenomics to Characterize Regional Genetic Heterogeneity in Glioblastoma. *Neuro Oncol* (2017) 19(1):128–37. doi: 10.1093/neuonc/now135
31. Lasocki A, Rosenthal MA, Roberts-Thomson SJ, Neal A, Drummond KJ. Neuro-Oncology and Radiogenomics: Time to Integrate? *AJNR Am J Neuroradiol* (2020) 41(11):1982–8. doi: 10.3174/ajnr.A6769
32. Rudie JD, Rauschecker AM, Bryan RN, Davatzikos C, Mohan S. Emerging Applications of Artificial Intelligence in Neuro-Oncology. *Radiology* (2019) 290(3):607–18. doi: 10.1148/radiol.2018181928
33. Lecun Y, Bengio Y, Hinton G. Deep Learning. *Nature* (2015) 521(7553):436–44. doi: 10.1038/nature14539
34. Litjens G, Kooi T, Bejnordi BE, Setio AAA, Ciompi F, Ghafoorian M, et al. A Survey on Deep Learning in Medical Image Analysis. *Med Image Anal* (2017) 42:60–88. doi: 10.1016/j.media.2017.07.005
35. Lao J, Chen Y, Li ZC, Li Q, Zhang J, Liu J, et al. A Deep Learning-Based Radiomics Model for Prediction of Survival in Glioblastoma Multiforme. *Sci Rep* (2017) 7(1):10353. doi: 10.1038/s41598-017-10649-8
36. Liu Z, Wang S, Dong D, Wei J, Fang C, Zhou X, et al. The Applications of Radiomics in Precision Diagnosis and Treatment of Oncology: Opportunities and Challenges. *Theranostics* (2019) 9(5):1303–22. doi: 10.7150/thno.30309
37. Kurc T, Bakas S, Ren X, Bagari A, Momeni A, Huang Y, et al. Segmentation and Classification in Digital Pathology for Glioma Research: Challenges and Deep Learning Approaches. *Front Neurosci* (2020) 14:27. doi: 10.3389/fnins.2020.00027
38. Jin L, Shi F, Chun Q, Chen H, Ma Y, Hameed NUF, et al. Artificial Intelligence Neuropathologist for Glioma Classification Using Deep Learning on Hematoxylin and Eosin Stained Slide Images and Molecular Markers. *Neuro Oncol* (2020) 23(1):42–52. doi: 10.1093/neuonc/noaa163 noaa163.
39. Tajbakhsh N, Shin JY, Gurudu SR, Hurst RT, Kendall CB, Gotway MB, et al. Convolutional Neural Networks for Medical Image Analysis: Full Training or Fine Tuning? *IEEE Trans Med Imaging* (2016) 35(5):1299–312. doi: 10.1109/tmi.2016.2535302
40. Kermany DS, Goldbaum M, Cai W, Valentim CCS, Liang H, Baxter SL, et al. Identifying Medical Diagnoses and Treatable Diseases by Image-Based Deep Learning. *Cell* (2018) 172(5):1122–1131.e9. doi: 10.1016/j.cell.2018.02.010
41. Li ZC, Bai H, Sun Q, Zhao Y, Lv Y, Zhou J, et al. Multiregional Radiomics Profiling From Multiparametric MRI: Identifying an Imaging Predictor of IDH1 Mutation Status in Glioblastoma. *Cancer Med* (2018) 7(12):5999–6009. doi: 10.1002/cam4.1863
42. Chang P, Grinband J. Deep-Learning Convolutional Neural Networks Accurately Classify Genetic Mutations in Gliomas. *AJNR Am J Neuroradiol* (2018) 39(7):1201–7. doi: 10.3174/ajnr.A5667
43. Zhang B, Chang K, Ramkissoon S, Tanguturi S, Bi WL, Reardon DA, et al. Multimodal MRI Features Predict Isocitrate Dehydrogenase Genotype in High-Grade Gliomas. *Neuro Oncol* (2017) 19(1):109–17. doi: 10.1093/neuonc/now121
44. Li L, Mu W, Wang Y, Liu Z, Liu Z, Wang Y, et al. A Non-invasive Radiomic Method Using (18)F-Fdg PET Predicts Isocitrate Dehydrogenase Genotype and Prognosis in Patients With Glioma. *Front Oncol* (2019) 9:1183. doi: 10.3389/fonc.2019.01183
45. Wei J, Yang G, Hao X, Gu D, Tan Y, Wang X, et al. A Multi-Sequence and Habitat-Based MRI Radiomics Signature for Preoperative Prediction of MGMT Promoter Methylation in Astrocytomas With Prognostic Implication. *Eur Radiol* (2019) 29(2):877–88. doi: 10.1007/s00330-018-5575-z
46. Li ZC, Bai H, Sun Q, Li Q, Liu L, Zou Y, et al. Multiregional Radiomics Features From Multiparametric MRI for Prediction of MGMT Methylation Status in Glioblastoma Multiforme: a Multicentre Study. *Eur Radiol* (2018) 28(9):3640–50. doi: 10.1007/s00330-017-5302-1

47. Qian J, Herman MG, Brinkmann DH, Laack NN, Kemp BJ, Hunt CH, et al. Prediction of MGMT Status for Glioblastoma Patients Using Radiomics Feature Extraction From 18f-DOPA-PET Imaging. *Int J Radiat OncologyBiologyPhys* (2020) 108(5):1339–46. doi: 10.1016/j.ijrobp.2020.06.073
48. Su X, Chen N, Sun H, Liu Y, Yang X, Wang W, et al. Automated Machine Learning Based on Radiomics Features Predicts H3 K27M Mutation in Midline Gliomas of the Brain. *Neuro Oncol* (2020) 22(3):393–401. doi: 10.1093/neuonc/noz184
49. Liu S, Shah Z, Sav A, Russo C, Berkovsky S, Qian Y, et al. Isocitrate Dehydrogenase (IDH) Status Prediction in Histopathology Images of Gliomas Using Deep Learning. *Sci Rep* (2020) 10(1):7733. doi: 10.1038/s41598-020-64588-y
50. Choi KS, Choi SH, Jeong B. Prediction of IDH Genotype in Gliomas With Dynamic Susceptibility Contrast Perfusion MR Imaging Using an Explainable Recurrent Neural Network. *Neuro Oncol* (2019) 21(9):1197–209. doi: 10.1093/neuonc/noz095
51. Choi SW, Cho HH, Koo H, Cho KR, Nenning KH, Langs G, et al. Multi-Habitat Radiomics Unravels Distinct Phenotypic Subtypes of Glioblastoma With Clinical and Genomic Significance. *Cancers* (2020) 12(7):1707–12. doi: 10.3390/cancers12071707
52. Zinn PO, Singh SK, Kotrotsou A, Abrol S, Thomas G, Mosley J, et al. Distinct Radiomic Phenotypes Define Glioblastoma TP53-PTEN-EGFR Mutational Landscape. *Neurosurgery* (2017) 64(CN_suppl_1):203–10. doi: 10.1093/neuros/nyx316
53. Beig N, Patel J, Prasanna P, Hill V, Gupta A, Correa R, et al. Radiogenomic Analysis of Hypoxia Pathway is Predictive of Overall Survival in Glioblastoma. *Sci Rep* (2018) 8(1):7. doi: 10.1038/s41598-017-18310-0
54. Beig N, Singh S, Bera K, Prasanna P, Singh G, Chen J, et al. Sexually Dimorphic Radiogenomic Models Identify Distinct Imaging and Biological Pathways That are Prognostic of Overall Survival in Glioblastoma. *Neuro Oncol* (2020) 23(2):251–63. doi: 10.1093/neuonc/noaa231 noaa231.
55. Beig N, Bera K, Tiwari P. Introduction to Radiomics and Radiogenomics in Neuro-Oncology: Implications and Challenges. *Neurooncol Adv* (2020) 2 (Suppl 4):iv3–iv14. doi: 10.1093/noajnl/vdaa148
56. Binder ZA, Thorne AH, Bakas S, Wileyto EP, Bilello M, Akbari H, et al. Epidermal Growth Factor Receptor Extracellular Domain Mutations in Glioblastoma Present Opportunities for Clinical Imaging and Therapeutic Development. *Cancer Cell* (2018) 34(1):163–177 e7. doi: 10.1016/j.ccell.2018.06.006
57. Itakura H, Achrol AS, Mitchell LA, Loya JJ, Liu T, Westbroek EM, et al. Magnetic Resonance Image Features Identify Glioblastoma Phenotypic Subtypes With Distinct Molecular Pathway Activities. *Sci Transl Med* (2015) 7(303):303ra138. doi: 10.1126/scitranslmed.aaa7582
58. Akbari H, Bakas S, Pisapia JM, Nasrallah MP, Rozycki M, Martinez-Lage M, et al. In Vivo Evaluation of EGFRvIII Mutation in Primary Glioblastoma Patients Via Complex Multiparametric MRI Signature. *Neuro Oncol* (2018) 20 (8):1068–79. doi: 10.1093/neuonc/noy033
59. Hsu JB, Lee GA, Chang TH, Huang SW, Le NQK, Chen YC, et al. Radiomic Immunophenotyping of GSEA-Assessed Immunophenotypes of Glioblastoma and Its Implications for Prognosis: a Feasibility Study. *Cancers* (2020) 12(10):3039–55. doi: 10.3390/cancers12103039
60. Dang L, White DW, Gross S, Bennett BD, Bittinger MA, Driggers EM, et al. Cancer-Associated IDH1 Mutations Produce 2-Hydroxyglutarate. *Nature* (2010) 465(7300):966. doi: 10.1038/nature09132
61. Sanson M, Marie Y, Paris S, Idbaih A, Laffaire J, Ducray F, et al. Isocitrate Dehydrogenase 1 Codon 132 Mutation is an Important Prognostic Biomarker in Gliomas. *J Clin Oncol* (2009) 27(25):4150–4. doi: 10.1200/jco.2009.21.9832
62. Xie C, Du R, Ho JW, Pang HH, Chiu KW, Lee EY, et al. Effect of Machine Learning Re-Sampling Techniques for Imbalanced Datasets in F-FDG PET-Based Radiomics Model on Prognostication Performance in Cohorts of Head and Neck Cancer Patients. *Eur J Nucl Med Mol Imaging* (2020) 47(12):2826–35. doi: 10.1007/s00259-020-04756-4
63. Bangalore Yogananda CG, Shah BR, Vejdani-Jahromi M, Nalawade SS, Murugesan GK, Yu FF, et al. A Novel Fully Automated MRI-based Deep-Learning Method for Classification of IDH Mutation Status in Brain Gliomas. *Neuro Oncol* (2020) 22(3):402–11. doi: 10.1093/neuonc/noz199
64. Hegi ME, Diserens AC, Gorlia T, Hamou MF, De Tribolet N, Weller M, et al. MGMT Gene Silencing and Benefit From Temozolomide in Glioblastoma. *N Engl J Med* (2005) 352(10):997–1003. doi: 10.1056/NEJMoa043331
65. Kaina B, Christmann M, Naumann S, Roos WP. MGMT: Key Node in the Battle Against Genotoxicity, Carcinogenicity and Apoptosis Induced by Alkylating Agents. *DNA Repair (Amst)* (2007) 6(8):1079–99. doi: 10.1016/j.dnarep.2007.03.008
66. Qian XC, Brent TP. Methylation Hot Spots in the 5' Flanking Region Denote Silencing of the O6-methylguanine-DNA Methyltransferase Gene. *Cancer Res* (1997) 57(17):3672–7.
67. Mansouri A, Hachem LD, Mansouri S, Nassiri F, Laperriere NJ, Xia D, et al. MGMT Promoter Methylation Status Testing to Guide Therapy for Glioblastoma: Refining the Approach Based on Emerging Evidence and Current Challenges. *Neuro Oncol* (2019) 21(2):167–78. doi: 10.1093/neuonc/noy132
68. Kazerooni AF, Bakas S, Saligheh Rad H, Davatzikos C. Imaging Signatures of Glioblastoma Molecular Characteristics: a Radiogenomics Review. *J Magnetic Resonance Imaging* (2019) 52(1):54–69. doi: 10.1002/jmri.26907
69. Lohmann P, Galldiks N, Kocher M, Heinzel A, Filss CP, Stegmayr C, et al. Radiomics in Neuro-Oncology: Basics, Workflow, and Applications. *Methods* (2020) 188:112–21. doi: 10.1016/j.ymeth.2020.06.003
70. Lotan E, Jain R, Razavian N, Fatterpekar GM, Lui YW. State of the Art: Machine Learning Applications in Glioma Imaging. *AJR Am J Roentgenol* (2019) 212(1):26–37. doi: 10.2214/AJR.18.20218
71. Xi YB, Guo F, Xu ZL, Li C, Wei W, Tian P, et al. Radiomics Signature: a Potential Biomarker for the Prediction of MGMT Promoter Methylation in Glioblastoma. *J Magn Reson Imaging* (2018) 47(5):1380–7. doi: 10.1002/jmri.25860
72. Sasaki T, Kinoshita M. Radiomics and MGMT Promoter Methylation for Prognostication of Newly Diagnosed Glioblastoma. *Sci Rep* (2019) 9: (1):14435. doi: 10.1038/s41598-019-50849-y
73. Kong Z, Lin Y, Jiang C, Li L, Liu Z, Wang Y, et al. (18)F-FDG-PET-Based Radiomics Signature Predicts MGMT Promoter Methylation Status in Primary Diffuse Glioma. *Cancer Imaging* (2019) 19(1):58. doi: 10.1186/s40644-019-0246-0
74. Chen X, Zeng M, Tong Y, Zhang T, Fu Y, Li H, et al. Automatic Prediction of MGMT Status in Glioblastoma Via Deep Learning-Based MR Image Analysis. *BioMed Res Int* (2020) 2020:9258649. doi: 10.1155/2020/9258649
75. Korfiatis P, Kline TL, Lachance DH, Parney IF, Buckner JC, Erickson BJ. Residual Deep Convolutional Neural Network Predicts MGMT Methylation Status. *J Digit Imaging* (2017) 30(5):622–8. doi: 10.1007/s10278-017-0009-z
76. Heimberger AB, Hlatky R, Suki D, Yang D, Weinberg J, Gilbert M, et al. Prognostic Effect of Epidermal Growth Factor Receptor and EGFRvIII in Glioblastoma Multiforme Patients. *Clin Cancer Res* (2005) 11(4):1462–6. doi: 10.1158/1078-0432.ccr-04-1737
77. Louis DN, Giannini C, Capper D, Paulus W, Figarella-Branger D, Lopes MB, et al. cIMPACT-NOW Update 2: Diagnostic Clarifications for Diffuse Midline Glioma, H3 K27M-Mutant and Diffuse Astrocytoma/Anaplastic Astrocytoma, IDH-Mutant. *Acta Neuropathol* (2018) 135(4):639–42. doi: 10.1007/s00401-018-1826-y
78. Aboian MS, Solomon DA, Felton E, Mabray MC, Villanueva-Meyer JE, Mueller S, et al. Imaging Characteristics of Pediatric Diffuse Midline Gliomas With Histone H3 K27M Mutation. *AJNR Am J Neuroradiol* (2017) 38(4):795–800. doi: 10.3174/ajnr.A5076
79. Liu TT, Achrol AS, Mitchell LA, Rodriguez SA, Feroze A, Iv M, et al. Magnetic Resonance Perfusion Image Features Uncover an Angiogenic Subgroup of Glioblastoma Patients With Poor Survival and Better Response to Antiangiogenic Treatment. *Neuro-oncology* (2017) 19(7):997–1007. doi: 10.1093/neuonc/now270
80. Colen RR, Wang J, Singh SK, Gutman DA, Zinn PO. Glioblastoma: Imaging Genomic Mapping Reveals Sex-Specific Oncogenic Associations of Cell Death. *Radiology* (2015) 275(1):215–27. doi: 10.1148/radiol.14141800
81. Lee JK, Wang J, Sa JK, Ladewig E, Lee HO, Lee IH, et al. Spatiotemporal Genomic Architecture Informs Precision Oncology in Glioblastoma. *Nat Genet* (2017) 49(4):594–9. doi: 10.1038/ng.3806
82. Hu LS, Hawkins-Daarud A, Wang L, Li J, Swanson KR. Imaging of Intratumoral Heterogeneity in High-Grade Glioma. *Cancer Lett* (2020) 477:97–106. doi: 10.1016/j.canlet.2020.02.025
83. Cho HR, Jeon H, Park CK, Park SH, Choi SH. Radiogenomics Profiling for Glioblastoma-Related Immune Cells Reveals CD49d Expression Correlation

With MRI Parameters and Prognosis. *Sci Rep* (2018) 8(1):16022. doi: 10.1038/s41598-018-34242-9
84. Lin P, Peng YT, Gao RZ, Wei Y, Li XJ, Huang SN, et al. Radiomic Profiles in Diffuse Glioma Reveal Distinct Subtypes With Prognostic Value. *J Cancer Res Clin Oncol* (2020) 146(5):1253–62. doi: 10.1007/s00432-020-03153-6
85. Wu J, Mayer AT, Li R. Integrated Imaging and Molecular Analysis to Decipher Tumor Microenvironment in the Era of Immunotherapy. *Semin Cancer Biol* (2020) 20(S1044-579X):30264–9. doi: 10.1016/j.semcancer.2020.12.005
86. Aslan K, Turco V, Blobner J, Sonner JK, Liuzzi AR, Núñez, et al. Heterogeneity of Response to Immune Checkpoint Blockade in Hypermutated Experimental Gliomas. *Nat Commun* (2020) 11(1):931. doi: 10.1038/s41467-020-14642-0
87. Booth TC, Williams M, Luis A, Cardoso J, Ashkan K, Shuaib H. Machine Learning and Glioma Imaging Biomarkers. *Clin Radiol* (2020) 75(1):20–32. doi: 10.1016/j.crad.2019.07.001
88. Liu X, Li Y, Sun Z, Li S, Wang K, Fan X, et al. Molecular Profiles of Tumor Contrast Enhancement: a Radiogenomic Analysis in Anaplastic Gliomas. *Cancer Med* (2018) 7(9):4273–83. doi: 10.1002/cam4.1672
89. Grossmann P, Narayan V, Chang K, Rahman R, Abrey L, Reardon DA, et al. Quantitative Imaging Biomarkers for Risk Stratification of Patients With Recurrent Glioblastoma Treated With Bevacizumab. *Neuro Oncol* (2017) 19 (12):1688–97. doi: 10.1093/neuonc/nox092
90. Petrova L, Korfiatis P, Petr O, Lachance DH, Parney I, Buckner JC, et al. Cerebral Blood Volume and Apparent Diffusion Coefficient - Valuable Predictors of non-Response to Bevacizumab Treatment in Patients With Recurrent Glioblastoma. *J Neurol Sci* (2019) 405:116433. doi: 10.1016/j.jns.2019.116433
91. Clark K, Vendt B, Smith K, Freymann J, Kirby J, Koppel P, et al. The Cancer Imaging Archive (TCIA): Maintaining and Operating a Public Information Repository. *J Digit Imaging* (2013) 26(6):1045–57. doi: 10.1007/s10278-013-9622-7
92. Edwards NJ, Oberti M, Thangudu RR, Cai S, Mcgarvey PB, Jacob S, et al. The CPTAC Data Portal: A Resource for Cancer Proteomics Research. *J Proteome Res* (2015) 14(6):2707–13. doi: 10.1021/pr501254j
93. Wang LB, Karpova A, Gritsenko MA, Kyle JE, Cao S, Li Y, et al. Proteogenomic and Metabolomic Characterization of Human Glioblastoma. *Cancer Cell* (2021) 39(4):509–528 e20. doi: 10.1016/j.ccell.2021.01.006
94. Puchalski RB, Shah N, Miller J, Dalley R, Nomura SR, Yoon JG, et al. An Anatomic Transcriptional Atlas of Human Glioblastoma. *Science* (2018) 360 (6389):660–3. doi: 10.1126/science.aaf2666
95. Zwanenburg A, Vallieres M, Abdalah MA, Aerts H, Andrearczyk V, Apte A, et al. The Image Biomarker Standardization Initiative: Standardized Quantitative Radiomics for High-Throughput Image-Based Phenotyping. *Radiology* (2020) 295(2):328–38. doi: 10.1148/radiol.2020191145
96. Shao L, Liu Z, Feng L, Lou X, Li Z, Zhang XY, et al. Multiparametric MRI and Whole Slide Image-Based Pretreatment Prediction of Pathological Response to Neoadjuvant Chemoradiotherapy in Rectal Cancer: a Multicenter Radiopathomic Study. *Ann Surg Oncol* (2020) 27(11):4296–306. doi: 10.1245/s10434-020-08659-4

Conflict of Interest: The authors declare that the research was conducted in the absence of any commercial or financial relationships that could be construed as a potential conflict of interest.

Copyright © 2021 Liu, Chen, Hu, Yang, Liu, Hu, Ge, Zhang and Liu. This is an open-access article distributed under the terms of the Creative Commons Attribution License (CC BY). The use, distribution or reproduction in other forums is permitted, provided the original author(s) and the copyright owner(s) are credited and that the original publication in this journal is cited, in accordance with accepted academic practice. No use, distribution or reproduction is permitted which does not comply with these terms.

frontiers in Oncology

ORIGINAL RESEARCH
published: 14 September 2021
doi: 10.3389/fonc.2021.741303

Fluorescence Lifetime Imaging and Spectroscopic Co-Validation for Protoporphyrin IX-Guided Tumor Visualization in Neurosurgery

*David Reichert[1,2], Mikael T. Erkkilae[1], Johanna Gesperger[1,3], Lisa I. Wadiura[4], Alexandra Lang[4], Thomas Roetzer[3], Adelheid Woehrer[3], Marco Andreana[1], Angelika Unterhuber[1], Marco Wilzbach[5], Christoph Hauger[5], Wolfgang Drexler[1], Barbara Kiesel[4], Georg Widhalm[4] and Rainer A. Leitgeb[1,2]**

[1] Center for Medical Physics and Biomedical Engineering, Medical University of Vienna, Vienna, Austria, [2] Christian Doppler Laboratory OPTRAMED, Medical University of Vienna, Vienna, Austria, [3] Division of Neuropathology and Neurochemistry, Department of Neurology, Medical University of Vienna, Vienna, Austria, [4] Department of Neurosurgery, Medical University of Vienna, Vienna, Austria, [5] Advanced Development Microsurgery, Carl Zeiss Meditec AG, Oberkochen, Germany

OPEN ACCESS

Edited by:
Alexandra Golby,
Harvard Medical School, United States

Reviewed by:
Evgenii Belykh,
Rutgers University, Newark, United States
Pablo Andres Valdes Quevedo,
Brigham and Women's Hospital, Harvard Medical School, United States

***Correspondence:**
Rainer A. Leitgeb
rainer.leitgeb@meduniwien.ac.at

Specialty section:
This article was submitted to Neuro-Oncology and Neurosurgical Oncology, a section of the journal Frontiers in Oncology

Received: 14 July 2021
Accepted: 24 August 2021
Published: 14 September 2021

Citation:
Reichert D, Erkkilae MT, Gesperger J, Wadiura LI, Lang A, Roetzer T, Woehrer A, Andreana M, Unterhuber A, Wilzbach M, Hauger C, Drexler W, Kiesel B, Widhalm G and Leitgeb RA (2021) Fluorescence Lifetime Imaging and Spectroscopic Co-Validation for Protoporphyrin IX-Guided Tumor Visualization in Neurosurgery. Front. Oncol. 11:741303. doi: 10.3389/fonc.2021.741303

Maximal safe resection is a key strategy for improving patient prognosis in the management of brain tumors. Intraoperative fluorescence guidance has emerged as a standard in the surgery of high-grade gliomas. The administration of 5-aminolevulinic acid prior to surgery induces tumor-specific accumulation of protoporphyrin IX, which emits red fluorescence under blue-light illumination. The technology, however, is substantially limited for low-grade gliomas and weakly tumor-infiltrated brain, where low protoporphyrin IX concentrations are outweighed by tissue autofluorescence. In this context, fluorescence lifetime imaging has shown promise to distinguish spectrally overlapping fluorophores. We integrated frequency-domain fluorescence lifetime imaging in a surgical microscope and combined it with spatially registered fluorescence spectroscopy, which can be considered a research benchmark for sensitive protoporphyrin IX detection. Fluorescence lifetime maps and spectra were acquired for a representative set of fresh *ex-vivo* brain tumor specimens (low-grade gliomas n = 15, high-grade gliomas n = 80, meningiomas n = 41, and metastases n = 35). Combining the fluorescence lifetime with fluorescence spectra unveiled how weak protoporphyrin IX accumulations increased the lifetime respective to tissue autofluorescence. Infiltration zones (4.1ns ± 1.8ns, $p = 0.017$) and core tumor areas (4.8ns ± 1.3ns, $p = 0.040$) of low-grade gliomas were significantly distinguishable from non-pathologic tissue (1.6ns ± 0.5ns). Similarly, fluorescence lifetimes for infiltrated and reactive tissue as well as necrotic and core tumor areas were increased for high-grade gliomas and metastasis. Meningioma tumor specimens showed strongly increased lifetimes (12.2ns ± 2.5ns, $p = 0.005$). Our results emphasize the potential of fluorescence lifetime imaging to optimize maximal safe resection in brain tumors in future and highlight its potential toward clinical translation.

Keywords: fluorescence-guided surgery, fluorescence lifetime imaging (FLIM), fluorescence spectroscopy, protoporphyrin IX, surgical microscope

INTRODUCTION

A large variety of different tumors might occur with the human brain. With an incidence rate of 7.1 and 16.7 per 100,000, around 25,000 primary malignant and 59,000 non-malignant brain and central nervous system tumors were expected to be diagnosed in the United States in 2020 (1). According to the current World Health Organization (WHO) classification of primary brain tumors, gliomas are classified as WHO grades II, III, and IV. Considering recent epidemiologic data, glioblastomas WHO grade IV account for 50 % of malignant brain tumors with a median survival of about 8 months (1). The median survival of lower-grade gliomas (LGG) including WHO grades II and III like diffuse astrocytomas and oligodendrogliomas ranges from 3 to 10 years, respectively (1). LGG account for approximately 20% of all primary brain tumors in adults (2). Meningiomas (MNG) represent the most common primary brain tumor accounting for approximately 38% of cases (1). Such tumors are divided into WHO grades I, II, and III, whereas MNG WHO grade I represents by far the most common tumor with a very good prognosis. Secondary brain tumors (metastases; MET) metastasizing frequently from lung, melanoma, renal, breast, or other cancers are common and characterized by poor patient prognosis (3).

Surgical resection is the treatment of choice in the initial management of gliomas and other brain tumor entities. The extent of resection (EoR) was found to be among the most important prognostic factors in both high-grade gliomas (HGG) and LGG, improving the overall and progression-free survival (4–7). Postoperative adjuvant radio- and/or chemotherapy is initiated dependent on the histopathological tumor diagnosis (8). Due to the proximity of brain tumors to eloquent neurological areas, precise surgical guidance in brain tumors is crucial. The infiltrative nature of glioma is a special challenge for the neurosurgeon. Further, the infiltration of brain tissue favors tumor recurrence, which together with the interdisciplinary treatment makes brain tumors the cancer group with the highest initial cost of care (9). In GBM, solid tumor tissue can be outlined by gadolinium contrast enhancement on preoperative magnetic resonance imaging (MRI) and used for intraoperative neuronavigation. Intraoperative MRI can be employed to update preoperative data and has shown to significantly improve the EoR (10). However, the technology as of now is expensive and not widely available. Novel surgical microscopes provide the possibility to integrate navigation data using preoperative imaging data in combination with intraoperative tumor visualization. In this context, optical imaging modalities are of particular interest. Protoporphyrin IX (PpIX) fluorescence guidance has been approved for medical use in both Europe and the United States and is well established for photodynamic diagnosis (PDD) of malignant glioma (11–13). In PDD, presurgical administration of 5-aminolevulinic acid (5-ALA) induces tumor-specific accumulation of the photosensitizer PpIX (14–16), which emits red fluorescence upon blue light illumination. The efficacy of PpIX for the resection of malignant glioma was first demonstrated in a multicenter phase III study (11). A multitude of subsequent studies has consolidated evidence for PDD to increase the EoR and to delineate tumorous tissue beyond gadolinium contrast enhancement especially in HGG (7, 12, 13, 17). Most LGG and weakly infiltrated tumor areas of HGG, however, lack visual fluorescence during surgical resection. Studies investigating on PpIX fluorescence guidance in LGG report visible fluorescence in about 0% to 20% of patients (17–20). Cases with visible fluorescence in radiologically suspected LGG were for the most part attributed to anaplastic foci, circumscribed intratumoral areas with a higher probability for malignant transformation (17, 20). This together with the frequent infiltrative growth makes complete resection of the fluid-attenuated inversion recovery (FLAIR)/T2 hyperintense lesion in LGG particularly challenging. Both optical-sectioning microscopy on a cellular level, scanning fiber endoscopes and spectroscopic PpIX quantification, however, had shown measurable accumulations of PpIX in LGG or at the boundaries of infiltrative gliomas which both lacked visible fluorescence during surgery (7, 21–24). As the weak PpIX fluorescence is outweighed by a dominating background of tissue autofluorescence in these cases, sensitive PpIX detection inherently requires distinction of PpIX from spectrally overlapping fluorophores. This essentially corresponds to the specificity of PpIX detection.

An alternate approach to measuring spectrally resolved fluorescence is time-resolved fluorescence measurements. The fluorescence lifetime is the average intramolecular time delay between excitation of a fluorophore and the emission of fluorescence. It is determined by the intrinsic molecular properties and the direct molecular environment. At the same time, it is independent of factors as excitation intensity or the method of measurement, which can be based on both time- and frequency-domain principles. The interested reader is referred to Marcu and Hartl (25) as well as Berezin and Achilefu (26). Fluorescence lifetime imaging (FLIM) of endogenous fluorophores like nicotinamide adenine dinucleotide (NADH) and flavin adenine dinucleotide (FAD) has been used in several studies to delineate tumor boundaries (25, 27). The lifetimes of these metabolic coenzymes are linked to the metabolic state of the respective tissue (28, 29). FLIM for macroscopic detection of PpIX, however, was proposed only recently (30). While the fluorescence lifetime of PpIX in organic solution (31) was measured to be 16.4ns, autofluorescence lifetimes of physiological parenchyma in murine and human brain were in the range of about 0.8 to 2 ns (detection > 580 nm) (32, 33). This is in good agreement with lifetimes of the individual endogenous fluorophores contributing to the overall autofluorescence in this spectral band (34).

Based on our previous results (32, 35), we hypothesize that weak PpIX concentrations as found in LGG and weakly infiltrated tumor tissue of HGG increase the fluorescence lifetime respective to non-pathological brain parenchyma when measured with frequency-domain (FD)-FLIM. To investigate the extent to which PpIX fluorescence can be distinguished from a dominating autofluorescence background, we developed a

multimodal surgical microscope. We combined FD-FLIM with spatially registered fluorescence spectroscopy, which can be considered a research benchmark for sensitive PpIX detection (7, 36). It is of note that while these studies accounted for optical tissue properties to quantify PpIX concentrations in tissue, our work relies on the raw fluorescence signal and employs the relative PpIX to autofluorescence signal contribution as a metric. To substantiate our hypothesis, we acquired a representative data set on freshly resected LGG, HGG, MNG, and MET. Next to emphasizing the capacity of FD-FLIM to delineate weak PpIX fluorescence, our second objective was to engineer the technology toward coherence with surgical workflows. We propose an updated fiber-optic-based implementation and demonstrate how both high-resolution tissue structure and FD-FLIM images can be delivered to the surgeon in real time through long working-distance surgical microscopes. This study emphasizes the potential of FLIM to improve maximal safe resection in brain tumor neurosurgery and highlights the feasibility of clinical translation.

MATERIALS AND METHODS

Multimodal FD-FLIM and Spectroscopy Setup

With the current setup (**Figure 1**), we expand on our previously published FD-FLIM system, integrated into a long working-distance (200 mm) surgical microscope (OPMI VISU 200, Carl Zeiss Meditec AG, Jena, Germany). Concisely, the FLIM engine consists of raster-scanning a modulated 405-nm laser (f_{mod} = 10MHz) for excitation and demodulating the emitted fluorescence signal *via* phase-sensitive detection. Upon correction of time-of-flight and electronic phase delays, the fluorescence lifetime τ is related to the measured phase by $\tau = \frac{\tan(\Phi)}{2\pi f_{mod}}$ (37). For a detailed description of the measurement setup and equipment, please refer to our previous work (38). A figure of the modified surgical microscope is depicted in **Supplementary Figure 1**. In the current iteration, we opted to couple the fluorescence into a 1,500-µm core multimode fiber (FP1500URT, 0.5NA, Thorlabs Inc., Newton, NJ, USA), rather than attaching the photomultiplier tube directly to the microscope. PpIX was detected in the band from 590 to 740 nm (665/150 BrightLine HC Semrock, Rochester, NY, USA). A single fluorescence lifetime frame with a lateral resolution of 25 µm (256 × 256 pixels) was acquired in 16 s. The excitation power on the sample was 6 mW and the fluorescence collection numerical aperture for a single stereoscopic path was 0.04. The 50/50 splitter in the right stereoscopic path was exchanged by a mirror to maximize fluorescence throughput. Further, the pixel dwell time and the integration time of the lock-in amplifier were set to 250 and 200 µs, respectively, to allow for sufficient settling of the low-pass filter's output. Fluorescence emission in the left stereoscopic path was split (50/50) and then coupled into a 1,500-µm core multimode fiber before detection by a spectrometer (CCS100/M, Thorlabs Inc.). Spectra were acquired

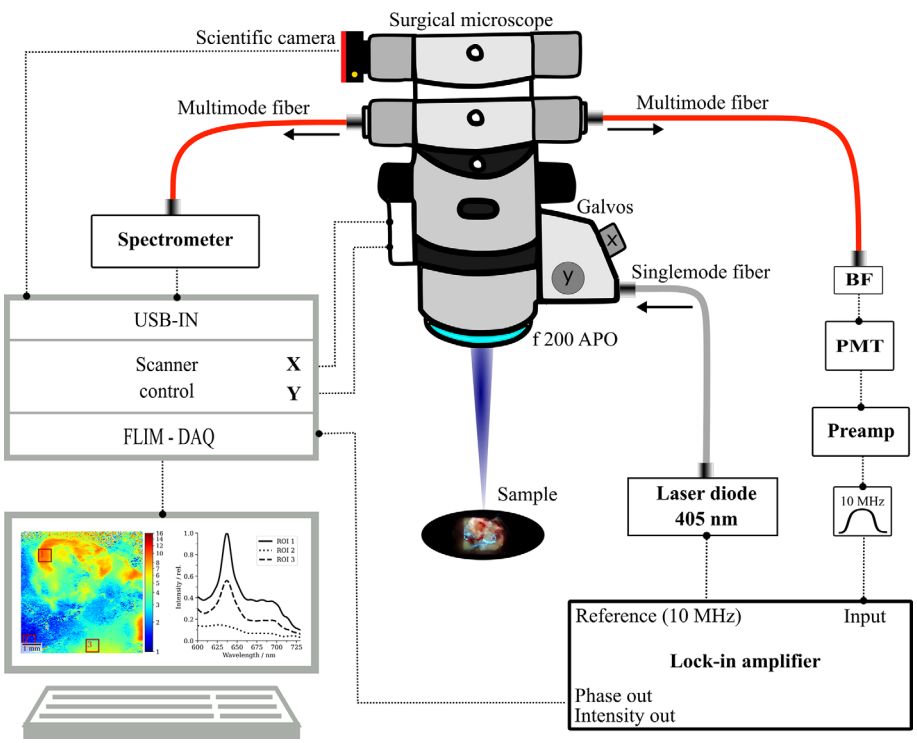

FIGURE 1 | Schematic sketch of the multimodal surgical microscope with integrated fluorescence lifetime imaging and spectroscopy channels. BF, bandpass filter; PMT, photomultiplier tube; DAQ, data acquisition system, f 200 APO, apochromatic objective.

only for selected regions of interest (ROIs) (size 600 μm^2) on the samples. To do so, arbitrary X/Y pixel coordinates were selected on a raster-scanned lifetime image and were then rendered into the corresponding scanner angles by a custom MATLAB script. The galvanometer mirrors then steered the laser on the respective ROIs. As spectra were acquired through a surgical microscope, integration time had to be increased up to 50 s to collect sufficient photons for weakly fluorescent tissue. Note that acquiring spatially correlated FD-FLIM and spectroscopic data would not have been possible with our previously published wide-field FD-FLIM setup (30), which is why we opted for the raster-scanning approach (38) within this work. We applied background correction and Gaussian filtering and could thereby recover spectra even for weak autofluorescence. Before the ocular, a 1.6-megapixel complementary metal-oxide-semiconductor camera (CS165CU1/M, Thorlabs Inc.) was attached to a second 50/50 splitter. Thus, images comparable to the surgeon's white-light tissue view could be acquired with the light source of the surgical microscope turned on. To acquire fluorescence images, the light source was turned off and the laser was scanned rapidly across the tissue. Camera integration time was then set to a long exposure time (2 s for most specimens). For both the camera and the spectrometer channels, light from the laser diode was blocked by a 430-nm longpass filter (430/LP BrightLine HC, Semrock).

Patient Cohort and Specimen Handling

Data were acquired in the laboratory in an *ex vivo* study on human brain tumor specimens from routine cytoreductive surgery. Diagnostic MRI was performed prior to surgery, with at least T1-weighted sequences with and without contrast media and T2-weighted sequences. Depending on tumor localization, additional sequences such as functional MRI and/or diffusion tensor imaging were conducted. Surgical resection was assisted by neuronavigation, white-light microscopy, and fluorescence guidance with 5-ALA administration 3 h before anesthesia. A small subset of patients without 5-ALA administration was included in the study. After resection, specimens were kept in a physiological environment (artificial cerebrospinal fluid, Landesapotheke Salzburg, 19C11S02) and imaged within 1 h. Histopathological diagnosis and representative H&E-stained slides were provided by experienced neuropathologists according to the WHO classification of CNS tumors from 2016.

In total, 15 LGG, 80 HGG, 41 MNG, and 35 MET specimens were included in the study. **Supplementary Tables 1–6** as well as **Supplementary Figure 4** provide a comprehensive overview of all specimens including WHO grade and patient-specific data as age and gender for the study cohort. Tumor entities were further categorized into core tumor (TUM), diffusely infiltrated brain (INF), necrosis (NEC), and reactive parenchyma (REA), according to the histopathological workup. Reactive tissue refers to non-infiltrated tissue with reactive alterations such as inflammatory responses. As non-pathological tissue usually is not resected, we only imaged one control sample resected on the access route to a tumor. For statistical purposes, we included two non-pathological specimens from our previous work (32, 35), resulting in three specimens in the non-pathological control (CTL) group. The study was approved by the ethics committee (EK419/2008 – Amendment 04/2018), and informed and written consent of patients was obtained.

Processing Routines and Statistical Analysis

Post-processing routines for reconstructing the fluorescence lifetime and intensity images from the lock-in amplifier's demodulated phase Θ and amplitude R were implemented in Jupyter Notebook. Scientific computations, statistical analysis, and data visualization were performed with Python's (RRID: SCR_008394) SciPy, Seaborn, and Matplotlib libraries. For spectra acquired on selected ROIs of the FLIM images, the relative PpIX signal contribution at the main emission peak (635 nm) was defined as a metric. A linear regression model was fit to the data points for wavelengths between 600 and 610 nm and 720 and 730 nm. Photon counts above the resulting fit were contributed to PpIX (S_{PpIX}) and below to tissue autofluorescence ($S_{Autofl.}$). The relative PpIX signal contribution (RSC_{PpIX}) was calculated as $RSC_{PpIX} = \frac{S_{PpIX}}{S_{Autofl.}+S_{PpIX}}$. About three to four spectra were measured for a total of 99 samples which resulted in 331 data points. Spectra were labeled according to the fluorescence status observed by the operating surgeon (visible/no visible fluorescence). For samples with inhomogeneous intraoperative fluorescence, the fluorescence status of the respective ROIs was additionally judged during imaging. A fifth-order polynomial model was fit to the data to approximate the relation between PpIX signal contribution and fluorescence lifetime. Confidence intervals (CI) (39) were calculated based on a two-sided 95% t-statistic, indicating the probability of the interval to contain the mean response of new data points.

$$CI = t_{DOF}^{0.975} \cdot \hat{\sigma} \cdot \sqrt{\frac{1}{n} + \frac{(x_0 - \bar{x})^2}{\Sigma_{i=1}^{n}(x_i - \bar{x})^2}}$$

The $t_{DOF}^{0.975}$- quantile was determined as a function of the degrees of freedom (DOF), and a two-sided 95% level of significance and $\bar{x}$ was the mean relative PpIX signal contribution. DOF were calculated as the sample size minus the number of parameters (6 for a fifth-order polynomial fit). The standard deviation of the error term $\hat{\sigma}$ was calculated as

$$\hat{\sigma} = \sqrt{\sum_{i=1}^{n} \frac{(y_i - y_{model,i})^2}{DOF}}$$

with $y_i - y_{model,i}$ being the residual error between a model estimation and the respective measured lifetime. Similarly, prediction intervals (PI) were determined, giving a 95% probability for a new observation to be within the PI.

$$PI = t_{DOF}^{0.975} \cdot \hat{\sigma} \cdot \sqrt{1 + \frac{1}{n} + \frac{(x_0 - \bar{x})^2}{\Sigma_{i=1}^{n}(x_i - \bar{x})^2}}$$

CI and PI were then added to the model predictions as $y_{model,i} \pm CI$ and $y_{model,i} \pm PI$ to form the respective bands.

Descriptive statistics on lifetime data included the mean and standard deviation as well as the median and first and third quartiles. The distribution of those values was visualized in violin plots according to the respective histopathological classification. To assure equal contribution of all specimens, the number of evaluated pixels per sample was normalized to the smallest specimen. This resulted in 21,733 randomly selected pixels per specimen being included in the analysis.

For inferential statistics on differences between the tumor entities and a control group containing non-pathological tissue, we employed a non-parametric Mann–Whitney U test. This decision was based on a low number of specimens within some subgroups (TUM, INF, NEC, REA) of tumor entities. Differences in the distributions among subgroups were ruled out with the Kolmogorov–Smirnov test after data normalization. This is a prerequisite when comparing medians with the Mann–Whitney U test. We considered differences between groups to be significant if $p < 0.05$, with the alternate hypothesis stating that the median fluorescence lifetime was significantly greater than in the non-pathological control group.

For FD-FLIM representation in images, we color-coded the lifetime with the python jet color map. Scaling this color map with the binary logarithm allowed for contrasting the dynamic range from tissue autofluorescence and LGG to strongly fluorescent tumors with constant color-map limits from 1 to 16 ns. This facilitated a convenient visual inter-specimen interpretability of images. Also, brain parenchyma was visualized in blue and strong PpIX fluorescence in red, which is in accordance with what surgeons are used to from conventional PpIX-guided surgery. Intermediate lifetimes for PpIX at the order of magnitude of tissue autofluorescence could then be contrasted according to their magnitude by turquoise, green, yellow, and orange shades. Fluorescence intensity measurements were visualized as grayscale images with the color-map limits being scaled from 0 to the maximum intensity within the image.

We also blended the color-coded fluorescence lifetime images onto the respective fluorescence intensity images of the same region, which allowed for visualizing tissue structure and the fluorescence lifetime in a single image. In particular, our algorithm implemented in Python involved the following processing steps. Both input images were converted from RGB to HSL (hue, saturation, lightness) color space and hue and saturation from the intensity image were replaced with the respective values from the lifetime image. The resulting image was then back-converted to RGB and subsequently converted to YPbPr color space. The chrominances Pb and Pr were kept, and the luminance Y was replaced by the luminance of the original intensity image, which again was obtained by a RGB to YPbPr conversion.

RESULTS

FD-FLIM Delineates Weak PpIX Fluorescence From Tissue Autofluorescence on Macroscale

In FD-FLIM, the measured lifetime is a composed average of the lifetimes of all excited and detected fluorophore emissions, weighted by their respective signal contributions. When measuring in 5-ALA-labeled tissue, both the autofluorescence and PpIX contribute to the overall fluorescence signal. To investigate the potential of delineating weak PpIX from the autofluorescence background, we combined FD-FLIM with spatially registered spectroscopic measurements. This allowed us to correlate the RSC_{PpIX} with the fluorescence lifetime, measured *ex vivo* in human brain tumor specimens. Three hundred thirty-one data points from 99 samples were evaluated, and a fifth-order polynomial fit together with CI and PI is shown in **Figure 2**. With the defined metric, strong intraoperative PpIX fluorescence was condensed at an RSC_{PpIX} of 1.0, with the fit indicating lifetimes of 14.1 ns ± 0.2 ns and 14.1 ns ± 2.1 ns for CI and PI, respectively. PpIX intraoperative fluorescence started becoming visible for RSC_{PpIX} of about 0.85 to 0.9, indicated through ROI A. This corresponded to lifetimes of about 8 to 16 ns, while the range from about 8 to 11ns mostly showed vague visible fluorescence. In ROI A, PpIX fluorescence was dominant respective to the autofluorescence background and could be visualized intraoperatively with a surgical microscope. More importantly, the interesting working range of FD-FLIM is highlighted in ROI B for RSC_{PpIX} from about 0.25 to 0.85. PpIX fluorescence was outweighed by autofluorescence and not visible during surgical resection. Yet, an increase in the RSC_{PpIX} led to an increase of the measured lifetime, facilitating the delineation of very weak PpIX fluorescence from the autofluorescence background. In ROI B, LGG and weakly infiltrated areas of other tumor entities as HGG and MET were found. Below an RSC_{PpIX} of 0.25 (ROI C), the fluorescence lifetime mostly stayed < 2 ns, which is on the order of magnitude expected for the autofluorescence of non-pathological brain parenchyma. Note that ROI C entailed very weak PpIX concentrations, which is examined in the context of methods for spectroscopic PpIX quantification in the discussion section.

Selected Clinical Cases Illustrate the Value of FD-FLIM for Tumor Delineation

In the previous section, we illustrated the full scope of FD-FLIM-enhanced tumor delineation by spectroscopic co-validation. Here, we provide a concise visualization of these findings with three selected clinical cases. **Figure 3A** shows an IDH-wild-type glioblastoma representing tumorous tissue commonly found within ROI A in **Figure 2**. Preoperatively MR images of the lesion in the left temporal lobe were performed demonstrating (I) a typical ring-like contrast enhancement in T1-weighted sequences and (II) a hyperintense appearance in FLAIR sequences. Intraoperative white-light and fluorescence surgical microscope images are shown in (III, IV), respectively. Strong intraoperative PpIX fluorescence was observed during surgery. Histopathology described characteristic cellular pleomorphism (CP), necrosis, and thrombosed vessels (TV; **Figure 3A**, V). Demodulated fluorescence intensity (in mV_{RMS}) and fluorescence lifetime (in ns) maps are shown in (VI, VII). The average lifetimes from ROI 1 to 3 were 14.8, 13.9, and 14.8 ns, respectively. Strong visible PpIX fluorescence of the resected specimen was confirmed by a scientific camera (VIII) while rapidly scanning the laser across the tissue and setting the integration time to 2 s. Measured spectra for the respective ROIs are shown in (IX). The RSC_{PpIX} was 1.0 for

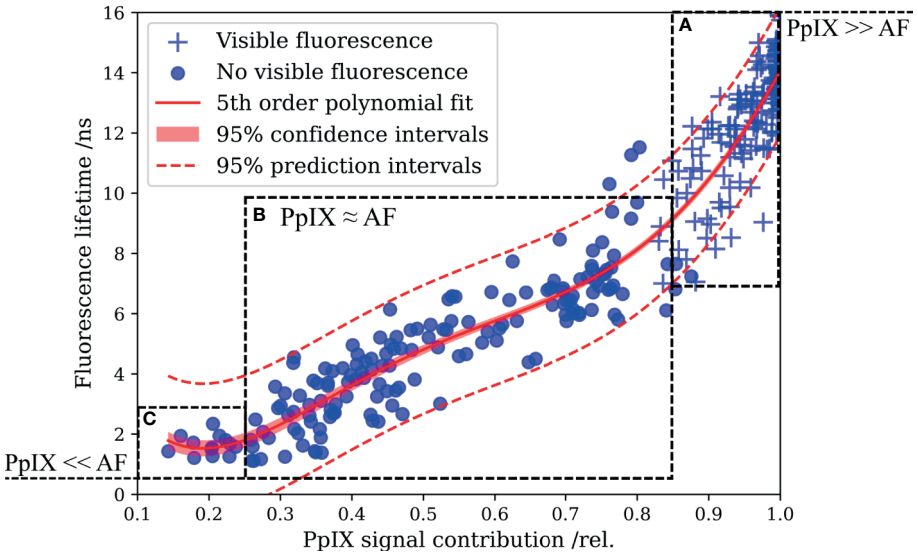

FIGURE 2 | Correlating the fluorescence lifetime with the relative PpIX signal contribution (RSC_{PpIX}) obtained from spatially registered spectroscopic measurements reveals the enhanced delineation of PpIX from tissue autofluorescence by means of FD-FLIM. **(A)** PpIX fluorescence exceeds tissue autofluorescence, and vague to strong intraoperative fluorescence was perceived from about 0.85 to 1.0 RSC_{PpIX}. **(B)** Autofluorescence dominates the overall signal and tissue lacked intraoperative PpIX fluorescence. Increased fluorescence lifetimes facilitate the delineation of PpIX fluorescence from the overall autofluorescence background. **(C)** Fluorescence lifetimes in the magnitude expected for tissue autofluorescence were measured for small $RSC_{PpIX} < 0.25$.

each of the ROIs, with the PpIX fluorescence being orders of magnitude higher than tissue autofluorescence.

Figure 3B shows a representative case of an LGG. The preoperative MR images of the right fronto-temporal tumor showed (I) no significant contrast enhancement on T1-weighted sequences, but (II) appeared as a hyperintense lesion on T2-weighted sequences. No visible fluorescence was observed during surgery (IV). Note that the ZEISS BLUE 400™ emission filter is partially transmissive to the excitation light to highlight the tissue structure in blue. The representative hematoxylin and eosin (H&E) stain entailed central nervous system tissue with infiltrates of an IDH-mutant diffuse glioma with clear-celled appearance (CCA; **Figure 3B**, V). Fluorescence lifetimes (VII) acquired on a resected specimen were increased in ROI 1 and 2 (4.1 and 3.4 ns). ROI 3 (1.6 ns) was chosen on a region with lifetimes on the order of magnitude of tissue autofluorescence, corresponding to what we observed for samples within ROI C of **Figure 2**. Spectroscopic measurements (IX) confirmed the accumulation of PpIX in ROI 1 and 2, with an RSC_{PpIX} of 0.37 and 0.31, respectively. RSC_{PpIX} on ROI 3 was 0.24 with very weak absolute PpIX fluorescence. In the camera image (VIII), PpIX fluorescence was outweighed by autofluorescence and a brighter white and a less intense region could be observed while integrating for 2 s.

Figure 3C depicts a metastasis of a bronchial carcinoma located in the right cerebellum. Preoperative MR images of the tumor demonstrated (I) contrast enhancement in T1-weighted sequences and (II) a hyperintense signal in T2-weighted sequences. Intraoperatively, no fluorescence was visible (IV). The histopathological workup described small, partly necrotic fragments of a carcinoma (CAR) with small- to middle-sized cells and expression of neuroendocrine markers (**Figure 3C**, V). Tissue partly appeared artificially squeezed due to the surgical intervention (AS). When integrating for 10 s with the scientific camera, slight PpIX fluorescence became visible in the upper and right-hand part of the resected sample (VIII). The fluorescence lifetime on the corresponding ROI 1 was 8.5 ns (VII), with the RSC_{PpIX} being 0.68 (VIII). PpIX fluorescence within ROI 1 therefore was slightly below the threshold for visible intraoperative fluorescence, considering the findings from **Figure 2**. ROI 3 entailed a fluorescence lifetime and RSC_{PpIX} of 4.5 ns and 0.61, respectively. Here, autofluorescence was dominant but spectrally and temporally resolved fluorescence clearly delineated PpIX in the tissue. ROI 3 (1.5 ns, $RSC_{PpIX} = 0.19$) visualizes a region with very little PpIX accumulation and lifetimes on the order of magnitude of tissue autofluorescence.

PpIX Fluorescence Lifetime Statistics of Gliomas, Meningiomas, and Metastasis

This section provides an overview of the fluorescence lifetimes measured for all specimens, including non-pathological tissue, LGG, HGG, MNG, and MET (**Figures 4A–D**). Tissue was further classified as reactive, infiltrated, necrotic, or core tumor, according to the histopathological workup. The descriptive statistics are visualized in violin plots, with the median and first and third quartiles indicated through dashed lines. Groups were tested for statistical significant differences against the non-pathological group, with the alternate hypothesis being that the median fluorescence lifetime was greater than what we observed in (A). Most importantly, both infiltration

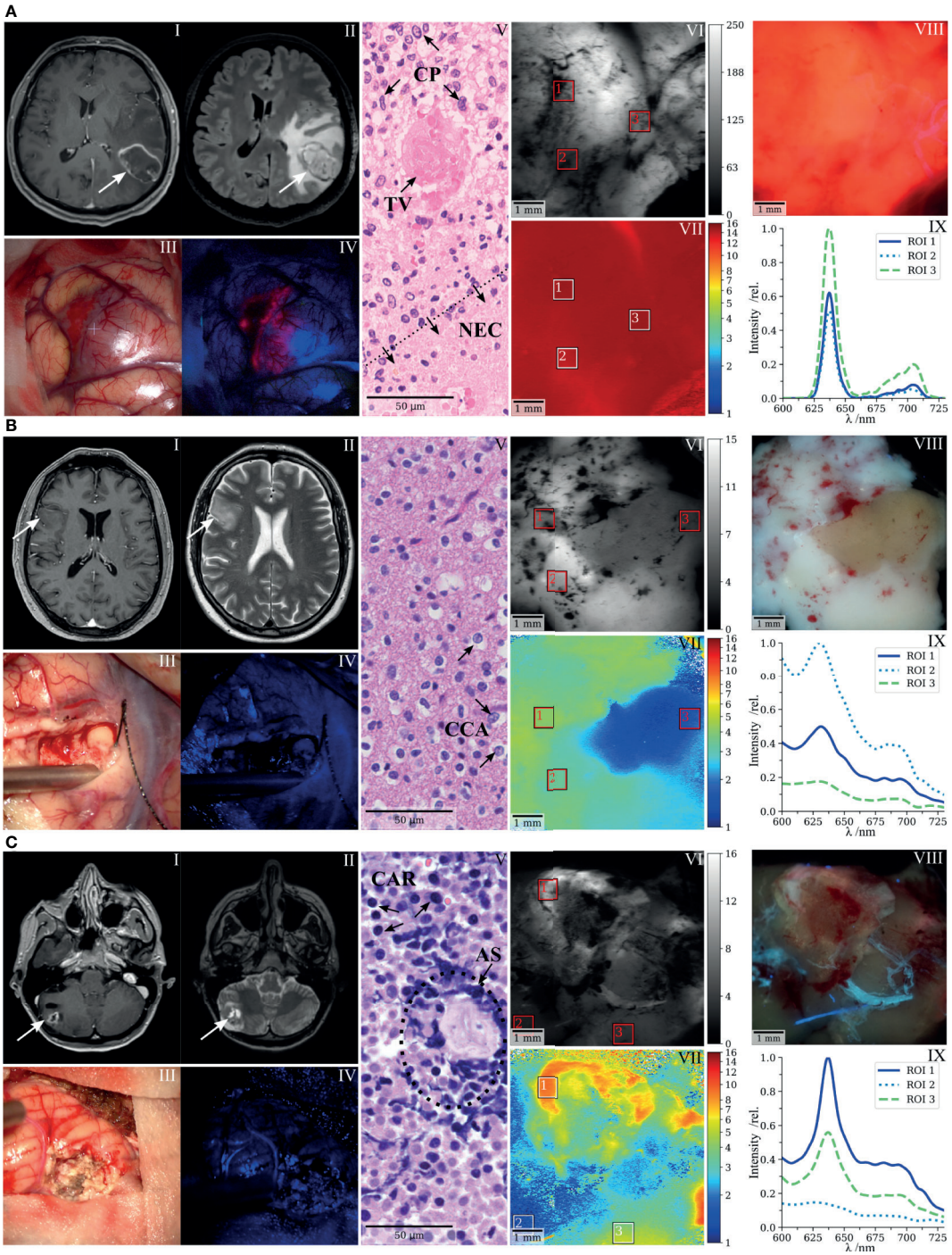

FIGURE 3 | FD-FLIM delineation of PpIX and spectroscopic co-validation illustrated with three selected clinical cases. **(A)** Glioblastoma, **(B)** low-grade glioma, and **(C)** bronchial carcinoma metastasized to the cerebellum. (I,II) Preoperative T1- and T2-weighted MRI, (III,IV) surgical microscope white light and BLUE 400 fluorescence images taken during cytoreductive surgery, (V) representative histopathological section stained with hematoxylin and eosin, (VI,VII) demodulated fluorescence intensity (in mV_{RMS}) and fluorescence lifetime (in ns) acquired on resected specimens with the raster-scanning FD-FLIM system, (VIII) fluorescence image of the respective specimens acquired with a scientific camera, and (IX) spectra acquired on the indicated ROIs in VI and VII; the fluorescence intensity (relative units) is plotted as a function of wavelength (in nm); CP, cellular pleomorphism; TV, thrombosed vessel; NEC, necrosis; CCA, clear-celled appearance; CAR, carcinoma cells; AS, artificially squeezed tissue.

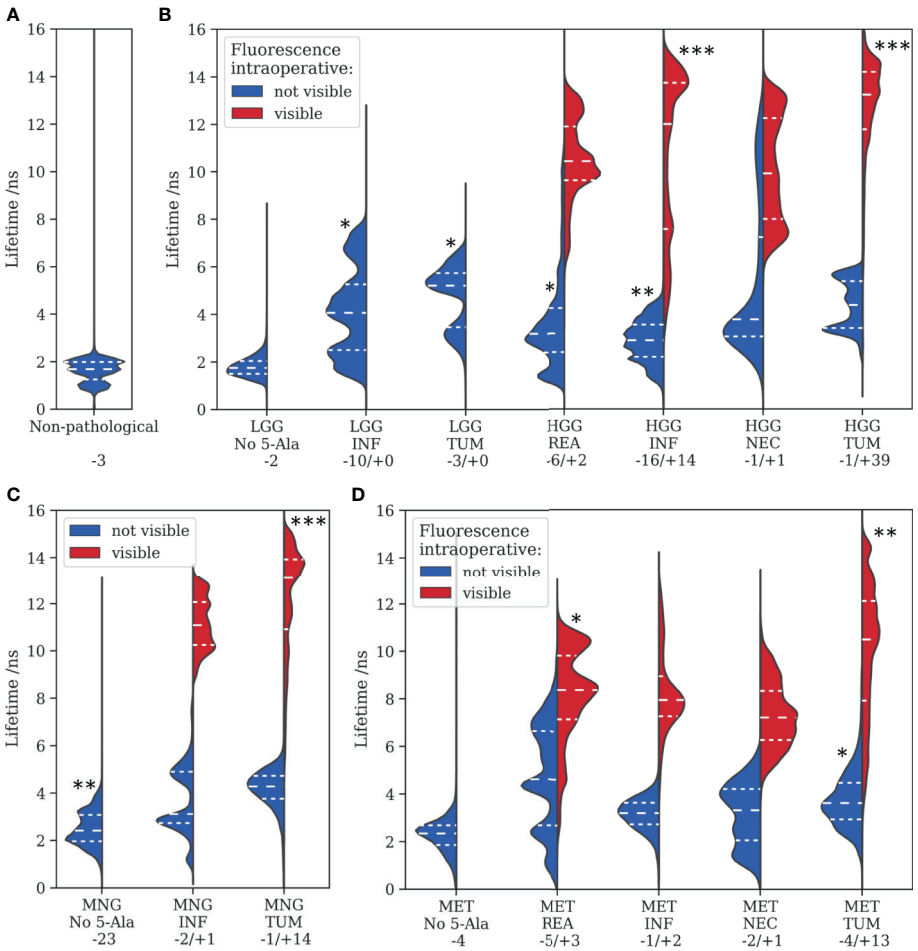

FIGURE 4 | Fluorescence lifetimes measured for various tumor entities are visualized with violin plots, where the dashed lines represent the median, 0.25 and 0.75 quartiles. **(A)** non-pathological tissue, **(B)** low- and high-grade gliomas, **(C)** meningiomas, and **(D)** metastasis. Tissue was further categorized into reactive (REA), infiltration zones (INF), necrotic regions (NEC), and core tumor areas (TUM) according to the histopathological workup. Statistical levels of significant difference to **(A)** of each subgroup are indicated with asterisks (*<0.05, **<0.01, ***<0.005). Numbers after a "– or "+" refer to the amount of samples without or with visible intraoperative fluorescence, respectively.

zones (median = 4.1 ns, first quantile = 2.5 ns, third quantile = 5.3 ns, $p = 0.017$) and core tumor areas (5.2 ns, 3.5 ns, 5.7 ns, $p = 0.040$) of LGG showed significantly increased lifetimes respective to the control group (1.7 ns, 1.3 ns, 2.0 ns). None of the LGG showed visible fluorescence during surgery. In infiltrated parenchyma of HGG, the number of samples for visible and non-visible intraoperative fluorescence was balanced with significantly increased median lifetimes, 2.9 ns ($p = 0.008$) and 12.0 ns ($p = 0.005$), respectively. Note that infiltrated tissue often showed heterogeneous visible fluorescence. This explains why about 30% of the measured tumor area in the "visible" group was below the identified threshold (**Figure 2**) for visible fluorescence of about 8 ns. While the majority of reactive parenchyma in HGG was visually non-fluorescent, 39 of 40 core tumor specimens showed strong fluorescence and clearly increased lifetimes (13.2 ns, 11.8 ns, 14.2 ns, $p = 0.002$). It is interesting to note that many MNG tumor specimens exhibited strong fluorescence with increased lifetimes (13.1 ns, 10.9 ns, 13.9 ns, $p = 0.005$), although a vast majority of those tumors was classified as benign (WHO grade I, **Supplementary Table 6**). Likewise, increased lifetimes were found for different tissue types of brain metastasis. Autofluorescence lifetimes of tumorous tissue without 5-ALA were clearly increased for both MNG (2.4 ns, 2.0 ns, 3.1 ns, $p = 0.010$) and MET (2.3 ns, 1.9 ns, 2.7 ns, $p = 0.056$), respective to autofluorescence lifetimes of physiological brain. Please refer to **Supplementary Table 2** for descriptive and inferential statistics of all tumor entities.

FD-FLIM and Structural Tissue Visualization in Neurosurgical Microscopes

In the previous sections, we outlined the capacity of FD-FLIM to delineate LGG and weakly fluorescent tumorous tissue on macroscale. The second imperative for successful clinical

translation is the coherence with surgical instrumentation and workflows. This section therefore covers important aspects related to engineering the technology toward clinical translation. For the simultaneous visualization of both tissue structure and fluorescence lifetime, we suggest color-blending FD-FLIM measurements on either a fluorescence intensity or a white-light camera image. The overlay algorithm is described in more detail in *Materials and Methods*. **Figure 5** illustrates how color-blending a fluorescence lifetime (II) on a highly resolved fluorescence intensity image (I) provides both tissue morphology and FD-FLIM contrast (III). In parallel, fusing lifetime and structural information is highly beneficial in terms of measurement speed. While the homodyne detection of FD-FLIM allows to recover weak signals from noise, the photon budget in surgical microscopes with long working distances is limited. This entails a trade-off between the field of view (FOV), the lateral resolution, and the frame rate. When reducing the resolution of the FD-FLIM image to 100 µm (IV, 64 × 64 pixels), acquisition time decreased to 1 s. The respective color-blended image (V) was highly comparable to (III), and the perceived image resolution was dominated by the luminance of the structural tissue image. For quantifying the similarity between II and IV as well as III and V, we employed the structural similarity index measure (SSIM). The SSIM takes both the perceived alteration of structural information as well as changes in luminance and contrast into account. While the SSIM was 0.895 for II and IV, it was 0.986 for III and V, confirming the visually perceived similarity. Note that when comparing two identical images, the SSIM would be 1.0.

For information on the measurement accuracy of FD-FLIM in tissue and the extent of PpIX bleaching under prolonged excitation, please refer to **Supplementary Figures 2** and **3**. We also propose an adjusted implementation of FD-FLIM for surgical microscopes with variable working distances (**Supplementary Materials Section 1.1**).

DISCUSSION

Maximal safe resection is of decisive importance in the management of brain tumors. PpIX fluorescence-guided surgery has improved neurosurgical resection in HGG but lacks sensitivity and specificity for the delineation of LGG and weakly infiltrated tumor areas of HGG. Our results emphasize the capacity of FD-FLIM to detect weak PpIX fluorescence and distinguish it from spectrally overlapping tissue autofluorescence on macroscale.

The benchmark for sensitive PpIX detection in tissue has been set by spectroscopic PpIX quantification, implemented both in handheld probes (7, 21) and in hyperspectral wide-field setups integrated in surgical microscopes (36, 40). While measuring spectrally resolved fluorescence facilitates clear distinction between weak PpIX and tissue autofluorescence, the technique has not been translated to clinical practice yet. This might be contributed to the size of the instrumentation and the spectral complexity of different physiochemical states of PpIX which hamper PpIX quantification especially in LGG (41). Wide-field PpIX quantification is also challenged by inhomogeneous illumination profiles across the field of view or resection cavities being not flat (42). The fluorescence lifetime is to a good degree parametrically independent to such perturbations as it is an intrinsic property of fluorophores (26). In this work, we combined fluorescence lifetime measurements of PpIX in brain tumor specimens with spatially registered spectroscopic measurements for the first time. We correlated FD-FLIM measurements with the respective PpIX signal contribution as

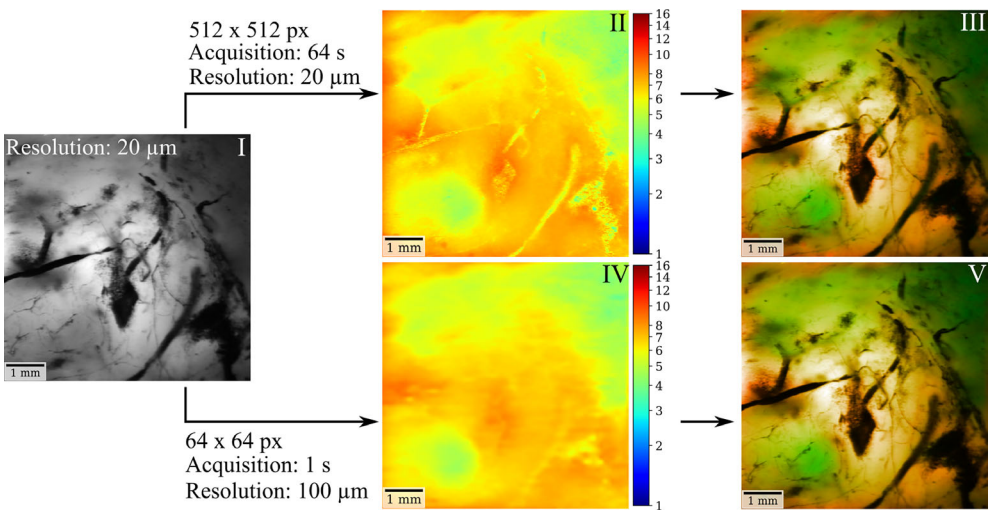

FIGURE 5 | FD-FLIM and structural tissue visualization in surgical microscopes can be achieved through color blending in near real time. Using a highly resolved fluorescence intensity (I) or a white-light camera image as a basis, color-blending the fluorescence lifetime (II) provides both structural tissue and lifetime information (III). When reducing the resolution of the FD-FLIM image to 100 µm (IV) acquisition time could be decreased to 1 sec. The corresponding color-blended image (V) yields comparable contrast to (III), with the perceived image quality and resolution being dominated by the luminance of the intensity image.

a ground truth. Autofluorescence lifetimes were found to be in the range of about 0.8 to 2 ns (32, 33), which was substantiated by a non-pathological sample within this study. The multimodal approach revealed how even weak PpIX concentrations in tissue led to an increase of the measured lifetime respective to tissue autofluorescence. While most HGG core tumor specimens exhibited strong intraoperative fluorescence, autofluorescence became dominant for LGG and weakly infiltrated, reactive, or necrotic tissue of HGG, MNG, and MET. At about 0.85 RSC_{PpIX} and below, PpIX was outweighed by the autofluorescence background and not visible during surgical resection. Down to an RSC_{PpIX} of about 0.25, the multimodal approach demonstrated enhanced FD-FLIM tumor delineation. The variations observed within the prediction intervals in **Figure 2** were expected as the autofluorescence background intensity and lifetimes varied among samples. This can be contributed to differences in absorption and scattering as well as to the known heterogeneity of metabolic strategies employed by brain tumors (43). Furthermore, porphyrins such as uroporphyrin and coproporphyrin (44) and various photoproducts of PpIX with shorter lifetimes (45) likely contributed to the overall signal.

Studies quantifying PpIX concentrations in tissue account for optical tissue properties as absorption and scattering and employ spectral unmixing to isolate the PpIX signal from the background fluorescence or photoproducts of PpIX (46). The relation between the PpIX concentration and the RSC_{PpIX} of the raw signal is therefore inherently non-linear. Nevertheless, we consider it helpful to put our work into this context, as the comparison enables the reader to get an estimate of the sensitivity of time-resolved fluorescence measurements in respect to spectroscopic PpIX quantification. It is worth mentioning that an RSC_{PpIX} below 0.25 was most likely linked to extremely weak PpIX concentrations. Widhalm et al. presented spectra for two LGG with PpIX being quantified to 13 and 35 ng/ml (7). We evaluated the RSC_{PpIX} in the corresponding processed spectra to be about 0.37 and 0.55, respectively. The non-pathological cortex entailed a PpIX concentration of 1 ng/ml, with a small peak corresponding to about 0.09 RSC_{PpIX} (7). Similarly, Valdés et al. showed spectra of two LGG with concentrations of 56 ng/ml (21) and 82 ng/ml (47), corresponding to about 0.57 and 0.67 RSC_{PpIX}, respectively. This suggests that the low concentrations within the presented LGG could have been contrasted by FD-FLIM. Note that reactive tissue accumulates PpIX and entails increased lifetimes which might be mistaken for infiltrated tumor regions. This might be seen as a general limitation for the specificity of methods basing their contrast on PpIX fluorescence. Combining FD-FLIM with other imaging modalities could provide valuable complementary information. A possible workflow might involve wide-field screening of the resection cavity with FD-FLIM and subsequent co-validation in the operating room by methods such as stimulated Raman histology (48) or confocal laser endomicroscopy (49, 50).

The proposed optical fiber-based architecture facilitates the integration of FD-FLIM into surgical microscopes with minor space requirements, which outlines the coherence of our method with surgical workflows. Nevertheless, the low collection efficiency at long working distances remains challenging for real-time visualization. Our setup allows for acquiring highly resolved (25 μm lateral resolution, 6.5 × 6.5 mm^2 FOV) FD-FLIM images at a working distance of 200 mm in about 16 s. This would allow for screening the resection cavity for residual tumor with a reasonable acquisition time. For enhanced visualization, we proposed to fuse FD-FLIM maps with a reduced lateral resolution with highly resolved white-light or fluorescence intensity images. With the proposed algorithm, tissue structure is visualized with high resolution and fluorescence lifetime contrast is provided with sufficient accuracy. In our setup, a reduction of the lateral FD-FLIM resolution to about 100 μm reduced the acquisition time to 1 s. A further reduction of the FD-FLIM resolution would be possible without sacrificing relevant information. Note that other approaches such as hand-held scanning with a point measurement probe achieved accuracies of 1 to 2 mm, with the need to correct for tissue motion with sophisticated algorithms (51). In the same manner, FD-FLIM scans could be acquired for the entire FOV within fractions of a second and then overlaid onto a continuous white-light video stream. The combination of image processing together with surgical microscopes designed with an optimized detection efficiency in the FLIM channel is promising for real-time intrasurgical FD-FLIM.

Apart from the capacity for sensitive intrasurgical tumor delineation, we found the value of PpIX lifetime imaging to be in the ease of interpretation. Independently of factors as excitation intensity and the FD-FLIM measurement instrumentation, the measured lifetime in tissue can expected to be in the range of about 0.5 to 16.4 ns. While a simple threshold at around 2 ns would provide excellent separation between PpIX and tissue autofluorescence, FD-FLIM is also promising to provide a robust input to machine learning classification models. In future, data acquired with various systems across a multitude of clinical centers could be fused to provide a big database for enhanced tumor delineation and classification. Aside from PpIX, label-free approaches measuring the fluorescence lifetime of endogenous tissue fluorophores as FAD or NADH provide a potential source of contrast for intrasurgical brain tumor delineation. Studies employing time-resolved two-photon microscopy showed increased mean NADH lifetimes in human glioma cell lines compared to non-pathological brain (52, 53). Alfonso-Garcia et al. intraoperatively demonstrated increased lifetimes for necrotic tissue respective to cortex as well as decreased lifetimes for an oligodendroglioma patient when comparing to the lifetimes of adjacent white matter (54). Higher mean NADH fluorescence lifetimes were also observed in glioblastomas respective to physiological brain (27, 55). The interested reader is also referred to Marcu and Hartl (25). Further studies are required to better understand the potential of endogenous fluorescence lifetimes for tumor delineation in the brain, and a special focus should be set on LGG and infiltrated tissue at tumor boundaries. In this respect, the heterogeneity of metabolic strategies employed by gliomas is particularly challenging (43).

Alongside these promising aspects, this study has to be seen under the following limitations. First, measurements were performed *ex vivo*. Larger studies with intrasurgical measurements

ultimately are required to investigate tissue *in vivo*. In this study, we intended to keep the state of tissue as close to *in vivo* as possible. We imaged within 1 h after resection and kept the specimens in artificial cerebrospinal fluid. More importantly, *ex vivo* imaging allowed us to validate FD-FLIM with spatially registered spectroscopy, as the long acquisition time of spectra and tissue motion would have complicated the method *in vivo*. Second, this implied a low number of non-pathological specimens, since biopsies few centimeters away from the tumor boundary are only feasible in very rare cases (for example the approach to deep-seated tumors). The small size of the control group in our study limited the explanatory power of statistical inference. Extended clinical trials will be necessary to account for this limitation. However, tissue in adequate distance to the MRI contrast-enhancing tumor boundary could be assumed to be non-pathological in future *in vivo* studies. While no histological confirmation would be possible without biopsy collection, we believe this approach to be reasonable for obtaining control measurements from the normal cortex. We emphasize that the value of this study lies in the multimodal co-validation, which coherently substantiates the capacity of FD-FLIM to delineate weak PpIX from the autofluorescence background. Third, the current laser power of 6 mW is compliant with laser safety norms (ANSI Z136.1) for tissue and safe for diffuse reflections toward the eye. However, specular reflections toward the eye could pose a problem in a worst-case scenario. As of now, at least optical density 1 laser safety protection is required. Considering a limiting aperture of 7 mm as specified for point-source ocular exposure, a maximum laser power of 1 mW is permissible at the eye. This suggests that the technology can be engineered toward an operation without any safety protection. Optimizing the surgical microscopes detection efficiency in the FLIM channel together with the proposed image processing methods would allow for decreasing the laser power. Alternatively, algorithmic safety measures can allow for detecting surgical instruments and reflecting surfaces based on the white-light video-stream and automatically shut down the laser before specular reflections can occur. Fourth, the homodyne detection inherent to FD-FLIM is to a good extent unaffected by unmodulated signal contributions as ambient light. Nevertheless, the relatively bright laboratory room light did increase the background signal at 10 MHz, which increased the noise and phase jitter for measurements of very weak tissue autofluorescence. We therefore turned off the light for an optimal signal-to-noise ratio. In the dimmed light conditions common to fluorescence-guided surgery, we would not expect this to pose a problem. Simultaneous white-light illumination during FD-FLIM measurements can be achieved by shaping the light source emission spectrum to not emit within the PpIX detection band.

To conclude, this study emphasizes the potential of FLIM to optimize maximal safe resection in brain tumors in the future and highlights its potential toward clinical translation. The advantage of PpIX for fluorescence guidance for tumor resection has been outlined also in other medical disciplines such as urology and gynecology. Evidently, the findings on FLIM for maximal safe tumor resection could initiate intensive research activities to be transferred to those areas as well.

DATA AVAILABILITY STATEMENT

The raw data supporting the conclusions of this article will be made available by the authors, without undue reservation.

ETHICS STATEMENT

The studies involving human participants were reviewed and approved by the Ethics Committee of the Medical University of Vienna (EK419/2008 – Amendment 04/2018). The patients/participants provided their written informed consent to participate in this study.

AUTHOR CONTRIBUTIONS

GW, BK, and LW resected the tumor specimens. JG, TR, and AW performed the histopathological workup. BK, LW, and AL organized the biopsy handling and preparation. MW and CH provided the technical consultation for modifications on the surgical microscope. ME and DR set up the FD-FLIM system under supervision of AU and MA. DR implemented the spectroscopy channel, performed the measurements, analyzed the data, and wrote the manuscript. ME, WD, GW, and RL initiated the project. All authors contributed to the article and approved the submitted version.

FUNDING

This project has received funding from the Austrian Christian Doppler Research Association as well as from the innovation board of the Carl Zeiss Meditec AG. TR is a recipient of a DOC Fellowship of the Austrian Academy of Sciences at the Division of Neuropathology and Neurochemistry (25262). JG is supported by an OeNB grant 16725 to AW. The financial support by the Austrian Federal Ministry for Digital and Economic Affairs and the National Foundation for Research, Technology and Development is gratefully acknowledged. This project has furthermore received funding from the European Union Horizon 2020 research and innovation program under the Marie Sklodowska-Curie grant agreement (MSCA grant 721766).

ACKNOWLEDGMENTS

We thank Tanja Peilnsteiner for consistent support with biopsy preparation.

SUPPLEMENTARY MATERIAL

The Supplementary Material for this article can be found online at: https://www.frontiersin.org/articles/10.3389/fonc.2021.741303/full#supplementary-material

REFERENCES

1. Ostrom QT, Patil N, Cioffi G, Waite K, Kruchko C, Barnholtz-Sloan JS. CBTRUS Statistical Report: Primary Brain and Other Central Nervous System Tumors Diagnosed in the United States in 2013–2017. *Neuro Oncol* (2020) 22: iv1–iv96. doi: 10.1093/neuonc/noaa200
2. Lombardi G, Barresi V, Castellano A, Tabouret E, Pasqualetti F, Salvalaggio A, et al. Clinical Management of Diffuse Low-Grade Gliomas. *Cancers (Basel)* (2020) 12:3008. doi: 10.3390/cancers12103008
3. Valiente M, Ahluwalia MS, Boire A, Brastianos PK, Goldberg SB, Lee EQ, et al. The Evolving Landscape of Brain Metastasis. *Trends Cancer* (2018) 4:176–96. doi: 10.1016/j.trecan.2018.01.003
4. Xia L, Fang C, Chen G, Sun C. Relationship Between the Extent of Resection and the Survival of Patients With Low-Grade Gliomas: A Systematic Review and Meta-Analysis. *BMC Cancer* (2018) 18:48. doi: 10.1186/s12885-017-3909-x
5. Albuquerque LAF, Almeida JP, de Macêdo Filho LJM, Joaquim AF, Duffau H. Extent of Resection in Diffuse Low-Grade Gliomas and the Role of Tumor Molecular Signature-S Systematic Review of the Literature. *Neurosurg Rev* (2020) 44(3):1371–89. doi: 10.1007/s10143-020-01362-8
6. Hervey-Jumper SL, Berger MS. Role of Surgical Resection in Low- and High-Grade Gliomas. *Curr Treat Options Neurol* (2014) 16:284. doi: 10.1007/s11940-014-0284-7
7. Widhalm G, Olson J, Weller J, Bravo J, Han SJ, Phillips J, et al. The Value of Visible 5-ALA Fluorescence and Quantitative Protoporphyrin IX Analysis for Improved Surgery of Suspected Low-Grade Gliomas. *J Neurosurg* (2019) 133 (1):79–88. doi: 10.3171/2019.1.JNS182614
8. Stupp R, Mason WP, van den Bent MJ, Weller M, Fisher B, Taphoorn MJB, et al. Radiotherapy Plus Concomitant and Adjuvant Temozolomide for Glioblastoma. *New Engl J Med* (2005) 352:987–96. doi: 10.1056/NEJMoa043330
9. Mariotto AB, Robin Yabroff K, Shao Y, Feuer EJ, Brown ML. Projections of the Cost of Cancer Care in the United States: 2010–2020. *J Natl Cancer Inst* (2011) 103:117–28. doi: 10.1093/jnci/djq495
10. Coburger J, Wirtz CR, König RW. Impact of Extent of Resection and Recurrent Surgery on Clinical Outcome and Overall Survival in a Consecutive Series of 170 Patients for Glioblastoma in Intraoperative High Field Magnetic Resonance Imaging. *J Neurosurg Sci* (2017) 61:233–44. doi: 10.23736/S0390-5616.16.03284-7
11. Stummer W, Pichlmeier U, Meinel T, Wiestler OD, Zanella F, Reulen H-J. Fluorescence-Guided Surgery With 5-Aminolevulinic Acid for Resection of Malignant Glioma: A Randomised Controlled Multicentre Phase III Trial. *Lancet Oncol* (2006) 7:392–401. doi: 10.1016/S1470-2045(06)70665-9
12. Suero Molina E, Schipmann S, Stummer W. Maximizing Safe Resections: The Roles of 5-Aminolevulinic Acid and Intraoperative MR Imaging in Glioma Surgery—Review of the Literature. *Neurosurg Rev* (2019) 42:197–208. doi: 10.1007/s10143-017-0907-z
13. Hadjipanayis CG, Widhalm G, Stummer W. What is the Surgical Benefit of Utilizing 5-Aminolevulinic Acid for Fluorescence-Guided Surgery of Malignant Gliomas? *Neurosurgery* (2015) 77:663–73. doi: 10.1227/NEU.0000000000000929
14. Teng L, Nakada M, Zhao S-G, Endo Y, Furuyama N, Nambu E, et al. Silencing of Ferrochelatase Enhances 5-Aminolevulinic Acid-Based Fluorescence and Photodynamic Therapy Efficacy. *Br J Cancer* (2011) 104:798–807. doi: 10.1038/bjc.2011.12
15. Belykh E, Shaffer KV, Lin C, Byvaltsev VA, Preul MC, Chen L. Blood-Brain Barrier, Blood-Brain Tumor Barrier, and Fluorescence-Guided Neurosurgical Oncology: Delivering Optical Labels to Brain Tumors. *Front Oncol* (2020) 10:739. doi: 10.3389/fonc.2020.00739
16. Stepp H, Stummer W. 5-ALA in the Management of Malignant Glioma. *Lasers Surg Med* (2018) 50:399–419. doi: 10.1002/lsm.22933
17. Widhalm G, Wolfsberger S, Minchev G, Woehrer A, Krssak M, Czech T, et al. 5-Aminolevulinic Acid Is a Promising Marker for Detection of Anaplastic Foci in Diffusely Infiltrating Gliomas With Nonsignificant Contrast Enhancement. *Cancer* (2010) 116:1545–52. doi: 10.1002/cncr.24903
18. Widhalm G, Kiesel B, Woehrer A, Traub-Weidinger T, Preusser M, Marosi C, et al. 5-Aminolevulinic Acid Induced Fluorescence is a Powerful Intraoperative Marker for Precise Histopathological Grading of Gliomas With Non-Significant Contrast-Enhancement. *PloS One* (2013) 8:e76988. doi: 10.1371/journal.pone.0076988
19. Jaber M, Ewelt C, Wölfer J, Brokinkel B, Thomas C, Hasselblatt M, et al. Is Visible Aminolevulinic Acid-Induced Fluorescence an Independent Biomarker for Prognosis in Histologically Confirmed (World Health Organization 2016) Low-Grade Gliomas? *Neurosurgery* (2019) 84:1214–24. doi: 10.1093/neuros/nyy365
20. Ewelt C, Floeth FW, Felsberg J, Steiger HJ, Sabel M, Langen K-J, et al. Finding the Anaplastic Focus in Diffuse Gliomas: The Value of Gd-DTPA Enhanced MRI, FET-PET, and Intraoperative, ALA-Derived Tissue Fluorescence. *Clin Neurol Neurosurg* (2011) 113:541–7. doi: 10.1016/j.clineuro.2011.03.008
21. Valdés PA, Jacobs V, Harris BT, Wilson BC, Leblond F, Paulsen KD, et al. Quantitative Fluorescence Using 5-Aminolevulinic Acid-Induced Protoporphyrin IX Biomarker as a Surgical Adjunct in Low-Grade Glioma Surgery. *J Neurosurg* (2015) 123:771–80. doi: 10.3171/2014.12.JNS14391
22. Wei L, Fujita Y, Sanai N, Liu JTC. Toward Quantitative Neurosurgical Guidance With High-Resolution Microscopy of 5-Aminolevulinic Acid-Induced Protoporphyrin IX. *Front Oncol* (2019) 9:592. doi: 10.3389/fonc.2019.00592
23. Belykh E, Miller EJ, Hu D, Martirosyan NL, Woolf EC, Scheck AC, et al. Scanning Fiber Endoscope Improves Detection of 5-ALA Induced Protoporphyrin IX Fluorescence at the Boundary of Infiltrative Glioma. *World Neurosurg* (2018) 113:e51–69. doi: 10.1016/j.wneu.2018.01.151
24. Meza D, Wang D, Wang Y, Borwege S, Sanai N, Liu JTC. Comparing High-Resolution Microscopy Techniques for Potential Intraoperative Use in Guiding Low-Grade Glioma Resections. *Lasers Surg Med* (2015) 47:289–95. doi: 10.1002/lsm.22347
25. Marcu L, Hartl BA. Fluorescence Lifetime Spectroscopy and Imaging in Neurosurgery. *IEEE J Selected Topics Quantum Electron* (2012) 18:1465–77. doi: 10.1109/JSTQE.2012.2185823
26. Berezin MY, Achilefu S. Fluorescence Lifetime Measurements and Biological Imaging. *Chem Rev* (2010) 110:2641–84. doi: 10.1021/cr900343z
27. Sun Y, Hatami N, Yee M, Phipps J, Elson DS, Gorin F, et al. Fluorescence Lifetime Imaging Microscopy for Brain Tumor Image-Guided Surgery. *J BioMed Opt* (2010) 15:056022. doi: 10.1117/1.3486612
28. Skala MC, Riching KM, Gendron-Fitzpatrick A, Eickhoff J, Eliceiri KW, White JG, et al. *In Vivo* Multiphoton Microscopy of NADH and FAD Redox States, Fluorescence Lifetimes, and Cellular Morphology in Precancerous Epithelia. *PNAS* (2007) 104:19494–9. doi: 10.1073/pnas.0708425104
29. Schaefer PM, Kalinina S, Rueck A, von Arnim CAF, von Einem B. NADH Autofluorescence-A Marker on its Way to Boost Bioenergetic Research. *Cytometry A* (2019) 95:34–46. doi: 10.1002/cyto.a.23597
30. Erkkilä MT, Bauer B, Hecker-Denschlag N, Medina MJM, Leitgeb RA, Unterhuber A, et al. Widefield Fluorescence Lifetime Imaging of Protoporphyrin IX for Fluorescence-Guided Neurosurgery: An *Ex Vivo* Feasibility Study. *J Biophotonics* (2019) 12:e201800378. doi: 10.1002/jbio.201800378
31. Russell JA, Diamond KR, Collins TJ, Tiedje HF, Hayward JE, Farrell TJ, et al. Characterization of Fluorescence Lifetime of Photofrin and Delta-Aminolevulinic Acid Induced Protoporphyrin IX in Living Cells Using Single- and Two-Photon Excitation. *IEEE J Selected Topics Quantum Electron* (2008) 14:158–66. doi: 10.1109/JSTQE.2007.912896
32. Erkkilä MT, Reichert D, Gesperger J, Kiesel B, Roetzer T, Mercea PA, et al. Macroscopic Fluorescence-Lifetime Imaging of NADH and Protoporphyrin IX Improves the Detection and Grading of 5-Aminolevulinic Acid-Stained Brain Tumors. *Sci Rep* (2020) 10:20492. doi: 10.1038/s41598-020-77268-8
33. Kantelhardt SR, Diddens H, Leppert J, Rohde V, Hüttmann G, Giese A. Multiphoton Excitation Fluorescence Microscopy of 5-Aminolevulinic Acid Induced Fluorescence in Experimental Gliomas. *Lasers Surg Med* (2008) 40:273–81. doi: 10.1002/lsm.20623
34. Croce AC, Bottiroli G. Autofluorescence Spectroscopy and Imaging: A Tool for Biomedical Research and Diagnosis. *Eur J Histochem* (2014) 58:2461. doi: 10.4081/ejh.2014.2461
35. Reichert D, Erkkilä MT, Holst G, Hecker-Denschlag N, Wilzbach M, Hauger C, et al. Towards Real-Time Wide-Field Fluorescence Lifetime Imaging of 5-ALA Labeled Brain Tumors With Multi-Tap CMOS Cameras. *BioMed Opt Express BOE* (2020) 11:1598–616. doi: 10.1364/BOE.382817

36. Valdes PA, Jacobs VL, Wilson BC, Leblond F, Roberts DW, Paulsen KD. System and Methods for Wide-Field Quantitative Fluorescence Imaging During Neurosurgery. *Opt Lett* (2013) 38:2786–8. doi: 10.1364/OL.38.002786
37. Lakowicz JR. *Principles of Fluorescence Spectroscopy*. Boston, MA: Springer Science & Business Media (2013).
38. Erkkilä MT, Reichert D, Hecker-Denschlag N, Wilzbach M, Hauger C, Leitgeb RA, et al. Surgical Microscope With Integrated Fluorescence Lifetime Imaging for 5-Aminolevulinic Acid Fluorescence-Guided Neurosurgery. *JBO* (2020) 25:71202. doi: 10.1117/1.JBO.25.7.071202
39. Montgomery DC, Runger GC. *Applied Statistics and Probability for Engineers*. John Wiley & Sons (2010).
40. Jermyn M, Gosselin Y, Valdes PA, Sibai M, Kolste K, Mercier J, et al. Improved Sensitivity to Fluorescence for Cancer Detection in Wide-Field Image-Guided Neurosurgery. *BioMed Opt Express* (2015) 6:5063–74. doi: 10.1364/BOE.6.005063
41. Montcel B, Mahieu-Williame L, Armoiry X, Meyronet D, Guyotat J. Two-Peaked 5-ALA-Induced PpIX Fluorescence Emission Spectrum Distinguishes Glioblastomas From Low Grade Gliomas and Infiltrative Component of Glioblastomas. *BioMed Opt Express BOE* (2013) 4:548–58. doi: 10.1364/BOE.4.000548
42. Belykh E, Miller EJ, Patel AA, Bozkurt B, Yağmurlu K, Robinson TR, et al. Optical Characterization of Neurosurgical Operating Microscopes: Quantitative Fluorescence and Assessment of PpIX Photobleaching. *Sci Rep* (2018) 8:12543. doi: 10.1038/s41598-018-30247-6
43. Strickland M, Stoll EA. Metabolic Reprogramming in Glioma. *Front Cell Dev Biol* (2017) 5:43. doi: 10.3389/fcell.2017.00043
44. Rück A, Dolp F, Hülshoff C, Hauser C, Scalfi-Happ C. Fluorescence Lifetime Imaging in PDT. An Overview. *Med Laser Appl* (2005) 20:125–9. doi: 10.1016/j.mla.2005.03.009
45. Yeh S-CA, Patterson MS, Hayward JE, Fang Q. Time-Resolved Fluorescence in Photodynamic Therapy. *Photonics* (2014) 1:530–64. doi: 10.3390/photonics1040530
46. Bravo JJ, Olson JD, Davis SC, Roberts DW, Paulsen KD, Kanick SC. Hyperspectral Data Processing Improves PpIX Contrast During Fluorescence Guided Surgery of Human Brain Tumors. *Sci Rep* (2017) 7:9455. doi: 10.1038/s41598-017-09727-8
47. Valdés PA, Leblond F, Kim A, Harris BT, Wilson BC, Fan X, et al. Quantitative Fluorescence in Intracranial Tumor: Implications for ALA-Induced PpIX as an Intraoperative Biomarker. *J Neurosurg* (2011) 115:11–7. doi: 10.3171/2011.2.JNS101451
48. Hollon TC, Pandian B, Adapa AR, Urias E, Save AV, Khalsa SSS, et al. Near Real-Time Intraoperative Brain Tumor Diagnosis Using Stimulated Raman Histology and Deep Neural Networks. *Nat Med* (2020) 26:52–8. doi: 10.1038/s41591-019-0715-9
49. Belykh E, Zhao X, Ngo B, Farhadi DS, Byvaltsev VA, Eschbacher JM, et al. Intraoperative Confocal Laser Endomicroscopy *Ex Vivo* Examination of Tissue Microstructure During Fluorescence-Guided Brain Tumor Surgery. *Front Oncol* (2020) 10:599250. doi: 10.3389/fonc.2020.599250
50. Acerbi F, Pollo B, De Laurentis C, Restelli F, Falco J, Vetrano IG, et al. *Ex Vivo* Fluorescein-Assisted Confocal Laser Endomicroscopy (CONVIVO® System) in Patients With Glioblastoma: Results From a Prospective Study. *Front Oncol* (2020) 10:606574. doi: 10.3389/fonc.2020.606574
51. Marsden M, Marsden M, Fukazawa T, Fukazawa T, Fukazawa T, Deng Y-C, et al. FLImBrush: Dynamic Visualization of Intraoperative Free-Hand Fiber-Based Fluorescence Lifetime Imaging. *BioMed Opt Express BOE* (2020) 11:5166–80. doi: 10.1364/BOE.398357
52. Kantelhardt SR, Leppert J, Krajewski J, Petkus N, Reusche E, Tronnier VM, et al. Imaging of Brain and Brain Tumor Specimens by Time-Resolved Multiphoton Excitation Microscopy *Ex Vivo*. *Neuro-Oncology* (2007) 9:103–12. doi: 10.1215/15228517-2006-034
53. Leppert J, Krajewski J, Kantelhardt SR, Schlaffer S, Petkus N, Reusche E, et al. Multiphoton Excitation of Autofluorescence for Microscopy of Glioma Tissue. *Neurosurgery* (2006) 58:759–67; discussion 759-767. doi: 10.1227/01.NEU.0000204885.45644.22
54. Alfonso-Garcia A, Bec J, Sridharan Weaver S, Hartl B, Unger J, Bobinski M, et al. Real-Time Augmented Reality for Delineation of Surgical Margins During Neurosurgery Using Autofluorescence Lifetime Contrast. *J Biophotonics* (2020) 13:e201900108. doi: 10.1002/jbio.201900108
55. Lukina M, Yashin K, Kiseleva EE, Alekseeva A, Dudenkova V, Zagaynova EV, et al. Label-Free Macroscopic Fluorescence Lifetime Imaging of Brain Tumors. *Front Oncol* (2021) 11:666059. doi: 10.3389/fonc.2021.666059

Conflict of Interest: MW and CH are employees of Carl Zeiss Meditec AG, Oberkochen, Germany. GW received restricted travel grants from NX Development Corp.

The remaining authors declare that the research was conducted in the absence of any commercial or financial relationships that could be construed as a potential conflict of interest.

Publisher's Note: All claims expressed in this article are solely those of the authors and do not necessarily represent those of their affiliated organizations, or those of the publisher, the editors and the reviewers. Any product that may be evaluated in this article, or claim that may be made by its manufacturer, is not guaranteed or endorsed by the publisher.

Copyright © 2021 Reichert, Erkkilae, Gesperger, Wadiura, Lang, Roetzer, Woehrer, Andreana, Unterhuber, Wilzbach, Hauger, Drexler, Kiesel, Widhalm and Leitgeb. This is an open-access article distributed under the terms of the Creative Commons Attribution License (CC BY). The use, distribution or reproduction in other forums is permitted, provided the original author(s) and the copyright owner(s) are credited and that the original publication in this journal is cited, in accordance with accepted academic practice. No use, distribution or reproduction is permitted which does not comply with these terms.

frontiers in Oncology

ORIGINAL RESEARCH
published: 23 September 2021
doi: 10.3389/fonc.2021.744318

Factors Associated With Dysfunction of Glymphatic System in Patients With Glioma

Cheng Hong Toh[1,2]* *and Tiing Yee Siow*[1]

[1] Department of Medical Imaging and Intervention, Chang Gung Memorial Hospital at Linkou, Tao-Yuan, Taiwan,
[2] Chang Gung University College of Medicine, Tao-Yuan, Taiwan

Objectives: Rodent experiments have provided some insights into the changes of glymphatic function associated with glioma growth. The diffusion tensor image analysis along the perivascular space (DTI-ALPS) method offers an opportunity for the noninvasive investigation of the glymphatic system in patients with glioma. We aimed to investigate the factors associated with glymphatic function changes in patients with glioma.

Materials and Methods: A total of 201 glioma patients (mean age = 47.4 years, 116 men; 86 grade II, 52 grade III, and 63 grade IV) who had preoperative diffusion tensor imaging for calculation of the ALPS index were retrospectively included. Information collected from each patient included sex, age, tumor grade, *isocitrate dehydrogenase 1* (*IDH1*) mutation status, peritumoral brain edema volume, tumor volume, and ALPS index. Group differences in the ALPS index according to sex, tumor grade, and *IDH1* mutation status were assessed using analysis of covariance with age adjustment. Linear regression analyses were performed to identify the factors associated with the ALPS index.

Results: Group comparisons revealed that the ALPS index of grade II/III gliomas was significantly higher than that of grade IV gliomas ($p < 0.001$). The ALPS index of *IDH1* mutant gliomas was significantly higher than that of *IDH1* wild-type gliomas ($p < 0.001$). On multivariable linear regression analysis, *IDH1* mutation ($\beta = 0.308$, $p < 0.001$) and peritumoral brain edema volume ($\beta = -0.353$, $p < 0.001$) were the two independent factors associated with the ALPS index.

Conclusion: *IDH1* wild-type gliomas and gliomas with larger peritumoral brain edema volumes were associated with a lower ALPS index, which may reflect impaired glymphatic function.

Keywords: glioma, glymphatic system, peritumoral brain edema, analysis along perivascular space (ALPS) index, diffusion tensor imaging

OPEN ACCESS

Edited by:
Nico Sollmann,
University of California, San Francisco, United States

Reviewed by:
Giuseppe Barisano,
University of Southern California, United States
Serena Pellegatta,
Fondazione IRCCS Istituto Neurologio Carlo Besta, Italy
Tobias Greve,
Ludwig Maximilian University of Munich, Germany

***Correspondence:**
Cheng Hong Toh
eldomtoh@hotmail.com

Specialty section:
This article was submitted to Neuro-Oncology and Neurosurgical Oncology, a section of the journal Frontiers in Oncology

Received: *20 July 2021*
Accepted: *02 September 2021*
Published: *23 September 2021*

Citation:
Toh CH and Siow TY (2021) Factors Associated With Dysfunction of Glymphatic System in Patients With Glioma. Front. Oncol. 11:744318. doi: 10.3389/fonc.2021.744318

INTRODUCTION

The glymphatic system has been recently recognized as a pathway for waste clearance and maintaining fluid balance in the brain parenchymal interstitium (1). Cerebrospinal fluid (CSF) from the subarachnoid space flows into the brain parenchyma through periarterial spaces of the penetrating arteries and, under the influence of aquaporin-4 (AQP4) water channels, mixes with parenchymal

interstitial fluid. The interstitial fluid and its solutes then move into the perivenous and perineuronal spaces, thereafter leaving the brain parenchyma. The discovery of the glymphatic system led to a new perspective into the pathogenesis of brain diseases such as neurodegeneration (2) and acute ischemic infarct (3). Recent studies have shown that the glymphatic system may play an essential role in brain tumor immunity and might be targeted in brain tumor immunotherapy (4).

Rodent experiments have provided some insights into the changes of glymphatic function associated with glioma growth. In rodent studies, reduced CSF efflux rate (5) and remodeling of the glymphatic pathway (4) were observed in glioma-bearing mice, and these changes may be associated with the formation of peritumoral brain edema. Despite substantial knowledge having been gained from animal studies, further research is necessary to confirm whether the findings regarding the glymphatic system of animals apply to humans. Noninvasive approaches such as the morphological assessment of intracranial perivascular spaces with structural magnetic resonance imaging (MRI) (6–9) and measurement of water diffusivity using diffusion MRI (10–12) have been proposed for the evaluation of human glymphatic function.

The analysis along the perivascular space (ALPS) index (10) is a diffusion metric derived from diffusion tensor imaging (DTI). It is thought to reflect the diffusivity along the perivascular spaces of medullary veins at the level of the lateral ventricle body and, thus, may serve as an estimate of human glymphatic function. Alterations of the ALPS index correlate with the Mini-Mental State Examination scores in patients with Alzheimer's disease and are thought to reflect glymphatic dysfunction. The ALPS index is also significantly lower in normal pressure hydrocephalus patients and points toward glymphatic dysfunction, as indicated by delayed clearance of intrathecally injected gadobutrol (13, 14).

The ALPS index offers an opportunity for the noninvasive investigation of the human glymphatic system. Thus, we took advantage of this method to evaluate the glymphatic system in patients with glioma. We aimed to investigate the correlations of glymphatic function with the volumes of tumor and peritumoral brain edema, tumor grades, and *isocitrate dehydrogenase 1* (*IDH1*) mutation status.

MATERIALS AND METHODS

Study Subjects

Approval for reviewing patients' clinical data and preoperative MRI studies was obtained from our Institutional Review Board. Between 2008 and 2018, a total of 239 consecutive patients with a histopathological diagnosis of grade II, III, or IV glioma underwent preoperative DTI at our institution. A total of 38 patients were excluded due to age younger than 18 years (n = 2), motion artifacts (n = 3), tumors limited to the infratentorial compartment (n = 4), and the *IDH1* mutation status not being available (n = 29). Thus, a total of 201 patients (85 women and 116 men, mean age = 47.4 ± 15.5 years, range = 18–91 years) were analyzed. None of the patients had begun corticosteroid treatment, radiation therapy, chemotherapy, or had previous brain surgery at the time of their MRI studies.

Clinical and Imaging Information

Patients' medical records and MRI studies were retrospectively reviewed to collect information including sex, age, tumor grade, and tumor *IDH1* mutation status. Histopathological diagnosis was made by a board-certified neuropathologist with 20 years of experience according to the 2007 WHO classification of central nervous system tumors before 2016 and thereafter based on the 2016 WHO classification.

MRI

All MRI studies were performed using a 3-T unit (Magnetom Tim Trio, Siemens, Erlangen, Germany) with a 12-channel phased-array head coil. All examinations included T2-weighted, susceptibility-weighted, DTI, and T1-weighted sequences acquired in the transverse plane before and after administration of 0.1 mmol/kg body weight gadopentetate dimeglumine (Magnevist; Schering, Berlin, Germany).

DTI was performed using a single-shot echo planar sequence (EPI) with the following parameters: repetition time/echo time (TR/TE), 5,800/83 ms; diffusion gradient encoding in 20 directions; b = 0, 1,000 s/mm^2; field of view (FOV), 256 × 256 mm; matrix size, 128 × 128; section thickness, 2 mm; and number of signals acquired, 4. A total of 50–60 sections without intersection gaps were used to cover the cerebral hemispheres, brainstem, and the cerebellum. Generalized autocalibrating partially parallel acquisitions (GRAPPA) with a reduction factor set at 2 were used during DTI acquisitions. Contrast-enhanced T1-weighted images [TR/TE = 2,000/2.63 ms, section thickness = 1 mm, inversion time (TI) = 900 ms, acquisition matrix = 224 × 256, and FOV = 224 × 256 mm] were acquired after completion of the DTI sequence.

Image Post-Processing and Analysis

The software nordicICE (nordic Image Control and Evaluation, version 2; Nordic Imaging Lab, Bergen, Norway) was used for all volume measurements. All images of each patient were co-registered based on a 3D non-rigid transformation and mutual information. The adequacy of registration was visually assessed and manual adjustments were performed by changing the transformation parameters of translation, rotation, and/or scaling, as necessary. The ALPS index was measured with 3D Slicer, version 4.10.2 (http://www.slicer.org). Blinded to histopathologic diagnoses, two neuroradiologists (with 16 and 6 years of experience) independently performed all measurements. If the tumors were found in both hemispheres, only those in the hemisphere with the larger tumor were selected for measurements of volumes. If multiple tumors or peritumoral brain edema areas were present, all were included as long as their sizes were larger than 1 × 1 cm^2.

Measurements of Volumes of Peritumoral Brain Edema, Whole Tumor, Enhancing Tumor Portions, Non-Enhancing Tumor Portions, Necrotic Portions, and Hemorrhagic Portions

One polygonal region of interest (ROI) was first placed on each T2-weighted image to include the entire peritumoral brain edema and

tumor, followed by another ROI drawn to include the entire tumor on each contrast-enhanced T1-weighted image. Subtracting the second ROI from the first ROI yielded the isolated peritumoral brain edema area. If non-enhancing, necrotic, and hemorrhagic tumor portions were present, they were measured by placing the ROIs on T2-weighted or contrast-enhanced T1-weighted images with reference to other pulse sequence images. In all the slices covering the whole tumor, the ROIs were drawn. Non-enhancing tumor portions were tumor components that showed T2-weighted/fluid-attenuated inversion recover (FLAIR) hyperintensity with corresponding T1-weighted hypointensity and no contrast enhancement. Necrotic tumor portions were tumor components that demonstrated central T2-weighted hyperintensity (i.e., fluid) with surrounding contrast enhancement. Hemorrhagic tumor portions were tumor components that had T1-weighted hyperintensity, T2-weighted hypointensity, or susceptibility-weighted hypointensity. Subtracting the ROIs of the non-enhancing, necrotic, and hemorrhagic tumor portions from the tumor ROI yielded the enhancing tumor area. The slice volume of each ROI was computed by multiplying the area by slice distance (slice thickness + slice gap). The total volumes of the peritumoral brain edema, whole tumor, enhancing tumor portion, non-enhancing tumor portion, necrotic portion, and hemorrhagic portion were calculated by summing up all the slice volumes. An example of ROI segmentation is shown in **Figure 1**.

Measurement of the ALPS Index

The diffusion tensor image analysis along the perivascular space (DTI-ALPS) method (10) was used to evaluate the glymphatic function. This method evaluates the diffusivity along with the perivascular space on a transverse slice at the level of the lateral ventricle body. The medullary veins, accompanied by their perivascular spaces, run perpendicular to the ventricular walls at the level of the lateral ventricular bodies in a right–left or a left–right direction (i.e., *x*-axis in the image coordinate). In this level, the corticofugal corona radiata projection fibers run in the craniocaudal direction (i.e., *z*-axis in the image coordinate) adjacent to the lateral ventricles. The superior longitudinal fascicle, which represents the association fibers, runs in the anterior–posterior direction (i.e., *y*-axis in the image coordinate) and is located lateral to the corona radiata. As the perivascular space is nearly perpendicular to both the projection fibers and association fibers, the mean *x*-axis diffusivity in both fibers (D_{xproj} and D_{xassoc} for *x*-axis diffusivity in the projection fiber and the association fiber, respectively) can reflect the change in perivascular flow, after being normalized to the mean diffusivity that is perpendicular to the *x*-axis and to the direction of the fiber tracts (*y*-axis for the projection fiber, where the diffusivity is denoted as D_{yproj}; *z*-axis for the association fiber, where the diffusivity is denoted as D_{zassoc}). To estimate the glymphatic activity, the ALPS index is defined as follows:

$$\text{ALPS index} = \frac{\text{mean}(D_{xproj}, D_{xassoc})}{\text{mean}(D_{yproj}, D_{zassoc})} \quad (1)$$

Diffusion metric images were generated by using 3D Slicer, version 4.10.2 (http://www.slicer.org). The diffusion tensor is calculated based on the "Diffusion Tensor Estimated function" in 3D Slicer. D*xx*, D*yy*, and D*zz* were extracted from the tensor data using a self-written Python script in the 3D Slicer Python interactor. The ROIs of the projection (mean size = 35 ± 19 mm^2) and association fibers (mean size = 30 ± 18 mm^2) ipsilateral to the tumors were drawn on a slice at the level of the lateral ventricular body based on a directionality encoded map. The ALPS index was computed according to Equation 1 above. An example of ROI placement for ALPS index measurement is shown in **Figure 1**.

Statistical Analysis

A commercially available statistical software package (SPSS 22; IBM, Armonk, NY, USA) was used for analysis, and *p*-values <0.05 were considered to indicate a statistical significance. Continuous variables are denoted as the mean ± standard deviation, unless otherwise noted. The Kolmogorov–Smirnov test was used to assess the normality of continuous variables.

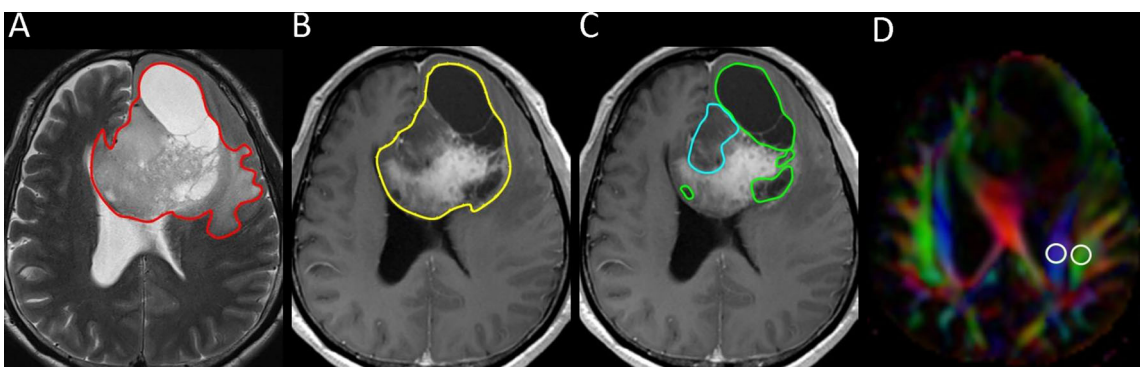

FIGURE 1 | Example of how regions of interest (ROIs) were segmented in a left frontal grade II glioma. **(A)** Transverse T2-weigthed image showing a manually drawn polygonal ROI (*red*) that includes the entire peritumoral brain edema and the whole tumor. **(B, C)** On contrast-enhanced T1-weighted images, the ROIs of whole tumor (*yellow*), non-enhancing tumor (*blue*), and necrotic portion (*green*) are shown. **(D)** Directionally encoded color map illustrating the ROIs of the projection (*blue area*) and association (*green area*) fibers in the left periventricular region for calculation of the analysis along the perivascular space (ALPS) index.

Variance inflation factors were used to detect multicollinearity. Interobserver variability in the measurements of volumes and the ALPS index was assessed by intraclass correlation coefficients (ICCs) with 95% confidence intervals (CIs) based on an absolute-agreement, two-way random-effects model. The final values of all measurements were obtained by taking the mean of the two observers' independent measurements.

Group differences in the ALPS index according to sex (man *vs*. woman), tumor grade (grade II *vs*. III *vs*. IV), and *IDH1* mutation status (mutant *vs*. wild-type) were assessed using analysis of covariance with age adjustment (15, 16). Additional Bonferroni correction was performed for tumor grade.

The associations of ALPS index with age, sex, histological grade, *IDH1* mutation status, whole tumor volume, enhancing tumor volume, non-enhancing tumor volume, necrotic portion volume, and hemorrhagic portion volume were first analyzed with univariable linear regression. All variables were entered as potential covariates in the stepwise multivariable linear regression analysis to identify independent factors associated with the ALPS index.

RESULTS

Table 1 summarizes the patients' characteristics and all measurements. Among the 201 patients with gliomas, 86 had grade II, 52 had grade III, and 63 had grade IV. A total of 107 (53.2%) tumors were *IDH1*-mutant. Eighty-four (41.8%) patients had glioma involving the right cerebral hemisphere.

There were excellent interobserver agreements (ICC = 0.822–0.948, $p < 0.001$) in the measurements of peritumoral brain edema volumes, whole tumor volumes, enhancing tumor volumes, non-enhancing tumor volumes, necrotic portions volumes, hemorrhagic portions volumes, and the ALPS index. The mean volumes (in cubic centimeters) of the peritumoral brain edema, whole tumor, enhancing tumor, non-enhancing tumor, necrotic portion, and hemorrhagic portion were 26.09 ± 30.38, 53.47 ± 39.40, 16.34 ± 18.58, 29.84 ± 38.25, 5.78 ± 14.65, and 3.82 ± 11.91, respectively. The mean ALPS index for grade II, grade III, and grade IV gliomas were 1.454 ± 0.186, 1.421 ± 0.214, and 1.220 ± 0.112, respectively.

The results of ALPS index comparisons according to sex, tumor grade, and *IDH1* mutation status with age adjustment are summarized in **Table 2**. The ALPS index of women was not significantly different from that of men ($p = 0.098$). The ALPS index of grade II and grade III gliomas was significantly higher than that of grade IV gliomas ($p < 0.001$). However, the ALPS index was not different between grade II and III gliomas ($p = 0.670$). The ALPS index of *IDH1* wild-type gliomas was significantly lower than that of *IDH1* mutant gliomas ($p < 0.001$). **Figure 2** shows the differences in the ALPS index according to sex, tumor grade, and *IDH1* mutation status.

The results of linear regression analyses of the factors associated with the ALPS index are summarized in **Table 3**. On univariable linear regression analysis, the ALPS index correlated with age ($\beta = -0.147$, $p = 0.038$), sex ($\beta = -0.139$, $p = 0.049$), tumor grade ($\beta = -0.361$, $p < 0.001$), *IDH1* mutation ($\beta = 0.384$, $p < 0.001$), peritumoral brain edema volume ($\beta = -0.439$, $p < 0.001$), enhancing tumor volume ($\beta = -0.348$, $p < 0.001$), and non-enhancing tumor volume ($\beta = 0.307$, $p < 0.001$). The associations of the ALPS index with whole tumor volume ($\beta = 0.101$, $p = 0.155$), necrotic portion volume ($\beta = -0.058$, $p = 0.410$), and hemorrhagic portion volume ($\beta = 0.002$, $p = 0.983$) were not statistically significant. **Figure 3** illustrates the correlations of the ALPS index with age, peritumoral brain edema volume, enhancing tumor volume, and non-enhancing tumor volume.

On stepwise multivariable linear regression analysis, *IDH1* mutation ($\beta = 0.308$; $p < 0.001$) and peritumoral brain edema volume ($\beta = -0.353$; $p < 0.001$) were the two independent factors associated with the ALPS index. A lower ALPS index was associated with *IDH1* wild-type gliomas and larger peritumoral brain edema volume.

TABLE 1 | Patient characteristics and all measurements.

Characteristics	Grade II	Grade III	Grade IV	All
No. of patients	86	52	63	201
Mean age ± SD (years)	41.4 ± 13.3	45.2 ± 13.6	57.5 ± 15.1	47.4 ± 15.5
Sex				
Woman	41	23	21	85
Man	45	29	42	116
Tumor location				
Right cerebral	37	16	31	84
Left cerebral	49	36	32	117
IDH1 mutation				
Wild-type	20	18	56	94
Mutant	66	34	7	107
Peritumoral edema volume (cm^3)	13.81 ± 18.36	17.04 ± 21.11	50.33 ± 35.70	26.09 ± 30.38
Whole tumor volume (cm^3)	52.82 ± 45.56	58.69 ± 40.92	50.04 ± 27.35	53.47 ± 39.40
Enhancing tumor volume (cm^3)	1.59 ± 6.21	12.27 ± 19.26	31.22 ± 15.46	16.34 ± 18.58
Non-enhancing tumor volume (cm^3)	47.02 ± 42.57	33.11 ± 30.57	3.69 ± 18.75	29.84 ± 38.25
Necrotic portion volume (cm^3)	1.94 ± 7.30	9.34 ± 22.39	8.10 ± 13.05	5.78 ± 14.65
Hemorrhagic portion volume (cm^3)	1.18 ± 10.95	3.05 ± 11.43	8.06 ± 12.55	3.82 ± 11.91
ALPS index	1.454 ± 0.186	1.421 ± 0.214	1.220 ± 0.112	1.372 ± 0.202

Except where indicated, data are numbers of patients.
SD, standard deviation; ALPS, analysis along the perivascular space.

TABLE 2 | Comparisons of the ALPS index according to sex, tumor grade, and *IDH1* mutation status with age adjustment.

Characteristics	ALPS index	Pairwise comparison	*p*-value	95% CI
Sex		Woman *vs*. man	0.098	–0.009 to 0.105
Woman	1.405 ± 0.216			
Man	1.348 ± 0.190			
Tumor grade		Grade II *vs*. III	0.670	–0.037 to 0.112
Grade II	1.454 ± 0.186	Grade II *vs*. IV	<0.001	0.178–0.333
Grade III	1.421 ± 0.214	Grade III *vs*. IV	<0.001	0.135–0.301
Grade IV	1.220 ± 0.112			
IDH1 mutation		Wild-type *vs*. mutant	<0.001	–0.235 to –0.097
Wild-type	1.311 ± 0.151			
Mutant	1.466 ± 0.201			

Data are the mean ± SD.

CI, confidence interval; ALPS, analysis along the perivascular space.

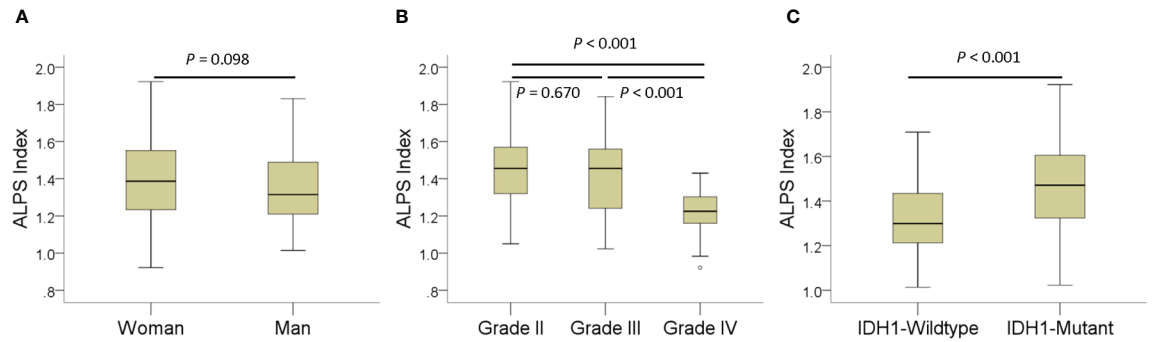

FIGURE 2 | Boxplots showing differences in the analysis along the perivascular space (ALPS) index according to sex **(A)**, tumor grade **(B)**, and *IDH1* mutation status **(C)**.

DISCUSSION

In the present study, the *IDH1* mutation status of gliomas and the peritumoral brain edema volume were two independent factors associated with the ALPS index. As reflected by a lower ALPS index, glymphatic function was impaired in *IDH1* wild-type gliomas and gliomas associated with larger peritumoral brain edema volumes. To our knowledge, this is the first study of human glymphatic function in patients with glioma.

The inverse correlation between the ALPS index and peritumoral brain edema volume was observed in meningiomas (17). It was proposed that tumor growth disrupts the balance between periarterial CSF influx and perivenous interstitial fluid efflux and results in the accumulation of interstitial fluid, i.e., peritumoral brain edema. A higher glymphatic function may facilitate interstitial fluid clearance and reduce or even prevent edema. In contrast, insufficient glymphatic function for interstitial fluid clearance may contribute to edema formation. Therefore, glymphatic dysfunction may explain the pathogenesis of peritumoral brain edema in meningiomas, which are extra-axial and have no direct contact with the brain interstitium.

The pathogenesis of peritumoral brain edema in gliomas is traditionally thought to represent the net transport of fluid from the intravascular compartment into the brain interstitium due to the proliferation of microvessels that have defects in their inter-endothelial tight junctions (18). However, this theory does not explain the formation of peritumoral brain edema in low-grade gliomas with intact tight junctions (19, 20). In our study, we also observed an inverse relationship between the ALPS index and peritumoral brain edema volume. This finding suggests that the peritumoral brain edema associated with intra-axial tumors (i.e., gliomas) may also be related to glymphatic dysfunction.

A recent study has shown that changes in the supporting structures of the blood–brain barrier, such as astrocytes, pericytes, and microglial cells, may also be associated with the influx of fluid into the brain interstitium (21). The astrocyte covering of brain microvessels seems to be rate limiting to water movement (21), and AQP4 water channels located on astrocytic foot processes may play a significant role in peritumoral brain edema formation. A strong correlation between peritumoral brain edema and upregulated astrocyte AQP4 expression in human gliomas suggests that increased AQP4 expression may be essential to the pathogenesis of peritumoral brain edema (22). Since AQP4 water channels are part of the glymphatic system, we speculate that there may an association between the ALPS index and the expression of AQP4 water channels. Further studies are needed to establish the role of the ALPS index as an imaging marker of AQP4 expression in gliomas.

The changes of glymphatic function associated with glioma growth have only been investigated in a few animal studies. In a study using an orthotopic xenograft glioma model (5), glioma

TABLE 3 | Univariable and multivariable linear regression analyses of factors associated with the ALPS index.

Characteristics	ALPS Index			
	Univariate linear regression		Multivariate linear regression	
	β	*p*-value	*β*	*p*-value
Age (years)	–0.147	0.038	0.075	0.351
Sex	–0.139	0.049	0.001	0.993
Tumor grade	–0.361	<0.001	–0.127	0.149
IDH1 mutation	0.384	<0.001	0.308	<0.001
Brain edema volume	–0.439	<0.001	–0.353	<0.001
Whole tumor volume	0.101	0.155	0.119	0.122
Enhancing tumor volume	–0.348	<0.001	0.024	0.778
Non-enhancing tumor volume	0.307	<0.001	0.108	0.187
Necrotic portion volume	–0.058	0.410	–0.033	0.653
Hemorrhagic portion volume	0.064	0.454	0.133	0.092

ALPS, analysis along the perivascular space; β, standardized coefficient.

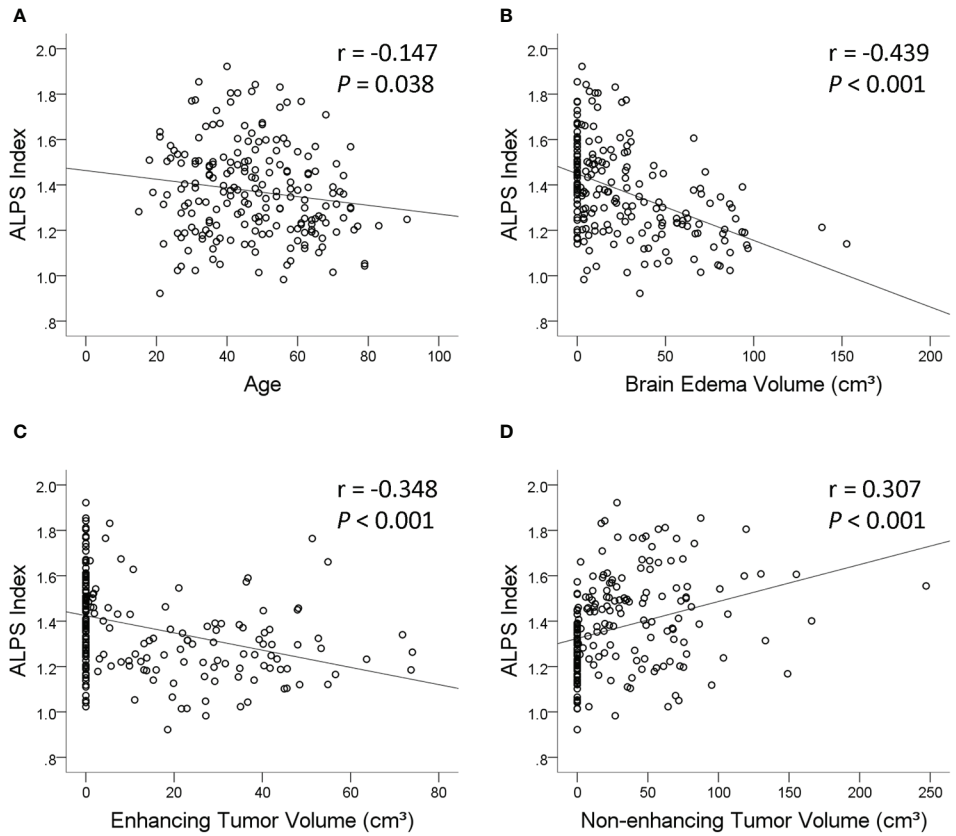

FIGURE 3 | Scatterplots with regression line showing the correlations of the analysis along the perivascular space (ALPS) index with age **(A)**, peritumoral brain edema volume **(B)**, enhancing tumor volume **(C)**, and non-enhancing tumor volume **(D)**.

growth caused glymphatic dysfunction with reduced CSF flow to the extracranial space. In our study, the glymphatic function of *IDH1* wild-type gliomas, measured with the ALPS index, was significantly lower than that of *IDH1* mutant gliomas. To the best of our knowledge, no human studies have reported the association between glymphatic function and the *IDH1* mutation status of gliomas.

IDH1 wild-type gliomas are known to behave more aggressively than *IDH1* mutant gliomas (23). We speculate that the spread of *IDH1* wild-type gliomas is associated with greater disruption to the flow of interstitial fluid and, consequently, lower glymphatic function. Alternatively, tumor-associated glymphatic pathway remodeling may be responsible for the differences in glymphatic function between *IDH1* wild-type and *IDH1* mutant gliomas. In mice

harboring gliomas, glymphatic function is increased for waste and fluid clearance by extensive growth of meningeal lymphatic vessels, which are downstream of the glymphatic pathway (4). A previous study showed that the growth of glioblastomas (mostly *IDH1* wild-type) from small to large tumors could take as short as 1.5 months (24). In contrast, *IDH1* mutant gliomas are known for longer survival and may be stable for years (25). We therefore speculate that the lower glymphatic function of *IDH1* wild-type gliomas may be related to their short duration of tumor growth, which does not allow extensive remodeling of the glymphatic pathway.

Although the mechanism for the association between glymphatic function and *IDH1* mutation status is unclear, the relationship has revealed some potential utilities for the ALPS index. Many MR imaging markers have been found to be useful in predicting the *IDH1* mutation status in gliomas (26–29). However, most of them are measured in the tumors, but may not be feasible when a large hemorrhage or necrosis is present. In contrast, the ALPS index is measured in the periventricular region outside of the tumor and, thus, may serve as an alternative marker for *IDH1* mutation prediction. Besides, the ALPS index may also be a prognostic factor for patient survival due to its correlation with *IDH1* mutation status. Further studies are needed to establish the predictive and prognostic roles of the ALPS index.

The anatomical relationship of the perivascular spaces, projection fibers, and association fibers in the periventricular region is the theoretical basis of the DTI-ALPS method. Although this method is based on a deductive model, it is frequently used to investigate human glymphatic function. Its potential to serve as an imaging marker of glymphatic activity has been reported in many clinical conditions such as Alzheimer's disease (10, 30), normal pressure hydrocephalus (31, 32), Parkinson disease (33, 34), age-related iron deposition (15), diabetic cognitive impairment (35), and meningioma-associated brain edema (17). However, there are limitations to this method and, consequently, our study. Firstly, the diffusion signal measured in clinical settings reflects overall changes in water mobility associated with many processes occurring at scales much smaller than typical MRI voxels. Therefore, we cannot definitely state that the ALPS index is a measure of glymphatic function. Secondly, the ALPS index could only measure the perivascular water flow that runs in a right-to-left direction and in the periventricular region. Further studies are needed to establish its correlation with overall glymphatic function. Finally, our study is a snapshot in time and does not include longitudinal data on temporal changes of the ALPS index and peritumoral brain edema volume following treatment. These pieces of information would be helpful to further establish the role of the glymphatic system in brain edema formation.

CONCLUSIONS

In conclusion, *IDH1* wild-type gliomas and gliomas with larger peritumoral brain edema volumes were associated with a lower ALPS index, which may reflect an impaired glymphatic function. The lower ALPS index in *IDH1* wild-type gliomas may suggest an association between glymphatic dysfunction and tumor aggressiveness. In addition, the correlation between larger peritumoral brain edema volumes and a lower ALPS index suggests that the formation of peritumoral brain edema may be related to glymphatic dysfunction.

DATA AVAILABILITY STATEMENT

The raw data supporting the conclusions of this article will be made available by the authors, without undue reservation.

ETHICS STATEMENT

The studies involving human participants were reviewed and approved by Chang Gung Medical Foundation Institutional Review Board. Written informed consent for participation was not required for this study in accordance with the national legislation and the institutional requirements.

AUTHOR CONTRIBUTIONS

CT and TS contributed to the conception and design of the study and to the acquisition and analysis of data. CT drafted the text, prepared the figures, and wrote the first draft of the manuscript. All authors read the final manuscript. All authors contributed to the article and approved the submitted version.

FUNDING

This study was funded by the National Science Council, Taiwan (NSC98-2314-B-182A-051-MY3 to CT).

REFERENCES

1. Rasmussen MK, Mestre H, Nedergaard M. The Glymphatic Pathway in Neurological Disorders. *Lancet Neurol* (2018) 17(11):1016–24. doi: 10.1016/s1474-4422(18)30318-1
2. Nedergaard M, Goldman SA. Glymphatic Failure as a Final Common Pathway to Dementia. *Science* (2020) 370(6512):50–6. doi: 10.1126/science.abb8739
3. Mestre H, Du T, Sweeney AM, Liu G, Samson AJ, Peng W, et al. Cerebrospinal Fluid Influx Drives Acute Ischemic Tissue Swelling. *Science* (2020) 367(6483):eaax7171. doi: 10.1126/science.aax7171
4. Hu X, Deng Q, Ma L, Li Q, Chen Y, Liao Y, et al. Meningeal Lymphatic Vessels Regulate Brain Tumor Drainage and Immunity. *Cell Res* (2020) 30 (3):229–43. doi: 10.1038/s41422-020-0287-8
5. Ma Q, Schlegel F, Bachmann SB, Schneider H, Decker Y, Rudin M, et al. Lymphatic Outflow of Cerebrospinal Fluid Is Reduced in Glioma. *Sci Rep* (2019) 9(1):14815. doi: 10.1038/s41598-019-51373-9
6. Ballerini L, Lovreglio R, Valdés Hernández MDC, Ramirez J, MacIntosh BJ, Black SE, et al. Perivascular Spaces Segmentation in Brain MRI Using Optimal 3d Filtering. *Sci Rep* (2018) 8(1):2132. doi: 10.1038/s41598-018-19781-5
7. Sepehrband F, Barisano G, Sheikh-Bahaei N, Cabeen RP, Choupan J, Law M, et al. Image Processing Approaches to Enhance Perivascular Space Visibility

and Quantification Using MRI. *Sci Rep* (2019) 9(1):12351. doi: 10.1038/s41598-019-48910-x
8. Zong X, Lian C, Jimenez J, Yamashita K, Shen D, Lin W. Morphology of Perivascular Spaces and Enclosed Blood Vessels in Young to Middle-Aged Healthy Adults at 7T: Dependences on Age, Brain Region, and Breathing Gas. *Neuroimage* (2020) 218:116978. doi: 10.1016/j.neuroimage.2020.116978
9. Barisano G, Sheikh-Bahaei N, Law M, Toga AW, Sepehrband F. Body Mass Index, Time of Day and Genetics Affect Perivascular Spaces in the White Matter. *J Cereb Blood Flow Metab* (2021) 41(7):1563–78. doi: 10.1177/0271678x20972856
10. Taoka T, Masutani Y, Kawai H, Nakane T, Matsuoka K, Yasuno F, et al. Evaluation of Glymphatic System Activity With the Diffusion MR Technique: Diffusion Tensor Image Analysis Along the Perivascular Space (DTI-ALPS) in Alzheimer's Disease Cases. *Jpn J Radiol* (2017) 35(4):172–8. doi: 10.1007/s11604-017-0617-z
11. Harrison IF, Siow B, Akilo AB, Evans PG, Ismail O, Ohene Y, et al. Non-Invasive Imaging of CSF-Mediated Brain Clearance Pathways *via* Assessment of Perivascular Fluid Movement With Diffusion Tensor MRI. *Elife* (2018) 7: e34028. doi: 10.7554/eLife.34028
12. Debacker C, Djemai B, Ciobanu L, Tsurugizawa T, Le Bihan D. Diffusion MRI Reveals *In Vivo* and Non-Invasively Changes in Astrocyte Function Induced by an Aquaporin-4 Inhibitor. *PloS One* (2020) 15(5):e0229702. doi: 10.1371/journal.pone.0229702
13. Ringstad G, Vatnehol SAS, Eide PK. Glymphatic MRI in Idiopathic Normal Pressure Hydrocephalus. *Brain* (2017) 140(10):2691–705. doi: 10.1093/brain/awx191
14. Eide PK, Ringstad G. Delayed Clearance of Cerebrospinal Fluid Tracer From Entorhinal Cortex in Idiopathic Normal Pressure Hydrocephalus: A Glymphatic Magnetic Resonance Imaging Study. *J Cereb Blood Flow Metab* (2019) 39(7):1355–68. doi: 10.1177/0271678x18760974
15. Zhou W, Shen B, Shen WQ, Chen H, Zheng YF, Fei JJ. Dysfunction of the Glymphatic System Might Be Related to Iron Deposition in the Normal Aging Brain. *Front Aging Neurosci* (2020) 12:559603. doi: 10.3389/fnagi.2020.559603
16. Zhang Y, Zhang R, Ye Y, Wang S, Jiaerken Y, Hong H, et al. The Influence of Demographics and Vascular Risk Factors on Glymphatic Function Measured by Diffusion Along Perivascular Space. *Front Aging Neurosci* (2021) 13:693787. doi: 10.3389/fnagi.2021.693787
17. Toh CH, Siow TY, Castillo M. Peritumoral Brain Edema in Meningiomas May Be Related to Glymphatic Dysfunction. *Front Neurosci* (2021) 15:674898. doi: 10.3389/fnins.2021.674898
18. Stummer W. Mechanisms of Tumor-Related Brain Edema. *Neurosurg Focus* (2007) 22(5):E8. doi: 10.3171/foc.2007.22.5.9
19. Belykh E, Shaffer KV, Lin C, Byvaltsev VA, Preul MC, Chen L. Blood-Brain Barrier, Blood-Brain Tumor Barrier, and Fluorescence-Guided Neurosurgical Oncology: Delivering Optical Labels to Brain Tumors. *Front Oncol* (2020) 10:739. doi: 10.3389/fonc.2020.00739
20. Nduom EK, Yang C, Merrill MJ, Zhuang Z, Lonser RR. Characterization of the Blood-Brain Barrier of Metastatic and Primary Malignant Neoplasms. *J Neurosurg* (2013) 119(2):427–33. doi: 10.3171/2013.3.jns122226
21. Haj-Yasein NN, Vindedal GF, Eilert-Olsen M, Gundersen GA, Skare Ø, Laake P, et al. Glial-Conditional Deletion of Aquaporin-4 (Aqp4) Reduces Blood-Brain Water Uptake and Confers Barrier Function on Perivascular Astrocyte Endfeet. *Proc Natl Acad Sci USA* (2011) 108(43):17815–20. doi: 10.1073/pnas.1110655108
22. Saadoun S, Papadopoulos MC, Davies DC, Krishna S, Bell BA. Aquaporin-4 Expression Is Increased in Oedematous Human Brain Tumours. *J Neurol Neurosurg Psychiatry* (2002) 72(2):262–5. doi: 10.1136/jnnp.72.2.262
23. Louis DN, Wesseling P, Aldape K, Brat DJ, Capper D, Cree IA, et al. cIMPACT-NOW Update 6: New Entity and Diagnostic Principle Recommendations of the cIMPACT-Utrecht Meeting on Future CNS Tumor Classification and Grading. *Brain Pathol* (2020) 30(4):844–56. doi: 10.1111/bpa.12832
24. Toh CH, Castillo M. Early-Stage Glioblastomas: MR Imaging-Based Classification and Imaging Evidence of Progressive Growth. *AJNR Am J Neuroradiol* (2017) 38(2):288–93. doi: 10.3174/ajnr.A5015
25. Toh CH, Castillo M, Wei KC, Chen PY. MRS as an Aid to Diagnose Malignant Transformation in Low-Grade Gliomas With Increasing Contrast Enhancement. *AJNR Am J Neuroradiol* (2020) 41(9):1592–8. doi: 10.3174/ajnr.A6688
26. Kim M, Jung SY, Park JE, Jo Y, Park SY, Nam SJ, et al. Diffusion- and Perfusion-Weighted MRI Radiomics Model may Predict Isocitrate Dehydrogenase (IDH) Mutation and Tumor Aggressiveness in Diffuse Lower Grade Glioma. *Eur Radiol* (2020) 30(4):2142–51. doi: 10.1007/s00330-019-06548-3
27. Leather T, Jenkinson MD, Das K, Poptani H. Magnetic Resonance Spectroscopy for Detection of 2-Hydroxyglutarate as a Biomarker for IDH Mutation in Gliomas. *Metabolites* (2017) 7(2):29. doi: 10.3390/metabo7020029
28. Choi KS, Choi SH, Jeong B. Prediction of IDH Genotype in Gliomas With Dynamic Susceptibility Contrast Perfusion MR Imaging Using an Explainable Recurrent Neural Network. *Neuro Oncol* (2019) 21(9):1197–209. doi: 10.1093/neuonc/noz095
29. Thust SC, Hassanein S, Bisdas S, Rees JH, Hyare H, Maynard JA, et al. Apparent Diffusion Coefficient for Molecular Subtyping of Non-Gadolinium-Enhancing WHO Grade II/III Glioma: Volumetric Segmentation Versus Two-Dimensional Region of Interest Analysis. *Eur Radiol* (2018) 28 (9):3779–88. doi: 10.1007/s00330-018-5351-0
30. Steward CE, Venkatraman VK, Lui E, Malpas CB, Ellis KA, Cyarto EV, et al. Assessment of the DTI-ALPS Parameter Along the Perivascular Space in Older Adults at Risk of Dementia. *J Neuroimaging* (2021) 31(3):569–78. doi: 10.1111/jon.12837\
31. Yokota H, Vijayasarathi A, Cekic M, Hirata Y, Linetsky M, Ho M, et al. Diagnostic Performance of Glymphatic System Evaluation Using Diffusion Tensor Imaging in Idiopathic Normal Pressure Hydrocephalus and Mimickers. *Curr Gerontol Geriatr Res* (2019) 2019:5675014. doi: 10.1155/2019/5675014
32. Bae YJ, Choi BS, Kim JM, Choi JH, Cho SJ, Kim JH. Altered Glymphatic System in Idiopathic Normal Pressure Hydrocephalus. *Parkinsonism Relat Disord* (2021) 82:56–60. doi: 10.1016/j.parkreldis.2020.11.009
33. Chen HL, Chen PC, Lu CH, Tsai NW, Yu CC, Chou KH, et al. Associations Among Cognitive Functions, Plasma DNA, and Diffusion Tensor Image Along the Perivascular Space (DTI-ALPS) in Patients With Parkinson's Disease. *Oxid Med Cell Longev* (2021) 2021:4034509. doi: 10.1155/2021/4034509
34. McKnight CD, Trujillo P, Lopez AM, Petersen K, Considine C, Lin YC, et al. Diffusion Along Perivascular Spaces Reveals Evidence Supportive of Glymphatic Function Impairment in Parkinson Disease. *Parkinsonism Relat Disord* (2021) 89:98–104. doi: 10.1016/j.parkreldis.2021.06.004
35. Yang G, Deng N, Liu Y, Gu Y, Yao X. Evaluation of Glymphatic System Using Diffusion MR Technique in T2DM Cases. *Front Hum Neurosci* (2020) 14:300. doi: 10.3389/fnhum.2020.00300

Conflict of Interest: The authors declare that the research was conducted in the absence of any commercial or financial relationships that could be construed as a potential conflict of interest.

Publisher's Note: All claims expressed in this article are solely those of the authors and do not necessarily represent those of their affiliated organizations, or those of the publisher, the editors and the reviewers. Any product that may be evaluated in this article, or claim that may be made by its manufacturer, is not guaranteed or endorsed by the publisher.

Copyright © 2021 Toh and Siow. This is an open-access article distributed under the terms of the Creative Commons Attribution License (CC BY). The use, distribution or reproduction in other forums is permitted, provided the original author(s) and the copyright owner(s) are credited and that the original publication in this journal is cited, in accordance with accepted academic practice. No use, distribution or reproduction is permitted which does not comply with these terms.

frontiers in Neuroscience

ORIGINAL RESEARCH
published: 27 September 2021
doi: 10.3389/fnins.2021.702353

Exploring Peritumoral Neural Tracts by Using Neurite Orientation Dispersion and Density Imaging

Shin Tai Chong[1], Xinrui Liu[2], Hung-Wen Kao[3,4], Chien-Yuan Eddy Lin[5], Chih-Chin Heather Hsu[1,6], Yi-Chia Kung[1], Kuan-Tsen Kuo[1], Chu-Chung Huang[7], Chun-Yi Zac Lo[8], Yunqian Li[2], Gang Zhao[2] and Ching-Po Lin[1,9]**

[1] Institute of Neuroscience, National Yang Ming Chiao Tung University, Hsinchu, Taiwan, [2] Department of Neurosurgery, First Hospital of Jilin University, Changchun, China, [3] Department of Medical Imaging, Hualien Tzu Chi Hospital, Buddhist Tzu Chi Medical Foundation, Hualien, Taiwan, [4] Department of Radiology, School of Medicine, Tzu Chi University, Hualien, Taiwan, [5] GE Healthcare, Taipei, Taiwan, [6] Center for Geriatrics and Gerontology, Taipei Veterans General Hospital, Taipei, Taiwan, [7] School of Psychology and Cognitive Science, Institute of Cognitive Neuroscience, East China Normal University, Shanghai, China, [8] Institute of Science and Technology for Brain-Inspired Intelligence, Fudan University, Shanghai, China, [9] Brain Research Center, National Yang Ming Chiao Tung University, Hsinchu, Taiwan

OPEN ACCESS

Edited by:
Nico Sollmann,
University of California,
San Francisco, United States

Reviewed by:
Andrey Zhylka,
Eindhoven University of Technology,
Netherlands
Sandro M. Krieg,
Technical University of Munich,
Germany
Giuseppe Barisano,
University of Southern California,
United States

***Correspondence:**
Ching-Po Lin
chingpolin@gmail.com
Hung-Wen Kao
cohimeow@gmail.com

Specialty section:
This article was submitted to Brain Imaging Methods, a section of the journal Frontiers in Neuroscience

Received: 29 April 2021
Accepted: 17 August 2021
Published: 27 September 2021

Citation:
Chong ST, Liu X, Kao H-W, Lin C-YE, Hsu C-CH, Kung Y-C, Kuo K-T, Huang C-C, Lo C-YZ, Li Y, Zhao G and Lin C-P (2021) Exploring Peritumoral Neural Tracts by Using Neurite Orientation Dispersion and Density Imaging. Front. Neurosci. 15:702353. doi: 10.3389/fnins.2021.702353

Diffusion Tensor Imaging (DTI) tractography has been widely used in brain tumor surgery to ensure thorough resection and minimize functional damage. However, due to enhanced anisotropic uncertainty in the area with peritumoral edema, diffusion tractography is generally not practicable leading to high false-negative results in neural tracking. In this study, we evaluated the usefulness of the neurite orientation dispersion and density imaging (NODDI) derived tractography for investigating structural heterogeneity of the brain in patients with brain tumor. A total of 24 patients with brain tumors, characterized by peritumoral edema, and 10 healthy counterparts were recruited from 2014 to 2021. All participants underwent magnetic resonance imaging. Moreover, we used the images obtained from the healthy participants for calibrating the orientation dispersion threshold for NODDI-derived corticospinal tract (CST) reconstruction. Compared to DTI, NODDI-derived tractography has a great potential to improve the reconstruction of fiber tracking through regions of vasogenic edema. The regions with edematous CST in NODDI-derived tractography demonstrated a significant decrease in the intracellular volume fraction (VF_{ic}, $p < 0.000$) and an increase in the isotropic volume fraction (VF_{iso}, $p < 0.014$). Notably, the percentage of the involved volume of the concealed CST and lesion-to-tract distance could reflect the motor function of the patients. After the tumor resection, four patients with 1–5 years follow-up were showed subsidence of the vasogenic edema and normal CST on DTI tractography. NODDI-derived tractography revealed tracts within the edematous area and could assist neurosurgeons to locate the neural tracts that are otherwise not visualized by conventional DTI tractography.

Keywords: neurite orientation dispersion and density imaging, diffusion tensor imaging, fiber tractography, vasogenic edema, brain tumor, neurosurgery

INTRODUCTION

The cerebral neoplasm may increase the intracranial pressure and cause neural tract deviation, infiltration, or destruction in the site of tumor growth and peritumoral areas (Assaf and Pasternak, 2008). Various magnetic resonance imaging (MRI) techniques are used to access and localize brain tumors to obtain a thorough resection and minimize functional loss. Among these techniques, diffusion tensor imaging (DTI) has been widely used to demonstrate the structural contents and peritumoral neural tracts. DTI is a non-invasive method that can probe the molecular diffusivity of water within the white matter to reflect the intravoxel architecture by measuring the water self-diffusion tensor (Basser et al., 1994; Basser, 1995). Herein, linking the anisotropic orientation determined by the principal eigenvector of the tensor has been widely applied to map the neuronal tracts (Mori et al., 1999; Mori and Van Zijl, 2002), which has also provided crucial information to neurosurgeons for neurosurgical planning and navigation (Berman et al., 2004; Bello et al., 2008). However, as a simplified model, DTI-derived tractography faces a substantial challenge in resolving the fiber tract within a voxel that comprises heterogeneous compartments including infiltrating cells and edematous tissues (Lecoeur et al., 2014; Chen et al., 2016; Gong et al., 2018; Ye et al., 2020).

Most aggressive brain tumors, such as malignant gliomas and metastatic tumors, are usually associated with peritumoral vasogenic edema (Lu et al., 2003). The latter generally infiltrates brain tissues with a lot of body fluid and alters the measures of diffusion characteristics, increasing the uncertainty of presurgical evaluation and leading to an enormous impact on patient management and surgical planning (Assaf and Pasternak, 2008; Lecoeur et al., 2014). Thus, it is crucial to identify the constituents of the infiltrated tissue and perform tractography within the area. However, the use of single ellipsoid DTI model makes this process challenging (Zhang et al., 2013). According to diffusion physics, diffusion-weighted images (DWI) with high *b*-value encoding can quantify the structural architecture and resolve structural heterogeneity (Callaghan et al., 1991; Lecoeur et al., 2014; Ye et al., 2020). Bi-exponential and higher-order models ascribe magnetic resonance (MR) signal attenuation into two processes, namely, restricted and hindered water diffusion in the intracellular and extracellular spaces, respectively, and provide a unique opportunity to reveal neural tracts within the hydro-environment compared with the conventional method. Previous studies have mentioned that multi-compartment diffusion models, such as the free water model (Lecoeur et al., 2013) and two-tensor unscented Kalman filter (UKF) (Chen et al., 2015, 2016) improve the tracking of the neuronal fiber in peritumoral vasogenic edema. This suggests that fiber tracking in the edema would benefit from the prior heterogeneity. Knowing the microstructure change in the peritumoral region may further help identify whether the fiber still existed, thus suggesting the need for an advanced biophysical diffusion model to explore the edematous fiber tracts (Liao et al., 2017).

Neurite orientation dispersion and density imaging (NODDI) is a clinically feasible three-compartment model that utilizes two *b*-value encodings (Zhang et al., 2012). The aforementioned model is capable of estimating three types of water diffusion behavior with different volume fractions, i.e., restricted (intracellular volume fraction), hindered (extracellular volume fraction), and free diffusion (isotropic volume fraction). These indices provide special measures that represent the axonal density and the dispersion of fiber orientations. NODDI is reportedly valuable for evaluating various neurological diseases, such as white matter microstructural changes in Alzheimer's disease (Fu et al., 2020) and Parkinson's disease (Mitchell et al., 2019). Moreover, it provides distinctive markers for multiple sclerosis (Crombe et al., 2018) and stroke (Adluru et al., 2014; Wang et al., 2019). Numerous studies have suggested that NODDI indices could provide unique contrast in brain tumors (Wen et al., 2015), which will help to differentiate between glioblastoma and solitary brain metastasis and reveal the differences between tumor infiltration and vasogenic edema (Kadota et al., 2020). Moreover, the NODDI indices are capable of characterizing white matter fibers involved in tumoral and edematous brain areas (Masjoodi et al., 2018), which implies that this multi-compartment model may potentially demonstrate neural tractography in peritumoral edema.

Although the peritumoral neural tracts involved in motor functions are crucial to neurosurgery, they are generally concealed by vasogenic edema and usually unseen with traditional diffusion modeling. Therefore, in this study, we aimed to use the NODDI model to investigate the structural heterogeneity in patients with vasogenic edema. First, we reconstructed the edematous corticospinal tract (CST) that were unseen with traditional diffusion modeling. Second, we provided evidence that the concealed tracts could reflect motor function, such as muscle strength, which would benefit surgical planning. Third, white matter integrity profiles were evaluated by the multi-compartment characteristics for better understanding the microstructure heterogeneity of the region of edema. Finally, we examined the disclosed tracts that could be detected following the release of the vasogenic edema.

MATERIALS AND METHODS

Participants

We recruited a total of 24 patients with brain tumor and 10 healthy participants from 2014 to 2021. The enrolled patients were diagnosed with cerebral neoplasm and a large volume of perilesional vasogenic edema in the motor area, primary somatosensory cortex, or premotor area that affected the CST. The vasogenic edema was determined by peritumoral hyperintensity on T2-weighted fluid-attenuated inversion recovery (T2-FLAIR) images and no evidence of restricted water diffusion on diffusion-weighted imaging (DWI). Each patient underwent muscle strength measurement by using the Medical Research Council (MRC) scale of muscle strength. Motor function decline was defined as abnormal if the MRC grading was 4 or less. This study was approved by the local institutional

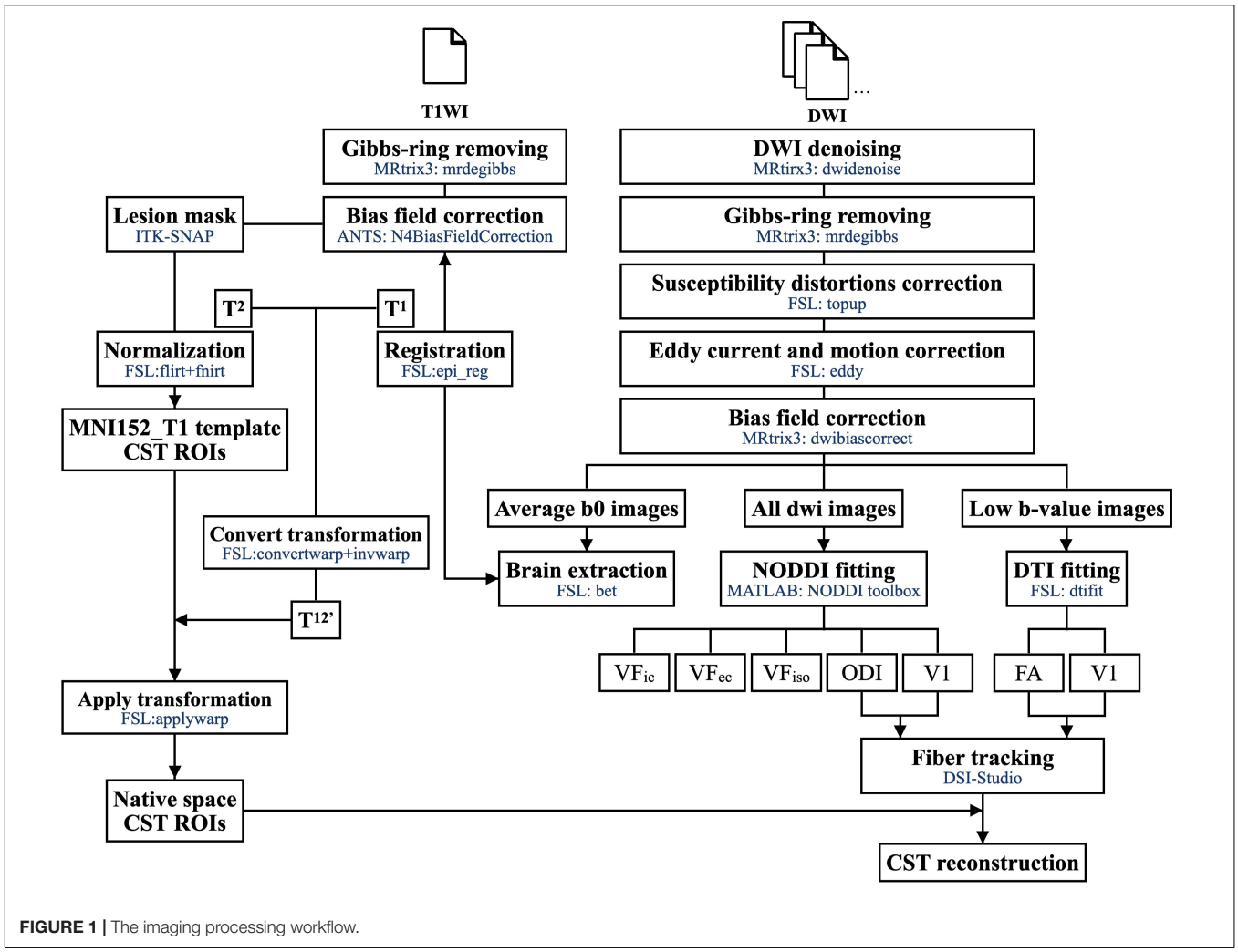

FIGURE 1 | The imaging processing workflow.

review board, and all participants provided informed consent for the surgery.

MRI Acquisition and Imaging Preprocessing

Data Set I

The first dataset enrolled six patients and five healthy participants at the Tri-Service General Hospital, Taipei, Taiwan. MRI data were acquired on a 3-T GE machine (Discovery MR 750, GE Healthcare, Milwaukee, United States) with an eight-channel head coil. The clinical routine MR scanning protocols included a high-resolution 3-D Fast Spoiled Gradient Echo T1-weighted images (T1-weighted images (T1WI); field of view (FOV) = 224 × 224 × 146 mm^3; voxel size = 1 × 1 × 1 mm^3; and TE/TR/TI = 4.2/10.2/450 ms), 2-D axial view fast recovery fast spin-echo T2-weighted images (T2-weighted images (T2WI); FOV = 250 × 250 × 150 mm^3; voxel size = 0.49 × 0.49 × 6 mm^3; and TE/TR = 100.7/5,619 ms), 2-D axial view FSE T2-FLAIR (FOV = 250 × 250 × 150 mm^3; voxel size = 0.49 × 0.49 × 6 mm^3; and TE/TR/TI = 118.3/12,000/2,200 ms), and 2-D axial view T1WI following the injection of gadolinium-based contrast agent (gadolinium-enhanced T1WI (Gd-T1WI); FOV = 250 × 250 × 150 mm^3; voxel size = 0.49 × 0.49 × 6 mm^3; and TE/TR/TI = 31.1/3,465.2/928.8 ms). Two-shelled DWI were acquired using a single-shot spin-echo planer imaging sequence (FOV = 240 × 240 × 112 mm^3; voxel size = 2.5 × 2.5 × 2.5 mm^3; TE/TR = 88/6,000 ms; four null images; 30 directions of b = 1,000 s/mm^2; and 60 directions of b = 2,000 s/mm^2).

Data Set II

The second dataset included 18 patients and five healthy participants at The First Hospital of Jilin University, Jilin, China. MRI data were acquired on a 3-T Siemens machine (Magnetom Verio, Siemens, Erlangen, Germany) with a 16-channel head coil. The clinical MR scanning protocol included a 2-D axial view T1WI (FOV = 230 × 230 × 117 mm^3; voxel size = 0.36 × 0.36 × 6.5 mm^3; and TE/TR/TI = 9/1,500/791.8 ms), 2-D axial view T2WI (FOV = 230 × 230 × 117 mm^3; voxel size = 0.6 × 0.6 × 6.5 mm^3; and TE/TR = 95/6,000 ms), 2-D axial T2-FLAIR (FOV = 230 × 230 × 117 mm^3; voxel size = 0.72 × 0.72 × 6.5 mm^3; and

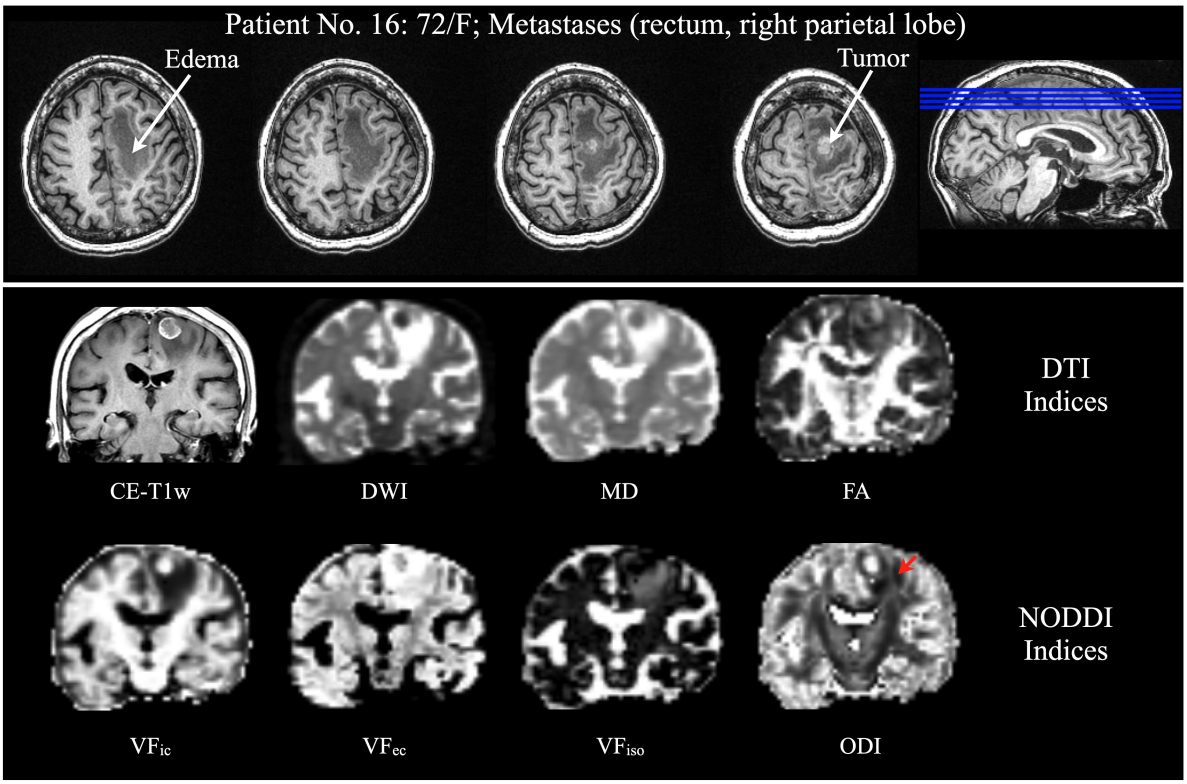

FIGURE 2 | Patient No. 16, a 72-year-old woman with rectum metastasis in the right parietal lobe. (Top) Axial view of CE-T1WI displays an enhancing tumor in the right superior frontal lobe, with significant vasogenic edema. (Bottom) Coronal view of CE-T1WI, DWI, DTI indices (MD, and FA), and NODDI indices (VF_{ic}, VF_{ec}, and VF_{iso}) could not reveal the CST except the ODI from NODDI (red arrow). CE-T1WI, contrast enhanced T1-weighted images; DWI, diffusion-weighted imaging; DTI, diffusion tensor imaging; MD, mean diffusivity; FA, fractional anisotropy; NODDI, neurite orientation dispersion and density imaging; VF_{ic}, intracellular volume fraction; VF_{ec}, extracellular volume fraction; and VF_{iso}, isotropic volume fraction; CST, corticospinal tract; and ODI, orientation dispersion index.

TE/TR/TI = 81/7,500/2,297.9 ms), and 3-D magnetization-prepared rapid gradient-echo Gd-T1WI (FOV = 250 × 250 × 160 mm^3; voxel size = 1 × 0.98 × 0.98 mm^3; and TE/TR/TI = 3.5/2,300/1,070 ms). Two-shelled DWI were acquired using a single-shot spin-echo planer imaging sequence (FOV = 250 × 250 × 160 mm^3; voxel size = 2.5 × 2.5 × 2.5 mm^3; and TE/TR = 95/16,700 ms; four null images; 30 directions of b = 1,000 s/mm^2; and 60 directions of b = 2,000 s/mm^2). We also acquired three null diffusion images with opposite polarity (phase encoding form posterior to anterior).

Imaging Preprocessing

All DWI data were processed by the in-house developed DWI preprocess pipeline (OGIO) that includes algorithms and functions from MRtrix3[1] FMRIB Software Library (FSL)[2] and ANTs[3]. The overall imaging preprocessing workflow is summarized in **Figure 1**.

First, we used dwidenoise (Veraart et al., 2016a,b; Cordero-Grande et al., 2019) and mrdegibbs (Kellner et al., 2016) functions in MRtrix3 (Tournier et al., 2019) for imaging denoising and removing the Gibbs ringing artifact from the DWI. To correct the susceptibility-included off-resonance field, image distortion induced by the fast-switching gradient, slight head motion, and FSL functions (Jenkinson et al., 2012) TOPUP and EDDY (Graham et al., 2017) were performed on DWIs acquired with two opposite polarities. Finally, dwibiascorrect (Tustison et al., 2010) was utilized to correct performing B1 field inhomogeneity in the DWI volume series. The Brain Extraction Tool function (Smith, 2002) from FSL was used to create a brain mask from the average null DWIs. For T1WI, we used the mrdegibbs (Kellner et al., 2016) function for removing the Gibbs ringing artifact and N4BiasFieldCorrection (Tustison et al., 2010) from ANTS for B1 field inhomogeneity correction.

Model Fitting

All images were fitted with the NODDI model using the NODDI MATLAB toolbox[4]. The low-*b*-value images (<1,500 s/mm^2) were used in DTI model fitting (with dtifit in FSL). We subsequently obtained the voxel-wise maps. We evaluated the first eigenvector for the principal directions on DTI tractography and used fractional anisotropy (FA) as the fiber tractography termination criteria. For NODDI-derived indices, we calculated

[1]https://www.mrtrix.org/

[2]https://fsl.fmrib.ox.ac.uk/fsl/fslwiki/

[3]http://picsl.upenn.edu/ANTS

[4]http://www.nitrc.org/projects/noddi_toolbox/

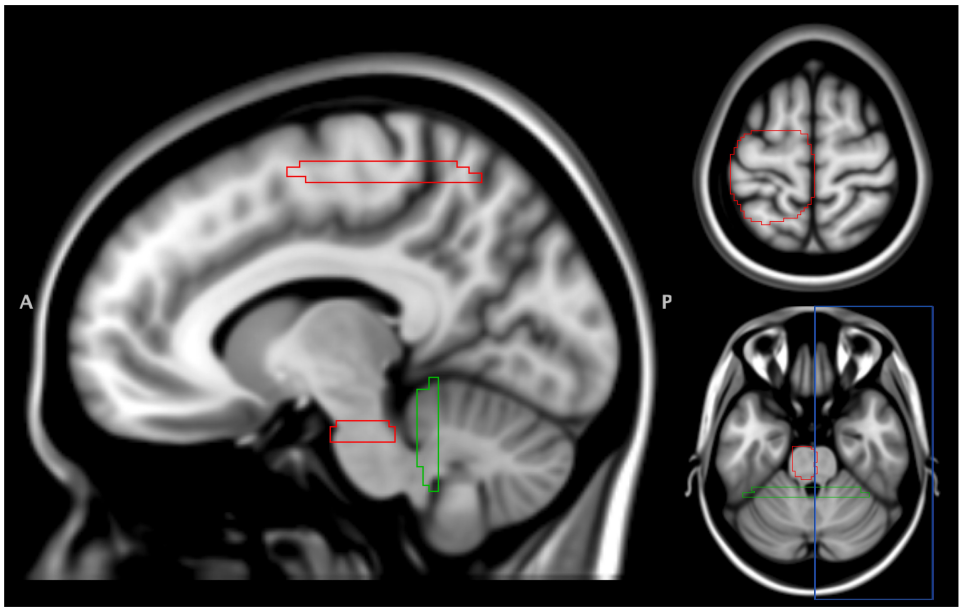

FIGURE 3 | Regions of interest for CST extraction. A total of 4 ROIs were defined in the MNI152 T1 space. Two ROIs (sensorimotor area and brainstem, red) were used for CST extraction. Another two ROIs for excluding streamlines into cerebellum (green) and cross-hemisphere connection (blue). ROI, region of interest; CST, corticospinal tract.

the orientation dispersion index (ODI), fiber orientation (the principal directions from NODDI model), and the three absolute volume fractions of NODDI (intracellular volume fraction, VF_{ic}; extracellular volume fraction, VF_{ec}; isotropic volume fraction, VF_{iso}), where $VF_{ic} + VF_{ec} + VF_{iso} = 1$ (**Figure 2**).

ROI Selection

For CST extraction, four regions of interest (ROIs) were manually drawn in the Montreal Neurological Institute (MNI) space according to previous study (Cooper et al., 2015). The first and second ROIs (axial view of sensorimotor area and brainstem) were used for CST extraction. The third and fourth ROIs were the exclusion ROIs for excluding streamlines into the cerebellum and cross-hemisphere connection (**Figure 3**). Following an inspection of T1WI, T2WI, T2-FLAIR, DWI, and Gd-T1WI, the ROIs of lesion and edema for each patient were manually drawn by using ITK-SNAP[5] (Yushkevich et al., 2006). All ROIs were manually drawn by a neuroradiologist (H-W Kao) with 15 years of experience.

Imaging Registration

To transform the ROIs from the MNI standard space to the individual space, T1WI was first co-registered with average null diffusion images using boundary-based registration to generate the transformation matrix from the DWI space to the T1WI space. Second, T1WI was then spatially normalized to the MNI152 T1 template in the standard space via linear affine transformation (FLIRT) and non-linear registration (FNIRT) (Zhang et al., 2001; Smith et al., 2004; Patenaude et al., 2011). The lesion mask was used to exclude the calculation in the nonlinear registration. Combining the two transformation matrices (DWI to T1WI and T1WI to MNI), we applied the inverse transformation matrix to obtain the ROIs in each individual's native DWI space with the nearest-neighbor interpolation. All the spatial registration and normalization procedures were implemented in FSL.

Fiber Tractography and ODI Threshold Calibration

CST was reconstructed from the directions identified by both DTI and NODDI. The NODDI-derived CSTs were reconstructed by modifying the FIB file of DSI-studio with NODDI's ODI and fiber orientation. All fiber tractography was done using the deterministic fiber algorithm (Yeh et al., 2013) implanted in the DSI-Studio[6]. Four ROIs (two for inclusion and two for exclusion, shown in **Figure 3**) were utilized for CST extraction. The step size was 0.5 mm; streamlines with lengths shorter than 30 mm or longer than 300 mm were discarded. A total of 3,000 streamlines were finally reconstructed.

To calibrate the ODI threshold, 10 healthy participants (five from each site) were included. We first reconstructed the DTI-derived CST with standard tracking termination criteria [fractional anisotropy (FA) $\leq$ 0.20; turning angle $\geq$ 60°] (Mori et al., 1999). Next, the NODDI-derived CSTs were reconstructed with ODI thresholds varying from 0.2 to 1. Moreover, the streamline similarity was evaluated using the dice similarity index (DSI) between DTI tractography and each ODI threshold CST. The DSI was defined as

[5]http://www.itksnap.org

[6]http://dsi-studio.labsolver.org

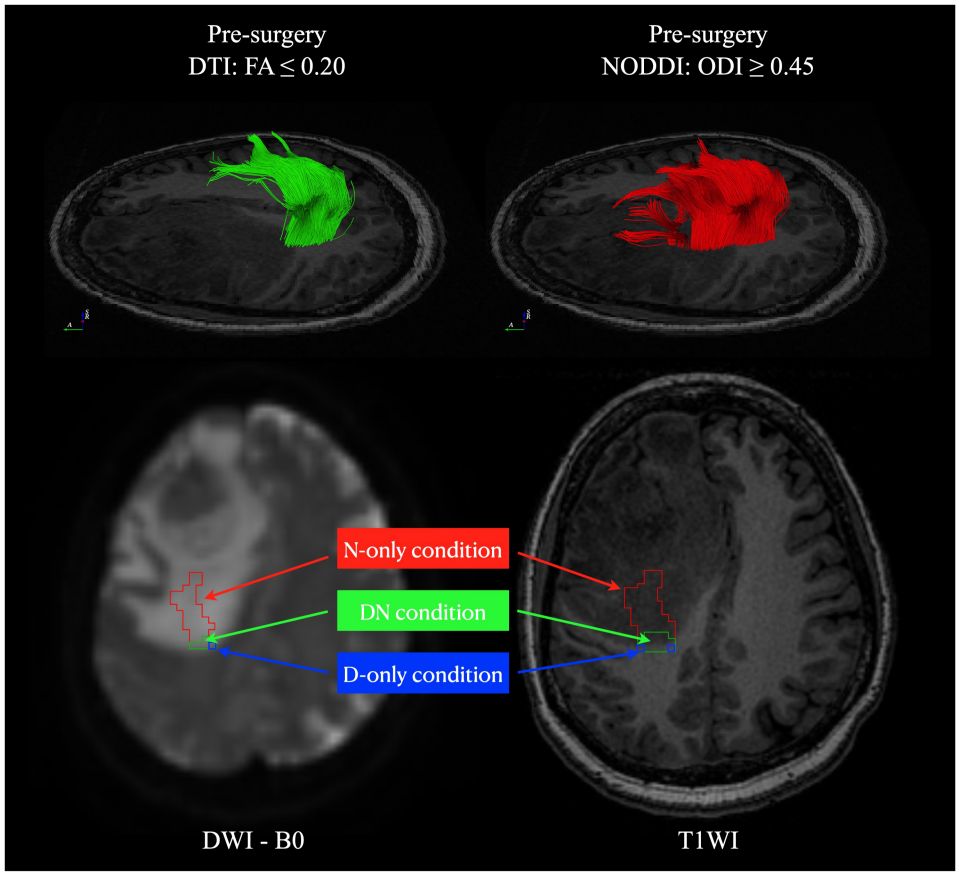

FIGURE 4 | The fiber tracts volume condition definition. Three conditions of the fiber tracts located in areas overlapping with peritumoral edema were classified in each patient: (1) DN condition: the volume of both DTI and NODDI-derived fiber tracts in the peritumoral edema (green); (2) D-only condition: the volume of only DTI fiber tracts in the peritumoral edema (blue); (3) N-only condition: the volume of only NODDI-derived fiber tracts in the peritumoral edema (red). DTI, diffusion tensor imaging; NODDI, neurite orientation dispersion and density imaging.

follows: $DSI = \frac{2(DT \cap NODDI)}{DTI+NODDI}$. The optimal ODI threshold was determined with the maximized overlap.

In this study, assessment of the differences between DTI and NODDI-derived tractography was achieved by comparing the DTI-derived CST with the standard FA threshold (FA $\leq$ 0.20), DTI-derived CST with low FA (FA $\leq$ 0.10), and NODDI-derived CST with optimal ODI threshold on 24 patients.

Statistical Analyses

To evaluate the microstructure changes in the edema region, we applied the edema mask for extracting the voxels with streamline pass through. The following three conditions of edematous fiber tracts were classified in each patient: (1) DN condition, the volume of both DTI and NODDI-derived fiber tracts in the peritumoral edema; (2) D-only condition, the volume of only DTI fiber tracts in the peritumoral edema; and (3) N-only condition, the volume of only NODDI-derived fiber tracts in the peritumoral edema (**Figure 4**). We calculated the percentage of involved volume (PIV) in the three conditions of CST to assess the patient's motor function. PIV was defined as follows: $PIV = \frac{volume\ of\ condition}{volume\ of\ CST}$. The volume of CST was defined as the total volume of CST in DTI and NODDI-derived reconstruction. Moreover, we measured the lesion-to-tract distance (LTD) from the lesion boundaries to the nearest CST in a three-dimensional view with the in-house-developed viewer (GoViewer). To integrate the evaluation index with LTD, the volume and PIV of each condition were divided by LTD as weighted.

We determined the diagnostic performance for differentiating the motor function using the receiver operating characteristic (ROC) curves. We calculated the sensitivity, specificity, and area under the ROC curve (AUC) to determine the diagnostic performance of each index. Moreover, Youden's J statistic was used for determining the optimal cutoff threshold for the ROC curve. The Youden index is defined as $J_{max} = max_t \{sensitivity(t) + specificity(t) - 1\}$, where t denotes the classification threshold for which J is maximal from the ROC curve. Furthermore, we extracted the mean NODDI-derived volume fractions (VF_{ic}, VF_{ec}, and VF_{iso}) in DN and N-only conditions. The Wilcoxon signed rank test was conducted to evaluate the differences in the microenvironment between the two conditions. All statistical analyses were analyzed

TABLE 1 | A summary of the clinical information, imaging features, and pathology of 24 patients.

					SI of solid portion		CE of solid portion			Lesion to tract distance	Motor function decline
Case	**Age/sex**	**Location**	**Edema**	**Edema volume**	**Gd–T1WI**	**T2WI**		**Pathology**	**WHO grading**		
1	65/F	Left frontal	S	18,658 mm^3	Hyper	Hyper	Hete	Meningioma	Grade I	37.2 mm	No
2	42/M	Right parietal	Mo	8,282 mm^3	Hyper	Iso	Homo	Meningioma	Grade I	12.9 mm	Yes
3	49/F	Left frontal	Mo	10,648 mm^3	Hyper	Iso	Homo	Meningioma	Grade I	17.4 mm	No
4	38/M	Right parietal	S	24,115 mm^3	Hyper	Hyper	Homo	Meningioma	Grade I	61.3 mm	No
5	36/M	Left frontal	S	29,935 mm^3	Hyper	Iso	Hete	Meningioma	Grade II	40.6 mm	No
6	57/F	Left frontal	S	27,435 mm^3	Hyper	Hyper	Homo	Meningioma	Grade II	23.5 mm	No
7	55/F	Right frontal	Mo	12,283 mm^3	Hyper	Iso	Homo	Meningioma	Grade II	16.4 mm	No
8	32/F	Right frontal	S	26,603 mm^3	Hypo	Iso	Hete	Glioma	Grade I	21.6 mm	No
9	43/M	Right parietal	Mo	1,870 mm^3	Hypo	Hyper	Homo	Glioma	Grade II	11.3 mm	No
10	56/M	Right frontal	S	17,733 mm^3	Hypo	Hyper	Homo	Glioma	Grade III	5.0 mm	No
11	55/F	Right parietal	Mo	9,557 mm^3	Hypo	Hyper	Homo	Glioma	Grade III–IV	10.0 mm	No
12	37/F	Right frontal	S	33,488 mm^3	Hyper	Hyper	Hete	Glioblastoma	Grade IV	19.4 mm	No
13	72/M	Left temporal	Mo	12,180 mm^3	Hyper	Hyper	Hete	Glioblastoma	Grade IV	3.8 mm	No
14	51/F	Right frontal	S	24,288 mm^3	Hyper	Hypo	Hete	Metastatic (lung)	Grade IV	34.7 mm	No
15	51/F	Left parietal	S	15,738 mm^3	Hyper	Hyper	Hete	Metastatic (lung)	Grade IV	4.8 mm	Yes
16	72/F	Right parietal	Mo	6,045 mm^3	Hyper	Hypo	Homo	Metastatic (rectum)	Grade IV	4.6 mm	Yes
17	69/F	Right frontal	S	30,948 mm^3	Hyper	Hypo	Hete	Metastatic (adenocarcinoma)	Grade IV	36.5 mm	No
18	59/F	Right frontal & temporal	Mo	5,535 mm^3	Hyper	Hypo	Hete	Metastatic (unknown)	Grade IV	15.2 mm	No
19	64/M	Left parietal	S	1,7875 mm^3	Hyper	Hypo	Hete	Metastatic (unknown)	Grade IV	16.4 mm	Yes
20	38/M	Right parietal	Mo	7,207 mm^3	Hypo	Hyper	Homo	Primitive neuroectodermal tumor	Grade IV	8.7 mm	Yes
21	53/F	Left frontal	S	21,523 mm^3	Hyper	Hypo	Homo	Malignant B-cell lymphoma	–	40.2 mm	No
22	55/F	Left parietal	Mo	8,680 mm^3	Hyper	Hypo	Hete	Ewing's sarcoma	–	7.7 mm	No
23	36/F	Left frontal	S	15,620 mm^3	Hyper	Hyper	Hete	Gliosis	–	2.3 mm	Yes
24	65/M	Left parietal	S	19,889 mm^3	Hyper	Hypo	Hete	Abscess	–	12.9 mm	Yes

CE, contrast enhancement; Hete, heterogeneous; Homo, homogeneous; Hyper, hyperintensity; Hypo, hypointensity; Iso, isointensity; Mo, moderate; S, severe; SI, signal intensity.

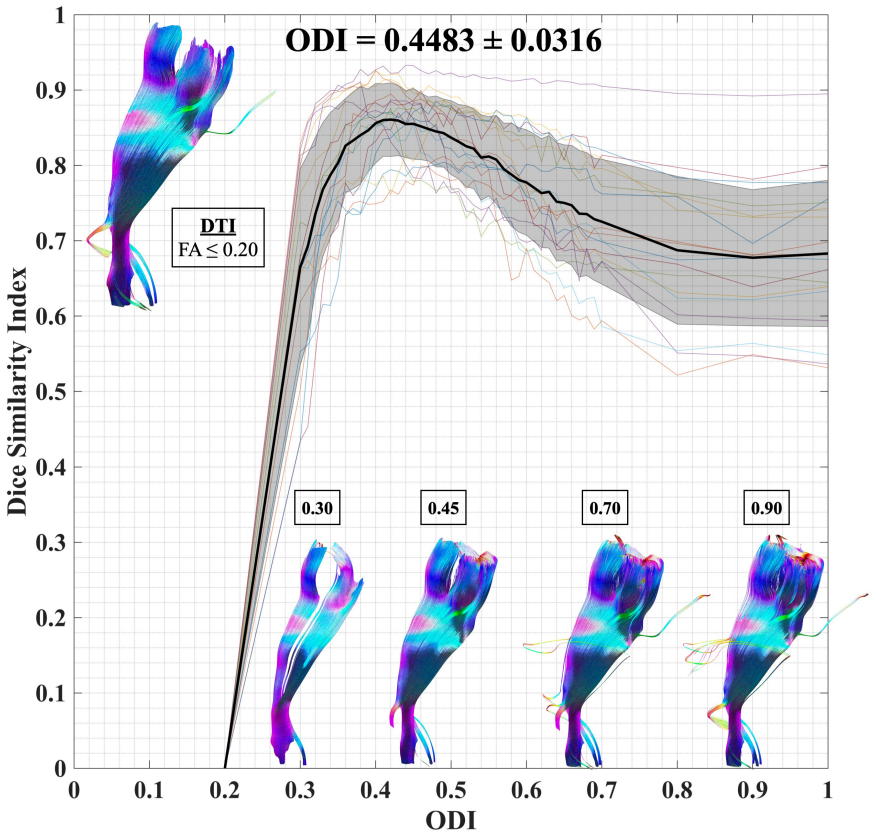

FIGURE 5 | ODI threshold calibration for CST. We have studied the dice similarity index at each considered ODI threshold compared to the standard DTI termination criteria (FA ≤ 0.2; turning angle ≥ 60°). An optimal ODI ≥ 0.45 has been set for CST reconstruction. ODI, orientation dispersion index; CST, corticospinal tract; and DTI, diffusion tensor imaging.

using statistical software (SPSS, version 25; SPSS, Chicago, Ill). p-values < 0.05 were considered statistically significant.

Follow-Up Comparison

A total of four patients were recruited after imaging showing subsidence of the vasogenic edema: two patients with 1 year (from data set II) and another two with 5 years (from data set I) after the tumor resection. MRI data acquisition and imaging processing were the same as the initial. The DTI tractography of CST reconstruction was performed with the standard FA criteria (FA $\leq$ 0.20; turning angle $\geq$60°). To quantify the restoration of the CST in the follow-up compared to initial DTI- and NODDI-derived tractography, we compared the fiber tractography between pre- and post-surgery. We registered the pre-surgery and follow-up data by using linear registration (FLIRT). DSI was used for the streamline similarity comparison.

RESULTS

The study included a total of 24 patients (9 men and 15 women). The mean age was 52 years, ranging from 32 to 72 years. Seven patients were diagnosed with meningiomas (four and three with grades I and II, respectively). Six patients had gliomas (one with grade I, one with grade II, and two each with grades III and IV). Six patients had metastases (two lung cancers, two rectal cancers, and two cancers of unknown origin). The other five patients had lymphoma, primitive neuroectodermal tumor, Ewing's sarcoma, abscess, and gliosis. Among our patients, six patients experienced motor function decline. **Table 1** summarizes the clinical information, imaging features, LTD, and pathological diagnoses of all patients.

ODI Threshold Calibration

The mean and maximum DSI values of CST reconstruction in the healthy participants were 0.8077 and 0.9164, respectively, with ODI $\geq$ 0.4482 $\pm$ 0.0316. We determined an optimal ODI threshold of 0.45 (**Figure 5**).

Comparison Between DTI and NODDI

We compared the differences between DTI and NODDI, predominantly found in regions with vasogenic edema. DTI-derived tractography with standard FA displayed non-stabilized performance in the regions of vasogenic edema, comprising only sparse tracts. DTI tractography with low FA revealed better performance but was accompanied by several noisy streamlines. NODDI-derived tractography could reveal the CST in the regions

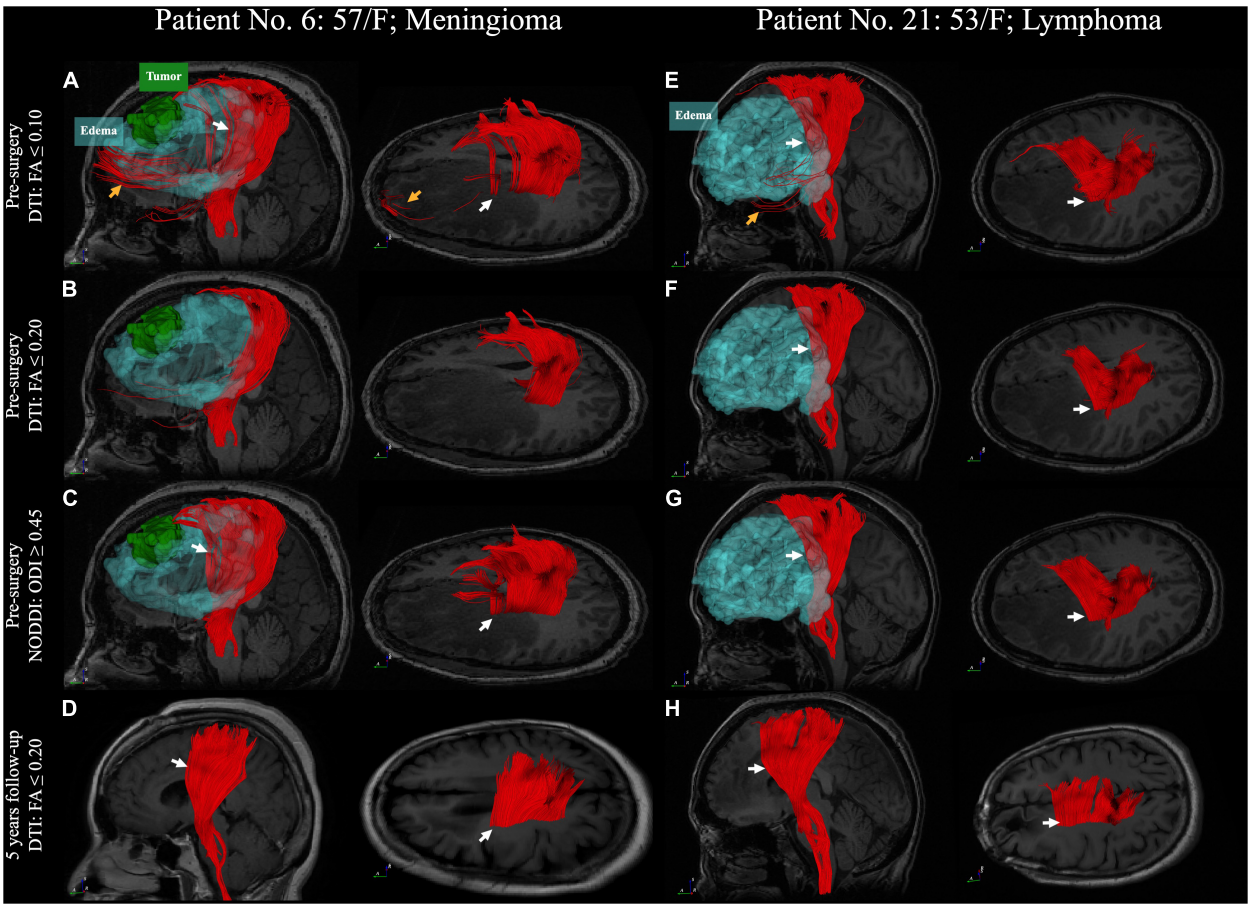

FIGURE 6 | A comparison between DTI and NODDI-derived CST reconstruction with 5 years follow-up. **(A–D)** Patient No. 6, a 57-year-old woman with a meningioma (WHO grade II) in the left frontal lobe. **(E–H)** Patient No. 21, a 53-year-old woman with malignant B-cell lymphoma. DTI tractography with standard termination criteria (FA $\leq$ 0.2) has failed to reconstruct the CST in the region with peritumoral edema in the first case. **(B)** However, the CST has been successfully reconstructed in the second case (**F**, white arrow). DTI tractography with low FA criteria (FA $\leq$ 0.1) displays better performance in the region with peritumoral edema (white arrow). Nonetheless, it is accompanied by noisy streamlines (**A,E**, yellow arrow). NODDI-derived tractography with ODI reveals better performance in the region with edema and less noisy streamlines (**C,G**, white arrow). The DTI tractography with standard termination criteria reveals a CST similar to the pre-surgery NODDI-derived CST after the vasogenic edema has subsided in 5 years **(D,H)**. DTI, diffusion tensor imaging; FA, fractional anisotropy; NODDI, neurite orientation dispersion and density imaging; CST, corticospinal tract; WHO, World Health Organization and ODI, orientation dispersion index.

of vasogenic edema, with fewer noisy streamlines (**Figures 6**, **7**). Two patients (patient nos. 2 and 15) failed to reconstruct any of the CST in the regions with vasogenic edema while using DTI tractography (**Supplementary Figure 1**).

ROC Diagnostic Performance Analysis

In ROC diagnostic performance analysis, we found that LTD, D-only volume, D-only PIV, N-only volume, N-only volume-LTD (N-only volume with weighted LTD), N-only PIV, and N-only PIV-LTDs (N-only PIV with weighted LTD) had significant differences between patients with and without surgery-related paresis. The PIV of the N-only condition weighted by LTD had the best diagnostic performance for determining the presence of motor function decline. The threshold value of >0.0128 yielded a sensitivity, specificity, and AUC of 100, 100%, and 1, respectively, for patients with motor function decline (**Figure 8**). The threshold value and diagnostic performance of each index in motor function decline are summarized in **Table 2**. The statistical details of group comparison between patients with and without motor function decline can be found in **Supplementary Table 2**.

NODDI Fraction Comparison

In a 2-D barycentric coordinate system, the distribution of the N-only condition (mean VF_{ic} = 0.1501; mean VF_{ec} = 0.5752; and mean VF_{iso} = 0.2738) was presented in the left upper shift relative to that in the DN condition (mean VF_{ic} = 0.2100; mean VF_{ec} = 0.5809; and mean VF_{iso} = 0.2091). The statistical comparison of NODDI indices between the N-only condition and DN condition showed no significant difference in VF_{ec} (p = 0.4751). Moreover, we observed a significant increase and decrease of VF_{iso} ($p < 0.0006$) and VF_{ic} ($p < 0.0036$) in the N-only condition when comparing it to the DN condition (**Figure 9**).

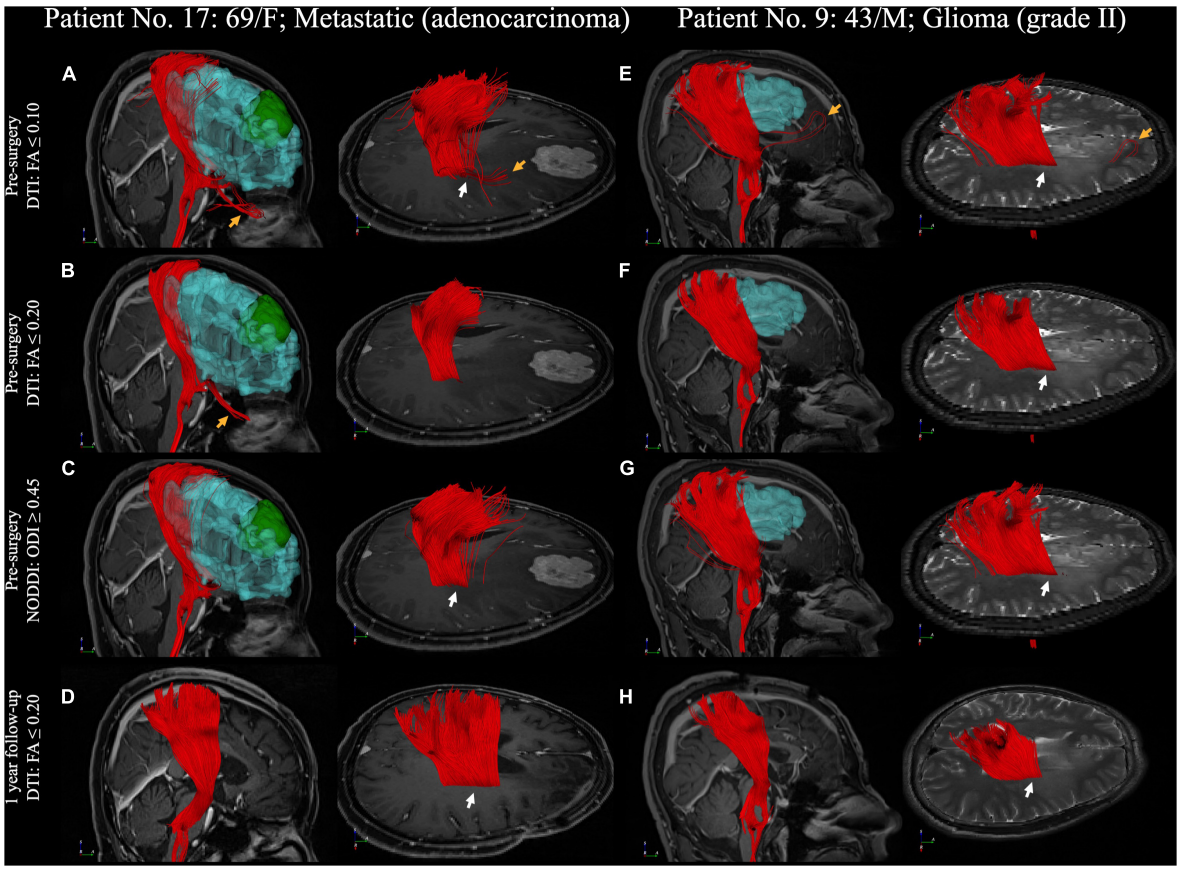

FIGURE 7 | A comparison between DTI and NODDI-derived CST reconstruction with 1-year follow-up. **(A–D)** Patient No. 17, a 69-year-old woman with an adenocarcinoma metastatic in the right frontal lobe. **(E–H)** Patient No. 9, a 43-year-old man with WHO grade II glioma in right parietal lobe. CST reconstruction in DTI and NODDI-derived tractography in pre-surgery and 1 year after tumor resection. White arrow indicated the fiber tracts in the peritumoral edema. DTI, diffusion tensor imaging; FA, fractional anisotropy; NODDI, neurite orientation dispersion and density imaging; CST, corticospinal tract; WHO, World Health Organization and ODI, orientation dispersion index.

Tract Verifications After Releasing the Vasogenic Edema

After the tumor resection, two patients with 5-year follow-up (**Figure 6**) and two with 1-year follow-up (**Figure 7**) showed reduced vasogenic edema and normal CST on DTI tractography with standard termination criteria (FA $\leq$ 0.20). The similarity comparison showed that NODDI-derived tractography performed the highest similarity and lowest standard deviation (0.607 $\pm$ 0.035) with post-surgery fiber tractography (**Figure 10**).

DISCUSSION

Specific functional tracts like CST that are concealed by peritumoral edema are meaningful to neurosurgeons. However, they have not yet been systematically disclosed. We applied an advanced NODDI model to different diffusion contents to highlight the neural anisotropy and tractography. Compared to conventional DTI tractography, NODDI-derived fiber tractography provided better performance in heterogeneous areas. Notably, the involved volume of the concealed tracts and LTD directly reflected their functional performance, which, in turn, would facilitate pre-surgery planning and post-surgery recovery assessment. After the vasogenic edema subsided, we verified the neural tracts in four patients during the 1–5-year follow-up.

DTI tractography effectively maps neural tracts within the human brain. However, it has been proven unreliable in revealing the fiber tracts in the peritumoral edema region (Zhang et al., 2013; Ye et al., 2020). Nonetheless, specific functional fiber tracts that are located in areas overlapping with peritumoral edema are crucial to the functional protection of the patients. Previous studies have mentioned that the single-tensor model has a high probability of failure in revealing the fiber tracts when the image voxel gets affected by the vasogenic edema (partial volume effect) (Lecoeur et al., 2013; Zhang et al., 2013; Liao et al., 2017). This necessitates the deconstruction of DWI signals. Lecoeur et al. (2013) proposed removing the free water compartment for tensor correction and achieved significantly improved tractography in the presence of edema. This concept was extended to further studies, such as free water modeling (Gong et al., 2018), two-tensor unscented UKF (Chen et al., 2015, 2016; Liao et al., 2017),

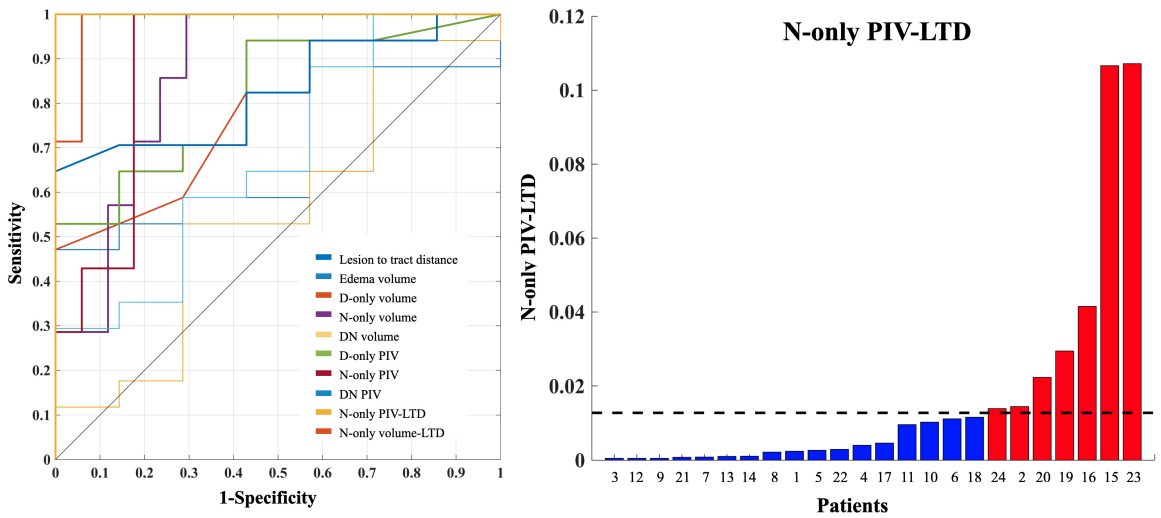

FIGURE 8 | The PIV-LTD of N-only condition and ROC diagnostic performance of motor functions. The PIV of N-only condition weighted by LTD had the best diagnostic performance for determining the presence of motor function decline (left, gold line). An optimal threshold of PIV-LTD of N-only condition >0.0128 has yielded a sensitivity, specificity, and AUC of 100%, 100%, and 1 for differentiating patients with motor function decline (right). The red and blue color bars indicate patients with and without motor function decline. The black dash line indicates the optimal threshold, determined by using the Youden index. PIV, percentage of involved volume; LTD, lesion-to-tract distance; ROC, receiver operating characteristic; AUC, area under the receiver operating characteristic curve.

TABLE 2 | The threshold value and diagnostic performance in motor function decline.

	Threshold value	Sensitivity	Specificity	AUC	Standard error	Significant	95% of confidence interval
Edema volume	20,260 mm^3	0.471	1	0.689	0.109	0.153	0.475–0.903
D-only volume	3.75 mm^3	0.941	0.571	0.798	0.096	0.024	0.609–0.987
N-only volume	665 mm^3	1	0.06	0.866	0.073	0.006	0.722–1
DN volume	2,281 mm^3	0.529	0.714	0.555	0.136	0.680	0.289–0.820
D-only PIV	0.035	0.529	1	0.815	0.090	0.017	0.638–0.992
N-only PIV	0.1742	1	0.824	0.891	0.067	0.003	0.759–1
DN PIV	0.0125	0.882	0.429	0.681	0.122	0.172	0.441–0.921
N-only volume-LTD	54.75	1	0.941	0.983	0.021	0.000	0.941–1
N-only PIV-LTD	0.0128	1	1	1	0	0.000	1–1
LTD	16.9 mm	0.647	1	0.828	0.084	0.013	0.664–0.992

PIV, percentage of involved volume; LTD, lesion-to-tract distance; AUC, area under the receiver operating characteristic curve.

and DBSI (Ye et al., 2020). Following the exclusion of the free water compartment, the above-mentioned models demonstrated the possibility of tracing a larger volume of fiber bundles. Derived from the NODDI model, the ODI summarized the angular variation of neurites by excluding the isotropic diffusivity. Therefore, the ODI showed a more apparent trend in fiber direction in the area with vasogenic edema when compared to the DTI-derived FA map (**Figure 2**). It also displayed higher sensitivity and specificity of CST reconstruction in the NODDI-derived tractography than did DTI tractography (**Figure 6**). We specified on CST reconstruction to systematically compare the results and validate them through follow-up data. Previous studies have suggested that the vasogenic edema may be resolved in 4 days after total removal and that it disappeared entirely by 2–3 weeks post-operation (Stevens et al., 1983; Shirotani et al., 1994). Despite a follow-up in only four patients, the tractography results and the similarity comparison suggested that free water fraction exclusion could improve fiber tracking in regions with vasogenic edema.

Conventionally, the FA threshold, one of the stopping criteria for DTI tractography, was chosen rather arbitrarily, ranging from 0.15 to 0.30 for general tracking purposes (Stadlbauer et al., 2007; Bello et al., 2008). Stadlbauer et al. (2007) conducted a study on brain tumor infiltration and associated vasogenic edema. They demonstrated that an increase in the FA threshold stepped up the distance between the reconstructed fiber bundles and the tumors and decreased the number of detectable fiber bundles. Accordingly, the FA threshold was usually selected at 0.15 or 0.10 to display the peritumoral neural tracts (Bello et al., 2008). Despite the high tracking sensitivity of low FA, low specificity increases the probability of noisy streamline reconstruction. This, in turn, concurrently increases the uncertainty of neurosurgery. Therefore, surgeons should be more careful while applying the results mentioned above in surgical planning and navigation.

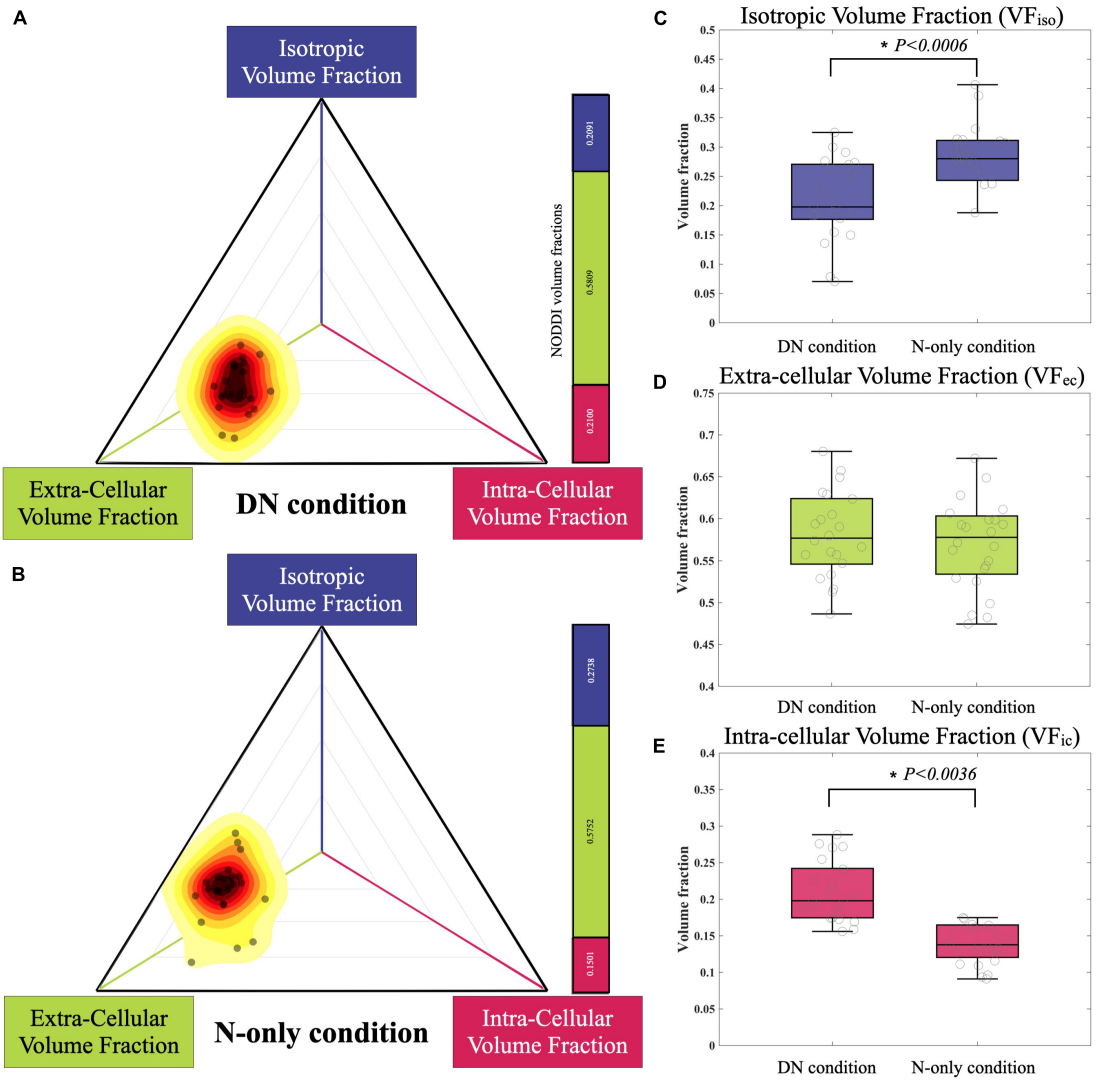

FIGURE 9 | The distribution of NODDI-derived volume fraction in the DN condition and N-only condition are plotted with a 2-D barycentric coordinate system. **(A)** The N-only condition and **(B)** distribution reveal a left upper shift in the coordinate system, compared to the DN condition. There is no significant difference in the VF_{ec} ($p = 0.4751$, **D**). However, there are significant differences in the VF_{ic} ($p < 0.0036$, **E**) and VF_{iso} ($p = 0.0006$, **C**). NODDI, neurite orientation dispersion and density imaging.

Following the exposure of the fiber tracts located in areas overlapping with peritumoral edema, we calculated the CST volume and LTD associated with motor functions. Numerous studies have suggested that the CST volume may reflect clinical outcomes, such as stroke recovery (Auriat et al., 2015) and amyotrophic lateral sclerosis (Wang et al., 2006). Sollmann et al. (2019) and Yu et al. (2020) suggested that the LTD was related to surgery-related transient impairment and may well be regarded as a presumptive predictor of outcome, attributable in part to tumor edema. In this study, we removed the edematous signal to highlight the percentage of the involved volume of the CST. The combination of PIV and LTD index revealed a direct association with motor function decline. Our results suggested that an increase in volume in the edema area and decrease in LTD may reflect motor function decline (**Figure 8**).

Furthermore, the fiber tracts located in areas overlapping with peritumoral edema that only existed in NODDI-derived tractography (N-only condition) significantly increased and decreased in VF_{iso} and VF_{ic} when compared with the DN-only condition (**Figure 9**). In the DTI model, the FA index was calculated by a total signal in each voxel. Unlike DTI, the NODDI model separated the total signal into three compartments: VF_{ic}, VF_{ec}, and VF_{iso}. However, in the calculation of NODDI's ODI, only VF_{ic} and VF_{ec} were used (Zhang et al., 2012). While comparing the NODDI indices between DN and N-only conditions, we found that there were no significant differences in the VF_{ec}, but there were in VF_{ic} and VF_{iso}. The region with increasing isotropic volume fraction (increased water content of the surrounding tissue) causes the FA's decrease and failure to reconstruct the CST in DTI tractography. This suggested that by

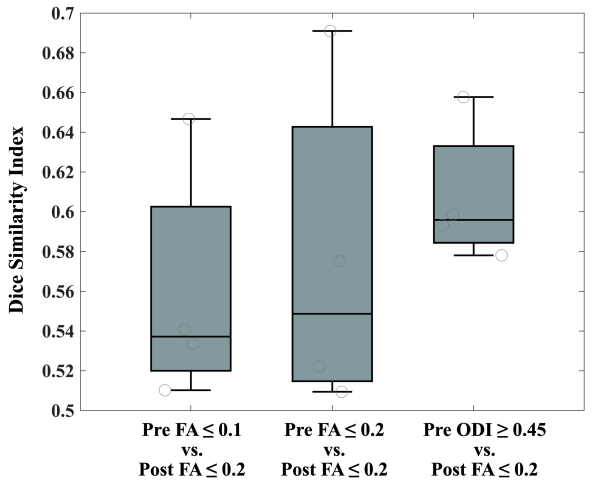

FIGURE 10 | The similarity comparison of CST reconstruction between pre- and post-surgery. CST, corticospinal tract.

excluding the isotropic volume fraction (edema effect), NODDI-derived tractography could reveal the fiber tracts located in areas overlapping with peritumoral edema. Based on the biophysical model, the increase in VF_{iso} may reflect the severity of vasogenic edema. Similarly, the decrease in VF_{ic} (neurite density index) may reflect focal neurologic deficits (neuron injury or axonal loss) and could also refer to the cognitive function decline (Kaal and Vecht, 2004; Parker et al., 2018). The edematous fiber tracts that only existed in DTI-derived tractography (D-only condition) found significant differences in the comparison between patients with and without motor function decline. However, as the D-only volume was relatively small (D-only volume = 31.45 ± 54.56 mm^3), the estimation of the differences within these regions may come from the variability of the fiber orientation estimated by the DTI model.

Limitations

Despite the good performance of the NODDI model in revealing the fiber tracts located in areas overlapping with peritumoral edema, our study has some limitations. First, our sample populations included a variety of tumor types. Previous studies have suggested that patients with glioma presumably had tumor-infiltrated edema, which was different from the pure vasogenic edema (Lu et al., 2003, 2004; Min et al., 2013). However, there were no significant differences found in the volume of edema with CST (DN-condition and N-only condition) in our dataset, which may suggest that patients in our dataset with edematous CST may not have infiltration by the tumor cell. The group comparison between vasogenic edema and edematous CST analysis can be found in **Supplementary Material**. Second, our MRI data were recruited from two different centers since these datasets were hard to obtain. Although the quantitative measurement that we used from the NODDI model, such as ODI, was normalized and calibrated from 10 healthy participants (five participants from each center), the variability from the different scanners still needed to be taken seriously. Third, our main purpose was to investigate the effect of edema on routinely employed tractography in clinical practice. The effect of crossing fiber in human white matter (Jeurissen et al., 2013) should be considered, and it would be necessary to utilize a model that focuses on solving crossing fiber-like constrained spherical deconvolution (CSD) (Tournier et al., 2008) in the future studies. Fourth, the NODDI protocol we used in this study is more time-consuming than the regular clinical DTI. The suggested NODDI protocol was encoded with two shells, 30 directions with 700 s/mm^2 and 60 directions with 2,000 s/mm^2 (Zhang et al., 2012), which involved approximately 15 min in our scanner with $|G_{max}| = 45$ mT/m. The balance of the trade-off between acquisition time and imaging resolution was shifted toward lower imaging resolution to decrease the acquisition time. Thus, we used 2.5 mm^3 as the isotropic voxel size, which is an acceptable protocol (Mohd Taib et al., 2017). Fifth, the optimal ODI threshold of 0.45 was only calibrated for the CST. The ODI thresholds were calibrated for the corpus callosum (0.478) and CST (0.467) in the study conducted by Figini et al. (2014), with values closer to our optimal values. However, the ODI threshold may differ while reconstructing other tracts. Finally, the correlation with intraoperative stimulation was absent. The changes of the post-operative CST examination in our study could be affected by multiple factors, especially the surgical approach. Future studies will require a larger sample size and direct cortical stimulation for validating the ability of NODDI-derived fiber tractography in the region of vasogenic edema in a more direct way.

CONCLUSION

Our results demonstrated that NODDI-derived fiber tractography had a great potential to improve the reconstruction of fiber tracking through regions of vasogenic edema. Increasing the isotropic volume fraction or decreasing the intracellular volume fraction may cause the DTI tractography failure to reveal the fiber tracts located in areas with peritumoral edema. Moreover, the volume of edematous CST that was reconstructed by NODDI-derived tractography could provide an accurate microstructure index for clinical quantitative measurements and diagnostic performance. Therefore, this technique may help neurosurgeons to define a better and safe margin for tumor resection.

DATA AVAILABILITY STATEMENT

The raw data supporting the conclusions of this article will be made available by the authors, without undue reservation.

ETHICS STATEMENT

The studies involving human participants were reviewed and approved by Institutional Review Board, Tri-Service General Hospital (TSGHIRB No. 1-102-05-109) Institutional Review Board, First Hospital of Jilin University (2017-465). The patients/participants provided their written informed consent to

participate in this study. Written informed consent was obtained from the individual (s) for the publication of any potentially identifiable images or data included in this article.

AUTHOR CONTRIBUTIONS

SC, H-WK, and C-PL contributed to the conception and design of the study. XL and H-WK organized the database. SC, C-YEL, C-CH, Y-CK, K-TK, C-CHH, and C-YL provided the methodology support. SC wrote the first draft of the manuscript. SC, H-WK and C-PL wrote sections of the manuscript. YL and GZ provide the additional clinical suggestions during the revision. All authors contributed to manuscript revision, read, and approved the submitted version.

FUNDING

C-YL was partially supported by the Shanghai Municipal Science and Technology Major Project (No.2018SHZDZX01), the National Key Research and Development Program of China (No. 2018YFC0910503), the Young Scientists Fund of the National Natural Science Foundation of China (No. 81801774), the Natural Science Foundation of Shanghai (No. 18ZR1403700), ZJ Lab, and Shanghai Center for Brain Science and Brain-Inspired Technology. C-PL was supported by the Ministry of Science and Technology (MOST) of Taiwan (grants MOST 110-2321-B-010-004, MOST 110-2321-B-010-007, MOST 108-2321-B-010-010-MY2, and MOST 110-2634-F-010-001), Veterans General Hospitals and University System of Taiwan Joint Research Program (VGHUST110-G1-1-3). This work was financially supported by the Brain Research Center, National Yang Ming Chiao Tung University from the Featured Areas Research Center Program within the framework of the Higher Education Sprout Project by the Ministry of Education (MOE) in Taiwan (110BRC-B501).

SUPPLEMENTARY MATERIAL

The Supplementary Material for this article can be found online at: https://www.frontiersin.org/articles/10.3389/fnins.2021.702353/full#supplementary-material

REFERENCES

Adluru, G., Gur, Y., Anderson, J. S., Richards, L. G., Adluru, N., and Dibella, E. V. R. (2014). "Assessment of white matter microstructure in stroke patients using NODDI," in *Proceedings of the 2014 36th Annual International Conference of the IEEE Engineering in Medicine and Biology Society*, (Piscataway, NY: IEEE).

Assaf, Y., and Pasternak, O. (2008). Diffusion tensor imaging (DTI)-based white matter mapping in brain research: a review. *J. Mol. Neurosci.* 34, 51–61. doi: 10.1007/s12031-007-0029-0

Auriat, A. M., Borich, M. R., Snow, N. J., Wadden, K. P., and Boyd, L. A. (2015). Comparing a diffusion tensor and non-tensor approach to white matter fiber tractography in chronic stroke. *Neuroimage Clin.* 7, 771–781. doi: 10.1016/j.nicl.2015.03.007

Basser, P. J. (1995). Inferring microstructural features and the physiological state of tissues from diffusion-weighted images. *NMR Biomed.* 8, 333–344. doi: 10.1002/nbm.1940080707

Basser, P. J., Mattiello, J., and Lebihan, D. (1994). MR diffusion tensor spectroscopy and imaging. *Biophys. J.* 66, 259–267. doi: 10.1016/s0006-3495(94)80775-1

Bello, L., Gambini, A., Castellano, A., Carrabba, G., Acerbi, F., Fava, E., et al. (2008). Motor and language DTI Fiber Tracking combined with intraoperative subcortical mapping for surgical removal of gliomas. *NeuroImage* 39, 369–382. doi: 10.1016/j.neuroimage.2007.08.031

Berman, J. I., Berger, M. S., Mukherjee, P., and Henry, R. G. (2004). Diffusion-tensor imaging—guided tracking of fibers of the pyramidal tract combined with intraoperative cortical stimulation mapping in patients with gliomas. *J. Neurosurg.* 101, 66–72. doi: 10.3171/jns.2004.101.1.0066

Callaghan, P. T., Coy, A., Macgowan, D., Packer, K. J., and Zelaya, F. O. (1991). Diffraction-like effects in NMR diffusion studies of fluids in porous solids. *Nature* 351, 467–469. doi: 10.1038/351467a0

Chen, Z., Tie, Y., Olubiyi, O., Rigolo, L., Mehrtash, A., Norton, I., et al. (2015). Reconstruction of the arcuate fasciculus for surgical planning in the setting of peritumoral edema using two-tensor unscented Kalman filter tractography. *NeuroImage Clin.* 7, 815–822. doi: 10.1016/j.nicl.2015.03.009

Chen, Z., Tie, Y., Olubiyi, O., Zhang, F., Mehrtash, A., Rigolo, L., et al. (2016). Corticospinal tract modeling for neurosurgical planning by tracking through regions of peritumoral edema and crossing fibers using two-tensor unscented Kalman filter tractography. *Int. J. Comput. Assisted Radiol. Surg.* 11, 1475–1486. doi: 10.1007/s11548-015-1344-5

Cooper, M., Thapar, A., and Jones, D. K. (2015). ADHD severity is associated with white matter microstructure in the subgenual cingulum. *Neuroimage Clin.* 7, 653–660. doi: 10.1016/j.nicl.2015.02.012

Cordero-Grande, L., Christiaens, D., Hutter, J., Price, A. N., and Hajnal, J. V. (2019). Complex diffusion-weighted image estimation via matrix recovery under general noise models. *NeuroImage* 200, 391–404. doi: 10.1016/j.neuroimage.2019.06.039

Crombe, A., Planche, V., Raffard, G., Bourel, J., Dubourdieu, N., Panatier, A., et al. (2018). Deciphering the microstructure of hippocampal subfields with in vivo DTI and NODDI: applications to experimental multiple sclerosis. *NeuroImage* 172, 357–368. doi: 10.1016/j.neuroimage.2018.01.061

Figini, M., Baselli, G., Riva, M., Bello, L., Zhang, H., and Bizzi, A. (2014). "NODDI performs better than DTI in brain tumors with vasogenic edema," in *Proceedings of the Joint Annual Meeting ISMRM-ESMRMB*, (Milan).

Fu, X., Shrestha, S., Sun, M., Wu, Q., Luo, Y., Zhang, X., et al. (2020). Microstructural white matter alterations in mild cognitive impairment and alzheimer's disease. *Clin. Neuroradiol.* 30, 569–579.

Gong, S., Zhang, F., Norton, I., Essayed, W. I., Unadkat, P., Rigolo, L., et al. (2018). Free water modeling of peritumoral edema using multi-fiber tractography: application to tracking the arcuate fasciculus for neurosurgical planning. *PLoS One* 13:e0197056. doi: 10.1371/journal.pone.0197056

Graham, M. S., Drobnjak, I., Jenkinson, M., and Zhang, H. (2017). Quantitative assessment of the susceptibility artefact and its interaction with motion in diffusion MRI. *PLoS One* 12:e0185647. doi: 10.1371/journal.pone.0185647

Jenkinson, M., Beckmann, C. F., Behrens, T. E. J., Woolrich, M. W., and Smith, S. M. (2012). FSL. *NeuroImage* 62, 782–790.

Jeurissen, B., Leemans, A., Tournier, J.-D., Jones, D. K., and Sijbers, J. (2013). Investigating the prevalence of complex fiber configurations in white matter tissue with diffusion magnetic resonance imaging. *Hum. Brain Map.* 34, 2747–2766. doi: 10.1002/hbm.22099

Kaal, E. C. A., and Vecht, C. J. (2004). The management of brain edema in brain tumors. *Curr. Opin. Oncol.* 16, 593–600.

Kadota, Y., Hirai, T., Azuma, M., Hattori, Y., Khant, Z. A., Hori, M., et al. (2020). Differentiation between glioblastoma and solitary brain metastasis using neurite orientation dispersion and density imaging. *J. Neuroradiol.* 47, 197–202. doi: 10.1016/j.neurad.2018.10.005

Kellner, E., Dhital, B., Kiselev, V. G., and Reisert, M. (2016). Gibbs-ringing artifact removal based on local subvoxel-shifts. *Magnet. Reson. Med.* 76, 1574–1581. doi: 10.1002/mrm.26054

Lecoeur, J., Caruyer, E., Elliott, M., Brem, S., Macyszyn, L., and Verma, R. (2014). "Addressing the challenge of edema in fiber tracking," in *Proceedings of the MICCAI 2014 DTI Tractography Challenge*, (Boston).

Lecoeur, J., Caruyer, E., Macyszyn, L., and Verma, R. (2013). "Improving white matter tractography by resolving the challenges of edema," in *Proceedings of the MICCAI 2013 DTI Tractography Challenge*, (Nagoya).

Liao, R., Ning, L., Chen, Z., Rigolo, L., Gong, S., Pasternak, O., et al. (2017). Performance of unscented Kalman filter tractography in edema: analysis of the two-tensor model. *NeuroImage Clin.* 15, 819–831. doi: 10.1016/j.nicl.2017.06.027

Lu, S., Ahn, D., Johnson, G., and Cha, S. (2003). Peritumoral diffusion tensor imaging of high-grade gliomas and metastatic brain tumors. *AJNR Am. J. Neuroradiol.* 24, 937–941.

Lu, S., Ahn, D., Johnson, G., Law, M., Zagzag, D., and Grossman, R. I. (2004). Diffusion-Tensor MR imaging of intracranial neoplasia and associated peritumoral edema: introduction of the tumor infiltration index. *Radiology* 232, 221–228. doi: 10.1148/radiol.2321030653

Masjoodi, S., Hashemi, H., Oghabian, M. A., and Sharifi, G. (2018). Differentiation of edematous, tumoral and normal areas of brain using diffusion tensor and neurite orientation dispersion and density imaging. *J. Biomed. Phys. Eng.* 8, 251–260.

Min, Z.-G., Niu, C., Rana, N., Ji, H.-M., and Zhang, M. (2013). Differentiation of pure vasogenic edema and tumor-infiltrated edema in patients with peritumoral edema by analyzing the relationship of axial and radial diffusivities on 3.0T MRI. *Clin. Neurol. Neurosurg.* 115, 1366–1370. doi: 10.1016/j.clineuro.2012.12.031

Mitchell, T., Archer, D. B., Chu, W. T., Coombes, S. A., Lai, S., Wilkes, B. J., et al. (2019). Neurite orientation dispersion and density imaging (NODDI) and free-water imaging in Parkinsonism. *Hum. Brain Map.* 40, 5094–5107. doi: 10.1002/hbm.24760

Mohd Taib, N., Kamil, W., Shuaib, I. L., Magosso, E., and Mat Isa, S. (2017). Determination of optimum combination of voxel size and b-value for brain diffusion tensor imaging. *Sains Malaysiana* 46, 67–74. doi: 10.17576/jsm-2017-4601-09

Mori, S., Crain, B. J., Chacko, V. P., and Van Zijl, P. C. (1999). Three-dimensional tracking of axonal projections in the brain by magnetic resonance imaging. *Ann. Neurol.* 45, 265–269. doi: 10.1002/1531-8249(199902)45:2<265::aid-ana21>3.0.co;2-3

Mori, S., and Van Zijl, P. C. M. (2002). Fiber tracking: principles and strategies - a technical review. *NMR Biomed.* 15, 468–480. doi: 10.1002/nbm.781

Parker, T. D., Slattery, C. F., Zhang, J., Nicholas, J. M., Paterson, R. W., Foulkes, A. J. M., et al. (2018). Cortical microstructure in young onset Alzheimer's disease using neurite orientation dispersion and density imaging. *Hum. Brain Map.* 39, 3005–3017. doi: 10.1002/hbm.24056

Patenaude, B., Smith, S. M., Kennedy, D. N., and Jenkinson, M. (2011). A Bayesian model of shape and appearance for subcortical brain segmentation. *NeuroImage* 56, 907–922. doi: 10.1016/j.neuroimage.2011.02.046

Shirotani, T., Shima, K., and Chigasaki, H. (1994). *Resolution of Peritumoral Brain Edema Following Excision of Meningioma*. Vienna: Springer, 416–418.

Smith, S. M. (2002). Fast robust automated brain extraction. *Hum. Brain Map.* 17, 143–155. doi: 10.1002/hbm.10062

Smith, S. M., Jenkinson, M., Woolrich, M. W., Beckmann, C. F., Behrens, T. E. J., Johansen-Berg, H., et al. (2004). Advances in functional and structural MR image analysis and implementation as FSL. *NeuroImage* 23, S208–S219.

Sollmann, N., Fratini, A., Zhang, H., Zimmer, C., Meyer, B., and Krieg, S. M. (2019). Associations between clinical outcome and tractography based on navigated transcranial magnetic stimulation in patients with language-eloquent brain lesions. *J. Neurosurg.* 132, 1033–1042. doi: 10.3171/2018.12.jns182988

Stadlbauer, A., Nimsky, C., Buslei, R., Salomonowitz, E., Hammen, T., Buchfelder, M., et al. (2007). Diffusion tensor imaging and optimized fiber tracking in glioma patients: histopathologic evaluation of tumor-invaded white matter structures. *NeuroImage* 34, 949–956. doi: 10.1016/j.neuroimage.2006.08.051

Stevens, J. M., Ruiz, J. S., and Kendall, B. E. (1983). Observation on peritumoural oedema in meningioma. Part I: distribution, spread and resolution of vasogenic oedema seen on computed tomography. *Neuroradiology* 25, 71–80. doi: 10.1007/bf00333295

Tournier, J.-D., Smith, R., Raffelt, D., Tabbara, R., Dhollander, T., Pietsch, M., et al. (2019). MRtrix3: a fast, flexible and open software framework for medical image processing and visualisation. *NeuroImage* 202:116137.

Tournier, J. D., Yeh, C.-H., Calamante, F., Cho, K.-H., Connelly, A., and Lin, C.-P. (2008). Resolving crossing fibres using constrained spherical deconvolution: validation using diffusion-weighted imaging phantom data. *NeuroImage* 42, 617–625. doi: 10.1016/j.neuroimage.2008.05.002

Tustison, N. J., Avants, B. B., Cook, P. A., Yuanjie, Z., Egan, A., Yushkevich, P. A., et al. (2010). N4ITK: improved N3 Bias Correction. *IEEE Trans. Med. Imaging* 29, 1310–1320. doi: 10.1109/tmi.2010.2046908

Veraart, J., Fieremans, E., and Novikov, D. S. (2016a). Diffusion MRI noise mapping using random matrix theory. *Magnet. Reson. Med.* 76, 1582–1593. doi: 10.1002/mrm.26059

Veraart, J., Novikov, D. S., Christiaens, D., Ades-Aron, B., Sijbers, J., and Fieremans, E. (2016b). Denoising of diffusion MRI using random matrix theory. *NeuroImage* 142, 394–406. doi: 10.1016/j.neuroimage.2016.08.016

Wang, S., Poptani, H., Bilello, M., Wu, X., Woo, J. H., Elman, L. B., et al. (2006). Diffusion tensor imaging in amyotrophic lateral sclerosis: volumetric analysis of the corticospinal tract. *Am. J. Neuroradiol.* 27, 1234–1238.

Wang, Z., Zhang, S., Liu, C., Yao, Y., Shi, J., Zhang, J., et al. (2019). A study of neurite orientation dispersion and density imaging in ischemic stroke. *Magnet. Reson. Imaging* 57, 28–33. doi: 10.1016/j.mri.2018.10.018

Wen, Q., Kelley, D.a.C, Banerjee, S., Lupo, J. M., Chang, S. M., Xu, D., et al. (2015). Clinically feasible NODDI characterization of glioma using multiband EPI at 7 T. *NeuroImage Clin.* 9, 291–299. doi: 10.1016/j.nicl.2015.08.017

Ye, Z., Gary, S. E., Sun, P., Mustafi, S. M., Glenn, G. R., Yeh, F. C., et al. (2020). The impact of edema and fiber crossing on diffusion MRI metrics assessed in an ex vivo nerve phantom: multi-tensor model vs. diffusion orientation distribution function. *NMR Biomed.* 34:e4414.

Yeh, F.-C., Verstynen, T. D., Wang, Y., Fernández-Miranda, J. C., and Tseng, W.-Y. I. (2013). Deterministic diffusion fiber tracking improved by quantitative anisotropy. *PLoS One* 8:e80713. doi: 10.1371/journal.pone.0080713

Yu, Q., Lin, K., Liu, Y., and Li, X. (2020). Clinical uses of diffusion tensor imaging fiber tracking merged neuronavigation with lesions adjacent to corticospinal tract : a retrospective cohort study. *J. Korean Neurosurg. Soc.* 63, 248–260. doi: 10.3340/jkns.2019.0046

Yushkevich, P. A., Piven, J., Hazlett, H. C., Smith, R. G., Ho, S., Gee, J. C., et al. (2006). User-guided 3D active contour segmentation of anatomical structures: significantly improved efficiency and reliability. *NeuroImage* 31, 1116–1128. doi: 10.1016/j.neuroimage.2006.01.015

Zhang, H., Schneider, T., Wheeler-Kingshott, C. A., and Alexander, D. C. (2012). NODDI: Practical in vivo neurite orientation dispersion and density imaging of the human brain. *NeuroImage* 61, 1000–1016. doi: 10.1016/j.neuroimage.2012.03.072

Zhang, H., Wang, Y., Lu, T., Qiu, B., Tang, Y., Ou, S., et al. (2013). Differences between generalized q-sampling imaging and diffusion tensor imaging in the preoperative visualization of the nerve fiber tracts within peritumoral edema in brain. *Neurosurgery* 73, 1044–1053.

Zhang, Y., Brady, M., and Smith, S. (2001). Segmentation of brain MR images through a hidden Markov random field model and the expectation-maximization algorithm. *IEEE Trans. Med. Imaging* 20, 45–57. doi: 10.1109/42.906424

Conflict of Interest: C-YEL was employed by GE Healthcare.

The remaining authors declare that the research was conducted in the absence of any commercial or financial relationships that could be construed as a potential conflict of interest.

Publisher's Note: All claims expressed in this article are solely those of the authors and do not necessarily represent those of their affiliated organizations, or those of the publisher, the editors and the reviewers. Any product that may be evaluated in this article, or claim that may be made by its manufacturer, is not guaranteed or endorsed by the publisher.

Copyright © 2021 Chong, Liu, Kao, Lin, Hsu, Kung, Kuo, Huang, Lo, Li, Zhao and Lin. This is an open-access article distributed under the terms of the Creative Commons Attribution License (CC BY). The use, distribution or reproduction in other forums is permitted, provided the original author(s) and the copyright owner(s) are credited and that the original publication in this journal is cited, in accordance with accepted academic practice. No use, distribution or reproduction is permitted which does not comply with these terms.

frontiers in Oncology

ORIGINAL RESEARCH
published: 04 October 2021
doi: 10.3389/fonc.2021.721821

Diagnostic and Prognostic Potential of ^{18}F-FET PET in the Differential Diagnosis of Glioma Recurrence and Treatment-Induced Changes After Chemoradiation Therapy

Monica Celli[1], Paola Caroli[1], Elena Amadori[2], Donatella Arpa[3], Lorena Gurrieri[4], Giulia Ghigi[3], Patrizia Cenni[2], Giovanni Paganelli[1] and Federica Matteucci[1]*

[1] Diagnostic Nuclear Medicine Unit, IRCCS Istituto Romagnolo per lo Studio dei Tumori (IRST) "Dino Amadori", Meldola, Italy, [2] Radiology MRI Unit, IRCCS Istituto Romagnolo per lo Studio dei Tumori (IRST) "Dino Amadori", Meldola, Italy, [3] Radiation Therapy Unit, IRCCS Istituto Romagnolo per lo Studio dei Tumori (IRST) "Dino Amadori", Meldola, Italy, [4] Oncology Unit, IRCCS Istituto Romagnolo per lo Studio dei Tumori (IRST) "Dino Amadori", Meldola, Italy

OPEN ACCESS

Edited by:
Alexandra Golby, Harvard Medical School, United States

Reviewed by:
Marco Riva, University of Milan, Italy
Nico Sollmann, University of California, San Francisco, United States

***Correspondence:**
Monica Celli
monica.celli@irst.emr.it

Specialty section:
This article was submitted to Neuro-Oncology and Neurosurgical Oncology, a section of the journal Frontiers in Oncology

Received: *07 June 2021*
Accepted: *09 September 2021*
Published: *04 October 2021*

Citation:
Celli M, Caroli P, Amadori E, Arpa D, Gurrieri L, Ghigi G, Cenni P, Paganelli G and Matteucci F (2021) Diagnostic and Prognostic Potential of ^{18}F-FET PET in the Differential Diagnosis of Glioma Recurrence and Treatment-Induced Changes After Chemoradiation Therapy. Front. Oncol. 11:721821. doi: 10.3389/fonc.2021.721821

Background: MRI-based differential diagnosis of glioma recurrence (GR) and treatment-induced changes (TICs) remain elusive in up to 30% of treated glioma patients. We aimed to determine ^{18}F-FET PET diagnostic performance in this clinical scenario, its outcome dependency on established prognostic factors, optimal ^{18}F-FET semi-quantitative thresholds, and whether ^{18}F-FET parameters may instantly predict progression-free survival (PFS) and overall survival (OS).

Methods: We retrospectively analyzed 45 glioma patients treated with chemoradiation therapy (32 males; mean age: 51 years, glioma grade: n=26 WHO4; n=15 WHO3; n=4 WHO2) who underwent ^{18}F-FET PET to resolve differential diagnosis of GR and TICs raised by MRI performed in the preceding 2 weeks and depicting any of the following changes in their radiation field: volumetric increase of contrast-enhancing lesions; new contrast-enhancing lesion; significant increase in T2/FLAIR non-enhancing lesion without reducing corticosteroids. ^{18}F-FET PET outcome relied on evaluation of maximum tumor-to-brain ratio (TBRmax), time-to-peak (TTP), and time-activity curve pattern (TAC). Metabolic tumor volume (MTV) and total tumor metabolism (TTM) were calculated for prognostic purposes. Standard of reference was repeat MRI performed 4–6 weeks after the previous MRI. Non-parametric statistics tested ^{18}F-FET-based parameters for dependency on established prognostic markers. ROC curve analysis determined optimal cutoff values for ^{18}F-FET semi-quantitative parameters. ^{18}F-FET parameters and prognostic factors were evaluated for PFS and OS by Kaplan-Meier, univariate, and multivariate analyses.

Results: ^{18}F-FET PET sensitivity, specificity, positive predictive value, negative predictive value were 86.2, 81.3, 89.3, 76.5%, respectively; higher diagnostic accuracy was yielded in IDH-wild-type glioma patients compared to IDH-mutant glioma patients (sensitivity:

81.8 *versus* 88.9%; specificity: 80.8 *versus* 81.8%). KPS was the only prognostic factor differing according to ^{18}F-FET PET outcome (negative *versus* positive). Optimal ^{18}F-FET cutoff values for GR were TBRmax ≥ 2.1, SUVmax ≥ 3.5, and TTP ≤ 29 min. PFS differed based on ^{18}F-FET outcome and related metrics and according to KPS; a different OS was observed according to KPS only. On multivariate analysis, ^{18}F-FET PET outcome was the only significant PFS factor; KPS and age the only significant OS factors.

Conclusion: ^{18}F-FET PET demonstrated good diagnostic performance. ^{18}F-FET PET outcome and metrics were significantly predictive only for PFS.

Keywords: ^{18}F-FET PET, treatment-related changes, treated gliomas, metabolic tumor volume, total tumor metabolism

1 INTRODUCTION

Gliomas are the most common primary brain malignancies, predominantly presenting as high-grade infiltrative tumors, almost ineluctably relapsing after multimodal treatment, which combines maximal surgical safe resection, concomitant chemoradiation, and adjuvant chemotherapy (1, 2).

After treatment, detection of glioma recurrence (GR) currently relies on RANO criteria integrating magnetic resonance imaging (MRI), patient performance status, and dosage of steroids.

MRI findings defining GR include the following: (i) ≥25% increase in the products of perpendicular diameters of measurable enhancing lesions compared with their smallest measurements obtained either at baseline (if no decrease) or at best response; (ii) the emergence of any new lesions; (iii) a significant increase in T2/FLAIR non-enhancing lesions on stable or increasing doses of corticosteroids compared with baseline scan or best response after initiation of therapy. Such MRI changes, however, are not strictly tumor specific (3, 4).

A proportion of 9–30% of treated glioma patients develops treatment-induced changes (TICs) simulating GR, potentially leading to misdiagnosis and inappropriate treatment modifications. TICs mimicking GR principally include two distinct patterns: pseudo-progression (PSP) and radio-necrosis (RN). PSP reflects inflammation and transiently increased permeability of tumor vasculature occurring within the first 6 months after chemoradiation appearing in the therapy field as new or increasing contrast-enhancing lesions and decreasing over time without any therapy change. RN lesions, implying brain tissue injury, necrosis, and vascular thrombosis, generally occur in the white matter not earlier than 1 year after having received any radiation or re-irradiation and generally do not subside (5–8).

Since TICs may mimic GR on conventional MRI, the ultimate diagnosis of TICs is retrospective as it requires a repeat MRI to be performed 4 weeks later demonstrating no further significant worsening of previously noted suspicious findings. This verification approach in two times may result in delayed diagnosis of GR.

In the attempt to promptly and confidently discriminate GR and TICs the PET-RANO and EANO working groups recommended evidence-based clinical use of amino-acid PET imaging as a metabolic integration to MRI (9).

The tyrosine analog ^{18}F-FET is an ^{18}F-labeled PET tracer highly specific for glioma. ^{18}F-FET uptake mechanism is driven by glioma overexpression of the active transmembrane L-type amino-acid transporter 2 (LAT2) and, to a minor extent, the lesser glioma-specific LAT1. An artificial amino-acid, ^{18}F-FET is not further metabolized within the cell and does not serve as substrate to protein synthesis. ^{18}F-FET uptake in inflammatory cells is low and negligible in the healthy brain. A large neutral amino-acid, ^{18}F-FET cannot cross the intact brain-blood-barrier (BBB), and glioma ^{18}F-FET uptake is not significantly influenced by changes in the BBB permeability (10–16).

These desirable features have led to wide clinical application of ^{18}F-FET-based imaging in glioma patients. With regards to differentiation of GR and TICs, few published studies, mainly retrospective and on small-sized cohorts of patients, documented high diagnostic accuracy of ^{18}F-FET PET imaging, encouraging its integration into the latest RANO working group guidelines and the drafting of intersocietal EANM/EANO/RANO practice guidelines and SNMMI procedure standards (17–25).

In this retrospective study, we aim to evaluate the diagnostic performance of PET-RANO-compliant ^{18}F-FET semiquantitative parameters in distinguishing TICs and GR in pretreated glioma patients with MRI findings suggestive, but not conclusive, for GR and the association of ^{18}F-FET outcome with established prognostic features. Additionally, we explore the potential prognostic value of ^{18}F-FET-based semiquantitative parameters.

2 MATERIALS AND METHODS

2.1 Ethics Statement

The present study involved the retrospective analysis of data from a study approved by the Ethics Committee IRST IRCCS AVR (approval number L2P1912 of 06/10/2015) and conducted in accordance with the Declaration of Helsinki and subsequent revisions. In accordance with the Italian legislation, written informed consent for observational retrospective studies conducted in Scientific Institutes for Research, Hospitalization and Healthcare (IRCCS) was not required.

TABLE 1 | Cohort characteristics.

Patients characteristics	Number/ (proportion)
Patients	45
Gender (male/female)	(32/13)
Median age; range	55 years; 21–76 years
Median KPS; range	90; 50–100
Glioma characteristics	
WHO IV glioblastoma	26
• IDH wild-type/IDH mutant	(21/5)
• MGMT methylated/non-methylated	(10/16)
WHO grade III gliomas	15
• anaplastic astrocytoma	7
• IDH wild-type/IDH mutant	(5/2)
• MGMT methylated/non-methylated	(1/6)
• oligodendroglioma	8
• IDH wild-type/IDH mutant	(0/8)
• MGMT methylated/non-methylated	(2/6)
WHO grade II astrocytoma	4
• IDH wild-type/IDH mutant	(3/1)
• MGMT methylated/non-methylated	(1/3)
Patients who had experienced glioma relapses prior to ^{18}F-FET PET	(34/45)
Treatments	
Patients who received primary surgery:	40
• partial resection	24
• grossly total resection	16
Patients who did not receive primary surgery (biopsy only)	5
Patients who received first-line chemoradiation therapy	45
Further treatments prior to ^{18}F-FET PET	
• surgical re-resection	6
• re-irradiation	24
• chemotherapy	20
• temozolomide	19
• PCV	3
• anti-VEGF	1
Median time from last RT to ^{18}F-FET PET; interquartile range	14 months; 5–22 months

IDH, isocitrate dehydrogenase; MGMT, O[6]-methylguanine-DNA methyltransferase; KPS, Karnofsky Performance Scale; PCV, procarbazine, lomustine, and vincristine; anti-VEGF, anti-vascular endothelial growth factor.

2.2 Patients

For this retrospective analysis, we searched our database (time span: October 2016–December 2020) for all treated glioma patients who were referred by the Area Vasta Romagna Neuro-Oncology Multidisciplinary Team for ^{18}F-FET PET imaging to assist MRI in differentiating GR and TICs.

Forty-five patients (32 males, 13 females; mean age: 51 years; range: 21–76) with treated gliomas were extracted. Of these, 26 patients had glioblastoma WHO4 (n=21 IDH-wildtype), 11 patients had astrocytoma (n=7 WHO3, of these 5 IDH-wildtype; n=4 WHO2, of these 3 IDH-wildtype), and 8 oligodendroglioma WHO3 (n=8 IDH-mutant). MGMT promoter methylation was present in 10/26 glioblastomas, in 4/11 astrocytomas, and in 2/8 oligodendrogliomas.

Out of 45 patients, 40 received primary surgery (grossly total resection in 16 patients; partial resection in 24 patients); in all patients, ^{18}F-FET PET was performed at least 12 weeks after any type of radiation therapy (**Table 1**).

2.3 MR Imaging

The MRI scans performed prior to ^{18}F-FET PET and afterward for clinical monitoring consisted of T1-weighted before and after contrast agent administration, T2-weighted/FLAIR, and diffusion-weighted imaging. Two neuroradiologists (CeP with 20 years' experience and AE with 5 years' experience) reported all post-radiation therapy MRI scans according to RANO interpretation criteria and reviewed MR images at multidisciplinary meetings. Suggestive MRI findings for GR included evidence of size-increasing contrast-enhanced lesions with at least 10 mm diameter (i.e., ≥25% increase in the product of perpendicular diameters compared with the nadir measurement obtained after radiation therapy); evidence of any new lesion within the radiation therapy field; significant increase in T2/FLAIR non-enhancing lesions compared with best response after therapy start and without decreasing corticosteroids. No significant clinical deterioration coexisted at the first evidence of the abovementioned findings.

2.4 ^{18}F-FET PET/CT Imaging

^{18}F-FET was commercially shipped with marketing authorization for the appropriate clinical indication of differentiating GR from TICs. ^{18}F-FET PET scans were performed within 2 weeks from the MRI depicting dubious findings for GR. ^{18}F-FET PET were acquired on a Biograph mCT Flow 64 PET/CT system (Siemens Healthineers, Germany).

Mean ^{18}F-FET activity of 3MBq/Kg of body weight was intravenously administered in bolus, and simultaneously, a 40-minute three-dimensional dynamic brain PET/CT scan was started. The dynamic brain ^{18}F-FET PET acquisition consisted of 35 frames (12 frames of 1 s, 6 frames of 10 s, 6 frames of 30 s, 5 frames of 1 min, and 6 frames of 5 min).

Late static brain images (summed images from 20 to 40 minutes post-injection) were generated from each dynamic ^{18}F-FET PET scan.

^{18}F-FET PET/CT images and the most recent MRI scan were reviewed on a syngo.via platform (Siemens Healthineers, Germany). Late static ^{18}F-FET PET images were rigidly co-registered with contrast-enhanced T1-weighted MRI images for lesion correlation.

^{18}F-FET PET scans were interpreted according to the joint practice guidelines collaboratively developed by the European Association of Nuclear Medicine (EANM), the Society of Nuclear Medicine and Molecular Imaging (SNMMI), the European Association of Neuro Oncology (EANO), and the working group for Response Assessment in Neuro Oncology with PET (PET-RANO).

A three-dimensional VOI with a 1.6 cm diameter was drawn on the ^{18}F-FET PET hottest index lesion to measure the SUVmax. The SUVmean of contralateral healthy brain tissue, measured with a similar VOI including gray and white matter, was used to generate the maximum tumor-to-background ratio (TBRmax). The index lesion VOI was copied onto the dynamic ^{18}F-FET acquisition to plot the time-activity curve (TAC), to extract the time-to-peak (TTP, minutes from the start of

dynamic acquisition up to lesion maximum SUVpeak), and to draw the TAC curve.

^{18}F-FET PET was considered positive for GR if the TBRmax was superior to the established cutoff value of 1.9 in the late period after radiation therapy (i.e., after 12 weeks from completion of RT). Early TTP (<20 min) and a TAC pattern with early peak and either wash-out (TAC pattern 1) or plateau (TAC pattern 2) were regarded as ancillary support of GR; late TTP (>20 min) with an accumulating curve pattern (TAC pattern 3) was deemed not suggestive of GR.

^{18}F-FET PET semiquantitative parameters SUVmax, TBRmax, and TTP were evaluated by receiver-operating-characteristic curve analysis to identify the optimal threshold values and their diagnostic performance.

In ^{18}F-FET PET scans documenting lesions consistent with GR, semiquantitative volumetric parameters were calculated for prognostic purposes. Metabolic tumor volume (MTV) and total tumor metabolism (i.e., TTM = MTV × lesion SUVmean) were semiautomatically calculated by drawing a VOI around the positive lesion on late static ^{18}F-FET PET, encompassing all SUVmax values returning a pathological TBRmax (i.e., TBRmax > 1.9).

To do so, reference minimum pathological SUV was obtained by multiplying the healthy brain SUVmean by the pathological TBRmax cutoff value of 1.9 (i.e., reference minimum pathological SUV = healthy brain SUVmean × 1.9). The resulting SUVmax value was considered the reference minimum pathological value for MTV contour thresholding.

2.5 Standard of Reference

2.5.1 Diagnosis of GR *versus* TIC

RANO-compliant diagnosis of GR in this study consisted in further worsening of MRI findings previously deemed suggestive for GR on the confirmatory MRI scan performed 4–6 weeks later.

The diagnosis of TICs was inferred whenever the initially worsening MRI findings stabilized on the subsequent confirmatory MRI scan. In six patients the histology results (surgical re-resection in five patients; biopsy in one patient) were made available for definitive confirmation of viable GR.

Clinical follow-up was interrogated for excluding any prior decrease or discontinuation of corticosteroids.

2.5.2 PFS and OS Calculation

PFS was computed from the date of ^{18}F-FET PET imaging to RANO-compliant evidence of confirmed progressive disease on MRI, namely, to the date of the confirmatory MRI documenting a second consecutive >25% increase in the product of lesion perpendicular diameters or any following MRI evidence of unequivocal GR. Follow-up MRI scans were performed every 2–4 months according to the disease status and clinical course.

Patients who did not meet RANO criteria for MRI-based GR or who were alive at last available clinical assessment were considered censored without event for PFS and OS, respectively.

2.6 Statistical Analysis

Statistical analysis was carried out with StatsDirect software. Diagnostic performance was calculated with 95% confidence intervals.

Shapiro-Wilk test was used to test data normality distribution. A two-sided Fisher's Exact test was used to test whether the ^{18}F-FET PET outcome (positive/negative) was significantly different according to dichotomous prognostic features, namely, IDH status (mutant *versus* wild-type) and MGMT methylation (methylated *versus* unmethylated).

A two-sided Mann-Whitney U test was used to define whether ordinal prognostic factors such as patient Karnofsky performance status (KPS), glioma WHO grade, and history of prior glioma relapses were randomly represented in ^{18}F-FET PET outcome.

^{18}F-FET parameters SUVmax, TBRmax, TTP, and TAC pattern of true positive glioma lesions were tested for any significant differences based on glial phenotype (Mann-Whitney) and WHO grade (Kruskal–Wallis).

Survival analysis for PFS and OS was carried out, and a log-rank test was used to identify different survival distributions based on ^{18}F-FET PET outcome and its related metrics and on other available prognostic factors. Cox-regression analysis was used to test the significance of PFS and OS hazard ratios for parameters found to significantly impact survival.

Results obtained by non-parametric tests and by survival analyses considered an α-error of 0.05 and reached statistical significance at $p < 0.035$.

3 RESULTS

Out of 45 patients presenting MRI findings suggestive for GR, 29 met RANO criteria for GR on subsequent MR evaluation performed 4–6 weeks later; of these, 25 were correctly identified by ^{18}F-FET PET (n = 12 WHO grade IV, n = 11 WHO grade III, n = 2 WHO grade II). The remaining 16 patients did not show immediate progression and were cautiously considered to harbor TICs; of these 16, ^{18}F-FET PET correctly identified 13 cases (n = 7 WHO grade IV, n = 4 WHO grade III, n = 2 WHO grade II).

In four cases ^{18}F-FET tested falsely negative. Subsequent MRI documented further increase in size of the previously noted MRI suspicious findings. Two patients experienced recurrence of GBM (IDH wild-type), and two patients had recurrent ODG (IDH-mutant). All four patients were off systemic treatment at time of ^{18}F-FET PET. One patient underwent re-resection confirming recurrence of GBM, two patients received re-irradiation of the growing lesions, and one patient was started on chemotherapy.

^{18}F-FET resulted falsely positive in three patients with IDH wild-type GBM. Follow-up MRI demonstrated stability of previously noted increasing lesions.

Overall, ^{18}F-FET PET diagnostic performance in differentiating GR and TICs returned sensitivity (SE) of 86.2% (95% CI: 68.3–96.1%), specificity (SP) of 81.3% (95% CI: 54.4–96.1%), positive predictive value (PPV) of 89.3% (95% CI: 71.8–97.7%), negative predictive value (NPV) of 76.5% (95% CI: 50.1–93.2%), positive likelihood ratio of 4.6 (95% CI: 2.0–13.2), and negative likelihood ratio of 0.2 (95% CI: 0.1–0.4).

^{18}F-FET PET diagnostic performance for detecting GR resulted higher for IDH-wild-type gliomas than IDH-mutant

gliomas (SE: 88.9 *versus* 81.8%; SP: 81.8 *versus* 80.8%; PPV: 88.9 *versus* 90%; NPV: 81.8 *versus* 66.7%).

^{18}F-FET PET outcome for GR (positive/negative) was not significantly different considering the glioma IDH status (p-value: 0.894) and MGMT methylation status (p-value: 0.996).

Patients' KPS significantly differed according to ^{18}F-FET PET outcome (p-value: 0.025), whereas glioma WHO grade, history of previous relapses, and age did not.

^{18}F-FET PET SUVmax, TBRmax, TTP, and TAC pattern for true positive lesions did not significantly differ across different glial phenotypes, WHO grades, nor did between IDH wild-type and mutant status and between MGMT methylated and unmethylated status (**Table 2**).

ROC analysis returned an optimal TBRmax cutoff value of 2.1 to discriminate GR and TICs (SE: 79.3%; SP: 75%; PPV: 85.2%; NPV: 66.7%; area-under-curve AUC: 78%). The best cutoff for SUVmax was 3.5 (SE: 48.3%; SP: 93.8%; PPV: 93.3%; NPV: 50%; area-under-curve AUC: 71.1%) and for TTP at 29 min (SE: 68.8%; SP: 82.8%; PPV: 85.2%; NPV: 66.7%; area-under-curve AUC: 70.4%). Cutoff values for volumetric parameters MTV (≥0.15 ml) and TTM (≥0.33 ml) were generated returning good diagnostic accuracy (SE: 86.2%; SP: 81.3%; AUC: 85.4%) (**Table 3**).

Median follow-up time after ^{18}F-FET PET was 7.5 months (interquartile range: 16.1 months). During follow-up, 31 patients eventually progressed (68.9%) and 11 patients died (24.4%). Survival univariate analysis documented statistically significant differences in PFS between ^{18}F-FET positive and ^{18}F-FET negative patients (PFS of 1.4 months and 14.7 months, respectively; log-rank test, $p < 0.0001$) and ^{18}F-FET-related metrics, and between patients with KPS < 80 and KPS ≥ 80 (PFS of 1.2 months *versus* 3.8 months, respectively; log-rank test, p: 0.0002). No significant differences in PFS were observed based on the IDH status (log-rank test, p: 0.588), MGMT status (log-rank test, p: 0.263), and WHO grade III/IV *versus* grade II (log-rank test, p: 0.872) (**Table 4**) (**Figures 1** and **2**).

In the sub-cohort of patients with high-performance status (i.e., KPS ≥ 80; n = 32 patients), ^{18}F-FET PET outcome significantly impacted on PFS (log-rank p: 0.0005) with a median PFS of 2.4 months for patients with positive ^{18}F-FET PET (n = 15) and a median PFS of 14.7 months for patients with negative ^{18}F-FET PET (n = 17).

Cox-regression analysis documented statistically significant PFS positive hazard ratio for ^{18}F-FET positive outcome (HR: 8.91; p = 0.0005), whereas no statistical significance was found for any pathology, treatment, and patient-related features. ^{18}F-FET cutoffs for volumetric parameters MTV and TTM did not significantly weigh on the PFS (HR: 1). OS-based survival analysis documented statistically significant differences only according to KPS < 80 and KPS ≥ 80 (median OS of 7.7 months and OS not reached; log-rank test, p = 0.0001). Neither ^{18}F-FET PET parameters nor pathology-related features were found to impact OS. Statistically significant OS positive hazard ratios were only detected for KPS (HR: 55.98; p = 0.003) and age at the time of ^{18}F-FET PET (HR: 11.4; p = 0.015) (**Table 5**).

4 DISCUSSION

The present study, stemming from our institution's initial experience on a small-sized cohort of patients undergoing ^{18}F-

TABLE 2 | Static semiquantitative ^{18}F-FET PET parameters.

	SUVmax ± SD	p-value	TBRmax ± SD	p-value
True Glioma Recurrence				
Glial phenotype				
• astrocytic	3.7 ± 1.7	0.591	3.4 ± 1.1	0.652
• oligodendroglial	4.2 ± 1.7		3.1 ± 0.6	
WHO grade				
• II	2.4 ± 1.7	0.542	3.1 ± 1.3	0.557
• III	3.9 ± 1.5		3.1 ± 0.9	
• IV	3.9 ± 1.9		3.6 ± 1.1	
IDH				
• wild-type	3.7 ± 1.7	0.782	3.3 ± 1.1	0.857
• mutant	3.9 ± 1.9		3.4 ± 0.9	
MGMT promoter				
• methylated	3.7 ± 1.4	0.904	3.1 ± 1.0	0.267
• unmethylated	3.8 ± 1.9		3.5 ± 1.0	
Treatment-induced changes	2.5 ± 0.5		1.9 ± 0.4	

TABLE 3 | GR diagnostic performance of static and dynamic ^{18}F-FET PET parameters.

	SUVmax	TBRmax	TTP	MTV	TLM
Cutoff Value	≥3.5	≥2.1	≤29 min	≥0.15 ml	≥0.33 ml
Sensitivity [95% CI]	48.3 [29.4–67.5]	79.3 [60.3–92.0]	68.8 [41.3–89.0]	86.2 [68.3–96.1]	86.2 [68.3–96.1]
Specificity [95% CI]	93.8 [69.8–99.8]	75.0 [47.6–92.7]	82.8 [64.2–94.2]	81.3 [54.3–95.9]	81.3 [54.3–95.9]
AUC ± SE	71.1 ± 0.08	78.0 ± 0.07	70.4 ± 0.09	85.4 ± 0.07	85.4 ± 0.06

TABLE 4 | Univariate analysis.

Parameters	Criterion	PFS		OS	
		p value	Median PFS time	p value	Median OS time
Age	≥50 years *vs.* <50 years	0.707	2.3 *vs.* 2.6 months	0.150	26.0 months *vs.* OS not reached
Resection	biopsy *vs.* complete/partial resection	0.782	2.3 *vs.* 5.5 months	0.607	26.0 months *vs.* OS not reached
WHO grade	IV *vs.* III/II	0.872	2.3 *vs.* 2.6 months	0.855	26.0 months *vs.* OS not reached
IDH status	mutant *vs.* wildtype	0.588	2.3 *vs.* 2.9 months	0.162	26 *vs.* 21.6 months
MGMT promoter	non-methylated *vs.* methylated	0.263	3.0 *vs.* 2.2 months	0.684	21.6 *vs.* 26 months
KPS	≥80 *vs.* <80	***0.0002***	3.8 *vs.* 1.2 months	***0.0013***	7.7 months *vs.* OS not reached
Prior relapses	yes/no	0.315	2.4 *vs.* 7.5 months	0.329	21.6 months *vs.* OS not reached
^{18}F-FET outcome	positive *vs.* negative	***<0.0001***	1.4 *vs.* 14.7 months	0.405	16.9 *vs.* 26.1 months
SUVmax	≥3.5 *vs.* <3.5	***0.0009***	1.2 *vs.* 3.6 months	0.094	10.4 months *vs.* OS not reached
TBRmax	≥2.1 *vs.* <2.1	***<0.0001***	1.7 *vs.* 14.3 months	0.300	21.6 months *vs.* OS not reached
TTP	<29 min *vs.* ≥29 min	***0.0044***	1.4 *vs.* 10.4 months	0.307	21.6 months *vs.* OS not reached
MTV	≥0.15 ml *vs.* <0.15 ml	***0.0001***	1.4 *vs.* 14.7 months	0.365	26.1 months *vs.* 16.9 months
TTM	≥0.33 ml *vs.* <0.33 ml	***0.0001***	1.4 *vs.* 14.7 months	0.405	26.1 months *vs.* 16.9 months

IDH, isocitrate dehydrogenase; MGMT, O[6]-methylguanine-DNA methyltransferase; KPS, Karnofsky Performance Scale; MTV, metabolic tumor volume; TTM, total tumor metabolism; PFS, progression-free survival; OS, overall survival. The bold italicized values means statistically significant.

FET PET, documents a diagnostic performance, slightly inferior to evidence from previously published literature with a sensitivity of 86.2% (95% CI: 68.3–96.1%) and a specificity of 81.3% (95% CI: 54.4–96.1%).

A recent meta-analysis by de Zwart et al. analyzed 10 studies on ^{18}F-FET PET (of these, three abstracts; 207 scans overall) in treated glioma patients with suspect GR, documenting a pooled sensitivity and specificity of 90% (95% CI, 81–95%) and 85% (95% CI, 71–93%). A meta-analysis from Kim et al. considering six studies on ^{18}F-FET PET (212 scans overall) in this clinical scenario found a pooled sensitivity and specificity of 89% (95% CI, 82–94%) and 88% (95% CI, 76–94%) (26, 27).

A recent retrospective study on a large cohort of treated WHO II-IV glioma patients (n = 127) by Maurer et al. also documented slightly inferior accuracy, with sensitivity, specificity, and accuracy of 86, 67, and 81%, respectively. The Authors found that ^{18}F-FET PET diagnostic performance, both in terms of sensitivity and specificity, was negatively affected by

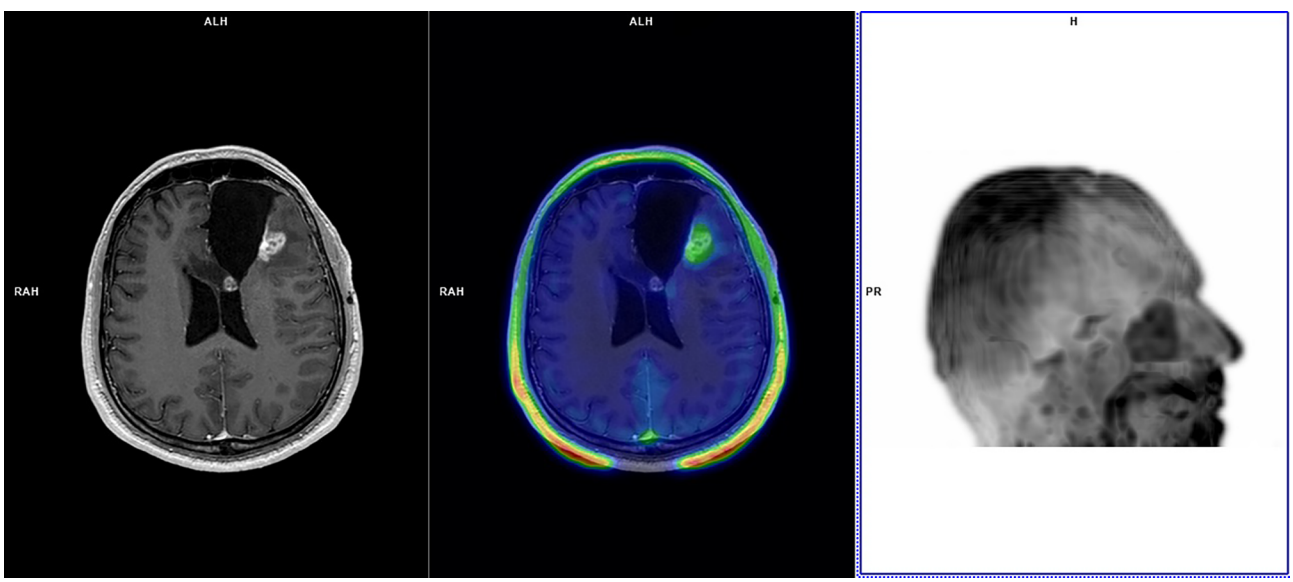

FIGURE 1 | A 35-year-old patient with left frontal glioblastoma (IDH wild-type; MGMT methylated) treated with partial resection in August 2017, chemoradiation (completed in November 2017), and four cycles of adjuvant temozolomide (last cycle in March 2018). In August 2018, left frontal cavity re-irradiation was performed for glioblastoma relapse. Follow-up MRI scans in November 2018 demonstrated an increasing pseudonodular area of contrast-enhancement along the left frontal surgical cavity without functional indices abnormalities, deemed dubious for GR. ^{18}F-FET PET performed in December 2018 demonstrated faint tracer uptake at late static imaging (TBRmax: 1.6) and TAC pattern 3 with TTP at 35 min. ^{18}F-FET PET was considered suggestive of TICs. MRI demonstrated disease progression in August 2019 (PFS: 8 months; OS not reached), and bevacizumab was commenced. At last MRI follow-up (January 2021) MRI demonstrated stable disease.

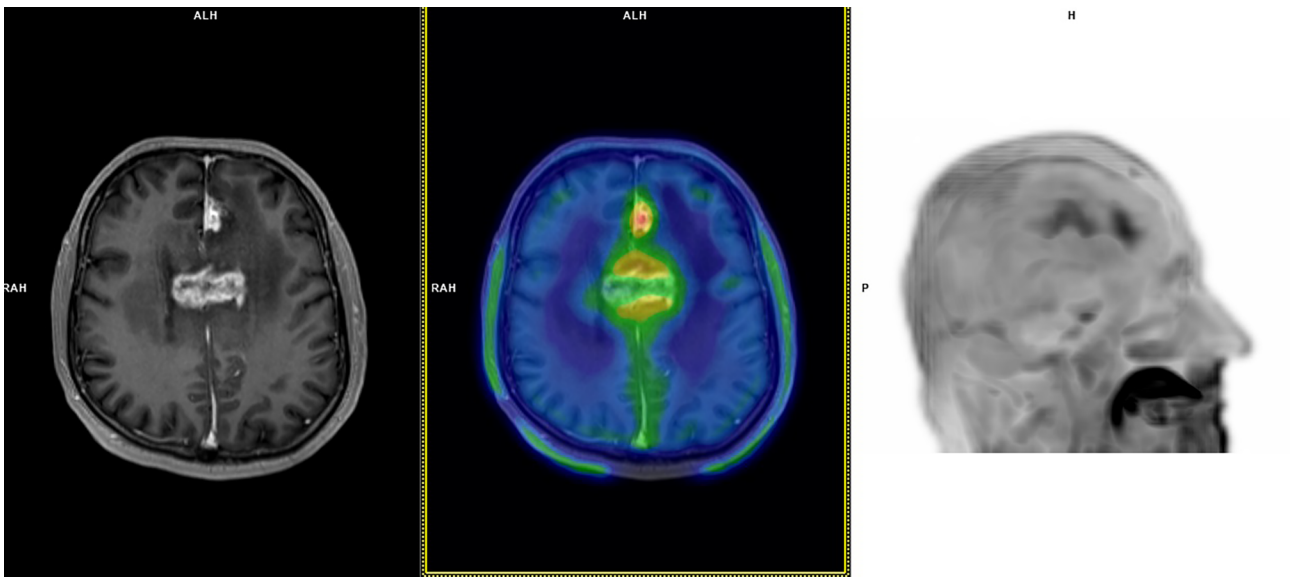

FIGURE 2 | A 60-year-old patient with bioptic diagnosis of astrocytoma WHO grade 3 with lesions in the left frontal lobe and corpus callosum (IDH wild-type; MGMT methylated) treated with chemoradiation (completed in March 2018) and re-irradiation in July 2018. Follow-up MRI scans in October 2018 documented an increasing T2/FLAIR signal and irregular contrast-enhancement at the medial aspect of the left frontal lobe and corpus callosum; no diffusion restriction was seen, and perfusion weighted imaging demonstrated slight increase in Ktrans e Ve values without abnormal Vp. MRI appearances were deemed dubious for GR, favouring the hypothesis of TICs. ^{18}F-FET PET performed in November 2018 demonstrated focal tracer uptake at late static imaging (TBRmax: 3.4), a TAC pattern with a TTP at 20 min and subsequent plateau (TAC pattern 2). ^{18}F-FET PET was considered suggestive of GR. MRI performed in January 2019 documented GR, and chemotherapy was started. This patient died in July 2019 (PFS: 1 month; OS: 8 months).

the presence of IDH mutations (diagnostic accuracy was 91% in IDH-wild-type gliomas and 67% in IDH-mutant gliomas; $p < 0.001$) (28).

In our study cohort, 16 patients (35.6% cases) had IDH-mutant gliomas, a proportion comparable to the 40% of IDH-mutant patients in Maurer's cohort. We could observe reduced ^{18}F-FET PET diagnostic accuracy for the identification of recurrent IDH-mutant gliomas compared to IDH-wild-type gliomas mainly due to decreased sensitivity (SE: 81.8 *versus* 88.9%; SP: 80.8 *versus* 81.8%). Irrespective of the IDH status, ^{18}F-FET PET false negativity may depend on low cellularity of GR, on small-sized viable glioma components, on GR low or defective expression of amino-acid transporter LAT2. We speculate that the relatively higher incidence of low ^{18}F-FET uptake in IDH-mutant gliomas may be consequent on metabolic reprogramming leading to reduced amino acid exchange *via* the LAT2 antiport. Glioma IDH-mutant genotype has also been found to induce immune quiescence in the tumor microenvironment, which also may account for furtherly reduced ^{18}F-FET non-specific uptake (29).

All three cases of ^{18}F-FET PET false positivity were IDH wild-type glioblastomas, and in one case hypofractionated re-

TABLE 5 | Multivariate analysis.

Parameters	Criteria	PFS [95% CI]		OS [95% CI]	
		Hazard ratio	p-value	Hazard ratio	p-value
Age	≥50 years	1.25 [0.54–2.89]	0.598	***11.43 [1.59–82.16]***	***0.015***
Primary Surgery	non-total resection	0.75 [0.15–3.73]	0.724	39.993	0.994
WHO grade	IV grade	0.92 [0.42–2.02]	0.834	0.40 [0.08–2.06]	0.275
IDH status	wild-type	0.35 [0.11–1.08]	0.069	0.07 [0.01–0.70]	0.023
MGMT promoter	unmethylated	1.29 [0.57–2.91]	0.543	0.47 [0.09–2.44]	0.373
Prior relapses	yes	0.81 [0.31–2.07]	0.656	4.20 [0.55–32.04]	0.166
KPS	<80	2.20 [0.87–5.53]	0.094	***55.98 [3.92–798.75]***	***0.003***
^{18}F-FET outcome	positive	***8.91 [2.62–30.29]***	***0.0005***	0.47 [0.04–5.24]	0.539
MTV	≥0.15 ml	1.0 [1.0–1.0]	<0.0001	1.0 [1.0–1.0]	<0.0001
TTM	≥0.33 ml	1.0 [1.0–1.0]	<0.0001	1.0 [1.0–1.0]	<0.0001

IDH, isocitrate dehydrogenase; MGMT, O[6]-methylguanine-DNA methyltransferase; KPS, Karnofsky Performance Scale; MTV, metabolic tumor volume; TTM, total tumor metabolism; PFS, progression-free survival; OS, overall survival.
The bold italicized values means statistically significant.

irradiation had been previously performed. Higher rates of radionecrosis have been associated with higher radiation doses, with volume of the target lesion, and with re-irradiation (30–32).

Radiation-induced injury involves a degree of inflammatory response, ischemia, and infarction of brain areas and may result in high ^{18}F-FET unspecific uptake (33–41).

As opposed to evidence from ^{18}F-FET PET studies conducted on newly diagnosed gliomas, in the post-treatment scenario, we did not observe any significant dependence of ^{18}F-FET metrics on WHO grade, glial type, and IDH status; this lack of association possibly depends on a more heterogeneous metabolic composition of post-treatment changes and GR.

^{18}F-FET outcome (positive or negative) was significantly different between patients with KPS ≥ 80 and KPS < 80, possibly representing a degree of association with GR-related clinical deterioration.

The ROC curve analysis obtained by comparison with the standard of reference in this late post-treatment scenario (i.e., more than 12 weeks from the last radiation treatment) returned a ^{18}F-FET TBRmax cutoff (≥2.1) slightly higher than that of 1.9 suggested by intersocietal practice guidelines, but equal or very similar to that found in the studies by Popperl (TBRmax ≥ 2.2), Galldiks (TBRmax ≥ 2.0), Kebir (TBRmax ≥ 2.1), Sogani (TBRmax ≥ 2.09), Bashir (TBRmax ≥ 2.0), and Maurer (TBRmax ≥ 1.95). TBRmax was found to be the most accurate ^{18}F-FET semiquantitative imaging biomarker for GR compared to lesion SUVmax and TTP, returning a sensitivity, specificity, and AUC of 79.3, 75.0, 78.0%, respectively (17, 20, 22, 24, 28).

Cutoffs for the ^{18}F-FET TBRmax-dependent volumetric parameters MTV and TTM were also found accurate with identical sensitivity, specificity, and AUC of 86.2, 81.3, 85.4%, respectively.

Given the possible co-existence of TICs and GR in the same patient, we introduced a new reproducible and patient-adapted method for segmenting ^{18}F-FET-based MTV and compute its derived parameter TTM. First, MTV was computable only in those cases where pathological TBRmax for GR was yielded, this prerequisite increasing specificity for GR segmentation. Secondly, to draw the presumed GR-specific MTV, we exclusively considered the lesion metabolic volume encompassing all SUVmax values that divided by the healthy brain SUVmean would return a TBRmax suggestive for GR. This condition was added in order to discard SUVmax values attributable to TICs. Survival-wise, this method easily produced volumetric metabolic parameters found to negatively impact PFS but not OS.

We believe that this inability of MTV and TTM to predict OS mainly depends on the heterogeneity of ^{18}F-FET PET timing in patients' clinical histories. In their retrospective study, Bashir et al. investigated the prognostic value of ^{18}F-FET-derived biological tumor volume (BTV) performed 6 months after radiation therapy completion in 146 glioblastoma patients (24). In their homogeneous cohort of patients, BTV (cutoff value = 0.55cc) was found to be a strong predictor of OS both at univariate (HR 1.303, $p < 0.0001$) and multivariate analyses (HR 1.339, $p < 0.0001$). A significant association with OS was demonstrated for patients' performance status, whereas the extent of surgery, age, MGMT promoter status, and IDH status did not predict patients' OS in glioma recurrence.

We caution on several limitations to this study. The retrospective design of the analysis may introduce selection bias. Only patients referred to multidisciplinary team discussions by internal medical and radiation oncologists had the chance to access FET PET imaging and exclusively in those cases where the review of MRI findings by the neuro-radiologists could not confidently discern the tumor or treatment-related nature of such findings. This preselection bias might limit the extrapolation of the present study results to the external clinical settings. In this study, the proportion of patients with confirmation of TIC was 35.5% (16 out of 45 patients), a datum falling at the highest end of the predicted incidence of pseudo-progression/radionecrosis. The standard of reference, prevalently based on repeat MRI and clinical follow-up, possibly leads to misclassification in some cases. The small sample size and its heterogeneity, the different type and number of treatments undergone by included patients. PFS and OS were calculated from the date of ^{18}F-FET PET. This computation may have potentially biased the prognostic weight of well-established prognostic metrics such as age at time of ^{18}F-FET (as this does not take into account the differing number of previous treatments), WHO grade, IDH status, MGMT status, and histotypes (astrocytic versus oligodendroglial).

In the present study, we could not evaluate associations between ^{18}F-FET PET and advanced MRI techniques or MRI spectroscopy. A small number of retrospective studies evaluated the feasibility and clinical value of simultaneous and sequential ^{8}F-FET PET/advanced MRI in differentiating GR from TIC. In a retrospective cohort of 104 treated glioma patients with suspected GR, Steidl et al. investigated the diagnostic performance of sequential perfusion-weighted MRI (PWI) and ^{18}F-FET PET. The authors found that high hyperperfusion defined by normalized maximum relative cerebral blood volume (rCBVmax: 2.85) could correctly identify GR in 42.3% of cases, whereas in the remaining 57.7% of cases, its poor negative predictive value (NPV = 36%) could be surpassed by the addition of static and dynamic ^{18}F-FET PET parameters, increasing diagnostic accuracy to 78%. The authors found that in the subgroup of IDH-mutant GR, PWI held superior diagnostic accuracy than ^{18}F-FET PET (PWI AUC: 80%; ^{18}F-FET AUC: 62%) (42).

In their retrospective study on 32 treated glioma patients undergoing simultaneous ^{18}F-FET PET/MRI and MRI spectroscopy to identify suspect GR, Sogani et al. found that the addition of ^{18}F-FET parameters slightly improved sensitivity of advanced MRI and magnetic resonance spectroscopy (MRS), with sensitivity, specificity, and diagnostic accuracy of 100, 85.7, and 96.87% for ^{18}F-FET PET/MRI and 96, 85.7, and 93.75% for advanced MRI and MRS (43).

The authors found significant positive correlations between TBR_{max} and TBR_{mean} and normalized $rCBV_{mean}$ and significant negative correlations between between $TBR_{max\ and}$ mean apparent diffusion coefficient ADC_{mean}. The spectroscopy-derived Choline/Creatinine ratio alone showed a sensitivity, specificity, and accuracy of 96, 85.7, 93.75%, respectively. No significant correlation was found between ^{18}F-FET TBRmax and TBR_{mean} and Choline/Creatinine ratio.

Despite the encouraging results of multimodal ^{18}F-FET PET/MRI, there remains a highly variable range of PWI parameter cutoffs, which strongly limits semiquantitative PWI reproducibility across centers.

Prospectively designed studies in larger and more homogeneous cohorts of pretreated glioma patients, possibly conjugating ^{18}F-FET PET and advanced MRI and MRS biomarkers, would better elucidate the complementary interplay of metabolic abnormalities underlying glioma recurrence and its prognosis.

5 CONCLUSIONS

^{18}F-FET PET demonstrated good diagnostic performance in discriminating GR and TICs, yielding higher accuracy in the assessment of IDH-wildtype gliomas as compared to IDH-mutant gliomas.

Among all considered prognostic parameters, only KPS was found to significantly differ according to ^{18}F-FET PET outcome.

^{18}F-FET PET outcome significantly predicted PFS in the whole studied cohort as well as in the sub-cohort of patients with high KPS.

Despite the heterogeneity of previous treatments, histological and molecular types of gliomas, and patient performance status, ^{18}F-FET PET-positive outcome remained the only predictor of PFS at multivariate analysis.

Neither ^{18}F-FET PET outcome/metrics nor volumetric metabolic parameters MTV and TTM were found instantly predictive of OS. KPS and age were the only predictors of OS in this cohort of patients.

DATA AVAILABILITY STATEMENT

The raw data supporting the conclusions of this article will be made available by the authors, without undue reservation.

ETHICS STATEMENT

The studies involving human participants were reviewed and approved by IRST IRCCS AVR. Written informed consent for participation was not required for this study in accordance with the national legislation and the institutional requirements.

AUTHOR CONTRIBUTIONS

MC, PCa, and FM reported ^{18}F-FET PET scans, designed the research, analyzed the results, and wrote the manuscript. EA and PCe reported brain MRI scans, verified the analytical methods, and supervised the findings of this work. DA, LG, GG, and GP contributed to the design and clinical implementation of this research. All authors discussed the results and contributed to the draft of this manuscript. All authors contributed to the article and approved the submitted version.

ACKNOWLEDGMENTS

The authors would like to thank Gráinne Tierney for her editorial assistance.

REFERENCES

1. Stupp R, Brada M, van den Bent MJ, Tonn JC, Pentheroudakis G, Group EGW. High-Grade Glioma: ESMO Clinical Practice Guidelines for Diagnosis, Treatment and Follow-Up. *Ann Oncol* (2014) 25 Suppl 3:iii93–101. doi: 10.1093/annonc/mdu050
2. Crocetti E, Trama A, Stiller C, Caldarella A, Soffietti R, Jaal J, et al. Epidemiology of Glial and Non-Glial Brain Tumours in Europe. *Eur J Cancer* (2012) 48(10):1532–42. doi: 10.1016/j.ejca.2011.12.013
3. van den Bent MJ, Wefel JS, Schiff D, Taphoorn MJ, Jaeckle K, Junck L, et al. Response Assessment in Neuro-Oncology (a Report of the RANO Group): Assessment of Outcome in Trials of Diffuse Low-Grade Gliomas. *Lancet Oncol* (2011) 12(6):583–93. doi: 10.1016/S1470-2045(11)70057-2
4. Chukwueke UN, Wen PY. Use of the Response Assessment in Neuro-Oncology (RANO) Criteria in Clinical Trials and Clinical Practice. *CNS Oncol* (2019) 8(1):CNS28. doi: 10.2217/cns-2018-0007
5. Brandsma D, Stalpers L, Taal W, Sminia P, van den Bent MJ. Clinical Features, Mechanisms, and Management of Pseudoprogression in Malignant Gliomas. *Lancet Oncol* (2008) 9(5):453–61. doi: 10.1016/S1470-2045(08)70125-6
6. Kruser TJ, Mehta MP, Robins HI. Pseudoprogression After Glioma Therapy: A Comprehensive Review. *Expert Rev Neurother* (2013) 13(4):389–403. doi: 10.1586/ern.13.7
7. Abbasi AW, Westerlaan HE, Holtman GA, Aden KM, van Laar PJ, van der Hoorn A. Incidence of Tumour Progression and Pseudoprogression in High-Grade Gliomas: A Systematic Review and Meta-Analysis. *Clin Neuroradiol* (2018) 28(3):401–11. doi: 10.1007/s00062-017-0584-x
8. Delgado-López PD, Riñones-Mena E, Corrales-García EM. Treatment-Related Changes in Glioblastoma: A Review on the Controversies in Response Assessment Criteria and the Concepts of True Progression, Pseudoprogression, Pseudoresponse and Radionecrosis. *Clin Transl Oncol* (2018) 20(8):939–53. doi: 10.1007/s12094-017-1816-x
9. Albert NL, Weller M, Suchorska B, Galldiks N, Soffietti R, Kim MM, et al. Response Assessment in Neuro-Oncology Working Group and European Association for Neuro-Oncology Recommendations for the Clinical Use of PET Imaging in Gliomas. *Neuro-Oncology* (2016) 18(9):1199–208. doi: 10.1093/neuonc/now058
10. Heiss P, Mayer S, Herz M, Wester HJ, Schwaiger M, Senekowitsch-Schmidtke R, et al. Investigation of Transport Mechanism and Uptake Kinetics of O-(2-[18F]Fluoroethyl)-L-Tyrosine *In Vitro* and *In Vivo*. *J Nucl Med* (1999) 40 (8):1367–73.
11. Langen K-J, Jarosch M, Mühlensiepen H, Hamacher K, Bröer S, Jansen P, et al. Comparison of Fluorotyrosines and Methionine Uptake in F98 Rat Gliomas. *Nucl Med Biol* (2003) 30(5):501–8. doi: 10.1016/S0969-8051(03)00023-4
12. Kobayashi K, Ohnishi A, Promsuk J, Shimizu S, Kanai Y, Shiokawa Y, et al. Enhanced Tumor Growth Elicited by L-Type Amino Acid Transporter 1 in Human Malignant Glioma Cells. *Neurosurgery* (2008) 62(2):493–503; discussion 4. doi: 10.1227/01.neu.0000316018.51292.19
13. Lahoutte T, Caveliers V, Camargo SM, Franca R, Ramadan T, Veljkovic E, et al. SPECT and PET Amino Acid Tracer Influx *via* System L (H4f2hc-Hlat1) and Its Transstimulation. *J Nucl Med* (2004) 45(9):1591–6.
14. Stöber B, Tanase U, Herz M, Seidl C, Schwaiger M, Senekowitsch-Schmidtke R. Differentiation of Tumour and Inflammation: Characterisation of [Methyl-3H]Methionine (MET) and O-(2-[18F]Fluoroethyl)-L-Tyrosine (FET) Uptake in Human Tumour and Inflammatory Cells. *Eur J Nucl Med Mol Imaging* (2006) 33(8):932–9. doi: 10.1007/s00259-005-0047-5
15. Stegmayr C, Oliveira D, Niemietz N, Willuweit A, Lohmann P, Galldiks N, et al. Influence of Bevacizumab on Blood-Brain Barrier Permeability and O-(2-18f-Fluoroethyl)-L-Tyrosine Uptake in Rat Gliomas. *J Nucl Med: Off Publication Soc Nucl Med* (2017) 58(5):700–5. doi: 10.2967/jnumed.116.187047

16. Stegmayr C, Willuweit A, Lohmann P, Langen KJ. O-(2-[18f]-Fluoroethyl)-L-Tyrosine (FET) in Neurooncology: A Review of Experimental Results. *Curr Radiopharm* (2019) 12(3):201–10. doi: 10.2174/1874471012666190111111046
17. Pöpperl G, Götz C, Rachinger W, Gildehaus FJ, Tonn JC, Tatsch K, et al. Value of O-(2-[18F]Fluoroethyl)- L-Tyrosine PET for the Diagnosis of Recurrent Glioma. *Eur J Nucl Med Mol Imaging* (2004) 31(11):1464–70. doi: 10.1007/s00259-004-1590-1
18. Rachinger W, Goetz C, Pöpperl G, Gildehaus FJ, Kreth FW, Holtmannspötter M, et al. Positron Emission Tomography With O-(2-[18F]Fluoroethyl)-L-Tyrosine *Versus* Magnetic Resonance Imaging in the Diagnosis of Recurrent Gliomas. *Neurosurgery* (2005) 57(3):505–11. doi: 10.1227/01.NEU.0000171642.49553.B0
19. Mehrkens JH, Pöpperl G, Rachinger W, Herms J, Seelos K, Tatsch K, et al. The Positive Predictive Value of O-(2-[18F]Fluoroethyl)-L-Tyrosine (FET) PET in the Diagnosis of a Glioma Recurrence After Multimodal Treatment. *J Neurooncol* (2008) 88(1):27–35. doi: 10.1007/s11060-008-9526-4
20. Galldiks N, Dunkl V, Stoffels G, Hutterer M, Rapp M, Sabel M, et al. Diagnosis of Pseudoprogression in Patients With Glioblastoma Using O-(2-[18F] Fluoroethyl)-L-Tyrosine PET. *Eur J Nucl Med Mol Imaging* (2015) 42 (5):685–95. doi: 10.1007/s00259-014-2959-4
21. Galldiks N, Stoffels G, Filss C, Rapp M, Blau T, Tscherpel C, et al. The Use of Dynamic O-(2-18F-Fluoroethyl)-L-Tyrosine PET in the Diagnosis of Patients With Progressive and Recurrent Glioma. *Neuro-oncology* (2015) 17(9):1293–300. doi: 10.1093/neuonc/nov088
22. Kebir S, Fimmers R, Galldiks N, Schäfer N, Mack F, Schaub C, et al. Late Pseudoprogression in Glioblastoma: Diagnostic Value of Dynamic O-(2-[18F] Fluoroethyl)-L-Tyrosine PET. *Clin Cancer Res* (2016) 22(9):2190–6. doi: 10.1158/1078-0432.CCR-15-1334
23. Kebir S, Khurshid Z, Gaertner FC, Essler M, Hattingen E, Fimmers R, et al. Unsupervised Consensus Cluster Analysis of [18F]-Fluoroethyl-L-Tyrosine Positron Emission Tomography Identified Textural Features for the Diagnosis of Pseudoprogression in High-Grade Glioma. *Oncotarget* (2017) 8(5):8294–304. doi: 10.18632/oncotarget.14166
24. Bashir A, Mathilde Jacobsen S, Mølby Henriksen O, Broholm H, Urup T, Grunnet K, et al. Recurrent Glioblastoma *Versus* Late Posttreatment Changes: Diagnostic Accuracy of O-(2-[18F]Fluoroethyl)-L-Tyrosine Positron Emission Tomography (18F-FET PET). *Neuro Oncol* (2019) 21(12):1595–606. doi: 10.1093/neuonc/noz166
25. Law I, Albert NL, Arbizu J, Boellaard R, Drzezga A, Galldiks N, et al. Joint EANM/EANO/RANO Practice Guidelines/SNMMI Procedure Standards for Imaging of Gliomas Using PET With Radiolabelled Amino Acids and [(18)F] FDG: Version 1.0. *Eur J Nucl Med Mol Imaging* (2019) 46(3):540–57. doi: 10.1007/s00259-018-4207-9
26. de Zwart PL, van Dijken BRJ, Holtman GA, Stormezand GN, Dierckx RAJO, Jan van Laar P, et al. Diagnostic Accuracy of PET Tracers for the Differentiation of Tumor Progression From Treatment-Related Changes in High-Grade Glioma: A Systematic Review and Metaanalysis. *J Nucl Med* (2020) 61(4):498–504. doi: 10.2967/jnumed.119.233809
27. Kim SJ, Ryul Shim S. Diagnostic Value of Radiolabeled Amino Acid PET for Detection of Pseudoprogression of Brain Tumor After Treatment: A Meta-Analysis. *Nucl Med Commun* (2019) 40(9):965–72. doi: 10.1097/MNM.0000000000001060
28. Maurer GD, Brucker DP, Stoffels G, Filipski K, Filss CP, Mottaghy FM, et al. F-FET PET Imaging in Differentiating Glioma Progression From Treatment-Related Changes: A Single-Center Experience. *J Nucl Med* (2020) 61(4):505–11. doi: 10.2967/jnumed.119.234757
29. Richardson LG, Choi BD, Curry WT. (R)-2-Hydroxyglutarate Drives Immune Quiescence in the Tumor Microenvironment of IDH-Mutant Gliomas. *Transl Cancer Res* (2019) 8(Suppl 2):S167–70. doi: 10.21037/tcr.2019.01.08
30. Shaw E, Scott C, Souhami L, Dinapoli R, Bahary JP, Kline R, et al. Radiosurgery for the Treatment of Previously Irradiated Recurrent Primary Brain Tumors and Brain Metastases: Initial Report of Radiation Therapy Oncology Group Protocol (90-05). *Int J Radiat Oncol Biol Phys* (1996) 34 (3):647–54. doi: 10.1016/0360-3016(95)02106-X
31. Korytko T, Radivoyevitch T, Colussi V, Wessels BW, Pillai K, Maciunas RJ, et al. 12 Gy Gamma Knife Radiosurgical Volume Is a Predictor for Radiation Necrosis in Non-AVM Intracranial Tumors. *Int J Radiat Oncol Biol Phys* (2006) 64(2):419–24. doi: 10.1016/j.ijrobp.2005.07.980
32. Blonigen BJ, Steinmetz RD, Levin L, Lamba MA, Warnick RE, Breneman JC, et al. Irradiated Volume as a Predictor of Brain Radionecrosis After Linear Accelerator Stereotactic Radiosurgery. *Int J Radiat Oncol Biol Phys* (2010) 77 (4):996–1001. doi: 10.1016/j.ijrobp.2009.06.006
33. Floeth FW, Pauleit D, Sabel M, Reifenberger G, Stoffels G, Stummer W, et al. 18f-FET PET Differentiation of Ring-Enhancing Brain Lesions. *J Nucl Med* (2006) 47(5):776–82.
34. Salber D, Stoffels G, Pauleit D, Reifenberger G, Sabel M, Shah NJ, et al. Differential Uptake of [18F]FET and [3H]L-Methionine in Focal Cortical Ischemia. *Nucl Med Biol* (2006) 33(8):1029–35. doi: 10.1016/j.nucmedbio.2006.09.004
35. Salber D, Stoffels G, Pauleit D, Oros-Peusquens AM, Shah NJ, Klauth P, et al. Differential Uptake of O-(2-18F-Fluoroethyl)-L-Tyrosine, L-3H-Methionine, and 3H-Deoxyglucose in Brain Abscesses. *J Nucl Med: Off Publication Soc Nucl Med* (2007) 48(12):2056–62. doi: 10.2967/jnumed.107.046615
36. Salber D, Stoffels G, Oros-Peusquens AM, Shah NJ, Reifenberger G, Hamacher K, et al. Comparison of O-(2-18F-Fluoroethyl)-L-Tyrosine and L-3H-Methionine Uptake in Cerebral Hematomas. *J Nucl Med* (2010) 51 (5):790–7. doi: 10.2967/jnumed.109.071423
37. Hutterer M, Ebner Y, Riemenschneider MJ, Willuweit A, McCoy M, Egger B, et al. Epileptic Activity Increases Cerebral Amino Acid Transport Assessed by 18F-Fluoroethyl-L-Tyrosine Amino Acid PET: A Potential Brain Tumor Mimic. *J Nucl Med* (2017) 58(1):129–37. doi: 10.2967/jnumed.116.176610
38. Langen KJ, Galldiks N. Reply to "[18F]-Fluoro-Ethyl-L-Tyrosine PET: A Valuable Diagnostic Tool in Neuro-Oncology, But Not All That Glitters Is Glioma" by Hutterer Et Al. *Neuro Oncol* (2013) 15(7):816–7. doi: 10.1093/neuonc/not059
39. Piroth MD, Prasath J, Willuweit A, Stoffels G, Sellhaus B, van Osterhout A, et al. Uptake of O-(2-[18F]Fluoroethyl)-L-Tyrosine in Reactive Astrocytosis in the Vicinity of Cerebral Gliomas. *Nucl Med Biol* (2013) 40(6):795–800. doi: 10.1016/j.nucmedbio.2013.05.001
40. Zinnhardt B, Pigeon H, Thézé B, Viel T, Wachsmuth L, Fricke IB, et al. Combined PET Imaging of the Inflammatory Tumor Microenvironment Identifies Margins of Unique Radiotracer Uptake. *Cancer Res* (2017) 77 (8):1831–41. doi: 10.1158/0008-5472.CAN-16-2628
41. Weiss HJ, Angiari S. Metabolite Transporters as Regulators of Immunity. *Metabolites* (2020) 10(10):418. doi: 10.3390/metabo10100418
42. Steidl E, Langen KJ, Hmeidan SA, Polomac N, Filss CP, Galldiks N, et al. Sequential Implementation of DSC-MR Perfusion and Dynamic. *Eur J Nucl Med Mol Imaging* (2020) 48(6):1956–65. doi: 10.1007/s00259-020-05114-0
43. Sogani SK, Jena A, Taneja S, Gambhir A, Mishra AK, D'Souza MM, et al. Potential for Differentiation of Glioma Recurrence From Radionecrosis Using Integrated 18F-Fluoroethyl-L-Tyrosine (FET) Positron Emission Tomography/Magnetic Resonance Imaging: A Prospective Evaluation. *Neurol India* (2017) 65(2):293–301. doi: 10.4103/neuroindia.NI_101_16

Conflict of Interest: The authors declare that the research was conducted in the absence of any commercial or financial relationships that could be construed as a potential conflict of interest.

Publisher's Note: All claims expressed in this article are solely those of the authors and do not necessarily represent those of their affiliated organizations, or those of the publisher, the editors and the reviewers. Any product that may be evaluated in this article, or claim that may be made by its manufacturer, is not guaranteed or endorsed by the publisher.

Copyright © 2021 Celli, Caroli, Amadori, Arpa, Gurrieri, Ghigi, Cenni, Paganelli and Matteucci. This is an open-access article distributed under the terms of the Creative Commons Attribution License (CC BY). The use, distribution or reproduction in other forums is permitted, provided the original author(s) and the copyright owner(s) are credited and that the original publication in this journal is cited, in accordance with accepted academic practice. No use, distribution or reproduction is permitted which does not comply with these terms.

frontiers in Oncology

ORIGINAL RESEARCH
published: 05 October 2021
doi: 10.3389/fonc.2021.735257

Dynamic ^{18}F-FDopa PET Imaging for Newly Diagnosed Gliomas: Is a Semiquantitative Model Sufficient?

*Timothée Zaragori[1,2], Matthieu Doyen[1,2], Fabien Rech[3,4], Marie Blonski[4,5], Luc Taillandier[4,5], Laëtitia Imbert[1,2] and Antoine Verger[1,2]**

[1] Department of Nuclear Medicine and Nancyclotep Imaging Platform, CHRU-Nancy, Université de Lorraine, Nancy, France, [2] IADI UMR 1254, INSERM, Université de Lorraine, Nancy, France, [3] Department of Neurosurgery, CHRU-Nancy, Université de Lorraine, Nancy, France, [4] Centre de Recherche en Automatique de Nancy CRAN UMR 7039, CNRS, Université de Lorraine, Nancy, France, [5] Department of Neuro-Oncology, CHRU-Nancy, Université de Lorraine, Nancy, France*

OPEN ACCESS

Edited by:
Sandro Krieg, Technical University of Munich, Germany

Reviewed by:
Thomas Pyka, Klinikum Dritter Orden, Germany
Nico Sollmann, University of California, San Francisco, United States

***Correspondence:**
Antoine Verger
a.verger@chru-nancy.fr

Specialty section:
This article was submitted to Neuro-Oncology and Neurosurgical Oncology, a section of the journal Frontiers in Oncology

Received: *02 July 2021*
Accepted: *06 September 2021*
Published: *05 October 2021*

Citation:
Zaragori T, Doyen M, Rech F, Blonski M, Taillandier L, Imbert L and Verger A (2021) Dynamic ^{18}F-FDopa PET Imaging for Newly Diagnosed Gliomas: Is a Semiquantitative Model Sufficient? Front. Oncol. 11:735257. doi: 10.3389/fonc.2021.735257

Purpose: Dynamic amino acid positron emission tomography (PET) has become essential in neuro-oncology, most notably for its prognostic value in the noninvasive prediction of isocitrate dehydrogenase (IDH) mutations in newly diagnosed gliomas. The 6-[^{18}F]fluoro-L-DOPA (^{18}F-FDOPA) kinetic model has an underlying complexity, while previous studies have predominantly used a semiquantitative dynamic analysis. Our study addresses whether a semiquantitative analysis can capture all the relevant information contained in time–activity curves for predicting the presence of IDH mutations compared to the more sophisticated graphical and compartmental models.

Methods: Thirty-seven tumour time–activity curves from ^{18}F-FDOPA PET dynamic acquisitions of newly diagnosed gliomas (median age = 58.3 years, range = 20.3–79.9 years, 16 women, 16 IDH-wild type) were analyzed with a semiquantitative model based on classical parameters, with (SQ) or without (Ref SQ) a reference region, or on parameters of a fit function (SQ Fit), a graphical Logan model with input function (Logan) or reference region (Ref Logan), and a two-tissue compartmental model previously reported for ^{18}F-FDOPA PET imaging of gliomas (2TCM). The overall predictive performance of each model was assessed with an area under the curve (AUC) comparison using multivariate analysis of all the parameters included in the model. Moreover, each extracted parameter was assessed in a univariate analysis by a receiver operating characteristic curve analysis.

Results: The SQ model with an AUC of 0.733 for predicting IDH mutations showed comparable performance to the other models with AUCs of 0.752, 0.814, 0.693, 0.786, and 0.863, respectively corresponding to SQ Fit, Ref SQ, Logan, Ref Logan, and 2TCM ($p \geq 0.10$ for the pairwise comparisons with other models). In the univariate analysis, the SQ time-to-peak parameter had the best diagnostic performance (75.7% accuracy) compared to all other individual parameters considered.

Conclusions: The SQ model circumvents the complexities of the ^{18}F-FDOPA kinetic model and yields similar performance in predicting IDH mutations when compared to the other models, most notably the compartmental model. Our study provides supportive evidence for the routine clinical application of the SQ model for the dynamic analysis of ^{18}F-FDOPA PET images in newly diagnosed gliomas.

Keywords: DOPA, PET, compartmental modeling, dynamic analysis, glioma, IDH mutation

INTRODUCTION

As an adjunct to magnetic resonance imaging (MRI), amino acid positron emission tomography (PET) imaging provides additional diagnostic and prognostic information in newly diagnosed gliomas (1). Amino acid PET is particularly helpful for gliomas exhibiting no contrast enhancement on MRI (2–4), which can, in some cases, conceal more aggressive gliomas (5). The most commonly used radiolabels, i.e., amino acids *O*-(2-[^{18}F]fluoroethyl)-L-tyrosine (^{18}F-FET) (6), ^{11}C-methionine (^{11}C-MET) (7), and 6-[^{18}F]fluoro-L-DOPA (^{18}F-FDOPA), were able to noninvasively characterize gliomas at the initial diagnosis (8). Dynamic acquisitions are started at the time of tracer injection, to follow the full kinetic path, and are most commonly performed with ^{18}F-FET and ^{18}F-FDOPA. Dynamic ^{11}C-MET acquisitions are rarely performed because of the limitations of the short (20 min) half-life of this radiolabeled amino acid (9).

Dynamic ^{18}F-FET and ^{18}F-FDOPA acquisitions have recently shown encouraging predictive performances for the noninvasive characterization of the mutation status of isocitrate dehydrogenase (IDH) in newly diagnosed gliomas (6, 8). This is considered to be one of the most important molecular parameters in gliomas according to the 2021 classification of the World Health Organization (WHO) (10). These results were obtained using a semiquantitative model, initially developed for dynamic ^{18}F-FET PET imaging, that can be easily transposed to the clinic (11). The model relies on the extraction of two parameters directly from the time–activity curve (TAC) without requiring any modeling of the underlying metabolism. These parameters are the time-to-peak (TTP), which is the time from the beginning of the dynamic acquisition to the maximal TAC value, and the late phase slope of the TAC. This simple model is currently recommended for dynamic ^{18}F-FET PET analyses (12) and has been reported to predict IDH mutation with an accuracy of 72% (6). The same dynamic analysis has also been successfully transposed to ^{18}F-FDOPA dynamic images, with the time-to-peak parameter demonstrating a promising 74% accuracy for predicting the presence of IDH mutations in newly diagnosed gliomas (8).

The simple dynamic ^{18}F-FET PET modeling approach can be applied because, unlike other radiolabeled amino acids, ^{18}F-FET is not metabolized by cells (13). Indeed, several studies have shown that ^{18}F-FET kinetics are best modeled using a one-tissue reversible compartmental model with reliable fit and stable kinetic parameters (14–16). The ^{18}F-FDOPA kinetics in glioma, however, involve a much more complex model that is, to date, only partially characterized (17, 18) because the initial models were developed in the context of assessing Parkinson's disease (19). The complexities of the ^{18}F-FDOPA kinetic model arise from its different peripheral and intracellular metabolic pathways. ^{18}F-FDOPA is metabolized into ^{18}F-labeled metabolites (METS) and ^{18}F-labeled L-3,4-dihydroxy-6-fluoro-3-*O*-methylphenylalanine (OMFD) in the periphery, with OMFD able to bidirectionally cross the blood–brain barrier. In addition, and unlike ^{18}F-FET, ^{18}F-FDOPA is metabolized *via* the dopaminergic pathway, even though it is unclear whether it is metabolized in the same way by tumor cells. A two-tissue compartmental model, only using one input function, has nevertheless been previously proven useful for the ^{18}F-FDOPA imaging of gliomas (17, 18). However, to the best of our knowledge, there are currently no studies that compare the semiquantitative dynamic model to other dynamic models, such as the compartmental ^{18}F-FDOPA PET imaging model in gliomas (17, 18).

Our current study assesses whether an ^{18}F-FDOPA semiquantitative dynamic analysis indeed captures all the relevant information contained in time–activity curves to predict the presence of IDH mutations compared to the more sophisticated graphical and compartmental models.

MATERIALS AND METHODS

Patients

We retrospectively selected newly diagnosed glioma patients for whom ^{18}F-FDOPA PET had been performed as part of the initial tumor characterization, in the Department of Nuclear Medicine at the CHRU of Nancy, between February 2018 and June 2020. The final selection included: i) patients with a neuropathological diagnosis based on the WHO 2016 classification (20) and with a maximum time interval of 150 days between the ^{18}F-FDOPA PET and the histological confirmation for diffuse grade II or III gliomas and 60 days for glioblastomas (6, 8); ii) patients with available raw data for *a posteriori* reconstruction; and iii) patients with a visually abnormal ^{18}F-FDOPA uptake, i.e., by excluding isometabolic and photopenic gliomas (21, 22). The institutional ethics committee (Comité d'Ethique du CHRU de Nancy—FRANCE) approved the evaluation of retrospective patient data on August 26, 2020. The trial was registered at ClinicalTrials.gov (NCT04469244). This research complied with the principles of the Declaration of Helsinki. Informed consent was obtained from all individuals included in the study.

^{18}F-FDopa PET Acquisition and Image Reconstruction

Patients were instructed to fast for at least 4 h prior to the examination and were pre-medicated with Carbidopa 1 h prior to the examination to increase tracer uptake in the brain (17). Patients were scanned with a digital Vereos PET/computed tomography (CT) camera (Vereos, Philips, Cleveland, OH, USA). Immediately after recording the CT images (100 kV, 80 mAs), a 30-min 3D list-mode PET acquisition was initiated concomitantly to the bolus injection of 2 MBq of ^{18}F-FDOPA per kilogram of body weight. Static PET images were reconstructed from the list-mode data acquired 10–30 min post-injection (12, 23). Dynamic images of all patients were reconstructed using two different temporal sampling protocols depending on the dynamic analyses carried out. For models requiring an input function, we used the recommended temporal sampling protocol from the EANM/SNMMI guidelines, i.e., 12 frames of 5 s, 6 frames of 10 s, 6 frames of 30 s, 5 frames of 60 s, and 4 frames of 300 s (12). This protocol was used because very short frames at the start of the acquisition are needed to capture the large variations of the radiotracer concentration in the blood that occur at the beginning of the acquisition. The temporal sampling protocol consisted of 30 × 60 s frames for models not requiring any input function (24). For models that do not require an input function, the short initial frames only contribute very noisy data points that do not contain any useful information because vascular phase data are not used. Moreover, using a uniform frame duration has the advantage of eliminating one source of noise due to the variations between the time points of the TACs.

Static images were reconstructed using the time-of-flight information and a high-resolution protocol with the Ordered Subset Expectation Maximization (OSEM) 3D algorithm [two iterations, 10 subsets, a deconvolution of the point spread function (PSF), and 256 × 256 × 164 voxels of 1 × 1 × 1 mm^3], while a protocol with a lower spatial resolution was used to limit the level of noise in dynamic images, i.e., three iterations, 15 subsets, without PSF, and 128 × 128 × 82 voxels of 2 × 2 × 2 mm^3 (25).

All images were corrected for attenuation using CT, dead time, and random and scattered coincidences during the reconstruction process.

Segmentation

Healthy brain uptake was initially measured from static images using a merged volume of interest (VOI) consisting of a crescent-shaped region of interest manually positioned on three consecutive slices of the semi-oval center of the unaffected hemisphere to include both white and gray matter. Tumor VOI was segmented semi-automatically from static images using a threshold of 1.6 healthy brain SUV_{mean}, as previously recommended (24, 26, 27). The arterial input function VOI was subsequently placed into the internal carotid using initial dynamic frames to identify the early vascular phases (28).

All volumes of interest were segmented using the LifeX software (lifexsoft.org) (29) and were visually inspected by an experienced physician (AV, nuclear physician with more than 10 years of experience) to ensure the quality of the methods applied. Healthy brain was considered as the reference region due to its nonspecific uptake, as required (26).

Extraction of Time–Activity Curves

For dynamic images reconstructed using the protocol with 30 × 60 s frames, each dynamic frame was first registered to the associated CT image in order to correct for any potential patient movement during the acquisition (30). These transformations, representing the evolution of the patient's movements over time, were interpolated to the time frames of the other protocol, for models involving an input function. Indeed, the first frames from images reconstructed with models involving an input function are very short and suffer from noise, which makes the registration very challenging.

Blood and brain TACs were extracted by retrieving the mean standard uptake value (SUV_{mean}) for each frame in the respective VOIs. Tumor TACs were computed by retrieving the SUV_{mean} for each frame in the volume corresponding to the SUV_{peak} of the tumor VOI on the static image in order to represent the most aggressive part of the tumor (24).

Input Function Pre-Processing

Since no arterial blood sampling was performed in this study, an image-derived input function was used for analyses that required one. TACs representing the evolution of the arterial blood activity were obtained from internal carotid VOIs and were fitted using linear interpolation to the peak followed by a tri-exponential function after the peak (31). The fitted blood TAC was then corrected for the spill-out effect, the coefficient of which had been estimated as 0.51 (32). In the case of ^{18}F-FDOPA, the plasma ^{18}F-FDOPA TAC was obtained after correcting for OMFD and other METS generated in the peripheral tissues (19). The plasma ^{18}F-FDOPA TAC can be obtained from the blood TAC if the hematocrit level and the proportion of each ^{18}F-labeled entity in the respective plasma TACs are known (18). These values were retrieved from the literature, specifically from Huang et al. (19), who used a hematocrit of 40%, and from Melega et al. (33), who reported the metabolite proportions for patients pre-medicated with 100 mg of Carbidopa, which is identical to the pre-medication schedule of our patients. To extrapolate the proportions of metabolites at any time, the measured fractions of plasma radioactivity were fitted using the following equations for the plasma fractions of DOPA, OMFD, and METS, respectively:

$$f_{DOPA}(t)_p = 1 - 0.36902735 \times (2 - e^{-0.03915133t} - e^{-0.03915214t})$$

$$f_{OMFD}(t)_p = 0.24080881 \times (1 - e^{-0.03251229t}) + 0.43768904 \times (1 - e^{-0.03251228t})$$

$$f_{METS}(t)_p = 1 - f_{OMFD}(t)_p - f_{DOPA}(t)_p$$

where t is the time in minutes.

Dynamic Models

The pre-processing steps and input data for each dynamic model are presented in **Figure 1**.

Semiquantitative Models

To overcome noise effects, tumor TACs were first fitted using nonlinear least square optimizations and a specific tumor vascularization function (patent WO/2008/053268, entitled "Method and System for Quantification of Tumoral Vascularization") (8, 24, 34):

$$SUV(t) = \begin{cases} 0, & t > t^* \\ a_0 + (a_1 + a_0)\left(\dfrac{A + \left(\frac{(t-t^*)}{a_2}\right)^p}{B + \left(\frac{(t-t^*)}{a_2}\right)^q}\right), & t \geq t^* \end{cases}$$

where t^* is the time interval from injection to the arrival of the radiotracer and a_0 the baseline intensity that is fixed at 0. a_1 and a_2 reflect the maximal value of contrast agent uptake and the time to peak intensity, respectively. p and q are coefficients related to the increase in intensity and the decrease in intensity, respectively. A and B are arbitrary parameters.

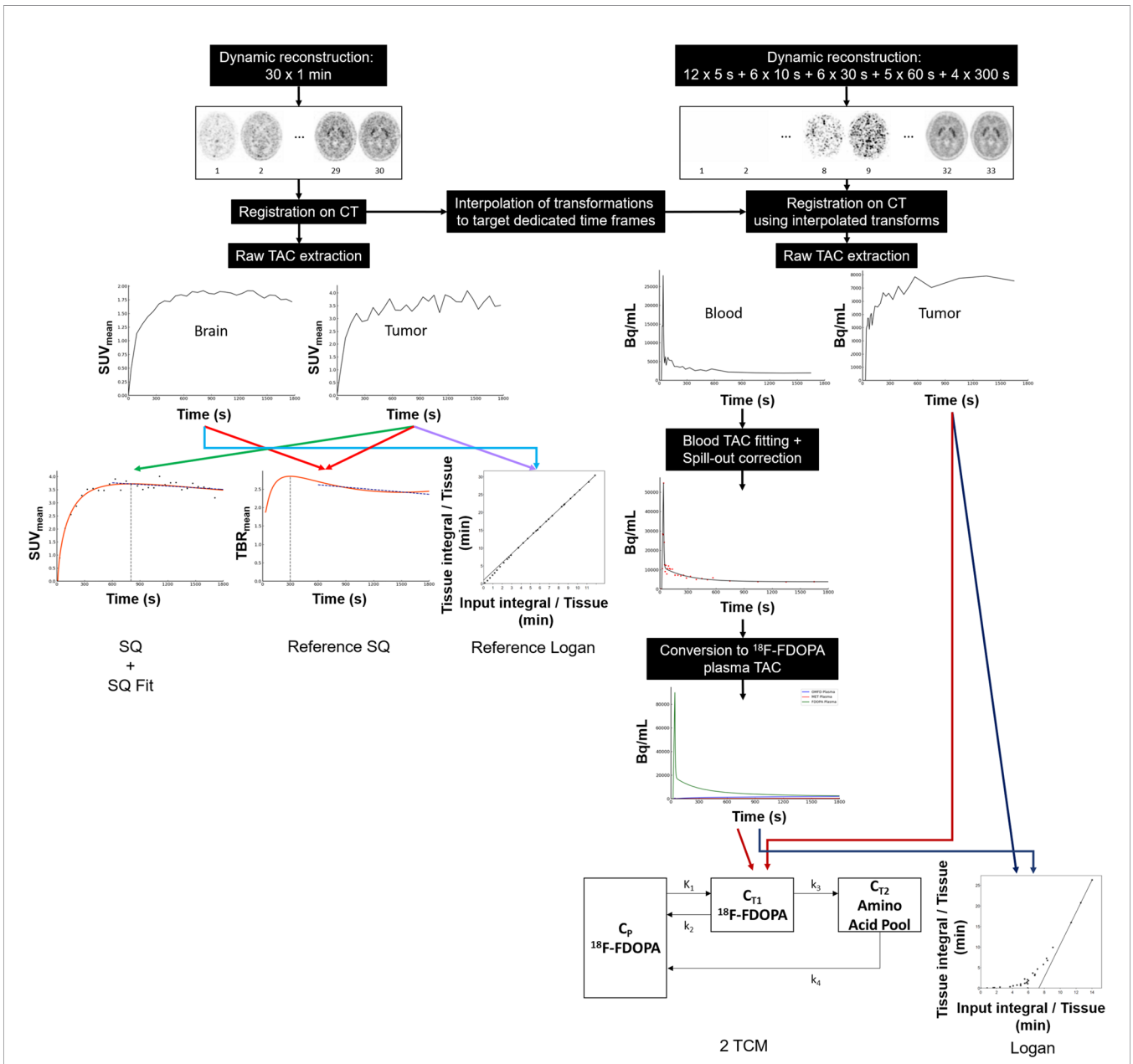

FIGURE 1 | Workflow showing the pre-processing steps required to perform dynamic analyses for all of the dynamic models used in this study: semiquantitative model (*SQ*) semiquantitative fitting parameters (*SQ Fit*), reference semiquantitative model (*Reference SQ*), Logan model with input function (*Logan*), Logan model with reference region (*Reference Logan*), and the two-tissue compartmental model (2TCM). *TBR*, tumor-to-brain ratio.

Semiquantitative (SQ) model parameters, time-to-peak (TTP) and slope, were respectively computed as the time from the beginning of the dynamic acquisition to the maximum uptake value and the slope of the linear regression of the data between the 10th and the 30th minute (8). Semiquantitative fitting parameters (SQ Fit)—a_1, a_2, p, q, A, and B—extracted from the equation of the fit were also assessed. The reference semiquantitative (Ref SQ) model was conducted as an assessment of other studies where the tumor-to-normal brain ratio dynamic values were used to overcome the Carbidopa effect (8, 24, 34), even though such normalization was not needed in this study. To achieve this, healthy brain TACs were fitted similarly to tumor TACs, and TAC ratios (TAC_{ratio}), representing the evolution of the ratios between tumor and brain fitted TACs, were computed. The TTP_{ratio} and $slope_{ratio}$ were computed from the TAC_{ratio} similarly to the tumor TACs.

Graphical Models

Among all graphical models available, the Logan graphical model (35) with the computation of the equilibrium volume of distribution is particularly suited to ^{18}F-FDOPA in gliomas since there is no evidence that ^{18}F-FDOPA is trapped in tumors (17). The Logan graphical model (Logan) was performed with the slope computed between 15 and 30 min post-injection, as previously suggested (17). The equilibrium volumes of distribution (V_{ed}) and Int_{Logan} were computed as the slope and the intercept of the graphical model, respectively. We also used the Logan graphical model with a healthy brain reference region (Ref Logan) similarly to the Patlak graphical model for ^{18}F-FDOPA PET imaging of parkinsonian syndromes (36). Two parameters, with regression between 15 and 30 min, were extracted from the Ref Logan model, namely, the distribution volume ratio (DVR) and the relative residence time (RRT), computed respectively as the slope and the negative intercept.

Compartmental Model

The model used was a simplified two-tissue compartmental model (2TCM) adapted from the original publication of Huang et al. (19) and previously used for the compartmental analysis of ^{18}F-FDOPA glioma imaging (18). Four rate constants (K_1, k_2, k_3, and k_4) and the blood volume fraction (V_b) were estimated by fitting the 2TCM to tumor TACs. The net influx rate constant, Ki, was computed from the previously estimated four rate constants as $Ki = (K_1 \times k_3) / (k_2 + k_3)$.

Statistical Analysis

Categorical variables are expressed as numbers and percentages and continuous variables as medians (first quartile to third quartile) because the variables did not follow a normal distribution. Intergroup comparisons were performed with the chi-squared test for categorical variables and the Mann–Whitney test for continuous variables.

For the overall comparison of the different kinetic models, parameters belonging to the same model were used to construct a multivariate model. This multivariate model was a general linear model with variables selected automatically in a stepwise manner with both forward and backward selections minimizing the Akaike information criterion. Comparisons between the performances of the final models were carried out with the one-sided comparison of superiority pairwise Delong tests (37).

The ability of each individually extracted parameter to predict an IDH mutation was assessed using receiver operating characteristic (ROC) curves from which the area under the curve (AUC), sensitivity, specificity, and accuracy were computed. The optimal threshold was determined by selecting the point on the curve closest to (0,1). Spearman's coefficients were calculated to assess the correlations between each extracted parameter of the different models.

P-values were adjusted using the Benjamini–Hochberg correction, and p-values lower than 0.05 were considered significant. Analyses were performed with the R software version 3.6.2 (R Foundation for Statistical Computing, Vienna, Austria).

RESULTS

Patients

Forty-five patients were initially selected, but eight patients should have been subsequently excluded because of issues in input function determination. The final population thus consisted of 37 patients [median age = 58.3 years, range = 20.3–79.9 years, 16 (43%) women]. According to the WHO 2016 classification of gliomas, 8 gliomas (22%) were classified as IDH-mutant astrocytomas (one was an anaplastic glioma), 7 (19%) as IDH-wild-type astrocytomas (four were anaplastic gliomas), 5 (14%) as IDH-mutant and 1p/19q co-deleted oligodendrogliomas, 16 (43%) as IDH-wild-type glioblastomas, and 1 (3%) as IDH-mutant glioblastoma.

Dynamic Models

The SQ model with an AUC of 0.733 showed similar performance to the other models with AUCs of 0.752, 0.814, 0.693, 0.786, and 0.863, respectively corresponding to SQ Fit, Ref SQ, Logan, Ref Logan, and 2TCM ($p \geq 0.10$ for the pairwise comparisons with the other models). We tested all the possible pairwise dynamic model combinations and found no significant differences ($p > 0.05$) (**Table 1** and **Figure 2**).

TABLE 1 | Results of the multivariate analyses for predicting isocitrate dehydrogenase (IDH) mutations with different dynamic models.

Dynamic model	AUC (95%CI)	Parameters included in the multivariate model
Semiquantitative	0.733 (0.564–0.901)	TTP
Semiquantitative fit	0.752 (0.590–0.913)	p
		a_2
		A
Reference semiquantitative	0.814 (0.671–0.956)	TTP_{ratio}
Logan	0.693 (0.496–0.889)	Int_{Logan}
Reference Logan	0.786 (0.620–0.951)	DVR
		RRT
Two-tissue compartmental	0.866 (0.737–0.996)	K_1
		k_3
		k_4

AUC, area under the curve; TTP, time-to-peak; DVR, distribution volume ratio; RRT, relative residence time.

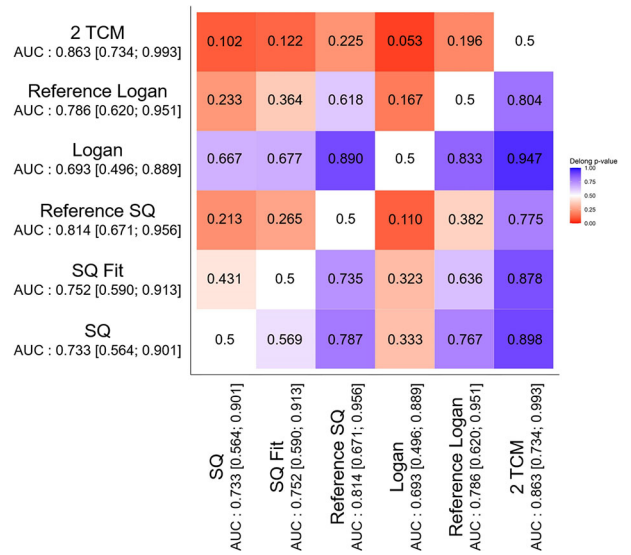

FIGURE 2 | Heatmap of the *p*-values for one-sided comparison of superiority pairwise Delong tests of the AUC multivariate analyses performed for each dynamic model. *AUC*, area under the curve; *SQ*, semiquantitative model; *SQ Fit*, semiquantitative fitting parameters; *Reference SQ*, reference semiquantitative model; *2TCM*, two-tissue compartmental model.

Detailed diagnostic performances of all individual parameters and the correlations between individual parameters are presented in **Table 2** and **Figure 3**, respectively. The TTP parameter from the SQ model showed the highest accuracy (75.7%) among all the parameters examined. The other SQ parameter, i.e., slope, also had a strong diagnostic performance, with an accuracy of 73.0%, which is within the range of performances for the parameters from the Ref SQ and Ref Logan models (respective accuracies of 73.0% and 70.3% for both TTP_{ratio} and $Slope_{ratio}$ and both DVR and RRT). Despite its high overall performance, none of the parameters obtained with the 2TCM were significant for predicting IDH mutations ($p > 0.14$). SQ parameters were highly correlated with Ref SQ $Slope_{ratio}$, the a_2 parameter from SQ Fit, and the intercepts from Logan and Ref Logan, namely, Int_{Logan} and RRT, respectively. The 2TCM parameters, however, did not correlate with any of the parameters from the other models. Most parameters extracted from the 2TCM were highly intra-correlated. Representative IDH-wild-type and IDH-mutant gliomas with all the models considered are shown in **Figure 4**.

DISCUSSION

The current study compared different ^{18}F-FDOPA kinetic models to assess whether the SQ model, which is currently recommended for amino acid PET in clinical routine practice, is specifically suited to a ^{18}F-FDOPA PET dynamic analysis (12). This comparison was performed on newly diagnosed gliomas for which the amino acid PET dynamic analysis had previously been shown to successfully predict the status of IDH mutation (6, 8, 24). The SQ model was found to have a similar performance to the other models, including the 2TCM, as previously reported for the dynamic ^{18}F-FDOPA PET imaging of gliomas (17, 18) (**Table 1** and **Figure 2**). Our study therefore provides supportive evidence for the application of the SQ model, to predict IDH mutations by ^{18}F-FDOPA PET imaging in newly diagnosed gliomas, in the clinic.

The SQ model has the advantage of being easily integrated into clinical routine practice with no need for heavy processing,

TABLE 2 | Results of the receiver operating characteristic (ROC) curve analyses for predicting isocitrate dehydrogenase (IDH) mutations using individual parameters.

Dynamic model	Parameter	*p*-value	AUC	Cutoff	Sensitivity (%)	Specificity (%)	Accuracy (%)
Semiquantitative	TTP	**0.020**	0.733	18.41 min	57.1	87.0	75.7
	Slope	**0.020**	0.730	–0.55 SUV h^{-1}	64.3	78.3	73.0
Semiquantitative fit	a_1	0.393	0.630	14.67	57.1	73.9	67.6
	a_2	0.390	0.652	936.86 s	71.4	60.9	64.9
	p	0.432	0.599	1.665	64.3	47.8	54.1
	q	0.390	0.668	0.299	71.4	65.2	67.6
	A	0.699	0.540	0	64.3	56.5	59.5
	B	0.432	0.593	2.21	50.0	78.3	67.6
Reference semiquantitative	TTP_{ratio}	**0.003**	0.814	5.28 min	78.6	69.6	73.0
	$Slope_{ratio}$	**0.024**	0.724	–0.37 h^{-1}	78.6	69.6	73.0
Logan	V_{ed}	0.147	0.646	1.51	64.3	69.6	67.6
	Int_{Logan}	0.107	0.693	–24.85 min	57.1	82.6	73.0
Reference Logan	DVR	**0.046**	0.699	2.41	78.6	65.2	70.3
	RRT	**0.030**	0.739	–0.71 min	78.6	65.2	70.3
Two-tissue compartmental	K_1	0.083	0.742	0.13 min^{-1}	71.4	69.6	70.3
	k_2	0.405	0.609	0.40 min^{-1}	64.3	52.2	56.8
	k_3	0.888	0.516	0.18 min^{-1}	57.1	56.5	56.8
	k_4	0.257	0.671	0.03 min^{-1}	71.4	65.2	67.6
	Ki	0.405	0.599	0.03 min^{-1}	64.3	56.5	59.5
	V_b	0.405	0.596	1.97	71.4	56.5	62.2

Bold p-values are significant Mann–Whitney tests for the comparison of IDH-wild-type and IDH-mutant gliomas.
AUC, area under the curve; SUV, standard uptake value; TTP, time-to-peak; DVR, distribution volume ratio; RRT, relative residence time.

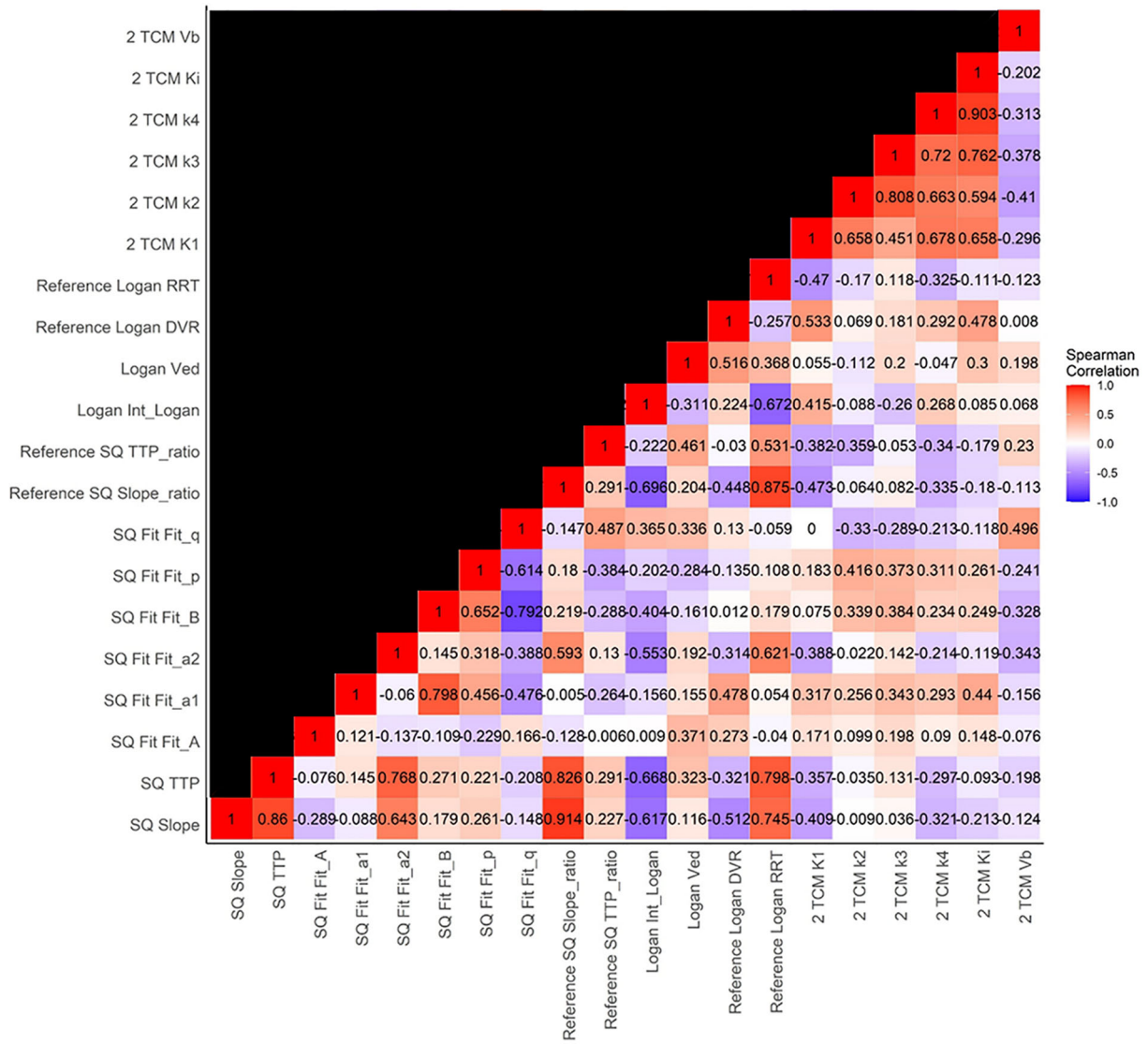

FIGURE 3 | Heatmap of Spearman's correlation coefficients for the individual parameters of each of the models.

a reference region, or an input function. Although compartmental analysis, which is considered the current gold standard, requires an input function, input functions are notoriously difficult to obtain in clinical routine practice because they either require blood sampling or, if extracted directly from images, heavy post-processing and many approximations (see **Figure 1**), which limits their use in the clinic.

There has been renewed interest in dynamic PET acquisitions because of the significant technological advances in the field, such as digital signal (38) and/or the longer field of view of PET devices. These improvements make dynamic acquisitions accessible to clinical routine practice (39). A simple dynamic model is thus preferable to harmonize protocols across different centers and to promote a wider acceptance in the scientific medical community, not only among nuclear physicians but also clinicians requiring access to easily understandable and interpretable data.

Our study confirms the high diagnostic performance of dynamic ^{18}F-FDOPA PET imaging using the SQ model to predict IDH mutations, with the TTP analysis yielding an accuracy of 75.7%. TACs with shorter TTPs may, in addition, identify more aggressive IDH-wild-type gliomas, which may correspond not only to tumors that express high concentrations of LAT transporters (40) but also those that are characterized by more extensive tracer perfusion, as shown for ^{18}F-FET (11) and discussed in our previous publications (8, 24). Such performances are within the range of previously published studies that reported accuracies of 74% for TTP alone (8) and 75% when associated with other specific radiomics features of ^{18}F-FDOPA PET imaging (24). It should nevertheless be noted

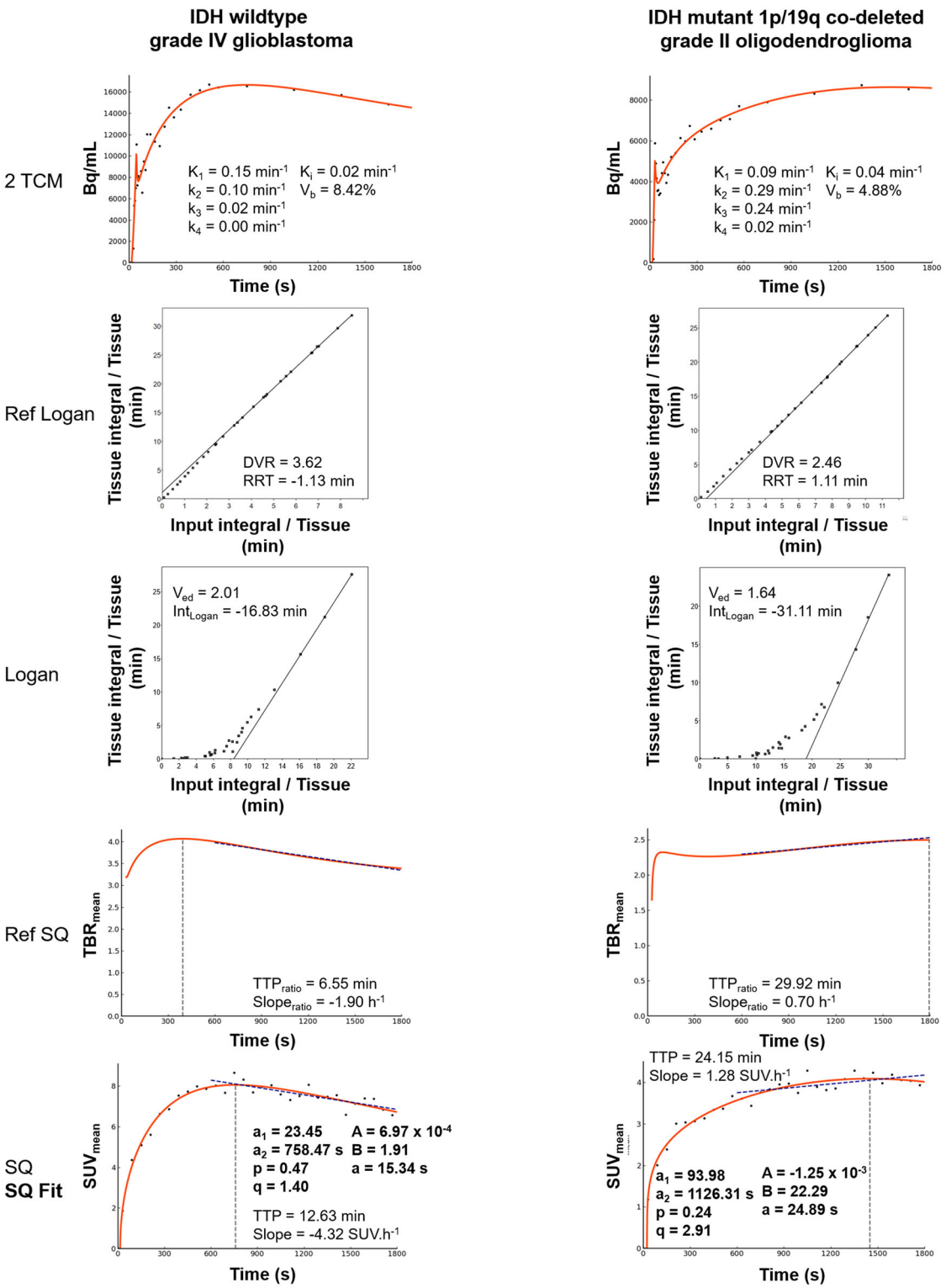

FIGURE 4 | Representative IDH-wild-type grade IV glioblastoma and an IDH-mutant 1p/19q co-deleted grade II oligodendroglioma. Fitted results and parameters extracted from all the dynamic models used in this study are displayed for each of the two patients: semiquantitative model (*SQ*), semiquantitative fitting parameters (*SQ Fit*), reference semiquantitative model (*Reference SQ*), Logan model with input function (*Logan*), Logan model with reference region (*Reference Logan*), and the two-tissue compartmental model (2TCM). *IDH*, isocitrate dehydrogenase; *TBR*, tumor-to-brain ratio.

that these latter two studies used a reference region for the SQ model to account for the population heterogeneity with regard to the Carbidopa pre-medication (8, 24, 34). In the current study, we report similar overall performances of the Ref SQ model and the SQ model (Ref SQ: AUC = 0.814, 95% CI = 0.671–0.956, p = 0.21, for the pairwise test with the SQ model). This is consistent with results from our previous dynamic ^{18}F-FDOPA PET studies (8, 24, 34). Even though no significant differences were observed between the different models studied, the 2TCM provided better performance (AUC = 0.863, range = 0.734–0.993, p = 0.11, for the pairwise test with the SQ model) with parameters that reflect different kinetic information compared to those from the other models (**Figure 3**). However, as explained above, adapting the 2TCM to clinical routine practice presents serious challenges and would make it more difficult to harmonize data sourced from different centers.

Among the radiolabeled amino acids recommended for the assessment of gliomas, ^{18}F-FET and ^{18}F-FDOPA have been demonstrated to have similar semiquantitative static parameters (41) but different kinetic parameters for tumor grading using compartmental modeling (28). When applying the WHO 2016 classification of gliomas, dynamic parameters for both radiotracers extracted from the SQ or the Ref SQ model, in the literature, showed similar performances in predicting IDH mutations. An accuracy of 72% was reported for the ^{18}F-FET TTP (6), while an accuracy of 74% was described for the ^{18}F-FDOPA TTP_{ratio} (8). These results were also confirmed in the Lohmann et al. radiomics study, which reported a model accuracy of 80% (42). The study of Lohmann et al. nevertheless showed that dynamic parameters were particularly pertinent in determining diagnostic performance. Since the underlying kinetic model of ^{18}F-FDOPA is much more complex than that of ^{18}F-FET, there was no evidence that a simple model such as the SQ model would suffice. Our current study showed that the SQ model is appropriate for interpreting ^{18}F-FDOPA kinetics and that it might be considered in future guidelines, as is currently the case for ^{18}F-FET imaging (12).

The main limitations of our study are related to the assumptions that underpin how the input function was determined. Since no blood sampling was performed for any of our patients, we extrapolated the input function from an image-derived blood TAC that was converted to a ^{18}F-FDOPA plasma TAC using a previously published method (18). This method is based on hematocrit data and the proportions of individual metabolites previously reported in the literature (19, 33). Since this assumption is not adapted to each patient, it may have a negative impact on the results from the model that are dependent on this input function. Moreover, our study used a digital PET device with high count sensitivity and improved dynamic image quality. The values of the different parameters may therefore not be directly comparable to those extracted from noisier dynamic images, captured with older PET devices. This may significantly affect the fitting process that is used for each dynamic model and, thus, affect the stability and the ability to directly extrapolate our results to other PET devices. The number of patients in this study was also limited, even though the diagnostic performances reported were similar to those of other amino acid dynamic PET studies. Although our population comprised a highly selected group of patients, it included representative proportions of the different types of gliomas (43).

CONCLUSION

Despite the complexities of the ^{18}F-FDOPA kinetic model, our study confirms that a simple semiquantitative analysis, which is currently recommended for amino acid PET imaging in clinical routine practice, captures all the relevant information contained in TACs to predict the presence of IDH mutations when compared to the more sophisticated graphical and compartmental models. Although dynamic parameters play important roles in the interpretation of radiolabeled amino acid PET imaging in gliomas, our current study shows that the application of this easily transposable method can be extended to ^{18}F-FDOPA PET imaging for the noninvasive characterization of newly diagnosed gliomas.

DATA AVAILABILITY STATEMENT

The original contributions presented in the study are included in the article/**Supplementary Material**. Further inquiries can be directed to the corresponding author.

ETHICS STATEMENT

The studies involving human participants were reviewed and approved by Comité d'Ethique du CHRU de Nancy - FRANCE. The patients/participants provided their written informed consent to participate in this study.

AUTHOR CONTRIBUTIONS

TZ, MD, and AV conceived and designed the study and analyzed the data. FR, MB, LT, and LI participated either in the study conception and design or the analysis and interpretation of the data. All authors helped with the drafting of the manuscript or revising it critically for important intellectual content. FR, MB, LT, LI, and AV approved the submitted version. All authors contributed to the article and approved the submitted version.

ACKNOWLEDGMENTS

The authors thank Petra Neufing for critical review of the manuscript.

SUPPLEMENTARY MATERIAL

The Supplementary Material for this article can be found online at: https://www.frontiersin.org/articles/10.3389/fonc.2021.735257/full#supplementary-material

Supplementary Table 1 | Raw_TACs_30x60s.

Supplementary Table 2 | Raw_TACs_compart_temp_sampling.

Supplementary Table 3 | Clinical_data.

Supplementary Table 4 | Parameters_results.

REFERENCES

1. Albert NL, Weller M, Suchorska B, Galldiks N, Soffietti R, Kim MM, et al. Response Assessment in Neuro-Oncology Working Group and European Association for Neuro-Oncology Recommendations for the Clinical Use of PET Imaging in Gliomas. *Neuro-Oncol* (2016) 18:1199–208. doi: 10.1093/neuonc/now058
2. Vettermann F, Suchorska B, Unterrainer M, Nelwan D, Forbrig R, Ruf V, et al. Non-Invasive Prediction of IDH-Wildtype Genotype in Gliomas Using Dynamic 18F-FET PET. *Eur J Nucl Med Mol Imaging* (2019) 46:2581–9. doi: 10.1007/s00259-019-04477-3
3. Kunz M, Albert NL, Unterrainer M, la Fougere C, Egensperger R, Schüller U, et al. Dynamic 18f-FET PET Is a Powerful Imaging Biomarker in Gadolinium-Negative Gliomas. *Neuro-Oncol* (2019) 21:274–84. doi: 10.1093/neuonc/noy098
4. Jansen NL, Graute V, Armbruster L, Suchorska B, Lutz J, Eigenbrod S, et al. MRI-Suspected Low-Grade Glioma: Is There a Need to Perform Dynamic FET PET? *Eur J Nucl Med Mol Imaging* (2012) 39:1021–9. doi: 10.1007/s00259-012-2109-9
5. Obara T, Blonski M, Brzenczek C, Mézières S, Gaudeau Y, Pouget C, et al. Adult Diffuse Low-Grade Gliomas: 35-Year Experience at the Nancy France Neurooncology Unit. *Front Oncol* (2020) 10:574679. doi: 10.3389/fonc.2020.574679
6. Verger A, Stoffels G, Bauer EK, Lohmann P, Blau T, Fink GR, et al. Static and Dynamic 18F–FET PET for the Characterization of Gliomas Defined by IDH and 1p/19q Status. *Eur J Nucl Med Mol Imaging* (2018) 45:443–51. doi: 10.1007/s00259-017-3846-6
7. Lopci E, Riva M, Olivari L, Raneri F, Soffietti R, Piccardo A, et al. Prognostic Value of Molecular and Imaging Biomarkers in Patients With Supratentorial Glioma. *Eur J Nucl Med Mol Imaging* (2017) 44:1155–64. doi: 10.1007/s00259-017-3618-3
8. Ginet M, Zaragori T, Marie P-Y, Roch V, Gauchotte G, Rech F, et al. Integration of Dynamic Parameters in the Analysis of 18F-FDopa PET Imaging Improves the Prediction of Molecular Features of Gliomas. *Eur J Nucl Med Mol Imaging* (2020) 47:1381–90. doi: 10.1007/s00259-019-04509-y
9. Nomura Y, Asano Y, Shinoda J, Yano H, Ikegame Y, Kawasaki T, et al. Characteristics of Time-Activity Curves Obtained From Dynamic 11C-Methionine PET in Common Primary Brain Tumors. *J Neurooncol* (2018) 138:649–58. doi: 10.1007/s11060-018-2834-4
10. Louis DN, Perry A, Wesseling P, Brat DJ, Cree IA, Figarella-Branger D, et al. The 2021 WHO Classification of Tumors of the Central Nervous System: A Summary. *Neuro-Oncol* (2021) 23(8):1231–51. doi: 10.1093/neuonc/noab106
11. Pöpperl G, Kreth FW, Herms J, Koch W, Mehrkens JH, Gildehaus FJ, et al. Analysis of 18F-FET PET for Grading of Recurrent Gliomas: Is Evaluation of Uptake Kinetics Superior to Standard Methods? *J Nucl Med* (2006) 47:393–403.
12. Law I, Albert NL, Arbizu J, Boellaard R, Drzezga A, Galldiks N, et al. Joint EANM/EANO/RANO Practice Guidelines/SNMMI Procedure Standards for Imaging of Gliomas Using PET With Radiolabelled Amino Acids and [18F]FDG: Version 1.0. *Eur J Nucl Med Mol Imaging* (2019) 46:540–57. doi: 10.1007/s00259-018-4207-9
13. Wester HJ, Herz M, Weber W, Heiss P, Senekowitsch-Schmidtke R, Schwaiger M, et al. Synthesis and Radiopharmacology of O-(2-[18F]Fluoroethyl)-L-Tyrosine for Tumor Imaging. *J Nucl Med* (1999) 40:205–12.
14. Debus C, Afshar-Oromieh A, Floca R, Ingrisch M, Knoll M, Debus J, et al. Feasibility and Robustness of Dynamic 18F-FET PET Based Tracer Kinetic Models Applied to Patients With Recurrent High-Grade Glioma Prior to Carbon Ion Irradiation. *Sci Rep* (2018) 8:14760. doi: 10.1038/s41598-018-33034-5
15. Bolcaen J, Lybaert K, Moerman L, Descamps B, Deblaere K, Boterberg T, et al. Kinetic Modeling and Graphical Analysis of 18F-Fluoromethylcholine (FCho), 18f-Fluoroethyltyrosine (FET) and 18F-Fluorodeoxyglucose (FDG) PET for the Fiscrimination Between High-Grade Glioma and Radiation Necrosis in Rats. *PloS One* (2016) 11:e0161845. doi: 10.1371/journal.pone.0161845
16. Thiele F, Ehmer J, Piroth MD, Eble MJ, Coenen HH, Kaiser H-J, et al. The Quantification of Dynamic FET PET Imaging and Correlation With the Clinical Outcome in Patients With Glioblastoma. *Phys Med Biol* (2009) 54:5525–39. doi: 10.1088/0031-9155/54/18/012
17. Schiepers C, Chen W, Cloughesy T, Dahlbom M, Huang S-C. 18f-FDOPA Kinetics in Brain Tumors. *J Nucl Med* (2007) 48:1651–61. doi: 10.2967/jnumed.106.039321
18. Wardak M, Schiepers C, Cloughesy TF, Dahlbom M, Phelps ME, Huang S-C. 18f-FLT and 18F-FDOPA PET Kinetics in Recurrent Brain Tumors. *Eur J Nucl Med Mol Imaging* (2014) 41:1199–209. doi: 10.1007/s00259-013-2678-2
19. Huang S-C, Yu D-C, Barrio JR, Grafton S, Melega WP, Hoffman JM, et al. Kinetics and Modeling of L-6-[^{18} F]Fluoro-DOPA in Human Positron Emission Tomographic Studies. *J Cereb Blood Flow Metab* (1991) 11:898–913. doi: 10.1038/jcbfm.1991.155
20. Louis DN, Perry A, Reifenberger G, von Deimling A, Figarella-Branger D, Cavenee WK, et al. The 2016 World Health Organization Classification of Tumors of the Central Nervous System: A Summary. *Acta Neuropathol (Berl)* (2016) 131:803–20. doi: 10.1007/s00401-016-1545-1
21. Galldiks N, Unterrainer M, Judov N, Stoffels G, Rapp M, Lohmann P, et al. Photopenic Defects on O-(2-[18F]-Fluoroethyl)-L-Tyrosine PET: Clinical Relevance in Glioma Patients. *Neuro-Oncol* (2019) 21:1331–8. doi: 10.1093/neuonc/noz083
22. Zaragori T, Castello A, Guedj E, Girard A, Galldiks N, Albert NL, et al. Photopenic Defects in Gliomas With Amino-Acid PET and Relative Prognostic Value: A Multicentric 11c-Methionine and 18F-FDOPA PET Experience. *Clin Nucl Med* (2021) 46:e36–7. doi: 10.1097/RLU.0000000000003240
23. Janvier L, Olivier P, Blonski M, Morel O, Vignaud J-M, Karcher G, et al. Correlation of SUV-Derived Indices With Tumoral Aggressiveness of Gliomas in Static 18f-FDOPA PET: Use in Clinical Practice. *Clin Nucl Med* (2015) 40:e429–35. doi: 10.1097/RLU.0000000000000897
24. Zaragori T, Oster J, Roch V, Hossu G, Chawki MB, Grignon R, et al. ^{18} F-FDOPA PET for the Non-Invasive Prediction of Glioma Molecular Parameters: A Radiomics Study. *J Nucl Med* (2021) jnumed.120.261545. doi: 10.2967/jnumed.120.261545
25. Salvadori J, Imbert L, Perrin M, Karcher G, Lamiral Z, Marie P-Y, et al. Head-To-Head Comparison of Image Quality Between Brain 18F-FDG Images Recorded With a Fully Digital Versus a Last-Generation Analog PET Camera. *EJNMMI Res* (2019) 9:61. doi: 10.1186/s13550-019-0526-5
26. Unterrainer M, Vettermann F, Brendel M, Holzgreve A, Lifschitz M, Zähringer M, et al. Towards Standardization of 18F-FET PET Imaging: Do We Need a Consistent Method of Background Activity Assessment? *EJNMMI Res* (2017) 7:48. doi: 10.1186/s13550-017-0295-y
27. Cicone F, Carideo L, Minniti G, Scopinaro F. The Mean Striatal 18F-DOPA Uptake Is Not a Reliable Cut-Off Threshold for Biological Tumour Volume Definition of Glioma. *Eur J Nucl Med Mol Imaging* (2019) 46:1051–3. doi: 10.1007/s00259-019-4276-4
28. Kratochwil C, Combs SE, Leotta K, Afshar-Oromieh A, Rieken S, Debus J, et al. Intra-Individual Comparison of 18F-FET and 18F-DOPA in PET Imaging of Recurrent Brain Tumors. *Neuro-Oncol* (2014) 16:434–40. doi: 10.1093/neuonc/not199
29. Nioche C, Orlhac F, Boughdad S, Reuzé S, Goya-Outi J, Robert C, et al. LIFEx: A Freeware for Radiomic Feature Calculation in Multimodality Imaging to Accelerate Advances in the Characterization of Tumor Heterogeneity. *Cancer Res* (2018) 78:4786–9. doi: 10.1158/0008-5472.CAN-18-0125
30. Ye H, Wong K-P, Wardak M, Dahlbom M, Kepe V, Barrio JR, et al. Automated Movement Correction for Dynamic PET/CT Images: Evaluation With Phantom and Patient Data. *PloS One* (2014) 9:e103745. doi: 10.1371/journal.pone.0103745
31. Zanotti-Fregonara P, Hirvonen J, Lyoo CH, Zoghbi SS, Rallis-Frutos D, Huestis MA, et al. Population-Based Input Function Modeling for [18F]

FMPEP-D2, an Inverse Agonist Radioligand for Cannabinoid CB1 Receptors: Validation in Clinical Studies. *PloS One* (2013) 8:e60231. doi: 10.1371/journal.pone.0060231
32. Martens C, Debeir O, Decaestecker C, Metens T, Lebrun L, Leurquin-Sterk G, et al. Voxelwise Principal Component Analysis of Dynamic [S-Methyl-11c] Methionine PET Data in Glioma Patients. *Cancers* (2021) 13:2342. doi: 10.3390/cancers13102342
33. Melega WP, Grafton ST, Huang S-C, Satyamurthy N, Phelps ME, Barrio JR. L-6-[^{18} F]Fluoro-DOPA Metabolism in Monkeys and Humans: Biochemical Parameters for the Formulation of Tracer Kinetic Models With Positron Emission Tomography. *J Cereb Blood Flow Metab* (1991) 11:890–7. doi: 10.1038/jcbfm.1991.154
34. Zaragori T, Ginet M, Marie P-Y, Roch V, Grignon R, Gauchotte G, et al. Use of Static and Dynamic [^{18}F]-F-DOPA PET Parameters for Detecting Patients With Glioma Recurrence or Progression. *EJNMMI Res* (2020) 10:1–10. doi: 10.1186/s13550-020-00645-x
35. Logan J. Graphical Analysis of PET Data Applied to Reversible and Irreversible Tracers. *Nucl Med Biol* (2000) 27:661–70. doi: 10.1016/s0969-8051(00)00137-2
36. Morbelli S, Esposito G, Arbizu J, Barthel H, Boellaard R, Bohnen NI, et al. EANM Practice Guideline/SNMMI Procedure Standard for Dopaminergic Imaging in Parkinsonian Syndromes 1.0. *Eur J Nucl Med Mol Imaging* (2020) 47:1885–912. doi: 10.1007/s00259-020-04817-8
37. DeLong ER, DeLong DM, Clarke-Pearson DL. Comparing the Areas Under Two or More Correlated Receiver Operating Characteristic Curves: A Nonparametric Approach. *Biometrics* (1988) 44:837. doi: 10.2307/2531595
38. Salvadori J, Odille F, Verger A, Olivier P, Karcher G, Marie P-Y, et al. Head-To-Head Comparison Between Digital and Analog PET of Human and Phantom Images When Optimized for Maximizing the Signal-to-Noise Ratio From Small Lesions. *EJNMMI Phys* (2020) 7:11. doi: 10.1186/s40658-020-0281-8
39. Dimitrakopoulou-Strauss A, Pan L, Sachpekidis C. Kinetic Modeling and Parametric Imaging With Dynamic PET for Oncological Applications: General Considerations, Current Clinical Applications, and Future Perspectives. *Eur J Nucl Med Mol Imaging* (2020) 48:21–39. doi: 10.1007/s00259-020-04843-6
40. Dadone-Montaudié B, Ambrosetti D, Dufour M, Darcourt J, Almairac F, Coyne J, et al. [18f] FDOPA Standardized Uptake Values of Brain Tumors Are Not Exclusively Dependent on LAT1 Expression. *PloS One* (2017) 12:e0184625. doi: 10.1371/journal.pone.0184625
41. Lapa C, Linsenmann T, Monoranu CM, Samnick S, Buck AK, Bluemel C, et al. Comparison of the Amino Acid Tracers 18F-FET and 18F-DOPA in High-Grade Glioma Patients. *J Nucl Med* (2014) 55:1611–6. doi: 10.2967/jnumed.114.140608
42. Lohmann P, Lerche C, Bauer EK, Steger J, Stoffels G, Blau T, et al. Predicting IDH Genotype in Gliomas Using FET PET Radiomics. *Sci Rep* (2018) 8:13328. doi: 10.1038/s41598-018-31806-7
43. Jiang H, Cui Y, Wang J, Lin S. Impact of Epidemiological Characteristics of Supratentorial Gliomas in Adults Brought About by the 2016 World Health Organization Classification of Tumors of the Central Nervous System. *Oncotarget* (2017) 131:803–20. doi: 10.18632/oncotarget.13555

Conflict of Interest: The authors declare that the research was conducted in the absence of any commercial or financial relationships that could be construed as a potential conflict of interest.

Publisher's Note: All claims expressed in this article are solely those of the authors and do not necessarily represent those of their affiliated organizations, or those of the publisher, the editors and the reviewers. Any product that may be evaluated in this article, or claim that may be made by its manufacturer, is not guaranteed or endorsed by the publisher.

Copyright © 2021 Zaragori, Doyen, Rech, Blonski, Taillandier, Imbert and Verger. This is an open-access article distributed under the terms of the Creative Commons Attribution License (CC BY). The use, distribution or reproduction in other forums is permitted, provided the original author(s) and the copyright owner(s) are credited and that the original publication in this journal is cited, in accordance with accepted academic practice. No use, distribution or reproduction is permitted which does not comply with these terms.

frontiers in Neuroscience

CASE REPORT
published: 27 October 2021
doi: 10.3389/fnins.2021.738708

Case Report: Disruption of Resting-State Networks and Cognitive Deficits After Whole Brain Irradiation for Singular Brain Metastasis

Martin Kocher[1,2,3*], *Christiane Jockwitz*[4,5], *Christoph Lerche*[1], *Michael Sabel*[3,6], *Philipp Lohmann*[1,2,3], *Gabriele Stoffels*[1], *Christian Filss*[1,7], *Felix M. Mottaghy*[3,7,8], *Maximilian I. Ruge*[2,3], *Gereon R. Fink*[3,9,10], *Nadim J. Shah*[1,11,12], *Norbert Galldiks*[3,9,10], *Svenja Caspers*[4,5] and *Karl-Josef Langen*[1,3,7,12]

[1] Institute of Neuroscience and Medicine (INM-4), Research Center Juelich, Juelich, Germany, [2] Department of Stereotaxy and Functional Neurosurgery, Center for Neurosurgery, Faculty of Medicine and University Hospital Cologne, Cologne, Germany, [3] Center of Integrated Oncology, Universities of Aachen, Bonn, Cologne and Duesseldorf, Cologne, Germany, [4] Institute of Neuroscience and Medicine (INM-1), Research Center Juelich, Juelich, Germany, [5] Institute for Anatomy I, Medical Faculty and University Hospital Düsseldorf, Heinrich Heine University Duesseldorf, Duesseldorf, Germany, [6] Department of Neurosurgery, Medical Faculty, Center of Neuro-Oncology, Heinrich-Heine-University Düsseldorf, Düsseldorf, Germany, [7] Department of Nuclear Medicine, University Hospital Aachen, Rheinisch-Westfaelische Technische Hochschule (RWTH) Aachen University, Aachen, Germany, [8] Department of Radiology and Nuclear Medicine, Maastricht University Medical Center, Maastricht, Netherlands, [9] Institute of Neuroscience and Medicine (INM-3), Research Center Juelich, Juelich, Germany, [10] Department of Neurology, Faculty of Medicine and University Hospital Cologne, University of Cologne, Cologne, Germany, [11] Department of Neurology, University Hospital Aachen, Rheinisch-Westfaelische Technische Hochschule (RWTH) Aachen University, Aachen, Germany, [12] Juelich-Aachen Research Alliance—Section JARA-Brain, Juelich, Germany

OPEN ACCESS

Edited by:
Sandro M. Krieg,
Technical University of Munich, Germany

Reviewed by:
Domenico Zaca,
Siemens, Italy
Denise Bernhardt,
Technical University, Munich, Germany

***Correspondence:**
Martin Kocher
martin.kocher@uk-koeln.de

Specialty section:
This article was submitted to Brain Imaging Methods, a section of the journal Frontiers in Neuroscience

Received: 09 July 2021
Accepted: 30 September 2021
Published: 27 October 2021

Citation:
Kocher M, Jockwitz C, Lerche C, Sabel M, Lohmann P, Stoffels G, Filss C, Mottaghy FM, Ruge MI, Fink GR, Shah NJ, Galldiks N, Caspers S and Langen K-J (2021) Case Report: Disruption of Resting-State Networks and Cognitive Deficits After Whole Brain Irradiation for Singular Brain Metastasis. Front. Neurosci. 15:738708. doi: 10.3389/fnins.2021.738708

Introduction: Long-term survivors of whole brain radiation (WBRT) are at significant risk for developing cognitive deficits, but knowledge about the underlying pathophysiological mechanisms is limited. Therefore, we here report a rare case with a singular brain metastasis treated by resection and WBRT that survived for more than 10 years where we investigated the integrity of brain networks using resting-state functional MRI.

Methods: A female patient with a left frontal non-small cell lung cancer (NSCLC) brain metastasis had resection and postoperative WBRT (30.0 in 3.0 Gy fractions) and stayed free from brain metastasis recurrence for a follow-up period of 11 years. Structural magnetic resonance imaging (MRI) and amino acid [O-(2-[^{18}F]fluoroethyl)-L-tyrosine] positron emission tomography (FET PET) were repeatedly acquired. At the last follow up, neurocognitive functions and resting-state functional connectivity (RSFC) using resting-state fMRI were assessed. Within-network and inter-network connectivity of seven resting-state networks were computed from a connectivity matrix. All measures were compared to a matched group of 10 female healthy subjects.

Results: At the 11-year follow-up, T2/FLAIR MR images of the patient showed extended regions of hyper-intensities covering mainly the white mater of the bilateral dorsal frontal and parietal lobes while sparing most of the temporal lobes. Compared to the healthy subjects, the patient performed significantly worse in all cognitive domains that included executive functions, attention and processing speed, while verbal

working memory, verbal episodic memory, and visual working memory were left mostly unaffected. The connectivity matrix showed a heavily disturbed pattern with a widely distributed, scattered loss of RSFC. The within-network RSFC revealed a significant loss of connectivity within all seven networks where the dorsal attention and fronto-parietal control networks were affected most severely. The inter-network RSFC was significantly reduced for the visual, somato-motor, and dorsal and ventral attention networks.

Conclusion: As demonstrated here in a patient with a metastatic NSCLC and long-term survival, WBRT may lead to extended white matter damage and cause severe disruption of the RSFC in multiple resting state networks. In consequence, executive functioning which is assumed to depend on the interaction of several networks may be severely impaired following WBRT apart from the well-recognized deficits in memory function.

Keywords: brain metastases, whole-brain radiotherapy, functional magnetic resonance imaging, cognitive function, case report

INTRODUCTION

In patients with singular brain metastases of primary solid tumors, neurosurgical resection followed by postoperative whole brain radiation therapy (WBRT) was a common therapeutic approach in the recent decades (Patchell et al., 1998; Gaspar et al., 2010). While WBRT increases local control at the resection site and reduces the number of newly occurring remote brain metastases (Patchell et al., 1998; Kocher et al., 2011; Brown et al., 2017), evidence is increasing that it may cause progressive cognitive deficits and impairment of quality of life especially in long-term survivors of the underlying metastatic cancer disease (Lin et al., 2013; Soffietti et al., 2013, 2017; Pinkham et al., 2015; Brown et al., 2017). Cognitive deficits following WBRT have been mainly observed in the domain of learning and memory function and are assumed to be caused by radiation-induced damage to the bilateral hippocampus (Chang et al., 2009), an insight that had led to the concept of hippocampal-sparing WBRT (Gondi et al., 2014; Brown et al., 2020; Giuseppe et al., 2020).

However, modern concepts of brain function suggest that cognitive performance in different domains does not rely solely on the function of specialized single cortical regions but rather depends on the interaction of multiple cortical regions organized in distributed functional networks. Several of these functional networks have been identified using resting-state functional MRI (rs-fMRI), and a set of cognitive functions have been assigned to them (Yeo et al., 2011; Schaefer et al., 2018). While alterations in whole-brain resting-state functional connectivity (RSFC) induced by chemotherapy of breast cancer patients ("chemo brain") have been studied to some extent (Bruno et al., 2012; Kesler et al., 2013; Piccirillo et al., 2015; Tao et al., 2017, 2020), reports regarding the effect of WBRT on RSFC are rare (Mitchell et al., 2020). Because WBRT, as chemotherapy, potentially affects multiple cortical regions and networks, it can be hypothesized that cognitive deficits after WBRT affect functional connectivity both within and between multiple networks and may result in deficits in multiple cognitive domains.

Therefore, we here took the rare opportunity to assess resting-state functional connectivity and cognitive performance in a long-term survivor of brain metastasis treated with WBRT who participated in a prospective study. The patient studied here suffered from a synchronous singular brain metastasis of a non-small cell cancer (NSCLC) and received resection and WBRT for the brain metastasis and resection and adjuvant chemotherapy for the primary tumor. The long survival and follow-up period of more than 10 years is rarely observed and put her at risk of developing the full extent of radiation-induced brain damage and associated cognitive deficits (Kocher et al., 2011; Brown et al., 2017). For comparison, we used RSFC and cognitive performance data from a closely matched group of healthy subjects from a population-based cohort.

CASE DESCRIPTION

In 2008, a 48-year old, left-handed female patient trained as a physician's assistant experienced a generalized seizure caused by a left frontal brain metastasis of a NSCLC (adenocarcinoma) of the lung. The metastasis was treated by neurosurgical resection and postoperative WBRT with a total dose of 30.0 Gy in 10 daily fractions of 3.0 Gy. After completion, the primary tumor was treated by upper lobe resection and mediastinal lymphonodectomy. Due to the involvement of mediastinal lymph nodes, four courses of adjuvant chemotherapy (cis-platin/vinorelbine) were applied and a complete remission at the intracranial and extracranial tumor sites could be achieved. During an 11-year follow up period, MR and FET PET brain imaging was conducted repeatedly. At the last follow up at the patient's age of 59.9 years, resting-state functional MRI (rs-fMRI) and cognitive testing were additionally performed. The timeline of the therapeutic interventions, diagnostics and outcomes is depicted in **Table 1**.

DIAGNOSTIC ASSESSMENT

Structural MR and PET Imaging

During the follow up period of the patient, structural MR and O-(2-[18F]fluoroethyl)-L-tyrosine (FET) PET images were

TABLE 1 | Timeline of diagnostics and therapeutic interventions.

Time (months from initial diagnosis)	Diagnostics/interventions	Outcome
0	Generalized seizure, structural brain MRI, and FET-PET	Left parietal, contrast-enhancing, and FET-PET-positive lesion
1	Resection of lesion	Singular metastasis, histopathological type: adenocarcinoma
2–3	Whole brain irradiation, 30 Gy in 10 fractions	Well tolerated
4	Right upper lobectomy for resection of primary tumor, mediastinal lymphadenectomy	NSCLC, involvement of mediastinal lymph nodes, Stage IV
6–9	Adjuvant chemotherapy, four courses of cisplatin/ vinorelbine	Complete remission of primary tumor
10–132	Follow-up including repeated chest CT and structural brain MRI and FET-PET, no further oncologic interventions	Complete remission of primary tumor and brain metastasis
132	Last follow-up, structural brain MRI, resting-state fMRI, and FET-PET	Development of bilateral white matter lesions

obtained using a high-resolution 3T hybrid PET/MR scanner equipped with a PET insert and a birdcage-like quadrature transmit head coil and an 8-channel receive coil (Siemens Tim-TRIO/ BrainPET, Siemens Medical Systems, Erlangen, Germany) (Herzog et al., 2011). MR imaging included a 3D T1-weighted magnetization-prepared rapid acquisition gradient-echo (MPRAGE) anatomical scan (176 sagittal slices, TR = 2,250 ms, TE = 3.03 ms, FoV = 256 × 256 mm^2, flip angle = 9°, voxel-size = 1 × 1 × 1 mm^3), a contrast-enhanced T1-weighted image (T1-CE) obtained from a second MPRAGE scan following the injection of gadolinium (0.1 mmol/kg, Dotarem^R, Guerbet GmbH, Sulzbach, Germany), and T2-weighted (T2-SPACE, 176 slices, TR = 3.2 s, TE = 417 ms, FoV = 256 × 256 mm^2, voxel-size = 1 × 1 × 1 mm^3) and fluid-attenuated inversion recovery structural images (FLAIR, 25 slices, TR = 9,000 ms, TE = 3.86 ms, FoV = 220 × 220 mm^2, flip angle = 150°, voxel-size = 0.9 × 0.9 × 4 mm^3).

Resting-State Functional MR Imaging

For rs-fMRI assessment, 300 functional volumes were acquired within 11 min using a gradient-echo echo planar imaging (GE-EPI) pulse sequence (36 axial slices, slice thickness 3.1 mm, repetition time TR = 2,200 ms, echo time TE = 30 ms, flip angle = 90°, FoV = 200 × 200 mm^2, in-plane voxel-size 3.1 × 3.1 mm^2). During image acquisition, the patient and the healthy subjects were instructed to relax and let their mind wander, but not to fall asleep. All MR protocols were exactly reproduced from a stand-alone 3T Siemens Tim-TRIO MR scanner used in the control group of the 1000BRAINS study (Caspers et al., 2014), and transferred to the hybrid scanner.

Determination of Resting-State Functional Connectivity

Functional images were subjected to the standard pre-processing steps of the SPM12/CONN toolbox (Whitfield-Gabrieli and Nieto-Castanon, 2012) comprising motion correction with removal of outliers and CSF/ white matter signals, slice timing correction, smoothing with 5 mm FWHM, bandpass-filtering to 0.008–0.09 Hz and denoising. All structural and functional images were non-rigidly co-registered to the MNI-152 standard brain template by means of the SPM12/CONN unified segmentation/registration algorithm. For determination of RSFC, a recently developed cortical parcellation (Schaefer et al., 2018) comprising 2 × 50 regions at the lowest resolution belonging to seven resting-state networks (visual, somato-motor, dorsal attention, ventral attention, limbic, fronto-parietal control, and default mode) was imported into the CONN toolbox and used to compute full connectivity matrices from the *z*-transformed Pearson correlation coefficients between the respective nodes. From these *z*-values, the within-network connectivity (sum of positive z-values for connections in the network/total number of nodes in the network) and inter-network connectivity (sum of positive *z*-values for connections to other networks/total number of connections to other networks) was computed for each of the seven networks (Stumme et al., 2020).

Cognitive Assessment

At the last follow up 11 years after initiation of therapy, the patient underwent a selection of neurocognitive tests using a subset of a test battery from the 1000BRAINS study (Caspers et al., 2014) that could be completed within 25–30 min and comprised the domains processing speed, attention, executive function, concept shifting, semantic word fluency, language processing, verbal working memory, visuo-spatial working memory and verbal episodic memory (Morris et al., 1989; Kalbe et al., 2004; Tombaugh, 2004).

Matched Cohort of Healthy Subjects

As pre-therapeutic cognitive data were not available for the patient, a reference group of healthy subjects was constructed from a population-based cohort study comprising over 1,300 patients. The cohort study investigated environmental and genetic influences on the inter-individual variability of brain structure, function, and connectivity in the aging brain [1000BRAINS study (Caspers et al., 2014)]. Due to a large variability of the factors gender, age and education in this large cohort which are known to impact both on cognitive performance and network measures (Jockwitz et al., 2017; Stumme et al., 2020; Jockwitz and Caspers, 2021), we aimed at selecting a subsample that resembled the patient as close as possible. For this purpose, only women that had the exactly the same level of education (tertiary, non-academic education, ISCED level 5B, 1997 ISCED scoring system, http://uis.unesco.

org/sites/default/files/documents/international-standard-classification-of-education-1997-en_0.pdf, accessed at 1.2.2018) and were of nearly the same age (±2 years) as the patient (59.9 years) were chosen from the entire cohort. This resulted resulting in a small cohort of 10 of healthy women with a mean age of 60.1 years (range 58.6–61.8 years). For comparison of cognitive test scores and within- and inter-network connectivity measures between the patient and the matched cohort, the (two-sided) one-sample *t*-test was applied (Kalpić et al., 2011). By applying this test, the observed value for the patient was assumed to represent the hypothetical mean of a patient population, and the probability distribution of the mean for the healthy cohort is compared to this value. $P < 0.05$ were regarded as significant.

OUTCOME

Clinical and Imaging Findings

During a follow-up period of 11 years, the patient stayed free from local tumor recurrence in the resection cavity, distant brain recurrence and further extracranial metastases. At the last follow up, she was in good general condition (ECOG performance score 0) and free from epileptic seizures and neurological deficits apart from a slight amnestic aphasia. She was still employed as a physician's assistant and reported to suffer from a significant reduction of working speed.

At initial diagnosis, the brain metastasis presented with localized MR contrast enhancement, increased uptake of FET and a well circumscribed, local T2/FLAIR hyperintensity covering the tumor and a small rim of normal brain tissue (**Figure 1**). At the last follow-up 11 years after brain metastasis resection and WBRT, the T1-weighted contrast enhanced MR and FET PET images showed no evidence of tumor recurrence, but in the T2/FLAIR MR images, extended regions of hyperintensities covering mainly the white mater of the bilateral dorsal frontal and parietal lobes while sparing most of the temporal lobes were found.

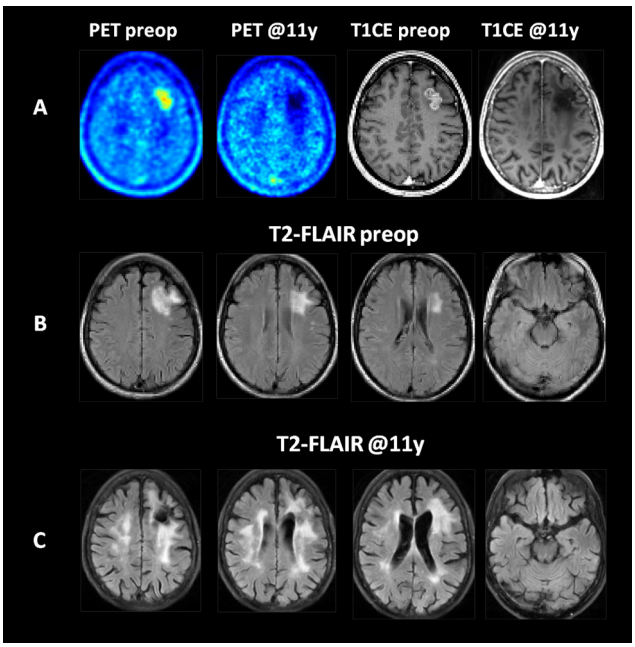

FIGURE 1 | Imaging findings at initial diagnosis and at 11 years of follow-up in a patient with a left frontal NSCLC (adenocarcinoma) brain metastasis treated by resection and whole brain radiotherapy. **(A)** The T1-weighted contrast enhanced MR (T1CE) and FET PET (PET) images revealed a contrast enhancing, PET-positive metastatic tumor with no evidence of recurrence in the brain or resection cavity during follow up. **(B)** The T2-FLAIR images at initial diagnosis. **(C)** At follow-up, extensive areas of T2-FLAIR hyperintensities developed in the white matter of the bilateral dorsal frontal and parietal lobes. All images are shown after elastic registration to the MNI-152 standard brain template.

Cognitive Test Results

Compared to the healthy subjects, the patient performed significantly worse in all cognitive domains that included executive functions, attention and processing speed (TMT-A 76 vs. 37 s, TMT-B 122 vs. 74 s, semantic word fluency test 19 vs. 29 items within 1 min), while most of the memory functions (verbal working memory, verbal episodic memory, and visual working memory) were left mostly unaffected, see **Figure 2**.

Resting-State Functional Connectivity

As depicted in **Figures 3A,B**, the mean RSFC matrix of the healthy subjects showed a clear pattern reflecting the structure of the underlying resting state networks. In contrast, the connectivity matrix of the patient showed a heavily disturbed pattern with a widely distributed, scattered loss of RSFC. The analysis of the within-network RSFC (**Figure 3C**) revealed a significant reduced connectivity within all seven networks. The dorsal attention and fronto-parietal control networks were the most severely affected and showed a reduction to <50% of the values in the healthy controls. As implied from the network structure of the brain, the inter-network RSFC was generally lower than the within-network connectivity in the healthy subjects, and was significantly further reduced in the patient for the visual, somato-motor, dorsal attention, and ventral attention networks.

DISCUSSION

In the present study, a NSCLC long-term survivor with metastatic brain disease who had WBRT developed extended white matter damage expressed by T2/FLAIR hyperintensities mainly covering the dorsal bilateral frontal and parietal lobes. Cognitive deficits were dominant in domains of executive functions, attention and processing speed but largely spared memory functions. The within-network connectivity of all 7 major resting state networks was significantly reduced, but the dorsal attention and fronto-parietal networks were most severely affected. A minor reduction of the inter-network connectivity was observed for the visual, somatomotor and attention networks.

Cognitive Deficits Following WBRT

The best evidence for the typical pattern of cognitive deficits induced by prophylactic or therapeutic WBRT was obtained from randomized clinical trials where appropriate neurocognitive test

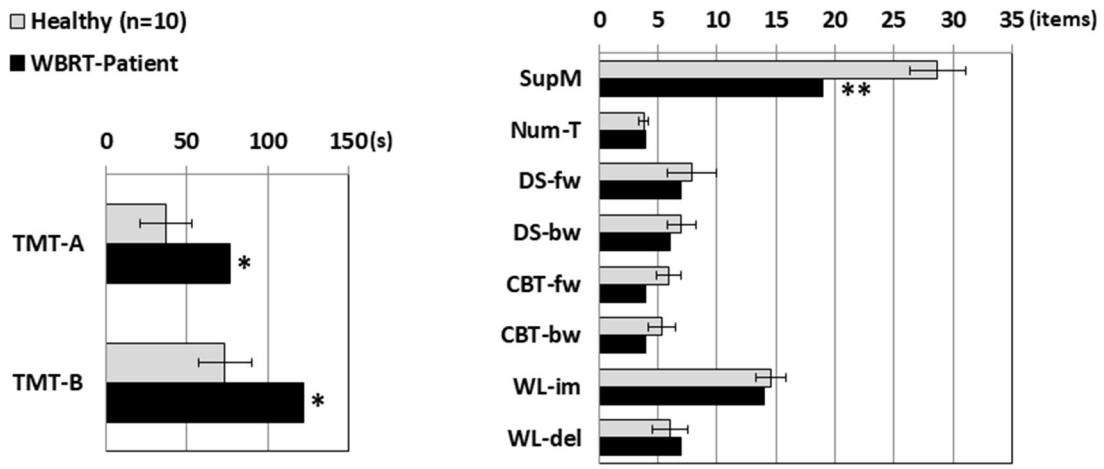

Test	Domain, Function
TMT-A: Trail-Making Test A, time in seconds	Processing Speed, Attention
TMT-B: Trail-Making Test B, time in seconds	Executive Function, Concept Shifting
SupM: Supermarket (DemTect), number of items named within 1 min	Semantic Word Fluency, Processing Speed
NumT: Number Transcoding (DemTect), number of correct items	Language Processing, Executive Function
DS-fw/bw: Digit Span for-/backward (DemTect), weighted number of items	Verbal Working Memory
CBT-fw/bw: CorsiBlock Tapping Test for- /backward (DemTect), weighted number of items	Visuo-Spatial Working Memory
WL-im/-del: Word List, immediate and delayed (DemTect) recall, number of items	Verbal Episodic Memory

FIGURE 2 | Cognitive test scores for Trail Making Tests A and B (measured in seconds, lower numbers mean better results) and for the tests scored by the number of items achieved (higher scores mean better results). Significant performance differences between the WBRT patient and the healthy subjects were observed for cognitive domains with a component of executive functioning (TMT-A: attention/ processing speed, TMT-B: executive function/concept shifting, supermarket test: semantic word fluency), while the scores for the memory domains were not significantly lowered. For the healthy subjects, means ± standard deviations are depicted; $^{*}p < 0.05$, $^{**}p < 0.01$, one-sample *t*-test.

sets have been applied (Tallet et al., 2012; McDuff et al., 2013). Recent trials found that, as in the present patient, not only memory, but also executive functioning is impaired as early as 3–6 months after WBRT (Brown et al., 2016, 2017). This view is also supported by a randomized trial on hippocampal-sparing WBRT where about 30% of the patients had memory deficits and a deterioration in the Trail-Making tests A (processing speed/attention) and B (concept shifting/executive function) at 6 months after WBRT (Brown et al., 2020).

Much less is known about the cognitive deficits developing after a follow-up time of 12 months or more after WBRT because only a small portion of patients survive this period, but it appears that verbal memory, executive functioning and processing speed are mostly affected (McDuff et al., 2013). Also, it is commonly assumed that injury to the white matter represents the major cause of cognitive deficits after WBRT and may progress beyond this time point (Greene-Schloesser et al., 2012). As in the case presented here, typical white matter changes detected by FLAIR MR imaging are dominantly located in the periventricular deep white matter and in the centrum semiovale and cover the dorsal frontal and parietal rather than the temporal lobes harboring the hippocampus (Fujii et al., 2006; Sabsevitz et al., 2013; Bovi et al., 2019). Therefore, it can be hypothesized that memory deficits are transient effects potentially caused by depletion of neuronal stem cells of the hippocampus (Peissner et al., 1999), whereas late cognitive deficits develop as a consequence of white matter injury to more distributed dorsal brain regions (Makale et al., 2017).

Functional Brain Connectivity Changes After WBRT

Regarding the changes in functional brain connectivity as determined by fMRI and induced by WBRT, to the best of our knowledge, only one other single case has been reported so far (Mitchell et al., 2020). This other reported patient also developed a decline in multiple cognitive domains including executive functions/visuo-constructional skills, naming, attention/calculations, memory and orientation 12 months after WBRT. The RSFC analysis was carried out 9 months after WBRT and revealed that most functional networks became aberrant where the medial temporal lobe network and the fronto-parietal network were affected most.

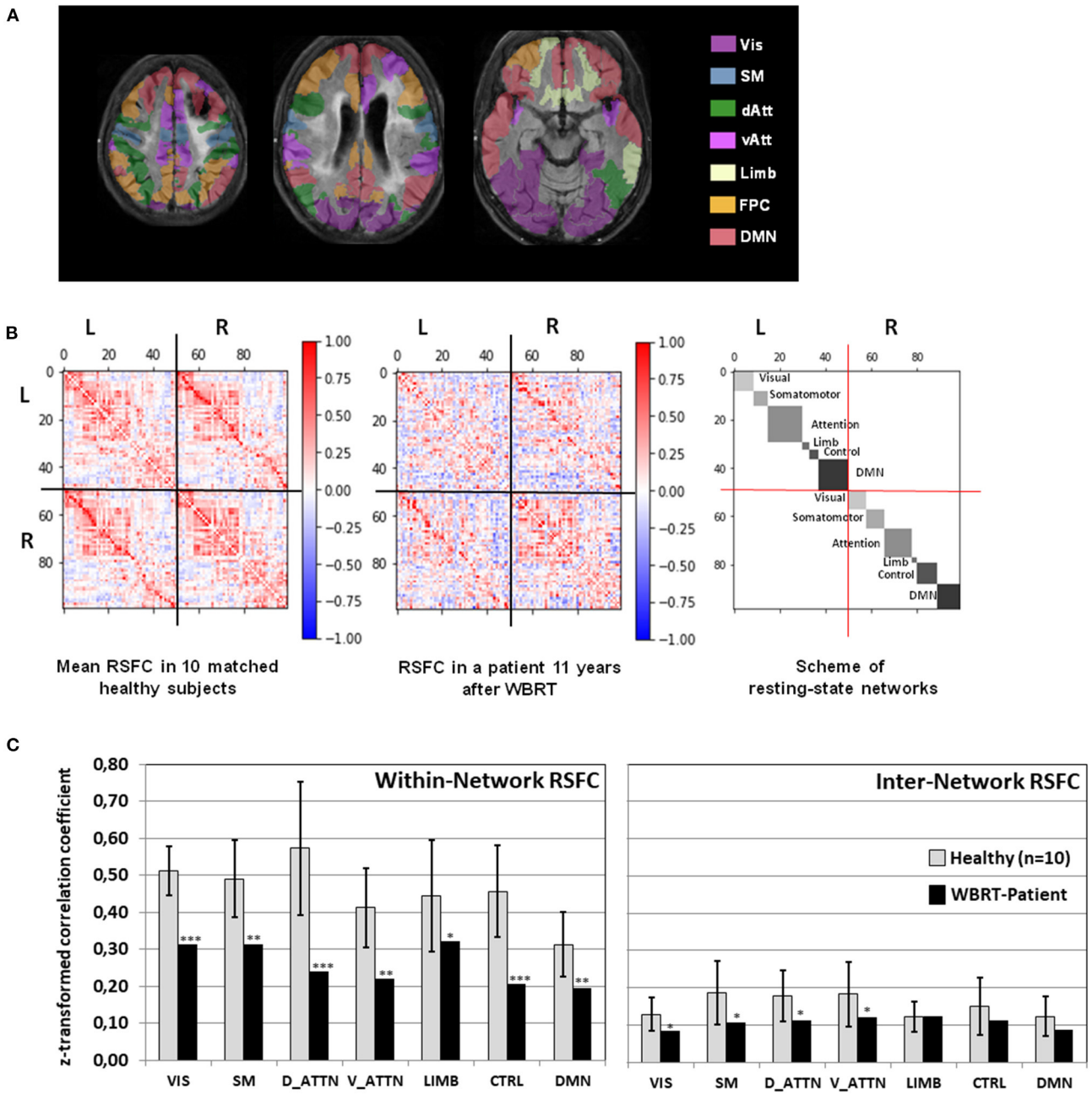

FIGURE 3 | (A) Overlay of the patient's FLAIR images registered to the MNI-152 space with the color-coded cortical areas belonging to 7 resting-state networks. **(B)** Mean resting-state functional connectivity in 10 healthy subjects and in the patient depicted together with the scheme of resting-state networks. **(C)** Within-network and inter-network resting state connectivity (RSFC, mean *z*-normalized Pearson correlation coefficient of positive-valued connections) for each of the seven resting-state networks in the whole brain radiotherapy (WBRT) patient compared to the healthy subjects. For the healthy subjects, means ± standard deviations are depicted. $^{*}p < 0.05$, $^{**}p < 0.01$, $^{***}p < 0.001$, one-sample *t*-test. Vis, Visual Network; SM, Somato-Motor Network; dAtt, Dorsal Attention Network; vAtt, Ventral Attention Network; Limb, Limbic Network; FPC, Fronto-Parietal Control Network; DMN, Default Mode Network.

In the patient of the present study, the within-network connectivity was primarily affected, a finding that has also been made in the aging brain (Stumme et al., 2020). Importantly, the dorsal attention network which is responsible for goal-directed, voluntary control of visuospatial attention (Corbetta and Shulman, 2002; Kincade et al., 2005; Vossel et al., 2012, 2014) and the fronto-parietal network which is involved in sustained attention, complex problem-solving and working memory (Menon, 2011) were affected most. This observation fits to the other results obtained here in two ways. First,

these networks are located in brain regions where the white matter was affected most. Second, the scores for cognitive tests that included a dominant component of executive functioning, directed attention and processing speed (TMT-A, TMT-B, and test verbal fluency test) were reduced strongest in the patient.

The slight reduction of inter-network connectivity after WBRT is probably also a consequence of radiation damage to the white matter. However, due to the network structure of the brain, inter-network connectivity can be expected to be lower than within-network connectivity, and has been found to show a compensatory increase as a response to diminishing within-network connectivity in older adults (Jockwitz and Caspers, 2021). Thus, a possible explanation for the pattern observed here at long time after WBRT may reflect the ability of the brain to partly compensate the irradiation-induced damage by functional reorganization.

Patients Perspective

At the last follow up, the patient was still employed as a physician's assistant and reported to live a satisfactory life. However, she claimed that performance speed for daily accomplishments at home and working tasks was significantly reduced which had caused some negative remarks from her colleagues. She did not regret her decision to have whole-brain radiation because, in her opinion, it had prevented the development of new brain metastases.

CONCLUSION

As demonstrated here in a patient with a metastatic NSCLC and long-term survival, WBRT may lead to extended damage to the white matter and cause severe disruption of the RSFC in multiple resting-state networks. Apart from well-recognized deficits in memory function, executive functioning and goal-directed attention which is assumed to depend on the interaction of several networks may be severely impaired as a result of WBRT. Although we assume that the patient presented here suffered the typical course of image changes and side effects induced by WBRT, more studies are clearly needed to confirm these findings.

DATA AVAILABILITY STATEMENT

The raw data supporting the conclusions of this article will be made available by the authors, without undue reservation.

ETHICS STATEMENT

The studies involving human participants were reviewed and approved by Ethics Committees of the Universities of Cologne and Essen, Germany. The patients/participants provided their written informed consent to participate in this study.

AUTHOR CONTRIBUTIONS

MK selected, analyzed, and interpreted the data and was a major contributor to writing the manuscript. CL, PL, FM, and NS provided the imaging methods and facilities. MS, GS, and CF treated and examined the patient. CJ and SC developed the network analysis methods and provided the control group data. MK, MR, GF, NG, and K-JL conceptualized the study. All authors read and approved the final manuscript.

FUNDING

The Wilhelm-Sander Stiftung, Germany, supported this work. This project was partially funded by the German National Cohort and the 1000BRAINS-Study of the Institute of Neuroscience and Medicine, Research Center Juelich, Germany and received funding from the European Union's Horizon 2020 Research and Innovation Programme under Grant Agreement No. 945539 (HBP SGA3; SC) as well as from the Initiative and Networking Fund of the Helmholtz Association (SC).

ACKNOWLEDGMENTS

The technical assistance of N. Judov, S. Frensch, K. Frey, T. Plum, E. Rota Kops, S. Schaden, J. Scheins, and L. Tellmann was gratefully acknowledged. We thank the Heinz Nixdorf Foundation (Germany) for the generous support of the Heinz Nixdorf Study. We thank the investigative group and the study staff of the Heinz Nixdorf Recall Study and 1000BRAINS.

SUPPLEMENTARY MATERIAL

The Supplementary Material for this article can be found online at: https://www.frontiersin.org/articles/10.3389/fnins.2021.738708/full#supplementary-material

REFERENCES

Bovi, J. A., Pugh, S. L., Sabsevitz, D., Robinson, C. G., Paulson, E., Mehta, M. P., et al. (2019). Pretreatment volume of MRI-determined white matter injury predicts neurocognitive decline after hippocampal avoidant whole-brain radiation therapy for brain metastases: secondary analysis of NRG oncology radiation therapy oncology group 0933. *Adv. Radiat. Oncol.* 4, 579–586. doi: 10.1016/j.adro.2019.07.006

Brown, P. D., Ballman, K. V., Cerhan, J. H., Anderson, S. K., Carrero, X. W., Whitton, A. C., et al. (2017). Postoperative stereotactic radiosurgery compared with whole brain radiotherapy for resected metastatic brain disease (NCCTG N107C/CEC.3): a multicentre, randomised, controlled, phase 3 trial. *Lancet Oncol.* 18, 1049–1060. doi: 10.1016/S1470-2045(17)30441-2

Brown, P. D., Gondi, V., Pugh, S., Tome, W. A., Wefel, J. S., Armstrong, T. S., et al. (2020). Hippocampal avoidance during whole-brain radiotherapy plus memantine for patients with brain metastases: phase III trial NRG oncology CC001. *J. Clin. Oncol.* 38, 1019–1029. doi: 10.1200/JCO.19.02767

Brown, P. D., Jaeckle, K., Ballman, K. V., Farace, E., Cerhan, J. H., Anderson, S. K., et al. (2016). Effect of radiosurgery alone vs radiosurgery with whole brain radiation therapy on cognitive function in patients with 1 to 3 brain metastases: a randomized clinical trial. *JAMA* 316, 401–409. doi: 10.1001/jama.2016.9839

Bruno, J., Hosseini, S. M., and Kesler, S. (2012). Altered resting state functional brain network topology in chemotherapy-treated breast cancer survivors. *Neurobiol. Dis.* 48, 329–338. doi: 10.1016/j.nbd.2012.07.009

Caspers, S., Moebus, S., Lux, S., Pundt, N., Schutz, H., Muhleisen, T. W., et al. (2014). Studying variability in human brain aging in a population-based German cohort-rationale and design of 1000BRAINS. *Front. Aging Neurosci.* 6:149. doi: 10.3389/fnagi.2014.00149

Chang, E. L., Wefel, J. S., Hess, K. R., Allen, P. K., Lang, F. F., Kornguth, D. G., et al. (2009). Neurocognition in patients with brain metastases treated with radiosurgery or radiosurgery plus whole-brain irradiation: a randomised controlled trial. *Lancet Oncol.* 10, 1037–1044. doi: 10.1016/S1470-2045(09)70263-3

Corbetta, M., and Shulman, G. L. (2002). Control of goal-directed and stimulus-driven attention in the brain. *Nat. Rev. Neurosci.* 3, 201–215. doi: 10.1038/nrn755

Fujii, O., Tsujino, K., Soejima, T., Yoden, E., Ichimiya, Y., and Sugimura, K. (2006). White matter changes on magnetic resonance imaging following whole-brain radiotherapy for brain metastases. *Radiat. Med.* 24, 345–350. doi: 10.1007/s11604-006-0039-9

Gaspar, L. E., Mehta, M. P., Patchell, R. A., Burri, S. H., Robinson, P. D., Morris, R. E., et al. (2010). The role of whole brain radiation therapy in the management of newly diagnosed brain metastases: a systematic review and evidence-based clinical practice guideline. *J. Neurooncol.* 96, 17–32. doi: 10.1007/s11060-009-0060-9

Giuseppe, Z. R., Silvia, C., Eleonora, F., Gabriella, M., Marica, F., Silvia, C., et al. (2020). Hippocampal-sparing radiotherapy and neurocognitive impairment: a systematic literature review. *J. Cancer Res. Ther.* 16, 1215–1222. doi: 10.4103/jcrt.JCRT_573_17

Gondi, V., Pugh, S. L., Tome, W. A., Caine, C., Corn, B., Kanner, A., et al. (2014). Preservation of memory with conformal avoidance of the hippocampal neural stem-cell compartment during whole-brain radiotherapy for brain metastases (RTOG 0933): a phase II multi-institutional trial. *J. Clin. Oncol.* 32, 3810–3816. doi: 10.1200/JCO.2014.57.2909

Greene-Schloesser, D., Robbins, M. E., Peiffer, A. M., Shaw, E. G., Wheeler, K. T., and Chan, M. D. (2012). Radiation-induced brain injury: a review. *Front. Oncol.* 2:73. doi: 10.3389/fonc.2012.00073

Herzog, H., Langen, K. J., Weirich, C., Rota Kops, E., Kaffanke, J., Tellmann, L., et al. (2011). High resolution BrainPET combined with simultaneous MRI. *Nuklearmedizin* 50, 74–82. doi: 10.3413/Nukmed-0347-10-09

Jockwitz, C., and Caspers, S. (2021). Resting-state networks in the course of aging-differential insights from studies across the lifespan vs. amongst the old. *Pflugers Arch.* 473, 793–803. doi: 10.1007/s00424-021-02520-7

Jockwitz, C., Caspers, S., Lux, S., Eickhoff, S. B., Jutten, K., Lenzen, S., et al. (2017). Influence of age and cognitive performance on resting-state brain networks of older adults in a population-based cohort. *Cortex* 89, 28–44. doi: 10.1016/j.cortex.2017.01.008

Kalbe, E., Kessler, J., Calabrese, P., Smith, R., Passmore, A. P., Brand, M., et al. (2004). DemTect: a new, sensitive cognitive screening test to support the diagnosis of mild cognitive impairment and early dementia. *Int. J. Geriatr. Psychiatry* 19, 136–143. doi: 10.1002/gps.1042

Kalpić, D., Hlupić N., and Lovrić M. (2011). "Student's t-tests," in *International Encyclopedia of Statistical Science*, ed M. Lovric (Berlin; Heidelberg: Springer). doi: 10.1007/978-3-642-04898-2_641

Kesler, S. R., Wefel, J. S., Hosseini, S. M., Cheung, M., Watson, C. L., and Hoeft, F. (2013). Default mode network connectivity distinguishes chemotherapy-treated breast cancer survivors from controls. *Proc. Natl. Acad. Sci. U. S. A.* 110, 11600–11605. doi: 10.1073/pnas.1214551110

Kincade, J. M., Abrams, R. A., Astafiev, S. V., Shulman, G. L., and Corbetta, M. (2005). An event-related functional magnetic resonance imaging study of voluntary and stimulus-driven orienting of attention. *J. Neurosci.* 25, 4593–4604. doi: 10.1523/JNEUROSCI.0236-05.2005

Kocher, M., Soffietti, R., Abacioglu, U., Villa, S., Fauchon, F., Baumert, B. G., et al. (2011). Adjuvant whole-brain radiotherapy versus observation after radiosurgery or surgical resection of one to three cerebral metastases: results of the EORTC 22952-26001 study. *J. Clin. Oncol.* 29, 134–141. doi: 10.1200/JCO.2010.30.1655

Lin, N. U., Wefel, J. S., Lee, E. Q., Schiff, D., van den Bent, M. J., Soffietti, R., et al. (2013). Challenges relating to solid tumour brain metastases in clinical trials, part 2: neurocognitive, neurological, and quality-of-life outcomes. A report from the RANO group. *Lancet Oncol.* 14, e407–e416. doi: 10.1016/S1470-2045(13)70308-5

Makale, M. T., McDonald, C. R., Hattangadi-Gluth, J. A., and Kesari, S. (2017). Mechanisms of radiotherapy-associated cognitive disability in patients with brain tumours. *Nat. Rev. Neurol.* 13, 52–64. doi: 10.1038/nrneurol.2016.185

McDuff, S. G., Taich, Z. J., Lawson, J. D., Sanghvi, P., Wong, E. T., Barker, F. G. 2nd, Hochberg, F. H., et al. (2013). Neurocognitive assessment following whole brain radiation therapy and radiosurgery for patients with cerebral metastases. *J. Neurol. Neurosurg. Psychiatry* 84, 1384–1391. doi: 10.1136/jnnp-2013-305166

Menon, V. (2011). Large-scale brain networks and psychopathology: a unifying triple network model. *Trends Cogn. Sci.* 15, 483–506. doi: 10.1016/j.tics.2011.08.003

Mitchell, T., Seitzman, B., Ballard, N., Petersen, S. E., Shimony, J., and Leuthardt, E. (2020). Human brain functional network organization is disrupted following whole-brain radiation therapy. *Brain Connect.* 10, 29–38. doi: 10.1089/brain.2019.0713

Morris, J. C., Heyman, A., Mohs, R. C., Hughes, J. P., van Belle, G., Fillenbaum, G., et al. (1989). The Consortium to Establish a Registry for Alzheimer's Disease (CERAD). Part I. Clinical and neuropsychological assessment of Alzheimer's disease. *Neurology* 39, 1159–1165. doi: 10.1212/WNL.39.9.1159

Patchell, R. A., Tibbs, P. A., Regine, W. F., Dempsey, R. J., Mohiuddin, M., Kryscio, R. J., et al. (1998). Postoperative radiotherapy in the treatment of single metastases to the brain: a randomized trial. *JAMA* 280, 1485–1489. doi: 10.1001/jama.280.17.1485

Peissner, W., Kocher, M., Treuer, H., and Gillardon, F. (1999). Ionizing radiation-induced apoptosis of proliferating stem cells in the dentate gyrus of the adult rat hippocampus. *Brain Res. Mol. Brain Res.* 71, 61–68. doi: 10.1016/S0169-328X(99)00170-9

Piccirillo, J. F., Hardin, F. M., Nicklaus, J., Kallogjeri, D., Wilson, M., Ma, C. X., et al. (2015). Cognitive impairment after chemotherapy related to atypical network architecture for executive control. *Oncology* 88, 360–368. doi: 10.1159/000370117

Pinkham, M. B., Sanghera, P., Wall, G. K., Dawson, B. D., and Whitfield, G. A. (2015). Neurocognitive effects following cranial irradiation for brain metastases. *Clin. Oncol.* 27, 630–639. doi: 10.1016/j.clon.2015.06.005

Sabsevitz, D. S., Bovi, J. A., Leo, P. D., Laviolette, P. S., Rand, S. D., Mueller, W. M., et al. (2013). The role of pre-treatment white matter abnormalities in developing white matter changes following whole brain radiation: a volumetric study. *J. Neurooncol.* 114, 291–297. doi: 10.1007/s11060-013-1181-8

Schaefer, A., Kong, R., Gordon, E. M., Laumann, T. O., Zuo, X. N., Holmes, A. J., et al. (2018). Local-global parcellation of the human cerebral cortex from intrinsic functional connectivity MRI. *Cereb. Cortex* 28, 3095–3114. doi: 10.1093/cercor/bhx179

Soffietti, R., Abacioglu, U., Baumert, B., Combs, S. E., Kinhult, S., Kros, J. M., et al. (2017). Diagnosis and treatment of brain metastases from solid tumors: guidelines from the European Association of Neuro-Oncology (EANO). *Neuro Oncol.* 19, 162–174. doi: 10.1093/neuonc/now241

Soffietti, R., Kocher, M., Abacioglu, U. M., Villa, S., Fauchon, F., Baumert, B. G., et al. (2013). A European Organisation for Research and Treatment of Cancer phase III trial of adjuvant whole-brain radiotherapy versus observation in patients with one to three brain metastases from solid tumors after surgical resection or radiosurgery: quality-of-life results. *J. Clin. Oncol.* 31, 65–72. doi: 10.1200/JCO.2011.41.0639

Stumme, J., Jockwitz, C., Hoffstaedter, F., Amunts, K., and Caspers, S. (2020). Functional network reorganization in older adults: graph-theoretical analyses of age, cognition and sex. *Neuroimage* 214:116756. doi: 10.1016/j.neuroimage.2020.116756

Tallet, A. V., Azria, D., Barlesi, F., Spano, J. P., Carpentier, A. F., Goncalves, A., et al. (2012). Neurocognitive function impairment after whole brain radiotherapy for brain metastases: actual assessment. *Radiat. Oncol.* 7:77. doi: 10.1186/1748-717X-7-77

Tao, L., Lin, H., Yan, Y., Xu, X., Wang, L., Zhang, J., et al. (2017). Impairment of the executive function in breast cancer patients receiving chemotherapy treatment: a functional MRI study. *Eur. J. Cancer Care (Engl.)* 26. doi: 10.1111/ecc.12553

Tao, L., Wang, L., Chen, X., Liu, F., Ruan, F., Zhang, J., et al. (2020). Modulation of interhemispheric functional coordination in breast cancer patients receiving chemotherapy. *Front. Psychol.* 11:1689. doi: 10.3389/fpsyg.2020.01689

Tombaugh, T. N. (2004). Trail Making Test A and B: normative data stratified by age and education. *Arch. Clin. Neuropsychol.* 19, 203–214. doi: 10.1016/S0887-6177(03)00039-8

Vossel, S., Geng, J. J., and Fink, G. R. (2014). Dorsal and ventral attention systems: distinct neural circuits but collaborative roles. *Neuroscientist* 20, 150–159. doi: 10.1177/1073858413494269

Vossel, S., Weidner, R., Driver, J., Friston, K. J., and Fink, G. R. (2012). Deconstructing the architecture of dorsal and ventral attention systems with dynamic causal modeling. *J. Neurosci.* 32, 10637–10648. doi: 10.1523/JNEUROSCI.0414-12.2012

Whitfield-Gabrieli, S., and Nieto-Castanon, A. (2012). Conn: a functional connectivity toolbox for correlated and anticorrelated brain networks. *Brain Connect* 2, 125–141. doi: 10.1089/brain.2012.0073

Yeo, B. T., Krienen, F. M., Sepulcre, J., Sabuncu, M. R., Lashkari, D., Hollinshead, M., et al. (2011). The organization of the human cerebral cortex estimated by intrinsic functional connectivity. *J. Neurophysiol.* 106, 1125–1165. doi: 10.1152/jn.00338.2011

Conflict of Interest: The authors declare that the research was conducted in the absence of any commercial or financial relationships that could be construed as a potential conflict of interest.

Publisher's Note: All claims expressed in this article are solely those of the authors and do not necessarily represent those of their affiliated organizations, or those of the publisher, the editors and the reviewers. Any product that may be evaluated in this article, or claim that may be made by its manufacturer, is not guaranteed or endorsed by the publisher.

Copyright © 2021 Kocher, Jockwitz, Lerche, Sabel, Lohmann, Stoffels, Filss, Mottaghy, Ruge, Fink, Shah, Galldiks, Caspers and Langen. This is an open-access article distributed under the terms of the Creative Commons Attribution License (CC BY). The use, distribution or reproduction in other forums is permitted, provided the original author(s) and the copyright owner(s) are credited and that the original publication in this journal is cited, in accordance with accepted academic practice. No use, distribution or reproduction is permitted which does not comply with these terms.

frontiers in Neuroscience

ORIGINAL RESEARCH
published: 29 October 2021
doi: 10.3389/fnins.2021.665016

Resting-State Functional Magnetic Resonance Imaging Networks as a Quantitative Metric for Impact of Neurosurgical Interventions

Peter H. Yang[1], Carl D. Hacker[1], Bhuvic Patel[1], Andy G. S. Daniel[2] and Eric C. Leuthardt[1,2,3,4,5]*

[1] *Department of Neurological Surgery, Washington University School of Medicine, St. Louis, MO, United States,* [2] *Department of Biomedical Engineering, Washington University in St. Louis, St. Louis, MO, United States,* [3] *Department of Neuroscience, Washington University School of Medicine, St. Louis, MO, United States,* [4] *Center for Innovation in Neuroscience and Technology, Washington University School of Medicine, St. Louis, MO, United States,* [5] *Brain Laser Center, Washington University School of Medicine, St. Louis, MO, United States*

Objective: Resting-state functional MRI (rs-fMRI) has been used to evaluate brain network connectivity as a result of intracranial surgery but has not been used to compare different neurosurgical procedures. Laser interstitial thermal therapy (LITT) is an alternative to conventional craniotomy for the treatment of brain lesions such as tumors and epileptogenic foci. While LITT is thought of as minimally invasive, its effect on the functional organization of the brain is still under active investigation and its impact on network changes compared to conventional craniotomy has not yet been explored. We describe a novel computational method for quantifying and comparing the impact of two neurosurgical procedures on brain functional connectivity.

Methods: We used a previously described seed-based correlation analysis to generate resting-state network (RSN) correlation matrices, and compared changes in correlation patterns within and across RSNs between LITT and conventional craniotomy for treatment of 24 patients with singular intracranial tumors at our institution between 2014 and 2017. Specifically, we analyzed the differences in patient-specific changes in the within-hemisphere correlation patterns of the contralesional hemisphere.

Results: In a post-operative follow-up period up to 2 years within-hemisphere connectivity of the contralesional hemisphere after surgery was more highly correlated to the pre-operative state in LITT patients when compared to craniotomy patients ($P = 0.0287$). Moreover, 4 out of 11 individual RSNs demonstrated significantly higher degrees of correlation between pre-operative and post-operative network connectivity in patients who underwent LITT (all $P < 0.05$).

Conclusion: Rs-fMRI may be used as a quantitative metric to determine the impact of different neurosurgical procedures on brain functional connectivity. Global and individual network connectivity in the contralesional hemisphere may be more highly preserved after LITT when compared to craniotomy for the treatment of brain tumors.

Keywords: functional neuroimaging, humans, laser therapy, magnetic resonance imaging, brain neoplasms/surgery, brain neoplasms/diagnostic imaging

OPEN ACCESS

Edited by:
Sandro M. Krieg, Technical University of Munich, Germany

Reviewed by:
Gaelle Eve Doucet, Boys Town National Research Hospital, United States
Domenico Zaca, Siemens, Italy

****Correspondence:***
Peter H. Yang
peter.yang@wustl.edu

Specialty section:
This article was submitted to Brain Imaging Methods, a section of the journal Frontiers in Neuroscience

Received: *06 February 2021*
Accepted: *05 October 2021*
Published: *29 October 2021*

Citation:
Yang PH, Hacker CD, Patel B, Daniel AGS and Leuthardt EC (2021) Resting-State Functional Magnetic Resonance Imaging Networks as a Quantitative Metric for Impact of Neurosurgical Interventions. Front. Neurosci. 15:665016. doi: 10.3389/fnins.2021.665016

INTRODUCTION

Resting-state functional MRI (rs-fMRI) is an imaging technique that has provided significant insight into the functional organization of the brain in both healthy and pathologic states. Functional MRI is based on measurements of changes in T2* signal that are dependent on the oxy/deoxyhemoglobin ratio; referred to as the blood oxygen level dependent (BOLD) signal. Traditionally, responses to experimental paradigms have been averaged across trials to investigate the topography of specific brain functions. However, even when no cognitive, language, or motor tasks are being performed, networks of brain regions demonstrate synchronous BOLD fluctuations (Biswal et al., 1995; Hacker et al., 2019). Extensive analyses of the correlation patterns of BOLD fluctuations have revealed networks such as the somatosensory, language, visual and auditory networks, among others (Power et al., 2011; Yeo et al., 2011). Importantly, these resting-state networks (RSNs) correspond anatomically to the topography of task-based fMRI activity (Smith et al., 2009; Hacker et al., 2019; Park et al., 2020). In the research setting, rs-fMRI has been used to evaluate network connectivity in disease states such as Parkinson's and Alzheimer's disease, providing insight into the impact of these diseases on brain function (Greicius et al., 2004; Hacker et al., 2012). Additionally, clinical outcomes after acute ischemic stroke have been correlated with inter-hemispheric connectivity measured using rs-fMRI. In a study of 13 patients who experienced subcortical stroke, rs-fMRI scans were taken at predetermined time points and compared with those from matched controls. The functional connectivity between the contralesional primary sensorimotor cortex and the bilateral primary sensorimotor cortex in patients who experienced stroke was found to initially decrease then increase over time and correlated with clinical recovery of motor function (Xu et al., 2014). This suggests that functional connectivity and neuroplasticity can be dynamically quantified after neurologic injury using rs-fMRI. Importantly, this demonstrates that the contralateral, non-lesional, hemisphere is useful in measuring changes in RSNs from intracranial lesions. Combined with diffusion tensor imaging for tractography, rs-fMRI is an emerging tool for preoperative neurosurgical planning as well as an intra-operative navigational technique for avoidance of eloquent structures (Dierker et al., 2017; Roland et al., 2017, 2019; Leuthardt et al., 2018).

Post-neurosurgical changes in network connectivity have been evaluated using rs-fMRI in several select applications, including after deep brain stimulation for Parkinson's disease, corpus callosotomy for epilepsy, and laser ablation of seizure foci (Johnston et al., 2008; Kahan et al., 2014; Boerwinkle et al., 2018). In all instances of studying rs-fMRI in neurosurgical procedures, the surgical intervention was intended to modify neural circuitry and rs-fMRI was used to describe those circuitry changes. However, there has not been a quantitative approach to comparing the functional impact of multiple surgical techniques in treating similar pathologies. With new and more widespread use of minimally invasive procedures such as stereotactic laser interstitial thermal therapy (LITT) to treat intracranial lesions, there is a need for quantifying and comparing the functional impact on brain connectivity to that of conventional open craniotomy.

LITT is a minimally invasive, ablative neurosurgical procedure that has gained significant traction over the past decade. Despite first being described by Bown (1983) the technique has only more recently become viable due to the development of MRI thermometry, which allows for real time monitoring of temperatures distant from the laser probe (De Poorter et al., 1995; Hawasli et al., 2013). The ability to create targeted, conformal thermal lesions in a minimally invasive manner makes LITT an attractive option for treating numerous central nervous system (CNS) lesions. LITT has been described for the treatment of epileptic foci, primary and metastatic brain tumors, and radiation necrosis, with new indications continuing to be developed (Hawasli et al., 2011, 2014; Torres-Reveron et al., 2013; Mohammadi et al., 2014; Kamath et al., 2017; Bijanki et al., 2020; Hafez et al., 2020; Remick et al., 2020). For example, rs-fMRI has been used at our institution during stereotactic LITT procedures both to plan a trajectory that avoids traversing eloquent cortex and to create an ablative lesion that spares eloquent cortex (Salehi et al., 2018). Anecdotally, LITT is presumed to be less disruptive to the overall functional brain connectivity because of the lack of brain retraction and manipulation which occur during open craniotomy, but the details of the differences in functional impact of LITT vs. standard craniotomy have not yet been quantified.

In this work, we demonstrate for the first time the use of a simple yet reproducible quantitative approach using rs-fMRI to illustrate the differences in impact that two surgical approaches have on the functional organization of the brain in patients with singular intra-axial brain tumors. Specifically, we show that the within-hemisphere resting-state Pearson correlation coefficients *contralateral* to the lesion in craniotomy and LITT patients can be directly compared and quantified while overcoming the challenges of tumor mass effect and post-surgical changes and while taking into account individual patient variations.

MATERIALS AND METHODS

Patient Selection

All aspects of this retrospective cohort study were approved by the Human Research and Protection Office Institutional Review Board (IRB) at our institution. Data including patient demographics, surgery types, surgery dates, radiation dates, rs-fMRI accession numbers, and tumor characteristics were retrospectively collected from patients who underwent craniotomy and/or LITT for intra-axial tumors between 2014 and 2017. Informed consent was not obtained due to the retrospective nature of the study. Treatment characteristics included whether patients underwent radiation between scans, prior stereotactic needle biopsy only, LITT, and craniotomy. Tumor characteristics included whether the tumor was intra-axial, type (metastatic or intrinsic glial neoplasm), WHO grade (if applicable), and volume (taken from radiology report). These characteristics were used to match patients between groups. Patients with evidence of bilateral tumor involvement, midline shift, or prior cranial surgery (except stereotactic needle biopsy)

were excluded. Patients with post-operative imaging up to 2 years were considered. Statistical analysis of continuous and categorical variables of patient and tumor characteristics were performed using the two-tailed Student's *t*-test and two-tailed Fisher's exact test, respectively, to calculate statistical significance (**Table 1**).

MRI Image Acquisition

All imaging was performed with a 3T Siemens Trio scanner. Patients were instructed to keep their eyes open and look at a single focus point during image acquisition. All patients remained awake during the scans. Structural imaging included one T1-weighted MP-RAGE [repetition time (TR) = 2,000 ms, echo time (TE) = 2.5 ms, flip angle = 12°, voxel size 1.0 × 1.0 × 1.0 mm] and one T2-weighted turbo-spin echo sequence [TR = 9,000 ms, TE = 115 ms, flip angle = 120°, voxel size 1.0 × 1.0 × 2.5 mm]. Rs-fMRI was acquired using an echo-planar imaging (EPI) sequence sensitive to BOLD contrast (TR = 2,070 ms, TE = 25 ms, flip angle = 90°, voxel size 4.0 × 4.0 × 4.0 mm). Two runs of 200 frames each (∼14 min total) were acquired in each subject.

Resting-State Functional Connectivity Preprocessing

fMRI preprocessing followed previously published preprocessing methods to ensure that artifacts were removed and that data was normalized (Shulman et al., 2010; Power et al., 2014; Leuthardt et al., 2018; Seitzman et al., 2020). This step corrected for head movement, normalized signal intensity across scans, and performed atlas transformation. Volumetric BOLD time series were registered to an isotropic 3 mm atlas space. In addition, spatial smoothing and voxel-wise temporal smoothing was performed for each run. Temporal frequencies < 0.1 Hz were retained. Time series sampled from regions of cerebrospinal fluid and white matter were used to reduce erroneous variations by regression of nuisance waveforms derived from motion correction. The whole-brain signal was removed as a nuisance regressor. Finally, frame censoring was performed. Volumetric frames in which the root-mean-square of voxel intensities within brain regions changed significantly compared to the previous frame (>0.5% of root-mean-square voxel intensities), the frame was censored to minimize the impact of head motion on functional connectivity computations. Scans were excluded if they failed preprocessing due to significant.

TABLE 1 | Baseline characteristics of craniotomy and laser interstitial thermal therapy patients.

Patient characteristics	Craniotomy	LITT	*P*-value
Patients	12	12	–
Mean age	46.7 (23.0–76.0)	48.7 (7.5–68.8)	0.8027
Female	6	5	1.0000
Tumor characteristics			
Intra-axial	12	12	–
Metastasis	3	3	0.8948
Intrinsic glial neoplasm	9	9	
WHO grade I/II	5	4	
WHO grade III/IV	4	5	
Mean tumor volume (cm^3)	14.3713	10.9382	0.6291
Treatment			
Radiation between scans	5	2	0.3707
No prior surgery	11	6	0.0686
Prior needle biopsy only	1	6	
Mean time between surgery and post-operative scan (days)	235.6667	206.3333	0.9076

WHO, World Health Organization; LITT, laser interstitial thermal therapy.
There was no significant difference between age, gender, tumor etiology, tumor volume, radiation treatment, prior surgery, and time between surgery and post-operative scan. Two tailed Student's t-test assuming unequal variances for continuous variables. Two-tailed Fisher's exact test for categorical variables.

Resting-State Functional Connectivity Analysis

A publicly available set of 300 cortical, subcortical, and cerebellar ROIs,[1] described in detail by Seitzman et al. (2020), was used in this study (Seitzman et al., 2020). This link also included a list of coordinates and consensus functional network labels. These ROIs and their corresponding network assignments were determined using a combination of seed-based correlation analysis and network community detection. The seed-based correlation analysis was performed to examine the spatial and temporal relationships between ROIs (**Figure 1**). In short, after image acquisition and preprocessing, the BOLD time series for each seed ROI were calculated as a correlation with all other ROIs in the brain, resulting in a Pearson's r matrix 300 × 300 in size. Community detection was used to determine the functional network membership of each ROI using the Infomap algorithm (Power et al., 2011). Thus, the 300 ROIs were assigned to one of 14 functional network communities: default mode, frontoparietal, cinguloopercular, salience, dorsal attention, ventral attention, visual, auditory, somatomotor dorsal, somatomotor lateral, parieto-medial, striatal orbitofrontal amygdalar, medial temporal lobe, and unlabeled. Because the latter 3 networks were less well-defined in literature, we selected to examine the former 11 well-defined networks for our study. A system called the Translational Imaging Portal (TIP), a customized version of the Extensible Neuroimaging Archive Toolkit (XNAT) imaging informatics software platform, was used to perform preprocessing and functional connectivity analysis (Leuthardt et al., 2018).

Analysis of Resting-State Functional Connectivity Resultant From Surgery

Given that postsurgical changes such as edema, pneumocephalus, hemorrhage, craniotomy plating systems, and other sources of artifact can produce noise that can significantly alter the BOLD signal, the entire hemisphere ipsilateral to the tumor was excluded in the correlation analysis. In other words, hemispheric and individual RSN correlation analysis was performed exclusively using within-hemisphere correlations *contralateral* to the lesion The 300 × 300 Pearson's *r* matrix of the whole brain was therefore truncated into a 150 × 150 hemispheric matrix prior to any statistical analysis.

[1] https://greenelab.ucsd.edu/data_software

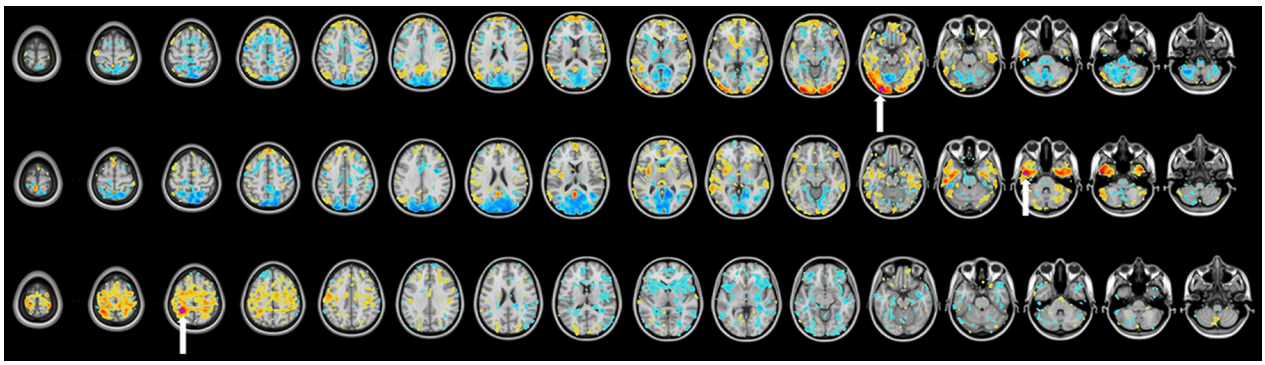

FIGURE 1 | Seed-based correlation map of a single patient with 3 representative ROIs (regions of interest) belonging to different RSNs (resting-state networks) projected onto a reference T1-weighted MRI. The purple dot (labeled with a white arrow) represents the seed ROI and warmer-colored regions represent positive correlation. Cooler colors represent negative correlation. 150 contralesional ROIs were isolated for analysis.

To control for the variability in tumor size and location between patients, hemispheric and individual RSN correlation analysis was performed using a pair of pre-operative and post-operative scans from the same patient. Specifically, the 2-dimensional correlation coefficient c was calculated between any pre-operative matrix (A) and the corresponding post-operative matrix (B), for each patient (shown below):

$$c_{x,y} = \frac{\sum_m \sum_n (A_{mn} - \overline{A})(B_{mn} - \overline{B})}{\sqrt{(\sum_m \sum_n (A_{mn} - \overline{A})^2)(\sum_m \sum_n (B_{mn} - \overline{B})^2)}}$$

Where $\overline{A}$ = mean of all values in matrix A and $\overline{B}$ = mean of all values in matrix B, m and n = column and row indices, x = patient number y = name of network represented by A and B

For example, the correlation coefficient between the pre-operative (A) and post-operative (B) matrices representing the somatodorsal network (SDN) for patient 1 in the LITT group is calculated by the following:

$$c_{LITT_1,SDN} = \frac{\sum_m \sum_n (A_{mn} - \overline{A})(B_{mn} - \overline{B})}{\sqrt{(\sum_m \sum_n (A_{mn} - \overline{A})^2)(\sum_m \sum_n (B_{mn} - \overline{B})^2)}}$$

Therefore, every comparison of interest between a pre-operative and post-operative network (matrix) y for an individual patient x can be represented by its correlation coefficient $c_{x,y}$. To quantify the changes for any given network y within each surgery group of N patients, the group-wise correlation coefficient G_y was calculated by taking the mean of all $c_{x,y}$ in each surgery group (i.e., $c_{LITT_1,y}$, $c_{LITT_2,y}$, . . . $c_{LITT_N,\ y}$).

Because craniotomy is the standard of care for tumor treatment, we tested the hypothesis that the functional networks in patients who underwent LITT were not more disrupted than those in patients who underwent craniotomy. When multiple post-operative rs-fMRI scans for a single patient were available, the most recent scan and therefore the longest time interval between scans was used to favor analysis of long-term network changes. The one-tailed Student's t-test, assuming unequal variances, was used to calculate statistical significance. A P-value less than 0.05 was taken to indicate significant difference. All matrix comparisons were calculated using MATLAB software (MATLAB and Statistics Toolbox Release 2016b, The MathWorks, Inc., Natick, Massachusetts, United States).

RESULTS

Patient and Tumor Characteristics

12 craniotomy patients and 12 LITT patients, each with one pre-operative and one post-operative scan, were included in this study. Patient demographics are shown in **Table 1**. The mean age and gender distributions were similar between groups. All tumors were intra-axial. Most tumors were intrinsic glial neoplasms and was no statistical difference between metastases and intrinsic glial neoplasms between groups. Patients who underwent LITT trended toward being likely to have had a prior needle biopsy compared to craniotomy patients. Patients who underwent craniotomy trended toward having larger tumor volumes but this was not statistically significant difference between the two groups. There was no significant difference between groups for the number of patients who underwent radiation between scans and the time intervals between surgery and post-operative scan.

Tumor Location

Tumor segmentation was performed using the T1-weighted post gadolinium contrast images. If the tumors did not have contrast enhancement, the region with FLAIR (fluid attenuated inversion recovery) hyperintensity was used. Tumor frequency maps illustrate the spatial distribution of tumor locations across patients (**Figure 2**). Tumors in the left hemisphere were reflected onto the right hemisphere for ease of visual comparison. **Supplementary Figure 1** delineates all regions with tumor-related changes (i.e., contrast enhancement plus surrounding FLAIR hyperintensity).

Network Analysis

ROIs for each patient were grouped into a total of 11 RSNs and one 150 × 150 hemispheric correlation matrix then compared between craniotomy patients and LITT patients (**Figures 3**, **4**).

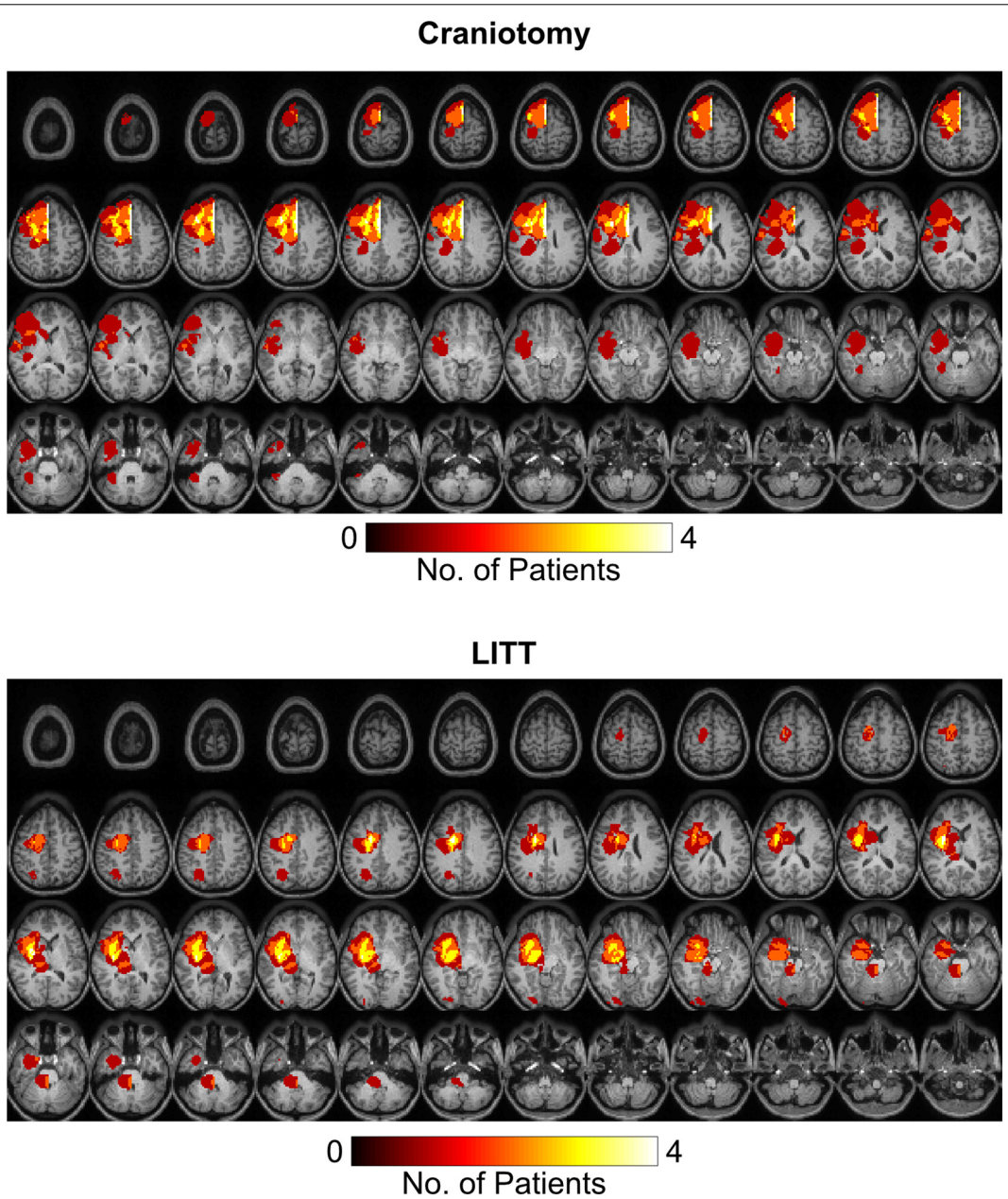

FIGURE 2 | Heat maps representing tumor locations in the craniotomy and LITT (laser interstitial thermal therapy) treatment groups. All tumors were mapped to the right hemisphere for a clearer illustration of tumor location. T1-weighted post-contrast images were used for tumors with contrast enhancement while FLAIR (fluid attenuated inversion recovery) hyperintensity was used for tumors without contrast enhancement.

The functional network names, abbreviations, and the number of ROIs comprising each network are shown in **Table 2**.

Histograms were generated to illustrate the group-wise 2-dimensional correlation coefficients of the pre-operative and post-operative contralesional hemispheres (**Figure 5**) and 11 RSNs (**Figure 6**) among patients who underwent craniotomy and those who underwent LITT. A correlation coefficient closer to 1 implies a network that is more similar to that of the pre-operative state. In our primary analysis, we found that the contralesional hemisphere showed a significantly higher degree of correlation between pre-operative and post-operative connectivity in the patients who underwent LITT compared to those who underwent craniotomy (**Figure 5**, $P = 0.0287$). In our secondary exploratory analysis, there was a higher degree of correlation in the connectivity of 4 networks (Somatomotor Dorsal, Fronto-Parietal, Salience, and Dorsal Attention) in patients who underwent LITT (**Table 2**, **Figure 6**). In majority of the remaining 7 comparisons, the RSNs in the LITT patients trended toward a greater degree of correlation compared to the craniotomy group.

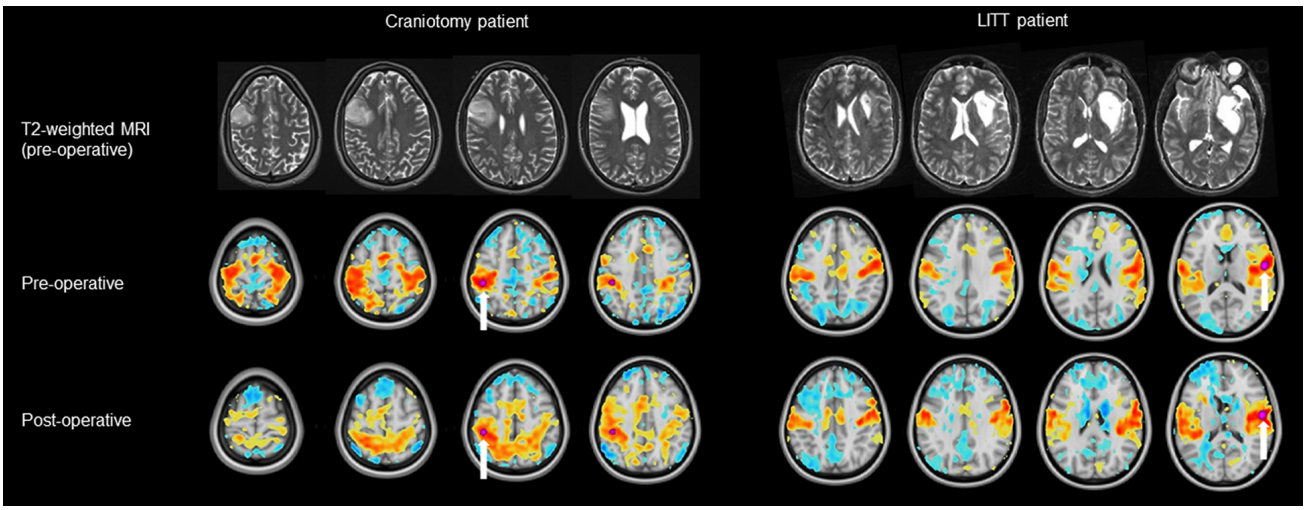

FIGURE 3 | Examples of a pre-operative and post-operative RSN (resting-state network) using a tumor-adjacent seed ROI (region of interest, labeled with a white arrow) on the contralesional hemisphere. The LITT (laser interstitial thermal therapy) patient (right) had a greater degree of correlation between the pre-operative and post-operative RSN than did the craniotomy patient (left). Note: clinical images use anatomic orientation while RSN projections use neurologic orientation.

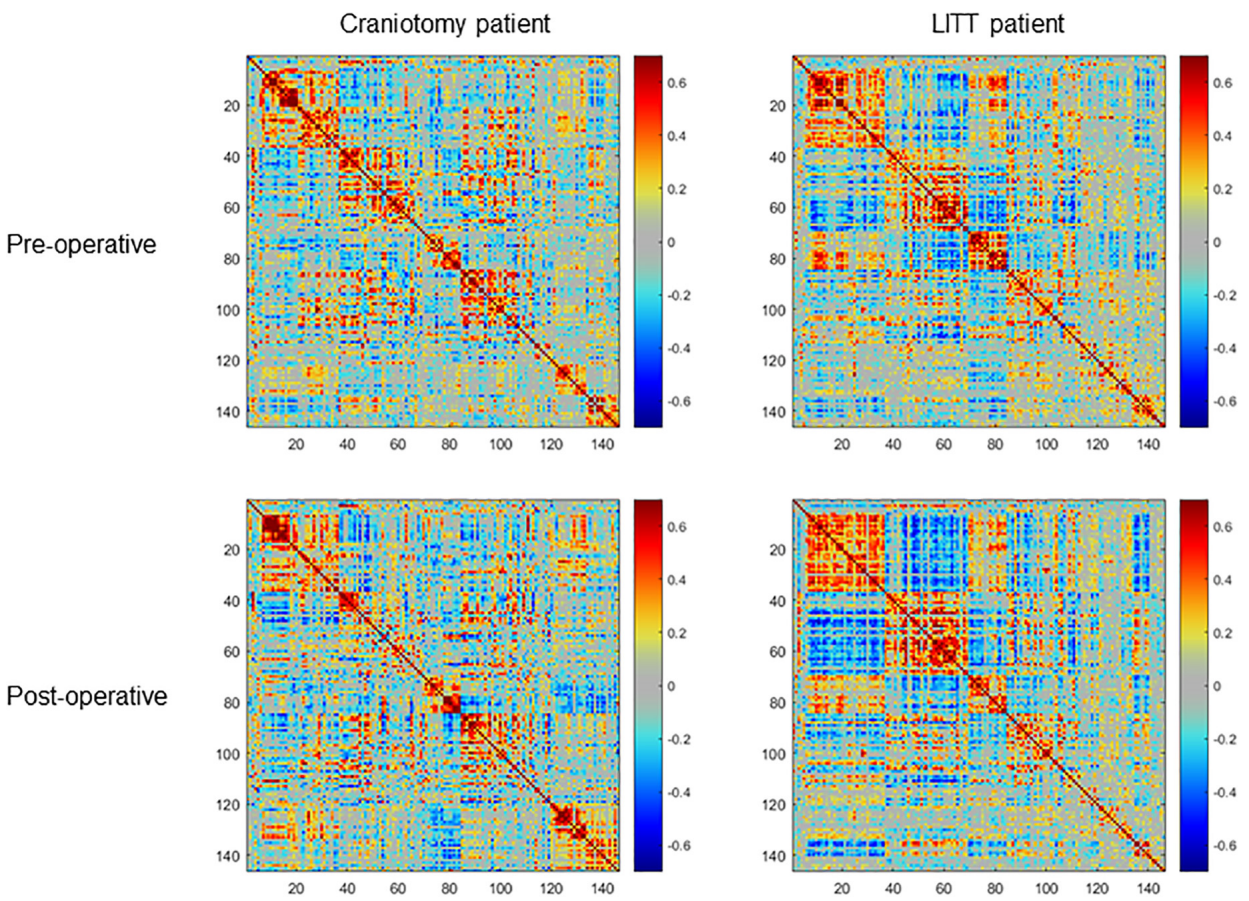

FIGURE 4 | Examples of pre-operative and post-operative within-hemisphere correlation matrices of the contralesional hemisphere (ROIs (regions of interest) = 150) of a single craniotomy patient (left) and a single LITT (laser interstitial thermal therapy) patient (right). The LITT patient had a greater degree of correlation between the pre-operative and post-operative matrices than did the craniotomy patient as determined by the 2-dimensional correlation coefficient.

TABLE 2 | Resting-state networks and group-wise two-dimensional correlation coefficients between pre-operative and post-operative scans.

Abbreviation	Resting-state network	ROIs	Craniotomy	LITT	*P*-value
SDN	Somatomotor Dorsal	17	0.667	0.741	**0.0343**
SLN	Somatomotor Lateral	3	0.969	0.965	0.4094
CON	Cingulo-Opercular	8	0.873	0.893	0.2263
AN	Auditory	6	0.816	0.818	0.4558
DMN	Default Mode	31	0.652	0.694	0.1308
PMN	Parieto-Medial	3	0.976	0.971	0.3445
VN	Visual	19	0.698	0.746	0.1164
FPN	Fronto-Parietal	15	0.710	0.825	**0.0001**
SN	Salience	8	0.792	0.880	**0.0081**
VAN	Ventral Attention	5	0.879	0.916	0.1360
DAN	Dorsal Attention	7	0.817	0.897	**0.0032**

One-tailed Student's t-test demonstrates a higher degree of correlation between the pre-operative and post-operative Somatomotor Dorsal, Fronto-Parietal, Salience, and Dorsal Attention resting-state networks in patients who underwent laser interstitial thermal therapy. ROIs, regions of interest; LITT, laser interstitial thermal therapy. Bold numbers indicate P < 0.05.

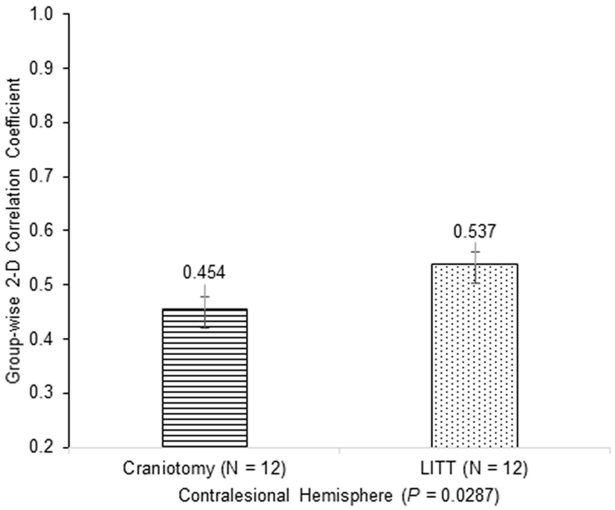

FIGURE 5 | Group-wise 2-dimensional correlation coefficients between pre-operative and post-operative hemispheres between patients who underwent craniotomy and LITT (laser interstitial thermal therapy). There was a greater degree of correlation in patients who underwent LITT (one-tailed Student's *t*-test, assuming unequal variances).

DISCUSSION

LITT has been shown to be safe and effective in the treatment of intracranial lesions (Shah et al., 2019; Kim et al., 2020). We have previously reported the outcomes and safety profile in using LITT as a frontline treatment for glioblastomas, metastases, low grade gliomas, epileptic foci, and radiation necrosis (Kamath et al., 2017, 2019; Salehi et al., 2018). While the thermal effects on tissues within the ablation target and the surrounding brain have been characterized, the impact of LITT on intrinsic functional organization of the brain, and specifically when compared to craniotomy, had not yet been explored (Mohammadi and Schroeder, 2014). Here we pilot a novel approach to quantify and compare the hemispheric and individual RSN changes from two surgical approaches while taking into account tumor mass effect, post-surgical changes, and individual patient variability. We found that relative to open craniotomy for tumor resection, LITT may have less of an impact on overall functional architecture, as measured by rs-fMRI connectivity. We found that in the follow-up period up to 2 years (average approximately 6 months) after surgery, the contralesional hemisphere and 4 RSNs showed a statistically significant difference in patients who underwent craniotomy vs. those who underwent LITT. Using this computational method, we found that the overall post-surgical brain functional connectivity in patients who underwent LITT was more similar to the pre-operative state than in patients who underwent craniotomy. These findings may not only provide evidence for the assumption that LITT may disrupt brain functional connectivity less than craniotomy, but that this analytical approach using rs-fMRI may be a useful objective tool for quantifying and comparing the effects that different neurosurgical interventions can have on the functional organization within a patient's brain.

Based on prior literature, it is reasonable to believe that rs-fMRI changes are clinically meaningful. In a longitudinal study of patients with Parkinson's disease, for example, Olde Dubbelink et al. (2014) found that FC changes were more pronounced in certain brain regions that corresponded to clinical measures of cognitive decline over time, which was independent from aging effects from the control group. Moreover, FC changes using rs-fMRI may also reflect the effect of therapeutic intervention. A randomized trial of cognitive rehabilitation in Parkinson's disease found that the intervention group showed increased FC between the bilateral dorsolateral prefrontal cortex and the left inferior temporal lobe, which correlated with measures of executive function. These effects in both FC and cognitive function were preserved at 18-month follow-up (Díez-Cirarda et al., 2018). These findings suggest that FC may correlate with neurocognitive status and serve as a diagnostic tool to monitor clinical change over time. As the overall practice of LITT continues to grow, it is important to understand the neurophysiological and neurocognitive consequences of this technology. The extent of network disruption in LITT as it compares to open resection can have implications not only on recovery after surgery, but potentially on survival. Preservation of motor and speech function after surgery have been show to predict overall survival after glioblastoma resections (McGirt et al., 2009; Gulati et al., 2011).

In considering rs-fMRI and network connectivity as it relates to the intervention, several variables as it relates to surgery were taken into consideration to best enable a fair comparison between the two interventions. First, laser ablation alters blood brain barrier (BBB) permeability which may have implications on glial-neuronal interactions that drive the BOLD signal. Our previous work has shown evidence that the BBB may be disrupted by hyperthermia, that peaks at 1–2 weeks after surgery and resolves by 4–6 weeks (Leuthardt et al., 2016). To reduce the potential effect of BBB permeability on BOLD signaling that might have unintended impact on detecting

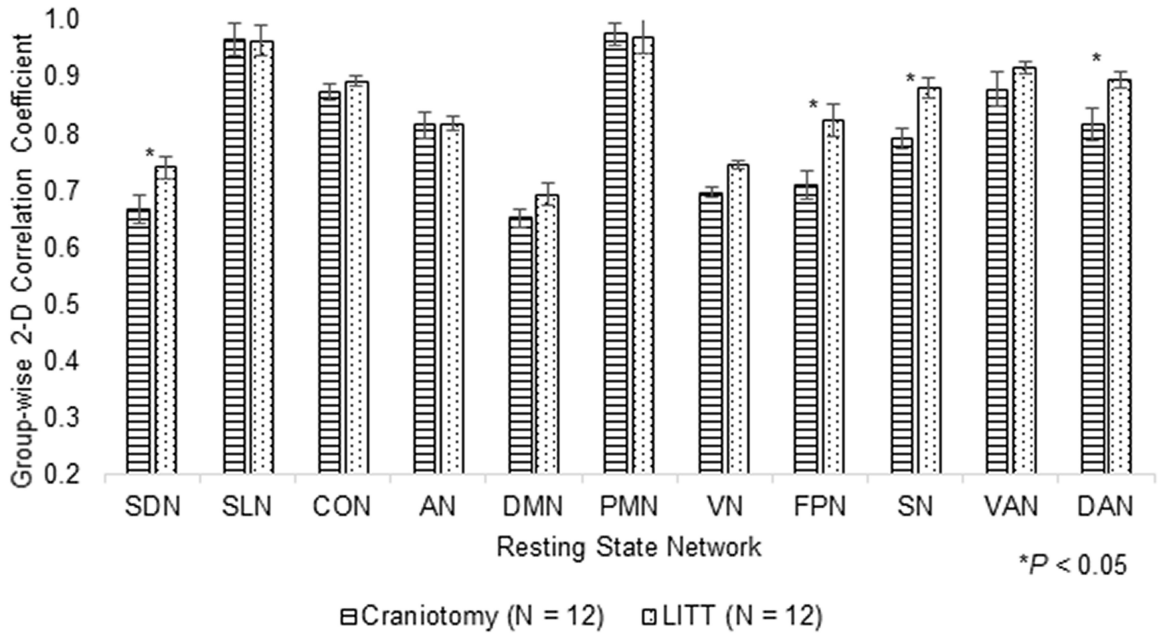

FIGURE 6 | Group-wise 2-dimensional correlation coefficients between pre-operative and post-operative RSNs (resting-state networks) between patients who underwent craniotomy and LITT (laser interstitial thermal therapy). 4 RSNs among LITT patients showed a higher degree of correlation between scans than among craniotomy patients (one-tailed Student's *t*-test, assuming unequal variances).

differences between RSNs, we selected scans from the most recent timepoint in order to minimize the impact of these changes when multiple post-operative scans were available. Second, the treated hemisphere is subject to a number of confounding variables that could impact network organization. The mass effect of the intracranial lesion on surrounding structures, peritumor edema, surgical plating systems, and post-surgical changes have posed challenges when studying RSNs. Prior studies investigating the changes in RSNs when there is brain asymmetry have used comparison methods using the *contralesional* hemisphere only (Park et al., 2011; Liu et al., 2020). Here, we used a similar approach, isolating and analyzing the within-hemisphere connectivity of RSNs of the contralesional hemisphere. This analytical technique makes the assumption that the intracranial pathology impacts the FC of the contralesional hemisphere, and importantly, this effect is indirect and nontrivial. This assumption is advantageous for the ease of mathematical analysis, but also indicates that local tissue disruption may have secondary global effects.

This study has several limitations including its retrospective nature, small patient cohort, and the lack of correlations to neurocognitive outcomes that might have clinical implications as mentioned above. Direct comparison of resting-state changes between craniotomy and LITT assumes similar baseline tumor characteristics, but in clinical practice there are likely inherent differences between these treatment groups such as tumor location and tumor volume which factor into the decision of which surgery is pursued. Therefore, the main limitation of this study is the inherent mismatch between treatment groups. However, this is the first study to use a quantitative approach to comparing the effect of open and minimally invasive tumor surgery on functional connectivity and to show that LITT may be less disruptive to intrinsic networks than conventional craniotomy using rs-fMRI as a quantitative metric. We demonstrated that analyzing the within-hemisphere connectivity within the contralesional hemisphere can be a useful strategy when comparing RSNs in the setting of mass effect, and patients serving as their own control can help reduce the individual variability when comparing patient groups. Future studies are warranted and include validating these results using patient cohorts matched by tumor location, volume, and type, quantifying the time course of RSN recovery after surgery, and correlating these changes to neurocognitive outcomes.

CONCLUSION

The purpose of this study was to use a novel method to quantify and compare changes in functional network connectivity in patients who underwent craniotomy and LITT for the treatment of intra-axial brain tumors. Global hemispheric connectivity and 4 individual RSNs were more well-preserved in patients who underwent LITT than those who underwent craniotomy in a follow-up period up to 2 years. Larger studies are warranted to validate these results and to determine their clinical implications.

DATA AVAILABILITY STATEMENT

The raw data supporting the conclusions of this article will be made available by the authors, without undue reservation.

ETHICS STATEMENT

The studies involving human participants were reviewed and approved by the Washington University in St. Louis. Written informed consent from the participants' legal guardian/next of kin was not required to participate in this study in accordance with the national legislation and the institutional requirements.

AUTHOR CONTRIBUTIONS

PY, BP, and EL contributed to hypothesis generation. PY and BP performed data collection and primary data analysis. PY was responsible for coding, statistical analysis, and manuscript writing. BP, CH, and EL performed manuscript editing. CH and AD assisted with secondary data analysis and visualization. All authors contributed to the article and approved the submitted version.

FUNDING

This work was supported by the National Institutes of Health (R25NS090978 to BP).

SUPPLEMENTARY MATERIAL

The Supplementary Material for this article can be found online at: https://www.frontiersin.org/articles/10.3389/fnins.2021.665016/full#supplementary-material

Supplementary Figure 1 | Heat maps representing tumor-affected regions in the craniotomy and LITT (laser interstitial thermal therapy) treatment groups. T1-weighted post-contrast images and surrounding FLAIR hyperintensity were used for tumors with contrast enhancement. FLAIR hyperintensity was used for tumors without contrast enhancement.

REFERENCES

Bijanki, K. R., van Rooij, S. J., Ely, T. D., Stevens, J. S., Inman, C. S., Fasano, R. E., et al. (2020). Case series: unilateral amygdala ablation ameliorates post-traumatic stress disorder symptoms and biomarkers. *Neurosurgery* 87, 796–802. doi: 10.1093/neuros/nyaa051

Biswal, B., Zerrin Yetkin, F., Haughton, V. M., and Hyde, J. S. (1995). Functional connectivity in the motor cortex of resting human brain using echo-planar MRI. *Magn. Reson. Med.* 34, 537–541. doi: 10.1002/mrm.1910340409

Boerwinkle, V. L., Vedantam, A., Lam, S., Wilfong, A. A., and Curry, D. J. (2018). Connectivity changes after laser ablation: resting-state fMRI. *Epilepsy Res.* 142, 156–160. doi: 10.1016/j.eplepsyres.2017.09.015

Bown, S. G. (1983). Phototherapy in tumors. *World J. Surg.* 7, 700–709. doi: 10.1007/BF01655209

De Poorter, J., De Wagter, C., De Deene, Y., Thomsen, C., Stahlberg, F., and Achten, E. (1995). Noninvasive MRI thermometry with the proton resonance frequency (PRF) method: in vivo results in human muscle. *Magn. Reson. Med.* 33, 74–81. doi: 10.1002/mrm.1910330111

Dierker, D., Roland, J. L., Kamran, M., Rutlin, J., Hacker, C. D., Marcus, D. S., et al. (2017). Resting-state functional magnetic resonance imaging in presurgical functional mapping: sensorimotor localization. *Neuroimaging Clin.* 27, 621–633. doi: 10.1016/j.nic.2017.06.011

Díez-Cirarda, M., Ojeda, N., Peña, J., Cabrera-Zubizarreta, A., Lucas-Jiménez, O., Gómez-Esteban, J. C., et al. (2018). Long-term effects of cognitive rehabilitation on brain, functional outcome and cognition in Parkinson's disease. *Eur. J. Neurol.* 25, 5–12. doi: 10.1111/ene.13472

Greicius, M. D., Srivastava, G., Reiss, A. L., and Menon, V. (2004). Default-mode network activity distinguishes Alzheimer's disease from healthy aging: evidence from functional MRI. *Proc. Natl. Acad. Sci. U.S.A.* 101, 4637–4642. doi: 10.1073/pnas.0308627101

Gulati, S., Jakola, A. S., Nerland, U. S., Weber, C., and Solheim, O. (2011). The risk of getting worse: surgically acquired deficits, perioperative complications, and functional outcomes after primary resection of glioblastoma. *World Neurosurg.* 76, 572–579. doi: 10.1016/j.wneu.2011.06.014

Hacker, C. D., Perlmutter, J. S., Criswell, S. R., Ances, B. M., and Snyder, A. Z. (2012). Resting state functional connectivity of the striatum in Parkinson's disease. *Brain* 135, 3699–3711. doi: 10.1093/brain/aws281

Hacker, C. D., Roland, J. L., Kim, A. H., Shimony, J. S., and Leuthardt, E. C. (2019). Resting-state network mapping in neurosurgical practice: a review. *Neurosurg. Focus* 47:E15. doi: 10.3171/2019.9.FOCUS19656

Hafez, D. M., Liekweg, C., and Leuthardt, E. C. (2020). Staged Laser Interstitial Thermal Therapy (LITT) treatments to left insular low-grade glioma. *Neurosurgery* 86, E337–E342. doi: 10.1093/neuros/nyz120

Hawasli, A. H., Bagade, S., Shimony, J. S., Miller-Thomas, M., and Leuthardt, E. C. (2013). Magnetic resonance imaging-guided focused laser interstitial thermal therapy for intracranial lesions: single-institution series. *Neurosurgery* 73, 1007–1017. doi: 10.1227/NEU.0000000000000144

Hawasli, A. H., Kim, A. H., Dunn, G. P., Tran, D. D., and Leuthardt, E. C. (2014). Stereotactic laser ablation of high-grade gliomas. *Neurosurg. Focus* 37:E1. doi: 10.3171/2014.9.FOCUS14471

Hawasli, A. H., Ray, W. Z., Murphy, R. K., Dacey, Jr RG, and Leuthardt, E. C. (2011). Magnetic resonance imaging-guided focused laser interstitial thermal therapy for subinsular metastatic adenocarcinoma: technical case report. *Oper. Neurosurg.* 70(suppl_2), onsE332–onsE338. doi: 10.1227/NEU.0b013e318232fc90

Johnston, J. M., Vaishnavi, S. N., Smyth, M. D., Zhang, D., He, B. J., Zempel, J. M., et al. (2008). Loss of resting interhemispheric functional connectivity after complete section of the corpus callosum. *J. Neurosci.* 28, 6453–6458. doi: 10.1523/JNEUROSCI.0573-08.2008

Kahan, J., Urner, M., Moran, R., Flandin, G., Marreiros, A., Mancini, L., et al. (2014). Resting state functional MRI in Parkinson's disease: the impact of deep brain stimulation on 'effective' connectivity. *Brain* 137(Pt 4), 1130–1144. doi: 10.1093/brain/awu027

Kamath, A. A., Friedman, D. D., Akbari, S. H. A., Kim, A. H., Tao, Y., Luo, J., et al. (2019). Glioblastoma treated with magnetic resonance imaging-guided laser interstitial thermal therapy: safety. Efficacy, and Outcomes. *Neurosurgery* 84, 836–843. doi: 10.1093/neuros/nyy375

Kamath, A. A., Friedman, D. D., Hacker, C. D., Smyth, M. D., Limbrick, D. D, Jr, Kim, A. H., et al. (2017). MRI-Guided interstitial laser ablation for intracranial lesions: a large single-institution experience of 133 cases. *Stereotact. Funct. Neurosurg.* 95, 417–428. doi: 10.1159/000485387

Kim, A. H., Tatter, S., Rao, G., Prabhu, S., Chen, C., Fecci, P., et al. (2020). Laser ablation of abnormal neurological tissue using robotic neuroblate system (LAANTERN): 12-month outcomes and quality of life after brain tumor ablation. *Neurosurgery* 87, E338–E346. doi: 10.1093/neuros/nyaa071

Leuthardt, E. C., Duan, C., Kim, M. J., Campian, J. L., Kim, A. H., Miller-Thomas, M. M., et al. (2016). Hyperthermic laser ablation of recurrent glioblastoma leads to temporary disruption of the peritumoral blood brain barrier. *PLoS One* 11:e0148613. doi: 10.1371/journal.pone.0148613

Leuthardt, E. C., Guzman, G., Bandt, S. K., Hacker, C., Vellimana, A. K., Limbrick, D., et al. (2018). Integration of resting state functional MRI into clinical

practice-a large single institution experience. *PLoS One* 13:e0198349. doi: 10.1371/journal.pone.0198349

Liu, D., Chen, J., Hu, X., Hu, G., Liu, Y., Yang, K., et al. (2020). Contralesional homotopic functional plasticity in patients with temporal glioma. *J. Neurosurg.* 134, 417–425.

McGirt, M. J., Mukherjee, D., Chaichana, K. L., Than, K. D., Weingart, J. D., and Quinones-Hinojosa, A. (2009). Association of surgically acquired motor and language deficits on overall survival after resection of glioblastoma multiforme. *Neurosurgery* 65, 463–470. doi: 10.1227/01.NEU.0000349763.42238.E9

Mohammadi, A. M., and Schroeder, J. L. (2014). Laser interstitial thermal therapy in treatment of brain tumors-the neuroblate system. *Expert Rev. Med. Devices* 11, 109–119. doi: 10.1586/17434440.2014.882225

Mohammadi, A. M., Hawasli, A. H., Rodriguez, A., Schroeder, J. L., Laxton, A. W., Elson, P., et al. (2014). The role of laser interstitial thermal therapy in enhancing progression-free survival of difficult-to-access high-grade gliomas: a multicenter study. *Cancer Med.* 3, 971–979. doi: 10.1002/cam4.266

Olde Dubbelink, K. T. E., Schoonheim, M. M., Deijen, J. B., Twisk, J. W. R., Barkhof, F., and Berendse, H. W. (2014). Functional connectivity and cognitive decline over 3 years in Parkinson disease. *Neurology* 83, 2046–2053. doi: 10.1212/WNL.0000000000001020

Park, C. H., Chang, W. H., Ohn, S. H., Kim, S. T., Bang, O. Y., Pascual-Leone, A., et al. (2011). Longitudinal changes of resting-state functional connectivity during motor recovery after stroke. *Stroke* 42, 1357–1362. doi: 10.1161/STROKEAHA.110.596155

Park, K. Y., Lee, J. J., Dierker, D., Marple, L. M., Hacker, C. D., Roland, J. L., et al. (2020). Mapping language function with task-based vs. resting-state functional MRI. *PLoS One* 15:e0236423. doi: 10.1371/journal.pone.0236423

Power, J. D., Cohen, A. L., Nelson, S. M., Wig, G. S., Barnes, K. A., Church, J. A., et al. (2011). Functional network organization of the human brain. *Neuron* 72, 665–678. doi: 10.1016/j.neuron.2011.09.006

Power, J. D., Mitra, A., Laumann, T. O., Snyder, A. Z., Schlaggar, B. L., and Petersen, S. E. (2014). Methods to detect, characterize, and remove motion artifact in resting state fMRI. *Neuroimage* 84, 320–341. doi: 10.1016/j.neuroimage.2013.08.048

Remick, M., McDowell, M. M., Gupta, K., Felker, J., and Abel, T. J. (2020). Emerging indications for stereotactic laser interstitial thermal therapy in pediatric neurosurgery. *Int. J. Hyperthermia* 37, 84–93. doi: 10.1080/02656736.2020.1769868

Roland, J. L., Griffin, N., Hacker, C. D., Vellimana, A. K., Akbari, S. H., Shimony, J. S., et al. (2017). Resting-state functional magnetic resonance imaging for surgical planning in pediatric patients: a preliminary experience. *J. Neurosurg. Pediatr.* 20, 583–590. doi: 10.3171/2017.6.PEDS1711

Roland, J. L., Hacker, C. D., Snyder, A. Z., Shimony, J. S., Zempel, J. M., Limbrick, D. D., et al. (2019). A comparison of resting state functional magnetic resonance imaging to invasive electrocortical stimulation for sensorimotor mapping in pediatric patients. *Neuroimage Clin.* 23:101850. doi: 10.1016/j.nicl.2019.101850

Salehi, A., Kamath, A. A., Leuthardt, E. C., and Kim, A. H. (2018). Management of intracranial metastatic disease with laser interstitial thermal therapy. *Front. Oncol.* 8:499. doi: 10.3389/fonc.2018.00499

Seitzman, B. A., Gratton, C., Marek, S., Raut, R. V., Dosenbach, N. U., Schlaggar, B. L., et al. (2020). A set of functionally-defined brain regions with improved representation of the subcortex and cerebellum. *Neuroimage* 206:116290. doi: 10.1016/j.neuroimage.2019.116290

Shah, A. H., Semonche, A., Eichberg, D. G., Borowy, V., Luther, E., Sarkiss, C. A., et al. (2019). The role of laser interstitial thermal therapy in surgical neuro-oncology: series of 100 consecutive patients. *Neurosurgery* 87, 266–275. doi: 10.1093/neuros/nyz424

Shulman, G. L., Pope, D. L. W., Astafiev, S. V., McAvoy, M. P., Snyder, A. Z., and Corbetta, M. (2010). Right hemisphere dominance during spatial selective attention and target detection occurs outside the dorsal frontoparietal network. *J. Neurosci.* 30, 3640–3651. doi: 10.1523/JNEUROSCI.4085-09.2010

Smith, S. M., Fox, P. T., Miller, K. L., Glahn, D. C., Fox, P. M., Mackay, C. E., et al. (2009). Correspondence of the brain's functional architecture during activation and rest. *Proc. Natl. Acad. Sci. U.S.A.* 106, 13040–13045. doi: 10.1073/pnas.0905267106

Torres-Reveron, J., Tomasiewicz, H. C., Shetty, A., Amankulor, N. M., and Chiang, V. L. (2013). Stereotactic laser induced thermotherapy (LITT): a novel treatment for brain lesions regrowing after radiosurgery. *J. Neurooncol.* 113, 495–503. doi: 10.1007/s11060-013-1142-2

Xu, H., Qin, W., Chen, H., Jiang, L., Li, K., and Yu, C. (2014). Contribution of the resting-state functional connectivity of the contralesional primary sensorimotor cortex to motor recovery after subcortical stroke. *PLoS One* 9:e84729. doi: 10.1371/journal.pone.0084729

Yeo, B. T., Krienen, F. M., Sepulcre, J., Sabuncu, M. R., Lashkari, D., Hollinshead, M., et al. (2011). The organization of the human cerebral cortex estimated by intrinsic functional connectivity. *J. Neurophysiol.* 106, 1125–1165. doi: 10.1152/jn.00338.2011

Conflict of Interest: EL is a consultant for Monteris Medical, E15, Acera, Alcyone, Intellectual Ventures, Medtronic Inc., Neurolutions, Osteovantage, Pear Therapeutics, Inc., Sante Ventures, and Microbot, owns equity in Neurolutions, General Sensing, Osteovantage, Pear Therapeutics, Face to Face Biometrics, Immunovalent, Caeli Vascular, Acera, Sora Neuroscience, Inner Cosmos, and Kinetrix, and is involved with licensing intellectual property in Neurolutions, Osteovantage, Caeli Vascular, Cerovations, and Intellectual Ventures. Washington University owns equity in Neurolutions. CH owns equity in Sora Neuroscience.

The remaining authors declare that the research was conducted in the absence of any commercial or financial relationships that could be construed as a potential conflict of interest.

Publisher's Note: All claims expressed in this article are solely those of the authors and do not necessarily represent those of their affiliated organizations, or those of the publisher, the editors and the reviewers. Any product that may be evaluated in this article, or claim that may be made by its manufacturer, is not guaranteed or endorsed by the publisher.

Copyright © 2021 Yang, Hacker, Patel, Daniel and Leuthardt. This is an open-access article distributed under the terms of the Creative Commons Attribution License (CC BY). The use, distribution or reproduction in other forums is permitted, provided the original author(s) and the copyright owner(s) are credited and that the original publication in this journal is cited, in accordance with accepted academic practice. No use, distribution or reproduction is permitted which does not comply with these terms.

frontiers in Neuroscience

ORIGINAL RESEARCH
published: 22 November 2021
doi: 10.3389/fnins.2021.783361

Assessment of Isocitrate Dehydrogenase 1 Genotype and Cell Proliferation in Gliomas Using Multiple Diffusion Magnetic Resonance Imaging

*Yan Xie[1], Shihui Li[1], Nanxi Shen[1], Tongjia Gan[1], Shun Zhang[1], Weiyin Vivian Liu[2] and Wenzhen Zhu[1]**

[1] Department of Radiology, Tongji Hospital, Tongji Medical College, Huazhong University of Science and Technology, Wuhan, China, [2] Magnetic Resonance Research, General Electric Healthcare, Beijing, China

Objectives: To compare the efficacy of parameters from multiple diffusion magnetic resonance imaging (dMRI) for prediction of isocitrate dehydrogenase 1 (IDH1) genotype and assessment of cell proliferation in gliomas.

Methods: Ninety-one patients with glioma underwent diffusion weighted imaging (DWI), multi-*b*-value DWI, and diffusion kurtosis imaging (DKI)/neurite orientation dispersion and density imaging (NODDI) on 3.0T MRI. Each parameter was compared between IDH1-mutant and IDH1 wild-type groups by Mann–Whitney *U* test in lower-grade gliomas (LrGGs) and glioblastomas (GBMs), respectively. Further, performance of each parameter was compared for glioma grading under the same IDH1 genotype. Spearman correlation coefficient between Ki-67 labeling index (LI) and each parameter was calculated.

Results: The diagnostic performance was better achieved with apparent diffusion coefficient (ADC), slow ADC (D), fast ADC (D*), perfusion fraction (f), distributed diffusion coefficient (DDC), heterogeneity index (α), mean diffusivity (MD), mean kurtosis (MK), and intracellular volume fraction (ICVF) for distinguishing IDH1 genotypes in LrGGs, with statistically insignificant AUC values from 0.750 to 0.817. In GBMs, no difference between the two groups was found. For IDH1-mutant group, all parameters, except for fractional anisotropy (FA) and D*, significantly discriminated LrGGs from GBMs ($P < 0.05$). However, for IDH1 wild-type group, only ADC statistically discriminated the two ($P = 0.048$). In addition, MK has maximal correlation coefficient ($r = 0.567$, $P < 0.001$) with Ki-67 LI.

Conclusion: dMRI-derived parameters are promising biomarkers for predicting IDH1 genotype in LrGGs, and MK has shown great potential in assessing glioma cell proliferation.

Keywords: diffusion magnetic resonance imaging, glioma, isocitrate dehydrogenase, cell proliferation, multi-parameter magnetic resonance image

OPEN ACCESS

Edited by:
Sandro M. Krieg, Technical University of Munich, Germany

Reviewed by:
Nguyen Minh Duc, Pham Ngoc Thach University of Medicine, Vietnam
Yan Zhou, Shanghai Jiao Tong University, China

****Correspondence:***
Wenzhen Zhu
zhuwenzhen8612@163.com

Specialty section:
This article was submitted to Brain Imaging Methods, a section of the journal Frontiers in Neuroscience

Received: *26 September 2021*
Accepted: *20 October 2021*
Published: *22 November 2021*

Citation:
Xie Y, Li S, Shen N, Gan T, Zhang S, Liu WV and Zhu W (2021) Assessment of Isocitrate Dehydrogenase 1 Genotype and Cell Proliferation in Gliomas Using Multiple Diffusion Magnetic Resonance Imaging. Front. Neurosci. 15:783361. doi: 10.3389/fnins.2021.783361

INTRODUCTION

In 2016, the World Health Organization classified levels of Central Nervous System tumors based on molecular features, specifically the isocitrate dehydrogenase 1 (IDH1) genotype (Karsy et al., 2017). IDH1 is a key enzyme involved in cellular metabolism, epigenetic regulation, redox, and DNA repair, existing in the cytoplasm and peroxisomes (Fu et al., 2010). Many studies have indicated a better prognosis of IDH1-mutant gliomas than IDH1 wild-type gliomas (Turkalp et al., 2014; Shen et al., 2020). Ye et al. (2013) found that IDH1 mutation causes a decrease in hypoxia-inducible factor −1α, which in turn leads to the inhibition of HIF-1α-mediated biological functions such as pro-angiogenesis, angiogenesis, migration, and motility of endothelial cells. Therefore, accurate identification of glioma IDH1 genotype facilitates the formulation of treatment plans and assessment of patient prognosis.

A nuclear protein, Ki-67, represents the proliferative activity of tumors and is closely associated with tumor differentiation and infiltration (Habberstad et al., 2011). The higher Ki-67 labeling index (LI) indicates faster tumor growth and poorer tissue differentiation. However, the cost of gene screening is high and not easy to broadly implement (Jiang et al., 2018). To obtain tumor pathology information and Ki-67 LI via surgery or pathological biopsy is not applicable for all gliomas, such as those in the brainstem and basal ganglia regions. Thus, an imaging approach to obtain anatomical details and tissue characteristics is essential for clinic diagnosis.

Diffusion magnetic resonance imaging (dMRI) is a non-invasive method to reflect microstructure information of diffusion of water molecules. The conventional mono-exponential diffusion-weighted imaging (DWI) reflects water motion paths *in vivo*. Diffusion tensor imaging (DTI) indicates the integrity of the white matter fiber tracts in the brain under the assumption of water random movements in Gaussian distribution (Maier et al., 2010). Since the complex cellular microenvironment in real organisms is limited by organelles, cell membranes, and extracellular gaps (Van Cauter et al., 2012; Jiang et al., 2015), water moves in non-Gaussian distribution and can be revealed by diffusion kurtosis imaging (DKI) (Wu and Cheung, 2010). DKI cannot reflect the intrinsic biophysical mechanisms such as the altered membrane permeability of axons, while neurite orientation dispersion and density imaging (NODDI) reflects a closer approximation to the real diffusion pattern of water molecules in the tissue microenvironment via characterizing the three main tissue cavities in the microstructural environment, namely, restricted diffusion of water within the neurite, hindered diffusion of water outside the neurite, and free diffusion of water in the cerebrospinal fluid (Zhang et al., 2012). In addition, the bi-exponential intravoxel incoherent motion (IVIM) imaging is able to separate the slow diffusive motion in response to intra- and extracellular water molecules as intra-tissue diffusion from the fast diffusive motion in response to intravascular water molecules as vascular perfusion (Shen et al., 2016), while the stretch-exponential DWI is able to describe the tissue heterogeneity and the continuous distribution of water molecules in the microstructure (Bennett et al., 2003).

Diffusion magnetic resonance imaging analyzed with different diffusion models reflects the complexity of tumor microstructure. Till now, few studies have been performed to compare the efficacy of these diffusion models in terms of IDH1 genotype. The purpose of this study was to assess IDH1 genotype and cell proliferation using mono-exponential, bi-exponential, stretch-exponential DWI, DTI, DKI, and NODDI models.

MATERIALS AND METHODS

Patient Population

This study was approved by local ethics committee and written informed consent was obtained from all subjects. Patients were included in the study if they met the following inclusion criteria: (a) pathologically confirmed primary gliomas; (b) preoperative DWI, multi-*b*-value DWI, and DKI/NODDI acquisition were performed; (c) IDH1 genotype measured by genetic screening or immunohistochemistry was available. The following were exclusion criteria: (a) purely cystic gliomas; (b) lack of routine MRI images. From July 2017 to December 2020, a total of 94 patients meeting the above inclusion criteria were enrolled in the study. Two cases with purely cystic glioma and one lack of routine images were excluded. In total, 91 patients were recruited into this study.

Image Data Acquisition

All MR images were performed on the a 3T MR system (Discovery MR750, GE Medical Systems, Milwaukee, WI, United States) with a 32-channel head coil. Routine axial sequences include T1 fluid-attenuated inversion recovery (FLAIR), T2 fast spin echo (FSE), T2 FLAIR, contrast-enhanced T1 weighted spin-echo.

Three diffusion imaging data were obtained using spin-echo echo-planar imaging sequences before the injection of contrast agents. The parameters of DWI were as follows: TR/TE = 3,000/70 ms, NEX = 1, matrix = 160 × 160, slice thickness = 5 mm, slice spacing = 1.5 mm, FOV = 240 mm × 240 mm, b = 0 and 1,000 s/mm^2, and acquisition time was 42 s. Multi-*b*-value DWI was performed with 20 *b*-values (b = 0, 20, 50, 80, 100, 150, 200, 400, 600, 800, 1,000, 1,200, 1,500, 2,000, 2,400, 2,800, 3,200, 3,600, 4,000, and 4,500 s/mm^2), for 0–1,000 s/mm^2, NEX = 1, for 1,200–2,800 s/mm^2, NEX = 2, and for 3,200–4,500 s/mm^2, NEX = 4, TR/TE = 3,200/90.6 ms, matrix = 160 × 160, slice thickness = 5 mm, spacing = 1.5 mm, FOV = 240 mm × 240 mm, acquisition time was 5 min 52 s. DKI/NODDI was performed with 3 *b*-values (b = 0, 1,250, and 2,500 s/mm^2) and 25 uniformly distributed directions for each nonzero *b*-value, TR/TE = 6,500/85, NEX = 1, matrix = 128 × 128, slice thickness = 3 mm, spacing = 0 mm, FOV = 240 mm × 240 mm, acquisition time was 5 min 45 s.

Image Processing and Regions of Interest Analysis

Mono-, bi-, and stretch-exponential DWI, IVIM, DTI, DKI parametric maps were processed using GE Advantage

workstation (version 4.5). After brain extraction of images by MRIcron (Version 12-12-2012), the NODDI parametric maps was processed using a MATLAB toolbox[1].

The apparent diffusion coefficient (ADC) map was obtained by the following mono-exponential model:

$$S(b)/S(0) = exp(-b \cdot ADC)$$

Where $S(b)$ and $S(0)$ represent the signal intensity for $b = 0$ and a non-zero b-value.

In bi-exponential intravoxel incoherent motion (IVIM) model, three maps of slow ADC (D), fast ADC (D*), perfusion fraction (f) were processed:

$$S(b)/S(0) = [f \cdot exp(-b \cdot D^*)] + [(1-f) \cdot exp(-b \cdot D)]$$

The maps of distributed diffusion coefficient (DDC) and heterogeneity index (α) were derived using a stretched-exponential model:

$$S(b)/S(0) = exp[-(b \cdot DDC^{\alpha})]$$

The DDC, which represents mean diffusion rate within voxels, can be considered as a composite of individual ADC values. The α varying between 0 and 1 reflects the degree of tissue heterogeneity.

The DTI quantitative maps including fractional anisotropy (FA) and mean diffusivity (MD) were calculated in a Gaussian-distributed model:

$$S(b)/S(0) = exp(-b \cdot D_{app})$$

The value of b is 1,250 mm^2/s in this study, and D_{app} is the ADC.

In addition, mean kurtosis (MK) map, a DKI parameter, was obtained in non-Gaussian-distributed model:

$$S(b)/S(0) = exp\left(-b \cdot D_{app} + 1/6b^2 \cdot D_{app}^2 \cdot k_{app}\right)$$

K_{app} is the diffusion kurtosis.

The NODDI model was processed using a MATLAB toolbox (see text footnote 1). NODDI with two shells (b = 1,250 and 2,500 mm^2/s) could obtain orientation dispersion index (ODI) and intracellular volume fraction (ICVF) maps. The full normalized signal S in NODDI can be written as:

$$S = (1 - V_{iso})(V_{ic}S_{ic} + (1 - V_{ic})S_{ec}) + V_{iso}S_{iso})$$

Where V_{ic} and S_{ic} is the non-Gaussian volume fraction and intracellular diffusion signal, V_{iso} and S_{iso} is the normalized volume fraction and signal for the isotropic Gaussian diffusion compartment. And S_{ec} is the extracellular normalized signal.

All parametric maps and routine MR images were analyzed using ImageJ software (version 1.52a, NIH, United States). Before drawing the regions of interest (ROIs), the size (256 × 256), number of slices (Raab et al., 2010), as well as canvas size (240 mm × 240 mm) of routine sequences images and all parameter maps were adjusted to ensure they had the same image resolution, number of slices, and FOV. Two neuroradiologists (both with 5 years of experience in neuroradiology) who were blinded to clinical data manually placed three to six ROIs (range, 29–98 pixels) in consensus in the solid parts of tumor parenchyma and avoided hemorrhage, calcification, edema, necrosis, and cystic lesions. The solid part of tumor parenchyma was defined as the area of enhancement on contrast-enhanced T1-weighted images. If there was no enhancement on contrast-enhanced T1-weighted images, the solid part was defined as the area of abnormal signal on T2 FLAIR and T2 FSE. Then, the ROI was copied to each parameter map to obtain the measurements for each parameter. Similar to the previous studies (Figini et al., 2018; Wang et al., 2019), the minimum ADC, D, f, DDC, a, MD, and maximum D*, MK, ODI, and ICVF from all ROIs for each patient were recorded.

[1]https://www.nitrc.org/projects/noddi_toolbox

Statistical Analysis

Chi-square tests or R × C columnar tables were used to test categorical variables. Mann–Whitney U test was used to test continuous variables. Receiver operating characteristic (ROC) curves were performed to evaluate the diagnostic efficacy of each parameter. And area under the curve (AUC) was compared by Z test. The correlation between each parameter and proliferation index was calculated by Spearman correlation analysis. All statistical analyses were performed with SPSS (Version 19.0.0, IBM, Armonk, NY, United States) and MedCalc (Version 15.8, MedCalc Software, Acacialaan, Ostend, Belgium). $P < 0.05$ was considered to connote statistical significance.

RESULTS

Patient Characteristics and Demographics

In this study, there were 42 patients with IDH1-mutant glioma and 49 patients with IDH1 wild-type glioma. Patients with IDH1-mutant glioma were younger than those with IDH1 wild-type glioma (P = 0.008). There was a significant difference of pathological grade distribution between IDH1-mutant group and IDH1 wild-type group ($P < 0.001$) (**Table 1**).

TABLE 1 | Patient characteristics and demographics.

Characteristics	IDH1-Mut	IDH1-WT	*P*-value
No. of patients	42	49	NA
Age (years), median (interquartile range)	53 (46.5, 58)	41 (34.75, 50.25)	0.001
Sex, *n* (%)			0.405
Male	20 (47.6%)	28 (57.1%)	
Female	22 (52.4%)	21 (42.9%)	
Pathological grading, *n* (%)			<0.001
II	19 (45.2%)	8 (16.3%)	
III	13 (31.0%)	7 (14.3%)	
IV	10 (23.8%)	34 (69.4%)	

F, female; M, male; Mut, mutant; WT, wild-type; NA, not applicable.

Correlation of Diffusion Magnetic Resonance Imaging Parameters With Isocitrate Dehydrogenase 1 Genotype and Grade

Figure 1 shows the contrast-enhanced T1-weighted images and dMRI parameter maps of typical IDH1-mutant and IDH1 wild-type glioma patients. In grade II and grade III lower-grade gliomas (LrGGs), IDH1 wild-type group showed significantly lower ADC, D, f, DDC, α, and MD values ($P < 0.05$) and higher D*, MK, and ICVF values ($P < 0.05$) than IDH1-mutant group. However, there was no significant difference in FA and ODI values ($P = 0.126$ and 0.164, respectively) between the two groups (**Figure 2**). **Table 2** shows the AUC values, sensitivity, specificity, and cutoff values for discriminating IDH1 genotype in LrGGs. ADC, D, D*, f, DDC, α, MD, MK, and ICVF all showed high diagnostic efficacy in predicting IDH1 genotype in LrGGs; however, their AUC values were not significantly different ($P > 0.05$) (**Figure 3**). For glioblastomas (GBMs), no significant difference of these parameters was found between IDH1-mutant and IDH1 wild-type groups.

The dMRI-derived parameters of tumor lesions in LrGGs and GBMs in the presence of the same IDH1 genotype are presented in **Table 3**. In IDH1-mutant group, all parameters of dMRI, except D*, and FA, can significantly distinguish LrGGs from GBMs ($P < 0.05$). In the IDH1 wild-type group, only ADC showed a critical statistical difference between LrGGs and GBMs ($P = 0.048$).

Correlation Between Diffusion Magnetic Resonance Imaging Parameters and Cell Proliferation Index

The expression of Ki-67 LI was detected by immunohistochemical staining in 87 patients in this study. **Figure 4** shows the Spearman correlation between Ki-67 LI and dMRI parameters in gliomas. Significant positive correlation was found between Ki-67 LI and D* ($r = 0.316$, $P = 0.003$), MK ($r = 0.567$, $P < 0.001$), ODI ($r = 0.300$, $P = 0.005$) as well as ICVF ($r = 0.528$, $P < 0.001$). In contrast, ADC, D, f, DDC, α and MD showed a significant negative correlation with Ki-67 LI ($r = -0.479$, $P < 0.001$; $r = -0.503$, $P < 0.001$; $r = -0.433$, $P < 0.001$; $r = -0.466$, $P < 0.001$; $r = -0.462$, $P < 0.001$; $r = -0.528$, $P < 0.001$, respectively). FA had no significant correlation with Ki-67 LI ($r = 0.201$, $P = 0.062$). MK has the maximal correlation coefficient and D* has the minimal.

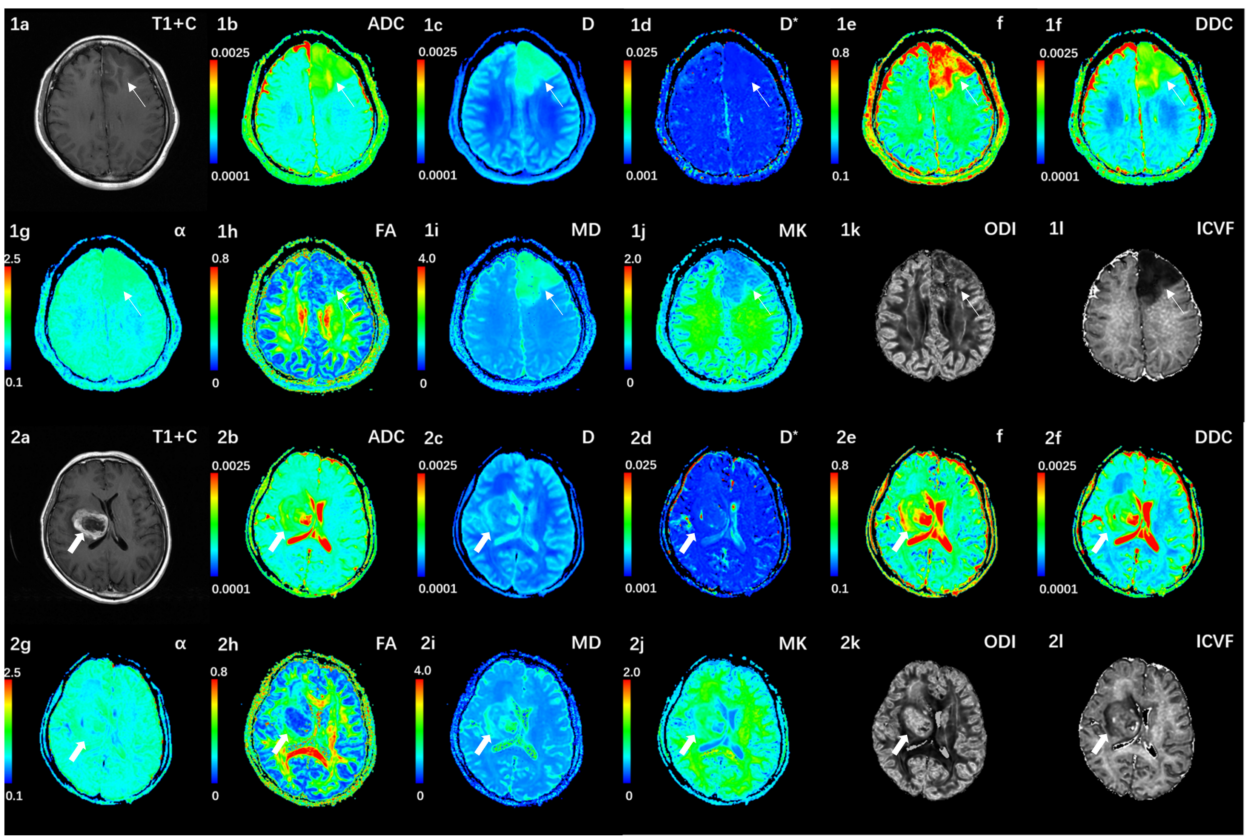

FIGURE 1 | (1a–l) Correspond to a 38-year-old female with a IDH1-mutant grade III glioma in the left frontal lobe (white thin arrow). The ADC, MD, D, f, and DDC as well as α maps show increased values in the solid part of the tumor, while D*, MK, ODI, and ICVF maps show decreased values. **(2a–l)** Corresponds to a 59-year-old female with a IDH1 wild-type grade III glioma in the right basal ganglia (white thick arrow). The ADC, MD, D, f, and DDC as well as α maps show decreased values in the solid part of the tumor, while D*, MK, ODI, and ICVF maps show increased values. ADC, D, D*, and DDC as well as MD are in units of 10^{-3} mm^2/s.

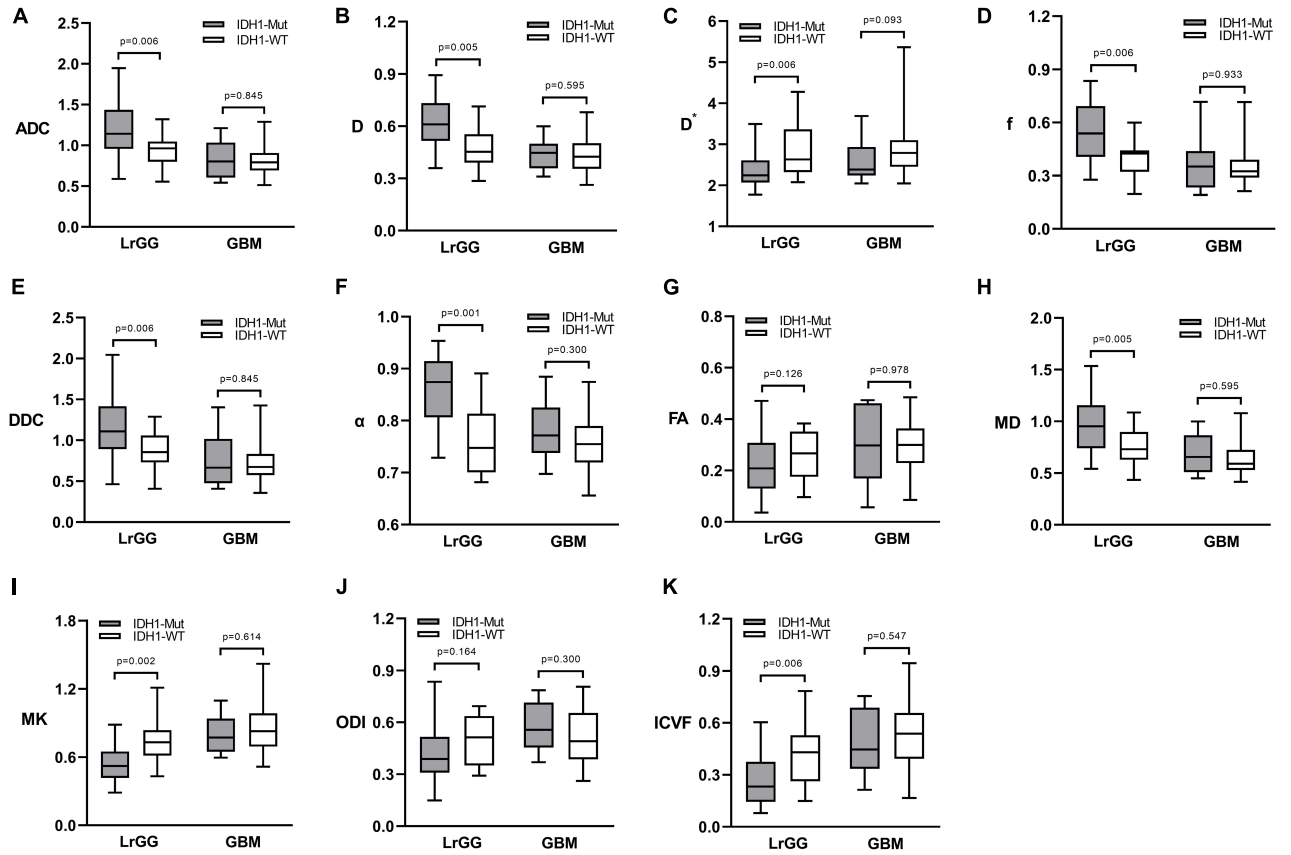

FIGURE 2 | Box and whisker plots of DWI **(A)**, IVIM **(B–D)**, stretched-exponential DWI **(E,F)**, DTI **(G,H)**, DKI **(I)**, and NODDI **(J,K)** parameter in LrGGs and GBMs stratified according to IDH1 genotype. Boxes represent the median ± quartiles, with whiskers extending to the maximum and minimum values. ADC, D, D*, and DDC as well as MD are in units of 10^{-3} mm^2/s. Mut, mutant; WT, wild-type; LrGG, lower-grade glioma; GBM, glioblastoma.

DISCUSSION

Our study showed the six diffusion models all provide at least one parameter with effective prediction performance on the IDH1 genotype in LrGGs. Also, dMRI parameters are promising in the assessment of cell proliferation, especially maximal correlation coefficient, found between MK and proliferation index.

TABLE 2 | ROC results of dMRI-derived parameter in differentiating IDH1 genotype in LrGGs.

Parameters	AUC	Sensitivity %	Specificity %	Cut-off value
ADC	0.750	59.38	93.33	1.084
D	0.758	68.75	80.00	0.553
D*	0.752	56.25	86.67	2.258
f	0.750	65.62	86.67	0.454
DDC	0.752	59.38	86.67	1.085
α	0.817	71.87	80.00	0.814
FA	0.640	87.50	40.00	0.318
MD	0.756	68.75	73.33	0.819
MK	0.788	71.87	80.00	0.613
ODI	0.627	81.25	46.67	0.518
ICVF	0.753	56.25	86.67	0.240

ADC, D, D, DDC, and MD are in units of 10^{-3} mm^2/s.*

Radiological differences were found between IDH1-mutant and wild-type groups in LrGGs. We suspected that IDH1 wild type existed in the LrGGs when more complex organizational structure, more abundant microvasculature, higher cell density, and more diffusion barriers appeared. However, none of the parameters showed significant differences in the identification of IDH1-mutant and wild-type groups in GBMs due to a single parameter with insufficient ability to discriminating diffusion and perfusion patterns of highly malignant and structurally complex. This hints that we should further explore differences in the GBM groups using a combination of multiple parameters in the future.

Previous studies have demonstrated the ability of conventional DWI and DTI to distinguish IDH-mutant gliomas from IDH wild-type gliomas (Xiong et al., 2016; Wu et al., 2018). In our study, ADC and MD values of IDH1 wild-type group were significantly lower than that of IDH1-mutant group in LrGGs. FA showed ineffective prediction on IDH1 genotype, possibly due to the high heterogeneity in FA values for the solid component of the tumor, which is consistent with the results of Tan et al. (2019).

Many studies have found that DKI has excellent efficacy in the grading diagnosis, differential diagnosis, molecular marker

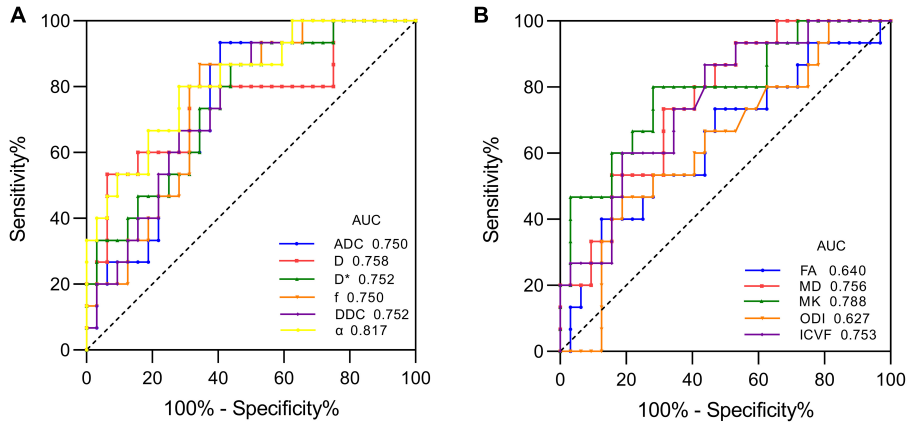

FIGURE 3 | ROC curves of each parameter for distinguishing mutant and wild-type IDH1 in LrGGs. **(A)** ROC curves of DWI, IVIM, and stretched-exponential DWI parameters. **(B)** ROC curves of DTI, DKI, and NODDI parameters.

TABLE 3 | dMRI-derived parameters in LrGGs and GBMs under the same IDH1 genotype.

Parameters	IDH1-Mut			IDH1-WT		
	LrGGs	GBMs	*P*-value	LrGGs	GBMs	*P*-value
ADC	1.142 (0.958, 1.436)	0.803 (0.606, 1.035)	0.003	0.963 (0.799,1.046)	0.792 (0.693,0.907)	0.095
D	0.611 (0.516, 0.732)	0.447 (0.358, 0.499)	<0.001	0.452 (0.390.0.553)	0.425 (0.354,0.503)	0.186
D*	2.242 (2.068, 2.611)	2.383 (2.241, 2.937)	0.140	2.630 (2.324,3.363)	2.791 (2.453,3.101)	0.558
f	0.539 (0.406, 0.693)	0.352 (0.234, 0.438)	0.007	0.425 (0.321,0.442)	0.325 (0.289,0.391)	0.165
DDC	1.110 (0.893,1.415)	0.665 (0.477, 1.017)	0.003	0.855 (0.730,1.060)	0.675 (0.575,0.834)	0.083
α	0.874 (0.807, 0.914)	0.771 (0.738, 0.825)	0.005	0.747 (0.701, 0.814)	0.755 (0.719, 0.790)	0.712
FA	0.208 (0.129, 0.307)	0.297 (0.169, 0.462)	0.125	0.267 (0.176, 0.352)	0.299 (0.229, 0.364)	0.386
MD	0.953 (0.740, 1.156)	0.655 (0.509, 0.865)	0.003	0.731 (0.629, 0.897)	0.590 (0.530, 0.724)	0.048
MK	0.522 (0.417, 0.649)	0.771 (0.647, 0.939)	<0.001	0.730 (0.613, 0.836)	0.827 (0.692, 0.984)	0.159
ODI	0.388 (0.309, 0.517)	0.556 (0.455, 0.714)	0.015	0.513 (0.351, 0.636)	0.491 (0.386, 0.655)	0.720
ICVF	0.233 (0.145, 0.376)	0.446 (0.334, 0.687)	0.002	0.430 (0.262, 0.528)	0.537 (0.392, 0.657)	0.073

*Each parameter is presented as median (interquartile range). Mut, mutant; WT, wild-type; LrGGs, lower-grade gliomas; GBMs, glioblastomas. *means the parameter "fast ADC".*

prediction, and prognostic assessment of glioma (Jiang et al., 2015; Pang et al., 2016; Hempel et al., 2018, 2019; Tan et al., 2019; Zhang et al., 2019; Haopeng et al., 2020). A DKI parameter MK reflects the complexity of the tissue microenvironment under the assumption of non-Gaussian distribution in the organism. Similar to the results reported by Zhao et al. (2019), our finding showed MK effectively discriminated IDH1-mutant group from wild-type group in LrGGs. IDH1-mutant gliomas have lower cell density, lower tissue complexity, and less aggressiveness, so they have decreased MK values, while IDH1 wild-type gliomas have a more heterogeneous tissue microenvironment, higher cell density, and more aggressive phenotype, resulting in significantly increased MK values.

Orientation dispersion index and ICVF computed based on the NODDI model represent neurite dispersion characteristics and neurite density, respectively. Maximov et al. (2017) found that two index parameters, ICVF and ODI, could identify low-grade glioma and high-grade glioma, and ICVF had the highest diagnostic efficacy and was significantly better than DTI. Li et al. (2019) considered NODDI to be a promising method for grading gliomas and predicting cell proliferation. Diffuse overgrowth of tumor cells with increased density leads to an increase in ICVF values. In addition, tumor cells grow infiltratively along adjacent vessels and around nerve axons, often accompanied by degradation and destruction of white matter nerve fiber bundles, causing microstructural changes and elevated dispersion in axonal bundles, leading to increased ODI. Our results showed only ICVF significantly distinguished IDH1-mutant group from IDH1 wild-type group in LrGGs. IDH1 wild-type gliomas may be more proliferative and aggressive due to more complex microstructure and thus possess higher ICVF values. Zhao et al. (2018) reported that the mean ICVF was significantly higher in GBMs with IDH1 mutation than that without IDH1 mutation. However, only four cases of IDH1-mutant GBMs were collected in their study, and the findings still need to be confirmed as even different to ours.

The IVIM model was proposed by Le Bihan et al. (1986), where D represents the diffusion movement of water molecules inside and outside the cell, D* reflects the blood perfusion of the microcirculation, and f represents the abundance of capillaries in the tissue. In recent years, IVIM has been widely used in the grading and differential diagnosis of glioma, reflecting

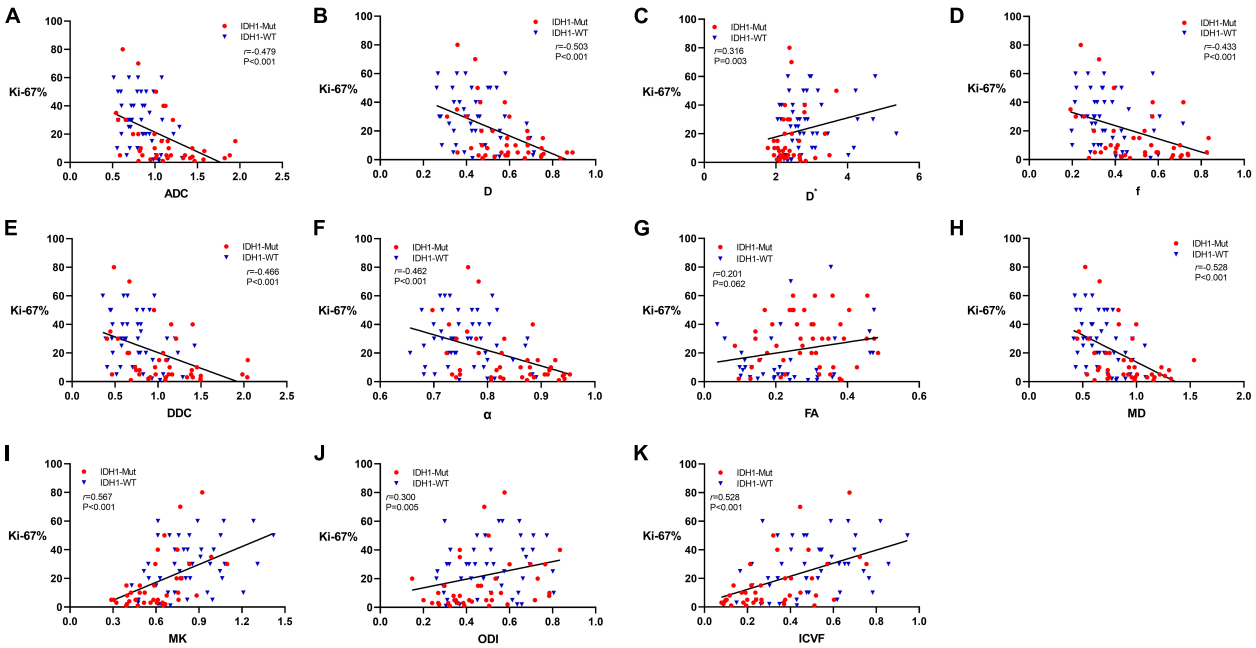

FIGURE 4 | Scatter diagrams demonstrating the correlations between Ki-67 labeling index and parameters of DWI **(A)**, IVIM **(B–D)**, stretched-exponential DWI **(E,F)**, DTI **(G,H)**, DKI **(I)**, and NODDI **(J,K)**. And *r* represents the Spearman correlation coefficient.

microscopic features such as tumor cell density and vascular proliferation (Bai et al., 2016; Shen et al., 2016; Kusunoki et al., 2020; Jiang and Minh Duc, 2021). Shen et al. (2016) studied the predictive efficacy of IVIM for glioma grading and considered that IVIM may be an imaging approach that combines arterial spin labeling (ASL) and ADC to assess tumor perfusion and diffusion. Minh Duc (Jiang and Minh Duc, 2021) found that IVIM has excellent diagnostic performance for distinguishing pilocytic astrocytoma from ependymoma. Increased D and f can reflect the pathological characteristics of pilocytic astrocytoma with low cell proliferation and high microvessel density, while decreased D and f reflects the high cell proliferation and low microvessel density of ependymoma. In the current study, the performance of D was slightly better than that of ADC in identifying the mutation status of IDH1 genotype in LrGGs perhaps due to D eliminates the influence of perfusion and more accurately reflects the diffusion and movement of water molecules. The D* value of IDH1 wild-type group is higher than that of IDH1-mutant group in LrGGs, indicating that IDH1 wild-type glioma has more abundant blood perfusion. Furthermore, *f*-value is higher in IDH1-mutant gliomas, inconsistent with Wang et al. (2019). The same contradictory results exist in studies of glioma grading, where *f*-values are higher in low-grade gliomas than in high-grade gliomas (Hu et al., 2014). Le Bihan (2019) suggested that the IVIM model is sensitive to fluid flow distributed within any voxel, not just blood flow. More relatively unrestricted water molecules outside the IDH1-mutant glioma cells may have contributed to the increase of *f*-values. Alternatively, these differences may be due to different IVIM model parameters, fitting methods, and ROI plotting methods (Cho et al., 2015).

The α is a parameter in stretched-exponential DWI that reflects the heterogeneity of the tissue. The high heterogeneity of tumor tissue, such as heterogeneous cells and proliferating vessels, leads to a decrease in α value (Chakhoyan et al., 2018; Chen et al., 2018). The DDC is a parameter reflecting diffusion in the stretched-exponential DWI, which is the weighted sum of ADC values. It can overcome the limitations of the biexponential DWI model regarding the assumption of fast and slow diffusion to reflect the diffusion characteristics of glioma, which is negatively correlated with tumor density. The stretched-exponential DWI model showed excellent efficacy in IDH1 genotype discrimination in our study, and α was able to distinguish IDH1 mutation status in LrGGs with the largest AUC value and high sensitivity and specificity. Lower α values indicate that the diffusion of water molecules in the tissue was inhomogeneous, and the heterogeneity of the tissue was higher (Bai et al., 2016). We speculate that the microenvironment of IDH1 wild-type glioma is more complicated, such as cell swelling and vascular proliferation, so it exhibits greater heterogeneity of intra-voxel diffusion.

In the ROC analysis of the diffusion parameters, we found that ADC, D, D*, f, DDC, α, MD, MK, and ICVF were all characterized by higher specificity and lower sensitivity in identifying LrGG IDH1 genotypes. Of these, α and MK had the highest sensitivity and AUC values. We therefore considered that α and MK may be more appropriate diffusion parameters for identifying LrGG IDH1 genotypes.

This is of great clinical importance for the prediction of IDH1 wild-type LrGGs, which have a malignant clinical course despite being pathologically relatively inert alterations. Therefore, accurate and non-invasive prediction of the IDH1 genotype in

LrGGs allows for timely treatment planning to impede malignant transformation of the disease.

We also investigated the prediction of glioma grading by dMRI under the same IDH1 genotype. Generally speaking, high-grade gliomas tend to be more heterogeneous, as shown in our findings. However, IDH1 wild-type LrGGs and GBMs showed only marginally statistically different ADC. Some studies have found that even in patients with IDH wild-type LrGG, tumors exhibit high levels of aggressiveness, with overall survival times similar to those of IDH wild-type GBM (Eckel-Passow et al., 2015; Wijnenga et al., 2017). This may explain our results, probably because the similar high heterogeneity and aggressiveness of IDH1 wild-type gliomas, resulting in most parameters that do not differ significantly between LrGGs and GBMs both with wild-type IDH1. In a word, with the increase of pathological grade, the tumor microstructure is more complex, with higher cell density and more disturbed water molecule movement, but IDH1 gene phenotype will affect the development of gliomas at a microscopic point of view. Compared with previous pathological grading studies (Bai et al., 2016), our study combined the pathological grading of gliomas with molecular phenotypes, which contributes to a more comprehensive understanding of the characteristics and microstructure of gliomas.

Nuclear protein Ki-67 is associated with cell proliferation specifically expressed in tumor cells (Alexiou et al., 2010; Gates et al., 2019). As the malignancy of the tumor increases, the blood supply becomes more abundant, the number of cells increases, malignant biological behavior ensues, such as hemorrhage and necrosis, and neovascularization forms further (Raab et al., 2010; Tietze et al., 2015). And these aforementioned alterations can affect the complexity and heterogeneity of tumor microstructure, when cellular gaps are smaller, water molecules diffusion is more restricted, and movement is more disturbed. Zhang et al. (2018) found MK and D have considerable potential to predict the degree of proliferation in diffuse astrocytomas. This is similar to our findings, where MK has maximal correlation coefficient with cell proliferation index. However, no significant correlation was found between FA and Ki-67 LI, which may be because the level of cell proliferation in response to Ki-67 only affects the size of the diffusion and not the pattern of diffusion routes.

We studied the predictive efficacy of multiple dMRI parameters for glioma IDH1 genotype and cell proliferation and found their great potential. However, dMRI still has some limitations that hinder its applicability in the routine clinical diagnosis of gliomas. There is currently no consensus on the optimal protocol parameters and post-processing methods for dMRI. This concerns acquisition parameters (e.g., number of directions, *b*-values) as well as post-processing methods. Further technical and methodological advances in the field of dMRI are necessary. Standardization and validation criteria for dMRI acquisition and post-processing techniques are needed in order to improve comparability between research centers.

Our study had some limitations. First, the sample size was small, especially for IDH1 wild-type LrGGs and IDH1-mutant GBMs. Although this is related to the uneven distribution of IDH1 mutation status in gliomas, future prospective studies with large samples are needed to ensure the accuracy of the experiment. Second, only one molecule, IDH1, was considered in this study, but many other molecules status such as 1p/19q codeletion and O6-methylguanine-DNA methyltransferase promoter methylation also play an important role in the development of gliomas, which needs to be further investigated. Finally, the ROI in this study was placed on the solid part of the tumor tissue; although this approach is more flexible and can better avoid areas of hemorrhage, necrosis, and calcification, it does not consider the tumor tissue as a whole. In the future, we can outline 3D ROIs on the parenchymal part of the whole tumor to validate our results of this study.

CONCLUSION

Our findings reveal the relationship between dMRI parameters and IDH1 genotype and proliferation index in gliomas. dMRI has great potential to provide imaging markers that are sensitive to microstructural changes in gliomas caused by IDH1 mutation and cell proliferation, thereby facilitating prognostic prediction and treatment of glioma patients.

DATA AVAILABILITY STATEMENT

The raw data supporting the conclusions of this article will be made available by the authors, without undue reservation.

ETHICS STATEMENT

The studies involving human participants were reviewed and approved by the Ethics Committee of Tongji Hospital, Tongji Medical College, Huazhong University of Science and Technology. Written informed consent to participate in this study was provided by the participants' legal guardian/next of kin.

AUTHOR CONTRIBUTIONS

YX and WZ: guarantor of integrity of the entire study. YX, SL, and WZ: study concepts and design. YX and NS: literature research. YX and TG: experimental studies and data analysis. YX, SZ, WL, and SL: manuscript preparation and editing. All authors contributed to the article and approved the submitted version.

FUNDING

This work was supported by the National Natural Science Foundation of China (Grant Number 81730049).

ACKNOWLEDGMENTS

This manuscript has been shared as a preprint on Research Square (https://doi.org/10.21203/rs.3.rs-468889/v1).

REFERENCES

Alexiou, G. A., Tsiouris, S., Kyritsis, A. P., Argyropoulou, M. I., Voulgaris, S., and Fotopoulos, A. D. (2010). Assessment of glioma proliferation using imaging modalities. *J. Clin. Neurosci.* 17, 1233–1238.

Bai, Y., Lin, Y., Tian, J., Shi, D., Cheng, J., Haacke, E. M., et al. (2016). Grading of gliomas by using monoexponential, biexponential, and stretched exponential diffusion-weighted MR imaging and diffusion kurtosis MR imaging. *Radiology* 278, 496–504. doi: 10.1148/radiol.2015142173

Bennett, K. M., Schmainda, K. M., Bennett, R. T., Rowe, D. B., Lu, H., and Hyde, J. S. (2003). Characterization of continuously distributed cortical water diffusion rates with a stretched-exponential model. *Magn. Reson. Med.* 50, 727–734. doi: 10.1002/mrm.10581

Chakhoyan, A., Woodworth, D. C., Harris, R. J., Lai, A., Nghiemphu, P. L., Liau, L. M., et al. (2018). Mono-exponential, diffusion kurtosis and stretched exponential diffusion MR imaging response to chemoradiation in newly diagnosed glioblastoma. *J. Neurooncol.* 139, 651–659. doi: 10.1007/s11060-018-2910-9

Chen, X., Jiang, J., Shen, N., Zhao, L., Zhang, J., Qin, Y., et al. (2018). Stretched-exponential model diffusion-weighted imaging as a potential imaging marker in preoperative grading and assessment of proliferative activity of gliomas. *Am. J. Transl. Res.* 10, 2659–2668.

Cho, G. Y., Moy, L., Zhang, J. L., Baete, S., Lattanzi, R., Moccaldi, M., et al. (2015). Comparison of fitting methods and b-value sampling strategies for intravoxel incoherent motion in breast cancer. *Magn. Reson. Med.* 74, 1077–1085. doi: 10.1002/mrm.25484

Eckel-Passow, J. E., Lachance, D. H., Molinaro, A. M., Walsh, K. M., Decker, P. A., Sicotte, H., et al. (2015). Glioma groups based on 1p/19q, IDH, and TERT promoter mutations in tumors. *N. Engl. J. Med.* 372, 2499–2508.

Figini, M., Riva, M., Graham, M., Castelli, G. M., Fernandes, B., Grimaldi, M., et al. (2018). Prediction of isocitrate dehydrogenase genotype in brain gliomas with MRI: single-shell versus multishell diffusion models. *Radiology* 289, 788–796. doi: 10.1148/radiol.2018180054

Fu, Y., Huang, R., Du, J., Yang, R., An, N., and Liang, A. (2010). Glioma-derived mutations in IDH: from mechanism to potential therapy. *Biochem. Biophys. Res. Commun.* 397, 127–130. doi: 10.1016/j.bbrc.2010.05.115

Gates, E. D. H., Lin, J. S., Weinberg, J. S., Hamilton, J., Prabhu, S. S., Hazle, J. D., et al. (2019). Guiding the first biopsy in glioma patients using estimated Ki-67 maps derived from MRI: conventional versus advanced imaging. *Neuro Oncol.* 21, 527–536. doi: 10.1093/neuonc/noz004

Habberstad, A. H., Gulati, S., and Torp, S. H. (2011). Evaluation of the proliferation markers Ki-67/MIB-1, mitosin, survivin, pHH3, and DNA topoisomerase IIalpha in human anaplastic astrocytomas–an immunohistochemical study. *Diagn. Pathol.* 6:43. doi: 10.1186/1746-1596-6-43

Haopeng, P., Xuefei, D., Yan, R., Zhenwei, Y., Wei, H., Ziyin, W., et al. (2020). Diffusion kurtosis imaging differs between primary central nervous system lymphoma and high-grade glioma and is correlated with the diverse nuclear-to-cytoplasmic ratio: a histopathologic, biopsy-based study. *Eur. Radiol.* 30, 2125–2137. doi: 10.1007/s00330-019-06544-7

Hempel, J. M., Brendle, C., Bender, B., Bier, G., Kraus, M. S., Skardelly, M., et al. (2019). Diffusion kurtosis imaging histogram parameter metrics predicting survival in integrated molecular subtypes of diffuse glioma: an observational cohort study. *Eur. J. Radiol.* 112, 144–152. doi: 10.1016/j.ejrad.2019.01.014

Hempel, J. M., Schittenhelm, J., Bisdas, S., Brendle, C., Bender, B., Bier, G., et al. (2018). In vivo assessment of tumor heterogeneity in WHO 2016 glioma grades using diffusion kurtosis imaging: diagnostic performance and improvement of feasibility in routine clinical practice. *J. Neuroradiol.* 45, 32–40. doi: 10.1016/j.neurad.2017.07.005

Hu, Y. C., Yan, L. F., Wu, L., Du, P., Chen, B. Y., Wang, L., et al. (2014). Intravoxel incoherent motion diffusion-weighted MR imaging of gliomas: efficacy in preoperative grading. *Sci. Rep.* 4:7208. doi: 10.1038/srep07208

Jiang, Q., and Minh Duc, N. (2021). The diagnostic function of intravoxel incoherent motion for distinguishing between pilocytic astrocytoma and ependymoma. *PLoS One* 16:e0247899. doi: 10.1371/journal.pone.0247899

Jiang, R., Jiang, J., Zhao, L., Zhang, J., Zhang, S., Yao, Y., et al. (2015). Diffusion kurtosis imaging can efficiently assess the glioma grade and cellular proliferation. *Oncotarget* 6, 42380–42393. doi: 10.18632/oncotarget.5675

Jiang, S., Rui, Q., Wang, Y., Heo, H. Y., Zou, T., Yu, H., et al. (2018). Discriminating MGMT promoter methylation status in patients with glioblastoma employing amide proton transfer-weighted MRI metrics. *Eur. Radiol.* 28, 2115–2123. doi: 10.1007/s00330-017-5182-4

Karsy, M., Guan, J., Cohen, A. L., Jensen, R. L., and Colman, H. (2017). New molecular considerations for glioma: IDH, ATRX, BRAF, TERT, H3 K27M. *Curr. Neurol. Neurosci. Rep.* 17:19. doi: 10.1007/s11910-017-0722-5

Kusunoki, M., Kikuchi, K., Togao, O., Yamashita, K., Momosaka, D., Kikuchi, Y., et al. (2020). Differentiation of high-grade from low-grade diffuse gliomas using diffusion-weighted imaging: a comparative study of mono-, bi-, and stretched-exponential diffusion models. *Neuroradiology* 62, 815–823. doi: 10.1007/s00234-020-02456-2

Le Bihan, D. (2019). What can we see with IVIM MRI? *Neuroimage* 187, 56–67. doi: 10.1016/j.neuroimage.2017.12.062

Le Bihan, D., Breton, E., Lallemand, D., Grenier, P., Cabanis, E., and Laval-Jeantet, M. (1986). MR imaging of intravoxel incoherent motions: application to diffusion and perfusion in neurologic disorders. *Radiology* 161, 401–407. doi: 10.1148/radiology.161.2.3763909

Li, S. H., Jiang, R. F., Zhang, J., Su, C. L., Chen, X. W., Zhang, J. X., et al. (2019). Application of neurite orientation dispersion and density imaging in assessing glioma grades and cellular proliferation. *World Neurosurg.* 131, e247–e254. doi: 10.1016/j.wneu.2019.07.121

Maier, S. E., Sun, Y., and Mulkern, R. V. (2010). Diffusion imaging of brain tumors. *NMR Biomed.* 23, 849–864.

Maximov, I. I., Tonoyan, A. S., and Pronin, I. N. (2017). Differentiation of glioma malignancy grade using diffusion MRI. *Phys. Med.* 40, 24–32. doi: 10.1016/j.ejmp.2017.07.002

Pang, H., Ren, Y., Dang, X., Feng, X., Yao, Z., Wu, J., et al. (2016). Diffusional kurtosis imaging for differentiating between high-grade glioma and primary central nervous system lymphoma. *J. Magn. Reson. Imaging* 44, 30–40. doi: 10.1002/jmri.25090

Raab, P., Hattingen, E., Franz, K., Zanella, F. E., and Lanfermann, H. (2010). Cerebral gliomas: diffusional kurtosis imaging analysis of microstructural differences. *Radiology* 254, 876–881. doi: 10.1148/radiol.09090819

Shen, G., Wang, R., Gao, B., Zhang, Z., Wu, G., and Pope, W. (2020). The MRI features and prognosis of gliomas associated with IDH1 mutation: a single center study in Southwest China. *Front. Oncol.* 10:852. doi: 10.3389/fonc.2020.00852

Shen, N., Zhao, L., Jiang, J., Jiang, R., Su, C., Zhang, S., et al. (2016). Intravoxel incoherent motion diffusion-weighted imaging analysis of diffusion and microperfusion in grading gliomas and comparison with arterial spin labeling for evaluation of tumor perfusion. *J. Magn. Reson. Imaging* 44, 620–632. doi: 10.1002/jmri.25191

Tan, Y., Zhang, H., Wang, X., Qin, J., Wang, L., Yang, G., et al. (2019). Comparing the value of DKI and DTI in detecting isocitrate dehydrogenase genotype of astrocytomas. *Clin. Radiol.* 74, 314–320. doi: 10.1016/j.crad.2018.12.004

Tietze, A., Hansen, M. B., Østergaard, L., Jespersen, S. N., Sangill, R., Lund, T. E., et al. (2015). Mean diffusional kurtosis in patients with glioma: initial results with a fast imaging method in a clinical setting. *AJNR Am. J. Neuroradiol.* 36, 1472–1478. doi: 10.3174/ajnr.A4311

Turkalp, Z., Karamchandani, J., and Das, S. (2014). IDH mutation in glioma: new insights and promises for the future. *JAMA Neurol.* 71, 1319–1325. doi: 10.1001/jamaneurol.2014.1205

Van Cauter, S., Veraart, J., Sijbers, J., Peeters, R. R., Himmelreich, U., De Keyzer, F., et al. (2012). Gliomas: diffusion kurtosis MR imaging in grading. *Radiology* 263, 492–501. doi: 10.1148/radiol.12110927

Wang, X., Chen, X. Z., Shi, L., and Dai, J. P. (2019). Glioma grading and IDH1 mutational status: assessment by intravoxel incoherent motion MRI. *Clin. Radiol.* 74, 651.e7–651.e14.

Wijnenga, M. M. J., Dubbink, H. J., French, P. J., Synhaeve, N. E., Dinjens, W. N. M., Atmodimedjo, P. N., et al. (2017). Molecular and clinical heterogeneity of adult diffuse low-grade IDH wild-type gliomas: assessment of TERT promoter mutation and chromosome 7 and 10 copy number status allows superior prognostic stratification. *Acta Neuropathol.* 134, 957–959. doi: 10.1007/s00401-017-1781-z

Wu, C. C., Jain, R., Radmanesh, A., Poisson, L. M., Guo, W. Y., Zagzag, D., et al. (2018). Predicting genotype and survival in glioma using standard clinical MR imaging apparent diffusion coefficient images: a pilot study from the Cancer Genome Atlas. *AJNR Am. J. Neuroradiol.* 39, 1814–1820. doi: 10.3174/ajnr.A5794

Wu, E. X., and Cheung, M. M. (2010). MR diffusion kurtosis imaging for neural tissue characterization. *NMR Biomed.* 23, 836–848.

Xiong, J., Tan, W., Wen, J., Pan, J., Wang, Y., Zhang, J., et al. (2016). Combination of diffusion tensor imaging and conventional MRI correlates with isocitrate dehydrogenase 1/2 mutations but not 1p/19q genotyping in oligodendroglial tumours. *Eur. Radiol.* 26, 1705–1715. doi: 10.1007/s00330-015-4025-4

Ye, D., Ma, S., Xiong, Y., and Guan, K. L. (2013). R-2-hydroxyglutarate as the key effector of IDH mutations promoting oncogenesis. *Cancer Cell* 23, 274–276. doi: 10.1016/j.ccr.2013.03.005

Zhang, H., Schneider, T., Wheeler-Kingshott, C. A., and Alexander, D. C. (2012). NODDI: practical in vivo neurite orientation dispersion and density imaging of the human brain. *Neuroimage* 61, 1000–1016. doi: 10.1016/j.neuroimage.2012.03.072

Zhang, J., Chen, X., Chen, D., Wang, Z., Li, S., and Zhu, W. (2018). Grading and proliferation assessment of diffuse astrocytic tumors with monoexponential, biexponential, and stretched-exponential diffusion-weighted imaging and diffusion kurtosis imaging. *Eur. J. Radiol.* 109, 188–195. doi: 10.1016/j.ejrad.2018.11.003

Zhang, J., Jiang, J., Zhao, L., Zhang, J., Shen, N., Li, S., et al. (2019). Survival prediction of high-grade glioma patients with diffusion kurtosis imaging. *Am. J. Transl. Res.* 11, 3680–3688.

Zhao, J., Li, J. B., Wang, J. Y., Wang, Y. L., Liu, D. W., Li, X. B., et al. (2018). Quantitative analysis of neurite orientation dispersion and density imaging in grading gliomas and detecting IDH-1 gene mutation status. *Neuroimage Clin.* 19, 174–181. doi: 10.1016/j.nicl.2018.04.011

Zhao, J., Wang, Y. L., Li, X. B., Hu, M. S., Li, Z. H., Song, Y. K., et al. (2019). Comparative analysis of the diffusion kurtosis imaging and diffusion tensor imaging in grading gliomas, predicting tumour cell proliferation and IDH-1 gene mutation status. *J. Neurooncol.* 141, 195–203. doi: 10.1007/s11060-018-03025-7

Conflict of Interest: The authors declare that the research was conducted in the absence of any commercial or financial relationships that could be construed as a potential conflict of interest.

Publisher's Note: All claims expressed in this article are solely those of the authors and do not necessarily represent those of their affiliated organizations, or those of the publisher, the editors and the reviewers. Any product that may be evaluated in this article, or claim that may be made by its manufacturer, is not guaranteed or endorsed by the publisher.

Copyright © 2021 Xie, Li, Shen, Gan, Zhang, Liu and Zhu. This is an open-access article distributed under the terms of the Creative Commons Attribution License (CC BY). The use, distribution or reproduction in other forums is permitted, provided the original author(s) and the copyright owner(s) are credited and that the original publication in this journal is cited, in accordance with accepted academic practice. No use, distribution or reproduction is permitted which does not comply with these terms.

frontiers in Neuroscience

ORIGINAL RESEARCH
published: 25 November 2021
doi: 10.3389/fnins.2021.743402

A Data-Based Approach for Selecting Pre- and Intra-Operative Language Mapping Tasks

Justyna O. Ekert[1], Matthew A. Kirkman[2], Mohamed L. Seghier[1,3], David W. Green[4] and Cathy J. Price[1]*

[1] Wellcome Centre for Human Neuroimaging, UCL Queen Square Institute of Neurology, London, United Kingdom, [2] Department of Neurosurgery, Queen's Medical Centre, Nottingham, United Kingdom, [3] Department of Biomedical Engineering, Khalifa University of Science and Technology, Abu Dhabi, United Arab Emirates, [4] Department of Experimental Psychology, University College London, London, United Kingdom

Background: Pre- and intra-operative language mapping in neurosurgery patients frequently involves an object naming task. The choice of the optimal object naming paradigm remains challenging due to lack of normative data and standardization in mapping practices. The aim of this study was to identify object naming paradigms that robustly and consistently activate classical language regions and could therefore be used to improve the sensitivity of language mapping in brain tumor and epilepsy patients.

Methods: Functional magnetic resonance imaging (fMRI) data from two independent groups of healthy controls (total = 79) were used to generate threshold-weighted voxel-based consistency maps. This novel approach allowed us to compare inter-subject consistency of activation for naming single objects in the visual and auditory modality and naming two objects in a phrase or a sentence.

Results: We found that the consistency of activation in language regions was greater for naming two objects per picture than one object per picture, even when controlling for the number of names produced in 5 s.

Conclusion: More consistent activation in language areas for naming two objects compared to one object suggests that two-object naming tasks may be more suitable for delimiting language eloquent regions with pre- and intra-operative language testing. More broadly, we propose that the functional specificity of brain mapping paradigms for a whole range of different linguistic and non-linguistic functions could be enhanced by referring to databased models of inter-subject consistency and variability in typical and atypical brain responses.

Keywords: neurosurgery, fMRI, brain mapping, direct electrical stimulation (DES), language, object naming

OPEN ACCESS

Edited by:
Alexandra Golby, Harvard Medical School, United States

Reviewed by:
Domenico Zaca, Siemens Italia, Italy
Saloni Krishnan, Royal Holloway, University of London, United Kingdom

****Correspondence:***
Justyna O. Ekert
justyna.ekert.14@ucl.ac.uk

Specialty section:
This article was submitted to Brain Imaging Methods, a section of the journal Frontiers in Neuroscience

Received: *18 July 2021*
Accepted: *01 November 2021*
Published: *25 November 2021*

Citation:
Ekert JO, Kirkman MA, Seghier ML, Green DW and Price CJ (2021) A Data-Based Approach for Selecting Pre- and Intra-Operative Language Mapping Tasks. Front. Neurosci. 15:743402. doi: 10.3389/fnins.2021.743402

INTRODUCTION

Awake craniotomy with intra-operative stimulation mapping is strongly advocated for patients with gliomas affecting eloquent brain regions (Hamer et al., 2012; Leon-Rojas et al., 2020). A growing body of evidence suggests that more extensive resection is associated with longer survival (Sanai and Berger, 2008a; Sanai et al., 2008; McGirt et al., 2009; Ius et al., 2012; Jakola et al., 2012, 2017). Nevertheless, to preserve the patient's

quality of life, the survival benefit conferred by more aggressive surgery needs to be balanced with the risk of post-operative deficits (referred to as the onco-functional balance) (Duffau et al., 2009). This is particularly challenging in patients with tumors in or adjacent to cortical language hubs, where resection may lead to life-changing impairments in communication skills (Jakola et al., 2011; Gabel et al., 2019). To attempt to preserve the integrity of language regions, intra-operative mapping with the use of direct electrical stimulation is performed (Ilmberger et al., 2008; De Witte and Mariën, 2013; Rofes et al., 2017b). The capacity to detect and evaluate function during surgery critically depends on the selection of sensitive and lesion-site specific testing paradigms that, at present, lack standardization (O'neill et al., 2020; Sefcikova et al., 2020; Young et al., 2021).

The purpose of this study is to demonstrate how functional consistency maps generated from large populations of neurotypical controls can be used to facilitate the selection of pre- and intra-operative language tasks that robustly and consistently activate core language areas. Below, we discuss the challenges related to current language mapping practices prior to illustrating how results from functional magnetic resonance imaging (fMRI) of neurotypical participants can be used to inform decision making.

Pre-operative Planning With fMRI

The complexity and wide distribution of language networks make it extremely challenging to predict how resection will affect language function. This is further complicated by inter-individual structural and functional variability, commonly observed in healthy individuals (Fedorenko and Blank, 2020) and exacerbated following tumor-induced reorganization. A common solution is to investigate language function prior to surgery using fMRI (Castellano et al., 2017). This provides potentially valuable, patient-specific information about the location and function of cortical language regions that may be at risk of damage, thereby enabling more targeted surgical approaches and reducing the operative duration (Sanai et al., 2008). In 2017, the American Society of Functional Neuroradiology published a white paper proposing two sets of language paradigms that balance the clinical usefulness and ease of application (Black et al., 2017). The recommended fMRI tasks for pre-surgical language assessment in adult patients included: sentence completion, silent word generation, rhyming, object naming, and/or passive story listening. The extent to which these guidelines have been adopted is currently unknown (Benjamin et al., 2018).

The reliability of fMRI has been examined in a meta-analysis of studies comparing fMRI with direct electrical stimulation for language mapping. The authors found that the sensitivity of fMRI for detecting language areas ranged from 59–100%, with 0–97% specificity (Giussani et al., 2010). It is also important to acknowledge three limitations of fMRI. First, detection of fMRI activation in a cortical area does not mean that the region is critical for a certain function and cannot be resected without post-operative functional deficits (Duffau, 2005; Silva et al., 2018) because the function of the region may be subsumed by another neural region/system. Second, when fMRI activation is not observed, true activation may have been missed because the blood-oxygen-level-dependent (BOLD) signal was compromised by pathology-related disruptions to neurovascular coupling. Third, the absence of fMRI activation in a region of interest may be due to an unsuitable paradigm that does not elicit robust activation at the individual subject level (Mahdavi et al., 2015; Pak et al., 2017), either because the region of interest is not strongly engaged or because of inter-subject variability in the degree to which a region is engaged.

Understanding inter-subject variability in neurologically normal subjects is important because it can arise for multiple reasons, such as differences in the hemodynamic response, differences in task performance or differences in the neural systems used for the same task (Seghier and Price, 2018). In this context, the absence of activation in a single patient might still be within the normal range but be treated as dysfunctional if located in a region that is significantly activated in a group-level study.

Given the above, the results from fMRI analyses are not a substitute for intra-operative stimulation mapping; however, they are useful for helping to select tasks that are most likely to evoke a response during intra-operative stimulation mapping.

Intraoperative Stimulation Mapping

The application of direct electrical stimulation (DES) for mapping of motor and sensory pathways in neuro-oncological surgery was described by Mitchel Berger in the nineties and it has subsequently become a part of the neurosurgeon's armamentarium (Berger et al., 1989; Berger and Ojemann, 1992). DES is the gold standard used to map the function of eloquent cortical regions and subcortical white matter tracts in neurosurgery patients, thereby facilitating maximum safe resection (Hamer et al., 2012). For intra-operative language mapping, the patient must be awakened or remain awake throughout the surgery so that they can engage in linguistic tasks such as object naming, counting, verbal fluency, and other (for review, see Young et al., 2021). A neuropsychologist or speech and language therapist monitors the patient's response to the task while the peritumoral tissue is stimulated to transiently disrupt its function (Klitsinikos et al., 2021). This involves bipolar stimulation with progressively increasing current intensity, typically from 1.5 to 6 mA and maintaining contact with neural tissue for 3 s at a time (Sanai et al., 2008). According to the standard protocol first established by Ojemann et al. (1989), each brain region should be stimulated at least 3 times (Sanai and Berger, 2008b; Sanai et al., 2008; Hervey-Jumper et al., 2015). A positive language site is identified when stimulation to the cortical region of interest results in an inability to successfully perform the task in 66% or more of the testing (Sanai and Berger, 2010).

Functional disturbances during electrical stimulation may indicate that the stimulated region was required for the task tested, but they may also reflect false positives. For example, a reduction in speed or accuracy may not be due to disturbance at the stimulus site; it could be a consequence of (a) disruption in distant task-related regions through the spread of electrical current along connecting axons (Matsumoto et al., 2004; Mandonnet et al., 2010), (b) patient fatigue, particularly during long testing sessions (Mandonnet et al., 2010), or (c) inadequate

task difficulty (Bu et al., 2021). Conversely, there are several reasons why the absence of an effect of DES may be a false negative: (1) the task was not appropriate to test the function of the stimulated region because it does not activate the region in the normal population; (2) the stimulated region was essential for the task in the patient because of normal inter-subject variability or pathology-induced functional reorganization; and (3) the stimulated region is required for the task but the stimulation intensity was insufficient to generate a response or the effect wasn't detected, e.g., if the effect was on response times or hesitation rather than speech arrest (Shimotake et al., 2015; O'neill et al., 2020). The successful interpretation of intra-operative DES is therefore critically dependent on selecting tasks that: (i) are easy to perform, particularly for patients who struggle to maintain focus during awake surgery; and (ii) robustly and consistently activate the targeted region in neurotypical individuals within the short timespan that DES can be safely applied.

At present, no standardized protocol exists to reliably identify and test language regions in neurosurgery patients with many institutions assessing only one task (Ruis, 2018; Sefcikova et al., 2020). A survey of the European Low-Grade Glioma Network showed that object naming was the most frequently utilized task for mapping language during awake surgery (Rofes et al., 2017a). However, choice of the object naming paradigms is highly variable across institutions ranging from in-house designed paradigms to use of one of a number of standardized tests for intra-operative language assessments, such as DO70/DO80, Picture Naming AAT, Boston Naming Test, Reitan Indiana Aphasia screening test, BDAE and the Snodgrass and Vanderwart collection, Laiacona–Capitani test (Rofes et al., 2015; Ruis, 2018; O'neill et al., 2020).

While stimulation mapping with visual picture naming is considered the gold standard, the choice of stimulus modality should be carefully considered, taking into account the site of the lesion. Hamberger et al. (2005) showed that sparing visual naming sites, without consideration of other sites, did not reliably prevent post-operative language decline in patients with temporal lobe epilepsy. Six out of seven patients who had auditory naming sites resected declined post-operatively, in comparison to three out of twelve patients with preserved auditory naming regions. Intra-operative language mapping may therefore require multiple tasks in order to prevent post-operative language deficits (Manan et al., 2020).

Current Study

The current study investigates how robustly and consistently different object naming paradigms engage sensory, motor and language regions in neurotypical individuals. As a proxy for neural activity, we used BOLD fMRI. By identifying object naming paradigms with the most consistent and robust BOLD responses, we generate hypotheses for optimal task selection for intra-operative and pre-operative surgical planning.

Specifically, we compared how consistently four different object naming tasks activated sensory, motor and language regions in neurotypical individuals at the voxel/region level. Three of the object naming tasks involved visual (picture) naming, the third involved auditory object naming (from the non-verbal sounds of objects and animals). For all four tasks, the number of stimuli presented and the fMRI acquisition time was controlled but, for two of the visual naming tasks, we presented objects in pairs every 5 s for a duration of 2.5 s, whereas in the other two tasks we presented one object at a time every 2.5 s for a duration of 1.5 s (**Figure 1**).

We expected that the requirement to name two objects on a trial, rather than one, would increase demand on the regions involved in speech production (e.g., those required to retrieve and produce names) and so yield more robust activation at the individual level. If the naming of two objects results in more consistent activation at the individual level in speech production regions compared to naming a single object, then future studies could investigate whether naming two objects increases test sensitivity for intraoperative and pre-operative language mapping.

Prior studies have aimed to compare the effectiveness of different language mapping fMRI paradigms (e.g., Unadkat et al., 2019) using traditional SPM{t} maps. However, this approach does not account for inter-subject variability (or consistency) and relies on selecting an arbitrary t-score threshold, leading to possible bias. In contrast, our functional consistency maps can be used to visualize activation over a range of different statistical thresholds and provide a score to indicate how consistently activation is observed across subjects in each voxel (Seghier and Price, 2016).

We used a large heterogeneous sample to deliberately maximize inter-subject variability (e.g., in age and gender). This heterogeneity makes our results more generalizable to clinical populations. As inter-subject variability in sample demographics was held constant across tasks, any task dependent differences in the degree to which a brain region is activated cannot be attributed to selection bias. Our goal was to identify tasks that result in the most consistent fMRI responses across participants, despite the heterogeneity in the subject characteristics. For tasks with low consistency (i.e., high inter-subject variability) in fMRI activation across the whole sample, we investigated whether consistency differed for younger compared to older participants.

MATERIALS AND METHODS

The data used in this experiment were selected from the PLORAS database (Seghier et al., 2016) rather than being acquired specifically for the purposes of the current experiment. Data collection was approved by the London Queen Square Research Ethics Committee. All subjects gave written informed consent prior to scanning.

Participant Groups

Our participants included 79 native English speakers, with normal or corrected-to-normal vision, and no history of neurological or psychiatric disorders. All were right handed according to the Edinburgh Handedness Inventory (Oldfield, 1971).

The 79 participants comprised two groups (Group 1 and Group 2). Group 1 (n = 24) performed two different object naming tasks, counterbalanced across participants. The first

object naming task (single visual object naming) involved overtly naming a single object in a picture (see **Figure 1**). Successive objects were semantically unrelated. The second object naming task (single auditory object naming) involved hearing the sound of an object or animal (e.g., a guitar playing) and overtly naming the object associated with the sound (e.g., "*guitar*"). Group 2 (n = 55) performed 4 object naming tasks including those performed by Group 1 (single visual object naming and single auditory object naming) and two tasks that presented two semantically unrelated objects per picture (see **Figure 1**). In one task, the objects were juxtaposed one above the other and participants named both objects aloud one after the other using a noun phrase (e.g., "*fox and boat*"). In the other task, the objects interacted to depict an event and participants were instructed to overtly name the two objects within a sentence that described how the objects were interacting (e.g., "*The cat is drinking from the jug*"). To do so they used one of four pre-specified verbs that described the interaction: "eating," "drinking," "jumping," or "falling." The set of acceptable verbs was restricted to minimize inter-subject variability in verb selection. Passive constructions were ruled out by requiring the agent of the action to be named first. We expected inter-subject consistency to be highest for sentence production because this is the most challenging task and therefore most demanding on the language system.

Other fMRI Tasks for Group 1

Group 1 participated in 16 different tasks including the visual and auditory single object naming tasks that we focus on in the current paper. In brief, the 16 tasks comprised a 2 × 2 × 2 × 2 factorial design (Hope et al., 2014). Factor 1 was visual or auditory stimuli, factor 2 was semantic content (stimuli were either meaningful or meaningless), factor 3 was phonological content (stimuli were either verbal or non-verbal) and factor 4 was task (either speech production or 1-back matching). The object naming tasks are examples of "non-verbal semantic stimuli." The verbal semantic stimuli were written or heard object names. The verbal non-semantic stimuli were written or heard pseudowords (e.g., "*wrundle*"). The non-verbal non-semantic stimuli were colored patterns in the visual modality and meaningless humming in the auditory modality. During speech production, participants: named the objects, read or repeated the words and pseudowords, named the color of the meaningless visual stimuli or named the gender of the humming voices in the auditory modality. During 1-back matching, participants indicated whether the stimulus was identical or different to the preceding stimulus. For each subject, the stimuli presented during speech production were identical to the stimuli presented during 1-back matching.

The order of the 16 tasks was counterbalanced across 24 subjects. Half the subjects performed the speech production tasks first and half performed the 1-back matching tasks first. Within each of these groups, half were presented the visual stimuli first, then auditory stimuli, the other half were presented with auditory stimuli first then visual stimuli. Within each of these groups, each type of stimulus (words, pseudowords, objects, colored patterns/humming) occurred an equal number of times first, second, third, or fourth (across subjects). As exactly the same stimuli were used for speech production and 1-back matching tasks, a direct comparison of fMRI activation for speech production and 1-back matching identified brain regions involved in speech production, after controlling for stimuli. The main effects of stimulus modality (visual versus auditory), semantics versus non-semantic, and phonological versus non-phonological are reported in Hope et al. (2014). The current study examines inter-subject consistency across the whole brain, and in language regions that are (a) activated by object naming compared to rest and (b) also activated when retrieving speech sounds, after controlling for task and perceptual processing (see "Regions of interest" below for details).

Other fMRI Tasks for Group 2

Group 2 participated in 13 different tasks (see **Figure 2**) including the 4 object naming tasks described above. The 13 tasks comprised 2 experiments. The first experiment involved 5 tasks that each presented two objects in a trial and were always presented in the following order: (1) visual semantic matching, (2) naming two objects, (3) verb naming, (4) sentence production and (5) auditory semantic matching. Tasks 1–4 presented two objects in each picture. In the visual semantic matching task, half the stimuli presented pairs of semantically related objects, and half presented pairs of objects that were not semantically related, with participants indicating this relationship with one finger press for semantically related and another for semantically unrelated. In the two-object naming task, the two objects in the picture were unrelated and non-interacting (e.g., "fox and boat"), see **Figures 1**, **2**. In the verb and sentence production tasks, the two objects in the picture were interacting and participants, either produced the verb describing the interaction ("Drinking") or generated a short sentence (as described above and in **Figures 1**, **2**). In auditory semantic matching, participants heard two object names that were either semantically related or not, indicating this relationship with a finger press response. Further details about the 5 tasks in Experiment 1 have been reported in Sanjuán et al. (2015). Here we focus on naming two objects in a phrase or in a sentence.

The second experiment in which Group 2 participated involved the 8 speech production tasks used with Group 1 (tasks 6–13 in **Figure 2**), including visual and auditory single object naming. These 8 tasks were always performed after the 5 Experiment 1 tasks. As in Experiment 1, the order of the 8 tasks in Experiment 2 was held constant. Moreover, the stimuli used in each task (Experiment 1 and 2) were identical for every subject in Group 2. This was to ensure that inter-subject variability, within task, could not be accounted for by stimulus effects. However, as Group 2 always performed Experiment 2 after Experiment 1, differences between tasks (e.g., naming two objects per trial in Experiment 1 vs. naming a single object per trial in Experiment 2) could reflect task order, see section on investigating the effect of task order below.

Stimulus Creation

The same selection of stimuli was presented to Groups 1 and 2. Stimulus creation was initiated by identifying 128 objects and animals with highly familiar names. Each was drawn and colored as realistically as possible by a professional artist (Eldad Druks).

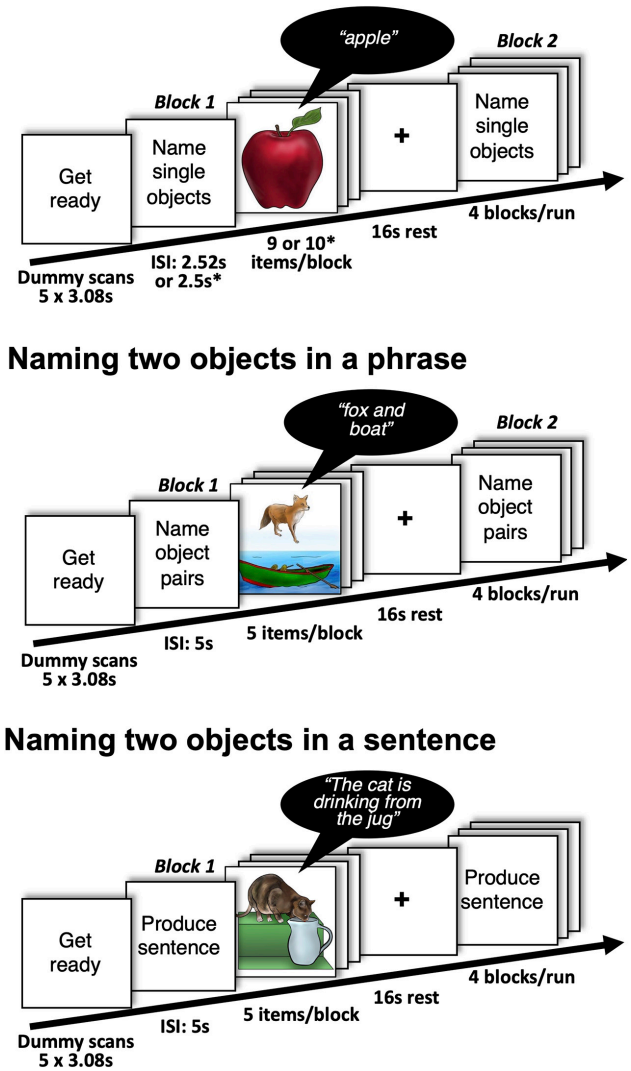

FIGURE 1 | Details of the experimental design with examples of stimuli and expected responses during naming single and two objects. Participants were also asked to perform a single auditory object naming task (naming objects from sounds). *presentation parameters used in Group 2.

Edges and features were outlined in black to ensure that the objects were easily recognizable in the scanner (see **Figure 1**), confirmed by high naming accuracy in pilot studies. The sounds of objects were taken from the NESSTI sound library (Hocking et al., 2013) but only 32 of the 128 objects in the pictures had sounds that were unambiguously related to one object or animal (e.g., there is no sound associated with a banana or table). Words were the written or spoken names associated with the objects. Pseudowords were created using a non-word generator (Duyck et al., 2004) that matched written pseudowords to the 128 objects names for bigram frequency, number of orthographic neighbors and word length. The colored patterns were created from the object pictures by scrambling the global and local features to render them unrecognizable and then manually editing the images to accentuate one of eight colors (brown, blue, orange, red, yellow, pink, purple, and green). We selected 32 different visual forms/patterns, with 4 shades of each of the 8 color categories (i.e., 8 different naming responses). In the auditory non-semantic-non-phonological task, there were 32 different humming sounds but only two possible responses (male/female).

The colors were not uniform in either the object naming or color naming tasks but pilot studies ensured that participants agreed on the predominant color of all the visual patterns. The stimuli used in the gender naming task (meaningless humming) were created by male or female voices humming with no phonological or semantic content.

Counterbalancing Objects Across Tasks

For Group 1, the 128 object names were assigned to four different sets of 32 stimuli (A, B, C, and D). Each set also included 4 repeat stimuli that needed to be detected during 1-back matching (i.e., total number of stimuli = 36). Sets A–C were rotated across pictures of objects, written object names and auditory object names, in different participants. Semantic and phonological content was therefore controlled across participants. Within participant, no stimulus set was repeated across the speech production tasks or across the 1-back matching tasks. Set D included the sounds of 32 objects that were always used during the object sound tasks and never used in any other task.

For Group 2, the 120 stimuli were assigned to 6 different sets of 20 stimuli (A-F), with 8 stimuli in set G. Each task, except auditory object naming, presented 2 different stimulus sets. In Experiment 1, the first task presented two novel sets (A and C), and the second to fifth presented one novel set (not presented in a previous task) and one repeated set (E and A, B and C, F and E, and D and F for tasks 2–5). In Experiment 2, visual object naming presented sets D and F. The pictures in set D were novel but their names had been presented during auditory semantic matching in Experiment 1. The pictures in set F were not novel as they had previously been presented for sentence production. For auditory object naming, participants were presented with 8 new stimuli from set G and 12 stimuli that had previously been seen or heard in Sets A to E.

Investigating the Effect of Stimulus Familiarity

As described above, the stimuli presented to Group 2 during two-object naming and sentence production (Experiment 1) were less familiar than the stimuli presented to Group 2 during auditory and visual single object naming (Experiment 2). Many prior studies have demonstrated how stimulus familiarity reduces neuronal responses, see Van Turennout et al. (2003) for an illustration during object naming. If the neuronal response is reduced by stimulus repetition, sensitivity to fMRI changes may be reduced possibly leading to less consistency in activation across subjects. To investigate the effect of familiarity, we compared inter-subject variability for single object naming in (A) Group 1 versus Group 2 and (B) subjects in Group 1 who performed speech production before (n = 12) vs. after

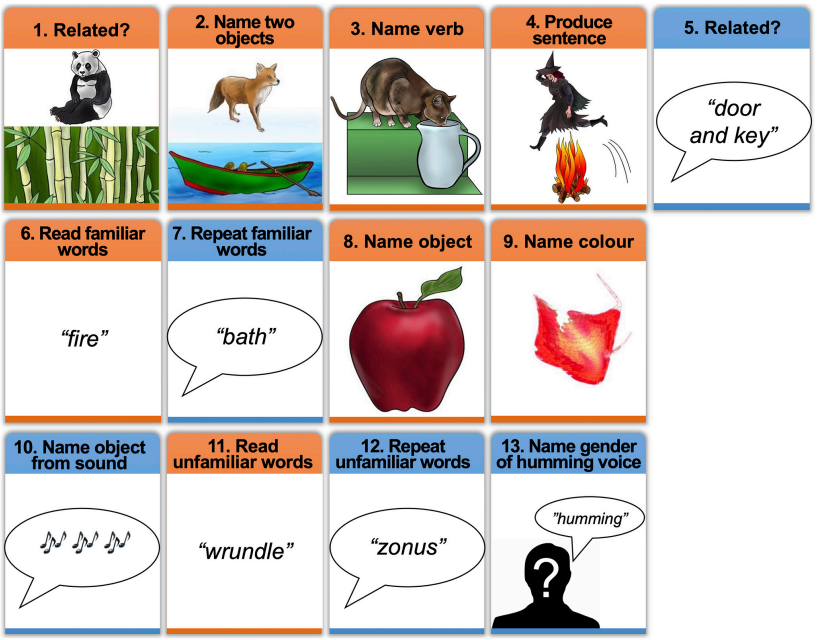

FIGURE 2 | Schematic of the experimental tasks with examples of stimuli. The order of tasks (1–13) was the same for all participants in Group 2. Tasks 6–13 were also presented to Group 1, in counterbalanced order. Orange boxes = tasks in the visual modality, Blue boxes = tasks in the auditory modality. In task 10 (naming object from sound), participants heard a sound (e.g., a guitar playing) and were asked to name the object that produced the sound (e.g., "guitar").

(n = 12) 1-back matching. For (A), the names of objects in the object naming tasks were completely novel for Group 1 but not for Group 2 (see above). For (B) the pictures of objects in the object naming tasks were completely novel for the 12 subjects who performed the speech production tasks first, but not novel for the 12 subjects who performed 1-back matching first.

Presentation Details

Each task (16 for Group 1 and 13 for Group 2) was presented in its own (separate) scanning run with 4 blocks of stimuli, each lasting 25 s, followed by 16 s of fixation. Within block, there were 9 stimuli of the same kind (8 novel, 1 repeat) for all Group 1 tasks; and 10 stimuli for all Group 2 tasks. The stimulus repeat in the Group 1 tasks only needed to be detected and responded to (with a finger press) in the 1-back matching tasks but was also present in the speech production tasks in order to keep the stimuli constant across tasks. The inter-stimulus interval was 2.52 s for Group 1, 2.5 s for Group 2 Experiment 2, and 5 s for Group 2 Experiment 1 (which presented pairs of object stimuli), see **Table 1** for further details of stimulus presentation parameters).

Procedure

Prior to scanning, we trained each participant on all tasks using a separate set of training stimuli except for the environmental sounds which remained the same. When in the scanner, participants were instructed to respond as fast as possible, keeping their body and head as still as possible and their eyes open and fixated on a cross in the middle of the display screen. Scanning started with the instructions "Get Ready" written on the in-scanner screen while five dummy scans were acquired (15.4 s in total). This was followed by a written instruction (e.g., "Name"), lasting 3.085 s, which indicated the forthcoming start of a new block and reminded participants of the task that needed to be performed.

Auditory stimuli were presented via MRI compatible headphones (MR Confon, Magdeburg, Germany), which filtered ambient in-scanner noise. Volume levels were adjusted for each participant before scanning. Spoken responses were recorded via a noise-canceling MRI microphone (FOMRI IIITM Optoacoustics, Or-Yehuda, Israel), and transcribed manually for off-line analysis. Correct responses were those that matched the target without delay or self-correction. For two-object naming and sentence production, the response was only correct if both objects were named correctly within the inter-trial interval. In addition, for sentence production, the correct verb also needed to be produced. For some stimuli, more than one response was considered correct. For example, a picture of a mug could be named "cup" or "mug." All other responses were categorized as incorrect. Response times for speech production were analyzed off-line but were only available for Group 2.

fMRI Data Analysis

Data for Group 1 and 2 were processed independently. All preprocessing and statistical analysis were performed in SPM12 (Wellcome Trust Centre for Neuroimaging, University College London, United Kingdom), running on MATLAB 2012a (Mathworks, MA, United States). Functional volumes were

spatially realigned to the first EPI volume and unwarped to compensate for non-linear distortions caused by head movement or magnetic field inhomogeneity. The unwarping procedure was used in preference to including the realignment parameters as linear regressors in the first-level analysis because unwarping accounts for non-linear movement effects by modeling the interaction between movement and any inhomogeneity in the T2* signal. After realignment and unwarping, the realignment parameters were checked to ensure that participants moved less than one voxel (3 mm) within each scanning run. The anatomical T1w images were co-registered to the mean EPI image generated during the realignment step and then spatially normalized to the MNI space using the unified normalization-segmentation routine in SPM12.

TABLE 1 | Experimental details for Group 1 and Group 2.

	Group 1	Group 2
Participants		
Number	25	59
Gender (n females/ n males)	12/12	34/25
Mean age in years (+/-SD)	31.44 (5.74)	44.5 (17.66)
Average number of syllables (SD)		
Reading words	1.53 (0.68)	1.55 (0.68)
Repeating words	1.53 (0.68)	1.68 (0.73)
Reading pseudowords	1.94 (0.92)	1.50 (0.51)
Repeating pseudowords	1.90 (0.84)	1.50 (0.51)
Naming pictures	1.55 (0.69)	1.48 (0.72)
Naming sounds	1.81 (0.92)	1.88 (0.94)
Naming gender	1.50 (0.51)	1.50 (0.51)
Naming colors	1.36 (0.49)	1.40 (0.50)
Average number of letters (+/-SD)		
Reading words	5.24 (1.68)	5.08 (1.61)
Repeating words	5.24 (1.68)	5.28 (1.38)
Reading pseudowords	5.28 (1.94)	4.40 (1.03)
Repeating pseudowords	5.35 (1.72)	4.35 (1.08)
Naming pictures	5.30 (1.75)	5.28 (1.75)
Naming sounds	5.64 (2.21)	5.65 (2.40)
Naming gender	5.00 (1.01)	5.00 (1.01)
Naming colors	4.89 (1.04)	4.80 (1.18)
Stimulus duration in sec (+/-SD)		
Sentence production	N/A	2.5
Two-object naming	N/A	2.5
Single visual object naming	1.5	1.5
Single auditory object naming	1.47 (0.12)	1.45 (0.15)
Inter-stimulus interval in sec		
Sentence production	N/A	5.0
Two-object naming	N/A	5.0
Single visual object naming	2.52	2.5
Single auditory object naming	2.52	2.5
Block length in sec		
Sentence production	N/A	25
Paired object naming	N/A	25
Single visual object naming	25.2	25
Single auditory object naming	25.2	25
Scanning parameters		
TR (sec)	3.085	3.085
Number of slices per image	44	44

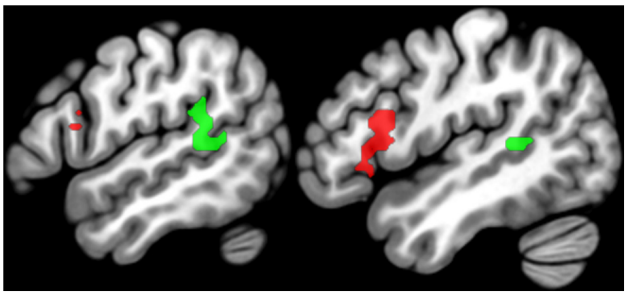

FIGURE 3 | Regions of interest. Sagittal slices (left x = –54, right x = –48) showing the group-level SPM{t} map for language regions of interest overlaid on a standard structural template in MNI space at $p < 0.05$ corrected for multiple comparisons. The SPM{t} map was generated using data from Group 1 only. Green = temporal regions of interest, Red = frontal regions of interest (see **Table 2** for details).

To spatially normalize all EPI scans to MNI space, the deformation field parameters that were obtained during the normalization of the anatomical T1w image were applied. The original resolution of the different images was maintained during normalization (voxel size $1 \times 1 \times 1$ mm^3 for structural T1w and $3 \times 3 \times 3$ mm^3 for EPI images). After normalization, functional images were spatially smoothed with a 6 mm full-width-half-maximum isotropic Gaussian Kernel to compensate for residual anatomical variability and to permit application of Gaussian random-field theory for statistical inference (Friston et al., 1995).

First Level Statistical Analyses

All preprocessed functional volumes were entered into a subject specific fixed effect analysis using the general linear model. Stimulus onset times were modeled as single events. For Group 1, we used 2 regressors per task, one modeling instructions, and the other modeling each stimulus. For Group 2, we used 4 regressors per task to model: (i) instructions, (ii) stimuli with correct responses, (iii) stimuli with incorrect responses and (iv) "other" responses (delayed, no response, or self-corrected). Stimulus functions were convolved with a canonical hemodynamic response function and high pass filtered with a cut-off period of 128 s.

For each scanning session/run (that alternated one task of interest with fixation), we generated a single contrast that compared activation in response to the stimuli and task of interest to resting with fixation. This resulted in 16 different contrasts (one per task) for each participant for Group 1 and 13 different contrasts for Group 2. Visual inspection ensured that there were no visible artifacts (e.g., edge effects, activation in ventricles) that might have been caused by within-scan head movements. These contrast images were then entered into a second-level analysis in SPM12 so that we could functionally segregate our core regions of interest.

TABLE 2 | Statistical details for regions of interest.

Region	Anatomical label (abbreviation)	MNI co-ordinates	Vx	Z-scores		
				Visual		
				SP	1-b	Conj.
				O > rest	W and P > O and C	(SP and 1-b)
Frontal	Pars triangularis (pTri)	−42, 30, −3	161	5.89	4.27	7.47
		−45, 24, 6		5.73	3.53	6.42
	Pars opercularis (pOp)	−48, 15, 18		5.86	3.67	6.63
Temporal	Anterior ascending terminal branch of the STS (atSTS)	−51, −45, 6	69	3.61	3.71	6.06
	Middle temporal gyrus (MTG)	−60, −48, 9		2.55	3.65	5.80
	Temporo-parietal junction (LTJ)	−54, −42, 21		5.41	3.09	5.76

SP = speech production, 1-b = 1-back matching. W = written words; P = written pseudowords; O = objects in pictures; C = colored patterns; Vx = number of voxels activated. Conj. = conjunction of SP O > rest and 1-b W and P > O and B.

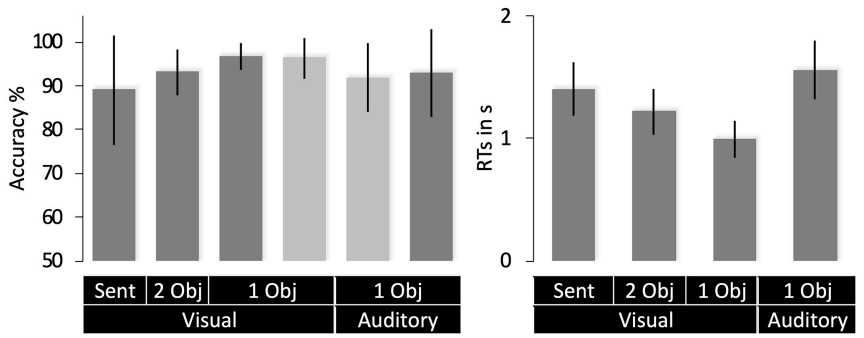

FIGURE 4 | Behavioral data (mean with SD). Accuracy scores for Group 1 are shown in light gray and Group 2 in dark gray. RTs (right) were only available for Group 1. 1 Obj = single object naming, 2 Obj = two-object naming, Sent = sentence production. RTs are for correct trials only.

Inter-Subject Consistency During Object Naming

Inter-subject consistency for all object naming tasks was evaluated, at every brain voxel, using threshold-weighted voxel-based consistency maps, as described in Seghier and Price (2016). These "functional consistency maps" quantify the proportion of subjects activating a particular voxel, and its nearest 6 neighbors, over a wide range of statistical thresholds ($p < 0.5$–0.001). Threshold-weighted consistency maps are generated by defining a complementary cumulative histogram of the number of subjects against the statistical threshold *th* at each voxel. Consistency is expressed as a single number by calculating the area under the curve of the complementary cumulative histogram. Prior to estimating the area under the curve, the generated histograms were multiplied by a linear weighting function W_{th} that monotonically increased with *th*:

$$W_{th} = \frac{2}{T_{max} - T_{min}} \times th$$

The histograms were thus linearly weighted to assign more weight to individual effects at higher statistical thresholds. The minimum threshold T_{min} was set to $p = 0.5$ (uncorrected) to exclude effects of non-interest. To account for the spatial dependency between neighboring voxels, the voxel-based consistency value summarized the effect at the voxel of interest and its 6 nearest neighbors using a spherical volume of interest with radius of 2 mm. A low consistency value (the proportion near 0) means that the voxel was consistently not activated in almost all subjects. When the proportion is 1, the voxel was activated in each subject irrespective of threshold within the range of statistical thresholds. A proportion less than 1, indicates either consistency across subjects at a low statistical threshold or that only a subset of participants activated the voxel, irrespective of threshold (for full discussion about the interpretation of intermediate consistency values, see Seghier and Price, 2016).

The "functional consistency maps" generated for each of our naming tasks allowed us to compare inter-subject consistency in activation, within language regions of interest (see below) and across the whole brain, for different tasks.

To investigate whether inter-subject variability is greater in older than younger participants, we split our 79 participants into two approximately equal sized groups (40 under 35 years old vs. 39 over 35 years old) and compared consistency across these groups for naming one object in (i) the visual modality and (ii) the auditory modality. In addition, we split the 55 participants who named two objects per condition and produced sentences into two approximately equal sized groups (27 under 40 years

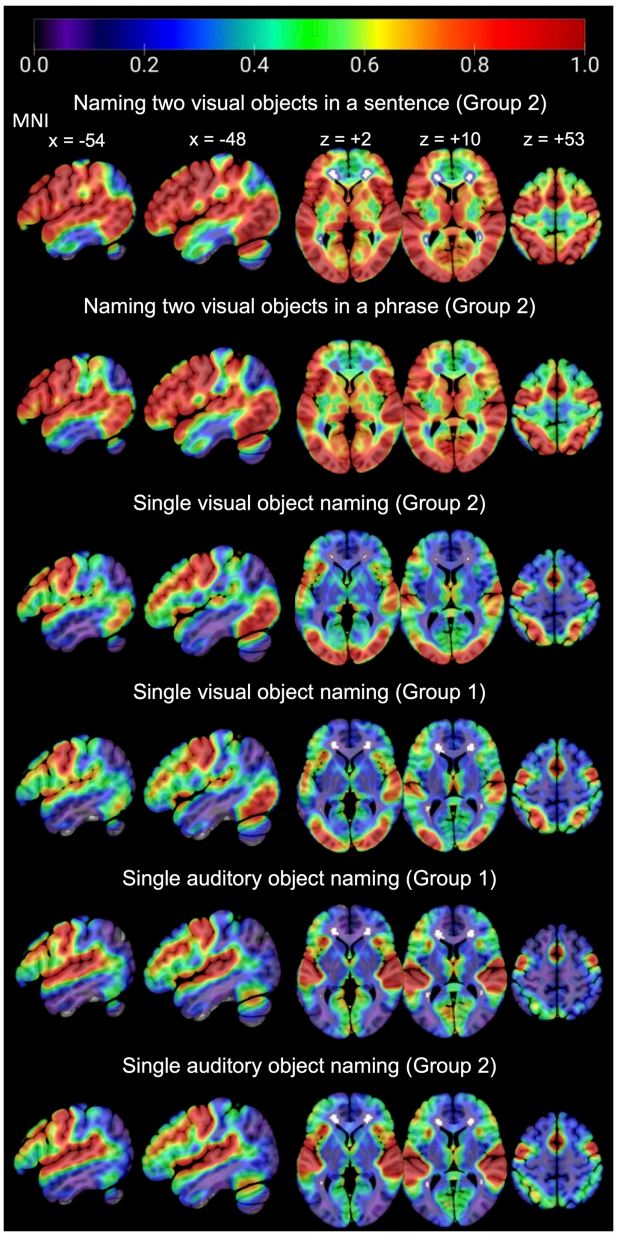

FIGURE 5 | Consistency of activation across the whole brain, for each task of interest in each group.

TABLE 3A | Consistency of activation in regions of interest.

Region	MNI co-ordinates	Naming objects					
		Two in a sentence	Two in a phrase	Single			
				Visual		Auditory	
		G2	G2	G1	G2	G1	G2
pTri	−42, 30, −3	90%	89%	59%	59%	64%	58%
	−45, 24, 6	84%	84%	53%	50%	55%	50%
pOp	−48, 15, 18	93%	85%	53%	55%	60%	62%
atSTS	−51, −45, 6	87%	87%	42%	47%	57%	69%
MTG	−60, −48, 9	90%	84%	42%	53%	67%	80%
TPJ	−54, −42, 21	92%	88%	43%	65%	75%	87%

TABLE 3B | Statistical comparison of naming one or two objects per trial.

Region	MNI co-ordinates	Odds ratios for naming two objects in a phrase compared to				
		Sentence	Single object naming			
			Visual		Auditory	
		G2	G1	G2	G1	G2
pTri	−42, 30, −3	0.93*	5.87	5.44	4.67	5.87
	−45, 24, 6	0.98*	4.58	5.11	4.26	4.93
pOp	−48, 15, 18	0.41*	5.27	4.90	3.92	3.63
atSTS	−51, −45, 6	0.99*	9.54	7.65	4.93	3.07*
MTG	−60, −48, 9	0.57*	7.11	4.58	2.49*	1.28*
TPJ	−54, −42, 21	0.64*	8.86	3.62	2.34*	1.00*

TABLE 3C | Statistical comparison of auditory and visual single object naming.

Region	MNI co-ordinates	Odds ratios for auditory compared to visual single object naming			
		Auditory G1 vs		Auditory G2 vs	
		Visual G1	Visual G2	Visual G1	Visual G2
pTri	−42, 30, −3	1.26*	1.17*	1.00*	0.93*
	−45, 24, 6	1.08*	1.20*	0.93*	1.04*
pOp	−48, 15, 18	1.34*	1.25*	1.45*	1.35*
atSTS	−51, −45, 6	1.94*	1.55*	3.11	2.49
MTG	−60, −48, 9	2.86	1.84*	5.57	3.59
TPJ	−54, −42, 21	3.78	1.55*	8.86	3.62

All odds ratios, except the values indicated with an asterisk, were significant ($p < 0.05$, 2 tailed), using both Chi Squared (Pearson) p values and Fischer's exact probability test. Consistency is expressed as a percentage (between 0–100%) rather than a value between 0 and 1. G1 = Group 1; G2 = Group 2. atSTS = anterior ascending terminal branch of the superior temporal sulcus, MTG = middle temporal gyrus, TPJ = temporo-parietal junction, pOp = pars opercularis, pTri = pars triangularis.

old versus 28 older than 40 years old) and compared consistency across age groups for the same tasks.

Regions of Interest

In addition to considering inter-subject consistency in activation at the whole brain level, we also home in on the core language areas that are involved in extracting and producing speech sounds, specifically the left posterior superior temporal cortex (Wernicke's area) and the left inferior frontal cortex (Broca's area). Using data from Group 1 only, these regions were segregated from the rest of the object naming network by searching for voxels that were activated during (A) object naming compared to rest and (B) 1-back matching of written words and pseudowords compared to object and color naming.

Contrast (B) has already been shown to activate areas involved in speech sound processing (Hope et al., 2014), consistent with expectation that skilled readers are highly trained to link written words and pseudowords to speech sounds and these "phonological codes" can be used to make 1-back matching decisions. Common activation for (Contrast A) and (Contrast B) segregates speech sound processing from the rest of the object naming system because (i) the 1-back matching task does not involve motor control of speech or auditory processing of the spoken response; and (ii) areas involved in visual perception are controlled by comparing visual 1-back matching of written words and pseudowords to visual objects and colored patterns.

Common activation for Contrasts (A) and (B) was identified by using a global conjunction in SPM with a statistical threshold of $p < 0.05$ after family wise error correction for multiple comparisons across the whole brain (in height). In addition, we checked and confirmed that the identified voxels were also activated by 1-back matching of words and pseudowords compared to rest.

The left temporal and frontal regions activated by the conjunction are illustrated in **Figure 3** and **Table 2**. The left frontal region included the pars opercularis (pOp) and pars triangularis (pTri). The left temporal region was in the left anterior ascending terminal branch of the superior temporal sulcus (atSTS), extending posteriorly into the left middle temporal gyrus (MTG) and dorsally into the left temporo-parietal junction (TPJ).

RESULTS

Behavioral Data

Average in-scanner accuracy was 89% or above for each object naming task in both groups (**Figure 4**). Response times were only available for Group 2. Within this group, response times were slower for single object naming in the auditory than visual modality (**Figure 4**) because auditory stimuli were delivered over time (sequential) while all parts of the visual stimuli were presented at the same time point (simultaneous).

Inter-Subject Consistency in Object Naming Activation

For naming single objects and two objects, activation was highly consistent in sensori-motor areas, including bilateral occipital, motor, and auditory cortices (see **Figure 5**). These regions were associated with the following functions in the group-level analysis reported by Hope et al. (2014): (i) bilateral occipito-temporal regions were associated with visual perception, (ii) left posterior middle temporal and parietal areas were associated with semantic associations, (iii) bilateral motor cortices, supplementary motor cortices, subcortical and cerebellar regions were associated with motor control of speech; and (iv) bilateral auditory cortices were associated with hearing stimuli or hearing the sound of the spoken response.

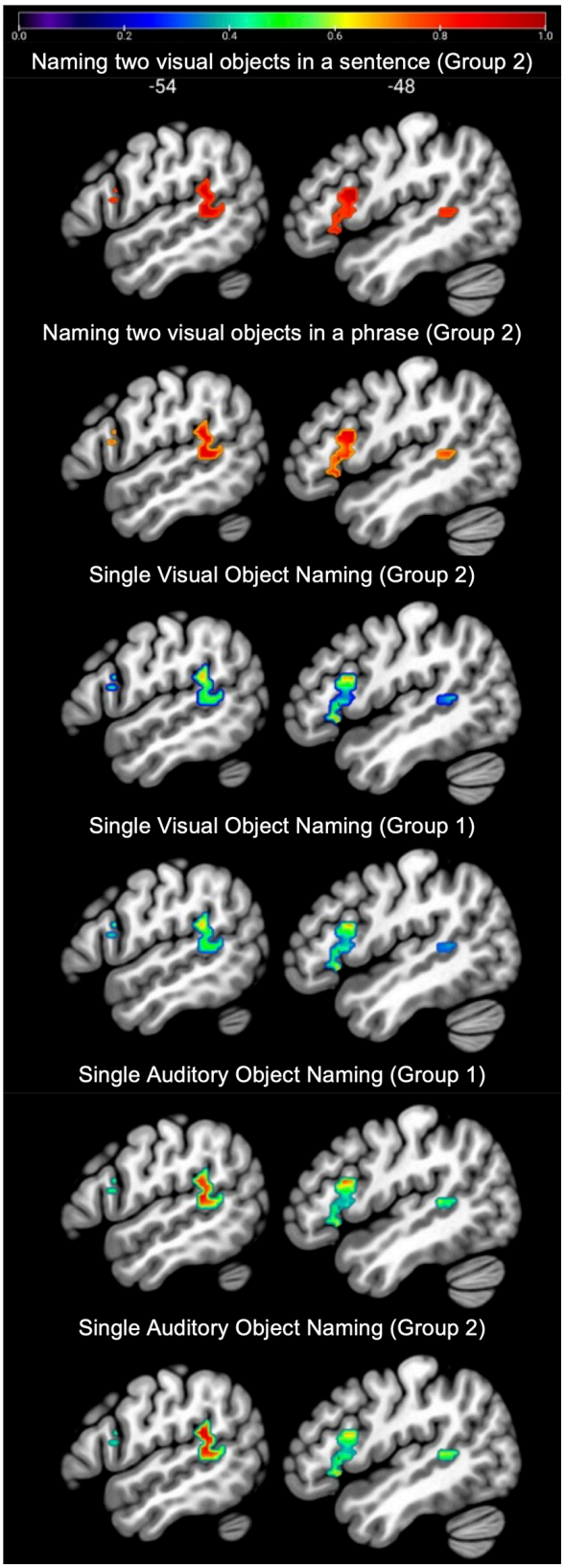

FIGURE 6 | Consistency in activation within language regions of interest.

TABLE 4 | Consistency of activation for younger versus older participants.

Region	MNI co-ordinates	Naming objects							
		Two in a sentence		Two in a phrase		Single			
		Visual				Visual		Auditory	
		Young	Older	Young	Older	Young	Older	Young	Older
		n = 27	*n* = 28	*n* = 27	*n* = 28	*n* = 40	*n* = 39	*n* = 40	*n* = 39
pTri	−42, 30, −3	84%	95%	80%	93%	59%	56%	56%	60%
	−45, 24, 6	80%	88%	84%	82%	56%	47%	51%	52%
pOp	−48, 15, 18	91%	96%	80%	93%	56%	59%	56%	70%
atSTS	−51, −45, 6	79%	95%	78%	93%	44%	48%	67%	64%
MTG	−60, −48, 9	87%	93%	80%	87%	52%	51%	79%	76%
TPJ	−54, −42, 21	87%	96%	82%	94%	65%	63%	86%	81%

*For abbreviations, see **Table 3**.*

In language regions of interest (left posterior superior temporal and inferior frontal regions associated with retrieving speech sounds, see **Figure 3**), activation was also highly consistent for naming two objects in a noun phrase and for naming two objects in a sentence (Group 2) but significantly less consistent for naming single visual objects in Groups 1 and 2, see **Table 3** and **Figure 6** for details. Auditory single object naming was significantly more consistent than visual single word object naming in temporal regions but not in frontal regions (see **Table 3C**).

Despite our expectation that sentence production would produce more consistent activation than two-object naming, there was no significant difference in the consistency of activation for producing two object names in a phrase compared to in a sentence (see **Table 3B**). We also found no significant difference in single object naming between (A) Group 1 (less familiar names) and Group 2 (more familiar names); or (B) subjects in Group 1 who performed speech production tasks before versus after 1-back matching on the same stimuli (mean consistency = 52% for both subgroups). Therefore, there was no evidence that differences in activation consistency for naming two objects rather than a single object arose from either condition order, stimulus familiarity or fatigue.

A comparison of inter-subject consistency for older and younger participants revealed remarkable similarity across older and younger participants for the single object naming tasks (see **Table 4** for details). For naming two objects in phrases and sentences, inter-patient consistency appeared higher for older than younger participants. However, this was neither anticipated nor significant using two-tailed Fisher's exact test. In summary, inter-patient consistency was significantly different between tasks for each age group, but not significant between age groups (for any of the tasks).

DISCUSSION

To select the optimal task for intra-operative mapping, a neurosurgeon needs confidence that the selected task typically and robustly engages the function of interest. In the case of object naming, our results strongly favor use of a two-object naming paradigm compared to a single object naming paradigm. Language regions are most consistently and robustly activated when participants name two objects in a picture using a phrase (e.g., "tap and pizza") or when they name two objects in a sentence (e.g., "The cat is drinking from the jug"). By contrast, activation is much less consistent when naming a single object from a picture (single visual object naming) or naming an object from its sound (single auditory object naming). These findings have implications for pre-operative and intra-operative language mapping in that such mapping may have improved sensitivity to language function if the task involves presenting two objects in the same picture rather than pictures of single objects.

We observed greater consistency in language-related activation for naming two objects rather than one even though the number of objects presented was held constant within 25 s blocks (10 for two-object naming and 10 for single object naming). The results cannot be explained by inter-subject differences in the BOLD response *per se*, because the hemodynamic response to neural activity is expected to stay constant within region and we are comparing inter-subject variability/consistency within region. Moreover, we found no evidence that this greater consistency was the consequence of familiarity/fatigue effects. Instead, we hypothesize that naming two objects increases demand on processes related to word retrieval and production yielding robust language-related activation at the individual subject level.

In the language regions of interest used in the current study (left posterior temporal and left posterior frontal areas involved in speech processing), activation did not show significantly more consistency for producing two object names in a sentence compared to a noun phrase (see **Figure 6** and **Table 3**). Therefore, the simpler two-object naming task was sufficient for investigating activation in our chosen language regions of interest. If, on the other hand, the regions of interest chosen were those involved in syntactic processing, the sentence

production task would be a better choice for pre-surgical planning. For example, in a series of 14 neurosurgery patients, Chang et al. (2018) used DES to identify stimulation sites associated with syntactic deficits during sentence production. Stimulation of regions in the pars opercularis and pars triangularis, which have not been identified during mapping with counting, naming or repetition, induced syntactic errors in 7/14 patients.

In the temporal lobe language region of interest, which included the temporo-parietal junction, middle and superior temporal cortex, activation was more consistent for auditory object naming than for visual object naming (see **Figure 6** and **Table 3C**). This is in line with prior studies (Hamberger et al., 2001, 2005) that reported a clinical benefit of utilizing single auditory object naming for language mapping in patients with temporal lobe epilepsy (TLE) (Hamberger et al., 2001, 2005). TLE patients often present with word finding difficulties and conversational speech impairments, despite normal performance on visual naming tasks. Carefully planned language testing, which takes into consideration the stimulus modality, is therefore crucial in preserving a patient's quality of life, particularly since a study by Moritz-Gasser et al. (2012) demonstrated that naming ability was significantly correlated with return to work in patients with low-grade gliomas.

In addition, our results show how consistently sensory and motor regions are activated by all four object naming tasks (**Figure 4**). This supports the notion that object naming can be used to probe the function of many different brain regions during intra-operative mapping. An impaired response to an object naming task during DES does not, however, indicate the function of the stimulated region as so many different types of processes are involved in object naming. To determine the function of a brain region, multiple different tasks are required to systematically manipulate the demands on different types of processing. This is possible within group fMRI studies (e.g., the 16 tasks administered to Group 1) but is not feasible for pre-operative planning because single patient pre-operative fMRI mapping needs to maximize repetitions of the same task for reliable estimation of signal to noise; and this necessitates minimizing the number of tasks unless the patient can return for multiple scanning sessions. In addition, interpretation of results from multitask fMRI studies is often challenging.

Our functional consistency maps offer a potential data-based solution for pre-surgical planning, accounting for inter-subject variability. Specifically, for each region of interest, functional consistency maps can be generated to calculate inter-subject consistency in response to multiple different tasks and task differences (contrasts). Neuro-surgical teams could then compare the location of regions planned for resection with the output from a database that indicates (i) which tasks engage the region; (ii) the consistency with which the region is engaged for these tasks across neurotypical individuals; and (iii) which tasks might be optimal for pre-operative fMRI or intra-operative DES.

Limitations and Future Directions

The current study explored the consistency of object naming activation in healthy controls. These findings may not necessarily translate to patient populations because the object naming networks may have already re-organized in patients with brain tumors or epilepsy (Fisicaro et al., 2016). To further investigate the effect of pathology on the consistency of object naming activation, future studies could investigate the consistency of language-task related activation in more heterogeneous participant samples, such as patients with brain tumors or drug-resistant epilepsy.

Our results suggest that successful implementation of the two-object naming paradigm in the intra-operative setting may allow for more sensitive language mapping. This motivates an explicit evaluation of whether the two-object naming paradigm provides a more reliable probe of language function than single object naming during intraoperative mapping. Further fMRI studies of neurotypical populations could also test how inter-subject variability/consistency changes with different inter-stimulus intervals. Based on the current results, our hypotheses are that (A) activation will be higher when participants are under time pressure but can still produce correct responses and (B) presenting two or more objects simultaneously provides a practical way to increase time pressure compared to presenting each object one at a time at a fast rate.

The approach illustrated in the current study can be extended to map networks of regions activated by different language tasks. For instance, Rofes and Miceli (2014) argued that verb naming might be more sensitive than object naming due to recruitment of additional networks involved in grammatical processing. Functional consistency maps could be used to compare the consistency of activation for verb naming relative to object naming and make further recommendations for intra-operative testing. This would contribute to data-based approaches for neurosurgical planning that will provide reliable and lesion-site specific brain mapping paradigms.

SUMMARY AND CONCLUSION

Object naming is a widely utilized task in patients undergoing neurosurgery and allows the mapping of a widely distributed network of speech production regions. In this study, we examined inter-subject consistency in activation during four different object naming tasks in neurotypical participants. Naming two depicted objects either in a phrase or in a sentence resulted in more consistent activation in core language areas (posterior temporal and inferior frontal) in comparison to single object naming (from visual or auditory stimuli). We therefore propose that requiring two objects to be named on a trial may optimize sensitivity to DES effects during awake language mapping. In addition, single object naming in the auditory modality (naming object from sounds) resulted in higher consistency of activation in temporal language regions in comparison to single object naming in the visual modality (naming objects from pictures). Our findings highlight the importance of selecting a stimulus modality based on lesion site.

DATA AVAILABILITY STATEMENT

The data that support the findings of this study are available upon request from the senior author CP.

ETHICS STATEMENT

The studies involving human participants were reviewed and approved by London Queen Square Research Ethics Committee. The patients/participants provided their written informed consent to participate in this study.

AUTHOR CONTRIBUTIONS

CP, JE, and MS contributed to conception and design of the study. JE performed the statistical analysis. JE and CP wrote the first draft of the manuscript. DG and MK wrote sections of the manuscript. All authors contributed to manuscript revision, read, and approved the submitted version.

FUNDING

This work was funded by Wellcome (203147/Z/16/Z and 205103/Z/16/Z, CP) and the Middlesex Hospital Medical School General Charitable Trust (JE).

ACKNOWLEDGMENTS

We thank Eldad Druks for creating the picture stimuli.

REFERENCES

Benjamin, C. F. A., Li, A. X., Blumenfeld, H., Constable, R. T., Alkawadri, R., Bickel, S., et al. (2018). Presurgical language fMRI: clinical practices and patient outcomes in epilepsy surgical planning. *Hum. Brain Mapp.* 39, 2777–2785. doi: 10.1002/hbm.24039

Berger, M. S., and Ojemann, G. A. (1992). Intraoperative brain mapping techniques in neuro-oncology. *Stereotact. Funct. Neurosurg.* 58, 153–161. doi: 10.1159/000098989

Berger, M. S., Kincaid, J., Ojemann, G. A., and Lettich, E. (1989). Brain mapping techniques to maximize resection, safety, and seizure control in children with brain tumors. *Neurosurgery* 25, 786–792. doi: 10.1097/00006123-198911000-00015

Black, D. F., Vachha, B., Mian, A., Faro, S. H., Maheshwari, M., Sair, H. I., et al. (2017). American society of functional neuroradiology–recommended fMRI paradigm algorithms for presurgical language assessment. *Am. J. Neuroradiol.* 38, E65–E73. doi: 10.3174/ajnr.A5345

Bu, L., Lu, J., Zhang, J., and Wu, J. (2021). Intraoperative cognitive mapping tasks for direct electrical stimulation in clinical and neuroscientific contexts. *Front. Hum. Neurosci.* 15:61. doi: 10.3389/fnhum.2021.612891

Castellano, A., Cirillo, S., Bello, L., Riva, M., and Falini, A. (2017). Functional MRI for surgery of gliomas. *Curr. Treat. Options Neurol.* 19, 1–23.

Chang, E. F., Kurteff, G., and Wilson, S. M. (2018). Selective interference with syntactic encoding during sentence production by direct electrocortical stimulation of the inferior frontal gyrus. *J. Cogn. Neurosci.* 30, 411–420. doi: 10.1162/jocn_a_01215

De Witte, E., and Mariën, P. (2013). The neurolinguistic approach to awake surgery reviewed. *Clin. Neurol. Neurosurg.* 115, 127–145. doi: 10.1016/j.clineuro.2012.09.015

Duffau, H. (2005). Lessons from brain mapping in surgery for low-grade glioma: insights into associations between tumour and brain plasticity. *Lancet Neurol.* 4, 476–486. doi: 10.1016/S1474-4422(05)70140-X

Duffau, H., Moritz-Gasser, S., and Gatignol, P. (2009). Functional outcome after language mapping for insular world health organization grade II gliomas in the dominant hemisphere: experience with 24 patients. *Neurosurg. Focus* 27:E7. doi: 10.3171/2009.5.FOCUS0938

Duyck, W., Desmet, T., Verbeke, L. P. C., and Brysbaert, M. (2004). Word gen: a tool for word selection and nonword generation in Dutch, English, German, and French. *Behav. Res. Methods, Instruments Comput.* 36, 488–499. doi: 10.3758/BF03195595

Fedorenko, E., and Blank, I. A. (2020). Broca's area is not a natural kind. *Trends Cogn. Sci.* 24, 270–284. doi: 10.1016/j.tics.2020.01.001

Fisicaro, R. A., Jost, E., Shaw, K., Brennan, N. P., Peck, K. K., and Holodny, A. I. (2016). Cortical plasticity in the setting of brain tumors. *Top. Magn. Reson. Imaging TMRI* 25:25. doi: 10.1097/rmr.0000000000000077

Friston, K. J., Frith, C. D., Turner, R., and Frackowiak, R. S. J. (1995). Characterizing evoked hemodynamics with fMRI. *Neuroimage* 2, 157–165. doi: 10.1006/nimg.1995.1018

Gabel, N., Altshuler, D. B., Brezzell, A., Briceno, E. M., Boileau, N. R., Miklja, Z., et al. (2019). Health related quality of life in adult low and high-grade glioma patients using the national institutes of health patient reported outcomes measurement information system (PROMIS) and neuro-QOL assessments. *Front. Neurol.* 10:212. doi: 10.3389/fneur.2019.00212

Giussani, C., Roux, F.-E., Ojemann, J., Sganzerla, E., Pirillo, D., and Papagno, C. (2010). Is preoperative functional magnetic resonance imaging reliable for language areas mapping in brain tumor surgery? Review of language functional magnetic resonance imaging and direct cortical stimulation correlation studies. *Neurosurgery* 66, 113–120. doi: 10.1227/01.NEU.0000360392.15450.C9

Hamberger, M. J., Goodman, R. R., Perrine, K., and Tamny, T. (2001). Anatomic dissociation of auditory and visual naming in the lateral temporal cortex. *Neurology* 56, 56–61. doi: 10.1212/wnl.56.1.56

Hamberger, M. J., Seidel, W. T., Mckhann, G. M., Perrine, K., and Goodman, R. R. (2005). Brain stimulation reveals critical auditory naming cortex. *Brain* 128, 2742–2749. doi: 10.1093/brain/awh621

Hamer, P. C. D. W., Robles, S. G., Zwinderman, A. H., Duffau, H., and Berger, M. S. (2012). Impact of intraoperative stimulation brain mapping on glioma surgery outcome: a meta-analysis. *J. Clin. Oncol.* 30, 2559–2565. doi: 10.1200/JCO.2011.38.4818

Hervey-Jumper, S. L., Li, J., Lau, D., Molinaro, A. M., Perry, D. W., Meng, L., et al. (2015). Awake craniotomy to maximize glioma resection: methods and technical nuances over a 27-year period. *J. Neurosurg.* 123, 325–339. doi: 10.3171/2014.10.JNS141520

Hocking, J., Dzafic, I., Kazovsky, M., and Copland, D. A. (2013). NESSTI: norms for environmental sound stimuli. *PLoS One* 8:e73382. doi: 10.1371/journal.pone.0073382

Hope, T. M. H., Prejawa, S., Parker Jones, O., Oberhuber, M., Seghier, M. L., Green, D. W., et al. (2014). Dissecting the functional anatomy of auditory word repetition. *Front. Hum. Neurosci.* 8:1–17. doi: 10.3389/fnhum.2014.00246

Ilmberger, J., Ruge, M., Kreth, F.-W., Briegel, J., Reulen, H.-J., and Tonn, J.-C. (2008). Intraoperative mapping of language functions: a longitudinal neurolinguistic analysis. *J. Neurosurg.* 109, 583–592. doi: 10.3171/JNS/2008/109/10/0583

Ius, T., Isola, M., Budai, R., Pauletto, G., Tomasino, B., Fadiga, L., et al. (2012). Low-grade glioma surgery in eloquent areas: volumetric analysis of extent of resection and its impact on overall survival. a single-institution experience in 190 patients. *J. Neurosurg.* 117, 1039–1052. doi: 10.3171/2012.8.jns12393

Jakola, A. S., Myrmel, K. S., Kloster, R., Torp, S. H., Lindal, S., Unsgård, G., et al. (2012). Comparison of a strategy favoring early surgical resection vs a strategy favoring watchful waiting in low-grade gliomas. *JAMA J. Am. Med. Assoc.* 308, 1881–1888. doi: 10.1001/jama.2012.12807

Jakola, A. S., Skjulsvik, A. J., Myrmel, K. S., Sjåvik, K., Unsgård, G., Torp, S. H., et al. (2017). Surgical resection versus watchful waiting in low-grade gliomas. *Ann. Oncol.* 28, 1942–1948. doi: 10.1093/annonc/mdx230

Jakola, A. S., Unsgård, G., and Solheim, O. (2011). Quality of life in patients with intracranial gliomas: the impact of modern image-guided surgery. *J. Neurosurg.* 114, 1622–1630. doi: 10.3171/2011.1.JNS101657

Klitsinikos, D., Ekert, J. O., Carels, A., and Samandouras, G. (2021). Mapping and anatomo-surgical techniques for SMA-cingulum-corpus callosum gliomas; how i do it. *Acta Neurochir. (Wien)* 163, 1239–1246. doi: 10.1007/s00701-021-04774-7

Leon-Rojas, J. E., Ekert, J. O., Kirkman, M. A., Sewell, D., Bisdas, S., and Samandouras, G. (2020). Experience with awake throughout craniotomy in tumour surgery: technique and outcomes of a prospective, consecutive case series with patient perception data. *Acta Neurochir. (Wien)* 162, 3055–3065. doi: 10.1007/s00701-020-04561-w

Mahdavi, A., Azar, R., Shoar, M. H., Hooshmand, S., Mahdavi, A., and Kharrazi, H. H. (2015). Functional MRI in clinical practice: assessment of language and motor for pre-surgical planning. *Neuroradiol. J.* 28, 468–473. doi: 10.1177/1971400915609343

Manan, H. A., Franz, E. A., and Yahya, N. (2020). Utilization of functional MRI language paradigms for pre-operative mapping: a systematic review. *Neuroradiology* 62, 353–367. doi: 10.1007/s00234-019-02322-w

Mandonnet, E., Winkler, P. A., and Duffau, H. (2010). Direct electrical stimulation as an input gate into brain functional networks: principles, advantages and limitations. *Acta Neurochir. (Wien)* 152, 185–193. doi: 10.1007/s00701-009-0469-0

Matsumoto, R., Nair, D. R., LaPresto, E., Najm, I., Bingaman, W., Shibasaki, H., et al. (2004). Functional connectivity in the human language system: a cortico-cortical evoked potential study. *Brain* 127, 2316–2330. doi: 10.1093/brain/awh246

McGirt, M. J., Chaichana, K. L., Gathinji, M., Attenello, F. J., Than, K., Olivi, A., et al. (2009). Independent association of extent of resection with survival in patients with malignant brain astrocytoma. *J. Neurosurg.* 110, 156–162.

Moritz-Gasser, S., Herbet, G., Maldonado, I. L., and Duffau, H. (2012). Lexical access speed is significantly correlated with the return to professional activities after awake surgery for low-grade gliomas. *J. Neurooncol.* 107, 633–641. doi: 10.1007/s11060-011-0789-9

O'neill, M., Henderson, M., Duffy, O. M., and Kernohan, W. G. (2020). The emerging contribution of speech and language therapists in awake craniotomy: a national survey of their roles, practices and perceptions. *Int. J. Lang. Commun. Disord.* 55, 149–162. doi: 10.1111/1460-6984.12510

Ojemann, G. A., Ojemann, J. G., Lettich, E., and Berger, M. (1989). Cortical language localization in left, dominant hemisphere: an electrical stimulation mapping investigation in 117 patients. *J. Neurosurg.* 71, 316–326.

Oldfield, R. C. (1971). The assessment and analysis of handedness: the Edinburgh inventory. *Neuropsychologia* 9, 97–113. doi: 10.1016/0028-3932(71)90067-4

Pak, R. W., Hadjiabadi, D. H., Senarathna, J., Agarwal, S., Thakor, N. V., Pillai, J. J., et al. (2017). Implications of neurovascular uncoupling in functional magnetic resonance imaging (fMRI) of brain tumors. *J. Cereb. Blood Flow Metab.* 37, 3475–3487. doi: 10.1177/0271678X17707398

Rofes, A., and Miceli, G. (2014). Language mapping with verbs and sentences in awake surgery: a review. *Neuropsychol. Rev.* 24, 185–199. doi: 10.1007/s11065-014-9258-5

Rofes, A., de Aguiar, V., and Miceli, G. (2015). A minimal standardization setting for language mapping tests: an Italian example. *Neurol. Sci.* 36, 1113–1119. doi: 10.1007/s10072-015-2192-3

Rofes, A., Spena, G., Talacchi, A., Santini, B., Miozzo, A., and Miceli, G. (2017b). Mapping nouns and finite verbs in left hemisphere tumors: a direct electrical stimulation study. *Neurocase* 23, 105–113. doi: 10.1080/13554794.2017.1307418

Rofes, A., Mandonnet, E., Godden, J., Baron, M. H., Colle, H., Darlix, A., et al. (2017a). Survey on current cognitive practices within the European low-grade glioma network: towards a European assessment protocol. *Acta Neurochir. (Wien)* 159, 1167–1178. doi: 10.1007/s00701-017-3192-2

Ruis, C. (2018). Monitoring cognition during awake brain surgery in adults: a systematic review. *J. Clin. Exp. Neuropsychol.* 40, 1081–1104. doi: 10.1080/13803395.2018.1469602

Sanai, N., and Berger, M. S. (2008a). Glioma extent of resection and its impact on patient outcome. *Neurosurgery* 62, 753–766. doi: 10.1227/01.neu.0000318159.21731.cf

Sanai, N., and Berger, M. S. (2008b). Mapping the horizon: techniques to optimize tumor resection before and during. *Clin. Neurosurg.* 55:14.

Sanai, N., and Berger, M. S. (2010). Intraoperative stimulation techniques for functional pathway preservation and glioma resection. *Neurosurg. Focus* 28:E1.

Sanai, N., Mirzadeh, Z., and Berger, M. S. (2008). Functional outcome after language mapping for glioma resection. *N. Engl. J. Med.* 358, 18–27. doi: 10.1056/nejmoa067819

Sanjuán, A., Hope, T. M. H., Parker Jones, O., Prejawa, S., Oberhuber, M., Guerin, J., et al. (2015). Dissociating the semantic function of two neighbouring subregions in the left lateral anterior temporal lobe. *Neuropsychologia* 76, 153–162. doi: 10.1016/j.neuropsychologia.2014.12.004

Sefcikova, V., Sporrer, J. K., Ekert, J. O., Kirkman, M. A., and Samandouras, G. (2020). High interrater variability in intraoperative language testing and interpretation in awake brain mapping among neurosurgeons or neuropsychologists: an emerging need for standardization. *World Neurosurg.* 141, e651–e660. doi: 10.1016/j.wneu.2020.05.250

Seghier, M. L., and Price, C. J. (2016). Visualising inter-subject variability in fMRI using threshold-weighted overlap maps. *Sci. Rep.* 6:20170. doi: 10.1038/srep20170

Seghier, M. L., and Price, C. J. (2018). Interpreting and utilising intersubject variability in brain function. *Trends Cogn. Sci.* 22, 517–530. doi: 10.1016/j.tics.2018.03.003

Seghier, M. L., Patel, E., Prejawa, S., Ramsden, S., Selmer, A., Lim, L., et al. (2016). The PLORAS database: a data repository for predicting language outcome and recovery after stroke. *Neuroimage* 124, 1208–1212. doi: 10.1016/j.neuroimage.2015.03.083

Shimotake, A., Matsumoto, R., Ueno, T., Kunieda, T., Saito, S., Hoffman, P., et al. (2015). Direct exploration of the role of the ventral anterior temporal lobe in semantic memory: cortical stimulation and local field potential evidence from subdural grid electrodes. *Cereb. Cortex* 25, 3802–3817. doi: 10.1093/cercor/bhu262

Silva, M. A., See, A. P., Essayed, W. I., Golby, A. J., and Tie, Y. (2018). Challenges and techniques for presurgical brain mapping with functional MRI. *NeuroImage Clin.* 17, 794–803. doi: 10.1016/j.nicl.2017.12.008

Unadkat, P., Fumagalli, L., Rigolo, L., Vangel, M. G., Young, G. S., Huang, R., et al. (2019). Functional MRI task comparison for language mapping in neurosurgical patients. *J. Neuroimaging* 29, 348–356. doi: 10.1111/jon.12597

Van Turennout, M., Bielamowicz, L., and Martin, A. (2003). Modulation of neural activity during object naming: effects of time and practice. *Cereb. Cortex* 13, 381–391. doi: 10.1093/cercor/13.4.381

Young, J. S., Lee, A. T., and Chang, E. F. (2021). A review of cortical and subcortical stimulation mapping for language. *Neurosurgery* 89, 331–342.

Conflict of Interest: The authors declare that the research was conducted in the absence of any commercial or financial relationships that could be construed as a potential conflict of interest.

Publisher's Note: All claims expressed in this article are solely those of the authors and do not necessarily represent those of their affiliated organizations, or those of the publisher, the editors and the reviewers. Any product that may be evaluated in this article, or claim that may be made by its manufacturer, is not guaranteed or endorsed by the publisher.

Copyright © 2021 Ekert, Kirkman, Seghier, Green and Price. This is an open-access article distributed under the terms of the Creative Commons Attribution License (CC BY). The use, distribution or reproduction in other forums is permitted, provided the original author(s) and the copyright owner(s) are credited and that the original publication in this journal is cited, in accordance with accepted academic practice. No use, distribution or reproduction is permitted which does not comply with these terms.

frontiers in Neuroscience

ORIGINAL RESEARCH
published: 30 November 2021
doi: 10.3389/fnins.2021.755327

Turbo Gradient and Spin Echo PROPELLER-Diffusion Weighted Imaging for Orbital Tumors: A Comparative Study With Readout-Segmented Echo-Planar Imaging

Qing Fu[1,2], Xiang-chuang Kong[1,2], Ding-Xi Liu[1,2], Kun Zhou[3], Yi-hao Guo[4], Zi-Qiao Lei[1,2†], Chuan-sheng Zheng[1,2*†] and Fan Yang[1,2*†]*

[1] Department of Radiology, Union Hospital, Tongji Medical College, Huazhong University of Science and Technology, Wuhan, China, [2] Hubei Province Key Laboratory of Molecular Imaging, Wuhan, China, [3] Siemens Shenzhen Magnetic Resonance Ltd., Shenzhen, China, [4] MR Collaboration, Siemens Healthcare Ltd., Guangzhou, China

Purpose: To qualitatively and quantitatively compare the image quality and diagnostic performance of turbo gradient and spin echo PROPELLER diffusion-weighted imaging (TGSE-PROPELLER-DWI) vs. readout-segmented echo-planar imaging (rs-EPI) in the evaluation of orbital tumors.

Materials and Methods: A total of 43 patients with suspected orbital tumors were enrolled to perform the two DWIs with comparable spatial resolution on 3T. The overall image qualities, geometric distortions, susceptibility artifacts, and lesion conspicuities were scored by using a four-point scale (1, poor; 4, excellent). Quantitative measurements, including contrast-to-noise ratios (CNRs), apparent diffusion coefficients (ADCs), geometric distortion rates (GDRs), and lesion sizes, were calculated and compared. The two ADCs for differentiating malignant from benign orbital tumors were evaluated. Wilcoxon signed-rank test, Kappa statistic, and receiver operating characteristics (ROC) curves were used.

Results: TGSE-PROPELLER-DWI performed superior in all subjective scores and quantitative GDR evaluation than rs-EPI ($p < 0.001$), and excellent interobserver agreement was obtained for Kappa value ranging from 0.876 to 1.000. ADC_{lesion} of TGSE-PROPELLER-DWI was significantly higher than those of rs-EPI ($p < 0.001$). Mean ADC of malignant tumors was significantly lower than that of benign tumors both in two DWIs. However, the AUC for differentiating malignant and benign tumors showed no significant difference in the two DWIs (0.860 vs. 0.854, $p = 0.7448$). Sensitivity and specificity could achieve 92.86% and 72.73% for TGSE-PROPELLER-DWI with a cutoff value of 1.23×10^{-3} mm^2/s, and 85.71% and 81.82% for rs-EPI with a cutoff value of 0.99×10^{-3} mm^2/s.

OPEN ACCESS

Edited by:
Nico Sollmann, University of California, San Francisco, United States

Reviewed by:
Matthew ManHin Cheung, CUHK Medical Centre, Hong Kong SAR, China
Dapeng Liu, Johns Hopkins University, United States
Robert Frost, Massachusetts General Hospital and Harvard Medical School, United States

***Correspondence:**
Zi-Qiao Lei
ziqiao_lei@hust.edu.cn
Chuan-sheng Zheng
hqzcsxh@sina.com
Fan Yang
fyang@hust.edu.cn
orcid.org/0000-0001-5718-9420

† These authors have contributed equally to this work

Specialty section:
This article was submitted to Brain Imaging Methods, a section of the journal Frontiers in Neuroscience

Received: *08 August 2021*
Accepted: *02 November 2021*
Published: *30 November 2021*

Citation:
Fu Q, Kong X-c, Liu D-X, Zhou K, Guo Y-h, Lei Z-Q, Zheng C-s and Yang F (2021) Turbo Gradient and Spin Echo PROPELLER-Diffusion Weighted Imaging for Orbital Tumors: A Comparative Study With Readout-Segmented Echo-Planar Imaging. Front. Neurosci. 15:755327. doi: 10.3389/fnins.2021.755327

Conclusion: Compared with rs-EPI, TGSE-PROPELLER-DWI showed minimized geometric distortion and susceptibility artifacts significantly improved the image quality for orbital tumors and achieved comparable diagnostic performance in differentiating malignant and benign orbital tumors.

Keywords: diffusion weighted imaging, apparent diffusion coefficient, orbit tumor, turbo gradient and spin echo PROPELLER diffusion-weighted imaging (TGSE-PROPELLER-DWI), readout-segmented echo-planar imaging (rs-EPI)

INTRODUCTION

Diffusion weighted imaging (DWI) is an essential MR sequence for diagnosing a broad spectrum of orbital diseases, enabling characteristics on morphological features of tissues with measurements of apparent diffusion coefficient (ADC). ADC is an additional noninvasive parameter for differentiation of malignant orbital tumors from benign lesions (Sepahdari et al., 2010; Razek et al., 2011; Intven et al., 2014).

The common single-shot echo-planar DWI (SS-EPI-DWI) collects k-space data with an echo-planar imaging (EPI) trajectory and has advantages of fast acquisition. However, it is very vulnerable to susceptibility artifacts, especially for the structures with air-bone-tissue interfaces because of relative long readout time and low bandwidth in phase-encoding direction (Turner et al., 1990; Li et al., 2015). Thus, SS-EPI-DWI usually results in unsatisfactory image quality with severe geometric distortions, signal pile-up or ghosting artifacts, and even misdiagnosis of anatomical structures/abnormalities, and lesions with small and/or irregular contour are difficult to be evaluated (White et al., 2006; Heidemann et al., 2010; Fu et al., 2021). Readout-segmented echo-planar imaging (rs-EPI) is an advanced DWI technique, in which the k-space is divided into several segments along the readout direction, and echo spacing and echo time were reduced (Porter and Heidemann, 2009). The previous studies (Bogner et al., 2012; Koyasu et al., 2014; Friedli et al., 2015; Xia et al., 2016; Zhao et al., 2016; Xu et al., 2017) demonstrated that rs-EPI showed reduced susceptibility-induced artifacts and T2* blurring compared with SS-EPI-DWI. However, it is unavoidable to suffer from the image distortions and susceptibility-induced artifacts (Bogner et al., 2012; Koyasu et al., 2014; Zhao et al., 2016; Xu et al., 2017; Sheng et al., 2020), challenging to distinguish small lesions from artifacts (Sheng et al., 2020).

Turbo gradient and spin echo PROPELLER diffusion-weighted imaging (TGSE-PROPELLER-DWI) is proposed recently, and its basic imaging principles have been introduced by Li et al. (2011); Zhou et al. (2018), and Hu et al. (2019). The fast turbo-gradient and spin-echo (TGSE) readout method in this technique helps reduce image distortions and magnetic susceptibility-induced artifacts; the phase-insensitive preparation module between diffusion preparation and the data acquisition was used to eliminate non-CPMG signal component; the gradient-spin echo is placed into each independent blade to minimize dephasing artifacts; the data is collected by rotating the blades, and the image is reconstructed with phase-error correction, achieving better robustness to motion artifacts. However, the signal-to-noise ratio (SNR) efficiency of TGSE-PROPELLER-DWI maybe lower than that of rs-EPI. It might be possible to reduce the acquisition time of TGSE-PROPELLER-DWI by using coils with higher channels, higher magnet field strength, and/or higher SNR (the parameters need to be optimized accordingly).

In clinical practice, TGSE-PROPELLER-DWI has been applied in the pediatric brain (Hu et al., 2019) and has also been previously compared with rs-EPI in clinical applications of middle ear (Sheng et al., 2020) and optic nerve (Yuan et al., 2020). Hu et al. (2019) suggested that TGSE-PROPELLER-DWI should be the first choice in patients where significant magnetic susceptibility artifacts are foreseen in some specific cases, for example, patients with orthodontia, postsurgical resection cavity, or shunts which are more susceptible to yield susceptibility artifacts. Sheng et al. (2020) and Yuan et al. (2020) found that TGSE-PROPELLER-DWI significantly improved image qualities by reducing geometric distortions, susceptibility artifacts, and less blurring compared with rs-EPI images in diagnosis of cholesteatoma and optic neuritis, but with a lower signal-to-noise ratio (SNR) than that of rs-EPI. However, the performance of TGSE-PROPELLER-DWI in depicting orbital tumors is still unknown. Whether it could decrease the geometric distortions and susceptibility artifacts or not is important to depict some small lesions, the extent of invasion and the diffusion characterization of orbital tumors accurately, and is also essential for the clinical treatment planning or even prognosis of the orbital tumors.

The purpose of the current study was to compare the clinical utility of TGSE-PROPELLER-DWI for depicting orbital tumors compared with rs-EPI. Specifically, image qualities of TGSE-PROPELLER-DWI and rs-EPI were compared subjectively and objectively, and their capacity for differentiating malignant from benign tumors was also evaluated.

MATERIALS AND METHODS

Study Population

This current prospective study was approved by the local medical ethics committee, and written informed consent was obtained prior to the MRI examinations. One of the patients was only 4 years old, and written informed consent was obtained from his legal guardians. Between September 1, 2020 and March 15, 2021, 43 patients (22 males and 21 females; mean age, 54.2 years; age range, 4–75 years) with suspected orbital tumors were enrolled in this study. Of those patients, 23 patients (10 males and

13 females; mean age, 49.3 years; age range, 4–69 years) with malignant tumors and 14 patients (10 males and 4 females; mean age, 60.6 years; age range, 49–71 years) with benign tumors were identified by pathological results 1–5 days after MR scanning. The remaining six patients were not found to have any orbital abnormalities.

Twenty-three benign orbital lesions comprised inflammatory pseudotumor (n = 5), cavernous malformation (n = 9), benign cyst (n = 3), dermoid cyst (n = 1), schwannoma (n = 2), meningioma (n = 2), and mucous cyst (n = 1). Fourteen malignant orbital lesions comprised lymphoma (n = 10), adenoid cystic carcinoma (n = 1), melanoma (n = 1), malignant solitary fibrous tumor (n = 1), and inflammatory myofibroblastic tumor (n = 1).

Magnetic Resonance Imaging Protocol

All MRI examinations were performed on a 3T MR scanner (MAGNETOM Skyra, Siemens Healthcare, Germany) equipped with a 45 mT/m achievable gradient strength and 200 T/m/s maximum slew rate using a dedicated 20-channel head-neck coil. Conventional MRI was required using the following sequences: coronal, axial and sagittal turbo spin-echo (TSE) T2-weighted imaging (T2WI) with fat suppression [repetition time/echo time (TR/TE): 5,220/37 ms, FOV: 200 mm × 200 mm, bandwidth: 220 Hz/pixel, slice thickness: 3 mm, flip angle = 160°, resolution 320 × 320, acquired voxel size = 0.63 mm × 0.63 mm × 3.0 mm]; axial and coronal TSE T1-weighted imaging (T1WI) without fat suppression (TR/TE: 600/6.4 ms, FOV: 180 mm × 180 mm, bandwidth: 391 Hz/pixel, slice thickness: 3 mm, flip angle = 150°, acquired voxel size = 0.35 mm × 0.35 mm × 3.0 mm); axial T1WI scanned by volume interpolated body examination (VIBE) with fat suppression before and after administration of contrast material (TR/TE: 18/3.69 ms, FOV: 180 mm × 180 mm, bandwidth: 180 Hz/pixel, slice thickness: 1 mm, flip angle = 9°, acquired voxel size = 0.63 mm × 0.63 mm × 1 mm).

Before contrast injection, the prototype TGSE-PROPELLER-DWI sequence and product rs-EPI were scanned with comparable spatial resolutions and similar acquisition time for all the enrolled patients. The detailed TGSE-PROPELLER-DWI parameters were as follows: TR/TE: 4,400/59 ms, FOV: 230 mm × 230 mm, bandwidth: 650 Hz/pixel, voxel size: 1.2 mm × 1.2 mm × 2.5 mm, number of slices: 16, matrix size: 192 × 192, PROPELLER coverage: 214.3%, PROPELLER number: 30, EPI factor: 5, turbo factor: 11, echo spacing: 13.9 ms, diffusion encoding mode: 4-scan-trace, b-values: 0 and 1,000 s/mm^2, averages: 1 for b = 0 s/mm^2 and 3 for b = 1,000 s/mm^2, turbo factor: 11, EPI factor: 5, and acquisition time: 5 min 51 s. The detailed parameters for rs-EPI were as follows: TR/TE: 6,670/68 ms, FOV: 200 mm × 200 mm, bandwidth: 780 Hz/pixel, voxel size: 1.1 mm × 1.1 mm × 2.5 mm, number of slices: 16, matrix size: 178 × 178, echo spacing: 0.4 ms, readout segments: 5, readout partial Fourier (Frost et al., 2012) was used: 3 readout segments acquired of 5 total (readout partial Fourier 5/8), generalized autocalibrating partially parallel acquisition (GRAPPA) was implemented to save time and reduce the effective echo-spacing, GRAPPA R:2, EPI factor: 89, diffusion encoding mode: 4-scan-trace, b-values: 0 and 1,000 s/mm^2, averages: 1 for b = 0 s/mm^2 and 3 for b = 1,000 s/mm^2, and acquisition time: 5 min 35 s. The phase-encoding directions for the two DWI methods were both set to be left-right.

Subjective Evaluations

Two experienced radiologists (with 15 and 25 years of experience working in neuroradiology) independently scored geometric distortions, susceptibility artifacts, lesion conspicuities, and the overall image qualities using a 4-point scale, as listed in **Table 1**. All the conventional T1WI and T2WI images were shown to the two radiologists, but images of TGSE-PROPELLER-DWI and rs-EPI of each patient were shown blindly. The order of patients and sequences (TGSE-PROPELLER-DWI or rs-EPI) was arranged in a random manner.

Objective Evaluations

Quantitative measurements, including contrast-to-noise ratios (CNRs), and apparent diffusion coefficients (ADCs), geometric distortion rates (GDRs), and lesion sizes of the two DWI sequences were calculated and compared.

The value of CNR was calculated by the following formula (Bogner et al., 2012): $\mathrm{CNR} = \frac{\mathrm{SI}_{\mathrm{lesion}} - \mathrm{SI}_{\mathrm{WM}}}{\sqrt{(\mathrm{SD}_{\mathrm{lesion}})^2 + (\mathrm{SD}_{\mathrm{WM}})^2}}$, SI_{lesion} and SI_{WM} represent the mean signal intensities of lesions and white matter.

In here, $\mathrm{SD}_{\mathrm{lesion}}$ and $\mathrm{SD}_{\mathrm{WM}}$ represent the standard deviation of lesions and white matter.

Apparent diffusion coefficients of orbital tumors were measured in ADC maps of both DWIs. The matching circular region-of-interest (ROI) on orbital tumors in the rs-EPI ADC map was copied to the corresponding region in the TGSE-PROPELLER-DWI ADC map, and the placement of ROIs would be moved slightly in order to achieve the matching region

TABLE 1 | Criteria for qualitative image quality comparisons between two DWIs.

Geometric distortion
1. Severe distortion
2. Moderate distortion
3. Mild distortion
4. No distortion
Susceptibility artifacts
1. Severe artifacts
2. Major artifacts
3. Only minor artifacts
4. No artifacts
Lesion conspicuity
1. Unable to evaluate
2. Acceptable for visualization
3. Obvious visibility
4. Excellent for visualization
Overall image quality
1. Poor, insufficient for diagnosis
2. Fair, adequate for diagnosis
3. Good for diagnosis
4. Excellent for diagnosis

between the two DWI methods. Then, the mean ADC values were generated automatically and recorded. All measurements were performed, avoiding signals from adjacent air, bone, susceptibility artifacts, and cystic or necrotic components of tumors.

Image fusions between the T2-weighted imaging (T2WI) and the two DWI sequences (b = 0 s/mm^2) were used as references for grading the extent of geometric distortions which was similar to strategies used by previous studies (Koyasu et al., 2014; Zhao et al., 2016; **Figure 1**). The value of GDR (Yokohama et al., 2019) was calculated as follows:

$$GDR = (|L_{DWI} - L_{T2}|)/L_{T2} \times 100\%$$

Where L_{T2} and L_{DWI} represent the maximum length of the vitreous body in T2WI and DWI, respectively. For lesion size, the maximum transversal and longitudinal length of tumors were measured in coronal T2WI, rs-EPI, and TGSE-PROPELLER-DWI images. The phase-encoding directions for the two DWI methods were both set to be left-right, so geometric distortion was mainly shown in this direction (left-right anatomically) especially in rs-EPI.

Statistical Analysis

Continuous variables were presented as the mean ± standard deviation (SD). If the subjective and objective parameters of the two DWIs conformed to normal distributions, paired t-test was used; otherwise, the Wilcoxon signed-rank test was used. Pearson correlation coefficients (r) were used to evaluate the correlations of lesion size on the two DWIs with that of T2WI. Inter-observer agreement between the two radiologists for the scores was analyzed using Kappa statistic (<0.40, poor; 0.40–0.59, moderate; 0.60–0.75, good; >0.75, excellent). Receiver operating characteristics (ROC) curves were used to evaluate the diagnostic performance of ADC values for differentiating orbital benign and malignant tumors, and the method by DeLong et al. (1988) was used to compare the area under curves (AUCs) of the two DWIs with 95% confidence intervals (CIs). Statistical analyses were performed with SPSS software (IBM SPSS 22, IBM Corp., Armonk, NY, United States) and MedCalc software (version 18.11.3; MedCalc Software, Ltd). A p-value <0.05 was considered statistically significant.

RESULTS

All the orbital lesions were detected successfully by the two DWIs. Mean lesion size was 1.93 cm × 1.86 cm in T2WI, 1.88 cm × 1.89 cm in TGSE-PROPELLER-DWI, and 1.91 cm × 1.91 cm in rs-EPI.

Subjective Scores and Inter-Observer Agreement Evaluations

As shown in **Table 2** and **Figure 2**, scores in TGSE-PROPELLER-DWI were significantly higher than those in rs-EPI for geometric distortions (3.9 ± 0.21, 2.14 ± 0.71, $z = -8.22$, $p < 0.001$), susceptibility artifacts (3.91 ± 0.36, 2.14 ± 0.60, $z = -8.32$, $p < 0.001$), lesion conspicuity (3.80 ± 0.52, 3.09 ± 0.88, $z = -5.50$, $p < 0.001$), and overall image quality (3.90 ± 0.31, 2.67 ± 0.52, $z = -8.20$, $p < 0.001$). No statistical difference in the interobserver variability for the qualitative scores was observed between the two radiologists (p-values >0.150). In addition, the Kappa value was 0.876–1.000, thus indicating excellent interobserver agreement.

Objective Analyses

As shown in **Table 3**, TGSE-PROPELLER-DWI showed significantly reduced geometric distortions compared with rs-EPI for quantitative GDR evaluation ($p < 0.001$) (**Figure 3**,

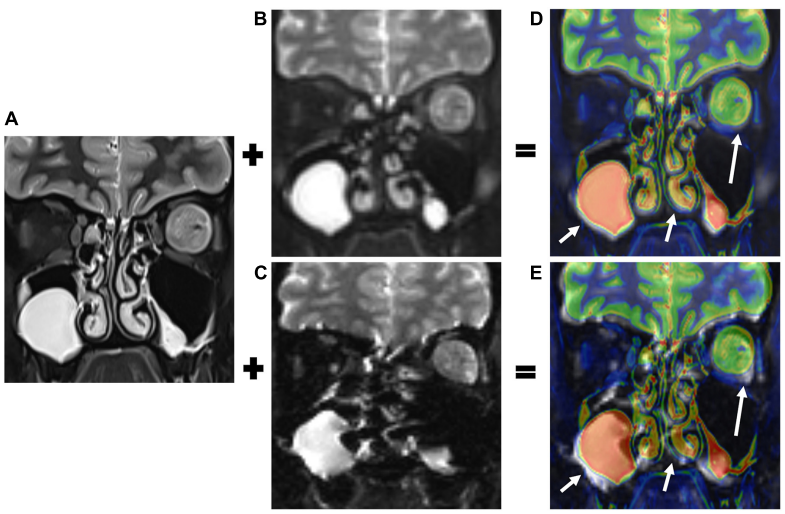

FIGURE 1 | T2-weighted imaging (T2WI, **A**), b0 images of TGSE-PROPELLER-DWI **(B)**, and rs-EPI **(C)** were fused. Color- and gray-coated images were derived from the T2WI and the two DWI b0 images **(D,E)**, respectively. The T2WI and TGSE-PROPELLER-DWI b0 images matched well, showing the left orbital tumor (long arrows in **D**) and ethmoid and maxillary sinuses (short arrows in **D**). The T2WI and rs-EPI b0 images were mismatched due to geometric distortions in the corresponding structures (arrows in **E**).

TABLE 2 | Qualitative scores for assessing image quality of the two DWIs.

Quantitative parameters	Reader 1				Reader 2				Inter-reader agreement (Kappa value)	
	TGSE-PROPELLER-DWI	rs-EPI	*z*	*P*	TGSE-PROPELLER-DWI	rs-EPI	*z*	*P*	TGSE-PROPELLER-DWI	rs-EPI
Geometric distortion	3.95 ± 0.21	2.12 ± 0.73	−5.82	<0.001	3.95 ± 0.21	2.16 ± 0.69	−5.84	<0.001	1.000	0.925
Susceptibility artifacts	3.91 ± 0.37	2.12 ± 0.63	−5.89	<0.001	3.91 ± 0.37	2.16 ± 0.57	−5.90	<0.001	1.000	0.912
Lesion conspicuity	3.81 ± 0.52	3.11 ± 0.88	−3.98	<0.001	3.78 ± 0.53	3.08 ± 0.89	−3.84	<0.001	0.898	0.960
Overall image quality	3.91 ± 0.29	2.67 ± 0.52	−5.85	<0.001	3.89 ± 0.32	2.67 ± 0.52	−5.77	<0.001	0.876	1.000

arrows); there was no significant difference in orbital tumor CNRs and white matter ADCs between the two DWI sequences ($p = 0.085$, $p = 0.110$, respectively); lesion ADC values of TGSE-PROPELLER-DWI were significantly higher than those of rs-EPI ($p < 0.001$). **Figure 3** shows a left orbital tumor (identified as solitary fibrous tumor by pathological result) which could be visualized clearly using the two DWIs. TGSE-PROPELLER-DWI showed minimized distortions and less susceptibility artifacts compared to rs-EPI. GDR values on TGSE-PROPELLER-DWI and rs-EPI were 0.036 and 0.171, respectively. ADC values of solid components on TGSE-PROPELLER-DWI and rs-EPI were 1.24×10^{-3} mm^2/s and 1.11×10^{-3} mm^2/s.

Correlation of TGSE-PROPELLER-DWI with conventional T2WI on the maximum transversal length and maximum longitudinal length ($r = 0.986$, $r = 0.969$, respectively) were both better than those of rs-EPI ($r = 0.941$, $r = 0.960$, respectively; **Table 4**). There was no significant difference in tumor size between TGSE-PROPELLER-DWI and rs-EPI ($p > 0.30$).

Apparent Diffusion Coefficient Analyses for Differentiating Malignant From Benign Orbital Tumors

Mean ADC value of malignant tumors was significantly lower than that of benign tumors both in TGSE-PROPELLER-DWI ($0.88 \pm 0.25 \times 10^{-3}$ mm^2/s, $1.46 \pm 0.55 \times 10^{-3}$ mm^2/s, $z = -2.86$, $p = 0.004$) and in rs-EPI ($0.78 \pm 0.26 \times 10^{-3}$ mm^2/s, $1.38 \pm 0.59 \times 10^{-3}$ mm^2/s, $z = -2.79$, $p = 0.005$) (**Figure 4**). Even though AUC value of TGSE-PROPELLER-DWI was slightly larger than that of rs-EPI (0.860 vs. 0.854, **Figure 5** and **Table 5**), there was no significant difference in the AUCs for both DWIs ($z = 0.326$, $p = 0.7448$). Sensitivity and specificity could achieve 92.86% and 72.73% for TGSE-PROPELLER-DWI (cutoff value: 1.23×10^{-3} mm^2/s), and 85.71% and 81.82% for rs-EPI (cutoff value: 0.99×10^{-3} mm^2/s) (**Table 5**).

DISCUSSION

This study demonstrated the feasibility and diagnostic performance of TGSE-PROPELLER-DWI for orbital tumors in clinical use. The data supported TGSE-PROPELLER-DWI to be superior than rs-EPI with regard to improved image quality and comparable capacity for differentiating malignant and benign orbital tumors.

In orbital DWI, TGSE-PROPELLER-DWI presented with minimized geometric distortions and susceptibility artifacts when compared with rs-EPI. According to various comparison studies between rs-EPI and SS-EPI-DWI, rs-EPI produced less image distortions, image blurring, and susceptibility artifacts in applications of orbital masses, sinonasal lesions, rectal cancer, head and neck, breast cancer, renal DWI by using semiquantitative scales or quantitative scores (Bogner et al., 2012; Koyasu et al., 2014; Friedli et al., 2015; Xia et al., 2016; Zhao et al., 2016; Xu et al., 2017), as well as increased sharpness of rs-EPI (Friedli et al., 2015; Zhao et al., 2016; Xu et al., 2017). However, partial volume effect, T2* blurring effect, and

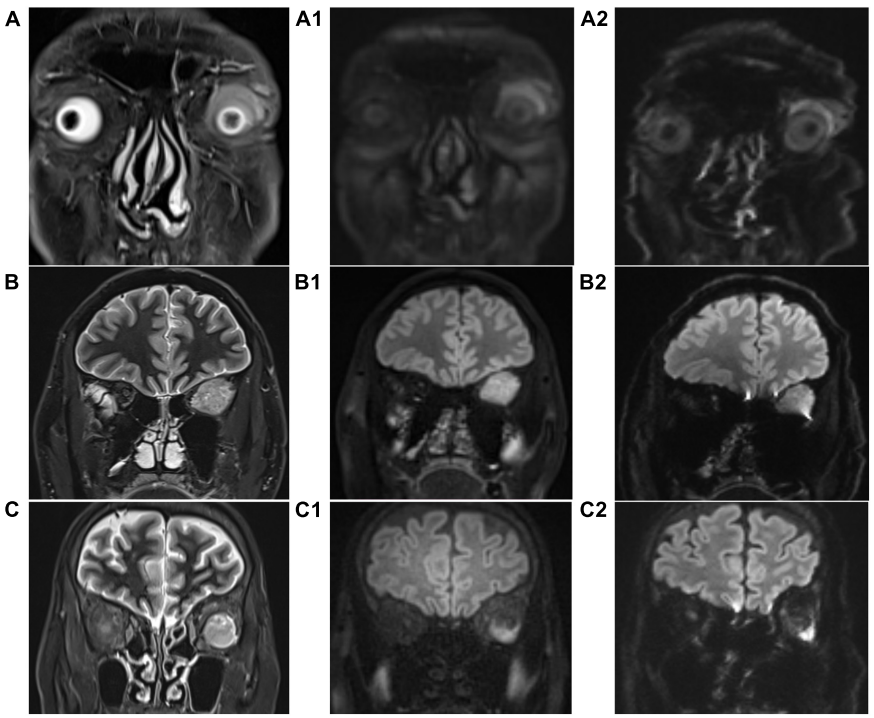

FIGURE 2 | Coronal T2-weighted imaging (T2WI) images **(A–C)**, coronal TGSE-PROPELLER-DWI b1000 images **(A1–C1)**, and coronal rs-EPI b1000 images **(A2–C2)**. **(A,A1,A2)**: patient 1, male, 62 years old, left orbital lymphoma, scores of geometric distortions, susceptibility artifacts, lesion conspicuity, and overall image quality of TGSE-BLADE-DWI were 4, 4, 4, and 4, respectively, while those of rs-EPI were 3, 2, 3, and 3, respectively. **(B,B1,B2)**: patient 2, male, 50 years old, left orbital fibroma, scores of geometric distortions, susceptibility artifacts, lesion conspicuity, and overall image quality of TGSE-BLADE-DWI were 4, 4, 4, and 4, respectively, while those of rs-EPI were 3, 3, 4, and 4, respectively. **(C,C1,C2)**: patient 3, female, 61 years old, left orbital hemangioma, scores of geometric distortions, susceptibility artifacts, lesion conspicuity, and overall image quality of TGSE-BLADE-DWI were 4, 4, 4, and 4, respectively, while those of rs-EPI were 2, 3, 2, and 2, respectively.

TABLE 3 | Quantitative parameters between TGSE-PROPELLER-DWI and rs-EPI.

Quantitative parameters	TGSE-PROPELLER-DWI	rs-EPI	*Z*-value	*P*-value
ADC ($\times 10^{-3}$ mm^2/s)				
White matter	0.78 ± 0.05	0.77 ± 0.05	−1.600	0.110
Lesion	1.23 ± 0.54	1.15 ± 0.56	−3.708	<0.001
CNR (b = 1,000 s/mm^2)	5.36 ± 4.82	4.13 ± 4.04	−1.720	0.085
GDR (%)	3.61 ± 3.58	17.14 ± 15.31	−5.580	<0.001
Lesion size (mm)				
Maximum transversal length	18.88 ± 9.21	19.13 ± 9.80	−0.770	0.441
Maximum longitudinal length	18.91 ± 10.07	19.08 ± 9.82	−1.001	0.317

geometric distortions could not be completely removed in rs-EPI (Bogner et al., 2012; Koyasu et al., 2014; Zhao et al., 2016; Xu et al., 2017; Sheng et al., 2020), which may lead to the failure to detect some small lesions (<2.5 mm) such as cholesteatomas (Sheng et al., 2020), because it was difficult to distinguish the small-sized lesions with the interference of susceptibility artifacts, especially in the air-tissue and bone-tissue interfaces. While TGSE-PROPELLER-DWI was immune to those artifacts in current study, subjective and objective assessments showed the minimized distortions and susceptibility artifacts of TGSE-PROPELLER-DWI for orbital DWI than rs-EPI, leading to the improved ability for depicting anatomical structures and lesions than rs-EPI. This result was consistent with a recent study, which focused on TGSE-PROPELLER-DWI for middle ear cholesteatoma with rs-EPI (Sheng et al., 2020) and another study which focused on TGSE-PROPELLER-DWI for the pediatric brain with SS-EPI-DWI (Hu et al., 2019). Different from the previous studies (Hu et al., 2019; Sheng et al., 2020), we also performed quantitative evaluations for geometric distortions. GDR of TGSE-PROPELLER-DWI was significantly lower than that of rs-EPI (0.036 vs. 0.171, $p < 0.001$) in the current study, which was in agreement with the subjective scores, supporting the superior performance of TGSE-PROPELLER-DWI with reduced distortions than rs-EPI.

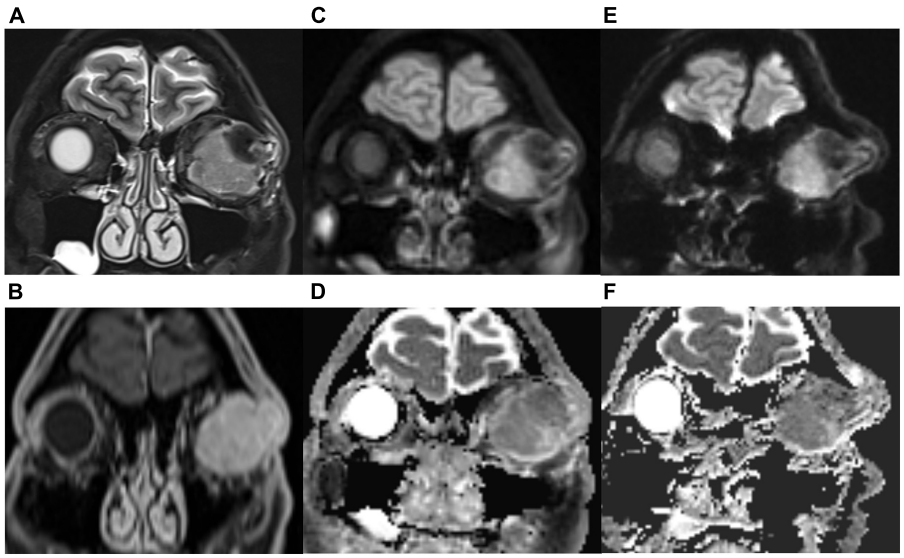

FIGURE 3 | A 50-year-old male with left solitary fibrous tumor. Compared with the T2-weighted imaging (T2WI, **A**) images and contrast-enhanced T1WI **(B)**, this lesion could be visualized clearly with TGSE-PROPELLER-DWI b1000 **(C)** and ADC map **(D)**; no geometric distortions were seen. Slight distortions were seen with rs-EPI b1000 **(E)** and ADC map **(F)**. More geometric distortions were observed in the frontal lobe and ethmoid sinus with rs-EPI.

TABLE 4 | Correlations of TGSE-PROPELLER-DWI and rs-EPI with conventional T2WI for evaluation of orbital tumor size.

Type	Maximum transversal length		Maximum longitudinal length	
	**r*	*p*	**r*	*p*
TGSE-PROPELLER-DWI	0.986	<0.001	0.969	<0.001
rs-EPI	0.941	<0.001	0.960	<0.001

**r, Pearson correlation coefficient.*

Even though DWI could observe and quantify biological structures based on diffusion properties of water molecules and improve lesion conspicuity (Prezzi et al., 2018), it has limited role for MR-guided planning in clinical practice mainly due to disadvantages in geometric integrity (Liney and Moerland, 2014). Decreased geometric distortions and susceptibility artifacts of DWI are essential for radiotherapy (RT) in matching or image fusions with other anatomical images for external beam planning, because high degree of accuracy is needed in RT applications (Bergen et al., 2020). Minimized geometric distortion is of critical importance to avoid excessive radiation dose to healthy tissues (Bergen et al., 2020). According to several published literatures (Chen et al., 2006; McPartlin et al., 2016; Studenski et al., 2016; Bergen et al., 2020), approximately 3 mm distortion would increase the doses in RT, and it would lead to significant dose errors if more than 1 cm and even affects the treatment outcomes. Results of the current study showed the superiority of TGSE-PROPELLER-DWI with minimized distortions and susceptibility artifacts, indicating the potential to be implemented in RT management. It would be meaningful to validate its performance and accuracy in the further research.

In orbital DWI, TGSE-PROPELLER-DWI was comparable in depicting tumor size and showed better lesion conspicuity when compared with rs-EPI. Even though the correlation of the lesion size in TGSE-PROPELLER-DWI with conventional T2WI was better than in rs-EPI-DWI, there was no significant difference in lesion sizes between the two DWIs, providing additional evidence of the new TGSE-PROPELLER-DWI for clinical use with the equivalent performance in depicting lesion sizes. With the help of the decreased artifacts and distortions mentioned above, lesions with better conspicuity and comparable CNR were observed in TGSE-PROPELLER-DWI, making a greatly improved image quality of TGSE-PROPELLER-DWI to rs-EPI in orbital imaging.

In orbital DWI, TGSE-PROPELLER-DWI ADCs could achieve comparable diagnostic performance for differentiation malignant from benign orbital tumors than rs-EPI ADCs. ADC value has been widely accepted as an effective biomarker for differential diagnosis of malignant and benign tumors in various body parts (Tsuruda et al., 1990; Yamasaki et al., 2005; Maeda and Maier, 2008; Sepahdari et al., 2010). Malignant tumors with restricted diffusion tend to have a lower ADC value, which may be related to their larger nuclei, higher cellularity, and decreased extracellular space, and benign tumors tend to display higher ADCs than malignant tumors (Tsuruda et al., 1990; Guo et al., 2002; EI Khouli et al., 2010). Our results demonstrated that the mean ADC value of malignant tumors was $0.88 \pm 0.25 \times 10^{-3}$ mm^2/s in

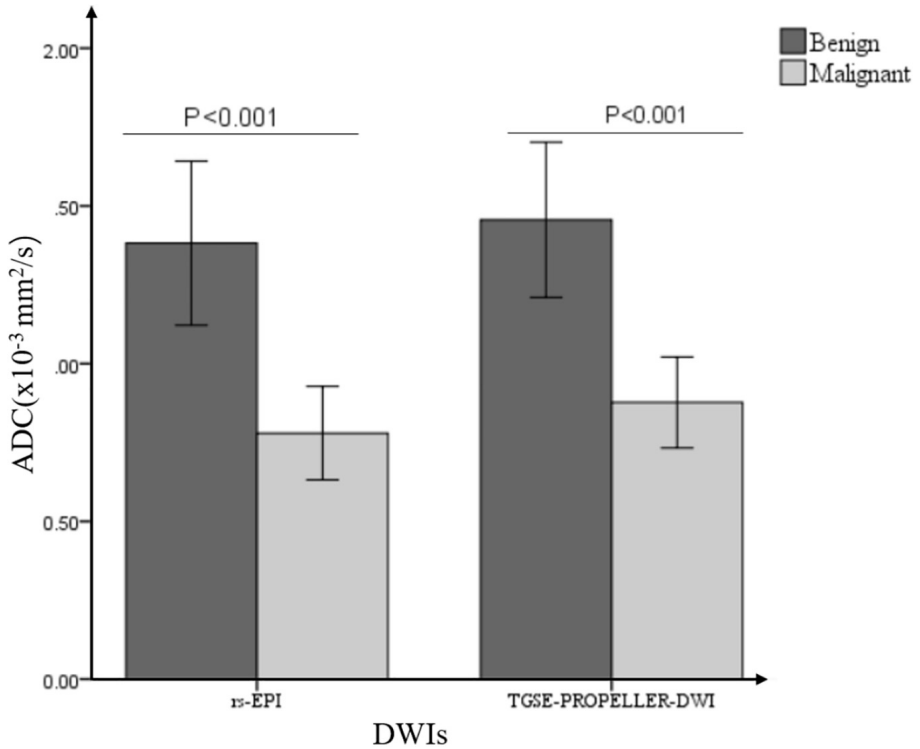

FIGURE 4 | Bar graph demonstrated the comparisons of ADC values between malignant and benign orbital tumors in two DWIs.

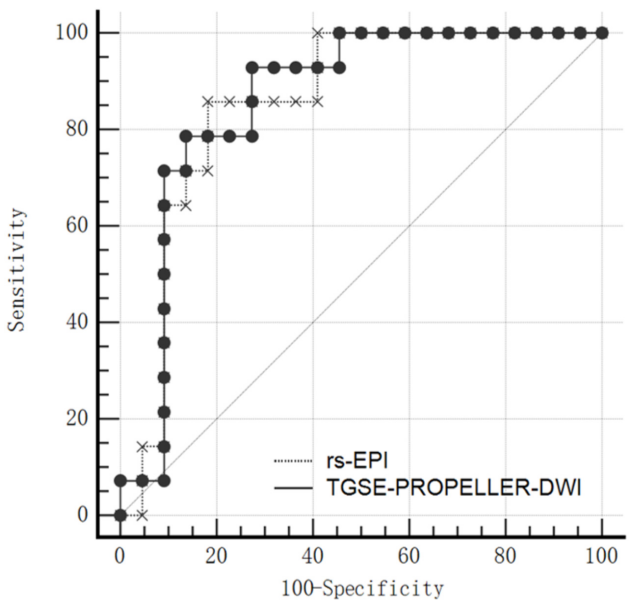

FIGURE 5 | ROC curve of the two DWI ADC values to differentiate malignant and benign orbital tumors.

TGSE-PROPELLER-DWI and 0.78 ± 0.26 × 10^{-3} mm^2/s in rs-EPI, and benign tumor was 1.46 ± 0.55 × 10^{-3} mm^2/s in TGSE-PROPELLER-DWI and 1.38 ± 0.59 × 10^{-3} mm^2/s in rs-EPI. This finding was in good agreement with published papers. Mean ADC of the two DWIs for malignant and benign orbital tumors was 0.84 ± 0.34 × 10^{-3} mm^2/s and 1.57 ± 0.33 × 10^{-3} mm^2/s, respectively, in Razek et al.'s (2011) report and 0.77 ± 0.38 × 10^{-3} mm^2/s and 1.23 ± 0.42 × 10^{-3} mm^2/s, respectively, in Fatima et al.'s (2014) report.

Several previous orbital DWI studies have reported different threshold values with different sensitivities and specificities. Razek et al. (2011) reported a cutoff value of 1.15 × 10^{-3} mm^2/s, with 95% sensitivity and 91% specificity for differentiating malignancy from benign lesions. Hemat (2017) reported cutoff value of 0.93 × 10^{-3} mm^2/s with 80% sensitivity, 83.3% specificity and 82% accuracy. Sepahdari et al. (2010) reported a threshold value of 1.0 × 10^{-3} mm^2/s with 63% sensitivity and 86% specificity. Bogner et al. (2012) reported an ADC threshold of 1.25 × 10^{-3} mm^3/s with 90% accuracy for discriminating malignant and benign lesions. While in the current study, when TGSE-PROPELLER-DWI ADC value of 1.23 × 10^{-3} mm^2/s was used as a cutoff value for differentiation of malignant from benign orbital tumors, sensitivity and specificity could achieve 92.86% and 72.73%, respectively, and rs-EPI ADC cutoff value was 0.99 × 10^{-3} mm^2/s with sensitivity 85.71% and specificity 81.82%.

Moreover, in the current work, the AUC value of TGSE-PROPELLER-DWI (AUC = 0.860) was similar to that of rs-EPI (AUC = 0.854) with no significant statistical difference

TABLE 5 | Receiver operating characteristic (ROC) curve analyses of ADC values for distinguishing orbital malignancy from benign tumors.

DWIs	AUC	95% CI	*z*	*P*-value	Youden index	Cutoff value ($\times 10^{-3}$ mm^2/s)	Sensitivity (95% CI)	Specificity (95% CI)
TGSE-PROPELLER-DWI	0.860	0.704–0.953	5.504	<0.0001	0.6558	1.23	92.86% (66.1–99.8)	72.73% (49.8–89.3)
rs-EPI	0.854	0.696–0.949	5.326	<0.0001	0.6753	0.99	85.71% (57.2–98.2)	81.82% (59.7–94.8)

AUC, area under curve; 95% CI, 95% confidence intervals.

($p > 0.700$), indicating a comparable diagnostic performance of the two DWIs for malignant and benign tumors differentiation. This data validated TGSE-PROPELLER-DWI to be a potential tool for characterizing orbital tumors as well as valuable differentiation of malignant from benign orbital tumors.

Our study had several limitations. First, the level of geometric distortion and susceptibility artifacts in rs-EPI is directly controlled by the echo-spacing which was set to 0.40 ms in this study where the scan time and number of averages were matched. Depending on other protocol details, e.g., decrease resolution or bandwidth, increase number of readout segment, the echo-spacing can be decreased which would reduce distortion and susceptibility artifacts. Second, we have set averages 1 for b = 0 s/mm^2 and 3 for b = 1,000 s/mm^2 in two DWIs by taking into account the specific characteristics of orbit for better image qualities, and acquisition times of TGSE-PROPELLER-DWI and rs-EPI were both 5–6 min. The longer examination time may yield unnecessary patient motion, resulting in motion artifacts and deterioration in image quality. Theoretically, TGSE-PROPELLER-DWI has the potential to reduce the motion artifacts to some extent due to the PROPELLER technique, but this was not investigated in current study. Further optimization of the sequence will be undertaken to decrease the scanning time for faster scanning procedure and patients' comfort, by integrating simultaneous multislice (SMS) or compressed sensing (CS) technologies if possible. Third, participant number was relatively limited with various pathological results. We have not discussed the capacities of two DWI ADCs for each tumor. The relationship between ADCs and tumor grades was not discussed either. Nonetheless, our preliminary data demonstrate the feasibility and potential benefits of TGSE-PROPELLER-DWI for orbital tumors in clinical practice. Moreover, further studies with a larger sample size with a broad spectrum of pathologies are still needed.

In conclusion, compared with rs-EPI, TGSE-PROPELLER-DWI showed minimized geometric distortions and susceptibility artifacts and significantly improved the image quality for characterizing orbital tumors. TGSE-PROPELLER-DWI is feasible for depicting orbital tumors and achieves comparable diagnostic performance in differentiating malignant and benign orbital tumors.

DATA AVAILABILITY STATEMENT

The original contributions presented in the study are included in the article/supplementary material, further inquiries can be directed to the corresponding author/s.

ETHICS STATEMENT

The studies involving human participants were reviewed and approved by the Medical Ethics Committee of Huazhong University of Science and Technology. Written informed consent to participate in this study was provided by the participants' legal guardian/next of kin. Written informed consent was obtained

from the individual(s) for the publication of any potentially identifiable images or data included in this article.

AUTHOR CONTRIBUTIONS

QF and FY: conception and design. QF, Y-HG, and KZ: administrative support. QF, X-CK, D-XL, and C-SZ: provision of study materials or patients. QF and X-CK: collection and assembly of data. QF, Z-QL, and FY: data analysis and interpretation. All authors contributed to study design, manuscript writing, study selection, data analysis, study quality evaluating, manuscript revising, and read and approved the final manuscript.

ACKNOWLEDGMENTS

The authors would like to thank Fan-li Jia (Department of Psychology, Seton Hall University, South Orange, NJ, United States) for his assistance in language editing.

REFERENCES

Bergen, R. V., Ryner, L., and Essig, M. (2020). Field-map correction in read-out segmented echo planar imaging for reduced spatial distortion in prostate DWI for MRI-guided radiotherapy applications. *Magn. Reson. Imaging* 67, 43–49. doi: 10.1016/j.mri.2019.12.005

Bogner, W., Pinker-Domenig, K., Bickel, H., Chmelik, M., Weber, M., Helbich, T. H., et al. (2012). Readout-segmented Echo-planar imaging improves the diagnostic performance of diffusion-weighted MR breast examinations at 3.0 T. *Radiology* 263, 64–76. doi: 10.1148/radiol.11111494

Chen, Z., Ma, C.-M., Paskalev, K., Li, J., Yang, J., Richardson, T., et al. (2006). Investigation of MR image distortion for radiotherapy treatment planning of prostate cancer. *Phys. Med. Biol.* 51, 1393–1403. doi: 10.1088/0031-9155/51/6/002

DeLong, E. R., DeLong, D. M., and Clarke-Pearson, D. L. (1988). Comparing the areas under two or more correlated receiver operating characteristic curves: a nonparametric approach. *Biometrics* 44, 837–845.

EI Khouli, R. H., Jacobs, M. A., Mezban, S. D., Huang, P., Kamel, I. R., Macura, K. J., et al. (2010). Diffusion-weighted imaging improves the diagnostic accuracy of conventional 3.0-T breast MR imaging. *Radiology* 256, 64–73. doi: 10.1148/radiol.10091367

Fatima, Z., Ichikawa, T., Ishigame, K., Motosugi, U., Waqar, A. B., Hori, M., et al. (2014). Orbital masses: the usefulness of diffusion-weighted imaging in lesion categorization. *Clin. Neuroradiol.* 24, 129–134. doi: 10.1007/s00062-013-0234-x

Friedli, I., Crowe, L. A., Viallon, M., Porter, D. A., Martin, P.-Y., de Seigneux, S., et al. (2015). Improvement of renal diffusion-weighted magnetic resonance imaging with readout-segmented echo-planar imaging at 3T. *Magn. Reson. Imaging* 33, 701–708. doi: 10.1016/j.mri.2015.02.023

Frost, R., Porter, D. A., Miller, K. L., and Jezzard, P. (2012). Implementation and assessment of diffusion-weighted partial fourier readout-segmented echo-planar imaging: implementation and assessment of diffusion-weighted partial fourier rs-EPI. *Magn. Reson. Med.* 68, 441–451. doi: 10.1002/mrm.23242

Fu, Q., Kong, X., Liu, D., Zhou, K., Guo, Y., Wang, M., et al. (2021). Clinical comparison of single-shot EPI, readout-segmented EPI and TGSE-BLADE for diffusion-weighted imaging of cerebellopontine angle tumors on 3 tesla. *Magn. Reson.* 84, 76–83. doi: 10.1016/j.mri.2021.09.009

Guo, Y., Cai, Y.-Q., Cai, Z.-L., Gao, Y.-G., An, N.-Y., Ma, L., et al. (2002). Differentiation of clinically benign and malignant breast lesions using diffusion-weighted imaging. *J. Magn. Reson. Imaging* 16, 172–178. doi: 10.1002/jmri.10140

Heidemann, R. M., Porter, D. A., Anwander, A., Feiweier, T., Heberlein, K., Knösche, T. R., et al. (2010). Diffusion imaging in humans at 7T using readout-segmented EPI and GRAPPA. *Magn. Reson. Med.* 64, 9–14. doi: 10.1002/mrm.22480

Hemat, E. M. (2017). Characterization of orbital masses by diffusion-weighted magnetic resonance imaging (DWI) and apparent diffusion coefficient (ADC) value. *Egypt. J. Radiol. Nucl. Med.* 48, 115–123. doi: 10.1016/j.ejrnm.2016.10.003

Hu, H. H., McAllister, A. S., Jin, N., Lubeley, L. J., Selvaraj, B., Smith, M., et al. (2019). Comparison of 2D BLADE turbo gradient- and spin-echo and 2D spin-echo echo-planar diffusion-weighted brain MRI at 3 T: preliminary experience in children. *Acad. Radiol.* 26, 1597–1604. doi: 10.1016/j.acra.2019.02.002

Intven, M., Reerink, O., and Philippens, M. E. P. (2014). Repeatability of diffusion-weighted imaging in rectal cancer: DWI repeatability in rectal cancer. *J. Magn. Reson. Imaging* 40, 146–150. doi: 10.1002/jmri.24337

Koyasu, S., Iima, M., Umeoka, S., Morisawa, N., Porter, D. A., Ito, J., et al. (2014). The clinical utility of reduced-distortion readout-segmented echo-planar imaging in the head and neck region: initial experience. *Eur. Radiol.* 24, 3088–3096. doi: 10.1007/s00330-014-3369-5

Li, L., Wang, L., Deng, M., Liu, H., Cai, J., Sah, V. K., et al. (2015). Feasibility study of 3-T DWI of the prostate: readout-segmented versus single-shot echo-planar imaging. *Am. J. Roentgenol.* 205, 70–76. doi: 10.2214/AJR.14.13489

Li, Z., Pipe, J. G., Lee, C.-Y., Debbins, J. P., Karis, J. P., and Huo, D. (2011). X-PROP: a fast and robust diffusion-weighted propeller technique: X-PROP. *Magn. Reson. Med.* 66, 341–347. doi: 10.1002/mrm.23033

Liney, G. P., and Moerland, M. A. (2014). Magnetic resonance imaging acquisition techniques for radiotherapy planning. *Sem. Radiat. Oncol.* 24, 160–168. doi: 10.1016/j.semradonc.2014.02.014

Maeda, M., and Maier, S. E. (2008). Usefulness of diffusion-weighted imaging and the apparent diffusion coefficient in the assessment of head and neck tumors. *J. Neuroradiol.* 35, 71–78. doi: 10.1016/j.neurad.2008.01.080

McPartlin, A. J., Li, X. A., Kershaw, L. E., Heide, U., Kerkmeijer, L., Lawton, C., et al. (2016). MRI-guided prostate adaptive radiotherapy – A systematic review. *Radiother. Oncol.* 119, 371–380. doi: 10.1016/j.radonc.2016.04.014

Porter, D. A., and Heidemann, R. M. (2009). High resolution diffusion-weighted imaging using readout-segmented echo-planar imaging, parallel imaging and a two-dimensional navigator-based reacquisition: EPI With Parallel Imaging and 2D Reacquisition. *Magn. Reson. Med.* 62, 468–475. doi: 10.1002/mrm.22024

Prezzi, D., Mandegaran, R., Gourtsoyianni, S., Owczarczyk, K., Gaya, A., Glynne-Jones, R., et al. (2018). The impact of MRI sequence on tumour staging and gross tumour volume delineation in squamous cell carcinoma of the anal canal. *Eur. Radiol.* 28, 1512–1519. doi: 10.1007/s00330-017-5133-0

Razek, A. A. K. A., Elkhamary, S., and Mousa, A. (2011). Differentiation between benign and malignant orbital tumors at 3-T diffusion MR-imaging. *Neuroradiology* 53, 517–522. doi: 10.1007/s00234-011-0838-2

Sepahdari, A. R., Aakalu, V. K., Setabutr, P., Shiehmorteza, M., Naheedy, J. H., and Mafee, M. F. (2010). Indeterminate Orbital Masses: Restricted Diffusion at MR Imaging with Echo-planar Diffusion-weighted Imaging Predicts Malignancy. *Radiology* 256, 554–564. doi: 10.1148/radiol.10091956

Sheng, Y., Hong, R., Sha, Y., Zhang, Z., Zhou, K., and Fu, C. (2020). Performance of TGSE BLADE DWI compared with RESOLVE DWI in the diagnosis of cholesteatoma. *BMC Med. Imaging* 20:40. doi: 10.1186/s12880-020-00438-7

Studenski, M. T., Valenciaga, Y., Abramowitz, M. C., Stoyanova, R., Bossart, E., Dogan, N., et al. (2016). Quantification of the margin required for treating intraprostatic lesions. *J. Appl. Clin. Med. Phys.* 17, 304–312. doi: 10.1120/jacmp.v17i3.6089

Tsuruda, J. S., Chew, W. M., Moseley, M. E., and Norman, D. (1990). Diffusion-weighted MR imaging of the brain: value of differentiating between

extraaxial cysts and epidermoid tumors. *AJR Am. J. Roentgenol.* 155, 1059–1065;discussion1066–1068. doi: 10.2214/ajr.155.5.2120936

Turner, R., Le Bihan, D., Maier, J., Vavrek, R., Hedges, L. K., and Pekar, J. (1990). Echo-planar imaging of intravoxel incoherent motion. *Radiology* 177, 407–414. doi: 10.1148/radiology.177.2.2217777

White, M. L., Zhang, Y., and Robinson, R. A. (2006). Evaluating tumors and tumorlike lesions of the nasal cavity, the paranasal sinuses, and the adjacent skull base with diffusion-weighted MRI. *J. Comput. Assist. Tomogr.* 30, 490–495. doi: 10.1097/00004728-200605000-00023

Xia, C., Liu, X., Peng, W., Li, L., Zhang, J., Meng, W., et al. (2016). Readout-segmented echo-planar imaging improves the image quality of diffusion-weighted MR imaging in rectal cancer: Comparison with single-shot echo-planar diffusion-weighted sequences. *Eur. J. Radiol.* 85, 1818–1823. doi: 10.1016/j.ejrad.2016.08.008

Xu, X., Wang, Y., Hu, H., Su, G., Liu, H., Shi, H., et al. (2017). Readout-segmented echo-planar diffusion-weighted imaging in the assessment of orbital tumors: comparison with conventional single-shot echo-planar imaging in image quality and diagnostic performance. *Acta Radiol.* 58, 1457–1467. doi: 10.1177/0284185117695667

Yamasaki, F., Kurisu, K., Satoh, K., Arita, K., Sugiyama, K., Ohtaki, M., et al. (2005). Apparent diffusion coefficient of human brain tumors at MR imaging. *Radiology* 235, 985–991. doi: 10.1148/radiol.2353031338

Yokohama, T., Iwasaki, M., Oura, D., Furuya, S., and Okuaki, T. (2019). The Reliability of reduced field-of-view DTI for highly accurate quantitative assessment of cervical spinal cord tracts. *MRMS* 18, 36–43. doi: 10.2463/mrms.mp.2017-0078

Yuan, T., Sha, Y., Zhang, Z., Liu, X., Ye, X., Sheng, Y., et al. (2020). "TGSE diffusion-weighted pulse sequence in the evaluation of optic neuritis: a comprehensive comparison of image quality with RESOLVE DWI," in *Proceedings of the Annual Meeting of the International Society for Magnetic Resonance in Medicine*, (Shenzhen).

Zhao, M., Liu, Z., Sha, Y., Wang, S., Ye, X., Pan, Y., et al. (2016). Readout-segmented echo-planar imaging in the evaluation of sinonasal lesions: A comprehensive comparison of image quality in single-shot echo-planar imaging. *Magn. Reson. Imaging* 34, 166–172. doi: 10.1016/j.mri.2015.10.010

Zhou, K., Liu, W., and Cheng, S. (2018). "Non-CMPG PROPELLER diffusion imaging: comparison of phase insensitive preparation with split acquisition," in *Proceedings of the Annual Meeting of the International Society for Magnetic Resonance in Medicine*, (Shenzhen).

Conflict of Interest: KZ was employed by the company Siemens Shenzhen Magnetic Resonance Ltd. China. Y-HG was employed by the company Siemens Healthcare Ltd. China.

The remaining authors declare that the research was conducted in the absence of any commercial or financial relationships that could be construed as a potential conflict of interest.

Publisher's Note: All claims expressed in this article are solely those of the authors and do not necessarily represent those of their affiliated organizations, or those of the publisher, the editors and the reviewers. Any product that may be evaluated in this article, or claim that may be made by its manufacturer, is not guaranteed or endorsed by the publisher.

Copyright © 2021 Fu, Kong, Liu, Zhou, Guo, Lei, Zheng and Yang. This is an open-access article distributed under the terms of the Creative Commons Attribution License (CC BY). The use, distribution or reproduction in other forums is permitted, provided the original author(s) and the copyright owner(s) are credited and that the original publication in this journal is cited, in accordance with accepted academic practice. No use, distribution or reproduction is permitted which does not comply with these terms.

frontiers in Neuroscience

ORIGINAL RESEARCH
published: 01 December 2021
doi: 10.3389/fnins.2021.782516

Assessment of Sodium MRI at 7 Tesla as Predictor of Therapy Response and Survival in Glioblastoma Patients

Daniel Paech[1†], Sebastian Regnery[2,3†], Tanja Platt[4], Nicolas G. R. Behl[4,5], Nina Weckesser[1], Paul Windisch[2], Katerina Deike-Hofmann[1], Wolfgang Wick[6], Martin Bendszus[7], Stefan Rieken[2,3], Laila König[2,3], Mark E. Ladd[4,8], Heinz-Peter Schlemmer[1], Jürgen Debus[2,3] and Sebastian Adeberg[2,3]*

[1] Division of Radiology, German Cancer Research Center (DKFZ), Heidelberg, Germany, [2] Department of Radiation Oncology, Heidelberg University Hospital, Heidelberg, Germany, [3] Clinical Cooperation Unit Radiation Oncology, German Cancer Research Center (DKFZ), Heidelberg, Germany, [4] Division of Medical Physics in Radiology, German Cancer Research Center (DKFZ), Heidelberg, Germany, [5] Siemens Healthcare GmbH, Erlangen, Germany, [6] Department of Neurology, Heidelberg University Hospital, Heidelberg, Germany, [7] Department of Neuroradiology, Heidelberg University Hospital, Heidelberg, Germany, [8] Faculty of Physics and Astronomy and Faculty of Medicine, University of Heidelberg, Heidelberg, Germany

OPEN ACCESS

Edited by:
Nico Sollmann,
University of California,
San Francisco, United States

Reviewed by:
Inge Compter,
Maastro Clinic, Netherlands
Esther Warnert,
Erasmus Medical Center, Netherlands

***Correspondence:**
Daniel Paech
d.paech@dkfz.de

† These authors have contributed equally to this work and share first authorship

Specialty section:
This article was submitted to Brain Imaging Methods, a section of the journal Frontiers in Neuroscience

Received: 24 September 2021
Accepted: 09 November 2021
Published: 01 December 2021

Citation:
Paech D, Regnery S, Platt T, Behl NGR, Weckesser N, Windisch P, Deike-Hofmann K, Wick W, Bendszus M, Rieken S, König L, Ladd ME, Schlemmer H-P, Debus J and Adeberg S (2021) Assessment of Sodium MRI at 7 Tesla as Predictor of Therapy Response and Survival in Glioblastoma Patients. Front. Neurosci. 15:782516. doi: 10.3389/fnins.2021.782516

The purpose of this work was to prospectively investigate sodium (^{23}Na) MRI at 7 Tesla (T) as predictor of therapy response and survival in patients with glioblastoma (GBM). Thus, 20 GBM patients underwent ^{23}Na MRI at 7T before, immediately after and 6 weeks after chemoradiotherapy (CRT). The median tissue sodium concentration (TSC) inside the whole tumor excluding necrosis was determined. Initial response to CRT was assessed employing the updated response assessment in neuro-oncology working group (RANO) criteria. Clinical parameters, baseline TSC and longitudinal TSC differences were compared between patients with initial progressive disease (PD) and patients with initial stable disease (SD) using Fisher's exact tests and Mann-Whitney-U-tests. Univariate proportional hazard models for progression free survival (PFS) and overall survival (OS) were calculated using clinical parameters and TSC metrics as predictor variables. The analyses demonstrated that TSC developed heterogeneously over all patients following CRT. None of the TSC metrics differed significantly between cases of initial SD and initial PD. Furthermore, TSC metrics did not yield a significant association with PFS or OS. Conversely, the initial response according to the RANO criteria could significantly predict PFS [univariate HR (95%CI) = 0.02 (0.0001–0.21), $p < 0.001$] and OS [univariate HR = 0.17 (0.04–0.65), $p = 0.005$]. In conclusion, TSC showed treatment-related changes in GBM following CRT, but did not significantly correlate with the initial response according to the RANO criteria, PFS or OS. In contrast, the initial response according to the RANO criteria was a significant predictor of PFS and OS. Future investigations need to elucidate the reasons for treatment-related changes in TSC and their clinical value for response prediction in glioblastoma patients receiving CRT.

Keywords: brain neoplasm/secondary cases, glioblastoma, response assessment, magnetic resonance imaging, ultra-high field (7 tesla), sodium MRI

INTRODUCTION

The overall prognosis of glioblastoma (GBM) remains poor despite gross tumor resection followed by chemoradiotherapy (CRT), but long-term survival can be achieved in a small subgroup of patients (Stupp et al., 2005, 2009). In this context, the early identification of tumor relapse remains a major challenge. Current assessment of response to therapy is based on the updated response assessment in neuro-oncology working group (RANO) criteria, which classify clinical follow-up MRI (Wen et al., 2010; Johnson et al., 2019). This approach suffers essential limitations due to the incidence of pseudo-progressions (PsPD) especially shortly after treatment (de Wit et al., 2004; Wen et al., 2010). Repeated imaging studies are necessary to rule out PsPD (Wen et al., 2010; Johnson et al., 2019), which impedes early identification of tumor relapse and delays potential 2nd-line therapies as part of personalized treatment approaches. Consequently, imaging techniques that enable an early or even real-time response assessment to guide therapy protocols are highly desirable.

Sodium (^{23}Na) MRI has been used within animal experiments (Schepkin et al., 2005, 2006) and mostly case reports (Thulborn et al., 2009; Laymon et al., 2012; Haneder et al., 2015) to monitor treatment associated changes in GBM consecutive to CRT. Here, ^{23}Na MRI demonstrated promising features as it seems to offer complementary information to routine imaging modalities (Laymon et al., 2012; Haneder et al., 2015; Regnery and Platt, 2021). Quite recently, an investigation of ^{23}Na MRI at 3 Tesla (T) in GBM patients suggested that the development of tissue sodium concentration (TSC) during CRT might reflect tumor cell kill (Thulborn et al., 2019). Thus, ^{23}Na MRI is a promising functional imaging technique in neuro-oncology (Regnery and Platt, 2021). However, ^{23}Na MRI is limited by a comparatively low signal-to-noise ratio (SNR) because ^{23}Na-ions are far less abundant than the protons used for conventional MRI techniques (Shah et al., 2016). Here, the advent of ultra-high field (UHF) MRI techniques opens new perspectives in ^{23}Na imaging by providing increased SNR (Konstandin and Schad, 2014; Shah et al., 2016). This longitudinal prospective study employed a 7T MRI scanner to investigate the development of TSC in 20 GBM patients following CRT. Based on previous reports, we explored the capacity of TSC to reflect therapy response and therefore predict progression free survival (PFS) as well as overall survival (OS).

PATIENTS AND METHODS

Patients

20 GBM patients prospectively underwent ^{23}Na imaging on a 7 Tesla MRI system before (t_0), immediately after (t_1) and 6 weeks after (t_2) (C)RT. Inclusion criteria were an age $\geq$ 18 years, histological proof of GBM, residual disease on clinical imaging after potential tumor resection, currently planned (C)RT and the absence of ferromagnetic or active implants unsuitable for 7 T. Ten patients (50%) received gross tumor resection before imaging and (C)RT. Eleven patients (55%) presented with newly diagnosed GBM and received CRT according to Stupp et al. (2005) or CRT modified to elderly age and decreased clinical performance according to Perry et al. (2017). Moreover, nine patients (45%) presented with recurrent GBM and received particle RT with or without systemic treatment. Detailed patient characteristics are shown in **Table 1**.

^{23}Na Magnetic Resonance Imaging at 7T

All ^{23}Na images were acquired on a 7T research scanner (Siemens Healthcare, Erlangen, Germany) with a double-resonant (^{1}H/^{23}Na) quadrature birdcage coil (RAPID Biomedical, Rimpar, Germany). The ^{23}Na data was obtained with a density-adapted 3D radial pulse sequence (Nagel et al., 2009) which yielded a nominal resolution of $(\Delta x)^3$ = (3 mm)^3 (TR/TE = 160 ms/0.35 ms, readout time = 10 ms, number of projections = 4,000, acquisition time = 10:40 min). TE was measured from the center of the RF pulse (shape: rectangular, duration: 600μs) to the start of the readout. Image reconstruction employed an iterative 3D Dictionary Learning Compressed Sensing algorithm (3D-DLCS) (Behl et al., 2016) (block size B = 3 × 3 × 3; dictionary size D = 80; number of samples = 500,000; regularization weighting factor μ = 0.5).

The tissue sodium concentration (TSC) was calculated using two reference vials (0.3–0.6% NaCl). Both B_1^+ and B_1^- corrections were applied to reduce transmit and receive inhomogeneities using the double angle method for the field estimations (Insko and Bolinger, 1993).

Clinical 3T Magnetic Resonance Imaging

All patients underwent clinical MRI at a field strength of 3T before initiation of (C)RT. Furthermore, clinical follow-up MRIs were performed approximately 4 and 12 weeks post-therapy. Routinely, clinical 3T MRI encompassed a pre- and post-contrast T1-weighted sequence (Gadolinium based contrast agent; TE = 4.04 ms, TR = 1,710 ms, FoV = 256 × 256 mm^2, matrix = 512 × 512, slice thickness = 1 mm) and a fluid-attenuated inversion recovery (FLAIR) sequence (TE = 135 ms, TR = 8,500 ms, FoV = 230 × 172 mm^2, matrix = 256 × 192, slice thickness = 5 mm) used for response assessment in accordance with the updated RANO criteria (Wen et al., 2010).

Image Processing

The clinical 3T MRI from the pre-therapy examination and the clinical 3T MRI from the 4-week post-therapy follow-up were co-registered to the radiotherapy planning CT scan by an automatic multi-modal rigid algorithm in MITK (Nolden et al., 2013). Subsequently, an experienced radiologist (DP, 8 years of experience) segmented the Gadolinium contrast enhancing (gdce) areas on T1-weighted 3T MRI together with hyperintense areas on FLAIR T2-weighted 3T MRI on pre- and post-therapy imaging. Necrosis was excluded carefully from the segmentation, resulting in the whole tumor area excluding necrosis. Finally, the segmentation derived from pre-therapy 3T MRI was co-registered to the initial (t_0) 7T ^{23}Na MRI, while the segmentation derived from the 4-week post-therapy 3T MRI was co-registered to 7T ^{23}Na MRI at both t_1 and t_2 to extract TSC values from the

TABLE 1 | Patient characteristics (*N* = 20).

	All patients (*N* = 20)	Initial progression (*N* = 9)	Initial stable disease (*N* = 7)	
Age (years)				
Median (IQR)	56.5 (47.8–61.2)	61 (58–68)	53 (45.5–60.5)	$p = 0.2$
Sex				
Male	11 (55%)	5	4	$p = 1.0$
Female	9 (45%)	4	3	
KPI (%)				
Median (IQR)	80 (70–90)	70 (70–92.5)	90 (85–90)	$p = 0.22$
IDH Status				
Wild type	18 (90%)	8	6	$p = 0.47$
Mutated	1 (5%)	0	1	
Unknown	1 (5%)	1		
MGMT methylation				
Not methylated	4 (20%)	1	2	$p = 1.0$
Methylated	10 (50%)	5	4	
Unknown	6 (30%)	3	1	
Recurrent disease				
Yes	9 (45%)	5	3	$p = 1.0$
No	11 (55%)	4	4	
Gross tumor resection				
Yes	10 (50%)	3	5	$p = 0.31$
No	10 (50%)	6	2	
RT				
60/2 Gy	9 (45%)	2	4	$p = 0.50$
40.05 Gy/2.67 Gy	2 (10%)	2	0	
Particle re-RT	9 (45%)	5	3	
Concurrent chemotherapy				
Yes	12 (60%)	5	5	$p = 0.63$
No	8 (40%)	4	2	
Initial response (3T MRI only)				
Progressive disease	9 (45%)	8	1	**$p = 0.002$**
Stable disease	5 (25%)	0	5	
Pseudoprogression	2 (10%)	1	1	
Not available	4	–	–	
OS (days)				
Median (IQR)	247.5 (150–389.8)	154 (124–258)	426 (322–576)	**$p = 0.005$**
PFS (days)				
Median (IQR)	92.5 (77.3–265.5)	78 (59–86)	267 (243–289)	**$p = 0.001$**
TSC				
Median (IQR)				
TSC t0 [absolute (mM)]	54.1 (46.6–58.1)	54.0 (39.2–58.8)	54.2 (50.1–58.3)	$p = 0.76$
TSC Δ t1–t0 (% of t0)	2.5 (−4.9 to 13.0)	1.1 (−5.8 to 9.6)	3.4 (−2.6 to 13.8)	$N = 7/7$, $p = 0.62$
TSC Δ t2–t0 (% of t0)	10.5 (1.1–22.5)	9.0 (−0.2 to 24.8)	11.9 (5.2–15.5)	$N = 5/5$, $p = 1.0$
TSC Δ t2–t1 (% of t1)	12.1 (3.2–19.2)	19.3 (14.0–24.3)	1.7 (−2.8 to 10.1)	$N = 5/5$, $p = 0.056$

Initial response to treatment was evaluated according to the response assessment in neuro-oncology working group (RANO) criteria. The tissue sodium concentration (TSC) was measured at three different time steps: t0, pre-treatment; t1, immediately post-treatment; t2, 6 weeks post-treatment. (N, total number; IQR, interquartile range; KPI, Karnofsky Performance Index; IDH, isocitrate-dehydrogenase; MGMT, O^6-methylguanine DNA methyltransferase; RT, radiotherapy; Gy, Gray; TMZ, Temozolomide; RBE, relative biological effectiveness; PD, progressive disease; SD, stable disease; PsPD, pseudoprogression; NA, not available; OS, overall survival; PFS, progression-free survival; TSC, tissue sodium concentration; Mm, mmol/l; Δ, difference).
Bold indicates statistically significant values with $p < 0.05$.

tumor region. An example of the tumor contouring and image registration procedures can be found in **Supplementary Figure 1**.

Response Assessment

Patients were routinely scheduled for clinical follow-up visits together with the 3T MRI examinations approximately 4 and 12 weeks post-therapy, as described above. These follow-up visits included thorough clinical examination as well as overall assessment of the radiological findings together with clinical information by a neurooncologist.

Study participants were classified as complete response (CR), partial response (PR), stable disease (SD), or progressive disease

(PD) based on radiographic findings and clinical information by the department of neuroradiology and neuro-oncology in accordance with the updated RANO criteria (Wen et al., 2010). To account for possible cases of PsPD, we followed the recommendations of the updated RANO criteria: Each PD in the first follow-up needed to be confirmed in the second follow-up or via biopsy (Wen et al., 2010). Performance of a biopsy was indicated clinically. If the second follow-up or biopsy did not confirm a PD, PsPD was stated. For further analysis, we additionally conducted a radiographic response assessment on clinical 3T MRI only with regard to signal changes (T1 pre- and post-contrast, T2-FLAIR) without using information on clinical status or histopathology (biopsy). A missed follow-up examination due to death or massive deterioration was counted as PD in both assessments.

PFS was calculated from the date of the baseline 7T ^{23}Na MRI (t_0) to the date of first progression or death from any cause. OS was calculated from the date of the baseline 7T ^{23}Na MRI (t_0) until death from any cause. At the time of statistical analysis, all patients had reached both endpoints.

Statistics

The median TSC inside the whole tumor area excluding necrosis was calculated at t_0, t_1, and t_2. Subsequently, the differences in median TSC between all-time steps were calculated. Those differences were normalized to the TSC of the earlier time step, yielding the normalized TSC changes. Clinical parameters, baseline median TSC at t_0 and the normalized TSC changes were compared between patients with initial SD and patients with initial PD using Fisher's exact test for non-continuous variables and Mann-Whitney *U*-tests for continuous variables. Furthermore, univariate proportional hazard models of PFS and OS were developed for different clinical and imaging parameters with the following predictor variables: patient age, sex, Karnofsky Performance Index (KPI), tumor recurrence (binary: recurrent, newly diagnosed), O^6-methylguanine DNA methyltransferase (MGMT) methylation (binary: yes, no), gross surgical resection (binary: yes, no), type of CRT (binary: standard of care, other), initial response according to RANO or radiographic findings only (binary: PD, SD), the baseline TSC at t_0 and the normalized TSC changes between all-time steps. The according hazard ratios (HR) and standard errors (SE) were calculated as maximum-likelihood estimates (MLE) and *p*-values were derived from the likelihood ratio test. In the proportional hazard model for PFS with RANO response status as predictor variable, MLEs for HRs did not converge and thus failed to yield a result. Hence, the corresponding univariate proportional hazard models employed Firth's penalized likelihood method and the computation of profile likelihood confidence intervals to yield valid estimates and *p*-values (Heinze and Ploner, 2002). All statistical evaluation employed R version 4.0.3.

Ethics

According to the declaration of Helsinki, this study received approval by the local ethics board (IRB number: S343/2016) and 7T MRI examinations were only initiated after a written informed consent was obtained from the patient.

RESULTS

According to the RANO criteria, the course of nine patients was classified as initial PD, whereas seven patients presented with initial SD, two of which with PsPD. One patient received post-treatment biopsy, which confirmed a PsPD. Four patients could not be classified due to cancelation of treatment or missing clinical follow-up. Classification according to changes on clinical 3T MRI only yielded similar results with two disagreements, thus showing a statistically significant association with the original RANO assessment ($p = 0.002$, **Table 1**).

Patients with initial PD showed a tendency toward higher age, lower KPI and fewer gross tumor resections, but no statistically significant differences were found between the initial PD and initial SD group concerning clinical baseline parameters. However, there was a statistically significant difference in PFS [Median PFS (IQR) (days): *PD* = 78 (59–86), *SD* = 267 (243–289), $p = 0.001$] and OS [Median OS (IQR) (days): *PD* = 154 (124–258), *SD* = 426 (322–576), $p = 0.005$] between the two groups (**Table 1**).

Descriptive analysis of TSC inside the whole tumor region excluding necrosis following treatment revealed a heterogeneous development over all patients (**Figure 1A**). The pre-therapy (t_0) median TSC did not differ significantly between cases of initial SD and initial PD according to RANO [Median TSC (IQR) (mM): *PD* = 54.04 (39.22–58.77), *SD* = 54.18 (50.14–58.34), $p = 0.76$]. Similarly, the normalized TSC changes did not show a statistically significant difference between cases of initial SD and initial PD according to RANO, but there was a tendency toward a stronger increase in TSC from t_1 to t_2 in early progressing tumors [Normalized ΔTSC_{t0-t1} (IQR): *PD* = 1.07% (−5.84 to 9.58%), *SD* = 3.42% (−2.62 to 13.8%), $p = 0.62$; normalized ΔTSC_{t0-t2} (IQR): *PD* = 8.99% (−0.24 to 24.84%), *SD* = 11.92% (5.15–15.49%), $p = 1$; normalized ΔTSC_{t1-t2} (IQR): *PD* = 19.27% (14.03–24.33%), *SD* = 1.68% (−2.83 to 10.11%), $p = 0.056$]. Similar results were obtained when analyzing uncorrected, absolute TSC values and differences (**Supplementary Figure 2** and **Supplementary Table 1**). **Table 1** and **Figure 1B** yield further details on the development of TSC following CRT for cases of initial SD and initial PD according to RANO. The discrepancy between findings on clinical 3T MRI and development of TSC is illustrated qualitatively for one patient case in **Figure 2**.

Univariate Cox proportional hazard models revealed that both the RANO criteria assessment of initial response as well as the 3T MRI only assessment of initial response yielded statistically significant predictors of PFS [RANO: HR (95% CI) = 0.02 (0.0001–0.21), $p = 7{\cdot}10^{-5}$; 3T MRI only: HR (95% CI) = 0.1 (0.02–0.49), $p = 0.0009$] and OS [RANO: HR (95% CI) = 0.17 (0.04–0.65), $p = 0.005$; 3T MRI only: HR (95% CI) = 0.26 (0.08–0.87), $p = 0.02$]. Furthermore, standard of care CRT was associated with significantly improved PFS [HR (95% CI) = 0.312 (0.1–1.0), $p = 0.046$]. Conversely, none of the TSC measures yielded a significant prediction of PFS or OS. **Table 2** provides detailed statistical findings of the survival analysis.

Since the evolution of TSC after treatment might have been influenced by prior treatments, we also conducted a descriptive analysis of TSC in newly diagnosed and recurrent tumors

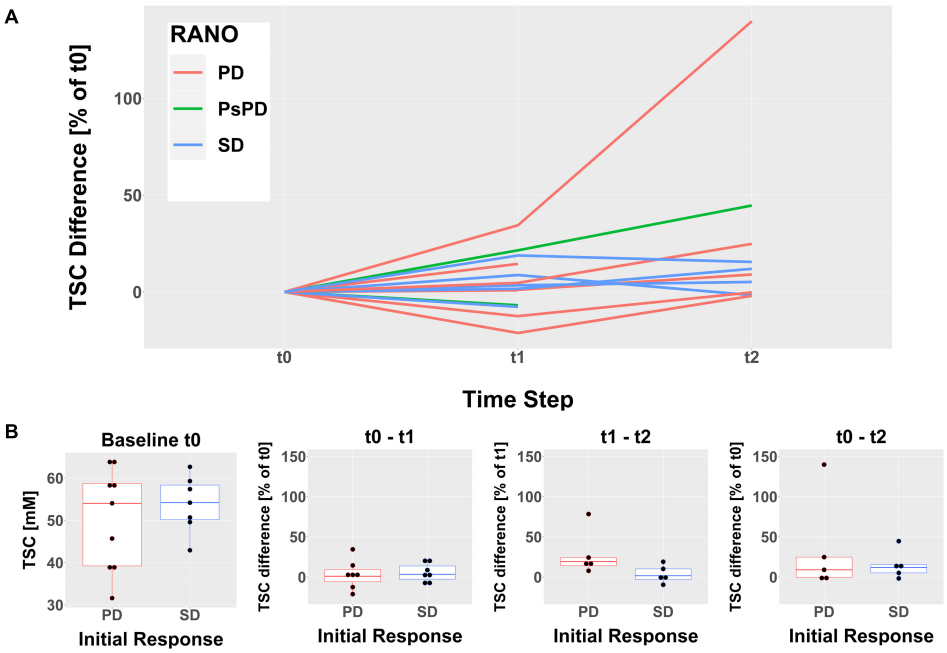

FIGURE 1 | Evolution of the median tissue sodium concentration (TSC) inside the whole tumor areas excluding necrosis following treatment. The time steps refer to the pre-therapy imaging (t_0), the follow-up immediately post-therapy (t_1) and the follow-up 6 weeks post-therapy (t_2). **(A)** The descriptive analysis shows a heterogeneous evolution of TSC for all patients that does not evidently reflect the RANO response evaluation. The differences between t_0 and t_1 (at time step t_1) as well as between t_0 and t_2 (at time step t_2) were normalized to the baseline TSC at t_0. **(B)** Boxplots showing the median TSC at t_0 (left) as well as the normalized TSC differences between all-time steps grouped by initial response according to RANO. None of the observed intergroup differences reached statistical significance.

separately. This small subgroup analysis did not reveal clear differences between newly diagnosed and recurrent tumors (**Supplementary Figure 3**).

DISCUSSION

To our knowledge, this is the first prospective investigation of ^{23}Na MRI at an ultra-high field strength of 7 T to evaluate treatment response in GBM patients. Our data demonstrates heterogeneous changes of TSC following CRT, which suggests that ^{23}Na MRI is sensitive to treatment-related effects. The TSC changes did not correlate with standard of care response assessment or clinical 3T MRI findings in general, so that ^{23}Na MRI might offer complementary biological information. However, the evaluation of TSC in the tumor did not enable a prediction of tumor progression or patient survival. Therefore, future investigations need to elucidate the reasons for treatment-related changes in TSC and their clinical value.

^{23}Na-Imaging and Origins of Altered Tissue Sodium Concentration

Compared to conventional proton MRI, ^{23}Na MRI is limited by a reduced SNR due to the approx. 10.000-fold lower concentration of ^{23}Na ions than protons in the human body (Shah et al., 2016; Regnery and Platt, 2021). SNR increases with increasing magnetic field strength, so that UHF-MRI scanners > 3T can significantly improve image quality in ^{23}Na MRI (Konstandin and Schad, 2014; Shah et al., 2016). Therefore, we employed an ultra-high field strength of 7T to optimize the SNR. Currently, more and more centers worldwide are acquiring UHF MRI scanners, which are likely to become increasingly applied in neuro-oncology, particularly to support ^{23}Na-imaging, in the near future (Platt et al., 2021).

TSC depends on intra- and extracellular volumes with the underlying ^{23}Na ion distribution (Ouwerkerk et al., 2003; Thulborn et al., 2009). Therefore, the significant elevation of TSC inside of gliomas (Turski et al., 1987; Ouwerkerk et al., 2003; Regnery et al., 2020) might be explained due to both higher intracellular ^{23}Na content of malignant cells (Cameron et al., 1980; Rotin et al., 1989) and enlarged extracellular space in gliomas (Bakay, 1970; Bruehlmeier et al., 2003; Zamecnik et al., 2004). The contribution of either compartment to the increased signal remains controversial (Ouwerkerk et al., 2003; Thulborn, 2016). Furthermore, it needs to be acknowledged that brain tumors can be accompanied by non-infiltrative peritumoral edema, blood brain barrier disruption and different tumor vascular structure, all of which might lead to an increased TSC as well (Turski et al., 1986, 1987; Driver et al., 2020).

Tissue Sodium Concentration as Response Predictor

Concerning treatment-related changes in TSC, previous findings from animal GBM models suggested that tumor TSC rises few days after an effective chemotherapy, which could reflect

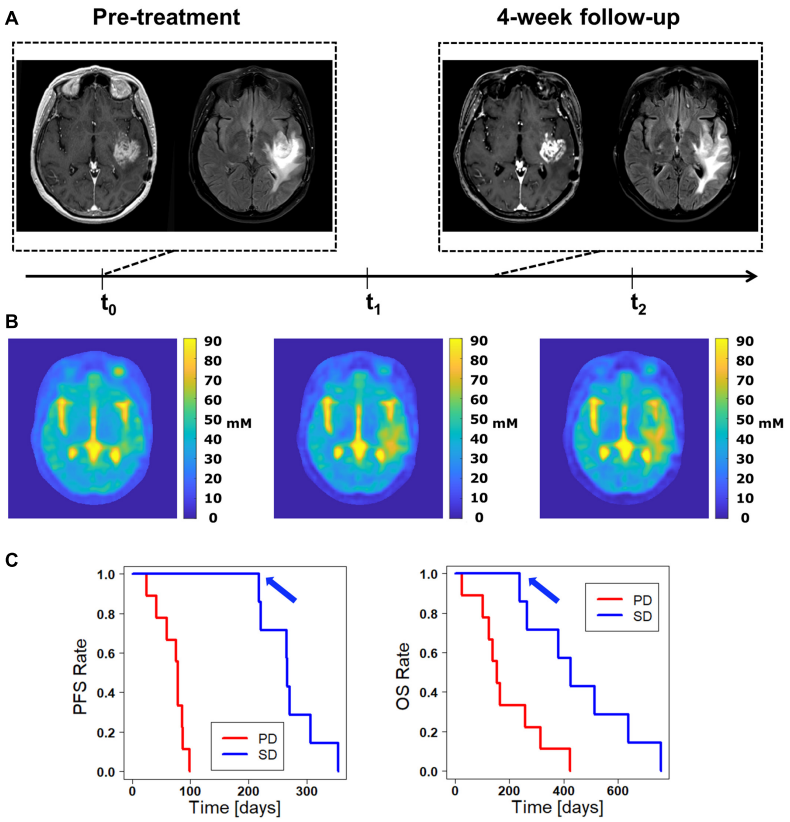

FIGURE 2 | Discrepancy between clinical 3T MRI and 7T ^{23}Na MRI. **(A)** The clinical 3T MRI of this patient presents only minor changes when comparing the pre-therapy baseline with the 4-week follow up, suggesting an initial stable disease (SD) according to the RANO criteria. **(B)** The tissue sodium concentration (TSC) shows a successive signal increase both inside the contrast enhancing region and within peritumoral edema. One could deduce a progressive disease (PD) with additional tumor infiltration and consecutively increased signal. On the other hand, a treatment response with successive tumor necrosis and reactive perifocal edema would also be a possible explanation. **(C)** The Kaplan-Meier curves for progression free survival (PFS, left) and overall survival (OS, right) show the significant prediction of PFS and OS by the RANO classification found in this study. Accordingly, the patient shown in A and B, which is rated as initial SD, lies on the favorable upper curve (blue arrow).

intracellular sodium overload or cellular shrinkage due to apoptosis and necrosis (Schepkin et al., 2005, 2006). Those preclinical studies investigated short time tumor response to few doses of chemotherapy without incorporating RT or a treatment protocol over several weeks. Nevertheless, similar tendencies were suggested by preliminary reports of clinical observations during radiotherapy (Thulborn et al., 2009). Moreover, several case reports revealed ^{23}Na signal changes inside gliomas following CRT which were different from findings in clinical imaging, but the underlying biochemical reasons remained undiscovered (Thulborn et al., 2009; Laymon et al., 2012; Haneder et al., 2015). Lastly, a recent clinical study of ^{23}Na MRI at 3T during concomitant CRT in GBM patients hypothesized that TSC may be used to measure tumor cell kill by longitudinal measurements of the brain volume with elevated TSC, representing the residual tumor volume, and its nominal TSC, which may be used to estimate the cell volume fraction (Thulborn et al., 2019).

This study found dichotomous changes of TSC-derived tumor volumes and suggested TSC as measure of tumor cell kill (Thulborn et al., 2019). However, a significant correlation between TSC and PFS was not found, which led the authors to conclude that tumor cell kill due to concomitant CRT alone might have a minor impact on survival when compared to the additional effect of adjuvant chemotherapy (Thulborn et al., 2019).

Our descriptive analysis revealed heterogeneous changes of TSC following (C)RT, which supports the idea that TSC quantifies different responses to treatment. Moreover, there was a trend toward a stronger TSC increase from t_1 to t_2 in early progressing tumors according to RANO criteria. Nevertheless, we did not find a significant correlation of the development of TSC with the clinical response assessments based on the RANO criteria. These findings agree with the previous reports which suggest that TSC generates information different from established clinical imaging (Laymon et al., 2012; Haneder et al., 2015; Thulborn et al., 2019). However, just as reported by the recent trial at 3T (Thulborn et al., 2019), TSC did not show a significant correlation with PFS or OS either. Our methods were complementary to this previous trial in many regards. TSC was measured at 7T, which provides a higher signal-to-noise-ratio (SNR). In addition, TSC was measured immediately after therapy (t_1) as well as 6-weeks post-therapy (t_2), therefore including later timepoints. Furthermore, our

TABLE 2 | Results of the statistical analysis: association with PFS and survival.

	Univariate proportional hazard model					
Variable	**Progression free survival**			**Overall survival**		
	N	**HR (95% CI)**	***p*-value**	**N**	**HR (95% CI)**	***p*-value**
Age	16	1.1 (1–1.1)	0.054	20	1 (0.99–1.1)	0.13
Sex	16	0.58 (0.19–1.8)	0.34	20	0.77 (0.29–2.1)	0.6
KPI	16	0.96 (0.92–1)	0.11	19	0.98 (0.94–1)	0.19
MGMT status	12	0.96 (0.25–3.7)	0.95	14	0.99 (0.3–3.3)	0.98
Recurrence	16	1.7 (0.57–5.1)	0.33	20	1.6 (0.65–4.2)	0.3
Resection	16	2.1 (0.71–6.0)	0.18	20	2.4 (0.94–6.2)	0.07
CRT	**16**	**0.31 (0.1–1)**	**0.046**	20	0.41 (0.16–1.1)	0.07
Response (RANO)	**16**	**0.02 (10^{-4}–0.21)***	**$6.6{\cdot}10^{-5}$***	**16**	**0.17 (0.04–0.65)**	**0.005**
Response (3T MRI w/o clinical data)	**16**	**0.1 (0.02–0.49)**	**0.0009**	**16**	**0.26 (0.08–0.87)**	**0.02**
TSC Median t0	16	0.98 (0.92–1.1)	0.62	20	1 (0.95–1.1)	0.85
TSC Δ t1–t0	14	0.97 (0.92–1)	0.27	14	0.97 (0.93–1)	0.24
TSC Δ t2–t0	10	1 (0.98–1)	0.83	10	0.99 (0.98–1)	0.51
TSC Δ t2–t1	10	1 (0.99–1.1)	0.25	10	1 (0.97–1)	0.96

N, number of patients; HR, hazard ratio; CI, confidence interval; KPI, Karnofsky Performance Index; MGMT, O^6-methylguanine DNA methyltransferase; CRT, chemoradiotherapy; TSC, tissue sodium concentration; Δ, relative TSC difference; t0, pre-therapy ^{23}Na MRI; t1, ^{23}Na MRI immediately post-therapy; t2, ^{23}Na MRI 6-weeks post-therapy.

**The corresponding analysis was based on Firth's penalized likelihood method with the computation of profile likelihood confidence intervals and p-values according to penalized likelihood ratio tests.*

Bold indicates statistically significant values with $p < 0.05$.

investigation encompassed the additional correlation of clinical classifications of response to therapy with PFS and OS, which yielded significant results.

Hence, TSC seems to reflect treatment effects which are not visible on clinical MRI, but a straightforward correlation with tumor cell kill has not been demonstrated yet. There was a trend toward a stronger TSC increase from t_1 to t_2 in early progressing GBM that could reach statistical significance in larger patient cohorts. However, TSC did not correlate with PFS and OS while clinical response correlated well with PFS and OS. Presumably, various factors besides mere tumor cell kill could have an overlapping influence on TSC, namely therapy-related non-infiltrative edema (Turski et al., 1986, 1987; Hashimoto et al., 1991; Ouwerkerk et al., 2003) and blood-brain-barrier disruption (Turski et al., 1986). Effective tumor cell kill may reduce blood brain barrier disruptions and brain edema, with a consecutive decrease of TSC in the corresponding regions (Thulborn et al., 2009). On the other hand, CRT itself can also cause blood brain barrier disruptions and brain edema, leading to the well-known pseudoprogressions with potential elevations of the TSC. Therefore, future approaches should aim to combine ^{23}Na MRI with proton MRI (e.g., diffusion-weighted imaging, perfusion-weighted imaging) to better understand different treatment effects besides tumor cell kill. Since ^{23}Na MRI offers information that is technically and biologically independent from established proton MRI applications, it might be highly useful in future multiparametric, machine-learning based approaches.

Limitations and Strengths

Several limitations of this study need to be acknowledged. Firstly, the patient cohort is relatively small and heterogeneous. Most patients had a comparatively poor prognosis due to a high number of relapsing tumors and only 50% gross tumor resections. This limits the power of our analysis. In addition, the use of different RT regimes could have led to different treatment reactions in normal tissues, e.g., different grades of blood brain barrier disruption. In particular, patients receiving (re-) radiotherapy of a relapsing GBM tend to experience pseudoprogressions and radionecrosis more often, and such treatment-related changes can confound the TSC. Nevertheless, all patients received RT as main treatment and the aim was to predict therapy response and survival, which should be possible if ^{23}Na MRI yields a straightforward measure of tumor cell kill. Clinical response assessments yielded a significant correlation with PFS and OS, whereas the TSC quantification in our setup failed to do so. However, it cannot be excluded that at higher SNR or higher spatial resolutions (e.g., due to $B_0 > 7$T, longer measurement times, use of array receiver coils) a correlation might become observable. Secondly, clinical 3T MRI and 7T ^{23}Na MRI were not performed at completely parallel follow-ups, which could have impeded the coregistration of the segmentations. In the past, different approaches have been used to analyze ^{23}Na MR images, mostly relying on segmentations defined on clinical MRI (Turski et al., 1986; Heinze and Ploner, 2002; Thulborn, 2016; Driver et al., 2020). A recent study investigating ^{23}Na MRI at 3T for response assessment in GBM patients used a semi-automatic approach to delineate tumor volumes directly on ^{23}Na images based on TSC cut-offs (which were created using clinical MRI) (Thulborn et al., 2019). This approach did not prove feasible in our data because of elevated TSC around CSF-spaces due to partial volume effects despite a high SNR at the 7T field strength. Lastly, the clinical assessment of treatment response might still be constrained by misclassifications due to pseudoprogression

despite following the RANO recommendations as current golden standard.

The strengths of this study include the prospective design and the use of a 7T ultra-high field scanner which offers high SNR compared to clinical field strengths. As opposed to previous studies that analyzed TSC changes over a short period of time, this study encompassed longitudinal TSC measurement up to 6 weeks after treatment. Furthermore, correlation with several clinical and radiographic parameters was performed to compare the predictive capacity of ^{23}Na MRI with clinical standard information.

DATA AVAILABILITY STATEMENT

The raw data supporting the conclusions of this article are available only upon scientific request because patient data are included. The corresponding author (DP) may be contacted to request the data.

ETHICS STATEMENT

The studies involving human participants were reviewed and approved by the University Heidelberg Institutional Review Board Alte Glockengießerei 11/1, 69115 Heidelberg, Germany. The patients/participants provided their written informed consent to participate in this study.

AUTHOR CONTRIBUTIONS

DP, SA, SRe, and NB: study conceptualization. NB and TP: technical methodology. DP, SRe, NB, and KD-H: examinations. SRe, NB, TP, NW, PW, and LK: data processing. SRe and DP: statistical analysis and writing first draft. SA, JD, H-PS, ML, SRi, WW, and MB: scientific supervision. All authors reviewing and editing first draft.

FUNDING

SRe was funded by the Physician-Scientist Program of Heidelberg University, Faculty of Medicine. DP receives funding from the German Research Foundation (DFG, project number 445704496).

ACKNOWLEDGMENTS

We thank Jessica Engelhart and Vanessa Peregovich for outstanding study assistance.

SUPPLEMENTARY MATERIAL

The Supplementary Material for this article can be found online at: https://www.frontiersin.org/articles/10.3389/fnins.2021.782516/full#supplementary-material

REFERENCES

Bakay, L. (1970). The extracellular space in brain tumours. I. Morphological considerations. *Brain* 93, 693–698. doi: 10.1093/brain/93.4.693

Behl, N. G., Gnahm, C., Bachert, P., Ladd, M. E., and Nagel, A. M. (2016). Three-dimensional dictionary-learning reconstruction of (23)Na MRI data. *Magn. Reson. Med.* 75, 1605–1616. doi: 10.1002/mrm.25759

Bruehlmeier, M., Roelcke, U., Blauenstein, P., Missimer, J., Schubiger, P. A., Locher, J. T., et al. (2003). Measurement of the extracellular space in brain tumors using 76Br-bromide and PET. *J. Nucl. Med.* 44, 1210–1218.

Cameron, I. L., Smith, N. K., Pool, T. B., and Sparks, R. L. (1980). Intracellular concentration of sodium and other elements as related to mitogenesis and oncogenesis in vivo. *Cancer Res.* 40, 1493–1500.

de Wit, M. C., de Bruin, H. G., Eijkenboom, W., Sillevis Smitt, P. A., and van den Bent, M. J. (2004). Immediate post-radiotherapy changes in malignant glioma can mimic tumor progression. *Neurology* 63, 535–537. doi: 10.1212/01.wnl.0000133398.11870.9a

Driver, I. D., Stobbe, R. W., Wise, R. G., and Beaulieu, C. (2020). Venous contribution to sodium MRI in the human brain. *Magn. Reson. Med.* 83, 1331–1338. doi: 10.1002/mrm.27996

Haneder, S., Giordano, F. A., Konstandin, S., Brehmer, S., Buesing, K. A., Schmiedek, P., et al. (2015). (2)(3)Na-MRI of recurrent glioblastoma multiforme after intraoperative radiotherapy: technical note. *Neuroradiology* 57, 321–326. doi: 10.1007/s00234-014-1468-2

Hashimoto, T., Ikehira, H., Fukuda, H., Yamaura, A., Watanabe, O., Tateno, Y., et al. (1991). In vivo sodium-23 MRI in brain tumors: evaluation of preliminary clinical experience. *Am. J. Physiol. Imaging* 6, 74–80.

Heinze, G., and Ploner, M. (2002). SAS and SPLUS programs to perform Cox regression without convergence problems. *Comput. Methods Programs Biomed.* 67, 217–223. doi: 10.1016/s0169-2607(01)00149-3

Insko, E. K., and Bolinger, L. (1993). Mapping of the Radiofrequency Field. *J. Magn. Reson. A.* 103, 82–85. doi: 10.1006/jmra.1993.1133

Johnson, D. R., Guerin, J. B., Ruff, M. W., Fang, S., Hunt, C. H., Morris, J. M., et al. (2019). Glioma response assessment: classic pitfalls, novel confounders, and emerging imaging tools. *Br. J. Radiol.* 92:20180730. doi: 10.1259/bjr.20180730

Konstandin, S., and Schad, L. R. (2014). 30 Years of sodium/X-nuclei magnetic resonance imaging. *MAGMA* 27, 1–4. doi: 10.1007/s10334-013-0426-z

Laymon, C. M., Oborski, M. J., Lee, V. K., Davis, D. K., Wiener, E. C., Lieberman, F. S., et al. (2012). Combined imaging biomarkers for therapy evaluation in glioblastoma multiforme: correlating sodium MRI and F-18 FLT PET on a voxel-wise basis. *Magn. Reson. Imaging* 30, 1268–1278. doi: 10.1016/j.mri.2012.05.011

Nagel, A. M., Laun, F. B., Weber, M. A., Matthies, C., Semmler, W., and Schad, L. R. (2009). Sodium MRI using a density-adapted 3D radial acquisition technique. *Magn. Reson. Med.* 62, 1565–1573. doi: 10.1002/mrm.22157

Nolden, M., Zelzer, S., Seitel, A., Wald, D., Muller, M., Franz, A. M., et al. (2013). The medical imaging interaction toolkit: challenges and advances : 10 years of open-source development. *Int. J. Comput. Assist. Radiol. Surg.* 8, 607–620. doi: 10.1007/s11548-013-0840-8

Ouwerkerk, R., Bleich, K. B., Gillen, J. S., Pomper, M. G., and Bottomley, P. A. (2003). Tissue sodium concentration in human brain tumors as measured with 23Na MR imaging. *Radiology* 227, 529–537. doi: 10.1148/radiol.2272020483

Perry, J. R., Laperriere, N., O'Callaghan, C. J., Brandes, A. A., Menten, J., Phillips, C., et al. (2017). Short-course radiation plus Temozolomide in elderly patients with glioblastoma. *N. Engl. J. Med.* 376, 1027–1037. doi: 10.1056/NEJMoa1611977

Platt, T., Ladd, M. E., and Paech, D. (2021). 7 Tesla and beyond: advanced methods and clinical applications in magnetic resonance imaging. *Invest. radiol.* 56, 705–725. doi: 10.1097/rli.0000000000000820

Regnery, S., Behl, N. G. R., Platt, T., Weinfurtner, N., Windisch, P., Deike-Hofmann, K., et al. (2020). Ultra-high-field sodium MRI as biomarker for tumor extent, grade and IDH mutation status in glioma patients. *Neuroimage Clin.* 28:102427. doi: 10.1016/j.nicl.2020.102427

Regnery, S., and Platt, T. (2021). [Perspectives of X-nuclei magnetic resonance imaging in neuro-oncology]. *Radiologe* 61, 36–42. doi: 10.1007/s00117-020-00753-8

Rotin, D., Steele-Norwood, D., Grinstein, S., and Tannock, I. (1989). Requirement of the Na+/H+ exchanger for tumor growth. *Cancer Res.* 49, 205–211.

Schepkin, V. D., Lee, K. C., Kuszpit, K., Muthuswami, M., Johnson, T. D., Chenevert, T. L., et al. (2006). Proton and sodium MRI assessment of emerging tumor chemotherapeutic resistance. *NMR Biomed.* 19, 1035–1042. doi: 10.1002/nbm.1074

Schepkin, V. D., Ross, B. D., Chenevert, T. L., Rehemtulla, A., Sharma, S., Kumar, M., et al. (2005). Sodium magnetic resonance imaging of chemotherapeutic response in a rat glioma. *Magn. Reson. Med.* 53, 85–92. doi: 10.1002/mrm.20332

Shah, N. J., Worthoff, W. A., and Langen, K. J. (2016). Imaging of sodium in the brain: a brief review. *NMR Biomed.* 29, 162–174. doi: 10.1002/nbm.3389

Stupp, R., Hegi, M. E., Mason, W. P., van den Bent, M. J., Taphoorn, M. J., Janzer, R. C., et al. (2009). Effects of radiotherapy with concomitant and adjuvant temozolomide versus radiotherapy alone on survival in glioblastoma in a randomised phase III study: 5-year analysis of the EORTC-NCIC trial. *Lancet Oncol.* 10, 459–466. doi: 10.1016/s1470-2045(09)70025-7

Stupp, R., Mason, W. P., van den Bent, M. J., Weller, M., Fisher, B., Taphoorn, M. J., et al. (2005). Radiotherapy plus concomitant and adjuvant temozolomide for glioblastoma. *N. Engl. J. Med.* 352, 987–996. doi: 10.1056/NEJMoa043330

Thulborn, K. R. (2016). Quantitative sodium MR imaging: a review of its evolving role in medicine. *Neuroimage* 168, 250-268. doi: 10.1016/j.neuroimage.2016.11.056

Thulborn, K. R., Lu, A., Atkinson, I. C., Damen, F., and Villano, J. L. (2009). Quantitative sodium MR imaging and sodium bioscales for the management of brain tumors. *Neuroimaging Clin. N. Am.* 19, 615–624. doi: 10.1016/j.nic.2009.09.001

Thulborn, K. R., Lu, A., Atkinson, I. C., Pauliah, M., Beal, K., Chan, T. A., et al. (2019). Residual tumor volume, cell volume fraction, and tumor cell kill during fractionated chemoradiation therapy of human glioblastoma using quantitative sodium MR imaging. *Clin. Cancer Res.* 25, 1226–1232. doi: 10.1158/1078-0432.ccr-18-2079

Turski, P. A., Houston, L. W., Perman, W. H., Hald, J. K., Turski, D., Strother, C. M., et al. (1987). Experimental and human brain neoplasms: detection with in vivo sodium MR imaging. *Radiology* 163, 245–249. doi: 10.1148/radiology.163.1.3029803

Turski, P. A., Perman, W. H., Hald, J. K., Houston, L. W., Strother, C. M., and Sackett, J. F. (1986). Clinical and experimental vasogenic edema: in vivo sodium MR imaging. Work in progress. *Radiology* 160, 821–825. doi: 10.1148/radiology.160.3.3090615

Wen, P. Y., Macdonald, D. R., Reardon, D. A., Cloughesy, T. F., Sorensen, A. G., Galanis, E., et al. (2010). Updated response assessment criteria for high-grade gliomas: response assessment in neuro-oncology working group. *J. Clin. Oncol.* 28, 1963–1972. doi: 10.1200/jco.2009.26.3541

Zamecnik, J., Vargova, L., Homola, A., Kodet, R., and Sykova, E. (2004). Extracellular matrix glycoproteins and diffusion barriers in human astrocytic tumours. *Neuropathol. Appl. Neurobiol.* 30, 338–350. doi: 10.1046/j.0305-1846.2003.00541.x

Conflict of Interest: NB was employed by the company Siemens Healthcare GmbH.

The remaining authors declare that the research was conducted in the absence of any commercial or financial relationships that could be construed as a potential conflict of interest.

Publisher's Note: All claims expressed in this article are solely those of the authors and do not necessarily represent those of their affiliated organizations, or those of the publisher, the editors and the reviewers. Any product that may be evaluated in this article, or claim that may be made by its manufacturer, is not guaranteed or endorsed by the publisher.

Copyright © 2021 Paech, Regnery, Platt, Behl, Weckesser, Windisch, Deike-Hofmann, Wick, Bendszus, Rieken, König, Ladd, Schlemmer, Debus and Adeberg. This is an open-access article distributed under the terms of the Creative Commons Attribution License (CC BY). The use, distribution or reproduction in other forums is permitted, provided the original author(s) and the copyright owner(s) are credited and that the original publication in this journal is cited, in accordance with accepted academic practice. No use, distribution or reproduction is permitted which does not comply with these terms.

frontiers in Neurology

ORIGINAL RESEARCH
published: 06 December 2021
doi: 10.3389/fneur.2021.747072

Combined Application of Sodium Fluorescein and Neuronavigation Techniques in the Resection of Brain Gliomas

*Zhan Xue[1], Lu Kong[2], Shuyu Hao[1], Yu Wang[1], Guijun Jia[1], Zhen Wu[1], Wang Jia[1], Junting Zhang[1] and Liwei Zhang[1]**

[1] Department of Neurosurgery, Beijing Tiantan Hospital, Capital Medical University, Beijing, China, [2] Department of Neurosurgery, Qingdao Municipal Hospital, Qingdao, China

Objectives: To explore the effectiveness and safety of the combined application of sodium fluorescein and neuronavigation techniques in the resection of brain gliomas in different locations and patients of different ages.

Methods: Fifty clinical cases of brain gliomas treated at the Department of Neurosurgery of Beijing Tiantan Hospital were collected from March 2014 to March 2019. These cases were divided into a supratentorial group (24 cases) and a brainstem group (26 cases) based on location and an adult group (28 cases) and a pediatric group (22 cases) based on age. Fluorescein-guided surgery was performed: the adult group received 5 mg/kg sodium fluorescein before opening the dura, while the pediatric group received 2.5 mg/kg during resection. Tumor visualization was evaluated by the enhancement of yellow fluorescein and considered "satisfactory" if the illumination demarcated the tumor boundary. Additionally, the consistency between fluorescein and neuronavigation was analyzed. The Karnofsky performance score (KPS) of all patients was recorded and assessed at admission, discharge, and the 6-month follow-up.

Results: In the 28 adult cases, 4 were unsatisfactory, while in the 22 pediatric cases, 2 were unsatisfactory; in 7 cases, there was an inconsistency between yellow fluorescein enhancement and neuronavigation, 6 were in the supratentorial group, and 1 was in the brainstem group. Statistical analysis showed no significant differences in the satisfactory rate between the adult and pediatric groups ($P = 0.575$), whereas there were significant differences inconsistency between the supratentorial group and brainstem group ($P = 0.031$). The mean KPS at admission was between 70 and 100, which was not significantly different from that at discharge ($P = 0.839$), but the KPS at the 6-month follow-up was significantly higher than that at admission ($P = 0.041$).

Conclusions: The consistency between sodium fluorescein and the neuronavigation system was higher in the brainstem group than in the supratentorial group; a half dose of sodium fluorescein (2.5 mg/kg) was sufficient for pediatric patients. The combined utilization of sodium fluorescein and neuronavigation techniques may confer glioma patients the opportunity to obtain better clinical outcomes after surgery.

Keywords: brain glioma, sodium fluorescein, fluorescein guided surgery, neuronavigation, treatment outcome

OPEN ACCESS

Edited by:
Alexandra Golby, Harvard Medical School, United States

Reviewed by:
Miguel Idoate, University of Seville, Spain
Neda Haj-Hosseini, Linköping University, Sweden

****Correspondence:***
Liwei Zhang
zlwtt@aliyun.com

Specialty section:
This article was submitted to Neuro-Oncology and Neurosurgical Oncology, a section of the journal Frontiers in Neurology

Received: *25 July 2021*
Accepted: *01 November 2021*
Published: *06 December 2021*

Citation:
Xue Z, Kong L, Hao S, Wang Y, Jia G, Wu Z, Jia W, Zhang J and Zhang L (2021) Combined Application of Sodium Fluorescein and Neuronavigation Techniques in the Resection of Brain Gliomas. Front. Neurol. 12:747072. doi: 10.3389/fneur.2021.747072

INTRODUCTION

Gliomas can occur in different locations and patients of different ages. For tumors located in the brain stem or adhering to supratentorial functional regions, the purpose of surgery should be to maximize tumor resection while preserving important neurological functions. Therefore, demarcation of the tumor boundary from surrounding normal tissue is essential for the safe removal of the lesion. In recent years, many techniques made great contributions to tumor positioning and imaging, such as sodium fluorescein (FL), 5-aminolevulinic acid (5-ALA), and neuronavigation, all of which resulted in much safer and more effective resection of brain gliomas, leading to better outcome to the patients (1–3). Because of low cost, sodium fluorescein technology is wider applied in developing countries than 5-ALA. However, because of the diversity of anatomic structures in different intracranial areas, the accuracy and consistency of fluorescence and neuronavigation technology in different brain locations is still undetermined. In addition, although it has been proven that 5 mg/kg sodium fluorescein is effective for demarcating the tumor margin in adults while 2.5 mg/kg is sufficient for pediatric patients, a comparative observation is still needed between adult and pediatric cases with different doses of sodium fluorescein to clarify the effect of imaging (4, 5).

In this study, we retrospectively analyzed 50 cases of intracranial gliomas treated in Beijing Tiantan Hospital, Capital Medical University, from March 2014 to March 2019 to evaluate the effectiveness and safety of the combined application of sodium fluorescein and neuronavigation systems in different tumor locations and patients of different ages.

EXPERIMENTAL SECTION

Patients Selection and Grouping

In this study, we retrospectively reviewed patients diagnosed with intracranial glioma who were treated in the Department of Neurosurgery of Beijing Tiantan Hospital between March 2014 and March 2019. Inclusion criteria were as follows: (1) newly diagnosed or suspicious, untreated gliomas; (2) the lesions were adhered to supratentorial areas or located in the brainstem areas; (3) brainstem lesions should be identified as a focal exophytic tumor and remarkably enhanced on MRI; (4) Karnofsky performance score (KPS) $\geq$ 70. Exclusion criteria included: (1) histological diagnosis other than glioma; (2) previously treated, recurrent tumors; (3) diffuse intrinsic or unresectable brainstem gliomas without or with mild enhancement on MRI after contrast; (4) KPS $<$ 70; (5) medical conditions that prevent the surgery or use of sodium fluorescein, such as coagulopathy, renal and hepatic dysfunction.

According to the inclusion and exclusion criteria, we identified 50 patients with gliomas (27 men and 23 women), such as 16 glioblastomas, 21 anaplastic astrocytomas, 8 oligodendrogliomas, and 5 pilocytic astrocytomas. All the patients were divided into a supratentorial group (24 cases) and a brainstem group (26 cases) based on tumor location, and an adult group (28 cases, mean age 50.5 years, range 21–64 years) and a pediatric group (22 cases, mean age 9.1 years, range 2–14 years) based on age.

Clinical and Radiological Evaluation

Clinical data at admission, discharge, and 3 months of follow-up were recorded and analyzed. For the supratentorial group, eight tumors were in the frontal lobe, six in the temporal lobe, seven in the thalamus, and three in the multiple lobes, with the main presenting symptoms being headache, movement disorder, and epilepsy (**Figure 1**). In the brainstem group, five tumors were in the midbrain, 16 in the pontine, and five in the medulla oblongata, and the main presenting symptoms were paralysis, diplopia, and dysphagia (**Figure 2**). Pre- and post-contrast MRI was performed no earlier than 5 days before the surgery and no later than 3 days after the surgery. Diffusion tensor imaging was merged into the neuronavigation system (StealthStation, Medtronic, Minneapolis, USA) if the tumor adhered to or infiltrated critical areas.

Surgical Protocol

After general anesthesia, 0.05 ml of 10% sodium fluorescein was used to perform a sensitivity test. The intraoperative use of sodium fluorescein was allowed if the test was negative. Before opening the dura, a dose of 5 mg/kg for the adult group and 2.5 mg/kg for the pediatric group was injected through the central vein. Microsurgery was performed under a PENTERO 900 microscope (Carl Zeiss, Oberkochen, Germany) equipped with a YELLOW 560 nm filter, which allowed for switching the illumination between fluorescence and white light. The neuronavigation system (Medtronic, Minneapolis, USA) was routinely used for approach planning, tumor localization, and margin demarcation. Electrophysiological monitoring was used for the tumors near or invading the functional areas. The surgical procedures were performed by the same group of neurosurgeons, and the chief surgeon was responsible for judging the effectiveness of sodium fluorescein as "satisfactory" or "unsatisfactory." "Satisfactory" was defined as the tumor being visualized as a yellow color by sodium fluorescein and clearly different from the surrounding normal tissue, while "unsatisfactory" was considered to be a mild enhancement, vague visualization, or blurred tumor-brain interface. The tumor was removed with standard microsurgical techniques. At the end of resection, the consistency between the fluorescein guide and the neuronavigation guide was carefully compared by detecting the tumor margin with the probe under the fluorescein mode of the microscope. A "consistency" was determined if the distance of the tumor margin measured by the two techniques was $<$2 mm, while 2 mm or more of a brain shift was considered an "inconsistency." All patients were followed up in the neurological intensive care unit after surgery and were transferred to the regular ward as soon as their condition became relatively stable.

Extent of Resection

Gross total resection (GTR) was defined as no residual tumors seen on postoperative MRI, near-total resection (NTR) was defined as $<$5% of the tumor volume compared with the

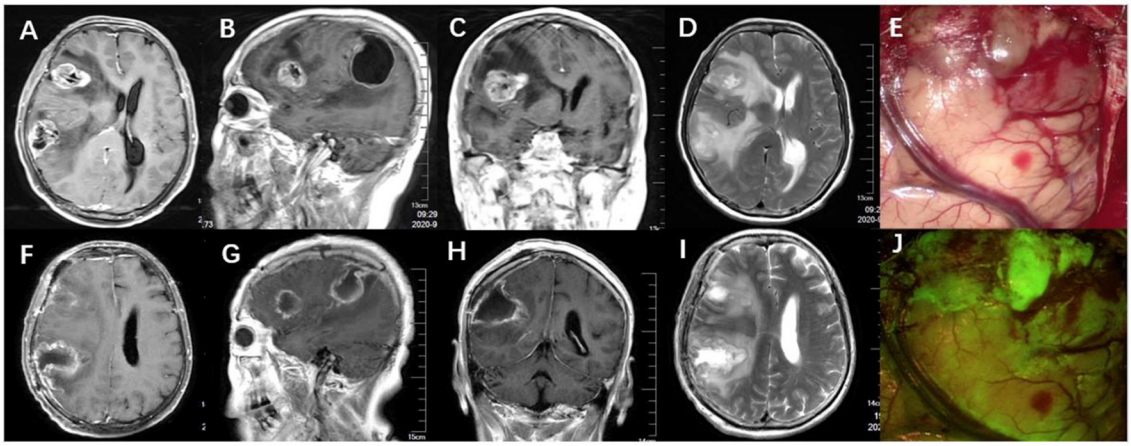

FIGURE 1 | (A–D) Preoperative MRI scan (axial, coronal, sagittal T1-weighted with gadolinium, and T2-weighted) showed adult multifocal glioblastoma. **(F–I)** Postoperative MRI showed complete tumor removal and relief of peritumoral edema. **(E,J)** During the surgery, the tumor tissue was stained yellowish green under the fluorescein mode of the microscope and was demarcated from normal brain tissue.

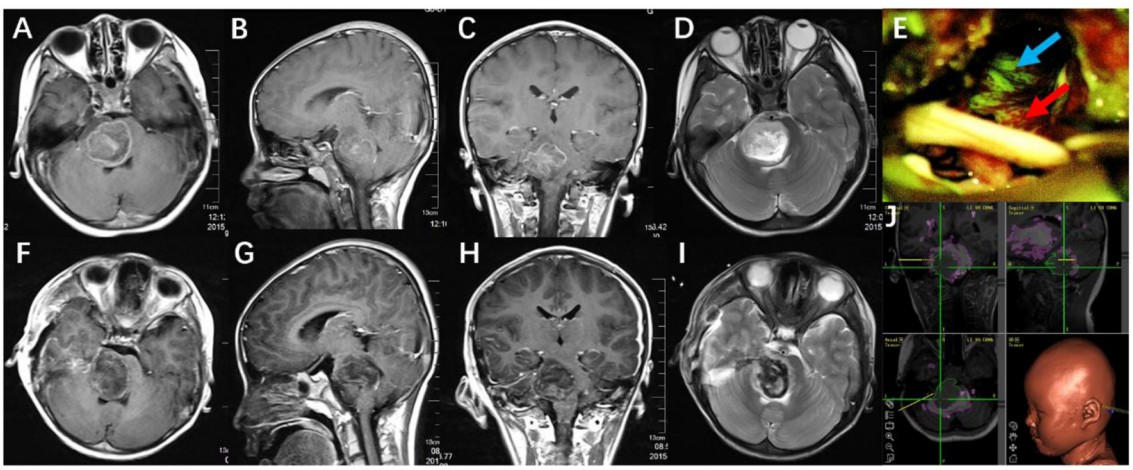

FIGURE 2 | (A–D) Preoperative MRI scan (axial, coronal, sagittal T1-weighted with gadolinium, and T2-weighted) showed a pediatric anaplastic astrocytoma in the right pons. **(F–I)** Postoperative MRI showed subtotal tumor resection. **(E)** Tumor was visualized under the YELLOW 560 nm filter (blue arrow showed tumor, red arrow showed brain tissue). **(J)** The surgical plan was made with the assistance of neuronavigation, revealing the relationship between the tumor, white matter tracts, and brainstem nuclei.

preoperative MRI, subtotal resection was defined as 5–10% residual tumor, and partial resection was defined as more than 10% of residual tumor. Tumor volume (V) was calculated by the formula $V = A \times B \times C/2$, which was determined by measuring the maximal length of axial (A), sagittal (B), and coronal (C) scans of preoperative and postoperative MRI by a vendor-provided software settled in the medical system.

Ethical Approval

The study was conducted in accordance with the *Declaration of Helsinki* and was approved by the Ethics Committee of Beijing Tiantan Hospital (No. KY 2019-115-01). Written informed consent was obtained from each patient (or the legal guardian of pediatric patients) before enrollment in the study.

RESULTS

Extent of Resection

All tumors showed enhancement on preoperative MRI, so the extent of resection (EOR) could be confirmed by comparing pre and postoperative MRI. In a total of 50 patients, GTR was achieved in 41 patients, constituting 82% of the cohort. Residual tumors (all defined as NTR) were detected in nine cases, mostly due to the remarkable adhesion or invasion of the tumors to the functional cerebral areas or brainstem nuclei.

Intraoperative Fluorescence and Navigation Characteristics

During the 50 tumor resection surgeries, 44 of the tumors were enhanced vividly by sodium fluorescein and stained

TABLE 1 | Visualization effect by fluorescence.

Group	Division	Satisfactory		Satisfactory rate	*P*
		Yes	No		
Age	Pediatric	20	2	90.91%	0.575
	Adult	24	4	85.71%	
Location	Supratentorial	20	4	83.33%	0.329
	Brainstem	24	2	92.31%	
Sex	Male	24	3	88.89%	0.834
	Female	20	3	86.96%	

TABLE 2 | Consistency between fluorescein and neuronavigation.

Group	Division	Consistency		*P*
		Consistent	Inconsistent	
Age	Pediatric	21	1	0.088
	Adult	22	6	
Location	Supratentorial	18	6	0.031
	Brainstem	25	1	
Sex	Male	22	5	0.318
	Female	21	2	

yellowish-green under the fluorescein mode of the microscope. Twenty-four tumors from the adult group and 20 from the pediatric group were identified as "satisfactory" by the neurosurgeons. Two "unsatisfactory" cases from the pediatric group were pilocytic astrocytomas, while four from the adult group were oligodendrogliomas. For the cases that identified "satisfactory," sodium fluorescein made the tumors recognizable enough to help the surgeons dissociate the lesion from the non-fluorescent surrounding tissue. No technical difficulties were found when switching the illumination between white light and fluorescence with one button on the grip. When comparing the consistency between fluorescein and neuronavigation, we found that the tumor margin distances measured independently by the two methods were not consistent in seven cases: six cases were from the supratentorial group and one from the brainstem group (**Figure 2**). Statistical analysis showed no significant differences between the adult group and pediatric group on the satisfactory visualization rate by fluorescence ($P = 0.575$), but significant differences were observed between the supratentorial group and brainstem group on consistency between fluorescein and neuronavigation ($P = 0.031$) (**Tables 1**, **2**).

Follow Up

The statistical analysis showed no significant differences between the patients' KPS at discharge and admission ($P = 0.839$), but the KPS of the patients at the 6-month follow-up was significantly higher than that at admission ($P = 0.041$) (**Table 3**).

TABLE 3 | Karnofsky performance score of the patients.

Observation time	KPS			
	70	80	90	100
Admission	10	15	16	9
Discharge	9	17	17	7
6 months follow up	1	17	20	12

DISCUSSION

Brain glioma is the most common malignant brain tumor occurring in both adult and pediatric patients. Glioma can grow in various locations in the brain tissue. For lesions found adhering to functional cerebral regions or focally invading the brain stem near important nuclei (often named exophytic brainstem gliomas), the treatment strategy remains challenging. Although there has been significant progress in radiotherapy, chemotherapy, and even immunotherapy, surgery is still considered the preferred treatment for cerebral or exophytic brainstem gliomas if the patients have no surgical contraindication (6–8). With the popularization of advanced adjuvant techniques, such as neuronavigation, neurophysiological monitoring, and intraoperative MRI, the safety and effectiveness of surgeries have greatly improved. However, for most neurosurgeons, "having a clear visual field" during tumor resection is one of the most essential principles, resulting in a higher resection rate, less risk of intraoperative hemorrhage, and better neurological status after surgery. Sodium fluorescein, indocyanine green (ICG), and 5-aminolevulinic acid (5-ALA) are the most often used reagents for intraoperative visualization during tumor removal. In 1998, 5-ALA was first reported in the resection of gliomas by Stummer et al. (9), which have significantly proven to improve the EOR of high-grade gliomas (2). Although 5-ALA has been approved by the FDA for glioma surgery in 2017 (10), in some developing countries like China, it is expensive in reagent purchasing and microscope upgrading. In comparison to ICG, fluorescein-guided surgery has obvious advantages, such as continued microsurgical work in filter mode, low cost, and easy preparation before surgery (11). The fluorescein technique was first introduced in 1947 for clinical use in brain tumor resection (12), and after the YELLOW 560 nm filter mode for microscopes was developed in 2012, the application of fluorescein-guided surgery blossomed. At present, the intraoperative fluorescein visualization technique has been applied in the resection of high-grade gliomas (1, 13), cerebral metastases (14, 15), primary central nervous system lymphomas (16), and gangliogliomas (11). Until February 2018, at least 1,099 patients with brain tumors underwent surgery with the assistance of fluorescein, mostly after 2012 (17).

The basic theory of fluorescence visualization for intracranial malignant tumors is that fluorescein can penetrate the incomplete blood–brain barrier. In 1982, Murray reported the application of sodium fluorescein for the resection of malignant brain tumors, with 84.7% sensitivity and 94.7% specificity for the fluorescein guidance (18). Shinoda and Koc also reported studies utilizing the sodium fluorescein in the glioblastoma surgery and found it "simple and safe" during the tumor resection (19, 20). In 2013, Acerbi first reported

that fluorescein-guided surgery for grade IV gliomas under a specific microscope equipped with a filter (YELLOW 560 nm) and concluded that advances in microscope technology could help better visualize the tumor (21). In 2017, the FLUOGLIO study confirmed that the fluorescein-guided technique with a dedicated filter on the surgical microscope is safe and enables a high percentage of contrast-enhancing tumors in patients with high-grade gliomas (22). Bowden analyzed the relationship between areas of fluorescence and pathology and showed that samples from areas of fluorescence demonstrated greater total cell density and higher Ki-67 (23). However, in the same study, they also found 11 cases of non-tumor tissue appeared illumination by the fluorescein. In our study, by utilizing sodium fluorescein, 44 cases (88%) were considered "satisfactory" in demarcating the tumor boundary, with a relatively high resection rate. The "unsatisfactory" cases in our study were pilocytic astrocytomas and oligodendrogliomas, which may verify the theory that the fluorescein cannot penetrate sufficiently through the blood–brain barrier in low-grade gliomas, which is in line with the published studies (1, 13, 21, 22). Also we found that the fluorescence characteristics were irrelevant to the location of the lesions, which may indicate that fluorescein is useful in various areas of brain tissue; luminance may only be correlated with malignancy.

Other factors that influence fluorescence visualization are the dose of sodium fluorescein and the delivery time (24). In the early stage of the study, the dose was 20 mg/kg to visualize the tumor by the naked eye and under the white light (15, 19, 20). However, some authors criticized that a high dose of sodium fluorescein may cause allergic shock (25). After using a microscope in the filter mode, the dose was further reduced to 5 mg/kg (1). In our previous report, 12 pediatric patients with exophytic brainstem glioma were given sodium fluorescein at 2.5 mg/kg and showed satisfactory fluorescence images without adverse effects (5). In this study, we found no differences between the adult group (5 mg/kg) and pediatric group (2.5 mg/kg) in the fluorescence visualization, which indicated that a half dose in children can achieve a similar degree of visualization as in the adult, which may further improve safety and reduce adverse effects. Sodium fluorescein was usually administered during anesthesia induction, incision of the scalp, opening of the dura, or exposure of the tumor (17). In our study, sodium fluorescein was administered intravenously when opening the dura, which was proven reasonable in achieving the satisfactory fluorescein images.

Neuronavigation has often been utilized during surgery for brain tumor resection since it was first developed and reported by Roberts in 1986 (26). One of the advantages of the neuronavigation to glioma surgery is that, with the help of a preoperative plan, it allows neurosurgeons to recognize nuclei and white matter fibers that are invisible under the microscope and thus may result in the better neurological outcomes. However, the primary disadvantage of neuronavigation is the "brain shift." In the older series, the shift was reported to be more than 10 mm (3). With the updates in navigation equipment, the range of system error was reduced. In our study, we identified 2 mm or less as the system error and found more inconsistency between fluorescein and navigation in tumors located in the supratentorial areas than in the brainstem areas. This may indicate that the accuracy for neuronavigation in the supratentorial area is not reliable and requires more attention when combined with sodium fluorescein.

In our study, EOR was not compared with the cases not applied with sodium fluorescein or navigation, which is beyond the scope of this study and will be evaluated in future research. The KPS is very important in measuring the quality of life of patients. In our study, the KPS at discharge was not higher than that at admission but significantly improved at the 6-month follow-up. The reason for this may be the vulnerability of the nerve tract and nuclei, which may be temporarily impaired shortly after the operation.

CONCLUSIONS

Our data and surgical experiences verified the feasibility and safety of sodium fluorescein in surgery for brain gliomas. For different tumor locations, the consistency between sodium fluorescein and neuronavigation techniques was higher in the brainstem group than in the supratentorial group. A half dose of sodium fluorescein (2.5 mg/kg) is adequate for the pediatric patients to obtain comparable images similar to that of adults. The combined utilization of sodium fluorescein and neuronavigation techniques may confer glioma patients with opportunities to obtain better clinical outcomes after surgery.

DATA AVAILABILITY STATEMENT

The original contributions presented in the study are included in the article/supplementary material, further inquiries can be directed to the corresponding authors.

ETHICS STATEMENT

The studies involving human participants were reviewed and approved by Ethics Committee of Beijing Tiantan Hospital. Written informed consent to participate in this study was provided by the participants' legal guardian/next of kin. Written informed consent was obtained from the individual(s), and minor(s)' legal guardian/next of kin, for the publication of any potentially identifiable images or data included in this article.

AUTHOR CONTRIBUTIONS

All authors listed have made a substantial, direct, and intellectual contribution to the work and approved it for publication.

FUNDING

This study was supported by grants from Beijing Hospital Authority Incubation Program (PX2019017).

REFERENCES

1. Acerbi F, Cavallo C, Broggi M, Cordella R, Anghileri E, Eoli M, et al. Fluorescein-guided surgery for malignant gliomas: a review. *Neurosurg Rev.* (2014) 37:547–57. doi: 10.1007/s10143-014-0546-6
2. Stummer W, Pichlmeier U, Meinel T, Wiestler OD, Zanella F, Reulen HJ. ALA-Glioma Study Group. Fluorescence-guided surgery with 5-aminolevulinic acid for resection of malignant glioma: a randomized controlled multicenter phase III trial. *Lancet Oncol.* (2006) 7:392–401. doi: 10.1016/S1470-2045(06)70665-9
3. Roberts DW, Hartov A, Kennedy FE, Miga MI, Paulsen KD. Intraoperative brain shift and deformation: a quantitative analysis of cortical displacement in 28 cases. *Neurosurgery.* (1998) 43:749–58; discussion 758–60. doi: 10.1097/00006123-199810000-00010
4. Rey-Dios R, Cohen-Gadol AA. Technical principles and neurosurgical applications of fluorescein fluorescence using a microscopeintegrated fluorescence module. *Acta Neurochir.* (2013) 155:701–6. doi: 10.1007/s00701-013-1635-y
5. Xue Z, Kong L, Pan CC, Wu Z, Zhang JT, Zhang LW. Fluorescein-guided surgery for pediatric brainstem gliomas: preliminary study and technical notes. *J Neurol Surg B.* (2018) 79:S340–6. doi: 10.1055/s-0038-1660847
6. Weller M, van den Bent M, Tonn JC, Stupp R, Preusser M, Cohen-Jonathan-Moyal E, et al. European Association for Neuro-Oncology (EANO) guideline on the diagnosis and treatment of adult astrocytic and oligodendroglial gliomas. *Lancet Oncol.* (2017) 18:e315–29. doi: 10.1016/S1470-2045(17)30194-8
7. Louis DN, Perry A, Reifenberger G, von Deimling A, Figarella-Branger D, Cavenee WK, et al. The 2016 World Health Organization Classification of Tumors of the Central Nervous System: a summary. *Acta Neuropathol.* (2016) 131:803–20. doi: 10.1007/s00401-016-1545-1
8. Teo C, Siu TL. Radical resection of focal brainstem gliomas: is it worth doing? *Childs Nerv Syst.* (2008) 24:1307–14. doi: 10.1007/s00381-008-0647-z
9. Stummer W, Stepp H, Möller G, Ehrhardt A, Leonhard M, Reulen HJ. Technical principles for protoporphyrin-IX-fluorescence guided microsurgical resection of malignant glioma tissue. *Acta Neurochir.* (1998) 140:995–1000. doi: 10.1007/s007010050206
10. Hadjipanayis CG, Stummer W. 5-ALA and FDA approval for glioma surgery. *J Neurooncol.* (2019). 141:479–86. doi: 10.1007/s11060-019-03098-y
11. Höhne J, Acerbi F, Falco J, Akçakaya MO, Schmidt NO, Kiris T, et al. Lighting up the Tumor-Fluorescein-Guided resection of Gangliogliomas. *J Clin Med.* (2020) 9:2405. doi: 10.3390/jcm9082405
12. Moore GE, Peyton WT, French LA, Walker WW. The clinical use of fluorescein in neurosurgery; the localization of brain tumors. *J Neurosurg.* (1948) 5:392–8. doi: 10.3171/jns.1948.5.4.0392
13. Schebesch KM, Proescholdt M, Höhne J, Hohenberger C, Hansen E, Riemenschneider MJ, et al. Sodium fluorescein guided resection under the YELLOW 560 nm surgical microscope filter in malignant brain tumor surgery–a feasibility study. *Acta Neurochir.* (2013) 155:693–9. doi: 10.1007/s00701-013-1643-y
14. Schebesch KM, Hoehne J, Hohenberger C, Proescholdt M, Riemenschneider MJ, Wendl C, et al. Fluorescein sodium-guided resection of cerebral metastases-experience with the first 30 patients. *Acta Neurochir.* (2015) 157:899–904. doi: 10.1007/s00701-015-2395-7
15. Okuda T, Kataoka K, Yabuuchi T, Yugami H, Kato A. Fluorescence-guided surgery of metastatic brain tumors using fluorescein sodium. *J Clin Neurosci.* (2010) 17:118–21. doi: 10.1016/j.jocn.2009.06.033
16. Schebesch KM, Hoehne J, Hohenberger C, Acerbi F, Broggi M, Proescholdt M, et al. Fluorescein sodium-guided surgery in cerebral lymphoma. *Clin Neurol Neurosurg.* (2015) 139:125–8. doi: 10.1016/j.clineuro.2015.09.015
17. Cavallo C, De Laurentis C, Vetrano IG, Falco J, Broggi M, Schiariti M, et al. The utilization of fluorescein in brain tumor surgery: a systematic review. *J Neurosurg Sci.* (2018) 62:690–703. doi: 10.23736/S0390-5616.18.04480-6
18. Murray KJ. Improved surgical resection of human brain tumors: Part I. A preliminary study. *Surg Neurol.* (1982) 17:316–9. doi: 10.1016/0090-3019(82)90298-1
19. Shinoda J, Yano H, Yoshimura S, Okumura A, Kaku Y, Iwama T, et al. Fluorescence-guided resection of glioblastoma multiforme by using high-dose fluorescein sodium. Technical note. *J Neurosurg.* (2003) 99:597–603. doi: 10.3171/jns.2003.99.3.0597
20. Koc K, Anik I, Cabuk B, Ceylan S. Fluorescein sodium-guided surgery in glioblastoma multiforme: a prospective evaluation. *Br J Neurosurg.* (2008) 22:99–103. doi: 10.1080/02688690701765524
21. Acerbi F, Broggi M, Eoli M, Anghileri E, Cuppini L, Pollo B, et al. Fluorescein-guided surgery for grade IV gliomas with a dedicated filter on the surgical microscope: preliminary results in 12 cases. *Acta Neurochir (Wien).* (2013) 155:1277–86. doi: 10.1007/s00701-013-1734-9
22. Acerbi F, Broggi M, Schebesch KM, Höhne J, Cavallo C, De Laurentiset C, et al. Fluorescein-Guided surgery for resection of high-grade gliomas: a multicentric prospective Phase II Study (FLUOGLIO). *Clin Cancer Res.* (2018) 24:52–61. doi: 10.1158/1078-0432.CCR-17-1184
23. Bowden SG, Neira JA, Gill B, Ung TH, Englander ZK, Zanazzi G, et al. Sodium fluorescein facilitates guided sampling of diagnostic tumor tissue in non-enhancing gliomas. *Neurosurg.* (2018) 82:719–27. doi: 10.1093/neuros/nyx271
24. Acerbi F, Broggi M, Broggi G, Ferroli P. What is the best timing for fluorescein injection during surgical removal of high-grade gliomas? *Acta Neurochir (Wien).* (2015) 157:1377–8. doi: 10.1007/s00701-015-2455-z
25. Dilek O, Ihsan A, Tulay H. Anaphylactic reaction after fluorescein sodium administration during intracranial surgery. *J Clin Neurosci.* (2011) 18:430–1. doi: 10.1016/j.jocn.2010.06.012
26. Roberts DW, Strohbehn JW, Hatch JF, Murray W, Kettenberger H. A frameless stereotaxic integration of computerized tomographic imaging and the operating microscope. *J Neurosurg.* (1986) 65:545–9. doi: 10.3171/jns.1986.65.4.0545

Conflict of Interest: The authors declare that the research was conducted in the absence of any commercial or financial relationships that could be construed as a potential conflict of interest.

Publisher's Note: All claims expressed in this article are solely those of the authors and do not necessarily represent those of their affiliated organizations, or those of the publisher, the editors and the reviewers. Any product that may be evaluated in this article, or claim that may be made by its manufacturer, is not guaranteed or endorsed by the publisher.

Copyright © 2021 Xue, Kong, Hao, Wang, Jia, Wu, Jia, Zhang and Zhang. This is an open-access article distributed under the terms of the Creative Commons Attribution License (CC BY). The use, distribution or reproduction in other forums is permitted, provided the original author(s) and the copyright owner(s) are credited and that the original publication in this journal is cited, in accordance with accepted academic practice. No use, distribution or reproduction is permitted which does not comply with these terms.

frontiers in Neuroscience

ORIGINAL RESEARCH
published: 08 December 2021
doi: 10.3389/fnins.2021.785969

Resting-State Electroencephalography Functional Connectivity Networks Relate to Pre- and Postoperative Language Functioning in Low-Grade Glioma and Meningioma Patients

*Nienke Wolthuis[1], Djaina Satoer[2], Wencke Veenstra[3], Marion Smits[4,5], Michiel Wagemakers[6], Arnaud Vincent[2], Roelien Bastiaanse[1,7], Perumpillichira J. Cherian[8,9] and Ingeborg Bosma[10]**

[1] Center for Language and Cognition Groningen, University of Groningen, Groningen, Netherlands, [2] Department of Neurosurgery, Erasmus MC – University Medical Center Rotterdam, Rotterdam, Netherlands, [3] Department of Rehabilitation Medicine, University Medical Center Groningen, University of Groningen, Groningen, Netherlands, [4] Department of Radiology & Nuclear Medicine, Erasmus MC – University Medical Center Rotterdam, Rotterdam, Netherlands, [5] Brain Tumour Centre, Erasmus MC Cancer Institute, Rotterdam, Netherlands, [6] Department of Neurosurgery, University Medical Center Groningen, Groningen, Netherlands, [7] National Research University Higher School of Economics, Moscow, Russia, [8] Department of Neurology, University Medical Center Rotterdam, Rotterdam, Netherlands, [9] Division of Neurology, Department of Medicine, McMaster University and Hamilton Health Sciences, Hamilton, ON, Canada, [10] Department of Neurology, University Medical Center Groningen, Groningen, Netherlands

Introduction: Preservation of language functioning in patients undergoing brain tumor surgery is essential because language impairments negatively impact the quality of life. Brain tumor patients have alterations in functional connectivity (FC), the extent to which brain areas functionally interact. We studied FC networks in relation to language functioning in glioma and meningioma patients.

Method: Patients with a low-grade glioma (N = 15) or meningioma (N = 10) infiltrating into/pressing on the language-dominant hemisphere underwent extensive language testing before and 1 year after surgery. Resting-state EEG was registered preoperatively, postoperatively (glioma patients only), and once in healthy individuals. After analyzing FC in theta and alpha frequency bands, weighted networks and Minimum Spanning Trees were quantified by various network measures.

Results: Pre-operative FC network characteristics did not differ between glioma patients and healthy individuals. However, hub presence and higher local and global FC are associated with poorer language functioning before surgery in glioma patients and predict worse language performance at 1 year after surgery. For meningioma patients, a greater small worldness was related to worse language performance and hub presence; better average clustering and global integration were predictive of worse outcome on language function 1 year after surgery. The average eccentricity, diameter

OPEN ACCESS

Edited by:
Nico Sollmann,
University of California,
San Francisco, United States

Reviewed by:
Kyung K. Peck,
Memorial Sloan Kettering Cancer Center, United States
Veit Stoecklein,
University Hospital of Munich, Germany
Kerstin Jütten,
University Hospital RWTH Aachen, Germany

***Correspondence:**
Ingeborg Bosma
i.bosma01@umcg.nl

Specialty section:
This article was submitted to Brain Imaging Methods, a section of the journal Frontiers in Neuroscience

Received: 29 September 2021
Accepted: 29 October 2021
Published: 08 December 2021

Citation:
Wolthuis N, Satoer D, Veenstra W, Smits M, Wagemakers M, Vincent A, Bastiaanse R, Cherian PJ and Bosma I (2021) Resting-State Electroencephalography Functional Connectivity Networks Relate to Pre- and Postoperative Language Functioning in Low-Grade Glioma and Meningioma Patients. Front. Neurosci. 15:785969. doi: 10.3389/fnins.2021.785969

and tree hierarchy seem to be the network metrics with the more pronounced relation to language performance.

Discussion: In this exploratory study, we demonstrated that preoperative FC networks are informative for pre- and postoperative language functioning in glioma patients and to a lesser extent in meningioma patients.

Keywords: language, network, functional connectivity, low-grade glioma, meningioma

INTRODUCTION

Primary brain tumors in the language dominant hemisphere are estimated to cause language impairment in nearly half of all patients (Davie et al., 2009). Language abilities are essential for everyday communication and for participation in society, hence, impairments negatively affect the quality of life (Hilari et al., 2012). As language covers a range of functions, several language modalities (speech production, comprehension, reading, and writing) and linguistic levels (e.g., phonology, concerning speech sounds; semantics, concerning meaning; and grammar, concerning word and sentence structure) are at risk in brain tumor patients.

The most frequently occurring primary brain tumors are gliomas and meningiomas. Gliomas are infiltrative tumors whereas the meningioma are extra-axially located Patients with a low-grade glioma involving eloquent brain areas generally undergo surgical resection by an awake procedure, to maximize the extent of resection while preventing additional impairment by surgical injury to eloquent brain areas. Patients of both groups have a relatively long life expectancy after surgery (Van Alkemade et al., 2012; Ho et al., 2014). Preservation of language functioning is crucial in these patients for successfully carrying out daily activities and maintaining work or continuing education. The incidence of language impairments after brain tumor surgery ranges between 10 and 70% (Santini et al., 2012; Antonsson et al., 2018; Di Cristofori et al., 2018; Van Kessel et al., 2020). Hence, it is important to gain more insight into the underlying mechanisms of language impairments in this group of patients, to identify at-risk patients and potentially prevent postoperative language decline.

Optimal functioning of the brain requires interactions between and within brain regions leading to a complex network organization. The properties of these interactions can be studied by using for instance diffusion tract imaging as a structural, and electroencephalography (EEG), magnetoencephalography (MEG) or functional magnetic resonance imaging (fMRI) as functional imaging techniques. Functional connectivity (FC) concerns the extent to which brain areas functionally interact, which is reflected by the level of synchronization of brain activity between different brain regions, characterized by any statistical interdependency between two signals (Aertsen et al., 1989).[1] Intracranial tumors can, due to the location, growth and treatment, lead to alterations in these functional interactions using EEG and MEG and therefore adjust their organization in the brain (network organization).[2] In brain tumor patients before surgery, FC tends to be increased in lower frequency bands (delta and theta) and decreased in higher frequency bands (beta and gamma) compared to healthy individuals using (MEG) (Bartolomei et al., 2006a,b; Van Dellen et al., 2012; Hu et al., 2013). For the (intermediate) alpha band, FC in brain tumor patients may be higher or lower than in a healthy population (Bartolomei et al., 2006a; Bosma et al., 2008), but appears to increase between pre- and postoperative assessments (Van Dellen et al., 2013; Lizarazu et al., 2020).

Network organization in brain tumor patients, as investigated with resting-state MEG, has been shown to relate to poorer cognitive functioning, such as verbal memory, working memory, attention, and executive functioning (Bosma et al., 2008, 2009; Van Dellen et al., 2012, 2013; Hu et al., 2013; Van Nieuwenhuizen et al., 2018; Derks et al., 2019). However, literature on language functioning in relation to FC network characteristics using EEG and MEG is scarce. Resting state fMRI on the other hand is a technique, believed to depend on the neurovascular uncoupling causing changes in neurometabolites. Language network studies done using resting state (rs) fMRI have shown differences in the network organization before and after surgery in glioma patients (Deverdun et al., 2020), and also, there is literature on the extent of the network involved in language function even in the contralateral hemisphere although impacting the core network to a lesser extent (Jin et al., 2021). MEG studies has reported that FC network alterations in the theta, alpha, and gamma bands are associated with poorer performance on a verbal fluency test in glioma patients (Van Dellen et al., 2012; Hu et al., 2013; Derks et al., 2019).[3] Furthermore, Lizarazu et al. (2020) assessed left-hemispheric, low-grade glioma patients with an object naming test and semi-spontaneous speech ratings, and registered resting-state MEG before, as well as at 3 and 6 months after surgery. No relations between FC change in the alpha band and language change scores were found, possibly because language performance did not significantly change between the

[1]The interpretation of FC network configurations is dependent on the investigated frequency band; brain activity in the delta and theta bands is considered pathological (this is usually absent in healthy adults while awake), whereas brain activity in the alpha and beta bands indicates normal physiological brain rhythms (Niedermeyer, 1999).

[2]The interpretation of FC network configurations is dependent on the investigated frequency band; brain activity in the delta and theta bands is considered pathological (this is usually absent in healthy adults while awake), whereas brain activity in the alpha and beta bands indicates normal physiological brain rhythms (Niedermeyer, 1999).

[3]Verbal fluency, in the form of category or letter fluency, is classified under language functioning instead of executive functioning here because the tests at least partly assess language processing (Whiteside et al., 2016; Aita et al., 2019).

time points. Nonetheless, studies in patients with non-tumor-related brain injury show that FC network characteristics predict the type of language impairment and the course of language recovery (Castellanos et al., 2010; Nicolo et al., 2015; Ranasinghe et al., 2017).

The aim of the study is to ascertain differences in network organization of patients with a presumed low-grade glioma and meningioma patients preoperatively, compared to healthy participants and the relation to language function. Our hypothesis is that network metrics are predictive of postoperative language performance in glioma patients.

MATERIALS AND METHODS

Participants

Patients with a presumed low-grade glioma and patients with a presumed grade I meningioma, who were planned to undergo surgery at the University Medical Centre Groningen (UMCG) or the Erasmus MC University Medical Centre Rotterdam (Erasmus MC), were invited to participate in the study and inclusion took place in 2017 and 2018.

Inclusion criteria were:

- intracranial, supratentorial, untreated tumor infiltrating into or pressing on the language-dominant hemisphere[4] (if language lateralisation was unknown: right-handed patients with left-sided tumor);
- tumor diameter > 3 cm (meningiomas only);
- age between 18 and 75 years;
- in case of epilepsy, seizures well-controlled with anticonvulsants.

Exclusion criteria were:

- non-native speaker of Dutch;
- history of a medical, neurological or psychiatric condition known to affect language or cognitive functioning;
- history of substance abuse;
- consistent use of dexamethasone preoperatively;
- previous brain surgery or cranial radiation therapy.

Glioma patients underwent tumor resection with an awake procedure and meningioma patients underwent surgery under general anesthesia. Healthy volunteers were invited to participate in the control group and matched for age, gender and education (often proxies of the patients). The same exclusion criteria applied for this group. This multicentre study was approved by the medical, ethical review board of the UMCG, which was also applicable to the Erasmus MC. All participants gave written informed consent.

Fifteen glioma and 15 healthy participants and 10 meningioma with 9 healthy participants were included in the study. Their specifics are given in the "Result" section.

[4]Edinburgh handedness inventory was used for handedness.

Procedure

Both patient groups underwent extensive language assessment at two time points: T1 = before surgery (glioma patients: mean 33 days, range 6–83; meningioma patients: mean 20 days, range 1–48); and T2 = 12 months after surgery (glioma patients: mean 12.61, range 11.05–15.22; meningioma patients: mean 11.97, range 11.21–12.49). EEG registration was performed at T1 and at T2 in glioma patients, at T1 in meningioma patients, and once in healthy participants.

Language Assessment

A selection of standardized language tests was conducted, assessing a wide range of linguistic abilities. Tests included object naming (De Witte et al., 2015), action naming in sentence context (Rofes, 2012), the shortened version of the Token Test (De Renzi and Faglioni, 1978), category fluency (Luteijn and Barelds, 2004), letter fluency (Schmand et al., 2008), reading and writing (Van Ierschot, 2018), and subtests of the Diagnostic Instrument for Mild Aphasia (DIMA; Satoer et al., 2019): repetition, semantic odd-picture-out, sentence completion), and sentence judgment (De Witte et al., 2015).

Raw scores were normalized by conversion to *z*-scores, using pre-existing normative data from a healthy population. Subsequently, eight language domains were created for the purpose of this study, as shown in **Table 1**. This was done for two reasons: (1) to reduce the number of statistical comparisons; and (2) to examine all language modalities (speech production, comprehension, reading, and writing), three linguistic levels (phonology, semantics, and grammar), and comprehension of two types of input (auditory and visual). A domain score equalled the average *z*-score of the tests in that domain for each patient. Domain scores below –1.5 indicated an impairment.

Electroencephalography Registration

Electroencephalography was registered using 44-channel Schwarzer amplifiers (Natus Europe GmbH, Munich). Twenty-one scalp electrodes were applied according to the International 10-20 System, with or without caps according to local protocol. Electrode positions are shown in **Figure 1**. Additional polygraphic electrodes were applied for artifact

TABLE 1 | Language domains under investigation with their corresponding tests.

Domains	Tests
(1) Production-Word retrieval	Object naming
(2) Production-Phonology	Repetition
	Letter fluency
(3) Production-Semantics	Semantic odd-picture-out
	Category fluency
(4) Production-Grammar	Sentence completion
	Action naming in sentence context
(5) Comprehension-Auditory input	Token Test
(6) Comprehension-Visual input	Sentence judgment (accuracy)
(7) Reading	Reading
(8) Writing	Writing

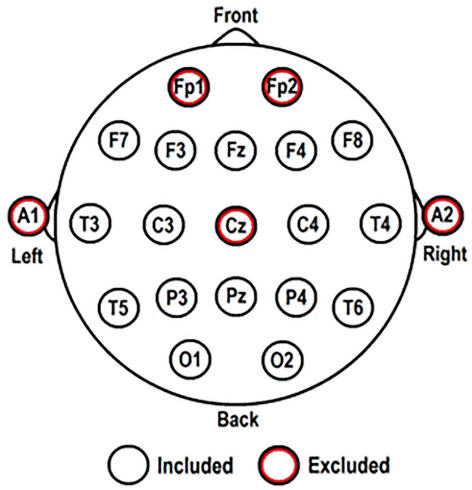

FIGURE 1 | Electrode positions according to the International 10-20 System. The five red-circled electrodes were excluded from all analyses.

detection: electrooculography (EOG; two diagonally placed electrodes for eye movements), electrocardiography (ECG; chest electrode), and respiration (abdominal movements). EEG was recorded with impedances $\leq$ 5 kΩ, a sampling frequency of 500 Hz, and with Cz as reference electrode.

At least 5 min of eyes-closed, resting-state EEG were registered for every participant. If there were many artifacts, the duration was prolonged to 10 min. Participants were instructed to refrain from moving and to stay alert. Alertness was continuously monitored and acoustic stimuli were given when signs of drowsiness appeared. For (glioma) patients with history of seizures and suspected epileptiform activity, the resting-state registration was followed by the standard clinical EEG registration of at least 30 min.

Electroencephalography Processing

Artifact-free EEG for analysis was selected by visual inspection (IB) and segmented into five epochs of 8.19 s (4096 samples) for each participant. Using BrainVision Analyzer 2.0 (Brain Products GmbH, 2013). EEG data were re-referenced to a new averaged reference consisting of 16 scalp electrodes: F3; F4; F7; F8; T3; T4; T5; T6; C3; C4; P3; P4; O1; O2; Fz; and Pz (excluding: Cz [reference electrode]; Fp1 and Fp2 [to minimize excess muscle activity and eye movement artifacts]; A1 and A2 [do not register brain activity]). Only these 16 electrodes were included for FC network analysis, described below (for more detailed explanations on FC network analysis see Van Straaten and Stam, 2013; Zhang et al., 2014; Van Diessen et al., 2015).

Functional Connectivity Network Analysis

Functional connectivity network analysis was performed in BrainWave software (version 0.9.152.12.26; Stam, 2018) for every EEG segment. The mean values of five segments for each participant were used in further (statistical) analyses. FC networks were analyzed in the theta (4–8 Hz) and alpha (8–13 Hz) frequency bands. These bands were selected based on previous literature (Van Dellen et al., 2012; Derks et al., 2019).

Functional connectivity network analysis was performed with the phase lag index (PLI), a correlation coefficient that measures synchronization of brain activity between different brain regions, by the consistency with which one signal is leading or lagging in phase with respect to another signal (Stam et al., 2007). As this is a phase-based technique, it does not depend on the amplitude of the signal. Other advantages of the PLI are that it analyses non-linear relations and that it is relatively insensitive to the effects of volume conduction, a phenomenon denoting that the activity recorded over different brain regions can be influenced by one single underlying source (Stam et al., 2007).

Analysis with the PLI results in values between 0 and 1 for every pair of signals. A PLI close to 0 demonstrates no/very weak synchronization between two signals recorded from different electrode sites, which indicates no/very weak functional interaction between the underlying brain areas. A PLI close to 1 indicates strong synchronization between two signals and a strong functional interaction between the underlying brain areas. PLI values form the basis for the FC networks, for both weighted and Minimum Spanning Tree (MST) networks, which provide complementary information. The organization of FC networks was quantified by network measures. Scores on these measures were referred to as network characteristics.

Graph Theory and Network Measures

All network measures used are based on graph theory (Watts and Strogatz, 1998). This is a mathematical approach by which a complex network is reduced to a 'graph,' an abstract representation of the network. A graph consists of nodes and connections, which are links between nodes. In our case, nodes refer to the electrode sites, which represent the underlying brain areas, and connections represent functional interactions between the underlying brain areas.

Different aspects of the network organization were evaluated by using network measures. First, connectivity of individual nodes was examined. Nodes with many connections and a central position in the network are called 'hubs.' Subsequently, short-distance or local FC, and long-distance or global FC were examined. Lastly, efficiency of the entire network configuration was examined.

Table 2 gives an overview of the network measures used, including examples corresponding to **Figure 2**. The first part of the table quantifies the original weighted networks, and the latter part quantifies the MST networks.

Weighted Networks

Weighted networks take the exact PLI values, the synchronization strength between signals, into account. Hence, it provides insight into all connections, weak and strong, on a continuous scale. For the visualization of weighted networks, several correlation thresholds were applied. PLI values above such threshold were included as connecting lines in a schematic

TABLE 2 | Network measures used for the quantification of the functional connectivity (FC) brain networks.

	Measure	Evaluation of	Description	Interpretation
PLI:	Phase Lag Index	Functional connectivity	Synchronization of activity (the consistency with which one signal is phase leading or lagging with respect to another signal), indicating the strength by which areas are functionally connected; mean of all channels	High PLI → high whole-brain FC
rC:	relative average Clustering coefficient	Local FC	Clustering coefficient: the extent to which neighbors of a node are connected to each other; Relative average clustering coefficient: the number of connections between the neighbors of a node divided by the total number of possible connections between them, averaged for all nodes, and for normalization, divided by the mean 'average clustering coefficient' of 50 surrogate random networks of identical density	High rC → high local FC
rL:	relative average path Length	Global FC	Path length: the number of connections between two nodes; Relative average path length: the number of connections in the shortest path to get from one node to another, averaged for all nodes, and for normalization, divided by the mean 'average path length' of 50 surrogate random networks of identical density	Low rL → high global FC
SWI:	Small-World Index	Entire network configuration	The extent to which rC and rL are in optimal balance (rC divided by rL)	Trade-off between a low SWI more in favor of local clustering and a high SWI more in favor of global integration
Degr:	Maximum Degree fraction	Connectivity of individual nodes	Degree fraction of a node: the number of connections that node has divided by the total number of connections; Maximum degree fraction: the highest degree fraction of all nodes	High Degr → presence of one/more hubs in the network
Ecc:	Average Eccentricity	Connectivity of individual nodes	Eccentricity of a node: the number of connections in the longest path[a] from that node to any other node, divided by the total number of connections; Average eccentricity: mean eccentricity of all nodes in the network	Low Ecc → presence of one/more hubs in the network
BC:	Maximum Betweenness Centrality	Connectivity of individual nodes	Betweenness centrality of a node: the number of paths going through that node divided by the total number of paths[a]; Maximum betweenness centrality: the highest BC of all nodes	High BC → presence of one/more hubs in the network
Leaf:	Leaf fraction	Local FC	Leaf number: the number of nodes in the network that have only one connection (degree = 1); Leaf fraction: leaf number divided by the total number of nodes	High Leaf → high local FC
Diam:	Diameter	Global FC	The number of connections in the longest path[a] between any two nodes in the network, and for normalization, divided by the maximum number of connections	Low Diam → high global FC
TH:	Tree Hierarchy	Entire network configuration	The balance between diameter reduction (a star-like configuration) and prevention from overloading central nodes (a line-like configuration); TH = leaf number/(2*(no. of nodes-1)*max BC)	Low TH[b] → line-like configuration (no risk of overloading central nodes) High TH[b] → star-like configuration (efficient FC)

When measures were averaged for all channels or nodes, this concerned the 16 remaining channels (electrode positions) as shown in ***Figure 1****.*
NA, not applicable.
[a]A path between any two nodes in a MST network is by definition the shortest path between these two nodes because the MST network only has one path between every two nodes (no cycles). Therefore, terms such as the 'longest shortest path' were avoided.
[b]TH close to 0 was considered to be low and TH close to 0.5 was considered to be high because TH ≥ 0.5 was not applicable in our data. See Boersma et al. (2013) for the full TH interpretation.

representation of the brain, and PLI values below the threshold were not included in the network figure. Weighted network figures were created at the group level and at the individual level.

Network measures that quantify weighted networks are influenced by network density, that is, the number of connections, while the number of nodes is equal between participants (Van Diessen et al., 2015). Therefore, weighted network measures were normalized by dividing their absolute values by the mean values of 50 surrogate random networks of the same density. This increased the comparability between networks.

Minimum Spanning Tree Networks

The MST (Stam et al., 2014) is a subnetwork of the weighted network. It has the same number of nodes as the weighted network (16 in our analysis), but the number of connections is limited to the number of nodes minus one (15 in our

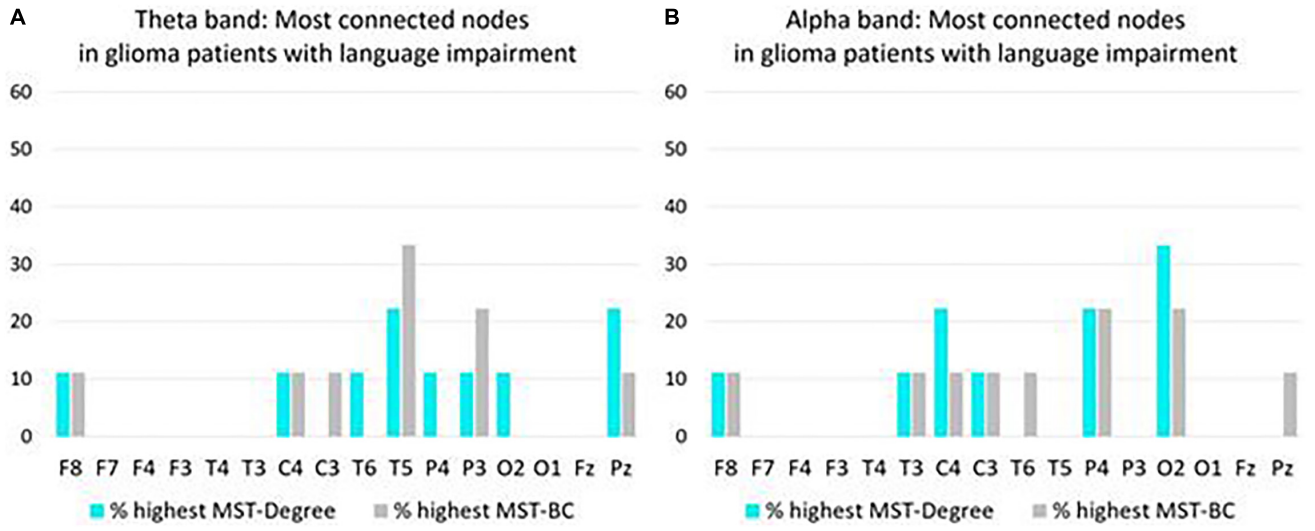

FIGURE 2 | Overview of most connected nodes in MST networks in the theta band **(A)** and in the alpha band **(B)** in preoperative glioma patients with language impairment ($N = 9$). For each node, the *y*-axis expresses the percentage of patients who have the highest Degree/Betweenness Centrality (BC) ranking for that node in their MST network. If a patient's network has two or more nodes with a shared highest ranking, all shared highest rankings are included in the figure.

analysis). Every node gets connected to at least one other node in the MST, without forming cycles. The selection of connections to be included in the MST follows the principle of minimum cost, which is the inverse of FC strength (1/PLI value). To illustrate, the highest PLI value between any of the 16 nodes, which indicates the strongest functional connection, has the lowest cost, and is, therefore, the first to be included in the MST. Next, the connection with the second highest PLI value is included, and so forth, while taking into account the above-mentioned criteria (all nodes have to be connected, no cycles, restricted number of connections). Creation of the MST was performed by Kruskal's algorithm (Kruskal, 1956) in BrainWave software.

As the MST is a binary network, it is independent of an (arbitrarily chosen) correlation threshold. Where a weighted network looks different for every other correlation threshold, the derived MST network always has one unique representation. Furthermore, MST networks are insensitive to the effect of network density because the number of nodes and connections remain the same. Both properties make MST networks well suited for comparisons between participants. A disadvantage of the MST network is that it includes a small portion of connections and does not provide information on weaker connections or local FC with cycles.

Statistical Analysis

Statistical tests were performed for each research question using IBM SPSS Statistics software (version 23, release 23.0.0.0). (1) Network characteristics of patient groups were compared to those of the control groups by Mann–Whitney *U* tests. (2) Kendall's tau-b correlation analyses were performed between preoperative network characteristics and preoperative language domain *z*-scores. (3) Network characteristics of patients with language impairment (z-score ≤ -1.5 on one or more language domains) were compared to those of patients without language impairment by means of Mann–Whitney *U* tests. Additionally, Degr and BC values were used to calculate which nodes were most often highly connected in patients with language impairment. (4) Kendall's tau-b correlation analyses were performed between preoperative network characteristics and 1 year postoperative language domain *z*-scores.

RESULTS

Participants

Demographic and clinical characteristics of the 15 glioma patients (matched to 15 healthy individuals) and the 10 meningioma patients (matched to nine healthy individuals) can be found in **Table 3**. At T2, there was a drop-out of two glioma patients, due to severe side effects of adjuvant treatment, and two meningioma patients, because they were no longer motivated to participate in the study.

Language Performance

T1 and T2

Pre- and postoperative language domain *z*-scores of the glioma patients are presented in **Table 4** and the performance of the meningioma patients on language domain *z*-scores are presented in **Table 5**.

Functional Connectivity Networks and Language Functioning

Taking into account the various aims posed, we will address each of them separately.

Functional Connectivity Network Characterization of Low-Grade Glioma and Meningioma Patients, Compared to the Network Organization in Healthy Individuals

Glioma Patients

T1

In the theta and alpha frequency band, there were no significant differences in the network characteristics between 15 patients and 15 healthy participants (**Appendix 1**).

T2

One year after surgery there was a significant difference in the small world index between the 13 glioma patients and the 15 healthy participants in the theta frequency band. Median of 1.102 in the patient population and 1.114 in the healthy participants (**Appendix 1**). For the healthy participants we have only one EEG registration which was used for both the analysis at T1 and T2 of the glioma patient group.

Meningioma Patients

In the preoperative setting, there were no significant differences in the network organization between the 10 meningioma patients and 9 healthy participants (**Appendix 2**).

Correlation of Network Organization to Preoperative Language Functioning

Glioma Patients

Correlation Analyses

In the theta band, we observed correlations between network metrics and language production. A positive correlation between MST-Ecc and P-Word Retrieval, P-Semantics and P-Grammar was found ($T = 0.43$, $p = 0.031$; $T = 0.40$, $p = 0.037$; and $T = 0.46$, $p = 0.019$). Another positive correlation was found with the same language tests for MST-Diam ($T = 0.45$, $p = 0.026$; $T = 0.50$, $p = 0.011$; and $T = 0.55$, $p = 0.005$). A negative correlation was found between P-Word Retrieval and MST-Leaf and MST-TH ($T = -0.42$, $p = 0.038$ and $T = -0.50$, $p = 0.012$). P-Grammar correlated negatively with the PLI ($T = -0.39$, $p = 0.047$).

In language comprehension, correlations were also found. C-Visual Input correlated negatively with SWI, MST-Degr and MST-BC ($T = -0.44$, $p = 0.04$; $T = -0.73$, $p = 0.001$; and $T = -0.44$, $p = 0.04$). C-Auditory Input was negatively correlated with relative path length ($T = -0.42$, $p = 0.035$). P-Writing was negatively correlated with the PLI ($T = -0.56$, $p = 0.016$) and positively correlated with MST-Diam ($T = 0.473$, $p = 0.042$).

In the alpha band correlations were mainly found with language comprehension. C-Visual Input showed a positive correlation with MST-Ecc and MST-Diam ($T = 0.44$, $p = 0.04$ and $T = 0.44$, $p = 0.046$) and a negative correlation was found with SWI, relative clustering and MST-TH ($T = -0.60$, $p = 0.005$; $T = -0.55$, $p = 0.022$; and $T = -0.46$, $p = 0.034$). In production, only a positive correlation was found with P-Grammar ($T = 0.39$, $p = 0.047$). See **Appendix 3**.

Meningioma Patients

Correlation Analyses

For meningioma patients, a negative correlation in the theta band was also found for C-Visual Input with the SWI ($T = -0.68$, $p = 0.033$) (**Appendix 4**).

Network Organization in the Language Impaired Patient Group

Glioma Patients

Patients With and Without Language Impairment

There were nine out of the 15 glioma patients with language impairment (z-score ≤ -1.5 on one or more language domains) and six out of 15 glioma patients without language impairment preoperatively. In the theta band, a lower eccentricity value (0.369 vs. 0.396, $p = 0.036$) and a less extended diameter (0.452 vs. 0.494, $p = 0.012$) was found in glioma patients with language impairments and a more star like hierarchy (0.422 vs. 0.388, $p = 0.036$) was related to patients with language impairment. No significant correlations were found in the alpha frequency band. **Appendix 5** presents all comparisons

Connectivity of Individual Nodes in Patients With Language Impairment

Nodes (electrode positions) with the highest Degr and the highest BC indicate the most connected and most centrally positioned nodes in the MST network. In order to further investigate network characteristics of patients with language impairment, the nodes with the highest Degr and the highest BC rankings were selected for every patient with impaired language performance. Consecutively for each node, the percentage of patients with that node having the highest Degr/BC was calculated (as in Boersma et al., 2013). These percentages are given in **Figure 2**. (Two right-hemispheric glioma patients were not included here because they were unimpaired).

In the theta band, T5, P3, and Pz most often had the highest Degree/BC rankings, representing the most connected nodes in the MST network of glioma patients with language impairment (**Figure 2A**).

In the alpha band, O2, P4, and C4 most often had the highest Degree/BC rankings, representing the most connected nodes in the MST network of glioma patients with language impairment (**Figure 2B**).

It must be emphasized that the language impaired patient group used in this analysis is rather small.

Meningioma Patients

Patients With and Without Language Impairment

There were four out of 10 meningioma patients with language impairment and six out of 10 meningioma patients without language impairment preoperatively. In the theta band a shorter average path length was associated with patients with language impairment (0.896 vs. 0.915, $p = 0.038$).

Connectivity of Individual Nodes in Patients With Language Impairment

In the theta band, C3 most often had the highest Degree/BC rankings, representing the most connected node in the MST

TABLE 3 | Demographic and clinical characteristics of the participants: number of participants (and percentage) or mean (and range).

	Glioma patients (*N* = 15)	Control group matched to glioma patients (*N* = 15)	Meningioma patients (*N* = 10)	Control group matched to meningioma patients (*N* = 9)
Gender – female	5 (33%)	6 (40%)	6 (60%)	4 (44%)
Mean age in years (range)	42.0 (22–60)	42.3 (20–59)	58.6 (50–69)	53.8 (46–59)
Mean education level[a] (range)	5.3 (4–7)	5.4 (4–7)	5.4 (3–7)	5.2 (4–7)
Handedness[b]				
Right	10 (67%)	12 (80%)	9 (90%)	8 (89%)
Left	4 (27%)	3 (20%)	0	1 (11%)
Ambidextrous	1 (7%)	0	1 (10%)	0
Mean 'diagnosis → surgery' time in months (range)	20.8 (1.1–167.3)	NA	8.0 (2.1–49.7)	NA
Tumor histology and grade[c]				
Diffuse astrocytoma, grade II	5 (33%)	NA	NA	NA
Oligodendroglioma, grade II	10 (67%)	NA	NA	NA
Meningioma, grade I	NA	NA	10 (100%)	NA
Tumor localization, hemisphere				
Left	13 (87%)	NA	10 (100%)	NA
Right	2 (13%)	NA	0	NA
Tumor localization, lobes				
Frontal	5 (33%)	NA	6 (60%)	NA
Fronto-temporal	1 (7%)	NA	0	NA
Fronto-parietal	1 (7%)	NA	0	NA
Temporal	1 (7%)	NA	0	NA
Temporo-insular	3 (20%)	NA	0	NA
Parietal	3 (20%)	NA	3 (30%)	NA
Parieto-temporal	1 (7%)	NA	0	NA
Parieto-occipital	0	NA	1 (10%)	NA
Extent of resection[d]				
Partial: 20–89%	7 (47%)	NA	1 (10%)	NA
Subtotal: 90–99%	6 (40%)	NA	1 (10%)	NA
Total: 100%	2 (13%)	NA	8 (80%)	NA
Use of anti-epileptic drugs at T1	13 (87%)	NA	6 (60%)	NA
Use of anti-epileptic drugs at T2	12/13 (92%)	NA	7/8 (88%)	NA
Postoperative glioma treatment (chemo/radiotherapy ongoing or completed at T2)	10/13 (77%)	NA	NA	NA

NA, not applicable; T1, before surgery; T2, one year after surgery. Some variables add up to 101% due to rounding.
[a]Education level was classified according to seven categories (1 = incomplete primary education; 2 = complete primary education; 3 = primary education and <2 years of low-level secondary education; 4 = complete low-level secondary education; 5 = complete average-level secondary education; 6 = complete high-level secondary education; 7 = complete university education; Verhage, 1964).
[b]Handedness was assessed by the Edinburgh Handedness Inventory (Oldfield, 1971).
[c]Based on the 2016 WHO (World Health Organisation) classification (Louis et al., 2016).
[d]Extent of resection was determined quantitatively by a neuroradiologist, based on pre- and postoperative tumor segmentation volumes.

network of meningioma patients with language impairment (**Figure 3A**). In the alpha band, T6 most often had the highest Degree/BC rankings, representing the most connected node in the MST network of meningioma patients with language impairment (**Figure 3B**).

Correlation of Preoperative Functional Connectivity Network Characteristics and Postoperative Language Outcome

Glioma Patients

Correlation Analyses

In the theta band, PLI, average clustering coefficient, MST-Ecc, MST-Degr, MST-leaf, MST-Diam, and MST-TH at T1 all are correlated with P-Word Retrieval 1 year after surgery. A positive correlation was found with MST-ECC and MST-diam ($T = 0.69$, $p = 0.001$ and $T = 0.73$, $p = 0.001$) and a negative correlation was observed with the PLI, average clustering coefficient, MST-Degr, MST-leaf and MST-TH ($T = -0.57$, $p = 0.008$; $T = -0.44$, $p = 0.042$; $T = -0.49$, $p = 0.022$; $T = -0.57$, $p = 0.009$; $T = -0.49$, $p = 0.023$). A significant correlation was found between PLI and P-Writing ($T = -0.47$, $p = 0.036$). These results indicate that poor performance on language 1 year after surgery is related to a more pronounced focal clustering and global integration on EEG in the preoperative setting.

In the alpha band, no significant correlations were found (**Appendix 7**).

TABLE 4 | Language domain *z*-scores of glioma patients at T1 and T2, including comparisons to normative data from a healthy population.

Language domain	T1: Language *z*-scores				Comparisons to the healthy population		T2: Language *z*-scores				Comparisons to the healthy population	
	N	*Mdn*	*Min*	*Max*	*Z*	*p*	*N*	*Mdn*	*Min*	*Max*	*Z*	*p*
P-Word Retrieval	15	– 1.64	–10.71	0.83	– 1.99	**0.023**	13	0.02	–7.18	0.88	– 1.23	0.110
P-Phonology	15	– 0.20	–5.28	0.95	– 2.27	**0.012**	13	– 0.84	–5.62	0.85	– 2.20	**0.014**
P-Semantics	15	– 0.60	–5.14	1.11	– 1.87	**0.031**	13	– 0.70	–3.99	0.91	– 1.85	**0.032**
P-Grammar	15	– 0.25	–8.33	0.74	– 1.53	0.063	13	– 0.59	–5.38	0.86	– 2.41	**0.008**
C-Auditory Input	15	– 0.69	–4.98	0.83	– 1.77	**0.039**	13	– 0.18	–3.97	0.83	– 0.88	0.191
C-Visual Input	13	0.19	–1.05	0.56	0.32	0.376	12	0.38	–0.72	0.57	0.94	0.173
Reading	14	0.28	–5.28	0.28	2.67	**0.004**	13	0.28	–2.50	0.28	– 0.69	0.247
Writing	13	– 0.79	–6.12	0.55	– 2.16	**0.016**	13	– 0.79	–7.45	0.55	– 2.78	**0.003**

P, production; C, comprehension; N, sample size; Mdn, median; Min, minimum value; Max, maximum value; Z, standardized test statistic of the one-sample Wilcoxon signed rank tests; p, p-value (one-sided). Significant effects ($p < 0.05$) are presented in bold font.

TABLE 5 | Language domain *z*-scores of meningioma patients at T1 and T2, including comparisons to normative data from a healthy population.

Language domain	T1: Language *z*-scores				Comparisons to the healthy population		T2: Language *z*-scores				Comparisons to the healthy population	
	N	*Mdn*	*Min*	*Max*	*Z*	*p*	*N*	*Mdn*	*Min*	*Max*	*Z*	*p*
P-Word Retrieval	10	– 0.58	–1.64	0.42	– 1.89	**0.030**	8	– 0.58	–8.44	0.88	– 1.40	0.081
P-Phonology	10	– 0.12	–1.34	1.16	– 0.97	0.167	8	– 0.11	–1.61	1.31	– 0.14	0.445
P-Semantics	10	– 0.48	–1.58	1.03	– 1.27	0.102	8	0.38	–1.34	1.43	1.26	0.104
P-Grammar	10	– 0.51	–1.29	– 0.35	– 2.81	**0.003**	8	– 0.16	–3.77	0.43	– 1.12	0.132
C-Auditory Input	10	0.07	–0.69	0.83	0.05	0.480	8	0.07	–1.19	0.83	0.28	0.390
C-Visual Input	7	– 0.07	–1.18	0.74	0.17	0.433	6	0.30	–0.53	0.51	0.73	0.232
Reading	9	0.28	–2.50	0.28	1.73	**0.042**	8	0.28	–2.50	0.28	1.51	0.066
Writing	9	– 0.79	–6.12	0.55	– 1.98	**0.024**	8	– 1.45	–6.12	0.55	– 1.69	**0.046**

P, production; C, comprehension; N, sample size; Mdn, median; Min, minimum value; Max, maximum value; Z, standardized test statistic of the one-sample Wilcoxon signed rank tests; p, p-value (one-sided). Significant effects ($p < 0.05$) are presented in bold font.

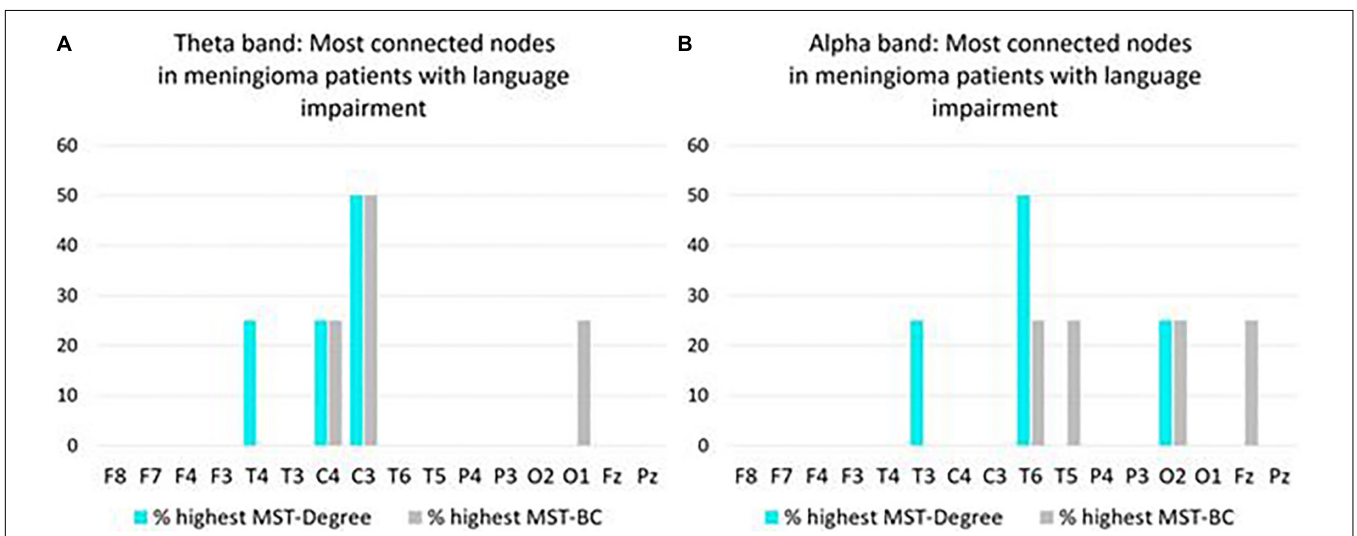

FIGURE 3 | Overview of most connected nodes in MST networks in the theta band **(A)** and in the alpha band **(B)** in pre operative meningioma patients with language impairment ($N = 4$). For each node, the *y*-axis expresses the percentage of patients who have the highest Degree/Betweenness Centrality (BC) ranking for that node in their MST network. If a patient's network has two or more nodes with a shared highest ranking, all shared highest rankings are included in the figure.

Meningioma Patients

Correlation Analyses

In the theta band, PLI was negatively correlated with P-Word Retrieval (T = –0.57, p = 0.048) and P-Semantics (T = –0.57, p = 0.048) In the alpha band, a positive correlation was found between P-Word Retrieval and MST-Ecc (T = 0.57, p = 0.048) and MST-Diam (T = 0.59, p = 0.044). A negative correlation was observed with P-Word Retrieval and MST-Degr (T = –0.64, p = 0.026) and between P-Writing and Betweenness (T = –0.57, p = 0.014). In the alpha band, no significant correlations were found. See **Appendix 8**.

DISCUSSION

In this first study on FC networks in relation to pre- and postoperative language functioning in glioma and meningioma patients, the results will be discussed below.

Functional Connectivity Network Characterization of Low-Grade Glioma and Meningioma Patients, Compared to the Network Organization in Healthy Individuals

Glioma and Meningioma Patients

The functional network in the preoperative setting of patients with the network metrics of healthy participants showed no difference in either the glioma or the meningioma patient population. It is possible that a difference could not be found by analyzing the patient group as a whole, including both patients with and without language impairment. It is possible that an evaluation in only language impaired patients could show a different network organization compared to healthy participants due to the neural plasticity which fails and give a language impairment. It is also possible that in patients without a language impairment will show a network organization which is more comparable to healthy participants because the tumor has not involved the language network or on the other hand will show differences because of the neural plasticity in which a patient will keep adequate language abilities.

Postoperative EEG was registered in glioma patients only, and a lower small-worldness was observed in the glioma patient population compared to healthy participants in the theta band. Studies on the theta band functional connectivity report increased theta-band FC before and after brain tumor surgery (Bosma et al., 2008, 2009; Van Dellen et al., 2012), particularly in the affected hemisphere (Bartolomei et al., 2006a). Higher FC in the theta band is likely to be indicative of more severe brain dysfunction, similar to brain activity in lower (delta and theta) frequency bands. This so-called 'slow-wave activity' during wakeful, resting conditions in adults generally represent pathological brain rhythms (Lüders and Noachtar, 2000) and it has been shown to be overrepresented in brain tumor patients (different tumor types and grades; Baayen et al., 2003; De Jongh et al., 2003; Oshino et al., 2007). When brain activity is highly present in a particular frequency band, one is more likely to find statistical interdependencies between brain signals, which provide more opportunities for high FC (Aertsen et al., 1989). Furthermore, increased theta-band FC may be related to epileptogenesis, a process by which the brain develops epilepsy. Our sample sizes were too small to verify this, but Douw et al. (2010) show that higher theta-band FC, especially in the temporal lobe, is associated with higher seizure frequency in glioma patients. The observation of the lower small-worldness in the glioma patients 1 year after surgery compared to the healthy participants may be explained by a shift toward a less optimal network organization with a higher local clustering in favor of global integration.

For the alpha band no relations were found although previous studies showed different results, Brain activity in the alpha band is representative of normal physiological brain rhythms (Lüders and Noachtar, 2000). Decreased alpha-band FC has previously been found in low-grade glioma patients (Bosma et al., 2008), and in patients with other types of brain injury, such as traumatic brain injury (Castellanos et al., 2010) and stroke (Dubovik et al., 2013). One study, however, has reported an increase of alpha-band FC in brain tumor patients (a mixed group of preoperative meningioma, low-grade glioma, and high-grade glioma patients; Bartolomei et al., 2006a). FC in higher frequency bands (beta and gamma) is generally reduced in brain tumor patients (Bartolomei et al., 2006a,b; Bosma et al., 2009; Hu et al., 2013). Hence, when the brain is affected by a tumor, FC in the alpha band may change in parallel with FC in higher frequency bands.

Correlation of Network Organization to Preoperative Language Functioning

Glioma Patients

Network metrics in the glioma patient population is related to the language function, both language comprehension and production and even writing. The relations are more pronounced in the theta frequency band. In the alpha band, the relations were mainly observed with comprehension. In the theta band, hub presence and higher focal and global FC are associated with poorer language functioning before surgery. The direction of this relationship is to be expected, considering that higher theta-band FC indicates more severe brain dysfunction (previous section). Similar findings are reported by Van Dellen et al. (2012), who demonstrated that FC alterations in the theta band, such as increased local FC, were related to poorer language performance in preoperative low-grade glioma patients. This applied to category fluency performance (production-semantics at the word level), whereas the current study shows associations with grammar, production of language, and comprehension of visual input, both of which concern language functioning at the sentence level and to a lesser extent to writing.

In the alpha band, a greater small-worldness coincides with higher local clustering can be seen as a representation moving a bit to a more organized network because path length did not change that much. It is associated with poorer language comprehension before surgery. This result is inconsistent with

previous findings, which demonstrated that lower global FC in the alpha band was related to poorer language production, as assessed with category fluency, in a group of preoperative low-grade and high-grade glioma patients (Derks et al., 2019). In addition, low alpha-band FC was related to poorer performance in several cognitive functions (e.g., verbal memory, information processing, and attention; Derks et al., 2019). The contrast with our result can be explained by the language task that was used to assess comprehension of visual input: sentence judgment (accuracy scores). This test was presumably too easy because it has a 50% chance of selecting the correct answer. Moreover, comprehension of visual input was the only language domain for which all patients were unimpaired preoperatively. Consequently, the correlation is based on small variation in unimpaired language performance and, therefore, may not be very informative.

Meningioma Patients

In the comprehension task of the meningioma patients, small-worldness again was negatively associated in the theta band. Less significant relations are presumably due to the nature of the tumor; meningiomas generally do not infiltrate the surrounding brain tissue (Wei et al., 2007). Therefore, they do not have a large direct destructive effect on brain tissue, which may be reflected by little or no FC alterations. Meningiomas can, however, cause language impairments, despite the absence of infiltrative injury (Gondar et al., 2021).

Network Organization in the Language Impaired Patient Group

Glioma and Meningioma Patients

The results indicate that in glioma patients, those with language impairments in the preoperative setting show hub presence, a more global integration and more star-like configuration compared to patients without a language impairment in the theta band. In the meningioma, patients with a language impairment show a shorter median relative path length.

A more descriptive analysis of individual nodes in the MST network suggests that, in left-hemispheric tumor patients with language impairment, theta-band FC is frequently highest in left-sided brain areas and alpha-band FC is frequently highest in right-sided brain areas. This must be interpreted with caution because the analysis is based on language-impaired subgroups, and the original numbers of glioma and meningioma patients were already small.

Overall, we showed indications that FC brain networks in the preoperative setting can signify presence of language impairment in brain tumor patients. The differences show a denser pattern of functional interactions with hubs which can lead to a more optimal global organization. Maybe this pattern in the preoperative setting is already a compensatory mechanism of the brain due to the slow growth of a glioma along the white matter tracts but is still failing. In patients with non-tumor-related, but neurodegenerative language impairment (i.e., primary progressive aphasia), the localisation of altered FC in resting-state MEG has been shown to be indicative of the type of language impairment, at least distinguishing phonological, semantic, and morphosyntactic impairments (Ranasinghe et al., 2017). It is possible that investigating FC of specific brain areas can provide more accurate insights into language impairments in brain tumor patients as well. The number of patients included in this analysis is rather small and the results therefore have to interpreted with caution.

Correlation of Preoperative Functional Connectivity Network Characteristics and Postoperative Language Outcome

Glioma Patients

In addition to the relation of the network metrics in the preoperative setting and language preoperatively, we also observed the same arrangement of language function 1 year after surgery, although no correction was performed on possible differences in tumor treatment or medication use. The results indicate again that poor performance on language 1 year after surgery is related to a more pronounced focal clustering and global integration on EEG in the preoperative setting. This was most pronounced with word retrieval, underlining the importance of an object naming task in the peri-operative phase of glioma surgery.

The correlation involving writing performance showed higher overall FC strength in the theta band before surgery may be associated with poorer writing after surgery. It is important to investigate this further because awake glioma surgery can induce writing impairments (Van Ierschot et al., 2018). In the current patient group, the number of preoperative versus 1 year postoperative writing impairments had doubled (Wolthuis et al., under review). Hence, the intraoperative procedure may benefit from a well-suited risk estimation on the basis of FC networks prior to surgery.

Alpha-band FC has no relation to language outcome in our study. This is in line with Lizarazu et al. (2020), who found no association between FC change in the alpha band and language change scores (object naming and semi-spontaneous speech ratings) between pre- and postoperative assessments in left-hemispheric, low-grade glioma patients. A reason for this may be that language performance did not change after surgery. The current study used language outcome scores 1 year after surgery (instead of language change scores) because performance at 1 year is most relevant for the postoperative approach, such as initiation of language intervention. To illustrate, a patient who shows no language change between pre- and postoperative assessments can either have continued unimpaired performance or persistent language impairments that require attention.

Meningioma Patients

Preoperative higher overall FC strength in the theta band, as well as hub presence and higher global FC in the alpha band, are associated with poorer language functioning (word retrieval, semantics, and writing) 1 year after surgery.

The functional reorganization in brain tumor patients with an impaired language performance tends to show a more pronounced local and global integration. It is possible that this configuration has arisen long before the surgery and can be seen as neural plasticity in slow growing tumors. However, this compensatory mechanism is not optimal as shown by worse language performance. It can be expected that the relation of preoperative network organization with language performance is similar to 1 year postoperatively taken into account that surgery is performed under the optimal conditions trying to preserve critical language areas.

Limitations and Future Directions

This study is underpowered, due to the combination of small groups, many variables and, as a consequence, many statistical comparisons that accompanied our exploratory design. However, the outcomes can assist selection of variables in future studies. Language domains that appear most promising in relation to FC networks are word retrieval (as assessed with object naming), grammar, and comprehension of visual input when using a sufficiently sensitive test (e.g., combination of accuracy and speed, Mooijman et al., 2021) and to a lesser extent semantics and writing. FC network characteristics that appear most promising in relation to language functioning are MST degree, eccentricity and diameter in the theta band, and weighted small-world index in the alpha band. Although the large number of network measures complement each other in quantifying FC network configurations, a disadvantage is that they are not all independent of each other (Van Diessen et al., 2015). This is another reason for limiting the number of network measures in future research.

Functional connectivity networks in the current study may have been influenced by tumor and treatment-related factors, such as tumor location, volume, histology, use of anti-epileptic drugs, and adjuvant treatment (only applicable to glioma patients at T2), but the sample sizes were too small to control for these variables. Apart from that, there were some EEG-related challenges. EEG registration is sensitive to conductivity errors, as conductivity of the skull and other tissues can blur the signal. Consequently, signals that are registered at the scalp may not originate from the brain areas directly underneath them. Although EEG has a high temporal resolution, when compared to network studies using techniques such as fMRI, further improvement to the spatial resolution could be made by using approaches such as source modeling. Moreover, electrical conduction properties of the human head vary between individuals. This results in differences in total FC strength, as measured with the PLI. We normalized the other weighted FC network measures to increase comparability between networks, although network comparisons are still not completely unbiased by using this method (Stam et al., 2014). MEG may be preferred to EEG for FC network investigations, because it will reduce the previous problems and increase spatial resolution. However, it is more expensive and less suitable for clinical use than EEG. Overall, future studies on this topic are likely to benefit from larger sample sizes and fewer variables, carefully selected on the basis of previous work.

CONCLUSION

Functional connectivity and network metrics in glioma patients and to a lesser extent in meningioma patients show significant correlations which all have the same direction. The most remarkable correlations were observed in the theta band. Hub presence and higher local and global FC are associated with poorer language functioning before surgery in glioma patients. In this exploratory study, these parameters predict worse language performance 1 year after surgery, although we have to be cautious about this finding due to a number of known and unknown patient and tumor related factors which could have influenced the results.

In meningioma patients, a greater small-worldness was related to language performance and hub presence, better average clustering and global integration were predictive of worse outcome on language function 1 year after surgery. The average eccentricity, diameter and tree hierarchy seems to be the network metrics with the more pronounced relation to language performance.

Overall, we present the first indications that FC networks are informative for language functioning in glioma patients undergoing surgery, but not (yet) to an extent that the outcomes are clinically applicable. Continuation of this line of research, especially the search for predictors of language outcome, has the potential to improve perisurgical patient care, such as treatment planning, counseling, and language rehabilitation.

DATA AVAILABILITY STATEMENT

The original contributions presented in the study are included in the article/**Supplementary Material**, further inquiries can be directed to the corresponding author/s.

ETHICS STATEMENT

The studies involving human participants were reviewed and approved by Medical Ethical Review Board University Medical Centre Groningen and Medical Ethical Review Board of Erasmus Medical Center in Rotterdam. The patients/participants provided their written informed consent to participate in this study.

AUTHOR CONTRIBUTIONS

RB, NW, DS, PC, IB, and WV contributed to conception and design of the study. NW organized the database, performed the statistical analysis, and wrote the first draft of the manuscript. RB, NW, DS, PC, and IB wrote sections of the manuscript. All authors contributed to manuscript revision, read, and approved the submitted version.

FUNDING

RB is partially supported by the Center for Language and Brain NRU Higher School of Economics, RF Government grant, ag. No 14.641.31.0004 and the EEG research reported was (partially) financially supported by the Dutch Aphasia Foundation (Stichting afasie Nederland).

ACKNOWLEDGMENTS

We thank the following people for contributing data and advice from the University Medical Center Groningen: Gea Drost, Esther Siero, and Hanne Rinck Jeltema and from the Erasmus University Medical Center Rotterdam: Marjan Scheltens-de Boer, Karla Biesheuvel, and Venny Pires, and Clemens Dirven, Joost Schouten, Evy Visch-Brink, and clinical neurophysiology technicians of both centers.

SUPPLEMENTARY MATERIAL

The Supplementary Material for this article can be found online at: https://www.frontiersin.org/articles/10.3389/fnins.2021.785969/full#supplementary-material

REFERENCES

Aertsen, A. M. H. J., Gerstein, G. L., Habib, M. K., and Palm, G. (1989). Dynamics of neuronal firingcorrelation: modulation of "effective connectivity." *J. Neurophysiol.* 61, 900–917. doi: 10.1152/jn.1989.61.5.900

Aita, S. L., Beach, J. D., Taylor, S. E., Borgogna, N. C., Harrell, M. N., and Hill, B. D. (2019). Executive, language, or both? An examination of the construct validity of verbal fluency measures. *Appl. Neuropsychol.* 26, 441–451. doi: 10.1080/23279095.2018.1439830

Antonsson, M., Jakola, A., Longoni, F., Carstam, L., Hartelius, L., Thordstein, M., et al. (2018). Post-surgical effects on language in patients with presumed low_grade glioma. *Acta Neurol. Scand.* 137, 469–480. doi: 10.1111/ane.12887

Baayen, J. C., De Jongh, A., Stam, C. J., De Munck, J. C., Jonkman, J. J., Kasteleijn-Nolst Trenité, D. G. A., et al. (2003). Localization of slow wave activity in patients with tumor-associated epilepsy. *Brain Topogr.* 16, 85–93. doi: 10.1023/B:BRAT.0000006332.71345.b7

Bartolomei, F., Bosma, I., Klein, M., Baayen, J. C., Reijneveld, J. C., Postma, T. J., et al. (2006a). Disturbed functional connectivity in brain tumour patients: evaluation by graph analysis of synchronization matrices. *Clin. Neurophysiol.* 117, 2039–2049. doi: 10.1016/j.clinph.2006.05.018

Bartolomei, F., Bosma, I., Klein, M., Baayen, J. C., Reijneveld, J. C., Postma, T. J., et al. (2006b). How do brain tumors alter functional connectivity? A magnetoencephalography study. *Ann. Neurol.* 59, 128–138. doi: 10.1002/ana.20710

Boersma, M., Smit, D. J. A., Boomsma, D. I., De Geus, E. J. C., Delemarre-van de Waal, H. A., and Stam, C. J. (2013). Growing trees in child brains: graph theoretical analysis of electroencephalography-derived minimum spanning tree in 5- and 7-year-old children reflects brain maturation. *Brain Connect.* 3, 50–60. doi: 10.1089/brain.2012.0106

Bosma, I., Douw, L., Bartolomei, F., Heimans, J. J., Van Dijk, B. W., Postma, T. J., et al. (2008). Synchronized brain activity and neurocognitive function in patients with low-grade glioma: a magnetoencephalography study. *Neuro Oncol.* 10, 734–744. doi: 10.1215/15228517-2008-034

Bosma, I., Reijneveld, J. C., Klein, M., Douw, L., Van Dijk, B. W., Heimans, J. J., et al. (2009). Disturbed functional brain networks and neurocognitive function in low-grade glioma patients: a graph theoretical analysis of resting-state MEG. *Nonlinear Biomed. Phys.* 3:9. doi: 10.1186/1753-4631-3-9

Brain Products GmbH (2013). *Brain Products GmbH, Solutions for Neurophysiological Research.* Available online at: brainproducts.com

Castellanos, N. P., Paúl, N., Ordóñez, V. E., Demuynck, O., Bajo, R., Campo, P., et al. (2010). Reorganization of functional connectivity as a correlate of cognitive recovery in acquired brain injury. *Brain* 133, 2365–2381. doi: 10.1093/brain/awq174

Davie, G. L., Hutcheson, K. A., Barringer, D. A., Weinberg, J. S., and Lewin, J. S. (2009). Aphasia in patients after brain tumour resection. *Aphasiology* 23, 1196–1206. doi: 10.1080/02687030802436900

De Jongh, A., Baayen, J. C., De Munck, J. C., Heethaar, R. M., Vandertop, W. P., and Stam, C. J. (2003). The influence of brain tumor treatment on pathological delta activity in MEG. *NeuroImage* 20, 2291–2301. doi: 10.1016/j.neuroimage.2003.07.030

De Renzi, E., and Faglioni, P. (1978). Normative data and screening power of a shortened version of the token test. *Cortex* 14, 41–49. doi: 10.1016/S0010-9452(78)80006-9

De Witte, E., Satoer, D., Robert, E., Colle, H., Verheyen, S., Visch-Brink, E., et al. (2015). The dutch linguistic intraoperative protocol: a valid linguistic approach to awake brain surgery. *Brain Lang.* 140, 35–48. doi: 10.1016/j.bandl.2014.10.011

Derks, J., Kulik, S., Wesseling, P., Numan, T., Hillebrand, A., van Dellen, E., et al. (2019). Understanding cognitive functioning in glioma patients: the relevance of IDH-mutation status and functional connectivity. *Brain Behav.* 9, 1–9. doi: 10.1002/brb3.1204

Deverdun, J., van Dokkum, L. E. H., Le Bars, E., Herbet, G., Mura, T., and Moritz, S. (2020). Languagereorganization after resection of low-grade gliomas, an fMRI task based connectivity study. *Brain Imaging Behav.* 14, 1779–1791.

Di Cristofori, A., Zarino, B., Bertani, G., Locatelli, M., Rampini, P., Carrabba, G., et al. (2018). Surgery in elderly patients with intracranial meningioma: neuropsychological functioning during a long term follow-up. *J. Neuro Oncol.* 137, 611–619. doi: 10.1007/s11060-018-2754-3

Douw, L., Van Dellen, E., De Groot, M., Heimans, J. J., Klein, M., Stam, C. J., et al. (2010). Epilepsy is related to theta band brain connectivity and network topology in brain tumor patients. *BMC Neurosci.* 11:103. doi: 10.1186/1471-2202-11-103

Dubovik, S., Ptak, R., Aboulafia, T., Magnin, C., Gillabert, N., Allet, L., et al. (2013). EEG alpha band synchrony predicts cognitive and motor performance in patients with ischemic stroke. *Behav. Neurol.* 26, 187–189. doi: 10.3233/BEN-2012-129007

Gondar, R., Patet, G., Schaller, K., and Meling, T. R. (2021). Meningiomas and cognitive impairment after treatment: a systematic and narrative review. *Cancers* 13:1846. doi: 10.3390/cancers13081846

Hilari, K., Needle, J. J., and Harrison, K. L. (2012). What are the important factors in health-related quality of life for people with aphasia? A systematic review. *Arch. Phys. Med. Rehabilit.* 93, S86–S95. doi: 10.1016/j.apmr.2011.05.028

Ho, V. K. Y., Reijneveld, J. C., Enting, R. H., Bienfait, H. P., Robe, P., Baumert, B. G., et al. (2014). Changing incidence and improved survival of gliomas. *Eur. J. Cancer* 50, 2309–2318. doi: 10.1016/j.ejca.2014.05.019

Hu, X. H., Lei, T., Xu, H. Z., Zou, Y. J., and Liu, H. Y. (2013). Resting-state magnetoencephalography study of "small world" characteristics and cognitive dysfunction in patients with glioma. *Onco Targets Ther.* 6, 311–313. doi: 10.2147/OTT.S42471

Jin, L., Li, C., Zhang, Y., Yuan, T., Ying, J., Zuo, Z., et al. (2021). The functional reorganization of language network modules in glioma patients: new insights from resting state fMRI study. *Front. Oncol.* 11:617179. doi: 10.3389/fonc.2021.617179

Kruskal, J. B. (1956). On the shortest spanning subtree of a graph and the traveling salesman problem. *Proc. Am. Math. Soc.* 7, 48–50. doi: 10.1090/S0002-9939-1956-0078686-7

Lizarazu, M., Gil-Robles, S., Pomposo, I., Nara, S., Amoruso, L., Quiñones, I., et al. (2020). Spatiotemporal dynamics of postoperative functional plasticity in patients with brain tumors in language areas. *Brain Lang.* 202:104741. doi: 10.1016/j.bandl.2019.104741

Louis, D. N., Perry, A., Reifenberger, G., von Deimling, A., Figarella-Branger, D., Cavenee, W. K., et al. (2016). The 2016 world health organization classification of tumors of the central nervous system: a summary. *Acta Neuropathol.* 131, 1–18. doi: 10.1007/s00401-016-1545-1

Lüders, H. O., and Noachtar, S. (2000). *Atlas And Classification Of Electroencephalography*. Philadelphia, PA: W. B. Saunders.

Luteijn, F., and Barelds, D. P. F. (2004). *Groninger Intelligentie Test – 2 (GIT-2)*. Amsterdam: Pearson.

Mooijman, S., Bos, L. S., Witte De, E., Vincent, A., Visch-Brink, E., and Satoer, D. (2021). Language processing in glioma patients: speed or accuracy as a sensitive measure? *Aphasiology* 1–25. doi: 10.1080/02687038.2021.1970099 [Epub ahead of print].

Nicolo, P., Rizk, S., Magnin, C., Di Pietro, M., Schnider, A., and Guggisberg, A. G. (2015). Coherent neural oscillations predict future motor and language improvement after stroke. *Brain* 138, 3048–3060. doi: 10.1093/brain/awv200

Niedermeyer, E. (1999). "The normal EEG of the waking adult," in *Electroencephalography: Basic Principles, Clinical Applications, And Related Fields*, 4th Edn, eds E. Niedermeyer and F. Lopes da Silva (Philadelphia, PA: Williams and Wilkins), 149–173.

Oldfield, R. C. (1971). The assessment and analysis of handedness: the edinburgh inventory. *Neuropsychologia* 9, 97–113. doi: 10.1016/0028-3932(71)90067-4

Oshino, S., Kato, A., Wakayama, A., Taniguchi, M., Hirata, M., and Yoshimine, T. (2007). Magnetoencephalographic analysis of cortical oscillatory activity in patients with brain tumors: synthetic aperture magnetometry (SAM) functional imaging of delta band activity. *NeuroImage* 34, 957–964. doi: 10.1016/j.neuroimage.2006.08.054

Ranasinghe, K. G., Hinkley, L. B., Beagle, A. J., Mizuiri, D., Honma, S. M., Welch, A. E., et al. (2017). Distinct spatiotemporal patterns of neuronal functional connectivity in primary progressive aphasia variants. *Brain* 140, 2737–2751. doi: 10.1093/brain/awx217

Rofes, A. (2012). *The Verb In Sentence Context Test: Standardization And Application In Awake Neurosurgery*. Ph.D. Dissertation. Groningen: University of Groningen.

Santini, B., Talacchi, A., Squintani, G., Casagrande, F., Capasso, R., and Miceli, G. (2012). Cognitive outcome after awake surgery for tumors in language areas. *J. Neuro Oncol.* 108, 319–326. doi: 10.1007/s11060-012-0817-4

Satoer, D., De Witte, E., Bastiaanse, R., Vincent, A., Mariën, P., and Visch-Brink, E. (2019). "Diagnostic Instrument for mild aphasia (DIMA): standardization and clinical application," in *Proceedings of the Conference Abstract: Academy of Aphasia 55th Annual Meeting*, Baltimore. doi: 10.3389/conf.fnhum.2017.223.00103

Schmand, B., Groenink, S. C., and Van den Dungen, M. (2008). Letterfluency: psychometrische eigenschappen en nederlandse normen. *Tijdschr. Gerontol. Geriatr.* 39, 65–77. doi: 10.1007/BF03078128

Stam, C. J. (2018). *BrainWave*. Available online at: http://home.kpn.nl/stam7883/brainwave.html (accessed 2020).

Stam, C. J., Nolte, G., and Daffertshofer, A. (2007). Phase lag index: assessment of functional connectivity from multi channel EEG and MEG with diminished bias from common sources. *Hum. Brain Mapping* 28, 1178–1193. doi: 10.1002/hbm.20346

Stam, C. J., Tewarie, P., Van Dellen, E., Van Straaten, E. C. W., Hillebrand, A., and Van Mieghem, P. (2014). The trees and the forest: characterization of complex brain networks with minimum spanning trees. *Int. J. Psychophysiol.* 92, 129–138. doi: 10.1016/j.ijpsycho.2014.04.001

Van Alkemade, H., De Leau, M., Dieleman, E. M. T., Kardaun, J. W. P. F., Van Os, R., Vandertop, W. P., et al. (2012). Impaired survival and long-term neurological problems in benign meningioma. *Neuro Oncol.* 14, 658–666. doi: 10.1093/neuonc/nos013

Van Dellen, E., De Witt Hamer, P. C., Douw, L., Klein, M., Heimans, J. J., Stam, C. J., et al. (2013). Connectivity in MEG resting-state networks increases after resective surgery for low-grade glioma and correlates with improved cognitive performance. *NeuroImage Clin.* 2, 1–7. doi: 10.1016/j.nicl.2012.10.007

Van Dellen, E., Douw, L., Hillebrand, A., Ris-Hilgersom, I. H. M., Schoonheim, M. M., Baayen, J. C., et al. (2012). MEG network differences between low- and high-grade glioma related to epilepsy and cognition. *PLoS One* 7:e50122. doi: 10.1371/journal.pone.0050122

Van Diessen, E., Numan, T., Van Dellen, E., Van der Kooi, A. W., Boersma, M., Hofman, D., et al. (2015). Opportunities and methodological challenges in EEG and MEG resting state functional brain network research. *Clin. Neurophysiol.* 126, 1468–1481. doi: 10.1016/j.clinph.2014.11.018

Van Ierschot, F. (2018). *Written Language In Awake Surgery – Monitoring Of Reading And Spelling In Glioma Patients Undergoing Awake Surgery*. Available online at: https://nvneuropsy.nl/uploads/prijzen/inzendingen/5abe08aaf035957a7a9e38858a3ce0b7.pdf (accessed 2020).

Van Ierschot, F., Bastiaanse, R., and Miceli, G. (2018). Evaluating spelling in glioma patients undergoing awake surgery: a systematic review. *Neuropsychol. Rev.* 28, 470–495. doi: 10.1007/s11065-018-9391-7

Van Kessel, E., Snijders, T. J., Baumfalk, A. E., Ruis, C., van Baarsen, K. M., Broekman, M. L., et al. (2020). Neurocognitive changes after awake surgery in glioma patients: a retrospective cohort study. *J. Neuro Oncol.* 146, 97–109. doi: 10.1007/s11060-019-03341-6

Van Nieuwenhuizen, D., Douw, L., Klein, M., Peerdeman, S. M., Heimans, J. J., Reijneveld, J. C., et al. (2018). Cognitive functioning and functional brain networks in postoperative WHO grade I meningioma patients. *J. Neuro Oncol.* 140, 605–613. doi: 10.1007/s11060-018-2987-1

Van Straaten, E. C. W., and Stam, C. J. (2013). Structure out of chaos: Functional brain network analysis with EEG, MEG, and functional MRI. *Eur. Neuropsychopharmacol.* 23, 7–18. doi: 10.1016/j.euroneuro.2012.10.010

Verhage, F. (1964). *Intelligentie En Leeftijd: Onderzoek BIJ Nederlanders Van 12 TOT 77 JAAR*. Assen: Van Gorkum.

Watts, D. J., and Strogatz, S. H. (1998). Collective dynamics of small-world networks. *Nature* 393, 440–442.

Wei, C. W., Guo, G., and Mikulis, D. J. (2007). Tumor effects on cerebral white matter as characterized by diffusion tensor tractography. *Can. J. Neurol. Sci.* 34, 62–68. doi: 10.1017/s0317167100005801

Whiteside, D. M., Kealey, T., Semla, M., Luu, H., Rice, L., Basso, M. R., et al. (2016). Verbal fluency: language or executive function measure? *Appl. Neuropsychol.* 23, 29–34. doi: 10.1080/23279095.2015.1004574

Zhang, X., Lei, X., Wu, T., and Jiang, T. (2014). A review of EEG and MEG for brainnetome research. *Cogn. Neurodyn.* 8, 87–98. doi: 10.1007/s11571-013-9274-9

Conflict of Interest: The authors declare that the research was conducted in the absence of any commercial or financial relationships that could be construed as a potential conflict of interest.

Publisher's Note: All claims expressed in this article are solely those of the authors and do not necessarily represent those of their affiliated organizations, or those of the publisher, the editors and the reviewers. Any product that may be evaluated in this article, or claim that may be made by its manufacturer, is not guaranteed or endorsed by the publisher.

Copyright © 2021 Wolthuis, Satoer, Veenstra, Smits, Wagemakers, Vincent, Bastiaanse, Cherian and Bosma. This is an open-access article distributed under the terms of the Creative Commons Attribution License (CC BY). The use, distribution or reproduction in other forums is permitted, provided the original author(s) and the copyright owner(s) are credited and that the original publication in this journal is cited, in accordance with accepted academic practice. No use, distribution or reproduction is permitted which does not comply with these terms.

frontiers in Oncology

ORIGINAL RESEARCH
published: 14 December 2021
doi: 10.3389/fonc.2021.761169

Tracking the Corticospinal Tract in Patients With High-Grade Glioma: Clinical Evaluation of Multi-Level Fiber Tracking and Comparison to Conventional Deterministic Approaches

Andrey Zhylka[1†], Nico Sollmann[2,3,4,5*†], Florian Kofler[3,6,7], Ahmed Radwan[8,9], Alberto De Luca[10,11], Jens Gempt[12], Benedikt Wiestler[3,7], Bjoern Menze[6,13], Sandro M. Krieg[4,12], Claus Zimmer[3,4], Jan S. Kirschke[3,4], Stefan Sunaert[8,9,14], Alexander Leemans[10] and Josien P. W. Pluim[1]*

[1] Biomedical Engineering, Eindhoven University of Technology, Eindhoven, Netherlands, [2] Department of Diagnostic and Interventional Radiology, University Hospital Ulm, Ulm, Germany, [3] Department of Diagnostic and Interventional Neuroradiology, School of Medicine, Klinikum rechts der Isar, Technical University of Munich, Munich, Germany, [4] TUM-Neuroimaging Center, Klinikum rechts der Isar, Technical University of Munich, Munich, Germany, [5] Department of Radiology and Biomedical Imaging, University of California, San Francisco, San Francisco, CA, United States, [6] Image-Based Biomedical Modeling, Department of Informatics, Technical University of Munich, Munich, Germany, [7] TranslaTUM - Central Institute for Translational Cancer Research, Technical University of Munich, Munich, Germany, [8] Department of Imaging and Pathology, Translational MRI, Katholieke Universiteit (KU) Leuven, Leuven, Belgium, [9] Department of Neurosciences, Leuven Brain Institute (LBI), Katholieke Universiteit (KU) Leuven, Leuven, Belgium, [10] Image Sciences Institute, University Medical Center Utrecht, Utrecht, Netherlands, [11] Neurology Department, UMC Utrecht Brain Center, University Medical Center Utrecht, Utrecht, Netherlands, [12] Department of Neurosurgery, School of Medicine, Klinikum rechts der Isar, Technical University of Munich, Munich, Germany, [13] Department of Quantitative Biomedicine, University of Zurich (UZ), Zurich, Switzerland, [14] Department of Radiology, Universitair Ziekenhuis (UZ) Leuven, Leuven, Belgium

While the diagnosis of high-grade glioma (HGG) is still associated with a considerably poor prognosis, neurosurgical tumor resection provides an opportunity for prolonged survival and improved quality of life for affected patients. However, successful tumor resection is dependent on a proper surgical planning to avoid surgery-induced functional deficits whilst achieving a maximum extent of resection (EOR). With diffusion magnetic resonance imaging (MRI) providing insight into individual white matter neuroanatomy, the challenge remains to disentangle that information as correctly and as completely as possible. In particular, due to the lack of sensitivity and accuracy, the clinical value of widely used diffusion tensor imaging (DTI)-based tractography is increasingly questioned. We evaluated whether the recently developed multi-level fiber tracking (MLFT) technique can improve tractography of the corticospinal tract (CST) in patients with motor-eloquent HGGs. Forty patients with therapy-naïve HGGs (mean age: 62.6 ± 13.4 years, 57.5% males) and preoperative diffusion MRI [repetition time (TR)/echo time (TE): 5000/78 ms, voxel size: 2x2x2 mm^3, one volume at b=0 s/mm^2, 32 volumes at b=1000 s/mm^2] underwent reconstruction of the CST of the tumor-affected and unaffected hemispheres

OPEN ACCESS

Edited by:
Alfredo Conti, University of Bologna, Italy

Reviewed by:
Enricomaria Mormina, Università degli Studi di Messina, Italy
Thomas Picht, Charité University Medicine Berlin, Germany

***Correspondence:**
Andrey Zhylka
a.zhylka@tue.nl
Nico Sollmann
nico.sollmann@tum.de

[†]These authors have contributed equally to this work and share first authorship

Specialty section:
This article was submitted to Neuro-Oncology and Neurosurgical Oncology, a section of the journal Frontiers in Oncology

Received: *19 August 2021*
Accepted: *15 November 2021*
Published: *14 December 2021*

Citation:
Zhylka A, Sollmann N, Kofler F, Radwan A, De Luca A, Gempt J, Wiestler B, Menze B, Krieg SM, Zimmer C, Kirschke JS, Sunaert S, Leemans A and Pluim JPW (2021) Tracking the Corticospinal Tract in Patients With High-Grade Glioma: Clinical Evaluation of Multi-Level Fiber Tracking and Comparison to Conventional Deterministic Approaches. Front. Oncol. 11:761169. doi: 10.3389/fonc.2021.761169

using MLFT in addition to deterministic DTI-based and deterministic constrained spherical deconvolution (CSD)-based fiber tractography. The brain stem was used as a seeding region, with a motor cortex mask serving as a target region for MLFT and a region of interest (ROI) for the other two algorithms. Application of the MLFT method substantially improved bundle reconstruction, leading to CST bundles with higher radial extent compared to the two other algorithms (delineation of CST fanning with a wider range; median radial extent for tumor-affected vs. unaffected hemisphere – DTI: 19.46° vs. 18.99°, p=0.8931; CSD: 30.54° vs. 27.63°, p=0.0546; MLFT: 81.17° vs. 74.59°, p=0.0134). In addition, reconstructions by MLFT and CSD-based tractography nearly completely included respective bundles derived from DTI-based tractography, which was however favorable for MLFT compared to CSD-based tractography (median coverage of the DTI-based CST for affected vs. unaffected hemispheres – CSD: 68.16% vs. 77.59%, p=0.0075; MLFT: 93.09% vs. 95.49%; p=0.0046). Thus, a more complete picture of the CST in patients with motor-eloquent HGGs might be achieved based on routinely acquired diffusion MRI data using MLFT.

Keywords: fiber tractography, diffusion MRI, brain tumor, corticospinal tract (CST), neurosurgery planning

INTRODUCTION

Gliomas represent the most common malignant brain tumors in adults, with an average annual age-adjusted incidence rate of ~4.67 to 5.73 per 100,000 population (1, 2). Anaplastic astrocytoma and glioblastoma are the major high-grade glioma (HGG) entities and peak in elderly subjects (1–3). Overall prognosis is poor, with a median survival below 2 years (1, 2, 4). HGGs can be regarded as chronic progressive diseases and typically show infiltrative growth behavior, which renders curative treatment almost impossible for the majority of affected patients (3, 5).

Nowadays, the standard treatment approach in patients harboring HGGs is a combination of neurosurgical resection, extended focal radiotherapy, and adjuvant chemotherapy (6–9). Nonetheless, multiple factors including histopathological characteristics, molecular tumor biology, as well as functional eloquence of the affected brain region contribute to individual therapy decision-making in clinical practice (9, 10). Regarding neurosurgical resection, a maximum extent of resection (EOR) has been associated with prolonged survival rates and better quality of life (11–17). However, mostly depending on individual tumor location, achieving a maximum EOR can be in conflict with preserving specific functions, such as the ability to move or speak without constraints. Thus, the principle of contemporary brain tumor surgery aims at an optimum EOR whilst avoiding surgery-related functional decline as far as possible (18, 19).

The gold-standard method for spatially resolved assessment of brain function is intraoperative direct electrical stimulation (DES), which can be applied as a strategy to guide neurosurgical resection and to avoid functional deficits in the course of tumor resection (8, 20–22). In addition to intraoperative DES, presurgical imaging is paramount to achieve an optimized onco-functional result. At the forefront of imaging techniques, multi-sequence magnetic resonance imaging (MRI) is applied to gather insights into spatial location, spread, and phenotyping of brain tumors (23–26). Lately, diffusion tensor imaging (DTI) in particular has seen increasing relevance as it allows identifying and delineating subcortical white matter (WM) structures non-invasively (27–31). In the neurosurgical context, DTI is frequently used for tracking of the corticospinal tract (CST), the main WM pathway subserving human motor function. The popularity of DTI can be explained by the low false-positive rate of tractography maps (32). Yet, the approach tends to produce underrepresented fiber bundles (33). Consequently, this causes an ongoing debate on whether conventional DTI methods are accurate and reliable enough to serve as a workable solution for delineating WM architecture in patients with glioma (34–37). Specifically, one main criticism is that the brain's WM architecture harbors numerous fiber crossings and further complex geometrical configurations, including fiber branching, which are hard to resolve (38, 39).

While deterministic tractography with DTI is the most common preoperative approach, a variety of models has been proposed to overcome the overall limitations of DTI-based tractography and improve the reconstruction of WM fiber organization as an attempt to further narrow the gap between imaging and reality, including diffusion kurtosis imaging and fiber orientation distribution (FOD)-based approaches using constrained spherical deconvolution (CSD) as the most prominent representative (40–42). At the same time, although these models are more capable of disentangling fiber

Abbreviations: 3D, three-dimensional; BraTS, Brain Tumor Segmentation; CSD, constrained spherical deconvolution; CST, corticospinal tract; DES, direct electrical stimulation; DTI, diffusion tensor imaging; EOR, extent of resection; FA, fractional anisotropy; FOD, fiber orientation distribution; FLAIR, fluid attenuated inversion recovery; HGG, high-grade glioma; MLFT, multi-level fiber tracking; MNI, Montreal Neurological Institute; MRI, magnetic resonance imaging; PACS, Picture Archiving and Communication System; ROI, region of interest; nTMS, navigated transcranial magnetic stimulation; SD, standard deviation; TFE, turbo field echo; TE, echo time; TR, repetition time; VBG, Virtual Brain Grafting; WM, white matter.

orientations, tractography algorithms commonly impose additional constraints that are set to achieve structurally plausible results, such as angular deviation and consideration of all the orientations as separate fibers. Consequently, either pathway propagation may be terminated, or a diverging branch may be pruned due to the angular limitations as well as related to spatial resolution constraints, which may artificially push the rate of false-negative findings (43). Thus, the possibility of incorporating fiber bifurcations with high angular deviations, such as those observed for the human CST, remains neglected. Probabilistic algorithms that are supposed to improve reconstructions by not just propagating into the peak FOD direction but sampling each step from the FOD could compensate for the angular resolution of the FOD model and capture certain pathway bifurcations. A series of previous publications has shown the ability of probabilistic tractography to improve the extent of the bundles over DTI-based tractography while highlighting microstructural changes induced by the tumor (44–46). However, usually direction samples are not drawn out of the whole FOD but from the segment defined by an angular deviation threshold (47). This introduces a limitation to probabilistic methods that is using higher angular deviation thresholds helps in reconstructing more complete bundles while also increasing the false-positive rate (32).

Against this background, we evaluate a novel method for improved fiber tractography of the CST in patients suffering from motor-eloquent HGGs, which aims to specifically tackle the issue of missing fiber branching of currently existing tractography procedures. We evaluate the recently developed multi-level fiber tracking (MLFT) approach that adds branches to the pathways that have been previously reconstructed, but do not reach a predefined target region (48, 49). Specifically, we hypothesize that the MLFT algorithm is capable of improving the reconstruction of the CST in the vicinity of a brain tumor when compared to conventionally used DTI-based tractography as well as tractography using CSD.

METHODS

Study Design and Patient Inclusion

This study was approved by the local institutional review board and was conducted in accordance with the Declaration of Helsinki. The requirement for written informed consent was waived due to the study's retrospective design.

Patients who underwent brain MRI using a multi-sequence imaging protocol for brain tumors according to clinical indication were retrospectively identified in the institutional Picture Archiving and Communication System (PACS). The time interval for PACS search ranged from February 2019 to February 2020 considering the time point of MRI acquisition. Inclusion criteria were 1) age above 18 years, 2) availability of preoperative 3-Tesla MRI including diffusion-weighted sequences, 3) diagnosis of a HGG (based on imaging findings and later confirmation by histopathological evaluation of biopsy probes or tumor tissue harvested during surgical resection), and 4) suspected motor-eloquent tumor location according to preoperative MRI (imaging suggesting infiltration or compression of anatomically suspected cortical motor-eloquent areas and/or suspected close proximity to the CST). The exclusion criteria were 1) artifacts due to implants or motion artifacts in imaging data according to visual image evaluation (e.g., non-diagnostic image quality due to patient movement during image acquisition), and 2) previous brain surgery.

Overall, 40 patients fulfilled the inclusion criteria and were considered for this study. Clinical details including demographics and final histopathological tumor grading were extracted from electronic health records of these patients.

Magnetic Resonance Imaging

Cranial MRI was performed in the preoperative routine setting. All imaging considered in this study was acquired on the same two 3-Tesla scanners (Achieva dStream or Ingenia; Philips Healthcare, Best, Netherlands) using a 32-channel head coil.

The standardized multi-sequence imaging protocol for brain tumors included a three-dimensional (3D) fluid attenuated inversion recovery (FLAIR) sequence (repetition time [TR]/ echo time [TE]: 4800/277 ms, 1 mm^3 isovoxel covering the whole head), an axial T2-weighted sequence (TR/TE: 3396/87 ms, voxel size of 0.36×0.36×4 mm^3), a diffusion-weighted sequence (TR/TE: 5000/78 ms, voxel size of 2x2x2 mm^3, one volume at b = 0 s/mm^2, 32 volumes at b = 1000 s/mm^2), and a 3D T1-weighted turbo field echo (TFE) sequence (TR/TE: 9/4 ms, 1 mm^3 isovoxel covering the whole head) without and with application of a contrast agent using a dose of 0.2 ml per kg body weight of gadoteric acid (Dotagraf 0.5 mmol/ml; Jenapharm GmbH & Co. KG, Jena, Germany). Further sequences not related to this study's analyses were acquired by default and used for radiological reporting and image-based diagnostics.

Data Processing

Co-Registration and Segmentation

First, to avoid errors in the automated structural parcellation due to the presence of pathology and related anatomical distortion, lesion filling for the T1-weighted images was done prior to structural parcellation, which substitutes the tumor volume in the image with data mimicking signal from the healthy tissue (either using noise or healthy tissue simulation). For robust parcellation, in this work we used automated Virtual Brain Grafting (VBG), which enables the generation of a virtual lesion-free T1-weighted image and structural parcellation using FreeSurfer recon-all (https://github.com/KUL-Radneuron/KUL_VBG/; KU Leuven, Department of Imaging and Pathology, Translational MRI, Leuven, Belgium) (50, 51). Lesion segmentation required for VBG was obtained fusing eight segmentation algorithms using majority voting from the Brain Tumor Segmentation (BraTS) toolkit (52, 53). The BraTS toolkit relies on a multi-modal input (non-contrast and contrast-enhanced T1-weighted images, FLAIR images, and T2-weighted images) and produces segmentation masks that enclose the tumor core (necrotic center and contrast-enhancing tumor parts) and FLAIR-hyperintense zones (edema/tumor infiltration), which were further used to compute the respective volumes (by accumulating volumes of each voxel in the respective masks) (52, 53). Before performing segmentations, all MRI data were transferred to

Montreal Neurological Institute (MNI) space (with an isotropic voxel size of 1 mm^3).

The diffusion-weighted MRI data of the individual patients were corrected for motion and eddy currents, and co-registered to the corresponding T1-weighted images using *ExploreDTI* (version 4.8.6; http://www.exploredti.com/; PROVIDI Lab, Utrecht, Netherlands) (54). The FODs were estimated using recursive calibration of the response function (55). We used a spherical harmonics order of $L_{max} = 6$. Motor cortex masks were assembled from precentral, postcentral, and paracentral lobule segmentations (**Figure 1A**) obtained with *FreeSurfer* (version 6.0.0; http://surfer.nmr.mgh.harvard.edu; Laboratory for Computational Neuroimaging, Charlestown, MA, USA) (51) using the Desikan-Killiany atlas (56). All image co-registrations and segmentations were visually inspected for quality and, in case of segmentations, manually corrected by a neuroradiologist when necessary.

Fiber Tacking Algorithms

Three deterministic tractography approaches were used in this study to reconstruct the CST of both hemispheres: DTI-based tractography, CSD-based tractography, and MLFT. DTI-based tractography was chosen since it is widely used in current clinical practice (36, 57). This algorithm propagates fiber streamlines into the main direction of the estimated diffusion tensor. However, it leads to issues with reconstructing pathways in certain complex situations (e.g., crossing or kissing fibers) when the estimated diffusion becomes closer to isotropic and the main tensor direction may not coincide with any of the underlying fiber orientations (38, 39). CSD-based tractography has improved the specificity compared to DTI-based tractography given higher angular resolution and an ability to disentangle more complex fiber configurations (41, 42). During pathway propagation each time the algorithm chooses an FOD peak that minimizes angular deviation from the previous step. The CSD approach was included as it has shown to be capable of adequately accounting for crossing fiber configurations, and it serves as a basis for the MLFT algorithm.

The recently proposed MLFT algorithm reconstructs bundles as multi-level structures, with the exact number of levels defined by the user (48, 49). Given a seed and a target region, MLFT aims to iteratively improve bundle reconstruction by adding pathways with high angulation reaching the target region (48, 49). At each iteration, MLFT propagates pathways from a set of seed points using deterministic CSD-based tractography that takes every step into the direction of a FOD peak the least deviating from the direction of the previous step. After propagation, the points of the pathways that did not reach the target region are used as seed points for the following iteration. Their initial directions are then defined as the peaks of the corresponding FODs that were ignored during propagation. If a seed point corresponds to multiple unused FOD peaks, it is duplicated to allow propagating each of the alternative directions. The rest of the pathways reaching the target region are forming a new level of the reconstruction. They are concatenated with the segment of the pathway they branched from that originates from the prior seed point set. This procedure is repeated for a predefined number of iterations. For the CST reconstruction, two levels (iterations) were used in this study. Thus, by extending the reconstruction with each new level, MLFT is attempting to account for branching fibers. It was also shown to preserve topography of the bundles (48, 49).

Additionally, it can be noticed that the reconstructions performed with deterministic CSD-based tractography are essentially the first level of the MLFT reconstructions. Thus, the extent of MLFT reconstructions will always at least cover that of the CSD-based algorithm.

Tractography Setup

To reconstruct the CST within each hemisphere, the seed region was placed in the single-slice transverse cross-section of the pontine level of the brain stem as obtained from brain parcellations (**Figure 1B**) (58). Motor cortex masks assembled from the segmentation of precentral, postcentral, and paracentral gyri of the left and right hemisphere, respectively, were set as target regions for MLFT and as a region of interest (ROI) to filter the results of DTI- and CSD-based tractography (**Figure 1A**). Five seed points were sampled per voxel in the seed mask at a single-slice level in the superior part of the brain stem, ensuring that all the points were on the same transverse plane. The tractography step was set to half a voxel size, the angular threshold was set to 45° (48, 49). For MLFT and CSD-based tractography the FOD peak threshold amplitude was set to 0.08, which was chosen empirically based on visual inspection of the results and with the aim to increase the volume of the reconstruction without introducing obvious false-positive

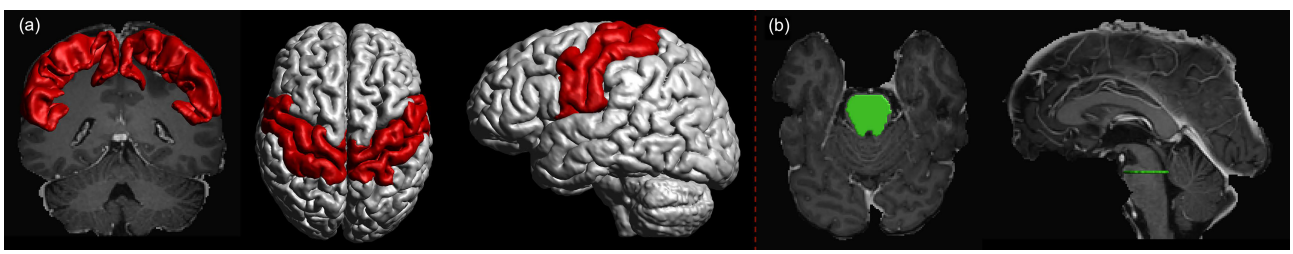

FIGURE 1 | **(A)** Motor cortex mask (red) was assembled using precentral, postcentral, and paracentral gyri as segmented using FreeSurfer. The motor cortex mask was used as a target region. **(B)** The seed region (green) was defined as a cross-section of the brain stem at the pontine level.

pathways. For DTI-based tractography the fractional anisotropy (FA) threshold was set to 0.1. The number of iterations was set to 2 for MLFT. Additionally, due to reconstruction of CST branches for the left and right hemisphere from the same seed region in the brain stem, interhemispheric connections were filtered out. Additional experiments evaluating algorithms on fine-grained target regions are provided in the **Supplementary Material**.

Fiber Tracking Evaluation

Qualitative Assessment

Visual image evaluation was performed by a neuroradiologist (7 years of experience in neuroradiological imaging) using *ExploreDTI*. The reconstructed bundles were rendered in the same scene as the contrast-enhanced T1-weighted images for an interactive assessment of the course of the CST and its relation to the tumor.

Patients were pseudonymized during all visual image evaluations. In detail, datasets stemming from DTI-based tractography, CSD-based tractography, and MLFT were opened during three rounds of evaluation, with each round randomly including one of those tractography results per patient. Between each round of assessment, an interval of at least two weeks was established to minimize recall bias. Both the tumor-affected and unaffected hemispheres were separately evaluated per patient. First, the course of the reconstructed CST through anatomical landmarks known to be key for the descending CST (ipsilateral internal capsule and cerebral crus at the level of the brain stem) was assessed in binary fashion (CST passing through/not passing through internal capsule and cerebral crus). Second, for tractography within the tumor-affected hemisphere, the neuroradiologist assessed whether the reconstructed CST appeared to be unaffected (no contact and no visually identifiable deviation), spatially deviated, infiltrated or split, or destroyed (entire or partial disintegration of the CST) due to the tumor mass, similar to previous work on qualitative evaluation of fiber tract anatomy (59).

Quantitative Assessment

Quantitative assessment of the CST bundles reconstructed with DTI-based, CSD-based tractography, and MLFT was performed, including radial extent and coverage of reconstructed fibers. The radial extent (in °) of the CST was calculated to show how much of the motor cortex is covered, which was achieved by computing the size of the segment of the coronal motor mask projection covered by the CST. Thus, the motor mask projection defines an arc of 90°, and the overlap of the bundle visitation mask on the motor cortex defines segments on the arc that constitute the radial extent. The difference in radial extents of the bundles reconstructed in tumor-affected and unaffected hemispheres was compared. Outliers in the difference distribution were detected as patients falling into the distribution tails and accounting for about 5% of the distribution. The threshold for the detection was calculated using the 2σ rule, where σ is the standard deviation (SD).

Given its wide use in clinical routine, DTI-based tractography was considered a baseline of comparison for the assessment of the algorithms regarding bundle trajectory. Thus, in order to assess the coherence of the CSD-based tractography and MLFT reconstructions with the DTI-based tractography results, coverage of the bundles generated with DTI-based tractography by the ones generated with CSD and MLFT was calculated. For calculation, binary visitation masks were created of the reconstructed bundles (with voxels being set to 1 if at least one pathway passed through it). Then, the part of the DTI-reconstructed bundle's mask intersecting with corresponding masks of the MLFT and the CSD-based reconstructions was calculated (in %, where 90% DTI coverage by MLFT would mean that 90% of the CST volume reconstructed by DTI-based tractography is also included in the respective reconstructed bundle when MLFT is used as the tractography algorithm in the same patient). The masks consisted of the voxels visited by the corresponding bundle (voxel contains at least one pathway point). All computations for quantitative image assessment were performed using in-house developed MATLAB scripts (version R2018b; The MathWorks Inc., Natick, MA, USA).

Statistics

For statistical data analyses, SPSS (version 26.0; IBM SPSS Statistics for Windows, IBM Corp., Armonk, NY, USA) and SciPy library [version 1.3.1; https://www.scipy.org/scipylib/ (60)] were used. In all statistical tests a significance level of $\alpha = 0.05$ was used.

Descriptive statistics included mean ± SD, ranges, and absolute or relative frequencies. For qualitative image assessment in the tumor-affected hemisphere, Chi-squared tests were conducted to test for differences in the spatial characteristics of the CST (unaffected, spatially deviated, infiltrated/split, or destroyed) between DTI-based tractography, CSD-based tractography, and MLFT. For quantitative image assessment, the tractography algorithms were first compared to each other based on the radial extents of the reconstructions, separately for the unaffected and tumor-affected hemispheres and for the right versus left hemispheres, using two-sided Wilcoxon signed-rank tests. Furthermore, Wilcoxon signed-rank tests were used to compare the radial extents achieved by the same algorithm in affected and unaffected hemispheres, respectively.

Additionally, the coverage of the DTI-based reconstruction of the CST by CSD-based tractography and MLFT was compared for unaffected and tumor-affected hemispheres using two-sided Wilcoxon signed-rank tests. This allowed to assess if the presence of the tumor and related mass effects caused a significant change in the results of MLFT and CSD-based tractography compared to DTI-based tractography for tract coverage. In addition, correlations between the ratio of DTI-based reconstructions of the CST covered by CSD-based tractography or MLFT with the tumor core volumes or FLAIR-hyperintensity zone volumes were calculated using Pearson correlation coefficients.

RESULTS

Patient Cohort

Forty patients (mean age: 62.6 ± 13.4 years, age range: 29.5 – 85.9 years, 17 females and 23 males) with a diagnosis of HGG and suspected motor-eloquent tumor location were included. **Table 1** provides further cohort details.

TABLE 1 | Characteristics of the study cohort.

Item		Value
Age		62.6 ± 13.4
(years; mean ± SD & range)		(29.5 – 85.9)
Sex	Male	57.5
(% of patients)	Female	42.5
Affected hemisphere	Left	40.0
(% of patients)	Right	60.0
Surgical procedure	Biopsy	22.5
performed	Resection	67.5
(% of patients)	Resection & intraoperative RTX	10.0
Extent of resection	STR	25.8
(% of patients)	GTR	74.2
Tumor grade	WHO grade III	12.5
(% of patients)	WHO grade IV	87.5
Tumor core volume		47,997.4 ± 39,098.9
(mm^3, mean ± SD & range)		(2,582 – 170,576)
Volume of FLAIR-hyperintense zone		64,727.3 ± 48,394.8
(mm^3, mean ± SD & range)		(4,625 – 184,127)

SD, standard deviation; WHO, World Health Organization; STR, subtotal resection; GTR, gross total resection; RTX, radiotherapy.

Qualitative Assessment

Representative exemplary cases for CST reconstruction by DTI-based tractography, CSD-based tractography, and MLFT are shown in **Figures 2**, **3**. The reconstructed CST passed through the internal capsule and cerebral crus as key anatomical landmarks for both hemispheres of all enrolled patients.

The reconstructed CST bundle was unaffected by or not in contact with the tumor mass in n=15, 8, and 4 patients for DTI-based tractography, CSD-based tractography, and MLFT, respectively, and did not fulfill the criteria of a disintegrated course in any of the patients. Furthermore, the reconstructed CST bundle was deviated in n=24, 26, and 22 patients, respectively. It appeared to be infiltrated/split in n=1, 6, and 14 patients when using DTI-based tractography, CSD-based tractography, or MLFT, respectively. There was a statistically significant difference in these spatial characteristics of the CST depending on the tractography approach chosen ($p = 0.0006$).

Quantitative Assessment

Radial Extent

The radial extents of the CST branches reconstructed with the three tractography algorithms are presented in **Figures 4**, **5**. The MLFT algorithm consistently provides increased radial extent when compared to both CSD-based and DTI-based tractography in all patients. In addition, when comparing radial extents between reconstructions from the three different tractography algorithms, results were statistically significant throughout (DTI vs. CSD/DTI vs. MLFT/CSD vs. MLFT: $p < 0.05$ each for tumor-affected vs. unaffected as well as right vs. left hemispheres; **Table 2**).

Each of the algorithms produced CST reconstructions with higher median radial extent of the reconstructions for the tumor-affected hemispheres as compared to the unaffected hemispheres, with a statistically significant difference only for MLFT (median radial extent for tumor-affected vs. unaffected hemisphere – DTI: 19.46° vs. 18.99°, $p = 0.8931$; CSD: 30.54° vs. 27.63°, $p = 0.0546$; MLFT: 81.17° vs. 74.59°, $p = 0.0134$).

Furthermore, the differences in radial extents of the CST bundles in tumor-affected and unaffected hemispheres were compared (**Figure 6**). Using 2σ, three outliers were identified (patients #8, #10, and #37), who were all characterized by extensive mass effect that caused deformation of the CST bundle within the tumor-affected hemisphere, and to a lesser extent also a deviation of the CST within the unaffected hemisphere (**Figure 7**). Midline shifts can be observed in these three outliers.

Coverage of DTI

The results on comparing the coverage of DTI-based reconstructions by the corresponding CSD-based and MLFT-based reconstructions are depicted in **Figure 8**. MLFT provides a higher fraction of coverage of the DTI reconstruction results of the CST when compared to CSD.

Both CSD-based and MLFT results more clearly coincide with DTI-based reconstructions in case of the unaffected hemispheres (median coverage for affected vs. unaffected hemisphere – CSD: 68.16% vs. 77.59%, $p = 0.0075$; MLFT: 93.09% vs. 95.49%; $p = 0.0046$), while the reconstructions in the tumor-affected hemisphere are characterized by a higher mismatch. Yet, for the MLFT median coverage is >90% for both the unaffected and tumor-affected hemisphere, which contrasts with the CSD-based reconstruction with a median coverage of <80%. The two patients that had the lowest DTI coverage (lower than 75%) in the tumor-affected hemisphere by the MLFT reconstructions were subjects with extensive mass effects and high tumor volume, namely patients #5 and #17. The lowest DTI coverage achieved with CSD-based tractography is also attributed to patient #5. For these patients, tumor volumes as well as volumes of the FLAIR-hyperintense zones ranged in the upper quartile.

The correlation coefficients of the DTI coverage by CSD-based tractography or MLFT with the tumor core (necrotic center and contrast-enhancing tumor parts) and FLAIR-hyperintense zones are shown in **Table 3**. There were statistically significant negative correlations between the

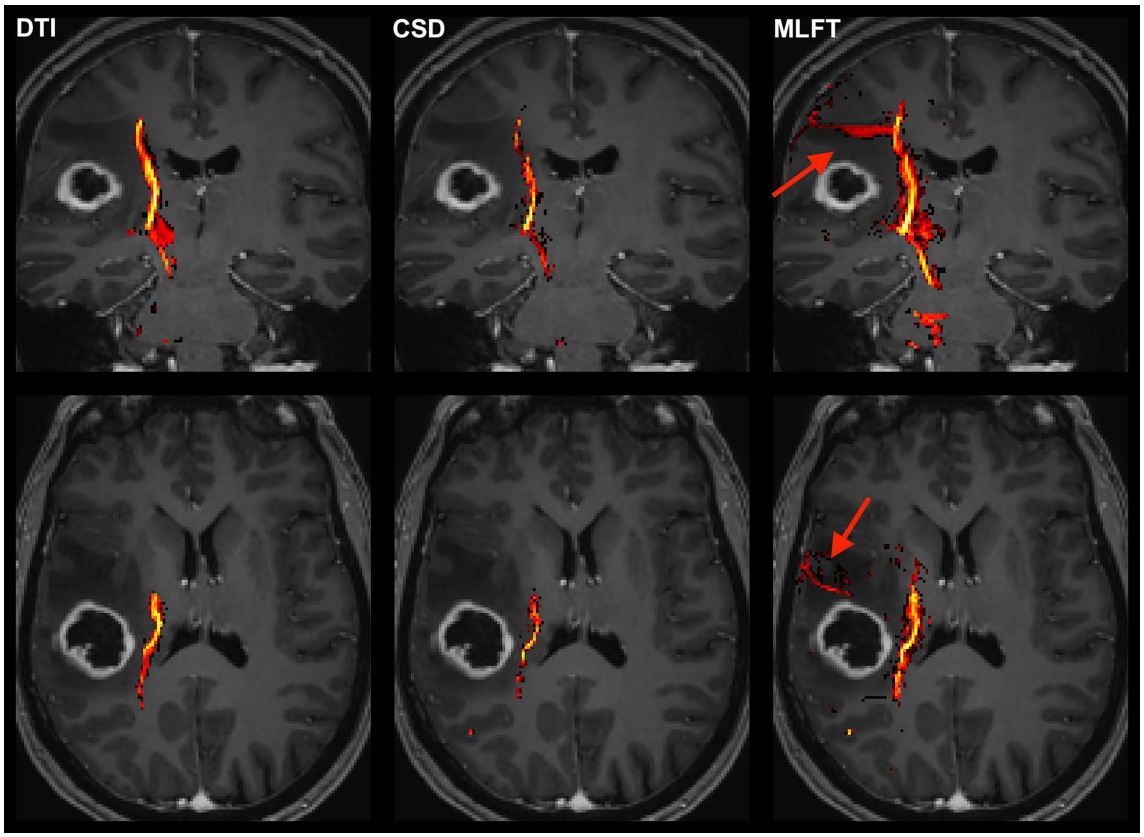

FIGURE 2 | Exemplary case for reconstruction of the corticospinal tract (CST) depending on the algorithm used for tractography. This illustrative exemplary case of a patient suffering from a right-sided high-grade glioma (HGG) shows the reconstructed CST within the tumor-affected hemisphere as derived from diffusion tensor imaging (DTI)-based tractography, constrained spherical deconvolution (CSD)-based tractography, and multi-level fiber tracking (MLFT). The CST reconstructions are fused with axial and coronal contrast-enhanced T1-weighted images to outline the lesion-to-CST relationship as well as the CST volume and course. The MLFT approach enables fiber tracking with a larger radial extent, thus displaying also fanning of the CST and fibers with acute angles (red arrow).

volume of the FLAIR-hyperintense zone and the DTI coverage (CSD: r = -0.52, p = 0.0006; MLFT: r = -0.52, p = 0.0005). Likewise, there were statistically significant negative correlations between the volume of the tumor core plus the volume of the FLAIR-hyperintense zone and DTI coverage (CSD: r = -0.48, p = 0.0018; MLFT: r = -0.47, p = 0.0021).

DISCUSSION

In this work we evaluated a novel tractography algorithm, MLFT, to achieve improved reconstruction of the CST in patients with motor-eloquent HGG. The MLFT algorithm was compared to deterministic DTI-based and deterministic CSD-based tractography of the CST of both hemispheres. The main findings are as follows: 1) the algorithm chosen for tractography had significant impact on the spatial course, volume, and shape of the CST, with MLFT-based reconstructions showing significantly higher radial extents; 2) compared to deterministic CSD-based tractography, MLFT showed higher coincidence with the DTI-based reconstructions, with a median coverage of >90% for both the tumor-affected as well as unaffected hemispheres; and 3) coverage of the CST as tracked by the DTI-based algorithm was significantly negatively associated with tumor-related mass effects (as estimated by volumes of tumor core and FLAIR-hyperintense zones) for both the CSD-based algorithm and MLFT.

Tractography of WM structures such as the CST is frequently employed for preoperative planning and intraoperative resection guidance in patients with intracranial neoplasms, using primarily DTI-based approaches (27–31). However, DTI-based tractography has several known limitations that may hamper value for clinical applications, including its limited ability to resolve geometrically complex situations such as crossing or kissing fibers (38, 39). Previous research has shown that using more advanced techniques, such as q-ball and CSD-based fiber tractography, may lead to improved results (37, 61, 62). In turn, the proposed MLFT algorithm is developed from CSD-based tractography and similarly propagates fiber pathways based on FOD peaks. However, unlike CSD-based tractography, MLFT assumes that FOD peaks represent not only fiber crossings, but also indicate fiber branching or high-angular deviation (48, 49). Without prior anatomical knowledge, such

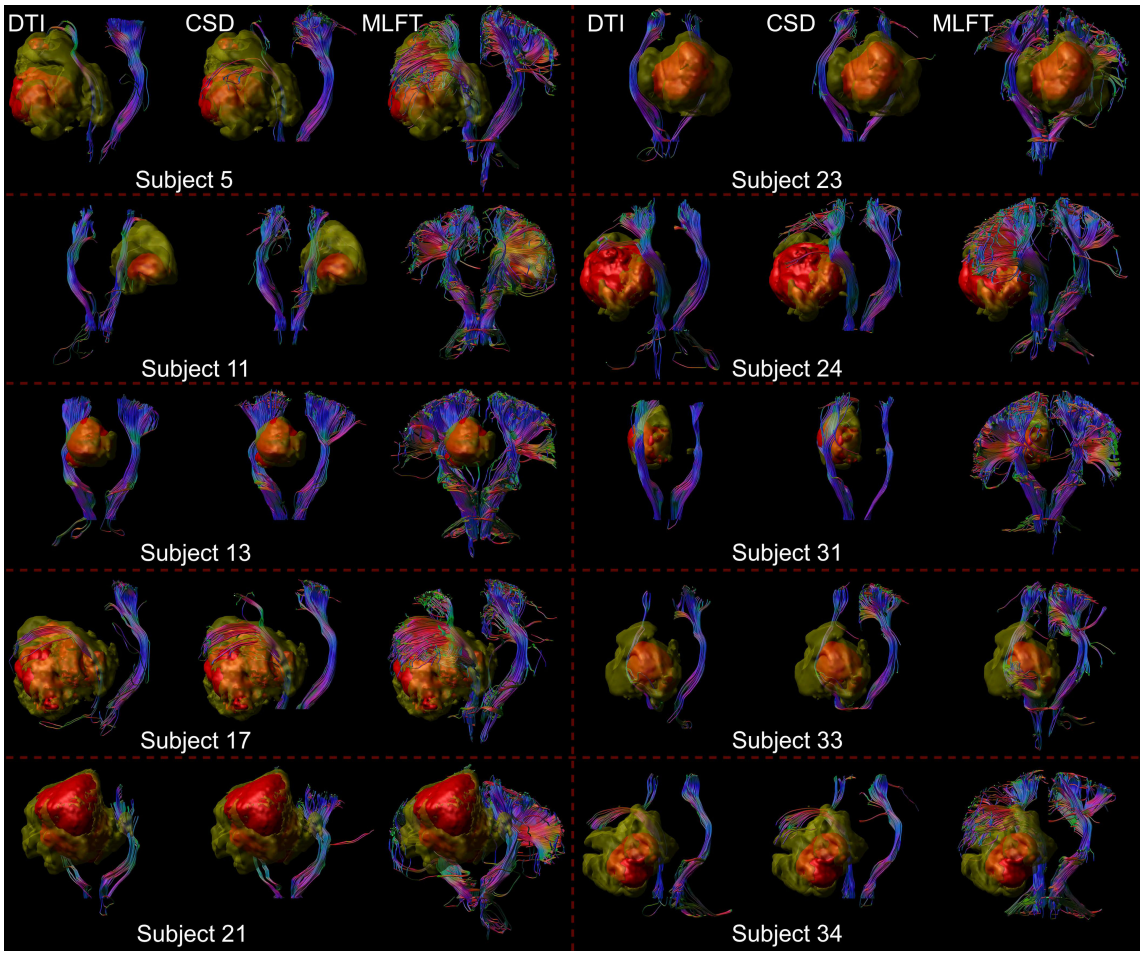

FIGURE 3 | Comparison of reconstructions of the corticospinal tract (CST) depending on the algorithm chosen for tractography. This figure shows reconstructions of the CST within the tumor-affected and unaffected hemispheres in a subset of 10 patients from the cohort, using diffusion tensor imaging (DTI)-based tractography, constrained spherical deconvolution (CSD)-based tractography, and multi-level fiber tracking (MLFT). The tumor core is shown as a red volume, the hyperintense zone in fluid attenuated inversion recovery (FLAIR) sequences is shown as a yellow volume. While CSD-based tractography provides reconstructions comparable to DTI-based tractography, MLFT is able to improve depiction of the extent of the CST fanning of both tumor-affected and unaffected hemispheres.

an approach would be at risk of generating multiple false-positive streamlines, which needs to be avoided particularly for ultimate clinical applicability. In order to prevent a high false-positive rate, MLFT requires well-defined target and seed regions, and if certain pathways do not enter the target area our algorithm checks if any deviation at the previous points would allow reaching the target region. Hence, using the algorithm gives some control over specificity while improving sensitivity.

Reconstructions of the CST using MLFT consistently showed the highest radial extent when compared to DTI- or CSD-based tractography (**Figure 3**). On average, CSD-based tractography achieved higher radial extent than the DTI-based algorithm (**Table 2**), while in some individual cases DTI-based tractography outperforms the CSD algorithm for this metric (**Figure 4**). Yet, MLFT provided CST branches with higher radial extents even for the tumor-affected hemispheres, which may indicate that a more complete reconstruction of particularly highly angulated parts of the CST close to its origin becomes possible when using MLFT (**Figures 4**, **5**). Indeed, based on simulations and preliminary *in-vivo* imaging in a cohort of healthy subjects, it has been suggested that the fanning close to the motor cortex can be well delineated with MLFT (48, 49). Considering the potential value of a broader fanning and reconstruction of laterally coursing fiber pathways, MLFT-derived reconstructions may be of merit since especially marginal fibers can be at risk for damage when aiming at a maximized EOR during surgery of motor-eloquent HGGs.

When comparing radial extents of tumor-affected and unaffected hemispheres, the observed differences are mostly comparable across the algorithms (**Figure 6**). Further, we separately explored the outliers with values above the mean + 2σ, given that they were of most interest, while any cases below the mean – 2σ were considered in the range of an expected result. As the unaffected hemisphere apparently does not show

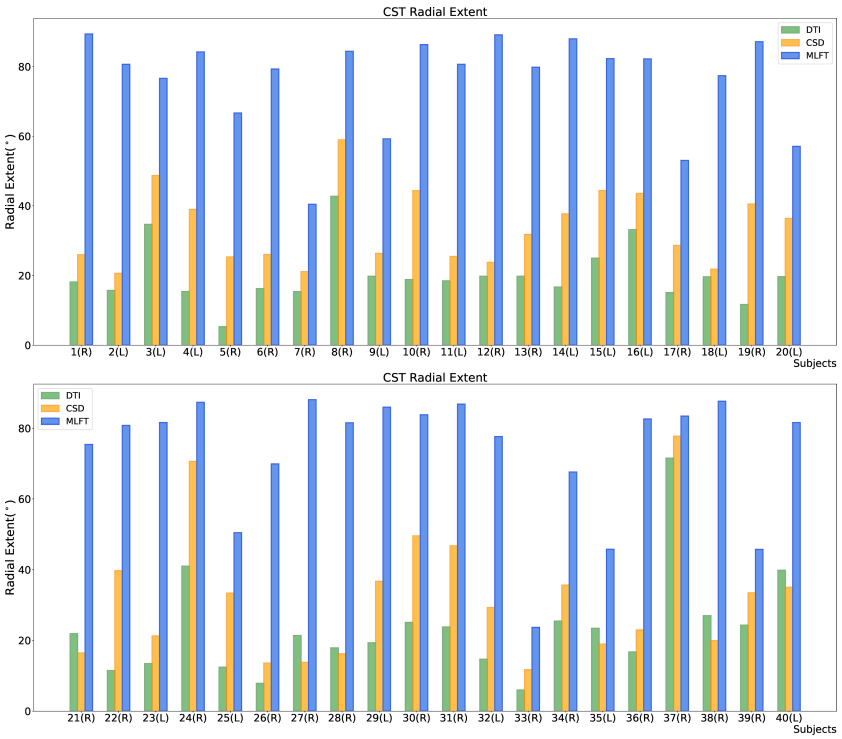

FIGURE 4 | Comparison of the radial extent of the corticospinal tract (CST) branches of the tumor-affected hemispheres. This figure illustrates the radial extent for CST reconstruction using diffusion tensor imaging (DTI)-based tractography (green), constrained spherical deconvolution (CSD)-based tractography (orange), and multi-level fiber tracking (MLFT; blue). The hemisphere affected by the tumor per patient is indicated next to the subject index (L – left, R – right). Using MLFT led to CST reconstructions with larger radial extent in all patients.

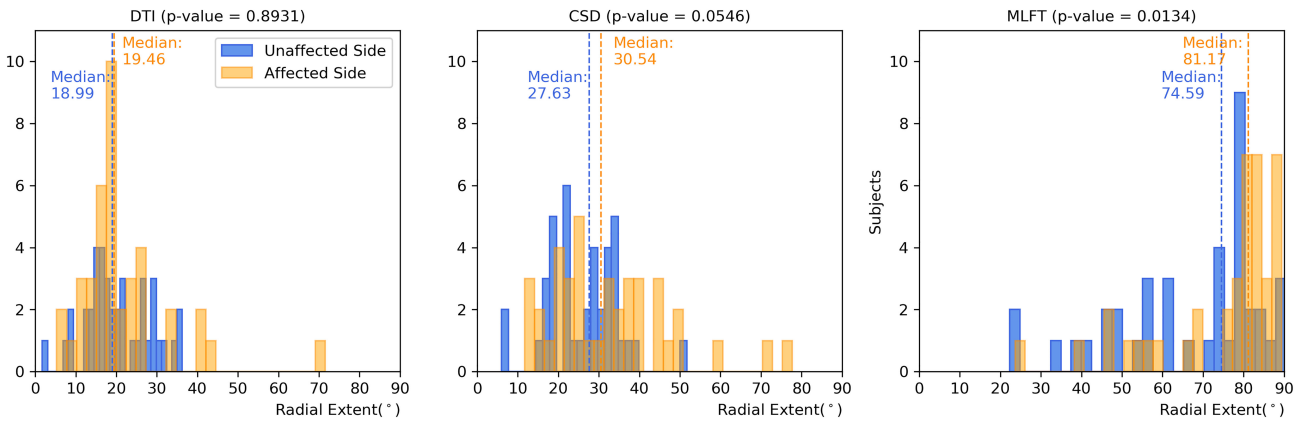

FIGURE 5 | Comparison of the radial extent of the corticospinal tract (CST) branches. This figure shows the radial extents (with median values as vertical dashed lines) for the CST reconstructions derived from diffusion tensor imaging (DTI)-based tractography, constrained spherical deconvolution (CSD)-based tractography, and multi-level fiber tracking (MLFT). Columns for the tumor-affected hemispheres are displayed in orange, columns for the unaffected hemispheres are depicted in blue. The affected hemispheres show higher radial extent in case of each of the used tractography algorithms. The p-values are derived from comparisons between hemispheres per tractography algorithm (Wilcoxon signed-rank paired tests with significance level α=0.05).

the same changes in microstructure related to a tumor, the CST extent there should be at least comparable. Patients with considerable radial extent differences (above the 2σ threshold) are all characterized by mass effects extensive enough to cause midline shift and introduce deformations to the bundle in unaffected hemispheres (**Figure 7**), while the opposite is not always true. Depending on the distinct location of the tumor, midline shift may not lead to higher radial extent of the CST in

TABLE 2 | Radial extent of fiber reconstructions.

Radial Extent Hemisphere	Mean ± SD, (°)			Range, (°)			P-value		
	DTI	CSD	MLFT	DTI	CSD	MLFT	CSD–DTI	MLFT–DTI	MLFT–CSD
Right	21.9 ± 11.7	30.0 ±14.6	73.8 ± 16.1	5.28 – 71.53	11.68 – 77.75	23.65 – 90.45	$5.5*10^{-5}$	$3.6*10^{-8}$	$3.6*10^{-8}$
Left	20.1 ± 8.3	28.9 ± 10.5	67.8 ± 18.3	1.75 – 39.84	5.97 – 51.72	22.31 – 90.07	$5.3*10^{-7}$	$3.6*10^{-8}$	$3.6*10^{-8}$
Affected	21.6 ± 11.7	32.8 ± 14.6	74.8 ± 15.6	5.28 – 71.53	11.68 – 77.75	23.65 – 89.41	$1.1*10^{-6}$	$3.6*10^{-8}$	$3.6*10^{-8}$
Unaffected	20.3 ± 8.0	26.1 ± 8.9	66.7 ± 17.9	1.75 – 36.22	5.97 – 51.72	22.31 – 90.45	$1.5*10^{-5}$	$3.6*10^{-8}$	$3.6*10^{-8}$

This table shows the mean ± SD and ranges for the radial extents of CST reconstructions with the three different algorithms used (DTI-based tractography, CSD-based tractography, and MLFT). Discrimination is made between left and right hemispheres as well as tumor-affected and unaffected hemispheres. P-values were computed for the comparisons of radial extents derived from the different algorithms (Wilcoxon signed-rank paired tests with significance level α=0.05). CST, corticospinal tract; SD, standard deviation; DTI, diffusion tensor imaging; CSD, constrained spherical deconvolution; MLFT, multi-level fiber tracking

the unaffected hemisphere; for instance, in cases of a more anterior tumor location and midline shift occurrence, no significant alteration was observed in radial extents. Regarding the reasons for the occurred differences, lateral components of the reconstructed CST pathways might be re-oriented as a result of WM compression causing smoothing of the acute angles of the fibers, which allowed the tractography algorithms to reconstruct them. Similarly, the CST pathways in the unaffected hemisphere could have been compressed and deviated in such a way that the angular resolution of the acquisition would not allow to resolve all fiber orientations properly, given that the acquired sequence only included 32 directions by default. In this regard, increasing the order of spherical harmonics used to estimate FODs would also increase the angular resolution, potentially solving the issue (41). Yet, this would require inclusion of a higher number of gradient directions in the sequence (63). At the same time, MLFT already reconstructs pathways closer to the tumor (**Figure 2**), hinting at potentially small tumor-to-CST distances that may exert impact on neurosurgical planning and have implications for patient outcome in terms of motor function and avoidance of surgery-related functional decline.

While the general trajectory and shape of the DTI-based reconstructions tend to be maintained by both MLFT and CSD-based tractography, MLFT improves the coverage of CST reconstructions as provided by DTI-based tractography over those taken from the CSD algorithm (**Figure 8**). Notably, the median coverage of DTI-based CST reconstructions by the CST as delineated with MLFT was higher than 90% for both tumor-affected and unaffected hemispheres. This indicates that the approach does not considerably increase the false-negative rate, while performing better than the CSD algorithm that provides a median coverage below 80%. At the same time, the coverage of the DTI-based CST reconstruction by MLFT as well as CSD-based tractography is inversely correlated to measures for tumor-related mass effects (as estimated by volumes of tumor core and FLAIR-hyperintense zones), which might reflect the effect of tumor-induced WM changes on the estimated orientation distribution by either of the used models (**Table 3**). However, the question arises which method comes closest to the *in-vivo* course and architecture of the CST. The gold standard to test this would be intraoperative DES, which has not been applied to evaluate CSD or MLFT results because of this study's retrospective design. Yet, there seems high agreement in neurosurgical oncology that techniques should move beyond DTI-based tractography to improve accuracy of tracking results (34–37).

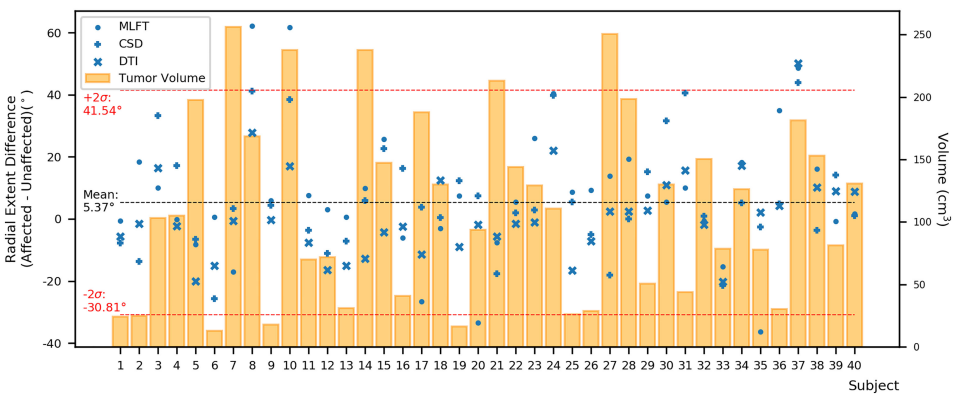

FIGURE 6 | Differences between the radial extent of tumor-affected and unaffected hemispheres. This figure shows the radial extent differences in relation to combined tumor and FLAIR-hyperintense zone volumes (orange) using the mean (black dashed line) with +/- 2 standard deviation (SD, provided as σ; red dashed lines) to identify potential outliers. Circles represent data points for the corticospinal tract (CST) as derived from multi-level fiber tracking (MLFT), while + represents data points derived from constrained spherical deconvolution (CSD)-based tractography and x represents data points stemming from diffusion tensor imaging (DTI)-based tractography. The outliers with positive radial extent difference are of most interest as they show unexpected behavior with higher radial extent in the tumor-affected hemisphere.

TABLE 3 | Correlations for coverage.

	CSD coverage of DTI		MLFT coverage of DTI	
	r	**P-value**	**r**	**P-value**
Tumor Core Volume	-0.25	0.12	-0.24	0.14
Volume of FLAIR-hyperintense zone	-0.52	<0.01	-0.52	<0.01
Volume of Tumor Core + FLAIR-hyperintense zone	-0.48	<0.01	-0.47	<0.01

This table shows the Pearson correlation coefficient (r) and related p-values for the correlations between tumor core volume, volume of FLAIR-hyperintense zone, and volume of tumor core plus FLAIR-hyperintense zone and coverage of the DTI-derived CST for reconstructions using CSD-based tractography or MLFT, respectively (significance level α=0.05). DTI, diffusion tensor imaging; CSD, constrained spherical deconvolution; MLFT, multi-level fiber tracking; FLAIR, fluid attenuated inversion recovery.

One aspect that may further improve tractography using the MLFT algorithm is to combine it with techniques that provide function-based ROIs for seeding. In this regard, previous work has used activation maps derived from functional MRI for ROI placements (64–66). More recently, motor maps derived from navigated transcranial magnetic stimulation (nTMS) have been used for ROI placements (67–72). Of note, it has been demonstrated that nTMS facilitates optimized tracking results for the CST, particularly when the primary motor cortex was in close vicinity of a brain tumor, suggesting that nTMS may be considered the method of choice to achieve proper ROI placements for CST tractography using DTI (71). Comparisons between the three algorithms using nTMS motor maps for seeding may help identify parts of the CST that are underrepresented by DTI- or CSD-based tractography but are evidently connected to the primary motor cortex, which might in particular include fibers with acute angles that could be better delineated with the MLFT method. Additionally, subcortical

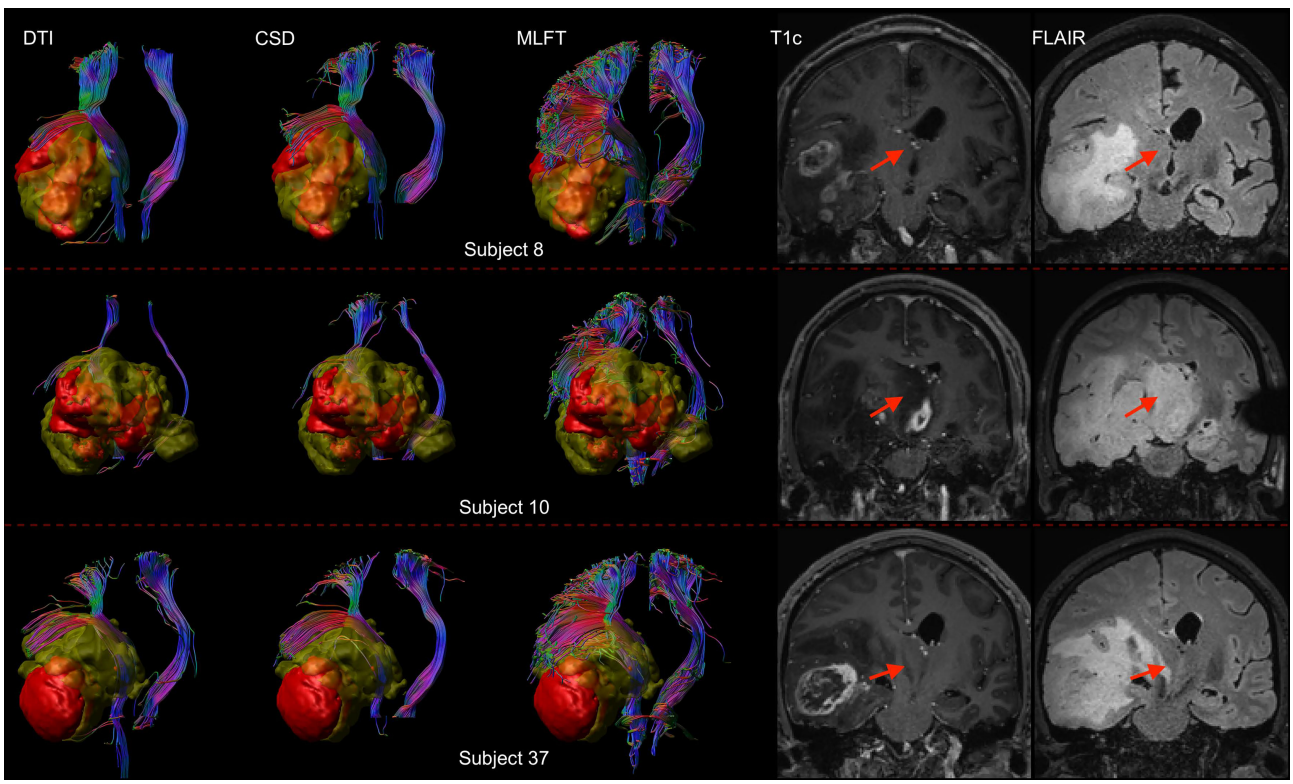

FIGURE 7 | Comparison of reconstructions of the corticospinal tract (CST) depending on the algorithm chosen for tractography in patients with high radial extent in the tumor-affected hemisphere. This figure shows reconstructions of the CST using diffusion tensor imaging (DTI)-based tractography, constrained spherical deconvolution (CSD)-based tractography, and multi-level fiber tracking (MLFT) within the tumor-affected and unaffected hemispheres in the subset of the three patients that were identified as outliers regarding radial extent within affected hemispheres (considering a 2σ threshold). The tumor core is shown as a red volume, the hyperintense zone in fluid attenuated inversion recovery (FLAIR) sequences is shown as a yellow volume. These patients were all characterized by extensive mass effect that caused deformation of the CST bundle within the tumor-affected hemisphere as well as, to a lesser extent, within the unaffected hemisphere with considerable midline shift (red arrow in coronal contrast-enhanced T1-weighted and coronal FLAIR images). In all cases, fanning is considerably improved particularly in the tumor-affected hemispheres when using the MLFT algorithm, with only few fibers with acute angles being displayed adjacent to the tumor masses when using DTI-based tractography.

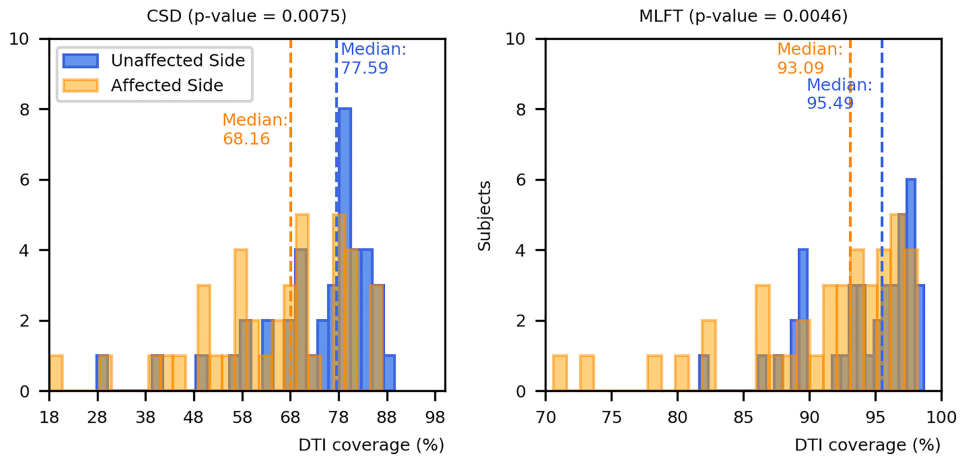

FIGURE 8 | Comparison of coverage for corticospinal tract (CST) branches. This figure shows the coverage (with median values as vertical dashed lines) of the CST reconstructions derived from diffusion tensor imaging (DTI)-based tractography by constrained spherical deconvolution (CSD)-based tractography or multi-level fiber tracking (MLFT). Columns for the tumor-affected hemispheres are displayed in orange, columns for the unaffected hemispheres are depicted in blue. The affected hemispheres show lower coverage compared to the tumor-unaffected hemispheres. The p-values are derived from comparisons between hemispheres per tractography algorithm (Wilcoxon signed-rank paired tests with significance level α=0.05).

language network analysis using nTMS-defined ROIs could be part of future work, as to date it has predominantly been performed with DTI-based tractography (68, 73–75).

The main limitation of the MLFT method is related to the accuracy of the estimated FODs in the WM. In a clinical setting neither the number of acquired directions nor b-values are routinely set high, and the accuracy of the fitted diffusion models may therefore be hampered, as the FODs have to be represented by lower-order spherical harmonics. Additionally, the FOD algorithm used does not estimate separate response functions for different tissues (55). An acquisition with multiple diffusion weightings (e.g., multi-shell imaging) would allow to use FOD estimation algorithms that are capable of differentiating multiple tissues (76). Another important limitation of this study is the absence of a correlation of the tractography results derived from CSD and MLFT to findings of intraoperative DES, as it would allow estimation of the sensitivity and specificity rates of these tractography algorithms. This is due to the study's retrospective character, while conventionally used DTI-based tractography for delineation of the CST has, however, been performed and considered for presurgical planning and intraoperative guidance within the scope of the standard of clinical care.

CONCLUSION

The results of this work suggest that tractography of the CST in patients harboring motor-eloquent HGGs may be improved using the proposed MLFT method. This advancement of the CSD principle enabled delineation of the CST with significantly increased radial extent for fibers close to the motor cortex, while maintaining coincidence with DTI-reconstructed CST bundles.

DATA AVAILABILITY STATEMENT

The data analyzed in this study is subject to the following licenses/restrictions: Analyzed dataset is a subject to medical secrecy and cannot be shared. The derivatives may be provided by the authors upon request. Requests to access these datasets should be directed to Andrey Zhylka, a.zhylka@tue.nl.

ETHICS STATEMENT

The studies involving human participants were reviewed and approved by the Ethikkommission der Technischen Universität München. Written informed consent for participation was not required for this study in accordance with the national legislation and the institutional requirements.

AUTHOR CONTRIBUTIONS

Conceptualization was performed by AZ, NS, ADL, AL, and JP. Methodology involved AZ, NS, and ADL. Software involved AZ, FK, AR, and AL. Validation was performed by NS. Formal analysis performed by AZ and NS. Investigation was performed by AZ and NS. Resources provided by JG, BW, BM, SK, CZ, JK, and SS. Data curation was performed by AZ and NS. Writing – original draft preparation was performed by AZ and NS. Writing – review and editing was performed by AZ, NS, FK, AR, ADL, JG, BW, BM, SK, CZ, JK, SS, AL, and JP. Visualization was performed by AZ and NS. Supervision was performed by NS, BM, CZ, JK, SS, AL, and JP. Project administration was performed by NS, CZ, and JK. All authors contributed to the article and approved the submitted version.

FUNDING

AZ is supported by the European Union's Horizon 2020 research and innovation program under the Marie Sklodowska-Curie grant agreement [765148]. BM, BW, and FK are supported through the SFB 824, subproject B12. This project was furthermore supported by the Deutsche Forschungsgemeinschaft (DFG) through TUM International Graduate School of Science and Engineering (IGSSE), GSC 81. The funders were not involved in the study design, collection, analysis, interpretation of data, the writing of this article or the decision to submit it for publication. All authors declare no other competing interests.

ACKNOWLEDGMENTS

We would like to thank Gabriel Girard for discussion and advice during analyses of data for this study.

SUPPLEMENTARY MATERIAL

The Supplementary Material for this article can be found online at: https://www.frontiersin.org/articles/10.3389/fonc.2021.761169/full#supplementary-material

REFERENCES

1. Ostrom QT, Bauchet L, Davis FG, Deltour I, Fisher JL, Langer CE, et al. The Epidemiology of Glioma in Adults: A "State of the Science" Review. *Neuro-Oncology* (2014) 16(7):896–913. doi: 10.1093/neuonc/nou087
2. Ostrom QT, Cote DJ, Ascha M, Kruchko C, Barnholtz-Sloan JS. Adult Glioma Incidence and Survival by Race or Ethnicity in the United States From 2000 to 2014. *JAMA Oncol* (2018) 4(9):1254–62. doi: 10.1001/jamaoncol.2018.1789
3. Wen PY, Kesari S. Malignant Gliomas in Adults. *N Engl J Med* (2008) 359 (5):492–507. doi: 10.1056/NEJMra0708126
4. Ostrom QT, Cioffi G, Gittleman H, Patil N, Waite K, Kruchko C, et al. CBTRUS Statistical Report: Primary Brain and Other Central Nervous System Tumors Diagnosed in the United States in 2012-2016. *Neuro-Oncology* (2019) 21(Suppl 5):v1–v100. doi: 10.1093/neuonc/noz150
5. Claes A, Idema AJ, Wesseling P. Diffuse Glioma Growth: A Guerilla War. *Acta Neuropathol* (2007) 114(5):443–58. doi: 10.1007/s00401-007-0293-7
6. Martinez-Garcia M, Alvarez-Linera J, Carrato C, Ley L, Luque R, Maldonado X, et al. SEOM Clinical Guidelines for Diagnosis and Treatment of Glioblastoma (2017). *Clin Trans Oncol Off Publ Fed Spanish Oncol Soc Natl Cancer Inst Mexico* (2018) 20(1):22–8. doi: 10.1007/s12094-017-1763-6
7. Stupp R, Mason WP, van den Bent MJ, Weller M, Fisher B, Taphoorn MJ, et al. Radiotherapy Plus Concomitant and Adjuvant Temozolomide for Glioblastoma. *N Engl J Med* (2005) 352(10):987–96. doi: 10.1056/NEJMoa043330
8. Sanai N, Berger MS. Surgical Oncology for Gliomas: The State of the Art. *Nat Rev Clin Oncol* (2018) 15(2):112–25. doi: 10.1038/nrclinonc.2017.171
9. Wang Y, Jiang T. Understanding High Grade Glioma: Molecular Mechanism, Therapy and Comprehensive Management. *Cancer Lett* (2013) 331(2):139–46. doi: 10.1016/j.canlet.2012.12.024
10. Khan MN, Sharma AM, Pitz M, Loewen SK, Quon H, Poulin A, et al. High-Grade Glioma Management and Response Assessment-Recent Advances and Current Challenges. *Curr Oncol* (2016) 23(4):e383–91. doi: 10.3747/co.23.3082
11. Molinaro AM, Hervey-Jumper S, Morshed RA, Young J, Han SJ, Chunduru P, et al. Association of Maximal Extent of Resection of Contrast-Enhanced and Non-Contrast-Enhanced Tumor With Survival Within Molecular Subgroups of Patients With Newly Diagnosed Glioblastoma. *JAMA Oncol* (2020) 6 (4):495–503. doi: 10.1001/jamaoncol.2019.6143
12. Brown PD, Maurer MJ, Rummans TA, Pollock BE, Ballman KV, Sloan JA, et al. A Prospective Study of Quality of Life in Adults With Newly Diagnosed High-Grade Gliomas: The Impact of the Extent of Resection on Quality of Life and Survival. *Neurosurgery* (2005) 57(3):495–504; discussion 495-504. doi: 10.1227/01.neu.0000170562.25335.c7
13. Haj A, Doenitz C, Schebesch KM, Ehrensberger D, Hau P, Putnik K, et al. Extent of Resection in Newly Diagnosed Glioblastoma: Impact of a Specialized Neuro-Oncology Care Center. *Brain Sci* (2017) 8(1):5. doi: 10.3390/brainsci8010005
14. Ammirati M, Vick N, Liao YL, Ciric I, Mikhael M. Effect of the Extent of Surgical Resection on Survival and Quality of Life in Patients With Supratentorial Glioblastomas and Anaplastic Astrocytomas. *Neurosurgery* (1987) 21(2):201–6. doi: 10.1227/00006123-198708000-00012
15. Hervey-Jumper SL, Berger MS. Evidence for Improving Outcome Through Extent of Resection. *Neurosurg Clin N Am* (2019) 30(1):85–93. doi: 10.1016/j.nec.2018.08.005
16. Lacroix M, Abi-Said D, Fourney DR, Gokaslan ZL, Shi W, DeMonte F, et al. A Multivariate Analysis of 416 Patients With Glioblastoma Multiforme: Prognosis, Extent of Resection, and Survival. *J Neurosurg* (2001) 95(2):190–8. doi: 10.3171/jns.2001.95.2.0190
17. Bloch O, Han SJ, Cha S, Sun MZ, Aghi MK, McDermott MW, et al. Impact of Extent of Resection for Recurrent Glioblastoma on Overall Survival: Clinical Article. *J Neurosurg* (2012) 117(6):1032–8. doi: 10.3171/2012.9.JNS12504
18. Duffau H, Mandonnet E. The "Onco-Functional Balance" in Surgery for Diffuse Low-Grade Glioma: Integrating the Extent of Resection With Quality of Life. *Acta Neurochirurgica* (2013) 155(6):951–7. doi: 10.1007/s00701-013-1653-9
19. Bush NA, Chang SM, Berger MS. Current and Future Strategies for Treatment of Glioma. *Neurosurg Rev* (2016) 40:1–14. doi: 10.1007/s10143-016-0709-8
20. Sanai N, Berger MS. Intraoperative Stimulation Techniques for Functional Pathway Preservation and Glioma Resection. *Neurosurg Focus* (2010) 28(2): E1. doi: 10.3171/2009.12.FOCUS09266
21. De Witt Hamer PC, Robles SG, Zwinderman AH, Duffau H, Berger MS. Impact of Intraoperative Stimulation Brain Mapping on Glioma Surgery Outcome: A Meta-Analysis. *J Clin Oncol Off J Am Soc Clin Oncol* (2012) 30 (20):2559–65. doi: 10.1200/JCO.2011.38.4818
22. Hervey-Jumper SL, Berger MS. Maximizing Safe Resection of Low- and High-Grade Glioma. *J Neuro-Oncol* (2016) 130(2):269–82. doi: 10.1007/s11060-016-2110-4
23. Villanueva-Meyer JE, Mabray MC, Cha S. Current Clinical Brain Tumor Imaging. *Neurosurgery* (2017) 81(3):397–415. doi: 10.1093/neuros/nyx103
24. Shukla G, Alexander GS, Bakas S, Nikam R, Talekar K, Palmer JD, et al. Advanced Magnetic Resonance Imaging in Glioblastoma: A Review. *Chin Clin Oncol* (2017) 6(4):40. doi: 10.21037/cco.2017.06.28
25. Overcast WB, Davis KM, Ho CY, Hutchins GD, Green MA, Graner BD, et al. Advanced Imaging Techniques for Neuro-Oncologic Tumor Diagnosis, With an Emphasis on PET-MRI Imaging of Malignant Brain Tumors. *Curr Oncol Rep* (2021) 23(3):34. doi: 10.1007/s11912-021-01020-2
26. Smits M. MRI Biomarkers in Neuro-Oncology. *Nat Rev Neurol* (2021) 17:486–500. doi: 10.1038/s41582-021-00510-y
27. Assaf Y, Pasternak O. Diffusion Tensor Imaging (DTI)-Based White Matter Mapping in Brain Research: A Review. *J Mol Neurosci* (2008) 34(1):51–61. doi: 10.1007/s12031-007-0029-0
28. Ulmer JL, Klein AP, Mueller WM, DeYoe EA, Mark LP. Preoperative Diffusion Tensor Imaging: Improving Neurosurgical Outcomes in Brain Tumor Patients. *Neuroimaging Clinics N Am* (2014) 24(4):599–617. doi: 10.1016/j.nic.2014.08.002
29. Ulmer JL, Salvan CV, Mueller WM, Krouwer HG, Stroe GO, Aralasmak A, et al. The Role of Diffusion Tensor Imaging in Establishing the Proximity of Tumor Borders to Functional Brain Systems: Implications for Preoperative Risk Assessments and Postoperative Outcomes. *Technol Cancer Res Treat* (2004) 3(6):567–76. doi: 10.1177/153303460400300606
30. Basser PJ, Mattiello J, LeBihan D. MR Diffusion Tensor Spectroscopy and Imaging. *Biophys J* (1994) 66(1):259–67. doi: 10.1016/S0006-3495(94)80775-1

31. Abdullah KG, Lubelski D, Nucifora PG, Brem S. Use of Diffusion Tensor Imaging in Glioma Resection. *Neurosurgical Focus* (2013) 34(4):E1. doi: 10.3171/2013.1.FOCUS12412
32. Maier-Hein KH, Neher PF, Houde JC, Cote MA, Garyfallidis E, Zhong J, et al. The Challenge of Mapping the Human Connectome Based on Diffusion Tractography. *Nat Commun* (2017) 8(1):1349. doi: 10.1038/s41467-017-01285-x
33. Farquharson S, Tournier JD, Calamante F, Fabinyi G, Schneider-Kolsky M, Jackson GD, et al. White Matter Fiber Tractography: Why We Need to Move Beyond DTI. *J Neurosurg* (2013) 118(6):1367–77. doi: 10.3171/2013.2.JNS121294
34. Nimsky C. Fiber Tracking–A Reliable Tool for Neurosurgery? *World Neurosurg* (2010) 74(1):105–6. doi: 10.1016/j.wneu.2010.05.014
35. Duffau H. Diffusion Tensor Imaging Is a Research and Educational Tool, But Not Yet a Clinical Tool. *World Neurosurg* (2014) 82(1-2):e43–5. doi: 10.1016/j.wneu.2013.08.054
36. Potgieser AR, Wagemakers M, van Hulzen AL, de Jong BM, Hoving EW, Groen RJ. The Role of Diffusion Tensor Imaging in Brain Tumor Surgery: A Review of the Literature. *Clin Neurol Neurosurg* (2014) 124:51–8. doi: 10.1016/j.clineuro.2014.06.009
37. Becker D, Scherer M, Neher P, Jungk C, Jesser J, Pfluger I, et al. Going Beyond Diffusion Tensor Imaging Tractography in Eloquent Glioma Surgery-High-Resolution Fiber Tractography: Q-Ball or Constrained Spherical Deconvolution? *World Neurosurg* (2020) 134:e596–609. doi: 10.1016/j.wneu.2019.10.138
38. Behrens TE, Berg HJ, Jbabdi S, Rushworth MF, Woolrich MW. Probabilistic Diffusion Tractography With Multiple Fibre Orientations: What Can We Gain? *NeuroImage* (2007) 34(1):144–55. doi: 10.1016/j.neuroimage.2006.09.018
39. Jeurissen B, Leemans A, Tournier JD, Jones DK, Sijbers J. Investigating the Prevalence of Complex Fiber Configurations in White Matter Tissue With Diffusion Magnetic Resonance Imaging. *Hum Brain Mapp* (2013) 34(11):2747–66. doi: 10.1002/hbm.22099
40. Jensen JH, Helpern JA, Ramani A, Lu H, Kaczynski K. Diffusional Kurtosis Imaging: The Quantification of Non-Gaussian Water Diffusion by Means of Magnetic Resonance Imaging. *Magnetic Reson Med Off J Soc Magnetic Reson Med / Soc Magnetic Reson Med* (2005) 53(6):1432–40. doi: 10.1002/mrm.20508
41. Tournier JD, Calamante F, Connelly A. Robust Determination of the Fibre Orientation Distribution in Diffusion MRI: Non-Negativity Constrained Super-Resolved Spherical Deconvolution. *NeuroImage* (2007) 35(4):1459–72. doi: 10.1016/j.neuroimage.2007.02.016
42. Jeurissen B, Leemans A, Jones DK, Tournier JD, Sijbers J. Probabilistic Fiber Tracking Using the Residual Bootstrap With Constrained Spherical Deconvolution. *Hum Brain Mapp* (2011) 32(3):461–79. doi: 10.1002/hbm.21032
43. Mortazavi F, Oblak AL, Morrison WZ, Schmahmann JD, Stanley HE, Wedeen VJ, et al. Geometric Navigation of Axons in a Cerebral Pathway: Comparing dMRI With Tract Tracing and Immunohistochemistry. *Cereb Cortex* (2018) 28(4):1219–32. doi: 10.1093/cercor/bhx034
44. Mormina E, Longo M, Arrigo A, Alafaci C, Tomasello F, Calamuneri A, et al. MRI Tractography of Corticospinal Tract and Arcuate Fasciculus in High-Grade Gliomas Performed by Constrained Spherical Deconvolution: Qualitative and Quantitative Analysis. *AJNR Am J Neuroradiol* (2015) 36(10):1853–8. doi: 10.3174/ajnr.A4368
45. Sheng Z, Yu J, Chen Z, Sun Y, Bu X, Wang M, et al. Constrained-Spherical Deconvolution Tractography in the Evaluation of the Corticospinal Tract in Glioma Surgery. *Front Surg* (2021) 8:646465. doi: 10.3389/fsurg.2021.646465
46. Mormina E, Arrigo A, Calamuneri A, Alafaci C, Tomasello F, Morabito R, et al. Optic Radiations Evaluation in Patients Affected by High-Grade Gliomas: A Side-by-Side Constrained Spherical Deconvolution and Diffusion Tensor Imaging Study. *Neuroradiology* (2016) 58(11):1067–75. doi: 10.1007/s00234-016-1732-8
47. Tournier JD, Smith R, Raffelt D, Tabbara R, Dhollander T, Pietsch M, et al. MRtrix3: A Fast, Flexible and Open Software Framework for Medical Image Processing and Visualisation. *NeuroImage* (2019) 202:116137. doi: 10.1016/j.neuroimage.2019.116137
48. Zhylka A, Leemans A, Pluim J, De Luca A. Anatomically Informed Multi-Level Fiber Tractography. *bioRxiv* (2020). doi: 10.1101/2020.12.16.423042.
49. Zhylka A, Leemans A, Pluim J, De Luca A. Anatomically Informed Multi-Level Fiber Tractography for Improved Sensitivity of White Matter Bundle Reconstruction in Diffusion MRI. *Proc Intl Soc Mag Reson Med* (2020) 28:855.
50. Radwan AM, Emsell L, Blommaert J, Zhylka A, Kovacs S, Theys T, et al. Virtual Brain Grafting: Enabling Whole Brain Parcellation in the Presence of Large Lesions. *NeuroImage* (2021) 229:117731. doi: 10.1016/j.neuroimage.2021.117731
51. Fischl B. FreeSurfer. *NeuroImage* (2012) 62(2):774–81. doi: 10.1016/j.neuroimage.2012.01.021
52. Kofler F, Berger C, Waldmannstetter D, Lipkova J, Ezhov I, Tetteh G, et al. BraTS Toolkit: Translating BraTS Brain Tumor Segmentation Algorithms Into Clinical and Scientific Practice. *Front Neurosci* (2020) 14:125. doi: 10.3389/fnins.2020.00125
53. Menze BH, Jakab A, Bauer S, Kalpathy-Cramer J, Farahani K, Kirby J, et al. The Multimodal Brain Tumor Image Segmentation Benchmark (BRATS). *IEEE Trans Med Imaging* (2015) 34(10):1993–2024. doi: 10.1109/TMI.2014.2377694
54. Leemans A, Jeurissen B, Sijbers J, Jones DK. ExploreDTI: A Graphical Toolbox for Processing, Analyzing, and Visualizing Diffusion MR Data. *Proc Intl Soc Mag Reson Med* (2009) 17:3537.
55. Tax CM, Jeurissen B, Vos SB, Viergever MA, Leemans A. Recursive Calibration of the Fiber Response Function for Spherical Deconvolution of Diffusion MRI Data. *NeuroImage* (2014) 86:67–80. doi: 10.1016/j.neuroimage.2013.07.067
56. Desikan RS, Segonne F, Fischl B, Quinn BT, Dickerson BC, Blacker D, et al. An Automated Labeling System for Subdividing the Human Cerebral Cortex on MRI Scans Into Gyral Based Regions of Interest. *NeuroImage* (2006) 31(3):968–80. doi: 10.1016/j.neuroimage.2006.01.021
57. Costabile JD, Alaswad E, D'Souza S, Thompson JA, Ormond DR. Current Applications of Diffusion Tensor Imaging and Tractography in Intracranial Tumor Resection. *Front Oncol* (2019) 9:426. doi: 10.3389/fonc.2019.00426
58. Weiss C, Tursunova I, Neuschmelting V, Lockau H, Nettekoven C, Oros-Peusquens AM, et al. Improved nTMS- and DTI-Derived CST Tractography Through Anatomical ROI Seeding on Anterior Pontine Level Compared to Internal Capsule. *NeuroImage Clin* (2015) 7:424–37. doi: 10.1016/j.nicl.2015.01.006
59. Jellison BJ, Field AS, Medow J, Lazar M, Salamat MS, Alexander AL. Diffusion Tensor Imaging of Cerebral White Matter: A Pictorial Review of Physics, Fiber Tract Anatomy, and Tumor Imaging Patterns. *AJNR Am J Neuroradiol* (2004) 25(3):356–69.
60. Virtanen P, Gommers R, Oliphant TE, Haberland M, Reddy T, Cournapeau D, et al. SciPy 1.0: Fundamental Algorithms for Scientific Computing in Python. *Nat Methods* (2020) 17(3):261–72. doi: 10.1038/s41592-019-0686-2
61. Tuch DS. Q-Ball Imaging. *Magnetic Reson Med Off J Soc Magnetic Reson Med / Soc Magnetic Reson Med* (2004) 52(6):1358–72. doi: 10.1002/mrm.20279
62. Bucci M, Mandelli ML, Berman JI, Amirbekian B, Nguyen C, Berger MS, et al. Quantifying Diffusion MRI Tractography of the Corticospinal Tract in Brain Tumors With Deterministic and Probabilistic Methods. *NeuroImage Clin* (2013) 3:361–8. doi: 10.1016/j.nicl.2013.08.008
63. Tournier JD, Calamante F, Gadian DG, Connelly A. Direct Estimation of the Fiber Orientation Density Function From Diffusion-Weighted MRI Data Using Spherical Deconvolution. *NeuroImage* (2004) 23(3):1176–85. doi: 10.1016/j.neuroimage.2004.07.037
64. Conturo TE, Lori NF, Cull TS, Akbudak E, Snyder AZ, Shimony JS, et al. Tracking Neuronal Fiber Pathways in the Living Human Brain. *Proc Natl Acad Sci USA* (1999) 96(18):10422–7. doi: 10.1073/pnas.96.18.10422
65. Guye M, Parker GJ, Symms M, Boulby P, Wheeler-Kingshott CA, Salek-Haddadi A, et al. Combined Functional MRI and Tractography to Demonstrate the Connectivity of the Human Primary Motor Cortex *In Vivo*. *NeuroImage* (2003) 19(4):1349–60. doi: 10.1016/s1053-8119(03)00165-4
66. Staempfli P, Reischauer C, Jaermann T, Valavanis A, Kollias S, Boesiger P. Combining fMRI and DTI: A Framework for Exploring the Limits of fMRI-Guided DTI Fiber Tracking and for Verifying DTI-Based Fiber Tractography Results. *NeuroImage* (2008) 39(1):119–26. doi: 10.1016/j.neuroimage.2007.08.025
67. Sollmann N, Wildschuetz N, Kelm A, Conway N, Moser T, Bulubas L, et al. Associations Between Clinical Outcome and Navigated Transcranial Magnetic

Stimulation Characteristics in Patients With Motor-Eloquent Brain Lesions: A Combined Navigated Transcranial Magnetic Stimulation-Diffusion Tensor Imaging Fiber Tracking Approach. *J Neurosurg* (2018) 128(3):800–10. doi: 10.3171/2016.11.JNS162322

68. Sollmann N, Zhang H, Fratini A, Wildschuetz N, Ille S, Schroder A, et al. Risk Assessment by Presurgical Tractography Using Navigated TMS Maps in Patients With Highly Motor- or Language-Eloquent Brain Tumors. *Cancers (Basel)* (2020) 12(5):1264. doi: 10.3390/cancers12051264
69. Frey D, Strack V, Wiener E, Jussen D, Vajkoczy P, Picht T. A New Approach for Corticospinal Tract Reconstruction Based on Navigated Transcranial Stimulation and Standardized Fractional Anisotropy Values. *NeuroImage* (2012) 62(3):1600–9. doi: 10.1016/j.neuroimage.2012.05.059
70. Krieg SM, Buchmann NH, Gempt J, Shiban E, Meyer B, Ringel F. Diffusion Tensor Imaging Fiber Tracking Using Navigated Brain Stimulation–a Feasibility Study. *Acta Neurochirurgica* (2012) 154(3):555–63. doi: 10.1007/s00701-011-1255-3
71. Weiss Lucas C, Tursunova I, Neuschmelting V, Nettekoven C, Oros-Peusquens AM, Stoffels G, et al. Functional MRI vs. Navigated TMS to Optimize M1 Seed Volume Delineation for DTI Tractography. A Prospective Study in Patients With Brain Tumours Adjacent to the Corticospinal Tract. *NeuroImage Clin* (2017) 13:297–309. doi: 10.1016/j.nicl.2016.11.022
72. Sollmann N, Meyer B, Krieg SM. Implementing Functional Preoperative Mapping in the Clinical Routine of a Neurosurgical Department: Technical Note. *World Neurosurg* (2017) 103:94–105. doi: 10.1016/j.wneu.2017.03.114
73. Sollmann N, Fratini A, Zhang H, Zimmer C, Meyer B, Krieg SM. Associations Between Clinical Outcome and Tractography Based on Navigated Transcranial Magnetic Stimulation in Patients With Language-Eloquent Brain Lesions. *J neurosurg* (2019) 132(4):1033–42. doi: 10.3171/2018.12.JNS182988
74. Sollmann N, Negwer C, Ille S, Maurer S, Hauck T, Kirschke JS, et al. Feasibility of nTMS-Based DTI Fiber Tracking of Language Pathways in Neurosurgical Patients Using a Fractional Anisotropy Threshold. *J Neurosci Methods* (2016) 267:45–54. doi: 10.1016/j.jneumeth.2016.04.002
75. Raffa G, Bahrend I, Schneider H, Faust K, Germano A, Vajkoczy P, et al. A Novel Technique for Region and Linguistic Specific nTMS-Based DTI Fiber Tracking of Language Pathways in Brain Tumor Patients. *Front Neurosci* (2016) 10:552. doi: 10.3389/fnins.2016.00552
76. De Luca A, Guo F, Froeling M, Leemans A. Spherical Deconvolution With Tissue-Specific Response Functions and Multi-Shell Diffusion MRI to Estimate Multiple Fiber Orientation Distributions (mFODs). *NeuroImage* (2020) 222:117206. doi: 10.1016/j.neuroimage.2020.117206

Conflict of Interest: NS received honoraria from Nexstim Plc (Helsinki, Finland) and Philips Healthcare (Best, The Netherlands). SK is consultant for Ulrich medical (Ulm, Germany) and Brainlab AG (Munich, Germany) and received honoraria from Nexstim Plc (Helsinki, Finland), Spineart Deutschland GmbH (Frankfurt, Germany), Medtronic (Meerbusch, Germany) and Carl Zeiss Meditec (Oberkochen, Germany).

The remaining authors declare that the research was conducted in the absence of any commercial or financial relationships that could be construed as a potential conflict of interest.

Publisher's Note: All claims expressed in this article are solely those of the authors and do not necessarily represent those of their affiliated organizations, or those of the publisher, the editors and the reviewers. Any product that may be evaluated in this article, or claim that may be made by its manufacturer, is not guaranteed or endorsed by the publisher.

Copyright © 2021 Zhylka, Sollmann, Kofler, Radwan, De Luca, Gempt, Wiestler, Menze, Krieg, Zimmer, Kirschke, Sunaert, Leemans and Pluim. This is an open-access article distributed under the terms of the Creative Commons Attribution License (CC BY). The use, distribution or reproduction in other forums is permitted, provided the original author(s) and the copyright owner(s) are credited and that the original publication in this journal is cited, in accordance with accepted academic practice. No use, distribution or reproduction is permitted which does not comply with these terms.

frontiers in Neurology

ORIGINAL RESEARCH
published: 14 January 2022
doi: 10.3389/fneur.2021.787140

Automatic Radiotherapy Planning for Glioblastoma Radiotherapy With Sparing of the Hippocampus and nTMS-Defined Motor Cortex

Michaela Schuermann[1], Yvonne Dzierma[1], Frank Nuesken[1], Joachim Oertel[2,3], Christian Rübe[1] and Patrick Melchior[1]*

[1] Department of Radiotherapy and Radiation Oncology, Saarland University Hospital, Homburg, Germany, [2] Faculty of Medicine, Saarland University, Saarbrücken, Germany, [3] Department of Neurosurgery, Saarland University Hospital, Homburg, Germany

Background: Navigated transcranial magnetic stimulation (nTMS) of the motor cortex has been successfully implemented into radiotherapy planning by a number of studies. Furthermore, the hippocampus has been identified as a radiation-sensitive structure meriting particular sparing in radiotherapy. This study assesses the joint protection of these two eloquent brain regions for the treatment of glioblastoma (GBM), with particular emphasis on the use of automatic planning.

Patients and Methods: Patients with motor-eloquent brain glioblastoma who underwent surgical resection after nTMS mapping of the motor cortex and adjuvant radiotherapy were retrospectively evaluated. The radiotherapy treatment plans were retrieved, and the nTMS-defined motor cortex and hippocampus contours were added. Four additional treatment plans were created for each patient: two manual plans aimed to reduce the dose to the motor cortex and hippocampus by manual inverse planning. The second pair of re-optimized plans was created by the Auto-Planning algorithm. The optimized plans were compared with the "Original" plan regarding plan quality, planning target volume (PTV) coverage, and sparing of organs at risk (OAR).

Results: A total of 50 plans were analyzed. All plans were clinically acceptable with no differences in the PTV coverage and plan quality metrics. The OARs were preserved in all plans; however, overall the sparing was significantly improved by Auto-Planning. Motor cortex protection was feasible and significant, amounting to a reduction in the mean dose by >6 Gy. The dose to the motor cortex outside the PTV was reduced by >12 Gy (mean dose) and >5 Gy (maximum dose). The hippocampi were significantly improved (reduction in mean dose: ipsilateral >6 Gy, contralateral >4.6 Gy; reduction in maximum dose: ipsilateral >5 Gy, contralateral >5 Gy). While the dose reduction using Auto-Planning was generally better than by manual optimization, the radiated total monitor units were significantly increased.

Conclusion: Considerable dose sparing of the nTMS-motor cortex and hippocampus could be achieved with no disadvantages in plan quality. Auto-Planning could further contribute to better protection of OAR. Whether the improved dosimetric protection

OPEN ACCESS

Edited by:
Sandro M. Krieg, Technical University of Munich, Germany

Reviewed by:
Thomas Picht, Charité University Medicine Berlin, Germany
S. Ottavio Tomasi, Paracelsus Medical University, Austria

****Correspondence:***
Michaela Schuermann
michaela.schuermann@uks.eu

Specialty section:
This article was submitted to Neuro-Oncology and Neurosurgical Oncology, a section of the journal Frontiers in Neurology

Received: *15 October 2021*
Accepted: *06 December 2021*
Published: *14 January 2022*

Citation:
Schuermann M, Dzierma Y, Nuesken F, Oertel J, Rübe C and Melchior P (2022) Automatic Radiotherapy Planning for Glioblastoma Radiotherapy With Sparing of the Hippocampus and nTMS-Defined Motor Cortex. Front. Neurol. 12:787140. doi: 10.3389/fneur.2021.787140

of functional areas can translate into improved quality of life and motor or cognitive performance of the patients can only be decided by future studies.

Keywords: navigated transcranial magnetic stimulation (nTMS), glioblastoma, hippocampus, Auto-Planning, radiotherapy

INTRODUCTION

While it has long been observed that brain radiotherapy can cause neurocognitive sequelae (1–5), only recently have technological advances, such as image-guided radiotherapy, intensity- and volumetric-modulated therapy, and improved treatment planning algorithms, i.e., automatic inverse optimization, allowed selective protection of critical brain structures. Hence, increasing focus is being placed on identifying structures vulnerable to radiation-induced deficits and protecting them by selective dose-shaping.

Most research in this area has focused on the hippocampus, whose dentate gyrus presents a neuronal progenitor cell niche in the adult brain, thus meriting particular dose sparing in radiotherapy (6). A higher dose to the hippocampus has been observed to correlate with neurocognitive deficits, particularly regarding verbal memory and higher cognitive functions (7–13). Possibly related to cognitive effects, a dose-dependent volume loss has been observed for a variety of cortical and subcortical regions (14–17). Nagtegaal et al. (17) reported 0.16% hippocampus volume loss per year and per Gray mean dose, translating this into an increase in hippocampal age (derived by a nomogram-based method) of between 2 and 20 years for doses up to 50 Gy.

Radiation-induced cortical atrophy of motor-eloquent regions, such as the precentral cortex, has furthermore been linked with impaired fine motor skills (18). In addition to motor deficits observed after stereotactic radiosurgery (19), dose to the precentral gyrus has been correlated with impaired verbal and working memory, attention, and executive functions (12).

Consequently, a number of studies have included the motor cortex as a radiosensitive organ in radiotherapy treatment planning (20–26). All these studies have employed navigated transcranial magnetic stimulation (nTMS) as a reliable technique to non-invasively define the motor cortex, which has proven useful in pre-surgical mapping (27–36). Most studies concentrated on the stereotactic treatment of metastases or arterio-venous malformations (AMV's); however, radiotherapy treatment planning of gliomas can be expected to offer even more optimization potential due to larger target volumes and highly modulated treatment plans as compared with stereotactic treatment. To our knowledge, only one study so far considered adjuvant radiotherapy for high-grade gliomas (21). Re-optimizing volumetric-modulated arc therapy (VMAT) treatment plans for 30 patients with an additional optimization objective on the nTMS-defined motor area, Diehl et al. could achieve a significant reduction of dose to the motor area by 14.3%.

The aim of our study is to further investigate the possibilities of motor cortex sparing in the treatment of high-grade gliomas. Beyond sparing the nTMS-defined motor cortex, we emphasize the importance of maintaining hippocampus sparing. In a previous study for brain metastases, we could show that the inclusion of motor cortex objectives in treatment planning without additional hippocampus objectives may even increase hippocampus dose (26). Hence, we here assess the possibility of the combined motor cortex and hippocampus optimization in radiotherapy treatment of glioblastoma (GBM).

Past years have witnessed an increasing use of automated planning algorithms to improve dose optimization, which have been shown to contribute to improved sparing of organs at risk (OAR) with no accompanying loss in target coverage (37–41). Therefore, in the present study, the manual re-optimization is compared with the results from an automated planning engine to assess whether further improvements in this highly complex scenario are achievable.

PATIENTS AND METHODS

In this retrospective study, patients with motor-eloquent GBMs who underwent nTMS-based surgical resection and radiotherapy between 2013 and 2018 were replanned and analyzed.

nTMS Mapping and Preparation in the Radiotherapy Treatment Planning System (TPS)

The nTMS of the patients was performed on a pre-operative MRI with contrast-enhanced T1-weighed Magnetization Prepared - RApid Gradient Echo (MP-RAGE) in the axial direction on a 1.5 or 3 T scanner (Magnetom Symphony-TIM 1.5 T, Magnetom Skyra 3.0 T, Siemens, Erlangen, Germany). The nTMS motor mapping was done using the Nexstim navigated brain stimulation (NBS) system 4.3 according to the protocol by Picht et al. (28). The patient was seated in a reclined position, and surface electromyography electrodes were attached to the abductor pollicis brevis, first dorsal interosseous, abductor digiti minimi, anterior tibial, and/or plantar muscles. The resting motor threshold (RMT) was identified by stimulating the presumed localization of the hand knob with different coil locations and orientations. The lowest nTMS stimulus intensity in which a 50 μV MEP response (peak-to-peak amplitude) is elicited in five out of 10 stimulations is generally defined as the RMT. The subsequent mapping was then carried out using 110–130% RMT, varying the coil position over the tumor and adjacent gyri. Positive responses were defined as MEP amplitudes above 50 μV and were marked as motor-eloquent stimulation on the MRI. The resulting collection of points is generally taken to represent the location of the primary motor cortex of the hand and lower extremity.

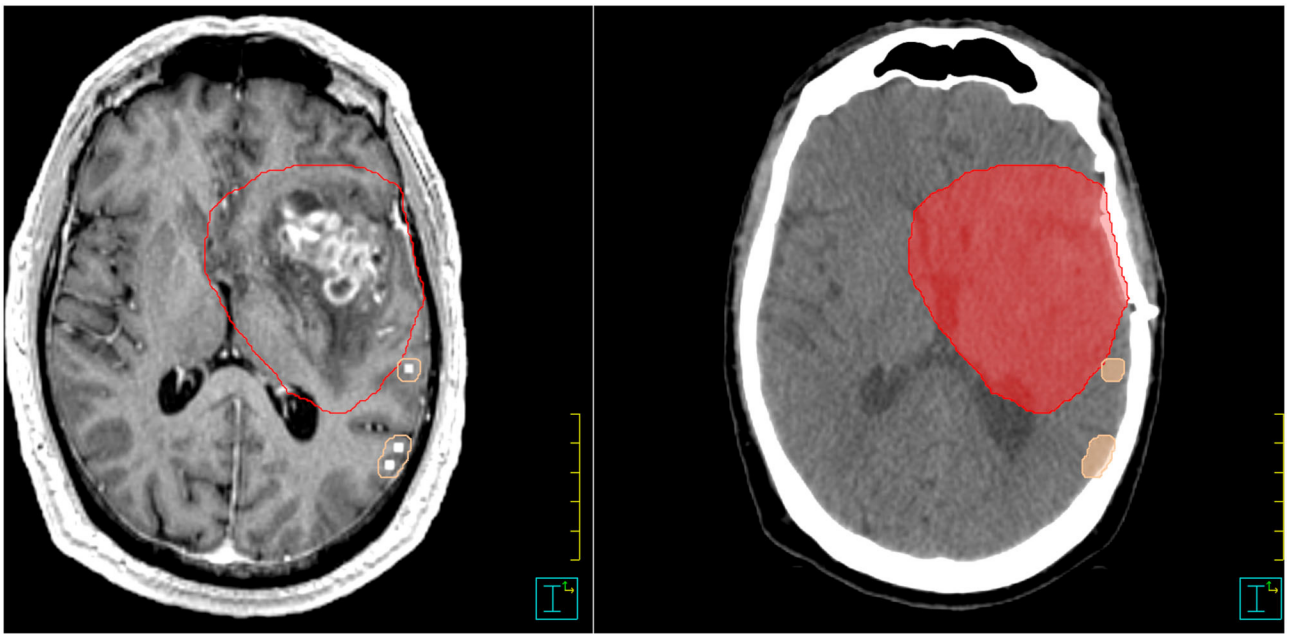

FIGURE 1 | Example for nTMS-mapping and contouring in Pinnacle. nTMS, navigated transcranial magnetic stimulation. PTV = red color; motor cortex = skin color.

For each patient, the nTMS mapping was imported as an additional secondary dataset into the original radiotherapy treatment plan in the Philips Pinnacle TPS V16.2. This image was rigidly co-registered to the primary data set (planning CT) and planning MRI (acquired post-operatively in both T1 MP-RAGE and T2 flair weighting sequence) based on a mutual information algorithm and then manually adjusted until the optimal alignment was achieved. Two radiation physicists and experienced radiation oncologists verified the co-registration independently. The original clinical target volume (CTV), the planning target volume (PTV), and OAR (lens, bulbus oculi, optic nerve, chiasma, medulla, brainstem, and cochlea) for brain irradiation as defined on the planning CT and planning MRI were reviewed, and the additional OARs were contoured: the hippocampi were defined based on T1-weighted planning MRI sequences according to delineation guidelines (42, 43). The nTMS-based motor cortex was contoured by a radiation oncologist by creating a new structure based on delineating the nTMS-positive eloquent points in a brush size slightly larger than the pixel size of the points so that a small margin around the motor-positive points is generated—this is just large enough so that adjacent motor-eloquent points coalesce into a unique structure as shown in **Figure 1**. No further post-processing of the nTMS-derived OAR was performed.

Treatment Planning

The original clinical plan for each patient was used, that is an intensity-modulated radiotherapy (IMRT) technique on a Siemens Artiste linear accelerator with 6 MV photon beams. For each patient, four re-optimized treatment plans were created in addition to the original clinically treated plan ("Original") using the Philips Pinnacle V16.2 TPS (Philips Healthcare, DA Best, Netherlands):

1. a re-optimized plan with sparing of the nTMS-defined motor cortex as an additional planning objective ("Manual Motor"),
2. a re-optimized plan with sparing of the nTMS-defined motor cortex and bilateral hippocampi as additional planning objectives ("Manual M+H"),
3. an automatically optimized plan sparing the nTMS-defined motor cortex ("Auto Motor"), and
4. an automatically optimized plan sparing both the nTMS-defined motor cortex and the bilateral hippocampi, referred to as "Auto M+H."

The normal plan optimization criteria are given in **Table 1**. For the manually optimized plans, the first optimization run was carried out using only the PTV and ring constructs; the OAR objectives were only added where the OARs fell close to the PTV and were not adequately spared in the first optimization.

The Auto-Planning algorithm of Pinnacle is a protocol-based automatic iterative optimization algorithm (39, 44). This algorithm tries to find the most effective balance between target coverage and OAR sparing based on user-defined priorities. Based on the user-defined contours, OAR objectives, and dose prescription for the target, the algorithm generates further optimization "help" structures in consideration of overlaps between PTV and OARs, ring structures for a controlled dose fall-off, and other structures to control target uniformity and dose spillage. Sequential optimization runs are used to best satisfy the user-defined dose objectives. Differently from library-based automatization algorithms, no knowledge of a set of other plans is required and the planning approach closely resembles

TABLE 1 | Standard optimization constraints for the "Original" plans and Auto-Planning plans.

	Structure	Objective
PTV and dose fall-off	PTV	Uniform dose 60 Gy (100%)
		D_{min} 57 Gy (95%)
		D_{max} 63 Gy
	PTV-Ring 1 (+0 to +5 mm)	D_{max} 57 Gy (95%)
	PTV-Ring 2 (+5 to +8 mm)	D_{max} 54 Gy (90%)
	External without PTV (+8 mm)	D_{max} 48 Gy (80%)
OAR's	Bulbi oculi	D_{mean} <35 Gy
	Lens	D_{max} <5 Gy
	Optic nerve	D_{max} <50 Gy
	Chiasma	D_{max} <50 Gy
	Brainstem	V_{54Gy} <10%
	Medulla	D_{max} <42 Gy
	Cochlea	D_{max} <35 Gy
	Spinal canal	D_{max} <42 Gy
New objectives	nTMS-defined motor cortex	As low as possible
	Hippocampus	As low as possible

If the PTV overlaps with an OAR or is near to it, an individual objective is required based on a clinical decision by the responsible radiation oncologist.
PTV, planning target volume; OAR, organs at risk; nTMS, navigated transcranial magnetic stimulation.

an experienced manual planner. The advantage of the Auto-Planning algorithm is the iterative nature and the inclusion of additional and automated help structures, which provides more complexity to the optimization than manually achievable. Furthermore, the algorithm does not stop once the pre-set objectives are satisfied, but rather tries to reduce the dose in the OARs below the demanded maximal dose (39, 41, 44).

The "Manual Motor" plan used the same optimization criteria as the "Original" plan and an additional criterion for the motor areas delineated by nTMS exteriorly to the PTV. Since none of the patients had the motor cortex located completely external to the PTV, the goal of this re-optimization was the reduction of the nTMS-based motor cortex mean dose without reducing the coverage of the PTV. The motor cortex dose was pushed as far as possible, accepting up to 0.5 Gy decrease in mean PTV dose.

The aims of the manual motor cortex and hippocampus sparing "Manual M+H" plan were the dose reduction of the motor cortex mean dose and the dose reduction in the hippocampi without reducing the coverage of the PTV. Here too, the optimization was carried out using the same optimization constraints as the "Original" plan adding the new constraints for the motor cortex and hippocampi.

Both the Auto-Planning "AP Motor" plan and the "AP M+H" plan were optimized using the Pinnacle Auto-Planning algorithm. The aims of "AP Motor" and "AP M+H" were the same as the aims of "Manual Motor" and "Manual M+H," respectively. Note that no automatization was included at the stage of motor cortex delineation, but only in the dose planning step.

The numbers of fields and the allowed segments in all re-optimized plans were equivalent to the used fields and segments of the "Original" plan. The direction of the fields was not changed. The final dose distributions were calculated using a collapsed cone (CC) convolution algorithm on a 2-mm dose grid. All plans were revised by experienced radiation oncologists and radiation physicists and were considered clinically acceptable.

Plan Evaluation

Different quality parameters were analyzed to evaluate the plan quality.

The Paddick conformity index (CI) (45–47).

$$CI = OR \bullet UR = \frac{TV_{PIV}^2}{PIV \bullet TV} \quad (1)$$

is the product of the Paddick overdose ratio (OR) and underdose ratio (UR). In the ideal plan, the CI is unity and decreases with decreasing plan quality.

The OR

$$OR = \frac{TV_{PIV}}{PIV} \quad (2)$$

is ideally 1, when the PTV volume inside the 95% isodose (TV_{PIV}) is the same size as the total volume irradiated with 95% of the total prescription (PIV).

The UR

$$UR = \frac{TV_{PIV}}{TV} \quad (3)$$

is ideally 1, when the PTV volume inside the 95% isodose (TV_{PIV}) is the same size as the total PTV volume (TV).

The homogeneity index (HI)

$$HI = \frac{PTV_{01\%} - PTV_{99\%}}{PTV_{mean}} \quad (4)$$

estimates the dose homogeneity inside the PTV by the ratio of the absolute dose difference ($PTV_{01\%}$ dose maximum and $PTV_{99\%}$ dose minimum) and the mean dose. In the ideal plan the HI equals 0.

The gradient index (GI)

$$GI = \frac{PIV}{V_{50\%}} \quad (5)$$

estimates the steepness of the dose fall-off by the ratio of the prescription isodose volume and the volume of half of this dose ($V_{50\%}$).

TABLE 2 | Overview of the overlap of motor cortex and PTV.

Percent of motor cortex in PTV	Number of patients
<24	3
25–49	1
50–74	1
75–94	5

PTV, planning target volume.

Besides these parameters, the maximum and the mean dose of the PTV and the OARs, especially the motor cortex and the hippocampi, are determined. For the motor cortex and the ipsilateral hippocampus, the intersection between the respective OAR and the different isodoses is analyzed.

Statistical Analyses

By an in-house Pinnacle script, the dose-volume histogram (DVH) values of each OAR, PTV, and motor cortex were exported into a comma separated variables (CSV) table. All calculations and statistical analyses were performed with MATLAB R2019b. A normal distribution could not be presumed, so Wilcoxon's signed-rank test of paired data with Bonferroni correction was used, reducing the level of significance to 0.005.

RESULTS

A total of 24 patients received radiation therapy and surgical resection at the authors' department. Only patients with a prescription of 30 fractions of 2 Gy were included to allow for a more homogeneous collective and more valid dosimetric comparison. Also, patients whose motor cortex was located to more than 95% inside the PTV were excluded from this study because a dose reduction was not reasonable. For the remaining 10 patients, the four re-optimized plans "Manual Motor," "AP Motor," "Manual M+H," and "AP M+H" were clinically acceptable. In **Table 2**, the distribution of the overlap of the motor cortex with the PTV is presented, while in **Figure 2**, an example for the resulting isodose distributions with the related DVH (**Figure 3**) is shown. In **Supplementary Table 1**, the metrics for plan quality and the dose to the PTV motor cortex and OARs are given.

PTV Coverage and Plan Quality Metrics

For the maximum dose and the mean dose to the PTV, there was no statistically significant difference between the five kinds of plans (**Figure 4**). The minimum dose decreased slightly for all re-optimized plans, but only reached statistical significance for the manual plans. From a clinical perspective, this decrease was deemed adequate and would not have impaired plan acceptability.

The brain without PTV received a slightly decreased mean dose (<1 Gy) in the re-optimized plans, which was statistically significant for the manually optimized plans, while the maximum dose remained almost the same.

For all plan quality parameters, there were hardly any significant differences between the five plans (**Figure 5**). The CI, OR, HI, and the GI appear slightly higher while the UR decreased; however, only the increase in HI for the motor cortex and hippocampus sparing plans is statistically significant and would not have resulted in the clinical rejection of the plans.

Organs at Risk

The OAR originally included in the clinical plans showed no significant or clinically relevant increase of the maximum or mean dose. The dose of all OARs in the "Original" plans was already below the clinical critical value. OAR near the hippocampi, such as brainstem or medulla, had a significant decrease in the maximum dose (up to 11 Gy for the brainstem in the "AP M+H" plan) and mean dose (up to 5.7 Gy for the brainstem in the "AP M+H" plan) for all re-optimized plans except for the "Manual Motor" plans, which did not optimize hippocampus dose. For most of the OARs, a significant further reduction of the maximum and mean doses was achieved by the Auto-Planning plans. Only if the doses in the "Original" plans were already very low (i.e., lenses located very far from the PTV), no significant reduction could be found.

Motor Cortex Sparing

For the motor cortex, a significant reduction in the mean dose for all four re-optimized plans could be achieved [from 54.3 ± 6.7 Gy ("Original") to 48.2 ± 10.2 Gy ("Manual Motor"), 46.8 ± 11.2 Gy ("AP Motor"), 48.1 ± 10.2 Gy ("Manual Motor+Hipp"), and 47.1 ± 11.4 Gy ("AP Motor+Hipp"), **Figure 6**], while there was no difference in the maximum dose (near the prescribed dose since this contour overlapped with the PTV). The overlap between the motor cortex and the 57, 54, 48, and 42 Gy isodoses is significantly reduced for all re-optimized plans (**Figure 7**). The improvement for the Auto-Planning plans was a little higher than for the manually optimized plans, but without reaching statistical significance. For the other isodoses, no significant changes occurred, given that the overlap for the lower doses with the motor cortex approached 100%.

If only the motor cortex outside the PTV is analyzed, then there is a significant reduction of the maximum dose and mean dose for all re-optimized plans (**Figure 8**). The maximum dose is reduced by around 3 Gy for the manually optimized plans and around 4 Gy for the Auto-Planning plans. The mean dose is reduced by 12 Gy for the manual plans and by 13 Gy for the Auto-Planning plans, and the difference between the manual and Auto-Planning plans is significant for both optimization goals.

Hippocampus Sparing

Taking the average of the maximum ipsilateral hippocampus dose over the collective of patients, a reduction of more than 5.5 Gy for the hippocampus-sparing plans could be seen ("Original" 46.6 ± 18.1 Gy, "Manual Motor" 46.3 ± 18.0 Gy, "AP Motor" 45.4 ± 19.7 Gy, vs. "Manual M+H" 40.9 ± 19.6 Gy, "AP M+H" 40.9 ± 20.9 Gy, **Figure 9**); however, given the large variability in maximum hippocampus doses over the collective statistical significance could only be proven between the "Manual M+H" plan and the "Original" and "Manual Motor" plans. For the mean

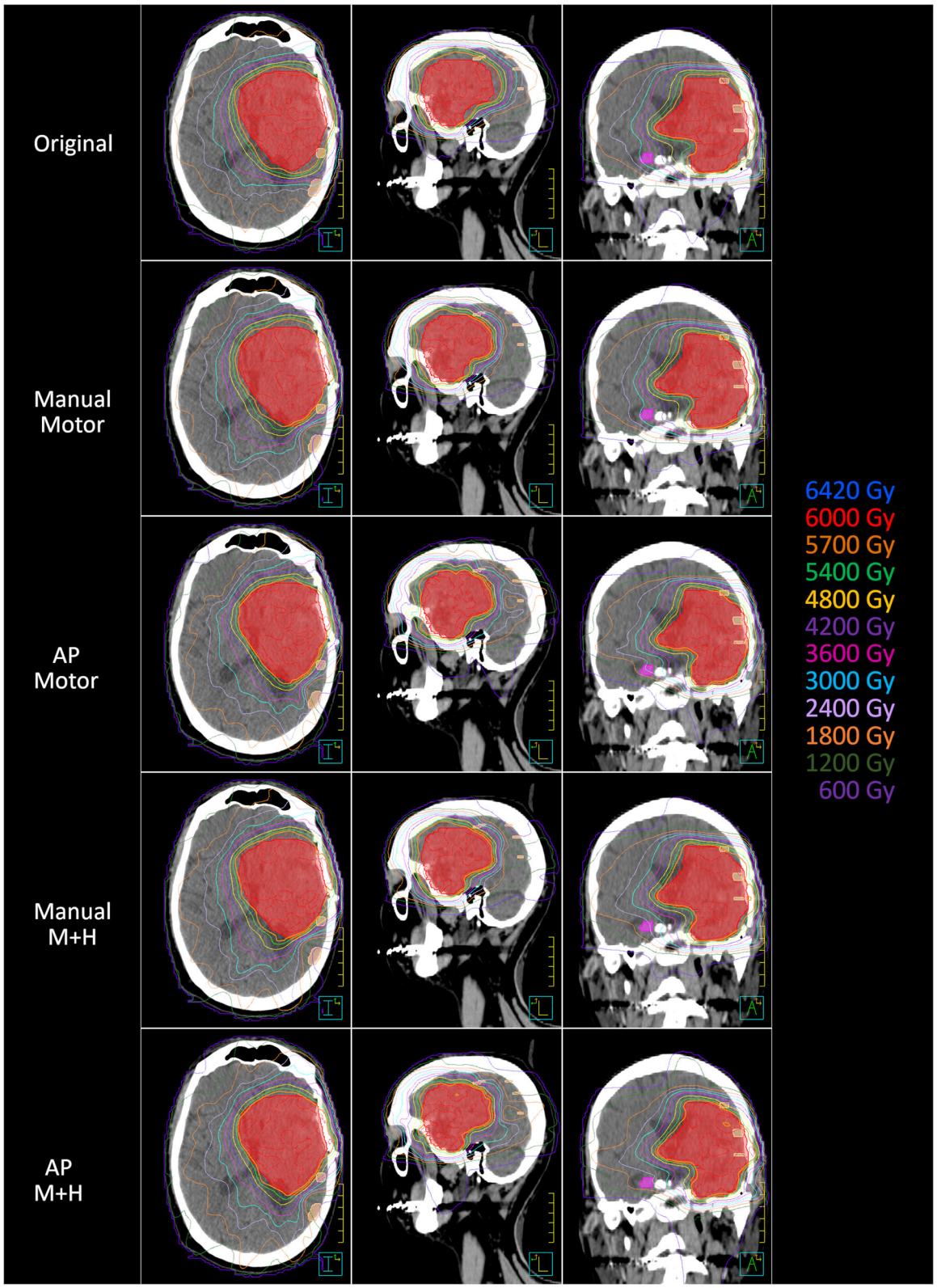

FIGURE 2 | Example of the dose distribution in the planning CT (axial, sagittal, and coronal axis) (left, middle, and right). PTV = red color, motor cortex = skin color, contralateral hippocampus = pink color.

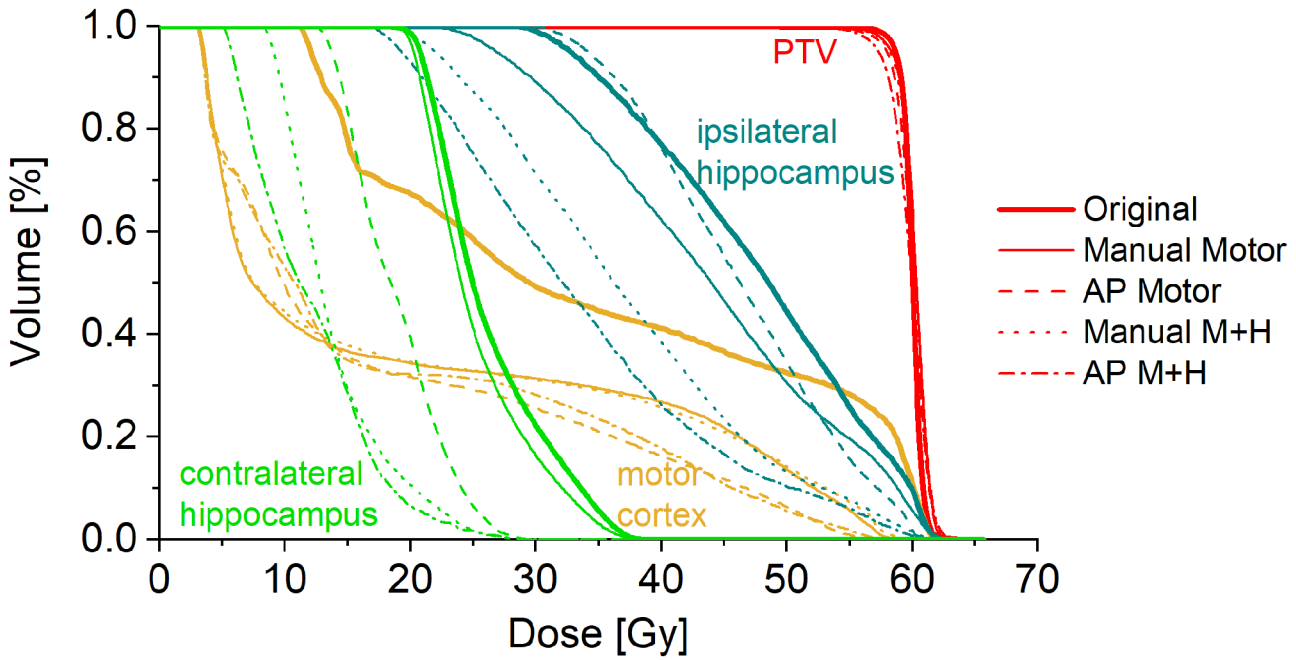

FIGURE 3 | Dose-volume histogram for the example patient in **Figure 1**.

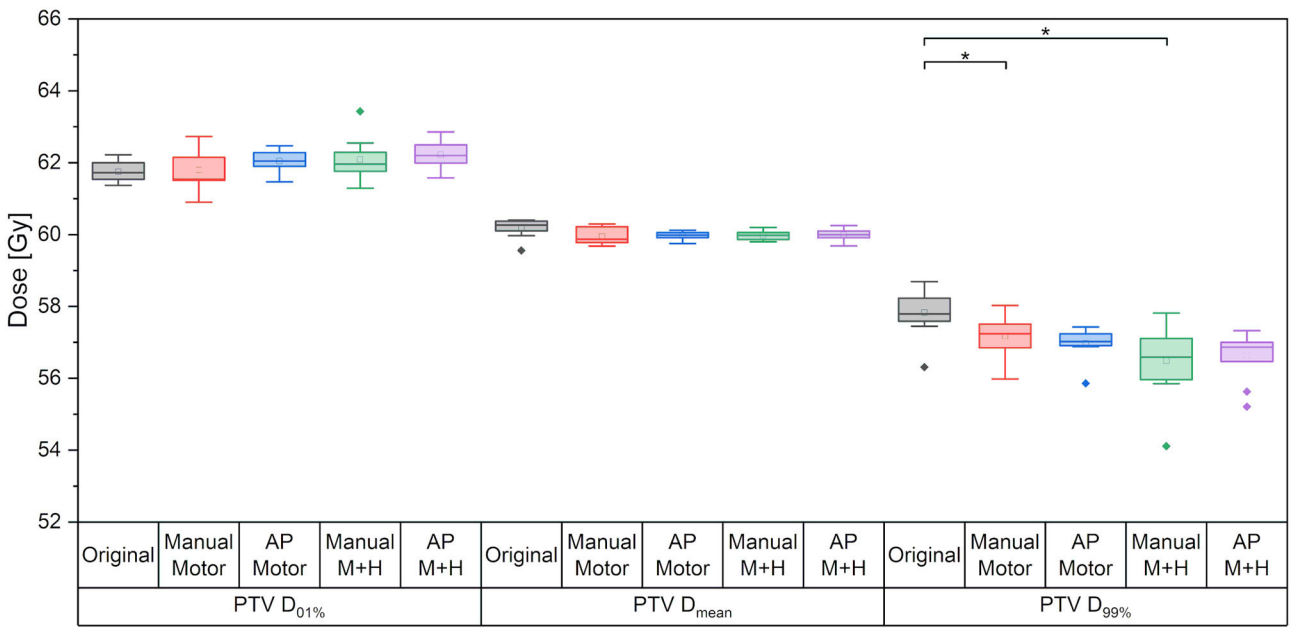

FIGURE 4 | Maximum dose ($D_{01\%}$), mean dose and minimum dose (D99%) to the PTV. Line = median value, square = mean value, diamond = outliers, star = statistically significant at $p < 0.005$.

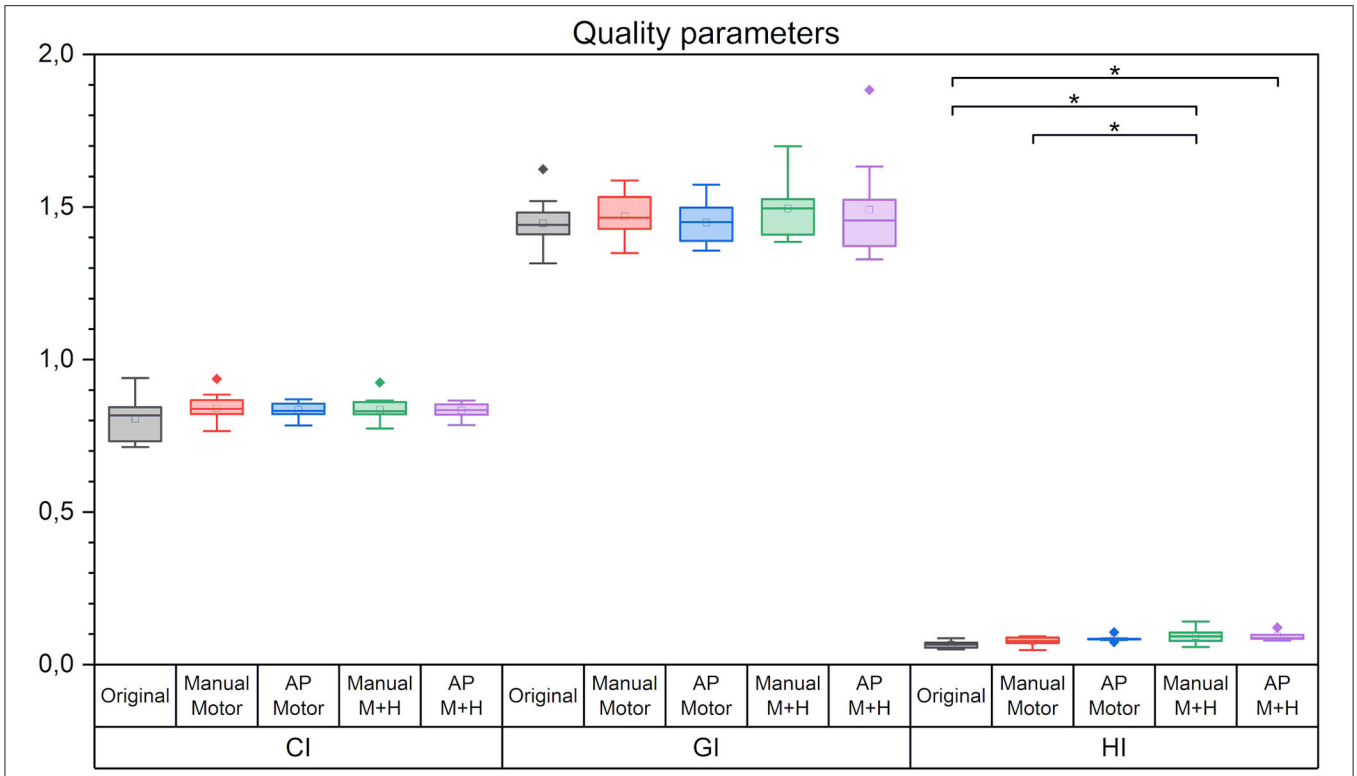

FIGURE 5 | Quality parameters conformity index (CI), gradient index (GI), and homogeneity index (HI). Line = median value, square = mean value, diamond = outliers. There were no statistically significant differences between the planning scenarios.

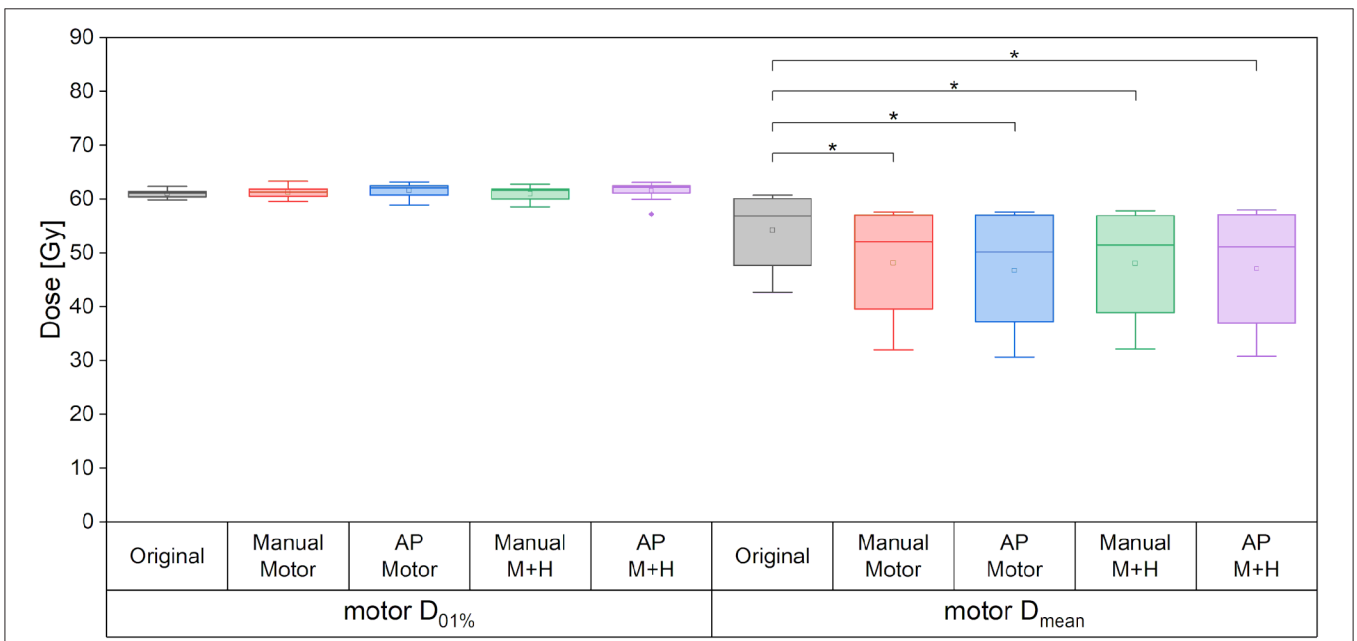

FIGURE 6 | Maximum and mean dose to the motor cortex. Line = median value, square = mean value, diamond = outliers, star = statistically significant at $p < 0.005$.

doses to the ipsilateral hippocampus, a significant improvement was observed in all re-optimized plans. The reduction of the only motor sparing plans was not as large as the reduction of the motor and hippocampi sparing plans, which was statistically

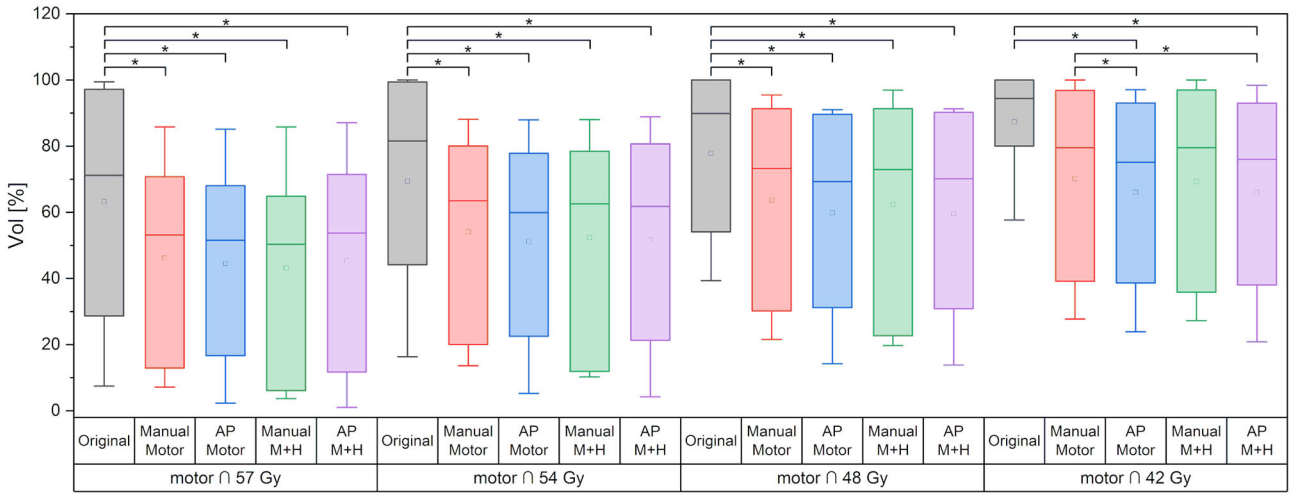

FIGURE 7 | Overlap of motor cortex and isodose levels. Line = median value, square = mean value, diamond = outliers, star = statistically significant at $p < 0.005$.

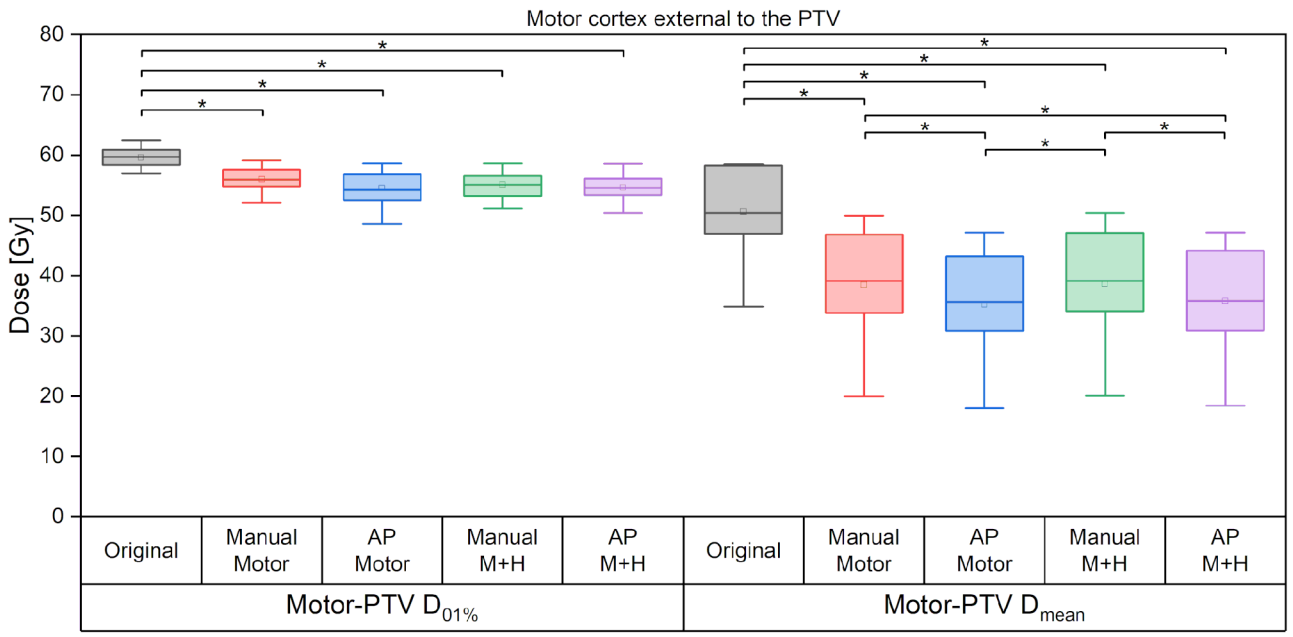

FIGURE 8 | Maximum and mean dose to the motor cortex. Line = median value, square = mean value, diamond = outliers, star = statistically significant at $p < 0.005$.

significant ("Original" 29.6 ± 18.3 Gy, "Manual Motor" 29.0 ± 17.3 Gy, "AP Motor" 25.4 ± 20.2 Gy, "Manual M+H" 23.0 ± 18.2 Gy, and "AP M+H" 21.1 ± 18.2 Gy). Meanwhile the Auto-Planning plans attained an even higher reduction than the manually optimized ones so that the "AP M+H" plan offered the largest improvement (statistically significant in comparison with all other plans).

Regarding the spatial overlap between the ipsilateral hippocampus and isodose levels, there were no significant differences between the plans, although it can be seen from **Figure 10** that the intersection between the hippocampus and higher isodose levels has decreased for the plans with motor cortex and hippocampus sparing.

For the motor cortex and hippocampi sparing plans, the maximum dose of the contralateral hippocampus was significantly reduced by more than 5.5 Gy and the mean dose by about 3.5 Gy as compared with the "Original" plan (**Figure 11**).

Plan Efficiency and Modulation

Figure 12 gives the required monitor units (MU) of the planning scenarios. For all re-optimized plans, the monitor units are significantly increased except for the "Manual Motor" plan for

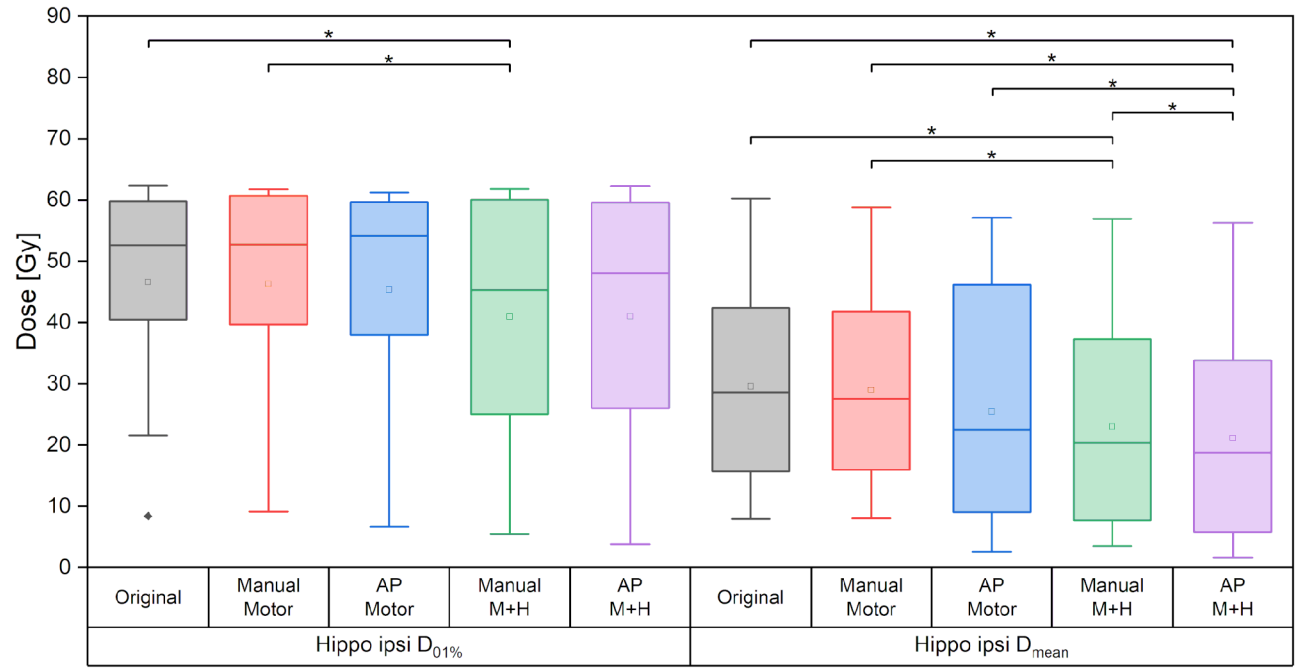

FIGURE 9 | Maximum and mean dose of the ipsilateral hippocampus. Line = median value, square = mean value, diamond = outliers, star = statistically significant $p < 0.005$.

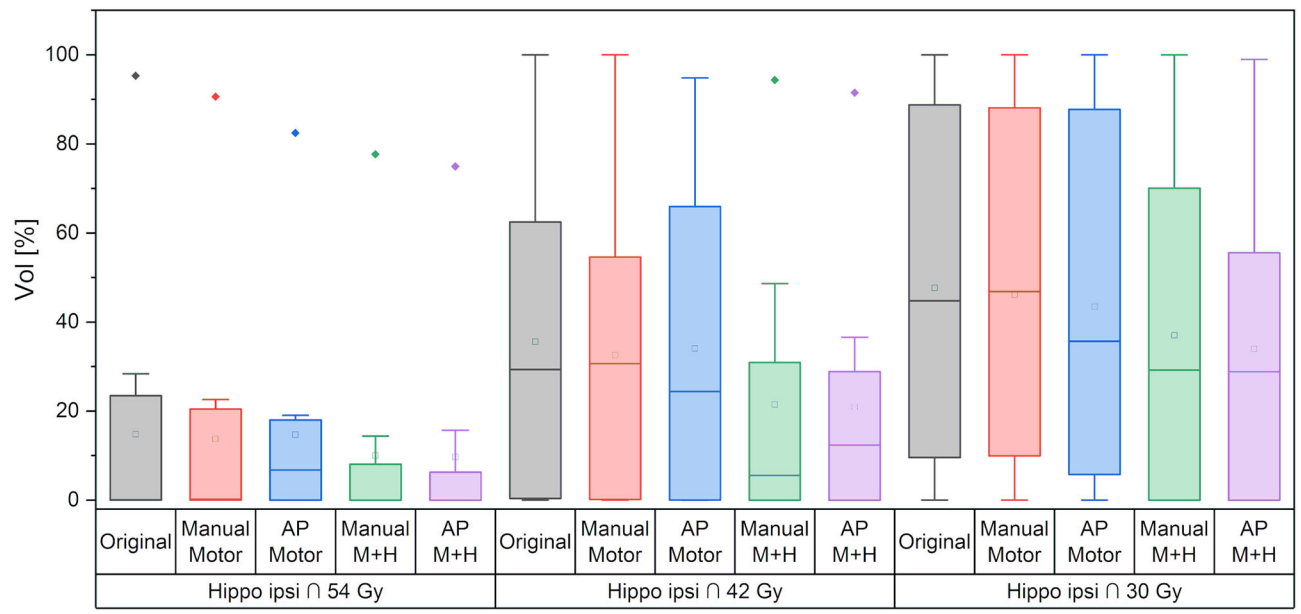

FIGURE 10 | Overlap of ipsilateral hippocampus and isodose levels. Line = median value, square = mean value, diamond = outliers, star = statistically significant $p < 0.005$.

which no significance could be proven. The increase for the plans which spare motor cortex and hippocampi, is significantly larger than for the plans which only consider the motor cortex. Also, the plans optimized with Auto-Planning require significantly higher monitor units, i.e., higher modulation of the beams.

DISCUSSION

Although we had only a small number of patients available for analysis, this was a homogeneous collective with very comparable clinical scenarios. For this cohort, a total of 50 treatment plans

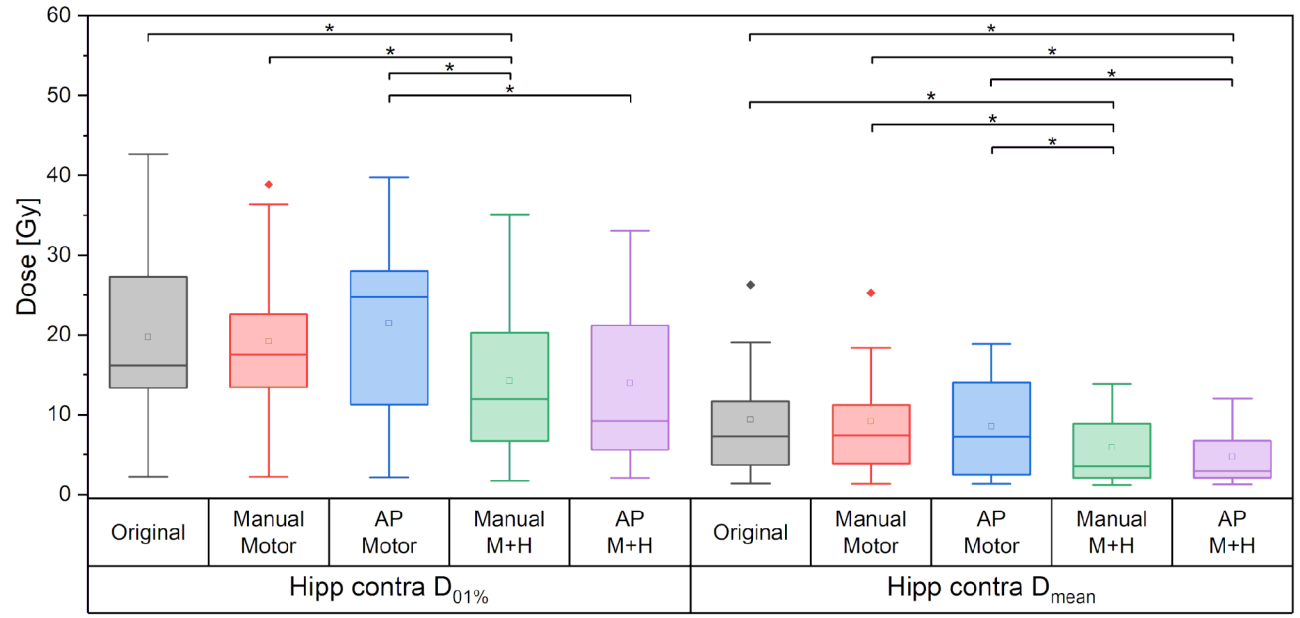

FIGURE 11 | Maximum and mean dose to the contralateral hippocampus. Line = median value, square = mean value, diamond = outliers, star = statistically significant $p < 0.005$.

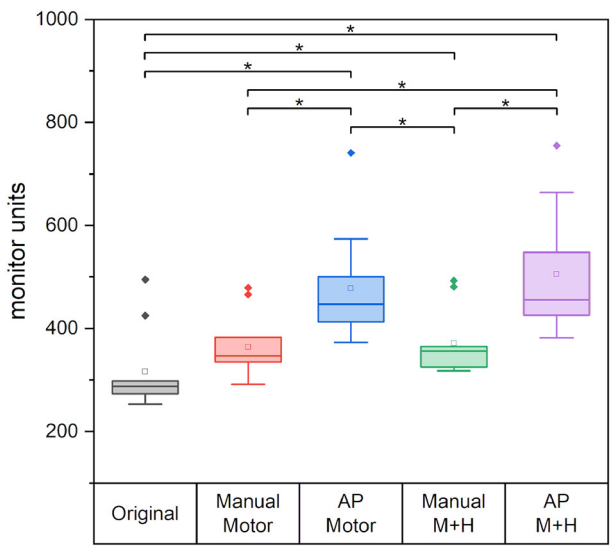

FIGURE 12 | The required monitor units for the different plans. Line = median value, square = mean value, diamond = outliers, star = statistically significant $p < 0.005$.

were compared, which were created in a reproducible manner and revised by an attending radiation oncologist and a senior medical physicist. This study could show that combined sparing of the nTMS-defined motor cortex and the hippocampus is feasible in the radiotherapeutic treatment of patients with GBM without compromising target coverage, plan quality metrics, or sparing of traditional OAR, even in a collective of patients where the motor cortex was partially included in the PTV.

The main goal, which was the sparing of the motor cortex and the hippocampi, could be achieved. The motor cortex mean dose was reduced by more than 10% (>6 Gy) in the whole nTMS-defined cortex and by up to 25% (>12 Gy) for the part of the motor cortex located outside of the PTV. A reduction of the maximum dose could expectedly not be achieved because the cortex overlaps largely with the PTV. However, the maximum dose of the motor cortex outside the PTV was significantly reduced for all plans by more than 3.5 Gy. Furthermore, the overlap of the motor cortex with high-dose isodoses could be significantly decreased.

For the ipsilateral and contralateral hippocampus, a reduction in the mean dose of over 20% (>6 Gy) and 40% (>4.6 Gy), respectively, could be achieved. The maximum doses were decreased significantly by over 10% (>5 Gy) and 20% (>5 Gy) for the ipsilateral and contralateral hippocampus, respectively.

Benefits of Automated Planning

Using the Auto-Planning algorithm, the motor cortex located outside the PTV could be better protected than in the manual plans; all other objectives (complete motor cortex, ipsilateral, and contralateral hippocampi) were equally satisfied by the manual and Auto-planning scenarios with no significant differences.

While several studies for different tumor entities have shown that Auto-Planning resulted in a better plan quality than manual plans [e.g., (38, 48)], this is not supported in our study collective. The PTV coverage and the plan quality defined through the plan quality parameters were the same for the "Original" plan and both kinds of planning. The similar plan quality indicates that the plan quality of the manual plans was good. However, the spread of the mean and maximum dose and the quality factors were smaller for the Auto-Planning. In addition, the variation

in dose to the healthy brain without PTV is smaller for Auto-Planning than manual. While only a reduction in measures of statistical spread (such as the interquartile range as seen in the box plots above) precludes a statistically significant difference between the manual and automated plans, this may point to better reproducibility and stability of the Auto-Planning results.

In contrast, the variation for the motor cortex dose is higher for Auto-Planning than for the manual plans. This effect could be due to the overlap of the motor cortex and the PTV. The conflicting objectives were not always achievable, which was a problem for the Auto-Planning algorithm, that could more consistently be solved manually by the informed decision of the planner. Nevertheless, on the average, the Auto-Planning performed slightly better.

Due to the different optimization parameters, the Auto-Planning reduced the dose for almost all other OARs significantly even when they were already below the constraints. This is one expressed aim of the Auto-Planning algorithm, as it strives to satisfy all the objectives and if possible to undercut them (41). The manual plans only aimed to reduce the dose in the other OARs if they were too high from a clinical point of view and ceased the efforts when the clinical objectives were reached. The second advantage of Auto-Planning is that one optimization is enough to produce a clinically acceptable plan, while for the manual plans, many optimization runs were normally needed. Hence, the clinical workflow was greatly relieved by knowing that an adequate plan could be reliably be created with the known set of objectives. In the clinical reality, this would also allow for a less experienced planner to create high-quality plans based on the Auto-Planning template, whereas an experienced planner invested considerable time and effort into the manual optimizations.

However, the good performance and partly even better sparing of the Auto-Planning scenarios come at the cost of higher intensity modulation expressed in the plan MU. While the manual plan with hippocampi sparing increased significantly by around 60 MU (−2 MU to +277 MU) when compared with the original plan, which amounts to about 19%, the increase for the Auto-Planning plans was significantly higher with over 185 MU (almost 60% higher than in the original plans, "AP Motor": +75 MU to +277 MU and "AP M+H": +84 MU to +367 MU). Such a large increase in irradiated dose will contribute to higher head scatter and leakage radiation, which is not precisely accounted for in the treatment plans and may be relevant from the perspective of radiation protection.

Comparison With Previous Studies on nTMS-Based Motor Cortex Optimization

A small number of studies have systematically evaluated the motor cortex as an optimization objective in radiotherapy treatment planning. As early as 2013, Conti et al. (23) used nTMS and functional MRI data and tractography of the motor and language system to optimize dose distributions in CyberKnife radiosurgery of 25 patients, achieving a 17% reduction in dose to functional areas. Focusing on the nTMS-defined motor cortex, Tokarev et al. (25) could reduce the maximum dose by up to 17% (average 6%) and the >12 Gy-volume by 2–78% (average 35.2%) in eight patients planned using GammaKnife. For linear-accelerator-based treatment of brain metastases, Schwendner et al. (22) reported a mean dose reduction to the nTMS-based motor cortex of 18% for a collective of 30 patients planned with VMAT, which corresponded to our own results for patients with metastases treated with IMRT, non-coplanar arcs, or static beams [sparing of about 30% in mean dose, but depending on planning technique and distance between the lesion and the motor cortex, (26)].

Only one study hitherto considered patients with malignant gliomas, which present a rather different patient collective with different needs for planning and optimization. In general, much larger target volumes are treated with modulated techniques in standard fractionations to 60 Gy or more, resulting in different necessities and possibilities for plan optimization. Diehl et al. (21) re-optimized plans for 30 patients with high-grade gliomas setting an objective of 45 Gy maximum dose to the nTMS-defined motor cortex outside the PTV [prescription 59.4 Gy/70 Gy in PTV/simultaneous integrated boost (SiB)]. The resulting mean dose to the motor maps was reduced by 12.8%, and the volumes of the motor maps receiving > 45 Gy decreased by 11.3%, without a relevant decrement in overall plan quality. We chose a somewhat modified approach in setting the motor map objectives as low as achievable for each patient before compromising PTV coverage. Still, a similar decrease in mean motor cortex dose (10%, 6 Gy) and a significant decrease in the overlap with the high dose isodoses are obtained. In particular, a further slight but statistically significant improvement in the overlap volumes could still be achieved using the Auto-Planning modality. Furthermore, for all patients, we could obtain the motor cortex dose protection not only without compromising PTV coverage and the sparing of other OAR but also when including additional constraints on the bilateral hippocampi.

Beyond the dosimetric optimization, such as the nTMS information into radiotherapy treatment planning, may offer further benefits. Picht et al. (20), presenting a mixed collective of 11 patients with metastases, meningiomas, and AMVs, evaluated whether the nTMS information on the motor cortex influenced patient counseling, contouring, and other treatment decisions from indication to dose prescription and optimization. All these factors except for the contouring were found to be at least somewhat influenced by the additional information in a large percentage of the patients. It can thus be presumed that the inclusion of nTMS information at an earlier stage than merely in dose optimization can provide further benefits for informed decisions.

Clinical Benefits of the Motor Cortex and Hippocampus Protection

In how far these dosimetric improvements can be translated into clinical endpoints is yet uncertain. First of all, the clinical effects

of radiotherapy may only become evident after some latency and may hence not occur within the remaining lifetime of patients with highly malignant glioma. In this case, an improvement in quality of life would not be achieved. However, several effects of ionizing radiation on the brain have been observed to occur within a time span of weeks to months, such as attention deficit and short-term memory loss (49, 50), or by >6 months after radiotherapy [general cognitive impairment and dementia in brain tumor survivors (50)]. In these patients, preservation of quality of life will be of paramount importance, if this can be achieved.

While motor skills have been reported to be decreased after radiotherapy (18, 19, 51), only little information is available on possible dose thresholds. In addition to the influence on motor skills, Peiffer et al. (12) found that the volume of the precentral gyrus covered by >40 Gy is a significant predictor for verbal immediate recall and trail making test performance, so an improvement in this value might translate into measurable cognitive improvement of the patients. In our paper, a significant reduction in the volume of the motor cortex overlapping with the high isodose levels (above 48 Gy and higher) could be achieved, and some sparing of lower isodose coverage was also feasible.

Regarding the hippocampus, Kim et al. (7) found impaired verbal learning performance for patients receiving a mean left hippocampus dose of between 38 and 43 Gy as compared with those receiving 11–12 Gy. While there was considerable variation in mean hippocampus dose in our patient collective, the hippocampus-optimized plans could reduce the dose to the contralateral hippocampus to <14 Gy in the manual and no more than 12 Gy in the Auto-Planning plans for all patients in our collective. The ipsilateral hippocampus mean dose ranged between 8 and 60 Gy (mean 30 Gy) in the original plans and could be reduced by 6.5 and 8.5 Gy in the manual and Auto-Planning optimizations so that it can be expected that some patients would be represented directly on the slope of a dose-response curve and hence benefit from dose reduction. Similarly, the maximum hippocampus dose varied greatly with distance from the PTV; however, it could still be reduced by about 5 Gy, which may be relevant for those patients close to a threshold dose of ca. 12 Gy, which was observed by Tsai et al. (8) to correlate with impaired verbal memory. Summing up the tenuous evidence on dose effects available so far, some tangible clinical and cognitive improvements may be achieved at least for a subset of the patients receiving radiotherapy. Most importantly, this dose sparing comes at no cost in plan quality regarding either PTV coverage and hence prognosis or sparing of "traditional" OAR. Therefore, to our opinion even a hypothetical and plausible – though as yet unproven – improvement in motor and the cognitive outcome would warrant the additional care in dose optimization.

CONCLUSION

Simultaneous dose reduction in the motor cortex and hippocampi is feasible while the PTV coverage, plan quality parameters, and sparing of other OAR are maintained or improved. The overall mean dose reduction to the nTMS-defined motor cortex was up to 10% (6 Gy), while the mean dose to the ipsilateral hippocampus was reduced by more than 20% (6 Gy) and the contralateral by more than 40% (4 Gy). Manual optimization and Auto-Planning achieved considerable dose protection, with slightly better performance of the Auto-Planning algorithms for most of the OAR coming at the cost of considerably higher dose modulation. No apparent disadvantages due to sparing the nTMS-defined motor cortex and hippocampi were found. Consequently, standardized sparing of these structures may be recommended for the clinical routine while the effects for the quality of life, motor function, and cognitive performance need to be determined in future studies.

DATA AVAILABILITY STATEMENT

The raw data supporting the conclusions of this article will be made available by the authors, without undue reservation.

ETHICS STATEMENT

Ethical review and approval was not required for the study on human participants in accordance with the local legislation and institutional requirements. The patients/participants provided their written informed consent to participate in this study.

AUTHOR CONTRIBUTIONS

YD designed the study concept. JO recruited the patients and was responsible for the surgical treatment of the patients and CR was responsible for the radiooncological treatment. Patient datasets were retrieved from the data base and retrospectively revised by YD. Import into the planning system and rigid registration with the planning CT was performed by YD and MS. PM and YD contoured the organs at risk. MS created the re-optimized radiotherapy treatment plans and performed the plan evaluation and statistical analysis. PM and FN evaluated the treatment plans. MS and YD wrote the manuscript and prepared the figures and tables. All authors were involved in the interpretation of the results and contributed to the article and approved the submitted version.

SUPPLEMENTARY MATERIAL

The Supplementary Material for this article can be found online at: https://www.frontiersin.org/articles/10.3389/fneur.2021.787140/full#supplementary-material

REFERENCES

1. Pendergrass JC, Targum SD. Harrison JE. Cognitive impairment associated with cancer: a brief review. *Inn Clin Neuroscience.* (2018) 15:36–44.

2. Saad S, Wang TJC. Neurocognitive deficits after radiation therapy for brain malignancies. *Am J Clin Oncol.* (2015) 38:634–40. doi: 10.1097/COC.0000000000000158

3. Greene-Schloesser D, Moore E, Robbins ME. Molecular pathways: radiation-induced cognitive impairment. *Clin Cancer Res.* (2013) 19:2294–300. doi: 10.1158/1078-0432.CCR-11-2903
4. Hladik D, Tapio S. Effects of ionizing radiation on the mammalian brain. *Mut Res*. (2016) 770:219–30. doi: 10.1016/j.mrrev.2016.08.003
5. Voshart DC, Wiedemann J, van Luijk P. Barazzuol L. Regional responses in radiation-induced normal tissue damage. *Cancers.* (2021) 13:367. doi: 10.3390/cancers13030367
6. Gondi V, Pugh SL, Tome WA, Caine C, Corn B, Kanner A, et al. Preservation of memory with conformal avoidance of the hippocampal neural stem-cell compartment during whole-brain radiotherapy for brain metastases (RTOG 0933): a phase II multi-institutional trial. *J Clin Onc*. (2014) 32:3810–6. doi: 10.1200/JCO.2014.57.2909
7. Kim KS, Wee CW, Seok JY, Hong JW, Chung JB, Eom KY, et al. Hippocampus-sparing radiotherapy using volumetric modulated arc therapy (VMAT) to the primary brain tumor: the result of dosimetric study and neurocognitive function assessment. *Radiat Oncol.* (2018) 13:29. doi: 10.1186/s13014-018-0975-4
8. Tsai PF, Yang CC, Chuang CC, Huang TY, Wu YM, Pai PC. et al. Hippocampal dosimetry correlates with the change in neurocognitive function after hippocampal sparing during whole brain radiotherapy: a prospective study. *Radiat Oncol.* (2015) 10:253. doi: 10.1186/s13014-015-0562-x
9. Gondi V, Hermann BP, Mehta MP. Tomé WA. Hippocampal dosimetry predicts neurocognitive function impairment after fractionated stereotactic radiotherapy for benign or low-grade adult brain tumors. *Int J Radiat Oncol Biol Phys.* (2013) 85:348–54. doi: 10.1016/j.ijrobp.2012.11.031
10. Ma TM, Grimm J, McIntyre R, Anderson-Keightly H, Kleinberg LR, Hales RK, et al. A prospective evaluation of hippocampal radiation dose volume effects and memory deficits following cranial irradiation. *Radiother Oncol.* (2017) 125:234–40. doi: 10.1016/j.radonc.2017.09.035
11. Okoukoni C, McTyre ER, Ayala Peacock DN, Pfeiffer AM, Strowd R, Cramer C, et al. Hippocampal dose volume histogram predicts hopkins verbal learning test scores after brain irradiation. *Adv Radiat oncol.* (2017) 2:624–9. doi: 10.1016/j.adro.2017.08.013
12. Peiffer AM, Leyrer CM, Greene-Schloesser DM, Shing E, Kearns WT, Hinson WH, et al. Neuroanatomical target theory as a predictive model for radiation-induced cognitive decline. *Neurology.* (2013) 80:747–53. doi: 10.1212/WNL.0b013e318283bb0a
13. Redmond KJ, Mahone EM, Terezakis S, Ishaq O, Ford E, McNutt T, et al. Association between radiation dose to neuronal progenitor cell niches and temporal lobes and performance on neuropsychological testing in children: a prospective stud. *Neuro-Oncol.* (2013) 15:360–9. doi: 10.1093/neuonc/nos303
14. Seiberg TM, Karunamuni R, Kaifi S, Burkeen J, Connor M, Krishnan A, et al. Cerebral cortex regions selectively vulnerably to radiation dose-dependent atrophy. *Int J Radiat Oncol Biol Phys.* (2017) 97:910–8. doi: 10.1016/j.ijrobp.2017.01.005
15. Gui C, Chintalapati N, Hales RK, Voong KR, Sair HI, Grimm J, et al. A prospective evaluation of whole brain volume loss and neurocognitive decline following hippocampal-sparing prophylactic cranial irradiation for limited-stage small-cell lung cancer. *J Neuro-Oncol.* (2019) 144:351–8. doi: 10.1007/s11060-019-03235-7
16. Nagtegaal SHJ, David S, Snijders TJ, Philippens MEP, Leemans A, Verhoeef JJC. Effect of radiation therapy on cerebral cortical thickness in glioma patients: treatment-induced thinning of the healthy cortex. *Neuro-Oncol Adv.* (2020) 2:1–8. doi: 10.1093/noajnl/vdaa060
17. Nagtegaal SHJ, David S, Philippens MEP, Snijders TJ, Leemans A, Verhoeff JJC. Dose-dependent volume loss in subcortical deep grey matter structures after cranial radiotherapy. *Clin Translational Radiat Oncol.* (2021) 26:35–41. doi: 10.1016/j.ctro.2020.11.005
18. Salans M, Tibbs MD, Karunamuni R, Yip A, Huynh-Le MP, Macari AC, et al. Longitudinal change in fine motor skills after brain radiotherapy and in vivo imaging biomarkers associated with decline. *Neuro-Oncol.* (2021) 23:1393–403. doi: 10.1093/neuonc/noab017
19. Minniti G, Clarke E, Lanzetta G, Osti MF, Trasimeni G, Bozzao A, et al. Stereotactic radiosurgery for brain metastases: analysis of outcome and risk of brain radionecrosis. *Radiat Oncol.* (2011) 6:48. doi: 10.1186/1748-717X-6-48
20. Picht T, Schilt S, Frey D, Vajkoczy P, Kufeld M. Integration of navigated brain stimulation data into radiosurgical planning: potential benefits and dangers. *Acta Neurochir*. (2014) 156:1125–33. doi: 10.1007/s00701-014-2079-8
21. Diehl CD, Schwendner MJ, Sollmann N, Oechsner M, Meyer B, Combs SE, et al. Application of presurgical navigated transcranial magnetic stimulation motor mapping for adjuvant radiotherapy planning in patients with high-grade gliomas. *Radiother Oncol*. (2019) 138:30–7. doi: 10.1016/j.radonc.2019.04.029
22. Schwendner MJ, Sollmann N, Diehl CD, Oechsner M, Meyer B, Krieg SM, et al. The role of navigated transcranial magnetic stimulation motor mapping in adjuvant radiotherapy planning in patients with supratentorial brain metastases. *Front Oncol*. (2018) 8:424. doi: 10.3389/fonc.2018.00424
23. Conti A, Pontoriero A, Ricciardi GK, Granata F, Vinci S, Angileri FF, et al. Integration of functional neuroimaging in CyberKnife radiosurgery: feasibility and dosimetric results. *Neurosurg Focus*. (2013) 34:E5. doi: 10.3171/2013.2.FOCUS12414
24. Islam M, Cooray G, Benmakhlouf H, Hatiboglu M, Sinclair G. Integrating navigated transcranial magnetic stimulation motor mapping in hypofractionated and single-dose gamma knife radiosurgery: a two-patient case series and a review of literature. *Surg Neurol Int*. (2020) 11:29. doi: 10.25259/SNI_406_2019
25. Tokarev AS, Rak VA, Sinkin MV, Evdokimova EL, Stepanov VN, Koynash GV, et al. Appliance of navigated transcranial magnetic stimulation in radiosurgery of brain metastases. *J Clin Neurophysiol*. (2020) 37:50–5. doi: 10.1097/WNP.0000000000000621
26. Dzierma Y, Schuermann M, Melchior P, Nuesken F, Oertel J, Rübe C, et al. Optimizing adjuvant stereotactic radiotherapy of motor-eloquent brain metastases: sparing the nTMS-defined motor cortex and the hippocampus. *Front Oncol.* (2021) 11:628007. doi: 10.3389/fonc.2021.628007
27. Picht T, Mularski S, Kuehn B, Vajkoczy P, Kombos T, Suess O. Navigated transcranial magnetic stimulation for preoperative functional diagnostics in brain tumor surgery. *Neurosurgery*. (2009) 65(Suppl. 6):93–8. doi: 10.1227/01.NEU.0000348009.22750.59
28. Picht T, Schmidt S, Brandt S, Frey D, Hannula H, Neuvonen T, et al. Preoperative functional mapping for rolanding brain tumor surgery: comparison of navigated transcranial magnetic stimulation to direct cortical stimulation. *Neurosurgery*. (2011) 69:581–9. doi: 10.1227/NEU.0b013e3182181b89
29. Frey D, Schilt S, Strack V, Zdunczyk A, Rösler J, Niraula B, et al. Navigated transcranial magnetic stimulation improves the treatment outcome in patients with brain tumors in motor eloquent locations. *Neuro Oncol.* (2014) 16:1365–72. doi: 10.1093/neuonc/nou110
30. Krieg SM, Sabih J, Bulubasova L, Obermueller T, Negwer C, Janssen I, et al. Preoperative motor mapping by navigated transcranial magnetic brain stimulation improves outcome for motor eloquent lesions. *Neuro Oncol.* (2014) 16:1274–82. doi: 10.1093/neuonc/nou007
31. Raffa G, Scibilia A, Conti A, Ricciardo G, Rizzo V, Morelli A, et al. The role of navigated transcranial magnetic stimulation for surgery of motor-eloquent brain tumors: a systematic review and meta-analysis. *Clin Neurol Neurosurg.* (2019) 180:7–17. doi: 10.1016/j.clineuro.2019.03.003
32. Picht T, Frey D, Thieme S, Kliesch S, Vajkoczy P. Presurgical navigated TMS motor cortex mapping improves outcome in glioblastoma surgery: a controlled observational study. *J Neurooncol.* (2016) 126:535–43. doi: 10.1007/s11060-015-1993-9
33. Krieg SM, Sollmann N, Obermueller T, Sabih J, Bulubas L, Negwer C, et al. Changing the clinical course of glioma patients by preoperative motor mapping with navigated transcranial magnetic brain stimulation. *BMC Cancer.* (2015) 15:231. doi: 10.1186/s12885-015-1258-1
34. Raffa G, Quattropiani MC, Germanò A. When imaging meets neurophysiology: the value of navigated meurophysiological mapping prior to brain tumor surgery. *Neurosurg Focus.* (2019) 47:E10. doi: 10.3171/2019.9.FOCUS19640
35. Hendrix P, Senber S, Griessenauer CJ, Simgen A, Schwerdtfeger K, Oertel J. Preoperative navigated transcranial magnetic stimulation in patients with motor eloquent lesions with emphasis on metastasis. *Clin Anat*. (2016) 29:925–31. doi: 10.1002/ca.22765

36. Hendrix P, Dzierma Y, Burkhardt B, Simgen A, Wagenpfeil G, Griessenauer CJ, et al. Preoperative navigated transcranial magnetic stimulation improves gross total resection rates in patients with motor-eloquent high-grade gliomas: a matched cohort study. *Neurosurg.*, (2021) 88:627–36 doi: 10.1093/neuros/nyaa486
37. Chatterjee A, Serban M, Abdulkarim B, Panet-Raymond V, Souhami L, Shenouda G, et al. Performance of knowledge-based radiation therapy planning for the glioblastoma disease site. *Int J Radiat Oncol Biol Phys.* (2017) 99:1021–8. doi: 10.1016/j.ijrobp.2017.07.012
38. Hansen CR, Bertelsen A, Hazell I, Zukauskaite R, Gyldenkerne N, Johansen J, et al. Automatic treatment planning improves the clinical quality of head and neck cancer plans. *Clin Translat Radiat Oncol.* (2016) 1:2–8. doi: 10.1016/j.ctro.2016.08.001
39. Hussein M, Heijmen BJ, Verellen D, Nisbet A. Automation in intensity modulated radiotherapy treatment planning – a review of recent innovation. *Br J Radiol.* (2018) 91:20180270. doi: 10.1259/bjr.20180270
40. McConnell KA, Marston T, Zehren BE, Lirani A, Stanley DN, Biship A, et al. Dosimetric evaluation of Pinnacle's automated treatment planning software to manually planned treatments, *Technology. Cancer Res Treat.* (2018) 17:1–7. doi: 10.1177/1533033818780064
41. Kusters JMAM, Bzdusek K, Kumar P, van Kollenburg PGM, Kunze-Busch MC, Wendling M, et al. Automated IMRT planning in Pinnacle: A study in head-and-neck cancer. *Strahlenther Onkol.* (2017) 193:1031–8. doi: 10.1007/s00066-017-1187-9
42. Eekers DBP, in't Ven L, Roelofs E, Postma A, Alapetite C, Burnet NG, et al. The EPTN consensus-based atlas for CT- and MR-based contouring in neuro-oncology. *Radiother Oncol.* (2018) 128:37–43. doi: 10.1016/j.radonc.2017.12.013
43. Scoccianti S, Detti B, Gadda D, Greto D, Furfaro I, Fiammetta M, et al. Organs at risk in the brain and their dose-constraints in adults and in children: a radiation oncologist's guide for delineation in everyday practice. *Radiother oncol.* (2015) 114:230–8. doi: 10.1016/j.radonc.2015.01.016
44. *Pinnacle Evolution: Improving Consistency With Automated Planning Algorithms Statements*. Available online at: www.philips.com/pinnacle (accessed November 8, 2021).
45. Shaw E, Kline R, Gillin M, Souhami L, Hirschfeld A, Dinapoli R, et al. Radiation Therapy Oncology Group: radiosurgery quality assurance guidelines. *Int J Radiat Oncol Biol Phys.* (1993) 27:1231–9. doi: 10.1016/0360-3016(93)90548-A
46. Paddick I, Lippitz B. A simple dose gradient measurement tool to complement the conformity index. *J Neurosurg.* (2006) 105(Suppl):194–201. doi: 10.3171/sup.2006.105.7.194
47. Paddick I. A simple scoring ratio to index the conformity of radiosurgical treatment plans. Technical note. *J Neurosurg.* (2000) 93(Suppl. 3):219–22. doi: 10.3171/jns.2000.93.supplement_3.0219
48. Hansen CR, Nielsen M, Bertelsen AS, Hazell I, Holtved E, Zukauskaite R, et al. Automatic treatment planning facilitates fast generation of high-quality treatment plans for esophageal cancer. *Acta Oncologica.* (2017) 56 1495–500. doi: 10.1080/0284186X.2017.1349928
49. Gondi V, Tome WA, Mehta MP. Why avoid the hippocampus? a comprehensive review. *Radiother Oncol.* (2010) 97:370–6. doi: 10.1016/j.radonc.2010.09.013
50. Greene-Schloesser D, Robbins ME, Peiffer AM, Shaw EG, Wheeler KT, Chan MD. Radiation-induced brain injury: a review. *Front Oncol.* (2012) 2:73. doi: 10.3389/fonc.2012.00073
51. Ris MD, Leisenring WM, Goodman P, Di C, Noll J, Levy W, et al. Neuropsychological and socioeconomic outcomes in adult survivors of pediatric low-grade glioma. *Cancer.* (2019) 125:3050–8 doi: 10.1002/cncr.32186

Conflict of Interest: The authors declare that the research was conducted in the absence of any commercial or financial relationships that could be construed as a potential conflict of interest.

Publisher's Note: All claims expressed in this article are solely those of the authors and do not necessarily represent those of their affiliated organizations, or those of the publisher, the editors and the reviewers. Any product that may be evaluated in this article, or claim that may be made by its manufacturer, is not guaranteed or endorsed by the publisher.

Copyright © 2022 Schuermann, Dzierma, Nuesken, Oertel, Rübe and Melchior. This is an open-access article distributed under the terms of the Creative Commons Attribution License (CC BY). The use, distribution or reproduction in other forums is permitted, provided the original author(s) and the copyright owner(s) are credited and that the original publication in this journal is cited, in accordance with accepted academic practice. No use, distribution or reproduction is permitted which does not comply with these terms.

frontiers in Oncology

ORIGINAL RESEARCH
published: 21 January 2022
doi: 10.3389/fonc.2021.788122

Dual-Task nTMS Mapping to Visualize the Cortico-Subcortical Language Network and Capture Postoperative Outcome—A Patient Series in Neurosurgery

Ann-Katrin Ohlerth[1,2], Roelien Bastiaanse[3], Lyndsey Nickels[4], Beate Neu[5], Wei Zhang[5], Sebastian Ille[5], Nico Sollmann[6,7,8] and Sandro M. Krieg[5,8]*

[1] Center for Language and Cognition Groningen, Groningen, Netherlands, [2] International Doctorate in Experimental Approaches to Language and Brain (IDEALAB, Universities of Groningen, Potsdam, Newcastle, and Macquarie University), Sydney, NSW, Australia, [3] Center for Language and Brain, Higher School of Economics, National Research University, Moscow, Russia, [4] School of Psychological Sciences, Faculty of Medicine, Health and Human Sciences, Macquarie University, Sydney, NSW, Australia, [5] Department of Neurosurgery, School of Medicine, Klinikum rechts der Isar, Technical University of Munich, Munich, Germany, [6] Department of Diagnostic and Interventional Radiology, University Hospital Ulm, Ulm, Germany, [7] Department of Diagnostic and Interventional Neuroradiology, School of Medicine, Klinikum rechts der Isar, Technical University of Munich, Munich, Germany, [8] TUM-Neuroimaging Center, Klinikum rechts der Isar, Technical University of Munich, Munich, Germany

OPEN ACCESS

Edited by:
Alireza Mansouri, The Pennsylvania State University (PSU), United States

Reviewed by:
Antonino F. Germano, University of Messina, Italy
S. Senthil Kumaran, All India Institute of Medical Sciences, India

***Correspondence:**
Ann-Katrin Ohlerth
a.ohlerth@rug.nl

Specialty section:
This article was submitted to Neuro-Oncology and Neurosurgical Oncology, a section of the journal Frontiers in Oncology

Received: *01 October 2021*
Accepted: *13 December 2021*
Published: *21 January 2022*

Citation:
Ohlerth A-K, Bastiaanse R, Nickels L, Neu B, Zhang W, Ille S, Sollmann N and Krieg SM (2022) Dual-Task nTMS Mapping to Visualize the Cortico-Subcortical Language Network and Capture Postoperative Outcome—A Patient Series in Neurosurgery. Front. Oncol. 11:788122. doi: 10.3389/fonc.2021.788122

Background: Perioperative assessment of language function in brain tumor patients commonly relies on administration of object naming during stimulation mapping. Ample research, however, points to the benefit of adding verb tasks to the testing paradigm in order to delineate and preserve postoperative language function more comprehensively. This research uses a case series approach to explore the feasibility and added value of a dual-task protocol that includes both a noun task (object naming) and a verb task (action naming) in perioperative delineation of language functions.

Materials and Methods: Seven neurosurgical cases underwent perioperative language assessment with both object and action naming. This entailed preoperative baseline testing, preoperative stimulation mapping with navigated Transcranial Magnetic Stimulation (nTMS) with subsequent white matter visualization, intraoperative mapping with Direct Electrical Stimulation (DES) in 4 cases, and postoperative imaging and examination of language change.

Results: We observed a divergent pattern of language organization and decline between cases who showed lesions close to the delineated language network and hence underwent DES mapping, and those that did not. The latter displayed no new impairment postoperatively consistent with an unharmed network for the neural circuits of both object and action naming. For the cases who underwent DES, on the other hand, a higher sensitivity was found for action naming over object naming. Firstly, action naming preferentially predicted the overall language state compared to aphasia batteries. Secondly, it more accurately predicted intraoperative positive language areas as

revealed by DES. Thirdly, double dissociations between postoperatively unimpaired object naming and impaired action naming and vice versa indicate segregated skills and neural representation for noun versus verb processing, especially in the ventral stream. Overlaying postoperative imaging with object and action naming networks revealed that dual-task nTMS mapping can explain the drop in performance in those cases where the network appeared in proximity to the resection cavity.

Conclusion: Using a dual-task protocol for visualization of cortical and subcortical language areas through nTMS mapping proved to be able to capture network-to-deficit relations in our case series. Ultimately, adding action naming to clinical nTMS and DES mapping may help prevent postoperative deficits of this seemingly segregated skill.

Keywords: language mapping, postoperative language state, navigated transcranial magnetic stimulation, action naming, object naming, direct electrical stimulation, case series

INTRODUCTION

Preoperative assessment of language and delineation of functional tissue in relation to a lesion is crucial to perform optimal neurosurgical intervention, while aiming to prevent post-operative deficits in brain tumor patients (1, 2). In addition to imaging tools such as functional magnetic resonance imaging (fMRI), preoperative language mapping with navigated transcranial magnetic stimulation (nTMS) has recently gained increasing interest. This non-invasive stimulation tool allows preoperative mapping of cortical functions by inducing transient lesions in small anatomical areas (3). This enables the mapping of areas associated with language disruption, which can be used in guiding surgical planning and intraoperative tumor resection (4–6). As the closest analogue to the gold standard of intraoperative mapping with direct electrical stimulation (DES), nTMS mapping as well relies on error elicitation during language production, and has shown superiority to fMRI by demonstrating a better overlap of nTMS results with DES results (4, 7–11).

The full potential of nTMS is reached in combination with fiber tracking, where language-positive nTMS spots can be employed for visualization of functionally involved subcortical white matter tracts (12–14). Using this preoperative visualization of the language network in relation to the lesion has proven its usefulness in neurosurgical practice by enlarging the extent of resection and the confidence of the surgeon, while leading to fewer language deficits at discharge (6, 13, 15).

Even though nTMS is generally established as a validated method that has been incorporated well in the clinical workflow in an increasing number of neuro-oncological centers (6, 15), one area that deserves further attention is the linguistic depth of the task commonly used during nTMS mapping and its influence on successfully preventing language deficits after surgery, given a task's crucial role for the resulting map of language-positive nTMS points. By solely employing object naming (ON), that targets noun production, for both cortical and subcortical delineation of function, more complex language skills may be neglected and endangered at the postoperative state. Consequently, it has been proposed that the addition of a simple second task of action naming (AN) may be beneficial (16, 17): By triggering the production of verbs in the context of a short sentence, grammatical and semantic skills can be tested that are not targeted by object naming and that, more importantly, are known to rely on anatomically distinct circuits (18–21). In DES mapping and in healthy participants using nTMS, this double dissociation, and the added value of action naming, have been shown to be especially important for the visualization of the semantically relevant ventral stream tracts (22–26). What is still missing, however, is the exploration of the use of both object and action naming tasks in nTMS prior to surgical procedures in tumor patients and the usefulness of this protocol for preventing postoperative language deficits. It is possible that better visualization of cortical and subcortical substrates of language functions may be achieved through addition of a second task, involving verbs.

In this case series, we deliver a description of our first experience with the dual-task mapping protocol in the clinical workflow of pre- (, intra-) and postoperative language testing considering nTMS mapping. As a first exploratory step, on the basis of patient cases harboring language-eloquent brain tumors, we evaluate the contribution of each task in (1) delineating the language state and network preoperatively, (2) informing and "predicting" the intraoperative mapping with DES through the nTMS maps, and (3) capturing the language state and network in relation to the acute postoperative outcome. We present seven cases, of which three were operated on the basis of only nTMS presurgical data and four with additional intraoperative mapping by DES in order to explore the issue of which patients may benefit from the administration of the dual-task protocol.

METHODS

Patient Population

Between March 2021 and August 2021, fourteen patients were included in the dual-task mapping protocol. Out of these, seven showed no proximity of the lesion to the language network as mapped out by nTMS (e.g., pre-frontal lesion) and are not included in this paper.

Inclusion criteria were that patients were right-handed and had an intracranial malignant tumor in the left hemisphere in the proximity of the language network as determined by nTMS mapping. Demographics, lesion characteristics and background language assessments of the seven cases are summarized in **Table 1**.

Preoperative MRI

Patients underwent preoperative MRI using a 3-Tesla MRI scanner (Achieva dStream or Ingenia, Philips Healthcare, Best, The Netherlands) with a 32-channel head coil. Among other sequences in the standard protocol for neuro-oncological imaging, acquisition included a three-dimensional (3D) fluid attenuated inversion recovery (FLAIR) sequence (TR/TE: 4800/277 ms, 1 mm^3 isovoxel covering the whole head), a 3D T1-weighted turbo field echo sequence (TR/TE: 9/4 ms, 1 mm^3 isovoxel covering the whole head) and/or 3D T1-weighted turbo spin echo black-blood sequence (TR/TE: 4000/35 ms, 1 mm^3 isovoxel covering the whole head) without and with administration of a contrast agent (Dotagraf, Jenapharm, Jena, Germany), and a diffusion tensor imaging (DTI) sequence (TR/TE 5000/78 ms, voxel size of 2 × 2 × 2 mm^3, 32 diffusion directions, one volume at b = 0 s/mm^2, 32 volumes at b = 1000 s/mm^2).

Preoperative Language Assessment with nTMS Mapping

In order to describe the overall language status of the patient, standardized language batteries [either Aachener Aphasie Test (AAT) or Aphasie Check List (ACL)] were carried out in most patients to identify pre-existing language impairments, when deemed appropriate by the medical team.

Preoperative language mapping was conducted using the Nexstim eXimia NBS system (version 5.1; Nexstim Plc, Helsinki, Finland) and following the protocol described by Krieg et al. (27). In addition to the standard ON task implemented in the system (e.g., the patient sees a black-and-white drawing of an object and has to name it: *apple*), AN in sentence context from the VAN-POP battery (16) was administered in a second block to trigger verb production (e.g., the patient sees a black-and-white drawing of a daily activity and has to name it: *the man reads*).

For both task blocks, the following steps were taken: firstly, on the day of nTMS mapping, the patient had to name all stimuli (80 ON items and 75 AN items) without stimulation in two baseline rounds to discard all items not fluently named (all items that were named with very late onset, could not be named at all or only on the second attempt were considered as errors). The score of correctly named items during the first baseline round comprised the preoperative baseline performance for that patient on ON and AN tasks.

Secondly, nTMS language mapping covering the majority of the left hemisphere cortical surface was performed using the patient-tailored stimuli list under a 5Hz/5 pulse protocol at 110% of the previously established resting motor threshold, as described previously for ON and for AN (24, 27). Stimuli were presented with a display time of 700 ms (ON) and 1000 ms (AN), as standardized in Ohlerth et al. (16), with an inter-picture-interval of 2500ms and a picture-trigger-interval of 0 ms. The ON block was always administered first.

Baseline and stimulation naming were video-recorded and afterwards examined for naming errors by a trained neuro-linguist (AKO) (24). All stimulation sequences leading to an error were counted (**Table 2**), marked as language-positive sites, and exported *via* DICOM format to the neuro-navigation planning unit (Brainlab Elements Net server version 3.0.6.14., Brainlab AG), resulting in two separate cortical language maps, one for ON and one for AN.

Fiber Tracking on the Basis of nTMS

Deterministic fiber tracking was performed on basis of a DTI sequence with 32 diffusion directions solely using the nTMS language-positive cortical sites as regions of interest (ROIs). For ROI creation, 5 mm rims were added to each language positive cortical site (12). Based on these ROIs, fiber tracking then visualized all fibers with a fiber length of 100 mm at a predetermined fractional anisotropy value of 0.15 and an angulation of 20° (12). This resulted in two separate language-related white matter network visualizations, one for ON and one for AN, that were visually inspected for presence of the known language tracts [Arcuate Fascicle (AF), Superior Longitudinal Fascicle (SLF), Frontal Aslant Tract (FAT), Uncinate Fascicle

TABLE 1 | Demographics of the patient cases.

Case	Age	Gender	Lesion site	Pathology	WHO grade	Awake surgery	Preoperative language status (ACL/AAT)
1	63	M	SFG	oligodendro-glioma	III	no	moderate impairment of auditory comprehension, and reading, mild semantic fluency impairment
2	70	M	prG	glioblastoma	III	no	not administered, no impairment in spontaneous speech
3	47	F	parietal white matter	metastasis of cervix carcinoma	–	no	not administered, no impairment in spontaneous speech
4	53	M	posterior STG	glioblastoma	III	yes	moderate impairment of production, mild writing impairment, mild impairment of phonological and semantic fluency
5	38	M	SFG	anaplastic astrocytoma	III	yes	no impairment, very mild semantic fluency impairment
6	57	M	middle ITG	astrocytoma	II	yes	mild impairment of comprehension and moderate impairment in phonological fluency
7	33	M	insula	astrocytoma	II	yes	no impairment

TABLE 2 | Proportion of induced errors during nTMS mapping of the left hemisphere with object naming (ON) and action naming (AN).

Case	Errors under nTMS in ON	Errors under nTMS in AN	Difference per Chi-square
1	0.15	0.09	0.13
2	0.15	0.15	0.87
3	0.11	0.09	0.54
4	0.04	0.09	0.05*
5	0.12	0.14	0.73
6	0.06	0.15	0.01*
7	0.16	0.25	0.07

Significant difference is marked by use of asterisk.

(UF), Inferior Longitudinal Fascicle (ILF), Inferior Fronto-Occipital Fascicle (IFOF)], the speech-articulatory tract [Cortico-nuclear tract, (CNT)], and commissural fibers (CF) and their proximity to the lesion (12, 26).

Intraoperative Mapping With DES

In order to establish an item list to be used during intraoperative mapping, for each patient, 91 new items for ON (those used in the hospital's standard neurosurgical procedure) and the same 75 items for AN from the VAN-POP were tested again one day prior to the surgery. Any errors were noted and those items were removed from the intraoperative stimulation trials.

During surgery, first an adequate level of anesthesia and sedation was administered to ensure the patient was unconscious while the head was placed in a Mayfield head clamp, and the cortex was exposed. Then neuro-navigation was used to localize and align the cortical and subcortical anatomy in relation to the preoperative scans and mapping results. Prior to language mapping, (general) analgesia and sedation were reduced to slowly awaken the patient. Once the patient was fully awake, calm, and cooperative, language mapping commenced using a bipolar stimulation electrode (distance 5mm) with a 4s stimulation output at an intensity of 4mA and a frequency of 50Hz. The entire exposed cortex was interrogated in 5-10mm steps and each stimulated site was tested at least 3 times. First, mapping was conducted with ON only, followed by a separate mapping with AN only. Cortical sites in which stimulation resulted in at least 2 errors from 3 stimulations were considered positive for the respective task, marked by number (1-digit = ON, 2-digit = AN) and their location was transferred to the navigation system. Resection was carried out sparing all positive areas (4, 28, 29).

Postoperative MRI and Image Co-Registration

Acquisition of MRI according to a standardized protocol in neuro-oncological patients was administered following the same sequences with the same parameters as in the preoperative stage within 48 hours of surgery. In order to assess the proximity of the resection cavity to the language networks for each task, the fiber tracking results were registered to the postoperative T1-weighted MRI datasets. Distortion correction and elastic fusion calculations were performed to account for brain shift (30). Pathological lesions, such as residual tumor or ischemia in the scans, the overlap of the cavity and the visualized language-positive cortical sites of nTMS, and/or the visualized white matter network were assessed. No case showed ischemic lesions.

Postoperative Language Assessment

On the third postoperative day, the language status was assessed by administering ON and AN without stimulation. Presentation of items followed the same procedure as the preoperative baseline naming. As for the preoperative assessment, all items that were not named correctly and fluently were scored as errors.

Analysis of Language State

Scores of each patient on the preoperative baseline naming and postoperative naming in ON and AN were compared to the performance of healthy control subjects [for ON performance, see (31), for AN performance, see (24)]. Results were analyzed using statistics designed for single case methodology (32) (**Table 3** and **Supplementary Material Table S1**). The change in pre- versus postoperative scores was evaluated using McNemar's/Fisher's exact tests. To assess the difference between ON and AN in the change in baseline versus postoperative accuracy, Wilcoxon' two-sample tests were applied to the difference in accuracy between baseline and postoperative test results for each test. Furthermore, Spearman correlations were used to examine the relationship between error patterns and several linguistic variables of the target words [ON: length, frequency, age of acquisition, animacy, and compound status; AN: length, frequency, age of acquisition, regularity, transitivity, instrumentality, name relatedness of the target verb to a noun (16)]. Bonferroni corrections were applied to correct for multiple comparisons in these correlations (**Supplementary Material Table S2**).

CASE DESCRIPTIONS

Clinical Case 1

This patient was a 63-year-old male, admitted to hospital after a general epileptic seizure. Scans showed a lesion in the superior frontal gyrus (SFG). During preoperative language assessment, the patient scored poorly on reading and displayed a moderate auditory comprehension impairment and mild semantic fluency deficiency. Baseline naming with ON and AN showed that AN was clinically impaired compared to healthy control participants as well as significantly worse than ON (**Table 3** and **Supplementary Material Table S1** for all scores and comparisons).

TABLE 3 | Proportion of correctly and fluently named items in ON and AN across testing points.

Case	Test	Baseline	1 Day Pre-operative	3 Days Post-operative	Difference between Baseline and Preoperative	Difference between Baseline and Postoperative	Difference in Decline between ON and AN (unpaired MWU)
1	ON	0.813*	N/A	0.838*	N/A	0.790	0.967
	AN	0.573*#	N/A	0.600*#	N/A	0.831	
2	ON	0.850	N/A	0.825	N/A	0.803	0.702
	AN	0.747	N/A	0.693#	N/A	0.522	
3	ON	0.975	N/A	0.988	N/A	0.999	0.567
	AN	0.880	N/A	0.867	N/A	0.999	
4	ON	0.925	0.868*	0.747*	0.147	0.037*	0.005*
	AN	0.773	0.653*#	0.427*#	0.039*	<0.001*	
5	ON	0.963*	0.934*	0.888	0.505	0.114	0.555
	AN	0.733*	0.680*#	0.707#	0.480	0.831	
6	ON	0.888	0.945*	0.350*#	0.263	<0.001*	0.004*
	AN	0.813	0.733*	0.533*#	0.286	<0.001*	
7	ON	0.913	0.967*	0.875*	0.192	0.606	0.040*
	AN	0.787	0.827*	0.587*#	0.580	0.009*	

[1]*Scores that indicate a significant impairment (p<.05) compared to healthy normative data (Singlims, Crawford et al., 2010) are marked by a hashtag (#). Healthy controls performed at 0.884 ± 0.046 (range 0.8-0.933) for ON (31) and at 0.852 ± 0.059 (range 0.667-0.933) for AN (26). Performance where the patients show a significantly bigger difference between tasks compared to controls (Revised Standardized Difference Test (RSDT), Crawford et al., 2010) are marked by an asterisk (*). All p values are 2-tailed. Cases 1-3 were not operated awake and, hence, the tests were not administered (N/A) 1 Day preoperatively.*

Preoperative nTMS mapping at baseline revealed language-positive nTMS spots for ON mostly in the frontal and the parietal lobe with one spot in proximity to the lesion (**Figure 1A**). Subsequent fiber tracking for ON included the AF, ILF, IFOF, CF and CNT (**Figure 1C**). Language-positive points for AN were more scarce and overlapped nearly entirely with ON points, resulting in a similar white matter visualization of the AF, IFOF, CF and CNT (**Figures 1B, D**).

Due to the prefrontal location of the tumor, which was only in proximity to the CNT of the delineated networks, the operation was performed asleep and without complications. Gross total resection was achieved.

On the third postoperative day, the patient showed a slight but not significant improvement in both ON and AN compared to preoperative testing, however, he was still impaired, and AN continued to be significantly worse than ON. Postoperative MRI confirmed that no language tract was in the vicinity of the resection cavity but only the articulatory speech tract CNT (**Figures 1E, F**). Case 1 was discharged on the sixth postoperative day. No additional cognitive nor physical impairments were noted.

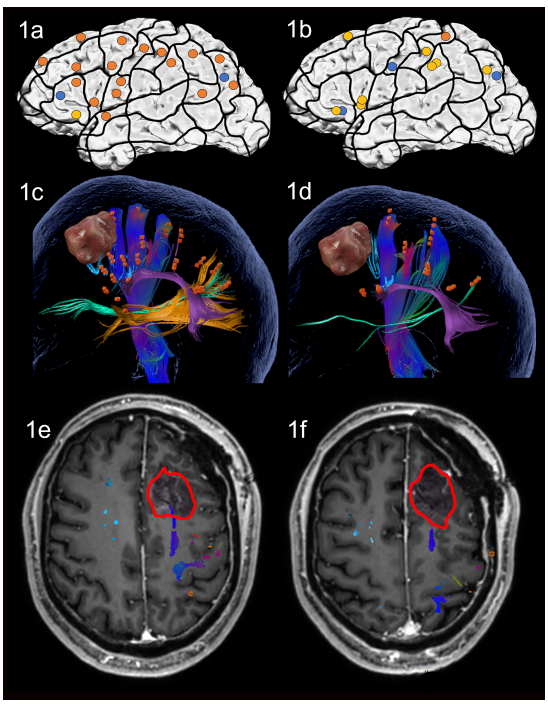

FIGURE 1 | Case 1. Left panels show ON results, right panels AN results. Panels **(A, B)** nTMS stimulation sites that induced errors; no response and hesitations in orange, semantic errors in yellow and performance errors in blue. Panels **(C, D)** Fiber tracking results including the lesion, nTMS cortical endpoints in orange and color-coded tracts with CNT in direction-coded, here dark blue, AF in purple, IFOF in turquoise, ILF in yellow, and CF in light blue. Panels **(E, F)** Overlap of tracking and postoperative T1-weighted imaging after elastic fusion with the resection cavity marked in red.

Clinical Case 2

Case 2 was a 70-year-old male, who presented having recently experienced the loss of fine motor skills in his right foot and hand. Imaging confirmed a lesion in the precentral gyrus (prG). Apart from these issues, his cognitive skills seemed intact at the preoperative stage, supported by normal scores for baseline naming of ON and AN (**Table 3** and **Supplementary Material Table S1**).

Preoperative nTMS mapping at baseline showed language-positive cortical areas for ON in the middle frontal regions, and in the middle temporal gyrus (MTG). There were few parietal points and 3 points in the prG itself, resulting in the visualized white matter of the CNT, ILF and IFOF (**Figures 2A, C**). For AN, nTMS mapping revealed language-positive spots in the middle and superior frontal gyrus, the superior and middle temporal gyrus, some parietal points and the poG, as well leading to visualization of the CNT, ILF and IFOF (**Figures 2B, D**). Despite language-positive points on the pre- and post central gyrus, the white matter networks of both tasks did not appear to be in proximity of the lesion. The surgery was therefore performed asleep and with no complications.

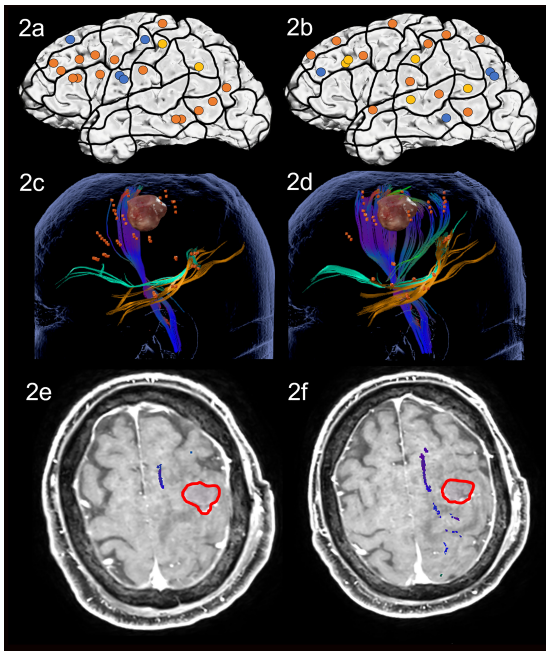

FIGURE 2 | Case 2. Left panels show ON results, right panels AN results. Panels **(A, B)** nTMS stimulation sites that induced errors; no response and hesitations in orange, semantic errors in yellow and performance errors in blue. Panels **(C, D)** Fiber tracking results including the lesion, nTMS cortical endpoints in orange and color-coded tracts with CNT in direction-coded, here dark blue, IFOF in turquoise, and ILF in yellow. Panels **(E, F)** Overlap of tracking and postoperative T1-weighted imaging after elastic fusion with the resection cavity marked in red.

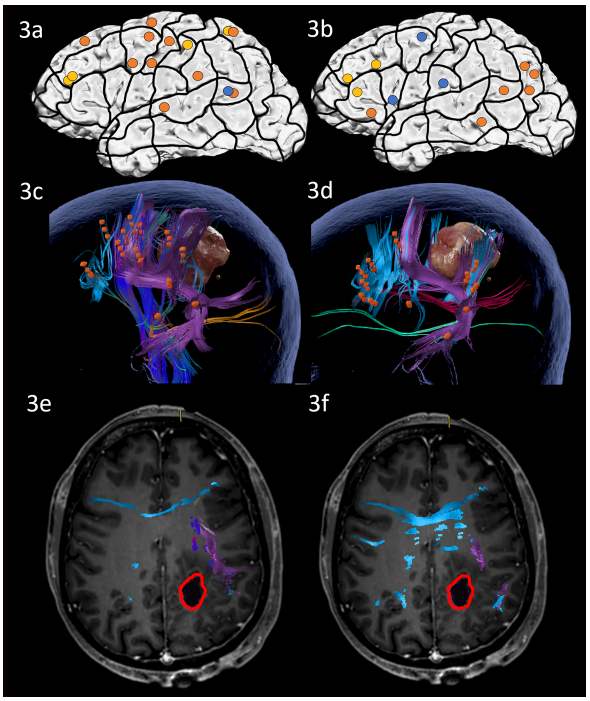

FIGURE 3 | Case 3. Left panels show ON results, right panels AN results. Panels **(A, B)** nTMS stimulation sites that induced errors; no response and hesitations in orange, semantic errors in yellow and performance errors in blue. Panels **(C, D)** Fiber tracking results including the lesion, nTMS cortical endpoints in orange and color-coded tracts with CNT in direction-coded, here dark blue, AF in purple, SLF in pink, IFOF in turquoise, ILF in yellow, and CF in light blue. Panels **(E, F)** Overlap of tracking and postoperative T1-weighted imaging after elastic with the resection cavity marked in red.

Postoperative assessment on the third postoperative day showed no significant change in the patient's performance, in agreement with results of postoperative MRI indicating no close distance between cavity and both the networks for ON and AN (**Figures 2E, F**).

Clinical Case 3

This patient was a 47-year-old female. She was admitted to the hospital after suffering from a focal seizure leaving her with temporary hemi-hypoesthesia and anomic aphasia, that resolved after 2 days. Scans were indicative of multiple metastases in both hemispheres, most likely secondary to a cervical carcinoma resected in 2008. Apart from three small lesions, the lesion to be resected at this point was situated in the left postcentral white matter. No cognitive or language functions seemed impaired preoperatively and she did not perform significantly differently to healthy controls for either ON or AN (**Table 3** and **Supplementary Material Table S1**).

Preoperative nTMS mapping at baseline revealed language-positive spots for ON in the superior frontal regions, as well as some parietal and superior temporal areas, resulting in visualization of a white matter network comprising the AF, ILF, CNT and CF (**Figures 3A, C**). Preoperative nTMS mapping with AN showed language-positive spots in more classical language areas such as the inferior frontal, and the posterior temporal and angular regions. These led to white matter visualization of the AF, SLF, IFOF and CF (**Figures 3B, D**). The surgery was performed asleep with no complications.

On the third postoperative day, the patient performed almost identically compared to the preoperative state in both ON and AN. MRI scanning demonstrated that the resection cavity did not overlap or approach the fiber tracts implicated in either ON nor AN (**Figures 3E, F**). The patient was discharged at the fifth postoperative day with no new impairments.

Clinical Case 4

Case 4 was a 53-year-old male who was referred following an episode of aphasia in the summer of 2020 and a second in February 2021. Scans in March 2021 revealed a lesion in the posterior superior temporal gyrus (STG), confirmed as a glioblastoma at biopsy. During preoperative assessment, he showed a mild to moderate impairment in language production, a mild impairment in writing as well as low scores in phonological and semantic fluency. He exhibited no significant impairment in accuracy on either ON or AN compared to healthy controls at this point. However, for two items in AN, he displayed a tendency to paraphrase verbs (*the man does ironing* instead of *the man irons*), a

pattern that is not observed in healthy controls. This worsened over the course of the month between biopsy and resection surgery: At preoperative testing one month later and one day prior to surgery, he was significantly worse, now clinically impaired on AN and displayed a tendency to paraphrase verbs in 5 items. ON remained unimpaired (**Table 3** and **Supplementary Material Table S1**).

Preoperative nTMS mapping at baseline with ON revealed only a few parietal, middle frontal and one temporal cortical language-positive spots, leading to white matter visualization of the AF, SLF, ILF and CNT (**Figures 4A, C**). During AN under nTMS mapping, middle frontal and several parietal cortical regions were uncovered, resulting in a similar white matter visualization of the AF, SLF, ILF and CNT (**Figures 4B, D**).

Due to the close location of the lesion to the language networks, an awake procedure including cortical DES mapping using both ON and AN tasks was performed. The craniotomy exposed inferior parietal and posterior STG regions. Stimulation of the exposed cortex led to only occasional errors with no site being repeatedly positive (2 out of 3 rule) in either of the tasks. Resection of the posterior STG and subsequently the underlying white matter was, therefore, carried out. There were no complications and intra-operative MRI confirmed a gross total resection.

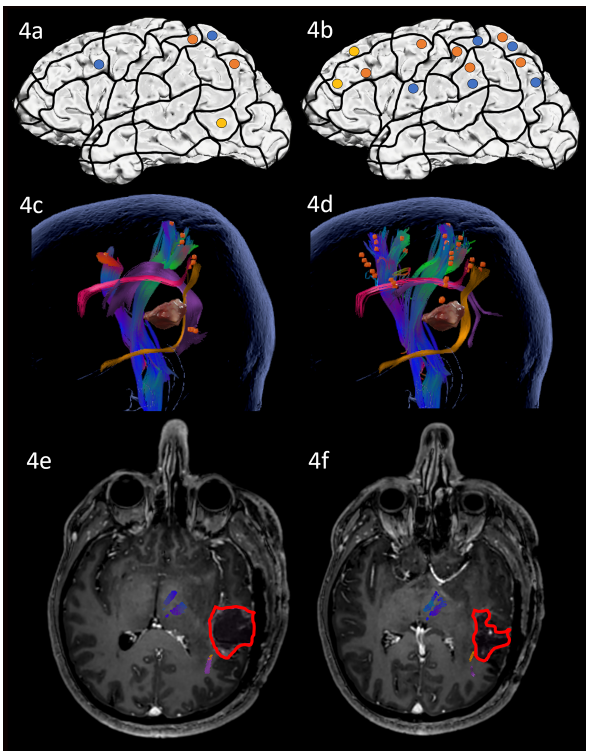

FIGURE 4 | Case 4. Left panels show ON results, right panels AN results. Panels **(A, B)** nTMS stimulation sites that induced errors; no response and hesitations in orange, semantic errors in yellow and performance errors in blue. Panels **(C, D)** Fiber tracking results including the lesion, nTMS cortical endpoints in orange and color-coded tracts with CNT in direction-coded, here dark blue, AF in purple, SLF in pink, and ILF in yellow. Panels **(E, F)** Overlap of tracking and postoperative T1-weighted imaging after elastic fusion with the resection cavity marked in red.

At postoperative assessment on the third postoperative day, the patient performed significantly more poorly on both ON and even poorer on AN compared to the preoperative state. AN seemed particularly affected and had declined significantly more severely than ON. The patient now paraphrased 14 verb items that were not troublesome at baseline. Moreover, poorer accuracy in AN correlated with transitivity, meaning that more complex verbs (*the man feeds the horse* vs. *the man sleeps*) were more problematic (**Supplementary Material Table S2**). Postoperative MRI scanning confirmed that the resection cavity left most of the white matter network unaffected, but was in proximity of the ILF, especially for AN (**Figures 4E, F**). This suggests that the vulnerable ventral stream may be responsible for the worsening in AN.

The patient was discharged on the third postoperative day with no further cognitive nor physical signs of impairment except for the reported language deficit.

Clinical Case 5

Case 5 was a 38-year-old male, who had suffered from severe headaches for a month with a subsequent general epileptic seizure. Scans revealed a large lesion in the superior frontal region. He scored within normal limits on the preoperative language batteries and on both ON and AN at the baseline, although AN was significantly less accurate than ON. A few days later, at preoperative testing one day prior to surgery, his performance was not significantly different, but now displaying impaired AN scores (**Table 3**; **Supplementary Material Table S1**).

During nTMS mapping at baseline, a large network was revealed for ON covering all three lobes and leading to a white matter visualization of the AF, ILF, CF and the Frontal Aslant Tract (**Figures 5A, C**). The nTMS mapping with AN led to many semantic errors and showed a similarly distributed network to ON with a high number of frontal areas and a white matter visualization of the AF, ILF, CNT, CF and Frontal Aslant Tract (**Figures 5B, D**).

Due to the close proximity to known frontal language areas and the visualized networks, the operation was performed awake with intraoperative DES mapping using both ON and AN tasks on the exposed frontal lobe. Intraoperative DES led to repeated errors in the pars opercularis under both tasks, which was spared during resection. Resection was achieved without complications and was extended deep into the white matter reaching the corpus callosum and head of caudate nucleus.

At testing on the third postoperative day, the patient's performance had slightly, but not significantly worsened in both tasks. MRI scanning confirmed that white matter damage was restricted to the Frontal Aslant Tract in both the ON and the AN network with all other language tracts arching posteriorly away from the resection cavity (**Figures 5E, F**). This suggests that the damage to the Frontal Aslant Tract did not influence naming, and that the majority of the language network remained untouched. The patient was discharged on the fourth postoperative day, with no further cognitive nor physical impairments.

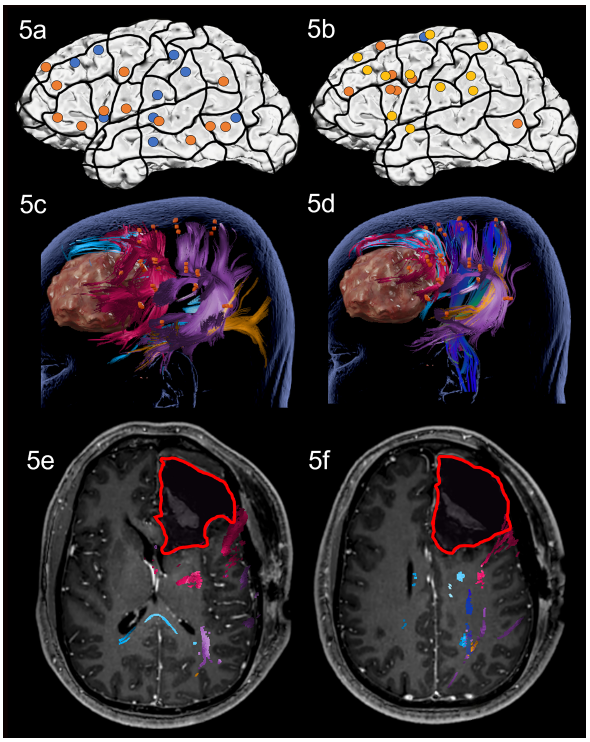

FIGURE 5 | Case 5. Left panels show ON results, right panels AN results. Panels **(A, B)** nTMS stimulation sites that induced errors; no response and hesitations in orange, semantic errors in yellow and performance errors in blue. Panels **(C, D)** Fiber tracking results including the lesion, nTMS cortical endpoints in orange and color-coded tracts with CNT in direction-coded, here dark blue, AF in purple, ILF in yellow, Frontal Aslant Tract in pink, and CF in light blue. Panels **(E, F)** Overlap of tracking and postoperative T1-weighted imaging after elastic fusion with the resection cavity marked in red.

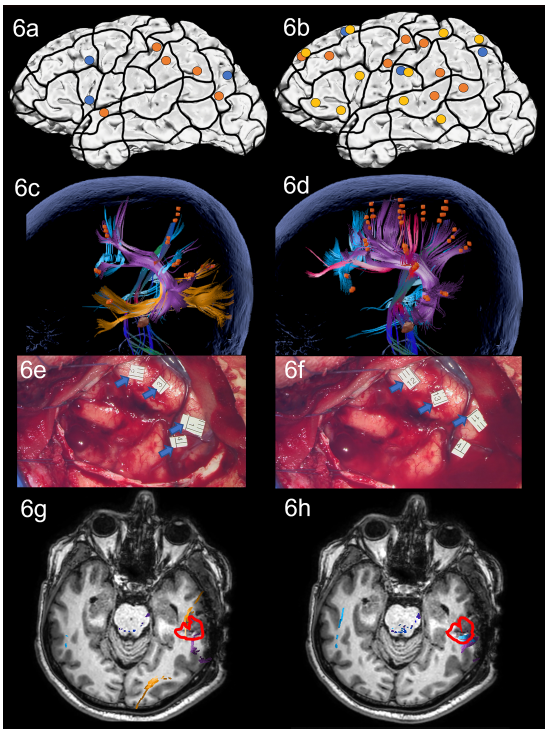

FIGURE 6 | Case 6. Left panels show ON results, right panels AN results. Panels **(A, B)** nTMS stimulation sites that induced errors; no response and hesitations in orange, semantic errors in yellow and performance errors in blue. Panels **(C, D)** Fiber tracking results including the lesion, nTMS cortical endpoints in orange and color-coded tracts with CNT in in direction-coded, here dark blue, AF in purple, SLF in pink, ILF in yellow, and CF in light blue. Panels **(E, F)** Screenshot of intraoperative positive cortical sites with tags 1-3 on the middle and posterior STG and tag 4 on the posterior MTG for ON, and tags 11-13 on the middle and posterior STG for AN. Panels **(G, H)** Overlap of tracking and postoperative T1-weighted imaging after elastic fusion with the resection cavity marked in red.

Clinical Case 6

Case 6 was a 57-year-old male, with a history of having been operated on for an astrocytoma WHO grade II in 2009. Following a biopsy in 2018 with subsequent radio- and chemotherapy, re-resection was now planned. Scans showed contrast-enhanced tumor growth along the previous resection cavity in the middle inferior temporal gyrus. On the preoperative language assessment, he displayed a mild comprehension deficit and moderate impairment in phonological fluency. ON and AN were not impaired at this point. At the preoperative testing day 2 weeks later (one day prior to surgery), his performance had not changed for ON. AN slightly worsened, which although still within normal limits, was now significantly worse than ON (**Table 3** and **Supplementary Material Table S1**).

During nTMS mapping at baseline, an ON network with parietal and frontal areas and one temporal cortical area was revealed, leading to white matter visualization of the AF, ILF, CNT and some parts of the CF (**Figures 6A, C**). AN resulted in many semantic errors and in an overall larger error rate with more frontal and temporal cortical sites and visualization of the AF, SLF, CNT, and CF, but no ventral stream tracts (**Figures 6B, D**).

Due to the spatial relation between the language network and the lesion, the patient was considered for awake surgery using the dual task ON and AN protocol under intraoperative DES. In the exposed middle and posterior temporal area, intraoperative DES led to errors in the STG in both tasks (**Figures 6E, F**: ON errors in tags 1-4; AN errors in tags 11-13), as predicted by nTMS mapping with AN. Moreover, the posterior MTG was found to include language-positive sites for ON (tag 4). Mapping results led to these regions being spared by the surgeon during access to the subcortical lesion. A gross total resection was achieved with no complications.

During testing on the third postoperative day, the patient's performance was significantly worse in both tasks compared to baseline. ON scores dropped severely to a clinically impaired score and worsened significantly more than AN. AN moderately worsened, with error production correlating with several linguistic values (**Supplementary Material Table S2**). Interestingly, verbs with values for instrumentality (e.g., *the man* ***cuts*** with the instrumental noun *knife*) were particularly affected. Postoperative MRI scans confirmed the overlap of the cavity and the ON network's AF and

ILF and the AN network's AF and CF (**Figures 6G, H**). This leads to the hypothesis that the harmed tissue in the intersection of the ILF and AF may be responsible for object semantics. Moreover, it could also be an account for the errors in AN for instrumental verbs, as these may be related to object semantics for the instrument.

The patient was discharged with no additional impairments on the third postoperative day.

Clinical Case 7

Case 7 was a 33-year-old male, admitted to the hospital after having recently suffered from two general epileptic seizures. A lesion was detected in the insular, fronto-basal and temporo-polar regions.

Preoperative baseline language assessment showed no language impairment, as well as normal scores on ON and AN. At the preoperative testing, 3 days later and one day prior to surgery, his performance had not changed significantly (**Table 3** and **Supplementary Material Table S1**).

Preoperative nTMS mapping at baseline revealed language-positive cortical sites for ON mainly in the prG and middle frontal gyrus (MFG) resulting in a white matter visualization of the AF, SLF, CNT and CF (**Figures 7A, C**). Apart from these regions, nTMS mapping with AN showed language-positive cortical areas in the parietal and temporal lobe and revealed semantic errors in all 3 lobes, leading to subcortical visualization of the AF, ILF, CNT and CF (**Figures 7B, D**).

Due to the close location of the lesion to the language networks, the surgical procedure included awake intraoperative cortical mapping with DES with ON and AN tasks. The craniotomy exposed inferior frontal and central regions and the anterior superior and middle temporal lobe. Intraoperative DES led to errors in ON in the middle postcentral gyrus (**Figure 7E**: tag 1). AN under DES confirmed this positive site and revealed a second region in the middle STG that repeatedly led to naming errors under stimulation only for AN (**Figure 7F**: tag 11 + 12) and as predicted by nTMS mapping with AN. Subsequent resection avoided these language-positive cortical areas and was extended into the insular lobe.

The patient's overall condition allowed postoperative testing only on the seventh postoperative day after the operation. His performance on ON had not changed compared to preoperative assessments. AN had significantly worsened and was now clinically impaired, with many semantically incorrect answers (e.g. "*The man … I guess he congratulates somebody*" instead of "*the man claps*" or "*The bird, well, how to say, it flaps its wings*" instead of the target "*The bird flies*"). These errors underlined the patient's inability to retrieve the target word, while being able to articulate and describe the situation. Postoperative MRI scans showed that the white matter network of ON had been spared entirely and was not in proximity of the cavity, while the AN network's ILF was in close proximity to the resected tissue (**Figures 7G, H**). The patient was discharged on Day 10, presenting with no further impairments.

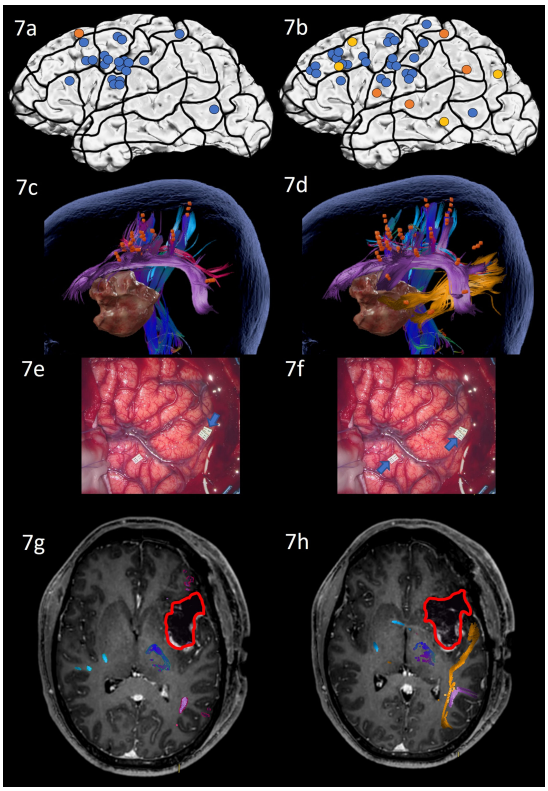

FIGURE 7 | Case 7. Left panels show ON results, right panels AN results. Panels **(A, B)** nTMS stimulation sites that induced errors; no response and hesitations in orange, semantic errors in yellow and performance errors in blue. Panels **(C, D)** Fiber tracking results including the lesion, nTMS cortical endpoints in orange and color-coded tracts with CNT in direction-coded, here dark blue, AF in purple, SLF in pink, ILF in yellow, and CF in light blue. Panels **(E, F)** Screenshot of intraoperative positive cortical sites with tag 1 PoG for ON, and tags 11 + 12 on PoG and the middle STG for AN. Panels **(G, H)** Overlap of tracking and postoperative T1-weighted imaging after elastic with the resection cavity marked in red.

DISCUSSION

Based on the neurolinguistic differences between, and supposed neuroanatomical segregation of, noun and verb knowledge, this series of cases set out to shed light on the benefits of nTMS language mapping from the use of a noun task (ON) and a verb task (AN) in perioperative language delineation in brain tumor patients. We have reported the details of seven cases, each described separately.

While this protocol had been successfully implemented using nTMS in healthy participants (24), the cases reported here show good feasibility of the dual task, ON and AN, protocol in the clinical population at hand: all patients were able to complete the addition of a second mapping with AN, and the extra task added a mere 15 min to the standard workflow of about 45-50 min. The potential added value of the addition of AN to the protocol for pre-, intra-, and postoperative delineation of language is discussed below.

Preoperative Delineation of the Language State and Network

Due to the higher processing load required during AN compared to ON, as well as AN requiring a larger neuroanatomical circuit

(18–21), we hypothesize that these two tasks may be differently affected by tumor growth even before surgical intervention. Moreover, the often milder impairments of glioma patients may not be detectable with ON alone, but only surface after more detailed screening through additional tools that screen, for instance, for more complex retrieval and grammatical skills (Wolthuis et al., subm.). Our study confirms this assumption: while Cases 2, 3, 5 and 7 performed well on ON and AN, as well as the more detailed AAT/ACL screening, the cases displaying a preexisting impairment (Cases 1, 4, and 6, **Table 1**) also performed significantly worse and/or were impaired in AN. This leads to the tentative conclusion that the AN task may be a more sensitive tool to spot the typically more subtle impairments of brain tumor patients. However, we do not suggest the exclusion of ON entirely: although not apparent in our sample, other patients may present with a dissociated deficit of unimpaired verb skills and impaired noun skills [for instance, see cases in (33)].

Regarding the added value of the AN task in preoperative visualization of the language network, the nTMS-only cases (Cases 1-3) show a different pattern to the cases who also underwent intraoperative DES (Cases 4-7). AN results either confirmed the functional cortical and subcortical tissue (Case 1 and 2), already detected during ON, or led to a more comprehensive white matter network with commissural fibers (Case 3). In all three cases, none of the visualized language network components appeared in close proximity to the to-be-resected regions.

In contrast, Cases 4-7 showed a much more divergent network visualization between the two tasks. Firstly, AN showed a higher sensitivity for detecting cortically positive areas in 2 cases (**Table 2**). The sentence context required by this task provides a greater opportunity for language to be disrupted by nTMS (i.e., more lexical items to be retrieved). However, the higher sensitivity of the AN task was still found in healthy participants, when both ON and AN were triggered in sentence context (24). This suggests that rather than an effect of the different context, the difference between ON and AN is that verb retrieval is likely more demanding and more easily disrupted under stimulation of nTMS.

Secondly, the difference in error type pattern between ON and AN further corroborates this: more semantic errors were elicited during AN in three out of our four cases (**Figures 5A, B**, **6A, B**, **7A, B**), originating from a disruption of the lexico-semantic retrieval of verbs. This further justifies the hypothesis that the AN task is lexico-semantically more demanding and is in line with previous findings reporting more semantic errors on the AN task under nTMS in healthy subjects, while errors at the sound level seem to be elicited to a similar degree in ON and AN (16, 17, 24).

In terms of the individual cases, this higher sensitivity for the AN task resulted in more language-positive cortical areas in Case 4, a similar distribution in Case 5, a clear profit from the combination of both tasks with AN for cortical and ON for subcortical visualization in Case 6, and AN was the better candidate for revealing functional cortical and subcortical matter in the proximity of the lesion in Case 7.

In summary, while the ON and AN networks showed high overlap and no close spatial relation to the lesion in Cases 1-3, the lesions of Cases 4-7 appeared rather close to the delineated networks on ON and AN and tumor growth seems to have affected them differently causing segregated reorganization of the two skills. In these cases, mapping with both ON and AN should be considered essential for risk stratification through error count, error quality and resulting white matter analysis after nTMS mapping.

Overlap With Intraoperative Mapping With DES

Often stressed as the "gold standard" for surgical decision making, DES intraoperative mapping remains the most direct tool for interrogating brain tissue and its functional involvement (34). However, not all patients are eligible for this highly invasive and costly procedure. Moreover, preoperative imaging and mapping aims to reliably predict intraoperative mapping results in order to shorten intraoperative time and to minimize the extent of the exposed cortex even further (4–6). Thus, the question arises how well the nTMS mapping results predicted DES maps in our four cases. The results are suggestive of more potent AN mapping for three cases. In Case 5, both ON and AN nTMS cortical maps failed to predict the negative DES results for most of the frontal lobe. For Case 4, nonetheless, the absence of positive cortical spots on the MFG during DES was in line with AN mapping (**Figures 4A, B**). The DES positive STG and middle MTG in Case 6 overlap with nTMS mapping of AN only (**Figures 6B, E, F**). Finally, in Case 7, AN based nTMS predicted the crucial middle STG region, an area known for verb representation (24, 35–37); this area was not revealed with ON under either DES nor nTMS (**Figures 7A, B, E, F**). The replicability of these results that point towards the higher sensitivity of AN-based nTMS compared ON-based nTMS and their overlap with DES mapping should next be evaluated in further patients with various lesion types and locations.

Visualization of Postoperative Outcome

The goal of clinical care for tumor patients is a gross total resection in combination with the lowest post-operative deficit. Therefore, our aim in exploring the dual-task ON and AN protocol was to analyze its ability to visualize the preoperative network in relation to the damage to it by the resection: If a network-to-deficit relationship can be captured through nTMS visualization, we may be able to predict and ultimately avoid postoperative language decline in future cases.

In the nTMS-only cases (1-3), this visualization of the functional network and its relation to the postoperative language state were achieved regardless of the task: in each case, the language networks for both ON and AN were spatially distant from the resection cavity. In conformity with this, no new language deficits were found following resection. This finding also underlines how accurately nTMS mapping and subsequent tracking registers the functional circuits of language and the changes to these circuits as a result of plasticity in the context of a tumor: For Cases 2 and 3 in particular, the lesions were located in what would have been thought to be highly eloquent cortical areas which would have rendered a

confident and safe tumor removal difficult. However, as nTMS captured the tumor-induced reorganization of the white matter, safe navigation and resection could be performed. These case observations are in agreement with the recent assumption that grey matter loss can be compensated for, while the focus should lie on the preservation of white matter integrity in order to avoid functional damage (38–40).

The added value of mapping with the second task of AN mapping becomes more evident in the remaining cases who additionally underwent intraoperative DES: In Case 4, both ON and AN networks were shown to be in the vicinity of the postoperative cavity (**Figures 4E, F**), particularly the AF and ILF for ON and even more so the ILF for AN. Previous data from DES and nTMS mapping have hinted towards the ventral stream's involvement in lexico-semantic retrieval (26, 38, 41–51). The presumed more lexico-semantically challenging AN task and network's close spatial relation to the lesion and cavity in this case are, therefore, in line with the patient's significant and even more marked drop in performance on AN compared to ON, highlighted further by his struggle with transitive verbs in particular: These verbs, that carry more semantic information about the constituents of the small sentence than intransitive verbs, seemed to be especially troublesome and substantiate the pattern of a lexico-semantic impairment of verbs and the fragility of the ventral stream visualized through AN.

In contrast, in Case 5 all major language white matter tracts showed to be unharmed by the resection, as the surgery could avoid damage to them due to their posteriorly pushed reorganization. Only the Frontal Aslant Tract, known to support fluency in spontaneous speech and not targeted by any of our tasks in particular (52), was depicted in the overlap with the postoperative cavity (**Figures 5E, F**). In accordance with this, no language impairment appeared in Case 5. We conclude that in this case no task was superior to the other in explaining postoperative language function, but that the overall reorganization captured by nTMS-based fiber tracking from both tasks was successful in predicting the postoperative state.

Lastly, Cases 6 and 7 displayed a mirrored pattern in language impairment with a significantly more severe decline in ON for Case 6 and a sole decline in AN for Case 7, while confirming the feasibility of nTMS-based fiber tracking in delineating the network and particularly the vulnerability of the ventral stream ILF. Even though both the AF and CF of the AN network and the AF of the ON network of Case 6 appeared to be damaged by the resection cavity (**Figures 6G, H**), we suspect the possible damage to the ILF of ON may explain the observed language deficit: the substantial drop in ON performance implies a severe deficit of object semantics not only in ON itself, but also affecting verb retrieval of those (instrumental) verbs that utilize objects [**Supplementary Material Table S2**, e.g. *The man **cuts** (with a knife)*]. This error pattern, that is consistent with a lexico-semantic retrieval deficit, is in accordance with a proposed temporal semantic hub for objects (53, 54). More importantly, however, this finding stresses the benefit of the dual-task protocol for a patient-tailored use of task: firstly, the ability of the method to show the network-to-deficit relationship was proven once more. Secondly, this error pattern of retrieval deficits in both ON and AN could only be substantiated by using the added information from linguistically standardized and marked protocols, that incorporate values such as instrumentality and frequency [for instance: the DULIP, ECCO, VAN-POP (16, 33, 55)].

Case 7, on the other hand, who showed unimpaired postoperative ON and newly impaired AN, is also consistent with the overlap of the network and the postoperative cavity (**Figures 7G, H**): All grey and white matter visualized by ON were unharmed, while, once more, the ILF of the AN network was in close proximity to the resection cavity and likely caused the low score on the AN task.

While our results are consistent with a temporal lobe hub for retrieval of semantics, these two cases stress the feasibility of using nTMS to highlight the vulnerability of the ventral stream on an individual basis: if preoperative visualization predicts proximity of the respective network to the tumor in these areas, special care should be taken of this language skill in order to minimize postoperative deficits even further.

Future Directions

The observed patterns of impairment of the cases reported here were based on post-operative testing on Day 3. This day often represents one of the first days of a stable cognitive function postoperatively, as well as one of the last days of in-house care before discharge. Even though a feasible and practical choice, this implies that we tested during a transient stage where some of the observed patterns may change or resolve over the next few weeks. However, especially in higher grade gliomas, a new worsening of the language state is also likely to follow due to regrowth of malignant tissue along the resection cavity. Those fragile network regions delineated at this early point in time might once more be affected. Nevertheless, future studies could opt for postoperative testing at the 3-months follow up to target an advanced recovered and possibly re-impaired point in time.

In addition, the implications we can draw at this point are based on a relatively small number of cases with an uneven distribution of lesion sites. Future studies may profit from analysis of larger case series with subgroups clustered by region to be able to make distinct claims of the benefit of each task in a specific region in question.

CONCLUSION

As a first instant of using a dual task for nTMS-based language mapping in a peri-operative setting, our case series including the second task of AN delivered promising results. We suggest that the verb task (AN) may be more sensitive in detecting minor pre-existing language impairments preoperatively and in predicting intraoperative positive mapping regions. However, the best grey and white matter visualization of functionally involved tissue may be achieved through implementation of both tasks, since double dissociations across cases are to be expected both behaviorally as well as anatomically.

The method delineated in our paper of nTMS-based mapping and fiber tracking proved capable of capturing network-to-deficit relations, particularly for white matter damage. We recommend that particular care should be dedicated to the preservation of the ventral stream tracts in order to avoid retrieval deficits for both nouns and verbs.

DATA AVAILABILITY STATEMENT

The raw data supporting the conclusions of this article will be made available by the authors, without undue reservation.

ETHICS STATEMENT

The studies involving human participants were reviewed and approved by the Institutional Review Board of the Technical University of Munich. The patients/participants provided their written informed consent to participate in this study.

AUTHOR CONTRIBUTIONS

A-KO, RB, LN, SI, NS, and SK contributed to the conception and design of the study. A-KO, BN, WZ, and NS performed the data collection and analysis. A-KO wrote the manuscript, with contributions and editing by all authors. All authors contributed to the article and approved the submitted version.

FUNDING

The study was financed by institutional grants from the Department of Neurosurgery, Klinikum rechts der Isar, School of Medicine, Technische Universität München, Munich, Germany. RB is supported by the Center for Language and Brain NRU Higher School of Economics, RF Government Grant, ag. No. 14.641.31.0004.

ACKNOWLEDGMENTS

The authors would like to express their gratitude to all patients for their time and efforts partaking in this study.

SUPPLEMENTARY MATERIAL

The Supplementary Material for this article can be found online at: https://www.frontiersin.org/articles/10.3389/fonc.2021.788122/full#supplementary-material

REFERENCES

1. Lefaucheur JP, Picht T. The Value of Preoperative Functional Cortical Mapping Using Navigated TMS. *Neurophysiol Clin* (2016) 46(2):125–33. doi: 10.1016/j.neucli.2016.05.001
2. Ottenhausen M, Krieg SM, Meyer B, Ringel F. Functional Preoperative and Intraoperative Mapping and Monitoring: Increasing Safety and Efficacy in Glioma Surgery. *Neurosurg Focus* (2015) 38(January):1–13. doi: 10.3171/2014.10.FOCUS14611.Disclosure
3. Hannula H, Ilmoniemi RJ. Basic Principles of Navigated TMS. In: *Navigated Transcranial Magnetic Stimulation in Neurosurgery*. Cham: Springer (2017). p. 3–29.
4. Picht T, Krieg SM, Sollmann N, Rösler J, Niraula B, Neuvonen T, et al. A Comparison of Language Mapping by Preoperative Navigated Transcranial Magnetic Stimulation and Direct Cortical Stimulation During Awake Surgery. *Neurosurgery* (2013) 72(5):808–19. doi: 10.1227/NEU.0b013e3182889e01
5. Sollmann N, Ille S, Hauck T, Maurer S, Negwer C, Zimmer C, et al. The Impact of Preoperative Language Mapping by Repetitive Navigated Transcranial Magnetic Stimulation on the Clinical Course of Brain Tumor Patients. *BMC Cancer* (2015) 15(1):261. doi: 10.1186/s12885-015-1299-5
6. Sollmann N, Kelm A, Ille S, Schröder A, Zimmer C, Ringel F, et al. Setup Presentation and Clinical Outcome Analysis of Treating Highly Language-Eloquent Gliomas *via* Preoperative Navigated Transcranial Magnetic Stimulation and Tractography. *Neurosurg Focus* (2018) 44(6):E2. doi: 10.3171/2018.3.FOCUS1838
7. Bährend I, Muench MR, Schneider H, Moshourab R, Dreyer FR, Vajkoczy P, et al. Incidence and Linguistic Quality of Speech Errors: A Comparison of Preoperative Transcranial Magnetic Stimulation and Intraoperative Direct Cortex Stimulation. *J Neurosurg* (2020) 134(5):1409–18. doi: 10.3171/2020.3.jns193085
8. Ille S, Sollmann N, Hauck T, Maurer S, Tanigawa N, Obermueller T, et al. Combined Noninvasive Language Mapping by Navigated Transcranial Magnetic Stimulation and Functional MRI and Its Comparison With Direct Cortical Stimulation. *J Neurosurg* (2015) 123(July):1–14. doi: 10.3171/2014.9.JNS14929
9. Krieg SM, Tarapore PE, Picht T, Tanigawa N, Houde J, Sollmann N, et al. Optimal Timing of Pulse Onset for Language Mapping With Navigated Repetitive Transcranial Magnetic Stimulation. *NeuroImage* (2014) 100:219–36. doi: 10.1016/j.neuroimage.2014.06.016
10. Takahashi S, Vajkoczy P, Picht T. Navigated Transcranial Magnetic Stimulation for Mapping the Motor Cortex in Patients With Rolandic Brain Tumors. *Neurosurg Focus* (2013) 34(4):1–7. doi: 10.3171/2013.1.FOCUS133
11. Tarapore PE, Findlay AM, Honma SM, Mizuiri D, Houde JF, Berger MS, et al. Language Mapping With Navigated Repetitive TMS: Proof of Technique and Validation. *NeuroImage* (2013) 82:260–72. doi: 10.1016/j.neuroimage.2013.05.018
12. Negwer C, Ille S, Hauck T, Sollmann N, Maurer S, Kirschke JS, et al. Visualization of Subcortical Language Pathways by Diffusion Tensor Imaging Fiber Tracking Based on rTMS Language Mapping. *Brain Imaging Behav* (2017) 11(3):899–914. doi: 10.1007/s11682-016-9563-0
13. Raffa G, Conti A, Scibilia A, Sindorio C, Quattropani M, Visocchi M, et al. Functional Reconstruction of Motor and Language Pathways Based on Navigated Transcranial Magnetic Stimulation and DTI Fiber Tracking for the Preoperative Planning of Low Grade Glioma Surgery: A New Tool for Preservation and Restoration of Eloquent Network. in. *Trends Reconstr Neurosurg - Neurorehabil Restor Reconstruction* (2017) 124:251–62. doi: 10.1007/978-3-319-39546-3_37
14. Sollmann N, Negwer C, Ille S, Maurer S, Hauck T, Kirschke JS, et al. Feasibility of nTMS-Based DTI Fiber Tracking of Language Pathways in Neurosurgical Patients Using a Fractional Anisotropy Threshold. *J Neurosci Methods* (2016) 267:45–54. doi: 10.1016/j.jneumeth.2016.04.002
15. Sollmann N, Meyer B, Krieg SM. Implementing Functional Preoperative Mapping in the Clinical Routine of a Neurosurgical Department: Technical Note. *World Neurosurg* (2017) 103:94–105. doi: 10.1016/j.wneu.2017.03.114
16. Ohlerth A-K, Valentin A, Vergani F, Ashkan K, Bastiaanse R. The Verb and Noun Test for Peri-Operative Testing (VAN-POP): Standardized Language

Tests for Navigated Transcranial Magnetic Stimulation and Direct Electrical Stimulation. *Acta Neurochir* (2020) 162(2):397–406. doi: 10.1007/s00701-019-04159-x
17. Rofes A, Miceli G. Language Mapping With Verbs and Sentences in Awake Surgery: A Review. *Neuropsychol Rev* (2014) 24(2):185–99. doi: 10.1007/s11065-014-9258-5
18. Bastiaanse R, Wieling M, Wolthuis N. The Role of Frequency in the Retrieval of Nouns and Verbs in Aphasia. *Aphasiology* (2016) 30(11):1221–39. doi: 10.1080/02687038.2015.1100709
19. Bastiaanse R, Van Zonneveld R. Broca's Aphasia, Verbs and the Mental Lexicon. *Brain Lang* (2004) 90(1–3):198–202. doi: 10.1016/S0093-934X(03)00432-2
20. Crepaldi D, Berlingeri M, Cattinelli I, Borghese NA, Luzzatti C, Paulesu E. Clustering the Lexicon in the Brain: A Meta-Analysis of the Neurofunctional Evidence on Noun and Verb Processing. *Front Hum Neurosci* (2013) 7:303 (JUN). doi: 10.3389/fnhum.2013.00303
21. Vigliocco G, Vinson DP, Druks J, Barber H, Cappa SF. Nouns and Verbs in the Brain: A Review of Behavioural, Electrophysiological, Neuropsychological and Imaging Studies. *Neurosci Biobehav Rev* (2011) 35:407–26. doi: 10.1016/j.neubiorev.2010.04.007
22. Havas V, Gabarrós A, Juncadella M, Rifa-Ros X, Plans G, Acebes JJ, et al. Electrical Stimulation Mapping of Nouns and Verbs in Broca's Area. *Brain Lang* (2015) 145:53–63. doi: 10.1016/j.bandl.2015.04.005
23. Lubrano V, Filleron T, Démonet J-F, Roux F-E. Anatomical Correlates for Category-Specific Naming of Objects and Actions: A Brain Stimulation Mapping Study. *Hum Brain Mapp* (2014) 35:429–43. doi: 10.1002/hbm.22189
24. Ohlerth A-K, Bastiaanse R, Negwer C, Sollmann N, Schramm S, Schröder A, et al. Bihemispheric Navigated Transcranial Magnetic Stimulation Mapping for Action Naming Compared to Object Naming in Sentence Context. *Submitted Publication* (2021) 11(9):1190. doi: 10.3390/brainsci11091190
25. Rofes A, Spena G, Talacchi A, Santini B, Miozzo A, Miceli G. *Mapping Nouns and Finite Verbs in Left Hemisphere Tumors: A Direct Electrical Stimulation Study Mapping Nouns and Finite Verbs in Left Hemisphere Tumors: A Direct Electrical Stimulation Study International Doctorate in Experimental Approaches to Language* (2017). Available at: https://doi.org/10.1080/13554794.2017.1307418.
26. Ohlerth AK, Bastiaanse R, Negwer C, Sollmann N, Schramm S, Schröder A, et al. Benefit of Action Naming Over Object Naming for Visualization of Subcortical Language Pathways in Navigated Transcranial Magnetic Stimulation-Based Diffusion Tensor Imaging-Fiber Tracking. *Front Hum Neurosci* (2021) 15:748274. doi: 10.3389/fnhum.2021.748274
27. Krieg SM, Lioumis P, Mäkelä JP, Wilenius J, Karhu J, Hannula H, et al. Protocol for Motor and Language Mapping by Navigated TMS in Patients and Healthy Volunteers; Workshop Report. *Acta Neurochir* (2017) 159(7):1187–95. doi: 10.1007/s00701-017-3187-z
28. Ojemann G, Ojemann J, Lettich E, Berger M. Cortical Language Localization in Left, Dominant Hemisphere. An Electrical Stimulation Mapping Investigation in 117 Patients. 1989. *J Neurosurg* (1989) 71(2):316–26. doi: 10.3171/JNS/2008/108/2/0411
29. Picht T, Kombos T, Gramm HJ, Brock M, Suess O. Multimodal Protocol for Awake Craniotomy in Language Cortex Tumour Surgery. *Acta Neurochir* (2006) 148(2):127–37. doi: 10.1007/s00701-005-0706-0
30. Ille S, Schwendner M, Zhang W, Schroeder A, Meyer B, Krieg SM. Tractography for Subcortical Resection of Gliomas Is Highly Accurate for Motor and Language Function: Iomri-Based Elastic Fusion Disproves the Severity of Brain Shift. *Cancers* (2021) 13(8):1787. doi: 10.3390/cancers13081787
31. Sollmann N, Fuss-Ruppenthal S, Zimmer C, Meyer B, Krieg SM. Investigating Stimulation Protocols for Language Mapping by Repetitive Navigated Transcranial Magnetic Stimulation. *Front Behav Neurosci* (2018) 12:197. doi: 10.3389/fnbeh.2018.00197
32. Crawford JR, Garthwaite PH, Porter S. Point and Interval Estimates of Effect Sizes for the Case-Controls Design in Neuropsychology: Rationale, Methods, Implementations, and Proposed Reporting Standards. *Cogn Neuropsychol* (2010) 27(3):245–60. doi: 10.1080/02643294.2010.513967
33. De Witte E, Satoer D, Robert E, Colle H, Verheyen S, Visch-Brink E, et al. The Dutch Linguistic Intraoperative Protocol: A Valid Linguistic Approach to Awake Brain Surgery. *Brain Lang* (2015) 140:35–48. doi: 10.1016/j.bandl.2014.10.011
34. De Witt Hamer PC, Robles SG, Zwinderman AH, Duffau H, Berger MS. Impact of Intraoperative Stimulation Brain Mapping on Glioma Surgery Outcome: A Meta-Analysis. *J Clin Oncol* (2012) 30(20):2559–65. doi: 10.1200/JCO.2011.38.4818
35. Corina DP, Gibson EK, Martin R, Poliakov A, Brinkley J, Ojemann GA. Dissociation of Action and Object Naming: Evidence From Cortical Stimulation Mapping. *Hum Brain Mapp* (2005) 24(1):1–10. doi: 10.1002/hbm.20063
36. Hauck T, Tanigawa N, Probst M, Wohlschlaeger A, Ille S, Sollmann N, et al. Task Type Affects Location of Language- Positive Cortical Regions by Repetitive Navigated Transcranial Magnetic Stimulation Mapping. *PloS One* (2015) 10(4):1–21. doi: 10.1371/journal
37. Hernandez-Pavon JC, Mäkelä N, Lehtinen H, Lioumis P, Mäkelä JP. Effects of Navigated TMS on Object and Action Naming. *Front Hum Neurosci* (2014) 8:660(660). doi: 10.3389/fnhum.2014.00660
38. Bello L, Gallucci M, Fava M, Carrabba G, Giussani C, Acerbi F, et al. Intraoperative Subcortical Language Tract Mapping Guides Surgical Removal of Gliomas Involving Speech Areas. *Neurosurgery* (2007) 60(1):67–80. doi: 10.1227/01.NEU.0000249206.58601.DE
39. Duffau H. The Huge Plastic Potential of Adult Brain and the Role of Connectomics: New Insights Provided by Serial Mappings in Glioma Surgery. *Cortex* (2014) 58:325–37. doi: 10.1016/J.CORTEX.2013.08.005
40. Trinh VT, Fahim DK, Shah K, Tummala S, McCutcheon IE, Sawaya R, et al. Subcortical Injury Is an Independent Predictor of Worsening Neurological Deficits Following Awake Craniotomy Procedures. *Neurosurgery* (2013) 72(2):160–9. doi: 10.1227/NEU.0b013e31827b9a11
41. Friederici AD. The Cortical Language Circuit: From Auditory Perception to Sentence Comprehension. *Trends Cogn Sci* (2012) 16(5):262–8. doi: 10.1016/j.tics.2012.04.001
42. Friederici AD. *White-Matter Pathways for Speech and Language Processing*. Vol 129. *1st ed*. Elsevier B.V (2015). doi: 10.1016/B978-0-444-62630-1.00010-X
43. Hickok G, Poeppel D. Dorsal and Ventral Streams: A Framework for Understanding Aspects of the Functional Anatomy of Language. *Cognition* (2004) 92(1–2):67–99. doi: 10.1016/j.cognition.2003.10.011
44. Hickok G, Poeppel D. The Cortical Organization of Speech Processing. *Nat Rev Neurosci* (2007) 8(5):393–402. doi: 10.1038/nrn2113
45. Ueno T, Saito S, Rogers TT, Ralph MA. Lichtheim 2: Synthesizing Aphasia and the Neural Basis of Language in a Neurocomputational Model of the Dual Dorsal-Ventral Language Pathways. *Neuron* (2011) 72(2):385–96. doi: 10.1016/j.neuron.2011.09.013
46. Bello L, Gambini A, Castellano A, Carrabba G, Acerbi F, Fava E, et al. Motor and Language DTI Fiber Tracking Combined With Intraoperative Subcortical Mapping for Surgical Removal of Gliomas. *Neuroimage* (2008) 39(1):369–82. doi: 10.1016/j.neuroimage.2007.08.031
47. Bello L, Castellano A, Fava E, Casaceli G, Riva M, Scotti G, et al. Intraoperative Use of Diffusion Tensor Imaging Fiber Tractography and Subcortical Mapping for Resection of Gliomas: Technical Considerations. *Neurosurg Focus* (2010) 28(2):1–14. doi: 10.3171/2009.12.FOCUS09240
48. De Witt Hamer PC, Moritz-Gasser S, Gatignol P, Duffau H. Is the Human Left Middle Longitudinal Fascicle Essential for Language? A Brain Electrostimulation Study. *Hum Brain Mapp* (2011) 32(6):962–73. doi: 10.1002/hbm.21082
49. Duffau H, Gatignol P, Mandonnet E, Peruzzi P, Tzourio-Mazoyer N, Capelle L. New Insights Into the Anatomo-Functional Connectivity of the Semantic System: A Study Using Cortico-Subcortical Electrostimulations. *Brain* (2005) 128(4):797–810. doi: 10.1093/brain/awh423
50. Leclercq D, Duffau H, Delmaire C, Capelle L, Gatignol P, Ducros M. Comparison of Diffusion Tensor Imaging Tractography of Language Tracts and Intraoperative Subcortical Stimulations: Clinical article. *J Neurosurg* (2010) 112(3):503–11. doi: 10.3171/2009.8.JNS09558
51. Maldonado IL, Moritz-Gasser S, de Champfleur NM, Bertram L, Moulinié G, Duffau H. Surgery for Gliomas Involving the Left Inferior Parietal Lobule: New Insights Into the Functional Anatomy Provided by Stimulation Mapping in Awake Patients: Clinical article. *J Neurosurg* (2011) 115(4):770–9. doi: 10.3171/2011.5.JNS112
52. Dick AS, Garic D, Graziano P, Tremblay P. The Frontal Aslant Tract (FAT) and Its Role in Speech, Language and Executive Function. *Frontal Aslant Tract*

(FAT) Its Role Speech Lang Exec Funct (2018) 111:148–63. doi: 10.1101/249912
53. Indefrey P. The Spatial and Temporal Signatures of Word Production Components: A Critical Update. *Front Psychol* (2011) 2:1–16. doi: 10.1016/j.cognition.2002.06.001
54. Indefrey P, Levelt WJM. The Neural Correlates of Language Production. *New Cogn Neurosci* (2000) 2000:845–65.
55. Rofes A, de Aguiar V, Miceli G. A Minimal Standardization Setting for Language Mapping Tests: An Italian Example. *Neuro Sci* (2015) 36(7):1113–9. doi: 10.1007/s10072-015-2192-3

Conflict of Interest: The authors declare that the research was conducted in the absence of any commercial or financial relationships that could be construed as a potential conflict of interest.

Publisher's Note: All claims expressed in this article are solely those of the authors and do not necessarily represent those of their affiliated organizations, or those of the publisher, the editors and the reviewers. Any product that may be evaluated in this article, or claim that may be made by its manufacturer, is not guaranteed or endorsed by the publisher.

Copyright © 2022 Ohlerth, Bastiaanse, Nickels, Neu, Zhang, Ille, Sollmann and Krieg. This is an open-access article distributed under the terms of the Creative Commons Attribution License (CC BY). The use, distribution or reproduction in other forums is permitted, provided the original author(s) and the copyright owner(s) are credited and that the original publication in this journal is cited, in accordance with accepted academic practice. No use, distribution or reproduction is permitted which does not comply with these terms.

frontiers in Neuroscience

ORIGINAL RESEARCH
published: 28 January 2022
doi: 10.3389/fnins.2021.791776

Radiomics Analysis Based on Magnetic Resonance Imaging for Preoperative Overall Survival Prediction in Isocitrate Dehydrogenase Wild-Type Glioblastoma

Shouchao Wang[1†], Feng Xiao[1†], Wenbo Sun[1], Chao Yang[2], Chao Ma[2], Yong Huang[3], Dan Xu[1], Lanqing Li[1], Jun Chen[4], Huan Li[1] and Haibo Xu[1]**

[1] Department of Radiology, Zhongnan Hospital of Wuhan University, Wuhan, China, [2] Department of Neurosurgery, Zhongnan Hospital of Wuhan University, Wuhan, China, [3] Department of Radiation and Medical Oncology, Zhongnan Hospital of Wuhan University, Wuhan, China, [4] Precision Health Institute, GE Healthcare, Shanghai, China

Purpose: This study aimed to develop a radiomics signature for the preoperative prognosis prediction of isocitrate dehydrogenase (IDH)-wild-type glioblastoma (GBM) patients and to provide personalized assistance in the clinical decision-making for different patients.

Materials and Methods: A total of 142 IDH-wild-type GBM patients classified using the new classification criteria of WHO 2021 from two centers were included in the study and randomly divided into a training set and a test set. Firstly, their clinical characteristics were screened using univariate Cox regression. Then, the radiomics features were extracted from the tumor and peritumoral edema areas on their contrast-enhanced T1-weighted image (CE-T1WI), T2-weighted image (T2WI), and T2-weighted fluid-attenuated inversion recovery (T2-FLAIR) magnetic resonance imaging (MRI) images. Subsequently, inter- and intra-class correlation coefficient (ICC) analysis, Spearman's correlation analysis, univariate Cox, and the least absolute shrinkage and selection operator (LASSO) Cox regression were used step by step for feature selection and the construction of a radiomics signature. The combined model was established by integrating the selected clinical factors. Kaplan–Meier analysis was performed for the validation of the discrimination ability of the model, and the C-index was used to evaluate consistency in the prediction. Finally, a Radiomics + Clinical nomogram was generated for personalized prognosis analysis and then validated using the calibration curve.

Results: Analysis of the clinical characteristics resulted in the screening of four risk factors. The combination of ICC, Spearman's correlation, and univariate and LASSO Cox resulted in the selection of eight radiomics features, which made up the radiomics signature. Both the radiomics and combined models can significantly stratify high- and low-risk patients ($p < 0.001$ and $p < 0.05$ for the training and test sets, respectively)

OPEN ACCESS

Edited by:
Nico Sollmann, University of California, San Francisco, United States

Reviewed by:
Yi Zhang, Zhejiang University, China
Hamza Farooq, University of Minnesota Twin Cities, United States
Yu Zeng, Central South University, China
Eman Helmy, Mansoura University, Egypt

***Correspondence:**
Huan Li
cntlh@whu.edu.cn
Haibo Xu
xuhaibo@whu.edu.cn

† These authors have contributed equally to this work

Specialty section:
This article was submitted to Brain Imaging Methods, a section of the journal Frontiers in Neuroscience

Received: *09 October 2021*
Accepted: *15 December 2021*
Published: *28 January 2022*

Citation:
Wang S, Xiao F, Sun W, Yang C, Ma C, Huang Y, Xu D, Li L, Chen J, Li H and Xu H (2022) Radiomics Analysis Based on Magnetic Resonance Imaging for Preoperative Overall Survival Prediction in Isocitrate Dehydrogenase Wild-Type Glioblastoma. Front. Neurosci. 15:791776. doi: 10.3389/fnins.2021.791776

and obtained good prediction consistency (C-index = 0.74–0.86). The calibration plots exhibited good agreement in both 1- and 2-year survival between the prediction of the model and the actual observation.

Conclusion: Radiomics is an independent preoperative non-invasive prognostic tool for patients who were newly classified as having IDH-wild-type GBM. The constructed nomogram, which combined radiomics features with clinical factors, can predict the overall survival (OS) of IDH-wild-type GBM patients and could be a new supplement to treatment guidelines.

Keywords: radiomics, isocitrate dehydrogenase wildtype, glioblastoma, MRI, nomogram

INTRODUCTION

Among all primary brain and other central nervous system tumors, gliomas account for about 26% (Ostrom et al., 2018). Among all malignant brain and other central nervous system tumors, glioblastoma (GBM) is the most common (Soomro et al., 2017). Despite the advances in surgery and chemoradiotherapy being great, the prognosis of GBM patients is still poor, with a median survival of only 12–14 months (Henson et al., 2005; Stupp et al., 2005; Van Meir et al., 2010; Lu et al., 2020; Soltani et al., 2021). In addition, several previous studies have confirmed that the status of isocitrate dehydrogenase (IDH) mutation has a great impact on the prognosis of GBM patients (Parsons et al., 2008; Hartmann et al., 2013; Reifenberger et al., 2014). According to the latest classification criteria of the World Health Organization (WHO) in 2021, the common diffuse gliomas of adults have been divided into only three types: astrocytoma, IDH-mutant; oligodendroglioma, IDH-mutant and 1p/19q-codeleted; and glioblastoma, IDH-wild type. IDH-wild-type diffuse astrocytic (NB: diffuse and astrocytic) tumors in adults, if microvascular proliferation or necrosis or telomerase reverse transcriptase (TERT) promoter mutation or epidermal growth factor receptor (*EGFR*) gene amplification or +7/-10 chromosome copy number changes are present, should be diagnosed as IDH-wild-type GBM. Based on the new classification criteria, a more reasonable and personalized prognosis analysis method can be constructed, which will directly affect the condition assessment, targeted treatment, and follow-up management of IDH-wild-type GBM patients (Louis et al., 2021).

In current clinical practice, several factors are usually combined to predict the prognosis of GBM patients, including age, gender, Karnofsky performance status (KPS; Buckner, 2003; Chambless et al., 2015), tumor location, and laterality (Field et al., 2014; Gately et al., 2018), molecular spectrum analysis (Binabaj et al., 2018; Schaff et al., 2020), and treatment plan (Stupp et al., 2009; Herrlinger et al., 2019), among others. In addition, it has been reported that the prognosis of malignant glioma may be affected by some basic characteristics of preoperative MRI, such as the extent of peritumoral edema (PTE), tumor crossing the midline, necrosis, enhancement, and the size of the cyst (Maldaun et al., 2004; Pope et al., 2005; Wu et al., 2015; Hansen et al., 2018). MRI is a non-invasive preoperative routine examination for GBM with the advantage of multi-parameter imaging and excellent soft tissue resolution, which can provide comprehensive structural and functional information of the tumor (Henson et al., 2005; Diehn et al., 2008). Currently, it has been proven that the MRI technology exhibits great potential in predicting the survival of patients with GBM (Gutman et al., 2013; Gevaert et al., 2014; Rao et al., 2016).

Radiomics transforms the subjective and semi-quantitative description of traditional imaging diagnosis (such as the enhancement degree, edema range, and space occupying effect) into objective and quantitative parameters (such as histogram features, and texture features) (Lambin et al., 2012; Peeken et al., 2017; Rogers et al., 2020). Compared to traditional imaging features, these quantitative radiomics features contain a number of invisible tumor biological information, such as tumor heterogeneity, oncogenic processes, invasion, and metastasis (Gillies et al., 2016; Limkin et al., 2017; Peeken et al., 2017; Liu et al., 2019). Therefore, a more effective and reliable method may be to analyze the prognosis of IDH-wild-type GBM by using a comprehensive multivariate model based on radiomics features and clinical risk factors.

This study aimed to develop machine learning models that can be used to predict the prognosis of IDH-wild-type GBM based on the radiomics features extracted from multicenter, multi-parameter MRI images. By constructing a combined Radiomics + Clinical nomogram, the overall survival of IDH-wild-type GBM patients was analyzed and predicted individually.

MATERIALS AND METHODS

Patients

Recruitment of the patients included in this study consisted of two parts. The first part was from our hospital (Zhongnan Hospital of Wuhan University), which was approved by the Medical Ethics Committee of the hospital (approval no. 2020181). Informed consent was waived because of the retrospective nature of the study. Using the Picture Archiving and Communications System (PACS), we searched and enrolled the patients admitted to hospital between June 2016 and December 2020. The second part was from the public databases The Cancer Genome Atlas (TCGA)/The Cancer Imaging Archive (TCIA; Clark et al., 2013). The patient identifiers in the databases were erased and approval of the Institutional Review Committee was not required. All patients were included and selected based

on the following exclusion criteria: (1) patients without any sequence of contrast-enhanced T1-weighted image (CE-T1WI), T2-weighted image (T2WI), or T2-weighted fluid-attenuated inversion recovery (T2-FLAIR) images; (2) patients who had received biopsy or operation; and (3) patients with large image artifacts and poor quality images, which may cause deviation in the follow-up process. Finally, a total of 142 patients from multiple centers were included in this study, among which 70 were from our hospital and 72 were from public databases. The detailed patient screening and grouping process is shown in **Supplementary Figure 1**, while the individual characteristics of these patients are shown in **Table 1**.

TABLE 1 | Clinical and traditional imaging characteristics of patients included in the study.

Characteristics	All subjects (*n* = 142)	Training set (*n* = 100)	Test set (*n* = 42)	*p*-value
Clinical				
Age (years), mean ± SD	58.72 ± 11.74	58.28 ± 10.86	59.76 ± 13.69	0.535
Gender, *n* (%)				0.870
Male	86 (60.56)	61 (61)	25 (59.52)	
Female	56 (39.44)	39 (39)	17 (40.48)	
KPS, median (range)	80 (40–100)	80 (40–100)	80 (40–100)	
Treatment, *n* (%)				0.802
Standard	120 (84.51)	85 (85)	35 (83.33)	
Non-standard	22 (15.49)	15 (15)	7 (16.67)	
Traditional imaging				
Location, *n* (%)				0.061
Frontal	61 (42.96)	45 (45)	16 (38.10)	
Temporal	39 (27.46)	27 (27)	12 (28.57)	
Parietal	23 (16.20)	11 (11)	12 (28.57)	
Occipital	5 (3.52)	5 (5)	0 (0)	
Others	14 (9.86)	12 (12)	2 (4.76)	
Number, *n* (%)				0.741
Single	109 (76.76)	76 (76)	33 (78.57)	
Multiple	33 (23.24)	24 (24)	9 (21.43)	
Tumor crossing the midline, *n* (%)				0.582
Yes	17 (11.97)	11 (11)	6 (14.29)	
No	125 (88.03)	89 (89)	36 (85.71)	
Maximum tumor diameter, mean ± SD	48.67 ± 16.33	49.77 ± 16.79	46.08 ± 15.05	0.202
Maximum edema diameter, mean ± SD	18.46 ± 10.55	18.99 ± 10.24	17.19 ± 10.28	0.377
PTE, *n* (%)				0.465
Minor, <1cm	38 (26.76)	25 (25)	13 (30.95)	
Major, ≥1cm	104 (73.24)	75 (75)	29 (69.05)	
Edema shape, *n* (%)				0.513
Rounded	65 (45.77)	44 (44)	21 (50.00)	
Irregular	77 (54.23)	56 (56)	21 (50.00)	
Edema diameter/tumor diameter, mean ± SD	0.43 ± 0.33	0.44 ± 0.36	0.39 ± 0.24	0.274
Necrosis, *n* (%)				0.744
No	14 (9.86)	9 (9)	5 (11.90)	
Mild	61 (42.96)	42 (42)	19 (45.24)	
Severe	67 (47.18)	49 (49)	18 (42.86)	
Cyst, *n* (%)				0.700
No	83 (58.45)	57 (57)	26 (61.90)	
Small	30 (21.13)	23 (23)	7 (16.67)	
Large	29 (20.42)	20 (20)	9 (21.43)	
Enhancement, *n* (%)				0.815
Not marked	63 (44.37)	45 (45)	18 (42.86)	
Marked	79 (55.63)	55 (55)	24 (57.14)	
OS, median (range)	306 (17–1,185)	296 (23–1,185)	322 (17–1,143)	

OS, overall survival.

Follow-Up

The overall survival (OS) of the patients from our hospital was calculated from the date of surgery to the last follow-up or death, and the preoperative image date was not long before the operation date. The minimum follow-up period to ascertain OS was 18 months after the date of surgery, if patients were still alive. The OS of the patients from TCGA/TCIA databases was obtained from support documents of the TCGA GBM Project.

Data Flowchart

As seen in **Figure 1**, the data processing of this study consisted of two modules: clinical characteristics and radiomics analysis modules. Clinical risk factors were screened one by one using univariate Cox regression, while radiomics analysis could be divided into five parts: image preprocessing, image segmentation, feature extraction, feature reduction, and step-by-9step model construction. The radiomics and combined (Radiomics + Clinical) models were constructed separately and then compared. Finally, the nomogram was generated as an effective tool to personally predict the 1- and 2-year survival of patients based on the model with better predictive performance.

As shown in **Table 1** and **Supplementary Figure 1**, all 70 samples from our hospital and 30 samples randomly selected from TCGA/TCIA made up the training set (a total of 100 cases), while the remaining 42 samples from TCGA/TCIA made up the test set. All feature analyses and modeling (clinical and radiomics) were operated on the training set and then validated on both the training and test sets.

Images Acquisition

All preoperative MRI images in our hospital were obtained with a 3.0-T scanner [Umr790 (Philips, Best, Netherlands) or MAGNETOM Trio (Siemens, Erlangen, Germany)] using an 8-channel array coil. The detailed acquisition parameters are summarized in **Supplementary Methods**.

Analysis of the Clinical Characteristics

Two radiologists reviewed the images with the double-blind method and negotiated the results together. Referring to a previously reported method (Wu et al., 2015), we collected radiological characteristics such as qualitative indicators (location, number, tumor crossing the midline, degree of edema, edema shape, degree of necrosis, degree of cystic change, and degree of enhancement) and quantitative indicators (maximum tumor diameter, maximum edema diameter, and maximum edema diameter/maximum tumor diameter). In addition to the above, information on the age, gender, KPS, and treatments were included in this study. Univariate Cox analysis was performed between OS and the clinical characteristics individually to screen the clinical risk factors.

Image Analysis

Before image analysis, T2-FLAIR images and CE-T1WI were strictly registered to T2WI using MATLAB software with

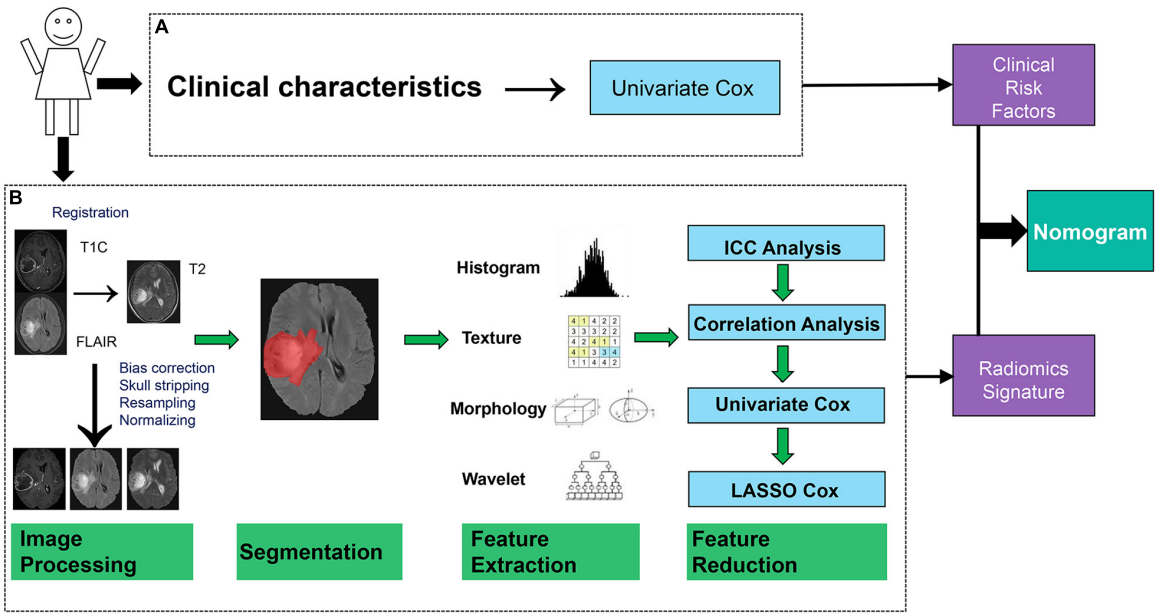

FIGURE 1 | Data flowchart of the study. **(A)** Module of the clinical characteristic analysis. **(B)** Module of the radiomics analysis.

SPM. Then, the CE-T1WI, T2WI, and the T2-FLAIR images were preprocessed using Analysis Kit software (GE Healthcare, Chicago, IL, United States). This included bias correction, skull stripping, and image resampling and normalization. One radiologist (SW) used ITK-SNAP to manually segment the regions of interest (ROIs). The region with a high signal on the T2-FLAIR image was drawn as the ROI.

For each MRI sequence (CE-T1WI, T2WI, and T2-FLAIR), 402 radiomics features were extracted for the ROI using AK Software (see **Supplementary Methods**). Then, all 1,206 features were combined for further modeling.

TABLE 2 | Univariate analysis of the clinical and traditional imaging factors with the overall survival (OS) of patients using Cox regression model.

Factors	HR	95% CI	*p*-value
Age	1.024	1.001–1.048	0.038*
Gender	1.064	0.697–1.623	0.774
KPS	0.987	0.976–0.998	0.021*
Treatment	0.708	0.442–1.134	0.151
Location	0.749	0.326–1.191	0.277
Number	1.18	0.778–1.788	0.436
Tumor crossing the midline	2.417	1.42–4.11	0.001*
Maximum tumor diameter	1.017	1.005–1.029	0.007*
Maximum edema diameter	0.996	0.979–1.013	0.626
PTE	0.896	0.604–1.327	0.583
Edema shape	1.069	0.753–1.518	0.708
Edema/tumor diameter	0.706	0.397–1.255	0.236
Necrosis	0.961	0.613–1.740	0.897
Cyst	1.108	0.717–1.484	0.815
Enhancement	0.942	0.663–1.337	0.737

*PTE, peritumoral edema. *p < 0.05.*

Twenty samples were randomly selected from all samples to test feature reliability and reproducibility. Feature extraction by two authors (SW and WS) was initially analyzed. The procedures were completed together to guarantee the productivity and stability of the features (see **Supplementary Methods**).

Feature Reduction and Radiomics Signature Construction

Four methods were used in the feature reduction and modeling processes (**Figure 1B**). Firstly, inter- and intra-class correlation coefficients (ICCs) were calculated to assess the stability and repeatability of each radiomics feature. Features with ICCs larger than 0.8 were considered to be robust and were retained for further analysis (see **Supplementary Methods**). Thereafter, Spearman's correlation coefficient for each pair of features was calculated. Two features with a correlation coefficient (r) larger than 0.9 meant that there is a high correlation between them, and one of these features was erased randomly.

Subsequently, univariate Cox analysis was performed on each radiomics feature to evaluate the ability of a single feature to predict OS. Features with p-values less than 0.05 were considered to be statistically significant and were retained in the least absolute shrinkage and selection operator (LASSO) Cox model for further analysis.

Least absolute shrinkage and selection operator Cox is a multivariate Cox method with L1 regularization. During modeling, the number of features could be reduced by imposing a penalty term to the feature weights. In this work, the key penalty coefficient of the LASSO Cox model was determined by the use of fivefold cross-validation.

The radiomics signature was established by a linear combination of the retained features (non-zero coefficients)

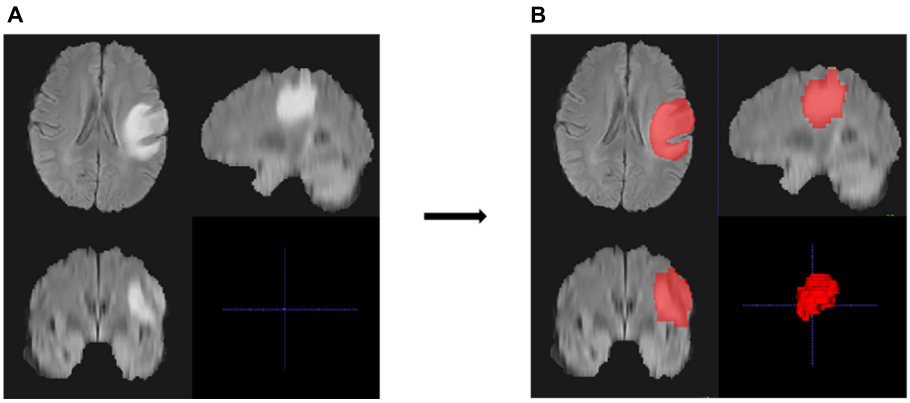

FIGURE 2 | An example of region of interest (ROI) and the segmentation results of the MRI images of one patient. **(A,B)** Cross-section views of images before segmentation **(A)** and after manual segmentation **(B)**. The lesion in the original image was high and showed a bright signal **(A)**, and the ROI of the lesion area is represented as red after segmentation **(B)**.

after LASSO Cox analysis. Kaplan–Meier (KM) survival curve analysis of OS based on the optimal cutoff value of the constructed radiomics and combined models was performed to stratify patients into high-risk and low-risk groups in the training set and test set, respectively. The optimal cutoff value of the radiomics signature was determined through traversing all values of the radiomics signature to obtain the best stratification result. The log-rank test was used for comparisons of the differences between the high- and low-risk patients stratified using the constructed models. Ultimately, the Radiomics + Clinical model was constructed using multivariate Cox analysis by combining the clinical risk factors and the radiomics signature. Proportionality assumption was tested based on the Schoenfeld residuals test. The consistency of model prediction was assessed using the C-index.

Nomogram Construction

The nomogram transformed the corresponding model into a simple and visual graph, making the results of the prediction model more distinct and of higher use value (see **Supplementary Methods**). Calibration curves were used to assess the consistency between the actual observation outcome and the nomogram prediction.

Statistical Analysis

The distributions of the clinical characteristics in the training and test sets were represented in the form of mean ± standard deviation or proportion according to the variable type. Group differences for these variables were compared using an independent samples *t*-test, chi-square test, or the Mann–Whitney U test according to the variable type and distribution.

Statistical analysis was performed using R software (version 3.6.3).[1] The following R packages were used: "glmnet" to perform the LASSO Cox regression analysis, the "survival" and "survminer" packages to implement the Kaplan–Meier analysis, and the "rms" package to implement the nomogram construction and calibration evaluation. A two-sided p-value < 0.05 was considered to be statistically significant for all statistical analyses.

[1]http://www.Rproject.org

RESULTS

Clinical Characteristics and Overall Survival

As presented in **Table 1**, no significant difference in the OS and clinical characteristics was found between the training and test sets. After univariate Cox analysis (**Table 2**), four independent risk factors, which included age, KPS, tumor crossing the midline and maximum tumor diameter significantly influenced the OS.

Image Analysis and Radiomics Signature Construction

Figure 2 shows an example of the lesion area segmented as ROI using the manual segmentation method. For the ROI in each MRI sequence image of a patient, 402 features were extracted. Thus, a total of 1,206 quantitative features were obtained for one patient, of which 614 features with ICC > 0.8 were retained for further analysis. Spearman's correlation analysis reduced the features to 241, and then by univariate Cox analysis to 45. **Figure 3** shows the results of feature reduction using LASSO Cox. Ultimately, 8 features were retained (**Table 3**), which made up the radiomics signature through linear combination.

Validation of Radiomics Models

As presented in **Figure 4** ($p < 0.001$ in the training set and $p < 0.05$ in the test set), both radiomics and Radiomics + Clinical models could effectively stratify the risk of OS. The C-index score in the range 0.74–0.86 (**Table 4**) in both the training and test sets meant good consistency of the model prediction. In addition, the Radiomics + Clinical model showed better predictive

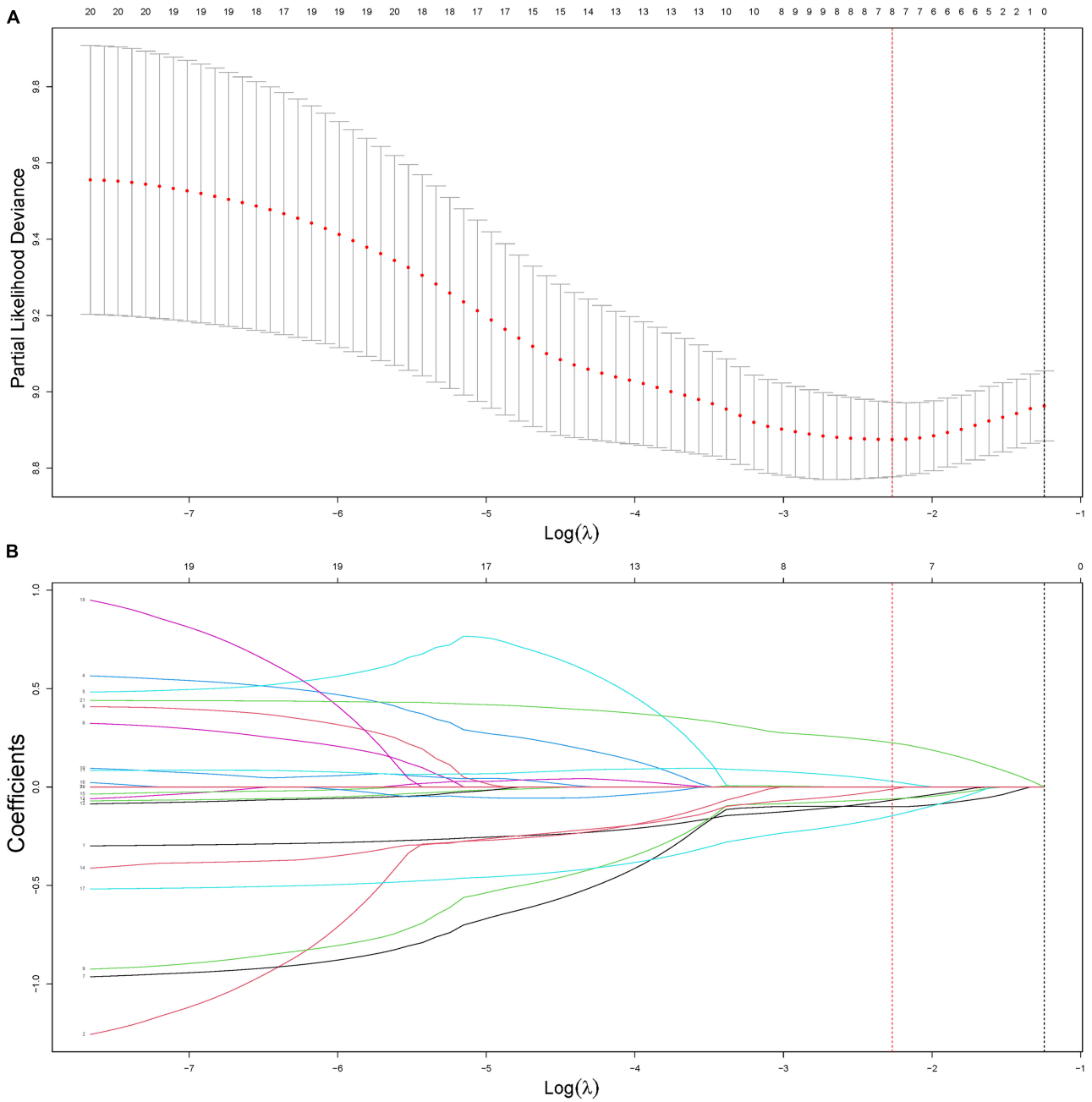

FIGURE 3 | Construction of the radiomics signature using least absolute shrinkage and selection operator (LASSO) Cox regression. **(A)** An optimal tuning parameter (λ) in the LASSO regression model was selected using fivefold cross-validation and the partial likelihood deviance rule. Two *vertical dashed lines* were drawn for two criteria: (1) the minimum of the partial likelihood deviance (lambda.min, *red dashed*) and the least feature number in the range of 1 standard error around lambda.min (lambda.1SE, *black dashed*). In this study, lambda.min (0.1035244) was selected to minimize the partial likelihood deviance. **(B)** LASSO coefficient profiles of the features. According to the fivefold cross-validation in panel **(A)**, the optimal λ value was determined at lambda.min, and the corresponding features with non-zero coefficients were included in the construction of the radiomics signature.

performance than the radiomics model, but the difference was not statistically significant. The overall Schoenfeld global test of the Radiomics + Clinical model was examined for proportional hazards (PH) assumption, which was met (p = 0.518). All covariates met the proportional hazards assumption (**Supplementary Figure 2**). To further evaluate the real performance of the model, we supplemented the 10 times tenfold cross-validation method to randomly divide the dataset 10 times, aiming to perform a more balanced model evaluation by calculating the average and standard deviation values of the model C-index. The C-index scores are shown in **Supplementary Table 2**.

TABLE 3 | Features and their corresponding coefficients in the radiomics signature.

	Feature category	Feature name	Coefficients
Radiomics	Contrast	C_ShortRunEmphasis_AllDirection_offset4_SD	−0.102
	T2	T2_ClusterShade_AllDirection_offset1_SD	−0.099
		T2_ClusterShade_AllDirection_offset7_SD	−0.073
		T2_Correlation_angle45_offset7	0.059
		T2_sumAverage	−0.047
		T2_Elongation	−0.198
	FLAIR	FLAIR_Elongation	0.001
		FLAIR_IntensityVariability	0.256

FLAIR, fluid-attenuated inversion recovery.

Radiomics Nomogram

Ultimately, the radiomics signature and four clinical risk factors (age, KPS, tumor crossing the midline, and maximum tumor diameter) were included in the nomogram (**Figure 5A**). The total score obtained by integrating the individual scores for age, KPS, tumor crossing the midline, maximum tumor diameter, and the radscore can be used to quantitatively predict the probability of a patient's 1- and 2-year survival (**Figure 5A**). The calibration curves of OS prediction at 1 and 2 years (**Figures 5B,C**) showed good agreement between the nomogram prediction and the actual observations.

DISCUSSION

In this study, we extracted more comprehensive features from CE-T1WI, T2WI, and T2-FLAIR sequences than those in previous studies so that we could mine radiological images in more depth. The radiomics signature has been identified as an independent prognostic biomarker of IDH-wild-type GBM. Therefore, we combined it with clinical risk factors (age, KPS, tumor crossing the midline, and maximum tumor diameter) to construct a combined model and nomogram as a personalized tool to estimate the OS of IDH-wild-type GBM patients. The models were constructed based on a multicenter training queue and verified based on a multicenter test set.

Traditional central nervous system tumor grading is mainly based on histological features, but now, some molecular markers can provide strong prognostic information. Therefore, molecular markers have been added as grading biomarkers and used to further evaluate the prognosis of several tumor types. The 2021 classification criteria of the WHO classified common adult diffuse gliomas into three types: astrocytoma, IDH-mutant; oligodendroglioma, IDH-mutant and 1p/19q-codeleted; and glioblastoma, IDH-wild type. In addition, it should be noted that IDH-wild-type diffuse astrocytic tumors in adults, if microvascular proliferation or necrosis or TERT promoter mutation or EGFR gene amplification or +7/−10 chromosome copy number changes are present, should be diagnosed as IDH-wild-type glioblastoma (Louis et al., 2017, 2021; Brat et al., 2018). Previous studies have explored the prognosis of glioblastoma according to the old classification (Alexander and Cloughesy, 2017; Chaddad et al., 2018; Rao et al., 2018; Zhang et al., 2019). Therefore, on this basis, according to the latest guidelines, we included some tumors previously considered to be of lower grade but now diagnosed with GBM into the study. This updates the prognosis prediction for such tumor patients and provides more real-time help with personalized treatment. This is a more complete and comprehensive retrospective study for patients with newly diagnosed IDH-wild-type GBM. Radiomics uses advanced computing methods to extract potential radiomics features from images and obtain more tumor information in a non-invasive manner. Previous studies have reported that radiomics features can predict the prognosis of gliomas. Bae et al. (2018) showed that radiomic MRI phenotyping can improve survival prediction when integrated with clinical and genetic profiles and thus has potential as a practical imaging biomarker. Tan et al. (2019) showed that radiomics can accurately reflect the heterogeneity of the tumor and edema areas of high-grade glioma so as to reflect the prognostic information to a certain extent. Compared with some previous studies, our model showed similar or even better predictive ability. The C-index of a model constructed for high-grade glioma was 0.764 (Tan et al., 2019). This may be related to the fact that we extracted more features from three different MRI sequences. The combination of multiple sources of information allows for an overall analysis of the tumor and better prognosis prediction. Except as mentioned above, it is more reasonable that multicenter data are adopted in the training and test processes. Although the performance of the constructed models is not the best among existing studies, they have stronger generalization ability, reproducibility, and usability. In addition, to further evaluate the real performance of the model, we supplemented the 10 times tenfold cross-validation method to randomly divide the data set 10 times, aiming to perform a more balanced model evaluation by calculating the average and standard deviation values of the model C-index.

We finally screened out 8 features, including 1 CE-T1WI feature, 5 T2WI features, and 2 T2-FLAIR features. The CE-T1WI sequence can well display the activity and necrotic area of the tumor, the T2WI sequence can reflect the anatomical location and cellularity of the tumor, and the T2-FLAIR sequence can depict the cellularity of the tumor and the density of tumor cells (Tan et al., 2019; Tian et al., 2020). The radiomics features of the combined sequences can represent the characteristics of tumors from different aspects and reflect the information of all aspects of tumors, evaluating tumors and their heterogeneity more comprehensively.

According to the latest classification, we excluded the IDH status and identified the constructed radiomics signature, age, KPS, tumor crossing the midline, and maximum tumor diameter as independent risk factors using multivariable Cox regression analysis. Both the radiomics and Radiomics + Clinical models could effectively stratify the risk of OS in IDH-wild-type GBM. The combined model showed better prediction effect than the single radiomics model, but the effect was limited. This indicates

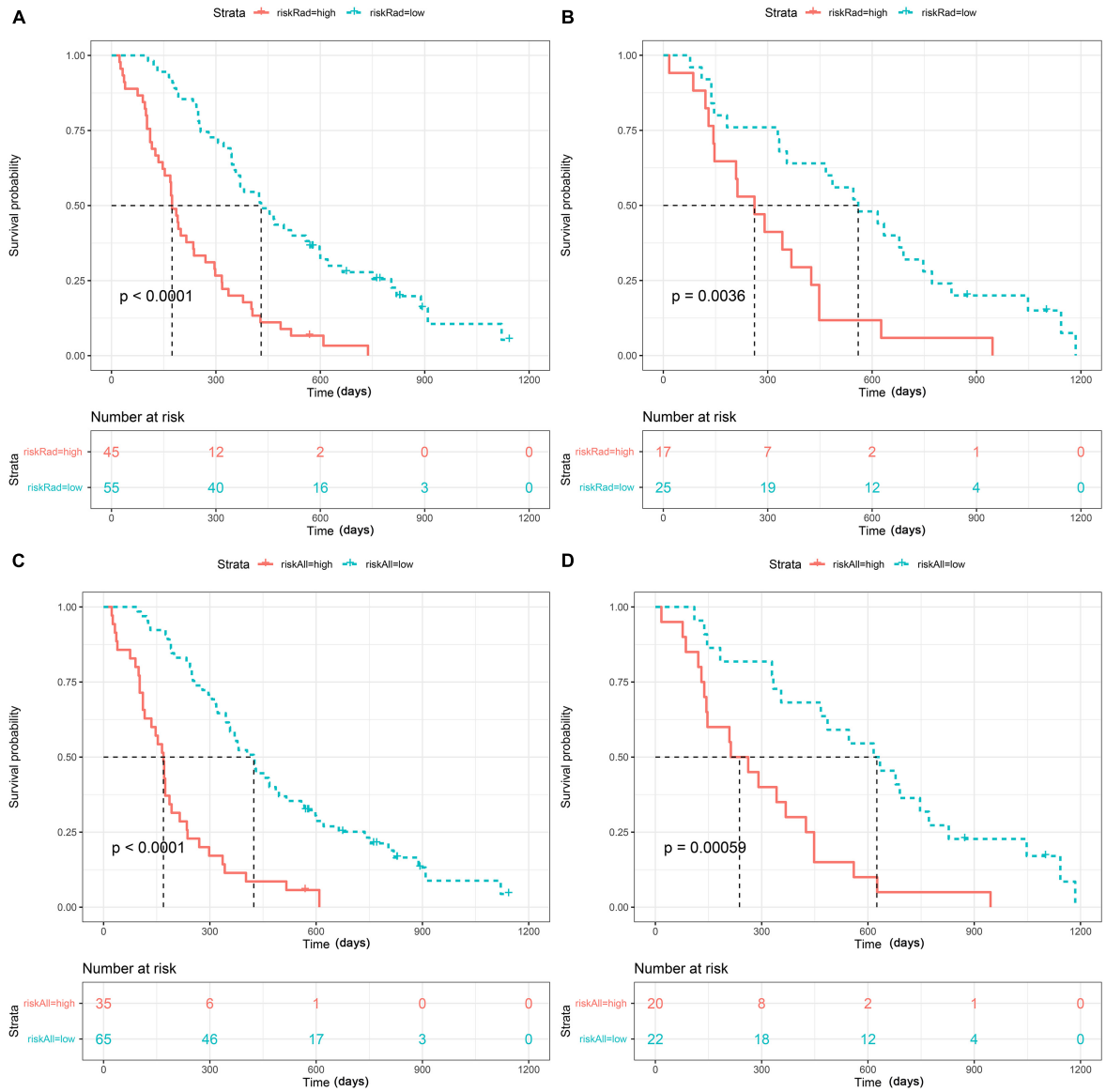

FIGURE 4 | Strata: index for risk stratification. Kaplan–Meier analysis of the overall survival (OS) of patients based on the radiomics model with optimal cutoff values (1.2311) in the training set **(A)** and the test set **(B)** and based on the Radiomics + Clinical model with optimal cutoff values (1.1489) in the training set **(C)** and the test set **(D)**.

that radiomics features may play a greater role in prognosis prediction. Moreover, it may be partly due to the IDH mutation status factor being reduced by including all IDH-wild-type patients according to the new classification, which may have reflected the importance of IDH mutation status in the prognosis of GBM patients. In addition, the nomogram built based on radiomics features and selected clinical features is a graphical representation of a statistical model and makes the results of the prediction model more prominent and of higher use value. By combining the scores of each risk factor in the nomogram, the 1- and 2-year survival probability of each patient can be estimated, making it a useful tool for the personalized diagnosis and treatment of IDH-wild-type GBM.

However, there are still some limitations in our study. Firstly, manual segmentation will produce personal errors. Automatic tumor segmentation based on deep learning will minimize user

TABLE 4 | Comparison of the predictive performance of the models using the C-index in the training and test sets.

Model	C-index (95%CI)	
	Training set	Test set
Radiomics	0.803 (0.744–0.861)	0.764 (0.680–0.848)
Radiomics + Clinical	0.836 (0.785–0.886)	0.799 (0.720–0.878)

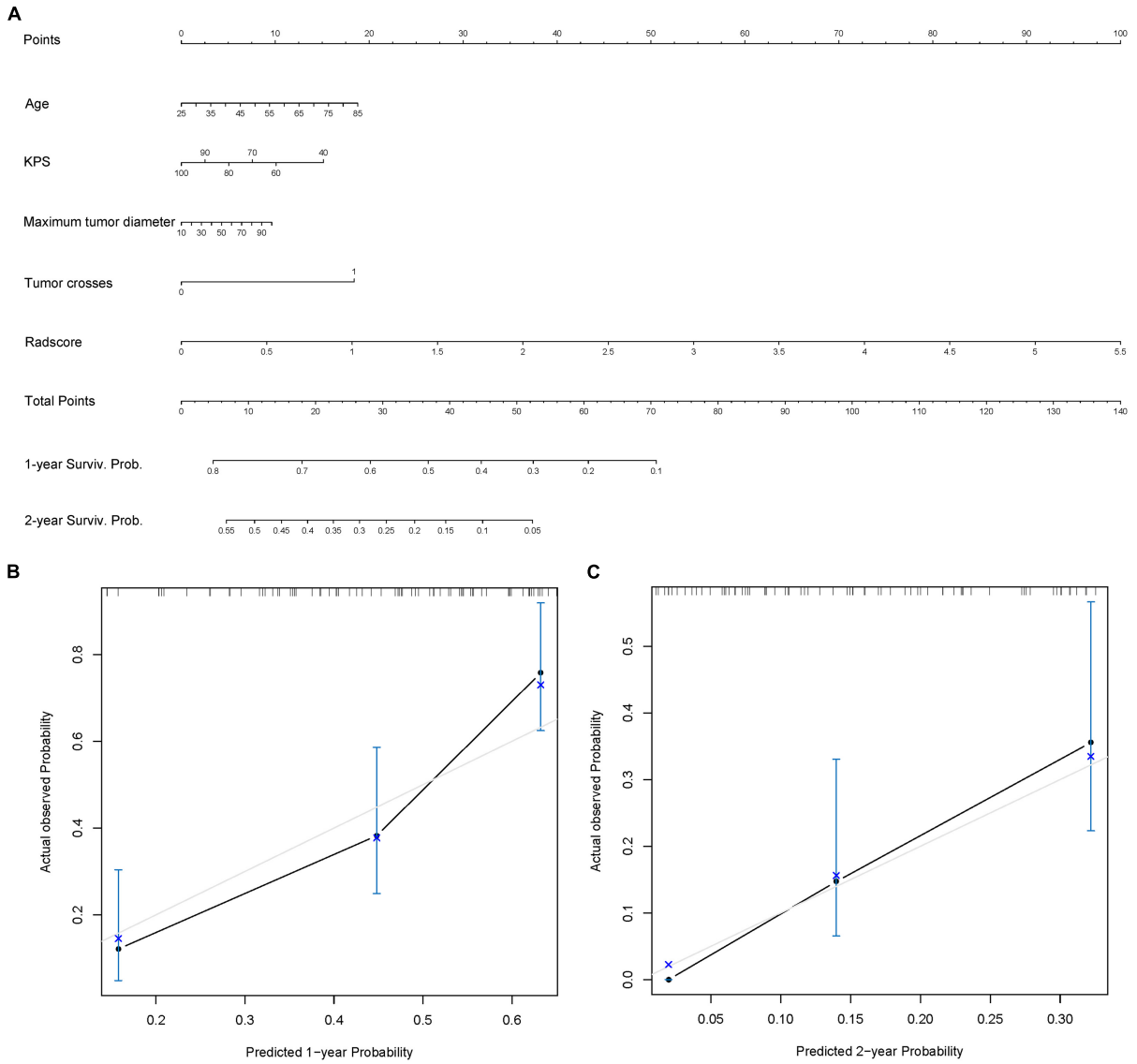

FIGURE 5 | Radiomics nomogram. **(A)** Radiomics + Clinical nomogram constructed by integrating the independent risk factors, including age, Karnofsky performance status (KPS), maximum tumor diameter, tumor crossing the midline, and radscore to predict the 1- and 2-year survival of patients with isocitrate dehydrogenase (IDH)-wild-type glioblastoma (GBM). **(B,C)** Calibration curves used to assess the prediction consistency of the nomogram in the training set **(B)** and the test set **(C)**.

bias and facilitate large-scale research. Secondly, due to the heterogeneity of the imaging parameters in the TCGA/TCIA databases, we only included conventional sequences, but did not analyze advanced MRI sequences. Finally, we did not consider the impact of various treatments on tumor progression after standard chemoradiotherapy in the analysis of OS.

CONCLUSION

In conclusion, for patients newly classified as IDH-wild-type GBM, radiomics features are still independent prognostic biomarkers, and age, KPS, tumor crossing the midline, and maximum tumor diameter can, to a certain degree, supplement radiomics features. The nomogram constructed by combining radiomics features and relevant clinical factors can improve the individualized prediction of survival of IDH-wild-type GBM patients, which provides help with personalized clinical treatment.

DATA AVAILABILITY STATEMENT

The original contributions presented in the study are included in the article/**Supplementary Material**, further inquiries can be directed to the corresponding authors.

ETHICS STATEMENT

The studies involving human participants were reviewed and approved by the Zhongnan Hospital, Wuhan, China (approval No.2020109). The patients/participants provided their written informed consent to participate in this study. Written informed consent was obtained from the individual(s) for the publication of any potentially identifiable images or data included in this article.

AUTHOR CONTRIBUTIONS

SW and FX performed the literature search and wrote the manuscript. WS, CY, CM, and YH helped with follow-up. DX, LL, and JC collected the data. HL and HX designed the manuscript structure and wrote the manuscript. All authors read and approved the final manuscript.

FUNDING

This work was supported by the National Natural Science Foundation of China (Grant No. 81801667), the National Key Research and Development Plan of China (Project 2017YFC0108803), the Improvement Project for Theranostic Ability on Difficulty Miscellaneous Disease (Tumor) (Grant No. ZLYNXM202016), and the Translational Medicine and Interdisciplinary Research Joint Fund of Zhongnan Hospital of Wuhan University (Grant No. ZNJC201911).

SUPPLEMENTARY MATERIAL

The Supplementary Material for this article can be found online at: https://www.frontiersin.org/articles/10.3389/fnins.2021.791776/full#supplementary-material

REFERENCES

Alexander, B. M., and Cloughesy, T. F. (2017). Adult glioblastoma. *J. Clin. Oncol.* 35, 2402–2409. doi: 10.1200/JCO.2017.73.0119

Bae, S., Choi, Y. S., Ahn, S. S., Chang, J. H., Kang, S. G., Kim, E. H., et al. (2018). Radiomic mri phenotyping of glioblastoma: improving survival prediction. *Radiology* 289, 797–806. doi: 10.1148/radiol.2018180200

Binabaj, M. M., Bahrami, A., ShahidSales, S., Joodi, M., Joudi, M. M., Hassanian, S. M., et al. (2018). The prognostic value of mgmt promoter methylation in glioblastoma: a meta-analysis of clinical trials. *J. Cell. Physiol.* 233, 378–386. doi: 10.1002/jcp.25896

Brat, D. J., Aldape, K., Colman, H., Holland, E. C., Louis, D. N., Jenkins, R. B., et al. (2018). Cimpact-now update 3: recommended diagnostic criteria for "diffuse astrocytic glioma, idh-wildtype, with molecular features of glioblastoma, who grade iv". *Acta Neuropathol.* 136, 805–810. doi: 10.1007/s00401-018-1913-0

Buckner, J. C. (2003). Factors influencing survival in high-grade gliomas. *Semin. Oncol.* 30(6 Suppl. 19), 10–14. doi: 10.1053/j.seminoncol.2003.11.031

Chaddad, A., Sabri, S., Niazi, T., and Abdulkarim, B. (2018). Prediction of survival with multi-scale radiomic analysis in glioblastoma patients. *Med. Biol. Eng. Comput.* 56, 2287–2300. doi: 10.1007/s11517-018-1858-4

Chambless, L. B., Kistka, H. M., Parker, S. L., Hassam-Malani, L., McGirt, M. J., and Thompson, R. C. (2015). The relative value of postoperative versus preoperative karnofsky performance scale scores as a predictor of survival after surgical resection of glioblastoma multiforme. *J Neurooncol.* 121, 359–364. doi: 10.1007/s11060-014-1640-x

Clark, K., Vendt, B., Smith, K., Freymann, J., Kirby, J., Koppel, P., et al. (2013). The cancer imaging archive (tcia): maintaining and operating a public information repository. *J. Digit. Imaging* 26, 1045–1057. doi: 10.1007/s10278-013-9622-7

Diehn, M., Nardini, C., Wang, D. S., McGovern, S., Jayaraman, M., Liang, Y., et al. (2008). Identification of noninvasive imaging surrogates for brain tumor gene-expression modules. *Proc. Natl. Acad. Sci. U S A.* 105, 5213–5218. doi: 10.1073/pnas.0801279105

Field, K. M., Rosenthal, M. A., Yilmaz, M., Tacey, M., and Drummond, K. (2014). Comparison between poor and long-term survivors with glioblastoma: review of an australian dataset. *Asia Pac. J. Clin. Oncol.* 10, 153–161. doi: 10.1111/ajco.12076

Gately, L., McLachlan, S. A., Philip, J., Ruben, J., and Dowling, A. (2018). Long-term survivors of glioblastoma: a closer look. *J. Neurooncol.* 136, 155–162. doi: 10.1007/s11060-017-2635-1

Gevaert, O., Mitchell, L. A., Achrol, A. S., Xu, J., Echegaray, S., Steinberg, G. K., et al. (2014). Glioblastoma multiforme: exploratory radiogenomic analysis by using quantitative image features. *Radiology* 273, 168–174. doi: 10.1148/radiol.14131731

Gillies, R. J., Kinahan, P. E., and Hricak, H. (2016). Radiomics: images are more than pictures, they are data. *Radiology* 278, 563–577. doi: 10.1148/radiol.2015151169

Gutman, D. A., Cooper, L. A., Hwang, S. N., Holder, C. A., Gao, J., Aurora, T. D., et al. (2013). Mr imaging predictors of molecular profile and survival: multi-institutional study of the tcga glioblastoma data set. *Radiology* 267, 560–569. doi: 10.1148/radiol.13120118

Hansen, S., Rasmussen, B. K., Laursen, R. J., Kosteljanetz, M., Schultz, H., Nørgård, B. M., et al. (2018). Treatment and survival of glioblastoma patients in denmark: the danish neuro-oncology registry 2009-2014. *J. Neurooncol.* 139, 479–489. doi: 10.1007/s11060-018-2892-7

Hartmann, C., Hentschel, B., Simon, M., Westphal, M., Schackert, G., Tonn, J. C., et al. (2013). Long-term survival in primary glioblastoma with versus without isocitrate dehydrogenase mutations. *Clin. Cancer Res.* 19, 5146–5157. doi: 10.1158/1078-0432.CCR-13-0017

Henson, J. W., Gaviani, P., and Gonzalez, R. G. (2005). Mri in treatment of adult gliomas. *Lancet Oncol.* 6, 167–175. doi: 10.1016/S1470-2045(05)01767-5

Herrlinger, U., Tzaridis, T., Mack, F., Steinbach, J. P., Schlegel, U., Sabel, M., et al. (2019). Lomustine-temozolomide combination therapy versus standard temozolomide therapy in patients with newly diagnosed glioblastoma with methylated mgmt promoter (ceteg/noa-09): a randomised, open-label, phase 3 trial. *Lancet* 393, 678–688. doi: 10.1016/S0140-6736(18)31791-4

Lambin, P., Rios-Velazquez, E., Leijenaar, R., Carvalho, S., van Stiphout, R. G., Granton, P., et al. (2012). Radiomics: extracting more information from medical images using advanced feature analysis. *Eur. J. Cancer* 48, 441–446. doi: 10.1016/j.ejca.2011.11.036

Limkin, E. J., Sun, R., Dercle, L., Zacharaki, E. I., Robert, C., Reuzé, S., et al. (2017). Promises and challenges for the implementation of computational medical imaging (radiomics) in oncology. *Ann. Oncol.* 28, 1191–1206. doi: 10.1093/annonc/mdx034

Liu, Z., Wang, S., Dong, D., Wei, J., Fang, C., Zhou, X., et al. (2019). The applications of radiomics in precision diagnosis and treatment of oncology: opportunities and challenges. *Theranostics* 9, 1303–1322. doi: 10.7150/thno.30309

Louis, D. N., Aldape, K., Brat, D. J., Capper, D., Ellison, D. W., Hawkins, C., et al. (2017). Cimpact-now (the consortium to inform molecular and practical approaches to cns tumor taxonomy): a new initiative in advancing nervous system tumor classification. *Brain Pathol.* 27, 851–852. doi: 10.1111/bpa.12457

Louis, D. N., Perry, A., Wesseling, P., Brat, D. J., Cree, I. A., Figarella-Branger, D., et al. (2021). The 2021 who classification of tumors of the central nervous system: a summary. *Neuro Oncol.* 23, 1231–1251. doi: 10.1093/neuonc/noab106

Lu, Y., Patel, M., Natarajan, K., Ughratdar, I., Sanghera, P., Jena, R., et al. (2020). Machine learning-based radiomic, clinical and semantic feature analysis for predicting overall survival and mgmt promoter methylation status in patients with glioblastoma. *Magn. Reson. Imaging* 74, 161–170. doi: 10.1016/j.mri.2020.09.017

Maldaun, M. V., Suki, D., Lang, F. F., Prabhu, S., Shi, W., Fuller, G. N., et al. (2004). Cystic glioblastoma multiforme: survival outcomes in 22 cases. *J. Neurosurg.* 100, 61–67. doi: 10.3171/jns.2004.100.1.0061

Ostrom, Q. T., Gittleman, H., Truitt, G., Boscia, A., Kruchko, C., and Barnholtz-Sloan, J. S. (2018). Cbtrus statistical report: primary brain and other central nervous system tumors diagnosed in the united states in 2011-2015. *Neuro Oncol.* 20(Suppl._4), v1–v86. doi: 10.1093/neuonc/noy131

Parsons, D. W., Jones, S., Zhang, X., Lin, J. C., Leary, R. J., Angenendt, P., et al. (2008). An integrated genomic analysis of human glioblastoma multiforme. *Science* 321, 1807–1812. doi: 10.1126/science.1164382

Peeken, J. C., Nüsslin, F., and Combs, S. E. (2017). "radio-oncomics" : the potential of radiomics in radiation oncology. *Strahlenther. Onkol.* 193, 767–779. doi: 10.1007/s00066-017-1175-0

Pope, W. B., Sayre, J., Perlina, A., Villablanca, J. P., Mischel, P. S., and Cloughesy, T. F. (2005). Mr imaging correlates of survival in patients with high-grade gliomas. *AJNR Am. J. Neuroradiol.* 26, 2466–2474.

Rao, A. M., Quddusi, A., and Shamim, M. S. (2018). The significance of mgmt methylation in glioblastoma multiforme prognosis. *J. Pak. Med. Assoc.* 68, 1137–1139.

Rao, A., Rao, G., Gutman, D. A., Flanders, A. E., Hwang, S. N., Rubin, D. L., et al. (2016). A combinatorial radiographic phenotype may stratify patient survival and be associated with invasion and proliferation characteristics in glioblastoma. *J. Neurosurg.* 124, 1008–1017. doi: 10.3171/2015.4.JNS142732

Reifenberger, G., Weber, R. G., Riehmer, V., Kaulich, K., Willscher, E., Wirth, H., et al. (2014). Molecular characterization of long-term survivors of glioblastoma using genome- and transcriptome-wide profiling. *Int. J. Cancer* 135, 1822–1831. doi: 10.1002/ijc.28836

Rogers, W., Thulasi, S. S., Refaee, T., Lieverse, R., Granzier, R., Ibrahim, A., et al. (2020). Radiomics: from qualitative to quantitative imaging. *Br. J. Radiol.* 93:20190948. doi: 10.1259/bjr.20190948

Schaff, L. R., Yan, D., Thyparambil, S., Tian, Y., Cecchi, F., Rosenblum, M., et al. (2020). Characterization of mgmt and egfr protein expression in glioblastoma and association with survival. *J. Neurooncol.* 146, 163–170. doi: 10.1007/s11060-019-03358-x

Soltani, M., Bonakdar, A., Shakourifar, N., Babaie, R., and Raahemifar, K. (2021). Efficacy of location-based features for survival prediction of patients with glioblastoma depending on resection status. *Front. Oncol.* 11:661123. doi: 10.3389/fonc.2021.661123

Soomro, S. H., Ting, L. R., Qing, Y. Y., and Ren, M. (2017). Molecular biology of glioblastoma: classification and mutational locations. *J. Pak. Med. Assoc.* 67, 1410–1414.

Stupp, R., Hegi, M. E., Mason, W. P., van den Bent, M. J., Taphoorn, M. J., Janzer, R. C., et al. (2009). Effects of radiotherapy with concomitant and adjuvant temozolomide versus radiotherapy alone on survival in glioblastoma in a randomised phase iii study: 5-year analysis of the eortc-ncic trial. *Lancet Oncol.* 10, 459–466. doi: 10.1016/S1470-2045(09)70025-7

Stupp, R., Mason, W. P., van den Bent, M. J., Weller, M., Fisher, B., Taphoorn, M. J., et al. (2005). Radiotherapy plus concomitant and adjuvant temozolomide for glioblastoma. *N. Engl. J. Med.* 352, 987–996. doi: 10.1056/NEJMoa043330

Tan, Y., Mu, W., Wang, X. C., Yang, G. Q., Gillies, R. J., and Zhang, H. (2019). Improving survival prediction of high-grade glioma via machine learning techniques based on mri radiomic, genetic and clinical risk factors. *Eur. J. Radiol.* 120:108609. doi: 10.1016/j.ejrad.2019.07.010

Tian, H., Wu, H., Wu, G., and Xu, G. (2020). Noninvasive prediction of tert promoter mutations in high-grade glioma by radiomics analysis based on multiparameter mri. *Biomed Res. Int.* 2020:3872314. doi: 10.1155/2020/3872314

Van Meir, E. G., Hadjipanayis, C. G., Norden, A. D., Shu, H. K., Wen, P. Y., and Olson, J. J. (2010). Exciting new advances in neuro-oncology: the avenue to a cure for malignant glioma. *CA Cancer J. Clin.* 60, 166–193. doi: 10.3322/caac.20069

Wu, C. X., Lin, G. S., Lin, Z. X., Zhang, J. D., Liu, S. Y., and Zhou, C. F. (2015). Peritumoral edema shown by mri predicts poor clinical outcome in glioblastoma. *World J. Surg. Oncol.* 13:97. doi: 10.1186/s12957-015-0496-7

Zhang, X., Lu, H., Tian, Q., Feng, N., Yin, L., Xu, X., et al. (2019). A radiomics nomogram based on multiparametric mri might stratify glioblastoma patients according to survival. *Eur. Radiol.* 29, 5528–5538. doi: 10.1007/s00330-019-06069-z

Conflict of Interest: JC was employed by the company GE Healthcare, Shanghai, China.

The remaining authors declare that the research was conducted in the absence of any commercial or financial relationships that could be construed as a potential conflict of interest.

Publisher's Note: All claims expressed in this article are solely those of the authors and do not necessarily represent those of their affiliated organizations, or those of the publisher, the editors and the reviewers. Any product that may be evaluated in this article, or claim that may be made by its manufacturer, is not guaranteed or endorsed by the publisher.

Copyright © 2022 Wang, Xiao, Sun, Yang, Ma, Huang, Xu, Li, Chen, Li and Xu. This is an open-access article distributed under the terms of the Creative Commons Attribution License (CC BY). The use, distribution or reproduction in other forums is permitted, provided the original author(s) and the copyright owner(s) are credited and that the original publication in this journal is cited, in accordance with accepted academic practice. No use, distribution or reproduction is permitted which does not comply with these terms.

frontiers in Oncology

ORIGINAL RESEARCH
published: 16 February 2022
doi: 10.3389/fonc.2022.840871

Decreasing Shortest Path Length of the Sensorimotor Network Induces Frontal Glioma-Related Epilepsy

Shengyu Fang[1,2], Lianwang Li[2], Shimeng Weng[2], Yuhao Guo[2], Zhong Zhang[1], Lei Wang[2], Xing Fan[2], Yinyan Wang[1]* and Tao Jiang[1,2,3]**

[1] Department of Neurosurgery, Beijing Tiantan Hospital, Capital Medical University, Beijing, China, [2] Beijing Neurosurgical Institute, Capital Medical University, Beijing, China, [3] Research Unit of Accurate Diagnosis, Treatment, and Translational Medicine of Brain Tumors, Chinese Academy of Medical Sciences, Beijing, China

Background: Glioma-related epilepsy (GRE) is a common symptom in patients with prefrontal glioma. Epilepsy onset is associated with functional network alterations. This study investigated alterations of functional networks in patients with prefrontal glioma and GRE.

Methods: Sixty-five patients with prefrontal lobe gliomas were retrospectively assessed and classified into GRE and non-GRE groups. Additionally, 25 healthy participants were enrolled after matching for general information. Imaging data were acquired within 72 h in pre-operation. The sensorimotor network was used to delineate alterations in functional connectivity (FC) and topological properties. One-way analysis of variance and *post-hoc* analysis with Bonferroni correction were used to calculate differences of FC and topological properties.

Results: All significant alterations were solely found in the sensorimotor network. Irrespective of gliomas located in the left or right prefrontal lobes, the edge between medial Brodmann area 6 and caudal ventrolateral Brodmann area 6 decreased FC in the GRE group compared with the non-GRE group [$p < 0.0001$ (left glioma), $p = 0.0002$ (right glioma)]. Moreover, the shortest path length decrease was found in the GRE group compared with the non-GRE group [$p = 0.0292$ (left glioma) and $p = 0.0129$ (right glioma)].

Conclusions: The reduction of FC between the medial BA 6 (supplementary motor area) and caudal ventrolateral BA 6 in the ipsilateral hemisphere and the shortening of the path length of the sensorimotor network were characteristics alterations in patients with GRE onset. These findings fill in the gap which is the relationship between GRE onset and the alterations of functional networks in patients with prefrontal glioma.

Significance Statement: Glioma related epilepsy is the most common symptom of prefrontal glioma. It is important to identify characteristic alterations in functional networks in patients with GRE. We found that all significant alterations occurred in the sensorimotor network. Moreover, a decreased FC in the supplementary motor area and a shortening of the path's length are additional characteristics of glioma-related epilepsy. We believe that our findings indicate new directions of research that will contribute to future investigations of glioma-related epilepsy onset.

Keywords: glioma, glioma-related epilepsy, functional network, graph theory, human

OPEN ACCESS

Edited by:
Sandro M. Krieg, Technical University of Munich, Germany

Reviewed by:
Feng Liu, Central South University, China
Jiu Chen, Nanjing Medical University, China

***Correspondence:**
Xing Fan
xingkongyaoxiang@163.com
Yinyan Wang
tiantanyinyan@126.com
Tao Jiang
taojiang1964@foxmail.com

Specialty section:
This article was submitted to Neuro-Oncology and Neurosurgical Oncology, a section of the journal Frontiers in Oncology

Received: *21 December 2021*
Accepted: *24 January 2022*
Published: *16 February 2022*

Citation:
Fang S, Li L, Weng S, Guo Y, Zhang Z, Wang L, Fan X, Wang Y and Jiang T (2022) Decreasing Shortest Path Length of the Sensorimotor Network Induces Frontal Glioma-Related Epilepsy. Front. Oncol. 12:840871. doi: 10.3389/fonc.2022.840871

INTRODUCTION

Tumor locations and low-grade glioma are susceptible factors for patients with glioma-related epilepsy (GRE) (1, 2). However, why prefrontal glioma is frequently induced GRE was still unknown. Extensive disruption of functional connectivity (FC) was thought to be related to patients with idiopathic epilepsy (3–5). Based on those studies, the investigation of epilepsy by analyzing the alterations in brain functional networks was proposed, which gives a new insight into the inspection of epilepsy.

The FC (6) and topological properties (7) are valuable to revealing the structure and conveying the ability of function networks based on resting-state functional magnetic resonance images (rs-fMRIs). Previous studies demonstrated that decreased inter-cortical FC in the different functional networks, such as sensorimotor (4), default mode (8), and visual networks (9), and decreased global efficiency were related to idiopathic epilepsy (4, 10, 11). However, different from idiopathic epilepsy only impairing functional networks, glioma not only was disrupted but also was able to reorganize functional networks (12, 13). Hence the previous conclusions that alterations of functional networks in patients with idiopathic epilepsy were not suitable for patients with glioma.

The decreasing shortest path lengths of the visual network (14) and language network (15) were markers to indicate that patients with left and right temporal lobe glioma suffered from GRE, respectively. However, it was still unknown what alterations of functional networks in patients with prefrontal glioma were related to GRE. Hence, in this study, we aimed to 1) explore how FC and topological properties alter in patients with prefrontal glioma and 2) find characteristic alterations in FC and topological properties of patients with GRE.

MATERIALS AND METHODS

The study protocol was approved by the local institutional review board.

Participants

Between January 2016 and July 2018, 70 patients from Tiantan Hospital with a primary diagnosis of prefrontal lobe glioma were retrospectively enrolled in the study. Inclusion criteria were as follows: (a) aged older than 18 years; (b) more than 6 years of school education; (c) no history of antiepileptic drug use; and (d) no history of biopsy, radiotherapy, or chemotherapy. The exclusion criteria were as follows: (a) contraindications for MRI; (b) head motion greater than 3 mm in translation or 3° in rotation; and (c) gliomas involving bilateral prefrontal lobes or leading midline shift.

Finally, 65 patients with prefrontal gliomas were enrolled in the study (29 male and 36 female, left hemisphere n = 35, right hemisphere n= 30). All patients were divided into the GRE and non-GRE groups. Preoperative electroencephalograms (4 hours) were performed in the patients who did not have a clear history of seizures (patients in non-GRE group, n = 36). Moreover, 25 right-handed healthy participants matched to the patients for age, sex, and education level which comprised the control group (12 men and 13 female).

Collection of Patient Clinical Characteristics

We retrospectively collected patient characteristics from inpatient records including age, sex, education level, Karnofsky performance status, histopathology, isocitrate dehydrogenase mutation status, the extent of tumor resection, information regarding preoperative seizures, type of seizure onset, and history of taking antiepileptic drugs. Follow-up information about epileptic control was obtained *via* telephone interviews at 1 year postoperatively.

MRI Acquisition

All MR images were acquired using a MAGNETOM Prisma 3T MRI scanner (Siemens, Erlangen, Germany). T1-magnetization prepared rapid acquisition gradient echo was applied to collect anatomical images [flip angle: 8°; repetition time (TR): 2,300 ms; echo time (TE): 2.3 ms; field of view (FOV): 240 × 240 mm^2; voxel size: 1.0 × 1.0 × 1.0 mm^3; slice number: 192]. T2-weighted sequences were used to acquire glioma images (flip angle: 150°; TR: 5,000 ms; TE: 105 ms; FOV: 240 × 240 mm^2; voxel size: 0.5 × 0.5 × 3 mm^3; slice number: 33). Finally, an echo-planar imaging sequence was applied for rs-fMRI (flip angle: 75°; TR: 2,000 ms; TE: 30 ms; FOV: 220 × 220 mm^2; voxel size: 3.0 × 3.0 × 5.0 mm^3; slice number: 30; acquisition duration: 8 min, closed eyes during scanning). We acquired all MRI data within 72 h before tumor resection.

Functional MRI Preprocessing

The Graph Theoretical Network Analysis software (https://www.nitrc.org/projects/gretna) (16) was applied for rs-fMRI preprocessing. For each participant, the steps of preprocessing were as follows: a) data transformation (from Digital Imaging and Communications in Medicine to Neuroimaging Informatics Technology Initiative); b) removal of the first five images; c) slice time correction; d) realignment; e) spatial normalization (normalized to echo-planar imaging template) (17); f) spatial smoothing (full width half maximum = 4 mm); g) temporal detrending (linear detrending); h) regressing out covariance (white matter signal: with WMMask_3 mm; cerebrospinal fluid signal: with CSFMask_3 mm; head motion: Friston—24 parameters); i) temporal filtering (0.01–0.1 Hz); and j) scrubbing (using default parameters and the interpolation strategy: linear interpolation, FD threshold = 0.5, previous time point number = 1, subsequent time point number = 2).

Regions of Tumor Invasion

The extent of low-grade glioma invasion was manually drawn based on the region of high signals on T2 fluid-attenuated inversion. All tumor masks were then normalized to the Montreal Neurological Institute standard space using the clinical toolbox package in SPM8 (http://www.fil.ion.ucl.ac.uk/spm/software/spm8/), which are shown in **Figure 1**. The tumor volume was calculated with the volumetric method based on the individual tumor mask.

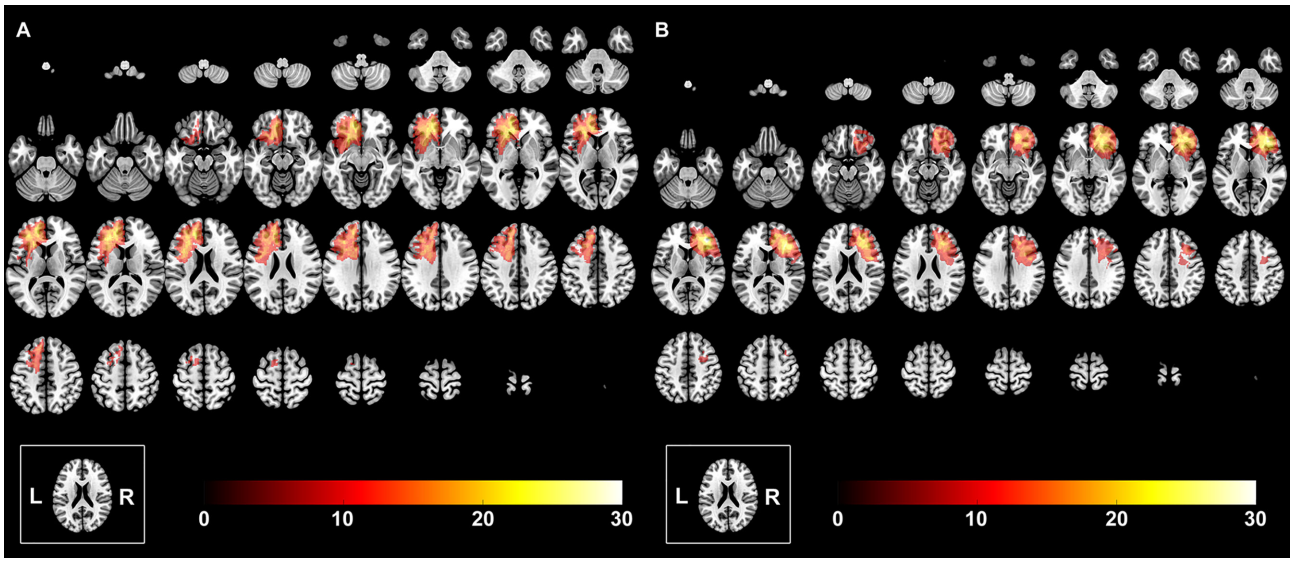

FIGURE 1 | The overlapping results of prefrontal lobe gliomas. The overlapping meant that we overlapped all the tumor masks of the left hemisphere into one template to show the quantitative distribution of the left hemispheric gliomas. The value of the color bar represents the number of patients with tumor located in the same region. **(A)** Tumor was in the left hemisphere. **(B)** Tumor was in the right hemisphere.

Regions of Interest

To calculate FC within cerebral functional networks, regions of interest (ROIs) were extracted from an open-access brain atlas, "brainnetome atlas" (http://www.brainnetome.org/) (18), which comprises 246 brain regions. To avoid the possibility that tumor invasion may affect the results of FC, the subnetworks that were invaded by gliomas and glioma-related edema were not analyzed. Therefore, in the current study, sub-templates were extracted, including the sensorimotor, visual, auditory, and left/right executive networks (based on tumor location). Details of ROIs are provided in **Tables S1**–**S5**.

Network Construction

Pearson's correlation coefficients were used to compare regional mean time series for all possible pairs of nodes that constructed the FC matrix. Consequently, four different FC matrices were generated from the four sub-templates of the sensorimotor, visual, auditory, and left/right executive networks.

Graph Theoretical Measures

Global and nodal topological properties, including cluster coefficient, global efficiency, the shortest path length, local efficiency, nodal efficiency, nodal local efficiency, and small-worldness properties, were calculated for the GRE, non-GRE, and healthy groups using the graph theory analysis (19). All matrices were transformed into absolute value matrices before calculating topological properties. A total of 10,000 random networks were used to calculate the topological properties.

Small-worldness properties, including gamma, lambda, and sigma, represent the efficiency of information delivery: gamma (γ) = C_{real}/C_{random} >> 1 (C represented cluster coefficient), lambda (λ) = L_{real}/L_{random} ~ 1 (L represented shortest path length), and sigma (σ) = γ/λ > 1 (20). A high value of sigma represents a high efficiency of information delivery.

Statistical Analyses

We compared the GRE, non-GRE, and healthy groups to identify which alterations were caused by each factor using SPSS (19.0 version, IBM) and GraphPad Prism 7 (GraphPad Software Inc., San Diego, USA). According to the type of data, clinical characteristics were compared between the GRE and non-GRE groups using a two-sample t-test, chi-square test, and one-way analysis of variance (ANOVA) which were used to compare among the GRE, non-GRE, and healthy groups.

When comparing the differences of FCs among the three groups, we used one-way ANOVA and *post-hoc* test with Bonferroni correction. Moreover, an eta-squared correlation was applied to explore the relationship between GRE onset and FC value.

Additionally, a series of sparsity thresholds (from 0.17 to 0.34, interval 0.01) was used to explore group differences in network topological properties, which was consistent with relevant studies (14, 15). For each property, one-way ANOVA was first applied. Subsequently, a *post-hoc* analysis with the Bonferroni correction was used if the results of ANOVA showed a significant difference (significant p-value was lower than 0.05). Clinical information (age, sex, and education level) was regressed out during statistical comparison in FC and topological properties.

RESULTS

Demographic Characteristics

Based on whether patients had preoperative GRE, 29 patients were included in the GRE group (15 and 14 patients with

prefrontal gliomas in the left and right hemisphere, respectively). Additionally, 36 patients comprised the non-GRE group (20 and 16 patients with prefrontal gliomas in the left and right hemispheres, respectively) (**Tables 1**, **2**). No significant differences were observed regarding age, sex, years of education, and Karnofsky performance status between the three groups. Moreover, no statistical difference in tumor volume and isocitrate dehydrogenase mutation status was found between the GRE and non-GRE groups. Furthermore, our postoperative follow-up data showed that no patient with preoperative GRE experienced epilepsy at 1 year after tumor resection. All patients achieved Engel class I.

Functional Connectivity Differences

The FC was compared among the GRE, non-GRE, and healthy groups in the matrices of sensorimotor, visual, auditory, and left/right executive networks (based on tumor location). Except for FC in the sensorimotor network, no significant differences in FC in the other three networks were noticed after Bonferroni correction. In total, 231 functional edges belonged to the sensorimotor network.

When gliomas were located in the left prefrontal lobe, all these six edges were significantly different among the three groups in *post-hoc* analysis with Bonferroni correction (**Figure 2** and **Table S6**).

Compared with the non-GRE group [0.357 ± 0.055 (mean ± mean standard error)], only one edge had lower FC in the GRE group (0.025 ± 0.057) after *post-hoc* analysis with Bonferroni correction ($p < 0.0001$), which connected A6m_L [medial Brodmann area (BA) 6 in the left hemisphere] and Acvl_L (caudal ventrolateral BA 6 in the left hemisphere). Moreover, compared with the healthy group, six edges were identified with significantly lower FC in the GRE group after *post-hoc* analysis with Bonferroni correction, which connected 1) A6m_L and Acvl_L (Healthy, 0.399 ± 0.037, $p < 0.0001$); 2) Acvl_R (caudal ventrolateral BA 6 in the right hemisphere) and A6m_L (GRE, 0.108 ± 0.050; Healthy, 0.418 ± 0.047, $p = 0.0027$); 3) A6m_R (medial BA 6 in the right hemisphere) and Acvl_L (GRE, 0.074 ± 0.064; Healthy, 0.428 ± 0.043, $p = 0.0003$); 4) A4tl_R (tongue and larynx region in the right hemisphere) and Acvl_L (GRE, 0.131 ± 0.047; Healthy, 0.436 ± 0.040, $p = 0.0069$); 5) A1/2/3tonla_R (tongue and larynx region of BA 1/2/3 in the right hemisphere)

TABLE 1 | Demographic and clinical characteristics of patients with left prefrontal gliomas.

Demographic and Clinical Characteristics	GRE (n = 15)	Non-GRE (n = 20)	Health (n = 25)	*p* value
Gender				
Male	8	6	12	0.32
Female	7	14	13	
Age (y)[a]	39.9 ± 2.7	43.9 ± 1.7	37.9 ± 2.0	0.10
Handness				
Right	15	20	25	-
Left	0	0	0	-
Preoperative KPS				
100	14	20	25	0.14
90~100	1	0	0	
Education level (y)[a]	13.0 ± 0.8	13.2 ± 0.6	12.6 ± 0.7	0.81
Histopathology				
Astrocytoma	5	7	–	0.92
Oligodendroglioma	10	13	–	
Tumor volume (mL)[a]	28.62 ± 3.85	26.67 ± 3.32	-	0.70
IDH status				
Mutation	13	16	-	0.68
Wild-type	2	4	-	
MGMT promoter methylation				
Methylation	11	13	-	0.72
Non-methylation	4	7	-	
TERT promoter mutation				
Mutation	10	11	-	0.73
Wild-type	5	9	-	
Type of seizure				
Secondary generalized	15	-	-	
Period from epilepsy first onset to rs-fMRI scan (days)	11.8 ± 1.5	-	-	-
Frequency before diagnosis				
Low (only once)	11	-	-	
Medium (2~3 times)	4	-	-	
Postoperative epileptic control				
Engel Class I	15	-	-	-

[a]*Values are means ± standard error of mean.*

KPS, Karnofsky performance status; MGMT, O^6-methylguanine DNA methyltransferase; TERT, telomerase reverse transcriptase gene; GRE, the group of patients with glioma-related epilepsy; non-GRE, the group of patients without glioma-related epilepsy.

The two-sample t-test was used to compare tumor volume between GRE and non-GRE groups. One-way ANOVA was used to compare age, education level, and Karnofsky performance status between GRE and non-GRE groups. Chi-square tests were used to compare gender, histopathology, and IDH status between GRE and non-GRE groups.

TABLE 2 | Demographic and clinical characteristics of patient with right prefrontal gliomas.

Demographic and Clinical Characteristics	GRE (n = 14)	Non-GRE (n = 16)	Health (n = 25)	*p* value
Gender				
Male	7	8	12	0.99
Female	7	8	13	
Age (y)[a]	37.2 ± 2.0	38.7 ± 2.2	37.9 ± 2.0	0.84
Handness				
Right	14	16	25	-
Left	0	0	0	-
Preoperative KPS				
100	12	16	25	0.07
90~100	2	0	0	
Education level (y)[a]	12.4 ± 1.0	13.6 ± 0.8	12.6 ± 0.7	0.64
Histopathology				
Astrocytoma	6	5	–	0.70
Oligodendroglioma	8	11		
Tumor volume (mL)[a]	35.84 ± 4.53	27.62 ± 3.52	-	0.16
IDH status				
Mutation	12	13	-	> 0.99
Wild-type	2	3	-	
MGMT promoter methylation				
Methylation	9	11	-	> 0.99
Non-methylation	5	5	-	
TERT promoter mutation				
Mutation	7	10	-	0.71
Wild-type	7	6	-	
Type of seizure				
Secondary generalized	14	-	-	
Period from epilepsy first onset to rs-fMRI scan (days)	14.2 ± 1.2	-	-	-
Frequency before diagnosis				
Low (only once)	13	-	-	
Medium (2~3 times)	1	-	-	
Postoperative epileptic control				
Engel Class I	14	-	-	-

[a]*Values are means ± standard error of mean.*

KPS, Karnofsky performance status; MGMT, O^6-methylguanine DNA methyltransferase; TERT, telomerase reverse transcriptase gene; GRE, the group of patients with glioma-related epilepsy; non-GRE, the group of patients without glioma-related epilepsy.

The two sample t-test was used to compare tumor volume between GRE and non-GRE groups. One-way ANOVA was used to compare age, education level, and Karnofsky performance status between GRE and non-GRE groups. Chi-square tests were used to compare gender, histopathology, and IDH status between GRE and non-GRE groups.

and Acvl_L (GRE, 0.063 ± 0.061; Healthy, 0.329 ± 0.050, p = 0.0091); and 6) A4ul_L (upper limb region of BA 4 in the left hemisphere) and A4ul_R (upper limb region of BA 4 in the right hemisphere) (GRE, 0.431 ± 0.077; Healthy, 0.812 ± 0.057, p = 0.0009). Moreover, no edge of FC was significantly different between the non-GRE and healthy groups.

When gliomas were located in the right prefrontal lobe, three edges of FC were significant different among the three groups in *post-hoc* analysis with Bonferroni test (**Figure 3** and **Table S7**).

Compared with the non-GRE group, two edges that were from A6m_R to Acvl_R (GRE, 0.118 ± 0.048; non-GRE, 0.437 ± 0.033, p = 0.0002) and A6m_R to A4hf_L (head and face regions of BA 4 in the left hemisphere; GRE, 0.252 ± 0.042; non-GRE, 0.657 ± 0.083, p = 0.0007) were identified with significantly lower FC in the GRE group. Moreover, compared with the healthy group, three edges were identified with significantly lower FC in the GRE group, which connected 1) A6m_R and Acvl_R (Healthy, 0.429 ± 0.048, p < 0.0001); 2) A4hf_L and A6m_R (Healthy, 0.575 ± 0.050, p = 0.0014); and 3) A1/2/3ulhf_R (upper limb, head, and face regions of BA 1/2/3 in the right hemisphere) and A4ul_L (GRE, 0.359 ± 0.089; Healthy, 0.691 ± 0.051, p = 0.0042). Additionally, no edge of FC was significantly different between the non-GRE and healthy groups.

The Relationship Between Functional Connectivity and Occurring GRE

Our results showed a negative correlation between FC of the functional edge connected A6m_L to Acvl_L when the glioma was located in the left hemisphere (r = -0.590, p < 0.0001, eta-squared correlation). A similar result was found when the glioma was located in the right hemisphere (functional edge: connected A6m_R and Acvl_R, r = -0.541, p < 0.0001).

Differences in Global Topological Properties

When gliomas were located in the left prefrontal hemisphere, there were some differences in global efficiency (p = 0.0118) and shortest path length (p = 0.0306) among the three groups in the sensorimotor network in one-way ANOVA (**Table S8** and **Figure 4**). After *post-hoc* analysis with Bonferroni correction, the non-GRE group (0.391 ± 0.009) showed weaker global efficiency than the GRE group (0.430 ± 0.012, p = 0.0113).

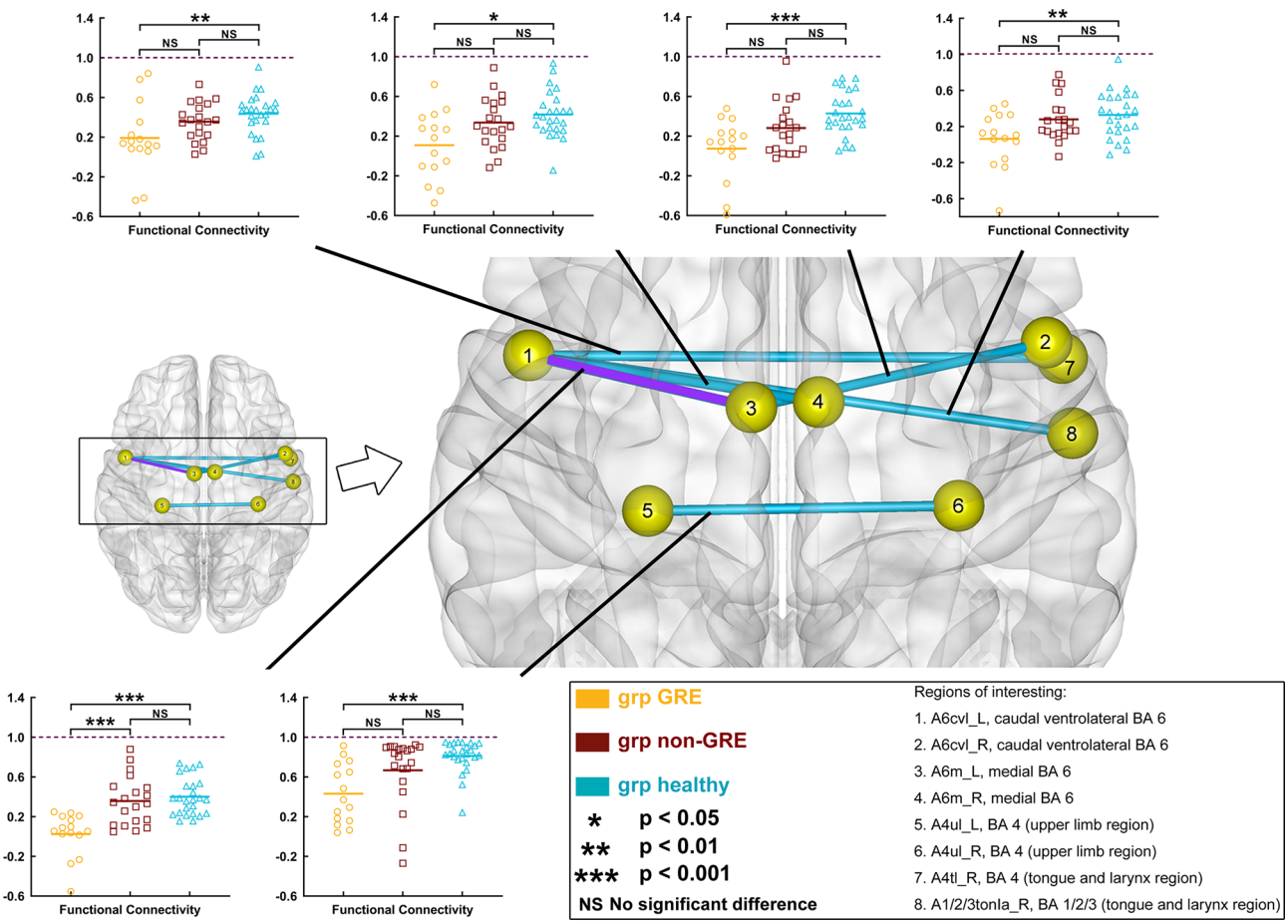

FIGURE 2 | Results of alterations in functional connectivity (FC) when gliomas grew in the left prefrontal lobe. The grp GRE (n = 15), group of patients with glioma-related epilepsy. The grp non-GRE (n = 20), group of patients without glioma-related epilepsy. The grp healthy (n = 25), group of healthy participants.

Moreover, compared with the non-GRE group (2.747 ± 0.081), the shortest path length was significantly shorter in the GRE group (2.473 ± 0.079, $p = 0.0292$).

When gliomas were located in the right prefrontal lobe, there were some differences in global efficiency ($p < 0.0001$), shortest path length ($p < 0.0001$), local efficiency ($p < 0.0001$), and clustering coefficient ($p < 0.0001$) among the three groups in the sensorimotor network by one-way ANOVA (**Table S9** and **Figure 5**). After a *post-hoc* analysis with Bonferroni correction, in the GRE group (0.521 ± 0.003), the global efficiency was significantly greater than those in the non-GRE group (non-GRE, 0.494 ± 0.007, $p = 0.0214$). Additionally, the shortest path length in the GRE group (1.958 ± 0.029) was shorter than in the non-GRE group (non-GRE, 2.170 ± 0.044, $p = 0.0129$). Moreover, compared with the healthy group, the GRE and non-GRE groups showed significantly greater global efficiency (hHealthy = 0.416 ± 0.006; GRE vs. healthy, $p < 0.0001$; and non-GRE vs. healthy, $p < 0.0001$), local efficiency (GRE = 0.662 ± 0.013, non-GRE = 0.624 ± 0.010, Healthy = 0.554 ± 0.010, GRE vs. healthy, $p < 0.0001$, and non-GRE vs. healthy, $p < 0.0001$), and clustering coefficient (GRE = 0.548 ± 0.012, non-GRE = 0.525 ± 0.009, Healthy = 0.475 ± 0.009; GRE vs. healthy, $p < 0.0001$, and non-GRE vs. healthy, $p = 0.0012$) after *post-hoc* analysis with Bonferroni correction. The shortest path length was significantly shorter in the GRE and non-GRE groups than in the healthy group (GRE, 1.959 ± 0.029, non-GRE, 2.170 ± 0.044, Healthy, 2.589 ± 0.047; GRE vs. healthy groups, $p < 0.0001$, and non-GRE vs. healthy groups, $p < 0.0001$).

In addition, the gamma ($p = 0.0021$) and lambda ($p < 0.0001$) values showed a significant difference among the three groups in one-way ANOVA. Furthermore, after the *post-hoc* analysis with the Bonferroni correction test, the value of gamma was found significantly higher in the healthy group (1.684 ± 0.088) than that in the non-GRE group (1.288 ± 0.050, $p = 0.0017$). The value of lambda was found significantly higher in the healthy group (1.143 ± 0.016) than in the GRE (1.029 ± 0.004, $p < 0.0001$) and non-GRE groups (1.054 ± 0.009, $p < 0.0001$).

No difference of global topological properties in the other three networks (visual, auditory, and left/right executive) was found among the three groups.

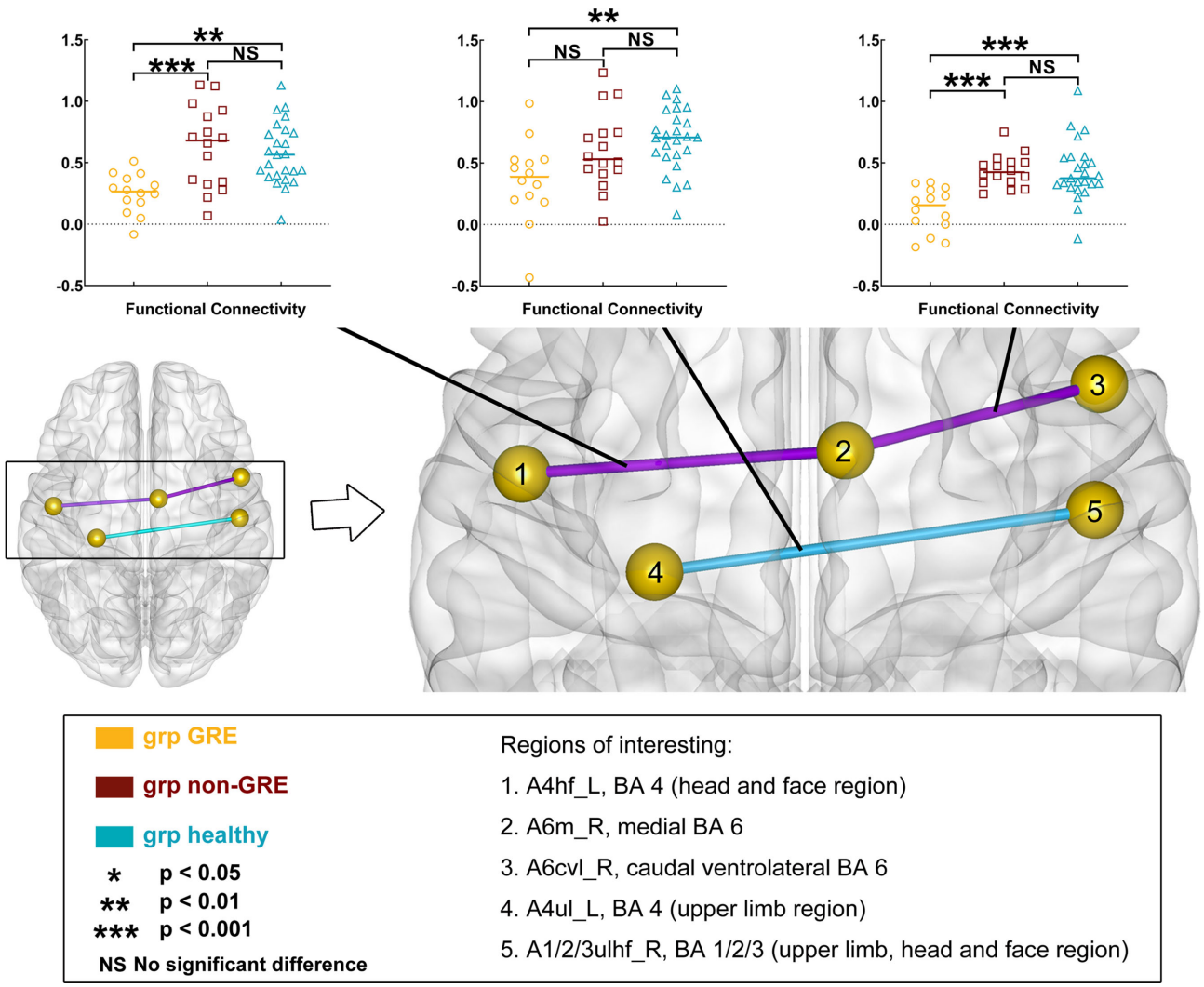

FIGURE 3 | Results of alterations in functional connectivity (FC) when gliomas grew in the right prefrontal lobe. The grp GRE (n = 14), group of patients with glioma-related epilepsy. The grp non-GRE (n = 16), group of patients without glioma-related epilepsy. The grp healthy (n = 25), group of healthy participants.

Differences in Nodal Topological Properties

We analyzed the nodal efficiency and nodal local efficiency among the three groups (**Tables S10**, **S11**) whether the gliomas were located in the left or right hemisphere. However, no significant difference was found among these three groups in nodal properties by one-way ANOVA. Moreover, no difference in nodal topological properties was found among these three groups in the other three networks (visual, auditory, and left/right executive).

DISCUSSION

This study investigated the characteristic alterations of functional networks in patients with prefrontal glioma and GRE. Our findings implied that gliomas located in different hemispheres may alter FC and topological properties in different ways. In addition, decreasing FC between ipsilateral medial BA 6 (supplementary motor area) and caudal ventrolateral BA 6 and shortening path length of the whole sensorimotor network were characteristic alterations in patients with GRE.

Seizure onset is associated with alterations in functional networks (14). In our previous studies, we found that the decreasing shortest path length was a marker to indicate that patients with temporal lobe glioma suffered from GRE. Nevertheless, the relationship between GRE onset and alterations of functional networks in patients with prefrontal glioma remains unclear. Whether glioma in the left or right prefrontal lobe, the edge connecting the medial BA 6 and caudal ventrolateral BA 6 areas in the ipsilateral hemisphere reduced their FC in the GRE group but insignificantly altered in the non-

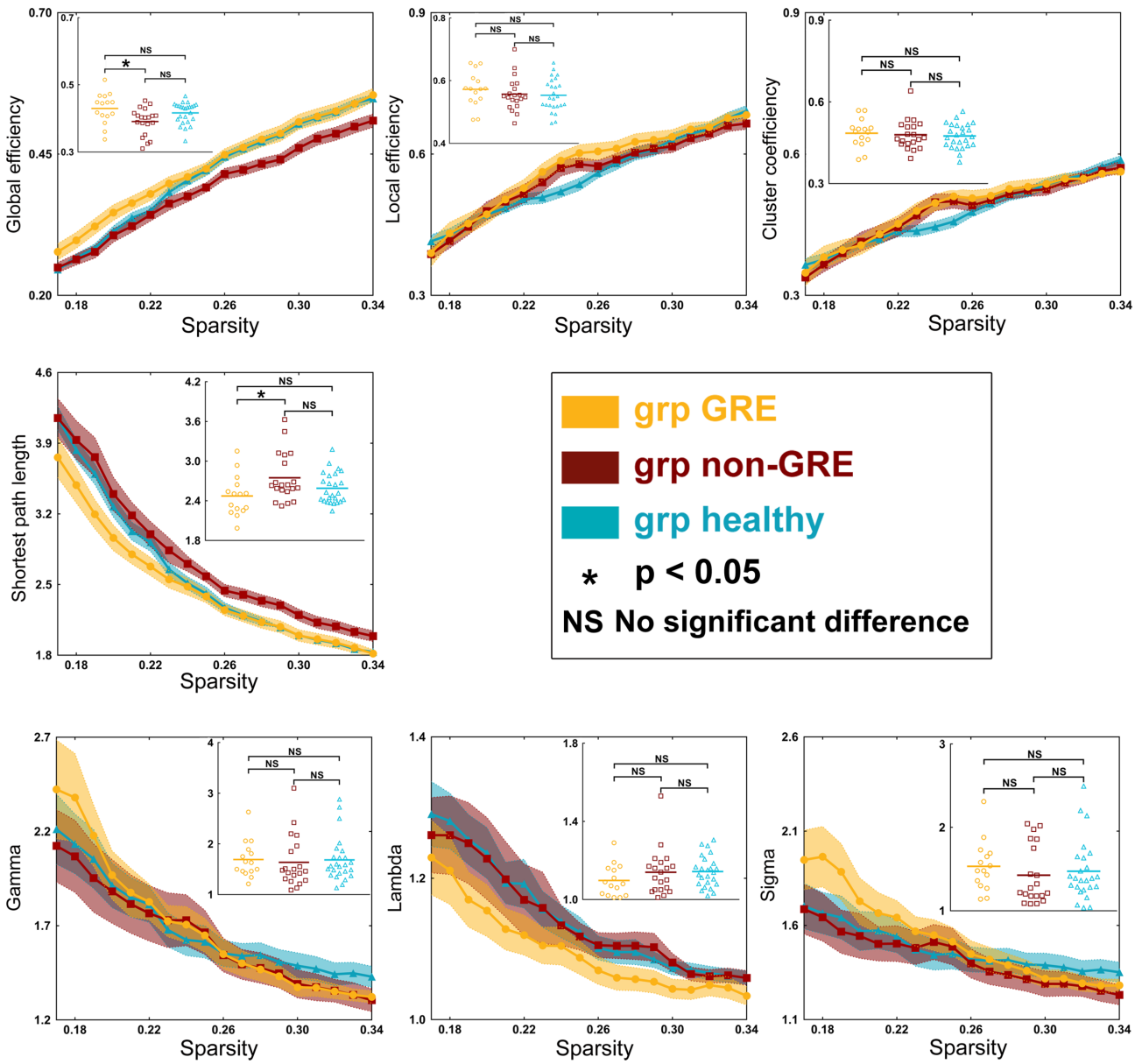

FIGURE 4 | Results of alterations in topological properties when gliomas grew in the left prefrontal lobe. Each property was analyzed with one-way ANOVA test and *post-hoc* test with least significant difference correction. The grp GRE (n = 15), group of patients with glioma-related epilepsy. The grp non-GRE (n = 20), group of patients without glioma-related epilepsy. The grp healthy (n = 25), group of healthy participants.

GRE group. The medial BA 6 area belongs to the supplementary motor area and the caudal ventrolateral BA 6 area belongs to the premotor area which is responsible for integrating and regulating motor information that controls the primary motor area to generate movement (21, 22). Moreover, our results of correlation analysis indicated a significant negative correlation between GRE onset and FC of this edge. Hence, we thought that glioma led some patients to decrease their FC in the BA 6 area, and this alteration was specifically related to GRE onset. Due to the FC reduction in the BA 6 area, the ability of motor functional control in the supplementary motor area is impaired. Hence, this alteration is presented in patients who suffer from GRE more easily. Simultaneously, this finding explained why the GRE was associated with their gliomas growing in or adjacent to the premotor area (23).

In our study, we found that the number of edges with FC significant alteration was different between the left and right gliomas. We thought that this difference was related to tumor locations. Our previous findings indicated that the left temporal glioma alters the visual network (14) but the right temporal glioma alters the language network (15). It meant different tumor location alters different networks. Hence, in this study, only the

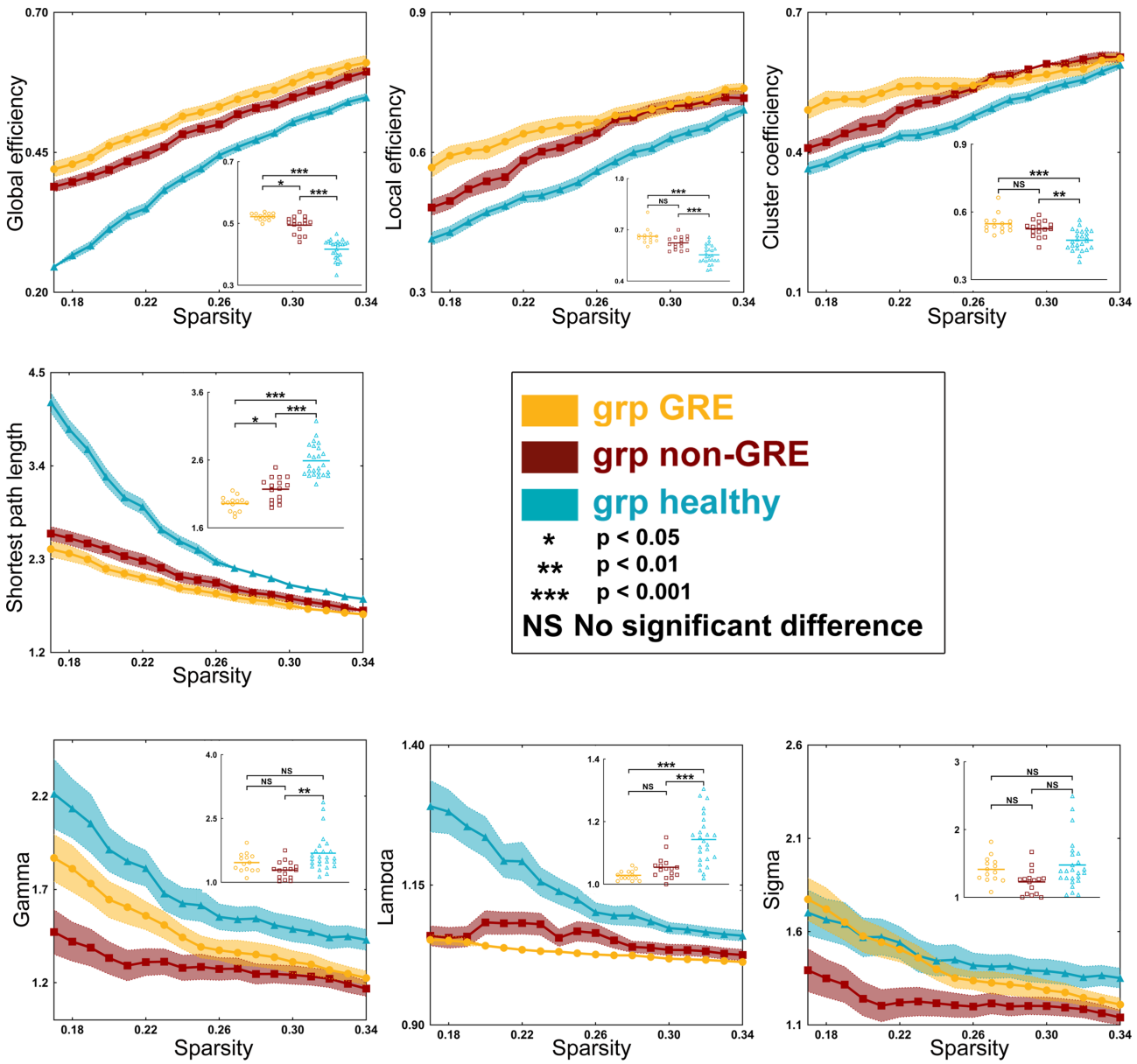

FIGURE 5 | Results of alterations in topological properties gliomas grew in the right prefrontal lobe. Each property was analyzed with one-way ANOVA test and *post-hoc* test with least significant difference correction. The grp GRE (n = 14), group of patients with glioma-related epilepsy. The grp non-GRE (n = 16), group of patients without glioma-related epilepsy. The grp healthy (n = 25), group of healthy participants.

sensorimotor network was altered by prefrontal glioma, but the alterations of edges were different. For this reason, we divided all patients into four groups based on the history of GRE and tumor location instead of making the tumor into the same hemisphere through flipping the rs-fMRI data like in a previous study (24).

An increase in the shortest path length was widely observed in patients with idiopathic epilepsy (25, 26). This change was related to long-term and frequent epilepsy onset that caused cortical sclerosis (27), gray matter atrophy (28), and cortical hypo-metabolism (29). These alterations of gray matter induce the pathways of information conveying disruption. However, different from idiopathic epilepsy, preoperative GRE was a relatively short-term symptom, since the glioma is being removed as soon as possible once the GRE appears, and most of GRE onset will be controlled (1). Hence, our findings that the shortest path length decreased and global efficiency increased in the GRE group were conversely to idiopathic epilepsy.

The alterations of topological property in glioma patients were related to network reorganization. Previous studies showed that glioma can induce network reorganization in cortices that are close to the lesion (30, 31). In the current study, all gliomas were located in the prefrontal lobe that was near the

sensorimotor network (especially near the supplementary motor area and premotor area). Hence, the topological properties of the sensorimotor network altered. For this reason, the FC of the edge between supplementary motor area and premotor area also altered.

Glioma-induced reorganization resulted in the shortest path length of sensorimotor networks being shortened (32, 33). A shorter network path contributed to a reduction in the convulsive threshold underlying epileptic seizures (34, 35). Conversely, longer network paths contributed to prolonging systematic response time that counteracted the rapid spread of local epileptic discharges (36). Compared with the non-GRE group, the patients in the GRE group have more significantly altered in the shortest path length. Thus, we thought that the shortened path length of the sensorimotor network was related to GRE onset.

Interestingly, the alterations of topological properties in patients with different hemispheric glioma were a little different when comparing the healthy group with the non-GRE group. We inferred that this discrepancy might be related to two reasons. On the one hand, all patients and healthy subjects in this study were right handed. Hence, different topological properties of sensorimotor network might exist between the left and right hemisphere. The left hemispheric motor cortices control right-sided motor functions, which were used more frequently and were more flexible than left-sided motor functions (37, 38). On the other hand, there might be some bias in selection since the sample size was relevant small, especially for patients with right gliomas.

Even though the number of patients was limited, the positive results identified in our study were reliable under strict statistical corrections. Here, the topological properties were calculated using functional matrices with absolute values as in previous studies (20, 39, 40). Moreover, all patients in our study did not use antiepileptic drugs before preoperative rs-fMRI scanning. Hence, we could not investigate how antiepileptic drugs could influence functional network alterations. Furthermore, the number of patients with other type of seizure was too small to analysis. Hence, we only investigated the patients with secondary generalized GRE in this study. In the future, we will enroll more patients to validate our findings.

In summary, the reduction of FC between the medial BA 6 (supplementary motor area) and caudal ventrolateral BA 6 in the ipsilateral hemisphere and a shortening of the path length of the sensorimotor network were characteristics alterations in patients with GRE onset. These findings reveal the relationship between GRE onset and alterations in brain functional networks in patients with prefrontal glioma.

DATA AVAILABILITY STATEMENT

The original contributions presented in the study are included in the article/**Supplementary Material**. Further inquiries can be directed to the corresponding authors.

ETHICS STATEMENT

The studies involving human participants were reviewed and approved by the IRB of Beijing Tiantan Hospital. The patients/participants provided their written informed consent to participate in this study.

AUTHOR CONTRIBUTIONS

Study concept and design: SF, LL, SW, and YG. Data acquisition and analysis: SF, LL, SW, ZZ, and YG. Statistics/verification of the analytical method: SF, XF, and YW. Writing of the first draft: SF, XF, LW, and YW. Supervision study: XF, YW, and TJ. All authors contributed to the article and approved the submitted version.

FUNDING

This work was supported by the Public Welfare Development and Reform Pilot Project of Beijing Medical Research Institute (PXM2019_026280_000008), Beijing Municipal Natural Science Foundation (No. 7202021), National Natural Science Foundation of China (No. 82001777), and Research Unit of Accurate Diagnosis, Treatment, and Translational Medicine of Brain Tumors Chinese (No. 2019-I2M-5-021).

ACKNOWLEDGMENTS

We thank Dr. Meng Lanxi for imaging data acquisition.

SUPPLEMENTARY MATERIAL

The Supplementary Material for this article can be found online at: https://www.frontiersin.org/articles/10.3389/fonc.2022.840871/full#supplementary-material

REFERENCES

1. You G, Sha Z, Jiang T. Clinical Diagnosis and Perioperative Management of Glioma-Related Epilepsy. *Front Oncol* (2020) 10:550353. doi: 10.3389/fonc.2020.550353
2. Liang S, Fan X, Zhao M, Shan X, Li W, Ding P, et al. Clinical Practice Guidelines for the Diagnosis and Treatment of Adult Diffuse Glioma-Related Epilepsy. *Cancer Med* (2019) 8(10):4527–35. doi: 10.1002/cam4.2362
3. Luo C, Li Q, Xia Y, Lei X, Xue K, Yao Z, et al. Resting State Basal Ganglia Network in Idiopathic Generalized Epilepsy. *Hum Brain Mapp* (2012) 33 (6):1279–94. doi: 10.1002/hbm.21286
4. Li Q, Chen Y, Wei Y, Chen S, Ma L, He Z, et al. Functional Network Connectivity Patterns Between Idiopathic Generalized Epilepsy With Myoclonic and Absence Seizures. *Front Comput Neurosci* (2017) 11:38. doi: 10.3389/fncom.2017.00038

5. Zhong C, Liu R, Luo C, Jiang S, Dong L, Peng R, et al. Altered Structural and Functional Connectivity of Juvenile Myoclonic Epilepsy: An fMRI Study. *Neural Plast* (2018) 2018:7392187. doi: 10.1155/2018/7392187
6. Negishi M, Martuzzi R, Novotny EJ, Spencer DD, Constable RT. Functional MRI Connectivity as a Predictor of the Surgical Outcome of Epilepsy. *Epilepsia* (2011) 52(9):1733–40. doi: 10.1111/j.1528-1167.2011.03191.x
7. Bernhardt BC, Chen Z, He Y, Evans AC, Bernasconi N. Graph-Theoretical Analysis Reveals Disrupted Small-World Organization of Cortical Thickness Correlation Networks in Temporal Lobe Epilepsy. *Cereb Cortex* (2011) 21 (9):2147–57. doi: 10.1093/cercor/bhq291
8. Yang T, Luo C, Li Q, Guo Z, Liu L, Gong Q, et al. Altered Resting-State Connectivity During Interictal Generalized Spike-Wave Discharges in Drug-Naive Childhood Absence Epilepsy. *Hum Brain Mapp* (2013) 34(8):1761–7. doi: 10.1002/hbm.22025
9. Cao X, Qian Z, Xu Q, Shen J, Zhang Z, Lu G. Altered Intrinsic Connectivity Networks in Frontal Lobe Epilepsy: A Resting-State fMRI Study. *Comput Math Methods Med* (2014) 2014:864979. doi: 10.1155/2014/864979
10. Liao W, Zhang Z, Pan Z, Mantini D, Ding J, Duan X, et al. Altered Functional Connectivity and Small-World in Mesial Temporal Lobe Epilepsy. *PloS One* (2010) 5(1):e8525. doi: 10.1371/journal.pone.0008525
11. Roland JL, Snyder AZ, Hacker CD, Mitra A, Shimony JS, Limbrick DD, et al. On the Role of the Corpus Callosum in Interhemispheric Functional Connectivity in Humans. *Proc Natl Acad Sci USA* (2017) 114(50):13278–83. doi: 10.1073/pnas.1707050114
12. Duffau H. Mapping the Connectome in Awake Surgery for Gliomas: An Update. *J Neurosurg Sci* (2017) 61(6):612–30. doi: 10.23736/S0390-5616.17.04017-6
13. Tate MC, Herbet G, Moritz-Gasser S, Tate JE, Duffau H. Probabilistic Map of Critical Functional Regions of the Human Cerebral Cortex: Broca's Area Revisited. *Brain* (2014) 137(Pt 10):2773–82. doi: 10.1093/brain/awu168
14. Fang S, Zhou C, Fan X, Jiang T, Wang Y. Epilepsy-Related Brain Network Alterations in Patients With Temporal Lobe Glioma in the Left Hemisphere. *Front Neurol* (2020) 11:684. doi: 10.3389/fneur.2020.00684
15. Fang S, Wang Y, Jiang T. Epilepsy Enhance Global Efficiency of Language Networks in Right Temporal Lobe Gliomas. *CNS Neurosci Ther* (2021) 27 (3):363–71. doi: 10.1111/cns.13595
16. Wang J, Wang X, Xia M, Liao X, Evans A, He Y. GRETNA: A Graph Theoretical Network Analysis Toolbox for Imaging Connectomics. *Front Hum Neurosci* (2015) 9:386. doi: 10.3389/fnhum.2015.00386
17. Calhoun VD, Wager TD, Krishnan A, Rosch KS, Seymour KE, Nebel MB, et al. The Impact of T1 Versus EPI Spatial Normalization Templates for fMRI Data Analyses. *Hum Brain Mapp* (2017) 38(11):5331–42. doi: 10.1002/hbm.23737
18. Fan L, Li H, Zhuo J, Zhang Y, Wang J, Chen L, et al. The Human Brainnetome Atlas: A New Brain Atlas Based on Connectional Architecture. *Cereb Cortex* (2016) 26(8):3508–26. doi: 10.1093/cercor/bhw157
19. Hart MG, Ypma RJ, Romero-Garcia R, Price SJ, Suckling J. Graph Theory Analysis of Complex Brain Networks: New Concepts in Brain Mapping Applied to Neurosurgery. *J Neurosurg* (2016) 124(6):1665–78. doi: 10.3171/2015.4.JNS142683
20. Gong Y, Wu H, Li J, Wang N, Liu H, Tang X. Multi-Granularity Whole-Brain Segmentation Based Functional Network Analysis Using Resting-State fMRI. *Front Neurosci* (2018) 12:942. doi: 10.3389/fnins.2018.00942
21. Vassal M, Charroud C, Deverdun J, Le Bars E, Molino F, Bonnetblanc F, et al. Recovery of Functional Connectivity of the Sensorimotor Network After Surgery for Diffuse Low-Grade Gliomas Involving the Supplementary Motor Area. *J Neurosurg* (2017) 126:1181–90. doi: 10.3171/2016.4.JNS152484
22. Fang S, Li Y, Wang Y, Zhang Z, Jiang T. Awake Craniotomy for Gliomas Involving Motor-Related Areas: Classification and Function Recovery. *J Neurooncol* (2020) 148(2):317–25. doi: 10.1007/s11060-020-03520-w
23. Wang Y, Qian T, You G, Peng X, Chen C, You Y, et al. Localizing Seizure-Susceptible Brain Regions Associated With Low-Grade Gliomas Using Voxel-Based Lesion-Symptom Mapping. *Neuro Oncol* (2015) 17(2):282–8. doi: 10.1093/neuonc/nou130
24. Vassal M, Charroud C, Deverdun J, Le Bars E, Molino F, Bonnetblanc F, et al. Recovery of Functional Connectivity of the Sensorimotor Network After Surgery for Diffuse Low-Grade Gliomas Involving the Supplementary Motor Area. *J Neurosurg* (2017) 126(4):1181–90. doi: 10.3171/2016.4.JNS152484
25. Besseling RM, Overvliet GM, Jansen JF, van der Kruijs SJ, Vles JS, Ebus SC, et al. Aberrant Functional Connectivity Between Motor and Language Networks in Rolandic Epilepsy. *Epilepsy Res* (2013) 107(3):253–62. doi: 10.1016/j.eplepsyres.2013.10.008
26. Lee C, Im CH, Koo YS, Lim JA, Kim TJ, Byun JI, et al. Altered Network Characteristics of Spike-Wave Discharges in Juvenile Myoclonic Epilepsy. *Clin EEG Neurosci* (2017) 48(2):111–7. doi: 10.1177/1550059415621831
27. Aparicio J, Carreno M, Bargallo N, Setoain X, Rubi S, Rumia J, et al. Combined (18)F-FDG-PET and Diffusion Tensor Imaging in Mesial Temporal Lobe Epilepsy With Hippocampal Sclerosis. *NeuroImage Clin* (2016) 12:976–89. doi: 10.1016/j.nicl.2016.05.002
28. Caciagli L, Bernasconi A, Wiebe S, Koepp MJ, Bernasconi N, Bernhardt BC. A Meta-Analysis on Progressive Atrophy in Intractable Temporal Lobe Epilepsy: Time Is Brain? *Neurology* (2017) 89(5):506–16. doi: 10.1212/WNL.0000000000004176
29. Celiker Uslu S, Yuksel B, Tekin B, Sariahmetoglu H, Atakli D. Cognitive Impairment and Drug Responsiveness in Mesial Temporal Lobe Epilepsy. *Epilepsy Behav* (2019) 90:162–7. doi: 10.1016/j.yebeh.2018.10.034
30. Pillai JJ. Insights Into Adult Postlesional Language Cortical Plasticity Provided by Cerebral Blood Oxygen Level-Dependent Functional MR Imaging. *AJNR Am J Neuroradiol* (2010) 31(6):990–6. doi: 10.3174/ajnr.A1896
31. Guerra-Carrillo B, Mackey AP, Bunge SA. Resting-State fMRI: A Window Into Human Brain Plasticity. *Neuroscientist* (2014) 20(5):522–33. doi: 10.1177/1073858414524442
32. van Dokkum LEH, Moritz Gasser S, Deverdun J, Herbet G, Mura T, D'Agata B, et al. Resting State Network Plasticity Related to Picture Naming in Low-Grade Glioma Patients Before and After Resection. *NeuroImage Clin* (2019) 24:102010. doi: 10.1016/j.nicl.2019.102010
33. Laura G, Silvia T, Nikolaos P, Patrizia P. The Role of fMRI in the Assessment of Neuroplasticity in MS: A Systematic Review. *Neural Plast* (2018) 2018:3419871. doi: 10.1155/2018/3419871
34. Ponten SC, Bartolomei F, Stam CJ. Small-World Networks and Epilepsy: Graph Theoretical Analysis of Intracerebrally Recorded Mesial Temporal Lobe Seizures. *Clin Neurophysiol* (2007) 118(4):918–27. doi: 10.1016/j.clinph.2006.12.002
35. Dyhrfjeld-Johnsen J, Santhakumar V, Morgan RJ, Huerta R, Tsimring L, Soltesz I. Topological Determinants of Epileptogenesis in Large-Scale Structural and Functional Models of the Dentate Gyrus Derived From Experimental Data. *J Neurophysiol* (2007) 97(2):1566–87. doi: 10.1152/jn.00950.2006
36. Ofer I, LeRose C, Mast H, LeVan P, Metternich B, Egger K, et al. Association Between Seizure Freedom and Default Mode Network Reorganization in Patients With Unilateral Temporal Lobe Epilepsy. *Epilepsy Behav* (2019) 90:238–46. doi: 10.1016/j.yebeh.2018.10.025
37. Rosazza C, Deleo F, D'Incerti L, Antelmi L, Tringali G, Didato G, et al. Tracking the Re-Organization of Motor Functions After Disconnective Surgery: A Longitudinal fMRI and DTI Study. *Front Neurol* (2018) 9:400. doi: 10.3389/fneur.2018.00400
38. Sgandurra G, Biagi L, Fogassi L, Sicola E, Ferrari A, Guzzetta A, et al. Reorganization of the Action Observation Network and Sensory-Motor System in Children With Unilateral Cerebral Palsy: An fMRI Study. *Neural Plast* (2018) 2018:6950547. doi: 10.1155/2018/6950547
39. Fornito A, Zalesky A, Bullmore ET. Network Scaling Effects in Graph Analytic Studies of Human Resting-State FMRI Data. *Front Syst Neurosci* (2010) 4:22. doi: 10.3389/fnsys.2010.00022
40. Mazrooyisebdani M, Nair VA, Garcia-Ramos C, Mohanty R, Meyerand E, Hermann B, et al. Graph Theory Analysis of Functional Connectivity Combined With Machine Learning Approaches Demonstrates Widespread Network Differences and Predicts Clinical Variables in Temporal Lobe Epilepsy. *Brain Connect* (2020) 10(1):39–50. doi: 10.1089/brain.2019.0702

Conflict of Interest: The authors declare that the research was conducted in the absence of any commercial or financial relationships that could be construed as a potential conflict of interest.

Publisher's Note: All claims expressed in this article are solely those of the authors and do not necessarily represent those of their affiliated organizations, or those of the publisher, the editors and the reviewers. Any product that may be evaluated in

this article, or claim that may be made by its manufacturer, is not guaranteed or endorsed by the publisher.

Copyright © 2022 Fang, Li, Weng, Guo, Zhang, Wang, Fan, Wang and Jiang. This is an open-access article distributed under the terms of the Creative Commons Attribution License (CC BY). The use, distribution or reproduction in other forums is permitted, provided the original author(s) and the copyright owner(s) are credited and that the original publication in this journal is cited, in accordance with accepted academic practice. No use, distribution or reproduction is permitted which does not comply with these terms.

frontiers in Neuroscience

REVIEW
published: 23 February 2022
doi: 10.3389/fnins.2022.787755

Advanced Imaging Techniques for Newly Diagnosed and Recurrent Gliomas

Luis R. Carrete[1], Jacob S. Young[2] and Soonmee Cha[3]*

[1] University of California San Francisco School of Medicine, San Francisco, CA, United States, [2] Department of Neurological Surgery, University of California, San Francisco, San Francisco, CA, United States, [3] Department of Radiology, University of California, San Francisco, San Francisco, CA, United States

Management of gliomas following initial diagnosis requires thoughtful presurgical planning followed by regular imaging to monitor treatment response and survey for new tumor growth. Traditional MR imaging modalities such as T1 post-contrast and T2-weighted sequences have long been a staple of tumor diagnosis, surgical planning, and post-treatment surveillance. While these sequences remain integral in the management of gliomas, advances in imaging techniques have allowed for a more detailed characterization of tumor characteristics. Advanced MR sequences such as perfusion, diffusion, and susceptibility weighted imaging, as well as PET scans have emerged as valuable tools to inform clinical decision making and provide a non-invasive way to help distinguish between tumor recurrence and pseudoprogression. Furthermore, these advances in imaging have extended to the operating room and assist in making surgical resections safer. Nevertheless, surgery, chemotherapy, and radiation treatment continue to make the interpretation of MR changes difficult for glioma patients. As analytics and machine learning techniques improve, radiomics offers the potential to be more quantitative and personalized in the interpretation of imaging data for gliomas. In this review, we describe the role of these newer imaging modalities during the different stages of management for patients with gliomas, focusing on the pre-operative, post-operative, and surveillance periods. Finally, we discuss radiomics as a means of promoting personalized patient care in the future.

Keywords: glioma, imaging, recurrence, progression, pseudoprogression, radiomics, PET scanning

OPEN ACCESS

Edited by:
Alexandra Golby, Harvard Medical School, United States

Reviewed by:
Jan Petr, Helmholtz Association of German Research Centres (HZ), Germany
Jens Gempt, Technical University of Munich, Germany
Georgios Naros, University of Tübingen, Germany
Giuseppe Barisano, University of Southern California, United States

****Correspondence:***
Jacob S. Young
Jacob.young@ucsf.edu

Specialty section:
This article was submitted to Brain Imaging Methods, a section of the journal Frontiers in Neuroscience

Received: *01 October 2021*
Accepted: *19 January 2022*
Published: *23 February 2022*

Citation:
Carrete LR, Young JS and Cha S (2022) Advanced Imaging Techniques for Newly Diagnosed and Recurrent Gliomas. Front. Neurosci. 16:787755. doi: 10.3389/fnins.2022.787755

Abbreviations: EOR, extend of resection; HGG, high-grade glioma; LGG, low-grade glioma; GBM, glioblastoma; MRI, magnetic resonance imaging; FLAIR, fluid-attenuated inversion recovery; BBB, blood-brain barrier; CE, contrast-enhancing; NCE, non-contrast enhancing; IDH, isocitrate dehydrogenase; MGMT, O6-methylguanine-DNA methyltransferase; DWI, diffusion-weighted imaging; ADC, apparent diffusion coefficient; SWI, susceptibility-weighted imaging; DSC, dynamic susceptibility contrast; DCE, dynamic contrast enhanced; ASL, arterial spin labeling; rCBV, relative cerebral blood volume; MRS, MR spectroscopy; DTI, diffusion tensor imaging; FA, fractional anisotropy; RCT, randomized controlled trial; GTR, gross total resection; iMRI, intraoperative MRI; fMRI, functional MRI; BOLD, blood oxygen level dependent; DES, direct electrical stimulation; MEG, magnetoencephalography; HFC, high functional connectivity; LFC, low functional connectivity; nTMS, navigated transcranial magnetic stimulation; nrTMS, navigated repetitive TMS; PFS, progression-free survival; OS, overall survival; PET, positron emission tomography; ^{18}F-FDG, 2-^{18}F-fluoro-2-deoxy-D-glucose; ^{18}F-FET, O-(2-^{18}F-fluoroethyl)-L-tyrosine; ^{11}C-MET, (S-^{11}C-methyl)-L-methionine; ^{18}F-FDOPA, 3,4-dihydroxy-6-^{18}F-fluoro-L-phenylalanine; AA PET, amino acid PET; TBR, tumor-background ratio.

INTRODUCTION

Gliomas are the most common primary brain tumor with varying prognosis depending on their grade and genomic profile (Louis et al., 2021). Patients often present with seizures and/or focal neurological deficit and undergo an imaging study, often an MRI scan, that reveals the neoplastic lesion. The standard of care for these patients begins with maximal safe resection followed by chemotherapy and radiation (Stupp et al., 2005; Molinaro et al., 2020). In the case of high grade glioma (HGG), there is substantial evidence to suggest that maximal extent of resection (EOR) of the contrast-enhancing (CE) regions of tumor on post-contrast T1 imaging, and in some cases resection of non-contrast enhancing (NCE) disease that extends beyond the CE tumor (i.e., a supratotal resection), improves survival (Li et al., 2016; Esquenazi et al., 2017; Molinaro et al., 2020).

In order to achieve a maximal safe resection of these infiltrative tumors, particularly when the goal is a supratotal resection, advanced imaging modalities, such as perfusion imaging, diffusion imaging, spectroscopy, and positron emission topography (PET) imaging, have become increasingly useful surgical adjuncts, especially when used in combination with intraoperative brain mapping. Nevertheless, despite aggressive treatments, these tumors almost always recur, and early detection of tumor recurrence remains critical for optimal patient management and evaluation of treatment options, including feasibility of repeat surgical resection. In the months following tumor resection and radiation therapy, the appearance of treatment effect or pseudoprogression, which is defined as the radiographic appearance of tumor growth that spontaneously resolves without additional anti-tumor therapy and is actually reflective of treatment response, can closely resemble the appearance of recurrent, progressive tumor on imaging. Therefore, it is critical to distinguish between these phenomena to best manage patients (Stupp et al., 2005, 2009, 2014). Additionally, distinguishing true progression from pseudoprogression is critical for proper patient enrollment in clinical trials at the time of recurrence. This distinction represents another key area where multimodal imaging studies can improve clinical decision-making (Chaskis et al., 2009). In this review, we describe the role for various imaging modalities for patients with primary brain tumors during the pre-operative and surveillance stages of treatment and highlight the emerging field of radiomics for gliomas.

PREOPERATIVE IMAGING AND SURGICAL PLANNING

After the initial diagnosis of lesion concerning for an intra-axial brain tumor is made, most institutions employ a standardized protocol for lesion characterization and pre-operative planning. 3-dimensional (3D) T1 pre- and post-contrast-enhanced, T2 contrast-enhanced, fluid-attenuated inversion recovery (FLAIR), and diffusion-weighted imaging (DWI) at a magnetic field strength of a minimum of 1.5 tesla (T) are commonly a part of these protocols (Ellingson et al., 2015). In the following section, we describe these common sequences and discuss how they can be used to clarify the diagnosis, determine the extent of tumor invasion, and maximize safety during tumor resection. For an overview of the various imaging techniques covered in this review, see **Table 1**.

T1 Pre- and Post-gadolinium and T2/T2 Fluid-Attenuated Inversion Recovery Sequences

T1-weighted pre- and post-contrast images as well as the T2 weighted images, particularly the fluid-attenuated inversion recovery (T2 FLAIR) sequence, are often the most critical for tumor visualization and are most frequently utilized intra-operatively with neuronavigation to assist with tumor resection. Aberrant vascular proliferation and tumor necrosis caused by high grade gliomas results in disruption of the blood-brain barrier (BBB) and vascular leakage of intravenously administered gadolinium contrast agent (Upadhyay and Waldman, 2011; Ellingson et al., 2017a; Hu et al., 2020). The contrast agent extravasation leads to T1 shortening and hyperintensity (i.e., "contrast-enhancement") on T1-weighted imaging (**Figure 1**; Hervey-Jumper and Berger, 2016; Hu et al., 2020).

In the case of glioblastoma (GBM), it is well-known that malignant cells invade past areas of contrast enhancement on T1 imaging (Berman et al., 2007). As mentioned above, a recent multicenter cohort study investigating maximal resection of CE and NCE tumors demonstrated that in addition to the survival benefit conferred by maximal resection of the CE tumor, additional resection of NCE tumor leads to improved overall survival (OS) regardless of isocitrate dehydrogenase (IDH) and O6-methylguanine-DNA methyltransferase (MGMT) methylation status in younger patients (Molinaro et al., 2020). This underscores the need for imaging modalities for HGG delineating tumor infiltration past areas of high contrast enhancement.

T2/FLAIR sequences are better suited for visualizing low-grade glioma (LGG) as well as areas of edema and tumor growth extending past CE areas on T1 typical of HGG. Low-grade tumors less frequently enhance on T1 post-contrast images given their lower rates of proliferation and intact BBB, making T2/FLAIR an important sequence in the evaluation of LGG (**Figure 1**; Sage and Wilson, 1994; Scott et al., 2002; Harpold et al., 2007; Gupta and Dwivedi, 2016). When LGGs do contrast enhance, the pattern is often patchy or wispy, which can indicate areas of malignant transformation (Whitfield et al., 2014; Zhang et al., 2021). Unlike, T1 sequences, T2/FLAIR functions by demonstrating hyperintensity in areas of prolonged transverse relaxation time due to increased water content (Upadhyay and Waldman, 2011; Ellingson et al., 2017a; Hu et al., 2020; Li J. et al., 2020). This property is useful in the visualization of peritumoral edema, an area containing infiltrating tumor cells and increased extracellular water due to plasma fluid leakage from aberrant tumor capillaries that surrounds the CE tumor core in HGG (Saadoun et al., 2002; Warth et al., 2007; Barajas et al., 2012, 2013). T2/FLAIR thus plays a valuable role in the planning of HGG resection given it reveals NCE areas of infiltrative

TABLE 1 | Imaging techniques for glioma imaging, utility, and limitations.

MRI technique	Clinical utility and findings
Preoperative Techniques for Tumor Characterization	
T1	Anatomic MRI- evaluates tissue architecture
Pre-contrast	Hyperintensity from fat, blood products, mineralization
Post-contrast	Demonstrates non-specific BBB breakdown
T2/FLAIR	Anatomic MRI- evaluates tissue architecture
	Hyperintensity in peritumoral edema, non-enhancing tumor, gliosis, white matter injury
DWI	Evaluates Brownian motion/diffusion of water molecules, can be presented as an ADC map
	Reduced diffusion (high signal intensity) in areas of increased cellularity due to tumor and in cytotoxic edema or postoperative injury
SWI	Sensitive to magnetic susceptibility of tissues
	Hypointense appearance from blood products, hyperintense appearance from calcification
MRS	Evaluate tumor biochemical/metabolic profile
	HGGs show higher Cho/NAA and Cho/Cr ratios than LGGs
Perfusion imaging	
DSC	Main metric is cerebral blood volume
	High blood volume suggestive of higher tumor grade or tumor recurrence
DCE	Main metric is k^{trans}, a measure of permeability
	High permeability suggests higher tumor grade
ASL	Main metric is cerebral blood flow
	High blood flow suggestive of higher-grade tumor. Does not require exogenous contrast.
PET	Investigates tumor rates of proliferation and metabolism using molecular tracers
FDG PET	Compares rates of tumor uptake of glucose metabolism relative to surrounding tissue; higher rates of glucose metabolism seen in higher tumor grades
AA PET	Compares rates of amino acid transport in tumors relative to surrounding brain tissue; higher rates of amino acid tracer metabolism indicative of higher tumor grade.
Imaging techniques for preoperative and intraoperative	
DTI	Examines the direction of diffusivity of water molecules along white matter tracts.
	Tractography demonstrates location of white matter tracts relative to infiltrative tumor to inform pre- and intra-operative planning
fMRI	Evaluate brain activation based on specific tasks based on regional changes in blood oxygenation levels
	Used for functional mapping of specific brain regions to help preserve areas critical to perform certain tasks by is limited by poor sensitivity and specificity and overall poor correlation with intraoperative direct electrical stimulation mapping
MEG	Detects magnetic fields generated by electrical currents from neuronal action potentials
	Registered with 3D MRI sequence to visualize functional neuronal activity
nTMS	Utilizes transcranial magnetic fields to non-invasively stimulate/inhibit brain cortex
	Transcranial magnetic fields applied through non-invasive image-guided method to generate functional maps to differentiate eloquent from non-eloquent cortex.

HGG, high-grade glioma; LGG, low-grade glioma; MRI, magnetic resonance imaging; FLAIR, fluid-attenuated inversion recovery; BBB, blood-brain barrier; DWI, diffusion-weighted imaging; SWI, susceptibility-weighted imaging; DSC, dynamic susceptibility contrast; DCE, dynamic contrast enhanced; ASL, arterial spin labeling; MRS, MR spectroscopy; DTI, diffusion tensor imaging; fMRI, functional MRI; MEG, magnetoencephalography; nTMS, navigated transcranial magnetic stimulation; PET, positron emission tomography; FDG PET, 2-^{18}F-fluoro-2-deoxy-D-glucose; AA PET, amino acid PET.

disease (Barajas et al., 2012; Henker et al., 2019; Hu et al., 2020; Verburg and de Witt Hamer, 2021). T2 and FLAIR sequences can also be used to predict clinically relevant molecular features of glioma, as is the case with T2/FLAIR mismatch sign. T2/FLAIR mismatch sign is characterized by a the presence of areas of hyperintensity on T2-weighted image paired with a relatively hypointense signal on FLAIR imaging with the exception of a hyperintense peripheral rim (**Figure 2**; Deguchi et al., 2020). This finding is strongly indicative of IDH-mutant, 1p/19q non-codeleted astroyctomas with a positive predictive value (PPV) ranging from 83 to 100% (Patel S. H. et al., 2017; Broen et al., 2018; Deguchi et al., 2020).

While T2 FLAIR and T1 post-contrast images- provide crucial information in the preoperative and intraoperative period, there are limitations to the information provided by these modalities. Despite the utility of T1-post contrast imaging for detecting HGG based on contrast extravasation, tumors such as GBM occasionally show no or minimal enhancement on T1 post-contrast imaging (**Figure 1**). Similarly T2 and FLAIR sequences are limited in their ability to distinguish between LGG and HGG (Scott et al., 2002; Maia et al., 2004). These limitations are addressed to a degree through the use of additional sequences and imaging modalities that serve to complement anatomic MR sequences in the assessment of gliomas to further characterize tumor grade.

Diffusion-Weighted Imaging

Diffusion-weighted imaging (DWI) is an MR sequence that measures random (Brownian) movement of water molecules and calculates diffusion metrics such as apparent diffusion coefficient

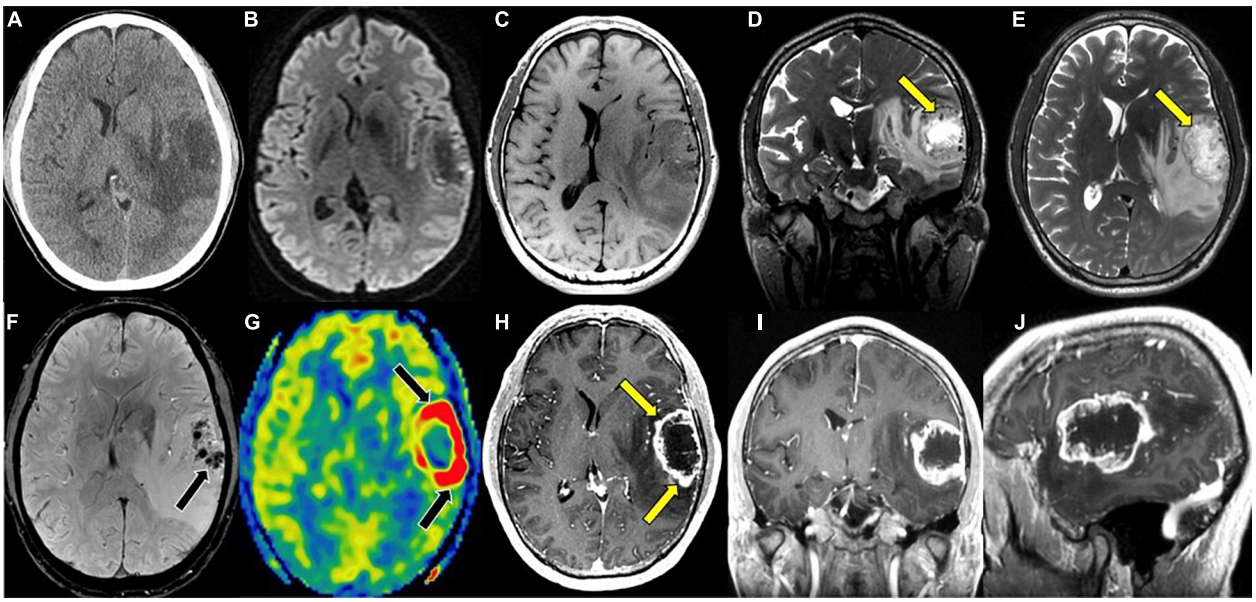

FIGURE 1 | Glioblastoma, IDH-wildtype. **(A)** Axial CT without contrast: Ill-defined hypodensity lesion centered in the left superior temporal gyrus; **(B)** axial DWI: No associated reduced diffusion; **(C)** axial T1 pre-contrast: hypointense mass; **(D)** coronal T2: heterogeneous mass with hypointense rim with prominent central necrosis (yellow arrow); **(E)** axial T2: heterogeneous mass with hypointense rim with prominent central necrosis (yellow arrow); **(F)** axial SWI: prominent blood products within the mass (black arrow); **(G)** axial ASL perfusion: marked hyperperfusion (black arrows) within the rim enhancing component of the mass; **(H)** axial T1 post-contrast: heterogeneous mass with thick rim enhancement (yellow arrows) and prominent central necrosis; **(I)** coronal T1 post-contrast: heterogeneous mass with thick rim enhancement and prominent central necrosis; **(J)** sagittal T1 post-contrast: heterogeneous mass with thick rim enhancement and prominent central necrosis. CT, Computed tomography; DWI, Diffusion-weighted imaging; SWI, Susceptibility-weighted imaging; ASL, Arterial spin labeling; MRS, Magnetic resonance spectroscopy.

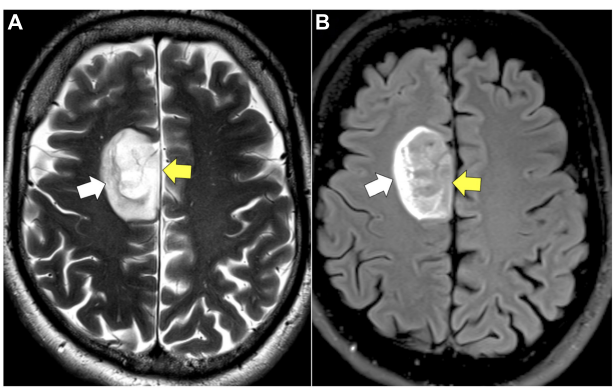

FIGURE 2 | T2/FLAIR mismatch. **(A)** Axial T2: homogenously hyperintense mass (yellow arrow). **(B)** Axial FLAIR: hypointense mass (yellow arrow) relative to T2 image with exception of a hyperintense peripheral rim (white arrow).

(ADC). In the context of glioma imaging, restricted diffusion (i.e., low ADC signal) indicates hypercellularity due to high tumor proliferation and restriction of water diffusion compared to tissues with lower cellular density. These areas of hypercellularity causing restricted water diffusion appear as bright signal on DWI (**Figure 3**; Schmainda, 2012). Several studies demonstrate an inverse relationship between ADC and cellular density with this inverse relationship also existing for ADC in relation to tumor proliferation (Ellingson et al., 2010; Schmainda, 2012). Notably, intratumoral heterogeneity and areas of necrosis can limit the utility of ADC values in certain regions of the tumor (Lam et al., 2002). Still, this property of detecting hypercellularity can detect early stages of malignant transformation that may not yet show contrast enhancement on T1 (Baehring et al., 2007; Schmainda, 2012).

A more recently developed technique of diffusion imaging known as diffusion kurtosis imaging (DKI) functions by quantifying the non-Gaussian nature of water molecules to develop several metrics that allow for a significantly better characterization of intratumoral heterogeneity relative to DWI. Recent studies propose that DKI is capable of detailing certain differences between tumor grades in gliomas, including differences between WHO grades II and III, and differences between grades III and IV (Raja et al., 2016). This emerging technology is not commonly used in clinical practice, but may play a role as a non-invasive means of evaluating a tumor's molecular characteristics (Raja et al., 2016).

Susceptibility-Weighted Imaging

Susceptibility-weighted imaging (SWI) is an MR sequence that shows differences in the local magnetic field susceptibility among neighboring tissues, allowing for visualization of substances such as deoxyhemoglobin in venous blood, iron deposition in the brain, or calcium, providing important diagnostic information (Löbel et al., 2010). SWI images are generated by processing data

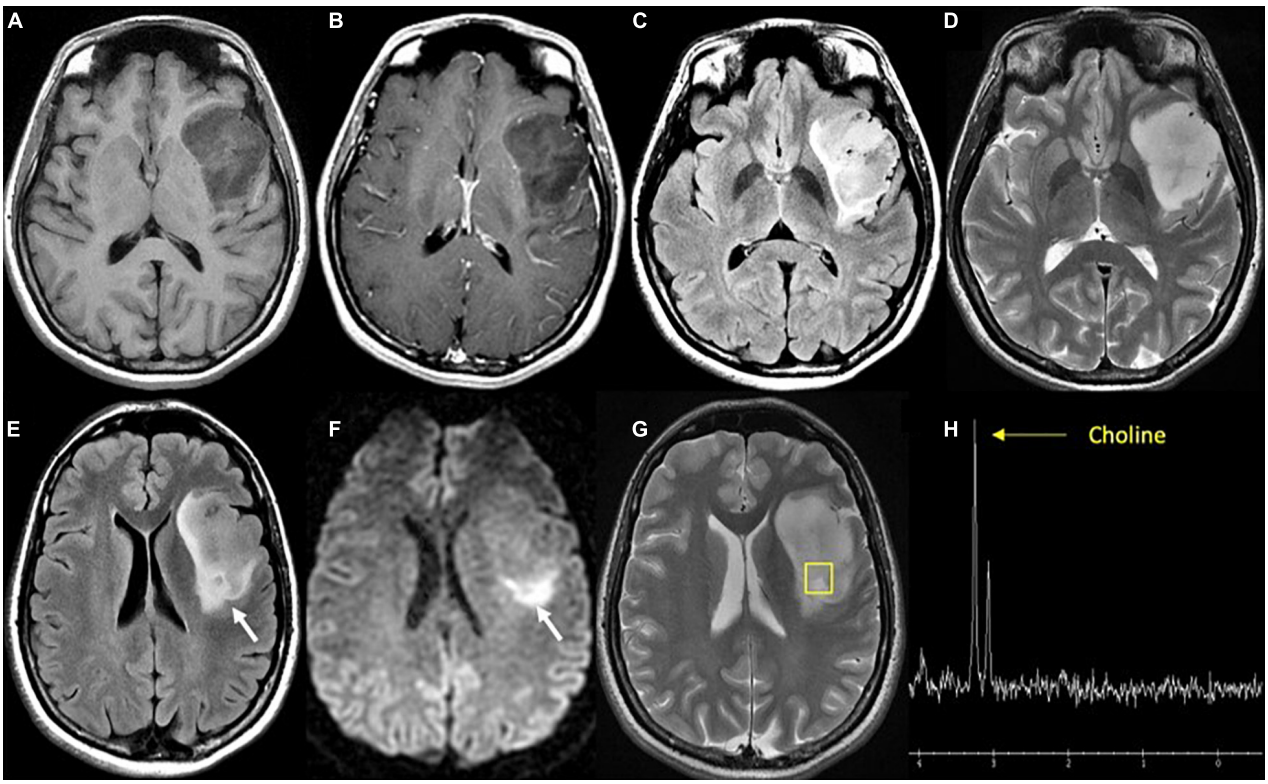

FIGURE 3 | Diffuse astrocytoma, IDH-wildtype. **(A)** Axial T1 pre-contrast: expansile hypointense left insular mass; **(B)** Axial T1 post-contrast: No associated enhancement; **(C)** axial FLAIR: heterogeneous mixed hyper- and hypointense signal intensity within the mass; **(D)** axial T2: homogeneous hyperintense mass; **(E)** axial FLAIR: hyperintense region of the tumor (white arrow) in the posterior aspect; **(F)** axial DWI: associated reduced diffusion in the posterior tumor (white arrow); **(G)** axial T2: localizer for single voxel MRS targeted to the posterior tumor; **(H)** proton MRS single voxel: pathologic increase in choline metabolite at 3.2 ppm (yellow arrow) and absent NAA metabolite (arrowhead) at 2 ppm consistent with proliferating process. Biopsy targeted to this region showed cellular astrocytoma. FLAIR, Fluid-attenuated inversion recovery.

that is acquired from methodology that includes a combination of high-resolution (3.0 T), a long echo time (TE), full-flow compensation, and a 3D gradient-echo. The acquired MR data is processed to detect susceptibility differences in substances within tissues such as those that are ferromagnetic (iron), paramagnetic (deoxyhemoglobin, clots), and diamagnetic (calcium) (Haacke et al., 2004). Magnetic fields applied to diamagnetic calcium appear bright while paramagnetic blood products appear dark on imaging (**Figure 1**). Based on these properties, SWI is the preferred modality for visualizing microhemorrhages, which becomes particularly valuable when trying to distinguish areas of necrosis or hemorrhage after radiation treatment, which will be discussed in more detail later in the review (Li et al., 2010; Löbel et al., 2010; Mohammed et al., 2013). The ability of SWI to identify calcium on imaging can also aid in predicting tumor histology and/or grade prior to pathological confirmation, particularly if a CT scan has not been obtained. Appearing as areas of low signal intensity, intratumoral calcification is most common in oligodendrogliomas, and can also be seen in gangliogliomas, pilocytic astrocytomas, and ependymomas (Emblem et al., 2008; Mohammed et al., 2013; Hsu et al., 2016). Additionally, there are studies that demonstrate that SWI can help differentiate brain abscess and necrotic GBM in cases where it is difficult to make a distinction on T1 post-contrast imaging (Toh et al., 2012).

In terms of limitations of this technique, multiple studies report long acquisition time of SWI as a limitation of this modality given that prolonged imaging can cause patient discomfort and is susceptible to motion artifact and image distortion (Sehgal et al., 2006; Tong et al., 2008; Fujima et al., 2010). Furthermore, while SWI is adept at imaging blood products and can depict blood vessels in both low-grade and high-grade glioma, the presence of calcium or hemorrhage within the tumor can serve as a susceptibility artifact that leads to underestimation of tumor perfusion; therefore, SWI is not as commonly used for visualizing microvessel density and tumor perfusion as other MR techniques (Willats and Calamante, 2013).

MR Perfusion Imaging

Dynamic susceptibility contrast (DSC), dynamic contrast enhanced (DCE), and arterial spin labeling (ASL) are the most commonly used MR perfusion techniques in clinical practice. DSC works by measuring transient decrease in brain signal intensity on T2*-weighted sequences after gadolinium contrast agent administration to generate a signal intensity time curve that is used to compute relative cerebral blood volume (rCBV)

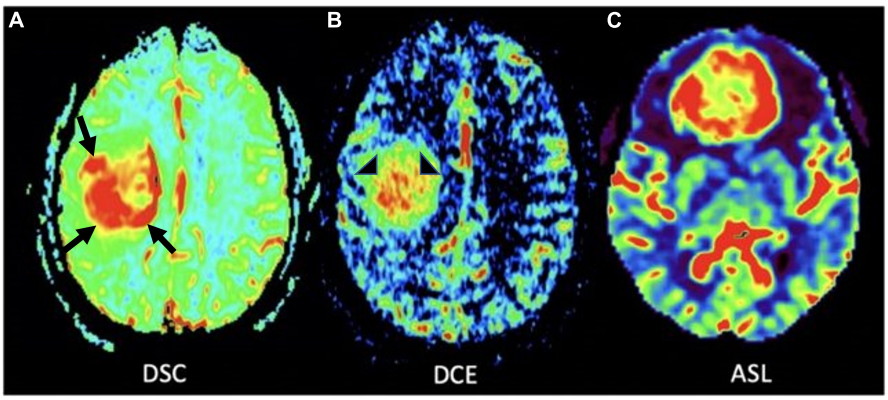

FIGURE 4 | MR perfusion sequences. **(A)** Axial DSC perfusion: Marked hyperperfusion within the lateral and posterior aspects of the mass (black arrows); **(B)** axial DCE perfusion: Marked capillary leakiness within the central aspect of the mass (arrowheads); **(C)** axial ASL perfusion: Marked hyperperfusion of a neoplasm in the frontal lobe. DSC, Dynamic susceptibility-weighted contrast-enhanced; DCE, Dynamic contrast enhanced; ASL, Arterial spin labeling.

for each voxel (Hu et al., 2012). rCBV signal correlates directly with microvessel volume and is seen as a marker of angiogenesis (**Figure 4**), serving to distinguish HGG from LGGs and non-neoplastic etiologies such as post-treatment effect with greater rCBV signal in higher grade gliomas (Danchaivijitr et al., 2008; Xiao et al., 2015). There is evidence to suggest that this modality is predictive of malignant transformation of LGGs (Maia et al., 2004) and overall survival, and can be particularly helpful in distinguishing tumor recurrence from post-treatment effect such as radiation necrosis, and pseudoprogression- defined as a transient increase in post-contrast enhancement within the treated tumor lesion that presents during the first 6 months after treatment, followed by spontaneous radiographic improvement or resolution without any changes to the treatment regimen (Law et al., 2006, 2008; Chaskis et al., 2009; Schmainda, 2012; van West et al., 2017).

The absolute quantification of cerebral blood flow, cerebral blood volume, and mean transit time using DSC is dependent on what is known as the arterial input function (AIF). The AIF describes contrast agent input to the brain through the measurement of contrast agent concentration as it flows through brain-feeding arteries. In clinical practice AIF is typically obtained by manually selecting a region of interest around a feeding artery (i.e., the internal carotid artery or middle cerebral artery), a process that is subjective, user-dependent, and can lead to variability between scans, affecting repeatability of DSC studies (Bleeker et al., 2011; Jafari-Khouzani et al., 2015).

DCE works by measuring dynamic signal changes on T1 weighted imaging after administration of intravenous contrast. In the context of glioma imaging, DCE is used to measure rates of capillary permeability caused by disordered tumor vasculature through the use of a volume transfer constant- k^{trans}. This metric can be informative in the process of tumor grading given that HGGs have greater vascular permeability relative to LGGs (Roberts et al., 2000; Patankar et al., 2005). Given that DCE is primarily used to provide insight into tumor vascular permeability (**Figures 4**, **5**), the utility of DCE is limited for the imaging of gliomas that do not exhibit BBB disruption or vascular leakage (Patankar et al., 2005; Essig et al., 2013).

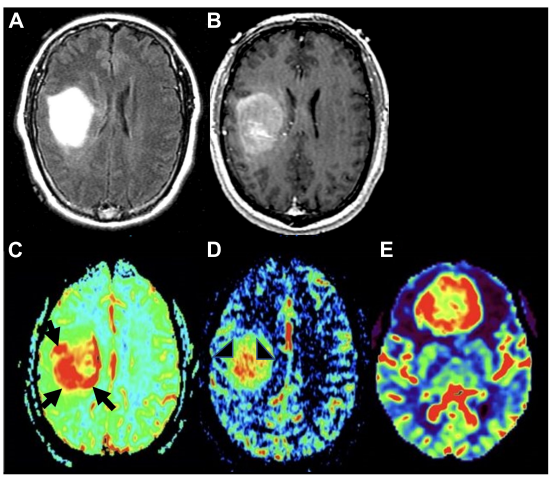

FIGURE 5 | Molecular glioblastoma. **(A)** Axial FLAIR: homogeneously hyperintense mass; **(B)** axial T1 post-contrast: mild enhancement within the mass without distinct area of necrosis; **(C)** axial DSC perfusion: marked hyperperfusion within the lateral and posterior aspects of the mass (black arrows); **(D)** axial DCE perfusion: marked capillary leakiness within the central aspect of the mass (arrowheads); **(E)** axial ASL perfusion: marked increase in cerebral blood flow and hyperperfusion of tumor in the frontal lobe (different tumor than the one depicted in panels **A–D**).

In contrast to DSC and DCE, ASL does not require intravenous injection of exogenous contrast (**Figures 1**, **4**, **6**). This technique quantitatively measures cerebral blood flow by inverting the magnetization of water protons in blood with a train of radiofrequency pulses in the carotid or vertebral arteries before blood enters the brain. Images are then collected and subsequently subtracted from a set of control static images, allowing for the quantification of cerebral blood flow (Zhang et al., 1995; Villanueva-Meyer et al., 2017; Hernandez-Garcia et al., 2019; Williams et al., 2019). Based on these properties, ASL can be used to differentiate HGG from LGG based on elevated perfusion (Kim et al., 2008; Cebeci et al., 2014; Villanueva-Meyer et al., 2017).

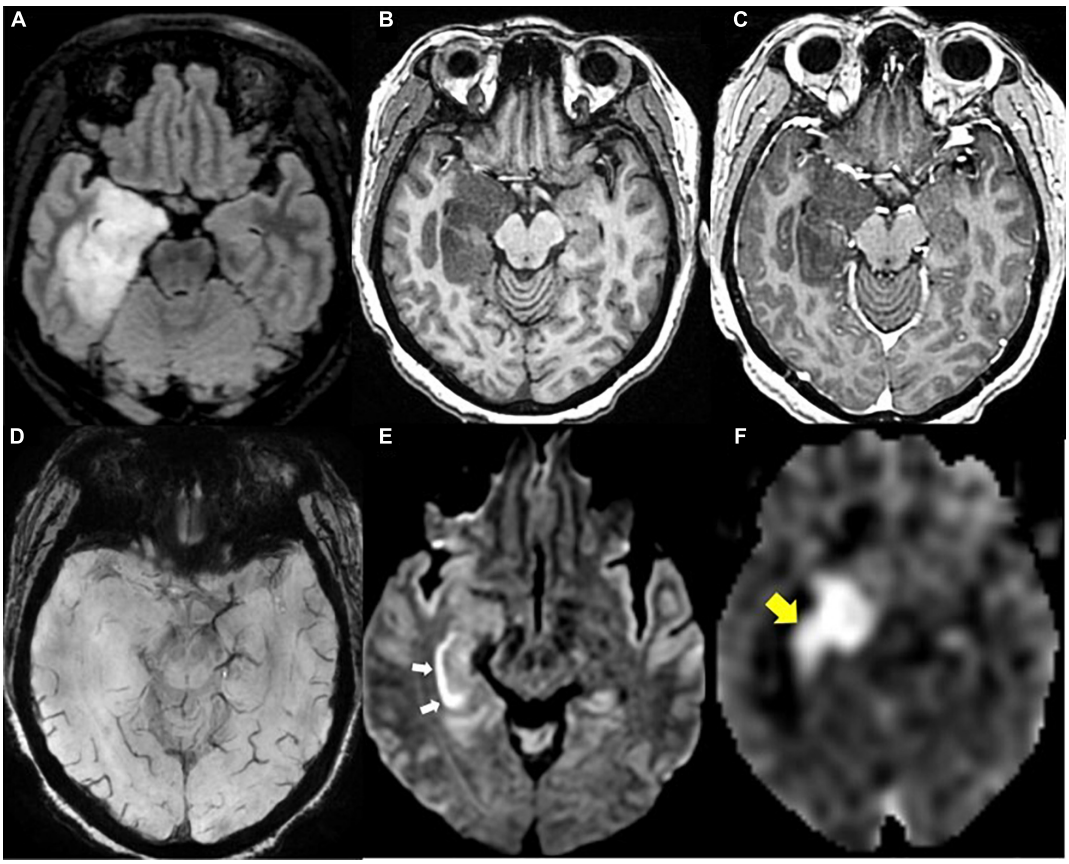

FIGURE 6 | Diffuse glioma, IDH-mutant. **(A)** Axial FLAIR: Expansile hyperintense mass in the right medial temporal lobe; **(B)** axial T1 pre-contrast: hypointense mass; **(C)** axial T1 post-contrast: no associated enhancement within the mass; **(D)** axial SWI: no blood products or calcium within the mass; **(E)** axial DWI: linear reduced diffusion (white arrows) in the right hippocampus due to recent seizure activity; **(F)** axial ASL perfusion: Marked hyperperfusion within the right hippocampus and medial temporal lobe due to recent seizure activity (yellow arrow).

On the other hand, ASL is limited by a low signal-to-noise ratio that results from the fact that labeled molecules in blood make up only 0.5–1.5% of the full static tissue signal, which can be improved by increasing total scan time. Additionally, absolute CBF quantification using ASL can be highly variable between patients due to differences in physiologic factors such as cardiovascular disease, age, sex, and hematocrit (Henriksen et al., 2013). Furthermore, a lack of standardization in postprocessing algorithms can result in variability in CBF measurements (Delgado et al., 2018). In order to develop a protocol for the widespread clinical use of ASL in the distinction between LGGs and HGGs, further standardization of absolute CBF quantification methods is warranted.

Of note, there are additional techniques that have emerged in more recent years that also can provide valuable information about glioma perfusion that are currently being explored as methods of improving the diagnostic accuracy of imaging. One such example is that of vessel architecture imaging (VAI) MRI, a technique that serves to describe the structural heterogeneity of microvasculature in the brain. VAI is used to examine differences in tumoral vasculature based on glioma type that helps in the distinction of LGG from HGG (Zhang et al., 2019).

Another technique that has been adopted in the imaging of gliomas is intravoxel incoherent motion (IVIM)- a technique that captures data on perfusion and diffusion of water molecules in brain tissue and associated capillary networks (Le Bihan et al., 1986; Shen et al., 2016; Togao et al., 2016; Zou et al., 2018). This sequence does not require the injection of exogenous contrast, and is utilized in certain studies to attempt to characterize glioma grade and IDH1 mutational status (Wang et al., 2019). Although these modalities are not used commonly in clinical practice, they may prove useful as adjuncts to the aforementioned MR perfusion techniques that are more widely used (DSC, DCE, and ASL).

MR Spectroscopy

MR spectroscopy (MRS) helps characterize the biochemical composition of regions of interest in the brain. This includes steady state concentrations of certain metabolites, metabolic reaction rates, and transport between cellular compartments. MRS provides insight into differences in biochemical composition between normal brain tissue and tumor. By tracking the presence of certain metabolites, such as choline (Cho), *N*-acetylaspartate (NAA), creatinine (Cr), lactate

(Lac), and myo-inositol (MI), MRS provides insight into cell membrane turnover (Cho), neuronal viability (NAA), normal cellular metabolism (Cr), tissue hypoxia (Lac), and astrocytic integrity (MI) (Herholz et al., 1992; Castillo et al., 2000; Gupta et al., 2000; Barker, 2001; Villanueva-Meyer et al., 2017). In the context of preoperative glioma assessment, Cho/NAA and Cho/Cr metabolite peaks exhibit a positive correlation with increasing tumor grade (**Figure 3**), and can be used to distinguish vasogenic edema from infiltrative edema (Fountas et al., 2004; Hourani et al., 2008; Villanueva-Meyer et al., 2017; Hu et al., 2020). Furthermore, emerging MRS technology allows for the detection of 2-hydroxyglutarate (2-HG), an oncometabolite that is produced by IDH mutant tumor cells serving as a non-invasive assessment of lesions where the diagnosis of LGG is uncertain (Choi et al., 2012). Histologically validated studies show that 2-HG detection through MRS can be used to distinguish IDH mutant from IDH wildtype glioma, albeit with variable sensitivity and specificity (Choi et al., 2016; Tietze et al., 2018). Limitations to this modality include the need for a relatively large lesion within a voxel, the lack of technical standardization in terms of acquisition techniques, and volume averaging (Burtscher et al., 2000; Villanueva-Meyer et al., 2017). Furthermore, low concentration of certain metabolites relative to water molecules makes detection of certain substances at clinical fields <3 T difficult, and can also lead to long acquisition times (Wu et al., 2016).

One novel MR technique that can also be used to investigate tissue metabolites is that of chemical exchange saturation transfer (CEST). CEST is capable of detecting a chemical compound of interest based on the exchange of magnetization between liable hydrogen protons of said compound and surrounding water molecules. This property allows for the detection of certain tissue metabolites with a higher spatial resolution than MRS (Hoefemann et al., 2021). In the case of glioma imaging, amide proton transfer (APT) CEST is the most common application of CEST, although not as widely available or commonly used as MRS. Elevated concentrations of proteins in glioma compared to surrounding tissues and the high rates of intracellular proton exchanges leads to an increased APT level. APT CEST can be used to differentiate between LGGs and HGGs (Choi et al., 2017), differentiation between regions of tumor and peritumoral edema (Wen et al., 2010), and is gaining interest as a method of investigating intratumoral heterogeneity (Warnert et al., 2021). One notable advantage of MRS over CEST is that MRS is able to simultaneously quantify multiple compounds, while CEST is only able to acquire one or two compounds at a time. Overlapping CEST effects from multiple metabolites also causes low specificity in CEST imaging for the measurement of specific tissue metabolites. The combination of CEST and MRS is currently being investigated, and may play a role in glioma imaging (Hoefemann et al., 2021).

Positron Emission Tomography as a Tool for Preoperative Planning

Positron emission tomography (PET) uses a variety of radio-labeled tracers to assess rates of cell proliferation, glucose metabolism, amino acid uptake, and membrane biosynthesis. This emerging clinical tool in the field of neuro-oncology thus provides valuable molecular, functional, and metabolic information about tumor biology. The most common molecular tracers utilized for PET imaging of gliomas include those that image glucose metabolism—2-^{18}F-fluoro-2-deoxy-D-glucose (^{18}F-FDG)—and those that image amino acid transport— O-(2-^{18}F-fluoroethyl)-L-tyrosine (^{18}F-FET), (S-^{11}C-methyl)-L-methionine (^{11}C-MET), and 3,4-dihydroxy-6-^{18}F-fluoro-L-phenylalanine (^{18}F-FDOPA) (Albert et al., 2016).

Positron emission tomography imaging with the glucose analog ^{18}F-FDG compares rates of cellular ^{18}F-FDG uptake in tumor cells relative to surrounding normal brain parenchyma. A high degree of ^{18}F-FDG PET uptake correlates with higher tumor grade and decreased survival (Padma et al., 2003). In the stage of primary tumor diagnosis, ^{18}F-FDG PET can also be used to distinguish between GBM and CNS lymphomas given markedly distinct rates of ^{18}F-FDG uptake between the two malignancies (Kosaka et al., 2008; Yamashita et al., 2013; Fink et al., 2015). However, there are significant limitations to the use of ^{18}F-FDG PET for glioma diagnosis. The high rate of glucose metabolism and ^{18}F-FDG uptake in normal brain cortex limits the diagnostic accuracy of ^{18}F-FDG PET (Albert et al., 2016). Moreover, this modality has limited specificity in distinguishing between gliomas, metastatic lesions, and even other non-neoplastic lesions like brain abscesses, neurosarcoidosis, and certain demyelinating CNS disorders (Omuro et al., 2006; Albert et al., 2016). Therefore, ^{18}F-FDG is not typically used in the presurgical planning period, instead amino acid PET tracers (AA PET) are preferred molecular tracers.

Tumor cells take up AA PET tracers at a higher rate than surrounding brain parenchyma; therefore, these tracers can provide greater tumor-to-background contrast than ^{18}F-FDG (Albert et al., 2016). Histology-validated series show that ^{18}F-FET, ^{11}C-MET, and ^{18}F-FDOPA are superior tracers to ^{18}F-FDG PET in delineating extent of glioma infiltration in both LGGs and HGGs. Of note, ^{18}F-FET is commonly used in the context of glioma characterization given that it has a high sensitivity in detection of WHO grade III and IV gliomas with the majority (>95%) of these tumors displaying high tracer uptake (Hutterer et al., 2013; Rapp et al., 2013; Jansen et al., 2015; Albert et al., 2016).

AA PET is also effective in visualizing tumor volumes that extend past areas of contrast enhancement on T1, and can also delineate tumor infiltration within non-specific areas of abnormal T2/FLAIR enhancement (Chen et al., 2006; Galldiks et al., 2006, 2011; Ledezma et al., 2009; Pafundi et al., 2013; Dunet et al., 2016). Furthermore, studies focused on examining intratumoral heterogeneity also show that AA PET is capable of identifying areas of higher cell proliferation within heterogenous glioma (Tanaka et al., 2009; Ewelt et al., 2011). AA PET thus could be used in the clinical setting to help optimize image-guided biopsy in the preoperative period by identifying areas of high cellularity and proliferation, and could also serve a role maximizing EOR by identifying areas

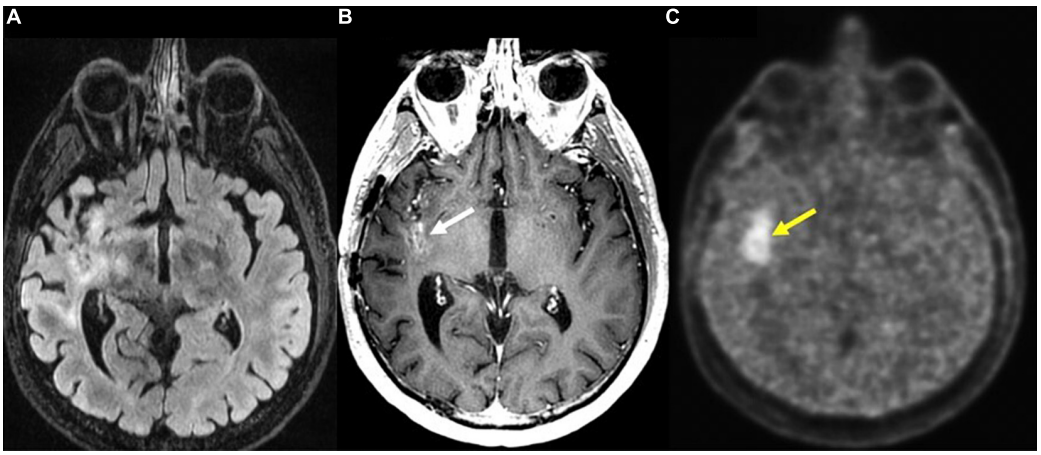

FIGURE 7 | Recurrent glioblastoma in right posterior insula (FMISO PET-MR). **(A)** Axial FLAIR: Ill-defined hyperintense area in the right posterior insula (black arrow); **(B)** axial T1 post-contrast: mild enhancement in the right posterior insula (white arrow); **(C)** axial ^{18}F-FMISO PET: avid uptake of FMISO tracer in the right posterior insular (yellow arrow). Biopsy targeted to this region showed recurrent glioblastoma. ^{18}F-FMISO, Fluoromisonidazole; PET, Positron emission tomography.

of infiltrating glioma not seen on anatomic MRI sequences (Ledezma et al., 2009).

PET can also be used as a tool for prognostication. Despite previously stated limitations of ^{18}F-FDG PET, this modality is reported to correlate with increased survival in patients with new GBM diagnosis (Albert et al., 2016; Sun et al., 2018). In the case of AA PET scans, earlier decrease in time-activity curves in dynamic (kinetic) ^{18}F-FET PET correlates with malignant transformation in the case of WHO grade II gliomas, and decreased overall survival in astrocytic HGGs (Jansen et al., 2015). Additionally, ^{18}F-fluoromisonidazole (^{18}F-FMISO), a PET imaging agent that selectively binds to hypoxic tissues, that is used to visualize degree of GBM tissue hypoxia also holds potential for prognostication (**Figure 7**). Given that higher pre-treatment ^{18}F-FMISO standardized uptake value peak (SUV_{peak}) is significantly associated with shorter OS (Gerstner et al., 2016).

Overall, PET is a powerful tool that has great clinical potential that is currently not commonly used in the preoperative planning period due to a lack of widespread utilization of AA PET in imaging centers, cost of use, and differences in methodology among studies investigating clinical use of PET (Albert et al., 2016).

ADJUNCTS TO ASSIST WITH INTRAOPERATIVE DECISION MAKING

Surgical planning through the use of the aforementioned MR modalities is essential for tumor characterization and localization. Gliomas can often involve brain structures that are critical for normal sensorimotor, visual, and cognitive function. Therefore, there must be a balance between resecting as much tumor as possible and preserving regions that are critical to optimize patient quality of life. In the following section, we describe MR and non-MR techniques that can help identify areas that are critical for neuronal function and thus guide preoperative and intraoperative decision making to maximize the safe resection of gliomas.

Diffusion Tensor Imaging

Diffusion tensor imaging (DTI) is a variant of DWI that also measures Brownian motion of water molecules but does so along a greater number of orthogonal planes. DTI can measure the directionality in diffusion of water molecules, a property that is particularly useful for the detection of large white matter tracts. The corticospinal tract, arcuate fasciculus, optic radiations, and fronto-occipital fasciculus are composed heavily myelinated axons that travel in parallel bundles, an architectural property that promotes the diffusion of water molecules along the direction of these white matter tracts (Cho and Jang, 2020). Furthermore, DTI calculates the metric of fractional anisotropy (FA), a numerical value based on the anisotropy of water molecules along axons that can provide insight into presence of intact myelinated white matter tracts (Le Bihan et al., 2001; Oh et al., 2005). For example, substantial decreases in FA are known to correlate with disruptions in white matter due to the presence of gliomas and peritumoral edema (Lu et al., 2004; Zolal et al., 2012; Fudaba et al., 2014).

The ability of DTI to delineate differences between subcortical white matter is useful during intra-operative navigation for identifying white matter fiber tracts and for defining the proximity to these anatomical tracts at the tumor resection margins (**Figures 8–12**; Berman et al., 2007; Zolal et al., 2012). One randomized controlled trial (RCT) comparing outcomes with and without preoperative DTI in 214 diffuse glioma patients with pyramidal tract involvement demonstrated that the use of DTI-based neuronavigation intraoperatively can help maximize safe rates of gross total resection (GTR) and improve outcomes for patients with low- and high-grade gliomas involving the pyramidal tract with significant post-operative functional benefits (Wu et al., 2007; Verburg and de Witt Hamer, 2021).

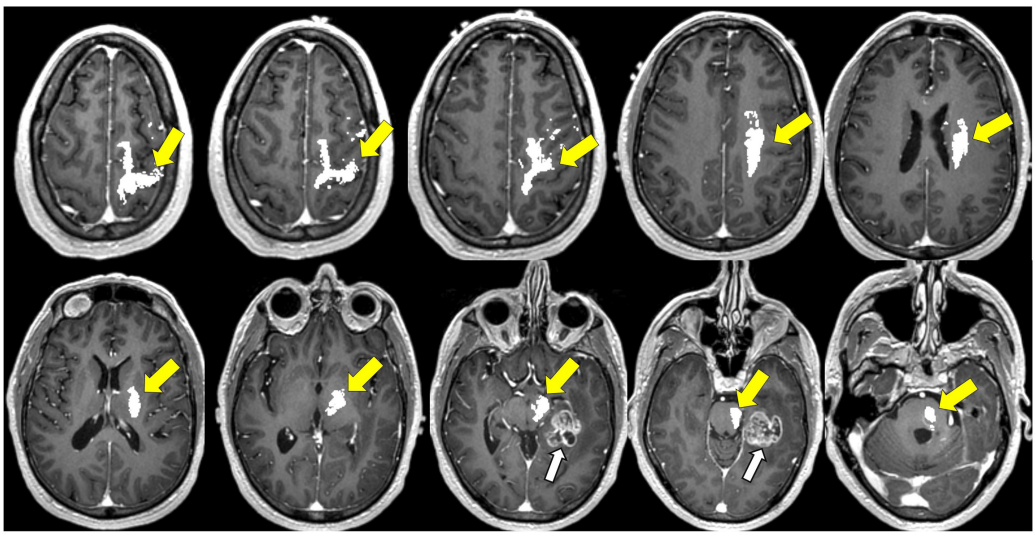

FIGURE 8 | Tractography corticospinal tract. Corticospinal tractography (yellow arrows) spanning from the superior motor cortex to pons overlaid on axial T1 post-contrast images showing enhancing necrotic glioblastoma (white arrows) in the left posterior parahippocampal gyrus.

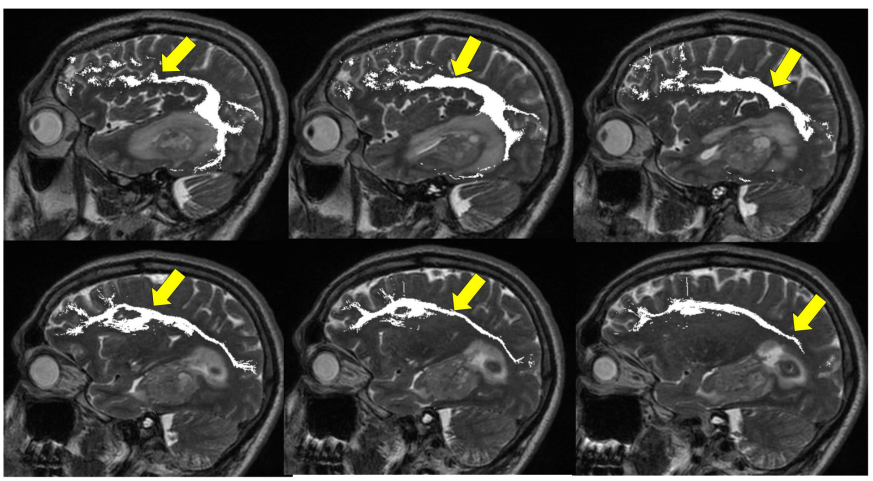

FIGURE 9 | Tractography: arcuate fasciculus. Arcuate fasciculus tractography (yellow arrows) overlaid on sagittal T2 images.

There are several limitations to this imaging modality when using it intra-operatively to assist with tumor resections. First, there can be great variability of tracking algorithm settings that can lead to white matter tract overestimation. Second, this modality can be user-dependent depending on region-of-interest placement (Verburg and de Witt Hamer, 2021).

One additional significant limitation of the use of DTI (and of any imaging modality where a preoperatively generated image is used for intraoperative neuronavigation) lies in the phenomenon of "brain shift" where the brain shifts intraoperatively away from the dural edge, and the spatial relationship of the brain is altered compared to the pre-operative images (Kuhnt et al., 2012). Glioma tumor volume has a significant correlation with brain shift, with one study reporting shift relative to preoperative imaging as high as 14.3 mm (Reinges et al., 2004). There is further evidence to suggest that length of surgery, craniotomy size, and supratentorial location correlate with greater brain shift (Reinges et al., 2004; Reinertsen et al., 2014). Intraoperative MRI (iMRI) has can be employed as a supplement to DTI and functional imaging as a method of compensating for brain shift and assessing the degree of tumor resection. Multiple studies show that this method increases EOR in glioma surgery with no significant increase in new postoperative deficits (Senft et al., 2011; Kuhnt et al., 2012).

Functional MRI

Functional MRI (fMRI) can be used to visualize neuronal activity by measuring the ratio of deoxyhemoglobin to oxyhemoglobin to generate a blood oxygen level dependent (BOLD) signal

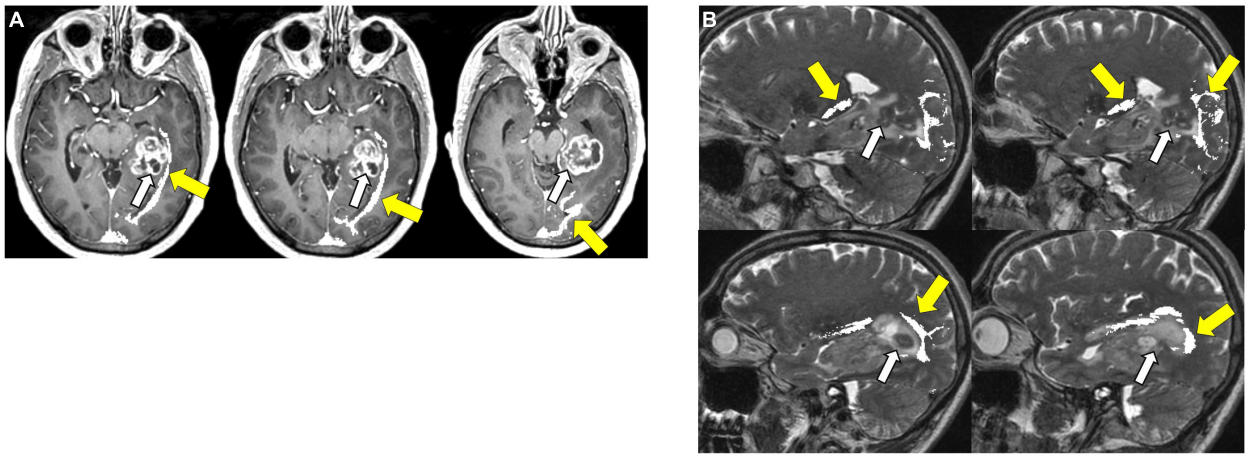

FIGURE 10 | Tractography: optic radiations. **(A)** Optic radiation tractography (yellow arrows) overlaid on axial T1 post-contrast images showing enhancing necrotic glioblastoma (white arrows) centered in the left posterior parahippocampal gyrus; **(B)** optic radiation tractography (yellow arrows) overlaid on sagittal T2 images.

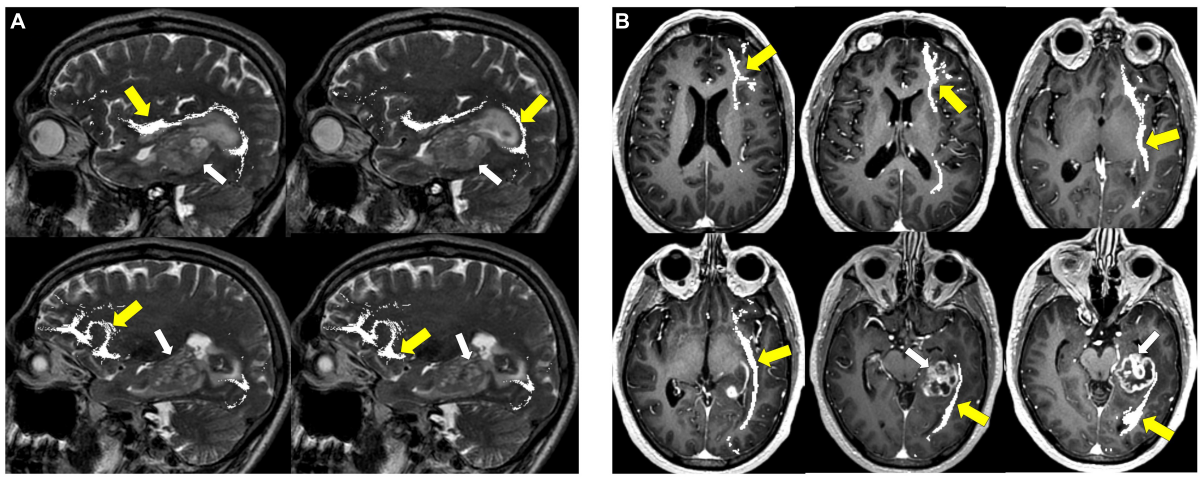

FIGURE 11 | Tractography: inferior fronto-occipital fasciculus. **(A)** Inferior fronto-occipital fasciculus tractography (yellow arrows) overlaid on sagittal T2 images. Left temporal glioblastoma (white arrows) is adjacent to but does not invade the tract. **(B)** Inferior fronto-occipital fasciculus tractography (yellow arrows) overlaid on axial T1 post-contrast images. Left temporal glioblastoma (white arrows) is adjacent to but does not invade the tract.

that allows for the spatiotemporal mapping of neuronal activity during periods of rest or cognitive tasks (Buchbinder, 2016). BOLD signal is determined by changes in the magnetic field surrounding red blood cells that depends on the state of oxygenation of hemoglobin. Oxyhemoglobin is diamagnetic and has a similar magnetic field relative to surrounding brain tissue. On the other hand, deoxyhemoglobin- which is at a higher concentration in brain tissue of high neuronal activity- is paramagnetic and forms local endogenous magnetic field gradients with strength that is dependent on deoxyhemoglobin concentration. These magnetic field gradients can be detected on T2 and T2* sequences (Thulborn et al., 1982; Ogawa et al., 1993). fMRI can be used in presurgical functional brain mapping, particularly when localizing areas of motor function (Krings et al., 2002; Bush et al., 2017).

Despite its utility in preoperative planning, a variety of challenges arise with the use of fMRI for glioma resection. First, vascular changes in HGGs can lead to neurovascular decoupling and BOLD signal loss that may not actually be reflective of absence of neuronal function, thus resulting in false negative fMRI signal loss (Fujiwara et al., 2004). Given this vulnerability of fMRI signal to microstructural alterations, task-based fMRI is reported to be more reliable in LGGs than HGGs (Castellano et al., 2017). Another limitation is that, compared to direct electrical stimulation (DES), fMRI is significantly limited in mapping the functional connectivity of language areas with sensitivity and specificity of 91 and 64% for identification of Broca's area and 93 and 18% for identification of Wernicke's area (Hervey-Jumper and Berger, 2016). Moreover, there is considerable variability between studies in the reported

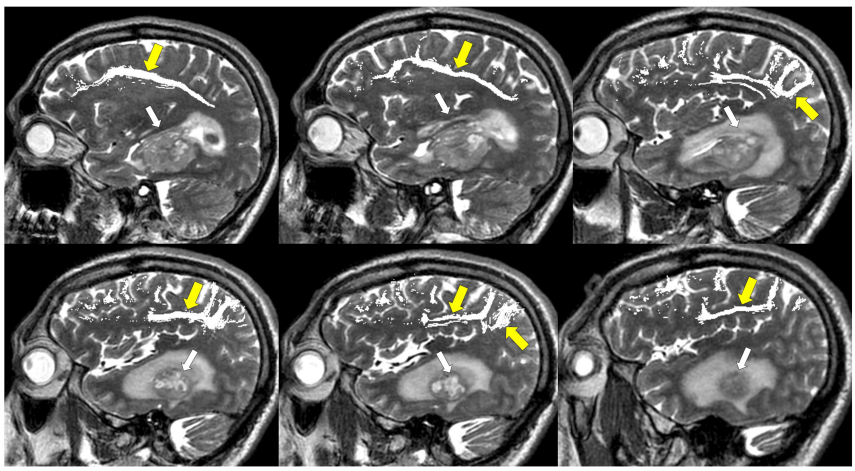

FIGURE 12 | Tractography: superior longitudinal fasciculus. Sagittal T2-weighted images show glioblastoma centered in the hippocampus and parahippocampal gyrus (white arrows). Overlay of tractography of superior longitudinal fasciculus (yellow arrows) demonstrates sparing of the tract by the tumor.

sensitivity and specificity for language mapping, a factor that can be attributed to differences in language paradigms investigated, a lack of standardization of distance thresholds when utilizing DES to confirm fMRI accuracy, and glioma grade heterogeneity (Morrison et al., 2016; Ellis et al., 2020).

Another important factor to consider when utilizing fMRI for clinical decision making is that sub-regions of functional areas are activated depending on a specific task, and while fMRI mapping suggests that certain areas are involved in particular tasks, it does not indicate whether said areas are necessary for function (Haller and Bartsch, 2009). Thus, surgical sparing of certain functional areas based on fMRI can often times preclude what may be a safe resection (Southwell et al., 2018). Therefore, while fMRI can be an adjunct for assessing surgical risk of tumor resection preoperatively, DES remains the gold standard for determining the location of function intraoperatively (Haller and Bartsch, 2009; Borchers et al., 2011; De Witt Hamer et al., 2012; Desmurget and Sirigu, 2015; Weiss Lucas et al., 2020).

Magnetoencephalography

Magnetoencephalography (MEG) detects magnetic fields that are generated by electrical currents from neuronal action potentials. MEG can be registered with a 3D MRI sequence to visualize functional neuronal activity with high spatiotemporal resolution- a spatial resolution of a few millimeters and a temporal resolution in milliseconds (Naeije et al., 2016). In addition to providing information regarding task-based neuronal activity, MEG is able to identify regions of high functional connectivity (HFC) and low functional connectivity (LFC) (Verburg and de Witt Hamer, 2021). This serves as a useful method of preoperatively evaluating function of tumoral and peritumoral brain tissue for surgical planning, particularly for preoperative somatosensory and motor mapping for which there are multiple validation studies (Yang et al., 1993; Schiffbauer et al., 2003; Lin et al., 2006; Nagarajan et al., 2008; Lee et al., 2020). Furthermore, MEG connectivity maps can reliably identify areas lacking in eloquent cortex, for LFC there is reportedly a negative predictive value of 100% for the presence of eloquent cortex during intraoperative DES (Martino et al., 2011). Therefore, MEG can detect areas near functional cortex that are amenable to resection while minimizing neurological deficits (Guggisberg et al., 2008).

Additionally, there is evidence to suggest that MEG may serve as an important supplement to DES during tumor resection in areas involving language processing. One study using MEG mapping to aid in LGG and HGG tumor resection found that surgical resection of HFC sites with negative response to intraoperative DES correlated with early transient postoperative functional decline in language processing that resolved within 3 months in patients who did not experience additional neurological insult such as stroke or early tumor progression. Although limited by a small sample size, these findings suggest that MEG can serve as a predictor of early transient decline in language processing following glioma resection (Lee et al., 2020). This modality is limited by cost, given that liquid helium is required to maintain the superconducting equipment of MEG machines, and availability is considerably limited (Hervey-Jumper and Berger, 2016).

The reliability of MEG in relation to fMRI as a method of functional mapping is an active area of research. One ongoing clinical trial reports that MEG has a higher specificity for motor and language mapping but a lower sensitivity for motor mapping than fMRI. Furthermore, this study reports that using MEG and fMRI in combination could potentially serve to increase the accuracy of motor mapping relative to the use of MEG and fMRI separately. While published data for this study has a low sample size, ongoing data collection may provide further insights into the clinical utility of combining MEG and fMRI (Ellis et al., 2020).

Navigated Transcranial Magnetic Simulation

Navigated transcranial magnetic stimulation (nTMS) is a technique that utilizes a wound copper coil to generate strong

magnetic pulses targeting a specific area of the brain. This coil is paired with a stereotactic image-guided system to generate highly accurate functional maps capable of differentiating eloquent from non-eloquent tissue through non-invasive stimulation and inhibition of specific cortical areas (Bush et al., 2017). nTMS is well-suited for preoperative identification of eloquent motor cortex, with a reported accuracy of nTMS for generating a functional motor map in relation to the gold standard, DES, of 99.7% (Picht, 2014). Importantly, the high accuracy of nTMS for generating a functional motor map is reported to be consistent between different examiners in the clinical setting (Picht et al., 2009; Forster et al., 2011; Krieg et al., 2012; Paiva et al., 2012; Tarapore et al., 2012; Picht, 2014; Haddad et al., 2020). In practice, nTMS influences preoperative plans for tumor resection by confirming or negating suspected involvement of primary motor cortex by the tumor, often leading to improved surgical outcomes for tumors involved with motor pathways (Frey et al., 2014; Picht, 2014; Picht et al., 2016). Furthermore, nTMS can be utilized to enhance accuracy of white matter tractography when used in conjunction with DTI. This technique can help diminish intraoperative injury in patients whose white matter tracts are closely involved with tumor, especially there are significant signal alterations in DTI due to peritumoral edema and vascular changes (Weiss et al., 2015). There is an abundance of clinical evidence to support favorable clinical outcome in patients receiving preoperative nTMS for resection of lesions involving motor cortex including greater improvement in postoperative motor function, lower rates of postoperative motor decline, and increased GTR (Krieg et al., 2014; Raffa et al., 2019). Therefore, employing nTMS for surgical planning in cases where gliomas involve motor cortex is an important consideration.

Language mapping is more challenging with this technology and usually relies on navigated repetitive TMS (nrTMS), which utilizes repetitive bursts of TMS and is better-suited for functional language mapping than the single pulses utilized for nTMS (Haddad et al., 2020). Similar to other functional mapping techniques, nrTMS has great variability in reported sensitivity and specificity for language mapping between studies (Picht et al., 2013; Tarapore et al., 2013). There are studies to suggest that combination of functional modalities such as fMRI or DTI with nrTMS may lead to improved functional mapping and clinical outcomes, but further investigation is needed to make these practices commonplace in the clinical setting (Ille et al., 2015; Könönen et al., 2015; Sollmann et al., 2018).

IMAGING FOR MONITORING TREATMENT RESPONSE AND TUMOR RECURRENCE

Despite the aggressive standard of care, nearly all diffuse gliomas eventually recur and postoperative surveillance imaging is critical to identify tumor recurrence as early as possible to provide treatment that can help slow down the rate of disease progression (Stupp et al., 2005, 2014; Le Rhun et al., 2016). There are several studies that show high rates of recurrence among LGGs within the 5 year postoperative period despite gross total tumor resection (Soffietti et al., 1998; Shaw et al., 2008; Chaichana et al., 2010). Early diagnosis of tumor recurrence in LGGs is critical to diminish chances of malignant transformation of recurrent LGGs (Duffau and Taillandier, 2015; Le Rhun et al., 2016). In the case of GBM, tumor recurrence is inevitable and can be difficult to manage. Common practice to attempt to manage recurrent GBM is the use of antiangiogenic agents (i.e., bevacizumab), nitrosourea alkylating agents, and/or repeat tumor resection (Wick et al., 2010; Batchelor et al., 2013; Johnson et al., 2013).

Postoperative surveillance for tumor recurrence and treatment-related changes is an ongoing challenge given that imaging characteristics of glioma recurrence and gliosis or treatment effect are similar in appearance on T1 and T2 sequences (Albert et al., 2016). Hyperintense signal on T1 post-contrast imaging within the resection cavity in the postoperative period is concerning for tumor recurrence, but can also be representative of ischemic brain tissue as well as devitalized tumor (Winter et al., 2020). Furthermore, inflammatory processes following chemoradiation can lead to a transient edematous process that can mimic signs of tumor recurrence in both HGG and LGG patients for several months after therapy. This process is often mistaken for tumor progression but does not represent true tumor recurrence and is thus termed pseudoprogression (**Figure 13**; Winter et al., 2020; Li et al., 2021).

Response Assessment in Neuro-Oncology Criteria for Differentiating Tumor Recurrence From Pseudoprogression

In an effort to distinguish tumor progression and pseudoprogression on imaging, the updated Response Assessment in Neuro-Oncology (RANO) criteria were developed in 2010. The RANO criteria state that tumor progression taking place during the 12 week period following the completion of radiotherapy can only be identified through imaging if new tumor enhancement arises outside of the radiation field (Wen et al., 2021). Clues to true progression cited in other articles include increased T2/FLAIR signal extending past the radiation field as well as involvement of the corpus callosum, signal that crosses midline, and subependymal involvement (Mullins et al., 2005; Abel et al., 2012; Strauss et al., 2019). Serial imaging over time can attempt to distinguish pseudoprogression from true tumor recurrence. Pseudoprogression on serial imaging is characterized by loss of post-contrast enhancement signal or volume over time (Li J. et al., 2020). However, this can be flawed as post-treatment effects slowly enlarge, usually over the span of the first 3–6 months after postoperative radiation therapy, and require many serial scans before finally regressing (**Figure 13**). The fact that the definitive distinction between pseudoprogression and tumor progression usually takes months, there is a risk that patients are under- or over-treated (Ellingson et al., 2017b). Obtaining early post-operative MRI scans (i.e., within 48 h of surgery) is critical for differentiating between pseudoprogression and true progression to avoid postsurgical confounders, such as tissue ischemia, that may alter signal intensity or enhancement on subsequent MRI scans. However, in

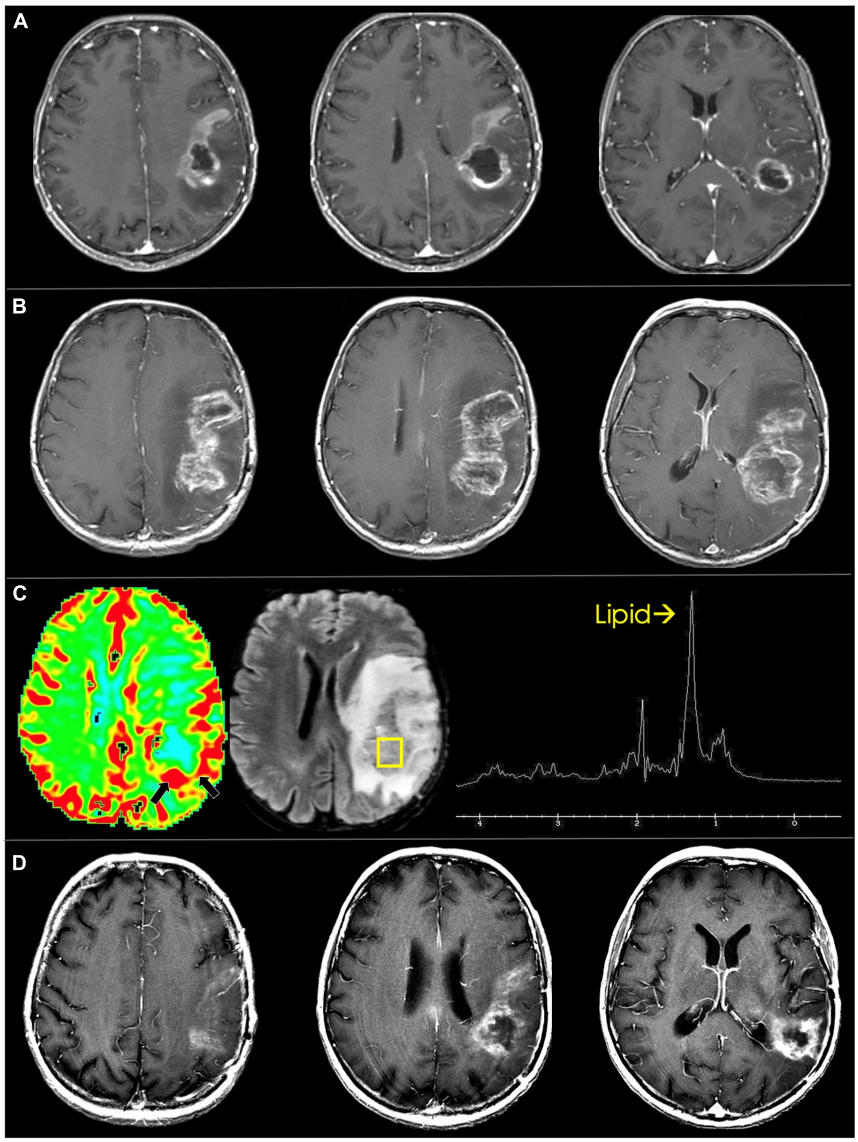

FIGURE 13 | Pseudoprogression in glioblastoma. **(A)** Immediate pre-radiotherapy: axial T1 post-contrast images show rim enhancing and centrally necrotic left frontoparietal glioblastoma. **(B)** Eight-week follow up: Immediate post-radiotherapy axial T1 post-contrast images show marked increase in enhancement and necrosis. **(C)** Dynamic susceptibility-weighted contrast-enhanced perfusion MRI shows mild increase in blood volume along the posterior rim (black arrows). Single voxel proton spectroscopy targeted to the posterior component shows markedly increased lipid peak suggesting tissue necrosis. **(D)** Three-months follow up: axial T1 post-contrast images show marked decrease in enhancement and necrosis of the treated glioblastoma.

most studies the sensitivity and specificity of anatomic (T1 and T2 weighted) MR sequences for detection of HGG progression are only 68 and 77%, respectively. Therefore, additional imaging modalities, like MR perfusion imaging, DWI and MRS, can be employed to aid in the diagnosis (van Dijken et al., 2017).

Advanced MR Sequences for Monitoring Tumor Recurrence

MR perfusion imaging is widely used to aid in distinguishing between recurrence and treatment effect as recurrent HGG exhibits higher rCBV values relative to post-treatment radiation effects (Sadeghi et al., 2008; Schmainda, 2012; Choi et al., 2013; Patel P. et al., 2017). DWI also plays a role in differentiating recurrent glioma from radiation treatment effects given that cell density is high in recurrent glioma tumors and low in areas of treatment changes. This translates to smaller ADC values in true glioma recurrence groups relative to pseudoprogression and post-radiation changes groups (Li C. et al., 2020). MRS can also be used to differentiate glioma from treatment effects. Particularly for HGGs, MRS shows an elevated Cho/Cr ratio in areas of tumor recurrence compared to areas of radiation-induced necrosis or treatment effect. There are also reported differences in Cho/NAA ratios between recurrent tumor and

areas of radiation-induced necrosis (Chuang et al., 2016). Despite these imaging modalities being more effective than anatomic MRI in helping distinguish between pseudoprogression, treatment effect, and true progression, their accuracy and efficacy is limited and often surgical biopsy with histopathological analysis is needed to confirm the diagnosis (Li et al., 2021).

Positron Emission Tomography Imaging for Monitoring Tumor Recurrence

Positron emission tomography also plays a role in the postoperative surveillance. Given that there is evidence to suggest that reduction in amino acid uptake is indicative of treatment response (Sun et al., 2018), there is interest in the use of AA PET as a method of facilitating the distinction between glioma recurrence and pseudoprogression (Galldiks et al., 2006; Jansen et al., 2013). Furthermore, ^{18}F-FET PET can be used to identify pseudoprogression within the first 3 months following chemoradiation therapy with an accuracy of 96% (Galldiks et al., 2015). Regarding the distinction between glioma recurrence and treatment-related changes there is evidence to suggest that the diagnostic accuracy of 11C-MET PET and ^{18}F-FET PET for differentiating recurrence from treatment-related changes is high with a sensitivity and specificity of 91 and 100% for both tracers (Grosu et al., 2011; Cui et al., 2021). Furthermore, a lower tumor-to-normal-uptake (T/N) ratio during AA PET analysis is associated with lower recurrence and longer OS (Galldiks et al., 2015; Patel P. et al., 2017; Deuschl et al., 2018). The use of ^{18}F-FDG for detection of tumor recurrence remains controversial, similar to its use at the time of diagnosis, but its wide availability warrants further investigation to attempt to optimize its clinical use (Wang et al., 2015).

IMAGING TO ASSESS FOR PSEUDORESPONSE FOLLOWING IMMUNOTHERAPY

Pseudoresponse refers to a decrease in contrast extravasation due to diminished leakiness of the BBB, resulting in markedly diminished CE on T1 post-contrast imaging. This is a finding that develops following treatment with antiangiogenic agents such as bevacizumab. Patients with GBM recurrence receiving bevacizumab immunotherapy. Anti-VEGF-A properties of bevacizumab often lead to a substantial, rapid radiologic response of contrast enhancement reduction and decreased edema just days after treatment; however, current evidence indicates that bevacizumab does not confer a benefit in OS (Norden et al., 2008). This is likely due to tumor adaptation to antiangiogenic therapy resulting in a hypoxic NCE invasive tumor phenotype that is capable of surviving despite decreased vascular proliferation. A return to CE from this period of NCE is associated with particularly poor outcome (Iwamoto et al., 2009; Galanis et al., 2012; Kim et al., 2015; Wick et al., 2016); therefore, an active area of investigation is geared toward developing a generalizable protocol for the identification of pseudoresponse in GBM.

Response Assessment in Neuro-Oncology Criteria for Assessing Pseudoresponse

The updated RANO criteria recommend the use of T2/FLAIR to assess for pseudoresponse, defined by the RANO criteria as an area of >50% reduction in CE without a significant decrease in the presence of NCE on T2/FLAIR. The RANO criteria provide an essential framework for the standardization of glioma surveillance following antiangiogenic therapy. Despite the existence of studies suggesting that DWI, MRS, and PET scans may play a valuable role in the identification of pseudoprogression, general experience with the use of these modalities for this purpose remains limited, and standardization of postoperative surveillance through incorporation of these modalities to the RANO criteria is an ongoing challenge (Boxerman et al., 2018).

One area of active investigation that shows how findings from the RANO group are being expanded upon is shown through immunotherapy response assessment in neuro-oncology (iRANO) criteria. iRANO integrates the framework of response assessment that the RANO group established for workup of LGG and HGG to establish guidelines for interpreting initial progressive imaging findings in patients with LGGs and HGGs on immunotherapy with goals of optimizing immunotherapy regimens (Okada et al., 2015). There may be a role in the incorporation of iRANO criteria in the context of pseudoresponse as these criteria continue to be refined and updated.

Positron Emission Tomography as a Tool for Assessing Pseudoresponse

Positron emission tomography also plays a role in differentiating pseudoresponse from treatment response in patients with GBM recurrence receiving bevacizumab immunotherapy. Anti-VEGF-A properties of bevacizumab often lead to a substantial, rapid radiologic response of contrast enhancement reduction and decreased edema just days after treatment; however, current evidence indicates that bevacizumab does not confer a benefit in OS (Norden et al., 2008). A large fraction of patients that originally exhibit radiological response eventually develop disease progression that can be tracked by increases in T2/FLAIR signal hyperintensities; however, objective measures of T2 FLAIR changes are challenging employ reliably (Boxerman et al., 2018). AA PET has been reported as a potentially viable adjunct in analyzing pseudoresponse. As a prognostication tool in the context of pseudoresponse, AA PET shows promise with existing evidence showing that persistent ^{18}FET-PET signal on NCE tumor during bevacizumab treatment is predictive of a significant decrease in OS (Wirsching et al., 2021).

EMERGENCE OF RADIOMICS

Radiomics is the practice of extracting and analyzing quantitative information from diagnostic images in a manner that can track subtleties in tumor characteristics and complex patterns

that are difficult to recognize by the human eye to produce prognostically important information such as treatment response vs. the likelihood of tumor progression and survival estimates (Mayerhoefer et al., 2020). Additionally, radiomics may be a method of characterizing heterogeneity throughout the entire tumor volume, compared to tumor biopsies that only capture heterogeneity within a specific, local region (Mayerhoefer et al., 2020). While detailing all of the different radiomics methodologies that can be employed to study tumor composition is beyond the scope of this review (Hu et al., 2020; Mayerhoefer et al., 2020), there are existing radiomics methods that have been employed to study intratumoral characteristics in the context of GBM. One example lies in one study where image-guided regional biopsies of GBM were collected, regional GBM driver genes were identified, and biopsy sites were co-registered with MRI and texture maps to match genetic regional status with specific imaging measurements (Hu et al., 2017). Machine learning algorithms were then employed to identify MRI signatures at the voxel level that correlated with GBM driver gene status within different regions of GBM tumor (Hu et al., 2017). This type of technique can thus serve to produce an imaging algorithm that can potentially capture tumoral molecular markers based on stereotyped imaging patterns.

Radiomics and Recurrence

One example of an integrated radiomics model for discriminating tumor recurrence from radiation necrosis in glioma patients has recently been developed by Wang et al. (2020). This model was developed in a primary cohort of 112 patients with pathologically confirmed gliomas and was validated by a cohort of 48 additional glioma patients. ^{18}F-FET PET and ^{11}C-MET PET along with individualized patient data and characteristics were utilized to generate a model predicting tumor recurrence. The integrated model consisted of 15 features that were identified as significant predictors of recurrence ($p < 0.001$) including variables like mean tumor-background ratio (TBR) of ^{18}F-FET, maximum TBR of ^{11}C-MET and patient age as well as a radiomics signature, was found to be highly predictive of recurrent glioma and accurate across both test and validation cohorts (Wang et al., 2020). More work will be needed to confirm radiomics based models are generalizable across different institutions with different scaling parameters, but this is an exciting emerging field that is advancing understanding of glioma behavior and developing valuable prognostic information in a non-invasive manner. Although there are still significant strides that remain to be made before broad clinical applications of emerging radiomics models, these are important initial steps in advancing individualized patient care for management of gliomas.

CONCLUSION

MR and PET scans have revolutionized the management of glioma patients. Upon diagnosis of intra-axial brain tumor, it is standard of care to obtain T1, T2/FLAIR, DWI, and susceptibility images to guide preoperative planning. Increasingly, this practice is being enhanced further through the use of advanced imaging modalities such as MR perfusion, diffusion, and spectroscopy and PET scans. Moreover, surgical resections are assisted by functional imaging assessments and intra-operative use of anatomical images and neuronavigation to maximize the safety of glioma resection. The monitoring of tumors during treatment through serial imaging is of great importance, but can be challenging, as distinguishing between treatment response and progression is often difficult. In the future it will be important to standardize the use of sequences like MR perfusion, diffusion, and spectroscopy and PET scans for postoperative tumor surveillance as they can dramatically improve interpretation of the underlying biologic process. Lastly, radiomics is emerging as an exciting big data tool for quantifying the information provided in the images and thereby potentially improving precision and accuracy, however the generalizability and role for radiomics for the management of gliomas is still unanswered.

AUTHOR CONTRIBUTIONS

All authors contributed to the manuscript and approved the final version of the manuscript.

FUNDING

JY was supported by the NREF Research Fellowship Grant.

REFERENCES

Abel, R., Jones, J., Mandelin, P., Cen, S., and Pagnini, P. (2012). Distinguishing pseudoprogression from true progression by FLAIR volumetric characteristics compared to 45 Gy isodose volumes in treated glioblastoma patients. *Int. J. Radiat. Oncol.* 84:S275. doi: 10.1016/j.ijrobp.2012.07.716

Albert, N. L., Weller, M., Suchorska, B., Galldiks, N., Soffietti, R., Kim, M. M., et al. (2016). Response assessment in neuro-oncology working group and european association for neuro-oncology recommendations for the clinical use of PET imaging in gliomas. *Neuro-Oncology* 18, 1199–1208. doi: 10.1093/neuonc/now058

Baehring, J. M., Bi, W. L., Bannykh, S., Piepmeier, J. M., and Fulbright, R. K. (2007). Diffusion MRI in the early diagnosis of malignant glioma. *J. Neurooncol.* 82, 221–225. doi: 10.1007/s11060-006-9273-3

Barajas, R. F., Hess, C. P., Phillips, J. J., Von Morze, C. J., Yu, J. P., Chang, S. M., et al. (2013). Super-Resolution track density imaging of glioblastoma: histopathologic correlation. *Am. J. Neuroradiol.* 34, 1319–1325. doi: 10.3174/ajnr.A3400

Barajas, R. F., Phillips, J. J., Parvataneni, R., Molinaro, A., Essock-Burns, E., Bourne, G., et al. (2012). Regional variation in histopathologic features of tumor specimens from treatment-naive glioblastoma correlates with anatomic and physiologic MR Imaging. *Neuro-Oncology* 14, 942–954. doi: 10.1093/neuonc/nos128

Barker, P. B. (2001). N-acetyl aspartate–a neuronal marker? *Ann. Neurol.* 49, 423–424.

Batchelor, T. T., Mulholland, P., Neyns, B., Nabors, L. B., Campone, M., Wick, A., et al. (2013). Phase III randomized trial comparing the efficacy of cediranib as monotherapy, and in combination with lomustine, versus lomustine alone in patients with recurrent glioblastoma. *J. Clin. Oncol.* 31, 3212–3218. doi: 10.1200/JCO.2012.47.2464

Berman, J. I., Berger, M. S., Chung, S., Nagarajan, S. S., and Henry, R. G. (2007). Accuracy of diffusion tensor magnetic resonance imaging tractography assessed

using intraoperative subcortical stimulation mapping and magnetic source imaging. *J. Neurosurg.* 107, 488–494. doi: 10.3171/JNS-07/09/0488

Bleeker, E. J. W., van Osch, M. J. P., Connelly, A., van Buchem, M. A., Webb, A. G., and Calamante, F. (2011). New criterion to aid manual and automatic selection of the arterial input function in dynamic susceptibility contrast MRI: new criterion for arterial input function selection. *Magn. Reson. Med.* 65, 448–456. doi: 10.1002/mrm.22599

Borchers, S., Himmelbach, M., Logothetis, N., and Karnath, H. O. (2011). Direct electrical stimulation of human cortex - the gold standard for mapping brain functions? *Nat. Rev. Neurosci.* 13, 63–70. doi: 10.1038/nrn3140

Boxerman, J. L., Zhang, Z., Safriel, Y., Rogg, J. M., Wolf, R. L., Mohan, S., et al. (2018). Prognostic value of contrast enhancement and FLAIR for survival in newly diagnosed glioblastoma treated with and without bevacizumab: results from ACRIN 6686. *Neuro-Oncology* 20, 1400–1410. doi: 10.1093/neuonc/noy049

Broen, M. P. G., Smits, M., Wijnenga, M. M. J., Dubbink, H. J., Anten, M. H. M. E., Schijns, O. E. M. G., et al. (2018). The T2-FLAIR mismatch sign as an imaging marker for non-enhancing IDH-mutant, 1p/19q-intact lower-grade glioma: a validation study. *Neuro-Oncol.* 20, 1393–1399. doi: 10.1093/neuonc/noy048

Buchbinder, B. R. (2016). Functional magnetic resonance imaging. *Handb. Clin. Neurol.* 135, 61–92. doi: 10.1016/B978-0-444-53485-9.00004-0

Burtscher, I. M., Skagerberg, G., Geijer, B., Englund, E., Ståhlberg, F., and Holtås, S. (2000). Proton MR spectroscopy and preoperative diagnostic accuracy: an evaluation of intracranial mass lesions characterized by stereotactic biopsy findings. *AJNR Am. J. Neuroradiol.* 21, 84–93.

Bush, N. A. O., Chang, S. M., and Berger, M. S. (2017). Current and future strategies for treatment of glioma. *Neurosurg. Rev.* 40, 1–14. doi: 10.1007/s10143-016-0709-8

Castellano, A., Cirillo, S., Bello, L., Riva, M., and Falini, A. (2017). Functional MRI for surgery of gliomas. *Curr. Treat Options Neurol.* 19, 34. doi: 10.1007/s11940-017-0469-y

Castillo, M., Smith, J. K., and Kwock, L. (2000). Correlation of myo-inositol levels and grading of cerebral astrocytomas. *AJNR Am. J. Neuroradiol.* 21, 1645–1649.

Cebeci, H., Aydin, O., Ozturk-Isik, E., Gumus, C., Inecikli, F., Bekar, A., et al. (2014). Assesment of perfusion in glial tumors with arterial spin labeling; comparison with dynamic susceptibility contrast method. *Eur. J. Radiol.* 83, 1914–1919. doi: 10.1016/j.ejrad.2014.07.002

Chaichana, K. L., McGirt, M. J., Laterra, J., Olivi, A., and Quiñones-Hinojosa, A. (2010). Recurrence and malignant degeneration after resection of adult hemispheric low-grade gliomas. *J. Neurosurg.* 112, 10–17. doi: 10.3171/2008.10.JNS08608

Chaskis, C., Neyns, B., Michotte, A., De Ridder, M., and Everaert, H. (2009). Pseudoprogression after radiotherapy with concurrent temozolomide for high-grade glioma: clinical observations and working recommendations. *Surg. Neurol.* 72, 423–428. doi: 10.1016/j.surneu.2008.09.023

Chen, W., Silverman, D. H. S., Delaloye, S., Czernin, J., Kamdar, N., Pope, W., et al. (2006). 18F-FDOPA PET imaging of brain tumors: comparison study with 18F-FDG PET and evaluation of diagnostic accuracy. *J. Nucl. Med. Off. Publ. Soc. Nucl. Med.* 47, 904–911.

Cho, M. K., and Jang, S. H. (2020). Diffusion tensor imaging studies on spontaneous subarachnoid hemorrhage-related brain injury: a mini-review. *Front. Neurol.* 11:283. doi: 10.3389/fneur.2020.00283

Choi, C., Ganji, S. K., DeBerardinis, R. J., Hatanpaa, K. J., Rakheja, D., Kovacs, Z., et al. (2012). 2-hydroxyglutarate detection by magnetic resonance spectroscopy in IDH-mutated patients with gliomas. *Nat. Med.* 18, 624–629. doi: 10.1038/nm.2682

Choi, C., Raisanen, J. M., Ganji, S. K., Zhang, S., McNeil, S. S., An, Z., et al. (2016). Prospective longitudinal analysis of 2-Hydroxyglutarate magnetic resonance spectroscopy identifies broad clinical utility for the management of patients with IDH-Mutant glioma. *J. Clin. Oncol.* 34, 4030–4039. doi: 10.1200/JCO.2016.67.1222

Choi, Y. J., Kim, H. S., Jahng, G. H., Kim, S. J., and Suh, D. C. (2013). Pseudoprogression in patients with glioblastoma: added value of arterial spin labeling to dynamic susceptibility contrast perfusion MR imaging. *Acta Radiol Stockh Swed.* 54, 448–454. doi: 10.1177/0284185112474916

Choi, Y. S., Ahn, S. S., Lee, S. K., Chang, J. H., Kang, S. G., Kim, S. H., et al. (2017). Amide proton transfer imaging to discriminate between low- and high-grade gliomas: added value to apparent diffusion coefficient and relative cerebral blood volume. *Eur. Radiol.* 27, 3181–3189. doi: 10.1007/s00330-017-4732-0

Chuang, M. T., Liu, Y. S., Tsai, Y. S., Chen, Y. C., and Wang, C. K. (2016). Differentiating radiation-induced necrosis from recurrent brain tumor using MR perfusion and spectroscopy: a meta-analysis. *PLoS One* 11:e0141438. doi: 10.1371/journal.pone.0141438

Cui, M., Zorrilla-Veloz, R. I., Hu, J., Guan, B., and Ma, X. (2021). Diagnostic accuracy of PET for differentiating true glioma progression from post treatment-related changes: a systematic review and meta-analysis. *Front. Neurol.* 12:671867. doi: 10.3389/fneur.2021.671867

Danchaivijitr, N., Waldman, A. D., Tozer, D. J., Benton, C. E., Brasil Caseiras, G., Tofts, P. S., et al. (2008). Low-grade gliomas: do changes in rCBV measurements at longitudinal perfusion-weighted MR imaging predict malignant transformation? *Radiology* 247, 170–178. doi: 10.1148/radiol.2471062089

De Witt Hamer, P. C., Robles, S. G., Zwinderman, A. H., Duffau, H., and Berger, M. S. (2012). Impact of intraoperative stimulation brain mapping on glioma surgery outcome: a meta-analysis. *J. Clin. Oncol.* 30, 2559–2565. doi: 10.1200/JCO.2011.38.4818

Deguchi, S., Oishi, T., Mitsuya, K., Kakuda, Y., Endo, M., Sugino, T., et al. (2020). Clinicopathological analysis of T2-FLAIR mismatch sign in lower-grade gliomas. *Sci. Rep.* 10:10113. doi: 10.1038/s41598-020-67244-7

Delgado, A. F., De Luca, F., Hanagandi, P., van Westen, D., and Delgado, A. F. (2018). Arterial spin-labeling in children with brain tumor: a meta-analysis. *AJNR Am. J. Neuroradiol.* 39, 1536–1542. doi: 10.3174/ajnr.A5727

Desmurget, M., and Sirigu, A. (2015). Revealing humans' sensorimotor functions with electrical cortical stimulation. *Philos. Trans. R. Soc. Lond. B Biol. Sci.* 370:20140207. doi: 10.1098/rstb.2014.0207

Deuschl, C., Kirchner, J., Poeppel, T. D., Schaarschmidt, B., Kebir, S., El Hindy, N., et al. (2018). 11C-MET PET/MRI for detection of recurrent glioma. *Eur. J. Nucl. Med. Mol. Imaging.* 45, 593–601. doi: 10.1007/s00259-017-3916-9

Duffau, H., and Taillandier, L. (2015). New concepts in the management of diffuse low-grade glioma: proposal of a multistage and individualized therapeutic approach. *Neuro-Oncology* 17, 332–342. doi: 10.1093/neuonc/nou153

Dunet, V., Pomoni, A., Hottinger, A., Nicod-Lalonde, M., and Prior, J. O. (2016). Performance of 18F-FET versus 18F-FDG-PET for the diagnosis and grading of brain tumors: systematic review and meta-analysis. *Neuro-Oncology* 18, 426–434. doi: 10.1093/neuonc/nov148

Ellingson, B. M., Bendszus, M., Boxerman, J., Barboriak, D., Erickson, B. J., Smits, M., et al. (2015). Consensus recommendations for a standardized Brain Tumor imaging protocol in clinical trials. *Neuro-Oncology* 17, 1188–1198. doi: 10.1093/neuonc/nov095

Ellingson, B. M., Malkin, M. G., Rand, S. D., Connelly, J. M., Quinsey, C., LaViolette, P. S., et al. (2010). Validation of functional diffusion maps (fDMs) as a biomarker for human glioma cellularity. *J. Magn. Reson. Imaging JMRI.* 31, 538–548. doi: 10.1002/jmri.22068

Ellingson, B. M., Chung, C., Pope, W. B., Boxerman, J. L., and Kaufmann, T. J. (2017a). Pseudoprogression, radionecrosis, inflammation or true tumor progression? challenges associated with glioblastoma response assessment in an evolving therapeutic landscape. *J. Neurooncol.* 134, 495–504. doi: 10.1007/s11060-017-2375-2

Ellingson, B. M., Wen, P. Y., and Cloughesy, T. F. (2017b). Modified criteria for radiographic response assessment in glioblastoma clinical trials. *Neurother J. Am. Soc. Exp. Neurother.* 14, 307–320. doi: 10.1007/s13311-016-0507-6

Ellis, D. G., White, M. L., Hayasaka, S., Warren, D. E., Wilson, T. W., and Aizenberg, M. R. (2020). Accuracy analysis of fMRI and MEG activations determined by intraoperative mapping. *Neurosurg. Focus.* 48:E13. doi: 10.3171/2019.11.FOCUS19784

Emblem, K. E., Scheie, D., Due-Tonnessen, P., Nedregaard, B., Nome, T., Hald, J. K., et al. (2008). Histogram analysis of MR imaging-derived cerebral blood volume maps: combined glioma grading and identification of low-grade oligodendroglial subtypes. *AJNR Am. J. Neuroradiol.* 29, 1664–1670. doi: 10.3174/ajnr.A1182

Esquenazi, Y., Friedman, E., Liu, Z., Zhu, J. J., Hsu, S., and Tandon, N. (2017). The survival advantage of "Supratotal" resection of glioblastoma using selective cortical mapping and the subpial technique. *Neurosurgery* 81, 275–288. doi: 10.1093/neuros/nyw174

Essig, M., Shiroishi, M. S., Nguyen, T. B., Saake, M., Provenzale, J. M., Enterline, D., et al. (2013). Perfusion MRI: the five most frequently asked technical questions. *AJR Am. J. Roentgenol.* 200, 24–34. doi: 10.2214/AJR.12.9543

Ewelt, C., Floeth, F. W., Felsberg, J., Steiger, H. J., Sabel, M., Langen, K. J., et al. (2011). Finding the anaplastic focus in diffuse gliomas: the value of Gd-DTPA enhanced MRI, FET-PET, and intraoperative, ALA-derived tissue fluorescence. *Clin. Neurol Neurosurg.* 113, 541–547. doi: 10.1016/j.clineuro.2011.03.008

Fink, J. R., Muzi, M., Peck, M., and Krohn, K. A. (2015). Multimodality brain tumor imaging: MR imaging, PET, and PET/MR imaging. *J. Nucl. Med.* 56, 1554–1561. doi: 10.2967/jnumed.113.131516

Forster, M. T., Hattingen, E., Senft, C., Gasser, T., Seifert, V., and Szelényi, A. (2011). Navigated transcranial magnetic stimulation and functional magnetic resonance imaging: advanced adjuncts in preoperative planning for central region tumors. *Neurosurgery* 68, 1317–1325. doi: 10.1227/NEU.0b013e31820b528c

Fountas, K. N., Kapsalaki, E. Z., Vogel, R. L., Fezoulidis, I., Robinson, J. S., and Gotsis. (2004). Noninvasive histologic grading of solid astrocytomas using proton magnetic resonance spectroscopy. *Stereotact. Funct. Neurosurg.* 82, 90–97. doi: 10.1159/000077458

Frey, D., Schilt, S., Strack, V., Zdunczyk, A., Rösler, J., Niraula, B., et al. (2014). Navigated transcranial magnetic stimulation improves the treatment outcome in patients with brain tumors in motor eloquent locations. *Neuro-Oncology* 16, 1365–1372. doi: 10.1093/neuonc/nou110

Fudaba, H., Shimomura, T., Abe, T., Matsuta, H., Momii, Y., Sugita, K., et al. (2014). Comparison of multiple parameters obtained on 3T pulsed arterial spin-labeling, diffusion tensor imaging, and MRS and the Ki-67 labeling index in evaluating glioma grading. *AJNR Am. J. Neuroradiol.* 35, 2091–2098. doi: 10.3174/ajnr.A4018

Fujima, N., Kudo, K., Terae, S., Hida, K., Ishizaka, K., Zaitsu, Y., et al. (2010). Spinal arteriovenous malformation: evaluation of change in venous oxygenation with susceptibility-weighted MR imaging after treatment. *Radiology* 254, 891–899. doi: 10.1148/radiol.09090286

Fujiwara, N., Sakatani, K., Katayama, Y., Murata, Y., Hoshino, T., Fukaya, C., et al. (2004). Evoked-cerebral blood oxygenation changes in false-negative activations in BOLD contrast functional MRI of patients with brain tumors. *NeuroImage* 21, 1464–1471. doi: 10.1016/j.neuroimage.2003.10.042

Galanis, E., Wu, W., Cloughesy, T., Lamborn, K., Mann, B., Wen, P. Y., et al. (2012). Phase 2 trial design in neuro-oncology revisited: a report from the RANO group. *Lancet Oncol.* 13, e196–e204. doi: 10.1016/S1470-2045(11)70406-5

Galldiks, N., Dunkl, V., Stoffels, G., Hutterer, M., Rapp, M., Sabel, M., et al. (2015). Diagnosis of pseudoprogression in patients with glioblastoma using O-(2-[18F]fluoroethyl)-L-tyrosine PET. *Eur. J. Nucl. Med. Mol. Imaging.* 42, 685–695. doi: 10.1007/s00259-014-2959-4

Galldiks, N., Kracht, L. W., Burghaus, L., Thomas, A., Jacobs, A. H., Heiss, W. D., et al. (2006). Use of 11C-methionine PET to monitor the effects of temozolomide chemotherapy in malignant gliomas. *Eur. J. Nucl. Med. Mol. Imaging.* 33, 516–524. doi: 10.1007/s00259-005-0002-5

Galldiks, N., Kracht, L. W., Dunkl, V., Ullrich, R. T., Vollmar, S., Jacobs, A. H., et al. (2011). Imaging of non- or very subtle contrast-enhancing malignant gliomas with [11C]-methionine positron emission tomography. *Mol. Imaging.* 10, 453–459.

Gerstner, E. R., Zhang, Z., Fink, J. R., Muzi, M., Hanna, L., Greco, E., et al. (2016). ACRIN 6684: assessment of tumor hypoxia in newly diagnosed glioblastoma using 18 F-FMISO PET and MRI. *Clin. Cancer Res.* 22, 5079–5086. doi: 10.1158/1078-0432.CCR-15-2529

Grosu, A. L., Astner, S. T., Riedel, E., Nieder, C., Wiedenmann, N., Heinemann, F., et al. (2011). An interindividual comparison of O-(2-[18F]fluoroethyl)-L-tyrosine (FET)- and L-[methyl-11C]methionine (MET)-PET in patients with brain gliomas and metastases. *Int. J. Radiat. Oncol. Biol. Phys.* 81, 1049–1058. doi: 10.1016/j.ijrobp.2010.07.002

Guggisberg, A. G., Honma, S. M., Findlay, A. M., Dalal, S. S., Kirsch, H. E., Berger, M. S., et al. (2008). Mapping functional connectivity in patients with brain lesions. *Ann. Neurol.* 63, 193–203. doi: 10.1002/ana.21224

Gupta, A., and Dwivedi, T. (2016). A simplified overview of world health organization classification update of central nervous system tumors. *J. Neurosci. Rural Pract.* 8, 629–641. doi: 10.4103/jnrp.jnrp_168_17

Gupta, R. K., Cloughesy, T. F., Sinha, U., Garakian, J., Lazareff, J., Rubino, G., et al. (2000). Relationships between choline magnetic resonance spectroscopy, apparent diffusion coefficient and quantitative histopathology in human glioma. *J. Neurooncol.* 50, 215–226. doi: 10.1023/a:1006431120031

Haacke, E. M., Xu, Y., Cheng, Y. C. N., and Reichenbach, J. R. (2004). Susceptibility weighted imaging (SWI). *Magn. Reson. Med.* 52, 612–618. doi: 10.1002/mrm.20198

Haddad, A. F., Young, J. S., Berger, M. S., and Tarapore, P. E. (2020). Preoperative applications of navigated transcranial magnetic stimulation. *Front. Neurol.* 11:628903. doi: 10.3389/fneur.2020.628903

Haller, S., and Bartsch, A. J. (2009). Pitfalls in FMRI. *Eur. Radiol.* 19, 2689–2706. doi: 10.1007/s00330-009-1456-9

Harpold, H. L. P., Alvord, E. C., and Swanson, K. R. (2007). The evolution of mathematical modeling of glioma proliferation and invasion. *J. Neuropathol. Exp. Neurol.* 66, 1–9. doi: 10.1097/nen.0b013e31802d9000

Henker, C., Hiepel, M. C., Kriesen, T., Scherer, M., Glass, A., Herold-Mende, C., et al. (2019). Volumetric assessment of glioblastoma and its predictive value for survival. *Acta Neurochir (Wien).* 161, 1723–1732. doi: 10.1007/s00701-019-03966-6

Henriksen, O. M., Kruuse, C., Olesen, J., Jensen, L. T., Larsson, H. B. W., Birk, S., et al. (2013). Sources of variability of resting cerebral blood flow in healthy subjects: a study using 133 Xe SPECT measurements. *J. Cereb. Blood Flow Metab.* 33, 787–792. doi: 10.1038/jcbfm.2013.17

Herholz, K., Heindel, W., Luyten, P. R., denHollander, J. A., Pietrzyk, U., Voges, J., et al. (1992). In vivo imaging of glucose consumption and lactate concentration in human gliomas. *Ann. Neurol.* 31, 319–327. doi: 10.1002/ana.410310315

Hernandez-Garcia, L., Lahiri, A., and Schollenberger, J. (2019). Recent progress in ASL. *NeuroImage* 187, 3–16. doi: 10.1016/j.neuroimage.2017.12.095

Hervey-Jumper, S. L., and Berger, M. S. (2016). Maximizing safe resection of low- and high-grade glioma. *J. Neurooncol.* 130, 269–282. doi: 10.1007/s11060-016-2110-4

Hoefemann, M., Döring, A., Fichtner, N. D., and Kreis, R. (2021). Combining chemical exchange saturation transfer and 1 H magnetic resonance spectroscopy for simultaneous determination of metabolite concentrations and effects of magnetization exchange. *Magn. Reson. Med.* 85, 1766–1782. doi: 10.1002/mrm.28574

Hourani, R., Brant, L. J., Rizk, T., Weingart, J. D., Barker, P. B., and Horská, A. (2008). Can proton MR spectroscopic and perfusion imaging differentiate between neoplastic and nonneoplastic brain lesions in adults? *AJNR Am. J. Neuroradiol.* 29, 366–372. doi: 10.3174/ajnr.A0810

Hsu, C. C. T., Watkins, T. W., Kwan, G. N. C., and Haacke, E. M. (2016). Susceptibility-Weighted imaging of glioma: update on current imaging status and future directions: susceptibility-weighted imaging of glioma. *J. Neuroimaging* 26, 383–390. doi: 10.1111/jon.12360

Hu, L. S., Eschbacher, J. M., Dueck, A. C., Heiserman, J. E., Liu, S., Karis, J. P., et al. (2012). Correlations between perfusion MR imaging cerebral blood volume, microvessel quantification, and clinical outcome using stereotactic analysis in recurrent high-grade glioma. *AJNR Am. J. Neuroradiol.* 33, 69–76. doi: 10.3174/ajnr.A2743

Hu, L. S., Hawkins-Daarud, A., Wang, L., Li, J., and Swanson, K. R. (2020). Imaging of intratumoral heterogeneity in high-grade glioma. *Cancer Lett.* 477, 97–106. doi: 10.1016/j.canlet.2020.02.025

Hu, L. S., Ning, S., Eschbacher, J. M., Baxter, L. C., Gaw, N., Ranjbar, S., et al. (2017). Radiogenomics to characterize regional genetic heterogeneity in glioblastoma. *Neuro-Oncology* 19, 128–137. doi: 10.1093/neuonc/now135

Hutterer, M., Nowosielski, M., Putzer, D., Jansen, N. L., Seiz, M., Schocke, M., et al. (2013). [18F]-fluoro-ethyl-L-tyrosine PET: a valuable diagnostic tool in neuro-oncology, but not all that glitters is glioma. *Neuro-Oncology* 15, 341–351. doi: 10.1093/neuonc/nos300

Ille, S., Sollmann, N., Hauck, T., Maurer, S., Tanigawa, N., Obermueller, T., et al. (2015). Combined noninvasive language mapping by navigated transcranial magnetic stimulation and functional MRI and its comparison with direct cortical stimulation. *J. Neurosurg.* 123, 212–225. doi: 10.3171/2014.9.JNS14929

Iwamoto, F. M., Abrey, L. E., Beal, K., Gutin, P. H., Rosenblum, M. K., Reuter, V. E., et al. (2009). Patterns of relapse and prognosis after bevacizumab failure in recurrent glioblastoma. *Neurology* 73, 1200–1206. doi: 10.1212/WNL.0b013e3181bc0184

Jafari-Khouzani, K., Emblem, K. E., Kalpathy-Cramer, J., Bjørnerud, A., Vangel, M. G., Gerstner, E. R., et al. (2015). Repeatability of cerebral perfusion using

dynamic susceptibility contrast MRI in glioblastoma patients. *Transl. Oncol.* 8, 137–146. doi: 10.1016/j.tranon.2015.03.002

Jansen, N. L., Suchorska, B., Schwarz, S. B., Eigenbrod, S., Lutz, J., Graute, V., et al. (2013). [18F]fluoroethyltyrosine-positron emission tomography-based therapy monitoring after stereotactic iodine-125 brachytherapy in patients with recurrent high-grade glioma. *Mol. Imaging* 12, 137–147.

Jansen, N. L., Suchorska, B., Wenter, V., Schmid-Tannwald, C., Todica, A., Egenbrod, S., et al. (2015). Prognostic significance of dynamic 18F-FET PET in newly diagnosed astrocytic high-grade glioma. *J. Nucl. Med.* 56, 9–15. doi: 10.2967/jnumed.114.144675

Johnson, D. R., Leeper, H. E., and Uhm, J. H. (2013). Glioblastoma survival in the United States improved after food and drug administration approval of bevacizumab: a population-based analysis. *Cancer* 119, 3489–3495. doi: 10.1002/cncr.28259

Kim, B. S., Kim, S. K., Choi, S. H., Lee, S. H., Seol, H. J., Nam, D. H., et al. (2015). Prognostic implication of progression pattern after anti-VEGF bevacizumab treatment for recurrent malignant gliomas. *J. Neurooncol.* 124, 101–110. doi: 10.1007/s11060-015-1808-z

Kim, M. J., Kim, H. S., Kim, J. H., Cho, K. G., and Kim, S. Y. (2008). Diagnostic accuracy and interobserver variability of pulsed arterial spin labeling for glioma grading. *Acta Radiol. Stockh Swed.* 49, 450–457. doi: 10.1080/02841850701881820

Könönen, M., Tamsi, N., Säisänen, L., Kemppainen, S., Määttä, S., Julkunen, P., et al. (2015). Non-invasive mapping of bilateral motor speech areas using navigated transcranial magnetic stimulation and functional magnetic resonance imaging. *J. Neurosci. Methods* 248, 32–40. doi: 10.1016/j.jneumeth.2015.03.030

Kosaka, N., Tsuchida, T., Uematsu, H., Kimura, H., Okazawa, H., and Itoh, H. (2008). 18F-FDG PET of common enhancing malignant brain tumors. *AJR Am. J. Roentgenol.* 190, W365–W369. doi: 10.2214/AJR.07.2660

Krieg, S. M., Sabih, J., Bulubasova, L., Obermuller, T., Negwer, C., Janssen, I., et al. (2014). Preoperative motor mapping by navigated transcranial magnetic brain stimulation improves outcome for motor eloquent lesions. *Neuro-Oncology* 16, 1274–1282. doi: 10.1093/neuonc/nou007

Krieg, S. M., Shiban, E., Buchmann, N., Gempt, J., Foerschler, A., Meyer, B., et al. (2012). Utility of presurgical navigated transcranial magnetic brain stimulation for the resection of tumors in eloquent motor areas: clinical article. *J. Neurosurg.* 116, 994–1001. doi: 10.3171/2011.12.JNS111524

Krings, T., Schreckenberger, M., Rohde, V., Spetzger, U., Sabri, O., Reinges, M. H. T., et al. (2002). Functional MRI and 18F FDG-Positron emission tomography for presurgical planning: comparison with electrical cortical stimulation. *Acta Neurochir (Wien).* 144, 889–899. doi: 10.1007/s00701-002-0992-8

Kuhnt, D., Bauer, M. H. A., and Nimsky, C. (2012). Brain shift compensation and neurosurgical image fusion using intraoperative MRI: current status and future challenges. *Crit. Rev. Biomed. Eng.* 40, 175–185. doi: 10.1615/critrevbiomedeng.v40.i3.20

Lam, W. W. M., Poon, W. S., and Metreweli, C. (2002). Diffusion MR imaging in glioma: does it have any role in the pre-operation determination of grading of glioma? *Clin. Radiol.* 57, 219–225. doi: 10.1053/crad.2001.0741

Law, M., Oh, S., Babb, J. S., Wang, E., Inglese, M., Zagzag, D., et al. (2006). Low-grade gliomas: dynamic susceptibility-weighted contrast-enhanced perfusion MR imaging–prediction of patient clinical response. *Radiology* 238, 658–667. doi: 10.1148/radiol.2382042180

Law, M., Young, R. J., Babb, J. S., Peccerelli, N., Chheang, S., Gruber, M. L., et al. (2008). Gliomas: predicting time to progression or survival with cerebral blood volume measurements at dynamic susceptibility-weighted contrast-enhanced perfusion MR imaging. *Radiology* 247, 490–498. doi: 10.1148/radiol.2472070898

Le Bihan, D., Breton, E., Lallemand, D., Grenier, P., Cabanis, E., and Laval-Jeantet, M. (1986). MR imaging of intravoxel incoherent motions: application to diffusion and perfusion in neurologic disorders. *Radiology* 161, 401–407. doi: 10.1148/radiology.161.2.3763909

Le Bihan, D., Mangin, J. F., Poupon, C., Clark, C. A., Pappata, S., Molko, N., et al. (2001). Diffusion tensor imaging: concepts and applications. *J. Magn. Reson. Imaging JMRI.* 13, 534–546. doi: 10.1002/jmri.1076

Le Rhun, E., Taillibert, S., and Chamberlain, M. C. (2016). Current management of adult diffuse infiltrative low grade gliomas. *Curr. Neurol Neurosci. Rep.* 16:15. doi: 10.1007/s11910-015-0615-4

Ledezma, C. J., Chen, W., Sai, V., Freitas, B., Cloughesy, T., Czernin, J., et al. (2009). 18F-FDOPA PET/MRI fusion in patients with primary/recurrent gliomas: initial experience. *Eur. J. Radiol.* 71, 242–248. doi: 10.1016/j.ejrad.2008.04.018

Lee, A. T., Faltermeier, C., Morshed, R. A., Young, J. S., Kakaizaa, S., Valdiva, C., et al. (2020). The impact of high functional connectivity network hub resection on language task performance in adult low- and high-grade glioma. *J. Neurosurg.* 134, 1102–1112. doi: 10.3171/2020.1.JNS192267

Li, C., Ai, B., Li, Y., Qi, H., and Wu, L. (2010). Susceptibility-weighted imaging in grading brain astrocytomas. *Eur. J. Radiol.* 75, e81–e85. doi: 10.1016/j.ejrad.2009.08.003

Li, C., Gan, Y., Chen, H., Chen, Y., Deng, Y., Zhan, W., et al. (2020). Advanced multimodal imaging in differentiating glioma recurrence from post-radiotherapy changes. *Int. Rev. Neurobiol.* 151, 281–297. doi: 10.1016/bs.irn.2020.03.009

Li, C., Yi, C., Chen, Y., Xi, S., Guo, C., Yang, Q., et al. (2021). Identify glioma recurrence and treatment effects with triple-tracer PET/CT. *BMC Med. Imaging.* 21:92. doi: 10.1186/s12880-021-00624-1

Li, J., Liu, S., Qin, Y., Zhang, Y., Wang, N., and Liu, H. (2020). High-order radiomics features based on T2 FLAIR MRI predict multiple glioma immunohistochemical features: a more precise and personalized gliomas management. *PLoS One* 15:e0227703. doi: 10.1371/journal.pone.0227703

Li, Y. M., Suki, D., Hess, K., and Sawaya, R. (2016). The influence of maximum safe resection of glioblastoma on survival in 1229 patients: can we do better than gross-total resection? *J. Neurosurg.* 124, 977–988. doi: 10.3171/2015.5.JNS142087

Lin, P. T., Berger, M. S., and Nagarajan, S. S. (2006). Motor field sensitivity for preoperative localization of motor cortex. *J. Neurosurg.* 105, 588–594. doi: 10.3171/jns.2006.105.4.588

Löbel, U., Sedlacik, J., Sabin, N. D., Sabin, N. D., Kocak, M., Broniscer, A., et al. (2010). Three-dimensional susceptibility-weighted imaging and two-dimensional T2*-weighted gradient-echo imaging of intratumoral hemorrhages in pediatric diffuse intrinsic pontine glioma. *Neuroradiology* 52, 1167–1177. doi: 10.1007/s00234-010-0771-9

Louis, D. N., Perry, A., Wesseling, P., Brat, D. J., Cree, I. A., Figarella-Branger, D., et al. (2021). The 2021 WHO classification of tumors of the central nervous system: a summary. *Neuro-Oncology* 23, 1231–1251. doi: 10.1093/neuonc/noab106

Lu, S., Ahn, D., Johnson, G., Law, M., Zagzag, D., and Grossman, R. I. (2004). Diffusion-tensor MR imaging of intracranial neoplasia and associated peritumoral edema: introduction of the tumor infiltration index. *Radiology* 232, 221–228. doi: 10.1148/radiol.2321030653

Maia, A. C. M., Malheiros, S. M. F., da Rocha, A. J., Stávale, J. N., Guimarães, I. F., Borges, L. R. R., et al. (2004). Stereotactic biopsy guidance in adults with supratentorial nonenhancing gliomas: role of perfusion-weighted magnetic resonance imaging. *J. Neurosurg.* 101, 970–976. doi: 10.3171/jns.2004.101.6.0970

Martino, J., Honma, S. M., Findlay, A. M., Guggisberg, A. G., Owen, J. P., Kirsch, H. E., et al. (2011). Resting functional connectivity in patients with brain tumors in eloquent areas. *Ann. Neurol.* 69, 521–532. doi: 10.1002/ana.22167

Mayerhoefer, M. E., Materka, A., Langs, G., Häggström, I., Szczypiński, P., Gibbs, P., et al. (2020). Introduction to radiomics. *J. Nucl. Med.* 61, 488–495. doi: 10.2967/jnumed.118.222893

Mohammed, W., Xunning, H., Haibin, S., and Jingzhi, M. (2013). Clinical applications of susceptibility-weighted imaging in detecting and grading intracranial gliomas: a review. *Cancer Imaging* 13, 186–195. doi: 10.1102/1470-7330.2013.0020

Molinaro, A. M., Hervey-Jumper, S., Morshed, R. A., Young, J. S., Han, S. J., Chunduru, P., et al. (2020). Association of maximal extent of resection of contrast-enhanced and non–contrast-enhanced tumor with survival within molecular subgroups of patients with newly diagnosed glioblastoma. *JAMA Oncol.* 6:495. doi: 10.1001/jamaoncol.2019.6143

Morrison, M. A., Tam, F., Garavaglia, M. M., Hare, G. M. T., Cusimano, M. D., Schweizer, T. A., et al. (2016). Sources of variation influencing concordance between functional mri and direct cortical stimulation in brain tumor surgery. *Front. Neurosci.* 10:461. doi: 10.3389/fnins.2016.00461

Mullins, M. E., Barest, G. D., Schaefer, P. W., Hochberg, F. H., Gonzalez, R. G., and Lev, M. H. (2005). Radiation necrosis versus glioma recurrence: conventional MR imaging clues to diagnosis. *AJNR Am. J. Neuroradiol.* 26, 1967–1972.

Naeije, G., Vaulet, T., Wens, V., Marty, B., Goldman, S., and De Tiège, X. (2016). Multilevel cortical processing of somatosensory novelty: a magnetoencephalography study. *Front. Hum. Neurosci.* 10:259. doi: 10.3389/fnhum.2016.00259

Nagarajan, S., Kirsch, H., Lin, P., Findlay, A., Honma, S., and Berger, M. S. (2008). Preoperative localization of hand motor cortex by adaptive spatial filtering of magnetoencephalography data. *J. Neurosurg.* 109, 228–237. doi: 10.3171/JNS/2008/109/8/0228

Norden, A. D., Young, G. S., Setayesh, K., Muzikansky, A., Klufas, R., Ross, G. L., et al. (2008). Bevacizumab for recurrent malignant gliomas: efficacy, toxicity, and patterns of recurrence. *Neurology* 70, 779–787. doi: 10.1212/01.wnl.0000304121.57857.38

Ogawa, S., Menon, R. S., Tank, D. W., Kim, S. G., Merkle, H., Ellermann, J. M., et al. (1993). Functional brain mapping by blood oxygenation level-dependent contrast magnetic resonance imaging. a comparison of signal characteristics with a biophysical model. *Biophys. J.* 64, 803–812. doi: 10.1016/S0006-3495(93)81441-3

Oh, J. S., Suk Park, K., Chan Song, I., Ju Kim, S., Hwang, J., Chung, A., et al. (2005). Fractional anisotropy-based divisions of midsagittal corpus callosum. *Neuroreport* 16, 317–320. doi: 10.1097/00001756-200503150-00002

Okada, H., Weller, M., Huang, R., Finocchiaro, G., Gilbert, M. R., Wick, W., et al. (2015). Immunotherapy response assessment in neuro-oncology: a report of the RANO working group. *Lancet Oncol.* 16, e534–e542. doi: 10.1016/S1470-2045(15)00088-1

Omuro, A. M., Leite, C. C., Mokhtari, K., and Delattre, J. Y. (2006). Pitfalls in the diagnosis of brain tumours. *Lancet Neurol.* 5, 937–948. doi: 10.1016/S1474-4422(06)70597-X

Padma, M. V., Said, S., Jacobs, M., Hwang, D. R., Dunigan, K., Satter, M., et al. (2003). Prediction of pathology and survival by FDG PET in gliomas. *J. Neurooncol.* 64, 227–237. doi: 10.1023/A:1025665820001

Pafundi, D. H., Laack, N. N., Youland, R. S., Parney, I. F., Lowe, V. J., Giannini, C., et al. (2013). Biopsy validation of 18F-DOPA PET and biodistribution in gliomas for neurosurgical planning and radiotherapy target delineation: results of a prospective pilot study. *Neuro-Oncology* 15, 1058–1067. doi: 10.1093/neuonc/not002

Paiva, W. S., Fonoff, E. T., Marcolin, M. A., Cabrera, H. N., and Teixeira, M. J. (2012). Cortical mapping with navigated transcranial magnetic stimulation in low-grade glioma surgery. *Neuropsychiatr. Dis. Treat.* 8, 197–201. doi: 10.2147/NDT.S30151

Patankar, T. F., Haroon, H. A., Mills, S. J., Balériaux, D., Buckley, D. L., Parker, G. J. M., et al. (2005). Is volume transfer coefficient (K(trans)) related to histologic grade in human gliomas? *AJNR Am. J. Neuroradiol.* 26, 2455–2465.

Patel, P., Baradaran, H., Delgado, D., Askin, G., Christos, P., John Tsiouris, A., et al. (2017). MR perfusion-weighted imaging in the evaluation of high-grade gliomas after treatment: a systematic review and meta-analysis. *Neuro-Oncology* 19, 118–127. doi: 10.1093/neuonc/now148

Patel, S. H., Poisson, L. M., Brat, D. J., Zou, Y., Cooper, L., Snuderl, M., et al. (2017). T2–FLAIR mismatch, an imaging biomarker for IDH and 1p/19q status in lower-grade gliomas: a TCGA/TCIA project. *Clin. Cancer Res.* 23, 6078–6085. doi: 10.1158/1078-0432.CCR-17-0560

Picht, T. (2014). Current and potential utility of transcranial magnetic stimulation in the diagnostics before brain tumor surgery. *CNS Oncol.* 3, 299–310. doi: 10.2217/cns.14.25

Picht, T., Frey, D., Thieme, S., Kliesch, S., and Vajkoczy, P. (2016). Presurgical navigated TMS motor cortex mapping improves outcome in glioblastoma surgery: a controlled observational study. *J. Neurooncol.* 126, 535–543. doi: 10.1007/s11060-015-1993-9

Picht, T., Krieg, S. M., Sollmann, N., Rösler, J., Niraula, B., Neuvonen, T., et al. (2013). A comparison of language mapping by preoperative navigated transcranial magnetic stimulation and direct cortical stimulation during awake surgery. *Neurosurgery* 72, 808–819. doi: 10.1227/NEU.0b013e3182889e01

Picht, T., Mularski, S., Kuehn, B., Vajkoczy, P., Kombos, T., and Suess, O. (2009). Navigated transcranial magnetic stimulation for preoperative functional diagnostics in brain tumor surgery. *Oper. Neurosurg.* 65(Suppl._6), 93–8; discussion 98-9. doi: 10.1227/01.NEU.0000348009.22750.59

Raffa, G., Scibilia, A., Conti, A., Ricciardo, G., Rizzo, V., Morelli, A., et al. (2019). The role of navigated transcranial magnetic stimulation for surgery of motor-eloquent brain tumors: a systematic review and meta-analysis. *Clin. Neurol. Neurosurg.* 180, 7–17. doi: 10.1016/j.clineuro.2019.03.003

Raja, R., Sinha, N., Saini, J., Mahadevan, A., Rao, K. N., and Swaminathan, A. (2016). Assessment of tissue heterogeneity using diffusion tensor and diffusion kurtosis imaging for grading gliomas. *Neuroradiology* 58, 1217–1231. doi: 10.1007/s00234-016-1758-y

Rapp, M., Heinzel, A., Galldiks, N., Stoffels, G., Felsberg, J., Ewelt, C., et al. (2013). Diagnostic performance of 18F-FET PET in newly diagnosed cerebral lesions suggestive of glioma. *J. Nucl. Med.* 54, 229–235. doi: 10.2967/jnumed.112.109603

Reinertsen, I., Lindseth, F., Askeland, C., Iversen, D. H., and Unsgård, G. (2014). Intra-operative correction of brain-shift. *Acta Neurochir (Wien).* 156, 1301–1310. doi: 10.1007/s00701-014-2052-6

Reinges, M. H. T., Nguyen, H. H., Krings, T., Hütter, B. O., Rohde, V., and Gilsbach, J. M. (2004). Course of brain shift during microsurgical resection of supratentorial cerebral lesions: limits of conventional neuronavigation. *Acta Neurochir (Wien).* 146, 369–377; discussion 377. doi: 10.1007/s00701-003-0204-1

Roberts, H. C., Roberts, T. P., Brasch, R. C., and Dillon, W. P. (2000). Quantitative measurement of microvascular permeability in human brain tumors achieved using dynamic contrast-enhanced MR imaging: correlation with histologic grade. *AJNR Am. J. Neuroradiol.* 21, 891–899.

Saadoun, S., Papadopoulos, M. C., Davies, D. C., Bell, B. A., and Krishna, S. (2002). Increased aquaporin 1 water channel expression in human brain tumours. *Br. J. Cancer* 87, 621–623. doi: 10.1038/sj.bjc.6600512

Sadeghi, N., D'Haene, N., Decaestecker, C., Levivier, M., Metens, T., Maris, C., et al. (2008). Apparent diffusion coefficient and cerebral blood volume in brain gliomas: relation to tumor cell density and tumor microvessel density based on stereotactic biopsies. *AJNR Am. J. Neuroradiol.* 29, 476–482. doi: 10.3174/ajnr.A0851

Sage, M. R., and Wilson, A. J. (1994). The blood-brain barrier: an important concept in neuroimaging. *AJNR Am. J. Neuroradiol.* 15, 601–622.

Schiffbauer, H., Berger, M. S., Ferrari, P., Freudenstein, D., Rowley, H. A., and Roberts, T. P. L. (2003). Preoperative magnetic source imaging for brain tumor surgery: a quantitative comparison with intraoperative sensory and motor mapping. *Neurosurg. Focus.* 15:E7. doi: 10.3171/foc.2003.15.1.7

Schmainda, K. M. (2012). Diffusion-weighted MRI as a biomarker for treatment response in glioma. *CNS Oncol.* 1, 169–180. doi: 10.2217/cns.12.25

Scott, J. N., Brasher, P. M. A., Sevick, R. J., Rewcastle, N. B., and Forsyth, P. A. (2002). How often are nonenhancing supratentorial gliomas malignant? A population study. *Neurology* 59, 947–949. doi: 10.1212/WNL.59.6.947

Sehgal, V., Delproposto, Z., Haddar, D., Haacke, E. M., Sloan, A. E., Zamorano, L. J., et al. (2006). Susceptibility-weighted imaging to visualize blood products and improve tumor contrast in the study of brain masses. *J. Magn. Reson. Imaging* 24, 41–51. doi: 10.1002/jmri.20598

Senft, C., Bink, A., Franz, K., Vatter, H., Gasser, T., and Seifert, V. (2011). Intraoperative MRI guidance and extent of resection in glioma surgery: a randomised, controlled trial. *Lancet Oncol.* 12, 997–1003. doi: 10.1016/S1470-2045(11)70196-6

Shaw, E. G., Berkey, B., Coons, S. W., Bullard, D., Brachman, D., Buckner, J. C., et al. (2008). Recurrence following neurosurgeon-determined gross-total resection of adult supratentorial low-grade glioma: results of a prospective clinical trial. *J. Neurosurg.* 109, 835–841. doi: 10.3171/JNS/2008/109/11/0835

Shen, N., Zhao, L., Jiang, J., Jiang, R., Su, C., Zhang, S., et al. (2016). Intravoxel incoherent motion diffusion-weighted imaging analysis of diffusion and microperfusion in grading gliomas and comparison with arterial spin labeling for evaluation of tumor perfusion. *J. Magn. Reson. Imaging JMRI.* 44, 620–632. doi: 10.1002/jmri.25191

Soffietti, R., Rudà, R., Bradac, G. B., and Schiffer, D. (1998). PCV chemotherapy for recurrent oligodendrogliomas and oligoastrocytomas. *Neurosurgery* 43, 1066–1073. doi: 10.1097/00006123-199811000-00035

Sollmann, N., Kelm, A., Ille, S., Schröder, A., Zimmer, C., Ringel, F., et al. (2018). Setup presentation and clinical outcome analysis of treating highly language-eloquent gliomas via preoperative navigated transcranial magnetic stimulation and tractography. *Neurosurg. Focus* 44:E2. doi: 10.3171/2018.3.FOCUS1838

Southwell, D. G., Birk, H. S., Han, S. J., Li, J., Sall, J. W., and Berger, M. S. (2018). Resection of gliomas deemed inoperable by neurosurgeons based on

preoperative imaging studies. *J. Neurosurg.* 129, 567–575. doi: 10.3171/2017.5.JNS17166

Strauss, S. B., Meng, A., Ebani, E. J., and Chiang, G. C. (2019). Imaging glioblastoma posttreatment: progression, pseudoprogression, pseudoresponse, radiation necrosis. *Radiol. Clin. North Am.* 57, 1199–1216. doi: 10.1016/j.rcl.2019.07.003

Stupp, R., Brada, M., van den Bent, M. J., Tonn, J. C., Pentheroudakis, G., Esmo Guidelines, et al. (2014). High-grade glioma: ESMO clinical practice guidelines for diagnosis, treatment and follow-up. *Ann. Oncol.* 25(Suppl. 3), iii93–iii101. doi: 10.1093/annonc/mdu050

Stupp, R., Hegi, M. E., Mason, W. P., van den Bent, M. J., Taphoorn, M. J. B., Janzer, R. C., et al. (2009). Effects of radiotherapy with concomitant and adjuvant temozolomide versus radiotherapy alone on survival in glioblastoma in a randomised phase III study: 5-year analysis of the EORTC-NCIC trial. *Lancet Oncol.* 10, 459–466. doi: 10.1016/S1470-2045(09)70025-7

Stupp, R., Mason, W. P., van den Bent, M. J., Weller, M., Fisher, B., Taphoorn, M. J. B., et al. (2005). Radiotherapy plus concomitant and adjuvant temozolomide for glioblastoma. *N. Engl. J. Med.* 352, 987–996. doi: 10.1056/NEJMoa043330

Sun, A., Liu, X., and Tang, G. (2018). Carbon-11 and Fluorine-18 labeled amino acid tracers for positron emission tomography imaging of tumors. *Front. Chem.* 5:124. doi: 10.3389/fchem.2017.00124

Tanaka, Y., Nariai, T., Momose, T., Aoyagi, M., Maehara, T., Tomori, T., et al. (2009). Glioma surgery using a multimodal navigation system with integrated metabolic images. *J. Neurosurg.* 110, 163–172. doi: 10.3171/2008.4.17569

Tarapore, P. E., Findlay, A. M., Honma, S. M., Mizuiri, D., Houde, J. F., Berger, M. S., et al. (2013). Language mapping with navigated repetitive TMS: proof of technique and validation. *NeuroImage* 82, 260–272. doi: 10.1016/j.neuroimage.2013.05.018

Tarapore, P. E., Tate, M. C., Findlay, A. M., Honma, S. M., Mizuiri, D., Berger, M. S., et al. (2012). Preoperative multimodal motor mapping: a comparison of magnetoencephalography imaging, navigated transcranial magnetic stimulation, and direct cortical stimulation. *J. Neurosurg.* 117, 354–362. doi: 10.3171/2012.5.JNS112124

Thulborn, K. R., Waterton, J. C., Matthews, P. M., and Radda, G. K. (1982). Oxygenation dependence of the transverse relaxation time of water protons in whole blood at high field. *Biochim Biophys. Acta* 714, 265–270. doi: 10.1016/0304-4165(82)90333-6

Tietze, A., Choi, C., Mickey, B., Maher, E. A., Parm Ulhøi, B., Sangill, R., et al. (2018). Noninvasive assessment of isocitrate dehydrogenase mutation status in cerebral gliomas by magnetic resonance spectroscopy in a clinical setting. *J. Neurosurg.* 128, 391–398. doi: 10.3171/2016.10.JNS161793

Togao, O., Hiwatashi, A., Yamashita, K., Kikuchi, K., Mizoguchi, M., Yoshimoto, K., et al. (2016). Differentiation of high-grade and low-grade diffuse gliomas by intravoxel incoherent motion MR imaging. *Neuro-Oncology* 18, 132–141. doi: 10.1093/neuonc/nov147

Toh, C. H., Wei, K. C., Chang, C. N., Hsu, P. W., Wong, H. F., Ng, S. H., et al. (2012). Differentiation of pyogenic brain abscesses from necrotic glioblastomas with use of susceptibility-weighted imaging. *Am. J. Neuroradiol.* 33, 1534–1538. doi: 10.3174/ajnr.A2986

Tong, K. A., Ashwal, S., Obenaus, A., Nickerson, J. P., Kido, D., and Haacke, E. M. (2008). Susceptibility-Weighted MR imaging: a review of clinical applications in children. *Am. J. Neuroradiol.* 29, 9–17. doi: 10.3174/ajnr.A0786

Upadhyay, N., and Waldman, A. D. (2011). Conventional MRI evaluation of gliomas. *Br. J. Radiol.* 84, S107–S111. doi: 10.1259/bjr/65711810

van Dijken, B. R. J., van Laar, P. J., Holtman, G. A., and van der Hoorn, A. (2017). Diagnostic accuracy of magnetic resonance imaging techniques for treatment response evaluation in patients with high-grade glioma, a systematic review and meta-analysis. *Eur. Radiol.* 27, 4129–4144. doi: 10.1007/s00330-017-4789-9

van West, S. E., de Bruin, H. G., van de Langerijt, B., Swaak-Kragten, A. T., van den Bent, M. J., and Taal, W. (2017). Incidence of pseudoprogression in low-grade gliomas treated with radiotherapy. *Neuro-Oncology* 19, 719–725. doi: 10.1093/neuonc/now194

Verburg, N., and de Witt Hamer, P. C. (2021). State-of-the-art imaging for glioma surgery. *Neurosurg. Rev.* 44, 1331–1343. doi: 10.1007/s10143-020-01337-9

Villanueva-Meyer, J. E., Mabray, M. C., and Cha, S. (2017). Current clinical brain tumor imaging. *Neurosurgery* 81, 397–415. doi: 10.1093/neuros/nyx103

Wang, K., Qiao, Z., Zhao, X., Li, X., Wang, X., Wu, T., et al. (2020). Individualized discrimination of tumor recurrence from radiation necrosis in glioma patients using an integrated radiomics-based model. *Eur. J. Nucl. Med. Mol. Imaging.* 47, 1400–1411. doi: 10.1007/s00259-019-04604-0

Wang, X., Chen, X. Z., Shi, L., and Dai, J. P. (2019). Glioma grading and IDH1 mutational status: assessment by intravoxel incoherent motion MRI. *Clin. Radiol.* 74, 651.e7-651.e14. doi: 10.1016/j.crad.2019.03.020

Wang, X., Hu, X., Xie, P., Li, W., Li, X., and Ma, L. (2015). Comparison of magnetic resonance spectroscopy and positron emission tomography in detection of tumor recurrence in posttreatment of glioma: a diagnostic meta-analysis: meta-analysis for glioma recurrence. *Asia Pac. J. Clin. Oncol.* 11, 97–105. doi: 10.1111/ajco.12202

Warnert, E. A. H., Wood, T. C., Incekara, F., Barker, G. J., Vincent, A. J. P., Schouten, J., et al. (2021). Mapping tumour heterogeneity with pulsed 3D CEST MRI in non-enhancing glioma at 3 T. *Magn. Reson. Mater. Phys. Biol. Med.* Online ahead of print. doi: 10.1007/s10334-021-00911-6

Warth, A., Simon, P., Capper, D., Goeppert, B., Tabatabai, G., Herzog, H., et al. (2007). Expression pattern of the water channel aquaporin-4 in human gliomas is associated with blood-brain barrier disturbance but not with patient survival. *J. Neurosci. Res.* 85, 1336–1346. doi: 10.1002/jnr.21224

Weiss Lucas, C., Nettekoven, C., Neuschmelting, V., Oros-Peusquens, A. M., Stoffels, G., Viswanathan, S., et al. (2020). Invasive versus non-invasive mapping of the motor cortex. *Hum. Brain Mapp.* 41, 3970–3983. doi: 10.1002/hbm.25101

Weiss, C., Tursunova, I., Neuschmelting, V., Locaku, H., Nettekoven, C., Oros-Peusquens, A. M., et al. (2015). Improved nTMS- and DTI-derived CST tractography through anatomical ROI seeding on anterior pontine level compared to internal capsule. *NeuroImage Clin.* 7, 424–437. doi: 10.1016/j.nicl.2015.01.006

Wen, J., Chen, W., Zhu, Y., and Zhang, P. (2021). Clinical features associated with the efficacy of chemotherapy in patients with glioblastoma (GBM): a surveillance, epidemiology, and end results (SEER) analysis. *BMC Cancer* 21:81. doi: 10.1186/s12885-021-07800-0

Wen, Z., Hu, S., Huang, F., Wang, X., Guo, L., Quan, X., et al. (2010). MR imaging of high-grade brain tumors using endogenous protein and peptide-based contrast. *NeuroImage* 51, 616–622. doi: 10.1016/j.neuroimage.2010.02.050

Whitfield, G. A., Kennedy, S. R., Djoukhadar, I. K., and Jackson, A. (2014). Imaging and target volume delineation in glioma. *Clin. Oncol.* 26, 364–376. doi: 10.1016/j.clon.2014.04.026

Wick, W., Chinot, O. L., Bendszus, M., Mason, W., Henriksson, R., Saran, F., et al. (2016). Evaluation of pseudoprogression rates and tumor progression patterns in a phase III trial of bevacizumab plus radiotherapy/temozolomide for newly diagnosed glioblastoma. *Neuro-Oncology* 18, 1434–1441. doi: 10.1093/neuonc/now091

Wick, W., Puduvalli, V. K., Chamberlain, M. C., van den Bent, M. J., Carpentier, A. F., Cher, L. M., et al. (2010). Phase III study of enzastaurin compared with lomustine in the treatment of recurrent intracranial glioblastoma. *J. Clin. Oncol.* 28, 1168–1174. doi: 10.1200/JCO.2009.23.2595

Willats, L., and Calamante, F. (2013). The 39 steps: evading error and deciphering the secrets for accurate dynamic susceptibility contrast MRI: THE 39 STEPS: TOWARDS ACCURATE DSC-MRI. *NMR Biomed.* 26, 913–931. doi: 10.1002/nbm.2833

Williams, V., Jayashree, M., Bansal, A., Baranwal, A., Nallasamy, K., Chandra Singhi, S., et al. (2019). Spontaneous intracranial haemorrhage in children—intensive care needs and predictors of in-hospital mortality: a 10-year single-centre experience. *Childs Nerv. Syst.* 35, 1371–1379. doi: 10.1007/s00381-019-04209-w

Winter, S. F., Vaios, E. J., Muzikansky, A., Martinez-Lage, M., Bussière, M. R., Shih, H. A., et al. (2020). Defining treatment-related adverse effects in patients with glioma: distinctive features of pseudoprogression and treatment-induced necrosis. *Oncologist* 25, e1221–e1232. doi: 10.1634/theoncologist.2020-0085

Wirsching, H. G., Roelcke, U., Weller, J., Hundsberger, T., Hottinger, A. F., von Moos, R., et al. (2021). MRI and 18FET-PET predict survival benefit from

bevacizumab plus radiotherapy in patients with isocitrate dehydrogenase wild-type glioblastoma: results from the randomized ARTE trial. *Clin. Cancer Res.* 27, 179–188. doi: 10.1158/1078-0432.CCR-20-2096

Wu, B., Warnock, G., Zaiss, M., Lin, C., Chen, M., Zhou, Z., et al. (2016). An overview of CEST MRI for non-MR physicists. *EJNMMI Phys.* 3:19. doi: 10.1186/s40658-016-0155-2

Wu, J. S., Zhou, L. F., Tang, W. J., Mao, Y., Hu, J., Song, Y. Y., et al. (2007). Clinical evaluation and follow-up outcome of diffusion tensor imaging-based functional neuronavigation: a prospective, controlled study in patients with gliomas involving pyramidal tracts. *Neurosurgery* 61, 935–948. doi: 10.1227/01.neu.0000303189.80049.ab

Xiao, H. F., Chen, Z. Y., Lou, X., Wang, Y. L., Gui, Q. P., Wang, Y., et al. (2015). Astrocytic tumour grading: a comparative study of three-dimensional pseudocontinuous arterial spin labelling, dynamic susceptibility contrast-enhanced perfusion-weighted imaging, and diffusion-weighted imaging. *Eur. Radiol.* 25, 3423–3430. doi: 10.1007/s00330-015-3768-2

Yamashita, K., Yoshiura, T., Hiwatashi, A., Togao, O., Yoshimoto, K., Suzuki, S. O., et al. (2013). Differentiating primary CNS lymphoma from glioblastoma multiforme: assessment using arterial spin labeling, diffusion-weighted imaging, and 18F-fluorodeoxyglucose positron emission tomography. *Neuroradiology* 55, 135–143. doi: 10.1007/s00234-012-1089-6

Yang, T. T., Gallen, C. C., Schwartz, B. J., and Bloom, F. E. (1993). Noninvasive somatosensory homunculus mapping in humans by using a large-array biomagnetometer. *Proc. Natl. Acad. Sci. U S A.* 90, 3098–3102. doi: 10.1073/pnas.90.7.3098

Zhang, K., Yun, S. D., Triphan, S. M. F., Sturm, V. J., Buschle, L. R., Hahn, A., et al. (2019). Vessel architecture imaging using multiband gradient-echo/spin-echo EPI. *PLoS One* 14:e0220939. doi: 10.1371/journal.pone.0220939

Zhang, W., Silva, A. C., Williams, D. S., and Koretsky, A. P. (1995). NMR measurement of perfusion using arterial spin labeling without saturation of macromolecular spins. *Magn. Reson. Med.* 33, 370–376. doi: 10.1002/mrm.1910330310

Zhang, Z., Tan, Z., Lv, Q., Wang, L., Yu, K., Yang, H., et al. (2021). High expression of C1ORF112 predicts a poor outcome: a potential target for the treatment of low-grade gliomas. *Front. Genet.* 12:710944. doi: 10.3389/fgene.2021.710944

Zolal, A., Hejčl, A., Vachata, P., Bartoš, R., Humhej, I., Malucelli, A., et al. (2012). The use of diffusion tensor images of the corticospinal tract in intrinsic brain tumor surgery: a comparison with direct subcortical stimulation. *Neurosurgery* 71, 331–340; discussion 340. doi: 10.1227/NEU.0b013e31825b1c18

Zou, T., Yu, H., Jiang, C., Wang, X., Jiang, S., Rui, Q., et al. (2018). Differentiating the histologic grades of gliomas preoperatively using amide proton transfer-weighted (APTW) and intravoxel incoherent motion MRI. *NMR Biomed.* 31:10.1002/nbm.3850. doi: 10.1002/nbm.3850

Conflict of Interest: The authors declare that the research was conducted in the absence of any commercial or financial relationships that could be construed as a potential conflict of interest.

Publisher's Note: All claims expressed in this article are solely those of the authors and do not necessarily represent those of their affiliated organizations, or those of the publisher, the editors and the reviewers. Any product that may be evaluated in this article, or claim that may be made by its manufacturer, is not guaranteed or endorsed by the publisher.

Copyright © 2022 Carrete, Young and Cha. This is an open-access article distributed under the terms of the Creative Commons Attribution License (CC BY). The use, distribution or reproduction in other forums is permitted, provided the original author(s) and the copyright owner(s) are credited and that the original publication in this journal is cited, in accordance with accepted academic practice. No use, distribution or reproduction is permitted which does not comply with these terms.

frontiers in Oncology

REVIEW
published: 28 February 2022
doi: 10.3389/fonc.2021.811425

High-Grade Glioma Treatment Response Monitoring Biomarkers: A Position Statement on the Evidence Supporting the Use of Advanced MRI Techniques in the Clinic, and the Latest Bench-to-Bedside Developments. Part 2: Spectroscopy, Chemical Exchange Saturation, Multiparametric Imaging, and Radiomics

Thomas C. Booth[1,2], Evita C. Wiegers[3], Esther A. H. Warnert[4], Kathleen M. Schmainda[5], Frank Riemer[6], Ruben E. Nechifor[7], Vera C. Keil[8], Gilbert Hangel[9], Patrícia Figueiredo[10], Maria Del Mar Álvarez-Torres[11] and Otto M. Henriksen[12] on behalf of the European Cooperation in Science Technology (COST) Glioma MR Imaging 2.0 (GliMR) initiative*

[1] School of Biomedical Engineering and Imaging Sciences, King's College London, St. Thomas' Hospital, London, United Kingdom, [2] Department of Neuroradiology, King's College Hospital NHS Foundation Trust, London, United Kingdom, [3] Department of Radiology, University Medical Center Utrecht, Utrecht, Netherlands, [4] Department of Radiology & Nuclear Medicine, Erasmus MC, Rotterdam, Netherlands, [5] Department of Biophysics, Medical College of Wisconsin, Milwaukee, WI, United States, [6] Mohn Medical Imaging and Visualization Centre (MMIV), Department of Radiology, Haukeland University Hospital, Bergen, Norway, [7] Department of Clinical Psychology and Psychotherapy International Institute for the Advanced Studies of Psychotherapy and Applied Mental Health, Babes-Bolyai University, Cluj-Napoca, Romania, [8] Department of Radiology and Nuclear Medicine, Amsterdam UMC, location VUmc, Amsterdam, Netherlands, [9] Department of Neurosurgery & High-Field MR Centre, Department of Biomedical Imaging and Image-Guided Therapy, Medical University Vienna, Vienna, Austria, [10] Department of Bioengineering and Institute for Systems and Robotics - Lisboa, Instituto Superior Técnico, Universidade de Lisboa, Lisbon, Portugal, [11] Biomedical Data Science Laboratory, ITACA, Universitat Politècnica de València, Valencia, Spain, [12] Department of Clinical Physiology, Nuclear medicine and PET, Copenhagen University Hospital Rigshospitalet, Copenhagen, Denmark

Objective: To summarize evidence for use of advanced MRI techniques as monitoring biomarkers in the clinic, and to highlight the latest bench-to-bedside developments.

Methods: The current evidence regarding the potential for monitoring biomarkers was reviewed and individual modalities of metabolism and/or chemical composition imaging discussed. Perfusion, permeability, and microstructure imaging were similarly analyzed in Part 1 of this two-part review article and are valuable reading as background to this article. We appraise the clinic readiness of all the individual modalities and consider methodologies involving machine learning (radiomics) and the combination of MRI approaches (multiparametric imaging).

OPEN ACCESS

Edited by:
Nico Sollmann, University of California, San Francisco, United States

Reviewed by:
Giuseppe Barisano, University of Southern California, United States
Daniel Paech, University Hospital Bonn, Germany

***Correspondence:**
Thomas C. Booth
tombooth@doctors.org.uk

Specialty section:
This article was submitted to Neuro-Oncology and Neurosurgical Oncology, a section of the journal Frontiers in Oncology

Received: *08 November 2021*
Accepted: *28 December 2021*
Published: *28 February 2022*

Citation:
Booth TC, Wiegers EC, Warnert EAH, Schmainda KM, Riemer F, Nechifor RE, Keil VC, Hangel G, Figueiredo P, Álvarez-Torres MDM and Henriksen OM (2022) High-Grade Glioma Treatment Response Monitoring Biomarkers: A Position Statement on the Evidence Supporting the Use of Advanced MRI Techniques in the Clinic, and the Latest Bench-to-Bedside Developments. Part 2: Spectroscopy, Chemical Exchange Saturation, Multiparametric Imaging, and Radiomics. Front. Oncol. 11:811425. doi: 10.3389/fonc.2021.811425

Results: The biochemical composition of high-grade gliomas is markedly different from healthy brain tissue. Magnetic resonance spectroscopy allows the simultaneous acquisition of an array of metabolic alterations, with choline-based ratios appearing to be consistently discriminatory in treatment response assessment, although challenges remain despite this being a mature technique. Promising directions relate to ultra-high field strengths, 2-hydroxyglutarate analysis, and the use of non-proton nuclei. Labile protons on endogenous proteins can be selectively targeted with chemical exchange saturation transfer to give high resolution images. The body of evidence for clinical application of amide proton transfer imaging has been building for a decade, but more evidence is required to confirm chemical exchange saturation transfer use as a monitoring biomarker. Multiparametric methodologies, including the incorporation of nuclear medicine techniques, combine probes measuring different tumor properties. Although potentially synergistic, the limitations of each individual modality also can be compounded, particularly in the absence of standardization. Machine learning requires large datasets with high-quality annotation; there is currently low-level evidence for monitoring biomarker clinical application.

Conclusion: Advanced MRI techniques show huge promise in treatment response assessment. The clinical readiness analysis highlights that most monitoring biomarkers require standardized international consensus guidelines, with more facilitation regarding technique implementation and reporting in the clinic.

Keywords: high-grade glioma, glioblastoma, treatment response, monitoring biomarker, MRI, spectroscopy, CEST, radiomics

1 INTRODUCTION

Contemporaneous, accurate, and reliable monitoring biomarkers are required for high-grade glioma treatment response assessment as important challenges limit the use of conventional structural MRI protocols. The current evidence regarding the potential for monitoring biomarkers based on advanced MRI techniques shows that the methodology has developed considerably. Although some techniques have evolved and matured over three decades, several new state-of-the-art methods are poised to contribute to the imaging armamentarium. However, limitations for all techniques remain. High level evidence (level 1 or 2) (1) of clinical diagnostic accuracy typically is lacking. Clinical implementation of standardized tools generally remains challenging, and some recent techniques are in their infancy. Many of these findings were shown following review of the modalities of perfusion, permeability, and microstructure imaging, described in Part 1 (*High-Grade Glioma Treatment Response Monitoring Biomarkers: A Position Statement on the Evidence Supporting the Use of Advanced MRI Techniques in the Clinic, and the Latest Bench-to-Bedside Developments. Part 1: Perfusion and Diffusion Techniques*) of this two-part review article.

The challenges limiting the use of conventional structural MRI protocols as monitoring biomarkers and the need for novel monitoring biomarkers are also described in Part 1. To complete a summary of the evidence for the use of advanced MRI techniques as monitoring biomarkers in the clinic, and to finish highlighting the latest bench-to-bedside developments, we now focus on the individual modalities of metabolism and/or chemical composition imaging. We also appraise the clinic readiness of all the individual modalities. Furthermore, we consider post-processing methodologies involving the combination of MRI approaches (multiparametric imaging) or machine learning (radiomics).

2 MATERIALS AND METHODS

The review method is described fully in Part 1. Briefly, experts in advanced MRI techniques applied to high-grade glioma treatment response assessment, convened through a European framework. The consensus decision was to focus on monitoring biomarkers that can reliably differentiate post-treatment-related effects (PTRE) from true tumor progression during (or before) the point when contrast enhancement on longitudinal relaxation time T_1-weighted MRI images first increases.

Advanced imaging technique analyses were compiled by subject matter experts and incorporated into a manuscript and circulated to the working group members.

To determine clinical diagnostic accuracy, we performed MEDLINE (including PubMed), Embase and Cochrane Register searches for recent systematic reviews and meta-analyses, favoring those which followed Preferred Reporting Items for Systematic Reviews and Meta-Analysis: Diagnostic

Test Accuracy (PRISMA-DTA) methodology (2). We also performed searches to analyze individual clinical studies related to each advanced imaging technique since the time of the included systematic review; if a systematic review was published before 2015, we confined our searches to 2015–2021.

3 RESULTS

3.1 Advanced MRI Techniques

3.1.1 Spectroscopy-Based Techniques

3.1.1.1 Methodology

Proton magnetic resonance spectroscopy (^{1}H MRS) is a technique that enables noninvasive characterization of certain biochemicals that are intermediates or end products of cellular metabolism, referred to as metabolites, within tissues based on the chemical shift of molecule resonances in relation to water. The area under a metabolite peak in a magnetic resonance (MR) spectrum is directly proportional to the tissue concentration of this metabolite. The major peaks in the brain include resonances of N-acetyl-aspartate (NAA), choline (Cho), creatine (Cre), and glutamate (Glu), but the total number of quantifiable metabolites depends mainly on the pulse sequence used, sequence parameters (e.g., echo time), and static magnetic field strength (3).

It is well known that spectra acquired from brain tumors are markedly different from spectra acquired from healthy brain tissue (4). An elevated Cho concentration and reduced NAA concentration can often be identified in tumors. A decrease in NAA is often interpreted as a loss or dysfunction of neural tissue, while increased Cho levels are thought to reflect the increased cell membrane turnover in tumors. Additional commonly used markers for tumor proliferation and tumor metabolism include increased lactate, myo-inositol, and lipid levels. In normal brain tissue, lactate is present in a barely MRS-detectable concentration. Elevated lactate levels may be the result of anaerobic glycolysis (i.e., the Warburg effect), necrosis, or ischemia. The exact role of myo-inositol is not fully elucidated, but studies have shown that it may reflect the number of viable glial cells in brain tumors (5). Lipid levels correlate with a breakdown of cell membranes through necrosis and, as such, are a marker for high-grade tumors (6). Because the direct estimation of biochemical concentrations in tumor tissue with *in vivo* MRS remains challenging, clinical and research outputs are normally described as ratios to NAA or Cr.

^{1}H MRS data can be acquired either as single voxel spectroscopy (SVS, **Figure 1**) or from multiple voxels by spectroscopic imaging [2D or 3D magnetic resonance spectroscopic imaging (MRSI), **Figure 2**]. SVS is easy to implement and less time consuming than MRSI. However, the acquisition of a single, rather large, voxel may result in either incomplete sampling of the tumor or the inclusion of peritumoral regions in the sample, which may confound the analysis of heterogeneous tumor tissue.

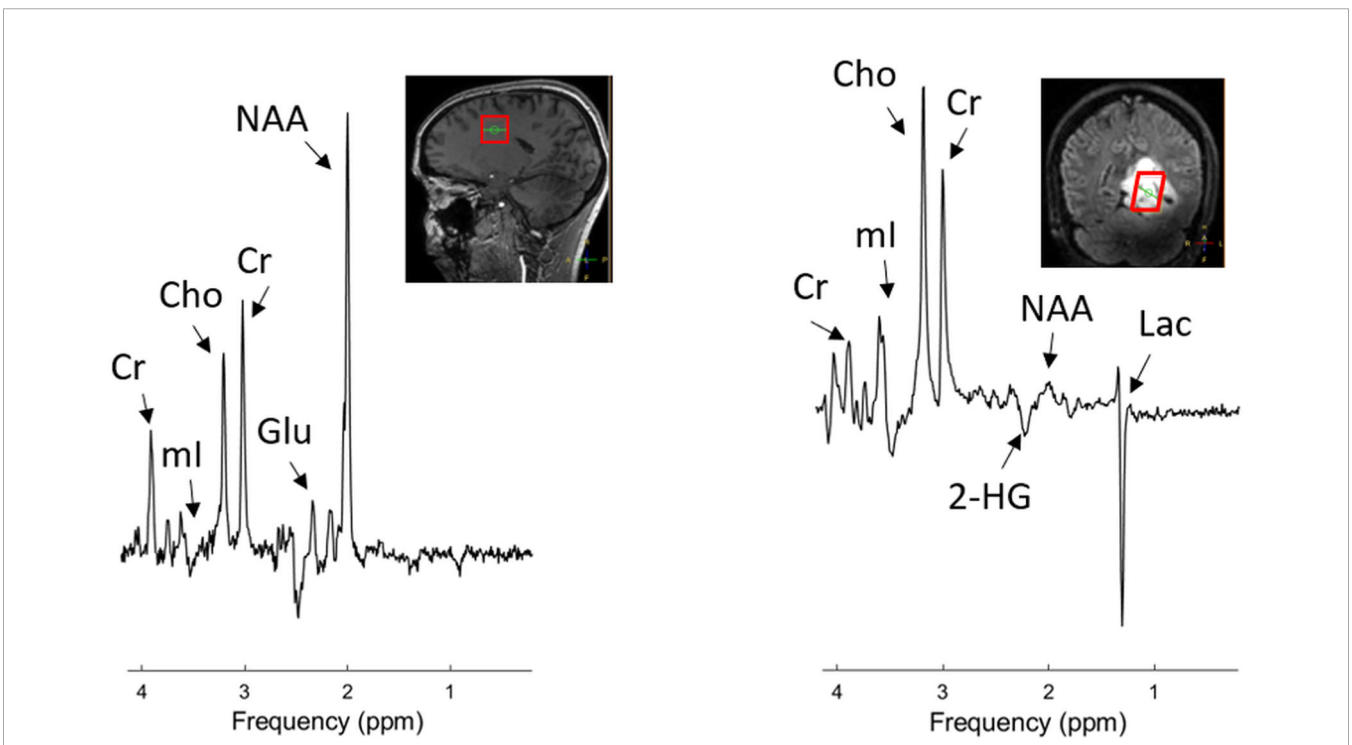

FIGURE 1 | Example of single-voxel ^{1}H MRS data acquired in a healthy volunteer (left) and a patient with diffuse astrocytoma with IDH-mutation, WHO grade 2. Data were acquired with a sLASER sequence at 7 T (TE 110 ms, TR 5000 ms) dedicated for detection of 2HG. The location of the MRS voxel is indicated by the red box in the structural images. An elevated Cho and Lac level and reduced NAA level are clearly visible in the tumor. Choline (Cho), Creatine (Cre), N-acetyl-aspartate (NAA), lactate (Lac), myo-Inositol (mI), glutamate (Glu). For illustrative purposes, a low-grade glioma is used.

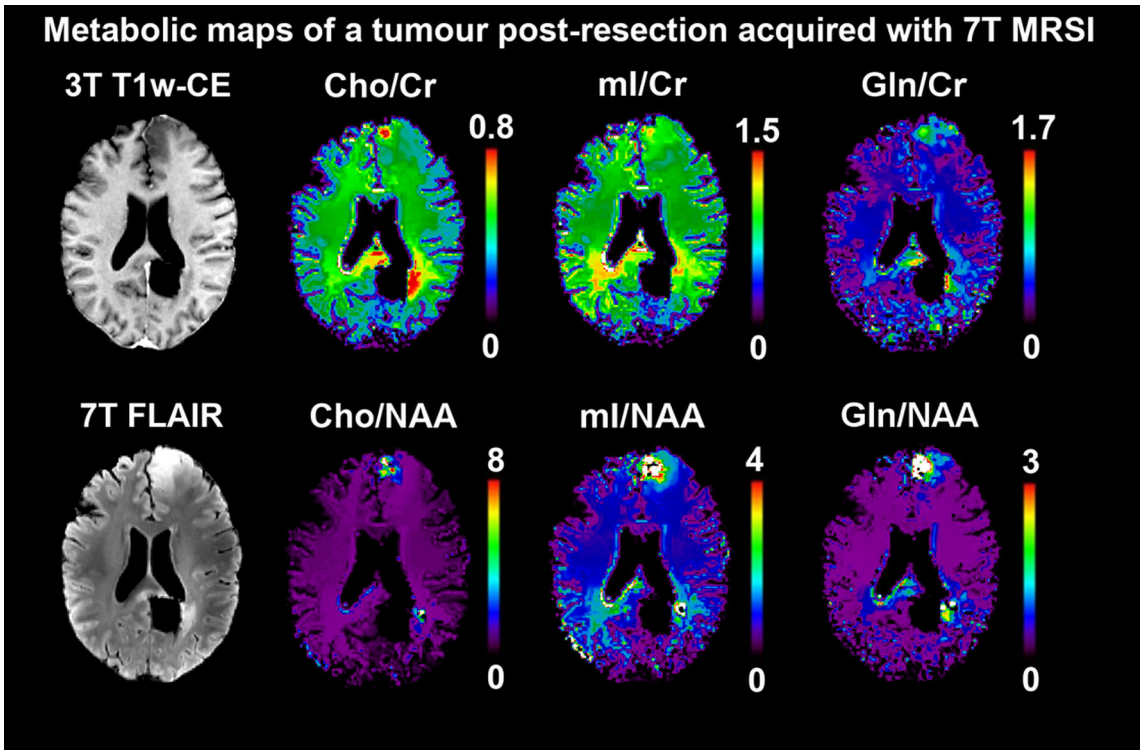

FIGURE 2 | Postsurgical 7 T MRSI scan of a patient with oligodendroglioma, IDH-mutant, 1p/19q deleted, grade 3. Free induction decay-acquisition and patch-based super-resolution, 3.4 × 3.4 × 8 mm^3 nominal resolution (7). The ratios of three metabolites (Cho, mI, Gln) to Cr and NAA as common references are mapped. Both in a left frontal second focus as well as around the primary focus resection cavity posterior to the splenium, increased ratios for all six are clearly discernible and relate to morphological findings. Specifically, for the Gln ratios, changes between normal-appearing brain tissues and suspected neoplastic growth are in the range of over a magnitude, making it an attractive potential biomarker, but will require ultra-high-field systems for quantification. Similar techniques could be applied for the spatial identification of neoplastic activity during therapy. Choline (Cho), Creatine (Cr), N-acetyl-aspartate (NAA), myo-Inositol (mI), glutamine (Gln).

Recently, the MRS community has tried to move forward and reach a standard consensus regarding MRS methodology developments of the last decade (8–11), but reproducibility studies have not been able to adequately reflect these recent discussions. In particular, multicenter reproducibility studies remain limited to only a few MRS applications (12, 13).

3.1.1.2 Evidence From Clinical Studies

The utility of MRS to distinguish recurrent tumors from radiation necrosis has been evaluated in two meta-analyses to date (**Table 1**). The first meta-analysis (23), comprising 13 studies, evaluated the diagnostic effectiveness of ^{1}H MRS (both SVS and MRSI) in differentiating recurrent tumor from radiation necrosis. This study showed that the Cho/Cr and Cho/NAA ratios are higher in tumor recurrence compared with radiation necrosis (pooled difference: 0.77, 95% CI = 0.57 to 0.98 for Cho/Cr; pooled difference: 1.02, 95% CI = 0.03 to 2.0 for Cho/NAA). In another meta-analysis of 18 studies (20), the pooled sensitivity and specificity of Cho/Cr and Cho/NAA in discriminating recurrent glioma and radiation necrosis are reported to be between 80–90%. Therefore, the authors recommended using MRS as an add-on to the structural MRI.

In a meta-analysis comparing the diagnostic accuracy of anatomical and advanced MRI [i.e., apparent diffusion coefficient (ADC), dynamic susceptibility contrast-enhanced (DSC), dynamic contrast enhanced (DCE), arterial spin labeling (ASL), and ^{1}H MRS (SVS and MRSI)] for treatment response assessment in high-grade gliomas, ^{1}H MRS was found to have the highest diagnostic accuracy, with a sensitivity of 91% and specificity of 95%, among all the advanced MRI techniques (21). Various metabolite ratios were used in the MRS studies included in this meta-analysis, but in the majority of the studies Cho/Cr turned out to be the best predictor to differentiate true tumor progression from PTRE. It is noteworthy that in all of the studies above, no explicit description was given as to which part of the tumor (e.g. contrast-enhancing, T_2-weighted hyperintense, or necrotic component) was assessed.

The utility of MRS to differentiate pseudoprogression from tumor recurrence is less well studied, but a few studies show its effectiveness. The potential of 3D MRSI was illustrated in a recent study using 3D echo planar spectroscopic imaging in glioblastoma patients (24). Here, Cho/NAA and Cho/Cr maps were co-registered to anatomical images and mapped on different regions of the neoplasm. Higher Cho/NAA and

TABLE 1 | Meta-analyses of advanced MRI treatment response monitoring biomarkers. Post-processing methodology meta-analyses are not included here, and are described in the relevant sections below.

Paper	Quality assessment	Period	Modality	Studies/ patient (n/n)	Sample size range(n-n)	Prospective Studies (n/n)	Progression compared to:	Pooled measure (n studies)	Sensitivity	Specificity
Yu et al. (14)	Q2	2012-2017	DWI/ADC	6/214	20-68	1/6	PSP	ADC mean (3) 5th centile ADC (2) relative ADC (1)	95 (89-98)	83 (72-91)
Zhang et al. (15)	Q2	2007-2014	DWI/ADC	9/284	20-210	1/9	RN	ADC ratio (7) ADC value (2)	82 (75-91)	84 (76-91)
Okuchi et al. (16)	Q2	2011-2015	DCE	9/298	14-79	3/9	PTRE	All	88 (74-95)	86 (78-91)
							–	K^{trans} (6)	75 (63-84)	79 (68-87)
							–	Toft/Extended Toft (6)	77 (65-86)	85 (75-92)
							–	Model independent (4)	94 (86-98)	85 (74-93)
Patel et al. (17)	Q2	2009-2015	DSC	15/897	9-169	7/28	PTRE	DSC best parameter	90 (85-94)	88 (83-92)
							–	DSC max nCBV (5)	93 (86-98)	76 (66-85)
							–	DSC mean nCBV (8)	88 (81-94)	88 (78-95)
		2011-2015	DCE	7/581	18-57	2/7	–	best parameter	89 (78-96)	85 (77-91)
Wan et al. (18)	Q2	2011-2016	DSC	11/116	20-68	1/11	PsP	nCBV	88 (84-92)	77 (89-84)
Deng et al. (19)	Q	1992-2013	DSC	7/174	10-57	0/18	No progression	rCBV (6)	88 (82-93)	85 (75-92)
Zhang et al. (20)	Q2		MRS	12/262	8-40	1/12	RN	Cho/Cr	83 (77-89)	83 (874-90)
				9/213	13-38	1/12	–	Cho/NAA	88 (81-93)	86 (76-93)
van Dijken et al. (21)	Q2	2009-2014	DSC	18/708	7-90	8/18	PTRE	Best parameter	87 (82-91)	87 (77-91)
		2011-2013	DCE	5/207	13-79	2/5	–	–	92 (73-98)	85 (76-92)
		2006-2014	MRS	9/203	12-40	4/9	–	–	91 (79-97)	95 (65-99)
		2010-2014	ADC	7/204	16-51	4/7	–	–	71 (60-80)	87 (77-93)
		2008-2013	Structural MRI	5/166	7-93	2/8	–	–	68 (51-81)	77 (45-93)
Wang et al. (22)	Q2	2009-2019	DSC	20/939	16-98	5/20	PTRE	nCBV (17) max rCBV (3)	83 (79-86)	83 (78-87)
		2013-2019	DCE	4/250	40-98	1/4	–	K^{trans}	73 (66-80)	80 (69-88)
		2013-2018	ASL	3/160	29-69	0/3	–	nCBF	79 (69-87)	78 (67-87)

RN, radiation necrosis; PSP, pseudoprogression; PTRE, post-treatment related effects; Q, QUADAS (Quality Assessment of Diagnostic Accuracy Studies) tool; Q2, QUADAS-2 tool.

Cho/Cr ratios specifically in the contrast-enhancing part of the tumor were found in patients with tumor progression compared with patients with pseudoprogression, with a discriminatory accuracy of 94%. Similar results were found in another MRSI study where a threshold of Cho/NAA ≥ 1.3 in the contrast-enhancing part of the tumor was proposed to determine tumor recurrence (25).

3.1.1.3 Strengths and Weaknesses

The main strength of MRS techniques for *in vivo* tumor assessment is the ability to acquire an array of metabolic alterations in one measurement and the flexibility to optimize methods for specific targets of interest. The main limitations of SVS and, to a lesser extent MRSI, are the relatively large voxel size and poor spatial coverage (3). This can lead to partial volume effects between active tumor, treatment-induced changes, and necrosis, as well as the omission of potentially neoplastic tissues. Furthermore, scan time is typically long, artifacts from transcranial lipids or susceptibility differences reduce spectral fitting reliability, and extensive offline processing is usually required. Advanced acquisition techniques can address most of these limitations but require expert operators and tools, and have led to a multitude of published methodologies lacking direct comparability. Therefore, MRS often is not included in routine clinical protocols. Recent initiatives for consensus on MRS methodology and applications are expected to lead to a more

"even playing field" and standardized approaches that will make future studies more comparable (9, 26, 27).

3.1.1.4 Future Developments

In most studies on PTRE, only the most prominent MRS peaks (i.e., NAA, Cho, and Cr) have been evaluated as these produce the most signal and are least affected by J-coupling under long echo times. The use of ultra-high field ^{1}H MRS (i.e., ≥ 7 Tesla [T]) results in an increased signal-to-noise ratio and an improved ability to separate overlapping peaks (28). Applying 3D MRSI may overcome the barrier of incomplete tumor sampling in SVS, and this has motivated the development of fast and high-resolution spectroscopic imaging sequences (29). With this, additional markers for tumor proliferation and tumor metabolism, including glycine (Gly), Glu, and glutamine (Gln), can be evaluated unambiguously (30). Recently, it was shown in preoperative patients that metabolic differences between tumor regions and peritumoral tissue, beyond decreased NAA levels and elevated Cho levels, could be detected at 7 T (31). For example, high levels of Gln and Gly (which are difficult to separate from Glu and myo-inositol, respectively, at lower fields) were found within the tumor region, which may reflect cancer cell proliferation in the case of Gly and malignant metabolic changes for Gln. Whether these high-resolution 3D metabolite maps could aid in identifying PTRE is yet to be determined. There are high expectations for the application of machine-learning-driven classification of neoplastic tissues that could help to reach this goal (32).

A specific metabolite of interest is 2-hydroxyglutarate (2HG). 2HG is an oncometabolite, produced in glial tumor cells bearing an isocitrate dehydrogenase (IDH) gene mutation, either IDH1 or IDH2. The discovery that 2HG can be detected *in vivo* by dedicated MRS sequences has led to several successful studies showing the ability to determine IDH status noninvasively by MRS (33). Additionally, a potential role for 2HG MRS has been proposed in treatment response imaging. In patients with IDH-mutant tumors, 2HG levels decrease following adjuvant radiation and chemotherapy (34, 35) and increase in the case of tumor progression (35). Furthermore, monitoring 2HG levels could be of specific interest in evaluating the effects of IDH-inhibitors, as was shown in a phase 1 clinical trial (36).

Although ^{1}H MRS gives insight into steady-state metabolite concentrations, protons are not the only nuclei with resonances of interest. Techniques using other nuclei can be used such as ^{31}P MRS and MRSI (37), deuterium metabolic imaging (DMI), and (hyperpolarized) ^{13}C MRS and MRSI, which enable the evaluation of tissue metabolism *in vivo* (**Figure 3**). For example, ^{31}P-MRSI has been applied to the imaging of inter- and intracellular pH in gliomas, finding increased pH values both at 7 T (37) and 9.4 T (38) in proof-of-concept studies.

These techniques can be used to detect different sets of molecules important to tumor metabolism, such as glucose or ATP, and there is the potential for deriving enzyme activity or acidity. Currently, these techniques are used mainly in a research setting but are potentially promising for distinguishing PTRE, as metabolic reprogramming is one the hallmarks of cancer. For example, it was shown that DMI can be used to visualize tumor tissue metabolism beyond glucose uptake and, thus, map the Warburg effect, which is typically only seen in active tumor cells (39). As such, DMI may be potentially useful to differentiate between treatment-induced necrosis and tumor progression.

3.1.2 Chemical Exchange Saturation Transfer

3.1.2.1 Methodology

Chemical exchange saturation transfer (CEST) MRI is a technique in which labile protons on endogenous proteins can be selectively targeted to generate contrast (40). In a typical CEST examination in patient studies at 3 T, B_1 saturation pulses are used with a range of off-resonance frequencies centered around on-resonance B_1 saturation pulses to generate a Z-spectrum. Labile protons that are bound to mobile proteins are hereby saturated and will lead to saturation of the free water pool when exchanging with the free water protons, depending on their abundance and exchange rate. Endogenous CEST effects that can be targeted include saturation transfer of protons in amide (3.5 ppm), amine (3 ppm), total creatine (Cre) (2 ppm), and hydroxyl (0.9 ppm) bonds. Additional effects of application of off-resonance saturation pulses that will be present within Z-spectra include broad magnetization transfer (MT) effects in semisolid macromolecules, relayed nuclear Overhauser enhancement (NOE) in mobile macromolecules (−1 to −4 ppm) (41), and direct saturation of free water protons (i.e. spillover effect) (42). Note that, in particular at 3 T due to broad spectral linewidths, these effects are either close to or even overlapping with the endogenous CEST effects that are often the target of CEST studies. Several approaches exist to best isolate all of the above effects, such that the CEST effect of interest can be measured. For instance, increasing main magnetic field strength, e.g. using 7 T instead of 3 T systems, aids in separation of all of these effects because it leads to decreased spectral linewidths of the individual effects. Optimizing duration and power of B_1 saturation pulses can be used to sensitize CEST experiments to protons exchanging with different rates. Analysis approaches include magnetization transfer ratio asymmetry (MTR_{asym}) (43), in which signals with off-resonance frequencies with matching positive and negative shift around 0 ppm are subtracted from one another (**Figure 4**), and multiple pool fitting approaches of the Z-spectrum which are used to explicitly isolate individual contributions, such as the NOE, spillover and broad magnetization transfer effects (41, 44). Additionally, a range of methodologies accounts for changes in parameters that will affect the CEST contrast generated. These include additional acquisitions and/or analysis to correct for inhomogeneities in the main magnetic (B_0) (45) and saturation (B_1) (46) field, or a change in the T_1 (47).

A full overview of CEST MRI acquisition and analysis approaches is beyond the scope of the current review and has been given previously (40). However, in using CEST MRI for brain tumor imaging some confounding factors do require explicit attention. For example, the T_1 relaxation time of the free water pool and the broad MT effect both directly affect the measured signal in CEST studies. In brain tumors, the T_1 relaxation time is often found to be increased compared to

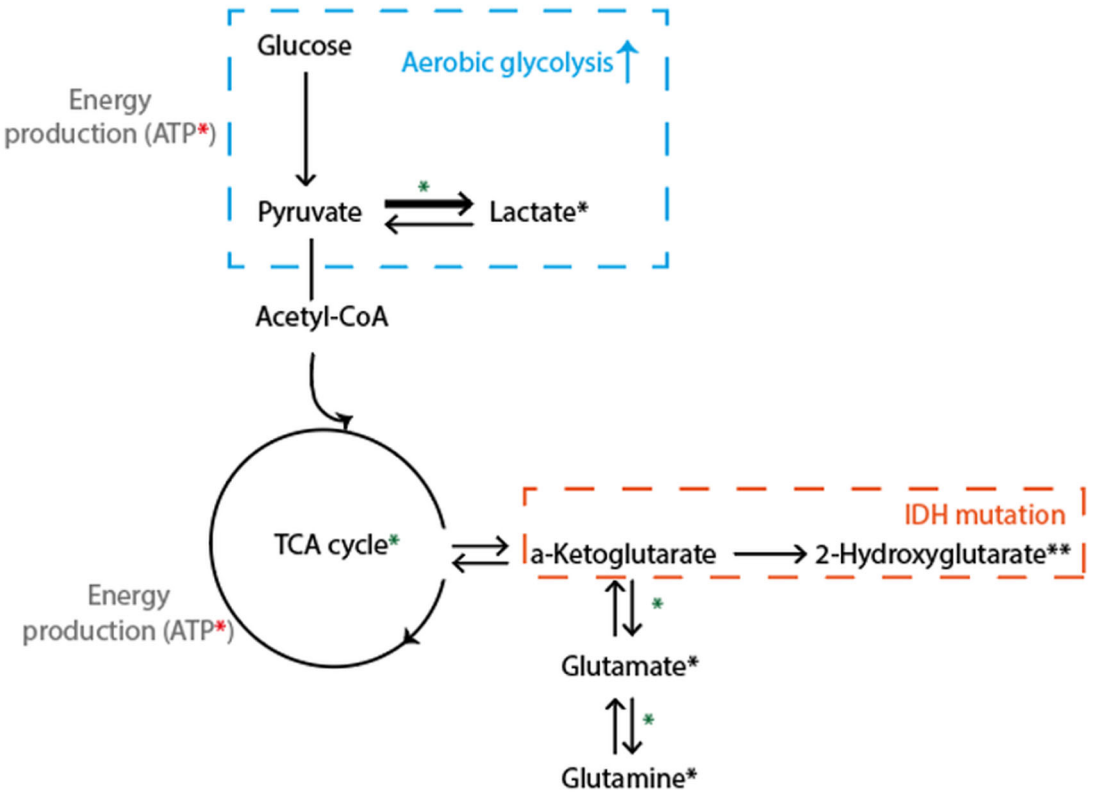

FIGURE 3 | Simplified schematic illustration of key metabolic pathways probed with spectroscopy. Glu (from brain-feeding arteries) is taken up by tumor cells and converted into pyruvate, which enters the tricarboxylic acid cycle and undergoes oxidative metabolism, for the production of energy (ATP). ^{1}H MRS visible metabolites are marked with a black *, where ** denotes that a dedicated MRS sequence is needed. Green *: includes pathways visible with ^{13}C or DMI. Red *: visible with ^{31}P MRS. Adenosine triphosphate (ATP), Glucose (Glu).

healthy white matter, which is generally attributed to increased tissue water content (48), while changes in macromolecular background in tumor tissue are thought to be the cause for commonly found decreases in MT in brain tumors (49–51). Additionally, B_1 saturation powers mostly used in CEST brain tumor studies are relatively low (< 2 μT), giving rise to strong NOE effects (41). However, NOE is known to change in brain tumors as well (52). The above highlights the difficulty of isolating the individual components contributing to CEST contrast and that care should be taken when changes in CEST contrasts are attributed to underlying physiological processes. This is an important aspect to keep in mind when reviewing the latest research in applications of CEST MRI to find biomarkers of treatment response in high-grade glioma.

Currently, imaging guidelines are not available (although in preparation). Some technical validation has been performed in healthy subjects in 7 T systems (53).

3.1.2.2 Evidence From Clinical Studies

Amide proton transfer (APT)-weighted CEST is the most investigated CEST technique to derive biomarkers of treatment response. In 2011, it was first shown in preclinical models that the APT-weighted signal of lesions immediately decreases when radiation necrosis occurs (in five animals) (54) or after treatment with temozolomide (five controls, six treated) (55). Increased APT-weighted signal within the lesion after treatment was thought to be indicative of increased cell proliferation in tumor progression, a hypothesis supported by a positive correlation between APT-weighted CEST and Ki67, an immunohistochemical marker of cell proliferation. This correlation has since been reproduced in human gliomas (56) and has led to the first results of increased APT-weighted CEST contrast after treatment to be associated with tumor progression rather than PTRE. However, the application of CEST MRI to differentiate tumor progression from PTRE is a relatively recent development, which has led to only a handful of clinical studies on this topic (see **Table S1**). Two research groups (57, 58) have found that in small cohorts of patients diagnosed with glioblastoma and scanned after chemoradiotherapy or radiotherapy alone, APT-weighted CEST improved differentiation of tumor response from PTRE compared with conventional imaging alone (with a combination of perfusion-weighted and APT-weighted CEST

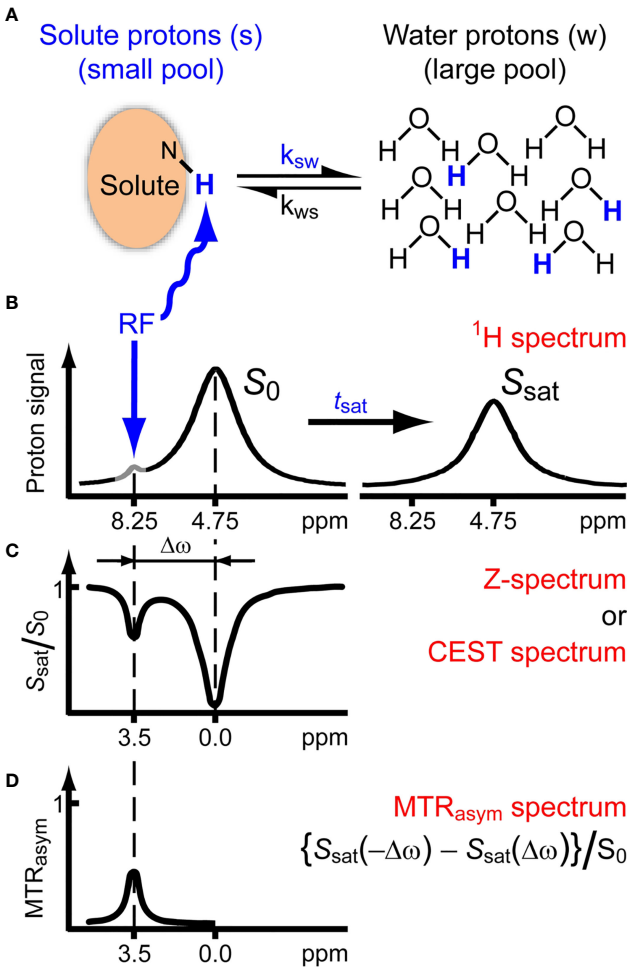

FIGURE 4 | Chemical exchange saturation transfer. **(A, B)** Solute protons (blue) are saturated at their specific resonance frequency in the proton spectrum (here 8.25 ppm for amide protons). This saturation is transferred to water (4.75 ppm) with exchange rate ksw and non-saturated protons (black) return. After a saturation period (t_{sat}), this effect becomes visible on the water signal (B, right). **(C)** The Z-spectrum, showing normalized water saturation (S_{sat}/S_0) as a function of irradiation frequency. When irradiating the water protons at 4.75 ppm, the signal disappears due to direct (water) saturation. This frequency is assigned to 0 ppm in Z-spectra. At short saturation times, only this direct saturation is apparent. At longer tsat, the CEST effect becomes visible at the frequency of the low-concentration exchangeable solute protons, now visible at 8.25 – 4.75 = 3.5 ppm in the Z-spectrum. **(D)** Result of MTR_{asym} analysis of the Z-spectrum with respect to the water frequency to remove the effect of direct saturation. Image adapted with permission from (42).

giving the best differentiation). An example of this is presented in **Figure 5**. One of these research groups showed that in even smaller cohorts, APT-weighted CEST outperformed ^{1}H MRS (59) and methionine positron emission tomography (PET) (60) at determining tumor progression. Retrospectively comparing APT-weighted CEST with diffusion and perfusion MRI biomarkers also indicated the added value of CEST to elucidate tumor progression in 36 glioblastoma patients treated with chemoradiotherapy or radiotherapy in a recent work (61). In another recent study where APT-weighted CEST was obtained in 32 patients within three months after treatment, increased APT-weighted CEST was seen in tumor progression with radiological confirmation after six months of follow-up (62). Moreover, in a previous, prospective study (50) 19 glioblastoma patients were systematically scanned before, during, and after chemoradiotherapy and an increase in APT-weighted CEST was shown to differentiate progressors from non-progressors as early as two weeks into treatment.

Although the above-referenced studies illustrate clinical findings of elevated APT-weighted CEST at 3 T by several research groups, recent work (63) did not find elevated APT-weighted CEST to be correlated to tumor progression in 12 glioblastoma patients scanned at 7 T. However, when these authors used a combination of image acquisition and analysis aimed at isolating the APT signal from the upfield relayed-nuclear Overhauser enhancement effects, they found that changes in the latter were able to differentiate tumor progression from PTRE. In line with this are the results of prospective studies (64, 65), where patients were scanned with CEST MRI at 7 T before treatment and APT was isolated from NOE effects. This showed that CEST contrasts before treatment are significantly correlated to overall and progression free survival (i.e., a prognostic biomarker). Taken together, these ultra-high field studies highlight the potential of CEST MRI to be used as a prognostic and monitoring biomarker candidate for treatment response assessment, although the different contrasts used indicate yet again that, although CEST contrasts can certainly differentiate active tumor tissue from PTRE, the exact mechanisms causing these contrasts remain to be elucidated.

Other studies optimize CEST image acquisition to be pH-weighted by including (66) or focusing on (67) amine proton exchange, which is thought to be more sensitive to pH changes than cell proliferation. Preclinical work (68) has shown that pH-weighted CEST contrast increases when intracellular pH decreases (i.e., becomes more acidic) in glioblastoma due to chemotherapy. Furthermore, clinical proof-of-concept of using pH-weighted CEST to assess treatment response has been demonstrated in patients after anti-angiogenic treatment (69) and patients treated with combined chemoradiotherapy (70).

3.1.2.3 Strengths and Weaknesses

A strength of CEST MRI for clinical diagnostics in tumor imaging is that those contrasts most explored for tumor imaging arise from endogenous markers and, therefore, no contrast agents are required. Additionally, the process of exchange inherently increases the signal-to-noise ratio of CEST imaging compared with MRS, which allows for a smaller voxel size to be used to probe heterogeneous tissues/pathologies, such as tumors. With these strengths, the potential of CEST MRI to improve differentiation of tumor progression from PTRE is clear. However, weaknesses include the multitude of options to acquire and analyze CEST MRI data, the variation in the timing of CEST MRI included during treatment, the retrospective nature of some

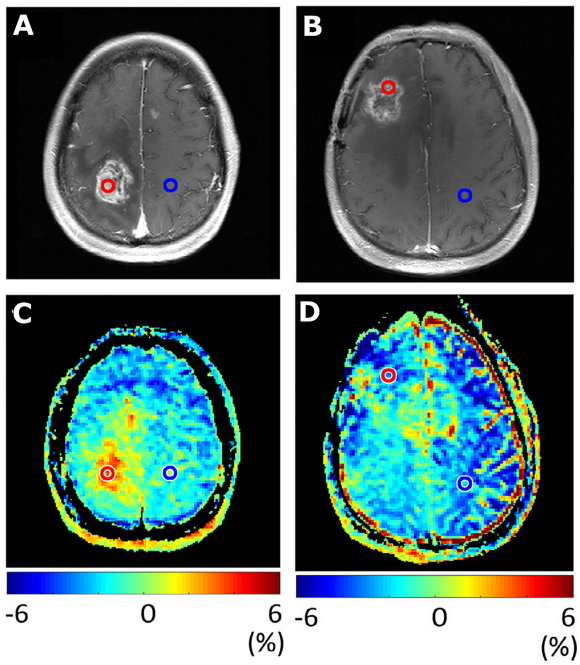

FIGURE 5 | Images illustrating APT-weighted imaging (MTR_{asym} at 3.5 ppm) in two patients after treatment with radiotherapy. Contrast enhancement on T_1-weighted images was seen in patient 1, 62 months after radiotherapy treatment and resection for grade 2 astrocytoma **(A)**. The additional increased MTR_{asym} in the same patient **(C)** illustrates tumor recurrence, which was confirmed as grade 4 glioblastoma after repeat surgery. Contrast enhancement on T_1-weighted images was seen in patient 2, 14 months after chemoradiotherapy of grade 3 astrocytoma, with regional anaplastic oligodendroglioma **(B)**. The additional MTR_{asym} in patient 2 **(D)** illustrates low values, indicating treatment effect, which was confirmed as radiation necrosis with histopathology after repeat surgery. Image adapted with permission from (58).

of the current clinical studies investigating APT-weighted CEST for tumor treatment response, and the small number of patients in the above-referenced studies. These weaknesses currently prevent a definitive summary of this imaging technique for treatment response assessment, in terms of indications for when to measure and which threshold values to use to separate tumor progression from PTRE.

3.1.2.4 Future Developments

To develop the application of CEST MRI for differentiation of treatment effects and tumor progression, a consensus from all relevant stakeholders regarding image acquisition and analysis is required to enable multicenter and multi-vendor trials. This is an area of active research, where a working group of international CEST experts is working toward an open source consensus CEST acquisition and analysis protocol (71).

3.1.3 Emerging MRI Techniques

There are several emerging techniques that may be shown to be monitoring biomarkers in future proof-of-concept studies. Here, we focus on some studies where proof-of-concept has already been shown.

3.1.3.1 Vascular Architecture Mapping and Oxygenation Imaging

Vessel caliber imaging, or vessel architecture mapping, is based on the fact that when a contrast agent passes through the vasculature and perturbs the local magnetic field, MRI signal from a gradient echo readout is sensitive to large arteries and capillaries, while with a spin echo readout signal is mostly sensitive to capillaries (72). Vessel architecture imaging hereby refers to the modelling framework that aims to assess subvoxel microvascular parameters, such as vessel density and vessel diameter, where vasculature with diameters < 200 μm are targeted (73). This imaging approach is included in recent "tumor microenvironment mapping," which combines vessel architecture imaging with oxygen metabolism imaging, i.e., measurement of the oxygen extraction fraction with quantitative blood oxygenation level dependent imaging. One study allowed five different tissue types within tumors to be identified (necrosis, hypoxia with/without neovascularization, oxidative phosphorylation, and glycolysis) (74). In 21 tumors scanned pre- and post-treatment, a change in the presence of these five metabolic profiles demonstrated recurrent glioblastoma. Although these results are still very preliminary, this proof-of-concept work shows the potential of this emerging technique to become a future monitoring biomarker.

3.1.3.2 Non-Proton MRI Techniques

Sodium (^{23}Na) imaging has established itself in MRI research due to the diverse role of sodium ions in tissue homeostasis (75). Unlike other non-proton techniques such as ^{31}P and ^{13}C, the ^{23}Na signal does not yield a metabolite spectrum, but only a single resonance in most environments such as human tissue (76). Therefore, imaging (as opposed to spectroscopy) is almost exclusively performed for ^{23}Na.

Although ^{23}Na MRI has been performed successfully in brain cancers since the late 1980s (77), more recent publications have shown its benefit in predicting IDH mutation status and tumor progression (78). Sodium concentration mapping has been performed in recurrent glioblastoma after radiotherapy (79) and also chemoradiotherapy (80). The authors of the former case report showed that the ^{23}Na images provided similar information as those contained in [^{18}F]fluoro-ethyl-tyrosine (FET) PET images and postulate that ^{23}Na images may therefore be able to provide a substitute for PET in MRI-only examination settings (79). Similarly, the authors of the second study noted that the 23Na images were sensitive to "real-time" changes in treatment volume that could be used to alter the course of treatment early on (80). Most recently, a study investigated whether whole tumor (excluding necrosis) measured immediately after chemotherapy with a follow-up 6 weeks later could predict stable or progressive disease, but did not find any significant correlations either with treatment response or overall survival (81). As with the other emerging techniques, ^{23}Na imaging is best considered as a proof-of-concept technique that may prove to be a future monitoring biomarker.

3.2 Advanced Handling of MRI Data

3.2.1 Multiparametric Imaging

3.2.1.1 Multiparametric Advanced MRI

The combination of multiple modalities may be of value for tissue characterization and help differentiate tumor from PTRE by providing complementary information of tumor biology and thus overcome limitations of individual techniques.

3.2.1.2 Evidence From Clinical Studies

A meta-analysis (82) of seven studies of multiparametric MRI (at least two of the following advanced MRI techniques: diffusion tensor imaging (DTI), diffusion-weighted imaging (DWI), DSC, DCE, ASL, and MRS) in patients with suspected pseudoprogression showed a pooled sensitivity and specificity of 84% and 95%, respectively, but the authors noted that the accuracy of multiparametric imaging was not different from that of monoparametric imaging determined in a meta-analysis of individual techniques (21). **Table S2** shows results of studies reporting separate and combined diagnostic performance of ≥ 2 parameters (e.g., PET, DWI, DSC, or MRS). The studies generally showed improved diagnostic accuracy when combining modalities, although the added value may be marginal when compared with the best performing single modality. Combined sensitivity and specificity may even be lower when compared with the single modality that has the highest sensitivity or specificity.

3.2.1.3 Strengths and Weaknesses

The main advantage of multiparametric imaging is related to reducing both false positive and false negative results of single modalities, either by providing complementary information on biology (e.g., perfusion and metabolism) or compensating for technical limitations of one modality (e.g., limited coverage of DSC in the presence of susceptibility artifacts). Interpreting advanced multiparametric data routinely in the clinic, however, may be difficult and time consuming due to the amount and complexity of data processing and integration. **Figure 6** illustrates the complexity of multiparametric imaging. Such a challenge may be particularly true for methods requiring longitudinal data such as relative cerebral blood volume and ADC parametric response maps

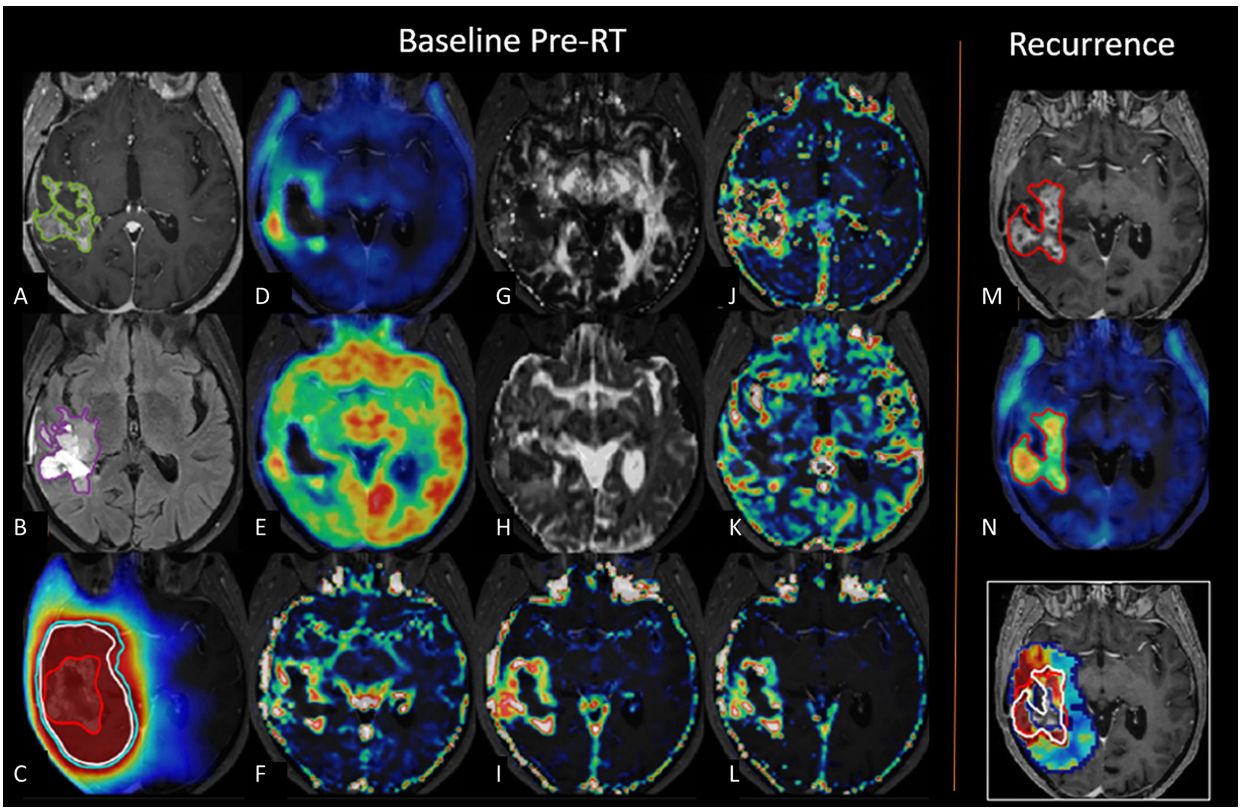

FIGURE 6 | Multiparametric imaging. Example of multiparametric imaging for prediction of tumor recurrence. Baseline images prior to radiotherapy in a patient with glioblastoma show contrast-enhancing lesion (green) on **(A)** post-contrast T_1-weighted images, **(B)** non-enhancing volumes (purple) on T_2 fluid attenuated inversion recovery, **(C)** radiotherapy dose plan with gross tumor volume (red), clinical target volume (white), and planning target volume (cyan), **(D)** [^{18}F]FET PET, **(E)** [^{18}F]FDG PET, **(F)** DCE blood volume, **(G)** DTI fractional anisotropy, **(H)** DTI mean diffusivity, **(I)** DCE extravascular extra-cellular volume, **(J)** DCE mean transit time, **(K)** DCE blood flow, **(L)** DCE permeability. Follow-up imaging shows recurrent tumor in red on **(M)** post-contrast T1-weighted images and **(N)** [^{18}F]FET PET imaging. Lower right image shows recurrence probability map superimposed on radiotherapy dose plan gross tumor volume (red) and actual recurrence boundary (white). Adapted with permission from (83).

combinations, which appear promising in determining treatment response (84). A further limitation is, as this review has shown, a paucity of high-level evidence for individual modalities especially relating to established frameworks for technical and clinical use as well as clear thresholds with understood confidence intervals to give a robust radiological outcome; therefore, combinations of individual modalities might compound error or lead to increased uncertainty of outcome.

3.2.1.4 Future Developments

One key area of development is to determine which modalities and parameters should be analyzed and integrated to give a clinically useful single diagnostic measure. One simple approach is to apply a scoring system, where each modality is rated as positive or negative, and the number of positive markers is added to a total score. One early study combining ASL, DCE, DSC, and MRS found that a score of ≥ 2 yielded a specificity of 94% as opposed to 77–84% for single modalities (85). To take into account lesion heterogeneity, one study of pseudoprgression compared to true progression applied scoring of different tumor components identified by automated voxel-based multiparametric clustering, resulting in final volume-weighted scores of the entire lesion. Applying this method in an independent test set, 87–89% of the lesions were correctly classified using the summed cluster score, compared with 76–83% using single modalities (86).

Others have applied machine learning approaches (described in more detail below) for automated voxel-wise classification of recurrence or pseudoprogression based on structural MRI, DSC, and ADC (87), or by providing maps predicting voxels where there will be downstream tumor progression (i.e., prognostic biomarkers) based on one-off multiparametric imaging prior to surgery (88) or radiotherapy (83), or through observing temporal changes in the images over time (89). A recent systematic review concluded that the integration of machine learning with multiparametric data was promising for visualization of diffusely infiltrating tumor cells before and after treatment. The review also concluded that because study cohorts are small, further studies are required to determine optimal methodology, and there is a need for larger cohorts to improve model performance (90). An advantage of machine learning is that wide data can be handled relatively easily (91) which might allow the wide spectrum of advanced imaging signatures to be captured together and thereby improve performance accuracy. However, to reiterate, a disadvantage when compared to a single modality approach is that combinations of outputs from individual modalities that are without frameworks for technical and clinical use, might compound inter-center variability and reduce generalizability considerably.

3.2.1.5 PET/MRI

PET is increasingly being used in the management of brain tumors as an adjunct to MRI. **Table 2** provides an overview of the most frequently applied (or methodologically relevant) PET tracers in gliomas, grouped according to the mechanism of uptake. PET data is most frequently obtained on standalone PET/computed tomography systems and then fused to MRI, but hybrid PET/MRI systems have the advantage of allowing the simultaneous acquisition of PET and both advanced and conventional MRI within a single imaging session. Among the available tracers, only the amino acid tracers, such as [^{18}F]fluoro-ethyl-tyrosine (FET), and the glucose analogue [^{18}F]fluoro-deoxy-glucose (FDG) PET have been included in joint European Association of Nuclear Medicine/European Association of Neuro-Oncology (EANO) guidelines (98, 99). Amino acid tracers are generally preferred over FDG due to more specific tumor uptake (as illustrated in **Figure 6**). Repeatability of amino acid PET using [^{18}F]FET has been investigated in animal models only (100). Because the main variability of PET imaging is related to the tracer and less so to the site or scanner, vendor-site-related differences are expected to be minor when consensus guidelines are followed, and PET tracers have been applied reliably in multicenter studies (101, 102).

Several reviews have highlighted the potential of combining PET acquired simultaneously with advanced MRI by using a hybrid PET/MRI system (**Figure 7**), but the number of studies actually investigating the value of multimodal approaches in distinguishing recurrent gliomas from PTRE is limited. Recent studies combining [^{18}F]FDG (105) or amino acid tracers (106–109) with DSC, DWI, and/or MRS (see **Table S2**) suggest that such multimodal imaging may provide complementary and additive information, leading to an improved overall diagnostic accuracy, but the optimal combination of modalities is not clear.

3.2.2 Machine Learning and Radiomics

3.2.2.1 Methodology

"Radiomics" (**Figure 8**) is the extraction of underlying quantitative information from the imaging dataset to develop biomarkers that may not be readily visible to individual human raters. Typically, radiomics consists of the following phases: preprocessing images, feature estimation (quantifying or characterizing the image), feature selection (dimensionality reduction to remove noise and random error in the underlying data, and, therefore, reduce overfitting), classification (decision or discriminant analysis), and evaluation (111). Evaluation in image analysis research initially consists of analytical validation, where the accuracy and reliability of the biomarker are assessed (112). Clinical validation is the subsequent clinical testing of biomarker performance, typically in a clinical trial.

Some studies have used applied statistical models, some have employed machine learning models, and many have leveraged both. The basic difference between them is that statistics draws population inferences from a sample, and machine learning finds generalizable predictive patterns (113). Recent work has made use of developments in technology to allow the use of much more complex supervised, unsupervised, and reinforcement machine learning, including the use of deep (multiple layered) neural networks, which allows automation of both feature estimation and selection steps (91).

3.2.2.2 Strengths and Weaknesses

Several barriers exist in translating machine learning high-grade glioma monitoring biomarkers to the clinic (114). These predominantly relate to the requirement of large datasets that have been accurately labeled to train models. However, machine learning has some additional weaknesses. Accuracy-driven performance metrics have led to a trend towards increasingly

TABLE 2 | Frequently studied PET tracers used to differentiate progression from post-treatment related effects.

Target Mechanism of uptake	Tracers	Clinical evidence[a]	Sensitivity (%-%)/ Specificity (%-%)[b]	Advantages/Disadvantages
Glucose metabolism				
GLUT 1/3 transport and hexokinase	[^{18}F]fluoro-deoxy-glucose (FDG)	+	S:43-100/40-100 M: 76-84/82-84	High availability High physiological uptake in normal structures and inflammatory foci
Amino acid transport				
Large amino acid transporters (LAT1 and LAT2)	[^{11}C]methionine (MET)	+	S:75-91/88-100 M:93-94/82	Short half-life and need for onsite cyclotron higher uptake in inflammatory lesions.
	[^{18}F]dihydroxy-phenylalanine (DOPA)	++	S: 84-100/61-100 M:86/72	Higher physiological in uptake basal ganglia
	[^{18}F]fluoro-ethyl-tyrosine (FET)	++	S: 84-100/86-100 M:90-92/85-88	Added accuracy of time activity curves from dynamic imaging
				All: extensively studies and used in clinical routine, low physiological uptake
Hypoxia				
Trapping in hypoxic cells	[^{18}F]fluoromisoinodazole (FMISO)	n.a	–	High background activity and need for delayed imaging
Profileration				
Thymidine kinase 1	[^{18}F]fluorothymidine (FLT)	+	S:82/50	Not superior to FDG Dot not cross BBB
Neuroinflammation				
Mitochondrial translocator protein (TSPO)	[^{11}C]PK11195	n.a.	–	[^{11}C]PK11195: short half-life and need for on-site cyclotron
	[^{18}F]GE-180	n.a.	–	heterogeneity and uptake in PTRE
Perfusion				
	[^{13}]NH3	(+)	S:78-83/86	Both: freely-diffusible tracers allows quantification of perfusion
	[^{15}O]H2O	n.a.	–	short half-life and need for on-site cyclotron
Vascular endothelium				
PSMA	[^{68}Ga]PSMA			
Cell membrane synthesis				
Choline	[^{11}C]Choline	+	S:74-92/88	[^{11}C]short half-life and need for on-site cyclotron uptake in non-tumor
	[^{18}F]Fluorocholine	+		Both: Uptake partially BBB dependent
Angiogenesis				
αvβ3 (RGD)	[^{18}F]FPPRRGD2	n.a.	–	Both: Do not cross BBB
Bevacizumab	[^{89}Zr]Bevacizumab	n.a.	–	
Cancer-associated fibroblast				
Fibroblast-activation protein	[^{68}Ga]FAPI02/04	n.a.	–	Possibly BBB dependent

Selection of tracers based on recent large/systematic reviews (92–95). Footnotes: [a]adapted from Werner et al. (95) where ++ = high diagnostic accuracy, + = limited diagnostic accuracy, (+) = limited data available, n.a. not applicable (only preliminary/no data available); [b]Range reported in single studies (S) or meta-analyses (M) reported in (92, 93, 96, 97). Also shown are some tracers of potential use for this indication.

opaque models (115), although recent developments in interpretability and explainability may help to mitigate this to some extent (116). Furthermore, linking the empirical data to a categorical analysis neglects an intrinsic ambiguity in the observed phenomena (117), which might adversely affect the intended performance (118). Also, algorithms may be unreliable due to several technical constraints: domain adaptation is currently limited, and more solutions are required to help algorithms extrapolate well to new centers. This is particularly true of advanced imaging where the lack of established frameworks for technical acquisition and clinical handling leads to spatial heterogeneity of data across hospital sites. Multi-parametric combinations of advanced imaging exacerbates the heterogeneity further and increases the challenge of model generalizability further. Robustness to unintended data, such as artifacts, is also a technical constraint that needs to be overcome. Finally, the presence of more than one pathology (e.g., abscess associated with a tumor following treatment) can also confound algorithms as these cases are scarce and often unlabeled.

Nonetheless, machine learning models have several key advantages. They require less formal statistical training given the huge developments in software (119), and the programming expertise for researchers has now been transformatively reduced, enabled by standardized implementations of open source software (120, 121). Machine learning models also have the ability to determine implicitly any complex nonlinear relationship between independent and dependent variables (119), and have the ability to determine all possible interactions between predictor variables (115).

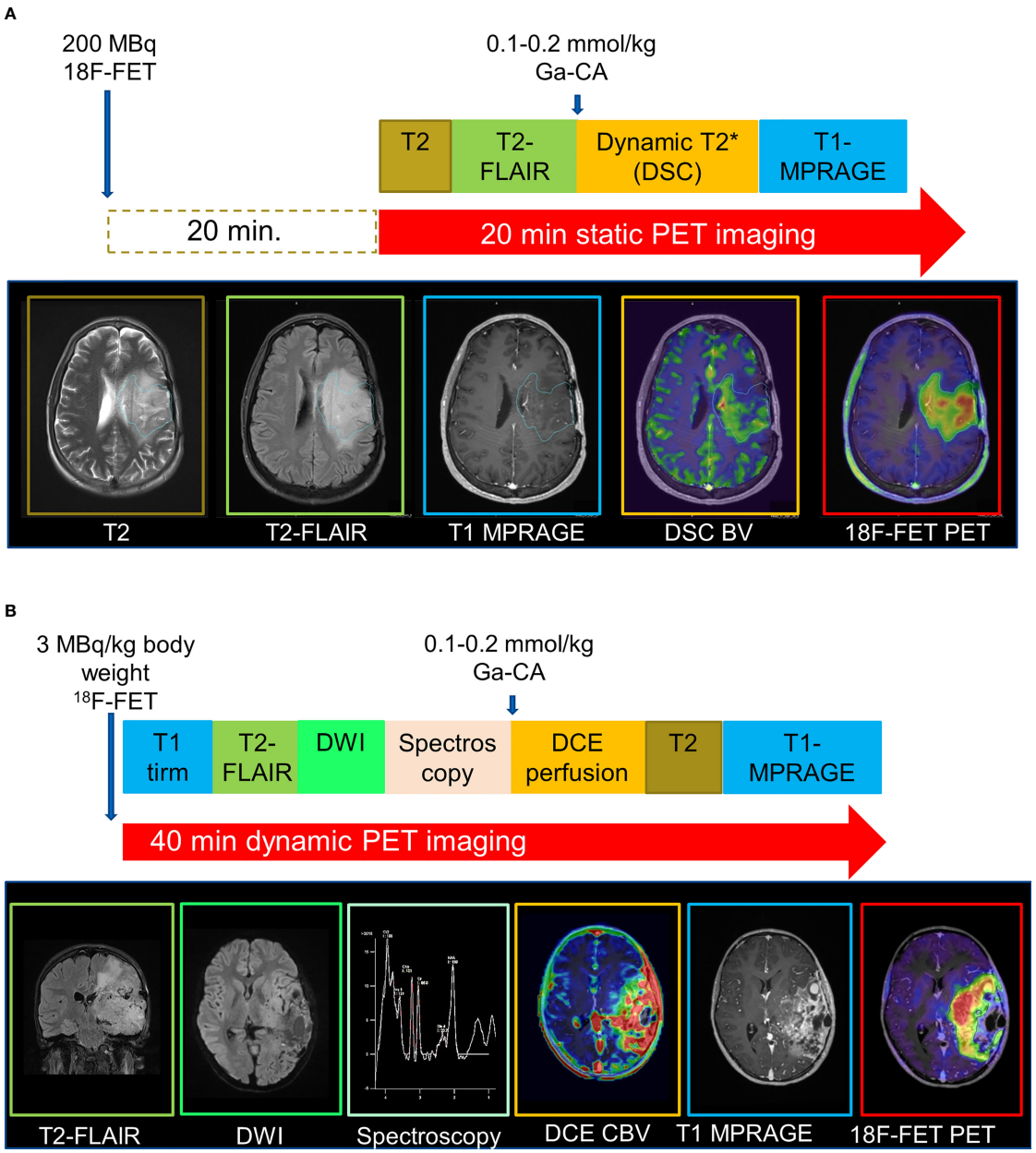

FIGURE 7 | Examples of hybrid PET/MRI protocols. MRI data were acquired during acquisition of **(A)** static 20-minute or **(B)** dynamic 40-minute PET data. Adapted with permission from (103) and (104), respectively.

3.2.2.3 Evidence From Clinical Studies

As shown elsewhere, multiple studies have attempted to develop monitoring biomarkers to determine treatment response. Many incorporate machine learning as a central pillar of the process. A review of studies up to 2018 (91), a systematic review of studies from 2018 – 2020 (122) using PRISMA-DTA methodology and a meta-analysis from 2018–2021 (123) indicated that those taking advantage of enhanced computational processing power to build monitoring biomarker models (e.g., using deep learning methods such as convolutional neural networks) have yet to show an advantage in performance compared with machine learning techniques using explicit feature engineering and less computationally expensive classifiers (e.g., using "classical" machine learning methods support vector machine). It is also notable that studies applying machine learning to build monitoring biomarker models have yet to show an overall advantage over those using traditional statistical methods. There is good diagnostic performance of machine learning models that use MRI features to distinguish between progressive disease and diagnostic accuracy measures comprise recall = 0.61 – 1.00,

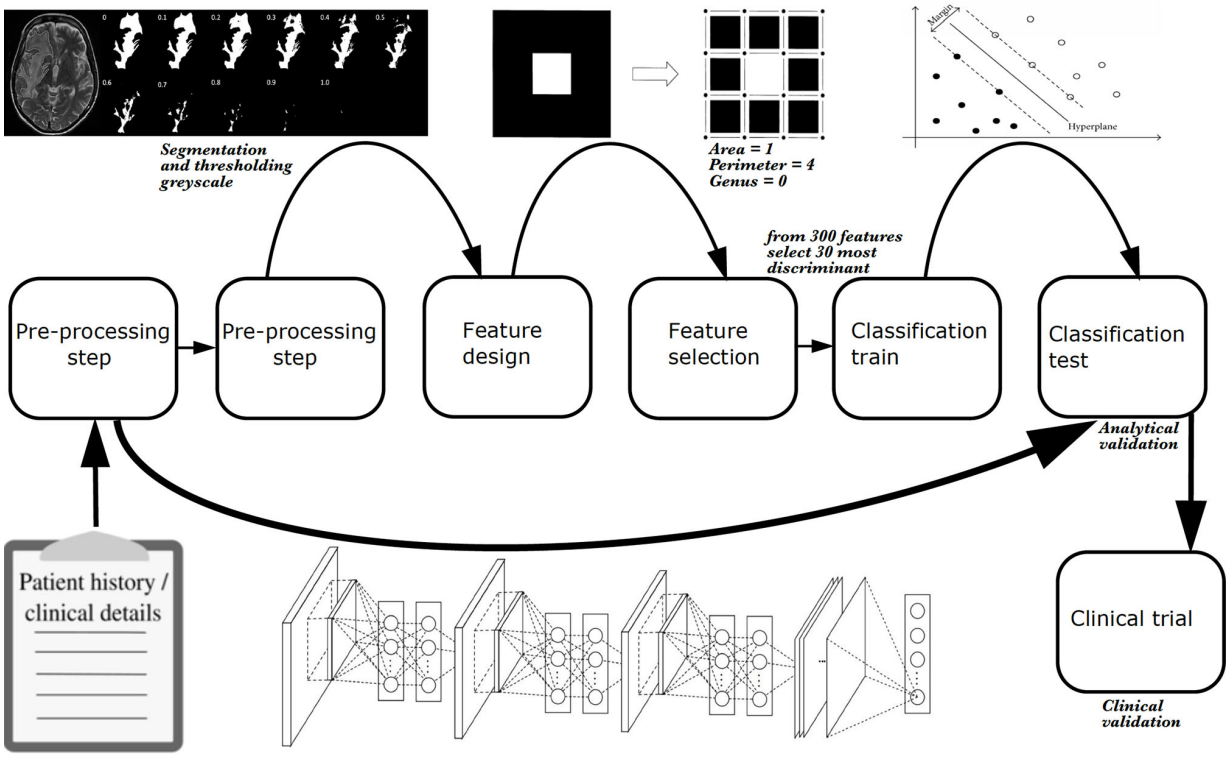

FIGURE 8 | The phases of a radiomics study. Explicit feature engineering is represented by a series of boxes from left to right, starting off with pre-processing and finishing with classification of a hold-out test set. Implicit feature engineering (deep learning) is represented below these boxes by a neural network which incorporates many steps of explicit feature engineering. As with explicit feature engineering, to achieve analytical validation, classification of a hold-out test set must be performed. Once analytical validation is achieved, ideally a clinical trial tests the model to achieve clinical validation in the same way a new therapeutic agent or surgical intervention is subject to a trial. Radiomics is image based, however, additional information can be incorporated such as clinical or demographic information. All studies require some pre-processing, whether that is data cleaning or converting file format from DICOM to NIfTI, for example. With explicit feature engineering, additional pre-processing is typically required such as image segmentation. In the example shown here, hyperintense voxels associated with a grade 4 glioblastoma in a T_2-weighted image are segmented as a region of interest for radiomic analysis. The mask is extracted using 11 different grey-scale thresholds to give binary combinations of black and white pixels. Thereafter, carefully designed image analysis features (or "estimated features") can be applied to the pixels. In the example shown, these are topological descriptors of image heterogeneity (white pixel area = 1; white pixel perimeter = 4; rings subtracted from holes, i.e., genus = 0) (110). The most discriminant features can be selected using statistical or machine learning techniques, and undergo classification using a machine learning algorithm. In the example shown, a support vector machine is used (the machine learning algorithm is described as "classical" to distinguish it and other similar algorithms from deep learning algorithms), and progression (solid black dots) and pseudoprogression (empty black dots) cases are determined.

specificity = 0.47 – 0.90, balanced accuracy = 0.54 – 0.83, precision = 0.58 – 0.88, F1 score = 0.59 – 0.94, and AUC = 0.65 – 0.85 (122, 123). The recent meta-analysis of ten studies showed a pooled true positive rate (sensitivity) = 0.769 (0.649 – 0.858), a false positive rate (1-specificity) = 0.352 (0.251 – 0.468) and a summary AUC-ROC = 0.765. Other pooled metrics showed derived measures of balanced accuracy = 0.706 (0.623–0.779); positive likelihood ratio = 2.220 (1.560–3.140); negative likelihood ratio = 0.366 (0.213–0.572); and diagnostic odds ratio = 6.670 (2.800–13.500) (123). It is noteworthy that the small numbers of patients included in these studies, the high-risk of bias and concerns of applicability in the study designs, and the low level of evidence given that the monitoring biomarker studies are retrospective, suggest that limited conclusions can be drawn from the data. The results show that glioblastoma treatment response monitoring biomarkers developed through machine learning are promising but are at an early phase of development and are not ready to be incorporated into clinical practice to distinguish tumor progression from PTRE. Furthermore, no practice guidelines exist for this specific application. All published studies would benefit from improvements in the methodology. Future studies would benefit from analytical validation using external hold-out tests, as well as from larger datasets to reduce overfitting.

3.2.2.4 Future Developments

Advances in brain tumor database curation will facilitate integration of imaging, clinical, demographic, and molecular marker information to create large databases which will allow machine learning models to be trained and tested at a greater scale to what has occurred previously (114). The capture of large volumes of data and the inclusion of a wider spectrum of imaging phenotypes typically results in improved diagnostic performance during machine learning or statistical tasks;

the relative improvement of deep learning model performance is particularly marked (124–126). For deep learning, the dependency on very large datasets can be reduced by data augmentation and transfer learning; the latter, where an already-developed model for a task is reused as the starting point for a model on a second task, is especially advantageous for medical tasks, since these pretrained models not only obviate the need for very large datasets but are less computationally expensive (116, 127, 128). One- or few-shot learning is related to this and allows classifiers to be built from very small labeled training sets (129).

Once established, incoming data from large-scale live repositories will allow ongoing refinement and assessment of outcomes. Furthermore, distributed machine learning approaches, in particular federated learning, will enable training on a large body of decentralized data (130). Federated learning is one instance of the more general approach of *bringing the code to the data, instead of the data to the code* and mitigates the fundamental problems of privacy, ownership, and locality of data. Although this technique is at the early research stage, federated learning appears to be fit-for-purpose for privacy-preserving medical applications (131, 132), and for high-grade glioma monitoring biomarkers in particular. However, the potential privacy and performance trade-off is unknown. Once established, federated learning will likely speed up the validation of the proposed methods, since fewer administrative data access requirements will be required, yet the sample will continue to be expanded by new data arriving from several sites.

3.3 Acceptance

3.3.1 Endorsement in Guidelines

Although diagnostic accuracies of most modalities appear high enough for clinical application, and this should encourage their clinical use, acceptance in clinical guidelines is limited for a variety of reasons associated with clinical readiness, which is summarized in **Table 3**. In the recent EANO/Society for Neuro-Oncology guidelines for management of glioblastoma (144) and EANO guidelines for diffuse gliomas (145), only perfusion MRI and amino acid PET are suggested as being helpful, and they are only mentioned in the case of suspected pseudoprogression. In the 2017 modified Response Assessment in Neuro-Oncology (RANO) criteria (141), it is noted that advanced MRI techniques, such as DSC, DCE, and amino acid PET, "have shown promise but additional work is necessary to standardize these approaches and improve their sensitivity and specificity" and "issues of cost and accessibility will need to be addressed before they can be widely adopted in clinical trials." Accordingly, the RANO criteria remain based on post-contrast T_1-weighted images only (and the T_2-weighted/fluid attenuated inversion recovery in 2010 RANO guidelines, albeit not quantified). In the proposed minimum imaging protocol from the Jumpstarting Brain Tumor Drug Development Coalition (143), designed to be widely applicable to a variety of MR scanners, only DWI (three b-values) is included in addition to these conventional structural sequences. DWI also has been included in the proposed minimum imaging protocol in the pediatric high-grade glioma RANO recommendations due to its widespread use and "potential benefit," while perfusion MRI and MRS are considered experimental (149). A summary of a survey of national imaging guidelines conducted among GliMR-associated countries are included within **Table 3** (methodology and results in **Supplementary Material**). Specifically, we determined whether there are guidelines for incorporation (routine or optional) of advanced MRI techniques in clinical practice for determining treatment response in high-grade gliomas.

3.3.2 Clinical Use of Advanced MRI

Published evidence of the current use of advanced MRI in daily clinical practice is limited. European surveys have reported that advanced MRI techniques are widely available (150) and also applied to brain tumor imaging (147, 151, 152) with substantial national differences. A survey of 220 European centers (3% survey yield) showed that despite widespread availability of advanced MRI techniques, to differentiate radiation necrosis from progressive disease, perfusion imaging is used most commonly (56% of centers), whereas MRS and DWI are used rarely (6% and 5% of centers, respectively) (147). A predominantly US survey of perfusion MRI (5% survey yield) reported widespread availability for brain imaging (all indications) offered by 81% of centers, with DSC being the most frequently offered (87%) followed by DCE (41%) and ASL (35%) (148). Among those offering perfusion MRI, the most frequent indication was post-treatment evaluation of intra-axial brain tumors (87%), in particular differentiating progression from radiation necrosis (96%) or pseudoprogression (84%). The authors note that perfusion imaging is widely adopted despite the lack of reimbursement and the limited support for perfusion imaging in guidelines at the time of the survey, suggesting that both the radiologist and the referring physician find value in these techniques. However, although there appears to be a wide adoption of advanced MRI, the results of the US and European surveys may be confounded by unrepresentative samples with > 95% of non-responders. A UK survey of post-operative imaging of all neuro-oncology centers (100% survey yield) showed that most centers (> 80%) included DWI in the standard protocol, while other advanced MRI techniques (DSC, DCE, or MRS) were applied routinely by only 10% of centers during follow-up, and in selected cases where there was possible pseudoprogression by 35% (153). Of interest, neuroradiologists were the main advocates for the use of advanced imaging, while neuro-oncologists were more likely to suggest that further evidence is needed.

4 CONCLUSION

The biochemical composition of high-grade gliomas is markedly different from healthy brain tissue. MRS allows the simultaneous acquisition of an array of metabolic alterations with Cho-based ratios appearing to be consistently discriminatory in treatment response assessment, although challenges remain in this technique despite it being mature. Promising directions relate to ultra-high field strengths and high-resolution MRSI, 2HG analysis, and the use of non-proton nuclei. Labile protons on endogenous proteins can be selectively targeted with CEST to give high-resolution images. The body of evidence for clinical application of APT imaging has been building for a decade, but more evidence is required to confirm the use of CEST as a monitoring biomarker. Multiparametric methodologies,

TABLE 3 | State of development of advanced MRI techniques.

	Track & Domain[a]	Perfusion			MRS		Diffusion		CEST	PET	Criteria		
		DSC (133)	DCE (133–136)	ASL (133, 137, 138)	Single	CSI	ADC	DTI	APT (53)	AA (100, 102, 139)	🟢	🟡	🔴
Technical validation													
Test-retest repeatability	T2	🟢	🟢	🟡	🟡	🟡	🟡	🟡	🟡	🟡	Yes, with current standard implementation	Yes, but with other implementation or patient group/animal model	None available
Cross-vendor reproducibility	T2	🟡	🔴	🟡	🟡	🟡	🟡	🟡	🟡	n.a.	Yes, with current standard implementation	Yes, but with other implementation or patient group	None available
Multisite reproducibility	T3	🟡	🟡	🟡	🟡	🟡	🟡	🟡	🟡	🔴	Yes, with current standard implementation	Yes, but with other implementation or patient group, phantom or analysis	None available
Clinical evidence													
Proof of concept in patients	C1	🟢	🟢	🟢	🟢	🟢	🟢	🟢	🟢	🟢	Differentiation tumor from PTRE	Differentiation tumor from normal brain	None available
Evaluated in clinical studies	C2-3	🟢	🟢	🟡	🟢	🟡	🟢	🟢	🟡	🟢	Multiple single center	Few or preliminary studies	None available
Evaluated in multi-center studies	C3	🟢	🟡	🔴	🔴	🔴	🟢	🟢	🔴	🟡	Good quality with relevant question	Small, preliminary or only method stability/ not relevant question	None available
Evaluated in meta-analysis		🟢	🟡	🟡	🟢	🔴	🟢	🟢	🔴	🟢	Consistent result with standard measures	Not standard measure/method, or low number studies/ patients	None available
Established diagnostic accuracy, cut-offs/criteria	C3	🟢	🟡	🔴	🔴	🔴	🟡	🟡	🔴	🟢	Consistent in multiple single center studies	Few or preliminary studies	None available
Acceptance													
Method guidelines/ recommendations	T	🟢	🟢	🟡	🟢	🔴	🟡	🟡	🔴	🟢	Available and updated	Available, but not updated or not specific for tumor imaging	None available
Included in clinical trial guidelines[b]		🟡	🔴	🔴	🔴	🔴	🟢	🟡	🔴	🟡	Included in suggested standard protocol	Mentioned, but clinical value uncertain	Not mentioned
Included in national imaging guideline		🟢	🟡	🟡	🟡	🟡	🟢	🟡	🔴	🟡	Endorsed by majority	Only endorsed but a minority	Not mentioned
Included in international clinical guidelines[c]		🟢	🔴	🔴	🔴	🔴	🔴	🔴	🔴	🟢	Endorsed by major international society guidelines	Mentioned, but clinical value uncertain	Not mentioned
In clinical use for brain tumor imaging[d]		🟢	🟡	🟡	🟢	🔴	🟢	🟡	🔴	n.a.	Widely implemented (>50%)	Intermediate (<50%)	Uncommon
In clinical use for PTRE vs glioma recurrence[d]		🟢	🟡	🔴	🔴	🔴	🟢	🟡	🔴	n.a.	Widely applied (>50%)	Intermediate (<50%)	Uncommon
Implementation													
Sequence availability	T2	🟢	🟢	🟡	🟢	🟡	🟢	🟢	🟡	n.a.	Comparable sequence available as clinical from all major vendors	No standard implementation or only work in progress	Research sequence at singles sites
Post-processing software availability	T2	🟡	🟡	🟡	🟢	🟡	🟢	🟢	🟡	🟢	On-line scanner/ reading work station with best practice implementation	Off-line, commercially available software	In-house software
Subjective ease of data acquisition (scanner operator e.g. clinical radiographer)	T2	🟢	🟢	🟢	🟡	🟡	🟢	🟢	🟡	🟢	Minimal need for training	Special training/ attention required	Difficult to obtain good quality data

(Continued)

TABLE 3 | Continued

	Track & Domain[a]	Perfusion			MRS		Diffusion		CEST	PET	Criteria		
		DSC (133)	DCE (133–136)	ASL (133, 137, 138)	Single	CSI	ADC	DTI	APT (53)	AA (100, 102, 139)	🟢	🟡	🔴
Subjective ease of post-processing (within clinical department e.g. clinical radiologist)		🟡	🟡	🟡	🟡	🔴	🟢	🟡	🔴	🟢	No post-processing needed	Extra processing/ training needed, but not time consuming	Expert or time intensive processing required
Subjective ease of data interpretation (clinician e.g. clinical radiologist)		🟢	🟢	🟡	🟡	🟡	🟡	🟡	🟡	🟢	Visual reading or only simple manual steps required	Special training/ expertise required	Highly specialized in single centers

[a]*Imaging biomarker roadmap (140);* [b]*Response assessment in neuro-oncology (RANO) (141), modified RANO criteria (142), standardized imaging protocol in clinical trials (143);* [c]*Society for Neuro-Oncology (SNO) and European Society of Neuro-Oncology (EANO) consensus review on management of glioblastoma (144), EANO guidelines on diffuse gliomas (145), EANO guideline on adult astrocytic and oligodendroglial gliomas (146);* [d]*European survey on advanced MRI (147), American Society of Neuroradiology survey on perfusion imaging (148).*
T, technical validation; C, clinical validation; Domain 1, discovery; Domain 2, validation (lower level evidence); Domain 3, validation (higher level evidence). Also included is amino acid PET. n.a., not applicable.

including the incorporation of nuclear medicine techniques, combine probes measuring different tumor properties. Although potentially synergistic, the limitations of each individual modality can also be compounded, particularly in the absence of standardization. Machine learning requires large datasets with high-quality annotation; currently, there is low-level evidence for monitoring biomarker clinical application.

In conclusion, advanced MRI techniques show huge promise in treatment response assessment. The clinical readiness analysis highlights that most monitoring biomarkers require standardized international consensus guidelines, with more facilitation regarding technique implementation and reporting in the clinic. The benefit of technique standardization will be multiplied in terms of multiparametric imaging and will also help leverage the enormous potential of machine learning tools.

AUTHOR CONTRIBUTIONS

Authors TB and OH served as overall editors. The individual sections were drafted by: Introduction (TB), DSC-MRI (KS and MÁ-T), DCE-MRI (OH), ASL (PF and VK), diffusion techniques (RN, FR, and VK), spectroscopy (ECW and GH), CEST (EAHW), multiparametric imaging (OMH), clinical readiness (OH), radiomics (TB), discussion (TB). All authors have contributed to the conception of the two parts of the article, revised them critically and approved the submitted versions.

FUNDING

This publication is part of the COST Action CA18206 Glioma MR Imaging 2.0 (www.glimr.eu), supported by COST (European Cooperation in Science and Technology), www.cost.eu. GliMR provided travel and accommodation for members who had travelled to early networking meetings.

- KS: National Institute of Health/National Cancer Institute R01 CA255123, U01 CA176110, UG3 CA247606, Medical College of Wisconsin Cancer Center.
- GH: Austrian Science Fund grant KLI-646.
- ECW: The Dutch Research Council (NWO) Talent Programme Veni: 18144
- EAHW: The Dutch Research Council (NWO) Talent Programme Veni: 91619121
- PF: The Portuguese Foundation for Science and Technology (FCT) Grant UIDB/50009/2020.
- RN: Babes-Bolyai University, Grant GTC No. 35277/18.11.2020.
- TB: The Wellcome/EPSRC Centre for Medical Engineering [WT 203148/Z/16/Z].
- MÁ-T: The ALBATROSS project (National Plan for Scientific and Technical Research and Innovation 2017-2020 and DPI2016-80054-R (Programa Estatal de Promoción del Talento y su Empleabilidad en I+D+i).

ACKNOWLEDGMENTS

The authors would like to thank Melissa Prah for assistance with obtaining figures, and Andrei Roman and Lydia Washechek for help with manuscript preparation. We also thank the national representatives who helped complete the national guideline survey (names listed in the **Supplementary Material**).

SUPPLEMENTARY MATERIAL

The Supplementary Material for this article can be found online at: https://www.frontiersin.org/articles/10.3389/fonc.2021.811425/full#supplementary-material

REFERENCES

1. Howick J, Chalmer I, Glasziou P, Greenhalgh T, Heneghan C, Liberati A. *Oxford Centre for Evidence-Based Medicine The Oxford 2011 Levels of Evidence*. Oxford (2016). Available at: http://www.cebm.net/index.aspx?o1/45653 (Accessed 1 August, 2018).
2. McInnes MDF, Moher D, Thombs BD, McGrath TA, Bossuyt PMthe PRISMA-DTA Group, et al. Preferred Reporting Items for a Systematic Review and Meta-Analysis of Diagnostic Test Accuracy Studies: The PRISMA-DTA Statement. *JAMA* (2018) 319:388–96. doi: 10.1001/jama.2017.19163
3. de Graaf RA. *In Vivo NMR Spectroscopy*. Chichester, UK: John Wiley & Sons, Ltd (2019). doi: 10.1002/9781119382461
4. Horská A, Barker PB. Imaging of Brain Tumors: MR Spectroscopy and Metabolic Imaging. *Neuroimaging Clin N Am* (2010) 20:293–310. doi: 10.1016/j.nic.2010.04.003
5. Castillo M, Smith JK, Kwock L. Correlation of Myo-Inositol Levels and Grading of Cerebral Astrocytomas. *AJNR Am J Neuroradiol* (2000) 21:1645–9.
6. Kuesel AC, Sutherland GR, Halliday W, Smith IC. 1h MRS of High Grade Astrocytomas: Mobile Lipid Accumulation in Necrotic Tissue. *NMR BioMed* (1994) 7:149–55. doi: 10.1002/nbm.1940070308
7. Hangel G, Jain S, Springer E, Hečková E, Strasser B, Považan M, et al. High-Resolution Metabolic Mapping of Gliomas *via* Patch-Based Super-Resolution Magnetic Resonance Spectroscopic Imaging at 7T. *Neuroimage* (2019) 191:587–95. doi: 10.1016/j.neuroimage.2019.02.023
8. Maudsley AA, Andronesi OC, Barker PB, Bizzi A, Bogner W, Henning A, et al. Advanced Magnetic Resonance Spectroscopic Neuroimaging: Experts' Consensus Recommendations. *NMR BioMed* (2021) 34:e4309. doi: 10.1002/nbm.4309
9. Wilson M, Andronesi O, Barker PB, Bartha R, Bizzi A, Bolan PJ, et al. Methodological Consensus on Clinical Proton MRS of the Brain: Review and Recommendations. *Magn Reson Med* (2019) 82:527–50. doi: 10.1002/mrm.27742
10. Kreis R, Boer V, Choi I, Cudalbu C, Graaf RA, Gasparovic C, et al. Terminology and Concepts for the Characterization of *In Vivo* MR Spectroscopy Methods and MR Spectra: Background and Experts' Consensus Recommendations. *NMR BioMed* (2021) 34:e4347. doi: 10.1002/nbm.4347
11. Near J, Harris AD, Juchem C, Kreis R, Marjańska M, Öz G, et al. Preprocessing, Analysis and Quantification in Single-Voxel Magnetic Resonance Spectroscopy: Experts' Consensus Recommendations. *NMR BioMed* (2021) 34:e4257. doi: 10.1002/nbm.4257
12. Považan M, Mikkelsen M, Berrington A, Bhattacharyya PK, Brix MK, Buur PF, et al. Comparison of Multivendor Single-Voxel MR Spectroscopy Data Acquired in Healthy Brain at 26 Sites. *Radiology* (2020) 295:171–80. doi: 10.1148/radiol.2020191037
13. van de Bank BL, Emir UE, Boer VO, van Asten JJA, Maas MC, Wijnen JP, et al. Multi-Center Reproducibility of Neurochemical Profiles in the Human Brain at 7 T. *NMR BioMed* (2015) 28:306–16. doi: 10.1002/nbm.3252
14. Yu Y, Ma Y, Sun M, Jiang W, Yuan T, Tong D. Meta-Analysis of the Diagnostic Performance of Diffusion Magnetic Resonance Imaging With Apparent Diffusion Coefficient Measurements for Differentiating Glioma Recurrence From Pseudoprogression. *Medicine (Baltimore)* (2020) 99:e20270. doi: 10.1097/MD.0000000000020270
15. Zhang H, Ma L, Shu C, Wang Y, Dong L. Diagnostic Accuracy of Diffusion MRI With Quantitative ADC Measurements in Differentiating Glioma Recurrence From Radiation Necrosis. *J Neurol Sci* (2015) 351::65–71. doi: 10.1016/j.jns.2015.02.038
16. Okuchi S, Rojas-Garcia A, Ulyte A, Lopez I, Ušinskienė J, Lewis M, et al. Diagnostic Accuracy of Dynamic Contrast-Enhanced Perfusion MRI in Stratifying Gliomas: A Systematic Review and Meta-Analysis. *Cancer Med* (2019) 8:5564–73. doi: 10.1002/cam4.2369
17. Patel P, Baradaran H, Delgado D, Askin G, Christos P, John Tsiouris A, et al. MR Perfusion-Weighted Imaging in the Evaluation of High-Grade Gliomas After Treatment: A Systematic Review and Meta-Analysis. *Neuro Oncol* (2017) 19:118–27. doi: 10.1093/neuonc/now148
18. Wan B, Wang S, Tu M, Wu B, Han P, Xu H. The Diagnostic Performance of Perfusion MRI for Differentiating Glioma Recurrence From Pseudoprogression. *Medicine (Baltimore)* (2017) 96:e6333. doi: 10.1097/MD.0000000000006333
19. Deng S-M, Zhang B, Wu Y-W, Zhang W, Chen Y-Y. Detection of Glioma Recurrence by 11C-Methionine Positron Emission Tomography and Dynamic Susceptibility Contrast-Enhanced Magnetic Resonance Imaging. *Nucl Med Commun* (2013) 34:758–66. doi: 10.1097/MNM.0b013e328361f598
20. Zhang H, Ma L, Wang Q, Zheng X, Wu C, Xu B. Role of Magnetic Resonance Spectroscopy for the Differentiation of Recurrent Glioma From Radiation Necrosis: A Systematic Review and Meta-Analysis. *Eur J Radiol* (2014) 83:2181–9. doi: 10.1016/j.ejrad.2014.09.018
21. van Dijken BRJ, van Laar PJ, Holtman GA, van der Hoorn A. Diagnostic Accuracy of Magnetic Resonance Imaging Techniques for Treatment Response Evaluation in Patients With High-Grade Glioma, a Systematic Review and Meta-Analysis. *Eur Radiol* (2017) 27:4129–44. doi: 10.1007/s00330-017-4789-9
22. Wang L, Wei L, Wang J, Li N, Gao Y, Ma H, et al. Evaluation of Perfusion MRI Value for Tumor Progression Assessment After Glioma Radiotherapy. *Medicine (Baltimore)* (2020) 99:e23766. doi: 10.1097/MD.0000000000023766
23. Chuang M-T, Liu Y-S, Tsai Y-S, Chen Y-C, Wang C-K. Differentiating Radiation-Induced Necrosis From Recurrent Brain Tumor Using MR Perfusion and Spectroscopy: A Meta-Analysis. *PloS One* (2016) 11:e0141438. doi: 10.1371/journal.pone.0141438
24. Verma G, Chawla S, Mohan S, Wang S, Nasrallah M, Sheriff S, et al. Three-Dimensional Echo Planar Spectroscopic Imaging for Differentiation of True Progression From Pseudoprogression in Patients With Glioblastoma. *NMR BioMed* (2019) 32:e4042. doi: 10.1002/nbm.4042
25. Kazda T, Bulik M, Pospisil P, Lakomy R, Smrcka M, Slampa P, et al. Advanced MRI Increases the Diagnostic Accuracy of Recurrent Glioblastoma: Single Institution Thresholds and Validation of MR Spectroscopy and Diffusion Weighted MR Imaging. *NeuroImage Clin* (2016) 11:316–21. doi: 10.1016/j.nicl.2016.02.016
26. Öz G, Deelchand DK, Wijnen JP, Mlynárik V, Xin L, Mekle R, et al. Advanced Single Voxel 1 H Magnetic Resonance Spectroscopy Techniques in Humans: Experts' Consensus Recommendations. *NMR BioMed* (2021) 34:e4236. doi: 10.1002/nbm.4236
27. Lin A, Andronesi O, Bogner W, Choi I, Coello E, Cudalbu C, et al. Minimum Reporting Standards for *In Vivo* Magnetic Resonance Spectroscopy (MRSinMRS): Experts' Consensus Recommendations. *NMR BioMed* (2021) 34:e4484. doi: 10.1002/nbm.4484
28. Gruber S, Heckova E, Strasser B, Považan M, Hangel GJ, Minarikova L, et al. Mapping an Extended Neurochemical Profile at 3 and 7 T Using Accelerated High-Resolution Proton Magnetic Resonance Spectroscopic Imaging. *Invest Radiol* (2017) 52:631–9. doi: 10.1097/RLI.0000000000000379
29. Bogner W, Otazo R, Henning A. Accelerated MR Spectroscopic Imaging—A Review of Current and Emerging Techniques. *NMR BioMed* (2021) 34:e4314. doi: 10.1002/nbm.4314
30. Ladd ME, Bachert P, Meyerspeer M, Moser E, Nagel AM, Norris DG, et al. Pros and Cons of Ultra-High-Field MRI/MRS for Human Application. *Prog Nucl Magn Reson Spectrosc* (2018) 109:1–50. doi: 10.1016/j.pnmrs.2018.06.001
31. Hangel G, Cadrien C, Lazen P, Furtner J, Lipka A, Hečková E, et al. High-Resolution Metabolic Imaging of High-Grade Gliomas Using 7T-CRT-FID-MRSI. *NeuroImage Clin* (2020) 28:102433. doi: 10.1016/j.nicl.2020.102433
32. Pedrosa de Barros N, Meier R, Pletscher M, Stettler S, Knecht U, Reyes M, et al. Analysis of Metabolic Abnormalities in High-Grade Glioma Using MRSI and Convex NMF. *NMR BioMed* (2019) 32:e4109. doi: 10.1002/nbm.4109
33. Branzoli F, Marjańska M. Magnetic Resonance Spectroscopy of Isocitrate Dehydrogenase Mutated Gliomas: Current Knowledge on the Neurochemical Profile. *Curr Opin Neurol* (2020) 33:413–21. doi: 10.1097/WCO.0000000000000833
34. Andronesi OC, Loebel F, Bogner W, Marjańska M, Vander Heiden MG, Iafrate AJ, et al. Treatment Response Assessment in IDH-Mutant Glioma Patients by Noninvasive 3d Functional Spectroscopic Mapping of 2-Hydroxyglutarate. *Clin Cancer Res* (2016) 22:1632–41. doi: 10.1158/1078-0432.CCR-15-0656

35. Choi C, Raisanen JM, Ganji SK, Zhang S, McNeil SS, An Z, et al. Prospective Longitudinal Analysis of 2-Hydroxyglutarate Magnetic Resonance Spectroscopy Identifies Broad Clinical Utility for the Management of Patients With IDH -Mutant Glioma. *J Clin Oncol* (2016) 34:4030–9. doi: 10.1200/JCO.2016.67.1222
36. Andronesi OC, Arrillaga-Romany IC, Ly KI, Bogner W, Ratai EM, Reitz K, et al. Pharmacodynamics of Mutant-IDH1 Inhibitors in Glioma Patients Probed by *In Vivo* 3d MRS Imaging of 2-Hydroxyglutarate. *Nat Commun* (2018) 9:1474. doi: 10.1038/s41467-018-03905-6
37. Korzowski A, Weinfurtner N, Mueller S, Breitling J, Goerke S, Schlemmer H, et al. Volumetric Mapping of Intra- and Extracellular pH in the Human Brain Using 31 P MRSI at 7T. *Magn Reson Med* (2020) 84:1707–23. doi: 10.1002/mrm.28255
38. Mirkes C, Shajan G, Chadzynski G, Buckenmaier K, Bender B, Scheffler K. (31)P CSI of the Human Brain in Healthy Subjects and Tumor Patients at 9.4 T With a Three-Layered Multi-Nuclear Coil: Initial Results. *MAGMA* (2016) 29:579–89. doi: 10.1007/s10334-016-0524-9
39. De Feyter HM, Behar KL, Corbin ZA, Fulbright RK, Brown PB, McIntyre S, et al. Deuterium Metabolic Imaging (DMI) for MRI-Based 3D Mapping of Metabolism In Vivo. *Sci Adv* (2018) 4:eaat7314. doi: 10.1126/sciadv.aat7314
40. van Zijl PCM, Lam WW, Xu J, Knutsson L, Stanisz GJ. Magnetization Transfer Contrast and Chemical Exchange Saturation Transfer MRI. Features and Analysis of the Field-Dependent Saturation Spectrum. *Neuroimage* (2018) 168:222–41. doi: 10.1016/j.neuroimage.2017.04.045
41. Jones CK, Huang A, Xu J, Edden RAE, Schär M, Hua J, et al. Nuclear Overhauser Enhancement (NOE) Imaging in the Human Brain at 7T. *Neuroimage* (2013) 77:114–24. doi: 10.1016/j.neuroimage.2013.03.047
42. van Zijl PCM, Yadav NN. Chemical Exchange Saturation Transfer (CEST): What is in a Name and What Isn't? *Magn Reson Med* (2011) 65:927–48. doi: 10.1002/mrm.22761
43. Zhou J. Amide Proton Transfer Imaging of the Human Brain. *Methods Mol Biol* (2011) 711:227–37. doi: 10.1007/978-1-61737-992-5_10
44. Windschuh J, Zaiss M, Meissner J-E, Paech D, Radbruch A, Ladd ME, et al. Correction of *B* 1-Inhomogeneities for Relaxation-Compensated CEST Imaging at 7 T. *NMR BioMed* (2015) 28:529–37. doi: 10.1002/nbm.3283
45. Kim M, Gillen J, Landman BA, Zhou J, van Zijl PCM. Water Saturation Shift Referencing (WASSR) for Chemical Exchange Saturation Transfer (CEST) Experiments. *Magn Reson Med* (2009) 61:1441–50. doi: 10.1002/mrm.21873
46. Schuenke P, Windschuh J, Roeloffs V, Ladd ME, Bachert P, Zaiss M. Simultaneous Mapping of Water Shift and B $_1$ (WASABI)—Application to Field-Inhomogeneity Correction of CEST MRI Data. *Magn Reson Med* (2017) 77:571–80. doi: 10.1002/mrm.26133
47. Zaiss M, Xu J, Goerke S, Khan IS, Singer RJ, Gore JC, et al. Inverse *Z* -Spectrum Analysis for Spillover-, MT-, and T_1 -Corrected Steady-State Pulsed CEST-MRI - Application to pH-Weighted MRI of Acute Stroke. *NMR BioMed* (2014) 27:240–52. doi: 10.1002/nbm.3054
48. Englund E, Brun A, Larsson EM, Györffy-Wagner Z, Persson B. Tumours of the Central Nervous System. Proton Magnetic Resonance Relaxation Times T1 and T2 and Histopathologic Correlates. *Acta Radiol Diagn (Stockh)* (1986) 27:653–9. doi: 10.1177/028418518602700606
49. Xu J, Li K, Zu Z, Li X, Gochberg DF, Gore JC. Quantitative Magnetization Transfer Imaging of Rodent Glioma Using Selective Inversion Recovery. *NMR BioMed* (2014) 27:253–60. doi: 10.1002/NBM.3058
50. Mehrabian H, Myrehaug S, Soliman H, Sahgal A, Stanisz GJ. Evaluation of Glioblastoma Response to Therapy With Chemical Exchange Saturation Transfer. *Int J Radiat Oncol Biol Phys* (2018) 101:713–23. doi: 10.1016/j.ijrobp.2018.03.057
51. Deshmane A, Zaiss M, Lindig T, Herz K, Schuppert M, Gandhi C, et al. 3D Gradient Echo Snapshot CEST MRI With Low Power Saturation for Human Studies at 3T. *Magn Reson Med* (2019) 81:2412–23. doi: 10.1002/mrm.27569
52. Zaiss M, Windschuh J, Paech D, Meissner JE, Burth S, Schmitt B, et al. Relaxation-Compensated CEST-MRI of the Human Brain at 7T: Unbiased Insight Into NOE and Amide Signal Changes in Human Glioblastoma. *Neuroimage* (2015) 112:180–8. doi: 10.1016/J.NEUROIMAGE.2015.02.040
53. Voelker MN, Kraff O, Brenner D, Wollrab A, Weinberger O, Berger MC, et al. The Traveling Heads: Multicenter Brain Imaging at 7 Tesla. *Magn Reson Mater Phys Biol Med* (2016) 29:399–415. doi: 10.1007/s10334-016-0541-8
54. Zhou J, Tryggestad E, Wen Z, Lal B, Zhou T, Grossman R, et al. Differentiation Between Glioma and Radiation Necrosis Using Molecular Magnetic Resonance Imaging of Endogenous Proteins and Peptides. *Nat Med* (2011) 17:130–4. doi: 10.1038/nm.2268
55. Sagiyama K, Mashimo T, Togao O, Vemireddy V, Hatanpaa KJ, Maher EA, et al. *In Vivo* Chemical Exchange Saturation Transfer Imaging Allows Early Detection of a Therapeutic Response in Glioblastoma. *Proc Natl Acad Sci* (2014) 111:4542–7. doi: 10.1073/pnas.1323855111
56. Togao O, Yoshiura T, Keupp J, Hiwatashi A, Yamashita K, Kikuchi K, et al. Amide Proton Transfer Imaging of Adult Diffuse Gliomas: Correlation With Histopathological Grades. *Neuro Oncol* (2014) 16:441–8. doi: 10.1093/neuonc/not158
57. Park KJ, Kim HS, Park JE, Shim WH, Kim SJ, Smith SA. Added Value of Amide Proton Transfer Imaging to Conventional and Perfusion MR Imaging for Evaluating the Treatment Response of Newly Diagnosed Glioblastoma. *Eur Radiol* (2016) 26:4390–403. doi: 10.1007/s00330-016-4261-2
58. Liu J, Li C, Chen Y, Lv X, Lv Y, Zhou J, et al. Diagnostic Performance of Multiparametric MRI in the Evaluation of Treatment Response in Glioma Patients at 3T. *J Magn Reson Imaging* (2020) 51:1154–61. doi: 10.1002/jmri.26900
59. Park JE, Kim HS, Park KJ, Kim SJ, Kim JH, Smith SA. Pre- and Posttreatment Glioma: Comparison of Amide Proton Transfer Imaging With MR Spectroscopy for Biomarkers of Tumor Proliferation. *Radiology* (2016) 278:514–23. doi: 10.1148/radiol.2015142979
60. Park JE, Lee JY, Kim HS, Oh J-Y, Jung SC, Kim SJ, et al. Amide Proton Transfer Imaging Seems to Provide Higher Diagnostic Performance in Post-Treatment High-Grade Gliomas Than Methionine Positron Emission Tomography. *Eur Radiol* (2018) 28:3285–95. doi: 10.1007/s00330-018-5341-2
61. Park YW, Ahn SS, Kim EH, Kang S-G, Chang JH, Kim SH, et al. Differentiation of Recurrent Diffuse Glioma From Treatment-Induced Change Using Amide Proton Transfer Imaging: Incremental Value to Diffusion and Perfusion Parameters. *Neuroradiology* (2021) 63:363–72. doi: 10.1007/s00234-020-02542-5
62. Ma B, Blakeley JO, Hong X, Zhang H, Jiang S, Blair L, et al. Applying Amide Proton Transfer-Weighted MRI to Distinguish Pseudoprogression From True Progression in Malignant Gliomas. *J Magn Reson Imaging* (2016) 44:456–62. doi: 10.1002/jmri.25159
63. Meissner J, Korzowski A, Regnery S, Goerke S, Breitling J, Floca RO, et al. Early Response Assessment of Glioma Patients to Definitive Chemoradiotherapy Using Chemical Exchange Saturation Transfer Imaging at 7 T. *J Magn Reson Imaging* (2019) 50:1268–77. doi: 10.1002/jmri.26702
64. Paech D, Dreher C, Regnery S, Meissner JE, Goerke S, Windschuh J, et al. Relaxation-Compensated Amide Proton Transfer (APT) MRI Signal Intensity is Associated With Survival and Progression in High-Grade Glioma Patients. *Eur Radiol* (2019) 29:4957–67. doi: 10.1007/s00330-019-06066-2
65. Regnery S, Adeberg S, Dreher C, Oberhollenzer J, Meissner JE, Goerke S, et al. Chemical Exchange Saturation Transfer MRI Serves as Predictor of Early Progression in Glioblastoma Patients. *Oncotarget* (2018) 9:28772–83. doi: 10.18632/oncotarget.25594
66. McVicar N, Li AX, Gonçalves DF, Bellyou M, Meakin SO, Prado MA, et al. Quantitative Tissue Ph Measurement During Cerebral Ischemia Using Amine and Amide Concentration-Independent Detection (AACID) With MRI. *J Cereb Blood Flow Metab* (2014) 34:690–8. doi: 10.1038/jcbfm.2014.12
67. Harris RJ, Cloughesy TF, Liau LM, Nghiemphu PL, Lai A, Pope WB, et al. Simulation, Phantom Validation, and Clinical Evaluation of Fast pH-Weighted Molecular Imaging Using Amine Chemical Exchange Saturation Transfer Echo Planar Imaging (CEST-EPI) in Glioma at 3 T. *NMR BioMed* (2016) 29:1563–76. doi: 10.1002/nbm.3611
68. McVicar N, Li AX, Meakin SO, Bartha R. Imaging Chemical Exchange Saturation Transfer (CEST) Effects Following Tumor-Selective Acidification Using Lonidamine. *NMR BioMed* (2015) 28:566–75. doi: 10.1002/nbm.3287
69. Yao J, Tan CHP, Schlossman J, Chakhoyan A, Raymond C, Pope WB, et al. pH-Weighted Amine Chemical Exchange Saturation Transfer Echoplanar Imaging (CEST-EPI) as a Potential Early Biomarker for Bevacizumab Failure

in Recurrent Glioblastoma. *J Neurooncol* (2019) 142:587–95. doi: 10.1007/s11060-019-03132-z
70. Harris RJ, Cloughesy TF, Liau LM, Prins RM, Antonios JP, Li D, et al. pH-Weighted Molecular Imaging of Gliomas Using Amine Chemical Exchange Saturation Transfer MRI. *Neuro Oncol* (2015) 17:1514–24. doi: 10.1093/neuonc/nov106
71. Herz K, Mueller S, Perlman O, Zaitsev M, Knutsson L, Sun PZ, et al. Pulseq-CEST: Towards Multi-Site Multi-Vendor Compatibility and Reproducibility of CEST Experiments Using an Open-Source Sequence Standard. *Magn Reson Med* (2021) 86:1845–58. doi: 10.1002/mrm.28825
72. Speck O, Chang L, DeSilva NM, Ernst T. Perfusion MRI of the Human Brain With Dynamic Susceptibility Contrast: Gradient-Echo Versus Spin-Echo Techniques. *J Magn Reson Imaging* (2000) 12:381–7. doi: 10.1002/1522-2586(200009)12:3<381::AID-JMRI2>3.0.CO;2-Y
73. Kiselev VG, Strecker R, Ziyeh S, Speck O, Hennig J. Vessel Size Imaging in Humans. *Magn Reson Med* (2005) 53:553–63. doi: 10.1002/MRM.20383
74. Stadlbauer A, Oberndorfer S, Zimmermann M, Renner B, Buchfelder M, Heinz G, et al. Physiologic MR Imaging of the Tumor Microenvironment Revealed Switching of Metabolic Phenotype Upon Recurrence of Glioblastoma in Humans. *J Cereb Blood Flow Metab* (2020) 40:528–38. doi: 10.1177/0271678X19827885
75. Tortora G, Derrickson B. *Principles of Anatomy and Physiology. 11th Ed*. Hoboken: Wiley (2006).
76. Ouwerkerk R. Sodium Magnetic Resonance Imaging: From Research to Clinical Use. *J Am Coll Radiol* (2007) 4:739–41. doi: 10.1016/j.jacr.2007.07.001
77. Feinberg DA, Crooks LA, Kaufman L, Brant-Zawadzki M, Posin JP, Arakawa M, et al. Magnetic Resonance Imaging Performance: A Comparison of Sodium and Hydrogen. *Radiology* (1985) 156:133–8. doi: 10.1148/radiology.156.1.4001399
78. Biller A, Badde S, Nagel A, Neumann J-O, Wick W, Hertenstein A, et al. Improved Brain Tumor Classification by Sodium MR Imaging: Prediction of IDH Mutation Status and Tumor Progression. *AJNR Am J Neuroradiol* (2016) 37:66–73. doi: 10.3174/ajnr.A4493
79. Haneder S, Giordano FA, Konstandin S, Brehmer S, Buesing KA, Schmiedek P, et al. ^{23}Na-MRI of Recurrent Glioblastoma Multiforme After Intraoperative Radiotherapy: Technical Note. *Neuroradiology* (2015) 57:321–6. doi: 10.1007/s00234-014-1468-2
80. Thulborn KR, Lu A, Atkinson IC, Pauliah M, Beal K, Chan TA, et al. Residual Tumor Volume, Cell Volume Fraction, and Tumor Cell Kill During Fractionated Chemoradiation Therapy of Human Glioblastoma Using Quantitative Sodium MR Imaging. *Clin Cancer Res* (2019) 25:1226–32. doi: 10.1158/1078-0432.CCR-18-2079
81. Paech D, Regnery S, Platt T, Behl NGR, Weckesser N, Windisch P, et al. Assessment of Sodium MRI at 7 Tesla as Predictor of Therapy Response and Survival in Glioblastoma Patients. *Front Neurosci* (2021) 15:1649. doi: 10.3389/fnins.2021.782516
82. Suh CH, Kim HS, Jung SC, Choi CG, Kim SJ. Multiparametric MRI as a Potential Surrogate Endpoint for Decision-Making in Early Treatment Response Following Concurrent Chemoradiotherapy in Patients With Newly Diagnosed Glioblastoma: A Systematic Review and Meta-Analysis. *Eur Radiol* (2018) 28:2628–38. doi: 10.1007/s00330-017-5262-5
83. Lundemann M, Munck af Rosenschöld P, Muhic A, Larsen VA, Poulsen HS, Engelholm S-A, et al. Feasibility of Multi-Parametric PET and MRI for Prediction of Tumour Recurrence in Patients With Glioblastoma. *Eur J Nucl Med Mol Imaging* (2019) 46:603–13. doi: 10.1007/s00259-018-4180-3
84. Galbán CJ, Chenevert TL, Meyer CR, Tsien C, Lawrence TS, Hamstra DA, et al. Prospective Analysis of Parametric Response Map–Derived MRI Biomarkers: Identification of Early and Distinct Glioma Response Patterns Not Predicted by Standard Radiographic Assessment. *Clin Cancer Res* (2011) 17:4751–60. doi: 10.1158/1078-0432.CCR-10-2098
85. Seeger A, Braun C, Skardelly M, Paulsen F, Schittenhelm J, Ernemann U, et al. Comparison of Three Different MR Perfusion Techniques and MR Spectroscopy for Multiparametric Assessment in Distinguishing Recurrent High-Grade Gliomas From Stable Disease. *Acad Radiol* (2013) 20:1557–65. doi: 10.1016/j.acra.2013.09.003
86. Park JE, Kim HS, Goh MJ, Kim SJ, Kim JH. Pseudoprogression in Patients With Glioblastoma: Assessment by Using Volume-Weighted Voxel-Based Multiparametric Clustering of MR Imaging Data in an Independent Test Set. *Radiology* (2015) 275:792–802. doi: 10.1148/radiol.14141414
87. Hu X, Wong KK, Young GS, Guo L, Wong ST. Support Vector Machine Multiparametric MRI Identification of Pseudoprogression From Tumor Recurrence in Patients With Resected Glioblastoma. *J Magn Reson Imaging* (2011) 33:296–305. doi: 10.1002/jmri.22432
88. Yan J-L, Li C, van der Hoorn A, Boonzaier NR, Matys T, Price SJ. A Neural Network Approach to Identify the Peritumoral Invasive Areas in Glioblastoma Patients by Using MR Radiomics. *Sci Rep* (2020) 10:9748. doi: 10.1038/s41598-020-66691-6
89. Kim M, Park JE, Kim HS, Kim N, Park SY, Kim Y-H, et al. Spatiotemporal Habitats From Multiparametric Physiologic MRI Distinguish Tumor Progression From Treatment-Related Change in Post-Treatment Glioblastoma. *Eur Radiol* (2021) 31:6374–83. doi: 10.1007/s00330-021-07718-y
90. d'Este SH, Nielsen MB, Hansen AE. Visualizing Glioma Infiltration by the Combination of Multimodality Imaging and Artificial Intelligence, a Systematic Review of the Literature. *Diagnostics* (2021) 11:592. doi: 10.3390/diagnostics11040592
91. Booth TC, Williams M, Luis A, Cardoso J, Ashkan K, Shuaib H. Machine Learning and Glioma Imaging Biomarkers. *Clin Radiol* (2020) 75:20–32. doi: 10.1016/j.crad.2019.07.001
92. Laudicella R, Quartuccio N, Argiroffi G, Alongi P, Baratto L, Califaretti E, et al. Unconventional Non-Amino Acidic PET Radiotracers for Molecular Imaging in Gliomas. *Eur J Nucl Med Mol Imaging* (2021) 48:3925–39. doi: 10.1007/s00259-021-05352-w
93. Moreau A, Febvey O, Mognetti T, Frappaz D, Kryza D. Contribution of Different Positron Emission Tomography Tracers in Glioma Management: Focus on Glioblastoma. *Front Oncol* (2019) 9:1134. doi: 10.3389/fonc.2019.01134
94. Drake LR, Hillmer AT, Cai Z. Approaches to PET Imaging of Glioblastoma. *Molecules* (2020) 25:568. doi: 10.3390/molecules25030568
95. Werner J-M, Lohmann P, Fink GR, Langen K-J, Galldiks N. Current Landscape and Emerging Fields of PET Imaging in Patients With Brain Tumors. *Molecules* (2020) 25:1471. doi: 10.3390/molecules25061471
96. de Zwart PL, van Dijken BRJ, Holtman GA, Stormezand GN, Dierckx RAJO, Jan van Laar P, et al. Diagnostic Accuracy of PET Tracers for the Differentiation of Tumor Progression From Treatment-Related Changes in High-Grade Glioma: A Systematic Review and Metaanalysis. *J Nucl Med* (2020) 61:498–504. doi: 10.2967/jnumed.119.233809
97. Cui M, Zorrilla-Veloz RI, Hu J, Guan B, Ma X. Diagnostic Accuracy of PET for Differentiating True Glioma Progression From Post Treatment-Related Changes: A Systematic Review and Meta-Analysis. *Front Neurol* (2021) 12:671867. doi: 10.3389/fneur.2021.671867
98. Law I, Albert NL, Arbizu J, Boellaard R, Drzezga A, Galldiks N, et al. Joint EANM/EANO/RANO Practice Guidelines/SNMMI Procedure Standards for Imaging of Gliomas Using PET With Radiolabelled Amino Acids and [18F]FDG: Version 1.0. *Eur J Nucl Med Mol Imaging* (2019) 46:540–57. doi: 10.1007/s00259-018-4207-9
99. Albert NL, Weller M, Suchorska B, Galldiks N, Soffietti R, Kim MM, et al. Response Assessment in Neuro-Oncology Working Group and European Association for Neuro-Oncology Recommendations for the Clinical Use of PET Imaging in Gliomas. *Neuro Oncol* (2016) 18:1199–208. doi: 10.1093/neuonc/now058
100. Stegmayr C, Schöneck M, Oliveira D, Willuweit A, Filss C, Galldiks N, et al. Reproducibility of O-(2-18F-Fluoroethyl)-L-Tyrosine Uptake Kinetics in Brain Tumors and Influence of Corticoid Therapy: An Experimental Study in Rat Gliomas. *Eur J Nucl Med Mol Imaging* (2016) 43:1115–23. doi: 10.1007/s00259-015-3274-4
101. Suchorska B, Jansen NL, Linn J, Kretzschmar H, Janssen H, Eigenbrod S, et al. Biological Tumor Volume in 18FET-PET Before Radiochemotherapy Correlates With Survival in GBM. *Neurology* (2015) 84:710–9. doi: 10.1212/WNL.0000000000001262
102. Galldiks N, Dunkl V, Ceccon G, Tscherpel C, Stoffels G, Law I, et al. Early Treatment Response Evaluation Using FET PET Compared to MRI in Glioblastoma Patients at First Progression Treated With Bevacizumab Plus Lomustine. *Eur J Nucl Med Mol Imaging* (2018) 45:2377–86. doi: 10.1007/s00259-018-4082-4

103. Henriksen OM, Marner L, Law I. Clinical PET/MR Imaging in Dementia and Neuro-Oncology. *PET Clin* (2016) 11:441–52. doi: 10.1016/j.cpet.2016.05.003
104. Henriksen OM, Larsen VA, Muhic A, Hansen AE, Larsson HBW, Poulsen HS, et al. Simultaneous Evaluation of Brain Tumour Metabolism, Structure and Blood Volume Using [18F]-Fluoroethyltyrosine (FET) PET/MRI: Feasibility, Agreement and Initial Experience. *Eur J Nucl Med Mol Imaging* (2016) 43:103–12. doi: 10.1007/s00259-015-3183-6
105. Pyatigorskaya N, Sgard B, Bertaux M, Yahia-Cherif L, Kas A. Can FDG-PET/MR Help to Overcome Limitations of Sequential MRI and PET-FDG for Differential Diagnosis Between Recurrence/Progression and Radionecrosis of High-Grade Gliomas? *J Neuroradiol* (2021) 48:189–94. doi: 10.1016/j.neurad.2020.08.003
106. Pyka T, Hiob D, Preibisch C, Gempt J, Wiestler B, Schlegel J, et al. Diagnosis of Glioma Recurrence Using Multiparametric Dynamic 18F-Fluoroethyl-Tyrosine PET-MRI. *Eur J Radiol* (2018) 103:32–7. doi: 10.1016/j.ejrad.2018.04.003
107. Sogani S, Jena A, Taneja S, Gambhir A, Mishra A, D'Souza M, et al. Potential for Differentiation of Glioma Recurrence From Radionecrosis Using Integrated ^{18} F-Fluoroethyl-L-Tyrosine (FET) Positron Emission Tomography/Magnetic Resonance Imaging: A Prospective Evaluation. *Neurol India* (2017) 65:293–301. doi: 10.4103/neuroindia.NI_101_16
108. Jena A, Taneja S, Gambhir A, Mishra AK, D'souza MM, Verma SM, et al. Glioma Recurrence Versus Radiation Necrosis. *Clin Nucl Med* (2016) 41:e228–36. doi: 10.1097/RLU.0000000000001152
109. Panagiotaki E, Walker-Samuel S, Siow B, Johnson SP, Rajkumar V, Pedley RB, et al. Noninvasive Quantification of Solid Tumor Microstructure Using VERDICT MRI. *Cancer Res* (2014) 74:1902–12. doi: 10.1158/0008-5472.CAN-13-2511
110. Booth TC, Larkin TJ, Yuan Y, Kettunen MI, Dawson SN, Scoffings D, et al. Analysis of Heterogeneity in T2-Weighted MR Images can Differentiate Pseudoprogression From Progression in Glioblastoma. *PloS One* (2017) 12:e0176528. doi: 10.1371/journal.pone.0176528
111. Kassner A, Thornhill RE. Texture Analysis: A Review of Neurologic MR Imaging Applications. *AJNR Am J Neuroradiol* (2010) 31:809–16. doi: 10.3174/ajnr.A2061
112. Cagney DN, Sul J, Huang RY, Ligon KL, Wen PY, Alexander BM. The FDA NIH Biomarkers, EndpointS, and Other Tools (BEST) Resource in Neuro-Oncology. *Neuro Oncol* (2018) 20:1162–72. doi: 10.1093/neuonc/nox242
113. Bzdok D, Altman N, Krzywinski M. Statistics Versus Machine Learning. *Nat Methods* (2018) 15:233–4. doi: 10.1038/nmeth.4642
114. Booth TC, Thompson G, Bulbeck H, Boele F, Buckley C, Cardoso J, et al. A Position Statement on the Utility of Interval Imaging in Standard of Care Brain Tumour Management: Defining the Evidence Gap and Opportunities for Future Research. *Front Oncol* (2021) 11:620070. doi: 10.3389/fonc.2021.620070
115. Tu JV. Advantages and Disadvantages of Using Artificial Neural Networks Versus Logistic Regression for Predicting Medical Outcomes. *J Clin Epidemiol* (1996) 49:1225–31. doi: 10.1016/s0895-4356(96)00002-9
116. Reyes M, Meier R, Pereira S, Silva CA, Dahlweid F-M, von Tengg-Kobligk H, et al. On the Interpretability of Artificial Intelligence in Radiology: Challenges and Opportunities. *Radiol Artif Intell* (2020) 2:e190043. doi: 10.1148/ryai.2020190043
117. Dharmarajan K, Strait KM, Tinetti ME, Lagu T, Lindenauer PK, Lynn J, et al. Treatment for Multiple Acute Cardiopulmonary Conditions in Older Adults Hospitalized With Pneumonia, Chronic Obstructive Pulmonary Disease, or Heart Failure. *J Am Geriatr Soc* (2016) 64:1574–82. doi: 10.1111/jgs.14303
118. Cabitza F, Rasoini R, Gensini GF. Unintended Consequences of Machine Learning in Medicine. *JAMA* (2017) 318:517–8. doi: 10.1001/jama.2017.7797
119. White H. Learning in Artificial Neural Networks: A Statistical Perspective. *Neural Comput* (1989) 1:425–64. doi: 10.1162/neco.1989.1.4.425
120. Ratib O, Rosset A, Heuberger J. Open Source Software and Social Networks: Disruptive Alternatives for Medical Imaging. *Eur J Radiol* (2011) 78:259–65. doi: 10.1016/j.ejrad.2010.05.004
121. *Medical Open Network for AI (MONAI)*. Available at: https://monai.io/ (Accessed 30 Dec 2020).
122. Booth TC, Akpinar B, Roman A, Shuaib H, Luis A, Chelliah A, et al. Machine Learning and Glioblastoma: Treatment Response Monitoring Biomarkers in 2021. In: Kia SM, et al. *Machine Learning in Clinical Neuroimaging and Radiogenomics in Neuro-Oncology. MLCN 2020, RNO-AI 2020. Lecture Notes in Computer Science, vol 12449*. Cham: Springer (2021). doi:10.1007/978-3-030-66843-3_21
123. Booth TC, Grzeda M, Chelliah A, Roman A, Al Busaidi A, Dragos C, et al. Imaging Biomarkers of Glioblastoma Treatment Response: A Systematic Review and Meta-Analysis of Recent Machine Learning Studies. *Front Oncol* (2022) 12:799662. doi: 10.3389/fonc.2022.799662
124. Hestness J, Narang S, Ardalani N, Diamos G, Jun H, Kianinejad H, et al. Deep Learning Scaling is Predictable, Empirically. *arXiv* (2017).
125. Sun C, Shrivastava A, Singh S, Gupta A. Revisiting Unreasonable Effectiveness of Data in Deep Learning Era. *arXiv* (2017).
126. Lei S, Zhang H, Wang K, Su Z. How Training Data Affect the Accuracy and Robustness of Neural Networks for Image Classification In: *Proc 2019 Int Conf Learn Represent (ICLR-2019)*. New Orleans, USA (2019). Available at: https://openreview.net/pdf?id=HklKWhC5F7.
127. Rudie JD, Rauschecker AM, Bryan RN, Davatzikos C, Mohan S. Emerging Applications of Artificial Intelligence in Neuro-Oncology. *Radiology* (2019) 290:607–18. doi: 10.1148/radiol.2018181928
128. Sotoudeh H, Shafaat O, Bernstock JD, Brooks MD, Elsayed GA, Chen JA, et al. Artificial Intelligence in the Management of Glioma: Era of Personalized Medicine. *Front Oncol* (2019) 9:768. doi: 10.3389/fonc.2019.00768
129. Paul A, Tang Y-X, Summers RM. Fast Few-Shot Transfer Learning for Disease Identification From Chest X-Ray Images Using Autoencoder Ensemble. In: Hahn HK, Mazurowski MA, editors. *Proc. SPIE Medical Imaging 2020: Computer-Aided Diagnosis*. Houston, USA (2020). Available at: https://www.spiedigitallibrary.org/conference-proceedings-of-spie/11314/2549060/Fast-few-shot-transfer-learning-for-disease-identification-from-chest/10.1117/12.2549060.short?SSO=1 (Accessed 18 Apr 2021).
130. Bonawitz K, Eichner H, Grieskamp W, Huba D, Ingerman A, Ivanov V, et al. Towards Federated Learning at Scale: System Design. *arXiv* (2019).
131. Brisimi TS, Chen R, Mela T, Olshevsky A, Paschalidis IC, Shi W. Federated Learning of Predictive Models From Federated Electronic Health Records. *Int J Med Inform* (2018) 112:59–67. doi: 10.1016/j.ijmedinf.2018.01.007
132. Li W, Milletarì F, Xu D, Rieke N, Hancox J, Zhu W, et al. Privacy-Preserving Federated Brain Tumour Segmentation. In: Suk HI, Liu M, Yan P, Lian C, editors. *Machine Learning in Medical Imaging. MLMI 2019. Lecture Notes in Computer Science*. (2019). Cham: Springer. vol 11861. doi: 10.1007/978-3-030-32692-0_16
133. Artzi M, Liberman G, Blumenthal DT, Bokstein F, Aizenstein O, Ben Bashat D. Repeatability of Dynamic Contrast Enhanced Vp Parameter in Healthy Subjects and Patients With Brain Tumors. *J Neurooncol* (2018) 140:727–37. doi: 10.1007/s11060-018-03006-w
134. Anzalone N, Castellano A, Cadioli M, Conte GM, Cuccarini V, Bizzi A, et al. Brain Gliomas: Multicenter Standardized Assessment of Dynamic Contrast-Enhanced and Dynamic Susceptibility Contrast MR Images. *Radiology* (2018) 287:933–43. doi: 10.1148/radiol.2017170362
135. Schmainda KM, Prah MA, Marques H, Kim E, Barboriak DP, Boxerman JL. Value of Dynamic Contrast Perfusion MRI to Predict Early Response to Bevacizumab in Newly Diagnosed Glioblastoma: Results From ACRIN 6686 Multicenter Trial. *Neuro Oncol* (2021) 23:314–23. doi: 10.1093/neuonc/noaa167
136. Quantitative Imaging Biomarkers Alliance. *QIBA Profile: 4 DCE-MRI Quantification (DCEMRI-Q)* (2017). Available at: http://qibawiki.rsna.org/index.php/Profiles (Accessed 30 July 2021).
137. Almeida JRC, Greenberg T, Lu H, Chase HW, Fournier J, Cooper CM, et al. Test-Retest Reliability of Cerebral Blood Flow in Healthy Individuals Using Arterial Spin Labeling: Findings From the EMBARC Study. *Magn Reson Imaging* (2018) 45:26–33. doi: 10.1016/j.mri.2017.09.004
138. Mutsaerts HJMM, van Osch MJP, Zelaya FO, Wang DJJ, Nordhøy W, Wang Y, et al. Multi-Vendor Reliability of Arterial Spin Labeling Perfusion MRI Using a Near-Identical Sequence: Implications for Multi-Center Studies. *Neuroimage* (2015) 113:143–52. doi: 10.1016/j.neuroimage.2015.03.043
139. Yamaguchi S, Hirata K, Okamoto M, Shimosegawa E, Hatazawa J, Hirayama R, et al. Determination of Brain Tumor Recurrence Using ^{11} C-Methionine Positron Emission Tomography After Radiotherapy. *Cancer Sci* (2021) 112:4246–56. doi: 10.1111/cas.15001

140. O'Connor JPB, Aboagye EO, Adams JE, Aerts HJWL, Barrington SF, Beer AJ, et al. Imaging Biomarker Roadmap for Cancer Studies. *Nat Rev Clin Oncol* (2017) 14:169–86. doi: 10.1038/nrclinonc.2016.162
141. Wen PY, Macdonald DR, Reardon DA, Cloughesy TF, Sorensen AG, Galanis E, et al. Updated Response Assessment Criteria for High-Grade Gliomas: Response Assessment in Neuro-Oncology Working Group. *J Clin Oncol* (2010) 28:1963–72. doi: 10.1200/JCO.2009.26.3541
142. Ellingson BM, Wen PY, Cloughesy TF. Modified Criteria for Radiographic Response Assessment in Glioblastoma Clinical Trials. *Neurotherapeutics* (2017) 14:307–20. doi: 10.1007/s13311-016-0507-6
143. Ellingson BM, Bendszus M, Boxerman J, Barboriak D, Erickson BJ, Smits M, et al. Consensus Recommendations for a Standardized Brain Tumor Imaging Protocol in Clinical Trials. *Neuro Oncol* (2015) 17:1188–98. doi: 10.1093/neuonc/nov095
144. Wen PY, Weller M, Lee EQ, Alexander BM, Barnholtz-Sloan JS, Barthel FP, et al. Glioblastoma in Adults: A Society for Neuro-Oncology (SNO) and European Society of Neuro-Oncology (EANO) Consensus Review on Current Management and Future Directions. *Neuro Oncol* (2020) 22:1073–113. doi: 10.1093/neuonc/noaa106
145. Weller M, van den Bent M, Preusser M, Le Rhun E, Tonn JC, Minniti G, et al. EANO Guidelines on the Diagnosis and Treatment of Diffuse Gliomas of Adulthood. *Nat Rev Clin Oncol* (2021) 18:170–86. doi: 10.1038/s41571-020-00447-z
146. Weller M, van den Bent M, Tonn JC, Stupp R, Preusser M, Cohen-Jonathan-Moyal E, et al. European Association for Neuro-Oncology (EANO) Guideline on the Diagnosis and Treatment of Adult Astrocytic and Oligodendroglial Gliomas. *Lancet Oncol* (2017) 18:e315–29. doi: 10.1016/S1470-2045(17)30194-8
147. Thust SC, Heiland S, Falini A, Jäger HR, Waldman AD, Sundgren PC, et al. Glioma Imaging in Europe: A Survey of 220 Centres and Recommendations for Best Clinical Practice. *Eur Radiol* (2018) 28:3306–17. doi: 10.1007/s00330-018-5314-5
148. Dickerson E, Srinivasan A. Multicenter Survey of Current Practice Patterns in Perfusion MRI in Neuroradiology: Why, When, and How Is It Performed? *Am J Roentgenol* (2016) 207:406–10. doi: 10.2214/AJR.15.15740
149. Erker C, Tamrazi B, Poussaint TY, Mueller S, Mata-Mbemba D, Franceschi E, et al. Response Assessment in Paediatric High-Grade Glioma: Recommendations From the Response Assessment in Pediatric Neuro-Oncology (RAPNO) Working Group. *Lancet Oncol* (2020) 21:e317–29. doi: 10.1016/S1470-2045(20)30173-X
150. Manfrini E, Smits M, Thust S, Geiger S, Bendella Z, Petr J, et al. From Research to Clinical Practice: A European Neuroradiological Survey on Quantitative Advanced MRI Implementation. *Eur Radiol* (2021) 31:6334–41. doi: 10.1007/s00330-020-07582-2
151. Mandonnet E, Wager M, Almairac F, Baron M-H, Blonski M, Freyschlag CF, et al. Survey on Current Practice Within the European Low-Grade Glioma Network: Where do We Stand and What is the Next Step? *Neurooncol Pract* (2017) 4:241–7. doi: 10.1093/nop/npw031
152. Freyschlag CF, Krieg SM, Kerschbaumer J, Pinggera D, Forster M-T, Cordier D, et al. Imaging Practice in Low-Grade Gliomas Among European Specialized Centers and Proposal for a Minimum Core of Imaging. *J Neurooncol* (2018) 139:699–711. doi: 10.1007/s11060-018-2916-3
153. Booth TC, Luis A, Brazil L, Thompson G, Daniel RA, Shuaib H, et al. Glioblastoma Post-Operative Imaging in Neuro-Oncology: Current UK Practice (GIN CUP Study). *Eur Radiol* (2021) 31:2933–433. doi: 10.1007/s00330-020-07387-3

Conflict of Interest: KS: Ownership interest in IQ-AI Ltd and financial interest in Imaging Biometrics LLC. TB speaker's bureau for AbbVie and Siemens Healthineers.

The remaining authors declare that the research was conducted in the absence of any commercial or financial relationships that could be construed as a potential conflict of interest.

Publisher's Note: All claims expressed in this article are solely those of the authors and do not necessarily represent those of their affiliated organizations, or those of the publisher, the editors and the reviewers. Any product that may be evaluated in this article, or claim that may be made by its manufacturer, is not guaranteed or endorsed by the publisher.

Copyright © 2022 Booth, Wiegers, Warnert, Schmainda, Riemer, Nechifor, Keil, Hangel, Figueiredo, Álvarez-Torres and Henriksen. This is an open-access article distributed under the terms of the Creative Commons Attribution License (CC BY). The use, distribution or reproduction in other forums is permitted, provided the original author(s) and the copyright owner(s) are credited and that the original publication in this journal is cited, in accordance with accepted academic practice. No use, distribution or reproduction is permitted which does not comply with these terms.

frontiers in Neuroscience

ORIGINAL RESEARCH
published: 01 March 2022
doi: 10.3389/fnins.2022.833073

Validation of Non-invasive Language Mapping Modalities for Eloquent Tumor Resection: A Pilot Study

*Matthew Muir[1], Rajan Patel[2], Jeffrey Traylor[3], Dhiego Chaves de Almeida Bastos[4], Sarah Prinsloo[1], Ho-Ling Liu[5], Kyle Noll[6], Jeffrey Wefel[6], Sudhakar Tummala[7], Vinodh Kumar[8] and Sujit Prabhu[1]**

[1] Department of Neurosurgery, The University of Texas MD Anderson Cancer Center, Houston, TX, United States, [2] Department of Neurosurgery, Baylor College of Medicine, Houston, TX, United States, [3] Department of Neurological Surgery, The University of Texas Southwestern Medical Center, Dallas, TX, United States, [4] Department of Neurosurgery, Cleveland Clinic, Cleveland, OH, United States, [5] Department of Imaging Physics, The University of Texas MD Anderson Cancer Center, Houston, TX, United States, [6] Department of Neuropsychology, The University of Texas MD Anderson Cancer Center, Houston, TX, United States, [7] Department of Neuro-Oncology, The University of Texas MD Anderson Cancer Center, Houston, TX, United States, [8] Department of Neuroradiology, The University of Texas MD Anderson Cancer Center, Houston, TX, United States

OPEN ACCESS

Edited by:
Sandro M. Krieg, Technical University of Munich, Germany

Reviewed by:
Jyrki Mäkelä, Hospital District of Helsinki and Uusimaa, Finland
Giovanni Pellegrino, McGill University, Canada

***Correspondence:**
Sujit Prabhu
sprabhu@mdanderson.org

Specialty section:
This article was submitted to Brain Imaging Methods, a section of the journal Frontiers in Neuroscience

Received: *10 December 2021*
Accepted: *13 January 2022*
Published: *01 March 2022*

Citation:
Muir M, Patel R, Traylor J, de Almeida Bastos DC, Prinsloo S, Liu H-L, Noll K, Wefel J, Tummala S Kumar V and Prabhu S (2022) Validation of Non-invasive Language Mapping Modalities for Eloquent Tumor Resection: A Pilot Study. Front. Neurosci. 16:833073. doi: 10.3389/fnins.2022.833073

Many studies have established a link between extent of resection and survival in patients with gliomas. Surgeons must optimize the oncofunctional balance by maximizing the extent of resection and minimizing postoperative neurological morbidity. Preoperative functional imaging modalities are important tools for optimizing the oncofunctional balance. Transcranial magnetic stimulation (TMS) and functional magnetic resonance imaging (fMRI) are non-invasive imaging modalities that can be used for preoperative functional language mapping. Scarce data exist evaluating the accuracy of these preoperative modalities for language mapping compared with gold standard intraoperative data in the same cohort. This study compares the accuracy of fMRI and TMS for language mapping compared with intraoperative direct cortical stimulation (DCS). We also identified significant predictors of preoperative functional imaging accuracy, as well as significant predictors of functional outcomes. Evidence from this study could inform clinical judgment as well as provide neuroscientific insight. We used geometric distances to determine copositivity between preoperative data and intraoperative data. Twenty-eight patients were included who underwent both preoperative fMRI and TMS procedures, as well as an awake craniotomy and intraoperative language mapping. We found that TMS shows significantly superior correlation to intraoperative DCS compared with fMRI. TMS also showed significantly higher sensitivity and negative predictive value than specificity and positive predictive value. Poor cognitive baseline was associated with decreased TMS accuracy as well as increased risk for worsened aphasia postoperatively. TMS has emerged as a promising preoperative language mapping tool. Future work should be done to identify the proper role of each imaging modality in a comprehensive, multimodal approach to optimize the oncofunctional balance.

Keywords: functional MRI, transcranial magnetic stimulation, direct cortical stimulation, gliomas, brain mapping, eloquent, aphasia

INTRODUCTION

Several studies have established a survival advantage to gross total resection in patients with intracranial malignancies (Molinaro et al., 2020). However, lesions in perieloquent language locations represent a unique challenge given risk of surgically acquired cognitive–linguistic deficits (Berger et al., 1994). The surgeon must balance an aggressive resection with preservation of eloquent structures in order to maximize survival as well as postoperative long term language function. Accumulating data has established that anatomy alone cannot predict functionality, indicating the need for functional mapping (Pouratian and Bookheimer, 2010). The introduction of direct cortical stimulation (DCS) during awake craniotomies has revolutionized this effort, allowing the surgeon to interrogate cortical language function by introducing transient electrical lesions (Ojemann et al., 2008). However, functional data can only be obtained intraoperatively, prohibiting the use of DCS for patient selection or surgical planning (Ojemann et al., 2008). In addition, various factors including young age, mental illness, and conscious sedation intolerance exclude patients for consideration for an awake craniotomy (Picht et al., 2013; Tarapore et al., 2013). Furthermore, this approach is invasive and associated with a risk of intraoperative seizures that can lead to an aborted operation (Serletis and Bernstein, 2007; Nossek et al., 2013a,b; Gonen et al., 2014; Eseonu et al., 2018). These considerations indicate the need for accurate preoperative mapping modalities.

Transcranial magnetic stimulation (TMS) has emerged as a method of non-invasively applying inhibitory stimulation to the cortex. The addition of stereotactic navigation to TMS has introduced the possibility of using TMS for preoperative lesion based cortical mapping (Ille et al., 2015a). Studies have shown an excellent correlation of TMS to DCS for motor mapping (Vitikainen et al., 2009; Picht et al., 2011; Krieg et al., 2012; Tarapore et al., 2012). In addition, studies have demonstrated the accuracy of preoperative imaging modalities such as electroencephalography and magnetoencephalography (Tarapore et al., 2012; Babajani-Feremi et al., 2014). However, the data analyzing TMS correlation with DCS for language mapping are sparse and limited to small patient cohorts (Picht et al., 2013; Tarapore et al., 2013). Functional magnetic resonance imaging (fMRI) is a preoperative mapping modality traditionally used for preoperative functional mapping (Picht et al., 2013). Because of a variety of proposed mechanisms, recent studies have shown poor correlation between fMRI and the gold standard of DCS for language mapping, especially in glioma patients (Giussani et al., 2010).

Data exploring the accuracy of both TMS and fMRI for language mapping in the same patient cohort would provide valuable insight into the proper role of each in a comprehensive multimodal mapping approach. Here we report our experience with preoperative language mapping using TMS compared with fMRI and intraoperative DCS in a pilot study of 28 patients.

MATERIALS AND METHODS

Inclusion and Exclusion Criteria

This study was approved by the institutional review board at our institution. Twenty-eight patients were included in this retrospective study with the following inclusion criteria: presence of left-sided glioma close to language eloquent structures according to Sawaya et al. (1998), underwent preoperative language mapping and awake craniotomy with DCS language mapping, and at least 18 years of age. Exclusion criteria consisted of severe aphasia per clinical neurological examination or contraindications to TMS mapping such as a pacemaker or cochlear implant (Rossi et al., 2009). All patients underwent preoperative TMS language mapping using an object-naming task paradigm up to a week before surgery and preoperative fMRI language mapping using three paradigms: sentence completion, letter fluency, and category fluency tasks. They also underwent preoperative neuropsychological evaluation.

Language Assessment

Preoperative language functioning was assessed within 1 week of planned surgical intervention with four different neuropsychological tests: Boston Naming Test (BNT), semantic fluency (Animals), Multilingual Aphasia Examination Controlled Oral Word Association (COWA), and the Multilingual Aphasia Examination Token Test (Token) (Spreen and Strauss, 1998). The BNT is an object naming task assessing expressive language, Animals and COWA are also expressive language measures interrogating lexical and semantic verbal fluency respectively, and Token is a measure of auditory comprehension aspects of receptive language. Patient performances on each task were converted to z scores (mean = 0, SD = 1) based on normative data stratified by age and education [see Noll et al. (2015) for sources of normative data]. Per common convention in neuropsychological research, a z score ≤ -1.5 was considered impaired. Frank postoperative aphasia was diagnosed *via* clinical neurologic examination and gathered from the postoperative clinical notes by the neurosurgery team in the week after surgery and again at 30-day follow-up. For appropriate comparison to postoperative status, binary measures of preoperative aphasia (i.e., present or absent) were also collected from the patient's chart. Postoperative aphasia immediately after surgery and that at 30-day follow-up were all recorded relative to preoperative aphasia and qualitatively recorded as the following categorical variables: "worsened" and "unchanged or improved" per record review.

Transcranial Magnetic Stimulation Mapping Protocol

A navigated TMS system was utilized in the present study (NBS System 3.2; Nexstim, Helsinki, Finland). TMS stimulation onset was simultaneous with presentation of the line drawing object (picture to trigger interval was 0.0 s). Time-locked rapid rate TMS trains were given for 5 Hz/5 pulses for 140 stimulations. The display time was 1,000 ms, and interpicture interval was

3,000 ms. We performed TMS language mapping according to the conventionally accepted protocol for TMS language mapping (Lioumis et al., 2012; Picht et al., 2013; Sollmann et al., 2013). The most likely location of the hand knob was identified anatomically. This area was then stimulated in a random pattern while systematically varying the rotation, tilt, and yaw of the magnetic field. The location of maximal motor evoked potential was identified. Resting motor threshold (RMT) was identified using this position (Krieg et al., 2012). Once determined, the individual's RMT was used as a basic value for the repetitive TMS language mapping procedure (Lioumis et al., 2012; Krieg et al., 2013; Picht et al., 2013; Sollmann et al., 2013). The patient then was baselined without stimulation on the object naming task, which consisted of presentation of line drawings of common objects and required the patient to verbally respond with the name of the pictured object. We used a common anterior/posterior coil orientation where the coil is oriented horizontally between the nasion and acoustic meatus. Pictures that elicited misnaming or hesitation were discarded. Baselining was repeated until a consistent baseline was obtained. Target dots 1 cm apart from each other were created in the surface of the three-dimensional (3D) brain reconstruction, based on the preoperative MRI, in a grid-like pattern. One centimeter was selected because a 1-cm radius of tissue is preserved around intraoperatively identified language-positive sites. The grid was created in the tumoral and peritumoral area. The pictures used on baseline were presented time locked to the TMS pulses while the coil was moved over the cerebral hemisphere. Each target dot was stimulated between four and five times non-consecutively. During this process, the patient was audiovisual-recorded. The audiovisual recordings were analyzed offline by the examiner who was also blind to the location of each stimulus in the 3D reconstruction. A site was considered a positive "hit" for language eloquence if disruption (e.g., speech arrest, hesitation, and paraphasic error) was observed on at least two of the trials. A hesitation was counted when the patient's response came after the TMS stimulation had ended for that picture. Positive sites were marked in the 3D brain surface as white dots, and this information was sent as a report to the surgeon. These sites were also exported in digital imaging and communications in medicine (DICOM) files to be uploaded in the Neuronavigation system (Elements; BrainLab, Munich, Germany).

Functional Magnetic Resonance Imaging Protocol

Magnetic Resonance Imaging scans were acquired on 3-T clinical scanners (GE Healthcare, Milwaukee, WI, United States), including fMRI scans using a T2*-weighted gradient-echo echo-planar imaging sequence (repetition time/echo time = 2,000/25 ms; matrix size = 64 × 64; field of view = 24 cm × 24 cm; 32 slices with 4-mm thickness and no gap; in-plane resolution = 3.75 mm^2 × 3.75 mm^2), and high-resolution T_2-weighted fluid-attenuated inversion recovery and 3D spoiled gradient-echo T1-weighted sequences were acquired for anatomic reference.

The fMRI scans included three task paradigms: letter fluency (LETT), category fluency (CAT), and sentence completion (SENT). All paradigms consisted of control and task blocks alternating for 20 s each. The task paradigms included six cycles of 20-s control and 20-s task blocks. For LETT, patients were presented with a letter of the alphabet and asked to generate words that started with that letter during each task block. For the control block, participants were asked to tap their index finger on their thumb bilaterally. For CAT, patients were presented with a category (e.g., cities or types of food) and asked to generate words related to the category. For the control block, participants were again asked to tap their index finger on their thumb bilaterally. For SENT, the task blocks consisted of incomplete sentences for which patients were asked to fill in a blank. For the control block, participants were given four gibberish sentences with a format resembling that in the active block (each lasting 5 s). Before the fMRI, all patients underwent practice trials according to our standard preoperative mapping guidelines to ensure that the patient could perform the tasks correctly. During fMRI acquisition, each paradigm was displayed using an MRI-compatible 32-inch liquid crystal display, and oral instructions were provided through an intercom.

The fMRI data were processed by using the DynaSuite Neuro software, version 3.0 (*Invivo*; Philips, Gainesville, FL, United States). Image preprocessing for fMRI included motion correction and spatial smoothing with a 4-mm full-width-at-half-maximum Gaussian kernel. A functional activation map was created using the correlation analysis of the task paradigms convolved with a canonical hemodynamic response function and the signal intensity time course for each voxel. Statistical thresholds ranging from corrected $p < 10^{-6}$–10^{-2} were applied to optimize the visualization of language areas.

Neuronavigation and Surgical Planning

Before the surgery, TMS points were imported to BrainLab Elements in DICOM image format. Processed fMRI data with blood oxygen level–dependent (BOLD) signal were sent to BrainLab Elements from the electronic medical records (EPIC). 3D objects were made of the TMS points as well as fMRI BOLD signal. The functional data were then coregistered to the preoperative structural MRI to create a comprehensive preoperative plan and sent to the surgeon. **Figure 1** shows an example of a 3D reconstruction of a preoperative plan.

Direct Cortical Stimulation

Following craniotomy and opening the dura, the patient was awakened with the removal of the laryngeal mask and was able to communicate with the neuroanesthesiologist and the surgeon *via* a microphone. Prior to stimulation, when the patients were deemed sufficiently alert, they were asked to perform an object naming task using picture cards for baselining. All the tasks were performed by either a neuropsychologist (KN) or a speech pathologist (JP) to facilitate the interpretation of errors during stimulation. Once a consistent baseline was established, patients were then asked to perform the same task during DCS. DCS was conducted by the surgeon synchronized with the tester. A leading phrase ("This is a. . .") would prompt the stimulation

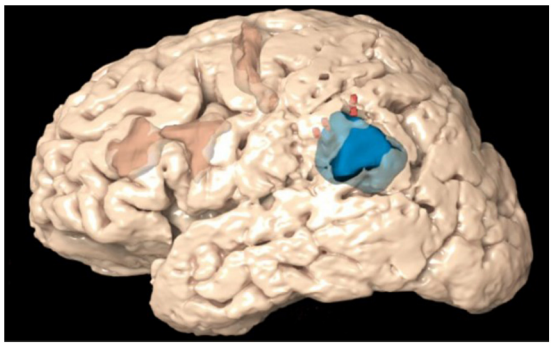

FIGURE 1 | 3D reconstruction of a preoperative plan depicting the transcranial magnetic stimulation (TMS) positive points (red) and blood oxygen level–dependent (BOLD) signal (orange) in context of the tumor (blue).

for approximately 2 s per stimulus starting at 1 mA. This process was repeated to stimulate the entire exposed surface of the brain. In addition, the patient was asked to generate words using phonemic and semantic categories similar to the fMRI verbal fluency paradigms. Any speech hesitation, dysnomia, paraphasic errors, and speech arrest were observed and noted. A site was considered a "hit" for language eloquence if any performance aberration was noted on at least two of three stimulations of the same site. An Ojemann stimulator (Radionics Inc., Burlington, MA, United States) was used with 5-mm spacing between the electrodes. For localization of the primary language and motor cortex, the stimulus was applied in increments of 1 mA, starting at 0.5 mA. The maximum stimulus needed to localize the language center was typically 4–6 mA. Positive DCS points were acquired using BrainLab and saved for offline analysis.

Data Analysis

The positive and negative TMS points were imported into the navigation software (BrainLab Elements) for analysis. Separate 3D objects were made of both the positive and negative points. The DICOM image was fused with the intraoperative T1 MRI containing the positive DCS points as well as a postoperative MRI. A 3D reconstruction of the craniotomy was generated from the postoperative MRI. TMS points lying outside the resection cavity were excluded from analyses as these areas were not examined intraoperatively with DCS. We recorded the relevant coordinates (negative TMS points, positive TMS points, and DCS points) from the resulting plan for statistical analysis.

Each positive TMS point was systematically measured for proximity to positive DCS points. A distance equation was utilized to determine if any DCS-positive points were located geometrically within 10 mm, which was considered a good correspondence between TMS and DCS. A distance of 10 mm was chosen because it is the widely accepted standard of error for DCS during language mapping (Haglund et al., 1994; Tharin and Golby, 2007; Sanai et al., 2008; Szelényi et al., 2010). Similar methodology was used for negative TMS points. If there were no positive DCS points within 10 mm, the point was counted as a true negative. If there was a positive DCS point within 10 mm of a negative TMS point, the point was counted as a false negative. In order to avoid labeling a portion of the cortex as both TMS positive and TMS negative, any point within 10 mm of a TMS-positive point was excluded from the analysis. Using DCS as the ground truth, positive predictive value (PPV), negative predictive value (NPV), sensitivity, and specificity were calculated from these values. **Figure 2** illustrates the visual analytic process for TMS compared with DCS.

For fMRI analysis, 10-mm spheres were manually drawn around positive DCS points. DCS spheres were visually inspected for overlap with fMRI BOLD signal for any of the fMRI paradigms utilized. If there was no BOLD signal within the craniotomy and also no positive points, a true negative was recorded. If there was BOLD signal within the craniotomy overlapping with a DCS sphere, a true positive was recorded. If there was BOLD signal within the craniotomy but separate from a DCS positive sphere, both a false positive and a false negative were recorded. Again, having DCS as ground truth, PPV, NPV, sensitivity, and specificity were calculated from these values. **Figure 3** illustrates the visual analytic process for fMRI compared with DCS.

Statistical Analysis

Analyses were performed with SPSS 24 (IBM, Armonk, NY, United States). True positives, false positives, true negatives, and false negatives for the entire cohort were added. We used these data to analyze each modality as binary classifiers in relation to DCS prediction using a single threshold of 10 mm, the standard error for both TMS and fMRI. Contingency tables were constructed to model the predictive value of both fMRI and TMS in relation to intraoperative DCS data and are shown in **Table 1**. The receiver operating characteristics sensitivity, specificity, NPV, and PPV were calculated for both modalities. Binary logistic regression was performed for each modality, and statistical significance was evaluated using the Hosmer-Lemeshow goodness-of-fit test at a significant level of $p < 0.05$.

Sensitivity of the preoperative modality (TMS or fMRI) represents the ability of the preoperative modality to correctly identify language-positive sites as determined by the ground truth intraoperative DCS. Specificity refers to the ability to correctly identify language-negative sites. PPV refers to the probability that language-positive site in terms of preoperative modalities will be defined as language positive by DCS. NPV refers to the probability that language-negative sites in terms of preoperative modalities will be defined as language negative by DCS.

χ^2 Tests were used to evaluate for preoperative factors that could be predictive of postoperative aphasia, such as age, location, cognitive status, or TMS variables. These variables were binarized. Age was binarized according to the median age (52). The total number of positive TMS points for each patient was also binarized according to the median (5). Location was binarized according to location (anterior vs. posterior). Tumor grade was binarized according to low- and high-grade tumors. Cognitive status was binarized according to impaired versus not impaired ($z < -1.5$ is impaired). Pearson product–moment correlation tests were used to evaluate preoperative factors such as tumor location (anterior vs. posterior), tumor grade, and

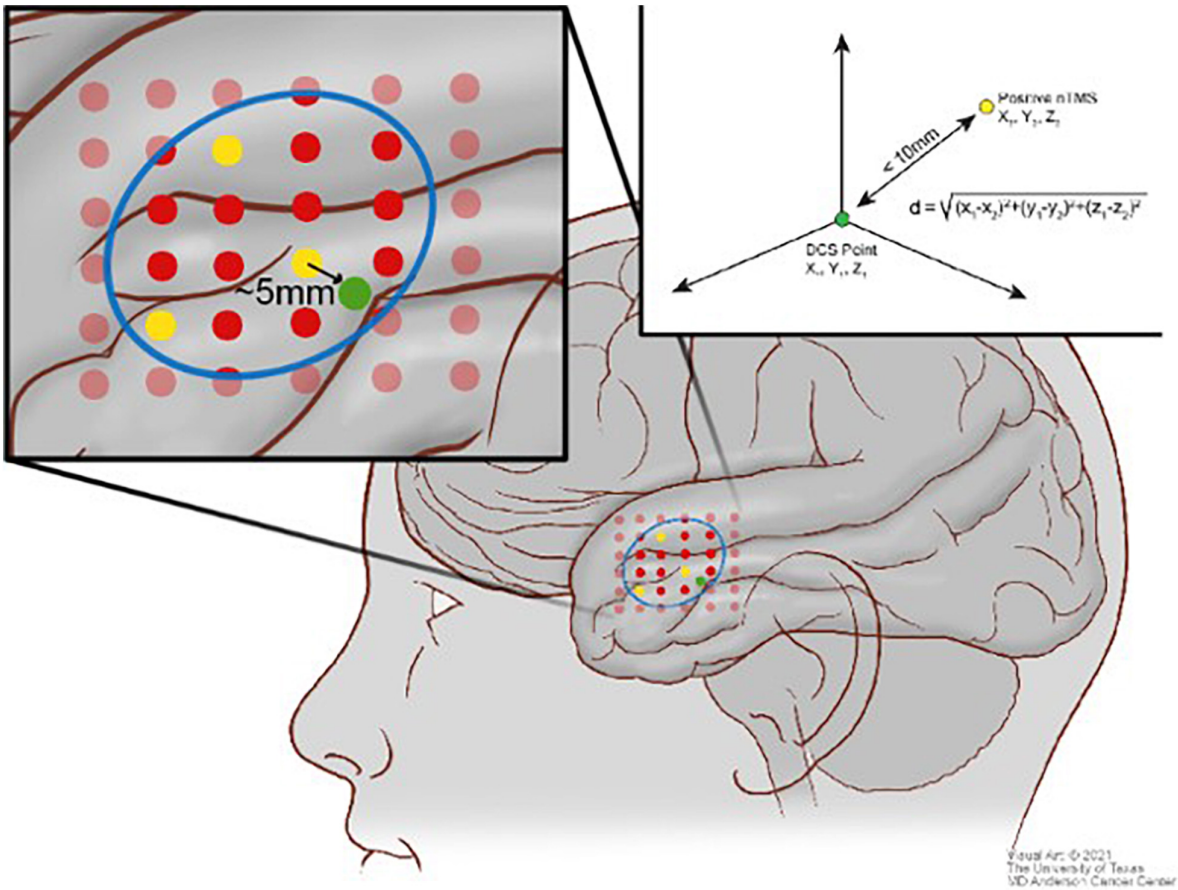

FIGURE 2 | Scheme illustrating the comparison between the direct cortical stimulation (DCS) points (green) and the transcranial magnetic stimulation (TMS) positive points (yellow) and TMS negative points (red) using the distance equation in context of the craniotomy (blue).

baseline neuropsychological language functioning that could be associated with TMS performance. Tumors were divided into anterior and posterior groups to evaluate for location-dependent accuracy of TMS. Tumors anterior to the terminal end of the central sulcus were defined as anterior and tumors posterior to the terminal end were defined as posterior. Given the exploratory nature of the study, an unadjusted $p \leq 0.05$ was considered statistically significant.

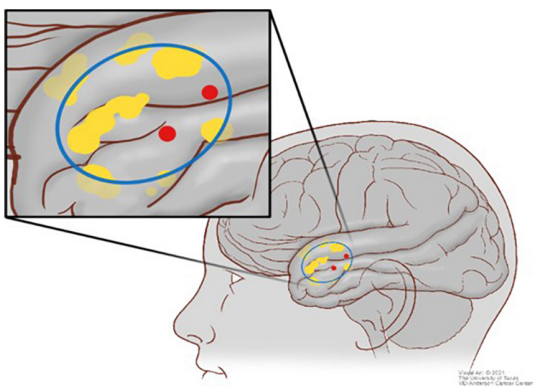

FIGURE 3 | Scheme illustrating the comparison between the direct cortical stimulation (DCS) points (red) and the blood oxygen level–dependent (BOLD) signal (yellow) in context of the craniotomy (blue).

RESULTS

Table 2 shows the patient characteristics, including preoperative and postoperative measures of aphasia. Twenty-eight patients were enrolled with surgeries between January 2017 and December

TABLE 1 | Confusion matrices for transcranial magnetic stimulation (TMS) versus direct cortical stimulation (DCS) (left) and functional magnetic resonance imaging (fMRI) versus DCS (right).

	DCS+	DCS−		DCS+	DCS−
TMS+	27	146	fMRI+	5	12
TMS−	4	302	fMRI−	2	8

The sensitivity of TMS for language mapping was 87%, specificity was 67%, positive predictive value was 16%, and negative predictive value was 99%.

The sensitivity of fMRI for language mapping was 71%, specificity was 40%, positive predictive value was 29%, and negative predictive value was 80%.

TABLE 2 | Patient characteristics.

Patient	Age (y)	Gender	Tumor histology	Location	Handedness	Preoperative aphasia	Postoperative aphasia?	Postoperative aphasia compared with preoperative	Postoperative aphasia at 1 month	1 month compared with preoperative
1	57	Female	Glioblastoma	Left temporal	Right	Yes	Yes	Aggravated	Yes	Aggravated
2	46	Female	Anaplastic astrocytoma	Left frontal	Right	No	Yes	Aggravated	Yes	Aggravated
3	45	Male	Diffuse glioma	Left temporal	Right	Yes	Yes	Aggravated	Yes	Aggravated
4	57	Male	Glioblastoma	Left temporoparietal	Right	Yes	Yes	Aggravated	Yes	Aggravated
5	28	Male	Anaplastic astrocytoma	Left temporal	Mixed	No	Yes	Aggravated	Yes	Aggravated
6	63	Female	Anaplastic oligodendroglioma	Left frontal	Right	No	Yes	Aggravated	Yes	Aggravated
7	60	Male	Glioblastoma	Left frontal	Right	No	Yes	Aggravated	Yes	Aggravated
8	69	Female	Anaplastic astrocytoma	Left frontal	Right	No	Yes	Aggravated	Yes	Aggravated
9	63	Female	Glioblastoma	Left temporal	Right	Yes	Yes	Aggravated	Yes	Aggravated
10	34	Male	Anaplastic astrocytoma	Left temporal	Right	Yes	Yes	Unchanged	Yes	Unchanged
11	58	Male	Glioblastoma	Left temporal	Right	Yes	Yes	Unchanged	No follow-up	N/A
12	35	Male	Anaplastic astrocytoma	Left temporal	Right	No	No	Unchanged	No	Unchanged
13	66	Female	Anaplastic oligodendroglioma	Left insular/temporal	Mixed	Yes	Yes	Aggravated	Yes	Unchanged
14	60	Male	Anaplastic astrocytoma	Left frontal	Right	No	Yes	Aggravated	No	Unchanged
15	56	Male	Glioblastoma	Left temporal	Right	No	Yes	Aggravated	No	Unchanged
16	43	Male	Diffuse astrocytoma	Left temporal	Right	No	No	Unchanged	No	Unchanged
17	22	Female	Glioblastoma	Left temporal	Right	No	Yes	Aggravated	No	Unchanged
18	31	Male	Diffuse astrocytoma	Left frontal	Right	No	No	Unchanged	No	Unchanged
19	70	Male	Glioblastoma	Left temporal	Right	Yes	Yes	Unchanged	No follow-up	N/A
20	71	Male	Glioblastoma	Left temporal	Right	No	Yes	Aggravated	No	Unchanged
21	23	Female	Diffuse astrocytoma	Left frontal	Right	No	No	Unchanged	No	Unchanged
22	61	Male	Glioblastoma	Left temporal	Right	No	Yes	Aggravated	Yes	Unchanged
23	27	Female	Diffuse astrocytoma	Left parietal	Right	No	No	Unchanged	No	Unchanged
24	67	Female	Glioblastoma	Left frontal	Right	No	No	Unchanged	No	Unchanged
25	71	Female	Glioblastoma	Left frontal	Right	No	No	Unchanged	No	Unchanged
26	40	Male	Anaplastic oligodendroglioma	Left frontal	Right	No	Yes	Aggravated	No follow-up	N/A
27	58	Female	Glioblastoma	Left temporal	Right	No	Yes	Aggravated	No follow-up	N/A
28	64	Female	Glioblastoma	Left frontal	Right	No	No	Unchanged	No	Unchanged

2018. The ages ranged from 25 to 71 years (mean = 52 years, SD = 16 years). Five patients (18%) had a diffuse astrocytoma World Health Organization grade II, 10 patients (36%) had an anaplastic astrocytoma grade III, and 14 patients (50%) had a glioblastoma.

Table 1 depicts contingency tables for both TMS and fMRI compared with DCS. The sensitivity of TMS was 83%, specificity was 67%, NPV was 99%, and PPV was 16%. The sensitivity of fMRI was 71%, specificity was 40%, NPV was 80%, and PPV was 29%. fMRI results were not used intraoperatively in four patients because of poor baseline limiting the patient's ability to comply with language mapping tasks (not severe enough to be excluded from TMS or the study). Eleven patients had no BOLD within the bounds of the craniotomy, consistent with negative intraoperative mapping with no DCS-positive points.

Table 3 shows binary logistic regression performed with fMRI and TMS in relation to predicting intraoperative DCS points using a single threshold of 10 mm. TMS showed statistically significant prediction of DCS points [odds ratio (OR) = 15.1, $p < 0.0001$], whereas fMRI did not show statistically significant prediction (OR = 1.7, $p = 0.59$).

Eight patients (29%) had preoperative aphasia per clinical neurologic examination. However, 86% of patients had at least one impaired score out of the four neuropsychological language tests. Regarding individual measures, 54% of patients were impaired on each verbal fluency measure, and 43% were

TABLE 3 | Univariate statistical analysis performed for each preoperative modality in relation to predicting intraoperative direct cortical stimulation (DCS) points.

	Odds ratio	95% Confidence interval	*p*-value
TMS	15.1	5.2–43.8	<0.0001
fMRI	1.7	0.26–10.8	0.59

TMS, transcranial magnetic stimulation; fMRI, functional magnetic resonance imaging.

impaired on confrontation naming, whereas comprehension was relatively preserved, with only 14% falling in the impaired range. On average, performances were lowest for verbal fluency [Animals (mean = −1.69, SD = 1.23); COWA (mean = −1.63, SD = 0.93)] and naming [BNT (mean = −1.37, SD = 1.35)], whereas comprehension was generally within normal limits [Token (mean = −0.20, SD = 1.23)]. Seventeen patients (61%) had transient worsened postoperative aphasia compared with preoperative status based on chart review. Twenty-four patients had 30-day follow-up; nine (38%) of these had worsened postoperative aphasia lasting longer than 30 days. Postoperative neuropsychological performances were not available for the majority of patients and thus were not analyzed. TMS-positive points were resected in 13 patients (46%). Five of these patients (38%) had postoperative aphasia lasting longer than 30 days. Eight (29%) had transient postoperative aphasia that subsided by 30-day follow-up. χ^2 Tests showed no association between resection of positive points and worsened postoperative aphasia, whether transient ($p = 0.60$) or persistent (> 30 days) ($p = 0.96$).

Table 4 summarizes preoperative variables along with TMS true positives, false positives, true negatives, and false negatives for each patient. A significant inverse correlation was found between baseline semantic fluency (animals) and false positives ($r_{26} = -0.46$, $p = 0.013$), indicating that patients with better baseline verbal fluency had fewer false-positive TMS results. Ten of 12 patients with impaired baseline semantic fluency ($z < -1.5$) had temporal tumors, while the other two had frontal lobe tumors. Eliminating patients with impaired baseline semantic fluency ($z < -1.5$) increased the specificity of TMS from 67 to 76% without significantly affecting the other measures.

No significant correlation was found between baseline naming on the BNT and number of true positives ($p = 0.37$), false positives ($p = 0.62$), or true negatives ($p = 0.97$). No significant correlation was found between baseline phonemic fluency (COWA) and false positives ($p = 0.40$), true positives ($p = 0.38$), or true negatives ($p = 0.24$). No significant correlation was found between baseline comprehension (Token) and false positives ($p = 0.88$), true

TABLE 4 | Preoperative variables used to perform univariate analysis of transcranial magnetic stimulation (TMS) performance along with false positives (FP), true positives (TP), true negatives (TN), and false negatives (FN) for each patient.

Patient	Age	Tumor grade	Tumor location	Boston naming test (*z* score)	Semantic fluency (*z* score)	Token test (*z* score)	MAE_COWA_Z (*z* score)	TP	FP	TN	FN
1	60	3	Posterior	−0.9	−1.6	0.4	−1.18	0	16	44	0
2	61	4	Anterior	−1.1	−0.8	−1.3	−2.13	0	10	18	0
3	57	4	Anterior	−3.3	−2	0.4	−3.12	0	4	46	0
4	63	4	Posterior	−1.4	−3.7	−0.7	−1.14	0	13	10	0
5	71	4	Anterior	−3	−3.7	0.9	−1.86	0	12	4	0
6	60	4	Anterior	−2.4	−1.4		−2.8	0	3	9	0
7	27	4	Anterior	−1.7	−2.7	0.9	−0.31	0	12	3	0
8	63	2	Anterior	−0.6	−3.2	−0.4	−2.22	7	6	0	0
9	56	3	Posterior	−3	−3.8	0.9	−1.93	0	8	19	0
10	22	4	Anterior	−3.3	−1.6	0.9	−0.73	1	3	8	0
11	46	4	Posterior	−3.3	−3.9	−1.3	−1.45	0	3	2	0
12	70	3	Posterior	−0.8	−0.9	−2	−2.5	3	5	4	2
13	31	4	Anterior	−0.7	−0.4	0.9	−0.86	0	3	15	0
14	23	2	Anterior	0.8	−0.2	0.9	−0.76	3	2	8	0
15	69	2	Posterior	−0.8	−2	−2.6	−3.53	0	4	7	0
16	35	3	Posterior	−2.9	−1.6	0.9	1.01	3	3	5	1
17	43	2	Anterior	−1.6	−1.1	−1.3	−1.72	0	3	0	0
18	58	4	Anterior	−0.7	0.1	−0.1	−1.38	0	0	11	0
19	57	4	Posterior	1.5	−1.8	−0.1	−0.82	1	4	13	0
20	66	3	Anterior	−2.5	−3.1	0.9	−1.72	0	4	3	0
21	45	2	Anterior	−0.2	−0.9	−1.3	−1.29	0	5	15	0
22	28	3	Posterior	N/A	−2.1	0.9	−1.4	5	5	3	0
23	58	4	Posterior	−1.7	0.2	−2.6	−1.4	1	2	11	1
24	64	4	Anterior	−0.6	−0.4	0.4	−1.52	0	3	15	0
25	67	4	Anterior	−1.4	−0.1	0.4	−1.66	1	6	12	0
26	40	3	Anterior	−2	−1.4	0.9	−1.72	2	3	1	0
27	71	4	Posterior	−0.9	−1.1	−2.6	−2.93	0	0	10	0
28	34	3	Anterior	1.5	−2.2	0.4	−2.54	0	4	6	0

positives ($p = 0.12$), or true negatives ($p = 0.94$). No significant correlation was found between age and false positives ($p = 0.67$), true positives ($p = 0.53$), or true negatives ($p = 0.85$). No significant correlation was found between tumor grade and false positives ($p = 0.33$), true positives ($p = 0.074$), or true negatives ($p = 0.73$). No significant correlation was found between location (anterior vs. posterior) and false positives ($p = 0.22$), true positives ($p = 0.95$), or true negatives ($p = 0.74$). False negatives were not included in the analysis because of their low occurrence.

The total number of positive TMS points was significantly correlated with persistent worsened postoperative aphasia (at 30-day follow-up) ($r_{26} = -0.60$, $p = 0.001$). However, the total number of positive DCS points was not significantly associated with persistent worsened postoperative aphasia ($p = 0.62$). A significant negative correlation was found between preoperative semantic fluency performance (animals) and risk for persistent worsened postoperative aphasia ($r_{26} = -0.56$, $p = 0.003$). No significant correlation was found between preoperative cognitive status assessed by the other three tests and risk for persistent postoperative aphasia.

DISCUSSION

Few studies have explored the correlation between preoperative TMS and intraoperative DCS, each with subtle differences in methodology. Tarapore et al. (2013) published a cohort of 12 patients with perisylvian glioma, finding sensitivity, specificity, and NPV greater than 90%. The authors spatially normalized each MRI and used a geometric distance of 10 mm to calculate copositivity between TMS and DCS sites. Picht et al. (2013) reported a sensitivity >80% and an NPV >90%, but low specificity and PPV. The authors used a cortical parcellation system to divide the cortex into functionally distinct regions and count TMS and DCS points as copositive if they fell within the same region. Jung et al. (2019) found TMS sensitivity greater than 60% and NPV greater than 70% using the same cortical parcellation system in a heterogeneous cohort of brain tumor patients.

A recent study by Bährend et al. (2020) found a sensitivity of 35%, specificity of 96%, an NPV of 96%, and a PPV of 16% using the geometric system. However, because of methodological differences, these results are difficult to interpret in the context of the previous studies. The authors noted a significantly increased number of stimulation sites compared with previous work (1,342 vs. 183 and 160), mainly due to larger craniotomies and smaller distances between stimulations. The dramatically increased number of stimulation sites led to a disproportionate amount of true negatives (1,138/1,342), which is the dominant factor when calculating specificity and NPV.

Results for TMS from our cohort showed an NPV exceeding 99% and a sensitivity of 83%, indicating that TMS consistently identifies language-positive sites defined by intraoperative mapping. However, the specificity and PPV were lower at 67 and 16%, respectively. These results support previous studies, providing further evidence for the utility of TMS for presurgical negative mapping. Sanai et al. (2008) were the first to report that intraoperative negative DCS mapping was sufficient to minimize long-term neurological deficits. Accumulating data showing the high sensitivity and NPV of TMS may point to a similar utility for preoperative negative TMS mapping. Ille et al. (2016) reported a case series of four patients who underwent resection for perieloquent lesions but were ineligible for an awake craniotomy. Only preoperative TMS was used for language mapping. At 3-month follow-up, none of the patients showed neurological sequelae, demonstrating the feasibility of resecting purely based on preoperative data (Ille et al., 2016).

Several possible reasons exist for the high sensitivity and high rate of false positives reported in most studies comparing TMS and DCS. Neuroimaging studies have demonstrated that TMS activates circuitry through transsynaptic spread, affecting downstream circuits outside the region of interest (Paus et al., 1997; Valero-Cabre and Pascual-Leone, 2005; Bestmann, 2008). Thus, a TMS-positive point may be the result of activation of a distant, functionally connected region, leading to false positives in non-essential locations. Preliminary studies using TMS for language lateralization would seem to support this hypothesis, as positive speech arrest sites were found in the non-dominant hemisphere (Pascual-Leone et al., 1991; Jennum et al., 1994; Michelucci et al., 1994; Epstein et al., 1999; Wassermann et al., 1999). Further study of optimal frequency, duration, and intensity of TMS may yield conditions that reduce this non-specific activation of non-essential intracortical pathways, resulting in fewer false positives (Picht et al., 2013). Other groups have explored the use of alternative language tests in order to reduce false positives, such as action naming and verb generation (Hernandez-Pavon et al., 2014; Hauck et al., 2015; Muthuraman et al., 2016).

Another reason for the high rate of false positives may be due to discrepancies between interpreting speech arrests during TMS or DCS stimulation. Intraoperative DCS speech arrests tend to be much more dramatic than TMS speech arrests, resulting in more ambiguity in calling TMS-positive points during stimulation. This could result in overcalling TMS-induced speech errors. Interestingly, better baseline semantic fluency, a measure of semantic network, and expressive language functioning, was associated fewer false positives on TMS. However, more than half the sample had baseline impairment in this domain. As such, increased false-positive rates for TMS may also be associated with baseline disruption of expressive language and semantic network integrity. Finally, it also possible that the higher rate of positive points observed in TMS could be due to identifying true language essential points that DCS did not identify. However, analyses of clinical sequelae of patients who underwent TMS-positive point resection do not support this idea. Tarapore et al. (2013) found that three of four of these patients had no permanent neurological deficit, whereas Picht et al. (2013) found that none of the 10 patients who had TMS-positive points resected showed permanent neurological deficits (Picht et al., 2013; Tarapore et al., 2013). Our cohort showed that 5 of the 13 patients with TMS-positive points resected showed worsened aphasia lasting longer than 30 days. However, there

was no correlation between resection of positive points and neurological outcome.

Interestingly, patient outcomes with respect to resection of positive TMS points seem to vary in motor cases versus language cases. Insight into this would provide information regarding whether TMS-positive points are truly essential for function. An analysis of a cohort of 43 patients by Moser et al. (2017) showed a direct correlation between the resection of TMS-positive motor points in prefrontal brain areas and postoperative motor function, whereas no such correlation has been found in TMS language studies to date (Picht et al., 2013; Tarapore et al., 2013; Moser et al., 2017). This could be due to different underlying neurophysiological mechanisms responsible for language versus motor function. Studies have shown that if more than one positive language site has been identified by DCS, one of them can be removed without permanent neurological sequel (Duffau, 2006; Robles et al., 2008). Neurological mechanisms for language seem to be far more complex than that of motor. Information coordinating movement is passed unidirectionally through long fiber tracks originating in M1 and terminating in spinal a-motor neurons, with modulating input from various other regions (Ries et al., 2019). In contrast, the anatomic distribution of sender and recipient neurons for language is organized in a mosaic pattern of discrete points, facilitating bidirectional communication, and redundant pathways (Chang et al., 2015). This more complex organization of the language system may be responsible for the unclear necessity of positive TMS and DCS language sites when compared with positive motor sites.

We also evaluated preoperative variables that could be predictive of TMS performance as well as risk for persistent worsened postoperative aphasia, finding mixed results. We found no correlation between age or tumor grade and TMS accuracy, using the outcomes of false positives, true positives, and false negatives. As noted previously, preoperative cognitive status assessed by semantic fluency (animal test) was found to be significantly correlated with false positives. Presumably, the TMS mapping process would be more impacted by a poor baseline than DCS because of the more subtle nature of errors induced by TMS. A poor baseline could lead to overcalling errors during preoperative mapping and more false positives. Eliminating patients with impaired semantic fluency test increased the specificity of TMS to 76% without significantly affecting the other measures of sensitivity, PPV, or NPV.

The total number of TMS-positive points upon preoperative mapping was significantly associated with risk for worsened postoperative aphasia at 30-day follow-up. Interestingly, the total number of DCS-positive points was not significantly associated with risk for persistent worsened postoperative aphasia. In addition, preoperative cognitive status assessed by semantic fluency was significantly associated with risk for persistent worsened postoperative aphasia. It is possible that compromise in baseline semantic fluency is an indicator of lesion proximity to eloquent networks, thus elevating risk of postoperative decline. These findings show that poor baseline status, whether captured by neuropsychological testing or TMS, is associated with postoperative neurological decline. More data concerning the impact of preoperative variables on TMS performance as well as risk for postoperative deficits could aid patient selection and risk stratification. Because of its superior correlations compared with the other three tests, the utility of the semantic fluency test should be further explored in the context of presurgical TMS language mapping.

Data regarding the utility of fMRI for presurgical language mapping in glioma patients are conflicting. A review of nine language mapping studies comparing fMRI to DCS showed widely varying levels of correlation (Giussani et al., 2010). The sensitivity ranged from 59 to 100%, whereas the specificity ranged from 0 to 97%. However, the results are difficult to interpret considering the heterogeneous patient populations (gliomas vs. benign tumors) and widely varying methodologies (Giussani et al., 2010). Some hypothesize that studies showing discrepancies between fMRI and DCS reflect methodological differences, as well as the pathophysiology of intracerebral lesions (Giussani et al., 2010). Picht et al. found that analyses of raw fMRI data by separate examiners can lead to different results, probably because fMRI relies on statistical thresholds that can vary by the individual patient as well as institution (Paus et al., 1997). In addition, gliomas diffusely infiltrate the brain parenchyma, decreasing the contact rate between glia and capillary cells, in turn decreasing the oxygen extraction fraction. These changes reduce the BOLD signal, rendering fMRI less accurate in cases involving intracerebral lesions (Feindel and Perot, 1965; Ojemann et al., 1998; Ulmer et al., 2003; Ulmer et al., 2004).

Despite these concerns, fMRI has shown significant utility for presurgical workup in glioma patients. Several groups have found good correlation between fMRI and intraoperative DCS for localizing motor, somatosensory, and visual areas (Roux et al., 2003; Majos et al., 2005; Li et al., 2006). Roux et al. (2003) showed that all of the 22 intraoperatively identified positive language sites were correlated to preoperative fMRI. A recent meta-analysis showed that preoperative fMRI decreases postoperative neurological morbidity (Luna et al., 2021), whereas a recent review found that fMRI has shown excellent utility for lateralizing language dominance, superior to the Wada test for many patients (Qadri et al., 2021). It is possible that combining task-based fMRI with cerebrovascular reactivity mapping (CVR) may help overcome some of the issues related to vascular uncoupling in the presence of brain tumors, although the impact of CVR mapping upon the accuracy of fMRI compared with DCS has not been adequately investigated to date.

Because of the widely varying patient populations and methodologies used in fMRI preoperative language mapping studies, considerable interest has turned to direct comparisons between the two main available preoperative modalities of TMS and fMRI within the same patient cohort. DCS maps the cortex by producing a transient virtual lesion, whereas fMRI maps by detecting changes in regional blood flow and oxygen extraction (Giussani et al., 2010). fMRI activations often overlie sulci, which hinders the ability of fMRI to precisely delineate between areas critical for language function versus areas merely participating,

obscuring which tissue must be preserved during surgery. This fundamental mechanistic difference between fMRI and the gold standard of DCS could account for much of the difficulty in correlating fMRI to DCS. TMS, like DCS, produces a transient virtual lesion and is seemingly unaffected by intracerebral lesions (Pascual-Leone et al., 1999; Sollmann et al., 2013). The mechanistic similarities of TMS to DCS could indicate that TMS has potential for superior correlation to intraoperative mapping data. While researchers have evolved fMRI protocols for many years, using TMS for presurgical mapping purposes is still in its infancy, except for a few specialized centers. More studies should further refine TMS language mapping protocols as well as optimize patient selection, with subsequent comparison to fMRI.

Ille et al. (2015b) were the first to show advantages of TMS for preoperative language mapping compared with fMRI within the same patient cohort. The authors emphasized the utility of fMRI for language studies in healthy patients but outlined the confounding impact of gliomas on fMRI data. However, our study seems to support these previous findings, showing higher sensitivity, specificity, and NPV in TMS compared with fMRI within the same patient cohort (Ille et al., 2015b). In addition, TMS showed statistically significant prediction of intraoperative DCS points, whereas fMRI did not. However, the statistical validity of these results remains in question because of the significant differences in data collection and aggregation between TMS and fMRI, leading to far more data points for TMS despite a similar number of patients. In addition, TMS lacks large, aggregated studies showing its clinical utility for preoperative language mapping (Luna et al., 2021). TMS also lacks comparable evidence to fMRI with respect to lateralizing language dominance (Qadri et al., 2021). While TMS has shown significant potential, the proper role of each modality for presurgical language mapping in brain tumor patients has yet to be determined.

Other groups have recently compared preoperative TMS language mapping to intraoperative DCS mapping. Our study has a few key methodological differences that should be noted. First, we utilized a geometric distance equation to detect and label copositive TMS and DCS locations instead of the cortical parcellation system used by Picht et al. (2013). Using the cortical parcellation system, the cortex is divided into functionally relevant divisions delineated by Corina et al. (2005). Two points are considered copositive only if they are in the same region, regardless of actual proximity. Although this approach may be beneficial for basic research, we believe that using geometric distance to determine copositivity is the more clinically relevant approach for a few reasons.

Intraoperative positive DCS points are treated as discrete points; the entire region is not avoided during resection. TMS points should be accordingly analyzed as discrete points in relation to DCS, instead of broader regions of interest, to achieve consistency. Furthermore, electrical stimulation studies have shown that language function resides in "mosaics" of connected points, often less than 1 cm, instead of broad clusters (Ojemann et al., 1989). Using the cortical parcellation system, detecting one of these points with TMS would inaccurately label the entire region as essential for language. Finally, the cortical parcellation system was derived from patients undergoing resection for epilepsy (Corina et al., 2005). The mass effect and cerebral edema produced by the tumor in patients undergoing glioma resection most likely distort the functionally defined anatomy derived from a different patient population.

Another methodological difference in our study was the exclusion of any TMS points outside of the craniotomy as well as negative TMS points within 10 mm of another positive TMS point. Preoperative TMS routinely stimulates the cortex in a wider distribution than the resection cavity exposes. Because the language-positive points identified by TMS were never tested by DCS, failure to exclude these points would falsely lower the specificity and PPV. Because we used a 10-mm margin of error between TMS and DCS points in the calculations, we eliminated negative TMS points within 10 mm of other positive TMS points. We wanted to avoid labeling a given point on the cortex as both language positive and language negative by TMS. It is unclear whether other groups using the geometric distance approach also performed this exclusion.

FUTURE DIRECTIONS AND LIMITATIONS

A significant methodological limitation in studies of this kind is the arbitrary selection of the threshold used to determine copositivity. Changing the threshold would change the calculated measures of accuracy. We chose 10 mm in accordance with Tarapore et al. (2012, 2013). Future studies should systematically vary the comparison threshold to document the effects on the accuracy of preoperative imaging modalities.

This study is limited by the retrospective nature of the data collection as well as a small sample size. A major limitation of studies focused on preoperative and intraoperative imaging modalities is the "brain shift" induced by the cerebral edema common to glioma patients. Once the skull flap has been removed, many patients experience a dramatic shift of the cortex in response to pressure differences and draining fluid (Gerard et al., 2017). This shift distorts the anatomy, producing a discrepancy between the preoperative MRI and intraoperative DCS point acquisition. This shift is even more pronounced when analyzing postoperative MRIs to investigate clinical sequelae of patients who had TMS-positive points resected. As a result, the veracity of the important analyses of these patients is questionable. Further work needs to be done to investigate innovative strategies to more accurately track the shift of the cortex from preoperative through postoperative imaging. In addition, further work stratifying the results based on anatomical regions as well as preoperative functional status could aid in optimal patient selection. Finally, further refining the TMS language mapping methodology could improve its clinical utility. Combining the TMS data with other modalities such as diffusion tensor imaging tractography could extend the map to subcortical structures. Future research should pursue methods to address the high rate of false positives, possibly by only reporting positive sites with multiple speech arrests at different stages of the procedure. Pursuing more objective methods of calling errors preoperatively during TMS stimulation could improve the correlation between modalities. Despite these limitations, our study provides valuable insight into the utility of presurgical mapping modalities, as well as novel methods of comparison.

CONCLUSION

TMS showed superior correlation with DCS compared with fMRI for preoperative language mapping in glioma patients. TMS showed high NPV and sensitivity, but comparably lower specificity and PPV. A poor cognitive baseline is associated with decreased TMS accuracy, as well as increased risk for persistent worsening postoperative aphasia. Future studies minimizing the confounding factor of brain shift, optimizing patient selection, and normalizing methods of error calling during TMS stimulation could increase the specificity and clinical utility of TMS.

DATA AVAILABILITY STATEMENT

The original contributions presented in the study are included in the article/supplementary material, further inquiries can be directed to the corresponding author.

ETHICS STATEMENT

The studies involving human participants were reviewed and approved by University of Texas MD Anderson Cancer Center Institutional Review Board (#2021-0856). The patients/participants provided their written informed consent to participate in this study.

AUTHOR CONTRIBUTIONS

MM and RP: conception and design, data analysis, writing, and editing. JT: data analysis and editing. DA and SPra: conception and design, data acquisition, and editing. SPri, VK, JW, and ST: data acquisition and editing. KN: conception and design, data analysis, and editing. All authors contributed to the article and approved the submitted version.

REFERENCES

Babajani-Feremi, A., Rezaie, R., Narayana, S., Choudhri, A. F., Fulton, S. P., Boop, F. A., et al. (2014). Variation in the topography of the speech production cortex verified by cortical stimulation and high gamma activity. *Neuroreport* 25, 1411–1417. doi: 10.1097/WNR.0000000000000276

Bährend, I., Muench, M. R., Schneider, H., Moshourab, R., Dreyer, F. R., Vajkoczy, P., et al. (2020). Incidence and linguistic quality of speech errors: a comparison of preoperative transcranial magnetic stimulation and intraoperative direct cortex stimulation. *J. Neurosurg.* 134, 1409–1418. doi: 10.3171/2020.3.JNS193085

Berger, M. S., Deliganis, A. V., Dobbins, J., and Keles, G. E. (1994). The effect of extent of resection on recurrence in patients with low grade cerebral hemisphere gliomas. *Cancer* 74, 1784–1791.

Bestmann, S. (2008). The physiological basis of transcranial magnetic stimulation. *Trends Cogn. Sci.* 12, 81–83.

Chang, E. F., Raygor, K. P., and Berger, M. S. (2015). Contemporary model of language organization: an overview for neurosurgeons. *J. Neurosurg.* 122, 250–261. doi: 10.3171/2014.10.JNS132647

Corina, D. P., Gibson, E. K., Martin, R., Poliakov, A., Brinkley, J., and Ojemann, G. A. (2005). Dissociation of action and object naming: evidence from cortical stimulation mapping. *Hum. Brain Mapp.* 24, 1–10. doi: 10.1002/hbm.20063

Duffau, H. (2006). New concepts in surgery of WHO grade II gliomas: functional brain mapping, connectionism and plasticity–a review. *J. Neurooncol.* 79, 77–115. doi: 10.1007/s11060-005-9109-6

Epstein, C. M., Meador, K. J., Loring, D. W., Wright, R. J., Weissman, J. D., Sheppard, S., et al. (1999). Localization and characterization of speech arrest during transcranial magnetic stimulation. *Clin. Neurophysiol.* 110, 1073–1079. doi: 10.1016/s1388-2457(99)00047-4

Eseonu, C. I., Rincon-Torroella, J., Lee, Y. M., ReFaey, K., Tripathi, P., and Quinones-Hinojosa, A. (2018). Intraoperative seizures in awake craniotomy for perirolandic glioma resections that undergo cortical mapping. *J. Neurol. Surg. A Cent Eur. Neurosurg.* 79, 239–246. doi: 10.1055/s-0037-1617759

Feindel, W., and Perot, P. (1965). Red cerebral veins: a report on arteriovenous shunts in tumors and cerebral scars. *J. Neurosurg.* 22, 315–325. doi: 10.3171/jns.1965.22.4.0315

Gerard, I. J., Kersten-Oertel, M., Petrecca, K., Sirhan, D., Hall, J. A., and Collins, D. L. (2017). Brain shift in neuronavigation of brain tumors: a review. *Med. Image Anal.* 35, 403–420. doi: 10.1016/j.media.2016.08.007

Giussani, C., Roux, F. E., Ojemann, J., Sganzerla, E. P., Pirillo, D., and Papagno, C. (2010). Is preoperative functional magnetic resonance imaging reliable for language areas mapping in brain tumor surgery? Review of language functional magnetic resonance imaging and direct cortical stimulation correlation studies. *Neurosurgery* 66, 113–120. doi: 10.1227/01.NEU.0000360392.15450.C9

Gonen, T., Grossman, R., Sitt, R., Nossek, E., Yanaki, R., Cagnano, E., et al. (2014). Tumor location and IDH1 mutation may predict intraoperative seizures during awake craniotomy. *J. Neurosurg.* 121, 1133–1138. doi: 10.3171/2014.7.JNS132657

Haglund, M. M., Berger, M. S., Shamseldin, M., Lettich, E., and Ojemann, G. A. (1994). Cortical localization of temporal lobe language sites in patients with gliomas. *Neurosurgery* 34, 567–576. discussion 576. doi: 10.1227/00006123-199404000-00001

Hauck, T., Tanigawa, N., Probst, M., Wohlschlaeger, A., Ille, S., Sollmann, N., et al. (2015). Task type affects location of language-positive cortical regions by repetitive navigated transcranial magnetic stimulation mapping. *PLoS One* 10:e0125298. doi: 10.1371/journal.pone.0125298

Hernandez-Pavon, J. C., Mäkelä, N., Lehtinen, H., Lioumis, P., and Mäkelä, J. P. (2014). Effects of navigated TMS on object and action naming. *Front. Hum. Neurosci.* 8:660. doi: 10.3389/fnhum.2014.00660

Ille, S., Sollmann, N., Butenschoen, V. M., Meyer, B., Ringel, F., and Krieg, S. M. (2016). Resection of highly language-eloquent brain lesions based purely on rTMS language mapping without awake surgery. *Acta Neurochir (Wien)* 158, 2265–2275. doi: 10.1007/s00701-016-2968-0

Ille, S., Sollmann, N., Hauck, T., Maurer, S., Tanigawa, N., Obermueller, T., et al. (2015a). Combined noninvasive language mapping by navigated transcranial magnetic stimulation and functional MRI and its comparison with direct cortical stimulation. *J. Neurosurg.* 123, 212–225. doi: 10.3171/2014.9.JNS14929

Ille, S., Sollmann, N., Hauck, T., Maurer, S., Tanigawa, N., Obermueller, T., et al. (2015b). Impairment of preoperative language mapping by lesion location: a functional magnetic resonance imaging, navigated transcranial magnetic stimulation, and direct cortical stimulation study. *J. Neurosurg.* 123, 314–324. doi: 10.3171/2014.10.JNS141582

Jennum, P., Friberg, L., Fuglsang-Frederiksen, A., and Dam, M. (1994). Speech localization using repetitive transcranial magnetic stimulation. *Neurology* 44, 269–273. doi: 10.1212/wnl.44.2.269

Jung, J., Lavrador, J. P., Patel, S., Giamouriadis, A., Lam, J., Bhangoo, R., et al. (2019). First United Kingdom experience of navigated transcranial magnetic stimulation in preoperative mapping of brain tumors. *World Neurosurg.* 122, e1578–e1587.

Krieg, S. M., Shiban, E., Buchmann, N., Gempt, J., Foerschler, A., Meyer, B., et al. (2012). Utility of presurgical navigated transcranial magnetic brain stimulation for the resection of tumors in eloquent motor areas. *J. Neurosurg.* 116, 994–1001. doi: 10.3171/2011.12.JNS111524

Krieg, S. M., Sollmann, N., Hauck, T., Ille, S., Foerschler, A., Meyer, B., et al. (2013). Functional language shift to the right hemisphere in patients with language-eloquent brain tumors. *PLoS One* 8:e75403. doi: 10.1371/journal.pone.0075403

Li, Z. X., Dai, J. P., Jiang, T., Li, S. W., Sun, Y. L., Liang, X. L., et al. (2006). [Function magnetic resonance imaging and diffusion tensor tractography in patients with brain gliomas involving motor areas: clinical application and outcome]. *Zhonghua Wai Ke Za Zhi* 44, 1275–1279.

Lioumis, P., Zhdanov, A., Mäkelä, N., Lehtinen, H., Wilenius, J., Neuvonen, T., et al. (2012). A novel approach for documenting naming errors induced by navigated transcranial magnetic stimulation. *J. Neurosci. Methods* 204, 349–354. doi: 10.1016/j.jneumeth.2011.11.003

Luna, L. P., Sherbaf, F. G., Sair, H. I., Mukherjee, D., Oliveira, I. B., and Köhler, C. A. (2021). Can preoperative mapping with functional MRI reduce morbidity in brain tumor resection? A systematic review and meta-analysis of 68 observational studies. *Radiology* 300, 338–349. doi: 10.1148/radiol.2021204723

Majos, A., Tybor, K., Stefańczyk, L., and Góraj, B. (2005). Cortical mapping by functional magnetic resonance imaging in patients with brain tumors. *Eur. Radiol.* 15, 1148–1158. doi: 10.1007/s00330-004-2565-0

Michelucci, R., Valzania, F., Passarelli, D., Santangelo, M., Rizzi, R., Buzzi, A. M., et al. (1994). Rapid-rate transcranial magnetic stimulation and hemispheric language dominance: usefulness and safety in epilepsy. *Neurology* 44, 1697–1700. doi: 10.1212/wnl.44.9.1697

Molinaro, A. M., Hervey-Jumper, S., Morshed, R. A., Young, J., Han, S. J., Chunduru, P., et al. (2020). Association of maximal extent of resection of contrast-enhanced and non-contrast-enhanced tumor with survival within molecular subgroups of patients with newly diagnosed glioblastoma. *JAMA Oncol.* 6, 495–503. doi: 10.1001/jamaoncol.2019.6143

Moser, T., Bulubas, L., Sabih, J., Conway, N., Wildschutz, N., Sollmann, N., et al. (2017). Resection of navigated transcranial magnetic stimulation-positive prerolandic motor areas causes permanent impairment of motor function. *Neurosurgery* 81, 99–110. doi: 10.1093/neuros/nyw169

Muthuraman, M., Hartwigsen, G., and Groppa, S. (2016). (Non-) invasive mapping of cortical language areas. *Clin. Neurophysiol.* 127, 1762–1763. doi: 10.1016/j.clinph.2015.12.006

Noll, K. R., Sullaway, C., Ziu, M., Weinberg, J. S., and Wefel, J. S. (2015). Relationships between tumor grade and neurocognitive functioning in patients with glioma of the left temporal lobe prior to surgical resection. *Neuro Oncol.* 17, 580–587. doi: 10.1093/neuonc/nou233

Nossek, E., Matot, I., Shahar, T., Barzilai, O., Rapoport, Y., Gonen, T., et al. (2013a). Failed awake craniotomy: a retrospective analysis in 424 patients undergoing craniotomy for brain tumor. *J. Neurosurg.* 118, 243–249. doi: 10.3171/2012.10.JNS12511

Nossek, E., Matot, I., Shahar, T., Barzilai, O., Rapoport, Y., Gonen, T., et al. (2013b). Intraoperative seizures during awake craniotomy: incidence and consequences: analysis of 477 patients. *Neurosurgery* 73, 135–140. discussion 140. doi: 10.1227/01.neu.0000429847.91707.97

Ojemann, G., Ojemann, J., Lettich, E., and Berger, M. (1989). Cortical language localization in left, dominant hemisphere. An electrical stimulation mapping investigation in 117 patients. *J. Neurosurg.* 71, 316–326. doi: 10.3171/jns.1989.71.3.0316

Ojemann, G., Ojemann, J., Lettich, E., and Berger, M. (2008). Cortical language localization in left, dominant hemisphere. An electrical stimulation mapping investigation in 117 patients. 1989. *J. Neurosurg.* 108, 411–421. doi: 10.3171/JNS/2008/108/2/0411

Ojemann, J. G., Neil, J. M., MacLeod, A. M., Silbergeld, D. L., Dacey, R. G. Jr., Petersen, S. E., et al. (1998). Increased functional vascular response in the region of a glioma. *J. Cereb. Blood Flow Metab.* 18, 148–153. doi: 10.1097/00004647-199802000-00004

Pascual-Leone, A., Bartres-Faz, D., and Keenan, J. P. (1999). Transcranial magnetic stimulation: studying the brain-behaviour relationship by induction of 'virtual lesions'. *Philos. Trans. R. Soc. Lond. B Biol. Sci.* 354, 1229–1238. doi: 10.1098/rstb.1999.0476

Pascual-Leone, A., Gates, J. R., and Dhuna, A. (1991). Induction of speech arrest and counting errors with rapid-rate transcranial magnetic stimulation. *Neurology* 41, 697–702. doi: 10.1212/wnl.41.5.697

Paus, T., Jech, R., Thompson, C. J., Comeau, R., Peters, T., and Evans, A. C. (1997). Transcranial magnetic stimulation during positron emission tomography: a new method for studying connectivity of the human cerebral cortex. *J. Neurosci.* 17, 3178–3184. doi: 10.1523/JNEUROSCI.17-09-03178.1997

Picht, T., Krieg, S. M., Sollmann, N., Rosler, J., Niraula, B., Neuvonen, T., et al. (2013). A comparison of language mapping by preoperative navigated transcranial magnetic stimulation and direct cortical stimulation during awake surgery. *Neurosurgery* 72, 808–819. doi: 10.1227/NEU.0b013e3182889e01

Picht, T., Schmidt, S., Brandt, S., Frey, D., Hannula, H., Neuvonen, T., et al. (2011). Preoperative functional mapping for rolandic brain tumor surgery: comparison of navigated transcranial magnetic stimulation to direct cortical stimulation. *Neurosurgery* 69, 581–588. discussion 588. doi: 10.1227/NEU.0b013e3182181b89

Pouratian, N., and Bookheimer, S. Y. (2010). The reliability of neuroanatomy as a predictor of eloquence: a review. *Neurosurg. Focus* 28:E3. doi: 10.3171/2009.11.FOCUS09239

Qadri, S., Dave, H., Das, R., and Alick-Lindstrom, S. (2021). Beyond the Wada: an updated approach to pre-surgical language and memory testing: an updated review of available evaluation techniques and recommended workflow to limit Wada test use to essential clinical cases. *Epilepsy Res.* 174:106673. doi: 10.1016/j.eplepsyres.2021.106673

Ries, S. K., Piai, V., Perry, D., Griffin, S., Jordan, K., Henry, R., et al. (2019). Roles of ventral versus dorsal pathways in language production: an awake language mapping study. *Brain Lang.* 191, 17–27. doi: 10.1016/j.bandl.2019.01.001

Robles, S. G., Gatignol, P., Lehéricy, S., and Duffau, H. (2008). Long-term brain plasticity allowing a multistage surgical approach to World Health Organization Grade II gliomas in eloquent areas. *J. Neurosurg.* 109, 615–624. doi: 10.3171/JNS/2008/109/10/0615

Rossi, S., Hallett, M., Rossini, P. M., and Pascual-Leone, A. (2009). Safety, ethical considerations, and application guidelines for the use of transcranial magnetic stimulation in clinical practice and research. *Clin. Neurophysiol.* 120, 2008–2039. doi: 10.1016/j.clinph.2009.08.016

Roux, F. E., Boulanouar, K., Lotterie, J. A., Mejdoubi, M., LeSage, J. P., and Berry, I. (2003). Language functional magnetic resonance imaging in preoperative assessment of language areas: correlation with direct cortical stimulation. *Neurosurgery* 52, 1335–1345. discussion 1345-1337. doi: 10.1227/01.neu.0000064803.05077.40

Sanai, N., Mirzadeh, Z., and Berger, M. S. (2008). Functional outcome after language mapping for glioma resection. *N. Engl. J. Med.* 358, 18–27. doi: 10.1056/NEJMoa067819

Sawaya, R., Hammoud, M., Schoppa, D., Hess, K. R., Wu, S. Z., Shi, W. M., et al. (1998). Neurosurgical outcomes in a modern series of 400 craniotomies for treatment of parenchymal tumors. *Neurosurgery* 42, 1044–1055. discussion 1055-1046. doi: 10.1097/00006123-199805000-00054

Serletis, D., and Bernstein, M. (2007). Prospective study of awake craniotomy used routinely and nonselectively for supratentorial tumors. *J. Neurosurg.* 107, 1–6. doi: 10.3171/JNS-07/07/0001

Sollmann, N., Picht, T., Makela, J. P., Meyer, B., Ringel, F., and Krieg, S. M. (2013). Navigated transcranial magnetic stimulation for preoperative language mapping in a patient with a left frontoopercular glioblastoma. *J. Neurosurg.* 118, 175–179. doi: 10.3171/2012.9.JNS121053

Spreen, O., and Strauss, E. (1998). *Compendium of Neuropsychological Tests, A*. Oxford: Oxford University Press.

Szelényi, A., Bello, L., Duffau, H., Fava, E., Feigl, G. C., Galanda, M., et al. (2010). Intraoperative electrical stimulation in awake craniotomy: methodological aspects of current practice. *Neurosurg. Focus* 28:E7. doi: 10.3171/2009.12.FOCUS09237

Tarapore, P. E., Findlay, A. M., Honma, S. M., Mizuiri, D., Houde, J. F., Berger, M. S., et al. (2013). Language mapping with navigated repetitive TMS: proof of technique and validation. *Neuroimage* 82, 260–272. doi: 10.1016/j.neuroimage.2013.05.018

Tarapore, P. E., Tate, M. C., Findlay, A. M., Honma, S. M., Mizuiri, D., Berger, M. S., et al. (2012). Preoperative multimodal motor mapping: a comparison of magnetoencephalography imaging, navigated transcranial magnetic stimulation, and direct cortical stimulation. *J. Neurosurg.* 117, 354–362. doi: 10.3171/2012.5.JNS112124

Tharin, S., and Golby, A. (2007). Functional brain mapping and its applications to neurosurgery. *Neurosurgery* 60, 185–201. discussion 201-182. doi: 10.1227/01.NEU.0000255386.95464.52

Ulmer, J. L., Hacein-Bey, L., Mathews, V. P., Mueller, W. M., DeYoe, E. A., Prost, R. W., et al. (2004). Lesion-induced pseudo-dominance at functional magnetic resonance imaging: implications for preoperative assessments. *Neurosurgery* 55, 569–579. discussion 580-561. doi: 10.1227/01.neu.0000134384.94749.b2

Ulmer, J. L., Krouwer, H. G., Mueller, W. M., Ugurel, M. S., Kocak, M., and Mark, L. P. (2003). Pseudo-reorganization of language cortical function at fMR imaging: a consequence of tumor-induced neurovascular uncoupling. *AJNR Am. J. Neuroradiol.* 24, 213–217.

Valero-Cabre, A., and Pascual-Leone, A. (2005). Impact of TMS on the primary motor cortex and associated spinal systems. *IEEE Eng. Med. Biol. Mag.* 24, 29–35. doi: 10.1109/memb.2005.1384097

Vitikainen, A. M., Lioumis, P., Paetau, R., Salli, E., Komssi, S., Metsahonkala, L., et al. (2009). Combined use of non-invasive techniques for improved functional localization for a selected group of epilepsy surgery candidates. *Neuroimage* 45, 342–348. doi: 10.1016/j.neuroimage.2008.12.026

Wassermann, E. M., Blaxton, T. A., Hoffman, E. A., Berry, C. D., Oletsky, H., Pascual-Leone, A., et al. (1999). Repetitive transcranial magnetic stimulation of the dominant hemisphere can disrupt visual naming in temporal lobe epilepsy patients. *Neuropsychologia* 37, 537–544. doi: 10.1016/s0028-3932(98)00102-x

Conflict of Interest: The authors declare that the research was conducted in the absence of any commercial or financial relationships that could be construed as a potential conflict of interest.

Publisher's Note: All claims expressed in this article are solely those of the authors and do not necessarily represent those of their affiliated organizations, or those of the publisher, the editors and the reviewers. Any product that may be evaluated in this article, or claim that may be made by its manufacturer, is not guaranteed or endorsed by the publisher.

Copyright © 2022 Muir, Patel, Traylor, de Almeida Bastos, Prinsloo, Liu, Noll, Wefel, Tummala, Kumar and Prabhu. This is an open-access article distributed under the terms of the Creative Commons Attribution License (CC BY). The use, distribution or reproduction in other forums is permitted, provided the original author(s) and the copyright owner(s) are credited and that the original publication in this journal is cited, in accordance with accepted academic practice. No use, distribution or reproduction is permitted which does not comply with these terms.

frontiers in Oncology

REVIEW
published: 03 March 2022
doi: 10.3389/fonc.2022.810263

High-Grade Glioma Treatment Response Monitoring Biomarkers: A Position Statement on the Evidence Supporting the Use of Advanced MRI Techniques in the Clinic, and the Latest Bench-to-Bedside Developments. Part 1: Perfusion and Diffusion Techniques

Otto M. Henriksen[1], María del Mar Álvarez-Torres[2], Patricia Figueiredo[3], Gilbert Hangel[4,5], Vera C. Keil[6], Ruben E. Nechifor[7], Frank Riemer[8], Kathleen M. Schmainda[9], Esther A. H. Warnert[10], Evita C. Wiegers[11] and Thomas C. Booth[12,13] on behalf of the European Cooperation in Science and Technology (COST) Glioma MR Imaging 2.0 (GliMR) Initiative*

[1] Department of Clinical Physiology, Nuclear Medicine and PET, Copenhagen University Hospital Rigshospitalet, Copenhagen, Denmark, [2] Biomedical Data Science Laboratory, ITACA, Universitat Politècnica de València, Valencia, Spain, [3] Department of Bioengineering and Institute for Systems and Robotics-Lisboa, Instituto Superior Técnico, Universidade de Lisboa, Lisbon, Portugal, [4] Department of Neurosurgery, Medical University, Vienna, Austria, [5] High-Field MR Centre, Department of Biomedical Imaging and Image-Guided Therapy, Medical University, Vienna, Austria, [6] Department of Radiology and Nuclear Medicine, Amsterdam UMC, Amsterdam, Netherlands, [7] International Institute for the Advanced Studies of Psychotherapy and Applied Mental Health, Department of Clinical Psychology and Psychotherapy, Babes-Bolyai University, Cluj-Napoca, Romania, [8] Mohn Medical Imaging and Visualization Centre (MMIV), Department of Radiology, Haukeland University Hospital, Bergen, Norway, [9] Department of Biophysics, Medical College of Wisconsin, Milwaukee, WI, United States, [10] Department of Radiology & Nuclear Medicine, Erasmus MC, Rotterdam, Netherlands, [11] Department of Radiology, University Medical Center Utrecht, Utrecht, Netherlands, [12] School of Biomedical Engineering and Imaging Sciences, St. Thomas' Hospital, King's College London, London, United Kingdom, [13] Department of Neuroradiology, King's College Hospital NHS Foundation Trust, London, United Kingdom

Objective: Summarize evidence for use of advanced MRI techniques as monitoring biomarkers in the clinic, and highlight the latest bench-to-bedside developments.

Methods: Experts in advanced MRI techniques applied to high-grade glioma treatment response assessment convened through a European framework. Current evidence regarding the potential for monitoring biomarkers in adult high-grade glioma is reviewed, and individual modalities of perfusion, permeability, and microstructure imaging are discussed (in Part 1 of two). In Part 2, we discuss modalities related to metabolism and/or chemical composition, appraise the clinic readiness of the individual modalities, and consider post-processing methodologies involving the combination of MRI approaches (multiparametric imaging) or machine learning (radiomics).

OPEN ACCESS

Edited by:
Nico Sollmann, University of California, San Francisco, United States

Reviewed by:
Harish Poptani, University of Liverpool, United Kingdom
Patrick W Hales, Great Ormond Street Hospital, United Kingdom

***Correspondence:**
Thomas C. Booth
tombooth@doctors.org.uk

Specialty section:
This article was submitted to Neuro-Oncology and Neurosurgical Oncology, a section of the journal Frontiers in Oncology

Received: *06 November 2021*
Accepted: *05 January 2022*
Published: *03 March 2022*

Citation:
Henriksen OM, del Mar Álvarez-Torres M, Figueiredo P, Hangel G, Keil VC, Nechifor RE, Riemer F, Schmainda KM, Warnert EAH, Wiegers EC and Booth TC (2022) High-Grade Glioma Treatment Response Monitoring Biomarkers: A Position Statement on the Evidence Supporting the Use of Advanced MRI Techniques in the Clinic, and the Latest Bench-to-Bedside Developments. Part 1: Perfusion and Diffusion Techniques. Front. Oncol. 12:810263. doi: 10.3389/fonc.2022.810263

Results: High-grade glioma vasculature exhibits increased perfusion, blood volume, and permeability compared with normal brain tissue. Measures of cerebral blood volume derived from dynamic susceptibility contrast-enhanced MRI have consistently provided information about brain tumor growth and response to treatment; it is the most clinically validated advanced technique. Clinical studies have proven the potential of dynamic contrast-enhanced MRI for distinguishing post-treatment related effects from recurrence, but the optimal acquisition protocol, mode of analysis, parameter of highest diagnostic value, and optimal cut-off points remain to be established. Arterial spin labeling techniques do not require the injection of a contrast agent, and repeated measurements of cerebral blood flow can be performed. The absence of potential gadolinium deposition effects allows widespread use in pediatric patients and those with impaired renal function. More data are necessary to establish clinical validity as monitoring biomarkers. Diffusion-weighted imaging, apparent diffusion coefficient analysis, diffusion tensor or kurtosis imaging, intravoxel incoherent motion, and other microstructural modeling approaches also allow treatment response assessment; more robust data are required to validate these alone or when applied to post-processing methodologies.

Conclusion: Considerable progress has been made in the development of these monitoring biomarkers. Many techniques are in their infancy, whereas others have generated a larger body of evidence for clinical application.

Keywords: magnetic resonance imaging, glioma, perfusion, diffusion, pseudoprogression, monitoring biomarkers, glioblastoma, high-grade glioma

1 INTRODUCTION

High-grade gliomas (adult-type diffuse WHO grade 3 and 4 gliomas) account for up to 85% of all new cases of malignant primary brain tumors diagnosed every year, with an incidence of approximately 5/100,000 person years in Europe and North America (1). Of these, approximately 70% are either "glioblastomas, isocitrate dehydrogenase (IDH)-wildtype" or "astrocytoma, IDH-mutant, grade 4" (2). Approximately 15% are "astrocytoma, IDH-mutant, grade 3" and approximately 10% are "oligodendroglioma, IDH-mutant and (chromosome) 1p/19q deleted, grade 3." Malignant primary brain tumors cause the greatest number of years of life lost than any other cancer (3). Grade 4 glioma is particularly devastating: The median survival without any treatment is less than six months and with standard-of-care treatment is only 14.6 months (4). In adults aged up to 70 years with good performance status, maximal safe tumor resection followed by radiotherapy with concomitant and adjuvant temozolomide has been recommended as the standard-of-care treatment for grade 4 glioma since 2005 (4–6).

During and after treatment, "monitoring biomarkers" are measured serially and are required to detect any change in the extent of glioma infiltration or provide evidence of treatment response (7). Magnetic resonance imaging (MRI) is particularly useful in determining treatment response as it is noninvasive and captures the entire tumor volume as well as adjacent tissues. Furthermore, in nearly all high-grade gliomas, the integrity of the blood-brain barrier (BBB) is disrupted. Following intravenous administration of gadolinium-based contrast agents (GBCA), the hydrophilic contrast molecules diffuse out of the vessel lumen and accumulate within the extravascular extracellular space, manifesting as contrast-enhancing hyperintense regions on T_1-weighted sequences (8). Subsequently, MRI has been incorporated into recommendations for determining treatment response in clinical trials (9). In these recommendations, treatment response assessment is based on simple linear metrics of contrast-enhancing tumor, specifically, the product of the maximal perpendicular cross-sectional dimensions (in "measurable" lesions, which are defined as > 10 mm in all perpendicular dimensions). The recommendations are based on expert opinion informed by observational studies and derived from the biologically plausible assumption that changes in tumor size identify progression of disease, potentially before it becomes clinically apparent, resulting in a lead time improvement for therapeutic intervention (10). Indeed, there may be benefits in changing management before the development of irreversible disability or before the extent of tumor precludes intervention. Some justification for enhancement as a disease proxy has been inferred from data showing that enhancing tumor size and extent of resection are "prognostic biomarkers" (7) at both first presentation and recurrence (11, 12).

The trial assessment recommendations, incorporated in a less stringent form during routine clinical assessment (13), allow for an early change in treatment strategy, for example, termination of ineffective treatments or switching to second-line therapies (14). However, there are four important challenges using conventional structural MRI protocols.

First, there is a paucity of evidence that earlier diagnosis of disease recurrence using conventional structural MRI influences prognosis (10). It is noted that individual enhancing tumor growth trajectories vary between individuals with the same histological tumor type.

Second, seemingly simple measurements can still be challenging because tumors have a variety of shapes, tumors may be confined to a cavity rim, and the edge of tumors may be difficult to define (15). For example, large, cyst-like gliomas are common and are often "non-measurable" unless a solid peripheral nodular component fulfils the above "measurable" criteria.

Third, there is a lack of biological specificity for contrast enhancement, which can lead to false positive, false negative, and indeterminate results, particularly relating to post-treatment related pseudophenomena in glioma (10). In high-grade glioma, pseudoprogression is an early post-treatment-related effect typically occurring within six months of finishing concomitant temozolomide and radiotherapy (**Figure 1**), whereas pseudoresponse typically occurs after anti-angiogenic agents such as bevacizumab have been administered. False positive progression and false negative treatment response are manifest as an increase or decrease in MRI contrast-enhancing volume, respectively. Delayed treatment effects, such as increased enhancement due to radiation necrosis, can similarly cause false positive progression. Other examples of non-specificity include post-operative peritumoral parenchymal enhancement following operative "tissue handling" or following operative infarction.

Fourth, due to the non-specificity of changes in contrast enhancing volume, treatment response assessment that is typically made in a retrospective manner as confirmatory imaging, is required to demonstrate a sustained increase (**Figure 1**) or a sustained decrease in enhancing volume. This leads to a delay in diagnosis.

Clearly, contemporaneous, accurate, and reliable monitoring biomarkers are required for high-grade glioma treatment response assessment. Due to the non-specific nature of contrast enhancement, histopathology is sometimes employed as a combined or alternative monitoring biomarker; often it is considered the reference standard of treatment response (**Figure 2**). However, there are several challenges when using histopathology as a monitoring biomarker. First, there is a paucity of evidence that earlier diagnosis of viable tumor using biopsy influences prognosis (2). Second, repeat tissue sampling has a high risk of procedure-related morbidity in patients with high-grade glioma compared to other systemic cancers (20). Third, biopsy has a potential drawback of sampling bias (21). Fourth, there is a need to improve and better systematize the application of histological and molecular analysis to diffuse glioma in the recurrent setting; currently, it is not standardized, causing a variety of inter-observer diagnostic interpretations given the background of extensive post-therapy-related changes (2).

An emerging alternative approach is to harness the potential value of circulating biomarkers (including circulating tumor cells, exosomes, and microRNAs) to monitor disease progression in glioma patients (22). For example, a recent study found that serum microRNA levels did not increase in cases of pseudoprogression, and increased levels were associated with tumor progression (23). However, as with any potential monitoring blood or cerebral spinal fluid biomarker, potential use requires further evaluation and validation in larger scale prospective studies before implementation into routine clinical practice can be envisaged.

Another promising approach, which concords with an impetus to derive an evidence-base for follow-up imaging of high-grade gliomas driven both by researchers as well as patients and caregivers (24–26), is to use advanced imaging techniques. Considerable technical developments have occurred in the last three decades; however, clinical translation is far from ubiquitous. A European survey in 2016 suggested dynamic susceptibility contrast-enhanced (DSC) MRI and ^{1}H-magnetic resonance spectroscopy was used in the clinic routinely in 82% and 80% of hospitals respectively (27). However, with only 3% survey response rate, it is unlikely to be representative of European practice. A 2020 survey of all UK neuro-oncology centers with 100% response rate from all three lead specialists (neuroradiology, neuro-oncology, and neurosurgery) within all centers showed that only 10% of centers routinely used any advanced MRI technique and a third of centers used such techniques in selected cases (13). It is noteworthy that many respondents suggested that advanced imaging techniques would improve their practice.

The purpose of this position statement is to summarize the evidence for the use of advanced MRI techniques as monitoring biomarkers in adult high-grade glioma in the clinic, and to highlight the latest bench-to-bedside developments.

2 MATERIALS AND METHODS

Clinicians, engineers, and physicists with expertise in advanced MRI techniques applied to high-grade glioma, convened virtually through the European Cooperation in Science and Technology (COST) Glioma MR Imaging 2.0 (GliMR) initiative (28) from July 2020 through July 2021, which also included experts from outside of Europe. A working group analyzed the available evidence for potential high-grade glioma monitoring biomarkers derived from advanced imaging techniques. The consensus decision was to focus on monitoring biomarkers that can reliably differentiate post-treatment-related effect from true tumor progression during (or before) the point when contrast enhancement on T_1-weighted MRI images first increases. False-negative progression (pseudoresponse) during second line treatment is a concern in the United States but rarely in Europe, as the European Medicines Agency concluded that progression-free survival bevacizumab trial outcome measures are inherently confounded and the use of bevacizumab is not supported (29). Therefore, pseudoresponse was not the focus of the position statement.

Potential biomarkers were derived predominantly from the individual image acquisition modalities of perfusion and/or permeability (using DSC MRI techniques, dynamic contrast enhanced [DCE] and arterial spin labeling [ASL]), microstructure (diffusion MRI techniques), metabolism and/or chemical

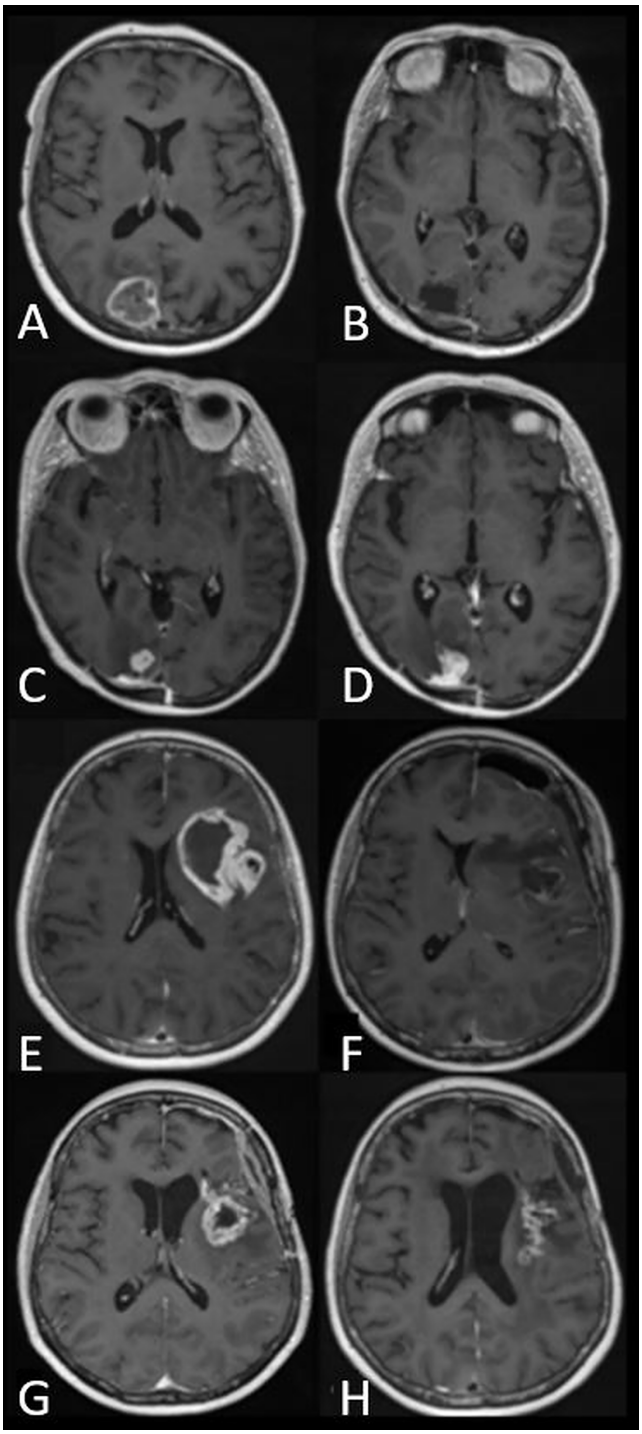

FIGURE 1 | Panels of axial T_1-weighted images after contrast administration in two patients with glioblastoma, IDH-wildtype. **(A–D)** demonstrate tumor progression. **(A)** Preoperative appearance of an occipital glioblastoma. **(B)** MRI performed five days after resection with no enhancement suggestive of residual tumor. **(C)** The patient continued with standard-of-care radiotherapy and temozolomide. Within three months of radiotherapy, a new enhancing lesion could be seen at the margin of the postoperative cavity. **(D)** The enhancing lesion had increased in size three months later and was confirmed to represent tumor recurrence after repeat surgery. **(E–H)** demonstrate pseudoprogression. **(E)** Preoperative appearance of an insular glioblastoma. **(F)** Postoperative appearance 24 hours after surgery showing blood degradation products, with no enhancement suggestive of residual tumor. **(G)** The patient continued with standard-of-care radiotherapy and temozolomide. MRI performed within six months of radiotherapy demonstrated a new, contrast-enhancing lesion. **(H)** Follow-up MRI at monthly intervals showed a gradual decrease in the size of the contrast-enhancing lesion without a change to standard-of-care temozolomide or corticosteroid use. The image shown here is the MRI performed four months later.

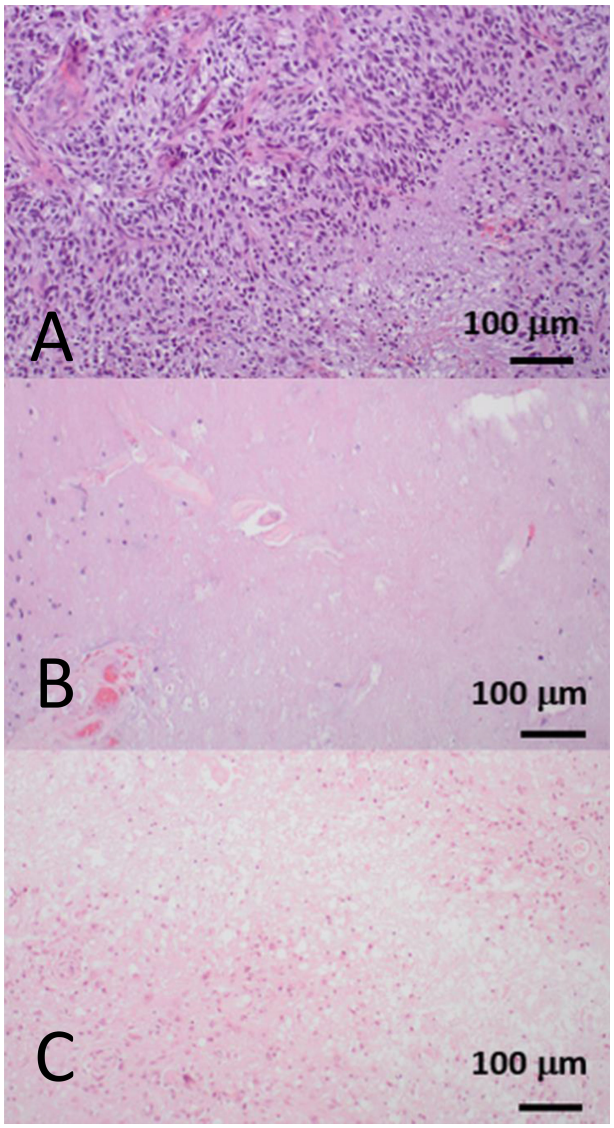

FIGURE 2 | Hematoxylin and eosin-stained biopsy samples showing three distinct histopathological patterns from three patients who were treated for glioblastoma, IDH-wildtype. All biopsies were obtained from a contrast-enhancing region that had increased in size on serial T_1-weighted images during follow-up imaging. **(A)** A fully viable tumor recurrence with dense cellularity and pseudopalisading necrosis. This corresponds to tumor progression. **(B)** Depopulated tumor with necrotizing treatment effect. This corresponds to the radiological appearances of pseudoprogression. **(C)** Nearly absent tumor cell compartment with extensive necrotizing treatment effect and hyalinizing vasculopathy. This corresponds to the delayed treatment effect, radiation necrosis. Pseudoprogression and radiation necrosis are two well-documented forms of "post-treatment related effect." Pseudoprogression generally occurs within the six months following completion of chemoradiotherapy, and resolves or stabilizes without additional treatment, whereas radiation necrosis generally occurs beyond six months, up to several years after radiotherapy, and is often more severe and progressive (16–19). Images courtesy of Dr. J Huse, Department of Pathology, MD Anderson Cancer Center, United States.

composition (magnetic resonance spectroscopy and chemical exchange saturation transfer [CEST] technique, and MRI combined with positron emission tomography [PET]). We also considered post-processing methodologies involving the combination of MRI approaches (multiparametric imaging) and image feature analysis techniques using machine learning (radiomics).

We agreed the work would be a *position statement* (30) promoting discussion on emerging topics and indicate the evidence gaps, strengths and limitations. Together this would provide the foundation for producing a multi-stakeholder downstream *guideline* (30) beyond the current position statement.

Specifically, it was agreed that advanced imaging technique analyses would

- summarize methodology,
- highlight strengths and weaknesses,
- determine clinical diagnostic accuracy, and
- expound the state-of-the-art and future developments.

Finally, we assessed the incorporation into national and/or international technical and/or clinical guidelines and indicated the current level of development and clinical readiness (presented in Part 2).

Advanced imaging technique analyses were compiled by subject matter experts and incorporated into a manuscript and circulated to the working group members. Edits and feedback were incorporated until all authors were in agreement with the content, and a position statement was produced summarizing the evidence for the use of advanced MRI techniques as monitoring biomarkers in the clinic, and highlighting the latest bench-to-bedside developments.

To determine clinical diagnostic accuracy, we performed MEDLINE (including PubMed), Embase and Cochrane Register searches for recent systematic reviews and meta-analyses, favoring those which followed Preferred Reporting Items for Systematic Reviews and Meta-Analysis: Diagnostic Test Accuracy (PRISMA-DTA) methodology (31). We also performed searches to analyze individual clinical studies related to each advanced imaging technique since the time of the included systematic review; if a systematic review was published before 2015, we confined our searches to 2015–2021. Search terms are listed in **Supplementary Table S1**. Given that the position statement describes a broad range of studies involving several imaging approaches (a range of MRI advanced techniques, PET, and post-processing methodologies) and several target conditions (pseudoprogression, radiation necrosis, or a combination of both) a PRISMA-DTA analysis addressing a specific question on diagnostic accuracy was beyond our remit. Nonetheless, components of the PRISMA-DTA methodology have been incorporated where practicable.

3 RESULTS

3.1 An Overview of Perfusion and Permeability

A hallmark of cancers is angiogenesis, the formation of new tumor vessels to sustain metabolic demands of the growing tumor (32). Its main trigger is hypoxia *via* HIF-1 (hypoxia inducible factor 1) release and cascades of other pro-angiogenic factors, e.g., vascular endothelial growth factor. Compared to normal vessels, tumor

vessels are larger, more irregular, and, importantly, highly permeable. The increased permeability leads to a disrupted BBB, allowing the extravasation of macromolecules (such as contrast agents) across the capillary wall (33). The glioma vasculature will thus exhibit increased perfusion, blood volume, and permeability compared with normal brain tissue.

Although the exact definition may depend on the method applied (34), perfusion is generally defined as the passage of blood through the tissue microcirculation. In the brain, cerebral blood flow (CBF) is traditionally used synonymously with perfusion, and both are measured in units of volume of blood per volume or weight of tissue per time (ml/100 ml/min or ml/100 mg/min). On the other hand, the term perfusion imaging is often used in a wider sense and also includes other aspects of the vascular function of an organ or tissue such as blood volume or vessel permeability. In the brain, the most commonly measured perfusion parameters are CBF and cerebral blood volume (CBV). In order to distinguish perfusion parameter maps (showing regional distribution within the brain) from global brain measurements, in imaging they are sometimes referred to as regional CBF and CBV (rCBF and rCBV, respectively). In a possibly confusing fashion, measures of CBF and CBV that are obtained voxelwise *relative* to the rest of the brain, but not in absolute units, are also often referred to as rCBF and rCBV, respectively. The latter definition of rCBF/rCBV is commonly used in the context of the perfusion imaging techniques described here. For this reason, we chose to use CBF and CBV to refer to absolute measurements of perfusion and blood volume, while keeping rCBF and rCBV for relative versions of these parameters. Moreover, perfusion imaging measurements of brain tumors are commonly normalized to a reference, for example healthy appearing brain of the contralateral hemisphere. In this case, normalized values are referred to as nRCBF/nRCBV, respectively. Another perfusion related parameter is vessel permeability, which may be quantified in terms of a transfer constant (K^{trans}) or a permeability surface area product (PS), depending on the measurement technique and associated modeling approach.

DSC and DCE techniques are based on dynamic MR imaging during the bolus passage of a GBCA to provide images of perfusion- and permeability-related parameters. DSC is a T_2/T_2* method most often used to assess vascular proliferation in terms of CBV. Conversely, DCE is a T_1-weighted method, which in its most widely used form provides information on a combination of tissue perfusion and vessel permeability as measured by K^{trans} in addition to plasma volume (Vp). Alternatively, arterial spin labeling (ASL) is a completely noninvasive and potentially quantitative technique without GBCA, which is based on labeling arterial water in order to provide an endogenous, freely diffusible perfusion tracer (35). ASL provides perfusion-weighted images, and it can be used to quantify tissue perfusion (CBF).

3.2 DSC-MRI

3.2.1 Methodology

With DSC-MRI, T_2- or T_2*-weighted images are acquired with high temporal resolution during the bolus administration of a GBCA (**Figure 3**). The bolus passage induces a gradient of susceptibility between the intravascular and extravascular tissue compartments causing a transient decrease in the signal intensity (36). Most often T_2*-weighted gradient-echo (GRE) echo planar imaging (EPI) methods are used, which are sensitive to vessels of all diameters (37). T_2-weighted images, obtained with spin-echo (SE) EPI methods, provide CBV maps primarily sensitive to microvessels. Subsequent descriptions will be given for GRE-based methods unless otherwise noted. The same basic principles for data acquisition and processing apply for SE-based methods.

As further illustrated in **Figure 3**, the DSC signal time course, S(t) is converted to a change in the T_2* relaxation rate ($\Delta R2^*(t)$),

$$\Delta R2^*(t) = \frac{-1}{TE}\ln\left(\frac{S(t)}{S_b}\right), \qquad \text{Equation 1}$$

where S_b is the mean of the baseline (pre-bolus) signal intensity whose integration provides an estimate of the relative cerebral blood volume (rCBV).

$$rCBV = \int \Delta R2^*(t)dt \qquad \text{Equation 2}$$

This measure is termed "relative" because it provides a voxelwise value *relative* to the rest of the brain.

Alternatively, an absolute measure of CBV can be determined from the ratio of the tissue ($C_t(t)$) (which is assumed equivalent to $\Delta R2^*(t)$) and arterial concentration-time curve ($C_a(t)$) first-pass areas,

$$CBV = \kappa\frac{\int C_t(\tau)d\tau}{\int C_a(\tau)d\tau}, \qquad \text{Equation 3}$$

where κ is the scale factor accounting for the density of brain tissue and the differences in hematocrit between capillaries and large vessels (38). As indicated, an absolute measure of CBV requires the determination of Ca(t), also referred to as the arterial input function (AIF). More often, for purposes of comparison, the rCBV will be normalized by dividing the rCBV in each image voxel by the mean rCBV determined from a reference tissue region of interest (ROI), such as normal appearing white matter giving normalized rCBV (nRCBV) values. Like absolute CBV, the nRCBV maps provide greater consistency for the comparison of rCBV across time and patients. Note that in some instances the term nRCBV may be used interchangeably with normalized CBV (nCBV), with the implicit assumption that the CBV is relative. In all cases, an explicit description of the steps used to create CBV should be provided, with clear definitions of nomenclature provided. Finally, another newer approach termed "standardization" has been devised to calibrate the rCBV maps directly (39) without requiring a normalizing ROI. Standardized rCBV (sRCBV) has demonstrated greater consistency across time (39) and improved repeatability compared with nRCBV (40). Both nRCBV and sRCBV have been used with success in several brain tumor clinical trials (41–43).

3.2.2 Correction for Leakage Effects

A key assumption of DSC-MRI is that GBCA remains compartmentalized within the intravascular space, causing a

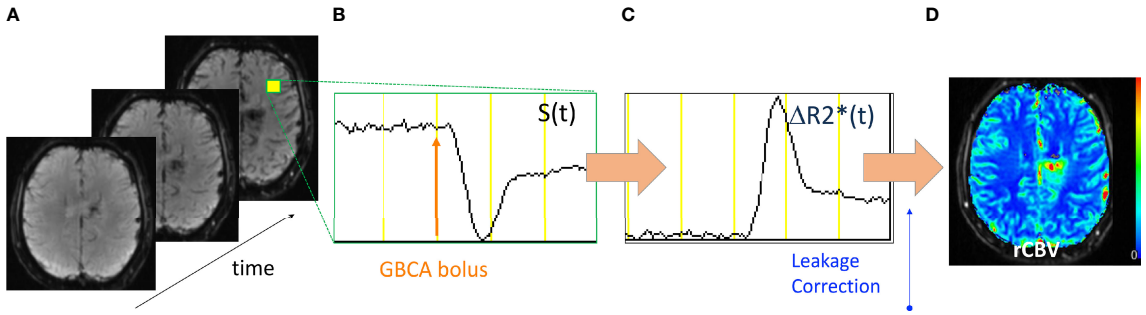

FIGURE 3 | Acquisition and processing of DSC-MRI data. **(A)** GRE-EPI images are collected with high temporal resolution. **(B)** The signal time course (S(t)) from a representative voxel shows the collection of baseline signal then the bolus injection of GBCA after which there is a transient decrease in S(t) and return toward baseline. **(C)** The S(t) is converted into the change in the T_2^* relaxation rate (ΔR2*(t)) from which **(D)** leakage-correction algorithms are applied and rCBV maps created.

susceptibility difference between the intravascular and extravascular compartments. However, with brain tumors, which often have a disrupted BBB, this assumption is violated. GBCA extravasation causes changes to the extravascular T_1 and T_2 (GBCA causes a change in the relaxation rate of the local tissue, which is inversely proportional to T_1 and T_2 [$R_1 = 1/T_1$; $R_2 = 1/T_2$]) in ways that can profoundly affect the DSC-MRI time course (44) and, thus, the accuracy of the rCBV estimate (45, 46). Therefore, different MRI acquisition and post-processing approaches have been used to diminish and/or correct for confounding GBCA leakage effects. One common approach is to administer a single-dose preload of GBCA before the collection of the DSC-MRI data, during which a second dose of GBCA is administered. The preload serves to diminish the effects of contrast extravasation that would occur during the DSC-MRI acquisition (45). One study demonstrated that use of a single-dose preload (0.1 mmol Gd/kg) with a 5-minute incubation time before the DSC-MRI dose, provided the best distinction in rCBV between tumor and treatment effect (47). Yet, even with a contrast agent preload, a correlation with tumor grade was only evident when a post-processing correction for leakage effects was also applied (46). The Boxerman-Schmainda-Weisskoff method (48) has become one of the most widely used leakage correction methods, but several modifications have since been proposed that deserve further consideration (49–51).

More recently, a population-based digital reference object of brain tumor tissue was developed to evaluate the entire parameter space of tissue condition and imaging parameter settings (52, 53). The digital reference object results confirmed that the double-dose approach using a single-dose (0.1 mmol/kg) preload and single-dose DSC with Boxerman-Schmainda-Weisskoff correction was the most accurate and most robust method, being fairly insensitive to slight variations in parameter settings. Yet, another potential lower GBCA dose method emerged. By simply using a lower flip angle (30°) with TE = 30 ms (at 3 Tesla [T]) or TE = 54 ms (at 1.5 T), it was predicted that rCBV results comparable to the double-dose reference standard could be obtained. This was experimentally confirmed at 3 T in a multisite study of brain tumor patients (54). These results helped to inform a recent consensus recommendation specifically for DSC-MRI data acquisition in high-grade glioma, which includes both the double-dose reference standard and single-dose methods (55). Clinical MRI results together with rCBV maps, obtained using the double-dose reference standard from a patient with a grade 2 oligodendroglioma, are shown in **Figure 4**.

3.2.3 Evidence from Clinical Studies

A systematic review and meta-analysis of studies between 2005 and 2015 included 17 DSC-MRI studies and concluded that individual studies, taken in an isolated form, showed encouraging results to differentiate tumor progression from treatment-related changes, with sensitivities and specificities in the 80%–90% range (56). Yet, widespread use has been hampered by the wide range of proposed rCBV thresholds reported (0.9–2.15). This variation is largely attributed to the statistically significant heterogeneity in how the DSC-MRI data are collected and analyzed (56). However, the studies reviewed preceded the recently published consensus recommendation that describes how best to acquire DSC-MRI data, and that a correction for leakage should be included. With widespread implementation of this consensus acquisition, it is hoped that greater consistency in mean rCBV thresholds will follow. A recent multisite study supports this contention (57). Several sites used their own post-processing platform to process the same DSC-MRI data whose acquisition was consistent with the subsequently published consensus recommendation regarding acquisition. A common threshold applicable to all sites could be determined to distinguish high- from low-grade tumor. This suggests that, with greater consistency in the acquisition of DSC-MRI data, agreement on thresholds to distinguish treatment-related effects from residual or recurrent tumor is also possible.

The practice of using the mean rCBV determined from the enhancing lesion ROI is another often-overlooked factor that may contribute to the wide range of reported rCBV thresholds. Rarely is a lesion composed of pure tumor or pure treatment effect. Instead, there is an admixture of tumor and treatment effect that will be unique for each patient and each cohort of patients. Yet, all studies described in the meta-analysis (56) used the mean rCBV from an ROI. Consequently, it is not surprising that each study reports a different threshold value because each

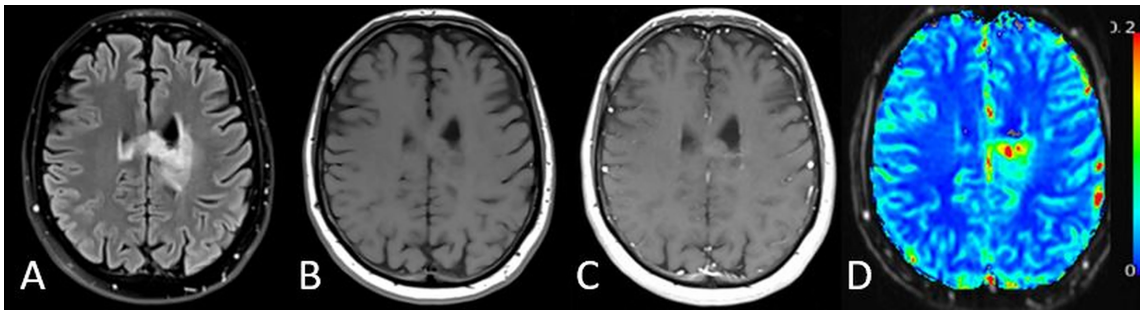

FIGURE 4 | MRI results from a 32-year-old patient with a grade 2 oligodendroglioma. **(A)** T_2-weighted FLAIR, **(B)** pre-contrast T_1-weighted, **(C)** post-contrast T_1-weighted (T_1+C) images along with the corresponding **(D)** sRCBV map for a representative image slice. Though this is a non-contrast-agent enhancing tumor, this example illustrates that DSC rCBV imaging may also provide information in non-enhancing tumors.

study comprises a unique set of patients. Even if the acquisition and post-processing methods were equivalent, it is still likely that each study would report a different threshold to distinguish tumor from treatment effect.

One proposed research solution to the determination of a widely accepted single threshold, is to use image-localized biopsy and spatially histopathologic correlation as described in two retrospective studies of high-grade brain tumors (58, 59). In these studies, only tissue confirmed to be either pure tumor or pure treatment effect were used to determine an rCBV threshold for distinction. In both studies, the consensus acquisition protocol was used, and the rCBV threshold was determined to be the same to distinguish high-grade tumor from treatment effect. A significant difference in tumor and treatment effect was also found for standardized rCBV (59). Biopsy-determined rCBV thresholds can be used to create voxelwise maps that distinguish tumor from non-tumor for the determination of the overall fraction of tumor burden within the enhancing lesion. These maps, referred to as fractional tumor burden (FTB) maps (60), provide a unique ability to visualize the admixture of tumor and post-treatment effects (**Figure 5**). The potential of FTB to predict response to treatment (61) and to distinguish between tumor or treatment effect, as confirmed by histopathologic examination of resected tissue samples (62), has been demonstrated. More recently, a prospective study (63) using image-localized biopsy tissue validated the ability of rCBV to predict tumor content (0–100%), demonstrating similar performance of nRCBV and sRCBV for the creation of FTB. Given that sRCBV does not require choosing a reference ROI, this represents an important step toward workflow optimization for the creation of FTB maps.

3.2.4 Future Developments

Other DSC-MRI perfusion metrics have also demonstrated promise for providing clinically relevant information to evaluate treatment response. In a preclinical study, the distribution of mean transit times, determined from DSC-MRI, was shown to be dose-dependent and predictive of response to the anti-angiogenic agent Sugen11657 (64). In a related study, capillary transit time heterogeneities together with indices of estimated tumor oxygenation, both determined from the DSC-MRI data, demonstrated promise for predicting unfavorable therapeutic effects in patients with recurrent glioblastoma (65). Combined GRE and SE sequences, which can provide measures of mean vessel diameter, have been shown to correlate with brain tumor grade (45, 46) and response to anti-angiogenic treatment (64). Multi-echo perfusion sequences, such as SPICE (44) or SAGE (66), measure GRE and/or SE at multiple echo times (TEs), enabling implicit correction of T_1 leakage effects and the data for determining both DSC-MRI and DCE-MRI perfusion parameters maps (67). Though the technology is still under development (68), these newer perfusion methods are likely to provide a wealth of information relevant to treatment monitoring in brain tumors. Furthermore, with the recent development of the brain tumor DSC-MRI digital reference object (52, 53), which can serve as a benchmark for all DSC-MRI methods (69), translation of these technologies for clinical use should take place more quickly than previously possible. The additional role to predict response to treatments is also emerging, as mentioned above, in the context of FTB.

3.2.5 Summary, Strengths, and Weaknesses

Measures of rCBV derived from DSC-MRI have consistently demonstrated the ability to provide information about brain tumor growth and response to treatment that is not available with current structural MRI methods. Of all advanced techniques, DSC is the most extensively studied for clinically utility. With a power-injector available and a cannula placed for contrast agent administration, DSC-MRI data are easy to collect using commonly available imaging methods and requires only an extra 2–3 minutes of scanning. Despite the ease of use and valuable information provided, the widespread clinical use of DSC-MRI has been hampered by the need to correct for confounding leakage effects, which in turn has led to a variety of ways to collect and process this data. However, great strides have been made to overcome these limitations, with a recent publication clearly outlining how best to collect this data (Boxerman consensus) and a strong recommendation that leakage correction must be used in the post-processing. In this

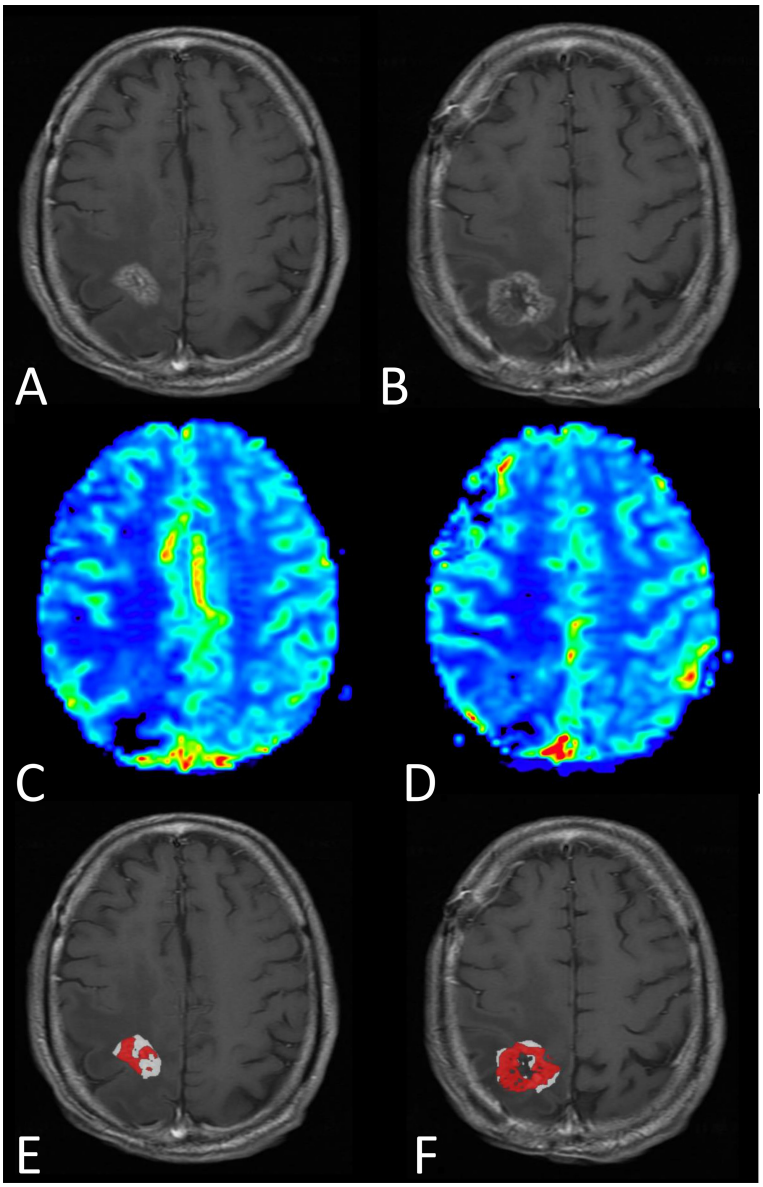

FIGURE 5 | MRI results from a male patient diagnosed four months earlier with glioblastoma, IDH-wildtype, and treated with surgery followed by standard-of-care radiotherapy and concomittant temozolomide. Progression was questioned at the time of this MRI exam (three days prior to re-do surgery). **(A, B)** Post-contrast T_1-weighted and **(C, D)** rCBV maps shown for two representative images slices. **(E, F)** FTB were created and show a mixture of tumor (red) and treatment effect (white), which is consistent with the pathologic diagnosis of tumor and treatment effect, respectively. Note that without the previously determined rCBV thresholds to distinguish tumor from treatment effect, the "blush" of higher rCBV noted on the rCBV maps would be difficult to interpret.

regard, the Boxerman-Schmainda-Weisskoff leakage correction (48) method has been the most commonly used and currently is the most widely recommended approach. Therefore, consensus regarding the collection and processing of DSC-MRI is being reached. Remaining challenges include the fact that the DSC-MRI acquisition is most often based on EPI. Although EPI provides the necessary temporal resolution, the spatial resolution is less good and significant signal dropout and geometric distortions can occur at air-tissue interfaces, such as near sinuses, with post-surgical blood products, or at resection sites. Therefore, efforts are underway to develop higher resolution fast imaging techniques with less sensitivity to these unwanted susceptibility effects. These efforts include the development of spiral-based sequences (44) or parallel imaging methods such as SENSE (70). With a complete solution composed of consistent acquisition and post-processing methods, all obtained with high temporal and spatial resolution, DSC-MRI should be widely accepted as a

robust addition to standard brain tumor exam to assess treatment response.

3.3 DCE-MRI

3.3.1 Methodology

DCE-MRI is based on dynamic T_1-weighted imaging after intravenous administration of a GBCA (**Figure 6**). The contrast agent will increase the relaxation rate $R_1 = 1/T_1$, and the change in relation rate is linearly related to the concentration of the contrast agent C by

$$R_1 = R_1^0 + r_1 C, \qquad \text{Equation 4}$$

where R_1^0 is the relaxation rate before arrival of the contrast agent and r_1 is the field strength specific relaxivity of the contrast agent. The exact relationship between signal (S) and change in relaxation rate depends on the sequence used. For the commonly used 3D T_1-weighted spoiled gradient recalled echo sequence, with short TE << T_2^* so that T_2^* effects are negligible, the measured signal is related to the contrast agent by:

$$S(t) = M_o \sin(\alpha) \frac{1 - e^{-\frac{TR}{T_1(t)}}}{1 - \cos(\alpha) e^{-\frac{TR}{T_1(t)}}}$$

$$= M_o \sin(\alpha) \frac{1 - e^{-TR(R_1^0 + r_1 C(t))}}{1 - \cos(\alpha) e^{-TR(R_1^0 + r_1 C(t))}}, \qquad \text{Equation 5}$$

where α is the flip angle and M_o is the equilibrium magnetization. Only T_1, and thus R_1^0, are unknown and are usually estimated by preceding T_1 mapping (typically obtained by performing T_1-weighted imaging at variable flip angles).

Various tracer kinetics models can be applied to the measured arterial and tissue concentration curves (see Ref. (71) for a comprehensive review). The choice (and complexity) of the model, and thus the requirements for the imaging protocol, are dependent on the tissue and pathology of interest. For brain tumors, the most widely applied three-parameter two-compartment model (i.e., the extended Tofts' model, **Figure 7**) provides voxelwise estimates of plasma volume fraction (V_p), interstitial volume (V_e), and K^{trans} (72), and thus information on permeability and blood volume, both indicators of neo-angiogenesis. For reliable estimation of K^{trans} from this model, a temporal resolution of < 10 sec (ideally ≤ 5 sec) and a total scan duration of 5 minutes following a single dose (0.1 mmol/kg) of GBCA are recommended in the proposed revised Quantitative Imaging Biomarkers Alliance (QIBA) profile (73). In the extended Tofts' model, the parameter K^{trans} reflects both tissue perfusion (F) and PS. Except in extreme cases where permeability is very low (F >> PS and $K^{trans} \approx$ PS) or very high (PS >> F and $K^{trans} \approx$ F), the parameter K^{trans} is a mixture of F and PS. The errors/bias of the parameter estimates derived from the extended Tofts' model may be substantial and depend on both the tissue (e.g., differences in low- compared to high-grade tumors) and the experimental conditions, e.g., temporal resolution (74). Still, this model may provide useful estimates of V_p, K^{trans}, and V_e also at low temporal resolution on 1.5 T systems.

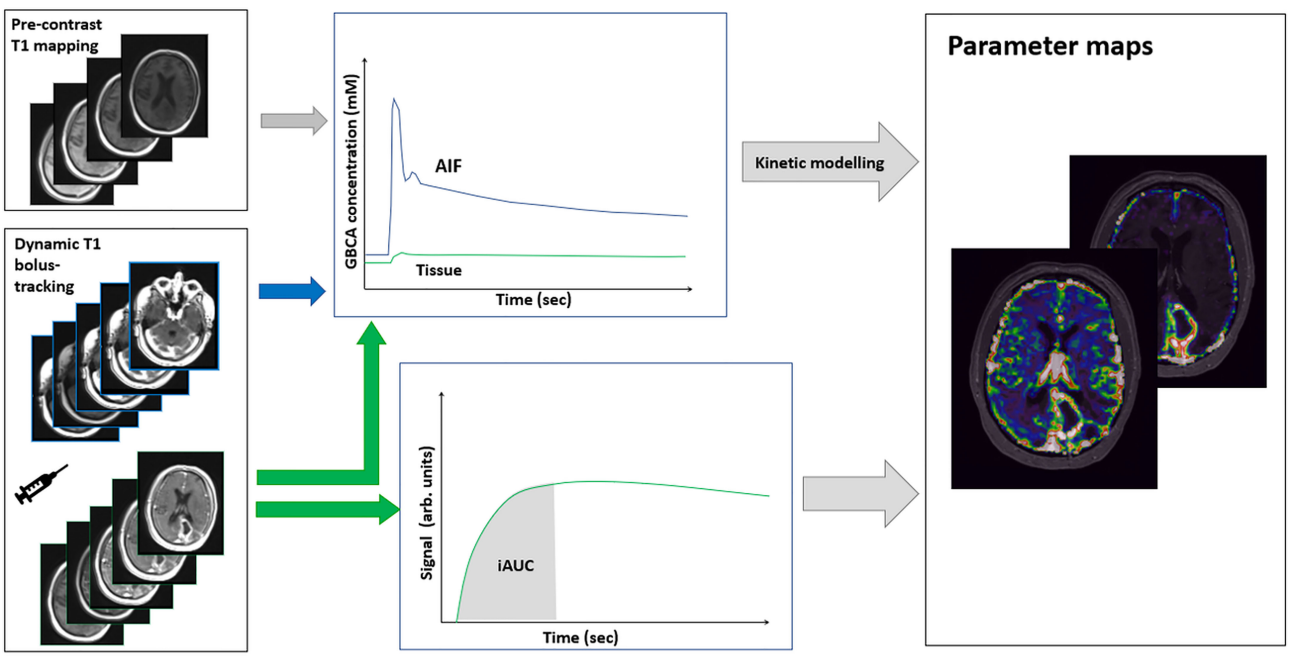

FIGURE 6 | Acquisition and processing of DCE-MRI data. Using dynamic T_1-weighted imaging, a signal increase is measured during bolus passage. From the preceding T_1 mapping obtained by T_1-weighted imaging at variable flip angles, the signal change can be converted into absolute concentrations of GBCA. From time concentration curves in arterial blood (AIF) and in tissue, absolute parameter maps can be produced by subsequent kinetic modeling. A simplified relative measure can be obtained from the area under the iAUC (initial part of the tissue signal curve), which reflects a mixture of blood flow, permeability, and blood volume.

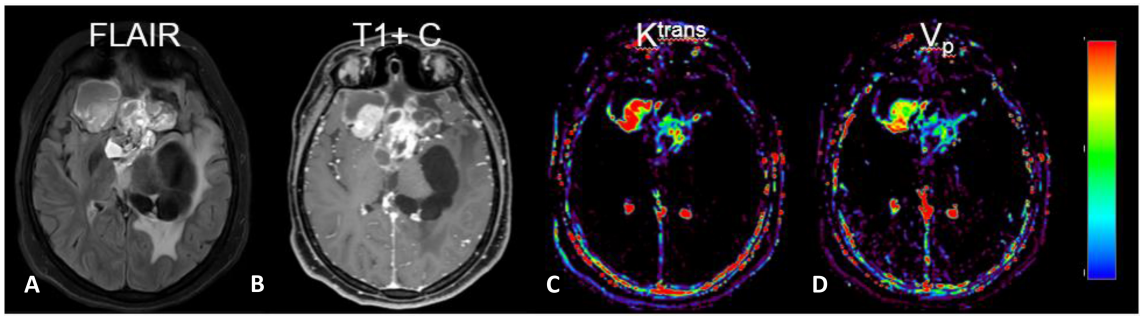

FIGURE 7 | MRI with DCE parameter maps. **(A)** FLAIR and **(B)** post-contrast T_1-weighted (T_1+C) images of a patient with a primary brain tumor. In addition, the extended Tofts' model was used to fit DCE-MRI data to generate parameter maps of **(C)** K^{trans} and **(D)** V_p. (Images are courtesy of Imaging Biometrics LCC).

Good repeatability of DCE using the extended Tofts' model has been reported in normal tissue of both healthy subjects and patients with brain tumors (75), and moderate-to-good repeatability of K^{trans} similar to that of DSC nRCBV was found in contrast enhancing lesions of patients with glioblastoma during treatment (76). Nonetheless, a cross-vendor and multisite reproducibility study of quantitative T_1-weighted imaging in a phantom found variable reproducibility dependent on both sequence and protocol used, field strength and range of T_1 values (77). Furthermore, whilst studies of DCE reading and analysis reported good to excellent inter- and intraobserver agreement (78, 79), there was considerable influence from the software used (78).

3.3.2 Future Developments

The current standard implementation of DCE using the extended Tofts' model described in the recent QIBA guidelines (73) may be considered state-of-the-art for DCE brain tumor imaging, but it has changed little in recent years. Methods taking advantage of better signal-to-noise ratio (SNR) at 3 T allow higher temporal resolution, permitting quantification of F, e.g., by model free-deconvolution (80), and thus separation of F and K^{trans} by the four-parameter two-compartment exchange models (2CXM) (81, 82). Estimation of F is (among other factors) highly sensitive to errors related to undersampling of the input function; therefore, high temporal resolution (ideally 1–2 sec) is required and may be achieved by limiting coverage or spatial resolution. Simpler (model independent) approaches are based on initial area under the signal curve (iAUC), and reflect the initial accumulation of contrast by the tissue (irrespective of the mechanism). This approach alleviates the need for T_1 mapping, measurement of arterial input function, and kinetic modeling, and it is possibly more robust across scanners and implementations (83, 84).

3.3.3 Strengths and Weaknesses

DCE-MRI is the standard perfusion method outside the brain, e.g., prostate and breast, but it is less widely used than DSC-MRI in the brain. Nonetheless, DCE-MRI has several advantages compared with DSC-MRI for post-treatment imaging of brain tumors. First, DCE-MRI is a T_1-weighted imaging technique and hence is less sensitive to the susceptibility artifacts in tissue adjacent to the skull base as well as within treated tumors that limit the coverage of T_2*-weighted imaging in DSC-MRI (85). In fact, DCE-MRI might provide useful image quality in > 80% of uninterpretable DSC-MRI cases (86). Second, unlike T_2*-weighted imaging, T_1-weighted contrast leakage effects are not a cause of error when using DCE-MRI. Instead, they allow explicit modeling of permeability and can provide absolute parameter maps of tissue microvascular properties. Third, T_1-weighted imaging in DCE allows easier and more accurate estimation of an AIF for kinetic modeling than EPI used for DSC-MRI. This and the conversion of blood and tissue signal to concentration of GBCA permit absolute quantification of physiological parameters, although quantitative parameter estimates probably are highly model specific. The main technical disadvantages of DCE-MRI compared with DSC-MRI are lower temporal resolution, need for T_1 mapping, and increased scan duration. Clinically, there are no generally established cut-off points or diagnostic criteria using the standard implementation (the extended Tofts' model). In the case of 2CXM analysis, a single small study investigated 2CXM DCE for pre-radiotherapy prediction of post-radiotherapy tumor progression (87), but no published clinical data regarding diagnostic accuracy are currently available, means of implementation are not standardized, and scanner and software solutions for advanced kinetic modeling are limited.

3.3.4 Evidence From Clinical Studies

Compared with DSC-MRI, the available evidence from clinical studies is more limited. **Supplementary Table S2** shows studies of diagnostic accuracy for differentiating disease progression related and treatment-related effects. Two partially overlapping meta-analyses (56, 88) calculated pooled sensitivity and specificity of 88–89% and 85–86%, respectively, based in combination on a total of 10 studies published from 2011 to 2015 including 371 patients. It is noteworthy that the diagnostic accuracy was higher in studies with model independent analysis (88) than in studies with two- or three-parameter models, while most recent studies (and clinical practice) typically employ three-parameter models. Clinical multicenter brain tumor studies

using DCE have been performed for tumor grading (79) and for evaluation of antiangiogenic treatment of recurrent glioma (76).

Several studies have made comparisons of the various DCE-MRI parameters with each other and with DSC-MRI. Optimal cut-off values determined by receiver operating curve (ROC) analysis and associated diagnostic accuracies from the individual studies are shown in **Supplementary Table S2**. Two large retrospective studies from the same group, each including more than 150 patients, found similar overall accuracy (area under receiver operating curve [AUROC]) of DSC-MRI and model free DCE-MRI for separation of progressive disease from pseudoprogression (89) and radiation necrosis (90), with DSC-MRI tending to provide higher specificity and lower sensitivity compared with DCE-MRI. Smaller retrospective studies comparing model-based analysis of DCE-MRI with DSC-MRI have reported variable findings, although single DCE-MRI parameters tend to provide lower diagnostic accuracy compared with DSC-MRI (**Supplementary Table S2**). The only prospective study comparing three-parameter analysis of DCE-MRI with DSC-MRI found AUROC of V_p and the model free analysis (iAUC) to be similar, and both slightly lower than DSC-CBV, whereas K^{trans} yielded the lowest AUROC (91). A prospective study including both high-grade glioma and metastases also found AUROC of V_p superior to K^{trans}, and suggest improved accuracy when combing the V_p and K^{trans} (92). Other, mainly smaller, retrospective studies of three-parameter analysis have suggested K^{trans} or V_e outperform V_p (**Supplementary Table S2**), while a single study found no diagnostic value of any DCE-MRI parameter (93). The evidence does not converge toward recommending a specific parameter or cut-off point, but a visual analysis of parameter maps comparing tumor to normal tissues may be a clinically acceptable approach (94).

In summary, clinical studies have proven the potential of DCE-MRI for distinguishing treatment-related effects from recurrence, but the optimal DCE acquisition protocol, mode of analysis, and parameter of highest diagnostic value and optimal cut-off points remain to be established.

3.4 ASL

3.4.1 Methodology

ASL is a perfusion imaging technique based on magnetically labeling water spins as they flow through the large brain-supplying arteries at the cervical spine level using radiofrequency (RF) pulses. An image of the brain is acquired after allowing for sufficient time for the labeled spins to reach the brain capillaries. The signal difference in magnetization between labeled images and non-labeled control images yields perfusion-weighted images using kinetic model estimations to calculate the quantitative CBF map (95). Typically, multiple label and control repetitions are acquired in alternating order, and their average subtraction value is used. A variety of ASL pulse sequences and associated analysis methods have been developed, which employ different strategies to control for unwanted labeling/subtraction effects and to overcome the intrinsically low SNR of the ASL signal. For a recent review focused on the ASL basic concepts and the current state-of-the-art acquisition and analysis approaches, see Ref. (35). New developments in ASL are also detailed by van Osch et al. (96).

3.4.1.1 Labeling Schemes

The two main labeling schemes are continuous ASL (CASL) (97) and pulsed ASL (PASL) (98, 99), illustrated in **Figure 8**. While CASL relies on the flow-driven adiabatic inversion of arterial water spins as they flow through the labeling plane under the continuous application of a RF field, PASL is based on the instantaneous inversion of water spins within a wide slab upon the application of an adiabatic inversion RF pulse. A derivation of CASL was more recently developed, pseudo-continuous ASL (pCASL), which uses a train of RF pulses to induce flow-driven adiabatic inversion of arterial water spins (100). In this way, it retains the SNR advantage of CASL compared with PASL while allowing implementation in standard clinical MRI systems not possible with CASL. The advantages of pCASL relative to both CASL and PASL have made this the labeling scheme of choice for clinical applications (95). More advanced and purpose-specialized labeling schemes employ non-spatially selective labeling, which can be achieved by inverting spins based on their velocity, or acceleration, rather than their spatial position: velocity-selective ASL and acceleration-selective ASL (101).

3.4.1.2 Image Acquisition

Fast image readout techniques should be employed, most commonly these are multi-slice 2D EPI but also segmented 3D methods such as 3D GRASE or 3D stack-of-spirals. While the latter are recommended for their higher SNR, the former is less sensitive to motion. Other acquisition parameters need to be selected, namely regarding background suppression and vascular crushing gradients, which may be used to minimize signal contributions from static and macrovascular spins, respectively. A critical choice is that of the time delay between labeling and image readout—post-labeling delay (PLD) in pCASL/CASL and inversion time (TI) in PASL (see **Figure 8A**). Most often, a single delay acquisition is performed: in this case, the delay should be long enough to ensure that the labeled spins have reached the tissues by the time signal is read out, so that it is not sensitive to variations in the arterial transit time or bolus arrival time, illustrated in **Figure 8**. Additionally, in PASL, saturation pulses should be applied in order to control the label duration, using QUIPSS II (102) or Q2TIPS (103) approaches (see **Figure 8A**). Because the label, and hence the perfusion signal, decay with longitudinal relaxation (T_1 of arterial blood up to the capillaries and T_1 of tissue after exchange), the trade-off between insensitivity to arterial transit time and sufficient SNR must be considered when choosing the value of PLD/TI. Alternatively, multiple delays may be sampled and an appropriate kinetic model fitted to the data to estimate CBF as well as arterial transit time. For multi-delay acquisitions, optimal sampling schemes (104, 105) or more efficient sampling schemes such as time-encoded pCASL (106), should be considered.

3.4.1.3 Perfusion Quantification

For perfusion quantification, tracer kinetic models have been developed with different levels of complexity. A standard kinetic model of ASL signals was originally developed by Buxton assuming a single well-mixed compartment and instantaneous exchange of water between blood and tissue (107) (see **Figure 8B**). Various

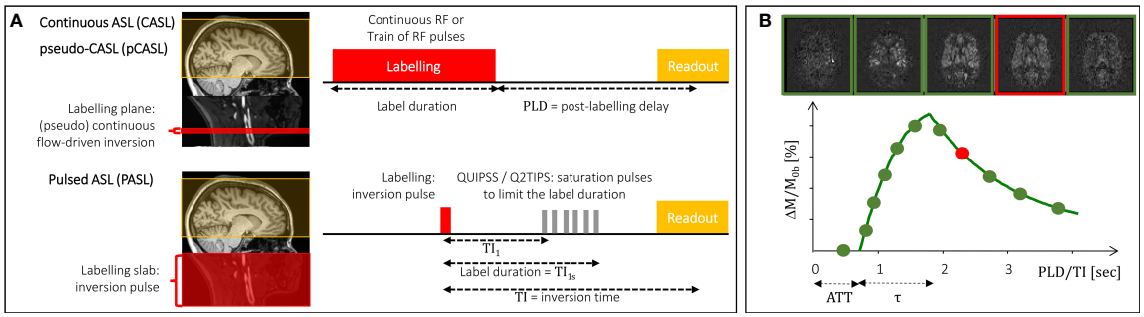

FIGURE 8 | Basic principles of ASL perfusion imaging. **(A)** The two main labeling schemes (CASL/pCASL and PASL) are illustrated, in terms of the location and extent of the labeling region (left) and associated pulse sequences and their timings (right). **(B)** The magnetization difference between label and control images is illustrated by the difference images for five representative delays (top) and the underlying kinetic curve obtained based on the standard kinetic model (bottom). The ATT (arterial transit time) and label bolus duration (τ) are indicated. The red box and dot indicate a typical PLD/TI value for a single-delay acquisition.

extensions of this model have since been proposed, namely to account for restricted water exchange/vessel permeability using two compartment models (108, 109), macrovascular (as well as microvascular) contributions (110), partial volume effects (111), or flow dispersion (112). Simplifications of the standard model have also been proposed (95) to obtain CBF measurements based on single-delay ASL acquisitions:

$$\text{In pCASL}: CBF = \frac{\lambda \Delta M e^{\frac{PLD}{T_{1b}}}}{2\alpha T_{1b} M_{0b}(1 - e^{-\frac{\tau}{T_{1b}}})} \qquad \text{Equation 6}$$

$$\text{In PASL}: CBF = \frac{\lambda \Delta M e^{\frac{TI}{T_{1b}}}}{2\alpha TI_1 M_{0b}} \qquad \text{Equation 7}$$

where ΔM is the control-label magnetization difference, M_{0b} is the equilibrium magnetization of arterial blood, T_{1b} [s] is the longitudinal relaxation time constant of arterial blood, λ is the blood/tissue partition coefficient for water, τ [s] is the label bolus duration, and α is the labeling efficiency. In order to quantify CBF in absolute units, calibration of ASL measurements must be performed. This involves normalizing the control-label difference images, ΔM, by the equilibrium magnetization of arterial blood, M_{0b} (113). Since M_{0b} cannot be measured directly *in vivo*, different methods have been proposed to estimate it based on the measurement of the tissue M_0, typically using a proton-density image acquired with the same readout as the ASL images but with a long repetition time (TR).

3.4.1.4 Consensus Recommendations

In an attempt to harmonize ASL perfusion measurements across studies, a consensus paper was published in 2015 with recommendations regarding the most appropriate implementation for clinical applications (95). In particular, the combination of pCASL with a segmented 3D readout was recommended for its superior SNR; however, PASL and 2D readouts still are often used. The use of background suppression without vascular crusher gradients is also recommended. Although ASL may be performed at 1.5 T, the recommended field strength is 3 T. In this paper, a calibration procedure and a simplified kinetic model were also proposed for CBF quantification based on single delay measurements. Although the consensus paper resulted in part from the efforts of a European network focused on dementia, the recommendations were made for clinical applications more generally. In fact, this consensus paper resulted in the implementation of a recommended sequence by MRI vendors, and this has indeed been adopted by an increasing number of studies. However, the consensus paper did not take tumor studies into key account, nor does it discuss peculiarities of tumor ASL imaging, which may influence the optimal application of ASL in tumor imaging under the recommended conditions. Several studies have assessed the test-retest repeatability of ASL CBF measurements, including the recommended single-delay pCASL implementation (114, 115) but also more complex protocols (116, 117). A reproducibility study has been performed for ASL CBF measurements obtained with commercial implementations of ASL across from major MRI vendors (118). This, however, preceded the consensus paper and results may be improved now that vendors have generally adopted these recommendations. Regarding multisite reproducibility, only one study has partially investigated this by assessing CBF in specific brain regions (115). All of these reliability studies have been performed on healthy subjects, and no studies in patients with brain tumors have been reported.

3.4.2 Strengths and Weaknesses

In contrast to DSC-MRI and DCE-MRI, ASL techniques do not require the injection of a contrast agent. As a consequence, fast repeated measurements on individual patients can be performed. Moreover, the absence of potential gadolinium deposition effects also allows ASL to be more widely used in pediatric patients and in patients with impaired renal function. Relative to DSC-MRI, ASL has the additional advantage that perfusion measurements are not tampered by BBB permeability effects. Even after leakage effects have been corrected for, DSC perfusion imaging is based on GBCA as an intravascular tracer, which limits its ability to yield true perfusion measurements. In contrast, ASL is based on water as a diffusible tracer, allowing it to truly measure perfusion at the capillary level (**Figure 9**). Additionally, susceptibility effects leading to signal dropout and geometric distortions are less prominent since shorter echo times are used.

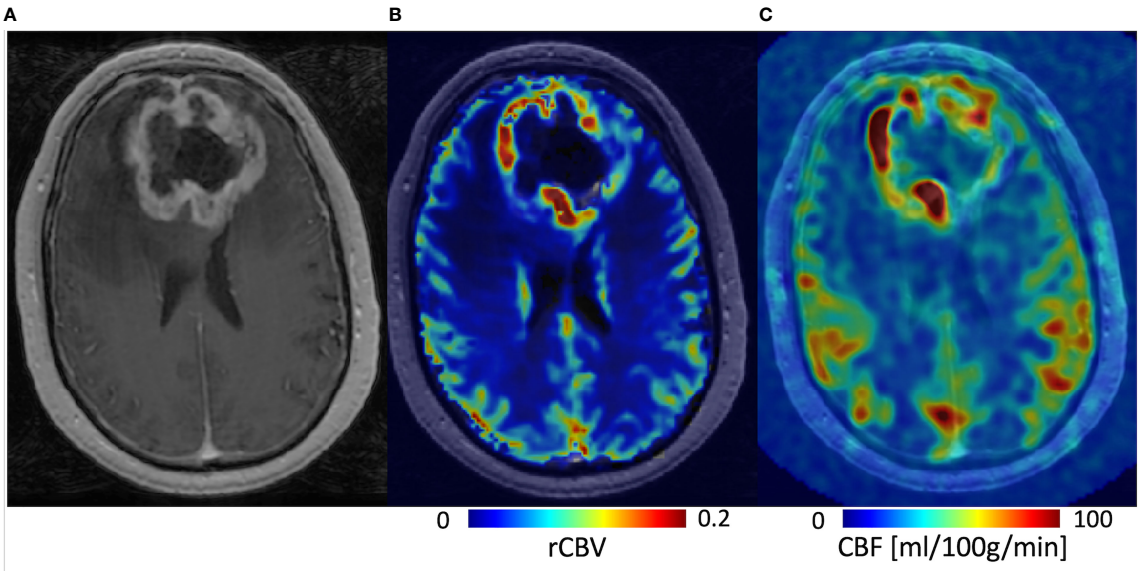

FIGURE 9 | Three-months post-radiotherapy follow-up in a 58-year-old patient diagnosed with a glioblastoma, IDH-wildtype, studied on a 3T GE MRI system. **(A)** The post-GBCA T_1-weighted series shows thick rim enhancement, which could theoretically also be pseudoprogression after recent completion of standard-of-care radiotherapy and concomittant temozolomide. **(B)** The DSC rCBV map, acquired with 2D EPI (TE/TR = 45/1500 ms), indicates general hyperperfusion of the enhancing outer tumor rim, which makes early true progression more likely and is thus decisive for further therapy planning. **(C)** The ASL CBF map, which was acquired with 3D pCASL using white paper settings, shows hyperperfusion concordant with the DSC rCBV map but without the need of gadolinium administration.

Despite the potential advantages relative to DSC-MRI and DCE-MRI, the main weakness of ASL remains its intrinsically low SNR. This has led to the proliferation of methodological options and limited accessibility in clinical sites, which have hindered its wider application so far. Besides the general lack of robustness that results from the low SNR, ASL is also more sensitive to motion artifacts than DSC-MRI or DCE-MRI, due to the inherent image subtraction as well as the frequent use of 3D readout. Additionally, single-delay ASL acquisitions may have macrovascular artifacts or underestimation of tissue perfusion in areas with prolonged arterial transit times, e.g., in patients with macrovascular stenosis.

3.4.3 Evidence From Clinical Studies

An overview of clinical studies published is provided in **Supplementary Table S3**. All studies employed commercial pCASL sequences with a single delay. Three of the listed studies were part of a recent meta-analysis of a total of 160 patients, which reported a pooled sensitivity and specificity of 79% and 78%, respectively to differentiate true progression from post-treatment related effects by ASL (119). All other studies also reported reported fair to good diagnostic accuracies for differentiating true progression from post-treatment related effects. The largest retrospective study included 69 patients (both low and high-grade gliomas) and reported sensitivity and specificity of 74% and 82%, respectively, for separation of progression from post-treatment related effects (120). In the two largest prospective studies, one study found both high sensitivity (94%) and specificity (92%) for separation of post-treatment related effects from true progression among 42 patients with treated high-grade gliomas (121), while the other reported low sensitivity (65%) but very high specificity (100%) among 58 patients (both low- and high-grade gliomas) in the context of pseudoprogression (122).

3.4.4 Future Developments

Studies exploring the utility of ASL for the identification of post-treatment related effects in high-grade glioma are limited to basic implementations of the technique and have technical and clinical variabilities as well as small sample sizes. Despite this, ASL continues to undergo substantial advances yet to be fully exploited in this context (96). In particular, advanced ASL techniques based on multiple-delay ASL measurements combined with appropriate kinetic models may be employed to obtain measurements of perfusion-related parameters besides rCBF (35). Of special interest in glioma is the putative possibility to obtain vessel permeability measurements by using multi-compartment kinetic models incorporating water exchange between blood and tissue (108, 109). For now, the biggest challenge is less the technical development and more the harmonization of current protocols, which would lead to clearer comparison between studies with the potential downstream effect of generating a higher level of evidence.

3.5 An Overview of Diffusion Techniques

Various diffusion MRI techniques can be applied to glioma treatment response assessment including standard diffusion-weighted imaging (DWI), apparent diffusion coefficient (ADC)

analysis, diffusion tensor imaging (DTI), diffusion kurtosis imaging (DKI), intravoxel incoherent motion (IVIM), as well as a multitude of microstructural modeling approaches, such as neurite orientation dispersion and density imaging (NODDI) (123) or restricted spectrum imaging (RSI) (124); free water imaging (FWI) (125); and vascular, extracellular and restricted diffusion for cytometry in tumors (VERDICT) (126).

The basic DWI sequence achieves diffusion contrast based on different gradient pulses in between the excitation and refocusing pulses of a basic SE experiment (127). This basic sequence produces images that highlight diffusional water molecule motion by signal loss. It has been extended to capture information of diffusion in different directions (128) and over different time periods. The gradient strength and duration are expressed in different b-values with a unit of s/mm^2. Typical b-values for brain imaging are up to a single (also called single-shell) b-value of 1000 s/mm^2 and the signal decay up to this b-value can be approximated by a Gaussian distribution. Notably, lower (50–250 s/mm^2) b-values are associated with signal from microvascular perfusion rather than Brownian diffusion motion, which is important in, for example, IVIM (129), a method that aims to recover the pseudo-diffusion coefficient of blood using several b-values (also called multi-shell) in its modeling approach. Note that multi-shell acquisitions may also be used in other modeling approaches. Higher b-values of > 1000 s/mm^2 are associated with more restricted and hindered environments employed in non-Gaussian (such as DKI) and microstructural models.

The ADC is the best-known diffusion parameter. By scaling the diffusion image with a non-weighted image, quantitative maps can be produced. This quantitative technique is available on any commercial MRI machine, which makes the integration in clinical trials attractive. Qualitative visual interpretation is also possible and gives an impression of cellular density and water content and can help in clinical differential diagnostics (**Figure 10**).

Extending the diffusion methodology to sensitize the signal over different directions, the DTI approach has seen widespread application due to its methodological and mathematical simplicity and elegance (130). DKI models (131) focus on the deviation from the Gaussian signal. This model is more sensitive to heterogeneity and complex tissue architecture, rendering parameters that are correlated with biological tissue properties and reflecting the organization of tissue microstructure (132). This approach may deliver biomarkers more relevant to disease interpretation, such as in heterogeneous environments, and dense architecture, such as solid tumors (133). A different approach to overcome the limitation of the Gaussian model is by explicitly modeling it. The FWI model can be used both to visualize the Gaussian signal (free water) and to remove it (free water corrected) (125) using a multi-shell acquisition. This may be useful to distinguish a large area of edema or necrosis from residual tumor and can be used to make DTI fiber tracking in the presence of such processes more accurate (134). Other multi-shell models aim to advance the understanding of neuronal diffusion parameters, such as NODDI (123) or RSI (124). Although NODDI has been designed entirely for use in normal brain tissue, the RSI model has been adapted for use in tumors (135).

3.6 DWI

3.6.1 Methodology

The b-value dependent diffusion signal in a classical diffusion acquisition is calculated based on the Stejskal-Tanner equation (127), where S_b is the signal depending on the apparent diffusion coefficient ADC and the diffusion gradient length δ, separation Δ, and strength G. The b-value is defined as $b = \gamma^2 \cdot G^2 \cdot \delta^2(\Delta - \frac{\delta}{3})$,

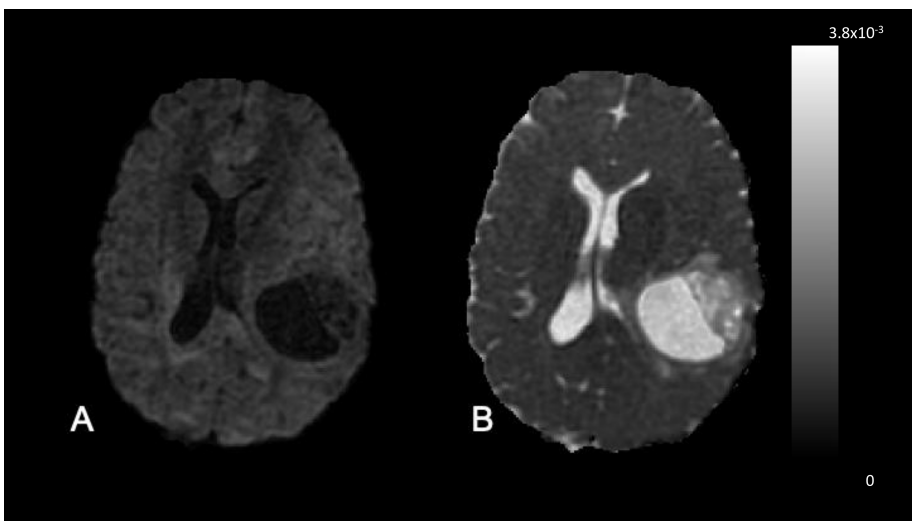

FIGURE 10 | DWI and ADC. These images were acquired in a 50-year-old treatment-naive female patient with glioblastoma, IDH-wildtype. **(A)** DWI (b = 1000 sec/mm^2). The necrotic cavity and necrotic rim are DWI hypointense, due to the diffusing spins having moved between the time of the excitation and the refocusing pulse. **(B)** ADC map. In the ADC map fast diffusion is highlighted by hyperintensity. The combined interpretation of both images gives the qualitative inference that this more likely represents a cavitating or cystic-like tumor with low cellularity rather than a brain abscess or lymphoma.

where γ is the gyromagnetic ratio. Assuming a pure Gaussian diffusion of water and a log-linear signal decay with increasing b-value:

$$S_b = S_0 e^{-b \cdot ADC} \quad \text{Equation 8}$$

By acquiring a diffusion weighted image S_b and an unweighted image S_0, the apparent diffusion coefficient ADC can be calculated as:

$$ADC = \log \frac{S_b}{S_0} \cdot -\frac{1}{b} \quad \text{Equation 9}$$

If more than one DWI S_b exists, ADC may also be derived by calculating a least squares fit to the Stejskal-Tanner equation.

To sensitize the diffusion image S_b, the diffusion gradient pulse may be played out on each of the three gradient axes individually, or on all three gradients at the same time (so-called tetrahedral scheme) (136). If played out on each axis individually, the images need to be averaged before the ADC map is calculated. Therefore, to calculate an ADC image, four separate volumes have to be acquired: the unweighted image S_0 and three S_b images for each of the individual gradient axes. To reduce the time it takes to acquire the sets of images, EPI (137) is commonly performed. EPI uses blipped line encoding to fill out k-space more quickly. Although this technique is incredibly fast, as with perfusion EPI acquisition, it is sensitive to susceptibility changes in the local magnetic field, often leading to artifacts near large tissue-air boundaries e.g., close to the frontal sinuses of the skull.

3.6.2 Strengths and Weaknesses

Diffusion-weighted sequences usually have a fast acquisition time, which makes them suitable for anxious or poorly compliant patients, both of which are common in the brain tumor patient population. DWI sequences are globally ubiquitous and well-standardized across centers with good dissemination of clinical knowledge of image interpretation compared to more advanced methods. They allow the discrimination of differential diagnoses such as stroke mimicking tumor progression or infection in the surgical cavity. On the other hand, DWI is affected by geometric distortions close to bone and air, which can affect diagnostic quality in adjacent brain structures. Similar artifacts can occur in the resected surgical cavity due to blood products.

3.6.3 Evidence From Clinical Studies

Progressive disease in high-grade gliomas is characterized by tumor hypercellularity manifesting as low ADC values (138–141), which confer poor survival (142–144). In contrast, an increase in ADC may indicate response to chemoradiotherapy (138, 145, 146) (**Figure 11**). Similar findings have been seen in other brain tumors, in tumors outside the central nervous system, and after high-grade glioma immunotherapy (138, 147–149). It is noteworthy that high ADC values have also been associated with the peritumoral T_2 hyperintensity of glioblastoma, albeit inconsistently. A variety of advanced analyses using histogram-based techniques, either at a fixed time or longitudinally, capture tumor heterogeneity and can be

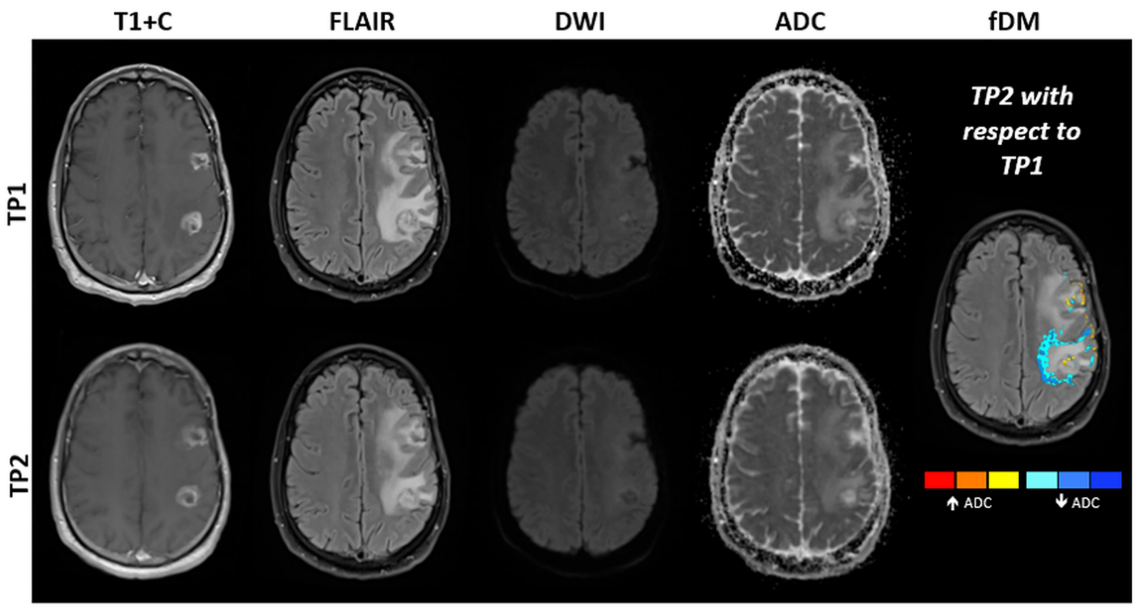

FIGURE 11 | MRI obtained in a 48-year-old patient with mulitfocal glioblastoma, IDH-wildtype. Shown are post-contrast T_1-weighted images, FLAIR images, DWI at b = 1000 s/mm^2 and ADC maps obtained at approximately two (TP1) and three months (TP2) after standard-of-care radiotherapy and concomittant temozolomide. Subtraction of ADC obtained at TP1 from ADC obtained at TP2 results in the creation of fDMs, which show where ADC is increasing (red to yellow) or decreasing (blue). Decreasing ADC (blue regions) is suggestive of increasing tumor cell density. Surgical resection performed one week after TP2 revealed an admixture of tumor recurrence and post-treatment related effects. Note that interpretation can be complicated by resolving edema between time points, which may also show decreased ADC.

applied to ADC maps to characterize therapy (138, 150, 151). One study showed that the fifth percentile on a cumulative histogram of ADC, obtained at a b-value of 3,000 sec/mm^2, was lower in progressive disease than in pseudoprogression ($P < 0.001$) (151). In two single-site studies, a clear cut-off of a mean ADC proved to be successful in predicting pseudoprogression (152, 153) with ADC $\leq 1300 \times 10^{-6}$ mm^2/s (sensitivity 100%, specificity 100%) and $\leq 1313 \times 10^{-6}$ mm^2/s (sensitivity 98.3%, specificity 100.0%), respectively for true progression.

A recent meta-analysis, which contained six eligible studies with a total of 214 patients, concluded that quantitative ADC is an effective approach for differentiation of glioma recurrence from pseudoprogression, and can be used as an auxiliary tool to diagnose glioma progression: sensitivity was 0.95 (95% confidence interval [CI] = 0.89 – 0.98), specificity was 0.83 (95% CI = 0.72 – 0.91) (154). Another meta-analysis showed that quantitative ADC has moderate diagnostic performance in differentiating glioma recurrence from radiation necrosis (sensitivity: 0.82 (95% CI: 0.75 - 0.87); specificity: 0.84 (95% CI: 0.76 - 0.91). The authors recommended not using diffusion MRI alone in differentiating between glioma recurrence and radiation necrosis (155). The latter analysis was supported by a meta-analysis comparing advanced imaging techniques that gave sensitivity and specificity results of 0.71 (95% CI: 0.60 - 0.80) and 0.84 (95% CI: 0.77 - 0.93), respectively, providing the lowest diagnostic accuracy among advanced MRI techniques analyzed (also MRS, DSC-MRI and DCE-MRI) (156). Ordinary ADC maps were found to be inferior in spatially discriminating treatment response compared with DSC-derived perfusion measures (59). Another study could not find any difference between perfusion and diffusion metrics in the ability to discriminate between recurrent tumor and pseudoprogression (157). In a different study, neither DSC-MRI nor DWI were found to be predictive of tumor recurrence (158).

Incorporating diffusion metrics into radiomics models improved diagnostic performance for identifying pseudoprogression over a model with only structural imaging volumes (89). A retrospective study employing a dictionary-learning approach was able to train its model to identify pseudoprogression from DTI data (159). The performance accuracy of radiomics and machine learning approaches in MRI are described in detail in Part 2.

3.6.4 Future Developments

A few studies have used longitudinal ADC maps, namely parametric response maps (PRMs) (160) or functional diffusion maps (fDMs, **Figure 11**) (145), to discriminate progression from pseudoprogression (161–163). Whilst these promising methods have been at the research stage for more than a decade, more evidence is required to translate these as routine clinical tools.

Since the initial development of fDMs (145, 164, 165), many other studies have assessed the potential of fDMs in treatment response evaluation in glioma (164, 166, 167). A study of 50 patients with glioma proved that the rate of change in fDM "hypercellular" volumes within hyperintense fluid-attenuated inversion recovery (FLAIR) regions of interest, predicted tumor progression, time-to-progression, and overall survival for both cytotoxic and antiangiogenic treatments earlier than standard anatomical imaging (167). Another study including 20 brain tumor patients found that fDMs predicted patient treatment response at three weeks from the start of chemoradiotherapy, revealing that early changes in tumor diffusion values could be used as a prognostic indicator of subsequent treatment response (146). The preliminary conclusion regarding fDMs is that this imaging biomarker has the potential to track treatment response in brain tumor patients in both enhancing and non-enhancing tumors. A recent study employing ADC histogram analysis, found that low-ADC tumor volume shrinkage has the same predictive power as fDMs (168).

A small study assessing the use of PRMs with "relative" ADC, where the relative ADC represents a ratio between tumor and contralateral normal-appearing tissue, showed the potential in differentiating true progression from pseudoprogression (169). Voxel-based PRMs of ADC were used to predict early tumor progression (170). Compared with traditional response criteria (Macdonald or RANO criteria (171)), a PRM has the potential to allow individualization of treatment seven to eight weeks earlier than the traditional response criteria (172), since PRM stratification can be determined during the radiotherapy and concomitant temozolomide treatment phase.

Given that DWI is acquired in most routine MRI examinations, post-processing methodologies leveraging multiparametric combinations, also described in Part 2, have often incorporated diffusion techniques. This may be with or without the application of machine learning approaches. For example, a machine learning model that used FLAIR and DWI images was able to predict tumor recurrence with higher accuracy than using either modality by itself (173). Likewise, analysis with a multiparametric clustering approach was shown to be superior to a single-modality approach (174, 175).

In summary, study designs will likely improve as large prospective studies are performed using published study protocols and this will provide a higher level of evidence for their translation as routine monitoring biomarkers for high-grade gliomas (176). Analyses are also likely to become more complex using histogram analyses or machine learning approaches, which can integrate longitudinal and multiparametric data. The beginnings of this development can already be seen (177).

3.7 IVIM and DKI

3.7.1 Methodology

IVIM and DKI are based on standard diffusion acquisition techniques. Standard DWI with ADC maps as a reference assume that water diffusion in tissues is Gaussian and that the diffusion signal will fall log-linearly with increasing b-value. However, the reality is different due to cell membrane interactions in anisotropic nerve fibers (and glial cells and their products such as myelin) and intravascular water in capillaries. Both IVIM and DKI try to assess the non-Gaussian and perfusion components in the diffusion signal, IVIM at the low end of the b-value axis of the signal-decay curve, assessing the perfusion-dependent component, and DKI on the high end of the b-value axis, above 1000 mm^2/s.

The physiological premise behind IVIM is that due to the complex networks of capillaries, the flowing water-bound

protons appear to move randomly, thereby simulating a Gaussian diffusion process. This pseudo-diffusion component can be expressed through various extensions of the basic Stejskal-Tanner equation, of which the biexponential model is possibly the most frequently applied in IVIM (178):

$$\frac{S(b)}{S(0)} = f \cdot e^{-b.(D^* + D_{blood})} + (1-f) \cdot e^{-b \cdot D_{tissue}} \quad \text{Equation 10}$$

with f being the capillary blood perfusion fraction in the diffusion signal, D* the pseudo-diffusion coefficient in the capillaries, and D true diffusion in either blood or tissue.

However, model fitting can become more stable, and thus reliable for application, if the model is simplified by separating diffusion into the fast pseudo-diffusion component of flowing water molecules, D*, and the slow component of water molecules moving by thermal diffusion, D, without further subdivision of tissue and blood components:

$$\frac{S(b)}{S(0)} = f \cdot e^{-b \cdot D^*} + (1-f) \cdot e^{-b \cdot D} \quad \text{Equation 11}$$

At high b-values, cell membranes become an influential factor on the diffusion signal. Therefore, the kurtosis effect, or the width and amplitude deformation of the Gaussian diffusion probability curve, needs to be incorporated as a dimensionless kurtosis factor K (131):

$$\frac{S(b)}{S(0)} = f \cdot e^{-bD^*} + (1 - D + f) \cdot e^{-bD + \frac{1}{6}b^2D^2K} \quad \text{Equation 12}$$

The choice of b-values influences the shape of the fitting curve and therefore the parameter results. For IVIM, this means that more b-values should be chosen in the spectrum below 250 mm^2/s. Currently, there is no consensus on how many or exactly which b-values should be chosen for IVIM and DKI measurements.

3.7.2 Strengths and Weaknesses

IVIM and DKI are both relevant techniques in neuro-oncological imaging because they can potentially assess important tumor tissue properties such as microperfusion and cellularity. They are also non-invasive. Multiple b-value acquisitions, however, can extend scan time. Choosing fewer b-values will shorten scan time but potentially will reduce the accuracy of the signal curve fit. Furthermore, IVIM and DKI, like all diffusion techniques, are heavily influenced by scanner-dependent field homogeneity as well as magnetic distortion caused by the tissue examined, which can limit their application e.g. in tissues close to air-filled spaces. There are many other limitations in the models used for post-processing, which can either underestimate or overestimate IVIM and DKI parameters. A detailed elaboration on the issues of fitting and parameter calculation for both IVIM and DKI was published in 2017 (131). The influence of model parameter selection to calculate the perfusion fraction in IVIM, for example, has been shown in gliomas (179).

3.7.3 Evidence From Clinical Studies

The ADC and perfusion fraction (f) extracted using a previously validated simplified IVIM model (150, 180) were used to assess the prediction of early progression in IDH-wildtype glioblastoma (181). Higher $ADC_{T2\text{-}FLAIR}$ at baseline, lower $f_{T2\text{-}FLAIR}$ at the 10th (of 30) radiation fraction, and lack of increase in $ADC_{T2\text{-}FLAIR}$ at the 20th radiation fraction compared with baseline, were associated with early progression. IVIM metrics were not associated with overall survival, while higher $f_{T2\text{-}FLAIR}$ at the 10th radiation fraction was associated with longer progression-free survival (181). In a study of 51 patients (182), a histogram analysis of IVIM metrics was able to differentiate true progression from pseudoprogression, with ROC analyses identifying the 90th percentile for perfusion to be discriminant with a sensitivity of 87.1%, and a specificity of 95.0%. A comparison study of different ADC modeling approaches found that all computed metrics, including those using the IVIM model, can differentiate tumor recurrence from pseudoprogression (100).

In a recent study of 32 glioblastomas, DKI showed high diagnostic accuracy, up to 88%, for differentiating between tumor progression and post-treatment related effects (183). In a comparison with DTI, DKI was found to be superior in predicting recurrence (184). DKI recently was applied to investigate treatment response and pseudoprogression in several studies (184–186) and these found that DKI was superior in assessing treatment response when compared to ADC and DTI. However, one of the studies found only limited benefit when compared to standard ADC measurements (185).

3.7.4 Future Developments

It is potentially possible to render a tumor angiogram and elastographic information based on IVIM and DKI measurements (178). Because vascular and elastographic tumor imaging are upcoming techniques in glioma imaging (187, 188), IVIM and DKI may be applied to such advanced applications. A more important development in the near future will be determning the optimal choice of the number of b values needed for a reliable fit for IVIM and DKI (189).

3.8 DTI

3.8.1 Methodology

By sampling the diffusion signal with at least six different directions, the information can be grouped into a so-called tensor, a multi-dimensional mathematical construct that adheres to mathematical operators (139) and can be used to determine diffusion magnitude (mean diffusivity) and degrees of diffusion anisotropy (fractional anisotropy [FA]). The estimated directionality can be visualized through post processing techniques using ellipsoids or fibers. DTI obtained by acquiring repeated DWI in different non-collinear directions can lead to some quantitative parameters, such as FA, mean diffusivity, axial diffusivity, and radial diffusivity. FA is an index between 0 and 1 to assess the degree of diffusion asymmetry in a voxel in terms of its eigenvalues. Because anatomical tracts are anisotropic, FA maps show where tracts are passing, or changing in disease, e.g., through destruction of these due to tumor cell invasion or sometimes treatment. A limitation of the diffusion tensor model is the assumption that the diffusion of water will always be Gaussian (190). This is true for diffusion within a singular environment (i.e., without different compartments), but

due to imaging voxels being relatively large, it rarely points to a complete picture in human tissue.

3.8.2 Strengths and Weaknesses

All scanner manufacturers have protocols to acquire DTI data and calculate mean diffusivity and FA maps as part of a post-processing step on the console. However, there is no common framework and a lack of consensus regarding how many directions or which b-values shells should be chosen. As in DWI, EPI-related artifacts such as geometric distortions and signal loss present challenges in superimposing DTI-derived maps on structural imaging. Although tractography is currently less relevant as a monitoring biomarker and largely beyond the scope of this position statement, it is noted that some scanner manufacturers offer the ability to perform tractography. These algorithms are often a "black-box," making comparison and reproducibility difficult. Commercial and non-commercial software packages exist, employing both deterministic and probabilistic algorithms. It is noteworthy that these require considerable training and present challenges when integrating the process with clinical workflows.

3.8.3 Evidence From Clinical Studies

After standard-of-care radiotherapy and concomittant temozolomide, when compared with pseudoprogression, the FA in contrast-enhancing tumor was higher in true tumor progression (162, 191, 192) and even appears to increase when compared to previous measurements (163). Whilst higher FA in progression has been postulated to occur due to the orientation of overproduced extracellular matrix in glioblastoma, other authors reported no difference in FA when pseudoprogression and progression were compared (141, 193). DTI-based maps of tissue isotropy and anisotropy have also been successfully used to predict recurrence of glioblastoma (194).

3.8.4 Future Developments

Clinical studies aiming to optimize the multiple b-value shells and number of directions selected, are required before consensus standardization will support translation into the clinic routinely. This is being enabled by the dissemination of sequences and greater accessibility of post-processing pipelines without the need for advanced programming skills.

3.9 Other Advanced Diffusion Techniques

3.9.1 Methodology

Multiple other advanced MRI techniques are based on DWI. Many of them focus on modeling diffusion in different tissue environments to disentangle the signal from "hindered, restricted, and isotropic compartments" (195). The hypothesis is that these compartments reflect actual tissue compartments, such as the extra-axonal or extracellular space (hindered diffusion), intra-cellular, or intra-axonal space (restricted), and fluid, such as edema or cerebrospinal fluid (isotropic). Many of these models, such as the NODDI technique, are designed based on assumptions in healthy white matter (123). Therefore, their use may be limited in glioblastomas. The RSI model (124) offers parametric indices to be calculated in a similar way to NODDI, such as with neurite density and dispersion indices, but RSI does allow more flexibility that may make it more appropriate for tumor imaging. While the tissue in RSI is modeled as cylinders, similar to other DWI-microstructure techniques targeted at white matter, the relatively large spectrum of size and orientation modeled makes it sensitive to a large range of geometries beyond the cylindrical shape (124). In addition, removal of the isotropic signal contribution can aid in disentangling enhancing tumor volume from edema. Disentangling the isotropic compartment is also of interest in the FWI technique. Here, a modeling approach that is initialized with a constant diffusivity of free water can be used to create maps of free water as well as produce a diffusion tensor that has the isotropic signal removed. Integration with the tensor approach lends its application to improving tractography results in the presence of a conspicuous amount of edema.

VERDICT is a model that infers tumor cell microstructure from DWI measurements (126). This model derives multiple compartments (intracellular, intravascular and extracellular–extravascular spaces) and has recently been used to investigate treatment response in animal models of glioma (196, 197). It has subsequently been adapted in human glioblastoma studies in treatment-naive patients (198). The VERDICT model assumes tumor cells are spherical and can model both cell radii and densities, making it an attractive option for the use in treatment response monitoring.

3.9.2 Strengths and Weaknesses

Even though the advanced radiological imaging and multiparametric imaging approach is promising in the context of post-treatment related effects or specifically for pseudoprogression and radiation necrosis, efforts to establish uniform practices and protocols are again necessary. As in DWI and DTI, geometric distortions are also a challenge and there is no consensus on how many directions and which b-value shells are optimal with which particular microstructural technique. Other factors, such as the choice of TE and TR that is limited by either hardware or sequence, also add difficulty to the reproduction of results.

Many microstructural imaging approaches require lengthy protocols or uncommon scanner hardware options, such as parallel transmit or head coils with a large number of channels. In addition, the high b-values required often necessitate imaging close to the noise baseline, which requires lengthy averaging or noise modeling in post-processing, which is not a trivial challenge in clinical imaging.

3.9.3 Evidence From Clinical Studies

The evidence in clinical studies of brain tumor treatment response is very limited. However, FWI has most recently been used to successfully predict glioblastoma recurrence (199). Furthermore, RSI has been used to show treatment effects (135, 200, 201) as well as investigating overall and progression-free survival in gliomas (202). NODDI has been used together with serial DTI imaging to observe tumor changes up to two months before recurrence (203). For completeness in describing these emerging techniques, it is also noted that RSI was used to differentiate true progression from immune-mediated pseudoprogression (**Figure 12**) in a proof-of-concept case

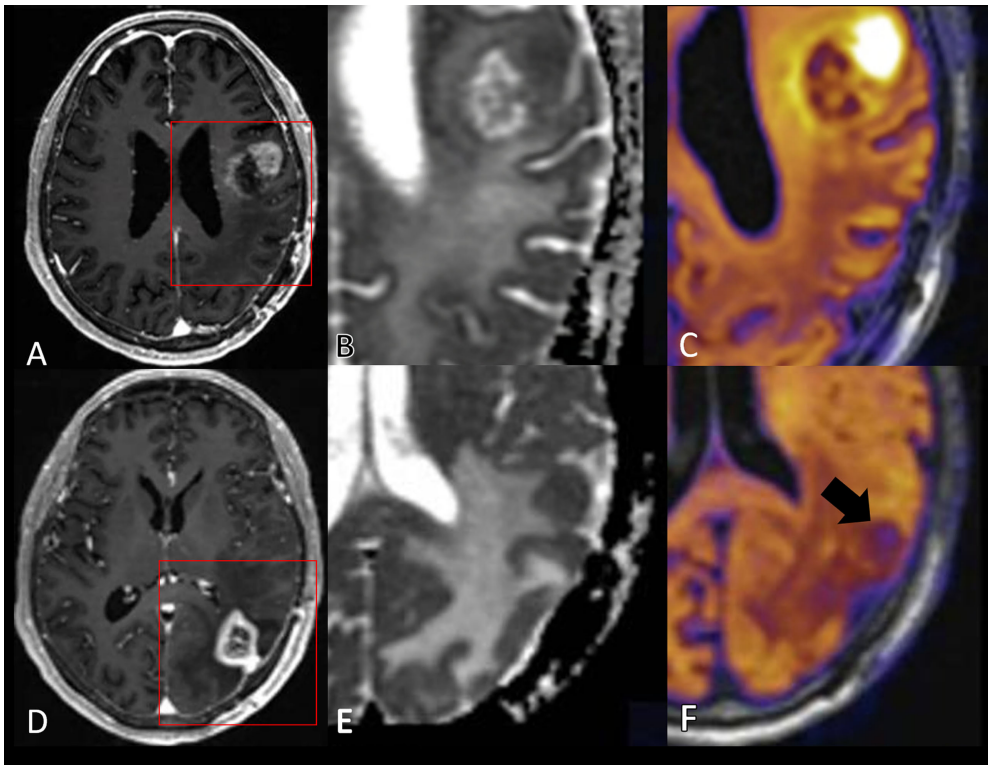

FIGURE 12 | A glioblastoma in a 64-year-old man after chemoradiation and immunotherapy with both true progression **(A–C)** and pseudoprogression **(D–F)** observed in the same patient at different time points. Red squares in the T1-weighted post contrast images **(A, D)** illustrate the magnified regions on ADC images **(B, E)** and RSI cellularity map **(C, F)**. **(A–C)** An enhancing frontolateral area **(A)** confirmed to represent true progression is shown to have low ADC **(B)** with hyperintensity in the RSI cellularity map with more subtle ring hyperintensity around the central necrosis **(C)**. Left parietal pseudoprogression in an enhancing solid focus **(D)** was shown to be hypointense on the RSI cellularity map **(F)**. The ADC map is not decisive here **(E)**. Adapted with kind permission by the authors (204).

study. A 64-year-old man had follow-up imaging over several months. He developed pathologically proven pseudoprogression as well as a secondary primary lesion in a separate location. The authors found that RSI was able to differentiate true progression from pseudoprogression while ADC could not (204). However, whilst RSI is supported by marginally more clinical evidence than these other emerging techniques, it has yet to be adopted in large-scale glioblastoma research studies, thereby allowing the strengths of the technique to be demonstrated.

4 DISCUSSION

Contemporaneous, accurate, and reliable monitoring biomarkers are required for high-grade glioma treatment response assessment as the use of conventional structural MRI protocols is limited by important challenges. The current evidence regarding the potential for monitoring biomarkers based on advanced MRI techniques is reviewed, and the individual modalities of perfusion, permeability, and microstructural imaging are described (these will be complemented by modalities related to metabolism and/or chemical composition discussed in Part 2). Considerable developments have been made in advanced MRI methodology. Although some techniques have evolved and matured over three decades, several new state-of-the-art methods are poised to contribute to the imaging armamentarium. However, limitations remain for all techniques. Good-quality evidence of clinical diagnostic accuracy is typically lacking. Clinical implementation of standardized tools generally remains challenging, and some recent techniques are in their infancy. The readiness of individual modalities in terms of technical validation, clinical evidence, acceptance and implementation are summarized in Part 2.

High-grade glioma vasculature exhibits increased perfusion, blood volume, and permeability compared with normal brain tissue. Measures of CBV derived from DSC-MRI have consistently provided information about brain tumor growth and response to treatment; it is the most clinically validated advanced technique. Clinical studies have proven the potential of DCE-MRI for distinguishing post-treatment related effects from recurrence, but the optimal acquisition protocol, mode of analysis, and parameter of highest diagnostic value and optimal cut-off points remain to be established. These same challenges are present to some extent with other perfusion techniques. ASL techniques do not require the injection of a contrast agent, and fast repeated measurements can be performed. Moreover, the absence of potential gadolinium

deposition effects allows widespread use in pediatric patients and those with impaired renal function. Although the current review is focused on adult high-grade glioma, several studies have shown the utility of ASL perfusion imaging in pediatric brain tumors (205). DWI, ADC, DTI, DKI, IVIM, and other microstructural modeling approaches also allow treatment response assessment; more robust data is required to validate these techniques alone or when applied to post-processing methodologies. (Post-processing methodologies involving the combination of MRI approaches [multiparametric imaging] or machine learning are summarized in Part 2). Finally, for all parametric imaging techniques, the clinical application of cutoffs based on the literature is complicated by differences in how a ROI is defined and what particular descriptive statistic value (maximum, mean, etc.) within the ROI is used. Using a fixed image analysis approach, a multi-center study did show that excellent agreement of cut-offs between sites and platforms may be achieved (57). Nevertheless, until methods are standardized, generally accepted cut-off values may be difficult to apply in the clinical setting. Alternatively, clinical departments may rely on replicating approaches for generation and analysis of parametric images described in individual studies reporting the cut-off used.

In conclusion, considerable progress has been made in the development of advanced MRI monitoring biomarkers. As we approach the mid-twenty-first century, the techniques will have matured and serve as robust clinic-ready assays for treatment response assessment in personalized medicine regimens, which themselves will evolve in parallel. For now, more research and collaboration are needed to provide standardized and evidenced-based tools for this uncommon but disproportionately devastating disease.

AUTHOR CONTRIBUTIONS

All authors have contributed to the conception of the two parts of the article, revised them critically and approved the submitted versions. Authors TB and OH served as overall editors. The individual sections were drafted by: Introduction (TB), DSC-MRI (KS and MÁ-T), DCE-MRI (OH), ASL (PF and VK), diffusion techniques (RN, FR, and VK), spectroscopy (ECW and GH), CEST (EAHW), multiparametric imaging (OH), clinical readiness (OH), radiomics (TB), discussion (TB). All authors contributed to the article and approved the submitted version.

FUNDING

This publication is part of the COST Action CA18206 Glioma MR Imaging 2.0 (www.glimr.eu), supported by COST (European Cooperation in Science and Technology), www.cost.eu. GliMR provided travel and accommodation for members who had travelled to early networking meetings. No participants were remunerated for their contribution. Funding support for KS: National Institute of Health/National Cancer Institute R01 CA255123, U01 CA176110, UG3 CA247606, Medical College of Wisconsin Cancer Center; GH: Austrian Science Fund grant KLI-646; ECW: The Dutch Research Council (NWO) Talent Programme Veni: 18144; EAHW: The Dutch Research Council (NWO) Talent Programme Veni: 91619121; PF: The Portuguese Foundation for Science and Technology (FCT) Grant UIDB/50009/2020; RN: Babes-Bolyai University, Grant GTC No. 35277/18.11.2020. TB was supported by the Wellcome/EPSRC Centre for Medical Engineering [WT 203148/Z/16/Z]. MÁ-T was supported by the ALBATROSS project (National Plan for Scientific and Technical Research and Innovation 2017-2020 and DPI2016-80054-R (Programa Estatal de Promoción del Talento y su Empleabilidad en I+D+i).

ACKNOWLEDGMENTS

The authors would like to thank Melissa Prah for assistance with obtaining figures, and Andrei Roman and Lydia Washechek for help with manuscript preparation. The authors also thank the national representatives who helped complete the national guideline survey (names listed in the **Supplementary Material** in Part 2).

SUPPLEMENTARY MATERIAL

The Supplementary Material for this article can be found online at: https://www.frontiersin.org/articles/10.3389/fonc.2022.810263/full#supplementary-material

REFERENCES

1. Ostrom QT, Gittleman H, Liao P, Rouse C, Chen Y, Dowling J, et al. CBTRUS Statistical Report: Primary Brain and Central Nervous System Tumors Diagnosed in the United States in 2007-2011. *Neuro Oncol* (2014) 16(Suppl 4):iv1–63. doi: 10.1093/neuonc/nou223
2. Haider AS, van den Bent M, Wen PY, Vogelbaum MA, Chang S, Canoll PD, et al. Toward a Standard Pathological and Molecular Characterization of Recurrent Glioma in Adults: A Response Assessment in Neuro-Oncology Effort. *Neuro Oncol* (2020) 22:450–6. doi: 10.1093/neuonc/noz233
3. Burnet NG, Jefferies SJ, Benson RJ, Hunt DP, Treasure FP. Years of Life Lost (YLL) From Cancer Is an Important Measure of Population Burden — and Should be Considered When Allocating Research Funds. *Br J Cancer* (2005) 92:241–5. doi: 10.1038/sj.bjc.6602321
4. Stupp R, Mason WP, van den Bent MJ, Weller M, Fisher B, Taphoorn MJB, et al. Radiotherapy Plus Concomitant and Adjuvant Temozolomide for Glioblastoma. *N Engl J Med* (2005) 352:987–96. doi: 10.1056/NEJMoa043330
5. Weller M, van den Bent M, Tonn JC, Stupp R, Preusser M, Cohen-Jonathan-Moyal E, et al. European Association for Neuro-Oncology (EANO) Guideline on the Diagnosis and Treatment of Adult Astrocytic and Oligodendroglial Gliomas. *Lancet Oncol* (2017) 18:e315–29. doi: 10.1016/S1470-2045(17)30194-8
6. Stupp R, Hegi ME, Mason WP, van den Bent MJ, Taphoorn MJB, Janzer RC, et al. Effects of Radiotherapy With Concomitant and Adjuvant Temozolomide Versus Radiotherapy Alone on Survival in Glioblastoma in a Randomised Phase III Study: 5-Year Analysis of the EORTC-NCIC Trial. *Lancet Oncol* (2009) 10:70025–7. doi: 10.1016/S1470-2045(09)70025-7

7. Cagney DN, Sul J, Huang RY, Ligon KL, Wen PY, Alexander BM. The FDA NIH Biomarkers, EndpointS, and Other Tools (BEST) Resource in Neuro-Oncology. *Neuro Oncol* (2018) 20:1162–72. doi: 10.1093/neuonc/nox242
8. Cao Y, Sundgren PC, Tsien CI, Chenevert TT, Junck L. Physiologic and Metabolic Magnetic Resonance Imaging in Gliomas. *J Clin Oncol* (2006) 24:1228–35. doi: 10.1200/JCO.2005.04.7233
9. Wen PY, Macdonald DR, Reardon DA, Cloughesy TF, Sorensen AG, Galanis E, et al. Updated Response Assessment Criteria for High-Grade Gliomas: Response Assessment in Neuro-Oncology Working Group. *J Clin Oncol* (2010) 28:1963–72. doi: 10.1200/JCO.2009.26.3541
10. Booth TC, Thompson G, Bulbeck H, Boele F, Buckley C, Cardoso J, et al. A Position Statement on the Utility of Interval Imaging in Standard of Care Brain Tumour Management: Defining the Evidence Gap and Opportunities for Future Research. *Front Oncol* (2021) 11:620070. doi: 10.3389/fonc.2021.620070
11. Ellingson BM, Harris RJ, Woodworth DC, Leu K, Zaw O, Mason WP, et al. Baseline Pretreatment Contrast Enhancing Tumor Volume Including Central Necrosis is a Prognostic Factor in Recurrent Glioblastoma: Evidence From Single and Multicenter Trials. *Neuro Oncol* (2017) 19:89–98. doi: 10.1093/neuonc/now187
12. Lacroix M, Abi-Said D, Fourney DR, Gokaslan ZL, Shi W, DeMonte F, et al. A Multivariate Analysis of 416 Patients With Glioblastoma Multiforme: Prognosis, Extent of Resection, and Survival. *J Neurosurg* (2001) 95:190–8. doi: 10.3171/jns.2001.95.2.0190
13. Booth TC, Luis A, Brazil L, Thompson G, Daniel RA, Shuaib H, et al. Glioblastoma Post-Operative Imaging in Neuro-Oncology: Current UK Practice (GIN CUP Study). *Eur Radiol* (2021) 31:2933–43. doi: 10.1007/s00330-020-07387-3
14. Dhermain FG, Hau P, Lanfermann H, Jacobs AH, van den Bent MJ. Advanced MRI and PET Imaging for Assessment of Treatment Response in Patients With Gliomas. *Lancet Neurol* (2010) 9. doi: 10.1016/S1474-4422(10)70181-2
15. Booth TC, Williams M, Luis A, Cardoso J, Ashkan K, Shuaib H. Machine Learning and Glioma Imaging Biomarkers. *Clin Radiol* (2020) 75. doi: 10.1016/j.crad.2019.07.001
16. Brandsma D, Stalpers L, Taal W, Sminia P, van den Bent MJ. Clinical Features, Mechanisms, and Management of Pseudoprogression in Malignant Gliomas. *Lancet Oncol* (2008) 9:453–61. doi: 10.1016/S1470-2045(08)70125-6
17. Booth TC, Larkin TJ, Yuan Y, Kettunen MI, Dawson SN, Scoffings D, et al. Analysis of Heterogeneity in T2-Weighted MR Images can Differentiate Pseudoprogression From Progression in Glioblastoma. *PloS One* (2017) 12:e0176528. doi: 10.1371/journal.pone.0176528
18. Radbruch A, Fladt J, Kickingereder P, Wiestler B, Nowosielski M, Bäumer P, et al. Pseudoprogression in Patients With Glioblastoma: Clinical Relevance Despite Low Incidence. *Neuro Oncol* (2015) 17:151–9. doi: 10.1093/neuonc/nou129
19. Booth TC, Waldman AD, Jefferies S, Jäger R. Comment on "The Role of Imaging in the Management of Progressive Glioblastoma. A Systematic Review and Evidence-Based Clinical Practice Guideline". *J Neurooncol* (2014) 118:435–60. doi: 10.1007/s11060-013-1330-0
20. Dhawan S, Venteicher AS, Butler WE, Carter BS, Chen CC. Clinical Outcomes as a Function of the Number of Samples Taken During Stereotactic Needle Biopsies: A Meta-Analysis. *J Neurooncol* (2021) 154:1–11. doi: 10.1007/s11060-021-03785-9
21. Müller DMJ, Robe PAJT, Eijgelaar RS, Witte MG, Visser M, de Munck JC, et al. Comparing Glioblastoma Surgery Decisions Between Teams Using Brain Maps of Tumor Locations, Biopsies, and Resections. *JCO Clin Cancer Inf* (2019) 3:1–12. doi: 10.1200/CCI.18.00089
22. Müller Bark J, Kulasinghe A, Chua B, Day BW, Punyadeera C. Circulating Biomarkers in Patients With Glioblastoma. *Br J Cancer* (2020) 122:295–305. doi: 10.1038/s41416-019-0603-6
23. Morokoff A, Jones J, Nguyen H, Ma C, Lasocki A, Gaillard F, et al. Serum microRNA is a Biomarker for Post-Operative Monitoring in Glioma. *J Neurooncol* (2020) 149:391–400. doi: 10.1007/s11060-020-03566-w
24. Lawrie TA, Kernohan A, Jenkinson MD, Thompson G. Interval Brain Imaging for Adults With Cerebral Glioma. *Cochrane Database Syst Rev* (2018) 12:CD013137. doi: 10.1002/14651858.CD013137.pub2
25. *The National Institute for Health and Care Excellence. Guideline Ng99* . Available at: https://www.nice.org.uk/guidance/ng99 (Accessed 1 March 2019).
26. *The James Lind Alliance Priority Setting Partnerships* . Available at: http://www.jla.nihr.ac.uk/priority-setting-partnerships/neuro-oncology/ (Accessed 1 August 2018).
27. Thust SC, Heiland S, Falini A, Jäger HR, Waldman AD, Sundgren PC, et al. Glioma Imaging in Europe: A Survey of 220 Centres and Recommendations for Best Clinical Practice. *Eur Radiol* (2018) 28:3306–31. doi: 10.1007/s00330-018-5314-5
28. Clement P, Booth T, Borovečki F, Emblem KE, Figueiredo P, Hirschler L, et al. GliMR: Cross-Border Collaborations to Promote Advanced MRI Biomarkers for Glioma. *J Med Biol Eng* (2021) 41:1–11. doi: 10.1007/s40846-020-00582-z
29. European Medicine Agency. *Refusal Assessment Report for Avastin* (2010). Available at: https://www.ema.europa.eu/en/documents/variation- report/avastin-h-c-582-ii-0028-epar-refusal-assessment-report-variation_en.pdf (Accessed 15 April 2019).
30. Europarat C of E. *Developing a Methodology for Drawing Up Guidelines on Best Medical Practices - Recommendation Rec13 and Explanatory Memorandum (2002)*. Strasbourg: Council of Europe Publications (2002).
31. McInnes MDF, Moher D, Thombs BD, McGrath TA, Bossuyt PMthe PRISMA-DTA Group, et al. Preferred Reporting Items for a Systematic Review and Meta-Analysis of Diagnostic Test Accuracy Studies: The PRISMA-DTA Statement. *JAMA* (2018) 319:388–96. doi: 10.1001/jama.2017.19163
32. Hanahan D, Weinberg RA. Hallmarks of Cancer: The Next Generation. *Cell* (2011) 144:646–74. doi: 10.1016/j.cell.2011.02.013
33. Ahir BK, Engelhard HH, Lakka SS. Tumor Development and Angiogenesis in Adult Brain Tumor: Glioblastoma. *Mol Neurobiol* (2020) 57:2461–78. doi: 10.1007/s12035-020-01892-8
34. Michael Peters A. The Precise Physiological Definition of Tissue Perfusion and Clearance Measured From Imaging. *Eur J Nucl Med Mol Imaging* (2018) 45:1139–41. doi: 10.1007/s00259-018-3982-7
35. Jezzard P, Chappell MA, Okell TW. Arterial Spin Labeling for the Measurement of Cerebral Perfusion and Angiography. *J Cereb Blood Flow Metab* (2018) 38:603–26. doi: 10.1177/0271678X17743240
36. Rosen BR, Belliveau JW, Vevea JM, Brady TJ. Perfusion Imaging With NMR Contrast Agents. *Magn Reson Med* (1990) 14:249–65. doi: 10.1002/mrm.1910140211
37. Boxerman JL, Bandettini PA, Kwong KK, Baker JR, Davis TL, Rosen BR, et al. The Intravascular Contribution to fMRI Signal Change: Monte Carlo Modeling and Diffusion-Weighted Studies *In Vivo*. *Magn Reson Med* (1995) 34:4–10. doi: 10.1002/mrm.1910340103
38. Perkio J, Aronen HJ, Kangasmaki A, Liu Y, Karonen J, Savolainen S, et al. Evaluation of Four Postprocessing Methods for Determination of Cerebral Blood Volume and Mean Transit Time by Dynamic Susceptibility Contrast Imaging. *Magn Reson Med* (2002) 47:973–81. doi: 10.1002/mrm.10126
39. Bedekar D, Jensen T, Schmainda KM. Standardization of Relative Cerebral Blood Volume (rCBV) Image Maps for Ease of Both Inter- and Intrapatient Comparisons. *Magn Reson Med* (2010) 64:907–13. doi: 10.1002/mrm.22445
40. Prah MA, Stufflebeam SM, Paulson ES, Kalpathy-Cramer J, Gerstner ER, Batchelor TT, et al. Repeatability of Standardized and Normalized Relative CBV in Patients With Newly Diagnosed Glioblastoma. *Am J Neuroradiol* (2015) 36:1654–61. doi: 10.3174/ajnr.A4374
41. Schmainda KM, Zhang Z, Prah M, Snyder BS, Gilbert MR, Sorensen AG, et al. Dynamic Susceptibility Contrast MRI Measures of Relative Cerebral Blood Volume as a Prognostic Marker for Overall Survival in Recurrent Glioblastoma: Results From the ACRIN 6677/RTOG 0625 Multicenter Trial. *Neuro Oncol* (2015) 17:1148–56. doi: 10.1093/neuonc/nou364
42. Gerstner ER, Zhang Z, Fink JR, Muzi M, Hanna L, Greco E, et al. ACRIN 6684: Assessment of Tumor Hypoxia in Newly Diagnosed Glioblastoma Using 18f-FMISO PET and MRI. *Clin Cancer Res* (2016) 22:5079–86. doi: 10.1158/1078-0432.CCR-15-2529
43. Schmainda KM, Prah MA, Marques H, Kim E, Barboriak DP, Boxerman JL. Value of Dynamic Contrast Perfusion MRI to Predict Early Response to Bevacizumab in Newly Diagnosed Glioblastoma: Results From ACRIN 6686

Multi-Center Trial. *Neuro Oncol* (2020) 23:314–23. doi: 10.1093/neuonc/noaa167
44. Paulson ES, Prah DE, Schmainda KM. Spiral Perfusion Imaging With Consecutive Echoes (SPICE) for the Simultaneous Mapping of DSC- and DCE-MRI Parameters in Brain Tumor Patients: Theory and Initial Feasibility. *Tomography* (2016) 2:295–307. doi: 10.18383/j.tom.2016.00217
45. Donahue KM, Krouwer HGJ, Rand SD, Pathak AP, Marszalkowski CS, Censky SC, et al. Utility of Simultaneously Acquired Gradient-Echo and Spin-Echo Cerebral Blood Volume and Morphology Maps in Brain Tumor Patients. *Magn Reson Med* (2000) 43:845–53. doi: 10.1002/1522-2594(200006)43:6<845::AID-MRM10>3.0.CO;2-J
46. Schmainda KM, Rand SD, Joseph AM, Lund R, Ward BD, Pathak AP, et al. Characterization of a First-Pass Gradient-Echo Spin-Echo Method to Predict Brain Tumor Grade and Angiogenesis. *Am J Neuroradiol* (2004) 25:1524–32.
47. Hu LS, Baxter LC, Pinnaduwage DS, Paine TL, Karis JP, Feuerstein BG, et al. Optimized Preload Leakage-Correction Methods to Improve the Diagnostic Accuracy of Dynamic Susceptibility-Weighted Contrast-Enhanced Perfusion MR Imaging in Posttreatment Gliomas. *Am J Neuroradiol* (2010) 31:40–8. doi: 10.3174/ajnr.A1787
48. Boxerman JL, Schmainda KM, Weisskoff RM. Relative Cerebral Blood Volume Maps Corrected for Contrast Agent Extravasation Significantly Correlate With Glioma Tumor Grade, Whereas Uncorrected Maps do Not. *Am J Neuroradiol* (2006) 27:859–67.
49. Bjornerud A, Sorensen AG, Mouridsen K, Emblem KE. T1- and T2*-Dominant Extravasation Correction in DSC-MRI: Part I–theoretical Considerations and Implications for Assessment of Tumor Hemodynamic Properties. *J Cereb Blood Flow Metab* (2011) 31:2041–53. doi: 10.1038/jcbfm.2011.52
50. Quarles CC, Ward BD, Schmainda KM. Improving the Reliability of Obtaining Tumor Hemodynamic Parameters in the Presence of Contrast Agent Extravasation. *Magn Reson Med* (2005) 53:1307–16. doi: 10.1002/mrm.20497
51. Leu K, Boxerman JL, Cloughesy TF, Lai A, Nghiemphu PL, Liau LM, et al. Improved Leakage Correction for Single-Echo Dynamic Susceptibility Contrast Perfusion MRI Estimates of Relative Cerebral Blood Volume in High-Grade Gliomas by Accounting for Bidirectional Contrast Agent Exchange. *AJNR Am J Neuroradiol* (2016) 37:1440–6. doi: 10.3174/ajnr.A4759
52. Semmineh NB, Bell LC, Stokes AM, Hu LS, Boxerman JL, Quarles CC. Optimization of Acquisition and Analysis Methods for Clinical Dynamic Susceptibility Contrast MRI Using a Population-Based Digital Reference Object. *Am J Neuroradiol* (2018) 39:1981–8. doi: 10.3174/ajnr.A5827
53. Semmineh NB, Stokes AM, Bell LC, Boxerman JL, Quarles CC. A Population-Based Digital Reference Object (DRO) for Optimizing Dynamic Susceptibility Contrast (DSC)-MRI Methods for Clinical Trials. *Tomography* (2017) 3:41–9. doi: 10.18383/j.tom.2016.00286
54. Schmainda KM, Prah MA, Hu LS, Quarles CC, Semmineh N, Rand SD, et al. Moving Toward a Consensus DSC-MRI Protocol: Validation of a Low-Flip Angle Single-Dose Option as a Reference Standard for Brain Tumors. *Am J Neuroradiol* (2019) 40:626–33. doi: 10.3174/ajnr.A6015
55. Boxerman JL, Quarles CC, Hu LS, Erickson BJ, Gerstner ER, Smits M, et al. Consensus Recommendations for a Dynamic Susceptibility Contrast MRI Protocol for Use in High-Grade Gliomas. *Neuro Oncol* (2020) 22:1262–75. doi: 10.1093/neuonc/noaa141
56. Patel P, Baradaran H, Delgado D, Askin G, Christos P, John Tsiouris A, et al. MR Perfusion-Weighted Imaging in the Evaluation of High-Grade Gliomas After Treatment: A Systematic Review and Meta-Analysis. *Neuro Oncol* (2017) 19:118–27. doi: 10.1093/neuonc/now148
57. Schmainda KM, Prah MA, Rand SD, Liu Y, Logan B, Muzi M, et al. Multisite Concordance of DSC-MRI Analysis for Brain Tumors: Results of a National Cancer Institute Quantitative Imaging Network Collaborative Project. *AJNR Am J Neuroradiol* (2018) 39:1008–16. doi: 10.3174/ajnr.A5675
58. Hu LS, Eschbacher JM, Dueck AC, Heiserman JE, Liu S, Karis JP, et al. Correlations Between Perfusion MR Imaging Cerebral Blood Volume, Microvessel Quantification, and Clinical Outcome Using Stereotactic Analysis in Recurrent High-Grade Glioma. *Am J Neuroradiol* (2012) 33:69–76. doi: 10.3174/ajnr.A2743
59. Prah MA, Al-Gizawiy MM, Mueller WM, Cochran EJ, Hoffmann RG, Connelly JM, et al. Spatial Discrimination of Glioblastoma and Treatment Effect With Histologically-Validated Perfusion and Diffusion Magnetic Resonance Imaging Metrics. *J Neurooncol* (2018) 136:13–21. doi: 10.1007/s11060-017-2617-3
60. Hu LS, Eschbacher JM, Heiserman JE, Dueck AC, Shapiro WR, Liu S, et al. Reevaluating the Imaging Definition of Tumor Progression: Perfusion MRI Quantifies Recurrent Glioblastoma Tumor Fraction, Pseudoprogression, and Radiation Necrosis to Predict Survival. *Neuro Oncol* (2012) 14:919–30. doi: 10.1093/neuonc/nos112
61. Prah MA, Connelly JM, Schmainda KM. MRI-Perfusion Derived Fractional Tumor Burden (FTB) is Predictive of Overall and Progression Free Survival in Newly Diagnosed Glioblastoma Following Concomitant Chemoradiotherapy. *Proc Int Soc Magnetic Resonance Med (Honolulu Hawaii)* 707.
62. Iv M, Liu X, Lavezo J, Gentles AJ, Ghanem R, Lummus S, et al. Perfusion MRI-Based Fractional Tumor Burden Differentiates Between Tumor and Treatment Effect in Recurrent Glioblastomas and Informs Clinical Decision-Making. *AJNR Am J Neuroradiol* (2019) 40:1649–57. doi: 10.3174/ajnr.A6211
63. Hoxworth JM, Eschbacher JM, Gonzales AC, Singleton KW, Leon GD, Smith KA, et al. Performance of Standardized Relative CBV for Quantifying Regional Histologic Tumor Burden in Recurrent High-Grade Glioma: Comparison Against Normalized Relative CBV Using Image-Localized Stereotactic Biopsies. *AJNR Am J Neuroradiol* (2020) 41:408–15. doi: 10.3174/ajnr.A6486
64. Quarles CC, Schmainda KM. Assessment of the Morphological and Functional Effects of the Anti-Angiogenic Agent SU11657 on 9L Gliosarcoma Vasculature Using Dynamic Susceptibility Contrast MRI. *Magn Reson Med* (2007) 57:680–7. doi: 10.1002/mrm.21193
65. Bonekamp D, Mouridsen K, Radbruch A, Kurz FT, Eidel O, Wick A, et al. Assessment of Tumor Oxygenation and its Impact on Treatment Response in Bevacizumab-Treated Recurrent Glioblastoma. *J Cereb Blood Flow Metab* (2017) 37:485–94. doi: 10.1177/0271678X16630322
66. Stokes AM, Quarles CC. A Simplified Spin and Gradient Echo Approach for Brain Tumor Perfusion Imaging. *Magn Reson Med* (2016) 75:356–62. doi: 10.1002/mrm.25591
67. Quarles CC, Gore JC, Xu L, Yankeelov TE. Comparison of Dual-Echo DSC-MRI- and DCE-MRI-Derived Contrast Agent Kinetic Parameters. *Magn Reson Imaging* (2012) 30:944–53. doi: 10.1016/j.mri.2012.03.008
68. Han M, Yang B, Fernandez B, Lafontaine M, Alcaide-Leon P, Jakary A, et al. Simultaneous Multi-Slice Spln- and Gradient-Echo Dynamic Susceptibility Perfusion-Weighted MRI of Gliomas. *Nmr BioMed* (2021) 34:e4399. doi: 10.1002/nbm.4399
69. Bell LC, Semmineh N, An H, Eldeniz C, Wahl R, Schmainda KM, et al. Evaluating the Use of rCBV as a Tumor Grade and Treatment Response Classifier Across NCI Quantitative Imaging Network Sites: Part II of the DSC-MRI Digital Reference Object (DRO) Challenge. *Tomogr (Ann Arbor Mich)* (2020) 6:203–8. doi: 10.18383/j.tom.2020.00012
70. Skinner JT, Robison RK, Elder CP, Newton AT, Damon BM, Quarles CC. Evaluation of a Multiple Spin- and Gradient-Echo (SAGE) EPI Acquisition With SENSE Acceleration: Applications for Perfusion Imaging in and Outside the Brain. *Magn Reson Imaging* (2014) 32:1171–80. doi: 10.1016/j.mri.2014.08.032
71. Sourbron SP, Buckley DL. Classic Models for Dynamic Contrast-Enhanced MRI. *NMR BioMed* (2013) 26:1004–27. doi: 10.1002/nbm.2940
72. Tofts PS, Brix G, Buckley DL, Evelhoch JL, Henderson E, Knopp MV, et al. Estimating Kinetic Parameters From Dynamic Contrast-Enhanced T1-Weighted MRI of a Diffusable Tracer: Standardized Quantities and Symbols. *J Magn Reson Imaging* (1999) 10:223–32. doi: 10.1002/(SICI)1522-2586(199909)10:3<223::AID-JMRI2>3.0.CO;2-S
73. *QIBA Profile: 4 DCE-MRI Quantification (DCEMRI-Q).* Available at: http://qibawiki.rsna.org/images/1/1f/QIBA_DCE-MRI_Profile-Stage_1-Public_Comment.pdf ref. accessed Feb 1, 2021
74. Luypaert R, Sourbron S, de Mey J. Validity of Perfusion Parameters Obtained Using the Modified Tofts Model: A Simulation Study. *Magn Reson Med* (2011) 65:1491–7. doi: 10.1002/mrm.22728
75. Artzi M, Liberman G, Blumenthal DT, Bokstein F, Aizenstein O, Ben Bashat D. Repeatability of Dynamic Contrast Enhanced Vp Parameter in Healthy

Subjects and Patients With Brain Tumors. *J Neurooncol* (2018) 140:727–37. doi: 10.1007/s11060-018-03006-w

76. Schmainda KM, Prah MA, Marques H, Kim E, Barboriak DP, Boxerman JL. Value of Dynamic Contrast Perfusion MRI to Predict Early Response to Bevacizumab in Newly Diagnosed Glioblastoma: Results From ACRIN 6686 Multicenter Trial. *Neuro Oncol* (2021) 23:314–32. doi: 10.1093/neuonc/noaa167
77. Bane O, Hectors SJ, Wagner M, Arlinghaus LL, Aryal MP, Cao Y, et al. Accuracy, Repeatability, and Interplatform Reproducibility of T_1 Quantification Methods Used for DCE-MRI: Results From a Multicenter Phantom Study. *Magn Reson Med* (2018) 79:2564–75. doi: 10.1002/mrm.26903
78. Conte GM, Castellano A, Altabella L, Iadanza A, Cadioli M, Falini A, et al. Reproducibility of Dynamic Contrast-Enhanced MRI and Dynamic Susceptibility Contrast MRI in the Study of Brain Gliomas: A Comparison of Data Obtained Using Different Commercial Software. *Radiol Med* (2017) 122. doi: 10.1007/s11547-016-0720-8
79. Anzalone N, Castellano A, Cadioli M, Conte GM, Cuccarini V, Bizzi A, et al. Brain Gliomas: Multicenter Standardized Assessment of Dynamic Contrast-Enhanced and Dynamic Susceptibility Contrast MR Images. *Radiology* (2018) 287:933–94. doi: 10.1148/radiol.2017170362
80. Larsson HBW, Hansen AE, Berg HK, Rostrup E, Haraldseth O. Dynamic Contrast-Enhanced Quantitative Perfusion Measurement of the Brain Usingt1-Weighted MRI at 3T. *J Magn Reson Imaging* (2008) 27:754–62. doi: 10.1002/jmri.21328
81. Sourbron S, Ingrisch M, Siefert A, Reiser M, Herrmann K. Quantification of Cerebral Blood Flow, Cerebral Blood Volume, and Blood-Brain-Barrier Leakage With DCE-MRI. *Magn Reson Med* (2009) 62:205–17. doi: 10.1002/mrm.22005
82. Larsson HBW, Courivaud F, Rostrup E, Hansen AE. Measurement of Brain Perfusion, Blood Volume, and Blood-Brain Barrier Permeability, Using Dynamic Contrast-Enhanced T_1 -Weighted MRI at 3 Tesla. *Magn Reson Med* (2009) 62:1270–81. doi: 10.1002/mrm.22136
83. Narang J, Jain R, Arbab AS, Mikkelsen T, Scarpace L, Rosenblum ML, et al. Differentiating Treatment-Induced Necrosis From Recurrent/Progressive Brain Tumor Using Nonmodel-Based Semiquantitative Indices Derived From Dynamic Contrast-Enhanced T1-Weighted MR Perfusion. *Neuro Oncol* (2011) 13:1037–46. doi: 10.1093/neuonc/nor075
84. Suh CH, Kim HS, Choi YJ, Kim N, Kim SJ. Prediction of Pseudoprogression in Patients With Glioblastomas Using the Initial and Final Area Under the Curves Ratio Derived From Dynamic Contrast-Enhanced T1-Weighted Perfusion MR Imaging. *Am J Neuroradiol* (2013) 34:2278–86. doi: 10.3174/ajnr.A3634
85. Henriksen OM, Larsen VA, Muhic A, Hansen AE, Larsson HBW, Poulsen HS, et al. Simultaneous Evaluation of Brain Tumour Metabolism, Structure and Blood Volume Using [18F]-Fluoroethyltyrosine (FET) PET/MRI: Feasibility, Agreement and Initial Experience. *Eur J Nucl Med Mol Imaging* (2016) 43:103–12. doi: 10.1007/s00259-015-3183-6
86. Heo YJ, Kim HS, Park JE, Choi C-G, Kim SJ. Uninterpretable Dynamic Susceptibility Contrast-Enhanced Perfusion MR Images in Patients With Post-Treatment Glioblastomas: Cross-Validation of Alternative Imaging Options. *PloS One* (2015) 10:e0136380. doi: 10.1371/journal.pone.0136380
87. Lundemann M, Munck af Rosenschöld P, Muhic A, Larsen VA, Poulsen HS, Engelholm S-A, et al. Feasibility of Multi-Parametric PET and MRI for Prediction of Tumour Recurrence in Patients With Glioblastoma. *Eur J Nucl Med Mol Imaging* (2019) 46:603–13. doi: 10.1007/s00259-018-4180-3
88. Okuchi S, Rojas-Garcia A, Ulyte A, Lopez I, Ušinskienė J, Lewis M, et al. Diagnostic Accuracy of Dynamic Contrast-Enhanced Perfusion MRI in Stratifying Gliomas: A Systematic Review and Meta-Analysis. *Cancer Med* (2019) 8:5564–73. doi: 10.1002/cam4.2369
89. Park JE, Kim HS, Goh MJ, Kim SJ, Kim JH. Pseudoprogression in Patients With Glioblastoma: Assessment by Using Volume-Weighted Voxel-Based Multiparametric Clustering of MR Imaging Data in an Independent Test Set. *Radiology* (2015) 275:792–802. doi: 10.1148/radiol.14141414
90. Kim HS, Goh MJ, Kim N, Choi CG, Kim SJ, Kim JH. Which Combination of MR Imaging Modalities Is Best for Predicting Recurrent Glioblastoma? Study of Diagnostic Accuracy and Reproducibility. *Radiology* (2014) 273:831–43. doi: 10.1148/radiol.14132868
91. Zakhari N, Taccone MS, Torres CH, Chakraborty S, Sinclair J, Woulfe J, et al. Prospective Comparative Diagnostic Accuracy Evaluation of Dynamic Contrast-Enhanced (DCE) vs. Dynamic Susceptibility Contrast (DSC) MR Perfusion in Differentiating Tumor Recurrence From Radiation Necrosis in Treated High-Grade Gliomas. *J Magn Reson Imaging* (2019) 50:573–82. doi: 10.1002/jmri.26621
92. Hatzoglou V, Yang TJ, Omuro A, Gavrilovic I, Ulaner G, Rubel J, et al. A Prospective Trial of Dynamic Contrast-Enhanced MRI Perfusion and Fluorine-18 FDG PET-CT in Differentiating Brain Tumor Progression From Radiation Injury After Cranial Irradiation. *Neuro Oncol* (2016) 18:873–80. doi: 10.1093/neuonc/nov301
93. Park YW, Ahn SS, Kim EH, Kang S-G, Chang JH, Kim SH, et al. Differentiation of Recurrent Diffuse Glioma From Treatment-Induced Change Using Amide Proton Transfer Imaging: Incremental Value to Diffusion and Perfusion Parameters. *Neuroradiology* (2021) 63:363–72. doi: 10.1007/s00234-020-02542-5
94. Fussell D, Young RJ. Role of MRI Perfusion in Improving the Treatment of Brain Tumors. *Imaging Med* (2013) 5:407–26. doi: 10.2217/iim.13.50
95. Alsop DC, Detre JA, Golay X, Günther M, Hendrikse J, Hernandez-Garcia L, et al. Recommended Implementation of Arterial Spin-Labeled Perfusion Mri for Clinical Applications: A Consensus of the ISMRM Perfusion Study Group and the European Consortium for ASL in Dementia. *Magn Reson Med* (2015) 73:102–16. doi: 10.1002/mrm.25197
96. van Osch MJP, Teeuwisse WM, Chen Z, Suzuki Y, Helle M, Schmid S. Advances in Arterial Spin Labelling MRI Methods for Measuring Perfusion and Collateral Flow. *J Cereb Blood Flow Metab* (2018) 38:1461–80. doi: 10.1177/0271678X17713434
97. Williams DS, Detre JA, Leigh JS, Koretsky AP. Magnetic Resonance Imaging of Perfusion Using Spin Inversion of Arterial Water. *Proc Natl Acad Sci USA* (1992) 89:212–6. doi: 10.1073/pnas.89.1.212
98. Kwong KK, Chesler DA, Weisskoff RM, Donahue KM, Davis TL, Ostergaard L, et al. Mr Perfusion Studies With T1-Weighted Echo Planar Imaging. *Magn Reson Med* (1995) 34:878–87. doi: 10.1002/mrm.1910340613
99. Kim S-G. Quantification of Relative Cerebral Blood Flow Change by Flow-Sensitive Alternating Inversion Recovery (FAIR) Technique: Application to Functional Mapping. *Magn Reson Med* (1995) 34:293–301. doi: 10.1002/MRM.1910340303
100. Liao D, Liu Y, Tang B, Wang D, Li X, Dai B, et al. Comparison of DWI Based on Monoexponential, Biexponential and Stretched-Exponential Models in Differentiating Tumor Recurrence and Pseudoprogression of Glioblastoma. *Chin J Med Imaging Technol* (2019) 35:1450–5. doi: 10.13929/j.1003-3289.201903059
101. Wong EC, Cronin M, Wu W-C, Inglis B, Frank LR, Liu TT. Velocity-Selective Arterial Spin Labeling. *Magn Reson Med* (2006) 55:1334–41. doi: 10.1002/MRM.20906
102. Wong EC, Buxton RB, Frank LR. Implementation of Quantitative Perfusion Imaging Techniques for Functional Brain Mapping Using Pulsed Arterial Spin Labeling. *NMR BioMed* (1997) 10:237–49. doi: 10.1002/(SICI)1099-1492(199706/08)10:4/5<237::AID-NBM475>3.0.CO;2-X
103. Luh W-M, Wong EC, Bandettini PA, Hyde JS. *QUIPSS II With Thin-Slice TI 1 Periodic Saturation: A Method for Improving Accuracy of Quantitative Perfusion Imaging Using Pulsed Arterial Spin Labeling* (1999). Available at: http://citeseerx.ist.psu.edu/viewdoc/download?doi=10.1.1.139.499&rep=rep1&type=pdf (Accessed December 7, 2018).
104. Woods JG, Chappell MA, Okell TW. A General Framework for Optimizing Arterial Spin Labeling MRI Experiments. *Magn Reson Med* (2018) 81:2474–248. doi: 10.1002/mrm.27580
105. Santos N, Sanches JM, Sousa I, Figueiredo P. Optimal Sampling and Estimation in PASL Perfusion Imaging. *IEEE Trans BioMed Eng* (2011) 58:3165–74. doi: 10.1109/TBME.2011.2164916
106. Teeuwisse WM, Schmid S, Ghariq E, Veer IM, Van Osch MJP. Time-Encoded Pseudocontinuous Arterial Spin Labeling: Basic Properties and Timing Strategies for Human Applications. *Magn Reson Med* (2014) 72:1712–22. doi: 10.1002/mrm.25083
107. Buxton RB, Frank LR, Wong EC, Siewert B, Warach S, Edelman RR. A General Kinetic Model for Quantitative Perfusion Imaging With Arterial Spin Labeling. *Magn Reson Med* (1998) 40:383–96. doi: 10.1002/mrm.1910400308

108. Lawrence KS St, Frank JA, McLaughlin AC. Effect of Restricted Water Exchange on Cerebral Blood Flow Values Calculated With Arterial Spin Tagging: A Theoretical Investigation. *Magn Reson Med* (2000) 44:440–9. doi: 10.1002/1522-2594(200009)44:3<440::AID-MRM15>3.0.CO;2-6
109. Parkes LM, Tofts PS. Improved Accuracy of Human Cerebral Blood Perfusion Measurements Using Arterial Spin Labeling: Accounting for Capillary Water Permeability. *Magn Reson Med* (2002) 48:27–41. doi: 10.1002/mrm.10180
110. Chappell MA, MacIntosh BJ, Donahue MJ, Günther M, Jezzard P, Woolrich MW. Separation of Macrovascular Signal in Multi-Inversion Time Arterial Spin Labelling MRI. *Magn Reson Med* (2010) 63:1357–65. doi: 10.1002/mrm.22320
111. Chappell MA, Groves AR, MacIntosh BJ, Donahue MJ, Jezzard P. Woolrich MW. Partial Volume Correction of Multiple Inversion Time Arterial Spin Labeling MRI Data. *Magn Reson Med* (2011) 65:1173–83. doi: 10.1002/mrm.22641
112. Chappell MA, Woolrich MW, Kazan S, Jezzard P, Payne SJ, MacIntosh BJ. Modeling Dispersion in Arterial Spin Labeling: Validation Using Dynamic Angiographic Measurements. *Magn Reson Med* (2013) 69:563–70. doi: 10.1002/mrm.24260
113. Pinto J, Chappell MA, Okell TW, Mezue M, Segerdahl AR, Tracey I, et al. Calibration of Arterial Spin Labeling Data—Potential Pitfalls in Post-Processing. *Magn Reson Med* (2020) 83:1222–34. doi: 10.1002/mrm.28000
114. Baas KPA, Petr J, Kuijer JPA, Nederveen AJ, Mutsaerts HJMM, van de Ven KCC. Effects of Acquisition Parameter Modifications and Field Strength on the Reproducibility of Brain Perfusion Measurements Using Arterial Spin-Labeling. *Am J Neuroradiol* (2021) 42:109–15. doi: 10.3174/ajnr.A6856
115. Almeida JRC, Greenberg T, Lu H, Chase HW, Fournier J, Cooper CM, et al. Test-Retest Reliability of Cerebral Blood Flow in Healthy Individuals Using Arterial Spin Labeling: Findings From the EMBARC Study. *Magn Reson Imaging* (2018) 45:26–33. doi: 10.1016/j.mri.2017.09.004
116. Mezue M, Segerdahl AR, Okell TW, Chappell MA, Kelly ME, Tracey I. Optimization and Reliability of Multiple Postlabeling Delay Pseudo-Continuous Arterial Spin Labeling During Rest and Stimulus-Induced Functional Task Activation. *J Cereb Blood Flow Metab* (2014) 34:1919–27. doi: 10.1038/jcbfm.2014.163
117. Sousa I, Vilela P, Figueiredo P. Reproducibility of the Quantification of Arterial and Tissue Contributions in Multiple Postlabeling Delay Arterial Spin Labeling. *J Magn Reson Imaging* (2014) 40:1453–62. doi: 10.1002/jmri.24493
118. Mutsaerts HJMM, van Osch MJP, Zelaya FO, Wang DJJ, Nordhøy W, Wang Y, et al. Multi-Vendor Reliability of Arterial Spin Labeling Perfusion MRI Using a Near-Identical Sequence: Implications for Multi-Center Studies. *Neuroimage* (2015) 113:143–52. doi: 10.1016/j.neuroimage.2015.03.043
119. Wang L, Wei L, Wang J, Li N, Gao Y, Ma H, et al. Evaluation of Perfusion MRI Value for Tumor Progression Assessment After Glioma Radiotherapy. *Med (Baltimore)* (2020) 99:e23766. doi: 10.1097/MD.0000000000023766
120. Wang YL, Chen S, Xiao HF, Li Y, Wang Y, Liu G, et al. Differentiation Between Radiation-Induced Brain Injury and Glioma Recurrence Using 3D pCASL and Dynamic Susceptibility Contrast-Enhanced Perfusion-Weighted Imaging. *Radiother Oncol* (2018) 129:68–74. doi: 10.1016/j.radonc.2018.01.009
121. Razek KAAA, El-Serougy L, Abdelsalam M, Gaballa G, Talaat M. Differentiation of Residual/Recurrent Gliomas From Postradiation Necrosis With Arterial Spin Labeling and Diffusion Tensor Magnetic Resonance Imaging-Derived Metrics. *Neuroradiology* (2018) 60:169–77. doi: 10.1007/s00234-017-1955-3
122. Pellerin A, Khalifé M, Sanson M, Rozenblum-Beddok L, Bertaux M, Soret M, et al. Simultaneously Acquired PET and ASL Imaging Biomarkers may be Helpful in Differentiating Progression From Pseudoprogression in Treated Gliomas. *Eur Radiol* (2021) 2021:1–11. doi: 10.1007/S00330-021-07732-0
123. Zhang H, Schneider T, Wheeler-Kingshott CA, Alexander DC. NODDI: Practical *In Vivo* Neurite Orientation Dispersion and Density Imaging of the Human Brain. *Neuroimage* (2012) 61:1000–16. doi: 10.1016/j.neuroimage.2012.03.072
124. White NS, Leergaard TB, D'Arceuil H, Bjaalie JG, Dale AM. Probing Tissue Microstructure With Restriction Spectrum Imaging: Histological and Theoretical Validation. *Hum Brain Mapp* (2013) 34:327–46. doi: 10.1002/hbm.21454
125. Pasternak O, Sochen N, Gur Y, Intrator N, Assaf Y. Free Water Elimination and Mapping From Diffusion MRI. *Magn Reson Med* (2009) 62:717–30. doi: 10.1002/mrm.22055
126. Panagiotaki E, Walker-Samuel S, Siow B, Johnson SP, Rajkumar V, Pedley RB, et al. Noninvasive Quantification of Solid Tumor Microstructure Using VERDICT MRI. *Cancer Res* (2014) 74:1902–12. doi: 10.1158/0008-5472.CAN-13-2511
127. Stejskal EO, Tanner JE. Spin Diffusion Measurements: Spin Echoes in the Presence of a Time-Dependent Field Gradient. *J Chem Phys* (1965) 42:288–92. doi: 10.1063/1.1695690
128. Moseley ME, Cohen Y, Kucharczyk J, Mintorovitch J, Asgari HS, Wendland MF, et al. Diffusion-Weighted MR Imaging of Anisotropic Water Diffusion in Cat Central Nervous System. *Radiology* (1990) 176:439–45. doi: 10.1148/radiology.176.2.2367658
129. Le Bihan D, Breton E, Lallemand D, Grenier P, Cabanis E, Laval-Jeantet M. MR Imaging of Intravoxel Incoherent Motions: Application to Diffusion and Perfusion in Neurologic Disorders. *Radiology* (1986) 161:401–7. doi: 10.1148/radiology.161.2.3763909
130. Alexander AL, Lee JE, Lazar M, Field AS. Diffusion Tensor Imaging of the Brain. *Neurotherapeutics* (2007) 4:316–29. doi: 10.1016/j.nurt.2007.05.011
131. Jensen JH, Helpern JA, Ramani A, Lu H, Kaczynski K. Diffusional Kurtosis Imaging: The Quantification of Non-Gaussian Water Diffusion by Means of Magnetic Resonance Imaging. *Magn Reson Med* (2005) 53:1432–40. doi: 10.1002/mrm.20508
132. Maiter A, Riemer F, Allinson K, Zaccagna F, Crispin-Ortuzar M, Gehrung M, et al. Investigating the Relationship Between Diffusion Kurtosis Tensor Imaging (DKTI) and Histology Within the Normal Human Brain. *Sci Rep* (2021) 11:8857. doi: 10.1038/s41598-021-87857-w
133. Raab P, Hattingen E, Franz K, Zanella FE, Lanfermann H. Cerebral Gliomas: Diffusional Kurtosis Imaging Analysis of Microstructural Differences. *Radiology* (2010) 254:876–81. doi: 10.1148/radiol.09090819
134. Gong S, Zhang F, Norton I, Essayed WI, Unadkat P, Rigolo L, et al. Free Water Modeling of Peritumoral Edema Using Multi-Fiber Tractography: Application to Tracking the Arcuate Fasciculus for Neurosurgical Planning. *PloS One* (2018) 13:e0197056. doi: 10.1371/journal.pone.0197056
135. Khan UA, Rennert RC, White NS, Bartsch H, Farid N, Dale AM, et al. Diagnostic Utility of Restriction Spectrum Imaging (RSI) in Glioblastoma Patients After Concurrent Radiation-Temozolomide Treatment: A Pilot Study. *J Clin Neurosci* (2018) 58:136–41. doi: 10.1016/j.jocn.2018.09.008
136. Conturo TE, McKinstry RC, Akbudak E, Robinson BH. Encoding of Anisotropic Diffusion With Tetrahedral Gradients: A General Mathematical Diffusion Formalism and Experimental Results. *Magn Reson Med* (1996) 35:399–412. doi: 10.1002/mrm.1910350319
137. Mansfield P. Multi-Planar Image Formation Using NMR Spin Echoes. *J Phys C Solid State Phys* (1977) 10:L55–8. doi: 10.1088/0022-3719/10/3/004
138. Aquino D, Gioppo A, Finocchiaro G, Bruzzone MG, Cuccarini V. MRI in Glioma Immunotherapy: Evidence, Pitfalls, and Perspectives. *J Immunol Res* (2017) 2017::5813951. doi: 10.1155/2017/5813951
139. Basser PJ, Mattiello J, LeBihan D. MR Diffusion Tensor Spectroscopy and Imaging. *Biophys J* (1994) 66:259–67. doi: 10.1016/S0006-3495(94)80775-1
140. Hrabe J, Kaur G, Guilfoyle D. Principles and Limitations of NMR Diffusion Measurements. *J Med Phys* (2007) 32:34–42. doi: 10.4103/0971-6203.31148
141. Sundgren PC, Fan X, Weybright P, Welsh RC, Carlos RC, Petrou M, et al. Differentiation of Recurrent Brain Tumor Versus Radiation Injury Using Diffusion Tensor Imaging in Patients With New Contrast-Enhancing Lesions. *Magn Reson Imaging* (2006) 24:1131–4. doi: 10.1016/j.mri.2006.07.008
142. Shiroishi MS, Boxerman JL, Pope WB. Physiologic MRI for Assessment of Response to Therapy and Prognosis in Glioblastoma. *Neuro Oncol* (2016) 18:467–78. doi: 10.1093/neuonc/nov179
143. Nakamura H, Murakami R, Hirai T, Kitajima M, Yamashita Y. Can MRI-Derived Factors Predict the Survival in Glioblastoma Patients Treated With Postoperative Chemoradiation Therapy? *Acta Radiol* (2013) 54:214–20. doi: 10.1258/ar.2012.120525
144. Saraswathy S, Crawford FW, Lamborn KR, Pirzkall A, Chang S, Cha S, et al. Evaluation of MR Markers That Predict Survival in Patients With Newly Diagnosed GBM Prior to Adjuvant Therapy. *J Neurooncol* (2009) 91:69–81. doi: 10.1007/s11060-008-9685-3

145. Moffat BA, Chenevert TL, Lawrence TS, Meyer CR, Johnson TD, Dong Q, et al. Functional Diffusion Map: A Noninvasive MRI Biomarker for Early Stratification of Clinical Brain Tumor Response. *Proc Natl Acad Sci* (2005) 102:5524–9. doi: 10.1073/pnas.0501532102
146. Østergaard L, Sorensen AG, Kwong KK, Weisskoff RM, Gyldensted C, Rosen BR. High Resolution Measurement of Cerebral Blood Flow Using Intravascular Tracer Bolus Passages. Part II: Experimental Comparison and Preliminary Results. *Magn Reson Med* (1996) 36. doi: 10.1002/mrm.1910360511
147. Vrabec M, Van Cauter S, Himmelreich U, Van Gool SW, Sunaert S, De Vleeschouwer S, et al. MR Perfusion and Diffusion Imaging in the Follow-Up of Recurrent Glioblastoma Treated With Dendritic Cell Immunotherapy: A Pilot Study. *Neuroradiology* (2011) 53:721–3. doi: 10.1007/s00234-010-0802-6
148. Song J, Kadaba P, Kravitz A, Hormigo A, Friedman J, Belani P, et al. Multiparametric MRI for Early Identification of Therapeutic Response in Recurrent Glioblastoma Treated With Immune Checkpoint Inhibitors. *Neuro Oncol* (2020) 22:1658–66. doi: 10.1093/neuonc/noaa066
149. Lupo JM. Diffusion MRI as an Early Marker of Response to Immune Checkpoint Inhibitors. *Neuro Oncol* (2020) 22:1557–8. doi: 10.1093/neuonc/noaa224
150. Schmainda KM. Diffusion-Weighted MRI as a Biomarker for Treatment Response in Glioma. *CNS Oncol* (2012) 1:169–80. doi: 10.2217/cns.12.25
151. Chu HH, Choi SH, Ryoo I, Kim SC, Yeom JA, Shin H, et al. Differentiation of True Progression From Pseudoprogression in Glioblastoma Treated With Radiation Therapy and Concomitant Temozolomide: Comparison Study of Standard and High- *B* -Value Diffusion-Weighted Imaging. *Radiology* (2013) 269:831–40. doi: 10.1148/radiol.13122024
152. Bulik M, Kazda T, Slampa P, Jancalek R. The Diagnostic Ability of Follow-Up Imaging Biomarkers After Treatment of Glioblastoma in the Temozolomide Era: Implications From Proton MR Spectroscopy and Apparent Diffusion Coefficient Mapping. *BioMed Res Int* (2015) 2015:641023. doi: 10.1155/2015/641023
153. Kazda T, Bulik M, Pospisil P, Lakomy R, Smrcka M, Slampa P, et al. Advanced MRI Increases the Diagnostic Accuracy of Recurrent Glioblastoma: Single Institution Thresholds and Validation of MR Spectroscopy and Diffusion Weighted MR Imaging. *NeuroImage Clin* (2016) 11:316–21. doi: 10.1016/j.nicl.2016.02.016
154. Yu Y, Ma Y, Sun M, Jiang W, Yuan T, Tong D. Meta-Analysis of the Diagnostic Performance of Diffusion Magnetic Resonance Imaging With Apparent Diffusion Coefficient Measurements for Differentiating Glioma Recurrence From Pseudoprogression. *Med (Baltimore)* (2020) 99:e20270. doi: 10.1097/MD.0000000000020270
155. Zhang H, Ma L, Shu C, Wang Y, Dong L. Diagnostic Accuracy of Diffusion MRI With Quantitative ADC Measurements in Differentiating Glioma Recurrence From Radiation Necrosis. *J Neurol Sci* (2015) 351:65–71. doi: 10.1016/j.jns.2015.02.038
156. van Dijken BRJ, van Laar PJ, Holtman GA, van der Hoorn A. Diagnostic Accuracy of Magnetic Resonance Imaging Techniques for Treatment Response Evaluation in Patients With High-Grade Glioma, a Systematic Review and Meta-Analysis. *Eur Radiol* (2017) 27:4129–44. doi: 10.1007/s00330-017-4789-9
157. Prager AJ, Martinez N, Beal K, Omuro A, Zhang Z, Young RJ. Diffusion and Perfusion MRI to Differentiate Treatment-Related Changes Including Pseudoprogression From Recurrent Tumors in High-Grade Gliomas With Histopathologic Evidence. *Am J Neuroradiol* (2015) 36:877–85. doi: 10.3174/ajnr.A4218
158. Khalifa J, Tensaouti F, Lotterie JA, Catalaa I, Chaltiel L, Benouaich-Amiel A, et al. Do Perfusion and Diffusion MRI Predict Glioblastoma Relapse Sites Following Chemoradiation? *J Neurooncol* (2016) 130:181–92. doi: 10.1007/s11060-016-2232-8
159. Zhang J, Yu H, Qian X, Liu K, Tan H, Yang T, et al. Pseudo Progression Identification of Glioblastoma With Dictionary Learning. *Comput Biol Med* (2016) 73:94–101. doi: 10.1016/j.compbiomed.2016.03.027
160. Galbán CJ, Chenevert TL, Meyer CR, Tsien C, Lawrence TS, Hamstra DA, et al. The Parametric Response Map is an Imaging Biomarker for Early Cancer Treatment Outcome. *Nat Med* (2009) 15:572–6. doi: 10.1038/nm.1919
161. Kashimura H, Inoue T, Beppu T, Ogasawara K, Ogawa A. Diffusion Tensor Imaging for Differentiation of Recurrent Brain Tumor and Radiation Necrosis After Radiotherapy—Three Case Reports. *Clin Neurol Neurosurg* (2007) 109:106–10. doi: 10.1016/j.clineuro.2006.04.005
162. Wang S, Martinez-Lage M, Sakai Y, Chawla S, Kim SG, Alonso-Basanta M, et al. Differentiating Tumor Progression From Pseudoprogression in Patients With Glioblastomas Using Diffusion Tensor Imaging and Dynamic Susceptibility Contrast MRI. *Am J Neuroradiol* (2016) 37:28–36. doi: 10.3174/ajnr.A4474
163. Qian X, Tan H, Zhang J, Zhao W, Chan MD, Zhou X. Stratification of Pseudoprogression and True Progression of Glioblastoma Multiform Based on Longitudinal Diffusion Tensor Imaging Without Segmentation. *Med Phys* (2016) 43:5889. doi: 10.1118/1.4963812
164. Hamstra DA, Chenevert TL, Moffat BA, Johnson TD, Meyer CR, Mukherji SK, et al. Evaluation of the Functional Diffusion Map as an Early Biomarker of Time-to-Progression and Overall Survival in High-Grade Glioma. *Proc Natl Acad Sci* (2005) 102:16759–64. doi: 10.1073/pnas.0508347102
165. Moffat BA, Chenevert TL, Meyer CR, Mckeever PE, Hall DE, Hoff BA, et al. The Functional Diffusion Map: An Imaging Biomarker for the Early Prediction of Cancer Treatment Outcome. *Neoplasia* (2006) 8:259–67. doi: 10.1593/neo.05844
166. Ellingson BM, Malkin MG, Rand SD, LaViolette PS, Connelly JM, Mueller WM, et al. Volumetric Analysis of Functional Diffusion Maps is a Predictive Imaging Biomarker for Cytotoxic and Anti-Angiogenic Treatments in Malignant Gliomas. *J Neurooncol* (2011) 102:95–103. doi: 10.1007/s11060-010-0293-7
167. Kelly PJ, Daumas-Duport C, Kispert DB, Kall BA, Scheithauer BW, Illig JJ. Imaging-Based Stereotaxic Serial Biopsies in Untreated Intracranial Glial Neoplasms. *J Neurosurg* (1987) 66:865–74. doi: 10.3171/jns.1987.66.6.0865
168. Chenevert TL, Malyarenko DI, Galbán CJ, Gomez-Hassan DM, Sundgren PC, Tsien CI, et al. Comparison of Voxel-Wise and Histogram Analyses of Glioma ADC Maps for Prediction of Early Therapeutic Change. *Tomogr (Ann Arbor Mich)* (2019) 5:7–14. doi: 10.18383/j.tom.2018.00049
169. Reimer C, Deike K, Graf M, Reimer P, Wiestler B, Omar Floca R, et al. Differentiation of Pseudoprogression and Real Progression in Glioblastoma Using ADC Parametric Response Maps. *PloS One* (2017) 12:e0174620. doi: 10.1371/journal.pone.0174620
170. Yoon RG, Kim HS, Kim DY, Hong GS, Kim SJ. Apparent Diffusion Coefficient Parametric Response Mapping MRI for Follow-Up of Glioblastoma. *Eur Radiol* (2016) 26:1037–47. doi: 10.1007/s00330-015-3896-8
171. Macdonald DR, Cascino TL, Schold SC, Cairncross JG. Response Criteria for Phase II Studies of Supratentorial Malignant Glioma. *J Clin Oncol* (1990) 8:1277–80. doi: 10.1200/JCO.1990.8.7.1277
172. Chenevert TL, Ross BD. Diffusion Imaging for Therapy Response Assessment of Brain Tumor. *Neuroimaging Clin N Am* (2009) 19:559–71. doi: 10.1016/j.nic.2009.08.009
173. Bacchi S, Zerner T, Dongas J, Asahina AT, Abou-Hamden A, Otto S, et al. Deep Learning in the Detection of High-Grade Glioma Recurrence Using Multiple MRI Sequences: A Pilot Study. *J Clin Neurosci* (2019) 70:11–3. doi: 10.1016/j.jocn.2019.10.003
174. Chang PD, Chow DS, Yang PH, Filippi CG, Lignelli A. Predicting Glioblastoma Recurrence by Early Changes in the Apparent Diffusion Coefficient Value and Signal Intensity on FLAIR Images. *Am J Roentgenol* (2017) 208:57–65. doi: 10.2214/AJR.16.16234
175. Yoon RG, Kim HS, Koh MJ, Shim WH, Jung SC, Kim SJ, et al. Differentiation of Recurrent Glioblastoma From Delayed Radiation Necrosis by Using Voxel-Based Multiparametric Analysis of MR Imaging Data. *Radiology* (2017) 285:206–13. doi: 10.1148/radiol.2017161588
176. Liu Z-C, Yan L-F, Hu Y-C, Sun Y-Z, Tian Q, Nan H-Y, et al. Combination of IVIM-DWI and 3D-ASL for Differentiating True Progression From Pseudoprogression of Glioblastoma Multiforme After Concurrent Chemoradiotherapy: Study Protocol of a Prospective Diagnostic Trial. *BMC Med Imaging* (2017) 17:10. doi: 10.1186/s12880-017-0183-y
177. Shin KE, Ahn KJ, Choi HS, Jung SL, Kim BS, Jeon SS, et al. DCE and DSC MR Perfusion Imaging in the Differentiation of Recurrent Tumour From Treatment-Related Changes in Patients With Glioma. *Clin Radiol* (2014) 69:e264–72. doi: 10.1016/j.crad.2014.01.016
178. Le Bihan D. What can We See With IVIM MRI? *Neuroimage* (2019) 187:56–67. doi: 10.1016/j.neuroimage.2017.12.062

179. Keil VC, Mädler B, Gielen GH, Pintea B, Hiththetiya K, Gaspranova AR, et al. Intravoxel Incoherent Motion MRI in the Brain: Impact of the Fitting Model on Perfusion Fraction and Lesion Differentiability. *J Magn Reson Imaging* (2017) 46:1187–99. doi: 10.1002/jmri.25615
180. Conklin J, Heyn C, Roux M, Cerny M, Wintermark M. Federau C. A Simplified Model for Intravoxel Incoherent Motion Perfusion Imaging of the Brain. *Am J Neuroradiol* (2016) 37:2251–7. doi: 10.3174/ajnr.A4929
181. Jabehdar Maralani P, Myrehaug S, Mehrabian H, Chan AKM, Wintermark M, Heyn C, et al. Intravoxel Incoherent Motion (IVIM) Modeling of Diffusion MRI During Chemoradiation Predicts Therapeutic Response in IDH Wildtype Glioblastoma. *Radiother Oncol* (2021) 156:258–65. doi: 10.1016/j.radonc.2020.12.037
182. Kim HS, Suh CH, Kim N, Choi CG, Kim SJ. Histogram Analysis of Intravoxel Incoherent Motion for Differentiating Recurrent Tumor From Treatment Effect in Patients With Glioblastoma: Initial Clinical Experience. *Am J Neuroradiol* (2014) 35:490–7. doi: 10.3174/ajnr.A3719
183. D'Amore F, Grinberg F, Mauler J, Galldiks N, Blazhenets G, Farrher E, et al. Combined 18f-FET PET and Diffusion Kurtosis MRI in Posttreatment Glioblastoma: Differentiation of True Progression From Treatment-Related Changes. *Neuro Oncol Adv* (2021) 3:vdab044. doi: 10.1093/noajnl/vdab044
184. Wu XF, Liang X, Wang XC, Qin JB, Zhang L, Tan Y, et al. Differentiating High-Grade Glioma Recurrence From Pseudoprogression: Comparing Diffusion Kurtosis Imaging and Diffusion Tensor Imaging. *Eur J Radiol* (2021) 135:109445. doi: 10.1016/j.ejrad.2020.109445
185. Chakhoyan A, Woodworth DC, Harris RJ, Lai A, Nghiemphu PL, Liau LM, et al. Mono-Exponential, Diffusion Kurtosis and Stretched Exponential Diffusion MR Imaging Response to Chemoradiation in Newly Diagnosed Glioblastoma. *J Neurooncol* (2018) 139:651–9. doi: 10.1007/s11060-018-2910-9
186. Baek HJ, Kim HS, Kim N, Choi YJ, Kim YJ. Percent Change of Perfusion Skewness and Kurtosis: A Potential Imaging Biomarker for Early Treatment Response in Patients With Newly Diagnosed Glioblastomas. *Radiology* (2012) 264:834–43. doi: 10.1148/radiol.12112120
187. Wang X, Li F, Wang D, Zeng Q. Diffusion Kurtosis Imaging Combined With Molecular Markers as a Comprehensive Approach to Predict Overall Survival in Patients With Gliomas. *Eur J Radiol* (2020) 128:108985. doi: 10.1016/j.ejrad.2020.108985
188. Juan-Albarracín J, Fuster-Garcia E, García-Ferrando GA, García-Gómez JM. ONCOhabitats: A System for Glioblastoma Heterogeneity Assessment Through MRI. *Int J Med Inform* (2019) 128:53–61. doi: 10.1016/j.ijmedinf.2019.05.002
189. Hu Y-C, Yan L-F, Han Y, Duan S-J, Sun Q, Li G-F, et al. Can the Low and High B-Value Distribution Influence the Pseudodiffusion Parameter Derived From IVIM DWI in Normal Brain? *BMC Med Imaging* (2020) 20:14. doi: 10.1186/s12880-020-0419-0
190. Niendorf T, Dijkhuizen RM, Norris DG, Van Lookeren Campagne M, Nicolay K. Biexponential Diffusion Attenuation in Various States of Brain Tissue: Implications for Diffusion-Weighted Imaging. *Magn Reson Med* (1996) 36:847–57. doi: 10.1002/mrm.1910360607
191. Xu J-L, Li Y-L, Lian J-M, Dou S, Yan F-S, Wu H, et al. Distinction Between Postoperative Recurrent Glioma and Radiation Injury Using MR Diffusion Tensor Imaging. *Neuroradiology* (2010) 52:1193–9. doi: 10.1007/s00234-010-0731-4
192. Alexiou GA, Zikou A, Tsiouris S, Goussia A, Kosta P, Papadopoulos A, et al. Comparison of Diffusion Tensor, Dynamic Susceptibility Contrast MRI and 99mtc-Tetrofosmin Brain SPECT for the Detection of Recurrent High-Grade Glioma. *Magn Reson Imaging* (2014) 32:854–9. doi: 10.1016/j.mri.2014.04.013
193. Agarwal A, Kumar S, Narang J, Schultz L, Mikkelsen T, Wang S, et al. Morphologic MRI Features, Diffusion Tensor Imaging and Radiation Dosimetric Analysis to Differentiate Pseudoprogression From Early Tumor Progression. *J Neurooncol* (2013) 112:413–20. doi: 10.1007/s11060-013-1070-1
194. Price SJ, Jena R, Burnet NG, Carpenter TA, Pickard JD, Gillard JH. Predicting Patterns of Glioma Recurrence Using Diffusion Tensor Imaging. *Eur Radiol* (2007) 17:1675–84. doi: 10.1007/s00330-006-0561-2
195. Panagiotaki E, Schneider T, Siow B, Hall MG, Lythgoe MF, Alexander DC. Compartment Models of the Diffusion MR Signal in Brain White Matter: A Taxonomy and Comparison. *Neuroimage* (2012) 59:2241–54. doi: 10.1016/j.neuroimage.2011.09.081
196. Roberts T, Hyare H, Hipwell B, Ianus A, Breen-norris J, Panagiotaki E, et al. Quantification of Tumour Microstructure in Low and High-Grade Brain Tumours Using VERDICT MRI: An Initial Feasibility Study. *Neuro Oncol* (2018) 20(Suppl. 1):i16. doi: 10.1093/neuonc/nox238.072
197. Roberts TA, Hyare H, Agliardi G, Hipwell B, d'Esposito A, Ianus A, et al. Noninvasive Diffusion Magnetic Resonance Imaging of Brain Tumour Cell Size for the Early Detection of Therapeutic Response. *Sci Rep* (2020) 10:9223. doi: 10.1038/s41598-020-65956-4
198. Zaccagna F, Riemer F, Priest AN, McLean MA, Allinson K, Grist JT, et al. Non-Invasive Assessment of Glioma Microstructure Using VERDICT MRI: Correlation With Histology. *Eur Radiol* (2019) 29:5559–66. doi: 10.1007/s00330-019-6011-8
199. Metz MC, Molina-Romero M, Lipkova J, Gempt J, Liesche-Starnecker F, Eichinger P, et al. Predicting Glioblastoma Recurrence From Preoperative MR Scans Using Fractional-Anisotropy Maps With Free-Water Suppression. *Cancers (Basel)* (2020) 12:728. doi: 10.3390/cancers12030728
200. McDonald CR, Delfanti RL, Krishnan AP, Leyden KM, Hattangadi-Gluth JA, Seibert TM, et al. Restriction Spectrum Imaging Predicts Response to Bevacizumab in Patients With High-Grade Glioma. *Neuro Oncol* (2016) 18:1579–90. doi: 10.1093/neuonc/now063
201. Farid N, Almeida-Freitas DB, White NS, McDonald CR, Muller KA, VandenBerg SR, et al. Restriction-Spectrum Imaging of Bevacizumab-Related Necrosis in a Patient With GBM. *Front Oncol* (2013) 3 SEP:258. doi: 10.3389/fonc.2013.00258
202. Latysheva A, Geier OM, Hope TR, Brunetti M, Micci F, Vik-Mo EO, et al. Diagnostic Utility of Restriction Spectrum Imaging in the Characterization of the Peritumoral Brain Zone in Glioblastoma: Analysis of Overall and Progression-Free Survival. *Eur J Radiol* (2020) 132:109289. doi: 10.1016/j.ejrad.2020.109289
203. Jin Y, Randall JW, Elhalawani H, Al Feghali KA, Elliott AM, Anderson BM, et al. Detection of Glioblastoma Subclinical Recurrence Using Serial Diffusion Tensor Imaging. *Cancers (Basel)* (2020) 12:568. doi: 10.3390/cancers12030568
204. Daghighi S, Bahrami N, Tom WJ, Coley N, Seibert TM, Hattangadi-Gluth JA, et al. Restriction Spectrum Imaging Differentiates True Tumor Progression From Immune-Mediated Pseudoprogression: Case Report of a Patient With Glioblastoma. *Front Oncol* (2020) 10:24. doi: 10.3389/fonc.2020.00024
205. Delgado AF, De Luca F, Hanagandi P, van Westen D, Delgado AF. Arterial Spin-Labeling in Children With Brain Tumor: A Meta-Analysis. *Am J Neuroradiol* (2018) 39:1536–42. doi: 10.3174/ajnr.A5727

Conflict of Interest: Author KS has ownership interest in IQ-AI Ltd and financial interest in Imaging Biometrics LLC. Author TB has participated in a speaker's bureau for AbbVie and Siemens Healthineers.

The remaining authors declare that the research was conducted in the absence of any commercial or financial relationships that could be construed as a potential conflict of interest.

Publisher's Note: All claims expressed in this article are solely those of the authors and do not necessarily represent those of their affiliated organizations, or those of the publisher, the editors and the reviewers. Any product that may be evaluated in this article, or claim that may be made by its manufacturer, is not guaranteed or endorsed by the publisher.

Copyright © 2022 Henriksen, del Mar Álvarez-Torres, Figueiredo, Hangel, Keil, Nechifor, Riemer, Schmainda, Warnert, Wiegers, and Booth. This is an open-access article distributed under the terms of the Creative Commons Attribution License (CC BY). The use, distribution or reproduction in other forums is permitted, provided the original author(s) and the copyright owner(s) are credited and that the original publication in this journal is cited, in accordance with accepted academic practice. No use, distribution or reproduction is permitted which does not comply with these terms.

frontiers in Oncology

CASE REPORT
published: 10 March 2022
doi: 10.3389/fonc.2022.858939

Case Report: ALK-Positive Histiocytosis With *KIF5B-ALK* Fusion in Cerebrum-Disseminated Lesions in a Child

Yi Guo[1,2], *Hai-bo Qu*[1,2], *Gang Ning*[1,2], *Feng-lin Jia*[1,2], *Hong Liu*[3], *Xin-mao Ma*[1,2] *and Yi Liao*[1,2*]

[1] Department of Radiology, West China Second University Hospital, Sichuan University, Chengdu, China, [2] Key Laboratory of Birth Defects and Related Diseases of Women and Children (Sichuan University), Ministry of Education, Chengdu, China, [3] Department of Integrated Traditional and Western Medicine, Center of Hemorrhoid and Fistula, West China Hospital of Sichuan University, Chengdu, China

OPEN ACCESS

Edited by:
Nico Sollmann, University of California, San Francisco, United States

Reviewed by:
Giorgio Inghirami, Cornell University, United States

***Correspondence:**
Yi Liao
connie0064@126.com

Specialty section:
This article was submitted to Neuro-Oncology and Neurosurgical Oncology, a section of the journal Frontiers in Oncology

Received: *20 January 2022*
Accepted: *11 February 2022*
Published: *10 March 2022*

Citation:
Guo Y, Qu H-b, Ning G, Jia F-l, Liu H, Ma X-m and Liao Y (2022) Case Report: ALK-Positive Histiocytosis With KIF5B-ALK Fusion in Cerebrum-Disseminated Lesions in a Child. Front. Oncol. 12:858939. doi: 10.3389/fonc.2022.858939

Background: Anaplastic lymphoma kinase (ALK)-positive histiocytosis is a rare type of histiocytosis that could affect multiple systems in children and adults. 10 cases of ALK-positive histiocytosis invading the central nervous system (CNS) have been reported. Herein, we report a case of ALK-positive histiocytosis invading the central nervous system and lungs and the details of follow-up of tumor dynamic changes during treatment.

Case Presentation: An 18-month-old boy was underweight and had slow growth of almost 3 months duration. The child could not stand and walk independently, and his language and intelligence development occurred later than those of his peers. Cranial magnetic resonance imaging revealed a giant suprasellar lesion with isosignal, measuring approximately 5.1× 3.6× 4.0 cm on T1-weighted imaging, with an obvious mass effect. Nodular, slightly low-signal shadows were also observed in the left temporal pole and left hippocampus, measuring approximately 1.0 cm × 0.7 cm× 0.5 cm and 0.9 cm× 0.8 cm × 0.5 cm on T1-weighted, respectively. The child underwent partial resection of the suprasellar lesion, and a diagnosis of ALK-positive histiocytosis was made histologically. Subsequently, the patient received chemotherapy (CHOP regimen) and anti-ALK therapy (crizotinib). The lesions were gradually shrinking without dissemination and the changes of intracranial and lung lesions were monitored with imaging during therapy. Unfortunately, the child died 8 months after the first surgery because of worsening intracranial infection.

Conclusion: ALK-positive histiocytosis may involve the central nervous system and disseminate intracranially. ALK-positive histiocytosis should be considered for the differential diagnosis of suprasellar lesions.

Keywords: ALK-positive histiocytosis, child, MRI, CT, brain, lung

INTRODUCTION

Anaplastic lymphoma kinase (ALK)-positive histiocytosis, which harbors a chromosomal translocation involving ALK at chromosome 2p23 (1), is a rare entity that can affect multiple systems, including the liver, spleen, digestive tract, bone marrow, skin, breast, and central nervous system (CNS) (2–5). ALK-positive histiocytosis can occur in both children and adults, while pediatric cases are more likely to have a disseminated disease that primarily affects the liver, spleen, or bone marrow (3). In adolescent patients, several symptoms can occur, including pallor, hepatosplenomegaly, thrombocytopenia, and anemia. When invading the CNS, ALK-positive histiocytosis can cause headache, vomiting, and seizures. According to a literature review of PubMed using keyword of ALK-positive histiocytosis, 10 cases of ALK-positive histiocytosis invading the CNS have been reported, and lesions located in the frontal lobe are more commonly reported (1, 3–7). Once the diagnosis of ALK-positive histiocytosis has been established, chemotherapy and anti-ALK therapy are generally applied. However, our review of the literature did not identify reports of imaging changes during treatment. Here, we report a rare case of intracranial disseminated ALK-positive histiocytosis in a child, mainly located in the suprasellar area, and discuss in detail the radiographic morphological changes occurring during chemotherapy and anti-ALK therapy.

CASE DESCRIPTION

An 18-month-old boy was underweight and had slow growth lasting for almost 3 months. On admission, the child's height and weight were 0.74 m and 8.0 kg, respectively (body mass index = 14.6 kg/m^2). No weight or height was gained despite increased feeding. The child could not stand and walk independently, and his language and intelligence development occurred later than do those of his peers. The boy was born in a natural birth and lived in Chengdu, Sichuan, China. He did not have any family history of congenital, allergic, or systemic diseases.

DIAGNOSIS, INTERVENTION, AND OUTCOME

Clinical Examination

Alpha-fetoprotein (AFP) and beta-human chorionic gonadotropin (β-hCG) levels were negative. Other examinations were unremarkable.

Imaging of Magnetic Resonance Imaging (MRI) and Computed Tomography (CT)

T1-weighted cranial MRI (PHILIPS INGENIA 3.0T) revealed a giant suprasellar lesion with isosignal protruding toward the third ventricle and measuring approximately 5.1cm × 3.6 cm× 4.0 cm, with an obvious mass effect. The structures adjacent to the lesion, including the pituitary stalk, optic chiasm, and midbrain were significantly compressed. Bilateral lateral ventricular dilatation with significant hydrocephalus was also present. Two nodular, slightly low-signal shadows were observed in the left temporal pole and the left hippocampus, respectively, measuring approximately 1.0cm × 0.7cm × 0.5 cm and 0.9cm × 0.8cm × 0.5 cm, respectively (**Figures 1A–E**). All these lesions showed slightly high signal intensity on T2-weighted images and significantly high signal intensity on fluid-attenuated inversion recovery images (aka FLAIR) (**Figures 1F–I**). The supra-sellar nidus showed mild peripheral edema on T2-weighted MRI. The supra-sellar nidus also showed significant heterogeneous and compressed Willis rings on contrast-enhanced T1-weighted MRI. The left-temporal-pole lesion showed significant circumferential enhancement with low signal centrally, while the left hippocampal lesion showed significant enhancement on contrast-enhanced T1-weighted MRI (**Figures 1J–N**). All these lesions showed slightly higher signal on diffusion-weighted imaging and had a diminished apparent diffusion coefficient (**Figures 1O–T**).

Chest CT (Neusoft, NeuViz128) showed multiple nodules in the lungs (8–9 lesions in the left lung and 9–10 lesions in the right). The largest was located in the anterior segment of the upper lobe of the right lung and measured approximately 1.0 cm× 0.9 cm (**Figures 3A–F**). There were no enlarged lymph nodes in the hilum or mediastinum after enhancement. Abdominal CT showed an enlarged liver and a slightly enlarged spleen, but no abnormal density or foci of enhancement were observed.

The changes in the intracranial lesions observed on MRI (PHILIPS ACHIEVA 1.5T) during chemotherapy and anti-ALK therapy are shown in **Figures 2 1A-L**. To quantify the changes in lesions, we calculated the volume as maximum height × maximum length × maximum width × π/6. The volume changes of the three lesions in the cerebrum are shown in **Figure 2-2A**. Although the tumors increased in size at the beginning of treatment, they gradually decreased with further treatment. The changes in the pulmonary lesions during treatment are shown in **Figures 2-2B**. As the treatment progressed, the tumor size in the lungs decreased significantly and seemed to show better efficacy than did the lesions in the cerebrum (**Figures 3G–X**).

Histology

The histiocytes were mostly epithelioid, partly round or foamy, with abundant cytoplasm, and had a low nucleoplasm ratio. Proliferative lesions with lymphocytic infiltration and scattered glial cells were observed in the tissue cells. Immunohistochemical analysis confirmed the histiocytic nature of the lesional cells, which were positive for CD68/PGM-1, CD20 (small subset), CD3 (subset), CD163, CD30, ALK-1, CD4, and Cyclin D1 and negative for S100, CD1a, p53, CD34, CD99, TdT, CXCL13, EGFR, SSTR2, SALL4, PLAP, and Langerin. The Ki-67 proliferation index was 5%. ALK1 expression was positive, and next-generation sequencing analysis revealed a KIF5B (exon 24)-ALK (exon 20) fusion. Finally, the patient was diagnosed with ALK-positive histiocytosis.

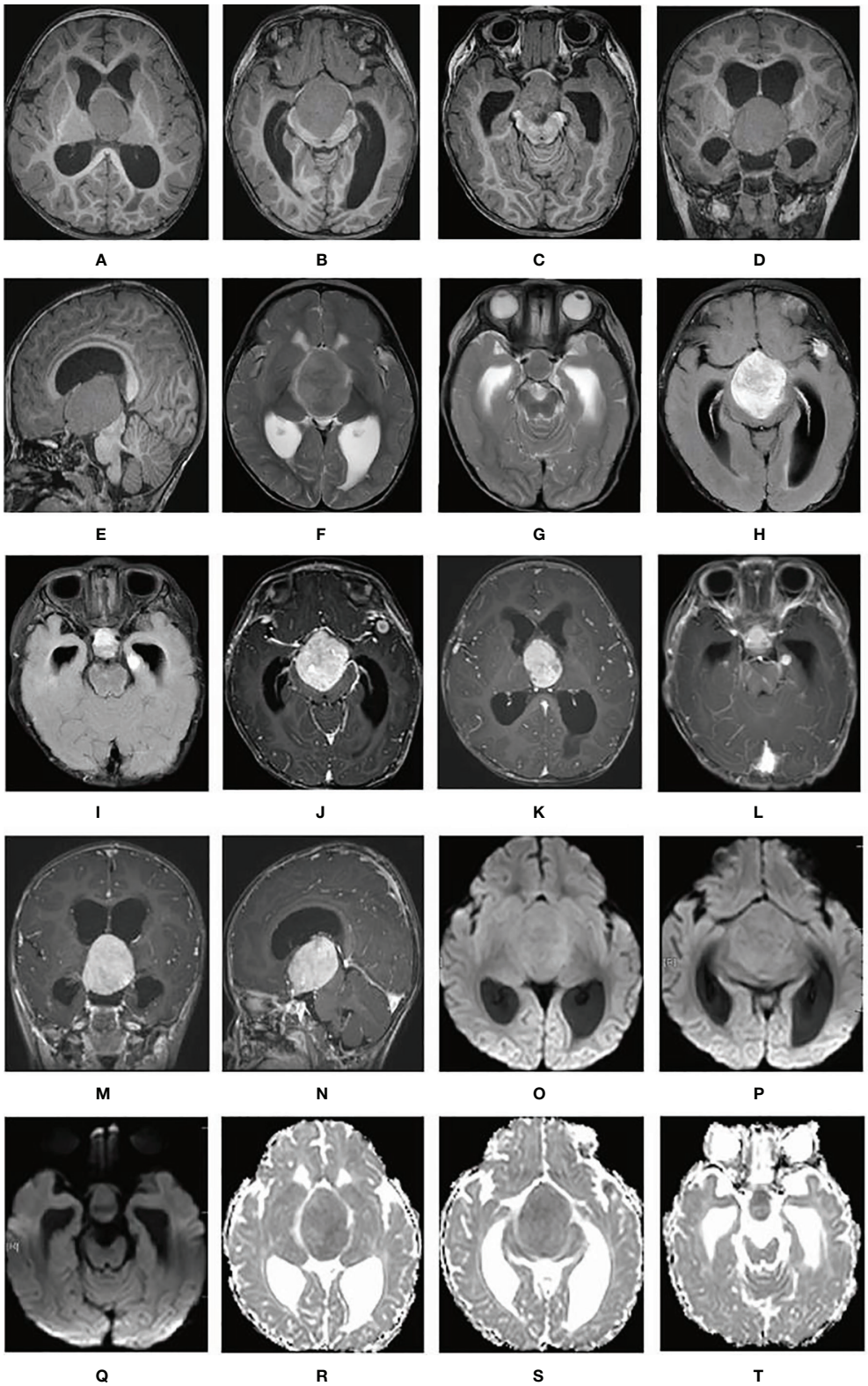

FIGURE 1 | Cerebral lesions are seen on MRI. **(A–E)** T1-weighted MRI; **(F, G)** T2-weighted MRI; **(H, I)** fluid-attenuated inversion recovery MRI; **(J–N)** contrast-enhanced T1-weighted MRI; **(O–Q)** diffusion-weighted imaging; and **(R–T)** apparent diffusion coefficient.

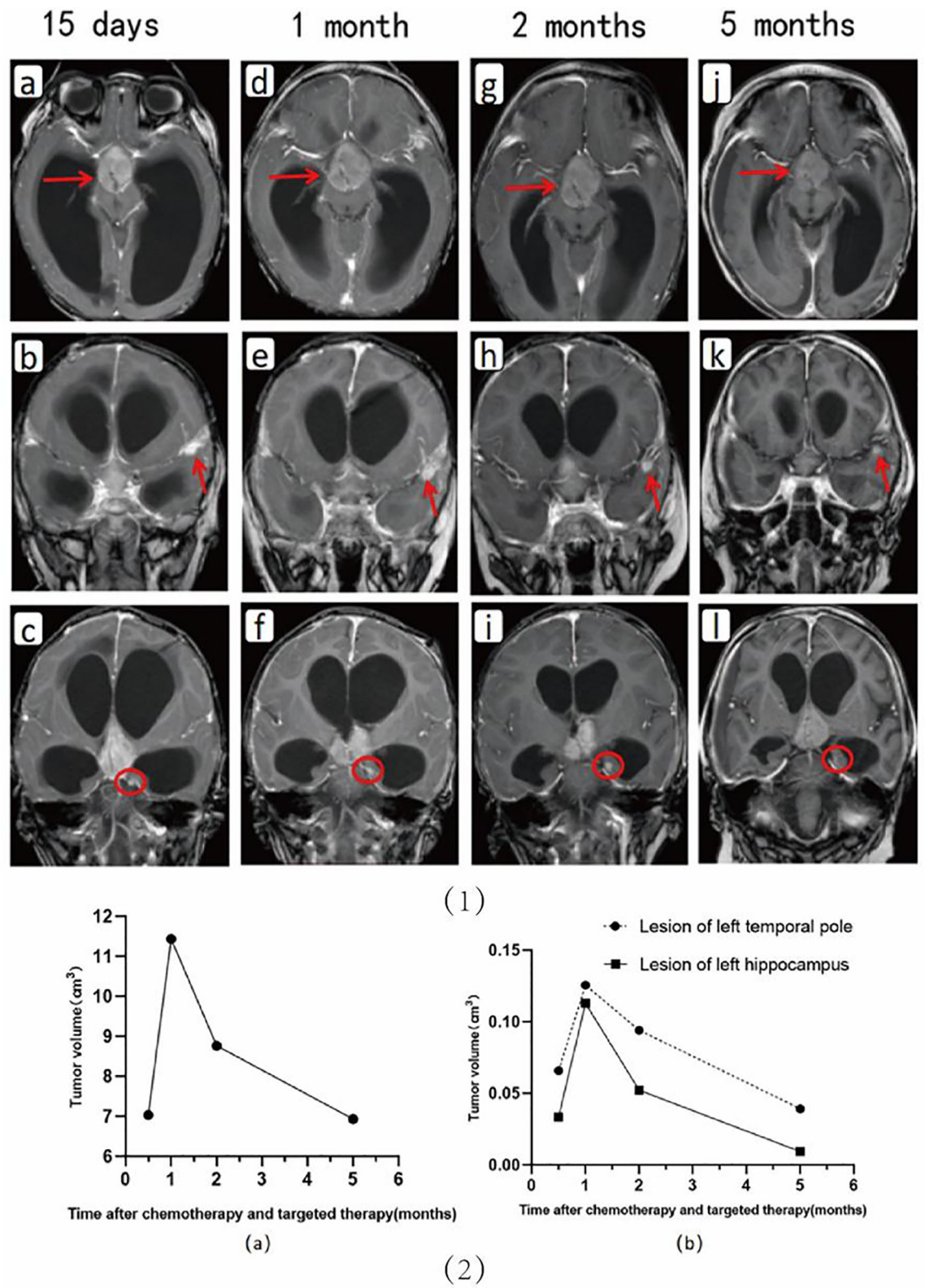

FIGURE 2 | Upper: Changes in the cerebral lesions are seen on imaging during chemotherapy and anti-ALK therapy. Shown are images at 15 days **(A–C)**, 1 month **(D–F)**, 2 months **(G–I),** and 5 months **(J–L)** after the start of drug therapy, respectively. Lower: Shown are the volumetric changes in the supra-sellar lesion **(A)** and in the lesions in the left temporal pole and hippocampus **(B)** during chemotherapy and targeted therapy.

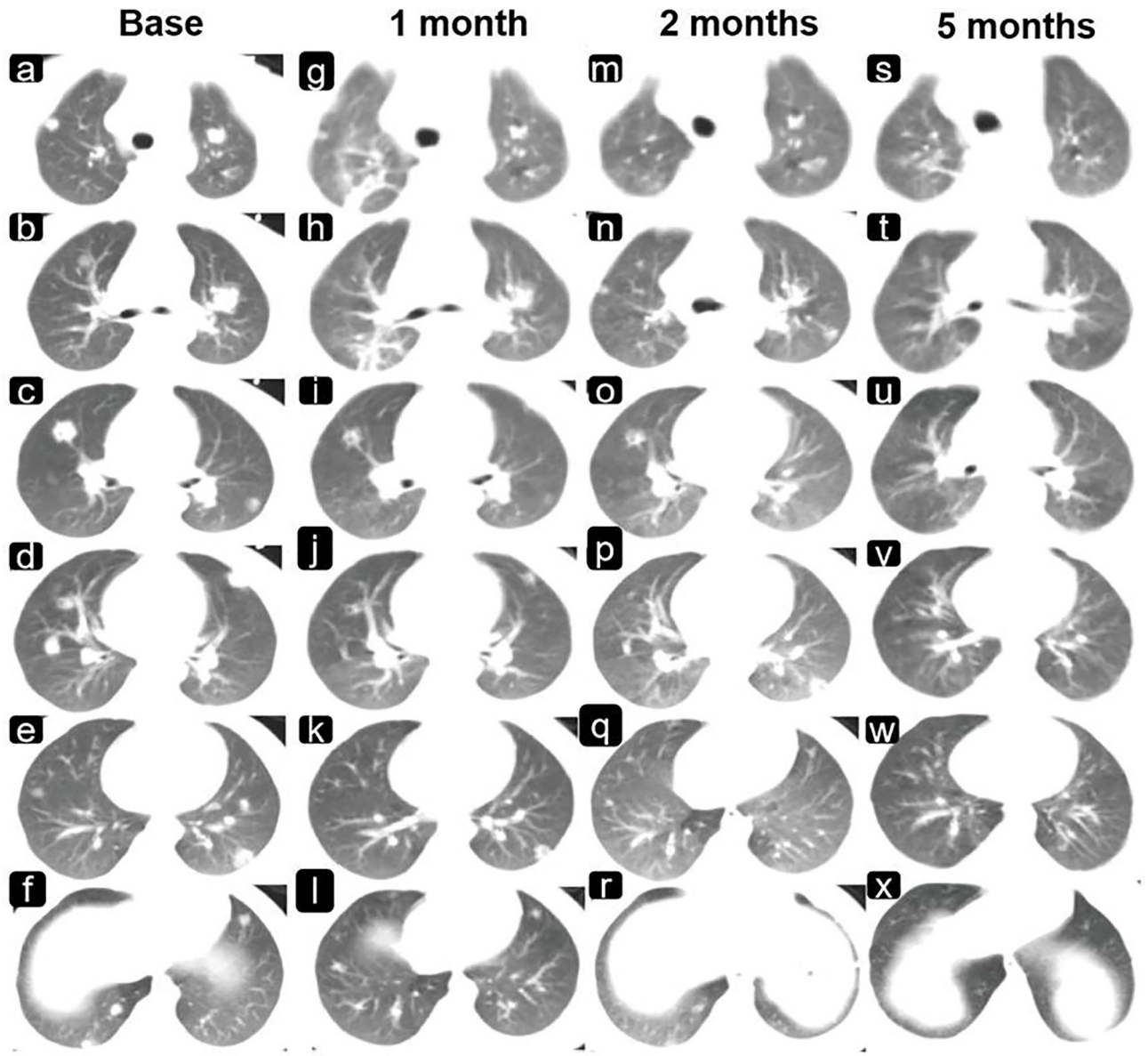

FIGURE 3 | Changes in the lung lesions are observed on imaging during chemotherapy and anti-ALK therapy. Shown are images of the lungs **(A–F)** before drug therapy and **(G–X)** after drug therapy (**G–L**, 1 month; **M–R**, 2 months; and **S–X**, 5 months).

Treatment

Subsequently, the child underwent partial resection of the suprasellar lesion to obtain a pathological biopsy. After surgery, the child developed hydrocephalus and intracranial infection and subsequently underwent right lateral ventricular borehole drainage and Omaya capsule placement, along with aggressive anti-infective therapy (ceftriaxone 400mg qd) and levetiracetam (100mg bid ivgtt) for seizure control. After 46 days, the child's condition stabilized, and he began to receive crizotinib (250mg qd po) for anti-ALK therapy and CHOP regimen (cyclophosphamide, doxorubicin, vincristine, prednisone) for chemotherapy. The patient received vincristine (0.35mg qiw ivgtt) and prednisone for induction chemotherapy for about 3 months. Subsequently, he received doxorubicin (15mg tiw ivgtt), vincristine (0.45-0.55mg qiw ivgtt), cyclophosphamide (100mg qd ivgtt) and prednisone for maintenance chemotherapy.

Intracranial infection of the child was progressively worsening. Cerebrospinal fluid culture was suggestive of *Bacillus cereus* 3 months later after the first surgery. Although the boy had received aggressive anti-infective treatment, including ceftriaxone, meropenem, and vancomycin combined with rifampin, along with external drainage of cerebrospinal fluid, the intracranial infection did not resolve completely.

Unfortunately, the child died 8 months after the first surgery because of worsening intracranial infection.

DISCUSSION

Histiocytoses are characterized by inflammation and accumulation derived from the monocyte and macrophage lineages, causing damage to various tissues (8). In recent years, ALK-positive histiocytosis, a rare type of histiocytosis, has occasionally been reported. Since Chan et al. reported the first case in 2008, almost 20 cases have been reported to date. Herein, we report a case of ALK-positive histiocytosis invading the respiratory and central nervous systems and report the results of dynamic and detailed follow-up of tumor changes. Despite poor prognosis of the child, the case is informative.

Although the prognosis of ALK-positive histiocytosis is generally good according to the literature, the child in this study died of intracranial infection despite receiving surgery, chemotherapy, anti-ALK, and anti-infective therapy. **Table 1** summarizes the literature reports of ALK-positive histiocytosis invading the CNS, and most patients benefited from regular therapy. Chang et al. reported a case of ALK-positive histiocytosis invading the CNS, intestine, and bone marrow (3). Although the boy received steroids and chemotherapy, he died of systemic disease. Usually, ALK-positive histiocytosis is a benign disease that can be controlled with regular therapy, including surgery, chemotherapy, and anti-ALK therapy. However, it is vital to be aware of possible complications during therapy, which could be a major cause of treatment failure.

AS ALK-positive histiocytosis can spread throughout the multiple systems, it can also disseminate intracranially. Qui et al. reported a Caucasian man with ALK-positive histiocytosis (1). The lesions of the patient were located in the left medial temporal lobe, right inferior frontal lobe and dural-based parasagittal right parietal convexity (1). Rossi et al. also reported a child with the same disease whose lesions were located in frontal and parietal lobes (7). It appears that disseminated growth is a characteristic of ALK-positive histiocytosis.

In the present case, it was necessary to differentiate ALK-positive histiocytosis from other types of histiocytosis. Classic Rosai–Dorfman disease (RDD) presents with massive bilateral, painless cervical lymphadenopathy with associated fever, weight loss, and night sweats (10). The average age at onset of RDD is approximately 20 years. Vaidya et al. has summarized 19 patients with RDD and find that lymphadenopathy is a common feature in imaging and bilateral uniformly enhancing cervical lymph node enlargement is the predominant abnormality on FDG-PET scans (11). Histologically, enlargement of the node with extensive sinusoidal expansion visible under low magnification is characteristic of RDD (12). Cells with abundant wispy cytoplasm and emperipolesis can be seen, alone or mixed with inflammatory cells, including lymphocytes and plasma cells (10). In general, RDD presents with S100 protein (+) and ALK (-) on immunohistochemistry. However, it may arise in cases of ALK-positive histiocytosis with diffuse cytoplasmic positivity of S-100 protein, especially when emperipolesis is also present (13).

Erdheim–Chester disease (ECD) was first described in 1930, and 1500 cases have been reported (14). ECD usually occurs in adults, and patients are more likely to be women (15, 16). The neuroimaging presentation of ECD is diverse, with varying degrees of meningeal, cranial, cerebral, and spinal cord involvement (17). ECD is characterized by patchy intensification within the lesion, which can last for several days (17). The histology characteristic of ECD is multisystemic proliferation of mature histiocytes on a background of inflammatory stroma (18). Pathology may present loose clusters of classical foamy or granular histiocytes with well-defined cell borders (18). Fibrosis is present in most cases with a few Touton-type cells (18).

ALK-positive histiocytosis can occur in both children and adults, and may involve multiple systems. In the current study, enhancement at T1-weighted with intracranial dissemination is characteristic of the ALK-positive histiocytosis. Histologically,

TABLE 1 | Literature search results on the clinical features and outcomes of ALK-positive histiocytosis involving the CNS.

Citation	Age	Sex	Location in CNS	Site of involvement	Therapy	Follow-up/ prognosis
Lucas et al. (6)	7 y	Female	Cerebellar vermis	No	Surgery	12 mo/well
Lucas et al. (6)	10 y	Female	Pericentral	No	Surgery	6 mo/well
Qiu et al. (1)	49 y	Male	Left temporal lobe, right frontal lobe	lungs, liver, bone pancreas, prostate, parotid gland, abdominal wall	GKRS, chemotherapy (lenalidomide), anti-ALK	2 mo/well
Rossi et al. (7)	10 mo	Male	Left frontal lobe, left parietal lobe	No	Surgery, chemotherapy (vinblastine), anti-ALK (alectinib)	7 mo/well
Rossi et al. (7)	11 y	Female	Right frontal lobe	No	Surgery	4 mo/well
Chang et al. (3)	33 mo	Male	NA	intestine, bone marrow	Steroids, chemotherapy (etoposide, cyclosporine, cytarabine, methotrexate)	2 mo/died
Chang et al. (3)	15 y	Male	Cavernous sinus	No	anti-ALK (crizotinib)	NA/well
Tian et al. (5)	51 y	Female	Left frontal lobe	Lungs, lymph nodes	Surgery, anti-ALK (alectinib)	10 mo/well
Takeyasu (4)	17 y	Female	Right frontal lobe	breast	anti-ALK (alectinib)	30 mo/well
Jaber (9)	27 y	Male	intradural extramedullary at the L3 level	No	Surgery	9 mo/well

ALK, anaplastic lymphoma kinase; GKRS, gamma knife radiosurgery; mo, months; y, years; NA, not available.

minimal cytologic atypia and focal spindled histiocytes are noted, along with scattered small lymphocytes and eosinophils (1). Touton-type multinucleated giant cells have been found in ALK-positive histiocytosis (9).

This case provides a new direction for the differential diagnosis of suprasellar tumors in radiology. In children with giant suprasellar tumors, the first diagnosis that comes to mind is craniopharyngioma (CP), which has two histological subtypes: adamantinomatous and papillary (19). The solid parts of CPs as well as calcified tissue and cyst walls can show a variety of T1 signals, from hypointense to hyperintense (20). CPs have generally been hypointense and hyperintense on T2weighted images. In addition, germinoma is a common intracranial tumor of children, in which the AFP and β-hCG levels are generally significantly high. Germinoma shows low to equal signal on T1weighted images and high signal on T2weighted images, which could be associated with necrosis and cystic degeneration, and significant enhancement on contrast-enhanced T1-weighted MRI. The ALK-positive histiocytosis reported in this study had a solid component without calcification or cystic changes, and enhancement scans showed significant enhancement, which differed somewhat from the above two tumor types.

The efficacy of chemotherapy and anti-ALK therapy here appeared to be greater in the lung than in the cerebrum. During the limited follow-up period of the current study, the regression speed of lesions located in the lungs was faster than that of lesions located in the CNS. Tian et al. reported a middle-aged female with ALK-positive histiocytosis located in the left frontal lobe, lungs, and lymph nodes (5). The cerebral lesion was removed surgically, and the patient received anti-ALK therapy (alectinib). Lesions of the lungs showed gradual regression during treatment as well. The lesions of the patient from Qiu et al.'s study involved multiple systems including the brain, lungs, liver, prostate, and bone (1). He received gamma knife treatment, lenalidomide-based chemotherapy, pembrolizumab, and anti-ALK therapy. The lesion was reported as stable, but additional information about the follow-up was lacking. Crizotinib and alectinib is an ALK-tyrosine kinase inhibitor that has been applied in the treatment of non-small-cell lung cancer (21). Several patients with ALK-positive histiocytosis have been benefit from crizotinib and alectinib as well (3–5, 7). The presence of the blood–brain barrier may affect the action of ALK-tyrosine kinase inhibitor in the CNS, but there is insufficient evidence to support the hypothesis that the efficacy of chemotherapy and anti-ALK therapy is greater for ALK-positive histiocytosis in the lung than in the cerebrum. Further studies are needed to address this question.

We conclude that ALK-positive histiocytosis can involve the central nervous system and disseminate intracranially. It is also worthy of consideration for the differential diagnosis of suprasellar lesions. Once the diagnosis of ALK-positive histiocytosis is confirmed, chemotherapy and anti-ALK therapy should be considered, but patients should be alerted to a risk of fatal complications.

ETHICS STATEMENT

We have obtained written informed consent from the patients' legal representatives for the publication.

AUTHOR CONTRIBUTIONS

YG and YL proposed the conception and design of the study. H-Bq and GN conducted data collection. YG and F-lJ conducted the literature search and data extraction. YG, HL, and X-mM were involved in picture production. YG and YL drafted the manuscript. All authors contributed to the article and approved the submitted version.

ACKNOWLEDGMENTS

The authors thank the patient and his family for their donation to medicine.

SUPPLEMENTARY MATERIAL

The Supplementary Material for this article can be found online at: https://www.frontiersin.org/articles/10.3389/fonc.2022.858939/full#supplementary-material

REFERENCES

1. Qiu L, Weitzman SP, Nastoupil LJ, Williams MD, Medeiros LJ, Vega F. Disseminated ALK-Positive Histiocytosis With KIF5B-ALK Fusion in an Adult. *Leukemia Lymphoma* (2021) 62(5):1234–8. doi: 10.1080/10428194.2020.1861273
2. Chan JK, Lamant L, Algar E, Delsol G, Tsang WY, Lee KC, et al. ALK+ Histiocytosis: A Novel Type of Systemic Histiocytic Proliferative Disorder of Early Infancy. *Blood* (2008) 112(7):2965–8. doi: 10.1182/blood-2008-03-147017
3. Chang KTE, Tay AZE, Kuick CH, Chen H, Algar E, Taubenheim N, et al. ALK-Positive Histiocytosis: An Expanded Clinicopathologic Spectrum and Frequent Presence of KIF5B-ALK Fusion. *Modern Pathol an Off J United States Can Acad Pathology Inc* (2019) 32(5):598–608. doi: 10.1038/s41379-018-0168-6
4. Takeyasu Y, Okuma HS, Kojima Y, Nishikawa T, Tanioka M, Sudo K, et al. Impact of ALK Inhibitors in Patients With ALK-Rearranged Nonlung Solid Tumors. *JCO Precis Oncol* (2021) 5:756–66. doi: 10.1200/PO.20.00383
5. Tian Y, Li J, Liu B, Xie H, Zheng M, Yao W. ALK-Positive Histiocytosis With Disseminated Disease Responded to Alectinib: A Case Report. *Ann Palliative Med* (2021) 10(9):10095–101. doi: 10.21037/apm-21-2117
6. Lucas CG, Gilani A, Solomon DA, Liang X, Maher OM, Chamyan G, et al. ALK-Positive Histiocytosis With KIF5B-ALK Fusion in the Central Nervous System. *Acta Neuropathologica* (2019) 138(2):335–7. doi: 10.1007/s00401-019-02027-7
7. Rossi S, Gessi M, Barresi S, Tamburrini G, Giovannoni I, Ruggiero A, et al. ALK-Rearranged Histiocytosis: Report of Two Cases With Involvement of the Central Nervous System. *Neuropathol Appl Neurobiol* (2021) 47(6):878–81. doi: 10.1111/nan.12739

8. Haroche J, Cohen-Aubart F, Rollins BJ, Donadieu J, Charlotte F, Idbaih A, et al. Histiocytoses: Emerging Neoplasia Behind Inflammation. *Lancet Oncol* (2017) 18(2):e113–25. doi: 10.1016/S1470-2045(17)30031-1
9. Jaber OI, Jarrah DA, Hiasat M, Hussaini MA. ALK-Positive Histiocytosis: A Case Report and Literature Review. *Turk Patoloji Dergisi* (2021) 37(2):172–7. doi: 10.5146/tjpath.2020.01507
10. Bruce-Brand C, Schneider JW, Schubert P. Rosai-Dorfman Disease: An Overview. *J Clin Pathol* (2020) 73(11):697–705. doi: 10.1136/jclinpath-2020-206733
11. Vaidya T, Mahajan A, Rane S. Multimodality Imaging Manifestations of Rosai-Dorfman Disease. *Acta Radiol Open* (2020) 9(8):2058460120946719. doi: 10.1177/2058460120946719
12. Rosai J, Dorfman RF. Sinus Histiocytosis With Massive Lymphadenopathy. A Newly Recognized Benign Clinicopathological Entity. *Arch Pathol* (1969) 87 (1):63–70.
13. Huang H, Gheorghe G, North PE, Suchi M. Expanding the Phenotype of ALK-Positive Histiocytosis: A Report of 2 Cases. *Pediatr Dev Pathol Off J Soc Pediatr Pathol Paediatric Pathol Soc* (2018) 21(5):449–55. doi: 10.1177/1093526617740784
14. Papo M, Emile JF, Maciel TT, Bay P, Baber A, Hermine O, et al. Erdheim-Chester Disease: A Concise Review. *Curr Rheumatol Rep* (2019) 21(12):66. doi: 10.1007/s11926-019-0865-2
15. Cohen-Aubart F, Emile JF, Carrat F, Helias-Rodzewicz Z, Taly V, Charlotte F, et al. Phenotypes and Survival in Erdheim-Chester Disease: Results From a 165-Patient Cohort. *Am J Hematol* (2018) 93(5):E114–e117. doi: 10.1002/ajh.25055
16. Estrada-Veras JI, O'Brien KJ, Boyd LC, Dave RH, Durham B, Xi L, et al. The Clinical Spectrum of Erdheim-Chester Disease: An Observational Cohort Study. *Blood Adv* (2017) 1(6):357–66. doi: 10.1182/bloodadvances.2016001784
17. Garg N, Lavi ES. Clinical and Neuroimaging Manifestations of Erdheim-Chester Disease: A Review. *J Neuroimaging* (2021) 31(1):35–44. doi: 10.1111/jon.12785
18. Ozkaya N, Rosenblum MK, Durham BH, Pichardo JD, Abdel-Wahab O, Hameed MR, et al. The Histopathology of Erdheim-Chester Disease: A Comprehensive Review of a Molecularly Characterized Cohort. *Modern Pathol an Off J United States Can Acad Pathol Inc* (2018) 31(4):581–97. doi: 10.1038/modpathol.2017.160
19. Muller HL, Merchant TE, Warmuth-Metz M, Martinez-Barbera JP, Puget S. Craniopharyngioma. *Nat Rev Dis Primers* (2019) 5(1):75. doi: 10.1038/s41572-019-0125-9
20. Rossi A, Cama A, Consales A, Gandolfo C, Garrè ML, Milanaccio C, et al. Neuroimaging of Pediatric Craniopharyngiomas: A Pictorial Essay. *J Pediatr Endocrinol Metab JPEM* (2006) 19(Suppl 1):299–319.
21. Peters S, Camidge DR, Shaw AT, Gadgeel S, Ahn JS, Kim DW, et al. Alectinib Versus Crizotinib in Untreated ALK-Positive Non-Small-Cell Lung Cancer. *N Engl J Med* (2017) 377(9):829–38. doi: 10.1056/NEJMoa1704795

Conflict of Interest: The authors declare that the research was conducted in the absence of any commercial or financial relationships that could be construed as a potential conflict of interest.

Publisher's Note: All claims expressed in this article are solely those of the authors and do not necessarily represent those of their affiliated organizations, or those of the publisher, the editors and the reviewers. Any product that may be evaluated in this article, or claim that may be made by its manufacturer, is not guaranteed or endorsed by the publisher.

Copyright © 2022 Guo, Qu, Ning, Jia, Liu, Ma and Liao. This is an open-access article distributed under the terms of the Creative Commons Attribution License (CC BY). The use, distribution or reproduction in other forums is permitted, provided the original author(s) and the copyright owner(s) are credited and that the original publication in this journal is cited, in accordance with accepted academic practice. No use, distribution or reproduction is permitted which does not comply with these terms.

frontiers in Neuroimaging

ORIGINAL RESEARCH
published: 29 March 2022
doi: 10.3389/fnimg.2022.838483

Automation of Cranial Nerve Tractography by Filtering Tractograms for Skull Base Surgery

Méghane Decroocq[1], Morgane Des Ligneris[1], Titouan Poquillon[1], Maxime Vincent[1], Manon Aubert[1], Timothée Jacquesson[1,2†] and Carole Frindel[1†]*

[1] Univ Lyon, INSA-Lyon, Université Claude Bernard Lyon 1, UJM-Saint Etienne, CNRS, INSERM, CREATIS UMR 5220, Lyon, France, [2] Skull Base Multi-Disciplinary Unit, Neurological Hospital Pierre Wertheimer, Hospices Civils de Lyon, Lyon, France

Fiber tractography enables the *in vivo* reconstruction of white matter fibers in 3 dimensions using data collected by diffusion tensor imaging, thereby helping to understand functional neuroanatomy. In a pre-operative context, it provides essential information on the trajectory of fiber bundles of medical interest, such as cranial nerves. However, the optimization of tractography parameters is a time-consuming process and requires expert neuroanatomical knowledge, making the use of tractography difficult in clinical routine. Tractogram filtering is a method used to isolate the most relevant fibers. In this work, we propose to use filtering as a post-processing of tractography to avoid the manual optimization of tracking parameters and therefore making a step forward automation of tractography. To question the feasibility of automated tractography of cranial nerves, we perform an analysis of main cranial nerves on a series of patients with skull base tumors. A quantitative evaluation of the filtering performance of two state-of-the-art and a new entropy-based methods is carried out on the basis of reference tractograms produced by experts. Our approach proves to be more stable in the selection of the optimal filtering threshold and turns out to be interesting in terms of computational time complexity.

Keywords: diffusion MR imaging, tractography, filtering accuracy, entropy, cranial nerve

OPEN ACCESS

Edited by:
Nico Sollmann, University of California, San Francisco, United States

Reviewed by:
Jan Egger, University Hospital Essen, Germany
Fan Zhang, Harvard Medical School, United States

****Correspondence:***
Carole Frindel
carole.frindel@creatis.insa-lyon.fr

† These authors have contributed equally to this work and share last authorship

Specialty section:
This article was submitted to Brain Imaging Methods, a section of the journal Frontiers in Neuroimaging

Received: *17 December 2021*
Accepted: *04 February 2022*
Published: *29 March 2022*

Citation:
Decroocq M, Des Ligneris M, Poquillon T, Vincent M, Aubert M, Jacquesson T and Frindel C (2022) Automation of Cranial Nerve Tractography by Filtering Tractograms for Skull Base Surgery. Front. Neuroimaging 1:838483. doi: 10.3389/fnimg.2022.838483

1. INTRODUCTION

Diffusion magnetic resonance imaging (MRI) allows to study the tissue microstructure *in vivo* non-invasively by detecting the movement of water molecules to generate specific contrast (Le Bihan and Johansen-Berg, 2012). This method has been widely used in the white matter of the brain, where the organization of axons is known to be consistent at the millimeter scale. Using diffusion MR images in a number of directions and suitable statistical models, the orientations of axonal bundles can be estimated (Tournier et al., 2011). These properties are then used to infer the structure of human brain tissue *in vivo*. From the tissue local orientations, it is possible to reconstruct a neural bundle by iteratively tracing these orientations until a termination criterion is reached. This process named "tractography" can be repeated from different starting points in a region of interest to produce an estimate of the structural connections of this region—referred to as a "tractogram" (Jeurissen et al., 2019). The biological precision of these reconstructions is however limited by the reconstruction mechanisms itself. The choice of the tractography algorithm, its settings and the tracing of local diffusion orientations can introduce biases in the tractograms which move them away from the underlying biological reality (Rheault et al., 2020).

Surgery of skull base tumors remains a challenge because it requires surgical approaches sparing the nervous tissue while allowing access to deep tumors in a complex anatomical environment made up of numerous nerves and cranial vessels (Samii and Gerganov, 2011). While cerebrovascular supply can be adequately assessed by MRI or angiography, the trajectory of the cranial nerves from the brainstem through the skull base and around tumors is not still achievable in routine clinical practice. Classic high-resolution T1 or T2 MRI sequences only allow visualization of the cisternal segment of the largest cranial nerves under normal conditions (Yousry et al., 2000). In this context, diffusion MRI and reconstruction by tractography of the path of cranial nerves displaced by tumors could be helpful for surgical planning, as attested by recent studies examining the trajectory of facial nerves in vestibular schwannomas surgery (Borkar et al., 2016; Song et al., 2016; Jacquesson et al., 2018a). Nonetheless, tractography involves a complex multi-step processing pipeline and is still difficult to apply to small-scale structures such as cranial nerves (Jacquesson et al., 2018b).

In order to extract the bundle of nerve fibers of interest, regions of interest (ROI) have to be manually delineated to initialize the tractography process. However, the design of ROI is time consuming and requires expert neuroanatomical knowledge. Besides, tractography parameters such as the minimum length of fibers, maximum angle, or fractional anisotropy (FA) threshold—used as a criterion for stopping the tractography process—also require a manual adjustment to perform an accurate reconstruction of the bundle. In this context, the automation of cranial nerve tractography arises from a growing need to save time and reduce its dependence on the user so that it can be applied systematically in clinical practice. A few studies compared fully automated tractography to user-driven tractography. The approaches chosen to automate the process mainly focus on ROI placement. In those studies, the imaging volumes were registered so that a standardized set of ROIs can be applied (Zhang et al., 2008, 2010). In their work, Nucifora et al. (2012) combined the use of an atlas-based set of ROI with post-processing treatment to filter the implausible "false" fibers. The results of this study suggest that filtering can help compensate for non-optimal ROIs and tracking parameters. In the case of cranial nerves, we believe that limitations related to the small size of the nerve fiber bundle and pathological displacement could be overcome by using filtering to discriminate nerve fibers from other structures selected involuntarily.

A number of tractogram filtering methods were proposed in the literature (Jörgens et al., 2021). The majority of approaches involve selecting the most relevant fibers based on a quality measure. This quality metric can be defined by the mean values of a diffusion metric along the fiber path (Yeh et al., 2021). This diffusion metric can be obtained from the diffusion tensor model (e.g., FA, axial, and radial diffusivities) (Everts et al., 2009), or from more sophisticated models such as constrained spherical deconvolution (CSD) (Smith et al., 2013, 2015) or other methods combining multiple approaches (Jörgens et al., 2021). Once the quality measure is defined, one way to filter tractograms consists of applying thresholds on the quality measure to filter out weak connections.

In this article, we propose to compare the performances of different filtering methods and evaluate their contribution in the context of the automation of cranial nerves tractography. To this end, a set of non-optimal tractograms is generated for five cranial nerves on a series of patients, by applying different transformations to the optimal ROI designed by the neurosurgeon, and varying the most sensitive parameters for the reconstruction of the tractograms. The non-optimal tractograms are filtered by two state-of-the-art approaches (Everts et al., 2009; Smith et al., 2013) and a new entropy-based method we propose. The non-optimal tractograms are compared to the ground truth tractograms produced by a neurosurgeon, before and after filtering. A quality metric based on Sørensen-Dice coefficient allows for a quantitative evaluation of the ability of the different filtering algorithms to isolate the cranial nerves in unfavorable cases.

2. MATERIAL

2.1. Cranial Nerves

Five cranial nerves or nerve groups were considered: the optic nerve (Chiasma); the oculomotor nerve (III); the trigeminal nerve (V); the acoustic facial bundle including nerves VII–VIII (AFB); and the lower nerves bundle including nerves IX, X, XI (LN). Their mean cisternal diameter was estimated (see **Table 1**) according to the known anatomy (Rhoton, 1979; Joo et al., 2014; Yoshino et al., 2016). The direction of their cisternal segment was oblique anteriorly and laterally for the optic and oculomotor nerves (Chiasma and III); straight anterior for the trigeminal nerve (V); straight lateral for the AFB bundle; and oblique laterally, anteriorly, and inferiorly for the LN bundle.

2.2. Patients

Patient data used in this work are based on the study carried out between December 2015 and December 2017 in Jacquesson et al. (2018a) (IRB Number 2015-A01113-46). Inclusion criteria were as follows: skull base tumor; at least two cranial nerves in contact with the tumor; legal capacity; consent provided after fair information; 3T MRI data with diffusion MRI (dMRI) acquisition. Exclusion criteria were as follows: MR contraindications. Eight patients showing a variability in the tumor location, size, and nerves in contact with the tumor were selected for our study.

2.3. MRI Acquisition

MR images were obtained using a 3T MRI Ingenia machine (Philips Medical Systems, Beth, The Netherlands) with a 32-channel head coil. Five sequences were acquired: post-contrast T1-weighted; high resolution and steady state T2-weighted; time of flight (TOF); diffusion; and AP-PA sequences (pair of $b = 0$ images with opposed phase encoding direction, Andersson et al., 2003). T1 post-contrast weighted sequence was used to manually segment the tumors and T2 steady state sequence as an anatomical reference. Diffusion images were acquired with following settings: TR = 3,956 ms; TE = 102 ms; b-value = 1,000 s.mm^{-}2; 32 directions; acquired voxel size = 2 mm isotropic; field of view: 224 mm; slice thickness = 2 mm; no slice gap; single-shot spin-echo sequence; 26 slices; and scan time 9 min 52 s.

TABLE 1 | Estimated diameter of the studied nerves from the literature.

Nerve definition	Optic	Oculomotor	Trigeminal	Acoustic-facial	Lower
Nerve abbreviation	Chiasma	III	V	AFN	LN
Diameter (*mm*)	10	5	7	3	2

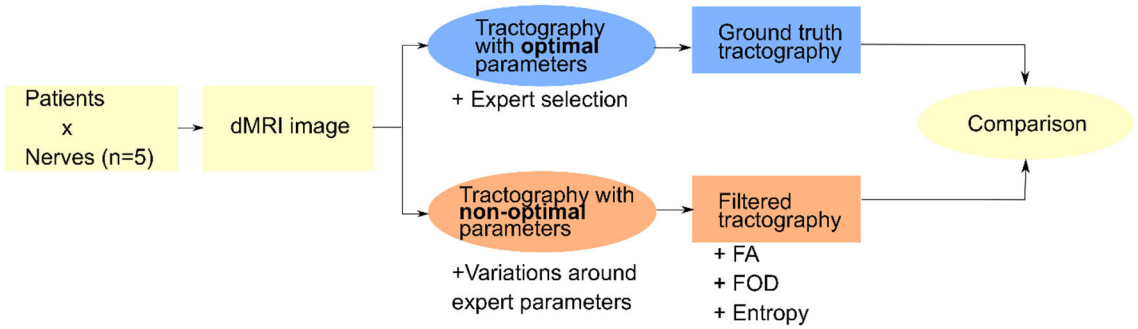

FIGURE 1 | General view of the pipeline used to test different filtering approaches on the basis of non-optimal tractograms with reference to a reference tractogram produced by an expert.

The limits of the acquisition box were the optic tracts superiorly and the foramen magnum inferiorly. Distortions were corrected using the top-up and eddy tools of the FMRIB software library (FSL) software (Smith et al., 2004).

2.4. Ground Truth Tractography

The tractography of the cranial nerves was carried out using the MRtrix3 software (Tournier et al., 2019). A brain mask was drawn to include the whole brainstem, the cisterns of cerebrospinal fluid, the skull base, and the orbits. A spherical constrained deconvolution (6 spherical harmonic terms) has been used to create a map of orientation distribution function (ODF). ROI for the initialization of the tractography were selected by overlaying the ODF map on the T2-weighted MRI in order to identify the cisternal trajectory of the cranial nerves with great precision. ROIs were placed on the best identifiable aspect of the cranial nerve in its cisternal segment in the three dimensions: axial, sagittal, and coronal. For each cranial nerve, a single ROI was used; ROIs were cubes and tailored to the anatomical features of each cranial nerve before initiating the tracking. A probabilistic tractography algorithm was used for the tracking of cranial nerves from the ROIs with the following optimized parameters (Jacquesson et al., 2018a): FA cut-off = 0.2–0.3; maximal curvature angle = 45°; minimum fiber length = 10 mm; step size = 0.1 mm. The number of fibers of each nerve to be reconstructed was set from 200 to 1,000 according to the estimated nerve diameter (see **Table 1**). These tractography results with optimized parameters serve as ground truth for the filtering methods detailed in Section 3.1. In post-treatment, some tractography reconstruction results were filtered manually by an expert in neuroanatomy in order to remove fibers that were away from the anatomy of the nerve.

3. METHODS

Three filtering methods are tested for their ability to remove erroneous fibers from the tractograms when the tractography parameters are not optimally adjusted. These filtering methods include two state-of-the-art approaches as well as an original approach: they are detailed and explained in section 3.1. Then in order to evaluate the filtering results, an evaluation pipeline is set up, where the filtering results (filtered tractograms) are compared to the reference tractogram as produced with a set of optimal parameters by a neuroanatomy expert. This pipeline is illustrated in **Figure 1** and its constituent steps are explained in section 3.2.

3.1. Filtering Methods

In this section, we describe the three filtering algorithms used in this study. Before filtering, these methods require the calculation of different parametric maps that are then used to compute—at the scale of a fiber—an indicator of its quality and thus decide whether or not to keep it in the final rendering.

Figure 2 illustrates filtering results by keeping different percentages of the total number of fibers, where the fiber sorting is performed in an order depending on the filtering method.

3.1.1. Fractional Anisotropy

FA measures the degree of anisotropy of the diffusion of water in a voxel. Without obstacles, water molecules freely diffuse in any direction. This pattern can however be modified by the presence of cell membranes or macromolecules. For example, if the water molecules are confined inside a cell, diffusion only occurs along the main axis of the cell and the diffusion is not isotropic, but anisotropic. The degree of anisotropy can be measured for each voxel of the diffusion MR images from the three eigenvalues (λ_1, λ_2, λ_3) of the diffusion tensor, which describes the diffusion of water using a Gaussian model:

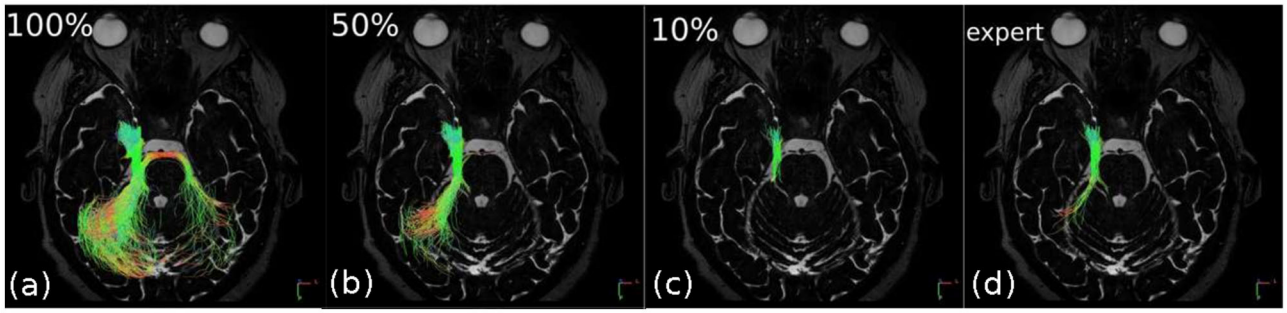

FIGURE 2 | Successive filtering obtained for different percentages of the total number of fibers sorted by decreasing entropy in the right trigeminal nerve (V). The "expert" image shows the result of "ground truth" tractography (for comparison purposes). In **(a)**, 100% of the fibers are depicted and it can be seen that the nerve, due to inaccurate regions of interest (ROI) positioning, has merged to the right with fibers that belong to a different structure of the brain. In **(b,c)**, 50 and 10% of the least entropic fibers are, respectively, displayed; this filtering allows to remove the false continuations and thus to tend toward **(d)** the expected "expert" result.

$$FA = \sqrt{\frac{1}{2}} \frac{\sqrt{(\lambda_1 - \lambda_2)^2 + (\lambda_2 - \lambda_3)^2 + (\lambda_3 - \lambda_1)^2}}{\sqrt{\lambda_1^2 + \lambda_2^2 + \lambda_3^2}}. \quad (1)$$

FA values range from 0 to 1, where 0 represents perfectly isotropic diffusion and 1 represents extremely anisotropic diffusion (Kingsley, 2006). FA values are unitless because they are a ratio of diffusion coefficients. As part of this study, the FA maps were calculated using the function `tensor2metric` of MRtrix3 software. The mean value of FA along the fibers is computed by trilinear interpolation with the `tcksample` function of MRtrix3. The fibers are then ranked in the descending order.

3.1.2. Fiber Orientation Distribution

The fiber orientation distribution (FOD) is a spherical probability density function that reveals the orientations and volumes of the underlying fiber bundles. Traditional methods include the estimation of a response function—signal expected in a voxel containing a single bundle of fibers all arranged in a coherent manner—which is then deconvolved from the dMRI signal in order to obtain the FOD (Tournier et al., 2007). The FOD is typically represented as lobes which provide information about the fraction of fibers in the voxel that are aligned along the direction of a lobe. Specifically, the fiber density is correlated with the integral of the FOD lobe and the bundle density to the sum of the segment lengths of fibers (in the voxel) assigned to this lobe. The goal of scale-invariant feature transform (SIFT) approach (Smith et al., 2013) is to assign fibers to the FOD lobes they pass through, so that all fibers contribute to the density of the bundles of the FOD lobes to which they are assigned, depending on their length (Smith et al., 2013) through the voxel of interest as well as a variable contributing weight (Smith et al., 2015):

$$\mu = \sum_{s\,:\,|s_l|>0} |s_l|.e_s^F, \quad (2)$$

where each fiber s that traverses the lobe l contributes the bundle density according to the product of its length $|s_l|$ through the voxel, and contributing weight e_s^F.

The underlying idea is to determine a vector of contributing weights F, such that when the contribution of each fiber is weighted accordingly in this vector, the bundle densities match the FOD lobe integrals throughout the all image. The FOD map is computed from the diffusion MR images using MRtrix3 `dwi2fod` function. On the basis of SIFT method, the associated F map is associated with the fibers by the `tcksift2` function of MRtrix3. The fibers are then ranked in the ascending order.

3.1.3. Entropy

We propose a third way of filtering on fibers which is based on entropy and is an original contribution proposed within the framework of this work. Shannon's entropy is used here to measure the homogeneity of the orientation of tractography fibers. The entropy of a vector field is defined by the entropy of the histogram of the vector orientations as follows:

$$e(X) = -\sum_{i=1\ldots n} p(x_i) log_2(p(x_i)), \quad (3)$$

where x_i is the bin i of the histogram of vector orientations and $p(x_i)$ the probability for a vector to be in the bin x_i. The probability $p(x_i)$ is calculated as:

$$p(x_i) = \frac{C(x_i)}{\sum_{i=1\ldots n} C(x_i)}, \quad (4)$$

with $C(xi)$ the number of vectors in the bin x_i. **Figure 3** illustrates this process in a two-dimensional case for a case of orientation disorder (**Figure 3A**: high entropy) and orientation coherence (**Figure 3B**: low entropy).

To compute the local entropy of tractograms, the fibers are first converted to a vector field encoding their 3D local orientations. This vector field could be obtained from the main eigenvector of the diffusion tensor estimated from the raw dMRI data. However, this method is very sensitive to noise, particularly because of the low resolution of the dMRI data (2 mm) compared to the diameter of the nerves (2–10 mm: see **Table 1**). We therefore propose to reconstruct a vector field from the fibers themselves. Considering that fibers are sampled more than 10 times finer than the dMRI voxel, the resolution of the final vector

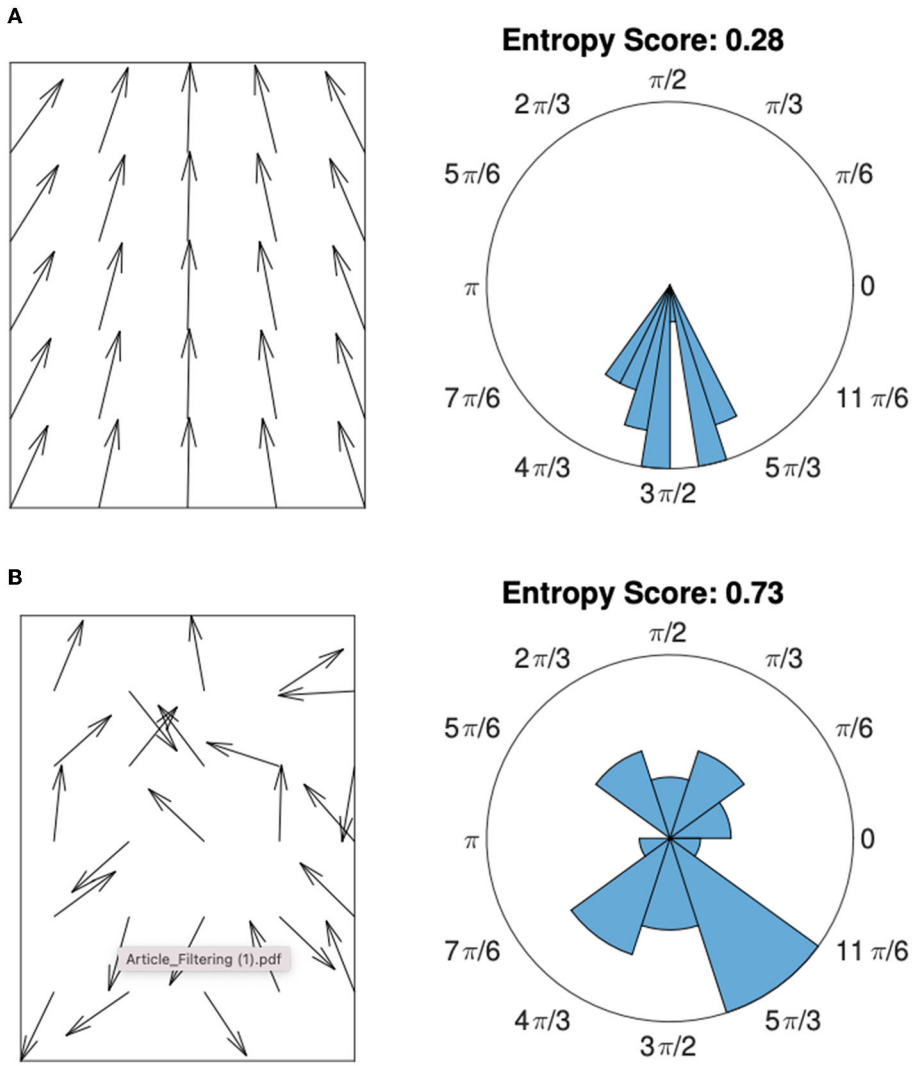

FIGURE 3 | Orientation histogram associated with vector fields of low entropy **(A)** and high entropy **(B)**. The score given in the right column corresponds to the entropy value of the central vector calculated using a 3 × 3 neighborhood and a circular orientation histogram with 10 bins. The more the vector field is scattered, the higher the entropy value.

field can be drastically improved. The fibers are transformed into a 3D image of local fiber density information, and a map of the maximum intensity gradient direction of this image is calculated using a $3 \times 3 \times 3$ neighborhood according to the method in Xu and Prince (1998). Since the gradient orientation is normal to the actual fiber orientation, the vectors are reoriented according to the average of the vector products of the central voxel and its neighbors in the $3 \times 3 \times 3$ neighborhood.

Then, each voxel of coordinates (x, y, z) in the vector field is associated to a small cubic neighborhood $n \times n \times n$. Considering 3D vectors, a spherical orientation histogram in the neighborhood of the considered voxel is computed. This is achieved in 3D by decomposing the unit sphere into patches of equal area (Leopardi, 2006), and using the cones connecting the patches to the center of the sphere as bins for the orientation histogram. The entropy is computed from the spherical orientation histogram as in Equation (3) and the entropy value is assigned to the corresponding voxel (x, y, z) in the 3D entropy map $E(x, y, z)$.

The entropy map depends on two parameters; the number of bins n used in the histogram and the size of the neighborhood considered to build the histogram. In our case, the parameters are chosen by taking into account priors on the dMRI acquisition and the anatomy of the cranial nerves. The number of bins corresponds roughly to the number of diffusion directions used in dMRI acquisition ($n = 32$) and the neighborhood size is proportional to the diameter of the considered nerve, as given in **Table 1**.

The coordinates of the fibers are re-written in the referential of the 3D vector field used to compute the entropy. Each fiber is

TABLE 2 | Values used for each tractography parameter in order to build the "non-optimal" database.

Parameter	Dataset 1	Dataset 2	Dataset 3	Dataset 4	Dataset 5
FA threshold	oFA	oFA-0.03	oFA-0.06	oFA-0.1	–
ROI size	$oROI_s$	$oROI_s$+$D/5$	$oROI_s$+$2D/5$	$oROI_s$+$3D/5$	$oROI_s$+$4D/5$
ROI vertical translation	$oROI_l$-$2D/5$	$oROI_l$-$D/5$	$oROI_l$	$oROI_l$+$D/5$	$oROI_l$+$2D/5$
ROI horizontal translation	$oROI_l$-$2D/5$	$oROI_l$-$D/5$	$oROI_l$	$oROI_l$+$D/5$	$oROI_l$+$2D/5$

D is the diameter of the nerve, as given in ***Table 1****. oFA, $oROI_s$, and $oROI_l$ stand for, respectively, optimal values of FA, regions of interest (ROI) size, and location.*

weighted by a score α. This score is computed from the entropy map E as follows:

$$\alpha = \frac{1}{|X|} \sum_{(x,y,z)\in X} E(x,y,z), \tag{5}$$

where X is the set of coordinates of the considered fiber.

3.2. Evaluation

3.2.1. Non-optimized Tractography Dataset

The performance of the proposed filtering methods is evaluated in a context of non-optimized tractography (i.e., non-expert operators). For this, a non-optimized database of cranial nerve tracking was generated. The ROI location and size and the FA threshold were identified as parameters of interest for this study because their optimal value strongly depends on the acquisition, pathology, and anatomical variability of the patient (Jacquesson et al., 2018b). They are likely to have a strong impact on the tractography results.

For each of the cranial nerves considered in this study, the fiber tacking is performed with non-optimal tractography parameters chosen as described in **Table 2**. The range of FA threshold values was selected with regard to recent state of the art (Jacquesson et al., 2018b) and the size and location of the ROI on the basis of inter-operator variability observed in previous work (Colon-Perez et al., 2016). It should be noted that FA threshold is only decreased and ROI size only increased because a high value of FA threshold or a very small size of ROI tend to truncate the nerve and therefore loose information, a case in which a filtering algorithm has little interest. The ROI size and position were impaired by applying dilation and translations to the optimal ROI designed by the expert. Such changes are done proportionally to the diameter D of the studied nerve (see **Table 1**) to have a comparable impact on each nerve. The influence of each tractography parameter is independently studied so that the other parameters are set to their default optimal values given in section 2.4.

Because we drift away from optimal parameters, in some cases only few or no fibers could be tracked by tractography. Filtering being is useless in such cases, they were excluded from our validation study.

3.2.2. Quality Metrics

The stochastic aspect of the probabilistic tractography algorithm makes it difficult to compare two tractograms. To allow a quantitative comparison, the performance of the filtering methods is assessed with a metric derived from the Sørensen-Dice score (Dice, 1945). The Sørensen-Dice score measures the similarity of two sets of elements as the ratio between the number of elements in their intersection and the sum of the elements in both sets. It ranges from 0 (the ensembles are disjoint) to 1 (the ensembles are overlapped). In this work, it is used to compare two tractograms; the ground truth tractogram X and the non-optimized tractogram Y. Due to the stochastic and continuous nature of tractography fibers, an original way to define their intersection, named Z, is proposed and illustrated in **Figure 4** on the top. The ground truth tractogram is first discretized on the basis of the original medical image voxels to produce a segmentation of the nerve of interest. The fibers of the non-optimized tractogram Y, which are included in the ground truth segmentation, forms the intersection set Z. We define our Sørensen-Dice score as :

$$SD = \frac{2|Z|}{|X| + |Y|}. \tag{6}$$

where X is ground truth tractogram and Y is one of the non-optimal tractograms (see **Table 2**), and Z is their intersection as defined above. The cardinality operator || refers to the number of fibers in the tractograms.

This metric is penalizing as it takes into account not only the position of the fibers but also their density. The maximum score can be obtained only if the number of fibers in the intersection and the number of fibers in the ground truth tractogram are the same. A tractogram containing only true positive fibers but with a lower number than in the ground truth is penalized. This is a welcomed feature in the design of our quality metric, as a too low fiber density may impair visualization of the nerve. This metric gives a lot of weight to false positive (i.e., spurious) fibers, which makes it is appropriate to measure the contribution of the filtering methods. However, it is not efficient for the detection of false negative fibers (i.e., missing nervous fibers), which cause incomplete or truncated nerves to obtain a high scores.

To take into account the truncature effect, we proposed another metric, that we call reverse Sørensen-Dice score *RSD*. It differs from the *SD* score in the way the intersection between X and Y is computed. In *RSD*, the non-optimized tractogram Y is segmented instead of X. The intersection, called *RZ*, is composed of the fibers of the ground truth X which are included

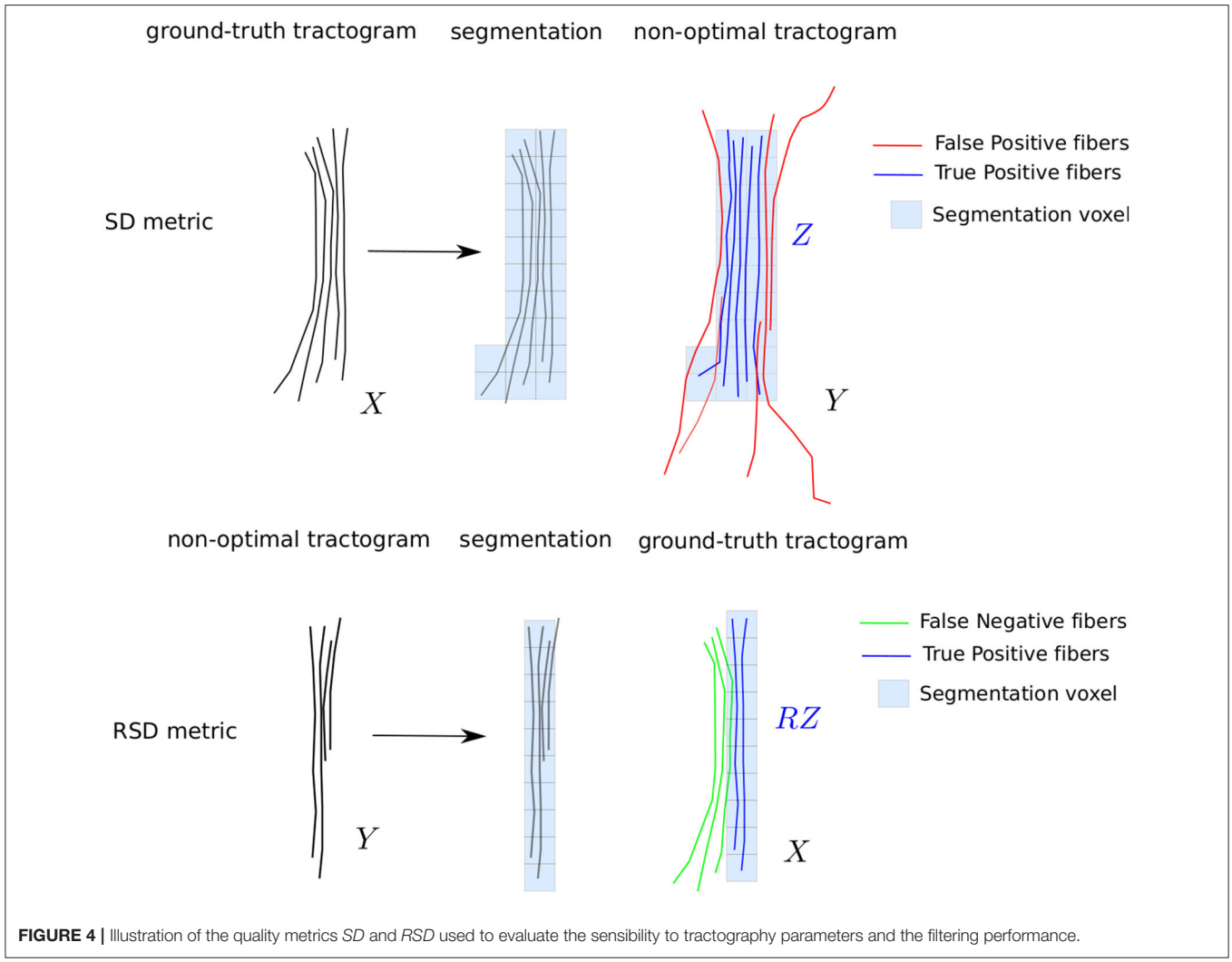

FIGURE 4 | Illustration of the quality metrics *SD* and *RSD* used to evaluate the sensibility to tractography parameters and the filtering performance.

in the segmentation of Y (see **Figure 4**). The *RSD* metric can be written as:

$$RSD = \frac{2|RZ|}{|X| + |Y|}. \tag{7}$$

This metric penalizes the false negative fibers; a truncated nerve will obtain a low score. In the next paragraph, we describe the specific metrics derived from *SD* and *RSD* in order to investigate (1) the sensitivity of tractogram to non-optimal tractography parameters and (2) the contribution of the filtering algorithms to improve the quality of the tractograms.

3.3. Sensitivity to Tractography Parameters

The study of the sensitivity to tractography parameter requires to evaluate both the unwanted fibers (false positive) and the missing fibers (false negative). In this case, both *RSD* and *SD* scores provide relevant information. This study does not investigate the filtering methods; we aim at comparing the non-optimized tractograms without any filtering, as described in section 3.2.1, to the ground truth. For this, two metrics are used. SD_{init} (respectively, RSD_{init}) refers to the *SD* score (respectively, *RSD* score) between the ground truth tractogram and non-optimized tractograms before filtering.

3.4. Filtering Performance

To evaluate the performance of the filtering methods, we will study two metrics based on the *SD* score. The maximum *SD* score between the ground truth tractogram and the non-optimized tractograms after filtering is noted SD_{max}. The score SD_{max} is the maximum of *SD* scores for filtering percentages that vary between 0 and 100% with a step of 1%. It represents the ability of the filtering algorithm to reach the expert result.

The performance of a filtering method is assessed by computing the difference $SD_{\text{diff}} = SD_{\text{max}} - SD_{\text{init}}$. SD_{diff} reflects the gain brought to the tractogram by the filtering method. If the initial tractogram is already of good quality, the gain will be low, whereas if the initial tractogram is noisy or erroneous, the gain might be more important. The most efficient filtering methods will achieve the highest gain.

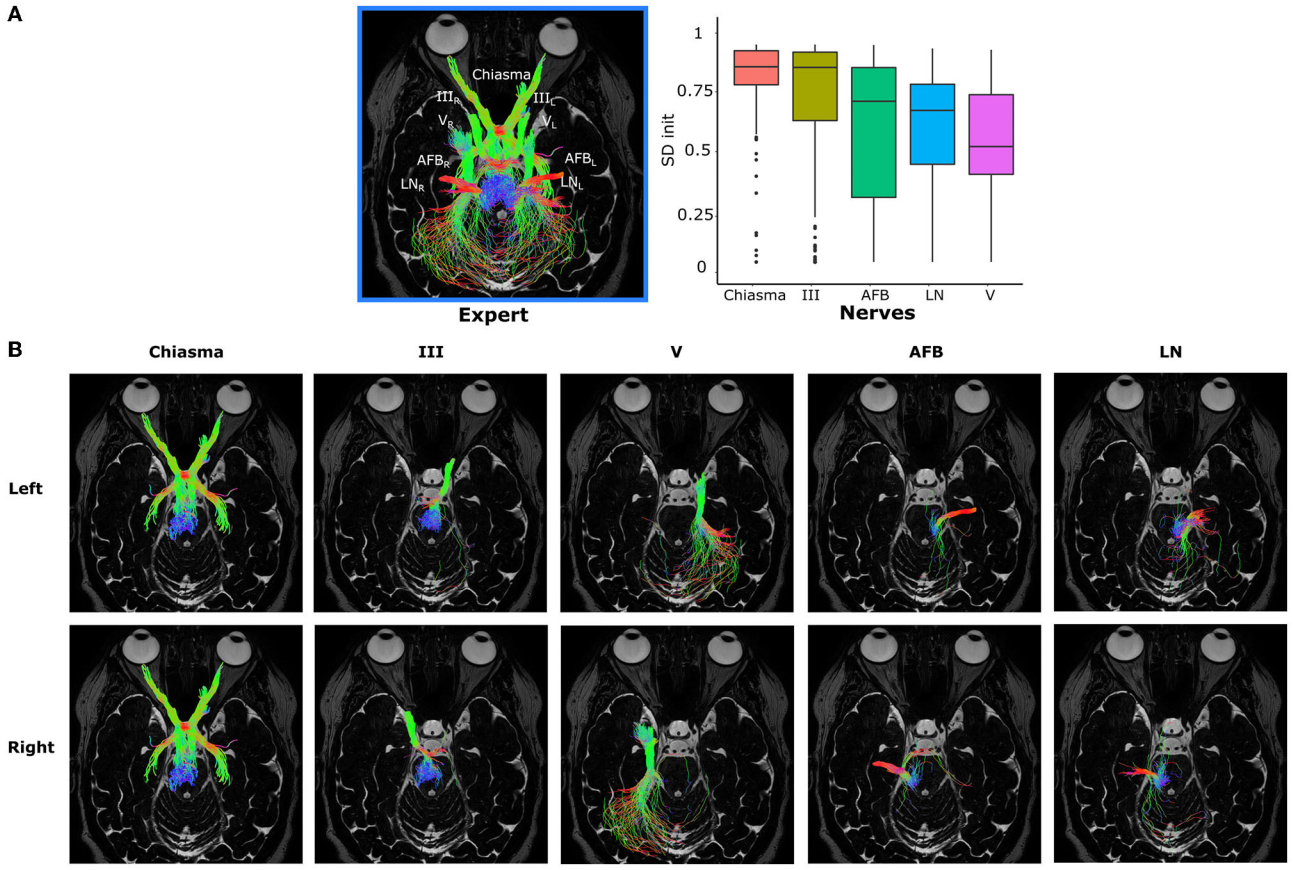

FIGURE 5 | (A) On the left, the five nerves of interest represented for a given patient and the two hemispheres (left L and right R). On the right, the distribution of SD_{init} according to the five nerves of interest for all patients and all the variations imposed around the values of optimal tractography parameters. **(B)** Independent representation of each nerve. The different nerves are represented in column according to the following order: Chiasma, III, V, AFB, LN, and in line according to the left then right hemisphere.

These two indices, SD_{max} and SD_{diff}, will be compared between nerves, tractography parameters, and filtering methods on the same data samples. The statistical test used is the paired Wilcoxon signed-rank test, since non-normality was observed for these data and samples are not independent.

4. RESULTS

In this section, we present the different results obtained. First, we observe the sensitivity of the tractograms with regard to the nerves and the variations applied to tractography parameters as given in **Table 2**. Then, we investigate the contribution of the filtering approaches from a general point of view and with regard to each tractography parameter variation. Finally, we study the optimal filtering threshold for each of the filtering methods for the sake of automation.

4.1. Sensitivity

Before looking at the performance of the filtering, we study the sensitivity of the tractograms to the variation of each tractography parameter with respect to the different nerves. This sensitivity is expressed by the SD_{init} index introduced in section 3.4.

4.1.1. Sensitivity to Nerves

Figure 5A shows on the left the different nerves in a patient for the left and right hemisphere. The disparity in the values of SD_{init} for the different nerves can be observed in **Figure 5A** on the right: this boxplot represents the distribution of SD_{init} for each of the nerves on the basis of all the disturbances created according to the non-optimal database detailed in section 3.2.1. **Table 3** gives the p-values associated with the Wilcoxon tests carried out two by two for each pair of nerves.

The nerves form two groups: one made up of Chiasma and III and another of V, LN, and AFB. The nerves Chiasma and III have roughly the same initial quality of tractography with a median of, respectively, $SD_{init} = 0.898$ and $SD_{init} = 0.895$ and are not significantly different (see **Table 3**). The median values for AFB ($SD_{init} = 0.739$), LN ($SD_{init} = 0.697$), and V ($SD_{init} = 0.531$) are significantly lower to Chiasma and III. Within the group made of AFB, LN, and V nerves, LN and AFB are not statistically different (see **Table 3**); V is statistically different from LN and AFB but

with *p*-values much lower than those obtained for the group of Chiasma and III nerves.

All this tends to say that the initial quality of the tractograms is not equal between the nerves: Chiasma and III are less sensitive to parameter variation than AFB, LN, and V. This fact can be explained by the localization of the nerves: in fact, AFB, LN, and V are closer to the back of the skull (as depicted in **Figure 5B**) and therefore to other nervous structures which can, if the tractography parameterization is not optimal, be reconstructed with the nerve of interest.

TABLE 3 | *P*-values from paired Wilcoxon signed-rank tests comparing two by two each nerve based on SD_{init} index.

	Chiasma	III	AFB	LN
III	0.18419			
AFB	6.4e-14	1.1e-12		
LN	< 2e-16	< 2e-16	0.17866	
V	< 2e-16	< 2e-16	0.00021	0.00229

4.1.2. Sensitivity to Tractography Parameters

The impact of the tractography parameters on the values of RSD_{init} and SD_{init} can be observed in **Figure 6**. In order to study the impact of each parameter variation more in detail, each parameter was varied independently, while the others are left at their optimal value. **Figure 6** represents the effect of the variation of each tractography parameter on the initial quality of the tractograms for all nerves together.

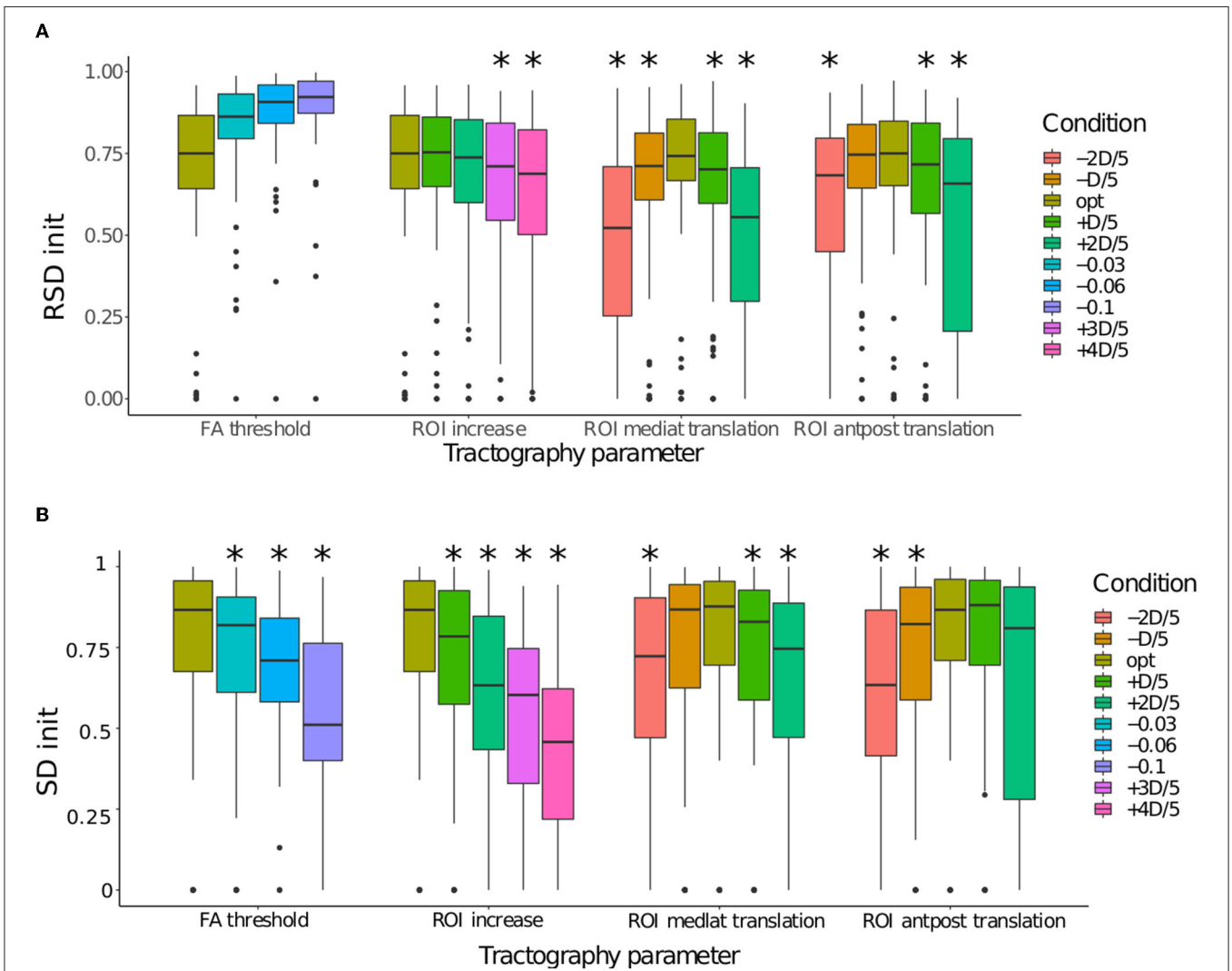

FIGURE 6 | (A) Comparison of the distributions of RSD_{init} according to each condition for the four tractography parameters: (1) FA threshold, (2) ROI size, (3) ROI mediolateral translation, and (4) ROI anteroposterior translation. **(B)** Comparison of the distributions of SD_{init} according to each condition for the four tractography parameters: (1) FA threshold, (2) ROI size, (3) ROI mediolateral translation, and (4) ROI anteroposterior translation. When a condition is significantly smaller to the optimal condition, it is marked with *.

The RSD_{init} score are given in the panel A of **Figure 6**, allowing to evaluate whether a change in parameters causes truncature of the nerve (low scores) or the fibers tracked covers the whole nerve (high scores). As it was expected, the decrease of the FA values causes the RSD_{init} to increase, as more spurious fibers are produced. The increasing of the ROI size also preserves the shape of the nerve, although the RSD_{init} score becomes significantly lower when the increase factor exceeds $+3D/5$. However, the ROI translation significantly lowers the RSD_{init}. Two types of displacement (mediolateral and anteroposterior translations) were modeled with two directions of translation with regard to the optimal one. This explains a non-monotonic evolution for these two ROI localization parameters. This drop was expected: as the ROI is moved away from its optimal position, fibers outside of the nerves are tracked, causing the nerve to appear incomplete. In such a case, the filtering algorithm might not be efficient as it can only remove the spurious fibers and not add the missing ones.

The SD_{init} score are given in the panel B of **Figure 6**, allowing to evaluate whether a change in parameters causes the generation of spurious fibers to be removed (low scores). It appears that for FA threshold the SD_{init} is already significantly lower for the tractograms with the smallest variation (FA-0.03). Same pattern of evolution is observed for the ROI size, with a slightly larger drop. In both cases, a lot of extra fibers are produced, hindering the visualization. In comparison, the variations observed for the position of the ROI seem smaller. For ROI with a mediolateral translation, the difference between all the tractograms is immediately significant for a lateral move (toward the right on the boxplot), but only for the value oROI_s-$2D/5$ for a move in the medial direction. For ROI with an anteroposterior translation, only the forward displacement is already significant from the value oROI_s-$D/5$. It should be noted that the RSD_{init} and SD_{init} scores of the optimal parameters is not at 1 because it includes the variability due to the probabilistic nature of the tractography algorithm used in this study (see section 2.4). In conclusion, lowering the FA parameter or increasing the ROI size results in the production of a lot of erroneous fibers while the ROI translation causes both a truncature of the nerve and erroneous fibers.

4.2. Filtering Contribution

In this section, we evaluate the ability of the three filtering methods described in section 3.1 to remove the erroneous fibers and thereby improve the non-optimized tractograms. This performance is expressed by the SD_{diff} index introduced in section 3.4.

4.2.1. General Performances

Regarding the overall performance of the three filtering methods evaluated using the $SD_{\mathit{mathrmdiff}}$ index and on the basis of all the tractograms of all nerves and patients, the median is equal to 0.049 for entropy, 0.018 for FA, and 0.067 for FOD. It therefore appears that the gain in filtering on the basis of the same data is in favor of the FOD and entropy methods.

Figure 7 represents the overall performance of the three filtering methods qualitatively for a patient and for all nerves combined. On the basis of visual observations made from **Figure 7A**, the quantitative results obtained are confirmed: the entropy and FOD methods give results closest to the ground truth and relatively equivalent quality, while the FA method produces a visually different filtering result which is less in agreement with the ground truth, in particular for the nerves identified in section 4.1 as the most variable, namely V, LN, and AFB. **Figure 7B** allows to study in more detail, nerve by nerve, the effect of the filtering. First observation, the nerves V and III are the most impacted by the increasing of ROI size and are therefore those which benefit the most from the filtering with the best results for the FOD and entropy methods, which make it possible to approach the ground truth more closely.

4.2.2. Tractography Parameters Influence

Figure 8 shows the performance of the three filtering methods according to the different tractography parameters based on the SD_{diff} index. In general, it can be observed that the further we move away from the optimal value of the parameter, the greater the filtering gain is, independently of the filtering method. This can be explained by the fact that tractograms produced with non-optimal parameters are more degraded. Their SD_{init} index is lower, which leaves more room for improvement by the filtering methods. If we compare the filtering methods according to the four tractography parameters, we can observe that FOD provides the best results in the ROI size increase case (significantly different from FA with a $p < 4.9\text{e-}14$ and entropy with a $p < 1.7\text{e-}08$) and better results but very close to entropy for the parameters related to the location of the ROI (significantly different from FA with a $p < 1.8\text{e-}11$ and entropy with a $p < 0.0478$). Concerning the parameter on the FA threshold, the entropy method is competitive or better. The FA method offers lower gains for the four tractography parameters, as observed in the overall performances.

Figure 9 gives a qualitative representation of the performance of the three filtering methods according to the different tractography parameters for different patients and nerves. The visual results presented in **Figure 9** confirm the quantitative results obtained from the analysis of **Figure 8**: the FOD method provides the best results in the case of a too large ROI (case of line 1), concerning the localization of the ROI the entropy and FOD methods are competitive (case of line 2), finally concerning the FA threshold the method based on the entropy provides the results closest to the ground truth.

To analyze more generally the contribution of filtering, we wanted to compare **Figure 6** before filtering with the results after filtering for the three tested methods. **Figure 10** shows whether the difference between the optimal condition and the degraded conditions of **Table 2** are still considered significant after filtering. It turns out that for the FA threshold and ROI size parameters, only the tractogram obtained with the parameter condition the furthest from the optimal remain significantly different (oFA-0.06, oFA-0.1 and oROI+3D/5, oROI+4D/5). In the case of the displacement of the ROI, for the entropy and FOD methods, none of the parameter variations trigger a significantly lower tractogram quality. The FA method is less efficient in this case. In conclusion, the filtering effectively makes it possible to move

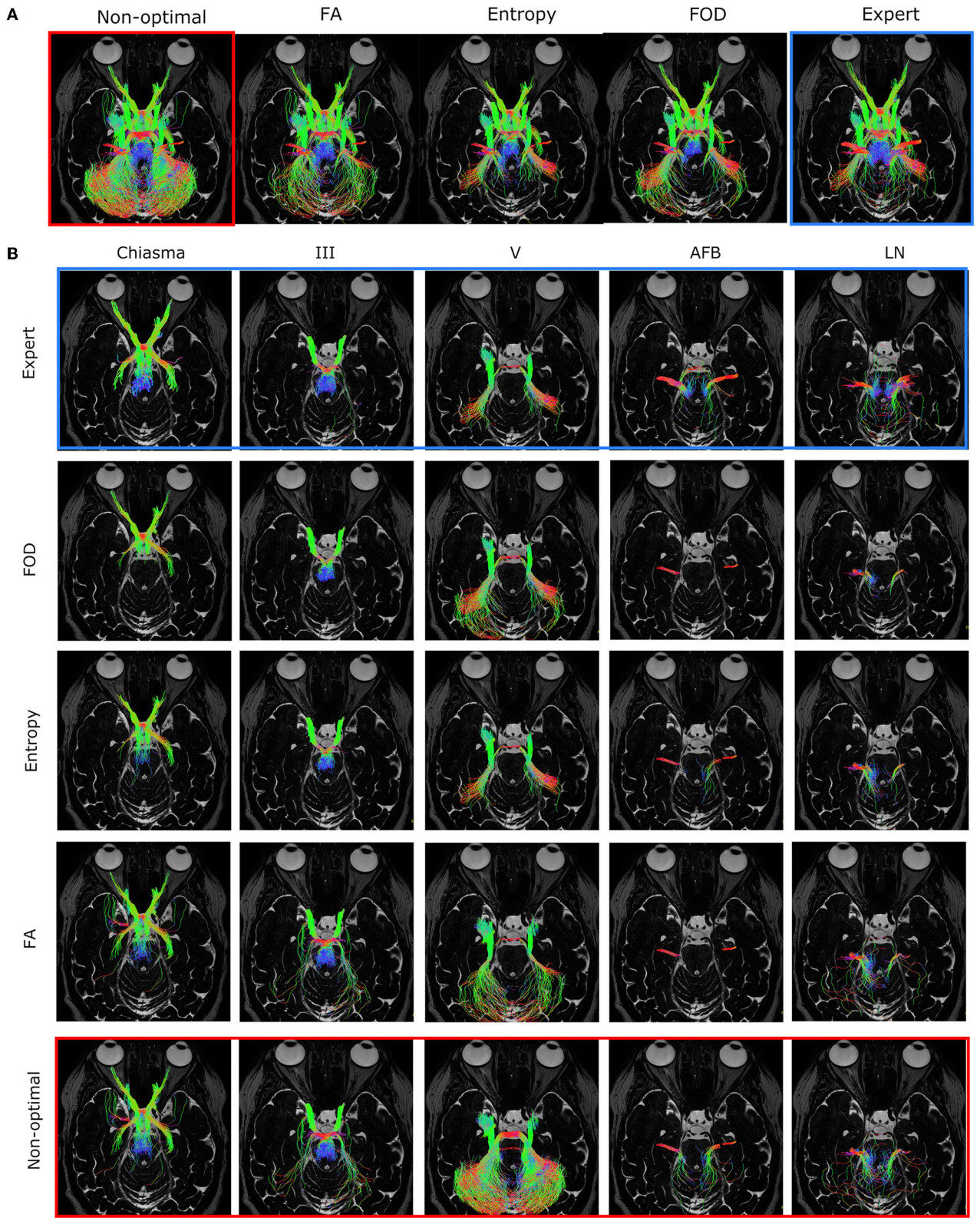

FIGURE 7 | (A) Optimal filtering obtained for the three different filtering methods [FA, entropy, and fiber orientation distribution (FOD), respectively] for all cranial nerves of a specific patient in the case of a regions of interest (ROI) that is too large. **(B)** Independent representation of each nerve. The different nerves are represented in column according to the following order: Chiasma, III, V, AFB, LN, and in line according to the different filtering methods. The "expert" image shows the result of the "ground truth" tractogram and was used for the choice of the optimal threshold. The "non-optimal" image shows a noisy tractogram obtained with poor initialization of the tractography parameters.

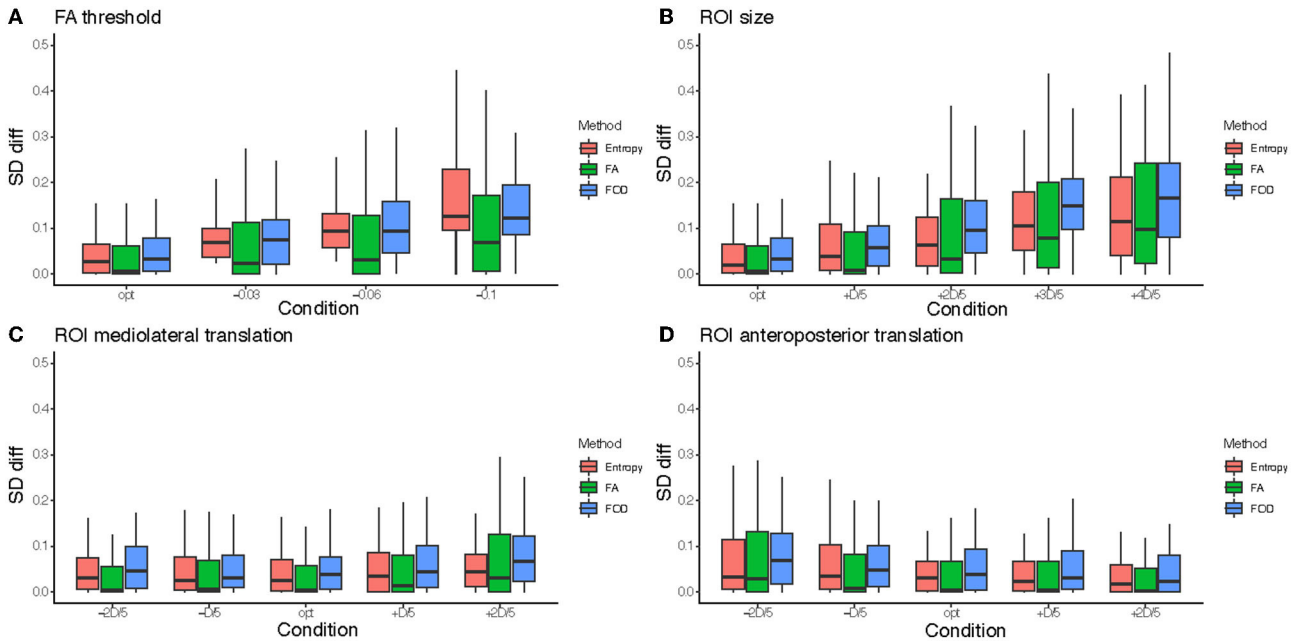

FIGURE 8 | Comparison of the distributions of SD_{diff} according to each condition for the four tractography parameters: **(A)** FA threshold, **(B)** regions of interest (ROI) size, **(C)** ROI mediolateral translation, and **(D)** ROI anteroposterior translation. For each parameter, SD_{diff} is displayed according to each condition and for all three methods [entropy, FA, and fiber orientation distribution (FOD)].

away from the optimal parameters while guaranteeing to find by post-processing tractograms close to those of the ground truth.

4.2.3. Optimal Filtering Threshold

Figure 11 shows, for each filtering method, the distribution of the optimal filtering thresholds in order to reproduce the ground truth as closely as possible (index SD_{max} introduced in section 3.4). These thresholds were normalized by patient with regard to the minimum and maximum indices of entropy, FA, and FOD maps, respectively. **Figure 11**, therefore, represents the variability of the adjustment of the optimal threshold for the different patients and the possibility of its automation. For the entropy, the median value is equal to 0.569, for FA to 0.676, and for FOD to 0.052. The distribution of the thresholds for the entropy method is evenly distributed around the median, while the interquartile distribution for the FA method is more spread above the median. The FOD distribution has a lower median than the other methods and has many values identified as outliers. These two points can make automation difficult for the FOD method.

5. DISCUSSION

In this study, we studied the impact of variations in the tractography parameters on the quality of the tractograms, with regard to the ground truth produced by an expert. The contribution of three filtering methods to correct these perturbations, including a new algorithm, was evaluated with several levels of observation. We have found that filtering increases the overlap with the tractograms produced by the expert, compensating efficiently for a poor tractography parameter optimization. The FOD method seems to be the most efficient filtering method, followed by the new entropy-based method we proposed, which benefits from an optimal threshold that is easier to select. These encouraging results pave the way for the automation of the tractography process.

5.1. Cranial Nerves and Tractography

Cranial nerves are particularly difficult to track because of their small sizes (2–10 mm, see **Table 1**) and their proximity to other structures, especially the brainstem, which can cause false continuations for the tracing of a specific nerve (Yoshino et al., 2016; Jacquesson et al., 2019). According to our study on the sensitivity of the tractograms on the basis of poorly optimized tractography parameters, the most sensitive nerves would be V, LN, and FN. This is in line with results from the literature, which show that the smaller structures tend to be more difficult to follow in tractography (Hodaie et al., 2010; Garcia-Fidalgo and Ortiz, 2013; Jeurissen et al., 2019).

Due to their anatomical characteristics, the cranial nerves are all the more difficult to follow when the tractography parameters are poorly optimized. In this context, it could be observed that it is the size of the ROI which seems the most critical, then the threshold of FA and finally the location of the ROI. As the ROI are drawn in the cisternal segment in the three dimensions, a slight displacement (as achieved in our study) results in a more limited distortion on the resulting tractogram. It should be noted that these significant distortions correspond to parameters that could be selected for the cranial nerves tractography—even by

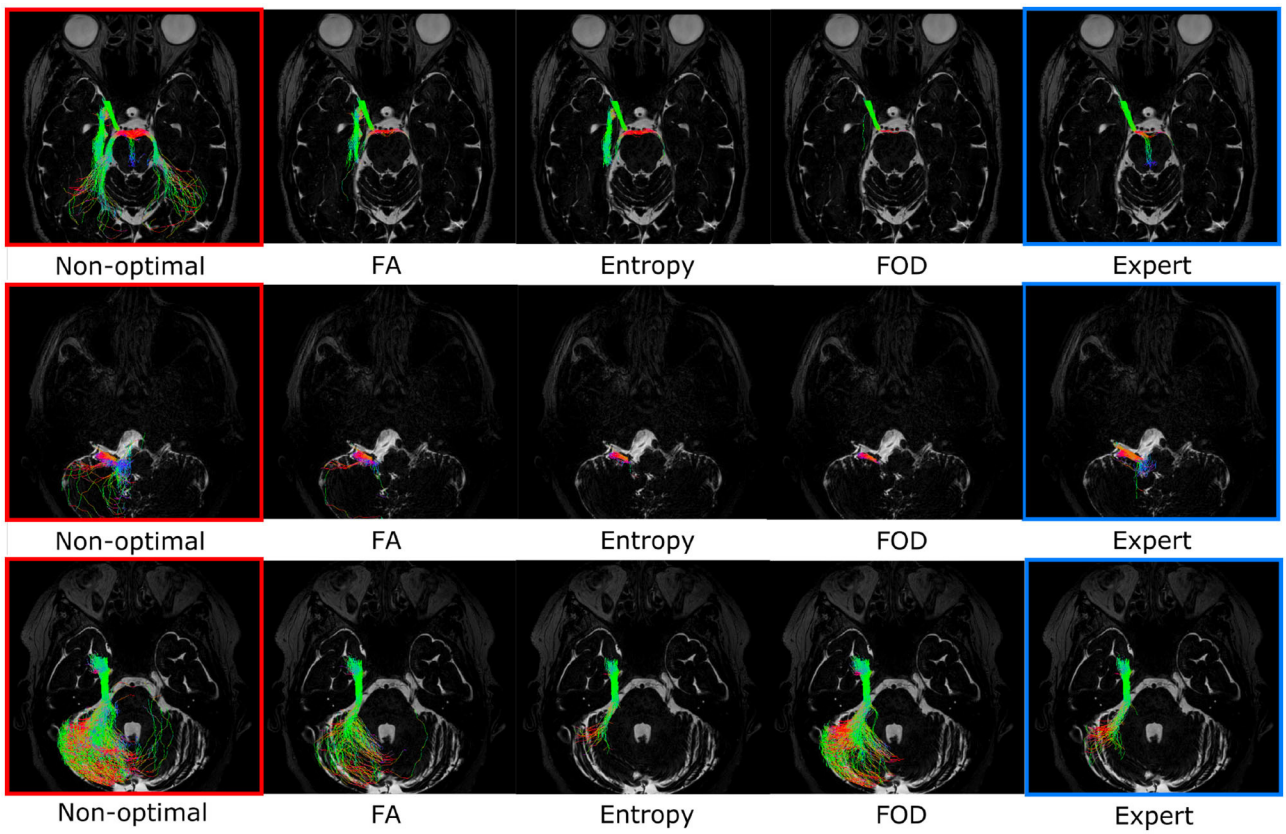

FIGURE 9 | Optimal filtering obtained for the different filtering methods (FA, entropy, and fiber orientation distribution [FOD], respectively) for specific cranial nerves and patients. The "expert" image shows the result of the ground truth tractogram. The "non-optimal" image shows the noisy tractogram obtained with poor initialization of the tractography parameters. **First line**: Illustration of the filtering on the right occulomotor nerve (III) in the case of regions of interest (ROI) that is too large. This case is more efficiently treated by the FOD-based method. **Second line**: Optimal filtering obtained for the right fascial and cochleo-vestibular nerves group (LN) in the case of poor placement of the ROI. This case is more efficiently treated by methods based on FOD and entropy. **Third line**: Optimal filtering obtained for the right trigeminal nerve (V) in the case of non-optimal FA threshold. This case is more efficiently treated by entropy-based method.

experts—with regard to the state of the art (Jacquesson et al., 2018b). More specifically, they can degrade expert tractograms by half on the Sørensen-Dice scale, which is normalized between 0 and 1. A Dice of 0.5 commonly reached in the case of the distortions tested in this work corresponds to an overlap of very poor quality in view of the ground truth. It is therefore important to note that the tractogram errors that we are trying to correct here are significant and lead to aberrant results as evidenced by the illustrations of the work.

A limitation of this study is the use of a unique tractography algorithm. However, this one (probabilistic tractography algorithm based on FOD) was chosen in accordance with the state of the art: He et al. (2021) demonstrate, in the case of the retinogeniculate visual pathway, that this algorithm provides the highest overall reconstruction rate and Xie et al. (2020) establish that a higher order model-based tractography algorithm had better performance on identifying true positive structures in comparison to the single-tensor tractography algorithm in the trigeminal nerve. Finally, this choice is confirmed by the recent study conducted on the same dataset used here (Jacquesson et al., 2018a) where all the cranial nerves could be tracked in the contralateral hemisphere of the tumor and with an 87% success rate on the displaced nerves.

5.2. Accuracy of Tractogram Filtering

The entropy and FOD methods have shown to be able to provide better filtering compared to the ground truth than the FA-based method. This is probably due to their more global nature. The FA-based method integrates punctual information along the fiber while entropy and FOD methods also integrate contextual information. In the case of FA method, the information is specific to each of the voxels without considering the contextual neighborhood, whereas in the case of the entropy and FOD methods, the information is, respectively, specific to a neighborhood adapted to the size of the nerve and to all the diffusion MR image. In addition, it should be noted that the entropy method—which is a statistical measure of the disorder—makes it possible to introduce an anatomical prior of coherence on the tractogram while the FOD method ensures to guarantee the fit between the fibers of the tractogram and the underlying MR diffusion image.

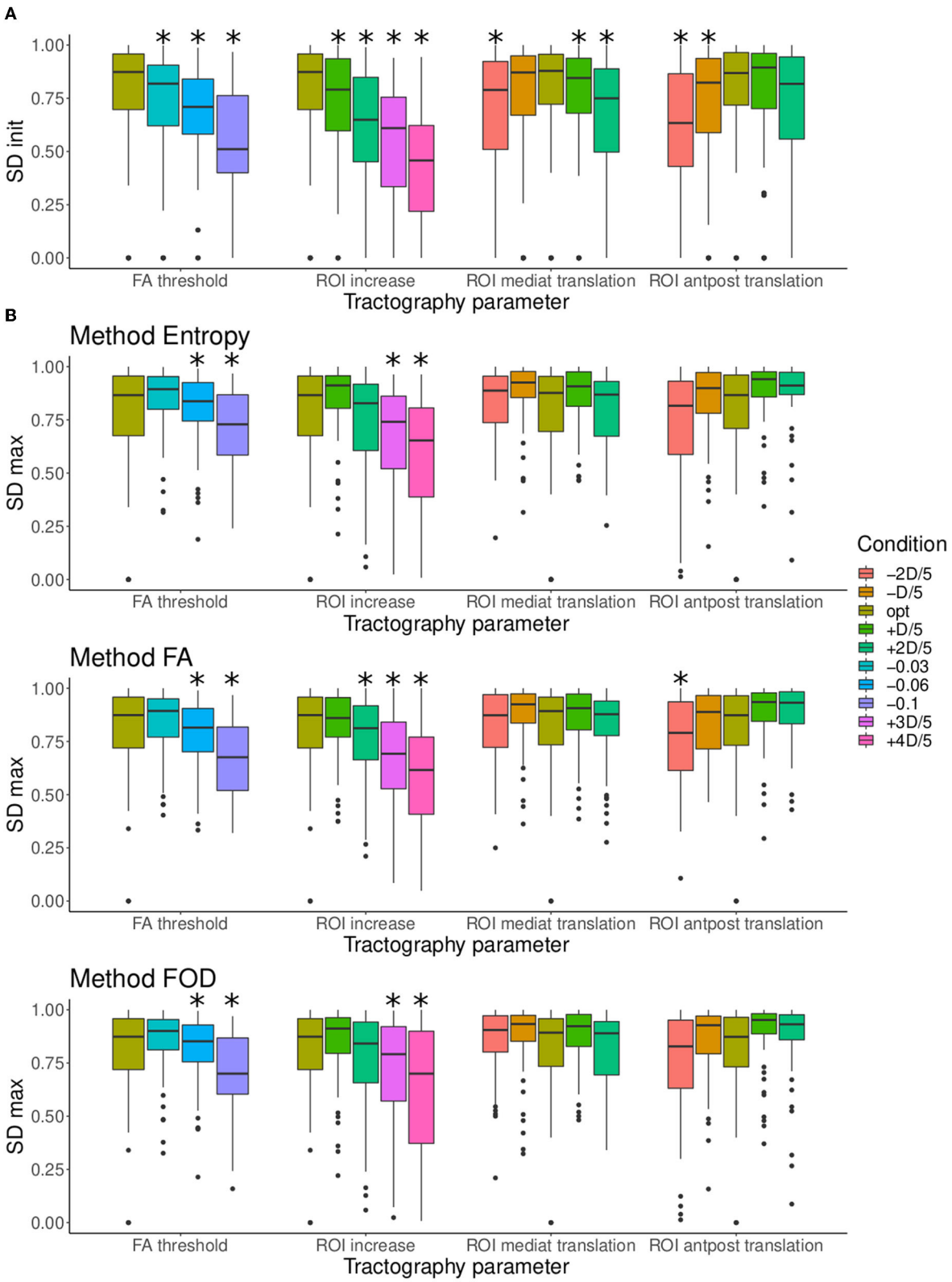

FIGURE 10 | (A) Comparison of the distributions of SD_{init} according to each condition for the four tractography parameters FA threshold, regions of interest (ROI) size, ROI mediolateral translation, and ROI anteroposterior translation. **(B)** Comparison of the distributions of SD_{max} (after filtering) according to each condition for the four

(Continued)

FIGURE 10 | tractography parameters and to the three filtering methods (entropy, FA, and FOD), each represented in a different row. It should be noted that in **(B)** for optimal conditions SD_{init} is given instead of SD_{max} because the optimal tractograms are not filtered. When a condition is significantly smaller to the optimal condition, it is marked with "*".

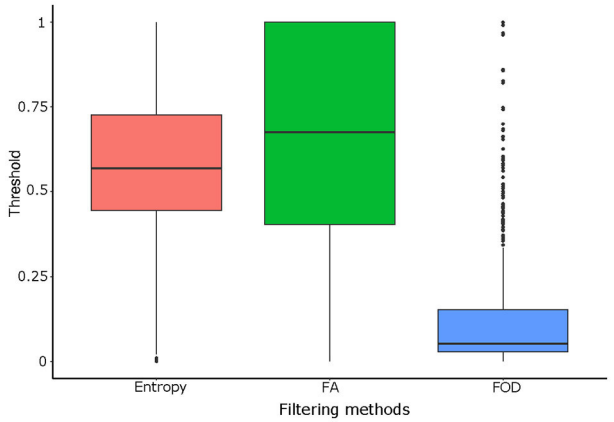

FIGURE 11 | Comparison of the distributions of the optimal filtering threshold according to each filtering method [entropy, FA, and fiber orientation distribution (FOD)].

These differences in the information that is embedded in the filtering approaches along the fiber is crucial. Indeed, when an ROI is misplaced in the cisternal cavity of the nerve, other very proximal bundles can be selected which the FOD and entropy can get rid of thanks to the contextual information from which they benefit. When the ROI is too large, on the other hand, the bundles selected in addition to the nerve of interest can be of very different nature. In this case, only very global information as produced by the FOD makes it possible to remove these bundles. Finally, in the context of a poor parameterization of the FA threshold, the tracing of the cranial nerve can continue for a longer time and in particular in the brainstem where white fibers mingle leading to spurious fibers. In this specific case, only the entropy method makes it possible to track a valid nerve because it encodes the coherence sought by the expert.

However, if the FOD method provides the best filtering results, the new approach developed (entropy) benefits of a reasonable complexity as it only integrates local information, adapted to the size of the nerve. Besides, as it does not depend on the original diffusion MR image, it can be generalized to other fibrous structures. We compared the FOD and entropy methods from a computational time point of view but they are not implemented in the same computer code and the FOD method is parallelized while ours is not yet.

5.3. Perspectives and Recommendations

To go further in the automation of the tractography in surgical planning, we plan to build a probabilistic atlas of ROIs by registering and merging the ROI data of the database used in this work (Jacquesson et al., 2018a). Since our filtering approach is able to deal with dilatation and translation of the ROIs, it seems adequate to compensate for the future use of such an ROI atlas and more particularly with possible patient-specific physiological variations, which would not be encoded in the atlas. From this study, especially the results depicted in **Figures 6**, **8**, we are able to identify the challenges linked to the automation of cranial nerve tractography for presurgical planning and make the following recommendations.

Our study demonstrates that filtering makes it possible to correct the distortions resulting from a bad parameterization of the tractography on the tractograms of cranial nerves. More precisely, we deduced from the results of **Figure 8** that the tolerated error (with regard to the optimal parameter) is 0.03 for FA, and $2D/5$ for the size of the ROI (where D is the size of the nerve of interest). We make more careful recommendations concerning the ROI translations. Unlike the variation of FA or ROI size, ROI translations tend to truncate the nerves, as shown in **Figure 5**. The filtering algorithms cannot compensate for this lack of nervous fibers. For this reason, we recommend to limit the translations as much as possible and to anticipate possible misplacement by increasing the size of the ROI. This information will be taken into account to build the ROI atlas.

5.4. Application in Neurosurgery

The patients included in this study presented tumors of the base of the skull, which displaced cranial nerves (on average, 2 nerves or more were affected by patient). The tractography parameters were adapted by the expert to track those displaced nerves (Jacquesson et al., 2018a). To know whether this displacement impacts in the sensitivity of the tractograms to parameter variation and the effect of the filtering, we consider independently the group of displaced and non-displaced nerves. **Figure 12** shows that the quality of the initial tractograms is not statistically different for the nerves displaced than the others ($p = 0.3$) and that the impact of filtering is similar for the two groups of nerves ($p = 0.22$). Filtering appears to be an automatic method for increasing the quality of tractograms for both intact nerves and displaced nerves. This opens up important perspectives for the targeted application in neurosurgery. A such filtering method could be directly implemented in navigation systems or tractography software to provide an accurate tractography with less user-related steps (Jacquesson et al., 2019). Entropy or FOD filtering could also improve the quality of selective brain fiber tracking in brain connectivity studies.

6. CONCLUSION

We have proposed a method to assess the quality of a filtering method applied to a cranial nerve tractogram. The filtering was carried out by an original approach that selects the fibers of the tractogram from a measurement of entropy applied in the neighborhood of each voxel in order to improve the biological

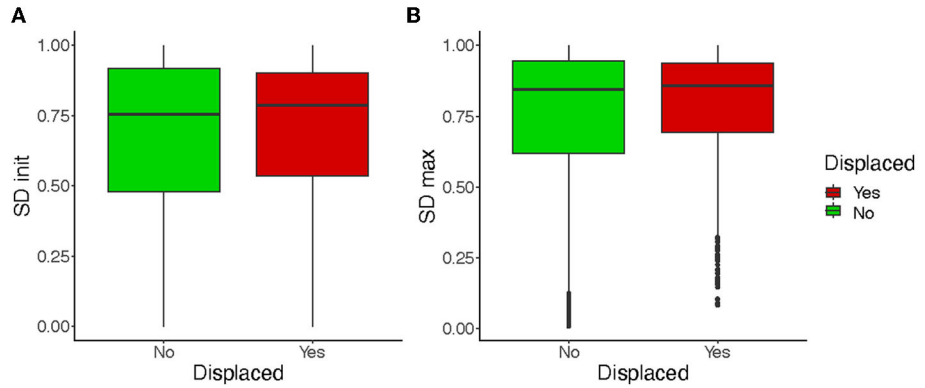

FIGURE 12 | Comparison of the distributions of SD_{init} **(A)** and SD_{max} **(B)** for displaced and non-displaced nerves. SD_{max} is given on average on the basis of all the filtering methods.

precision of the tractogram. This method was compared with two classical other approaches: a method based on FA which integrates only local information and the more recent method based on the FOD which integrates information on the entire diffusion MR image. We show that by removing the fibers considered to be detrimental to the quality of the tractogram given the ground truth, the bias of incorrect parameterization of the tractography is reduced in the filtered datasets and the biological plausibility of the tractograms is improved. Our filtering approach offers filtering performance exceeding the FA approach and similar to the FOD except in the case of too large ROI size. It also offers great possibilities in terms of automation with an optimal threshold that is easier to set and a more modest algorithmic complexity.

DATA AVAILABILITY STATEMENT

The Entropy filtering code is available in the following GitHub project: https://github.com/megdec/tractography-visualization. It also includes a test dataset. Patient data is not available but may be available on special request and under conditions relating to the protection of personal data. Further inquiries can be directed to the corresponding author.

ETHICS STATEMENT

The studies involving human participants were reviewed and approved by CPP SUD-EST II, Bâtiment Pinel, Groupement Hospitalier Est, 59 Boulevard Pinel 69500 BRON. The patients/participants provided their written informed consent to participate in this study. Written informed consent was obtained from the individual(s) for the publication of any potentially identifiable images or data included in this article.

AUTHOR CONTRIBUTIONS

MDec, TJ, and CF contributed to the conception and design of the study. MDec, TP, MV, and MA organized the database and performed the numerical experiments. MA produced the illustrations on the patients. MDes performed the statistical analysis. MDec wrote the first draft of the manuscript. MDec, MDes, TJ, and CF wrote sections of the manuscript. All authors contributed to manuscript revision, read, and approved the submitted version.

FUNDING

Support was received from the Servier Institute; the Hospices Civils de Lyon; the French Society of Neurosurgery; the Medtronic, and Nuovo Soldatis Foundations.

ACKNOWLEDGMENTS

The authors would like to thank the Biosciences Department of INSA Lyon for allowing students TP and MV to carry out their end-of-studies internship on the data of this research work, thus contributing to the completion of this work.

REFERENCES

Andersson, J. L., Skare, S., and Ashburner, J. (2003). How to correct susceptibility distortions in spin-echo echo-planar images: application to diffusion tensor imaging. *Neuroimage* 20, 870–888. doi: 10.1016/S1053-8119(03)00336-7

Borkar, S. A., Garg, A., Mankotia, D. S., Joseph, S. L., Suri, A., Kumar, R., et al. (2016). Prediction of facial nerve position in large vestibular schwannomas using diffusion tensor imaging tractography and its intraoperative correlation. *Neurol. India* 64, 965. doi: 10.4103/0028-3886.190270

Colon-Perez, L., Triplett, W., Bohsali, A., Corti, M., Nguyen, P., Patten, C., et al. (2016). A majority rule approach for region-of-interest-guided streamline fiber tractography. *Brain Imaging Behav.* 10, 1137–1147. doi: 10.1007/s11682-015-9474-5

Dice, L. R. (1945). Measures of the amount of ecologic association between species. *Ecology* 26, 297–302. doi: 10.2307/1932409

Everts, M. H., Bekker, H., and Roerdink, J. B. (2009). Depth-dependent halos: illustrative rendering of dense line data. *IEEE Trans. Visual. Comput. Graph.* 15, 1299–1306. doi: 10.1109/TVCG.2009.138

Garcia-Fidalgo, E., and Ortiz, A. (2013). "Probabilistic appearance-based mapping and localization using visual features," in *Iberian Conference on Pattern Recognition and Image Analysis* (Madeira: Springer), 277–285. doi: 10.1007/978-3-642-38628-2_33

He, J., Zhang, F., Xie, G., Yao, S., Feng, Y., Bastos, D. C., et al. (2021). Comparison of multiple tractography methods for reconstruction of the retinogeniculate visual pathway using diffusion MRI. *Hum. Brain Mapp.* 42, 3887–3904. doi: 10.1002/hbm.25472

Hodaie, M., Quan, J., and Chen, D. Q. (2010). *In vivo* visualization of cranial nerve pathways in humans using diffusion-based tractography. *Neurosurgery* 66, 788–796. doi: 10.1227/01.NEU.0000367613.09324.DA

Jacquesson, T., Cotton, F., Attyé, A., Zaouche, S., Tringali, S., Bosc, J., et al. (2018a). Probabilistic tractography to predict the position of cranial nerves displaced by skull base tumors: value for surgical strategy through a case series of 62 patients. *Neurosurgery* 85, E125–E136. doi: 10.1093/neuros/nyy538

Jacquesson, T., Frindel, C., Kocevar, G., Berhouma, M., Jouanneau, E., Attyé, A., et al. (2018b). Overcoming challenges of cranial nerve tractography: a targeted review. *Neurosurgery* 84, 313–325. doi: 10.1093/neuros/nyy229

Jacquesson, T., Yeh, F.-C., Panesar, S., Barrios, J., Attyé, A., Frindel, C., et al. (2019). Full tractography for detecting the position of cranial nerves in preoperative planning for skull base surgery. *J. Neurosurg.* 132, 1642–1652. doi: 10.3171/2019.1.JNS182638

Jeurissen, B., Descoteaux, M., Mori, S., and Leemans, A. (2019). Diffusion mri fiber tractography of the brain. *NMR Biomed.* 32, e3785. doi: 10.1002/nbm.3785

Joo, W., Yoshioka, F., Funaki, T., and Rhoton, A. L. (2014). Microsurgical anatomy of the trigeminal nerve. *Clin. Anat.* 27, 61–88. doi: 10.1002/ca.22330

Jörgens, D., Descoteaux, M., and Moreno, R. (2021). "Challenges for tractogram filtering," in *Anisotropy Across Fields and Scales* (Cham: Springer), 149. doi: 10.1007/978-3-030-56215-1_7

Kingsley, P. B. (2006). Introduction to diffusion tensor imaging mathematics: Part II. anisotropy, diffusion-weighting factors, and gradient encoding schemes. *Concepts Magnet. Reson. A* 28, 123–154. doi: 10.1002/cmr.a.20049

Le Bihan, D., and Johansen-Berg, H. (2012). Diffusion MRI at 25: exploring brain tissue structure and function. *Neuroimage* 61, 324–341. doi: 10.1016/j.neuroimage.2011.11.006

Leopardi, P. (2006). "A partition of the unit sphere into regions of equal area and small diameter," in *Electronic Transactions on Numerical Analysis*, 309–327.

Nucifora, P. G., Wu, X., Melhem, E. R., Gur, R. E., Gur, R. C., and Verma, R. (2012). Automated diffusion tensor tractography: implementation and comparison to user-driven tractography. *Acad. Radiol.* 19, 622–629. doi: 10.1016/j.acra.2012.01.002

Rheault, F., Poulin, P., Caron, A. V., St-Onge, E., and Descoteaux, M. (2020). Common misconceptions, hidden biases and modern challenges of dmri tractography. *J. Neural Eng.* 17, 011001. doi: 10.1088/1741-2552/ab6aad

Rhoton, A. L. (1979). Microsurgical anatomy of the posterior fossa cranial nerves. *Clin. Neurosurg.* 26:398–462. doi: 10.1093/neurosurgery/26.CN_suppl_1.398

Samii, M., and Gerganov, V. M. (2011). Petroclival meningiomas: quo vadis? *World Neurosur.* 75, 424. doi: 10.1016/j.wneu.2010.12.035

Smith, R. E., Tournier, J.-D., Calamante, F., and Connelly, A. (2013). Sift: Spherical-deconvolution informed filtering of tractograms. *Neuroimage* 67:298–312. doi: 10.1016/j.neuroimage.2012.11.049

Smith, R. E., Tournier, J.-D., Calamante, F., and Connelly, A. (2015). Sift2: Enabling dense quantitative assessment of brain white matter connectivity using streamlines tractography. *Neuroimage* 119, 338–351. doi: 10.1016/j.neuroimage.2015.06.092

Smith, S. M., Jenkinson, M., Woolrich, M. W., Beckmann, C. F., Behrens, T. E., Johansen-Berg, H., et al. (2004). Advances in functional and structural mr image analysis and implementation as FSL. *Neuroimage* 23, S208–S219. doi: 10.1016/j.neuroimage.2004.07.051

Song, F., Hou, Y., Sun, G., Chen, X., Xu, B., Huang, J. H., et al. (2016). *In vivo* visualization of the facial nerve in patients with acoustic neuroma using diffusion tensor imaging-based fiber tracking. *J. Neurosurg.* 125, 787–794. doi: 10.3171/2015.7.JNS142922

Tournier, J.-D., Calamante, F., and Connelly, A. (2007). Robust determination of the fibre orientation distribution in diffusion mri: non-negativity constrained super-resolved spherical deconvolution. *Neuroimage* 35, 1459–1472. doi: 10.1016/j.neuroimage.2007.02.016

Tournier, J.-D., Mori, S., and Leemans, A. (2011). Diffusion tensor imaging and beyond. *Magnet. Reson. Med.* 65, 1532. doi: 10.1002/mrm.22924

Tournier, J.-D., Smith, R., Raffelt, D., Tabbara, R., Dhollander, T., Pietsch, M., et al. (2019). MRtrix3: A fast, flexible and open software framework for medical image processing and visualisation. *Neuroimage* 2019, 116137. doi: 10.1016/j.neuroimage.2019.116137

Xie, G., Zhang, F., Leung, L., Mooney, M. A., Epprecht, L., Norton, I., et al. (2020). Anatomical assessment of trigeminal nerve tractography using diffusion MRI: a comparison of acquisition b-values and single-and multi-fiber tracking strategies. *Neuroimage Clin.* 25, 102160. doi: 10.1016/j.nicl.2019.102160

Xu, C., and Prince, J. L. (1998). Snakes, shapes, and gradient vector flow. *IEEE Trans. Image Process.* 7, 359–369.

Yeh, C.-H., Jones, D. K., Liang, X., Descoteaux, M., and Connelly, A. (2021). Mapping structural connectivity using diffusion MRI: Challenges and opportunities. *J. Magnet. Reson. Imaging* 53, 1666–1682. doi: 10.1002/jmri.27188

Yoshino, M., Abhinav, K., Yeh, F.-C., Panesar, S., Fernandes, D., Pathak, S., et al. (2016). Visualization of cranial nerves using high-definition fiber tractography. *Neurosurgery* 79, 146–165. doi: 10.1227/NEU.0000000000001241

Yousry, I., Camelio, S., Schmid, U., Horsfield, M., Wiesmann, M., Brückmann, H., et al. (2000). Visualization of cranial nerves I-XII: value of 3D CISS and T2-weighted fse sequences. *Eur. Radiol.* 10, 1061–1067. doi: 10.1007/s003300000452

Zhang, W., Olivi, A., Hertig, S. J., van Zijl, P., and Mori, S. (2008). Automated fiber tracking of human brain white matter using diffusion tensor imaging. *Neuroimage* 42, 771–777. doi: 10.1016/j.neuroimage.2008.04.241

Zhang, Y., Zhang, J., Oishi, K., Faria, A. V., Jiang, H., Li, X., et al. (2010). Atlas-guided tract reconstruction for automated and comprehensive examination of the white matter anatomy. *Neuroimage* 52, 1289–1301. doi: 10.1016/j.neuroimage.2010.05.049

Conflict of Interest: The authors declare that the research was conducted in the absence of any commercial or financial relationships that could be construed as a potential conflict of interest.

Publisher's Note: All claims expressed in this article are solely those of the authors and do not necessarily represent those of their affiliated organizations, or those of the publisher, the editors and the reviewers. Any product that may be evaluated in this article, or claim that may be made by its manufacturer, is not guaranteed or endorsed by the publisher.

Copyright © 2022 Decroocq, Des Ligneris, Poquillon, Vincent, Aubert, Jacquesson and Frindel. This is an open-access article distributed under the terms of the Creative Commons Attribution License (CC BY). The use, distribution or reproduction in other forums is permitted, provided the original author(s) and the copyright owner(s) are credited and that the original publication in this journal is cited, in accordance with accepted academic practice. No use, distribution or reproduction is permitted which does not comply with these terms.

frontiers | Frontiers in Neurology

SYSTEMATIC REVIEW
published: 05 April 2022
doi: 10.3389/fneur.2022.857825

Ultra-High-Field MRI in the Diagnosis and Management of Gliomas: A Systematic Review

*Annabelle Shaffer[1], Susanna S. Kwok[1], Anant Naik[1], Aaron T. Anderson[2,3], Fan Lam[2,4,5], Tracey Wszalek[2,3], Paul M. Arnold[1,6] and Wael Hassaneen[1,6]**

[1] Carle Illinois College of Medicine, University of Illinois at Urbana-Champaign, Champaign, IL, United States, [2] Beckman Institute for Advanced Science and Technology, University of Illinois at Urbana-Champaign, Champaign, IL, United States, [3] Carle Illinois Advanced Imaging Center, University of Illinois and Carle Health, Urbana, IL, United States, [4] Department of Bioengineering, University of Illinois at Urbana-Champaign, Champaign, IL, United States, [5] Cancer Center at Illinois, University of Illinois at Urbana-Champaign, Champaign, IL, United States, [6] Carle Department of Neurosurgery, Carle Foundation Hospital, Urbana, IL, United States

Importance: Gliomas, tumors of the central nervous system, are classically diagnosed through invasive surgical biopsy and subsequent histopathological study. Innovations in ultra-high field (UHF) imaging, namely 7-Tesla magnetic resonance imaging (7T MRI) are advancing preoperative tumor grading, visualization of intratumoral structures, and appreciation of small brain structures and lesions.

Objective: Summarize current innovative uses of UHF imaging techniques in glioma diagnostics and treatment.

Methods: A systematic review in accordance with PRISMA guidelines was performed utilizing PubMed. Case reports and series, observational clinical trials, and randomized clinical trials written in English were included. After removing unrelated studies and those with non-human subjects, only those related to 7T MRI were independently reviewed and summarized for data extraction. Some preclinical animal models are briefly described to demonstrate future usages of ultra-high-field imaging.

Results: We reviewed 46 studies (43 human and 3 animal models) which reported clinical usages of UHF MRI in the diagnosis and management of gliomas. Current literature generally supports greater resolution imaging from 7T compared to 1.5T or 3T MRI, improving visualization of cerebral microbleeds and white and gray matter, and providing more precise localization for radiotherapy targeting. Additionally, studies found that diffusion or susceptibility-weighted imaging techniques applied to 7T MRI, may be used to predict tumor grade, reveal intratumoral structures such as neovasculature and microstructures like axons, and indicate isocitrate dehydrogenase 1 mutation status in preoperative imaging. Similarly, newer imaging techniques such as magnetic resonance spectroscopy and chemical exchange saturation transfer imaging can be performed on 7T MRI to predict tumor grading and treatment efficacy. Geometrical distortion, a known challenge of 7T MRI, was at a tolerable level in all included studies.

Conclusion: UHF imaging has the potential to preoperatively and non-invasively grade gliomas, provide precise therapy target areas, and visualize lesions not seen on conventional MRI.

Keywords: ultra-high field imaging, ultra-high field MRI, 3-Tesla MRI, 7-Tesla MRI, brain tumors, gliomas, glioblastoma

OPEN ACCESS

Edited by:
Nico Sollmann, University of California, San Francisco, United States

Reviewed by:
Daniel Paech, University Hospital Bonn, Germany
Antonio Di Ieva, Macquarie University, Australia
Cornelia Brendle, Kantonsspital Münsterlingen, Switzerland

***Correspondence:**
Wael Hassaneen
wael.mostafa@carle.com

Specialty section:
This article was submitted to Neuro-Oncology and Neurosurgical Oncology, a section of the journal Frontiers in Neurology

Received: *19 January 2022*
Accepted: *02 March 2022*
Published: *05 April 2022*

Citation:
Shaffer A, Kwok SS, Naik A, Anderson AT, Lam F, Wszalek T, Arnold PM and Hassaneen W (2022) Ultra-High-Field MRI in the Diagnosis and Management of Gliomas: A Systematic Review. Front. Neurol. 13:857825. doi: 10.3389/fneur.2022.857825

INTRODUCTION

Gliomas are tumors arising from glial cells—astrocytes, oligodendrocytes, microglia—and make up approximately one-third of primary central nervous system (CNS) tumors. Physiologically, glial cells contribute to many essential tasks, including supporting neuronal metabolic function, contributing to the blood-brain barrier, and myelinating axons (1). Gliomas are characterized by the glial cell type underlying the neoplastic change and biomarkers, such as key genes or altered molecular pathways (2). Additionally, like other tumors, gliomas are further graded *via* the World Health Organization (WHO) criteria that utilizes histological and molecular genotypic features to assess the degree of malignancy on a scale of CNS WHO grade 1 (low grade, slow growing) to 4 (high grade, very aggressive) (2, 3). However, many studies referenced here utilize terminology from prior WHO classification criteria.

Early and accurate identification of gliomas is critical in diagnostics, prognostics, and strategic tailoring of individual therapy. Therapy can include a combination of surgery, radiotherapy, and chemotherapy. This characterization is especially important to the treatment of highly aggressive tumors, such as glioblastoma (GBM), which has a <5% 5-year survival probability (4). Presently, tissue biopsy is required for tumor grading and genotyping whereby assessment of glial fibrillary acidic protein production, isocitrate dehydrogenase 1 (IDH) mutational status, presence of 1p/19q codeletion, epidermal growth factor receptor (EGFR) expression, E3 ubiquitin-protein-ligase-Mdm2 encoding gene mutation status, and other neoplastic changes within gliomas enables the more robust characterization that is critical to the development of individualized treatment associated with improved clinical outcomes (2–4). For example, IDH mutations have improved survival outcomes compared to IDH-wildtype (WT) (5), and O(6)-methylguanine-DNA methyltransferase (MGMT) promoter methylation is a favorable prognostic factor in GBM (6).

However, histopathology necessitates surgical collection of brain tissue and must be preceded by extensive clinical workup to confirm the presence of cancerous tissue. An integral part of clinical workup is brain imaging, ideally MRI, which is used to confirm the presence of a lesion, its location, and to generate a plan for intraoperative navigation (7). Traditional low field MRI (1.5T or 3T, found in most clinical settings) has been shown to significantly improve the extent of glioma resection (8). Advances in low field MRI acquisition and processing, including innovative uses of diffusion-weighted imaging (DWI) and magnetic resonance spectroscopic imaging (MRS/I) algorithms, have enabled both more accurate delineation of tumors margins and pre-operative assessment of biomolecular characteristics associated with gliomas that was previously only feasible through histologic assessment of biopsied brain tissue. These imaging sequences, along with numerous other advancements (4), have demonstrated the ability of MRI to provide information for enhanced tumor characterization and improved predictions of treatment efficacy that traditionally relied on surgical biopsy.

Ultra-high field (UHF) MRI systems are defined as having a magnetic field strength of 7T or higher (9, 10) and different applications are displayed in **Figure 1**. The enhanced sensitivity and stronger gradient systems have allowed for the acquisition of higher resolution images of the brain with clinically acceptable acquisition times (11), as well as more accurate quantification of tissue biophysical parameters and disease states (12). Variations in image acquisition and processing enable unique characterization of gliomas at UHF may improve diagnosis and treatment efficacy prediction without the need for tissue biopsy. Numerous studies have demonstrated the utility of UHF imaging on patients with glioma. To further our understanding of the potential clinical benefits of UHF imaging on gliomas, we seek to summarize such studies in this concise, systematic review.

Ultra-High Field MRI: A Cost Benefit Analysis

UHF systems offer a variety of benefits in assessing tissue. First, the signal-to-noise ratio (SNR) has been found to scale up to super-linearly with static magnetic field strength (B0) enabling higher spatial resolution and enhanced gray vs. white matter contrast (10, 13–15). Second, UHF imaging provides higher resolution molecular data that can be used in the characterization of non-structural neoplastic changes (such as metabolic activity, angiogenesis, and protein synthesis) in the brain which, at low-field, has been severely limited by poor resolution and long acquisition time (16–19). Third, spectral resolution is enhanced due to elevated SNR and separation of metabolite peaks allowing for more metabolites to be detected (20).

The cost of UHF systems is significantly greater than lower field systems as each Tesla costs ∼$1 million (9). Other upfront costs include larger space to house the scanner, reinforced flooring to support the weight of the magnet, and more steel for magnetic shielding. In our institution's experience of acquiring a 7T MRI, we have encountered increased service costs due to less expertise available for 7T MRI technical support and increased time required to optimize imaging protocols compared to lower field systems. Costs for cooling the superconducting magnet are unchanged due to its zero-boil-off nature which eliminates the need for helium refills. Hospital revenue for MRI scans is also unchanged as there is only one rate available. However, as 7T imaging becomes more specific for different pathologies, the need for other tests may decline, reducing the overall costs incurred.

METHODS

We performed a systematic review adherent to PRISMA guidelines. A search on PubMED was performed on March 30th, 2021 using the following terms: *((Ultra high field) OR ("7-Tesla" OR "7Tesla" OR "7 Tesla") OR ((("7T" OR "7-T" OR "7 T") AND (MRI)))) AND ((Glioblastoma) OR (GBM) OR (Glioma)).* Articles were also subsequently added after citation matching and a more updated literature search. We sought to obtain articles that utilized various UHF MRI techniques for

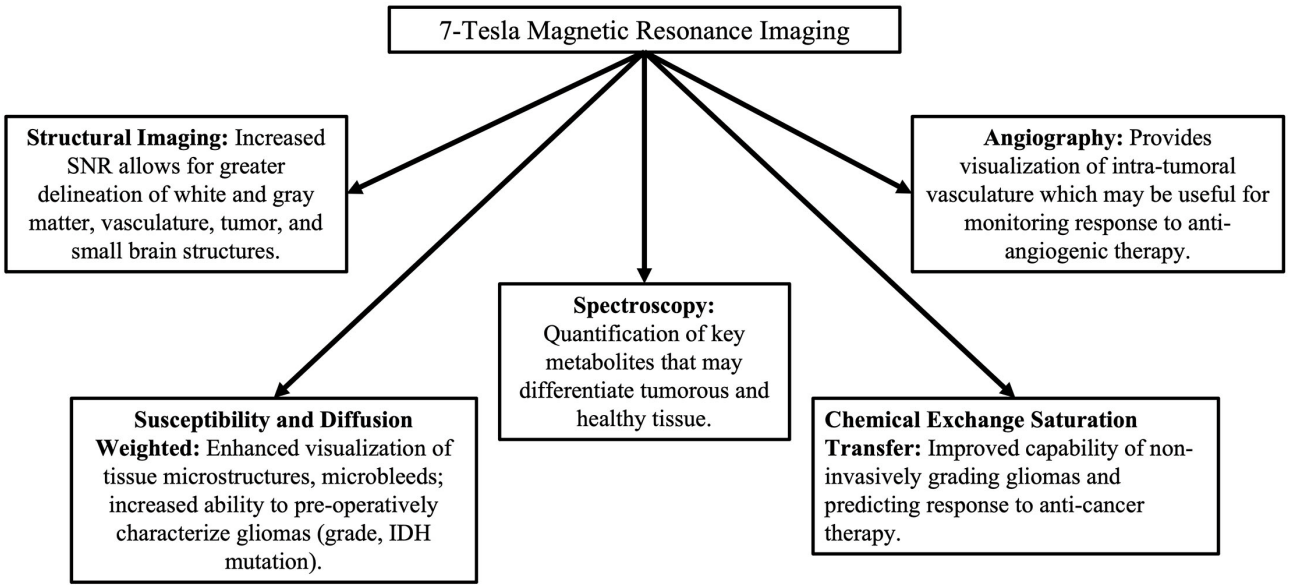

FIGURE 1 | Types of advanced imaging techniques and their benefits in comparison to lower-field MRI.

the characterization of glioma. We included case reports, case series, retrospective and prospective observational studies, and randomized controlled trials. Clinical evidence was prioritized over preclinical models. Non-full length and non-English records were excluded. No date constraints were imposed. **Figure 2** summarizes the search strategy and subsequent inclusion and exclusion parameters utilized in this systematic review. **Supplementary Table 1** summarizes characteristics of all included human studies. We examined several previously defined outcomes. First, we sought to investigate a comparable improvement in signal-to-noise ratio, yielding better diagnostic capacity across multiple imaging modalities. Second, we sought to expand diagnostic impact, which was defined by any possible alterations in clinical management by the use of UHF imaging. This included impact on patient mortality, progression free survival, degree of tumor resection, and selection of treatment modality post-operatively.

RESULTS

From an initial 472 articles obtained through databases, elimination of non-duplicates, reviews and meta-analyses yielded 381 articles whose title, abstract and additional meta-data were screened against the inclusion criteria defined. One hundred and ninety-four full-length articles were screened, yielding 46 for consideration for final meta-analysis, of which 11 articles were discovered with an updated search and citation matching.

Structural Imaging

The advent of *in vivo* non-invasive structural imaging revolutionized medical practice, enabling the visualization of anatomic changes related to disease without autopsy. Due to its ability to provide high-contrast in soft tissue, MRI has been the cornerstone of assessing structural changes in the brain. Improvements to traditional, low-field structural imaging *via* UHF has improved SNR ratios, providing higher resolution contrast to enhance delineation of smaller white matter, gray matter, vasculature, and other brain structures (11, 21). Image acquisition at 7T can be clinically feasible with durations of 7:30 min and minimal side effects (11). Compter et al. (21) demonstrated the ability of 7T MRI to depict micro-vascularization in GBM. Furthermore, this study showed that incorporation of these images into neurosurgical navigation and radiotherapy treatment planning systems was not only technically feasible, but suggested that its use, following clinical-use optimization, may improve surgical outcomes compared to systems guided by low-resolution computed tomography images (21). In a study that assessed pre-operative GBM, Regnery et al. (11) compared fluid-attenuated inversion recovery (FLAIR) sequenced images obtained at 3T compared to 7T. This study found higher SNR in white matter and greater contrast of healthy white matter to GBM tissue with the subsequent conclusion that UHF FLAIR may enhance visualization of tumor infiltration into neighboring white matter tracts (11). They found demarcation of tumor boundaries through UHF significantly reduced calculated GBM volume by 7.4%, implying that UHF has the potential to spare more healthy brain tissue (11).

Challenges to structural imaging at 7T include poor image quality and the presence of ghosting artifacts in structures nearest the skull base (**Figure 3**), namely the frontal and temporal lobes, which may be attributed to signal heterogeneity caused by the transition of tissue type (21). These challenges, which are similarly described at lower field strengths, may be overcome through image correction specific to sequences obtained, usage of dielectric pads, and improvements in hardware (11, 21–23).

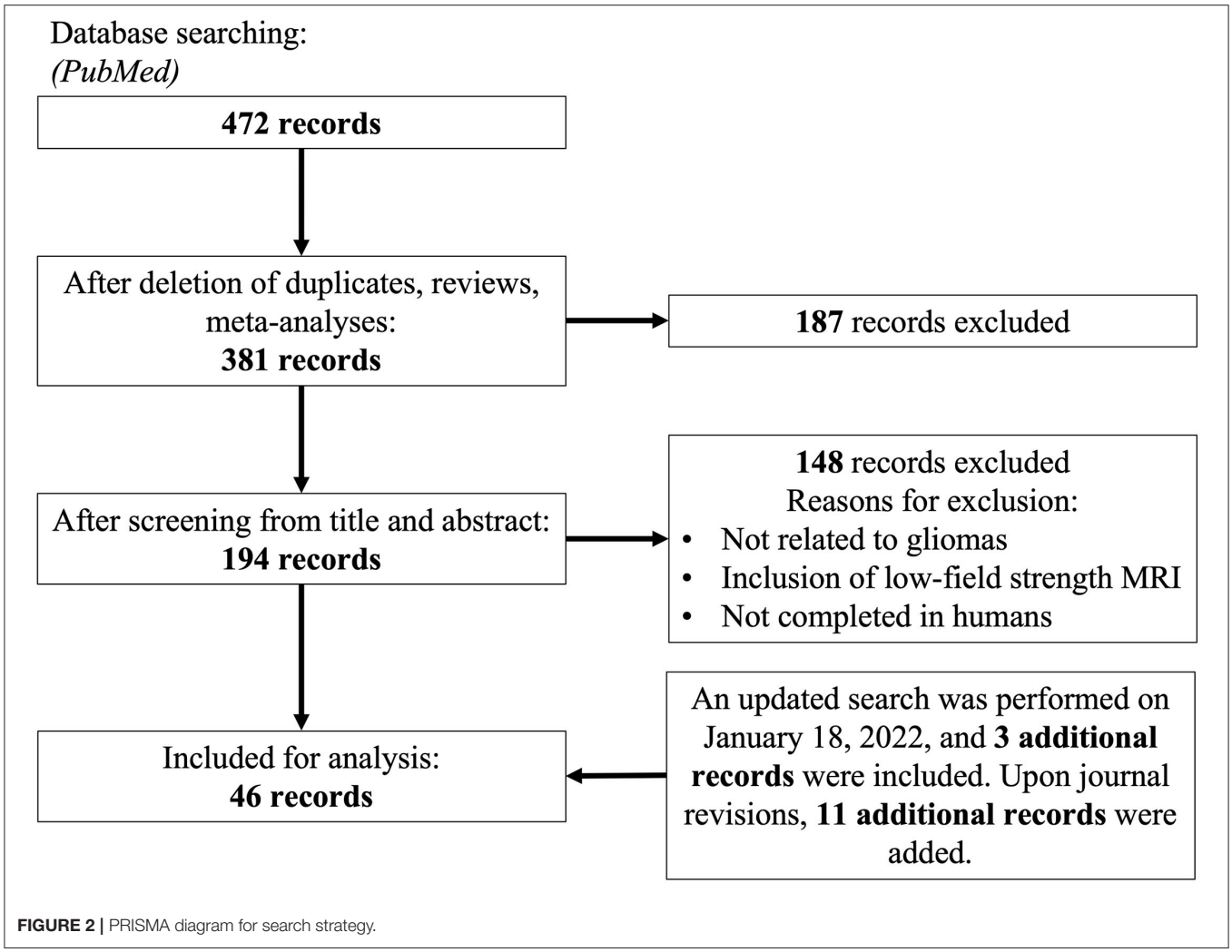

FIGURE 2 | PRISMA diagram for search strategy.

Diffusion and Susceptibility-Weighted Imaging

Susceptibility weighted imaging (SWI) combines both the magnitude and phase components of MRI data to generate images, while standard diagnostic images only make use of magnitude information. SWI is sensitive to diamagnetic, paramagnetic, and ferromagnetic substances due to the phase shifts that these substances cause. DWI also uses MRI to visualize tissue microstructures, such as axons and glial cells, through the random motion of water particles. Both imaging techniques have been utilized to analyze small structures in the brain, such as microbleeds after radiation therapy and intra-tumoral vasculature. As outlined below, usage of these techniques could provide enhanced estimation of pre-operative tumor grade, characterization of tumor microstructures, and visualization of radiation therapy injury.

Currently, diagnosis of a glioma requires histopathological analysis of a surgical biopsy obtained. MRIs can also provide an estimation of a tumor's grade based on the contrast-enhancement present (24). However, MRI estimation of tumor grade is limited by inconsistency of contrast enhancement in benign and malignant gliomas and contraindications to the use of contrast (24). As such, new preoperative imaging techniques are being developed to estimate tumor grade more accurately.

Neovascularization is a distinguishing feature of highly malignant gliomas (25), such as GBM, and can be visualized through SWI. Venous structures can also be visualized *via* SWI 7T (26). Two case series (25, 27) utilized longitudinal SWI 7T MRI to identify changes in tumor vasculature during administration of an anti-angiogenic therapy, bevacizumab, to patients with a GBM or anaplastic astrocytoma. Grabner et al. (27) visualized changes in brain edema in four of five patients, microhemorrhages in one patient, and increased intratumoral irregularities in one patient. In another patient, intratumoral changes were difficult to visualize due to scarring (27). Similarly, SWI 7T MRI and fractal dimension analysis was used to quantify changes in intratumoral vasculature and complexity (25, 28). Fractal dimensions describe an object's geometric complexity and have been used in neuroradiology to detect lesions (25, 28). In a four patient case series, one patient had neurological

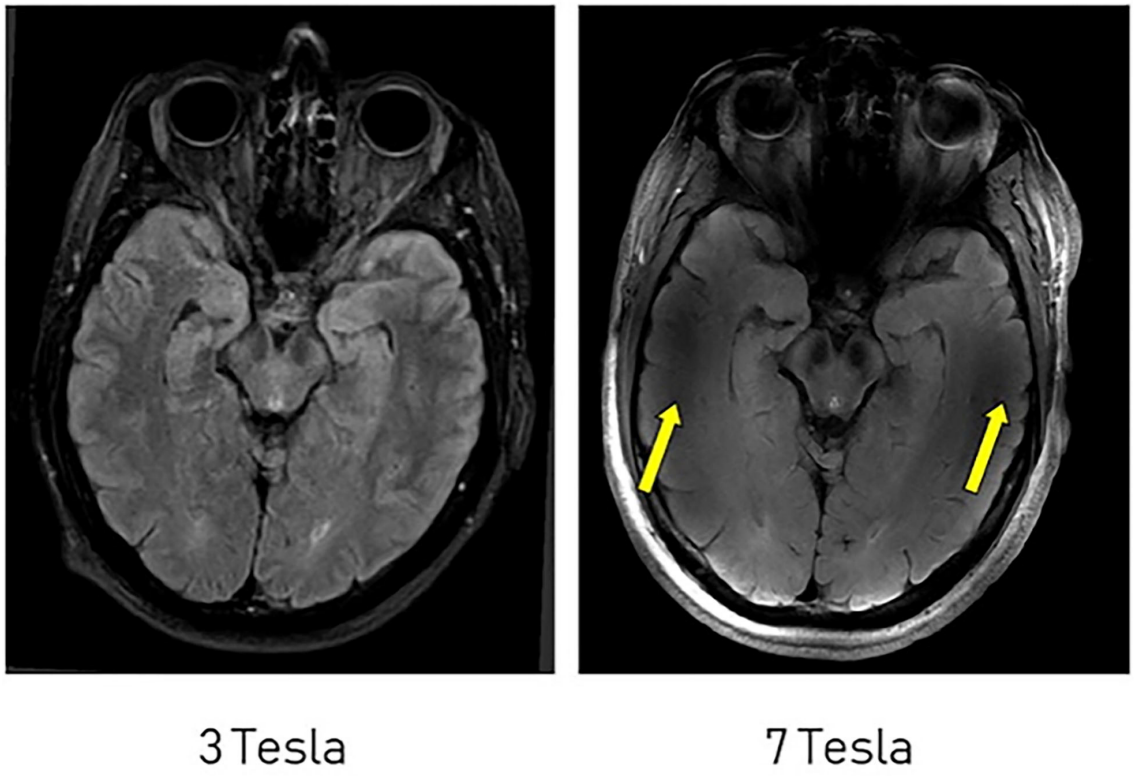

FIGURE 3 | Comparison of FLAIR imaging at 3T and 7T. Artifacts are more significant near the skull base at 7T (yellow arrows). This figure is used with permission from Regnery et al. (11).

improvements alongside a decreased fractal dimensions value following anti-angiogenic therapy (25). In a 36 patient series, a significant difference in fractal dimension values was identified between WHO grade 2 and grade 4 gliomas (28).

In addition to tumor vascularity, molecular markers, such as IDH, are useful in tumor grading and prognosis. IDH-mutant is associated with gliomas of lesser grades and greater progression-free survival time (24). Median survival time of GBM patients with an IDH mutation was 16 months more than those with IDH-WT (15 vs. 31 months) (29). Grabner et al. (24) utilized local image variance (LIV) of hypo-intensities seen on SWI 7T MRI and compared LIV values to tumor grade and IDH-mutant status. In a 30 patient study, where half had an IDH mutation, LIV values were significantly increased in WHO grade 3 and 4 gliomas and significantly correlated with numerical grading. Furthermore, significantly higher LIV values were found in IDH-WT gliomas vs. IDH-mutant gliomas (24).

SWI MRI has also been utilized to assess radiation therapy-induced injury to the brain. Lupo et al. (30) and Bian et al. (31) assessed cerebral microbleeds after radiation therapy using 7T SWI MRI and found microbleeds only in glioma patients who had undergone radiation therapy. Glioma patients who had exclusive chemotherapy did not present with these lesions. Additionally, Bian et al. (31) compared microbleed detection in SWI 3T and SWI 7T MRI. SWI MRI at 3T and 7T strengths detected significantly more microbleeds than magnitude-only images. However, there were insignificant differences in microbleeds detected by SWI 7T MRI vs. SWI 3T MRI when both deep-brain ($n = 3$) and non-deep-brain tumors ($n = 7$) were considered (31). When only non-deep-brain tumors were considered, SWI 7T MRI detected significantly more microbleeds than SWI 3T MRI (31).

Due to DWI's ability to visualize tissue microstructures, it has been used to evaluate many brain disease processes including gliomas. Wen et al. (32) described the clinical feasibility of acquiring DWI 7T MRI and the comparability to images acquired with DWI at 3T MRI. The images at 7T provided unique contrast that supported better visualization of tissue complexity.

Spectroscopy

Structural MRI uses signals from water protons (^{1}H) to generate an anatomic depiction of the brain by voxel. It is also used to map data acquired through other modalities such as magnetic resonance spectroscopy (MRS). MRS has been traditionally used to identify biomolecules through ^{1}H signals acquired in waveforms with unique resonance frequency differences. When MRS for a specified nucleus is collected voxel-by-voxel and mapped onto a structural MRI image, spectroscopy enables visualization of specific biomolecules within the brain as MRS/I. This enables the quantification and mapping of various molecules relevant to brain metabolism, possibly without

exogenous contrast agents. Besides ^{1}H, other nuclei can also be imaged by MRS/I, e.g., carbon (^{13}C), deuterium (^{2}H), fluorine (^{19}F), phosphorus (^{31}P), and sodium (^{23}Na) (latter two have FDA-approved coils) enabling broad biomolecular profiling or depiction of molecular concentrations within a volume both at a given timepoint and longitudinally. MRS/I generates output in the form of spatially-resolved MR spectra, from which the detection of specific molecules of interest and quantification of molecular composition can be performed. The use of non-^{1}H nuclei, due to low *in-vivo* concentrations, has had limited success at lower field-strength MRI; however, the use of UHF offers the unique advantage of capturing small concentrations of non-^{1}H nuclei at high resolution.

Cancer is associated with a myriad of biomolecular changes that, in theory, make MRS/I uniquely suitable to non-invasively characterize tumors and contribute to treatment planning (33). However, the clinical applications of MRS/I have been greatly hindered by long acquisition times, low image resolution, and poor SNR. The improved instrumentation offered by UHF systems provides unique opportunities to address these long-standing challenges. Combined with the results from studies optimizing image acquisition and processing, 7T MRS/I has the potential to provide robust biomolecular information that could improve clinical diagnostics, evaluation of progression, and assessment of therapeutic responses of gliomas.

Currently, studies on 7T MRS/I in brain tumors can be categorized as either those that evaluate the efficacy of non-^{1}H-MRS in tumor characterization (34–38) or those that modify image acquisition or processing methods to optimize ^{1}H-MRS for clinical use (namely to increase SNR and decrease acquisition time) (39–43). Apart from ^{1}H, 7T MRS/I using ^{17}O, ^{31}P, ^{35}Cl, and ^{23}Na NMR have been acquired on patients with gliomas to evaluate feasibility compared to existing methods (34–37). The use of non-^{1}H nuclei enables the study of specific pathophysiologic processes involved in neurologic cancers: ^{17}O allows for the depiction of oxygen-consumption correlated to changes in cerebral metabolic rate associated with glioma (44, 45); ^{31}P enables visualization of ATP[1] and pH (46, 47); ^{35}Cl and ^{23}Na enable the visualization of ion-pump and ion-channel activity related to electrochemical conduction (35, 36). Additionally, ^{23}Na has demonstrated the ability to reflect both IDH mutation status and tumor grade (48). However, another study showed that ^{23}Na in 7T MRI could not predict progression-free nor overall survival, but changes in total sodium content in GBM patients undergoing chemoradiotherapy were appreciated (49). Additional studies have sought to identify biomolecules specifically associated with gliomas using metabolic mapping on 7T MRS/I compared to 3T MRS/I (38, 39). These studies found that metabolites, including creatinine, choline, glutamate, glutamine, glutathione, myoinositol, N-acetylaspartate (NAA), N-acetyl-aspartylglutamine (NAAG), and taurine, could be visualized with 7T MRS/I (38, 39). Differences in metabolic profiles may distinguish tumorous tissue and healthy brain tissue (50).

UHF ^{1}H-MRS/I studies also focus on overcoming the limitations of 3T MRS/I through adopting better instrumentation and tailored acquisitions such as the use of different MRI head coils (36), use of short and ultrashort echo times (40–43, 51), better localization (42), dual-readout alternated gradients (51), and adiabatic selective refocusing (43). Several of these studies utilize ^{1}H-MRS/I to specifically evaluate 2-hydroxyglutarate (2HG) due to its up-regulation in patients with an IDH mutation (38, 42, 43, 51). GBMs with IDH-mutant status have increased NADPH activity which increases the production of 2HG and may subsequently be associated with more favorable outcomes (38, 42, 43, 51, 52). Overall, these studies show that enhanced visualization of 2HG can be obtained. Optimization of ^{1}H-MRS/I allows for detection of 2HG in concentrations as low as 0.5 mM (52). Therefore, further optimizations and improvements may achieve higher resolution and better robustness to enable clinical use in diagnostics and prognostics.

Although the use of 7T MRS/I to differentiate between glioma recurrence vs. radiation necrosis has not been described in any currently published study, the use of MRS/I in 3T MRI can distinguish between glioma recurrence and radiation necrosis. For example, choline to NAA ratio, choline to creatine ratio, and choline to lipid ratio have been shown to be significantly elevated in glioma recurrence compared to radiation necrosis on 3T MRS in multiple studies (53, 54). Therefore, given the propensity of studies to have similar results when moved from 3T to 7T imaging, it is probable that UHF imaging will yield similar results with greater sensitivity and specificity. However, the exact results and the advantages that UHF MRS/I may provide will require future investigation. Additionally, given the difference in physiologic function between necrotic tissue and neoplastic tissue, MRS/I with other nuclei to assess ion channel function and biochemicals specific to cell growth, proliferation, and angiogenesis as opposed to those that are affiliated with cell death and apoptosis, may enhance the ability of MRS/I to delineate between glioma recurrence and radiation necrosis.

Chemical Exchange Saturation Transfer

Chemical exchange saturation transfer (CEST) is a contrast enhancement technique that enables the detection of specific molecules containing amides, amines, or hydroxyl protons exchangeable with bulk water (19, 55–61). Depending on the molecule targeted for saturation and their *in-vivo* concentrations, CEST has multiple variants that are useful in tumor grading and prediction of treatment efficacy: amide-proton-transfer CEST (APT-CEST) that detects and images amide and amine groups, glutamate-CEST that images glutamate, D-glucose CEST (glucose-CEST) that images glucose, and acidoCEST that images pH changes in GBM. As CEST requires the application of frequency-selective radiofrequency (RF) radiation to the exchangeable proton groups, the increased frequency dispersion at UHF is expected to improve signal detection specificity. The molecular imaging nature of CEST shows promise for improved capability for tumor grading and treatment efficacy prediction. The asymmetrical MTR parameter is most commonly used for CEST quantification; however, it is affected by other CEST pools, such as nuclear Overhauser effects (NOE), and technical issues, such as direct water saturation and magnetization transfer contrast. More sophisticated quantification methods discussed here seek to accurately depict proton concentrations while

maximizing sensitivity to microenvironmental changes (such as pH and temperature) *in-vivo* through the use of various fitting algorithms and corrections (62–64).

NOE mediated CEST at 7T MRI was compared to standard contrast-enhanced MR images in GBM patients (55). Compared to normal-appearing contralateral tissue, regions of tumor tissue, radiation necrosis, and peritumoral hyperintensities had significantly greater NOE-CEST signal (55). Additional areas of hyperintensity, not seen on standard imaging, were also identified using NOE-CEST, indicating NOE-CEST likely provides further structural detail (55). Similarly, Zaiss et al. (19) found that by utilizing a correction algorithm for apparent exchange-dependent relaxation (AREX), NOE-CEST shows a significantly greater contrast between tumorous and necrotic tissue and between tumor and healthy tissue. Utilization of amide-CEST in the same study did not result in significant contrast (19). Later, a follow-up study concluded that APT-CEST could generate unique contrast that overlaps with gadolinium weighted T1 imaging if it was corrected for AREX and downfield-aliphatic-related NOE signal was suppressed (56). However, NOE and other magnetization transfer effects have been shown to be significantly different in tumors compared to healthy tissue. These findings suggest that further elucidation of CEST differences and implementation of corrections are necessary to accurately visualize characteristic differences between gliomas and healthy tissue (56, 64).

CEST at 7T MRI has also been investigated for its ability to predict tumor grade, IDH mutation status, and MGMT promoter methylation. Comparing pre-surgical NOE- and APT-CEST 7T MR images and histopathological biopsy in 10 patients, Heo et al. (58) identified significantly less NOE-CEST signal in gliomas vs. contralateral healthy tissue ($p < 0.01$). Additionally, the NOE-CEST signal differed significantly in WHO grade 2 vs. WHO grade 3-4 gliomas ($p < 0.05$) (58). Differences in APT-CEST signals across tissue types were not appreciated (58). A similar study that analyzed biopsy samples from 15 patients with glioblastoma showed improved visualization of cellularity using NOE-CEST compared to diffusion-weighted MRI (65).

Utilizing downfield NOE-suppressed APT-CEST (dns-APT), Paech et al. (57) predicted IDH mutation status and differentiated gliomas of low and high grades but could not predict MGMT promoter methylation (57). APT-CEST signals were significantly greater in gliomas localized to the right hemisphere than the left ($p < 0.05$), and NOE-CEST signals were significantly greater in gliomas with subventricular zone contact ($p < 0.05$) (59). Healthy controls did not exhibit hemisphere differences in signals (59). While subventricular zone contact can indicate a poor prognosis, no histopathological characteristics, including cell density and ki67, were significantly associated with location (59). An inverse relationship between survival and APT values was demonstrated using relaxation-compensated APT-CEST (66). Furthermore, APT-CEST signal differences correlate with treatment response. Using pre-treatment, post-treatment, and 6 months post-treatment groups, Meissner et al. showed that 7T dns-APT CEST signal was significantly different between chemoradiotherapy treatment-responsive and treatment-non-responsive groups; however, this was only appreciable between the pre-treatment group and immediate post-treatment group (61).

CEST 7T MRI may be a mechanism to predict clinical characteristics and anti-cancer treatment response. Neal et al. (60) conducted a study on the effectiveness of glutamate-CEST (**Figure 4**) to detect both the aggressiveness of the glioma and determine the risk of having glioma-associated seizures. Increased peritumoral glutamate-CEST contrast was significantly associated with recent seizure ($p = 0.038$) and drug-refractory epilepsy ($p = 0.029$) (60). This data suggests that glutamate-CEST contrast may indicate the likelihood of glioma-associated seizures.

Gadolinium-based contrast agents are frequently used in MRI of the brain and other tissues; however, there is renewed concern about its safety profile due to reports of nephrogenic systemic fibrosis and deposition of gadolinium in tissues. As such, there is interest in developing non-metallic and biodegradable contrast agents. D-glucose may offer a biodegradable contrast agent. Xu et al. (67) and Schuenke et al. (68) demonstrated the feasibility of gluco-CEST and glucose-CESL (chemical exchange sensitive spin-lock), respectively, at 7T in patients with gliomas. Paech et al. (69) found that glucose-CESL signals were significantly increased in tumor tissue compared to contralateral normal tissue and that areas of glucose-CESL intensity correlated to areas of tumor tissue seen on gadolinium-enhanced images (69). Case studies have also demonstrated better identification of tumor borders (68) and enhanced contrast between tumor and normal tissue (70) using glucose-CESL methods. Animal models of glucose-based agents are discussed in Preclinical Models and Future Directions.

Angiography

There exists few studies utilizing angiography at 7T MRI to visualize tumoral vasculature in humans. Limited data exists in rodent models as well (71). Radbruch et al. (72) utilized time-of-flight angiography at 7T MRI to visualize tumor vessels in 12 patients with GBM. All patients were imaged prior to surgical resection or treatment with anti-cancer therapies. Tumor vessels were found to be clearly visible in all patients. Using multiscale vessel enhancement filtering and segmentation, tumor vasculature was characterized and compared to healthy white matter. Tumor vasculature had significantly greater vessel surface area ($p < 0.035$) and number of branches ($p < 0.001$) but had lesser vessel length ($p < 0.001$). It was also observed that tumors had an insignificantly greater density of vessels ($p < 0.078$). Visualization and quantification of tumor vasculature could offer a monitoring method for anti-angiogenic therapy and tumor grading.

Preclinical Models and Future Directions

Murine model studies are currently underway to improve imaging and non-invasive tumor characterization. Sehgal et al. (73) investigated the use of 3-O-methyl-D-glucose (3-OMG), a non-metabolizable analog of glucose, as a contrast agent in MRI studies using CEST. In a murine glioma model, contrast enhancement using 3-OMG was found to be nearly double the contrast enhancement seen when using D-glucose (2.5–5.0% vs.

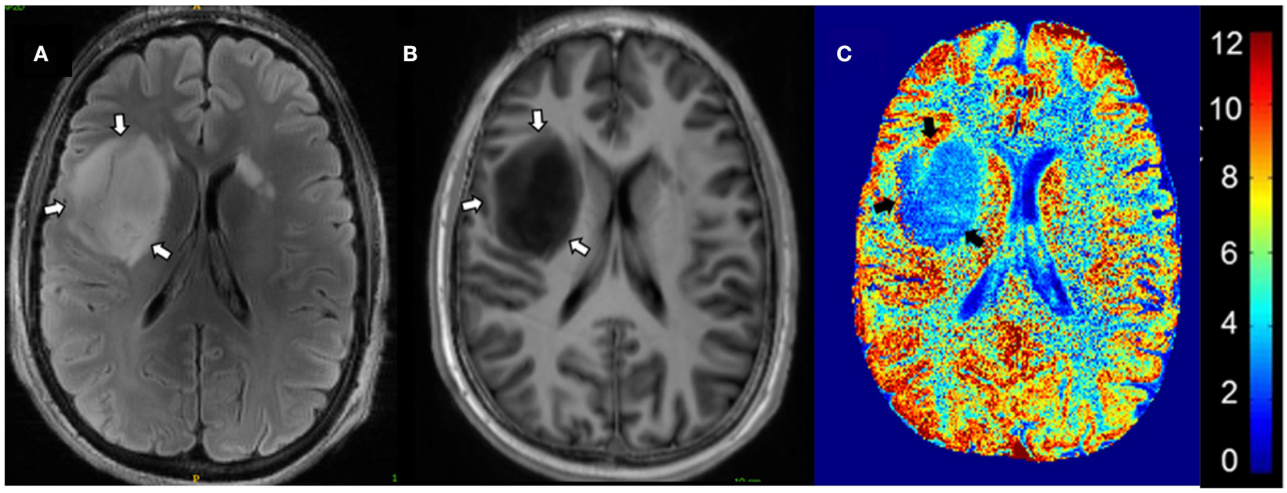

FIGURE 4 | Glutamate-CEST imaging of a diffuse astrocytoma. **(A)** 3T FLAIR with tumors identified by white arrows. **(B)** 7T FLAIR with tumors identified by white arrows. **(C)** Glutamate-CEST contrast map with tumors identified by black arrows and CEST contrast gradient on the right. Figure used with permission from Neal et al., 2019 (60).

1.5–3.0%). Unlike gadolinium agents that require a disrupted blood brain barrier to diffuse into the brain, glucose transporters in the brain can uptake 3-OMG. Being non-metabolized, 3-OMG is not affected by metabolism or insulin's response. While a toxicity profile of infused 3-OMG is needed, it has been used orally in human nutrient absorption studies indicating it is likely without evidence of safety issues.

In a murine study utilizing 11.7T MRI to study a variety of tumors (glioma, neuroblastoma, and breast cancer cell lines), Tanoue et al. (74) found differences in APT signaling based on tumor type and histopathological characteristics. It was found that APT signaling was elevated in tumors with greater proliferative potential. Additionally, regions of bleeding also correlated to regions of elevated APT signaling.

A critical challenge of GBM is recurrence due to its infiltrative nature. Cellular infiltration into healthy regions is difficult to quantify using conventional MRI. Utilizing 7T MRI perfusion images, Vallatos et al. (75) demonstrated a negative correlation between tumor cell infiltration and perfusion near tumor margins. Perfusion imaging identified a larger abnormal brain region surrounding the murine GBM compared to relaxation and diffusion-based techniques. Perfusion imaging was more sensitive to abnormal tissue, but less specific than other modalities. Perfusion imaging techniques may provide a therapy target region that is more inclusive of remote cellular infiltrate although further work is necessary.

LIMITATIONS

In addition to added costs and limited availability, several limitations exist for 7T MRI use in gliomas. 7T MRI can contribute to patient side effects, such as peripheral nerve stimulation, localized heating, vestibular effects, and increased RF energy deposition in tissues which carries unknown long term health effects (21, 76). Poor image quality and image distortions are often seen, especially when imaging structures deep within the brain and nearest the skull base (21, 31). These distortions are related to differences of magnetic susceptibility between air cavities of the skull and brain (77). Motion artifacts are frequently seen because the increased SNR in 7T MRI also increases its sensitivity to patient motion during the scan, such as breathing and heartbeats (77). SNR decreases from the center to the periphery of the brain (77). RF head coils, such as the commercial distributed 1-channel quadrature birdcage 32-channel receive head coil by Nova Medical (Wilmington, MA) and the pTx version for research purposes, allow for increased SNR (78). Innovations in head coil designs are also underway to better visualize cerebellum structures (78). Lastly, advanced imaging analysis, such as fractal dimensions, is likely infeasible in current clinical settings.

DATA AVAILABILITY STATEMENT

The original contributions presented in the study are included in the article/**Supplementary Material**, further inquiries can be directed to the corresponding authors.

AUTHOR CONTRIBUTIONS

AS, SK, and AN contributed to conception of the study and execution of systematic review. AA, FL, TW, PA, and WH contributed to critical revisions of the manuscript. All authors contributed to the article and approved the submitted version.

SUPPLEMENTARY MATERIAL

The Supplementary Material for this article can be found online at: https://www.frontiersin.org/articles/10.3389/fneur.2022.857825/full#supplementary-material

REFERENCES

1. Ferris SP, Hofmann JW, Solomon DA, Perry A. Characterization of gliomas: from morphology to molecules. *Virchows Arch.* (2017) 471:257–69. doi: 10.1007/s00428-017-2181-4
2. Louis DN, Perry A, Wesseling P, Brat DJ, Cree IA, Figarella-Branger D, et al. The 2021 WHO classification of tumors of the central nervous system: a summary. *Neuro Oncol.* (2021) 23:1231–51. doi: 10.1093/neuonc/noab106
3. Wesseling P, Capper D. WHO 2016 classification of gliomas. *Neuropathol Appl Neurobiol.* (2018) 44:139–50. doi: 10.1111/nan.12432
4. Wei RL, Wei XT. Advanced diagnosis of glioma by using emerging magnetic resonance sequences. *Front Oncol.* (2021) 11:694498. doi: 10.3389/fonc.2021.694498
5. Sun H, Yin L, Li S, Han S, Song G, Liu N, et al. Prognostic significance of IDH mutation in adult low-grade gliomas: a meta-analysis. *J Neurooncol.* (2013) 113:277–84. doi: 10.1007/s11060-013-1107-5
6. Hegi ME, Diserens AC, Gorlia T, Hamou MF, de Tribolet N, Weller M, et al. MGMT gene silencing and benefit from temozolomide in glioblastoma. *N Engl J Med.* (2005) 352:997–1003. doi: 10.1056/NEJMoa043331
7. McGirt MJ, Villavicencio AT, Bulsara KR, Friedman AH. MRI-guided stereotactic biopsy in the diagnosis of glioma: comparison of biopsy and surgical resection specimen. *Surg Neurol.* (2003) 59:277–81; discussion 81–2. doi: 10.1016/S0090-3019(03)00048-X
8. Senft C, Franz K, Ulrich CT, Bink A, Szelenyi A, Gasser T, et al. Low field intraoperative MRI-guided surgery of gliomas: a single center experience. *Clin Neurol Neurosurg.* (2010) 112:237–43. doi: 10.1016/j.clineuro.2009.12.003
9. Ladd ME, Bachert P, Meyerspeer M, Moser E, Nagel AM, Norris DG, et al. Pros and cons of ultra-high-field MRI/MRS for human application. *Prog Nucl Magn Reson Spectrosc.* (2018) 109:1–50. doi: 10.1016/j.pnmrs.2018.06.001
10. Ugurbil K. Magnetic resonance imaging at ultrahigh fields. *IEEE Trans Biomed Eng.* (2014) 61:1364–79. doi: 10.1109/TBME.2014.2313619
11. Regnery S, Knowles BR, Paech D, Behl N, Meissner JE, Windisch P, et al. High-resolution FLAIR MRI at 7 Tesla for treatment planning in glioblastoma patients. *Radiother Oncol.* (2019) 130:180–4. doi: 10.1016/j.radonc.2018.08.002
12. Platt T, Ladd ME, Paech D. 7 tesla and beyond: advanced methods and clinical applications in magnetic resonance imaging. *Invest Radiol.* (2021) 56:705–25. doi: 10.1097/RLI.0000000000000820
13. Shokrollahi P, Drake JM, Goldenberg AA. Signal-to-noise ratio evaluation of magnetic resonance images in the presence of an ultrasonic motor. *Biomed Eng Online.* (2017) 16:45. doi: 10.1186/s12938-017-0331-1
14. Trattnig S, Springer E, Bogner W, Hangel G, Strasser B, Dymerska B, et al. Key clinical benefits of neuroimaging at 7T. *Neuroimage.* (2018) 168:477–89. doi: 10.1016/j.neuroimage.2016.11.031
15. Pohmann R, Speck O, Scheffler K. Signal-to-noise ratio and MR tissue parameters in human brain imaging at 3, 7, and 94 tesla using current receive coil arrays. *Magn Reson Med.* (2016) 75:801–9. doi: 10.1002/mrm.25677
16. Beisteiner R, Robinson S, Wurnig M, Hilbert M, Merksa K, Rath J, et al. Clinical fMRI: evidence for a 7T benefit over 3T. *Neuroimage.* (2011) 57:1015–21. doi: 10.1016/j.neuroimage.2011.05.010
17. Goncalves NR, Ban H, Sanchez-Panchuelo RM, Francis ST, Schluppeck D, Welchman AE. 7 tesla FMRI reveals systematic functional organization for binocular disparity in dorsal visual cortex. *J Neurosci.* (2015) 35:3056–72. doi: 10.1523/JNEUROSCI.3047-14.2015
18. Bogner W, Otazo R, Henning A. Accelerated MR spectroscopic imaging-a review of current and emerging techniques. *NMR Biomed.* (2021) 34:e4314. doi: 10.1002/nbm.4314
19. Zaiss M, Windschuh J, Paech D, Meissner JE, Burth S, Schmitt B, et al. Relaxation-compensated CEST-MRI of the human brain at 7T: unbiased insight into NOE and amide signal changes in human glioblastoma. *Neuroimage.* (2015) 112:180–8. doi: 10.1016/j.neuroimage.2015.02.040
20. Balchandani P, Naidich TP. Ultra-High-Field MR Neuroimaging. *Am J Neuroradiol.* (2015) 36:1204–15. doi: 10.3174/ajnr.A4180
21. Compter I, Peerlings J, Eekers DB, Postma AA, Ivanov D, Wiggins CJ, et al. Technical feasibility of integrating 7 T anatomical MRI in image-guided radiotherapy of glioblastoma: a preparatory study. *MAGMA.* (2016) 29:591–603. doi: 10.1007/s10334-016-0534-7
22. Teeuwisse WM, Brink WM, Webb AG. Quantitative assessment of the effects of high-permittivity pads in 7 Tesla MRI of the brain. *Magn Reson Med.* (2012) 67:1285–93. doi: 10.1002/mrm.23108
23. Winkler SA, Schmitt F, Landes H, de Bever J, Wade T, Alejski A, et al. Gradient and shim technologies for ultra high field MRI. *Neuroimage.* (2018) 168:59–70. doi: 10.1016/j.neuroimage.2016.11.033
24. Grabner G, Kiesel B, Wohrer A, Millesi M, Wurzer A, God S, et al. Local image variance of 7 Tesla SWI is a new technique for preoperative characterization of diffusely infiltrating gliomas: correlation with tumour grade and IDH1 mutational status. *Eur Radiol.* (2017) 27:1556–67. doi: 10.1007/s00330-016-4451-y
25. Di Ieva A, Matula C, Grizzi F, Grabner G, Trattnig S, Tschabitscher M. Fractal analysis of the susceptibility weighted imaging patterns in malignant brain tumors during antiangiogenic treatment: technical report on four cases serially imaged by 7 T magnetic resonance during a period of four weeks. *World Neurosurg.* (2012) 77:785e11–21. doi: 10.1016/j.wneu.2011.09.006
26. Di Ieva A, Tschabitscher M, Galzio RJ, Grabner G, Kronnerwetter C, Widhalm G, et al. The veins of the nucleus dentatus: anatomical and radiological findings. *Neuroimage.* (2011) 54:74–9. doi: 10.1016/j.neuroimage.2010.07.045
27. Grabner G, Nobauer I, Elandt K, Kronnerwetter C, Woehrer A, Marosi C, et al. Longitudinal brain imaging of five malignant glioma patients treated with bevacizumab using susceptibility-weighted magnetic resonance imaging at 7 T. *Magn Reson Imaging.* (2012) 30:139–47. doi: 10.1016/j.mri.2011.08.004
28. Di Ieva A, God S, Grabner G, Grizzi F, Sherif C, Matula C, et al. Three-dimensional susceptibility-weighted imaging at 7 T using fractal-based quantitative analysis to grade gliomas. *Neuroradiology.* (2013) 55:35–40. doi: 10.1007/s00234-012-1081-1
29. Han S, Liu Y, Cai SJ, Qian M, Ding J, Larion M, et al. IDH mutation in glioma: molecular mechanisms and potential therapeutic targets. *Br J Cancer.* (2020) 122:1580–9. doi: 10.1038/s41416-020-0814-x
30. Lupo JM, Chuang CF, Chang SM, Barani IJ, Jimenez B, Hess CP, et al. 7-Tesla susceptibility-weighted imaging to assess the effects of radiotherapy on normal-appearing brain in patients with glioma. *Int J Radiat Oncol Biol Phys.* (2012) 82:e493–500. doi: 10.1016/j.ijrobp.2011.05.046
31. Bian W, Hess CP, Chang SM, Nelson SJ, Lupo JM. Susceptibility-weighted MR imaging of radiation therapy-induced cerebral microbleeds in patients with glioma: a comparison between 3T and 7T. *Neuroradiology.* (2014) 56:91–6. doi: 10.1007/s00234-013-1297-8
32. Wen Q, Kelley DA, Banerjee S, Lupo JM, Chang SM, Xu D, et al. Clinically feasible NODDI characterization of glioma using multiband EPI at 7 T. *Neuroimage Clin.* (2015) 9:291–9. doi: 10.1016/j.nicl.2015.08.017
33. Oz G, Alger JR, Barker PB, Bartha R, Bizzi A, Boesch C, et al. Clinical proton MR spectroscopy in central nervous system disorders. *Radiology.* (2014) 270:658–79. doi: 10.1148/radiol.13130531
34. Bogner W, Chmelik M, Andronesi OC, Sorensen AG, Trattnig S, Gruber S. *In vivo* 31P spectroscopy by fully adiabatic extended image selected *in vivo* spectroscopy: a comparison between 3 T and 7 T. *Magn Reson Med.* (2011) 66:923–30. doi: 10.1002/mrm.22897
35. Nagel AM, Lehmann-Horn F, Weber MA, Jurkat-Rott K, Wolf MB, Radbruch A, et al. *In vivo* 35Cl MR imaging in humans: a feasibility study. *Radiology.* (2014) 271:585–95. doi: 10.1148/radiol.13131725
36. Biller A, Badde S, Nagel A, Neumann JO, Wick W, Hertenstein A, et al. Improved brain tumor classification by sodium mr imaging: prediction of IDH mutation status and tumor progression. *Am J Neuroradiol.* (2016) 37:66–73. doi: 10.3174/ajnr.A4493
37. Gruber S, Heckova E, Strasser B, Povazan M, Hangel GJ, Minarikova L, et al. Mapping an extended neurochemical profile at 3 and 7 T using accelerated high-resolution proton magnetic resonance spectroscopic imaging. *Invest Radiol.* (2017) 52:631–9. doi: 10.1097/RLI.0000000000000379
38. Hangel G, Jain S, Springer E, Heckova E, Strasser B, Povazan M, et al. High-resolution metabolic mapping of gliomas *via* patch-based super-resolution magnetic resonance spectroscopic imaging at 7T. *Neuroimage.* (2019) 191:587–95. doi: 10.1016/j.neuroimage.2019.02.023
39. Li Y, Larson P, Chen AP, Lupo JM, Ozhinsky E, Kelley D, et al. Short-echo three-dimensional H-1 MR spectroscopic imaging of patients with glioma at 7 Tesla for characterization of differences in metabolite levels. *J Magn Reson Imaging.* (2015) 41:1332–41. doi: 10.1002/jmri.24672

40. Ganji SK, An Z, Tiwari V, McNeil S, Pinho MC, Pan E, et al. *In vivo* detection of 2-hydroxyglutarate in brain tumors by optimized point-resolved spectroscopy (PRESS) at 7T. *Magn Reson Med.* (2017) 77:936–44. doi: 10.1002/mrm.26190
41. An Z, Tiwari V, Ganji SK, Baxter J, Levy M, Pinho MC, et al. Echo-planar spectroscopic imaging with dual-readout alternated gradients (DRAG-EPSI) at 7 T: application for 2-hydroxyglutarate imaging in glioma patients. *Magn Reson Med.* (2018) 79:1851–61. doi: 10.1002/mrm.26884
42. Berrington A, Voets NL, Larkin SJ, de Pennington N, McCullagh J, Stacey R, et al. A comparison of 2-hydroxyglutarate detection at 3 and 7 T with long-TE semi-LASER. *NMR Biomed.* (2018) 31:3886. doi: 10.1002/nbm.3886
43. Esmaeili M, Stockmann J, Strasser B, Arango N, Thapa B, Wang Z, et al. An integrated RF-receive/B0-shim array coil boosts performance of whole-brain MR spectroscopic imaging at 7 T. *Sci Rep.* (2020) 10:15029. doi: 10.1038/s41598-020-71623-5
44. Paech D, Nagel AM, Schultheiss MN, Umathum R, Regnery S, Scherer M, et al. Quantitative dynamic oxygen 17 MRI at 70 T for the cerebral oxygen metabolism in glioma. *Radiology.* (2020) 295:181–9. doi: 10.1148/radiol.2020191711
45. Hoffmann SH, Begovatz P, Nagel AM, Umathum R, Schommer K, Bachert P, et al. A measurement setup for direct 17O MRI at 7 T. *Magn Reson Med.* (2011) 66:1109–15. doi: 10.1002/mrm.22871
46. Ren J, Sherry AD, Malloy CR. (31)P-MRS of healthy human brain: ATP synthesis, metabolite concentrations, pH, and T1 relaxation times. *NMR Biomed.* (2015) 28:1455–62. doi: 10.1002/nbm.3384
47. Ren J, Shang T, Sherry AD, Malloy CR. Unveiling a hidden (31) P signal coresonating with extracellular inorganic phosphate by outer-volume-suppression and localized (31) P MRS in the human brain at 7T. *Magn Reson Med.* (2018) 80:1289–97. doi: 10.1002/mrm.27121
48. Regnery S, Behl NGR, Platt T, Weinfurtner N, Windisch P, Deike-Hofmann K, et al. Ultra-high-field sodium MRI as biomarker for tumor extent, grade and IDH mutation status in glioma patients. *Neuroimage Clin.* (2020) 28:102427. doi: 10.1016/j.nicl.2020.102427
49. Paech D, Regnery S, Platt T, Behl NGR, Weckesser N, Windisch P, et al. Assessment of sodium MRI at 7 Tesla as predictor of therapy response and survival in glioblastoma patients. *Front Neurosci.* (2021) 15:782516. doi: 10.3389/fnins.2021.782516
50. Korzowski A, Weckesser N, Franke VL, Breitling J, Goerke S, Schlemmer HP, et al. Mapping an extended metabolic profile of gliomas using high-resolution (31)P MRSI at 7T. *Front Neurol.* (2021) 12:735071. doi: 10.3389/fneur.2021.735071
51. Li Y, Liu X, Xu K, Qian Z, Wang K, Fan X, et al. MRI features can predict EGFR expression in lower grade gliomas: a voxel-based radiomic analysis. *Eur Radiol.* (2018) 28:356–62. doi: 10.1007/s00330-017-4964-z
52. Shams Z, van der Kemp WJM, Emir U, Dankbaar JW, Snijders TJ, de Vos FYF, et al. Comparison of 2-hydroxyglutarate detection with sLASER and MEGA-sLASER at 7T. *Front Neurol.* (2021) 12:718423. doi: 10.3389/fneur.2021.718423
53. Chuang MT, Liu YS, Tsai YS, Chen YC, Wang CK. Differentiating radiation-induced necrosis from recurrent brain tumor using MR perfusion and spectroscopy: a meta-analysis. *PLoS ONE.* (2016) 11:e0141438. doi: 10.1371/journal.pone.0141438
54. Anbarloui MR, Ghodsi SM, Khoshnevisan A, Khadivi M, Abdollahzadeh S, Aoude A, et al. Accuracy of magnetic resonance spectroscopy in distinction between radiation necrosis and recurrence of brain tumors. *Iran J Neurol.* (2015) 14:29–34.
55. Paech D, Zaiss M, Meissner JE, Windschuh J, Wiestler B, Bachert P, et al. Nuclear overhauser enhancement mediated chemical exchange saturation transfer imaging at 7 Tesla in glioblastoma patients. *PLoS ONE.* (2014) 9:e104181. doi: 10.1371/journal.pone.0104181
56. Zaiss M, Windschuh J, Goerke S, Paech D, Meissner JE, Burth S, et al. Downfield-NOE-suppressed amide-CEST-MRI at 7 Tesla provides a unique contrast in human glioblastoma. *Magn Reson Med.* (2017) 77:196–208. doi: 10.1002/mrm.26100
57. Paech D, Windschuh J, Oberhollenzer J, Dreher C, Sahm F, Meissner JE, et al. Assessing the predictability of IDH mutation and MGMT methylation status in glioma patients using relaxation-compensated multipool CEST MRI at 70 T. *Neuro Oncol.* (2018) 20:1661–71. doi: 10.1093/neuonc/noy073
58. Heo HY, Jones CK, Hua J, Yadav N, Agarwal S, Zhou J, et al. Whole-brain amide proton transfer (APT) and nuclear overhauser enhancement (NOE) imaging in glioma patients using low-power steady-state pulsed chemical exchange saturation transfer (CEST) imaging at 7T. *J Magn Reson Imaging.* (2016) 44:41–50. doi: 10.1002/jmri.25108
59. Dreher C, Oberhollenzer J, Meissner JE, Windschuh J, Schuenke P, Regnery S, et al. Chemical exchange saturation transfer (CEST) signal intensity at 7T MRI of WHO IV degrees gliomas is dependent on the anatomic location. *J Magn Reson Imaging.* (2019) 49:777–85. doi: 10.1002/jmri.26215
60. Neal A, Moffat BA, Stein JM, Nanga RPR, Desmond P, Shinohara RT, et al. Glutamate weighted imaging contrast in gliomas with 7Tesla magnetic resonance imaging. *Neuroimage Clin.* (2019) 22:101694. doi: 10.1016/j.nicl.2019.101694
61. Meissner JE, Korzowski A, Regnery S, Goerke S, Breitling J, Floca RO, et al. Early response assessment of glioma patients to definitive chemoradiotherapy using chemical exchange saturation transfer imaging at 7 T. *J Magn Reson Imaging.* (2019) 50:1268–77. doi: 10.1002/jmri.26702
62. Zhou IY, Wang E, Cheung JS, Zhang X, Fulci G, Sun PZ. Quantitative chemical exchange saturation transfer (CEST) MRI of glioma using image downsampling expedited adaptive least-squares (IDEAL) fitting. *Sci Rep.* (2017) 7:84. doi: 10.1038/s41598-017-00167-y
63. Liu D, Zhou J, Xue R, Zuo Z, An J, Wang DJ. Quantitative characterization of nuclear overhauser enhancement and amide proton transfer effects in the human brain at 7 tesla. *Magn Reson Med.* (2013) 70:1070–81. doi: 10.1002/mrm.24560
64. Windschuh J, Zaiss M, Meissner JE, Paech D, Radbruch A, Ladd ME, et al. Correction of B1-inhomogeneities for relaxation-compensated CEST imaging at 7 T. *NMR Biomed.* (2015) 28:529–37. doi: 10.1002/nbm.3283
65. Paech D, Burth S, Windschuh J, Meissner JE, Zaiss M, Eidel O, et al. Nuclear Overhauser Enhancement imaging of glioblastoma at 7 Tesla: region specific correlation with apparent diffusion coefficient and histology. *PLoS ONE.* (2015) 10:e0121220. doi: 10.1371/journal.pone.0121220
66. Paech D, Dreher C, Regnery S, Meissner JE, Goerke S, Windschuh J, et al. Relaxation-compensated amide proton transfer (APT) MRI signal intensity is associated with survival and progression in high-grade glioma patients. *Eur Radiol.* (2019) 29:4957–67. doi: 10.1007/s00330-019-06066-2
67. Xu X, Yadav NN, Knutsson L, Hua J, Kalyani R, Hall E, et al. Dynamic glucose-enhanced (DGE) MRI: translation to human scanning and first results in glioma patients. *Tomography.* (2015) 1:105–14. doi: 10.18383/j.tom.2015.00175
68. Schuenke P, Koehler C, Korzowski A, Windschuh J, Bachert P, Ladd ME, et al. Adiabatically prepared spin-lock approach for T1rho-based dynamic glucose enhanced MRI at ultrahigh fields. *Magn Reson Med.* (2017) 78:215–25. doi: 10.1002/mrm.26370
69. Paech D, Schuenke P, Koehler C, Windschuh J, Mundiyanapurath S, Bickelhaupt S, et al. T1rho-weighted dynamic glucose-enhanced MR imaging in the human brain. *Radiology.* (2017) 285:914–22. doi: 10.1148/radiol.2017162351
70. Schuenke P, Paech D, Koehler C, Windschuh J, Bachert P, Ladd ME, et al. Fast and quantitative T1rho-weighted dynamic glucose enhanced MRI. *Sci Rep.* (2017) 7:42093. doi: 10.1038/srep42093
71. Doblas S, He T, Saunders D, Pearson J, Hoyle J, Smith N, et al. Glioma morphology and tumor-induced vascular alterations revealed in seven rodent glioma models by *in vivo* magnetic resonance imaging and angiography. *J Magn Reson Imaging.* (2010) 32:267–75. doi: 10.1002/jmri.22263
72. Radbruch A, Eidel O, Wiestler B, Paech D, Burth S, Kickingereder P, et al. Quantification of tumor vessels in glioblastoma patients using time-of-flight angiography at 7 Tesla: a feasibility study. *PLoS ONE.* (2014) 9:e110727. doi: 10.1371/journal.pone.0110727
73. Sehgal AA, Li Y, Lal B, Yadav NN, Xu X, Xu J, et al. CEST MRI of 3-O-methyl-D-glucose uptake and accumulation in brain tumors. *Magn Reson Med.* (2019) 81:1993–2000. doi: 10.1002/mrm.27489
74. Tanoue M, Saito S, Takahashi Y, Araki R, Hashido T, Kioka H, et al. Amide proton transfer imaging of glioblastoma, neuroblastoma, and breast cancer cells on a 117T magnetic resonance imaging system. *Magn Reson Imaging.* (2019) 62:181–90. doi: 10.1016/j.mri.2019.07.005
75. Vallatos A, Al-Mubarak HFI, Birch JL, Galllagher L, Mullin JM, Gilmour L, et al. Quantitative histopathologic assessment of perfusion MRI as a marker of

glioblastoma cell infiltration in and beyond the peritumoral edema region. *J Magn Reson Imaging.* (2019) 50:529–40. doi: 10.1002/jmri.26580
76. Vachha B, Huang SY. MRI with ultrahigh field strength and high-performance gradients: challenges and opportunities for clinical neuroimaging at 7 T and beyond. *Eur Radiol Exp*. (2021) 5:35. doi: 10.1186/s41747-021-00216-2
77. Barisano G, Sepehrband F, Ma S, Jann K, Cabeen R, Wang DJ, et al. Clinical 7 T MRI: are we there yet? A review about magnetic resonance imaging at ultra-high field. *Br J Radiol.* (2019) 92:20180492. doi: 10.1259/bjr.20180492
78. Kraff O, Quick HH. Radiofrequency coils for 7 tesla MRI. *Top Magn Reson Imaging.* (2019) 28:145–58. doi: 10.1097/RMR.0000000000000206

Conflict of Interest: The authors declare that the research was conducted in the absence of any commercial or financial relationships that could be construed as a potential conflict of interest.

Publisher's Note: All claims expressed in this article are solely those of the authors and do not necessarily represent those of their affiliated organizations, or those of the publisher, the editors and the reviewers. Any product that may be evaluated in this article, or claim that may be made by its manufacturer, is not guaranteed or endorsed by the publisher.

Copyright © 2022 Shaffer, Kwok, Naik, Anderson, Lam, Wszalek, Arnold and Hassaneen. This is an open-access article distributed under the terms of the Creative Commons Attribution License (CC BY). The use, distribution or reproduction in other forums is permitted, provided the original author(s) and the copyright owner(s) are credited and that the original publication in this journal is cited, in accordance with accepted academic practice. No use, distribution or reproduction is permitted which does not comply with these terms.

frontiers | Frontiers in Neuroscience

REVIEW
published: 19 April 2022
doi: 10.3389/fnins.2022.881661

Multiparametric Intraoperative Ultrasound in Oncological Neurosurgery: A Pictorial Essay

Francesco Prada[1,2,3,4], Riccardo Ciocca[4,5], Nicoletta Corradino[4,5], Matteo Gionso[4,6], Luca Raspagliesi[4,7], Ignazio Gaspare Vetrano[1], Fabio Doniselli[8,9], Massimiliano Del Bene[1,10] and Francesco DiMeco[1,11,12]*

[1] Department of Neurosurgery, Fondazione IRCCS Istituto Neurologico Carlo Besta, Milan, Italy, [2] Department of Neurological Surgery, University of Virginia, Charlottesville, VA, United States, [3] Focused Ultrasound Foundation, Charlottesville, VA, United States, [4] Acoustic Neuroimaging and Therapy Laboratory, Fondazione IRCCS Istituto Neurologico Carlo Besta, Milan, Italy, [5] Faculty of Medicine and Surgery, Università degli Studi di Milano, Milan, Italy, [6] Faculty of Medicine and Surgery, Humanitas University, Pieve Emanuele, Italy, [7] Department of Neurosurgery, Humanitas Clinical and Research Center, Milan, Italy, [8] Neuroradiology Unit, Fondazione IRCCS Istituto Neurologico Carlo Besta, Milan, Italy, [9] Department of Biomedical Sciences for Health, Università degli Studi di Milano, Milan, Italy, [10] Department of Experimental Oncology, IEO, European Institute of Oncology IRCCS, Milan, Italy, [11] Department of Pathophysiology and Transplantation, University of Milan, Milan, Italy, [12] Johns Hopkins Medical School, Baltimore, MD, United States

OPEN ACCESS

Edited by:
Nico Sollmann,
University of California,
San Francisco, United States

Reviewed by:
Santiago Cepeda,
Hospital Universitario Río Hortega,
Spain
Jan Coburger,
Ulm University Medical Center,
Germany
Andrej Steno,
Comenius University, Slovakia

***Correspondence:**
Francesco Prada
francesco.prada@istituto-besta.it

Specialty section:
This article was submitted to Brain Imaging Methods, a section of the journal Frontiers in Neuroscience

Received: 22 February 2022
Accepted: 16 March 2022
Published: 19 April 2022

Citation:
Prada F, Ciocca R, Corradino N, Gionso M, Raspagliesi L, Vetrano IG, Doniselli F, Del Bene M and DiMeco F (2022) Multiparametric Intraoperative Ultrasound in Oncological Neurosurgery: A Pictorial Essay. Front. Neurosci. 16:881661. doi: 10.3389/fnins.2022.881661

Intraoperative ultrasound (ioUS) is increasingly used in current neurosurgical practice. This is mainly explained by its affordability, handiness, multimodal real-time nature, and overall by its image spatial and temporal resolution. Identification of lesion and potential residue, analysis of the vascularization pattern, and characterization of the nature of the mass are only some of the advantages that ioUS offers to guide safe and efficient tumor resection. Technological advances in ioUS allow to achieve both structural and functional imaging. B-mode provides high-resolution visualization of the lesion and of its boundaries and relationships. Pioneering modes, such as contrast-enhanced ultrasound (CEUS), ultrasensitive Doppler, and elastosonography, are tools with great potential in characterizing different functional aspects of the lesion in a qualitative and quantitative manner. As already happening for many organs and pathologies, the combined use of different US modalities offers new insights in a multiparametric fashion. In this study, we present the potential of our multiparametric approach for ioUS during neuro-oncological surgery. In this effort, we provide a pictorial essay focusing on the most frequent pathologies: low- and high-grade gliomas, meningiomas, and brain metastases.

Keywords: intraoperative ultrasound, contrast-enhanced ultrasound, Doppler, B-mode, elastography, glioma, meningioma, metastasis

INTRODUCTION

Forward

Image-guided surgery (IGS) is one of the cornerstones of modern neurosurgery. In this context, intraoperative ultrasound (ioUS) is becoming progressively more diffused. Once the shield of bone is removed, the mechanical viscoelastic properties of the brain allow an excellent propagation of US waves and the application of most ultrasonographical techniques. While the main downside

is represented by the steep learning curve, ioUS provides a versatile, real-time, close-hand, and multipurpose tool to explore and characterize the operative field beyond a simply morphological perspective (Rubin and Dohrmann, 1983; Newman and Rozycki, 1998; Chacko et al., 2003; Ng and Swanevelder, 2011). A growing body of literature supports IoUS application to achieve gross total removal (GTR) in low-grade and high-grade gliomas, as this parameter is associated with progression-free survival and overall survival improvement (D'Amico et al., 2017). Clinical trials are emerging to evaluate the impact of ioUS on the extent of resection: the first randomized controlled trial on ioUS B-mode was published by Incekara et al. (2021). Furthermore, in recent years, technological advances and pioneering research have been widening the ioUS range of use beyond the mere assessment of the extent of resection.

Multiparametric Intraoperative Ultrasound

At present, different advanced US techniques are available to provide both anatomical and functional information in real-time during surgery. The complementary application of different US techniques is defined as the multiparametric ultrasound (mpUS) approach. The mpUS approach is an already established technique for the pre-operative and intraoperative evaluation of focal lesions in various organs, especially the liver. For instance, the mpUS in hepatology is used for non-invasive staging of liver fibrosis, detection and classification of portal hypertension and esophageal varices, prognosis in chronic liver diseases, and characterization of focal liver lesions (FLLs) (Grgurevic et al., 2019). Brain ultrasound is going in the same direction (Prada et al., 2016a; Wang et al., 2019; Newsome and Dayton, 2020). In neurosurgery, intraoperative mpUS encompasses gray-scale B-mode, conventional Doppler (color, power, spectral) with ultrasensitive Doppler (usDoppler), strain elastosonography (SE), shear wave elastosonography (SWE), and contrast-enhanced ultrasound (CEUS) with microbubbles (MBs) (Moiyadi, 2016; Pang et al., 2017; Kim et al., 2018; Mannaerts et al., 2018; Grgurevic et al., 2019).

The intrinsic added value of multiparametric imaging is the possibility to exploit each modality to emphasize different characteristics of a lesion, such as its perfusion pattern, its consistency, edema, fibrosis, extension, and relationships, with surrounding structures. In a similar fashion as multiparametric MRI, mpUS aims to give a 360-degree analysis of a lesion with the advantage of being an intraoperative technique with real-time navigation.

B-mode, the oldest and most diffused US modality, is mainly structural imaging. It has achieved an excellent spatial and temporal resolution, even comparable to MRI (Ng and Swanevelder, 2011; Chan et al., 2021), allowing to visualize the tumor, to study the surrounding structures, to assess the extent of resection, and to characterize some aspects of the tumor (e.g., necrosis and solid components) (Prada et al., 2016b; Incekara et al., 2021).

Doppler imaging (color-, power, spectral-) is the other workhorse of ioUS in neurosurgery. It allows to visualize and characterize the blood flow and perfusion pattern from the arterial side, through the capillary district to the venous collectors of virtually every kind of lesion (Prada et al., 2016b). In this setting, the newest algorithms and instruments permit advanced usDoppler techniques, which enable the operator to visualize and characterize tumoral micro-vascularization. Xflow is a high-resolution, high-definition Doppler technology, which maximizes spatial resolution and Doppler signal penetration capabilities. MicroV represents the state-of-the-art sensitivity for superficial and deeper vessels for real-time microvascular perfusion analysis even in the case of very low flow signal (**Figure 1**; Yoo et al., 2020; Kloth et al., 2021).

Among the most advanced techniques, the use of ultrasound contrast agents (UCAs) has opened the door to numerous applications. UCAs dynamics inform on the arterial or venous nature of a vessel, also allowing to characterize the perfusion pattern finally leading to tumor visualization, assessment of the extent of resection, and tumor characterization (Prada et al., 2014a,b, 2016a; Sidhu et al., 2018; Wang et al., 2019; della Pepa et al., 2019; Newsome and Dayton, 2020; Incekara et al., 2021). Notably, the possibility to quantify MBs distribution in the human brain to quantitatively discriminate between tumoral and normal brain tissues has recently been demonstrated (**Figure 2**; Prada et al., 2021). The application of the CEUS sequence MIP (maximum-intensity projection) permits a detailed evaluation of intratumoral vascularization (**Figure 3**). In some preclinical studies, CEUS seems to even permit a real high-definition "acoustic angiography" to visualize the microvascular neo-angiogenesis of tumors (Newsome and Dayton, 2020). The use of CEUS during neuro-oncological procedures has been included in the guidelines from the European Federation of the Societies for Ultrasound in Medicine and Biology (EFSUMB) in 2017, representing a paradigm shift for the use of US in neurosurgery (Sidhu et al., 2018).

Another fundamental technique for an exhaustive evaluation of a lesion is elastosonography. It can provide details about the mechanical properties of the tumor compared with the parenchyma of the surrounding normal brain. For instance, the use of algorithms based on elastosonography appears to be more accurate than those from B-mode in differentiating intraoperatively HGGs and metastasis (Cepeda et al., 2021b). Technically, two methodologies, namely, strain elastography (SE) and shear wave elastography (SWE), are available. SE applies a mechanical force to measure lesions' stiffness, which is expressed on a color scale for qualitative assessment. Differently, SWE provides a quantitative assessment. This technique exploits a US stimulus to induce tissue displacement, thus providing a quantitative representation of the stiffness. In the current practice, elastosonography seems useful mainly in gliomas and meningiomas characterization (**Figure 4**; Prada et al., 2015, 2016b, 2019; della Pepa et al., 2020; Cepeda et al., 2021a; Chan et al., 2021; Menna et al., 2021; Yin et al., 2021).

Each ioUS technique has not only advantages but also limitations (Šteňo et al., 2021), which foster the need for a multiparametric approach. IoUS has still a low level of evidence at this time (Fountain et al., 2021), although it has an interesting potential not only in characterizing the lesion but also in permitting quantitative measurements, which are important tools for research, laying the foundations for algorithm-based

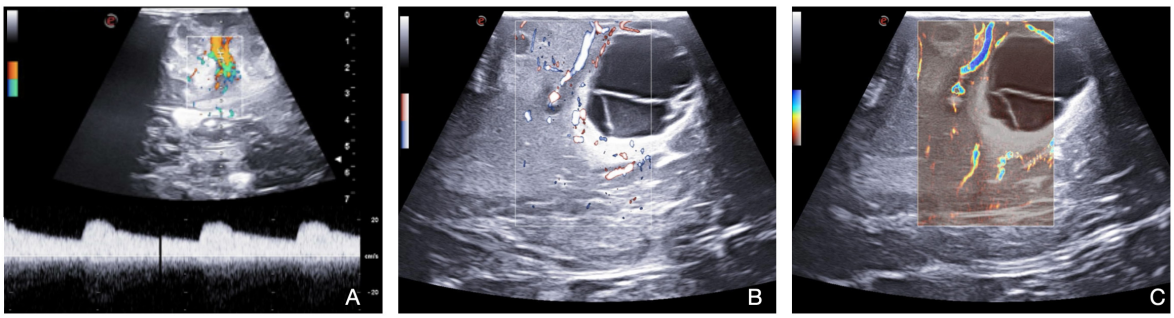

FIGURE 1 | Doppler techniques (Color-Doppler, X-Flow, Micro-V). Color Doppler and spectral Doppler **(A)** bring information about flow direction and velocity with quantification of the velocity through spectral Doppler. X-Flow **(B)** maximizes spatial resolution and Doppler signal penetration capabilities. Micro-V **(C)** permits real-time micro-vascular perfusion analysis, identifying low flow signals.

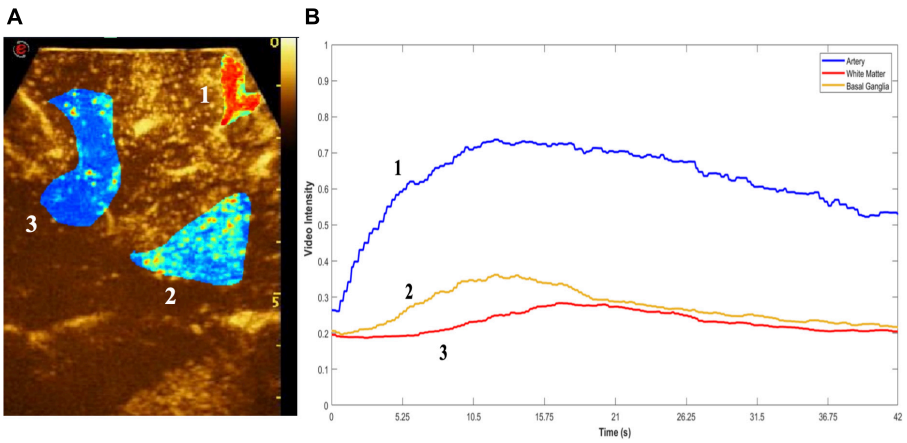

FIGURE 2 | Quantitative CEUS. Quantitative analysis of MBs distribution. **(A)** Region of interest (ROI) is drawn on key structures (1, artery-blue; 2, white matter-red; 3, basal ganglia-yellow), following which peak enhancement and time-intensity curves (TICs) were quantified **(B)**. This enables discernment between different types of brain tumors as well as regions and structures within the brain.

characterization of brain lesions (Kim et al., 2018; Wang et al., 2019; Prada et al., 2021).

ULTRASOUND EQUIPMENT AND ACQUISITION MODALITIES

Intraoperative ultrasound in neuro-oncological surgery is dynamic and requires tailoring of the US settings and probes several times during the operation. For instance, various probes exist to address almost every situation: high-frequency probes for superficial tumors, linear or convex multifrequency probes for more deep-seated lesions, micro-convex or hockey-stick probes for exploring surgical cavities, and dedicated pituitary probes (Prada et al., 2016b; Cabrilo et al., 2021). The spectrum of available US techniques depends both on the probe employed and on the scanner to which they are connected. In everyday practice, we mainly use the last generation US device (MyLab 9, Esaote, Genoa, GE, Italy) with an integrated magnetic fusion imaging system for virtual navigation (MedCom GmbH, Darmstadt, DE, Germany). Concerning the probes, our workhorses are a 3–11 Hz linear probe and a micro-convex intracavitary probe (Prada et al., 2016b).

After the craniotomy and before the dural opening, the probe is wrapped in a sterile plastic sheath with coupling sterile US gel in standard fashion. The first US acquisition is usually performed *trans*-durally for a preliminary inspection of the operative field, landmarks identification, lesion localization, and characterization and finally to identify the best surgical corridor to the lesion. The surgical field is continuously irrigated with sterile saline solution to allow US coupling and to reduce artifacts related to air or blood clots. Multiple US scans are performed throughout the surgery not only to guide surgical removal but also to assess the extent of resection, perfusion changes, or complications occurrence. A standard multiparametric US exam is based on the following modalities. B-Mode is usually the first employed technique, as it allows a high-resolution structural characterization of lesions and surrounding structures. Conventional Doppler techniques are used for main vessels identification: color- and spectral-Doppler are combined to identify and characterize whether the blood flow is present.

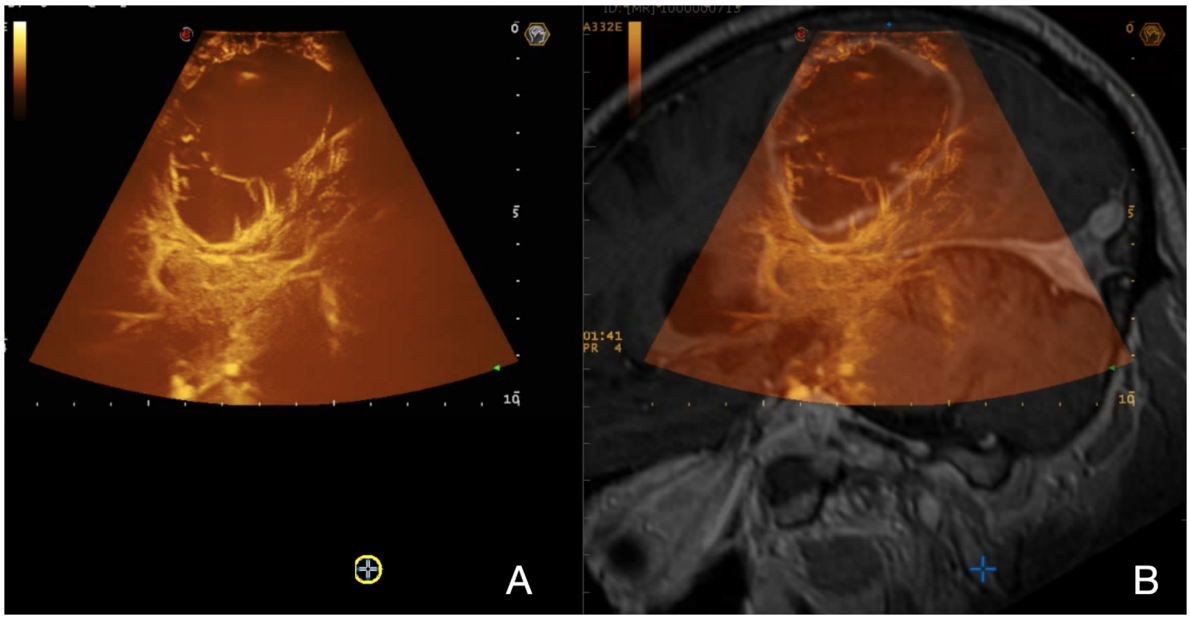

FIGURE 3 | Navigated MIP-CEUS. **(A)** On the left, a real-time MIP-CEUS sequence is displayed; **(B)** on the right, the corresponding pre-operative MRI is fused with real-time ioUS. The signal obtained throughout the MBs distribution can be depicted in a MIP image to describe the entire vascular-tree including smaller vessels under structural and functional aspects, giving detailed representation of the CE pattern.

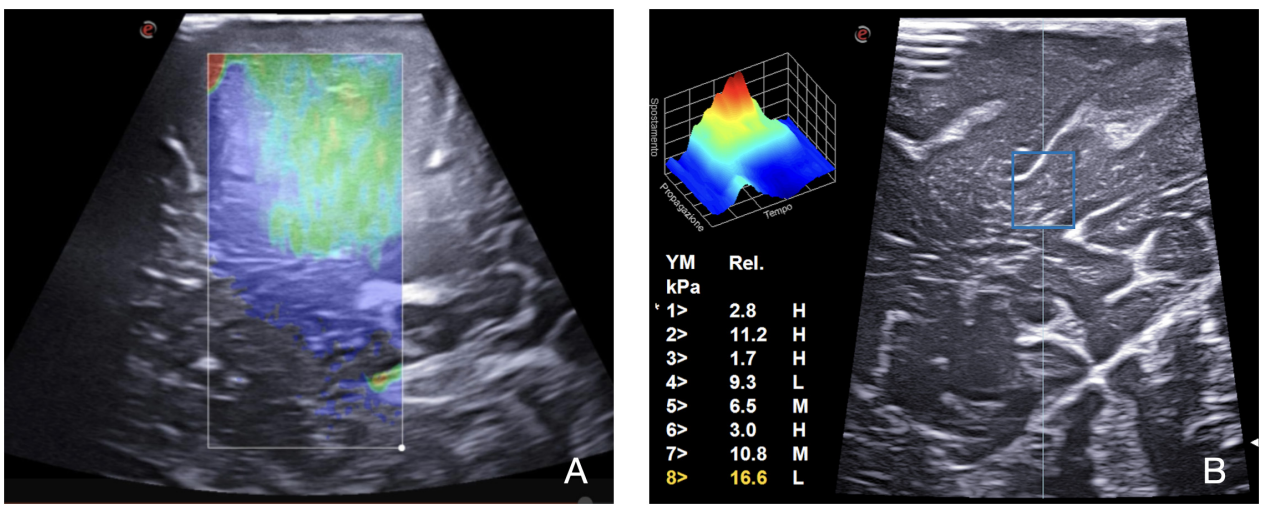

FIGURE 4 | SE and SWE. Elastosonography provides information regarding the tumor and surrounding parenchyma mechanical properties through qualitative and quantitative evaluation. **(A)** On the left, SE in a case of metastasis: a mechanical force is applied to measure lesion stiffness, which is expressed on a color scale for qualitative assessment. **(B)** On the right, SWE, using the QElaxto algorithm, provides a quantitative assessment of stiffness of a specific ROI inside the lesion.

Ultrasensitive usDoppler techniques (Xflow, MicroV, Esaote, Genoa, GE, Italy) are employed to study the perfusion pattern and capillary angio-architecture of the tumor and surrounding parenchyma. Elastosonography provides information regarding the tumor and surrounding parenchyma mechanical features through qualitative and quantitative evaluation (SE, SWE). Finally, CEUS, relying on UCAs (Sonovue), allows to observe tumor and parenchyma perfusion patterns, characteristically recognizing 4 phases: "wash in" representing the arterial signal, "parenchymal perfusion" giving an overall idea about capillary bed perfusion distribution, "peak" which is the maximum contrast intensity associated with tumor perfusion, and "wash out" corresponding to venous outflow. The signal obtained throughout the four phases can be depicted in a MIP image to describe the entire vascular tree including smaller vessels under structural and functional aspects.

At this point, neurosurgeons proceed in lesion removing, practicing multiple multiparametric scans for a real-time

evaluation of the neighboring structures, residual tumor, and changes occurrence.

Once the lesion is completely removed, a final multiparametric scan is performed to evaluate potential hidden residual tumor and potential complications occurrence.

In the following paragraph, we sought to summarize the main applications, values, and issues, together with our considerations concerning the use of multiparametric ioUS in the four, most relevant, entities in oncological surgery, namely, low-grade gliomas (LGGs), high-grade gliomas (HGGs), meningiomas, and brain metastases.

LOW-GRADE GLIOMA

Low-grade glioma (LGG, WHO, 2021 grade 2) (Louis et al., 2021) represents a real challenge for neurosurgeons. LGGs are hardly discernible from surrounding healthy brain parenchyma at macroscopic inspection. Likewise, as these lesions do not show contrast enhancement at MR imaging, the definition of surgical margins is most often left to FLAIR-hyperintense areas representative of neoplastic cells' infiltration and perilesional vasogenic edema. In our experience, in B-Mode, LGGs appear as slightly hyperechoic owing to homogeneous echo signals with blurred margins (**Figure 5**). Therefore, the distinction of neoplastic infiltration from perilesional edema remains an open challenge (Solheim et al., 2010; Prada et al., 2014a,b; del Bene et al., 2018). However, several papers have demonstrated the positive impact of B-mode US on the extent of resection in LGGs (Sastry et al., 2017; Zhang et al., 2017; del Bene et al., 2018; Munkvold et al., 2018; Mazzucchi et al., 2020). The issue of artifacts occurrence in intra-axial brain tumor surgery should be mentioned. This phenomenon can lead to the impossibility of distinguishing between tumor residue and artifact related to surgical manipulation (Šteňo et al., 2021).

Contrast-enhanced US highlights the perfusion pattern of the tissues, allowing to identify not only neoplastic areas, where vessels are more represented, but also higher grade spots, such as anaplastic foci, thus guiding surgical decision-making (Prada et al., 2014a). In particular, the parenchymal phase of CEUS enhancement can be helpful in the identification of residual tumors depending on the specific perfusion pattern of the tumor (Prada et al., 2016a). As presented in **Figure 5**, LGGs show a mild, dotted contrast-enhanced image with a diffuse appearance. The pattern is homogenous as there are no necrotic cores or cystic and hemorrhagic areas, while arterial, parenchymal, and venous phases are slower than high-grade gliomas. These considerations may allow an intraoperative glioma WHO grade characterization even in dubious cases (Prada et al., 2014b, 2021; Cheng et al., 2016; del Bene et al., 2018; Wu et al., 2019).

In LGGs surgery, conventional Doppler techniques are exploited to visualize main neighboring vessels in strict relationship with the tumor. With color- and spectral-Doppler, it is possible to define the flow velocity and to distinguish arteries from veins. Concerning tumor perfusion patterns, it is not possible to identify tumoral macrovessels in LGGs. Xflow and MicroV Doppler can explore the micro-vasculature, which in LGGs is usually scarce (**Figure 5**). For this reason, in the case of LGGs, usually CEUS is much more informative than Doppler techniques (Ng and Swanevelder, 2011; Prada et al., 2014b, 2015; Cepeda et al., 2021b).

Finally, elastosonography is another useful US tool to characterize the nature and to visualize the lesion. LGGs, in most cases, appear stiffer than the surrounding healthy brain as shown in **Figure 5**. This characteristic can help the neurosurgeon in defining its borders and eventually post-resection residue (Chauvet et al., 2016; Prada et al., 2019; Chan et al., 2021; Yin et al., 2021).

In the case of oligodendrogliomas, specific considerations must be made: B-mode scans are often characterized by intratumoral calcifications depicted as highly echogenic spots. CEUS shows faster contrast enhancement (CE) and better-defined borders than other LGGs, and all the phases are slower than that in anaplastic astrocytomas. CE patterns are homogeneous even with the presence of intralesional calcification and cysts (Prada et al., 2014b; del Bene et al., 2018).

Multiparametric approach provides the surgeon with last-generation instruments to intraoperatively visualize, characterize, and identify lesions and surrounding structures. In our practice, combining different techniques is preferred to standard B-mode alone, as this allows to predict tumor biology and to better visualize tumor, relationships, and residues, which could lead to safer and more effective surgery: despite the potential of mpUS, more trials are needed to demonstrate cost-effectiveness benefits from this approach (Prada et al., 2014a, 2016b; Cheng et al., 2016; del Bene et al., 2018).

HIGH-GRADE GLIOMA

High-grade gliomas (WHO, 2021, 3 and 4) (Louis et al., 2021) are easily recognizable in intraoperative B-mode as their appearance is inhomogeneous due to their necro-cystic or hemorrhagic component, their irregular shape, and unclear borders. In our experience, HGGs are usually characterized by hyperechoic margins mixed with iso-ipoechoic central necrotic areas and infiltrative patterns (**Figure 6**). In general, the margins are more identifiable than that in LGGs even it is still difficult to differentiate between tumor boundaries and peri-lesional edema. However, B-mode is highly informative in HGG resection as demonstrated in numerous papers (Chacko et al., 2003; Solheim et al., 2010; del Bene et al., 2018; Carai et al., 2021; Incekara et al., 2021; Yin et al., 2021). At first, it allows a real-time anatomical study of the lesion, surrounding structures, and tumor architecture even before the dural opening. Furthermore, as the dural opening is accompanied by a brain shift, the anatomy could be modified. B-mode is used to navigate again to identify the lesion, the anatomical landmarks, and the vital structures to be preserved. In addition, the neurosurgeon can observe which gyrus is infiltrated and thus tailoring the corticectomy preserving the spared gyrus. During surgery, B-mode US can be repeated multiple times to guide the surgery and estimate the extent of resection (Solheim et al., 2010; Prada et al., 2014b, 2016b; del Bene et al., 2018; Incekara et al., 2021; Yin et al., 2021).

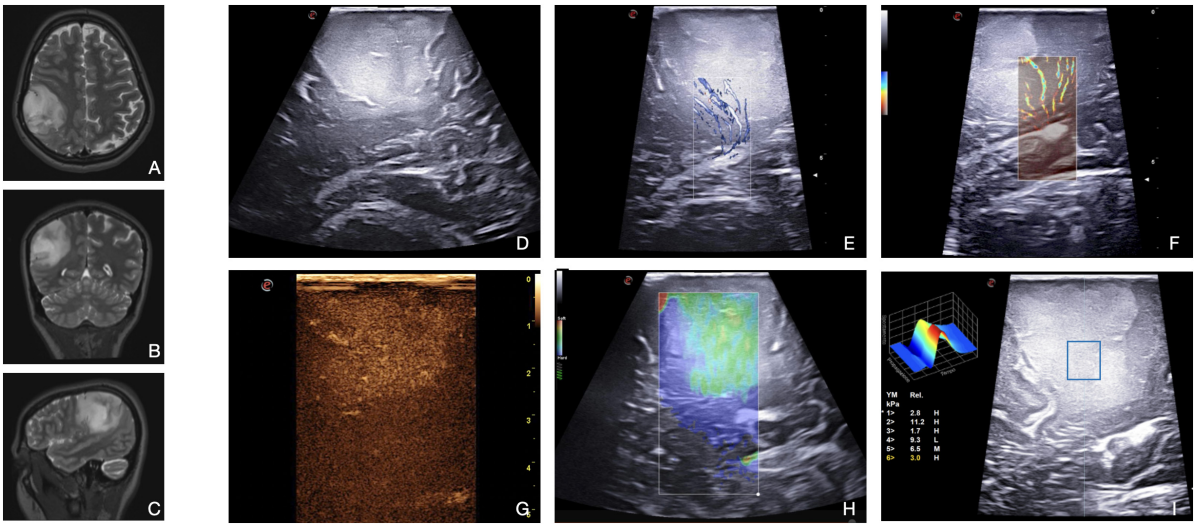

FIGURE 5 | Illustrative case of a diffuse astrocytoma (Grade 2 WHO, 2021). **(A–C)** Pre-operative MRI demonstrates a right frontal-temporal-parietal low-grade, non-enhancing intra-axial tumor. **(D)** In B-mode, LGG appears as a hyperechoic diffuse mass with blurred margins. Both X-flow Doppler **(E)** and Micro-V **(F)** demonstrate the venous drainage toward the ependyma. CEUS **(G)** allows to differentiate peritumoral edema from tumoral tissue. Typically, LGG shows a mild, dotted CE with homogenous pattern. SE **(H)** and SWE **(I)** allow a qualitative and quantitative evaluation, respectively, of the stiffness of the lesion. This information can be exploited to identify the interface between tumor and brain as shown in image **(H)** (the lesion appears green-softer than the parenchyma beneath).

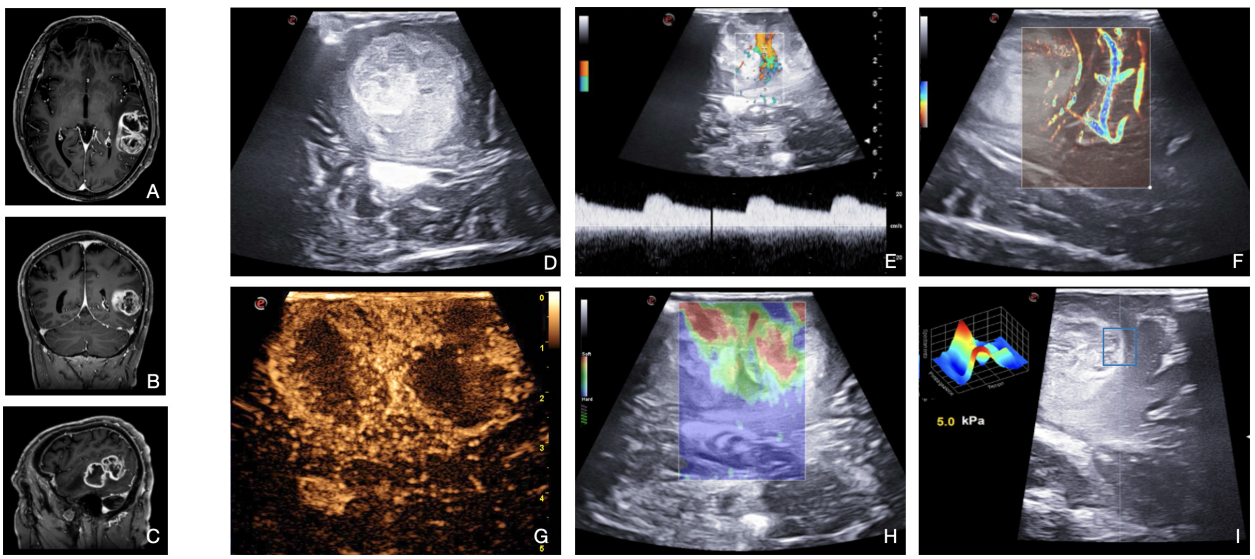

FIGURE 6 | Illustrative case of glioblastoma (Grade 4 WHO, 2021). **(A–C)** Pre-operative MRI demonstrates a left temporal high-grade, enhancing intra-axial tumor. **(D)** B-mode provides mainly structural information on the lesion and on the main relationships with surrounding structures. B-mode shows the presence of a vast hypoechoic necrotic core within the lesion. Color-Doppler **(E)** and MicroV **(F)** depict the main vessels and create a map of the vascular tree. Spectral-Doppler characterizes the flow inside a vessel, thus providing information on the nature and relevance: in panel **(E)** an artery between the two lesion's necrotic core with a flow velocity of 20 cm/s. MicroV highlights the surrounding vessels and the smaller capillaries inside the lesion. CEUS **(G)** provides a representation of the anatomical and functional architecture of the entire vascular tree. The image acquired at the peak phase is suggestive for the entity of perfusion of HGG, also dissecting the components of the lesion: two intense CE ring-shaped areas of vital tissue delineating two central low CE necrotic cores. Qualitative **(H)** and quantitative **(I)** elastosonography inform on the stiffness of the different components of the lesion (e.g., necrosis vs. vital tissue) and on the interface between tumor and brain. SE shows two soft areas (red) surrounded by stiffer areas (green-blue). SWE, using the QElaxto algorithm, can define the stiffness of a specific ROI inside or outside the lesion.

Doppler ultrasound is applied to acquire more information about the vascularization of the lesion and the relationships with the surrounding vessels. In addition, it can be helpful for the orientation of the surgical field and the preparation of the corridor. While spectral-Doppler and color-Doppler are used to identify the vessels and understand their arterial or venous

nature, power-Doppler is exploited to better highlight the smaller branches from the surrounding vessels (**Figure 6**). However, conventional Doppler alone gives limited information (Prada et al., 2016b, 2018; Šteňo et al., 2016). Application of usDoppler (Xflow, MicroV) is particularly useful for the surgeon, as the sensitivity and high-definition of these techniques permit to visualize and estimate more accurately HGG's smallest vessels and the entity of neoangiogenesis (**Figure 6**).

Elastosonography demonstrates HGGs to be usually softer than the healthy brain parenchyma (**Figure 6**), thus helping to discern between HGGs and LGGs (Cepeda et al., 2021b). Quantitative analysis made possible by SWE is particularly interesting for the creation of algorithms to discern intraoperatively the nature of the lesion, such as distinguishing HGGs from solitary brain metastases (Prada et al., 2016b, 2019; Cepeda et al., 2021b; Yin et al., 2021). SE and SWE are useful even for assisting tumoral resection (Newman and Rozycki, 1998).

Finally, CEUS allows a real-time angiosonography of the HGG which provides an in-depth analysis of the anatomical and functional organization of the vascular tree, also identifying their relationship with the neighboring arteries and veins. As shown in **Figure 6**, HGGs commonly display intense CE signal characterized by fast perfusion patterns. The arterial phase shows macro-vessels supplying the mass and a peripheral enhancement that moves toward the inner areas of the lesion. While the proliferating areas have high CE, the necrotic areas don't show any. The MIP sequence emphasizes the smaller vessels, giving a detailed representation of this CE pattern. As regards glioblastomas (GBM, WHO, 2021 grade 4), there are generally two different CE patterns: the peripheral CE surrounding a necrotic core or a more nodular and heterogeneous high CE within the lesion alternated by small spots of necrosis (Ng and Swanevelder, 2011; Prada et al., 2016a; Sidhu et al., 2018; Cepeda et al., 2021a; Menna et al., 2021).

In general, HGG borders are always better visualized after MBs administration than in B-mode due to the different vascularization of the tumor with respect to the normal brain tissue (Schrope and Newhouse, 1993). Thanks to these characteristics, CEUS has been exploited to identify tumor remnants after resection in different studies: CEUS shows persistent CE in nodular tissue around the surgical cavity, while B-mode alone can be unclear (Ng and Swanevelder, 2011; Fountain et al., 2021; Menna et al., 2021).

MENINGIOMA

Most intracranial meningiomas are benign tumors with a good prognosis after standard treatment. However, under structural and functional aspects they may differ enormously, also contracting threatening relationships with vital structures (Solheim et al., 2009). MpUS provides valuable information for tumor identification, enabling analysis of the tumor location, relationships, mechanical properties, and vascularization (Prada et al., 2015; Menna et al., 2021).

In our experience, meningiomas are generally recognizable in B-mode as hyperechoic lesions with a homogeneous pattern, a granular aspect, and fine trabeculation (WHO 1-2) (**Figure 7**) or with several hypoechoic areas of necrotic degeneration (WHO 3). When present, intratumoral calcifications are depicted as highly echogenic components. In addition, meningioma margins are generally well defined even though, especially in the case of brain invasion, surrounding brain parenchyma can also be hyperechoic (Prada et al., 2015, 2016b). Through the careful interpretation of the B-mode signal, it is possible to achieve an initial overview of tumor mechanical features, of the nature of the interfaces and relationships, and of gross extension. Traditional color- and spectral-Doppler show the presence, direction, and velocity of the flow in surrounding or encased large vessels, enabling the surgeon to rapidly create a real-time flow map to avoid them during surgery. This consideration is particularly true in the case of deep-seated meningiomas close to basal veins, vital arteries, or in meningiomas invading or strictly adherent to dural sinuses. Solheim et al. (2009) examined the application of power-Doppler in meningioma surgery concluding that in most cases, this US modality could be helpful in visualizing feeding arteries and adjacent important vessels leading to safe preservation of them. Anyway, the authors recognized this technique to be limited by the difficulty to study low-flow vessels. Conversely, micro-Doppler (Xflow, MicroV) magnifies slow flow also in smaller vessels, providing the surgeon with information about the entity of meningioma vascularization and location of main feeders, which can be useful to plan resection (**Figure 7**).

Contrast-enhanced ultrasound allows a reliable intraoperative visualization of the peritumoral and intratumoral vascular tree, providing real-time dynamic images of intrinsic tumor perfusion, visualizing "wash in" velocity, parenchymal perfusion, and peak and venous "wash out." Thanks to the most recent algorithms for quantitative CEUS, we expect its intraoperative application to change meningioma surgery in the near future (Prada et al., 2021). Usually, the CEUS pattern for meningiomas consists of an intense and rapid contrast enhancement with an impressive peak, especially for higher grades, a slow venous, and not always visible (Prada et al., 2015). MIP on the CEUS image sequence can be used to obtain better visualization of intra-tumoral vascular tree and higher definition of the lesions' borders, even allowing a better understanding of the relationship between tumors and surrounding vessels in relationship with it (**Figure 7**). CEUS in meningioma surgery offers two main advantages. The boundaries of the lesion are easily identified, also enabling easier detection of residual tissue. Second, the main arterial feeders and surrounding vessels are visualized and characterized, thus providing pivotal information for tumor debulking and resection. These data can be valuable in guiding surgical decision-making and planning, for instance, by targeting the arterial feeders first to obtain a complete tumor devascularization before debulking. In addition, CEUS might be repeated to evaluate the degree of remaining vascularization from other feeders outside the main dural supply.

Meningiomas encompass quite a wide spectrum of textures and brain-tumor interfaces which unavoidably play a fundamental role during resection; however, MR imaging is not always predictive of these aspects. Elastosonography instead, by directly calculating the lesions' Young modulus, provides real-time, intuitive imaging of meningiomas' stiffness and relation to

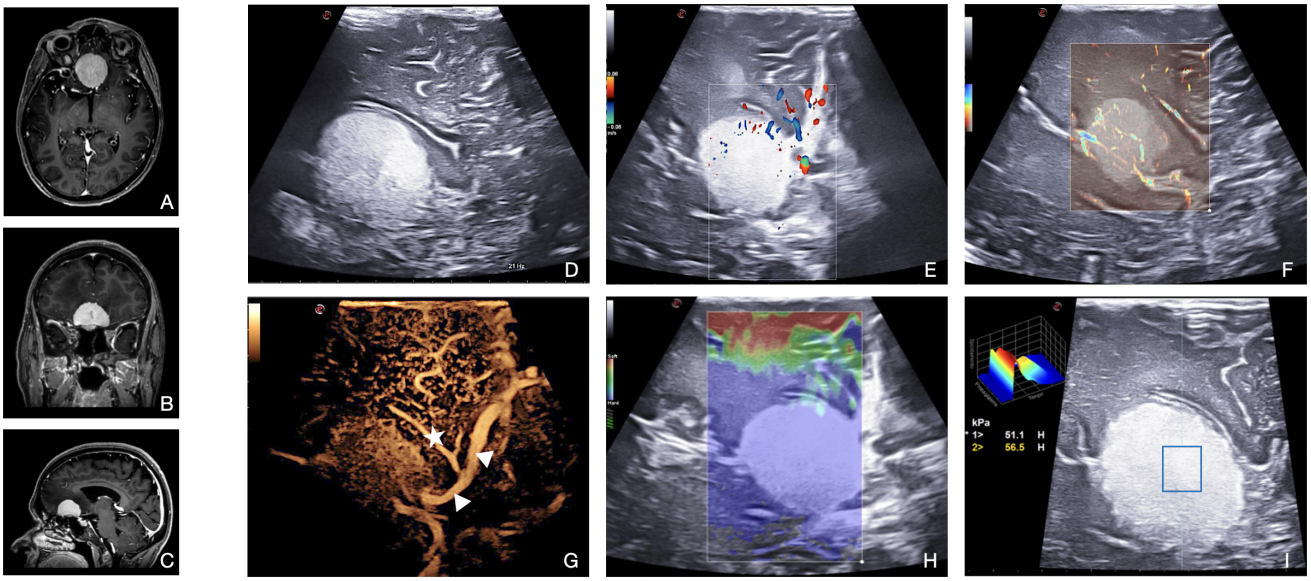

FIGURE 7 | Illustrative case of atypical meningioma (Grade 2 WHO, 2021). **(A–C)** Pre-operative MRI demonstrates a Planum Sphenoidale, enhancing, extra-axial tumor. **(D)** Standard B-mode: meningioma appears hyperechoic, compared with normal brain parenchyma, with a homogeneous pattern and a granular aspect. Tumor margins are sharply defined. **(E)** Color- and spectral-Doppler show the presence, direction, and velocity of flow of the vessels of the anterior circulation. **(F)** Micro-V depicts also slow flow in small-diameter vessels within the lesion, providing information about the entity of perfusion/vascularization. **(G)** CEUS enhances the findings of Doppler modalities representing a peritumoral and intratumoral vascular tree. In this patient, we can appreciate the relationships between meningioma and anterior cerebral artery (arrowheads) and Heubner's artery (star). The basal portion of the lesion cannot be properly studied due to calcification within the meningioma itself. In meningioma surgery, elastosonography informs on lesion mechanical features, thus guiding surgical decision-making. In this case, **(H)** SE shows meningioma with a higher stiffness than the surrounding tissues. **(I)** SWE confirms the higher stiffness also providing a quantitative evaluation: Young's modules in the ROI of 56 kPa.

surrounding structures. From our experience, this feature plays a pivotal role in the planning of resection strategy, to the point of influencing the choice of a particular instrument or approach (**Figure 7**; Prada et al., 2015; della Pepa et al., 2020).

BRAIN METASTASES

Brain metastases are generally recognizable in B-mode as distinctly hyperechoic lesions with a diffuse granular or heterogeneous aspect (e.g., peripheral ring and central necrosis or nodule and cystic areas). The most frequent B-mode pattern encompasses solid components and cystic or necrotic areas varying in size and owing well-demarcated boundaries even in the case of surrounding edema (**Figure 8**).

Conventional Doppler techniques allow to visualize main neighboring vessels and to characterize the blood flow features. Xflow and MicroV techniques usually depict relevant perfusion at the capillary level through several centripetal feeders from the surrounding parenchyma.

Then, CEUS defines a rapid contrast enhancement, with a fast arterial phase and contrast enhancement peak. Contrast enhancement is intense and persistent with a delayed venous phase and irregular and heterogeneous CE pattern (**Figure 8**). CEUS depicts with detail the nature of the tissues (e.g., necrotic vs. vital) in virtue of the degree of CE. The arterial supply is frequently centripetal with many macrovessels within the lesion, whose visualization can be magnified through MIP sequence. As such, CEUS can aid brain metastases resection by identifying feeding arteries, draining veins, and tumor vasculature.

Elastosonography allows to characterize the mechanical properties of the lesion and to plan the surgical approach. In general, brain metastases may be stiffer (kidney, colon) or softer (lung, endometrial) than a normal brain. As described by Chauvet et al. (2016), brain metastases have a low mean elasticity value–partially due to central necrosis. Furthermore, elastosonography can guide the differential diagnosis between metastasis and HGGs (Prada et al., 2016a; Wu et al., 2019).

In particular, in bran metastases, IoUS plays a major role at the beginning of the resection, to understand the relationships and the feeders and to orientate in the surgical field, or in case of piecemeal resections when en-bloc removal is not feasible, to assess the extent of resection and residue presence.

MULTIPARAMETRIC ULTRASOUND LIMITATIONS

Although mpUS owns great potential, certainly it is limited by some relevant aspects which should be taken into account. The learning curve of mpUS is certainly steep or even steeper if compared with standard B-mode. Specific courses and resources should be promoted and supported. Research in this field is still at the dawn, thus still not allowing to demonstrate the

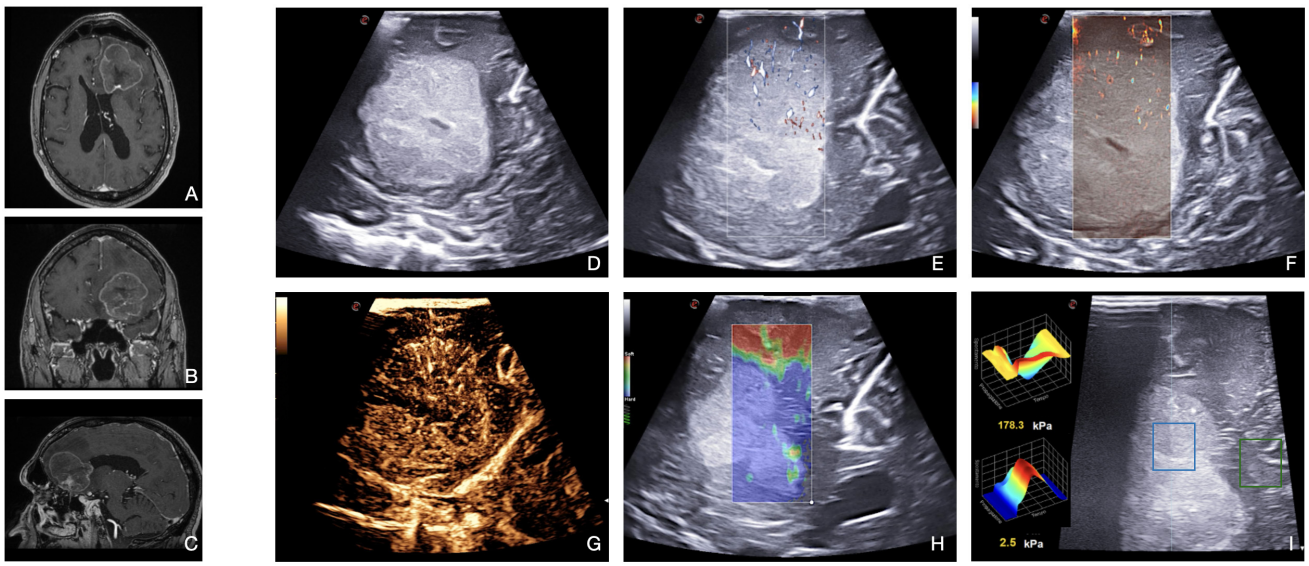

FIGURE 8 | Illustrative case of brain metastasis of lung carcinoma. **(A–C)** Pre-operative MRI demonstrates a left frontal, enhancing, intra-axial tumor. **(D)** B-mode: the lesion appears distinctly hyperechoic with a diffuse granular and heterogeneous aspect. The central core is necrotic. Tumor/brain interface is recognizable. **(E,F)** Micro-Doppler techniques (X-Flow and micro-V) demonstrate the presence of intratumoral microvascularization, thus informing on perfusion pattern. **(G)** CEUS shows a moderate and heterogeneous contrast enhancement pattern with centripetal dynamics. The central necrotic core is highlighted. In general, metastasis may appear as stiffer or milder than a healthy brain. In this case, **(H,I)** SE shows a high stiffness (blue) in the neoplastic region analyzed, while SWE quantifies the stiffness in specific ROI (the central blue ROI has a stiffness of 2.5 kPa, while the peripheral green ROI of 178.3 kPa).

real reach of this approach. Another intrinsic limitation of this approach is the necessity of the last generation US device, which hinder the spreading of the technique. Each modality employed in multiparametric evaluation has specific limitations that should always be considered when evaluating the reliability of this methodology. As for standard applications of US, acoustic enhancement artifacts (AEAs) are a major issue that could hamper the visualization of tumor borders and residue presence after debulking. To overcome this problem, new approaches are under investigation, such as the use of dedicated coupling fluids, micro-probes to study the cavity from inside, CEUS applications, navigated US, and the exploiting of surrounding healthy brain to study the surgical cavity. Finally, being neurosurgery a new field of application of mpUS, the level of evidence for this approach is still low, and further investigations are warranted to exploit the full potential (Solheim et al., 2010; Prada et al., 2016b; Šteňo et al., 2016, 2021; Unsgård et al., 2019).

CONCLUSION

Ultrasound brain imaging applications have been historically limited by the presence of bone shielding, thus shifting diagnostics and research to CT and MRI applications. As a matter of fact, a craniotomy opens a window that allows US imaging of the brain as for other US accessible body organs where multiparametric US has been exploited for several years to obtain structural and functional information about tumoral biology before histopathological examination. IoUS has many advantages in neuro-oncological surgery. Due to the multiparametric approach, it is possible to study the tumor and the surrounding parenchyma under structural and functional aspects in real-time and dynamically during the operation. The different ioUS techniques can be exploited both in malignant and benign tumors providing the operators with crucial information to optimize surgery, identifying the remnants, and facilitating maximal resection. The impressive spreading of ioUS among different neurosurgical centers all over the world testifies the potential of multiparametric ioUS in neuro-oncological surgery. To this end, we sought that every craniotomy performed, not only for brain tumors but also for other neurosurgical cases, such as trauma, epilepsy, or vascular cases, will be used as an opportunity to better understand brain physiopathology in real-time. Closing up the patients with prosthesis that allow for post-operative imaging, and eventually therapy, will allow to carry this opportunity in a post-operative setting as well (del Bene et al., 2022). Nevertheless, further research and efforts regarding improvements, training, standardization, and reproducibility of intraoperative ultrasound modalities as stand-alone tools and in a multiparametric fashion are still required.

AUTHOR CONTRIBUTIONS

FP contributed to acquisition of data, study concept, and design. FP and MD contributed to critical revision of the manuscript for intellectual content. RC and NC contributed to original draft preparation. FP, RC, NC, MG, LR, FD, IV, MD, and FDM contributed to reviewing and editing. All authors contributed to the article and approved the submitted version.

REFERENCES

Cabrilo, I., Delaunay, R., Heaysman, C. L., Ourselin, S., Vitiello, V., Vercauteren, T., et al. (2021). A novel intraoperative ultrasound probe for transsphenoidal surgery: first-in-human study. *Surg. Innov.* 1–7. doi: 10.1177/15533506211031091

Carai, A., de Benedictis, A., Calloni, T., Onorini, N., Paternò, G., Randi, F., et al. (2021). Intraoperative ultrasound-assisted extent of resection assessment in pediatric neurosurgical oncology. *Front. Oncol.* 11:660805. doi: 10.3389/fonc.2021.660805

Cepeda, S., García-García, S., Arrese, I., Fernández-Pérez, G., Velasco-Casares, M., Fajardo-Puentes, M., et al. (2021b). Comparison of intraoperative ultrasound b-mode and strain elastography for the differentiation of glioblastomas from solitary brain metastases. an automated deep learning approach for image analysis. *Front. Oncol.* 10:590756. doi: 10.3389/fonc.2020.590756

Cepeda, S., Arrese, I., García-García, S., Velasco-Casares, M., Escudero-Caro, T., Zamora, T., et al. (2021a). Meningioma consistency can be defined by combining the radiomic features of magnetic resonance imaging and ultrasound elastography. a pilot study using machine learning classifiers. *World Neurosurg.* 146, e1147–e1159. doi: 10.1016/j.wneu.2020.11.113

Chacko, A. G., Kumar, N. K. S., Chacko, G., Athyal, R., Rajshekhar, V., and Unsgaard, G. (2003). Intraoperative ultrasound in determining the extent of resection of parenchymal brain tumours – a comparative study with computed tomography and histopathology. *Acta Neurochir.* 145, 743–748. doi: 10.1007/s00701-003-0009-2

Chan, H. W., Uff, C., Chakraborty, A., Dorward, N., and Bamber, J. C. (2021). Clinical application of shear wave elastography for assisting brain tumor resection. *Front. Oncol.* 11:619286. doi: 10.3389/fonc.2021.619286

Chauvet, D., Imbault, M., Capelle, L., Demene, C., Mossad, M., Karachi, C., et al. (2016). In vivo measurement of brain tumor elasticity using intraoperative shear wave elastography. *Ultraschall Med.* 37, 584–590. doi: 10.1055/s-0034-1399152

Cheng, L. G., He, W., Zhang, H. X., Song, Q., Ning, B., Li, H. Z., et al. (2016). Intraoperative contrast enhanced ultrasound evaluates the grade of glioma. *BioMed Res. Int.* 2016:2643862. doi: 10.1155/2016/2643862

D'Amico, R. S., Englander, Z. K., Canoll, P., and Bruce, J. N. (2017). Extent of resection in glioma–a review of the cutting edge. *World Neurosurg.* 103, 538–549. doi: 10.1016/j.wneu.2017.04.041

del Bene, M., Perin, A., Casali, C., Legnani, F., Saladino, A., Mattei, L., et al. (2018). Advanced ultrasound imaging in glioma surgery: beyond gray-scale b-mode. *Front. Oncol.* 8:576. doi: 10.3389/fonc.2018.00576

del Bene, M., Raspagliesi, L., Carone, G., Gaviani, P., Silvani, A., Solbiati, L., et al. (2022). Cranial sonolucent prosthesis: a window of opportunity for neuro-oncology (and neuro-surgery). *J. Neuro Oncol.* 156, 529–540. doi: 10.1007/s11060-021-03929-x

della Pepa, G. M., Menna, G., Stifano, V., Pezzullo, A. M., Auricchio, A. M., Rapisarda, A., et al. (2020). Predicting meningioma consistency and brain-meningioma interface with intraoperative sstrain ultrasound elastography: a novel application to guide surgical strategy. *Neurosurg. Focus* 50, 1–11. doi: 10.3171/2020.10.FOCUS20797

della Pepa, G. M., Sabatino, G., and la Rocca, G. (2019). "Enhancing vision," in high grade glioma surgery: a feasible integrated 5-ala + ceus protocol to improve radicality. *World Neurosurg.* 129, 401–403. doi: 10.1016/j.wneu.2019.06.127

Fountain, D. M., Bryant, A., Barone, D. G., Waqar, M., Hart, M. G., Bulbeck, H., et al. (2021). Intraoperative imaging technology to maximise extent of resection for glioma: a network meta-analysis. *Cochrane Database Syst. Rev.* 2021:CD013630. doi: 10.1002/14651858.CD013630.pub2

Grgurevic, I., Tjesic Drinkovic, I., and Pinzani, M. (2019). Multiparametric ultrasound in liver diseases: an overview for the practising clinician. *Postgrad. Med. J.* 95, 425–432. doi: 10.1136/postgradmedj-2018-136111

Incekara, F., Smits, M., Dirven, L., Bos, E. M., Balvers, R. K., Haitsma, I. K., et al. (2021). Intraoperative B-mode ultrasound guided surgery and the extent of glioblastoma resection: a randomized controlled trial. *Front. Oncol.* 11:649797. doi: 10.3389/fonc.2021.649797

Kim, H. J., Kim, S. M., Kim, B., la Yun, B., Jang, M., Ko, Y., et al. (2018). Comparison of strain and shear wave elastography for qualitative and quantitative assessment of breast masses in the same population. *Sci. Rep.* 8:6197. doi: 10.1038/s41598-018-24377-0

Kloth, C., Kratzer, W., Schmidberger, J., Beer, M., Clevert, D. A., and Graeter, T. (2021). Ultrasound 2020 – diagnostics & therapy: on the way to multimodal ultrasound: contrast-enhanced ultrasound (ceus), microvascular doppler techniques, fusion imaging, sonoelastography, interventional sonography. *RoFo* 193, 23–32. doi: 10.1055/a-1217-7400

Louis, D. N., Perry, A., Wesseling, P., Brat, D. J., Cree, I. A., Figarella-Branger, D., et al. (2021). The 2021 WHO classification of tumors of the central nervous system: a summary. *Neuro-Oncology* 23, 1231–1251. doi: 10.1093/neuonc/noab106

Mannaerts, C. K., Wildeboer, R. R., Postema, A. W., Hagemann, J., Budäus, L., Tilki, D., et al. (2018). Multiparametric ultrasound: evaluation of greyscale, shear wave elastography and contrast-enhanced ultrasound for prostate cancer detection and localization in correlation to radical prostatectomy specimens. *BMC Urol.* 18:98. doi: 10.1186/s12894-018-0409-5

Mazzucchi, E., la Rocca, G., Ius, T., Sabatino, G., and della Pepa, G. M. (2020). Multimodality imaging techniques to assist surgery in low-grade gliomas. *World Neurosurg.* 133, 423–425. doi: 10.1016/j.wneu.2019.10.120

Menna, G., Olivi, A., and della Pepa, G. M. (2021). Integration of different intraoperative ultrasound modalities in meningioma surgery: a 4-step approach. *World Neurosurg.* 146, 376–378. doi: 10.1016/j.wneu.2020.12.005

Moiyadi, A. V. (2016). Intraoperative ultrasound technology in neuro-oncology practice—current role and future applications. *World Neurosurg.* 93, 81–93. doi: 10.1016/j.wneu.2016.05.083

Munkvold, B. K. R., Jakola, A. S., Reinertsen, I., Sagberg, L. M., Unsgård, G., and Solheim, O. (2018). The diagnostic properties of intraoperative ultrasound in glioma surgery and factors associated with gross total tumor resection. *World Neurosurg.* 115, e129–e136. doi: 10.1016/j.wneu.2018.03.208

Newman, P. G., and Rozycki, G. S. (1998). The history of ultrasound. *Surg. Clin. North Am.* 78, 179–195. doi: 10.1016/S0039-6109(05)70308-X

Newsome, I. G., and Dayton, P. A. (2020). Visualization of microvascular angiogenesis using dual-frequency contrast-enhanced acoustic angiography: a review. *Ultrasound Med. Biol.* 46, 2625–2635. doi: 10.1016/j.ultrasmedbio.2020.06.009

Ng, A., and Swanevelder, J. (2011). Resolution in ultrasound imaging. *Contin. Educ. Anaesth. Crit. Care Pain* 11, 186–192. doi: 10.1093/bjaceaccp/mkr030

Pang, T., Huang, L., Deng, Y., Wang, T., Chen, S., Gong, X., et al. (2017). Logistic regression analysis of conventional ultrasonography, strain elastosonography, and contrast-enhanced ultrasound characteristics for the differentiation of benign and malignant thyroid nodules. *PLoS One* 12:e0188987. doi: 10.1371/journal.pone.0188987

Prada, F., del Bene, M., Fornaro, R., Vetrano, I. G., Martegani, A., Aiani, L., et al. (2016a). Identification of residual tumor with intraoperative contrast-enhanced ultrasound during glioblastoma resection. *Neurosurg. Focus* 40:E7. doi: 10.3171/2015.11.FOCUS15573

Prada, F., Solbiati, L., Martegani, A., and DiMeco, F (eds) (2016b). *Intraoperative Ultrasound (IOUS) in Neurosurgery: From Standard B-mode to Elastosonograpy*. Cham: Springer International Publishing.

Prada, F., del Bene, M., Mauri, G., Lamperti, M., Vailati, D., Richetta, C., et al. (2018). Dynamic assessment of venous anatomy and function in neurosurgery with real-time intraoperative multimodal ultrasound: technical note. *Neurosurg. Focus* 45:E6. doi: 10.3171/2018.4.FOCUS18101

Prada, F., del Bene, M., Moiraghi, A., Casali, C., Legnani, F. G., Saladino, A., et al. (2015). From grey scale b-mode to elastosonography: multimodal ultrasound imaging in meningioma surgery – pictorial essay and literature review. *BioMed Res. Int.* 2015:925729. doi: 10.1155/2015/925729

Prada, F., del Bene, M., Rampini, A., Mattei, L., Casali, C., Vetrano, I. G., et al. (2019). Intraoperative strain elastosonography in brain tumor surgery. *Oper. Neurosurg.* 17, 227–236. doi: 10.1093/ons/opy323

Prada, F., Gennari, A. G., Linville, I. M., Mutersbaugh, M. E., Chen, Z., Sheybani, N., et al. (2021). Quantitative analysis of in-vivo microbubble distribution in the human brain. *Sci. Rep.* 11:11797. doi: 10.1038/s41598-021-91252-w

Prada, F., Mattei, L., del Bene, M., Aiani, L., Saini, M., Casali, C., et al. (2014a). Intraoperative cerebral glioma characterization with contrast enhanced ultrasound. *BioMed Res. Int.* 2014:484261. doi: 10.1155/2014/484261

Prada, F., Perin, A., Martegani, A., Aiani, L., Solbiati, L., Lamperti, M., et al. (2014b). Intraoperative contrast-enhanced ultrasound for brain tumor surgery. *Neurosurgery* 74, 542–552. doi: 10.1227/NEU.0000000000000301

Rubin, J. M., and Dohrmann, G. J. (1983). Intraoperative neurosurgical ultrasound in the localization and characterization of intracranial masses. *Radiology* 148, 519–524. doi: 10.1148/radiology.148.2.6867352

Sastry, R., Bi, W. L., Pieper, S., Frisken, S., Kapur, T., Wells, W., et al. (2017). Applications of ultrasound in the resection of brain tumors. *J. Neuroimaging* 27, 5–15. doi: 10.1111/jon.12382

Schrope, B. A., and Newhouse, V. L. (1993). Second harmonic ultrasonic blood perfusion measurement. *Ultrasound Med. Biol.* 19, 567–579. doi: 10.1016/0301-5629(93)90080-8

Sidhu, P., Cantisani, V., Dietrich, C., Gilja, O., Saftoiu, A., Bartels, E., et al. (2018). The EFSUMB guidelines and recommendations for the clinical practice of contrast-enhanced ultrasound (CEUS) in non-hepatic applications: update 2017 (long version). *Ultraschall Med. Eur. J. Ultrasound* 39, e2–e44. doi: 10.1055/a-0586-1107

Solheim, O., Selbekk, T., Jakola, A. S., and Unsgård, G. (2010). Ultrasound-guided operations in unselected high-grade gliomas-overall results, impact of image quality and patient selection. *Acta Neurochir.* 152, 1873–1886. doi: 10.1007/s00701-010-0731-5

Solheim, O., Selbekk, T., Lindseth, F., and Unsgård, G. (2009). Navigated resection of giant intracranial meningiomas based on intraoperative 3D ultrasound. *Acta Neurochir.* 151, 1143–1151. doi: 10.1007/s00701-009-0395-1

Šteňo, A., Buvala, J., Babková, V., Kiss, A., Toma, D., and Lysak, A. (2021). Current limitations of intraoperative ultrasound in brain tumor surgery. *Front. Oncol.* 11:659048. doi: 10.3389/fonc.2021.659048

Šteňo, A., Jezberová, M., Holl*ı*, V., Timárová, G., and Šteňo, J. (2016). Visualization of lenticulostriate arteries during insular low-grade glioma surgeries by navigated 3D ultrasound power doppler: technical note. *J. Neurosurg.* 125, 1016–1023. doi: 10.3171/2015.10.JNS151907

Unsgård, G., Sagberg, L. M., Müller, S., and Selbekk, T. (2019). A new acoustic coupling fluid with ability to reduce ultrasound imaging artefacts in brain tumour surgery—a phase I study. *Acta Neurochir.* 161, 1475–1486. doi: 10.1007/s00701-019-03945-x

Wang, J., Yang, Y., Liu, X., and Duan, Y. (2019). Intraoperative contrast-enhanced ultrasound for cerebral glioma resection and the relationship between microvascular perfusion and microvessel density. *Clin. Neurol. Neurosurg.* 186:105512. doi: 10.1016/j.clineuro.2019.105512

Wu, D. F., He, W., Lin, S., Han, B., and Zee, C. S. (2019). Using real-time fusion imaging constructed from contrast-enhanced ultrasonography and magnetic resonance imaging for high-grade glioma in neurosurgery. *World Neurosurg.* 125, e98–e109. doi: 10.1016/j.wneu.2018.12.215

Yin, L., Cheng, L., Wang, F., Zhu, X., Hua, Y., and He, W. (2021). Application of intraoperative B-mode ultrasound and shear wave elastography for glioma grading. *Quant. Imaging Med. Surg.* 11, 2733–2743. doi: 10.21037/qims-20-1368

Yoo, J., Je, B. K., and Choo, J. Y. (2020). Ultrasonographic demonstration of the tissue microvasculature in children: microvascular ultrasonography versus conventional color doppler ultrasonography. *Korean J. Radiol.* 21, 146–158. doi: 10.3348/kjr.2019.0500

Zhang, G., Li, Z., Si, D., and Shen, L. (2017). Diagnostic ability of intraoperative ultrasound for identifying tumor residual in glioma surgery operation. *Oncotarget* 8, 73105–73114. doi: 10.18632/oncotarget.20394

Conflict of Interest: The authors declare that the research was conducted in the absence of any commercial or financial relationships that could be construed as a potential conflict of interest.

Publisher's Note: All claims expressed in this article are solely those of the authors and do not necessarily represent those of their affiliated organizations, or those of the publisher, the editors and the reviewers. Any product that may be evaluated in this article, or claim that may be made by its manufacturer, is not guaranteed or endorsed by the publisher.

Copyright © 2022 Prada, Ciocca, Corradino, Gionso, Raspagliesi, Vetrano, Doniselli, Del Bene and DiMeco. This is an open-access article distributed under the terms of the Creative Commons Attribution License (CC BY). The use, distribution or reproduction in other forums is permitted, provided the original author(s) and the copyright owner(s) are credited and that the original publication in this journal is cited, in accordance with accepted academic practice. No use, distribution or reproduction is permitted which does not comply with these terms.

frontiers | Frontiers in Oncology

ORIGINAL RESEARCH
published: 22 April 2022
doi: 10.3389/fonc.2022.882313

Contralesional Sensorimotor Network Participates in Motor Functional Compensation in Glioma Patients

Shengyu Fang[1,2], Lianwang Li[2], Shimeng Weng[2], Yuhao Guo[2], Zhang Zhong[1], Xing Fan[1], Tao Jiang[1,2,3]* and Yinyan Wang[1,2]**

[1] Department of Neurosurgery, Beijing Tiantan Hospital, Capital Medical University, Beijing, China, [2] Beijing Neurosurgical Institute, Capital Medical University, Beijing, China, [3] Research Unit of Accurate Diagnosis, Treatment and Translational Medicine of Brain Tumors, Chinese Academy of Medical Sciences, Beijing, China

OPEN ACCESS

Edited by:
Sandro M. Krieg,
Technical University of Munich,
Germany

Reviewed by:
Guangxiang Chen,
The Affiliated Hospital of Southwest Medical University, China
S. Ottavio Tomasi,
Paracelsus Medical University, Austria

***Correspondence:**
Xing Fan
xingkongyaoxiang@163.com
Tao Jiang
taojiang1964@foxmail.com
Yinyan Wang
tiantanyinyan@126.com

Specialty section:
This article was submitted to Neuro-Oncology and Neurosurgical Oncology, a section of the journal Frontiers in Oncology

Received: 23 February 2022
Accepted: 11 March 2022
Published: 22 April 2022

Citation:
Fang S, Li L, Weng S, Guo Y, Zhong Z, Fan X, Jiang T and Wang Y (2022) Contralesional Sensorimotor Network Participates in Motor Functional Compensation in Glioma Patients. Front. Oncol. 12:882313. doi: 10.3389/fonc.2022.882313

Background: Some gliomas in sensorimotor areas induce motor deficits, while some do not. Cortical destruction and reorganization contribute to this phenomenon, but detailed reasons remain unclear. This study investigated the differences of the functional connectivity and topological properties in the contralesional sensorimotor network (cSMN) between patients with motor deficit and those with normal motor function.

Methods: We retrospectively reviewed 65 patients (32 men) between 2017 and 2020. The patients were divided into four groups based on tumor laterality and preoperative motor status (deficit or non-deficit). Thirty-three healthy controls (18 men) were enrolled after matching for sex, age, and educational status. Graph theoretical measurement was applied to reveal alterations of the topological properties of the cSMN by analyzing resting-state functional MRI.

Results: The results for patients with different hemispheric gliomas were similar. The clustering coefficient, local efficiency, transitivity, and vulnerability of the cSMN significantly increased in the non-deficit group and decreased in the deficit group compared to the healthy group ($p < 0.05$). Moreover, the nodes of the motor-related thalamus showed a significantly increased nodal efficiency and nodal local efficiency in the non-deficit group and decreased in the deficit group compared with the healthy group ($p < 0.05$).

Conclusions: We posited the existence of two stages of alterations of the preoperative motor status. In the compensatory stage, the cSMN sacrificed stability to acquire high efficiency and to compensate for impaired motor function. With the glioma growing and the motor function being totally damaged, the cSMN returned to a stable state and maintained healthy hemispheric motor function, but with low efficiency.

Keywords: resting-state functional magnetic resonance images, graph theory, brain reorganization, topological property, glioma

HIGHLIGHTS

This study investigated how the contralesional hemispheric sensorimotor network (cSMN) was altered in glioma patients with different motor status (deficit or normal). Two potential stages (compensated and decompensated) of motor function alteration were found. When the glioma initially appeared and the motor function of patients was normal, the cSMN sacrificed stability to acquire high efficiency in order to compensate for the impaired motor function induced by glioma. With the glioma growing and the degree of disruption of motor function being high, the damaged motor function was unable to be compensated by the cSMN; the cSMN, therefore, returned to a stable state and maintained healthy hemispheric motor function, but with low efficiency. Our findings verified that the contralesional hemispheric cortex participated in the motor functional compensation through altering the functional brain network.

INTRODUCTION

Motor function is essential for daily life, and motor dysfunction induced by a glioma has a major impact on a patient's quality of life (1). Owing to neural plasticity and functional compensation, some deficits can be recovered (2–4). Normal cortices surrounding lesions (5) and mirror-symmetrical cortices in the contralesional hemisphere are recruited to compensate for the dysfunction (4–6). However, since primary sensorimotor cortices are responsible for a sole function, remodeling through surrounding areas and then compensating for the damaged motor function are difficult (7). Accordingly, it becomes crucial to investigate network remodeling in the mirror-symmetrical sensorimotor cortices to understand the compensation for motor deficits.

Many multimodal imaging studies have demonstrated that cortical compensation in the contralesional hemisphere was related to functional recovery (8–11). Glioma is a progressive disease. It is probable for a glioma that grew on the sensorimotor network to induce preoperative motor deficit, but not all gliomas do. Cortical destruction and reorganization are related to this phenomenon, but the detailed mechanisms remain unclear. Hence, we investigated how alterations of the contralesional sensorimotor network (cSMN) in patients with different preoperative motor status help in understanding the mechanisms of motor functional compensation.

Resting-state functional MRI (rs-fMRI) is widely used to delineate functional networks. Accumulating rs-fMRI studies investigated the correlations between alterations of functional connectivity (FC) and glioma-induced functional plasticity in glioma patients (8, 12). In addition to FC, topological properties are another dimension to delineate network connections (13), which show the hierarchical connections of nodes in a network and represent the characteristics of information conveying (14, 15). Thus, the topological properties of functional networks are expected to provide a new perspective in explaining functional compensation. The current study aimed to 1) reveal how the cSMN is altered in patients with gliomas that have invaded sensorimotor-related structures and 2) identify relevant changes between the topological properties and preoperative motor deficits by comparing patients with different motor status. Subsequently, we hoped to provide some evidence for recovery treatments by identifying crucial nodes of the cSMN.

MATERIALS AND METHODS

This study was reviewed and approved by the institutional review board of the Beijing Tiantan Hospital. Written informed consent was obtained from all patients for their original treatments.

Participants

We retrospectively reviewed the medical records of 70 patients who were diagnosed with gliomas in sensorimotor function-related areas between August 2017 and March 2020 at Beijing Tiantan Hospital. The inclusion criteria were as follows: 1) adult patients and 2) a primary glioma without any history of treatment. The exclusion criteria were as follows: 1) head motion >1 mm in translation or 1° in rotation, 2) lesions located bilaterally, and 3) tumor resulting in midline shifting.

All enrolled patients were first divided based on tumor location and were subsequently classified into a deficit and a non-deficit group based on their preoperative motor status. The muscle strength of each patient was tested using the British Medical Research Council scale and by neurosurgeons who have over 10 years of work experience in clinical neurosurgery. If the muscle strength of any limbs was lower than grade 5, the patient would be defined as having preoperative motor deficit. After matching for age, sex, and educational status, 33 healthy participants were enrolled as controls (men, $n = 18$). The handedness of all patients and participants was examined using the Edinburgh Handedness Inventory test. All of them were right-handed.

MRI Acquisition

In the current study, a Siemens 3.0-T MR scanner (MAGNETOM Prisma, Erlangen, Germany) was used to collect imaging data. The parameters for the T1 magnetization-prepared rapid acquisition gradient echo with gadolinium enhancement were as follows: repetition time (TR) = 2,300 ms, echo time (TE) = 2.3 ms, field of view (FOV) = 240 × 240 mm^2, flip angle (FA) = 8°, slice number = 192, and voxel size = 1.0 × 1.0 × 1.0 mm^3. The parameters for the T2-weighted fluid-attenuated inversion recovery (T2-FLAIR) sequence were: TR = 5,000 ms, TE = 387 ms, FOV = 220 × 220 mm^2, FA = 150°, slice number = 128, thickness = 0.9 mm, and voxel size = 0.4 × 0.4 × 0.9 mm^3.

The rs-fMRI images were acquired with an echo planar imaging sequence. The parameters were as follows: TR = 2,000 ms, TE = 30 ms, FOV = 220 × 220 mm^2, FA = 90°, slice number = 30, voxel size = 3.0 × 3.0 × 3.0 mm^3, and acquisition duration = 8 min. Participants were asked to get monitored without thinking about anything during rs-fMRI acquisition.

Regions of Tumor Invasion

Two neuroradiologists independently reviewed the MR images using MRIcron software (http://www.mccauslandcenter.sc.edu/mricro/mricron/) to manually determine the extent of glioma

invasion (shown in **Figures 1**, **2**) (16). The tumor masks of lower-grade glioma (grades II and III) and glioblastoma (grade IV) were drawn based on the high-intensity regions of FLAIR and the enhancement regions of the contrast-enhanced T1-weighted images, respectively. If there was a more than 5% difference in the region drawn by the two neuroradiologists, a third neuroradiologist with 25 years of experience made the final decision. All tumor masks were normalized to the MNI-152 T1 template using SPM 8 software (University College London, London, UK; http://www.fil.ion.ucl.ac.uk/spm/). The tumor volumes were calculated with a volumetric measurement.

Functional MRI Preprocessing

We used GRETNA (https://www.nitrc.org/projects/gretna) (17, 18) to preprocess the rs-fMRI data. Information of the preprocessing pipeline and the parameters in each step were as follows: 1) transformation to a NIFTI file; 2) removal of the first images (time point number to remove = 5); 3) slice timing correction; 4) realignment; 5) spatial normalization (normalized to echo planar imaging template) (19); 6) smoothing (full width at half maximum = 4 mm); 7) temporal detrending (linear detrending); 8) regressing out the covariance (white matter signal: with WMMask_3mm; CSF signal: with CSFMask_3mm; head motion: Friston, 24 parameters); 9) temporal filtering (0.01–0.08 Hz); and 10) scrubbing (using default parameters and the interpolation strategy: linear interpolation; FD threshold, 0.5; previous time point number, 1; subsequent time point number, 2).

Regions of Interest

Tumor occupation can induce a mismatch during the step of normalization, and neurovascular uncoupling decreases the accuracy of blood oxygen signals (20–22). Accordingly, the results related to the lesional sensorimotor network would be inaccurate with the effects of these factors. To avoid these effects,

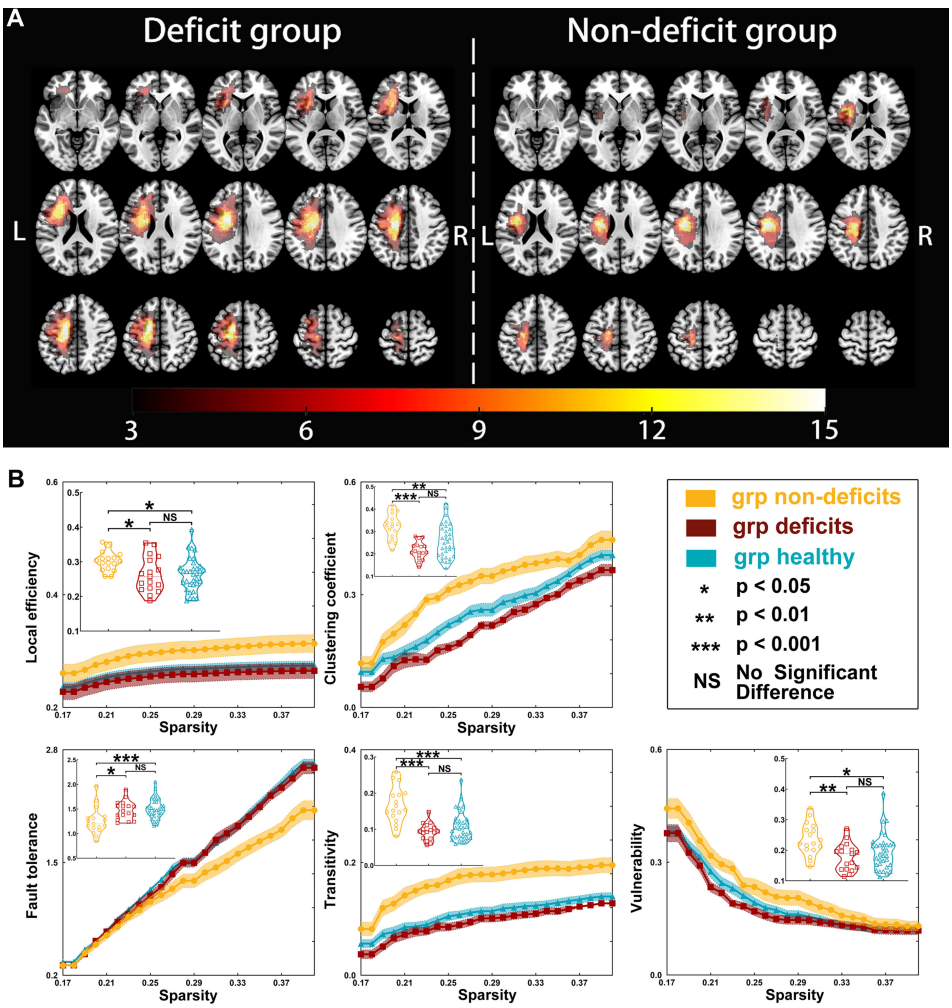

FIGURE 1 | Tumor location and global properties of patients with left hemispheric gliomas. **(A)** Overlapping results of gliomas in the left hemisphere. The *value of the color bar* represents the number of patients with tumors located in a same region. **(B)** Differences in global topological properties of the sensorimotor network in the contralesional hemisphere among the three groups.

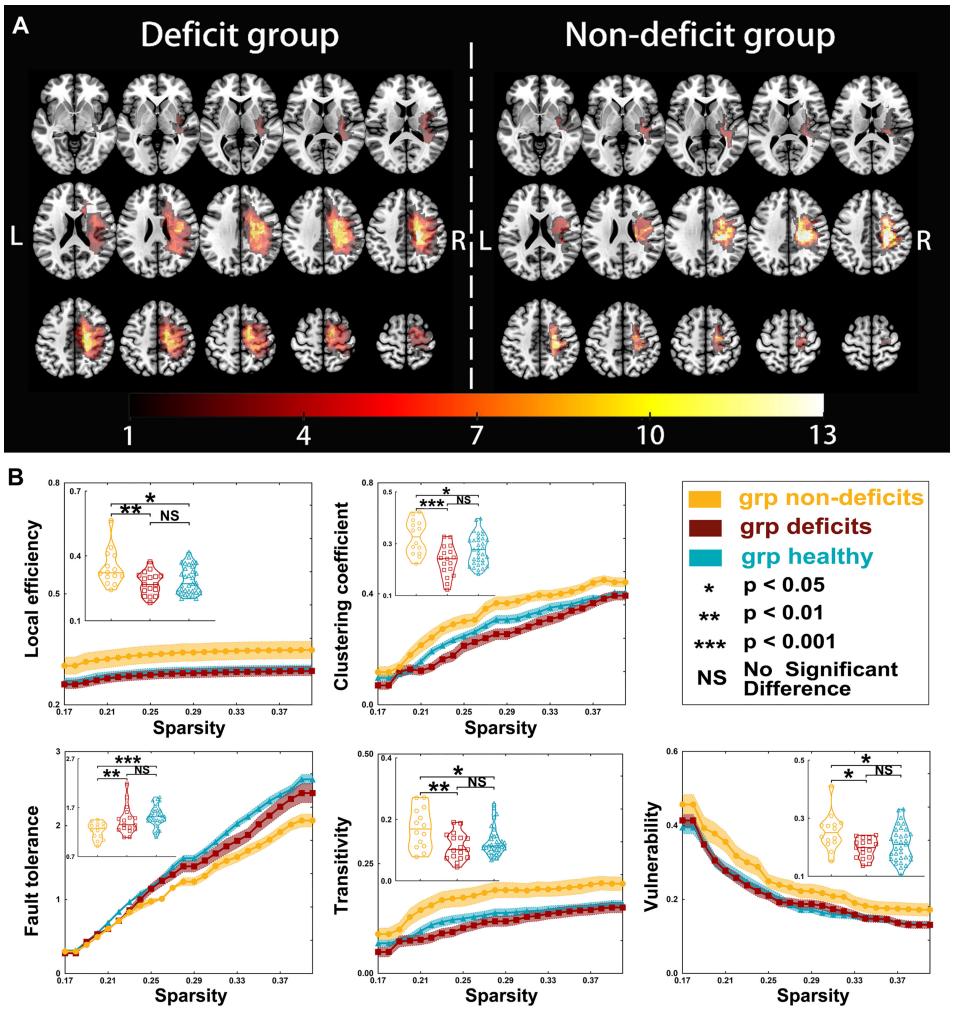

FIGURE 2 | Tumor location and global properties of patients with right hemispheric gliomas. **(A)** Overlapping results of gliomas in the right hemisphere. The *value of the color bar* represents the number of patients with tumors located in a same region. **(B)** Differences in global topological properties of the sensorimotor network in the contralesional hemisphere among the three groups.

the regions of interest in the cSMN that were unrelated to these factors, to keep our results reliable, were extracted from a brain atlas (http://www.brainnetome.org/) (23) using the BRANT software. The seeds were generated as 5-mm spheres based on the coordinates of the sensorimotor network. Finally, 14 nodes were extracted to construct a cSMN template (**Supplementary Tables S1, S2**).

Network Construction

Pearson's correlation coefficients were applied to construct the FC matrices by calculating the regional mean time series for all extracted nodes of the sensorimotor networks.

Graph Theoretical Measures

Graph theoretical measurement is a reliable method to quantitatively reveal topological properties (24, 25). In this study, all weighted matrices were transformed into absolute to calculate the topological properties, including local efficiency, clustering coefficient, global efficiency, the shortest path length, small-worldness (gamma, lambda, and sigma), fault tolerance, transitivity, vulnerability, nodal efficiency, nodal local efficiency, nodal cluster coefficient, and betweenness centrality (24, 26–28). Detailed information of each property is shown in the **Supplementary Material**.

Statistical Analyses

We used SPSS 25.0 software (Microsoft®, IBM Corp., Armonk, NY, USA) to perform statistical analyses. The clinical characteristics were compared between the patient and control groups using Student's *t*-test, Mann–Whitney *U* test, chi-square test, and one-way ANOVA according to the type of data. To explore group differences in network topological properties, we applied a series of sparsity thresholds (from 0.17 to 0.40, interval = 0.01) consistent with the literature (29). We selected the tumor volume and malignancy grade as covariates during the

comparison of the FCs and topological properties among the groups. Bonferroni correction was used to correct the FC results. The topological properties were compared among the groups using one-way ANOVA. Bonferroni correction was subsequently used for *post-hoc* analysis when the results of one-way ANOVA were significantly different. A p-value <0.05 was considered as significant. Furthermore, we analyzed the correlation between the preoperative muscle strength of deficit hand and topological properties using Spearman's correlation.

RESULTS

Sixty-five right-handed patients (men, n = 32) met the inclusion criteria. The preoperative Karnofsky performance scores of the non-deficit group were higher than those of the deficit group (p < 0.001). Moreover, the tumor volumes were larger in the deficit group than those in the non-deficit group (left hemisphere, p = 0.016; right hemisphere, p = 0.033). No differences were observed in age, sex, or educational status among the three groups (**Table 1**). The differences in FC are shown in the **Supplementary Material**.

Differences in Global Topological Properties

Regarding left hemispheric gliomas (for detailed results, see **Table 2** and **Figure 1**), the local efficiency (p = 0.0138), clustering coefficient (p < 0.0001), fault tolerance (p = 0.0009), transitivity (p < 0.0001), and vulnerability (p = 0.0074) were different among the three groups (non-deficit, deficit, and healthy groups). *Post-hoc* analysis with Bonferroni correction showed that the non-deficit group had greater local efficiency than the deficit (p = 0.0461) and healthy (p = 0.0181) groups. Moreover, compared to the non-deficit group, the clustering coefficient and transitivity decreased in the deficit (p < 0.0001 and p < 0.0001, respectively) and healthy (p = 0.0022 and p < 0.0001, respectively) groups. Additionally, compared to the non-deficit group, the fault tolerance increased in the deficit (p = 0.0138) and healthy (p = 0.0008) groups. Furthermore, the vulnerability was weaker in the deficit (p = 0.0077) and healthy (p = 0.0439) groups than that in the non-deficit group.

Regarding right hemispheric gliomas (for detailed results, see **Table 3** and **Figure 2**), the local efficiency (p = 0.0063), clustering coefficient (p = 0.0003), fault tolerance (p = 0.0008), transitivity (p = 0.0045), and vulnerability (p = 0.0130) were different among the three groups. *Post-hoc* analysis with Bonferroni correction revealed that the local efficiency was weaker in the deficit (p = 0.0084) and healthy (p = 0.0191) groups than that in the non-deficit group. Moreover, compared with the non-deficit group, the clustering coefficient and transitivity decreased in the deficit (p = 0.0002 and p = 0.0048, respectively) and healthy (p = 0.0386 and p = 0.0199, respectively) groups. Additionally, compared to the non-deficit group, the fault tolerance increased in the deficit (p = 0.0035) and healthy (p = 0.0005) groups. Furthermore, the vulnerability was weaker in the deficit (p = 0.0141) and healthy (p = 0.0469) groups than that in the non-deficit group.

Small-World Properties

There were some differences in the gamma (left-sided glioma, p = 0.0289; right-sided glioma, p = 0.0001) and sigma (left-sided

TABLE 1 | Demographic and clinical characteristics.

Demographic and clinical characteristics	Left hemisphere		Right hemisphere		Healthy (n = 33)	Left hemisphere p-value	Right hemisphere p-value
	Non-deficit group (n = 17)	Deficit group (n = 17)	Non-deficit group (n = 14)	Deficit group (n = 17)			
Gender							
Male	8	10	6	8	18	0.782	0.735
Female	9	7	8	9	15		
Age (years)*	40.4 ± 2.2	39.8 ± 3.0	41.8 ± 3.4	43.4 ± 2.2	37.2 ± 1.5	0.487	0.088
Handedness							
Right	17	17	14	17	33	–	–
Left	0	0	0	0	0		
KPS score (preoperative)							
100	15	0	5	0	33		
90	2	0	9	0	0	<0.001	<0.001
80	0	14	0	14	0		
70	0	3	0	3	0		
Motor deficit duration (months)	–	1.9 ± 0.3	–	2.3 ± 0.4	–	–	–
Education period (years)*	13.5 ± 0.8	13.4 ± 0.7	12.5 ± 0.7	13.2 ± 0.82	13.4 ± 0.6	0.994	0.654
Tumor grade					–		
II	6	4	7	7		0.708	0.725
III	11	13	7	10			
Tumor volume (ml)*	57.66 ± 8.66	92.39 ± 10.54	60.63 ± 7.71	87.98 ± 9.08	–	0.016	0.033

Motor deficit duration was the time from outpatient diagnosis to inpatient functional MRI scan.

KPS, Karnofsky Performance Scale.

**Values are the mean ± SEM. Student's t-test was used to compare the differences of the tumor volume and the Karnofsky Performance Scale scores between the deficit and non-deficit groups. One-way ANOVA was used to compare the differences of age and education period between the deficit, non-deficit, and healthy groups. Fisher's test was used to compare the differences of gender and tumor grade between the deficit and non-deficit groups. The deficit group comprised patients with preoperative motor deficit; the non-deficit group was composed of patients without preoperative motor deficit.*

TABLE 2 | Global properties compared between the patient and healthy groups for tumors located on the left hemisphere.

	Non-deficit group	Deficit group	Healthy group	One-way ANOVA (*p*-value)	*Post-hoc* analysis (*p*-value)		
					Deficit *vs.* non-deficit	Non-deficit *vs.* healthy	Deficit *vs.* healthy
Local efficiency	0.301 ± 0.007	0.263 ± 0.012	0.264 ± 0.008	0.0138	0.0461	0.0181	>0.9999
Clustering coefficient	0.322 ± 0.014	0.215 ± 0.010	0.256 ± 0.013	<0.0001	<0.0001	0.0022	0.0935
Global efficiency	0.304 ± 0.017	0.285 ± 0.015	0.275 ± 0.009	0.2628	–	–	–
Shortest path length	4.525 ± 0.240	4.748 ± 0.229	4.917 ± 0.153	0.3677	–	–	–
Gamma	1.025 ± 0.020	0.931 ± 0.027	1.000 ± 0.014	0.0289	0.0344	>0.9999	0.0963
Lambda	0.988 ± 0.002	0.988 ± 0.003	0.991 ± 0.002	>0.9999	–	–	–
Sigma	1.039 ± 0.020	0.942 ± 0.037	1.001 ± 0.014	0.0299	0.0271	0.6955	0.1913
Fault tolerance	1.255 ± 0.066	1.475 ± 0.046	1.508 ± 0.035	0.0009	0.0138	0.0008	>0.9999
Transitivity	0.166 ± 0.012	0.094 ± 0.006	0.108 ± 0.007	<0.0001	<0.0001	<0.0001	0.6810
Vulnerability	0.235 ± 0.013	0.178 ± 0.011	0.195 ± 0.010	0.0074	0.0077	0.0439	0.8297

Global properties were calculated with one-way ANOVA. If the results of one-way ANOVA were significant, post-hoc analysis with Bonferroni correction was subsequently applied.

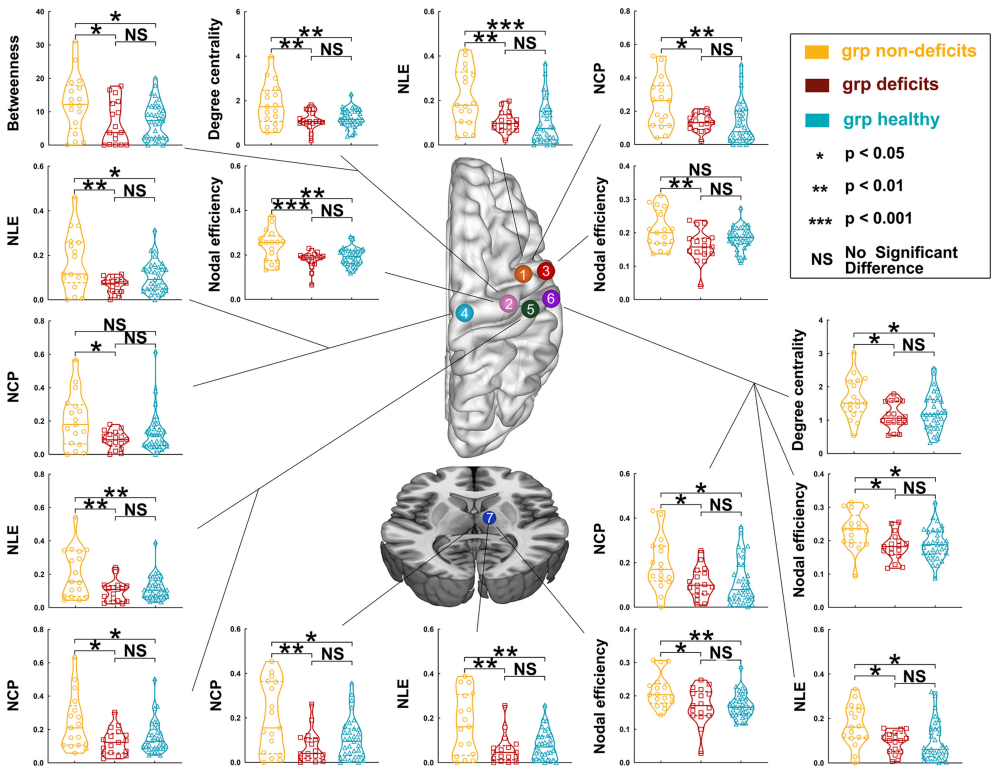

FIGURE 3 | Differences in nodal topological properties of the sensorimotor network in the contralesional hemisphere among the three groups, with left hemisphere glioma. *Orange node* (No. 1), caudal dorsolateral Brodmann area (BA) 6 (A6cdl); *pink node* (No. 2), upper limb of BA 4 (A4ul); *red node* (No. 3), tongue and larynx of BA 4 (A4tl); *light blue node* (No. 4), lower limb region of BA 4 (A4ll); *green node* (No. 5), upper limb, head, and face regions of BA 1/2/3 (A1/2/3ulhf); *purple node* (No. 6), tongue and larynx of BA 1/2/3 (A1_2_3tonla); and *dark blue node* (No. 7), premotor-related thalamus (mPMtha).

glioma, $p = 0.0299$; right-sided glioma, $p = 0.0153$) values among the three groups (for detailed results, see **Tables 2** and **3**). However, there was no difference in the lambda (left-sided glioma, $p > 0.9999$; right-sided glioma, $p > 0.9999$) values among the three groups.

Regarding left hemispheric gliomas, the gamma value was greater in the non-deficit group than that in the deficit group ($p = 0.0344$) after *post-hoc* analysis with Bonferroni correction. Moreover, the sigma value was greater in the non-deficit group than that in the deficit group ($p = 0.0271$).

TABLE 3 | Global properties compared between the patient and healthy groups for tumors located on the right hemisphere.

	Non-deficit group	Deficit group	Healthy group	One-way ANOVA (*p*-value)	*Post-hoc* analysis (*p*-value)		
					Deficit *vs.* non-deficit	Non-deficit *vs.* healthy	Deficit *vs.* healthy
Local efficiency	0.347 ± 0.023	0.273 ± 0.013	0.288 ± 0.011	0.0063	0.0084	0.0191	>0.9999
Clustering coefficient	0.326 ± 0.018	0.233 ± 0.014	0.277 ± 0.010	0.0003	0.0002	0.0386	0.0536
Global efficiency	0.353 ± 0.026	0.293 ± 0.014	0.301 ± 0.012	0.0595	–	–	–
Shortest path length	4.000 ± 0.246	4.610 ± 0.222	4.607 ± 0.153	0.0896	–	–	–
Gamma	1.112 ± 0.017	1.031 ± 0.031	1.006 ± 0.011	0.0002	0.0212	0.0001	>0.9999
Lambda	1.047 ± 0.011	1.041 ± 0.035	1.000 ± 0.012	0.0582	–	–	–
Sigma	1.062 ± 0.013	0.986 ± 0.013	1.006 ± 0.011	<0.0001	0.0233	0.0498	>0.9999
Fault tolerance	1.232 ± 0.045	1.441 ± 0.070	1.517 ± 0.036	0.0008	0.0035	0.0005	0.7915
Transitivity	0.172 ± 0.017	0.112 ± 0.011	0.127 ± 0.008	0.0045	0.0048	0.0199	0.9784
Vulnerability	0.254 ± 0.017	0.196 ± 0.008	0.211 ± 0.010	0.0130	0.0141	0.0469	>0.9999

Global properties were calculated with one-way ANOVA. If the results of one-way ANOVA were significant, post-hoc analysis with Bonferroni correction was subsequently applied.

Regarding right hemispheric gliomas, the gamma value was greater in the non-deficit group than that in the deficit (p = 0.0212) and healthy (p = 0.0001) groups after *post-hoc* analysis with Bonferroni correction. Moreover, the sigma value was greater in the non-deficit group than that in the deficit (p = 0.0233) and healthy (p = 0.0498) groups.

Nodal Topological Properties

Regarding left hemispheric gliomas, among the three groups (for detailed results, see **Supplementary Tables S3–S7** and **Figure 3**), the nodal local efficiency values of five nodes—caudal dorsolateral Brodmann area (BA) 6 (A6cdl), lower limb BA 4 (A4ll), upper limb and face BA 1/2/3 (A1_2_3ulhf), tongue and larynx of BA 1/2/3 (A1_2_3tonIa), and premotor thalamus (mPMtha)—were significantly altered on *post-hoc* tests with Bonferroni correction. Compared with the non-deficit group, the nodal local efficiency of these nodes decreased in the deficit (A6cdl, p = 0.0048; A4ll, p = 0.0014; A1_2_3ulhf, p = 0.0044; A1_2_3tonIa, p = 0.0270; and mPMtha, p = 0.0011) and healthy (A6cdl, p = 0.0005; A4ll, p = 0.0278; A1_2_3ulhf, p = 0.0075; A1_2_3tonIa, p = 0.0119; and mPMtha, p = 0.0019) groups. Similarly, the nodal clustering coefficients of these nodes (except node A4ll) were greater in the non-deficit group than those in the deficit (A6cdl, p = 0.0212; A1_2_3ulhf, p = 0.0113; A1_2_3tonIa, p = 0.0394; and mPMtha, p = 0.0027) and healthy (A6cdl, p = 0.0034; A1_2_3ulhf, p = 0.0342; A1_2_3tonIa, p = 0.0300; and mPMtha, p = 0.0138) groups. Moreover, the nodal efficiency values of three nodes—upper limb BA 4 (A4ul), A1_2_3tonIa, and mPMtha—were significantly altered. Compared with the non-deficit group, the nodal efficiency of these nodes decreased in the deficit (A4ul, p = 0.0007; A1_2_3tonIa, p = 0.0134; and mPMtha, p = 0.0182) and healthy (A4ul, p = 0.0030; A1_2_3tonIa, p = 0.0174; and mPMtha, p = 0.0058) groups. Additionally, the degree centrality of two nodes (A4ul and A1_2_3tonIa) was significantly altered. Compared with the non-deficit group, the degree centrality decreased in the deficit (A4ul, p = 0.0020; A1_2_3tonIa, p = 0.0146) and healthy (A4ul, p = 0.0023; A1_2_3tonIa, p = 0.0436) groups. Furthermore, the betweenness centrality of node A4ul was significantly altered. Compared with the non-deficit group, the betweenness centrality decreased in the deficit (p = 0.0379) and healthy (p = 0.0402) groups.

Regarding right hemispheric gliomas, among the three groups (for detailed results, see **Supplementary Tables S8–S12** and **Figure 4**), the nodal local efficiency values of four nodes—A6cdl, A4tl, A1_2_3tonIa, and mPMtha—were significantly altered on *post-hoc* tests with Bonferroni correction. Compared with the non-deficit group, the nodal local efficiency values of these nodes decreased in the deficit (A6cdl, p = 0.0172; A4tl, p = 0.0210; A1_2_3tonIa, p < 0.0001; and mPMtha, p = 0.0056) and healthy (A6cdl, p = 0.0492; A4tl, p = 0.0057; A1_2_3tonIa, p = 0.0027; and mPMtha, p = 0.0158) groups. The nodal clustering coefficient of node A1_2_3tonIa was greater in the non-deficit group than that in the deficit (p = 0.0027) and healthy (p = 0.0500) groups. Moreover, the nodal efficiency values of four nodes—A6cdl, A4ul, trunk BA 1/2/3 (A1_2_3tru), and mPMtha—were significantly altered. Compared with the non-deficit group, the nodal efficiency of these nodes decreased in the deficit (A6cdl, p = 0.0187; A4ul, p = 0.0175; A1_2_3tru, p = 0.0445; and mPMtha, p = 0.0065) and healthy (A6cdl, p = 0.0213; A4ul, p = 0.0215; A1_2_3tru, p = 0.0003; and mPMtha, p < 0.0001) groups. Additionally, the degree centrality of node A1_2_3tonIa was significantly altered. Compared with the non-deficit group, the degree centrality decreased in the deficit group (p = 0.0248). Furthermore, the betweenness centrality of node A1_2_3ulhf was significantly altered. Compared with the non-deficit group, the betweenness centrality decreased in the deficit (p = 0.0468) and healthy (p = 0.0050) groups.

Correlation Between Muscle Strength and Topological Properties

Regarding patients with left glioma, the clustering coefficient (r = 0.805, p < 0.0001), local efficiency (r = 0.356, p = 0.0390), gamma (r = 0.695, p < 0.0001) and sigma (r = 0.677, p < 0.0001) values, transitivity (r = 0.741, p < 0.0001), and vulnerability (r = 0.540, p = 0.0010) were positively correlated with muscle strength of deficit hand. Similarly, regarding patients with right glioma, the clustering coefficient (r = 0.704, p < 0.0001), local efficiency (r = 0.477, p =

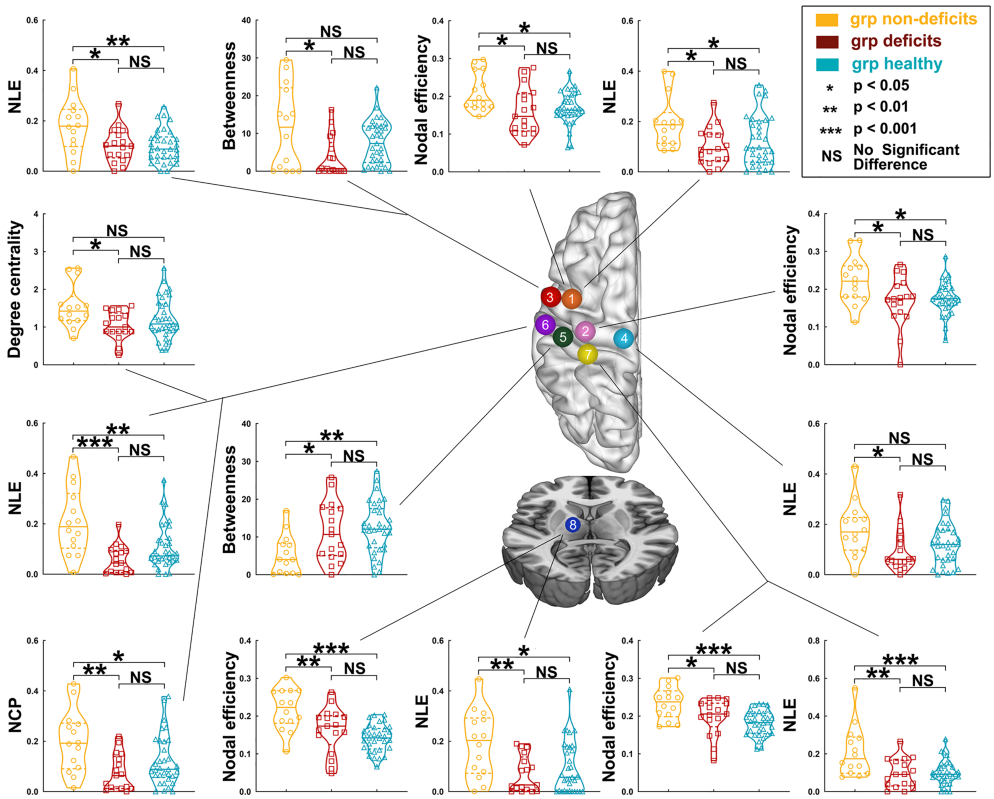

FIGURE 4 | Differences in nodal topological properties of the sensorimotor network in the contralesional hemisphere among the three groups, with right hemisphere glioma. *Orange node* (No. 1), caudal dorsolateral Brodmann area (BA) 6 (A6cdl); *pink node* (No. 2), upper limb of BA 4 (A4ul); *red node* (No. 3), tongue and larynx of BA 4 (A4tl); *light blue node* (No. 4), lower limb region of BA 4 (A4ll); *green node* (No. 5), upper limb, head, and face regions of BA 1/2/3 (A1/2/3ulhf); *purple node* (No. 6), tongue and larynx of BA 1/2/3 (A1_2_3tonla); *yellow node* (No. 7), trunk region of BA 1/2/3 (A1_2_3tru); and *dark blue node* (No. 8), premotor-related thalamus (mPMtha).

0.0067), gamma ($r = 0.702$, $p < 0.0001$) and sigma ($r = 0.711$, $p < 0.0001$) values, transitivity ($r = 0.603$, $p = 0.0003$), and vulnerability ($r = 0.510$, $p = 0.0034$) were positively correlated with the muscle strength of deficit hand (**Supplementary Figure S1**).

DISCUSSION

This study investigated the alterations of the cSMN in patients with gliomas and with different preoperative motor status. The results revealed that the FC of the cSMN was not different between the patient and healthy groups (for detailed information, see part 2 of the **Supplementary Material**). However, the topological properties of the cSMN were significantly different between patients with and without motor deficits.

In our study, the network properties (such as the clustering coefficient and local efficiency) in the non-deficit group were greater than those in the healthy group. The clustering coefficient represents the ratio between the number of actual edges and the maximum number of possible edges in a network (26). Thus, compared with the healthy group, the increased clustering coefficient in the non-deficit group meant that the network was remodeled through increasing the number of actual edges. The remodeling networks implied that the mirrored motor cortices on the contralesional hemisphere participated in functional compensation in the non-deficit group, and this compensation process resulted in normal motor function when the glioma involved the primary motor area (2, 7, 30).

How do contralesional cortices compensate for motor function? The tendency of alterations of the topological properties among the three groups indicated that two stages of motor functional compensation might exist.

In our study, the cSMN in the non-deficit group showed small-world properties and was significantly increased compared with that of the healthy group, but the cSMN in the deficit group did not have small-world properties ($\sigma < 1$). Small-world properties were calculated based on the clustering coefficient and shortest path length (31–33). The small-world properties were found to be increased in the non-deficit group and decreased in the deficit group compared with the healthy group. Specifically, the clustering coefficient was changed and the shortest path length was unchanged. The inverse tendency of alterations of the clustering coefficients between the non-deficit and deficit groups was determined by the different degrees of network disruption. The

network disruptions were more serious in the deficit group than those in the non-deficit group, as patients in the deficit group had larger tumor volumes (30, 34, 35). The different degrees of network disruptions also explained that the local efficiency, clustering coefficient, gamma and sigma values, and transitivity were positively correlated with the muscle strength of contralesional hemisphere limbs. Moreover, the contralesional primary motor area is necessary for recovery if a lesion invaded large parts of the motor area (36). Since the contralateral cortex is persistently involved in compensating for impaired motor function, we believed that the reason patients suffer from preoperative motor deficits was that this compensated motor function was further damaged by growing gliomas. In addition, the shortest path length was insignificantly changed both in the deficit and non-deficit groups. Accordingly, similar to stroke patients increasing the small-worldness of the network after recovery training (29). Based on the evidence we found in patients with glioma, we hypothesized that the cSMN firstly acquired a high conveying efficiency (improved small-worldness of the cSMN) to participate in compensating for the damaged motor function in the lesional hemisphere (non-deficit stage). Subsequently, the cSMN developed a low conveying efficiency (reduced small-worldness in the cSMN) because the compensatory motor function was further damaged by the growing glioma (deficit stage). Furthermore, this finding does not contradict the conventional theory that motor function is controlled by the contralateral hemisphere. Despite the participation of the contralesional hemisphere in motor functional compensation, patients would still suffer from motor deficits as the disease progresses in the lesional hemisphere.

Vulnerability evaluates the stability of a network (14), which represents the alterations of the conveying efficiency if each node in a network is replaced (28, 37). In our study, the vulnerability of the cSMN increased in the non-deficit group, but was insignificantly altered in the deficit group. This finding indicates that the cSMN in the deficit group was more stable than that in the non-deficit group.

Tumor grade is not a determined factor for the different network alterations in the deficit and non-deficit groups. The theory of compensatory functions in glioma patients is that, when a glioma appears, the functional network begins remodeling to compensate for the damaged functions (8). This compensation firstly recruits tissues surrounding the glioma, and then the homotopic areas in the contralesional hemisphere if the damaged function cannot be compensated by surrounding tissues (3). This theory supports the existence of the compensatory stage of motor function in glioma patients. Some studies revealed that high-grade gliomas (HGGs), as well as low-grade gliomas (LGGs), were able to induce contralateral network reorganization (38–41) and neuroplasticity (42–44). Unlike stoke, gliomas are relatively slow growing; therefore, the brain tissue around the tumor has enough time to develop neuroplasticity, which may occur earlier in HGG than in LGG due to its high invasiveness (2, 40). In order to identify the differences of brain networks between the compensatory and decompensated stages, patients with HGGs are a good model since those with LGGs often have normal function at surgery. Moreover, the clinical manifestations of patients showed that the influence of HGGs is also gradually aggravated (45). To avoid bias, the tumor volume and tumor grade were regressed out as covariates in this study.

Some patients with HGGs suffered from motor deficits, which meant that the compensation of motor function was insufficient (46). Therefore, combined with the alterations of conveying efficiency in the different stages (compensatory and decompensatory stages), we concluded that the cSMN sacrificed stability to exchange conveying efficiency in order to compensate for the damaged motor function in the compensatory stage. Meanwhile, the healthy hemisphere maintained its own motor function with low conveying efficiency. In the decompensatory stage, when the motor function in the lesional hemisphere was completely destroyed by the growing glioma, the conveying efficiency of the contralesional hemisphere was unable to recover and remained low, and the cSMN returned to a stable status.

Regarding the alterations in nodal properties, we found that most of the alterations focused on the primary sensorimotor areas and motor-related thalamus. We found an increasing tendency of alterations of nodal properties in the non-deficit group and an unchanging tendency in the deficit group compared with the healthy group. This finding further verified that the contralesional sensorimotor cortices are crucial for motor functional compensation (47, 48). Moreover, our results showed that, regardless of the glioma location, the nodal efficiency, nodal clustering coefficient, and nodal local efficiency of the nodes (premotor-related thalamus) increased in the non-deficit group and decreased in the deficit group. These findings indicated that the premotor-related thalamus played an important role in compensating for the damaged motor function in the non-deficit stage and significantly decreased the conveying efficiency in the deficit stage. Previous studies showed that the contralesional motor-related thalamus participated in motor plasticity by changing pathways and building midline-crossing contralesional corticospinal fibers (47, 48). Hence, our findings verified this theory through functional networks and differed from previous verification through structural networks. Furthermore, as previous studies have shown, the motor-related thalamus is crucial for the modulation of motor function (30, 49–51). Our findings might provide a target for further protection in operations and for stimulating treatment using repetitive transcranial magnetic stimulation post-operation.

An important point that should be raised is that our study did not investigate the interhemispheric alterations of FCs or topological properties in order to avoid negative effects from neurovascular uncoupling and tumor occupation as much as possible. In this study, we chose the cSMN because the origin of blood supply in each hemisphere is different. Consequently, the interhemispheric FC, as well as the topological properties of the entire sensorimotor network, could not be investigated. Previous studies showed that neurovascular uncoupling affects the results of rs-fMRI (52), but we considered that their conclusions were biased due to the calculation of interhemispheric FCs (53). In fact, no significant difference in the FCs of the cSMN between the patient and healthy groups was found in previous glioma-relevant studies (53–55). Our findings in FCs are consistent with these previous studies.

The most important limitation of this study is that, although our findings are encouraging, they are still conjectures based on the controversial theory that the symmetric cortex is able to compensate for the damaged function in the lesional hemisphere (55, 56). The use of transcranial magnetic stimulation may validate our findings in the future.

In summary, alteration of the topological properties of the cSMN is a dynamic process in patients with gliomas. Two stages of motor functional alterations may exist. In the compensatory stage, the cSMN sacrificed stability to acquire high conveying efficiency and to compensate for the damaged motor function of the lesional hemisphere. With tumor growth and deterioration, patients enter the decompensatory stage, and motor dysfunction on the affected side arises. The cSMN returns to a stable state and maintains healthy hemispheric motor function, but with low efficiency.

DATA AVAILABILITY STATEMENT

The raw data supporting the conclusions of this article will be made available by the authors, without undue reservation.

ETHICS STATEMENT

The studies involving human participants were reviewed and approved by the IRB of Beijing Tiantan Hospital. The patients/participants provided written informed consent to participate in this study.

AUTHOR CONTRIBUTIONS

SF, LL, SW, and YG: study concept and design. SF, LL, SW, ZZ, and YG: data acquisition and analysis. SF, XF, and YW: statistics/verified analytical method. SF, XF, and YW: writing the first draft. XF, YW, and TJ: study supervision. All authors contributed to the article and approved the submitted version.

FUNDING

This work was supported by the Public Welfare Development and Reform Pilot Project of Beijing Medical Research Institute (PXM2019_026280_000008), Beijing Municipal Natural Science Foundation (No. 7202021), National Natural Science Foundation of China (No. 82001777), and the Research Unit of Accurate Diagnosis, Treatment, and Translational Medicine of Brain Tumors (No. 2019-I2M-5-021).

ACKNOWLEDGMENTS

We thank Dr. Meng Lanxi for imaging data acquisition.

SUPPLEMENTARY MATERIAL

The Supplementary Material for this article can be found online at: https://www.frontiersin.org/articles/10.3389/fonc.2022.882313/full#supplementary-material

REFERENCES

1. Jiang T, Nam DH, Ram Z, Poon WS, Wang J, Boldbaatar D, et al. Clinical Practice Guidelines for the Management of Adult Diffuse Gliomas. *Cancer Lett* (2020) 499:60–72. doi: 10.1016/j.canlet.2020.10.050
2. Almairac F, Duffau H, Herbet G. Contralesional Macrostructural Plasticity of the Insular Cortex in Glioma Patients. *Neurology* (2018) 91(20):e1902–8. doi: 10.1212/wnl.0000000000006517
3. Duffau H. Brain Plasticity and Tumors. *Adv Tech Stand Neurosurg* (2008) 33:3–33. doi: 10.1007/978-3-211-72283-1_1
4. Payne BR, Lomber SG. Reconstructing Functional Systems After Lesions of Cerebral Cortex. *Nat Rev Neurosci* (2001) 212:911–9. doi: 10.1038/35104085
5. Heiss WD, Thiel A, Kessler J, Herholz K. Disturbance and Recovery of Language Function: Correlates in PET Activation Studies. *Neuroimage* (2003) 20 Suppl 1:S42–9. doi: 10.1016/j.neuroimage.2003.09.005
6. Duffau H. Hodotopy, Neuroplasticity and Diffuse Gliomas. *Neurochirurgie* (2017) 633:259–65. doi: 10.1016/j.neuchi.2016.12.001
7. Herbet G, Maheu M, Costi E, Lafargue G, Duffau H. Mapping Neuroplastic Potential in Brain-Damaged Patients. *Brain* (2016) 139(Pt 3):829–44. doi: 10.1093/brain/awv394
8. Duffau H. Functional Mapping Before and After Low-Grade Glioma Surgery: A New Way to Decipher Various Spatiotemporal Patterns of Individual Neuroplastic Potential in Brain Tumor Patients. *Cancers (Basel)* (2020) 129. doi: 10.3390/cancers12092611
9. Li Q, Dong JW, Del Ferraro G, Petrovich Brennan N, Peck KK, Tabar V, et al. Functional Translocation of Broca's Area in a Low-Grade Left Frontal Glioma: Graph Theory Reveals the Novel, Adaptive Network Connectivity. *Front Neurol* (2019) 10:702. doi: 10.3389/fneur.2019.00702
10. Stretton J, Sidhu MK, Winston GP, Bartlett P, McEvoy AW, Symms MR, et al. Working Memory Network Plasticity After Anterior Temporal Lobe Resection: A Longitudinal Functional Magnetic Resonance Imaging Study. *Brain* (2014) 137(Pt 5):1439–53. doi: 10.1093/brain/awu061
11. Polania R, Paulus W, Antal A, Nitsche MA. Introducing Graph Theory to Track for Neuroplastic Alterations in the Resting Human Brain: A Transcranial Direct Current Stimulation Study. *Neuroimage* (2011) 543:2287–96. doi: 10.1016/j.neuroimage.2010.09.085
12. Liu D, Chen J, Hu X, Hu G, Liu Y, Yang K, et al. Contralesional Homotopic Functional Plasticity in Patients With Temporal Glioma. *J Neurosurg* (2020) 1–9. doi: 10.3171/2019.11.JNS191982
13. Hart MG, Ypma RJ, Romero-Garcia R, Price SJ, Suckling J. Graph Theory Analysis of Complex Brain Networks: New Concepts in Brain Mapping Applied to Neurosurgery. *J Neurosurg* (2016) 1246:1665–78. doi: 10.3171/2015.4.JNS142683
14. Fang S, Zhou C, Fan X, Jiang T, Wang Y. Epilepsy-Related Brain Network Alterations in Patients With Temporal Lobe Glioma in the Left Hemisphere. *Front Neurol* (2020) 11:684. doi: 10.3389/fneur.2020.00684
15. Yun JY, Boedhoe PSW, Vriend C, Jahanshad N, Abe Y, Ameis SH, et al. Brain Structural Covariance Networks in Obsessive-Compulsive Disorder: A Graph Analysis From the ENIGMA Consortium. *Brain* (2020) 1432:684–700. doi: 10.1093/brain/awaa001
16. Fang S, Zhou C, Wang L, Fan X, Wang Y, Zhang Z, et al. Characteristic Alterations of Network in Patients With Intraoperative Stimulation-Induced Seizures During Awake Craniotomy. *Front Neurol* (2021) 12:602716. doi: 10.3389/fneur.2021.602716
17. Wang J, Wang X, Xia M, Liao X, Evans A, He Y. Corrigendum: GRETNA: A Graph Theoretical Network Analysis Toolbox for Imaging Connectomics. *Front Hum Neurosci* (2015) 9:458. doi: 10.3389/fnhum.2015.00458

18. Wang J, Wang X, Xia M, Liao X, Evans A, He Y. GRETNA: A Graph Theoretical Network Analysis Toolbox for Imaging Connectomics. *Front Hum Neurosci* (2015) 9:386. doi: 10.3389/fnhum.2015.00386
19. Calhoun VD, Wager TD, Krishnan A, Rosch KS, Seymour KE, Nebel MB, et al. The Impact of T1 Versus EPI Spatial Normalization Templates for fMRI Data Analyses. *Hum Brain Mapp* (2017) 3811:5331–42. doi: 10.1002/hbm.23737
20. Hadjiabadi DH, Pung L, Zhang J, Ward BD, Lim WT, Kalavar M, et al. Brain Tumors Disrupt the Resting-State Connectome. *NeuroImage Clin* (2018) 18:279–89. doi: 10.1016/j.nicl.2018.01.026
21. Agarwal S, Sair HI, Pillai JJ. The Problem of Neurovascular Uncoupling. *Neuroimaging Clin N Am* (2021) 311:53–67. doi: 10.1016/j.nic.2020.09.003
22. Sun H, Vachha B, Laino ME, Jenabi M, Flynn JR, Zhang Z, et al. Decreased Hand Motor Resting-State Functional Connectivity in Patients With Glioma: Analysis of Factors Including Neurovascular Uncoupling. *Radiology* (2020) 2943:610–21. doi: 10.1148/radiol.2019190089
23. Fan L, Li H, Zhuo J, Zhang Y, Wang J, Chen L, et al. The Human Brainnetome Atlas: A New Brain Atlas Based on Connectional Architecture. *Cereb Cortex* (2016) 268:3508–26. doi: 10.1093/cercor/bhw157
24. Bernhardt BC, Chen Z, He Y, Evans AC, Bernasconi N. Graph-Theoretical Analysis Reveals Disrupted Small-World Organization of Cortical Thickness Correlation Networks in Temporal Lobe Epilepsy. *Cereb Cortex* (2011) 219:2147–57. doi: 10.1093/cercor/bhq291
25. He Y, Wang J, Wang L, Chen ZJ, Yan C, Yang H, et al. Uncovering Intrinsic Modular Organization of Spontaneous Brain Activity in Humans. *PloS One* (2009) 44:e5226. doi: 10.1371/journal.pone.0005226
26. Mazrooyisebdani M, Nair VA, Garcia-Ramos C, Mohanty R, Meyerand E, Hermann B, et al. Graph Theory Analysis of Functional Connectivity Combined With Machine Learning Approaches Demonstrates Widespread Network Differences and Predicts Clinical Variables in Temporal Lobe Epilepsy. *Brain Connect* (2020) 101:39–50. doi: 10.1089/brain.2019.0702
27. Paldino MJ, Zhang W, Chu ZD, Golriz F. Metrics of Brain Network Architecture Capture the Impact of Disease in Children With Epilepsy. *NeuroImage Clin* (2017) 13:201–8. doi: 10.1016/j.nicl.2016.12.005
28. Latora V, Marchiori M. Vulnerability and Protection of Infrastructure Networks. *Phys Rev E Stat Nonlin Soft Matter Phys* (2005) 71(1 Pt 2):15103. doi: 10.1103/PhysRevE.71.015103
29. Laney J, Adali T, McCombe Waller S, Westlake KP. Quantifying Motor Recovery After Stroke Using Independent Vector Analysis and Graph-Theoretical Analysis. *NeuroImage Clin* (2015) 8:298–304. doi: 10.1016/j.nicl.2015.04.014
30. Aswendt M, Pallast N, Wieters F, Baues M, Hoehn M, Fink GR. Lesion Size- and Location-Dependent Recruitment of Contralesional Thalamus and Motor Cortex Facilitates Recovery After Stroke in Mice. *Transl Stroke Res* (2021) 12 (1):87–97. doi: 10.1007/s12975-020-00802-3
31. Sporns O, Zwi JD. The Small World of the Cerebral Cortex. *Neuroinformatics* (2004) 22:145–62. doi: 10.1385/NI:2:2:145
32. Ponten SC, Bartolomei F, Stam CJ. Small-World Networks and Epilepsy: Graph Theoretical Analysis of Intracerebrally Recorded Mesial Temporal Lobe Seizures. *Clin Neurophysiol* (2007) 1184:918–27. doi: 10.1016/j.clinph.2006.12.002
33. Qi S, Mu YF, Cui LB, Zhang J, Guo F, Tan QR, et al. Anomalous Gray Matter Structural Networks in Recent Onset Post-Traumatic Stress Disorder. *Brain Imaging Behav* (2018) 122:390–401. doi: 10.1007/s11682-017-9693-z
34. Hendrix P, Hans E, Griessenauer CJ, Simgen A, Oertel J, Karbach J. Neurocognitive Status in Patients With Newly-Diagnosed Brain Tumors in Good Neurological Condition: The Impact of Tumor Type, Volume, and Location. *Clin Neurol Neurosurg* (2017) 156:55–62. doi: 10.1016/j.clineuro.2017.03.009
35. Noll KR, Sullaway C, Ziu M, Weinberg JS, Wefel JS. Relationships Between Tumor Grade and Neurocognitive Functioning in Patients With Glioma of the Left Temporal Lobe Prior to Surgical Resection. *Neuro Oncol* (2015) 174:580–7. doi: 10.1093/neuonc/nou233
36. Di Pino G, Pellegrino G, Assenza G, Capone F, Ferreri F, Formica D, et al. Modulation of Brain Plasticity in Stroke: A Novel Model for Neurorehabilitation. *Nat Rev Neurol* (2014) 1010:597–608. doi: 10.1038/nrneurol.2014.162
37. Hart MG, Price SJ, Suckling J. Connectome Analysis for Pre-Operative Brain Mapping in Neurosurgery. *Br J Neurosurg* (2016) 305:506–17. doi: 10.1080/02688697.2016.1208809
38. De Baene W, Rutten GJM, Sitskoorn MM. The Temporal Pattern of a Lesion Modulates the Functional Network Topology of Remote Brain Regions. *Neural Plast* (2017) 2017:3530723. doi: 10.1155/2017/3530723
39. Fandino J, Kollias SS, Wieser HG, Valavanis A, Yonekawa Y. Intraoperative Validation of Functional Magnetic Resonance Imaging and Cortical Reorganization Patterns in Patients With Brain Tumors Involving the Primary Motor Cortex. *J Neurosurg* (1999) 912:238–50. doi: 10.3171/jns.1999.91.2.0238
40. Cargnelutti E, Ius T, Skrap M, Tomasino B. What do We Know About Pre- and Postoperative Plasticity in Patients With Glioma? A Review of Neuroimaging and Intraoperative Mapping Studies. *NeuroImage Clin* (2020) 28:102435. doi: 10.1016/j.nicl.2020.102435
41. Zimmermann M, Rossler K, Kaltenhauser M, Grummich P, Brandner N, Buchfelder M, et al. Comparative fMRI and MEG Localization of Cortical Sensorimotor Function: Bimodal Mapping Supports Motor Area Reorganization in Glioma Patients. *PloS One* (2019) 143:e0213371. doi: 10.1371/journal.pone.0213371
42. Conway N, Wildschuetz N, Moser T, Bulubas L, Sollmann N, Tanigawa N, et al. Cortical Plasticity of Motor-Eloquent Areas Measured by Navigated Transcranial Magnetic Stimulation in Patients With Glioma. *J Neurosurg* (2017) 1275:981–91. doi: 10.3171/2016.9.JNS161595
43. Zhang N, Xia M, Qiu T, Wang X, Lin CP, Guo Q, et al. Reorganization of Cerebro-Cerebellar Circuit in Patients With Left Hemispheric Gliomas Involving Language Network: A Combined Structural and Resting-State Functional MRI Study. *Hum Brain Mapp* (2018) 3912:4802–19. doi: 10.1002/hbm.24324
44. Majos A, Bryszewski B, Kosla KN, Pfaifer L, Jaskolski D, Stefanczyk L. Process of the Functional Reorganization of the Cortical Centers for Movement in GBM Patients: fMRI Study. *Clin Neuroradiol* (2017) 271:71–9. doi: 10.1007/s00062-015-0398-7
45. Rossi M, Conti Nibali M, Vigano L, Puglisi G, Howells H, Gay L, et al. Resection of Tumors Within the Primary Motor Cortex Using High-Frequency Stimulation: Oncological and Functional Efficiency of This Versatile Approach Based on Clinical Conditions. *J Neurosurg* (2019) 1–13. doi: 10.3171/2019.5.JNS19453
46. Duffau H. The Huge Plastic Potential of Adult Brain and the Role of Connectomics: New Insights Provided by Serial Mappings in Glioma Surgery. *Cortex* (2014) 58:325–37. doi: 10.1016/j.cortex.2013.08.005
47. Snyder DB, Beardsley SA, Schmit BD. Role of the Cortex in Visuomotor Control of Arm Stability. *J Neurophysiol* (2019) 1225:2156–72. doi: 10.1152/jn.00003.2019
48. Chowdhury RH, Glaser JI, Miller LE. Area 2 of Primary Somatosensory Cortex Encodes Kinematics of the Whole Arm. *Elife* (2020) 9. doi: 10.7554/eLife.48198
49. DeSimone JC, Archer DB, Vaillancourt DE, Wagle Shukla A. Network-Level Connectivity is a Critical Feature Distinguishing Dystonic Tremor and Essential Tremor. *Brain* (2019) 1426:1644–59. doi: 10.1093/brain/awz085
50. Klingner CM, Brodoehl S, Witte OW, Guntinas-Lichius O, Volk GF. The Impact of Motor Impairment on the Processing of Sensory Information. *Behav Brain Res* (2019) 359:701–8. doi: 10.1016/j.bbr.2018.09.016
51. Wahl AS, Omlor W, Rubio JC, Chen JL, Zheng H, Schroter A, et al. Neuronal Repair. Asynchronous Therapy Restores Motor Control by Rewiring of the Rat Corticospinal Tract After Stroke. *Science* (2014) 3446189:1250–5. doi: 10.1126/science.1253050
52. Agarwal S, Sair HI, Yahyavi-Firouz-Abadi N, Airan R, Pillai JJ. Neurovascular Uncoupling in Resting State fMRI Demonstrated in Patients With Primary Brain Gliomas. *J Magn Reson Imaging* (2016) 43(3):620–6. doi: 10.1002/jmri.25012
53. Mallela AN, Peck KK, Petrovich-Brennan NM, Zhang Z, Lou W, Holodny AI. Altered Resting-State Functional Connectivity in the Hand Motor Network in Glioma Patients. *Brain Connect* (2016) 68:587–95. doi: 10.1089/brain.2016.0432
54. Agarwal S, Lu H, Pillai JJ. Value of Frequency Domain Resting-State Functional Magnetic Resonance Imaging Metrics Amplitude of Low-Frequency Fluctuation and Fractional Amplitude of Low-Frequency Fluctuation in the Assessment of Brain Tumor-Induced Neurovascular Uncoupling. *Brain Connect* (2017) 76:382–9. doi: 10.1089/brain.2016.0480
55. Fox ME, King TZ. Functional Connectivity in Adult Brain Tumor Patients: A Systematic Review. *Brain Connectivity* (2018) 87:381–97. doi: 10.1089/brain.2018.0623

56. Hillary FG, Grafman JH. Injured Brains and Adaptive Networks: The Benefits and Costs of Hyperconnectivity. *Trends Cognit Sci* (2017) 215:385–401. doi: 10.1016/j.tics.2017.03.003

Conflict of Interest: The authors declare that the research was conducted in the absence of any commercial or financial relationships that could be construed as a potential conflict of interest.

Publisher's Note: All claims expressed in this article are solely those of the authors and do not necessarily represent those of their affiliated organizations, or those of the publisher, the editors and the reviewers. Any product that may be evaluated in this article, or claim that may be made by its manufacturer, is not guaranteed or endorsed by the publisher.

Copyright © 2022 Fang, Li, Weng, Guo, Zhong, Fan, Jiang and Wang. This is an open-access article distributed under the terms of the Creative Commons Attribution License (CC BY). The use, distribution or reproduction in other forums is permitted, provided the original author(s) and the copyright owner(s) are credited and that the original publication in this journal is cited, in accordance with accepted academic practice. No use, distribution or reproduction is permitted which does not comply with these terms.

frontiers | Frontiers in Neurology

ORIGINAL RESEARCH
published: 02 May 2022
doi: 10.3389/fneur.2022.866274

Non-Invasive Prediction of Survival Time of Midline Glioma Patients Using Machine Learning on Multiparametric MRI Radiomics Features

Da-Biao Deng[1,2], Yu-Ting Liao[3], Jiang-Fen Zhou[4], Li-Na Cheng[2], Peng He[2], Sheng-Nan Wu[2], Wen-Sheng Wang[2] and Quan Zhou[1]**

[1] Department of Radiology, Third Affiliated Hospital of Southern Medical University (Academy of Orthopedics Guangdong), Guangzhou, China, [2] Imaging Department of Guangdong 999 Brain Hospital, Guangzhou, China, [3] GE Healthcare, Guangzhou, China, [4] Department of Neuro-Oncology of Guangdong 999 Brain Hospital, Guangzhou, China

Objectives: To explore the feasibility of predicting overall survival (OS) of patients with midline glioma using multi-parameter magnetic resonance imaging (MRI) features.

Methods: Data of 84 patients with midline gliomas were retrospectively collected, including 40 patients with OS > 12 months (28 cases were adults, 14 cases were H3 K27M-mutation) and 44 patients with OS < 12 months (29 cases were adults, 31 cases were H3 K27M-mutation). Features were extracted from the largest slice of tumors, which were manually segmented on T2-weighted (T2w), T2 fluid-attenuated inversion recovery (T2 FLAIR), and contrast-enhanced T1-weighted (T1c) images. Data were randomly divided into training (70%) and test cohorts (30%) and normalized and standardized using Z-scores. Feature dimensionality reduction was performed using the variance method and maximum relevance and minimum redundancy (mRMR) algorithm. We used the logistic regression algorithm to construct three models for T2w, T2 FLAIR, and T1c images as well as one combined model. The test cohort was used to evaluate the models, and receiver operating characteristic (ROC) curves, areas under the curve (AUCs), sensitivity, specificity, and accuracy were calculated. The nomogram of the combined model was built and evaluated using a calibration curve. Decision curve analysis (DCA) was used to evaluate the clinical application value of the four models.

Results: A total of 1,316 features were extracted from T2w, T2 FLAIR, and T1c images, respectively. And then the best non-redundant features were selected from the extracted features using the variance method and mRMR. Finally, five features were extracted each from T2w, T2 FLAIR, and T1c images, and 12 features were extracted for the combined model. Four models were established using the optimal features. In the test cohort, the combined model performed the best out of all models. The AUCs of the T2w, T2 FLAIR, T1c, and combined models were 0.73, 0.78, 0.74, and 0.87, respectively, and accuracies were 0.72, 0.76, 0.72, and 0.84, respectively. The ROC curves and DCA showed that the combined model had the highest efficiency and most favorable clinical benefits.

OPEN ACCESS

Edited by:
Nico Sollmann,
University of California, San Francisco, United States

Reviewed by:
Jun Shen,
Sun Yat-sen University, China
Ting Song,
Third Affiliated Hospital of Guangzhou Medical University, China
Jayant Jagtap,
Symbiosis Institute of Technology, India
Vera Catharina Keil,
VU Medical Center, Netherlands
Xiangrong Yu,
Zhuhai People's Hospital, China

***Correspondence:**
Wen-Sheng Wang
wws161616@sina.com
Quan Zhou
zhouquan3777@smu.edu.cn

Specialty section:
This article was submitted to Neuro-Oncology and Neurosurgical Oncology, a section of the journal Frontiers in Neurology

Received: 31 January 2022
Accepted: 31 March 2022
Published: 02 May 2022

Citation:
Deng D-B, Liao Y-T, Zhou J-F, Cheng L-N, He P, Wu S-N, Wang W-S and Zhou Q (2022) Non-Invasive Prediction of Survival Time of Midline Glioma Patients Using Machine Learning on Multiparametric MRI Radiomics Features. Front. Neurol. 13:866274. doi: 10.3389/fneur.2022.866274

Conclusion: The combined radiomics model based on multi-parameter MRI features provided a reliable non-invasive method for the prognostic prediction of midline gliomas.

Keywords: machine learning, radiomics, MRI, midline glioma, overall survival

INTRODUCTION

Diffuse midline gliomas (DMGs) with an H3 K27M mutation are a group of tumors newly defined in 2016 and amended to DMGs with an H3 K27-altered in 2021 (1, 2). They occur commonly in the brainstem of children, although they are not uncommon in adults. The median survival time of patients with a DMG with H3 K27M mutation is shorter than that of patients without H3 K27M mutation (3). Furthermore, H3 K27M mutation not only have prognostic implications but may also represent a potential new immunotherapeutic target (4). However, because of the high risk of operating on the midline area, most patients only undergo radiotherapy or chemotherapy (5, 6). Without information regarding H3 K27-altered, predicting the survival of patients with midline gliomas is challenging. Therefore, it is of significant clinical value to develop a non-invasive method to evaluate the survival of patients with midline gliomas.

In clinical practice, magnetic resonance imaging (MRI) is one of the most valuable methods for evaluating the survival of patients with midline gliomas before and during treatment. MRI findings of tumors often help clinicians adjust treatment strategies. Furthermore, the World Health Organization's classification of tumors of the central nervous system began integrating molecular and genetic profiling in 2016, with gradual improvements being made continuously. However, the relationship between macroscopic MRI findings and molecular subtyping of tumors remains uncertain. H3 K27M mutant patients has shorter survival time than those of wild type, and several studies have shown no significant correlation between H3 K27M mutant- and wild-type DMGs in terms of tumor necrosis, patterns of enhancement, edema, infiltrative features, or diffusion characteristics (3, 7, 8). This suggests that macroscopic MRI findings, such as tumor location, size, signal intensity, contrast enhancement, and advanced MRI techniques, such as diffusion-weighted imaging, do not currently meet the clinical needs of evaluation of DMG survival. On the other hand, according to the 2021 WHO classification of tumors of the central nervous system, DMGs, H3 K27-altered include H3 wild type with enhancer of zeste homolog inhibitory protein (EZHIP) overexpression and epidermal growth factor receptor (EGFR) mutation in addition to H3 K27M mutation (2). Therefore, the prediction of H3 K27M mutation alone in the past cannot accurately evaluate the prognosis of patients with DMG. Thus, there is an urgent need for better and more advanced tools to explore biological information hidden in traditional MR images, which would have substantial clinical implications, such as avoiding inappropriate treatments.

One such tool is radiomics, which involves the non-invasive extraction of a large amount of quantitative information from medical images that cannot be perceived by human vision. To date, radiomics has been demonstrated to be valuable in predicting the molecular genetic characteristics, tumor grading, differential diagnosis, and prognostic evaluation of gliomas (6, 9–14). Numerous studies have accurately predicted the survival of gliomas using radiomics. Prasanna et al. (15) found that radiomic features from the peritumoral brain parenchyma on routine pre-operative MRI can predict long- vs. short-term survival in glioblastomas. Senders et al. (16) have trained fifteen statistical and machine learning algorithms based on 13 demographic, socioeconomic, clinical, and radiographic features to predict overall survival, 1-year survival status of glioblastomas, and found the accelerated failure time model demonstrated superior performance compared to Cox proportional hazards regression and other machine learning algorithms. Therefore, we investigated the feasibility of predicting the overall survival (OS) of patients with midline gliomas using machine learning to offer an alternative method to non-invasively predict prognoses of midline glioma patients.

MATERIALS AND METHODS

Patients

This study was approved by the hospital ethics committee, and the requirement for obtaining informed consent was waived. We retrospectively collected data of patients with a midline glioma treated at Guangdong 999 Brain Hospital between January 2017 and October 2020. The inclusion criteria were: (1) glioma located in the midline area (e.g., vermis, brainstem, thalamus, corpus callosum, sellar region, and basal ganglia); (2) patients had undergone surgical resection or biopsy, and the pathological diagnosis was certain; and (3) patients underwent T2-weighted (T2w), T2 fluid-attenuated inversion recovery (T2 FLAIR), and contrast-enhanced T1-weighted (T1c) imaging at our hospital before the operation. Exclusion criteria were: (1) missing T2w, T2 FLAIR, or T1c images; (2) uncertain pathological diagnosis; and (3) poor image quality. Poor image quality is defined as obvious motion artifacts; the vascular pulsation artifact in the posterior fossa was obvious after enhancement; and (4) patients who had received related preoperative treatments, such as radiotherapy or chemotherapy; (5) patients who had been followed up for $<$12 months.

Initially, 161 cases were included, of whom 77 were excluded; 20 had received treatment before surgery, 11 had uncertain pathology, 12 had incomplete imaging data, 6 had poor image quality, and 28 were followed up for $<$12 months. Finally, a total of 84 cases were included. The OS of 40 cases was $>$12 months (long-term group) and the OS of 44 cases was $<$12 months (short-term group) (**Figure 1**).

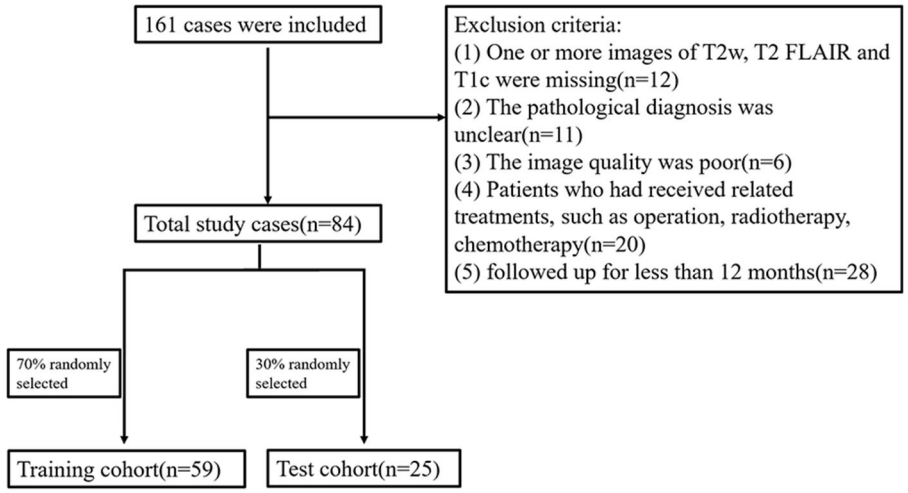

FIGURE 1 | Flowchart of patient inclusion and patient groupings.

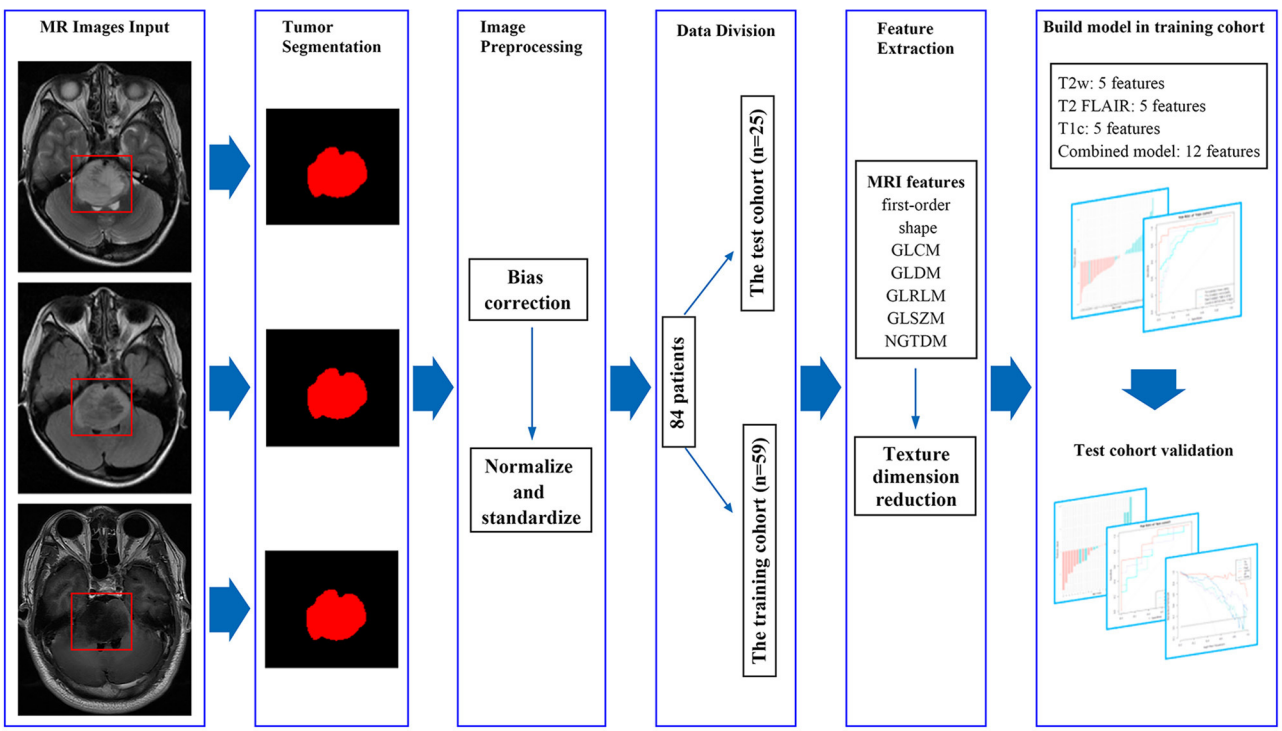

FIGURE 2 | MRI feature extraction and machine learning flow chart. By manually segmenting the tumors, we extracted 1,316 imaging features from masked preoperative T2w, T2 FLAIR, and T1c images. The variance method and maximum relevance and minimum redundancy were used to select the best features, and the four models were established. The test cohort was then used to verify the model.

T1w, T2w, T2 FLAIR, and T1c Images Acquisition

All patients were scanned using a GE HDxt 3.0T MR (General Electric, Milwaukee, WI, USA) or Philips Intera 1.5T MR (Royal Philips Electronics, Amsterdam, Netherlands) scanner. Imaging sequences included T1w, T2w, T2 FLAIR, and T1c sequences. The 3.0T MRI scan parameters were: repetition time (TR) 1,900 ms, echo time (TE) 24 ms, and inversion time (TI) 780 ms for T1w imaging; TR 4,480 ms and TE 120 ms for T2w imaging; TR 9,480 ms, TE 120 ms, and TI 2,300 ms for T2 FLAIR imaging. The T1w, T2w, and T2 FLAIR imaging sequences on the 3.0T scanner used the following parameters: field of view (FOV): 240

TABLE 1 | Clinical characteristics of 84 patients in the short-term and long-term groups.

Variable		Cases	Short-term group ($n = 44$)	Long-term group ($n = 40$)	Statistical value	p-value
Men		62	35 (79.55%)	27 (67.50%)	1.573	0.21
Women		22	9 (20.45%)	13 (32.50%)		
Age		84	27.25 ± 17.51	28.25 ± 15.19	−0.278	0.781
	Age (<18 years)	27	15 (34.09%)	12 (30.0%)	0.161	0.688
	Age (≥18 years)	57	29 (65.91%)	28 (70.0%)		
Tumor classification						
	WHO* 1	14	2 (4.55%)	12 (30.0 %)	11.868	0.001
	WHO 2	21	9 (20.45%)	12 (30.0 %)		
	WHO 3	19	12 (27.27 %)	7 (17.50 %)		
	WHO 4	30	21 (47.73 %)	9 (22.50 %)		
H3 K27M-mutation		45	31 (70.45%)	14 (35.00%)	10.589	0.001
H3 K27M wild-type		39	13 (29.55%)	26 (65.00%)		
Tumor location						
	Sellar region	4	2 (4.55%)	2 (5.0%)	0.029	0.865
	Basal ganglia	4	2 (4.55%)	2 (5.0%)		
	Brainstem	32	15 (34.09%)	17 (42.50%)		
	Corpus callosum	8	5 (11.36%)	3 (7.50%)		
	Thalamus	31	20 (45.45%)	11 (27.50%)		
	Cerebellar vermis	5	0	5 (12.50%)		
Operation						
	Biopsy	21	14 (31.82%)	7 (17.50%)	3.377	0.066
	Partial resection	31	16 (36.36%)	15 (37.50%)		
	Subtotal resection	23	12 (27.27%)	11 (27.50%)		
	Total resection	9	2 (4.55%)	7 (17.50%)		
Treatment						
	Radiotherapy	55	22 (50.0%)	33 (82.50%)	9.79	0.002
	Without radiotherapy	29	22 (50.0%)	7 (17.50%)		
	Chemotherapy	38	13 (29.55%)	25(62.50%)	1.285	0.257
	Chemotherapy + targeted therapy	11	8 (18.18%)	3 (7.50%)		
	Without chemotherapy	35	23 (52.27%)	12 (30.0%)		
OS**		84	5.16 ± 5.38	25.34 ± 9.46	−11.865	< 0.001

*World Health Organization.
**Overall survival.

× 240 mm, matrix: 256 × 256, slice thickness: 5.5 mm, slice gap: 1.0 mm, number of excitations (NEX): 1. The 1.5T MRI scan parameters were: TR 488 ms, TE 15 ms, and matrix: 152 × 121 for T1w imaging; TR 3,980 ms, TE 110 ms, and matrix: 230 × 130 for T2w imaging; TR 6,000 ms, TE 120 ms, TI 2,000 ms, and matrix: 192 × 115 for T2 FLAIR imaging. The T1w, T2w, and T2 FLAIR imaging sequences on the 1.5T scanner used the following parameters: FOV: 230 × 182 mm, slice thickness: 5.5 mm, slice gap: 1.0 mm, NEX: 1. T1c imaging on the 1.5T and 3.0T MRI scanners was performed after the administration of Gadolinium-Diethylenetriaminepentaacetic Acid (Gd-DTPA) (Kangchen Company, Guangzhou, China) or Gd diamine (GE Pharmaceuticals, USA) at a dose of 0.1 mmol/kg body weight.

Tumor Segmentation

All images were saved as Digital Imaging and Communications in Medicine (DICOM) and imported into the ITK-SNAP software (version 3.8.0, http://www.itksnap.org) for segmentation. Some studies have shown that one slice (2D) with the largest cross-section of the tumor and the entire tumor volume (3D) for segmentation has comparable diagnostic performance, and there are also some studies that use one slice for tumor segmentation (17–20). So, in this study, the regions of interest (ROIs) were manually segmented (**Figure 2**) on the axial slice with the largest cross-section of the tumors on T2w, T2 FLAIR, and T1c images by two authors (S Wu and P He, with 4 and 6 years of diagnostic experience in neuroradiology, respectively) who were blinded to histological results.

The final ROIs were calculated using the overlapping segmentations generated by the two authors. If the overlap rate was <90%, the ROI was defined by L Cheng, who had >10 years of diagnostic experience in neuroradiology (16, 21). The ROIs included cystic and necrotic components which may reflect tumor heterogeneity.

Imaging Feature Extraction

A total of 1,316 texture parameters were extracted from T2w, T2 FLAIR, and T1c images using the open-source package

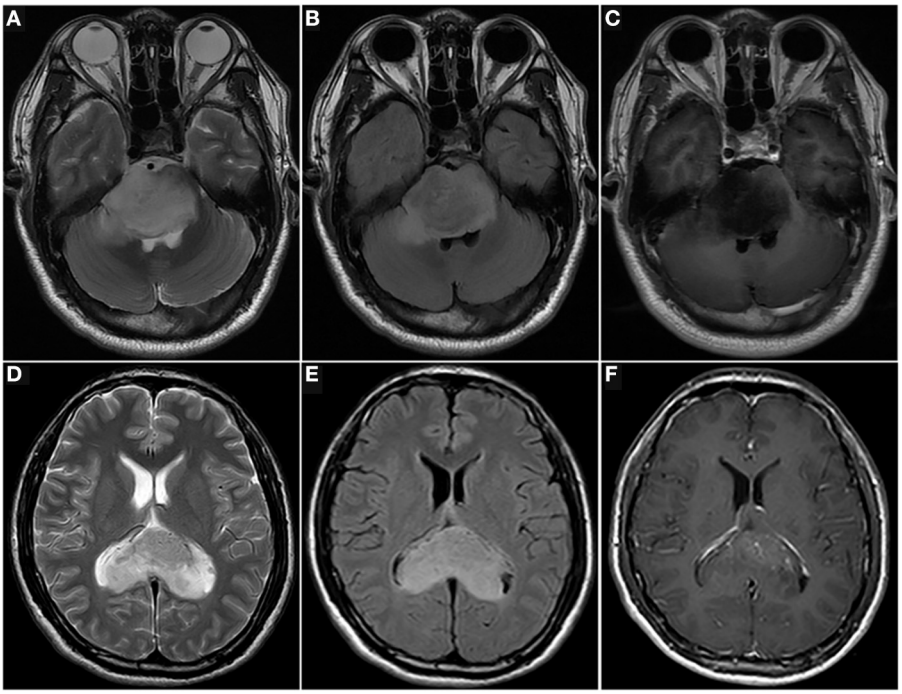

FIGURE 3 | Images of patients with midline gliomas. T2w **(A)**, T2 FLAIR **(B)**, and T1c **(C)** images of a 34-year-old man with a pontine diffuse midline glioma with a H3 K27M mutation (WHO 4), and histopathology of diffuse astrocytoma. He underwent a biopsy and was treated with radiotherapy and chemotherapy. The overall survival of the patient was 4.4 months. T2w **(D)**, T2 FLAIR **(E),** and T1c **(F)** images of a 33-year-old man with corpus callosum diffuse astrocytoma (WHO 2). He underwent a biopsy and was treated with radiotherapy and chemotherapy. The overall survival of the patient was 39 months (up to October 2020).

Pyradiomics (version 3.0.1, https://github.com/Radiomics/pyradiomics) on Python (version 3.5.6, https://www.python.org) and included first-order statistical features, shape features, gray level co-occurrence matrix, gray level dependence matrix, gray level run length matrix, gray level size zone matrix, and neighboring gray tone dependence matrix (22). The median and block methods were used to replace missing values and outliers.

Data Cohort Division and Preprocessing

Data were randomly divided into training (70%; 59 patients including the long-term group 31 patients and the long-term group 28 patients) and test (30%; 25 patients including the long-term group13 patients and the long-term group 12 patients) cohorts. All features extracted from the ROIs were normalized using Z-scores.

Feature Dimensionality Reduction and Selection of Optimal Features

The variance method was used to calculate the variance of features extracted from imaging. When the variance of the feature was 0, the feature was removed. The maximum relevance and minimum redundancy (mRMR) method was used to select the best non-redundant features from the extracted features.

Radiomics Feature Model and Evaluation

Logistic regression was used to establish the model. According to the best features of the T2w, T2 FLAIR, and T1c images, three models for T2w, T2 FLAIR, and T1c images and one combined model (T2w + T2 FLAIR + T1c) were constructed. Receiver operating characteristic (ROC) curve analysis and decision curve analysis (DCA) were used to assess the performance of the models (**Figure 2**).

Statistical Analysis

All statistical analyses were performed using R (version 3.5.1, http://www.R-project.org) and Python (version 3.5.6, https://www.python.org/). Chi-squared or Fisher's exact tests were used for nominal variables. Kruskal–Wallis H tests were used for ordinal variables. Student's t-tests were used for continuous variables. The variance method and mRMR were used for feature dimensionality reduction. Logistic regression was used to establish the model and construct a nomogram. ROC curve analysis was used to assess the established models according to accuracy (AC), area under the curve (AUC), sensitivity, and specificity values. DCA was used to evaluate the application value of the models. A $p < 0.05$ was considered statistically significant.

RESULTS

Patient Characteristics

A total of 84 patients with a midline glioma were enrolled in the study (62 men and 22 women; mean age 27.73 $\pm$ 16.36 years; range 1–63 years). The clinical characteristics of the long-term and short-term groups are shown in **Table 1**, **Figure 3**. There

TABLE 2 | Clinical characteristics of 84 patients in the training and test cohorts.

Variable		Cases	Training cohort	Test cohort	Statistical value	*p*-value
Men		62	45 (76.27%)	17 (68.0%)	0.621	0.431
Women		22	14 (23.73%)	8 (32.0%)		
Age		84	29.15 ± 17.07	24.36 ± 14.29	−1.232	0.222
	Age (< 18 years)	27	18 (30.51%)	9 (36.0%)	0.243	0.622
	Age (≥ 18 years)	57	41 (69.49%)	16 (64.0%)		
Tumor classification						
	WHO* 1	14	8 (13.56%)	6 (24.0%)	0.146	0.703
	WHO 2	21	15 (25.42%)	6 (24.0%)		
	WHO 3	19	16 (27.12%)	3 (12.0%)		
	WHO 4	30	20 (33.90%)	10 (40.0%)		
H3 K27M-mutation		45	30 (50.85%)	15 (60.00%)	0.591	0.442
H3 K27M wild-type		39	29 (49.15%)	10 (40.00%)		
Tumor location						
	Sellar region	4	4 (6.78%)	0	1.53	0.216
	Basal ganglia	4	4 (6.78%)	0		
	Brainstem	32	21 (35.59%)	11 (44.0%)		
	Corpus callosum	8	7 (11.86%)	1 (4.0%)		
	Thalamus	31	20 (33.90%)	11 (44.0%)		
	Cerebellar vermis	5	3 (5.08%)	2 (8.0%)		
Operation						
	Biopsy	21	17 (28.81%)	4 (16.0%)	3.767	0.052
	Partial resection	31	23 (38.98%)	8 (32.0%)		
	Subtotal resection	23	15 (25.42%)	8 (32.0%)		
	Total resection	9	4 (6.78%)	5 (20.0%)		
Treatment						
	Radiotherapy	55	43 (72.88%)	12 (48.0%)	4.809	0.028
	Without Radiotherapy	29	16 (27.12%)	13 (52.0%)		
	Chemotherapy	38	30 (50.85%)	8 (32.0%)	2.172	0.141
	Chemotherapy + targeted therapy	11	8 (13.56%)	3 (12.0%)		
	Without chemotherapy	35	21 (35.59%)	14 (56.0%)		
OS**		84	14.48 ± 12.20	15.45 ± 13.89	0.32	0.75

*World Health Organization.
**Overall survival.

was a significant difference in radiotherapy between the long-term group and the short-term group ($p = 0.002$). The patients with H3 K27M mutation in short-term group outnumbered those in long-term group significantly ($p = 0.001$). There was also a significant difference in OS between the short-term and long-term groups (5.16 ± 5.38 months vs. 25.34 ± 9.46 months, $p < 0.001$). The clinical characteristics of the training and test cohorts are shown in **Table 2**. The patients who underwent radiotherapy in the training outnumbered those in the test cohort significantly ($p = 0.0028$).

Feature Selection and Model Comparison

The extracted texture parameters needed to be normalized and standardized to reduce bias due to the missing values and outliers. The best non-redundant features were then selected from the extracted features using the variance method and mRMR. Finally, five features were extracted each from T2w, T2 FLAIR, and T1c images, and 12 features were extracted for the combined model (**Table 3**).

The three separate models and the combined model performed well on both the training and test cohorts, shown by the high AC. The performance of each model on the training and test cohorts, respectively, were: T2w: AUC = 0.86 vs. 0.734, AC = 0.84 vs. 0.72; T2 FLAIR: AUC = 0.89 vs. 0.78, AC = 0.90 vs. 0.76; T1c: AUC = 0.84 vs. 0.74, AC = 0.76 vs. 0.72; combined model: AUC = 0.96 vs. 0.87, AC = 0.93 vs. 0.84 (**Table 4**). The combined model had the best performance. The ROC curves of the T2w, T2 FLAIR, T1c, and combined models are shown in **Figure 4**. DCA of the four models showed that the combined model offered the largest net benefit (**Figure 5**). The radiomics nomogram of the combined model applied to the training cohort showed that it directly predicted the probability of OS > 12 months in patients with midline gliomas (**Figure 6**).

DISCUSSION

In this study, for the reproducibility and replicability of feature extraction, we used an open-source Pyradiomics 3.0.1 package

of Python to calculate the features. To minimize the bias stemming from the use of data acquired at a single center and parameters of a single machine, we collected MRI data from different suppliers and different imaging protocols to recognize the diversity of data. Finally, we obtained optimal radiomics characteristics of T2w, T2 FLAIR, and T1c images to construct four models to non-invasively predict the prognosis of patients with midline gliomas. We compared the four models in terms of ROC curve, AUC, AC, sensitivity, and specificity and found that all models performed well on both the training and test cohorts, showing high AC. Among these, the combined model had the best performance. Moreover, DCA showed that the combined model offered the highest net benefit and application value. Our results demonstrate the feasibility of evaluating prognoses of patients with midline gliomas using traditional MRI radiomics. Furthermore, the fusion of radiomics characteristics obtained from different imaging sequences may improve the performance of the predictive model.

Numerous studies have shown that a single radiomics predictive model performs worse than a fusion radiomics model. Fusion radiomics models perform better and include more useful features, demonstrating the multimodal images play an important role in the prognostic evaluation of gliomas (23, 24). In this study, we constructed a machine learning model based on multi-parameter MRI data to predict the OS of patients with midline gliomas. Our results also showed that the fusion model performed better than the single radiomics model. In our training cohort, the combined model included 12 radiomics features (three features from T1c data, four features from T2 FLAIR data, and five features from T2w data), which were mainly derived from second- and higher-order texture features. The higher-order texture features can capture deeper imaging heterogeneity and provide information on tissue microstructure and local tumor microenvironment, which can help predict patient survival time (25, 26). Higher-order radiomics characteristics have also been shown to be closely related to genetic changes in tumors (6, 27–31). Five features in our combined model come from T2w, indicating that T2w images may provide more valuable texture features than T2 FLAIR and T1c images for evaluating survival time, which may explain why most studies prefer T2w sequences as the first choice for separate or joint analyses (26). However, T2 FLAIR and T1c images can offer additional details to the model and are thus indispensable (6, 27, 28). Therefore, we chose these three sequences. In addition, we applied the 12 features of the combined model to

TABLE 3 | Best characteristic parameters of the four models.

Dataset	Number	Characteristic parameters
T2w	5	T2w_wavelet.HLL_first order_10 Percentile T2w _exponential_glszm_Gray Level NonUniformity T2w _gradient_glcm_MCC T2w _exponential_glcm_Inverse Variance T2w_wavelet.LHH_glszm_Low Gray Level Zone Emphasis
T2 FLAIR	5	T2 FLAIR_square_glszm_Small Area Low Gray Level Emphasis T2 FLAIR_wavelet.HLH_first order_Skewness T2 FLAIR_wavelet.LHH_gldm_Small Dependence High Gray Level Emphasis T2 FLAIR_wavelet.HHH_glszm_High Gray Level Zone Emphasis T2 FLAIR_wavelet.HHL_glcm_MCC
T1c	5	T1c_exponential_glszm_Small Area Low Gray Level Emphasis T1c _wavelet.HHH_glcm_Cluster Shade T1c _logarithm_glszm_Gray Level NonUniformity T1c _wavelet.LHH_gldm_Large Dependence High Gray Level Emphasis T1c _wavelet.LHH_glszm_Gray Level Variance
Combined model	12	T1c_exponential_glszm_Small Area Low Gray Level Emphasis T2 FLAIR_square_glszm_Low Gray Level Zone Emphasis T2 FLAIR_wavelet.HLH_first order_Skewness T2w_exponential_glszm_Gray Level NonUniformity T2 FLAIR_gradient_glszm_Small Area Low Gray Level Emphasis T1c_wavelet.HHH_glcm_ClusterShade T2 FLAIR_wavelet.HHH_glszm_High Gray Level Zone Emphasis T2w_wavelet.LHH_glszm_Low Gray Level Zone Emphasis T2w_wavelet.HLL_gldm_Dependence NonUniformity Normalized T1c_wavelet.HLH_glszm_High Gray Level Zone Emphasis T2w_gradient_glcm_MCC T2w_exponential_glcm_Inverse Variance

TABLE 4 | Comparison of the diagnostic efficiency between the four models.

Dataset		AUC (95% CI)	Accuracy	Sensitivity	Specificity
T2w	Training cohort	0.859 (0.764–0.955)	0.814	0.857	0.774
	Test cohort	0.737 (0.537–0.937)	0.72	0.917	0.538
T2 FLAIR	Training cohort	0.888 (0.798–0.979)	0.898	0.929	0.871
	Test cohort	0.776 (0.582–0.969)	0.76	0.583	0.923
T1c	Training cohort	0.844 (0.743–0.945)	0.763	0.786	0.742
	Test cohort	0.737 (0.532–0.942)	0.72	0.917	0.538
Combined model	Training cohort	0.961 (0.904–1.0)	0.932	0.893	0.968
	Test cohort	0.865 (0.722–1.0)	0.84	0.667	1.0

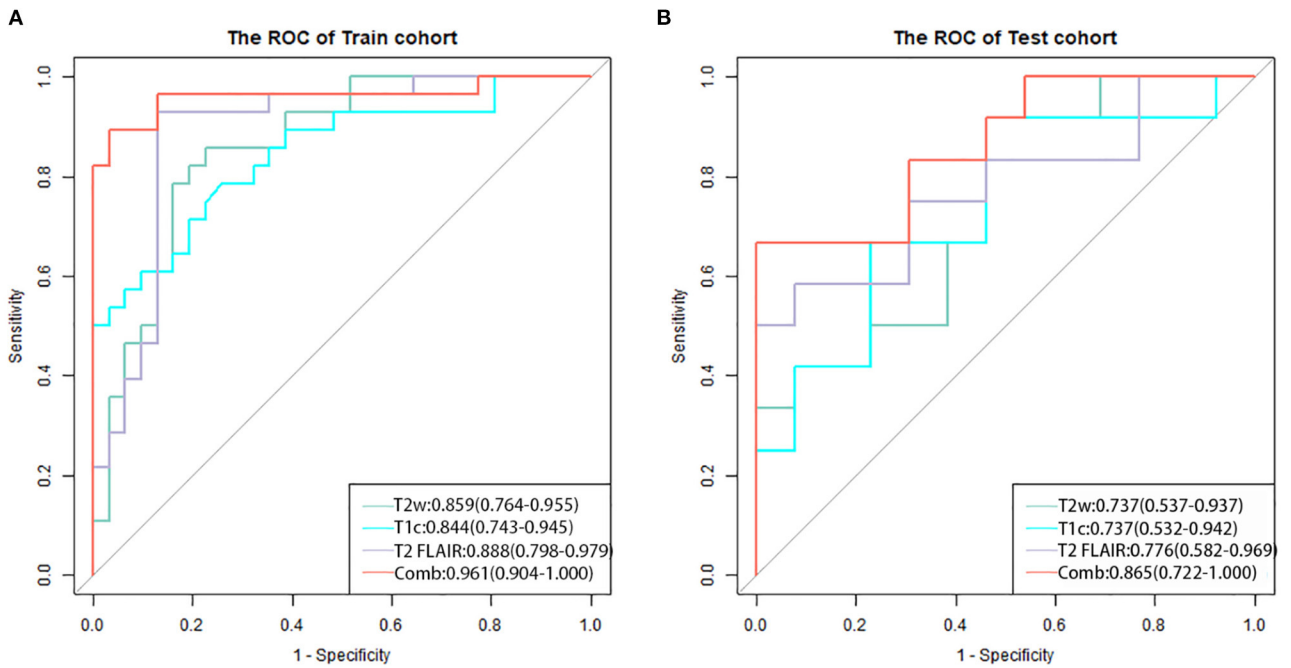

FIGURE 4 | The receiver operating characteristic curves of the four models for the training **(A)** and test **(B)** cohorts. The combined model (red line) applied to the training and test cohorts had the best performance.

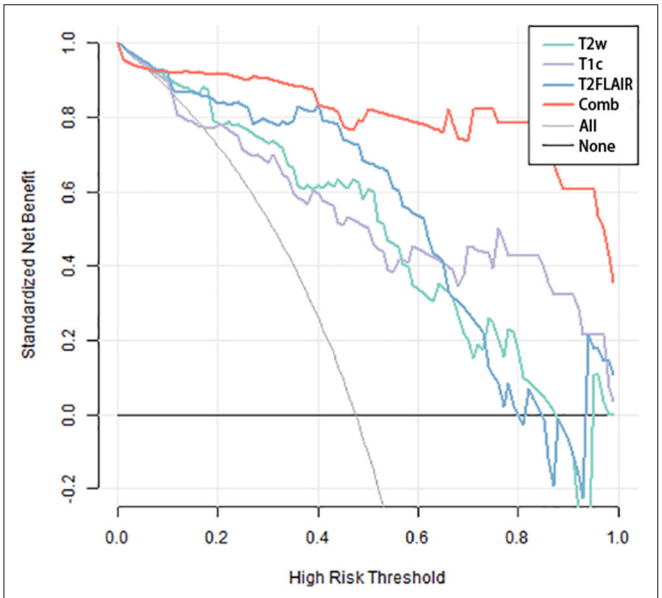

FIGURE 5 | Decision-curve analysis of the four models. The x-axis represents the threshold probability, and the y-axis represents the net benefit. The combined model (red line) had a higher net benefit and better application value for predicting the survival time of patients with midline gliomas.

the nomogram, which enabled a more intuitive prediction of survival time.

To the best of our knowledge, the H3 K27M mutation, an independent prognostic factor, is common in midline gliomas. Several studies on the prediction of H3 K27M mutation status using machine learning based on radiomics features extracted from MRI data have been conducted to date. Su et al. (32) retrospectively studied 100 patients with midline gliomas and built 10 models using the Tree-based Pipeline Optimization Tool-based automated machine learning algorithm with radiomics features extracted from T2 FLAIR images. The AC of the best pipeline ranged from 0.788 to 0.867 in the training cohort and from 0.60 to 0.84 in the testing cohort. Pan et al. (14) retrospectively evaluated 151 brainstem gliomas and built a prediction model that incorporated 36 MRI features and three clinical features using a random forest algorithm. The model achieved an AC of 84.44% in the test cohort. Moreover, they constructed a simplified model that achieved an AC of 75.55% in the test cohort. Kandemirli et al. (33) developed an extreme gradient boosting algorithm classifier based on machine learning to predict the H3 K27M mutation using conventional MRI sequences. The model had an AUC of 0.791 in the training set and 0.737 in the test set, and the AC of the model was 73% in the test set. Furthermore, Li et al. (34) explored visually accessible MRI features of 30 patients with DMGs with and without the H3 K27M mutation using principal component analysis based on radiomics and found that T2w sequences may be more valuable and that cystic formation may be a biomarker for diagnosing DMGs with an H3 K27M mutation.

In addition to predicting the mutation status of H3 K27M, several researchers have evaluated the OS of patients with midline glioma using texture analysis. Szychot et al. (35) retrospectively analyzed 32 children with DMGs using a T2w

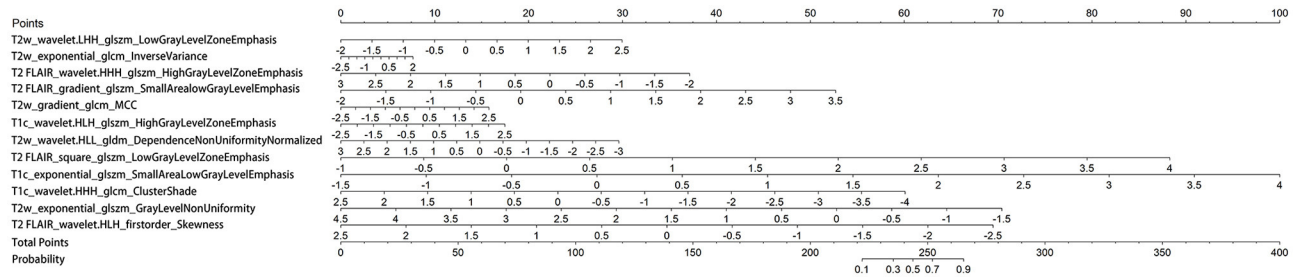

FIGURE 6 | Nomogram of the combined model. A vertical line was drawn from each predictor to the point to obtain the score of the predictor. The scores of each predictor are then added, and a vertical line is drawn from the total score to the survival probability axis. The total score corresponds to the probability of >12 months survival.

imaging and apparent diffusion coefficient map-based texture analysis to predict outcomes of patients with DMG and found that the best predictor was mean of positive pixels, which could divide patients into poor and good prognosis groups according to a median survival time of 7.5 and 17.5 months, respectively. In this article, we included a larger number of cases to predict the OS of midline glioma patients using machine learning based on multiparametric MRI radiomics features, and our ACs were similar to those of the abovementioned machine learning studies. Thus, our model may offer an alternative method to predict the OS of patients with midline gliomas.

The current study has several limitations. First, a relatively small sample size and lack of an independent external test dataset in this study, which we will take as the key work in the next step. Second, the use of a single center may have introduced some bias. The next step is to conduct a multicenter study to improve the performance of the predictive model using more data. Third, only one method was used to build the model. If multiple methods were used to build and verify the models, a better model could be developed with improved AC. Forth, the patients who underwent radiotherapy in the long-term group are more than those in the short-term group, and some RT patients were treated with chemotherapy and/or targeted therapy at the same time, so it cannot be simply considered that RT can better predict the survival. In the next step, more cases need to be collected for subgroup analysis to detect the impact of RT on predicting the survival of DMG. Fifth, At present, there are many methods for extracting image features, such as local binary pattern (LBP), local ternary pattern (LTP), histogram of oriented gradients (HOG), etc. We used only one conventional method for feature extraction in this study due to the issues with overfitting and related techniques, In the future, we will try to use more methods to extract image features for further research.

Our radiomics model based on traditional MRI sequence data, especially the fusion radiomics model, may offer a reliable and non-invasive method to predict the survival time of patients with midline gliomas. Although there are several limitations, our findings provide a reference for the preoperative prediction and individualized treatment of gliomas as well as for further radiomics research on midline gliomas.

DATA AVAILABILITY STATEMENT

The original contributions presented in the study are included in the article/**Supplementary Material**, further inquiries can be directed to the corresponding authors.

ETHICS STATEMENT

The studies involving human participants were reviewed and approved by IRB of Guangdong Sanjiu Brain Hospital. Written informed consent from the participants' legal guardian/next of kin was not required to participate in this study in accordance with the national legislation and the institutional requirements. Written informed consent was obtained from the individual(s), and minor(s)' legal guardian/next of kin, for the publication of any potentially identifiable images or data included in this article.

AUTHOR CONTRIBUTIONS

D-BD and QZ: conceptualization. D-BD: methodology, formal analysis, and writing—original draft preparation. Y-TL: software. W-SW and QZ: validation. J-FZ: investigation. PH: resources. S-NW, PH, and L-NC: data curation. W-SW: visualization. QZ: supervision and project administration. All authors: writing—review and editing, read, and agreed to the submission of the manuscript.

SUPPLEMENTARY MATERIAL

The Supplementary Material for this article can be found online at: https://www.frontiersin.org/articles/10.3389/fneur.2022.866274/full#supplementary-material

REFERENCES

1. Louis DN, Perry A, Reifenberger G, von Deimling A, Figarella-Branger D, Cavenee WK, et al. The 2016 World Health Organization Classification of tumors of the central nervous system: a summary. *Acta Neuropathol.* (2016) 131:803–20. doi: 10.1007/s00401-016-1545-1
2. Louis DN, Perry A, Wesseling P, Brat DJ, Cree IA, Figarella-Branger D, et al. The 2021 WHO classification of tumors of the central nervous system: a summary. *Neuro Oncol.* (2021) 23:1231-51. doi: 10.1093/neuonc/noab106
3. Qiu T, Chanchotisatien A, Qin Z, Wu J, Du Z, Zhang X, et al. Imaging Characteristics of Adult H3 K27M-mutant Gliomas. *J Neurosurg.* (2019) 15:1–9. doi: 10.3171/2020.2.JNS191920a
4. Ochs K, Ott M, Bunse T, Sahm F, Bunse L, Deumelandt K, et al. K27M-mutant Histone-3 as a Novel Target for Glioma Immunotherapy. *Oncoimmunology.* (2017) 6:e1328340. doi: 10.1080/2162402X.2017.1328340
5. Liu Z, Feng S, Li J, Cao H, Huang J, Fan F, et al. The Epidemiological Characteristics and Prognostic Factors of Low-Grade Brainstem Glioma: a Real-World Study of Pediatric and Adult Patients. *Front Oncol.* (2020) 10:391. doi: 10.3389/fonc.2020.00391
6. Huang RY, Guenette JP. Non-invasive Diagnosis of H3 K27M Mutant Midline Glioma. *Neuro Oncol.* (2020) 22:309–10. doi: 10.1093/neuonc/noz240
7. Aboian MS, Solomon DA, Felton E, Mabray MC, Villanueva-Meyer JE, Mueller S, et al. Imaging Characteristics of Pediatric Diffuse Midline Gliomas with Histone H3 K27M Mutation. *AJNR Am J Neuroradiol.* (2017) 38:795–800. doi: 10.3174/ajnr.A5076
8. Aboian MS, Tong E, Solomon DA, Kline C, Gautam A, Vardapetyan A, et al. Diffusion Characteristics of Pediatric Diffuse Midline Gliomas with Histone H3-K27M Mutation Using Apparent Diffusion Coefficient Histogram Analysis. *Am J Neuroradiol.* (2019) 40:1804–10. doi: 10.3174/ajnr.A6302
9. Zhang X, Tian Q, Wang L, Liu Y, Li B, Liang Z, et al. Radiomics Strategy for Molecular Subtype Stratification of Lower-Grade Glioma: Detecting IDH and TP53 Mutations Based on Multimodal MRI. *J Magn Reson Imaging.* (2018) 48:916–26. doi: 10.1002/jmri.25960
10. Peng H, Huo J, Li B, Cui Y, Zhang H, Zhang L, et al. Predicting Isocitrate Dehydrogenase (IDH) Mutation Status in Gliomas Using Multiparameter MRI Radiomics Features. *J Magn Reson Imaging.* (2021) 53:1399–407. doi: 10.1002/jmri.27434
11. Zhang S, Sun H, Su X, Yang X, Wang W, Wan X, et al. Automated machine learning to predict the co-occurrence of isocitrate dehydrogenase mutations and O6-methylguanine-DNA methyltransferase promoter methylation in patients with gliomas. *J Magn Reson Imaging.* (2021) 54:197–205. doi: 10.1002/jmri.27498
12. Zhou H, Vallières M, Bai HX, Su C, Tang H, Oldridge D, et al. MRI Features Predict Survival and Molecular Markers in Diffuse Lower-grade Gliomas. *Neuro Oncol.* (2017) 19:862–70. doi: 10.1093/neuonc/now256
13. Kocak B, Durmaz ES, Ates E, Sel I, Turgut Gunes S, Kaya OK, et al. Radiogenomics of Lower-grade Gliomas: Machine Learning-based MRI Texture Analysis for Predicting 1p/19q Codeletion Status. *Eur Radiol.* (2020) 30:877–86. doi: 10.1007/s00330-019-06492-2
14. Pan CC, Liu J, Tang J, Chen X, Chen F, Wu YL, et al. A Machine Learning-based Prediction Model of H3K27M Mutations in Brainstem Gliomas Using Conventional MRI and Clinical Features. *Radiother Oncol.* (2019) 130:172–79. doi: 10.1016/j.radonc.2018.07.011
15. Prasanna P, Patel J, Partovi S, Madabhushi A, Tiwari P. Radiomic features from the peritumoral brain parenchyma on treatment-naïve multi-parametric MR imaging predict long versus short-term survival in glioblastoma multiforme: Preliminary findings. *Eur Radiol.* (2017) 27:4188–97. doi: 10.1007/s00330-016-4637-3
16. Senders JT, Staples P, Mehrtash A, Cote DJ, Taphoorn MJB, Reardon DA, et al. An Online Calculator for the Prediction of Survival in Glioblastoma Patients Using Classical Statistics and Machine Learning. *Neurosurgery.* (2020) 86:2:E184–E192. doi: 10.1093/neuros/nyz403
17. Li S, Liu J, Xiong Y, Han Y, Pang P, Luo P, et al. Application Values of 2D and 3D Radiomics Models Based on CT Plain Scan in Differentiating Benign from Malignant Ovarian Tumors. *Biomed Res Int.* (2022) 2022:5952296. doi: 10.1155/2022/5952296
18. Lubner MG, Stabo N, Lubner SJ, del Rio AM, Song C, Halberg RB, et al. CT textural analysis of hepatic metastatic colorectal cancer: pre-treatment tumor heterogeneity correlates with pathology and clinical outcomes. *Abdom Imaging.* (2015) 40:2331–7. doi: 10.1007/s00261-015-0438-4
19. Akkus Z, Ali I, Sedlár J, Agrawal JP, Parney IF, Giannini C, et al. Predicting Deletion of Chromosomal Arms 1p/19q in Low-Grade Gliomas from MR Images Using Machine Intelligence. *J Digit Imaging.* (2017) 30:469-476. doi: 10.1007/s10278-017-9984-3
20. Han Y, Xie Z, Zang Y, Zhang S, Gu D, Zhou M, et al. Non-invasive genotype prediction of chromosome 1p/19q co-deletion by development and validation of an MRI-based radiomics signature in lower-grade gliomas. *J Neurooncol.* (2018) 140:297–306. doi: 10.1007/s11060-018-2953-y
21. Kniep HC, Madesta F, Schneider T, Hanning U, Schönfeld MH, Schön G, et al. Radiomics of Brain MRI: Utility in Prediction of Metastatic Tumor Type. Radiology (2019) 290:2:479-87. doi: 10.1148/radiol.2018180946
22. van Griethuysen JJM, Fedorov A, Parmar C, Hosny A, Aucoin N, Narayan V, et al. Computational Radiomics System to Decode the Radiographic Phenotype. *Cancer Res.* (2017) 77:e104–e107. doi: 10.1158/0008-5472.CAN-17-0339
23. Jiang C, Kong Z, Liu S, Feng S, Zhang Y, Zhu R, et al. Fusion Radiomics Features from Conventional MRI Predict MGMT Promoter Methylation Status in Lower Grade Gliomas. *Eur J Radiol.* (2019) 121:108714. doi: 10.1016/j.ejrad.2019.108714
24. Li ZC, Bai H, Sun Q, Li Q, Liu L, Zou Y, et al. Multiregional Radiomics Features from Multiparametric MRI for Prediction of MGMT Methylation Status in Glioblastoma Multiforme: a Multicentre Study. *Eur Radiol.* (2018) 28:3640–50. doi: 10.1007/s00330-017-5302-1
25. Aerts HJ, Velazquez ER, Leijenaar RT, Parmar C, Grossmann P, Carvalho S, et al. Decoding Tumour phenotype by Noninvasive Imaging Using a Quantitative Radiomics approach. *Nat Commun.* (2014) 5:4006. doi: 10.1038/ncomms5006
26. Qian Z, Li Y, Sun Z, Fan X, Xu K, Wang K, et al. Radiogenomics of Lower-grade Gliomas: a Radiomic Signature as a Biological Surrogate for Survival Prediction. *Aging.* (2018) 10:2884–99. doi: 10.18632/aging.101594
27. Seow P, Wong JHD, Ahmad-Annuar A, Mahajan A, Abdullah NA, Ramli N. Quantitative Magnetic Resonance Imaging and Radiogenomic Biomarkers for Glioma Characterisation: a Systematic Review. *Br J Radiol.* (2018) 91:20170930. doi: 10.1259/bjr.20170930
28. Sasaki T, Kinoshita M, Fujita K, Fukai J, Hayashi N, Uematsu Y, et al. Radiomics and MGMT Promoter Methylation for Prognostication of Newly Diagnosed Glioblastoma. *Sci Rep.* (2019) 9:14435. doi: 10.1038/s41598-019-50849-y
29. Tian H, Wu H, Wu G, Xu G. Noninvasive Prediction of TERT Promoter Mutations in High-Grade Glioma by Radiomics Analysis Based on Multiparameter MRI. *Biomed Res Int.* (2020) 2020:3872314. doi: 10.1155/2020/3872314
30. Patel SH, Poisson LM, Brat DJ, Zhou Y, Cooper L, Snuderl M, et al. T2-FLAIR Mismatch, an Imaging Biomarker for IDH and 1p/19q Status in Lower-grade Gliomas: A TCGA/TCIA Project. *Clin Cancer Res.* (2017) 23:6078-85. doi: 10.1158/1078-0432.CCR-17-0560
31. Li Y, Qian Z, Xu K, Wang K, Fan X, Li S, et al. MRI Features Predict p53 Status in Lower-grade Gliomas via a Machine-learning Approach. *Neuroimage Clin.* (2017) 17:306–11. doi: 10.1016/j.nicl.2017.10.030
32. Su X, Chen N, Sun H, Liu Y, Yang X, Wang W, et al. Automated Machine Learning Based on Radiomics Features Predicts H3 K27M Mutation in Midline Gliomas of the Brain. *Neuro Oncol.* (2020) 22:393-401. doi: 10.1093/neuonc/noz184
33. Kandemirli SG, Kocak B, Naganawa S, Ozturk K, Yip SSF, Chopra S, et al. Machine learning-based multiparametric magnetic resonance imaging radiomics for prediction of H3K27M mutation in midline gliomas. *World Neurosurg.* (2021) 151:e78–85. doi: 10.1016/j.wneu.2021.03.135
34. Li Q, Dong F, Jiang B, Zhang M. Exploring MRI Characteristics of Brain Diffuse Midline Gliomas With the H3 K27M Mutation Using Radiomics. *Front Oncol.* (2021) 11:646267. doi: 10.3389/fonc.2021.646267
35. Szychot E, Youssef A, Ganeshan B, Endozo R, Hyare H, Gains J, et al. Predicting outcome in childhood diffuse midline gliomas using magnetic resonance imaging based texture analysis. *J Neuroradiol.* (2020) 48:243–7. doi: 10.1016/j.neurad.2020.02.005

Conflict of Interest: Y-TL was employed by GE Healthcare.

The remaining authors declare that the research was conducted in the absence of any commercial or financial relationships that could be construed as a potential conflict of interest.

Publisher's Note: All claims expressed in this article are solely those of the authors and do not necessarily represent those of their affiliated organizations, or those of the publisher, the editors and the reviewers. Any product that may be evaluated in this article, or claim that may be made by its manufacturer, is not guaranteed or endorsed by the publisher.

Copyright © 2022 Deng, Liao, Zhou, Cheng, He, Wu, Wang and Zhou. This is an open-access article distributed under the terms of the Creative Commons Attribution License (CC BY). The use, distribution or reproduction in other forums is permitted, provided the original author(s) and the copyright owner(s) are credited and that the original publication in this journal is cited, in accordance with accepted academic practice. No use, distribution or reproduction is permitted which does not comply with these terms.

frontiers | Frontiers in Neuroscience

ORIGINAL RESEARCH
published: 04 May 2022
doi: 10.3389/fnins.2022.837349

Intraoperative Real-Time Near-Infrared Image-Guided Surgery to Identify Intracranial Meningiomas *via* Microscope

Jun Muto[1]†, Yutaka Mine[2], Yuya Nishiyama[1], Kazuhiro Murayama[3], Seiji Yamada[4], Daijiro Kojima[1], Motoharu Hayakawa[1], Kazuhide Adachi[1], Mitsuhiro Hasegawa[1], John Y. K. Lee[5] and Yuichi Hirose[1]*

[1] Department of Neurosurgery, Fujita Health University, Toyoake, Japan, [2] Department of Neurosurgery, Saiseikai Yokohamashi Tobu Hospital, Yokohama, Japan, [3] Department of Radiology, Fujita Health University, Toyoake, Japan, [4] Department of Pathology, Fujita Health University, Toyoake, Japan, [5] Department of Neurosurgery, University of Pennsylvania, Philadelphia, PA, United States

OPEN ACCESS

Edited by:
Sandro M. Krieg,
Technical University of Munich, Germany

Reviewed by:
Neda Haj-Hosseini,
Linköping University, Sweden
Vassiliy Tsytsarev,
University of Maryland, College Park, United States

***Correspondence:**
Jun Muto
muto@fujita-hu.ac.jp

†Present address:
Jun Muto,
Tokyo Medical Center, Tokyo, Japan

Specialty section:
This article was submitted to Brain Imaging Methods, a section of the journal Frontiers in Neuroscience

Received: 16 December 2021
Accepted: 08 February 2022
Published: 04 May 2022

Citation:
Muto J, Mine Y, Nishiyama Y, Murayama K, Yamada S, Kojima D, Hayakawa M, Adachi K, Hasegawa M, Lee JYK and Hirose Y (2022) Intraoperative Real-Time Near-Infrared Image-Guided Surgery to Identify Intracranial Meningiomas via Microscope. Front. Neurosci. 16:837349. doi: 10.3389/fnins.2022.837349

Meningiomas are a common pathology in the central nervous system requiring complete surgical resection. However, in cases of recurrence and post-irradiation, accurate identification of tumor remnants and a dural tail under bright light remains challenging. We aimed to perform real-time intraoperative visualization of the meningioma and dural tail using a delayed-window indocyanine green (ICG) technique with microscopy. Fifteen patients with intracranial meningioma received 0.5 mg/kg ICG a few hours before observation during the surgery. We used near-infrared (NIR) fluorescence to identify the tumor location. NIR fluorescence could visualize meningiomas in 12 out of 15 cases. Near-infrared visualization during the surgery ranged from 1 to 4 h after the administration of ICG. The mean signal-to-background ratio (SBR) of the intracranial meningioma in delayed-window ICG (DWIG) was 3.3 ± 2.6. The ratio of gadolinium-enhanced T1 tumor signal to the brain (T1BR) (2.5 ± 0.9) was significantly correlated with the tumor SBR (p = 0.016). K^{trans}, indicating blood–brain barrier permeability, was significantly correlated with tumor SBR ($p < 0.0001$) and T1BR (p = 0.013) on dynamic contrast-enhanced magnetic resonance imaging (MRI). DWIG demonstrated a sensitivity of 94%, specificity of 38%, positive predictive value (PPV) of 76%, and negative predictive value (NPV) of 75% for meningiomas. This is the first pilot study in which DWIG fluorescence-guided surgery was used to visualize meningioma and dural tail intraoperatively with microscopy. DWIG is comparable with second-window ICG in terms of mean SBR. Gadolinium-enhanced T1 tumor signal may predict NIR fluorescence of the intracranial meningioma. Blood–brain barrier permeability as shown by K^{trans} on dynamic contrast-enhanced MRI can contribute to gadolinium enhancement on MRI and to ICG retention and tumor fluorescence by NIR.

Keywords: enhanced permeability retention, intracranial meningioma, metabolic navigation, near-infrared, second window indocyanine green, fluorescence

INTRODUCTION

Meningiomas are the most frequently occurring intracranial tumors in adults, accounting for one third of all cases. The gold standard treatment for symptomatic meningioma is resection (Mirimanoff et al., 1985), but even after removal and maximal adjunctive radiation therapy, the median time to radiological progression is 12, 7, and 2 years for World Health Organization (WHO) grades I, II, and III meningiomas, respectively (Olar et al., 2015).

Currently, the differentiation between the dural or adjacent bone invasion and reactive tissue in meningioma seems to be limited. Chances of safe gross total resection without neurological defects may decrease due to the tumor's location, invasion of the dura and/or bone, and involvement of neurovascular structures. Fluorescence-guided surgery may be a helpful tool in evaluating the extent of resection, especially in patients with complex meningiomas. 5-Aminolevulinic acid (5-ALA), a prodrug in the porphyrin family, has been shown to facilitate tumor identification, improve tumor resection rates in meningioma (Dijkstra et al., 2019; Valdes et al., 2019), and prolong overall survival in glioblastoma (Stummer et al., 2000, 2006). However, 5-ALA has limitations, i.e., fluorescence in the visible light spectrum (400–700 nm) is highly absorbed by endogenous fluorophores, a lack of tissue penetrance, and confounding with background brain autofluorescence (Stummer et al., 2006).

Fluorescence-guided neurosurgery is useful, especially for recurrent and radiated cases, where it is difficult to identify the exact tumor location by direct observation under a bright light. Indocyanine green (ICG) has been used in neurosurgery as a vascular contrast agent in the evaluation of aneurysms by facilitating the assessment of arterial and venous flow (Hide et al., 2015). Intraoperative video angiography shows real-time blood flow during surgery with a bolus of 5–25 mg per operation (Ueba et al., 2013). Recently, second-window ICG (SWIG) for tumor lesions was reported in which a high dose of 5 mg/kg of ICG was administered to a patient harboring a brain tumor up to 24 h before surgery, and near-infrared (NIR) fluorescence from the tumor itself could be observed during the surgery. The usefulness of SWIG has been shown in meningioma (Lee et al., 2017a), glioblastoma (Lee et al., 2016), and metastatic tumors (Lee et al., 2017b; Muto et al., 2021).

However, SWIG requires a dose administration of ICG corresponding to the maximum safe capacity for biological use, which may cause side effects and limit its application to patients and require administration 1 day before observation. We modified the dose and timing of administration to 0.5 mg/kg ICG during the surgery, and NIR fluorescence can be observed more than 1 h after administration. We defined this modified technique as "delayed window ICG (DWIG)." The reason for the observation time was that Zeh et al. (2017) found that NIR fluorescence in glioblastomas in a mouse model peaked at 1 h post-infusion and plateaued 24 h post-infusion. Currently, 0.5 mg/kg of ICG administered intraoperatively has been used to evaluate real-time blood flow in neurosurgery with a few side effects. Using the DWIG technique, fluorescence from the tumor can be detected more than 1 h after intraoperative administration of 25 mg of ICG. Considering these findings, we hypothesized that (1) the administration of ICG more than 1 h before surgery might be feasible for visualizing the tumor and dural tail compared with the normal brain parenchyma, (2) there is a correlation between gadolinium-enhanced magnetic resonance imaging (Gd-MRI) and ICG fluorescence of the lesions, and (3) the mechanism of ICG fluorescence is implicated by vascular permeability.

We aimed to use DWIG after administering 0.5 mg/kg of ICG intraoperatively with delayed observation for intracranial meningioma and the dural tail, evaluate its efficacy, and clarify its mechanism in this pilot study.

MATERIALS AND METHODS

Study Design and Ethical Approval

This prospective study was approved by the Fujita Health University Clinical Research Ethical Committee (CRB4180003) and Saiseikai Yokohamashi Tobu Hospital (20200137). Informed consent was obtained from all patients.

Patient Population

Fifteen meningiomas in 15 patients were enrolled in this study. All patients underwent Gd-MRI, computed tomography scan, and surgical resection with intravenous ICG administration.

Near-Infrared Imaging System

The KINEVO microscope (KINEVO 900, Carl Zeiss Meditec AG, Jena Germany) was used for the 15 patients, with the FLOW 800 application that utilized an NIR excitation light source (805 nm) and camera (820–860 nm). NIR images were captured and stored for further evaluation.

Surgery and Delayed-Window Indocyanine Green Technique

Each patient received intravenous ICG (0.5 mg/kg) ($C_{43}H_{47}N_2NaO_6S_2$, Daiichi Sankyo, Tokyo, Japan) mixed with 10 ml of 0.9% saline during the craniotomy at the beginning of the surgery. NIR visualization ranged from 1 to 4 h after the administration of ICG. After exposing the dura mater, the microscope was introduced, the operating room was dimmed, and light in the NIR wavelength was irradiated from the illumination system. The NIR fluorescence was sometimes detected over the dura mater in cases where the tumor was attached to the convex side of the dura. Then the dura mater was incised, and the intradural tumor was exposed. Subsequently, NIR fluorescence was detected from the tumor itself using an illumination system. Fluorescence excitation and exposure were registered when the tumor was exposed for the first time. At that point, the tumor seemed to be most visible compared with the normal brain parenchyma, and fluorescence excitation and imaging settings were sustained throughout the remainder of the surgery. The tumors and dural tail were dissected and totally removed under DWIG based on the fluorescence guidance.

Dynamic Contrast-Enhanced Magnetic Resonance Imaging Examination and Post-processing

Magnetic resonance imaging (MRI) examinations were performed using a 3T MRI system (Vantage Titan 3T; Canon Medical Systems Corporation, Otawara, Tochigi, Japan) with a 32-channel head coil. Axial dynamic contrast-enhanced (DCE) MRI was performed after intravenous administration of a contrast agent using a 3D fast field echo quick sequence that provided coverage of the whole brain tumor using the following parameters: matrix size, zero-filling matrix 512 × 512 (acquisition matrix 186 × 256); field of view, 220 mm × 220 mm; repetition time, 5.5 ms; echo time, 2.5 ms; flip angle, 15°; and section thickness, 5 mm. Thirty-one dynamic consecutive volumes, each including 21 sections to cover the tumor based on T2-weighted images, were obtained every 10 s, giving a total measurement time of 5 min and 4 s. The contrast agent gadobutrol (Gadovist; Bayer, Osaka, Japan, 0.05 ml/kg body weight) was injected intravenously as a bolus through a driven autoinjector (Sonic Shot GX; Nemoto, Japan) at a rate of 1 ml/s, followed by an intravenous bolus injection of 30 ml of physiological saline solution at 1 ml/s. Post-processing of DCE perfusion MR images was performed using dedicated post-processing software (Olea Sphere V3.0, Olea Medical, Vitrea Workstation V7.1, Canon Medical Systems Corporation). The pharmacokinetic model introduced by Tofts et al. can also be used to calculate the volume transfer constant K^{trans} (/min) from the intravascular to the extravascular space, K^{ep} (= K^{trans}/V^{e})(/min)from the extravascular to the intravascular space, the volume of the extravascular extracellular space V^{e} (ml/100 ml of tissue), and fractional plasma volume V^{p} (ml/100 ml of tissue) (Tofts and Kermode, 1991; Tofts et al., 1999). The two-compartment pharmacokinetic model proposed by the extended model (Tofts et al., 1999) asserts that blood vessels and tissues are regarded as independent compartments. Each parameter is calculated from the relationship between contrast media concentrations at the target and reference sites based on this two-compartment model with the following parameters: the rate constant for tissue migration of contrast media (K^{trans}), the volume ratio of the extracellular space outside the vessel (V^{e}), and the volume ratio of the intravascular component (V^{p}). Based on this two-compartment pharmacokinetic model for DCE-MRI, we used the perfusion analysis method to calculate the permeability parameter (Tofts and Kermode, 1991) as only K^{trans}. A schematic of K^{trans}, K^{ep}, V^{e}, and V^{p} is depicted in **Figure 1**.

Image Analysis and Statistical Analysis

In all cases, DCE-MRI and ICG-NIR videos were stored to assess the feasibility and efficacy of real-time ICG-NIR imaging for intracranial meningioma and analyze the correlation between DCE-MRI and ICG-NIR. We obtained a background reading from the adjacent normal brain to generate a signal-to-background ratio (SBR). Additionally, region of interest (ROI) analysis was performed to quantify the amount of fluorescence from the tissues. We selected five ROIs corresponding to the tumor lesions and normal tissue lesions on the images and analyzed their average values. We drew five ROIs on Gd-enhanced T1 MRI to compare the enhanced tumor with the normal brain parenchyma and analyzed their average values, which we called the T1-Gd enhancement to normal brain ratio (T1BR) using ImageJ software (NIH Image, Bethesda, MD, United States). Univariate analyses were conducted using the chi-square or Fisher's exact test to compare categorical variables and the unpaired t-test or Mann–Whitney rank-sum test and simple linear regression analysis for continuous variables. Statistical significance was set at $p < 0.05$. Statistical analyses were performed using JMP 14.1.0 (SAS Institute Inc., Cary, NC, United States).

Pathological Evaluation

Frozen tumor sections were prepared in a standard fashion. We collected samples of the dura mater and tumor, and numbered each sample during surgery. Histopathological analyses were performed, and tissue samples were examined and cataloged. Permanent sections were chemically fixed and embedded in paraffin blocks at a 5 μm thickness. Vertical sectioning was performed along with hematoxylin and eosin staining. Each tissue sample was assessed for the presence of tumor-specific cells by certified pathologists and correlated with fluorescence during surgery by neurosurgeons separately.

Representative Cases

Case 1 (Patient No. 5)

An 80-years-old woman, who had undergone two surgical removals and two gamma knife radiations, presented with seizures and consulted with our department. The tumor was pathologically diagnosed as an anaplastic meningioma. Preoperative Gd-MRI revealed convexity meningioma recurrence (axial in **Figure 2A** and coronal in **Figure 2B**), which showed moderate intensity on K^{trans} (**Figure 2C**), low intensity on K^{ep} (**Figure 2D**), low intensity on V^{p} (**Figure 2E**), and moderate intensity on V^{e} (**Figure 2F**) on DCE-MRI. She received 0.5 mg/kg of ICG 1 h before the observation during surgery. During surgery, the tumor could be seen at the dura mater with granulation (**Figure 2G**). NIR fluorescence could be detected in the dural view and was confirmed by NIR before the dura incision (**Figure 2H**). In recurrent cases, it is difficult to distinguish tumor recurrence from normal dura mater with granulation under bright light. Following tumor resection with a margin, there was no tumor remnant under bright light in this case (**Figure 2I**) and no NIR fluorescence at the end of surgery, which confirmed that the tumor had been completely removed (**Figure 2J**). NIR fluorescence helped surgeons find the lesions that were difficult to identify under bright light, especially in recurrent and radiated cases. Post-operative Gd-MRI showed gross total resection (**Figures 2K,L**). There was no recurrence of symptoms for 8 months (**Supplementary Video 1**).

Case 2 (Patient No. 14)

A 72-years-old woman presented with hearing disturbance and gait instability and was referred to our hospital. Her Gd-MRI revealed an enhanced mass (35 mm in maximum diameter) at the

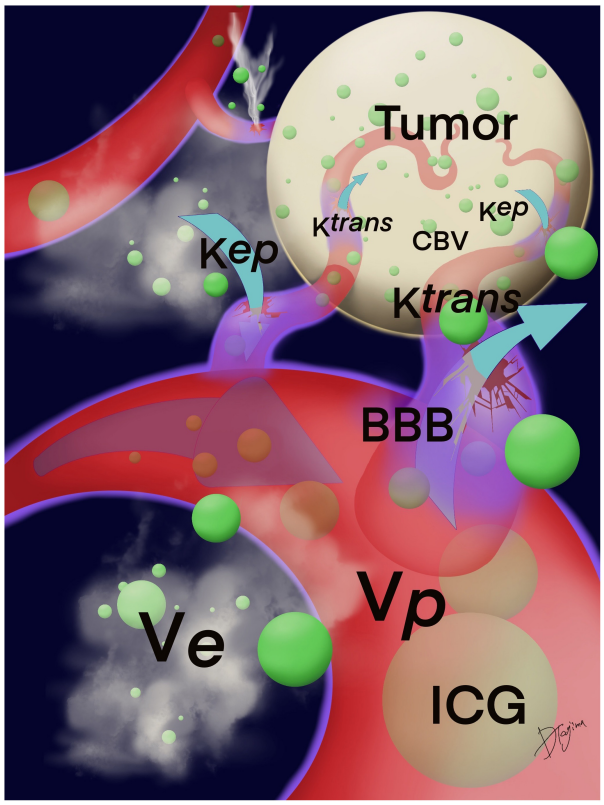

FIGURE 1 | Schema of K^{trans}, K^{ep}, V^e, and V^p. K^{trans} indicates the permeability from the intravascular to the extravascular space; K^{ep}, from the extravascular to the intravascular space; V^e, the volume of the extravascular extracellular space; and V^p, the fractional plasma volume. The BBB around the tumor was damaged, and ICG may leak from vascular structures at the compromised BBB that were calculated by the permeability. Green circles are ICG particles. BBB, blood–brain barrier; ICG, indocyanine green.

right cerebellum, suggesting meningioma (**Figure 3A**). It showed moderate intensity on K^{trans} (**Figure 3B**), low intensity on K^{ep} (**Figure 3C**), moderate intensity on V^p (**Figure 3D**), and low intensity on V^e (**Figure 3E**) on DCE-MRI.

The intracranial tumor was surgically treated with neuronavigation and NIR in the same manner as in Case 1. After the craniotomy, the dura mater was exposed (**Figure 3F**), and NIR fluorescence detected the tumor at the dural view, which helped determine the dural incision (**Figure 3G**). During tumor removal, the surgeon could identify the tumor under bright light (**Figure 3H**) and confirm its exact location during resection: in addition, residual tumor could be identified using NIR fluorescence.

Residual tumor could be identified, as well as that of the residual tumor, using NIR (**Figure 3I**).

After tumor removal, no residual tumor was observed under bright light (**Figure 3J**) and NIR (**Figure 3K**). Post-operative Gd-MRI showed no enhanced mass (**Figure 3L**). The patient's symptoms improved dramatically after surgery, and she was discharged from the hospital without any neurological deficits (**Supplementary Video 2**).

RESULTS

Delayed-Window Indocyanine Green Shows Near-Infrared Fluorescence of Intracranial Meningioma *via* Microscope

Fifteen patients were enrolled in this study. Eleven patients were female, and their mean age was 60 years (range 28–81 years). In total, 15 meningiomas were treated (total removal: 12; partial removal: 3). Patient characteristics are summarized in **Table 1**. Two representative cases are shown in **Figure 2** (convexity) and **Figure 3** (cerebellopontine angle). As mentioned previously, in this study, we modified the SWIG technique, in which a high dose of 5 mg/kg of ICG is administered up to 24 h before surgery to a patient harboring a brain tumor, to DWIG, in which 0.5 mg/kg of ICG is administered during surgery and observation of fluorescence occurs more than 1 h after administration.

Delayed-window ICG could detect and determine the location of meningiomas by NIR fluorescence. The average time from ICG infusion to observation was 2.1 ± 0.2 h (**Table 1**). Twelve out of 15 (80%) patients showed stronger NIR fluorescence in the tumor than in the surrounding brain parenchyma. The SBR from the tumor itself was 3.3 ± 2.6 (**Table 2**).

In cases with NIR-positive meningiomas, no residual tumor was observed after surgery by NIR. Moreover, post-operative MRI did not show any residual lesions, implying that ICG-NIR can detect residual tumor during surgery. The SBR was not significantly correlated with some variables inherent to the tumor such as Ki-67 ($p = 0.79$), tumor size ($p = 0.42$), and maximum diameter ($p = 0.40$) (data not shown). Blood tests and physical and neurological examinations did not reveal any side effects for 3 months after the administration of ICG.

T1-Gd Enhancement to Normal Brain Ratio on Magnetic Resonance Imaging

Preoperative Gd enhancement may predict NIR fluorescence (Lee et al., 2016). Next, we assessed the correlation between Gd-MRI and NIR fluorescence. The mean T1-Gd enhancement to normal brain ratio (T1BR) was 2.5 ± 0.9. We evaluated the relationship between T1BR and SBR using linear regression analysis. T1BR was significantly correlated with the SBR of NIR fluorescence ($p = 0.016$, $R^2 = 0.36$) as shown in **Figure 4** but not with Ki-67 ($p = 0.28$), tumor size ($p = 0.47$), and diameter ($p = 0.27$) (data not shown).

Blood–Brain Barrier Permeability May Cause Near-Infrared Fluorescence

The mechanism of Gd-MRI can only be influenced by vascular permeability (Montagne et al., 2016). Thus, we calculated the parameters K^{trans}, K^{ep}, V^e, and V^p using DCE-MRI to assess the relationship between permeability and NIR fluorescence. The SBR of NIR fluorescence was significantly positively correlated with K^{trans} ($p < 0.0001$, $R^2 = 0.76$) (**Figure 5** and **Table 2**) but not K^{ep} ($p = 0.64$), V^e ($p = 0.30$), and V^p ($p = 0.32$) (**Table 2**). **Figure 6**

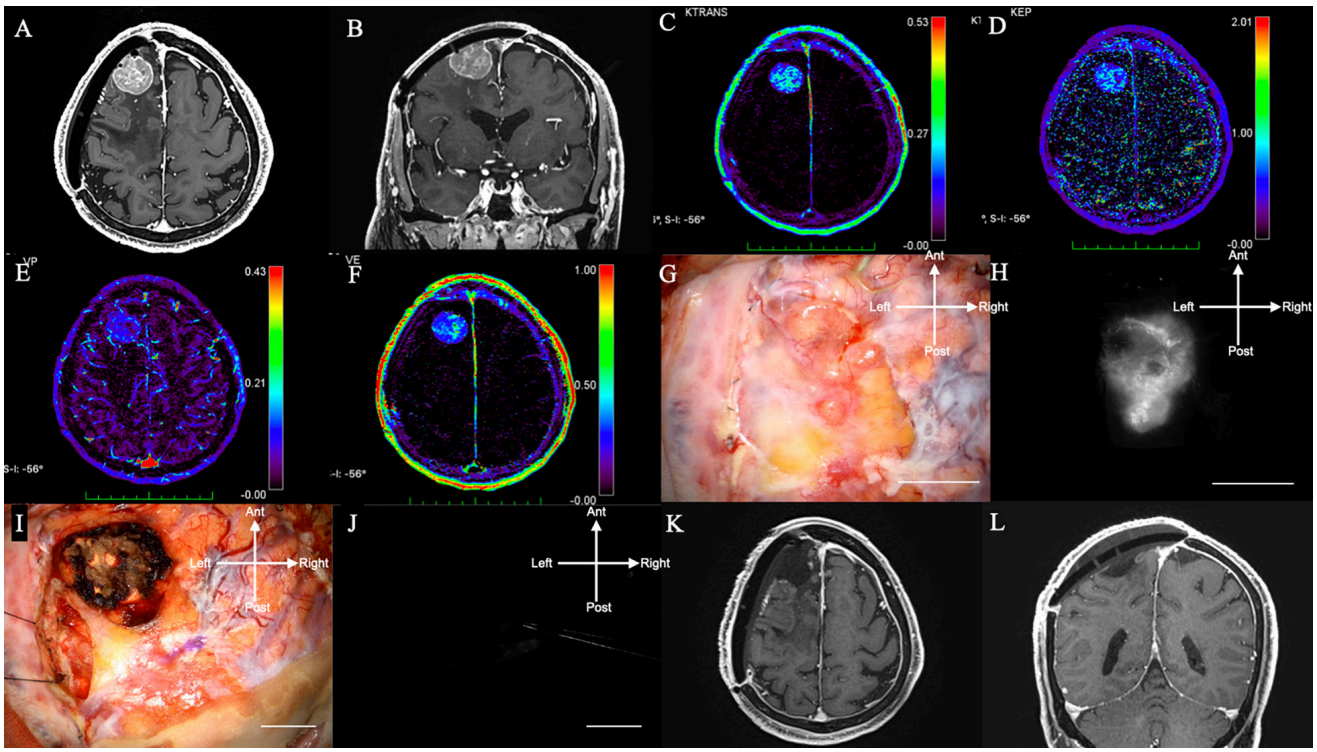

FIGURE 2 | (Case 5). Convexity meningioma in the right frontal lobe displaying NIR fluorescence using a KINEVO microscope. **(A)** Axial and **(B)** sagittal Gd-enhanced T1-weighted pre-operative MRI showing the ring enhanced lesion in the left frontal lobe. **(C)** K^{trans}, **(D)** K^{ep}, **(E)** V^e, and **(F)** V^p on additional MRI. **(G)** Bright light image of the dura mater. **(H)** NIR fluorescence of the dura mater showing NIR fluorescence localized to the tumor. **(I)** Bright light image. **(J)** No NIR fluorescence after resection. **(K)** Axial and **(L)** sagittal Gd-enhanced T1-weighted postoperative MRI showing no residual lesion. NIR, near-infrared; Gd, gadolinium; MRI, magnetic resonance imaging; K^{trans}, volume transfer constant; K^{ep}, rate constant; V^e, volume of the extravascular extracellular space; V^p, vascular plasma volume.

shows a significant correlation between T1BR on MRI and K^{trans} (p = 0.0013, R^2 = 0.56). The linear regression plot revealed no significant association of T1BR with K^{ep} (p = 0.70), V^e (p = 0.96), or V^p (p = 0.44) (**Table 2**).

Near-Infrared Contrast Dye to Detect Margins

Finally, we tried to confirm whether ICG-NIR could detect the tumor and the dural tail by pathological examination. In 12 out of 15 cases, we collected 25 specimens of the surrounding dura mater that was the edge of the tumor attachment and the dural tail on preoperative MRI. We excluded three cases of inverted SBR because the surrounding dura mater showed lower fluorescence than the normal brain parenchyma. Then these specimens were pathologically diagnosed without knowing the results of the NIR fluorescence (**Table 3**). By using the NIR camera, 21 of 25 specimens were positive, and four were negative. In margin specimens, 17 were pathologically positive, and eight were negative. The ICG-NIR fluorescence system had a sensitivity of 94% [95% confidence interval (CI), 84.2–98.9], but its specificity decreased to 38% (95% CI, 16.4–47.6) (**Table 3**). The PPV was 76% (95% CI, 68.2–80.1), and the NPV was 75% (95% CI 32.9–95.3) (**Table 3**).

DISCUSSION

Indocyanine Green Dose and Near-Infrared Fluorescence Intensity

Indocyanine green combines with albumin and is metabolized in the liver. Its biological halflife (t1/2) in blood and normal tissue is 3–4 min (De Gasperi et al., 2016). Prior to vascular surgery, 25 mg of ICG was intravenously administered to visualize the arterial, capillary, and venous flow. ICG has also been used for patients with brain tumors in the same manner (Ferroli et al., 2011; Kim et al., 2011); however, its use was not sufficient.

Previous studies of NIR using SWIG on tumors have affirmed its feasibility and usefulness. SWIG protocols described by Madajewski et al. (Madajewski et al., 2012) and Lee et al. (Lee et al., 2016, 2017a,b) include the administration of 5.0 mg/kg of ICG 24 h before surgery. We referred to a prior SWIG protocol (Hide et al., 2015) for several brain tumors carried out *via* a VisionSense exoscope and microscope (Lee et al., 2017b; Muto et al., 2021). However, Zeh et al. (2017) reported that the NIR-SBR in gliomas peaked at 1 h post-infusion, not 24 h. Considering these findings, we hypothesized that the administration of ICG more than 1 h before surgery might be enough and feasible for visualizing the tumor.

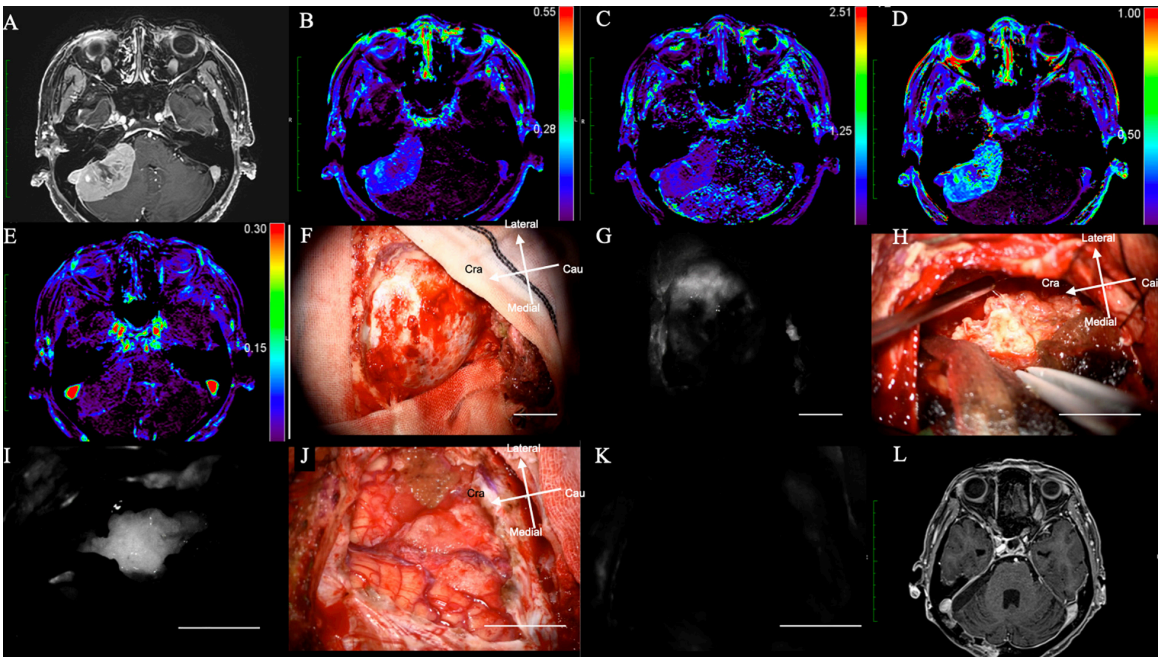

FIGURE 3 | (Case 14). Meningioma at the right cerebellopontine angle displaying NIR fluorescence by microscope using a KINEVO microscope. **(A)** Axial Gd-enhanced T1-weighted preoperative MRI showing the ring enhanced lesion in the right frontal lobe; **(B)** K^{trans}, **(C)** K^{ep}, **(D)** V^{e}, and **(E)** V^{p} on additional MRI. **(F)** Bright light image of the dura mater. **(G)** NIR fluorescence of the dura mater. **(H)** Tumor location during resection under bright light. **(I)** NIR fluorescence of the dura mater showing the exact tumor location with brain shift during tumor resection. **(J)** Bright light image. **(K)** No NIR fluorescence after tumor resection showing total removal of the tumor. **(L)** Axial Gd-enhanced T1-weighted postoperative MRI showing no residual lesion. NIR, near-infrared; Gd, gadolinium; MRI, magnetic resonance imaging; K^{trans}, volume transfer constant; K^{ep}, rate constant; V^{e}, volume of the extravascular extracellular space; V^{p}, vascular plasma volume.

To verify our hypothesis, we intraoperatively administered 0.5 mg/kg of ICG with observation at ≥1 h post-injection in this study (DWIG). The mean time from injection to observation was 2.1 ± 0.9 h. We could observe fluorescence from the tumor after the intensity of the fluorescence decreased in the vascular structures and normal brain parenchyma. Delayed excretion occurred inside the tumor and may have been caused by enhanced permeability and retention (EPR) effects. EPR likely intensifies the difference in fluorescence intensity between the tumor and normal parenchyma. This study showed that DWIG was sufficient in differentiating NIR fluorescence in meningioma compared with normal brain parenchyma. In fact, the mean SBR of the intracranial meningioma in DWIG was 3.3 ± 2.6 compared with 5.6 ± 1.7 in SBR in SWIG (Lee et al., 2017a). The SBR in DWIG was slightly weaker than the SBR in SWIG in meningioma visualization but enough for differentiation between the tumor and normal brain parenchyma. This may improve the boost excitation of NIR (Li et al., 2019). Moreover, a lower dose of ICG in DWIG resulted in fewer effects. In the 15 cases in this study, there were no hematological and clinical side effects due to ICG usage. Thus, our technique could be useful for intraoperative real-time imaging in different populations including adolescents, young and older patients, patients with hepatic or renal dysfunction, and patients with other complications. Our findings suggested that NIR with microscopy is feasible for identifying intracranial meningiomas and a dural tail, although optimizing the settings is necessary to improve the visualization of tumor fluorescence. The procedure for DWIG is easier than that for SWIG, with a lower potential for side effects.

Fluorophores in Intracranial Meningioma Resection

Neuronavigation is now popular for intracranial tumor removal. It facilitates surgical planning before surgery; however, the brain is displaced after opening the dura mater and during tumor removal. This decreases the accuracy of the tumor location. In fact, the fluorescence of ICG revealed unexpected lesions in the bright light field in a recurrent case after radiation therapy (Case 4). Thus, the NIR fluorescence technique would be beneficial as an adjunct for tumor removal.

Previous studies have reported that fluorescein, 5-ALA, and ICG are currently available as fluorescent agents, and fluorescein and 5-ALA are used for meningioma detection.

Indocyanine green has been used as a vascular angiography technique in patients with meningioma (Ueba et al., 2013). To date, 25 mg of ICG was intravenously administered to visualize the arterial, capillary, and venous flow. Nonetheless, SWIG with ICG has been used in recent years. Lee et al. (2017a) reported using the SWIG technique for meningioma with a VisionSense exoscope. SWIG involves the administration of 5 mg/kg of ICG 24 h before surgery. The maximum safe dosage of ICG for humans (Raabe et al., 2005) is 5 mg/kg. The usage of this

TABLE 1 | Data of 15 patients with intracranial meningioma, including age, gender, tumor location, pathology, tumor grade, MIB-1(%), time from ICG injection (hours), resection rate.

	Age	Gender	Location	Pathology	Tumor grade	MIB-1(%)	Observation time (hours)	Resection
1	57	M	Convexity	Angiomatous	1	9.5	1	GTR
2	28	F	Convexity	Meningothelial	1	4.5	3	PR*1
3	64	F	Sphenoid Ridge	Secretory	1	2.7	2	GTR
4	81	F	Sphenoid Ridge	Meningothelial	1	1.5	3	GTR
5	80	M	Convexity	Anaplastic	3	37.5	1	GTR
6	53	F	Sphenoid Ridge	Fibrous	1	1	2	GTR
7	76	F	Falx	Secretory	1	1.7	2	GTR
8	54	M	Plunum sphenoidale	Fibrous	1	2.4	2	GTR
9	55	M	Petroclival	Transitional	1	2.3	4	PR(*1)
10	62	F	Petroclival	Transitional	1	4.5	2	PR(*1)
11	54	F	Convexity	Angiomatous	1	2.7	1	GTR
12	36	F	Sphenoid Ridge	Meningothelial	1	5	2	GTR
13	53	F	Petroclival	Meningothelial	1	0.8	1	PR(*1)
14	72	F	CP Angle	Fibrous	1	2.3	3	GTR
15	77	F	Convexity	Atypical	2	8.2	2	GTR

ICG, indocyanine green; M, male; F, female; GTR, gross tumor resection; PR, partial resection.

TABLE 2 | Data of 15 patients with intracranial meningioma, including fluorescence, NIR tumor SBR, ratio of Gd-enhanced T1 tumor to normal brain, signal intensity of fluorescence in NIR and the scores of K^{trans}, K^{ep}, V^{e}, and V^{p} on MRI.

Case	Fluorescence	SBR	T1BR	Signal visible with near-infrared camera	K^{trans}	K^{ep}	V^{e}	V^{p}
1	No	0.7	2.4	Weak	0.1	1.2	0.01	0.63
2	Positive	1.9	1.8	Moderate	0.16	0.62	0.28	0.25
3	No	0.8	1.9	Weak	0.9	1.7	0.52	0.24
4	Positive	1.8	2.7	Moderate	0.11	0.040	0.45	0.42
5	Positive	3.2	1.9	Strong	0.15	0.53	0.28	0.08
6	Positive	2.3	2.9	Strong	0.18	0.3	0.05	0.81
7	Positive	8.6	3.9	Strong	0.4	0.71	0.57	0.11
8	Positive	2.0	2.6	Moderate	0.21	2.02	0.97	0.03
9	Positive	2.7	2.9	Strong	0.24	0.71	0.95	0.24
10	Positive	3.7	1.7	Strong	0.22	0.46	0.46	0.49
11	No	0.006	2.1	Weak	0.06	0.07	0.08	0.47
12	Positive	7.0	2.5	Strong	0.36	0.51	0.15	0.2
13	Positive	7.5	5.3	Strong	0.52	0.59	0.88	0.46
14	Positive	4.0	1.6	Strong	0.13	0.40	0.36	0.06
15	Positive	3.6	1.9	Strong	0.3	1.7	0.48	0.1

NIR, near-infrared; SBR, signal-to-background ratio; Gd, gadolinium; K^{trans}, volume transfer constant; K^{ep}, rate constant; V^{e}, volume of the extravascular extracellular space; V^{p}, vascular plasma volume; MRI, magnetic resonance imaging; T1BR, ratio of gadolinium-enhanced T1 tumor signal to the brain.

maximum dosage in SWIG results in a metabolic burden on the liver and kidneys. To avoid side effects, such as liver and kidney dysfunction, patients younger than 18 years and pregnant women should not be considered for SWIG. In DWIG, these side effects are not a concern. ICG works by passive accumulation within tumor tissues *via* a delayed EPR effect. The benefits of fluorescence guidance with ICG are the negligible tissue autofluorescence in the NIR optical region, the low cost, and the long history of use in the neurosurgery field for monitoring blood flow during surgery. The drawbacks of ICG are that it is not a receptor-specific fluorophore, it has non-specific liver uptake, and it cannot be used in patients with iodine allergy, liver disease, or uremia. Lee and colleagues also demonstrated a sensitivity of 96.4%, specificity of 38.9%, PPV of 71.1%, and NPV of 87.5% (Lee et al., 2017a). The current study of DWIG showed a sensitivity of 94%, but its specificity decreased to 38%. The PPV and NPV were 76 and 75%, respectively, in intracranial meningiomas using a microscope, indicating that results are almost the same as SWIG. This pilot study confirmed the usefulness of DWIG in intracranial meningiomas using a microscope.

5-ALA is a cellular metabolic fluorophore in the heme biosynthesis pathway. 5-ALA-induced fluorescence is also influenced by the vascularity of the tumor, blood–brain barrier (BBB) permeability, tumor cell proliferative activity, and cellular density (Leon et al., 1996; Stummer et al., 1998). Although sensitivity and specificity rates in 5-ALA

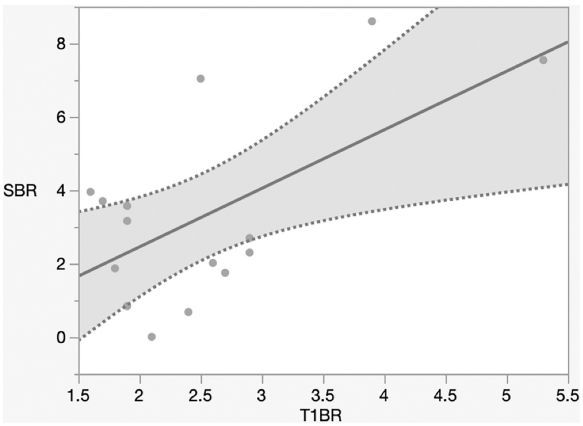

FIGURE 4 | Linear regression plot of NIR. SBR of the tumor versus magnetic resonance imaging signal intensity ratio of the tumor on T1-contrast scan. The SBR increased with the ratio of gadolinium-enhanced T1 tumor signal to the normal brain ($p = 0.016$, $R^2 = 0.36$). NIR, near-infrared; SBR, signal–background ratio; K^{trans}, volume transfer constant; T1BR, ratio of gadolinium-enhanced T1 tumor signal to the brain.

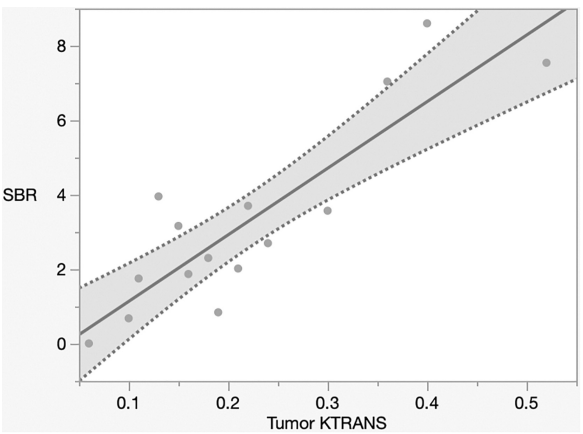

FIGURE 5 | Linear regression plot of NIR; SBR of tumor from the brain surface versus K^{trans}. The SBR increased with K^{trans} on magnetic resonance imaging ($p < 0.0001$, $R^2 = 0.77$). NIR, near-infrared; SBR, signal–background ratio; K^{trans}, volume transfer constant.

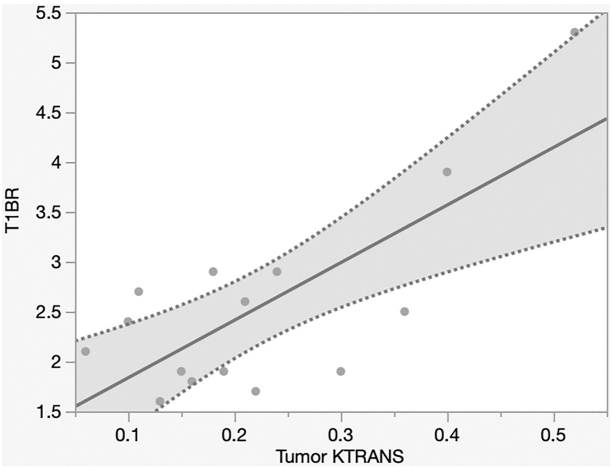

FIGURE 6 | Linear regression plot of NIR; MRI signal intensity ratio of the tumor on T1-contrast scan versus K^{trans} on MRI. T1BR increased with K^{trans} ($p = 0.013$, $R^2 = 0.56$). NIR, near-infrared; MRI, magnetic resonance imaging; SBR, signal–background ratio; K^{trans}, volume transfer constant; T1BR, ratio of gadolinium-enhanced T1 tumor signal to the brain.

were inconsistent between studies, 5-ALA helps to visualize intracranial meningiomas with a sensitivity of 92–98% and a specificity of 95% (Dijkstra et al., 2019). There is no correlation between fluorescence intensity and WHO grade or histological subtype, and fluorescence is often heterogenic (Motekallemi et al., 2015; Foster and Eljamel, 2016). The drawbacks are phototoxicity and higher costs. 5-ALA fluorescence in different parts of the same tumor can present a different fluorescent pattern. Additionally, in dural imaging, 20% of patients with histologically confirmed meningioma invasion showed fluorescence in the dural tail (Wilbers et al., 2014). Most publications report cases or case series evaluating fluorescence status in intracranial meningiomas. Thus, the use of 5-ALA remains experimental, especially in cases of tumor recurrence, and it seems difficult to draw conclusions regarding the role of 5-ALA in meningioma surgery (Motekallemi et al., 2015; Foster and Eljamel, 2016).

Fluorescein sodium has been commonly used in identifying and monitoring intracranial angiography. Fluorescein sodium is able to penetrate the tumor because of the impaired BBB and tends not to diffuse into the normal brain. Although it can extend beyond Gd contrast-enhanced regions probably because of its smaller molecular weight, it corresponds to Gd uptake on MRI (Neira et al., 2017). Its merit is colorimetric separation, and the drawbacks are rapid photobleaching and non-specific high background. It has been safely used in humans for many years, predominantly in ophthalmology for retinal angiography, and the cost of fluorescein sodium is relatively low when compared with the cost of 5-ALA (Acerbi et al., 2014). Fluorescein sodium is usually visible to the naked eye at high dosages (20 mg/kg body weight) and is observable through the yellow 560-nm filter at lower doses, allowing better tissue discrimination with more natural colors (Schwake et al., 2015). Fluorescein sodium, like ICG, rapidly accumulates within tumor regions; however, the fluorescence may persist for hours aiding in the visualization of meningioma (Hadjipanayis, 2019). Fluorescein sodium has also been used in fluorescence-guided neurosurgery of glioblastoma and metastatic brain tumors (Okuda et al., 2010); however, the usefulness of fluorescein sodium is still controversial in intracranial meningioma surgery. In 30 patients, 88% of meningiomas showed homogenous tumor fluorescence, and 12% were heterogenous under a yellow, 560-nm wavelength filter (Akcakaya et al., 2017). Only three reports have been published about the experimental use of fluorescein sodium in meningioma surgery (da Silva et al., 2014a,b; Akcakaya et al., 2017).

Other fluorophores that can be directly targeted to specific receptors have been developed. BLZ-100 is a conjugate of the tumor-specific peptide chlorotoxin paired with an NIR

TABLE 3 | Dura mater samples from the dural tail on pre-operative MRI in 25 samples from 12 patients.

	NIR fluorescence			Sensitivity (95%CI)	Specificity (95%CI)	PPV (95%CI)	NPV (95%CI)
Tumor pathology		**Positive**	**Negative**				
	Positive	16	1	94% (84.2–98.0)	38% (16.4–47.6)	76% (68.2–80.1)	75% (32.9–95.3)
	Negative	5	3				

Sensitivity: 94%, Specificity: 38%, Positive predictive value: 76%, Negative predictive value: 75%.
MRI, magnetic resonance imaging; NIR, near-infrared; PPV, positive predictive value; NPV, negative predictive value; CI, confidence interval.

fluorophore for use with recurrent glioblastoma and pediatric brain tumor (Patil et al., 2019). Alkylphosphocholine analogs are small synthetic phospholipid ether molecules, which may target specific tumor types including osteosarcoma, pancreatic adenocarcinoma, and glioblastoma (Weichert et al., 2014).

Epidermal growth factor receptor (EGFR) may be conjugated with fluorescent dyes, allowing for targeted cell-surface fluorescence (Seekell et al., 2013). While no clinical studies have been performed to date, preclinical studies have intravenously administered fluorescently conjugated anti-EGFR antibodies into rats and observed safe doses up to 24.5 mg/kg of an IRDye 800CW anti-EGFR antibody (ABY-029, Affibody, Sweden) (Samkoe et al., 2017).

Sprayable activatable fluorescent probes for glioblastoma have been developed. The fluorescent probe proline–arginine–HMRG reacts with calpain-1, which is highly expressed in glioblastoma cell line U87, and can distinguish tumors from peritumoral tissues *in vitro* (Hu et al., 2018). These fluorophores are still in the experimental stage and have been developed to mainly target glioblastoma, not meningioma. Hence, the fluorophores for meningioma are currently limited. Therefore, ICG-induced fluorescence enables feasible meningioma identification during surgery.

Mechanism of Indocyanine Green Fluorescence

We hypothesized that ICG retention in diseased tissue was caused by the EPR effect, which, in turn, disturbs the lymphatic drainage system and increases vessel permeability through defective endothelial cells with wide fenestrations caused by an increase in agents from tumor cells (Maeda et al., 2016). ICG administration could be feasible for the optical monitoring of BBB disruption (Ergin et al., 2012). DCE-MRI can be used to evaluate BBB permeability and fluid and molecular exchange between the interstitial extracellular and intracellular fluid matrix (Tofts et al., 1999). In the dura mater, the BBB does not exist; thus, the mechanism of Gd and ICG retention in the dura mater seems to be different from that in brain tumors. The K^{trans} score showed permeability from the intravascular to the extravascular space. We analyzed K^{trans}, K^{ep}, V^e, V^p, and cerebral blood volume on DCE-MRI. The mechanism of each parameter is illustrated in **Figure 1**. Only K^{trans} showed a significant difference between the SBR and T1BR, but K^{ep}, V^e, and V^p were not significantly different. Thus, only BBB permeability is correlated with ICG and Gd retention (Montagne et al., 2016). An improved DCE-MRI method using Gd-based contrast agents with an individual arterial input function curve has been developed to measure the BBB permeability constant K^{trans} in the healthy brain as K^{trans} values in a healthy brain are typically 10 to 100 times lower than those in patients with brain tumors, stroke, or infections. In our study, all patients with $K^{trans} > 0.1$ showed visible fluorescence from ICG. Thus, $K^{trans} > 0.1$ may be the threshold for the fluorescent visualization of intracranial meningioma.

Ratio of T1–Gadolinium Enhancement to Normal Brain Ratio and Signal-to-Background Ratio

Some publications reported that T1BR is associated with the intensity of NIR fluorescence (Lee et al., 2017a; Muto et al., 2021). Our data demonstrated a correlation between T1BR and SBR and no correlation between T1BR and the maximum tumor diameter and tumor volume. These results suggest that T1BR might predict the efficacy of DWIG in tumor visualization before surgery. Additionally, the mechanism of Gd-MRI in brain tumors can only be influenced by vascular permeability (Montagne et al., 2016). This supports the hypothesis that retention of ICG occurs through the EPR effect in areas of enhanced vascular permeability (Maeda et al., 2000; Ergin et al., 2012). Accumulating data imply that BBB permeability is correlated with the fluorescent intensity in DWIG.

Inverse Signal-to-Background Ratio

Three patients demonstrated an inverse pattern of NIR fluorescence in the current study. Lee et al. (2017a) previously reported this phenomenon and found no predictive factor for it. We observed significant differences between inversion and K^{trans} and no difference in K^{ep}, V^e, V^p, maximum diameter, tumor volume, T1BR, location, and WHO grade. K^{trans}, indicating BBB permeability, may predict the inversion pattern, as well as the feasibility of SBR in intracranial meningiomas.

Limitations of Delayed-Window Indocyanine Green

Our current study is a pilot study; therefore, the study sample was small. The sensitivity and specificity tests are largely determined by sample size, and thus, accurate test calculation was limited. Tumor location and surgical manipulations also might influence visualization by ICG. Because the concepts of SWIG and DWIG are new, a comparison study has not yet been performed. ICG is neither a receptor-bound nor a receptor-specific agent. Therefore, a lack of specificity is a concern for this method. The KINEVO system has an automatic exposure feature that can average the pixel intensity to normalize the background and

assign it a neutral gray color. The camera tries to balance the exposure when set to the automatic exposure mode. To resolve these problems, we fixed the gain and illumination manually at the tumor view, resulting in the avoidance of false-positive tumor margins. Furthermore, the scores of these parameters can be used throughout the surgery. However, the scores are relative and not absolute values. Thus, the distance between the lens and the target was different each time when observing NIR fluorescence.

CONCLUSION

This pilot study revealed the usefulness of the DWIG technique in identifying intracranial meningiomas and the dural tail in real time during surgery. NIR fluorescence of ICG can, on average, provide 3.3 ± 2.6 times stronger fluorescence in the meningioma than in normal brain parenchyma compared with 5.6 ± 1.7 in SWIG as reported previously. Gd-enhanced T1 tumor signals may predict NIR fluorescence of the intracranial meningioma. The BBB permeability as shown by K^{trans} on DCE-MRI can contribute to Gd enhancement on MRI and to ICG retention and tumor fluorescence by NIR. This pilot study established the protocol for the main study. Further evaluation is needed to solve limitations for clinical use; however, we believe that the procedure for DWIG can be easier than that for SWIG, with a lower potential for side effects.

DATA AVAILABILITY STATEMENT

The original contributions presented in the study are included in the article/**Supplementary Material**, further inquiries can be directed to the corresponding author.

ETHICS STATEMENT

The studies involving human participants were reviewed and approved by Fujita Health University Clinical Research Ethical Committee (CRB4180003) and Saiseikai Yokohamashi Tobu Hospital (20200137). The patients/participants provided their written informed consent to participate in this study.

AUTHOR CONTRIBUTIONS

JM, YM, KM, SY, DK, and MoH: editing and drafting the manuscript and abstract. JM, YM, MiH, JL, and YH: critically revising the work and reviewed the submitted version of the work. YH: supervision. JM and YM: conception and design. JM: approved the final version of the work on behalf of all authors.

FUNDING

Funding for this study was provided by the Japan Research Foundation for Clinical Pharmacology, Japan, April 2020 (JM) and MEST KAKENHI grant number 21K09140, Japan, April 2020 (JM).

ACKNOWLEDGMENTS

We thank Yu Nakagawa, Masahiro Joko, Hiroshi Kagami, and Makoto Inaba.

SUPPLEMENTARY MATERIAL

The Supplementary Material for this article can be found online at: https://www.frontiersin.org/articles/10.3389/fnins.2022.837349/full#supplementary-material

Supplementary Video 1 | The movie of Case 1 shows the exact tumor location under bright light and near-infrared (NIR). At the end of surgery, we confirmed that the entire tumor was removed as no fluorescence was emitted from the tumor under bright light and NIR. NIR illumination can help surgeons to find lesions that are difficult to identify under bright light, especially in recurrent and radiated cases.

Supplementary Video 2 | The movie of Case 2 demonstrates the tumor under bright light and near-infrared (NIR). At the end of surgery, we confirmed total tumor removal under bright light and NIR, and no fluorescence from the tumor and the dura mater remained.

REFERENCES

Acerbi, F., Broggi, M., Eoli, M., Anghileri, E., Cavallo, C., Boffano, C., et al. (2014). Is fluorescein-guided technique able to help in resection of high-grade gliomas? *Neurosurg. Focus* 36:E5. doi: 10.3171/2013.11.Focus13487

Akcakaya, M. O., Goker, B., Kasimcan, M. O., Hamamcioglu, M. K., and Kiris, T. (2017). Use of sodium fluorescein in meningioma surgeryp under the YELLOW-560 nm surgical microscope filter: feasibility and preliminary results. *World Neurosurg.* 107, 966–973. doi: 10.1016/j.wneu.2017.07.103

da Silva, C. E., da Silva, V. D., and da Silva, J. L. (2014a). Convexity meningiomas enhanced by sodium fluorescein. *Surg. Neurol. Int.* 5:3.

da Silva, C. E., da Silva, V. D., and da Silva, J. L. (2014b). Sodium fluorescein in skull base meningiomas: a technical note. *Clin. Neurol. Neurosurg.* 120, 32–35. doi: 10.1016/j.clineuro.2014.02.015

De Gasperi, A., Mazza, E., and Prosperi, M. (2016). Indocyanine green kinetics to assess liver function: ready for a clinical dynamic assessment in major liver surgery? *World J. Hepatol.* 8, 355–367.

Dijkstra, B. M., Jeltema, H. J. R., Kruijff, S., and Groen, R. J. M. (2019). The application of fluorescence techniques in meningioma surgery-a review. *Neurosurg. Rev.* 42, 799–809. doi: 10.1007/s10143-018-01062-4

Ergin, A., Wang, M., Zhang, J. Y., Bruce, J. N., Fine, R. L., Bigio, I. J., et al. (2012). The feasibility of real-time *in vivo* optical detection of blood-brain barrier disruption with indocyanine green. *J. Neurooncol.* 106, 551–560.

Ferroli, P., Acerbi, F., Albanese, E., Tringali, G., Broggi, M., Franzini, A., et al. (2011). Application of intraoperative indocyanine green angiography for CNS tumors: results on the first 100 cases. *Acta Neurochir. Suppl.* 109, 251–257. doi: 10.1007/978-3-211-99651-5_40

Foster, N., and Eljamel, S. (2016). ALA-induced fluorescence image guided surgery of meningiomas: a meta-analyses. *Photodiagnosis Photodyn. Ther.* 15, 73–78.

Hadjipanayis, C. G. S. W. (2019). *Fluorescence-Guided Neurosurgery: Neuro-Oncology and Cerebrovascular Applications*. New York, NY: Thieme publisher.

Hide, T., Yano, S., Shinojima, N., and Kuratsu, J. (2015). Usefulness of the indocyanine green fluorescence endoscope in endonasal transsphenoidal surgery. *J. Neurosurg.* 122, 1185–1192. doi: 10.3171/2014.9.jns14599

Hu, S., Kang, H., Baek, Y., El Fakhri, G., Kuang, A., and Choi, H. S. (2018). Real-time imaging of brain tumor for image-guided surgery. *Adv. Healthc. Mater.* 7:e1800066. doi: 10.1002/adhm.201800066

Kim, E. H., Cho, J. M., Chang, J. H., Kim, S. H., and Lee, K. S. (2011). Application of intraoperative indocyanine green videoangiography to brain tumor surgery. *Acta Neurochir.* 153, 1487–1495. doi: 10.1007/s00701-011-1046-x

Lee, J. Y. K., Pierce, J. T., Thawani, J. P., Zeh, R., Nie, S., Martinez-Lage, M., et al. (2017a). Near-infrared fluorescent image-guided surgery for intracranial meningioma. *J. Neurosurg.* 128, 380–390. doi: 10.3171/2016.10.JNS161636

Lee, J. Y. K., Pierce, J. T., Zeh, R., Cho, S. S., Salinas, R., Nie, S., et al. (2017b). Intraoperative near-infrared optical contrast can localize brain metastases. *World Neurosurg.* 106, 120–130. doi: 10.1016/j.wneu.2017.06.128

Lee, J. Y. K., Thawani, J. P., Pierce, J., Zeh, R., Martinez-Lage, M., Chanin, M., et al. (2016). Intraoperative near-infrared optical imaging can localize gadolinium-enhancing gliomas during surgery. *Neurosurgery* 79, 856–871. doi: 10.1227/neu.0000000000001450

Leon, S. P., Folkerth, R. D., and Black, P. M. (1996). Microvessel density is a prognostic indicator for patients with astroglial brain tumors. *Cancer* 77, 362–372. doi: 10.1002/(sici)1097-0142(19960115)77:2<362:Aid-cncr20<3.0.Co;2-z

Li, C., Buch, L., Cho, S., and Lee, J. Y. K. (2019). Near-infrared intraoperative molecular imaging with conventional neurosurgical microscope can be improved with narrow band "boost" excitation. *Acta Neurochir.* 161, 2311–2318. doi: 10.1007/s00701-019-04054-5

Madajewski, B., Judy, B. F., Mouchli, A., Kapoor, V., Holt, D., Wang, M. D., et al. (2012). Intraoperative near-infrared imaging of surgical wounds after tumor resections can detect residual disease. *Clin. Cancer Res.* 18, 5741–5751. doi: 10.1158/1078-0432.CCR-12-1188

Maeda, H., Tsukigawa, K., and Fang, J. A. (2016). retrospective 30 years after discovery of the enhanced permeability and retention effect of solid tumors: next-generation chemotherapeutics and photodynamic therapy–problems, solutions, and prospects. *Microcirculation* 23, 173–182. doi: 10.1111/micc.12228

Maeda, H., Wu, J., Sawa, T., Matsumura, Y., and Hori, K. (2000). Tumor vascular permeability and the EPR effect in macromolecular therapeutics: a review. *J. Control. Release* 65, 271–284. doi: 10.1016/s0168-3659(99)00248-5

Mirimanoff, R. O., Dosoretz, D. E., Linggood, R. M., Ojemann, R. G., and Martuza, R. L. (1985). Meningioma: analysis of recurrence and progression following neurosurgical resection. *J. Neurosurg.* 62, 18–24. doi: 10.3171/jns.1985.62.1.0018

Montagne, A., Toga, A. W., and Zlokovic, B. V. (2016). Blood-brain barrier permeability and gadolinium: benefits and potential pitfalls in research. *JAMA Neurol.* 73, 13–14. doi: 10.1001/jamaneurol.2015.2960

Motekallemi, A., Jeltema, H. R., Metzemaekers, J. D., van Dam, G. M., Crane, L. M., and Groen, R. J. (2015). The current status of 5-ALA fluorescence-guided resection of intracranial meningiomas-a critical review. *Neurosurg. Rev.* 38, 619–628. doi: 10.1007/s10143-015-0615-5

Muto, J., Mine, Y., Nakagawa, Y., Joko, M., Kagami, H., Inaba, M., et al. (2021). Intraoperative real-time near-infrared optical imaging for the identification of metastatic brain tumors *via* microscope and exoscope. *Neurosurg. Focus* 50:E11. doi: 10.3171/2020.10.FOCUS20767

Neira, J. A., Ung, T. H., Sims, J. S., Malone, H. R., Chow, D. S., Samanamud, J. L., et al. (2017). Aggressive resection at the infiltrative margins of glioblastoma facilitated by intraoperative fluorescein guidance. *J. Neurosurg.* 127, 111–122. doi: 10.3171/2016.7.JNS16232

Okuda, T., Kataoka, K., Yabuuchi, T., Yugami, H., and Kato, A. (2010). Fluorescence-guided surgery of metastatic brain tumors using fluorescein sodium. *J. Clin. Neurosci.* 17, 118–121. doi: 10.1016/j.jocn.2009.06.033

Olar, A., Wani, K. M., Sulman, E. P., Mansouri, A., Zadeh, G., Wilson, C. D., et al. (2015). Mitotic index is an independent predictor of recurrence-free survival in meningioma. *Brain Pathol.* 25, 266–275. doi: 10.1111/bpa.12174

Patil, C. G., Walker, D. G., Miller, D. M., Butte, P., Morrison, B., Kittle, D. S., et al. (2019). Phase 1 safety, pharmacokinetics, and fluorescence imaging study of tozuleristide (BLZ-100) in adults with newly diagnosed or recurrent gliomas. *Neurosurgery* 85, E641–E649. doi: 10.1093/neuros/nyz125

Raabe, A., Beck, J., and Seifert, V. (2005). Technique and image quality of intraoperative indocyanine green angiography during aneurysm surgery using surgical microscope integrated near-infrared video technology. *Zentralbl. Neurochir.* 66, 1–6. doi: 10.1055/s-2004-836223

Samkoe, K. S., Gunn, J. R., Marra, K., Hull, S. M., Moodie, K. L., Feldwisch, J., et al. (2017). Toxicity and pharmacokinetic profile for single-dose injection of ABY-029: a fluorescent anti-EGFR synthetic affibody molecule for human use. *Mol. Imaging Biol.* 19, 512–521. doi: 10.1007/s11307-016-1033-y

Schwake, M., Stummer, W., Suero Molina, E. J., and Wolfer, J. (2015). Simultaneous fluorescein sodium and 5-ALA in fluorescence-guided glioma surgery. *Acta Neurochir.* 157, 877–879. doi: 10.1007/s00701-015-2401-0

Seekell, K., Lewis, S., Wilson, C., Li, S., Grant, G., and Wax, A. (2013). Feasibility study of brain tumor delineation using immunolabeled gold nanorods. *Biomed. Opt. Express* 4, 2284–2295. doi: 10.1364/BOE.4.002284

Stummer, W., Novotny, A., Stepp, H., Goetz, C., Bise, K., and Reulen, H. J. (2000). Fluorescence-guided resection of glioblastoma multiforme by using 5-aminolevulinic acid-induced porphyrins: a prospective study in 52 consecutive patients. *J. Neurosurg.* 93, 1003–1013. doi: 10.3171/jns.2000.93.6.1003

Stummer, W., Pichlmeier, U., Meinel, T., Wiestler, O. D., Zanella, F., and Reulen, H. J. (2006). Fluorescence-guided surgery with 5-aminolevulinic acid for resection of malignant glioma: a randomised controlled multicentre phase III trial. *Lancet Oncol.* 7, 392–401. doi: 10.1016/s1470-2045(06)70665-9

Stummer, W., Stepp, H., Moller, G., Ehrhardt, A., Leonhard, M., and Reulen, H. J. (1998). Technical principles for protoporphyrin-IX-fluorescence guided microsurgical resection of malignant glioma tissue. *Acta Neurochir.* 140, 995–1000. doi: 10.1007/s007010050206

Tofts, P. S., Brix, G., Buckley, D. L., Evelhoch, J. L., Henderson, E., Knopp, M. V., et al. (1999). Estimating kinetic parameters from dynamic contrast-enhanced T(1)-weighted MRI of a diffusable tracer: standardized quantities and symbols. *J. Magn. Reson. Imaging* 10, 223–232. doi: 10.1002/(sici)1522-2586(199909)10:3<223:aid-jmri2<3.0.co;2-s

Tofts, P. S., and Kermode, A. G. (1991). Measurement of the blood-brain barrier permeability and leakage space using dynamic MR imaging. 1. Fundamental concepts. *Magn. Reson. Med.* 17, 357–367. doi: 10.1002/mrm.1910170208

Ueba, T., Okawa, M., Abe, H., Nonaka, M., Iwaasa, M., Higashi, T., et al. (2013). Identification of venous sinus, tumor location, and pial supply during meningioma surgery by transdural indocyanine green videography. *J. Neurosurg.* 118, 632–636. doi: 10.3171/2012.11.Jns121113

Valdes, P. A., Millesi, M., Widhalm, G., and Roberts, D. W. (2019). 5-aminolevulinic acid induced protoporphyrin IX (ALA-PpIX) fluorescence guidance in meningioma surgery. *J. Neurooncol.* 141, 555–565. doi: 10.1007/s11060-018-03079-7

Weichert, J. P., Clark, P. A., Kandela, I. K., Vaccaro, A. M., Clarke, W., Longino, M. A., et al. (2014). Alkylphosphocholine analogs for broad-spectrum cancer imaging and therapy. *Sci. Transl. Med.* 6:240ra75.

Wilbers, E., Hargus, G., Wolfer, J., and Stummer, W. (2014). Usefulness of 5-ALA (Gliolan(R))-derived PPX fluorescence for demonstrating the extent of infiltration in atypical meningiomas. *Acta Neurochir.* 156, 1853–1854. doi: 10.1007/s00701-014-2148-z

Zeh, R., Sheikh, S., Xia, L., Pierce, J., Newton, A., Predina, J., et al. (2017). The second window ICG technique demonstrates a broad plateau period for near infrared fluorescence tumor contrast in glioblastoma. *PLoS One* 12:e0182034. doi: 10.1371/journal.pone.0182034

Conflict of Interest: JL owned stock options in Visionsense.

The remaining authors declare that the research was conducted in the absence of any commercial or financial relationships that could be construed as a potential conflict of interest.

Publisher's Note: All claims expressed in this article are solely those of the authors and do not necessarily represent those of their affiliated organizations, or those of the publisher, the editors and the reviewers. Any product that may be evaluated in this article, or claim that may be made by its manufacturer, is not guaranteed or endorsed by the publisher.

Copyright © 2022 Muto, Mine, Nishiyama, Murayama, Yamada, Kojima, Hayakawa, Adachi, Hasegawa, Lee and Hirose. This is an open-access article distributed under the terms of the Creative Commons Attribution License (CC BY). The use, distribution or reproduction in other forums is permitted, provided the original author(s) and the copyright owner(s) are credited and that the original publication in this journal is cited, in accordance with accepted academic practice. No use, distribution or reproduction is permitted which does not comply with these terms.

frontiers | Frontiers in Neuroscience

ORIGINAL RESEARCH
published: 09 May 2022
doi: 10.3389/fnins.2022.883584

Navigated Intraoperative 3D Ultrasound in Glioblastoma Surgery: Analysis of Imaging Features and Impact on Extent of Resection

Benjamin Saß[1], Darko Zivkovic[1], Mirza Pojskic[1], Christopher Nimsky[1,2] and Miriam H. A. Bopp[1,2]*

[1] Department of Neurosurgery, University of Marburg, Marburg, Germany, [2] Center for Mind, Brain and Behavior (CMBB), Marburg, Germany

Background: Neuronavigation is routinely used in glioblastoma surgery, but its accuracy decreases during the operative procedure due to brain shift, which can be addressed utilizing intraoperative imaging. Intraoperative ultrasound (iUS) is widely available, offers excellent live imaging, and can be fully integrated into modern navigational systems. Here, we analyze the imaging features of navigated i3D US and its impact on the extent of resection (EOR) in glioblastoma surgery.

Methods: Datasets of 31 glioblastoma resection procedures were evaluated. Patient registration was established using intraoperative computed tomography (iCT). Pre-operative MRI (pre-MRI) and pre-resectional ultrasound (pre-US) datasets were compared regarding segmented tumor volume, spatial overlap (Dice coefficient), the Euclidean distance of the geometric center of gravity (CoG), and the Hausdorff distance. Post-resectional ultrasound (post-US) and post-operative MRI (post-MRI) tumor volumes were analyzed and categorized into subtotal resection (STR) or gross total resection (GTR) cases.

Results: The mean patient age was 59.3 ± 11.9 years. There was no significant difference in pre-resectional segmented tumor volumes (pre-MRI: 24.2 ± 22.3 cm^3; pre-US: 24.0 ± 21.8 cm^3). The Dice coefficient was 0.71 ± 0.21, the Euclidean distance of the CoG was 3.9 ± 3.0 mm, and the Hausdorff distance was 12.2 ± 6.9 mm. A total of 18 cases were categorized as GTR, 10 cases were concordantly classified as STR on MRI and ultrasound, and 3 cases had to be excluded from post-resectional analysis. In four cases, i3D US triggered further resection.

Conclusion: Navigated i3D US is reliably adjunct in a multimodal navigational setup for glioblastoma resection. Tumor segmentations revealed similar results in i3D US and MRI, demonstrating the capability of i3D US to delineate tumor boundaries. Additionally, i3D US has a positive influence on the EOR, allows live imaging, and depicts brain shift.

Keywords: glioblastoma, intraoperative ultrasound, intraoperative imaging, brain shift, neuronavigation, extent of resection

OPEN ACCESS

Edited by:
Sandro M. Krieg, Technical University of Munich, Germany

Reviewed by:
Hamza Farooq, University of Minnesota Twin Cities, United States
Neda Haj-Hosseini, Linköping University, Sweden

****Correspondence:***
Benjamin Saß
sassb@med.uni-marburg.de

Specialty section:
This article was submitted to Brain Imaging Methods, a section of the journal Frontiers in Neuroscience

Received: *25 February 2022*
Accepted: *08 April 2022*
Published: *09 May 2022*

Citation:
Saß B, Zivkovic D, Pojskic M, Nimsky C and Bopp MHA (2022) Navigated Intraoperative 3D Ultrasound in Glioblastoma Surgery: Analysis of Imaging Features and Impact on Extent of Resection. Front. Neurosci. 16:883584. doi: 10.3389/fnins.2022.883584

INTRODUCTION

With a total of 49.1%, glioblastomas are the most common malignant primary brain tumors in the United States, accounting for 14.3% of all primary brain tumors, while showing the lowest median survival time of 8 months (Ostrom et al., 2021), in spite of advances in therapy, including surgery, radiation, chemotherapy (Stupp et al., 2005, 2009), and alternating electric fields [tumor treating fields (TTFs)] (Burri et al., 2018). The extent of resection (EOR) and residual tumor volume are known to be significant factors influencing the patient overall survival time as demonstrated by several studies supporting the superiority of gross total resection (GTR) over subtotal resection (STR) or biopsy (Grabowski et al., 2014; Brown et al., 2016). In fact, compared to STR, GTR increases the likelihood of 1-year survival about 61% and the likelihood of 2-year survival about 19% (Brown et al., 2016). Furthermore, resection of fluid-attenuated inversion recovery (FLAIR) abnormalities beyond the boundaries of T1 contrast-enhancing tumor regions was found to additionally prolong median survival (Li et al., 2016). In contrast, extended resection increases the risk of neurological impairment (Stummer et al., 2011), which in turn decreases the likelihood of consequent adjuvant therapy (Gulati et al., 2011). Modern neurosurgical intraoperative setups include neuronavigational systems, multimodal magnetic resonance imaging data, if available intraoperative MRI (iMRI), intraoperative stimulation mapping, and 5-aminolevulinic acid supported techniques to minimize the risk of neurological deterioration while maximizing the EOR (Stummer et al., 2006; De Witt Hamer et al., 2012; Wen et al., 2020). Because neuronavigational systems are mainly based on pre-operative imaging, they harbor the risk of an increasing inaccuracy during the operative course due to brain shift, a phenomenon, which can be attributed to influences of gravity, brain retraction and swelling, tissue removal, and loss of cerebrospinal fluid (Roberts et al., 1998; Nimsky et al., 2000). Attempts to quantify intraoperative brain shift were made as early as by Kelly et al. (1986) who developed an approach using radiographic imaging for the detection of movement of intracranially inserted reference balls. Others tested systems based on the analysis of video images and microscope tracking (Roberts et al., 1998), optical scanning (Audette et al., 1999), or simply a navigated pointer (Dorward et al., 1998; Hill et al., 1998). Intraprocedural displacement of cortical and deeper located structures is not correlated, demonstrating the complexity of brain deformation (Hastreiter et al., 2004). Moreover, the phenomenon occurs throughout the surgical procedure and, consequently, only repetitive intraoperative imaging can provide the basis for accurate image guidance (Nabavi et al., 2001).

The two major modalities in intraprocedural imaging are iMRI and intraoperative ultrasound (iUS) (Wirtz et al., 1997; Nimsky et al., 2000, 2001; Nabavi et al., 2001). Despite the indisputable advantage of excellent imaging quality, iMRI has its shortcomings, such as limited availability, high costs, the need for a special training of the staff, structural requirements, and high time consumption (Nimsky et al., 2004; Reinertsen et al., 2014). In contrast, today iUS is widely available, cost effective, straightforward in use, and even multiple image acquisitions can be easily integrated into the surgical procedure (Sastry et al., 2017). Although iUS was already introduced (Chandler et al., 1982) and routinely used by some neurosurgeons in the 1980s (Knake et al., 1982), it was not widely accepted until neuronavigational systems and high imaging quality iUS coalesced (Gronningsaeter et al., 2000; Ohue et al., 2010). The consistent further development of navigated intraoperative 3D ultrasound (i3D US) (Tronnier et al., 2001; Unsgaard et al., 2002) allows comfortable sequentially updating of 3D imaging maps during surgery (Unsgaard et al., 2002) and thus may be a supportive measure for estimating brain shift and the EOR in glioma surgery during the procedure (Munkvold et al., 2018).

In our institution, i3D US has become an integral part of the surgical routine for intracranial space-occupying lesions. In cases of brain metastasis, we have shown that i3D US clearly delineates tumor boundaries, allows live imaging updates, and identifies brain deformation reliably (Saß et al., 2020). In contrast to metastases, gliomas feature less well-defined boundaries and, apparently, depicting these in iUS is more difficult. Thus, we initially conceptualized a proof-of-concept study, which demonstrated the use of intraoperative Doppler for the visualization of the shift of vascular structures as an instrument for brain shift estimation in glioma surgery. However, this approach did not provide direct information on the tumor itself or the EOR (Sass et al., 2021). Consequently, here we present our analysis of 31 prospectively obtained intraoperative computed tomography (iCT) registration-based navigated i3D US datasets in glioblastoma patients. By addressing tumor volume, shape, and shifting when compared to pre-operative MRI (pre-MRI), as well as the subjective impression of imaging quality, and the impact of i3D US on EOR, we describe the benefits as well as the drawbacks and pitfalls of navigated i3D US in a modern multimodal setup.

MATERIALS AND METHODS

This prospective study encompasses all surgical cases of primary or recurrent glioblastoma in 2020 operated with iCT-based registration for a total of 31 cases in 29 patients (case nos. 9 and 10, and case nos. 5 and 26 were the same patients, respectively). In all cases, surgery was recommended by a neuro-oncological tumor board, and all patients provided written informed consent. Ethics approval for archiving clinical and technical data applying intraoperative imaging and navigation was obtained (study no. 99/18).

Within a few days before surgery, all patients underwent a pre-operative stocktickerMRI, encompassing at least native and contrast-enhanced T1-weighted, T2-weighted, and FLAIR sequences. Pre-operative imaging was transferred to the navigational system (Brainlab, Munich, Germany), which consisted of a ceiling-mounted double monitor (Curve, Brainlab, Munich, Germany), two wall-embedded screens (Buzz, Brainlab, Munich, Germany), the navigational camera, server, and software (Elements, Brainlab, Munich, Germany). Within the software, the computer-assisted outlining tool called smart brush was used to

segment the tumor masses in the T1-weighted contrast-enhanced stocktickerMRI, or in cases of little enhancement, in T2-weighted or FLAIR sequences. In this application, the user marks roughly the tumor in one slice and the software automatically delineates the tumor boundaries. To create a 3D object, the same procedure is repeated in a perpendicular plane. Then, the 3D object is reviewed by the surgeon and if necessary edited to achieve the best possible segmentation result. Additionally, eloquent regions at risk were outlined either using the smart brush application or the automatic cranial segmentation application, which features automated, knowledge-based anatomical contouring.

The surgical procedures were conducted under general anesthesia. All patients received 40 mg of dexamethasone after narcosis induction and perioperative antibiotic prophylaxis. The patients then were positioned on an operating room (OR) table and the head was fixed to the table using a radiolucent DORO® Skull with metal pins. Whenever possible, the pins were positioned in a manner that the surgical field could be scanned between the pins, reducing metal artifacts. A reference array with four reflective markers was attached to the head clamp. The registration scan was either performed before skin incision or after craniotomy. If performed before skin incision, three fiducial markers were placed within the anticipated scanning region. The navigation camera was then aligned to the reference array and reflective markers on the iCT. Next, the OR table was rotated 90° to the mobile 32-slice CT-scanner (AIRO, Brainlab, Munich) and a low-dose registration scan (0.042 mSv) of 62 mm scan length was performed, while the camera detected the reference array and reflective markers on the scanner. Once the scan was completed, the table was turned back, and the camera was adjusted to detect the reference array. The iCT datasets were automatically transferred to the navigational system and fused to the pre-operative imaging data for automatic patient registration. The three fiducial markers were used to determine the registration accuracy. To accomplish this, the tip of a navigational pointer was placed in the divot of each fiducial marker, cross-checked, and saved to the navigational system, which allowed the calculation of the target registration error (TRE) as the Euclidean offset of the pointer tip subsequently. The navigational system was then ready to use, and the cranial approach could be planned. Details of the iCT-based registration procedure were published before (Carl et al., 2018).

After team time-out, skin disinfection, and sterile draping the skin was incised and the cranial bone exposed. Immediately before the craniotomy was performed, the patient received 125 ml of 15% mannitol. In cases where the registration scan was performed after craniotomy, the approach was planned based on anatomical landmarks. In these cases, the scanning procedure itself was similar to the one mentioned above, but under sterile conditions, and an additional scout scan was performed to define the 62 mm scan region. This modified procedure did not allow the aforementioned TRE calculation, and the registration accuracy had to be reviewed comparing landmarks at the patient's head (e.g., at the edge of the craniotomy or superficial cortical vessels) to the displayed navigational data.

Reasoned by our experience that the imaging quality is the highest before dural opening, and to allow as less potentially harmful direct contact of the ultrasound probe and the brain surface as possible, the first navigated i3D US datasets were acquired directly after bone removal but before dura incision utilizing the bk5000 system (bk medical, Herlev, Denmark) connected to the navigational system. The scan was performed with an immersible, sterilizable high-resolution small footprint transducer (N13C5, bk medical, Herlev, Denmark), which has a 29 mm × 10 mm convex scanning surface and a scanning range from 5 to 13 MHz. Saline was administered as a coupling fluid, then the pre-calibrated transducer, which was equipped with a reference array, was smoothly moved over the dura generating 2D slices, which were automatically transferred to the navigational system. Here, the 0.3 mm 2D slices were automatically processed to co-registered 3D datasets, which could be further displayed as an overlay with the pre-operative imaging, side-by-side, or as a stand-alone and could be reformatted into any orientation.

After tumor removal, a saline depot was filled in the resection cavity as coupling fluid and a second 3D scan was performed and evaluated. In some cases, when residual tumor volume was detected and resection was thereof extended, another scan was carried out. Additional scans were acquired at any time during surgery if deemed necessary by the surgeon. **Figure 1** illustrates the above-mentioned steps of i3D US application.

During the surgical procedure, the overlay or side-by-side view of pre-MRI and i3D US datasets was helpful in the rough estimation of brain shift. For more detailed analysis, the lesions or residual tumor volumes were segmented in the navigational software using the smart brush application. Pre-operative and intraoperative data were exported to MeVisLab (MeVis Medical Solutions AG, Bremen, Germany) for further processing, analogous to the procedure we described for brain metastases (Saß et al., 2020).

An estimation of the displacement of the segmented object was investigated by calculation of the Euclidean offset of the geometric centers of gravity (CoG), which were calculated by summing up the coordinates of voxels and dividing them by the number of voxels. The following formula was used to calculate the CoG, where A_{US} and B_{MR} are sets of voxels of the segmented objects in US and MRI datasets, and a and b are the coordinates of the voxels:

$$CoG_{US} = \frac{1}{|A_{US}|} \times \sum_{a \in A_{US}} a \; and \; CoG_{MR} = \frac{1}{|B_{MR}|} \times \sum_{b \in B_{MR}} b$$

The geometric CoG is a robust measure under rotation, scaling, and skewing, not susceptible to random noise (Flusser and Suk, 1994), and has thus been used for similar displacement measurements before (Paul et al., 2015).

As a similarity measure, the spatial overlap of the segmented object was determined using the Dice coefficient (C_{DSC}) (Dice, 1945; Zou et al., 2004; Nitsch et al., 2019):

$$C_{Dsc} = \frac{2\,|A_{US} \bigcap B_{MR}|}{|A_{US}| + |B_{MR}|}$$

The C_{DSC} is a value between 0 and 1, where 0 indicates no overlap and 1 indicates an exact match (Nitsch et al., 2019).

The resemblance of objects was evaluated with the Hausdorff distance, which measures the distance of each voxel of one segmentation that is the farthest from any point of the other segmentation and *vice versa* (Huttenlocher et al., 1993) and is defined as

$$H(A_{US},\ B_{MR}) = \max\{d_{max}(A_{US},\ B_{MR}), d_{max}(B_{MR}, A_{US})\} \quad (1)$$

$$\text{with } d_{max} = \max_{a \in A_{US}} \min_{b \in B_{MR}} ||a - b|| \quad (2)$$

(Huttenlocheret al., 1993; Nitschet al., 2019).

The Hausdorff distance, which is measured in millimeter, is smaller the more the segmentations resemble each other (Nitsch et al., 2019).

Data were statistically analyzed with GraphPad Prism 8.4.3 (GraphPad Software, San Diego, CA, United States) for Mac OS. The D'Agostino-Pearson test was used for testing for normal distribution. The Wilcoxon matched-pairs signed-rank test was used for not normally distributed, paired data analysis.

A p-value of < 0.05 was considered statistically significant.

RESULTS

A total of 31 cases in 29 patients (12 females, 17 males) were included in this study. The mean ± standard deviation (SD) age at time of surgery was 59.3 ± 11.9 years, ranging from 29.4 to 77.9 years. The most common glioblastoma location was the frontal lobe (12; right:left = 9:3) followed by temporal (9; right:left = 6:3), temporo-parieto-occipital (6; right:left = 5:1), parietal (2; right:left = 1:1), occipital (1: right), and cerebellar (1; right). Histological workup revealed isocitrate dehydrogenase (IDH) wild-type-glioblastoma WHO grade IV in 29 cases, of which case no. 20 featured a giant cell component, case no. 26 was described as infiltration zone of a known glioblastoma, and histology in case no. 30 was mainly necrosis. Case nos. 2 and 15 were IDH-mutant glioblastoma grade IV. For more details on patient characteristics, refer to **Table 1**.

Due to low imaging quality in pre-resectional i3D US (pre-US), case no. 15 had to be excluded from pre-resectional analysis. In 14 cases (registration scan performed prior to skin incision), the mean TRE was calculated, resulting in a mean ± SD of 0.91 ± 0.53 mm, which is comparable to our previous published data (Carl et al., 2018). The imaging quality of i3D US was subjectively judged as excellent in 17 cases (55%), good in 8 cases (26%), sufficient in 5 cases (16%), and poor in 1 case (3%), depending on the amount of artifacts and the quality of established of contact between the probe's surface and the dural layer.

The mean pre-operative tumor volume segmented in MRI (Vol pre-MRI) was 24.2 ± 22.3 cm^3 (mean ± SD) with a median of 16.3 cm^3 compared to 24.0 ± 21.8 cm^3 (mean ± SD) with a median of 17.6 cm^3 when segmented in the pre-resectional ultrasound datasets (Vol pre-US;, refer to **Figure 2A**). Both groups were not normally distributed (D'Agostino-Pearson test), and the two-tailed Wilcoxon matched-pairs test demonstrated no

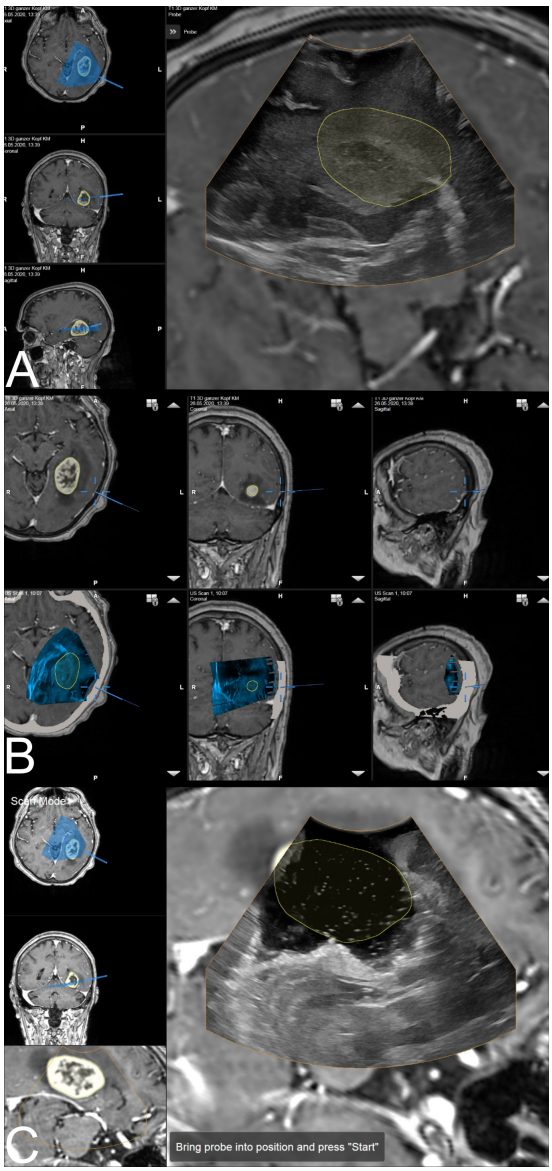

FIGURE 1 | The ultrasound application: intraoperative display of i3D US over MRI data. **(A)** The first intraoperative ultrasound before dural opening is displayed as an overlay. The yellow line shows the tumor borders segmented on pre-MRI, which are not correspondent with i3D US, indicating brain deformation. Corresponding axial, coronal, and sagittal view of pre-MRI data is shown on the left side, including a visualization of localization and orientation of the recent i3D US. **(B)** After i3D US acquisition, the ultrasound application automatically displays pre-operative imaging (upper row: pre-MRI) and intraoperative imaging (lower row: i3D US as an overlay in pre-MRI) simultaneously in an axial, coronal, and sagittal slice depending on the position of the navigated transducer (cursor). Besides this, the arrows on the right side of each view allow for scrolling through the co-registered i3D US and pre-MRI sets to further explore the data. **(C)** The second navigated intraoperative ultrasound after resection (post-US) is displayed as an overlay on the pre-MRI. Analogous to **(A)**, the tumor outlines based on the pre-MRI data are visualized in yellow demonstrating the tumor boundaries to be completely within the resection cavity. For comparison of live ultrasound images and pre-MRI data, the scan mode view is chosen. In this case, the left-hand side of the image shows the axial and coronal view, as well as the inline view of the pre-MRI dataset, on which the ultrasound data is superimposed, without the overlay.

significant difference (p = 0.8752) with a median of differences of −0.005 cm^3, whereas the median of the magnitude of the differences, which was calculated to overcome the issue of balancing negative and positive values, was 0.95 cm^3.

Pre-resectionally, the Euclidean distance of the CoG was 3.9 ± 3.0 mm (mean ± SD) with a median of 3.3 mm, whereas the Hausdorff distance was 12.3 ± 6.9 mm (mean ± SD) with a median of 10.7 mm (**Figures 2B,C**). The mean Dice coefficient C_{DSC} was 0.71 ± 0.21 (mean ± SD) with a median of 0.79 (**Figure 2D**). The lowest C_{DSC} was found in case no. 25, where the tumor volume was extraordinarily small (Vol pre-MRI: 0.5 cm^3). However, C_{DSC} did not correlate with tumor size in pre-operative MRI (r = 0.34, p = 0.0675, non-parametric Spearman correlation) or pre-resectional i3D US (r = 0.33, p = 0.0738, non-parametric Spearman correlation).

Three cases had to be excluded from statistical analysis of post-resectional volumes for different reasons (see below). The post-operative tumor volume segmented in MRI (Vol post-MRI) was 1.3 ± 3.5 cm^3 (mean ± SD), which is similar to the post-resectional tumor volume segmented in the last ultrasound (Vol post-US), which was 1.2 ± 3.3 cm^3. In 18 of 28 cases, the last acquired i3D US tumor volume was 0.0 cm^3 (complying with GTR), but in 10 cases i3D US revealed remaining tumor volume, but no further resection was indicated, thus, those cases were classified as STR. Vol post-US in these cases was 3.5 ± 4.9 cm^3 (mean ± SD) with a median of 2.1 cm^3 and Vol post-MRI was 3.5 ± 5.2 cm^3 (mean ± SD) with a median 2.4 cm^3, and did not significantly differ (two-tailed Wilcoxon matched-pairs test, p = 0.8457). Additionally, in four cases where total resection was planned (GTR-cases), i3D US demonstrated a significant remaining tumor, which led to extension of tumor resection.

The excluded cases were case nos. 7 and 8, which had corrupted post-resectional i3D US datasets and case no. 9, which was excluded, because it was the same patient as case no. 10, who underwent surgery two times within 5 days. In this case, tumor progression with a volume of 3.0 cm^3 was identified in the post-operative MRI (post-MRI) after the first surgery compared to the pre-operative MRI, which was performed at a relatively large interval prior to resection (8 days before surgery). Retrospectively, an additional tumor volume of 3.1 cm^3 outside

TABLE 1 | Patient characteristics.

Case	Age [years]	Sex	Localization/Site	Neuropathological diagnosis/IDH status	Primary/Recurrent
1	58.16	f	Temporal/r	GBM grade IV/IDH wt	P
2	29.38	m	Frontal/l	GBM grade IV/IDH mut	P
3	61.63	f	Frontal/l	GBM grade IV/IDH wt	P
4	47.50	m	Parietal/r	GBM grade IV/IDH wt	R
5	44.52	m	Frontal/r	GBM grade IV/IDH wt	R
6	62.39	m	Temporal/r	GBM grade IV/IDH wt	P
7	67.74	f	Frontal/r	GBM grade IV/IDH wt	P
8	52.43	m	Tpo/r	GBM grade IV/IDH wt	R
9	63.22	f	Frontal/r	GBM grade IV/IDH wt	R
10	63.23	f	Frontal/r	GBM grade IV/IDH wt	R
11	68.98	m	Cerebellar/r	GBM grade IV/IDH wt	R
12	57.88	f	Temporal/r	GBM grade IV/IDH wt	P
13	77.91	f	Temporal/l	GBM grade IV/IDH wt	P
14	73.96	f	Tpo/r	GBM grade IV/IDH wt	R
15	40.76	m	Temporal/r	GBM grade IV/IDH mut	R
16	47.63	m	Parietal/l	GBM grade IV/IDH wt	P
17	68.91	m	Frontal/l	GBM grade IV/IDH wt	P
18	76.62	f	Frontal/r	GBM grade IV/IDH wt	P
19	68.99	m	Frontal/r	GBM grade IV/IDH wt	R
20	54.53	m	Temporal/l	GBM grade IV/IDH wt (with a giant cell component)	P
21	73.09	f	Temporal/r	GBM grade IV/IDH wt	R
22	55.38	m	Tpo/r	GBM grade IV/IDH wt	R
23	61.69	m	Frontal/r	GBM grade IV/IDH wt	P
24	64.48	m	Occipital/r	GBM grade IV/IDH wt	P
25	66.82	m	Temporal/l	GBM grade IV/IDH wt	P
26	45.17	m	Frontal/r	GBM grade IV/IDH wt (infiltration zone)	R
27	75.90	m	Tpo/l	GBM grade IV/IDH wt	P
28	55.58	f	Temporal/r	GBM grade IV/IDH wt	P
29	64.77	f	Tpo/r	Necrosis, GBM grade IV/IDH wt	R
30	43.25	m	Tpo/r	GBM grade IV/IDH wt	R
31	47.25	f	Frontal/r	GBM grade IV/IDH wt	P

f, female; GBM, glioblastoma; IDH, isocitrate dehydrogenase; m, male; mut, mutant; P, primary; R, recurrent; tpo, temporo-parieto-occipital; wt, wildtype.

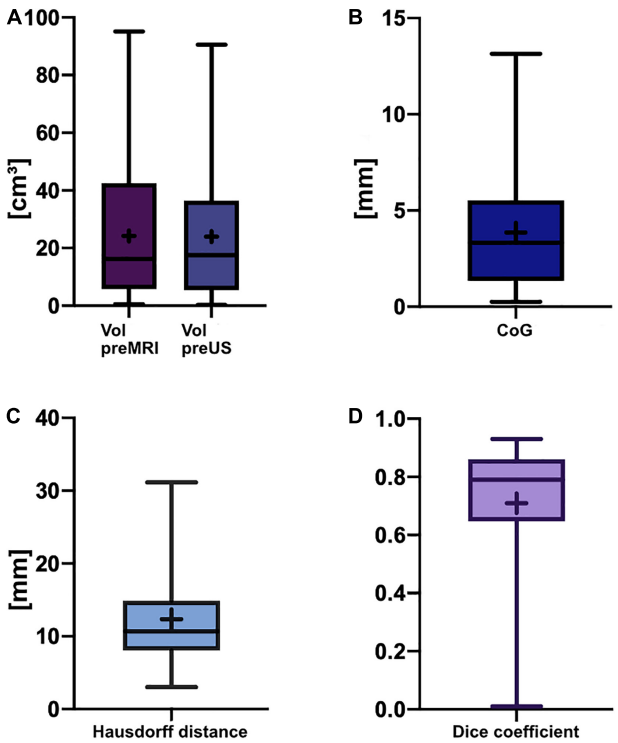

FIGURE 2 | Box-and-whisker plots of pre-resectional data. The lines indicate the medians, boxes extend from the 25th to 75th percentile, the whiskers encompass the range; + indicates the mean. **(A)** Tumor volumes: Vol pre-MRI 24.2 ± 22.3 cm^3 (mean ± SD) and median 16.3 cm^3, Vol pre-US 24.0 ± 21.8 cm^3 (mean ± SD) and median 17.6 cm^3; no significant difference (p = 0.8752, two-tailed Wilcoxon-matched pairs test). **(B)** Euclidean distance of the center of gravity: 3.9 ± 3.0 mm (mean ± SD), median of 3.3 mm. **(C)** Hausdorff distance: 12.3 ± 6.9 mm (mean ± SD), median of 10.7 mm. **(D)** Dice coefficient: 0.71 ± 0.21 (mean ± SD), median of 0.79 (unitless).

the tumor boundaries segmented in MRI could have been already detected in pre-resectional i3D US but was not interpreted as pathological tissue during surgery. We excluded this case, because, on the one hand, the planned resection was completed, but, on the other hand, remaining tumor could have been seen in i3D US. For more details on tumor object characteristics, refer to **Table 2**.

DISCUSSION

The dilemma of discordance between pre-operative imaging and intraoperative findings is well known and has been the subject of research in the neurosurgical field for decades. Attempts to overcome this issue reach back to the 1980s, when radiographic imaging of intraoperatively inserted reference objects was used to detect brain movement during surgery (Kelly et al., 1986). Later, landmark studies on brain shift suggested (serial) iMRI for visualization and compensation of deformation during surgical procedures (Nimsky et al., 2000; Nabavi et al., 2001), but in recent years iUS has evolved into a real alternative lacking most of the disadvantages of iMRI (Sastry et al., 2017), such as time consumption, limited availability, high costs, and the need for specialized personnel (Nimsky et al., 2001). In a current retrospective study in 23 patients with different brain tumor entities comparing intraoperative characteristics of iUS and iMRI, Bastos et al. reported a good concordance of tumor localization and margins in iUS with pre-operative MRI and 100% agreement between iUS and iMRI in the prediction of the extent of tumor resection, meaning either STR or GTR as classified by a neuroradiologist in post-MRI (Bastos et al., 2021). This is consistent with our findings of 18 cases classified as GTR and 10 cases as STR in both post-resectional iUS and post-MRI in glioblastoma patients; however, we additionally analyzed the remaining tumor volume in the STR cases, which was 3.5 ± 4.9 cm^3 (mean ± SD) in i3D US and 3.5 ± 5.2 cm^3 in post-MRI, showing no significant difference (p = 0.8457). This underpins the accuracy of iUS compared to MRI. Further, we identified 4 out of 18 cases (22.2%) in the GTR-group, where i3D US depicted tumor remnants and resection was extended, resulting in no evident remaining tumor in post-resectional iUS or post-MRI.

In light of this and, in contrast, the fact that tumor remnants were reliably identified in all ten STR cases, and in addition, resection was extended in four other cases based on i3D US imaging data, we conclude that although the imaging quality of i3D US is excellent under optimal conditions and may contribute to intraoperative extension of EOR, it cannot replace post-MRI.

Pre-requisite for the evaluation of spatial overlap and potential shifting is a sufficient image fusion and patient registration, which was quantified using the TRE in those 14 cases that received iCT before craniotomy. The TRE of 0.91 ± 0.53 mm is in line with our previously published experience in 200 cases of iCT-based registration in cranial procedures (Carl et al., 2018). The US probe was pre-calibrated, establishing a so-called rigid registration based on spatial position information (Lunn et al., 2003; Prada et al., 2015), and thus, once acquired, i3D US datasets were automatically co-registered to the other imaging modalities. This was analogous to the procedure we described for i3D US in brain metastasis, where we additionally calculated the technical accuracy of US probe pre-calibration to be 1.33 ± 0.33 mm (mean ± SD) utilizing a US phantom containing wires. These were identified in the US image and compared to the expected positions (Saß et al., 2020). In our opinion, reliable registration accuracy can be concluded based on these data, and thus, the presented Dice coefficient C_{DSC} of 0.71 ± 0.21 (mean ± SD; median 0.79), which indicates a large spatial overlap, cannot be attributed to the registration procedure to a larger extent. However, multiple factors influence the C_{DSC} hindering its approximation toward a value of 1, the so-called perfect match, which one would expect assuming a similar imaging quality in pre-US and pre-MRI. The segmentation procedure itself is error-prone and observer-dependent as shown by Nitsch et al., who had three experts segmenting the same structures in iUS and found a C_{DSC} of 0.52–0.83 between the segmentation results and a C_{DSC} of 0.74, when an automatic segmentation algorithm was compared to expert segmentation (Nitsch et al., 2019). Another group found wide ranges of C_{DSC} reaching from 0.49 to 0.97 for segmentation of brain tumors

in MRI when performed by an expert manually or with a semi-automated probabilistic fractional segmentation algorithm (Zou et al., 2004). Similarly, the Multimodal Tumor Image Segmentation Benchmark (BRATS) study, which was designed to compare different automatic segmentation algorithm for brain tumors MRI, analyzed, as a baseline for later comparison with algorithms, the segmentation results of experts and revealed in this regard a considerable disagreement resulting in a C_{DSC} of 0.74–0.85 (Menze et al., 2015). Additionally, spatial overlap, and hence the C_{DSC}, is dependent on the spatial displacement of the segmented object after craniotomy. We chose to determine the spatial shift utilizing the Euclidean distance of the geometric CoG, which resulted in a mean ± SD of 3.9 ± 3.0 mm and a median of 3.3 mm, which is in accordance with our results in brain metastasis surgery, where an Euclidean distance of CoG of 3.7 ± 2.5 mm (mean ± SD, median: 3.0 mm) was seen (Saß et al., 2020). Although it is commonly believed among neurosurgeons that most brain deformation occurs after dural opening, there are several reports claiming a significant shift as early as after craniotomy but before dura incision. Ohue et al. (2010) investigated brain shift by marking reference points in pre-operative imaging and intraoperative US and measuring the distance at different time points. The mean overall shift of all measured structures before dural opening was 2.8 mm, increasing to 4.2 mm immediately before tumor resection, and reached a maximum of 6.8 mm during or after tumor removal (Ohue et al., 2010). Interestingly, when focusing on the measurements made at the tumor margins, which yielded a shift of 3.4 ± 1.9 mm (range: 0.4–10.8 mm) before dural opening, the results of Ohue et al. (2010) are comparable to our measurements. While Ohue et al. (2010) described a significant increase after dura incision, Letteboer et al. (2005) who also

TABLE 2 | Pre-resectional tumor characteristics and iUS quality.

Case	Vol pre-MRI (cm^3)	Vol pre-US (cm^3)	Vol res. iUS (cm^3)	Vol post-US (cm^3)	Vol post-MRI (cm^3)	Euclidean Δ CoG (mm)	Hausdorff distance (mm)	Dice coefficient (unitless)	US quality
1	2.4	1.8		0	0	1.11	5.39	0.72	Excellent
2	57.8	57.7	0.2	0	0	4.08	10.20	0.80	Excellent
3	47.9	50.4		17.0	18.1	3.75	15.39	0.80	Excellent
4	5.5	4.84		2.0	1.7	3.35	30.41	0.75	Excellent
5	16.1	15.9		0.8	0.5	1.26	13.34	0.79	Excellent
6	47.8	48.5		0	0	2.06	6.48	0.86	Good
7	18.8	18.4		–	–	3.48	8.06	0.80	Sufficient
8	2.2	2.1		–	–	7.31	9.54	0.36	Good
9	16.4	19.3		0*	0/3.0**	3.19	8.60	0.54	Excellent
10	3.0**	3.1		0	0	7.87	13.89	0.51	Excellent
11	2.4	2.5		0	0	1.23	3.00	0.87	Excellent
12	95.1	90.5		0	0	3.29	8.66	0.86	Good
13	15.7	16.7		0	0	6.07	15.81	0.66	Excellent
14	26.0	24.8		0	0	1.37	9.43	0.77	Sufficient
15	43.9	–		2.1	3.2	–	–	–	Poor
16	22.1	23.1		0.6	0.9	2.40	12.57	0.84	Good
17	6.0	5.6	1.0	0	0	1.21	4.12	0.89	Excellent
18	16.2	16.5		0	0	0.25	19.82	0.92	Excellent
19	30.8	28.7		0	0	3.36	8.06	0.80	Excellent
20	19.7	21.8	3.0	0	0	5.96	31.16	0.64	Sufficient
21	9.2	10.5		0.7	0.1	13.14	14.04	0.29	Sufficient
22	11.0	11.2		2.2	1.7	0.61	4.47	0.91	Good
23	50.8	62.1	2.8	0	0	3.78	11.18	0.79	Good
24	9.6	13.2		2.7	3.3	5.37	14.73	0.69	Sufficient
25	0.5	0.3		0	0	7.64	9.00	0.01	Excellent
26	4.1	4.3		0	0	4.11	13.38	0.50	Excellent
27	51.8	47.1		3.5	2.7	10.63	24.54	0.65	Excellent
28	40.8	35.8		0	0	1.75	13.04	0.86	Good
29	13.0	10.1		0	0	1.96	8.06	0.82	Excellent
30	49.7	38.4		3.7	2.7	3.04	16.79	0.65	Good
31	33.6	34.5		0	0	1.19	7.07	0.93	Excellent

*Vol pre-MRI, volume pre-operative segmented in MRI; Vol pre-US, volume pre-resectional segmented in US; Vol res. iUS, volume of residual tumor segmented in i3D US leading to further extension of resection; Vol post-US, volume segmented in last acquired i3D US; Vol post-MR, volume in post-operative MRI; Euclidean Δ CoG, Euclidean difference of geometric center of gravity. Case nos. 9 and 10 are in the same patient within 5 days: * no residual tumor was detected in post-US in case no. 9, but was out of the scanning field and could have been seen in pre-US; ** indicates that no tumor was detected within the pre-operatively segmented area, but a tumor volume of 3.0 cm^3 was detected in the adjacent in post-MRI (which is also pre-MRI for case no. 10). US quality according to the first author's subjective assessment.*

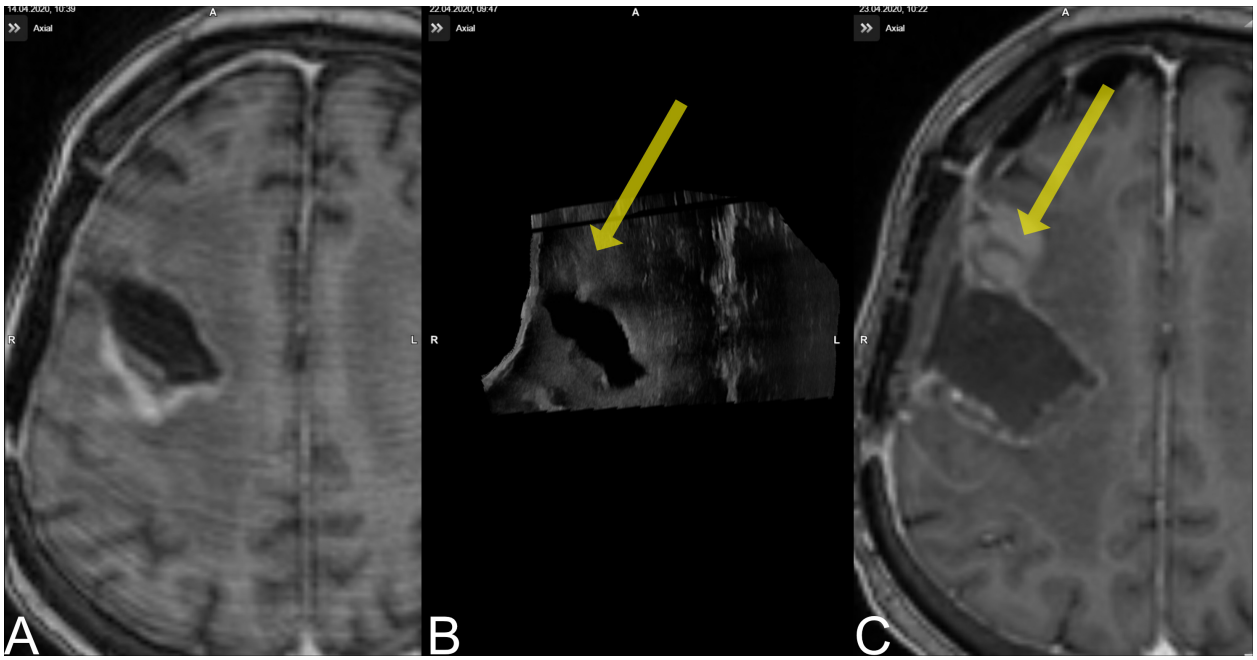

FIGURE 3 | Case no. 9. **(A)** The pre-MRI (8 days prior to surgery) demonstrated a contrast-enhancing lesion occipital to the resection cavity. **(B)** The pre-US demonstrated a lesion rostral to the resection cavity (yellow arrow) that was missed during surgery. **(C)** The new lesion is evident on post-MRI.

measured a shift of 3.0 mm parallel to the direction of gravity, only found additional shifting of 0.2 mm after dura incision. The phenomenon of a higher degree of shifting before than after durotomy can be discussed to be attributed to calibration errors or true shift (Sastry et al., 2017). Because we found the registration error and calibration error of the US probe to be low, we do not expect these factors to affect our measurements to any great extent.

In our experience, mainly three factors can contribute to dissimilarity when comparing pre-operative to intraoperative imaging data, namely, segmentation inaccuracy, pressure applied with a probe during image acquisition, and true brain deformation. While C_{DSC} and similar segmentation volumes indicate a good segmentation accuracy, it remains difficult to distinguish between the latter two. To minimize the impact of the probe's contact with the brain, we used a saline depot as a coupling fluid and applied as little pressure as possible, but still enough to achieve good contact and image quality. However, even the Euclidean distance of the geometric CoG might be to some degree influenced by the probe's pressure. To further analyze the degree of resemblance of the pre-MRI and pre-US segmentations, we used the Hausdorff distance (Huttenlocher et al., 1993). Here, we found a mean ± SD of 12.3 ± 6.9 mm (and a median of 10.7 mm), which is more than we previously published in case of brain metastasis (mean ± SD: 8.1 mm ± 2.9; median: 8.1 mm) (Saß et al., 2020), but it fits well with the study of Nitsch et al. (2019) who found a Hausdorff distance of 12.2 mm between expert and automated segmentation. To our knowledge, there is no clear definition of when the Hausdorff distance is considered excellent, good, or sufficient. Considering that the Nitsch et al. (2019) results are regarded as "reasonable and acceptable segmentation results," we interpret our results in the same direction, although the resemblance of tumor objects in pre-MRI and pre-US was higher in brain metastasis (Saß et al., 2020).

Besides our interpretation of tumor volumes, C_{DSC}, Euclidean distance of CoG, and Hausdorff distance, one must not underestimate the benefit of displaying i3D US datasets as an overlay or site-by-site on the navigational screen, which allows a rough estimation of brain shift and registration coherence. In cases where the registration would become imprecise for any reason, e.g., due to movement of the reference array during the operative course, this could also be detected immediately on the navigational screen. Additionally, in cases where an update of the registration cannot be achieved, it is possible to navigate based on i3D US datasets alone.

The overall tumor identification and delineation was rated by investigators as much more difficult and time consuming than for brain metastases despite the fact that imaging quality was rated to be excellent or good in 25 cases (81%). Keeping this in mind, we interpret the C_{DSC}, similarity in tumor volume segmentations, and eventually also the Hausdorff distance to indicate a good to excellent segmentation result. We did not use contrast-enhanced ultrasound for our study, which has been shown to improve the capability of distinguishing between tumor and normal brain tissue (Prada et al., 2016). This technique may help refine segmentation results in future studies, but, in contrast, first must be thoroughly integrated into the surgical workflow.

A limitation of this study is the exclusion of one case from pre-resectional and three cases from the post-resectional

analysis; case no. 15 was a recurrent temporal GBM grade IV, IDH mutant, where we were not able to establish a good contact of the US probe and the scarred dural layer, resulting in exclusion from pre-resectional evaluation; case nos. 7 and 8 were excluded due to corrupted data, case no. 9, which was in the same patient as in case no. 10, is worth a closer scrutiny (**Figure 3**). The 63–year-old female patient suffered from a recurrent IDH wildtype glioblastoma located at the right frontal lobe. The patient received the pre-MRI 8 days before surgery, and the whole procedure was tailored to the segmented tumor object in pre-MRI. Retrospectively, pre-US during the first surgery documented additional tumor volume (3.1 cm^3) outside the MRI-segmented object boundaries but was misinterpreted during surgery. The post-US-scanning field, however, did not encompass the additional tumor tissue but was only able to document the MRI-segmented tumor to be completely resected. The tumor mass was then detected in the post-MRI (3.0 cm^3), and registration to the pre-MRI demonstrated it to be tumor progression. This case is interesting insofar as it demonstrates one of the weaknesses of i3D US; no matter how good the imaging quality of iUS is, the scanning field is limited compared to MRI, and if the examiner focuses only on the pre-operatively segmented areas, pathologies can easily be missed.

CONCLUSION

Navigated i3D US in glioblastoma surgery is a helpful tool that allows rough estimation of brain shift and the registration accuracy at a glance even during the surgical procedure, while it can be easily implemented in the surgical workflow. We found a high imaging quality, an excellent concordance of tumor object segmentations compared to post-MRI, and a reliable estimation of residual tumor, which triggered extension of EOR in every fifth case.

DATA AVAILABILITY STATEMENT

The raw data supporting the conclusions of this article will be made available by the authors, without undue reservation.

ETHICS STATEMENT

The studies involving human participants were reviewed and approved by the Ethics Committee of the Medical Faculty of the Philipps-University Marburg. The patients/participants provided their written informed consent to participate in this study. Written informed consent was obtained from the individual(s) for the publication of any potentially identifiable images or data included in this article.

AUTHOR CONTRIBUTIONS

BS, CN, and MB: conceptualization and supervision. MB and BS: methodology and visualization and writing – original draft preparation. DZ, CN, and MP: validation. BS, MB, and DZ: investigation and data curation. MB, DZ, CN, MP, and BS: resources. MB, MP, and CN: writing – review and editing. MB: project administration. All authors have read and agreed to the published version of the manuscript.

FUNDING

Open Access funding was provided by the Open Access Publication Fund of Philipps-Universität Marburg with the support of the Deutsche Forschungsgemeinschaft (DFG, German Research Foundation).

REFERENCES

Audette, M. A., Siddiqi, K., and Peters, T. M. (eds) (1999). *Level-Set Surface Segmentation and Fast Cortical Range Image Tracking for Computing Intrasurgical Deformations*. Berlin: Springer Berlin Heidelberg.

Bastos, D. C. A., Juvekar, P., Tie, Y., Jowkar, N., Pieper, S., Wells, W. M., et al. (2021). Challenges and opportunities of intraoperative 3D ultrasound with neuronavigation in relation to intraoperative MRI. *Front. Oncol.* 11:656519. doi: 10.3389/fonc.2021.656519

Brown, T. J., Brennan, M. C., Li, M., Church, E. W., Brandmeir, N. J., Rakszawski, K. L., et al. (2016). Association of the extent of resection with survival in glioblastoma: a systematic review and meta-analysis. *JAMA Oncol.* 2, 1460–1469. doi: 10.1001/jamaoncol.2016.1373

Burri, S. H., Gondi, V., Brown, P. D., and Mehta, M. P. (2018). The evolving role of tumor treating fields in managing glioblastoma: guide for oncologists. *Am. J. Clin. Oncol.* 41, 191–196. doi: 10.1097/COC.0000000000000395

Carl, B., Bopp, M., Sass, B., and Nimsky, C. (2018). Intraoperative computed tomography as reliable navigation registration device in 200 cranial procedures. *Acta Neurochir.* 160, 1681–1689. doi: 10.1007/s00701-018-3641-6

Chandler, W. F., Knake, J. E., McGillicuddy, J. E., Lillehei, K. O., and Silver, T. M. (1982). Intraoperative use of real-time ultrasonography in neurosurgery. *J. Neurosurg.* 57, 157–163. doi: 10.3171/jns.1982.57.2.0157

De Witt Hamer, P. C., Robles, S. G., Zwinderman, A. H., Duffau, H., and Berger, M. S. (2012). Impact of intraoperative stimulation brain mapping on glioma surgery outcome: a meta-analysis. *J. Clin. Oncol.* 30, 2559–2565. doi: 10.1200/JCO.2011.38.4818

Dice, L. R. (1945). Measures of the amount of ecologic association between species. *Ecology* 26, 297–302. doi: 10.2307/1932409

Dorward, N. L., Alberti, O., Velani, B., Gerritsen, F. A., Harkness, W. F., Kitchen, N. D., et al. (1998). Postimaging brain distortion: magnitude, correlates, and impact on neuronavigation. *J. Neurosurg.* 88, 656–662. doi: 10.3171/jns.1998.88.4.0656

Flusser, J., and Suk, T. (1994). A moment-based approach to registration of images with affine geometric distortion. *IEEE Trans. Geosci. Remote Sens.* 32, 382–387. doi: 10.1109/36.295052

Grabowski, M. M., Recinos, P. F., Nowacki, A. S., Schroeder, J. L., Angelov, L., Barnett, G. H., et al. (2014). Residual tumor volume versus extent of resection: predictors of survival after surgery for glioblastoma. *J. Neurosurg.* 121, 1115–1123. doi: 10.3171/2014.7.JNS132449

Gronningsaeter, A., Kleven, A., Ommedal, S., Aarseth, T. E., Lie, T., Lindseth, F., et al. (2000). SonoWand, an ultrasound-based neuronavigation system. *Neurosurgery* 47, 1373–1379. discussion 9-80. doi: 10.1093/neurosurgery/47.6.1373

Gulati, S., Jakola, A. S., Nerland, U. S., Weber, C., and Solheim, O. (2011). The risk of getting worse: surgically acquired deficits, perioperative complications, and functional outcomes after primary resection of glioblastoma. *World Neurosurg.* 76, 572–579. doi: 10.1016/j.wneu.2011.06.014

Hastreiter, P., Rezk-Salama, C., Soza, G., Bauer, M., Greiner, G., Fahlbusch, R., et al. (2004). Strategies for brain shift evaluation. *Med. Image Anal.* 8, 447–464. doi: 10.1016/j.media.2004.02.001

Hill, D. L., Maurer, C. R. Jr., Maciunas, R. J., Barwise, J. A., Fitzpatrick, J. M., and Wang, M. Y. (1998). Measurement of intraoperative brain surface deformation under a craniotomy. *Neurosurgery* 43, 514–526. discussion 27-8. doi: 10.1097/00006123-199809000-00066

Huttenlocher, D. P., Klanderman, G. A., and Rucklidge, W. J. (1993). Comparing images using the hausdorff distance. *IEEE Trans. Pattern Anal. Mach. Intell.* 15, 850–863. doi: 10.1109/34.232073

Kelly, P. J., Kall, B. A., Goerss, S., and Earnest, F. (1986). Computer-assisted stereotaxic laser resection of intra-axial brain neoplasms. *J. Neurosurg.* 64, 427–439. doi: 10.3171/jns.1986.64.3.0427

Knake, J. E., Chandler, W. F., McGillicuddy, J. E., Silver, T. M., and Gabrielsen, T. O. (1982). Intraoperative sonography for brain tumor localization and ventricular shunt placement. *AJR Am. J. Roentgenol.* 139, 733–738. doi: 10.2214/ajr.139.4.733

Letteboer, M. M., Willems, P. W., Viergever, M. A., and Niessen, W. J. (2005). Brain shift estimation in image-guided neurosurgery using 3-D ultrasound. *IEEE Trans. Biomed. Eng.* 52, 268–276. doi: 10.1109/TBME.2004.840186

Li, Y. M., Suki, D., Hess, K., and Sawaya, R. (2016). The influence of maximum safe resection of glioblastoma on survival in 1229 patients: can we do better than gross-total resection? *J. Neurosurg.* 124, 977–988. doi: 10.3171/2015.5.JNS142087

Lunn, K. E., Paulsen, K. D., Roberts, D. W., Kennedy, F. E., Hartov, A., and West, J. D. (2003). Displacement estimation with co-registered ultrasound for image guided neurosurgery: a quantitative in vivo porcine study. *IEEE Trans. Med. Imaging* 22, 1358–1368. doi: 10.1109/TMI.2003.819293

Menze, B. H., Jakab, A., Bauer, S., Kalpathy-Cramer, J., Farahani, K., Kirby, J., et al. (2015). The multimodal brain tumor image segmentation benchmark (BRATS). *IEEE Trans. Med. Imaging* 34, 1993–2024.

Munkvold, B. K. R., Jakola, A. S., Reinertsen, I., Sagberg, L. M., Unsgard, G., and Solheim, O. (2018). The diagnostic properties of intraoperative ultrasound in glioma surgery and factors associated with gross total tumor resection. *World Neurosurg.* 115, e129–e136.

Nabavi, A., Black, P. M., Gering, D. T., Westin, C. F., Mehta, V., Pergolizzi, R. S. Jr., et al. (2001). Serial intraoperative magnetic resonance imaging of brain shift. *Neurosurgery* 48, 787–797. discussion 97-8. doi: 10.1097/00006123-200104000-00019

Nimsky, C., Ganslandt, O., Cerny, S., Hastreiter, P., Greiner, G., and Fahlbusch, R. (2000). Quantification of, visualization of, and compensation for brain shift using intraoperative magnetic resonance imaging. *Neurosurgery* 47, 1070–1079. discussion 9-80. doi: 10.1097/00006123-200011000-00008

Nimsky, C., Ganslandt, O., Hastreiter, P., and Fahlbusch, R. (2001). Intraoperative compensation for brain shift. *Surg. Neurol.* 56, 357–364. discussion 64-5. doi: 10.1016/s0090-3019(01)00628-0

Nimsky, C., Ganslandt, O., Von Keller, B., Romstock, J., and Fahlbusch, R. (2004). Intraoperative high-field-strength MR imaging: implementation and experience in 200 patients. *Radiology* 233, 67–78. doi: 10.1148/radiol.2331031352

Nitsch, J., Klein, J., Dammann, P., Wrede, K., Gembruch, O., Moltz, J. H., et al. (2019). Automatic and efficient MRI-US segmentations for improving intraoperative image fusion in image-guided neurosurgery. *Neuroimage Clin.* 22:101766. doi: 10.1016/j.nicl.2019.101766

Ohue, S., Kumon, Y., Nagato, S., Kohno, S., Harada, H., Nakagawa, K., et al. (2010). Evaluation of intraoperative brain shift using an ultrasound-linked navigation system for brain tumor surgery. *Neurol. Med. Chir.* 50, 291–300. doi: 10.2176/nmc.50.291

Ostrom, Q. T., Cioffi, G., Waite, K., Kruchko, C., and Barnholtz-Sloan, J. S. (2021). CBTRUS statistical report: primary brain and other central nervous system tumors diagnosed in the United States in 2014-2018. *Neuro Oncol.* 23(12 Suppl. 2), iii1–iii105. doi: 10.1093/neuonc/noab200

Paul, K., Graessl, A., Rieger, J., Lysiak, D., Huelnhagen, T., Winter, L., et al. (2015). Diffusion-sensitized ophthalmic magnetic resonance imaging free of geometric distortion at 3.0 and 7.0 T: a feasibility study in healthy subjects and patients with intraocular masses. *Invest. Radiol.* 50, 309–321. doi: 10.1097/RLI.0000000000000129

Prada, F., Bene, M. D., Fornaro, R., Vetrano, I. G., Martegani, A., Aiani, L., et al. (2016). Identification of residual tumor with intraoperative contrast-enhanced ultrasound during glioblastoma resection. *Neurosurg. Focus.* 40:E7. doi: 10.3171/2015.11.FOCUS15573

Prada, F., Del Bene, M., Mattei, L., Lodigiani, L., DeBeni, S., Kolev, V., et al. (2015). Preoperative magnetic resonance and intraoperative ultrasound fusion imaging for real-time neuronavigation in brain tumor surgery. *Ultraschall. Med.* 36, 174–186. doi: 10.1055/s-0034-1385347

Reinertsen, I., Lindseth, F., Askeland, C., Iversen, D. H., and Unsgard, G. (2014). Intra-operative correction of brain-shift. *Acta Neurochir.* 156, 1301–1310. doi: 10.1007/s00701-014-2052-6

Roberts, D. W., Hartov, A., Kennedy, F. E., Miga, M. I., and Paulsen, K. D. (1998). Intraoperative brain shift and deformation: a quantitative analysis of cortical displacement in 28 cases. *Neurosurgery* 43, 749–758. discussion 58-60. doi: 10.1097/00006123-199810000-00010

Sass, B., Pojskic, M., Zivkovic, D., Carl, B., Nimsky, C., and Bopp, M. H. A. (2021). Utilizing intraoperative navigated 3D color doppler ultrasound in glioma surgery. *Front. Oncol.* 11:656020. doi: 10.3389/fonc.2021.656020

Sastry, R., Bi, W. L., Pieper, S., Frisken, S., Kapur, T., Wells, W. III, et al. (2017). Applications of ultrasound in the resection of brain tumors. *J. Neuroimaging.* 27, 5–15. doi: 10.1111/jon.12382

Saß, B., Carl, B., Pojskic, M., Nimsky, C., and Bopp, M. (2020). Navigated 3D ultrasound in brain metastasis surgery: analyzing the differences in object appearances in ultrasound and magnetic resonance imaging. *Appl. Sci.* 10:7798. doi: 10.3390/app10217798

Stummer, W., Pichlmeier, U., Meinel, T., Wiestler, O. D., Zanella, F., Reulen, H. J., et al. (2006). Fluorescence-guided surgery with 5-aminolevulinic acid for resection of malignant glioma: a randomised controlled multicentre phase III trial. *Lancet Oncol.* 7, 392–401. doi: 10.1016/S1470-2045(06)70665-9

Stummer, W., Tonn, J. C., Mehdorn, H. M., Nestler, U., Franz, K., Goetz, C., et al. (2011). Counterbalancing risks and gains from extended resections in malignant glioma surgery: a supplemental analysis from the randomized 5-aminolevulinic acid glioma resection study. Clinical article. *J. Neurosurg.* 114, 613–623. doi: 10.3171/2010.3.JNS097

Stupp, R., Hegi, M. E., Mason, W. P., van den Bent, M. J., Taphoorn, M. J., Janzer, R. C., et al. (2009). Effects of radiotherapy with concomitant and adjuvant temozolomide versus radiotherapy alone on survival in glioblastoma in a randomised phase III study: 5-year analysis of the EORTC-NCIC trial. *Lancet Oncol.* 10, 459–466. doi: 10.1016/s1470-2045(09)70025-7

Stupp, R., Mason, W. P., van den Bent, M. J., Weller, M., Fisher, B., Taphoorn, M. J., et al. (2005). Radiotherapy plus concomitant and adjuvant temozolomide for glioblastoma. *N. Engl. J. Med.* 352, 987–996.

Tronnier, V. M., Bonsanto, M. M., Staubert, A., Knauth, M., Kunze, S., and Wirtz, C. R. (2001). Comparison of intraoperative MR imaging and 3D-navigated ultrasonography in the detection and resection control of lesions. *Neurosurg. Focus.* 10:E3. doi: 10.3171/foc.2001.10.2.4

Unsgaard, G., Ommedal, S., Muller, T., Gronningsaeter, A., and Nagelhus Hernes, T. A. (2002). Neuronavigation by intraoperative three-dimensional ultrasound: initial experience during brain tumor resection. *Neurosurgery* 50, 804–812. discussion 12. doi: 10.1097/00006123-200204000-00022

Wen, P. Y., Weller, M., Lee, E. Q., Alexander, B. M., Barnholtz-Sloan, J. S., Barthel, F. P., et al. (2020). Glioblastoma in adults: a society for neuro-oncology (SNO) and European society of neuro-oncology (EANO) consensus review on current management and future directions. *Neuro Oncol.* 22, 1073–1113. doi: 10.1093/neuonc/noaa106

Wirtz, C. R., Bonsanto, M. M., Knauth, M., Tronnier, V. M., Albert, F. K., Staubert, A., et al. (1997). Intraoperative magnetic resonance imaging to update interactive navigation in neurosurgery: method and preliminary

experience. *Comput. Aided Surg.* 2, 172–179. doi: 10.3109/10929089709148110

Zou, K. H., Warfield, S. K., Bharatha, A., Tempany, C. M., Kaus, M. R., Haker, S. J., et al. (2004). Statistical validation of image segmentation quality based on a spatial overlap index. *Acad. Radiol.* 11, 178–189. doi: 10.1016/s1076-6332(03)00671-8

Conflict of Interest: CN and MB are consultants for Brainlab.

The remaining authors declare that the research was conducted in the absence of any commercial or financial relationships that could be construed as a potential conflict of interest.

Publisher's Note: All claims expressed in this article are solely those of the authors and do not necessarily represent those of their affiliated organizations, or those of the publisher, the editors and the reviewers. Any product that may be evaluated in this article, or claim that may be made by its manufacturer, is not guaranteed or endorsed by the publisher.

Copyright © 2022 Saß, Zivkovic, Pojskic, Nimsky and Bopp. This is an open-access article distributed under the terms of the Creative Commons Attribution License (CC BY). The use, distribution or reproduction in other forums is permitted, provided the original author(s) and the copyright owner(s) are credited and that the original publication in this journal is cited, in accordance with accepted academic practice. No use, distribution or reproduction is permitted which does not comply with these terms.

frontiers | Frontiers in Oncology

ORIGINAL RESEARCH
published: 11 May 2022
doi: 10.3389/fonc.2022.886968

Differentiation of Meningiomas and Gliomas by Amide Proton Transfer Imaging: A Preliminary Study of Brain Tumour Infiltration

Han-Wen Zhang[1], Xiao-Lei Liu[1], Hong-Bo Zhang[2], Ying-Qi Li[3], Yu-li Wang[1], Yu-Ning Feng[1], Kan Deng[4], Yi Lei[1], Biao Huang[5]* and Fan Lin[1]**

[1] Department of Radiology, The First Affiliated Hospital of Shenzhen University, Health Science Center, Shenzhen Second People's Hospital, Shenzhen, China, [2] Department of Radiology, The Seventh Affiliated Hospital, Sun Yat-sen University, Shenzhen, China, [3] Department of Radiology, Songgang People's Hospital, Shenzhen, China, [4] Research Department, Philips Healthcare, Guangzhou, China, [5] Department of Radiology, Guangdong Provincial People's Hospital, Guangdong Academy of Medical Sciences, Guangdong, China

OPEN ACCESS

Edited by:
Nico Sollmann,
University of California,
San Francisco, United States

Reviewed by:
Guolin Ma,
China-Japan Friendship Hospital,
China
Yanwei Miao,
Dalian Medical University, China
Tianming Qiu,
Fudan University, China

***Correspondence:**
Yi Lei
13602658583@163.com
Biao Huang
huangbiao@gdph.org.cn
Fan Lin
foxetfoxet@gmail.com

Specialty section:
This article was submitted to Neuro-Oncology and Neurosurgical Oncology, a section of the journal Frontiers in Oncology

Received: 01 March 2022
Accepted: 07 April 2022
Published: 11 May 2022

Citation:
Zhang H-W, Liu X-L, Zhang H-B, Li Y-Q, Wang Y-l, Feng Y-N, Deng K, Lei Y, Huang B and Lin F (2022) Differentiation of Meningiomas and Gliomas by Amide Proton Transfer Imaging: A Preliminary Study of Brain Tumour Infiltration. Front. Oncol. 12:886968. doi: 10.3389/fonc.2022.886968

Background: Gliomas are more malignant and invasive than meningiomas.

Objective: To distinguish meningiomas from low-grade/high-grade gliomas (LGGs/HGGs) using amide proton transfer imaging (APT) combined with conventional magnetic resonance imaging (MRI) and to explore the application of APT in evaluating brain tumour invasiveness.

Materials and Methods: The imaging data of 50 brain tumors confirmed by pathology in patients who underwent APT scanning in our centre were retrospectively analysed. Of these tumors, 25 were meningiomas, 10 were LGGs, and 15 were HGGs. The extent of the tumour-induced range was measured on APT images, T2-weighted imaging (T2WI), and MRI enhancement; additionally, and the degree of enhancement was graded. Ratios ($R^{APT/T2}$ and $R^{APT/E}$) were obtained by dividing the range of changes observed by APT by the range of changes observed *via* T2WI and MR enhancement, respectively, and APT_{mean} values were measured. The Mann–Whitney U test was used to compare the above measured values with the pathological results obtained for gliomas and meningiomas, the Kruskal-Wallis test was used to compare LGGs, HGGs and meningiomas, and Dunn's test was used for pairwise comparisons. In addition, receiver operating characteristic (ROC) curves were drawn.

Results: The Mann–Whitney U test showed that APT_{mean} (p=0.005), $R^{APT/T2}$ (p<0.001), and $R^{APT/E}$ (p<0.001) values were statistically significant in the identification of meningioma and glioma. The Kruskal-Wallis test showed that the parameters APT_{mean}, $R^{APT/T2}$, $R^{APT/E}$ and the degree of enhancement are statistically significant. Dunn's test revealed that $R^{APT/T2}$ (p=0.004) and $R^{APT/E}$ (p=0.008) could be used for the identification of LGGs and meningiomas. APT_{mean} (p<0.001), $R^{APT/T2}$ (p<0.001), and $R^{APT/E}$ (p<0.001) could be used for the identification of HGGs and meningiomas. APT_{mean} (p<0.001) was statistically

significant in the comparison of LGGs and HGGs. ROC curves showed that $R^{APT/T2}$ (area under the curve (AUC)=0.947) and $R^{APT/E}$ (AUC=0.919) could be used to distinguish gliomas from meningiomas.

Conclusion: APT can be used for the differential diagnosis of meningioma and glioma, but APT_{mean} values can only be used for the differential diagnosis of HGGs and meningiomas or HGGs and LGGs. Gliomas exhibit more obvious changes than meningiomas in APT images of brain tissue; this outcome may be caused by brain infiltration.

Keywords: amide proton transfer, differential diagnosis, glioma, meningioma, MRI, tumour invasion

ADVANCES IN KNOWLEDGE

1. APT combined with conventional MR can be very good for the differential diagnosis of gliomas and meningiomas. APT can be used to differentiate among LGGs, HGGs and meningiomas.
2. Glioma APT images are larger than conventional MR images; therefore, gliomas are more obvious on these images than relatively benign meningiomas. This may be related to the infiltration of brain tumors.

1 INTRODUCTION

The Warburg effect, the theory that tumors metabolize acidic substances, is increasingly recognized by an increasing number of scientists studying tumors (1). In cutting-edge research, scientific experiments involving the abnormal accumulation of a series of acidic metabolites, such as methylglutaric acid, have repeatedly verified this viewpoint (2, 3). In the field of gliomas, Varun Venkataramani et al. proposed that glutamatergic synaptic input of glioma cells drives brain tumour progression, especially glioma progression (4). Compared with meningiomas with a significantly better survival prognosis, gliomas undoubtedly have a stronger ability to infiltrate the brain.

Due to the high recurrence rate and poor prognosis, gliomas have become a research hotspot in medicine (5). The main reason for the high recurrence rate of gliomas is the inability to effectively measure the boundary of the tumour infiltrated so that the gliomas cannot be radically removed (6). Neither long-term temozolomide chemotherapy nor radiotherapy in the later stage can effectively cure patients (7, 8). However, most meningiomas originating from the meninges, except for a very small number of malignant meningiomas, can be cured by excision. Meningiomas are directly supplied by meningeal blood vessels and show significant enhancement on enhanced magnetic resonance (MR) scans, and high-grade glioma (HGG)-induced blood–brain barrier (BBB) disruption can achieve a similar degree of enhancement (9).

According to the Warburg effect, malignant tumors cause acidic substances to accumulate in the infiltrating area. At present, clinical imaging technologies that can measure acidic metabolites include MR spectroscopy (MRS) and amide proton transfer imaging (APT) based on chemical exchange saturation transfer (CEST) (10, 11). APT technology can measure the amide proton content and indirectly reflect the protein content and pH value of a substance (12). At present, research on APT in gliomas mainly focuses on the use of the APT value for the evaluation of preoperative tumour malignancy and the identification of postoperative recurrence and pseudo-progression (13–15). However, there are only two studies on meningiomas, one on the content of Ki-67 in meningiomas and the other on the differential diagnosis of typical and atypical meningiomas (16, 17). At present, there is no research on the differential diagnosis of gliomas and meningiomas using APT technology.

In this study, APT was used to evaluate gliomas and meningiomas to obtain APT values, and the range of APT changes caused by tumors was measured and compared with the range of changes observed by conventional imaging of tumors. These analyses were performed to explore whether the changes in APT values and ranges caused by meningiomas and gliomas can be used for differential diagnosis.

2 MATERIALS AND METHODS

2.1 Patients

From January 2021 to February 2022, one hundred brain tumour patients who underwent Philips Ingenia 3.0 Tesla (T) MR imaging (MRI) scans were collected in our centre. Inclusion criteria were as follows (1): complete clinical data, no history of trauma and radiotherapy and chemotherapy (2); complete routine imaging before surgery, including T1-weighted imaging (T1WI), T2-weighted imaging (T2WI), enhanced scan, diffusion-weighted imaging (DWI) and APT, with satisfactory image quality diagnosis requirements; and (3) patients with postoperative pathological diagnosis of meningioma or glioma after surgical treatment.

Finally, 50 patients (25 males and 25 females) were included, including 25 patients with meningioma (12 males and 13 females) and 25 patients with gliomas (13 males and 12 females), aged 16-71 (48 ± 13) years old. This retrospective study was approved by the regional ethics committee and exempted from informed consent.

2.2 MRI

We scanned patients with a Philips Healthcare 3.0T Ingenia MR scanner (Philips Healthcare, Amsterdam, The Netherlands) using a

20-channel head coil. Patients fasted for 4-6 h before scanning. The localization line was located at the inferior border of the corpus callosum, and the scanning range was the whole brain. T1WI, T2WI, T2W-fluid attenuated inversion recovery (FLAIR), DWI, and APT scans were performed first, and then enhanced scans were performed.

2.2.1 Conventional MR Sequence

1. Axial T1WI parameters were as follows: repetition time (TR)/ echo time (TE) = 2034/20 milliseconds (ms), section thickness = 5 mm, field of vision (FOV) = 230×210 mm, and matrix = 328×258. 2. Axial T2WI parameters were as follows: TR/TE = 3000/105 ms, section thickness = 5 mm, FOV = 230×210 mm, and matrix = 328×258. 3. Coronal T2W-FLAIR parameters were as follows: TR/ TE = 9000/81 ms, section thickness = 5 mm, inversion time = 2500 ms, FOV = 230 × 210 mm, and matrix = 328 × 258). 4. Axial DWI parameters were as follows: the B value of DWI is B = 0 and B = 1000 s/mm2, TR/TE = 3741/80 ms, section thickness = 5 mm, FOV = 230×210 mm, FOV = phase 100%, and matrix = 128 ×97.

2.2.2 APT and T1W-Enhanced Sequence

1. APT images were acquired axially (TR/TE=6306/8.3 ms, section thickness=5 mm, FOV=230×180 mm, and matrix=128×100).
2. An intravenous injection of gadodiamide (Omniscan, GE Healthcare, Dublin, Ireland) was carried out at an injection rate of 3.5 mL/s *via* a power injector (0.1 mmol/kg), followed by flushing with 10 mL of normal saline. Sagittal T1WI-enhanced parameters were as follows (TR/TE=6.8/3.1 ms, section thickness=1 mm, FOV=240×240 mm, and matrix=240×240).

2.3 Pathological Results

The pathological data of all patients included intraoperative pathology and immunohistochemical results. The pathological results of all glioma patients with complete molecular sequencing included isocitrate dehydrogenase, O6-methylguanine-DNA methyltransferase, telomere reverse transcriptase, etc.

The final pathological findings of the patients were obtained according to the 2016 edition of the CNS Tumour Classification.

2.4 Image Analysis

Conventional MR images were used for tumour extent measurements using ITK-SNAP-3.8.0 (University of Pennsylvania, Philadelphia, PA). The localization of the solid area of the tumour was performed on the T1WI structural image by three senior physicians, and the T2WI and enhanced scans were delineated. T2WI scans were marked, and the enhancement range was denoted as R^{T2} and R^{E}. A region of interest (ROI) was selected to avoid surrounding blood vessels, tumour necrosis and regions of cystic degeneration. At the same time, for the enhanced scan images, we scored the degree of enhancement on a 1-4 scale (1-no enhancement, 2-slight enhancement, 3-moderate enhancement, and 4-significant enhancement).

APT mean (APT_{mean}) and range measurements (R^{APT}) were performed on APT images of tumors using IntelliSpace Portal 10.0 (Philips Medical, The Netherlands). T1WI structural images and the contralateral normal tissue areas served as references for the delineation of the range of APT image changes caused by tumors.

Finally, we compared R^{APT} with R^{T2} and R^{E} to obtain the corresponding ratios ($R^{APT/E}$ and $R^{APT/T2}$) to determine whether the range of APT increased.

2.5 Statistical Analysis

We used the Statistical Package for the Social Sciences (SPSS v.19, Chicago, IL, USA) for data statistics. The intra/interclass correlation coefficients (ICCs) were used to calculate consistency between reviewers. Two-sided p values<0.05 were considered statistically significant. All data were calculated using the Shapiro-Wilk test, and the result was $p<0.05$, indicating that the data did not conform to a normal distribution. Because the data did not follow a normal distribution, the Mann–Whitney U test was used to evaluate differences in enhancement and APT images based on APTmean, $R^{APT/T2}$, and $R^{APT/E}$ between gliomas and meningiomas. The Kruskal-Wallis test was used to compare LGGs, HGGs and meningiomas, and Dunn's test was used for pairwise comparisons. The area under the curve (AUC), confidence interval (CI) and cut-off values of the different types were calculated by receiver operating characteristic (ROC) curve analysis and the Youden Index. Following Bonferroni correction, $p<0.01$ indicated statistical significance. All statistical graphs were made using GraphPad Prism 7 (Prism 7, La Jolla, California).

3 RESULTS

3.1 Patients

The age and sex of the patients and the range of imaging (R^{T2}, R^{E}, and R^{APT}) were not statistically significant. The interobserver agreement of all measurements between the three reviewers was excellent, with ICC values greater than 0.80. Basic patient information and imaging information are shown in **Table 1**.

3.2 Differentiation of Meningiomas and Gliomas by APT

Mann–Whitney U test results showed that the degree of enhancement ($p=0.011$), APT_{mean} values ($p=0.005$), $R^{APT/E}$ values ($p<0.001$) and $R^{APT/T2}$ values ($p<0.001$) were statistically significant. This shows that $R^{APT/E}$ and $R^{APT/T2}$ can be used to distinguish gliomas and meningiomas to a better degree, and the change in APT range induced by gliomas is more obvious than that of meningiomas. Thus, the APT_{mean} and enhancement degree can help differentiate gliomas from meningiomas.

The ROC curve analysis (**Figure 1A**) demonstrated that the $R^{APT/E}$ (AUC=0.947, CI: 0.886-1.000) and $R^{APT/T2}$ (AUC=0.919, CI: 0.886-1.000) values were significantly different between patients in the glioma and meningioma groups ($p<0.001$), which allowed a high diagnostic efficiency. The cut-off value for $R^{APT/E}$ was 1.116, with a sensitivity of 92% and a specificity of 92%. The cut-off value of $R^{APT/T2}$ was 1.092, with a sensitivity of 92% and a specificity of 88%. This shows that the changes in the APT range of most gliomas increased by more than 11.6% in contrast-enhanced images, and this change reached more than 9.2% when compared with that of T2WI images.

TABLE 1 | Clinical characteristics, tumour range of MR imaging and parameters related to APT based on differences in patients with glioma and meningioma.

Variable Clinical characteristics	Glioma (n=25)	Meningioma (n=25)	*p*
Age, years	48.68 ± 12.77	47.44 ± 15.08	0.793
Sex			0.779
Male	13 (52%)	12 (48%)	
Female	12 (48%)	13 (52%)	
MR information			
Degree of enhancement	2.84 ± 0.94	3.48 ± 0.51	0.011
Tumor range of MRI (mm^2)			
R^{T2}	1394.00 ± 1097.50	1720.00 ± 1699.00	0.831
R^{E}	1558.00 ± 1083.50	1764.00 ± 1678.00	0.992
R^{APT}	2175.00 ± 1219.00	1764.00 ± 1723.00	0.200
Parameters related to APT			
APT_{mean}	4.28 ± 2.43	2.52 ± 0.63	0.005
$R^{APT/T2}$	120.5% ± 23.0%	103.5% ± 6.0%	<0.001
$R^{APT/E}$	127.0% ± 32.0%	102.4% ± 6.0%	<0.001

Ps: p<0.05 indicates statistical significance. Values are the median ± Interquartile Range (IQR).

**Degree of enhancement does not represent a specific value. Meningiomas are generally moderately or significantly enhanced, while gliomas can have various degrees of enhancement; LGGs are generally slightly or moderately enhanced, and HGGs are generally moderately or significantly enhanced.*

(1-no enhancement, 2-slight enhancement, 3-moderate enhancement, 4-significant enhancement).

3.3 Differentiation of Meningiomas, LGGs and HGGs by APT

The Kruskal-Wallis test showed that the parameters APT_{mean}, $R^{APT/T2}$, $R^{APT/E}$ and the degree of enhancement were statistically significant (p<0.001).

3.3.1 Differentiation of Meningiomas From LGGs by APT

Dunn's test results showed that the degree of enhancement (p<0.001), $R^{APT/E}$ values (p=0.008) and $R^{APT/T2}$ values (p=0.004) were statistically significant, but not APT_{mean} (p>0.01). Hence, the degree of enhancement, $R^{APT/E}$ and $R^{APT/T2}$ can be used to distinguish LGGs from meningiomas. The enhancement degree of meningiomas is obviously stronger than that of LGGs, and the changes in APT images induced by LGGs are more obvious than those of meningiomas. However, since the APT_{mean} of LGGs is close to that of meningiomas, this value cannot be used for differential diagnosis. **Figure 2** shows a comparison of APT and conventional MR images of LGGs and meningiomas.

The ROC curve analysis (**Figure 1B**) demonstrated that the $R^{APT/E}$ (AUC=0.908, CI: 0.809-1.000), $R^{APT/T2}$ (AUC=0.930, CI: 0.840-1.000), degree of enhancement (AUC=0.924, CI: 0.779-1.000) were significantly different between patients in the LGG and meningioma groups (p<0.01), which allowed high diagnostic efficiency. The cut-off value for $R^{APT/E}$ was 1.104, with a sensitivity of 90% and a specificity of 86%. The cut-off value of $R^{APT/T2}$ was 1.095, with a sensitivity of 90% and a specificity of 92%. This shows that the changes in the APT range of most LGGs increased by more than 10.4% on contrast-enhanced images, and this change also reached more than 9.5% when compared with that of T2WI images. The enhanced image had a cut-off value of 1.5, a sensitivity of 100% and a specificity of 80%. This indicates that the enhancement of meningiomas is significantly stronger than that of LGGs.

3.3.2 Differentiation of Meningiomas From HGGs by APT

Dunn's test results showed that the APT_{mean} (p<0.001), $R^{APT/E}$ (p<0.001) and $R^{APT/T2}$ (p<0.001) values were statistically significant. However, the degree of enhancement was not statistically significant (p>0.01). This shows that APT_{mean}, $R^{APT/E}$ and $R^{APT/T2}$ can be used to distinguish HGG and meningioma to a better degree. The APT_{mean} of HGG is significantly higher than that of meningioma, and the changes in the APT image range brought by HGG are more obvious than those of meningioma. The enhancement degree of meningioma and HGG is mostly moderate or marked enhancement, so the degree of enhancement cannot be used to distinguish these two diseases.

In the ROC curve analysis (**Figure 1C**), $R^{APT/E}$ (AUC=0.973, CI: 0.932-1.000), $R^{APT/T2}$ (AUC=0.912, CI: 0.782-1.000), APT_{mean} (AUC=0.976, CI: 0.938-1.000) values were significantly different between patients in the HGG and meningioma groups (p<0.001), which allowed a high diagnostic efficiency. The cut-off value for $R^{APT/E}$ was 1.123 with a sensitivity of 93.3% and a specificity of 88.0%. The cut-off value of $R^{APT/T2}$ was 1.101, the sensitivity was 86.7%, and the specificity was 92.0%. This shows that compared to that on enhanced images, the change in the APT range of HGGs increased by more than 12.3%, and this change also reached more than 10.1% compared with that on T2WI scans. The cut-off of the APT value was 3.840, the sensitivity was 93.3%, and the specificity was 92.0%. This finding indicated that the APT_{mean} of HGGs was significantly higher than that of meningiomas.

3.3.3 Differential Diagnosis of LGGs and HGGs by APT

Dunn's test results showed that the degree of enhancement (p=0.001) and APT_{mean} (p<0.001) were statistically significant. However, $R^{APT/E}$ (p=0.299) and $R^{APT/T2}$(p=0.969) were not statistically significant (p>0.01). This shows that the APT_{mean} and the enhancement degree can better distinguish HGGs and LGGs. HGGs usually have a high degree of enhancement, and the APTmean is also higher than that of LGGs.

The ROC curve analysis (**Figure 1D**) demonstrated that the enhancement (AUC=0.920, CI: 0.768-1.000) and APT_{mean} (AUC=0.913, CI: 0.720-1.000) were significantly different between

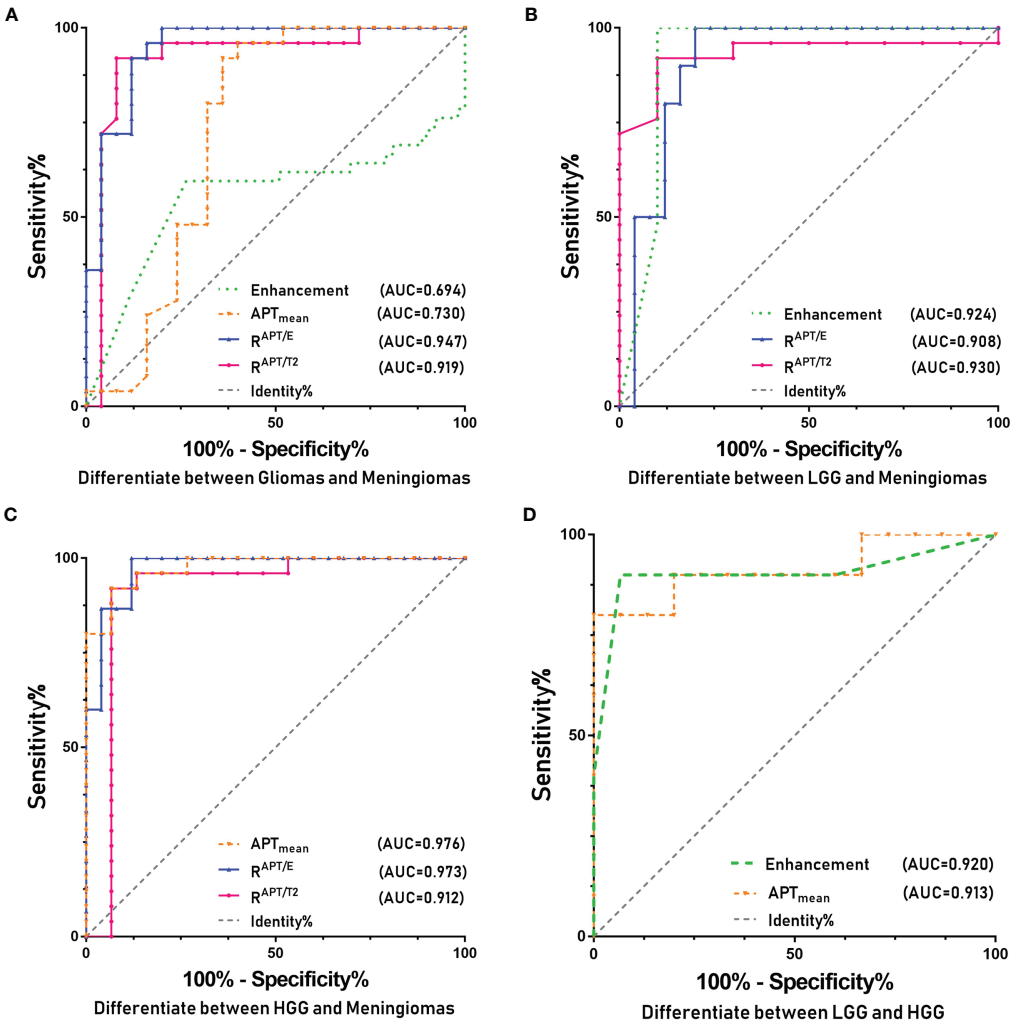

FIGURE 1 | ROC curves of the various parameters of APT and for identifying different types of tumors. **(A)** Glioma and meningioma. **(B)** LGG and meningioma. **(C)** HGG and meningioma. **(D)** LGG and HGG.

patients in the HGG and LGG groups ($p \leq 0.001$), which allowed a high diagnostic efficiency. The cut-off value of the APT value was 3.520, the sensitivity was 93.3%, and the specificity was 80.0%. The cut-off value for the degree of enhancement was 1.5, with a sensitivity of 100% and a specificity of 80%. This shows that the APT_{mean} of HGGs is higher, and the enhancement degree is above moderate enhancement.

We briefly summarize the above statistical results in **Table 2** for the differential diagnosis of HGG, LGG and meningioma. We sorted the invasiveness of glioma, LGG, and HGG compared with meningioma, as shown in **Figure 3**.

4 DISCUSSION

APT technology was first established by Zhou et al. of Johns Hopkins University by applying the most classic two-pool model, namely, a free water pool (solution) and an amide proton pool (solute) (18). Since peptides and proteins in the body generally contain amide bonds (-NH), the resonance frequency of hydrogen protons is 0 ppm, the resonance frequency of amide protons is 3.5 ppm, and the asymmetrical magnetization transfer rate (MTRasym) calculated by using the Z-spectrum can reflect the APT rate (19). Amide protons were saturated under continuous selective saturating radio frequency (RF) pulse irradiation. Exchange with free water *via* chemical shifts resulted in a reduction in the water signal. The reduction in this signal can indirectly reflect the changes in metabolites and pH changes in the substance; hence, it can be used to determine the content of amide protons in this region (20). This study used APT technology to study patients with gliomas and meningiomas and found an interesting phenomenon. The changes in the range of APT images caused by gliomas were more obvious than those of relatively benign meningiomas.

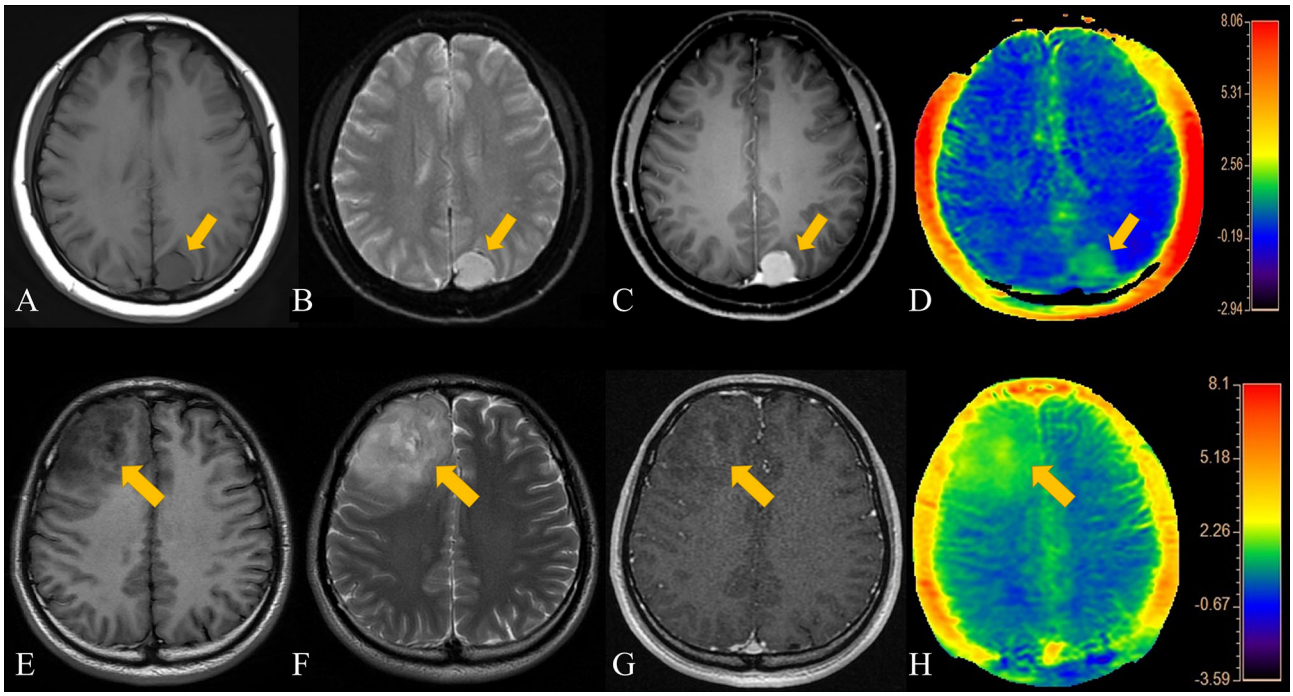

FIGURE 2 | Patient 1, a 44-year-old female, presented with a left parietal lobe meningioma. The patient's T2WI, contrast-enhanced MRI, and APT range were similar. **(A)** T1-weighted imaging showed an iso-slightly low signal. **(B)** T2-weighted imaging showed an iso-slightly high signal. **(C)** Enhanced MR imaging showed marked enhancement. **(D)** APT imaging shows a slightly higher rate of amide proton transfer. Patient 2, a 34-year- old male, had an LGG in the right frontal lobe. The APT signal range of the patient was slightly larger than that on both the T2WI and enhanced scans. **(E)** T1-weighted imaging showed an iso-slightly low signal. **(F)** T2-weighted imaging showed an iso-slightly high signal. **(G)** Enhanced MRI showed mild enhancement. **(H)** APT imaging showed that the amide proton transfer rate slightly increased.

TABLE 2 | APT and enhancement features to differentiate LGGs, HGGs, and meningiomas.

	LGGs and meningiomas	HGGs and meningiomas	LGGs and HGGs
Degree of enhancement	√, Enhancement degree of meningiomas is higher	X, Both were mainly significant enhancement	√, Enhancement degree of HGG is higher
APT_{mean}	X, Both have relatively low APT_{mean}	√, The APT_{mean} of HGG is significantly higher	√, HGG is significantly higher than LGG
$R^{APT/T2}$	√, LGG changes are more pronounced	√, HGG changes are more pronounced	X, Both LGGs and HGGs have strong tumour invasiveness to the brain
$R^{APT/E}$	√, LGG changes are more pronounced	√, HGG changes are more pronounced	X, Both LGGs and HGGs have strong tumour invasiveness to the brain

Ps: √-statistically significant, X-not statistically significant. (p<0.01 indicates statistical significance).

The use of conventional MRI for the diagnosis of glioma and meningioma is quite mature. For example, typical meningiomas have some obvious signs, such as the "meningeal tail " sign, which can be used for differential diagnosis. However, for the diagnosis of atypical meningioma or meningeal enhancement caused by glioma, APT technology can assist in the differential diagnosis to a certain extent. At the same time, combining APT with conventional MRI images has been shown to yield better diagnostic performance. For example, compared with significantly enhanced meningiomas, HGG has a higher APT_{mean} value, and the change range of APT images is larger than that of conventional images. APT measurements can help differentiate gliomas from meningiomas; however, these measurements are less effective for differentiating LGGs with a lower MTRasym from meningiomas. However, the enlargement range of APT compared with traditional MR images caused by HGGs or LGGs is more obvious than that of meningiomas. We cannot directly conclude that this is the extent of glioma brain infiltration. Moreover, we have no pathological confirmation, but this change does exist compared to more benign meningiomas. Our study can only indicate that APT imaging may have some value in the determination of malignant brain tumour boundaries, but there is no doubt that this approach can be used in the differential diagnosis between gliomas and meningiomas.

In fact, the use of APT in the differential diagnosis of brain tumors is well established, but its use has mainly focused on the differentiation of solitary brain metastases (SBMs) and

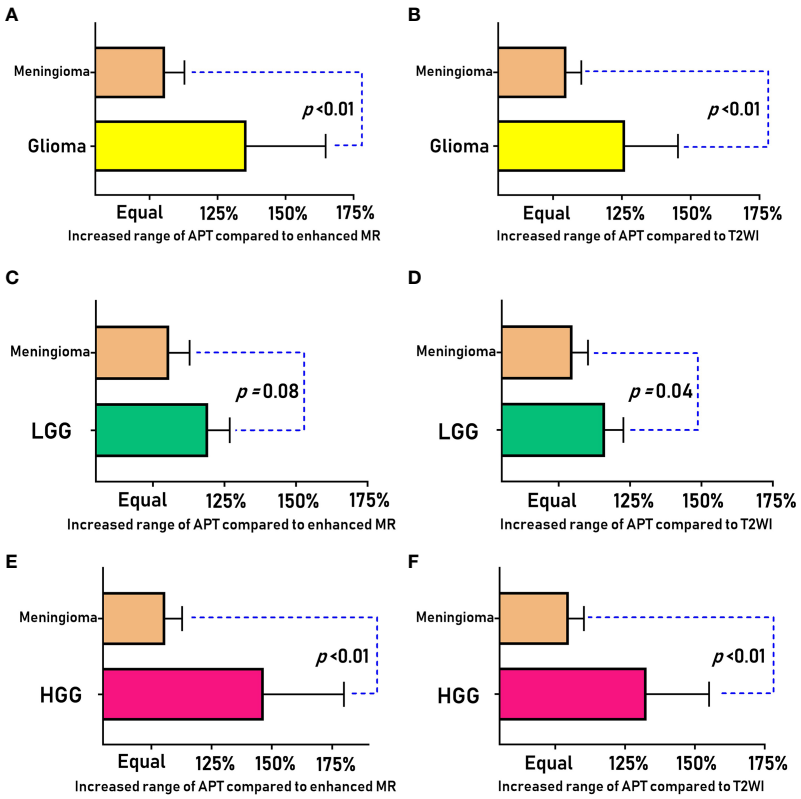

FIGURE 3 | Comparison of the APT enlargement range ($R^{APT/T2}$ and $R^{APT/E}$) between meningiomas and gliomas (LGG and HGG).

glioblastomas (GBMs) (21). Both Yu and Kamimura's studies found that the APT value of GBMs was higher than that of SBMs, which can be used for the differential diagnosis of GBMs (22, 23). However, it is interesting that, in Kamimura's study, we found that the APT value in the nonenhanced T2WI-increased area around GBMs was significantly higher than that in the corresponding T2WI-increased area of SBMs. Our study on gliomas and meningiomas also had similar results. Relatively benign meningiomas had lower APT values, but we found that gliomas caused changes in the APT range that were even larger than the range detected by T2WI, and LGGs also had similar performance to HGGs. The range of these changes was more than 9%, and these changes can even be directly judged by the naked eye. Combined with the enhancement degree and APT value, these changes can effectively help clinicians accurately identify gliomas and meningiomas.

"Ischaemic penumbra" is a concept of acute cerebral ischaemia, referring to the area of brain tissue that can be recovered with prompt medical treatment, usually referring to the area of brain tissue between DWI and perfusion-weighted imaging (PWI) (24). Gliomas also lead to the appearance of similar areas of tissue due to tumour brain infiltration, that is, the areas shown by conventional MR and the true borders of gliomas. The delineation of this boundary determines the extent of the operation and the prognosis of the patient's survival (25). Similar to the use of intraoperative fluorescent probes, tumors can be radically removed as much as possible while preserving the patient's normal brain tissue area (26). Our thinking is similar to that of most scholars; the changes in gliomas should first be the infiltration of microscopic tumour cells and the accumulation of metabolites and then the formation of tumors and corresponding tumor blood vessels (27). Notably, there are many techniques used in the preoperative evaluation of brain stromal tumors, including PWI, DWI, MRS, etc. Compared with the improved enhancement caused by the destruction of the BBB (usually HGGs are more likely to cause BBB disruption than LGGs), PWI can more effectively respond to the blood supply of gliomas, and the range of APT that can respond to substance metabolism should be larger than that of PWI (28, 29). Some of our patients also underwent PWI. For example, the suitable range for PWI in the patient with HGG in **Figure 4** was also significantly smaller than that of APT. If enough similar patients are evaluated, this result should be verifiable. Compared with PWI, DWI or conventional MRI, APT may have higher sensitivity in the early stage of brain tumour infiltration, and it also has a certain role in determining the tumour infiltration boundary. Thus, it is helpful for determining the scope of surgery.

Importantly, there are two main ways to verify the imaging boundary of glioma brain infiltration: 1. Pathological examination of the area showing changes on images; if the corresponding pathological results could be obtained, they could be directly confirmed. However, the main difficulty of this method lies in the extended clinical resection and the correspondence between pathological tissue and imaging. 2. For the correspondence

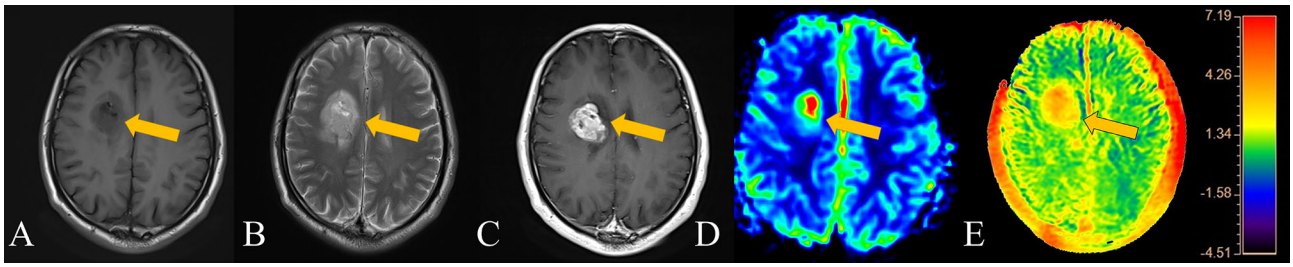

FIGURE 4 | Patient 3, a 62-year-old male, has an HGG in the right basal ganglia. The APT signal range of the patient was obviously larger than that on both T2WI and enhanced scans and larger than that on PWI. **(A)** T1-weighted imaging showed an iso-slightly low signal. **(B)** T2-weighted imaging showed an iso-slightly high signal. **(C)** Enhanced MR imaging showed obvious enhancement. **(D)** PWI showed marked hyper-perfusion. **(E)** APT imaging shows that the amide proton transfer rate obviously increased.

between the scope of resection and preoperative images, the patients were followed up for recurrence, and the survival time was recorded. At present, many studies have proven that APT can be applied to the judgement of recurrence and pseudo-progression. However, if the lesions can be completely removed before surgery, the patients' prognosis and treatment can be improved, and the need for a second surgery can be reduced (30).

Limitations of our research: 1. The number of patients was relatively small. 2. There was a lack of pathological results for whether the enlarged area of APT compared with conventional MR was a brain area infiltrated with tumors. 3. At present, this was only a study comparing APT and conventional MR images; if adequate functional imaging evaluation can be added, it will be possible to evaluate patients with brain tumors more comprehensively.

In conclusion, this study found that $R^{APT/E}$, $R^{APT/T2}$ and APT_{mean} can be better for the differential diagnosis of glioma and meningioma. APT combined with conventional imaging enhancement can better differentiate between LGGs, HGGs and meningiomas.

DATA AVAILABILITY STATEMENT

The raw data supporting the conclusions of this article will be made available by the authors, without undue reservation.

ETHICS STATEMENT

The studies involving human participants were reviewed and approved by Clinical Research Ethics Committee of Shenzhen Second People's Hospital. Written informed consent from the participants' legal guardian/next of kin was not required to participate in this study in accordance with the national legislation and the institutional requirements.

AUTHOR CONTRIBUTIONS

H-WZ contributed to the conception of the study; H-BZ, Y-QL, and X-LL contributed significantly to analysis and manuscript preparation; KD, FL, and Y-LW performed the data analyses and wrote the manuscript; YL, BH, and Y-NF helped perform the analysis with constructive discussions. All authors contributed to the article and approved the submitted version.

FUNDING

This study is supported by a grant from National Natural Science Foundation of China (Grant Number: 82071871),Youth Exploration Fund of Shenzhen Health Economics Society (Grant Number: 202211), Clinical Research Project of Shenzhen Second People's Hospital, China (Grant Number: 20193357021), and Clinical Research Project of Shenzhen Second People's Hospital, China (Grant Number: 20203357036).

ACKNOWLEDGMENTS

We would like to thank Ms. Siling Gu for her help in this research.

REFERENCES

1. Heiden MGV, Cantley LC, Thompson CB. Understanding the Warburg Effect: The Metabolic Requirements of Cell Proliferation. *Science* (2009) 324 (5930):1029–33. doi: 10.1126/science.1160809
2. Gomes AP, Ilter D, Low V, Endress JE, Fernández-García J, Rosenzweig A, et al. Age-Induced Accumulation of Methylmalonic Acid Promotes Tumour Progression. *Nature* (2020) 585(7824):283. doi: 10.1038/s41586-020-2630-0
3. Ohshima K, Morii E. Metabolic Reprogramming of Cancer Cells During Tumor Progression and Metastasis. *Metabolites* (2021) 11(1):28. doi: 10.3390/metabo11010028
4. Venkataramani V, Tanev DI, Strahle C, Studier-Fischer A, Fankhauser L, Kessler T, et al. Glutamatergic Synaptic Input to Glioma Cells Drives Brain Tumour Progression. *Nature* (2019) 573(7775):532. doi: 10.1038/s41586-019-1564-x
5. Smits M, van den Bent MJ. Imaging Correlates of Adult Glioma Genotypes. *Radiology* (2017) 284(2):316–31. doi: 10.1148/radiol.2017151930

6. Patel SH, Poisson LM, Brat DJ, Zhou Y, Cooper L, Snuderl M, et al. T2-FLAIR Mismatch, an Imaging Biomarker for IDH and 1p/19q Status in Lower-Grade Gliomas: A TCGA/TCIA Project. *Clin Cancer Res* (2017) 23(20):6078–85. doi: 10.1158/1078-0432.CCR-17-0560
7. Kumari N, Thakur N, Cho HR, Choi SHJSR. Assessment of Early Therapeutic Response to Nitroxoline in Temozolomide-Resistant Glioblastoma by Amide Proton Transfer Imaging: A Preliminary Comparative Study With Diffusion-Weighted Imaging. *Sci Rep* (2019) 9(1):5585. doi: 10.1038/s41598-019-42088-y
8. Suh CH, Kim HS, Jung SC, Choi CG, Kim SJ. Multiparametric MRI as a Potential Surrogate Endpoint for Decision-Making in Early Treatment Response Following Concurrent Chemoradiotherapy in Patients With Newly Diagnosed Glioblastoma: A Systematic Review and Meta-Analysis. *Eur Radiol* (2018) 28(6):2628–38. doi: 10.1007/s00330-017-5262-5
9. Yu J, Chen FF, Zhang HW, Zhang H, Luo SP, Huang GD, et al. Comparative Analysis of the MRI Characteristics of Meningiomas According to the 2016 WHO Pathological Classification. *Technol Cancer Res Treat* (2020) 19:1533033820983287. doi: 10.1177/1533033820983287
10. Dreher C, Oberhollenzer J, Meissner JE, Windschuh J, Schuenke P, Regnery S, et al. Chemical Exchange Saturation Transfer (CEST) Signal Intensity at 7T MRI of WHO IV Degrees Gliomas is Dependent on the Anatomic Location. *J Magn Reson Imaging* (2019) 49(3):777–85. doi: 10.1002/jmri.26215
11. Su C, Zhao L, Li S, Jiang J, Cai K, Shi J, et al. Amid Proton Transfer (APT) and Magnetization Transfer (MT) MRI Contrasts Provide Complimentary Assessment of Brain Tumors Similarly to Proton Magnetic Resonance Spectroscopy Imaging (MRSI). *Eur Radiol* (2019) 29(3):1203–10. doi: 10.1007/s00330-018-5615-8
12. Dai H, Jiang C, Wu G, Huang R, Jin X, Zhang Z, et al. A Combined DTI and Resting State Functional MRI Study in Patients With Postherpetic Neuralgia. *Japanese J Radiol* (2020) 38(5):440–50. doi: 10.1007/s11604-020-00926-4
13. Sotirios B, Demetriou E, Topriceanu CC, Zakrzewska Z. The Role of APT Imaging in Gliomas Grading: A Systematic Review and Meta-Analysis. *Eur J Radiol* (2020) 133:109353. doi: 10.1016/j.ejrad.2020.109353
14. Suh CH, Park JE, Jung SC, Choi CG, Kim SJ, Kim HS., et al. Amide Proton Transfer-Weighted MRI in Distinguishing High- and Low-Grade Gliomas: A Systematic Review and Meta-Analysis. *Neuroradiology* (2019) 2019(1):525–34. doi: 10.1007/s00234-018-02152-2
15. Park JE KH, Park SY JS, Kim JH HH. Identification of Early Response to Anti-Angiogenic Therapy in Recurrent Glioblastoma: Amide Proton Transfer-Weighted and Perfusion-Weighted MRI Compared With Diffusion-Weighted MRI. *Radiology* (2020) 295(2):397–406. doi: 10.1148/radiol.2020191376
16. Yu H, Wen X, Wu P, Chen Y, Zou T, Wang X, et al. Can Amide Proton Transfer-Weighted Imaging Differentiate Tumor Grade and Predict Ki-67 Proliferation Status of Meningioma? *Eur Radiol* (2019) 29(10):5298–306. doi: 10.1007/s00330-019-06115-w
17. Joo B, Han K, Choi YS, Lee SK, Ahn SS, Chang JH, et al. Amide Proton Transfer Imaging for Differentiation of Benign and Atypical Meningiomas. *Eur Radiol* (2018) 28(1):331–9. doi: 10.1007/s00330-017-4962-1
18. Zhou J, Heo HY, Knutsson L, Zijl PV, Jiang S. APT-Weighted MRI: Techniques, Current Neuro Applications, and Challenging Issues. *J Magn Reson Imaging* (2019) 50(2):347–64. doi: 10.1002/jmri.26645
19. Heo H-Y, Jones CK, Hua J, Yadav N. Whole-Brain Amide Proton Transfer (APT) and Nuclear Overhauser Enhancement (NOE) Imaging in Glioma Patients Using Low-Power Steady-State Pulsed Chemical Exchange Saturation Transfer (CEST) Imaging at 7T. *J Magn Reson Imaging* (2016) 40(9):41–50. doi: 10.1002/jmri.25108
20. Jiang S, Yu H, Wang X, Lu S, Li Y, Feng L, et al. Molecular MRI Differentiation Between Primary Central Nervous System Lymphomas and High-Grade Gliomas Using Endogenous Protein-Based Amide Proton Transfer MR Imaging at 3 Tesla. *Eur Radiol* (2016) 26(1):64–71. doi: 10.1007/s00330-015-3805-1
21. Yang Y, Qu X, Huang Y, Afsar K, Yan G, Guo G, et al. Preliminary Application of 3.0 T Magnetic Resonance Chemical Exchange Saturation Transfer Imaging in Brain Metastasis of Lung Cancer. *BMC Med Imaging* (2020) 20(1):4. doi: 10.1186/s12880-019-0400-y
22. Yu H, Lou H, Zou T, Wang X, Jiang S, Huang Z, et al. Applying Protein-Based Amide Proton Transfer MR Imaging to Distinguish Solitary Brain Metastases From Glioblastoma. *Eur Radiol* (2017) 27(11):4516–24. doi: 10.1007/s00330-017-4867-z
23. Kamimura K, Nakajo M, Yoneyama T, Fukukura Y, Hirano H, Goto Y, et al. Histogram Analysis of Amide Proton Transfer-Weighted Imaging: Comparison of Glioblastoma and Solitary Brain Metastasis in Enhancing Tumors and Peritumoral Regions. *Eur Radiol* (2019) 29(8):4133–40. doi: 10.1002/mrm.28764
24. Bhattacharjee R, Gupta RK, Das B, Dixit VK, Gupta P, Singh A. Penumbra Quantification From MR SWI-DWI Mismatch and its Comparison With MR ASL PWI-DWI Mismatch in Patients With Acute Ischemic Stroke. *Nmr Biomed* (2021) 34(7):e4526. doi: 10.1002/nbm.4526
25. Gao XH, Li C. Nanoprobes Visualizing Gliomas by Crossing the Blood Brain Tumor Barrier. *Small* (2014) 10(3):426–40. doi: 10.1002/smll.201301673
26. Yan H, Wang L, Wang J, Weng X, Lei H, Wang X, et al. Two-Order Targeted Brain Tumor Imaging by Using an Optical/Paramagnetic Nanoprobe Across the Blood Brain Barrier. *ACS Nano* (2012) 6(1):410–20. doi: 10.1021/nn203749v
27. Zhang XY, Zhai YT, Jin ZY, Li C, Sun PZ, Wu Y. Preliminary Demonstration of *In Vivo* Quasi-Steady-State CEST Postprocessing-Correction of Saturation Time and Relaxation Delay for Robust Quantification of Tumor MT and APT Effects. *Magn Reson Med* (2021) 86(2):943–53. doi: 10.1002/mrm.28764
28. Zhang HW, Lyu GW, He WJ, Lei Y, Lin F, Feng YN, et al . Differential Diagnosis of Central Lymphoma and High-Grade Glioma: Dynamic Contrast-Enhanced Histogram. *Acta Radiol* (2020) 61(9):1221–27. 284185119896519. doi: 10.1177/0284185119896519
29. Zhang HW, Lyu GW, He WJ, Lei Y, Lin F, Wang MZ, et al. DSC and DCE Histogram Analyses of Glioma Biomarkers, Including IDH, MGMT, and TERT, on Differentiation and Survival. *Acad Radiol* (2020) 27(12):e263–e271. doi: 10.1016/j.acra.2019.12.010
30. Wong KK, Rostomily R, Wong STC. Prognostic Gene Discovery in Glioblastoma Patients Using Deep Learning. *Cancers (Basel)* (2019) 11 (1):53. doi: 10.3390/cancers11010053

Conflict of Interest: The authors declare that the research was conducted in the absence of any commercial or financial relationships that could be construed as a potential conflict of interest.

Publisher's Note: All claims expressed in this article are solely those of the authors and do not necessarily represent those of their affiliated organizations, or those of the publisher, the editors and the reviewers. Any product that may be evaluated in this article, or claim that may be made by its manufacturer, is not guaranteed or endorsed by the publisher.

Copyright © 2022 Zhang, Liu, Zhang, Li, Wang, Feng, Deng, Lei, Huang and Lin. This is an open-access article distributed under the terms of the Creative Commons Attribution License (CC BY). The use, distribution or reproduction in other forums is permitted, provided the original author(s) and the copyright owner(s) are credited and that the original publication in this journal is cited, in accordance with accepted academic practice. No use, distribution or reproduction is permitted which does not comply with these terms.

frontiers | Frontiers in Neurology

ORIGINAL RESEARCH
published: 12 May 2022
doi: 10.3389/fneur.2022.895638

Surgical Effects of Resecting Skull Base Tumors Using Pre-operative Multimodal Image Fusion Technology: A Retrospective Study

Zhi-heng Jian[1†], Jia-yan Li[1†], Kai-hua Wu[1], Yu Li[1], Shi-xue Li[1], Hai-dong Chen[2] and Gang Chen[1]*

[1] Department of Neurosurgery, Zhuhai People's Hospital (Zhuhai Hospital Affiliated With Jinan University, China), Zhuhai, China, [2] Department of Radiology, Zhuhai's People Hospital, Zhuhai, China

Objectives: To analyze the surgical effects of resecting skull base tumors using multimodal three-dimensional (3D) image fusion technology in the neurosurgery department and present some typical cases.

Methods: From October 2019 to October 2021, we included 47 consecutive patients with skull base tumors in the Neurosurgery Department at Zhuhai People's Hospital in this study. Pre-operative head computed tomography and magnetic resonance imaging data acquisition was performed using the GE AW workstation software for registration fusion, image fusion, and 3D reconstruction. The surgical approach and surgical plan were designed based on the multimodal 3D image, and the resection rate, complication rate, and operative time of the surgery using the multimodal image fusion technique were analyzed.

Results: The reconstructed multimodal 3D images precisely demonstrated the size, location, and shape of the tumor along with the anatomical relationship between the tumor and surrounding structures, which is consistent with the intraoperative findings. Among 47 patients, 39 patients (78.7%) underwent total resection, 5 (14.9%) underwent subtotal resection, and 3 (6.4%) underwent partial resection. The mean operative time was 4.42 ± 1.32 h. No patient died during the inpatient period. Post-operative complications included 6 cases of cerebrospinal fluid leakage (14.9%), 3 cases of intracranial infection (6.4%), 6 cases of facial paralysis (12.8%), 2 cases of dysphagia (4.3%), and 1 case of diplopia (2.1%), all of which were improved after symptomatic treatment. The application value of pre-operative 3D image fusion technology was evaluated as outstanding in 40 cases (85.1%) and valuable in 7 cases (14.9%).

Conclusions: Pre-operative multimodal image fusion technology can provide valuable visual information in skull base tumor surgery and help neurosurgeons design the surgical incision, choose a more rational surgical approach, and precisely resect the tumor. The multimodal image fusion technique should be strongly recommended for skull base tumor surgery.

Keywords: image infusion, skull base tumor, cerebral fluid leakage, skull base reconstruction, micro-surgical procedure, neurosurgery

OPEN ACCESS

Edited by:
Sandro M. Krieg, Technical University of Munich, Germany

Reviewed by:
Mirza Pojskic, University Hospital of Giessen and Marburg, Germany
Jan Egger, University Hospital Essen, Germany

***Correspondence:**
Gang Chen
jhy_501@163.com

[†] *These authors share first authorship*

Specialty section:
This article was submitted to Neuro-Oncology and Neurosurgical Oncology, a section of the journal Frontiers in Neurology

Received: *14 March 2022*
Accepted: *04 April 2022*
Published: *12 May 2022*

Citation:
Jian Z-h, Li J-y, Wu K-h, Li Y, Li S-x, Chen H-d and Chen G (2022) Surgical Effects of Resecting Skull Base Tumors Using Pre-operative Multimodal Image Fusion Technology: A Retrospective Study. Front. Neurol. 13:895638. doi: 10.3389/fneur.2022.895638

INTRODUCTION

Skull base tumors are a spectrum of tumor deriving from bone structure, dura mater, brain tissue, and outer cranial tissue adjoin with the skull base. They also have a large number of branching vessels involved in the blood supply, so intraoperative bleeding can easily cause an unclear surgical field (1–3). Moreover, some skull base tumors are accompanied by destruction of the skull base bone structure (4, 5). The total resection rate varies from 57 to 77% (6–10). Skull base tumor surgery requires a high order of neuroanatomical knowledge and a substantial surgical experience; therefore, it has been recognized as one of the most challenging types of neurosurgery. Yet, single-mode imaging has been unable to meet the soaring demand of microinvasion and precise resection in neurosurgery, especially in skull base tumor resection. Multimodal image fusion is a three-dimensional (3D) reconstruction of multiple image data on the same image that provides a clear, intuitive, and overall display of the tumor and its spatial relationship with peripheral vessels, nerves, and brain tissue, as well as the skull structure related to the surgical approach. By applying to this technique, neurosurgeons can design a more rationale surgical approach to skull base tumor surgery, avoid unexpected injury, better protect the normal skull structure, and reduce complications (11–14). This technology was introduced in our department in October 2019. The present study aimed to analyze the surgical effects of resecting skull base tumors using multimodal 3D image fusion technology in the neurosurgery department and present some typical cases.

MATERIALS AND METHODS

Ethics Statements

This study was approved by the Medical Ethics Committee of Zhuhai People's Hospital (Number: ZY.no20201001B06011231).

Study Design and Patient Population

In total, 47 consecutive patients with skull base tumors who were admitted to the Neurosurgery Department of Zhuhai People's Hospital underwent microcraniotomy from October 2019 to September 2021 and were screened for the present retrospective study.

Image Data Collection and Examination Methods

A computed tomography (CT) examination was performed using a GE Revolution CT (128-row) scanner (Boston, MA, USA) with a scan thickness of 1 mm. A Philips 3.0T Achieva TX MR scanner (Amsterdam, the Netherlands) was used for the magnetic resonance imaging (MRI) examination, and the imaging sequence included T1-weighted imaging (T1WI), T1WI 3D turbo field echo, T2-weighted imaging 3D fluid-attenuated inversion recovery (FLAIR), 3D phase contrast angiography magnetic resonance (MR) venography (MRV), contrast-enhance magnetic resonance angiography (MRA), 3D time of flight MRA, etc.

Image Acquisition and Multimodal Image Fusion

CT and MR image data (Digital Imaging and Communications in Medicine format) of all patients were downloaded from the HIS information system, and then the image data were uploaded to the GE AW workstation. Corresponding image sequences were opened in the workstation to complete registration fusion and 3D reconstruction. Automatic registration and manual registration are used for registration. Automatic alignment imports required image data such as MR sequences and CT data, and then the Infusion function was selected for automatic matching. Manual registration uses characteristic anatomical markers (e.g., the center of the eyeball, pituitary fossa, sinuses, mastoid apex, digastric sulcus apex, etc.) as reference points. Three to five reference points were used for each case. The Smart Brush function was used to draw the outline of the tumor, and then the MRA, MRV, and other images were fused with the tumor to form the 3D digital anatomical image of the tumor and vessels. Finally, the 3D reconstruction image of the skull was added to the 3D image of the tumor with blood vessels by CT to complete the multimodal image fusion.

Surgical Treatment Assisted by Multimodal Image Fusion Technology

All patients were operated by one senior surgeon. Multimodal image fusion and 3D reconstruction were used to demonstrate the spatial relationship of the tumor and surrounding structures (**Figure 1A**). Specific details such as bony defection was evaluated (**Figure 1B**). Approach stimulation was performed based on the 3D reconstructed image (**Figure 1C**). The incision design was based on the stimulation result (**Figure 1D**). Intraoperative resection was performed along the tumor boundary, and attention was paid to protect the tumor and important tissues, such as the surrounding arteries, veins, and nerves, to achieve the maximum possible total tumor resection. For tumors invading the cavernous sinus, internal carotid artery, cranial nerves, and other tissues, subtotal resection or partial resection can be performed, and stereotactic radiotherapy should be performed after to detect residual tumors (**Figure 1E**). The post-operative image was used to evaluate the surgical effect (**Figure 1F**).

Evaluation Criteria of the Application Value

The evaluation method of the application value of multimodal image fusion technology was based on Oishi et al.'s (15) study. All patients were operated by one senior surgeon and the overall application value was estimated by the surgeon after surgery. The evaluation grade was divided into three levels:

(1) Prominent: pre-operative multimodal image fusion technology is important to completion of the operation, and the expected surgical effect cannot be achieved by using single modal images only;
(2) Supportive: a single modal image can also achieve the expected surgical effect, but multimodal image fusion technology can provide a clearer and more intuitive demonstration of fine structures, which can reduce the injury of surgical collateral and benefit surgery; and

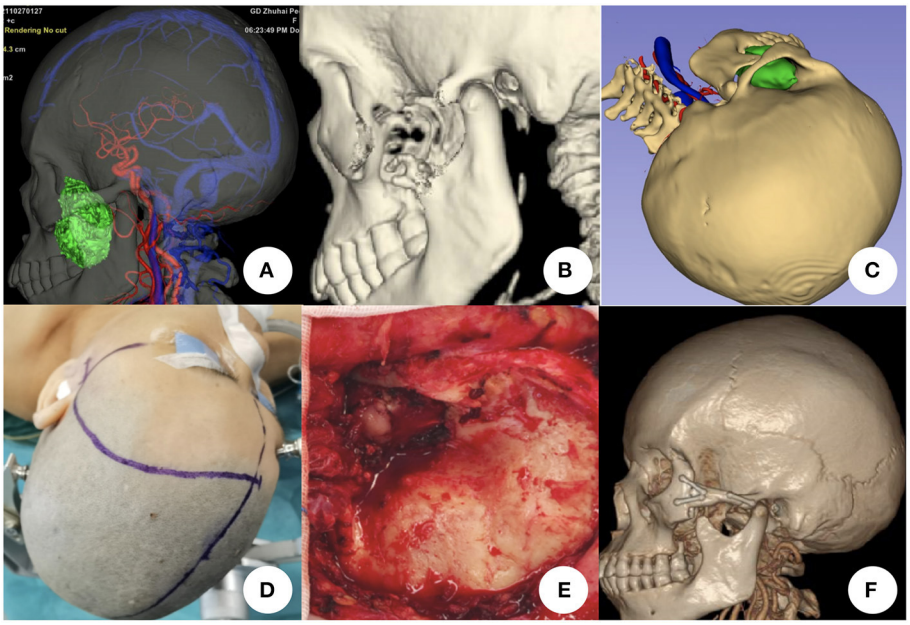

FIGURE 1 | Surgical plan for resecting skull base tumors using multimodal image fusion technology. **(A)** Tumor in the left infra-temporal fossa shown by multimodal image fusion [combined with head computed tomography (CT), magnetic resonance imaging, magnetic resonance angiography, and magnetic resonance venography]. **(B)** Bony defect is demonstrated by head CT three-dimensional (3D) reconstruction. **(C)** Simulation of the surgical plan using multimodal fusion and 3D images. **(D)** Incision design based on simulated approach. **(E)** Tumor exposure and resection during the surgical procedure; the zygomatic arch is removed. **(F)** Post-operative head CT scan and 3D reconstruction showing that the tumor was totally resected and the zygomatic arch was reconstructed.

(3) No value: surgery can be completed as expected through using of a single modal image only, without the assistance of multimodal image fusion technology.

The evaluation criteria were as follows:

(1) whether the choice of surgical approach was appropriate;
(2) whether the judgment of spatial location of tumor was accurate;
(3) whether the location and adjacent relationship of vessels were accurate;
(4) whether the adjacent relationship between the tumor and venous sinus was accurate;
(5) whether the exposure of bone window was sufficient; and
(6) whether the surgical procedure was consistent with the pre-operative judgment.

Surgical Resection Rate, Post-operative Complication Rate, and Follow-Up

Surgical Resection Rate

The total resection rate was determined based on the following brain MR examination results within 1–3 days after the operation (1):

(1) total resection (100% tumor resection with no radiographic residue);
(2) subtotal resection (more than 90% tumor volume reduction); and
(3) partial resection (0–90% tumor volume reduction) and unresection.

Complication Rate

The incidence of surgical complications during the perioperative period included olfactory disorders, blurred vision, protruding eyes, epistaxis, nasal obstruction, hearing loss, facial numbness, facial paralysis, eyelid closure, limb sensory, and limb motor disorders.

Operative Time

The operative time was estimated from the incision of the scalp to completion of tumor resection. The overall mean operative time was measured and analyzed.

Follow-Up

Patients were followed up within 3–12 months after surgery. Brain MR enhancement was reviewed to evaluate whether the tumor recurred or increased and assess whether there are new complications.

Statistical Analysis

The t-test and χ^2-test were used to compare the mean or frequency between the patient groups, respectively. Statistical analysis was performed using SPSS 25.0 (IBM Corp., Armonk, NY, USA). A P-value < 0.05 was considered to be statistically significant.

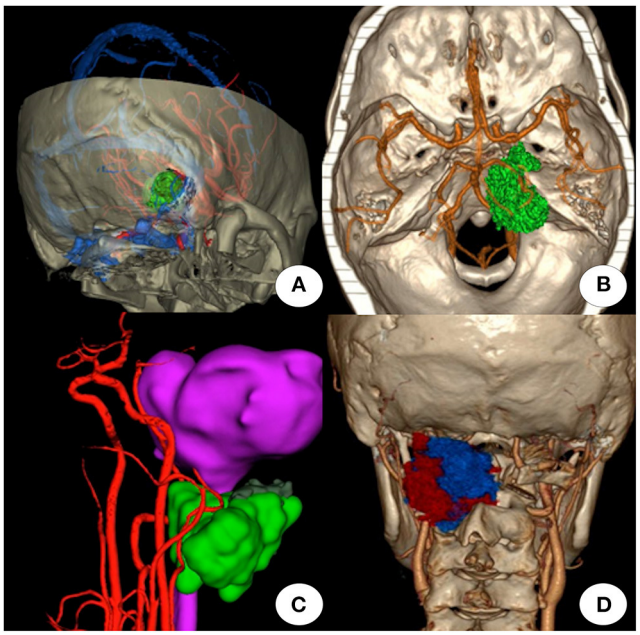

FIGURE 2 | Effectiveness of multimodal image fusion technology. **(A)** Surgical plan of the retrosigmoid approach using a multimodal image fusion image (combined with head computed tomography, magnetic resonance imaging, magnetic resonance angiography, and magnetic resonance venography). **(B)** Multimodal image fusion demonstrates the spatial relationship of the tumor and surrounding structures. **(C)** Multimodal image fusion demonstrates the relationship between the left vertebral artery and tumor (green). **(D)** Multimodal image fusion demonstrates the spatial relationship between the tumor (red and blue), artery, and surrounding bony structures.

RESULTS

Demographic and Clinical Characteristics

Forty-seven patients (19 men and 28 women) were included. Patients' average age was 51.11 ± 12.62 years (range, 12–77 years).

Multimodal Image Fusion Outcome

Pre-operative multimodal image fusion and reconstruction were completed in all 47 patients with skull base tumors. The 3D image after multimodal image fusion could be rotated arbitrarily, and the surface structure became transparent or translucent to show the internal structure of interest, when enabled design of the surgical approach and plan (**Figure 2A**). The spatial relationship of the tumor and surrounding structures (**Figure 2B**), spatial relationship of the vessels and lesions (**Figure 2C**), and demonstration of the intracranial communication lesion (**Figure 2D**) were all consistent with the intraoperative findings.

Clinical Outcome

Tumor Characteristics

(1) Anterior skull base: There were left cranio-orbital communication tumors in 2 cases, olfactory groove/sphenoid platform meningiomas in 6 cases (left side, 3 cases; right side, 2 cases), and sphenoid ridge meningiomas in 3 cases (right side, 3 cases).
(2) Middle skull base: There were tumors in the saddle area/cavernous sinus area in 8 cases (left cavernous sinus area, 6 cases; right cavernous sinus area, 2 cases), temporal base/inferior temporal fossa in 6 cases (left side, 2 cases; right side, 4 cases), and petroclival area in 5 cases (left side, 4 cases; right side, 1 case).
(3) Posterior skull base: There were tumors in the cerebellopontine angle (CPA) area in 10 cases (left side, 5 cases; right side, 5 cases), jugular foramen in 2 cases (left side, 2 cases), and occipitocervical junction in 4 cases (left side, 2 cases; right side, 2 cases).
(4) There were 14 cases of intracranial communication and 33 cases of non-intracranial communication. Recurrent tumors developed in 9 cases, and malignancy occurred in 6 cases. The volume of the mass was >3 cm^3 in 32 cases (**Table 1**).

Pathology of the Tumors

There were meningiomas in 23 cases, schwannomas in 14 cases, metastatic tumors in 3 cases, a spindle cell tumor in 1 case, mesenchymal malignant tumor in 1 case, giant cell granuloma in 1 case, cholesteatoma in 1 case, squamous cell carcinoma of the left external auditory canal with petrosal bone and temporal base infiltration in 1 case, pituitary adenoma in 1 case, and choroid plexus papilloma in 1 case (**Table 2**).

Outcome of Surgical Resection

Total resection was performed in 39 cases (39/47, 78.7%), subtotal resection in 5 cases (7/47, 14.9%), and partial resection in 3 cases (3/47, 6.4%). No perioperative deaths occurred. The cases of subtotal resection included a left trigeminal schwannoma in 1 case, right cavernous sinus meningioma in 1 case, breast cancer and brainstem metastasis in 1 case, and olfactory groove meningioma in 2 cases with ethmoid sinus infiltration in the maxillary sinus. Cases of partial resection included a left optic canal meningioma in 1 case, external auditory canal squamous cell carcinoma with left petrosal bone–temporal base infiltration in 1 case, and petroclival meningioma in 1 case. The differences of the tumor size, malignancy, recurrence and position of tumors were not statistical significant except the total resection rate of intracranial and extracranial communication tumors was lower than that of non-intracranial and extracranial communication tumors (71.4 and 87.9%, respectively, $P = 0.001$).

Operative Time

The mean operative time was 4.42 ± 1.32 h. The mean operative times in the anterior skull base group, middle skull base group, and posterior skull base group were 4.72 ± 0.98 h, 5.32 ± 1.28 h, and 3.92 ± 1.73 h, respectively. The differences of the tumor size, malignancy, recurrence and position of tumors were not statistical significant except the operation time of intracranial and extracranial communication tumors is longer than non-intracranial and extracranial communication tumors (5.72 ± 1.53 h and 4.12 ± 1.33 h, respectively, $P = 0.012$).

Complications

Six cases of cerebrospinal fluid leakage were cured by lumbar cistern drainage. Three cases of intracranial infection were treated with lumbar cistern drainage and antibiotic treatment. One case of intracranial hematoma was a meningioma of the

TABLE 1 | Characteristic of the 47 cases of tumors.

Position	Side		Communication		Tumor volume		Recurrence		Malignancy	
	Left	Right	Positive	Negative	>3 cm^3	<3 cm^3	Positive	Negative	Positive	Negative
Anterior	**5**	**5**	**3**	**7**	**7**	**3**	**3**	**7**	**2**	**8**
Frontal-orbital area	2	0	2	0	1	1	1	1	1	4
Planum sphenoidale	3	2	1	4	4	1	1	4	1	4
Sphenoid ridge	0	3	0	3	2	1	1	2	0	3
Middle	**12**	**7**	**7**	**12**	**12**	**7**	**3**	**16**	**3**	**16**
Cavernous sinus	6	2	3	5	6	2	2	6	0	8
Infra-temporal fossa	2	4	3	3	3	3	1	5	3	3
Petroclival region	4	1	1	4	3	2	0	5	0	5
Posterior	**10**	**8**	**4**	**14**	**13**	**5**	**3**	**15**	**1**	**17**
CPA region	5	5	0	10	8	2	1	9	0	10
Jugular foramen	2	0	0	2	2	0	0	2	0	2
Occipital-cervical region	2	2	4	0	3	1	2	2	0	4
Brain stem	1	1	0	2	0	2	0	2	1	1
Total	**27**	**20**	**14**	**33**	**32**	**15**	**9**	**38**	**6**	**41**

CPA, cerebello-pontine angle.

anterior skull base, so a secondary operation was performed to evacuate the hematoma and decompress the bone flap. One case of infraction was an olfactory groove meningioma that was cured by conservative treatment. There were 9 cases of cranial nerve dysfunction, including 6 cases of facial paralysis, 2 cases of dysphagia, and 1 case of oculomotor nerve paralysis; 6 patients improved after symptomatic treatment and hormone shock therapy. Two patients with posterior cranial nerve paralysis underwent tracheotomy and recovered after discharge.

Follow-Up

Forty-five cases were successfully followed up after discharge, and 2 cases missed follow-up. The 45 patients were followed up for 3–12 months, with an average of 7 months. One patient with metastatic lung cancer died. Among 39 patients who underwent total resection of the tumor, 2 patients had recurrence after surgery, namely 1 patient with a malignant meningioma of the anterior skull base and 1 patient with a trigeminal schwannoma. There were no new complications in the remaining 44 cases except 1 mortality.

Application Value of Multimodal Image Fusion Technology

Among 47 cases of skull base tumors, 40 cases were evaluated as prominent and 7 cases as supportive. The multimodal image fusion-assisted pre-operative approach was reasonable in all cases. The spatial location and surrounding tissue structure of the tumor reconstructed in all cases were consistent with the intraoperative findings. The reconstructed vessels, venous sinuses, and cranial nerves in all cases were consistent with the intraoperative findings. Two cases had overexposure of the bone window (**Table 3**).

TABLE 2 | Pathology of the tumors.

Pathology	Position			Total
	Anterior	Middle	Posterior	
Meningioma	8	12	3	23
Schwannoma	0	2	12	14
Metastasis	1	1	1	3
Spindle cell tumor	1	0	0	1
Cholesteatoma	0	0	1	1
Squamous carcinoma	0	1	0	1
Mesenchymal malignancy	0	1	0	1
Giant cell granuloma	0	1	0	1
Pituitary adenoma	0	1	0	1
Choroid plexus papilloma	0	0	1	1
Total	**10**	**19**	**18**	**47**

Representative Cases

Case 1: A 32-year-old man with a recurrent C2 schwannoma (**Supplementary Video 1**).

Case 27: A 52-year-old man with a recurrent spindle cell tumor of the left cranio-orbital communication (**Supplementary Video 2**).

Case 46: A 57-year-old woman with a lobular malignant tumor of the left infratemporal fossa (**Supplementary Video 3**).

DISCUSSION

Multimodal image fusion technology benefits pre-operative surgical planning and resection in all types of skull base tumor cases (16–18). In cases in which the retrosigmoid approach as used, we made the incision based on the multimodal fusion

TABLE 3 | Summary of cases, pre-surgical plan, and surgical outcomes.

Case no.	Location	Given evaluation	Spatial aspects of tumor	Arterial information	Venous information	Bone window	Surgical resection	Achievement
1	Occipital-cervical region	Prominent	Satisfactory	Satisfactory	Satisfactory	Reasonable	GTR	As planned
2	Frontal-orbital area	Prominent	Extension to the bone	Satisfactory	Satisfactory	Reasonable	PR	Inefficient removal due to extension to the bone
3	Planum sphenoidale	Supportive	Satisfactory	Satisfactory	Satisfactory	Reasonable	STR	Inefficient removal due to bleeding
4	Cavernous sinus	Prominent	Satisfactory	Satisfactory	Satisfactory	Reasonable	GTR	As planned
5	Sphenoid ridge	Supportive	Satisfactory	Satisfactory	Satisfactory	Reasonable	GTR	As planned
6	Cavernous sinus	Prominent	Satisfactory	Satisfactory	Satisfactory	Reasonable	GTR	As planned
7	Infra-temporal fossa	Prominent	Satisfactory	Satisfactory	Satisfactory	Reasonable	GTR	As planned
8	Petroclival region	Prominent	Extension to the bone	Satisfactory	Satisfactory	Reasonable	PR	Inefficient removal due to bleeding
9	Cavernous sinus	Prominent	Satisfactory	Satisfactory	Satisfactory	Reasonable	STR	Inefficient removal due to brain swelling
10	CPA region	Supportive	Satisfactory	Satisfactory	Damage to the petrosal vein	Reasonable	GTR	As planned
11	Jugular foramen	Prominent	Satisfactory	Satisfactory	Satisfactory	Reasonable	GTR	As planned
12	Planum sphenoidale	Prominent	Satisfactory	Satisfactory	Satisfactory	Overexposure	STR	Inefficient removal due to brain swelling
13	Occipital-cervical region	Prominent	Satisfactory	Satisfactory	Satisfactory	Reasonable	GTR	As planned
14	Planum sphenoidale	Supportive	Satisfactory	Satisfactory	Satisfactory	Reasonable	GTR	As planned
15	Planum sphenoidale	Prominent	Satisfactory	Satisfactory	Satisfactory	Reasonable	GTR	As planned
16	Cavernous sinus	Supportive	Extension to the major artery	Unable to fully demonstrate the degree of adhesion	Satisfactory	Reasonable	STR	Inefficient removal due to location of ICA and tumor
17	Sphenoid ridge	Prominent	Satisfactory	Satisfactory	Satisfactory	Reasonable	GTR	As planned
18	Cavernous sinus	Prominent	Satisfactory	Satisfactory	Satisfactory	Reasonable	GTR	As planned
19	Infra-temporal fossa	Prominent	Extension to the bone	Satisfactory	Satisfactory	Reasonable	PR	Inefficient removal due to bleeding
20	Petroclival region	Prominent	Satisfactory	Satisfactory	Satisfactory	Reasonable	GTR	As planned
21	CPA region	Prominent	Satisfactory	Satisfactory	Satisfactory	Reasonable	GTR	As planned
22	CPA region	Prominent	Satisfactory	Satisfactory	Satisfactory	Reasonable	GTR	As planned
23	Jugular foramen	Prominent	Satisfactory	Satisfactory	Satisfactory	Reasonable	GTR	As planned
24	Occipital-cervical region	Prominent	Satisfactory	Satisfactory	Satisfactory	Reasonable	STR	Inefficient removal due to bleeding
25	Occipital-cervical region	Supportive	Satisfactory	Satisfactory	Satisfactory	Reasonable	GTR	As planned
26	CPA region	Supportive	Satisfactory	Satisfactory	Satisfactory	Reasonable	GTR	As planned
27	Frontal-orbital area	Prominent	Satisfactory	Satisfactory	Satisfactory	Reasonable	GTR	As planned
28	Planum sphenoidale	Prominent	Satisfactory	Satisfactory	Satisfactory	Reasonable	GTR	As planned
29	Cavernous sinus	Prominent	Satisfactory	Satisfactory	Satisfactory	Reasonable	GTR	As planned
30	CPA region	Prominent	Satisfactory	Satisfactory	Satisfactory	Reasonable	GTR	As planned
31	Cavernous sinus	Prominent	Satisfactory	Satisfactory	Satisfactory	Reasonable	GTR	As planned
32	Infra-temporal fossa	Prominent	Satisfactory	Satisfactory	Satisfactory	Reasonable	GTR	As planned
33	Petroclival region	Prominent	Satisfactory	Satisfactory	Satisfactory	Reasonable	GTR	As planned
34	Cavernous sinus	Prominent	Satisfactory	Satisfactory	Satisfactory	Reasonable	GTR	As planned
35	CPA region	Prominent	Satisfactory	Satisfactory	Satisfactory	Reasonable	GTR	As planned
36	CPA region	Prominent	Satisfactory	Satisfactory	Satisfactory	Overexposure	GTR	As planned
37	CPA region	Prominent	Satisfactory	Satisfactory	Satisfactory	Reasonable	GTR	As planned
38	CPA region	Prominent	Satisfactory	Satisfactory	Satisfactory	Reasonable	GTR	As planned

(Continued)

TABLE 3 | Continued

Case no.	Location	Given evaluation	Spatial aspects of tumor	Arterial information	Venous information	Bone window	Surgical resection	Achievement
39	CPA region	Prominent	Satisfactory	Satisfactory	Satisfactory	Reasonable	GTR	As planned
40	Sphenoid ridge	Prominent	Satisfactory	Satisfactory	Satisfactory	Reasonable	GTR	As planned
41	Petroclival region	Prominent	Satisfactory	Satisfactory	Satisfactory	Reasonable	GTR	As planned
42	Infra-temporal fossa	Prominent	Satisfactory	Satisfactory	Satisfactory	Reasonable	GTR	As planned
43	CPA region	Prominent	Satisfactory	Satisfactory	Satisfactory	Reasonable	GTR	As planned
44	Petroclival region	Prominent	Satisfactory	Satisfactory	Satisfactory	Reasonable	GTR	As planned
45	CPA region	Prominent	Satisfactory	Satisfactory	Satisfactory	Reasonable	GTR	As planned
46	Infra-temporal fossa	Prominent	Satisfactory	Satisfactory	Satisfactory	Reasonable	GTR	As planned
47	Infra-temporal fossa	Prominent	Satisfactory	Satisfactory	Satisfactory	Reasonable	GTR	As planned

No., number; GTR, gross total resection; STR, sub-total resection; PR, partial resection; CPA, cerebello-pontine angle; ICA, internal carotid artery.

image, which clearly displayed the spatial relationship of the tumor, transverse sinus, and sigmoid sinus. The bone flap could also be precisely designed in all 47 cases, except for 2 cases of overexposure. In both cases (1 case of an olfactory groove meningioma and 1 case of an acoustic schwannoma), unexpected intraoperative brain swelling occurred and hampered the surgical site exposure. Overall, the main arteries and veins were consistent with the intraoperative findings. We evaluated the application value of every case involved in our study individually based on the evaluation criteria. Forty cases were prominent, which was substantial for the resection procedure, and 7 cases were supportive. In 7 supportive cases, 1 case was a cholesteatoma in the CPA region, 2 cases were meningiomas of the planum sphenoidale, and 1 case was a meningioma of the sphenoid ridge. Those 4 cases were both clearly located with no bone deconstruction, and no significant nerves or arteries were adhered to the tumor; this could be seen on the two-dimensional MR or CT scan. In 1 acoustic tumor case, the volume of the tumor was small and the auditory canal was not penetrated, so total resection was possible based on only the pre-operative MR image. In 1 case of an occipital-cervical schwannoma that was not adhered to the vertebral artery, the tumor was fully visible in the outer dura mater on the MR scan. Except 1 case of a squamous cell carcinoma of the left external auditory canal with petrosal bone and temporal base infiltration, the partial resection plan could only be determined intraoperatively due to the inability to fully observe the degree of adhesion between the tumor, internal cortical artery, and petrosal segment pre-operatively. In that case, a supportive evaluation was given. However, in MR T2-FLAIR sequence, the moisture content could be demonstrated so the degree of hardness could be primarily evaluated (19). In that case, a primary comprehensive MR image is still needed.

The total resection rate was 78.7%, which was mildly higher than that previously reported without the multimodal image fusion technique. In most previous cases, the number of intracranial and extracranial communication tumors and malignant tumors was lower than that of non-intracranial and extracranial communication tumors and benign tumors. Our study showed a similar result. Generally, when tumors have a high degree of adhesion with major blood vessels, the total resection rate is low. There were two post-operative cases shifted to radiotherapy department due to partial resection which were petroclival region meningioma for one case and infra-temporal fossa meningioma for one case. Both of those two cases were occurred unexpected intraoperative bleeding due to high adhesion.

The mean operative time was mildly shorter than that in some previous reports in which the multimodal image fusion technique were not applied (20–22). The operative time in the posterior skull base in the present study was shorter than that in other case reports (23, 24). In one study, the original craniotomy technique of the posterior sigmoid sinus keyhole approach was used by the surgeon's team, and the new method kept the craniotomy time within 22–25 min (25).

In the current study, there were 3 cases of intracranial infection including 2 cases of middle skull base tumors. Extracranial communication and malignant tumors were mostly accompanied by bony defects and severe adhesion (26, 27); thus, the long operative time and difficult resection would increase the complication rate. Post-operative complications of the posterior skull base were mainly facial paralysis, most of which improved after symptomatic treatment. Two patients with dysphagia underwent post-operative tracheotomy, but their swallowing function recovered after discharge.

Skull base reconstruction is the key to preventing cerebral fluid leakage and intracranial infection, and is one of the important factors for successful intracranial base resection (28, 29). In this study, we used the multimodal image fusion technique to evaluate the reconstruction plan, and bone defects were fully visible and titanium plates for reconstruction were formed pre-operatively. Only 6 cases of cerebrospinal fluid leakage occurred post-operatively, mainly due to severe damage of the skull base fracture and failure to repair damaged meninges intraoperatively. Skull base reconstruction should be fully comprehensible based on the pre-operative incision design. Intraoperative separation of tumors adhered to the meninges should be performed carefully and gently to minimize damage to their structural integrity. During intraoperative resection of the tumor, attention should be paid to preserving the meningeal residual margin of the skull base and not to overexcising the meningeal residual margin by emphasizing total tumor resection. There should be enough cap-shaped aponeurosis and periosteum for dural repair. For

skull defects <4 cm in diameter, the dural was closely repaired using a pedicled bone valve or cap aponeurosis without skull reconstruction. Cranial reconstruction should be considered for skull defects ≥4 cm in diameter. If cerebral fluid leakage occurs after surgery, lumbar cistern drainage is feasible; if cerebral fluid leakage still exists after 1 month of conservative operation, a secondary operation to fix the leakage is needed (30).

At present, multimodal image fusion technology still has some limitations, as it is difficult to reconstruct tiny vessels. However, 3D reconstruction has high requirements for image inspection, such as a scanning layer thickness >2 mm, which may lead to a roughly reconstructed image and affect the reference value.

CONCLUSIONS

The multimodal image fusion technique can achieve satisfactory results and should be strongly recommended for skull base tumor surgery. Derived from this technique, mixed virtual reality technology has broad prospects for assisted surgery of skull base tumors in the future. A follow-up study is ongoing by our team.

DATA AVAILABILITY STATEMENT

The original contributions presented in the study are included in the article/**Supplementary Material**, further inquiries can be directed to the corresponding author.

ETHICS STATEMENT

The studies involving human participants were reviewed and approved by Medical Ethics Committee of Zhuhai People's Hospital (Number: ZY.no20201001B06011231). The patients/participants provided their written informed consent to participate in this study. Written informed consent was obtained from the individual(s) for the publication of any potentially identifiable images or data included in this article.

AUTHOR CONTRIBUTIONS

GC and Z-hJ contributed to the study concept and design. J-yL and H-dC contributed to the acquisition of data. YL and K-hW contributed to the analysis and interpretation of data. Z-hJ contributed to the drafting of the manuscript. All authors read and approved the final manuscript.

FUNDING

This work was supported by Soochow Key Health Talents Project of Jiangsu Province, 2014, GC and Zhuhai People's Hospital Scientific Research Initiation Project No. 2021KYQD-02 to GC.

ACKNOWLEDGMENTS

The authors thank the participants and all who were involved in our study.

SUPPLEMENTARY MATERIAL

The Supplementary Material for this article can be found online at: https://www.frontiersin.org/articles/10.3389/fneur.2022.895638/full#supplementary-material

REFERENCES

1. Savardekar AR, Patra DP, Bir S, Thakur JD, Mohammed N, Bollam P, et al. Differential tumor progression patterns in skull Base versus Non-Skull base meningiomas: a critical analysis from a long-term follow-up study and review of literature. *World Neurosurg.* (2018) 112:e74–83. doi: 10.1016/j.wneu.2017.12.035
2. Kettner M, Szczygielski J. Operative skull base approaches. *Radiologe.* (2019) 59:1080–7. doi: 10.1007/s00117-019-00601-4
3. Cannizzaro D, Sabatino G, Mancarella C, Revay M, Revay M, Pecchioli G, et al. Management and surgical approaches of brainstem cavernous malformations: our experience and literature review. *Asian J Neurosurg.* (2019) 14:131–9. doi: 10.4103/ajns.AJNS_290_17
4. de Cates C, Borsetto D, Scoffings D, O'Donovan D, Donnelly NN. Skull base parachordoma/myoepithelioma. *J Int Adv Otol.* (2020) 16:278–81. doi: 10.5152/iao.2020.7203
5. Brokinkel B, Stummer W, Sporns P. Simpson grade IV resections of skull base meningiomas: does the postoperative tumor volume impact progression? *J Neurooncol.* (2018) 137:219–21. doi: 10.1007/s11060-017-2715-2
6. Schuknecht B. Patterns of perineural skull base tumor extension from extracranial tumors. *Neuroimaging Clin N Am.* (2021) 31:473–83. doi: 10.1016/j.nic.2021.05.007
7. Combs SE, Baumert BG, Bendszus M, Bozzao A, Brada M, Fariselli L, et al. ESTRO ACROP guideline for target volume delineation of skull base tumors. *Radiother Oncol.* (2021) 156:80–94. doi: 10.1016/j.radonc.2020.11.014
8. Passer JZ, Alvarez-Breckenridge C, Rhines L, DeMonte F, Tatsui C, Raza SM. Surgical management of skull base and spine chordomas. *Curr Treat Options Oncol.* (2021) 22:40. doi: 10.1007/s11864-021-00838-z
9. Yang JX, Aygun N, Nadgir RN. Imaging of the postoperative skull base and cerebellopontine angle. *Neuroimaging Clin N Am.* (2022) 32:159–74. doi: 10.1016/j.nic.2021.08.005
10. Mehta GU, Muelleman TJ, Brackmann DE, Gidley PW. Temporal bone resection for lateral skull-base malignancies. *J Neurooncol.* (2020) 150:437–44. doi: 10.1007/s11060-020-03445-4
11. Zhang H, Liu G, Tong XG, Hang W. Application of three-dimensional printing technology in the surgical treatment of nasal skull base tumor. *Zhonghua Er Bi Yan Hou Tou Jing Wai Ke Za Zhi.* (2018) 53:780–4. doi: 10.3760/cma.j.issn.1673-0860.2018.10.012
12. Hernández DA, Zaloff Dakoff JM, Auad C, et al. Stereotactic brain radiosurgery in the treatment of skull base tumors. *Med (B Aires).* (2019) 79:453–60.
13. Mehta GU, Raza SM. Management of skull base metastases. *Neurosurg Clin N Am.* (2020) 31:659–66. doi: 10.1016/j.nec.2020.06.013
14. Sato M, Tateishi K, Murata H, Kin T, Suenaga J, Takase H, et al. Three-dimensional multimodality fusion imaging as an educational and planning tool for deep-seated meningiomas. *Br J Neurosurg.* (2018) 32:509urga doi: 10.1080/02688697.2018.1485877
15. Oishi M, Fukuda M, Yajima N, Yoshida K, Yoshida K, Hiraishi T, et al. Interactive presurgical simulation applying advanced 3D imaging and modeling techniques for skull base and deep tumors. *J Neurosurg.* (2013) 119:94–105. doi: 10.3171/2013.3.JNS121109

16. Hamasaki T, Morioka M, Nakamura H, Yano S, Hirai T, Kuratsu J. A 3-dimensional computed tomographic procedure for planning retrosigmoid craniotomy. *Neurosurgery*. (2009) 64(Suppl. 2):241–5; discussion 245–6. doi: 10.1227/01.NEU.0000336763.90656.2B
17. Yoshida K, Akiyama T, Takahashi S, Miwa T, Horiguchi T, Sasaki H, et al. Cone-beam computed tomography fusion technique for vascular assessment of skull base meningiomas. *World Neurosurg*. (2021) 151:61–9. doi: 10.1016/j.wneu.2021.04.065
18. Hwang RS, Turner RC, Radwan W, Singh R, Lucke-Wold B, Tarabishy A, et al. Relationship of the sinus anatomy to surface landmarks is a function of the sinus size difference between the right and left side: Anatomical study based on CT angiography. *Surg Neurol Int*. (2017) 8:58. doi: 10.4103/sni.sni_351_16
19. Shukla G, Alexander GS, Bakas S, Nikam R, Talekar K, Palmer JD, et al. Advanced magnetic resonance imaging in glioblastoma: a review. *Chin Clin Oncol*. (2017) 6:40. doi: 10.21037/cco.2017.06.28
20. Yang R, Lu H, Wang Y, Peng X, Mao C, Yi Z, et al. CT-MRI image fusion-based computer-assisted navigation management of communicative tumors involved the infratemporal-middle cranial fossa. *J Neurol Surg B Skull Base*. (2021) 82:e321–9. doi: 10.1055/s-0040-1701603
21. Kolakshyapati M, Ikawa F, Abiko M, Mitsuhara T, Takeda M, Shrestha T, et al. Usefulness of preoperative simulation in skull base approach: a case report. *J Neurol Surg B Skull Base*. (2018) 79:S378–82. doi: 10.1055/s-0038-1660843
22. Lv GH, Zou MX, Liu FS, Zhang Y, Huang W, Ye A, et al. Clinicopathological and prognostic characteristics in extra-axial chordomas: an integrative analysis of 86 cases and comparison with axial chordomas. *Neurosurgery*. (2019) 85:E527–42. doi: 10.1093/neuros/nyz073
23. Sade B, Mohr G, Dufour JJ. Vascular complications of vestibular schwannoma surgery: a comparison of the suboccipital retrosigmoid and translabyrinthine approaches. *J Neurosurg*. (2006) 105:200–4. doi: 10.3171/jns.2006.105.2.200
24. Krasic D, Stojanovic M, Petrovic V, Pesic Z. Extracranial meningiomas in the head- and- neck region: a 15 years' experience. *Niger J Clin Pract*. (2018) 21:1078–80. doi: 10.4103/njcp.njcp_439_17
25. Jian ZH, Sheng MF Li JY, An DZ, Weng ZJ, Chen G. Developing a method to precisely locate the Keypoint during craniotomy using the retrosigmoid keyhole approach: Surgical anatomy and technical nuances. *Front Surg*. (2021) 8:700777. doi: 10.3389/fsurg.2021.700777
26. Sarwal A. Neurologic complications in the postoperative neurosurgery patient. *Continuum (Minneap Minn)*. (2021) 27:1382–404. doi: 10.1212/CON.0000000000001039
27. Safdarian M, Safdarian M, Chou R, Hashemi SMR, Rahimi-Movaghar V. A systematic review about the position-related complications of acoustic neuroma surgery *via* suboccipital retrosigmoid approach: Sitting versus lateral. *Asian J Neurosurg*. (2017) 12:365–73. doi: 10.4103/1793-5482.185069
28. Grau S, Kellermann S, Faust M, Perrech M, Beutner D, Drzezga A, et al. Repair of cerebrospinal fluid leakage using a transfrontal, radial Adipofascial flap: an individual approach supported by three-dimensional printing for surgical planning. *World Neurosurg*. (2018) 110:315–8. doi: 10.1016/j.wneu.2017.11.083
29. Tan J, Song R, Huan R, Huang N, Chen J. Intraoperative lumbar drainage can prevent cerebrospinal fluid leakage during transsphenoidal surgery for pituitary adenomas: a systematic review and meta-analysis. *BMC Neurol*. (2020) 20:303. doi: 10.1186/s12883-020-01877-z
30. Graupman P, Nussbaum ES, Patel PD. Preventing cerebral spinal fluid leakage following endoscopy through a burr hole using a novel watertight closure: technical note. *Br J Neurosurg*. (2021). doi: 10.1080/02688697.2021.1903392. [Epub ahead of print].

Conflict of Interest: The authors declare that the research was conducted in the absence of any commercial or financial relationships that could be construed as a potential conflict of interest.

Publisher's Note: All claims expressed in this article are solely those of the authors and do not necessarily represent those of their affiliated organizations, or those of the publisher, the editors and the reviewers. Any product that may be evaluated in this article, or claim that may be made by its manufacturer, is not guaranteed or endorsed by the publisher.

Copyright © 2022 Jian, Li, Wu, Li, Li, Chen and Chen. This is an open-access article distributed under the terms of the Creative Commons Attribution License (CC BY). The use, distribution or reproduction in other forums is permitted, provided the original author(s) and the copyright owner(s) are credited and that the original publication in this journal is cited, in accordance with accepted academic practice. No use, distribution or reproduction is permitted which does not comply with these terms.

frontiers | Frontiers in Human Neuroscience

ORIGINAL RESEARCH
published: 16 May 2022
doi: 10.3389/fnhum.2022.803163

The Effect of Right Temporal Lobe Gliomas on Left and Right Hemisphere Neural Processing During Speech Perception and Production Tasks

Adam Kenji Yamamoto[1,2], Ana Sanjuán[3,4], Rebecca Pope[4], Oiwi Parker Jones[4,5], Thomas M. H. Hope[4], Susan Prejawa[4,6,7], Marion Oberhuber[4], Laura Mancini[1,2], Justyna O. Ekert[4], Andrea Garjardo-Vidal[4,8], Megan Creasey[4], Tarek A. Yousry[1,2], David W. Green[9] and Cathy J. Price[4]*

[1] Neuroradiological Academic Unit, Department of Brain Repair and Rehabilitation, UCL Queen Square Institute of Neurology, University College London, London, United Kingdom, [2] Lysholm Department of Neuroradiology, National Hospital for Neurology and Neurosurgery, London, United Kingdom, [3] Neuropsychology and Functional Imaging Group, Departamento de Psicología Básica, Clínica y Psicobiología, Universitat Jaume I, Castellón de La Plana, Spain, [4] Wellcome Centre for Human Neuroimaging, UCL Queen Square Institute of Neurology, University College London, London, United Kingdom, [5] FMRIB Centre and Jesus College, University of Oxford, Oxford, United Kingdom, [6] Faculty of Medicine, Collaborative Research Centre 1052 "Obesity Mechanisms", University Leipzig, Leipzig, Germany, [7] Department of Neurology, Max Planck Institute for Human Cognitive and Brain Sciences, Leipzig, Germany, [8] Faculty of Health Sciences, Universidad del Desarrollo, Concepcion, Chile, [9] Experimental Psychology, University College London, London, United Kingdom

OPEN ACCESS

Edited by:
Nico Sollmann, University of California, San Francisco, United States

Reviewed by:
Roelien Bastiaanse, University of Groningen, Netherlands
Layla Gould, University of Saskatchewan, Canada
Nicole Brennan, Montefiore Medical Center, United States
Jinsong Wu, Huashan Hospital, Fudan University, China

***Correspondence:**
Adam Kenji Yamamoto
a.yamamoto@ucl.ac.uk

Specialty section:
This article was submitted to Brain Imaging and Stimulation, a section of the journal Frontiers in Human Neuroscience

Received: *27 October 2021*
Accepted: *28 March 2022*
Published: *16 May 2022*

Citation:
Yamamoto AK, Sanjuán A, Pope R, Parker Jones O, Hope TMH, Prejawa S, Oberhuber M, Mancini L, Ekert JO, Garjardo-Vidal A, Creasey M, Yousry TA, Green DW and Price CJ (2022) The Effect of Right Temporal Lobe Gliomas on Left and Right Hemisphere Neural Processing During Speech Perception and Production Tasks. Front. Hum. Neurosci. 16:803163. doi: 10.3389/fnhum.2022.803163

Using fMRI, we investigated how right temporal lobe gliomas affecting the posterior superior temporal sulcus alter neural processing observed during speech perception and production tasks. Behavioural language testing showed that three pre-operative neurosurgical patients with grade 2, grade 3 or grade 4 tumours had the same pattern of mild language impairment in the domains of object naming and written word comprehension. When matching heard words for semantic relatedness (a speech perception task), these patients showed under-activation in the tumour infiltrated right superior temporal lobe compared to 61 neurotypical participants and 16 patients with tumours that preserved the right postero-superior temporal lobe, with enhanced activation within the (tumour-free) contralateral left superior temporal lobe. In contrast, when correctly naming objects (a speech production task), the patients with right postero-superior temporal lobe tumours showed higher activation than both control groups in the same right postero-superior temporal lobe region that was under-activated during auditory semantic matching. The task dependent pattern of under-activation during the auditory speech task and over-activation during object naming was also observed in eight stroke patients with right hemisphere infarcts that affected the right postero-superior temporal lobe compared to eight stroke patients with right hemisphere infarcts that spared it. These task-specific and site-specific cross-pathology effects highlight the importance of the right temporal lobe for language processing and motivate

further study of how right temporal lobe tumours affect language performance and neural reorganisation. These findings may have important implications for surgical management of these patients, as knowledge of the regions showing functional reorganisation may help to avoid their inadvertent damage during neurosurgery.

Keywords: gliomas, fMRI, language, speech perception, speech production, right temporal lobe, neurosurgery

INTRODUCTION

This study investigates how right temporal lobe gliomas, a type of primary brain tumour, alter the neural networks supporting speech perception and production tasks. Typically, gliomas present with epileptic type seizures rather than speech impairment (Laws et al., 1984; Chang et al., 2008; Ius et al., 2012), particularly in right handed patients who have tumours in the right cerebral hemisphere and so it is often assumed that the right cerebral hemisphere is less important for language function. Although early patient studies found that right hemispheric tumours do result in subtle language impairments (Gainott et al., 1981; Thomson et al., 1998), much of the previous research over the past 20 years has focused on tumours affecting the left hemisphere. Nevertheless, functional imaging of the healthy brain has increasingly shown that the right superior temporal lobe responds to human sounds (Belin et al., 2000), voice processing (Kriegstein and Giraud, 2004; Lattner et al., 2005; Andics et al., 2010), auditory feedback during speech production (Tourville et al., 2008; Behroozmand et al., 2015; Yamamoto et al., 2019b) and speech comprehension (Gajardo-Vidal et al., 2018). One region of the right superior temporal lobe in particular, the posterior superior temporal sulcus (RpSTS), is activated during both speech perception and production tasks and we have recently proposed that it is involved in integrating auditory expectations with auditory input (Yamamoto et al., 2019b).

Here we test the causal relevance of the right superior temporal lobe, in particular the RpSTS, for supporting speech perception and production, in patients with gliomas affecting this region. First we assess whether these patients have impaired language. Second, using fMRI, we investigate how the tumour may have altered the functioning of the neural networks during specific language tasks: auditory semantic matching (a speech perception task) and object naming (a speech production task). Brain injury occurring due to a tumour offers a unique insight into brain plasticity, as the potential for functional recovery is far greater with slow growing tumours than after an acute-onset insult to the brain such as occurs with a stroke (Desmurget et al., 2007). The rationale for our approach is as follows: if regions within the right superior temporal lobe typically support accurate and efficient speech processing then perturbed function resulting from the glioma will manifest as detectable performance deficits on detailed language assessment unless other brain areas, such as in the contralateral hemisphere, are able to support the function as has been shown in patients harboring left hemispheric lesions (Thiel et al., 2006, 2005; Krieg et al., 2013). In the current study three patients all with right temporal lobe gliomas of differing grades (grade 2, 3, 4) were assessed using a detailed language assessment to identify whether any had subtle language impairments which may not have been evident on clinical neurological examination performed at the bedside. A prior study (Noll et al., 2016), reported the results of three language tests administered to patients with right temporal lobe gliomas. Impaired performance was noted for 42% on verbal memory (Hopkins Verbal Learning Test), 10% on phonemic (letter) fluency and 7% on object naming; and these impairments were noted to be less severe than those reported in patients with left temporal lobe gliomas. Although there is less evidence that glioma grade influences performance on language tasks in patients (like ours) who have right hemisphere gliomas (Antonsson et al., 2018), prior studies have reported that cognitive and language impairments are more common (Bizzi et al., 2012), more severe (Zhang et al., 2018) or both (Noll et al., 2015a) for patients with left hemispheric high grade gliomas (HGGs) compared with low grade gliomas (LGGs). We therefore expected that language abilities would differ across our three patients given their different glioma grades.

We then performed fMRI to investigate the functioning of the speech perception and speech production networks in each of the three patients by comparing task related activation to that observed in 61 neurotypical control participants. This involved identifying: (a) any regions that the patients activated significantly more than the control participants when performing the same language task (Thiel et al., 2006) and (b) how such effects depended on the task. Enhanced activation in the patients compared to the control participants could either be within (intra-tumoural) or close to (peri-tumoural) the tumour or it could occur distant to the damage either within the ipsilateral or contra-lateral hemisphere (Duffau, 2005; Thiel et al., 2006; Desmurget et al., 2007). For example, the patients with right temporal lobe tumours might have abnormally high activation within or around the tumour-infiltrated right temporal lobe or they might have increased activation in homologue areas within the contralateral left superior temporal lobe (Thiel et al., 2005; Turkeltaub et al., 2011).

We focused on changes in task-specific brain activation that replicated across the three patients with right temporal lobe gliomas. Finally, we investigated whether these changes were: site-specific, pathology specific, both or neither by conducting the same investigations on three other patient groups: 16 patients with gliomas not involving the right postero-superior temporal

Abbreviations: BOLD, blood oxygenation level dependent; fMRI, functional magnetic resonance imaging; LGG, low grade glioma WHO (World Health Organization) grade 1-2; GOI, glioma patients of interest; GC, glioma control patients; HGG, high grade glioma WHO (World Health Organization) grade 3-4; MEG, Magnetoencephalography; PET, Positron emission tomography; pSTS, posterior superior temporal sulcus; PT, planum temporale; RpSTS, right posterior superior temporal sulcus; SC, stroke control patients; SOI, stroke patients of interest; TMS, transcranial magnetic stimulation.

lobe, eight stroke patients with right hemisphere infarcts affecting the right postero-superior temporal lobe and eight stroke patients with right hemisphere infarcts sparing it.

MATERIALS AND METHODS

Participants

A total of 96 adults participated in an ethics committee approved fMRI study at the UCL Queen Square Institute of Neurology and the National Hospital for Neurology and Neurosurgery. 19 were patients, prospectively enrolled following referral for further management of their brain tumour. In 18 of these the diagnosis of glioma (WHO grade 1–4) was confirmed following surgery. 16 were patients who had previously suffered a right hemisphere infarct and were enrolled in the fMRI study after behavioural assessment and brain imaging for the PLORAS study (Seghier et al., 2016) confirmed that they were able to perform the fMRI tasks with high accuracy. The remaining 61 participants were neurologically intact (neurotypical control participants: NC). The patients were assigned to one of four groups:

Glioma Patients of Interest

Three adult neurosurgical patients (two male, one female) were the only patients enrolled in this time-limited fMRI study who had circumscribed tumours in the right postero-superior temporal lobe that infiltrated the right pSTS region that we have previously identified as involved in speech perception and production (Yamamoto et al., 2019b; see lesion overlap map in **Figure 1**). We refer to these patients as A, B and C, with A studied first and C studied last. The histological diagnoses of these patients are described below with demographic data provided in **Table 1**.

Glioma Control Patients

All other patients with supratentorial gliomas were assigned to this group (n = 16). One patient in this group did not proceed to surgery however they were included because imaging appearances of their tumour were consistent with a glioma. The histological diagnoses of these patients and additional demographic data are provided in **Supplementary Appendix 1**.

Stroke Patients of Interest

This group included eight patients with right hemisphere infarcts that (i) involved the right postero-superior temporal lobe and (ii) had activation in the F-map ($p < 0.001$) in the right postero-superior temporal region that we have previously identified as involved in speech perception and production (Yamamoto et al., 2019b). An additional four patients with right posterior temporal lobe damage participated in the fMRI paradigm but were not included in the current study because there was no residual parenchyma evident on MRI or no fMRI response (F-map from first level analysis thresholded at $p < 0.001$ uncorrected) in the region of interest within the right postero-superior temporal lobe. Demographic details for the eight included patients are provided in **Table 1**. An anatomical description of each infarct site is provided in **Supplementary Appendix 2**. Structural MR images, and the fMRI response are shown for each patient in **Supplementary Appendix 3**.

Stroke Control Patients

This group (n = 8) included the stroke patients with right hemisphere infarcts that preserved the right postero-superior temporal lobe according to (i) structural imaging and (ii) the F-map from the first level fMRI analysis (see **Table 1** and **Supplementary Appendix 2** for further details).

Clinical Details of Patients of Interest With Right Postero-Superior Temporal Gliomas

Both patient A and patient C's tumours were discovered on imaging shortly after the onset of generalised seizures. Patient B's tumour was discovered incidentally on brain imaging performed 3 years previously for a different indication and had been subsequently monitored with imaging and shown to be gradually increasing in size. The onset of generalised seizures during this period of observation had resulted in referral to our institution. All patients were seizure free at the time of study participation (3 weeks for patient A, 9 months for patient B and 15 months for patient C) and were on anticonvulsant medication (levetiracetam for patient A, lamotrigine for patient B, sodium valproate and topiramate for patient C). None of the patients had previously received or were receiving treatment with corticosteroids at the time of the study.

Patients A and C were right handed. Patient B was left handed but we found no evidence that Patient B had right lateralised language responses. To the contrary, their language fMRI activation was entirely consistent with that observed in the two right handed patients. As is standard practice in our institution an experienced neuroradiologist provided a clinical fMRI report on two additional fMRI tasks which are acquired as part of standard clinical management. These were reported as being in keeping with left hemisphere dominance for all three patients.

None of the three patients reported any motor or visual symptoms. Patient B self-reported subtle changes in auditory function such as difficulty holding simultaneous conversations and understanding speech in the presence of other auditory stimuli. Patient C self-reported a decline in memory and concentration following diagnosis. None of the patients complained of difficulties with speech production.

Patient A's tumour was centred on the middle temporal gyrus (MTG) and inferior temporal gyrus with the tumour extending to the superior temporal sulcus and medially into the deep and periventricular white matter bordering the lateral ventricle (**Figure 1**). Patient B's tumour was the smallest, centred on the superior temporal lobe involving the superior temporal gyrus (STG) and planum temporale (PT) immediately adjacent to Heschl's gyrus (HG). Unlike patients A and C, patient B's tumour was surrounded by confluent white matter signal abnormality, which extended further into the anterior temporal lobe, medially to the periventricular white matter and superiorly into the inferior parietal lobule. Patient C's tumour was the largest and was also centred on the right superior temporal lobe involving

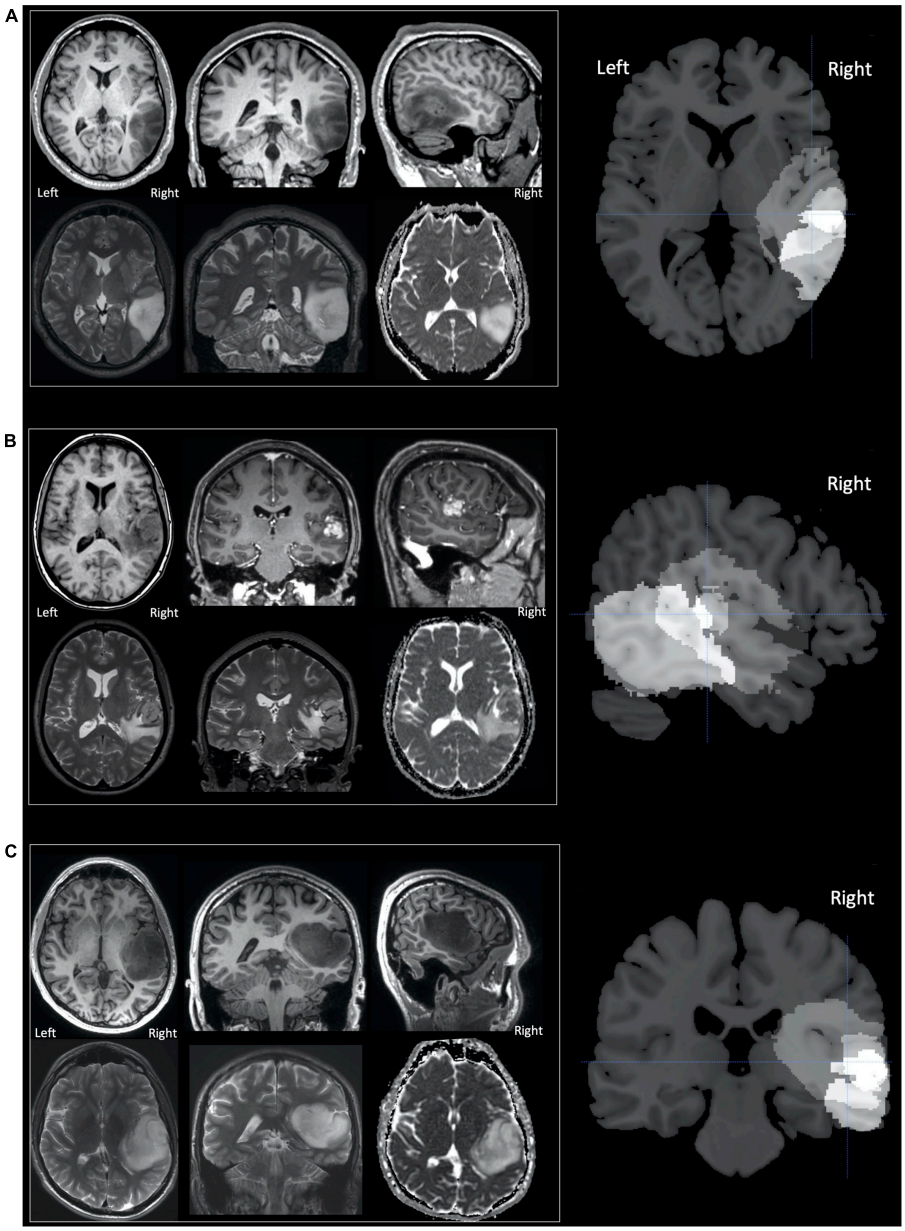

FIGURE 1 | Tumours in patients **(A–C)**. Selected MR images for patients **(A–C)** are shown in neurological convention, with the right of the image corresponding to the right of the patient. The upper row, for each patient, displays (from left to right) axial, coronal and sagittal T1-weighted images. For patients A and C only unenhanced sequences are shown as their tumours were both non-enhancing. For patient B the coronal and sagittal images T1-weighted images are contrast enhanced and display a central enhancing component. The lower row for each patient (from left to right), displays axial and coronal T2-weighted images and the axial apparent diffusion coefficient (ADC) image from the diffusion weighted imaging (DWI). The right column of images shows sections from the lesion overlap map demonstrating the three tumours superimposed on one another—brighter voxels indicate more overlap between the three tumours. The overlap was greatest in the region of the superior temporal sulcus with the cross hair centred at [+51 −25 +5] which showed significantly altered activation during the speech perception and production tasks (see section "Results").

HG, PT and STG. Medially, the tumour extended into the posterior insula.

Based upon the World Health Organization 2016 classification (Louis et al., 2016) which was in use at the time of this study, the histological diagnosis of glioma was confirmed in patient A (WHO grade 2 oligoastrocytoma IDH mutant, 19q deletion), patient B (WHO grade 4 glioblastoma IDH wildtype) and patient C (WHO grade 3 anaplastic astrocytoma IDH mutant). The volume of each patient's tumour ranged from 11 to 97cm^3 (see **Figure 1**). The structural imaging performed in patients A and C demonstrated non-enhancing tumours. Patient's B tumour demonstrated enhancement consistent with higher grade features at the time of study though the tumour had been present for at least 3 years prior to referral. Patients A and B underwent

TABLE 1 | Participant details.

Neurotypical control participants (NC)	**Group 1 (MRI 1)**	**Group 2 (MRI 2)**	
Number	51	10	
Gender (n female/n male)	31/20	7/3	
Median age in years (range)	37.1 (20–75.6)	23 (20.3–28.5)	
Handedness (right/left)	51/0	5/5	
RpSTS glioma patients (GOI) (MRI 2)	**A**	**B**	**C**
Age	25.5	41.2	19.8
Gender	M	F	M
Handedness	R	L	R
Clinical presentation	Seizure	Seizure	Seizure
Tumour type	OA (2)	GBM (4)	AA (3)
Tumour volume/cm^3	60	11	97
Glioma control patients (GC) (MRI 2)			
Number	16		
Gender (n female/n male)	8/8		
Median age in years (range)	42.6 (21.6–58.5)		
Handedness (right/left)	13/3		
Stroke patients (MRI 1)	**RpSTS damage (SOI)**	**RpSTS preserved (SC)**	
Number	8	8	
Gender (n female/n male)	2/6	2/6	
Median age in years (range)	61.5 (45–73)	54.5 (26–72)	
Handedness (right/left)	7/1	8/0	
Median Years post stroke (range)	5.0 (1.9–14.2)	3.9 (0.8–15.4)	

Demographic and clinical data for the different participant groups. MRI 1, imaged at location 1; MRI 2, imaged at location 2. Gender F, female; M, male. Handedness R, right; L, left. Tumour type (with WHO histological grading in brackets): OA, oligoastrocytoma; GBM, glioblastoma; AA, anaplastic astrocytoma (based upon the 2016 criteria; Louis et al., 2016). Tumour volume is in cm^3 with measurement performed using manual segmentation in ITK-SNAP 3.6.0 (Yushkevich et al., 2006) by a neuroradiologist (author A.K.Y.).

surgery shortly afterward in our institution, this was performed in the intra-operative MRI surgical suite. Given the pre-operative clinical fMRI findings of left hemispheric dominance, both surgeries were performed under general anesthesia without intra-operative language mapping. Patient C underwent surgery in a different institution, this was performed after one further year of observation.

Language Testing

Each patient (glioma and stroke) underwent behavioural testing performed by a speech and language therapist using the Comprehensive Aphasia Test (CAT) (Swinburn et al., 2004) which consists of twenty one language related tests and six cognitive non-language tasks taking approximately 1–2 h to complete, depending on ability. Each task generates raw scores which are expressed as T-scores relative to a reference group of 113 aphasic patients and 27 controls. This classifies each patient's performance as being either normal or impaired. Lower scores indicate lower performance.

fMRI

Experimental Design

All participants (all patients and NC) performed the same language fMRI paradigm with five different conditions that have previously been described (Sanjuán et al., 2015) with further examples of the fMRI tasks illustrated in Ekert et al. (2021). We report data from three tasks. The first task required participants to listen to pairs of spoken object names that were either semantically related (e.g., pizza and tomato) or unrelated (e.g., fridge and camera), recognise the spoken objects (speech perception), hold these names in auditory short-term memory and press a button to indicate if the two objects referred to were semantically related or not. The index finger on the dominant hand was used if the objects were semantically related and the middle finger of the same hand was used if the two objects were semantically unrelated. The second task involved naming aloud two objects in each of a series of pictures and also linking these with "and" (e.g., "cup and piano"). The third task was a control condition that involved seeing pictures of two objects (as in Task 2) and semantically matching them (as in Task 1).

Semantically related items were either from the same category (e.g., elephant and giraffe, grapes and pear, harp and piano) or the same location (e.g., dolphin and sea; mermaid and rocks; crab and shell). Half the stimuli in Tasks 1 and 3 presented semantically related objects. None of the object pairs used for object naming (Task 2) were semantically related. The two remaining conditions presented pictures of two objects interacting with one another (e.g., camera falling off the chair);

and required either the production of a full sentence ("the camera is falling off the chair") or the verb only ("falling"). We did not include these conditions in the current study because they were not matched, for content, to the visual and auditory semantic matching conditions. However, we note here that there was (a) no significant difference ($p > 0.001$) in activation for sentence production and object naming in any of the regions reported in this study and (b) significantly less activation in these regions for verb naming compared to object naming. This was expected given that only 4 verbs were used (eating, drinking, jumping, falling) and each response involved only one of these words (as opposed to two object names).

Different stimuli were presented in different conditions, but there was no rotation of stimuli across conditions in different participants and there was no counterbalancing of conditions across participants. This is because the aim of the study was to test how brain responses differ across participants and to interpret inter-subject differences, we therefore needed to hold all other experimental details (stimuli and task order) constant across participants. All participants (patients and controls) were each presented with five conditions in the following order: (1) visual semantic matching on pictures of two objects (our baseline task); (2) naming the objects in pictures (our speech production task); (3) naming the verb in a picture of an event; (4) producing a sentence to describe the event in a picture; and (5) auditory semantic matching on two heard object names (our speech perception task).

Stimulus Selection/Preparation

Across the experiment, each participant was presented with 120 animal or object concepts, either in picture format or as spoken speech. The names associated with these objects had one to four syllables in English (mean 1.59; standard deviation (SD) 0.73). To ensure that all participants recognised the objects and produced highly accurate behavioural responses, a prior pilot study was conducted on 26 young healthy adults and inter-subject variability was evaluated in (i) the name associated with each object and animal, and (ii) whether two objects were considered to be semantically related. On the basis of the pilot results, all the objects/animals that were most consistently named during object naming were assigned to the object naming condition. From the remaining stimuli, those with the strongest semantic associations were assigned as related pairs in the semantic matching conditions (visual or auditory). The remaining stimuli were assigned as unrelated pairs.

Stimulus Presentation

Each task was presented in a separate scan run with four blocks of five object pairs, presented at a rate of one every 5 seconds (s) (i.e., 10 objects in 25s blocks). Every stimulus block was preceded by a written instruction (e.g., "Name objects"), lasting 3.08s (equivalent to one interscan interval), which indicated the start of a new block and reminded subjects of the task. Within each semantic matching block (auditory and visual), there were two or three semantically related pairs and three or two semantically unrelated pairs.

All visual stimuli (pictures of objects) were presented via an LCD projector, and an adjustable head-coil mirror, onto a screen that was clearly visible to the subject. Together they subtended a visual angle of 7.4 degrees with 1,024 × 768 resolution after scaling to 350 × 350 pixels. The duration of each visual stimulus was 2.5 s, with 3.5 s fixation between stimuli (i.e., 5 s interstimulus interval).

All auditory stimuli were presented for 1.76–2.5 s via MRI compatible headphones (MR Confon, Magdeburg, Germany), which filtered ambient in-scanner noise. The mean duration of the auditory stimuli (two object names linked with "and") was 1.92 s from the onset of the first word to the offset of the second word (standard deviation of 0.13 s). Volume levels were adjusted for each subject before scanning. During stimulus presentation, participants fixated on a cross centred on the screen to control.

Each stimulus block was followed by 16 s resting periods, during which participants fixated on a cross centred on the screen. These resting with fixation periods allowed activation to return to baseline between blocks, therefore ensuring maximum sensitivity to all effects of interest.

Behavioural Response Acquisition

Prior to scanning, all participants were instructed as to the task requirements and familiarised with the procedure using pictures and auditory stimuli which were separate to those being used in the scanner. During scanning, participants were reminded to keep their eyes open for all tasks, including the auditory task. They were also frequently reminded to remain as still as possible to prevent movement-induced acquisition noise.

Spoken responses were recorded for each subject via a noise-canceling MRI microphone (FOMRI III^{TM} Optoacoustics, Or-Yehuda, Israel), and transcribed manually for off-line analysis. For auditory and visual semantic decision tasks, participants used two fingers of the same hand (left hand for 15 subjects) to press one of two buttons on an fMRI compatible button box.

Behavioural Data Processing

Responses to each stimulus were transcribed at the time of imaging and scored for accuracy off-line by listening to the audio files (for object naming) and by reviewing the recorded data from the button press tasks. Each response was categorised as correct (when the response matched the target) or incorrect. If >10% of participants across the study produced a spoken response that did not match the target but did match the meaning (e.g., target = mug, response = cup), responses for these participants were also marked as "correct." Other (i.e., atypical responses) were classified as "incorrect."

Reaction times (RTs) for spoken responses were obtained from the audio files. To compute them, we used an adaptive moving window filter that was tailored to each subject. The optimal window length (i.e., the width which maximally smoothed the audio stream) was based on a portion of the audio file collected during rest. After smoothing the whole time series, we defined the onset of speech as a rise in the absolute amplitude of the smoothed audio stream beyond 1.5 standard deviations from the mean.

Accuracy and response times (from stimulus onset to response) were successfully collected for all trials for all participants except for one missing response time for visual semantic matching of one participant in the NC group; five missing responses at the end of visual semantic matching (the control task) for Patient C; and 11 missing response times from Patient C during object naming because of technical failures in the voice recording system. When semantic matching responses were missing (six in total), we could not be sure they were correct, therefore these trials were excluded from the behavioural and also fMRI statistical analyses that focused on correct responses using an event-related analysis. Accuracy during object naming was recorded by listening to participant responses during scanning and this indicated that all the object naming trials with missing response times were accurate. These trials were therefore only excluded from the analysis of in-scanner response times and not from the accuracy or fMRI analyses. Although loss of data points can influence the sensitivity of statistical contrasts, it has no bearing on the interpretation of significant effects that replicate across all three of our patients.

MRI Acquisition

Functional and structural research sequences were performed using the same acquisition technique on 3T Siemens scanners (Erlangen, DE) with 12-channel head coils. Data were acquired at two different locations: The Wellcome Centre for Human Neuroimaging (location 1) and the National Hospital for Neurology and Neurosurgery (location 2). Location 1 was used for 51 of the NC group and all the stroke patients (n = 16); location 2 was used for the remaining 10 of the NC group and all the patients with gliomas (n = 19). Total scanning time was approximately 1 h and 30 min per subject, including set up and the acquisition of a structural scan.

Functional images for all participants were acquired using a gradient echo (GE) echo planar imaging (EPI) sequence with in plane resolution = 3 × 3 mm^2, repetition time TR = 3,080 ms, echo time TE/flip angle = 30 ms/90°, field of view (FOV) = 192 × 192 mm^2 and matrix size = 64 × 64. The TR (3,080 ms) was chosen to maximise whole-brain coverage and allowed us to asynchronise the slice acquisition with stimulus onset (5,000 ms) to allow for distributed sampling of stimulus onsets across slices in each condition (Veltman et al., 2002). For example, when the first stimulus in a block was presented at the start of the TR (slice 1 of 44), subsequent stimuli were presented at slices: 11, 22, 27, and 38.

For locations 1 and 2 respectively, slice thickness = 2 mm/2.5 mm, interslice gap = 1 mm/0.5 mm, number of slices = 44/49 (for whole brain coverage), volumes per time series within run = 66/64, with 5/3 dummy scans (to allow for T1 equilibration effects).

At location 1, T1-weighted anatomical images were acquired after the EPI sequences, using a 3-D modified driven equilibrium Fourier transform sequence (TR/TE/TI/flip angle = 7.92 ms/2.48 ms/910 ms/16°, voxel size = 1 × 1 × 1 mm^3,176 slices). At location 2, T1-weighted anatomical images were acquired with a magnetisation prepared rapid acquisition gradient echo (MPRAGE) sequence (Mugler and Brookeman, 1990) in the sagittal plane (TR/TE/TI/flip angle = 2,200 ms/2.88 ms/900 ms/10°, voxel size = 1.1 × 1.1 × 1.1 mm^3, 176 slices). Clinical MRI sequences were performed as part of routine pre-neurosurgical management.

fMRI Data Pre-processing

We performed the fMRI data analysis in SPM12 (Wellcome Centre for Human Neuroimaging, London, United Kingdom), running on MATLAB 2012a (MathWorks, Natick, MA, United States). Functional volumes were (a) spatially realigned to the first EPI volume and (b) un-warped to compensate for non-linear distortions caused by the interaction between head movement and magnetic field inhomogeneity. The anatomical T1-weighted image was (c) co-registered to the mean EPI image which had been generated during the realignment step and then spatially normalised to the Montreal Neurological Institute (MNI) space using the new unified normalisation-segmentation tool of SPM12. To spatially normalise all EPI scans to MNI space, (d) we applied the deformation field parameters that were obtained during the normalisation of the anatomical T1 image. The original resolution of the different images was maintained during normalisation (voxel size 1 × 1 × 1 mm^3 for the structural T1-weighted and 3 × 3 × 3 mm^3 for the EPI images). Due to the presence of the right temporal tumours, the co-registration and normalisation images were carefully reviewed by a neuroradiologist (A.K.Y) to ensure that there were no mis-registrations apparent to the eye. After the normalisation procedure, (e) functional images were spatially smoothed with a 6 mm full-width-half-maximum isotropic Gaussian Kernel to compensate for residual anatomical variability and to permit application of Gaussian random-field theory for statistical inference (Friston et al., 1995).

First Level Statistical Analyses

In the first-level statistical analyses, each pre-processed functional volume was entered into a subject specific fixed-effect analysis using the general linear model. An event-related analysis was performed, which allows for the modeling of brain responses for correct trials with the exclusion of incorrect trials (Mechelli et al., 2003). All stimulus onset times were modeled as single events, with only the correct response trials as regressors of interest and three extra regressors that included the instructions, incorrect or "other" (self-corrected, delayed or no-response) trials. Stimulus functions were then convolved with a canonical hemodynamic response function. To exclude low-frequency confounds, the data were high-pass filtered using a set of discrete cosine basis functions with a cut-off period of 128 s. The contrasts of interest compared each of the different conditions (correct trials only) to fixation.

Second Level Statistical Analyses

Second Level Analysis 1

To identify regions of interest, we compared the fMRI response for our three tasks of interest in the three patients with gliomas of

interest (GOI) to the 61 NC. The patients were modeled as three independent groups (one patient per group) and the NC were modeled as two independent groups (51 scanned at location 1 and 10 scanned at location 2). We then identified group differences in activation for: (1) auditory semantic matching vs. rest, (2) visual object naming vs. rest, (3) auditory semantic matching vs. visual semantic matching, and (4) visual object naming vs. visual semantic matching. Contrasts (3) and (4) allowed us to focus on activation that was more likely to be related to speech perception and production respectively (after controlling for semantic and perceptual or motor responses).

We only report group differences that are (i) highly significant ($p < 0.05$ with family wise error correction across the whole brain) when comparing activation across the three patients to that across the two NC groups; (ii) also significant for each patient compared to the NC groups (using an uncorrected threshold of $p < 0.05$) and (iii) not sensitive to scanner differences (i.e., at location 1 or 2). The combination of statistical criteria that all needed to be satisfied to infer abnormal activation are detailed in **Table 2**.

Second Level Analysis 2

To identify site specific and pathology specific effects, the results from second level analysis 1 were further investigated in a *post hoc* analysis that included the first level contrasts for the auditory semantic matching and object naming tasks for all 96 participants. These two tasks were modeled separately for 5 groups: NC ($n = 61$), GOI ($n = 3$), GC ($n = 16$), SOI ($n = 8$) and SC ($n = 8$). Focusing on regions of interest from Second level analysis 1, we plot the data from each task for each participant and report the significance of the statistics for the interactions between task (object naming vs. auditory semantic matching) and group (GOI vs. GC and SOI vs. SC).

RESULTS

The Effect of Right Posterior Superior Temporal Sulcus Damage on Standardised Language Scores

All three patients with RpSTS gliomas had non-aphasic scores on test of speech comprehension and object recognition including: word-to-picture matching, sentence-to-picture matching, sentence repetition, semantic matching (with pictures) and paragraph comprehension. However, they had reduced scores (in the mildly impaired range) when naming objects in pictures and when matching written words to pictures (a written word comprehension test). There was no evidence to suggest these impairments could be explained by difficulties in recognising pictures or semantic matching because all three patients had normal scores when matching pictures on the basis of their semantic relationships and when matching heard speech (spoken words and sentences) to complex pictures. Patient C also had impaired scores on repeating phonologically complex words, reading words aloud, and recognition memory (see **Table 3**). Importantly the overall scores between the three patients for written comprehension and object naming were very similar, with patient B with the grade 4 glioma no more impaired than patient A with the grade 2 glioma.

For stroke patients with damage to RpSTS, we found that, like the patients with RpSTS gliomas none had impaired speech comprehension, object recognition or semantic matching. Mild impairments were recorded for: comprehension of written words ($n = 2$); repetition of words ($n = 2$) and repetition of non-words ($n = 1$). However, unlike the patients with RpSTS gliomas, none of the stroke patients with RpSTS damage had impaired object naming scores. Plausibly, this is because they were all tested years after their strokes (1.9–14.2 years) (see **Table 1** and **Supplementary Appendix 2**).

In Scanner Behavioural Results

All but three participants scored at least 75% correct on each task. The exceptions were one stroke control patient who scored 60% on the auditory semantic matching, one neurotypical control participant who scored 70% for object naming and another neurotypical control participant who scored 55% for visual semantic matching. Accuracy for patients of interest (with RpSTS gliomas or stroke patients) was within the normal range for each of the three tasks. **Table 4** summarises the in scanner behavioural performance for the NC group and patients with RpSTS gliomas.

fMRI Results

Auditory Semantic Matching (Second Level Analysis 1)

In NC, auditory semantic matching increased activation (compared to rest and visual semantic matching) in bilateral superior temporal gyri (red and cyan regions in **Figure 2**) with no significant difference between those imaged in Location 1 or 2.

Compared to the NC group, the three patients with right pSTS gliomas showed significantly less activation in the right superior temporal lobe (**Table 5A**). This was observed, for all three patients, in the region infiltrated by the tumours, sited between the right posterior superior temporal sulcus (pSTS) and right planum temporale (PT) (red cluster in **Figure 3**) with peaks at MNI [+51 −25 +5] and [+45 −28 +5]. In contrast, activation in the left homologue, bordering the left pSTS and left PT [−39 −34 +5], was higher (enhanced) in each of the patients compared to the controls (**Table 5A**, blue clusters **Figure 3**). These group and individual patient effects were seen for auditory semantic matching compared to both rest and visual semantic matching (**Table 5A**).

Individual responses, from all three patients with right pSTS gliomas and 61 controls, are plotted in **Figure 4** to illustrate that each patient showed reduced and increased activation relative to the average control response within the right and left superior temporal lobes respectively. This effect is most notable at [+51 −25 +5] where all three patients' responses were below the normal range. Outside the auditory cortices, there were no other significant abnormalities in activation during auditory semantic matching that were observed in each of the three patients.

TABLE 2 | Statistical criteria and thresholds used for identifying abnormal activation.

Task:	**Auditory semantic matching**		**Object naming**	
Baseline:	**>Rest**	**>Vis Sem Mat**	**>Rest**	**>Vis Sem Mat**
Abnormally low activation				
(1) NC only	$p < 0.05$c	$p < 0.05$c	$p < 0.05$c	$p < 0.05$c
(2) NC > All 3 Patients	$p < 0.05$c	$p < 0.05$c	$p < 0.05$c	$p < 0.05$c
(3) NC > Patient A	$p < 0.05$u	$p < 0.05$u	$p < 0.05$u	$p < 0.05$u
(4) NC > Patient B	$p < 0.05$u	$p < 0.05$u	$p < 0.05$u	$p < 0.05$u
(5) NC > Patient C	$p < 0.05$u	$p < 0.05$u	$p < 0.05$u	$p < 0.05$u
Abnormally high activation				
(1) All 3 patients	$p < 0.05$c	$p < 0.05$c	$p < 0.05$c	$p < 0.05$c
(2) All 3 Patients > NC	$p < 0.05$c	$p < 0.05$c	$p < 0.05$c	$p < 0.05$c
(3) Patient A > NC	$p < 0.05$u	$p < 0.05$u	$p < 0.05$u	$p < 0.05$u
(4) Patient B > NC	$p < 0.05$u	$p < 0.05$u	$p < 0.05$u	$p < 0.05$u
(5) Patient C > NC	$p < 0.05$u	$p < 0.05$u	$p < 0.05$u	$p < 0.05$u

*The table lists the statistical criteria used to identify regions of abnormal activation in the glioma patients of interest (GOI) compared to the neurotypical control participants (NC) for auditory semantic matching > rest/visual semantic matching; and object naming > rest/visual semantic matching. Group effects (contrasts 1-2) were assessed at a statistical threshold of $p < 0.05$ with family wise error correction across the whole brain ($p < 0.05$c) and individual patient effect (contrasts 3–5) were assessed, within these regions, at an uncorrected threshold of $p < 0.05$ ($p < 0.05$u). Results are reported for contrast (2) to (5) in **Tables 5A,B**.*

TABLE 3 | CAT test results for patients with gliomas of interest.

CAT Test		**Cut-off**	**A**	**B**	**C**
Written comprehension	Words Ts	54	**50**†	**53**†	**51**†
	Raw score	27/30	**25**	**27**	**26**
Speech production	Reading words Ts	61	69	69	**57**†
	Raw score	45/48	48	48	**42**
	Object naming Ts	61	**61**†	**60**†	**61**†
	Raw score	43/48	**42**	**41**	**43**
	Repeating complex words Ts	61	62	62	**55**†
	Raw score	5/6	6	6	**5**
Cognitive	Recognition memory Ts	47	48	59	**32**†
	Raw score	8/10	9	10	**4**

*Results from the Comprehensive Aphasia Test (CAT) are shown for the subtests that were impaired for patients A, B and C. Raw scores are converted to T-scores following comparison to a reference population of 113 patients. If the score is equal or below the cut-off value, this is classified as impaired performance, marked by † in **bold**. The raw score indicates how many errors the patients made, or in the cut-off column, the total number of points available (denominator), and the highest number associated with impaired performance (numerator). The patients performed in the normal range for the remainder of the subtests from the CAT.*

TABLE 4 | In scanner behavioural performance for patients with RpSTS gliomas.

Task		**NC group 1**	**NC group 2**	**A**	**B**	**C**
Auditory matching	Accuracy	96 (4) [85–100]	96 (6) [80–100]	95	100	100
	RT	2,600 (203) [2,250–3,291]	2,539 (194) [2,248–2,945]	2,404	2,366	2,517
Object naming	Accuracy	94 (5) [80–100]	91 (10) [70–100]	90	80	100
	RT	1,310 (157) [1,006–1,917]	996 (380) [426–1,803]	1,126	1,107	n/a
Visual matching	Accuracy	96 (7) [55–100]	99 (2) [95–100]	95	100	93
	RT	1,287 (263) [860–2,212]	1,131 (189) [881–1,386]	1,180	1,262	1,037

NC groups 1 and 2 refer to the two groups of neurotypical control participants (according to the location used for data acquisition). A, B, and C refer to the three patients with RpSTS gliomas. Accuracy is the mean percentage of correct responses for each task with (standard deviation) and [range]. RT is the response time in milliseconds with (standard deviation) and [range]. n/a = not applicable because the response times could not be collected for technical reasons as detailed in the Materials and Methods section.

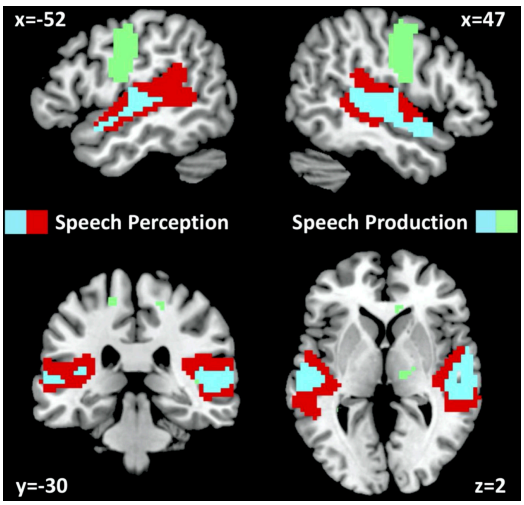

FIGURE 2 | fMRI activation for neurotypical control participants. fMRI activation clusters are shown for the 61 neurotypical control participants (NC) for the speech perception task (auditory semantic matching > visual semantic matching) and the speech production task (object naming > visual semantic matching). Cyan represents activated voxels for both auditory semantic matching and object naming. Red represents activated voxels for auditory semantic matching only and green represents activated voxels for object naming only. The statistical threshold was $p < 0.05$ with family wise error correction across the whole brain.

Object Naming (Second Level Analysis 1)

In NC, visual object naming (compared to either rest or visual semantic matching) increased activation in bilateral superior temporal gyri, pre-central and post-central gyri and supero-inferior medial cerebellar and subcortical regions (green and cyan regions in **Figure 2**). The only activation difference for NC imaged at Location 1 or 2 was in bilateral cerebellum which is not relevant to the current results.

Across the three patients with right pSTS gliomas, there were no brain regions, including RpSTS that were consistently less activated than the neurotypical control participants. Even more surprisingly, patients showed higher than normal activation in RpSTS during naming where we found lower than normal activation during auditory semantic matching (see **Table 5** and **Figures 3**, **4**). **Table 5C** shows the significance of this task by group interaction, along with the opposite pattern of effects in the left superior temporal lobe where patient activation was significantly higher than normal during auditory semantic matching, but not during object naming (see plots in **Figures 3**, **4**).

Other Patient Groups (Second Level Analysis 2)

Our final analysis demonstrated that the task dependent group differences in RpSTS (under-activation during auditory semantic matching and over-activation during object naming) were also observed when (i) our three patients with RpSTS gliomas were compared to 16 patients with gliomas that spared RpSTS and (ii) in the comparison of right hemisphere stroke patients with damage vs. preservation of RpSTS (**Table 6**). **Figure 5** compares the group and individual responses at the peak RpSTS region [+51, −25, +5]. Almost all the control participants (61 neurotypical and 22 patients) show more or equivalent activation for auditory semantic matching (light brown) than object naming (blue). This pattern reverses for the three patients with RpSTS gliomas and the eight patients with (incomplete) RpSTS stroke damage.

In the left temporal lobe, enhanced activation during auditory semantic matching was observed for our three glioma patients of interest (with RpSTS damage) compared to the 16 patients with gliomas that spared RpSTS ($Z = 6.5$; $p < 0.05$ corrected at −39, −34, +5), but activation in this region was not higher than normal in any of the 16 stroke patients during either task.

DISCUSSION

The aim of this study was to investigate if gliomas within the right postero-superior temporal lobe, involving speech sensitive language regions, result in language impairment and how they affect the functioning of the neural networks involved in the perception and production of speech. We searched for atypical neural activation that was common to patients with three differing grades of right temporal lobe gliomas (grade 2, 3, 4) compared to (i) neurotypical control participants and (ii) patients with gliomas in other supratentorial regions. We also tested whether the same effects were observed when comparing brain activation from patients with right hemisphere stroke damage that affected, or did not affect, the right postero-superior temporal lobe. This revealed cross-pathology effects that were task specific and site specific. Below, we describe the effect of RpSTS gliomas on speech and language abilities and the neural processing associated with speech perception and production tasks in the context of prior literature, before discussing the role of tumour plasticity, study limitations and clinical implications.

The Effect of Right Posterior Superior Temporal Sulcus Damage on Speech and Language Behaviour

Despite having tumours that infiltrated the right temporal lobe regions implicated in speech perception and production, none of the three patients with RpSTS gliomas showed language impairments on clinical examination or speech perception impairments on standardised speech and language assessments. However, all three of these patients had mild impairments on tests of object naming and written comprehension. This finding complements and extends prior literature. For example, Noll et al. (2016) found that 2/29 (7%) of their patients with right temporal lobe gliomas had object naming impairments, 3/29 (10%) had letter fluency impairments and 12/30 (40%) had impaired verbal learning (total recall). Antonsson et al. (2018) also reported the pre-operative results of language assessment in a patient who had a tumour that infiltrated the temporal lobe (in addition to frontal, insula and thalamic regions) with this patient having below cut off scores on word definitions and comprehension of logico-grammatical sentences and sentence analysis but not object naming.

TABLE 5 | Comparison of patients with RpSTS gliomas to neurotypical control participants.

(A) Auditory semantic matching				
Contrast	**Patients**	**NC > Patients**		**Patients > NC**
		+51 −25 +5	**+45 −28 +5**	**−39 −34 +5**
Auditory semantic matching > Rest	A, B, and C	**5.1**	**5.4**	**6.8**
	Patient A	2.7	3.2	1.9
	Patient B	3.2	3.5	5.1
	Patient C	3.3	3.0	5.4
Auditory > Visual semantic matching	A, B, and C	**5.9**	**4.5**	**5.1**
	Patient A	3.5	3.3	1.7
	Patient B	4.8	3.0	3.7
	Patient C	2.4	1.9	4.1
(B) Object naming				
Contrast	**Patients**	**Patients > NC**		
		+51 −25 +5	**+42 −34 −4**	**+39 −40 +11**
Object naming > Rest	A, B, and C	**5.2**	**5.5**	**7.9**
	Patient A	3.3	5.3	8.5
	Patient B	5.3	2.0	1.8
	Patient C	ns	2.8	2.7
Object naming > Visual semantic matching	A, B, and C	ns	**4.9**	**7.4**
	Patient A	1.8	3.9	7.9
	Patient B	3.8	1.9	2.7
	Patient C	ns	2.3	2.3
(C) Task by group interactions				
Contrast	**Patients**	**Patients > NC**		
		+51 −25 +5	**+45 −28 +5**	**−39 −34 +5**
Auditory semantic matching > Naming	A, B, and C	ns	ns	3.6
	Patient A	ns	ns	1.7
	Patient B	ns	ns	2.2
	Patient C	ns	ns	2.9
Naming > Auditory semantic matching	A, B, and C	**7.1**	**5.3**	ns
	Patient A	4.2	4.1	ns
	Patient B	5.9	3.3	ns
	Patient C	3.1	2.3	ns

*Group differences in fMRI activation, for patients with RpSTS gliomas (A, B, C) compared to 61 neurotypical control participants (NC) for: (A) auditory semantic matching, (B) object naming and (C) the interaction of auditory semantic matching and object naming. Co-ordinates (MNI) are from the comparison of all three patients (A, B, and C) to NC. Z-scores for individual patients are all within a 3 mm sphere of these co-ordinates. Statistical thresholds: Z scores ≥ 4.8 = $p < 0.05$ after family wise error correction across the whole brain (shown in bold), ≥ 3.1 = $p < 0.001$ uncorrected and ≥ 1.7 = $p < 0.05$ uncorrected. ns = not significant at $p < 0.05$ uncorrected. See **Figure 3** and text for anatomical localisation.*

Variability in the effect of right temporal lobe damage on language function was also observed in our sample of eight patients with stroke damage to RpSTS, half of which had mild impairments with written comprehension and/or repetition of words/non-words. Further studies are required to understand whether the variability observed in our own data and prior studies is the consequence of: the degree and location of damage within the right temporal lobe and the extent of damage to other brain regions, the histological grading and speed of growth of the tumours and the degree of functional re-organisation of the language networks which is likely to depend on pathology duration.

Neural Processing Associated With Speech Perception and Production Tasks

Evidence that the neural processing of speech perception and production was altered in patients with RpSTS gliomas,

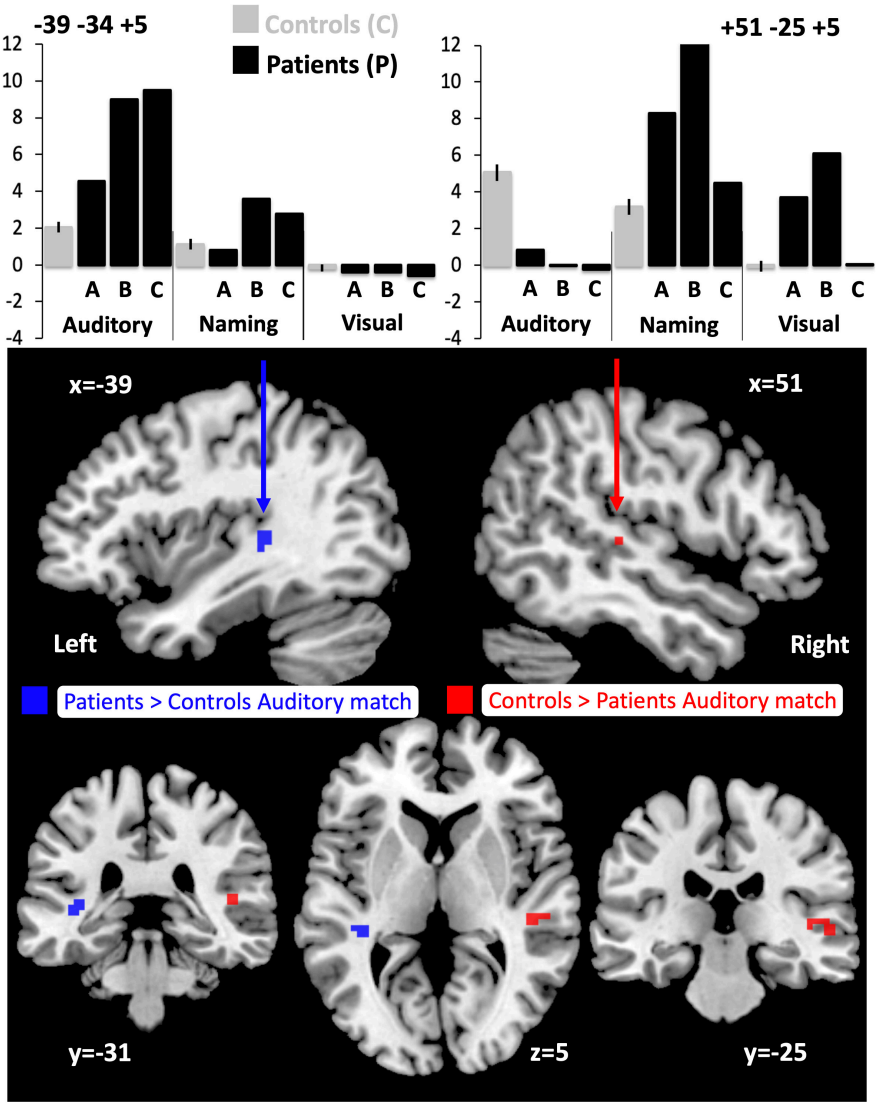

FIGURE 3 | Altered responses during auditory semantic matching, object naming and visual semantic matching in the three RpSTS glioma patients compared with neurotypical control participants. The plots (top) illustrate the fMRI responses in the left [−39 −34 +5] and right [+51 −25 +5] superior temporal lobes for the three fMRI tasks: auditory semantic matching (auditory), object naming (naming) and visual semantic matching (visual). Y-axis represent the fMRI responses (first eigenvariate extracted from SPM). The images below show the sites of abnormal fMRI activation ($p < 0.05$ after family wise error correction across the whole brain) in the patients compared to the neurotypical controls participants (NC), overlaid on a normalised T1-weighted image in neurological convention (right of subject on right of image). Blue indicates the left superior temporal region where patients showed an enhanced response during auditory semantic matching (11 voxels). Red (in the right pSTS) shows where the patients under-activated during auditory semantic matching compared to NC (19 voxels).

compared to a large sample of neurotypical control participants and a large sample of control patients with gliomas affecting other parts of the cerebrum, was identified in the left and right temporal lobes. The left superior temporal cortex showed enhanced activation during auditory semantic matching but not object naming; and the right superior temporal cortex showed abnormally low activation during auditory semantic matching but enhanced activation during object naming. These atypical effects cannot be explained by patients failing to perform the fMRI tasks (Price and Friston, 1999) because (i) the fMRI tasks were, by design, not particularly challenging and patients had accuracy in the range of the controls and (ii) the analysis was based on correct trials only. Nor can they be explained by tumour related disruptions to the hemodynamic response (Jiang et al., 2010; Wang et al., 2012) because (i) we observed abnormal responses in the tumour free left cerebral hemisphere; and (ii) the abnormalities in the right superior temporal cortex observed were task-specific in all three patients. Additionally, these effects were not seen in any of the further 16 patients with gliomas within other parts of the cerebrum indicating this is not a sequela of a non-specific tumour-induced disruption to language networks. Alternative interpretations are considered below.

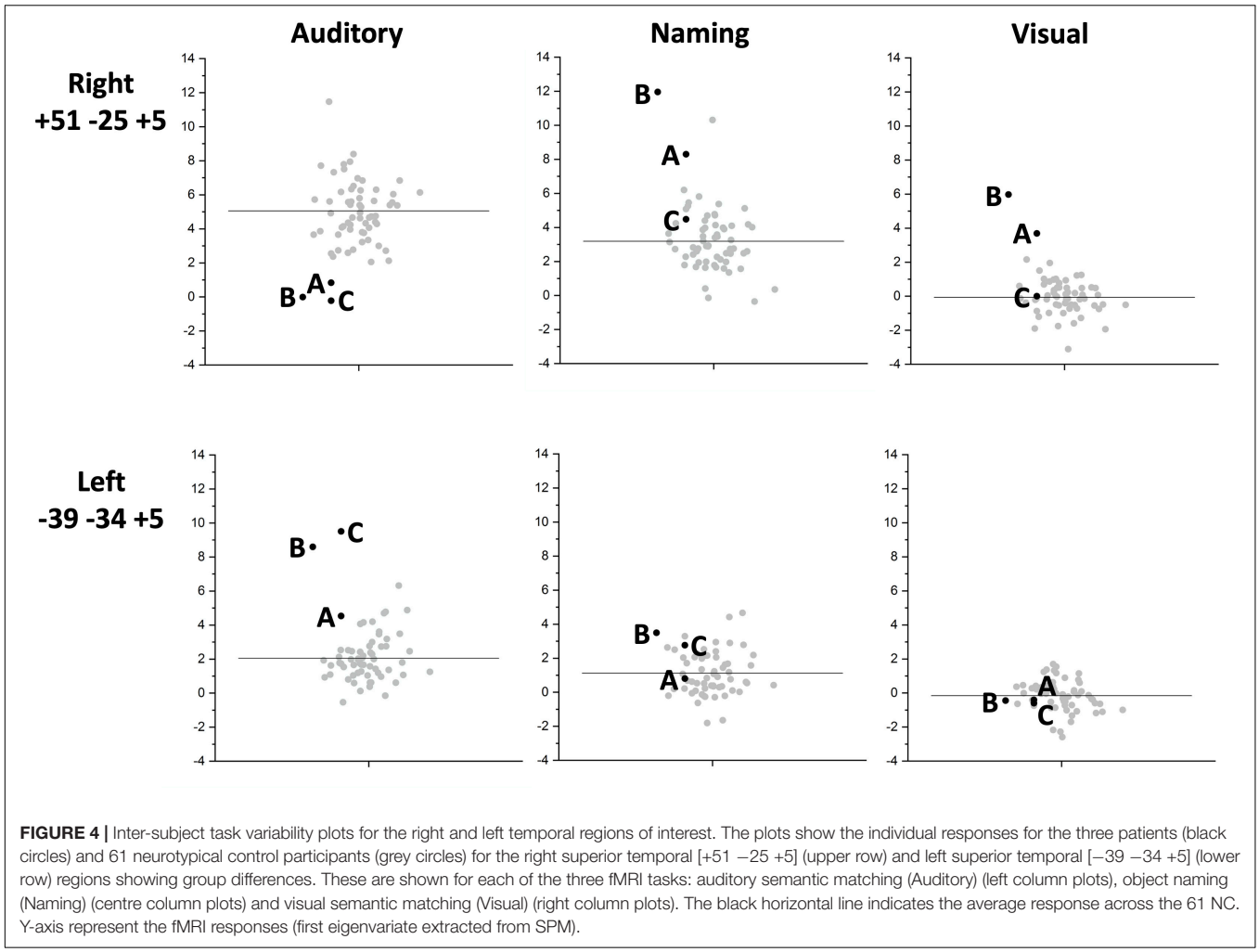

FIGURE 4 | Inter-subject task variability plots for the right and left temporal regions of interest. The plots show the individual responses for the three patients (black circles) and 61 neurotypical control participants (grey circles) for the right superior temporal [+51 −25 +5] (upper row) and left superior temporal [−39 −34 +5] (lower row) regions showing group differences. These are shown for each of the three fMRI tasks: auditory semantic matching (Auditory) (left column plots), object naming (Naming) (centre column plots) and visual semantic matching (Visual) (right column plots). The black horizontal line indicates the average response across the 61 NC. Y-axis represent the fMRI responses (first eigenvariate extracted from SPM).

TABLE 6 | Enhanced right temporal lobe activation for object naming > auditory semantic matching.

	+51 −25 +5	+45 −28 +5	+39 −40 +11	+42 −34 −4
GOI > GC	4.6	3.5	4.3	2.2
SOI > SC	5.6	5.9	4.1	1.7

*Statistical significance (Z scores) of group differences in activation for object naming more than (>) auditory semantic matching at each of the right temporal lobe co-ordinates identified in the comparison of RpSTS gliomas to neurotypical control participants (see **Table 5** for details). The results are shown for the comparisons of the Glioma patients of interest (GOI) > Glioma control patients (GC) (upper row) and the Stroke patients of interest (SOI) > Stroke control patients (SC).*

Abnormal fMRI Activation During Auditory Semantic Matching

Auditory input to each ear normally results in bilateral responses in the auditory cortices because ascending sensory afferent fibers from the brainstem cochlear nuclei project to both ipsilateral and contralateral auditory cortices (Parker Jones and Schnupp, 2021). In the context of right postero-superior temporal tumours or ischemic damage, it is not surprising that we observed reduced activation during auditory processing in the right auditory cortex. Although this did not result in abnormally slow responses or low accuracy during the auditory semantic matching task, speech perception impairments might have been observed with more stringent assessments, particularly when stimuli are only presented to the left ear given prior evidence that the crossed connections between ascending sensory afferent fibers and contralateral auditory cortices are more effective and functionally more important (Kimura, 1961; Nakasato et al., 1997; Jafari et al., 2016). For example, Nakasato et al. (1997) demonstrated that the presence of a tumour in the superior temporal lobe delays the auditory evoked potential to a stimulus when it is presented in the ear contralateral to the tumour but not when it is presented in the ear ipsilateral to the tumour.

Plausibly, normal behavioural responses during auditory semantic matching in the context of abnormally low responses in the right auditory cortex could be explained by the exaggerated response we observed in the undamaged left superior temporal lobe in the patients with right postero-superior temporal gliomas. For example, the enhanced response in the left hemisphere during auditory semantic matching might reflect enhanced, selective attention to right ear processing in the left temporal lobe

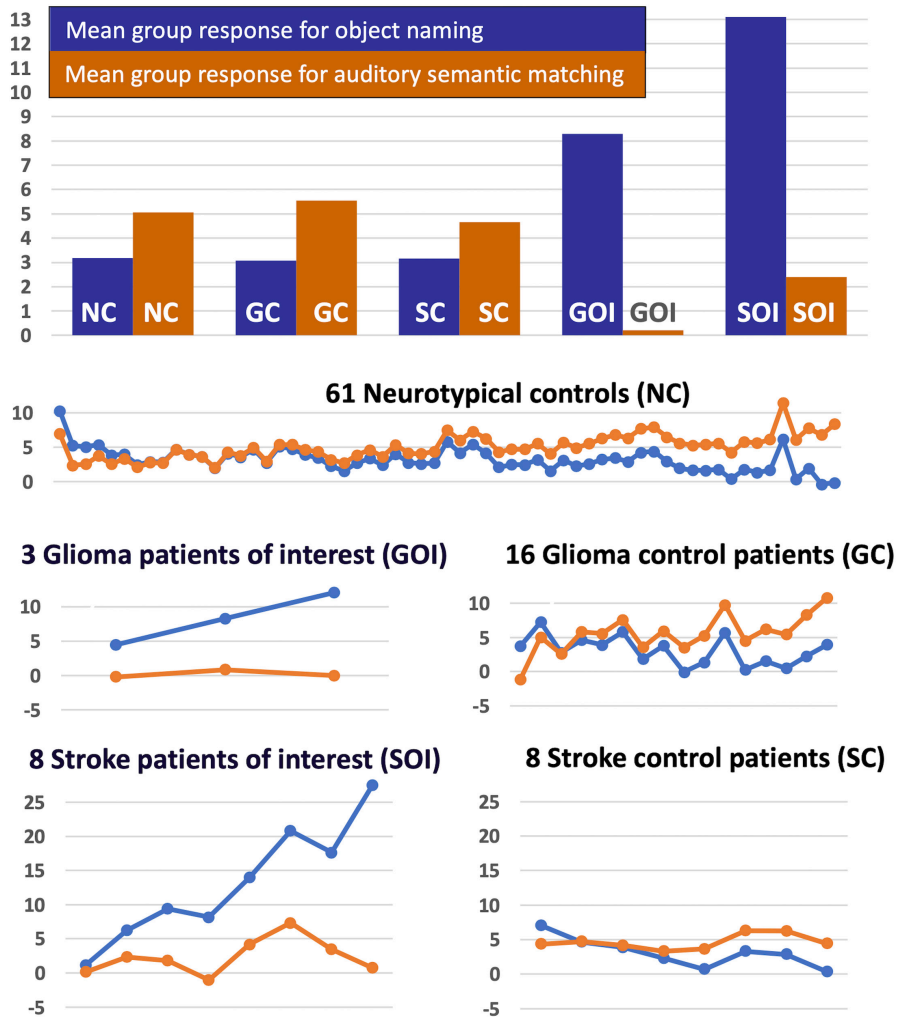

FIGURE 5 | Task-specific fMRI response in RpSTS [+51 −25 +5]. The task-specific responses (blue = object naming, light brown = auditory semantic matching) in Right pSTS [+51 −25 +5] are shown for the five groups of participants (NC, GC, SC, GOI, and SOI). The uppermost chart shows the mean group response for the two tasks for each of the five groups. The lower plots show the individual responses for the two tasks for each participant in each of the five groups (in total $n = 96$). Y-axis represent the fMRI responses (first eigenvariate extracted from SPM).

because of impaired right temporal lobe function (Hugdahl and Andersson, 1986). Neurophysiologically, this can be supported through the presence of both ascending cochlear afferents projecting to bilateral auditory cortices and the presence of cortico-fugal projections to subcortical structures (Suga and Ma, 2003) through which top-down modulation can occur (Yan and Suga, 1998; Zhang and Suga, 2000). In our patients, these top-down effects are likely to be strategic because enhanced left temporal activation was not observed during object naming, even though bilateral auditory cortices are involved in processing the sound of the spoken response. Enhanced left temporal lobe activation was also not observed in any of the stroke patients even though three had no detectable activation in their right auditory cortex during auditory semantic matching. Plausibly this is because most of these patients were imaged at least 2 years following the time of their stroke. Future fMRI studies of stroke patients with right temporal lobe infarcts are required to test whether left temporal lobe activation is enhanced during auditory semantic matching in the immediate period following the onset of damage rather than later on following recovery.

An alternative explanation of enhanced left temporal lobe activation is that it represents contralateral disinhibition (Bloom and Hynd, 2005) from the damaged right auditory cortex but this would not explain why left temporal activation was not enhanced during object naming or in any of the stroke patients who had damage to the right auditory cortex. As we were only able to study three patients with right postero-superior temporal lobe gliomas, further studies are needed to determine whether enhanced left temporal activation during speech perception tasks is a result of (a) different neuroplasticity mechanisms following gliomas and infarcts; or (b) other

individual differences (e.g., strategic, functional anatomy) that are independent of pathology.

Abnormal fMRI Activation During Object Naming

Given the reduction in the right pSTS response during auditory semantic matching, it is surprising that no such reduction was observed during the speech production task (object naming). To the contrary, RpSTS activation during object naming was either higher than normal (patients A,B) or in the high normal range (patient C). This enhanced RpSTS activation during object naming, but not during the auditory semantic matching task was also observed in stroke patients with right hemisphere infarcts affecting, but not destroying, the right postero-superior temporal lobe. In other words, it was observed across two pathologies that are associated with different onsets (slow vs. acute), neuroplasticity mechanisms (continuous in the context of actively progressing damage with growing tumours vs. time limited in the case of a suddenly occurring infarct).

The fact that right temporal lobe object naming activation is not reduced within tumour infiltrated auditory cortex is informative in three ways. The first is that, despite RpSTS being infiltrated by the tumours, its task-specific activation during object naming indicates that it could still respond during accurate (in-scanner) speech production. Second, this task-specific effect (under-activation during auditory semantic matching, enhanced activation during object naming) is unlikely to represent the sequela of a perturbed hemodynamic response function which has been described when functional imaging has been performed in patients with brain tumours (Ojemann et al., 1998; Jiang et al., 2010; Wang et al., 2012). To the contrary, the task-specific responses provide evidence that the RpSTS region is functionally active despite being infiltrated by tumour. This is in keeping with previous studies demonstrating preserved function within tumour infiltrated cortices using intra-operative mapping in both low (Duffau et al., 2003; Benzagmout et al., 2007) and high grade gliomas (Ojemann et al., 1996), magnetoencephalography (MEG) (Schiffbauer et al., 2001) and fMRI (Krainik et al., 2003). It is also in keeping with our observations that the same pattern of response (under-activation during auditory semantic matching and enhanced activation during object naming) was observed in patients with RpSTS gliomas and stroke patients with right postero-superior temporal lobe infarcts. Third, if activity within tumour infiltrated auditory cortex does support object naming, complete loss of RpSTS (e.g., after resection) may result in more object naming errors, especially given that deficits were already detectable on behavioural language testing in all three patients.

In terms of how RpSTS contributes to object naming, we have previously proposed that it is normally responsive to auditory bottom up inputs and top down attention to the expected auditory output during speech production (Yamamoto et al., 2019b). Both these observations implicate RpSTS in the auditory monitoring of one's own spoken response, which is necessary to ensure that sounds produced by the subjects' articulators correspond to the sounds they were intended to produce (Yamamoto et al., 2019b). This is consistent with the current observation that RpSTS is a speech perception area that responds during auditory semantic matching and object naming but not visual semantic matching (see cyan areas in **Figure 2**). Prior studies have also shown how RpSTS activation increases when the auditory feedback is perturbed during speech production creating a mismatch between heard speech and intended speech (Houde and Jordan, 1998; Tourville et al., 2008; Zheng et al., 2010; Niziolek and Guenther, 2013; Behroozmand et al., 2015).

According to this theoretical account of RpSTS function, the continued RpSTS activation in our patients with RpSTS damage, during object naming but not auditory semantic matching, might reflect the increased demands on a disrupted speech monitoring system that attempts to minimises error-prone speech by increasing attention to top-down predictions relative to the perturbed auditory inputs from their own speech (brought about by the tumour). Such a top-down processing mechanism is more effective during speech production than speech perception because the patients can predict the sounds they are about to produce but cannot so easily predict the auditory signals produced during speech perception tasks (Blank et al., 2018).

Tumour-Related Plasticity in the Patients With Low and High Grade Gliomas

Our findings of altered fMRI activation that was common across all three patients may be surprising given the generally held view that more slowly growing low grade gliomas have the potential for neural plasticity (Duffau, 2006, 2005; Desmurget et al., 2007) while more aggressive high grade gliomas have limited potential for remodeling. On the other hand, there have been previous reports of both low and high grade gliomas inducing the same pattern of reorganisation in language networks. This has been demonstrated with intra-operative mapping (Lubrano et al., 2010), positron emission tomography (Thiel et al., 2001), repetitive transcranial magnetic stimulation (Thiel et al., 2005), language fMRI (Bizzi et al., 2012) and resting state fMRI (Briganti et al., 2012). Tumour grading alone is therefore not sufficient to predict the potential for tumour-related plasticity, which likely relates to a multitude of factors which include the tumour's rate of growth, its size, location and which eloquent brain regions are infiltrated.

LIMITATIONS AND FUTURE DIRECTIONS

The main limitation of this study was the small cohort size of patients with right postero-superior temporal gliomas. We attempted to mitigate the reporting of spurious (subject specific) findings, by focusing on fMRI abnormalities that were consistent across all three participants despite differences in their age, tumour histology and size. We also demonstrate that the task specific responses in RpSTS were observed in stroke patients with right hemisphere infarcts that involved the right postero-superior temporal lobe. Nevertheless, future studies are required to determine how well our findings replicate over larger cohorts

of patients with right postero-superior temporal gliomas, and any factors that influence functional reorganisation of language processing in these patients. Repeated longitudinal language testing would also help determine whether progressive language impairments in speech production tasks are accompanied by a reduction in compensatory RpSTS activation and whether this is accompanied by contra-lateral hemispheric functional reorganisation, as observed during speech perception. Additional studies will also be required post-operatively to determine the effect of the tumour resection on both language assessment and the pattern of fMRI activation. Whilst the effect on language function is not as severe as with left temporal lobe resection, decline in verbal learning and memory and letter fluency have still been observed in 31% and 26% of patients undergoing resection of right temporal gliomas (Noll et al., 2015b). The aim will be to determine if any post-operative decline in language function is influenced by the presence or absence of altered activation in right pSTS.

A second potential limitation is that abnormal fMRI responses may reflect dysfunctional neurovascular coupling. Previous studies performed in patients with gliomas have demonstrated reduced fMRI BOLD activation across the tumour affected hemisphere (Jiang et al., 2010; Wang et al., 2012). This has been proposed to be due to tumour-related perturbation of the normal brain environment leading to neurovascular uncoupling (Zacà et al., 2014) that impacts the assessment of language hemispheric dominance (Ulmer et al., 2004). An altered BOLD response resulting from close proximity of a glioma is however not always the case (Yamamoto et al., 2019a) and even high grade gliomas have been shown to retain the normal task-evoked response resulting in localised cerebral oxygenation alteration and preserved BOLD activation close to the tumour (Fujiwara et al., 2004). Additional MRI perfusion studies could help to assess whether perfusion is abnormal within and/or close to tumour-infiltrated parenchyma. Examination of resting state fMRI in the RpSTS region would also be informative. The atypical language activations observed in the current study are however unlikely to be the consequence of neurovascular uncoupling because the direction of the BOLD response in the tumour affected hemisphere varied between tasks (**Figure 4**). Future experiments are, nonetheless, required to investigate whether right postero-superior temporal intra-tumoural fMRI activation, during object naming, represents preserved intra-tumoural function. This could be achieved using a non-invasive technique such as navigated-TMS or could also be performed intra-operatively with electrical stimulation techniques for cortical mapping (Picht et al., 2013).

SUMMARY AND CONCLUSION

The current study found evidence for mild language impairments and atypical language activation in patients with gliomas (low and high grade) infiltrating the right postero-superior temporal lobe. Neural differences that were consistent across patients, compared to neurotypical controls participants and glioma control patients, were observed both within the tumour infiltrated right temporal lobe and within the contra-lateral hemisphere, representing two of the previously proposed patterns of plasticity (Desmurget et al., 2007).

One of the most striking results was that atypical neural activation in all three patients was task specific with abnormally low RpSTS activation during auditory semantic matching that was not seen during object naming. Our explanation for these effects is as follows. During auditory semantic matching, the processing of auditory inputs to right auditory cortex is perturbed. The abnormally high activation we observed in the left auditory cortex for the patients with right temporal lobe gliomas but none of the eight patients with right temporal lobe stroke damage suggest individual differences in the strategic re-directing of attention to the left auditory cortex but further studies are required to confirm this. In contrast during object naming, activation with right postero-superior temporal damage increases rather than decreases in the RpSTS, a region which is implicated in speech production in the healthy brain (Tian and Poeppel, 2013, 2010; Tian et al., 2016; Yamamoto et al., 2019b). We propose that these results are being driven top-down, rather than bottom up, and reflect the special role that RpSTS plays in monitoring self-generated speech.

CLINICAL IMPLICATIONS

Our findings have several clinical implications. First, to reduce the risk of post-operative language deficits it is important for neurosurgeons to understand which brain regions might be compensating for the function of the region affected by the tumour so that these compensatory regions can be preserved during resection (Duffau, 2006, 2005). In addition to performing routine clinical fMRI tasks which can help to identify interhemispheric lateralisation of language activation (Black et al., 2017; Bargalló et al., 2020) additional preoperative fMRI tasks could be tailored depending upon which particular brain regions are affected by the tumour, and what is known about the function of these regions in the neurologically intact brain. For tumours affecting the right postero-superior temporal lobe, given the pre-existing knowledge of the function of RpSTS and the findings from this study, we would recommend using a two-object naming task performed with overt speech production (as has been used in this study) which has high consistency of reproducible activation across participants (Ekert et al., 2021).

In addition to fMRI, both intra-tumoural and peri-tumoural functional centres could be further assessed pre-operatively with other non-invasive techniques such as MEG (Zimmermann et al., 2019) and navigated-TMS (Ille et al., 2015). This combined increased pre-operative knowledge of sites of language function could lead to modification of the surgical technique such as the decision to perform the surgery awake with intra-operative mapping of the language system, particularly for right hemispheric tumours which are more likely to be

operated on under general anesthesia than those in the left hemisphere (Hervey-Jumper et al., 2015; Vilasboas et al., 2017). If atypical activation occurs in the contra-lateral hemisphere as was shown with speech perception, it may also be important to confirm that these regions have been recruited prior to surgery in order to minimise any post-operative deficit. It has been suggested that surgery performed for low grade gliomas, particularly in patients with no or only minimal deficits, should be performed awake irrespective of the hemisphere (Duffau, 2018). If pre-operative investigations, fMRI with corroborative evidence from MEG/TMS, do identify right intra- or peri-tumoural language centres then we would be in agreement with this recommendation, which should also be extended to include patients with higher grade tumours such as those reported in the current study.

Second, insight into the mechanisms which support speech perception and production could allow for better predictions of long term outcomes for future patients. For example, if we know which regions can compensate for loss of another region infiltrated with tumour, then recovery or maintenance of function will depend on whether the tumour has spared compensatory pathways.

Finally, our study motivates further pre-operative language fMRI studies of patients with right hemispheric tumours which has historically not been the case (Manan et al., 2020). These may further reveal how right sided gliomas alter language performance and reorganisation within the language network.

DATA AVAILABILITY STATEMENT

The raw data supporting the conclusions of this article are available upon request from the senior author CJP, c.j.price@ucl.ac.uk.

ETHICS STATEMENT

The studies involving human participants were approved by the NHS Research Ethics Committee–London Bridge and the London Queen Square Research Ethics Committee. The patients/participants provided their written informed consent to participate in this study.

AUTHOR CONTRIBUTIONS

AKY and CJP conceived, designed the study, analysed and interpreted the tumour patient and control data, drafted the manuscript. AKY, RP, and LM acquired and processed the tumour patient data. AGV and MC were involved with the acquisition and analysis of the stroke patient data with CJP. JE was involved with the analysis of the patient fMRI data. AS, OPJ, TMHH, SP, and MO acquired and processed the control data. AS, OPJ, TMHH, SP, CJP, DWG, and MO designed and optimised the fMRI paradigms. TAY provided overview to the study. All authors contributed to the article and approved the submitted version.

FUNDING

This research was funded by Wellcome (205103/Z/16/Z; 203147/Z/16/Z) and a grant provided by the National Institute for Health Research (NIHR) UCLH/UCL Comprehensive Biomedical Research Centre (Project Award reference 74).

ACKNOWLEDGMENTS

For the purpose of Open Access, the author has applied a CC BY public copyright license to any author accepted manuscript version arising from this submission. We thank Eldad Druks for creating the picture stimuli.

SUPPLEMENTARY MATERIAL

The Supplementary Material for this article can be found online at: https://www.frontiersin.org/articles/10.3389/fnhum.2022.803163/full#supplementary-material

REFERENCES

Andics, A., McQueen, J. M., Petersson, K. M., Gál, V., Rudas, G., and Vidnyánszky, Z. (2010). Neural mechanisms for voice recognition. *Neuroimage* 52, 1528–1540. doi: 10.1016/j.neuroimage.2010.05.048

Antonsson, M., Longoni, F., Jakola, A., Tisell, M., Thordstein, M., and Hartelius, L. (2018). Pre-operative language ability in patients with presumed low-grade glioma. *J. Neurooncol.* 137, 93–102. doi: 10.1007/s11060-017-2699-y

Bargalló, N., Cano-López, I., Rosazza, C., Vernooij, M. W., Smits, M., Vitali, P., et al. (2020). Clinical practice of language fMRI in epilepsy centers: a European survey and conclusions by the ESNR Epilepsy Working Group. *Neuroradiology* 62, 549–562. doi: 10.1007/s00234-020-02397-w

Behroozmand, R., Shebek, R., Hansen, D. R., Oya, H., Robin, D. A., Howard, M. A., et al. (2015). Sensory-motor networks involved in speech production and motor control: an fMRI study. *Neuroimage* 109, 418–428. doi: 10.1016/j.neuroimage.2015.01.040

Belin, P., Zatorre, R. J., Lafaille, P., Ahad, P., and Pike, B. (2000). Voice-selective areas in human auditory cortex. *Nature* 403, 309–312. doi: 10.1038/35002078

Benzagmout, M., Gatignol, P., and Duffau, H. (2007). Resection of world health organization Grade II gliomas involving Broca's area: methodological and functional considerations. *Neurosurgery* 61, 741–753. doi: 10.1227/01.NEU.0000280069.13468.B2

Bizzi, A., Nava, S., Ferrè, F., Castelli, G., Aquino, D., Ciaraffa, F., et al. (2012). Aphasia induced by gliomas growing in the ventrolateral frontal region: assessment with diffusion MR tractography, functional MR imaging and neuropsychology. *Cortex* 48, 255–272. doi: 10.1016/j.cortex.2011.11.015

Black, D. F., Vachha, B., Mian, A., Faro, S. H., Maheshwari, M., Sair, H. I., et al. (2017). American Society of Functional Neuroradiology- recommended fMRI paradigm algorithms for presurgical language assessment. *Am. J. Neuroradiol.* 38, E65–E73. doi: 10.3174/ajnr.A5345

Blank, H., Spangenberg, M., and Davis, M. H. (2018). Neural prediction errors distinguish perception and misperception of speech. *J. Neurosci.* 38, 6076–6089. doi: 10.1523/JNEUROSCI.3258-17.2018

Bloom, J. S., and Hynd, G. W. (2005). The role of the corpus callosum in Interhemispheric Transfer of Information: Excitation or Inhibition? *Neuropsychol. Rev.* 15, 59–71. doi: 10.1007/s11065-005-6252-y

Briganti, C., Sestieri, C., Mattei, P. A., Esposito, R., Galzio, R. J., Tartaro, A., et al. (2012). Reorganization of functional connectivity of the language network in patients with brain gliomas. *Am. J. Neuroradiol.* 33, 1983–1990. doi: 10.3174/ajnr.A3064

Chang, E. F., Potts, M. B., Keles, G. E., Lamborn, K. R., Chang, S. M., Barbaro, N. M., et al. (2008). Seizure characteristics and control following resection in 332 patients with low-grade gliomas. *J. Neurosurg.* 108, 227–235. doi: 10.3171/JNS/2008/108/2/0227

Desmurget, M., Bonnetblanc, F., and Duffau, H. (2007). Contrasting acute and slow-growing lesions: a new door to brain plasticity. *Brain* 130, 898–914. doi: 10.1093/brain/awl300

Duffau, H. (2018). Is non-awake surgery for supratentorial adult low-grade glioma treatment still feasible? *Neurosurg. Rev.* 41, 133–139. doi: 10.1007/s10143-017-0918-9

Duffau, H. (2006). New concepts in surgery of WHO grade II gliomas: functional brain mapping, connectionism and plasticity - a review. *J. Neurooncol.* 79, 77–115. doi: 10.1007/s11060-005-9109-6

Duffau, H. (2005). Lessons from brain mapping in surgery for low-grade glioma: insights into associations between tumour and brain plasticity. *Lancet Neurol.* 4, 476–486. doi: 10.1016/S1474-4422(05)70140-X

Duffau, H., Capelle, L., Denvil, D., Sichez, N., Gatignol, P., Lopes, M., et al. (2003). Functional recovery after surgical resection of low grade gliomas in eloquent brain: hypothesis of brain compensation. *J. Neurol. Neurosurg. Psychiatry* 74, 901–907. doi: 10.1136/jnnp.74.7.901

Ekert, J. O., Kirkman, M. A., Seghier, M. L., Green, D. W., and Price, C. J. (2021). A Data-based approach for selecting pre- and intra-operative language mapping tasks. *Front. Neurosci.* 15:743402. doi: 10.3389/fnins.2021.743402

Friston, K. J., Frith, C. D., Turner, R., and Frackowiak, R. S. (1995). Characterizing evoked hemodynamics with fMRI. *Neuroimage* 2, 157–165. doi: 10.1006/nimg.1995.1018

Fujiwara, N., Sakatani, K., Katayama, Y., Murata, Y., Hoshino, T., Fukaya, C., et al. (2004). Evoked-cerebral blood oxygenation changes in false-negative activations in BOLD contrast functional MRI of patients with brain tumors. *Neuroimage* 21, 1464–1471. doi: 10.1016/j.neuroimage.2003.10.042

Gainott, G., Caltagirone, C., Miceli, G., and Masullo, C. (1981). Selective semantic-lexical impairment of language comprehension in right brain damaged patients. *Brain Lang.* 13, 201–211. doi: 10.1016/0093-934X(81)90090-0

Gajardo-Vidal, A., Lorca-Puls, D. L., Hope, T. M. H., Parker Jones, O., Seghier, M. L., Prejawa, S., et al. (2018). How right hemisphere damage after stroke can impair speech comprehension. *Brain* 141, 3389–3404. doi: 10.1093/brain/awy270

Hervey-Jumper, S. L., Li, J., Lau, D., Molinaro, A. M., Perry, D. W., Meng, L., et al. (2015). Awake craniotomy to maximize glioma resection: methods and technical nuances over a 27-year period. *J. Neurosurg.* 123, 325–339. doi: 10.3171/2014.10.jns141520

Houde, J. F., and Jordan, M. I. (1998). Sensorimotor adaptation in speech production. *Science* 279, 1213–1216. doi: 10.1126/science.279.5354.1213

Hugdahl, K., and Andersson, L. (1986). The "forced-attention paradigm" in dichotic listening to CV-syllables: a comparison between adults and children.". *Cortex* 22, 417–432. doi: 10.1016/S0010-9452(86)80005-3

Ille, S., Sollmann, N., Hauck, T., Maurer, S., Tanigawa, N., Obermueller, T., et al. (2015). Combined noninvasive language mapping by navigated transcranial magnetic stimulation and functional MRI and its comparison with direct cortical stimulation. *J. Neurosurg.* 123, 212–225. doi: 10.3171/2014.9.JNS14929

Ius, T., Isola, M., Budai, R., Pauletto, G., Tomasino, B., Fadiga, L., et al. (2012). Low-grade glioma surgery in eloquent areas: volumetric analysis of extent of resection and its impact on overall survival. A single-institution experience in 190 patients: clinical article. *J. Neurosurg.* 117, 1039–1052. doi: 10.3171/2012.8.JNS12393

Jafari, Z., Esmaili, M., Delbari, A., Mehrpour, M., and Mohajerani, M. H. (2016). Auditory temporal processing deficits in chronic stroke: a comparison of brain damage lateralization effect. *J. Stroke Cerebrovasc. Dis.* 25, 1403–1410. doi: 10.1016/j.jstrokecerebrovasdis.2016.02.030

Jiang, Z., Krainik, A., David, O., Salon, C., Troprès, I., Hoffmann, D., et al. (2010). Impaired fMRI activation in patients with primary brain tumors. *Neuroimage* 52, 538–548. doi: 10.1016/j.neuroimage.2010.04.194

Kimura, D. (1961). Some effects of temporal-lobe damage on auditory perception. *Can. J. Psychol.* 15, 156–165. doi: 10.1037/h0083218

Krainik, A., Lehéricy, S., Duffau, H., Capelle, L., Chainay, H., Cornu, P., et al. (2003). Postoperative speech disorder after medial frontal surgery: role of the supplementary motor area. *Neurology* 60, 587–594. doi: 10.1212/01.WNL.0000048206.07837.59

Krieg, S. M., Sollmann, N., Hauck, T., Ille, S., Foerschler, A., Meyer, B., et al. (2013). Functional language shift to the right hemisphere in patients with language-eloquent brain tumors. *PLoS One* 8:e75403. doi: 10.1371/journal.pone.0075403

Kriegstein, K. V., and Giraud, A.-L. (2004). Distinct functional substrates along the right superior temporal sulcus for the processing of voices. *Neuroimage* 22, 948–955. doi: 10.1016/j.neuroimage.2004.02.020

Lattner, S., Meyer, M. E., and Friederici, A. D. (2005). Voice perception: sex, pitch, and the right hemisphere. *Hum. Brain Mapp.* 24, 11–20. doi: 10.1002/hbm.20065

Laws, E. R., Taylor, W. F., Clifton, M. B., and Okazaki, H. (1984). Neurosurgical management of low-grade astrocytoma of the cerebral hemispheres. *J. Neurosurg.* 61, 665–673. doi: 10.3171/jns.1984.61.4.0665

Louis, D. N., Perry, A., Reifenberger, G., von Deimling, A., Figarella-Branger, D., Cavenee, W. K., et al. (2016). The 2016 World Health Organization classification of tumors of the central nervous system: a summary. *Acta Neuropathol.* 131, 803–820. doi: 10.1007/s00401-016-1545-1

Lubrano, V., Draper, L., and Roux, F. E. (2010). What makes surgical tumor resection feasible in Broca's area? Insights into intraoperative brain mapping. *Neurosurgery* 66, 868–875. doi: 10.1227/01.NEU.0000368442.92290.04

Manan, H. A., Franz, E. A., and Yahya, N. (2020). Utilization of functional MRI language paradigms for pre-operative mapping: a systematic review. *Neuroradiology* 62, 353–367. doi: 10.1007/s00234-019-02322-w

Mechelli, A., Henson, R. N., Price, C. J., and Friston, K. J. (2003). Comparing event-related and epoch analysis in blocked design fMRI. *Neuroimage* 18, 806–810. doi: 10.1016/S1053-8119(02)00027-7

Mugler, J. P., and Brookeman, J. R. (1990). Three-dimensional magnetization-prepared rapid gradient-echo imaging (3D MP RAGE). *Magn. Reson. Med.* 15, 152–157. doi: 10.1002/mrm.1910150117

Nakasato, N., Kumabe, T., Kanno, A., Ohtomo, S., Mizoi, K., and Yoshimoto, T. (1997). Neuromagnetic evaluation of cortical auditory function in patients with temporal lobe tumors. *J. Neurosurg.* 86, 610–618. doi: 10.3171/jns.1997.86.4.0610

Niziolek, C. A., and Guenther, F. H. (2013). Vowel category boundaries enhance cortical and behavioral responses to speech feedback alterations. *J. Neurosci.* 33, 12090–12098. doi: 10.1523/JNEUROSCI.1008-13.2013

Noll, K. R., Sullaway, C., Ziu, M., Weinberg, J. S., and Wefel, J. S. (2015a). Relationships between tumor grade and neurocognitive functioning in patients with glioma of the left temporal lobe prior to surgical resection. *Neuro Oncol.* 17, 580–587. doi: 10.1093/neuonc/nou233

Noll, K. R., Weinberg, J. S., Ziu, M., Benveniste, R. J., Suki, D., and Wefel, J. S. (2015b). Neurocognitive changes associated with surgical resection of left and right temporal lobe glioma. *Neurosurgery* 77, 777–785. doi: 10.1227/NEU.0000000000000987

Noll, K. R., Ziu, M., Weinberg, J. S., and Wefel, J. S. (2016). Neurocognitive functioning in patients with glioma of the left and right temporal lobes. *J. Neurooncol.* 128, 323–331. doi: 10.1007/s11060-016-2114-0

Ojemann, J. G., Miller, J. W., and Silbergeld, D. L. (1996). Preserved function in brain invaded by tumor. *Neurosurgery* 39, 253–258. doi: 10.1097/00006123-199608000

Ojemann, J. G., Neil, J. M., MacLeod, A.-M., Silbergeld, D. L., Dacey, R. G., Petersen, S. E., et al. (1998). Increased functional vascular response in the region of a Glioma. *J. Cereb. Blood Flow Metab.* 18, 148–153. doi: 10.1097/00004647-199802000-00004

Parker Jones, O., and Schnupp, J. (2021). "How does the brain represent speech?," in *The Handbook of Speech Perception*, eds L. C. Nygaard, J. S. Pardo, D. B. Pisoni, and R. E. Remez (Oxford: Wiley-Blackwell).

Picht, T., Krieg, S. M., Sollmann, N., Rösler, J., Niraula, B., Neuvonen, T., et al. (2013). A Comparison of language mapping by preoperative navigated transcranial magnetic stimulation and direct cortical stimulation during awake surgery. *Neurosurgery* 72, 808–819. doi: 10.1227/NEU.0b013e3182889e01

Price, C. J., and Friston, K. J. (1999). Scanning patients with tasks they can perform. *Hum. Brain Mapp* 8, 102–108. doi: 10.1002/(sici)1097-0193(1999)8:2/3<102::aid-hbm6>3.0.co;2-j

Sanjuán, A., Hope, T. M. H., Parker Jones, O., Prejawa, S., Oberhuber, M., Guerin, J., et al. (2015). Dissociating the semantic function of two neighbouring subregions in the left lateral anterior temporal lobe. *Neuropsychologia* 76, 153–162. doi: 10.1016/j.neuropsychologia.2014.12.004

Schiffbauer, H., Ferrari, P., Rowley, H. A., Berger, M. S., and Roberts, T. P. (2001). Functional activity within brain tumors: a magnetic source imaging study. *Neurosurgery* 49, 1313–1320. doi: 10.1097/00006123-200112000-00005

Seghier, M. L., Patel, E., Prejawa, S., Ramsden, S., Selmer, A., Lim, L., et al. (2016). The PLORAS database: a data repository for predicting language outcome and recovery after stroke. *Neuroimage* 124, 1208–1212. doi: 10.1016/j.neuroimage.2015.03.083

Suga, N., and Ma, X. (2003). Multiparametric corticofugal modulation and plasticity in the auditory system. *Nat. Rev. Neurosci.* 4, 783–794. doi: 10.1038/nrn1222

Swinburn, K., Porter, G., and Howard, D. (2004). *The Comprehensive Aphasia Test*. Hove: Psychology Press.

Thiel, A., Habedank, B., Herholz, K., Kessler, J., Winhuisen, L., Haupt, W. F., et al. (2006). From the left to the right: how the brain compensates progressive loss of language function. *Brain Lang.* 98, 57–65. doi: 10.1016/j.bandl.2006.01.007

Thiel, A., Habedank, B., Winhuisen, L., Herholz, K., Kessler, J., Haupt, W. F., et al. (2005). Essential language function of the right hemisphere in brain tumor patients. *Ann. Neurol.* 57, 128–131. doi: 10.1002/ana.20342

Thiel, A., Herholz, K., Koyuncu, A., Ghaemi, M., Kracht, L. W., Habedank, B., et al. (2001). Plasticity of language networks in patients with brain tumors: a positron emission tomography activation study. *Ann. Neurol.* 50, 620–629. doi: 10.1002/ana.1253

Thomson, A. M., Taylor, R., and Whittle, I. R. (1998). Assessment of communication impairment and the effects of resective surgery in solitary, right-sided supratentorial intracranial tumours: a prospective study. *Br. J. Neurosurg.* 12, 423–429. doi: 10.1080/02688699844628

Tian, X., and Poeppel, D. (2013). The effect of imagination on stimulation: the functional specificity of efference copies in speech processing. *J. Cogn. Neurosci.* 25, 1020–1036. doi: 10.1162/jocn_a_00381

Tian, X., and Poeppel, D. (2010). Mental imagery of speech and movement implicates the dynamics of internal forward models. *Front. Psychol.* 1:166. doi: 10.3389/fpsyg.2010.00166

Tian, X., Zarate, J. M., and Poeppel, D. (2016). Mental imagery of speech implicates two mechanisms of perceptual reactivation. *Cortex* 77, 1–12. doi: 10.1016/j.cortex.2016.01.002

Tourville, J. A., Reilly, K. J., and Guenther, F. H. (2008). Neural mechanisms underlying auditory feedback control of speech. *Neuroimage* 39, 1429–1443. doi: 10.1016/j.neuroimage.2007.09.054

Turkeltaub, P. E., Messing, S., Norise, C., and Hamilton, R. H. (2011). Are networks for residual language function and recovery consistent across aphasic patients? *Neurology* 76, 1726–1734. doi: 10.1212/WNL.0b013e31821a44c1

Ulmer, J. L., Hacein-Bey, L., Mathews, V. P., Mueller, W. M., DeYoe, E. A., Prost, R. W., et al. (2004). Lesion-induced pseudo-dominance at functional magnetic resonance imaging: implications for preoperative assessments. *Neurosurgery* 55, 569–579. doi: 10.1227/01.NEU.0000134384.94749.B2

Veltman, D. J., Mechelli, A., Friston, K. J., and Price, C. J. (2002). The importance of distributed sampling in blocked functional magnetic resonance imaging designs. *Neuroimage* 17, 1203–1206. doi: 10.1006/nimg.2002.1242

Vilasboas, T., Herbet, G., and Duffau, H. (2017). Challenging the myth of right nondominant hemisphere: lessons from corticosubcortical stimulation mapping in awake surgery and surgical implications. *World Neurosurg.* 103, 449–456. doi: 10.1016/j.wneu.2017.04.021

Wang, L., Chen, D., Olson, J., Ali, S., Fan, T., and Mao, H. (2012). Re-examine tumor-induced alterations in hemodynamic responses of BOLD fMRI: implications in presurgical brain mapping. *Acta Radiol.* 53, 802–811. doi: 10.1258/ar.2012.120118

Yamamoto, A. K., Parker Jones, O., Hope, T. M. H., Prejawa, S., Oberhuber, M., Ludersdorfer, P., et al. (2019b). A special role for the right posterior superior temporal sulcus during speech production. *Neuroimage* 203:116184. doi: 10.1016/j.neuroimage.2019.116184

Yamamoto, A. K., Magerkurth, J., Mancini, L., White, M. J., Miserocchi, A., McEvoy, A. W., et al. (2019a). Acquisition of sensorimotor fMRI under general anaesthesia: assessment of feasibility, the BOLD response and clinical utility. *Neuroimage Clin.* 23, 8–11. doi: 10.1016/j.nicl.2019.101923

Yan, W., and Suga, N. (1998). Corticofugal modulation of the midbrain frequency map in the bat auditory system. *Nat. Neurosci.* 1, 54–58. doi: 10.1038/255

Yushkevich, P. A., Piven, J., Hazlett, H. C., Smith, R. G., Ho, S., Gee, J. C., et al. (2006). User-guided 3D active contour segmentation of anatomical structures: significantly improved efficiency and reliability. *Neuroimage* 31, 1116–1128. doi: 10.1016/j.neuroimage.2006.01.015

Zacà, D., Jovicich, J., Nadar, S. R., Voyvodic, J. T., and Pillai, J. J. (2014). Cerebrovascular reactivity mapping in patients with low grade gliomas undergoing presurgical sensorimotor mapping with BOLD fMRI. *J. Magn. Reson. Imaging* 40, 383–390. doi: 10.1002/jmri.24406

Zhang, N., Xia, M., Qiu, T., Wang, X., Lin, C. P., Guo, Q., et al. (2018). Reorganization of cerebro-cerebellar circuit in patients with left hemispheric gliomas involving language network: a combined structural and resting-state functional MRI study. *Hum. Brain Mapp* 39, 4802–4819. doi: 10.1002/hbm.24324

Zhang, Y., and Suga, N. (2000). Modulation of responses and frequency tuning of thalamic and collicular neurons by cortical activation in mustached bats. *J. Neurophysiol.* 84, 325–333. doi: 10.1152/jn.2000.84.1.325

Zheng, Z. Z., Munhall, K. G., and Johnsrude, I. S. (2010). Functional overlap between regions involved in speech perception and in monitoring one's own voice during speech production. *J. Cogn. Neurosci.* 22, 1770–1781. doi: 10.1162/jocn.2009.21324

Zimmermann, M., Rössler, K., Kaltenhäuser, M., Grummich, P., Brandner, N., Buchfelder, M., et al. (2019). Comparative fMRI and MEG localization of cortical sensorimotor function: bimodal mapping supports motor area reorganization in glioma patients. *PLoS One* 14:e0213371. doi: 10.1371/journal.pone.0213371

Conflict of Interest: The authors declare that the research was conducted in the absence of any commercial or financial relationships that could be construed as a potential conflict of interest.

Publisher's Note: All claims expressed in this article are solely those of the authors and do not necessarily represent those of their affiliated organizations, or those of the publisher, the editors and the reviewers. Any product that may be evaluated in this article, or claim that may be made by its manufacturer, is not guaranteed or endorsed by the publisher.

Copyright © 2022 Yamamoto, Sanjuán, Pope, Parker Jones, Hope, Prejawa, Oberhuber, Mancini, Ekert, Garjardo-Vidal, Creasey, Yousry, Green and Price. This is an open-access article distributed under the terms of the Creative Commons Attribution License (CC BY). The use, distribution or reproduction in other forums is permitted, provided the original author(s) and the copyright owner(s) are credited and that the original publication in this journal is cited, in accordance with accepted academic practice. No use, distribution or reproduction is permitted which does not comply with these terms.

frontiers | Frontiers in Neuroscience

ORIGINAL RESEARCH
published: 26 May 2022
doi: 10.3389/fnins.2022.876587

3D Amide Proton Transfer Weighted Brain Tumor Imaging With Compressed SENSE: Effects of Different Acceleration Factors

Nan Zhang[1,2], Haonan Zhang[1], Bingbing Gao[1], Yanwei Miao[1], Ailian Liu[1], Qingwei Song[1], Liangjie Lin[3] and Jiazheng Wang[3]*

[1] Department of Radiology, First Affiliated Hospital of Dalian Medical University, Dalian, China, [2] Department of Radiology, Zhongshan Hospital of Fudan University, Shanghai, China, [3] MSC Clinical and Technical Solutions, Philips Healthcare, Beijing, China

OPEN ACCESS

Edited by:
Alexandra Golby, Harvard Medical School, United States

Reviewed by:
Rongwen Tain, University of California, Irvine, United States
Andrew S. Nencka, Medical College of Wisconsin, United States

****Correspondence:***
Qingwei Song
songqw1964@163.com

Specialty section:
This article was submitted to Brain Imaging Methods, a section of the journal Frontiers in Neuroscience

Received: *15 February 2022*
Accepted: *13 April 2022*
Published: *26 May 2022*

Citation:
Zhang N, Zhang H, Gao B, Miao Y, Liu A, Song Q, Lin L and Wang J (2022) 3D Amide Proton Transfer Weighted Brain Tumor Imaging With Compressed SENSE: Effects of Different Acceleration Factors. Front. Neurosci. 16:876587. doi: 10.3389/fnins.2022.876587

Objectives: The aim of the current study was to evaluate the performance of compressed SENSE (CS) for 3D amide proton transfer weighted (APTw) brain tumor imaging with different acceleration factors (AFs), and the results were compared with those of conventional SENSE.

Methods: Approximately 51 patients with brain tumor (22 males, 49.95 ± 10.52 years) with meningiomas (n = 16), metastases (n = 12), or gliomas (n = 23) were enrolled. All the patients received 3D APTw imaging scans on a 3.0 T scanner with acceleration by CS (AFs: CS2, CS3, CS4, and CS5) and SENSE (AF: S1.6). Two readers independently and subjectively evaluated the APTw images relative to image quality and measured confidence concerning image blur, distortion, motion, and ghosting artifacts, lesion recognition, and contour delineation with a 5-point Likert scale. Mean amide proton transfer (APT) values of brain tumors (APT_{tumor}), the contralateral normal-appearing white matter (APT_{CNAWM}), and the peritumoral edema area (if present, APT_{edema}) and the tumor volume (V_{APT}) were measured for objective evaluation and determination of the optimal AF. The Ki67 labeling index was also measured by using standard immunohistochemical staining procedures in samples from patients with gliomas, and the correlation between tumor APT values and the Ki67 index was analyzed.

Results: The image quality of AF = CS5 was significantly lower than that of other groups. V_{APT} showed significant differences among the six sequences in meningiomas (p = 0.048) and gliomas (p = 0.023). The pairwise comparison showed that the V_{APT} values of meningiomas measured from images by CS5 were significantly lower, and gliomas were significantly larger than those by SENSE1.6 and other CS accelerations, ($p < 0.05$). APT_{tumor} (p = 0.191) showed no significant difference among the three types of tumors. The APT_{tumor} values of gliomas measured by APTw images with the

SENSE factor of 1.6 and the CS factor of 2, 3, and 4 (except for CS5) were all positively correlated with Ki67.

Conclusion: Compressed SENSE could be successfully extended to accelerated 3D APTw imaging of brain tumors without compromising image quality using the AF of 4.

Keywords: amide proton transfer, brain tumor, compressed SENSE, acceleration factor, peritumoral edema

INTRODUCTION

Although head magnetic resonance imaging (MRI) is an established tool for head tumor diagnosis in clinical practice, standard MRI sequences (such as T2 weighted imaging, T2W; fluid-attenuated inversion recovery, FLAIR; diffusion-weighted imaging, DWI; and gadolinium-enhanced T1-weighted imaging, Gd-T1W) can provide plentiful information for detection and differentiation of brain tumors. However, the diagnostic specificity is still limited in differentiating grades of brain tumors and predicting proliferation potential. When diagnosing malignant gliomas, T2W hyperintensity may represent both peritumoral vasogenic edema and infiltrating tumor. Gd-T1W also could not reliably distinguish the lesions of necrotic and highly cell-infiltrating tumors (Eidel et al., 2017). Besides, different kinds of perfusion, diffusion and MR spectroscopic imaging (MRSI) methods have been introduced to clinical or research protocols, but their stability and accuracy are still controversial.

Chemical exchange saturation transfer (CEST) imaging is a novel magnetic resonance molecular imaging method derived from magnetization transfer (MT) technology (van Zijl et al., 2018). Selective pre-saturation is carried out by applying saturation radio-frequency (RF) pulses to endogenous or exogenous specific substances, and the interexchange between saturated hydrogen protons and hydrogen protons in free water molecules causes the attenuation of free water signals (van Zijl and Yadav, 2011; Zhou et al., 2019). The degree of water signal attenuation is proportional to the number of targeted compounds with exchangeable protons; therefore, CEST enables indirect measurement of tissue metabolites, as well as a reflection of the physical and chemical properties of tissues that affect the chemical exchange (van Zijl and Yadav, 2011; Pankowska et al., 2019). Amide proton transfer-weighted (APTw) MR imaging, as a kind of CEST technology targeting amide protons (resonating at 3.5 ppm downfield from water), has provided a tool for non-invasive detection of endogenous free proteins and polypeptide molecules in the cytoplasm, and hence, the indirect measurement of metabolic changes and pathophysiological information in living cells (Zhou et al., 2013; Lin et al., 2018; Ishimatsu et al., 2019; Debnath et al., 2020). APTw MRI was introduced in 2003 for imaging brain tumors (Zhou et al., 2003). Currently, the most common application of APTw MRI is for the study of human brain tumors (Wen et al., 2010; Jiang et al., 2016; Yu et al., 2017; Joo et al., 2018), where it starts to impact grade (Xu et al., 2021), recurrence (Park et al., 2020), and chemotherapy response (Joo et al., 2018) of glioma, differentiation of meningiomas (Scott et al., 2002) and brain metastases (Yu et al., 2017). Numerous studies from different institutions (Scott et al., 2002; Park et al., 2021; Xu et al., 2021) indicate that APTw imaging may add important value to brain cancer diagnosis. The added value of APTw MRI in enhancing the non-invasive diagnosis of brain tumors at a molecular level can potentially aid in guiding brain tumor therapies, such as surgery, radiotherapy, and local chemotherapy.

However, CEST imaging, including APTw MRI, can be much slower than conventional qualitative imaging because the saturated image needs to be repeated at multiple saturation frequencies, especially when the three-dimensional acquisition is required for whole-brain coverage (Zhu et al., 2010). Even longer scan times are required to obtain a higher spectral resolution Z spectrum with a wide bias frequency range (Zhang et al., 2020). The extensive clinical applications of APTw MRI require rapid volume imaging. Volume (3D) acquisition is more inclined to minimize the difference in saturation loss caused by T1 relaxation between slices (Zhu et al., 2010). Zhu et al. (2010) developed a whole-brain 3D APTw MRI method with a higher spatial resolution that had great advantages, especially for describing intra-tumor heterogeneity. But it is subject to a long scanning time. Patients with brain tumors are poorly tolerated and can be predisposing to a motion artifact and limiting the ability to incorporate such pulse sequences into clinical imaging time slots. APTw imaging is very sensitive to movement. Therefore, shortening the scanning time is very necessary for APTw imaging.

Therefore, scan time is one of the key factors that limit the application of CEST-MRI in clinical use. Compressed sensing (CS; Candes et al., 2006; Donoho, 2006) is a new framework for data acquisition and signal recovery. It allows measuring sparse and compressible signals at a rate close to their intrinsic information rate rather than their Nyquist rate. These signals can be reconstructed exactly from very few incoherent measurements by a non-linear procedure (Donoho, 2006; Candès et al., 2007). CS aims to reconstruct signals and images from significantly fewer measurements than were traditionally thought necessary. Magnetic Resonance Imaging is an essential medical imaging tool burdened by an inherently slow data acquisition process. The application of CS to MRI has the potential for significant scan time reductions, with benefits for patients and health care economics. Previous studies (Togao et al., 2017; Heo et al., 2019) have demonstrated the

Abbreviations: CS/CS-SENSE, compressed SENSE; APTw, amide proton transfer weighted; AF, acceleration factors; APT_{tumor}, mean APT value of brain tumors; APT_{CNAWM}, mean APT value of the contralateral normal appearing white matter; APT_{edema}, mean APT value of the peritumoral edema area; V_{APT}, tumor volume.

feasibility of compressed sensing (CS) for accelerated CEST-MRI in healthy volunteers and patients with brain tumors with an acceleration factor (AF) of 4 (Gawlitza et al., 2017), but whether different accelerators have effects on APTw imaging remains to be further explored. The current study aimed to explore the performance of the compressed SENSE (CS-SENSE) technique (Heo et al., 2019) for the acceleration of brain tumor APTw imaging using different AFs and to find the optimal AF.

MATERIALS AND METHODS

Patients

The study was approved by the Local Ethics Committee, and all the patients were informed and gave their written consent to participate in this study. Between October 2019 and March 2021, a total of 73 patients were included with the criteria of (1) previously untreated; (2) underwent a complete multiparametric MRI exam consisting of APTw and Gd-enhanced T1W imaging; and (3) histopathological confirmation was obtained by gross total or partial surgical resection and by stereotactic biopsy after the multiparametric MRI exam. Approximately, 22 patients were excluded from the study for the following reasons: 1. Postoperative pathology revealed other tumors except for meningioma, metastatic tumor, and glioma (12 cases); 2. Poor lesion visibility caused by patient movement on APTw images (10 cases). Finally, 51 patients [22 males, age: 49.95 ± 10.52 (24–68) years] were included in the study, who were divided into three groups (**Figure 1**): 1. Meningiomas (n = 16), including 5 pathologically diagnosed with atypical meningioma, and 11 with benign meningioma; 2. Metastases (n = 12), the primary sites of cancer included lung (n = 6), breast (n = 2), kidney (n = 1), colon (n = 1), and liver (n = 2); 3. Gliomas (n = 23), including Grade II(n = 6), Grade III(n = 7), Grade IV(n = 10).

Surgery and Pathologic Evaluation

Histopathological confirmation was obtained by gross total or partial surgical resection and by stereotactic biopsy. Tumor types were determined based on the pathological diagnosis of the surgical specimens according to the 2016 World Health Organization (WHO) classification. Gliomas were classified with Grades II, III, and IV. The Ki67 labeling index was also measured by using standard immunohistochemical staining procedures in samples from patients with gliomas. Tumor sections were reviewed and Ki67 was quantified based on the percentage of positive cells in the highest density of the stained areas; all cells with nuclear staining of any intensity were considered positive, and the Ki67 labeling index was defined as the percentage of positive cells among the total number of counted cells.

Magnetic Resonance Imaging Protocol

Magnetic resonance examinations were performed on a 3.0 T MR scanner (Ingenia CX, Philips Healthcare, Netherlands) with a 32-channel head coil. Each patient was placed in a supine position without compression to the head. The APTw images were acquired in addition to the conventional imaging protocols (T1W, T2W, FLAIR, and Gd-T1W), with imaging parameters detailed in **Table 1**. The CS acceleration factors used in this study included 2, 3, 4, and 5. For APTw imaging, a 2-s saturation pulse was applied with 2-μT B1 amplitude at each of the following 6 frequencies for a Z spectrum: ±2.7 ppm, ±3.5 ppm, and ±4.3 ppm, where 0 ppm was defined as the water proton resonance. A reference acquisition was performed with the radio frequency (RF) at −1,560 ppm. Three acquisitions were made with the RF saturation at +3.5 ppm and with echo shifts to generate a B0 map for voxel-wise frequency correction to the Z spectra. To ensure acceptable spectral selectivity, we enforced a spectral resolution smaller than 100 Hz measured as the full width at half maximum by acquiring spectral signals before each APTw scan. The APTw sequences were scanned before the injection of the gadolinium contrast agent (Gadodiamide, Bayer AG, Bayer Leverkusen, Germany).

Image Analysis

Amide proton transfer weighted images were automatically reconstructed on the MR console after the data acquisition according to APTw imaging theory and a previously published algorithm (Togao et al., 2017) and transferred to the IntelliSpace Portal (ISP v7.0, Philips Healthcare, Netherlands) workstation for amide proton transfer (APT) value measurements. For each patient, the threshold extraction method for segmentation of the tumors as a whole was carried out according to the following steps independently by two neuroradiologists (both with 3 years of experience): 1. The 3D tumor structure was first automatically segmented on GD-T1W images using the MR segmentation software on ISP; 2. Manual adjustment was implemented for the tumor segmentation to ensure the inclusion of all tumor; 3. The threshold within the range of 0–1% to 5–8% was manually selected to remove structures of blood vessels and necrosis; 4. The segmentations were copied to APTw images for measurement of tumor volumes (V_{APT}) and the mean APT values of tumors (APT_{tumor}). The whole tumor volumes (ROIs) were distributed within the Gd-enhancing tumor area, as well as within the peritumoral brain zone based on the Gd-T1WI and T2WI co-registered with the APTw image (Zhang et al., 2016). Also, the ROIs (with a size about 50 mm^2) were manually defined on the solid parts of tumors in the contralateral normal-appearing white matter (CNAWM) area to get APT_{CNAWM} values. The peritumoral edema (surrounding non-enhancing areas with T2-prolongation, if present) was manually segmented using threshold fitting on the T2W images; tumor and necrosis were removed manually according to GD-T1W images. The segmented regions were also copied to APTw images for measurement of APT_{edema} values.

Quantitative Analysis

Two readers independently and subjectively evaluated the APTw images relative to image quality and measured

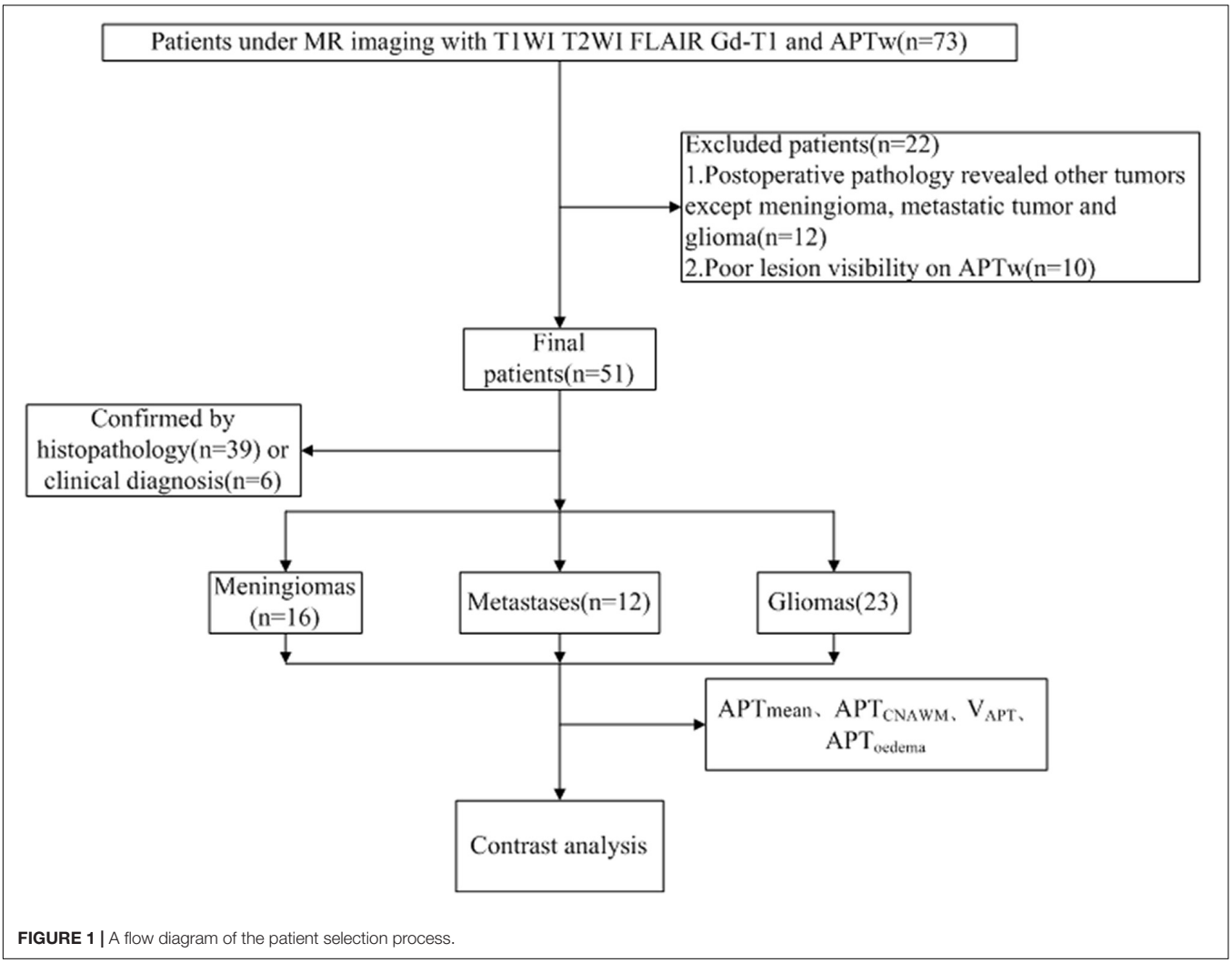

FIGURE 1 | A flow diagram of the patient selection process.

TABLE 1 | Magnetic resonance (MR) parameters of all sequences of brain imaging.

	T1W	T2W	T2 FLAIR	Gd-T1W	APTw
Scan mode	TSE	TSE	TSE	TFE	TSE
Repetition time, TR (ms)	2095	4000	9000	260	7280
Echo time, TE (ms)	15	122	125	4.6	7.8
Field of view, FOV (mm^2)	230 × 230	230 × 230	230 × 187	240 × 240	230 × 180 × 70
Acquisition voxel size (mm^3)	0.8 × 0.88	0.6 × 0.6	0.75 × 1.04	0.65 × 0.8	1.8 × 1.8 × 7
Recon voxel size (mm^3)	0.48 × 0.48	0.45 × 0.45	0.53 × 0.53	0.45 × 0.45	0.9 × 0.9 × 7
Flip angle (degree)	110	90	110	11	90
Slice thickness (mm)	6.5	6.5	6.5	0.96	7
Gap (mm)	1	1	1	−0.48	0
TSE/TFE factor	7	30	39	64	174
Acceleration mode/factor R	SENSE2	SENSE2	SENSE2.1	SENSE1.5	SENSE: 1.6 CS: 2, 3, 4, 5
Saturation B1 amplitude (μT)	–	–	–	–	2
Saturation duration (s)	–	–	–	–	2
Scan time (s)	88	96	81	44	219, 219, 166, 113, 59.3

confidence with respect to image blur, distortion, motion and ghosting artifacts, lesion recognition, and contour delineation with a 5-point Likert scale: 5, good image quality with tumor detectable and lesion contour delineated on APTw images without reference to contrast-enhanced MR images; 4, tumor lesion could be recognized on APTw images, but contour was not so well delineated, reference information on contrast-enhanced MR images; 3, tumor undetectable without reference to contrast-enhanced MR; 2, poor APTw image quality with obvious artifacts, although the tumor lesion was revealed on T2WI or DWI images; 1, no lesions were identified on any contrast-enhanced MR or APTw images.

Statistical Analyses

All statistical analyses were performed using the statistical package SPSS 21.0. Intraclass correlation coefficient (ICC) was used to evaluate measurement consistency. An ICC greater than 0.75 was considered to indicate good agreement. For image quality assessment, interobserver agreement was evaluated by ICC. ICC values of less than 0.4, 0.41–0.75, and greater than 0.75 were considered to indicate positive but poor, fair, and good agreement, respectively. Friedman test was used to compare the difference in image quality score data and multiple comparisons were performed between each pair of different AFs with Bonferroni correction. Repeated ANOVA was used to test the APT measurement results by sequences with different SENSE/CS AFs. ANOVA was used to compare the APT_{tumor} values measured for different types of tumors. Pairwise comparisons were carried out using a Wilcoxon signed-rank test with the p values corrected by Bonferroni correction. Spearman's correlation coefficient was used to analyze the correlation between APTw and Ki67 expressions. $P < 0.05$ was recognized as statistically significant.

RESULTS

Qualitative Analysis

The subjective scores of the two observers for APTw images with different AFs were consistent (ICC value >0.75). The data by the senior observer were selected for analysis, and the image scores of different AFs were 4.9 ± 0.6, 4.3 ± 0.3, 4.1 ± 0.5, 4.0 ± 0.6, and 2.3 ± 0.4, respectively. There was a statistical difference in image scores among different AFs ($p < 0.001$). The image quality of AF = CS5 was significantly lower than those of other groups (**Table 2**).

TABLE 2 | Pairwise comparison between different AF scan image quality evaluation groups (p-value).

	S1.6	CS2	CS3	CS4	CS5
S1.6	–	1.000	0.875	0.324	<0.001
CS2	1.000	–	0.822	0.214	<0.001
CS3	0.875	0.822	–	0.360	<0.001
CS4	0.324	0.214	0.360	–	<0.001
CS5	<0.001	<0.001	<0.001	<0.001	–

Comparison of Quantitative Measurements From Amide Proton Transfer Weighted Images With Different Acceleration Factors

Figures 2–6 showed the measurements of APT_{tumor}, APT_{CNAWM} and V_{APT} values in the three types of tumors. APT_{CNAWM} and APT_{tumor} showed no significant difference among results by 3D APTw imaging with acceleration by CS (AFs = 2–5) and SENSE (AF = 1.6) in all the three types of tumors ($p > 0.05$), while the V_{APT} value showed significant differences among the six sequences in meningiomas ($p = 0.048$) and gliomas ($p = 0.023$) (**Tables 3–5**). The pairwise comparison showed that the V_{APT} values of meningiomas measured from images by CS5 were significantly lower than those by SENSE1.6 and other CS accelerations ($p < 0.05$) (**Table 6**), and the V_{APT} values of gliomas measured from images by CS5 were significantly larger than those by SENSE1.6 and other CS accelerations ($p < 0.05$) (**Table 7**).

TABLE 3 | Comparisons of quantitative amide proton transfer (APT) values for meningiomas among CS and SENSE scans.

	APT_{CNAWM}	APT_{tumor}	V_{APT} (mm^3)
SENSE1.6	0.81 ± 0.49	2.84 ± 0.74	10.03 ± 6.50
CS2	1.15 ± 0.51	3.08 ± 0.52	9.53 ± 6.41
CS3	0.99 ± 0.36	2.76 ± 0.53	9.94 ± 6.09
CS4	1.10 ± 0.60	2.85 ± 0.46	10.04 ± 6.22
CS5	1.04 ± 0.46	2.68 ± 0.27	2.28 ± 1.16
p	0.500	0.482	0.048

TABLE 4 | Comparisons of quantitative APT values for metastasis among CS-SENSE and SENSE scans.

	APT_{CNAWM} (%)	APT_{tumor} (%)	V_{APT} (mm^3)
SENSE1.6	1.08 ± 0.6	3.02 ± 0.90	7.23 ± 4.02
CS2	0.96 ± 0.55	2.89 ± 0.81	7.04 ± 4.52
CS3	0.83 ± 0.53	3.26 ± 0.80	6.97 ± 4.56
CS4	0.95 ± 0.55	2.72 ± 0.70	6.87 ± 4.70
CS5	0.38 ± 1.22	2.88 ± 0.72	5.23 ± 1.12
p	0.375	0.882	0.442

TABLE 5 | Comparisons of quantitative APT values for gliomas between CS-SENSE and SENSE scans.

	APT_{CNAWM} (%)	APT_{tumor} (%)	V_{APT} (mm^3)
SENSE1.6	0.93 ± 0.61	2.96 ± 0.63	110.23 ± 66.23
CS2	0.85 ± 0.61	2.76 ± 0.59	110.19 ± 62.22
CS3	0.87 ± 0.58	2.96 ± 0.48	109.89 ± 54.12
CS4	1.08 ± 0.42	2.92 ± 0.45	109.89 ± 43.18
CS5	0.79 ± 0.48	2.75 ± 0.61	140.23 ± 66.23
p	0.247	0.853	0.023

TABLE 6 | The pairwise comparison of V_{APT} of meningiomas (*p*-value).

	S1.6	CS2	CS3	CS4	CS5
S1.6	–	0.482	0.634	0.543	0.012
CS2	0.482	–	0.563	1.000	0.014
CS3	0.634	0.563	–	0.562	0.023
CS4	0.543	1.000	0.562	–	0.021
CS5	0.012	0.014	0.023	0.021	–

TABLE 7 | The pairwise comparison of gliomas of V_{APT} (*p*-value).

	S1.6	CS2	CS3	CS4	CS5
S1.6	–	1.000	0.943	0.654	0.032
CS2	1.000	–	0.762	0.832	0.026
CS3	0.634	0.762	–	0.743	0.024
CS4	0.654	0.832	0.743	–	0.034
CS5	0.032	0.026	0.024	0.034	–

Comparison of Image Features From Amide Proton Transfer Weighted Images With Different Acceleration Factors

We assessed the radiologic characteristic of the meningiomas, metastases, and gliomas, using conventional (T1W, T2W, FLAIR, and Gd-T1W) and APTw sequences. For the meningiomas (16 cases), 11 cases showed homogenous enhancement and 5 showed heterogeneous enhancement on the Gd-T1W images. The tumor cores showed hyperintensities (relative to the CNAWM) on the APTw images, and the hyperintense areas on APTw images were approximately equal to the lesions shown on the Gd-T1W (**Figure 2**).

The Gd-T1W and APTw images for a patient with metastasis are illustrated in **Figure 3**. The tumor cores showed hyperintensities (relative to the CNAWM) on the APTw images, and the hyperintense areas on APTw images were approximately equal to the lesions shown on the Gd-T1W image.

The Gd-T1W and APTw images for a patient with glioma are illustrated in **Figure 4**. The APTw images overall showed visually homogenous APTw hyperintensities (spatially compared to the CNAWM) in the region with Gd enhancement on the Gd-T1W images.

Comparison of Amide Proton Transfer Values Measured by the Optimal Acceleration Factor Among the Three Types of Tumors

The optimal AF of CS-SENSE determined in this study for 3D APTw brain tumor imaging was 4, which will be discussed later. **Figures 2–4** show the measurements of APT_{tumor}, APT_{CNAWM}, and V_{APT} in the three types of tumors on images by the optimal AF of CS-SENSE. APT_{tumor} was higher than APT_{CNAWM} in all three types of tumors ($p = 0.024$). APT_{CNAWM} ($p = 0.205$) and APT_{tumor} ($p = 0.191$) showed no significant difference among the three types of tumors.

Histological Composition of Different Magnetic Resonance Imaging Classifications

Of the total 23 gliomas (Grade II: $n = 6$, Grade III: $n = 7$, and Grade IV: $n = 10$), the APT_{tumor} values measured by APTw images with the SENSE factor of 1.6 and the CS factor of 2, 3, and 4 (except for CS5) were all positively correlated with Ki67 (**Table 8**).

DISCUSSION

In the current study, brain APTw imaging accelerated by CS-SENSE with increased acceleration factors (AFs 2–5) was compared with results by conventional SENSE acceleration with an AF of 1.6. According to our results, the image quality was significantly reduced when the AF was increased to CS5, where the quantitatively measured volume (V_{APT}) of the tumor was also significantly changed. Therefore, the acceleration factor 4 for CS-SENSE was recommended without significantly compromising image quality, saving at least 48.86% scan time compared to the SENSE acceleration.

Heo et al. (2019) have tried to apply compressed sensing for the reconstruction of fast scanned 3D APTw images (15 slices, slice thickness = 4 mm, plane spatial resolution = 1.8 mm^2 × 1.8 mm^2, and scan duration = 130 s) on patients with glioma based on the conventional parallel under-sampling scheme (GRAPPA). In contrast, the compressed SENSE method used in this study adopts an acquisition scheme of variable-density random under-sampling, and the sensitivity information from multi-channel coils was also included for the CS image reconstruction (Candes et al., 2006). Moreover, we presented a more comprehensive evaluation of the application of the compressed SENSE technique for accelerated 3D APTw imaging (with different acceleration factors ranging from 2-to 5) on an extended cohort of patients with a brain tumor. Also, the compressed SENSE with an acceleration factor of 4 (113 s) was recommended for 3D APTw brain tumor imaging without compromising image quality.

In previous studies, the APT values were usually measured from ROIs drawn on one single slice (Gawlitza et al., 2017; Yu et al., 2017; Xu et al., 2021), which might not be representative of tumors associated with strong heterogeneity. For each patient in this study, the 3D enhanced regions were automatically segmented on 3D Gd-T1W images using threshold fitting, and the segmented ROIs were copied to 3D APTw images. Therefore, the APT values measured in this study were from a 3D volume of the whole tumor, which can be more representative, especially for tumors with inhomogeneity.

The image quality of AF = CS5 was significantly lower than that of other groups. The APTw imaging with CS5 showed that the tumor undetectable without a reference to conventional MR images, the APT image of the tumor part only had decreased edge sharpness and signal drift, and the APT value was not affected.

Tumor volume was also studied in this study; the V_{APT} values of meningioma measured on APTw images by CS5 were

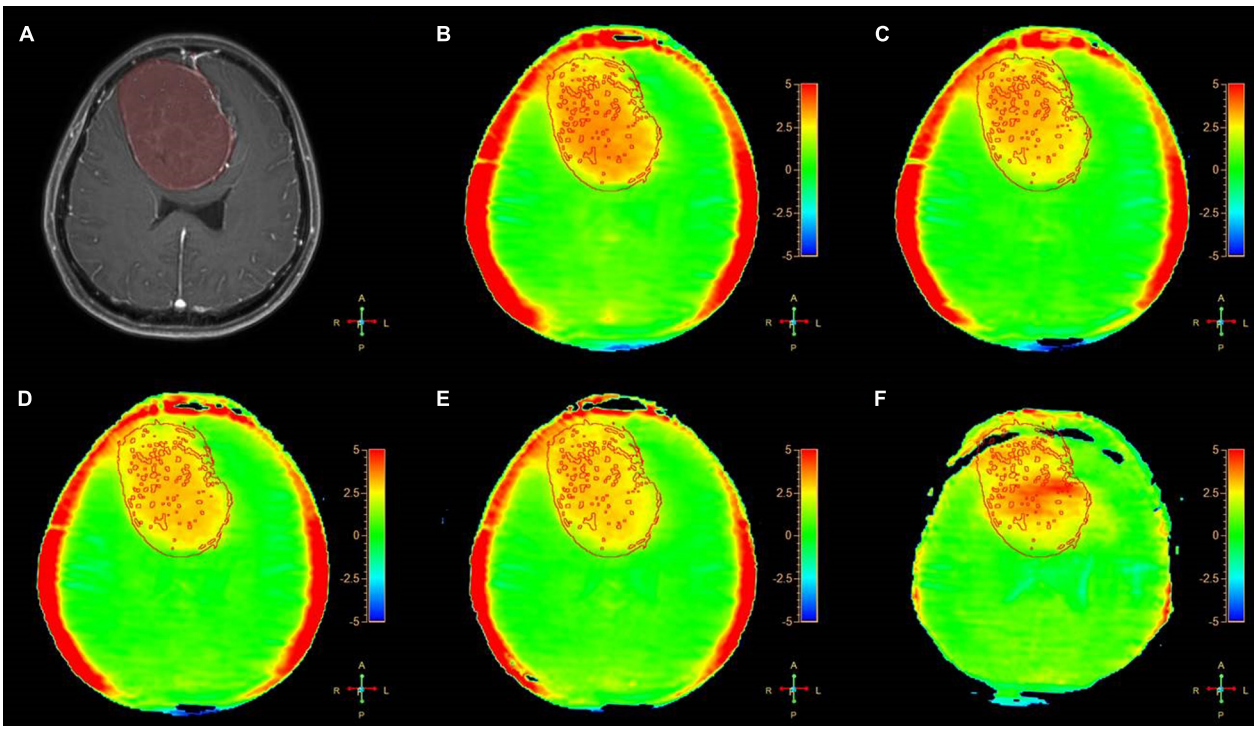

FIGURE 2 | A 54-year-old female patient with meningiomas in brain: **(A)** Gd-T1W; **(B–F)** APTw images by SENSE (AF 1.6) and CS-SENSE (AFs of 2, 3, 4, and 5). The ROIs were obtained manually on the Gd-T1W image and copied to the others as shown.

significantly smaller than those measured on APTw images by other accelerations, and V_{APT} values of gliomas were larger than others. Gliomas may have peritumoral edema and necrosis. The APT values in peritumoral edema were significantly higher for gliomas than for meningiomas, which may represent the higher tumor cell infiltration of gliomas. This finding is consistent with Jiang et al. (2016). The V_{APT} values measured for metastasis showed no difference among all sequences. This indicates that the high CS acceleration factor (AF = 5) would have a significant influence on the display of glioma tumor volume. Numerous studies indicated that (Scott et al., 2002) gadolinium-enhanced MRI was limited in differentiation between low- and high-grade gliomas that some high-grade gliomas (roughly 10% of glioblastomas and 30% of anaplastic astrocytoma) demonstrate no gadolinium enhancement. Some cases of tumors in this study were observed with a larger area of hyperintense regions on APTw images than on Gd-T1W images. It can be seen that the size of APT hyperintense regions is of great significance to the display of tumor information, so the influence of excessive AF on the display of tumor volume cannot be ignored.

The peritumoral edema of meningioma was well displayed on the APTw images of the present study. Peritumoral edema in meningiomas was dependent on the expression of AQP-4 (Gawlitza et al., 2017). Joo et al. (2018) showed that both the peritumor edema of typical meningioma and benign meningioma could be observed on APTw images. Yu et al. (2019) showed that the mean APT value of peritumoral edema was not associated with tumor grade, but the APT_{min} and $APT_{max-min}$ values of peritumoral edema were significantly different between WHO Grade I and Grade II meningiomas. The larger hyperintense regions in APTw maps than in Gd-T1W images in the cases of malignancies were observed in the current study, which may be attributed to the enhanced APT signals of peritumoral edema in malignancies.

For the metastases, the APT signal showed a high signal on peritumoral edema. Our results showed that the APT_{tumor} values in the enhancing areas ($3.32 \pm 1.09\%$) were significantly higher than APT_{edema} values ($1.73 \pm 0.2\%$). Previous studies (Zhou et al., 2013) have found that, in solitary brain metastases, the mean APT values in both the enhancing and edema areas were significantly higher than those in normal-appearing white matter. This study further investigated the APTw signal of peritumoral edema in metastatic tumors with accelerated 3D APTw imaging. The heterogeneity of the APTw signal was related to the heterogeneity of metastatic tumors, indicating that APTw imaging could reflect the necrosis of the metastatic tumor.

For the gliomas, the APT signal showed the peritumoral edema well, and the APT_{mean} with different AFs of the enhancement area was significantly different from that of the APT_{edema}. The previous study by Jiang et al. (2016) has demonstrated that APT values of the peritumoral edema were significantly lower for primary central nervous system lymphomas than for high-grade gliomas. APT values of the peritumoral edema can be valuable for the differentiation

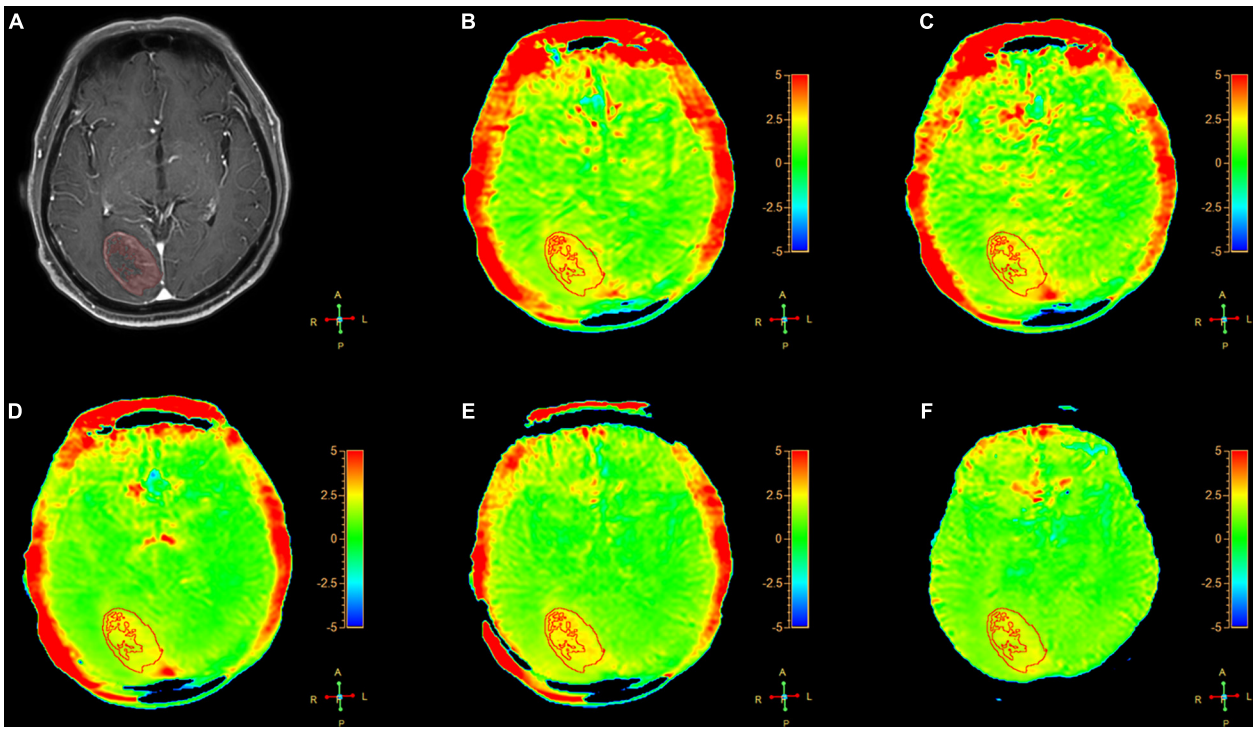

FIGURE 3 | A 64-year-old female patient with metastasis in brain: **(A)** Gd-T1W; **(B–F)** APTw images by SENSE (AF 1.6) and CS-SENSE (AFs of 2, 3, 4, and 5). The ROIs were obtained manually on the Gd-T1W image and copied to the others as shown.

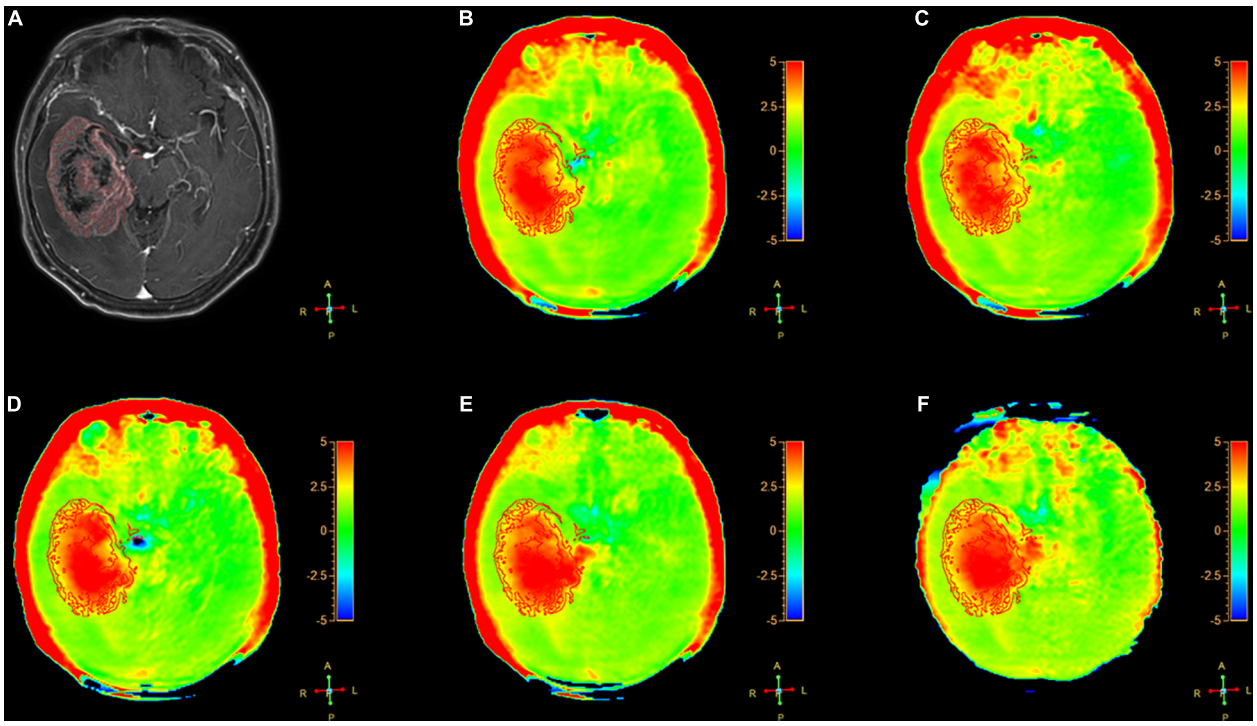

FIGURE 4 | A 54-year-old female patient with gliomas tumors (Grade III) in brain: **(A)** Gd-T1W; **(B–F)** APTw images by SENSE (AF 1.6) and CS-SENSE (AFs of 2, 3, 4, and 5). The ROIs were obtained manually on the Gd-T1W image and copied to the others as shown.

TABLE 8 | Correlation between APT_{tumor} and Ki67.

AF	APT_{tumor} (%)	*r*	*p*
SENSE1.6	2.96 ± 0.63	0.573	0.016
CS2	2.76 ± 0.59	0.590	0.013
CS3	2.96 ± 0.48	0.610	0.009
CS4	2.92 ± 0.45	0.621	0.008
CS5	2.75 ± 0.61	0.396	0.116

of glioma from other tumors. When compared to DCE images, hyperintensity lesions on APTw maps were with more heterogeneous features, and similar results have been observed in previous studies (Jiang et al., 2016) for central nervous system lymphomas and gliomas. APTw imaging would be a valuable MRI biomarker by which to diagnose brain cancer. The Ki67 is a nuclear protein associated with tumor cell proliferation and the expression of ribosomal RNA. With a relatively short half-life, Ki67 serves as a sensitive marker for the proliferation of tumor cells. It has been demonstrated that Ki67 is positively correlated with the malignant degree of glioma (Wolfesberger et al., 2010), yet the relationship between Ki67 and the prognosis of glioma remains largely unknown. The sample size of this study is small, and it is only preliminary to conclude that Ki67 is related to the proliferation of glioma cells. In this study, the relationship between APT value and the positive expression rate of Ki67 was

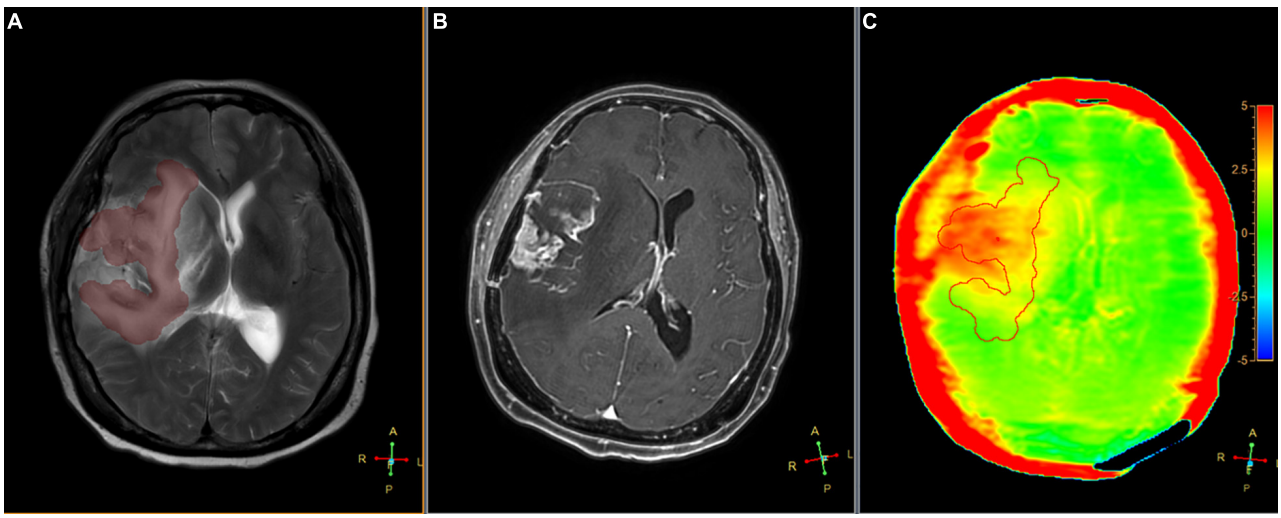

FIGURE 5 | Segmented peritumoral high signal intensity areas and the peritumoral areas in a 63-year-old male with gliomas (Grade IV) overlaid onto coregistered T2W **(A)**, Gd-T1W **(B)**, and APTw **(C)** images (SENSE AF = 1.6). The APT_{edema} was 2.47%.

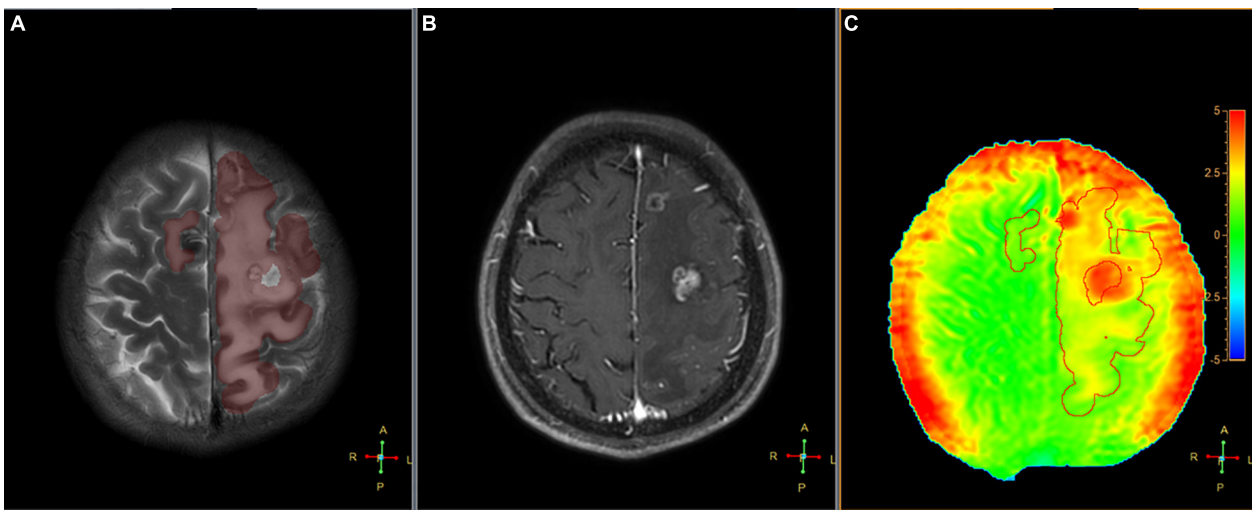

FIGURE 6 | Segmented peritumoral high signal intensity areas and the peritumoral areas in a 45-year-old male with a metastasis (the primary site of cancer was lung) overlaid onto coregistered T2W **(A)**, Gd-T1W **(B)**, and APTw **(C)** images (SENSE AF = 1.6). The APT_{edema} was 2.54%.

analyzed and results showed that APT_{tumor} values of gliomas measured by APTw images with the SENSE factor of 1.6 and the CS factor of 2, 3, and 4 (except for CS5) were all positively correlated with Ki67 ($p < 0.05$).

There are some limitations or weaknesses in this study. The tumor types included in this study were limited, and the sample size for each type of tumor was limited, which may be the reason for the lack of difference in APT_{tumor} among the three types of tumors. Further studies on the three types of tumors should be carried out with larger subjects.

CONCLUSION

The compressed SENSE with an acceleration factor of 4 was recommended for 3D APTw imaging without compromising image quality for brain tumor imaging, and saving at least 48.86% scan time compared to the conventional SENSE acceleration. The APTw imaging can obtain molecule-level information about brain tumors, and the acceleration by compressed SENSE would benefit its clinical applications.

DATA AVAILABILITY STATEMENT

The original contributions presented in the study are included in the article/supplementary material, further inquiries can be directed to the corresponding author.

ETHICS STATEMENT

The studies involving human participants were reviewed and approved by the Ethics Committee of First Affiliated Hospital of Dalian Medical University. The patients/participants provided their written informed consent to participate in this study.

AUTHOR CONTRIBUTIONS

NZ and QS conceived the study. NZ and HZ participated in the sequence alignment and scanning. BG and JW collected the clinical materials and data. AL and YM processed and analyzed the data. NZ wrote the first draft of the manuscript. LL revised the manuscript. All authors commented on previous versions of the manuscript and read and approved the final manuscript.

FUNDING

This study was supported by the National Natural Science Foundation of China (81671646), Horizontal Research Project (2021HZ006), and Research Project of Education Department of Liaoning Province (LJKZ0856).

REFERENCES

Candes, E. J., Romberg, J., and Tao, T. (2006). Robust uncertainty principles: exact signal reconstruction from highly incomplete frequency information. *IEEE Transac. Inform. Theory* 52, 489–509. doi: 10.1109/TIT.2005.862083

Candès, E., Braun, N., and Wakin, M. (2007). "Sparse signal and image recovery from compressive samples," in *IEEE International Symposium on Biomedical Imaging* (Arlington, VA), 976–979. doi: 10.1109/ISBI.2007.357017

Debnath, A., Gupta, R. K., and Singh, A. (2020). Evaluating the role of Amide Proton Transfer (APT)-weighted contrast, optimized for normalization and region of interest selection, in differentiation of neoplastic and infective mass lesions on 3T MRI. *Mol. Imaging Biol.* 22, 384–396. doi: 10.1007/s11307-019-01382-x

Donoho, D. L. (2006). Compressed sensing. *IEEE Transac. Inform. Theory* 52, 1289–1306. doi: 10.1109/TIT.2006.871582

Eidel, O., Burth, S., Neumann, J. O., Kieslich, P. J., Sahm, F., Jungk, C., et al. (2017). Tumor infiltration in enhancing and non-enhancing parts of glioblastoma: a correlation with histopathology. *PLoS One* 12:e169292. doi: 10.1371/journal.pone.0169292

Gawlitza, M., Fiedler, E., Schob, S., Hoffmann, K. T., and Surov, A. (2017). Peritumoral brain edema in meningiomas depends on Aquaporin-4 expression and not on tumor grade, tumor volume, cell count, or Ki-67 labeling index. *Mol. Imaging Biol.* 19, 298–304. doi: 10.1007/s11307-016-1000-7

Heo, H. Y., Xu, X., Jiang, S., Zhao, Y., Keupp, J., Redmond, K. J., et al. (2019). Prospective acceleration of parallel RF transmission-based 3D chemical exchange saturation transfer imaging with compressed sensing. *Magn. Reson. Med.* 82, 1812–1821. doi: 10.1002/mrm.27875

Ishimatsu, K., Nishie, A., Takayama, Y., Asayama, Y., Ushijima, Y., Kakihara, D., et al. (2019). Amide proton transfer imaging for differentiating benign ovarian cystic lesions: potential of first time right. *Eur. J. Radiol.* 120:108656. doi: 10.1016/j.ejrad.2019.108656

Jiang, S., Yu, H., Wang, X., Lu, S., Li, Y., Feng, L., et al. (2016). Molecular MRI differentiation between primary central nervous system lymphomas and high-grade gliomas using endogenous protein-based amide proton transfer MR imaging at 3 Tesla. *Eur. Radiol.* 26, 64–71. doi: 10.1007/s00330-015-3805-1

Joo, B., Han, K., Choi, Y. S., Lee, S. K., Ahn, S. S., Chang, J. H., et al. (2018). Amide proton transfer imaging for differentiation of benign and atypical meningiomas. *Eur. Radiol.* 28, 331–339. doi: 10.1007/s00330-017-4962-1

Lin, G., Zhuang, C., Shen, Z., Xiao, G., Chen, Y., Shen, Y., et al. (2018). APT weighted MRI as an effective imaging protocol to predict clinical outcome after acute ischemic stroke. *Front. Neurol.* 9:901. doi: 10.3389/fneur.2018.00901

Pankowska, A., Kochalska, K., Lazorczyk, A., Dyndor, K., Koziol, P., Zienczuk, B., et al. (2019). Chemical exchange saturation transfer (CEST) as a new method of signal obtainment in magnetic resonance molecular imaging in clinical and research practice. *Pol. J. Radiol.* 84, e147–e152. doi: 10.5114/pjr.2019.84242

Park, J. E., Kim, H. S., Park, S. Y., Jung, S. C., Kim, J. H., and Heo, H. Y. (2020). Identification of early response to anti-angiogenic therapy in recurrent glioblastoma: amide proton transfer-weighted and perfusion-weighted MRI compared with diffusion-weighted MRI. *Radiology* 295, 397–406. doi: 10.1148/radiol.2020191376

Park, Y. W., Ahn, S. S., Kim, E. H., Kang, S. G., Chang, J. H., Kim, S. H., et al. (2021). Differentiation of recurrent diffuse glioma from treatment-induced change using amide proton transfer imaging: incremental value to diffusion and perfusion parameters. *Neuroradiology* 63, 363–372. doi: 10.1007/s00234-020-02542-5

Scott, J. N., Brasher, P. M., Sevick, R. J., Rewcastle, N. B., and Forsyth, P. A. (2002). How often are nonenhancing supratentorial gliomas malignant? A population study. *Neurology* 59, 947–949. doi: 10.1212/wnl.59.6.947

Togao, O., Keupp, J., Hiwatashi, A., Yamashita, K., Kikuchi, K., Yoneyama, M., et al. (2017). Amide proton transfer imaging of brain tumors using a self-corrected 3D fast spin-echo dixon method: comparison with separate B0 correction. *Magn. Reson. Med.* 77, 2272–2279. doi: 10.1002/mrm.26322

van Zijl, P. C. M., and Yadav, N. N. (2011). Chemical exchange saturation transfer (CEST): what is in a name and what isn't? *Magn. Reson. Med.* 65, 927–948. doi: 10.1002/mrm.22761

van Zijl, P., Lam, W. W., Xu, J., Knutsson, L., and Stanisz, G. J. (2018). Magnetization transfer contrast and chemical exchange saturation transfer MRI. features and analysis of the field-dependent saturation spectrum. *Neuroimage* 168, 222–241. doi: 10.1016/j.neuroimage.2017.04.045

Wen, Z., Hu, S., Huang, F., Wang, X., Guo, L., Quan, X., et al. (2010). MR imaging of high-grade brain tumors using endogenous protein and peptide-based contrast. *Neuroimage* 51, 616–622. doi: 10.1016/j.neuroimage.2010.02.050

Wolfesberger, B., Tonar, Z., Gerner, W., Skalicky, M., Heiduschka, G., Egerbacher, M., et al. (2010). The tyrosine kinase inhibitor sorafenib decreases cell number and induces apoptosis in a canine osteosarcoma cell line. *Res. Vet. Sci.* 88, 94–100. doi: 10.1016/j.rvsc.2009.06.009

Xu, Z., Ke, C., Liu, J., Xu, S., Han, L., Yang, Y., et al. (2021). Diagnostic performance between MR amide proton transfer (APT) and diffusion kurtosis imaging (DKI) in glioma grading and IDH mutation status prediction at 3T. *Eur. J. Radiol.* 134:109466. doi: 10.1016/j.ejrad.2020.109466

Yu, H., Lou, H., Zou, T., Wang, X., Jiang, S., Huang, Z., et al. (2017). Applying protein-based amide proton transfer MR imaging to distinguish solitary brain metastases from glioblastoma. *Eur. Radiol.* 27, 4516–4524. doi: 10.1007/s00330-017-4867-z

Yu, H., Wen, X., Wu, P., Chen, Y., Zou, T., Wang, X., et al. (2019). Can amide proton transfer-weighted imaging differentiate tumor grade and predict Ki-67 proliferation status of meningioma? *Eur. Radiol.* 29, 5298–5306. doi: 10.1007/s00330-019-06115-w

Zhang, Y., Heo, H. Y., Lee, D. H., Zhao, X., Jiang, S., Zhang, K., et al. (2016). Selecting the reference image for registration of CEST series. *J. Magn. Reson. Imaging* 43, 756–761. doi: 10.1002/jmri.25027

Zhang, Y., Yong, X., Liu, R., Tang, J., Jiang, H., Fu, C., et al. (2020). Whole-brain chemical exchange saturation transfer imaging with optimized turbo spin echo readout. *Magn. Reson. Med.* 84, 1161–1172. doi: 10.1002/mrm.28184

Zhou, J., Heo, H. Y., Knutsson, L., van Zijl, P., and Jiang, S. (2019). APT-weighted MRI: techniques, current neuro applications, and challenging issues. *J. Magn. Reson. Imaging* 50, 347–364. doi: 10.1002/jmri.26645

Zhou, J., Hong, X., Zhao, X., Gao, J. H., and Yuan, J. (2013). APT-weighted and NOE-weighted image contrasts in glioma with different RF saturation powers based on magnetization transfer ratio asymmetry analyses. *Magn. Reson. Med.* 70, 320–327. doi: 10.1002/mrm.24784

Zhou, J., Lal, B., Wilson, D. A., Laterra, J., and van Zijl, P. C. (2003). Amide proton transfer (APT) contrast for imaging of brain tumors. *Magn. Reson. Med.* 50, 1120–1126. doi: 10.1002/mrm.10651

Zhu, H., Jones, C. K., van Zijl, P. C., Barker, P. B., and Zhou, J. (2010). Fast 3D chemical exchange saturation transfer (CEST) imaging of the human brain. *Magn. Reson. Med.* 64, 638–644. doi: 10.1002/mrm.22546

Conflict of Interest: LL and JW are employee of Philips Healthcare, China.

The remaining authors declare that the research was conducted in the absence of any commercial or financial relationships that could be construed as a potential conflict of interest.

Publisher's Note: All claims expressed in this article are solely those of the authors and do not necessarily represent those of their affiliated organizations, or those of the publisher, the editors and the reviewers. Any product that may be evaluated in this article, or claim that may be made by its manufacturer, is not guaranteed or endorsed by the publisher.

Copyright © 2022 Zhang, Zhang, Gao, Miao, Liu, Song, Lin and Wang. This is an open-access article distributed under the terms of the Creative Commons Attribution License (CC BY). The use, distribution or reproduction in other forums is permitted, provided the original author(s) and the copyright owner(s) are credited and that the original publication in this journal is cited, in accordance with accepted academic practice. No use, distribution or reproduction is permitted which does not comply with these terms.

frontiers | Frontiers in Oncology

ORIGINAL RESEARCH
published: 27 May 2022
doi: 10.3389/fonc.2022.874631

Surgery of Motor Eloquent Glioblastoma Guided by TMS-Informed Tractography: Driving Resection Completeness Towards Prolonged Survival

Carolin Weiss Lucas[1†], Andrea Maria Faymonville[1,2†], Ricardo Loução[1,3,4], Catharina Schroeter[1], Charlotte Nettekoven[1], Ana-Maria Oros-Peusquens[4], Karl Josef Langen[4], N. Jon Shah[4,5,6], Gabriele Stoffels[4], Volker Neuschmelting[1], Tobias Blau[6,7], Hannah Neuschmelting[8], Martin Hellmich[9], Martin Kocher[1,3,4], Christian Grefkes[4,10] and Roland Goldbrunner[1]*

[1] Department of General Neurosurgery, Center of Neurosurgery, Faculty of Medicine and University Hospital Cologne, University of Cologne, Cologne, Germany, [2] Department of Neurosurgery, University Hospital Mannheim, Mannheim, Germany, [3] Department of Stereotaxy and Functional Neurosurgery, Center of Neurosurgery, Faculty of Medicine and University Hospital Cologne, University of Cologne, Cologne, Germany, [4] Institute of Neuroscience and Medicine (INM-4), Forschungszentrum Julich, Juelich, Germany, [5] JARA - BRAIN - Translational Medicine, Aachen, Germany, [6] Department of Neurology, RWTH Aachen University, Aachen, Germany, [7] Institute of Neuropathology, Faculty of Medicine and University Hospital Cologne, University of Cologne, Cologne, Germany, [8] Institute of Pathology and Neuropathology, University Hospital Essen, Essen, Germany, [9] Institute for Diagnostic and Interventional Radiology, Faculty of Medicine and University Hospital Cologne, University of Cologne, Cologne, Germany, [10] Institute for Medical Statistics and Computational Biology, Faculty of Medicine and University Hospital Cologne, University of Cologne, Cologne, Germany, [11] Department of Neurology, Faculty of Medicine and University Hospital Cologne, University of Cologne, Cologne, Germany

OPEN ACCESS

Edited by:
Nico Sollmann,
University of California, San Francisco, United States

Reviewed by:
Georgios Naros,
University of Tübingen, Germany
Jose Pedro Lavrador,
King's College Hospital NHS Foundation Trust, United Kingdom
Thomas Picht,
Charité Universitätsmedizin Berlin, Germany

***Correspondence:**
Carolin Weiss Lucas
carolin.weiss@uk-koeln.de

[†]These authors have contributed equally to this work and share first authorship

Specialty section:
This article was submitted to Neuro-Oncology and Neurosurgical Oncology, a section of the journal Frontiers in Oncology

Received: 12 February 2022
Accepted: 21 March 2022
Published: 27 May 2022

Citation:
Weiss Lucas C, Faymonville AM, Loução R, Schroeter C, Nettekoven C, Oros-Peusquens A-M, Langen KJ, Shah NJ, Stoffels G, Neuschmelting V, Blau T, Neuschmelting H, Hellmich M, Kocher M, Grefkes C and Goldbrunner R (2022) Surgery of Motor Eloquent Glioblastoma Guided by TMS-Informed Tractography: Driving Resection Completeness Towards Prolonged Survival. Front. Oncol. 12:874631. doi: 10.3389/fonc.2022.874631

Background: Surgical treatment of patients with glioblastoma affecting motor eloquent brain regions remains critically discussed given the risk–benefit dilemma of prolonging survival at the cost of motor-functional damage. Tractography informed by navigated transcranial magnetic stimulation (nTMS-informed tractography, TIT) provides a rather robust estimate of the individual location of the corticospinal tract (CST), a highly vulnerable structure with poor functional reorganisation potential. We hypothesised that by a more comprehensive, individualised surgical decision-making using TIT, tumours in close relationship to the CST can be resected with at least equal probability of gross total resection (GTR) than less eloquently located tumours without causing significantly more gross motor function harm. Moreover, we explored whether the completeness of TIT-aided resection translates to longer survival.

Methods: A total of 61 patients (median age 63 years, m = 34) with primary glioblastoma neighbouring or involving the CST were operated on between 2010 and 2015. TIT was performed to inform surgical planning in 35 of the patients (group T; vs. 26 control patients). To achieve largely unconfounded group comparisons for each co-primary outcome (i.e., gross-motor functional worsening, GTR, survival), (i) uni- and multivariate regression analyses were performed to identify features of optimal outcome prediction; (ii),

optimal propensity score matching (PSM) was applied to balance those features pairwise across groups, followed by (iii) pairwise group comparison.

Results: Patients in group T featured a significantly higher lesion-CST overlap compared to controls (8.7 ± 10.7% vs. 3.8 ± 5.7%; p = 0.022). The frequency of gross motor worsening was higher in group T, albeit non-significant (n = 5/35 vs. n = 0/26; p = 0.108). PSM-based paired-sample comparison, controlling for the confounders of preoperative tumour volume and vicinity to the delicate vasculature of the insula, showed higher GTR rates in group T (77% vs. 69%; p = 0.025), particularly in patients with *a priori* intended GTR (87% vs. 78%; p = 0.003). This translates into a prolonged PFS in the same PSM subgroup (8.9 vs. 5.8 months; p = 0.03), with GTR representing the strongest predictor of PFS (p = 0.001) and OS (p = 0.0003) overall.

Conclusion: The benefit of TIT-aided GTR appears to overcome the drawbacks of potentially elevated motor functional risk in motor eloquent tumour localisation, leading to prolonged survival of patients with primary glioblastoma close to the CST.

Keywords: high grade glioma, HGG, rolandic, CST, transcranial magnetic stimulation, functional outcome, diffusion tensor imaging, DTI

INTRODUCTION

Despite the availability of advanced functional imaging techniques, the decision whether or not to resect high-grade gliomas in highly eloquent locations like the primary motor system remains a continued matter of debate. In addition to the risk of compromising health-related quality of life, the decision-making process is influenced by the concern that patients in whom motor function deteriorates after surgery may subsequently become ineligible for adjuvant tumour treatment, which could negate the beneficial effect of surgical tumour tissue reduction on survival (1, 2). In consequence, many patients with tumours closely adjacent to the corticospinal tract (CST) are treated by biopsy and definitive radio-chemotherapy, although there is substantial evidence that the complete removal of contrast-enhancing (CE-) tumour tissue (i.e., gross total tumour resection; GTR) improves the survival of glioblastoma patients (1).

Modern preoperative imaging techniques can inform the surgical decision-makers with valuable data regarding the individual location of functionally important structures at risk, e.g., the CST. The CST represents an essential component of the primary motor system with comparatively little potential of functional reorganisation to compensate for motor deficits in case of structural harm (3). Its individual localisation can be challenging in glioblastoma patients due to tumour mass effects. Tractography based on diffusion tensor imaging (DTI) can provide a robust estimate of individual CST localisation also in the neighbourhood of brain tumours, especially if informed by functional localisation techniques like neuronavigated transcranial magnetic stimulation (nTMS) (4).

The use of functional localisers like nTMS to define the primary motor cortex (M1) as the starting region of interest (ROI) for tractography is of particular importance in motor eloquent brain tumours since not only physiological variability (5) but also tumour-related functional reorganisation and anatomical shifts hamper its localisation based on pure brain atlas information (6, 7).

The pre- and intraoperative use of advanced functional localiser techniques such as nTMS and nTMS-informed tractography (TIT) can affect surgical decision-making (8). However, the question of whether the application of those techniques is associated with a more aggressive resection and might—as a consequence—influence survival, remains controversially debated (8, 9) and cannot be adequately addressed by comparison with historical cohorts due to substantial changes in the general surgical strategy and the availability of pre- and intraoperative aids.

In this cohort study, we investigated the effect of TIT-aided neuronavigation on gross-motor functional outcome and completeness of resection linked to survival in patients with motor eloquent glioblastoma. Results were compared to matched cases from the same period and institution. We hypothesised that the use of TIT allows for tumour resection in comparatively critical location (i.e., close to the CST) without a major increase in gross motor function risk. Moreover, we hypothesised that the preoperative planning based on TIT allows for realistic expectations regarding the intraoperative findings, leading to resection completeness (i.e., GTR rate) noninferior to a control group with comparatively less motor eloquent tumour location. Lastly, we set out to explore to which extent the surgical success translates to improved progression-free and overall survival (PFS and OS, respectively).

METHODS

General Study Design

In this hospital-based cohort study of 61 patients with first diagnosed primary, motor eloquent glioblastoma, we, first, investigated differences in the characteristics of group T,

receiving preoperative TIT for surgery planning upon request by the responsible neurosurgeon, compared to the control group C. As a consequence, we expected an overall more motor eloquent localisation of tumours in group T (i.e., higher overlap with the CST). Second, the influence of TIT-aided surgery planning and other potential factors on postoperative functional changes were explored (primary outcome: gross motor function; secondary outcome: Karnofsky Perfromance Status, KPS). Third, factors influencing GTR were analysed; propensity score matching (PSM) was applied to balance significant confounders across groups before comparing GTR outcome groups T and C (cf. section *Data Analysis*). Finally, uni- and multivariate Cox Proportional Hazards regression models were used to explore the influencing factors on survival (PFS, OS) in this specific cohort; PSM was applied to achieve a largely unbiased comparison of survival outcomes between patients with vs. without GTR.

Patients

Between July 2010 and May 2015, a consecutive group of patients with primary glioblastoma was allocated to this single-centre study cohort, characterised by scheduled tumour resection (following the decision of an interdisciplinary tumour board) and tumour infiltration of the posterior frontal and/or the anterior parietal lobes, thus showing the proximity of the tumour margins to M1 and/or the CST. Exclusion criteria were poor general performance [KPS <50%; (10)] and contraindications for magnetic resonance imaging (MRI). Part of the patients received preoperative nTMS mapping of the motor cortex together with TIT of the corticospinal/corticobulbar tract as part of the preoperative functional diagnostics (TI**T** group T), whereas others did not receive tractography (**c**ontrol group C), based on the individual decision of the responsible neurosurgeon. All patients receiving nTMS and/or tractography in addition to established pre-/intraoperative aids were prospectively filed in an institutional registry, which was approved by the local ethics committee, and provided written informed consent. Of note, epilepsy was not considered a contraindication to single-pulse nTMS as long as effective anticonvulsant treatment was provided, consistent with current safety data (11). The decision of whether or not a patient with suspected glioblastoma neighbouring M1/the CST would receive TIT was made by the responsible team of neurosurgeons on an individual risk estimation basis. Of important note, during the allocation period, preoperative TIT was not yet regarded as an essential prerequisite of state-of-the-art neuro-oncological surgery in motor-eloquent location, and was not always actively requested by the responsible team of neurosurgeons; moreover, logistic reasons and the ineligibility or unwillingness of some patients to undergo TMS can be held responsible for the non-performance of TIT, altogether explaining why not all patients received preoperative TIT.

All patients underwent neuro-oncological surgery according to current standards, including surgery performed or directly supervised by a senior neurosurgeon specialised in neuro-oncological surgery, and the routine use of 5-aminolevulinic acid (5-ALA) for fluorescence-guided resection, intraoperative ultrasound, and usually intraoperative neuronavigation. Intraoperative neuromonitoring was performed according to the preference of the neurosurgeon, and generally consisted of direct cortical stimulation (DCS) using a monopolar probe. Only very sporadically, additional subcortical stimulation was performed (using the train-of-five technique). In patients of the T group, DCS was guided by the nTMS data, with functional hotspots serving as starting points for determination of the DCS intensities [cf. (12)]. Generally, the surgical strategy aimed at the complete removal of solid tumour tissue, characterised by bright 5-ALA fluorescence, and the additional removal of moderately/weakly fluorescent tissue in tumour regions regarded non-eloquent. Of note, an essential prerequisite for indicating tumour resection was the expected achievability of GTR without relevant functional harm. Exceptionally, large tumours with intracranial mass effect (associated with clinical symptoms and/or non-eligibility for radiooncological treatment) were also considered for surgery even if the functionally critical localisation of CE-tumour parts (e.g., involving the basal ganglia) led to the *a priori* intention of subtotal resection.

The histological diagnosis of all patients eligible for the study was retrospectively re-evaluated according to the World Health Organisation (WHO) classification of 2016 [cf. (13) for review] by a senior neuropathologist (co-author TB) based on the available information regarding the isocitrate dehydrogenase (IDH) 1/2 gene mutation status.

This study was conducted in accordance with the ethical standards of the Declaration of Helsinki (first adopted in 1969, last revised in 2013).

nTMS Motor Mapping and nTMS-Informed Tractography

nTMS was conducted to map M1 using the eXimia NBS system (version 4.2, Nexstim Ltd., Helsinki, Finland) equipped with a figure-of-eight-shaped coil for biphasic magnetic stimulation and an integrated neuronavigation system using the individual T1-weighted (T1w) MRI sequence, as previously described (14). In brief: depending on the tumour location and clinical motor deficits, motor-evoked potentials (MEPs) were recorded from the abductor pollicis brevis muscle, the plantar toe flexor muscles and/or the anterior lateral third of the tongue using surface electrodes (Ambu Neuroline, Bad Nauheim, Germany). For mapping, the stimulation intensity was adjusted to 110% of the resting motor threshold (RMT) of the respective muscles. Starting at the centre (hotspot) of each body part representation, mapping was continued radially until no more nTMS-elicited MEPs (of at least 50 μV peak-to-peak amplitude) were found. After mapping, MEP data were manually cleared from data points with implausible latencies or unintended voluntary reinnervation [cf. (15)]. All surviving map data points and the corresponding map centres (hotspots) were exported as binary image files, and were made available for surgical planning (by integration in the neuronavigation software IplanNet®; Brainlab, Feldkirchen).

The somatotopic map centre volumes of interest corresponding to M1 were enlarged by a radius of 5 mm and

served as origins for tractography of the somatotopic "core fibres" (terminating at a second region of interest in the anterior pontine region; **Figure 1**). Additionally, the total map extent was used as an alternative starting region of interest (to achieve a supposedly less specific but more sensitive tractography result). Tractography was performed by a deterministic algorithm using the software tool iPlanNet (Brainlab, Feldkirchen), based on the clinical DTI data (cf. MRI and Volumetric Analysis). Two patients with group T received tractography based on anatomical ROI seeding due to unavailability of nTMS data (including one case [ID 4] with a severe preoperative motor deficit impeding to elicit MEP by nTMS within the safety limits of stimulation intensity).

MRI and Volumetric Analysis

All MRIs were obtained for clinical reasons. Preoperative MRI scans were acquired within ten days before surgery and included a T1w image sequence with and without gadolinium-based CE (post contrast), T2-weighted and fluid-attenuated inversion recovery (FLAIR) image sequences, and DTI meeting with current quality standards [i.e., ≥30 diffusion weighting directions (17)]. Postoperative scans were performed within 48 h after surgery, and comprised an additional DWI sequence, but no DTI.

The resection extent was determined based on the postoperative MRI. Here, any positive CE within brain tissue was assigned to tumour residual. GTR was considered the primary surgical outcome parameter due to its huge relevance for tumour control and survival of glioblastoma patients. Moreover, a quantitative, volumetric analysis tool (iPlan®, Brainlab, Feldkirchen, Germany) was used to measure the preoperative CE-tumour volume (PTV) and the residual CE-tumour volume (RTV) as follows (providing the volume in cm^3): (i) based on CE-T1w MRI, all CE-tissue within the mask of the tumour region was labelled using auto-segmentation, (ii) vessels, bone and dural structures were excluded from the labelled volume, (iii) based on the fused non-CE-T1w MRI, all hyperintense structures included in the volume were removed. Thereafter, tumour volumes were exported and converted into NIfTI format for further postprocessing steps (cf. *Standardised Estimation of Tumour Eloquence*). Of note, in two cases images were unavailable in digital format (only as printed films); here, PTV was estimated based on two-dimensional measurements and the assumption of a spherical tumour model. GTR, PTV and RTV were independently assessed by two neurosurgeons (CS or AF, and CWL) and a certified neuroradiologist (HN) blinded to the group affiliation of the respective patient (T vs. C). Tumour mass reduction (i.e., the proportional extent of resection) was defined by '1-RRTV', with the relative RTV (RRTV) representing the ratio between RTV and PTV.

Standardised Estimation of Tumour Eloquence

To provide a standardised estimate of the motor eloquence of the tumour location across all subjects, normalised CE-tumour volumes were overlaid with a population-based atlas template of the CST [(18) **Figure 2**]. Moreover, tumour overlap with the insula—representing a structure of high surgical risk due to the high likelihood of critical vascular damage—was assessed based on a standard atlas (19). To this end, tumour volumes were co-registered to Montreal Neuroimaging Institute (MNI) template space by linear and elastic registration of the underlying anatomical scans using the Advanced Normalisation Tools [ANTs (20)], which are comparatively robust to (tumour-induced) alterations of the cortical surface (21). This algorithm uses diffeomorphisms of both the input image (T1w of the patient) and the reference image (template T1w), commonly referred to as symmetric normalisation [SyN (20)], allowing for both small and large deformations. It is coupled with a difference metric, which evaluates the cross-correlation in neighbourhoods of voxels, and a multi-resolution optimisation. Visual inspection using well-known anatomical landmarks (e.g., corpus callosum, frontal horns of the lateral ventricles, central sulcus, outer brain margins) confirmed that normalisation was adequate. Proportional overlap volumes (i.e., overlap volume between tumour and the ipsilateral atlas template in relation to the respective atlas template volume) were calculated regarding the CST (CST-overlap) and the insular cortex (insula-overlap) by a custom-made Matlab script [using the "Tools for NIfTI and ANALYZE image" toolbox in MATLAB R2018b, The Mathworks, Massachusetts, IL, USA (22)].

The same script was applied to detect overlap (yes/no) between the tumour volume and other anatomical brain regions (frontal, parietal, temporal). A tumour extension to the temporal lobe was considered indicative of Sylvian fissure involvement—representing a second structure associated with increased risk of vascular damage –, and was manually checked on the original anatomical MRI (by CWL).

Clinical Functional Assessment

To test the functional outcome, every patient underwent a neurological examination before surgery, on postoperative day 7 ± 3, and at follow-up after three months (i.e., 12 ± 4 weeks). Pre- and postoperative motor deficits were graded into four categories of muscle strength assessed from the most affected body part, based on the British Medical Research Council system for manual grading of muscle strength [MRC (23)], which was, however, developed for lesions of the peripheral nervous system: category 1 = no deficit (MRC 5/5); category 2 = slight deficit (MRC 4/5), category 3 = moderate deficit (MRC 3/5), and category 4 = severe deficit (MRC 0-2/5). To consider also the overall clinical condition, the KPS was assessed at each time point. Relative changes in gross motor function and KPS were described on a three-level ordinal scale (better, idem, worse). It is noteworthy that comorbidity (e.g., assessed by the Charlson Comorbidity Index) was excluded due to (i) lacking evidence regarding its impact on mortality and morbidity in patients with brain metastasis (24), and (ii) its relevance for glioma patients being critically debated (25).

Survival

PFS and OS data were gathered by clinical follow-up documentation, or were obtained from the general practitioners of the patients, or from the designated mortality registry. The date

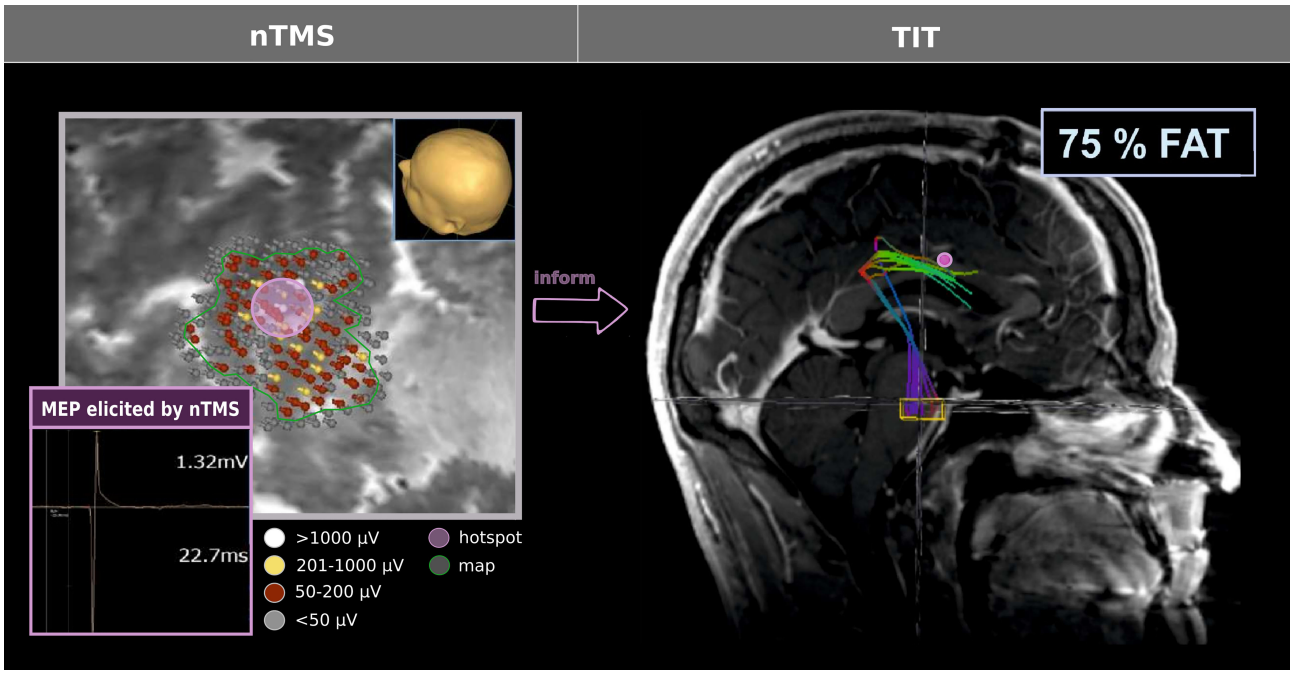

FIGURE 1 | TIT workflow. nTMS was performed to achieve a functional map of the respective somatotopic area (here: hand representation). All map coordinates (corresponding to MEP of ≥50 µV peak-to-peak amplitude, i.e., labelled in red, yellow, or white) and the centre/hotspot coordinate (yielding the highest reproducible peak-to-peak amplitude; violet) were exported to inform tractography, serving as starting points for the deterministic algorithm. Notably, the centre/hotspot was enlarged by 5 mm; a second cubic region of interest was set in the anterior pontine region [yellow box; cf. Weiss Lucas et al. (15)]. Tractography was performed by adjusting the cut-off of fractional anisotropy values to the 75% of the fractional anisotropy threshold [FAT, according to Frey et al. (79)], exemplified here with the map centre/hotspot serving as the origin.

of PFS was determined by the date of the MRI scan, which led to the statement of progressive disease (PD), or by the date of death, irrespective of its cause. PD statements were based on multidisciplinary consent in the weekly tumour board meeting. For the analysis of survival data, those long-term survivors, which were still alive at the time of manuscript preparation (n = 2), were censored. The time point of censoring was set to the date of the most recent patient contact.

Data Analysis

The statistical analyses were performed using R (R Studio, Version 2021.09.2, based on R v4.1.2; libraries: psych, MASS, SURVIVAL, MatchIt, dplyr, optmatch, ggplot2).

The selection of features considered relevant in this study was based on evidence from previous studies, and was tailored to include all presumably independent factors, which were assessable before or at the time of surgery and had a potential influence on the chosen endpoints. Thus, the following factors were included:

Functional outcome: age (continuous), preoperative gross motor status (4 levels), PTV (continuous), CST-overlap (continuous), insula-overlap (continuous), involvement of the Sylvian fissure (dichotomous), tumour hemisphere (dichotomous), TIT (dichotomous).

Resection outcome: anti-oedematous drugs (dichotomous), PTV (continuous), CST-overlap (continuous), insula-overlap (continuous), involvement of the Sylvian fissure (dichotomous), tumour hemisphere (dichotomous), TIT (dichotomous).

Survival outcome: age (continuous), gender (dichotomous), promotor status of the O6-Methylguanin-DNS-Methyltransferase (MGMT; dichotomous), preoperative gross motor function (4 levels), preoperative KPS (11 levels), PTV (continuous), CST-overlap (continuous), insula-overlap (continuous), involvement of the Sylvian fissure (dichotomous), tumour hemisphere (dichotomous), TIT (dichotomous), GTR (dichotomous), RTV (continuous).

Data were analysed applying the following steps:

(i) Regression analysis and feature selection: Uni- followed by multivariate regression analyses were performed to select features (for survival: Cox proportional-Hazards regression using the "coxph" function from the {survival} library in R; for resection outcome: generalised linear logistic regression model using the "glm" function from the {MASS} library in R); here, a liberal statistical threshold of $p \leq 0.1$ was applied to qualify factors for inclusion in the NULL model.

(ii) Model simplification: The NULL model was optimised stepwise by removal and addition of factors, based on the Akaike information criterion [AIC (26)] to compare the predictive value of models. Here, the automised "stepAIC" function (from the {MASS} library in R) was used. The increase in model complexity was only accepted if the improvement of the AIC was at least at

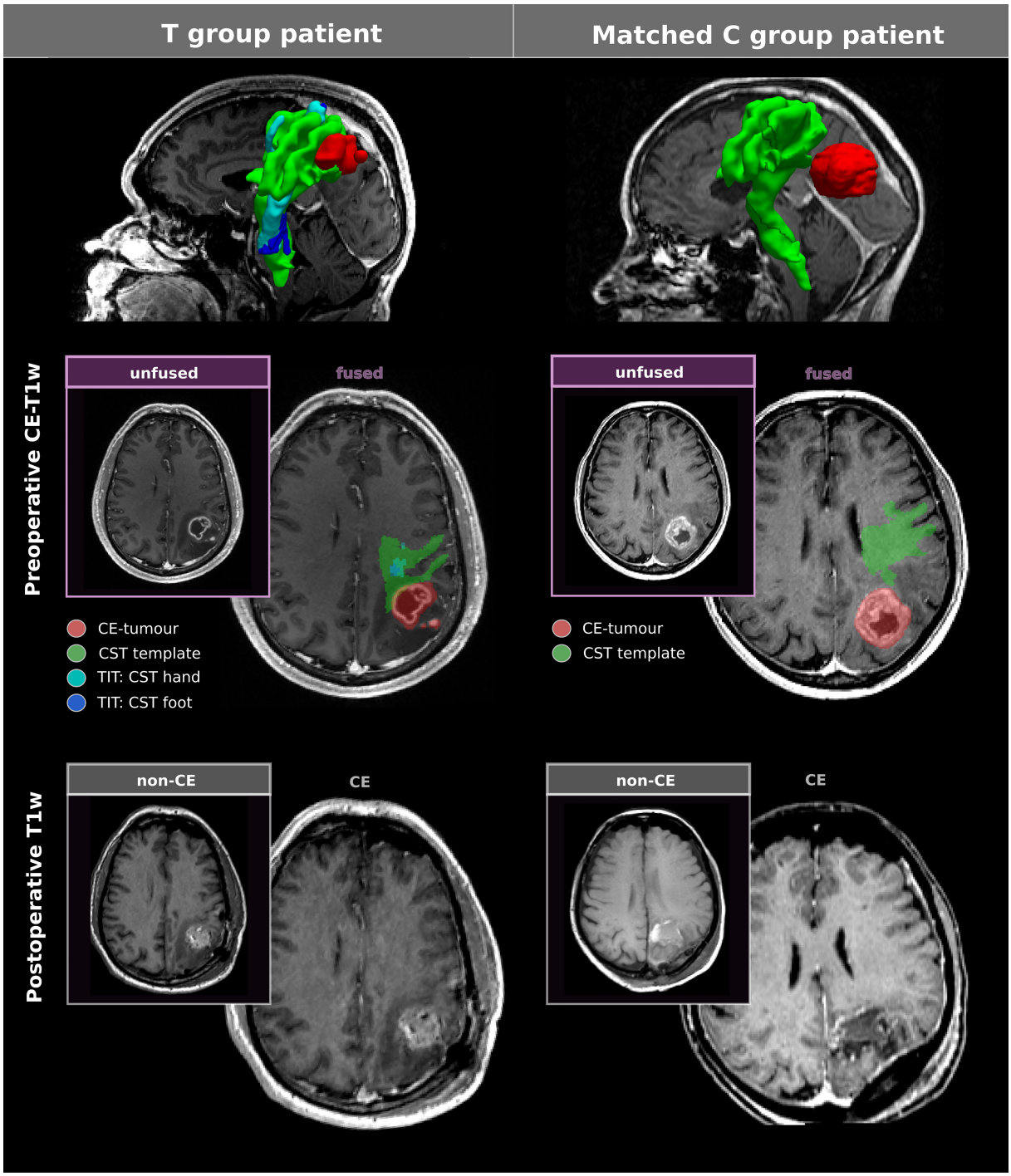

FIGURE 2 | Illustration of clinical and experimental methodology. To investigate the influence of TIT on GTR, patients from group T (TIT) and control group C were pairwise matched according to the CE-tumour volume (PTV) and the insula-overlap. The figure illustrates the clinical and methodological imaging results in a PSM-paired couple of patients (IDs 35 and 48; **Supplementary Table S1**). In patients from group T (left), somatotopic CST fibres (cyan: hand; blue: foot) were reconstructed using TIT and were integrated in the neuronavigation system for surgery planning and intraoperative guidance. For a standardised assessment of tumour eloquence across groups, a probabilistic standard CST template (green) was used to compute the CST-overlap, i.e., the proportion of the CST template overlapped with the tumour volume (red). Case 35 (left): 50 year-old male patient presenting with focal motor seizures and coordination deficits responsive to oral antiepileptic and anti-oedematous drugs who underwent GTR aided by TIT, 5-ALA and DCS without postoperative gross motor deficits (PFS 7.3 months; OS 10.0 months). Case 48 (right): The 78 year-old female patient without preoperative motor deficits underwent GTR guided by neuronavigation and 5-ALA fluorescence without postoperative gross motor deficits (PFS 5.8 months; OS 8.6 months).

the statistical level of p <0.1. The final model is referred to as the "winning model" throughout the manuscript. Whenever the winning model included factors other than the stratifying variable, PSM was performed in the following to control for confounders.

(iii) *PSM:* The concept of the PSM itself and of comparable methods have been implemented to improve data quality, comparability and estimation of treatment effects of groups by reduction or elimination of confounding effects [cf., e.g., (27)]. Therefore, this method has been widely regarded as the current gold standard for the analysis of observational data (28) and is of particular interest for the comparison of relatively small groups. Here, patients from the (larger) T group were matched pairwise according to the factors of the winning model to patients from the C group, based on their propensity scores. Here, the "matchit" function in R ({MatchIt} library, optimal matching method) was applied. The covariate balance in the matched sample was checked using paired-sample *post hoc* tests to exclude a significant group difference (with p <0.1 leading to rejection of the PSM result). This workflow (i–iii) was repeated for each distinct outcome (i.e., postoperative worsening of gross motor function, GTR, PFS, OS). Notably, TIT and GTR were stratifying factors for PFS/OS and thus not included in the PSM for these endpoints.

(iv) Matched pair analysis: Given optimal PSM regarding all variables of the winning model, tests for paired data (within-subject design) were applied for this part of the group comparisons (27): To test group differences between optimally matched dichotomous variables, McNemar's chi-square test was used. Group comparisons regarding normally distributed (according to the Shapiro–Wilk test), continuous variables, were performed using two-sided t-tests. The Wilcoxon signed-rank test was applied for group comparison between rank scaled (e.g., KPS) and not normally distributed continuous paired data. Log-rank tests were applied for group comparison of survival models (using the "survdiff" function from the {survival} library in R).

A level of significance was set at p <0.05 (except for step [i] feature selection). For histograms, bin width was selected according to the rule of Freedman–Diaconis (29).

RESULTS

Patients

A total of 61 patients (median age = 63 [32–87] years, 34 men) were included in the full data set (**Table 1**). Most patients (56% overall) presented with a preoperative gross motor deficit and received anti-oedematous medication (i.e., oral dexamethasone; 72% overall) before surgery; however, most patients were in good overall clinical status (median KPS = 90). Due to the inclusion criteria, patients were generally diagnosed with an IDH 1/2 wildtype glioblastoma, and 32% (n = 19) showed a promoter methylation of the MGMT gene (**Table 1**).

According to the tumour vicinity to the motor cortex and/or pyramidal tract, all tumours were characterised by frontal and/or parietal localisation, and partly involved the temporal lobe (25%), and/or reached the insula (33%), and/or the Sylvian fissure (12%). Notably, tumour infiltration reaching the insula and/or the Sylvian fissure (36% overall) was considered at increased risk of vascular damage (**Table 1**). Probable involvement of the CST and/or M1 was confirmed by the overlap of the normalised PTV with a standard CST map in 49 (82%) of the cases.

Surgery was almost always supported by intraoperative neuronavigation (93%) and 5-ALA fluorescence imaging (97%). The two remaining cases without 5-ALA administration (due to unexpected glioblastoma diagnosis; both T group) were not considered for PSM to avoid bias. Approximately 64% of the patients received intraoperative neuromonitoring, which generally consisted of DCS (except for two cases for which phase reversal was used to identify the central sulcus, and another two cases with additional use of subcortical stimulation). More than half of the patients were investigated by nTMS motor mapping (61%) and/or DTI-tractography (57%; group T) for surgery planning (**Table 1**). Notably, the size of the control group C was comparatively small (n = 26; 43%) since, in a given time frame, most patients with posterior frontal and/or anterior parietal tumour location were scheduled for TIT.

A comparison of means revealed no significant differences between cohort T (n = 35; median age = 60 [32–80] years, 18 men) and cohort C (n = 26; median age = 68 [51–87] years, 16 men) regarding the patient/tumour characteristics except for younger age (p = 0.046) and higher CST-overlap in group T (8.7 ± 10.7% vs. 3.8 ± 5.7%; p = 0.022; **Figure 3**). Moreover, the rate of applied imaging/mapping techniques was higher in group T: intraoperative DCS (83% vs. 39%; p <0.0001), and preoperative nTMS (94% vs. 15%; p <0.0001)—both linked to the grouping variable TIT.

Gross Motor Functional and General Clinical Outcome

For the entire group of patients, the postoperative gross motor status was not significantly different from the preoperative condition (full cohort; mean ± SD: 0.8 ± 0.9 vs. 0.7 ± 0.9; p = 0.33). Accordingly, in most patients, gross motor function remained at least unchanged after surgery (n = 54 [89%]; **Table 2**). Twelve (20%) of those patients showed gross motor functional improvement. In contrast, seven patients (11%) presented a deterioration of gross motor function at the time of discharge (**Table 2**); in two of the cases, the cause was not directly related to the removal of tumour tissue in motor eloquent location (case 18: sinus venous thrombosis with fatal outcome; case 34: ischemia inside the posterior limb of the internal capsule, outside the tumour volume, due to vascular damage in the posterior insular region). Of the remaining five cases (8%), four had a pre-existing motor deficit. In all five cases, the degree of deterioration was limited to one scale level.

Compared to the preoperative time point, also the general clinical condition of the patients remained statistically unchanged at the time of discharge (both median KPS = 90 [50, 100]; p = 0.6), but deteriorated until the follow-up visit after three months (median KPS = 80 [40, 100]; p = 0.017; **Table 2**). As

TABLE 1 | Patient characteristics.

General	
Age (median in years *[range]*)	63 *[32;87]*
Gender	
N males (%)	34 (56%)
N females (%)	27 (44%)
Steroids preoperative (%)	44 (72%)
Biological tumour characteristics	
MGMT promoter methylated (%)	19 (32%)
IDH-1/2 status	
IDH1 R132H wildtype, immunohistochemical analysis (%)	55 (90%)
IDH1/IDH 2 wildtype, molecular genetic analysis (%)	39 (63%)
Wildtype unknown (%)	5 (8%)
CE-tumour location & size	
Left hemisphere (%)	30 (49%)
Size (ccm, mean ± SD)	24 ± 20
Frontal[§] (%)	47 (77%)
Parietal[§] (%)	46 (75%)
Temporal[§] (%)	15 (25%)
Insula[§] (%)	20 (33%)
Sylvian fissure (%)	7 (12%)
Elevated vascular risk (i.e., insula and/or Sylvian fissure)	*22 (36%)*
CST involvement[§] (%)	49 (82%)
Insula-overlap in mean ‰ ± SD	0.35‰ ± 0.11‰
CST-overlap in mean % ± SD	6.7% ± 9.2%
Gross-motor function and general clinical condition	
Any preoperative gross motor deficit (%)	34 (56%)
slight gross motor deficit (MRC 4/5)	19 (31%)
moderate gross motor deficit (MRC 3/5)	11 (18%)
severe gross motor deficit (MRC 0–2/5)	3 (5%)
KPS preoperative (median *[range; 0–100]*)	90 *[50;100]*
Functional and tumour mapping/imaging	
Preoperative	
NTMS	61%
DTI	57%
Intraoperative	
5-ALA	97%
Neuronavigation	93%
Intraoperative neuromonitoring (DCS)	64%

Pre- and intraoperative characteristics of the full patient cohort (n = 61) are provided. [§]According to overlap between tumour volume and atlas template (yes/no). SD, standard deviation.

far as evaluable, none of the patients with postoperative worsening of gross motor function had fully recovered within three months (permanent deficit: n = 4; prior death: n = 1; lost to neurological follow-up: n = 2).

As expected, the degrees of gross motor functional deficit and KPS were negatively correlated, both pre- (r = −0.396; p = 0.002) and postoperatively (r = −0.371; p = 0.003).

Univariate and subsequent multivariate analysis of our data (full cohort) identified the CST-overlap, which was strongly correlated with the (preoperative) degree of gross motor deficit (Spearman's rho = 0.518; p = 0.00002), as the best predictor of postoperative gross motor function worsening. Accordingly, *post hoc* Wilcoxon tests showed a statistical trend towards a higher CST-overlap in the group with gross motor worsening (W = 196; p = 0.080). Moreover, a significant Spearman correlation was observed between the CST-overlap and the degree of postoperative gross motor deficit (rho = 0.382; p = 0.003).

Despite the significantly more probable tumour infiltration of the CST in group T according to statistical overlap analysis (cf. *Patients*), there was no significant difference between groups (T vs. C) regarding the resection-related change in gross motor function (p = 0.108) or KPS (p = 0.939; **Table 3**). Accordingly, there was no significant difference between groups T vs. C regarding the relative change of the gross motor functional deficit (0.0 ± 0.7 vs. −0.2 ± 0.5; p = 0.192). Notably, cases 18 and 34 were excluded from group comparisons to minimise bias.

Resection Outcome

GTR was achieved in 72% of all cases (**Table 2**, translating to n = 17 subtotal resections overall). Six of the subtotal resection (T group: n = 3; C group: n = 3) were planned as partial resections, due to a clinically critical tumour mass effect combined with the existence of distant/satellite CE-tumour lesions (n = 2) or CE-tumour infiltration of functionally very eloquent midline structures (n = 4). In another three cases of subtotal resection (including one T group patient), parts of M1 were spared, according to intraoperative confirmation by DCS. In the remaining eight cases, other intraoperative findings led to a less rigorous surgical strategy (n = 4), or the cause of incomplete resection remained unclear (n = 4).

According to the high GTR rates, RTV was low (mean: 0.8 ± 2.0 ccm; **Table 2**), corresponding to an average RRTV of 3% ± 7% across all patients (n = 61).

Chi-squared tests to compare GTR between groups T and C showed no significant difference overall (T: 74% vs. C: 69%; p = 0.883) and for the subgroup of n = 55 patients with *a priori* intended GTR (i.e., excluding the six cases with intended incomplete tumour debulking; T: 81% vs. C: 78%; p = 1.000; **Table 4**), thus supporting the hypothesis of non-inferiority of the T group despite the higher average CST-overlap.

To identify and rule out potential confounders, univariate and subsequent multivariate logistic regression analysis and model simplification according to AIC was performed, showing that the best prediction of GTR could be made by the insula-overlap (p = 0.090) with the preoperative tumour volume (p = 0.017). When excluding, however, the six patients with *a priori* intended subtotal resection, the single best predictor was the insula-overlap (p = 0.096). To control for the influence of both parameters, PSM was performed and identified optimally matched pairs between groups T and C based on full patient cohort (i.e., full match, n = 52; **Supplementary Table S1**) and on the reduced dataset of patients with intended GTR (n = 46; **Supplementary Table S2**).

Comparison of GTR across the optimally matched patient pairs showed higher GTR in the T group, for the full match (T: 77% vs. C: 69%; p = 0.025) and for the matched patients with intended GTR (T: 87% vs. C: 78%; p = 0.003; **Table 4**).

Survival Outcome

The median PFS was 7.6 months (95% confidence interval [CI] = 5.6–9.5 months) and the median OS was 15.0 months (CI = 12.0–18.0 months; **Table 2**; **Figure 4**). Two female patients (ages 32 and 50 years) were still alive, progression-free and in good clinical status at the time of manuscript preparation (i.e., 117 and 91 months postoperatively). Three patients (with the first two affiliated to the T group) suffered from early postoperative death due to therapy complications (case 18: thrombosis of transverse

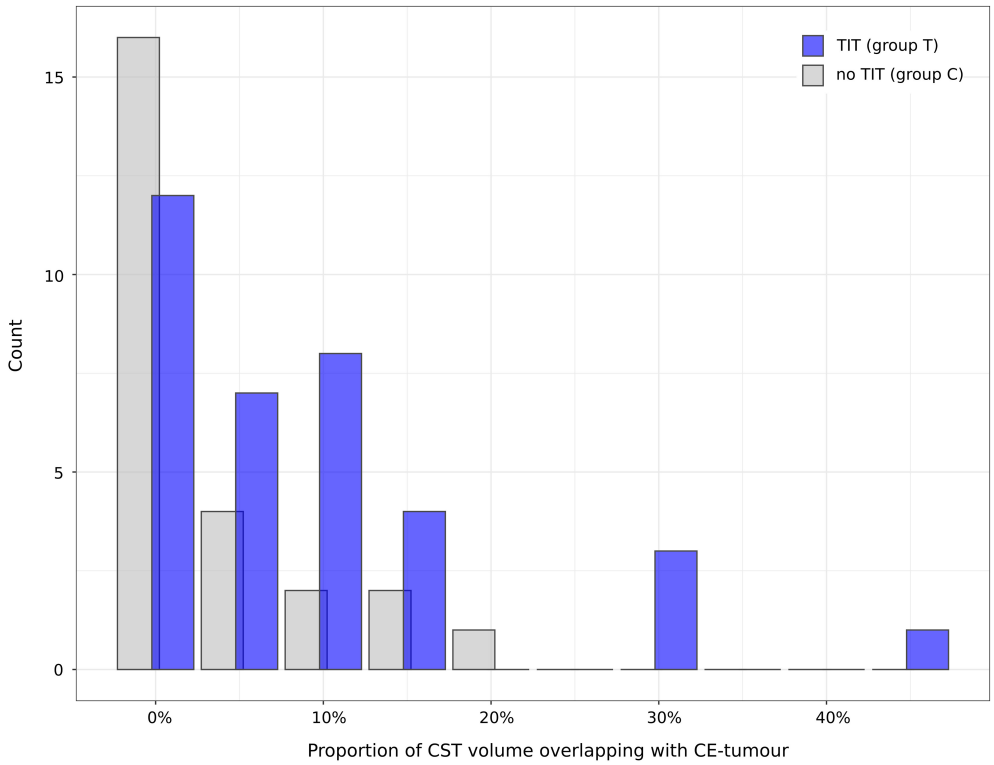

FIGURE 3 | Groupwise distribution of CST-overlap. The histogram displays the distribution of the proportional CST volume overlapping with CE-tumour (CST-overlap), grouped by TIT. The Wilcoxon test revealed a higher mean CST-overlap in group T compared to group C (8.7% ± 10.7% vs. 3.8% ± 5.7%; p = 0.022). X-axis: percentage of CST-overlap. Y-axis: count. Blue: group T (TIT; n = 35). Grey: group C (control, no TIT; n = 26).

sinus, 8 days OS; case 22: colostasis/ileus with secondary complications during radiochemotherapy, 88 days OS; case 21: subdural hygroma with trapping valve mechanism, complicated re-surgery and subsequent death, OS 129 days). Another patient from group T (case 2) underwent partial tumour resection to achieve mass reduction but remained in too limited general clinical condition (i.e., KPS 60 postoperatively) to receive adjuvant treatment; he died before the first follow-up time point (OS 45 days), probably due to tumour progression. All other patients were alive at the time point of the first follow-up MRI three months postoperatively. Of note, median survival times in the PSM-paired subset of 46 patients with *a priori* intended GTR (cf. *Resection Outcome*) were 8.12 [5.92, 9.72] months (PFS) and 14.9 [12.1, 17.5] months (OS).

We hypothesised that the achievement of tumour mass reduction, positively influenced by the use of TIT, could lead to improved survival. Uni- and multivariate Cox proportional hazards regression analysis followed by standardised model simplification identified GTR as the only variable, which significantly predicted PFS (p = 0.002; **Table 5**). In contrast, the optimal model to predict OS was composed of GTR and age (Wald test p = 0.00007; **Table 5**). Thus, for OS analysis, PSM was performed leading to an optimal pairwise balance of age (median 60 vs. 59 years; p = 0.961) between groups with vs. without GTR (2:1 match; cf. **Supplementary Table S3**), hence allowing largely unconfounded group comparison.

The stratified log-rank test showed GTR to be significantly associated with longer PFS (p = 0.0007; data base: full cohort of n = 60) and with longer OS (p = 0.002; data base: age-matched sample of n = 51; **Figures 5A, B**).

Notably, for the subgroup of patients with intended GTR, controlled for the bias of PTV and insula-overlap, the use of TIT was not only associated with slightly higher GTR rates (cf. *Resection Outcome*) but also with prolonged PFS (p = 0.030; dataset: PTV/Insula-matched sample of n = 46 with intended GTR; **Figures 5C, D**).

DISCUSSION

In a consecutive single-centre cohort of 61 patients first diagnosed with motor eloquent glioblastoma, we tested the hypothesis that at least equally high GTR rates can be achieved for tumours in comparatively close relationship to the CST without causing major functional harm, when using TIT for comprehensive and individualised resection planning. Moreover, we explored the consequences of TIT-aided resection for survival.

TABLE 2 | Patient outcome.

Extent of resection	
GTR	44 (72%)
RTV (ccm, mean ± SD)	0.8 ± 2.0
RRTV (%, mean ± SD	3% ± 7%
Gross-motor function and general clinical condition	
KPS at discharge (median [range])	90 [50;100]
Better	13 (22%)
Same	30 (50%)
Worse [by ≥20 pts]	17 (28%)
KPS after 3 months (median [range])	80 [40;100]
Better	15 (25%)
Same	17 (28%)
Worse [by ≥20 pts]	28 (46%)
Gross motor deficit at discharge	
Absolute (median grade 0–3 [range])	1 [0-3]
Any gross motor deficit	31 (51%)
Slight gross motor deficit (MRC 4/5)	20 (33%)
Moderate gross motor deficit (MRC 3/5)	7 (12%)
Severe gross motor deficit (MRC 0–2/5)	4 (7%)
Relative	
Better	11 (18%)
Same	43 (71%)
Worse	7 (12%)
[related to tumour tissue removal]	*[5 (8%)]*
Due to vascular lesion (distant ischemia)	1 (3%)
Due to sinus thrombosis	1 (3%)
Survival	
OS in months (median *[CI]*)	15.0 *[12.0;18.0]*
Death events (percent of total)	59 (97%)
Due to surgery-related complications	2 (3%)
[prior to discharge]	*[1(2%)]*
Due to surgery-unrelated complications	1 (2%)
PFS in months (median *[CI]*)	7.6 *[5.6;9.5]*
Progression or death events (percent of total)	59 (97%)
N patients progression-free alive (rate)	2 (3%)
Death prior to first routine MRI (within 3 months)	5 (8%)
[prior to first follow-up]	*[6 (10%)]*

Outcome data are provided for the full patient cohort (n = 61). CI: 95% confidence interval. SD, standard deviation.

Our results showed that, despite a more critical tumour localisation regarding the CST-overlap, higher GTR rates could be achieved using TIT compared to controls in a PSM-paired sample balanced for all significant independent confounders (i.e., PTV and insula-overlap). This achievement in tumour control was at the cost of a nonsignificantly higher proportion of resection-induced worsening of gross-motor function. Even in this specific cohort of patients with glioblastoma in highly motor eloquent localisation, GTR—optimisable by TIT-aided surgery—still represents the strongest predictor of PFS and OS. Also, the application of TIT translated into a significant increase in PFS.

Maintenance of Gross Motor and General Clinical Functioning

Our data confirm the expectation of a correlation between general clinical functioning (according to KPS) and gross motor function, none of both parameters yielded statistically significant differences between groups (T vs. C). The significant deterioration in KPS three months postoperatively compared to the status at discharge, however, seems primarily attributable to early tumour recurrence and may additionally reflect the clinical correlates of the adverse effects of radiochemotherapy. With overall five cases of gross motor function worsening caused by direct mechanical injury (8% overall, 15% in group T), corresponding to at least three cases of permanent deficits (5% overall, 9% in group T), overall our results conform to previous publications. Other authors reported permanent deficit rates between 6% (30) and 22% (31, 32) in patients with similar characteristics and technical aids [cf. (8)]. A recently published, comparatively large bi-centric dataset including n = 165 patients with motor eloquent gliomas by Rosenstock et al. (33) found permanent deficits in 13% of all cases, closely agreeing with our findings. Although the difference in directly resection-induced functional outcome between groups C and T did not meet the level of statistical significance (p = 0.108), possibly due to the rareness of the events and the limited sample size (cf. *Strengths and Limitations*), all patients with an unfavourable motor outcome were part of the T group. This can be interpreted as a consequence of the closer relationship between tumour and CST in the T group, thus confirming the results of Rosenstock et al. (33) who identified the structural integrity of the CST (expressed by the average fractional anisotropy) and strongly correlated distance between tumour and CST as the co-principal components of a risk stratification model predicting motor functional outcome in glioma surgery. This corresponds to the

TABLE 3 | Contingency tables showing group-wise distribution of functional outcome.

		Postoperative change					
		Gross motor function			KPS		
		better	**same**	**worse**	**better**	**same**	**worse**
Group	**T** (n = 33)	7	21	5	8	17	8
	C (n = 26)	5	21	0	5	15	6
Overall (n = 59)		12 (20%)	42 (71%)	5 (8%)	13 (22%)	32 (54%)	14 (24%)

The two 3 × 2 contingency tables demonstrate the postoperative change of gross motor function (left) and of the KPS (right) across groups T vs. C. Fisher's exact test showed no significant group influence on gross motor (p = 0.108) or KPS outcome (p = 0.939). Group T, TIT. Group C, control, no TIT. Cases 18 and 34 (with postoperative deficits unrelated to direct mechanical injury of the CST/M1) were excluded. cf. ***Supplementary Table S4*** *for a complementary statistical analysis in the subgroup of patients with intraoperative neuromonitoring (which largely agreed with the key results presented here).*

TABLE 4 | Contingency tables showing group-wise distribution of resection completeness.

		Patient cohort			
		Full (n = 61)		GTR intended (n = 55)	
		GTR	subtotal	GTR	subtotal
Unmatched groups	**T**	26	9	26	6
	C	18	8	18	5
		Full Match (n = 52)*		Match GTR intended (n = 46)**	
		GTR	subtotal	GTR	subtotal
PSM-paired groups	**T**	20	6	20	3
	C	18	8	18	5

Four-fold contingency tables for the unmatched groups (upper part) failed to show an association of TIT with the extent of resection in the full (unmatched) patient cohort (left; Pearson's $\chi^2 = 0.02$; $p = 0.883$) and in the subset of patients with a-priori intention of GTR (right; Pearson's $n = 55$; $\chi^2 = 1.2 \times 10^{-30}$, $p = 1.000$). PSM-paired groups (lower part): the tables demonstrate the distribution of GTR amongst groups matched pairwise using PSM (cf. ***Supplementary Tables S1, S2****), pointing towards a higher probability of GTR in the T group for both the full PSM cohort (McNemar's $\chi^2 = 5.04$; $p = 0.025$) and for the subgroup with intended GTR (McNemar's $\chi^2 = 9.33$; $p = 0.003$). Of note, these findings are largely confirmed also for the subgroup of patients with intraoperative neuromonitoring (cf.* ***Supplementary Table S5*** *for an overview of the complementary data). *p <0.05; **p <0.01.*

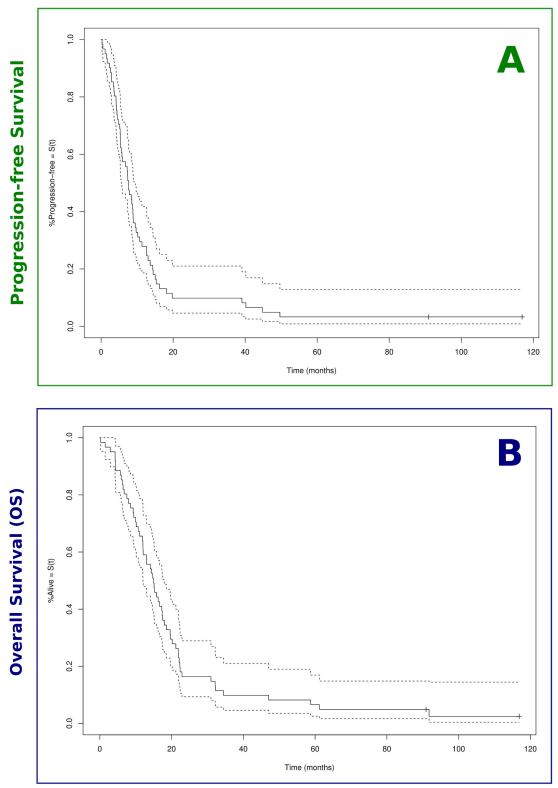

FIGURE 4 | Kaplan–Meier survival curves. Estimated survival proportions according to Kaplan–Meier are displayed for the full patient cohort (n = 61). **(A)** Median progression-free survival (PFS) was 7.6 months. **(B)** Overall survival (OS) was 15.0 months (OS; cf. **Table 2**). The associated lower and upper bounds of the 95% confidence interval are displayed as dashed lines. Censoring events are indicated by vertical 'ticks'.

results of uni- and multivariable regression analyses of our data identifying the CST-overlap as the best predictor of gross motor functional worsening, which was strongly correlated with the preoperative functional deficit. Moreover, the utmost incomplete recovery of all patients with gross motor functional deterioration who could be neurologically re-evaluated three months later (n = 4) mirrors the evidence from stroke research: the functional reorganisation potential after CST lesion, principally mediated by the recruitment of secondary motor network components, seems largely inefficient (3) and depends critically on the degree of structural CST damage (34).

Notably, the valuable technique of intraoperative (semi-) continuous dynamic mapping of the CST (35) based on the principle of intermittent monopolar subcortical stimulation (36) was established for routine use in our centre only after the period of patient allocation to this study. Recent data from Seidel et al. (37) using this innovative technique in n = 182 cases of motor eloquent brain lesions showed permanent surgery-induced motor deficits in 3% overall, and in 1.7% of the patients caused by direct mechanical injury. Despite limited comparability of their dataset with ours (e.g., due to centre effects and heterogeneous tumour entities including only 45% glioblastoma), it can be assumed that the use of (semi-) continuous dynamic mapping might help to further improve the balance between resection completeness and avoidance of functional harm.

Towards an Optimised Degree of Resection

Intraoperative fluorescence-guidance of resection (usually by 5-ALA), which was applied in all except for two cases in our study, was a milestone in the history of high-grade glioma surgery (38, 39). To date, 5-ALA fluorescence represents a standard intraoperative tool but not a common outcome measure, since objective quantification methods for residual fluorescence have not yet been established. However, the prognostic value of (quantitative) intraoperative metabolic imaging represents an interesting subject to future investigations. Although there is substantial agreement that fluorescence-guidance improves the completeness of resection (and, thus, hampers comparison with historical cohorts before the introduction of 5-ALA), GTR rates reported in the literature vary strongly in the range between 50 and 80%, even in cohorts with routine use of 5-ALA [cf. (40) for review]. Regardless of the

TABLE 5 | Cox proportional hazards regression models best describing survival outcomes.

Outcome	Feature	Coefficients			Wald statistic	
		Estimate	Hazard ratio	SE	z value	*p*-value
PFS	GTR	−1.011	0.364	0.308	−3.284	0.001**
OS	Age	0.040	1.041	0.012	3.238	0.001**
	GTR	−1.125	0.325	0.311	−3.612	0.0003***

*Results of the winning cox proportional Hazards regression models are shown for PFS (upper line) and OS (lower lines). The respective features were considered for PSM. SE, standard error. **p <0.01; ***p <0.001.*

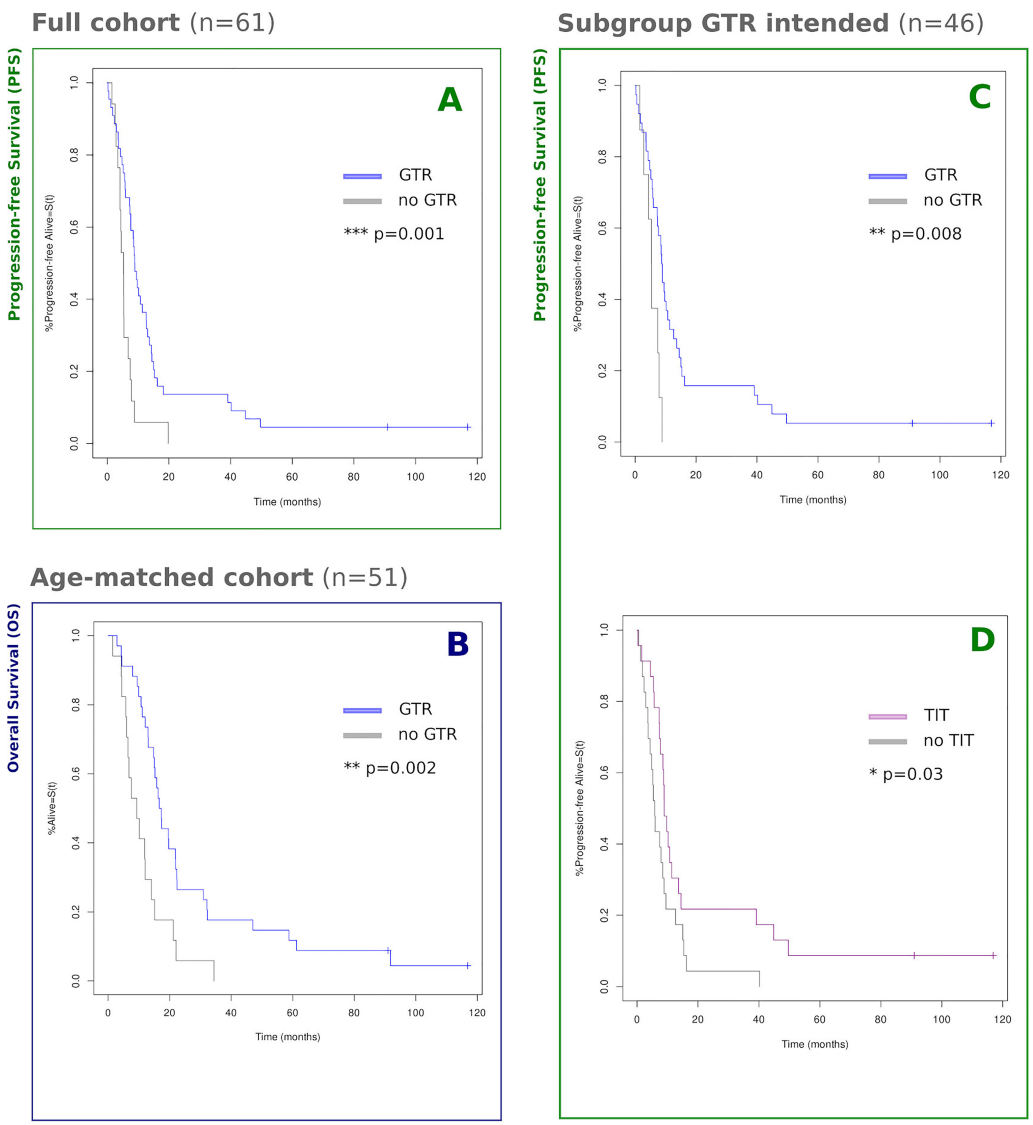

FIGURE 5 | Kaplan–Meier survival curves by group. Estimated survival proportions according to Kaplan–Meier statistics are displayed, grouped by GTR/TIT. Censoring events are indicated by vertical 'ticks'. **(A)** Full cohort of n = 61, GTR vs. no GTR: 8.9 vs. 5.3 months [χ^2 = 10.6; p = 0.001]; **(B)** PSM age-paired cohort of n = 51, GTR vs. no GTR: 17.0 vs. 9.3 months [χ^2 = 9.7; p = 0.002]; **(C, D)** Subgroup of n = 46 patients a-priori eligible for GTR, pairwise balanced for PTV and insula-overlap using PSM. **(C)** GTR vs. no GTR: 8.8 vs 5.5 months [chi2 = 7.1; p = 0.008] ("p = " is missing); **(D)** TIT vs. no TIT: 8.9 vs. 5.8 months [χ^2 = 4.7; p = 0.030]. For an overview of PSM raw data, cf. **Supplementary Tables S3 (B)** and **S2 (C, D)**. *p <0.05; **p <0.01; ***p <0.001.

eloquent tumour locations, resection outcomes in our study cohort reached 72% overall (74% in the T group) and 80% GTR in the subgroup with *a priori* intended GTR. Other groups applying similar CST visualisation techniques (including tractography) to inform motor eloquent tumour resections reported GTR rates between 50% (31) and 73–74% (33, 41) in mixed cohorts mainly including high-grade glioma patients, which, however, limits direct comparisons with our study results. Comparing GTR rates between groups with vs. without TIT, we found a significant difference (T: 77% vs. C: 69%; p = 0.025) when using PSM to control for the confounding effects of PTV and insula involvement. This effect appears mainly attributable to TIT rather than to nTMS (alone), i.e., according to the results of Raffa et al. (42) who found a significant improvement in GTR with the use of TIT but nonsignificantly by nTMS alone in a case-control study with three diagnostic arms. Although generally supporting the results of other groups who also found higher GTR rates in patient cohorts of DTI-informed surgery, the resection outcome in our control group was still favourable compared to the previously reported control GTR rates, e.g., in the range of 51–53% (41, 43). This might be due to a better control of confounders in this matched control group taken from the same period. For instance, the use of intraoperative neuronavigation, being inevitably linked to the intraoperative use of functional data like TIT, has been increasingly used over the past decades, and can *per se* contribute to improving the extent of resection. In our study, only four patients (of the control group) were operated without intraoperative neuronavigation (two of them with GTR outcome), thus reducing this bias to a minimum.

The still considerable advantage of TIT-informed surgery (planning), regarding resection completeness, could be explained by (i) better patient selection regarding the objective of GTR without causing relevant functional harm. This primary hypothesis is supported by the fact that two surgeries (8%) in group C vs. only one surgery in group T (3%) were switched to subtotal resection based on intraoperative DCS results. Another explanation is (ii) a higher degree of confidence of the neurosurgeon towards the CST localisation due to the intraoperative availability of functional neuronavigation including TIT results, leading to a more aggressive surgical strategy, at least at a supposedly "safe" distance from the expected location of the CST [generally corresponding to a distance of ≥3–5 mm, dependent on the local anatomy/vascularisation (37)]. Whether or not this effect of TIT could be similarly achieved by the routine use of intraoperative (semi-) continuous dynamic mapping remains to be investigated in direct comparison of both methods.

Survival

With an overall median OS of 15.0 months and the median PFS of 7.6 months overall, our survival results are in the upper field compared to larger-scale studies of surgically treated primary glioblastoma patients with unspecified tumour localisation reporting median PFS in the range of 6–7 months and median OS between 12 and 15 months (44–48). We hypothesise that the motor eloquent location of tumours predisposes patients for comparatively early tumour detection due to the association with motor symptoms and focal seizures (49), mostly still in a stage eligible for GTR. This assumption is supported by the facts that (i) in our dataset, comparatively high GTR rates were achieved (cf. *Discussion*, *Resection Outcome*), and that (ii) OS outcome data in our GTR subgroup (i.e., median 17.0 months) are in close agreement with median OS of patients with completely resected primary glioblastoma of random localisation [e.g., Kreth et al. (GTR: n = 125): 17.1 months (46); Stummer et al. (GTR: n = 137): 17.9 months (38)].

Regarding the effect of the extent of resection on survival, which is the subject of an ongoing debate [cf., e.g., (50)], we identified GTR but not RTV as the strongest influenceable predictor of survival. Similarly, Kreth et al. (46) found GTR but not subtotal resection to be associated with prolonged survival. Hence, also in motor eloquent tumours, GTR represents the key player to improve survival. Local tumour recurrence (facilitated by incomplete resection) likely affects motor function and, thus, the general clinical condition of the patients, and offers limited second-line local therapy options due to the regional eloquence. Our conclusions are supported by recent data of Hendrix et al. (43), who also identified older age and subtotal resection as the primary hazards for overall survival of patients with motor eloquent high-grade gliomas (although in a mixed cohort of WHO grade 3/4 gliomas).

Strengths and Limitations

As far as we are aware, this is the first study to systematically assess survival outcome in a consecutive patient cohort composed exclusively of primary motor eloquent glioblastoma patients treated by TIT-guided tumour resection, allowing for first-time demonstration of a significant effect of TIT-driven GTR on survival. This could be achieved using an optimal PSM and a rigorous strategy of data-driven statistical analysis (i.e., selecting features for matching based on regression analysis), particularly well-suited for small-sample studies in rare diseases like motor eloquent glioblastoma.

The non-randomised design, however, remains an important limitation of this study and explains the larger proportion of CST-overlap in the T group, as patients with tumours close to the CST were more likely subjected to TIT than patients with comparatively CST-distant tumours. Even despite this confound, as stated above, we still found a longer PFS in patients undergoing TIT. Therefore, our study supports the idea of a prospective randomised controlled trial to prove the benefits of TIT in glioblastoma surgery. Alternatively, a large multicentre study (combined with PSM-based statistical analysis) could serve to confirm the results, offering a better balance between the sample size and the large variety of potential confounding factors.

Since DTI was performed only in the T group, a direct assessment of the distance/overlap between the tumour and the CST by individual tractography was impossible for both groups. To allow, however, for a group-wise comparison, a standard CST template overlaid with normalised CE-T1w tumour volumes was used. Although being justified by the issue of between-group comparability, this approach comes with the limitation of providing a less precise estimate of motor eloquence (tending to its over-estimation) compared with individual DTI and might not always agree with expert assessments of the scans.

TIT in our study was performed according to the current state-of-the-art in clinical routine, i.e., based on standard DTI and

deterministic data processing representing rather robust tools for CST visualisation (4). However, the precision of the tractography results might be further improved by the use of more advanced techniques of (i) diffusion MRI acquisition, (ii) postprocessing and (iii) co-registration techniques, for instance. (i) The use of optimised b-values and kurtosis tensor strategies (51, 52), high angular resolution diffusion imaging (HARDI)/q-ball imaging (53, 54), neurite orientation dispersion and density imaging [NODDI (55, 56)] can improve the tractography results especially in regions of fibre crossings, at the cost of acquisition time [cf. (57)]. This drawback, however, could be at least partly alleviated using accelerated acquisition schemes such as compressed sensing (58). (ii) In addition to image acquisition techniques, probabilistic tractography algorithms (59, 60) and (iii) elastic fusion in addition to linear co-registration of diffusion imaging and structural MRI contribute substantially to precision improvement, especially in the context of brain tumours, where tumour-related changes in cellular water content interfere with diffusion metrics (61). Furthermore, echo planar imaging (EPI)-based diffusion and fMRI acquisitions can be tailored to display the same image distortions, thus rendering the nonlinear registration unnecessary and allowing for a precise seed region definition.

Concerning functional localisation, recent advancements in fMRI acquisition and analysis, such as high-resolution fMRI [cf. (62)] and high-field fMRI/mesoscopic brain mapping (63, 64) might qualify fMRI techniques, along with magnetoencephalography [MEG (65, 66)], as an acceptable alternative to nTMS as a functional localised to inform CST-tractography in the future.

Even when achieving optimal precision in the estimation of the CST localisation using non-invasive techniques like TIT, its intraoperative validity is hampered by the nonlinear brain shift induced by skull/dura opening, which increases along with the loss of cerebrospinal fluid and the quantity of tumour tissue removed [cf. (67)]. This fallacious co-registration mismatch concerning intraoperative neuronavigation can be at least partly overcome by intraoperative renewal of the co-registration with intraoperative imaging [cf. (68)], i.e., intraoperative MRI [iMRI (69)], CT [iCT (70, 71)] and 3D ultrasound [iUS (72–74)]. However, intraoperative neuromonitoring techniques remain the gold standard in the resection of motor-eloquent gliomas (75), and their partial use in this study represents another limitation. For instance, intraoperative neuromonitoring by cortex stimulation and (semi-) continuous dynamic mapping in particular (36, 76) provide excellent tools for repeated estimation of the CST distance from the resection cavity, e.g., guided by TIT-integrated neuronavigation. These techniques are especially appropriate if patients are not monitored behaviourally in an awake surgery setting, which allows the additional monitoring of higher-order brain functions such as motor control (16, 77, 78). It is possible that the *intraoperative* effect of TIT is at least partly outperformed by a comprehensive and rigorous intraoperative neuromonitoring.

Conclusions

This study shows that incorporating TIT into the pre- and intraoperative workflow enhances the completeness of resection in GTR-eligible motor eloquent primary glioblastoma. This achievement is associated with a non-significant increase in directly resection-related motor function deficits, and leads to prolonged PFS—with subtotal resection representing the primary influenceable hazard of PFS and OS in this patient cohort. A controlled prospective trial is needed to ultimately prove the benefit of TIT in glioblastoma surgery.

DATA AVAILABILITY STATEMENT

The raw data supporting the conclusions of this article will be made available by the authors, without undue reservation.

ETHICS STATEMENT

The studies involving human participants were reviewed and approved by the Ethics Committee of the Medical Faculty of the University of Cologne. The participants receiving nTMS and/or TIT were filed in an institutional registry, and provided their written informed consent.

AUTHOR CONTRIBUTIONS

CWL: study design, data acquisition, data analysis, manuscript draft & editing. AMF: study design, data acquisition, manuscript draft & editing. RL: data analysis; manuscript editing. CN: manuscript editing. CS, AMOP, KJL, NJS, GS, and VN: data acquisition, manuscript editing. TB and HN: data analysis, manuscript editing. MH: proofing of data analysis, manuscript editing. MK: data analysis and manuscript editing. CG: study design and manuscript editing. RG: study design, data acquisition and manuscript editing. All authors listed have made a substantial, direct, and intellectual contribution to the work and approved it for publication.

FUNDING

CWL and RG received funding from the German Research Foundation (DfG) for the purchase of the nTMS device (INST 1856/50-1) and as support for the Article Processing Charge (491454339). CWL received additional funding from the Faculty of Medicine of the University of Cologne (Koeln Fortune/Gerok 8/2016).

ACKNOWLEDGMENTS

We thank the MR staff of the Forschungszentrum Jülich and all patients for their support. Moreover, we thank Lukas Hensel (Cologne) and Shiva Vishwanathan (Jülich) for providing first drafts of custom Matlab scripts in the context of standardised anatomical tumour localisation.

SUPPLEMENTARY MATERIAL

The Supplementary Material for this article can be found online at: https://www.frontiersin.org/articles/10.3389/fonc.2022.874631/full#supplementary-material

REFERENCES

1. McGirt MJ, Mukherjee D, Chaichana KL, Than KD, Weingart JD, Quinones-Hinojosa A. Association of Surgically Acquired Motor and Language Deficits on Overall Survival After Resection of Glioblastoma Multiforme. *Neurosurgery* (2009) 65(3):463–70. doi: 10.1227/01.NEU.0000349763.42238.E9
2. Brown TJ, Brennan MC, Li M, Church EW, Brandmeir NJ, Rakszawski KL, et al. Association of the Extent of Resection With Survival in Glioblastoma: A Systematic Review and Meta-Analysis. *JAMA Oncol* (2016) 2(11):1460–9. doi: 10.1001/jamaoncol.2016.1373
3. Ward NS, Newton JM, Swayne OB, Lee L, Thompson AJ, Greenwood RJ, et al. Motor System Activation After Subcortical Stroke Depends on Corticospinal System Integrity. *Brain* (2006) 129(Pt 3):809–19. doi: 10.1093/brain/awl002
4. Weiss Lucas C, Tursunova I, Neuschmelting V, Nettekoven C, Oros-Peusquens AM, Stoffels G, et al. Functional MRI vs. Navigated TMS to Optimize M1 Seed Volume Delineation for DTI Tractography. A Prospective Study in Patients With Brain Tumours Adjacent to the Corticospinal Tract. *NeuroImage Clin* (2016) 23:13:297–309. doi: 10.1016/j.nicl.2016.11.022
5. Farrell DF, Burbank N, Lettich E, Ojemann GA. Individual Variation in Human Motor-Sensory (Rolandic) Cortex. *J Clin Neurophysiol* (2007) 24 (3):286–93. doi: 10.1097/WNP.0b013e31803bb59a
6. Duffau H, Capelle L, Denvil D, Sichez N, Gatignol P, Lopes M, et al. Functional Recovery After Surgical Resection of Low Grade Gliomas in Eloquent Brain: Hypothesis of Brain Compensation. *J Neurol Neurosurg Psychiatry* (2003) 74(7):901–7. doi: 10.1136/jnnp.74.7.901
7. Tozakidou M, Wenz H, Reinhardt J, Nennig E, Riffel K, Blatow M, et al. Primary Motor Cortex Activation and Lateralization in Patients With Tumors of the Central Region. *NeuroImage Clin* (2013) 2:221–8. doi: 10.1016/j.nicl.2013.01.002
8. Umana GE, Scalia G, Graziano F, Maugeri R, Alberio N, Barone F, et al. Navigated Transcranial Magnetic Stimulation Motor Mapping Usefulness in the Surgical Management of Patients Affected by Brain Tumors in Eloquent Areas: A Systematic Review and Meta-Analysis. *Front Neurol* (2021) 12:644198. doi: 10.3389/fneur.2021.644198
9. Barone DG, Lawrie TA, Hart MG. Image Guided Surgery for the Resection of Brain Tumours. *Cochrane Database Syst Rev* (2014) 2014(1):CD009685. doi: 10.1002/14651858.CD009685.pub2
10. Karnofsky DA, Burchenal JH. The Clinical Evaluation of Chemotherapeutic Agents in Cancer. In: CM MacLeod, editor. *Evaluation of Chemotherapeutic Agents*. New York: Columbia University Press (1949). p. 196–6.
11. Tarapore PE, Picht T, Bulubas L, Shin Y, Kulchytska N, Meyer B, et al. Safety and Tolerability of Navigated TMS for Preoperative Mapping in Neurosurgical Patients. *Clin Neurophysiol* (2016) 127(3):1895–900. doi: 10.1016/j.clinph.2015.11.042
12. Weiss Lucas C, Nettekoven C, Neuschmelting V, Oros-Peusquens AM, Stoffels G, Viswanathan S, et al. Invasive Versus non-Invasive Mapping of the Motor Cortex. *Hum Brain Map* (2020) 41(14):3970–83. doi: 10.1002/hbm.25101
13. Louis DN, Perry A, Reifenberger G, von Deimling A, Figarella-Branger D, Cavenee WK, et al. The 2016 World Health Organization Classification of Tumors of the Central Nervous System: A Summary. *Acta Neuropathol* (2016) 131(6):803–20. doi: 10.1007/s00401-016-1545-1
14. Weiss C, Nettekoven C, Rehme AK, Neuschmelting V, Eisenbeis A, Goldbrunner R, et al. Mapping the Hand, Foot and Face Representations in the Primary Motor Cortex - Retest Reliability of Neuronavigated TMS Versus Functional MRI. *Neuroimage* (2013) 66:531–42. doi: 10.1016/j.neuroimage.2012.10.046
15. Weiss C, Tursunova I, Neuschmelting V, Lockau H, Nettekoven C, Oros-Peusquens AM, et al. Improved nTMS- and DTI-Derived CST Tractography Through Anatomical ROI Seeding on Anterior Pontine Level Compared to Internal Capsule. *NeuroImage Clin* (2015) 7:424–37. doi: 10.1016/j.nicl.2015.01.006
16. Bello L, Freyschlag CF, Rech F. Motor Control. In: E Mandonnet, G Herbet, editors. *Intraoperative Mapping of Cognitive Networks*, vol. 1 . Cham: Springer (2021). p. 3–19. doi: 10.1007/978-3-030-75071-8
17. Jones DK. The Effect of Gradient Sampling Schemes on Measures Derived From Diffusion Tensor MRI: A Monte Carlo Study. *Magn Reson Med* (2004) 51(4):807–15. doi: 10.1002/mrm.20033
18. Chenot Q, Tzourio-Mazoyer N, Rheault F, Descoteaux M, Crivello F, Zago L, et al. A Population-Based Atlas of the Human Pyramidal Tract in 410 Healthy Participants. *Brain Struct Funct* (2019) 224(2):599–612. doi: 10.1007/s00429-018-1798-7
19. Mazziotta J, Toga A, Evans A, Fox P, Lancaster J, Zilles K, et al. A Probabilistic Atlas and Reference System for the Human Brain: International Consortium for Brain Mapping (ICBM). *Philos Trans R Soc Lond B Biol Sci* (2001) 356 (1412):1293–322. doi: 10.1098/rstb.2001.0915
20. Avants BB, Epstein CL, Grossman M, Gee JC. Symmetric Diffeomorphic Image Registration With Cross-Correlation: Evaluating Automated Labeling of Elderly and Neurodegenerative Brain. *Med Image Anal* (2008) 12(1):26–41. doi: 10.1016/j.media.2007.06.004
21. Ou Y, Akbari H, Bilello M, Da X, Davatzikos C. Comparative Evaluation of Registration Algorithms in Different Brain Databases With Varying Difficulty: Results and Insights. *IEEE Trans Med Imaging* (2014) 33(10):2039–65. doi: 10.1109/TMI.2014.2330355
22. Shen J. *Tools for NIfTI and Analyse Image*. Available at: https://www.mathworks.com/matlabcentral/fileexchange/8797-tools-for-nifti-and-analyse-image (Accessed February 2, 2022).
23. Medical Research Council. *Aids to the Investigation of the Peripheral Nervous System*. London: Her Majesty's Stationary Office (1943). Medical Research Council.
24. Ening G, Schmieder K, Brenke C. Adjunct Preoperative Factors Impacting Brain Metastasis Patient's Morbidity and Mortality. *J Neurol Neurosci* (2015) 6 (2):13. doi: 10.21767/2171-6625.100013
25. Fiorentino A, Ricchetti F, Mazzola R, Fersino S, Giaj Levra N, Alongi F. Regarding Ening Et al. Charlson Comorbidity Index: An Additional Prognostic Parameter for Preoperative Glioblastoma Patient Stratification. *J Cancer Res Clin Oncol* (2015) 141(6):1139–40. doi: 10.1007/s00432-015-1944-z
26. Akaike H. (1973). Information Theory as an Extension of the Maximum Likelihood Principle, in: *2nd International Symposium on Information Theory*, Akademiai Kiado, Budapest, Hungary: Akademiai Kiado. pp. 167–281. doi: 10.1007/978-1-4612-1694-0_15
27. Austin PC. Comparing Paired vs Non-Paired Statistical Methods of Analyses When Making Inferences About Absolute Risk Reductions in Propensity-Score Matched Samples. *Stat Med* (2011) 30(11):1292–301. doi: 10.1002/sim.4200
28. Shadish WR, Cook TD, Campbell DT. Experimental and Quasi-Experimental Designs for Generalized Causal Inference. *Boston: Houghton Mifflin* (2001). doi: 10.1002/pam.10129
29. Freedman D, Diaconis P. On the Histogram as a Density Estimator:L2 Theory. *Z für Wahrscheinlichkeitstheorie und Verwandte Gebiete* (1981) 57:453–76. doi: 10.1007/BF01025868
30. Frey D, Schilt S, Strack V, Zdunczyk A, Rösler J, Niraula B, et al. Navigated Transcranial Magnetic Stimulation Improves the Treatment Outcome in Patients With Brain Tumors in Motor Eloquent Locations. *Neuro Oncol* (2014) 16:1365–72. doi: 10.1093/neuonc/nou110
31. Rosenstock T, Grittner U, Acker G, Schwarzer V, Kulchytska N, Vajkoczy P, et al. Risk Stratification in Motor Area-Related Glioma Surgery Based on Navigated Transcranial Magnetic Stimulation Data. *J Neurosurg* (2017) 126:1227–37. doi: 10.3171/2016.4.JNS152896
32. Sollmann N, Zhang H, Fratini A, Wildschuetz N, Ille S, Schröder A, et al. Risk Assessment by Presurgical Tractography Using Navigated TMS Maps in Patients With Highly Motor- or Language-Eloquent Brain Tumors. *Cancers* (2020) 12(5):1264. doi: 10.3390/cancers12051264
33. Rosenstock T, Hani L, Grittner U, Schlinkmann N, Ivren M, Schneider H, et al. Bicentric Validation of the Navigated Transcranial Magnetic Stimulation Motor Risk Stratification Model. *J Neurosurg* (2021) 1-13. doi: 10.3171/2021.3.JNS2138
34. Stinear CM, Barber PA, Smale PR, Coxon JP, Fleming MK, Byblow WD. Functional Potential in Chronic Stroke Patients Depends on Corticospinal Tract Integrity. *Brain* (2007) 130(Pt 1):170–80. doi: 10.1093/brain/awl333
35. Raabe A, Beck J, Schucht P, Seidel K. Continuous Dynamic Mapping of the Corticospinal Tract During Surgery of Motor Eloquent Brain Tumors: Evaluation of a New Method. *J Neurosurg* (2014) 120(5):1015–24. doi: 10.3171/2014.1.JNS13909
36. Duffau H. Contribution of Cortical and Subcortical Electrostimulation in Brain Glioma Surgery: Methodological and Functional Considerations. *Neurophysiol Clin* (2007) 37(6):373–82. doi: 10.1016/j.neucli.2007.09.003

37. Seidel K, Schucht P, Beck J, Raabe A. Continuous Dynamic Mapping to Identify the Corticospinal Tract in Motor Eloquent Brain Tumors: An Update. *J Neurol Surg A Cent Eur Neurosurg* (2020) 81(2):105–10. doi: 10.1055/s-0039-1698384
38. Stummer W, Pichlmeier U, Meinel T, Wiestler OD, Zanella F, Reulen HJ, et al. Fluorescence-Guided Surgery With 5-Aminolevulinic Acid for Resection of Malignant Glioma: A Randomised Controlled Multicentre Phase III Trial. *Lancet Oncol* (2006) 7(5):392–401. doi: 10.1016/S1470-2045(06)70665-9
39. Díez Valle R, Hadjipanayis CG, Stummer W. Established and Emerging Uses of 5-ALA in the Brain: An Overview. *J Neurooncol* (2019) 141(3):487–94. doi: 10.1007/s11060-018-03087-7
40. Eatz TA, Eichberg DG, Lu VM, Di L, Komotar RJ, Ivan ME. Intraoperative 5-ALA Fluorescence-Guided Resection of High-Grade Glioma Leads to Greater Extent of Resection With Better Outcomes: A Systematic Review [Published Online Ahead of Print, 2022 Jan 6]. *J Neurooncol* (2022) 156(2):233–56. doi: 10.1007/s11060-021-03901-9
41. Raffa G, Scibilia A, Conti A, Cardali SM, Rizzo V, Terranova C, et al. Multimodal Surgical Treatment of High-Grade Gliomas in the Motor Area: The Impact of the Combination of Navigated Transcranial Magnetic Stimulation and Fluorescein-Guided Resection. *World Neurosurg* (2019) 128:e378–90. doi: 10.1016/j.wneu.2019.04.158
42. Raffa G, Conti A, Scibilia A, Cardali SM, Esposito F, Angileri FF, et al. The Impact of Diffusion Tensor Imaging Fiber Tracking of the Corticospinal Tract Based on Navigated Transcranial Magnetic Stimulation on Surgery of Motor-Eloquent Brain Lesions. *Neurosurgery* (2018) 83(4):768–82. doi: 10.1093/neuros/nyx554
43. Hendrix P, Dzierma Y, Burkhardt BW, Simgen A, Wagenpfeil G, Griessenauer CJ, et al. Preoperative Navigated Transcranial Magnetic Stimulation Improves Gross Total Resection Rates in Patients With Motor-Eloquent High-Grade Gliomas: A Matched Cohort Study. *Neurosurgery* (2021) 88(3):627–36. doi: 10.1093/neuros/nyaa486
44. Stupp R, Mason WP, van den Bent MJ, Weller M, Fisher B, Taphoorn MJ, et al. Radiotherapy Plus Concomitant and Adjuvant Temozolomide for Glioblastoma. *N Engl J Med* (2005) 352(10):987–96. doi: 10.1056/NEJMoa043330
45. Sanai N, Polley MY, McDermott MW, Parsa AT, Berger MS. An Extent of Resection Threshold for Newly Diagnosed Glioblastomas. *J Neurosurg* (2011) 115(1):3–8. doi: 10.3171/2011.2.jns10998
46. Kreth FW, Thon N, Simon M, Westphal M, Schackert G, Nikkhah G, et al. Gross Total But Not Incomplete Resection of Glioblastoma Prolongs Survival in the Era of Radiochemotherapy. *Ann Oncol* (2013) 24(12):3117–23. doi: 10.1093/annonc/mdt388
47. Chaichana KL, Jusue-Torres I, Navarro-Ramirez R, Raza SM, Pascual-Gallego M, Ibrahim A, et al. Establishing Percent Resection and Residual Volume Thresholds Affecting Survival and Recurrence for Patients With Newly Diagnosed Intracranial Glioblastoma. *Neuro Oncol* (2014) 16(1):113–22. doi: 10.1093/neuonc/not137
48. Grabowski MM, Recinos PF, Nowacki AS, Schroeder JL, Angelov L, Barnett GH, et al. Residual Tumor Volume Versus Extent of Resection: Predictors of Survival After Surgery for Glioblastoma. *J Neurosurg* (2014) 121(5):1115–23. doi: 10.3171/2014.7.JNS132449
49. Akeret K, Stumpo V, Staartjes VE, Vasella F, Velz J, Marinoni F, et al. Topographic Brain Tumor Anatomy Drives Seizure Risk and Enables Machine Learning Based Prediction. *NeuroImage Clin* (2020) 28:102506. doi: 10.1016/j.nicl.2020.102506
50. Wen PY, Weller M, Lee EQ, Alexander BM, Barnholtz-Sloan JS, Barthel FP, et al. Glioblastoma in Adults: A Society for Neuro-Oncology (SNO) and European Society of Neuro-Oncology (EANO) Consensus Review on Current Management and Future Directions. *Neuro Oncol* (2020) 22(8):1073–113. doi: 10.1093/neuonc/noaa106
51. Marrale M, Collura G, Brai M, Toschi N, Midiri F, La Tona G, et al. Physics, Techniques and Review of Neuroradiological Applications of Diffusion Kurtosis Imaging (DKI). *Clin Neuroradiol* (2016) 26(4):391–403. doi: 10.1007/s00062-015-0469-9
52. Bopp MHA, Emde J, Carl B, Nimsky C, Saß B. Diffusion Kurtosis Imaging Fiber Tractography of Major White Matter Tracts in Neurosurgery. *Brain Sci* (2021) 11(3):381. doi: 10.3390/brainsci11030381
53. Tuch DS, Reese TG, Wiegell MR, Makris N, Belliveau JW, Wedeen VJ. High Angular Resolution Diffusion Imaging Reveals Intravoxel White Matter Fiber Heterogeneity. *Magn Reson Med* (2002) 48(4):577–82. doi: 10.1002/mrm.10268
54. Tuch DS. Q-Ball Imaging. *Magn Reson Med* (2004) 52(6):1358–72. doi: 10.1002/mrm.20279
55. Zhang H, Schneider T, Wheeler-Kingshott CA, Alexander DC. NODDI: Practical *In Vivo* Neurite Orientation Dispersion and Density Imaging of the Human Brain. *Neuroimage* (2012) 61(4):1000–16. doi: 10.1016/j.neuroimage.2012.03.072
56. Pieri V, Sanvito F, Riva M, Petrini A, Rancoita PMV, Cirillo S, et al. Along-Tract Statistics of Neurite Orientation Dispersion and Density Imaging Diffusion Metrics to Enhance MR Tractography Quantitative Analysis in Healthy Controls and in Patients With Brain Tumors. *Hum Brain Mapp* (2021) 42(5):1268–86. doi: 10.1002/hbm.25291
57. Caiazzo G, Trojsi F, Cirillo M, Tedeschi G, Esposito F. Q-Ball Imaging Models: Comparison Between High and Low Angular Resolution Diffusion-Weighted MRI Protocols for Investigation of Brain White Matter Integrity. *Neuroradiology* (2016) 58(2):209–15. doi: 10.1007/s00234-015-1616-3
58. Michailovich O, Rathi Y, Dolui S. Spatially Regularized Compressed Sensing for High Angular Resolution Diffusion Imaging. *IEEE Trans Med Imaging* (2011) 30(5):1100–15. doi: 10.1109/TMI.2011.2142189
59. Jbabdi S, Johansen-Berg H. Tractography: Where do We Go From Here? *Brain Connect* (2011) 1(3):169–83. doi: 10.1089/brain.2011.0033
60. Bucci M, Mandelli ML, Berman JI, Amirbekian B, Nguyen C, Berger MS, et al. Quantifying Diffusion MRI Tractography of the Corticospinal Tract in Brain Tumors With Deterministic and Probabilistic Methods. *NeuroImage Clin* (2013) 3:361–8. doi: 10.1016/j.nicl.2013.08.008
61. Ellingson BM, Cloughesy TF, Lai A, Nghiemphu PL, Pope WB. Nonlinear Registration of Diffusion-Weighted Images Improves Clinical Sensitivity of Functional Diffusion Maps in Recurrent Glioblastoma Treated With Bevacizumab. *Magn Reson Med* (2012) 67(1):237–45. doi: 10.1002/mrm.23003
62. Goense J, Bohraus Y, Logothetis NK. fMRI at High Spatial Resolution: Implications for BOLD-Models. *Front Comput Neurosci* (2016) 10:66. doi: 10.3389/fncom.2016.00066
63. Huber L, Tse DHY, Wiggins CJ, Uludağ K, Kashyap S, Jangraw DC, et al. Ultra-High Resolution Blood Volume fMRI and BOLD fMRI in Humans at 9.4 T: Capabilities and Challenges. *Neuroimage* (2018) 178:769–79. doi: 10.1016/j.neuroimage.2018.06.025
64. Bandettini PA, Huber L, Finn ES. Challenges and Opportunities of Mesoscopic Brain Mapping With fMRI. *Curr Op Behav Sci* (2021) 40:189–200. doi: 10.1016/j.cobeha.2021.06.002
65. Tarapore PE, Tate MC, Findlay AM, Honma SM, Mizuiri D, Berger MS, et al. Preoperative Multimodal Motor Mapping: A Comparison of Magnetoencephalography Imaging, Navigated Transcranial Magnetic Stimulation, and Direct Cortical Stimulation. *J Neurosurg* (2012) 117(2):354–62. doi: 10.3171/2012.5.JNS112124
66. Bowyer SM, Pang EW, Huang M, Papanicolaou AC, Lee RR. Presurgical Functional Mapping With Magnetoencephalography. *Neuroimaging Clin N Am* (2020) 30(2):159–74. doi: 10.1016/j.nic.2020.02.005
67. Gerard IJ, Kersten-Oertel M, Petrecca K, Sirhan D, Hall JA, Collins DL. Brain Shift in Neuronavigation of Brain Tumors: A Review. *Med Image Anal* (2017) 35:403–20. doi: 10.1016/j.media.2016.08.007
68. Bayer S, Maier A, Ostermeier M, Fahrig R. Intraoperative Imaging Modalities and Compensation for Brain Shift in Tumor Resection Surgery [Published Correction Appears in Int J Biomed Imaging. 2019 Oct 1;2019:9249016]. *Int J BioMed Imaging* (2017) 2017:6028645. doi: 10.1155/2017/6028645
69. Nimsky C, Ganslandt O, Merhof D, Sorensen AG, Fahlbusch R. Intraoperative Visualization of the Pyramidal Tract by Diffusion-Tensor-Imaging-Based Fiber Tracking. *Neuroimage* (2006) 30(4):1219–29. doi: 10.1016/j.neuroimage.2005.11.001
70. Uhl E, Zausinger S, Morhard D, Heigl T, Scheder B, Rachinger W, et al. Intraoperative Computed Tomography With Integrated Navigation System in a Multidisciplinary Operating Suite. *Neurosurgery* (2009) 64(5 Suppl 2):231–40. doi: 10.1227/01.NEU.0000340785.51492.B5
71. Senova S, Lefaucheur JP, Brugières P, Ayache SS, Tazi S, Bapst B, et al. Case Report: Multimodal Functional and Structural Evaluation Combining Pre-Operative nTMS Mapping and Neuroimaging With Intraoperative CT-Scan and Brain Shift Correction for Brain Tumor Surgical Resection. *Front Hum Neurosc* (2021) 15:646268. doi: 10.3389/fnhum.2021.646268

72. Rasmussen IA Jr, Lindseth F, Rygh OM, Berntsen EM, Selbekk T, Xu J, et al. Functional Neuronavigation Combined With Intra-Operative 3D Ultrasound: Initial Experiences During Surgical Resections Close to Eloquent Brain Areas and Future Directions in Automatic Brain Shift Compensation of Preoperative Data. *Acta Neurochir* (2007) 149(4):365–78. doi: 10.1007/s00701-006-1110-0
73. Morin F, Courtecuisse H, Reinertsen I, Le Lann F, Palombi O, Payan Y, et al. Brain-Shift Compensation Using Intraoperative Ultrasound and Constraint-Based Biomechanical Simulation. *Med Image Anal* (2017) 40:133–53. doi: 10.1016/j.media.2017.06.003
74. Saß B, Pojskic M, Zivkovic D, Carl B, Nimsky C, Bopp MHA. Utilizing Intraoperative Navigated 3D Color Doppler Ultrasound in Glioma Surgery. *Front Oncol* (2021) 11:656020. doi: 10.3389/fonc.2021.656020
75. You H, Qiao H. Intraoperative Neuromonitoring During Resection of Gliomas Involving Eloquent Areas. *Front Neurol* (2021) 12:658680. doi: 10.3389/fneur.2021.658680
76. Schucht P, Seidel K, Jilch A, Beck J, Raabe A. A Review of Monopolar Motor Mapping and a Comprehensive Guide to Continuous Dynamic Motor Mapping for Resection of Motor Eloquent Brain Tumors. *Neurochirurgie* (2017) 63(3):175–80. doi: 10.1016/j.neuchi.2017.01.007
77. Freyschlag CF, Duffau H. Awake Brain Mapping of Cortex and Subcortical Pathways in Brain Tumor Surgery. *J Neurosurg Sci* (2014) 58(4):199–213.
78. Duffau H. Mapping the Connectome in Awake Surgery for Gliomas: An Update. *J Neurosurg Sci* (2017) 61(6):612–30. doi: 10.23736/S0390-5616.17.04017-6
79. Frey D, Strack V, Wiener E, Jussen D, Vajkoczy P, Picht T. A New Approach for Corticospinal Tract Reconstruction Based on Navigated Transcranial Stimulation and Standardized Fractional Anisotropy Values. *Neuroimage* (2012) 62(3):1600–9. doi: 10.1016/j.neuroimage.2012.05.059

Conflict of Interest: The authors declare that the research was conducted in the absence of any commercial or financial relationships that could be construed as a potential conflict of interest.

Publisher's Note: All claims expressed in this article are solely those of the authors and do not necessarily represent those of their affiliated organizations, or those of the publisher, the editors and the reviewers. Any product that may be evaluated in this article, or claim that may be made by its manufacturer, is not guaranteed or endorsed by the publisher.

Copyright © 2022 Weiss, Lucas, Faymonville, Loução, Schroeter, Nettekoven, Oros-Peusquens, Langen, Shah, Stoffels, Neuschmelting, Blau, Neuschmelting, Hellmich, Kocher, Grefkes and Goldbrunner. This is an open-access article distributed under the terms of the Creative Commons Attribution License (CC BY). The use, distribution or reproduction in other forums is permitted, provided the original author(s) and the copyright owner(s) are credited and that the original publication in this journal is cited, in accordance with accepted academic practice. No use, distribution or reproduction is permitted which does not comply with these terms.

GLOSSARY

AIC	Akaike information criterion
5-ALA	5-aminolevulinic
ANTs	Advanced Normalisation Tools
CE	Contrast-enhanced/-ing
CST	Corticospinal tract
CST-overlap	Proportional overlap volume between tumour and the ipsilateral corticospinal tract (CST) relative to the respective CST volume
DCS	Direct cortical stimulation
DTI	Diffusion tensor imaging
EPI	Echo planar imaging
FLAIR	Fluid-attenuated inversion recovery
GLM	Generalised linear model
GTR	Gross total resection
iCT	Intraoperative CT
IDH	Isocitrate dehydrogenase
iMRI	Intraoperative MRI
Insula-overlap	Proportional overlap volume between tumour and the ipsilateral insular cortex relative to the respective insular cortex volume
iUS	Intraoperative ultrasound
KPS	Karnofsky performance scale
M1	Primary motor cortex
MEG	Magnetoencephalography
MEP	Motor evoked potential
MGMT	O6-Methylguanin-DNS-Methyltransferase
MNI	Montreal Neuroimaging Institute
MRC	(British) Medical Research Council
MRI	Magnetic resonance imaging
nTMS	Navigated transcranial magnetic stimulation
OS	Overall survival
PD	Progressive disease
PFS	Progression-free survival
PSM	Propensity score matching
PTV	Preoperative CE-tumour volume
RMT	Resting motor threshold
ROI	Region of interest
RRTV	Relative residual CE-tumour volume
RTV	Residual CE-tumour volume
SD	Standard deviation
TIT	TMS-informed tractography
T1w	T1-weighted
WHO	World Health Organisation

frontiers | Frontiers in Neuroscience

ORIGINAL RESEARCH
published: 16 June 2022
doi: 10.3389/fnins.2022.837624

Laterality and Sex Differences of Human Lateral Habenula Afferent and Efferent Fiber Tracts

Frederick L. Hitti[1], Drew Parker[2], Andrew I. Yang[1], Steven Brem[1] and Ragini Verma[1,2]*

[1] Department of Neurosurgery, University of Pennsylvania, Philadelphia, PA, United States, [2] Diffusion and Connectomics in Precision Healthcare Research Lab, Department of Radiology, University of Pennsylvania, Philadelphia, PA, United States

Introduction: The lateral habenula (LHb) is an epithalamic nucleus associated with negative valence and affective disorders. It receives input *via* the stria medullaris (SM) and sends output *via* the fasciculus retroflexus (FR). Here, we use tractography to reconstruct and characterize this pathway.

Methods: Multi-shell human diffusion magnetic resonance imaging (dMRI) data was obtained from the human connectome project (HCP) (n = 20, 10 males) and from healthy controls (n = 10, 6 males) scanned at our institution. We generated LHb afferents and efferents using probabilistic tractography by selecting the pallidum as the seed region and the ventral tegmental area as the output target.

Results: We were able to reconstruct the intended streamlines in all individuals from the HCP dataset and our dataset. Our technique also aided in identification of the LHb. In right-handed individuals, the streamlines were significantly more numerous in the left hemisphere (mean ratio 1.59 ± 0.09, p = 0.04). In left-handed individuals, there was no hemispheric asymmetry on average (mean ratio 1.00 ± 0.09, p = 1.0). Additionally, these streamlines were significantly more numerous in females than in males (619.9 ± 159.7 vs. 225.9 ± 66.03, p = 0.04).

Conclusion: We developed a method to reconstruct the SM and FR without manual identification of the LHb. This technique enables targeting of these fiber tracts as well as the LHb. Furthermore, we have demonstrated that there are sex and hemispheric differences in streamline number. These findings may have therapeutic implications and warrant further investigation.

Keywords: probabilistic tractography, lateral habenula, depression, human brain asymmetry, stria medullaris, fasciculus retroflexus, sex differences

OPEN ACCESS

Edited by:
Sandro M. Krieg, Technical University of Munich, Germany

Reviewed by:
Lauren Jean O'Donnell, Harvard Medical School, United States
Jack Webster, University of Strathclyde, United Kingdom
Chuyang Ye, Beijing Institute of Technology, China

****Correspondence:***
Frederick L. Hitti
Frederick.Hitti@pennmedicine.upenn.edu

Specialty section:
This article was submitted to Brain Imaging Methods, a section of the journal Frontiers in Neuroscience

Received: *16 December 2021*
Accepted: *27 May 2022*
Published: *16 June 2022*

Citation:
Hitti FL, Parker D, Yang AI, Brem S and Verma R (2022) Laterality and Sex Differences of Human Lateral Habenula Afferent and Efferent Fiber Tracts. Front. Neurosci. 16:837624. doi: 10.3389/fnins.2022.837624

INTRODUCTION

The lateral habenula (LHb) is a well-conserved epithalamic nucleus that participates in value-based decision-making (Hikosaka, 2010). LHb neurons are more active during punishment or following the absence of an expected reward. In this manner, LHb activity signals the negative valence associated with a decision (Hikosaka et al., 2008; Hikosaka, 2010; Metzger et al., 2017). Moreover, increased activity of the LHb is seen in response to chronic stress (Hikosaka, 2010;

Nuno-Perez et al., 2018). In humans, positron emission tomography has been used to demonstrate that LHb activity is associated with depressed mood (Morris et al., 1999). In rodents, inhibition of the LHb has been shown to reverse social withdrawal and despair seen in animals subjected to chronic stress (Winter et al., 2011; Sachs et al., 2015; Tchenio et al., 2017). Finally, modulation of the LHb with DBS has been demonstrated to be an effective therapy in a patient with treatment resistant depression (TRD) (Sartorius et al., 2010). For these reasons, the LHb may be an important therapeutic target for depression.

To employ neuromodulation of the LHb for therapeutic purposes, its anatomy in humans must be characterized and targeted. The LHb receives input from a number of brain regions *via* the stria medullaris (SM). Predominant inputs include the ventral pallidum and the globus pallidus internus (GPi) which is homologous to the rodent entopeduncular nucleus (Knowland et al., 2017; Hu et al., 2020; Liu et al., 2020). Prior studies in the social defeat mouse model of depression have also demonstrated that these inputs mediate depression-like behavior (Knowland et al., 2017; Liu et al., 2020). Furthermore, the LHb serves as a regulator of the dopaminergic system *via* the fasciculus retroflexus (FR) which connects the LHb to the ventral tegmental area (VTA) (Wise, 2004; Hikosaka et al., 2008). To characterize these fiber tracts in human subjects, we utilized diffusion magnetic resonance imaging (dMRI). Prior studies have reconstructed the SM with dMRI using the LHb as a seed region for probabilistic tractography (Strotmann et al., 2014; Kochanski et al., 2016, 2018; Grodd et al., 2020). While effective, this strategy does not allow for selection of specific input and output tracts that may be associated with depressive symptomatology. Additionally, this strategy requires manual selection of the LHb which can be difficult due to its small size. Here, we selected the pallidum as the seed region and the VTA as the target region to reconstruct the SM and FR. This strategy allowed us to reconstruct these tracts without manual selection of the LHb and enabled characterization of the specific fiber tracts implicated in depression.

MATERIALS AND METHODS

Datasets

Multi-shell 3T dMRI (1.25 mm isotropic resolution, b = 1000, 2000, and 3000 s/mm^2, 90 directions each) and structural MRI (3T T1/T2, 0.7 mm isotropic resolution) data was obtained from the WU-Minn HCP 1200 Subjects Data Release (Van Essen et al., 2012; Glasser et al., 2013). 5 right-handed individuals of each sex (Edinburgh inventory [EI] (Oldfield, 1971) score of 100) and 5 left-handed individuals of each sex (EI score < -80) that contained a complete set of structural and diffusion data were selected. Other than the handedness and data completeness criteria, subject selection was random. To assess the feasibility of our tractography strategy on "clinical grade" data, we selected 10 healthy control individuals (6 males, 4 females) scanned at our institution. This dataset contained 3T T1 structural MRI data (1 mm isotropic resolution) and 3T multi-shell dMRI data (2 mm isotropic resolution, b = 300 [15 directions], b = 800 [30 directions], and b = 2000 [64 directions] s/mm^2). The number of subjects was selected based on our prior experience with diffusion tractography of small white matter tracts (Yang et al., 2022).

Probabilistic Tractography

All dMRI data was pre-processed with the "eddy" tool in the FMRIB Software Library (FSL) to correct for eddy current distortions and subject motion and the "topup" tool to correct for EPI distortion (Jenkinson et al., 2012; Andersson and Sotiropoulos, 2016). This data was then further processed using FSL's bedpostx_gpu followed by probtrackx_gpu for probabilistic tractography (Jenkinson et al., 2012; Hernández et al., 2013; Hernandez-Fernandez et al., 2019). Pre-processed bedpostx_gpu data was available for the HCP dataset. This processing was done with the default settings other than the following parameters: burnin = 3000, zeppelins deconvolution model (Sotiropoulos et al., 2016), gradient non-linearity correction, and Rician noise assumption (Andersson, 2008). For the clinical grade data, the default settings were used for bedpostx_gpu processing except Rician noise was selected (Andersson, 2008; Jbabdi et al., 2012). probtrackx_gpu was used for probabilistic tractography with the ipsilateral pallidum set as the seed region (**Supplementary Figure 1**). This region of interest (ROI) was generated using FreeSurfer's subcortical segmentation feature (Fischl, 2012). The VTA was used as the termination mask (**Supplementary Figure 2**). The VTA ROI was manually drawn as described by Coenen et al. (2012) using T2 structural images (HCP data) or mean b0 images (clinical grade data).

To ensure selection of LHb afferents and efferents, a waypoint mask that contains the LHb was also included. The rostral half of a 6 mm radius sphere centered at the posterior commissure was selected as the waypoint ROI (**Supplementary Figure 3**). The posterior commissure was chosen as a reference point due to its anatomical proximity to the LHb and ease of identification. To investigate the feasibility of this tractography strategy on single-shell dMRI data, the b = 800 data was extracted from the multi-shell clinical grade dataset and processed with bedpostx_gpu and probtrackx_gpu as described above. The b = 800 shell was chosen since it was closest to the b = 1000 shell used in most clinical studies. For streamline visualization of both the multi-shell and single-shell tractography, the fdt_paths output files from probtrackx_gpu were loaded into FSLeyes, pseudocolored, and overlayed on the structural T1 images. The lower threshold of the fdt_paths display/clipping range was set as 5% of the total number of streamlines generated. To investigate hemispheric differences, the total number of streamlines generated for each hemisphere was compared to the contralateral hemisphere within each subject in the HCP dataset. For sex difference comparisons, the total number of streamlines generated for each hemisphere was summed for each individual in the HCP dataset. The number of generated streamlines was obtained from the waytotal output file.

Statistical Analysis

Statistical analysis was performed using the GraphPad Prism software. Averages are presented as the mean ± standard deviation (SD) for demographic data and mean ± standard error

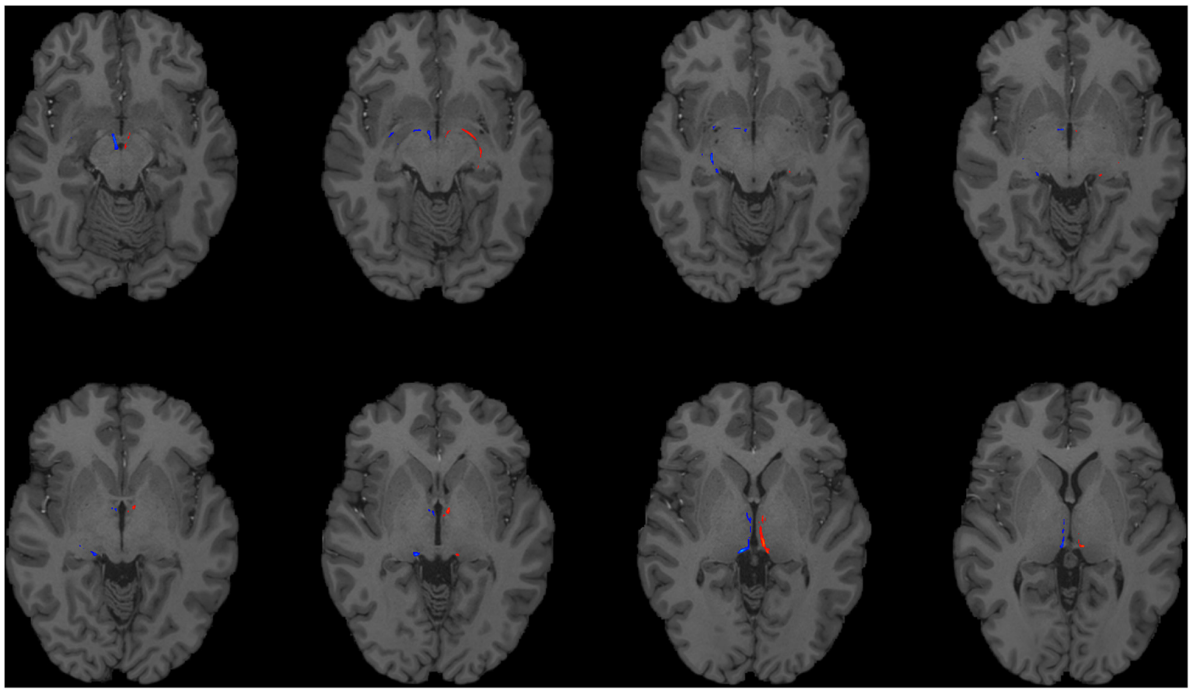

FIGURE 1 | Using HCP dMRI data to reconstruct the afferent and efferent tracts of the LHb. Axial T1 MR images with superimposed streamline density maps of LHb fiber tracts are shown for a representative HCP subject. Left hemisphere streamlines are colored in red and right hemisphere streamlines are colored in blue.

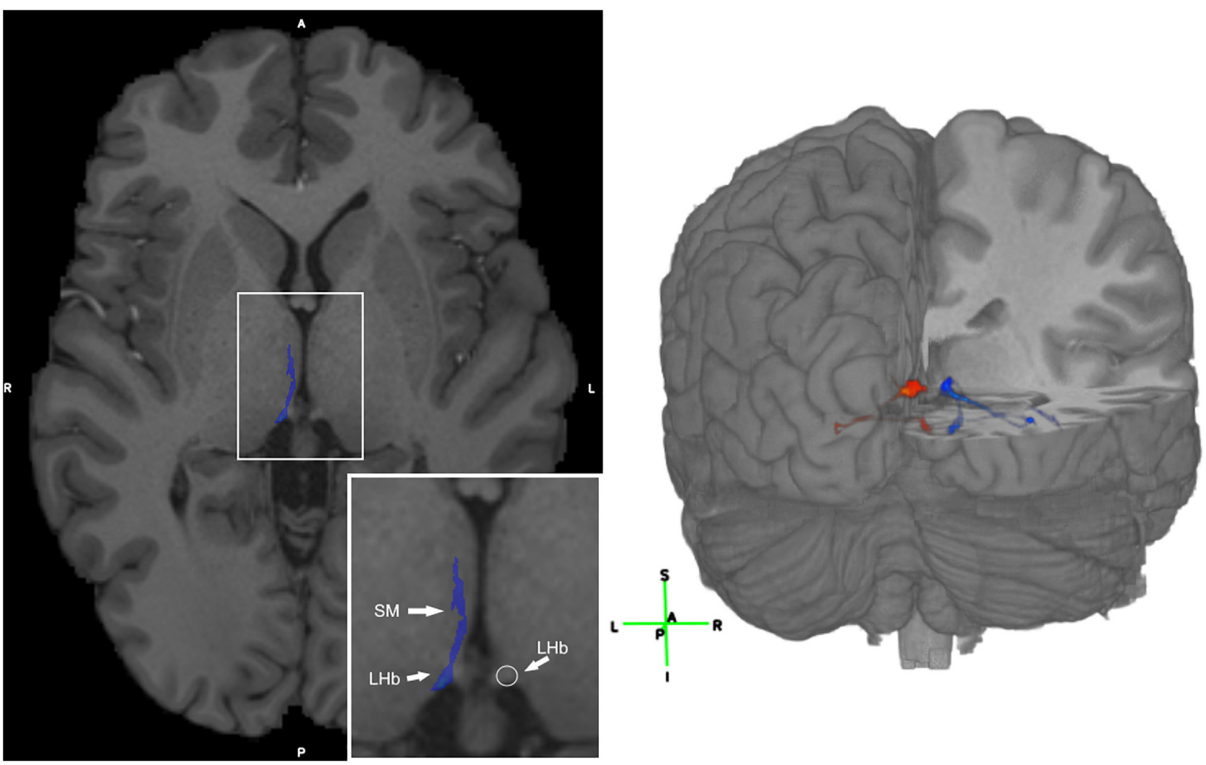

FIGURE 2 | Visualization of the LHb and 3D visualization of the SM and FR streamlines. **(Left)** Axial T1 image with the SM labeled in blue in a representative subject. The LHb is depicted on the image as the area of highest streamline density. **(Right)** 3D visualization of the SM and FR streamlines in a representative HCP subject. Legend: anterior (A), posterior (P), right (R), left (L), superior (S), inferior (I).

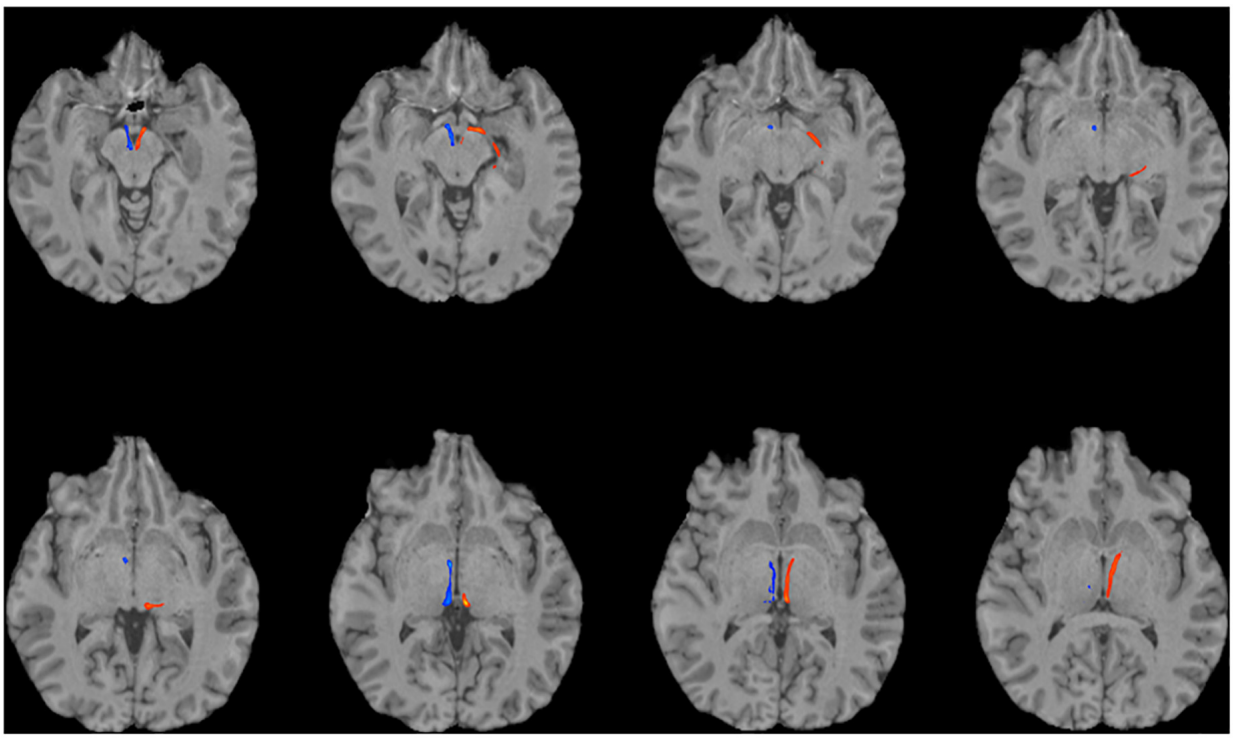

FIGURE 3 | Using multi-shell "clinical grade" dMRI data to reconstruct the afferent and efferent tracts of the LHb. Axial T1 MR images with superimposed streamline density maps of LHb fiber tracts are shown for a representative subject. Left hemisphere streamlines are colored in red and right hemisphere streamlines are colored in blue.

of the mean (SEM) otherwise. Ratio paired, two-tailed *t*-tests were used to test the significance of hemispheric differences in streamline number. An unpaired, two-tailed *t*-test was used to test for sex differences. Statical significance was defined as $p < 0.05$.

RESULTS

Subject Demographics

For the HCP dataset, 10 individuals of each sex, with a full set of dMRI and structural MRI data, were selected. The mean age was 28.7 ± 3.3 years old (range 22–34). Half of the individuals were right-handed (EI score of 100), and half were left-handed (average EI score of −94 ± 6.6, range −100 to −85). The 10 subjects (6 male, 4 female) in our "clinical grade" dataset had an average age of 39.5 ± 8.2 years old (range 26–56).

Probabilistic Tractography of the Stria Medullaris and Fasciculus Retroflexus

To reconstruct the SM and FR, we employed probabilistic tractography using FSL's bedpostx and probtrackx programs. We used the pallidum as the seed region (**Supplementary Figure 1**), because the GPi and ventral pallidum project to the LHb *via* the SM. The VTA, a major target of the LHb, was selected as a termination mask to reconstruct the FR (**Supplementary Figure 2**). A waypoint mask that contained the LHb (but did not require manual outlining of the LHb, see the section "Materials and Methods") was included to ensure specificity of the tractography (**Supplementary Figure 3**). Given the relatively small caliber of these tracts, we first investigated the feasibility of this strategy on the high quality dMRI data obtained as part of the HCP. We were able to successfully reconstruct the intended tracts in all HCP subjects (n = 20, **Figures 1**, **2**). To explore the generalizability of this strategy and its potential application for clinical purposes, we performed probabilistic tractography on lower resolution "clinical grade" multi-shell dMRI data obtained at our institution. We successfully reconstructed the SM and FR tracts on this data as well in all subjects (n = 10, **Figure 3**). To determine if multi-shell and/or high *b*-value dMRI data is required for the reconstruction of these tracts, we extracted one shell from our multi-shell dataset and employed the tractography strategy detailed above on the single-shell dMRI data. This dMRI data was intended to simulate dMRI data obtained during routine clinical studies. While a number of streamlines were generated, the SM and FR tracts were not reconstructed as robustly using this single-shell and lower *b*-value data (**Figure 4**).

Hemispheric Asymmetry of Lateral Habenula Afferents/Efferents

To study possible hemispheric differences in LHb connectivity, we compared the total number of streamlines generated per

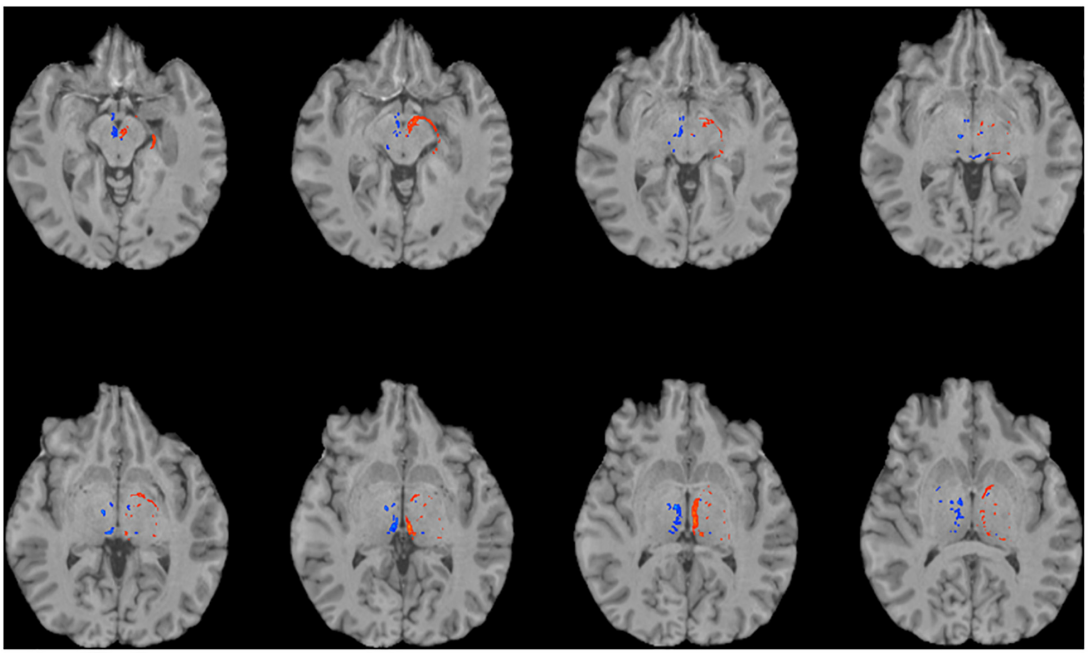

FIGURE 4 | Using single-shell "clinical grade" dMRI data to reconstruct the afferent and efferent tracts of the LHb. Axial T1 MR images with superimposed streamline density maps of LHb fiber tracts are shown for a representative subject. Single-shell/lower *b*-value dMRI does not reconstruct the streamlines as faithfully as the multi-shell/higher *b*-value data. Left hemisphere streamlines are colored in red and right hemisphere streamlines are colored in blue.

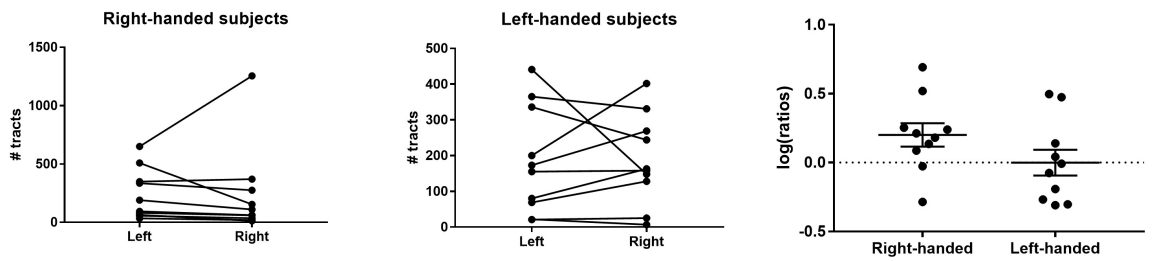

FIGURE 5 | Hemispheric asymmetry of LHb afferents/efferents. **(Left)** The majority (80%) of right-handed individuals had a greater number of streamlines in the left hemisphere. **(Middle)** Left-handed individuals did not demonstrate a consistent hemispheric asymmetry in streamline count. **(Right)** The log of the left:right streamline ratio for each individual is shown along with the group geometric mean. The geometric mean was significantly greater than 0 for right-handed individuals but not for left-handed subjects.

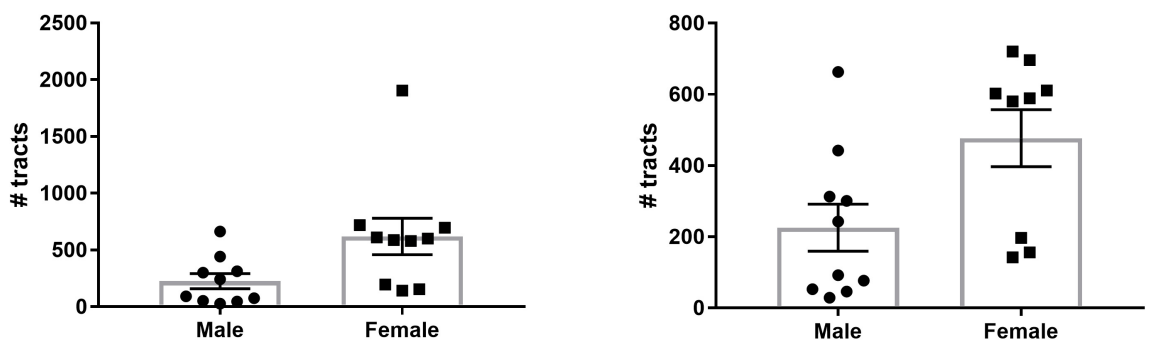

FIGURE 6 | Sex differences in LHb afferent/efferent streamline count. **(Left)** The number of streamlines for each subject as well as the group means are shown. There are a significantly greater number of LHb streamlines in female brains compared to male brains. **(Right)** Even with the outlier removed, the mean number of streamlines in females remains significantly greater than in males.

hemisphere within each subject. We found that 80% of right-handed individuals had a greater number of streamlines in the left hemisphere (**Figure 5**). In these subjects, there was a significant difference in the mean number of streamlines between hemispheres (geometric mean ratio 1.59 ± 0.09, $p = 0.04$, **Figure 5**). Conversely, there was no statistically significant hemispheric asymmetry on average in left-handed subjects (geometric mean ratio 1.00 ± 0.09, $p = 1.0$, **Figure 5**).

Lateral Habenula Afferent/Efferent Sex Differences

To investigate potential sex differences of SM/FR streamline count, we summed the total number of streamlines for the two hemispheres of each individual and calculated the group mean. On average, the total number of streamlines was significantly greater in females than in males (619.9 ± 159.7 vs. 225.9 ± 66.03, $p = 0.04$, $n = 10$ for each group, **Figure 6**). One of the female subjects was an outlier (>2 SD from mean) and the variances of the groups were significantly different ($F = 5.85$, $p = 0.02$). After removal of this subject, the variances of the groups were not significantly different and the means remained significantly different (477 ± 79.71 vs. 225.9 ± 66.03, $p = 0.03$, **Figure 6**).

DISCUSSION

In this study, we describe a novel method for reconstruction of the human afferent (SM) and efferent (FR) tracts of the LHb using dMRI data. Prior studies used the LHb itself as a seed region to generate the putative afferent and efferent tracts of this epithalamic nucleus (Strotmann et al., 2014; Kochanski et al., 2016, 2018; Grodd et al., 2020). The LHb is a very small brain region; therefore, manual selection is difficult and may lead to operator dependent variability and inconsistencies in tractography results (Schilling et al., 2021). Our technique employs a seed region automatically generated by FreeSurfer (Fischl, 2012) segmentation, thereby making this method more reliable and operator independent. While the strategy employed here does require manual outlining of the VTA, this region is larger than the LHb and multiple anatomic landmarks exist to identify this region in a consistent manner (Coenen et al., 2012).

Given the LHb's relevance in affective dysfunction (Hu et al., 2020), targeting this nucleus and/or the SM/FR may be important for therapeutic purposes. The method employed here allows for identification of these tracts for surgical targeting. One limitation of this technique is that the streamlines include both the afferents and efferents, so they are not easily separable. Notably, other previously published techniques have this limitation as well. Furthermore, the LHb itself may be identified as the brain region adjacent to the third ventricle with the highest streamline density (**Figure 2**). We first used the high quality HCP dMRI data to develop and validate our tractography method and then demonstrated that this method is generalizable to dMRI data that may be acquired in a clinical setting. Hence, this tractography strategy may potentially be used for treatment purposes in the future.

After developing a strategy to generate the SM/FR tracts, we then proceeded to further characterize these tracts. We found hemispheric asymmetry in the number of streamlines generated in a majority of individuals, and this asymmetry was statistically significant in right-handed subjects. The LHb is a well-conserved epithalamic nucleus found in all vertebrates (Bianco and Wilson, 2009). Structural studies in multiple species, including humans, have demonstrated that there are hemispheric differences in the volume of the lateral habenular nucleus (Bianco and Wilson, 2009; Ahumada-Galleguillos et al., 2017). Interestingly in many species of fish, the right LHb is much larger than the left; however, in mammals the hemispheric difference is less pronounced and the left LHb is often larger than the right (Bianco and Wilson, 2009; Ahumada-Galleguillos et al., 2017). To our knowledge, our study is the first to demonstrate in living human subjects that the input and output streamlines of the LHb exhibit hemispheric asymmetry.

In addition to structural asymmetry, several groups have reported differences in LHb function between the two hemispheres (Lawson et al., 2014; Hennigan et al., 2015; Amiri et al., 2021). One group used resting state functional MRI (fMRI) to show that patients with TRD had increased functional connectivity of the left LHb compared to controls (Amiri et al., 2021), while another group demonstrated decreased node degree of the right LHb in individuals with subclinical depression relative to controls (Zhu et al., 2019). Other groups have explored the role of the LHb using fMRI in healthy subjects and have demonstrated that LHb activity is associated with an aversive stimulus (shock) (Lawson et al., 2014; Hennigan et al., 2015). While both studies demonstrated asymmetric LHb activation, Hennigan et al. (2015) reported increased activity of the left LHb compared to the right, but Lawson et al. (2014) reported increased activity of the right LHb, not the left. Lawson and colleagues suggested that they observed right LHb activation because the shock was delivered to the subjects' left hand (Lawson et al., 2014). In contrast, the Hennigan et al. study reported left LHb activation with shocks delivered to the subjects' left foot (Hennigan et al., 2015). These authors did not speculate regarding the cause of asymmetric LHb activation, but their results do not support the hypothesis that the location of the noxious stimulus dictates which LHb nucleus is activated. Considered together, the structural and functional data suggest that the left LHb is dominant in most individuals. Neither of the fMRI studies reported the handedness of their subjects. Our structural data suggest that handedness may potentially explain the divergent findings of these studies. Although the streamline count was greater on the left in 80% of right-handed subjects, there were some subjects with a greater streamline count on the right. Asymmetric LHb volume or afferent/efferent streamline number may correlate with functional LHb asymmetry, and future studies could explore the correlation between LHb structure and function within individuals.

Psychological studies have demonstrated that individuals associate positive valence to objects/individuals in the space in which their dominant hand acts more easily (i.e., right-handed individuals associate positive valence to objects in rightward

space) (Casasanto, 2009). It is intriguing to speculate that LHb functional/structural asymmetry may contribute to this behavior. While a recent meta-analysis did not find handedness to be a risk factor for depression (Packheiser et al., 2021), hemispheric differences in the treatment of depression using transcranial magnetic stimulation (TMS) have been observed (Chung et al., 2015) suggesting that LHb streamline asymmetry may be of therapeutic importance as well.

After exploring hemispheric asymmetry, we next investigated sex differences in LHb streamline number. We found that women have a greater number of SM/FR streamlines on average compared to men. Our group has previously demonstrated that significant structural and functional differences exist between the male and female human brain (Ingalhalikar et al., 2014; Tunç et al., 2016). The current study supports and extends these findings by revealing increased LHb afferent/efferent streamline count in females compared to males. Female sex is a well-known risk factor for depression and TRD (Taipale et al., 2020). Given the LHb's role in processing stimuli of negative valence, it is intriguing to speculate that increased LHb streamline number may contribute to susceptibility to depression. One limitation of this study is that the streamlines were not reconstructed in individuals with a diagnosis of major depressive disorder. Future studies could more thoroughly explore the relationship between sex, LHb streamline count, and depression.

CONCLUSION

Using the input and output brain regions of the LHb, we have developed a method to reconstruct the afferent and efferent tracts of this epithalamic nucleus without having to identify it manually, which is challenging and error prone due to its small size. This technique enables surgical targeting of the SM and FR tracts as well as indirect LHb targeting. Furthermore, we have demonstrated that these streamlines are more prominent in the female human brain and that most right-handed individuals have a greater number of streamlines in the left hemisphere. These findings may have therapeutic implications for treating affective disorders such as TRD and warrant further investigation in larger studies that have clinical measures for correlation.

DATA AVAILABILITY STATEMENT

The raw data supporting the conclusions of this article will be made available by the authors, without undue reservation.

ETHICS STATEMENT

Ethical review and approval was not required for the study on human participants in accordance with the local legislation and institutional requirements. Written informed consent for participation was not required for this study in accordance with the national legislation and the institutional requirements.

AUTHOR CONTRIBUTIONS

FH: conceptualization, methodology, formal analysis, writing – original draft, and visualization. DP: resources and data curation. AY: writing – review and editing and conceptualization. SB: writing – review and editing, supervision, and funding acquisition. RV: conceptualization, writing – review and editing, supervision, and funding acquisition. All authors contributed to the article and approved the submitted version.

FUNDING

Data were provided in part by the Human Connectome Project, WU-Minn Consortium (Principal Investigators: David Van Essen and Kamil Ugurbil; 1U54MH091657) funded by the 16 NIH Institutes and Centers that support the NIH Blueprint for Neuroscience Research; and by the McDonnell Center for Systems Neuroscience at Washington University. The healthy control data was collected at UPenn and supported by the NIH grant #R01 NS096606 (PI: Verma and Brem).

SUPPLEMENTARY MATERIAL

The Supplementary Material for this article can be found online at: https://www.frontiersin.org/articles/10.3389/fnins.2022.837624/full#supplementary-material

REFERENCES

Ahumada-Galleguillos, P., Lemus, C. G., Díaz, E., Osorio-Reich, M., Härtel, S., and Concha, M. L. (2017). Directional asymmetry in the volume of the human habenula. *Brain Struct. Funct.* 222, 1087–1092. doi: 10.1007/s00429-016-1231-z

Amiri, S., Arbabi, M., Kazemi, K., Parvaresh-Rizi, M., and Mirbagheri, M. M. (2021). Characterization of brain functional connectivity in treatment-resistant depression. *Prog. Neuropsychopharmacol. Biol. Psychiatry* 111:110346. doi: 10.1016/j.pnpbp.2021.110346

Andersson, J. L. R. (2008). Maximum a posteriori estimation of diffusion tensor parameters using a Rician noise model: why, how and but. *NeuroImage* 42, 1340–1356. doi: 10.1016/j.neuroimage.2008.05.053

Andersson, J. L. R., and Sotiropoulos, S. N. (2016). An integrated approach to correction for off-resonance effects and subject movement in diffusion MR imaging. *NeuroImage* 125, 1063–1078. doi: 10.1016/j.neuroimage.2015.10.019

Bianco, I. H., and Wilson, S. W. (2009). The habenular nuclei: a conserved asymmetric relay station in the vertebrate brain. *Philos. Trans. R. Soc. B Biol. Sci.* 364, 1005–1020. doi: 10.1098/rstb.2008.0213

Casasanto, D. (2009). Embodiment of abstract concepts: good and bad in right- and left-handers. *J. Exp. Psychol. Gen.* 138, 351–367. doi: 10.1037/a0015854

Chung, S. W., Hoy, K. E., and Fitzgerald, P. B. (2015). Theta-Burst Stimulation: a New Form of TMS Treatment for Depression? *Depress. Anxiety* 32, 182–192. doi: 10.1002/da.22335

Coenen, V. A., Panksepp, J., Hurwitz, T. A., Urbach, H., and Mädler, B. (2012). Human Medial Forebrain Bundle (MFB) and Anterior Thalamic Radiation (ATR): imaging of Two Major Subcortical Pathways and the Dynamic Balance of Opposite Affects in Understanding Depression. *J. Neuropsychiatry Clin. Neurosci.* 24, 223–236. doi: 10.1176/appi.neuropsych.11080180

Fischl, B. (2012). FreeSurfer. *NeuroImage* 62, 774–781. doi: 10.1016/j.neuroimage.2012.01.021

Glasser, M. F., Sotiropoulos, S. N., Wilson, J. A., Coalson, T. S., Fischl, B., Andersson, J. L., et al. (2013). The minimal preprocessing pipelines for the Human Connectome Project. *NeuroImage* 80, 105–124. doi: 10.1016/j.neuroimage.2013.04.127

Grodd, W., Kumar, V. J., Schüz, A., Lindig, T., and Scheffler, K. (2020). The anterior and medial thalamic nuclei and the human limbic system: tracing the structural connectivity using diffusion-weighted imaging. *Sci. Rep.* 10:10957. doi: 10.1038/s41598-020-67770-4

Hennigan, K., D'Ardenne, K., and McClure, S. M. (2015). Distinct Midbrain and Habenula Pathways Are Involved in Processing Aversive Events in Humans. *J. Neurosci.* 35, 198–208. doi: 10.1523/JNEUROSCI.0927-14.2015

Hernández, M., Guerrero, G. D., Cecilia, J. M., García, J. M., Inuggi, A., Jbabdi, S., et al. (2013). Accelerating Fibre Orientation Estimation from Diffusion Weighted Magnetic Resonance Imaging Using GPUs. *PLoS One* 8:e61892. doi: 10.1371/journal.pone.0061892

Hernandez-Fernandez, M., Reguly, I., Jbabdi, S., Giles, M., Smith, S., and Sotiropoulos, S. N. (2019). Using GPUs to accelerate computational diffusion MRI: from microstructure estimation to tractography and connectomes. *NeuroImage* 188, 598–615. doi: 10.1016/j.neuroimage.2018.12.015

Hikosaka, O. (2010). The habenula: from stress evasion to value-based decision-making. *Nat. Rev. Neurosci.* 11, 503–513. doi: 10.1038/nrn2866

Hikosaka, O., Sesack, S. R., Lecourtier, L., and Shepard, P. D. (2008). Habenula: crossroad between the Basal Ganglia and the Limbic System. *J. Neurosci.* 28, 11825–11829. doi: 10.1523/JNEUROSCI.3463-08.2008

Hu, H., Cui, Y., and Yang, Y. (2020). Circuits and functions of the lateral habenula in health and in disease. *Nat. Rev. Neurosci.* 21, 277–295. doi: 10.1038/s41583-020-0292-4

Ingalhalikar, M., Smith, A., Parker, D., Satterthwaite, T. D., Elliott, M. A., Ruparel, K., et al. (2014). Sex differences in the structural connectome of the human brain. *Proc. Natl. Acad. Sci.U. S. A.* 111, 823–828. doi: 10.1073/pnas.1316909110

Jbabdi, S., Sotiropoulos, S. N., Savio, A. M., Graña, M., and Behrens, T. E. J. (2012). Model-based analysis of multishell diffusion MR data for tractography: how to get over fitting problems. *Magn. Reson. Med.* 68, 1846–1855. doi: 10.1002/mrm.24204

Jenkinson, M., Beckmann, C. F., Behrens, T. E. J., Woolrich, M. W., and Smith, S. M. (2012). FSL. *NeuroImage* 62, 782–790. doi: 10.1016/j.neuroimage.2011.09.015

Knowland, D., Lilascharoen, V., Pacia, C. P., Shin, S., Wang, E. H.-J., and Lim, B. K. (2017). Distinct Ventral Pallidal Neural Populations Mediate Separate Symptoms of Depression. *Cell* 170, 284.e–297.e18. doi: 10.1016/j.cell.2017.06.015

Kochanski, R. B., Dawe, R., Eddelman, D. B., Kocak, M., and Sani, S. (2016). Identification of the stria medullaris thalami using diffusion tensor imaging. *NeuroImage Clin.* 12, 852–857. doi: 10.1016/j.nicl.2016.10.018

Kochanski, R. B., Dawe, R., Kocak, M., and Sani, S. (2018). Identification of Stria Medullaris Fibers in the Massa Intermedia Using Diffusion Tensor Imaging. *World Neurosurg.* 112, e497–e504. doi: 10.1016/j.wneu.2018.01.066

Lawson, R. P., Seymour, B., Loh, E., Lutti, A., Dolan, R. J., Dayan, P., et al. (2014). The habenula encodes negative motivational value associated with primary punishment in humans. *Proc. Natl. Acad. Sci.U. S. A.* 111, 11858–11863. doi: 10.1073/pnas.1323586111

Liu, B., Cao, Y., Wang, J., and Dong, J. (2020). Excitatory transmission from ventral pallidum to lateral habenula mediates depression. *J. World Fed. Soc. Biol. Psychiatry* 21, 627–633. doi: 10.1080/15622975.2020.1725117

Metzger, M., Bueno, D., and Lima, L. B. (2017). The lateral habenula and the serotonergic system. *Pharmacol. Biochem. Behav.* 162, 22–28. doi: 10.1016/j.pbb.2017.05.007

Morris, J. S., Smith, K. A., Cowen, P. J., Friston, K. J., and Dolan, R. J. (1999). Covariation of Activity in Habenula and Dorsal Raphé Nuclei Following Tryptophan Depletion. *NeuroImage* 10, 163–172. doi: 10.1006/nimg.1999.0455

Nuno-Perez, A., Tchenio, A., Mameli, M., and Lecca, S. (2018). Lateral Habenula Gone Awry in Depression: bridging Cellular Adaptations With Therapeutics. *Front. Neurosci* 12:485. doi: 10.3389/fnins.2018.00485

Oldfield, R. (1971). The assessment and analysis of handedness: the Edinburgh inventory. *Neuropsychologia* 9, 97–113. doi: 10.1016/0028-3932(71)90067-4

Packheiser, J., Schmitz, J., Stein, C. C., Pfeifer, L. S., Berretz, G., Papadatou-Pastou, M., et al. (2021). Handedness and depression: a meta-analysis across 87 studies. *J. Affect. Disord.* 294, 200–209. doi: 10.1016/j.jad.2021.07.052

Sachs, B. D., Ni, J. R., and Caron, M. G. (2015). Brain 5-HT deficiency increases stress vulnerability and impairs antidepressant responses following psychosocial stress. *Proc. Natl. Acad. Sci.U. S. A.* 112, 2557–2562. doi: 10.1073/pnas.1416866112

Sartorius, A., Kiening, K. L., Kirsch, P., von Gall, C. C., Haberkorn, U., Unterberg, A. W., et al. (2010). Remission of Major Depression Under Deep Brain Stimulation of the Lateral Habenula in a Therapy-Refractory Patient. *Biol. Psychiatry* 67, e9–e11. doi: 10.1016/j.biopsych.2009.08.027

Schilling, K. G., Rheault, F., Petit, L., Hansen, C. B., Nath, V., Yeh, F.-C., et al. (2021). Tractography dissection variability: what happens when 42 groups dissect 14 white matter bundles on the same dataset? *NeuroImage* 243:118502. doi: 10.1016/j.neuroimage.2021.118502

Sotiropoulos, S. N., Hernández-Fernández, M., Vu, A. T., Andersson, J. L., Moeller, S., Yacoub, E., et al. (2016). Fusion in diffusion MRI for improved fibre orientation estimation: an application to the 3T and 7T data of the Human Connectome Project. *NeuroImage* 134, 396–409. doi: 10.1016/j.neuroimage.2016.04.014

Strotmann, B., Heidemann, R. M., Anwander, A., Weiss, M., Trampel, R., Villringer, A., et al. (2014). High-resolution MRI and diffusion-weighted imaging of the human habenula at 7 tesla. *J. Magn. Reson. Imaging* 39, 1018–1026. doi: 10.1002/jmri.24252

Taipale, H., Reutfors, J., Tanskanen, A., Brandt, L., Tiihonen, J., DiBernardo, A., et al. (2020). Risk and risk factors for disability pension among patients with treatment resistant depression- a matched cohort study. *BMC Psychiatry* 20:232. doi: 10.1186/s12888-020-02642-9

Tchenio, A., Lecca, S., Valentinova, K., and Mameli, M. (2017). Limiting habenular hyperactivity ameliorates maternal separation-driven depressive-like symptoms. *Nat. Commun.* 8:1135. doi: 10.1038/s41467-017-01192-1

Tunç, B., Solmaz, B., Parker, D., Satterthwaite, T. D., Elliott, M. A., Calkins, M. E., et al. (2016). Establishing a link between sex-related differences in the structural connectome and behaviour. *Philos. Trans. R. Soc. B Biol. Sci.* 371:20150111. doi: 10.1098/rstb.2015.0111

Van Essen, D. C., Ugurbil, K., Auerbach, E., Barch, D., Behrens, T. E. J., Bucholz, R., et al. (2012). The Human Connectome Project: a data acquisition perspective. *NeuroImage* 62, 2222–2231. doi: 10.1016/j.neuroimage.2012.02.018

Winter, C., Vollmayr, B., Djodari-Irani, A., Klein, J., and Sartorius, A. (2011). Pharmacological inhibition of the lateral habenula improves depressive-like behavior in an animal model of treatment resistant depression. *Behav. Brain Res.* 216, 463–465. doi: 10.1016/j.bbr.2010.07.034

Wise, R. A. (2004). Dopamine, learning and motivation. *Nat. Rev. Neurosci.* 5, 483–494. doi: 10.1038/nrn1406

Yang, A. I., Parker, D., Vijayakumari, A. A., Ramayya, A. G., Donley-Fletcher, M. P., Aunapu, D., et al. (2022). Tractography-Based Surgical Targeting for Thalamic Deep Brain Stimulation: a Comparison of Probabilistic vs Deterministic Fiber Tracking of the Dentato-Rubro-Thalamic Tract. *Neurosurgery* 90, 419–425. doi: 10.1227/NEU.0000000000001840

Zhu, Y., Qi, S., Zhang, B., He, D., Teng, Y., Hu, J., et al. (2019). Connectome-Based Biomarkers Predict Subclinical Depression and Identify Abnormal Brain Connections With the Lateral Habenula and Thalamus. *Front. Psychiatry* 10:371. doi: 10.3389/fpsyt.2019.00371

Conflict of Interest: The authors declare that the research was conducted in the absence of any commercial or financial relationships that could be construed as a potential conflict of interest.

Publisher's Note: All claims expressed in this article are solely those of the authors and do not necessarily represent those of their affiliated organizations, or those of the publisher, the editors and the reviewers. Any product that may be evaluated in this article, or claim that may be made by its manufacturer, is not guaranteed or endorsed by the publisher.

Copyright © 2022 Hitti, Parker, Yang, Brem and Verma. This is an open-access article distributed under the terms of the Creative Commons Attribution License (CC BY). The use, distribution or reproduction in other forums is permitted, provided the original author(s) and the copyright owner(s) are credited and that the original publication in this journal is cited, in accordance with accepted academic practice. No use, distribution or reproduction is permitted which does not comply with these terms.

frontiers | Frontiers in Oncology

ORIGINAL RESEARCH
published: 17 June 2022
doi: 10.3389/fonc.2022.902612

Evaluation of HIF-1α Expression in a Rat Glioma Model Using Intravoxel Incoherent Motion and R2* Mapping

Dongdong Wang[1†], Yiping Lu[1†], Xuanxuan Li[1†], Nan Mei[1], Pu-Yeh Wu[2], Daoying Geng[1], Hao Wu[3] and Bo Yin[1*]*

[1] Department of Radiology, Huashan Hospital, Fudan University, Shanghai, China, [2] Department of MR Research, GE Healthcare, Shanghai, China, [3] Department of Dermatology, Huashan Hospital, Fudan University, Shanghai, China

OPEN ACCESS

Edited by:
Sandro M. Krieg,
Technical University of Munich,
Germany

Reviewed by:
Carlos Perez-Torres,
Virginia Tech, United States
Lixiong Dai,
University of Chinese Academy of
Sciences, China

***Correspondence:**
Hao Wu
seaseewh@163.com
Bo Yin
yinbo@fudan.edu.cn

[†]These authors have contributed
equally to this work

Specialty section:
This article was submitted to
Neuro-Oncology and
Neurosurgical Oncology,
a section of the journal
Frontiers in Oncology

Received: 23 March 2022
Accepted: 16 May 2022
Published: 17 June 2022

Citation:
Wang D, Lu Y, Li X, Mei N, Wu P-Y,
Geng D, Wu H and Yin B (2022)
Evaluation of HIF-1α Expression in a
Rat Glioma Model Using Intravoxel
Incoherent Motion and R2* Mapping.
Front. Oncol. 12:902612.
doi: 10.3389/fonc.2022.902612

Accurate evaluation of HIF-1α levels can facilitate the detection of hypoxia niches in glioma and treatment decisions. To investigate the feasibility of intravoxel incoherent motion (IVIM) and R2* Mapping for detecting HIF-1α expression levels, sixteen rats with intracranial C6 gliomas were subjected to IVIM and R2* Mapping using a 7 Tesla MRI scanner. For each model, the brain tissue on the HIF-1α-stained slices was subdivided into multiple square regions of interest (ROIs) with areas of 1 mm^2, for which HIF-1α expression was assessed by HALO software to form a maps of HIF scores with a 0–300 range. The IVIM and R2* Mapping images were processed to create maps of the D, D*, f and R2* that were then paired with the corresponding HIF score maps. The average D, D*, f, perfusion (f × D*) and R2* values were calculated for the ROIs in the tumor and normal brain regions with different HIF-1α levels and used in further analysis. In this study, the average tumor size of sixteen C6 model rats was 458 ± 46.52 mm^3, and the 482 included ROIs consisted of 280 tumoral and 202 normal ROIs. The average HIF score for the tumor regions was significantly higher than normal brain tissue ($p < 0.001$), and higher HIF scores were obtained for the central part of tumors than peripheral parts ($p=0.03$). Compared with normal brain tissues, elevated perfusion and f values were observed in tumor regions ($p = 0.021$, 0.004). In tumoral ROIs, the R2* values were higher in the group with high HIF-1α expression than in the group with low HIF-1α expression ($p = 0.003$). A correlation analysis revealed a positive correlation between the R2* value and HIF scores ($r = 0.43$, $p < 0.001$) and a negative correlation between D* and the HIF scores ($r = -0.30$, $p = 0.001$). Discrepancies in HIF-1α expression were found among different intratumoral areas, and IVIM and R2* Mapping were found to be promising means of noninvasive detection of the distribution and expression level of HIF-1α.

Keywords: glioma, IVIM, hypoxia, HIF - 1α, R2* mapping

INTRODUCTION

Glioma is the most common and malignant primary brain tumor in humans and has a specific histological hallmark of microvascular proliferation (1). Dysfunctional neoangiogenesis is believed to contribute to a hypoxic microenvironment in glioma and resistance to chemoradiotherapy (2–5). Molecular responses to hypoxia are predominantly mediated by increased activity of hypoxia-inducible factors (HIFs), predominantly HIF-1α (5). Accurate evaluation of HIF-1α levels can facilitate the detection of hypoxia niches in glioma and treatment decisions. Traditionally, invasive methods, including oxygen electrodes and biopsy-derived techniques, have been used to assess HIF-1α expression in glioma, but have accuracies that largely depend on tissue sampling and cannot reflect the oxygenation status of the whole tumor due to the heterogeneous distribution of tumor hypoxia (6, 7). Noninvasive and convenient methods for assessing HIF-1α expression and accurate assessment of whole-tumor hypoxia would be extremely useful.

Two noninvasive and contrast-free functional MRI techniques, named intravoxel incoherent motion (IVIM) and R2* Mapping, have made it possible to visualize hypoxic regions. IVIM was first introduced by Le Bihan et al. (8) and can be used to distinguish the incoherent motion of water molecules within capillaries from extravascular molecular diffusion. The true diffusion coefficient (D), pseudodiffusion coefficient (D*), and perfusion fraction (f) were calculated by applying a biexponential model to multiple b-value diffusion images. Previous reports have demonstrated that IVIM could serve as an important guide for the quantitative assessment of HIF-1α expression in solid prostate cancer (9). The other technique, R2* Mapping, has been used to determine tissue oxygen bioavailability by measuring alterations in deoxyhemoglobin, an endogenous MR imaging marker with the property of paramagnetism (10). It was proven that R2* Mapping can detect alterations in oxygenation status, and a significant correlation between R2* and HIF-1α expression in the kidney was also reported (11). To date, no research has been performed on evaluating the usage of IVIM and R2* Mapping to visualize HIF-1α expression in glioma.

Therefore, the aim of this study was to use IVIM and R2* Mapping parameters (D, D*, f, perfusion and R2*) to determine HIF-1α expression levels in rat glioma models, investigate the feasibility of these two potential hypoxia imaging methods, and evaluate the corresponding application potential for further clinical practice.

MATERIALS AND METHODS

All studies were approved by the Institutional Animal Care and Use Committee of the Medical School of Fudan University.

Rat Model

Male Wistar rats (age 6–10 weeks, n = 16) were anesthetized by intraperitoneal injection of medetomidine (0.4 mg/kg) and ketamine (70 mg/kg). Approximately 1×10^6 cells in 5 μl were stereotactically injected into the basal ganglia (3 mm left of the bregma at a 4.5-mm depth in the brain). Metamizol (50 mg/kg) was injected subcutaneously to prevent postoperative pain. The rats were monitored for mood behavior and activity levels throughout the entire experiment using the volume of droppings as a surrogate measurement.

MRI Examination

Seven days after the rats were injected with tumor cells, T2WI MRI scanning was performed to evaluate the volume of each tumor every two days. On the 14th day after being injected with tumor cells, the rats were anaesthetized by intraperitoneal injection of medetomidine and ketamine, and subsequently intubated and maintained under anesthesia with isoflurane using active ventilation. To improve the stability and repeatability of image acquisition, the rat body temperature was maintained at 37.0°C using a heating pad, and the respiratory rate was maintained at 50–70 breaths per minute using a mixture of air containing 1%–2% isoflurane to minimize breathing artifacts while sustaining normal oxygen delivery.

MR imaging was performed on a 7.0 T small-animal MR unit (Bruker PharmaScan, Ettlingen, Germany) equipped with a transmit-receive quadrature volume coil with an inner diameter of 3.8 cm. Anatomical T2-weighted images were obtained using a 2D fast spin echo sequence (three orthogonal directions; TR = 3000; TE = 33 ms; 7 echoes; field of view (FOV) = 25.6×25.6mm^2; matrix size = 96×96; slice thickness = 0.5 mm; 20 slices). IVIM images were acquired using a free-breathing single-shot echo-planar imaging pulse sequence with 10 b values (TR = 2000 ms; TE = 23 ms; FOV = 25.6×25.6 mm^2; matrix size = 96×96; slice thickness = 1 mm; 10 slices; b = 0, 25, 50, 75, 100, 150, 200, 300, 1000, 1500, 2000 mm^2/s; scan time = 3 min 20 seconds). R2* Mapping was performed with a 3D spoiled gradient-echo sequence (TR = 160 ms; TE = 3.4, 9.3, 15.2, 21.2, 27.1, 33, 38.9, 44.8, 50.7, 56.6, 62.5, 68.5, 74.4, 80.3, 86.2, 92.1 ms; FOV =25.6×25.6 mm^2; matrix size=96×96; slice thickness = 1 mm; 10 slices; NEX = 2; scan time = 6 min 20 seconds). The IVIM and R2* Mapping sequences were registered with the T2WI images.

Postprocessing

The IVIM-DWI data was postprocessed using Functool-MADC software on an Advantage Workstation (Version 4.6; GE Health care, Milwaukee, WI, USA). An IVIM-DWI biexponential model was defined as $SI/SI_0 = (1–f) \times \exp(–bD) + f \times \exp(–bD^*)$, where SI_0 is the mean signal intensity of the ROI under consideration at b = 0 mm^2/s, and SI is the signal intensity at higher b values. D denotes the diffusion coefficient of water molecules (the true diffusion coefficient), D* represents the microcirculation perfusion (pseudodiffusion) coefficient, f is the perfusion fraction, and f multiplied by D* represents the perfusion (12). We also obtained R2* values from the R2* Mapping images using the Functool-R2* mapping software on the Advantage Workstation(Version 4.6; GE Health care, Milwaukee, WI, USA) as well. The R2* maps for each tumor were calculated and R2* values were calculated as the reciprocal of the T2* values.

Immunohistochemistry

The rats were sacrificed after the MRI scans were taken. The rats were overdosed with ketamine and medetomidine and then transcardially perfused with 4% paraformaldehyde in PBS. The rat brains were removed, postfixed in 4% paraformaldehyde in PBS overnight, dissected and embedded in paraffin. Five-micrometer brain sections were cut using a sliding microtome and processed.

The sections were stained with hematoxylin and eosin as per standard protocol. The stained slides were deparaffined in xylene, dehydrated through graded alcohol concentrations, and washed in Tris buffer (pH = 7.0). Antigen retrieval was performed by heat mediation in citrate buffer (pH = 6.2) for 1 hour at 90°C and then blocked using 5% skim milk. The sections were incubated with a rabbit monoclonal anti-human HIF-1α antibody (1/50, ab51608, Abcam, Cambridge, UK) for 16 hours at 4°C. Undiluted horseradish peroxidase-conjugated antirabbit IgG (ab150081, Abcam) was used as the secondary antibody. All specimens were investigated by HALO image analysis software.

MR and Pathological Analysis

The largest tumor section on coronal T2WI was selected, and the corresponding coronal pathological slices were measured with electronic calipers at the largest cross-sectional area of the lesion. Subsequently, the corresponding slices of the IVIM and R2* Mapping images were selected.

The HIF-1α scores, including the percent of positive HIF-1α cells and coloring strength, for all the rectangular ROIs were automatically evaluated by HALO image analysis software using the IHC v1.6 algorithm module (Indica Labs, NM) (13). All the ROIs had an area of 1 mm^2 (14). The scores for the coloring strength and percentage of positive cells were multiplied together to produce final HIF-1α scores with a 0-300 range. An intratumoral region with a score over 150 was considered a region with high HIF-1α expression, whereas a score less than 150 was considered to indicate a region with low HIF-1α expression. The inclusion criteria for ROIs was as follows: (a) the ROI contained only tumor or normal tissue and (b) the proportion of the components of vessels, necrosis or calcification was less than 25%, without air. An ROI with a center less than 1 mm from the edge of the tumor was classified as a peripheral intratumoral part and was otherwise classified as a central intratumoral part.

An in-house MATLAB (Mathworks, Natick, MA, USA) script was used to perform a quantitative analysis. The IVIM/R2* Mapping images were subdivided into multiple ROIs corresponding to the subdivision of the corresponding pathological slices. The imaging parameters of all the areas were automatically output. The imaging parameters and corresponding HIF-1α scores were recorded for statistical analyses. The basic workflow of our study is illustrated in **Figure 1**.

Statistical Analysis

Statistical analysis was performed using R software (Version 3.5.3; R Foundation for Statistical Computing, Vienna, Austria). The imaging parameters for the low- and high-expression groups were compared using the Mann–Whitney U-test. A p value less than 0.05 was considered statistically significant. The Spearman correlation coefficient was used to assess the relationships between the imaging parameters, including the D, D*, f, perfusion and R2* values and the HIF-1α scores for the tumor and normal tissue on the contralateral side. A simple linear regression analysis was performed to illustrate the relationship between imaging parameters and HIF-1α expression.

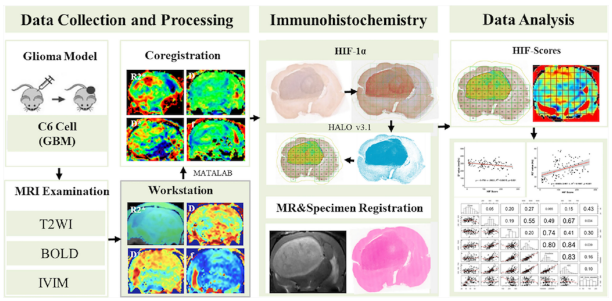

FIGURE 1 | Workflow of the study.

RESULTS

In this study, the average tumor size of sixteen rats was 458 ± 46.52 mm^3, and the 482 included ROIs consisted of 280 ROIs of tumor tissue and 202 ROIs of normal brain tissue.

1. Tumor Tissue vs. Normal Brain Tissues

The HIF-1α expression level in tumor tissue was higher than that in normal tissue (123.73 ± 70.18 vs. 21.13 ± 19.14, $p < 0.001$), and the f and perfusion values of the tumor tissue were also higher than those of normal tissue (46.29 ± 2.75 vs. 51.09 ± 8.58, $p = 0.004$; 1277.09 ± 228.64 vs. 1463.88 ± 378.67, $p = 0.021$). There was no significant difference between the R2*, D, and D* values of tumor and normal tissues (**Table 1**).

2. The Spatial Distribution of Pathological and Imaging Features

HIF-1α expression in the central intratumoral area was higher than that in the peripheral areas (137.17 ± 76.23 vs. 108.77 ± 59.98, $p = 0.03$), and the perfusion, f, and D* values in the central intratumoral area were lower than those in the peripheral areas (1385.03 ± 427.17 vs. 1551.65 ± 296.05, $p = 0.003$; 50.00 ± 9.87 vs. 52.31 ± 6.76, $p = 0.026$; 2749.23 ± 487.95 vs. 2962.53 ± 363.06, $p = 0.044$) (**Figure 2**). There was no significant difference in the spatial distributions of the R2* or D values between the tumor and normal tissue (**Table 2**).

3. The Distribution of Imaging Parameters in Groups With High and Low HIF-1α Expression

The mean R2* was higher in the group with high HIF-1α expression than in the low-expression group (40.95 ± 6.46 vs. 36.49 ± 9.62, $p = 0.003$) (**Figure 3**). There was no significant difference in the D, f, and D* values for the intratumoral areas with high- and low-expression of HIF-1α (**Table 3**).

TABLE 1 | Mean parameter values for tumor and normal brain tissues.

Imaging/Pathological Parameter	Normal Brain Area (Mean ± SD, N = 202)	Tumor Region (Mean ± SD, N = 280)	P
R2* (Hz)	36.74 ± 9.35	38.24 ± 8.76	0.502
D (×10^{-6} mm^2/s)	414.21 ± 53.38	419.50 ± 81.97	0.721
D* (×10^{-6} mm^2/s)	2755.02 ± 441.42	2850.23 ± 444.48	0.373
f (%)	46.29 ± 2.75	51.09 ± 8.58	**0.004***
Perfusion (×10^{-6} mm^2/s)	1277.09 ± 228.64	1463.88 ± 378.67	**0.021***
HIF-Score	21.13 ± 19.14	123.73 ± 70.18	**<0.001***

** and bold values means p<0.05 was considered statistically significant.*

4. Regression Analysis Between the HIF Score and Imaging Parameters

A Pearson correlation analysis revealed a negative correlation between D* and the HIF-1α expression levels (r = -0.30, p = 0.001). There was a positive correlation between the R2* value and the HIF-1α expression level (r = 0.43, p < 0.001) (**Figure 4**). There was no significant correlation between the HIF-1α expression level and the D, f and perfusion values.

DISCUSSION

Hypoxia is an important microenvironmental feature of glioma that can be categorized into chronic and acute hypoxia. Chronic or "diffusion-limited" hypoxia applies to tumor cells at a distance from blood vessels and can be detected by pimonidazole staining (15). "Acute" or "transient" hypoxia results from local fluctuations in blood perfusion and the oxygen supply and can be detected by HIF-1α staining: HIF-1α was found to be more diffusely distributed in tumors than pimonidazole. After 5 hours of hypoxia exposure, HIF-1α reaches maximal expression levels and returns to basal levels at 12 hours (16). Hypoxia is a clinical problem that contributes to therapy resistance, and acute hypoxia may be particularly dangerous because high HIF-1α expression upregulates canonical stem cell genes and facilitates plasticity toward a stem-like state. Especially in glioblastoma (GBM), the hypoxic microenvironment may enable GBM cells under certain inhibitor treatments to maintain a stem-like phenotype (17). Thus, the accurate detection of HIF-1α expression in glioma facilitates making individual treatment plans, especially regarding the usage of anti-hypoxia drugs. In this study, we found satisfactory feasibility for using the noninvasive methods of R2* Mapping and IVIM imaging to detect HIF-1α expression in glioma.

We quantitatively analyzed immunohistochemical images using HALO software to calculate a density heatmap of HIF-1α, including quantitatively determining the staining intensity and the corresponding percentage of positive cells. The automatic calculation of HIF scores prevents the introduction of bias from different pathologists calculating HIF scores. In addition, the corresponding parameter values of all the areas of the MRI images were automatically output by an in-house MATLAB script, which also circumvents the introduction of bias from manually drawing ROIs. Christen et al. (18, 19) drew an ROI around a whole tumor and compared the imaging parameters of the tumor with those of the contralateral striatum, neglecting GBM heterogeneity. In this study, we divided the tumor into multiple rectangular ROIs of equal sizes to prevent the introduction of bias from tumor heterogeneity and increase the accuracy of the results.

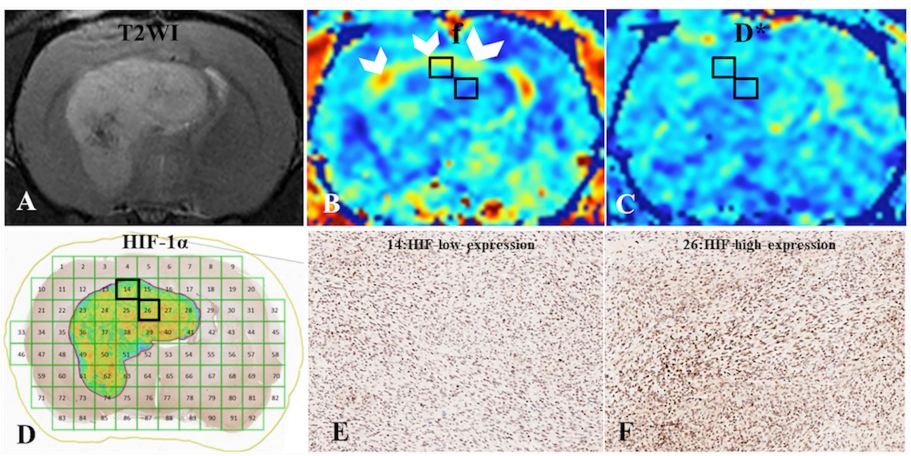

FIGURE 2 | **(A)** C6-cell glioma tissue was observed in a T2WI image. **(B, C)** f and D* maps. **(D)** ROI locations in the tumor area correspond to 14 and 26 (HIF-1α map), for which the f values were 59% and 47%, respectively; the D* values were 341.69 ×10-6 mm2/s and 281.41 ×10-6 mm2/s, respectively; and the HIF-scores were 122.89 and 174.12, respectively. A high f value was found for the peripheral intratumoral tissue (white arrow). **(E, F)** Immunohistochemical staining images (× 400) showed low and high expression of HIF-1α in the tumor for ROIs 14 and 26, respectively, on the HIF-1α map.

TABLE 2 | Mean parameter values for the spatial distribution of pathological and imaging features.

Imaging/Pathological Parameter	Central Part of Tumor (Mean ± SD, N = 171)	Peripheral Part of Tumor (Mean ± SD, N = 109)	P
R2* (Hz)	38.23 ± 8.64	38.25 ± 8.98	0.989
D ($\times 10^{-6}$ mm^2/s)	415.66 ± 78.99	423.77 ± 85.72	0.605
D* ($\times 10^{-6}$ mm^2/s)	2749.23 ± 487.95	2962.53 ± 363.06	**0.044***
f (%)	50.00 ± 9.87	52.31 ± 6.76	**0.026***
Perfusion ($\times 10^{-6}$ mm^2/s)	1385.03 ± 427.17	1551.65 ± 296.05	**0.003***
HIF-Score	137.17 ± 76.23	108.77 ± 59.98	**0.030***

** and bold values means p<0.05 was considered statistically significant.*

R2* Mapping is a noninvasive method that offers a unique advantage in being able to realize dynamic and repeated detection of altered tissue oxygenation without the use of ionizing radiation and has exhibited good reproducibility in the kidneys of rabbit models (10, 11, 20, 21). In this study, no significant difference was found between the R2* values of tumor and uninvolved contralateral brain tissue, which was consistent with the results of a previous study (18). However, as mentioned above, we compared the ROIs in intratumor tissue with high and low expression of HIF-1α and found the R2* value was useful for determining the HIF-1a distribution. This result can be explained by the dependence of R2* on the deoxyhemoglobin content, where increased paramagnetic deoxyhemoglobin generation in tumors contributed to increased R2* values. Due to tumor vasculature destruction or increased oxygen demand for tumor regeneration, the R2* values of intratumoral tissue zones with high HIF expression were higher than for those with low HIF expression. In addition, a significant positive correlation was observed between R2* and HIF-1α in the glioma model, suggesting that R2* Mapping can be used to detect different levels of glioma tissue oxygenation.

In fact, hypoxia is promoted by high oxygen consumption in tumor regions with increased cellularity and decreased oxygen supply because of impaired vascular structure. Our results showed higher HIF-1α expression in the central tumor area than in peripheral tumor parts and normal tissue, and the perfusion, f, and D* values in the central tumor parts were lower than those in the peripheral parts. However, no significant difference between the D values of the central and peripheral tissue was found in this study. The D value is a measure of the diffusion of water molecules and the cell density. Thus, the higher HIF-1α expression in central intratumor tissue may be caused by impaired vessels, which is consistent with the perivascular and vascular-invasive niches of glioblastoma (22).

The results of this study also showed that the IVIM parameters could be used to detect HIF-1α expression levels in glioma tissue. The negative correlation between D* and HIF-1α expression levels could be attributed to D* mainly being a measure of microcirculation perfusion. A high D* corresponds to high supply of blood and oxygen. A disorganized and functionally impaired vasculature in glioma can contribute to decreasing D*, and the metabolic demand of tumor cells leads to increased HIF-1α expression. However, in this study, D and f were poor indicators for assessing HIF-1α expression because technical limitations, such as data instability and a low SNR, made it difficult to measure f and D accurately, which may be the main reason for why these parameters were not useful for predicting HIF-1α expression (23).

Our study had several limitations. First, IVIM and R2* Mapping could not be used to measure tissue oxygen levels directly. The R2* and D values were not in agreement with the PtO_2 levels and were compromised by the absence of direct quantification (18, 21, 24). Second, we did not observe dynamic changes in R2* and the IVIM parameters during glioma

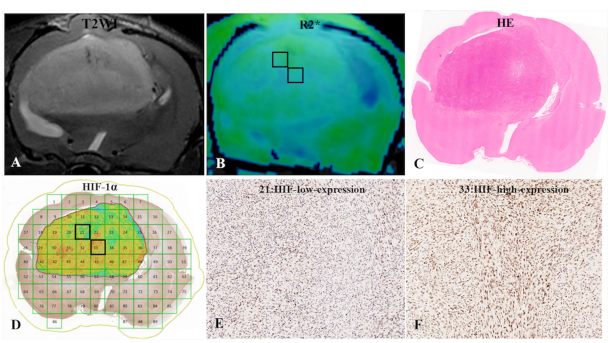

FIGURE 3 | **(A)** C6-cell glioma tissue was observed in a T2WI image. **(B)** the post-processing R2* value of c6-cell glioma. **(C)** H&E staining. **(D)** ROI locations in the tumor area on the R2* map correspond to 21 and 33 (HIF-1a map), for which the R2* values were 33.50 Hz and 45.87 Hz, respectively, and the HIF-scores were 104.87 and 200.95, respectively. **(E, F)** Immunohistochemical staining images (× 400) showed low and high expression of HIF-1a in the tumor for ROIs 21 and 33, respectively, on the HIF-1a map.

TABLE 3 | Mean parameter values for the distribution of imaging parameters in high- and low-expression groups.

Imaging Parameter	Regions with High HIF-1a Expression (Mean ± SD, N = 143)	Regions with Low HIF-1a Expression (Mean ± SD, N = 137)	P
R2* (Hz)	40.95 ± 6.46	36.49 ± 9.62	**0.003***
D (×10^{-6} mm^2/s)	415.87 ± 77.37	421.85 ± 85.29	0.702
D* (×10^{-6} mm^2/s)	2746.46 ± 533.77	2917.34 ± 364.43	0.106
f (%)	50.91 ± 8.04	51.21 ± 8.97	0.856
Perfusion (×10^{-6} mm^2/s)	1408.84 ± 411.43	1499.49 ± 354.45	0.233

** and bold values means p<0.05 was considered statistically significant.*

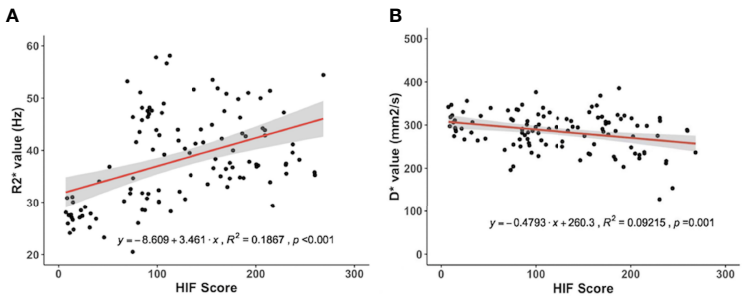

FIGURE 4 | Correlations for the hypoxia-inducible factor 1α (HIF-1α) with the pseudodiffusion coefficient (D*) and the apparent transverse relaxation rate (R2*). **(A)** HIF-1α correlated positively with the R2* value (r = 0.43, p < 0.001). **(B)** HIF-1α correlated negatively with D* (r = -0.30, p = 0.001).

development, and further study is necessary before this technique can be extensively used in clinical practice.

In conclusion, there was heterogeneity of HIF-1α expression in glioma tissue, and IVIM and R2* Mapping were found to be promising methods for the noninvasive detection of the distribution and expression level of HIF-1α. Both the D* parameter of IVIM and the R2* parameter of R2* Mapping were significantly correlated with HIF-1α expression and could be useful for the assessment and mapping of HIF-1a expression.

DATA AVAILABILITY STATEMENT

The raw data supporting the conclusions of this article will be made available by the authors, without undue reservation.

ETHICS STATEMENT

The animal study was reviewed and approved by Institutional Animal Care and Use Committee of the Medical School of Fudan University.

AUTHOR CONTRIBUTIONS

BY and HW mainly conceived the project and designed the study. DW, YL, and XL performed all experiments, participated in the experimental design, and drafted the manuscript. NM and P-YW analyzed and interpreted part of the data. DG mainly contributed to the conception and revised the manuscript. All authors read and approved the final manuscript.

FUNDING

This study has received funding by Youth Program of National Natural Science Foundation of China (Fund No. 81901697), the Youth Medical Talents –Medical Imaging Practitioner Program [Grant number SHWRS(2020)_087] to YL, Shanghai Sailing Program (Grant No. 21YF1404800) to XL, Youth Program of Special Project for Clinical Research of Shanghai Municipal Health Commission Health industry(Grant No. 20204Y0421) to DW and Science and Technology Innovation Action Plan of Shanghai Science and Technology Commission(Grant No. 22S31905900) to BY.

REFERENCES

1. Hambardzumyan D, Bergers G. Glioblastoma: Defining Tumor Niches. *Trends Cancer.* (2015) 1:252–65. doi: 10.1016/j.trecan.2015.10.009
2. Stadlbauer A, Oberndorfer S, Zimmermann M, Renner B, Buchfelder M, Heinz G, et al. Physiologic MR Imaging of the Tumor Microenvironment Revealed Switching of Metabolic Phenotype Upon Recurrence of Glioblastoma in Humans. *J Cereb Blood Flow Metab* (2020) 40:528–38. doi: 10.1177/0271678X19827885
3. Stadlbauer A, Eyüpoglu I, Buchfelder M, Dörfler A, Zimmermann M, Heinz G, et al. Vascular Architecture Mapping for Early Detection of Glioblastoma Recurrence. *Neurosurg Focus.* (2019) 47:E14. doi: 10.3171/2019.9.FOCUS19613
4. Guo H, Kang H, Tong H, Du X, Liu H, Tan Y, et al. Microvascular Characteristics of Lower-Grade Diffuse Gliomas: Investigating Vessel Size

Imaging for Differentiating Grades and Subtypes. *Eur Radiol* (2019) 29:1893–902. doi: 10.1007/s00330-018-5738-y
5. Schito L, Semenza GL. Hypoxia-Inducible Factors: Master Regulators of Cancer Progression. *Trends Cancer.* (2016) 2:758–70. doi: 10.1016/j.trecan.2016.10.016
6. Lin CS, Liu TC, Lee MT, Yang SF, Tsao TC. Independent Prognostic Value of Hypoxia-Inducible Factor 1-Alpha Expression in Small Cell Lung Cancer. *Int J Med Sci* (2017) 14:785–90. doi: 10.7150/ijms.19512
7. Maralani PJ, Das S, Mainprize T, Phan N, Bharatha A, Keith J, et al. Hypoxia Detection in Infiltrative Astrocytoma: Ferumoxytol-Based Quantitative BOLD MRI With Intraoperative and Histologic Validation. *Radiology.* (2018) 288:821–9. doi: 10.1148/radiol.2018172601
8. Zhu M, Zhang C, Yan J, Sun J, Zhao X, Zhang L, et al. Accuracy of Quantitative Diffusion-Weighted Imaging for Differentiating Benign and Malignant Pancreatic Lesions: A Systematic Review and Meta-Analysis. *Eur Radiol* (2021) 31:7746–59. doi: 10.1007/s00330-021-07880-3
9. Hompland T, Hole KH, Ragnum HB, Aarnes EK, Vlatkovic L, Lie AK, et al. Combined MR Imaging of Oxygen Consumption and Supply Reveals Tumor Hypoxia and Aggressiveness in Prostate Cancer Patients. *Cancer Res* (2018) 78:4774–85. doi: 10.1158/0008-5472.CAN-17-3806
10. Wang Y, Zhang X, Hua Z, Xie L, Jiang X, Wang R, et al. Blood Oxygen Level-Dependent Imaging and Intravoxel Incoherent Motion MRI of Early Contrast-Induced Acute Kidney Injury in a Rabbit Model. *Kidney Blood Press Res* (2019) 44:496–512. doi: 10.1159/000500052
11. Wang Y, Zhang X, Wang B, Xie Y, Wang Y, Jiang X, et al. Evaluation of Renal Pathophysiological Processes Induced by an Iodinated Contrast Agent in a Diabetic Rabbit Model Using Intravoxel Incoherent Motion and Blood Oxygenation Level-Dependent Magnetic Resonance Imaging. *Korean J Radiol* (2019) 20:830–43. doi: 10.3348/kjr.2018.0757
12. Fujiwara S, Mori Y, de la Mora DM, Akamatsu Y, Yoshida K, Shibata Y, et al. Feasibility of IVIM Parameters From Diffusion-Weighted Imaging at 11.7T MRI for Detecting Ischemic Changes in Common Carotid Artery Occlusion Rats. *Sci Rep* (2020) 10:8404. doi: 10.1038/s41598-020-65310-8
13. Yasuda Y, Ozasa H, Kim YH, Yamazoe M, Ajimizu H, Yamamoto Funazo T, et al. MCL1 Inhibition is Effective Against a Subset of Small-Cell Lung Cancer With High MCL1 and Low BCL-XL Expression. *Cell Death Dis* (2020) 11:177. doi: 10.1038/s41419-020-2379-2
14. Dewhirst MW, Birer SR. Oxygen-Enhanced MRI Is a Major Advance in Tumor Hypoxia Imaging. *Cancer Res* (2016) 76:769–72. doi: 10.1158/0008-5472.CAN-15-2818
15. Masaki Y, Shimizu Y, Yoshioka T, Feng F, Zhao S, Higashino K, et al. Imaging Mass Spectrometry Revealed the Accumulation Characteristics of the 2-Nitroimidazole-Based Agent "Pimonidazole" in Hypoxia. *PloS One* (2016) 11:e0161639. doi: 10.1371/journal.pone.0161639
16. Boyd NH, Tran AN, Bernstock JD, Etminan T, Jones AB, Gillespie GY, et al. Glioma Stem Cells and Their Roles Within the Hypoxic Tumor Microenvironment. *Theranostics.* (2021) 11:665–83. doi: 10.7150/thno.41692
17. Janssen HL, Haustermans KM, Sprong D, Blommestijn G, Hofland I, Hoebers FJ, et al. HIF-1A, Pimonidazole, and Iododeoxyuridine to Estimate Hypoxia and Perfusion in Human Head-and-Neck Tumors. *Int J Radiat Oncol Biol Phys* (2002) 54:1537–49. doi: 10.1016/s0360-3016(02)03935-4
18. Christen T, Lemasson B, Pannetier N, Farion R, Remy C, Zaharchuk G, et al. Is T2* Enough to Assess Oxygenation? Quantitative Blood Oxygen Level-Dependent Analysis in Brain Tumor. *Radiology.* (2012) 262:495–502. doi: 10.1148/radiol.11110518
19. Lemasson B, Christen T, Serduc R, Maisin C, Bouchet A, Le Duc G, et al. Evaluation of the Relationship Between MR Estimates of Blood Oxygen Saturation and Hypoxia: Effect of an Antiangiogenic Treatment on a Gliosarcoma Model. *Radiology* (2012) 265:743–52. doi: 10.1148/radiol.12112621
20. Chang D, Wang YC, Xu TT, Peng XG, Cai Y, Wang L, et al. Noninvasive Identification of Renal Hypoxia in Experimental Myocardial Infarctions of Different Sizes by Using BOLD MR Imaging in a Mouse Model. *Radiology.* (2018) 286:129–39. doi: 10.1148/radiol.2017161998
21. Abumoawad A, Saad A, Ferguson CM, Eirin A, Woollard JR, Herrmann SM, et al. Tissue Hypoxia, Inflammation, and Loss of Glomerular Filtration Rate in Human Atherosclerotic Renovascular Disease. *Kidney Int* (2019) 95:948–57. doi: 10.1016/j.kint.2018.11.039
22. Stadlbauer A, Zimmermann M, Doerfler A, Oberndorfer S, Buchfelder M, Coras R, et al. Intratumoral Heterogeneity of Oxygen Metabolism and Neovascularization Uncovers 2 Survival-Relevant Subgroups of IDH1 Wild-Type Glioblastoma. *Neuro Oncol* (2018) 20:1536–46. doi: 10.1093/neuonc/noy066
23. Li X, Wu S, Li D, Yu T, Zhu H, Song Y, et al. Intravoxel Incoherent Motion Combined With Dynamic Contrast-Enhanced Perfusion MRI of Early Cervical Carcinoma: Correlations Between Multimodal Parameters and HIF-1α Expression. *J Magn Reson Imaging.* (2019) 50:918–29. doi: 10.1002/jmri.26604
24. Li Y, Ye J, Zhou S, Bai R, Fu G, Zhang W, et al. Multi-Parameter MRI to Investigate Vasculature Modulation and Photo-Thermal Ablation Combination Therapy Against Cancer. *Nanomedicine.* (2018) 14:2179–89. doi: 10.1016/j.nano.2018.07.008

Conflict of Interest: Author PW was employed by company GE Healthcare.

The remaining authors declare that the research was conducted in the absence of any commercial or financial relationships that could be construed as a potential conflict of interest.

Publisher's Note: All claims expressed in this article are solely those of the authors and do not necessarily represent those of their affiliated organizations, or those of the publisher, the editors and the reviewers. Any product that may be evaluated in this article, or claim that may be made by its manufacturer, is not guaranteed or endorsed by the publisher.

Copyright © 2022 Wang, Lu, Li, Mei, Wu, Geng, Wu and Yin. This is an open-access article distributed under the terms of the Creative Commons Attribution License (CC BY). The use, distribution or reproduction in other forums is permitted, provided the original author(s) and the copyright owner(s) are credited and that the original publication in this journal is cited, in accordance with accepted academic practice. No use, distribution or reproduction is permitted which does not comply with these terms.

frontiers | Frontiers in Neurology

SYSTEMATIC REVIEW
published: 24 June 2022
doi: 10.3389/fneur.2022.882334

Diagnostic Accuracy of the Diffusion-Weighted Imaging Method Used in Association With the Apparent Diffusion Coefficient for Differentiating Between Primary Central Nervous System Lymphoma and High-Grade Glioma: Systematic Review and Meta-Analysis

Xiaoli Du[1], *Yue He*[2] *and Wei Lin*[1]*

[1] *Department of Radiology, Chengdu First People's Hospital, Chengdu, China,* [2] *Department of Orthopedics, Chengdu First People's Hospital, Chengdu, China*

OPEN ACCESS

Edited by:
Sandro M. Krieg, Technical University of Munich, Germany

Reviewed by:
Constantin-Cristian Topriceanu, University College London, United Kingdom
Na Li, Shandong Cancer Hospital, China

***Correspondence:**
Wei Lin
linwei_image@sina.com

Specialty section:
This article was submitted to Neuro-Oncology and Neurosurgical Oncology, a section of the journal Frontiers in Neurology

Received: *23 February 2022*
Accepted: *27 May 2022*
Published: *24 June 2022*

Citation:
Du X, He Y and Lin W (2022) Diagnostic Accuracy of the Diffusion-Weighted Imaging Method Used in Association With the Apparent Diffusion Coefficient for Differentiating Between Primary Central Nervous System Lymphoma and High-Grade Glioma: Systematic Review and Meta-Analysis. Front. Neurol. 13:882334. doi: 10.3389/fneur.2022.882334

Background: It is difficult to differentiate between a few primary central nervous system lymphoma (PCNSL) and high-grade glioma (HGG) using conventional magnetic resonance imaging techniques. The purpose of this study is to explore whether diffusion-weighted imaging (DWI) can be effectively used to differentiate between these two types of tumors by analyzing the apparent diffusion coefficient (ADC).

Research Design and Methods: Data presented in Pubmed, Embase, Web of Science, Cochrane Library, China National Knowledge Infrastructure (CNKI), Wanfang Database, and China Science and Technology Journal Database (CQVIP) were analyzed. High-quality literature was included, and the quality was evaluated using the quality assessment of diagnostic accuracy studies-2 (QUADAS-2) tool, and the studies were based on the inclusion and exclusion rules. The pooled sensitivity, pooled specificity, pooled positive likelihood ratio (PLR), pooled negative likelihood ratio (NLR), pooled diagnostic odds ratio (*DOR*), area under the curve (AUC) of the summary operating characteristic curve (SROC), and corresponding 95% confidence interval (*CI*) were calculated using the bivariate mixed effect model. Meta-regression analysis and subgroup analysis were used to explore the sources of heterogeneity. The publication bias was evaluated by conducting Deek's test.

Results: In total, eighteen high-quality studies were included. The pooled sensitivity was 0.82 (95% CI: 0.75–0.88), the pooled specificity was 0.87 (95% CI: 0.84–0.90), the pooled positive likelihood ratio was 6.49 (95% CI: 5.06–8.32), the pooled NLR was 0.21 (95% CI: 0.14–0.30), the pooled *DOR* was 31.31 (95% CI: 18.55–52.86), and the pooled AUC was 0.90 (95% CI: 0.87–0.92). Sample size, language and country of publication, magnetic field strength, region of interest (ROI), and cut-off values of different types of

ADC can potentially be the sources of heterogeneity. There was no publication bias in this meta-analysis.

Conclusions: The results obtained from the meta-analysis suggest that DWI is characterized by high diagnostic accuracy and thus can be effectively used for differentiating between PCNSL and HGG.

Keywords: diffusion-weighted imaging, meta-analysis, lymphoma, diagnosis, high-grade glioma

INTRODUCTION

Primary central nervous system lymphoma (PCNSL) is a variant of the non-Hodgkin lymphoma of the central nervous system. PCNSL is a disease in which cancer cells form in the primary brain, spinal cord, and eye (1). The origin of 3–5% of intracranial tumors can be attributed to PCNSL. It has been observed that the incidence rate of PCNSL is increasing each year (2). The clinical manifestations are similar to the clinical manifestations observed for intracranial gliomas. Apart from the process of pathological biopsy, imaging techniques are also used to differentiate between the two types of tumors. At present, the recommended PCNSL treatment method involves the use of chemotherapy combined with immunotherapy. Generally, surgery is not recommended (3, 4). HGG is primarily resected surgically, and the process is supplemented by radiotherapy and chemotherapy (5). The choice of the treatment plan heavily relies on the accurate identification of the two types of tumors.

A significant number of uniformly enhanced masses or nodules are observed in the deep parts of the brain near the midline structure when the MRI technique is used to study the manifestation of PCNSL. Atypical MRI manifestations, which overlap with the manifestations observed for HGG, are observed in some cases, making the accurate identification of the tumors difficult. This can potentially result in misdiagnosis. Diffusion-weighted imaging (DWI) is a new MRI technology that was developed in the middle of the 1990s. It is the only non-invasive method that can be used to detect the diffusion of water molecules in living tissues (6). DWI does not involve the process of contrast agent imaging. This process can be used to diagnose patients allergic to contrast agents or patients suffering from abnormal renal function. The results obtained using this technique are better than the result obtained using other techniques, such as enhanced MRI. The apparent diffusion coefficient (ADC) value can eliminate the effects of the T2 penetration effect and diffusion-sensitive gradient. This value can accurately and truly reflect the diffusion ability of water molecules in tumor tissues. The ADC value can quantitatively reflect the density and malignancy of tumor cells. Hence, it is widely used in clinical diagnosis (7). We hypothesized that the ADC value could be used to distinguish between the two types of tumors as the extents of blood flow characterizing PCNSL and HGG are different. Based on the current research status, we conducted a systematic meta-analysis to evaluate the comprehensive diagnostic value of DWI combined with ADC for accurately identifying PCNSL and HGG.

MATERIALS AND METHODS

Search Strategy

Chinese and English databases were primarily searched. The English databases include Pubmed, Embase, Web of Science, and Cochrane Library, and the Chinese databases include China National Knowledge Infrastructure (CNKI), Wanfang Database, and China Science and Technology Journal Database (CQVIP). The keywords used were glioma, lymphoma, DWI, and ADC. We can obtain the relevant "Medical Subject Headings" from https://www.ncbi.nlm.nih.gov/mesh/?term=. For different databases, different Boolean logic retrieval formulae were used. The period for database retrieval covered the period from the establishment of each retrieval database to March 2022.

Inclusion and Exclusion Criteria

There were several inclusion criteria: 1) The patient should have pathologically confirmed PCNSL and high-grade glioma (the WHO grade III or grade IV). 2) The patient should not have been exposed to any treatment methods prior to being subjected to the imaging conditions. 3) The patient should have undergone DWI–MRI sequence tests. 4) Studies with sufficient data to calculate true-positive (TP), false-positive (FP), false-negative (FN), and true-negative (TN) values should be considered. For example, the considered for the studies contains raw data for all patients. The reports present the sensitivity and specificity achieved using DWI during the diagnosis of the two diseases. Sensitivity is expressed as TP/(TP+FN), and specificity is expressed as TN/(TN+FP). These formulae can be used to obtain the relevant data (4) The sample sizes greater than 10 should be considered. The were several exclusion criteria applied. 1) Cases, where animal experiments or other basic experiments were conducted, were not considered. 2) Data from non-original research articles, such as the data presented in review articles, conference reports, abstracts, comments, letters, and case reports were excluded. 3) Patients from the same cohort were not considered. When the research samples are from the same cohort, we consciously consider and choose the latest study reported or the study with the largest sample size.

Data Collection and Quality Assessment

During the process, two researchers are selected. If there are differences among the authors, the differences are resolved through discussion within the group. The extraction parameters primarily include the author of the study, the year of publication, the sample size (control group and case group sizes), the average

age and gender of the patients in the control and case groups, research type (whether it is a retrospective study or a prospective study), imaging parameters corresponding to DWI, sensitivity, specificity, cut-off value, and the TP, FP, TN, and FN values of each study.

The quality of the included literature reports was evaluated based on the guidelines presented by the quality assessment of diagnostic accuracy studies-2 (QUADAS-2) tool and a Newcastle-Ottawa Scale (NOS). The QUADAS-2 scale was divided into various factors: 1) patient selection; 2) index test; 3) reference standard; and 4) flow and timing (8). The software Review Manager (version 5.2) was used to determine the bias and quality of the included studies. The literature quality evaluation chart was also drawn. The answers "yes," "unclear," and "no" corresponded to "high risk," "unclear risk," or "low risk," respectively, and indicated the bias risk level. The risk levels were denoted in red, yellow, and green, respectively, in the quality evaluation chart. The NOS was used to assess the quality of included case-control and cohort studies and each item of NOS is assigned 1 or 2 points. Studies with a score of 5 or more are considered to be of high quality.

Statistical Analysis

The data were analyzed using Stata 15.1 (64-bit), Review manager 5.2, and MetaDiSc 1.4. The pooled sensitivity, pooled specificity, pooled positive likelihood ratio (PLR), pooled negative likelihood ratio (NLR), pooled diagnostic odds ratio (*DOR*), summary receiver operating characteristic (SROC), area under the curve (AUC), and corresponding 95% confidence interval (*CI*) of DWI for the differentiation of PCNSL and HGG were calculated using the bivariate mixed effect model (9). The relationships among prior-test probability, likelihood ratio, and post-test probability were studied to certify using Fagan's nomogram. The heterogeneity of the study was assessed by conducting the Cochran-Q and I^2 tests (10). A $p < 0.05$ was considered statistically significant. When I^2 was > 50%, high heterogeneity among the studies was suggested. MetaDiSc 1.4 software was used to calculate the Spearman correlation coefficient between the logarithm of sensitivity and the logarithm of 1-specificity to determine whether the threshold effect results in heterogeneity. A strong positive correlation indicates the generation of a threshold effect (11). The literature publication bias was evaluated by analyzing the Deeks' funnel plot (12). Sensitivity analysis, meta-regression analysis, and subgroup analysis methods were used to identify the source of heterogeneity. The value of $p < 0.05$ was considered statistically significant.

RESULTS

Literature Search and Quality Evaluation

We have preliminarily identified 261 documents (duplicate documents were excluded) for our studies by searching the Chinese and English databases. After reading the abstract and judging the literature type, we excluded 169 non-original studies (literature and review articles unrelated to this field of study). After thoroughly reading the remaining literature reports, we included a total of 18 literature reports (13–30) for meta-analysis. A total of 372 patients with PCNSL and 701 patients with glioma were included in the study. A total of 32 lesions (14 glioblastomas and 18 PCNSL) were studied by Anwar et al. (24). Hence, a total of 380 lesions characterized by PCNSL and 704 lesions characterized by glioma were included in the meta-analysis. The process of literature screening is presented in **Figure 1**, and the basic characteristics of the included literature reports are shown in **Tables 1**, **2**. Results obtained from QUADAS-2 are presented in **Figure 2**, and the quality evaluation of NOS are shown in **Supplementary Table 1**. The quality of the included studies was found to be satisfactory.

Meta-Analysis: Results

The results of the heterogeneity test were obtained ($Q = 3.409$, $df = 2.00$, $p = 0.091$, $I^2 = 41\%$; 95% *CI* was in the range of 0–100). It was observed that moderate levels of heterogeneity existed between the included studies. The results of the threshold effect test revealed that the Spearman correlation coefficient was 0.048 ($p = 0.851$). This indicated that a threshold effect did not result in heterogeneity. The pooled sensitivity of DWI (used to differentiate PCNSL from HGG) was 0.82 (95% CI: 0.75–0.88), the pooled specificity was 0.87 (95% CI: 0.84–0.90), the pooled PLR was 6.49 (95% CI: 5.06–8.32), the pooled NLR was 0.21 (95% CI: 0.14–0.30), and the pooled DOR was 31.31 (95% CI: 18.55–52.86). The forest maps of pooled results are shown in **Figures 3A–E**. The results obtained by analyzing the SROC are presented in **Figure 3F**. The AUC of SROC was 0.90 (95% CI 0.87–0.92). Analysis of the Fagan diagram (**Figure 4**) reveals that the probability before the prediction is 50%. Under conditions of positive DWI, the probability of diagnosing PCNSL would increase the post-test probability to 87%. When the result was negative, the probability of diagnosing PCNSL would decrease the post-test probability to 17%.

Meta-Regression and Subgroup Analysis

We conducted a meta-regression analysis to find the potential source of heterogeneity. Various variables were considered: sample size (>50 vs. <50), language (English vs. Chinese), country (Asia vs. other continents), magnetic field strength (3.0 vs. 1.5 T), the necessity of using ADC ratios, ADC_{min}, and ADC_{mean} as the cut-off value (Yes vs. No), and ROI placement (solid portion vs. the whole tumor). This is presented in **Figure 5**. Some of the variables (sample size, language, and necessity of using ADC_{min} as the cut-off value) are the sources of heterogeneity for sensitivity and specificity, while others (country, magnetic field strength, necessity of using ADC ratios, ADC_{mean} as the cut-off values, and ROI placement) are the sources of heterogeneity observed in specificity.

For subgroup analysis (**Table 3**), the results of studies with a pooled literature whose sample size is less than 50 have a high sensitivity of 0.93 (95% CI: 0.86–0.99) and a specificity of 0.89 (95% CI: 0.83–0.95). Results from pooled studies conducted with Chinese language literature revealed that a high sensitivity of 0.88 (95% CI: 0.80–0.97) and a specificity of 0.92 (95% CI: 0.87–0.97) was achieved. Low sensitivity of 0.78 (95% CI: 0.70–0.85) was achieved in cases where ADC ratios were not used as the cut-off values. When ADC_{min} was not used as the cut-off value, high

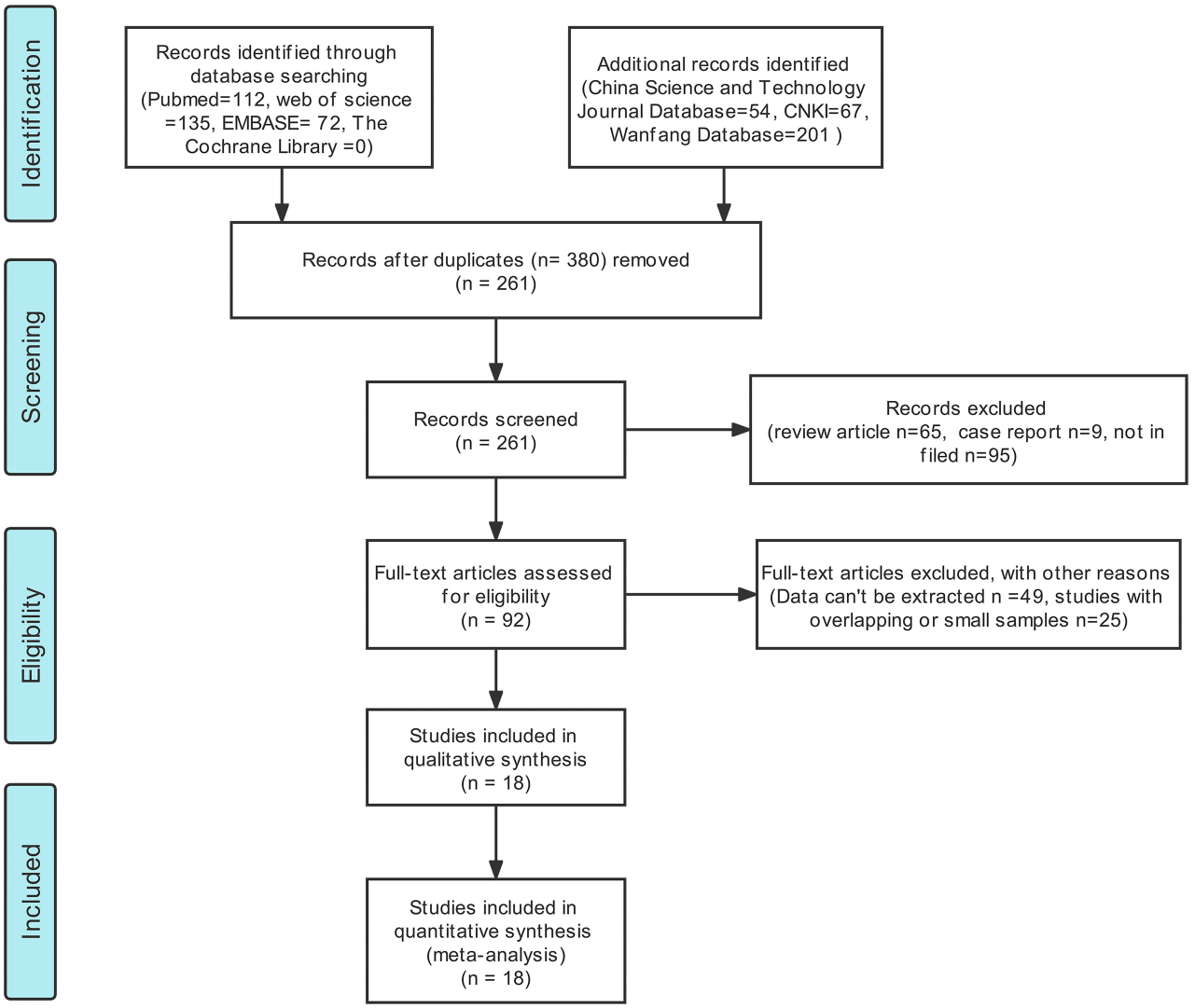

FIGURE 1 | A Flowchart representing the literature selection process.

sensitivity of 0.83 (95% CI: 0.77–0.89) and low specificity of 0.87 (95% CI: 0.84–0.90) was achieved. In cases where ADC_{mean} was not used as the cut-off value, high sensitivity of 0.83 (95% CI: 0.76–0.90) and low specificity of 0.86 (95% CI: 0.83–0.89) were achieved. When ROI placement reflected a solid tumor, a low sensitivity of 0.79 (95% CI: 0.68–0.90) was achieved.

Sensitivity Analysis and Publication Bias

Results from sensitivity analysis revealed that the goodness of fit and bivariate normality tests should be conducted using the bivariate mixed effect model for the meta-analysis (**Figure 6**). Four influential outliers were identified. No other outliers could be identified by conducting outlier detection tests. The four abnormal studies were excluded, and significant changes in sensitivity (0.83 vs. 0.82), specificity (0.85 vs. 0.87), PLR (5.65 vs. 6.49), NLR (0.20 vs. 0.21), AUC (0.86 vs. 0.90) and *DOR* (27.72 vs. 31.31) were not observed. This indicated that the combined results were relatively stable. Deek's test was performed to assess the publication bias (**Figure 7**). The number of studies on both sides of the dividing line was roughly equal and symmetrical ($p = 0.09$), indicating the absence of publication bias. Besides, the funnel plot was shown in **Supplementary Figure 1**.

DISCUSSION

We thoroughly searched and studied the Chinese and English databases to perform the meta-analyses. We selected a total of 18 relevant literature reports for the studies after thoroughly reading the literature reports (taking into account the inclusion and exclusion criteria). The pooled sensitivity, specificity, PLR, NLR, and DOR were 0.82, 0.87, 6.5, 0.21, and 31, respectively. The AUC was 0.90, indicating that DWI can

TABLE 1 | Basic clinical characteristics and parameters of the included literature.

First author	Year	Language	Country	Study design	Type of magnetic resonance equipment	B values (s/mm^2)	PCNSL			HGG		
							No. of patients	Mean age	SEX (Male/ Female)	No. of patients	Mean age	SEX (Male/ Female)
Toh CH	2008	English	China	Retrospective	Siemens 3.0T	0, 1,000	10	53.3	4/6	10	51.9	5/5
Doskaliyev A	2012	English	Japan	Retrospective	GE 3.0T	0, 1,000, 4,000	10	59.7	4/6	14	60.2	7/7
Yamashita K	2013	English	Japan	Retrospective	Philips 3.0T	0, 1,000	19	64.8	Unknown	37	58.5	Unknown
Ahn SJ	2014	English	Korea	Retrospective	Philips 3.0T	0, 1,000	25	60	10/15	62	56.7	34/28
Nakajima S	2015	English	Japan	Retrospective	Siemens 3.0T	0, 1,000	11	70	4/7	23	56.5	13/10
Ko CC	2016	English	China	Retrospective	Siemens 1.5T	0, 1,000	22	59	9/13	104	60	58/46
Li D	2017	Chinese	China	Retrospective	Siemens 3.0T	0, 1,000	22	55	14/8	27	51	19/8
Lin X	2017	English	USA	Retrospective	GE 3.0T	1,000	18	68.7	11/7	36	68.6	22/4
Lu S	2017	English	China	Retrospective	Siemens 3.0T	0, 1,000	18	56.8	12/6	42	54.5	27/15
Luo L	2018	Chinese	China	Retrospective	Siemens 3.0T	0, 1,000	38	57	17/21	30	51	17/13
Xue X	2019	Chinese	China	Retrospective	GE 1.5T or 3.0T	0, 1,000	15	52.53	8/7	26	60.65	15/11
Anwar SSM	2019	English	Pakistan	Retrospective	Siemens 1.5T or 3.0T	0, 500, 1,000	10 (14)	56.8	3/7	11 (18)	52.0	8/3
Eisenhut F	2020	English	Germany	Retrospective	Siemens 3.0T	0, 1,000	37	68.7	24/13	37	67.9	25/12
Mehrnahad M	2020	English	Iran	Retrospective	Siemens 1.5T	0, 1,000	20	57	Unknown	50	54	Unknown
Geng L	2021	Chinese	China	Retrospective	GE 3.0T	0, 1,000	30	59.13	20/10	35	50.6	23/12
Eyüboglu I	2021	English	Turkey	Retrospective	Siemens 1.5T	0, 1,000	16	Unknowm	Unknown	55	Unknowm	Unknown
Ozturk K	2021	English	USA	Retrospective	Siemens 3.0T	0, 1,000	31	64	18/13	57	59	35/22
Zhang S	2022	English	China	Retrospective	GE 3.0T	0, 1,000	20	60.8	8/12	45	55.4	29/16

TABLE 2 | Characteristic of primary diagnostic studies.

First author	Year	Tp	Fp	Fn	Tn	Sensitivity	Specificity	Cut-off value	ROI placement
Toh CH	2008	10	0	0	10	100	100	ADC ratios 1.060	Solid portion
Doskaliyev A	2012	9	1	1	13	90.9	91.7	ADC_{min} 0.5*10^{-3}mm^2/s	Solid portion
Yamashita K	2013	11	5	8	32	58.8	86.5	ADC_{min} 0.62*10^{-3}mm^2/s	Solid portion
Ahn SJ	2014	21	6	4	56	85	90	ADC_{mean} 0.98*10^{-3}mm^2/s	Whole tumor
Nakajima S	2015	11	6	0	17	100	73.9	$ADC_{5\%}$ 0.68*10^{-3}mm^2/s	Whole tumor
Ko CC	2016	14	17	8	87	64	84	ADC_t 0.77*10^{-3}mm^2/s	Solid portion
Li D	2017	21	4	1	23	95.5	85.2	ADC_c 0.77*10^{-3}mm^2/s	Whole tumor
Lin X	2017	12	4	6	32	69	89	ADC_{mean} 1.3*10^{-3}mm^2/s	Whole tumor
Lu S	2017	14	7	4	35	76.2	83.3	ADC ratios 1.317	Whole tumor
Luo L	2018	32	4	6	26	84.21	86.87	$ADC_{50\%}$ 1.1*10^{-3}mm^2/s	Whole tumor
Xue X	2019	10	0	5	26	66.7	100	ADC_{mean} 0.69*10^{-3}mm^2/s	Solid portion
Anwar SSM	2019	18	2	0	12	100	85.7	ADC ratios 1.05	Solid portion
Eisenhut F	2020	33	4	11	26	89	70	ADC_{max} 1.314*10^{-3}mm^2/s	Whole tumor
Mehrnahad M	2020	15	7	5	43	76	85	ADC_{median} 1.035*10^{-3}mm^2/s	Solid portion
Geng L	2021	29	2	1	33	96.7	95.7	ADC ratios 1.045	Whole tumor
Eyüboglu I	2021	12	12	4	43	76	78	ADC_{tch} 0.82*10^{-3}mm^2/s	Solid portion
Ozturk K	2021	23	7	8	50	73.7	87.1	ADC ratios 0.825	Whole tumor
Zhang S	2022	20	45	14	2	6	43	ADC_{min} 0.89*10^{-3}mm^2/s	Whole tumor

ADC_{min}, minimum apparent diffusion coefficient; ADC_{meaan}, mean apparent diffusion coefficient; $ADC_{5\%}$, $_{fifth}$ percentile value of cumulative apparent diffusion coefficient histogram; ADC_t, apparent diffusion coefficient of the most strongly-enhanced tumor area; ADC_c, corrected apparent diffusion coefficient; $ADC_{50\%}$, fiftieth percentile value of cumulative apparent diffusion coefficient histogram; ADC_{tch}, apparent diffusion coefficient of tumor circumference hyperintensities.

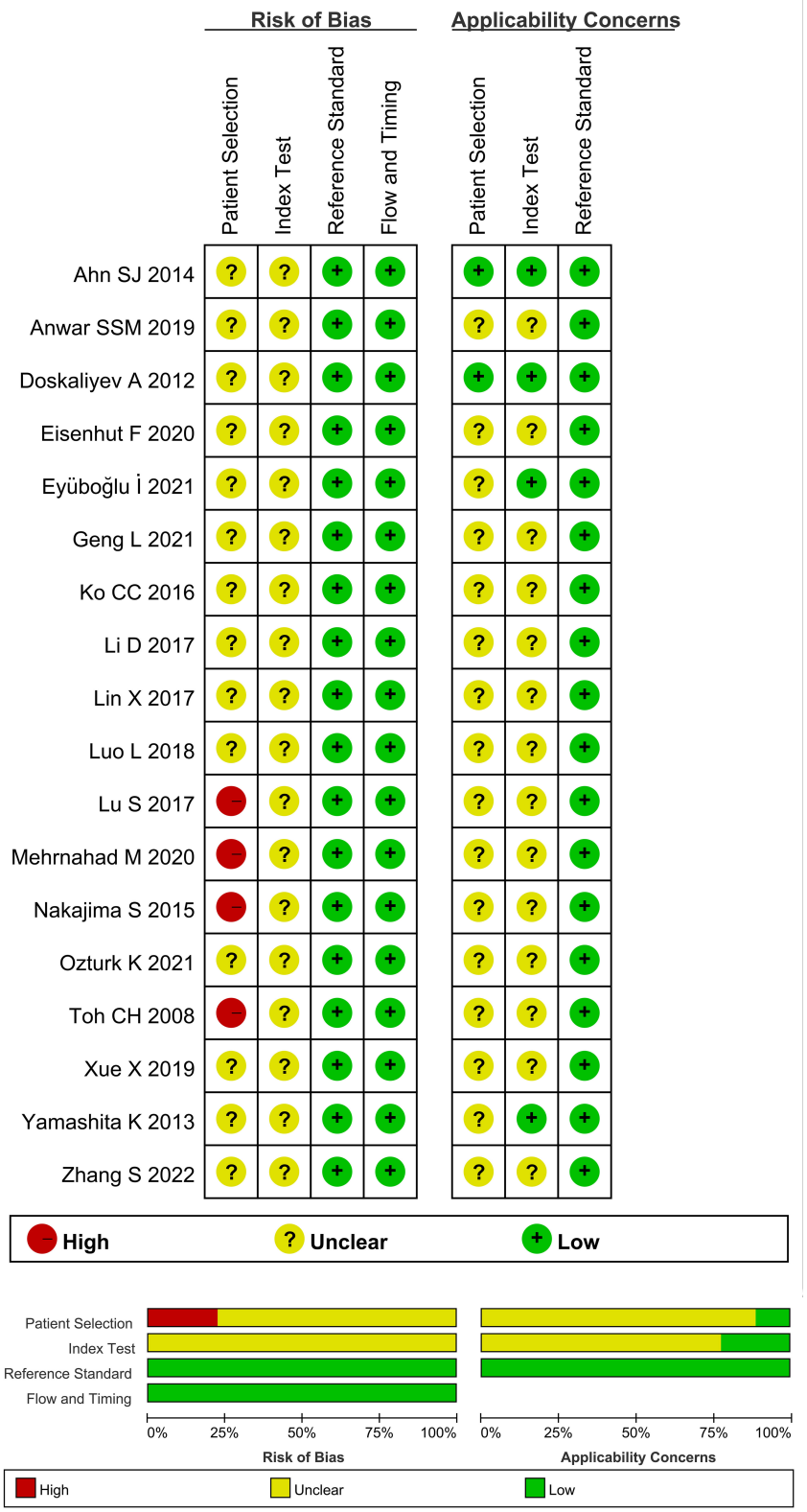

FIGURE 2 | A document quality evaluation chart prepared using the QUADAS-2 tool.

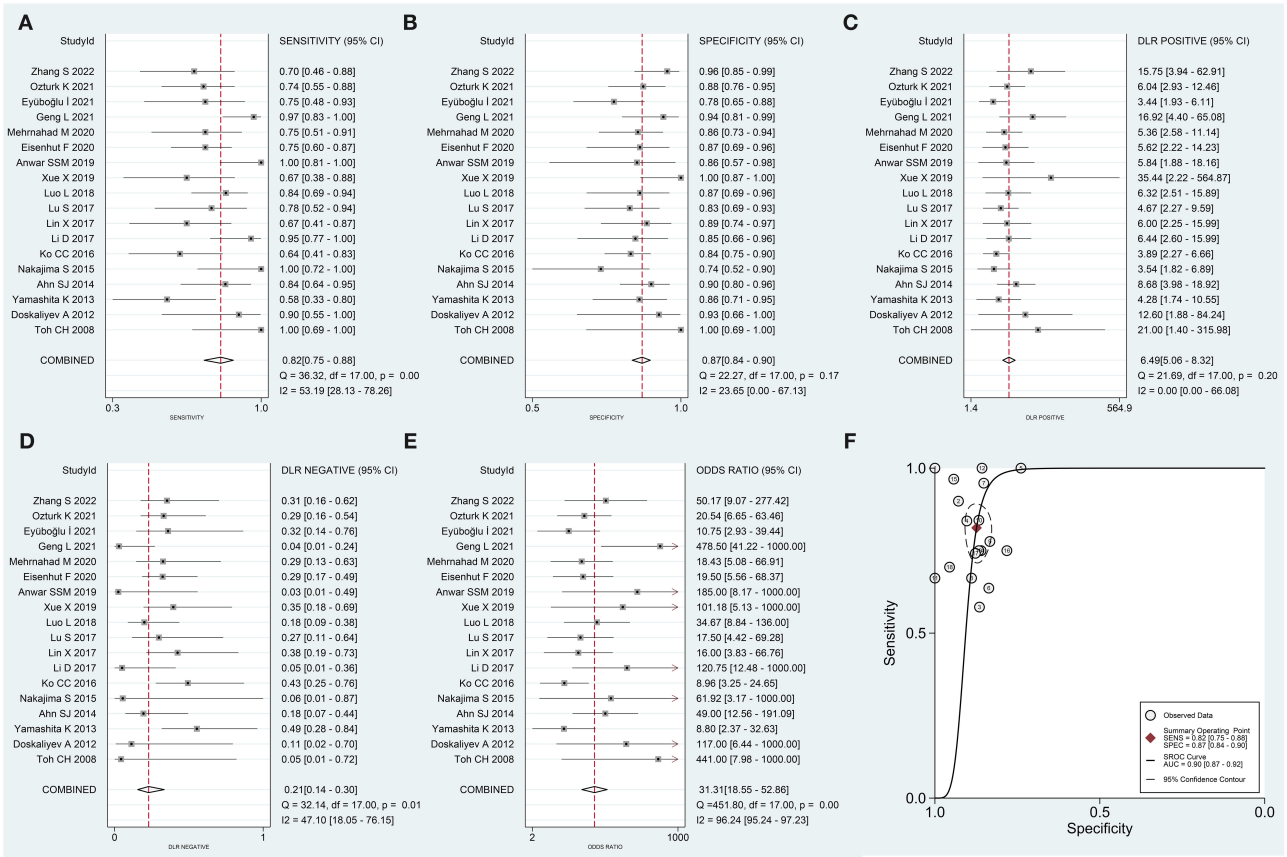

FIGURE 3 | Forest plot generated for pooled **(A)** sensitivity, **(B)** specificity, **(C)** positive likelihood ratio (PLR), **(D)** negative likelihood ratio (NLR), **(E)** diagnostic odds ratio (DOR), and **(F)** area under the curve (AUC) recorded for the summary receiver operating characteristic (SROC) curve.

effectively distinguish between PCNSL and HGG. The *DOR* is a single performance indicator that combines sensitivity and specificity for diagnostic testing. As the pooled *DOR* of the 18 studies selected by us was 31, it was advantageous to use DWI to distinguish PCNSL from HGG. Moderate levels of heterogeneity were obtained post meta-analysis. and there was no publication bias.

Primary central nervous system lymphoma and HGG are characterized by a similar location of onset, high cell density, multi-center onset, and invasive growth. Thus, there is a high chance of misdiagnosis (31). PCNSL can often be found in the deep brain parenchyma near the intracranial midline. It is mostly found on the tentorium. a slightly lower or equal T1 signal, equal or slightly higher T2 signal, highly intense DWI signal, low-intensity ADC signal, low incidence of internal cystic necrosis, mild to moderate peritumoral edema, and space-occupying effects can be observed using the MRI technique compared with other intracranial tumors (32). HGG invades a wide area (usually involving two or more lobes of the cerebral hemisphere). The invasion can be primarily observed in the white matter. Analysis of the images recorded using the MRI technique revealed the diffuse infiltration of the tumor cells and/or demyelination of the white matter. The signal was uniform, the boundary was unclear, and the tumor infiltration and edema could not be distinguished (33).

It has been previously reported that the density of the micro-vessel in PCNSL is significantly less than the density of the micro-vessels in HGG (34). This indicates that the tumor is deficient in blood. The rate of growth of these tumors is slow, resulting in less severe internal cystic necrosis. Glioma, especially HGG, is characterized by the high blood supply and rapid growth of tumor cells. The release of the cystic swelling factor (from the tumor cells) can result in a significant extent of cystic necrosis of the tumor tissues. The special anatomical position of some PCNSLs results in an adequate extent of blood supply. Under these conditions, the manifestations are complex and diverse. Hence, atypical MRI signals are obtained. The signals corresponding to PCNSL overlap with the atypical signals corresponding to glioma. Hence, it is difficult to accurately identify the two types of tumors using conventional MRI techniques. In recent years, the DWI method has been widely used in clinical settings as a non-invasive, rapid, and reproducible quantitative evaluation method to identify benign tumors, determine the degree of malignancy, and evaluate cell density.

Diffusion-weighted imaging is a non-invasive MRI-based functional imaging method that can be used to observe the

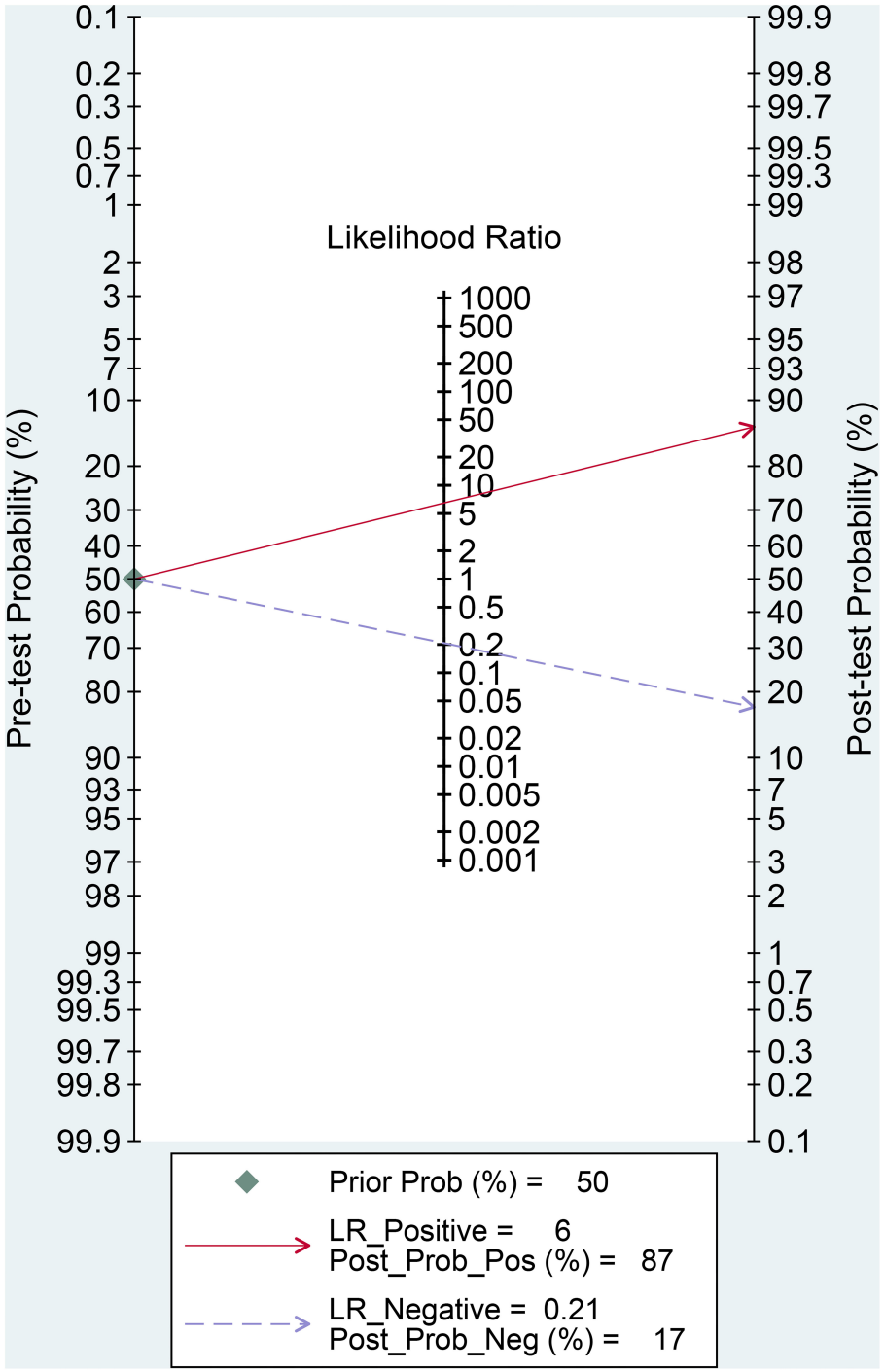

FIGURE 4 | Fagan's nomogram for evaluating the post-test probability.

microscopic dispersion state of water molecules present in tissues. The method can also be used for quantitative analysis in association with the ADC value. The ADC value can be used to eliminate the effects of the T2 penetration effect, diffusion sensitivity gradient, and other factors. This value efficiently and accurately quantifies the dispersion ability of the water molecules present in tumor tissues (35). ADC can quantitatively reflect the density and malignancy of tumor cells. In the past, most studies have used the average ADC of tumor parenchyma for comparison, but there is heterogeneity due to

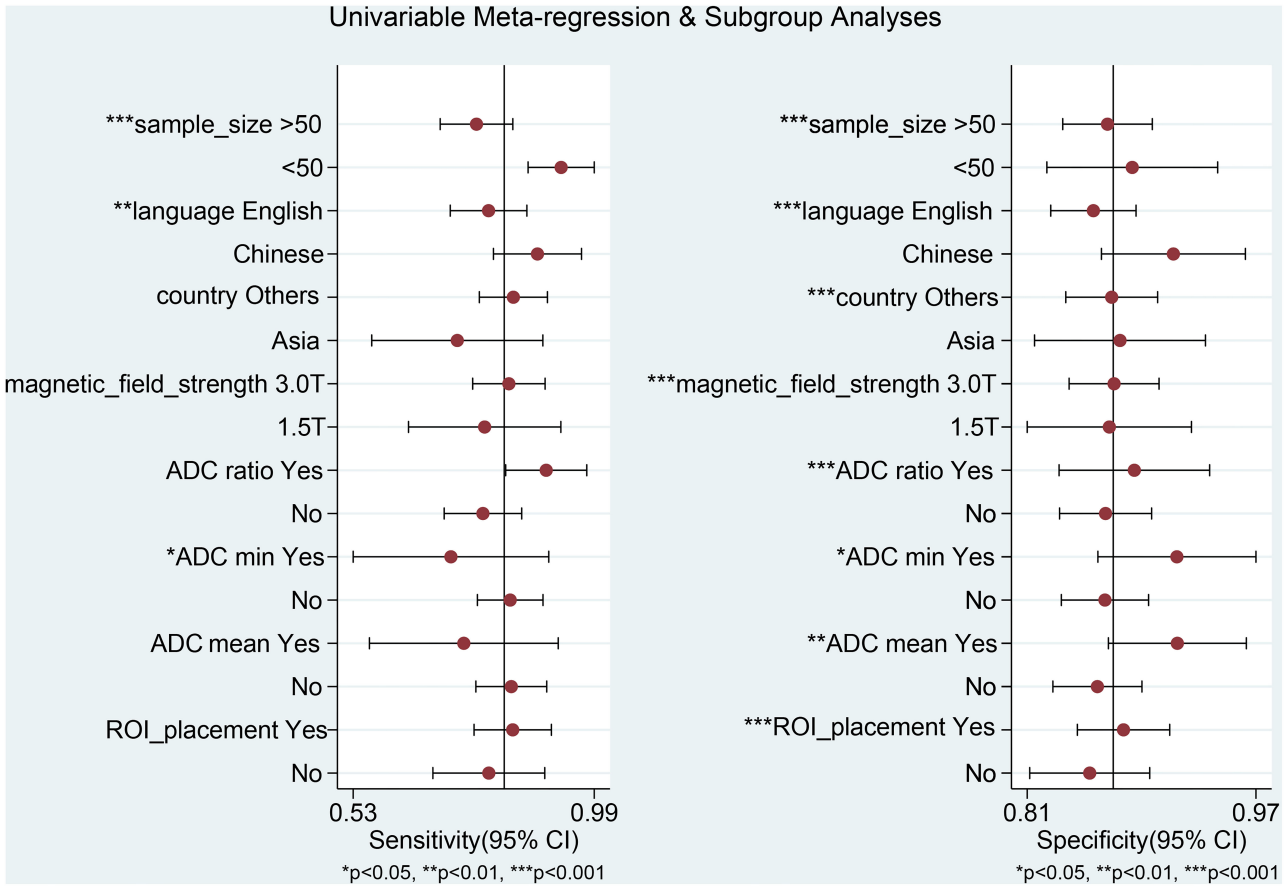

FIGURE 5 | Univariable meta-regression analysis for the sensitivity and specificity of DWI for differentiating between primary central nervous system lymphoma (PCNSL) and high-grade glioma (HGG).

the different degrees of internal differentiation of tumor tissues. Only a single average ADC index cannot truly and accurately reflect the biological behavior and malignancy of tumors. In addition, results from the subgroup analysis also suggested that the sensitivity achieved using the ADC_{min} and ADC_{mean} values decreased significantly, while the sensitivity and specificity achieved using the ADC ratio increased. This further indicated that the ADC ratio could be effectively used to eliminate the influence of microcirculation injection and white matter fiber dispersion in different directions. It can also help increase the degree of comparability between different individuals and reduce systematic error. Therefore, a more comprehensive and effective performance should be achieved before the method is applied in clinical settings. A universal ADC value and specific ADC parameters to set the cut-off values are yet to be identified. The cut-off value for ADC varies from study to study. We should comprehensively analyze the images recorded for the patient to determine the specific ADC cut-off value. It has been reported that although large non-tumor parenchymal areas can be avoided to measure the average ADC values corresponding to tumor parenchyma, microcapsule formation, microcalcification, and bleeding in tumor parenchymal areas (potentially resulting in the deviation in the average ADC values) cannot be avoided in the region of interest. This hinders the reflection of tumor micropathology (28).

Previously reported results that were obtained by conducting meta-analyses have been combined and analyzed for the accurate identification of PCNSL and glioma using the MRI technique. For example, a meta-analysis conducted with 598 participants (pooled from 14 studies) revealed that the perfusion-weighted imaging (PWI) method could be effectively used to distinguish between HGG and PCNSL. The results were highly accurate (pooled AUC: 0.9415). The dynamic susceptibility contrast (DSC) value is potentially the best index that can be used to distinguish between HGG and PCNSL (36). Results from a meta-analysis involving 704 participants (pooled over 13 studies) revealed the absence of a significant difference in AUC [between DSC and susceptibility-weighted imaging (SWI)]. The Z-test was conducted, and the combined results suggested that a high and similar rate of diagnostic accuracy could be achieved using the DSC-MRI and SWI techniques. Thus, these methods could be effectively used to distinguish between HGG and PCNSL (37). Researchers have also conducted meta-analyses using the DWI technique to identify the two types of tumors. All eight studies

TABLE 3 | Results of subgroup analysis and meta-regression analysis.

Covariate		No. of studies	Sensitivity [95%CI]	P1	Specificity [95%CI]	P2	$\chi 2$	*P*
Sample_size	>50	12	0.77 [0.70–0.83]	<0.01	0.87 [0.84–0.90]	<0.01	8.32	0.02
	<50	6	0.93 [0.86–0.99]		0.89 [0.83–0.95]			
Language	English	14	0.79 [0.72–0.86]	<0.01	0.86 [0.83–0.89]	<0.01	4.89	0.09
	Chinese	4	0.88 [0.80–0.97]		0.92 [0.87–0.97]			
Country	Asia	15	0.84 [0.77–0.90]	0.67	0.87 [0.84–0.90]	<0.01	1.82	0.40
	Others	3	0.73 [0.57–0.89]		0.88 [0.82–0.94]			
Magnetic field strength	3.0T	14	0.83 [0.76–0.90]	0.32	0.87 [0.84–0.91]	<0.01	0.36	0.83
	1.5T	4	0.78 [0.64–0.93]		0.87 [0.81–0.93]			
Parameter	ADC ratios	5	0.90 [0.82–0.97]	0.66	0.89 [0.84–0.94]	<0.01	4.40	0.11
	Others	13	0.78 [0.70–0.85]		0.87 [0.84–0.90]			
Parameter	ADC_{min}	3	0.72 [0.53–0.90]	0.03	0.92 [0.86–0.97]	0.02	4.19	0.12
	Others	15	0.83 [0.77–0.89]		0.87 [0.84–0.90]			
Parameter	ADC_{mean}	3	0.74 [0.56–0.92]	0.05	0.92 [0.87–0.97]	0.01	4.49	0.11
	Others	15	0.83 [0.76–0.90]		0.86 [0.83–0.89]			
ROI_placement	Whole tumor	10	0.83 [0.76–0.91]	0.13	0.88 [0.85–0.91]	<0.01	1.14	0.56
	Solid portion	8	0.79 [0.68–0.90]		0.86 [0.81–0.90]			

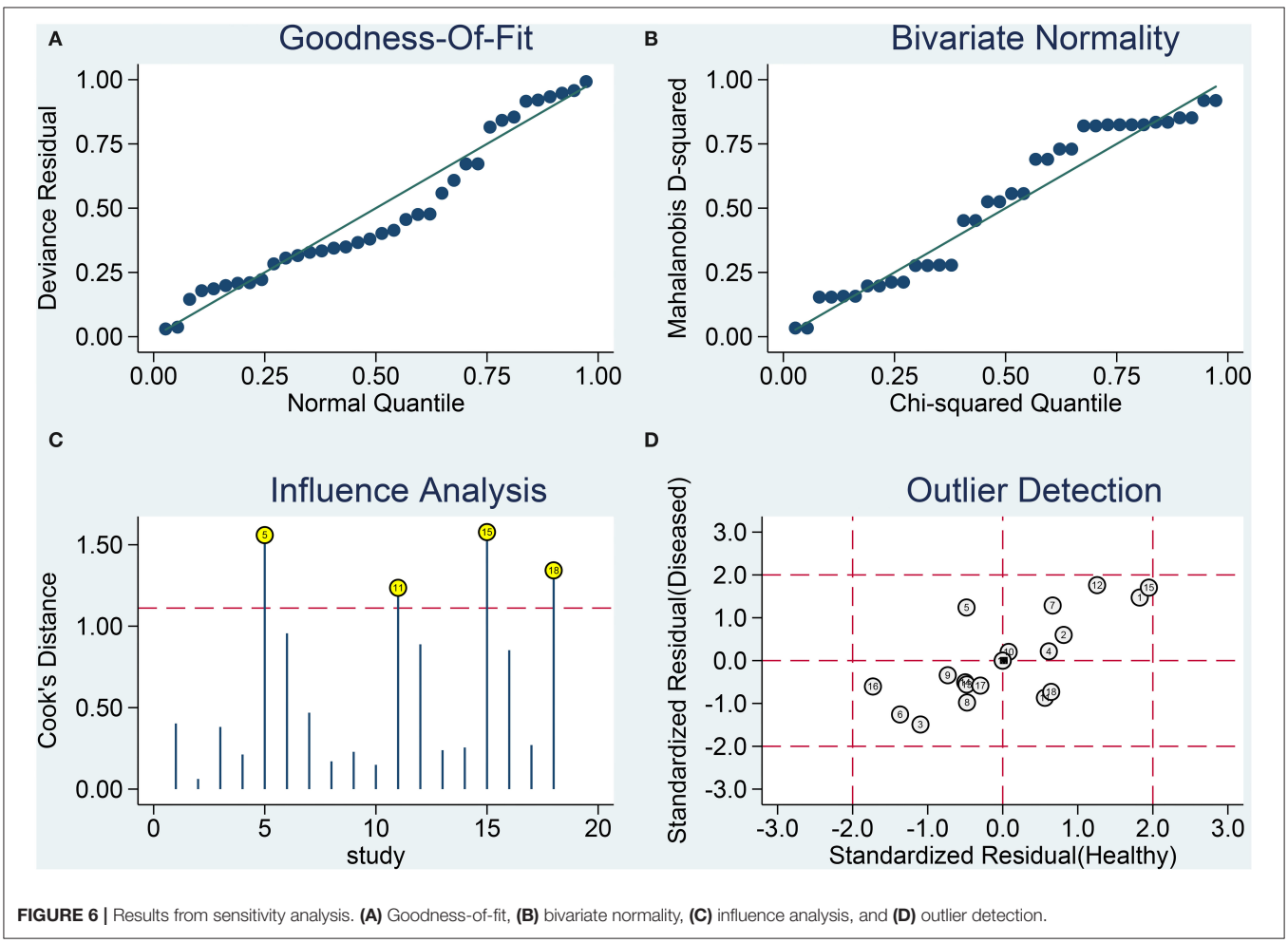

FIGURE 6 | Results from sensitivity analysis. **(A)** Goodness-of-fit, **(B)** bivariate normality, **(C)** influence analysis, and **(D)** outlier detection.

were conducted on a total of 461 patients. The results obtained confirmed that the DWI method could be effectively used to accurately identify the two types of tumors. However, significant heterogeneity was observed, and the combined sensitivity, specificity, and other indicators were lower than those reported by us (38).

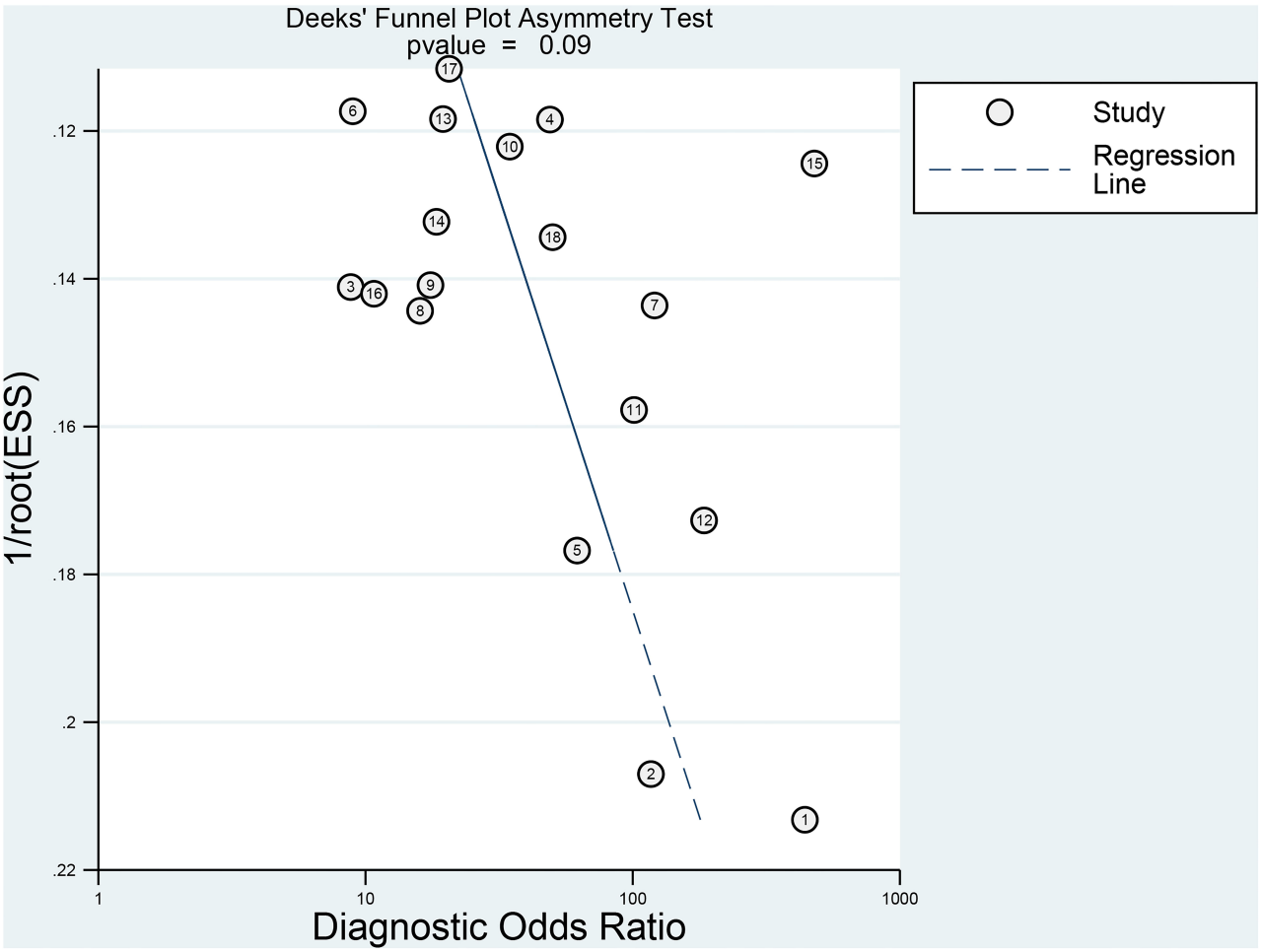

FIGURE 7 | Publication bias determined by conducting Deeks' test.

The ^{18}F-fluorodeoxyglucose (FDG)-positron emission tomography/computed tomography (PET/CT) technique can be used to simultaneously reflect the anatomical and metabolic information of the focus. The use of the PET/CT technique can result in a significant increase in the diagnostic accuracy achieved for the central nervous system lymphoma (39). Uchinomura S et al. retrospectively analyzed the PET/CT scanning results of 13 patients with PCNSL and 62 patients with glioblastoma before they were subjected to treatment methods. It was found that the diagnostic AUC value of PETCT could be as high as 0.9 (39). A retrospective analysis was carried out by Zhou W et al. They reported that the maximum standardized uptake (SUVmax) value and tumor to normal contralateral cortex activity (T/N) ratio calculated using the PET/CT technique could be used as reliable indices to distinguish between PCNSL and glioblastoma multiforme (40). Currently, an increasing number of studies are being conducted using the machine learning (ML) technique to image brains and distinguish between PCNSL and HGG. Results obtained from a meta-analysis of 8 relevant literature reports suggest that the efficiency of the ML algorithm-based method was at par, or in some cases, better than the efficiency of radiologists. The pooled AUC was approximately 0.9 (41).

There are several limitations of the studies. First, the sample sizes in some of the literature reports considered for the studies were <50, and most of the studies were reported by researchers working in Asia. These factors also result in heterogeneity. Second, we included retrospective studies to conduct our studies, and prospective studies were not considered. In retrospective studies, it is difficult to avoid selection bias. It is also difficult to determine the time sequence of exposure and disease. The authenticity of information is debatable, and all these factors affect the accuracy of the final results. Third, it is better to establish a unified method using the DWI method as the differences in the imaging parameters, fluctuations in the field strength, and differences in the efficiencies of the post-processing software used may result in the generation of inaccurate ADC values. Thus, the result can potentially be affected.

CONCLUSION

The results obtained by conducting the meta-analysis reveal that the DWI method is characterized by high sensitivity, specificity, and diagnostic accuracy. This method can be effectively used to distinguish between PCNSL and HGG. It is suggested that

samples of patients suffering from PCNSL and HGG should be analyzed using the DWI to effectively distinguish between the two types of tumors as soon as possible. Further research on the diagnostic performance of DWI requires more well-designed and prospective studies involving a larger number of patients.

DATA AVAILABILITY STATEMENT

The original contributions presented in the study are included in the article/**Supplementary Material**, further inquiries can be directed to the corresponding author.

AUTHOR CONTRIBUTIONS

XD and YH conceived and designed the study, acquired and analyzed the data, and wrote the manuscript. WL contributed to data analysis and manuscript preparation. All authors read and approved the manuscript and agree to be accountable for all aspects of the research in ensuring that the accuracy or integrity of any part of the work is appropriately investigated and resolved.

ACKNOWLEDGMENTS

We thank Bullet Edits Limited for the linguistic editing and proofreading of the manuscript.

SUPPLEMENTARY MATERIAL

The Supplementary Material for this article can be found online at: https://www.frontiersin.org/articles/10.3389/fneur.2022.882334/full#supplementary-material

Supplementary Figure 1 | A funnel plot representing the publication bias.

Supplementary Table 1 | The results of study quality and bias judged by the Newcastle-Ottawa Scale (NOS) checklist.

REFERENCES

1. Fox CP, Phillips EH, Smith J, Linton K, Gallop-Evans E, Hemmaway C, et al. Guidelines for the diagnosis and management of primary central nervous system diffuse large B-cell lymphoma. *Br J Haematol.* (2019) 184:348–63. doi: 10.1111/bjh.15661
2. Chukwueke UN, Nayak L. Central nervous system lymphoma. *Hematol Oncol Clin North Am.* (2019) 33:597–611. doi: 10.1016/j.hoc.2019.03.008
3. Alcantara M, Fuentealba J, Soussain C. Emerging landscape of immunotherapy for primary central nervous system lymphoma. *Cancers (Basel).* (2021) 13:5061. doi: 10.3390/cancers13205061
4. Chukwueke U, Grommes C, Nayak L. Primary central nervous system lymphomas. *Hematol Oncol Clin North Am.* (2022) 36:147–59. doi: 10.1016/j.hoc.2021.09.004
5. Chen R, Smith-Cohn M, Cohen AL, Colman H. Glioma subclassifications and their clinical significance. *Neurotherapeutics.* (2017) 14:284–97. doi: 10.1007/s13311-017-0519-x
6. Lima J, Mehta T, Datta N, Bakradze E, Staff I, Beland D, et al. Migraine history: a predictor of negative diffusion-weighted imaging in IV-tPA-treated stroke mimics. *J Stroke Cerebrovasc Dis.* (2019) 28:104282. doi: 10.1016/j.jstrokecerebrovasdis.2019.06.040
7. Wang QP, Lei DQ, Yuan Y, Xiong NX. Accuracy of ADC derived from DWI for differentiating high-grade from low-grade gliomas: systematic review and meta-analysis. *Medicine (Baltimore).* (2020) 99:e19254. doi: 10.1097/MD.0000000000019254
8. Whiting PF, Rutjes AW, Westwood ME, Mallett S, Deeks JJ, Reitsma JB, et al. QUADAS-2: a revised tool for the quality assessment of diagnostic accuracy studies. *Ann Intern Med.* (2011) 155:529–36. doi: 10.7326/0003-4819-155-8-201110180-00009
9. Vogelgesang F, Schlattmann P, Dewey M. The evaluation of bivariate mixed models in meta-analyses of diagnostic accuracy studies with SAS, Stata and R. *Methods Inf Med.* (2018) 57:111–9. doi: 10.3414/ME17-01-0021
10. Cohen JF, Chalumeau M, Cohen R, Korevaar DA, Khoshnood B, Bossuyt PM. Cochran's Q test was useful to assess heterogeneity in likelihood ratios in studies of diagnostic accuracy. *J Clin Epidemiol.* (2015) 68:299–306. doi: 10.1016/j.jclinepi.2014.09.005
11. Zamora J, Abraira V, Muriel A, Khan K, Coomarasamy A. Meta-DiSc: a software for meta-analysis of test accuracy data. *BMC Med Res Methodol.* (2006) 6:31. doi: 10.1186/1471-2288-6-31
12. Deeks JJ, Macaskill P, Irwig L. The performance of tests of publication bias and other sample size effects in systematic reviews of diagnostic test accuracy was assessed. *J Clin Epidemiol.* (2005) 58:882–93. doi: 10.1016/j.jclinepi.2005.01.016
13. Toh CH, Castillo M, Wong AM, Wei KC, Wong HF, Ng SH, et al. Primary cerebral lymphoma and glioblastoma multiforme: differences in diffusion characteristics evaluated with diffusion tensor imaging. *AJNR Am J Neuroradiol.* (2008) 29:471–5. doi: 10.3174/ajnr.A0872
14. Doskaliyev A, Yamasaki F, Ohtaki M, Kajiwara Y, Takeshima Y, Watanabe Y, et al. Lymphomas and glioblastomas: differences in the apparent diffusion coefficient evaluated with high b-value diffusion-weighted magnetic resonance imaging at 3T. *Eur J Radiol.* (2012) 81:339–44. doi: 10.1016/j.ejrad.2010.11.005
15. Yamashita K, Yoshiura T, Hiwatashi A, Togao O, Yoshimoto K, Suzuki SO, et al. Differentiating primary CNS lymphoma from glioblastoma multiforme: assessment using arterial spin labeling, diffusion-weighted imaging, and ^{1}8F-fluorodeoxyglucose positron emission tomography. *Neuroradiology.* (2013) 55:135–43. doi: 10.1007/s00234-012-1089-6
16. Ahn SJ, Shin HJ, Chang JH, Lee SK. Differentiation between primary cerebral lymphoma and glioblastoma using the apparent diffusion coefficient: comparison of three different ROI methods. *PLoS ONE.* (2014) 9:e112948. doi: 10.1371/journal.pone.0112948
17. Nakajima S, Okada T, Yamamoto A, Kanagaki M, Fushimi Y, Okada T, et al. Primary central nervous system lymphoma and glioblastoma: differentiation using dynamic susceptibility-contrast perfusion-weighted imaging, diffusion-weighted imaging, and (18)F-fluorodeoxyglucose positron emission tomography. *Clin Imaging.* (2015) 39:390–5. doi: 10.1016/j.clinimag.2014.12.002
18. Ko CC, Tai MH, Li CF, Chen TY, Chen JH, Shu G, et al. Differentiation between glioblastoma multiforme and primary cerebral lymphoma: additional benefits of quantitative diffusion-weighted MR imaging. *PLoS ONE.* (2016) 11:e0162565. doi: 10.1371/journal.pone.0162565
19. Li D, Li Z. Value of conventional MR and diffusion weighted imaging in differentiating primary central nervous system lymphoma and glioblastoma. *Int Med Health Guidance News.* (2016) 23:2906–9.
20. Lin X, Lee M, Buck O, Woo KM, Zhang Z, Hatzoglou V, et al. Diagnostic Accuracy of T1-Weighted Dynamic Contrast-Enhanced-MRI and DWI-ADC for Differentiation of Glioblastoma and Primary CNS Lymphoma. *AJNR Am J Neuroradiol.* (2017) 38:485–91. doi: 10.3174/ajnr.A5023
21. Lu S, Wang S, Gao Q, Zhou M, Li Y, Cao P, et al. Quantitative evaluation of diffusion and dynamic contrast-enhanced magnetic resonance imaging for differentiation between primary central nervous system lymphoma and glioblastoma. *J Comput Assist Tomogr.* (2017) 41:898–903. doi: 10.1097/RCT.0000000000000622
22. Luo L, Ren C, Zhang Y, Cheng J, Wang W, Gao X. Analysis of histogram of T2WI, ADC and enhanced T1WI in the differential diagnosis of pimary central nervous system lymphoma and glioblastoma. *Radiol Practice.* (2018) 33:658–63.

23. Xue X, Zhang J, Yang R, Liu Y, Li J, Han T. Valuation of combination use of single voxel long echo 1H-MRS and ADC in distinguishing primary central nervous system lymphoma from high grade gliomas. *J Clin Radiol.* (2019) 38:2194–9.
24. Anwar S, Baig MZ, Laghari AA, Mubarak F, Shamim MS, Jilani UA, et al. Accuracy of apparent diffusion coefficients and enhancement ratios on magnetic resonance imaging in differentiating primary cerebral lymphomas from glioblastoma. *Neuroradiol J.* (2019) 32:328–34. doi: 10.1177/1971400919857556
25. Zhang S, Wang J, Wang K, Li X, Zhao X, Chen Q, et al. Differentiation of high-grade glioma and primary central nervous system lymphoma: multiparametric imaging of the enhancing tumor and peritumoral regions based on hybrid (18)F-FDG PET/MRI. *Eur J Radiol.* (2022) 150:110235. doi: 10.1016/j.ejrad.2022.110235
26. Eisenhut F, Schmidt MA, Putz F, Lettmaier S, Fröhlich K, Arinrad S, et al. Classification of primary cerebral lymphoma and glioblastoma featuring dynamic susceptibility contrast and apparent diffusion coefficient. *Brain Sci.* (2020) 10:886. doi: 10.3390/brainsci10110886
27. Mehrnahad M, Rostami S, Kimia F, Kord R, Taheri MS, Rad HS, et al. Differentiating glioblastoma multiforme from cerebral lymphoma: application of advanced texture analysis of quantitative apparent diffusion coefficients. *Neuroradiol J.* (2020) 33:428–36. doi: 10.1177/1971400920937382
28. Geng L, Sun Y, Zhao Y, Wan J, Xu L, Ye Y, et al. Application of ADC values and rADC values in the diagnosis and differentiation of primary central nervous system lymphoma and its correlation with Ki-67. *J Pract Med.* (2021) 37:2530–4.
29. Eyüboglu I, Çakir IM, Aslan S, Sari A. Diagnostic efficacy of apparent diffusion coefficient measurements in differentiation of malignant intra-axial brain tumors. *Turk J Med Sci.* (2021) 51:256–67. doi: 10.3906/sag-2006-1
30. Ozturk K, Soylu E, Cayci Z. Differentiation between primary CNS lymphoma and atypical glioblastoma according to major genomic alterations using diffusion and susceptibility-weighted MR imaging. *Eur J Radiol.* (2021) 141:109784. doi: 10.1016/j.ejrad.2021.109784
31. Chiavazza C, Pellerino A, Ferrio F, Cistaro A, Soffietti R, Rudà R. Primary CNS lymphomas: challenges in diagnosis and monitoring. *Biomed Res Int.* (2018) 2018:3606970. doi: 10.1155/2018/3606970
32. Küker W, Nägele T, Korfel A, Heckl S, Thiel E, Bamberg M, et al. Primary central nervous system lymphomas (PCNSL): MRI features at presentation in 100 patients. *J Neurooncol.* (2005) 72:169–77. doi: 10.1007/s11060-004-3390-7
33. Almansory KO, Fraioli F. Combined PET/MRI in brain glioma imaging. *Br J Hosp Med (Lond).* (2019) 80:380–6. doi: 10.12968/hmed.2019.80.7.380
34. Chakhoyan A, Yao J, Leu K, Pope WB, Salamon N, Yong W, et al. Validation of vessel size imaging (VSI) in high-grade human gliomas using magnetic resonance imaging, image-guided biopsies, and quantitative immunohistochemistry. *Sci Rep.* (2019) 9:2846. doi: 10.1038/s41598-018-37564-w
35. Gatidis S, Schmidt H, Martirosian P, Nikolaou K, Schwenzer NF. Apparent diffusion coefficient-dependent voxelwise computed diffusion-weighted imaging: an approach for improving SNR and reducing T2 shine-through effects. *J Magn Reson Imaging.* (2016) 43:824–32. doi: 10.1002/jmri.25044
36. Xu W, Wang Q, Shao A, Xu B, Zhang J. The performance of MR perfusion-weighted imaging for the differentiation of high-grade glioma from primary central nervous system lymphoma: a systematic review and meta-analysis. *PLoS ONE.* (2017) 12:e0173430. doi: 10.1371/journal.pone.0173430
37. Wu Y, Den Z, Lin Y. Accuracy of susceptibility-weighted imaging and dynamic susceptibility contrast magnetic resonance imaging for differentiating high-grade glioma from primary central nervous system lymphomas: meta-analysis. *World Neurosurg.* (2018) 112:e617–e623. doi: 10.1016/j.wneu.2018.01.098
38. Lu X, Xu W, Wei Y, Li T, Gao L, Fu X, et al. Diagnostic performance of DWI for differentiating primary central nervous system lymphoma from glioblastoma: a systematic review and meta-analysis. *Neurol Sci.* (2019) 40:947–56. doi: 10.1007/s10072-019-03732-7
39. El-Galaly TC, Villa D, Gormsen LC, Baech J, Lo A, Cheah CY. FDG-PET/CT in the management of lymphomas: current status and future directions. *J Intern Med.* (2018) 284:358–76. doi: 10.1111/joim.12813
40. Zhou W, Wen J, Hua F, Xu W, Lu X, Yin B, et al. (18)F-FDG PET/CT in immunocompetent patients with primary central nervous system lymphoma: differentiation from glioblastoma correlation with DWI. *Eur J Radiol.* (2018) 104:26–32. doi: 10.1016/j.ejrad.2018.04.020
41. Nguyen AV, Blears EE, Ross E, Lall RR, Ortega-Barnett J. Machine learning applications for the differentiation of primary central nervous system lymphoma from glioblastoma on imaging: a systematic review and meta-analysis. *Neurosurg Focus.* (2018) 45:E5. doi: 10.3171/2018.8.FOCUS18325

Conflict of Interest: The authors declare that the research was conducted in the absence of any commercial or financial relationships that could be construed as a potential conflict of interest.

Publisher's Note: All claims expressed in this article are solely those of the authors and do not necessarily represent those of their affiliated organizations, or those of the publisher, the editors and the reviewers. Any product that may be evaluated in this article, or claim that may be made by its manufacturer, is not guaranteed or endorsed by the publisher.

Copyright © 2022 Du, He and Lin. This is an open-access article distributed under the terms of the Creative Commons Attribution License (CC BY). The use, distribution or reproduction in other forums is permitted, provided the original author(s) and the copyright owner(s) are credited and that the original publication in this journal is cited, in accordance with accepted academic practice. No use, distribution or reproduction is permitted which does not comply with these terms.

frontiers | Frontiers in Neuroscience

ORIGINAL RESEARCH
published: 13 July 2022
doi: 10.3389/fnins.2022.885291

Decoding the Heterogeneity of Malignant Gliomas by PET and MRI for Spatial Habitat Analysis of Hypoxia, Perfusion, and Diffusion Imaging: A Preliminary Study

*Michele Bailo[1,2], Nicolò Pecco[3], Marcella Callea[4], Paola Scifo[5], Filippo Gagliardi[2], Luca Presotto[5], Valentino Bettinardi[5], Federico Fallanca[5], Paola Mapelli[1,5], Luigi Gianolli[5], Claudio Doglioni[4], Nicoletta Anzalone[1,3], Maria Picchio[1,5], Pietro Mortini[1,2], Andrea Falini[1,3] and Antonella Castellano[1,3]**

[1] Vita-Salute San Raffaele University, Milan, Italy, [2] Department of Neurosurgery and Gamma Knife Radiosurgery, IRCCS Ospedale San Raffaele, Milan, Italy, [3] Neuroradiology Unit and CERMAC, IRCCS Ospedale San Raffaele, Milan, Italy, [4] Pathology Unit, IRCCS Ospedale San Raffaele, Milan, Italy, [5] Department of Nuclear Medicine, IRCCS Ospedale San Raffaele, Milan, Italy

OPEN ACCESS

Edited by:
Alexandra Golby,
Harvard Medical School,
United States

Reviewed by:
Shanshan Jiang,
Johns Hopkins Medicine,
United States
Alberto De Luca,
University Medical Center Utrecht,
Netherlands

***Correspondence:**
Antonella Castellano
castellano.antonella@hsr.it

Specialty section:
This article was submitted to Brain Imaging Methods, a section of the journal Frontiers in Neuroscience

Received: 27 February 2022
Accepted: 14 June 2022
Published: 13 July 2022

Citation:
Bailo M, Pecco N, Callea M, Scifo P, Gagliardi F, Presotto L, Bettinardi V, Fallanca F, Mapelli P, Gianolli L, Doglioni C, Anzalone N, Picchio M, Mortini P, Falini A and Castellano A (2022) Decoding the Heterogeneity of Malignant Gliomas by PET and MRI for Spatial Habitat Analysis of Hypoxia, Perfusion, and Diffusion Imaging: A Preliminary Study. Front. Neurosci. 16:885291. doi: 10.3389/fnins.2022.885291

Background: Tumor heterogeneity poses major clinical challenges in high-grade gliomas (HGGs). Quantitative radiomic analysis with spatial tumor habitat clustering represents an innovative, non-invasive approach to represent and quantify tumor microenvironment heterogeneity. To date, habitat imaging has been applied mainly on conventional magnetic resonance imaging (MRI), although virtually extendible to any imaging modality, including advanced MRI techniques such as perfusion and diffusion MRI as well as positron emission tomography (PET) imaging.

Objectives: This study aims to evaluate an innovative PET and MRI approach for assessing hypoxia, perfusion, and tissue diffusion in HGGs and derive a combined map for clustering of intra-tumor heterogeneity.

Materials and Methods: Seventeen patients harboring HGGs underwent a pre-operative acquisition of MR perfusion (PWI), Diffusion (dMRI) and ^{18}F-labeled fluoroazomycinarabinoside (^{18}F-FAZA) PET imaging to evaluate tumor vascularization, cellularity, and hypoxia, respectively. Tumor volumes were segmented on fluid-attenuated inversion recovery (FLAIR) and T1 post-contrast images, and voxel-wise clustering of each quantitative imaging map identified eight combined PET and physiologic MRI habitats. Habitats' spatial distribution, quantitative features and histopathological characteristics were analyzed.

Results: A highly reproducible distribution pattern of the clusters was observed among different cases, particularly with respect to morphological landmarks as the necrotic core, contrast-enhancing vital tumor, and peritumoral infiltration and edema, providing valuable supplementary information to conventional imaging. A preliminary analysis, performed on stereotactic bioptic samples where exact intracranial coordinates were available, identified a reliable correlation between the expected microenvironment of the different spatial habitats and the actual histopathological features. A trend

toward a higher representation of the most aggressive clusters in WHO (World Health Organization) grade IV compared to WHO III was observed.

Conclusion: Preliminary findings demonstrated high reproducibility of the PET and MRI hypoxia, perfusion, and tissue diffusion spatial habitat maps and correlation with disease-specific histopathological features.

Keywords: high-grade glioma, PET, MRI, habitats, hypoxia imaging, perfusion-weighted imaging, diffusion-weighted imaging, tumor heterogeneity

INTRODUCTION

Tumor heterogeneity poses a major clinical challenge in brain tumors and its enhanced assessment can be pivotal to understand treatment failure in high-grade gliomas (HGGs) (O'Connor et al., 2015; Stadlbauer et al., 2018b). Indeed, in HGGs, the regional diversity both at the level of DNA mutation and gene expression profiles may ultimately alter phenotype by influencing tumor cell metabolism, apoptosis, and angiogenesis processes (Louis et al., 2016; Komori et al., 2018). At the individual patient level, the heterogeneous biology of malignant gliomas challenges tools that rely on single biopsy criteria for making disease-wide assessments and poses a problem in planning effective subsequent treatments. Furthermore, tumor heterogeneity is reflected in differential and dynamical response during therapy, eventually causing the failure of previously effective alkylating drugs or targeted therapies, as resistant clones invariably emerge and proliferate (Sottoriva et al., 2013; Stadlbauer et al., 2018b).

Non-invasive imaging can provide multiple biomarkers with insight into the malignancy and biology of gliomas. Conventional magnetic resonance imaging (cMRI) is routinely employed in the diagnosis and clinical management of malignant gliomas: beside the tumor features described by cMRI sequences, advanced physiological MRI techniques such as diffusion MRI (dMRI) and perfusion-weighted imaging (PWI) add important structural, physiological and hemodynamic information to measure biological properties quantitatively and non-invasively and correlate with patients' outcome (Castellano and Falini, 2016). Similarly, positron emission tomography (PET) imaging reflects fundamental metabolic patterns throughout the tumor. In particular, PET using tracers from nitroimidazoles family, such as ^{18}F-labeled fluoroazomycinarabinoside (^{18}F-FAZA) or ^{18}F-labeled fluoromisonidazole (^{18}F-FMISO), identifies areas of hypoxic tissue that have been shown as related to treatment resistance, thus negatively impacting on patient outcome and survival (Preibisch et al., 2017; Abdo et al., 2019).

Furthermore, with the application of advanced mathematical modeling, it is also possible to divide neoplasms into definite subregions comprehending clusters of voxels with comparable radiomics features. This method is defined as "habitat imaging" and is considered a way to characterize and measure the heterogeneity of the tumoral microenvironment (Gatenby et al., 2013). Habitat imaging has been currently mainly employed on cMRI sequences, although it could hypothetically be applied to any neuroimaging method, comprising advanced MRI techniques such as PWI and dMRI as well as PET imaging with different radiotracers (Zhou et al., 2014; Hu et al., 2015; Lee et al., 2015a,b; O'Connor et al., 2015; Cui et al., 2016; Sauwen et al., 2016; Dextraze et al., 2017; Kim and Gatenby, 2017; Zhou et al., 2017; Fathi Kazerooni et al., 2018; Fuster-Garcia et al., 2018; Ismail et al., 2018; Juan-Albarracin et al., 2018; Li et al., 2018a,b; John et al., 2019; Juan-Albarracin et al., 2019; Li et al., 2019; Stringfield et al., 2019; Wang et al., 2019; Wei et al., 2019; Zhang et al., 2019; Beig et al., 2020; Del Mar Alvarez-Torres et al., 2020; Verma et al., 2020; Wu et al., 2020; Kim et al., 2021; Park et al., 2021).

To date, the spatial relationship between areas of hypoxia, neoangiogenesis, and altered tissue microstructure and cellularity has not been completely elucidated in HGGs using advanced neuroimaging. The aim of the present study is to evaluate an innovative, PET and MRI approach for the assessment of hypoxia, perfusion, and tissue diffusion in HGG and derive a combined spatial habitat map for clustering of intra-tumor heterogeneity. To the best of our knowledge, this represents the first study combining the aforementioned parameters to define brain tumor habitats.

Abbreviations: ^{18}F-FAZA, ^{18}F-labeled fluoroazomycinarabinoside; ADC, apparent diffusion coefficient; CE, contrast-enhanced; CT, computed tomography; DCE, dynamic contrast-enhanced; DSC, dynamic susceptibility contrast-enhanced; cMRI, conventional magnetic resonance imaging; dMRI, diffusion magnetic resonance imaging techniques; DTI, diffusion tensor imaging; DWI, diffusion-weighted imaging; FLAIR, fluid-attenuated inversion recovery; HGG, high-grade glioma; HIF-1α, hypoxia-inducible factor 1α; IDH, isocitrate dehydrogenase; Ktrans, volume transfer constant; MD, mean diffusivity; MGMT, O6-methylguanine-DNA methyltransferase; MRI, magnetic resonance imaging; PET, positron emission tomography; PWI, perfusion-weighted magnetic resonance imaging; rCBV, relative cerebral blood volume; VEGF, vascular-endothelial growth factor; Vp, plasma volume; WHO, World Health Organization.

MATERIALS AND METHODS

Patients

In this study the PET and MRI datasets of twenty patients harboring brain lesions with MRI features suggestive for HGG were analyzed, previously recruited in a prospective study on hypoxia tracers at San Raffaele Scientific Institute from April 2016 to October 2017. The local research ethics committee approved the study, and informed consent was obtained from all patients. All the subjects underwent advanced MRI acquisition and ^{18}F-FAZA PET/CT before surgery, except for two patients that were withdrawn from the study due to technical problems related to radiotracer synthesis. Another patient was eventually excluded

from the analysis since the final histopathological diagnosis was brain metastases from lung cancer.

PET/CT

The procedure of ^{18}F-FAZA radiotracer production followed the technique previously reported by Savi et al. (2017). Every recruited patient had an intravenous administration of about 372 ± 17 (minimum 340, maximum 407) MBq of ^{18}F-FAZA. The PET/CT scan acquisition and analysis were conducted as previously reported by Mapelli and Picchio (2020) and Mapelli et al. (2021).

MRI Acquisition

Pre-operative MRI datasets were acquired (1–5 days prior to the surgical procedure) on a 1.5 T scanner (Philips Achieva–Philips Healthcare, Best, Netherlands) in 12/17 cases, and on a 3.0 T (Ingenia CX scanner, Philips Healthcare, Best, Netherlands) on 5/17 patients.

Imaging acquisition included the following sequences:

1. 3D-FLAIR (fluid-attenuated inversion recovery) and Contrast-enhanced (CE) 3D-T1 weighted images, for morphological evaluation and tumor segmentation (**Figures 1A,B**);
2. Diffusion Tensor Imaging (DTI) sequence to detect microstructural features of the tumor tissue. DTI data were obtained using a single-shot echo planar sequence with diffusion gradients applied along 15 or 32 axes, using *b*-values of 0 and 1000 s/mm^2. After correcting for distortions due to eddy currents and head motion, maps of Mean Diffusivity (MD) (**Figure 1C**) were derived from DTI acquisitions by fitting the diffusion tensor model within each voxel using the FMRIB Diffusion Toolbox (FDT tool, FMRIB Software Library [FSL] version 6.0.0[1]);
3. Perfusion-weighted magnetic resonance imaging including dynamic contrast-enhanced (DCE) and dynamic susceptibility contrast-enhanced (DSC) MRI, to characterize tumor vascularization and neoangiogenic processes, according to a previously descripted protocol (Santarosa et al., 2016; Anzalone et al., 2018). PWI analysis was performed with Olea Sphere (v 3.0, Olea Medical Solutions, France) to obtain the parametric maps of volume transfer constant (Ktrans) and plasma volume (Vp), derived from DCE, and relative cerebral blood volume (rCBV), derived by DSC, as described in Conte et al. (2017) (**Figures 1D–F**). Pre-processing steps included automatic motion correction by a rigid-body registration, automatic spatial smoothing, and background segmentation.

The complete acquisition parameters of all the sequences are reported in the **Supplementary Tables 1**, **2**.

Image Processing

For each patient, all the radiological studies and maps were imported, coregistered to the reference 3D-T1 CE sequence (two consecutive automatic rigid registration processes, with 6 degrees of freedom and 0.1 as percentage of samples, were performed after initial manual adjustment, then carefully checked for the eventual necessity of minor manual correction) and reformatted to the same matrix (voxel 1 × 1 × 1 mm) in the image processing software 3D Slicer[2] (Fedorov et al., 2012), creating a single dataset for each patient. Two different tumor masks were segmented manually using 3D Slicer, being carefully checked repeatedly by the first author (MB) and an experienced neuroradiologist (AC): one including only the enhancing tissue and necrotic core on the post-gadolinium 3D-T1 images (CE-tumor, green contour in **Figure 1A**), the second including, additionally, the peritumoral infiltrative edema as identified on 3D-FLAIR images (FLAIR-tumor, orange contour in **Figure 1B**). Care was taken, while comparing data from multiple coregistered sequences (e.g., Susceptibility-weighted imaging, T2-weighted, PWI maps, MD maps, T1-weighted images with and without contrast enhancement, CT) not to include non-tumoral structures that could jeopardize subsequent analyses (e.g., subarachnoid cisterns, sulci, ventricular space, choroid plexus, ependyma, significant vascular structures, dural folds, calcifications).

The feasibility of deriving a combined spatial habitat map was then exploited by using the automatic Otsu thresholding algorithm method developed in Matlab2019a (The MathWorks, Inc., Natick, MA, United States). The Otsu algorithm was chosen for its simplistic approach in dividing ROI tumoral voxels into two clusters with high and low-intensity (Zhou et al., 2014, 2017; Napel et al., 2018; Stringfield et al., 2019), thus maintaining the clinical significance of each map subregion. The Otsu algorithm calculates a global threshold T from each of the grayscale tumoral ROI (perfusion, diffusion, and hypoxia, **Figures 1C–G**) by minimizing intra-class intensity variance, or equivalently, by maximizing inter-class variance as described in Otsu (1979).

For each subject the three tumoral ROIs were imported in Matlab2019a and voxels included inside the tumor ROI [excluding those outside the range of mean ± 3 standard deviations, as described in Collewet et al. (2004)] were clustered into two disjoint subregions with the automatic Otsu's algorithm. Therefore, given three tumor-masked maps (D_1, D_2, and D_3), they were clustered as follows:

$$D_1 \rightarrow [D_{1L}, D_{1H}], D_2 \rightarrow [D_{2L}, D_{2H}], \textit{and } D_3 \rightarrow [D_{3L}, D_{3H}]$$

$$D_{1L} \cap D_{1H} = \emptyset, D_{2L} \cap D_{2H} = \emptyset, \textit{and } D_{3L} \cap D_{3H} = \emptyset$$

In this way, 2 clusters for each map ("high" and "low" expression of a parameter) were obtained. Then, spatial habitat maps were composed in each patient by defining as a different 'habitat' each possible combination of clusters (see **Supplementary Figure 1**). Thus, the cluster that groups together all high-intensity cluster sequences (HHH) is defined as:

$$Habitat(HHH) : [D_{1H} \cap D_{2H} \cap D_{3H}]$$

The different habitats were eventually represented with different colors (**Figures 1H,I**) to ease visual identification,

[1]https://fsl.fmrib.ox.ac.uk/

[2]http://www.slicer.org

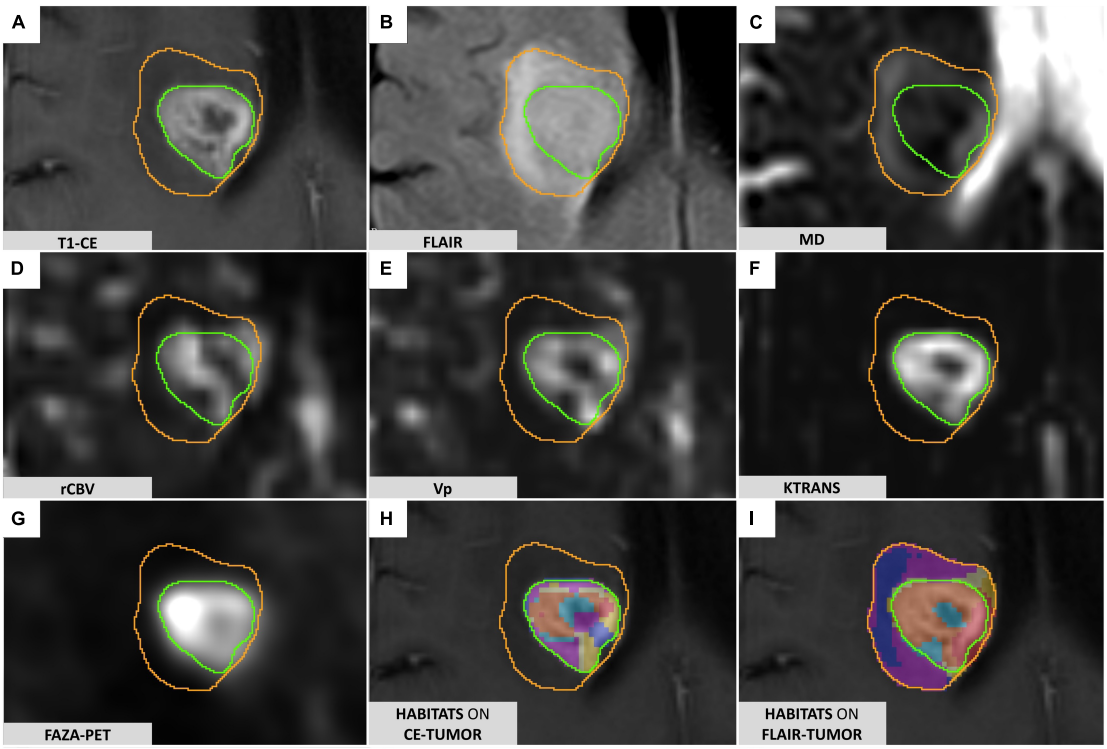

FIGURE 1 | FLAIR-tumor and CE-tumor segmentations on different MRI sequences. **(A)** T1-weighted contrast-enhanced imaging: the CE-tumor volume is contoured in green, including the enhancing tissue and necrotic core only. **(B)** FLAIR images: FLAIR-tumor is contoured in orange, including both the CE-tumor and the peritumoral hyperintensity. **(C)** MD map elaborated from DTI acquisition. **(D)** rCBV map elaborated from DSC MR perfusion acquisition. **(E)** VP map elaborated from DCE MR perfusion acquisition **(F)** Ktrans map elaborated from DCE MR perfusion acquisition. **(G)** 18F-FAZA-PET uptake showing hypoxic areas. **(H)** Prototype of clusters resulting from the application of the spatial habitat imaging algorithm only to the contrast-enhanced tumor volume (CE-tumor); clusters obtained this way were considered too small and fragmented in order to be reliably correlated to histology, and therefore not suitable for the purpose of the present study. **(I)** Habitats obtained applying the spatial habitat imaging algorithm to the FLAIR-tumor volume (which included the contrast-enhanced tumor core along with the surrounding area of FLAIR hyperintensity) were able to divide the whole tumor in a more reproducible way, with larger clusters amenable to a reliable histological correlation with the bioptic samples obtained; for the aforementioned reasons we selected FLAIR-tumor as the final tumor mask to be investigated and all the results presented in our paper are based on its analysis.

yield regions with different combinations of perfusion, diffusion, and hypoxia, supposedly reflecting different physiological microenvironments within the tumor.

Surgical Procedure and Histopathological Evaluation

All patients underwent the surgical procedure at the Neurosurgery Department of the IRCCS San Raffaele Hospital (Milan, Italy). Patients were considered for maximum safe resection or stereotactic needle biopsy according to tumor location/extension and patient characteristics (e.g., age, comorbidities, and performance status).

In the case of stereotactic biopsy, the procedure commenced with the fixation of the MRI-compatible Leksell stereotactic frame to the patient's skull (Model G, Elekta, Stockholm, Sweden), under mild intravenous sedation (midazolam) and local anesthesia (lidocaine and mepivacaine). The patient then underwent the acquisition of an axial 3D-T1 MRI after gadolinium administration (Voxel 1 × 1 mm, slice thickness 1 mm, Matrix 256 × 256 mm) using the appropriate fiducial system on a Philips Achieva 1.5 Tesla MR scanner (Philips Medical Systems, Best, Netherlands). In most of the cases, a 3D T2-weighted series was also obtained. All the relevant imaging and parameter maps were then imported into the stereotactic planning software Leksell SurgiPlan® (Elekta Instruments AB, Stockholm, Sweden) and coregistered to the newly acquired stereotactic images.

Since the final tumor habitats were not available to the neurosurgeon pre-operatively, the designation of target sites for biopsy sites and the needle path were planned according to the best clinical practice in order to maximize patient safety while ensuring final diagnosis. During the procedure, a Sedan needle (2.5 mm diameter and 10 mm of bioptic window) was used to acquire a minimum of two bioptic samples. Considering the macroscopical aspect and size of the sample obtained and the procedure-related risks/complications, a median of 3 cylindrical tissue biopsies (median length 8 mm, range 4–11 mm) were obtained. The accuracy of the bioptic sampling was eventually verified in all cases through the co-registration of the pre-operative imaging and planned trajectory with the post-operative CT images inside the SurgiPlan software; the

stereotactic coordinates of the exact, final sites of the biopsy were then imported in the 3D Slicer Dataset.

The tissue samples obtained were directly fixed in a 10% formalin solution and referred to the pathology department, where they were processed the same day or the following one if the procedures were performed in the late afternoon. The final diagnosis was established according to the 2016 World Health Organization (WHO) classification (Louis et al., 2016). A descriptive analysis of the microscopic morphology of each sample was performed by an expert neuropathologist (MC) attended by a neurosurgeon (MB), repeating the whole evaluation at three distant time points (blinded from previously reported values and patient's case) in order to enhance the reproducibility of the results. Additionally, to address the issue of the length variability among different bioptic specimens and to maximize the correspondence with the target point set on the stereotactic planning system, only the central portion (extending 5 mm along the greatest axis of the specimen in its largest section available) was analyzed in each sample.

The following parameters were semi-quantitatively graded similarly to a previously reported work (Mikkelsen et al., 2018), despite the adoption of a higher number of classes dividing each feature in the present analysis: cellularity, the extent of necrosis, and the number of hyperplastic vessels counted. Cellularity was graded with a score from 1 (seemingly normal representation) to 5 (extremely high cellular density). Classes adopted for necrosis (expressed as a rate over the whole area considered for each specimen) were the following: 0 (0%), 1 ($\leq$10%), 2 (11–25%), 3 (26–50%), 4 (51–75%), and 5 (76–100%).

In the 10/17 patients who underwent needle biopsy, the stereotactic coordinates of the sampling sites were imported in the 3D Slicer Dataset as a 5 mm diameter spherical volume, similarly to what was previously described by other authors (Jun et al., 2006; Barajas R. F. et al., 2012; Gates et al., 2019; Rotkopf et al., 2020), in order to take into account the maximum reported accuracy error in Euclidean distance reported in the literature (Roth et al., 2018). Each histopathological specimen, labeled according to the order of resection, was then analyzed in comparison to the corresponding voxels and habitats in the 3D Slicer Dataset.

Statistical Analysis

Statistical analysis was performed with IBM SPSS Statistics, version 23.0 (IBM Corp., Armonk, NY, United States), Prism 9 version 3.1 (GraphPad Software, LLC) and Matlab2019a (MathWorks, Natick, MA, United States). The threshold of statistical significance was defined as two-sided $P = 0.05$. Distribution normality was assessed with the Kolmogorov–Smirnov test.

The following variables were tested for possible associations: quantitative values across different habitats for each parametric map, CE-tumor volume, FLAIR-tumor volume, representation of the different habitats (absolute volume, rate over total), patient's age, WHO tumor grading, MGMT methylation, 1p19q codeletion, IDH-1 status. The distribution of mean values of Vp, ^{18}F-FAZA and MD parametric maps in each habitat was displayed by means of boxplots.

A Kruskal–Wallis test was conducted to determine if there were differences among different habitats in voxel-wise parametric values for each PET and MRI map. The percentage of habitats' representation according to tumor grade and molecular status was assessed by boxplots' visual inspection. Pairwise comparisons were performed using Dunn's procedure with Bonferroni correction for multiple comparisons.

RESULTS

Patients and Lesion Characteristics

The study population (data summarized in **Table 1**) was composed of 5 female and 12 male patients, with ages ranging from 41 to 81 years old (mean 66 years).

A single contrast-enhancing (CE) lesion was detected in 13/17 patients; 3/17 patients harbored multiple CE lesions, while in one patient no definite CE tumor core was confidently identifiable. The average cumulative CE-tumor volume (per patient) was 25.3 $\pm$ 24.4 cm^3 (range 0–79.1 cm^3). Mean cumulative FLAIR-tumor volume (per patient) was 94.2 $\pm$ 58.7 cm^3 (range 10.2–185.4 cm^3). The mean rate between CE-tumor and FLAIR-tumor volume was 0.30 $\pm$ 0.20 (range 0–0.7).

Maximum safe resection was performed in 7/17, while a stereotactic biopsy was obtained in 10/17 patients. Four out of individuals harbored an anaplastic astrocytoma (WHO grade III), one had an anaplastic oligodendroglioma (1p/19q co-deleted, WHO grade III) and 12/17 patients had grade IV glioblastoma, according to WHO 2016 classification (Louis et al., 2016). Three tumors retained an IDH-1 mutation. Histopathological and molecular data are summarized in **Table 1**.

Mean overall survival (**Table 1**) was 53.1 $\pm$ 67 weeks (median 21 weeks, range 8–222 weeks). Two patients were still alive at the last follow-up assessment (49 and 51 months, respectively). The remaining 15 patients died during follow-up due to causes directly (e.g., tumor progression increasing mass effect on cerebral structures) or indirectly (e.g., aspiration pneumonia) associated with the disease.

Map Selection

The ideal number of maps to be included simultaneously in the algorithm was thoroughly evaluated. The possible complementary information gathered by adding a higher number of maps had to be balanced with the exponential increase in the number of significantly smaller and fragmented clusters, resulting in an unreliable surgical targeting and histological correlation. For the aforementioned reasons, after examining the possible complementarity of the maps, "8" (from the combination of three different parametric maps) was identified as the ideal number of clusters for the purpose of the project. Among the available parametric perfusion maps, the intra-vascular plasma volume derived from DCE-MRI, that quantifies tumor neoangiogenesis similarly to rCBV (Alcaide-Leon et al., 2015), was selected as the most appropriate for the purpose of the study due to the lower sensitivity to susceptibility artifacts and to the presence of intralesional hemorrhagic foci, as well as

for the better capability to discriminate surrounding macrovessel from true intralesional neoangiogenic hotspots on Vp parametric maps, especially in cortical tumors growing in proximity to large vessels (Santarosa et al., 2016). Furthermore, DCE-derived Vp maps have higher spatial resolution compared to DSC-derived rCBV maps and yield an absolute quantification of perfusion parameters (Anzalone et al., 2018). Vp also allows a more informative representation of the FLAIR-tumor volume outside of the CE region compared to Ktrans (Nguyen et al., 2016; Zhang et al., 2017; Anzalone et al., 2018).

Positron emission tomography (PET) with the ^{18}F-flouroazomycin arabinoside (^{18}F-FAZA) radiotracer has been previously used for the non-invasive assessment of tumor hypoxia (Mapelli et al., 2021), and was chosen due to its high perfusion, high biological half-life time and fast clearance from blood, with subsequent improved tumor-to-background ratio (Mapelli and Picchio, 2020).

Among the DTI-derived maps, MD was selected as one of the simplest and most validated parameters in radiomics to distinguish tumor grade and cellular proliferation in brain gliomas (Miloushev et al., 2015). MD quantifies water molecular mobility, averaged over all the obtained directions, within tissues impeded by cell membranes and tortuosity of the extracellular space (Maier et al., 2010). This parameter is equivalent to the apparent diffusion coefficient (ADC) generated from DWI acquisitions and shows a negative correlation with tissue cellularity, as previously reported in literature (Ellingson et al., 2010; Maier et al., 2010; Chen et al., 2013; Sanvito et al., 2021).

Habitats' Analysis

Eight habitats were generated from cluster intersection by combining all possible HIGH (H) and LOW (L) intensity regions of each map (Vp + ^{18}F-FAZA + MD) and the final tumor habitat map was composed (**Figure 1**).

TABLE 1 | Patient demographic, histopathologic, and survival data.

No.	Age (yrs)	Sex	Tumor vol. CE (cm^3)	Tumor vol. FLAIR (cm^3)	No. of distinct lesions	Surgical procedure	Histology (grade)	p53	ATRX	GFAP	KI-67	MGMT methylation	IDH-1 status	OS (wks)
1	71	F	23.4	67.8	1	Resection	GBL (WHO IV)	20%	+	+	10%	+	−	40
2	58	M	4.4	10.2	1	Biopsy	GBL (WHO IV)	15%	+	+	20%	N/A	+	76
3	56	M	25.0	111.6	1	Resection	GBL (WHO IV)	5%	+	+	25%	+	−	214
4	61	M	1.1	10.9	1	Resection	AA (WHO III)	5%	−	+	30%	+	−	71
5	73	F	61.4	130.2	1	Biopsy	GBL (WHO IV)	5–10%	+	+	7%	N/A	−	21
6	77	M	56.1	184.0	1	Resection	GBL (WHO IV)	0	+	+	15%	+	−	16
7	79	M	79.1	185.4	1	Resection	GBL (WHO IV)	10%	−	+	20%	+	−	26
8	69	F	1.6	50.1	5	Biopsy	AA (WHO III)	5%	+	+	3%	N/A	−	13
9	64	M	2.6	91.1	3	Biopsy	GBL (WHO IV)	10%	+	+	35%	N/A	−	21
10	81	M	34.4	98.1	4	Biopsy	AO (WHO III)	0	+	++	15%	N/A	+	10
11	65	M	30.3	136.5	1	Resection	GBL (WHO IV)	0	+	+	15%	+	−	44
12	77	M	5.4	23.4	1	Biopsy	GBL (WHO IV)	N/A	+	N/A	5%	N/A	−	13
13	41	M	0.0	146.5	1	Biopsy	AA (WHO III)	3%	+	+	10%	+	+	10
14	64	M	53.0	70.8	1	Biopsy	AA (WHO III)	<1%	+	−	20%	−	−	8
15	61	M	26.8	102.9	1	Resection	GBL (WHO IV)	40%	+	+	40%	N/A	−	88
16	57	F	8.0	18.8	1	Biopsy	GBL (WHO IV)	<5%	+	+	5%	N/A	−	222
17	44	F	16.8	162.3	1	Biopsy	GBL (WHO IV)	70%	−	+	25%	N/A	−	9

Immunohistochemical analysis displayed was performed on a single sample considered as the most representative by the referring neuropathologist.

In the preliminary analysis of our experiment, we investigated the application of the same clustering algorithm to either the CE- or FLAIR-tumor, since both of them have been considered for habitat imaging studies previously published, and we assessed the obtained habitats. Clusters obtained from CE-tumor volume alone were considered too small and fragmented in order to be reliably correlated to histology, and therefore they were not deemed suitable for the purpose of the present study (**Figure 1H**). On the contrary, habitats obtained from FLAIR-tumor volume (which included the CE region along with the surrounding FLAIR hyperintensity) were able to divide the whole tumor in a more reproducible way, with a larger cluster amenable to a reliable histological correlation with the bioptic samples obtained (**Figure 1I**). For these reasons, we selected FLAIR-tumor as the final tumor mask to be investigated and all the results presented in our paper are based on its analysis. The radiological characteristics of the 8 clusters, and their volumetric representation, are summarized in **Table 2** and depicted in **Figure 2**. Median voxel values among different maps (Vp, ^{18}F-FAZA, and MD) and Habitats (1–8) are reported in **Table 3**. Boxplots of the quantitative distribution of mean values of Vp, ^{18}F-FAZA and MD parametric maps in each environment are shown in **Figure 3**.

Figure 4 depicts habitats distribution in four different cases of the present series. **Figures 5**, **6** present two illustrative cases showing the consistency between the functional spatial tumor habitats and the microscopic morphology of the corresponding tissue. The microscopic semi-quantitative analysis (cellularity, extent of necrosis, number of hyperplastic vessels) of each sample and the corresponding Habitats on imaging are reported in **Table 4**. **Table 5** and **Figures 7**, **8** report habitats' prevalence according to grade and molecular features. Habitats' descriptions and characteristics are analyzed below.

Habitat 1, characterized by high perfusion (the highest Vp values among all clusters, **Figure 3**), high hypoxia, and high diffusivity, corresponded to areas of mild hyperintensity on T2/FLAIR sequences and intense enhancement on T1–CE sequences; Habitat 1 voxels were localized inside of CE-tumor segmentation in 92% of the cases overall. No areas of necrosis were identifiable on cMRI sequences inside this cluster. This cluster was often located at the periphery of the CE-tumor, leaving other aggressive clusters more internally in the tumor core. **Habitat 2** was denoted by elevated perfusion, hypoxia, and restricted diffusion, representing, alone, about half of CE-tumor volume overall. On cMRI it was denoted by a mild hyperintensity on T2/FLAIR sequences and no visible necrosis. Similarly to Habitat 1, this cluster was localized inside of CE-tumor segmentation in 89% of the cases overall, usually in close proximity to the previous one; however, when compared to the first cluster, Habitat 2 was much more represented (12.1% vs. 4.5%), harboring a less intense contrast enhancement on T1-CE sequences, lower perfusion values, more reduced diffusivity (possibly reflecting higher cellularity) and, generally (in 12/17 patients), higher hypoxia (^{18}F-FAZA-uptake). At histopathology these first two habitats were largely associated with a higher number of hyperplastic

TABLE 2 | Habitats' characteristics and volumetric representation.

	Habitats' characteristics			Habitats representation among cases (% of total tumor volume)																
				Patient number																Row Aver.
n	Perfusion (Vp)	Hypoxia (FAZA)	Diffusivity (MD)	1	2	3	4	5	6	7	8	9	10	11	12	13	14	15	16	17	
1	**High**	**High**	**High**	0.2	11.1	2.0	1.3	8.0	6.7	4.8	1.9	2.6	1.7	5.4	1.9	4.4	6.7	11.1	6.4	0.7	4.5
2	**High**	**High**	*Low*	25.1	10.2	13.6	9.1	7.4	11.6	16.0	3.1	2.1	23.6	3.1	16.2	11.7	6.8	6.7	25.8	14.5	12.1
3	**High**	*Low*	**High**	2.0	4.8	3.5	16.8	1.4	1.1	1.4	10.6	9.5	2.1	3.3	2.6	6.6	5.2	1.7	2.4	1.3	4.5
4	**High**	*Low*	*Low*	5.0	12.9	2.2	4.9	1.5	1.4	2.6	9.4	12.0	5.1	6.0	3.1	7.1	4.3	2.3	7.2	1.6	5.2
5	*Low*	**High**	**High**	0.3	5.7	1.9	1.2	10.4	3.7	6.2	0.6	0.9	2.1	4.3	0.4	8.5	12.4	7.1	5.6	0.3	4.2
6	*Low*	**High**	*Low*	6.3	3.7	4.1	2.8	23.0	4.6	8.1	0.7	1.0	7.7	3.4	5.9	11.8	18.6	2.2	7.0	9.3	7.1
7	*Low*	*Low*	**High**	45.3	7.0	54.8	34.3	21.2	37.0	31.4	41.5	28.9	15.4	12.8	35.1	33.9	21.1	37.7	18.0	43.2	30.5
8	*Low*	*Low*	*Low*	15.7	44.7	17.8	29.6	27.2	33.8	29.3	32.1	43.1	42.2	61.7	34.7	15.9	24.7	31.2	27.7	29.1	31.8

Aver, average row value; Diffus, diffusivity; FAZA, ^{18}F-FAZA; Perfus, perfusion.

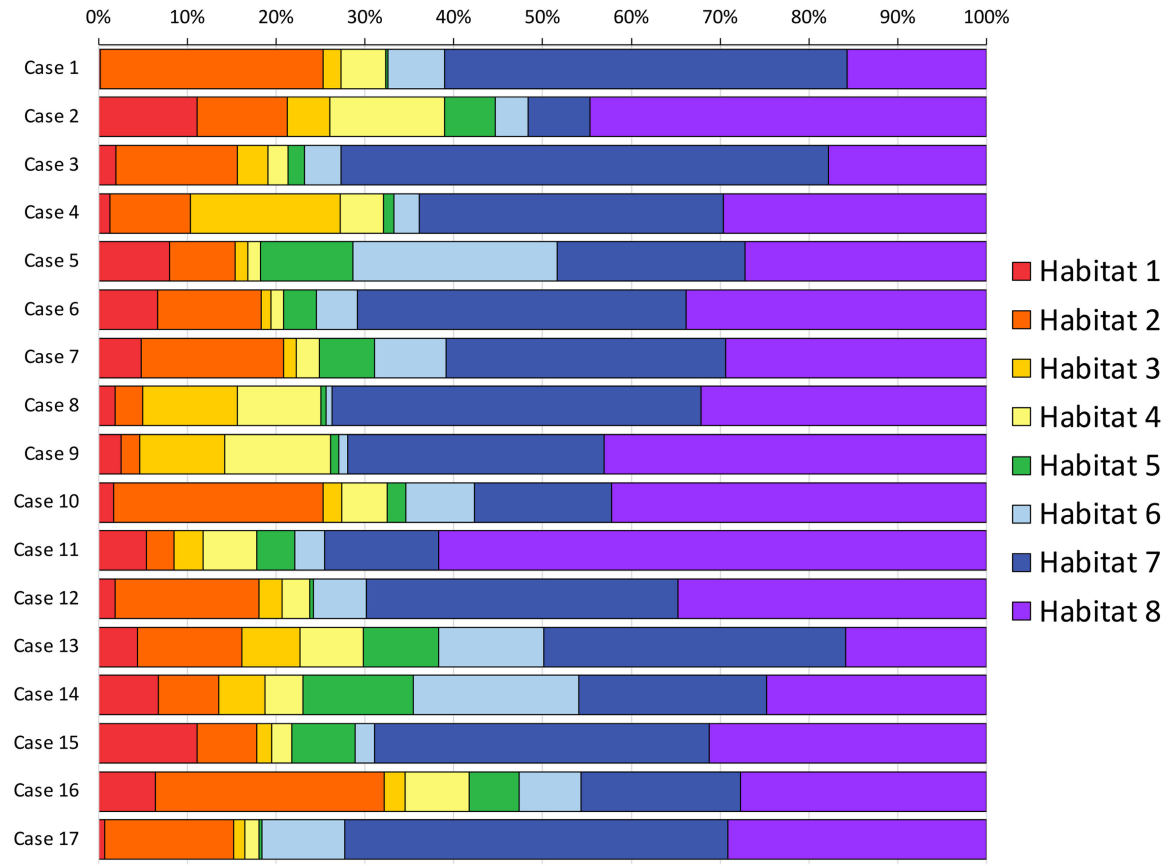

FIGURE 2 | Habitats volumetric representation. The relative volumetric representation of each habitat (expressed as a percentage of the whole FLAIR-tumor volume) is reported for each case included in the series.

vessels and cellularity, whereas a very low rate of necrosis. Moreover, their relative prevalence was higher among WHO grade IV gliomas.

Habitats 3 and **4**, both sharing low hypoxia and high perfusion, while a different degree of diffusivity, were extremely fragmented and poorly represented among all cases (4.5 and 5.2% of the tumor volume, respectively). They were mostly grouped together, often located either at the interface between tumor CE core and the surrounding area of FLAIR-hyperintensity with no CE, adjacent to large vessels or close to the cerebral cortex. Only about 25% of the voxels of these clusters were located inside of CE-tumor segmentation.

Habitat 5 was characterized by high hypoxia, low perfusion, and increased diffusivity (possibly denoting low cellularity). It was located inside of CE-tumor segmentation in 93% of cases, characterized by necrotic areas at both cMRI and histopathology. This was the least prevalent habitat, with an average representation of 4.2% (range 0.3–12.4%) among the considered tumors; however, it appeared more represented in WHO grade IV (4%) compared to WHO grade III tumors (2.1%).

Habitat 6 (low perfusion, reduced diffusivity, and high hypoxia) had a relatively high representation compared to the aforementioned clusters (average 7.1%, range 0.7–23%), being mostly localized inside of CE-tumor segmentation (75% of the cases). It was predominantly identified as areas of less intense CE inside the tumor core, being closely related to Habitat 5 (located more internally) and Habitat 2 (located more externally), as well perceivable in **Figures 4C,D**. Conversely, in different cases, this cluster was identified as areas of faint contrast-enhancement outside the main tumor cores, as one could appreciate in **Figures 4A,B**. At histopathology this habitat showed features of intermediate aggressiveness.

The remaining two clusters had the largest volumetric representation (each one representing over 30% of the total FLAIR-tumor volume) and were both found in areas with no CE in roughly 95% of the cases. **Habitat 7** was, possibly, the least aggressive one inside the tumor mask due to its low values in all the considered parameters; it was characterized by the highest absolute MD values among all clusters (possibly reflecting the lowest cellularity) and it was located in areas of markedly hyperintense FLAIR signal (**Figures 4B,D**). The distribution of Habitat 7 was significantly higher (mean 33.3% vs. 18.8%, median 34.7% vs. 15.4% $P = 0.05$, independent sampled Mann-Whitney U test) in IDH-1 wild-type tumor compared to IDH-1 mutated (see **Table 5** and **Figure 8**). **Habitat 8** was characterized, on the contrary, by reduced diffusivity; moreover, perfusion

TABLE 3 | Plasma volume (Vp), ^{18}F-labeled fluoroazomycinarabinoside (^{18}F-FAZA), and mean diffusivity (MD) voxel median values among different habitats.

Map	Habitat*	Case 1	Case 2	Case 3	Case 4	Case 5	Case 6	Case 7	Case 8	Case 9	Case 10	Case 11	Case 12	Case 13	Case 14	Case 15	Case 16	Case 17	Row average
Vp	1-**H**HH	5.90	8.80	3.72	0.98	7.67	7.04	5.85	2.86	6.42	2.32	4.90	2.00	1.28	9.25	7.51	6.60	5.95	5.24
	2-**H**HL	5.39	8.43	3.40	1.16	5.14	5.15	6.55	2.63	5.36	2.27	4.47	1.91	1.36	7.48	8.45	6.71	6.67	4.85
	3-**H**LH	4.79	8.16	2.66	1.22	5.20	4.37	5.45	1.72	3.14	2.07	3.52	1.75	1.08	7.80	5.95	5.91	4.77	4.09
	4-**H**LL	4.74	7.46	2.84	1.10	4.82	4.41	5.25	1.69	2.97	1.91	3.25	1.55	1.10	7.04	6.18	6.12	4.59	3.94
	5-**L**HH	2.65	4.90	1.28	0.68	2.18	0.92	2.48	1.13	1.21	0.97	1.22	0.65	0.24	2.40	2.69	3.06	2.36	1.82
	6-**L**HL	2.79	5.76	1.45	0.71	2.71	2.08	2.96	1.20	1.16	1.28	1.26	0.71	0.34	2.47	2.96	3.71	2.86	2.14
	7-**L**LH	0.86	4.44	0.64	0.51	1.26	0.01	1.17	1.03	1.03	0.65	0.94	0.11	0.18	1.77	0.47	1.30	1.16	1.03
	8-**L**LL	1.66	4.80	0.66	0.47	1.75	0.15	1.46	0.99	1.02	0.91	1.07	0.21	0.33	1.92	0.84	2.15	1.72	1.30
	Whole tumor mask	1.94	5.89	0.83	0.64	2.32	0.25	1.88	1.14	1.40	1.14	1.23	0.31	0.43	2.81	1.15	3.84	1.67	1.70
^{18}F-FAZA	1-H**H**H	0.77	1.55	1.26	0.73	1.97	1.73	2.08	1.38	1.06	1.52	0.84	1.38	0.41	3.45	1.48	1.43	1.05	1.42
	2-H**H**L	1.00	1.26	1.86	1.13	1.95	1.87	2.48	1.14	1.90	1.76	0.83	2.00	0.44	3.45	1.38	1.48	1.38	1.61
	3-H**L**H	0.30	0.70	0.69	0.33	1.03	0.81	1.04	0.42	0.37	0.61	0.31	0.46	0.26	1.28	0.54	0.84	0.47	0.62
	4-H**L**L	0.45	0.70	0.65	0.34	1.12	0.88	0.99	0.39	0.37	0.65	0.30	0.78	0.26	1.21	0.57	0.83	0.66	0.66
	5-L**H**H	0.73	1.69	1.64	0.66	1.81	1.66	1.92	0.74	0.69	1.76	0.64	1.22	0.37	3.46	1.33	1.27	0.87	1.32
	6-L**H**L	0.84	1.29	1.97	0.77	1.75	2.21	2.09	0.73	0.88	1.68	0.65	1.52	0.40	3.44	1.15	1.38	0.97	1.40
	7-L**L**H	0.13	0.43	0.12	0.27	0.56	0.16	0.23	0.37	0.33	0.31	0.25	0.22	0.25	0.44	0.15	0.40	0.30	0.29
	8-L**L**L	0.22	0.46	0.16	0.26	0.88	0.21	0.28	0.36	0.32	0.33	0.20	0.29	0.26	0.56	0.19	0.56	0.45	0.35
	Whole tumor mask	0.24	0.63	0.18	0.31	1.31	0.25	0.47	0.38	0.34	0.45	0.24	0.35	0.30	1.79	0.26	0.92	0.42	0.52
MD[§]	1-HH**H**	1.60	1.05	1.54	1.22	0.97	1.49	1.64	0.49	1.26	1.24	1.45	1.28	1.48	1.46	1.70	1.24	0.95	1.30
	2-HH**L**	0.99	0.85	1.13	0.86	0.81	1.13	1.15	0.40	1.03	0.90	1.08	0.95	1.19	1.12	1.20	0.88	0.76	0.97
	3-HL**H**	1.68	1.05	1.65	1.33	1.04	1.45	1.65	0.50	1.20	1.30	1.40	1.39	1.51	1.46	1.64	1.27	0.99	1.32
	4-HL**L**	1.10	0.79	1.15	1.02	0.73	1.14	1.23	0.40	0.98	0.93	1.01	1.03	1.21	1.15	1.20	0.89	0.81	0.99
	5-LH**H**	1.51	1.28	1.61	1.20	0.95	1.57	1.70	0.51	1.23	1.29	1.71	1.27	1.50	1.42	1.84	1.31	0.95	1.34
	6-LH**L**	0.98	0.83	1.25	0.89	0.78	1.09	1.21	0.41	0.98	0.92	1.04	0.92	1.22	1.15	1.30	0.97	0.71	0.98
	7-LL**H**	1.85	1.04	1.72	1.26	1.01	1.53	1.63	0.49	1.17	1.36	1.40	1.37	1.56	1.46	1.61	1.31	0.99	1.34
	8-LL**L**	1.22	0.78	1.30	1.00	0.72	1.15	1.27	0.41	1.00	0.95	0.96	1.06	1.26	1.13	1.23	0.97	0.83	1.01
	Whole tumor mask	1.41	0.84	1.58	1.14	0.84	1.33	1.39	0.46	1.07	0.97	1.02	1.13	1.41	1.27	1.50	1.01	0.88	1.13

**"H" and "L" correspond, respectively, to the High and Low-intensity cluster of the considered parametric maps.*

[§]Median values are here reported with a multiplication factor of 10^3.

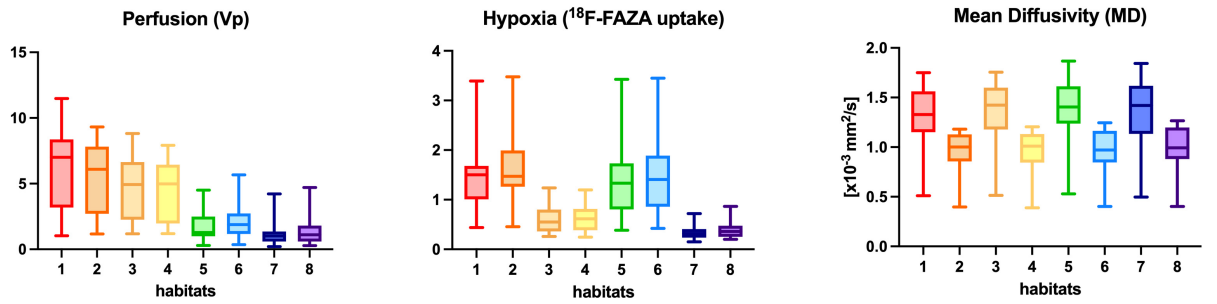

FIGURE 3 | Perfusion (Vp), ^{18}F-FAZA, and Diffusivity (MD) quantitative values within each habitat for the whole group of patients. Boxplots shows the distribution of mean values of Vp, ^{18}F-FAZA, and MD parametric maps in each environment.

values and hypoxia values tended to be higher than those of Habitat 7 (**Table 3**). **Habitat 8** was also identified in the setting of hemorrhagic foci or necrotic areas with micro-hemorrhagic components (as identified on susceptibility weighted imaging, SWI) or viscous mucinous components, due to low MD values resulting from extravascular blood components or liquefactive necrosis (Kang et al., 2001; Chen et al., 2018; Ono et al., 2018) (yellow arrow on **Figures 4A,B**). Additionally, as easily noticeable in **Figures 4C,D**, the localization of Habitat 8 in cortical areas distant from the tumor core is likely related to the lower MD values of the cerebral cortex, compared to underlying edematous white matter. When considering bioptic samples obtained outside the CE-tumor these last two habitats were characterized by histological features of low cellularity and no signs of necrosis or neovascularization. Conversely, they showed extensive necrosis with no viable tissue, in those cases biopsied inside the CE-tumor.

DISCUSSION

In this study, quantitative radiomic parameters from PET and MR images were derived for the assessment of hypoxia, perfusion, and tissue diffusion in a cohort of high-grade glioma patients, and a pipeline for a voxel-wise analysis to combine them in a number of discrete spatial tumor habitats was implemented for the clustering of highly hypoxic areas as well as areas of similar perfusion and diffusion characteristics. By this approach, eight regions were consistently highlighted within the tumor volume, reflecting the intra-tumor heterogeneity of physiological and histopathological microenvironments. Spatial tumor habitats demonstrated high reproducibility across patients and correlation with disease-specific histopathological and cMRI features. To the best of our knowledge, this represents the first study combining the aforementioned parameters to define tumor habitats.

Combined PET and MRI Hypoxia, Perfusion, and Diffusion Spatial Habitats' Features

Of the eight habitats identified, we might speculate that the first two could identify the "vital" core of the tumor, with the second cluster being, hypothetically, the most aggressive component. Interestingly, **Habitat 1**, characterized by the highest Vp values (**Figure 3**), was often located more peripherally than **Habitat 2**, which is in line with the fact that perfusion values tend to be higher at the periphery of the tumor core (Ponte et al., 2017). These two habitats also showed the highest hypoxia values, data in accordance with previously reported studies (Ponte et al., 2017). The fact that the tumor "vital core" represents, at the same time, the most perfused and most hypoxic area, although it might seem paradoxical, is likely related to the functionally and structurally abnormal vascularity that characterizes HGGs, unable to provide sufficient perfusion and oxygen supply (Ponte et al., 2017; Rosinska and Gavard, 2021). The higher hyperintensity on T1-weighted CE sequences noticed inside **Habitat 1** could be related to higher perfusion and/or vascular permeability, as confirmed by the significantly higher Vp, but also rCBV and Ktrans values noted in this cluster. The higher MD values of **Habitat 1**, when compared to **Habitat 2,** could imply lower tissue cellularity but also the presence of stronger vasogenic edema due to blood-brain barrier leakage. As somehow expected, the distribution of these habitats, together with the other most "aggressive" biologic cluster representing areas of tumor necrosis (Habitat 5), was higher in WHO grade IV tumors compared to WHO III.

The poor representation of **Habitat 3** and **4** might be related to the low prevalence of well-oxygenated areas inside the tumor core. Since a certain degree of hypoxia is required to trigger neoangiogenesis (and thus increased perfusion), it is unlikely to find highly perfused but scarcely hypoxic clusters within HGGs (Huang et al., 2016; Ponte et al., 2017).

Habitat 5 represents necrotic areas still including some degree of vital tissue, since the ^{18}F-FAZA-PET tracer needs hypoxic, yet vital, cells in order to be reduced to reactive oxygen radicals and remain locally trapped (Halmos et al., 2014; Mapelli and Picchio, 2020).

Habitat 6, when colocalizing with areas of faint contrast-enhancement outside the tumor "vital" and necrotic cores, was interpreted by the authors as new tumoral seeds progressing toward higher malignancy, since it harbored reduced diffusivity and increased hypoxia, but not yet a significantly augmented vascularization. On the contrary, when **Habitat 6** was identified inside of the tumor core, it was interpreted as regions where

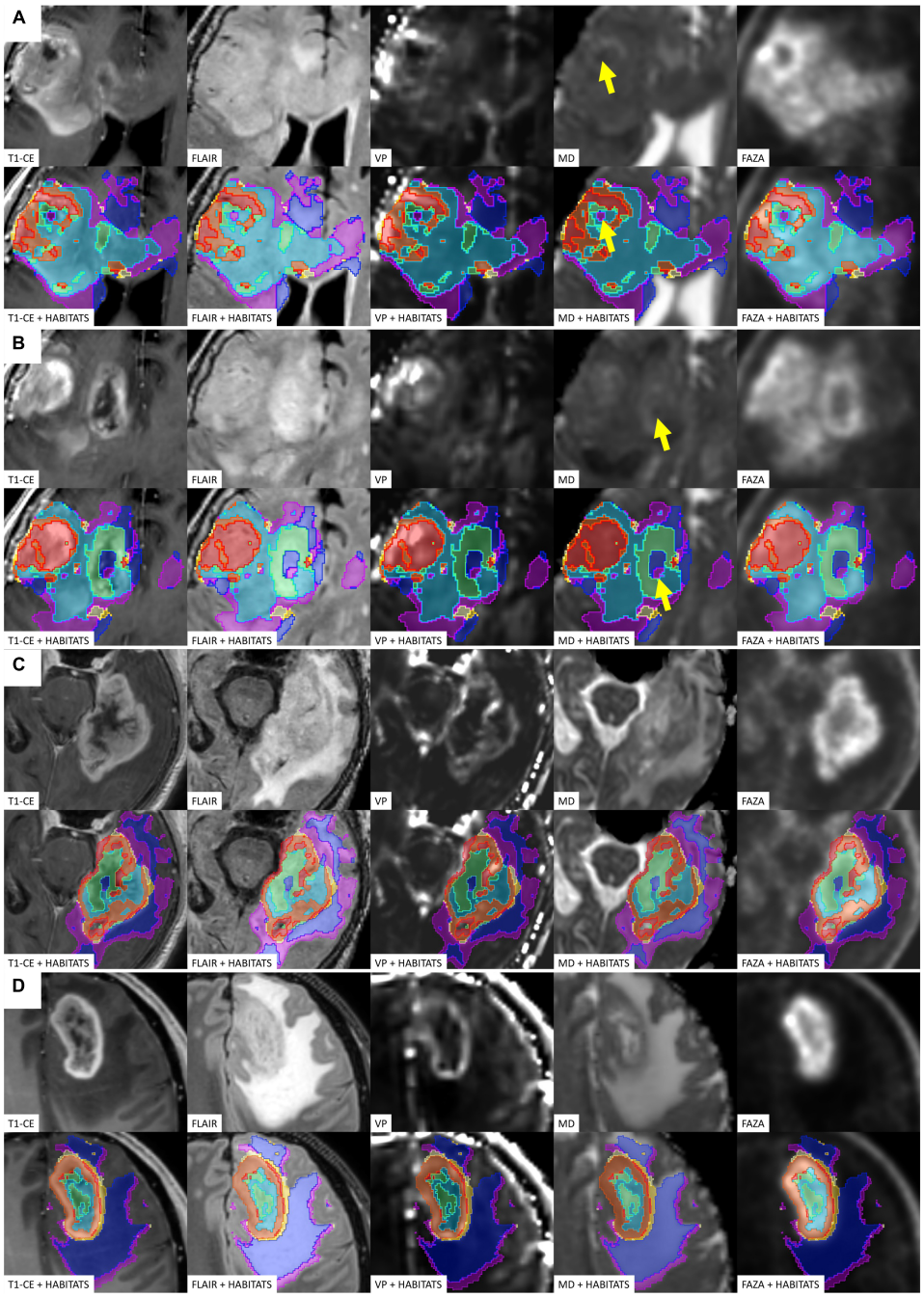

FIGURE 4 | Four different illustrative cases **(A–D)** showing habitats distribution and reproducibility of spatial habitat imaging maps. A table listing the key colors (1–red, 2–orange, 3–gold, 4–yellow, 5–aquamarine, 6–light blue, 7–dark blue, and 8–violet) assigned to each habitat is reported in **Figure 5**. The yellow arrows shows point areas of microhemorragic foci resulting in a MD signal restriction.

tumor growth exceeded neovascularization and that were close to evolving into necrosis.

Finally, we suggested that **Habitat 8**, due to its reduced diffusivity, might identify areas of tumor infiltration beyond the CE vital core, while **Habitat 7** areas of vasogenic edema (with no, or less prominent, tumor infiltration). Interestingly, in our series, the relative volume of pure edema (Habitat 7) was significantly higher in IDH-1 wild-type tumors, compared to IDH-1 mutated lesions, similarly to other recent studies (Dubinski et al., 2021).

Considering the known models of tumor progression (Holash et al., 1999; Brat et al., 2002; Hardee and Zagzag, 2012; Stadlbauer et al., 2018b), we may hypothesize a possible evolution over the time of the identified PET/MRI habitats:

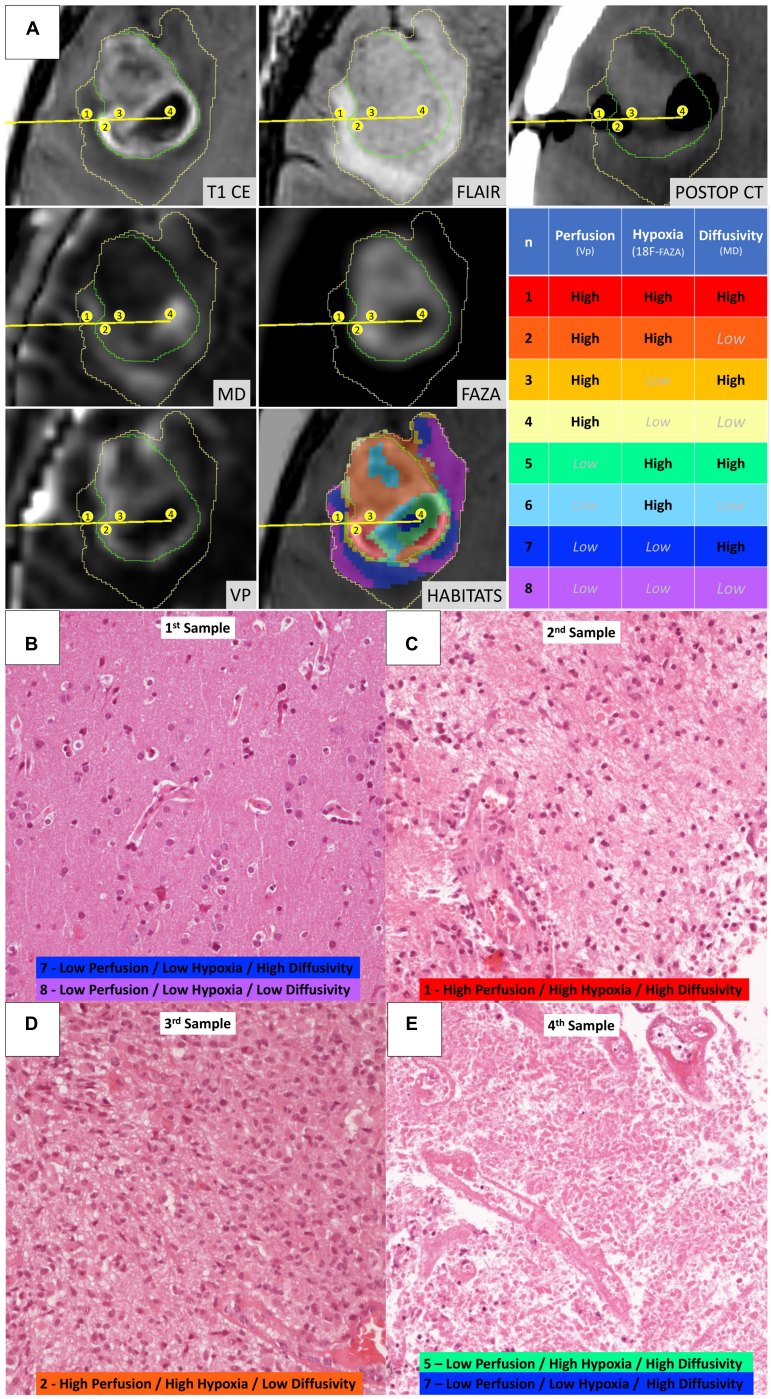

FIGURE 5 | Illustrative case of a 57-year-old female patient (case 16 in **Table 1**) who underwent stereotactic biopsy. **(A)** The trajectory path (yellow line) and the four consecutive sampling sites (enumerated in the yellow circles) are displayed in axial formatted pre-operative T1-CE, FLAIR, MD, ^{18}F-FAZA, Vp, and post-operative CT images; the spatial distribution of the identified habitats and the assigned key colors are also displayed (1–red, 2–orange, 3–gold, 4–yellow, 5–aquamarine, 6–light blue, 7–dark blue, and 8–violet). **(B)** Microscopic slide [20× magnification, Hematoxylin and Eosin (H&E)] from the first sampling (corresponding to Habitat 7–Low Perfusion/Low Hypoxia/High Diffusivity and Habitat 8–Low Perfusion/Low Hypoxia/Low Diffusivity) showing a cortical/subcortical area with normal tissue architecture, presence of normal vessel and no significant increase in cellularity, but rather mild reactive gliosis. **(C)** Microscopic slide (20× magnification, H&E) from the second sampling (Habitat 1–High Perfusion/High Hypoxia/High Diffusivity) showing a clearly pathological area of white matter with increased cellularity, disruption of the physiological tissue architecture, and abnormal vessels. **(D)** Microscopic slide (20× magnification, H&E) from the third sampling (Habitat 2–High Perfusion/High Hypoxia/Low Diffusivity) showing neoplastic tissue with cytoarchitecture disruption, elevated cellularity with the presence of gemistocytic astrocytes, nuclear atypia, abundant eosinophilic cytoplasm, abnormal vascularization. **(E)** Microscopic slide (20× magnification, H&E) from the fourth sampling (Habitat 5–Low Perfusion/High Hypoxia/High Diffusivity and Habitat 7–Low Perfusion/Low Hypoxia/High Diffusivity) showing tissue with extensive necrosis.

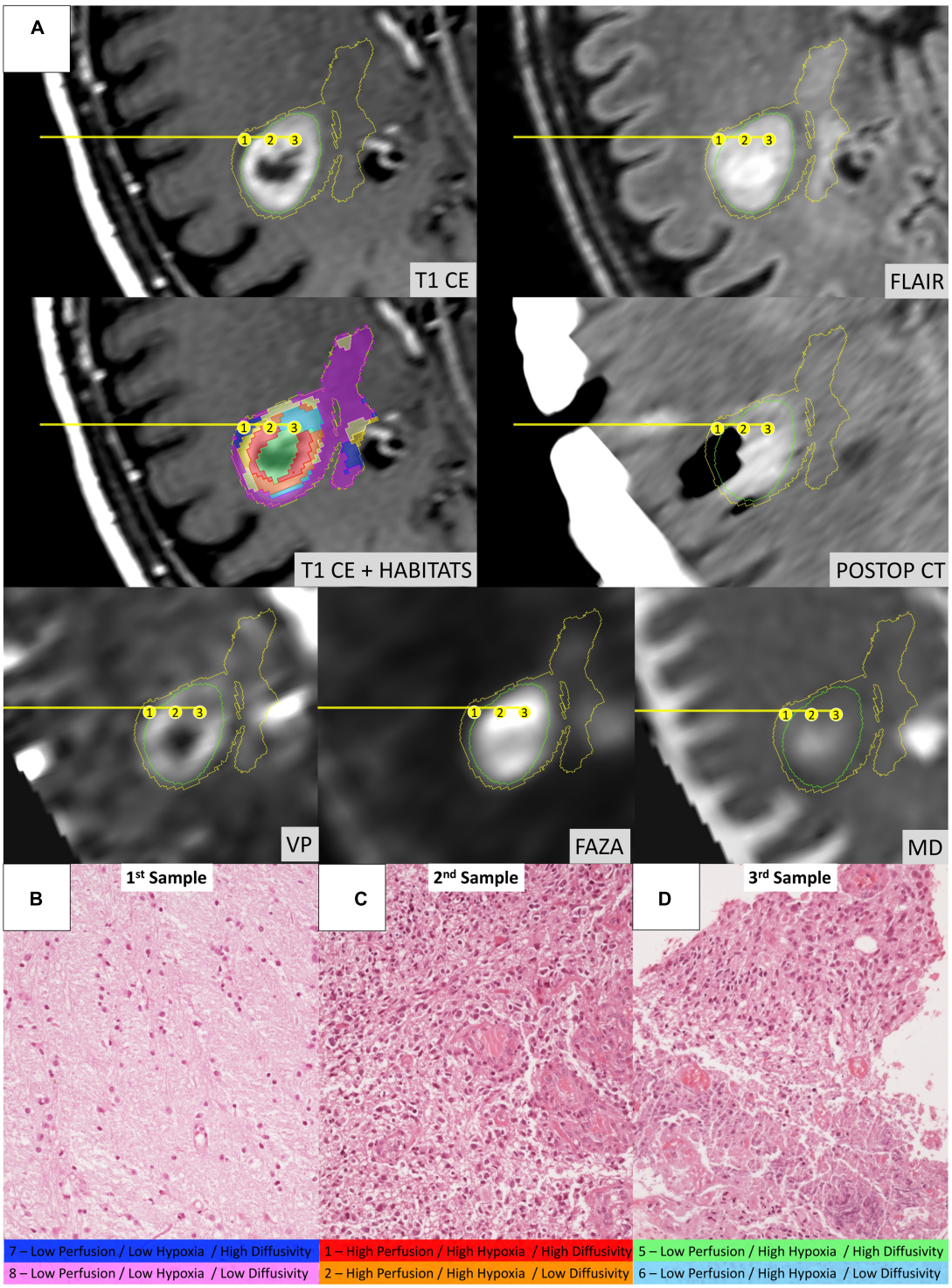

FIGURE 6 | Illustrative case of a 58-year-old male patient (Case 2 in **Table 1**) who underwent stereotactic biopsy. **(A)** The trajectory path (yellow line) and the three consecutive sampling sites (enumerated in the yellow circles) are displayed in axial formatted pre-operative T1-CE, FLAIR, MD, ^{18}F-FAZA, Vp, and post-operative CT images; habitats were identified using the same key-color described in **Figure 5**. **(B)** Microscopic slide [20× magnification, Hematoxylin and Eosin (H&E)] from the first sampling (Habitat 7–Low Perfusion/Low Hypoxia/High Diffusivity and Habitat 8–Low Perfusion/Low Hypoxia/Low Diffusivity) showing a seemingly normal white matter architecture. **(C)** Microscopic slide (20× magnification, H&E) from the second sampling (Habitat 1–High Perfusion/High Hypoxia/High Diffusivity and Habitat 2–High Perfusion/High Hypoxia/Low Diffusivity) showing evident hypercellularity with nuclear atypias and marked vascular proliferation. **(D)** Microscopic slide (20× magnification, H&E) from the third sampling (Habitat 5–Low Perfusion/High Hypoxia/High Diffusivity and Habitat 6–Low Perfusion/High Hypoxia/Low Diffusivity) areas of vital tumoral tissue (on the upper part) mixed with areas of necrosis (on the lower part).

TABLE 4 | Semi-quantitative histopathologic analysis for each bioptic sample obtained.

Case number	Sample	Cellularity[a] (1–5)	Class of necrosis[b] (0–5)	Number of hyperplastic vessels counted (*n*)	Habitats involved (ordered by prevalence inside VOI)[c]
2	A	1	0	0	7, 8
	B	4	0	43	2
	C	4	1	21	5
5	A	3	2	1	6
	B	4	4	1	2, 5
	C	3	5	3	5, 7, 8
	D§	3	3	6	5, 6
8	A	2	0	0	1
	B	2	0	0	1
	C	2	0	1	1
	D	2	0	0	1
9	A	5	2	20	1
	B	5	2	19	1
10	A	1	0	0	7, 8
	B	3	1	8	2
12	A	1	0	4	8, 2, 6
	B	3	2	4	2, 6
	C	4	1	8	2
13	A	1	0	0	7
	B	1	0	0	5
	C	3	0	0	3
	D	3	0	2	1,3
14	A	3	0	5	7,8,6
	B	4	0	11	6
16	A	1	0	0	7, 8
	B	3	0	28	1
	C	5	1	11	2
	D	N/A*	5	N/A*	5, 7
17	A	4	0	6	2
	B	4	1	7	2
	C	4	0	4	6, 2

Features assessed in the present analysis were: cellularity, extent of necrosis, and number of hyperplastic vessels counted.
To address the issue of length variability among different bioptic specimens and to maximize the correspondence with the target point set on the stereotactic planning system, only the central portion (extending 5 mm along the greatest axis of the specimen in its largest section available) was analyzed in each sample.
The corresponding spatial tumor imaging habitats involved are reported in the last column, ordered accordingly to their relative prevalence inside of the 5 mm diameter volume of interest.
N/A, not applicable.
[a]*Cellularity was graded with a score from 1 (seemingly normal representation) to 5 (extremely high cellular density).*
[b]*Classes considered for necrosis (expressed as a rate over the whole area considered for each specimen) were the following: 0 (0%), 1 (≤10%), 2 (11–25%), 3 (26–50%), 4 (51–75%), 5 (76–100%).*
[c]*A 5 mm diameter volume of interest (VOI) was drawn according to the exact stereotactic coordinates of each target and needle window orientation, then carefully verified also in the coregistered in the early post-operative CT scan. In this column, the included habitats are reported. Since the spatial habitat maps were not available at the time of planning, final sampling VOI ended at the intersection of multiple clusters in many cases; in the latter case, clusters are listed in order of maximum volumetric representation inside of the VOI.*
§This sample was only 4 mm long.
**It was not possible to calculate these features since the sample was completely represented by necrosis.*

areas of tumor infiltration in the white matter (**Habitat 8**) might eventually develop some degree of hypoxia (**Habitat 6**), which, in turn, trigger neovascularization possibly through tumor cells secretion of mediators such as HIF-1α and VEGF (Stadlbauer et al., 2018b) and increased perfusion values, becoming a tumor "vital core": **Habitat 1** and (perhaps subsequently) **Habitat 2**. In due course, the tumor growth in the vital core will overwhelm its abnormal vascularization, leading toward areas in a pre-necrotic state (**Habitat 6**); as the necrosis progresses, cellularity will decrease (**Habitat 5**) eventually turning into liquefactive necrosis, with no remaining vital cells and showing, consequently, a concomitant drop in hypoxia signaling and ^{18}F-FAZA-tracer uptake (**Habitat 7**). The aforementioned "habitat progression" is easily perceivable in **Figures 4C,D**, where a somehow concentric distribution of the clusters is identifiable.

Potential Clinical Applications

Advanced neuroimaging techniques such as PWI, dMRI, or PET with different radiotracers are usually evaluated independently in the clinics or are rather combined into an average parameter for the entire region of interest, discarding important spatial

TABLE 5 | Mean and median representation of the eight different habitats according to IDH-1 status and WHO 2016 grade.

Habitats characteristics				Habitats' representation (% of total tumor volume) according to							
				IDH-1 status				WHO 2016 grading			
n	Perfusion (Vp)	Hypoxia (^{18}F-FAZA)	Diffusivity (MD)	Wild-type		Mutated		III		IV	
				Mean (%)	Median (%)	Mean (%)	Median (%)	Mean (%)	Median (%)	Mean (%)	Median(%)
1	**High**	**High**	**High**	4.3	3.7	5.8	4.4	3.2	1.9	5.1	5.1
2	**High**	**High**	*Low*	11.5	10.3	15.2	11.7	10.9	9.1	12.7	12.6
3	**High**	*Low*	**High**	4.5	2.5	4.5	4.8	8.3	6.6	2.9	2.2
4	**High**	*Low*	*Low*	4.6	3.7	8.4	7.1	6.2	5.1	4.8	2.9
5	*Low*	**High**	**High**	4.0	2.8	5.4	5.7	4.9	2.1	3.9	4.0
6	*Low*	**High**	*Low*	6.9	5.3	7.8	7.7	8.3	7.7	6.6	5.3
7	*Low*	*Low*	**High**	33.0	34.7	18.8	15.4	29.3	33.9	31.0	33.2
8	*Low*	*Low*	*Low*	31.3	29.5	34.2	42.2	28.9	29.6	33.0	30.3

Data are expressed as a percentage of the cumulative tumor volume of the whole series.

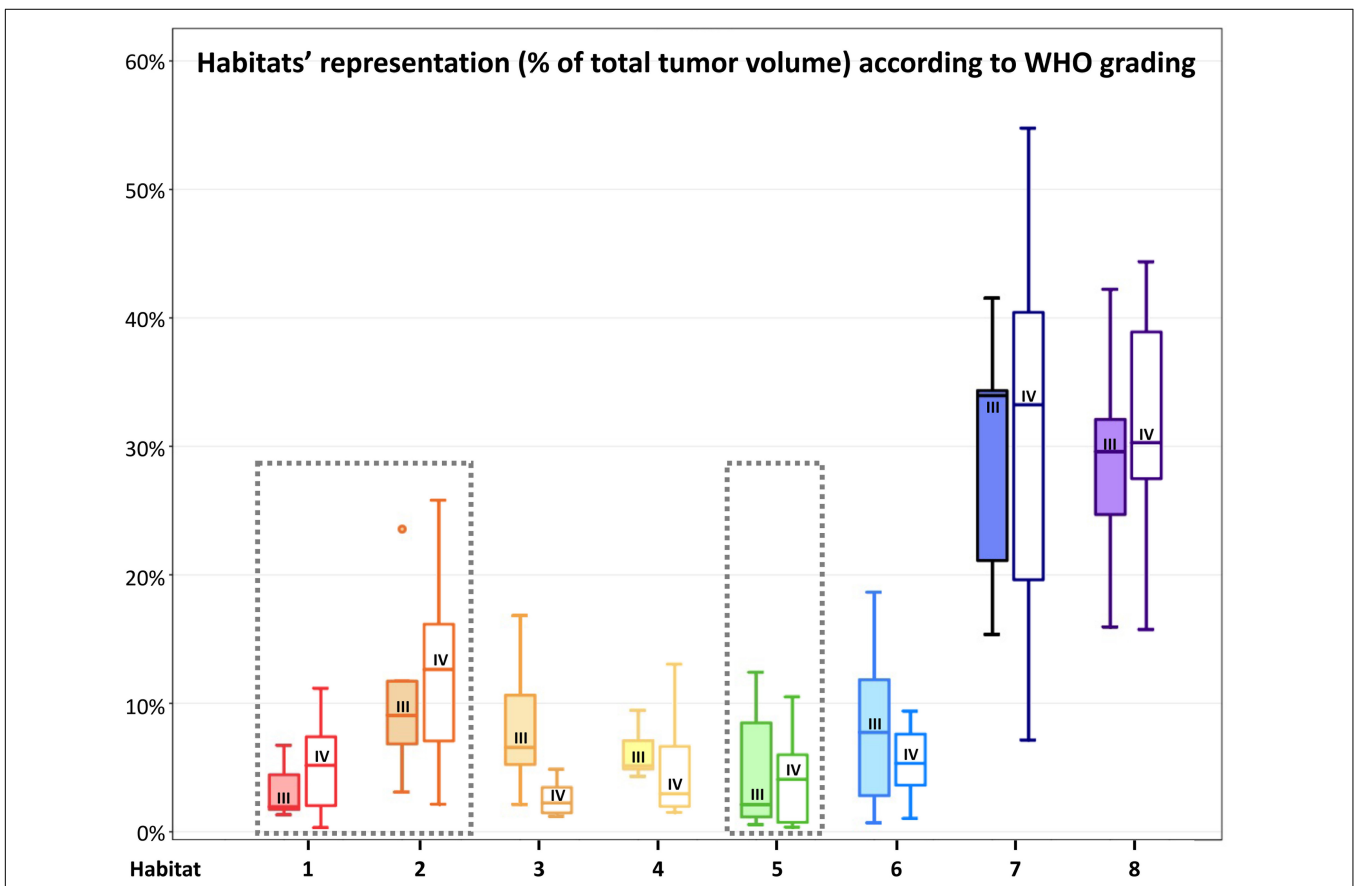

FIGURE 7 | Habitats' representation (% of total tumor volume) according to WHO 2016 grade. For each habitat, the boxplot on the left (with filled color) represents WHO grade III tumors, while the boxplot on the right (not filled with color) represents WHO grade IV tumors. WHO grade IV gliomas had a higher (although not statistically significant) representation of Habitat 1 and 2 (considered the most aggressive clusters from a metabolic point of view) and Habitat 5 (mostly associated with necrotic areas). The most aggressive clusters are surrounded by a gray box with a dashed line.

information (O'Connor et al., 2015; Napel et al., 2018). The simultaneous combination of diverse imaging modalities into a single habitat map leverages the information of the individual imaging datasets, possibly enhancing the ability to capture subtle physiological differences within tumor tissue and better revealing the complexity of spatial and temporal heterogeneity, both at

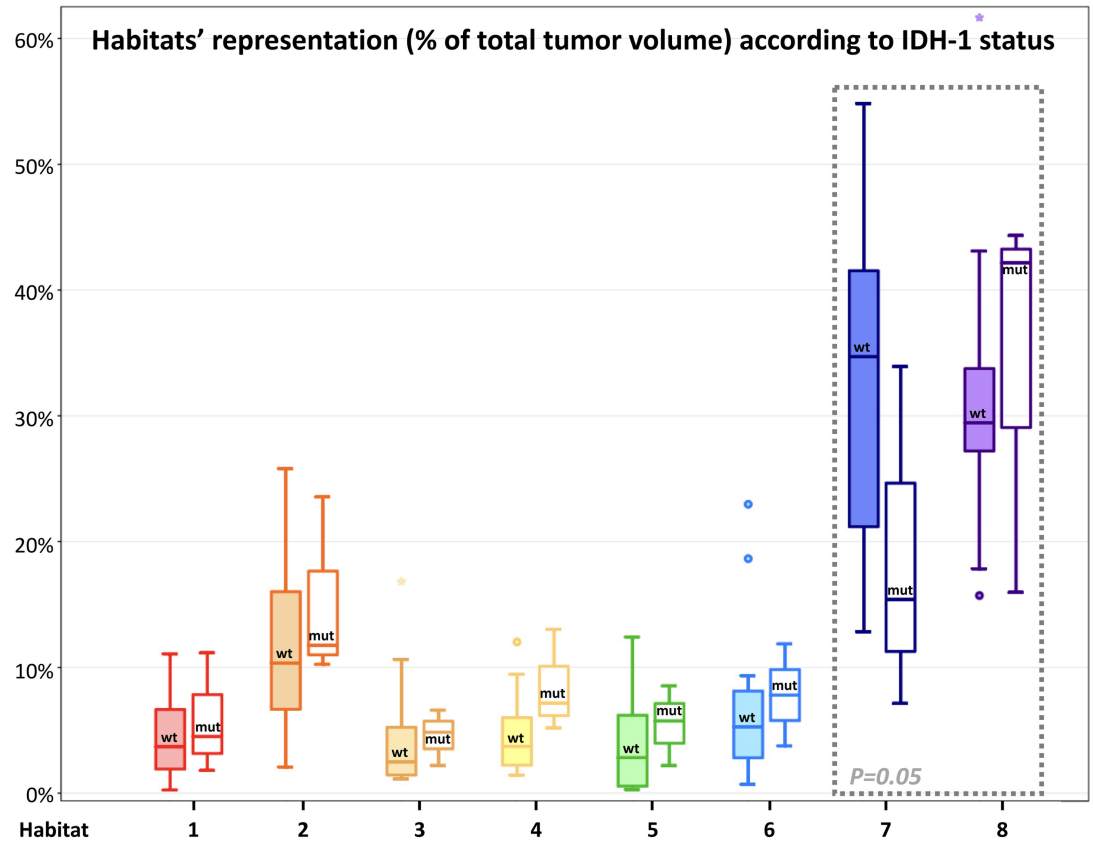

FIGURE 8 | Habitats' representation (% of total tumor volume) according to IDH-1 status. For each habitat, the boxplot on the left (with filled color) represents IDH-1 Wild-type tumors, while the boxplot on the right (not filled with color) represents IDH-1 mutated tumors. Main differences were found in the representation of Habitat 7 (possibly embodying pure vasogenic edema) and 8 (possibly representing infiltrative edema). The former was significantly ($P = 0.05$) higher in IDH wild-type tumors, while the latter was higher (not significantly) in IDH-mutated lesions; these latter two habitats were surrounded by a gray box with a dashed line to highlight the differences.

initial diagnosis and during follow-up (Yip et al., 2017; Napel et al., 2018).

Furthermore, the heterogeneous biology of HGGs challenges the reliability of limited needle biopsy sampling for making disease-wide characterization. Nevertheless, needle biopsies are utilized, to date, in about a third of cases to define HGG diagnosis. The rate of non-diagnostic (to be repeated) stereotactic biopsies is 7–10% (Lu et al., 2015; Sciortino et al., 2019), and complete diagnostic accuracy has been reported as low as 33–64% of cases (compared to pathologic analysis obtained with the subsequent gross-total resection of the same lesion) (Jackson et al., 2001; Muragaki et al., 2008; Reithmeier et al., 2013). Integrating spatial tumor habitats into a bioptic planning system might better guide the neurosurgeon in sampling the most relevant functional regions of the tumor, especially by virtue of the much easier perception/understanding of the colored maps of a limited number of habitats, compared to the thorough expertise in advanced neuroimaging needed to interpret multiple coregistered parametric maps elaborated from PWI, dMRI, or PET radiotracers (as depicted in the illustrative cases of **Figures 5**, **6**). This might be particularly valuable in those gliomas showing poor or no enhancement on T1-CE sequences, since about one-third of non-enhancing gliomas contain aggressive areas that, if correctly included in the pathologic analysis, may lead to classify the lesion into a higher-grade tumor, with consequently remarkable differences on treatment management and prognosis. In these cases, the few samples achievable *via* needle biopsy might easily underestimate the actual tumor grade if not adequately guided to the most aggressive areas.

We believe that further exploration of hypoxia-, perfusion-, and diffusion-derived habitats might provide precious, holistic information about intra-tumor heterogeneity, unveiling regional diversity both at the level of DNA mutation and gene expression profiles, helping in prognosis stratification and, perhaps, in future, treatment selection. The precise identification of the areas with the highest perfusion, microstructural alteration and cellularity, and hypoxia inside and outside the tumor contrast enhancement component could represent an enormous aid in surgical and radiotherapy planning. In the former case, the identification of an aggressive habitat might induce the surgeon to seek its maximum safe resection rate even if not showing evident contrast enhancement. In

the latter case, radiation dose painting with boosts on the most aggressive and resistant clusters represents one of the most appealing perspectives for the next future (Castellano et al., 2021). Finally, the identified habitats could represent a precious tool in monitoring the dynamical spatio-temporal modification in glioma heterogeneity during therapies and follow-up and could identify more clearly areas of tumor response or progression.

Limitations and Future Work

One main drawback of the present work is the limited number of cases analyzed and their heterogeneity (e.g., tumor histology, grading, molecular characteristics, volume, location, patient's age, comorbidities, type of surgery) which have likely hampered the achievement of conclusive associations between the variables involved (parametric map values, habitats, histopathological data, and patient outcome/survival).

In the subgroup of 10 patients undergoing a stereotactic biopsy, we were able to identify a qualitative correlation between the expected microenvironment of the different habitats and the actual histopathologic morphology, although only a preliminary analysis was possible in this small and heterogenous series and no definitive, statistically significant, conclusion could be drawn. The designation of biopsy target spots and path was planned in order to maximize patient safety while ensuring final diagnosis, according to the best clinical practice, by means of the minimum amount of sampling deemed necessary, due to ethical concerns. This, along with the fact that the spatial tumor habitats were not available to the neurosurgeon pre-operatively, prevented the acquisition of a sufficient variety of sampled habitats in the same lesion and frequently ended in sampling over multiple clusters at once, therefore limiting the possibility of direct associations. A thorough evaluation of prospectively and systematically collected data is clearly necessary to correlate the identified clusters with histopathological, immunohistochemical, and molecular biomarkers.

Multiparametric analysis on a per-voxel basis to generate habitats maps remains challenging, because this requires spatial registration of all imaging sequences, which can be hampered by the resolution differences and deformations that can occur between different acquisition modalities (Winfield et al., 2016; Napel et al., 2018). In the future, the use of a fully hybrid PET/MR scanner could further enhance the quality and spatial discrimination of the data obtained from dMRI and PWI while optimizing scanning time and image coregistration. Moreover, considerable processing and analyses were required initially for the generation of the final spatial tumor habitats, which demanded intensive labor and both clinical imaging scientist and informatics/engineering expertise. This requirement could be particularly critical in clinical practice when a short time in-between imaging and surgery is available. However, we believe that this could be overcome in the future *via* dedicated flow-charts with automated algorithms, providing the benefit of a much easier data interpretation for the neurosurgeon in charge of planning the procedure.

A limitation of the applied algorithm was the possible colocalization of the same radiological habitat in different tumor microenvironments. This mainly derived from the fact that MD, despite it has been proved to be inversely correlated to tissue cellularity, also depends on other parameters such as free water, perfusion/ischemia, temperature, and the presence of blood or mucinous components (Maier et al., 2010; Chen et al., 2018; Ono et al., 2018). For instance, Habitat 8 (which was thought to mainly represent areas of increased cellularity due to tumor infiltration of the surrounding white matter) was also found in proximity to microhemorrhagic foci, liquefactive necrosis including viscous mucinous components or cerebral vessels and cortex. On the other hand, perfusion values may be partly influenced by the presence of macrovessels passing through the analyzed tissue. A possible solution to the issues above could be leaving a larger margin from the aforementioned regions while segmenting tumor mask, adding/modifying the parametric maps utilized in the procedure, or identifying different cut-offs or algorithms for the clustering analysis.

The adopted Otsu algorithm is an easy-to-apply method able to find the optimal binary threshold for a single parametric map and outputting two disjoint regions, with high and low-intensity voxels. This allows combining different map subregions to obtain clusters of possible clinical significance. However, this method is limited in capturing all of the variety of tissues present in the tumoral ROI due to the net cut-off of the binary threshold, and it inherently assumes that all maps contain only two tissue classes, neglecting the fact that some maps could be sensitive to multiple tissue microenvironments. Moreover, this technique quickly leads to challenges when trying to combine multiple maps: the addition of more than 3 maps to the computation was found inadequate of the purpose of the study, due to the exponential increase of clusters number, making them excessively small and fragmented within the tumor ROI to offer a reliable correlation with bioptic specimens. The adoption of more refined data-driven clustering methods such as k-means, which allow to consider multiple parametric maps at the same time while preventing over-segmentation would have, perhaps, better addressed this particular issue. However, for the purposes of the present work, the generated clusters needed to be consistent in number and quantitative features among the different cases, in order to allow a possible biological interpretation of the individual habitats.

The alternative adoption of novel advanced MR techniques capable of assessing tissue hypoxia could represent another extremely appealing eventuality, since it would avoid the need for PET hypoxia radiotracers (such as ^{18}F-FMISO or ^{18}F-FAZA) that can be difficult to be gathered from specialized manufacturers or produced locally, expensive, time-consuming, and still problematic to be implemented in common practice due to the lack of a thorough clinical validation and institutional authorization. Indeed, in more recent years, resting-state blood oxygen level-dependent (BOLD) acquisitions have been successfully employed in the detection of areas of neurovascular uncoupling and hypoxia inside of tumoral tissue (Stadlbauer et al., 2011, 2018a,b; Pillai and Zaca, 2012; Englander et al., 2018).

These maps could be easily acquired in the same MRI protocol together with morphological sequences, dMRI, and PWI, and can be eventually integrated into our algorithm to generate spatial tumor imaging habitats.

This study represents a preliminary analysis, as part of a feasibility study: additional future work will involve performing a systematic correlation of spatial habitat analysis with patients' outcome, survival and recurrence, in a larger, prospective clinical series. Moreover, it would be interesting to follow-up patients over the course of the disease with the tumor habitat maps in order to monitor spatio-temporal changes and be able to validate the speculated spatio-temporal evolution of the PET/MRI tumor habitats.

CONCLUSION

This study shows the feasibility of an innovative PET and MRI approach for the assessment of hypoxia, perfusion, and diffusion in HGGs to derive combined habitats for the clustering of intra-tumor heterogeneity. The high consistence and reproducibility of the proposed spatial habitat imaging approach, as well as the correlation of the identified habitats with disease-specific histopathological features suggest that this approach can be valuable to decode metabolic, structural, and physiological patterns at same moment and non-invasively, in order to identify different areas within heterogeneous tumors. A systematic, prospective validation of this combined PET and MRI hypoxia, perfusion, and diffusion spatial tumor habitat map in a larger cohort of malignant glioma patients is warranted to define its impact on individualized therapy planning, prediction of prognosis and follow-up.

DATA AVAILABILITY STATEMENT

All data generated and analysed during the current study are available from the corresponding author on reasonable request.

ETHICS STATEMENT

The studies involving human participants were reviewed and approved by the Institutional Ethics Committee of Ospedale San Raffaele, Milan, Italy. Patients provided their written informed consent to participate in this study and for the publication of any potentially identifiable images or data included in this article.

AUTHOR CONTRIBUTIONS

AC and MB: conception and design of the study, imaging dataset creation and coregistration on 3D Slicer, tumor segmentation, and habitat analysis. MB and PMa: patient enrollment and clinical data collection. PS, VB, FF, NA, and AC: imaging acquisition and ^{18}F-FAZA-PET, PWI, and DTI map generation. MB, NP, and AC: data management and statistical analysis. MB: map implementation in surgical planning, correlations with surgical data, and writing first draft of the manuscript. NP and LP: creation and execution of MATLAB scripts for map binarization and habitats generation. MC and MB: histopathological analysis. AC: conceived the original idea and was in charge of the overall direction and revision of the study. NA, MP, PMo, and AF: helped to supervise the project. All authors contributed to manuscript revision, read, and approved the submitted version.

FUNDING

This research was funded by the Italian Ministry of Health, grant number GR-2018-12365670. We also acknowledge the support received from the Italian Association for Cancer Research (AIRC grant IG 2014 Id.1524).

ACKNOWLEDGMENTS

The present work was performed by MB in partial fulfillment of the requirements for obtaining the Ph.D. degree at Vita-Salute San Raffaele University, Milano, Italy.

SUPPLEMENTARY MATERIAL

The Supplementary Material for this article can be found online at: https://www.frontiersin.org/articles/10.3389/fnins.2022.885291/full#supplementary-material

REFERENCES

Abdo, R. A., Lamare, F., Fernandez, P., and Bentourkia, M. (2019). Analysis of hypoxia in human glioblastoma tumors with dynamic 18F-FMISO PET imaging. *Aust. Phys. Eng. Sci. Med.* 42, 981–993. doi: 10.1007/s13246-019-00797-8

Alcaide-Leon, P., Pareto, D., Martinez-Saez, E., Auger, C., Bharatha, A., and Rovira, A. (2015). Pixel-by-pixel comparison of volume transfer constant and estimates of cerebral blood volume from dynamic contrast-enhanced and dynamic susceptibility contrast-enhanced mr imaging in high-grade gliomas. *AJNR Am. J. Neuroradiol.* 36, 871–876. doi: 10.3174/ajnr.A4231

Anzalone, N., Castellano, A., Cadioli, M., Conte, G. M., Cuccarini, V., Bizzi, A., et al. (2018). Brain gliomas: multicenter standardized assessment of dynamic contrast-enhanced and dynamic susceptibility contrast MR images. *Radiology* 287, 933–943.

Barajas, R. F. Jr., Phillips, J. J., Parvataneni, R., Molinaro, A., Essock-Burns, E., Bourne, G., et al. (2012). Regional variation in histopathologic features of tumor specimens from treatment-naive glioblastoma correlates with anatomic and physiologic MR Imaging. *Neuro Oncol.* 14, 942–954. doi: 10.1093/neuonc/nos128

Beig, N., Bera, K., Prasanna, P., Antunes, J., Correa, R., Singh, S., et al. (2020). Radiogenomic-based survival risk stratification of tumor habitat on GD-T1W MRI is associated with biological processes in glioblastoma. *Clin. Cancer Res.* 26, 1866–1876. doi: 10.1158/1078-0432.CCR-19-2556

Brat, D. J., Castellano-Sanchez, A., Kaur, B., and Van Meir, E. G. (2002). Genetic and biologic progression in astrocytomas and their relation to angiogenic

dysregulation. *Adv. Anat. Pathol.* 9, 24–36. doi: 10.1097/00125480-200201000-00004

Castellano, A., and Falini, A. (2016). Progress in neuro-imaging of brain tumors. *Curr. Opin. Oncol.* 28, 484–493. doi: 10.1097/CCO.0000000000000328

Castellano, A., Bailo, M., Cicone, F., Carideo, L., Quartuccio, N., Mortini, P., et al. (2021). Advanced imaging techniques for radiotherapy planning of Gliomas. *Cancers (Basel)* 13:1063. doi: 10.3390/cancers13051063

Chen, L., Liu, M., Bao, J., Xia, Y., Zhang, J., Zhang, L., et al. (2013). The correlation between apparent diffusion coefficient and tumor cellularity in patients: a meta-analysis. *PLoS One* 8:e79008. doi: 10.1371/journal.pone.0079008

Chen, L.-P., Jiang, X.-Q., Zhao, Z., and Wang, X.-H. (2018). Apparent diffusion coeffcient value for prediction of hemorrhagic transformation in acute ischemic infarction. *Int. J. Clin. Exp. Med.* 11, 109–117.

Collewet, G., Strzelecki, M., and Mariette, F. (2004). Influence of MRI acquisition protocols and image intensity normalization methods on texture classification. *Magn. Reson. Imaging* 22, 81–91. doi: 10.1016/j.mri.2003.09.001

Conte, G. M., Castellano, A., Altabella, L., Iadanza, A., Cadioli, M., Falini, A., et al. (2017). Reproducibility of dynamic contrast-enhanced MRI and dynamic susceptibility contrast MRI in the study of brain gliomas: a comparison of data obtained using different commercial software. *Radiol. Med.* 122, 294–302. doi: 10.1007/s11547-016-0720-8

Cui, Y., Tha, K. K., Terasaka, S., Yamaguchi, S., Wang, J., Kudo, K., et al. (2016). Prognostic imaging biomarkers in glioblastoma: development and independent validation on the basis of multiregion and quantitative analysis of MR images. *Radiology* 278, 546–553. doi: 10.1148/radiol.2015150358

Del Mar Alvarez-Torres, M., Juan-Albarracin, J., Fuster-Garcia, E., Bellvis-Bataller, F., Lorente, D., Reynes, G., et al. (2020). Robust association between vascular habitats and patient prognosis in glioblastoma: an international multicenter study. *J. Magn. Reson. Imaging* 51, 1478–1486. doi: 10.1002/jmri.26958

Dextraze, K., Saha, A., Kim, D., Narang, S., Lehrer, M., Rao, A., et al. (2017). Spatial habitats from multiparametric MR imaging are associated with signaling pathway activities and survival in glioblastoma. *Oncotarget* 8, 112992–113001. doi: 10.18632/oncotarget.22947

Dubinski, D., Won, S. Y., Rauch, M., Behmanesh, B., Ngassam, L. D. C., Baumgarten, P., et al. (2021). Association of isocitrate dehydrogenase (IDH) status with edema to tumor ratio and its correlation with immune infiltration in glioblastoma. *Front. Immunol.* 12:627650. doi: 10.3389/fimmu.2021.627650

Ellingson, B. M., Malkin, M. G., Rand, S. D., Connelly, J. M., Quinsey, C., LaViolette, P. S., et al. (2010). Validation of functional diffusion maps (fDMs) as a biomarker for human glioma cellularity. *J. Magn. Reson. Imaging* 31, 538–548. doi: 10.1002/jmri.22068

Englander, Z. K., Horenstein, C. I., Bowden, S. G., Chow, D. S., Otten, M. L., Lignelli, A., et al. (2018). Extent of bold vascular dysregulation is greater in diffuse gliomas without isocitrate dehydrogenase 1 R132H mutation. *Radiology* 287, 965–972. doi: 10.1148/radiol.2017170790

Fathi Kazerooni, A., Nabil, M., Zeinali Zadeh, M., Firouznia, K., Azmoudeh-Ardalan, F., Frangi, A. F., et al. (2018). Characterization of active and infiltrative tumorous subregions from normal tissue in brain gliomas using multiparametric MRI. *J. Magn. Reson. Imaging* 48, 938–950. doi: 10.1002/jmri.25963

Fedorov, A., Beichel, R., Kalpathy-Cramer, J., Finet, J., Fillion-Robin, J. C., Pujol, S., et al. (2012). 3D slicer as an image computing platform for the quantitative imaging network. *Magn. Reson. Imaging* 30, 1323–1341. doi: 10.1016/j.mri.2012.05.001

Fuster-Garcia, E., Juan-Albarracin, J., Garcia-Ferrando, G. A., Marti-Bonmati, L., Aparici-Robles, F., and Garcia-Gomez, J. M. (2018). Improving the estimation of prognosis for glioblastoma patients by MR based hemodynamic tissue signatures. *NMR Biomed* 31, e4006. doi: 10.1002/nbm.4006

Gatenby, R. A., Grove, O., and Gillies, R. J. (2013). Quantitative imaging in cancer evolution and ecology. *Radiology* 269, 8–15. doi: 10.1148/radiol.13122697

Gates, E. D. H., Lin, J. S., Weinberg, J. S., Hamilton, J., Prabhu, S. S., Hazle, J. D., et al. (2019). Guiding the first biopsy in glioma patients using estimated Ki-67 maps derived from MRI: conventional versus advanced imaging. *Neuro Oncol.* 21, 527–536. doi: 10.1093/neuonc/noz004

Halmos, G. B., Bruine de Bruin, L., Langendijk, J. A., van der Laan, B. F., Pruim, J., and Steenbakkers, R. J. (2014). Head and neck tumor hypoxia imaging by 18F-fluoroazomycin-arabinoside (18F-FAZA)-PET: a review. *Clin. Nucl. Med.* 39, 44–48.

Hardee, M. E., and Zagzag, D. (2012). Mechanisms of glioma-associated neovascularization. *Am. J. Pathol.* 181, 1126–1141. doi: 10.1016/j.ajpath.2012.06.030

Holash, J., Maisonpierre, P. C., Compton, D., Boland, P., Alexander, C. R., Zagzag, D., et al. (1999). Vessel cooption, regression, and growth in tumors mediated by angiopoietins and VEGF. *Science* 284, 1994–1998. doi: 10.1126/science.284.5422.1994

Hu, L. S., Ning, S., Eschbacher, J. M., Gaw, N., Dueck, A. C., Smith, K. A., et al. (2015). Multi-parametric MRI and texture analysis to visualize spatial histologic heterogeneity and tumor extent in glioblastoma. *PLoS One* 10:e0141506. doi: 10.1371/journal.pone.0141506

Huang, W. J., Chen, W. W., and Zhang, X. (2016). Glioblastoma multiforme: effect of hypoxia and hypoxia inducible factors on therapeutic approaches. *Oncol. Lett.* 12, 2283–2288. doi: 10.3892/ol.2016.4952

Ismail, M., Hill, V., Statsevych, V., Huang, R., Prasanna, P., Correa, R., et al. (2018). Shape features of the lesion habitat to differentiate brain tumor progression from pseudoprogression on routine multiparametric MRI: a multisite study. *AJNR Am. J. Neuroradiol.* 39, 2187–2193. doi: 10.3174/ajnr.A5858

Jackson, R. J., Fuller, G. N., Abi-Said, D., Lang, F. F., Gokaslan, Z. L., Shi, W. M., et al. (2001). Limitations of stereotactic biopsy in the initial management of gliomas. *Neuro Oncol.* 3, 193–200. doi: 10.1093/neuonc/3.3.193

John, F., Bosnyak, E., Robinette, N. L., Amit-Yousif, A. J., Barger, G. R., Shah, K. D., et al. (2019). Multimodal imaging-defined subregions in newly diagnosed glioblastoma: impact on overall survival. *Neuro Oncol.* 21, 264–273. doi: 10.1093/neuonc/noy169

Juan-Albarracin, J., Fuster-Garcia, E., Garcia-Ferrando, G. A., and Garcia-Gomez, J. M. (2019). ONCOhabitats: a system for glioblastoma heterogeneity assessment through MRI. *Int. J. Med. Inform.* 128, 53–61. doi: 10.1016/j.ijmedinf.2019.05.002

Juan-Albarracin, J., Fuster-Garcia, E., Perez-Girbes, A., Aparici-Robles, F., Alberich-Bayarri, A., Revert-Ventura, A., et al. (2018). Glioblastoma: vascular habitats detected at preoperative dynamic susceptibility-weighted contrast-enhanced perfusion MR imaging predict survival. *Radiology* 287, 944–954. doi: 10.1148/radiol.2017170845

Jun, P., Garcia, J., Tihan, T., McDermott, M. W., and Cha, S. (2006). Perfusion MR imaging of an intracranial collision tumor confirmed by image-guided biopsy. *AJNR Am. J. Neuroradiol.* 27, 94–97.

Kang, B. K., Na, D. G., Ryoo, J. W., Byun, H. S., Roh, H. G., and Pyeun, Y. S. (2001). Diffusion-weighted MR imaging of intracerebral hemorrhage. *Korean J. Radiol.* 2, 183–191. doi: 10.3348/kjr.2001.2.4.183

Kim, J. Y., and Gatenby, R. A. (2017). Quantitative clinical imaging methods for monitoring intratumoral evolution. *Methods Mol. Biol.* 1513, 61–81. doi: 10.1007/978-1-4939-6539-7_6

Kim, M., Park, J. E., Kim, H. S., Kim, N., Park, S. Y., Kim, Y. H., et al. (2021). Spatiotemporal habitats from multiparametric physiologic MRI distinguish tumor progression from treatment-related change in post-treatment glioblastoma. *Eur. Radiol.* 31, 6374–6383. doi: 10.1007/s00330-021-07718-y

Komori, T., Muragaki, Y., and Chernov, M. F. (2018). Pathology and genetics of gliomas. *Prog. Neurol. Surg.* 31, 1–37. doi: 10.1159/000466835

Lee, J., Narang, S., Martinez, J., Rao, G., and Rao, A. (2015a). Spatial habitat features derived from multiparametric magnetic resonance imaging data are associated with molecular subtype and 12-month survival status in glioblastoma multiforme. *PLoS One* 10:e0136557. doi: 10.1371/journal.pone.0136557

Lee, J., Narang, S., Martinez, J. J., Rao, G., and Rao, A. (2015b). Associating spatial diversity features of radiologically defined tumor habitats with epidermal growth factor receptor driver status and 12-month survival in glioblastoma: methods and preliminary investigation. *J. Med. Imaging (Bellingham)* 2:041006. doi: 10.1117/1.JMI.2.4.041006

Li, C., Yan, J. L., Torheim, T., McLean, M. A., Boonzaier, N. R., Zou, J., et al. (2019). Low perfusion compartments in glioblastoma quantified by advanced magnetic resonance imaging and correlated with patient survival. *Radiother. Oncol.* 134, 17–24. doi: 10.1016/j.radonc.2019.01.008

Li, Z. C., Bai, H., Sun, Q., Li, Q., Liu, L., Zou, Y., et al. (2018a). Multiregional radiomics features from multiparametric MRI for prediction of MGMT methylation status in glioblastoma multiforme: a multicentre study. *Eur. Radiol.* 28, 3640–3650. doi: 10.1007/s00330-017-5302-1

Li, Z. C., Bai, H., Sun, Q., Zhao, Y., Lv, Y., Zhou, J., et al. (2018b). Multiregional radiomics profiling from multiparametric MRI: identifying an

imaging predictor of IDH1 mutation status in glioblastoma. *Cancer Med.* 7, 5999–6009. doi: 10.1002/cam4.1863

Louis, D. N., Perry, A., Reifenberger, G., von Deimling, A., Figarella-Branger, D., Cavenee, W. K., et al. (2016). The 2016 world health organization classification of tumors of the central nervous system: a summary. *Acta Neuropathol.* 131, 803–820. doi: 10.1007/s00401-016-1545-1

Lu, Y., Yeung, C., Radmanesh, A., Wiemann, R., Black, P. M., and Golby, A. J. (2015). Comparative effectiveness of frame-based, frameless, and intraoperative magnetic resonance imaging-guided brain biopsy techniques. *World Neurosurg.* 83, 261–268. doi: 10.1016/j.wneu.2014.07.043

Maier, S. E., Sun, Y., and Mulkern, R. V. (2010). Diffusion imaging of brain tumors. *NMR Biomed.* 23, 849–864. doi: 10.1002/nbm.1544

Mapelli, P., and Picchio, M. (2020). 18F-FAZA PET imaging in tumor hypoxia: a focus on high-grade glioma. *Int. J. Biol. Markers* 35(1_suppl), 42–46. doi: 10.1177/1724600820905715

Mapelli, P., Callea, M., Fallanca, F., Castellano, A., Bailo, M., Scifo, P., et al. (2021). 18F-FAZA PET/CT in pretreatment assessment of hypoxic status in high-grade glioma: correlation with hypoxia immunohistochemical biomarkers. *Nucl. Med. Commun.* 42, 763–771. doi: 10.1097/MNM.0000000000001396

Mikkelsen, V. E., Stensjoen, A. L., Berntsen, E. M., Nordrum, I. S., Salvesen, O., Solheim, O., et al. (2018). Histopathologic features in relation to pretreatment tumor growth in patients with glioblastoma. *World Neurosurg.* 109, e50–e58. doi: 10.1016/j.wneu.2017.09.102

Miloushev, V. Z., Chow, D. S., and Filippi, C. G. (2015). Meta-analysis of diffusion metrics for the prediction of tumor grade in gliomas. *AJNR Am. J. Neuroradiol.* 36, 302–308. doi: 10.3174/ajnr.A4097

Muragaki, Y., Chernov, M., Maruyama, T., Ochiai, T., Taira, T., Kubo, O., et al. (2008). Low-grade glioma on stereotactic biopsy: how often is the diagnosis accurate? *Minim. Invasive Neurosurg.* 51, 275–279. doi: 10.1055/s-0028-1082322

Napel, S., Mu, W., Jardim-Perassi, B. V., Aerts, H. J., and Gillies, R. J. (2018). Quantitative imaging of cancer in the postgenomic era: radio (geno) mics, deep learning, and habitats. *Cancer* 124, 4633–4649. doi: 10.1002/cncr.31630

Nguyen, T. B., Cron, G. O., Bezzina, K., Perdrizet, K., Torres, C. H., Chakraborty, S., et al. (2016). Correlation of tumor immunohistochemistry with dynamic contrast-enhanced and DSC-MRI parameters in patients with gliomas. *AJNR Am. J. Neuroradiol.* 37, 2217–2223. doi: 10.3174/ajnr.A4908

O'Connor, J. P., Rose, C. J., Waterton, J. C., Carano, R. A., Parker, G. J., and Jackson, A. (2015). Imaging intratumor heterogeneity: role in therapy response, resistance, and clinical outcome. *Clin. Cancer Res.* 21, 249–257. doi: 10.1158/1078-0432.CCR-14-0990

Ono, Y., Chernov, M. F., Muragaki, Y., Maruyama, T., Abe, K., and Iseki, H. (2018). Imaging of Intracranial Gliomas. *Prog. Neurol. Surg.* 30, 12–62. doi: 10.1159/000464376

Otsu, N. (1979). A threshold selection method from gray-level histograms. *IEEE Trans. Syst Man Cybern.* 9, 62–66. doi: 10.1109/TSMC.1979.4310076

Park, J. E., Kim, H. S., Kim, N., Park, S. Y., Kim, Y. H., and Kim, J. H. (2021). Spatiotemporal heterogeneity in multiparametric physiologic MRI Is associated with patient outcomes in IDH-wildtype glioblastoma. *Clin. Cancer Res.* 27, 237–245. doi: 10.1158/1078-0432.CCR-20-2156

Pillai, J. J., and Zaca, D. (2012). Comparison of BOLD cerebrovascular reactivity mapping and DSC MR perfusion imaging for prediction of neurovascular uncoupling potential in brain tumors. *Technol. Cancer Res. Treat.* 11, 361–374. doi: 10.7785/tcrt.2012.500284

Ponte, K. F., Berro, D. H., Collet, S., Constans, J. M., Emery, E., Valable, S., et al. (2017). In vivo relationship between hypoxia and angiogenesis in human glioblastoma: a multimodal imaging study. *J. Nucl. Med.* 58, 1574–1579. doi: 10.2967/jnumed.116.188557

Preibisch, C., Shi, K., Kluge, A., Lukas, M., Wiestler, B., Gottler, J., et al. (2017). Characterizing hypoxia in human glioma: a simultaneous multimodal MRI and PET study. *NMR Biomed.* 30, e3775. doi: 10.1002/nbm.3775

Reithmeier, T., Lopez, W. O., Doostkam, S., Machein, M. R., Pinsker, M. O., Trippel, M., et al. (2013). Intraindividual comparison of histopathological diagnosis obtained by stereotactic serial biopsy to open surgical resection specimen in patients with intracranial tumours. *Clin. Neurol. Neurosurg.* 115, 1955–1960. doi: 10.1016/j.clineuro.2013.05.019

Rosinska, S., and Gavard, J. (2021). Tumor vessels fuel the fire in glioblastoma. *Int. J. Mol. Sci.* 22:6514. doi: 10.3390/ijms22126514

Roth, A., Buttrick, S. S., Cajigas, I., Jagid, J. R., and Ivan, M. E. (2018). Accuracy of frame-based and frameless systems for deep brain stimulation: a meta-analysis. *J. Clin. Neurosci.* 57, 1–5. doi: 10.1016/j.jocn.2018.08.039

Rotkopf, L. T., Wiestler, B., Preibisch, C., Liesche-Starnecker, F., Pyka, T., Norenberg, D., et al. (2020). The wavelet power spectrum of perfusion weighted MRI correlates with tumor vascularity in biopsy-proven glioblastoma samples. *PLoS One* 15:e0228030. doi: 10.1371/journal.pone.0228030

Santarosa, C., Castellano, A., Conte, G. M., Cadioli, M., Iadanza, A., Terreni, M. R., et al. (2016). Dynamic contrast-enhanced and dynamic susceptibility contrast perfusion MR imaging for glioma grading: preliminary comparison of vessel compartment and permeability parameters using hotspot and histogram analysis. *Eur. J. Radiol.* 85, 1147–1156. doi: 10.1016/j.ejrad.2016.03.020

Sanvito, F., Castellano, A., and Falini, A. (2021). Advancements in neuroimaging to unravel biological and molecular features of brain tumors. *Cancers (Basel)* 13:424. doi: 10.3390/cancers13030424

Sauwen, N., Acou, M., Van Cauter, S., Sima, D. M., Veraart, J., Maes, F., et al. (2016). Comparison of unsupervised classification methods for brain tumor segmentation using multi-parametric MRI. *Neuroimage Clin.* 12, 753–764. doi: 10.1016/j.nicl.2016.09.021

Savi, A., Incerti, E., Fallanca, F., Bettinardi, V., Rossetti, F., Monterisi, C., et al. (2017). First evaluation of pet-based human biodistribution and dosimetry of (18)F-FAZA, a tracer for imaging tumor hypoxia. *J. Nucl. Med.* 58, 1224–1229. doi: 10.2967/jnumed.113.122671

Sciortino, T., Fernandes, B., Conti Nibali, M., Gay, L. G., Rossi, M., Lopci, E., et al. (2019). Frameless stereotactic biopsy for precision neurosurgery: diagnostic value, safety, and accuracy. *Acta Neurochir. (Wien)* 161, 967–974. doi: 10.1007/s00701-019-03873-w

Sottoriva, A., Spiteri, I., Piccirillo, S. G., Touloumis, A., Collins, V. P., Marioni, J. C., et al. (2013). Intratumor heterogeneity in human glioblastoma reflects cancer evolutionary dynamics. *Proc. Natl. Acad. Sci. U.S.A.* 110, 4009–4014. doi: 10.1073/pnas.1219747110

Stadlbauer, A., Buchfelder, M., Doelken, M. T., Hammen, T., and Ganslandt, O. (2011). Magnetic resonance spectroscopic imaging for visualization of the infiltration zone of glioma. *Cent. Eur. Neurosurg.* 72, 63–69. doi: 10.1055/s-0030-1253410

Stadlbauer, A., Zimmermann, M., Doerfler, A., Oberndorfer, S., Buchfelder, M., Coras, R., et al. (2018b). Intratumoral heterogeneity of oxygen metabolism and neovascularization uncovers 2 survival-relevant subgroups of IDH1 wild-type glioblastoma. *Neuro Oncol.* 20, 1536–1546. doi: 10.1093/neuonc/noy066

Stadlbauer, A., Mouridsen, K., Doerfler, A., Bo Hansen, M., Oberndorfer, S., Zimmermann, M., et al. (2018a). Recurrence of glioblastoma is associated with elevated microvascular transit time heterogeneity and increased hypoxia. *J. Cereb. Blood Flow Metab.* 38, 422–432. doi: 10.1177/0271678X17694905

Stringfield, O., Arrington, J. A., Johnston, S. K., Rognin, N. G., Peeri, N. C., Balagurunathan, Y., et al. (2019). Multiparameter MRI predictors of long-term survival in glioblastoma multiforme. *Tomography* 5, 135–144. doi: 10.18383/j.tom.2018.00052

Verma, R., Correa, R., Hill, V. B., Statsevych, V., Bera, K., Beig, N., et al. (2020). Tumor habitat-derived radiomic features at pretreatment mri that are prognostic for progression-free survival in glioblastoma are associated with key morphologic attributes at histopathologic examination: a feasibility study. *Radiol. Artif. Intell.* 2:e190168. doi: 10.1148/ryai.2020190168

Wang, Q., Li, Q., Mi, R., Ye, H., Zhang, H., Chen, B., et al. (2019). Radiomics nomogram building from multiparametric MRI to predict grade in patients with glioma: a cohort study. *J. Magn. Reson. Imaging* 49, 825–833. doi: 10.1002/jmri.26265

Wei, J., Yang, G., Hao, X., Gu, D., Tan, Y., Wang, X., et al. (2019). A multi-sequence and habitat-based MRI radiomics signature for preoperative prediction of MGMT promoter methylation in astrocytomas with prognostic implication. *Eur. Radiol.* 29, 877–888. doi: 10.1007/s00330-018-5575-z

Winfield, J. M., Payne, G. S., Weller, A., and deSouza, N. M. (2016). DCE-MRI, DW-MRI, and MRS in cancer: challenges and advantages of implementing qualitative and quantitative multi-parametric imaging in the clinic. *Top. Magn. Reson. Imaging* 25, 245–254. doi: 10.1097/RMR.0000000000000103

Wu, H., Tong, H., Du, X., Guo, H., Ma, Q., Zhang, Y., et al. (2020). Vascular habitat analysis based on dynamic susceptibility contrast perfusion MRI predicts IDH

mutation status and prognosis in high-grade gliomas. *Eur. Radiol.* 30, 3254–3265. doi: 10.1007/s00330-020-06702-2

Yip, C., Weeks, A., Shaw, K., Siddique, M., Chang, F., Landau, D. B., et al. (2017). Magnetic resonance imaging (MRI) of intratumoral voxel heterogeneity as a potential response biomarker: assessment in a HER2+ esophageal adenocarcinoma xenograft following trastuzumab and/or cisplatin therapy. *Transl. Oncol.* 10, 459–467. doi: 10.1016/j.tranon.2017.03.006

Zhang, J., Liu, H., Tong, H., Wang, S., Yang, Y., Liu, G., et al. (2017). Clinical applications of contrast-enhanced perfusion mri techniques in gliomas: recent advances and current challenges. *Contrast Media Mol. Imaging* 2017:7064120. doi: 10.1155/2017/7064120

Zhang, X., Lu, H., Tian, Q., Feng, N., Yin, L., Xu, X., et al. (2019). A radiomics nomogram based on multiparametric MRI might stratify glioblastoma patients according to survival. *Eur. Radiol.* 29, 5528–5538. doi: 10.1007/s00330-019-06069-z

Zhou, M., Chaudhury, B., Hall, L. O., Goldgof, D. B., Gillies, R. J., and Gatenby, R. A. (2017). Identifying spatial imaging biomarkers of glioblastoma multiforme for survival group prediction. *J. Magn. Reson. Imaging* 46, 115–123. doi: 10.1002/jmri.25497

Zhou, M., Hall, L., Goldgof, D., Russo, R., Balagurunathan, Y., Gillies, R., et al. (2014). Radiologically defined ecological dynamics and clinical outcomes in glioblastoma multiforme: preliminary results. *Transl. Oncol.* 7, 5–13. doi: 10.1593/tlo.13730

Conflict of Interest: The authors declare that the research was conducted in the absence of any commercial or financial relationships that could be construed as a potential conflict of interest.

Publisher's Note: All claims expressed in this article are solely those of the authors and do not necessarily represent those of their affiliated organizations, or those of the publisher, the editors and the reviewers. Any product that may be evaluated in this article, or claim that may be made by its manufacturer, is not guaranteed or endorsed by the publisher.

Copyright © 2022 Bailo, Pecco, Callea, Scifo, Gagliardi, Presotto, Bettinardi, Fallanca, Mapelli, Gianolli, Doglioni, Anzalone, Picchio, Mortini, Falini and Castellano. This is an open-access article distributed under the terms of the Creative Commons Attribution License (CC BY). The use, distribution or reproduction in other forums is permitted, provided the original author(s) and the copyright owner(s) are credited and that the original publication in this journal is cited, in accordance with accepted academic practice. No use, distribution or reproduction is permitted which does not comply with these terms.

frontiers | Frontiers in Oncology

CASE REPORT
published: 22 July 2022
doi: 10.3389/fonc.2022.866622

Case Report: Atypical Solitary Brain Metastasis: The Role of MR Spectroscopy In Differential Diagnosis

Dusko Kozic[1,2], *Nebojsa Lasica*[1,3], *Danica Grujicic*[4,5,6], *Savo Raicevic*[7], *Natasa Prvulovic Bunovic*[1,2], *Igor Nosek*[2] *and Jasmina Boban*[1,2]*

[1] Faculty of Medicine, University of Novi Sad, Novi Sad, Serbia, [2] Oncology Institute of Vojvodina, Center for Diagnostic Imaging, Sremska Kamenica, Serbia, [3] Clinic of Neurosurgery, Clinical Center of Vojvodina, Novi Sad, Serbia, [4] Faculty of Medicine, University of Belgrade, Belgrade, Serbia, [5] Neuro-Oncology Department, Clinic of Neurosurgery Clinical Center of Serbia, Belgrade, Serbia, [6] Pediatric Oncology Department, Institute of Oncology and Radiology of Serbia, Belgrade, Serbia, [7] Department of Pathology, Clinical Center of Serbia, Belgrade, Serbia

OPEN ACCESS

Edited by:
Alexandra Golby, Harvard Medical School, United States

Reviewed by:
S. Ottavio Tomasi, Paracelsus Medical University, Austria
Fahd Derkaoui Hassani, Cheikh Zaid International University Hospital, Morocco

***Correspondence:**
Jasmina Boban
jasmina.boban@mf.uns.ac.rs

Specialty section:
This article was submitted to Neuro-Oncology and Neurosurgical Oncology, a section of the journal Frontiers in Oncology

Received: *31 January 2022*
Accepted: *17 June 2022*
Published: *22 July 2022*

Citation:
Kozic D, Lasica N, Grujicic D, Raicevic S, Prvulovic Bunovic N, Nosek I and Boban J (2022) Case Report: Atypical Solitary Brain Metastasis: The Role of MR Spectroscopy In Differential Diagnosis. Front. Oncol. 12:866622. doi: 10.3389/fonc.2022.866622

Background: Metastatic brain tumors are typically located at the cerebral hemispheres or the cerebellum and most frequently originate from primary breast or lung tumors. Metastatic lesions are usually associated with blood–brain barrier disruption, solid or ring-like contrast enhancement, and perilesional vasogenic edema on brain imaging. Even in cases where metastases are predominantly cystic, enhancement of the minor solid component can be detected. In contrast, non-enhancing secondary brain tumors were only reported in a patient after antiangiogenic treatment with bevacizumab.

Case report: We report a case of a 54-year-old male who presented with left-sided weakness and multiple seizures. Brain magnetic resonance imaging revealed a T2-weighted heterogeneous solid tumor in the right frontoparietal parasagittal region, with no apparent enhancement on T1-weighted post-contrast images and no evident perilesional edema. Further MRS analysis revealed markedly increased choline and lipid peaks. The patient underwent craniotomy for tumor removal. Histopathology revealed findings consistent with metastatic non-microcellular neuroendocrine lung cancer. positron emission tomography/computed tomography (PET/CT) revealed a stellate lesion within the right upper lung lobe, compatible with primary lung cancer.

Conclusion: Non-enhancing brain metastatic tumors are rarely reported in the literature, usually following antiangiogenic treatment. Here, we report the first ever case of a non-enhancing metastatic brain tumor with no prior history of antiangiogenic treatment, with particular emphasis on the importance of MRS analysis in atypical brain lesions.

Keywords: brain metastasis, nonenhancing, magnetic resonance spectroscopy, case report, neuroendocrine tumor

BACKGROUND

Magnetic resonance imaging (MRI) is the method of choice for detection of brain metastases (1). Majority of metastatic brain tumors are located in the cerebral hemispheres and the cerebellum, whereas breast and lungs are the most frequent primary origin of the neoplastic dissemination (1, 2). Metastatic foci are associated with blood–brain barrier disruption, solid or ring-like contrast enhancement, and perilesional vasogenic edema are usually evident. Even when cerebral metastatic foci are predominantly cystic, enhancement of the minor solid component can be detected. Non-enhancing solid components of brain neoplasms are usually evident in World Health Organization (WHO) grade II and grade III astrocytomas but seldom in metastatic lesions (3–5). Karimi et al. reported non-enhancing metastases in a patient with lung cancer, following antiangiogenic effects of bevacizumab (Avastin) (5).

To the best of our knowledge, this is the first report of a non-enhancing solid component of metastatic brain tumor and the benefits and importance of the magnetic resonance spectroscopy (MRS) as a supportive non-invasive diagnostic tool in the diagnostic algorithm.

CASE PRESENTATION

A 54-year-old male presented with a 4-week history of the left arm and leg weakness and clumsiness followed by multiple seizures 2 weeks prior to admission. The patient had no past medical history or history of hereditary diseases. Physical examination was unremarkable. Neurological examination revealed left-sided weakness with no sensory deficits.

Brain MRI revealed a dural-based mass in the right frontoparietal region, extending to the intraaxial compartment, measuring 46 mm in antero-posterior, 34 mm in cranio-caudal, and 23 mm in the lateral dimension. The mass was heterogeneous on the T2-weighted sequence with no significant post-contrast enhancement of the solid tumor component after intravenous administration of gadolinium-diethylenetriamine pentaacetic acid. Tortuous peripheral enhancement correlated with dislocated cortical venous vessels. Markedly increased choline (Cho) and lipid peak were noted on MRS (**Figures 1A–D**). No surrounding edema was noted. Imaging findings mainly were consistent with a solitary fibrous tumor.

After usual prepping of the operative field, right parasagittal craniotomy was performed for tumor resection. The lesion was in the right parietal parasagittal region in contact with falx, pink in color, with an approximate largest diameter of 3.5 cm. Gross total resection was performed with the assistance of neuromonitoring. Tissue samples were taken intraoperatively and sent for frozen section and histopathology examination. The patient postoperative course was uneventful.

On histopathological examination tumor cells manifested scant to moderate amounts of eosinophilic cytoplasm and irregular nuclei with "salt and pepper" chromatin. Brisk mitotic activity was noted (**Figure 1A**). Immunohistochemical staining revealed that tumor cells nuclei strongly and diffusely expressed TTF-1 (**Figure 1B**) associated with high proliferative Ki-67 index (**Figure 2C**). These features were compatible with non-microcellular neuroendocrine lung cancer metastatic disease. PET/CT revealed a stellate lesion, with spicules radiating out from the central portion of the mass, within the right upper lung lobe, compatible with primary lung cancer, measuring 17 mm × 2 8mm (**Figure 3**).

Patient remained progression free for 2 years, developing multiple metastases in cerebral and cerebellar hemispheres, lungs, and adrenal glands. Further institutional protocol-based adjuvant therapy included etoposide with cisplatin chemotherapy (EP) and radiation treatment for the tumoral bed with fractioned external beam irradiation to a total dose of 40 Gy divided into 20 fractions, which was interrupted after 17th fraction due to patient's personal will. Extensive dissemination of malignant disease resulted in lethal outcome three years after the initial diagnosis had been established.

DISCUSSION

Non-enhancing cerebral metastatic foci are seldomly reported and poorly understood. Typically, metastatic lesions to the central nervous system demonstrate a strong contrast enhancement and are detected on post-contrast T1-weighted images, whereas plain and post-contrast FLAIR sequences are found to be most sensitive in identifying leptomeningeal secondary malignant involvement (6, 7). However, occasionally leptomeningeal metastases may exhibit minimal or even absent contrast enhancement, particularly if there is a presence of tumor hemorrhage as reported earlier by Rumboldt et al. (8); these lesions, however, usually show precontrast T1W hyperintensity, which allows for better initial detection. Early detection of brain metastases may improve disease control and life expectancy due to prompt implementation of adequate treatment (9, 10).

Neovascularization of the metastatic lesions and hyperemia is a major cause of contrast enhancement, associated with blood volume and blood flow increase. An additional contributing factor in metastatic tumors enhancement is compatible with alterations in blood–brain barrier because blood vessels supplying the tumor tissue are typically immature and "leaky" (11–13).

The most likely reason for the non-enhancement of cerebral metastases, documented in the literature, is associated with the antiangiogenic effects of anticancer treatment and monoclonal antibodies (5, 14). Another reason is associated with delayed or even completely blocked permeability of the blood–brain barrier to gadolinium chelate due to tiny fenestrations, diminished local blood flow, and the size capillary surface area (15, 16).

However, our patient presented with no clinical history of oncologic disease or anticancer, biological, or immunosuppressive treatment. The tumor on non-enhanced MRI study was rather voluminous, most compatible with

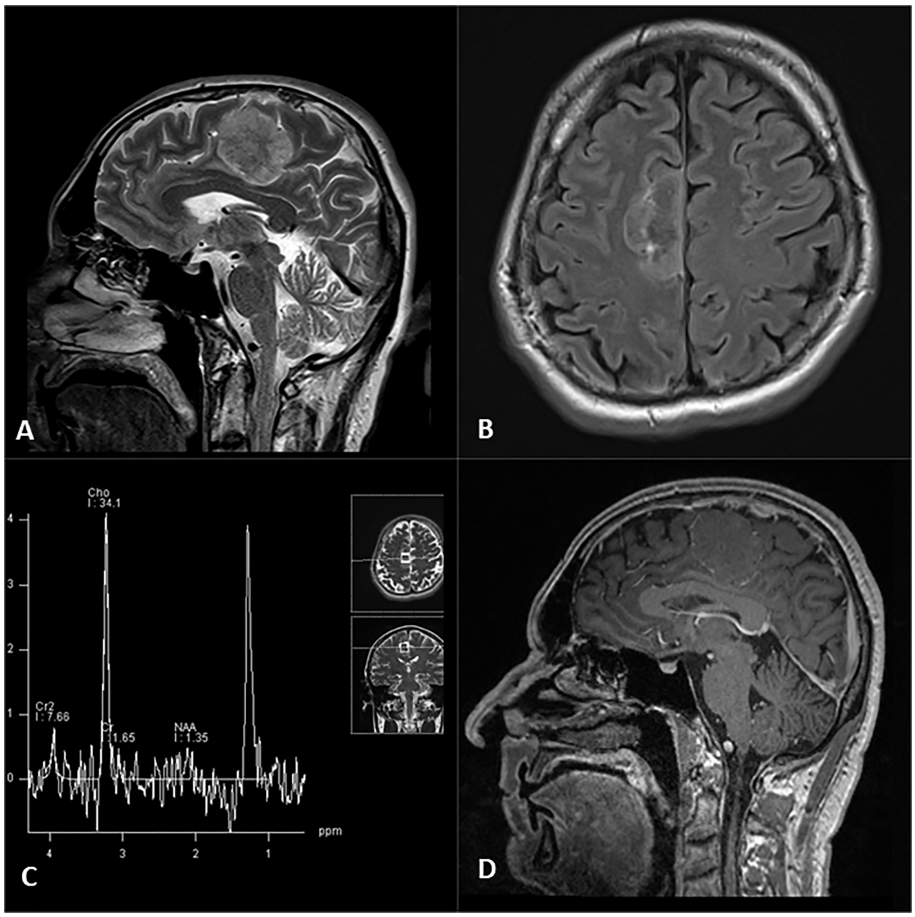

FIGURE 1 | Right frontal parafalcine tumor evident on T2 sagittal **(A)** and FLAIR axial images **(B)**, associated with typical high choline and lipid peaks on single-voxel MR spectroscopy **(C)** and lack of expected enhancement on post contrast T1 sagittal image **(D)**.

meningioma, or less likely, metastatic neoplastic process. Primary brain tumor, with the secondary invasion of the dura, was also considered. The absence of expected vivid contrast enhancement practically excluded meningioma and metastatic lesion from the differential diagnosis. However, the neurometabolic profile revealed on MRS noted high peaks of Cho and lipid and no identification of N-acetyl aspartate (NAA) and creatine (Cr). Such a pattern is most compatible with metastasis.

MRS is a non-invasive diagnostic modality that evaluates the cerebral metabolic profile by determining different neurochemical concentrations. NAA, seen at 2.06 ppm in the proton spectrum of a healthy person, is a marker of neuronal integrity and function. The increased Cho concentration

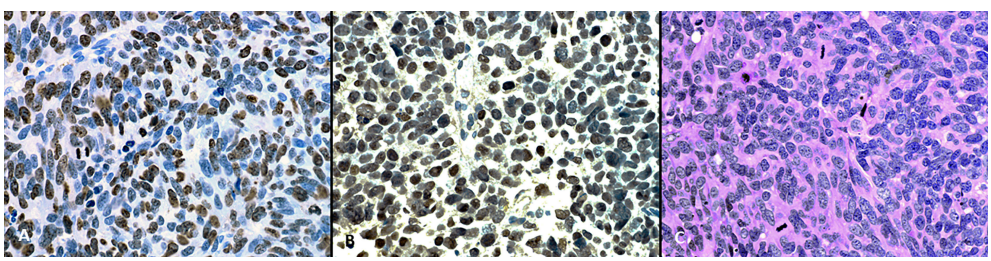

FIGURE 2 | **(A)** On hematoxylin and eosin staining tumor cells have scant to moderate amount of eosinophillic cytoplasm, and irregular nuclei with "salt and pepper" chromatin. Brisk mitotic activity can be seen. **(B)** On immunohistochemical staining tumor cells nuclei strongly and diffusely express TTF-1. **(C)** The proliferative Ki-67 index is high (magnification, x400).

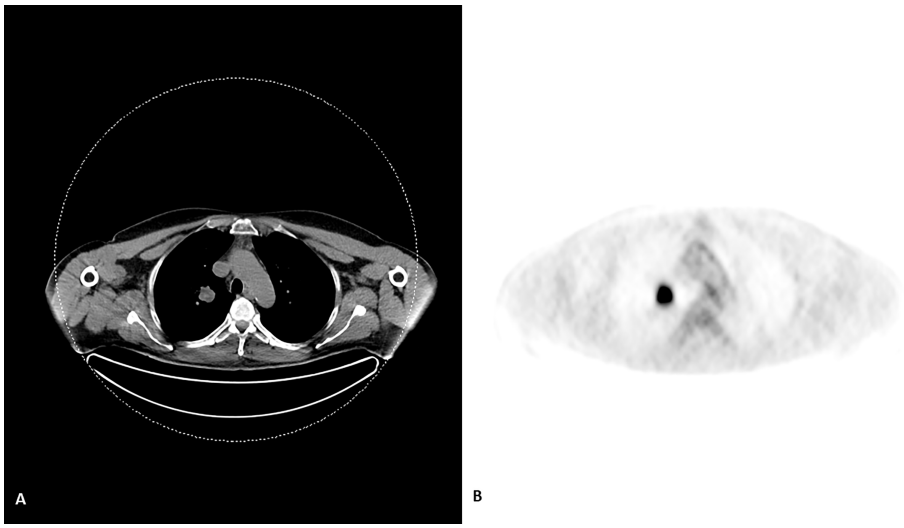

FIGURE 3 | An evident lesion in the upper lobe of the right lung on CT scan **(A)** with an avid FDG uptake **(B)** of the compatible with cancer on PET scan.

indicates the presence of increased cell membrane turnover. The elevated lactate peak is associated with increased macrophage activation and anaerobic glycolysis. The level of Cr seems to be related to cerebral energy reserves. Recent studies suggested that the determination of absolute concentrations of each metabolite substantially increases the accuracy and understanding of the altered brain physiology (17). In almost all patients with brain tumors, MRS shows metabolic ratio alterations (18).

The decreased level of NAA is consistent with the destroyed neuronal tissue, neuronal dysfunction, or rarefaction. The increased Cho peak in primary and metastatic brain tumors is associated with accelerated cell proliferation and cell membrane turnover (19). The rise of the myo-inositol peak in the neoplastic tissue is most compatible with glial proliferation in less aggressive gliomas (grade 2), whereas complete lack of NAA and Cr peaks may suggest a non-glial origin of the neoplasm (20).

Elevated Cho and lipid peaks, with absent peaks of NAA and Cr, are typical of metastatic disease of the brain, whereas a Cho-only spectrum is characteristic of non-glial intra-axial neoplasms and extra-axial tumors. The additional presence of alanine is seen in meningiomas (21). This pattern, characteristic for metastatic brain tumors, was evident in our patient, increasing the role of MR spectroscopy, especially in atypical appearances of different cerebral neoplastic diseases of glial and non-glial nature.

CONCLUSION

In previous studies, non-enhancing brain metastatic tumors were only reported following antiangiogenic treatment. To best of our knowledge, this is the first ever case of a non-enhancing solid component of metastatic brain tumor with no prior history of antiangiogenic treatment, with particular emphasis on the importance of MRS analysis in atypical brain lesions.

DATA AVAILABILITY STATEMENT

The raw data supporting the conclusions of this article will be made available by the authors, without undue reservation.

ETHICS STATEMENT

The studies involving human participants were reviewed and approved by Ethical Review Board of the Clinical Center Serbia. The patients/participants provided their written informed consent to participate in this study. Written informed consent was obtained from the individual(s) for the publication of any potentially identifiable images or data included in this article.

AUTHOR CONTRIBUTIONS

DK, DG, and NL wrote the manuscript. SR undertook the pathological analysis of the specimens. DK, NPB and IN undertook the radiological diagnosis. DG carried out surgical and the clinical management of the patient. JB was involved in data analysis and critical revision of the drafted manuscript. All authors contributed to the article and approved the submitted version.

REFERENCES

1. Achrol AS, Rennert RC, Anders C, Soffietti R, Ahluwalia MS, Nayak L, et al. Brain Metastases. *Nat Rev Dis Primers* (2019) 5(1):5.144. doi: 10.1038/s41572-018-0055-y
2. Patchell RA. The Management of Brain Metastases. *Cancer Treat Rev* (2003) 29(6):533–40.146. doi: 10.1016/s0305-7372(03)00105-1
3. Percy DB, Ribot EJ, Chen Y, McFadden C, Simedrea C, Steeg PS, et al. *In Vivo* Characterization of Changing Blood-Tumor Barrier Permeability in a Mouse Model of Breast Cancer Metastasis: A Complementary Magnetic Resonance Imaging Approach. *InvestRadiol* (2011) 46(11):718–25. doi: 10.1097/RLI.0b013e318226c427
4. Lemasson B, Serduc R, Maisin C, Bouchet A, Coquery N, Robert P, et al. Monitoring Blood-Brain Barrier Status in a Rat Model of Glioma Receiving Therapy: Dual Injection of Low-Molecular-Weight and Macromolecular MR Contrast Media. *154 Radiol* (2010) 257(2):342–52. doi: 10.1148/radiol.10092343
5. Karimi S, Lis E, Gilani S, D'Ambrosio N, Holodny A. Nonenhancing Brain Metastases. *J Neuroimaging* (2011) 21(2):184–7. doi: 10.1111/j.1552-6569.2009.00389.x
6. Singh SK, Agris JM, Leeds NE, Ginsberg LE. Intracranial Leptomeningeal Metastases: Comparison of Depiction at FLAIR and Contrast-Enhanced MR Imaging. *Radiology* (2000) 159 217(1):50–3. doi: 10.1148/radiology.217.1.r00oc3550
7. Singh SK, Leeds NE, Ginsberg LE. MR Imaging of Leptomeningeal Metastases: Comparison of Three Sequences. *AJNR Am J Neuroradiol* (2002) 23(5):817–21.
8. Rumboldt Z, Lambert L, Talan-Hranilovic J, Marjan D, Sajko T. Nonenhancing Spinal Subdural Metastatic Tumor. *AJNR Am J Neuroradiol* (2005) 26(9):2406–9.
9. Groves MD. Leptomeningeal Disease. *Neurosurg Clin N Am* (2011) 22(1):67–78-vii. 165. doi: 10.1016/j.nec.2010.08.006
10. Clarke JL, Perez HR, Jacks LM, Panageas KS, Deangelis LM. Leptomeningeal Metastases in 167 the MRI Era. *Neurology* (2010) 74(18):1449–54. doi: 10.1212/WNL.0b013e3181dc1a69
11. Smirniotopoulos JG, Murphy FM, Rushing EJ, Rees JH, Schroeder JW. Patterns of Contrast Enhancement in the Brain and Meninges. *Radiographics* (2007) 27(2):525–51. doi: 10.1148/rg.272065155
12. Sage MR, Wilson AJ, Scroop R. Contrast Media and the Brain. The Basis of CT and MR Imaging Enhancement. *Neuroimaging Clin N Am* (1998) 8(3):695–707.
13. Jain R, Griffith B, Narang J. Blood-Brain-Barrier Imaging in Brain Tumors: Concepts and 174 Methods. *Neurographics* (2012) 2(2):48–59. doi: 10.3174/ng.21200285
14. Kleinschmidt-DeMasters BK, Damek DM. The Imaging and Neuropathological Effects of Bevacizumab (Avastin) in Patients With Leptomeningeal Carcinomatosis. *J Neurooncol* (2010) 96(3):375–84. doi: 10.1007/s11060-009-9969-2
15. Sorensen AG. Science to Practice: Blood-Brain Barrier Leakage—One Size Does Not Fit All. *Radiology* (2010) 257(2):303–4. doi: 10.1148/radiol.101691
16. Ueno M. Molecular Anatomy of the Brain Endothelial Barrier: An Overview of the Distributional Features. *Curr Med Chem* (2007) 14(11):1199–206. doi: 10.2174/092986707780597943
17. Kozić D, Bjelan M, Boban J, Ostojić J, Turkulov V, Todorović A, et al. A Prominent Lactate Peak as a Potential Key Magnetic Resonance Spectroscopy (MRS) Feature of Progressive Multifocal Leukoencephalopathy (PML): Spectrum Pattern Observed in Three Patients. *Bosn J Basic Med Sci* (2017) 17(4):349–54. doi: 10.17305/bjbms.2017.2092
18. Kozić D, Nagulić M, Samardzić M, Ostojić J, Rasulić L, Cvetković-Dozić D. Intrapontine Malignant Nerve Sheath Tumor: MRI and MRS Features. *Acta Neurol Belg* (2008) 108(2):67–71.
19. Kozic D, Medic-Stojanoska M, Ostojic J, Popovic L, Vuckovic N. Application of MR Spectroscopy and Treatment Approaches in a Patient With Extrapituitary Growth Hormone Secreting Macroadenoma. *Neuro Endocrinol Lett* (2007) 28(5):560–4.
20. Kozić D, Ostojić J, Bjelan M, Koprivšek K. The Role of MR Spectroscopy in Neurooncology. *Prilozi* (2012) 33(1):425–33.
21. Vucković N, Kozić D, Vuleković P, Vucković D, Ostojić J, Semnic R. MR and MRS Characteristics of Intraventricular Meningioma. *J Neuroimaging* (2010) 20(3):294–6. doi: 10.1111/j.1552-6569.2008.00345.x4

Conflict of Interest: The authors declare that the research was conducted in the absence of any commercial or financial relationships that could be construed as a potential conflict of interest.

Publisher's Note: All claims expressed in this article are solely those of the authors and do not necessarily represent those of their affiliated organizations, or those of the publisher, the editors and the reviewers. Any product that may be evaluated in this article, or claim that may be made by its manufacturer, is not guaranteed or endorsed by the publisher.

Copyright © 2022 Kozic, Lasica, Grujicic, Raicevic, Prvulovic Bunovic, Nosek and Boban. This is an open-access article distributed under the terms of the Creative Commons Attribution License (CC BY). The use, distribution or reproduction in other forums is permitted, provided the original author(s) and the copyright owner(s) are credited and that the original publication in this journal is cited, in accordance with accepted academic practice. No use, distribution or reproduction is permitted which does not comply with these terms.

frontiers | Frontiers in Oncology

TYPE Systematic Review
PUBLISHED 01 August 2022
DOI 10.3389/fonc.2022.852076

Check for updates

OPEN ACCESS

EDITED BY
Sandro M. Krieg,
Technical University of Munich, Germany

REVIEWED BY
Pallavi Tiwari,
Case Western Reserve University, United States
Yi Zhang,
Zhejiang University, China
Martin Kocher,
University of Cologne, Germany

*CORRESPONDENCE
Hua-Long She
hlsxnxy@dingtalk.com

†These authors have contributed equally to this work and share first authorship

SPECIALTY SECTION
This article was submitted to Neuro-Oncology and Neurosurgical Oncology, a section of the journal Frontiers in Oncology

RECEIVED 10 January 2022
ACCEPTED 29 June 2022
PUBLISHED 01 August 2022

CITATION
Chen K, Jiang X-W, Deng L-j and She H-L (2022) Differentiation between glioma recurrence and treatment effects using amide proton transfer imaging: A mini-Bayesian bivariate meta-analysis.
Front. Oncol. 12:852076.
doi: 10.3389/fonc.2022.852076

COPYRIGHT
© 2022 Chen, Jiang, Deng and She. This is an open-access article distributed under the terms of the Creative Commons Attribution License (CC BY). The use, distribution or reproduction in other forums is permitted, provided the original author(s) and the copyright owner(s) are credited and that the original publication in this journal is cited, in accordance with accepted academic practice. No use, distribution or reproduction is permitted which does not comply with these terms.

Differentiation between glioma recurrence and treatment effects using amide proton transfer imaging: A mini-Bayesian bivariate meta-analysis

Kai Chen[1†], Xi-Wen Jiang[2†], Li-jing Deng[3] and Hua-Long She[2*]

[1]Department of Medical Imaging, Shenzhen Samii Medical Center, Shenzhen, China, [2]Department of Medical Imaging, Affiliated Hospital of Xiangnan University (Clinical College), Chenzhou, China, [3]Department of Neonatology, Shenzhen Third People's Hospital, Second Hospital Affiliated to Southern University of Science and Technology, Shenzhen, China

Background: Amide proton transfer (APT) imaging as an emerging MRI approach has been used for distinguishing tumor recurrence (TR) and treatment effects (TEs) in glioma patients, but the initial results from recent studies are different.

Aim: The aim of this study is to systematically review and quantify the diagnostic performance of APT in assessing treatment response in patients with post-treatment gliomas.

Methods: A systematic search in PubMed, EMBASE, and the Web of Science was performed to retrieve related original studies. For the single and added value of APT imaging in distinguishing TR from TEs, we calculated pooled sensitivity and specificity by using Bayesian bivariate meta-analyses.

Results: Six studies were included, five of which reported on single APT imaging parameters and four of which reported on multiparametric MRI combined with APT imaging parameters. For single APT imaging parameters, the pooled sensitivity and specificity were 0.85 (95% CI: 0.75–0.92) and 0.88 (95% CI: 0.74–0.97). For multiparametric MRI including APT, the pooled sensitivity and specificity were 0.92 (95% CI: 0.85–0.97) and 0.83 (95% CI: 0.55–0.97), respectively. In addition, in the three studies reported on both single and added value of APT imaging parameters, the combined imaging parameters further improved diagnostic performance, yielding pooled sensitivity and specificity of 0.91 (95% CI: 0.80–0.97) and 0.92 (95% CI: 0.79–0.98), respectively, but the pooled sensitivity was 0.81 (95% CI: 0.65-0.93) and specificity was 0.82 (95% CI: 0.61–0.94) for single APT imaging parameters.

Conclusion: APT imaging showed high diagnostic performance in assessing treatment response in patients with post-treatment gliomas, and the addition

of APT imaging to other advanced MRI techniques can improve the diagnostic accuracy for distinguishing TR from TE.

KEYWORDS

amide proton transfer (APT) imaging, glioma, tumor recurrence, treatment effect, pseudoprogression, radiation necrosis (RN)

Introduction

Glioma is the most common primary brain tumor with a poor prognosis. Radiotherapy and chemotherapy are important post-treatments for glioma patients. As the treatments often produce new lesions that may mimic tumor recurrence (TR) on imaging, differentiating TR from treatment effects (TEs) remains a major clinical challenge that often leads to delay termination of ineffective therapies or premature termination of effective therapies. Hence, patients with suspected TR are frequently confirmed by stereotactic biopsy or surgery.

Tumor pseudoprogression and radiation necrosis are the major treatment-induced changes. Pseudoprogression is mainly a radiological definition, as a new or enlarging area of contrast agent enhancement, without argument of true tumor progression, which will decrease or stabilize without additional therapy (1). Pseudoprogression cases occur considerably in the first 12 weeks after the end of treatment (2), while 30% of pseudoprogression cases may occur after more than 3 months. Radiation necrosis generally occurs 3–12 months after radiotherapy, which is characterized histopathologically by fibrinoid necrosis of blood vessel walls, with adjacent perivascular parenchymal coagulative necrosis (3).

In recent years, several functional and molecular magnetic resonance (MR) imaging techniques have been applied to identify a more accurate imaging marker for tumor tissues, such as diffusion-weighted imaging (DWI), arterial spin labeling (ASL) imaging, dynamic susceptibility contrast-enhanced (DSC) imaging, MR spectroscopy (MRS), and amide proton transfer (APT) weighted imaging. Apparent diffusion coefficient (ADC) was quantified from DWI due to increased cellularity and extracellular space tortuosity. Relative cerebral blood flow (rCBF) quantified from ASL is a useful index for assessing tumor-induced neovascularization. Similar to the mechanism of rCBF, relative cerebral blood volume (rCBV) quantified from DSC seems to be a reliable technique to better identify glioma recurrence (4, 5). MRS is a molecular imaging technique that can invasively obtain information about cellular metabolism. A previous meta-analysis (6) reported that of the novel MR imaging techniques for assessing treatment response in high-grade gliomas, MRS showed the highest diagnostic accuracy; however, APT imaging was not included. APT imaging is a newly emerging molecular MR imaging technique that enables indirect measurement of endogenous mobile proteins and peptides in tissue, by detecting the magnetization transfer ratio (MTR) asymmetry at the offsets of ±3.5 ppm with respect to the water signal (7). Recent studies (8–10) have demonstrated the capability of APT imaging in assessment of post-treatment gliomas, which is a superior imaging technique to MRS (8), predominantly based on the fact that active tumors have higher protein/peptide content compared to areas of treatment-related effects due to tumor vascular endothelial damage, cytotoxicity and mutagenicity of alkylating agents, and reduced cell density (11). Positron emission tomography (PET) with the amino acid tracers is one of the most popular known to reflect protein metabolism in gliomas and has high accuracy in the diagnosis of patients with recurrent glioma (9). However, repeated radiation exposure from PET is not desirable for patients requiring long-term follow-up. Therefore, APT imaging has substantial benefit in that it uses an off-resonance radiofrequency (RF) pulse to detect endogenous mobile proteins and peptides within recurrent gliomas without ionizing radiation. Another clinical advantage of APT imaging is that it is non-invasive with no need for exogenous contrast and is a reproducible technique, which can be a potential alternative to DSC perfusion, especially in patients where contrast agent is contraindicated (12).

However, the diagnostic performance of APT imaging in assessing the response of glioma after treatment has not been systematically evaluated. Therefore, the purpose of this meta-analysis study was to evaluate the single and added value of APT imaging in differentiating TR from TE in patients with post-treatment gliomas.

Materials and methods

This meta-analysis followed the recommendations of the Preferred Reporting Items for Systematic Reviews and Meta-Analyses to diagnostic test accuracy checklist (13). Two reviewers (Kai Chen and Xi-wen Jiang) performed the article search, study selection, data extraction, and quality assessment independently. Disagreements were resolved by consensus-

based discussion with a third reviewer (Hua-Long She, with 13 years of neuroimaging experience).

Literature search

The search process follows the guide of PICOS criteria (13). A systematic search in PubMed, Web of Science, and Embase databases was performed to find original studies relevant to the research question. We used the search query combined synonyms for glioma, APT, and TEs (see Supplementary Table S1). The search was performed on 2 December 2021, without a start date limit, and was restricted to studies published in English.

Inclusion and exclusion criteria

The original research articles included were required to meet the following criteria: (1) the patients who were confirmed as gliomas on pathology examination; (2) those who had received total or subtotal tumor resection followed by either chemoradiotherapy (CCRT) or radiation therapy (RT); (3) suspected recurrent glioma on follow-up MRI; (4) used APT imaging to assess the enlarged lesion; (5) pathological or serial clinico-radiological follow-up results were used as the reference standard; (6) the true positive (TP), false positive (FP), false negative (FN), and true negative (TN) values could be extracted from articles or obtained from the authors.

Exclusion criteria were as follows: (1) studies among pediatric patients (<18 years); (2) review articles, guidelines, consensus statements, letters, editorials, and conference abstracts; (3) MRI ≤1.5 T; (4) a partially overlapping patient population; and (5) insufficient data for reconstruction of 2 × 2 tables. In the case of an overlapping study population, the study of the largest and most recent study population was included.

Data extraction and quality assessment

Extracted data contained general characteristics (including authors, publication year, study period, total number of patients, the rate of glioma recurrence, and patient age), study characteristics (including study design, tumor histology, and time interval between post-treatment and APT imaging), MRI characteristics [including the evaluation parameters and the cutoff values, MR manufacturer, magnet field strength, MRI sequences used for APT, region of interest (ROI) selection, and combined techniques for multiparametric MRI], and key data (TP, FP, FN, and TN). When provided data were insufficient to 2 × 2 contingency tables, we contacted the corresponding author to request the original data. If the diagnostic performances of several APT parameters were separately evaluated, the results with the highest diagnostic performance were selected.

Quality Assessment of Diagnostic Accuracy Studies 2 (QUADAS-2) was used to assess the methodological quality of the included studies in Review Manager 5.3 software (Cochrane). QUADAS-2 defined quality as the risk of bias and applicability of a study in the following domains: patient selection, index tests, reference standard, flow, and timing, mainly including the level to which estimates of diagnostic accuracy avoided risk of bias, and the degree to which studies are applicable to the research question in the review (14).

Statistical analysis

First of all, exploration of threshold effect was performed using Meta-Disc 1.4 (Ramony Cajal Hospital, Madrid, Spain) software, and then the heterogeneity of sensitivity and specificity between studies was assessed using a combination of Cochran Q and the I^2 factor with $p < 0.05$ considered significant. $I^2 > 50\%$ indicates substantial inter-study heterogeneity. As the number of studies involved was small, we used the package "meta4diag" in R version 3.6.0 (R Core Team, 2019) to perform the Bayesian approach meta-analysis. The pooled sensitivity, specificity, and their corresponding 95% confidence intervals (95% CI) were calculated to assess the diagnostic accuracy of single APT imaging parameters and its added value for multiparametric MRI, respectively. If there were overlapping data between studies, data from the largest and most appropriate study were selected for inclusion in quantitative analysis. Summarized data were represented using summary receiver operating characteristic (SROC) plots.

Results

Literature search

A total of 185 records were initially identified through systematic literature search. After the removal of 37 duplicates, and screening the publication type, 13 conference abstracts, 6 case reports, and 28 reviews and meta-analyses were excluded. There were 23 nonhuman studies, 69 unrelated studies, and 1 study with insufficient information to construct 2 × 2 tables. Full-text reviews were performed, and two studies that had a shared study population with the other study were excluded.

Finally, six studies (11, 15–19) were included in the meta-analysis. Of them, five studies (11, 15, 16, 18, 19) used single APT imaging parameters and four studies (16–19) used multiparametric MRI combined with APT imaging parameters to differentiate between glioma recurrence and TEs. The detailed literature selection process is summarized in Figure 1.

Characteristics of the included studies

The patient and study characteristics are described in Table 1. The size of the study ranged from 21 to 74 subjects, with the percentage of subjects with TR ranged from 53.33% to 85.71%. One study (16) only included patients with glioblastoma, while two studies (11, 19) included patients with high-grade gliomas (WHO III and IV). The studies using single APT imaging parameters for quantitative synthesis included a total of 184 subjects and using multiparametric MRI combined with APT imaging parameters included a total of 205 subjects. The study design was perspective in three studies (11, 17, 19) and not explicit in one study (15). Only one study (15) enrolled patients restricted to those with suspected tumor progression within the first 3 months after chemotherapy. In five studies that reported on the single value of APT (%) between TR and TE group, one study (16) used the 90% histogram intensity for the APT (APT90) as the diagnostic parameter, and the others used the mean value for the APT (APT mean).

In the four studies that reported on multiparametric MRI, three studies (16–18) used DSC imaging, including two studies (16, 18) that used normalized rCBV (nCBV) as a parameter. The rCBV was normalized by dividing the rCBV value in the region of interest by the rCBV value of contralateral side (5). One study (18) also combined DWI and DTI, using ADC and fractional anisotropy (FA) as parameters. In addition, one study (19) only combined rCBF quantified from ASL.

APT imaging uses a series of frequency-selective RF pulses tuned at 3.5 ppm upfield of the water resonance labeling the amide protons. APT signal intensity is reported as a percentage change in the bulk water signal intensity, which depends on the pulse sequence features and parameters used. According to the recent consensus (20), we summarized the MR hardware and APT imaging techniques, as shown in Table 2. The Philips Achieva 3.0-T MR scanner was the most used device in five studies. In the pulse sequence of APT imaging, the pulse train was used in four studies as RF saturation. 3D pulse sequence readout was used for image acquisition in five studies and 3D gradient and spin-echo (3D-GRASE) was the most used sequence. Only one study (19) used 2D single-shot spin-echo planar imaging (SE-EPI) readout to acquire images, which had the lowest values of APT (1.56 ± 1.14% TR vs. −0.44 ± 1.34% TE).

Quality assessment

The QUADAS-2 scores of each study are presented in Figure 2. Overall, all included studies had a low to unclear risk of bias and minimal concerns regarding applicability. In the first domain

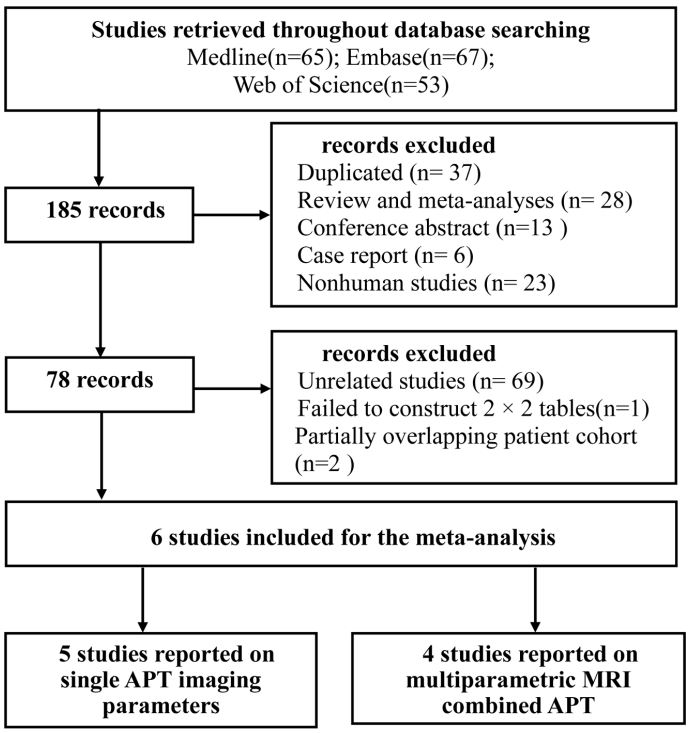

FIGURE 1
Flowchart depicting study selection.

10.3389/fonc.2022.852076

TABLE 1 Characteristics of the included studies.

Author (year)	Study period	Design	Subjects	TR, *n* (%)	Age (years)	Tumor grade	Time interval	Diagnostic parameter	APT value (TR vs TE)	ROI selection	Cutoff value of APT	Multi-parametric MRI
Jiang S S et al. (2019) (11)	April 2010–October 2015	Pros	21	18 (85.71%)	54.6 ± 17	III–IV	353 days (43–1,311)	APTmean	2.71% ± 0.91% vs. 1.24% ± 0.29%	2–5 ROIs	1.79%	NA
Liu J et al. (2020) (19)	Unknown	Pros	30	16 (53.33%)	47.6 ± 11.4 (TR) 40.5 ± 15.0 (TE)	III–IV	20.9 ± 17.8 (weeks TR) 27.4 ± 31.9 (weeks TE)	APTmean	1.56 ± 1.14% vs. −0.44 ± 1.34%	2–5 ROIs	NA	APT + rCBF
Ma B et al. (2016) (15)	Unknown	unknown	32	20 (62.5%)	56.5 (22-78)	I–IV	3 months (1–12 months)	APTmean	2.75 ± 0.42% vs. 1.56 ± 0.42%	3–5 ROIs	2.42%	NA
Paprottka K J et al. (2021) (17)	December 2017–April 2020	Pros	74	57 (77.03%)	54.91 ± 12.2	I–IV	102 days	NA	NA	New or enlarged lesion	1.79%	APT+ rCBV
Park K J et al. (2016) (16)	August 2013–March 2015	Retro	65	37 (56.92%)	54.3(24-77)	IV	39.1 ± 11.5 (weeks TR) 57.3 ± 14.1 (weeks TE)	APT90	3.87 ± 1.72% vs. 1.38 ± 1.14%	Whole contrast-enhancing lesion	2.88%	APT + nCBV
Park Y W et al. (2021) (18)	July 2017–September 2019	Retro	36	25 (69.44%)	52.3 ± 13.7 (TR) 57.1 ± 14.8 (TE)	II–IV	77.7 ± 141.3 (weeks TR) 31.7 ± 30.1 (weeks TE)	APTmean	3.18% vs. 1.77%	One ovoid ROI	2.11%	ADC + FA + nCBV + APT

Pros, prospective; Retro, retrospective; TR, tumor recurrence; TE, treatment effects; APTmean, the mean value for the APT; APT90, 90% histogram intensity for the APT; T, Tesla; NA, not available; ROI, region of interest; ADC, apparent diffusion coefficient; rCBV, relative cerebral blood volume; nCBV, normalized cerebral blood volume; rCBF, relative cerebral blood flow; FA, fractional anisotropy.
Time interval: interval between completion of post-treatment and APT imaging.

regarding patient selection, four studies (11, 15, 18, 19) had unclear risk of bias due to concerns about not explicitly mentioning whether patient enrollment was consecutive. In the index test domain, all studies had a low risk of bias. Four studies (15–17, 19) had an unclear risk of bias for the reference standard domain, because it was unmentioned whether the results of the reference standard were interpreted without knowledge of the index test. In the flow and timing domain, all studies had a low risk of bias.

Regarding the applicability assessment, one study (17) had an unclear applicability concern in patient selection, as 4/74 cases did not receive radiotherapy. We had no concerns that the conduct and interpretation of the index test and the reference standard do not match our review questions in any of the studies.

Data analysis

The results of the diagnostic threshold analysis demonstrated that no significant threshold effect existed.

The five studies using the single APT imaging parameters to differentiate TR from TE showed no significant heterogeneity in sensitivity (p = 0.445, I^2 = 0%) and limited heterogeneity in specificity (p = 0.156, I^2 = 39.8%). The estimated sensitivities and specificities of the five included individual studies were 0.80–0.87 and 0.81–0.90, respectively. The pooled sensitivity and specificity were 0.85 (95% CI: 0.75–0.92) and 0.88 (95% CI: 0.74–0.97), respectively. The forest plot demonstrated mild heterogeneity between studies

TABLE 2 APT imaging technique of the included studies using MTR asymmetry (at 3.5 ppm) on MRI systems.

Author (year)	Hardware	Pulse sequence			
		RF saturationapproach	RF saturationparameters	Readout	Acquisitionprotocol
Jiang S S et al. (2019) (11)	Philips Achieva 3.0 T	Pulse train	t_p = 200 ms, t_d = 10 ms, n = 4, DCsat = 95%, Tsat = 830 ms, B1 = 2 μT	3D-GRASE	Z-spectrum
Liu J et al. (2020) (19)	GE, Discovery MR750 3.0 T	Pulse train	t_p = 400 ms, t_d = 0 ms, n = 3, DCsat = 100%, Tsat = 1.2 s, B1 = 1.5 μT	Single-slice, SE-EPI	Z-spectrum
Ma B et al. (2016) (15)	Philips Achieva 3.0 T	Pulse train	tp = 200 ms, t_d = 10 ms, n = 4, DCsat = 95%, Tsat = 830 ms, B1 = 2 μT	3D-GRASE	Z-spectrum
Paprottka K J et al. (2021) (17)	Philips Achieva or Ingenia 3.0 T	Time-interleaved pTX	t_p = 50 ms, t_d = 0 ms, n = 40, DCsat = 100%, Tsat = 2 s, B1 = 2 μT	3D-FSE	6-offset
Park K J et al. (2016) (16)	Philips Achieva 3.0 T	Time-interleaved pTX	t_p = 70 ms, t_d = 70 ms, n = 30, DCsat = 50%, Tsat = 4.2 s, B1 = 1 μT	3D-GRE	Z-spectrum
Park Y W et al. (2021) (18)	Philips Achieva or Ingenia 3.0 T	Pulse train	t_p = 200 ms, t_d = 0 ms, n = 4, DCsat = 100%, Tsat = 800 ms, B1 = 2 μT	3D-GRASE	6-offset

pTX, parallel transmit; t_p, individual pulse element duration in a pulse train; t_d, interpulse delay; n, number of pulse element-delay repetitions; DCsat, saturation duty cycle (= $t_p/[t_p + t_d]$); Tsat, total RF saturation time; B1, RF saturation field strength.
Z-spectrum, normalized water saturation signal (S_{sat}/S_0) as a function of frequency offset relative to the water resonance, where S_{sat} and S_0 are water signal intensities with and without RF saturation, respectively; 6-offset, APT MRI saturation at the saturation frequency offsets (± 3.0, ± 3.5, ± 4.0 ppm) from water and without saturation, for example.
SE, spin-echo acquisition; FSE, fast spin echo; EPI, echo planar imaging; GRE, gradient echo; GRASE, gradient and spin-echo acquisition.

(Figure 3); in addition, the SROC curve (Figure 5A) showed a difference between the 95% credible region and prediction region. The estimated sensitivities were higher in studies with a smaller total sample of patients (N < 50), and estimated specificities were also slightly higher in the two studies (11, 15) that used 3D gradient and spin-echo (GRASE) APT imaging sequence.

The four studies (16–19) using multiparametric MRI combined with APT imaging parameters to differentiate TR from TE showed no significant heterogeneity in sensitivity (p = 0.796, I^2 = 0%), but substantial heterogeneity in specificity (p < 0.001, I^2 = 84.0%). The pooled sensitivity and specificity of the four studies were 0.92 (95% CI: 0.85–0.97) and 0.83 (95% CI: 0.55–0.97), respectively. The forest plot (Figure 4) and the SROC plot (Figure 5B) showed that the primary source of heterogeneity was the study (17) that has a slightly higher sensitivity and extremely low specificity. With the exception of that study, the remaining three studies (16, 18, 19) showed no significant heterogeneity in sensitivity (p = 0.846, I^2 = 0%) and specificity (p = 0.978, I^2 = 0%). Moreover, the three studies had both reported on single APT imaging parameters and multiparametric MRI combined with APT in differentiating TR from TE, and APT parameters added to multiparametric MRI improved diagnostic performance, yielding pooled sensitivity and specificity of 0.91 (95% CI: 0.80–0.97) and 0.92 (95% CI: 0.79–0.98), respectively (Figure 6), while the pooled sensitivity was 0.81 (95% CI: 0.65–0.93) and specificity was 0.82 (95% CI: 0.61–0.94) for single APT imaging parameters (Figure S1).

Discussion

In this meta-analysis, we evaluated the value of APT imaging in the evaluation of post-treatment response in glioma patients. Our results indicate that APT imaging is an exciting prospect in distinguishing glioma recurrence from TE, especially when combined with other multiparametric MRI parameters.

Compared to the previous mate analysis (6), we found that the diagnostic accuracy of APT imaging was similar to the nCBV derived from DSC and higher than the ADC derived from DWI, but was lower than MRS, both of which were commonly used imaging biomarkers in multiparametric MRI for the determination of treatment response after chemoradiotherapy in patients with glioblastoma (5). However, these were indirect comparisons, and only allowing all techniques to be tested in the same population would overcome the main limitation.

Mixed response in post-treatment glioma can result from a variety of nontumorous processes, including ischemia, postsurgical changes, treatment-related inflammation, subacute radiation effects, and radiation necrosis (17). rCBV and rCBF were useful indices for assessing tumor-induced neovascularization. Nevertheless, inflammation can

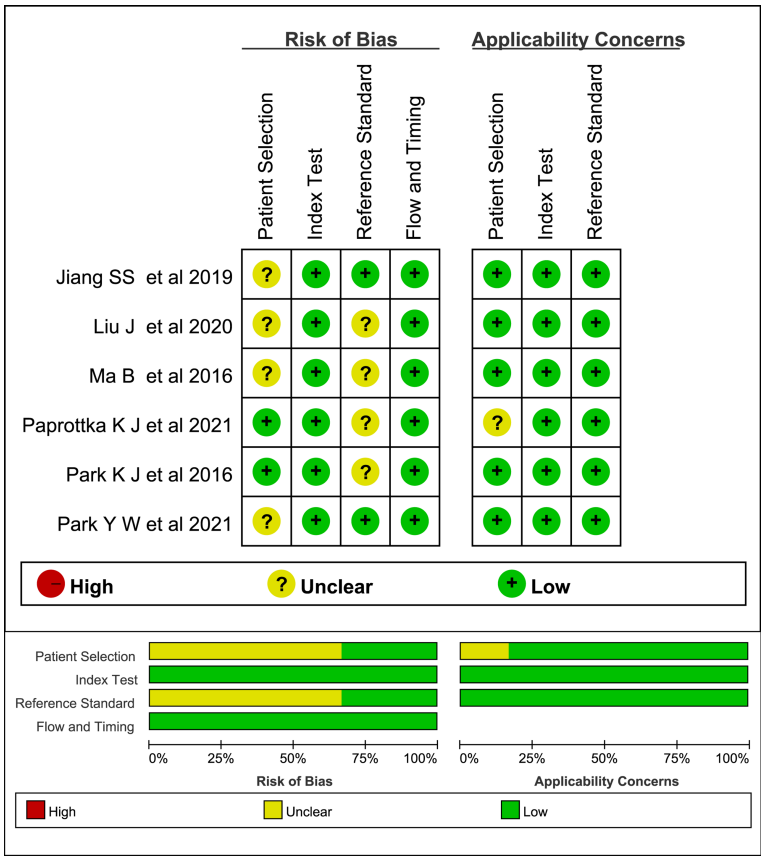

FIGURE 2
Stacked bar charts of Quality Assessment of Diagnostic Accuracy Studies 2 scores of methodologic study quality.

also lead to increased value. On DWI, recurrent tumors may show reduced ADC due to increased cellularity and extracellular space tortuosity, but radiation necrosis may also show diffusion restriction, presumably due to intracellular edema and viscous material in the transition zone (21). Consequently, increased rCBV and rCBF does not always mean viable tumor angiogenesis, and decreased ADC values do not always mean high cellularity. Various metabolic ratios

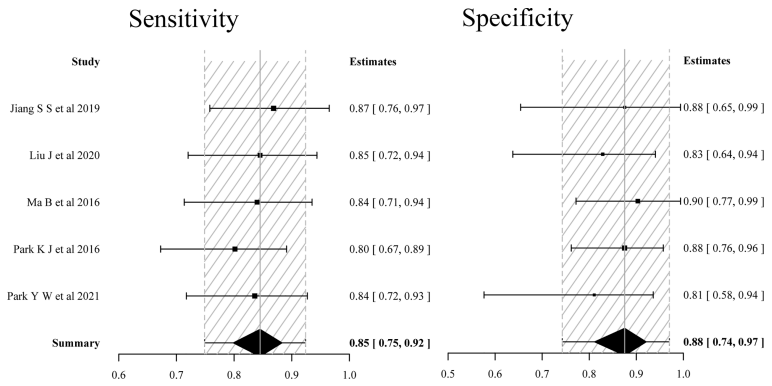

FIGURE 3
Forest plots of the sensitivity and specificity of single APT imaging parameters for differentiating tumor recurrence and treatment effects in patients with post-treatment glioma.

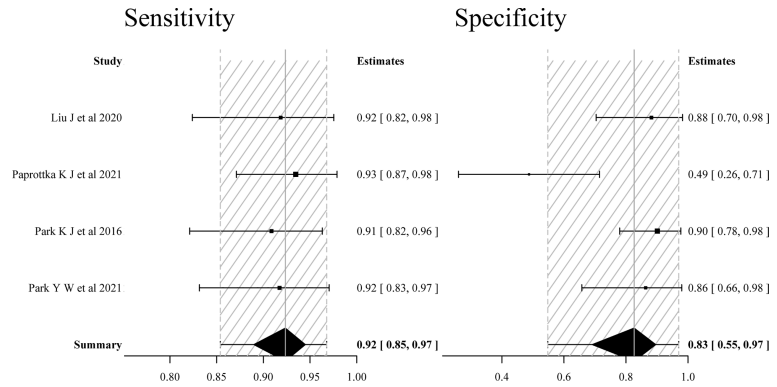

FIGURE 4
Forest plots of the sensitivity and specificity of multiparametric MRI including APT imaging parameters for differentiating tumor recurrence and treatment effects in patients with post-treatment glioma.

were used in the MRS studies. However, choline (Cho)/creatine (Cr) peak-area ratio was identified as the best predictor in identifying recurrent glioma after the post-treatment (6). Cho peak is one of the most important indicators in evaluating brain tumor proliferation. Cr peak maintains certain stability in the development of many diseases; thus, it is often used as a reference. In practice, MRS is more technically challenging and the voxel sizes are relatively large. Ideally, any technique that can reliably detect glioma proliferation within a larger area of TEs should cover the entire radiation volume.

APT imaging provides different regional information and increases the diagnostic value for multiparametric MRI, while the best cutoff values for the advance MRI techniques precisely distinguishing post TR from TE were arbitrary because of the heterogeneity in the biological activity of glioma and the use of different MRI systems. Of the four studies using multiparametric MRI combined with APT, one study (17) used the predefined thresholds from the literature by using the following cutoff values: APT > 1.79 (11) and rCBV > 5.6 (22), resulting in a slight increase in sensitivity, but a significant decrease in specificity. After excluding the study, the heterogeneities across the three studies in terms of pooled sensitivity and specificity were significantly reduced (Figure 4), whereas the diagnostic performance was not significantly superior to the results reported in a previous meta-analysis (5), which used multiparametric MRI but not combined with APT, with a pooled sensitivity and specificity of 0.84 (95% CI: 0.74–0.91) and 0.95 (95% CI: 0.83–0.99), respectively. However, the fact that meta-analysis only evaluated the value of multiparametric MRI for the determination of early treatment response, the studies containing mixed TE cases, such as pseudoprogression occurring after more than 3 months and radiation necrosis,

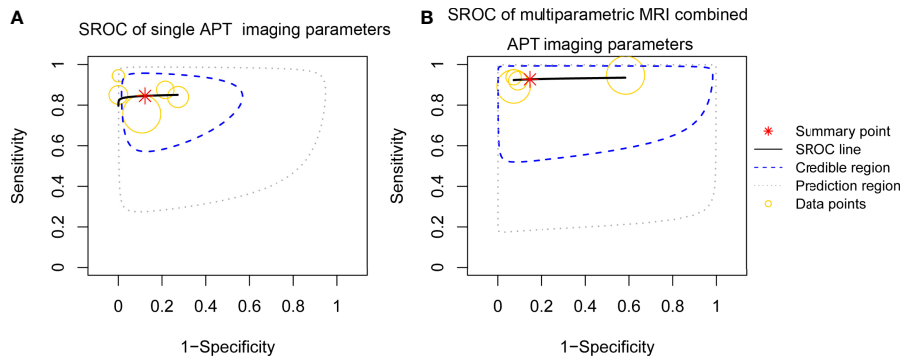

FIGURE 5
Summary receiver operating characteristic (SROC) curve of the diagnostic performance of single APT imaging parameters and multiparametric MRI including APT imaging parameters for differentiating tumor recurrence and treatment effects in patients with post-treatment glioma. **(A)** SROC curve of single APT imaging parameters (estimate of AUC was 0.863). **(B)** SROC curve of multiparametric MRI including APT imaging parameters (estimate of AUC was 0.933).

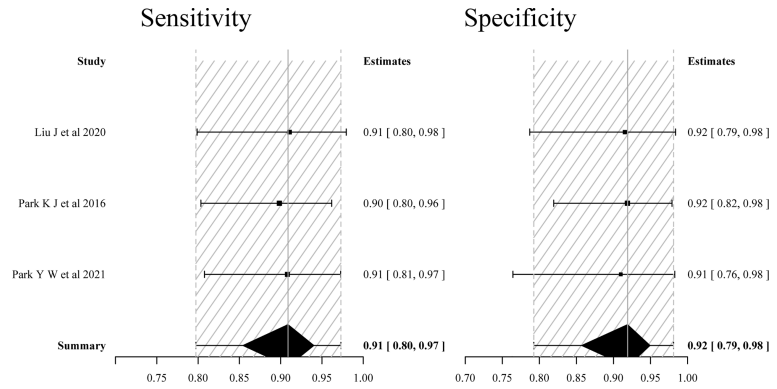

FIGURE 6
Forest plots of the sensitivity and specificity of multiparametric MRI including APT imaging parameters (only included three studies reported on both the single and added value of APT imaging parameters) for differentiating tumor recurrence and treatment effects in patients with post-treatment glioma.

were excluded. A potential source of heterogeneity among the studies using single APT imaging parameters to differentiate TR from TE might be the use of different sequences. One study used 2D SE-EPI sequence, which has low signal intensity and small differences between TR and TE groups, while relatively high estimated sensitivity and specificity were obtained in the studies using a 3D GRASE sequence. The 3D GRASE APT imaging technique has been confirmed to have reliable image quality and reasonable scan time (23).

This mate analysis used the Bayesian approach. Bayesian inference adds a small amount of informative priors that can stabilize the analysis without overwhelming data (24), as opposed to the frequentist methods that express the initial uncertainty with a prior distribution. Bayesian bivariate meta-analyses have advantages in estimating the heterogeneity among studies and pooled effect, especially when the number of studies included is small (25).

The limitations of this study include a relatively small number of studies. In addition, the mean intervals between the end of post-treatment and APT imaging were varied among studies, leading to the inclusion of several stages of treatment-related changes. However, a previous meta-analysis found no difference between early follow-up studies and studies that were conducted more than 3 months after CCRT (6). Additionally, we did not evaluate the publication bias, and another study raised a similar concern about the studies using APT in differentiating TR from TE, which consistently report positive results (26). Lastly, the repeatability of APT signal was excellent in supratentorial locations, while it was poor in infratentorial locations due to severe B0 inhomogeneity and susceptibility, which affects MTR asymmetry (27), and the locations of the glioma were not mentioned in the included studies. Nevertheless, caution is required when applying our results to daily clinical practice.

Conclusion

This mini-Bayesian bivariate meta-analysis disclosed that APT imaging has high diagnostic performance in evaluating treatment response in patients with post-treatment gliomas, and the addition of APT imaging to other advanced MRI techniques can improve the diagnostic accuracy for distinguishing TR from TE. However, based on the current evidence from a small number of studies, further evaluation is required.

Data availability statement

The original contributions presented in the study are included in the article/**Supplementary Material**. Further inquiries can be directed to the corresponding author.

Author contributions

H-LS contributed to the study design, KC and X-WJ contributed to literature search, collection, and assembly of data. Data analysis was performed by KC and L-JD. KC wrote the first draft of the manuscript. H-LS and L-JD revised and edited the manuscript. All authors read and approved the final version.

Funding

This work was supported by the Science and Technology Planning Project of Chenzhou City, Hunan Province [zdyf 201973 and zdyf 20201811].

Conflict of interest

The authors declare that the research was conducted in the absence of any commercial or financial relationships that could be construed as a potential conflict of interest.

Publisher's note

All claims expressed in this article are solely those of the authors and do not necessarily represent those of their affiliated organizations, or those of the publisher, the editors and the reviewers. Any product that may be evaluated in this article, or claim that may be made by its manufacturer, is not guaranteed or endorsed by the publisher.

Supplementary material

The Supplementary Material for this article can be found online at: https://www.frontiersin.org/articles/10.3389/fonc.2022.852076/full#supplementary-material

SUPPLEMENTARY FIGURE 1
Forest plots of the sensitivity and specificity of single APT imaging parameters (only included three studies reported on both the single and added value of APT imaging parameters) for differentiating tumor recurrence and treatment effects in patients with post-treatment glioma

References

1. Garcia GCTE, Dhermain F. Pseudoprogression in gliomas: the use of advanced MRI for treatment decisions. *Curr Treat Options Neurol* (2020) 22:23. doi: 10.1007/s11940-020-00630-8

2. Wen PY, Macdonald DR, Reardon DA, Cloughesy TF, Sorensen AG, Galanis E, et al. Updated response assessment criteria for high-grade gliomas: response assessment in neuro-oncology working group. *J Clin Oncol* (2010) 28(11):1963–72. doi: 10.1200/jco.2009.26.3541

3. Zikou A, Sioka C, Alexiou GA, Fotopoulos A, Voulgaris S, Argyropoulou MI. Radiation necrosis, pseudoprogression, pseudoresponse, and tumor recurrence: Imaging challenges for the evaluation of treated gliomas. *Contrast Media Mol Imaging* (2018) 2018:6828396. doi: 10.1155/2018/6828396

4. Wang S, Martinez-Lage M, Sakai Y, Chawla S, Kim SG, Alonso-Basanta M, et al. Differentiating tumor progression from pseudoprogression in patients with glioblastomas using diffusion tensor imaging and dynamic susceptibility contrast MRI. *AJNR Am J Neuroradiol* (2016) 37(1):28–36. doi: 10.3174/ajnr.A4474

5. Suh CH, Kim HS, Jung SC, Choi CG, Kim SJ. Multiparametric MRI as a potential surrogate endpoint for decision-making in early treatment response following concurrent chemoradiotherapy in patients with newly diagnosed glioblastoma: a systematic review and meta-analysis. *Eur Radiol* (2018) 28:2628–38. doi: 10.1007/s00330-017-5262-5

6. van Dijken BRJ, van Laar PJ, Holtman GA, van der Hoorn A. Diagnostic accuracy of magnetic resonance imaging techniques for treatment response evaluation in patients with high-grade glioma, a systematic review and meta-analysis. *Eur Radiol* (2017) 27:4129–44. doi: 10.1007/s00330-017-4789-9

7. Sotirios B, Demetriou E, Topriceanu CC, Zakrzewska Z. The role of APT imaging in gliomas grading: A systematic review and meta-analysis. *Eur J Radiolo* (2020) 133:109353. doi: 10.1016/j.ejrad.2020.109353

8. Park JE, Kim HS, Park KJ, Kim SJ, Kim JH, Smith SA. Pre- and posttreatment glioma: Comparison of amide proton transfer imaging with MR spectroscopy for biomarkers of tumor proliferation. *Radiology* (2016) 278(2):514–23. doi: 10.1148/radiol.2015142979

9. Park JE, Lee JY, Kim HS, Oh JY, Jung SC, Kim SJ, et al. Amide proton transfer imaging seems to provide higher diagnostic performance in post-treatment high-grade gliomas than methionine positron emission tomography. *Eur Radiol* (2018) 28(8):3285–95. doi: 10.1007/s00330-018-5341-2

10. Meissner J-E, Korzowski A, Regnery S, Goerke S, Breitling J, Floca RO, et al. Early response assessment of glioma patients to definitive chemoradiotherapy using chemical exchange saturation transfer imaging at 7 T. *J Magnet Reson Imaging* (2019) 50(4):1268–77. doi: 10.1002/jmri.26702

11. Jiang SS, Eberhart CG, Lim M, Heo HY, Zhang Y, Blair L, et al. Identifying recurrent malignant glioma after treatment using amide proton transfer-weighted MR imaging: A validation study with image-guided stereotactic biopsy. *Clin Cancer Res* (2019) 25(2):552–61. doi: 10.1158/1078-0432.Ccr-18-1233

12. Friismose AI, Markovic L, Nguyen N, Gerke O, Schulz MK, Mussmann BR. Amide proton transfer-weighted MRI in the clinical setting–correlation with dynamic susceptibility contrast perfusion in the post-treatment imaging of adult glioma patients at 3T. *Radiography* (2022) 28(1):95–101. doi: 10.1016/j.radi.2021.08.006

13. Moher D, Shamseer L, Clarke M, Ghersi D, Liberati A, Petticrew M, et al. Preferred reporting items for systematic review and meta-analysis protocols (PRISMA-p) 2015 statement. *Syst Rev* (2015) 4(1):1. doi: 10.1186/2046-4053-4-1

14. Whiting PF, Rutjes AW, Westwood ME, Mallett S, Deeks JJ, Reitsma JB, et al. QUADAS-2: a revised tool for the quality assessment of diagnostic accuracy studies. *Ann Intern Med* (2011) 155(8):529–36. doi: 10.7326/0003-4819-155-8-201110180-00009

15. Ma B, Blakeley JO, Hong X, Zhang H, Jiang S, Blair L, et al. Applying amide proton transfer-weighted MRI to distinguish pseudoprogression from true progression in malignant gliomas. *J Magnet Reson Imaging* (2016) 44(2):456–62. doi: 10.1002/jmri.25159

16. Park KJ, Kim HS, Park JE, Shim WH, Kim SJ, Smith SA. Added value of amide proton transfer imaging to conventional and perfusion MR imaging for evaluating the treatment response of newly diagnosed glioblastoma. *Eur Radiol* (2016) 26(12):4390–403. doi: 10.1007/s00330-016-4261-2

17. Paprottka KJ, Kleiner S, Preibisch C, Kofler F, Schmidt-Graf F, Delbridge C, et al. Fully automated analysis combining f-18 -FET-PET and multiparametric MRI including DSC perfusion and APTw imaging: a promising tool for objective evaluation of glioma progression. *Eur J Nucl Med Mol Imaging* (2021) 48(13):4445–55. doi: 10.1007/s00259-021-05427-8

18. Park YW, Ahn SS, Kim EH, Kang SG, Chang JH, Kim SH, et al. Differentiation of recurrent diffuse glioma from treatment-induced change using amide proton transfer imaging: incremental value to diffusion and perfusion parameters. *Neuroradiology* (2021) 63(3):363–72. doi: 10.1007/s00234-020-02542-5

19. Liu J, Li C, Chen Y, Lv X, Lv Y, Zhou J, et al. Diagnostic performance of multiparametric MRI in the evaluation of treatment response in glioma patients at 3T. *J Magn Reson Imaging* (2020) 51(4):1154–61. doi: 10.1002/jmri.26900

20. Zhou J, Zaiss M, Knutsson L, Sun PZ, Ahn SS, Aime S, et al. Review and consensus recommendations on clinical APT-weighted imaging approaches at 3T: Application to brain tumors. *Magn Reson Med* (2022) 88(2):546–74. doi: 10.1002/mrm.29241

21. Verma N, Cowperthwaite MC, Burnett MG, Markey MK. Differentiating tumor recurrence from treatment necrosis: a review of neuro-oncologic imaging strategies. *Neuro Oncol* (2013) 15(5):515–34. doi: 10.1093/neuonc/nos307

22. Göttler J, Lukas M, Kluge A, Kaczmarz S, Gempt J, Ringel F, et al. Intralesional spatial correlation of static and dynamic FET-PET parameters with MRI-based cerebral blood volume in patients with untreated glioma. *Eur J Nucl Med Mol Imaging* (2017) 44(3):392–7. doi: 10.1007/s00259-016-3585-0

23. Zhou J, Zhu H, Lim M, Blair L, Quinones-Hinojosa A, Messina SA, et al. Three-dimensional amide proton transfer MR imaging of gliomas: Initial experience and comparison with gadolinium enhancement. *J Magnet Reson Imaging* (2013) 38(5):1119–28. doi: 10.1002/jmri.24067

24. Guo J, Riebler A and Rue H. Bayesian Bivariate meta-analysis of diagnostic test studies with interpretable priors. *Stat Med* (2017) 36(19):3039–58. doi: 10.1002/sim.7313

25. Martin E, Geitenbeek RTJ, Coert JH, Hanff DF, Graven LH, Grünhagen DJ, et al. A Bayesian approach for diagnostic accuracy of malignant peripheral nerve sheath tumors: a systematic review and meta-analysis. *Neuro Oncol* (2021) 23(4):557–71. doi: 10.1093/neuonc/noaa280

26. Okuchi S, Hammam A, Golay X, Kim M and Thust S. Endogenous chemical exchange saturation transfer MRI for the diagnosis and therapy response assessment of brain tumors: A systematic review. *Radiol Imaging Cancer* (2020) 2(1):e190036. doi: 10.1148/rycan.2020190036

27. Akbari H, Kazerooni AF, Ware JB, Mamourian E, Anderson H, Guiry S, et al. Quantification of tumor microenvironment acidity in glioblastoma using principal component analysis of dynamic susceptibility contrast enhanced MR imaging. *Sci Rep* (2021) 11(1):15011. doi: 10.1038/s41598-021-94560-3

frontiers | Frontiers in Oncology

TYPE Original Research
PUBLISHED 13 September 2022
DOI 10.3389/fonc.2022.897147

Check for updates

OPEN ACCESS

EDITED BY
Sandro M. Krieg,
Technical University of Munich, Germany

REVIEWED BY
Giovanni Raffa,
University of Messina, Italy
Tianming Qiu,
Fudan University, China
Junfeng Lu,
Fudan University, China

*CORRESPONDENCE
Giorgio Carrabba
giorgio.carrabba@unimib.it

SPECIALTY SECTION
This article was submitted to Neuro-Oncology and Neurosurgical Oncology, a section of the journal Frontiers in Oncology

RECEIVED 15 March 2022
ACCEPTED 14 July 2022
PUBLISHED 13 September 2022

CITATION
Carrabba G, Fiore G, Di Cristofori A, Bana C, Borellini L, Zarino B, Conte G, Triulzi F, Rocca A, Giussani C, Caroli M, Locatelli M and Bertani G (2022) Diffusion tensor imaging, intra-operative neurophysiological monitoring and small craniotomy: Results in a consecutive series of 103 gliomas.
Front. Oncol. 12:897147.
doi: 10.3389/fonc.2022.897147

COPYRIGHT
© 2022 Carrabba, Fiore, Di Cristofori, Bana, Borellini, Zarino, Conte, Triulzi, Rocca, Giussani, Caroli, Locatelli and Bertani. This is an open-access article distributed under the terms of the Creative Commons Attribution License (CC BY). The use, distribution or reproduction in other forums is permitted, provided the original author (s) and the copyright owner(s) are credited and that the original publication in this journal is cited, in accordance with accepted academic practice. No use, distribution or reproduction is permitted which does not comply with these terms.

Diffusion tensor imaging, intra-operative neurophysiological monitoring and small craniotomy: Results in a consecutive series of 103 gliomas

Giorgio Carrabba[1,2]*, Giorgio Fiore[3], Andrea Di Cristofori[1], Cristina Bana[4], Linda Borellini[4], Barbara Zarino[3], Giorgio Conte[5], Fabio Triulzi[5], Alessandra Rocca[1,2], Carlo Giussani[1,2], Manuela Caroli[3], Marco Locatelli[3,6] and Giulio Bertani[3]

[1]Neurosugery, Azienda Socio Sanitaria Territoriale Monza - Ospedale San Gerardo di Monza, Monza, Italy, [2]Dipartimento di Medicina e Chirurgia, Università degli Studi di Milano-Bicocca, Milan, Italy, [3]Neurosurgery, Fondazione IRCCS Ca' Granda Ospedale Maggiore Policlinico, Università degli Studi di Milano, Milan, Italy, [4]Neurophysiopathology, Fondazione IRCCS Ca' Granda Ospedale Maggiore Policlinico, Università degli Studi di Milano, Milano, Italy, [5]Neuroradiology, Fondazione IRCCS Ca' Granda Ospedale Maggiore Policlinico, University of Milano, Milano, Italy, [6]Department of Medical-Surgical Physiopathology and Transplantation, University of Milan, Milan, Italy

Diffusion tensor imaging (DTI) allows visualization of the main white matter tracts while intraoperative neurophysiological monitoring (IONM) represents the gold standard for surgical resection of gliomas. In recent years, the use of small craniotomies has gained popularity thanks to neuronavigation and to the low morbidity rates associated with shorter surgical procedures. The aim of this study was to review a series of patients operated for glioma using DTI, IONM, and tumor-targeted craniotomies. The retrospective analysis included patients with supratentorial glioma who met the following inclusion criteria: preoperative DTI, intraoperative IONM, tumor-targeted craniotomy, pre- and postoperative MRI, and complete clinical charts. The DTI was performed on a 3T scanner. The IONM included electroencephalography (EEG), transcranial (TC) and/or cortical motor-evoked potentials (MEP), electrocorticography (ECoG), and direct electrical stimulation (DES). Outcomes included postoperative neurological deficits, volumetric extent of resection (EOR), and overall survival (OS). One hundred and three patients (61 men, 42 women; mean age 54 ± 14 years) were included and presented the following WHO histologies: 65 grade IV, 19 grade III, and 19 grade II gliomas. After 3 months, only three patients had new neurological deficits. The median postoperative volume was 0cc (IQR 3). The median OS for grade IV gliomas was 15 months, while for low-grade gliomas it was not reached. In our experience, a small craniotomy and a tumor resection supported by IONM and DTI permitted to

achieve satisfactory results in terms of neurological outcomes, EOR, and OS for glioma patients.

KEYWORDS

glioma, neurosurgery, neurophysiological monitoring (IOM), DTI - diffusion tensor imaging, mini craniotomy, glioblastoma multiforme (GBM), low grade glioma (LGG)

Introduction

Diffusion tensor imaging (DTI) is an advanced neuroimaging technique that allows the 2D and 3D reconstruction of important white matter tracts such as cortico-spinal tract (CST), superior longitudinal fascicles (SLFs), and inferior frontal-occipital (IFO) fascicles (1–4). Preservation of white matter tracts is crucial for patients' neurological integrity and, probably, even more than the preservation of certain cortical areas. Several publications on DTI confirm its reliability and role in planning neurosurgical resection of brain tumors (1–3, 5, 6). Knowing in advance the tridimensional architecture of the main fiber bundles surrounding a brain tumor can help in choosing the best approach to the tumor and preserve essential white matter tracts (2, 7, 8). As a consequence, DTI can contribute to decreasing the postoperative neurological deficit, reducing surgical invasiveness, and helping in tailoring the most appropriate craniotomy (9–11).

When considering brain tumor resections, intraoperative neurophysiological monitoring (IONM) and brain mapping techniques represent the gold standard for surgical management of primary CNS neoplasms (12, 13). These neurophysiological techniques allow to identify and preserve important cortical and subcortical functional sites while monitoring fundamental neurological functions (e.g., MEP and SSEP - (1, 5, 14–16)). Brain mapping usually requires the exposure of a large area of the brain cortex to identify the different eloquent sites (e.g., primary motor strip, speech arrest sites). Eloquent areas are determined by positive responses to direct electrical stimulation (DES) of the motor areas or by the interference of speech for language (17, 18). Thus, relatively large classic frontotemporal craniotomies are generally performed to obtain enough space for tumor removal and positive mapping. Nevertheless, in recent years the use of small craniotomies targeted on the tumor has gained popularity thanks to neuro-navigation systems and the low morbidity rates associated with shorter surgical procedures, reduced anesthetic drug administration, and consequently shorter patients' hospitalization (7, 8, 19, 20). Only recently, some authors have advocated the utility of negative mapping without necessarily obtaining positive sites to have safer tumor resections (15, 21).

Few studies are available in the literature dealing with the intriguing technical topic of the combination of mini-craniotomy (or tumor-targeted craniotomy or again small craniotomy) and the use of IONM. The two techniques are somehow considered mutually exclusive (how can you have a positive response site when you perform a tumor-targeted craniotomy)? or compatible in a small number of cases (e.g., tumor nearby of eloquent sites).

In this work, we present the experience of the authors in a consecutive series of 103 patients affected by astrocytoma grades I to IV operated combining DTI, IOM, and minimally invasive craniotomy. Technical aspects will be presented, together with neurological outcomes, surgical complications, the extent of resection, and patients' survival data.

Materials and methods

A cohort of patients who received surgical treatment for supratentorial gliomas between May 2011 and February 2016 at the Fondazione IRCCS Ca' Granda Ospedale Maggiore Policlinico of Milano were retrospectively assessed for inclusion in this study.

Inclusion criteria

The following criteria needed to be met for patient inclusion:

1) age superior to 18 years;
2) supratentorial gliomas;
3) tumor tissue available for histological and molecular diagnoses according to the WHO 2016 CNS brain tumors' classification;
4) pre- and postoperative (obtained within 72 h) T2-weighted (w) images, T2-weighted fluid-attenuated inversion recovery (FLAIR) images, T1-weighted images before and after gadolinium intravenous administration, and diffusion-weighted images (DWI) available for radiological evaluation and volumetric analysis;

5) a tailored "small-craniotomy" as a surgical approach to the tumor;
6) surgical resection guided by intraoperative DTI and IONM;
7) completeness of the clinical chart during the review process by the Authors;
8) informed consent for participating in the study.

Patients suffering from recurrent tumors were also included in this study, in case the aforementioned inclusion criteria were met. These patients were classified as revision resections.

Ethical approval was waived by the local Ethics Committee of "Università degli Studi di Milano," because of the retrospective nature of the study, and all the procedures being performed were part of routine care.

Histopathological and molecular diagnoses

Tumor samples were formalin-fixed and analyzed by dedicated neuropathologists. Tumor grade and molecular profile were reported according to both the WHO 2016 and 2021 CNS brain tumor classifications (22).

MGMT was considered to be methylated when it showed more than 9% of promoter methylation as previously described (23).

Clinical features

Baseline demographic features, preoperative KPS, length of the in-ward stay, postoperative neurological deficits, postoperative seizures' rate—as their incidence during the in-ward stay and at follow-up (FU), destination at discharge, and neurological deficits still present at 3-month FU were collected from electronic clinical records and registers, and outpatient neuro-oncological evaluations.

The occurrence of a new postoperative neurological deficit was graded according to severity (severe or mild/moderate). The following deficits were considered severe: severe muscle strength deficit (grade 1–3 Medical Research Council Scale), hemianopia, and aphasia. All other neurological deficits were considered mild/moderate. Deficits still present at 3-month FU were considered definitive.

All patients underwent extensive pre- and postoperative neuropsychological testing using the battery of neuropsychological tests as reported previously (24–26).

Radiological features

Preoperative MRI scans were performed on a 3T Philips Achieva (Best, the Netherlands) scanner, using a 32-channel phased-array head coil.

As part of daily care at our Institution, all patients suffering from intracranial tumors received preoperative and postoperative (within 72 h) brain MRIs. T2-weighted (w) images, T2w fluid-attenuated inversion recovery (FLAIR) images, T1w images before and after gadolinium intravenous administration, and diffusion-weighted images (DWI) were assessed for radiological feature extraction. Baseline radiological characteristics included tumor location—as affected cerebral lobe and side—contrast enhancement (CE), and preoperative and postoperative tumor volumes. Volumetric tumor measures were addressed by a trained resident neurosurgeon (G.F.) and reviewed by an experienced neurosurgeon (G.C.), both of them blinded to clinical information. We used the open-source software Horos (www.horosproject.org; Horos Project) for manual segmentation which allowed us to manually delineate, slice by slice, the tumor contour, thus creating a ROI dataset from which the tumor volume (cm^3) was calculated. For CE tumors (i.e., ring-like contrast-enhancement pattern), regions of interest (ROIs) contoured CE boundaries. For tumors without CE or with patchy CE, ROIs contoured FLAIR alteration areas.

The extent of resection (EOR) was calculated as: [(preoperative tumor volume – postoperative tumor volume)/preoperative tumor volume] × 100 (27).

Postoperative DWI was checked for ischemic damage and postoperative pre-contrast T1w for hyperintense blood products.

DTI imaging

Diffusion tensor imaging (DTI) acquisition included an axial single-shot spin-echo echo-planar imaging (EPI) sequence (TR 7,866 ms; TE 74 ms) with 64 diffusion-encoding directions. A diffusion gradient was applied using two b factors (0 and 1,000 s/mm^2), with a sensitivity encoding reduction factor (SENSE) of 2 and a flip angle equal to 90°. Isotropic voxel dimensions of 2 × 2 × 2 mm^3 were obtained by using a field of view of 225 × 225 mm^2 and a matrix of 112 × 110. Seventy slices were obtained, with a thickness of 2 mm, with no gap. DTI data motion artifacts were adjusted using the installed software on the scanner. The total acquisition time was 8 min 47 s.

Fiber tracking

Deterministic (28) fiber tracking based on DTI was performed using the iPlan 3.0 cranial planning software (Brainlab AG, Munich, Germany). DTI sequences were automatically corrected for head motion and eddy current distortions.

Fiber tracking of the corticospinal tract (CST) was obtained by placing a cubic box region of interest (ROI) along the precentral gyrus and a second one along the anterior pons.

The SLF was reconstructed by placing a first ROI on the high-anisotropy region laterally to the central part of the lateral ventricle on a coronal section; the second ROI was placed on the peri-trigonal area at the level of the descending branch of the tract (1). To reconstruct the arcuate fasciculus (AF), three cubic seed ROIs were placed along the subcortical white matter of the opercular part of the inferior frontal gyrus, the inferior part of the precentral gyrus, the supramarginal gyrus, and the superior and medial temporal gyrus (19). To reconstruct the inferior frontal-occipital fasciculus (IFOF) and the uncinate fasciculus (UF), we constructed an ROI on the anterior floor of the external capsule at the junction of the frontal and temporal lobes, where the IFOF narrows in the section being contiguous to UF (29). To reconstruct the inferior longitudinal fasciculus (ILF), two ROIs were located along the subcortical white matter of the anterior temporal region and the occipital one (30). The frontal aslant tract (FAT) was reconstructed by placing an ROI on the opercular frontal cortex (inferior frontal gyrus) and a second one in the supplementary motor area (SMA) and pre-SMA cortices (superior frontal gyrus).

Fiber tracking was performed with a fractional anisotropy (FA) minimum threshold value of 0.15 (mainly 0.18–0.21), an angular threshold of 45° (not editable by the user), and a variable minimum fiber length of 30–50 mm.

IONM methods

The armamentarium used for IONM has already been described elsewhere by our group (25, 31). The neurophysiological techniques included transcranial corkscrew electrodes for transcranial (TC) motor-evoked potentials (MEPs); DES with monopolar and bipolar probes for mapping motor and language functions; cortical strip for electrical stimulation of the cortex and cortical MEP monitoring; cortical strip for electrocorticography (ECoG); and electromyography (EMG) for continuous monitoring of motor functions.

The IONM was performed by dedicated neurophysiologists and technicians (FC, GA, LB, MV). The monitoring technique was performed as described previously (25, 31).

Anesthesiological technique

In all patients, a total intravenous anesthesia protocol was performed with remifentanil and propofol, as previously reported. No curare or curare-like drugs were used in this series. In the case of awake craniotomy, the surgical opening was performed in an asleep–awake fashion with a laryngeal mask (5, 32).

Surgical technique

IONM

The type of IONM was tailored to tumor location and patients' characteristics, with regard to functional anatomy, as depicted by DTI-FT, and cognitive status, according to neuropsychological evaluation. EEG and EMG monitoring of motor response was used in all the cases, as described elsewhere (33).

In the revision process, we tried to simplify our IONM choices, as reported in Table 1. Briefly, tumors were classified according to the hemisphere and lobe being affected. Tumors in the dominant hemisphere were generally operated on awake to allow language and complex neurological function mapping and monitoring (asleep–awake technique). Tumors in the frontal or parietal lobe were simplistically considered tumors affecting the motor areas, and as previously described, IONM was decided based on the distance of the tumor from the motor cortex (M1) or CST [more than 3 cm or less than 3 cm (1, 15, 16, 34, 35)]. Gliomas located more than 3 cm away from the CST or M1 were monitored with continuous transcranial MEPs, with DES being applied mostly subcortically using a monopolar probe. Temporal and insular tumors were operated on with awake or asleep surgery according to their location in the dominant or non-dominant hemisphere, respectively. Non-dominant temporal tumors were operated on with transcranial MEP (TC MEP) monitoring and subcortical monopolar DES to check the distance from the midline structures while facing the medial part of the temporal lobe. Dominant temporal lobe tumors required bipolar DES at cortical and subcortical levels (similarly to dominant frontal lobe tumors) to map cortical language sites and important subcortical fiber bundles. Insular lobe tumors, considering their well-known surgical complexity, were generally approached using all the IONM armamentariums, especially when located in the dominant hemisphere (25). Occipital lobe tumors were treated with minimal IONM (TC MEP, rarely with subcortical monopolar DES), and their resection was generally guided by DTI with the reconstruction of the optic pathways (2).

Definition of small craniotomy

In our series, as "small craniotomy" we defined a craniotomy that did not extend beyond 1 cm from the maximal tumor diameters if the tumor was cortical or immediately subcortical or that did not extend beyond 1 cm of the maximal cortical tumor projections in case of a deep-seated location. In other words, no brain other than the strictly necessary to allow tumor resection was exposed. Some intraoperative pictures are available in Figure 1, showing a complete IONM despite the size of the craniotomy and surgical tailoring as aforementioned. The functional areas surrounding the tumor were not necessarily exposed.

TABLE 1 The scheme used for IONM choice according to the surgical procedure to be performed.

Lobe	Distance tumor/ CST	Awake yes/ no	MEP		DES - Cortical		DES - Subcortical		EcoG	EEG	EMG
			TC	Strip	Monopolar	Bipolar	Monopolar	Bipolar			
Frontal	> 3cm	no	■	▒	▒	□	■	□	▒	■	■
	> 3cm	yes	■	▒	▒	■	■	■	■	■	■
	< 3cm	no	▒	■	■	▒	■	▒	▒	■	■
	< 3cm	yes	▒	■	■	■	■	■	■	■	■
Parietal	> 3cm	no	■	▒	▒	□	■	□	▒	■	■
	> 3cm	yes	■	▒	▒	■	■	■	■	■	■
	< 3cm	no	▒	■	■	▒	■	▒	▒	■	■
	< 3cm	yes	▒	■	■	■	■	■	■	■	■
Temporal		no	■	□	□	□	▒	□	▒	■	■
		yes	■	□	▒	■	▒	■	■	■	■
Occipital			■	□	□	□	▒	□	▒	■	■
Insular		no	■	■	■	▒	■	▒	▒	■	■
		yes	■	■	■	■	■	■	■	■	■

■ indicates that the neurophysiological technique was always used.

▒ indicates that the neurophysiological technique was NOT always used.

□ indicates that the neurophysiological technique was never used.

10.3389/fonc.2022.897147

Surgical resection of tumors close (≤3cm) to the motor area

In the case of Rolandic and peri-Rolandic gliomas (as defined by Berger in 2004 (16)), a small craniotomy was planned according to DTI and neuro-navigation (Brainlab, Munich, Germany). The craniotomy was performed over the tumor aiming to expose the lesion and the strictly necessary cortex, which, in this case, could or could not include M1 (Figure 1). After opening the dura, we mostly employed a monopolar low-intensity and high-frequency (HF) electrical stimulation to identify the cortical (M1) and subcortical motor pathways. When a stable cortical motor response was achieved, the intensity of stimulation was further decreased to the threshold (36), to enhance M1 detection. If increased focality/specificity of cortical stimulation was needed to discriminate M1 from premotor or sensitive areas, a bipolar low-frequency (LF) electrical stimulation was also exploited.

A cortical strip with four to six platinum contacts (Integra, Princeton, NJ, USA) was placed on the motor cortex to allow monitoring of the motor function throughout the procedure. In case the motor cortex was not fully exposed, then the cortical strip was made to slide under the dura with care. After the localization of M1, then brain mapping was performed around the tumor to exclude the presence of peritumoral motor functioning areas. After the required corticectomy was performed, continuous monitoring of the motor pathway was achieved with cortical MEPs with a cortical or subdural strip. At this point, DTI was employed to help in the neurophysiological definition of the CST. Subcortical resection close to the motor pathways was performed alternating mapping with the monopolar probe and the aspiration (eventually with CUSA) of tumoral/peritumoral areas as far as it was considered safe, according to brain/tumor visual appearance. Tumor resection was continued until a positive response at the intensity of 2–3 mA with the monopolar probe was obtained.

Surgical resection of tumors in frontal or parietal lobe not close to the cortical motor areas

In the case of gliomas located in the frontal or parietal lobe but not close to the Rolandic area, the craniotomy was placed right over the tumor (or over its cortical projections), with minimal brain exposure. In this way, the motor area was not generally exposed and positioning cortical electrodes under the dura and over the motor area strip (for cortical MEP monitoring) was in most cases not possible. For this reason, before surgery, corkscrew electrodes were placed on the scalp, in the skin area that was over the projection of the motor area. Occasionally, DTI reconstruction of the CST was used to help the technician in the definition of the area and correct positioning of the corkscrew electrodes. Continuous TC MEPs were monitored during surgery. After exposure of the lesion, the resection started with a corticectomy (when necessary) and subsequent dissection of the tumor from the normal brain

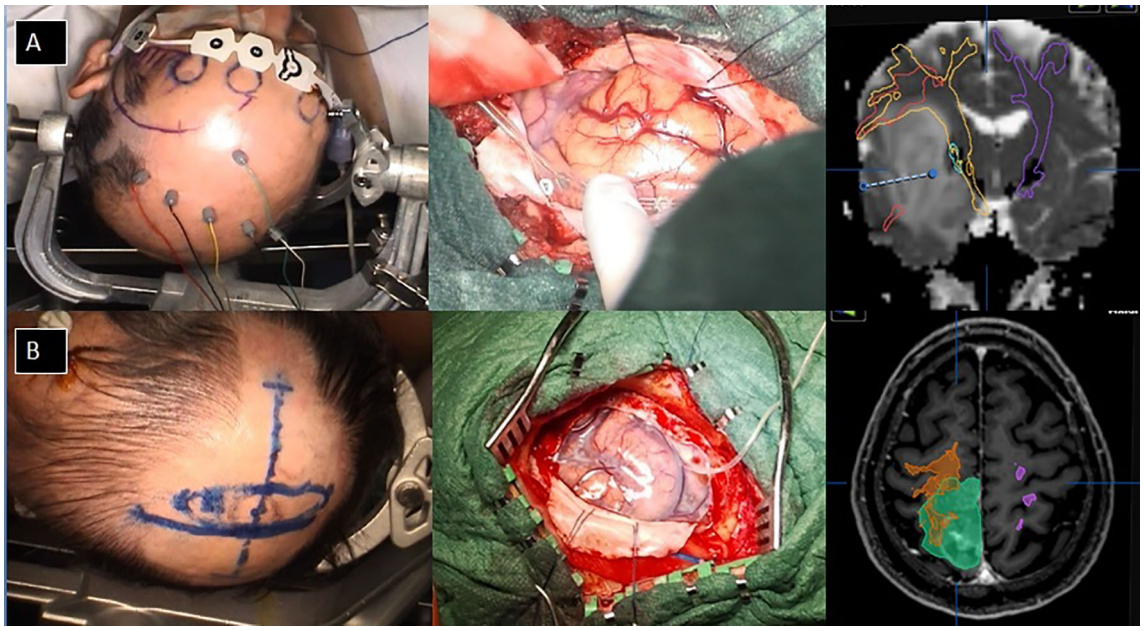

FIGURE 1
Examples of small craniotomy tailored on DTI and tumor projection to the cortex. **(A)** a case of an insula tumor with the intraoperative view and the neuronavigational planning; **(B)** a case of a parietal tumor with the intraoperative view and the surgical planning.

parenchyma using Penfield dissectors and CUSA from time to time. During the resection of the deeper part of the tumor, monopolar stimulation was used to assess the distance from the CST. During surgical resection of larger lesions, phenomena of brain shift and pneumocephalus may decrease TC MEP responses. At this point, positioning a cortical strip for cortical MEP monitoring became generally possible.

Surgical resection of tumors in the temporal or occipital lobe in the non-dominant hemisphere

In the case of gliomas located in non-dominant temporal and occipital lobes, the surgical resection was carried out similarly to what was done for frontal or parietal lobe tumors located >3 cm away from the Rolandic area. Essentially, motor monitoring was performed using TC MEP with corkscrew electrodes and monopolar DES was done subcortically. In addition to DTI for the CST, in occipital lobe tumors, the resection was planned and carried out taking into consideration the DTI reconstruction of the optic pathways, as described elsewhere (2).

Surgical resection of tumors in the dominant hemisphere operated with asleep–awake technique

In the case of tumors, located in the dominant hemisphere affecting frontal and temporal lobes and, at times, parietal and occipital lobes, the asleep–awake technique was used for surgical resection. As extensively published, the awake technique is the most reliable and safest technique to preserve complex functions in patients with brain tumors in the dominant hemisphere. In particular, it allows intraoperative testing of the patients with specific tasks for language expression and comprehension as well as customized tasks for the preservation of other skills such as music, cognitive functions, and social recognition. The authors applied awake surgery in all the cases of LGG affecting the dominant hemisphere and in most cases of HGG. The utility of the awake technique in HGG has been extensively debated (37, 38), and, in this series, it was used in selected HGG patients after multidisciplinary evaluation by neurosurgeons, neuropsychologists, and anesthesiologists.

In the asleep–awake setting, a tumor-targeted craniotomy was performed as well (Figure 2). Then, the patient was awakened, the laryngeal mask was removed, and once the patient was collaborative, the brain mapping for language and other functions was performed using bipolar DES (Penfield's technique). When the lesion was in proximity to the motor area, then the MEP monitoring was performed using a cortical strip; on the contrary, when the lesion was not close to the Rolandic area, TC MEP was employed. Bipolar DES was applied also subcortically, using a generally slight increase in the 60-Hz currents (10%–20%). Monopolar DES was used for motor mapping at both the cortical and subcortical levels.

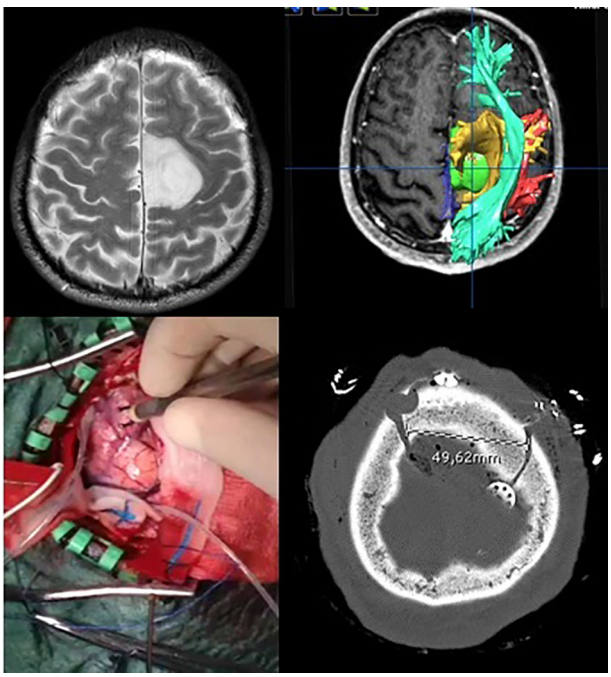

FIGURE 2
Example of awake surgery for a left frontal low-grade glioma performed with a targeted small craniotomy sized about 4.5 cm.

DTI was used to plan the craniotomy and to help in the definition of the lesion as it regards its relationship with the CST but also the main language fiber bundles. In particular, as described elsewhere, the IFO and the arcuate fasciculus were reconstructed using DTI and defined intraoperatively by DES.

Surgical resection of tumors located in the insular lobe

The insula is located deeply in the Sylvian fissure, and the resection of these gliomas is among the most challenging. Given these premises, it is clear that the greatest efforts were made preoperatively to get complete DTI reconstruction of the important white matter tracts and intraoperatively to obtain a reliable and complete IONM (Figure 3).

In addition to EEG, TC MEPs were always applied. The most commonly used approach to the insular lobe was the trans-opercular approach. On the non-dominant side, this approach required cortical brain mapping (using monopolar DES) to avoid the motor area of the face, while in the dominant hemisphere awake surgery was necessary to avoid injury to the language function. The technique in the dominant hemisphere was similar to the one adopted for dominant frontal or parietal gliomas in terms of brain mapping and monitoring of language functions. Nevertheless, the technical difficulties due to perforating branches of the middle cerebral artery, the length of surgery, and the deeper location of these tumors require higher technical skills than other gliomas.

Intraoperative variables

Data concerning surgical procedures were retrieved from digital operative registers. The following variables of interest were collected: type of anesthesia (asleep vs. asleep–awake or asleep–awake–asleep), type of intraoperative neurophysiological monitoring (IONM), surgical procedure duration, and occurrence of intraoperative seizures.

The use of the following IONM techniques was analyzed and collected: transcranial electrical stimulation (TC) with motor-evoked potentials (MEPs) and somatosensory-evoked potentials (SSEPs), electroencephalography (EEG), electrocorticography (ECoG), direct electrical stimulation (DES), monopolar stimulation for subcortical mapping, and bipolar stimulation for cortical mapping.

Intraoperative seizures were classified according to their clinical manifestation—as electrical or symptomatic—and the treatment needed to stop them—cold water irrigation or drugs (32).

In the case of recurrent tumor resection, it was recorded if an extension of the previous mini-craniotomy was required.

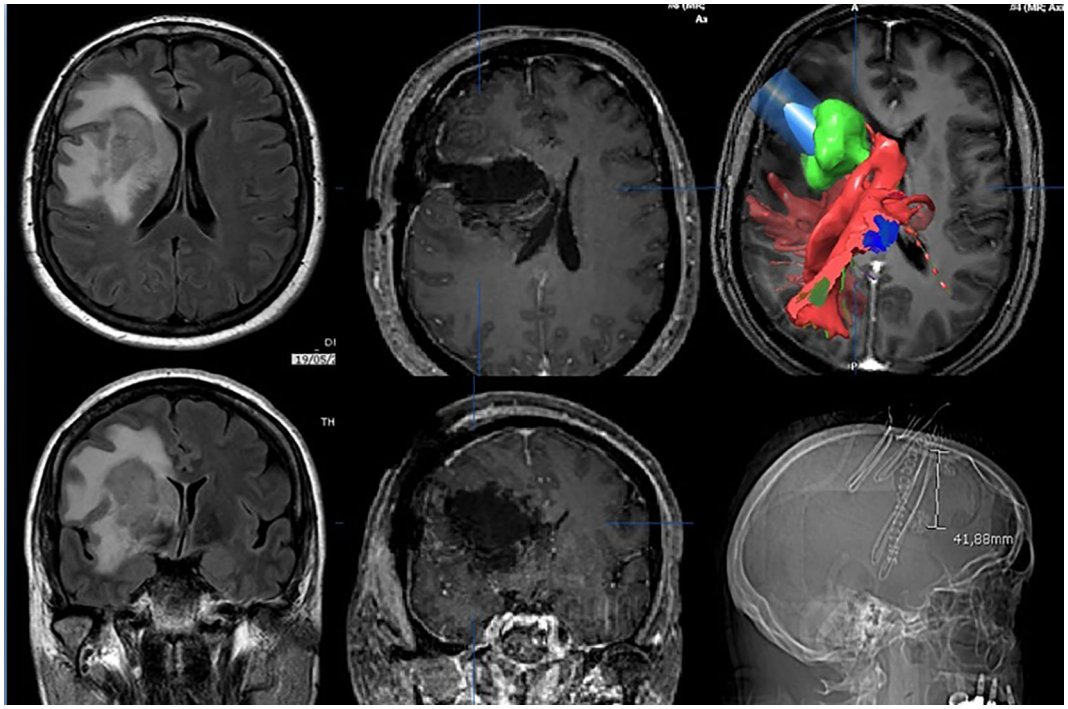

FIGURE 3
Fronto-opercular approach to an insular high-grade glioma targeted according DTI and IONM.

Outcome measures

Three outcome measures were assessed for the patients: overall survival (OS), progression-free survival (PFS), and rate of definitive neurological deficits (deficits that did not regress at the 3-month follow-up). The postoperative tumor volume and EOR were identified as the main surgical outcomes.

OS was defined as the time from surgery to death. PFS was defined as the time from surgery to tumor progression. We referred to RANO criteria for gliomas to assess disease progression (39).

Patients who did not experience death or disease progression were censored at their last scan date, during OS and PFS analyses.

Statistical analyses

Variables of interest were reported and compared as follows:

- Frequencies were reported as a percentage and compared by chi-square/Fisher exact test;
- Continuous variables were checked for normal distribution through skewness, kurtosis, and Shapiro–Wilks normality test;
- The continuous normally distributed variables were reported as mean ± standard deviation and compared through Student's t-test or variance analyses.
- The continuous skewed distributed variables were reported as median (interquartile range, IQR) and compared *via* Mann–Whitney U-test and Kruskal–Wallis test.

A multiple linear regression model (using the Enter method) was settled to assess the predicting value of explanatory variables on the surgical predicted outcome (postoperative volume and EOR). The explanatory variables were chosen based on recent literature as well as on the statistical significance of the univariate analysis. Multicollinearity was assessed at each step through tolerance and the variance inflation factor (VIF). Residuals were checked for normality.

OS and PFS as a function of time were calculated by the Kaplan–Meier method.

Univariate analysis of risk factors influencing PFS and OS was assessed by the proportional hazard regression model. Variables associated with PFS and OS in univariate analyses ($p < 0.05$) were included in the multivariate Cox proportional hazard regression model. All statistical analyses were performed using IBM SPSS version 25.0, International Business Machines Corp, New York, USA.

Results

In the period between May 2011 and February 2016, 265 patients received surgical treatment for supratentorial gliomas. One hundred and three patients met the inclusion criteria for the study. Of these, 21 patients received a revision resection. The overall median follow-up was 19 months (range from 3 to 108 months). Follow-up ended in November 2021. The main variables of interest are summarized in Table 2.

Histopathological tumor features

According to WHO 2016 brain tumor classification (22), 65 patients suffered from WHO grade IV gliomas (63%), 19 patients from WHO grade III gliomas (19%), and 19 patients from WHO grade II gliomas (19%). WHO grade III gliomas included 15 astrocytomas (6 IDH 1 or 2 mutated) and four oligodendrogliomas (all IDH 1/2 mutated). WHO grade II

TABLE 2 Clinical and histological features of our series.

Patient Population	103
First Resection	82
Revision Surgery	21
WHO 2016	
Grade IV	65
Grade III	19
Grade II	19
WHO 2021	
oligodendroglioma	14
astrocytoma	9
GBM -like	80
Age	54 ± 14
Sex (male)	61
Preoperative KPS (median)	80
Length of in-ward Stay (days)	7 (IQR 4)
Intraoperative Symptomatic Seizures	7
Post-operative Seizures	9
New Postoperative Deficits	31
3-month Follow-up Deficits	3

tumors embedded eight astrocytomas (2 IDH 1 or 2 mutated) and 11 oligodendrogliomas (all IDH 1 or 2 mutated).

The MGMT gene promoter methylation showed superiority at 9% in 55 cases (53%).

All the patients with WHO grade IV tumors received chemoradiotherapy according to the Stupp protocol except eight patients (6 received only temozolomide, 1 fotemustine, and 1 did not receive any adjuvant treatment). All the patients with WHO grade III tumors received chemoradiotherapy except three patients (2 received only temozolomide and 1 did not receive any adjuvant treatment). Among patients with WHO grade II tumors, only four patients received adjuvant chemoradiotherapy.

According to WHO 2021 brain tumor classification, we identified 14 patients with a molecular oligodendroglioma profile (IDH1 or 2 mutations, and 1p–19q chromosomal arm heterozygosity loss), of which 10 are WHO grade II and four WHO grade III. Nine patients showed a molecular astrocytoma profile (IDH1 or 2 mutations, with intact 1p–19q), among which three showed WHO grade II histological features and six with WHO grade III histological characteristics. Eighty patients showed glioblastoma (GBM)-like features: IDH1 and 2 wild types (wt) and imbalance of chromosome 7 and chromosome 10q loss of heterozygosity, or telomerase reverse transcriptase (TERT) promoter mutation, or epidermal growth factor receptor (EGFR) amplification (40). All the patients with GBM molecular features received chemoradiotherapy except 12 patients (7 received only temozolomide and 5 did not receive any adjuvant treatment). Among patients with astrocytoma molecular features, five patients received adjuvant chemoradiotherapy. Among patients with oligodendroglioma molecular features, four patients received adjuvant temozolomide.

Patients population

The mean age was 54 ± 14 years. Sixty-one patients (59%) were men. The mean preoperative KPS was 80. One-way ANOVA showed a statistically significant variance among age means of the different WHO tumor grades ($F = 4$; $p = 0.002$) as well as among the three molecular subtypes ($F = 7$; $p = 0.001$). *Post-hoc* analyses using the LSD method revealed greater age means among WHO grade IV glioma carriers (58 ± 12 years), compared to others (45 ± 15 years), and among patients with GBM and GBM-like molecular profiles (57 ± 13 years), in comparison to those with oligodendroglioma (46 ± 14 years) and astrocytoma (43 ± 16 years) molecular features.

Chi-square analyses revealed a higher incidence of preoperative KPS rates inferior to 80 among glioblastoma carriers (51%), in comparison to those suffering from lower-grade gliomas (7%–33%), and among patients with a GBM-like molecular profile (46%) when compared with both of those with astrocytoma (0%) and oligodendroglioma (7%).

Clinical characteristics

The median length of the in-ward stay was 7 (IQR 4) days. Nine patients (9%) experienced seizures during the in-ward stay, requiring an antiepileptic drug increase and/or multidrug association. All but two of these patients experienced partial epileptic events. One patient suffered from a generalized seizure, while another from a delayed postoperative awakening.

Postoperative neurological deficits occurred in 31 patients, of which 14 were severe. Ten patients showed an improved neurological status at postoperative evaluations. At the 3-month FU, only three neurological deficits were still present (3%). Seventeen patients (17%) were discharged to a rehabilitation facility.

Intraoperative variables

Thirty-three patients underwent craniotomy under asleep–awake anesthesia. All patients underwent mini-craniotomy with at least EEG, EMG, and TC MEP as IONM. In 77 patients (75%), ECoG was used. DES was exploited in 51 patients (50%). Cortical mapping required monopolar and bipolar stimulation in 24 cases (23%). Subcortical monopolar stimulation was exploited in 33 cases (32%).

Fourteen patients (13.6%) experienced intraoperative seizures, of which eight (7.7%) were only electrically evident. Seven patients (6,8%) experienced intraoperative symptomatic (partial) seizures which required cold irrigation as a unique treatment, while two patients (2%) experienced symptomatic (partial) seizures that required pharmacological treatment.

The exact Fisher chi-square test revealed a statistical correlation between the incidence of intraoperative seizures and the employment of bipolar stimulation for brain cortical mapping (8/24 patients, $p = 0.003$).

Among the 21 revision resection cases, only one needed an extension of the previous craniotomy.

Volumetric analyses

The median preoperative volume was 24 cc (IQR 42). The median postoperative volume was 0 cc (IQR 3). The median EOR among all gliomas was 100% (IQR 10%).

The following explanatory variables were put in the multiple linear regression model to predict postoperative volume values: preoperative volume, WHO 2016 gliomas' classification type, and tumor side and location (as affected encephalic lobe). Increasing preoperative volume ($R^2 = 0.5$; $b = 0.15$; $ES = 0.03$; $ß = 0.5$; $p = 0.0001$), WHO grade II IDH wt gliomas ($R^2 = 0.5$; $b = 13.7$; $ES = 3$; $ß = 0,3$; $p = 0.0001$), and insular gliomas ($R^2 = 0.5$; $b = 5$; $ES = 2$; $ß = 0.2$; $p = 0.023$) were related to greater postoperative tumor volumes.

The same regression analysis was conducted to predict EOR: WHO grade II IDH wt (R^2 = 0.5; b = -24; ES = 5; ß = -0.4; p = 0.0001) and mut (R^2 = 0.5; b = -14; ES = 3; ß = -0.3; p = 0.0001) gliomas and WHO grade III IDH mut (R^2 = 0.5; b = -15; ES = 3.6; ß = -0.3; p = 0.0001), insular (R^2 = 0.5; b = -11; ES = 3; ß = -0.3; p = 0.0001), and thalamic (R^2 = 0.5; b = -10.5; ES = 6; ß = -0.1; p = 0.0001) gliomas were related to lower EOR.

Postoperative volumes resulted to be predicted by the preoperative ones, as a function of a cubic regression line (R2: 0.7; Figure 4).

First resection

Preoperative volume medians of the different WHO tumor grades and molecular subtypes were compared, without any difference between groups being shown. The WHO grade II IDH1/2wt tumors had the largest preoperative volume median (38 cc, IQR 70), while the WHO grade III IDH1/2wt gliomas had the minimum preoperative volume median (15 cc, IQR 21).

Glioblastomas and WHO grade III IDH wt gliomas showed the lowest postoperative volume medians, equal to 0 cc, reaching statistical significance at medians' comparison (p = 0.0001, Figure 5).

EOR medians resulted to be statistically different among WHO tumor grades, with the highest EOR values among grade IV gliomas (p = 0.0001, Figure 6). When EOR medians were compared among the three molecular subtypes, no statistically significant differences were noted, with a positive trend of higher EOR rates among GBM and GBM-like gliomas (p = 0.067, Figure 7).

Revision surgery

The preoperative and postoperative volume medians' comparison among the different WHO tumor grades and molecular subtypes in revision surgery cases did not reach statistical significance in Kruskal–Wallis tests (respectively p = 0.138 and p = 0.112).

The comparison of EOR medians among different WHO grades as well as among the three different molecular subtypes demonstrated significantly higher rates among grade IV gliomas (p = 0.038) and GBM/GBM-like gliomas (p = 0.036).

Overall survival analyses

The log-rank test using the Kaplan–Meier method indicated a statistically significant OS difference among all WHO grades (p = 0.0001). The median OS for WHO grade III IDH1/2mt gliomas was 74 months, for WHO grade III IDH1/2wt gliomas 20 months, and for WHO grade IV gliomas 14 months. For WHO grade II IDH1/2mt and wt gliomas, the median OS was not reached.

A statistically significant difference was also demonstrated among the OS of the three molecular groups (p = 0.0001). The median OS for GBM and GBM–like gliomas was 15 months. The median OS for astrocytomas and oligodendrogliomas was not reached.

The log-rank test using the Kaplan–Meier method was also employed to assess PFS, showing a statistically significant difference among all WHO grades (p = 0.0001). The median PFS for the WHO grade III IDH1/2wt gliomas was 12 months and for the WHO grade IV gliomas 10 months. For the WHO grade II IDH1/2mt and wt gliomas as well as for the WHO grade III IDH1/2mt ones, the median PFS was not reached. As for the OS, a statistically significant difference was noted among the three molecular groups (p = 0.0001). The median PFS for GBM and GBM–like gliomas was 12 months. For astrocytomas and oligodendrogliomas, the median PFS was not reached.

First resection

Survival analyses were repeated on the only first resected gliomas.

The log-rank test using the Kaplan–Meier method showed a statistically significant difference among the OS of all WHO grades (p = 0.0001, SM 11A). The median OS for WHO grade III IDH1/2mt gliomas was 74 months, for WHO grade III IDH1/2wtgliomas 15 months, and for WHO grade IV gliomas 14 months. For WHO grade II IDH1/2mtand wt gliomas, the median OS was not reached (Figure 8).

The 1-, 2-, and 5-year OS rates were 100%, 100%, and 90% for WHO grade II IDH1/2mt gliomas, 67%, 67%, and 17% for WHO grade II IDH1/2wt gliomas, 100%, 100%, and 75% for WHO grade III IDH1/2mt gliomas, 37.5%, 12.5%, and 12.5% for WHO grade III IDH1/2wt gliomas, and 58.8%, 25%, and 4% for WHO grade IV gliomas.

As for OS, the log-rank test using the Kaplan–Meier method was used to assess PFS, showing a statistically significant difference among all WHO grades (p = 0.0001, SM 11B). The median PFS for the WHO grade III IDH1/2wt gliomas was 12 months and for the WHO grade IV gliomas 9 months. For the WHO grade II IDH1/2mtand wt gliomas as well as for the WHO grade III IDH1/2mt ones, the median PFS was not reached Figure 9.

The 1-, 2-, and 5-year PFS rates were respectively 100%, 100%, and 90% for WHO grade II IDH1/2mt gliomas, 67%, 67%, and 17% for WHO grade II IDH1/2wt gliomas, 100%, 100%, and 75% for WHO grade III IDH1/2mt gliomas, 37.5%, 12.5%, and 12.5% for WHO grade III IDH1/2wt gliomas, and 39%, 20%, and 4% for WHO grade IV gliomas.

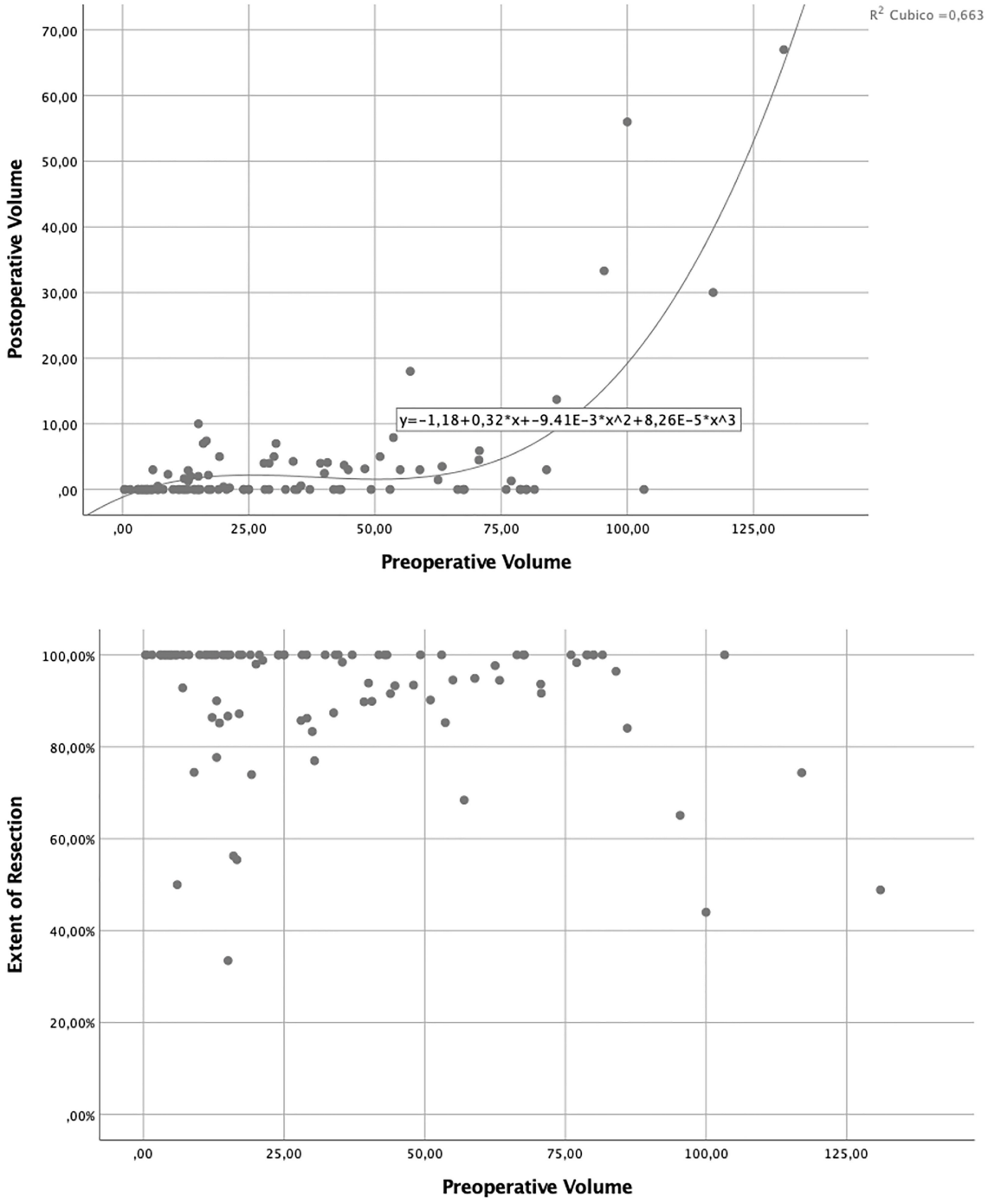

FIGURE 4
Volumetric analysis showing relations between preoperative tumor volume, residual tumor volume, and extent of resection.

Concerning molecular subtypes, the log-rank test using the Kaplan–Meier method showed statistically different OS among the three molecular groups (p = 0.0001 Figure 10). The median OS for GBM and GBM–like gliomas was 15 months. The median OS for astrocytomas and oligodendrogliomas was not reached.

The 1-, 2-, and 5-year OS rates were respectively of 60%, 28%, and 10% for GBM and GBM–like gliomas, 100%, 100%,

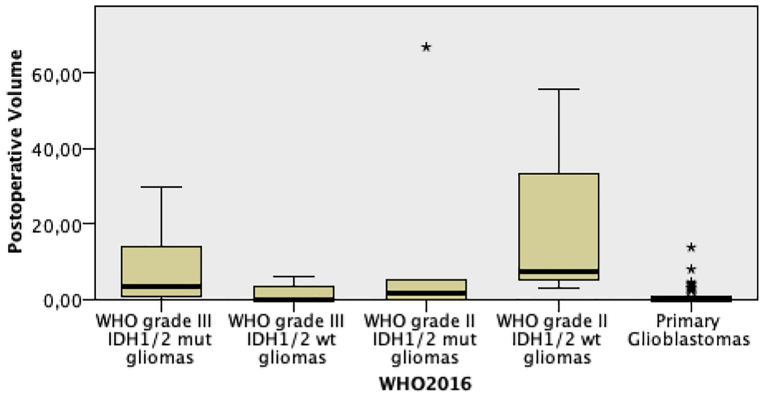

FIGURE 5
Postoperative volume comparison among the different WHO 2016 grade gliomas. * means outlayer.

and 78% for astrocytomas, and 100%, 100%, and 88% for oligodendrogliomas.

The survival analysis was repeated to address PFS, showing a statistically significant difference among the three molecular groups (p = 0.0001 Figure 11). The median PFS for GBM and GBM–like gliomas was 10 months. For astrocytomas and oligodendrogliomas, the median PFS was not reached.

The 1-, 2-, and 5-year PFS rates were 42%, 23%, and 6% for GBM and GBM–like gliomas, 100%, 100%, and 78% for astrocytomas, and 100%, 100%, and 88% for oligodendrogliomas.

Age, affected side, preoperative KPS, and WHO 2016 gliomas' classification affected PFS and OS at univariate analysis using the proportional hazard regression model. In the Cox proportional hazard multivariate regression model, only preoperative KPS (p = 0.006) and WHO 2016 grade II (p = 0.009) and III (p = 0.021) IDH1/2 mut gliomas confirmed a statistical correlation with the overall PFS and OS.

Revision surgery

The survival analyses through the log-rank test using the Kaplan–Meier method were not performed on the revision surgery group due to the limited sample size.

The 1-, 2-, and 5-year OS rates were 100%, 100%, and 75% for WHO grade II IDH1/2mt gliomas; 100%, 100%, and 50% for WHO grade III IDH1/2mt gliomas; 100%, 0%, and 0% for WHO grade III IDH1/2wt gliomas; and 50%, 7%, and 0% for WHO grade IV gliomas.

The 1-, 2-, and 5-year PFS rates were 100%, 100%, and 50% for WHO grade II IDH1/2mt gliomas, 100%, 50%, and 50% for WHO grade III IDH1/2mt gliomas, 100%, 0%, and 0% for WHO grade III IDH1/2wt gliomas, and 42%, 7%, and 0% for WHO grade IV gliomas.

The 1-, 2-, and 5-year OS rates were of 53%, 7%, and 0% for GBM and GBM–like gliomas and 100%, 100%, and 67% for oligodendrogliomas.

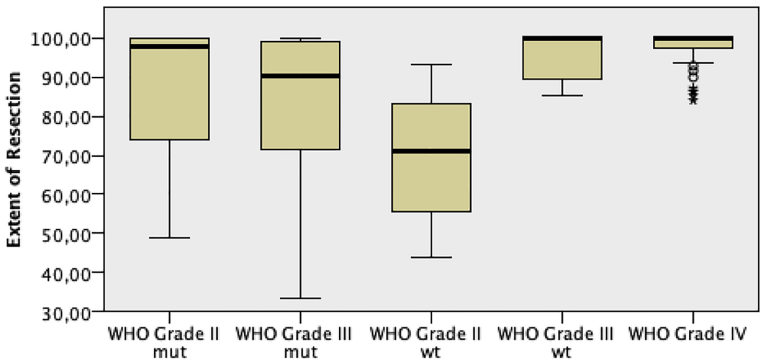

FIGURE 6
EOR comparison among the different WHO 2016 grade gliomas.

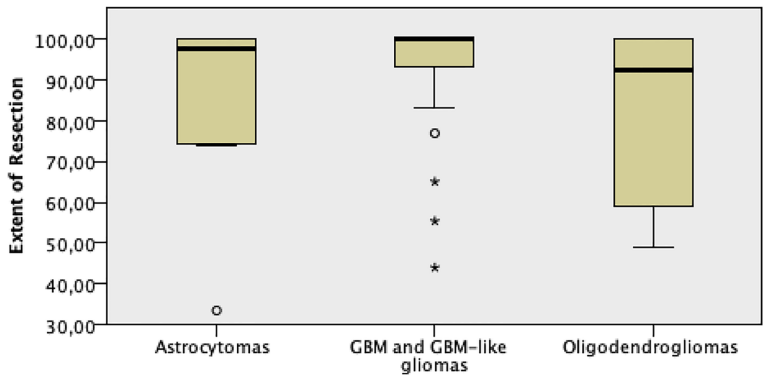

FIGURE 7
EOR comparison among the different molecular subtype gliomas.

The 1-, 2-, and 5-year PFS rates were of 47%, 7%, and 0% for GBM and GBM–like gliomas and 100%, 84%, and 50% for oligodendrogliomas.

Discussion

In the last 20 years, the importance of white matter tracts has been rediscovered in neurosurgery (3, 6, 15, 35, 41, 42). Before, it was a common belief that the preservation of cortical functional areas was the most important surgical target when resecting a brain tumor. Nowadays, it is well known that damaging subcortical white matter tracts can bring severe neurological deficits and affect patients' outcomes even more negatively than a cortical injury (5, 7, 35). For example, a CST interruption can bring irreversible hemiplegia while cortical damage of the motor strip may result "only" in a focal motor deficit. As it concerns language, a similar consideration can be done: in fact, the classical localist view of "well-defined" Broca's and Wernicke's areas has shifted to a hodotopical view (41, 43, 44). In this novel understanding of language organization, there are two major subcortical complex networks constituted by the dorsal stream which is responsible for phonological tasks and a ventral stream in charge of semantic functions (43, 45). Such language organization emphasizes the role of subcortical connections rather than the importance of definite cortical areas (44, 46–48). Moreover, it has been shown that cortical areas can undergo brain plasticity phenomena, much more relevant than white

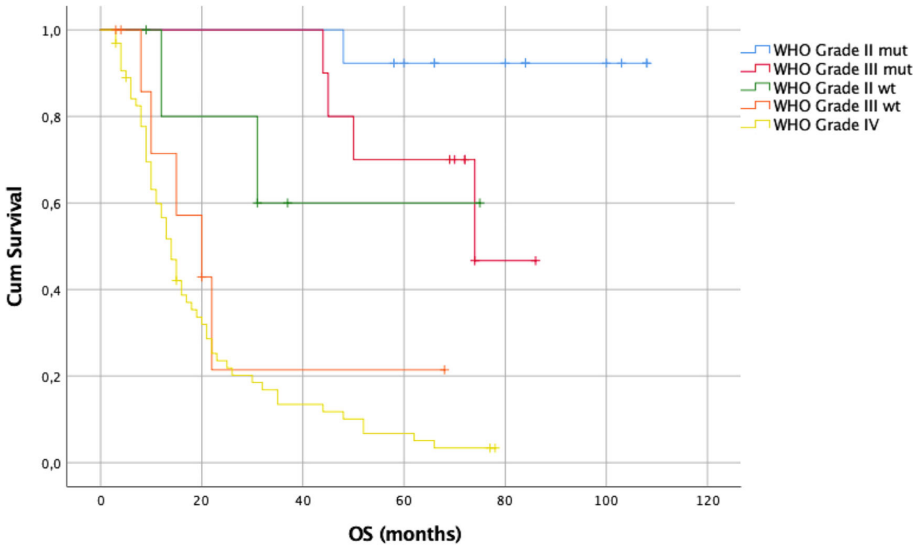

FIGURE 8
Kaplan–Meier curves of OS of patients at first resection.

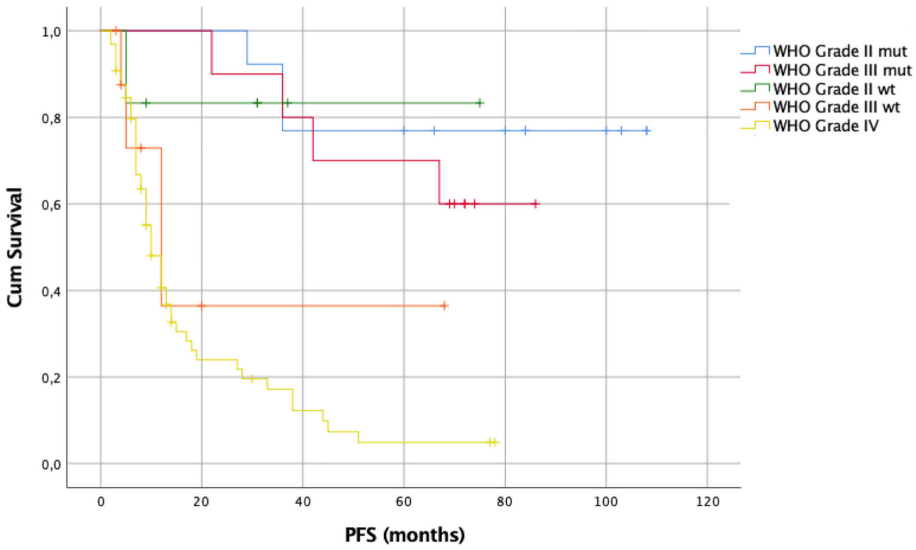

FIGURE 9
Kaplan–Meier curves of PFS of patients at first resection.

matter tracts (6, 49). Based on these considerations, it becomes clear that the possibility to know in advance the location of the main white matter tracts and their relationships with a brain tumor constitutes a fundamental help for neurosurgeons approaching a brain tumor resection (50–53). DTI allows to reconstruct and visualize the most important white matter tracts on anatomical MR images of patients, permitting to build a personalized and complete surgical planning. The tractography and the 2D reconstructions of the main fiber bundles can be uploaded on neuronavigation devices (which may be integrated with intraoperative ultrasounds) giving also real-time imaging of the white matter tracts during surgery.

Nevertheless, all the DTI surgical information has to be verified by IONM and it is nowadays unacceptable to operate close to the main fiber bundles (or eloquent cortical areas) without IONM (13, 34, 35, 45, 54). The scientific evidence

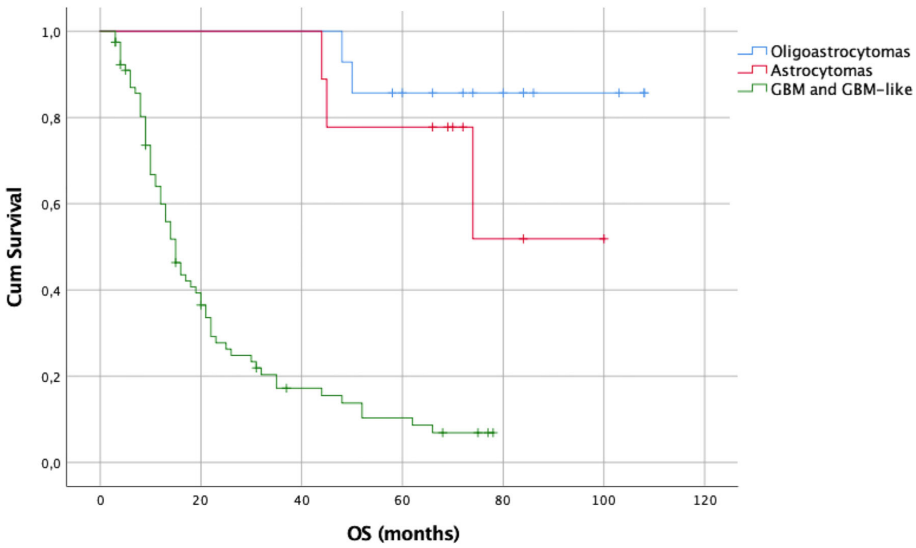

FIGURE 10
Kaplan–Meier curves of OS according to glioma molecular subtypes at first resection.

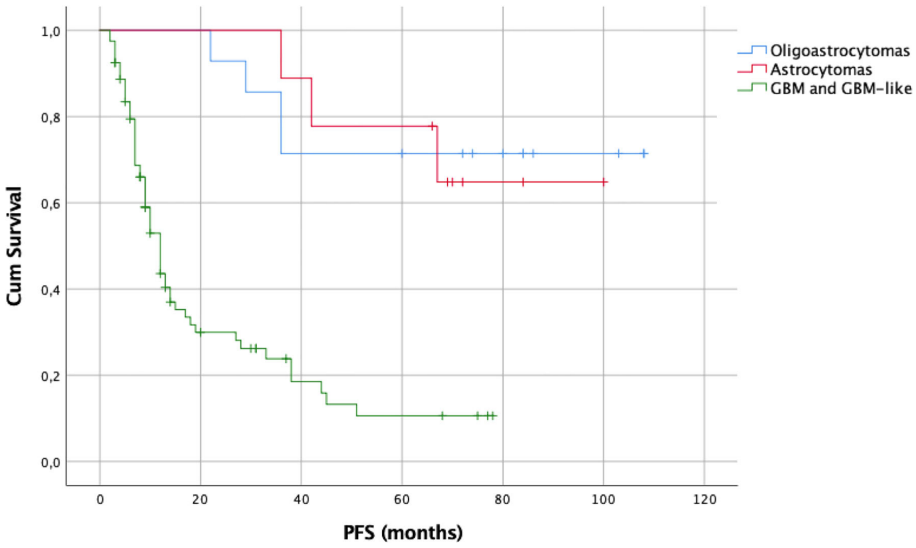

FIGURE 11
Kaplan–Meier curves of PFS according to glioma molecular subtypes at first resection.

supporting the use of IONM has been growing in recent years, and many studies have shown that patients' permanent morbidity is reduced and tumor EOR is increased when IONMs are applied (12, 31, 55). Parallelly, multiple studies have demonstrated that the EOR correlates positively with OS for both LGG and HGG pushing more and more surgeons toward maximal or even supra-maximal tumor resections according to function boundaries (56–58). To date, no standardization exists regarding IONM and great variability occurs in their application to the surgical setting. Some authors use only cortical and subcortical brain mapping while others apply extensively neurophysiological techniques to have the maximal information in the operating room (31, 34, 59).

Given these premises (usefulness of DTI and need of IONM) but also the trend toward reduced invasiveness of surgical procedures, our group tried to combine IONM (fundamental), DTI (useful), and small craniotomy to verify their possibility of combination and the patients' outcomes in a large consecutive series of gliomas. Minimally invasive neurosurgery has gained popularity thanks to several technical advancements including preoperative advanced imaging (MRI, fMRI, DTI), neuronavigation, intraoperative imaging techniques (MRI, CT, US), and microscopic and endoscopic refinements. For brain tumors, the limited invasiveness has brought to propose even day surgery plans with doubtless advantages for patients and healthcare systems (60–62). Other clear advantages of small or limited craniotomy include reduced surgical times, shorter anesthesia, and probably fewer complications (63, 64). Despite that few data are available in the neurosurgical literature regarding complications, it appears reasonable that infections, postoperative hematomas, wound problems, and consequently, neurological outcomes could be positively affected by reduced invasiveness. An indirect proof of concept stands in the observation that most, if not all, neurosurgical departments have progressively reduced the size of the craniotomy in the last 20 years with shorter operating room times (31, 60–62, 65). Parallelly, in all other surgeries (abdominal, thoracic, etc.), the rate of minimally invasive procedures is constantly growing as compared to traditional open surgery.

The first result of our series of 103 gliomas is that, in all the cases, a tumor-targeted approach resulted to be feasible without affecting the EOR or the surgical outcomes. In particular, despite most centers using IONM performing large craniotomies to allow exposure of eloquent areas to be sure of not obtaining falsely negative brain mapping, we deliberately chose to minimize the craniotomy (without reducing the IONM) considering the expertise and trust in IONM. In other words, our confidence in IONMs and our team of neurophysiologists was so high that we were confident that a negative mapping, even without observing positive responses, was a real negative. Such confidence was supported by the extensive use of DTI which, through the reconstruction of the white matter bundles' tridimensional architecture, allowed us to tailor the craniotomy and the type of IONM, as well as the surgical corridor, for a safer and faster surgical resection. In this paper, we were also able to summarize the type of IONM according to the location of the tumor and the distance from CST (>3 cm or less than 3 cm) to make our experience reproducible by other neurosurgical centers (Table 1). Briefly, our technique, being relatively mini-invasive, pointed out that satisfactory motor monitoring can be

achieved through TC MEPs when the lesion is not nearby the motor area. Nevertheless, in this setting DES of subcortical tracts is fundamental and should be better performed with the monopolar stimulator. On the other hand, when the tumor is near the motor area then TC MEP may not be useful and MEP should be performed with a cortical strip while mapping with monopolar and, in case, bipolar stimulation. HF monopolar stimulation demonstrated to be an efficient and reliable tool with equal safety and efficacy when compared to bipolar stimulation techniques (66, 67). Furthermore, HF monopolar stimulation showed high reliability even when CST is infiltrated by the tumor (68). HF stimulation is also related to reduced incidence of intraoperative seizures and easy transition to continuous monitoring of motor pathways during surgical resection (69). In the case of tumors located in M1, of which the macroscopic localization on the cortex is not evident, we associated a cortical bipolar LF electrical stimulation to confine the corticectomy to the minimum necessary, then switched to HF monopolar electrical stimulation when the corticectomy was completed (34). When the tumor clearly reached the cortical surface, we did not recur to LF bipolar stimulation since the cortical entry point was obviously represented by the pathological cortex and more focality of the stimulus was not needed.

Awake surgery, in our experience, was not incompatible with small craniotomies and indeed appeared to be faster and very tolerated by the patients as well. Even if the absence of positive responses may be disturbing for the surgeon, we did not recur to higher stimulation intensities or repeated stimulations to achieve positive responses, thus keeping the rates of intraoperative electric complications low. In our experience and, as already published, the use of the currents able to induce motor response was the key for having a reliable mapping.

Our experience suggests that negative mapping is safe and feasible. In this view, intraoperative DTI guidance of DES allowed us to focus the cortical and subcortical mapping to the regions of strict relationship between the tumor and the main fiber bundles and increased our trust in mapping results, even for negative mapping, since we rarely experienced major discrepancies between the two localizing techniques. Nevertheless, we always kept in mind the limitations of DTI fiber reconstruction, carefully exploring by DES the regions of uncertainty, affected by peritumoral edema or marked anatomical disruption, where DTI-FT may fail to adequately reconstruct essential bundles. In doubtful cases, resection was ultimately guided by IONM results. The neurological deficits in our series, in fact, were similar to the best available literature since only 3% of patients experienced a permanent neurological worsening (12, 70). The rate of definitive neurological deficits is related not only to preservation of white matter fiber bundles but also to safe manipulation of vascular structures. Small craniotomies and tailored surgical corridors can reduce the exposure of vessels and, consequently, undesired injury to them. This might have contributed to the low rate of definitive neurological deficits.

The EOR was not affected by the small craniotomy since the median EOR was 100% among different types of gliomas. As consequent, and again in line with the literature, OS was relatively good with a median of 15 months for GBM (or GBM-like) and as it concerns LGG, median OS was not reached after a median follow-up of 19 months (range 3–108). Kaplan–Meier survival curves are available in Figures 8–11 and in supplementary materials Figures 10A, B, Figures 11A, B.

Finally, we believe that DTI and the expertise reached by our group in the use of IONM played a major role in permitting the use of small craniotomies as well as negative mapping techniques. These latter considerations may constitute a limit of our paper and may justify the reason why limited literature is available on the topic.

The effect of brain shift on preoperative DTI needs also to be discussed, even if small craniotomies are theoretically less affected by it. Since the displacement of major white matter tracts is somehow unpredictable, the authors strongly suggest checking their position during tumor resection by IONM, increasing the employment of DES mostly in the deepest part of the resection cavity, where the effects of brain shifts are likely to be amplified. Intraoperative ultrasounds and CT might be employed to correct the brain shift, as improving guidance of DES, while intraoperative MRI could even allow intraoperative DTI and fiber tracking.

As last consideration, in selected cases, the small craniotomies, as defined above, could be extended a little more to nearby non-eloquent areas, as per preoperative DTI and functional assessment, to allow more extensive resection when feasible.

Conclusion

Reduced invasiveness (in general) and patient integrity represent surgical aims we should all try to pursue, despite technical difficulties, in the primary interest of our patients. Extensive preoperative workout, including DTI and patient cognitive assessment, allows tailoring craniotomies and IONMs to patient needs, reducing surgical invasiveness while guaranteeing optimal functional and survival outcomes. Like all surgical techniques, a learning curve is needed for relying on negative mapping as, in our experience, we found its dependability to be related to expertise, confidence, and cooperation among all the involved professionals.

Other preoperative tools have gained popularity in recent years, such as the preoperative transcranial magnetic stimulation (TMS) (71–76). As a future perspective, our team aims at evaluating and validating the preoperative TMS as a

useful tool to improve reduced invasiveness and reliable negative mapping.

Data availability statement

The original contributions presented in the study are included in the article/Supplementary Material. Further inquiries can be directed to the corresponding author.

Ethics statement

Ethical review and approval were not required for the study on human participants in accordance with the local legislation and institutional requirements. Written informed consent for participation was not required for this study in accordance with the national legislation and the institutional requirements.

Author contributions

GCa, GF, AC: concept and drafting. CB, LB: neurophysiological monitoring and data collection. BZ, GF: statistical analysis. GCo, FT: DTI reconstructions; data collections; imaging revision. AR, MC, GB: clinical records analysis and data collection. ML; CG; GCa: critical review of the manuscript. All authors contributed to the article and approved the submitted version.

Funding

This study was supported by "Associazione Amici della Clinica Neurochirurgica" and "Università degli studi di Milano-Bicocca".

Conflict of interest

The authors declare that the research was conducted in the absence of any commercial or financial relationships that could be construed as a potential conflict of interest.

Publisher's note

All claims expressed in this article are solely those of the authors and do not necessarily represent those of their affiliated organizations, or those of the publisher, the editors and the reviewers. Any product that may be evaluated in this article, or claim that may be made by its manufacturer, is not guaranteed or endorsed by the publisher.

Supplementary material

The Supplementary Material for this article can be found online at: https://www.frontiersin.org/articles/10.3389/fonc.2022.897147/full#supplementary-material

References

1. Bello L, Gambini A, Castellano A, Carrabba G, Acerbi F, Fava E, et al. Motor and language DTI fiber tracking combined with intraoperative subcortical mapping for surgical removal of gliomas. *Neuroimage* (2008) 39:369–82. doi: 10.1016/j.neuroimage.2007.08.031

2. Bertani GA, Bertulli L, Scola E, Di Cristofori A, Zavanone M, Triulzi F, et al. Optic radiation diffusion tensor imaging tractography: An alternative and simple technique for the accurate detection of meyer's loop. *World Neurosurg* (2018) 117: e42–56. doi: 10.1016/j.wneu.2018.05.131

3. Duffau H. Lessons from brain mapping in surgery for low-grade glioma: insights into associations between tumour and brain plasticity. *Lancet Neurol* (2005) 4:476–86. doi: 10.1016/S1474-4422(05)70140-X

4. Leclercq D, Duffau H, Delmaire C, Capelle L, Gatignol P, Ducros M, et al. Comparison of diffusion tensor imaging tractography of language tracts and intraoperative subcortical stimulations: Clinical article. *JNS* (2010) 112:503–11. doi: 10.3171/2009.8.JNS09558

5. Bello L, Gallucci M, Fava M, Carrabba G, Giussani C, Acerbi F, et al. INTRAOPERATIVE SUBCORTICAL LANGUAGETRACT MAPPING GUIDES SURGICAL REMOVALOF GLIOMAS INVOLVING SPEECH AREAS. *Neurosurgery* (2007) 60:67–82. doi: 10.1227/01.NEU.0000249206.58601.DE

6. Duffau H. Brain plasticity: From pathophysiological mechanisms to therapeutic applications. *J Clin Neurosci* (2006) 13:885–97. doi: 10.1016/j.jocn.2005.11.045

7. Krieg SM, Lioumis P, Mäkelä JP, Wilenius J, Karhu J, Hannula H, et al. Protocol for motor and language mapping by navigated TMS in patients and healthy volunteers; workshop report. *Acta Neurochir* (2017) 159:1187–95. doi: 10.1007/s00701-017-3187-z

8. Raffa G, Conti A, Scibilia A, Sindorio C, Quattropani MC, Visocchi M, et al. Functional reconstruction of motor and language pathways based on navigated transcranial magnetic stimulation and DTI fiber tracking for the preoperative planning of low grade glioma surgery: A new tool for preservation and restoration of eloquent networks. In: M Visocchi, HM Mehdorn, Y Katayama and KRH von Wild, editors. *Trends in reconstructive neurosurgery. acta neurochirurgica supplement*. Cham: Springer International Publishing (2017). p. 251–61. doi: 10.1007/978-3-319-39546-3_37

9. Voets NL, Pretorius P, Birch MD, Apostolopoulos V, Stacey R, Plaha P. Diffusion tractography for awake craniotomy: accuracy and factors affecting specificity. *J Neurooncol* (2021) 153:547–57. doi: 10.1007/s11060-021-03795-7

10. Soni N, Mehrotra A, Behari S, Kumar S, Gupta N. Diffusion-tensor imaging and tractography application in pre-operative planning of intra-axial brain lesions. *Cureus* (2017) 9(10): e1739. doi: 10.7759/cureus.1739

11. Alexopoulos G, Cikla U, El Tecle N, Kulkarni N, Pierson M, Mercier P, et al. The value of white matter tractography by diffusion tensor imaging in altering a neurosurgeon's operative plan. *World Neurosurg* (2019) 132:e305–13. doi: 10.1016/j.wneu.2019.08.168

12. De Witt Hamer PC, Robles SG, Zwinderman AH, Duffau H, Berger MS. Impact of intraoperative stimulation brain mapping on glioma surgery outcome: A meta-analysis. *JCO* (2012) 30:2559–65. doi: 10.1200/JCO.2011.38.4818

13. Yordanova YN, Moritz-Gasser S, Duffau H. Awake surgery for WHO grade II gliomas within "noneloquent" areas in the left dominant hemisphere: toward a "supratotal" resection: Clinical article. *JNS* (2011) 115:232–9. doi: 10.3171/2011.3.JNS101333

14. Rossi M, Sciortino T, Conti Nibali M, Gay L, Viganò L, Puglisi G, et al. Clinical pearls and methods for intraoperative motor mapping. *Neurosurg* (2021) 88:457–67. doi: 10.1093/neuros/nyaa359

15. Han SJ, Morshed RA, Troncon I, Jordan KM, Henry RG, Hervey-Jumper SL, et al. Subcortical stimulation mapping of descending motor pathways for perirolandic gliomas: assessment of morbidity and functional outcome in 702 cases. *J Neurosurg* (2019) 131:201–8. doi: 10.3171/2018.3.JNS172494

16. Keles GE, Lundin DA, Lamborn KR, Chang EF, Ojemann G, Berger MS. Intraoperative subcortical stimulation mapping for hemispheric perirolandic gliomas located within or adjacent to the descending motor pathways: evaluation of morbidity and assessment of functional outcome in 294 patients. *J Neurosurg* (2004) 100:369–75. doi: 10.3171/jns.2004.100.3.0369

17. Roux F-E, Djidjeli I, Quéhan R, Réhault E, Giussani C, Durand J-B. Intraoperative electrostimulation for awake brain mapping: how many positive interference responses are required for reliability? *J Neurosurg* (2020) 133:1191–201. doi: 10.3171/2019.6.JNS19925

18. Rossi M, Puglisi G, Conti Nibali M, Viganò L, Sciortino T, Gay L, et al. Asleep or awake motor mapping for resection of perirolandic glioma in the nondominant hemisphere? development and validation of a multimodal score to tailor the surgical strategy. *J Neurosurg* (2022) 136:16–29. doi: 10.3171/2020.11.JNS202715

19. Negwer C, Sollmann N, Ille S, Hauck T, Maurer S, Kirschke JS, et al. Language pathway tracking: comparing nTMS-based DTI fiber tracking with a cubic ROIs-based protocol. *JNS* (2017) 126:1006–14. doi: 10.3171/2016.2.JNS152382

20. Raffa G, Quattropani MC, Germanò A. When imaging meets neurophysiology: the value of navigated transcranial magnetic stimulation for preoperative neurophysiological mapping prior to brain tumor surgery. *Neurosurgical Focus* (2019) 47:E10. doi: 10.3171/2019.9.FOCUS19640

21. Tamura M, Kurihara H, Saito T, Nitta M, Maruyama T, Tsuzuki S, et al. Combining pre-operative diffusion tensor images and intraoperative magnetic resonance images in the navigation is useful for detecting white matter tracts during glioma surgery. *Front Neurol* (2022) 12:805952. doi: 10.3389/fneur.2021.805952

22. Louis DN, Perry A, Reifenberger G, von Deimling A, Figarella-Branger D, Cavenee WK, et al. The 2016 world health organization classification of tumors of the central nervous system: a summary. *Acta Neuropathol* (2016) 131:803–20. doi: 10.1007/s00401-016-1545-1

23. Fontana L, Tabano S, Bonaparte E, Marfia G, Pesenti C, Falcone R, et al. *MGMT*- methylated alleles are distributed heterogeneously within glioma samples irrespective of *IDH* status and chromosome 10q deletion. *J Neuropathol Exp Neurol* (2016) 75:791–800. doi: 10.1093/jnen/nlw052

24. Papagno C, Casarotti A, Comi A, Gallucci M, Riva M, Bello L. Measuring clinical outcomes in neuro-oncology. a battery to evaluate low-grade gliomas (LGG). *J Neuro-Oncol* (2012) 108:269–75. doi: 10.1007/s11060-012-0824-5

25. Zarino B, Sirtori MA, Meschini T, Bertani GA, Caroli M, Bana C, et al. Insular lobe surgery and cognitive impairment in gliomas operated with intraoperative neurophysiological monitoring. *Acta Neurochir* (2021) 163:1279–89. doi: 10.1007/s00701-020-04643-9

26. Zarino B, Di Cristofori A, Fornara GA, Bertani GA, Locatelli M, Caroli M, et al. Long-term follow-up of neuropsychological functions in patients with high grade gliomas: can cognitive status predict patient's outcome after surgery? *Acta Neurochir (Wien)* (2020) 162:803–12. doi: 10.1007/s00701-020-04230-y

27. Sanai N, Polley M-Y, McDermott MW, Parsa AT, Berger MS. An extent of resection threshold for newly diagnosed glioblastomas. *J Neurosurg* (2011) 115:3–8. doi: 10.3171/2011.7.JNS10238

28. Henderson F, Abdullah KG, Verma R, Brem S. Tractography and the connectome in neurosurgical treatment of gliomas: the premise, the progress, and the potential. *Neurosurgical Focus* (2020) 48:E6. doi: 10.3171/2019.11.FOCUS19785

29. Catani M, Howard RJ, Pajevic S, Jones DK. Virtual *in vivo* interactive dissection of white matter fasciculi in the human brain. *NeuroImage* (2002) 17:77–94. doi: 10.1006/nimg.2002.1136

30. Wu Y, Sun D, Wang Y, Wang Y. Subcomponents and connectivity of the inferior fronto-occipital fasciculus revealed by diffusion spectrum imaging fiber tracking. *Front Neuroanat* (2016) 10:88. doi: 10.3389/fnana.2016.00088

31. Carrabba G, Bertani G, Cogiamanian F, Ardolino G, Zarino B, Di Cristofori A, et al. Role of intraoperative neurophysiologic monitoring in the resection of thalamic astrocytomas. *World Neurosurg* (2016) 94:50–6. doi: 10.1016/j.wneu.2016.06.049

32. Conte V, Magni L, Songa V, Tomaselli P, Ghisoni L, Magnoni S, et al. Analysis of Propofol/Remifentanil infusion protocol for tumor surgery with intraoperative brain mapping. *J Neurosurgical Anesthesiol* (2010) 22:119–27. doi: 10.1097/ANA.0b013e3181c959f4

33. Bertani G, Fava E, Casaceli G, Carrabba G, Casarotti A, Papagno C, et al. Intraoperative mapping and monitoring of brain functions for the resection of low-grade gliomas: technical considerations. *FOC* (2009) 27:E4. doi: 10.3171/2009.8.FOCUS09137

34. Gogos AJ, Young JS, Morshed RA, Avalos LN, Noss RS, Villanueva-Meyer JE, et al. Triple motor mapping: transcranial, bipolar, and monopolar mapping for supratentorial glioma resection adjacent to motor pathways. *J Neurosurg* (2021) 134:1728–37. doi: 10.3171/2020.3.JNS193434

35. Carrabba G, Fava E, Giussani C, Acerbi F, Portaluri F, Songa V, et al. Cortical and subcortical motor mapping in rolandic and perirolandic glioma surgery: impact on postoperative morbidity and extent of resection. *J Neurosurg Sci* (2007) 51:45–51.

36. Rossi M, Nibali MC, Viganò L, Puglisi G, Howells H, Gay L, et al. Resection of tumors within the primary motor cortex using high-frequency stimulation: oncological and functional efficiency of this versatile approach based on clinical conditions. *J Neurosurg* (2020) 133:642–54. doi: 10.3171/2019.5.JNS19453

37. Giussani C, Di Cristofori A. Awake craniotomy for glioblastomas: is it worth it? considerations about the article entitled "Impact of intraoperative stimulation mapping on high-grade glioma surgery outcome: a meta-analysis". *Acta Neurochir* (2020) 162:427–8. doi: 10.1007/s00701-019-04173-z

38. Gravesteijn BY, Keizer ME, Vincent AJPE, Schouten JW, Stolker RJ, Klimek M. Awake craniotomy versus craniotomy under general anesthesia for the surgical treatment of insular glioma: choices and outcomes. *Neurol Res* (2018) 40:87–96. doi: 10.1080/01616412.2017.1402147

39. Wen PY, Macdonald DR, Reardon DA, Cloughesy TF, Sorensen AG, Galanis E, et al. Updated response assessment criteria for high-grade gliomas: response assessment in neuro-oncology working group. *J Clin Oncol* (2010) 28:1963–72. doi: 10.1200/JCO.2009.26.3541

40. Louis DN, Perry A, Wesseling P, Brat DJ, Cree IA, Figarella-Branger D, et al. The 2021 WHO classification of tumors of the central nervous system: a summary. *Neuro-Oncology* (2021) 23:1231–51. doi: 10.1093/neuonc/noab106

41. Duffau H. Hodotopy, neuroplasticity and diffuse gliomas. *Neurochirurgie* (2017) 63:259–65. doi: 10.1016/j.neuchi.2016.12.001

42. Duffau H. Stimulation mapping of white matter tracts to study brain functional connectivity. *Nat Rev Neurol* (2015) 11:255–65. doi: 10.1038/nrneurol.2015.51

43. Chang EF, Raygor KP, Berger MS. Contemporary model of language organization: an overview for neurosurgeons. *JNS* (2015) 122:250–61. doi: 10.3171/2014.10.JNS132647

44. Di Cristofori A, Basso G, de Laurentis C, Mauri I, Sirtori MA, Ferrarese C, et al. Perspectives on (A)symmetry of arcuate fasciculus. a short review about anatomy, tractography and TMS for arcuate fasciculus reconstruction in planning surgery for gliomas in language areas. *Front Neurol* (2021) 12:639822. doi: 10.3389/fneur.2021.639822

45. Rahimpour S, Haglund MM, Friedman AH, Duffau H. History of awake mapping and speech and language localization: from modules to networks. *Neurosurgical Focus* (2019) 47:E4. doi: 10.3171/2019.7.FOCUS19347

46. Sarubbo S, De Benedictis A, Merler S, Mandonnet E, Balbi S, Granieri E, et al. Towards a functional atlas of human white matter: Functional atlas of white matter. *Hum Brain Mapp* (2015) 36:3117–36. doi: 10.1002/hbm.22832

47. Sarubbo S, De Benedictis A, Merler S, Mandonnet E, Barbareschi M, Dallabona M, et al. Structural and functional integration between dorsal and ventral language streams as revealed by blunt dissection and direct electrical stimulation: Anatomo-functional integration of language. *Hum Brain Mapp* (2016) 37:3858–72. doi: 10.1002/hbm.23281

48. De Benedictis A, Duffau H, Paradiso B, Grandi E, Balbi S, Granieri E, et al. Anatomo-functional study of the temporo-parieto-occipital region: dissection, tractographic and brain mapping evidence from a neurosurgical perspective. *J Anat* (2014) 225:132–51. doi: 10.1111/joa.12204

49. Duffau H. Does post-lesional subcortical plasticity exist in the human brain? *Neurosci Res* (2009) 65:131–5. doi: 10.1016/j.neures.2009.07.002

50. Jiao Y, Lin F, Wu J, Li H, Fu W, Huo R, et al. Plasticity in language cortex and white matter tracts after resection of dominant inferior parietal lobule arteriovenous malformations: a combined fMRI and DTI study. *J Neurosurg* (2020), 134(3), 1–8. doi: 10.3171/2019.12.JNS191987

51. Matsumoto R, Okada T, Mikuni N, Mitsueda-Ono T, Taki J, Sawamoto N, et al. Hemispheric asymmetry of the arcuate fasciculus: a preliminary diffusion tensor tractography study in patients with unilateral language dominance defined by wada test. *J Neurol* (2008) 255:1703–11. doi: 10.1007/s00415-008-0005-9

52. Thiebaut de Schotten M, ffytche DH, Bizzi A, Dell'Acqua F, Allin M, Walshe M, et al. Atlasing location, asymmetry and inter-subject variability of white matter tracts in the human brain with MR diffusion tractography. *NeuroImage* (2011) 54:49–59. doi: 10.1016/j.neuroimage.2010.07.055

53. Ius T, Angelini E, Thiebaut de Schotten M, Mandonnet E, Duffau H Evidence for potentials and limitations of brain plasticity using an atlas of

functional resectability of WHO grade II gliomas: Towards a "minimal common brain". *NeuroImage* (2011) 56:992–1000. doi: 10.1016/j.neuroimage.2011.03.022

54. Picht T, Krieg SM, Sollmann N, Rösler J, Niraula B, Neuvonen T, et al. A comparison of language mapping by preoperative navigated transcranial magnetic stimulation and direct cortical stimulation during awake surgery. *Neurosurgery* (2013) 72:808–19. doi: 10.1227/NEU.0b013e3182889e01

55. Kim SS, McCutcheon IE, Suki D, Weinberg JS, Sawaya R, Lang FF, et al. AWAKE CRANIOTOMY FOR BRAIN TUMORS NEAR ELOQUENT CORTEX. *Neurosurgery* (2009) 64:836–46. doi: 10.1227/01.NEU.0000342405.80881.81

56. Pessina F, Navarria P, Cozzi L, Ascolese AM, Simonelli M, Santoro A, et al. Maximize surgical resection beyond contrast-enhancing boundaries in newly diagnosed glioblastoma multiforme: is it useful and safe? a single institution retrospective experience. *J Neurooncol* (2017) 135:129–39. doi: 10.1007/s11060-017-2559-9

57. Hervey-Jumper SL, Berger MS. Maximizing safe resection of low- and high-grade glioma. *J Neurooncol* (2016) 130:269–82. doi: 10.1007/s11060-016-2110-4

58. Molinaro AM, Hervey-Jumper S, Morshed RA, Young J, Han SJ, Chunduru P, et al. Association of maximal extent of resection of contrast-enhanced and non–Contrast-Enhanced tumor with survival within molecular subgroups of patients with newly diagnosed glioblastoma. *JAMA Oncol* (2020) 6:495. doi: 10.1001/jamaoncol.2019.6143

59. Boetto J, Bertram L, Moulinié G, Herbet G, Moritz-Gasser S, Duffau H. Low rate of intraoperative seizures during awake craniotomy in a prospective cohort with 374 supratentorial brain lesions: Electrocorticography is not mandatory. *World Neurosurg* (2015) 84:1838–44. doi: 10.1016/j.wneu.2015.07.075

60. Carrabba G, Venkatraghavan L, Bernstein M. Day surgery awake craniotomy for removing brain tumours: Technical note describing a simple protocol. *Minim Invasive Neurosurg* (2008) 51:208–10. doi: 10.1055/s-2008-1073132

61. Whiting BB, Lee BS, Mahadev V, Borghei-Razavi H, Ahuja S, Jia X, et al. Combined use of minimal access craniotomy, intraoperative magnetic resonance imaging, and awake functional mapping for the resection of gliomas in 61 patients. *J Neurosurg* (2020) 132:159–67. doi: 10.3171/2018.9.JNS181802

62. Cordella R, Acerbi F, Broggi M, Vailati D, Nazzi V, Schiariti M, et al. Intraoperative neurophysiological monitoring of the cortico-spinal tract in image-guided mini-invasive neurosurgery. *Clin Neurophysiol* (2013) 124:1244–54. doi: 10.1016/j.clinph.2012.11.005

63. Reisch R, Stadie A, Kockro RA, Hopf N. The keyhole concept in neurosurgery. *World Neurosurg* (2013) 79:S17.e9–S17.e13. doi: 10.1016/j.wneu.2012.02.024

64. Reisch R, Perneczky A. Ten-year experience with the supraorbital subfrontal approach through an eyebrow skin incision. *Operative Neurosurg* (2005) 57:ONS–242-ONS-255. doi: 10.1227/01.NEU.0000178353.42777.2C

65. Fernandes de Oliveira Santos B, de Araujo Paz D, Fernandes VM, dos Santos JC, Chaddad-Neto FEA, Sousa ACS, et al. Minimally invasive supratentorial neurosurgical approaches guided by smartphone app and compass. *Sci Rep* (2021) 11:6778. doi: 10.1038/s41598-021-85472-3

66. Aaronson DM, Martinez Del Campo E, Boerger TF, Conway B, Cornell S, Tate M, et al. Understanding variable motor responses to direct electrical stimulation of the human motor cortex during brain surgery. *Front Surg* (2021) 8:730367. doi: 10.3389/fsurg.2021.730367

67. Kombos T, Suess O, Kern BC, Funk T, Hoell T, Kopetsch O, et al. Comparison between monopolar and bipolar electrical stimulation of the motor cortex. *Acta Neurochirurgica* (1999) 141:1295–301. doi: 10.1007/s007010050433

68. Bello L, Riva M, Fava E, Ferpozzi V, Castellano A, Raneri F, et al. Tailoring neurophysiological strategies with clinical context enhances resection and safety and expands indications in gliomas involving motor pathways. *Neuro-Oncology* (2014) 16:1110–28. doi: 10.1093/neuonc/not327

69. Tate MC, Guo L, McEvoy J, Chang EF. Safety and efficacy of motor mapping utilizing short pulse train direct cortical stimulation. *Stereotactic Funct Neurosurg* (2013) 91:379–85. doi: 10.1159/000350020

70. Gerritsen JKW, Arends L, Klimek M, Dirven CMF, Vincent AJ-PE. Impact of intraoperative stimulation mapping on high-grade glioma surgery outcome: a meta-analysis. *Acta Neurochirurgica* (2019) 161:99–107. doi: 10.1007/s00701-018-3732-4

71. Rosenstock T, Tuncer MS, Münch MR, Vajkoczy P, Picht T, Faust K. Preoperative nTMS and intraoperative neurophysiology - a comparative analysis in patients with motor-eloquent glioma. *Front Oncol* (2021) 11:676626. doi: 10.3389/fonc.2021.676626

72. Ius T, Somma T, Baiano C, Guarracino I, Pauletto G, Nilo A, et al. Risk assessment by pre-surgical tractography in left hemisphere low-grade gliomas. *Front Neurol* (2021) 12:648432. doi: 10.3389/fneur.2021.648432

73. Haddad AF, Young JS, Berger MS, Tarapore PE. Preoperative applications of navigated transcranial magnetic stimulation. *Front Neurol* (2021) 11:628903. doi: 10.3389/fneur.2020.628903

74. Raffa G, Picht T, Büki A, Germanò A. Editorial: nTMS, connectivity and neuromodulation in brain tumor patients. *Front Neurol* (2022) 13:885773. doi: 10.3389/fneur.2022.885773

75. Sollmann N, Krieg SM, Säisänen L, Julkunen P. Mapping of motor function with neuronavigated transcranial magnetic stimulation: A review on clinical application in brain tumors and methods for ensuring feasible accuracy. *Brain Sci* (2021) 11(7):897. doi: 10.3390/brainsci11070897

76. Sollmann N, Zhang H, Fratini A, Wildschuetz N, Ille S, Schröder A, et al. Risk assessment by presurgical tractography using navigated TMS maps in patients with highly motor- or language-eloquent brain tumors. *Cancers (Basel).* (2020) 12 (5):1264. doi: 10.3390/cancers12051264

frontiers | Frontiers in Neuroscience

TYPE Original Research
PUBLISHED 21 September 2022
DOI 10.3389/fnins.2022.886465

Check for updates

OPEN ACCESS

EDITED BY
Alexandra Golby,
Harvard Medical School, United States

REVIEWED BY
Miriam H. A. Bopp,
University of Marburg, Germany
Kristin Huntoon,
University of Texas MD Anderson Cancer Center, United States

*CORRESPONDENCE
David Kis
kisdavid@gmail.com

†These authors share first authorship

SPECIALTY SECTION
This article was submitted to Brain Imaging Methods, a section of the journal Frontiers in Neuroscience

RECEIVED 28 February 2022
ACCEPTED 16 August 2022
PUBLISHED 21 September 2022

CITATION
Kis D, Szivos L, Rekecki M, Shukir BS, Mate A, Hideghety K and Barzo P (2022) Predicting the true extent of glioblastoma based on probabilistic tractography.
Front. Neurosci. 16:886465.
doi: 10.3389/fnins.2022.886465

COPYRIGHT
© 2022 Kis, Szivos, Rekecki, Shukir, Mate, Hideghety and Barzo. This is an open-access article distributed under the terms of the Creative Commons Attribution License (CC BY). The use, distribution or reproduction in other forums is permitted, provided the original author(s) and the copyright owner(s) are credited and that the original publication in this journal is cited, in accordance with accepted academic practice. No use, distribution or reproduction is permitted which does not comply with these terms.

Predicting the true extent of glioblastoma based on probabilistic tractography

David Kis[1*†], Laszlo Szivos[1†], Mark Rekecki[1], Bayan Salam Shukir[1], Adrienn Mate[1], Katalin Hideghety[2] and Pal Barzo[1]

[1]Department of Neurosurgery, Faculty of Medicine, University of Szeged, Szeged, Hungary, [2]Department of Oncology, Faculty of Medicine, University of Szeged, Szeged, Hungary

Glioblastoma is the most frequent type of primary brain tumors. Despite the advanced therapy, most of the patients die within 2 years after the diagnosis. The tumor has a typical appearance on MRI: a central hypointensity surrounded by an inhomogeneous, ring-shaped contrast enhancement along its border. Too small to be recognized by MRI, detached individual tumor cells migrate along white matter fiber tracts several centimeters away from the edge of the tumor. Usually these cells are the source of tumor recurrence. If the infiltrated brain areas could be identified, longer survival time could be achieved through supratotal resection and individually planned radiation therapy. Probabilistic tractography is an advanced imaging method that can potentially be used to identify infiltrated pathways, thus the real extent of the glioblastoma. Our study consisted of twenty high grade glioma patients. Probabilistic tractography was started from the tumor. The location of tumor recurrence on follow-up MRI was considered as the primary infiltrated white matter tracts. The results of probabilistic tractography were evaluated at thirteen different thresholds. The overlap with the tumor recurrence of each threshold level was then defined to calculate the sensitivity and specificity. In the group level, sensitivity (81%) and specificity (90%) were the most reliable at 5% threshold level. There were two outliers in the study group, both with high specificity and very low sensitivity. According to our results, probabilistic tractography can help to define the true extent of the glioblastoma at the time of diagnosis with high sensitivity and specificity. Individually planned surgery and irradiation could provide a better chance of survival in these patients.

KEYWORDS

probabilistic tractography, glioblastoma, tumor recurrence, extended survival, infiltration

Introduction

Glioblastoma is the most frequent type of primary brain tumors. The majority of patients die within 16–20 months after the diagnosis despite all the advanced therapy (Yan et al., 2009). Currently, the gold standard therapy for glioblastoma consists of maximum safe resection (more than 90% of the tumor mass should be removed) that is followed by the Stupp protocol (Stupp et al., 2005; Louis et al., 2021; Ostrom et al., 2021).

Glioblastoma is a rapidly growing, infiltrative malignant tumor originating from the glial cells of the white matter. Tumor cells tend to propagate along white matter fiber tracts. In an advanced stage, the tumor can infiltrate gray matter as well (Wirsching et al., 2016). Histologically, glioblastoma is characterized by atypical cells, a high mitotic rate, glomeruloid vascular proliferation, and necrosis (Demuth and Berens, 2004).

Currently, the most sensitive *in vivo* diagnostic modality is contrast-enhanced T1 MRI. The appearance of the tumor on MRI images is very typical. Irregular ring-shaped contrast enhancement can be seen with a hypointense necrotic center, usually with prominent peritumoral edema and mass effect (Young, 2007; Shukla et al., 2017). Previous studies have shown that the tumor mass identifiable on the MRI images does not correspond to the true extent of the tumor (Demuth and Berens, 2004). Due to the tumor's infiltrative growth, glioblastoma cells can be present at a distance of 5 to 10 cm from the contrast-enhancing border. Some studies have demonstrated that glioblastoma cells can be present anywhere in the brain, including the contralateral hemisphere (Tonn and Goldbrunner, 2003).

Tumor cells are migrating from the tumor mass along fiber tracts, invading brain regions far away from the original site of the tumor. Although the tumor mass and infiltrative part form one structural unit, only the tumor mass can be visualized easily on standard MRI images (Petrecca et al., 2013; Lemee et al., 2015). The infiltrative component can be considered as an abnormal "fiber tract" that first invades and then destroys normal brain (Virga et al., 2019).

The recurrence of glioblastoma usually originates from these infiltrative tumor cells, which is supported by the observation that tumor progression often appears in the white matter surrounding the resection cavity (Milano et al., 2010; Petrecca et al., 2013).

This aggressive, infiltrative feature of the tumor makes the available treatment options less effective. The surgical resection is aimed at removing the tumor mass visible on the MRI images. The remaining tumor cells, which may be present in significant amounts even if the post-operative MRI shows a "tumor-free" status, are treated with irradiation and chemotherapy (Stupp et al., 2005). After a gross total or subtotal resection, the patients' survival depends on how the remaining tumor cells respond to oncological treatment. These treatments are more effective if the residual tumor volume is lower (Roelz et al., 2016).

As opposed to chemotherapy, which is a systematic treatment, surgery and irradiation are focal treatments. In the case of glioblastoma, these modalities are individually tailored to achieve the best results. Surgery is considered successful if no contrast enhancement is visible on the post-operative MRI images or if the residual tumor is less than 10% of its original size. Radiation therapy typically has a standard planning protocol. Irradiation is focused to an area that exceeds the border of the resection cavity/the residual tumor margins by 1 to 3 cm to destroy the remaining infiltrative glioblastoma cells (Barani and Larson, 2015).

There are several factors that define the patients' survival, such as age, comorbidities, extent of resection, location of tumor, Karnofsky Performance Scale and molecular markers (e.g., MGMT promoter methylation, IDH mutant or wild type) (Lacroix et al., 2001; Bauchet et al., 2010). Recent studies have shown that gross total resection is an independent prognostic factor associated with improved clinical outcome (Wykes et al., 2021). Theoretically, better therapeutic effects and longer survival would be possible if the residual tumor volume could be minimized. It can be accomplished through supratotal tumor resection (when the resection margins exceed the contrast-enhancing border) or individually planned irradiation that focuses the beam to brain regions actually infiltrated by the tumor (De Bonis et al., 2013). The problem is that standard MRI sequences cannot identify infiltrated brain regions, that is, cannot determine the true extent of the tumor (Shukla et al., 2017; de Leeuw and Vogelbaum, 2019). FLAIR and MR Spectroscopy (MRS) are two MRI modalities which were introduced in the last decade to identify the infiltrative part of the glioblastoma. Although both sequences have promising results, their routine application is limited. Using FLAIR to guide surgical resection and irradiation has not resulted in longer survival (Garrett et al., 2017; Altieri et al., 2019). MRS has a low resolution which makes it challenging to use for such precise image guided procedures (Deviers et al., 2014).

Abbreviations: AAL3, automated anatomical labeling atlas 3; ASSET, array coil spatial sensitivity encoding; BEDPOSTX, bayesian estimation of diffusion parameters obtained using sampling techniques; DICOM, digital imaging and communications in medicine; DTI, diffusion tensor imaging; DWI, diffusion weighted images; F-DOPA, fluoro-dihydroxyphenylalanine; F-FET, F-Fluoro-Ethyl-Tyrosine; FDT, FMRIB's diffusion toolbox; FLAIR, fluid attenuation inversion recovery; FMRIB, Functional magnetic resonance imaging of the brain; FOV, field of view; FSL, FMRIB software library; FSPGR, fast spoiled gradient echo; GE, general electric; GPU, graphical processing unit; IDH, isocitrate dehydrogenase mutation; JHU-ICMB-DTI, Johns Hopkins University, international consortium of brain mapping, diffusion tensor imaging; LNR, lactate/N-acetylaspartate ratio; MGMT, O^6-methylguanine-DNA methyltransferase; MNI152, Montreal neurological institute 152; MRI, magnetic resonance imaging; MRS, magnetic resonance spectroscopy; NIFTI, neuroimaging informatics technology initiative; OS, overall survival; PET-CT, positron emission tomography, computed tomography; PFS, progression free survival; PROBTRACX, probabilistic tracking with crossing fibers; SWI, susceptibility weighted images; TC, tumor connection; TE, time of echo; TR, time of repetition.

Tractography is an advanced application of diffusion MRI. Based on the diffusion movement pattern of the water molecules, white matter fiber tracts can be visualized (Le Bihan et al., 1992; Mascalchi et al., 2005). The diffusion pattern is characterized by anisotropy. A more directional diffusion results in higher anisotropy. Hence fiber tract reconstruction is more certain in those brain regions with high anisotropy. In the last decade tractography has an evolving role in preoperative mapping and image guided therapy of brain tumors (Costabile et al., 2019). There are two types of tractography algorithms, the deterministic and probabilistic methods (Yamada et al., 2009).

Conventional diffusion tensor imaging-based deterministic tractography can visualize the major white matter pathways reliably (Mori and van Zijl, 2002; Mukherjee et al., 2008). Therefore, it can be used to identify white matter fibers around the tumor (e.g., corticospinal tract) and help to plan the surgical trajectory to avoid injuring important pathways. The main limitation of deterministic tractography is that in regions with low anisotropy values, such as cortical and subcortical gray matter, branching pathways and crossing fibers, it cannot identify fibers reliably (Yamada et al., 2009).

The ball and sticks model-based probabilistic tractography has several advantages and overcomes the above limitation. It tracks fibers in regions with low anisotropy values and visualizes crossing fibers. Moreover, it provides quantitative measures representing the connectivity distribution of the seed region. It can be thresholded to exclude false positive results (Behrens et al., 2003b, 2007). Probabilistic tractography is a powerful tool to identify white matter fiber tracts with a high certainty. Potentially, it can be also used to identify white matter fiber tracts that are infiltrated by the tumor (Behrens et al., 2007; Kis et al., 2014).

In our study, we aimed to identify the true extent of glioblastoma using probabilistic tractography in a retrospective manner. Tumor recurrence was identified on follow-up MRI images, and its sites were considered the brain regions that had originally been infiltrated by the tumor. Probabilistic tractography was performed on the preoperative MRI images, and the results were compared with the location of tumor recurrence at different threshold levels.

Materials and methods

Patient population

Patients were included in the study retrospectively from those who had undergone surgical treatment at our department between 2010 and 2021. Inclusion criteria were the followings: 1, The diagnosis were primary glioblastoma or grade III anaplastic oligodendroglioma. 2, All patients underwent either subtotal or total tumor resection during the primary surgery. Based on post-operative MRI images (acquired within 48 h), subtotal resection was defined as the remaining contrast-enhancing tumor was less than 10% of its original volume, while greater extent of remaining tumor is considered partial resection. Total resection was achieved when no contrast enhancement was visible (Ahmed et al., 2019). The surgical resection was followed by the Stupp protocol (Stupp et al., 2005). 3, All patients had preoperative DTI scans in addition to the routine head MRI protocol. 4, Follow-up MRI scans were acquired every 3 months. A total of 96 adult (>18 years) patients were screened and 20 were enrolled to the study. All of them had preoperative DTI. The two main reason why patients were excluded are 1, lost to follow-up or 2, partial surgical resection.

The first follow-up MRI was used to identify infiltrated fiber tracts that had prominent tumor recurrence in the white matter surrounding the resection cavity. The study was approved by the institutional review board, and written informed consent was obtained from all patients.

Patients' data are summarized in **Table 1**.

Imaging

Preoperative and follow-up MRI images were used in this study. Scanning was performed using a 3-T GE Signa Excite scanner. Two sequences of preoperative MRI were used: (1) contrast-enhanced high-resolution 3D axial FSPGR-T1; and (2) DTI images. For the follow-up MRI, only the contrast-enhanced high-resolution 3D axial FSPGR-T1 sequence was used.

Contrast-enhanced high-resolution T1-weighted scan parameters: 3D FSPGR fast spoiled gradient echo: repetition time [TR]/echo time [TE], 10.3/4.2 ms; flip angle, 15°; ASSET 2; field of view [FOV], 25 cm × 25 cm; matrix, 256 × 256; slice thickness, 1 mm.

Diffusion-weighted image parameters: DTI: TR/TE, 11,500/98.4 ms; flip angle, 90°; FOV, 24 cm × 24 cm; matrix, 80 × 80; slice thickness, 3 mm; ASSET: 2; b-value = 1,000 s/mm^2, in 25 independent directions and 1 non-gradient set (b-value = 0 s/mm^2).

Scans covered the whole head. Total scan time was 18–27 min, including all sequences (FLAIR, non-contrast and contrast-enhanced T1, T2, DWI, DTI, SWI).

Data pre-processing

According to the method previously described by Behrens et al., MRI data were processed using tools from the FMRIB Software Library (FSL, version 5.0.7; Oxford Centre for Functional MRI of the Brain (FMRIB), United Kingdom)[1] (Behrens et al., 2003a). Compressed NifTI images were created from the original DICOM files using Chris Rordens'

1 www.fmrib.ox.ac.uk/fsl

TABLE 1 Patients' clinical data are summarized in this table.

	Age (years) and Sex	PFS (months)	OS (months)	Time of diagnosis	Date of recurrence	Date of last follow-up/Death	Side	Localization	Histology
1.	52 Male	5	26	2012. 09	2013. 02	2014. 11	Left	Temporalis	Glioblastoma
2.	53 Male	4	12	2011. 02	2011. 06	2012. 02	Left	Temporo-parietalis	Glioblastoma
3.	47 Male	4	20	2010. 09	2011. 01	2012. 05	Left	Frontalis	Glioblastoma
4.	68 Male	13	20	2013. 01	2014. 02	2014. 09	Left	Temporalis	Glioblastoma
5.	54 Female	34	35	2010. 04	2013. 02	2013. 03	Left	Frontalis	Glioblastoma
6.	67 Male	5	12	2012. 02	2012. 07	2013. 02	Left	Temporalis	Glioblastoma
7.	26 Male	28	46	2010. 03	2012. 08	2014. 01	Right	Frontalis	Glioblastoma
8.	29 Male	47	64	2012. 05	2016. 04	2017. 09	Left	Fronto-parietalis	Oligodendroglioma –Gr 3
9.	34 Male	6	11	2010. 12	2011. 05	2011. 10	Left	Frontalis	Glioblastoma
10.	67 Female	37	37	2012. 06	2015. 07	2015. 07	Right	Frontalis	Oligodendroglioma –Gr 3
11.	51 Female	61	72	2011. 02	2016. 03	2017. 02	Left	Parietalis	Oligodendroglioma –Gr 3
12.	39 Male	22	47	2010. 07	2012. 05	2014. 06	Right	Parieto-occipitalis	Glioblastoma
13.	55 Male	2	4	2021. 02	2021. 04	2021. 06	Right	Temporo-parieto-occipitalis	Glioblastoma
14.	77 Female	8	10	2019. 10	2020. 06	2020. 08	Left	Temporo-parietalis	Glioblastoma
15.	68 Male	8	10	2020. 04	2021. 12	2022. 02	Left	Frontalis	Oligodendroglioma –Gr 3
16.	59 Male	2	3	2021. 10	2021. 12	2022. 02	Left	Frontalis	Glioblastoma
17.	56 Male	2	28	2019. 11	2020. 01	2022. 03	Left	Parietalis	Glioblastoma
18.	46 Female	1	2	2021. 12	2022. 01	2022. 02	Left	Parietalis	Glioblastoma
19.	36 Male	3	6	2020. 10	2021. 01	2021. 04	Left	Parietalis	Glioblastoma
20.	46 Male	4	15	2019. 11	2020. 03	2021. 02	Right	Frontalis	Glioblastoma

PFS, progression free survival; OS, overall survival.

MRICron software (Rorden et al., 2007). Diffusion images were visually checked for artifacts. Data quality was satisfactory in all subjects; therefore, no volume was discarded. The standard preprocessing steps were taken: eddy current and motion correction (affine registration of the diffusion volumes to the b0 volume), adaptation of the b-matrix (Leemans and Jones, 2009) by eddy tool (FSL 6.0.1) (Andersson and Sotiropoulos, 2016), skull stripping, reconstruction of diffusion tensors, and estimation of diffusion parameters (Smith, 2002). For each patient, DTI images and preoperative FSPGR–T1-weighted images were registered to each other (6 degrees of freedom, cost function: mutual information, interpolation: trilinear). For analyses in the standard space, affine registration (12 degrees of freedom, cost function: correlation ratio, interpolation: trilinear) of each patient's preoperative and follow-up FSPGR-T1 to standard T1 images (Montreal Neurological Institute, MNI152 1 mm brain) was done. Transformation matrices were created in every registration step. Image registration was performed with FMRIB's linear registration tool (FLIRT) (Jenkinson and Smith, 2001; Jenkinson et al., 2002).

Defining masks

In this study, we used two types of masks: (1) tumor masks (primary tumor and tumor recurrence masks); and (2) cortical and subcortical white matter masks.

Tumor masks were used to identify the true extension of the glioblastoma. The primary tumor mask served as a seed mask for probabilistic tractography, and the tumor recurrence mask was considered to represent the primary infiltrated brain regions.

The cortical and subcortical white matter masks were used to identify brain regions infiltrated by the tumor and where the tumor recurred.

Cortical and subcortical white matter masks

The standard brain was divided into distinct subcortical and cortical subregions. The standard JHU ICBM–DTI–white matter–81 labels map was used to segment the white matter into 54 subregions in the left and right hemispheres each, and 6 midline structures (Mori et al., 2008). The standard AAL3 map was used to segment the cortex into 84 subregions on either side (Rolls et al., 2020). The JHU–ICBM–DTI–white matter–81

labels and AAL3 maps were in the MNI152 1 mm space (Hua et al., 2008; Rolls et al., 2020). **Figures 1A,B**

Tumor masks

The primary tumor and the tumor recurrence masks were created on the patients' preoperative and follow-up T1 images, respectively. The contrast-enhancing part was considered to be the tumor, and it was manually delineated by two independent researchers. The primary tumor mask was used as the seed mask for tractography analyses. **Figures 2–4**.

Tractography analyses

Based on a multifiber model, probabilistic tractography was performed using the primary tumor mask (Behrens et al., 2007). The default settings of the FDT (5,000 samples, 0.5-mm step length, curvature threshold = 0.2) were applied (Behrens et al., 2003a,b). It resulted in a probabilistic tract which is a set of voxels with different probabilities of connection to the original seed mask. The tractography result was called tumor connection (TC).

To eliminate low-probability connections (false positive results), threshold levels were set to include only those voxels that represented a connectivity value equal to or greater than a certain percentage of the maximum connectivity voxel of the TC (Bennett et al., 2011; Khalsa et al., 2014).

In this work, we defined connectivity as the total number of successful samples per voxel. Thirteen threshold levels were tested resulting in thirteen TCs: 1, 5, 10, 15, 20, 25, 30, 40, 50, 60, 70, 80, and 90% (**Figures 2–4**). We assessed which of the above threshold levels has the highest sensitivity and specificity in predicting the true extent of the tumor. The area of tumor recurrence was considered the primary infiltrated brain area, which therefore corresponded to the original true extent of the glioblastoma.

Defining sensitivity and specificity

To validate the reliability of this method in the prediction of glioblastoma recurrence, sensitivity and specificity were defined at each threshold level in each patient. Individual and group results were also calculated.

All thirteen thresholded TCs and the tumor recurrence mask were transformed to the standard space.

The standard cortical and subcortical brain regions were projected on the patients' brain in the MNI152 space and it was then assessed how many of them overlapped with the thirteen different TCs and the tumor recurrence mask.

Brain regions that overlapped with the TCs but not with the tumor recurrence mask were considered false positive results.

Brain regions that overlapped with the tumor recurrence mask but not with the TCs were considered false negative results.

Sensitivity and specificity were calculated using the following formula:

Sensitivity = A/(A + C)

Specificity = D/(D + B)

A: number of brain regions covered by both TC and tumor recurrence mask.

B: number of brain regions only covered by the TC.

C: number of brain regions only covered by the tumor recurrence mask.

D: number of brain regions covered by neither the TC nor the tumor recurrence mask.

The complete analysis (preprocessing steps, defining masks, tractography) took approximately 1 h for each patient. Probabilistic tractography was performed using a GPU-based implementation of BEDPOSTX and PROBTRAKX.

Results

In our study group female-to-male ratio was 1:3. Average age was 51.5 years. A total of 50% of the patients was between 45 and 60 years old. Most frequently the tumor was located in the left hemisphere (75%) and in the frontal lobe (45%). The two most common neurological deficit was hemiparesis (35%) and speech disturbancies (25%). A total of 40% of the patients did not have severe neurological symptoms preoperatively. The average KPS was 73% preoperatively and 80% at 2 months after the operation. Navigation guided (Medtronic Inc StealthStation iNav or S8) individually planned minimal invasive craniotomy was performed in all cases. Total (70%) or subtotal (30%) resection was achieved in all patients. Four patients (20%) had grade III anaplastic oligodendroglioma (**Table 1**). The progression-free and overall survival periods, age, and female-to-male ratio corresponded to the literature (Ostrom and Barnholtz-Sloan, 2011; Michaelsen et al., 2018).

There were two outliers in the study group (Patients 1 and 20) who showed remarkably lower sensitivity than the rest of the patients (**Table 2** and **Figures 3**, **4**). Their results were excluded from the group analyses as it is explained in the section "Discussion."

A total of 18 patients' data were averaged and evaluated. TCs with higher threshold levels were associated with higher specificity and lower sensitivity. The maximum sensitivity and specificity were observed at 1 and 90%, respectively (**Table 3**).

The TC with the 5% threshold level seems to give the most reliable results. In the majority of the patients (72.2%), sensitivity was higher than 75%. Additionally, in 77.7% of patients, specificity was greater than 85%. At the group level, both measures were higher than 80%. Average sensitivity was 81% and average specificity was 90% at the 5% threshold (**Table 3** and **Graph 1** and **Figure 2**).

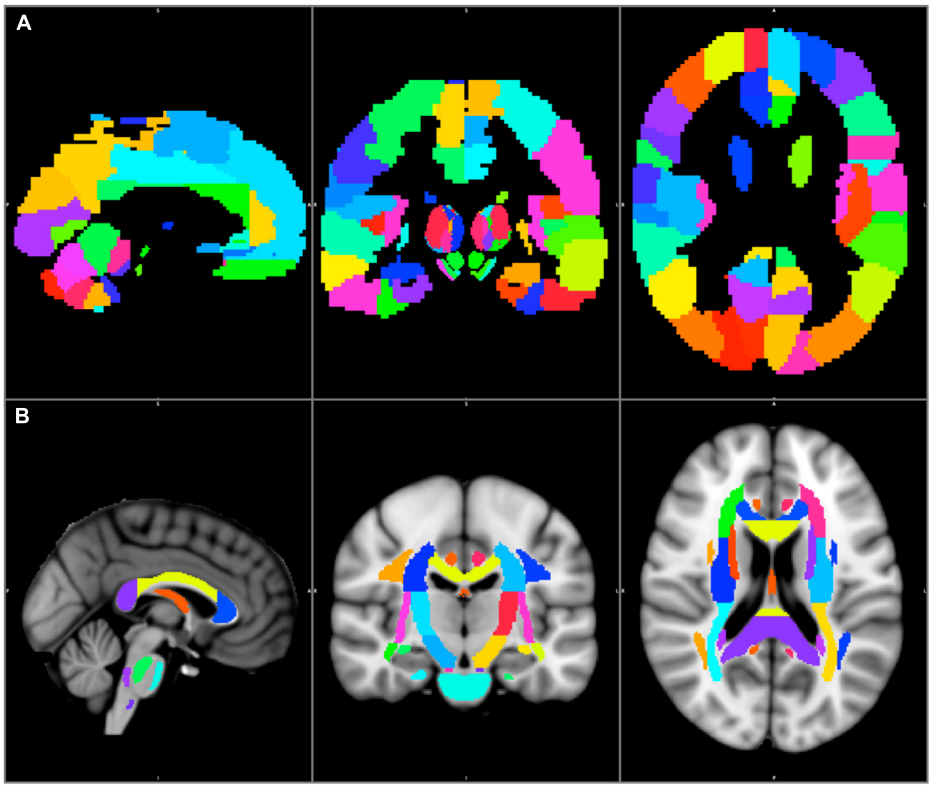

FIGURE 1
The AAL3 cortical **(A)** and the JHU–ICBM–DTI–81 white matter labels subcortical **(B)** regions are shown in the MNI152 1 mm space.

Tumor volume varied between 6.2 and 116.4 cm^3. The volume of the recurrent tumor also showed high variability, as it ranged from 7.8 to 140.2 mm^3.

Discussion

Glioblastoma is often considered the most aggressive type of cancer. Overall survival is 18 months and only 1% of the patients are alive 5 years after the diagnosis.

The gold standard therapy for glioblastoma is maximum safe resection followed by oncological and oncoradiological treatment. There is a positive correlation between the extent of primary tumor resection and the overall survival (Wykes et al., 2021).

In oncological surgery, an extended safety margin is used to remove the primary tumor and all the infiltrated surrounding tissues. Unfortunately, this approach cannot be employed in the case of primary brain tumors. Resection should be limited to the tumor mass-normal tissue border (Yasargil, 1994). The removal of healthy brain tissue is likely to cause severe neurological symptoms and a reduced quality of life. The remaining tumor cells infiltrating the normal brain tissue should be treated with oncological procedures, such as irradiation and chemotherapy (Stupp et al., 2005).

Glioblastoma, which is the most aggressive type of these infiltrative primary brain tumors, recurs from the remaining infiltrative tumor cells (Petrecca et al., 2013). Currently, the radiological modality with the highest sensitivity for glioblastoma is MRI (Shukla et al., 2017). The tumor mass is visible on the contrast-enhanced T1 images, but the cells infiltrating the otherwise normal brain tissue (which can be at a distance of several centimeters from the contrast enhancing border) are not.

Theoretically, if the true extent of the glioblastoma can be revealed, prolonged progression-free and overall survival periods can be achieved with supratotal resection and individually planned radiation therapy.

In the recent decade, FLAIR, MRS and amino acid-based PET-CT were introduced to identify the true extent of glioblastoma as potential imaging modalities.

In case of glioblastoma the hyperintense volume in the FLAIR images corresponds to microscopic tumor infiltration and edema, and usually exceeds the contrast enhancing volume (Watanabe et al., 1992). Preoperative FLAIR images can be used to plan surgical resection and irradiation therapy but there is no clear evidence that it has a positive prognostic

10.3389/fnins.2022.886465

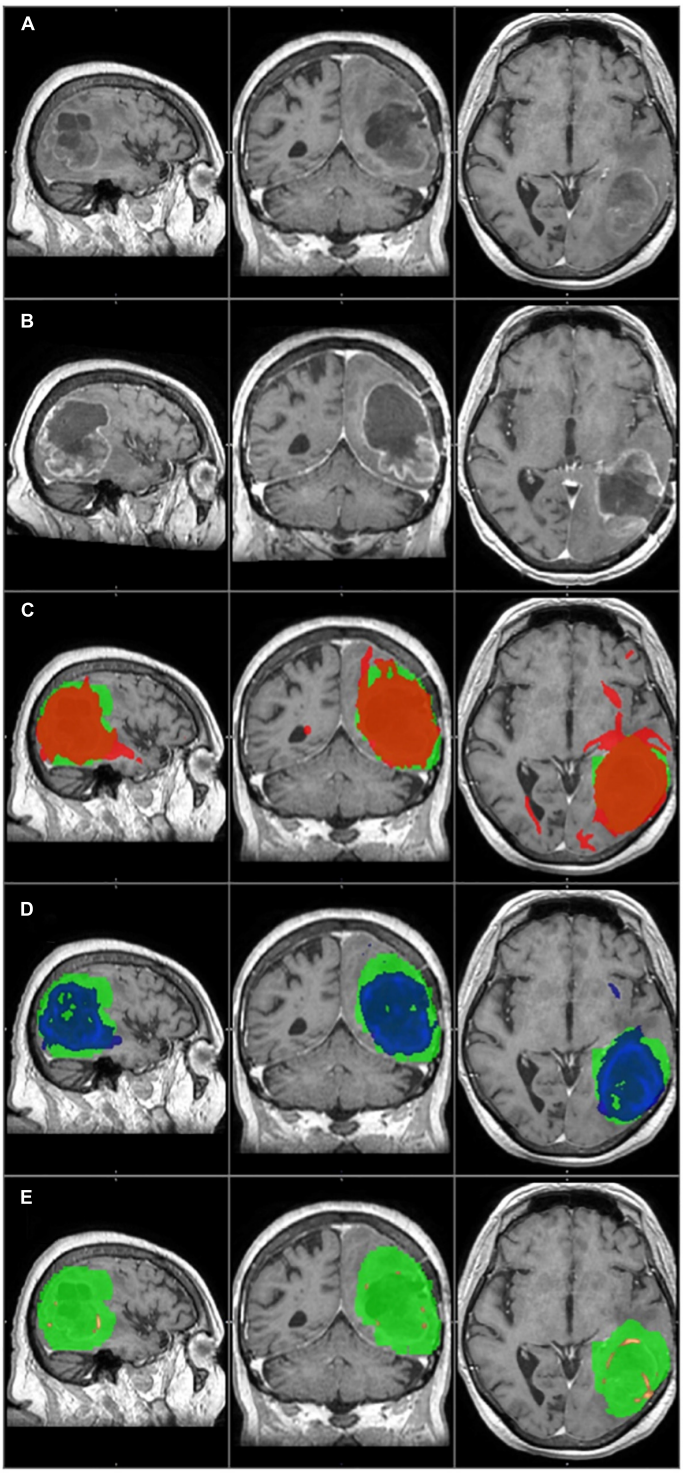

FIGURE 2
The primary tumor, the recurrence tumor, and the overlap between the different TCs and the tumor recurrence mask of the representative case of Patient 14 are displayed in this figure. All images are transformed to the MNI152 1 mm space. **(A)** The preoperative contrast enhanced T1 image. A huge tumor with ring shaped contrast enhancement can be seen in the left temporo-parito-occipital region. **(B)** The size and the location of the tumor recurrence. **(C)** The 1% TC (red) is overlapped on the tumor recurrence mask (green). **(D)** The 5% TC (blue) is overlapped on the tumor recurrence mask (green). **(E)** The 40% TC (red-yellow) is overlapped on the tumor recurrence mask (green). **(C–E)** Are on the preoperative T1 images. Although the sensitivity is higher at 1% than at 5%, the specificity is lower due to the greater number of false positive regions. The best overlap can be seen at the 5% threshold level. At 40%, the TC is almost invisible and covers only a small portion of the tumor recurrence mask resulting in high specificity but low sensitivity.

10.3389/fnins.2022.886465

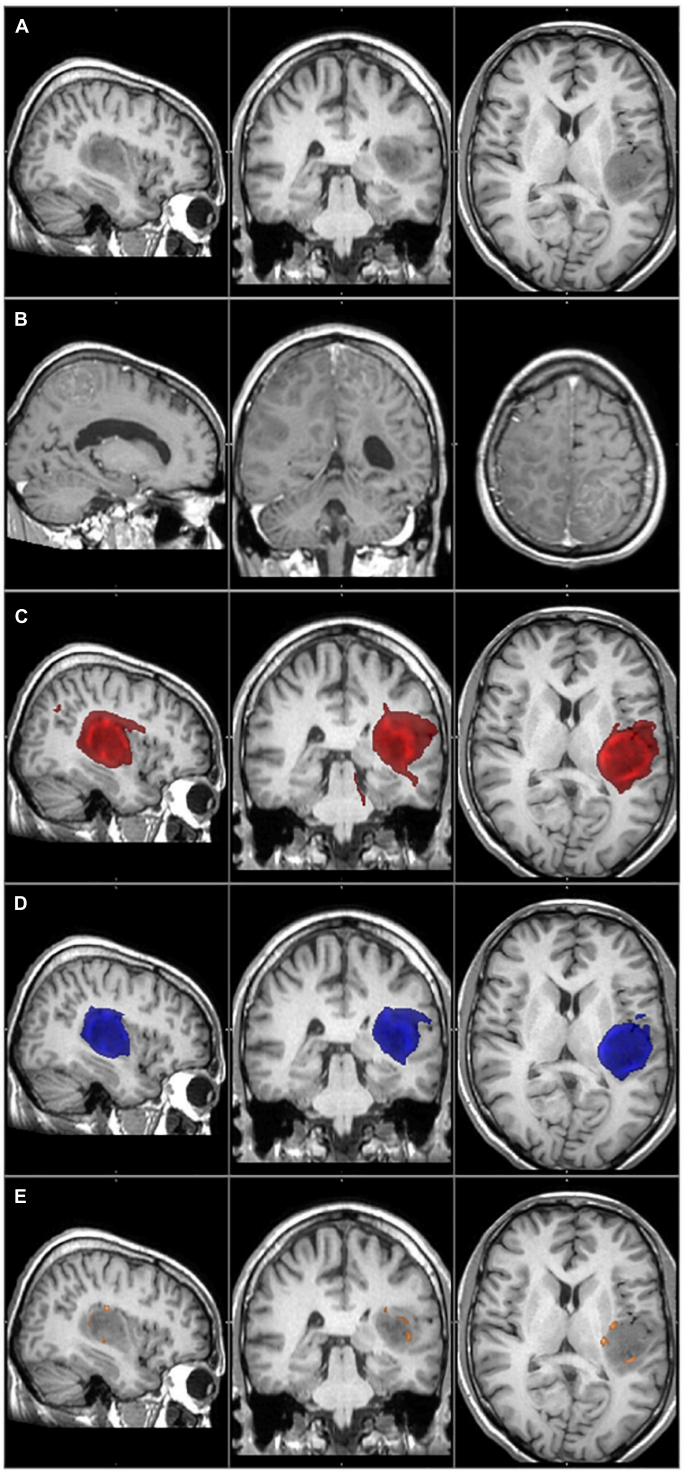

FIGURE 3
The primary tumor, the recurrence tumor, and the overlap between the different TCs and the tumor recurrence mask of the representative case of Patient 1 are displayed in this figure. All images are transformed to the MNI152 1 mm space. **(A)** The preoperative contrast enhanced T1 image. The tumor is located in the left temporo-parietal region and does not enhance the contrast agent, but histology verified the glioblastoma. **(B)** The size and the location of the tumor recurrence. **(C)** The 1% TC (red) is overlapped on the tumor recurrence mask (green). **(D)** The 5% TC (blue) is overlapped on the tumor recurrence mask (green). **(E)** The 40% TC (red-yellow) is overlapped on the tumor recurrence mask (green). **(C–E)** Are on the preoperative T1 images. The main part of the recurrence is far away from the original tumor location, which leads to very low sensitivity even at the 1% threshold level.

10.3389/fnins.2022.886465

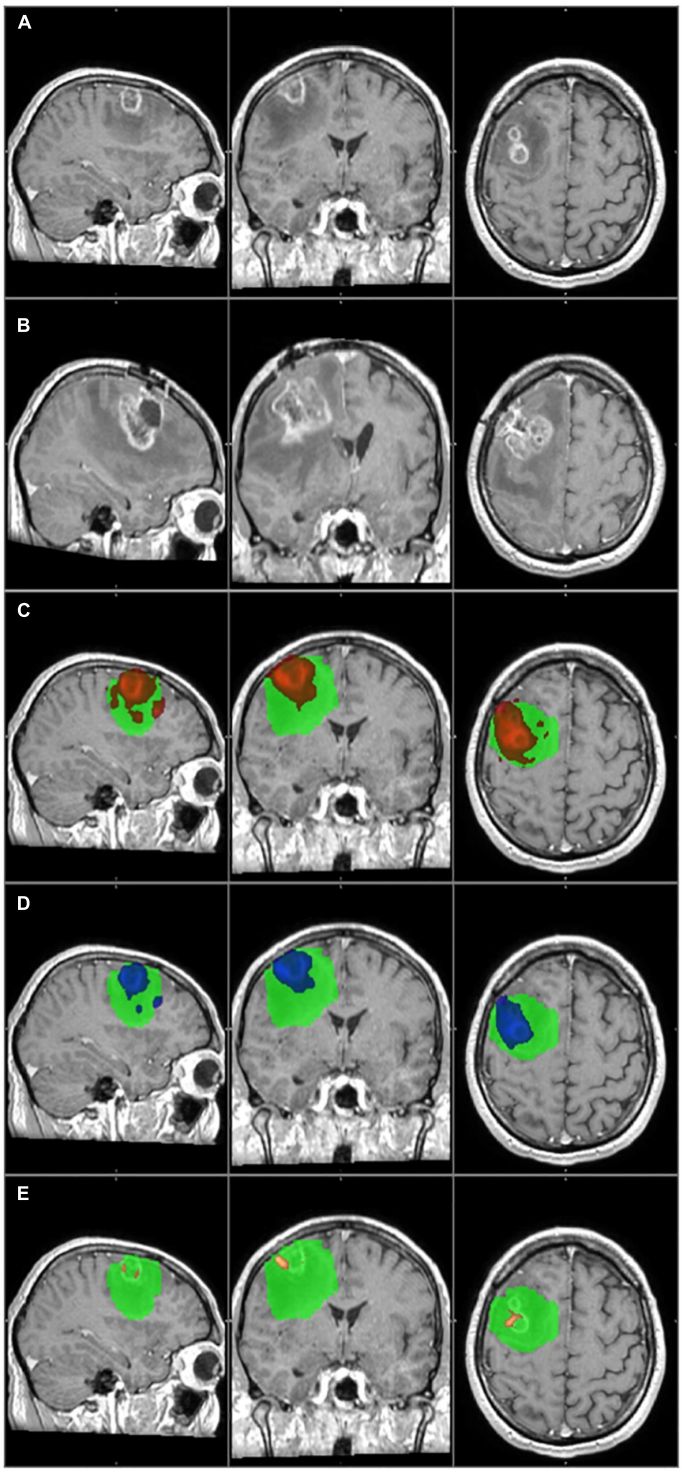

FIGURE 4
The primary tumor, the recurrence tumor, and the overlap between the different TCs and the tumor recurrence mask of the representative case of Patient 20 are displayed in this figure. All images are transformed to the MNI152 1 mm space. **(A)** The preoperative contrast enhanced T1 image. Two small tumors with ring shaped contrast enhancement can be seen in the right frontal region. **(B)** The size and the location of the tumor recurrence. **(C)** The 1% TC (red) is overlapped on the tumor recurrence mask (green). **(D)** The 5% TC (blue) is overlapped on the tumor recurrence mask (green). **(E)** The 40% TC (red-yellow) is overlapped on the tumor recurrence mask (green). **(C–E)** Are on the preoperative T1 images. As it can be seen, the TCs are fully overlapping with the tumor recurrence mask and therefore the specificity is 100% at every threshold. On the other hand the recurrence remarkably exceeds the border of the TCs, and the sensitivity is low, even at 1%. Please note that the direction of the recurrence is in correspondence with the TCs, and the low sensitivity is the result of the fast tumor progression.

TABLE 2 The sensitivity and specificity values are listed in this table at each threshold level of the three example cases.

	1%	5%	10%	15%	20%	25%	30%	40%	50%	60%	70%	80%	90%
A													
Sensitivity	0,94	0,80	0,77	0,74	0,66	0,63	0,57	0,46	0,23	0,20	0,14	0,11	0,09
Specificity	0,85	0,96	0,98	0,99	1,00	1,00	1,00	1,00	1,00	1,00	1,00	1,00	1,0
B													
Sensitivity	0,36	0,27	0,23	0,23	0,23	0,23	0,18	0,18	0,09	0,09	0,09	0,05	0
Specificity	0,79	0,85	0,89	0,90	0,90	0,90	0,91	0,91	0,92	0,94	0,96	0,99	0,99
C													
Sensitivity	0,44	0,25	0,25	0,19	0,19	0,19	0,19	0,19	0,19	0,19	0,13	0,13	0
Specificity	1	1	1	1	1	1	1	1	1	1	1	1	1

A: The results of Patient 14 are in concordance with the group average sensitivity and specificity values. B: The sensitivity and specificity of Patient 1. Please note that the specificity is high but the sensitivity is low even at 1% threshold level. This is because there is a smaller part of the recurrent tumor at the original site, which is covered by the TCs, therefore the ratio of the false positive results is low. The main part of the recurrence is far away from the original site, and this will result in a high false negative result. C: The results of Patient 20 are summarized in this table. The specificity is 100% at all threshold level while the sensitivity is very low even at 1%. This is due to the extensive local tumor recurrence which overlaps totally with all TCs. It also exceeds its borders and affects several other brain regions resulting in a high rate of false negative results.

TABLE 3 The group average sensitivity and specificity values (with standard error of the mean) are listed in this table at each threshold level.

	1%	5%	10%	15%	20%	25%	30%	40%	50%	60%	70%	80%	90%
Sensitivity (Avg ± SEM)	0,91 ± 0,03	0,81 ± 0,04	0,73 ± 0,04	0,67 ± 0,05	0,61 ± 0,05	0,60 ± 0,05	0,58 ± 0,06	0,50 ± 0,06	0,35 ± 0,05	0,31 ± 0,06	0,21 ± 0,06	0,14 ± 0,05	0,13 ± 0,06
Specificity (Avg ± SEM)	0,81 ± 0,03	0,9 ± 0,02	0,93 ± 0,02	0,95 ± 0,01	0,96 ± 0,01	0,96 ± 0,02	0,92 ± 0,05	0,93 ± 0,05	0,98 ± 0,01	0,94 ± 0,05	0,94 ± 0,05	0,94 ± 0,05	0,94 ± 0,05

As the threshold increases the sensitivity decreases and the specificity increases. The highest values can be seen at 1 and 5% threshold levels.

value (Garrett et al., 2017; Altieri et al., 2019). The extent of FLAIR signal hyperintensity prior to the initial surgery is not associated with survival. On the other hand, overall survival is significantly affected by the preoperative contrast enhancement volume (Altieri et al., 2019). In addition, FLAIR images can identify tumor progression earlier than contrast enhanced T1 on the follow-up MRI and associated with progression free and overall survival (Garrett et al., 2017). It is hard or even impossible to differentiate where microscopic tumor infiltration ends within the edema. Identifying the exact borders of the infiltrative part of the glioblastoma is challenging on FLAIR. Therefore the true extent of the tumor can be overestimated due to false positive hyperintense regions. Probabilistic tractography has the advantage that its result can be thresholded, and not like on FLAIR, the false positive results can be ruled out.

Magnetic resonance spectroscopy has promising results to predict the site of GBM recurrence. In one study LNR MRS has 88.8% sensitivity and 97.6% specificity to detect tumor vs. normal brain tissue and 71% true and 10% false positive ratio to predict the site of glioblastoma recurrence (Deviers et al., 2014). The spatial resolution of MRS was very low (6.25 mm × 6.25 mm × 25.0 mm = 976,5 mm^3) in this study (Ken et al., 2013). These factors make it challenging to use MRS results in routine patient care and image guided surgical and radiation therapy. Diffusion MRI based tractography on the other hand has much better resolution, which makes it a more feasible method.

^{11}C- Methionin-, ^{18}F-DOPA, and ^{18}F-FET-PET have been introduced for primary and secondary brain tumor detection. The increased uptake in brain tumors is based on the overexpression of the amino acid transporter in the tumor cells and in the tumor supplying vessels, which is independent from the blood-brain barrier (BBB). Therefore, these amino-acid based PET methods are appropriate for the following goals: to help differentiate necrosis and tumors, provide information on changed biochemical processes prior to the appearance of morphological changes, and to characterize the residual brain tumor volume for more accurate post-operative radiotherapy.

^{18}F-FET-PET has been used in some studies to determine the tumor and/or residual tumor volume for radiotherapy. In most cases, the target volume for irradiation determined this way was larger than the one determined with MRI alone (Munck Af Rosenschold et al., 2015). Post-operative ^{18}F-FET-PET scans had a higher sensitivity for detecting residual tumor than MRI (Buchmann et al., 2016). Nonetheless, ^{18}F-FET-PET had a sensitivity of 87% and a specificity of 68% for detecting glial tumors (Hutterer et al., 2013). These results make ^{18}F-FET-PET a potential diagnostic tool to identify the true extent of glioblastomas.

There are several disadvantages of ^{18}F-FET-PET that make its routine clinical use difficult. It is quite expensive, time-consuming (the total examination time can be several hours), and exposes the patient to radiation. Also, spatial resolution is limited to 5 mm. MRI, on the other hand, uses no radiation, has high spatial resolution (<1 mm), and takes about 15–20 min. It

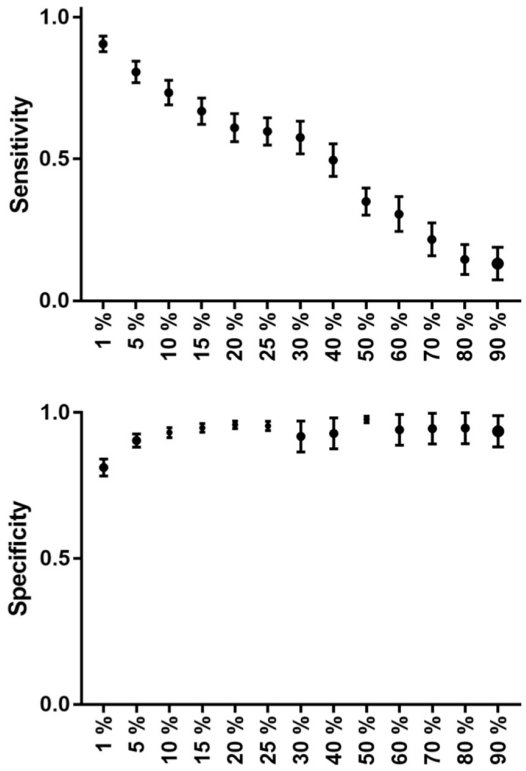

GRAPH 1
The group average sensitivity and specificity values (with standard error of mean) can be seen on this graph at each threshold level. Sensitivity decreases in a nearly linear fashion, while specificity has a nearly parabolic increase along the increasing threshold levels.

is also a part of the standard diagnostic protocol for glioblastoma and therefore does not require any extra procedures. If an MRI modality that is suitable for identifying the true extent of glioblastomas could be found, it would be a much more feasible examination to be used in clinical practice than ^{18}F-FET-PET (Muoio et al., 2018).

Tractography is an advanced MRI imaging modality. It is based on diffusion MRI images. The direction of the diffusion movement of water molecules in the brain can be reconstructed. In the white matter, this movement tends to be parallel to the fiber tract orientation. Using this information, white matter pathways can be reconstructed mathematically. The major drawback of tractography is that the diffusion direction can be uncertain in several important brain regions (e.g., white and gray matter border, gray matter, basal ganglia, crossing fiber tracts, tumor, peritumoral edema) and, therefore, the result is unreliable (Bammer, 2003; Wakana et al., 2004; Johansen-Berg and Behrens, 2006). Probabilistic tractography is one possible algorithm to overcome this limitation. It takes the uncertainty of water diffusion into account. The result of probabilistic tractography is a set of voxels. Each voxel has a value representing the probability that the given voxel belongs to the visualized white matter fiber tract. This basically means that all voxels can be identified, even the ones that have the lowest chance of being connected to the tract. It also means that there are a lot of false positive results. Therefore, an optimal threshold level must be defined to exclude the highest number of false positive and false negative voxels.

Glioblastoma originates from a core. As it progresses, a tumor mass and an infiltrative part of the tumor develop (Wick et al., 2018). Due to the fast-growing nature of the tumor, the center of the mass is often necrotized, and the edges consist of viable tumor (Young, 2007). The infiltrative part is a mixture of tumor cells and white matter fiber tracts. The two parts form a structural unit and can be considered an abnormal fiber tract that has several connections with the surrounding pathways (Osswald et al., 2015). This makes probabilistic tractography a potential tool to identify the connections between the tumor and its pathways, furthermore, the infiltrated brain regions and, more importantly, the true extent of the tumor could be pinpointed (Mukherjee et al., 2008).

The problem is that when probabilistic tractography is performed, the infiltrative tumor part is invisible on standard MRI images (Lasocki and Gaillard, 2019).

When the remaining tumor cells become resistant to the oncological treatment, they start to proliferate (Milano et al., 2010; Petrecca et al., 2013). The infiltrative part increases in volume and then becomes visible on conventional MRI images. Intuitively, the tumor becomes visible in the brain regions where it was invisible on the initial and previous follow-up images. The identified tumor recurrence then can be used for comparison with the TCs identified using probabilistic tractography.

We had to find a method that would allow us to reliably compare the TCs with the tumor recurrence mask. It would be a simple way to define the overlapping volume of the two and then, based on the ratio of the overlap, calculate sensitivity and specificity. Unfortunately, this method would not give us a reliable result because of the following two limiting factors. First, in most of the cases, the anatomy of the brain gradually changes during the time between the preoperative and the follow-up MRI scan. It is challenging, even with non-linear registration, to create perfect alignment between the preoperative and follow-up MRI images because of the mass effect of the tumor. Therefore, a direct comparison of the anatomical location of the TCs and the tumor recurrence mask is unreliable. The second limitation is due to the nature of tractography and the natural course of glioblastomas. TC volumes change by thresholding. The recurrence volume depends on when the follow-up MRI scan was performed. Contrast enhancement first appears along the fiber tracts, then the tumor gets thicker and soon exceeds the volume of the fiber tract. Accordingly, infiltrated fiber tracts may be visible on the tractography

images, but the volume may differ remarkably from the tumor recurrence mask.

Therefore, instead of using the volumes for comparison, we identified brain regions affected by both the tumor and the TCs. According to the JHU ICBM–DTI–81 white matter label and AAL3 standard atlases, the standard brain was divided into subcortical and cortical regions, and the number of affected regions was calculated.

At the group level, we found high sensitivity (81%) and specificity (90%) rates at the 5% threshold level. Our results suggest that the presented method is a reliable and clinically feasible way to predict the true extent of glioblastomas.

On the other hand, there are several limiting factors of this method that can affect the final result.

As it has been previously mentioned, the preoperative and follow-up MRI images do not align perfectly with the standard MRI images. This means that the TCs and the tumor recurrence mask are not completely in an anatomically identical location. This problem cannot be completely eliminated by neither of the widely available registration algorithms. The misalignment can only be minimized to have the least effect on the results (Kocher et al., 2021).

Sensitivity and specificity are directly determined by the volume and extension of the tumor recurrence mask, which depend on the time of the follow-up MRI scan. In case of a later MRI scan, the tumor volume can be significantly higher; consequently the calculated sensitivity and specificity can also be different.

To overcome these two limitations, we did not make a direct comparison between the volumes of the TCs and the tumor recurrence mask but counted the number of affected cortical and subcortical areas within the standard space. Registering the preoperative and follow-up MRI images to the standard space reduces the anatomical distortion between the two to the possible minimum. Even if the TCs and the tumor recurrence mask are in an anatomically identical location, the volume difference between the two can change the results. Therefore, we did not compare the volumes but the number of the affected brain areas instead. This way, if either the TC or the tumor recurrence mask reached one area, it was counted as positive. The difference in the volumes reaching the same location did not matter. Only the positive hit counts. Unfortunately, even this technique cannot perfectly rule out the above mentioned limitations. A good example for this is the case of Patient 20 (see below).

There is another limitation to the presented method, which is related to the nature of the tumor recurrence. The two outlier patients are perfect examples to that. The appearance of the recurrence on the follow-up MRI was not eligible to determine which part of the brain was infiltrated preoperatively. In their case, the presented method was unreliable to define the specificity and sensitivity. Their data were excluded from the group average to avoid false distortion of the results.

Patient 1 had a rare type of tumor progression. The recurrence appeared in a multifocal fashion, far away from the original site (**Figure 3**).

Patient 20 had a recurrence in the white matter around the resection cavity. The contrast enhancing part of the original tumor was very small (6.2 cm^3) if compared to the recurrence volume (54.9 cm^3). A huge area of the frontal lobe was included by the tumor recurrence mask but not by TCs (**Figure 4**), and there was a considerable difference in the number of affected brain regions.

In both cases, the special anatomical situations mentioned above resulted in a low level of overlap between the TCs and the tumor recurrence masks, therefore they decreased the sensitivities. In the case of Patient 1, the distant infiltrated areas could not be identified based on the tractography images, and the low sensitivity value was real. However, in the case of Patient 20, it was a partially false result. At the time of the follow-up MRI tumor progression was significant. The TCs overlapped with several brain regions where the recurrence appeared, and the direction of the recurrence was in concordance with the TCs. On the other hand, the tumor recurrence also contained many brain regions away from the original site. This resulted in a high number of false negative results and low sensitivity, even though tractography predicted the location of the recurrence well. The case of Patient 20 enlightens the importance of the timing of the follow-up MRI in our methodology. An earlier follow-up MRI with a less prominent tumor progression may have resulted in a better correlation with the TCs. In conclusion we believe that in the case of Patient 20, the TC with the 5% threshold level would give us reliable information regarding the true extent of the tumor, but because of the reason discussed above, the calculated sensitivity is low (**Table 2** and **Figure 4**).

On the other hand, the two outlier patients also highlight the limitation of the applicability of the presented method. It provides useful information in only those glioblastoma patients who have typical progression pattern and the recurrence appears within the close proximity of the resection cavity. According to the literature 90–95% of the patients belongs to that group (De Bonis et al., 2013). Our study group is in concordance with that, as 90% of the patients had the recurrence around the resection cavity.

In our study, we presented a probabilistic tractography-based method to identify the true extent of glioblastomas at the time of diagnosis. With the presented method, we were able to visualize the infiltrated brain areas on the preoperative MRI images in most patients with high sensitivity and specificity rates. It may help achieve more radical tumor resection and individually planned radiation therapy, which may lead to prolonged survival. As the presented work was a pilot study to validate the methods' reliability in terms of identification of the true extent of the glioblastoma, a prospective study is planned to investigate the potential positive effect of its application on the survival of glioblastoma patients.

Data availability statement

The original contributions presented in this study are included in the article/supplementary material, further inquiries can be directed to the corresponding author.

Ethics statement

The studies involving human participants were reviewed and approved by the Local Ethical Review Board of the University of Szeged, Szeged, Hungary. The patients/participants provided their written informed consent to participate in this study.

Author contributions

DK contributed to conception, design and study, data analyses, and wrote the first version of the manuscript. LS, BS, and MR organized the database. LS performed statistical analyses and created figures and tables. KH and AM collected patients' data and created tables. PB organized the study. All authors contributed to the article and approved the submitted version.

Conflict of interest

The authors declare that the research was conducted in the absence of any commercial or financial relationships that could be construed as a potential conflict of interest.

Publisher's note

All claims expressed in this article are solely those of the authors and do not necessarily represent those of their affiliated organizations, or those of the publisher, the editors and the reviewers. Any product that may be evaluated in this article, or claim that may be made by its manufacturer, is not guaranteed or endorsed by the publisher.

References

Ahmed, F. I., Abdullah, K. G., Durgin, J., Salinas, R. D., O'Rourke, D. M., and Brem, S. (2019). Evaluating the Association Between the Extent of Resection and Survival in Gliosarcoma. *Cureus* 11:e4374. doi: 10.7759/cureus.4374

Altieri, R., Melcarne, A., Soffietti, R., Rudá, R., Franchino, F., Pellerino, A., et al. (2019). Supratotal Resection of Glioblastoma: Is Less More? *Surg. Technol. Int.* 10, 432–440.

Andersson, J. L. R., and Sotiropoulos, S. N., (2016). An integrated approach to correction for off-resonance effects and subject movement in diffusion MR imaging. *NeuroImage* 125, 1063–1078. doi: 10.1016/j.neuroimage.2015.10.019

Bammer, R. (2003). Basic principles of diffusion-weighted imaging. *Eur. J. Radiol.* 45, 169–184. doi: 10.1016/s0720-048x(02)00303-0

Barani, I. J., and Larson, D. A. (2015). Radiation therapy of glioblastoma. *Cancer Treat. Res.* 163, 49–73. doi: 10.1007/978-3-319-12048-5_4

Bauchet, L., Mathieu-Daudé, H., Fabbro-Peray, P., Rigau, V., Fabbro, M., Chinot, O., et al. (2010). Oncological patterns of care and outcome for 952 patients with newly diagnosed glioblastoma in 2004. *Neuro Oncol.* 12, 725–735. doi: 10.1093/neuonc/noq030

Behrens, T. E. J., Berg, H. J., Jbabdi, S., Rushworth, M. F. S., and Woolrich, M. W. (2007). Probabilistic diffusion tractography with multiple fibre orientations: What can we gain? *Neuroimage* 34, 144–155. doi: 10.1016/j.neuroimage.2006.09.018

Behrens, T. E. J., Johansen-Berg, H., Woolrich, M. W., Smith, S. M., Wheeler-Kingshott, C. A. M., Boulby, P. A., et al. (2003a). Non-invasive mapping of connections between human thalamus and cortex using diffusion imaging. *Nat. Neurosci.* 6, 750–757. doi: 10.1038/nn1075

Behrens, T. E. J., Woolrich, M. W., Jenkinson, M., Johansen-Berg, H., Nunes, R. G., Clare, S., et al. (2003b). Characterization and propagation of uncertainty in diffusion-weighted MR imaging. *Magn. Reson. Med.* 50, 1077–1088. doi: 10.1002/mrm.10609

Bennett, I. J., Madden, D. J., Vaidya, C. J., Howard, J. H. J., and Howard, D. V. (2011). White matter integrity correlates of implicit sequence learning in healthy aging. *Neurobiol. Aging* 32, 2317.e1–12. doi: 10.1016/j.neurobiolaging.2010.03.017

Buchmann, N., Kläsner, B., Gempt, J., Bauer, J. S., Pyka, T., Delbridge, C., et al. (2016). (18)F- fluoroethyl-l-thyrosine positron emission tomography to delineate tumor residuals after glioblastoma resection: A comparison with standard postoperative magnetic resonance imaging. *World Neurosurg.* 89, 420–426. doi: 10.1016/j.wneu.2016.02.032

Costabile, J. D., Alaswad, E., D'Souza, S., Thompson, J. A., and Ormond, D. R. (2019). Current Applications of Diffusion Tensor Imaging and Tractography in Intracranial Tumor Resection. *Front. Oncol.* 9:426. doi: 10.3389/fonc.2019.00426

De Bonis, P., Anile, C., Pompucci, A., Fiorentino, A., Balducci, M., Chiesa, S., et al. (2013). The influence of surgery on recurrence pattern of glioblastoma. *Clin. Neurol. Neurosurg.* 115, 37–43. doi: 10.1016/j.clineuro.2012.04.005

de Leeuw, C. N., and Vogelbaum, M. A. (2019). Supratotal resection in glioma: A systematic review. *Neuro Oncol.* 21, 179–188. doi: 10.1093/neuonc/noy166

Demuth, T., and Berens, M. E. (2004). Molecular mechanisms of glioma cell migration and invasion. *J. Neurooncol.* 70, 217–228. doi: 10.1007/s11060-004-2751-6

Deviers, A., Ken, S., Filleron, T., Rowland, B., Laruelo, A., Catalaa, I., et al. (2014). Evaluation of the lactate-to-N-acetyl-aspartate ratio defined with magnetic resonance spectroscopic imaging before radiation therapy as a new predictive marker of the site of relapse in patients with glioblastoma multiforme. *Int. J. Radiat. Oncol. Biol. Phys.* 90, 385–393. doi: 10.1016/j.ijrobp.2014.06.009

Garrett, M. D., Yanagihara, T. K., Yeh, R., McKhann, G. M., Sisti, M. B., Bruce, J. N., et al. (2017). Monitoring Radiation Treatment Effects in Glioblastoma: FLAIR Volume as Significant Predictor of Survival. *Tomography* 3, 131–137. doi: 10.18383/j.tom.2017.00009

Hua, K., Zhang, J., Wakana, S., Jiang, H., Li, X., Reich, D. S., et al. (2008). Tract probability maps in stereotaxic spaces: Analyses of white matter anatomy and tract-specific quantification. *Neuroimage* 39, 336–347. doi: 10.1016/j.neuroimage.2007.07.053

Hutterer, M., Nowosielski, M., Putzer, D., Jansen, N. L., Seiz, M., Schocke, M., et al. (2013). [18F]-fluoro-ethyl-L-tyrosine PET: A valuable diagnostic tool in neuro-oncology, but not all that glitters is glioma. *Neurooncology* 15, 341–351. doi: 10.1093/neuonc/nos300

Jenkinson, M., and Smith, S. (2001). A global optimisation method for robust affine registration of brain images. *Med. Image Anal.* 5, 143–156. doi: 10.1016/s1361-8415(01)00036-6

Jenkinson, M., Bannister, P., Brady, M., and Smith, S. (2002). Improved optimization for the robust and accurate linear registration and motion correction of brain images. *Neuroimage* 17, 825–841. doi: 10.1016/s1053-8119(02)91132-8

Johansen-Berg, H., and Behrens, T. E. J. (2006). Just pretty pictures? What diffusion tractography can add in clinical neuroscience. *Curr. Opin. Neurol.* 19, 379–385. doi: 10.1097/01.wco.0000236618.82086.01

Ken, S., Vieillevigne, L., Franceries, X., Simon, L., Supper, C., Lotterie, J. A., et al. (2013). Integration method of 3D MR spectroscopy into treatment planning system for glioblastoma IMRT dose painting with integrated simultaneous boost. *Radiat. Oncol.* 8:1. doi: 10.1186/1748-717X-8-1

Khalsa, S., Mayhew, S. D., Chechlacz, M., Bagary, M., and Bagshaw, A. P. (2014). The structural and functional connectivity of the posterior cingulate cortex: Comparison between deterministic and probabilistic tractography for the investigation of structure-function relationships. *Neuroimage* 102, 118–127. doi: 10.1016/j.neuroimage.2013.12.022

Kis, D., Máté, A., Kincses, Z. T., Vörös, E., and Barzó, P. (2014). The role of probabilistic tractography in the surgical treatment of thalamic gliomas. *Neurosurgery* 10, 262–272. doi: 10.1227/NEU.0000000000000333

Kocher, M., Jockwitz, C., Lohmann, P., Stoffels, G., Filss, C., Mottaghy, F. M., et al. (2021). Lesion-Function Analysis from Multimodal Imaging and Normative Brain Atlases for Prediction of Cognitive Deficits in Glioma Patients. *Cancers* 13:2373. doi: 10.3390/cancers13102373

Lacroix, M., Abi-Said, D., Fourney, D. R., Gokaslan, Z. L., Shi, W., DeMonte, F., et al. (2001). A multivariate analysis of 416 patients with glioblastoma multiforme: Prognosis, extent of resection, and survival. *J. Neurosurg.* 95, 190–198. doi: 10.3171/jns.2001.95.2.0190

Lasocki, A., and Gaillard, F. (2019). Non-Contrast-Enhancing Tumor: A New Frontier in Glioblastoma Research. *AJNR. Am. J. Neuroradiol.* 40, 758–765. doi: 10.3174/ajnr.A6025

Le Bihan, D., Turner, R., Douek, P., and Patronas, N. (1992). Diffusion MR imaging: Clinical applications. *AJR* 159, 591–599. doi: 10.2214/ajr.159.3.1503032

Leemans, A., and Jones, D. K. (2009). The B-matrix must be rotated when correcting for subject motion in DTI data. *Magn. Reson. Med.* 61, 1336–1349. doi: 10.1002/mrm.21890

Lemee, J. M., Clavreul, A., and Menei, P. (2015). Intratumoral heterogeneity in glioblastoma: Don't forget the peritumoral brain zone. *Neuro Oncol.* 17, 1322–1332. doi: 10.1093/neuonc/nov119

Louis, D. N., Perry, A., Wesseling, P., Brat, D. J., Cree, I. A., Figarella-Branger, D., et al. (2021). The 2021 WHO Classification of Tumors of the Central Nervous System: A summary. *Neuro Oncol.* 23, 1231–1251. doi: 10.1093/neuonc/noab106

Mascalchi, M., Filippi, M., Floris, R., Fonda, C., Gasparotti, R., and Villari, N. (2005). Diffusion-weighted MR of the brain: Methodology and clinical application. *Radiol. Med.* 109, 155–197.

Michaelsen, S. R., Urup, T., Olsen, L. R., Broholm, H., Lassen, U., and Poulsen, H. S. (2018). Molecular profiling of short-term and long-term surviving patients identifies CD34 mRNA level as prognostic for glioblastoma survival. *J. Neurooncol.* 137, 533-542. doi: 10.1007/s11060-017-2739-7

Milano, M. T., Okunieff, P., Donatello, R. S., Mohile, N. A., Sul, J., Walter, K. A., et al. (2010). Patterns and timing of recurrence after temozolomide-based chemoradiation for glioblastoma. *Int. J. Radiat. Oncol. Biol. Phys.* 78, 1147–1155. doi: 10.1016/j.ijrobp.2009.09.018

Mori, S., and van Zijl, P. C. M. (2002). Fiber tracking: Principles and strategies - a technical review. *NMR Biomed.* 15, 468–480. doi: 10.1002/nbm.781

Mori, S., Oishi, K., Jiang, H., Jiang, L., Li, X., Akhter, K., et al. (2008). Stereotaxic white matter atlas based on diffusion tensor imaging in an ICBM template. *Neuroimage* 40, 570–582. doi: 10.1016/j.neuroimage.2007.12.035

Mukherjee, P., Berman, J. I., Chung, S. W., Hess, C. P., and Henry, R. G. (2008). Diffusion tensor MR imaging and fiber tractography: Theoretic underpinnings. *AJNR. Am. J. Neuroradiol.* 29, 632–641. doi: 10.3174/ajnr.A1051

Munck Af Rosenschold, P., Costa, J., Engelholm, S. A., Lundemann, M. J., Law, I., Ohlhues, L., et al. (2015). Impact of [18F]-fluoro-ethyl-tyrosine PET imaging on target definition for radiation therapy of high-grade glioma. *Neurooncology* 17, 757–763. doi: 10.1093/neuonc/nou316

Muoio, B., Giovanella, L., and Treglia, G. (2018). Recent Developments of 18F-FET PET in Neuro-oncology. *Curr. Med. Chem.* 25, 3061–3073. doi: 10.2174/0929867325666171123202644

Osswald, M., Jung, E., Sahm, F., Solecki, G., Venkataramani, V., Blaes, J., et al. (2015). Brain tumour cells interconnect to a functional and resistant network. *Nature* 528, 93–98. doi: 10.1038/nature16071

Ostrom, Q. T., and Barnholtz-Sloan, J. S. (2011). Current state of our knowledge on brain tumor epidemiology. *Curr. Neurol. Neurosci. Rep.* 11, 329–335. doi: 10.1007/s11910-011-0189-8

Ostrom, Q. T., Cioffi, G., Waite, K., Kruchko, C., and Barnholtz-Sloan, J. S. (2021). CBTRUS Statistical Report: Primary Brain and Other Central Nervous System Tumors Diagnosed in the United States in 2014-2018. *Neuro Oncol.* 23:iii1–iii105. doi: 10.1093/neuonc/noab200

Petrecca, K., Guiot, M. C., Panet-Raymond, V., and Souhami, L. (2013). Failure pattern following complete resection plus radiotherapy and temozolomide is at the resection margin in patients with glioblastoma. *J. Neurooncol.* 111, 19–23. doi: 10.1007/s11060-012-0983-4

Roelz, R., Strohmaier, D., Jabbarli, R., Kraeutle, R., Egger, K., Coenen, V. A., et al. (2016). Residual Tumor Volume as Best Outcome Predictor in Low Grade Glioma-A Nine-Years Near-Randomized Survey of Surgery vs. Biopsy. *Sci. Rep.* 6:32286. doi: 10.1038/srep32286

Rolls, E. T., Huang, C. C., Lin, C. P., Feng, J., and Joliot, M. (2020). Automated anatomical labelling atlas 3. *Neuroimage* 206:116189. doi: 10.1016/j.neuroimage.2019.116189

Rorden, C., Karnath, H.-O., and Bonilha, L. (2007). Improving lesion-symptom mapping. *J. Cogn. Neurosci.* 19, 1081–1088. doi: 10.1162/jocn.2007.19.7.1081

Shukla, G., Alexander, G. S., Bakas, S., Nikam, R., Talekar, K., and Palmer, J. D. (2017). Advanced magnetic resonance imaging in glioblastoma: A review. *Chin. Clin. Oncol.* 6:40. doi: 10.21037/cco.2017.06.28

Smith, S. M. (2002). Fast robust automated brain extraction. *Hum. Brain Mapp.* 17, 143–155. doi: 10.1002/hbm.10062

Stupp, R., Mason, W. P., van den Bent, M. J., Weller, M., Fisher, B., Taphoorn, M. J., et al. (2005). Radiotherapy plus concomitant and adjuvant temozolomide for glioblastoma. *N. Engl. J. Med.* 352, 987–996. doi: 10.1056/NEJMoa043330

Tonn, J. C., and Goldbrunner, R. (2003). Mechanisms of glioma cell invasion. *Acta Neurochir. Suppl.* 88, 163–167.

Virga, J., Szivos, L., Hortobágyi, T., Chalsaraei, M. K., Zahuczky, G., Steiner, L., et al. (2019). Extracellular matrix differences in glioblastoma patients with different prognoses. *Oncol. Lett.* 17, 797–806. doi: 10.3892/ol.2018.9649

Wakana, S., Jiang, H., Nagae-Poetscher, L. M., van Zijl, P. C. M., and Mori, S. (2004). Fiber tract-based atlas of human white matter anatomy. *Radiology* 230, 77–87. doi: 10.1148/radiol.2301021640

Watanabe, M., Tanaka, R., and Takeda, N. (1992). Magnetic resonance imaging and histopathology of cerebral gliomas. *Neuroradiology* 34, 463–469. doi: 10.1007/BF00598951

Wick, W., Osswald, M., Wick, A., and Winkler, F. (2018). Treatment of glioblastoma in adults. *Ther. Adv. Neurol. Disord.* 11:1756286418790452. doi: 10.1177/1756286418790452

Wirsching, H. G., Galanis, E., and Weller, M. (2016). Glioblastoma. *Handb. Clin. Neurol.* 134, 381–397. doi: 10.1016/B978-0-12-802997-8.00023-2

Wykes, V., Zisakis, A., Irimia, M., Ughratdar, I., Sawlani, V., and Watts, C. (2021). Importance and Evidence of Extent of Resection in Glioblastoma. *J. Neurol. Surg.* 82, 75–86. doi: 10.1055/s-0040-1701635

Yamada, K., Sakai, K., Akazawa, K., Yuen, S., and Nishimura, T. (2009). MR tractography: A review of its clinical applications. *Magn. Reson. Med. Sci.* 8, 165–174. doi: 10.2463/mrms.8.165

Yan, H., Parsons, D. W., Jin, G., McLendon, R., Rasheed, B. A., Yuan, W., et al. (2009). IDH1 and IDH2 mutations in gliomas. *N. Engl. J. Med.* 360, 765–773. doi: 10.1056/NEJMoa0808710

Yasargil, M. G. (1994). "Neuropathology," in *Microneurosurgery Vol. 3B*, (New York, NY: Georg Thieme Verlag), 115–192.

Young, G. S. (2007). Advanced MRI of adult brain tumors. *Neurol. Clin.* 25, 947–973. doi: 10.1016/j.ncl.2007.07.010

frontiers | Frontiers in Neuroscience

TYPE Original Research
PUBLISHED 13 October 2022
DOI 10.3389/fnins.2022.860208

Check for updates

OPEN ACCESS

EDITED BY
Sandro M. Krieg,
Technische Universität München,
Germany

REVIEWED BY
Hamza Farooq,
University of Minnesota Twin Cities,
United States
Spyridon Bakas,
University of Pennsylvania,
United States

*CORRESPONDENCE
Mariam Aboian
Mariam.aboian@yale.edu
Khaled Bousabarah
KBousabarah@visageimaging.com

SPECIALTY SECTION
This article was submitted to
Brain Imaging Methods,
a section of the journal
Frontiers in Neuroscience

RECEIVED 22 January 2022
ACCEPTED 13 July 2022
PUBLISHED 13 October 2022

CITATION
Aboian M, Bousabarah K, Kazarian E, Zeevi T, Holler W, Merkaj S, Cassinelli Petersen G, Bahar R, Subramanian H, Sunku P, Schrickel E, Bhawnani J, Zawalich M, Mahajan A, Malhotra A, Payabvash S, Tocino I, Lin M and Westerhoff M (2022) Clinical implementation of artificial intelligence in neuroradiology with development of a novel workflow-efficient picture archiving and communication system-based automated brain tumor segmentation and radiomic feature extraction.
Front. Neurosci. 16:860208.
doi: 10.3389/fnins.2022.860208

COPYRIGHT
© 2022 Aboian, Bousabarah, Kazarian, Zeevi, Holler, Merkaj, Cassinelli Petersen, Bahar, Subramanian, Sunku, Schrickel, Bhawnani, Zawalich, Mahajan, Malhotra, Payabvash, Tocino, Lin and Westerhoff. This is an open-access article distributed under the terms of the Creative Commons Attribution License (CC BY). The use, distribution or reproduction in other forums is permitted, provided the original author(s) and the copyright owner(s) are credited and that the original publication in this journal is cited, in accordance with accepted academic practice. No use, distribution or reproduction is permitted which does not comply with these terms.

Clinical implementation of artificial intelligence in neuroradiology with development of a novel workflow-efficient picture archiving and communication system-based automated brain tumor segmentation and radiomic feature extraction

Mariam Aboian[1]*, Khaled Bousabarah[2]*, Eve Kazarian[1], Tal Zeevi[3], Wolfgang Holler[2], Sara Merkaj[1], Gabriel Cassinelli Petersen[1], Ryan Bahar[1], Harry Subramanian[1], Pranay Sunku[1], Elizabeth Schrickel[1], Jitendra Bhawnani[3], Mathew Zawalich[3], Amit Mahajan[3], Ajay Malhotra[3], Sam Payabvash[3], Irena Tocino[3], MingDe Lin[4] and Malte Westerhoff[2]

[1]Department of Radiology and Biomedical Imaging, Brain Tumor Research Group, Yale School of Medicine, Yale University, New Haven, CT, United States, [2]Visage Imaging, GmbH, Berlin, Germany, [3]Department of Radiology and Biomedical Imaging, Yale School of Medicine, Yale University, New Haven, CT, United States, [4]Department of Radiology, Yale University and Visage Imaging, New Haven, CT, United States

Purpose: Personalized interpretation of medical images is critical for optimum patient care, but current tools available to physicians to perform quantitative analysis of patient's medical images in real time are significantly limited. In this work, we describe a novel platform within PACS for volumetric analysis of images and thus development of large expert annotated datasets in parallel with radiologist performing the reading that are critically needed for development of clinically meaningful AI algorithms. Specifically, we implemented a deep learning-based algorithm for automated brain tumor segmentation and radiomics extraction, and embedded it into PACS to accelerate a supervised, end-to- end workflow for image annotation and radiomic feature extraction.

Materials and methods: An algorithm was trained to segment whole primary brain tumors on FLAIR images from multi-institutional glioma BraTS 2021 dataset. Algorithm was validated using internal dataset from Yale New

Haven Health (YHHH) and compared (by Dice similarity coefficient [DSC]) to radiologist manual segmentation. A UNETR deep-learning was embedded into Visage 7 (Visage Imaging, Inc., San Diego, CA, United States) diagnostic workstation. The automatically segmented brain tumor was pliable for manual modification. PyRadiomics (Harvard Medical School, Boston, MA) was natively embedded into Visage 7 for feature extraction from the brain tumor segmentations.

Results: UNETR brain tumor segmentation took on average 4 s and the median DSC was 86%, which is similar to published literature but lower than the RSNA ASNR MICCAI BRATS challenge 2021. Finally, extraction of 106 radiomic features within PACS took on average 5.8 ± 0.01 s. The extracted radiomic features did not vary over time of extraction or whether they were extracted within PACS or outside of PACS. The ability to perform segmentation and feature extraction before radiologist opens the study was made available in the workflow. Opening the study in PACS, allows the radiologists to verify the segmentation and thus annotate the study.

Conclusion: Integration of image processing algorithms for tumor auto-segmentation and feature extraction into PACS allows curation of large datasets of annotated medical images and can accelerate translation of research into development of personalized medicine applications in the clinic. The ability to use familiar clinical tools to revise the AI segmentations and natively embedding the segmentation and radiomic feature extraction tools on the diagnostic workstation accelerates the process to generate ground-truth data.

KEYWORDS

artificial intelligence (AL), machine learning (ML), PACS (picture archiving and communication system), brain tumor, segmentation, feature extraction, glioma, BraTS

Introduction

Artificial intelligence (AI) is a powerful technology that has significant potential impact in the development of personalized medicine solutions in medical imaging, but only a few of these algorithms are readily available in standard clinical practice, regardless of whether they are FDA approved (ACR Data Science Institute, n.d.; Benjamens et al., 2020; Garderen et al., 2021). One of the major limitations in successful translation of AI algorithms into clinical practice is the lack of multicenter annotated datasets that allow sufficient training of the algorithm to be for clinical translation. Solutions to this problem include data sharing agreements, development of image databank consortiums (MIDRC, TCIA, BraTS), and federated learning (MIDRC, n.d.; Clark et al., 2013; Menze et al., 2015; Bakas et al., 2017a,b, 2018; Sheller et al., 2020). While these methods provide important advances for algorithm development, the need for building large databases of individual hospital data for algorithm translation to specific patient population that the hospital serves still remains.

While one can retrospectively curate these databases, a more workflow efficient method is to develop these databases in real time. That is, to have a platform for clinically incorporated tools that allow building of large radiologist annotated clinical datasets. Several studies evaluated methods outside of clinical PACS that provide potential solutions for incorporation of ML into clinical practice, with some of the studies demonstrating role of ML in changing clinical decisions such as administration of contrast (Combès et al., 2021; Garderen et al., 2021; Thakur et al., 2022). These approaches are early adapters of ML in clinical practice and are demonstrating potential for future approaches.

Deep learning algorithms have proven themselves to be effective in various aspects of glioma imaging, including tumor segmentation and classifying tumor grade and genetic subtypes in gliomas. Central nervous system (CNS) malignancy

is expected to be diagnosed in 24,530 patients this year, with 18,600 patients dying from this disease (Siegel et al., 2020, 2021). The most common CNS malignancy is glioma, which are clinicopathologically graded as glioblastoma (IDH wildtype, Grade 4), astrocytoma (IDH-mutant grade 4, 3, 2) according to the World Health Organization 2021 (WHO) grading scale (Louis et al., 2021). The glioma grade represents the overall malignant potential of the tumor and can be determined based on pathologic evaluation and molecular analysis, with most recent classification describing significant changes in 2021 (Gonzalez Castro and Wesseling, 2020; Louis et al., 2021; Rushing, 2021). While glioblastomas are the most aggressive tumor type with a median survival of 14.6 months after treatment, grade 1-3 gliomas and IDH-mutant grade 4 astrocytomas have better outcomes with mean survival times ranging 2–8 years (Claus et al., 2015; Liang et al., 2020; Poon et al., 2020). Molecular subtypes play an important role in response to treatment and overall survival. For instance, MGMT mutation in GBM can improve treatment response to alkylating agents (Hegi et al., 2005). In addition, IDH mutation is an important prognostic factor for patients with improved survival rates compared to IDH wildtype glioblastomas (Xia et al., 2015; Chen et al., 2016).

Brain segmentation and radiomic feature extraction tools have shown promising results for incorporation in clinical practice in the field of neuro-oncology, but clinical translation has been significantly hampered due to limited available annotated datasets and decreased performance of algorithms on geographically distinct validation datasets (Subramanian et al., 2021; Cassinelli Petersen et al., 2022; Jekel et al., 2022).

Systematic reviews on application of Machine Learning in Gliomas identified 695 studies on this area, however, none of them described routine clinical implementation of these tools (Subramanian et al., 2021; Cassinelli Petersen et al., 2022; Jekel et al., 2022). While these tools have shown promising results in tumor segmentation and generation of high throughput quantitative data, several challenges are preventing their integration into clinical practice (Rudie et al., 2019). These challenges include incorporation of these tools into clinical workflow, making them user-friendly to radiologists, making the algorithm assessment of tumors time efficient, and coordinating the software output with radiology report software. To incorporate glioma segmentation tools into existing clinical workflows, we developed automated and efficient tumor segmentation and feature extraction tools and integrated them into PACS that is used at our hospital system, thus connecting an inference system which handles calls from the PACS, and presents the segmentation results to the attending radiologists in an easily accessible manner within a suitable hanging protocol. This method has potential to accelerate clinical implementation of ML by incorporating the ML algorithm into the software that is used by radiologists. This approach also has potential for development of large annotated datasets during real-time clinical practice.

Materials and methods

After IRB approval, pre-operative images were obtained from the Yale New Haven Hospital database in adult patients with pathologically proven gliomas grade 3 and 4. The MR imaging was performed before surgical diagnosis of these patients. The images were reviewed retrospectively and the patients were grouped into high and low grade glioma. The DICOM data was transferred, and automatically anonymized, from our clinical PACS to our research PACS (Visage AI Accelerator, Visage Imaging, Inc., San Diego, CA, United States) (Lin, 2020). On the research PACS, 3D segmentation of the whole tumor with surrounding edema was performed manually by a board certified neuroradiologist (MSA) who was blinded to the glioma grading and outcome (**Supplementary Figure 1**). This manual segmentation served as the reference standard to which the AI based automatic segmentation tool was tested. Specifically, an algorithm was trained to delineate the whole glioma portion on MRI FLAIR images. The AI network was trained using the BraTS 2021 dataset, which contains multi-institutional and multi-sequence MRI scans of gliomas (Menze et al., 2015; Bakas et al., 2017a,b). The algorithm was subsequently trained on an internal dataset from Yale New Haven Health. For a deep-learning network architecture we chose UNET Transformer (UNETR), which uses a transformer in the encoder instead of a classical convolutional layer because this has improved performance compared to other architectures for this task (Hatamizadeh et al., 2022). The algorithm was trained using volumetric patches of size 128 × 128 × 64 with a spacing of 1.5 cm^3 × 1.5 cm^3 × 2 cm^3 using trilinear interpolation with sampling of the patches (Benjamens et al., 2020; ACR Data Science Institute, n.d.). All preprocessing was performed once per volume and this intermediary data was cached to use for training.

The UNETR has a larger VRAM consumption than the NNUNET. The NNUNET samples a patch with size 128 × 128 × 128 from the 1 mm^3 × 1 mm^3 × 1 mm^3 image resulting in an effective size of cropped volume of 128 mm^3, which would not fit into the available VRAM (24GB, NVIDIA TITAN RTX). To achieve a similar volume, we resampled in the z-direction from 1 to 2, which allowed us to reduce the patch size to 128 × 128 × 64. The automatically segmented brain tumor was pliable for manual modification using the existing segmentation tools available in Visage 7.

The trained AI network was natively embedded using Docker and the NVIDIA Triton inference platform. The Docker container has access to the current protocol content and processes the data retrieved from the PACS. To ensure that the developed algorithm is deployed in a safe manner which is

crucial in a clinical environment we adhered to the standards described by the Open Web Application Security Project (OWASP) (GitHub, Inc., n.d.). Their checklist includes good practices to secure Docker containers such as frequent updates, not exposing the docker daemon, limit user permissions and resources usage etc. (OWASP Cheat Sheet Series, n.d.). For preprocessing, brain extraction was performed (Isensee et al., 2019), the cropped data was reoriented, resampled using trilinear interpolation and the voxel intensities normalized using z-score normalization. The preprocessed image data was then passed to the inference platform through an HTTP request. The platform utilized mixed precision and TensorRT to boost inference speed. Inference was performed using a sliding window and test-time-augmentation in the form of flipping along each axis. The result was then passed back to the Docker container which converted the results to an overlay visible in Visage 7 (**Figure 1**). To reduce the burden on the radiologist in these tasks, several improvements were implemented into the Visage PACS client (Visage 7-1-18). These included a Quad multi-planar reformat comparison layout with 3D registration (automatic viewer registration tool) to facilitate viewing and segmentation. Given that certain aspects of the tumor are best segmented in specific MR sequences, it was critical to develop the function to copy/paste segmentation masks across MR sequences and ensure that the exact segmentation is transposed.

The resulting segmentation can be saved in PACS as a DICOM presentation state.

In a second step, we natively embedded PyRadiomics (Harvard Medical School, Boston, MA, United States) for feature extraction from those segmentations (Griethuysen et al., 2017). The algorithm utilizes both automatically and manually delineated structures present in the viewer content and calculates their radiomic features. Upon completion, the results are available to the researcher in JSON format, which can be stored locally. To validate our implementation, we compared the extracted values to a reference implementation which used locally stored data. The overall workflow is depicted in **Figure 1**.

The accuracy of the AI algorithm was measured based on DSC (between a board certified neuroradiologist's manual segmentations and the AI algorithm's result) and the correctness of the feature extraction was measured by calculating relative difference compared to a reference implementation.

Results

The UNETR autosegmentation algorithm was trained on FLAIR images from the BraTS 2021 dataset, all 1251 FLAIR series with whole tumor segmentations were used. The training data was split into 1,151 samples for training and 100 for validation. The test set only contained data from YNNH, which was 73 pathologically proven high grade gliomas. Training was stopped after 250 epochs and the model with the best mean DSC (0.90) on the validation dataset was chosen. The model stopped improving after the 170 epoch. On the test dataset, the DSC was lower, but the algorithm still provided a solid baseline segmentation with median DSC of 0.86 and a mean of 0.81. A sample segmentation is depicted in **Figure 2**.

The developed model was deployed using the NVIDIA Triton inference platform and integrated into the Visage AI Accelerator. The average overall processing time after activating the segmentation algorithm was 2.33 s on our system (NVIDIA TITAN RTX, Intel(R) Core(TM) i7-6900K CPU @ 3.20GHz, 64 GB RAM).

Interaction between the PACS and the algorithm, including image retrieval and storing the resulting segmentation took 0.33 seconds, preprocessing and postprocessing (including brain extraction, image reorientation and resampling) took 1.48 s and the actual inference of the AI model took 0.52 s. Afterward, the segmentation is displayed and modifiable within the client workstation using the same, familiar tools available on the diagnostic workstation.

The extraction of radiomic features is then started from the same interface using the embedded PyRadiomics module, with an average computation time of 4 s. The extracted radiomic features can then be exported as JSON files. To confirm the stability of the embedded feature extraction algorithm, it was compared to a reference implementation (EK, TZ). Initially, the features that were extracted from the demonstrated up to 1.4% difference in absolute values with 17 features being different among 106 features total. After inspecting each implementation, a minor version difference was identified. Using the same version (3.0) of the PyRadiomics module resulted in complete agreement, bringing the absolute error to zero (**Figure 3**). After confirming the correct implementation of PACS based feature extraction, we also performed separate feature extraction on three different time points and found zero error among those separate extraction steps.

Overall, the integration of the glioma segmentation algorithm and feature extraction algorithm into the standard PACS viewer resulted in a workflow efficient and interactive way for users to generate datasets of annotated medical images and corresponding radiomic data. The combination of the image viewer's standard tools and the availability of algorithms in the form of a button makes advanced quantitative image volume analysis much more accessible in clinical practice.

Discussion

In this work, we demonstrate that implementation of AI tools into PACS is feasible and provides tools for annotation of medical images and extraction of quantitative imaging features to radiologists in a format that is the same as the clinical workflow. An AI-based workflow including auto-segmentation and radiomic feature-extraction was integrated into a PACS

platform and made available to clinicians. The radiologists can use the same PACS interface that they use in clinical practice, thus not requiring additional training or data export for image analysis with ML algorithms. The set of tools interacts with the content visible in the clinical viewer and produces annotations which can be modified using existing tools. The workflow is fast with a total computation time of below five seconds for running both the automatic AI glioma 3D segmentation and radiomic feature extraction tools and easily accessible through buttons integrated into the workstation's interface.

The quality of the automatically generated whole tumor segmentations from the FLAIR sequence is good with a median DSC 0.86 measured using gold standard segmentations performed by a board certified neuroradiologist. The tool produced quick baseline segmentations which can be approved or modified by the clinician and subsequently is stored in the PACS. The overall result is a fast and interactive pipeline of PACS-integrated tumor segmentation and feature extraction, which is available to the clinician immediately after opening a study. The workflow uses familiar tools and does not require

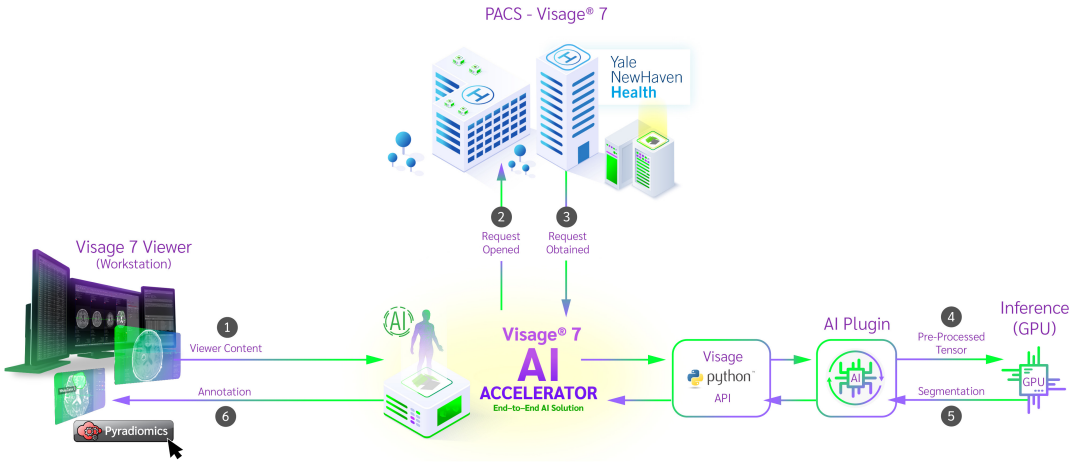

FIGURE 1
Schematic diagram of auto-segmentation and feature extraction tools incorporated into clinical PACS on Visage Imaging platform. From the workstation, the viewer content is passed to the Python API and the corresponding image data is retrieved from the PACS system. After preprocessing, a request is sent to the inference platform and a segmentation is returned. The segmentation is added to the study by the Python API and the result is displayed in the workstation. After reviewing the segmentation, the physician now has the ability to run radiomic feature extraction on the curated dataset.

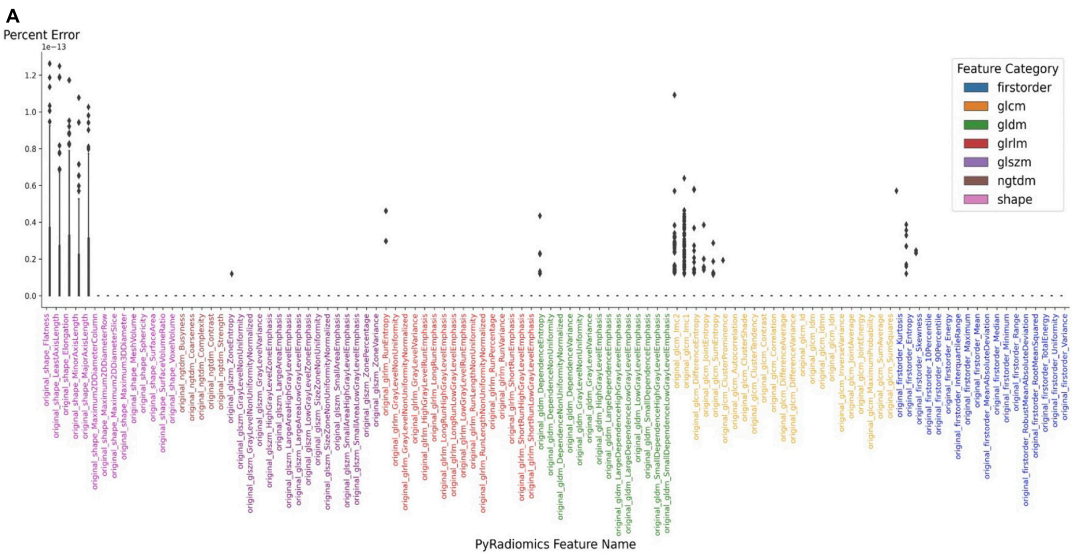

FIGURE 2
(Continued)

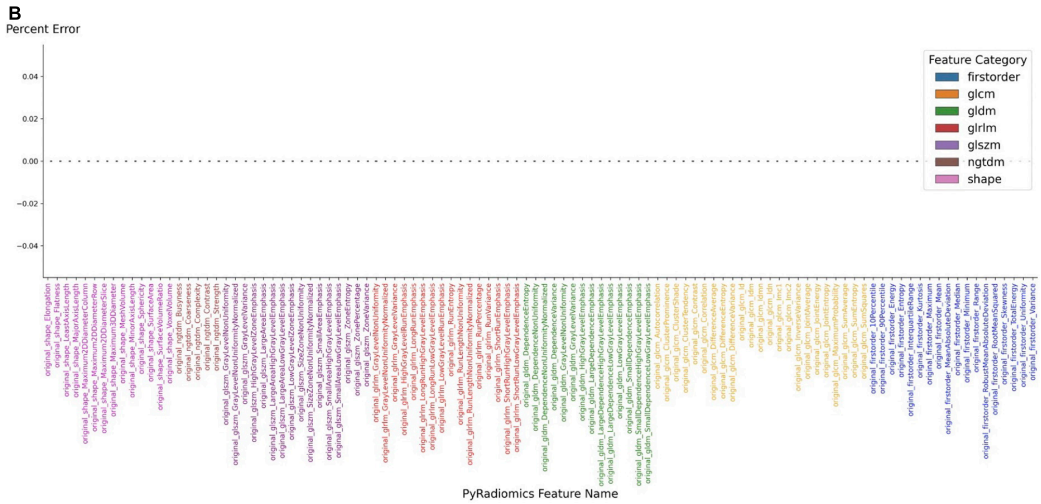

FIGURE 2
Auto-segmentation tool delineates the borders of tumor and surrounding edema and is similar to manual segmentation of the tumor by neuroradiologist **(A)**. **(B)** Accuracy of segmentation measured using DICE coefficient, Jaccard index, Positive Predictive Value (PPV), True Positive Rate (TPR), and True Negative Rate (TNR).

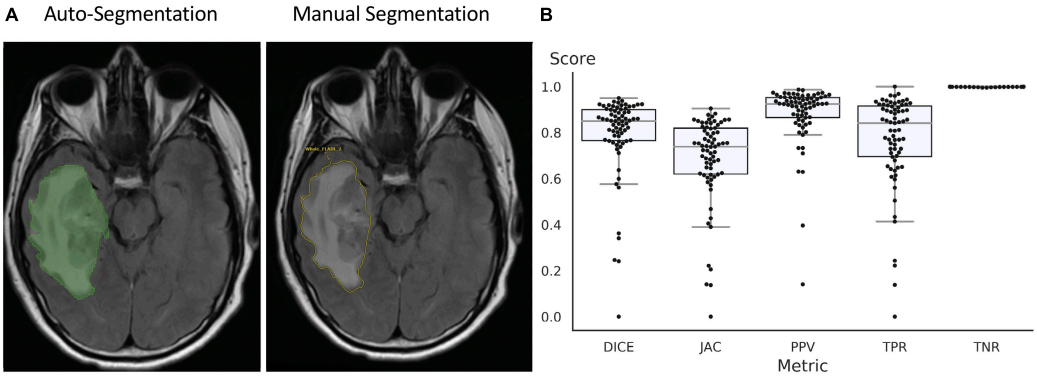

FIGURE 3
Accuracy of feature extraction using PyRadiomics. **(A)** Features extracted using PyRadiomics incorporated into PACS were compared to features extracted using external PyRadiomic script. The version of the PyRadiomics were v3.0 and v3.0.post3.dev0+ge100f1d. **(B)** The error was brought to zero after the versions of PyRadiomics were matched.

any additional software or coding knowledge. While higher DSC scores were reported in the RSNA ASNR MICCAI BRATS glioma segmentation challenge, our dataset is different due to inclusion of motion degraded but clinically relevant images. Future work will include implementation of advanced algorithms, such as nnUNET which show higher DSC scores.

Currently machine learning in medical imaging is a hot topic with a large spike in publications starting in 2017 (Subramanian et al., 2021; Afridi et al., 2022; Avery et al., 2022; Bahar et al., 2022; Cassinelli Petersen et al., 2022; Jekel et al., 2022). Multiple works demonstrated high accuracy with use of ML for tumor segmentation, identification of images with brain tumors from other pathologies, glioma grade and molecular subtype prediction, differentiation of gliomas from lymphoma or brain metastases. These results suggest that clinical implementation of these algorithms is imminent and will be seen in the clinical practice in the next few years (Subramanian et al., 2021; Afridi et al., 2022; Avery et al., 2022; Bahar et al., 2022; Cassinelli Petersen et al., 2022; Jekel et al., 2022; Tillmanns et al., 2022). The next frontier in neuro-oncology imaging is identification of clinical applications of ML algorithms in clinical practice and determining the aspects of clinical care that can be improved with predictions that can be generated by these algorithms. The best method to achieve adoption, is to bring the ML tools into the hands of everyday radiologists who may or may not have the expertise in computer science or ML, but have extensive expertise in manipulating clinical PACS. PACS has rapidly evolved since its implementation into clinical practice

in early 2000s. It has changed the face of clinical practice for radiologists and significantly affected how radiologists interact with the referring providers and hospital staff. The toolset we present in our paper is the first step toward this new reality in clinical practice and will serve as the platform for data curation, annotation/labeling, and AI algorithm implementation.

In addition to enable AI-based interactive workflows, another goal is to develop AI which can run unsupervised on each eligible study. While in most cases AI is not there yet, the persistent and safe storage of segmentations, imaging and clinical parameters in the PACS system enables building of large libraries of datasets. The work in our laboratory is underway to expand the training to additional studies from our institution. Those kinds of datasets accelerate the process of developing and validating such models. The additional information could also already be leveraged for patient management, such as tracking of individual lesions with existing segmentations (Kickingereder et al., 2019).

Our paper has several limitations, which include focus on FLAIR based segmentations for accuracy assessment. The algorithm was originally trained on a BraTS dataset but tested on our single institution data that consists of multiple individual hospitals. The small dataset has been expanded to a larger glioma dataset of 430 cases for development of clinical applications of these tools at our hospital. Another limitation of our study is use of only one feature extraction method (PyRadiomics), which is one of the many methods available (Zwanenburg et al., 2020). The strength of our system is that other feature extraction algorithms can be incorporated in our system, based on the needs of the algorithm that is being used and clinical service where it is being incorporated into.

We present a novel method for implementation of AI algorithms into clinical practice by incorporating a deep learning algorithm for glioma segmentation and radiomic feature extraction into clinical PACS. We validated this method on a single institutional glioma dataset and demonstrate reproducibility of feature extraction. This work has potential for accelerating the translation of research concepts to routine clinical use.

Data availability statement

The raw data supporting the conclusions of this article will be made available by the authors, without undue reservation.

Ethics statement

The studies involving human participants were reviewed and approved by Yale IRB. Written informed consent from the participants' legal guardian/next of kin was not required to participate in this study in accordance with the national legislation and the institutional requirements.

Author contributions

MA, ML, MW, KB, IT, and AjM contributed to conception and design of the study. SM, GC, RB, HS, PS, ES, and AmM organized the database. KB, WH, ML, and MW developed the PACS platform. KB, TZ, and EK performed the statistical analysis. MA wrote the first draft of the manuscript. MA, KB, EK, and ML wrote sections of the manuscript. JB and MZ contributed to the Yale IT specifications details. All authors contributed to manuscript revision, read, and approved the submitted version.

Funding

This study received funding from the American Society of Neuroradiology Fellow Award 2018 (MA). This publication was made possible by KL2 TR001862 (MA) from the National Center for Advancing Translational Science (NCATS), components of the National Institutes of Health (NIH), and NIH roadmap for Medical Research. SM received funding in part from the Biomedical Education Program (BMEP). RB received funding in part from the National Institute of Diabetes and Digestive and Kidney Disease of the National Institutes of Health under Award Number: T35DK104689. SP has grant support from NIH/NINDS K23NS118056, The Foundation of the American Society of Neuroradiology (ASNR) #1861150721, Doris Duke Charitable Foundation (DDCF) #2020097, and NVIDIA.

Conflict of interest

ML was an employee and stockholder of Visage Imaging, Inc. KB, WH, and MW were employees of Visage Imaging, GmbH.

The remaining authors declare that the research was conducted in the absence of any commercial or financial relationships that could be construed as a potential conflict of interest.

Publisher's note

All claims expressed in this article are solely those of the authors and do not necessarily represent those of their affiliated

organizations, or those of the publisher, the editors and the reviewers. Any product that may be evaluated in this article, or claim that may be made by its manufacturer, is not guaranteed or endorsed by the publisher.

Author disclaimer

The content of this article is solely the responsibility of the authors and do not necessarily represent the official view of NIH.

Supplementary material

The Supplementary Material for this article can be found online at: https://www.frontiersin.org/articles/10.3389/fnins.2022.860208/full#supplementary-material

SUPPLEMENTARY FIGURE 1
Segmentations performed on Visage Software with whole, core, and necrotic portions of the tumor segmented. The whole segmentation **(A)** included tumor core and surrounding edema and infiltrating tumor. The core **(B)** segmentation included the outer margin of the enhancing component of the tumor. The necrotic **(C)** segmentation included the internal necrotic component of the enhancing portion of the tumor.

References

Afridi, M., Jain, A., Aboian, M., and Payabvash, S. (2022). Brain tumor imaging: applications of artificial intelligence. *Semin Ultrasound CT MR* 43, 153–169.

ACR Data Science Institute (n.d.). *Empowering machine learning in radiology*. Available online at: https://www.acrdsi.org

Avery, E., Sanelli, P., Aboian, M., and Payabvash, S. (2022). Radiomics: a primer on processing workflow and analysis. *Semin Ultrasound CT MR* 43, 142–146.

Bahar, R., Merkaj, S., Cassinelli Petersen, G., Tillmanns, N., Subramanian, H., Brim, W., et al. (2022). Machine learning models for classifying high- and low-grade gliomas: a systematic review and quality of reporting analysis. *Front. Oncol.* 12:856231. doi: 10.3389/fonc.2022.856231

Bakas, S., Akbari, H., Sotiras, A., Bilello, M., Rozycki, M., Kirby, J., et al. (2017a). Advancing the cancer genome atlas glioma MRI collections with expert segmentation labels and radiomic features. *Sci. Data* 4:170117. doi: 10.1038/sdata.2017.117

Bakas, S., Akbari, H., Sotiras, A., Bilello, M., Rozycki, M., Kirby, J., et al. (2017b). Segmentation labels for the pre-operative scans of the TCGA-GBM collection. *Cancer Imaging Arch.* doi: 10.7937/K9/TCIA.2017.KLXWJJ1Q

Bakas, S., Reyes, M., Jakab, A., Bauer, S., Rempfler, M., Crimi, A., et al. (2018). Identifying the best machine learning algorithms for brain tumor segmentation, progression assessment, and overall survival prediction in the BRATS challenge. *arXiv* [Preprint]. arXiv: 1811.02629.

Benjamens, S., Dhunnoo, P., and Meskó, B. (2020). The state of artificial intelligence-based FDA-approved medical devices and algorithms: an online database. *NPJ Digital Med.* 3:118. doi: 10.1038/s41746-020-00324-0

Cassinelli Petersen, G., Shatalov, J., Verma, T., Brim, W., Subramanian, H., Brackett, A., et al. (2022). Machine learning in differentiating gliomas from primary CNS lymphomas: a systematic review. reporting quality, and risk of bias assessment. *Am. J. Neuroradiol.* 43, 526–533. doi: 10.3174/ajnr.A7473

Chen, J., Yao, Y., Xu, H., and Qin, Z. (2016). Isocitrate dehydrogenase (IDH)1/2 mutations as prognostic markers in patients with glioblastomas. *Medicine* 95:e2583.

Clark, K., Vendt, B., Smith, K., Freymann, J., Kirby, J., Koppel, P., et al. (2013). The Cancer Imaging Archive (TCIA): maintaining and operating a public information repository. *J. Digit. Imaging* 26, 1045–1057. doi: 10.1007/s10278-013-9622-7

Claus, E., Walsh, K., Wiencke, J., Molinaro, A., Wiemels, J., Schildkraut, J., et al. (2015). Survival and low-grade glioma: the emergence of genetic information. *Neurosurg. Focus* 38:E6.

Combès, B., Kerbrat, A., Pasquier, G., Commowick, O., Le Bon, B., Galassi, F., et al. (2021). A clinically-compatible workflow for computer-aided assessment of brain disease activity in multiple sclerosis patients. *Front. Med.* 8:740248. doi: 10.3389/fmed.2021.740248

Garderen, K., Voort, S., Versteeg, A., Koek, M., Gutierrez, A., Straten, M., et al. (2021). EASE: clinical implementation of automated tumor segmentation and volume quantification for adult low-grade glioma. *Front. Med.* 8:738425. doi: 10.3389/fmed.2021.738425

GitHub, Inc. (n.d.). Available online at: https://github.com/OWASP/Docker-Security

Gonzalez Castro, L., and Wesseling, P. (2020). The cIMPACT-NOW updates and their significance to current neuro-oncology practice. *Neuro-Oncol. Practice* 8, 4–10. doi: 10.1093/nop/npaa055

Griethuysen, J., Fedorov, A., Parmar, C., Hosny, A., Aucoin, N., Narayan, V., et al. (2017). Computational radiomics system to decode the radiographic phenotype. *Cancer Res.* 77, e104–e107. doi: 10.1158/0008-5472.CAN-17-0339

Hatamizadeh, A., Tang, Y., Nath, V., Yang, D., Myronenko, A., Landman, B., et al. (2022). "Unetr: Transformers for 3d medical image segmentation," in *Proceedings of the IEEE/CVF winter conference on applications of computer vision*, 574–584.

Hegi, M., Diserens, A. C., Gorlia, T., Hamou, M. F., Tribolet, N., Weller, M., et al. (2005). MGMT gene silencing and benefit from temozolomide in glioblastoma. *New England J. Med.* 352, 997–1003.

Isensee, F., Schell, M., Pflueger, I., Brugnara, G., Bonekamp, D., Neuberger, U., et al. (2019). Automated brain extraction of multisequence MRI using artificial neural networks. *Hum. Brain Mapp.* 40, 4952–4964. doi: 10.1002/hbm.24750

Jekel, L., Brim, W., Reppert, M., Staib, L., Cassinelli Petersen, G., Merkaj, S., et al. (2022). Machine learning applications for differentiation of glioma from brain metastasis-a systematic review. *Cancers* 14:1369. doi: 10.3390/cancers14061369

Kickingereder, P., Isensee, F., Tursunova, I., Petersen, J., Neuberger, U., Bonekamp, D., et al. (2019). Automated quantitative tumour response assessment of MRI in neuro-oncology with artificial neural networks: a multicentre, retrospective study. *Lancet Oncol.* 20, 728–740. doi: 10.1016/S1470-2045(19)30098-1

Liang, J., Lv, X., Lu, C., Ye, X., Chen, X., Fu, J., et al. (2020). Prognostic factors of patients with gliomas – an analysis on 335 patients with glioblastoma and other forms of Gliomas. *BMC Cancer* 20:35. doi: 10.1186/s12885-019-6511-6

Lin, M. (2020). Accelerating the translation of artificial intelligence from ideas to routine clinical workflow. *Acad. Radiol.* 27, 121–122. doi: 10.1016/j.acra.2019.08.019

Louis, D., Perry, A., Wesseling, P., Brat, D., Cree, I., Figarella-Branger, D., et al. (2021). The 2021 WHO classification of tumors of the central nervous system: a summary. *Neuro Oncol.* 23, 1231–1251.

Menze, B., Jakab, A., Bauer, S., Kalpathy-Cramer, J., Farahani, K., Kirby, J., et al. (2015). The multimodal brain tumor image segmentation benchmark (BRATS). *IEEE Trans. Med. Imaging* 34, 1993–2024.

MIDRC (n.d.). Available online at: https://www.midrc.org/midrc-acknowledgements

OWASP Cheat Sheet Series (n.d.). Available online at: https://cheatsheetseries.owasp.org/cheatsheets/Docker_Security_Cheat_Sheet.html

Poon, M., Sudlow, C., Figueroa, J., and Brennan, P. (2020). Longer-term (≥ 2 years) survival in patients with glioblastoma in population-based studies pre- and post-2005: a systematic review and meta-analysis. *Sci. Rep.* 10:11622. doi: 10.1038/s41598-020-68011-4

Rudie, J., Rauschecker, A., Bryan, R., Davatzikos, C., and Mohan, S. (2019). Emerging applications of artificial intelligence in neuro-oncology. *Radiology* 290, 607–618.

Rushing, E. (2021). WHO classification of tumors of the nervous system: preview of the upcoming 5th edition. *memo - Magazine Eur. Med. Oncol.* 14, ages188–ages191.

Sheller, M., Edwards, B., Reina, G., Martin, J., Pati, S., Kotrotsou, A., et al. (2020). Federated learning in medicine: facilitating multi-institutional collaborations without sharing patient data. *Sci. Rep.* 10:12598. doi: 10.1038/s41598-020-69250-1

Siegel, R., Miller, K., and Jemal, A. (2020). Cancer statistics, 2020. *CA Cancer J. Clin.* 70, 7–30.

Siegel, R., Miller, K., Fuchs, H., and Jemal, A. (2021). Cancer Statistics, 2021. *CA Cancer J. Clin.* 71, 7–33.

Subramanian, H., Dey, R., Brim, W., Tillmanns, N., Cassinelli Petersen, G., Brackett, A., et al. (2021). Trends in development of novel machine learning methods for the identification of gliomas in datasets that include non-glioma images: a systematic review. *Front. Oncol.* 11:788819. doi: 10.3389/fonc.2021.788819

Thakur, S., Schindler, M., Bilello, M., and Bakas, S. (2022). Clinically deployed computational assessment of multiple sclerosis lesions. *Front. Med.* 9:797586. doi: 10.3389/fmed.2022.797586

Tillmanns, N., Lum, A., Cassinelli, G., Merkaj, S., Verma, T., Zeevi, T., et al. (2022). Identifying clinically applicable machine learning algorithms for glioma segmentation: recent advances and discoveries. *Neuro-oncol. Adv.* 4:vdac093. doi: 10.1093/noajnl/vdac093

Xia, L., Wu, B., Fu, Z., Feng, F., Qiao, E., Li, Q., et al. (2015). Prognostic role of IDH mutations in gliomas: a meta-analysis of 55 observational studies. *Oncotarget* 6, 17354–17365. doi: 10.18632/oncotarget.4008

Zwanenburg, A., Vallières, M., Abdalah, M. A., Aerts, H. J. W. L., Andrearczyk, V., Apte, A., et al. (2020). The image biomarker standardization initiative: standardized quantitative radiomics for high-throughput image-based phenotyping. *Radiology* 295, 328–338. doi: 10.1148/radiol.2020191145

Advantages of publishing in Frontiers

OPEN ACCESS
Articles are free to read for greatest visibility and readership

FAST PUBLICATION
Around 90 days from submission to decision

HIGH QUALITY PEER-REVIEW
Rigorous, collaborative, and constructive peer-review

TRANSPARENT PEER-REVIEW
Editors and reviewers acknowledged by name on published articles

Frontiers
Avenue du Tribunal-Fédéral 34
1005 Lausanne | Switzerland

Visit us: www.frontiersin.org
Contact us: frontiersin.org/about/contact

REPRODUCIBILITY OF RESEARCH
Support open data and methods to enhance research reproducibility

DIGITAL PUBLISHING
Articles designed for optimal readership across devices

FOLLOW US
@frontiersin

IMPACT METRICS
Advanced article metrics track visibility across digital media

EXTENSIVE PROMOTION
Marketing and promotion of impactful research

LOOP RESEARCH NETWORK
Our network increases your article's readership